Giulia Viggiani, editor

GEOTECHNICAL ASPECTS OF UNDERGROUND CONSTRUCTION IN SOFT GROUND

CRC Press
Taylor & Francis Group
A BALKEMA BOOK

GEOTECHNICAL ASPECTS OF UNDERGROUND CONSTRUCTION
IN SOFT GROUND

This page intentionally left blank

PROCEEDINGS OF THE 7TH INTERNATIONAL SYMPOSIUM ON GEOTECHNICAL ASPECTS OF UNDERGROUND CONSTRUCTION IN SOFT GROUND, ROMA, ITALY, 17–19 MAY 2011

Geotechnical Aspects of Underground Construction in Soft Ground

Editor
Giulia Viggiani
Università di Roma Tor Vergata, Roma, Italy

CRC Press
Taylor & Francis Group
Boca Raton London New York Leiden

CRC Press is an imprint of the
Taylor & Francis Group, an **informa** business
A BALKEMA BOOK

CRC Press
Taylor & Francis Group
6000 Broken Sound Parkway NW, Suite 300
Boca Raton, FL 33487-2742

Version Date: 20120829

International Standard Book Number-13: 978-0-203-80358-5 (eBook - PDF)

Visit the Taylor & Francis Web site at
http://www.taylorandfrancis.com

and the CRC Press Web site at
http://www.crcpress.com

Geotechnical Aspects of Underground Construction in Soft Ground – Viggiani (ed)
© 2012 Taylor & Francis Group, London, ISBN 978-0-415-68367-8

Table of contents

Preface xiii

Organisation xv

Sponsors xvii

Special lectures

Mexico City deep eastern drainage tunnel 3
M.A. Aguilar-Téllez, R. Méndez-Marroquin, J.L. Rangel-Núñez, M. Comulada-Simpson, U. Maidl & G. Auvinet-Guichard

Long-term tunnel settlement mechanisms of Metro Line 2 in Shanghai 21
C.W.W. Ng, Q. Li & G.B. Liu

Deep excavations for Amsterdam Metro North-South line: An update and lessons learned 37
A.F. van Tol & M. Korff

Evaluating the effects of tunnelling on historical buildings: The example of a new subway in Rome 47
S. Rampello, L. Callisto, F.M. Soccodato & G.M.B. Viggiani

Keiichi Fujita lecture

TC204 proposal for 'Keiichi Fujita Lecture' 65
R. Kastner

Tribute to Professor Keiichi Fujita by ISSMGE Technical Committee 204 (formerly TC28) on Underground Construction in Soft Ground 67
R.J. Mair & H. Akagi

Session reports

Construction, design and measured performance of bored tunnels 71
C.O. Menkiti

Numerical and physical modelling of tunnels and deep excavations 79
S.W. Jacobsz

Construction, design and measured performance of deep excavations 87
J.R. Standing

Design methods and predictive tools for deep excavations and bored tunnels 97
L. Callisto

Construction, design, and measured performance of bored tunnels

Application of the image and laser sensors based tunnel scanning system 105
M. Sagong, T.H. Koh, B.S. Chun, B.H. Lee & Y.S. Byun

Manipulations of the sticky clays regarding EPB tunnel driving 111
G. Spagnoli, M. Feinendegen, R. Ernst & M. Weh

The effects of anisotropy and of unhomogeneity of stress state on the lining of road tunnel in a Flysch formation 119
V.M. Santoro

Foam conditioning in EPB tunnelling 127
M. Thewes, C. Budach & A. Bezuijen

High-resolution multichannel seismic survey for the excavation of the new headrace tunnel for the Crevola Toce III hydropower scheme in the Ossola Valley, Italy 137
M. Sapigni, A.M. Baldi, F. Bianchi & J. De Luca

Geotechnical instrumentation data management 149
J.L. Gilby, P. Eng & M. Socol

Design and construction of a sewer tunnel in difficult site conditions 157
P. Croce, S. Di Maio, G. Speciale & L. Cassibba

Prediction and performance of a ground freezing application to the rehabilitation works of an existing tunnel 165
A. Pigorini, A. Sciotti, G. Zoppo & G. Calabresi

Flow around a TBM: A Comparison of analytical and numerical models 173
A. Bezuijen, F. Nagel & G. Meschke

Design of jet-grouting for tunnel waterproofing 181
M. Arroyo, A. Gens, P. Croce & G. Modoni

Modelling a deep tunnel excavation in a low-porosity tectonised clay 189
D. Boldini & A. Graziani

Micro-measurement and monitoring system for ageing underground infrastructure (Underground M3) 197
K. Soga, A. Ledesma, A. Roncaglia & I. Vaníček

Settlement monitoring and tunnelling process adaptation—case of South Toulon tunnel 205
J.P. Janin, D. Daniel, R. Kastner, F. Emeriault, A. Guilloux & H. Lebissonnais

Backcalculation of internal forces in the segmental lining of a tunnel: The experience of Line 1 in Naples 213
E. Bilotta & G. Russo

Backanalysis of measured movements in ageing tunnels 223
C. de Santos, A. Ledesma & A. Gens

Modelling and monitoring of a urban underground excavation 231
A. Cantone, R. Fico, F. Cavuoto & A. Mandolini

The Line 3 of the Metro of Cairo 239
P. Patrizi

Methods of monitoring of metro lining in Prague 247
M. Vaníček, S. Chamra, D. Jirásko, J. Macháček, I. Vaníček, J. Záleský, A. Hada, K. Chaiyasarn & K. Soga

Two adjacent railway tunnels underneath the historic city of Mainz 257
H. Quick, J. Michael, S. Meissner & U. Arslan

Aicha-Mauls on the Brenner Base Tunnel—status of the works and results 263
H. Quick, J. Michael, K. Bergmeister & E. Facchin

A new tunnel bored in alluvial soft soil under the Malaga Airport 271
C.S. Oteo, J. García Pérez, H. Moreno, P. de La Fuente & J. Oteo Escobar

Analysis of convergence data and 3D numerical modelling of tunnels excavated in fine-grained soils 281
P. Perazzelli, T. Rotonda, D. Boldini, A.M. Ajmone-Cat & P.M. Gianvecchio

Back-fill grout with two component mix in EPB tunneling to minimize surface settlements: Rome Metro—Line C case history 291
S. Pelizza, D. Peila, R. Sorge & F. Cignitti

Deep excavation of Malatesta Station in Rome: Design, construction and measures 301
E. Romani, R. Sorge, G. Guiducci, A. Lucarelli & G. Furlani

Line C in Rome: Remote monitoring system 309
R. Sorge, S. Moretti & O. Tripoli

Physical and numerical modelling of deep excavations and bored tunnels

Review of Newtonian and non-Newtonian fluids behaviour in the context of grouts 321
S. Kazemian, A. Prasad & B.B.K. Huat

Stability of cohesive-frictional soils with square underground openings 327
K. Yamamoto, A.V. Lyamin, D.W. Wilson, A.J. Abbo & S.W. Sloan

Bearing capacity analysis of cohesive-frictional soils with dual circular tunnels 335
K. Yamamoto, A.V. Lyamin, D.W. Wilson, A.J. Abbo & S.W. Sloan

Centrifuge modelling of the response of buildings to tunnelling 343
R.P. Farrell & R.J. Mair

Tunnelling-induced deformation on a masonry structure: A numerical approach 353
A. Amorosi, D. Boldini, G. de Felice & M. Malena

The dynamic behavior of shield circular tunnels and surrounding granular soils during earthquakes 361
M. Hatambeigi, Y. Pashang Pisheh & M. Pashang Pisheh

An investigation into Inclined Struts method as a type of shoring 369
A. Fakher & S. Sadeghian

Understanding ground deformation mechanisms during multi-propped excavation in soft clay 377
S.Y. Lam, S.K. Haigh & M.D. Bolton

Face stability control for EPB tunnels in a non homogeneous till formation with highly permeable layers 387
A. Graziani, A. Lembo-Fazio, M. Moccichino & P. Romualdi

Numerical simulation of long-term twin-tunnel behaviour at St James's park 395
R.G. Laver & K. Soga

The efficiency of compensation grouting in sands 403
K. Soga, A. Bezuijen & K. Eisa

Tunneling in stratified soft ground: Experimental study on 1g EPBS reduced scale model 411
N. Berthoz, D. Branque, H. Wong, G. Généreux, D. Subrin & E. Humbert

Effects of the excavation procedure on the stability of diaphragm wall panels 417
D. L'Amante & A. Flora

Water table lowering effects on excavations 425
N.P. Raposo & A.T. Gomes

Influence of leakage on tunnel behavior in soft soils 433
D.M. Zhang, H.W. Huang & Z.Y. Fan

Effect of soil stratification on pipe behaviour due to tunnelling-induced ground movements based on the displacement controlled method 441
Z.G. Zhang, M.S. Huang, M.X. Zhang & W.D. Wang

Influence of overcut length on jack force and acting earth pressure during pipe jacking 449
A. Asanprakit, M. Sugimoto & J. Chen

Assessment of building damage induced by excavation using plate analogy 455
E. Namazi & H. Mohamad

Comparing the limit equilibrium method and the numerical stress analysis method of tunnel face stability assessment 463
P. Perazzelli & G. Anagnostou

An analytical method to control tunnel lining settlements 471
A.D. Garini

Interaction between tunnelling and bridge foundation—3D numerical investigation 477
C. Yoo & S.J. Wu

Numerical analysis of precast tunnel segmental lining supported by full-scale experimental tests 481
F. Cignitti, R. Sorge, A. Meda, F. Nerilli & Z. Rinaldi

The ground movement simulator: An interesting facility for the study of the behavior of buildings submitted to ground subsidence 489
M. Caudron, M. Al Heib, B. Hor & F. Emeriault

Experimental and numerical study of grout injections in silty soils 495
L. Masini, S. Rampello, G.M.B. Viggiani & K. Soga

3D finite element analysis of deep excavations with cross-walls 505
S. Rampello & S. Salvatori

A 3D numerical study of deep excavations in clayey soils 515
E. Erbì & F.M. Soccodato

Construction, design, and measured performance of deep excavations

Interaction of retaining structure with adjacent building: Multi-stage numerical analysis 523
E.M. Comodromos & M.C. Papadopoulou

Effect of pressurized grouting on anchor behavior in residual soils 529
T.-S. Kim, B.-K. Sim, J.-S. Kim, S.-W. Lee & I.-M. Lee

Design and construction of anchored diaphragm walls and dewatering system for the excavation of a two-level basement car park at the Al Ghazala Hotel Intercontinental in Tripoli—Libya 537
C. Asioli, M. Agostini & T. Minotti

Underground car parks in Italian urban areas: Not an easy task! 545
G. Pagotto, P. Silvi & F. Casadei

Recent uses of directional drilling technology in the construction field 553
D. Vanni, M. Siepi, M. Croce, F. Melli & V. Specchio

Leak detection in complex underground structures using an innovative geophysical method 559
D. Vanni & E. Geutebrück

Construction of a large underground parking in Bari downtown 567
R. Granata, F. Gioia & V. Cotecchia

Seepage experiences for deep urban excavation at the TBM Malatesta shaft, Rome 577
A. Capata & V. Capata

Spatial effects on excavations in deep soft lacustrine clay 585
P. Becker, G. Berhane & H.-G. Kempfert

Detection of imperfections in diaphragm walls with geophysical measurements 593
R. Spruit, V. Hopman & A.F. van Tol

An integrated monitoring and risk management system for civil construction works 599
E.P.T. Smits

The study of displacements of diaphragm walls built in Warsaw Quaternary soils 605
A. Siemińska-Lewandowska, M. Mitew-Czajewska & U. Tomczak

Design control and monitoring of a jet grouted excavation bottom plug 611
N. Eramo, G. Modoni & M.A.A. de Toledo

Dewatering tests results for underground C Line stations construction 619
M. Grisolia, G. Iorio & A. Zechini

Evaluation of negative skin friction on sheet pile walls at the Rio Grande dry dock, Brazil 627
C.M. Santana, F.A.B. Danziger, F.R. Lopes, L.B. Becker & R.J.L. Pereira

Challenging demands on the geotechnical design and first monitoring results of the T185 in Frankfurt 633
S. Meissner, H. Quick, J. Michael & U. Arslan

Geotechnical design of a railway tunnel and an underground station supporting the new city hall, Delft, The Netherlands 639
M.J.C. Everaars, E. Kwast, C.M. Meulblok, S. Delfgaauw & H. Mortier

CSM-cutter soil mixing—worldwide experiences of a young soil mixing method in soft soils 647
F.-W. Gerressen & T. Vohs

The construction of deep excavation ditch in weak soil in St. Petersburg 653
R. Mangushev, E. Lashkova, V. Smolenkov & A. Osokin

Effect of staged dewatering and excavation on the heave of soil beneath deep excavation 659
G. Zheng & Z. Li

Design and construction of deep excavations in Shanghai 667
W.D. Wang & Z.H. Xu

3-D finite element modeling and construction aspects for vertical shafts in Metro C Rome 685
G. Furlani, G. Guiducci, A. Lucarelli, A. Carrettucci & R. Sorge

Effect of cement on tropical peat stabilized by deep mixing method 693
S. Kazemian, A. Prasad & B.B.K. Huat

Design methods and predictive tools for deep excavations and bored tunnels

Effects of tunnelling on a single pile: Three-dimensional design tool 701
J.Q. Surjadinata, T.S. Hull & J.P. Carter

Prediction method of the displacement of surrounding ground during excavation 709
Y. Motoi

Numerical modeling of diaphragm wall behavior in Bangkok soil using hardening soil model 715
N. Phien-wej, M. Humza & Z.Z. Aye

A nonlinear soil spring model considering ground stress and strain change during excavation 723
T. Sakamoto & Y. Katsura

How to analyse walls for deep excavations 729
A. Hettler & T. Schanz

Prediction of tunnel-induced settlements in soft ground 735
J. Fillibeck & N. Vogt

Strains and failure characteristics of pyroclastic materials in deep excavation 743
A. Lombardi & A. Capata

Simplified numerical method for tunnel design under seismic condition: Some examples about Istanbul Metro design, Kadikoy-Kartal Line 751
G.M. Gaspari, G. Quaglio, V. Floria

FEM analyses of deep excavations and earth retaining structures in soft clay 765
T. Kono & Y. Shigeno

The influence of jet-grout constitutive modelling in excavation analyses 773
M. Ciantia, M. Arroyo, R. Castellanza & A. Gens

Pile-group response due to tunnelling 781
F. Basile

Prediction of surface settlements induced by TBM using Artificial Neural Networks method 791
R. Boubou, F. Emeriault & R. Kastner

Durability of calcarenitic hypogea in the underground cultural heritage of Palermo (Sicily) 799
M. Zimbardo, L. Ercoli & N. Nocilla

Deep excavation in Bulgaria—comparison of measured and computed performance 807
A.E. Totsev

Tunnel-boring process in urban environment: Modeling for reliability—a kinematic study 813
D. Festa, W. Broere, S.v.d. Woude & J.W. Bosch

Mechanical analysis of jet grouted supporting structures 819
A. Flora, S. Lirer, G.P. Lignola & G. Modoni

3D simulations of a NATM tunnel in stiff clays with soil parameters optimised using monitoring data from exploratory adit 829
T. Svoboda & D. Mašín

Numerical analysis of 20.5 m deep excavation with anchored diaphragm wall 835
J. Josifovski, S. Gjorgjevski & M. Jovanovski

Performance of deep excavations in the Taipei Basin 843
R.N. Hwang & Z.C. Moh

Geotechnical issues related to dry maintenance of open cut excavations below groundwater table in soft soils: Reliability of a simplified calculation model 851
F. Carnevale, R. Gallotti, F. Caneparo & P. Pampanin

Ground movements, interaction with existing structures and mitigation measures

Compensation grouting: Mechanisms determining the shape of the grout body 861
A. Bezuijen & A.F. van Tol

Analysis of ground movements induced by tunnels in sand based on contract CR3 in Kaohsiung metro 869
B.C.B. Hsiung

The response of buildings to tunnelling: A case study 877
R.P. Farrell, R.J. Mair, A. Sciotti, A. Pigorini & M. Ricci

The response of piled buildings to deep excavations 887
M. Korff, R.J. Mair, A.F. van Tol & F.J. Kaalberg

The horizontal response of framed buildings on individual footings to excavation-induced movements 895
K.H. Goh & R.J. Mair

The response of buildings to movements induced by deep excavations 903
K.H. Goh & R.J. Mair

3D numerical modelling and settlement monitoring during excavation of the Metro-Torino South extension 911
G. Barla, M. Barla & G. Leuzzi

3D Numerical modelling of tunnelling intersecting piles 919
S.W. Lee, C.K.M. Choy, S.C. Tse, F.R. van Gool, W.W.L. Cheang & R.B.J. Brinkgreve

Geotechnical cut-off diaphragms for built-up area protection in urban underground development 927
N.S. Nikiforova & D.A. Vnukov

Greater Metro Line 3, Cairo: Installation of underground construction pits using cut-off-wall and soft-gel-grouting 933
L. Liersch & M. Baltruschat

An interpretation of jet grouting effects on the retaining structures of a deep excavation and on adjacent buildings 941
E. Fontanella, L. Callisto, A. Desideri, A. Sciotti & C. Ottaviani

Compensation grouting of piled foundations to mitigate tunneling settlements 949
F.J. Kaalberg, R.D. Essler & R. Kleinlugtenbelt

Settlement behaviour after compensation and corrective grouting 955
A. Bezuijen, F.J. Kaalberg, R. Kleinlugtenbelt & R.D. Essler

South Toulon tunnel: Analysis of an instrumented section 963
J.P. Janin, D. Dias, R. Kastner, F. Emeriault, A. Guilloux & H. Lebissonnais

Prediction of the effects induced by the Metro C construction on an old masonry building 971
F. Buselli, A. Logarzo, S. Miliziano, F. Formato, G. Simonacci & A. Zechini

Ground movements induced by tunnel boring in Naples 979
E. Bilotta & G. Russo

EPB tunnelling in deltaic deposits: Observations of ground movements 987
A. Gens, A. Di Mariano & M.T. Yubero

Mitigation of the effects induced by shallow tunneling in urban environment: The use of 'compensation grouting' in the underground Line B1 works in Rome 995
A. Sciotti, A. Desideri, G. Saggio & C. Kummerer

Jacked piles as mitigation measure of surface settlements due to tunneling in clay 1003
M. Marchi, G. Gottardi, G. Marchi, P.M. Masoli, L. Zambianchi & G. Zattoni

Observed and predicted settlements induced by the construction of hydraulic tunnels in Buenos Aires 1011
A. Logarzo, S. Miliziano, V. Floria & M. Pescara

On the effects of Line 6 tunnel excavation in Naples 1019
B. Bitetti, A. Mandolini, A.F.V. Tol, W. Broere & R.B.J. Brinkgreve

Long term environmental effect of tunnel construction in weak soils 1027
M. Mets, R. Raudsepp & T. Ruben

Soft ground tunneling in urban areas—proximity effects 1033
J.F. Chang, H.C. Chao & Z.C. Moh

Activities of TC204 working groups

Urban tunnels in soft ground: Review of current design practice 1047
V. da Mota Wedekin, R. Kastner, A. Guilloux, A. Bezuijen, J. Standing & A. Negro Jr.

Guidelines for comparing field or physical model observations with numerical simulations 1065
G.M.B. Viggiani

A predictive exercise on the behaviour of tunnels under seismic actions 1071
E. Bilotta & F. Silvestri

Author index 1079

This page intentionally left blank

Geotechnical Aspects of Underground Construction in Soft Ground – Viggiani (ed)
© 2012 Taylor & Francis Group, London, ISBN 978-0-415-68367-8

Preface

Technical Committee 204: "Underground Construction in Soft Ground" of the International Society for Soil Mechanics and Geotechnical Engineering (ISSMGE) was first established as TC28 in 1989 to provide a forum for interchange of ideas and discussion amongst representative from different countries with an active interest in tunnelling and deep excavations in the urban environment. In 1994, under the Chairmanship of Prof. Keiichi Fujita, TC28 organised its first symposium as a satellite event to the ISSMGE International Conference in New Delhi. Since then, the host society of TC28 was handed over from the Japanese Geotechnical Society to the British Geotechnical Society, under the Chairmanship of Prof. Robert Mair, and then to the French Geotechnical Society, under the Chairmanship of Prof. Richard Kastner.

Over the years TC28 has always kept its commitment towards collecting information concerning the geotechnical aspects of the design, construction and analysis of deep excavations, tunnels, and large underground structures in the urban environment, with particular emphasis on the development, effects and control of ground movements, their interaction with existing structures, mitigation measures and risk management. The success of the New Delhi symposium led to the strong feeling that organising regular events would be both well received and productive so that five more International Symposia on "Geotechnical Aspects of Underground Construction in Soft Ground" have been organised by TC28 since 1994. These were held every three years in London (1996), Tokyo (1999), Toulouse (2002), Amsterdam (2005), and Shanghai (2008). This volume of Proceedings is the outcome of the seventh symposium of the series, which was held in Roma in May 2011. During the Symposium the Chairmanship of TC204 was handed over from Prof. Kastner to Prof. Adam Bezuijen from the Netherlands.

The themes for the Roma Symposium were in line with the terms of reference of Technical Committee TC204 and included tunnelling in soft ground, deep excavations, monitoring, numerical analysis, and mitigating measures. The call for papers drew an overwhelming response and over 200 abstracts were received, resulting in 116 technical papers accepted for publication in the proceedings and the attendance of nearly 180 delegates from 30 Countries.

As customary, the first two days of the symposium consisted of technical discussion sessions, covering:

1. Construction, design, and measured performance of bored tunnels
2. Physical and numerical modelling of deep excavations and bored tunnels
3. Construction, design, and measured performance of deep excavations
4. Design methods and predictive tools for deep excavations and bored tunnels
5. Ground movements, interaction with existing structures and mitigation measures

During each of these sessions, a general report was presented together with a small number of selected individual papers. Oral presentations were followed by open debate and discussion.

At the beginning and at the end of each of the first two days four invited special lectures were delivered by dr. Mario Aguillar Tellez (Mexico), Prof. Charles W.W. Ng (Hong Kong), Prof. Frits van Tol (the Netherlands) and Prof. Sebastiano Rampello. Their lectures were devoted to the geotechnical aspects of construction of the new Mexico City deep sewerage system (as a special contribution of TC214 "Soft Soils"), the long-term settlement mechanisms of tunnels in Shanghai, the lessons learned from the deep excavations for North-South Line in Amsterdam, and the evaluation of the effects of tunnel excavation on historical buildings, drawing from experience gathered during construction of a subway line C in Roma.

In addition to standard technical sessions, two special sessions also took place during the first two days of the Symposium, one devoted to an illustration of current activities of TC204 Working Groups, and another one to an overview of Roma and Napoli underground extension projects.

On the third day of the Symposium technical visits were organised to the work sites of Line C of Roma Underground, under construction at the time of the Symposium; for those delegates willing to stay, extra

technical visits to the construction sites of Linea 1 and Linea 6 of Napoli Underground were organised on the fourth day.

This volume contains 128 papers, including the written versions of the reports on the activities of TC204 working groups, of the general reports and of the invited lectures. All the papers that were submitted were peer-reviewed on a voluntary basis by members of TC204.

The success of the symposium must be attributed to the authors of the papers, the speakers at the symposium, the delegates who travelled to Roma to present their work orally or in the poster sessions and to take part in the discussion, and to friends and colleagues who accepted to act as chairmen of the technical sessions for their task of keeping everybody (more or less) to time. All the same, the Symposium would not have been possible without the efficiency and hard work of ing. Claudio Soccodato and Ms. Susanna Antonielli, and the tremendous support of the then Chairman and Secretary of TC204, Prof. Richard Kastner and dr. Jamie Standing.

Finally, thanks are due to the companies, both from Italy and from abroad, that were willing to give financial support to the organisation of the Symposium and that chose to use the Symposium as a showcase for their products and services; a list of the main sponsors and of the exhibitors is included in this volume of proceedings.

Stefano Aversa
Chairman AGI
Chairman Local Organising Committee

Giulia Viggiani
Editor

Geotechnical Aspects of Underground Construction in Soft Ground – Viggiani (ed)
© 2012 Taylor & Francis Group, London, ISBN 978-0-415-68367-8

Organisation

The Symposium of Technical Committee 204 on "Geotechnical Aspects of Underground Construction in Soft Ground" was organised by the Italian Geotechnical Society (AGI) under the Auspices of the International Society for Soil Mechanics and Geotechnical Engineering and of the Italian Ministry for Public Works.

TECHNICAL COMMITTE 204

Prof. Richard Kastner, *Chairman*
Dr. Jamie Standing, *Secretary*

CORE MEMBERS

Prof. Hirokazu Akagi (Japan)
Dr. Adam Bezuijen (The Netherlands)
Dr. Storer Boone (Canada)
Mr Eric Hudson-Smith (Australia)
Prof. Robert Mair (UK)
Dr. Jozsef Mecsi (Hungary)
Prof. Arsenio Negro (Brazil)
Prof. Charles Ng (Hong Kong)

MEMBERS

Mr. Ervin Paci (Albania)
Ing. Alejo Sfriso (Argentina)
Dr. Jeff Hsi (Australia)
Mr. Christian Schroeder (Belgium)
Prof. Jean-François Thimus (Belgium)
Prof. Andre Assis (Brazil)
Prof. Hongwei Huang (China)
Prof. Ivo Herle (Czech & Slovak)
Dr. Petr Kouldelka (Czech & Slovak)
Dr. Omar Ezzeldine (Egypt)
Dr. Alain Guilloux (France)
Mr. Jacques Robert (France)
Prof. Achim Hettler (Germany)
Prof. Hubert Quick (Germany)
Mr. Bernd Schuppener (Germany)
Prof. Norbert Vogt (Germany)
Mrs. Stavroula Schina (Greece)
Mrs. Panagiotis Vettas (Greece)
Prof. Kazuhito Komiya (Japan)
Dr. M. Sugimoto (Japan)
Prof. Zh. Masanov (Kazakhstan)
Dr. M. Ukshebaev (Kazakhstan)
Prof. In Mo Lee (Korea)
Prof. Chung Sik Yoo (Korea)
Dr. Klaas Jan Bakker (Netherlands)
Mr. EA Kwast (Netherlands)
Prof. Frits van Tol (Netherlands)
Prof. Anna Sieminska-Lewandowska (Poland)
Mr. Jorge Almeida e Sousa (Portugal)
Mr. Pedro Guedes de Melo (Portugal)
Dr. Horatiu Popa (Romania)
Prof. V. Petrukhin (Russia)
Dr. Nadezda Nikiforova (Russia)
Mr. Peter Day (South Africa)
Prof. César Sagaseta (Spain)
Dr. Manuel Romana (Spain)

Dr. Richard Pang (Hong Kong)
Mr. P. György (Hungary)
Dr. Nitin Som (India)
Dr. Mahmood Vafaeian (Iran)
Dr. Marco Barla (Italy)
Dr. Walter Steiner (Switzerland)
Dr. N. Phienwej (Thailand)
Prof. Neil Taylor (UK)
Prof. Richard Finno (USA)
Prof. Giulia Viggiani (Italy)

LOCAL ORGANISING COMMITTEE

Chairman Secretary

Prof. Stefano Aversa, *AGI*
ing. Claudio Soccodato, *AGI*

Members

Ing. Enrico Arini, *Metropolitana Milanese*
Prof. Giovanni Barla, *Politecnico di Torino*
Dr. Marco Barla, *Politecnico di Torino*
Dr. Daniela Boldini, *Università di Bologna*
Dr. Federico Bortoli, *Roma Metropolitane*
Prof. Alberto Burghignoli, *Università di Roma La Sapienza*
Ing. Franco Cristini, *Metro C*
Dr. Giuseppe Cozza, *Metropolitana Milanese*
Ing. Antonello de Risi, *MN Metropolitana di Napoli*
Prof. Michele Jamiolkowski, *Politecnico di Torino*
Prof. Alessandro Mandolini, *Seconda Università di Napoli*
Prof. Gianpiero Russo, *Università di Napoli Federico II*
Ing. Giannegidio Silva, *MN Metropolitana di Napoli*
Ing. Giovanni Simonacci, *Roma Metropolitane*
Dr. Fabio Maria Soccodato, *Università di Cagliari*
Ing. Filippo Stinellis, *Metro C*
Prof. Giulia Viggiani, *Università di Roma Tor Vergata*

Geotechnical Aspects of Underground Construction in Soft Ground – Viggiani (ed)
© 2012 Taylor & Francis Group, London, ISBN 978-0-415-68367-8

Sponsors

MAIN SPONSORS

ASTALDI

METROPOLITANA DI NAPOLI SpA

AnsaldoSTS

EXHIBITORS

JobSoil GEOTECHNICAL INNOVATION & RESEARCH

DMS GEOTECHNICAL ENGINEERING

HARPACEAS Tecnologie per le tue idee

Leica Geosystems

MAE

PLAXIS

SISGEO

This page intentionally left blank

Special lectures

This page intentionally left blank

Geotechnical Aspects of Underground Construction in Soft Ground – Viggiani (ed)
© 2012 Taylor & Francis Group, London, ISBN 978-0-415-68367-8

Mexico City deep eastern drainage tunnel

M.A. Aguilar-Téllez & R. Méndez-Marroquin
Ingenieros Civiles Asociados, Mexico

J.L. Rangel-Núñez
Universidad Autónoma Metropolitana, Mexico

M. Comulada-Simpson & U. Maidl
Maidl Tunnel Consultants, Mexico

G. Auvinet-Guichard
Universidad Nacional Autónoma de México

ABSTRACT: The Eastern Drainage Tunnel project (Túnel Emisor Oriente, TEO) of Mexico City, a deep drainage system for mixed storm water and sewage, with a length of 62 km and interior diameter of 7 m, is being built mainly through lacustrine, alluvial and volcanic soil deposits with a wide range of mechanical characteristics and, along some short stretches, through volcanic rocks. The tunnel's construction also requires excavating 24 shafts with 12–16 m interior diameter and depth ranging from 28 to 155 m. The poor properties of some of the soils encountered, their expected seismic response, the foreseeable effects of regional subsidence on the tunnel in the lacustrine zone, and the high water pressure registered in some geological formations make this project particularly challenging. This paper describes the main features of the project, presents a brief summary of the soil properties, and discusses briefly the geotechnical criteria and analysis methods that were adopted for the design of the typical shafts and tunnel sections, as well as some of the construction methods that are being implemented.

1 INTRODUCTION

The Mexico City valley is a closed basin without a natural water outlet. As a matter of fact, Mexico City was originally built on a small island of the Texcoco lake. Starting in the XVII Century, large artificial dewatering works were undertaken to avoid recurrent flooding of the city (Auvinet, 2010). The Nochistongo trench was opened in 1789 in the northern part of the valley and, in 1900, the Gran canal with a length of 47.5 km leading to the Tequisquiac tunnel was inaugurated. Due to the growth of the urban area and to the pumping-induced general subsidence of the lacustrine zone of the valley, this system soon proved to be inadequate. The Gran canal progressively lost most of its capacity to operate by gravity flow. From 1967 to 1975, a deep drainage tunnel known as Túnel Emisor Central (TEC) with an original capacity of 290 m^3/s was built as part of a new deep drainage system (Ref. 03). To reduce the city's vulnerability to flooding in case of problems in the TEC and in order to attend drainage requirements in newly populated areas, it has been considered necessary to build a second deep drainage tunnel, known as Túnel Emisor Oriente (TEO). This new tunnel will introduce a welcome degree of redundancy in the drainage system, allowing maintenance works to be performed on existing installations. This is the largest civil work being built in Mexico now and probably the largest tunnel in the world built in soft soils.

This paper presents the main features of the project, describes briefly the geological-geotechnical conditions prevailing along the tunnel and discusses the geotechnical criteria and analysis methods adopted for design. Two main aspects are enhanced in this presentation: problems related to construction in the very soft lacustrine clays of Mexico City, affected by regional subsidence and presenting seismic amplification, and the construction of deep parts of the tunnel (down to 150 m) in areas with water pressure as high as 0.75 MPa.

2 GENERAL DESCRIPTION OF THE PROJECT

The TEO is being built in the northeastern part of the Mexico City valley. This tunnel is 62 km

long with interior diameter of 7 m and exterior diameter of 8.4 m for the first 21 km and 8.6 m for the rest of the tunnel. The slope in the north direction is initially 0.19%, reduced to 0.16% after the km 13+460 section (Fig. 1).

Overburden thickness over the tunnel's crown varies from 28 m in the south part (L-0) to 155 m close to the north exit (L-20). Due to the tunnel's length and depth, a wide range of geomaterials are encountered: soft plastic lacustrine clays submitted to regional consolidation and to seismic amplification in the south part, sandy and clayey soils of alluvial or volcanic origin with higher shear strength and lower compressibility in the central part and finally, highly consolidated soils with lenses of boulders inserted in a clayey and silty matrix in the north part. Locally, basaltic lava flows will be encountered. Close to the north end of the tunnel, an aquifer with pressures as high as 0.75 MPa has been detected.

The TEO is being constructed using seven Tunnel Boring Machines (TBM) of the Earth Pressure Balance type (EPBS) and 24 deep shafts will also be constructed, five with internal diameter of 16 m (for assembly and disassembly of TBM) and the rest of 12 m (for operation and maintenance of the tunnel). The distance between contiguous shafts is typically 2.5 km, depth varying from 28 to 155 m. The TEO's north portal is located near the TEC outlet, and in both cases water is discharged into El Salto River, Hidalgo State.

The construction procedure of the shafts varies depending on the soil profile. Three different construction methods are typically used: 1) walls cast in place for the shaft's entire depth, 2) mixed procedure (wall cast in place down to a certain depth followed by construction with conventional techniques in deeper competent materials (Fig. 2) and 3) use

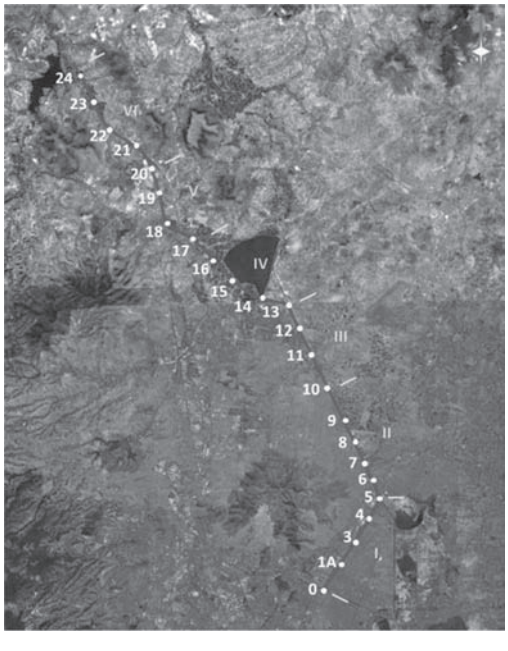

Figure 1. General layout of the Túnel Emisor Oriente (Google-Earth, 2011).

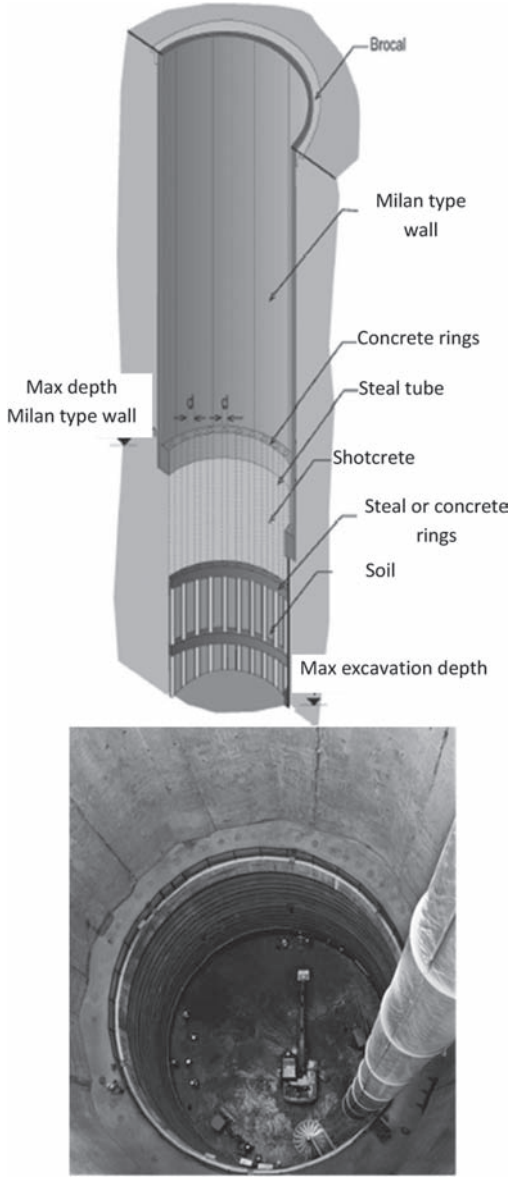

Figure 2. Construction process and lining of shafts (Contreras *et al.*, 2010).

of conventional techniques for the shaft's entire depth.

The tunnel support system (Fig. 3) consists of a primary lining constituted by prefabricated concrete segments and a secondary reinforced concrete lining, cast in place at a second stage. Between shafts L-0 and L-10 (km 21+635.101) the tunnel's exterior diameter is 8.4 m, and the thickness of both the primary and secondary linings is 0.35 m (Fig. 3a); from L-10 to the portal, the exterior diameter is 8.6 m and the thickness of both primary and secondary linings is 0.4 m (Fig. 3b).

For construction purposes, the TEO was divided in six parts (Fig. 1). I: shafts L-0 to L-5, 10.1 km; II: shafts L-5 to L-10, 11.6 km; III: shafts L-10 to L-13, 9.2 km; IV: shafts L-13 to L-17, 10.2 km, V: shafts L-17 to L-20, 8.6 km and VI: shafts L-20 to portal, 12.4 km. These stretches do not correspond to any particular geological or geotechnical zoning.

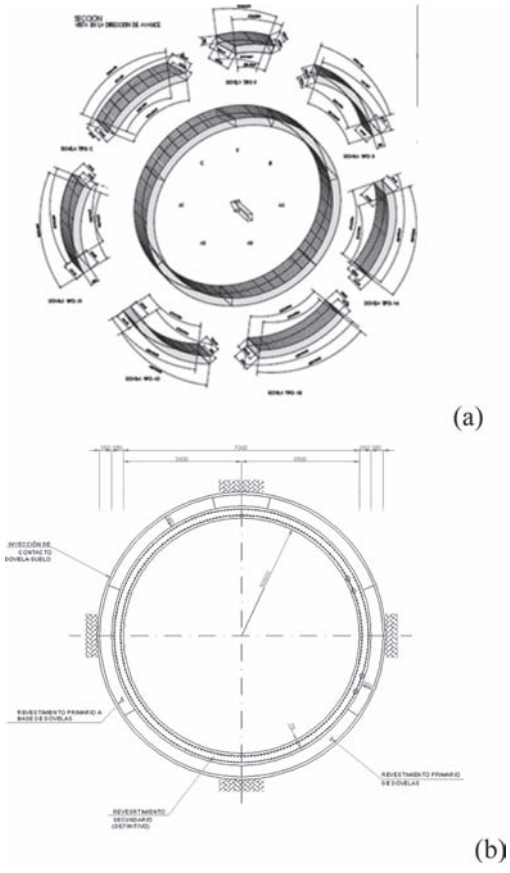

Figure 3. Tunnel support system: primary (a) and combined (b) linings.

3 GEOLOGICAL AND GEOTECHNICAL EXPLORATION

The geological and geotechnical exploration campaign was very ambitious; close to 250 borings (25,000 m) were performed. The campaign was divided into three stages: primary, principal and detailed exploration; some exploration works are still under way.

The following exploration methods have been used:

- Borings: Standard Penetration Test (SPT) and Cone Penetration Test (CPT)
- Soil sampling: Shelby and Denison tubes and triple swivel sampler
- In situ testing: piezometers, permeability tests, pressuremeter, phicometer tests
- Geophysical methods: Cross-hole and SPAC compression and shear wave velocity profile measurements
- Laboratory testing: index and mechanicals properties.

Difficulties were encountered for deep explorations (from 100 to 200 m), particularly for undisturbed sampling of silty sand with gravels, clayey silts with sand, and volcanic tuffs. Therefore, in many cases, in situ tests were preferred.

Special studies were also performed to assess the rate of regional subsidence in the lacustrine zone, for the characterization of aquifers and aquitards, for environmental impact, *etc*.

The interpretation of the soil exploration and specialized studies was a challenging task, based mainly on geological maps of the Mexico valley (Mooser *et al*., 1996). Correlation, estimation and simulation analyses were performed along the tunnel, using geostatistical methods (Auvinet, 2002) in order to assess spatial variability of the geomaterials (Fig. 4) (Juárez *et al.,* 2010).

4 GEOLOGICAL AND HYDRAULIC CONDITIONS

The TEO course was defined trying to minimize hard rock excavation and overburden thickness. As a consequence, the tunnel initially crosses through poorly consolidated Quaternary deposits of the northern part of the Mexico basin along the first 40 km, and then through tertiary tuffs from the consolidated Nochistongo mountain range along 21.3 km.

4.1 *General geology*

From south to north, in the first 2.5 km the tunnel will be excavated through Quaternary lacustrine

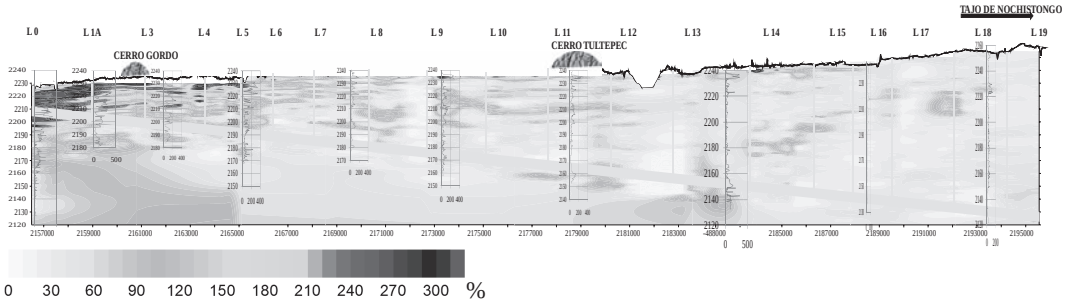

Figure 4. Soil water content in field along the tunnel, as estimated by geostatistical methods.

deposits of the Mexico basin, and then it will cut through a Pliocene formation of the Nochistongo mountain range. Next, the tunnel passes through Pliocene lacustrine deposits of the Taxhimay formation which are divided into tectonic blocks covered by alluvial fans. Some basaltic lava flows will be encountered occasionally (Fig. 5).

4.2 *Geological formations*

The tunnel will cross six different main formations, namely:

1. Lacustrine Formation of the Mexico basin (upper Quaternary, 300,000 years old: km 0 to 21+140; strata 1, green, 2, yellow, and 10, light blue). It consists of clays interbedded with silts and sands derived mostly from rains of acidic pumices during volcanic eruptions, which were deposited in shallow fresh water lakes in layers 1 to 2 m thick. At the south end of the tunnel, excavation will be performed along a 2.5 km stretch of typical Mexico City lacustrine clays. Lenses and hard layers of clastic materials within the clay deposit may tend to deflect the TBM course.
2. Basalt Formation (Quaternary: km 21+140 to 30+300; strata 3, brown, 7, pink, and 9, red): Basaltic lavas and ash from the north flank of the Nochistongo mountain range and Tultepec hill.

   These basalt or ash lenses are found within the lacustrine and al luvial deposits. Due to their high permeability and transmissibility, significant water flow is expected.
3. Sub-lacustrine soils formation (km 30+300 to 38+000; stratum 4, light brown). It consists of alluvial soils, i.e. sandy silts with sand lenses, and occasionally fluvial gravels. There is neither tectonic faulting nor significant water flow.
4. Alluvial fans formation (Plio-Quaternary, Nochistongo mountain range: km 38+000 to 40+350; stratum 6, blue). These deposits are composed of very compact sand and gravel layers. There is no tectonic faulting and permeability and transmissibility are low.
5. Huehuetoca volcanic formation (upper Pliocene: km 40+350 to 46+000; stratum 7, pink). These deposits are contained in alluvial fans from the south flank of the Nochistongo mountain range, and consist of a thick sequence of semi-hard ignimbrite and compact tuffs. Lavas, pyroclastic flows and gravels with boulders could be encountered. There is not evidence of tectonic faults. It is important to note that, at the bottom of this formation, contiguous to the Taxhimay formation, layers of sandy gravels and silty boulders have been detected, where hydraulic loads are important.
6. Taxhimay Formation (middle Pliocene, 2 million years old: km 46+000 to portal; upper 5s, light green; lower 5i, dark green). This is a much consolidated old lacustrine deposit with clay, silty clay, sandy silt, and occasionally layers of pumice or fluvial sands and tuffs. This formation is divided into two units: the lower one is highly consolidated dark green lacustrine clay, the upper one is less consolidated clay. Permeability and transmissibility are low. However, intense tectonic activity has affected the Taxhimay formation, giving rise to the formation of a block structure which increases permeability. Significant amounts of water, suddenly changing from low to high, can be expected.

4.3 *Geohydrology*

The TEO will intercept three different aquifers:

- Mexico City aquifer. The tunnel will remain in the upper aquitard that confines the deep Mexico City aquifer. This aquitard consists mostly of impervious lacustrine materials such as clays, with lenses or thin layers of silts and sands.

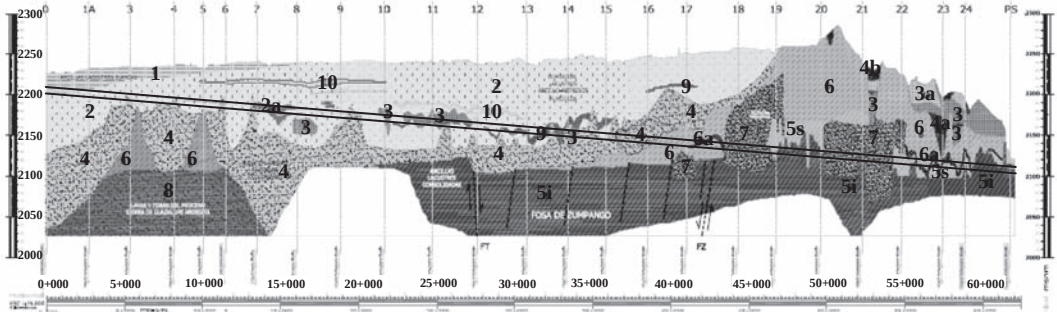

Figure 5. Geology (Mooser, 2010).

- Cuautitlán-Pachuca aquifer, located in Mexico State. This aquifer contains both lacustrine and alluvial sediments as well as rock of volcanic origin.
- Valle del Mezquital aquifer, located in Hidalgo State. This aquifer will be intercepted in the TEO's final stretch.

In both the Mexico City and Cuautitlán-Pachuca aquifers, significant drawdown is observed due to intense water-pumping for local consumption of potable water. Drawdown of the static level registered in some wells can reach 1.3 to 1.6 m/year in the TEO's south part. This has induced, among other effects, subterranean water drainage in the southeast flank of the Sierra de Guadalupe range and the generation of large drawdown cones. On the other hand, in the north part, close to Huehuetoca, in the Mezquital aquifer, drawdown observed is generally less than 0.35 m/year to 1.0 m/year.

The stretch between shafts L-10 and L-18 corresponds to a semi-confined (multilayered) aquifer in lacustrine-type sediments such as sands, silts and clays. At a depth of less than 60 m are perched aquifers that required special attention during the construction of shafts. The hydrostatic level corresponding to the regional aquifer level is found below 65 m. The subsoil is a highly heterogeneous stratified medium with low hydraulic conductivity (1×10^{-4} cm/s). The hydraulic head over the tunnel's crown varies from 5 m to 45 m and estimated potential flow towards the tunnel varies from 0.03 l/s/m to 1.6 l/s/m.

The aquifer between shaft L-18 and exit is semi-confined and located within granular materials such as sands and gravel and sediments of volcanic origin. The granular materials present a medium hydraulic conductivity and are interbedded with fine material with permeability as low as 1×10^{-3} to 1×10^{-4} cm/s, with lateral continuity. The hydraulic head in this stretch was the highest registered along the entire tunnel reaching values as high as 35 m to 75 m over the tunnel keystone, with estimated subterranean flow toward the tunnel of 0.3l to 0.98 l/s/m.

5 GEOTECHNICAL CHARACTERIZATION

From a geotechnical point of view, 95% of the tunnel will be excavated through soils of alluvial-fluvial and volcanic origin and the rest through igneous extrusive rocks such as basalts.

In the first stretch, between shafts L-0 and L1A, the tunnel is located in very compressible clays with low shear strength affected by a pumping-induced consolidation process, known for their amplification of seismic waves. Subsequently, the clayey layers disappear progressively and the tunnel enters a zone of volcanic tuffs formed by sandy silts, or silty sands, occasionally with partially saturated clay, in which the piezometric level has suffered partial or total drawdown, with lenses of sand containing some gravel and very compact volcanic ashes. Between shafts L-10 and L-14 the soil profile changes abruptly and in the tunnel's excavation front it is mixed, with, in the upper part, a basalt flow from Tultepec hill resting on a cemented volcanic ash lying in turn on the volcanic tuff previously mentioned. In this area, piezometric levels are higher. From shaft L-14 to L-16 the tunnel crosses alluvial pre-lacustrine soils composed principally of sandy silts with sand lenses and, locally, fluvial gravel. A specific feature of this zone is that in the lower part of the tunnel section a deformable layer with low shear strength is found, and piezometric levels present an almost total drawdown. Between shafts L-16 and L-19 the soil is a material of alluvial origin, generally sands or silty gravel interbedded with sandy silts, in which, locally, thin layers of boulders contained in a weakly cemented silty matrix are found, with significant water head. From this section onward piezometric pressures increase. From L-19 to the portal the tunnel is

located in the Taxhimay formation, constituted by highly consolidated clays with low deformability and high shear strength; however, the last part of the tunnel is near the contact between the Taxhimay formation and volcanic fans in which a layer of gravel and boulders is found with pore pressures as high as 0.75 MPa and where serious problems for tunnel excavation, control of water and stability of the support system are expected.

In order to give a general idea of the soil quality from the tunneling point of view, Figure 6 presents the depth variation to the tunnel's axis along the tunnel, geostatic total vertical stress and pore pressure, average shear strength, the stability ratio and the safety factor of the tunnel's excavation (Tamez, 1997 and Rangel *et al.*, 2005 and 2007).

The lowest safety factors are obtained in the first stretch of the TEO, which crosses the very soft Mexico City clays presenting high deformability and low shear strength. In this zone, it is necessary to use TBM with pressure control in the excavation front, place primary lining timely, and apply grouting pressure equal to the in situ stress in order to avoid unacceptable settlements of soil surface. Although geo material properties improve as tunnel depth increases, in some zones the tunnel will cross lenses of soft clays with abated pore pressure leading to low safety factors. In these zones, using TBM with the characteristics already described is also necessary. From shaft L-10 onward, but principally between shafts L-19 and L-24, where a layer

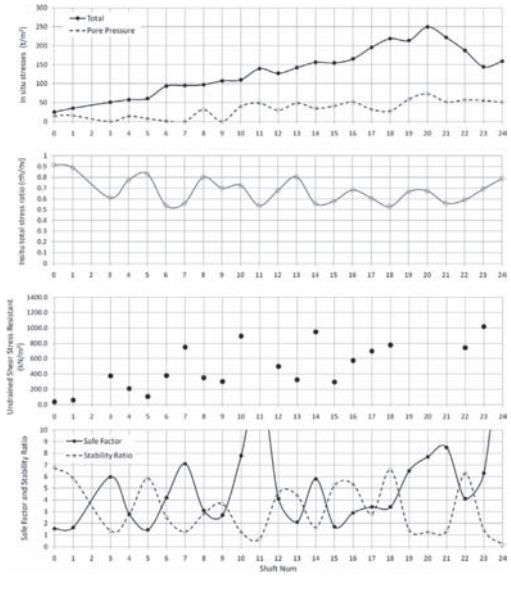

Figure 6. In situ stresses, in situ total stress ratio, undrained shear strength, safety factor according to Tamez (1997) and stability ratio (Rangel, 2005 and 2007).

of boulders contained in a silt matrix is encountered, hydraulic head with values as high as 0.5 to 0.75 MPa will represent a difficult challenge for the EPBS machines.

A detailed geotechnical description for each tunnel is as follows:

Section I (L-0 to L-5). The overburden thickness varies from 16 to 40 m, and the tunnel is situated mainly in the Mexico City lacustrine zone, where high plasticity clays are found. These highly deformable materials are suffering a consolidation process due to deep water pumping and are known to present strong soil movement amplifications during earthquakes. The water table is found at a depth between 2 and 5 m, and the hydrostatic pressure presents some drawdown in the first 4 km (L-0 to L-3); then the tunnel crosses deeper hard silt and sandy silt deposits with lenses of soft silts with large water pressure drawdown (L-3 to L-5). The main problems from a design point of view are:

- Shaft and tunnel construction in very soft saturated soils, with high deformability and low shear strength.
- Subsidence rate of soil surface around 18 cm/year.
- Seismic amplification
- Presence of cracks in the clay layers.

A typical subsoil profile of this zone is shown in Figure 7, where high water content is correlated to very low undrained shear-resistant and stress-strain modules.

In very soft soils, pressures on the primary lining must be of the same order as those prevailing in geostatic conditions. If this objective is not attained, plastic zones and large radial deformations are generated around the tunnel, leading to unacceptable surface settlement. Furthermore, the primary lining's structural capacity is strongly affected by large radial displacements and by contrasts between horizontal and vertical pressures.

In the first part of this section, the water table is only between 2 and 5 m deep, and no drawdown is registered at depth, so the lining works mainly in compression. However, in the second part of this stretch, water pressures are depleted (Fig. 6) and low ratios (0.7) have developed between the horizontal and vertical stresses, inducing important bending moments in the dowel ring.

The effect of regional subsidence on the primary lining is unfavorable since anisotropic vertical and horizontal effective stresses are induced. For design purposes it was assumed that water pressure drawdown at the hard layer level would increase 9 kN/m^2 during the 18 month period before the final lining was installed.

Another particular design issue in this zone is the seismic amplification of clay deposits. Figure 8 shows

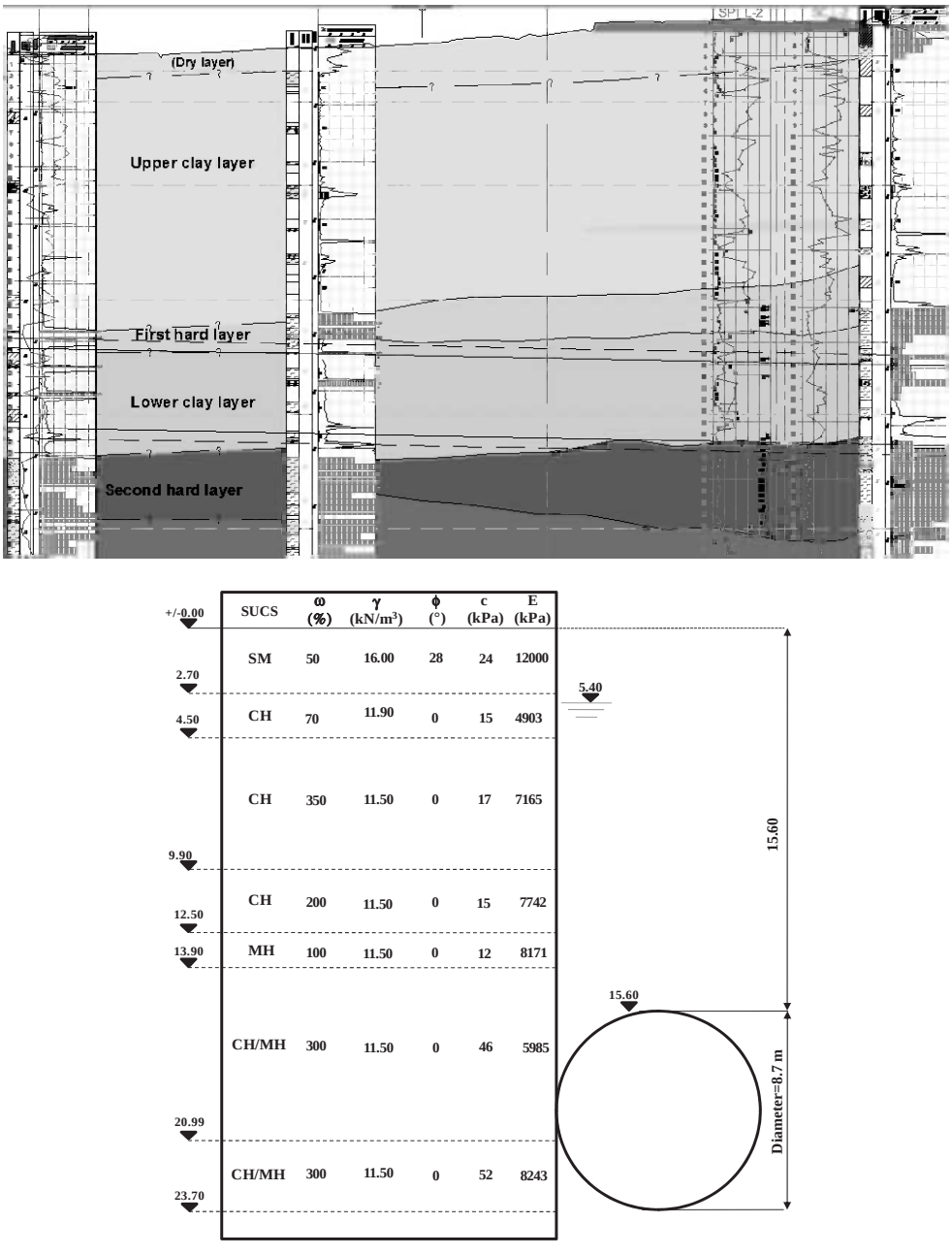

Figure 7. Borings close to shaft L1 (typical soft soil profile).

characteristics of the earthquake and soil deposit design response for Mexico City clay deposits in this TEO zone: a) is the acceleration spectral of the bed rock motion for the Mexico City valley for two return period events (for 47.5 and 475 years, short and long term seismic design periods); b) is the transfer function for the clay deposit and c) the acceleration spectral at the top of the clay deposit at the beginning of the TEO (L-1). Note a very high amplification, up to 10 times, and free field acceleration at the top of clay deposits around 300 cm/s^2, which is a typical average value for Mexico City clay deposits.

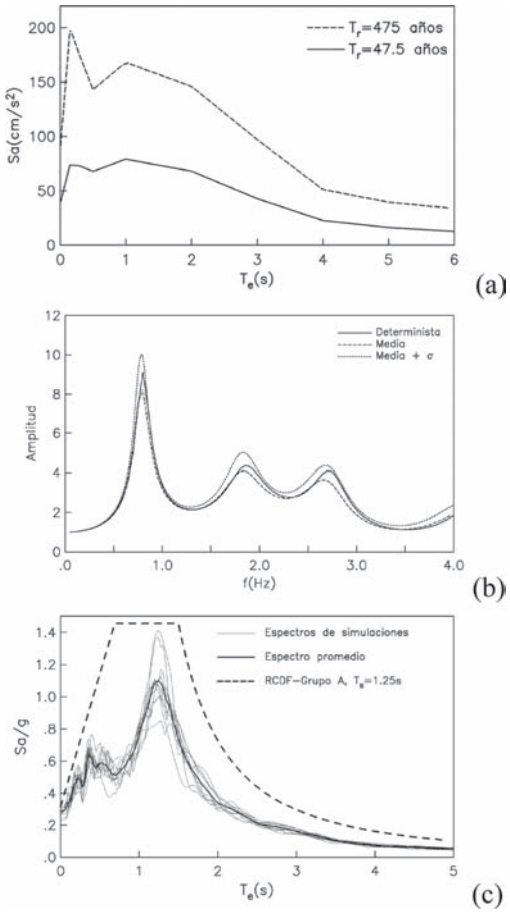

Figure 8. (a) Spectrals of uniform danger in rock for the Mexico valley, (b) transfer function in clayey deposits of the Mexico valley and (c) response spectral in clayey deposits in a return period of 475 years.

Seismic movements affect mainly shafts in the longitudinal direction, and tunnels in the transverse section, but the main effect of earthquakes is in the connection between tunnels and shafts.

Section II (L-5 to L-10). The soil above this part of the tunnel is between 40 m and 70 m thick and consists of volcanic tuffs with low hydraulic conductivity formed by interbedded silts and sandy silts with silty sand lenses. A soft clay lens is found at the tunnel level. Pore pressure in these materials is almost completely depleted, especially between shafts L-6 and L-9 and the ratio between horizontal and vertical stresses is estimated to be as low as 0.7. (Fig. 6). These geostatic stresses and the presence of the soft clay lens are very unfavorable conditions for the primary support's structural work as, given such contrast, the tunnel lining tends to bend like an oval in the horizontal direction and since the clayey stratum is very deformable, important deformations are also generated on the lining that is formed by dowels. Also, given the important contrast between the deformability of silty strata and that of the clayey lens, high shear stresses are generated at this border on the primary lining. On this stretch there is no soil deposit seismic amplification and the subsidence phenomenon is low.

Section III (L-10 to L-13). Section III, with overburden between 70 and 83 m, is similar to section II since volcanic tuffs are the predominant materials but the hydraulic head tends to increase. This is particularly conspicuous in a basalt lens resting on a sand layer that is found within the silty material. In this zone, a mixed excavation front (saturated basalt and volcanic tuffs) will be encountered. The strong contrast between the moduli of these two materials leads to serious problems in the analysis of lining behavior. Due to depth, geostatic stresses are high. To reduce stresses on the lining, some radial deformation of the soil can be allowed before installation of the support system. This is achieved controlling the pressure in the excavation front and the grouting pressure for the mortar placed in the space between soil and primary lining. However, radial displacements should not lead to development of plastic zones in the soil. Finally, the subsidence and dynamic amplification phenomena are not present in section III. Again, no significant seismic amplification nor noticeable general subsidence are expected.

Section IV (L-13 to L-17). Overburden varies between 83 m and 115 m. The hydraulic head reaches 0.5 MPa and the ratio between total vertical and horizontal stresses is expected to be less than 0.7. The tunnel will cross different geological formations: first clayey and sandy lacustrine deposits with a volcanic ash lens close to the tunnel's crown (shaft L-13); then fine soils and sand with gravel will be found (shafts L-14 and L-15), and at the end of the stretch, the presence of an alluvial fan will probably induce a significant flow of water towards the tunnel (shafts L-16 and L-17). Constructive problems should be expected due to large hydraulic head and sandy layers. On the other hand, due to the low ratio between vertical and horizontal stress, the primary lining will be subjected to important mechanical actions. As far as shafts are concerned, in L-13 alternating sandy silts and silty sands will be found at depths between 70 m and 80 m, and safety factors regarding bottom failure and excavation conditions without support are also expected to be large since the tunnel reaches its largest depth in this area (155 m). To avoid crossing large boulders and fractured volcanic rocks, some significant changes have been introduced in the project based on a large number

of borings. The strategy consists of trying to stay within the Taxhimay formation and sound volcanic rocks as long as possible. In shaft L-20, interbedded silty sand and sandy silts between 62 m and 85 m and clays between 85 m and 112 m may lead to low safety factors during construction. Just as in section III, the tunnel's attack is expected to be of mixed front, especially at the end of the stretch. The consolidation process and seismic amplification here are expected be low due to the absence of compressible clayey soil deposits. In shaft L-17, clays will be found between 50 m and 60 m and sandy clays will appear between 85 m and 95 m, which will also lead to low safety factors.

Section V (L-17 to L-20). Overburden varies between 115 m and 155 m; the tunnel will cross alluvial fans and the Taxhimay formation, constituted by impervious clayey and sandy deposits with low water content. In this zone there are no highly compressible soils so no consolidation or seismic amplification problems are to be expected.

Section VI (L-20 to L-24). Overburden varies between 80 m and 155 m. The tunnel will be built in the Nochistongo zone of the Tepozotlan range, within the upper and lower Taxhimay formations, alluvial fans and "volcanitas humaredas". A faulting system orthogonal to the tunnel will be encountered, especially in the Taxhimay formation (Fig. 5). Hydraulic head as high as 7.5 MPa has been registered. Geostatic pressures are also expected to be large since the tunnel reaches its largest depth in this area (155 m). To avoid crossing large boulders and fractured volcanic rocks, some significant changes have been introduced in the project based on a large number of borings. The strategy consists of trying to stay within the Taximay formation and sound volcanic rocks as long as possible. In shaft L-20, interbedded silty sand and sandy silts between 62 and 85 m and clays between 85 and 112 m may lead to low safety factors during construction. As section III, a mixed excavation front will be encountered, mainly at the end of this section. The consolidation process and seismic amplification here are expected be low due to the absence of compressible clayey soil deposits.

6 ANALYSIS OF THE TUNNEL SUPPORT SYSTEM

The tunnel support system is built in two stages: a primary lining consisting of six to seven prefabricated segments is being installed in the back part of the tunneling machine as the excavation proceeds while, in a second stage, a final concrete lining is cast using a sliding formwork (Fig. 3).

To represent adequately this constructive process and its mechanical effects in the surrounding soil and in the lining, evolutionary Finite Element models are used. A structural analysis of the lining is based on the stiffness method. The main stages of the analysis are as follows (Fig. 8):

i. *Evaluation of geostatic stresses.*
ii. *Construction of primary lining*. Evaluation of changes in the original stress and strain conditions in the subsoil, including induced pore pressures, and resulting mechanical actions in the tunnel primary lining. Evaluation of changes in these conditions, including dissipation of pore pressures, and of the support system's behavior during the expected life of the primary lining before the final lining is cast (18 months)
iii. *Construction of secondary lining*. Evaluation of changes in the original stress and strain conditions in the subsoil, and resulting mechanical actions in the tunnel's primary and secondary linings considering an operation period of 50 years, taking into account the probable evolution of the hydraulic conditions within the soil during this period.

6.1 *Determination of the geostatic stresses*

Initial subsoil stresses (effective, pore pressure and total) are determined based on the soil's volumetric weight, measurements of field pore pressures with open and electronic piezometers for the most unfavorable condition, and evaluating the at rest quotient value by means of the following expressions:

$$k_0 = \begin{cases} \dfrac{\nu'}{1-\nu'} & \textit{Continuum theory} \\ (1-\sin\phi')OCR & \textit{Jacky} \text{ (1944) } \textit{and Meyerhof} \text{ (1976)} \end{cases}$$

where ν' is the effective Poisson ratio and ϕ' the effective internal friction angle.

In the lacustrine clayey strata the Poisson ratio value was $\nu' \approx 0.5$, whereas in sandy strata (tuffs), agglomerates and rocks it was considered that $0.3 < \nu' < 0.4$.

6.2 *Construction of the primary lining*

Starting with the subsoil's geostatic conditions and applying surface overburden, changes in the state of stresses and subsoil deformations during the tunnel's excavation with earth pressure balance tunnel boring machines and construction of the primary lining formed by voussoir rings were determined with the two-dimensional Finite Element Method (2D FEM).

At this stage the important points to consider in the construction process modeling are: front pressure, injection pressure, characteristics of mortar or bi-component that is placed in the existing space between lining and medium just after the shield's passing, and the primary lining's rigidity and resistance. For 2D finite element models the soil's radial displacement around the tunnel prior to installing the primary lining is calculated considering the factors previously mentioned, except the last one. A preliminary evaluation of this radial deformation is analyzed by the characteristics curves method, in order to assess the limit conditions of the plastic radii and their corresponding deformations. It is important to mention that this method is widely used in Mexico because of the results obtained in the practice of tunnel-making.

In plastic and very deformable soils located at the start of the outline, it was sought to have the construction process cause very slight changes in the state of geostatic stresses in the surrounding medium in order to diminish to the utmost the surface settlements generated by tunneling; therefore, radial displacements generated on the tunnel's periphery were almost exclusively generated by the deformability of the primary lining's rings, which were less than 1% of the tunnel's diameter, to avoid cracks on the primary support.

For sections where the tunnel has such depth that surface settlements are minimal, a moderate decrease of geostatic stresses is considered, taking care that the plastic zones generated do not indicate failure mechanisms and that radial displacements produced on the lining were always below 1% of tunnel diameter. In these sections, there were problems during the design of the primary lining when the tunnel is located in very deformable soil strata and with null or almost no pore pressure, given that under these conditions the lining's structural work is high for ko values indicated before, and loss of the lining's confinement caused by the water. There were also design problems with the mixed excavation front condition, where the contrast between deformation modules of basalt and tuffs is high.

A third case of difficult primary lining design is in the condition of very deep tunnel, with variable coverage between 50 m and 160 m, pore pressure up to 7.5 bars, and located in deformable soils. In this case the construction process and primary support were designed considering an important relaxation of gesostatic stresses, and the generation of corresponding plasticization zones around the tunnel. Defining this decrease was critical and it depended on the magnitude of plasticization generated, and the soil's total displacement value on the tunnel's periphery.

Modeling with 2D FEM has the following main analysis stages (Fig. 9):

1. Determination of the state of geostatic stresses and application of surface overburden (0.15 kN/m^2).

2 & 3. Evaluation of the change in the state of geostatic stresses due to the shield's passing. At this stage the soil elements are removed from the tunnel's zone and the shield is placed. First, the medium is excavated with a frontal shield weighing 323 kN/m^3 and then the radial displacement induced by the shield's skirting zone, where weight changes to 240 kN/m^3, is determined. Tunnel emersion and a pore pressure increase are generated at this stage. It is important to point out that the analysis considers pore pressure dissipation as immediate.

4. The primary lining is placed modeled with a continuous cylinder with real dimensions, meaning that the presence of longitudinal or transverse joints is not considered at all, so effective radial and tangential stresses are determined at this stage, pore pressure at the lining-soil interface for different flexibility ratios of the primary lining, EI, and a constant value of axial rigidity, EA = 8.4 kN/m^3. The detailed structural analysis of the primary lining is done afterward using a model of rigidities formed by two rings, starting with the state of stresses around the tunnel determined at this stage (Comulada and Maidl, 2010). Also, a radial displacement is applied to the soil located in the tunnel's periphery, whose value depends on the characteristics of the filling at the space left by the shield's progress, the injection pressure and the pressure value at the excavation's front, taking care to avoid radial displacements and plastic zones of such magnitude that there are soil failure mechanisms.

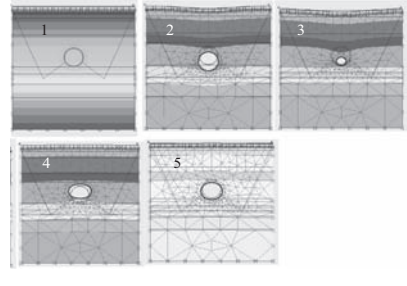

Figure 9. 2D Finite Element Method model for tunneling and placement of primary lining.

5. Primary lining work at 18 months. During this design stage pore pressures are made to descend according to the history of the place. Effective stresses are also determined at the interface located between lining and soil, and pore pressures for later analysis.

Having determined the stresses with incidence on the primary lining at stages 4 and 5 mentioned before (placing the lining and consolidation at 18 months), we proceeded to analyze their behavior taking into account the presence of the longitudinal and transverse sections on the dowel rings. For that, the double ring model developed by Maidl is used (Comulada and Maidl, 2010), in which dowels are modeled with beam elements and the transverse joints with Winkler rotational elements (Fig. 10). The presence of contiguous rings is represented in the model with a second ring connected to the first by Winkler elements. The characteristics of the Winkler elements are determined experimentally. Both rings of the model are supported on Winkler elements so the system is stable, but the rigidity of these elements is insignificant because the state of stresses that have incidence on the support and obtained with the FEM is in equilibrium, so the presence of Winkler elements is only to counteract any maladjustment of numerical origin, and thus the value of the rigidities of these models is very low.

It is important to point out that at the tunnel's first section, limiting radial displacements to low values before placing the support is sought in order to avoid important surface settlement; therefore, the stresses that had incidence on the lining were high and slightly lower than the geostatic ones. For the TEO's final sections, the design strategy was the opposite. In effect, inducing radial displacement on the land before placing the primary support was sought, as well as abating pore pressures in order to diminish pressures acting on that support, but avoiding the generation of important radial displacements and plastic zones around the tunnel.

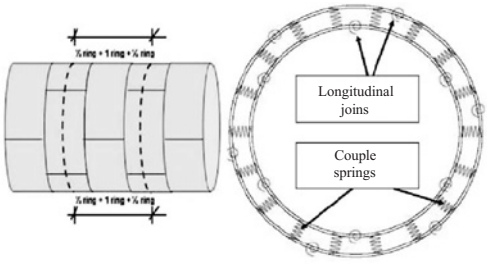

Figure 10. Double ring structural model (Comulada and Maidl, 2010).

Figure 11 shows the results obtained wit respect to the primary lining at the end of the analysis. We have the following comments:

- Cases representative of critical conditions obtained for each section are shown with solid blocks. A critical condition is understood as that which presents an inadmissible deformation.
- Variable contractions (1% to 2%) were applied to represent the land's displacement before placing the lining. There are special cases with low values of 0.2% to 0.5% and high values of 3.5% to 4%.
- Flexing rigidity of the continuous support was reduced to values of 10% to 20% to take into account transverse and longitudinal joints between dowels. There are cases, such as in shafts 18 and 20, where the percentage was 40%.
- Axial force on the primary lining was increased from 900 to 6,500 kN/m, as the tunnel's cover was increased, keeping the shear value almost constant at interval 50, and 200 kN/m. The value of the flexing moment did not show a tendency like that of the axial force or the shear; it varied between 30 and 360 kN-m/m.

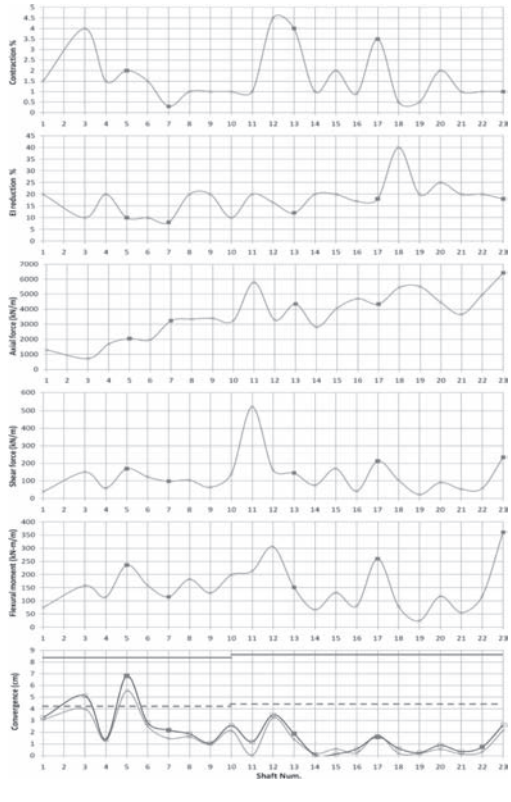

Figure 11. Results obtained from the analysis of TEO temporal lining.

- Horizontal and vertical convergences oscillated but in general were below 0.5% of the tunnel's diameter (4.2 cm and 4.3 cm) except in the cases of shafts L-3 and L-5, whose value was slightly higher although still below 1% of the diameter. This last indicates when the lining begins to crack significantly.

For the analysis of the lining under long term conditions at 18 months (stage 5, Fig. 9), which is the life span assigned to the primary lining, a variable pore pressure abatement between 5 kN/m^2 and 10 kN/m^2 was considered, only for the tunnel's initial section (L-0 to L-1A). Also considered is a model with uniform axial load, obtained from the previous state of stresses, with the horizontal pressure decreasing with the abatement proposed at 18 months and using the soil's long term deformability models. This is derived from the field observation indicating that with the tunnel's short term deformation, stress around the tunnel is redistributed uniformly.

6.3 *Construction of the secondary lining*

The secondary lining is born in a state of stresses caused only by its own weight, although at the soil-primary lining border there is a pseudo-homogenous stress, and the secondary lining will only support stress changes generated in the long term, 50 years, such as remaining stresses caused by placing the secondary lining prior to the primary lining's total stabilization, those caused by the subsidence phenomenon and/or changes in water table levels, and the incidence of seismic waves.

The numerical analysis considers that the primary lining contributes to the tunnel support's work in the long term. For the tuffs and sandy silts zones, apart from the primary lining's remaining work originated by placing the secondary lining at 18 months, two possible long term work conditions are analyzed: total recovery of pore pressures and elimination of that pressure. In the case of lacustrine clays, consolidation development is considered at 50 years. Finally, also considered in all the cases analyzed is the increase of stresses at the support, caused by earthquakes for a return period of 475 years.

Currently, the design of the tunnel's secondary lining is being carried out; nonetheless, preliminary analyses indicate that the lining's critical working conditions are located in the zones where the tunnel is deeper.

Seismic analysis. It is carried out for two working conditions: at a return period of 47.5 years for the primary lining's dynamic analysis (short term) and 475 years for the secondary lining (long term), using the method proposed by Wang and Parson (1993). Results indicate that deformation induced on the concrete ring is very low, in the order of $\varepsilon = 0.001$, for the longitudinal movement, and circumferential deformation of $\varepsilon = 0.0003$ by oval shaping.

6.4 *Special cases and studies*

There are particular structures in the project that required a special design, such as in the assembly galleries. On occasions it was not possible to assemble the tunneling machine at surface, so assembly galleries had to be set up, with a horseshoe section 11.7 m high and 12.4 m wide, 25.5 m long. These galleries were built with a conventional tunneling system, meaning that at every step of the excavation, usually 1.5 m long, lining was installed. The support consisted of a layer of shotcrete 0.30 m thick, with steel arches set at 1 m intervals. Due to the tunnel geometry and soil's mechanical characteristics, tunnel excavation was done using a top heading and bench approach, and according to the soil's undrained shear resistance, fully grouted fiberglass dowels parallel to the tunnel axes were used to reinforce the excavation front.

These structures were analyzed with 3D numerical models of finite elements considering each constructive stage (Fig. 12).

On the other hand, special studies are being carried out on the behavior of dowels rings on the secondary lining using physical models (Fig. 13) (Aguilar *et al.*, 2010).

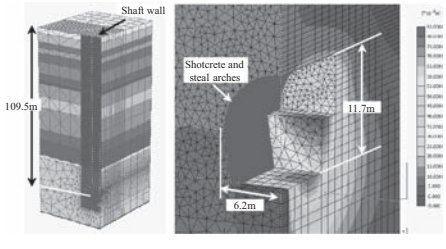

Figure 12. 3D numerical model of the analysis of the assembly gallery at L-17.

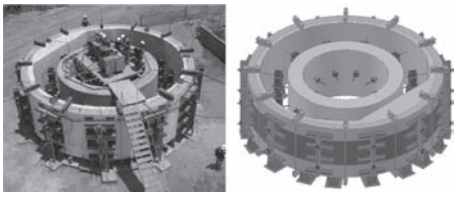

Figure 13. Study with instrumented physical models of the structural work of the voussoirs coupled to the secondary lining.

7 ANALYSIS AND DESIGN OF THE SHAFT EXCAVATION PROCESS AND LINING

In order to ensure the stability of the excavation and good construction and service conditions, attention must be paid to a number of ultimate and serviceability states (Auvinet *et al*., 2010).

The failure mechanisms analyzed were: depth, lateral extrusion, sub-pressure, flotation, kicking, excavation advance without support.

Ultimate states include:

a. *Soil fracturing and slurry losses*. During the excavation of the annular trench, some incidents have been reported such as fluid losses or fracturing of the soil due to slurry pressure. In Mexico City soft clays, fracturing may appear when the slurry level is raised only one meter above the water table level. The construction of a concentric plastic concrete annular wall is helpful to prevent fracturing.
b. *Excavation stability*. The general stability of the excavation (progressive or total excavation, bottom general failure, kicking) can be assessed using standard analytical limit analysis methods such as those proposed by Nash & Jones (1963), Alberro & Auvinet (1984) and Tamez (2001). However, numerical methods are now generally preferred. Using for example the finite element method, it is possible to take into account the geometric and mechanical details of the problem with great accuracy. In this type of analysis, the selection of an adequate constitutive model is extremely important (Hejazi *et al*., 2008). The most critical shear failure mechanism is generally a wall failure (Fig. 14a), although local extrusion of soft layers is also known to have happened in other excavations for the Mexico City subway system. On the other hand, when a concrete wall is built around a previous the excavation, bottom shear failure is most critical (Fig. 14b). When analyzing this mechanism, the fact that the bottom of the excavation's expansion induces a progressive increase of the water content and a reduction of the soil's shear strength should be taken into account.
c. *Bottom uplift failure*. In most cases, the bottom of the excavation is located slightly above the first hard layer. In this relatively pervious layer (typical permeability coefficient $k = 10^{-6}$ m/s), pore pressure is generally partially abated due to pumping of potable water for the city. Failure of the excavation bottom due to the uplift pressure is however a clear possibility. The safety factor can be obtained comparing the uplift pressure with the weight of the soil in the excavation bottom and of the slurry if it was used. It should however be taken into account that the weight of the slurry induces a pore pressure increment in the pervious layer. The transient conditions prevailing when the slurry level suddenly goes down can lead to the development of unfavorable seepage forces towards the excavation. This situation can be easily simulated performing transient flow analyses using the finite element method (Fig. 15a).

   When the excavation rests directly on the hard layer, the granular material of this layer can present a boiling condition when the vertical gradient due to lowering of the slurry level reaches a critical value.

   To cancel any possibility of uplift failure and buoyancy condition, electrosmotic water pumping from the hard layer has been used by one of the contractors to control hard layer pore pressure. Finite element modeling and instrumentation with piezometers have been used to assess the efficiency of this solution (Fig. 15b).
d. *Floating of finished structure*. When the construction of the shaft is finished the structure may float in certain conditions. This happens when the Archimedes thrust is larger than the sum of the weight of the structure and the lateral friction between soil and concrete developed on the shaft's surface perimeter. This is more likely to

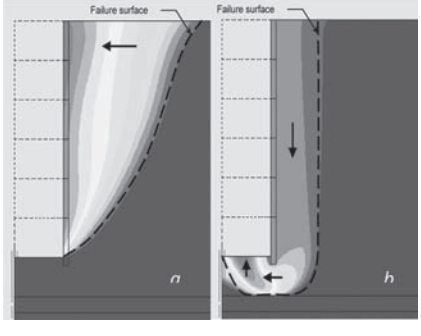

Figure 14. Potential shear failure mechanisms (Contour displacements): (a) without concrete wall (b) with concrete wall.

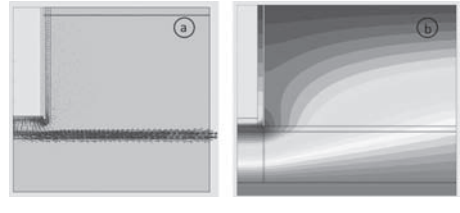

Figure 15. FEM simulations of: (a) Transient flow conditions in pervious layer and (b) Pumping in the hard layer to control uplift thrust (hydraulic head contours).

happen with shafts of large diameter, since lateral friction is proportional to shaft diameter, whereas the Archimedes thrust grows as the diameter squared. When necessary, the structure must be ballasted and/or the shaft wall's thickness increased to avoid flotation.

e. *Behavior of shafts against negative friction*. If the pore pressure decreases in superficial clay deposits located down to 40 m depth, it will generate negative friction on the shaft skin. The negative friction could be calculated using the following equation (Zeevaert, 1983):

$$NF = \pi D \cdot K_{\phi} \cdot \int \sigma_0 \cdot dz_i$$

where, NF is the negative friction on the shaft skin, D is exterior diameter, K_{ϕ} is the long term lateral earth pressure for each stratum, $K_{\phi} \approx 0.3$, and $\int \sigma_0 \, dz_i$ is the area of the diagram of vertical effective stresses according to the total abatement. It is also possible to evaluate the effect of this lateral force using FE Method.

Serviceability limit states are also important:

f. *Movements induced in neighboring buildings during construction*. In an urban environment, neighbors are frequently worried that soil displacements induced during shaft construction could damage their property. Careful attention must be given to this problem. However, displacements computed using finite element modeling are small and, in normal conditions, excavation by the flotation method should not affect other constructions. This has been confirmed by instrumentation measurements on many sites.

g. *Long term behavior*. A much more critical aspect is the apparent protruding of the shaft with respect to the surrounding ground that may occur due to the contribution of the upper clay formation to the regional subsidence. A protruding rate of 18 cm per year may be expected in shafts L-0 and L-1. This is a very compelling reason to keep the shaft away from important constructions whenever possible.

h. *Seismic behavior*. The seismic behavior of the shafts considering an event with return period of 475 years was also studied using an analytical approach proposed by Pérez & Avilés (2010). Results show that seismic loads are the most critical condition, mainly in deep shafts, but using 3D numerical modeling the working conditions of the support are substantially lower (Fig. 16, Rangel *et al.*, 2010).

A very important point during an earthquake is the behavior of the tunnel-shaft joint because these structures are moving in a different way. Due to high stress concentration during seismic loads this project does not consider the joint between tunnel and shaft.

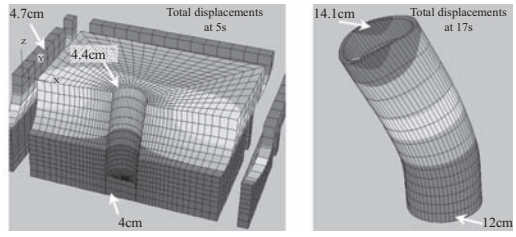

a) Whole numerical model b) Detail of shaft model

Figure 16. Three dimensional numerical difference finite model using flac3D. Total displacement diagrams determined at 5 s (a) and 17 s (b) of the earthquake signal.

8 MONITORING AND BEHAVIOR

The TEO instrumentation program includes the following measurements:

a. Convergences. Using extensometers, the shortening and lengthening of each of the tunnel's primary lining rings are measured on the vertical and horizontal axes.
b. Surface leveling. Measurement of settlements on lines transverse to the tunnel's outline, and edifications.
c. Instrumented dowels rings. Along the already built tunnel five dowel rings have been instrumented by means of: seven joint measurers, four pressure cells, eight deformation meters for steel, and eight deformation meters for concrete.
d. Measurement of pore pressure in the soil.
e. Measurement of subsoil movements with inclination meters.
f. Measurement of the tunneling process variables: front pressure, advance speed, alignment, volume and pressure of injection mortar, etc.

Currently, the primary support has been excavated and placed in almost all the shafts, whereas the tunnel is excavated with the primary lining only on its first 243 m from shaft L-0.

8.1 *Tunnel*

The zone where the tunnel has already been excavated is characterized by consisting totally of very compressible clays, with low shear resistance and maximum humidity contents of 400% and regional subsidence of 18 cm/year. Also, this zone is the most critical from the point of view of affectation to the existing infrastructure and the edifications at the surface (mainly homes). In effect, the tunnel's

keystone is located between 15 m and 25 m depth, and a vehicle bridge with piles is crossed passing only 2.5 m away from the piles of one of the supports.

Therefore, this section has been extensively instrumented: there are instrumented dowel rings approximately every 30 cm, leveling lines have been installed at surface and buildings, and the convergences on each ring are measured with more frequency.

Fig 17 shows a summary of the convergence, injection pressure and volume measurements carried out during 8 months. It shows that the tendency of the measurements of vertical and horizontal convergences is to stabilize between the values of 4 cm and 5.5 cm, save at some special points that report values of up to 7 cm. It is important to comment that no cracks or fissures haven observed on the body of any ring, or aperture of the joints, transverse of longitudinal, nor any filtrations that lead to a condition of loss of sealing.

It has also been observed that there are abrupt convergence increases that are correlated with these events:

- Extraordinary event, tunnel flooding: between 4 and 5 February 2010
- Start of rain season: June 2010
- Earthquake 6.4°: 30 June 2010
- Excavation resumed: 4 August 2010

These events caused convergence increases in small time lapses. For example: in the case of ring No. 37, Figure 18, the first period, that corresponds December-January, the record shows a deformation speed $\Delta\delta h = 16$ mm/month, presenting a jump at the end of the period that coincides with the tunnel's flooding. Then, the deformation speed tends toward 4 mm/month between February and May, and drops to 2.3 mm/month from May onward, with a tendency to stabilization. The events marking the start of the rain season and the earthquake have been reflected with small convergence increases.

The cases where high convergence values (between 4.5 cm and 7 cm) occur are associated with deficiencies in the constructive process, such as injection pressure or volume decrease of the project at this section, 1.5 bar and 7.55 cm^3 respectively. In particular cases, such as the tunnel's nearness to the bridge's foundation piles, injection volume increases have been measured of up to 12.5 m^3.

Average convergences measured to date at this section, 4 cm to 5.5 cm, are slightly higher than the design measurements of 3 cm to 4.2 cm.

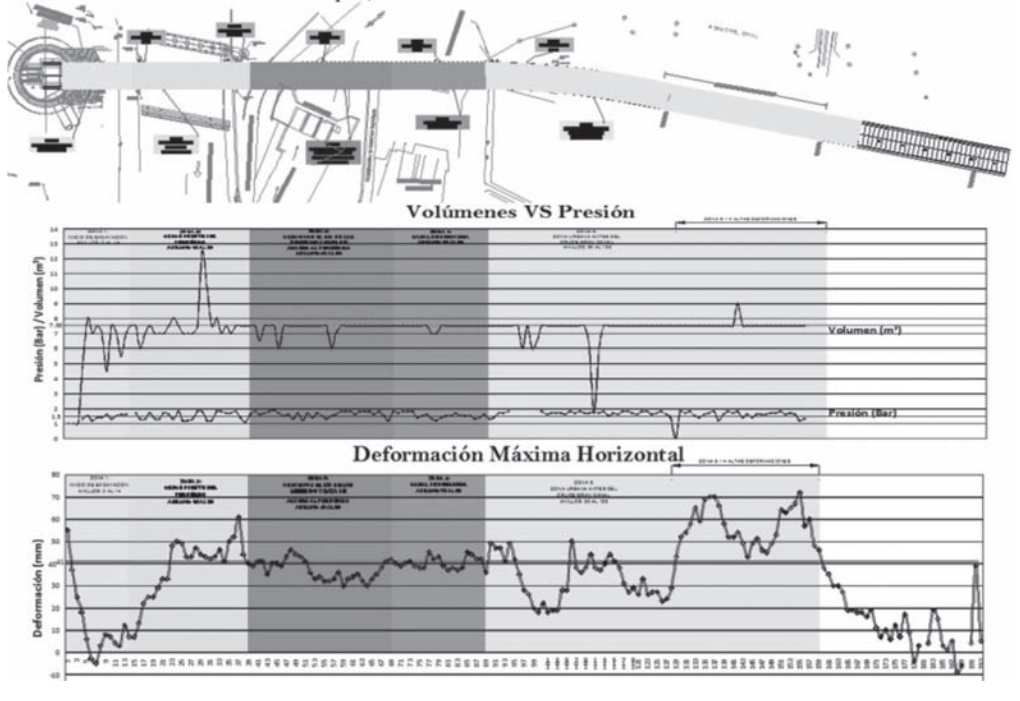

Figure 17. Measurements made at the tunnel after 8 months of construction: (a) plan location, (b) injection pressures and volume, (c) horizontal convergence and (d) vertical convergence.

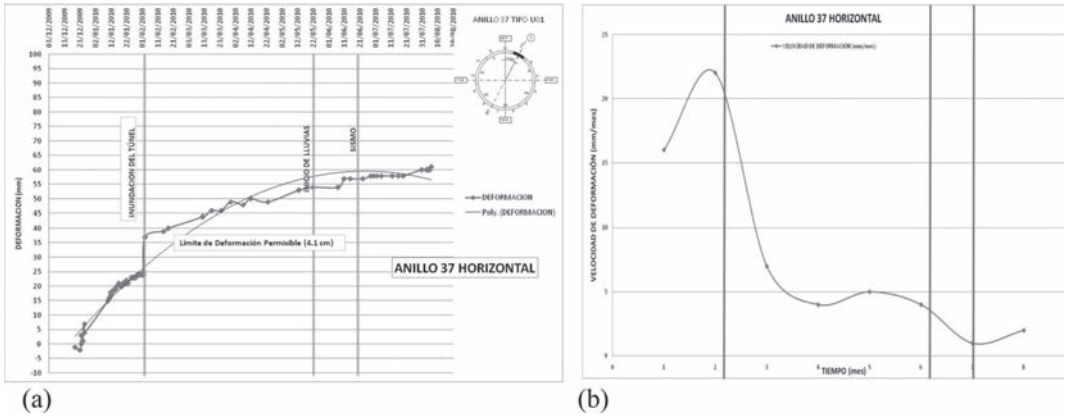

Figure 18. Convergence measured at voussoir ring 37: (a) time vs horizontal convergence diagram, (b) time vs deformation speed diagram.

With respect to surface land settlements, two zones have been observed: the first, at between 0 and 50 m of tunnel, settlements are in the order of 13 cm, with a maximum of 14.3 cm, whereas for the second, between 50 m and 243 m, reported settlements were of the order of 4.4 cm, with a maximum of 6.4 cm. Settlements measured at the first zone are important, and are a product of the vehicle bridge-tunnel's interaction.

8.2 *Shafts*

Shaft behavior in general has been satisfactory from the point of view of stability during construction and useful life; nonetheless, there have been constructive problems, mainly with the tolerance of deviation of each diaphragm wall panel and entrapment of the trench excavating machine.

The cases where these problems occurred were at shaft L-5, after crossing a very hard stratum, and then when finding a soft and deformable stratum, and at the deepest shafts, as in L-20, of 155 m depth, where a diaphragm wall was built for the first 120 m and then using the conventional method and immediate placing of the support.

9 CONCLUSIONS AND RECOMMENDATIONS

Exploration: Exploration techniques for samples and lab tests used in conventional Mexican engineering produced adequate results at depths of less than 60 m. For more depth, new technologies were required, such as measuring shear wave velocity by means of the SPAC geophysical technique, the use of a presiometer, phicometer, triple barrel samplers, etc.

Design: The design strategy has been congruous with what has been observed during the development of the construction work, with convergences similar to what was indicated at the design stage, and observing the integrity of the dowel rings.

In the section of clayey soils and coverage between 28 m and 40 m, it was observed that the value of flexion rigidity EI used to consider the joints between dowels and dowel rings varies between 10% and 15%.

Instrumentation: It was observed that pore pressure dissipation with the passing of the tunneling machine in clayey soils was quick, taking a day at most. The calculations have been consistent with what the observed during the construction.

Constructive processes: For the tunnels excavated in clayey soils, surface settlements are fully related to the tunnel's constructive process. In effect, the adequate selection of pressure, volume and type of dosage of the injection mixture for the annular space between dowel and soil avoids generating important settlements, as otherwise these settlements can affect neighboring buildings. Other aspects to care for are the pressure applied at the excavation front, and an homogenous injection process along the entire space. For the case of the TEO, minimal pressure to apply at the front was determined following these criteria:

- $p_f = u + 0.5$ kg/cm^2
- $p_f = \sigma_v \times k_a + u + 20$ kPa.

Also, it was considered that $p_{iny} = p_f$.

Geotechnical issues: The main geotechnical problems during the design and construction in soft soils were:

- The dynamic amplification and subsidence problems in Mexico City clays
- Tunneling in an urban area with very soft soils
- Tunneling soils at 50 m and 155 m deep
- Having mixed soil condition like sandy silt and basalts lens or clay lens in sandy silt hard layers
- The construction of deep shafts (up to 160 m) in difficult soil condition

For tunneling in soft soils, the surface settlements are fully associated with the tunnel construction process. In fact, the proper selection of pressure, volume and the grout for the annular injection between soil and lining prevent the generation of unacceptable settlements. Other aspects to take into account are the pressure applied on the excavation face and be careful to have a uniform injection around the tunnel.

ACKNOWLEDGEMENTS

We would like to thank to the organizing committee for the invitation to this symposium, especially to Professor Richard Kastner and Professor Stefano Aversa. A recognition as well to the working team who dedicate most of their time to the construction of this important project.

This article is a contribution of technical committee TC-214.

REFERENCES

Aguilar, O., L. Mendoza, E.A. Tavera, Y. Alberto and J. Morelos (2010), Load test on a real scale model of a tunnel with secondary lining, *National Soil Mechanics Meeting*.

Alberro, J. and G. Auvinet (1984), Construcción de estaciones de Metro a gran profundidad en las arcillas del Valle de México (Construction of deep subway stations in Mexico City valley clays), *Technical Report* to COVITUR, December, Mexico.

Arias, F. (1997), Confiabilidad de trincheras estabilizadas con lodo (Reliability of slurry trenches), *Master degree thesis*, División de Estudios de Posgrado de la Facultad de Ingeniería, UNAM, Mexico.

Auvinet, G. and J.F. Rodríguez (2004), Análisis de lumbreras cilíndricas sometidas a cargas locales (Analysis of shafts subjected to local loads), *Proceedings, XXII National Soil Mechanics Meeting*, Sociedad Mexicana de Mecánica de Suelos, Vol 2, Guadalajara, Mexico, pp 317–322.

Auvinet-Guichard G., J.F. Rodríguez-Rebolledo and J.L. Rangel-Núñez (2010), Construction of deep tunnel shafts in Mexico City soft clays by the flotation method, *Acta Geotechnica*, 5, Springer-Verlag, DOI 10.1007/s11440-010-0115-2, pp 63–68.

Auvinet Guichard, G. (2010), Doscientos años en la historia de la ingeniería en México (Two hundred years in the history of engineering in Mexico), *Separata,* Fundación ICA, Mexico, DF.

Comulada-Simpson, M., and U. Maidl (2010), Design and structural analysis of lining segments in soft soils. *International symposium on Tunnels and Shafts*, Mexican Society of Soils Mechanics and Mexican Association of Underground Works and Tunnel Engineering, Mexico, DF.

Farjeat Paramo, E. (1975), Memoria Técnica de las Obras del Drenaje Profundo del Distrito Federal, *TUNEL S.A. de C.V*., Mexico DF.

Google-Earth (2011), Electronic maps.

Hejazi Y., Dias D. and Kastner R. (2008) Impact of constitutive models on the numerical analysis of underground constructions, *Acta Geotechnica*, 3.251-258 DOI 10.1007/s11440-008-0056-1.

Jaky, J. (1944), The coefficient of earth pressure at rest, *J. Soc. Hungarian Architects Eng.,* 7–355–358.

Jaw-Nan Wang and Parsons Brinckerhoff Inc. (1993), *Seismic design of tunnels: a simple state-of-the-art design approach*, Parsons Brinckerhoff Inc., One Penn Plaza, New York.

Juárez, M., G. Auvinet, F. Hernández and E. Méndez (2010), Contribución a la caracterización geotécnica de la zona norte de la cuenca de México (Contribution to geotechnical characterization of the north part of Mexico Basin), *Memorias Técnicas, XXV Reunión Nacional de Mecánica de Suelos e Ingeniería Geotécnica*, Sociedad Mexicana de Ingeniería Geotécnica, Acapulco, Gro., Mexico.

Mooser, F., A. Montiel and A. Zúñiga (1996), Nuevo mapa geológico de las cuencas de México, Toluca y Puebla (New geological map for Mexico, Toluca and Puebla basins), *Comisión Federal de Electricidad*, ISBN: 968-7780-00-2, Mexico DF.

Mooser, F. (2010) Modelo Geológico del Túnel Emisor Oriente (Geological model of TEO), COMISSA, Mexico, DF.

Nash J.K.T.L. and G.K. Jones (1963), The support of trenches using fluid mud, grouts and drilling muds in Engineering Practice, Butterworths, London, pp 177–180.

Perez-Rocha, L.E. and J. Avilés López (2010), Determination of seismic actions in shafts buried in soft soils, *International Symposium of Tunnels and Shafts* in Mexico City, SMIG and AMITOS, Mexico.

Rangel, J.L., U. Iturrarán V, A.G. Ayala and F. Cervantes (2005), Tunnel Stability analysis during construction using a neuro-fuzzy system, *Int. Jour. Num. An. Meth. in Geomech.*, 29: 1434–1456.

Rangel-Núñez, J.L., G. Auvinet-Guichard and E. Tamez-González (2007), A simple criterion to evaluate tunnel stability during construction, ECCOMAS Thematic Conference on Computational Methods in Tunneling, J. Eberhardsteiner et al (eds.), Vienna, Austria.

Rangel-Núñez, J.L., S. Martínez Galvan, N. Salmiento-Solano and E. Ovando-Shelley (2010), "Dynamic analysis of shafts in Mexico City deposits," *International Symposium of Tunnels and Shafts* in Mexico City, SMIG and AMITOS, Mexico.

Tamez, E., J.L. Rangel Núñez and E. Holguín (1997), *Diseño Geotécnico de Túneles (Geotechnical design of tunnels)*, TGC Geotecnia, Mexico DF. ISBN 9685571007.

Tamez, E. (2001) *Ingeniería de Cimentaciones. Conceptos Básicos de la Práctica* (Foundation Engineering. Basic Practice Principles), TGC Geotecnia, Mexico.

Wilson, E. (1965), *Structural Analysis of Axisymmetric Solids*, American Institute of Aeronautics and Astronautics Journal, Vol. 3–12 December, USA, pp 2269–2273.

Zeevaert, L. (1983), Foundation Engineering for Difficult Subsoil Conditions, 2nd ed., Van Nostrand Reinhold.

Geotechnical Aspects of Underground Construction in Soft Ground – Viggiani (ed)
© 2012 Taylor & Francis Group, London, ISBN 978-0-415-68367-8

Long-term tunnel settlement mechanisms of Metro Line 2 in Shanghai

C.W.W. Ng & Q. Li
The Hong Kong University of Science and Technology, HKSAR, China

G.B. Liu
Tongji university, Shanghai, China

ABSTRACT: Non-uniform excessive tunnel settlements and relatively small tunnel heaves have been observed along Shanghai Metro Lines 1 and 2 over the last 15 years. Tunnels of the Metro lines were constructed using an Earth Pressure Balance (EPB) machine. It is well-known that significant long-term tunnel settlements may pose a threat to the serviceability and safety of the underground metro systems. However, the mechanisms of the observed large long-term tunnel settlements up to 144 mm at some stations are still not fully understood. In this paper, measured tunnel settlements of the 16.4 km long Metro Line 2 from 1999 to 2007 are studied together with groundwater pumping records from 1920s. Four possible causes including the effects of tunnel construction, secondary compression of soft clay, cyclic loading due to running trains, and groundwater pumping for the observed large tunnel settlements at some stations are investigated based on desk study, results of static and cyclic laboratory tests and coupled consolidation finite element analyses. The likely mechanism for the observed long-term tunnel settlement is identified and discussed.

1 INTRODUCTION

Shanghai is the largest financial centre in China with a population of about 23 millions. In order to alleviate the increasingly severe congestion problems in this city, underground metro network has been developed in stages in Shanghai. Since the first metro line (Line 1) was started in operation in 1995, there are 11 metro lines (excluding the Shanghai Maglev airport link) and 267 stations built. All tunnels of these 11 metro lines were driven using an Earth Pressure Balance (EPB) machine. The external diameter (D) of tunnel is typically 6.2 m and is located at relatively shallow depths (about 13 m below ground) in soft clay. The total length of tunnels in operation is 410 km in 2010 (see Fig. 1), making the Shanghai metro network the longest in the world. It is anticipated that a total of 510 km long of track will be in operation by 2012 and further increased to 877 km long by 2020.

Since the operation of Metro Lines 1 and 2, non-uniform tunnel settlements and heaves have been observed at various stations along the two lines. Water leakages at various joints of concrete linings were observed resulting from excessive tunnel settlements along the two lines (see Fig. 2). It is well-recognized that excessive tunnel settlements may lead to structural cracking and tunnel misalignment, which greatly affect the safety of under ground metro system (Schmidt and Grantz, 1979;

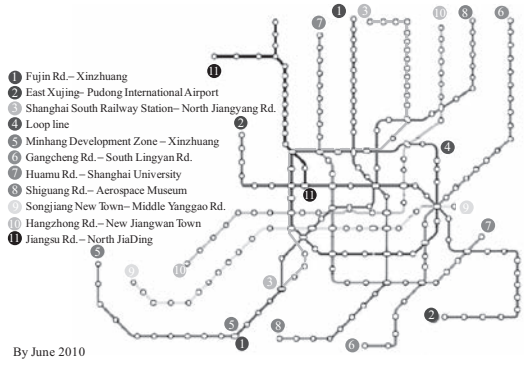

Figure 1. Map of Shanghai metro system.

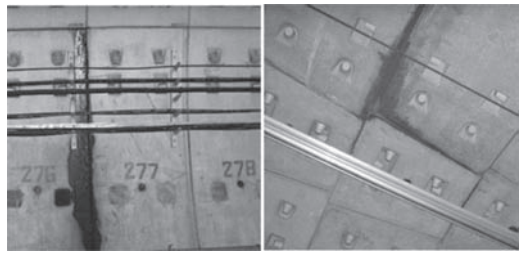

Figure 2. Typical leakage at joints of metro tunnels in Shanghai.

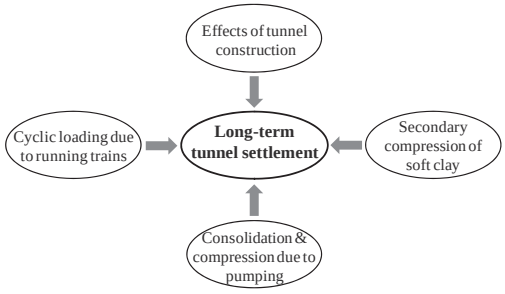

Figure 3. Possible causes of large long-term tunnel settlements in Shanghai.

Grantz, 2001a). Dalgıç (2002) monitored and reported the deformation of Bolu rock tunnel. It was found that considerable tunnel settlement developed in a thrust fault zone (poor ground condition) during construction. Grantz (2001) reported long-term tunnel settlements of several rectangular immersed tunnels during operation. The author proposed some possible reasons for the observed large tunnel settlements such as extraction of water gas and oil from underlying strata, poor subsoil conditions and large tidal variations.

In this paper, measured non-uniform tunnel settlements and heaves along the 16.4 km Metro Line 2 (Phase I) between December 1999 and May 2007 (i.e., 7.5 years) are studied and discussed. Some possible causes investigated (see Fig. 3) to explain the observed large long-term tunnel settlements include the effects of tunnel construction, secondary compression of soft clays, cyclic loading due to running trains, and groundwater pumping in aquifers. Based on desk study of tunnel settlements and groundwater pumping records, laboratory static and cyclic element test results, and coupled consolidation finite element analyses, the likely principal mechanism leading to the observed large long-term tunnel settlements is identified and verified.

2 GEOLOGICAL CONDITIONS AND SOIL PROPERTIES ALONG METRO LINE 2

2.1 *Geological conditions*

Shanghai is located on the Yangtze River delta in the eastern part of China. Figure 4 shows the location of Metro Line 2 (Phase I). The construction of Phase I was started in December 1995 and completed in February 1999. The Metro consists of 16.4 km long twin tunnels running from the Zhongshan Park in the west to Longyang Road in the east. A total of 12 stations are available for Phase I at an average interval of 1.4 km along the line. Subsequently, Line 2 has been extended to include a total of

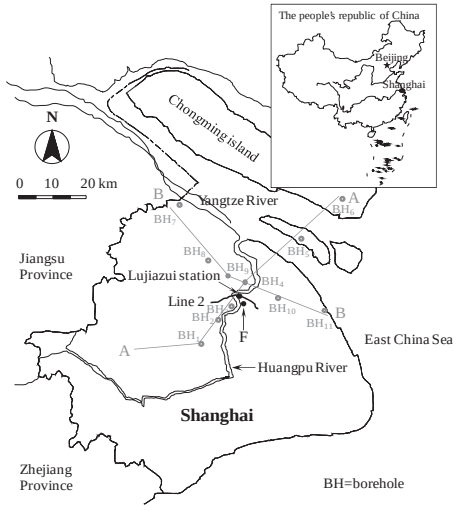

Figure 4. Locations of Shanghai Metro Line 2 (Phase I) and 11 boreholes along sections A-A and B-B.

31 stations connected by 60 km long track, running from the Puxi area in the west, across the Huangpu River underneath, to the Pudong area in the east. For the construction of metro lines in Shanghai, various deep boreholes (over 300 m) were sunk. The locations of 11 boreholes, BH_1 to BH_{11}, along sections A-A and B-B are also shown in the figure.

Figure 5(a) shows the geological profile along section A-A. The geology consists mainly of alluvial and marine sediments deposited during the Quaternary period (Shanghai Geology Office, 1979). The 300–350 m thick deposits contain six clayey strata sandwiched by five aquifers (i.e., sand deposits). They were formed under alternating warm and cold climates and changes of sea levels during the last three-million years. It can be seen that the uppermost three aquifers are interconnected at some locations. For Aquifer IV, the thickness varies from place to place.

The geological profile along section B-B is shown in Figure 5(b). The location of Metro Line 2 is projected and indicated on the section for illustrative purposes. Since the depth of the tunnel axis is about 13 m below ground surface, the C/D ratio is approximately 1.6, where C is the cover depth of the tunnel. Similar to section A-A, the geology along section B-B also consists of sandwiched alluvial and marine sediments, comprising six clayey layers, which are sandwiched by five aquifers (i.e., sand deposits). Considerable variations of the thickness of each soil layer can be seen. The thickness of each soil layer is not known for sure. The main ground water table is generally located at 1 m below ground surface in Shanghai. Figure 6 shows

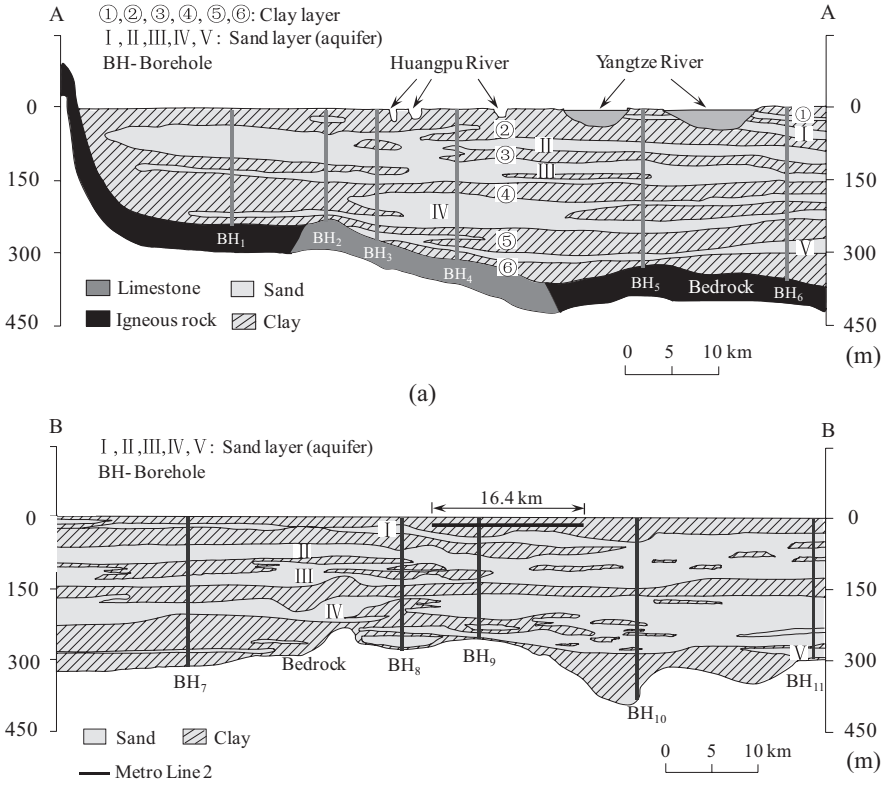

Figure 5. Shanghai geological profiles: (a) along section A-A; (b) along section B-B (from Shanghai Geology Office, 1979).

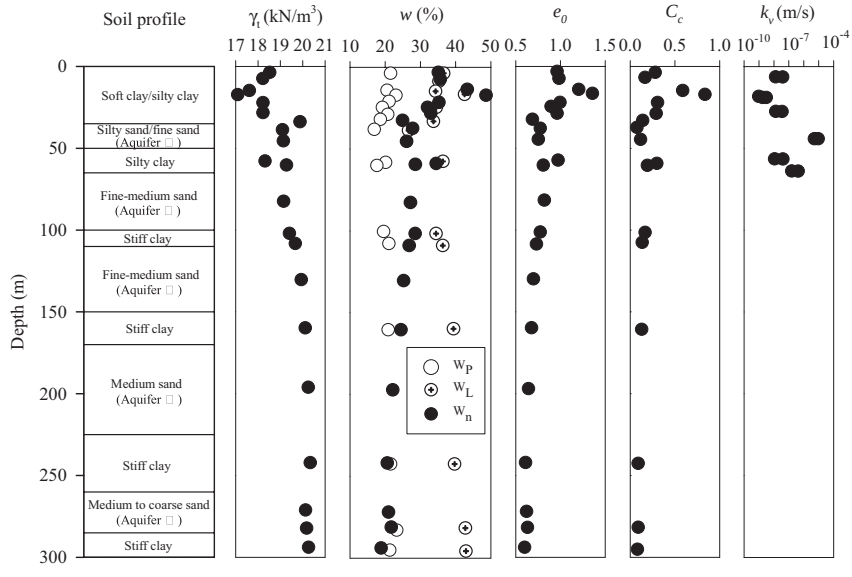

Figure 6. Typical soil profile and properties in Shanghai (modified from Chai et al., 2004).

a typical soil profile and properties in Shanghai. The uppermost stratigraphy (top 50 m of soils) is mostly encountered in engineering practice. It generally consists of 2 m thick of fill underlain by a soft clay layer ranging from 3 to 22 m. It should be noted that Metro Line 2 is located in this soft clay layer. The soft clay is followed by a layer of 20 m thick silty sand/fine sand layer and then followed by a 20 m thick silty clay stratum. The first fine-medium sand (Aquifer I) is located at about 40 m below ground. Although the depth and thickness of each aquifer can vary considerably from place to place, Aquifers, II, III, IV and V may be found at 60 m, 110 m, 170 m and 260 m below ground, respectively.

As shown in the figure, unit weight (γ_t) of soils decreases from 19 kN/m^3 near ground surface to 17 kN/m^3 at 22 m in the soft/silty clay layer, and it then increases to 20 kN/m^3 at about 150 m and it remains almost constant thereafter. Over the upper 50 m, the measured natural water contents (w_n) are close to the liquid limit of each soil, suggesting the soft and compressible nature of the soils. The variations of measured void ratio (e_0) and compression index (C_c) with depth are consistent with the profiles of γ_t and w_n. Below 50 m, measured natural water content of clayey soils decreases with depth and it reaches its corresponding plastic limit at 150 m below ground. As illustrated in the figure, the variations of vertical permeability (k_v) of soft clay layer fall between 10^{-7} and 10^{-9} m/s, whereas the k_v value for silty sand/fine sand can be as high as 10^{-4} m/s.

2.2 *Secondary compressibility of soft clay*

In order to investigate long-term tunnel settlement mechanism of Metro Line 2 located in the first soft clay layer, block samples with dimensions of 300 × 300 × 300 mm^3 were taken at depths of 8.5 m and 15.5 m from a basement in Shanghai. One-dimensional consolidation and secondary compression tests on natural clay samples were carried out in accordance with BS 1377-5 (BSI, 1990) in standard oedometers using a steel ring of 69 mm internal diameter and 19 mm height. Two conventional Incremental Loading (IL) tests and four long-term consolidation tests up to 70 days were carried out on the natural soft clay specimens. For comparisons, an IL test was also performed on a reconstituted specimen prepared according to the procedures suggested by Burland (1990).

Figure 7 compares measured secondary compression indices (C_α) of the Shanghai soft clay with four other different natural soft soils published in the literature. It can be seen from the figure that average ratios of C_α/C_c are 0.034 and 0.030 for natural and reconstituted Shanghai clay, respectively.

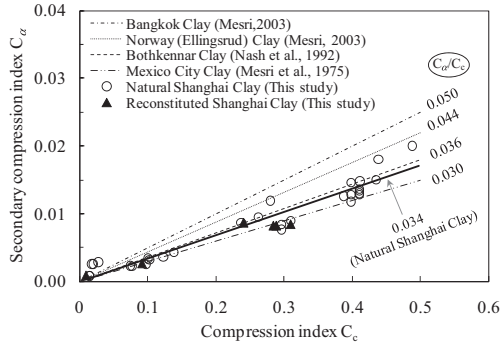

Figure 7. Comparison of C_α/C_c value of Shanghai Clay with other soft clays worldwide (Ng et al., 2011).

By comparing the C_α/C_c values ranging from 0.01 and 0.07 (Terzaghi et al., 1996) for a variety of natural geo-materials and the comparisons shown in the figure, it is clear that the Shanghai clay does not exhibit distinctive large secondary compression characteristics as commonly assumed by many researchers and engineers in the mainland China. On the contrary, the secondary compressibility of Shanghai soft clay is low.

To further compare and quantify the secondary compressibility of the Shanghai soft clay, the coefficient of secondary compression defined as $\varepsilon_\alpha = C_\alpha / (1 + e)$ is adopted. As suggested by Mesri (1973) (see Table 1), geotechnical materials may be classified ranging from very low to extremely high secondary compressibility based on the values of ε_α.

Figure 8 shows relationship of ε_α versus natural water content w_n for natural Shanghai clay. For comparisons, other 13 different natural soil deposits are also included in the figure. It can be seen that the coefficients of secondary compression of Shanghai clay fall within the range of 0.2%–0.8%, which can be classified by Mesri (1973) as a soil with low to medium secondary compressibility as indicated in Table 1. The laboratory measured results on the natural clay are consistent with measured ground settlements due to deep excavations in Shanghai (Liu et al., 2005). The measured low to medium ε_α values of the Shanghai soft clay seem to imply that any observed long-term soil and tunnel settlements are not likely attributed to the low secondary compression characteristics of the clay. More discussion is given in section 5.2 later.

2.3 *Cyclic triaxial tests on soft clay*

In order to investigate the effects of running trains on compression of soft clay and hence any possibility of induced tunnel settlement, cyclic triaxial

Table 1. Classification of soils based on secondary compressibility (from Mesri, 1973).

ε_α (%)	Secondary compressibility
<0.2	Very low
0.4	Low
0.8	Medium
1.6	High
3.2	Very high
>6.4	Extremely high

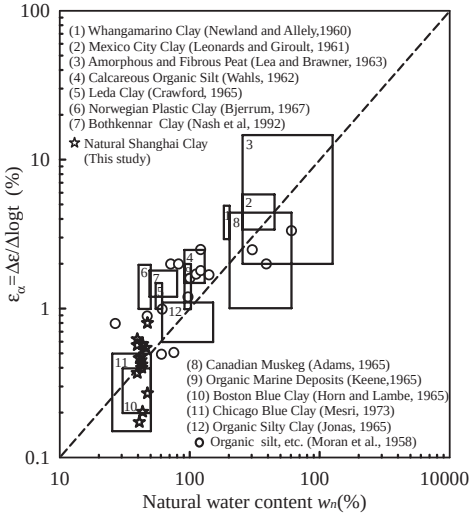

Figure 8. Comparison of secondary compression index of Shanghai soft clay with other clays worldwide (Ng et al., 2011).

tests were carried out by Liu (2006) in Tongji university. Natural soft clay samples were taken at about 10 m depth from a basement. Three cyclic tests with different cyclic stress ratios (CSRs), i.e., ratio of cyclic deviatoric stress to undrained shear strength, of 0.18, 0.35, and 0.53 were carried out by using a GDS multi-function dynamic triaxial apparatus. The undrained shear strength of the clay was 57 kPa. The sizes of each specimen were 39 mm in diameter and 89 mm in height. Each specimen was subjected to 10,000 cycles of one-way undrained compression at 1 Hz.

Figure 9(a) shows the development of axial strain with number of cycles of compression. At lower CSRs of 0.18 and 0.35, each specimen tends to reach a steady value of axial strain (less than 0.05%) after about 1,000 cycles of compression at 1 Hz. On the contrary, the specimen subjected to CSR of 0.53, its axial strain keeps increasing and fails to reach a steady value even after 10,000 cycles of compression.

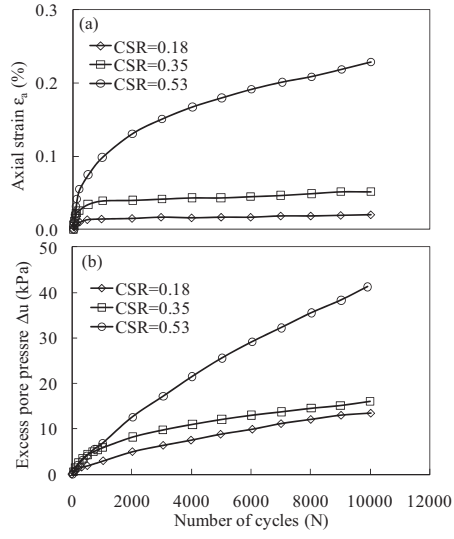

Figure 9. Development of (a) axial strain with number of cycles; (b) excess pore pressure with number of cycles (modified from Liu, 2006).

Consistently with the observed small cumulative strains, measured excess pore pressures (Δu) for the tests under two lower CSRs of 0.18 and 0.35 are fairly limited, i.e., only up to about 15 kPa after 10,000 cycles of compression at 1 Hz (see Figure 9(b)). On the other hand, measured Δu increases continuously with number of cyclic compression at a CSR of 0.53 and excessive pore water pressure reaches about 40 kPa at 10,000 cycles without showing a clear sign of reducing Δu during each cycle.

According to the reported cyclic test results shown in Figures 9(a) and (b), it is not difficult to deduce that running trains would have a minimal effect on the accumulation of axial strains and hence any significant long-term soil and tunnel settlements in Shanghai soft clay, if CSR induced by running trains is low. Some more details are given and discussion in section 5.2 later.

3 METHOD OF TUNNEL CONSTRUCTION AND INSTRUMENTATION

3.1 *Method of tunnel construction*

The EPB tunnelling method has been used to drive all metro tunnels in Shanghai so far. The diameter and length of each EPB shield are 6.34 m and 6.24 m, respectively. Compensation grouting was often undertaken to minimize ground surface settlements and to control volume losses ranging from 0.5% to 2% (Chen et al., 2008).

Figure 10 shows a typical cross-section of precast reinforced concrete tunnel lining for Metro Line 2. Each tunnel lining consists of six concrete segments bolted together by 12 and 17 steel bolts in the circumferential and longitudinal directions (Lee et al., 1999). The length and the thickness of each concreted lining are 1.0 m and 0.35 m, respectively.

3.2 *Instrumentation*

Various instruments were installed to monitor groundwater pressures, surface, subsurface and tunnel settlements. Figure 11(a) shows the layout of instrumentation adopted in this study. To record water pressure in each aquifer, a standpipe piezometer was used. Monitoring of ground surface settlements was carried out by precise levelling of markers installed at spacing of about 1 km along the metro line. To measure compression of a soil stratum (either a clay layer or an aquifer), a pair of rod extensometers were placed at the top and bottom of each soil stratum. A schematic diagram of a rod extensometer is shown in Figure 11(b). Depending on the depth and thickness of a soil stratum to be measured, the length of extensometers varied in different boreholes in which they were installed. Depending on the length of each extensometer required, up to three different diameters of steel rods were installed to cover the depth of each borehole.

For measuring tunnel settlements, stainless steel levelling points as illustrated in Figure 10 were set up in the middle of each concrete track. These levelling points were placed approximately at every 25 m along the longitudinal axis of an entire length of each tunnel of Metro Line 2. To minimize the influence of general ground settlements, benchmarks for measuring tunnel settlements were installed in the bedrock underneath Line 2. The monitoring of Metro Line 2 was started from December 1999 and the frequency of monitoring was once about every six months. The last tunnel settlement record obtained for this paper is May 2007.

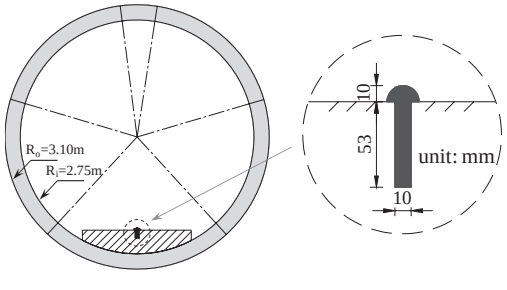

Figure 10. Cross-section of tunnel lining.

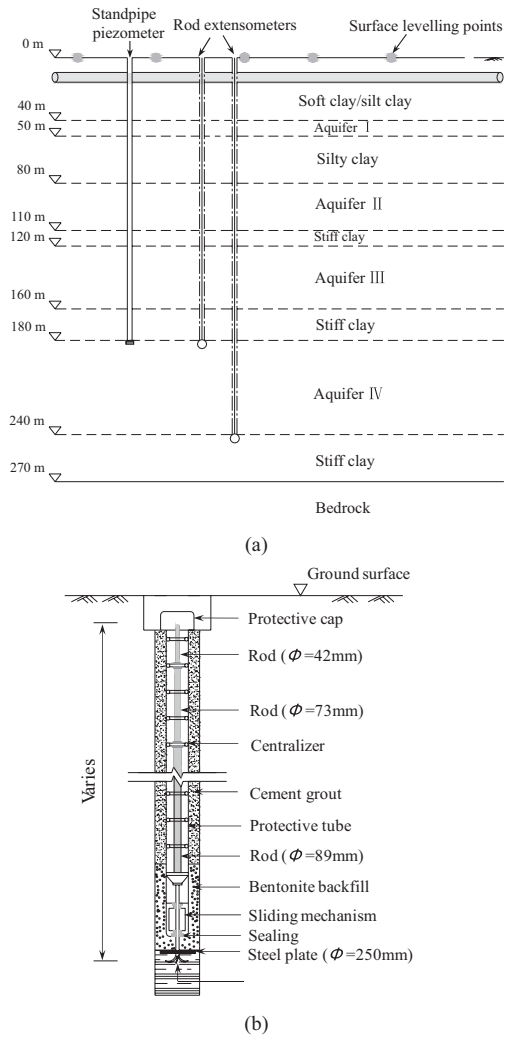

Figure 11. (a) Layout of instrumentation and estimated geological profile from BH_3 and BH_9; (b) Schematic diagram of a rod extensometer.

4 MEASURED LONG-TERM TUNNEL SETTLEMENTS AND HEAVES

Figure 12(a) and (b) show measured tunnel settlements and heaves along the east and west bounds of Metro Line 2, respectively. The Zhongshan Park station is taken as the reference for chainage Calculations. Non-uniform vertical tunnel movements (i.e., settlements and heaves) can be found consistently at any chainage of both tunnels. As the distance between the eastbound and the westbound tunnels is only about 17 m apart, it is not surprising to observe such similar trends and magnitudes

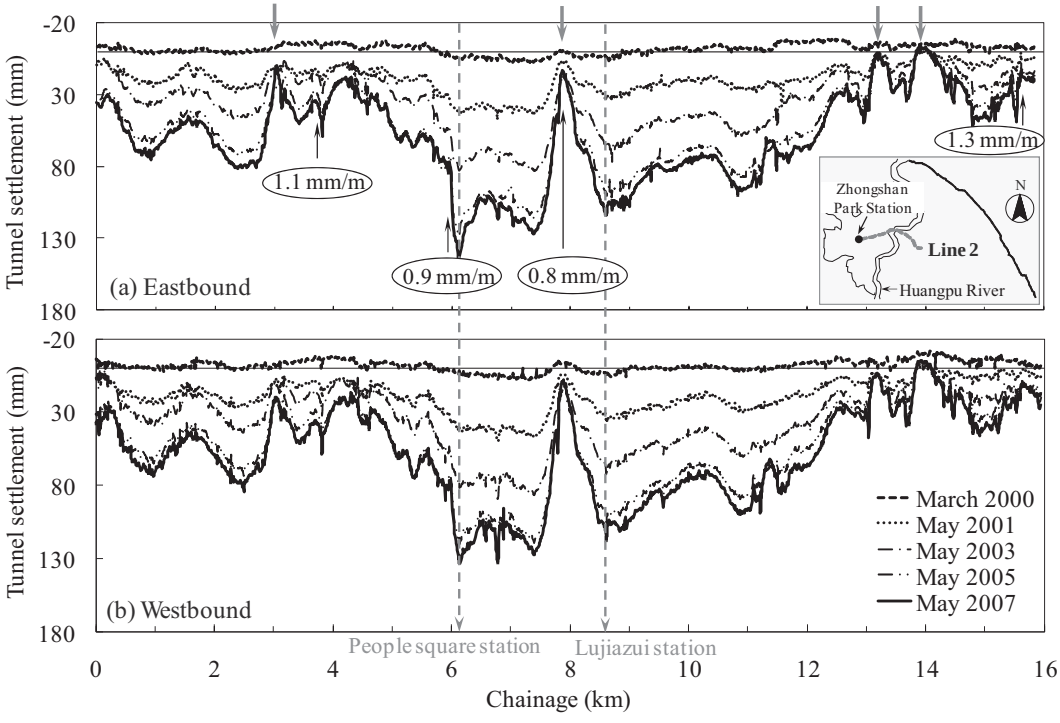

Figure 12. Measured tunnel settlements and heaves of Metro Line 2.

of tunnel movements at each chainage of the two bound tunnels. The maximum measured tunnel settlements of the eastbound and the westbound are 144 mm and 133 mm at chainage 6.1 km (near the People square station) in May 2007, respectively. It should be noted that the monitoring of tunnel settlement of Line 2 was started from December 1999, i.e., nine months after tunnel construction. Therefore, the actual tunnel settlements could be even larger than the measured values.

Although non-uniform tunnel settlements are not surprising along Metro Line 2, there are four unusual locations where tunnel settlements are generally smaller than 25 mm (marked by arrows in Figure 12(a)). These observed tunnel settlements are even smaller than the measured short-term consolidation settlements (90 days) reported by Lee et al. (1999) near the People square station of Metro Line 2. There is no sufficient evidence to suggest that the geological conditions (see Figure 5(b)) at these four locations are greatly different from those of others. This is because the distance between boreholes is too far apart. These unusual small tunnel settlements are difficult to be understood and explained.

On the contrary, initial upward tunnel heaves were measured at several chainages as shown in the figures. The maximum measured tunnel heaves of the eastbound and the westbound are 8.9 mm and 11.8 mm at chainages 12.4 km and 14.0 km in March 2000 (i.e., within 13 months after tunnel construction), respectively. These initial tunnel heaves might be attributed to unloading effects induced by nearby underground construction activities like excavation in these areas. From July 2000 onwards, the observed tunnel heaves began to settle, probably because of clay consolidation.

For assessing the serviceability and safety of a tunnel, it is more important and relevant to investigate differential rather than total settlements of a tunnel. Along Metro Line 2, four critical chainages with maximum gradients (i.e., 0.11%, 0.09%, 0.08%, and 0.13%) of differential tunnel settlements are indicated in Figure 12(a). The gradient or angular distortion is defined as differential tunnel settlement between two consecutive measurements divided by the distance between them. Grantz (2001) reported that water leakage was found at joints of an immersed Baytown tunnel where the gradient of differential tunnel settlement was 0.16%, which is slightly larger than the maximum value of 0.13% observed in Metro Line 2 up to May 2007. Although the magnitude of angular

distortion that Metro Line 2 can resist without inducing leakage is not known, one should perhaps pay attention to its increasing trend.

To investigate consolidation settlement behaviour of Metro Line 2, the locations where large settlements were measured, the People square station and Lujiazui station at chainages 6.1 km and 8.7 km, are selected respectively. Figure 13 shows the variations of tunnel settlement with logarithm of time at these two selected stations over a period of 7.5 years. It appears that the observed tunnel settlements just reached the end of primary consolidation stage. Since long-term monitoring data of tunnel settlement is rarely available in literature, ground surface settlement over tunnel at Grimsby (O'Reilly et al., 1991) located in soft clay is also included in the figure for comparisons. It can be seen that the measured tunnel settlements of Metro line 2 at the two selected stations are significantly larger than the measured long-term ground surface settlements over the Grimsby tunnel. Given that tunnel settlement is generally smaller than the corresponding ground surface settlement, the difference of tunnel settlements at Grimsby and Shanghai should be even larger. This seems to suggest that the observed large tunnel settlements in Shanghai would not possibly be caused by consolidation of the soft clay only.

It is worth noting that the rate of tunnel settlement for Metro Line 2 appears to decrease from 2004. Taking the People square station (at chainage 6.1 km) as an example, the eastbound tunnel settled 83 mm for the first 4.5 yeas since December 1999 (or 18.4 mm/year). For the period between 2004 and 2007, tunnel settlement only increased from 83 mm to 113 mm (or 10 mm/year). The reduction in the rate of tunnel settlement is attributed to the reducing amount of ground water pumping from Aquifer IV. Details are discussed later.

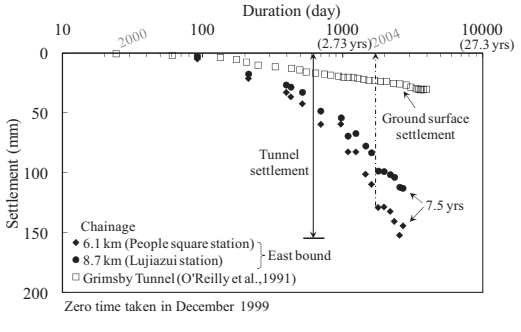

Figure 13. Development of tunnel settlement with logarithm of time at chainages of 6.1 km and 8.7 km.

5 POSSIBLE MECHANISMS OF LONG-TERM TUNNEL SETTLEMENTS

5.1 *Effect of tunnel construction on long-term tunnel settlement*

Tunnelling in soft clay would inevitably cause soil disturbance leading to settlements. In addition, consolidation of pressurized grouting material during construction may give rise to tunnel and ground surface settlements. To investigate the effect of EPB shield tunnelling on ground surface settlements, a cross section near the People square station of Metro Line 2 (see Figure 4) was heavily instrumented and monitored during its construction (Lee et al., 1999).

Figure 14 shows the development of ground surface settlement with time. According to the observed ground surface settlement, Lee et al. (1999) identified and divided the influence of tunnel construction process into five phases, namely, Phase I—the approach of tunnel shield; Phase II—the passing of shield body; Phase III—tail void closure; Phase IV—consolidation of grouted material and disturbed soils; and Phase V—secondary consolidation of disturbed soils. As illustrated in the figure, the majority of ground surface settlement occurred in the first 60 days after the EPB shield body passed the monitoring section (Phase IV). Since compensation grouting was adopted at this station, the settlement occurred during this period was mainly caused by consolidation of grouted material and disturbed soils. The consolidation was reported to cease about 60 days after the shield body passage (Lee et al., 1999). Due to the secondary consolidation of disturbed soils, a further small ground surface settlement was observed. It is evident that the primary consolidation of grouted materials and disturbed soils was almost completed within two months after tunnelling and the effect

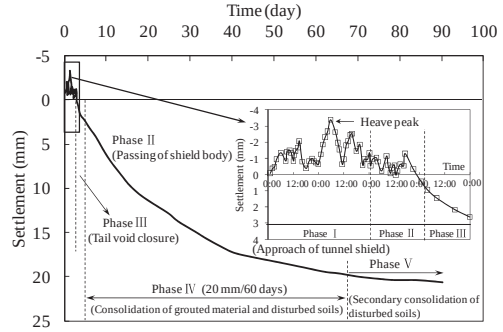

Figure 14. Development of ground surface settlement with time near People square station of Metro Line 2 (modified from Lee et al., 1999).

of secondary consolidation of soft clay was not significant. Three months after tunnel construction, the observed total ground surface settlement was less than 25 mm. Based on the observations made near the People square station as reported by Lee et al. (1999), the effects of tunnel construction alone cannot explain the large observed long-term tunnel settlements of 144 mm and 133 mm in the eastbound and westbound tunnels at the People square station over a period of 7.5 years, respectively (see Figures 12(a) and (b)).

5.2 *Effects of secondary compression of soft clay and cyclic loading on long-term tunnel settlement*

Based on the results of 70-day one-dimensional consolidation tests on natural block samples described in section 2.2, the secondary compression (or creep) characteristics of Shanghai soft clay may be classified as a soil with low to medium secondary compressibility as suggested by Mesri (1973) (see Table 1). This finding and classification are consistent with field monitoring results of an excavation in Shanghai by Liu et al. (2005) who found that ground settlements were mainly caused by dissipation of excess pore pressures rather than the secondary compression or creep during a period of 60 days. Further evidence is also provided by Lee et al. (1999) that the effects of secondary compression of Shanghai soft clay on tunnel settlement are not significant. It is therefore reasonable to conclude that the secondary compression of Shanghai soft clay should not be the main cause of the observed large long-term tunnel settlements.

In Shanghai, each running train for Metro Line 2 generally consists of eight carriages. Each carriage is 22.8 m long and 3 m wide with a weight of 54,500 kg. Hence, an estimated cyclic loading due to passing trains is about 8 kPa. Given that the undrained shear strength of Shanghai soft clay is 57 kPa, an estimate of CSR is 0.14. Comparing with the cyclic test results at CSR of 0.18 shown in Figure 9, it is reasonable to conclude that the effects of cyclic loading imposed by passing trains on cumulative strains and excess pore pressures should not be significant. Therefore, cyclic loading imposed by running trains cannot be the major reason for the measured large tunnel settlements along Metro Line 2.

5.3 *Effect of groundwater pumping on long-term tunnel settlement*

Due to shortage of water resources, groundwater pumping in Aquifers (I–IV) has been the main vehicle to sustain industrial and economical growth, and to provide potable water for people in Shanghai over the last 90 years. Therefore, Shanghai has been severely suffered from excessive land subsidence due to groundwater pumping.

As illustrated in Figure 5(b), Metro Line 2 is located in the top soft clay stratum, which is underlain by Aquifers (I–IV) and other clay deposits. It is expected that pumping groundwater from these aquifers would inevitably result in compression of aquifers and consolidation settlements of clay layers, inducing tunnel settlements. In order to explore whether groundwater pumping from aquifers is the main reason for the observed large tunnel settlements at the Lujianzu and People square stations, measurements from extensometers and standpipe piezometers installed at location F (refer to Figure 4), which is the closest monitoring point to these two stations, are studied. Based on the geological information obtained from BH_3 and BH_9, which are the two closest ones to location F, the estimated geological profiles and thickness of each soil stratum shown in Figure 11(a) are used in the interpretation and analysis of long-term tunnel settlements at the two stations in this paper.

5.3.1 *Measured groundwater pressure heads and compressions of soil layers at location F (1985–2007)*

Prior to 1965, groundwater pumping was mainly taking place in Aquifers II and III for industrial uses in Shanghai (Shi et al., 2008). Due to excessive ground subsidence observed, pumping in these two upper aquifers was greatly reduced, leading to the recovery of groundwater (and hence pressure heads) in these two aquifers. To meet the increasing demands of water, however, major groundwater extraction was turned to Aquifer IV after 1965. Figure 15(a) shows the variations of measured pressure head of each aquifer by standpipe piezometers from 1985 to 2007. It can be seen that the measured pressure heads in Aquifers I to III are fairly consistent and they have remained almost unchanged till 1990. These measured heads suggest that the main ground water table was located a few metres below ground surface and hydrostatic down to a depth of about 160 m (i.e., Aquifer III) below ground. Subsequently, the measured pressure heads decrease slightly due to groundwater extraction in these aquifers afterwards.

For Aquifer IV, the measured pressure head was about 13 m below ground in 1985 due to major groundwater extraction started in 1965 and it declined significantly and reached its lowest level of about 32 m below ground surface in 1997. However, it gradually recovered, especially between 2004 and 2007 during which the pressure head increased by four metres. The recovery of pressure head was attributed to the reduction of groundwater extraction.

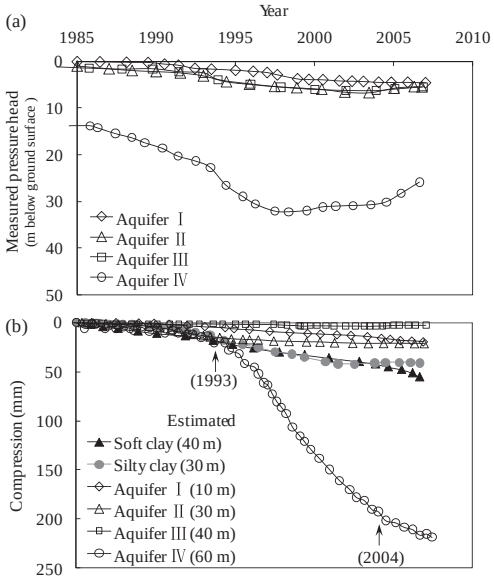

Figure 15. (a) Measured pressure head of each aquifer; (b) Measured compressions of soil layers at location F.

Figure 15(b) shows the corresponding measured compression of each soil layer by extensometers over the same period. The numeric number following each soil type denotes an estimated thickness of each stratum. As expected, the largest compression occurred in Aquifer IV, apparently consistent with the significant declining of pressure head in this sand layer. Despite of the large reduction of pressure heads prior to 1997 due to groundwater extraction, the compression of Aquifer IV, similar to those in Aquifers I–III, appeared to be relatively mild and it varied fairly linearly with time until 1993. This sand stratum seemed to compress elastically resulting from a reduction in groundwater pressure. After 1993, however, the compression of Aquifer IV increased significantly. The compression continued even though the groundwater pressure was recovered gradually after 1997. This significant increase in compression may be attributed to plastic yielding of the sand stratum. However, the rate of compression seemed to slow down after 2004. This is consistent with the development of tunnel settlements at the Lujiazui and People square stations at which a reduction in the rate of tunnel settlement was also observed after 2004 (see Figure 13).

Comparing with the compression of Aquifer IV, the magnitude of compressions in Aquifers I, II and III are substantially smaller. The response of these three sand aquifers is consistent with the pressure changes as shown in Figure 15(a), suggesting elastic behaviour of these three aquifers.

Regarding the compressions of the 40 m thick soft clay and 30 m thick of silty clay, their responses are generally similar and consistent with the measured groundwater heads in Aquifers I and II. This is because they are sandwiched with these two sand layers. By comparing with the compression (i.e., 218 mm) of Aquifer IV in 2007, the measured compression in either clay layer was only about 50 mm (less than 25% of that in aquifer), suggesting that the observed large tunnel settlements were unlikely caused by the primary and secondary consolidation of these two clay strata.

5.3.2 *Comparison of ground surface settlements and tunnel settlements of Metro Line 2 (2001–2005)*

Figure 16(a) and (b) show contours of measured ground surface settlement and tunnel settlements from 2001 to 2005 along Metro Line 2, respectively. It is generally recognized that ground surface settlement are mainly caused by groundwater pumping from aquifers in Shanghai (Chai et al., 2004; Shi et al., 2008). It can be seen from the figures that measured ground surface settlements are fairly consistent with tunnel settlements. The consistency of these two independent sets of measurements is vital since it provides the authors more confidence in the measured tunnel settlements. For instance, along the route of Line 2 from A (i.e., West Nanjing Road Station) to B (i.e, Shanghai Science and Technology Museum Station), two large settlement zones (i.e., SC_1 and SC_2) can be identified in Figure 16(a). Similarly,

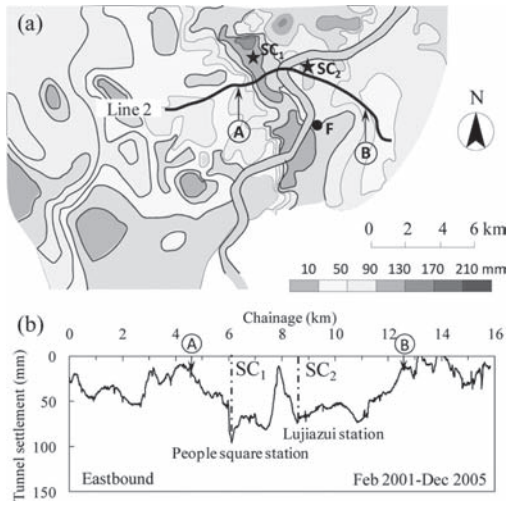

Figure 16. (a) Contours of measurd ground surface settlements; (b) Measured tunnel settlement of eastbound tunnel from 2001 to 2005.

large tunnel settlements can also be found close to SC_1 and SC_2 (refer to Figure 16(b)). The largest measured tunnel settlements at chainage 6.1 km and 8.7 km, which are close to SC_1 and SC_2, are 95 mm and 73 mm, respectively (see Figure 16(b)). These measured tunnel settlements correspond well with the contours of ground surface settlement. As the tunnels of Metro Line 2 are located at relatively shallow depths, it is obvious that the ground surface and the tunnels would have settled simultaneously, due to the compressions of aquifers and clay layers underneath Metro Line 2. Considering the compression of Aquifer IV is the largest among all soils (refer to Figure 15(b)), it is reasonable to attribute the observed large ground surface and tunnel settlements to the significant compression of the aquifer. Details of the mechanism leading to the significant compression are discussed and verified in the following sections.

5.3.3 *Compression mechanism of aquifers (1985–2007)*

To investigate possible yielding of each aquifer, an average vertical effective stress in each soil layer is estimated. Figure 17 shows the relationship of measured compression from 1985 to 2007 and corresponding estimated vertical effective stress of each aquifer. Computed compressions by finite element analysis shown in the figure are to be discussed later. For Aquifers I to III, measured compression of each aquifer increased linearly with an increase in vertical effective stress, indicating the uppermost three aquifers were elastic.

As reported by Shi et al. (2008), pressure heads dropped to their lowest levels in Aquifers II and III in 1965 (i.e., 30 m below ground surface) and recovered to about 5 m below ground surface in early 1970s. Thus, the increase in vertical effective stress in Aquifers II and III between 1985 and 2007 due to groundwater pumping followed an elastic re-loading stress path, i.e., no soil yielding was expected and identified. This is consistent with the results shown in Figure 17.

For Aquifer IV, a linear relationship is also observed between compression and vertical effective stress from 1985 to 1993. However, the measured compression of Aquifer IV begins to increase significantly after 1993.

Prior to the 1990s, the historical lowest pressure head in Aquifer IV was 21 m below ground surface as reported by Shi et al. (2008). Thus, the groundwater pumping to 22 m below ground surface in Aquifer IV exceeded its lowest historical pressure in 1993 (refer to Figure 15(a)) and hence induced the largest vertical effective stress in the sand stratum (see insert in Figure 17), resulting in soil yielding. It is reasonable to postulate that Aquifer IV yielded at 2,174 kPa in 1993. Subsequently, plastic compression in the aquifer occurred between 1993 and 1997 (see Figure 17) as groundwater pumping continued until 1997. Despite there was a reduction of groundwater pumping in Aquifer IV giving rise to decreasing measured pressure head (see Figure 15(a)), the aquifer compressed continuously even though its vertical effective stress remained almost constant between 1997 and 2004 and reduced subsequently. The observed large compression after 1997 may be caused by secondary compression of the aquifer.

If secondary compression indeed occurred in Aquifer IV at location F, one would expect to observe similar compression behaviour somewhere else in Shanghai. Figure 18 explores and compares measured vertical compressive strains of Aquifer IV at F and other two locations in Shanghai. The shapes of compression curves of the aquifer are very similar at these three locations and the estimated yield stresses vary from 2,174 kPa to 2,205 kPa. Unlike what commonly assumed that the compression of an aquifer is elastic, noticeable plastic and secondary compressions were found in

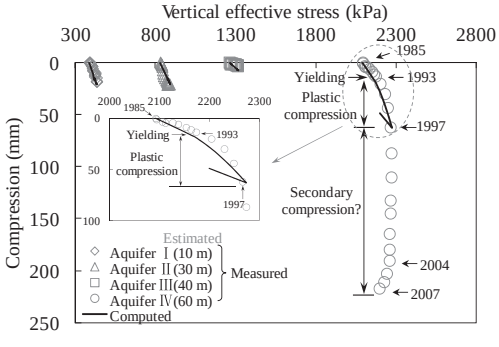

Figure 17. Relationship of measured compression and estimated vertical effective stress of each aquifer (from 1985 to 2007).

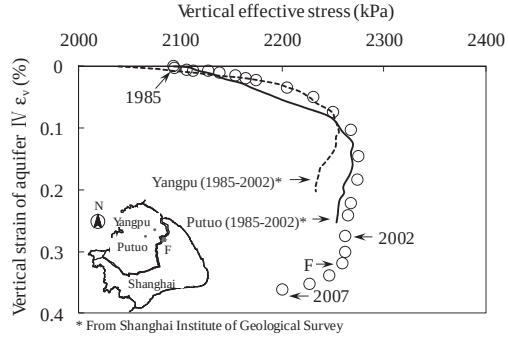

Figure 18. Comparison of compressions of Aquifer IV at various locations.

Aquifer IV in Shanghai. Besides these three sites, similar phenomenon was also observed for several other locations in Shanghai, where extensometers and piezometers were installed (Zhang et al., 2006). Therefore, it is evident to conclude that this type of secondary compression behaviour may be a key feature of Aquifer IV in some areas of Shanghai and hence the large observed tunnel settlements are mainly attributed to secondary compression of this aquifer.

Due to insufficient tunnelling records and no precise geological data available from largely spaced deep boreholes, it is not clear to the authors whether Aquifer IV is all inter-connected in entire Shanghai or not. Also the thickness of each aquifer is not known for sure since it varies from place to place. It is, therefore, not possible to investigate and explain with confidence in observed small long-term tunnel settlements (less than 25 mm) at some locations along the route of Metro Line 2.

6 NUMERICAL ANALYSIS OF SOIL COMPRESSIONS AT LOCATION F

In order to improve our understanding of the observed large tunnel settlements and compression mechanism of aquifers, one-dimensional coupled consolidation analysis of soil strata at location F was carried out by using the finite element software ABAQUS version 6.8 (2008) for a period from 1920 to 2007 since it is known that extensive ground water exploitation started from 1920 in Shanghai (Shi et al., 2008). Computed results are discussed and compared with available measurements of surface and tunnel settlements and compressions of aquifers for the period from 1985 to 2007.

6.1 *Finite element mesh and initial and boundary conditions*

Figure 19 shows the Finite Element (FE) mesh of the soil profile at location F. This mesh consists of 1,350 eight-node quadrilateral elements. Except the top two soil layers, the thickness of each other soil stratum is not known for sure but estimated from BH_3 and BH_9 only. The two lateral boundaries are modelled as rollers while the bottom boundary is specified as pinned supports. The top surface is modelled as a free drainage boundary. Both lateral boundaries and the bottom of the mesh are set to be impermeable. It is assumed that the initial water table was located at the ground surface in 1920 and hydrostatic throughout the depth, and all soil strata were normally consolidated.

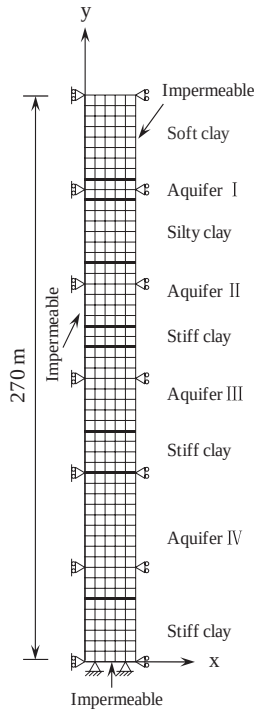

Figure 19. Finite element mesh and boundary conditions adopted in numerical analysis.

6.2 *Constitutive models and parameters*

In this study, each clay stratum and each sand layer (MCC) and Drucker-Prager/Cap (DPC) models, respectively.

For the MCC model, the gradient of normal consolidation line, $\lambda = 0.2$ and the gradient of swelling line, $\kappa = 0.02$ in e-ln p' space for the soft clay were deduced from one-dimensional consolidation tests on natural Shanghai Clay (Ng et al., 2011). For the rest of clay stratum, λ and κ values were estimated from compression index C_c provided by Chai et al. (2004). The slope of the critical stress ratio or M-line in p'-q space (where q is deviatoric stress and p' is mean effective stress) and Poisson's ratio υ were assumed to be 1.24 and 0.2, respectively.

For the DPC model used for each aquifer, the yield surface of the model comprises of a Drucker-Prager shear failure surface, an elliptical cap which intersects the mean effective stress axis, and a transition surface connecting the shear failure surface and the cap (ABAQUS, 2008). For this model, there are two elastic parameters, Young's Modulus (E) and Poisson's ratio (υ) and six plastic parameters, cohesion (d), friction angle (β), cap eccentricity (R), initial yield surface position ($\varepsilon_{\text{vol}}^{\text{in}}\big|_0$),

transition surface radius (α) and flow stress ratio K. Details of the definition for each parameter are given by ABAQUS (2008). It should be noted that β value used in this study is 43.3°, which is equivalent to an internal angle of friction of 35°. A summary of material parameters used in the FE analyses is given in Table 2.

According to site investigation, the permeability of soft clay and Aquifer I are 3×10^{-9} m/s and 1×10^{-5} m/s, respectively. For silty clay and stiff clay layers, the permeability is estimated by the following equation (Taylor, 1948) to take account of the effect of void ratio:

$$k = k_0 \times 10^{(e-e_0)/C_k} \quad (1)$$

Where k_0 is the initial permeability; e_0 is the initial void ratio; k and e are the permeability and void ratio of current clay layer, respectively; C_k is equal to $0.5e_0$ (Terzaghi et al., 1996). In this study, k_0 and e_0 are assumed to be 3×10^{-8} m/s and 1.0, respectively For Aquifers II to IV, the permeability of 1×10^{-4}, 1×10^{-5}, 2×10^{-5} m/s reported by Shi et al. (2008) are used, respectively.

6.3 *Modelling procedures*

Based on measured pressure heads, consolidation and compression of soils due to groundwater pumping were simulated by specifying the measured pore water pressure in each aquifer. Since only piecewise records of pressure head of each aquifer is available prior to 1985, the history and modelling of pressure head variations from 1920 to 1985 is divided into three periods, namely, 1920–1965, 1965–1975, and 1975–1985 for simplicity. In 1920, groundwater pressures in aquifers were assumed to be hydrostatic from ground surface (see Fig. 20). Pressure heads in Aquifers I, II and III declined to 5 m, 30 m, 30 m below ground surface in 1965, whereas pressure head in Aquifer IV fell to 21 m below ground surface in 1960. From 1965 to 1975, the pore pressures in all aquifers recovered to be hydrostatic from ground surface were adopted, except Aquifer IV, in which the pore pressure was increased by 11 m pressure head till 1975. From 1975 to 1985, pressure heads in Aquifers I, II and III changed slightly, whereas the pressure head in Aquifer IV was declining as shown in the figure. After 1985, continuous measured pressure head of each aquifer (refer to Figure 15(a)) was used for the coupled consolidation FE analysis.

6.4 *Computed results*

The computed compression of each aquifer during the period of 1985 to 2007 is shown by solid line in Figure 17. It can be seen that the computed results agree fairly well with the measured compressions of the uppermost three aquifers. For Aquifer IV, by assuming the initial yield surface position $\varepsilon_{vol}^{in}\big|_0 = 0.135$, the computed compressions are comparable to measured results during the period of 1985 to 1997 (refer to the inset), except the occurrence of soil yielding in 1997. As expected, when pressure head rose gradually after 1997, effective stress decreased and Aquifer IV swelled in numerical simulation. This swelling behaviour is contrast to the measured significant compression of the aquifer as the DPC model is not supposed to be able to capture any secondary compression behaviour of soil.

Since the locations of the Lujiazui station and location F are about 2 km apart (refer to Figure 4) with similar ground conditions, it is reasonable to make a comparison of settlements between these two locations. Figure 21 shows the comparison of

Table 2. Summary of material parameters adopted in finite element analyses.

	γ_{sat} (kN/m^3)	e_0	k (10^{-9} m/s)	E (MPa)	υ	λ	κ	d (kPa)	β (°)	R	$\varepsilon_{vol}^{in}\big\|_0$	α	K
Soft clay	18.5	1.2	3.0	N/A	0.2	0.02	0.002	N/A					
Silty clay	19.0	0.9	2.2			0.19	0.038						
Stiff clay (110 m–120 m)	19.8	0.8	1.5			0.06	0.006						
Stiff clay (160 m–180 m)	20.0	0.7	0.9			0.04	0.004						
Stiff clay (240 m–270 m)	20.5	0.6	0.6			0.04	0.004						
Aquifer I	19.0	1.0	10000	20	0.15	N/A	N/A	0.001	43.3	0.02	0.092	0.01	1.0
Aquifer II	19.0	0.9	100000	80							0.119		
Aquifer III	20.0	0.8	10000	200							0.127		
Aquifer IV	20.5	0.7	20000	300							0.135		

Note: N/A, not applicable.

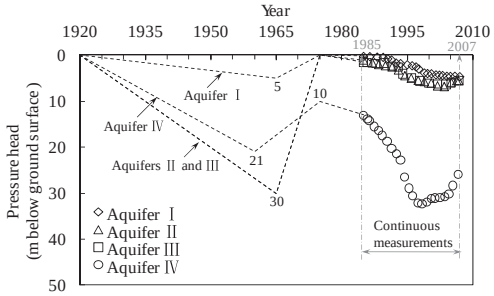

Figure 20. Specified pressure head in each aquifer for numerical analysis.

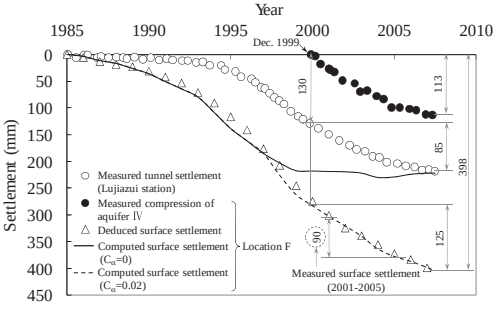

Figure 21. Comparison of measured tunnel settlement at the Lujiazui station and computed surface settlements at location F.

measured tunnel settlement at the Lujiazui station and computed surface settlement at location F. The measured compression of Aquifer IV at F is also shown for comparison. It can be seen the shape of measured tunnel settlement curve is remarkably consistent with the measured compression of Aquifer IV, except that the aquifer has an extra of 130 mm compression measured from 1985 to December 1999. Clearly, no measurement of tunnel settlement is available prior to December 1999 on the contrary. From December 1999 to May 2007, the measured tunnel settlement is 113 mm, while the measured compression of Aquifer IV is 85 mm, which makes up 75% of the measured tunnel settlement. This means the observed tunnel settlement of at Lujiazui station was mainly caused by the compression of Aquifer IV. The remaining 25% of tunnel settlement might be attributed to consolidation settlements of clay strata and compressions of other aquifers.

The deduced total surface settlement curve illustrated by open triangles in the figure is obtained by summing all the measured compressions in soft and silty clay layers and four aquifers as shown in Figure 15(b), and estimated compressions of the three relatively thin stiff clay strata shown in Figure 19. The estimation is necessary because no measured compressions of the three stiff clay layers are available at location F.

To estimate compression of each stiff clay layer and hence to deduce the total surface settlement, the strain of each stiff clay layer is assumed to be half of measured value in the silty clay layer. As shown in Figure 21, the deduced total surface settlement is 398 mm from 1985 to 2007, whereas the deduced surface settlement is 125 mm during the recent 7.5-year monitoring period (i.e., December 1999 to May 2007). As expected, the recent measured 125 mm of surface settlement is larger than the measured tunnel settlement. This is because the twin tunnels of Line 2 are embedded about 13 m below ground surface. Soil consolidation and compressions should have taken place over the tunnels during this monitoring period.

Despite the good agreement between the computed and deduced total surface settlements before 1997, the computed surface settlement (for $C_\alpha = 0$ analysis) is substantially underestimated by about 40 mm at the end of monitoring period in May 2007. It should be noted that no significant secondary compression of Aquifer IV is measured before 1997 (see Figure 17). This may explain why there is a good agreement between computed and deduced settlements between 1985 and 1997.

To account for the influence of secondary compression of Aquifer IV on computed results (i.e., $C_\alpha = 0$ analysis), the following equation is used to estimate the amount of secondary compression in the aquifer (Δ_s):

$$\Delta_s = \frac{C_\alpha H}{1+e_p}\log\left(\frac{t}{t_p}\right) \tag{2}$$

where C_α is secondary compression index; H is thickness of Aquifer IV; e_p, t_p and t are the initial void ratio, elapsed time at the beginning and elapsed time at any stage of secondary compression, respectively. Refer to Figure 17, it is reasonable to deduce that the secondary compression of Aquifer IV started in 1997. With this deduction, e_p and t_p are 0.65 and 4,380 days in 1997, respectively. By using $C_\alpha = 0.02$ for Aquifer IV in Equation (2), Δ_s value for each year (i.e., from 1997 to 2007) is calculated and added to the corresponding computed value obtained from the $C_\alpha = 0$ analysis to provide the computed surface settlement curve marked with $C_\alpha = 0.02$ in Figure 21. In order to verify this surface settlement curve using $C_\alpha = 0.02$, measured surface settlement of 90 mm between 2001 and 2005 (obtained from measurements shown in Figure 16(a)) is marked in the figure for comparisons, it can be seen that the

computed settlement of 85 mm assuming $C_\alpha = 0.02$ agrees fairly well with the measured value during the same period.

Further comparisons are made between the computed values using $C_\alpha = 0.02$ assumption and deduced surface settlements (denoted by open triangles) in Figure 21, an excellent agreement is obtained. However, this $C_\alpha = 0.02$ value requires verification by carrying out laboratory tests on high quality samples taken from Aquifer IV.

It is evident that the majority of measured tunnel settlement resulted from the compression of Aquifer IV, which was rarely realized and recognized before. It is urgent and necessary to control groundwater pumping from this aquifer to prevent further tunnel settlements. In addition, comprehensive laboratory tests on high quality samples from Aquifer IV should be obtained and tested to verify and confirm the deduced long-term tunnel settlement mechanism for Metro Line 2 in Shanghai.

7 CONCLUSIONS

After EPB tunnelling, non-uniform long-term tunnel settlements and heaves have been measured along Metro Line 2 in Shanghai. Measured data between 1999 and 2007 were studied in detail to investigate possible settlement mechanisms of the EPB shield tunnels. Four possible settlement mechanisms including effects of tunnel construction, consolidation and secondary compression of soft clay (creep), cyclic loading due to running trains, and groundwater pumping in aquifers were investigated. Based on the results of desk study, laboratory tests and numerical FE back-analysis, the following conclusions may be drawn:

1. It is evident that compression characteristics of aquifers in Shanghai can change from "elastic" to "plastic" when its historical vertical effective stress (or overburden pressure) is exceeded due to a sufficient reduction of pore water pressure in an aquifer resulting from groundwater pumping. After soil yielding, noticeable secondary compression was found in Aquifer IV in Shanghai. Careful control of groundwater pumping is necessary to avoid an induction of plastic yielding and hence large secondary compression.
2. Among the four possible causes investigated, it is evident that groundwater pumping in Aquifer IV is the most likely principal reason for the large observed long-term tunnel settlements along Metro Line 2 in Shanghai. Controlling groundwater pumping in this aquifer is, therefore, vital to minimize further tunnel settlements.
3. Measured large long-term tunnel settlements along Metro Line 2 are primarily attributed to compression of Aquifer IV, which accounts for 75% of the measured total tunnel settlement over the monitoring period of 7.5 years.
4. There is not enough information such as detailed tunnelling records and accurate geological data from more closely spaced deep boreholes to investigate and understand the measured small long-term tunnel settlements (less than 25 mm) and unusual heaves along the route of Metro Line 2.
5. The mechanical properties of Aquifers II, III and IV such as yield stress, primary and secondary compression characteristics (i.e., C_α, values) should be investigated by using high quality of samples and field testing.

ACKNOWLEDGEMENTS

The authors would like to acknowledge research grants 617608 and 617410 provided by the Research Grants Council of HKSAR. The field monitoring works were undertaken by Shanghai Institute of Geology Survey. The support by Shanghai Shentong Metro Co., Ltd is gratefully acknowledged. The authors would also like to thank Mr Li Xiangyu for assisting in collecting the field monitoring data.

REFERENCES

ABAQUS (2008). ABAQUS user's and theory manual. Version 6.8. *Dassault Sytemes Simulia Corp*.

BSI (1990). BS1377: Methods of test for soils for civil engineering purposes. Part 5—Compressibility, permeability and durability tests. *British Standard Institution, London.*

Burland, J.B. (1990). On the compressibility and shear strength of natural clays. *Géotechnique,* 40(3), 329–378.

Chai, J.C., Shen, S.L., Zhu, H.H. & Zhang, X.L. (2004). Land subsidence due to groundwater drawdown in Shanghai. *Géotechnique,* 54(2), 143–147.

Chen, Y.F., Zhang, Q.H., Zhang, Y. & Zhen, J. (2008). In-situ monitoring and analyzing on construction of three closely spaced parallel shiled tunnels. *Chinese Journal of Underground Space and Engineering,* 4(2), 335–340.

Dalgıç, S. (2002). Tunneling in squeezing rock, the Bolu tunnel, Anatolian Motorway, Turkey. *Engineering Geology,* 67(1–2), 73–96.

Grantz, W.C. (2001a). Immersed tunnel settlements Part 1: Nature of settlements. *Tunnelling and Underground Space Technology,* 16(3), 195–201.

Grantz, W.C. (2001b). Immersed tunnel settlements Part 2: Case histories. *Tunnelling and Underground Space Technology,* 16(3), 203–210.

Lee, K.M., Ji, H.W., Shen, C.K., Liu, J.H. & Bai, T.H. (1999). Ground response to the construction of Shanghai Metro Tunnel-Line 2. *Soils and Foundations,* 39(3), 113–134.

Liu, G.B., Ng, C.W.W. & Wang, Z.W. (2005). Observed performance of a deep multistrutted excavation in Shanghai soft clays. *Journal of Geotechnical and Geoenvironmental Engineering,* 131(8), 1004–1013.

Liu, M. (2006). Study on the dynamic constitutive model of saturated soft clay and the effect of train loading on the long-term tunnel settlement. *Ph.D thesis, Tongji University, Shanghai, China*.

Mesri, G. (1973). Coefficient of secondary compression. *ASCE J Soil Mech Found Div-v 99,* (SM1), 123–137.

Ng, C.W.W., Li, Qing & Liu, G.B. (2011). Characteristics of one-dimensional compressibility of Shanghai Clay. *Chinese Journal of Geotechnical Engineering,* 33(4), 630–636.

O'Reilly, M.P., Mair, R.J. & Alderman, G.H. (1991). Long-term settlements over tunnels: an eleven-year study at Grimsby. *Proc. Tunneling '91. London, 55–64*.

Schmidt, B. & Grantz, W.C. (1979). Settlements of immersed tunnels. *ASCE J Geotech Eng Div,* 105(9), 1031–1047.

Shanghai Geology Office (1979). Hydrogeological map of Shanghai, Hydrogeological in Atlas of China, No. 45. *China Map Publisher. Beijing.*

Shi, X., Wu, J., Ye, S., Zhang, Y., Xue, Y., Wei, Z., Li, Q. & Yu, J. (2008). Regional land subsidence simulation in Su-Xi-Chang area and Shanghai City, China. *Engineering Geology,* 100(1–2), 27–42.

Taylor, D.W. (1948). Fundametals of soil mechanics. *John Willey & Sons Inc. New York*.

Terzaghi, K., Peck, R.B. & Mesri, G. (1996). Soil Mechanics in Engineering Practice. *John Wiley and Sons, Inc., New York*, 43–44.

Zhang, Y., Xue, Y.Q., Wu, J.C. & Li, Q.F. (2006). Characteristics and parameters of sand strata deformation due to groundwater pumping in Shanghai *Journal of Hydraulic Engineering,* 37(5), 560–566.

Geotechnical Aspects of Underground Construction in Soft Ground – Viggiani (ed)
© 2012 Taylor & Francis Group, London, ISBN 978-0-415-68367-8

Deep excavations for Amsterdam Metro North-South line: An update and lessons learned

A.F. van Tol
Deltares, Delft University of Technology, Delft, The Netherlands

M. Korff
Deltares, Delft, The Netherlands/Cambridge University, Cambridge, UK

ABSTRACT: The North-South line in Amsterdam is being built underneath the historic centre of the city. Three deep stations are constructed in deep excavations supported by diaphragm walls. During the excavation for Vijzelgracht Station, leakage through the wall resulted in large settlements of and damage to monumental buildings, which threatened the support of the authorities for the project. With the application of robust preventive measures at two of the deep stations, it was possible to continue the project. This paper reports on the events, the counter measures, the monitoring, the repair of the buildings and the lessons learned for the project and for the foundation sector to avoid future failures in D-walls. Moreover, effort is made to improve quality assessment and measuring techniques to detect potential leakages in advance.

1 INTRODUCTION

1.1 *North South line Amsterdam*

The North-South Line in Amsterdam is 9.5 kilometres long. This metro line starts at street level in the North of Amsterdam and passes under the historical centre of the city in a twin shield tunnel. South of the historic centre, the line re-emerges at street level between the RAI conference centre and the existing railway station South/WorldTradeCentre. Five underground stations are under construction. Diaphragm walls support the excavations of the three deep inner city stations: Rokin (RKN), Vijzelgracht (VZG) and Ceintuurbaan (CTB). This paper deals with the leakages that occurred at Vijzelgracht resulting in severe settlement of monumental buildings, exceeding project budgets and time schedule. After a short description of the events the paper will focus on the lessons learned.

1.2 *Ground conditions*

At Vijzelgracht Station, there are fill deposits and soft Holocene clay deposits to a level of about (Dutch reference level) NAP –12.5 m (ground level is around NAP +1.5 m). These are underlain by the 1st sand layer, from NAP –12.5 m to NAP –14/–15 m, which is on top of a 2.5 m thick sandy silt stratum (the Allerød). The 2nd sand layer is found at about NAP –17/–18 m, extending to NAP –26 m. Below the 2nd sand layer, there is a stiff clay layer that is approximately 15 m thick (the Eem clay). The piezometric head in the 1st and 2nd sand layer is about NAP –2.0 m. Details of the construction and soil profiles can be found in Salet et al. (2006).

1.3 *Construction method*

The stations are being built top-down to a depth of about NAP –31 m at Vijzelgracht, with 1.2 m thick diaphragm walls extending to a depth of approximately NAP –45 m. See Figure 1. The diaphragm

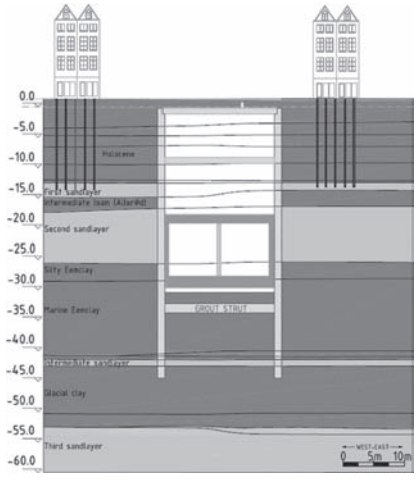

Figure 1. Cross-section of Vijzelgracht Station.

walls consist of panels with lengths of approximately 2.8 m and 5.2 m. Traditional grabs and steel stop ends with water bars (PVC strips) are used to a depth of NAP –36 m to provide waterproofing. The Eem clay layer below NAP –26 m provides a seal off for the bottom of the excavation. Ground improvement works with lean concrete columns took place before installing the walls to remove obstacles in the Holocene deposits.

2 EVENTS

2.1 *Leakages of D-walls*

At Vijzelgracht Station in particular, and to some extent at Rokin Station, numerous joints in the D-wall panels leaked during the excavation up to about NAP –12 m. These leaks varied from damp patches to more significant water flows, but up to that depth the wall did not leak much. A standard procedure of drilling in the wall and polyurethane injections stopped these leakages.

2.2 *First event*

There was severe inflow of water and soil through a panel joint for the first time on the 19th of June 2008 in the west wall of Vijzelgracht Station. The excavation depth was approximately NAP –12 m at that time. The leak was attributed to a steel stop end which could not be removed at this location and the failure of the jet grouting repair method. This leak of water and soil resulted in substantial settlement—up to 140 mm—and damage in the adjacent buildings. To stabilise the historic buildings a timber framework was installed, see Figure 2. More details of the damage to the adjacent buildings are described in Korff et al. (2009). The settlement was mainly the result of ground loss into the excavation causing a strong reduction of the cone-resistance of the first sand layer, the bearing strata of the wooden pile foundations; consolidation effects due to pore pressure reduction were minor. It was possible to stop the inflow only after substantial backfill and polyurethane injection.

Figure 2. A timber framework was installed to stabilise the historical buildings after severe settlements.

On the 17th of June, two days before the described event, a large bentonite inclusion (measuring approximately 0.4 × 1.0 m) was discovered during excavation just next to a panel joint in the east wall. Immediately after the discovery, water with soil or bentonite started to flow in. Fortunately, the contractor was able to stop the intrusion of water by immediate backfilling in front of the joint.

2.3 *Geophysical leakage detection*

After these events occurred geophysical leakage detection was carried out by the multi-sensor survey system (ECR®) with application of spatially targeted electrical impulses (EFT®). Analysis of these measurements showed that there were many small leakages to be expected along the wall, but none of the joints showed major leakage. The work resumed with trial excavations.

2.4 *Second event*

On the 10th of September 2008, another severe leakage of soil and water occurred, resulting in settlement in adjacent buildings of up to 250 mm. This leak was caused by a large bentonite inclusion next to panel joint 69/70 in the west wall during a trial excavation from NAP –13 to –17 m. The maximum width of the inclusion was approximately 0.2 m and the height was at least 2 m. When the contractor noticed the inclusion, it was dry (no leakage). In the next 4 hours the contractor made preparations for retaining the bentonite inclusion with steel plates. After holes had been drilled to anchor the third plate in the wall, water suddenly started to flow. Within half an hour, the flow of water and soil was almost impossible to control and it took hours to stop it. After 12 hours the contractor, municipal officials and back office consultants concluded that the situation was stable. During those 12 hours, almost 700 litres of polyurethane had been injected and approximately 450 m^3 of soil had been backfilled.

3 TECHNICAL ANALYSES

3.1 *Quality of the D-walls*

These serious events originate technically to two main causes, the first is the presence of a large bentonite inclusion in the D-wall and second the fact that the bentonite inclusion was not classified as a possible big risk. As a consequence, the resulting inflow of water and sand could not be stopped

directly or in a restricted time span to prevent serious erosion effects outside the excavation.

Unfortunately, the precise cause of the bentonite inclusions could not be identified. A visual inspection (of the excavated area) indicates that the quality of the D-walls at Vijzelgracht Station was significantly worse than at Rokin and Ceintuurbaan, even though they were installed by the same contractor. The overall quality of the walls at Vijzelgracht was worse than might reasonably have been expected. The presence of three large bentonite inclusions and many smaller ones has led to doubts about the workmanship and quality control.

3.2 *Bentonite inclusions*

The bentonite inclusions are most likely caused by a combination of suboptimal circumstances during the installation of the walls, such as delays after removing the steel stop ends, after cleaning the bentonite slurry, the inclination of the stop ends and very thick reinforcement bars relative to the aggregate size of the concrete. Moreover the bentonite slurry had to be replaced entirely in several panels when it became too viscous probably because of an unfavourable interaction with the soft mix, used to stabilise the very soft top-layers and to replace bored obstacles. In addition, cleaning the bentoniet in the trench with the 5.2 m-wide panels from just one pump position and concreting with only one tremie pipe could have contributed to the development of a large bentonite inclusion. All the causes listed here attributed to the trench being not fully cleaned with fresh bentonite just before concreting (Figure 3a). During concreting, the thick bentonite was therefore not removed by the concrete, as seen in Figure 3b. The result is a bentonite inclusion in the concrete, as shown in Figure 3c.

Up to the first event no specific measures were taken to control the situation in case of a serious leak. The normal procedure with PU-injection and placing of steel plates in case of more severe leakage was applied. After the first event and the geophysical leakage detection, which showed many (probably) small leakages it was decided to start the next stage of excavation (from NAP –13 to –17 m) with small inspection pits at the joints between the panels in order to be able to fill back in case of severe inflow of water and to obtain in such a way a validation of the (ECR®)/(EFT®) measurements. The second event occurred when the mentioned inclusion was found in the inspection pit but as no water flow was observed it was not considered as a serious problem and in stead of back filling the contractor started drilling holes in the adjacent concrete to connect steel plates. The inclusion probably liquefied due to the drilling, resulting in the mentioned inflow of water and sand that could not be stopped for many hours.

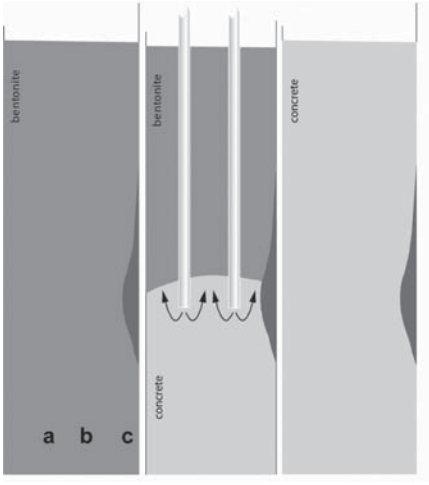

Figure 3. Forming of a bentonite inclusion during the concreting of a panel in three subsequent stages.

4 CONTINUATION OF THE EXCAVATIONS

4.1 *Freezing of all joints*

An attempt has been made—using an analysis of the panel production data, the construction log books, the (ECR®)/(EFT®) measurements and the observations during the performed excavation—to obtain reliable information prior to further excavation about the quality of the wall, and about the severity and the locations of possible bad spots in the diaphragm walls. The analysis focused particularly on determining in advance which suspect locations (i.e. anomalies) are so serious that they will fail immediately upon excavation, resulting in a breakthrough of water and sand, since this will dictate how the work can be resumed safely.

It followed from the analysis that qualitative relationships could be established between the quality of the joints on the one hand, and the (ECR®)/(EFT®) measurements, construction data and logbooks on the other. However, it was not possible to establish any direct, unambiguous relationship between the construction data, the (ECR®)/(EFT®) results and the observed quality of the joints up to the excavation level. In order to ensure an adequate level of certainty during the subsequent excavations, each joint had to be considered a severe potential leak. It was decided that it was necessary to seal all joints before further excavation could start.

Because of the impossibility or unacceptability to carry out works from street level, it was decided to seal the joints from inside the excavation by freezing the joints. Adjacent to every joint two freezing pipes were installed. After reaching a frozen body—consisting of frozen soil, D-wall and

Table 1. Overview of measured width of D-wall joints at three deep excavations.

Joint width [mm]	Ceintuurbaan number	Rokin number	Vijzelgracht number
0–20	126	65	32
20–50		28	69
50–100			2
100–300			5
>300			1

possible inclusions in the wall—that fulfilled the requirements, the staged excavation was continued in layers of about 4 m. During such a stage, the joints were excavated first and covered with steel plates, while the freezing process continued deeper down for the next stage of excavation.

4.2 *Present situation*

This process started in the spring of 2010 and is ongoing at present, May 2011. This preventive sealing covers all sand layers in the height of the excavation. Excavation in the Eem-clay is considered to pose no severe leakage risk.

The same procedure was adopted for Rokin Station as this excavation was at the same level at the time of the events and the risk analysis was similar to the one at Vijzelgracht. At Rokin Station, the excavations are finished and the concrete floor slab has been installed. At Ceintuurbaan Station, the excavation already reached the Eem-clay layer before the Vijzelgracht incidents and therefore no additional measures were taken and no severe leakages occurred.

During the excavations of the frozen joints the width of the joint (=thickness of bentonite cake or inclusion) on the inside face of the wall were measured after freezing the cover of the D-walls. Table 1 presents the results of the three excavations. The results from Rokin Station and Ceintuurbaan Station are based on the full excavation, while Vijzelgracht is at 75% of the final excavation depth. It appears that at Ceintuurbaan all joints have a width of 20 mm maximum and at Rokin of 50 mm. At Vijzelgracht 8 joints exceed the width of 50 mm. The maximum width exceeds 250 mm.

5 BUILDINGS

5.1 *Effect on the soil around the excavation*

Investigations were undertaken, including Cone Penetration Tests (CPTs) to determine the amount of soil disturbance, which reached about 20 m away from the joint where the soil inflow occurred, see Figure 4. Examination of CPTs performed immediately after the first incident (see Figure 5) indicates that there is clear evidence of the 1st sand layer (between NAP –12 and –14) having been disturbed in the region of the panel joint 89/90. The second sand layer also shows disturbance.

The CPT's show cone resistance, q_c, values of the 1st sand layer to have reduced significantly adjacent to houses 4 to 8 Vijzelgracht. The largest reduction to 6–7 MPa was found at the location of the houses 4 and 6 Vijzelgracht. Other CPTs at greater distance from this region show q_c values in excess of 20 MPa.

The reduced q_c values of the 1st sand layer are consistent with considerable loosening caused by a significant volume of sand being washed through the leaking panel joint. During the second incident, some disturbance of the second sand layer was also evident from the CPTs.

The settlement was therefore mainly the result of ground loss into the excavation resulting in loosening and strong reduction of the cone-resistance of the first sand layer, which is the bearing stratum of the wooden pile foundations. consolidation effects due to pore pressure reduction were minor.

5.2 *Damage to the buildings*

The houses influenced by both incidents are historic buildings from around 1670. The buildings all have a semi-basement, a raised ground floor,

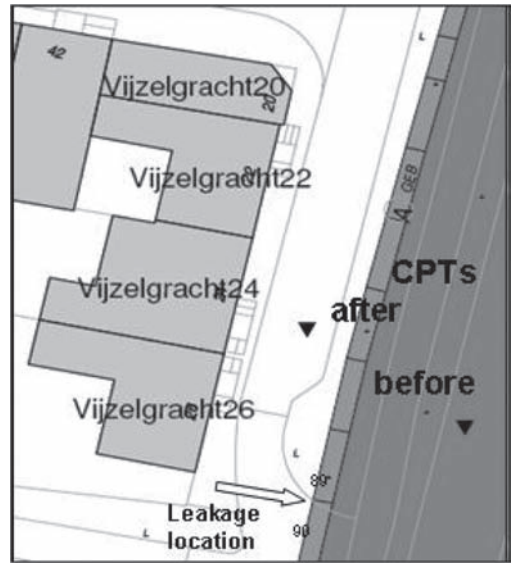

Figure 4. Situation of CPT's at first incident.

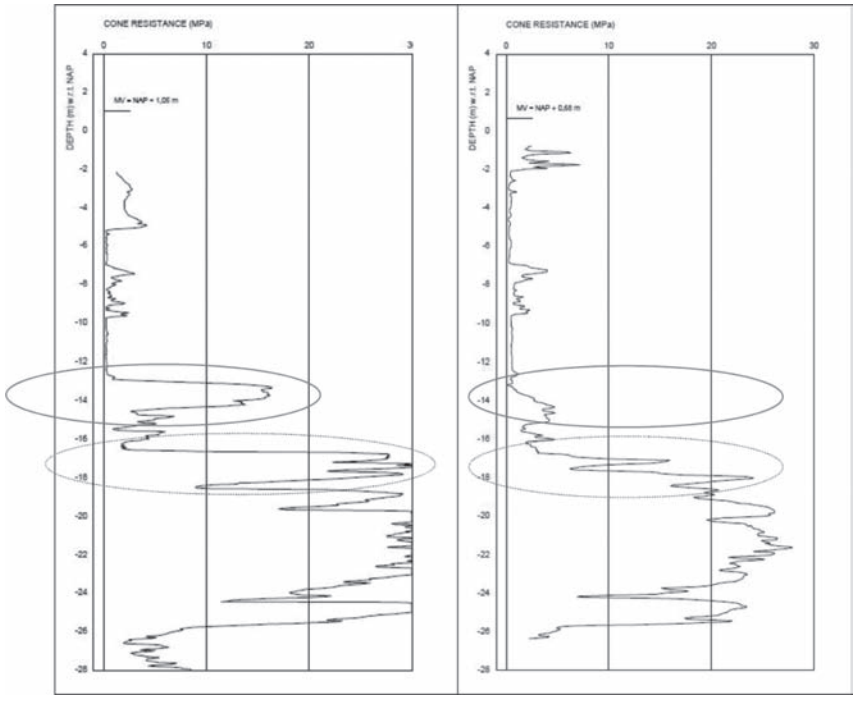

Figure 5. CPT's before (left) and after (right) first incident.

and a first floor with a vaulted roof. The height of the buildings is about 9 m. The original foundation consisted of 52 timber piles per house in rows of 2 wooden piles under the brick walls extends to the first sand layer at a level of around NAP −13 m. Before construction of the North South Line these buildings were equipped with monitoring instruments, comprising optical prisms for total station surveying at two levels and manual levelling bolts at street level.

The block of houses Vijzelgracht 20–26 settled a maximum of 150 mm as a consequence of the first incident in June 2008. The building tilted towards the corner of VZG 26, and towards the excavation and the location of the leakage. A slight sagging was found between VZG 26 and VZG 24 and hogging towards VZG 22.

Block Vijzelgracht 4–10 settled a maximum of 240 mm directly after the second leakage incident. The foundations of Vijzelgracht 4–8 had been renewed before the construction activities started. The new steel piles and the old timber piles are both founded in the first sand layer.

The most important damage indicators are presented in Table 2. According to Korff et al. (2011) the actual damage derived from the observations for both blocks (VZG 20–26 and VZG 4–8) would be category 5, very severe (Burland et al. 1977).

Table 2. Deformations after first and second incident.

Damage indicators	VZG 20–26	VZG 4–8
Max slope	1:111	1:51
Max relative rotation	1:160	1:125
Deflection ration	0.47%	0.40%
Horizontal strain	0.04%	0.12%

5.3 *Repair of the buildings*

5.3.1 *Corrective grouting of the buildings affected by the first incident*

After bracing the buildings, it was decided to apply corrective grouting to increase the bearing capacity of the sand and to lift the buildings. For the final restoration of the buildings a new foundation will be installed. It was implicitly demonstrated that the end bearing capacity of the pile foundations had been restored, when lifting of the buildings proved possible and stability of the building had been assured. Moreover, it showed that it was possible to apply further grouting to compensate for future settlements from ongoing construction of the station.

Although lifting of the buildings was successful, it appeared that for these conditions (loose sand

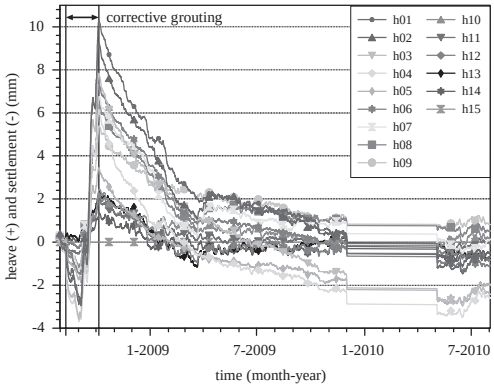

Figure 6. Results of corrective grouting underneath Block VZG 20–26, from Bezuijen et al. (2011).

due to ground loss) the efficiency of the corrective grouting process was very low. Ongoing settlements were found up to at least 5 months after finishing the grouting, see Figure 6. The buildings responded to the grouting in a relatively stiff manner, probably due to the temporary stabilizing timber cross beams, which made analysis of the grouting process difficult. Details of the corrective grouting can be found in Bezuijen et al. (2011).

5.3.2 *Lifting the buildings affected by the second incident*

Since the buildings of the second incident already had foundation renewal prior to the start of construction, it was decided to test the remaining capacity of the piles by pile load tests. Most of the piles had an ultimate capacity above 400 kN, which was the test level. The original pile load is about 250 to 280 kN. For a group of piles close to the leakage the ultimate capacities ranged from 300 to 350 kN. A few piles further away had capacities as low as 125 up to 225 kN, which could either be due to an irregular shape of the leakage effect or due to an originally low capacity. From the load tests it appeared that only a few piles had insufficient bearing capacity. It was decided to lift the whole block by jacking the piles; 5 piles were added in Vijzelgracht 6 to compensate for the loss of bearing capacity of the affected piles. The maximum lift to be obtained was 220 mm at the corner of Vijzelgracht 4. The procedure for lifting the buildings is described in De Nijs & Kaalberg (2010).

6 MONITORING

6.1 *Settlements and pore pressures*

One of the questions after the events occurred was the role of the monitoring system. Public as well as political concern arose as it became clear that the monitoring system did not warn for the severe incident. At the start of the project, during the political debate about impact, costs and risks, the monitoring system was presented as a tool that warned for deviations from the predicted behaviour.

The large settlements during the first event were however not preceded by smaller settlements that could have indicated the coming calamity. First the data from the robotic total stations, monitoring the prism's at the buildings required a processing time of 4 hours. After the first event it was decided to shorten that period to 2 hours.

Another possible early warning could be the readings from the piezometers installed in the different aquifers. These data were recorded every hour. Figure 7 shows the pore pressure readings (left axis) in the first and second sand layer during the first events as well as the total station reading as the manual levelling system (right axis). These measurements can be compared to the data from the diaries of the supervisors during the first incident:

13:10 h	First inflow, at excavation NAP –14 m
14:00 h	Start of grouting in joint, mounting steel plates and backfilling
16:00 h	Steel plates fixed (NAP –12 to –14 m). Inflow decreases; more back filling
18:45 h	Flow stopped almost
21:30 h	Increase of flow
22:00 h	Grouting from outside
01:00 h	Grouting in second sand layer
03:15 h	No more flow visible

At 13.00 the pore pressures first show signs of leakage by a draw down of nearly 1 m in the closest observation wells. Ten minutes later (13.10) the first inflow was recorded. So in this case neither the prism's nor the pore pressure transducers showed any early sign of the coming event.

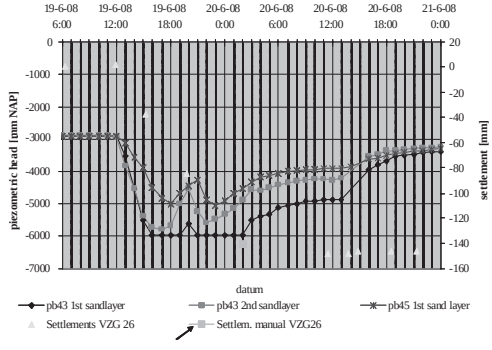

Figure 7. Monitoring data during first event.

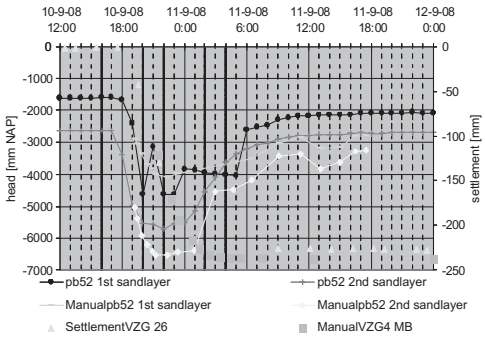

Figure 8. Monitoring data during second event.

Figure 8 shows the monitoring data during the second event.

The observations from supervisors are as follows:

12:00 h	At NAP –17 m big inclusion found. No leakage was observed!
16:30 h	Start mounting steel plates
18:00 h	1st plate was mounted, 2nd at 18.30 h and the 3rd was mounted at 18.45 h
18:45 h	Small leakage from behind plates
18:50 h	Water breakthrough ➔ injecting in D-wall,
7:00 h	After back filling 450 m^3, and massive PU-injection, leakages is stopped

During the second incident, the pore pressure transducers in the second sand layer show a first draw down of nearly 1 m at 18.00 hours, while the first inflow of water was observed at 18.45 h. This could have been a signal for immediate back filling instead of going on with mounting plates.

At one other deep excavation for the North-South Line, at Central Station a leakage in the D-wall was detected prior to the excavations due to careful monitoring of piezometers outside the excavation during test pumping inside the excavation. Due to the somewhat lower permeability of the sand layers at that location and a tight grid of observation wells it was possible to localise a leakage prior to the excavation and to mitigate it.

6.2 *Conclusions regarding the monitoring*

1. Leakage through D-walls develops with ongoing excavation, so the inflow before excavation might be negligible.
2. Accurate analyses of continuous pore pressure registration may reveal a leakage at an early stage. This depends on flow and permeability of aquifers outside the excavation.
3. If such accurate monitoring does not reveal a leakage it has not been proven that there is none. But, if this monitoring shows a reaction outside the excavation, there definitely is a leakage.

7 LESSONS LEARNED

The lessons learned from the described events consider different levels. At the project level the organisational structure has been adapted, with other and new personal and new working methods as well. At the level of the foundation sector, clients, consultants and contractors united in a CUR-committee (CUR is comparable with CIRIA) to improve the D-wall installation and excavation process. At scientific level, Delft University of Technology started a research project into improvement of leakage detecting and quality assessment systems to detect bad spots, in particular in D-walls prior to the excavation.

7.1 *Project level*

The measures taken at organisation level are: (i) the appointment of project leaders for each of the three deep stations, (ii) more specific geotechnical expertise involved in both day-to-day construction control as well as independent reviewers (iii) application of risk management in a structured way in particular for soil related risks, (iv) open communication with the community; house owners, shop owners and other inhabitants.

7.2 *Sector level*

Van Tol et al. (2010) reported their findings related to D-wall problems in the Netherlands and in Belgium over the last years, including the Vijzelgracht events. Subsequently the foundation sector formed a CUR-committee and concluded a number of lessons learned and the following recommendations, which are reported in the recently published CUR-report 231 (CUR, 2010). Handbook Diaphragm walls:

1. Panel installation data should be reported in more detail. This will improve the quality of D-wall panels. After calamities, these data are extremely useful to determine the cause. The time schedule with all relevant start and stop times as part of the panel data: excavating, removing steel stop end, cleaning trench, concreting. Delays, weekend, and so on are indications for higher risk?
2. All the positions of the grab must be measured (and the envelope of all positions must be reported) during excavation instead of only measuring when the trench is at full depth,

in order to control the accuracy of the excavation and to reduce the risk of "enclosed concrete"
3. Bentonite must be tested with the soil from the site (and possible additives from ground treatment)
4. Time between removing steel stop end and concreting should be as short as possible to minimize the bentonite cake to the adjacent panel
5. All the joints must be jetted or swept to remove accumulated impurities, when the trench is open for more than 24 hours (the handbook states 'in case of delays')
6. Adequate risk management should consider the consequences of an inflow and prepare counter measures
7. The present leakage detection systems (EFT®/ ECR®) are not yet able to detect bentonite inclusions and do not discriminate between small leakages and large bentonite inclusion
8. Also known facts from common practice, sometimes disregarded, are re-confirmed,:
   – A one-phase or three phase panel is more accurate than a two-phase panel
   – The trench must be cleaned by moving the pump over the full length of the trench
   – The slump value of every truck mixer load has to be determined immediately before concreting
   – Horizontal inclination of concrete level must be monitored
   – Openings in reinforcement cages should be at least seven times the maximum aggregate size.

Van Tol et al. (2010) argue that diaphragm walls are still a thorough solution for retaining walls in deep excavations in urban areas. A more detailed monitoring of the execution process in accordance with EN1538, supplemented by the lessons learned, is necessary. When only limited general information is available, good quality control is impossible, for both the contractor and the supervisors. If the execution process is monitored in detail, the quality of the product can be guaranteed and the risks of severe leaks will be minimised.

7.3 *At scientific level*

Delft University started two research projects: one focuses on improvements of the installation process and the second investigates the feasibility of sonic logging and geophysical logging of panels and across joints to check the wall for anomalies before the start of the excavation. Sonic logging is a standard procedure to check the consistency of the concrete for one panel or a bored pile. The feasibility of using this technique across the joint is relatively unknown. The first experiments on a test specimen (a piece of D-wall with an intended soft soil inclusion) show promising results.

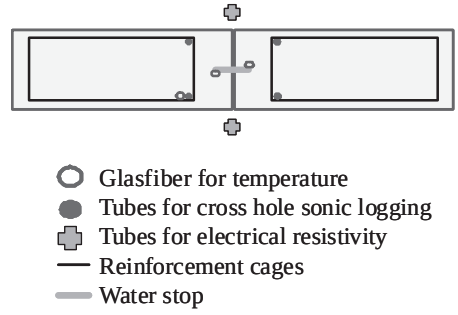

Figure 9. The position of monitoring systems (Spruit, 2011).

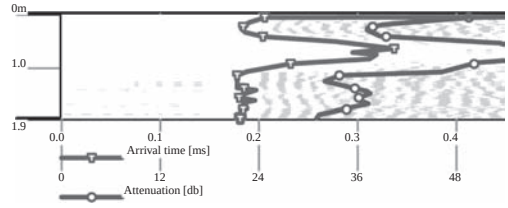

Figure 10. The response of Cross-Hole-Sonic-Logging over a D-wall joint, partly filled with an inclusion (Spruit, 2011).

Figure 9 shows the layout of different monitoring systems at the joint between two D-wall panels as recently applied in a test in a D-wall project in Rotterdam and on a regular base at a D-wall project in Delft, Netherlands. The cross-hole seismic logging method was validated using a D-wall test block with a height of 2 m with a known inclusion. The measurements, see Figure 10, showed a clear increase of arrival time and of attenuation of the sonic waves (Spruit, 2011).

The present leakage detection systems (ECR® and EFT®) proved to be successful in excavations supported with sheet pile walls. In case of D-walls it was not possible to distinguish between very small and insignificant leaks and very serious bentonite inclusions. The research at Delft University aims to improve this technique for D-walls.

ACKNOWLEDGEMENT

The authors were in charge of an independent survey of the cause of the incidents and the necessary repair methods (see Korff et al. (2008)). The Dienst NoordZuidlijn and the contractor Max Bögl are greatly acknowledged for their support for sharing these lessons learned.

REFERENCES

Burland, J.B., Broms, B.B., de Mello, V.F.B., 1977. Behaviour of Foundations and Structures. *Ninth International Conference on Soil Mechanics and Foundation Engineering*, Tokyo, Japan. 495–546.

Bezuijen, A. Kleinlugtenbelt, R.E, Kaalberg, F.J. and Essler R.D. (2011), Settlement behaviour after compensation and corrective grouting, *Proceedings of TC28, International Symposium, Geotechnical aspects of underground construction in soft ground, Roma, Italy*.

CUR-report 231, 2010, Handbook Diaphragm-walls, design and installation, CUR/COB, Gouda, The Netherlands (in Dutch).

De Nijs, R., Kaalberg, F.J., 2010. Recovery of pile bearing capacity (In Dutch; Herstel paaldraagvermogen). *Cement* 2010/8. 48–53.

Korff, M., Mair, R.J. and Van Tol, A.F., 2009, Building damage examples due to leakage at a deep excavation in Amsterdam. *Int. Conference of Soil Mechanics and Geotechnical Engineering, Alexandria, Egypt.*

Korff, M., Veenbergen, V. & Van Tol, A.F., 2008, Summary Deltares reports for Vijzelgracht Station, Deltares report 435691-0003 (in Dutch).

Korff, M, Mair, R.J., Van Tol, A.F. and Kaalberg, F. 2011, Building damage and repair due to leakage in a deep excavation, *Proceedings of the Institution of Civil Engineers journal Forensic Engineering, accepted for publication*.

Salet, Th.A.M., De Kort, P.J.C.M. & Crawley, J.D., 2006. Amsterdam North South Line, Metro-construction of deep diaphragm walls for three underground stations. *Proc. Tenth International Conference on Piling and Deep Foundation, Linderberg, Bottiau & van Tol (Eds), Amsterdam. DFI, Emap*.

Spruit, R., 2011, Diaphragm walls Kruisplein, Proceedings of TC28, *International Symposium, Geotechnical aspects of underground construction in soft ground, Roma, Italy*.

Van Tol, A.F., Veenbergen, V. & Maertens, J. 2010, Diaphragm Walls, A reliable solution for Deep Excavations in Urban Areas? DFI/EFFC, *Proc. of the 11th International Conference (electronic version), DFI, London*.

This page intentionally left blank

Geotechnical Aspects of Underground Construction in Soft Ground – Viggiani (ed)
© 2012 Taylor & Francis Group, London, ISBN 978-0-415-68367-8

Evaluating the effects of tunnelling on historical buildings: The example of a new subway in Rome

S. Rampello & L. Callisto
Dipartimento di Ingegneria Strutturale e Geotecnica, Sapienza Università di Roma, Italy

F.M. Soccodato
Dipartimento di Geoingegneria e Tecnologie Ambientali, Università di Cagliari, Italy

G.M.B. Viggiani
Dipartimento di Ingegneria Civile, Università di Roma Tor Vergata, Italy

ABSTRACT: Contracts T2 and T3 of the new Line C of Roma underground will be constructed in the historical centre of the city, in an area of great archaeological, historical and artistic value. Significant problems connected to buried archaeological remnants, the geotechnical characteristics of the soil, excavation below the water table, and the necessity of minimising the effects on the historical and monumental heritage are therefore expected. This lecture illustrates the methods adopted to evaluate the effects of tunnelling on the existing monuments and historical buildings, with particular reference to contract T2. The study of the interaction between construction activities and the built environment was carried out following procedures of increasing complexity: Level 1 green-field analyses were used for a preliminary evaluation of the potential damage; Level 2 2D and 3D FE analyses accounted for the presence of existing buildings and considered possible long-term effects induced by drainage through the tunnels lining. The lecture illustrates the main aspects of this procedure, using the example case study of Palazzo Grazioli.

1 INTRODUCTION

Public demand for transport facilities to improve the quality of life in larger cities is constantly growing. One of the main objectives of many European administrations has been that of rendering the many different functions of city life accessible through the creation of sustainable and extended nets of public transport, such that the use of private transport becomes an option rather than a necessity. Often, the only means to safeguard the formal, material and historical integrity of ancient cities is that of going underground. In Italy there are several underground train lines currently under construction or at the design stage in many major cities, such as, for instance, Napoli, Torino and Roma.

The construction of new underground railway lines and the extension of existing ones requires open excavation and bored tunnelling to be carried out in the urban environment, generally in difficult ground, such as soft soils and weak rocks, often below the water table, and almost always in close vicinity of existing buildings and structures. In these conditions, the main design requirement is that of limiting ground deformations caused by the changes of total stress due to excavation and of ground water pressures during excavation and in the long term.

This is particularly relevant for cases where existing structures are of monumental and historical value.

Figure 1 shows the existing network of underground connections in Roma and the extensions currently under construction or at the design stage. At present, only two lines intersect each other at Termini Central Railway Station. Line B is relatively shallow as it was built during the 1930s mostly by cut-and-cover techniques, whereas the bored tunnels of Line A were constructed in the 1970s. A northward extension of Line B, connecting Piazza Bologna to Conca d'Oro, is currently under construction. Also under construction is the new Line C, whose preliminary design was approved by the Municipality of Roma in October 2002. Line C runs North West to South East of the city, for a total length of more than 25 km and 33 stations, reaching out to the eastern suburbs and coming to the surface at Giardinetti station. The easternmost part of the line (contracts T4 to T7) is presently under construction, while the central part of the route (contracts T2 and T3) is currently at the detailed design stage.

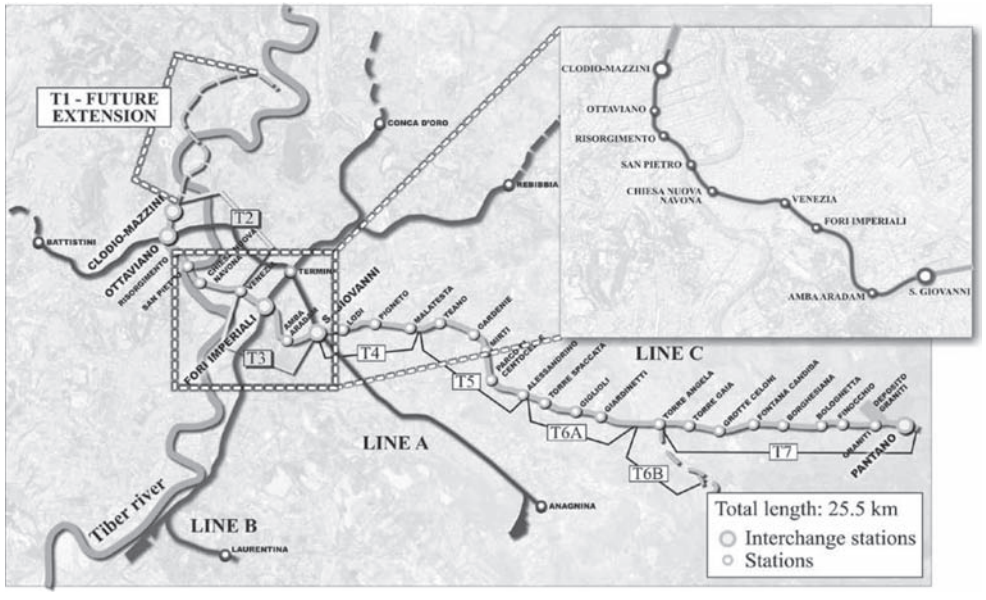

Figure 1. Existing underground connections in Roma and planned extensions.

Construction of this part of the route is more problematic than the previous stretches, as the running tunnels and the stations will have to be built in the historical centre of the city, with significant problems connected to buried archaeological remnants, the geotechnical characteristics of the soil, construction below the water table, and the necessity of minimising the effects at the surface on the historical and monumental heritage.

Contract T3 interacts mainly with monuments of Roman Age (I ÷ V century). The most significant of these are: the Aurelian Walls at Porta Asinaria and Porta Metronia, the Church of Santo Stefano Rotondo, the Acquedotto Celimontano, the Anfiteatro Flavio (Coliseum), the Basilica di Massenzio, the Colonnacce, and the Foro di Cesare.

Contract T2 starts at Piazza Venezia, where there are important monuments built over a period of time spanning from the II to the XX century, such as the Colonna Traiana (II cent.), the Church of Santa Maria di Loreto (XVI cent.), and the Vittoriano (XIX-XX cent.), and then runs along the Corso Vittorio heading towards the Tiber river, in close vicinity of a large number of ancient masonry buildings of historical and artistic value built between the XV and the XIX century, such as Palazzo Venezia and Palazzo Grazioli, at the beginning of the contract; the Church of Sant'Andrea della Valle and Palazzo Massimo alle Colonne, in its central portion; the Church of Chiesa Nuova, Palazzo della Cancelleria and Palazzo Sforza Cesarini in the final part of the contract.

2 GROUND CONDITIONS

Figure 2 shows a geological section of Contract T2, from piazza Venezia to the river Tiber. Starting from the bottom, it is possible to recognise a thick deposit of stiff and overconsolidated clay of Pliocene age (*APl*), at depths of about 60 m b.g.l., overlain by a layer of gravel and sand of Pleistocene age (*SG*), with a thickness of about 10 m, and then by the alluvium deposits of the river Tiber of Holocene age, for a total average thickness of 50 m. The alluvia are very variable in grading and include fine-grained layers of clayey silt and silty clay (*Ag*, *LAv*), layers of medium to coarse sand (*S*), and layers of silty sand and sandy silt (*SLv*) or medium to fine sand and sandy-clayey silt (*SLg*). At surface, the geological profile is completed by a layer of made ground (*R*), consisting mainly of coarse-grained material, sand and gravel, with a thickness of about 10 m.

The ground water pressure is nearly hydrostatic with a hydraulic head located at depths of about 8 to 10 m below ground level and subject to periodic fluctuations connected to the hydrometric level of the river Tiber.

To avoid direct intersections with the archaeological layer, the running tunnels will be excavated at depths between 25 and 40 m b.g.l. (deepening towards the river) using EPB tunnel boring machines with an outer diameter of 6.7 m. In the initial and final stretches of Contract T2 the tunnels will be mostly contained in fine grained soils, while

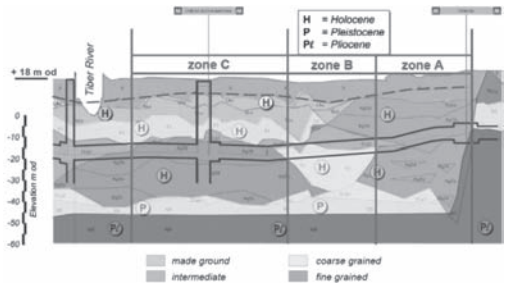

Figure 2. Geological section of contract T2.

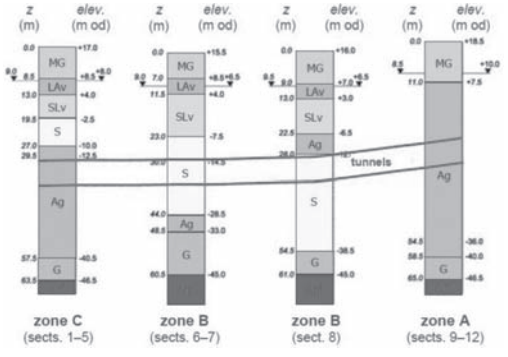

Figure 3. Soil profile and tunnel depths in contract T2.

in the central portion of the contract, excavation will be carried out essentially in the sandy soils.

The geotechnical investigation included deep boreholes and cross-hole tests, cone penetration tests with piezocone, down-hole tests and dilatometer tests; in addition to conventional laboratory tests, undrained and drained triaxial compression and extension tests were also carried out using triaxial cells instrumented with bender elements and local axial strain transducers; finally resonant column tests were performed for an accurate estimate of the small-strain shear stiffness.

Careful consideration of the results of all borehole logs and *in situ* and laboratory tests carried out between 1999 and 2009 permitted to identify three zones characterised by typical soil profiles, shown in Figures 2 and 3 as zones A, B, and C.

The fine-grained soils consist mainly of normally consolidated clayey silts (*LAv*), found below the made ground for a thickness of about 5 m in zones B and C, and by a thick layer of silty clays (*Ag*) overlying the deep gravel layer in zones A and C. Because of the relative position of the tunnels and the fine-grained layers, it can be anticipated that long-term effects will only be significant in zones A and C.

3 INTERACTION OF THE NEW LINE WITH EXISTING BUILDINGS

Because of the exceptional archaeological and historical value of the structures potentially affected by the construction of the line, the design had to include a detailed study of the interaction between the construction activities and the monuments.

As prescribed by the grantor of the project (Roma Metropolitane), the general contractor (Metro C) set up a multidisciplinary steering technical committee, with the assignment of implementing all necessary procedures to safeguard the historical buildings.

More in detail, the main tasks of the steering committees are as follows: evaluate, also through numerical analyses, the influence of the construction of Line C on the existing monuments and historical buildings; suggest, where necessary, appropriate mitigation measures of geotechnical or/and structural nature; develop a comprehensive and redundant monitoring scheme to follow in real time the response of the buildings to construction; assist the general contractor in the evaluation of the monitoring data to optimise construction sequences or/and procedures, during construction.

To accomplish these tasks, five working groups were set up, whose activities were coordinated by the steering committee, including experts in preservation and restoration of monuments, tunnelling, geology, structural and geotechnical engineering, geomatics and monitoring.

The Geotechnical Engineering Working Group was charged with the tasks of the mechanical characterisation of the deposits and the definition of the relevant soil parameters, the prediction of the displacement field affecting the different buildings during and after construction, the evaluation of the feasibility of different mitigation measures to be implemented when the soil-structure analyses yielded unacceptable displacement fields, and the development of a geotechnical monitoring scheme. Moreover, in close co-operation with the Structural Engineering Group, the Geotechnical Engineering Group was also required to develop a consistent and scientifically sound methodological approach to be followed to evaluate how the construction of the line would affect the existing historical buildings, thus assessing the expected damage category.

3.1 *Soil-structure interaction analyses*

The analysis of the interaction between construction activities and built environment was carried out following procedures of increasing complexity.

At a first stage, simplified analyses (Level 1), based on empirical procedures, were performed computing surface and near-surface displacements

by semi-empirical methods in green field conditions, *i.e.* neglecting the effects of the presence of the buildings on the displacement field (Attewell & Woodman, 1982, Attewell *et al*. 1986). The resulting displacement field was applied by the group of structural engineering to a 3D linear elastic finite element model of the structure under examination. Both groups made independent evaluations of potential damage to the building. Depending on the outcome of these evaluations the study was stopped at this level or continued to a more complex level of analysis (Level 2).

At this second stage, the interaction between the tunnels and the historical buildings was studied by numerical 2D or 3D finite element analyses in which the building characteristics were included using a simplified representation of the building as an equivalent solid entirely embedded into the soil. The new computed displacement field was applied to the structural model of the building and damage was re-evaluated, independently, by both groups. Depending on the results, either the computed level of damager was considered acceptable or remedial measures were eventually proposed.

4 LEVEL 1 ANALYSES

The available field evidence indicates that, in green field conditions, the shape of the surface settlement trough is well described by a Gaussian distribution curve, in a section transversal to the tunnel axis and at sufficient distance from the face to assume plane strain conditions, and by a cumulative probability function in the longitudinal direction, see Figure 4 (Peck, 1969, O'Reilly and New, 1982).

The transverse surface settlement trough, see Fig. 4(a), can be written as:

$$w(y) = w_{\max} \cdot \exp\left(\frac{-y^2}{2 \cdot i^2}\right) \tag{1}$$

Where w is the vertical displacement a distance y from the tunnel axis, $w_{\max}$ is the maximum vertical displacement, and i is the distance of the point of inflection of the Gaussian curve from the tunnel axis.

Integrating the plane strain settlement trough at surface (eq. (1)), it is possible to express $w_{\max}$ as:

$$w_{\max} = \frac{\sqrt{\pi}}{4\sqrt{2}} \frac{V_L D^2}{i} \tag{2}$$

Where D is the tunnel diameter and V_L is the volume loss, *i.e.* the volume of the settlement through at surface divided by the nominal volume

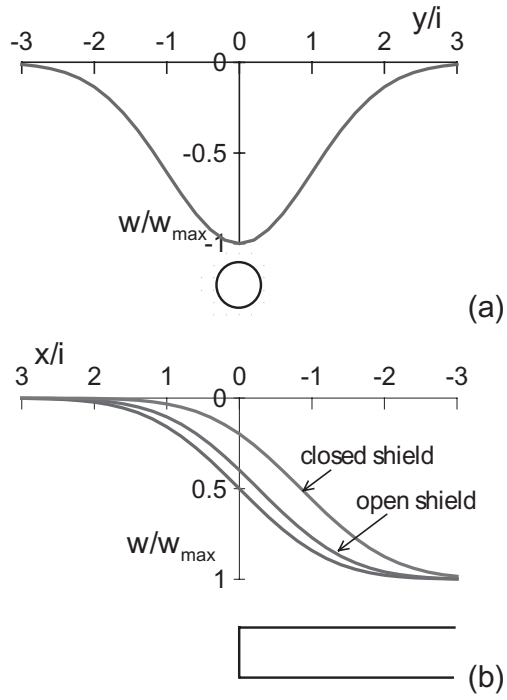

Figure 4. Level 1 profiles of vertical displacements: (a) transversal and (b) longitudinal.

of the excavated tunnel. In this study, settlements were computed using values of the volume loss between 0.5% (contractual requirement) and 1.0% (worst case scenario) as tunnel excavation will be carried out using EPB (Earth Pressure Balance) tunnel boring machines.

For relatively deep tunnels, *i.e*. tunnels with a cover at least equal to one diameter, the value of i at surface is proportional to the depth of the tunnel axis, z_0 (O'Reilly e New, 1982):

$$i_0 = K \cdot z_0 \tag{3}$$

through a coefficient, K, depending essentially on the soil type; in this case values of K of 0.4 to 0.5 were assumed.

In the longitudinal direction, the shape of the profile of vertical displacements is well represented by the cumulative probability function (O'Reilly & New, 1982, Attewell & Woodman, 1982), but the profile is shifted, see Fig. 4(b), so that the settlement at the tunnel face is only 0.2–0.4 of the maximum settlement at distance from the tunnel face, depending on whether the tunnel is excavated by closed or open shield.

Forgroundmovementsatdepthitistypicallyassumed (O'Reilly & New, 1982; Grant & Taylor, 2000) that

the shape of the settlement trough is still Gaussian so that the same eq. (1) can be used to compute the profiles of vertical displacements at any depth z below ground surface, as long as w_{max} and the variation of $i = K(z) \cdot (z_0 - z)$ are defined.

Several relationships to evaluate i at depth have been proposed (Mair *et al*., 1993; Moh & Huang, 1996, Mair & Taylor, 2001). In this study the expression by Moh *et al*. (1996):

$$i(z) = b \cdot D \cdot \left(\frac{z_0 - z}{D} \right)^m \tag{4}$$

was adopted, with values of the exponent m ranging between 0.4, recommended for silty-sands, and 0.8 for silty-clays. Parameter b can be obtained from the value of i at surface:

$$i(z = 0) = i_0 = b \cdot D \cdot \left(\frac{z_0}{D} \right)^m \tag{5}$$

or:

$$i(z) = i_0 \cdot \left(\frac{z_0 - z}{z_0} \right)^m \tag{6}$$

Equations (5) and (6) indicate that the relative width of the settlement trough, K, increases with depth, as shown in Figure 5.

Horizontal displacements were always computed assuming that the vectors of ground movements point towards the tunnel axis (O'Reilly & New, 1982).

To account for changes of direction in plan and of depth, the tunnels were divided into rectilinear portions, and each portion further subdivided into horizontal segments at constant depths. The displacements caused by each segment were computed as the difference of those caused by two tunnels of semi-infinite length and the total displacements obtained by superposition. With same logic, the presence of multiple tunnels was accounted for by superposition of the effects of each tunnel.

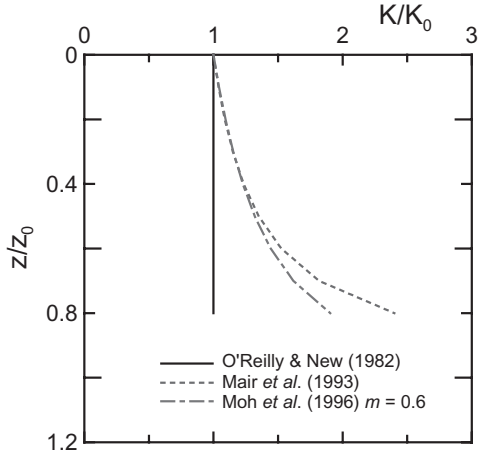

Figure 5. Level 1 variation of K with depth.

5 LEVEL 2 ANALYSES

In Level 2 analyses, the interaction between the soil, the tunnels, and the buildings was explicitly accounted for through numerical analyses in which the building characteristics were included.

The soil profile, the pore water pressure regime and the mechanical properties of the soil were obtained from the results of *in situ* and laboratory investigations; the process of tunnel excavation, including long term effects, was explicitly modelled in 2D or 3D finite element analyses, in which the building stiffness, weight and embedded depth of foundation were accounted for as detailed in the following.

The analyses were carried out in terms of effective stresses modelling the clay layers as undrained and the granular soils as drained.

5.1 *Soil constitutive model*

The mechanical behaviour of all soils was described using an elastic–plastic rate independent constitutive model with isotropic hardening and Mohr Coulomb failure criterion. This is the Hardening Soil model (Schanz *et al*., 1999), implemented in the finite element codes Plaxis and Tochnog which were used for the numerical analyses. The elastic behaviour is defined by isotropic elasticity using a stress dependent Young's modulus:

$$E' = E^{ref} \left(\frac{c' \cdot \cot \varphi' + \sigma_3'}{c' \cdot \cot \varphi' + p^{ref}} \right)^m \tag{7}$$

were σ'_3 is the minimum principal effective stress, c' is the effective cohesion, φ' is the angle of shearing resistance and $p^{ref} = 100$ kPa is a reference pressure, and E^{ref} and m are model parameters.

The model has a deviatoric and a volumetric yield surfaces with independent isotropic hardening depending on deviatoric plastic strain and volumetric plastic strain, respectively. The flow rule is associated for the volumetric yield surface, and non-associated for the deviatoric yield surface.

The elastic Young's modulus, representing the initial tangent stiffness, was related to the small-strain shear modulus, G_0, obtained from

cross-hole tests. Appropriate values of E^{ref} and m were obtained by best fitting cross hole test results with eq. (7) and assuming $\nu' = 0.2$.

Figure 6 show the profiles of G_0 obtained by three cross-hole tests carried out in zone A, together with the values of G_0 obtained from triaxial tests instrumented with bender elements and from resonant column tests. The continuous line in Figure 6 represents the profile of G_0 used in the finite element analyses, computed using the parameters given in Tables 1 and 2; the values of the horizontal effective stress σ'_3 were obtained using the values of the coefficient of earth pressure at rest K_0 listed in Table 1. In the context of strain hardening plasticity, the overconsolidation ratio must be regarded as a yield stress ratio, so that values of OCR > 1 can be specified also for geologically normally consolidated soil layers exhibiting a yield stress larger than the in situ stress; this was the case for the granular soils such as the made ground and the layers of sand and gravel.

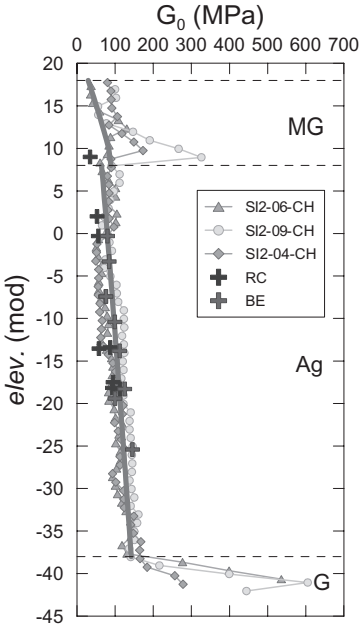

Figure 6. Measured and computed profiles of G_0.

Non linear stress-strain behaviour is described in the model by two parameters, E'_{50} and E'_{oed} controlling the volumetric and deviatoric hardening rules, respectively. Both parameters are defined by expression similar to eq. (7) but, in contrast to E', they are not used within a concept of elasticity, and were evaluated by best fitting the stress-strain curves obtained from triaxial tests carried out using local axial-strain transducers.

As an example, Figure 7 shows the results of three drained triaxial tests carried out on undisturbed samples retrieved from the silty clay (*Ag*) and sheared from values of effective cell pressure equal to the estimated mean effective stress *in situ,* together with the model predictions computed using the parameters listed in Table 2.

5.2 *Modelling tunnel excavation.*

In plane strain conditions, tunnel excavation can be simulated either by reducing the nodal forces acting at the tunnel boundary by a factor λ, or by imposing a given displacement field, characterised by a displacement δ at the tunnel crown. Both the reduction factor λ or the displacement δ can be calibrated to obtain a given volume loss at surface.

However, it is well known that imposing uniform unloading or uniform radial contraction of the tunnel boundary, yields settlement troughs that

Table 1. Strength and stress history parameters for soils in zone A.

Soil	γ (kN/m³)	C' (kPa)	φ′ (°)	OCR	K_0^{nc}	K_0^{oc}
R	18.5	15	29	2.00	0.515	–
Ag	18.4	20	26	1.35	0.577	0.655

Table 2. Stiffness parameters for soils in zone A.

Soil	E'^{ref} (MPa)	m	E'/E'_{50}	E'_{oed}/E'_{50}	E'^{ref}_{50} (MPa)	E'^{ref}_{oed} (MPa)
R	240	0.8	10	1.0	24.0	24.0
Ag	150	0.8	20	1.5	7.5	11.3

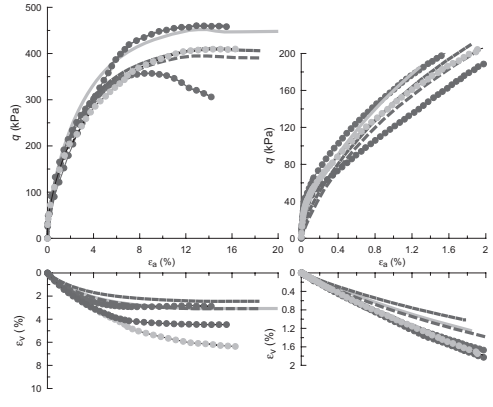

Figure 7. Observed (symbols) and computed (lines) stress-strain relationships.

are wider and with a lower maximum displacement than observed in practice. Therefore, in this study, a modified displacement approach was adopted, in which a set of vertical displacements were imposed at the upper portion of the tunnel while leaving the invert fixed (Fig. 8), and then the conditions on the displacements were removed after activating the tunnel lining. The displacement field still depends on only one scalar parameter, namely the vertical displacement at the tunnel crown, but a better agreement is achieved between the numerical and the empirical predictions for green-field conditions.

A simplified procedure was used to simulate tunnel construction in 3D, extending the technique used for the plane strain analyses. At any stage, the tunnel cavity is wholly lined by the shield or the permanent lining but for the face, where a support pressure equal to the total horizontal stress at rest is applied, Figure 9(a). The shield extends for 4 vertical mesh slices, for a total length of 8 m, and the permanent lining is installed two slices behind (4 m).

Tunnelling is modelled in discrete steps by removing 1 slice of soil (2 m) and advancing the support pressure and the shield by an equivalent length, while removing the same length of permanent lining at the shield tail. In this manner a region of unlined soil is created at the tail of the shield

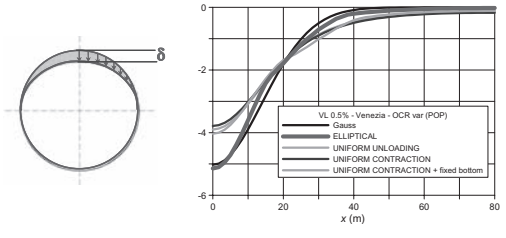

Figure 8. 2D analyses: imposed ground movements at tunnel boundary and predicted settlement trough.

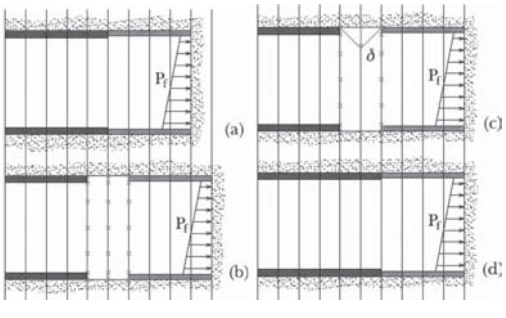

Figure 9. Simplified procedure adopted for simulating the process of tunnelling excavation in 3D.

with three lines of nodes that have all degrees of freedom removed, Figure 9(b).

After reaching equilibrium, a displacement field similar to that used in the 2D analyses is imposed to the central line of nodes, Figure 9(c), such that a required value of volume loss at the shield is achieved.

Once the final values of the displacements are achieved, the final lining is installed and the degrees of freedom of the three lines of nodes are reactivated before letting the system reach a new equilibrium condition for the following excavation step, Figure 9(d).

The values of the displacement δ at the tunnel crown were determined by trial and error to meet the requirement that the design volume loss was attained at the ground surface for stationary conditions.

Figure 10 shows a view of the green-field three-dimensional mesh used for calibration, carried out modelling a rectilinear and horizontal tunnel, in a layered soil. The displacement δ imposed at the tunnel crown was changed in order to obtain a volume loss of 0.5% at ground surface.

The settlement trough computed at ground surface by numerical analysis at the end of calibration compares well with that obtained using the empirical method (for $K = 0.4$) both in terms of maximum settlement and width of settlement trough.

The same values of δ obtained from model calibration in green-field conditions were then used

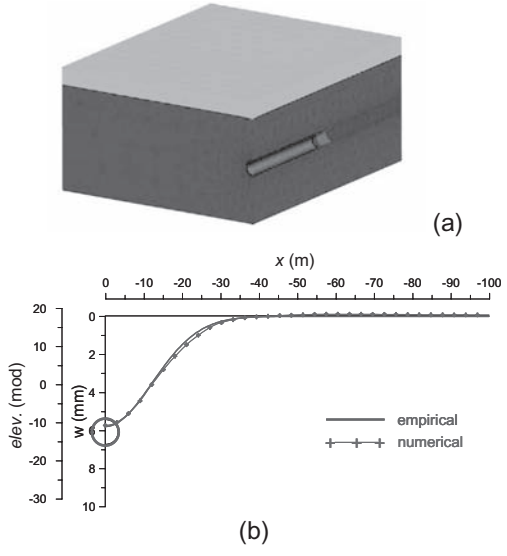

Figure 10. (a) 3D view of the mesh used for calibration and (b) comparison of numerical and Gaussian settlement troughs.

in the interaction analyses, in which the building effects were included.

5.3 *Long term effects*

When tunnelling is carried out in fine-grained soils, an increase of settlements with time can occur due to the change in the hydraulic conditions at the tunnel boundary, where pore pressures are equal to zero. Reviewing the long-term settlements measured in clays after tunnel construction, Mair and Taylor (1997) concluded that the major factors affecting the development of long term settlements are the initial pore water pressure distribution, the excess pore water pressure induced by tunnel construction, the compressibility of the clay and, more than anything else, the ratio of the permeability of the tunnel lining and of the soil.

The key factors affecting long term settlements may be isolated considering the simple scheme of one-dimensional flow through two porous media representing the soil and the tunnel lining. In Figure 11, h is the hydraulic head at a distance L from the tunnel lining, where the hydraulic head reduction is negligible, h_e is the hydraulic head at the interface of the lining and the soil, h_i ($= h - \Delta h$), is the hydraulic head at the internal boundary of the lining, where the pore water pressure is zero, and t_L is the thickness of the lining. Of course, Figure 11 shows the stationary conditions that are achieved slowly with time, in the long-term.

The long term hydraulic head at the soil-lining interface can be computed as:

$$h_e = h - \frac{\alpha}{1+\alpha} \cdot \Delta h = h - \psi \cdot \Delta h \tag{10}$$

where parameter α:

$$\alpha = \frac{k_{lining}}{k_{soil}} \cdot \frac{L}{t_L} \tag{11}$$

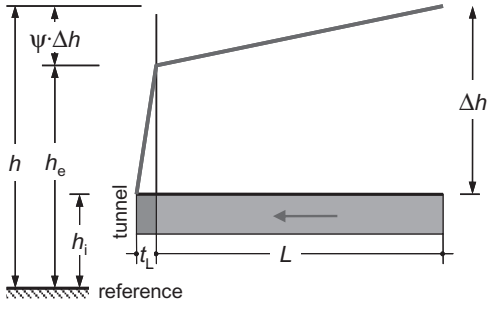

Figure 11. Scheme of one-dimensional flow through tunnel lining.

quantifies the importance of the long-term effects.

For large values of α, the hydraulic head h_e at the external boundary of the lining decreases, the effective stress in the soil increases and, therefore the long term-settlements in the soil. For $\alpha \to \infty$, the condition of fully permeable lining is attained. On the other hand, for low values of α, the total head in the soil tends to h, that is the tunnel lining approaches the condition of fully impermeable boundary, the long-term pore water pressures are not altered, and the long term settlements become negligible. In practice, a numerical study carried out by Wongsaroy (2005) showed that long-term settlements become increasingly relevant for values of α larger than about 0.1.

Reliable estimates of α require reliable estimates of both soil and lining permeability. For the case at hand, the permeability of the silty clay was estimated using the results of piezocone (CPTU) dissipation tests, while the permeability of the tunnel lining was estimated using results of permeability tests carried out on samples of the grout injected behind the lining, and assuming typical values for the precast concrete segments. This resulted in average values of $k_{soil} = 2\times10^{-10}$ m/s and $k_{lining} = 1.5 \times 10^{-11}$ m/s, or a permeability ratio $k_{lining}/k_{soil} \cong 0.1$. Based on the soil profile in zone A, the seepage length was $L = 10$–20 m, so that, for a lining thickness $t_L = 0.4$–0.5 m, values of α ranging from 2 to 5 were computed. For zone C, where a permeable layer of silty sand is found about 4 m above the tunnel crown, L ≅ 4 m, and $\alpha \cong 1.0$; it follows that long-term effects are likely to be less significant for zone C.

In the numerical analyses, long-term conditions were reproduced by modelling the tunnel lining as a porous material and setting the pore water pressure equal to zero at its internal boundary. Long-term settlements computed for zone A using the estimated permeability ratio $k_{lining}/k_{soil} \cong 0.1$ were substantially larger than the short-term settlements computed at the end of tunnel construction, and the computed settlement trough was much wider. For a lower permeability ratio, $k_{lining}/k_{soil} = 0.01$ the long-term effects would be negligible.

Figure 12 shows the pore water pressure profiles immediately after tunnel construction and in the long term. In undrained conditions a reduction of pore pressure is computed above the crown and at the sides of the tunnel, for distances of about 5 m, while at larger distances there is an increase of pore water pressure. In the long term, there is a reduction of the pore water pressures, that for $k_{lining}/k_{soil} = 0.1$ is quite marked, due to the draining effect of the tunnel lining. For a larger soil permeability ($k_{lining}/k_{soil} = 0.01$), the long term pore water pressure is close to the initial distribution and the long term settlements are negligible.

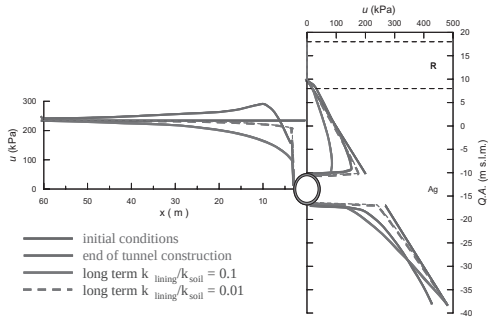

Figure 12. Profiles of pore water pressure on the centre line and at axis level of the tunnel at the end of construction and in the long term.

5.4 *Equivalent solids for buildings*

In Level 2 numerical analyses the building is transformed in an Equivalent Solids (ES) with simpler geometry and appropriate mechanical properties. This equivalent solid is fully embedded into the soil and is assumed to behave as a linear elastic material: the assumption of linear elastic behaviour can be considered sufficiently accurate only for relatively small volume losses, that is when the structure undergoes small distortions.

In order that the building and its simplified representation through an elastic solid may be considered equivalent, they should show a similar response to a given perturbation. For the present problem, the perturbation consists of imposed vertical displacements at foundation level (computed with a green-field analysis) and the response is the corresponding distribution of the nodal forces at the same level.

In the simple assumption of isotropic elasticity, the mechanical behaviour of the equivalent solid is completely described by the Poisson's ratio (assumed to be equal to 0.3) and the Young's modulus. This is found iteratively, to produce a distribution of nodal forces at the foundation level that matches the distribution computed using a complete structural model of the building.

The equivalent solid is introduced in the finite element analyses with its stiffness and a weight that reproduces that of the complete building, and a new displacement field is computed that accounts for the presence of the building. This displacement field is applied to the complete structural model for a final evaluation of the effects induced by tunnel construction.

In plane strain conditions, a number of further simplifying assumptions are needed. The building was taken to be transversal to the tunnel axis and only the contribution of the transversal walls was accounted for in the analysis. In this case, the equivalent solid refers to a single embedded wall, of given thickness, b, and height, H; as in the plane strain analyses the structure is continuous in the longitudinal direction, it was necessary to scale the equivalent stiffness and weight by the ratio b/s_{av}, in which s_{av} is the spacing between two contiguous walls, in order to spread the stiffness and weight in the longitudinal direction.

Notwithstanding the efforts to accommodate complex geometrical layouts into a simple plane-strain scheme, in some cases the curvilinear trajectories of the tunnels and the significant skew of the buildings relative to the tunnel required three dimensional finite element studies. Moreover, it was recognised that in several instance the density of heavy and stiff buildings was so high that a mutual interference of several buildings could not be ruled out.

The definition of the equivalent solids in a 3D analysis posed a specific problem arising from a difference between the geotechnical and the structural meshes: while the geotechnical 3D equivalent solids were made of solid brick elements, the structural models use bi-dimensional shell elements. Therefore, the node layout in the two models did not match, and it was not possible to compare directly the nodal forces. In this case the search for Young's modulus of the equivalent soil was based on the minimisation of cumulative reactions computed on a transversal vertical section of the building.

6 CASE STUDY: PALAZZO GRAZIOLI

Palazzo Grazioli (XIX century), located at the start of Contract T2, near Piazza Venezia, will be used as a case study to illustrate the application of the procedures outlined above. Figure 13 shows a plan view of the building, indicating the position of the tunnel axes and the main masonry walls; the façade of the building on via degli Astalli is highlighted as an orange line.

The local ground conditions at Palazzo Grazioli. consist of made ground, about 10 m thick, overlying a thick layer (46 m) of slightly overconsolidated silty clay, where the tunnels are to be excavated, at a depth of about 28.5 m. At larger depths, there is the layer of gravel with a thickness of 5 to 7 m, and that of the stiff Pliocenic overconsolidated clay. The distribution of pore water pressure is nearly hydrostatic with a hydraulic head at a depth of about 8.0 m below ground surface. The foundation level is at a depth of about 9 m below ground surface.

Figure 14 shows the contours of green-field settlements computed using the empirical relationships (Level 1 analyses), at foundation level

Figure 13. Plan view of Palazzo Grazioli, showing the relative position of the building and the tunnels axes.

for different stages of excavation of the two tunnels.

The settlements Figure 14 are computed for a volume loss V_L = 0.5%, and are end-of-construction values, for undrained soil behaviour. Figure 15 shows the settlement troughs along a transversal section at the end of construction of the first and the second tunnel for V_L = 0.5% and 1%. The maximum settlements occur above the tunnel axes and are equal to about 7 mm for V_L = 0.5% and twice this value (14 mm) for V_L = 1%. The interaction between the tunnels is negligible. The evaluation of the potential damage for the buildings involved the evaluation of all the components of the displacement field underneath the four facades of the building, also considering intermediate position of the tunnels face.

For Level 2 interaction studies, both two- and three-dimensional finite element analyses were performed, predicting the short-term settlements at the end of tunnel construction and the long-term settlements associated to partial drainage through the tunnel lining. These analyses considered explicitly the effects of the weight and stiffness of the stiffness through the inclusion of appropriate equivalent solids.

The plane strain analyses studied the façade of Palazzo Grazioli on via degli Astalli. To obtain an equivalent solid representing the building, the structural engineering group applied the green-field displacements to finite element models of both the entire façade and the equivalent solid shown in the upper part and the lower part of Figure 16(a),

Figure 14. Palazzo Grazioli—level 1 analyses: contours of short-term settlements at the depth of foundations (z = 9.0 m).

representing only the embedded portion of the wall. The Young's modulus of the equivalent solid was found as the value that minimised the differences between the node reactions at the base of the two solids, as shown in Figure 16(b). This procedure yielded an equivalent Young's modulus E_{ES} = 3.9 GPa, against an actual Young's modulus for the masonry E = 2.5 GPa. Further scaling for compatibility with

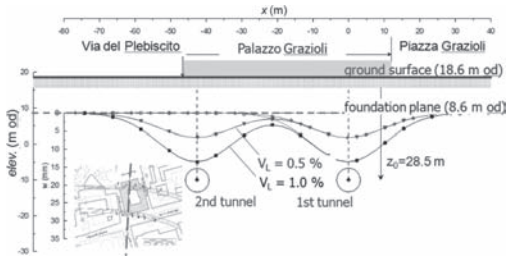

Figure 15. Palazzo Grazioli—Level 1 analyses: short-term subsurface settlement troughs computed in a section transversal to the tunnels.

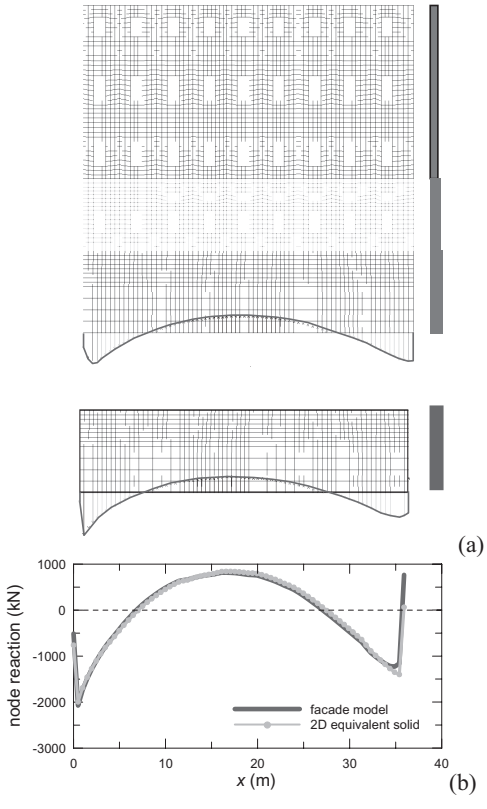

Figure 16. Palazzo Grazioli—façade on via degli Astalli: (a) finite element model of the entire façade (top) and of the equivalent solid (bottom) and (b) node reactions-based equivalence for the structural equivalent solid in plane strain analyses.

a plane strain analysis produced a Young's modulus of E_{ES} = 1.2 GPa to be used in the two-dimensional interaction finite element analyses.

Figure 17 shows the settlement troughs computed under the façade assuming a volume loss of 0.5%, at the end of construction of the first and the second tunnel, and in the long-term.

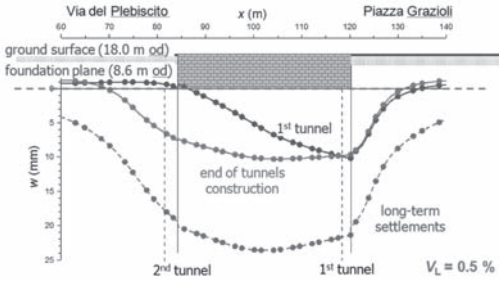

Figure 17. Palazzo Grazioli—2D Level 2 analyses: short- and long-term settlement troughs computed in a section transversal to the tunnels.

The results of these two-dimensional computations are quite different from those obtained from Level 1 analyses, illustrating the role played by soil-structure interaction. In the short term, they provide similar values of maximum settlement, but a completely different deflection pattern for the façade, that undergoes sagging rather than hogging, with a much lower curvature than predicted with empirical methods.

Parametric analyses were carried out to isolate and evaluate the influence of the building stiffness and weight on the computed settlement trough, acting primarily on the Young's modulus of the equivalent solid and on building weight. In fact, it was found that the differences between the empirical evaluations and the results of the numerical computations depend both on the interaction between the tunnels and on the weight and stiffness of the building. Numerical analyses predict a significant interaction between the tunnels, that cannot be reproduced by simple superposition of the effects of single tunnels as significant plastic strains are induced by the excavation and the problem becomes strongly non-linear. Building weight is mainly responsible for the slightly larger maximum computed settlements, as it induces an increase in deviatoric stress thus mobilising a lower stiffness. Finally, the stiffness of the building affects mainly the shape of the settlement trough, reducing its curvature.

The computed ratio of long term settlements (dashed line in Fig. 17) and end-of-construction settlements is as high as about 2.5; however, the increase in settlements is associated with negligible changes in the curvature of the settlement trough, and therefore does not produce significant damage to the façade.

Figure 18 shows a view of a number of buildings located close to piazza Venezia, including Palazzo Grazioli. It is clear that this is one of those situations in which the mutual interference of sev-

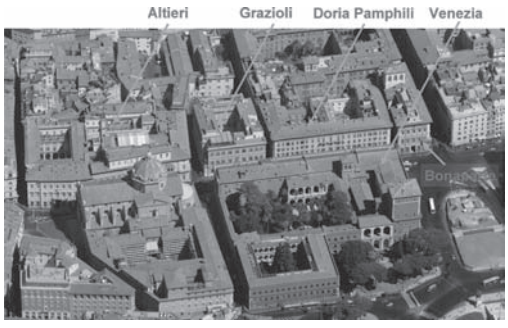

Figure 18. Aerial view of the historical buildings in zone A, close to piazza Venezia.

eral heavy and stiff buildings cannot be ignored, as it is likely to increase substantially the initial state of stress in the soil and modify the settlement profiles obtained in green field conditions. Moreover, at Piazza Venezia the route comes to a wide curve so that there is significant skew between the tunnels axis and the buildings façades, suggesting the opportunity to carry out 3D interaction analyses using a large model including all the relevant buildings located in the area.

Figure 19 illustrates the complete structural model and the equivalent solid used to represent Palazzo Grazioli in the 3D finite element analyses. The Young's modulus for the equivalent solid, E_{ES}, was obtained minimising the difference between the cumulative nodal forces deriving from the application of the full three-dimensional greenfield displacement distribution at the foundation base, along a transversal section through the building. In this case, the optimum Young's modulus of the equivalent solid was $E_{ES} = 2.38$ GPa, only slightly smaller than the value of $E = 2.5$ GPa used for the complete model of the building, but this is not a general result.

Figure 20(a) shows a plan view of the region that was analysed in the study, with an area of about 300 m^2. Figure 20(b) shows a view of the domain with the equivalent solids for the buildings and the two tunnels following their curved trajectories that deepen towards the river Tiber. Some simplifications were introduced in the model: the thickness of the made ground was taken to be equal to 8 m, and the equivalent solids extend exactly down to the contact of the made ground with the silty clay. The mesh includes the made ground and the silty clay, down to a depth of 56 m, whereas the top of the layer of the gravel is modelled as a rigid boundary.

In the analyses the progressive advancement of tunnel face was modelled, and the deformations of the buildings computed for different positions

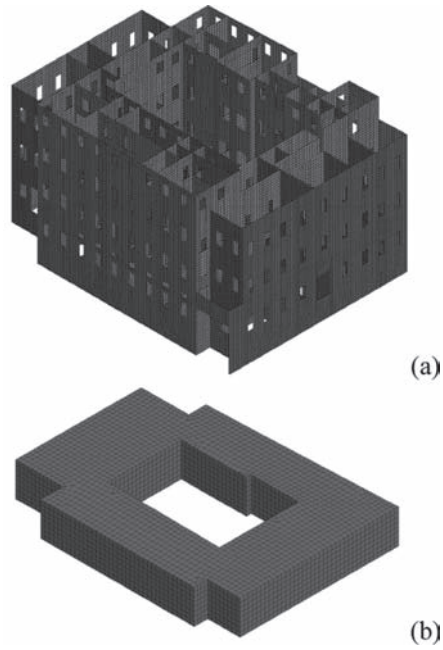

Figure 19. Palzzo Grazioli—3D Level 2 analyses: (a) complete FE model of the building, (b) FE model of equivalent solid.

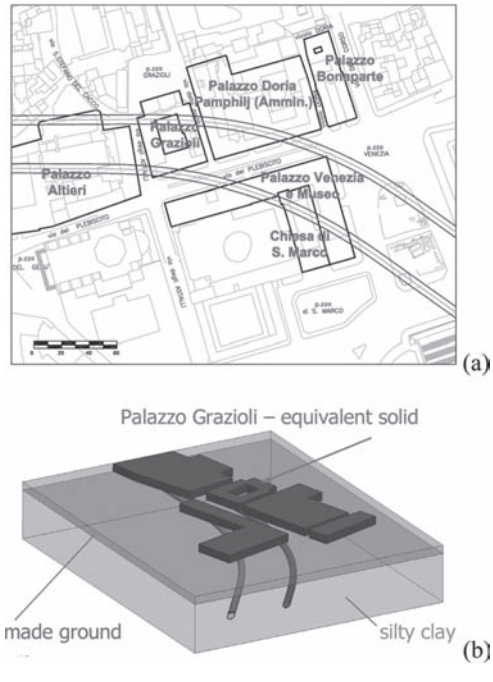

Figure 20. Piazza Venezia- 3D Level 2 analyses: (a) plan view of the area and (b) 3D view of the domain with embedded equivalent solids.

of the tunnel face, to define the most critical conditions for the buildings. In general, the most critical deflected shapes were computed along sections transversal to the tunnel axes.

Figures 21(a)–(c) show the contours of short-term settlements computed for different tunnel advancement. At the end of tunnel construction, the maximum settlements are about 13 mm and the width of the settlement trough at foundation level varies from about 70 m to about 90 m depending on the distance between the tunnels. The contours of long-term settlements are plotted in Figure 21(d); the maximum values are about 22 mm, or 1.7 times the end of construction settlements, while the width of the settlement trough at foundation level increases to about 130 m.

Figure 22 compares the short-term settlements of the façade of Palazzo Grazioli computed in Level 1 and in Level 2 analyses, for V_L = 0.5%. Both 2D and 3D FE analyses predict maximum settlements of about 10 mm to 11 mm, about 1.5 times those computed using empirical methods. Green-field and 3D FE analyses predict some hogging at the base of the façade, but the curvature obtained from numerical analysis is significantly smaller than predicted using empirical methods. Two-dimensional analyses predict sagging, but with very low curvature.

The horizontal tensile strains computed from the FE analyses are lower than those computed using empirical relationships, particularly for the three-dimensional analyses; this is mainly due to the significant stiffness of the building in the horizontal direction, that prevents transmission of horizontal strain.

The assessment of potential damage was carried out following the procedure proposed by Burland and Wroth (1974) and Burland (1995). Specifically, the interaction diagrams proposed by the Authors, that relate the computed values of deflection ratio and horizontal tensile strain to six damage categories were used. The values of limiting tensile strain adopted in this study to identify the damage categories were lower than those proposed by Boscardin and Cording (1989), to account for the historical value of the buildings (Table 3).

Figure 23(a) shows the results obtained using empirical methods and numerically, for values of volume loss of 0.5% and 1%. In all cases, the points fall within damage category zero (negligible), with the only exception of green-field evaluations that, in hogging and for a volume loss of 1%, predict damage category 1 or 2 depending on whether the average or the maximum computed horizontal strain is used in the damage assessment. The comparison between the results of empirical methods and numerical analyses is limited to deflections in sagging and shows clearly that explicit consid-

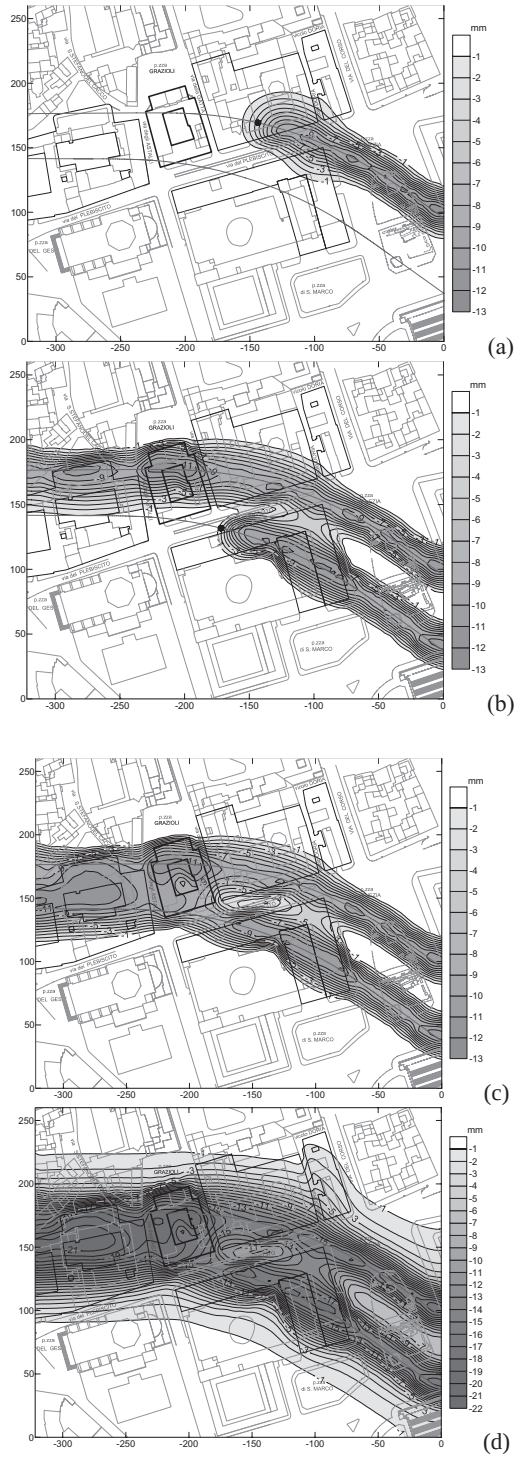

Figure 21. Piazza Venezia- 3D Level 2 analyses: contours of (a)–(c) short term and (d) long-term settlements at the foundation depth (z = 9.0 m).

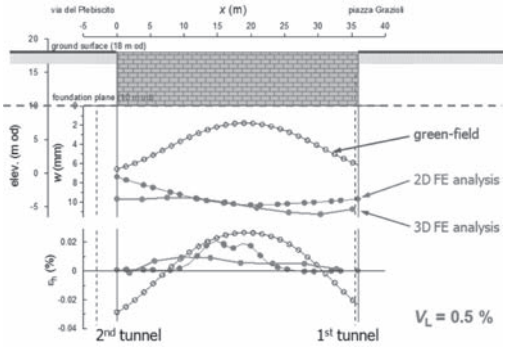

Figure 22. Palazzo Grazioli—façade on via degli Astalli: comparison of short-term settlements computed in a section transversal to the tunnels by Level 1 and Level 2 analyses.

Table 3. Adopted damage categories (modified from Boscardin and Cording, 1989).

Damage category	Damage level	ε_{lim}
0	Negligible	$<4 \times 10^{-4}$
1	Very slight	$4 \times 10^{-4} - 6 \times 10^{-4}$
2	Slight	$6 \times 10^{-4} - 10 \times 10^{-4}$
3	Moderate	$10 \times 10^{-4} - 20 \times 10^{-4}$
4–5	Severe to very severe	$>20 \times 10^{-4}$

eration of soil-structure interaction reduced the potential damage estimated for the building.

The results of the full 3D analysis are shown in blue in Figure 23(b); in this case, the comparison is limited to a volume loss of 0.5%, but is carried out for both sagging and hogging. Again, numerical analyses predict a lesser category of damage compared with green-field evaluations and this is particularly evident when the building deforms in hogging, as both deflection ratio and horizontal tensile strain are substantially lower than those computed using empirical methods.

The procedure proposed by Burland and Wroth (1974) provides only an average estimate of potential damage to the buildings, as it does not provide any distribution of strain within the structure. Some insight into the building response could be obtained from the stress analyses that were carried out by the structural engineering working group, in which the displacement field computed at foundation level was applied to a detailed three-dimensional linear model of the building. Figure 24 shows the contours of the increments of the tensile maximum principal stress σ_1 computed in the façade. The first two plots show the contours of σ_1 obtained after application of the end-of-construction displacements

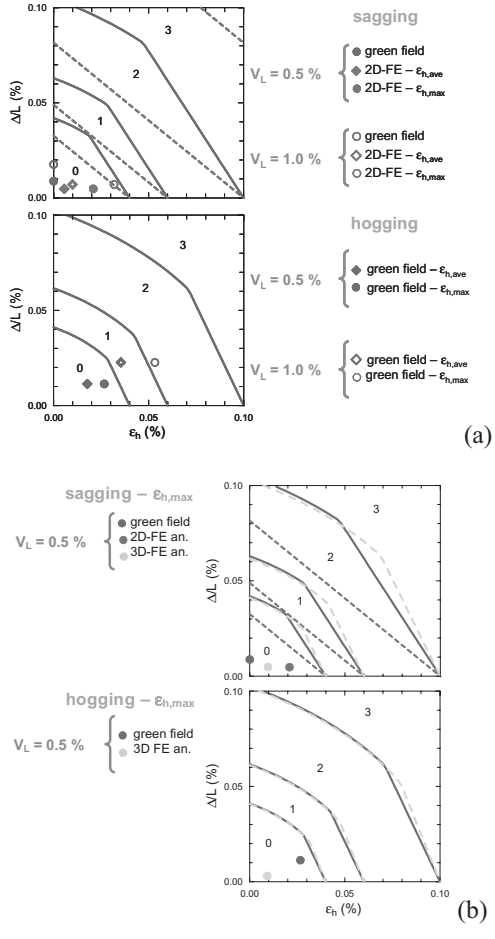

Figure 23. Palazzo Grazioli—façade on via degli Astalli: evaluation of potential damage.

from either Level 1 green-field analyses or Level 2 FE interaction analyses. Green-field displacements induce the largest values of σ_1 (0.8 ÷ 1.2 MPa), localised mainly near the windows of the ground and first floor, providing a maximum tensile strain of $\varepsilon = 3 \times 10^{-4}$ to 5×10^{-4} for a Young's modulus of 2.5 GPa. Application of the displacements computed from the FE soil structure interaction produce smaller values of tensile strain, by as much as 70%. The corresponding maximum tensile strain becomes as small as about $\varepsilon = \times 10^{-5}6$ to 9×10^{-5}. As the conventional threshold strain that separates damage 0 category from damage 1 category is equal to 4×10^{-5}, it is evident that the two independent evaluations of potential damage, carried out with the Burland and Wroth (1974) method and with a three-dimensional structural analysis, are in a substantial agreement. Long-term settlements,

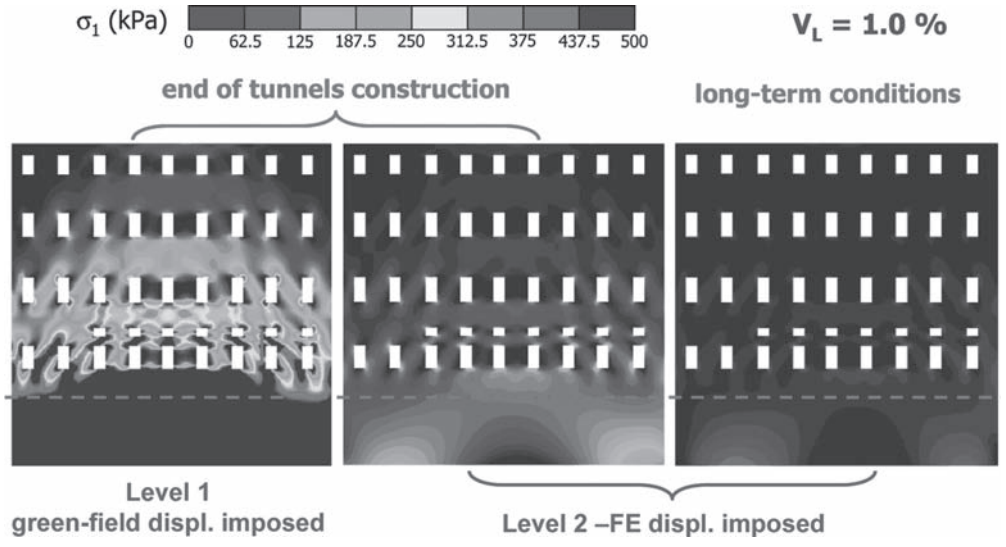

Figure 24. Palazzo Grazioli—façade on via degli Astalli: contours of maximum principal tensile stress induced by given displacement fields applied at the foundation plane.

although of a larger magnitude result in a slight reduction of the curvature and do not produce any appreciable damage.

7 CONCLUSIONS

Contract T2 of the new line C of Rome underground underpasses the historical centre of the city where masonry buildings of particular relevance are present, mostly built between the XV and the XIX centuries. A reliable evaluation of potential damage induced by tunnel excavation to the existing building was then essential in order proceed with design implementing, where necessary, appropriate mitigation techniques.

The procedure for evaluating these effects hinged on the geotechnical analyses, starting from a careful geotechnical characterisation based on in situ and laboratory tests and including the use of reliable computation models, but promoted a fruitful interaction of the geotechnical and structural engineers. At several stages, parallel evaluation of the damage to the buildings were carried out by both groups using the tunnelling-induced displacement fields computed in the geotechnical analyses. These independent estimates by the geotechnical and the structural engineers always provided consistent results.

Evaluation of tunnelling-induced effects was carried out following procedures of increasing level of complexity. Namely, Level 1 green-field evaluations were carried out using empirical relationships and assuming that the buildings follow the ground displacements; at a subsequent stage, depending on the results of Level 1 analyses and on the specific relevance of the building, Level 2 FE interaction analyses were carried out in which the influence of the weight and the stiffness of the building was explicitly considered using a simplified description of the building through an equivalent solid entirely embedded into the soil, down to the foundation level. These analyses were often carried out assuming plane strain conditions, but in several cases the geometrical complexities called for a three-dimensional analysis. In addition to the study of the soil-structure interaction, these numerical analyses permitted to evaluate the long-term settlements that may develop when tunnels are excavated in fine-grained soils of very low permeability.

As a general result, explicit consideration of stiffness and weight of the building resulted in somewhat larger settlements but smaller distortions, and therefore predicted a lower damage if compared with the green-field computations. Long-term settlements were estimated to be relevant in zone A, where tunnels are to be excavated in a thick layer of low-permeability silty clay. The ratio of long-term to immediate settlements computed in 2D and 3D numerical analyses was in the range of 2.0 to 2.5 and the width of the long-term settlement trough was about 1.4–1.9 times larger than the one computed in the short-term. In any case, the reduction in the curvature of long-term settlement troughs resulted in a reduction of the predicted damage to the buildings.

ACKNOWLEDGEMENTS

The Authors are grateful to Roma Metropolitane s.r.l. and Metro C S.p.a. that made this study possible. Profs. Michele Jamiolkowski, Alberto Burghignoli and Kalman Kovary, of the Steering Technical Committee, shared the efforts to develop the methodological approach, engaging in stimulating discussions and providing useful suggestions during its development; Prof. Fabrizio Vestroni and Mr Vittorio Lucarelli contributed to the definition of the equivalent solids form the structural end. Thanks are due to Mrs Francesca Buono, Dr Gennaro Landi and Dr Nunzio Losacco for performing some of the numerical analyses.

REFERENCES

Attewell P.B. and Woodman J.P. (1982). Predicting the dynamics of ground settlement and its derivatives caused by tunnelling in soil. *Ground Engineering*, 15(8): 13–22.

Attewell P.B., Yeates J. and Selby A.R. (1986). Soil movements induced by tunnelling and their effects on pipelines and structures. Glasgow: Blakie.

Boscardin M.D. and Cording E.J. (1989). Building response to excavation—induced settlement. *Journal of Geotechnical Engineering*, ASCE, 65(1), 1–21.

Burghignoli A. (2012). Conferenza "Arrigo Croce", L'attraversamento sotterraneo del centro storico di Roma. *Rivista Italiana di Geotecnica*, 45(4), 13–50.

Burghignoli A., Jamiolkowski M. and Viggiani C. (2007). Geotechnics for the preservation of historic cities and monuments: components of a multidisciplinary approach. Invited Lecture, *XIV Europ. Conf. on Soil Mech. and Geotechn. Engng*., Madrid, 1, 3–38.

Burghignoli A., Di Paola F., Jamiolkowski M. and Simonacci G. (2010). New Rome metro line C: approach for safeguarding ancient monuments. Invited Lecture, *Int. Conf. on Geotechnical Challenges in Megacities*, Moscow, 1–24.

Burland J.B. and Wroth C.P. (1974). Settlement of buildings and associated damage. *Proc. Conf on Settlement of Structures*, Cambridge, UK, 611–654.

Burland J.B. (1995). Assessment of risk of damage to buildings due to tunnelling and excavation. *1st Int. Conf. on Earthquake Geotechnical Engineering*, Tokio, 1189–1201.

Grant R.J. and Taylor R.N. (2000). Tunnelling-induced ground movements in clay. *Geotechnical Engineering*, Proc. Institution of Civil Engineers, 143, 43–55.

Mair R.J. (2008). 46th Rankine Lecture. Tunnelling and geotechnics: new horizons. *Géotechnique*, 58(9): 695–736.

Mair R.J. and Taylor R.N. (1997). Bored tunnelling in the urban environment. State-of-the-art report and theme lecture. *Proc. 14th Int. Conf. of Soil Mechanics and Foundation Engineering, Hamburg*, 4, 2353–2385.

Mair R.J. and Taylor R.N. (2001). Elizabeth House: settlement predictions. Building response to tunnelling. In *Case studies from construction of the Jubilee Line Extension, London, Vol. 1: Projects and methods* (eds J.B. Burland, J.R. Standing and F.M. Jardine), 195–215, London, Thomas Telford, CIRIA spec. publ. 200.

Mair R.J., Taylor R.N. and Bracegirdle A. (1993). Subsurface settlement profiles above tunnels in clays. *Géotechnique* 43(2), 315–320

Moh Z.C., Huang R.N. and Ju D.H. (1996). Ground movements around tunnels in soft ground. *Proc. Int. Symp. on Geotechnical Aspects of Underground Construction in Soft Ground*, London, 725–730.

O'Reilly M.P. and New B.M. (1982). Settlements above tunnels in the United Kindom—Their magnitudes and prediction. *Proc. Tunnelling '82 Symp*., London, 173–181.

Peck R.B. (1969). Deep excavation and tunnelling in soft ground. State-of-the-art-report, Mexico City, State of the Art Volume, *Proc. 7th Int. Conf. on Soil Mechanics and Foundation Engineering*, 225–290.

Schanz T., Vermeer P.A. and Bonnier P.G. (1999). Formulation and verification of the Hardening—Soil model. *Proc. Plaxis Symp. on Beyond 2000 in Computational Geotechnics*, Amsterdam, 281–296.

Wongsaroy J. (2005). Three-dimensional finite elements analysis of short- and long-term ground response to open face tunnelling in stiff clay. PhD Thesis, Cambridge University.

Keiichi Fujita lecture

This page intentionally left blank

Geotechnical Aspects of Underground Construction in Soft Ground – Viggiani (ed)
© 2012 Taylor & Francis Group, London, ISBN 978-0-415-68367-8

TC204 proposal for 'Keiichi Fujita Lecture'

Following the death of Professor Fujita at the end of July 2010, our current TC204 chairman, Professor Richard Kastner, proposed the idea of introducing a prestigious lecture to be entitled the 'Keiichi Fujita Lecture'. The intention with the lecture was to recognise the enormous contribution made by Professor Fujita in setting up TC 28 (as it was then), taking on the responsibility of chairman and participating in many other roles, both technical and organisational.

The proposal is that the lecture be given at future TC204 International Symposia which have been held every three years since Prof Fujita set up TC28. A suitably deserving and distinguished speaker would be chosen by current members of TC204 following nominations from within the group.

Given below is a tribute to Professor Fujita, prepared by former TC28 chairman, Professor Robert Mair. Within this tribute the proposal to set up a prestigious lecture in honour of Prof Fujita is also described. This tribute and the proposal were sent to all members of TC204 for comment. Only very positive responses were received. The tribute was read by Professor Hirokazu Akagi at the remembrance service for Prof Fujita, held on 8th September 2010 along with condolences on behalf of members of TC204.

Professor Richard Kastner (Chairman TC204)
Dr Jamie Standing (Secretary TC204)

This page intentionally left blank

Geotechnical Aspects of Underground Construction in Soft Ground – Viggiani (ed)
© 2012 Taylor & Francis Group, London, ISBN 978-0-415-68367-8

Tribute to Professor Keiichi Fujita by ISSMGE Technical Committee 204 (formerly TC28) on Underground Construction in Soft Ground

All members of TC 204 are very saddened to learn of the passing away of Professor Keiichi Fujita on 31st July 2010. He was a very distinguished engineer who achieved an enormous amount in his very active and highly successful career. He was not only an expert on tunnelling and deep excavations, but also on piled foundations and many other aspects of geotechnical engineering. He was the author of many State-of-the-Art reports and delivered many Keynote Lectures at ISSMGE conferences. Much has been achieved by ISSMGE's Technical Committee 204 on Underground Construction in Soft Ground (formerly TC28) and this is in large part due to the inspirational leadership of Professor Fujita. In 1994, under his leadership as Chairman, Professor K. Fujita organized a one-day International Symposium in New Delhi—just before the 13th ICSMGE. This was an outstanding success, bringing together specialists in underground construction from many countries.

Following the success of Professor Fujita's initiative, it was decided to initiate a series of two-day International Symposia on Geotechnical Aspects of Underground Construction in Soft Ground, with a third day devoted to technical site visits to underground construction projects. These International Symposia have been held every three years over the past 10 years as follows: 1996 London, 1999 Tokyo, 2002 Toulouse, 2005 Amsterdam, 2008 Shanghai

For each of these International Symposia there has been a wealth of information published in the Proceedings, with many hundreds of papers published on a wide variety of underground construction topics of major technical interest, mainly on case histories and new research. Professor Fujita was the inspiration for these highly successful International Symposia, and we all owe him a great debt of gratitude.

At the next International Symposium in May 2011 to be held in Rome, we will fondly remember Professor Fujita as the father of TC28 and a great inspiration to us all. It will be proposed that a prestigious lecture in memory of Professor Fujita, to be named the **'Keiichi Fujita Lecture'**, will be delivered at each subsequent International Symposium on Geotechnical Aspects of Underground Construction in Soft Ground. The 'Keiichi Fujita Lecture' will be a lasting tribute to Professor Fujita's remarkable contributions.

Professor Fujita's wisdom and experience, combined with extraordinary energy and a great sense of humour, will be sorely missed. We extend our heartfelt condolences to Mrs Fujita and her family.

Professor Robert Mair
Professor Hirokazu Akagi

This page intentionally left blank

Session reports

This page intentionally left blank

Geotechnical Aspects of Underground Construction in Soft Ground – Viggiani (ed)
© 2012 Taylor & Francis Group, London, ISBN 978-0-415-68367-8

Construction, design and measured performance of bored tunnels

C.O. Menkiti
Geotechnical Consulting Group, London, UK

ABSTRACT: This report reviews 24 papers submitted to the Symposium under Session TS1: Construction, Design and Measured Performance of Bored Tunnels. The papers are reviewed in three groups: Design (and Analysis), Construction and Measured Performance.

1 INTRODUCTION

The realization of any tunnelling project involves at least four phases:

- Feasibility studies,
- Design (and analysis)
- Construction
- Maintenance over the asset life span.

This General Report focuses on design and analysis, construction and measured performance. Measured performance or monitoring is important for several reasons. Monitoring is important for validation of the design assumptions, for control of construction processes and quality, for mitigation of risk to nearby infrastructure and people, for optimization of the construction process (speed and cost) and following construction for the management of the tunnel asset through the remainder of its life cycle.

A total of 24 papers from 10 countries were submitted under Session TS1: Construction Design and Measured Performance of Bored Tunnels. The breakdown of the papers is given in Table 1. Included is a count of whether the papers present information on collapses, because it is often when failures occur that we learn the most.

This General Report is divided into three sections covering; Design and Analysis (Section 2), Construction (Section 3) and Monitored Performance (Section 4). Conclusions are given in Section 5. The purpose of the General Report is to give a broad overview of the papers within the subject area. The intention is to provide the reader with an outline of the information presented in this session and to guide them efficiently to the papers of specific interest to them, which can then be consulted for more detailed information. A brief critique of the papers is also presented.

Table 1. Summary of presented papers.

Theme	No. of papers	Case history?	Information about collapse?
Design & analysis	7	6	2
Construction	10	10	3
Measured performance	7	6	0

2 DESIGN AND ANALYSIS

2.1 *General*

Arroyo et al: Design of jet grouting for tunnel waterproofing. This paper presents a case history from Barcelona. A new high speed rail tunnel was excavated in quaternary deposits, dominated by paleochannels of water bearing sands and gravel. The high speed rail tunnel was constructed at depths of 6–25 m and passed beneath the still active existing railway lines. Ground water level was at 10–15 m below ground level. Jet grouting was used to mitigate the danger of sudden collapse and inundation, which was the primary risk. (Settlement, if slow, could be tolerated due to an active ballast maintenance programme.) Several jet configurations are considered. The paper focuses on sub-horizontal single fluid pipe canopy and floor slabs configurations, used where vertical access was not available. Details of field trials and other design tools used to successfully construct the tunnel are given in the paper. Figure 1 shows the probabilistic assessment used to verify the continuity of the jet grout canopy—a key design requirement.

Bilotta & Russo: Back-calculation of internal forces in the segmental lining of a tunnel. The authors provide good information on the strains and loads in segmental lined tunnels from production to tunnel construction. The aim of the paper is to better inform the design process. Naples Line 1 tunnels were instrumented (6.75 m dia EPB; wedge block lining with water proof gaskets).

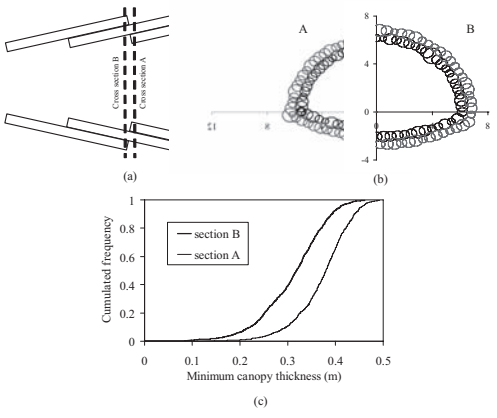

Figure 1. Probabilistic analysis of the continuity of tunnel canopy (a. longitudinal section; b. example of cross section simulation; c. cumulated frequency distributions of the minimum thickness of the canopy)—from Arroyo et al.

Tunnel segments were instrumented with VW strain gauges to measure bending and axial load in transverse & longitudinal directions. Ground conditions comprised sands below the water table. The tunnel depth at the monitoring sections was 14–19.5 m. The obtained results show load development during ring build and shove, as the instrumented ring and subsequent rings are built (Fig. 2).

Boldini et al: Modelling a deep tunnel in a low-porosity tectonised clay. For tunnels in clay soils, undrained behaviour is usually assumed during construction. In deep tunnels in clay soils, stress relief induces a large plastic zone around the tunnel within which pore water pressures may reduce to large negative values. In pervasively fissured, very stiff scaly clays, the actual behaviour may be different—because fissures could open up on unloading and saturation may be lost. The authors have developed four different models, representing a range of feasible pore pressure responses, and use these to study this phenomenon in the short and long term after pore pressure dissipation/equalization (Fig. 3). Their study is made with reference to the Raticosa tunnel. Boldini and co-authors conclude that the various models have little impact on the predicted lining load.

Sapigni et al: High resolution multi channel seismic survey for the excavation of the new headrace tunnel for Crevola Toce II hydropower scheme. The paper reports seismic refraction & reflection surveys that were conducted through gneiss and interlayered metasediments. These investigations were augmented with downhole seismic tests to 400 m depth. The authors state that interpretation of the collated information allowed improved geological

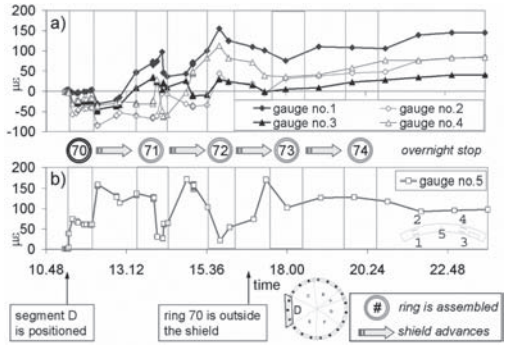

Figure 2. Typical strains measured during installation: a) circumferential; b) longitudinal (Bilotta & Russo).

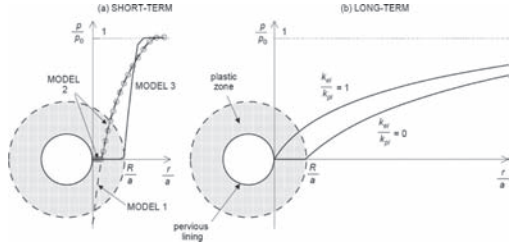

Figure 3. Possible schemes of pore-pressure distribution for short (a) and long-term situation (b). "a" is the tunnel radius, R the plastic radius and p_0 the undisturbed in situ pore pressure (Boldini et al).

modelling. The authors also argue that this information can inform feasibility studies of various tunnel alignments to allow the avoid weak zones.

Bezuijen et al: A comparison of analytical and numerical models. The authors highlight that bentonite and grout flow around a TBM shield affect the settlement trough. Yet, most settlement models assume that the soil is in contact with the shield. Bezuijen and co-workers argue that numerical models that ignore the bentonite/grout layer may therefore over prediction of settlement. To investigate this phenomenon, 1D and 3D models developed by the authors are described and their results compared. On this basis, Bezuijen et al conclude that flow of process fluids around the TBM has a significant effect on volume loss, but only for cases where volume loss is already relatively low (i.e. <1%).

Perazzelli et al: *Analysis of convergence data and 3D numerical modelling in fine-grained soils*. These authors present data for Santa Maria Twin tunnels in Calabria, constructed using sequential excavation and support with sprayed concrete lining (the variant often referred to as the traditional "Italian Method"). the tunnel face area was 120–180 m^2 at depths up to 120 m. The ground was alternating layers of silty clay,

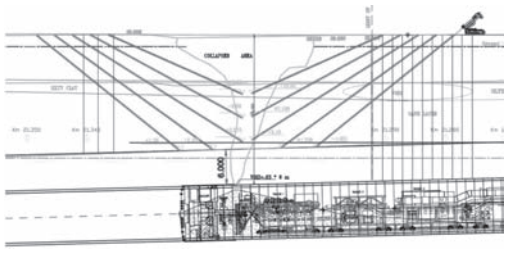

Figure 4. Compaction grouting above the collapse area—longitudinal section (Patrizi).

sand and silt. Presented ground water information is limited. Convergence measurements were analysed using "closure analysis". This technique attempts to relate tunnel lining displacement to the distance from face and to time. Comparisons were made to FLAC 3D analyses results to give an insight into the tunnel behaviour during construction.

P. Patrizi: *The Line 3 of the Metro of Cairo*. This paper presents a useful case history example located in the alluvial flood plain of the River Nile. Ground conditions comprised variable fill over layers of sands, alternating with clay and gravel. Ground water is 2–20 m bgl. Diaphragm wall station boxes were constructed first, before slurry TBM passage (9.15 m o.d.). A grout plug was used to seal the base of boxes before excavation, and the seal was verified by pumping tests. In Phase 1 of the project, a collapse occurred on 3/9/2009. A sinkhole extended to the surface and the TBM was flooded and buried (Fig. 4). The recovery of the TBM after the collapse is described. Recovery was by primarily by ground freezing (brine, 4 weeks for ice wall closure). Many other interesting details of the project are also given in the paper.

2.2 *Conclusions reached—design & analysis*

The papers reviewed under the Design and Analysis section have brought out a few key points. The pore pressures response of stiff highly fissured clays is complex—but is beginning to be better understood. It is likely that the lining loads of a segmental lined tunnel would vary over a wide range simply due to small variations in ring build. Bentonite and grout flow around the TBM shield is now better understood. Some good case histories are provided.

3 CONSTRUCTION

3.1 *General*

Pelizza et al: Back-fill grout with two-component mix in EPB tunnelling to minimise surface settlements: *Rome Metro—Line C case history*. The authors list the functions of tailskin grouting as; void filling to minimise settlement, locking the segmental lining into place to resist loads from self weight, TBM thrust and TBM back-up train, ensuring uniform contact between the ring and the surrounding ground, avoiding puncture loads and complimenting the tunnel waterproofing system. To achieve these, clear design criteria must be met. The two component mix is essentially a super fluid mortar, stabilised so that it can survive the period from batching to injection. At the injection point, an accelerator admixture is introduced so that the grout gels a few seconds afterwards. The authors describe the experience of using the two component mix at Rome Metro C, where four EPM machines of 6.71 m excavation diameter were used in variable ground conditions. The mix utilised is reported to comprised 700–820 kg of water with 30–60 kg of bentonite, 310–350 kg of cement 3–7 litres of retarding agent, and 50–100 litres of accelerator. The quality and continuity of the grout backfill was verified by quality testing, which included in-tunnel coring and geophysical surveys.

Spagnoli et al and Thewes et al: examine the problem of EBP TBM conditioning in various ground conditions, as it relates to optimization of TBM performance. Spagnoli and co-workers consider the clogging in high PI clays. They examine the mineralogy and electro-chemistry of four soils prone to clogging. These workers use a cone pull-out test and other laboratory tests to measure adherence and thus to assess the potential for clogging. The authors describe a new "Clogging Test System" (CloggTS) which they argue mimics some aspects of the material cutting and handling in a TBM. Thewes et al examine foam conditioning for sandy soils. They describe the background and previous work on assessing foam injections for EPB-TBMs. The authors then report on the experimental investigation of foam generation and soil-foam mixtures. Thewes and co-researchers find a dependence of foam quality on the size of the foam gun and conclude that industrial size foam generators are needed in laboratory investigations in order to replicate site conditions.

Oteo et al: A new tunnel bored in alluvial soft soil under Malaga Airport. An extension of Malaga Airport required the diversion of a rail line below the River Guadalhorce. The paper describes the construction of this diversion tunnel. Construction was by EPB machine and cut and cover methods. Large deformations occurred at the start of the project and this served as an early warning, triggering additional ground investigations and an augmented design. The encountered ground conditions were mixed, comprising quaternary sands, gravels and clays. Various ground improvement applications

were utilised, and these are described in the paper. With these ground improvements, settlements were better controlled (up to 50 mm) as compared the case without treatment (50–200 mm, see Fig. 5).

Santoro: The effects of anisotropy and of inhomogeneity of stress state on the lining of road tunnel in a Flysch formation. The author describes an 80 m^2 tunnel constructed with SCL using the sequential excavation method colloquially known as the "Italian traditional method". The tunnel was in Fortore, Campbasso, Italy. The tectonised ground generated "squeezing" conditions and large settlement of the top heading. This necessitated the use of micropiles and novel ground anchors (referred to as "TFEG"). FE analyses were used to better understand the tunnel-ground response—particularly for sections near a slope which were subject to an initially anisotropic stress conditions.

Romani et al: *Deep excavation of Malatesta Station in Rome: design, construction and mitigation measures.* This paper presents a good case history. The ground conditions comprised made ground and alluvium over fluvially sedimented pyroclastics. The pyroclastics (Tuff) had the consistency of a fine to granular soil with some cementation. The station was constructed top-down in diaphragm wall supported boxes. The walls extended significantly below final excavation level in order to cut-off ground water flow. Therefore internal dewatering was all that was needed to aid construction. Design was supported by 3D FE analysis and monitoring was used to verify the design and allow optimization. Temperature correction of monitoring results was found to be an important factor. Figure 6 presents a summary of the measured ground movements.

Quick et al & Pigorini et al discuss the rehabilitation of existing tunnel. Quick and co-workers present the case of two adjacent railway tunnels beneath the historic city of Mainz, at a depth of 26 m. The tunnels were in clay silt and marl, with

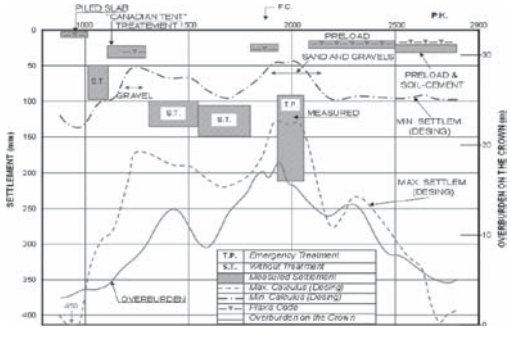

Figure 5. Comparison of subsidence—predicted and measured (Oteo et al).

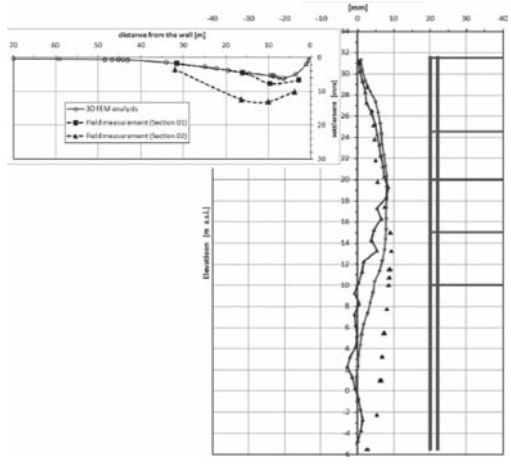

Figure 6. Predicted and monitored ground surface settlements and horizontal wall movement (Romani et al).

the water table at or below invert level. Various in-tunnel measures and surface grouting were undertaken to minimise settlement and the effect on buildings (see Fig. 7). Measured settlements were up to 100 mm.

Pigorini et al present the re-profiling of the Cassia-Monte Mario railway (8.8 m i.d.). The tunnel was under the water table, at depths of up to 76 m. There was a need to demolish and reconstruct the invert. An earlier attempt in 2004 had led to a serious breech and flooding of tunnel. A revised approach using ground freezing was adopted (target temp −10°C). Field trials and numerical analyses were used to support the design. The construction sequence meant that some freeze pipes would be cut through during the excavation and support work (Fig. 8). The ground was frozen for 45 days, then the freeze pipes were cut and excavation carried out before excessive thawing occurred (Fig. 9). Further useful information can be found in the paper.

Croce et al and Quick et al present more case histories of tunnels construction in difficult sites. Croce and his colleagues describe the construction of a sewer in difficult ground with shallow cover, beneath existing buildings and utilities. Quick et al present the construction of the rescue tunnel for the Brenner Base Tunnel. The rescue tunnel provided geological and monitoring information and dewatering access, in advance of the construction of the main tunnels.

3.2 *Conclusions reached—construction*

The papers examined in the Construction section raise several useful points which are now summarised.

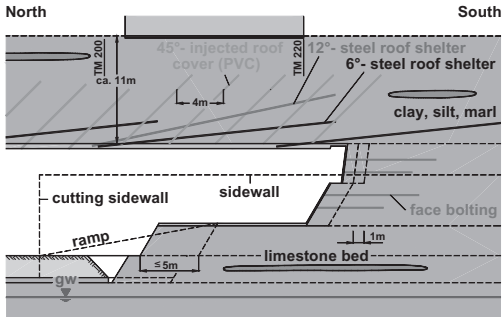

Figure 7. Undercrossing of a hotel; driving concept and securing measures (Quick et al, quoting Steiger et al. 1999).

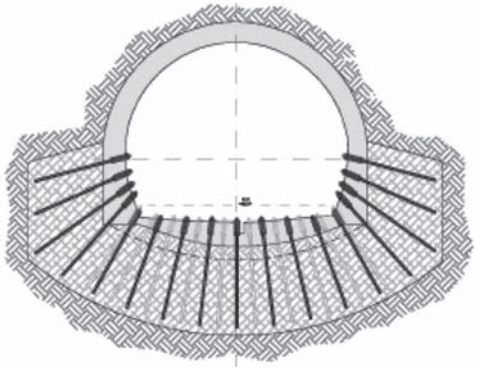

Figure 8. Freeze pile layout and tunnel cross-section. (Pigorini et al).

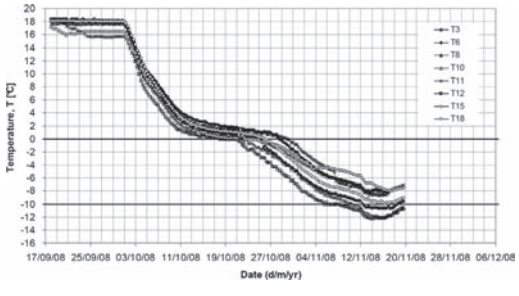

Figure 9. Variation of temperature with time during ground freezing. Data from intermediate sensors at the side walls in section n° 1 (Pigorini et al).

Many useful case histories are described highlighting good practice but also problems and challenges. A large range of ground treatment solutions are presented. Useful developments in EPM conditioning and testing are also described.

4 MEASURED PERFORMANCE

4.1 *General*

Measured performance of tunnelling works is usually obtained by monitoring. For the reasons given in Section 1, monitoring is required both during and after construction. Increasingly, monitoring is also undertaken long after construction, in aged tunnels, to assist asset management and maintenance. This section of the General report considers monitoring through all stages of the tunnel asset lifecycle.

Soga et al and Vanicek et al: draw on recent advances in technology to effectively monitor the condition of ageing metro infrastructure in London, Prague and Barcelona. The new technologies they harness are; Micro-Electro-Mechanical Systems (MEMS), Wireless Sensor Networks (WSN), laser scanning and computer vision. The monitoring systems they have developed involve a two-tier approach; (i) mico-detection of defects using computer vision, and (ii) micro-monitoring and communications using MEMS and WSN technologies. The authors claim that these technologies are potentially low-cost. They therefore allow the possibility of reducing maintenance costs of "end-of-life" structures (such as aged tunnels). An example of a MEMS sensor is shown in Figure 10.

Figure 11 shows deployment of MEMS sensors and WSN communications in a tunnel. Much useful detail is given in both papers.

Sagong et al: Application of the image & laser sensors based tunnel scanning system. These authors highlight that old tunnelling are traditionally managed through labour intensive tunnel inspections. They present a new "opto-laser" monitoring system that incorporates two 2 components—a bank of cameras which capture surface defects that are

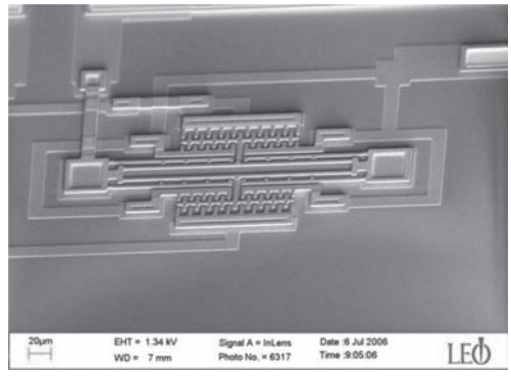

Figure 10. Double-ended tuning fork (DETF) parallel-plate resonators, e.g. as used for crackmeter devices (Soga et al).

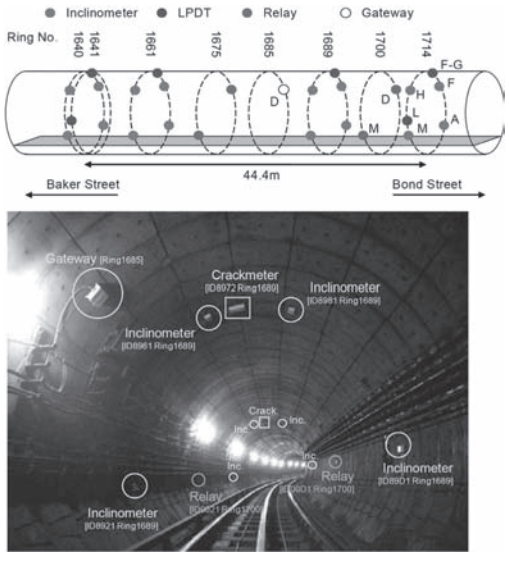

Figure 11. WSN in London underground tunnel (Soga et al).

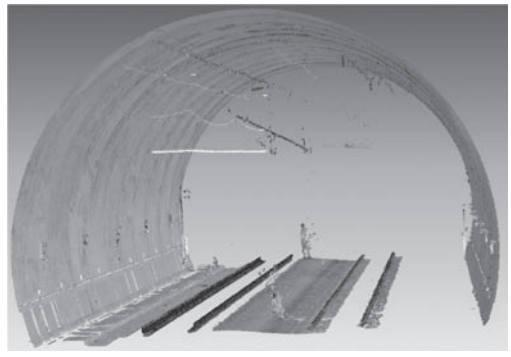

Figure 12. Laser scanning data set after digital filtering (Sagong et al).

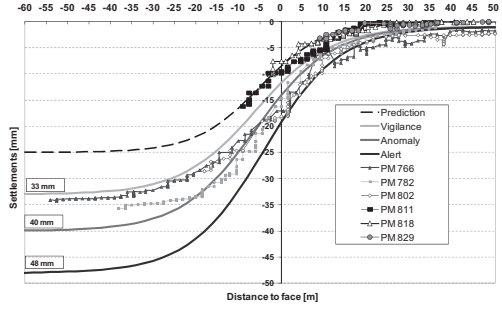

Figure 13. Example of tunnelling process adaptation to settlements predictions (Janin et al).

then automatically identified by computer, and a bank of spot lasers that scan the tunnel intrados to give 3-D geometric and radiometric representations. Radiometric representations provide information on surface characteristics such as wetness, surface cracks, etc. Useful information on the details and capabilities of this system, together with the interpretation processes are presented in the paper. An example of a laser representation from a laser scan is shown in Figure 12.

Janin et al: Settlement monitoring and tunnelling process adaptation—case of south Toulon Tunnel. These authors describe an observational method tunnelling case history. Settlements were controlled by adjusting lining support measures in direct response to the observed settlements and settlement trends. Adjusted support measures included; (i) modification of face bolting detail, modification of umbrella pipe arch details, and (iii) further sub-division and sequential excavation of the tunnel face. An analytical equation was derived for the evolution of surface settlement at a point, as the tunnel approached and passes. This profile of predicted settlement was then used as a basis to adjust the tunnel support measures in order to keep the observed settlements within prescribed thresholds (see Fig. 13).

De Santos et al: Back-analysis of measured movements in ageing tunnels. Other papers in this session (Soga et al & Vanicek et al) have dealt with improved monitoring of ageing tunnels. De Santos and co-workers build on this work to develop a method of using such data in back-analyses to derive critical parameters for the ageing tunnel. The variables monitored in ageing tunnels are typically displacements such as opening of cracks, joint rotations, etc. De Santos et al argue that such data could be used as input information to assess or infer the loads on the lining and thus the reason(s) for damage to the ageing tunnel. This is the reverse of normal analysis/assessment where you start with forces and stiffnesses and calculate displacements. For a set of measured displacements, several solutions are feasible. Optimisation techniques are therefore used by the authors to find the most likely answer. The method was illustrated using a section of the Jubilee Line tunnel in London containing rings with domed segment joints (Fig. 14). The earth pressure at rest (K_o) and the joint stiffness were inferred from the measured displacements by this technique (Fig. 15).

Sorge et al, and *Gilby & Socol* present papers on monitoring systems for new tunnels. Sorge and his fellow workers discuss the monitoring for Metro Line C in Rome. Some 933 instrument groups were needed, with about 20,000 devices and 23 km of

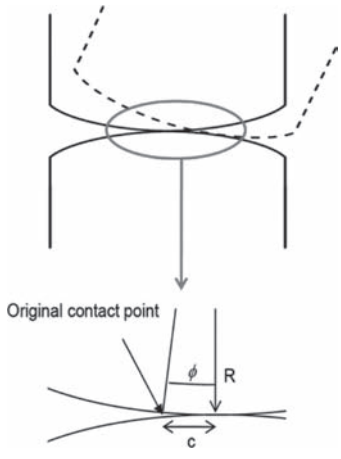

Figure 14. Rotation between two segments in tunnel ring that was assessed by De Santos et al.

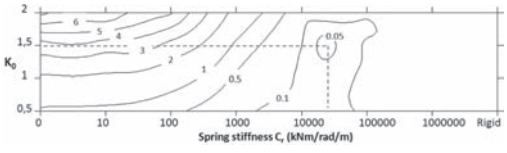

Figure 15. Optimisation of the objective function F (Cr, K_0, De Santos et al).

cables. Monitoring had to provide complete, reliable and prompt information, while minimising the risk of human error and allowing flexibility. Gilby & Socol discuss a web based platform (GECMS) for managing construction and monitoring data. A different platform for geotechnical interpretation is also discussed.

4.2 *Conclusions reached—measured performance*

Automated and semi automated systems are now available to monitor new and ageing assets (e.g. for London Underground some assets are up to150 yrs old). Very large amounts of data are now routinely generated with monitoring (e.g. laser range finder scans tunnel lings at a frequency of 200,000 readings per second). Interpretation, searching and locating critical information are problems that are likely to have increasing importance in the future. Several good case histories also provided.

5 OVERALL CONCLUSIONS

There have been many recent developments in tunnel design and analysis, tunnel construction and measured performance. The key trend drivers appear to be:

- Pressures associated with economic and safe management of ageing infrastructure;
- Cost pressures (project construction costs and whole-life-cycle costs);
- Programme pressures (faster delivery);
- Technological advances, and
- Increasing public and client expectations.

There has been marked improvement in:

- Monitoring and data management capabilities. Is there a risk of data overload?
- The speed of data acquisition and the ability to respond to the observed measurements has increased substantially and is now in the order of minutes. Is this a new era of the application of the Observational Method?
- Use of numerical modelling, particularly 3D modelling is growing. Is this matched with growth in the availability of competent analysts and comparable high quality ground investigation data?

REFERENCES

Arroyo M., Gens A. and Croce P. and Modoni G. Design of jet-grouting for tunnel waterproofing.

Bezuijen A., Nagel F. and Meschke G. Flow around a TBM: A Comparison of analytical and numerical models.

Bilotta E. and Russo G. Backcalculation of internal forces in the segmental lining of a tunnel: the experience of Line 1 in Naples.

Boldini D. and Graziani A. Modelling a deep tunnel excavation in a low-porosity tectonised clay.

Croce P., Di Maio S., Speciale G. and Cassibba L. Design and construction of a sewer tunnel in difficult site conditions.

de Santos C., Ledesma A. and Gens A. Backanalysis of measured movements in ageing tunnels.

Gilby J. L and Socol M. Geotechnical Instrumentation Data Management.

Janin J.P., Daniel D., Kastner R., Emeriault F., Guilloux A. and Lebissonnais H. Settlement monitoring and tunnelling process adaptation—case of South Toulon Tunnel.

Oteo C.S., García Pérez J., Moreno H., de La Fuente P. and Escobar J.O. A new tunnel bored in alluvial soft soil under the Malaga Airport.

Patrizi P. The Line 3 of the Metro of Cairo.

Pelizza S., Peila D., Sorge R. and Cignitti F. Back-fill grout with two component mix in EPB tunnelling to minimize surface settlements: Rome Metro—Line C case history.

Perazzelli P., Rotonda T., Boldini D., Ajmone-Cat A.M. and Gianvecchio P.M. Analysis of convergence data and 3D numerical modelling of tunnels excavated in fine-grained soils.

Pigorini A., Sciotti A., Zoppo G. and Calabresi G. Prediction and performance of a ground freezing application to the rehabilitation works of an existing tunnel.

Quick H., Michael J., Bergmeister K., Facchin E. and Facchin E. Aicha-Mauls on the Brenner Base Tunnel—status of the works and results.

Quick H., Michael J., Meissner S. and Arslan U. Two adjacent railway tunnels underneath the historic city of Mainz.

Romani E., Sorge R., Guiducci G., Lucarelli A. and Furlani G. Deep excavation of Malatesta Station in Rome: design, construction and measures.

Sagong M., Koh T.H., Chun B.S., Lee B.H. and Byun Y.S. Application of the image and laser sensors based tunnel scanning system.

Santoro V.M. The effects of anisotropy and of unhomogeneity of stress state on the lining of road tunnel in a Flysch formation.

Sapigni M., Baldi A.M., Bianchi F. and De Luca J. High-resolution multichannel seismic survey for the excavation of the new headrace tunnel for the Crevola Toce III hydropower scheme in the Ossola Valley, Italy.

Soga K., Ledesma A., Roncaglia A. and Vaníček I. Micro-measurement and monitoring system for ageing underground infrastructure (UndergroundM3).

Sorge R., Moretti S., and Tripoli O. Line C in Rome: remote monitoring system.

Spagnoli G., Feinendegen M., Ernst R. and Weh M. Manipulations of the sticky clays regarding EPB tunnel driving.

Steiger, H., Theissen-Wenzel, C., Quick, H. 1999. *Neuer Mainzer Tunnel—Behandlung geotechnischer Grenzfälle in der Planung und Ausführung*—Vorträge zum 6. Darmstädter Geotechnik-Kolloquium, Darmstadt, 11. März 1999, Mitteilungen des Institutes und der Versuchsanstalt für Geotechnik der Technischen Universität Darmstadt, Heft Nr. 44.

Symposium Papers Reviewed in this Report.

Thewes M., Budach C. and Bezuijen A. Foam Conditioning in EPB Tunnelling.

Vaníček M., S. Chamra, D. Jirásko, J. Macháček, Vaníček I., Záleský J., Hada A., Chaiyasarn K. and Soga K. Methods of monitoring of metro lining in Prague.

Geotechnical Aspects of Underground Construction in Soft Ground – Viggiani (ed)

Numerical and physical modelling of tunnels and deep excavations

S.W. Jacobsz
University of Pretoria, Pretoria, South Africa

ABSTRACT: This paper presents an overview of the papers submitted for the session on numerical and physical modelling of tunnels and deep excavations, submitted for the proceedings of the Fifth International Symposium on Geotechnical Aspects of Underground Construction in Soft Ground, held from 16 to 18 May 2011 in Rome.

1 INTRODUCTION

A total of 26 papers were submitted for the session on numerical and physical modelling of tunnels and deep excavations. The subjects covered, affiliation of authors and methods of investigation followed by the various researchers are presented in this paper. This is followed by a review of the individual papers submitted, after which the papers selected for presentation at the symposium are reviewed.

1.1 *Aspects covered*

Aspects covered by the papers in this session are summarised in Table 1 below, indicating the number of papers received covering the subjects listed. Aspects related to tunnelling were the most common topic, followed by aspects of excavations, subsidence of buildings and others.

1.2 *Affiliations of authors*

Papers were received both from academics and practitioners, with a total of 18 papers received from academics, 6 produced by academics and practitioners working together and 2 papers by practitioners only. The reason for the relatively small number of practitioners taking part in this session is probably related to the theoretical nature of this session, i.e. numerical and physical modelling, which appears to be most at home in an academic environment.

The authors are from 14 countries, mostly located in Asia and Europe. The following countries are represented: Australia, China, France, India, Iran, Italy, Japan, Korea, Malaysia, the Netherlands, Portugal, Switzerland, Taiwan and the United Kingdom.

1.3 *Investigative approach*

The methods applied by the authors to investigate the problems forming the subjects of their papers are summarised in Table 2 below.

Interestingly, most papers were based on work carried out using numerical modelling, with fewer papers discussing physical modelling. The reason is likely to be attributable to an abundance of software packages now available for the analysis of geotechnical problems. Four papers presented the results from mathematical or closed form solutions.

Four of the papers on physical modelling were based on the results of 1G modelling, with only

Table 1. Aspects covered by papers.

Topic	Number of papers
Excavations	5
Grouting	2
Materials	2
Pipe jacking	1
Subsidence of buildings	3
Various aspects of tunnelling	13

Table 2. Investigative approached adopted by authors.

Method	Number of papers
Numerical modelling	13
Mathematical or closed for solutions	4
Physical modelling at 1G	4
Physical modelling in the centrifuge	2
Both numerical and physical modelling	3
Literature review	1

two papers presenting the results of centrifuge modelling. It is the opinion of the session reviewer that the authors of papers which are based on 1G modelling should indicate how the results from their models can be extrapolated to the prototype scale without attempting to replicate the stress distribution in the prototype.

2 OVERVIEW OF INDIVIDUAL PAPERS

In this section an overview of the various papers contained in the session on numerical and physical modelling of tunnels and deep excavations is presented. The papers are grouped according to the topics which they discuss as listed in Table 1.

The discussion of each paper focuses briefly on the problem investigated, the approach followed to investigate the problem, followed by a short summary of the most important findings. Readers are referred to the individual papers for detail.

2.1 *Papers on excavations*

2.1.1 *An investigation into inclined struts method as type of shoring by Fakher & Sadeghian*

The authors reported that limited information was available in the literature regarding the use of inclined struts to support buildings adjacent to open excavations. The bottom end of the strut was located in the excavation, supporting the building at the edge of the excavation. Different strut geometries were investigated.

The problem was investigated by means of a three dimensional finite difference analysis and followed on earlier two dimensional work by the authors. The struts were modelled as beams and the soil as a linear elastic—perfectly plastic material obeying a Mohr-Coulomb failure criterion.

It was found that the building displacements were dependant on the sequence of excavation. The best performance in terms of displacements was achieved when the excavation was carried out, leaving some material behind, then installing the strut and then removing the material left behind.

2.1.2 *Understanding ground deformation mechanisms during multi-propped excavation in soft clay by Lam, Haigh & Bolton*

The authors investigated the performance of a propped excavation in slightly over-consolidated clay. They examined the effects of wall stiffness, the effect of the depth to the stiff stratum and the effect of toe fixity conditions.

The problem was investigated by means of a sophisticated centrifuge model in which the construction of a multi-propped retaining wall could be modelled. Pore pressures, ground settlements and wall deflections were monitored. Instrumentation used comprised LVDTs and PIV.

The maximum wall displacement was found to be a non-linear function of the wall stiffness. It was observed that stiffening of the wall was not the most economical method for the reduction of wall movements. The fixity at the base of the wall was found to have a very significant effect on the control of wall movement below the final excavation level. Control of toe movement of the wall was reported to be important to limit adjacent soil deformation.

2.1.3 *Water table lowering effects on excavations by Raposo & Topa Gomes*

This paper investigates the effect of how the lowering of the water table in the residual granites in Porto, Portugal was modelled on the predicted behaviour of the excavation. Lowering of the water table results in an increase in the strength and stiffness of the soil and is common practice in Porto.

The problem was investigated by means of numerical modelling in which the lowering of the water table was modelled by different means. Wall bending moments, wall displacements and surface displacements were examined.

The consideration of non-saturated conditions resulted in reduced bending moments, wall deflections and surface settlements. Realistic analysis of unsaturated conditions was found to be important, resulting in less conservative designs. The authors recommended *in situ* tests for the evaluation of the relationship between soil stiffness and suctions.

2.1.4 *3D finite element analysis of deep excavations with cross-walls by Rampello & Salvatori*

The effect of leaving cross-walls of different geometries supporting diaphragm walls was investigated in the soil profile of ancient Rome.

The work was carried out using finite element analyses and examined wall deflections and ground settlement behind the diaphragm walls. Different cross-wall spacings and lengths were investigated and results were compared with the results of 2D analyses. The walls were modelled using brick elements, the soil using a non-linear, elastic-plastic model (the Plaxis Hardening Model) and the wall-soil contact was modelled using interface elements.

It was found that cross-walls reduce wall deflections and ground settlements. For small cross-wall spacings, 2D and 3D results predicted similar deflections down to the excavation depth. It was however found that 2D analyses over-estimated deflections

below excavation depth and over-estimated soil settlement behind the wall. Large differences between 2D and 3D analyses were reported for large wall spacings.

2.1.5 *Effects of excavation procedure on the stability of diaphragm wall panels by L'Amante & Flora*

The paper investigated the effect of the position of the excavator carrying out the excavation of a diaphragm panel on the stability of the panel.

A case study was presented illustrating an excavation panel failure that occurred when the excavator was standing adjacent to the long side of the diaphragm wall. The case study was analysed using a 2D and 3D finite element parametric study using the Plaxis Hardening Soil Model.

It was found that the position of the machine can play a positive *or* negative roll on panel stability. It was found that it was generally more favourable for the excavator to be standing along short side of the panel.

2.2 *Papers on grouting*

2.2.1 *The efficiency of compensation grouting in sands by Soga, Bezuijen & Eisa*

The authors investigated effects of the following aspects on the compensation efficiency achieved during the grouting of sands:

- Water/cement ratio
- Bentonite content
- Injection rate

The work was carried out using parallel physical modelling at the Universities of Delft and Cambridge. Models were set up to measure grouting efficiency in fine saturated sand.

Reasonable agreement between the Cambridge and Delft results were reported. Efficiency was found to be correlated with sand density, with low densities yielding low efficiencies. Higher water/cement ratios also resulted in lower efficiencies and increasing bentonite content resulting in increased efficiency and less pressure filtration.

2.2.2 *Experimental and numerical study of grout injections in silty soils by Masini, Rampello, Viggiani & Soga*

This study investigated the efficiency of compensation grouting in silty soils.

The problem was investigated by means of physical modelling using an 850 mm circular tub containing 400 mm of silica flour into which grout was injected. The injection volumes, heave and pore pressure responses were measured. Numerical analyses were carried out to attempt replication of the physical model. For the purposes of the numerical model, the silt was modelled as a non-linear elastic-plastic model using the Plaxis Hardening Model and the grout was modelled as a non-porous linear elastic material modelling cavity expansion. Soil parameters were calibrated by comparison with triaxial test data.

Compensation efficiencies of well below unity were found and it was found that efficiencies reduced with time. The initial loss due to pressure filtration was, however, small. The numerical analysis could replicate stress changes and induced excess pore pressures outside the injection body relatively well. The authors reported that it is important to take large strains into account when modelling grout injections numerically.

2.3 *Modelling of materials*

2.3.1 *Analysis of excavation using a stress path dependent undrained soil model by Ou & Hsieh*

The development of a total stress constitutive model for excavations was presented. The model is a variation on the Duncan and Chang (1970) model and requires 6 parameters.

The authors presented the model and results, validating it against laboratory data and a case history. Because the model is a total stress model, it does not conform with the effective stress principle. Parameters therefore have to be determined empirically. The model and parameters must take stress path effects into account in order to be realistic. Advantages of such a model are that it is relatively simple, disregarding anisotropy, small strain behaviour, pore pressures etc. However, it is important that parameters must be obtained from stress paths comparable to what will be analysed.

2.3.2 *Review of Newtonian and non-Newtonian fluids behaviour in the context of grouts by Kazemian, Prasad & Huat*

This paper examined various rheological models for grouts. Rheological models describe the relationship between shear stress and shear rate of the material under consideration. These properties naturally change in cementitious grouts as hydration takes place.

A literature review was carried out and an overview of Newtonian and non-Newtonian fluids were presented looking at the behaviour of pseudo-plastic fluids, dilatant fluids, viscoplastic fluids and thixotropic fluids.

The authors mention that no single model is available that characterises the behaviour of cementitious grouts during all its phases of hydration. It is difficult to find a rheological model to characterise cement grout adequately, e.g. the Bingham model is also not exact.

2.4 *Paper on pipe jacking*

2.4.1 *Influence of overcut length on jack force and acting earth pressure during pipe jacking by Asanprakit, Sugimoto & Chen*

The effect of overcutting on jacking force required during pipe jacking was examined. The authors reported that most available models do not consider overcutting.

A 3D finite element pipe jack model was set up in which the soil was modelled as springs, the tunnel lining as shell elements and the lining-soil interface using a Mohr-Coulomb criterion.

It was reported that the model was adequate i.t.o. the predicted earth pressure acting on the pipe, the jacking force and the frictional resistance encountered. It was found that overcutting greatly influences loads on the jacked pipe and the jacking resistance.

2.5 *Subsidence of buildings*

2.5.1 *Assessment of building damage induced by excavation using plate analogy by Namazi & Mohamad*

A model for the prediction of damage to buildings caused by nearby excavations was presented. Most existing models are based on tensile strain, deflection ratio (ω) and the angular distortion (β) suffered by the building under consideration. It reported that in 3D, twist increases bending and diagonal strains, resulting in greater tensile strains.

In their model, the authors proposed that the building be modelled as a thick, uniformly loaded, rectangular plate. The model accounts for warping and twisting using Levinson elastic plate theory to calculate tensile strains. It does, however, not account for soil structure interaction.

It was reported that when the length/widht ratio exceeds 3, beam analogy is sufficiently accurate to model the building. It was recommended that the method be validation against case studies.

2.5.2 *The ground movement simulator: an interesting facility for the study of the behaviour of buildings submitted to ground subsidence by Caudron, Heib, Hor & Emeriault*

This study examined the effect of soil subsidence on overlying development (soil-structure interaction).

A 1G model study of subsidence under buildings using Fontainebleau sand was carried out. Stress levels were not modified. A model platform measuring 3 m × 2 m, comprising 48 retractable (250 × 250 mm) jacks when complete was described. Subsidence could be created at any location in the model by retracting the desired jack. Surface settlements were measured using stereo imagery. Buildings were modelled using a hollow "waffle" frame with lead powder. This was sized to posses the correct stiffness and exert the correct stress. A parametric study, looking at buildings at different locations w.r.t. the zone of subsidence, was carried out. Building behaviour was compared with the settlement of the greenfield.

The authors concluded that it is important that soil structure interaction be taken into account.

2.5.3 *Centrifuge modelling of the response of buildings to tunnelling by Farrel & Mair*

Modelling of building response due to tunnelling was the topic of this paper.

The problem was investigated using centrifuge modelling looking at soil structure interaction effects and examined both elastic and non-elastic buildings. Model buildings of various geometries and stiffnesses were investigated (using aluminium, micro concrete and masonry). The authors examined building settlement in relation to the greenfield settlement, the effect of building embedment on horizontal behaviour and the subsequent damage.

It was reported that buildings do not deform as the greenfield, with the greenfield response being modified both vertically and horizontally. The interaction depends on the relative building stiffness. It was found that negligible horizontal strains were transferred into model buildings even for buildings with extremely low horizontal stiffness. This could have implications for existing damage criteria which depend on tensile strains. It was reported that it is generally over-conservative to estimate damage based on greenfield settlement and horizontal distortions.

2.6 *Aspects of tunnelling*

2.6.1 *Tunnelling induced deformation of a masonry structure: a numerical approach by Amorosi, Boldini, de Felice & Malena*

This paper focuses on the prediction of damage to ancient structures due to underground construction.

A numerical model of tunnelling under a masonry structure was created. Initially, the free field was modelled to validate the model, after which the masonry structure was included. The soil was modelled as a linear elastic-perfectly plastic undrained material. The masonry model took the discrete nature of a brick wall into account and was based on a linear elastic-perfectly plastic model with anisotropic elasticity and strength.

It was found that the settlement trough was wider than predicted by a closed form solution at 0.7% volume loss. Better agreement was, however, reported at 2.3% volume loss. The presence of building

changes the greenfield deformations. Plastic strains were reported in the in masonry wall.

2.6.2 *Stability of cohesive-frictional soils with square underground openings by Yamamoto, Lyamin, Wilson, Abbo & Sloan*

The stability of twin square openings in plane strain conditions was investigated using rigorous upper and lower bound numerical limit analysis from plasticity theory. Results were compared with several rigid block upper bound mechanisms and a parametric study, examining different tunnel depths and tunnel spacings, was carried out. The soil was modelled as a drained Mohr-Coulomb material. (This is valid for soils obeying the associated flow rule).

Good correlations were reported between the upper bound and lower bound predictions for relatively shallow tunnel depths at close spacing and when the value of the effective friction angle (ϕ') was small. It was reported that upper bound mechanisms performed better for square openings than circular openings. Future work will include the refinement of an upper bound model giving realistic results for high ϕ' values and openings at larger spacings.

2.6.3 *Bearing capacity analysis of cohesive-frictional soil with dual circular tunnels by Yamamoto, Lyamin, Wilson, Abbo & Sloan*

This paper is similar to the paper discussed in Section 2.6.2 above, but investigated circular tunnels rather the square tunnels. As mentioned above, it was found that upper bound mechanisms performed better for square openings than circular openings.

2.6.4 *The dynamic behaviour of shield circular tunnels and surrounding granular soils during earthquakes by Hatambeigi, Pashang Pisheh & Pashang Pisheh*

The performance of a shield tunnel during an earthquake was investigated by means of a 2D dynamic numerical model. An 8 m diameter tunnel, centred at 12 m depth in medium dense sandy soil under a volume loss of 2% was modelled. A parametric study was carried out in which various soil and lining properties were varied. The soil was modelled as an elastic-plastic Mohr-Coulomb material and the lining as an elastic material. The model was first validated using a static analysis, after which the acceleration record of the 1940 El Centro earthquake was applied at the model base.

It was found that ground and tunnel deformation decreased with increasing soil and lining stiffness, cohesion and damping ratio. A stiffer lining resulted in larger lining forces.

2.6.5 *Face stability control for EPB tunnels in a non-homogeneous till formation with highly permeable layers by Graziani, Lembo-Fazio, Moccichino and Romualdi*

This paper examined the influence of muck permeability in a TBM head chamber on face stability.

The problem was investigated by means of a 3D finite difference modelling of a mixed face of till with a sandy layer in-between, representative of the situation in Vancouver. The conditioned soil in the head chamber and screw conveyor was explicitly modelled. The soil was modelled as a linear elastic-perfectly plastic material with a Mohr-Coulomb yield criterion. The tunnel excavation was first modelled without and then with the TBM in place. The conditioned soil properties and associated ground response, water pressure drawdown and minimum support pressures required to ensure face stability were investigated.

It was found that when the muck permeability was equal or less than the in situ permeability, drawdown effects associated with the tunnel excavation were avoided. It is important to control muck conditioning and the most important factor governing the soil response to tunnelling was found to be the permeability of the conditioned soil.

2.6.6 *Influence of leakage on tunnel behaviour in soft soils by Zhang, Huang & Fan*

The authors investigated the effects of tunnel leakage on tunnel settlement and lining moments over time by means of a small scale models in saturated sand at 1G. Both permeable and impermeable tunnels were modelled.

Tunnels with permeable tunnel linings were found to settle, while tunnels with impermeable tunnel linings were found to rise (float). Leakage resulted in differential settlement along the tunnel. Moments in the tunnel lining were reported to increase with time in the case of permeable tunnels, but remained constant for impermeable tunnels.

2.6.7 *Effect of soil stratification on pipe behaviour due to tunnelling-induced ground movements based on the displacement controlled method by Zhang, Huang, Zhang & Wang*

This paper investigated the effects of tunnelling near pipes in a anisotropic soil by means of numerical modelling. Results were compared to centrifuge data from Cambridge.

The numerical model incorporated stiffness anisotropy, but modelled the soil as linear elastic. Imposed greenfield soil movements were based on the model by Loganathan and Poulos (1998).

It was reported that good correlation was obtained between the centrifuge data and the

predictions from the proposed model for pipe settlement and bending moments in isotropic soil at small volume losses. Poorer correlation was, however, obtained when anisotropy was modelled. The authors concluded that the consideration of soil anisotropy is important when studying tunnelling under pipes.

2.6.8 *An analytical method to control the tunnel lining settlements by Garini*

The author proposed to use pre-stressed anchorages at points on a tunnel lining to reduce lining convergence under soil pressure. He then presented a structural analysis method to analyse the stability of the tunnel lining segments using virtual work principles. For the application of the method, the tunnel lining arch is subdivided into sub-arches, each with a span of less than 90°. The paper contains the mathematical background and the author reported that the method is suitable for applications in soft soils and shallow bored tunnels. The method can be applied in either force or displacement form.

2.6.9 *Interaction between tunnelling and bridge foundation—3D numerical investigation by Yoo & Wu*

This paper examined the effects of tunnelling under a pile-supported bridge that was studied by means of a 3D finite element model. The piles, pile caps and piers were modelled explicitly. A pile-soil interface was introduced which allowed slip. The soil was modelled using an elastic-plastic Mohr-Coulomb material with a non-associated flow rule.

It was found that the mobilised load on piles close to tunnel reduces due to downward movement relative to soil. Loads on piles further away were found to increase due to load redistribution in the bridge.

2.6.10 *Numerical analysis of precast tunnel segmental lining supported by full-scale experimental results by Cignitti, Sorge, Meda, Nerilli & Rinaldi*

The behaviour of precast tunnel segments under TBM jacking loads was investigated by means of numerical analysis and full-scale load tests on lining segments in the laboratory. The numerical model incorporated a non-linear fracture mechanics approach to model cracking in lining segments. The lining concrete and reinforcement steel, as well as the jacking shoes and teflon interface plates, were modelled explicitly. The numerical modelling first focussed on one segment and then a complete ring.

In the full-scale laboratory tests, single lining segments could be loaded up to 4000 kN per jacking shoe. First crack initiation and the subsequent development with increasing load were investigated.

Cracking was found to initiate between jacking shoes and not under them. It was reported that, at crack initiation, similar loads were predicted for single segments and completed rings. Good correlation between the numerical and physical trials were reported regarding the replication of crack onset.

3 PAPERS PRESENTED

The following three papers were selected for presentation at the symposium. It was the intention to invite presentations from a variety of topics, subject to the availability of authors attending the symposium to present their work.

3.1 *Numerical simulation of long-term twin-tunnel behaviour at St James's Park by Laver & Soga*

It was reported that long term settlements still occur at an unexpectedly high rate in St James's Park, London above the twin-tunnels of the Jubiliee Line Extension. This was attributed to creep or unexpected soil softening. The authors presented work modelling the long term performance of the twin-tunnels using coupled consolidation finite element analysis.

The effect of different soil and lining permeabilities on the long term consolidation above the tunnels was investigated and included a study of the effect of soil anisotropy. Also examined was the performance of a fissure softening model recently developed after observing softening on fissures in triaxial extension tests and softer than expected behaviour observed under torsional shearing in the hollow cylinder apparatus.

The authors reported that by adjusting the permeability of the soil and the lining, the deformation around tunnel could not quite be matched. Unexpectedly high permeability anisotropy values had to be applied at the tunnel crown, perhaps indicative of stress induced permeability changes.

It was reported that the fissure model developed gave a narrower settlement trough than conventional finite element models and this is more representative of field observations.

3.2 *Tunnelling in stratified soft ground: experimental study on 1g EPBS reduced scale model by Berthoz, Branque, Wong, Généreux, Subrin & Humbert*

The authors presented results obtained from reduced scale modelling of an Earth Pressure

Balanced Shield, tunneling in soft ground at 1G. Surface settlements and arching effects around the TBM were examined in homogeneous and stratified soils, paying particular attention to the influences of face pressure and the soil mass composition. Face collapse mechanisms in homogeneous pure frictional and frictional-cohesive materials, as well as stratified soils (two and three-layered soils), were also presented. In the stratified profiles, the frictional soil was located above the tunnel axis, with frictional-cohesive material below the tunnel axis. Similar failure mechanisms were observed in the homogeneous and stratified profiles, although failure tended to take place in stages in the case of a three-layered soil.

3.3 *Comparing the limit equilibrium method and the numerical stress analysis method of tunnel face stability assessment by Parazzelli & Anagnostou*

Two approaches for the evaluation of tunnel face stability of tunnel faces reinforced by bolts were investigated, i.e. a limit equilibrium method (Anagnostou & Serafeimidis, 2007) and a numerical stress analysis method. Comparative calculations were carried out modelling a dry cohesive-frictional soil using the finite difference code FLAC3D. The soil was modelled as an elastic—perfectly plastic material obeying the Mohr-Coulomb yield criterion.

The first results presented apply to an unreinforced tunnel face and compares the predicted tunnel support pressure. The influence of tunnel shape, in situ stress and dilatancy was investigated. It was found that the limit equilibrium method and the numerical stress analysis method provided results comparable with those from other analysis methods.

The reinforcing effect of the bolts was investigated in the second part of the paper. The numerical stress analysis method indicated that shear failure of the soil around the bolts controlled the bolt-soil interaction ahead of the face. This suggests that the bond strength (i.e. the resistance of the interface between grouted bolt and soil) used in the limit equilibrium analysis should account for the shear resistance of the ground and thus the normal stresses ahead of the face. A simplified procedure was presented by which this can be achieved.

4 CONCLUSIONS

A total of 26 papers have been received in the field of numerical and physical modelling of tunnels and deep excavations. The most popular topic was aspects of tunnelling, with a total of 13 papers received. This was followed by 5 papers on various aspects of excavation, 3 papers on the subsidence of buildings, 2 each on materials and grouting and 1 paper on pipe jacking.

In terms of modelling approaches, the most popular method was numerical modelling, followed by 1G modelling and mathematical and closed form solutions. Three papers were based on both physical and numerical modelling. Only 2 papers presented the results of centrifuge modelling. One paper comprised a literature review.

The majority of authors in this session were from an academic environment, with a relatively small number from industry.

A brief review of the individual papers are included above.

REFERENCES

Anagnostou, G., Serafeimidis, K. (2007). The dimensioning of tunnel face reinforcement. *ITA-AITES World Tunnel Congress* "Underground Space—the 4th Dimension of Metropolises", Prague.

Duncan, J.M. & Chang, C.Y. 1970. Nonlinear analysis of stress and strain in soils. *Journal of the Soil Mechanics and Foundations Division ASCE* 96(5): 637–659.

Loganathan, N., and Poulos, H.G. 1998. Analytical prediction for tunneling-induced ground movements in clays. *Journal of Geotechnical and geoenvironmental engineering,* ASCE, 124(9): 846–856.

This page intentionally left blank

Geotechnical Aspects of Underground Construction in Soft Ground – Viggiani (ed)
© 2012 Taylor & Francis Group, London, ISBN 978-0-415-68367-8

Construction, design and measured performance of deep excavations

J.R. Standing
Imperial College, London, UK

ABSTRACT: This paper presents an overview of the papers submitted for the session on Construction, Design and Measured Performance of Deep Excavations, submitted for the proceedings of the Seventh International Symposium on Geotechnical Aspects of Underground Construction in Soft Ground, held from 16 to 18 May 2011 in Rome.

1 OVERVIEW

There are 22 papers within this session with authors from twelve countries: Italy, Germany, Holland, China, Greece, India, Korea, Malaysia, Poland, Russia and the United Kingdom. Authors of four of the papers are from academia, nine from industry and nine from a healthy mixture of both.

The papers have been broadly divided into four groups, although there is inevitably some overlap between groups. The first covers case studies with monitoring data and information on the design and construction of deep excavations. The second group relates to the study of deep excavations by numerical analyses. Several of the papers discuss issues concerning seepage, leakages and/or dewatering and these have been placed in a third group. The fourth group includes papers that describe ground improvement methods or new technologies for facilitating deep excavations.

2 DEEP EXCAVATION CASE STUDIES

In all deep excavation works it is necessary to estimate and try to control deformations, especially in the urban environment where existing structures and infrastructure need to be protected. Monitoring plays a key role in checking the expected outcomes from design and analysis, modifying these and ultimately checking and controlling the construction processes to minimise deformations.

All of the papers within this first grouping mention the monitoring that was performed and usually give some quantification of the displacements that were observed during the works.

The first paper considered, by Smits (2011), discussing the Rotterdam Randstad Rail project, sets the scene well within this context. The project involved 0.7 km of bored and 2.3 km of cut and cover tunnels and deep excavations supported using diaphragm walls. Ground improvement techniques, such as in-place soil mixing, jet grouting, ground replacement and ground freezing, were implemented within the soft Holocene soils encountered. As the new construction would potentially affect a number of existing structures and services a risk management system was set up involving hazard levels. The integrated monitoring and risk management system for the construction works is described and discussed with examples in the context of protecting the 'surroundings', adjusting the monitoring system and anticipating the finances that might be required as part of implementing mitigation measures.

The control of ground and structural displacements can frequently be controlled by adopting more substantial (and expensive) construction techniques. The paper by Wang and Xu (2011) provides a very extensive coverage of the construction techniques adopted for many deep excavations in Shanghai during the past two decades. The geotechnical ground conditions are described initially—in doing this the reader immediately understands the challenges of constructing within the extensive depths of very soft recent soils. Figure 1, from the paper, showing a bird's-eye view of part of the city, highlights the density of very large and high structures that need to be protected during underground works. The paper is very valuable as it collates a wide scope of methods for constructing retaining walls (see Fig. 2), lateral and vertical support systems with clear and helpful sketches and photographs and discussion on their benefits and limitations. It goes on to describe a number of benchmark deep excavations in Shanghai, e.g. the largest and deepest deep excavation, the largest circular excavation. In order to control deformations approaches such as performance-based design and

practical construction methodologies are described and discussed, such as top-down method, advanced reinforcing soils within the excavation area and adopting zoned excavations.

The authors, Pagotto, Silvi and Casadei (2011), of the paper 'Underground car parks in Italian urban areas—not an easy task!' are also very familiar with the various issues of constructing deep circular excavations for car parking in the urban environment. They give a comprehensive breakdown of a number of practical items to consider, ranging from interaction with the neighbours, assessing the condition of the adjacent structures through to facilitating archaeological investigations. They also stress the importance of subsurface services, saying that in some cases the cost of dealing with these precludes financially the excavation going ahead. Technical issues are then dealt with including ground conditions (with seismic considerations in Italy), modelling loads, checking pile position and the need for corrective measures and waterproofing. New construction methods are also briefly described and their advantages discussed.

Figure 1. A birds-eye view of part of Shanghai city showing numerous skyscrapers (from Wang and Xu).

Moving back to the Netherlands, Everaars, Kwast, Meulblok, Delfgaauw and Mortier (2011) describe a project currently underway to provide a new cut-and-cover railway tunnel and station in the city of Delft. Of particular interest is the fact that the diaphragm walls which support the excavation for the tunnel and station have also been designed to carry the vertical loads of a new city hall to be built above them. They also need to be impermeable. The diaphragm walls in certain areas have such large bending moments that it was not possible to provide sufficient gaps between the necessary reinforcing steel. Trials were performed using shallow diaphragm wall shaped excavations to assess the optimal concrete mixture and casting method. High vertical loads and the potential for differential settlement were overcome by adopting spreading beams at the top of the diaphragm walls and barrettes in conjunction with varying their toe levels. An important consideration raised by the authors is the need to check the integrity of the diaphragm wall joints to avoid leakages and the consequent risks associated with them. This subject is dealt with later in this session (papers by Vanni and Geutebrűck, 2011 and Spruit *et al*. 2011).

Meissner, Quick, Michael and Arslan (2011) describe the challenges of constructing the foundations for a 200 m high tower block T185 in Frankfurt. A piled-raft solution was selected with a combination of diaphragm and secant-pile retaining walls supporting the walls of the two levels of basement. Advantages of using a piled-raft foundation are given, an important one

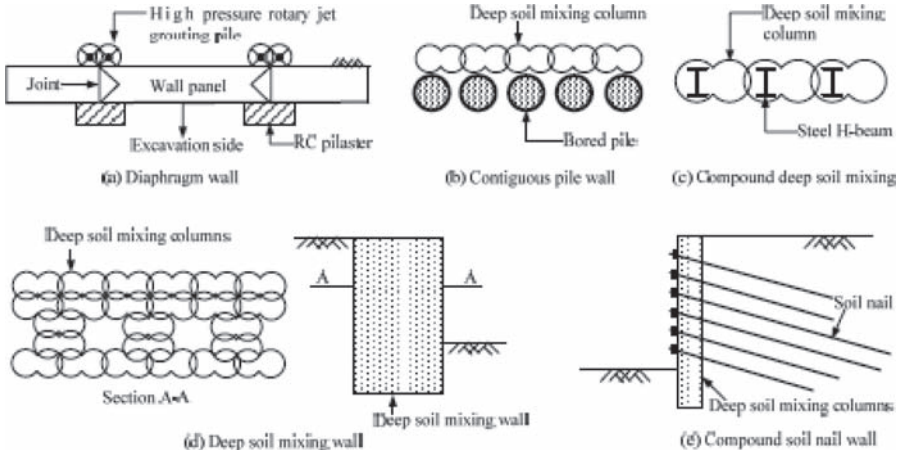

Figure 2. Sketches showing some typical retaining wall types used in Shanghai (from Wang and Xu).

being the reduction of settlements and differential settlements. An optimised foundation design was achieved using 3-D finite element analysis. Measurements of settlements and wall head displacements relating to the stage of construction at the time of writing, corresponded well with calculated values. The latter were greatly reduced (only ~5 mm) where inclined struts were adopted in the vicinity of an existing subway line.

Three case studies from St Petersburg, Russia involving deep excavations are described by Mangushev, Lashkova, Smolenkov and Osokin (2011). The soils are weak, sensitive, they occasionally contain boulders and often have high water tables. Each of the three cases involved excavations deeper than 12 m and involved the use of sheet piles, sometimes semi-circular in section and sometimes installed within a cement-clay solution, subsequently replaced by concrete—to provide what is termed 'wall-in-the-ground' structures. In all cases it was necessary to install piles to prevent base uplift. Generally the deformations of the walls were deemed acceptable and adjacent structures were not damaged—in some cases these buildings had their foundations reinforced by Titan piles—there is an interesting contrast in the Stockmann trade centre case where one building that was not reinforced in this way required some subsequent restoration work.

Deep excavations in the urban environment where there are nearby structures that need protecting is often achieved using diaphragm walls. Predicting the lateral displacements of these walls is an important component of assessing potential building damage. To achieve this, the geology needs to be understood and representative soil parameters are required for numerical analysis. In many instances this is not possible, e.g. where the geology changes rapidly. Back-analyses of monitored wall movements provides a method of quantifying displacements in complex ground conditions. Siemińska-Lewan-dowska, Mitew-Czajewska and Tomczak (2011) present data from 18 case studies involving diaphragm walls providing a useful range of typical movements for the various ground conditions encountered in Warsaw. The case studies have been divided into three groups involving different construction methods with: (i) anchors, (ii) props and (iii) top-down construction, illustrating typical ranges of movement to expect with different soil conditions under controlled construction procedures.

Challenging groundwater conditions in the very close proximity of the sea had to be overcome in order to construct the two-level basement for a major hotel complex in Tripoli, Libya. The paper by Asioli, Agostini and Minotti (2011) describes the approach used to control the ground water flow into the excavation (through permeable soils), designed in conjunction with consideration of the diaphragm wall depth. Another important consideration was to keep the water level outside the excavation as high as possible to avoid damage to nearby structures. Preliminary numerical analyses were performed to assess the best approach to construct the excavation considering three scenarios. This illustrated that increasing the depth of the diaphragm walls did not provide much additional benefit and that it was best to pump from within the excavation. More detailed numerical analyses were then performed to design the walls, accounting for local and global stability and the anchors used and the dewatering system. The project was successfully completed in good time, illustrating the effectiveness of the design and good teamwork between the parties involved.

The effect of staged dewatering in conjunction with staged top-down excavation is discussed by Zheng and Li (2011) who provide monitoring data from a deep excavation in Tianjin, China (see Fig. 3). They explain how the staged construction processes result in an increase in effective stresses in the silty clay and silts present at the site, thus reducing the compressibility of the soils and reducing the heave of the soil at the base of the excavation. They back up their hypothesis using

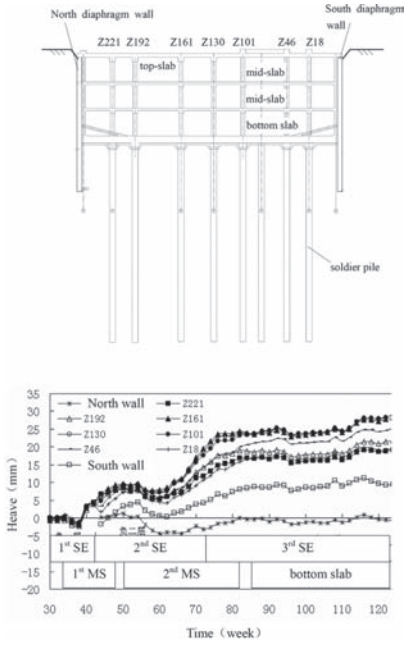

Figure 3. Profile of excavation using top-down construction and monitoring date showing heave of diaphragm walls and piles (n.b. SE = staged excavation, MS = mid-span construction) (from Zheng and Li).

triaxial tests performed following stress paths simulating the anticipated ground response during construction at points close to and away from the diaphragm walls. The monitoring data presented can be interpreted within the framework of their hypothesis and experimental results. The paper therefore emphasises the importance of taking staged construction into account.

3 STUDY OF DEEP EXCAVATIONS BY NUMERICAL ANALYSES

The complex soil-structure interaction processes involved with deep excavations and often their three-dimensional nature mean that for most cases the only way to predict and understand the mechanisms taking place is to perform sophisticated numerical analyses.

Numerical analyses have been used more and more in recent years with increased computing power, improved numerical techniques and more comprehensive constitutive models. Great care is required in such analyses along with a fundamental understanding of the soils, the constitutive models and the analyses themselves. It also has to be remembered that the more complex the constitutive model, generally the more soil parameters that are required, necessitating extensive sophisticated laboratory test programmes.

Three papers are included in this section. They provide comprehensive details about analyses performed to model the construction of deep basements. They also contain details about construction methods and present monitoring data for comparison.

In the paper by Becker, Berhane and Kempfert (2011) numerical back-analysis has been used to investigate the effects of factors such as construction and excavation stages on the deformations of a secant-pile wall supporting a 5.9 m deep excavation in soft lacustrine clays. The development of the measured displacements and pore water pressure changes are compared with results from the 2-D finite element analysis which accounts for the use of a waling beam cast around the inner perimeter of the top of the wall and the sequence of excavation steps (Fig. 4).

In particular the progressive mobilisation of the different support measures (walls, steel props and base slab) is considered with the developing displacements. An important factor accounted for is the anticipated stress path followed during the construction (similar to the paper just described by Zheng and Li)—the ground has been spilt into different zones subjected to a variety of stress paths as indicated in Figure 5. The comparison between the measured and calculated displacements

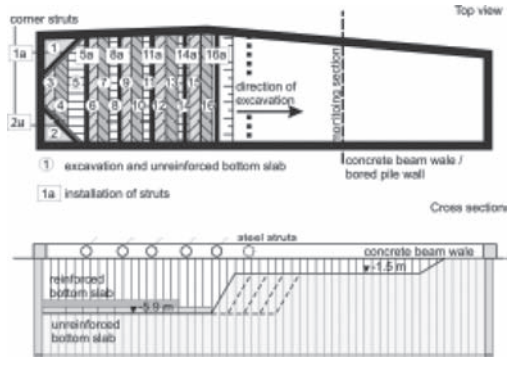

Figure 4. Top view and cross-section of excavation site with idealized construction stages (from Becker *et al.*).

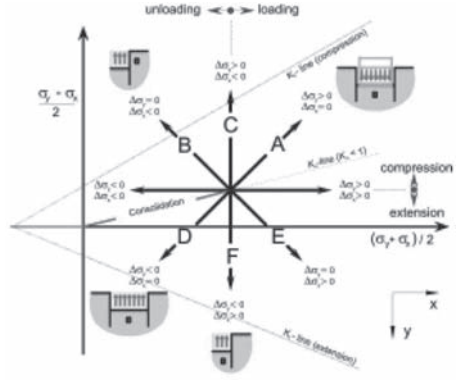

Figure 5. Idealized stress paths for triaxial tests (from Becker *et al.*).

indicates the improvement of the analysis when the appropriate stress path is considered.

A numerical analysis using the finite difference approach was implemented to help with the design of protective measures during the excavation of a 12 m deep four-level basement for parking adjacent to an existing building in Thessaloniki, Greece. Comodromos and Papadopoulou (2011) report that the existing building started to move unacceptably during demolition of the building that previously occupied the site. Attempts were made to underpin the existing building using jet-grouting but the ground (primarily sands and gravels) was so weak that the stress relief that took place prior to the grout hardening caused further movements and rotations.

A different approach using a curtain wall of steel tubes beneath the existing foundation was investigated (see Fig. 6) and designed using the analysis and all stages of the subsequent works were also modelled. The plane-strain analysis indicated that

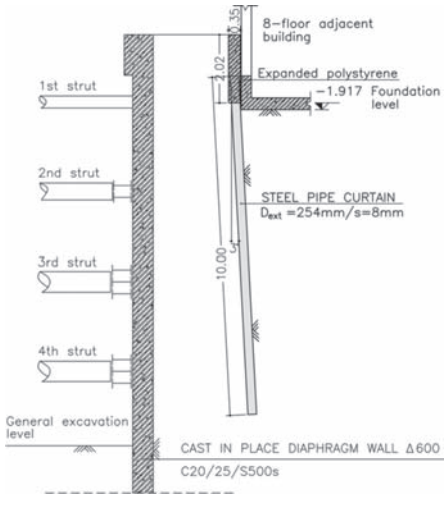

Figure 6. Support measures used to protect building prior to adjacent excavation (from Comodromos and Papadopoulou).

the curtain wall would reduce displacements and rotations and that to minimise them further the steel props should be prestressed with 500 kN. There was good agreement between the horizontal displacement measured at the top of the adjacent building with that predicted.

Furlani, Guiducci, Lucarelli, Carrettucci and Sorge (2011) describe the construction processes used to sink two large shafts (15.7 m inner diameter) about 5 m apart and 45 m deep forming part of the Metro C works in Rome. The shafts acted as TBM reception chambers and were then incorporated into the metro system for ventilation. They were sunk in complex ground conditions comprising strata of volcanic formation, altered tuffs and pyroclastic materials. A particular concern was the medium to high permeability of the strata as the base of the excavation was 24 m below the water table. This was dealt with by grouting the base of the diaphragm walls to create a zone in the form of an inverted arch. Comprehensive 3-D numerical finite element analyses with advanced constitutive models were used to assess effects such as the interaction of the shafts, the effects of ground treatment in the vicinity of the openings for the TBMs and the stress redistribution once the TBMs broke through. The analyses revealed that the latter process was the most critical structurally for the shafts themselves. Monitoring showed that the grouted base of the shafts worked well and that ground movements associated with TBM works were greatest, those from shaft construction being negligible.

4 STUDIES RELATED TO SEEPAGE, DEWATERING AND LEAKAGE

In any deep excavation, water ingress into the excavation and the potential destabilising effects water has on both the retaining walls and the base are all major concerns to anticipate. The papers discussed so far—in particular the paper just described by Furlani *et al.*—all allude to some degree to the subject of water ingress, while it is the main focus of the following papers within this group.

The very complex stratigraphy of Rome and its effect on the distribution of permeability values is described and discussed by Grisolia, Iorio and Zechini (2011) with particular reference to the dewatering works for the three stations Teano, Mirti and Gardenie along the Metro Line C. The stratigraphy of the beds is frequently not continuous and the range of permeabilities as established from LeFranc tests spans five orders of magnitude (10^{-8} to 10^{-3} m/sec).

Dewatering field tests were performed to compare with estimated pumping rates necessary and in two of the stations (Mirti and Gardenie) the rate of pumping was much greater than expected and it was still not possible to draw down the water level within the station boxes themselves to adequate levels (comparisons were made between water conditions within and outside of the excavations). Reasons for these differences are identified from seepage flow analysis as being due to different flow regimes within the strata and around the walls. In order to reduce the flow in the two stations, grout curtains were installed (using the same technology as described by Furlani *et al.* 2011). A 2-D numerical steady-state flow analysis was performed to compare average permeability values within the strata before and after grouting, using pumping rates to calibrate the values. It is felt by the authors that these analyses were more useful than the LeFranc tests for the complex ground conditions encountered. The grout curtains worked well in reducing permeability value.

Still considering the Line C of the Rome Metro Line C, Capata and Capata (2011) provide further information about the groundwater conditions beneath Rome, this time considering the Malatesta shaft. Again the complex stratigraphy is described but there is more emphasis in this paper on the design of the wells themselves considering their depth, diameter and spacing. Dewatering trials were performed—an essential exercise when the ground conditions are so complex and varied. Two water table depths were confirmed separated by a low permeability silty layer. In this case study the pumping tests indicated that the diaphragm walls penetrated into substantially impermeable strata and that they were themselves well constructed. Comparisons are made with the experience from

the Gardenie station (discussed in the previous paper by Grisolia *et al*. 2011) where the extent of the fractured tuff was such that it was not completely sealed by the diaphragm walls, hence requiring the installation of a grout wall to reduce permeability values and flow rates.

In the next paper considered in this group we move further south in Italy to the coastal city of Bari. Granata, Gioia and Cotecchia (2011) describe the geology of the area which comprises primarily 'Bari Limestone' which extends to great depths and comprises sequences of limestone, dolomitic limestone and dolomite. Comprehensive ground investigations were performed to establish hydrogeological and geomechanical conditions. Of significance is the frequently karstic and open-fractured nature of the Bari Limestone (permeability at the site was established as 10^{-4} to 10^{-3} m/sec). The excavation was to extend to 7 m below the natural ground water level. The geotechnical characteristics of the limestone were also estimated for assessing, using numerical analysis, the stability of the excavation during and on completion of the works. Detailed information is given about the grouts and grouting operations that were implemented to reduce the permeability of the strata both within and beneath and around the perimeter of the excavation. Three grout mixes were used, selected to suit the nature of the fracturing and voids and the grouting operation sequences. The grouting very effectively reduced the overall permeability of the ground with an average value being estimated as about 10^{-7} m/sec. Following these operations the excavation was completed successfully under safe and dry conditions and no damage to the adjacent historic buildings is reported.

The next two papers in this group discuss methods of detecting leaks and imperfections in diaphragm walls. Clearly this would be of great benefit to establish before excavating.

Vanni and Geutebrűck (2011) explain a new technology for detecting leaks and provide a case study where it was used. The method works by measuring ion flow within electrical fields. A series of sensors are placed within the excavation area, set out in a grid arrangement and in the case study pairs of boreholes outside and within the excavation were used to induce flow of artificial electrical tracers (see Fig. 7). The sensors detect where there is greater flow and hence potential points where leakages through the diaphragm wall may be occurring. The case study is the Gondar station on the new Line B1 of the Rome Metro. It was realised during construction that instrumentation within the hydromill was faulty during construction of certain panels and the 'multi sensor leak detection' technology was used to confirm the exact location. It was able to show competent areas and allow grouting works to be carried out inside and outside the retaining walls prior to excavation works. Excavation of the station box was subsequently completed without any leakage problems. Such technology clearly has a very important role in such cases from viewpoints of stability during excavation, safeguarding of nearby structures and significant cost savings. The second paper covering the issue of leaks and imperfections in diaphragm walls is by Spruit, Hopman and van Tol (2011) who report on investigations using four techniques applied to a full-scale constructed wall and smaller-scale panels cast in a laboratory environment. Temperature was monitored and found to have most benefit during the bentonite replacement and concrete casting stages, allowing potential defects to be identified during production. Natural gamma radiation measurements were found to have only limited

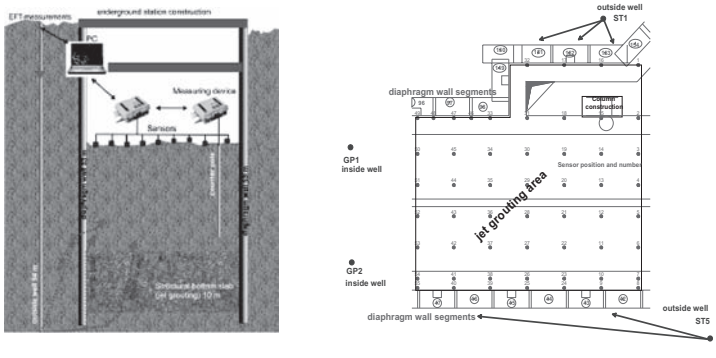

Figure 7. Schematic illustration of the leak detection method for deep structures and the sensor grid map for Gondar station with 55 sensors outside EFT-energy wells and inside counter poles on excavation level (from Vanni and Geutebrűck).

application for the case studied. Cross-hole seismic tomography was found to be efficient: tubes are required within the panels but these allow defects within the joints to be detected (where they occur most frequently). The fourth approach involved measuring electrical resistivity and this indicated an anomaly at the same location as the previous (CHST) method. It proved more efficient to use the full-scale panels for assessing the methods and confirmation of what was detected will be possible during excavation within the volume enclosed by the diaphragm walls. Therefore what is presented in this paper constitutes a class-A prediction!

5 GROUND IMPROVEMENT METHODS AND NEW TECHNOLOGIES FOR FACILITATING DEEP EXCAVATIONS

In this final section four papers covering quite different topics have been grouped as they all broadly relate to ground improvement.

Jet grouting is sometimes adopted for the improvement of the ground for tunnelling and deep excavations. However, there are sometimes uncertainties about how to control the effectiveness of such works. Eramo, Modoni and Arroyo (2011) explain the approaches that are available for controlling uncertainties in design and optimising site operations. In some cases the control is by specifying diameter, unit weight and strength of columns while an alternative is to focus on field trials. A case study from Barcelona is described where a base plug for a large excavation to form a station box was formed using jet grouting. A number of field trials were performed using different jet-grouting systems and these were assessed in a variety of ways (rotary coring and testing of samples etc) to define the best technique to adopt. A statistical analysis was used to facilitate the assessment of the results. Ground surface movements were also monitored, which allowed some significant settlements to be identified for certain grouting systems (in particular it was found that systems where large amounts of cement were injected resulted in large settlements). The field trials and monitoring thus allowed the jet-grouting method to be optimised and adverse effects, such as settlement, to be minimised using a rational and objective procedure.

A new technology involving 'Cutter-Soil-Mixing' (CSM) is described by Gerressen and Vohs (2011) who say that it offers an alternative to jet-grouting. The method of deep mixing uses rotating cutting/mixing elements that rotate about a horizontal rather than the usual vertical axis (see Fig. 8). Details are given concerning the construction steps and the range of sizes that can be dealt with. Comparisons

Figure 8. Mixing wheels and housing for hydraulic gear drives of a CSM unit (from Gerressen and Vohs).

are made with other techniques and a number of advantages to the new system are highlighted. Various case studies are then presented to illustrate the application of the system, i.e. for retaining walls, foundations and soil improvement. It seems that there is potentially a great diversity of applications that can be achieved with the CSM to considerable depths requiring less space for the plant.

Another technology, developed within the oil industry and now applied to geotechnical engineering challenges, is directional drilling. Vanni, Siepi, Croce, Melli and Specchio (2011) describe historic uses of such a technology and then go on to describe some new applications, illustrating them with case studies. The previous uses were to allow pipelines to be installed beneath urban areas or rivers where open-cut excavations were not practicable or to implement compensation grouting without the need to construct shafts from which to install the TAMs and inject the grout. They then describe two case studies where directional drilling was used to repair two dams (in New Zealand and the US) by constructing cut-off walls. A particularly challenging application involved containment of contaminated ground at two sites in Italy. It was discovered that there was no base protective membrane at the base of the contaminated ground. The ground could be effectively sealed using walls but initially it seemed that the only way to seal the base was to remove the contaminated material, install an appropriate membrane and then replace it. The new approach allowed the underlying calcarenite to be grouted, thus sealing off any potentially harmful leachates without having to disturb the waste material (see Fig. 9).

Anchors are often used in earth-retaining structures to increase stability and reduce deformations.

value calcium silicate hydrate crystals are formed

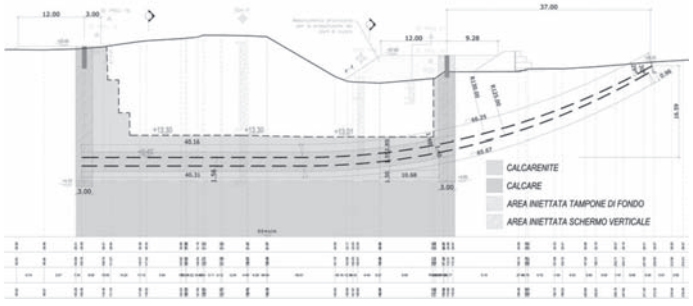

Figure 9. Base slab construction, allowing contaminated ground above to be sealed (from Vanni *et al.*).

The effect of pressurised grouting of compression anchors in residual soils has been investigated and is reported by Kim, Sim, Kim, Lee and Lee (2011). They describe a study involving (i) cavity expansion theory, with and without incorporating the permeation characteristics of the grout; (ii) laboratory small-scale model studies and (iii) field tests. Three residual soils commonly found in Korea were investigated. Using and comparing the results from these three lines of study, the authors conclude that the grout penetration should be used in conjunction with the cavity expansion theory when the ground permeability is greater than 10^{-5} m/sec. Increases in ultimate pull-out resistance can be gained for weaker soils for which SPT values are less than 50 but there is little benefit for stronger soils. It is suggested that the results could be applied to other residual soils.

The final paper within this session under the heading of ground improvement, by Kazemain, Prasad and Huat (2011), discusses the effect of cement on tropical peat from Malaysia stabilised by deep mixing. Three peat types were investigated: fibrous, hemic and sapric which have reducing water contents (~505%, 325% and 190% respectively), organic contents and fibre contents. Samples were prepared, with a central core of cement-mixed soil, which were then left submerged for 28 days to cure and then tested in Rowe cells to investigate the effect of cement content on primary and secondary compression characteristics (Cc and $C\alpha$). These tests were supplemented by microstructural studies using an SEM. All three types of peat showed a reduction in compressibility (Cc and $C\alpha$) with increasing cement content. Calcium and hydroxide ions are generated during the cement hydration process and when their concentration reaches a certain threshold value calcium silicate hydrate crystals are formed which bond soil particles and increase shear strength. The SEM analyses confirmed this effect and showed that it occurred most beneficially in the sapric peat.

6 CONCLUSIONS

The papers within this session have provided some excellent examples of field data, construction technology and design and analysis. The use of numerical analysis to understand how loads and stresses are redistributed in and around deep excavations and the resulting deformations that occur continues to increase in popularity. Field monitoring plays an essential role in validating the results from such analyses and controlling the works during excavation/construction. There are a number of excellent examples within this session illustrating this approach.

There is still an important need to try to make sure that published papers providing monitoring data include sufficient additional information to allow readers to use the data to validate their own independent numerical analyses. Defining the scope of information that is typically required to achieve this is the goal of one of TC204's Working Groups. Another closely linked Working Group is involved with the creation of a database where such information can be stored, again trying to make sure that sufficient information is provided. Details concerning both of these working group activities can be found on the TC204 website.

Some of the papers provide very useful statistical information about the effectiveness of various construction techniques, along with typical ranges of wall deflections etc—the papers by Wang and Xu (2011) and Siemińska-Lewandowska *et al.* (2011) are good examples.

In terms of construction technology, there are two papers that deal with the important topic of leaks through diaphragm walls. There are a number of case studies reported in the literature where such leaks have caused serious problems. The papers by Vanni and Geutebrűck (2011) and Spruit *et al.* (2011) discuss new techniques to detect such leaks and cite case studies where different approaches have been used.

This concludes the general report on papers grouped under the heading of 'Construction, design and measured performance of deep excavations'. Readers are encouraged to read the individual papers within the proceedings for more detailed information and references.

REFERENCES

Asioli C., Agostini M. and Minotti T. 2011. Design and construction of anchored diaphragm walls and dewatering system for the excavation of a two-level basement car park at the Al Ghazala Hotel Intercontinental in Tripoli—Libya. *Proceedings of 7th International Conference of TC28: Geotechnical aspects of underground construction in soft soils*. Roma.

Becker P., Berhane G. and Kempfert H.-G. 2011. Spatial effects on excavations in deep soft lacustrine clay. *Proceedings of 7th International Conference of TC28: Geotechnical aspects of underground construction in soft soils*. Roma.

Capata A. and Capata V. 2011. Seepage experiences for deep urban excavation at the TBM Malatesta shaft, Rome. *Proceedings of 7th International Conference of TC28: Geotechnical aspects of underground construction in soft soils*. Roma.

Comodromos E.M. and Papadopoulou M.C 2011. Interaction of retaining structure with adjacent building: multi-stage numerical analysis. *Proceedings of 7th International Conference of TC28: Geotechnical aspects of underground construction in soft soils*. Roma.

Eramo N., Modoni G. and Arroyo Alvarez de Toledo M. 2011. Design control and monitoring of a jet grouted excavation bottom plug. *Proceedings of 7th International Conference of TC28: Geotechnical aspects of underground construction in soft soils*. Roma.

Everaars M.J.C., Kwast E., Meulblok C.M., Delfgaauw S. and Mortier H. 2011. Geotechnical design of a railway tunnel and underground station supporting the new city hall, Delft, The Netherlands. *Proceedings of 7th International Conference of TC28: Geotechnical aspects of underground construction in soft soils*. Roma.

Furlani G., Guiducci G., Lucarelli A., Carrettucci A. and Sorge R. 2011. 3-D finite element modelling and construction aspects for vertical shafts in Metro C, Rome. *Proceedings of 7th International Conference of TC28: Geotechnical aspects of underground construction in soft soils*. Roma.

Gerressen F.-W. and Vohs T. 2011. CSM-cutter soil mixing—worldwide experiences of a young soil mixing method in soft soils. *Proceedings of 7th International Conference of TC28: Geotechnical aspects of underground construction in soft soils*. Roma.

Granata R., Gioia F. and Cotecchia V. 2011. Construction of a large underground parking in Bari downtown. Proceedings of 7th International Conference of TC28: Geotechnical aspects of underground construction in soft soils. Roma.

Grisolia M., Iorio G. and Zechini A. 2011. Dewatering tests results for underground C Line stations construction. *Proceedings of 7th International Conference of TC28: Geotechnical aspects of underground construction in soft soils*. Roma.

Kazemain S., Prasad A. and Huat B.B.K. 2011. Effect of cement on tropical peat stabilized by deep mixing method. *Proceedings of 7th International Conference of TC28: Geotechnical aspects of underground construction in soft soils*. Roma.

Kim T.-S., Sim B.-K., Kim J.-S., Lee S.-W. and Lee I.-M. 2011. Effect of pressurized grouting on anchor behaviour in residual soils. *Proceedings of 7th International Conference of TC28: Geotechnical aspects of underground construction in soft soils*. Roma.

Mangushev R., Lashkova E., Smolenkov V.Ju. and Osokin A. 2011. The construction of deep excavation ditch in weak soil in St. Petersburg. *Proceedings of 7th International Conference of TC28: Geotechnical aspects of underground construction in soft soils*. Roma.

Meissner S., Quick H., Michael J. and Arslan U. 2011. Challenging demands on the geotechnical design and first monitoring results of the T185 in Frankfurt. *Proceedings of 7th International Conference of TC28: Geotechnical aspects of underground construction in soft soils*. Roma.

Pagotto G., Silvi P. and Casadei F. 2011. Underground car parks in Italian urban areas: not an easy task! Proceedings of 7th International Conference of TC28: Geotechnical aspects of underground construction in soft soils. Roma.

Siemińska-Lewandowska A., Mitew-Czajewska M. and Tomczak U. 2011. The study of displacements of diaphragm walls built in Warsaw Quaternary soils. *Proceedings of 7th International Conference of TC28: Geotechnical aspects of underground construction in soft soils*. Roma.

Smits E.P.T. 2011. An integrated monitoring and risk management system for civil construction works. Proceedings of 7th International Conference of TC28: Geotechnical aspects of underground construction in soft soils. Roma.

Spruit R., Hopman V. and van Tol A.F. 2011. Detection of imperfections in diaphragm walls with geophysical measurements. *Proceedings of 7th International Conference of TC28: Geotechnical aspects of underground construction in soft soils*. Roma.

Vanni D. and Geutebrück E. 2011. Leak detection in complex underground structures at the Gondar Metro station, Rome, Italy. *Proceedings of 7th International Conference of TC28: Geotechnical aspects of underground construction in soft soils*. Roma.

Vanni D., Siepi M., Croce M., Melli F. and Specchio V. 2011. Recent uses of directional drilling technology in the construction field. *Proceedings of 7th International Conference of TC28: Geotechnical aspects of underground construction in soft soils*. Roma.

Wang W.D. and Xu Z.H. 2011. Design and construction of deep excavations in Shanghai. Proceedings of 7th International Conference of TC28: Geotechnical aspects of underground construction in soft soils. Roma.

Zheng G. and Li Z. 2011. Effect of staged dewatering and excavation on the heave of soil beneath deep excavation. *Proceedings of 7th International Conference of TC28: Geotechnical aspects of underground construction in soft soils*. Roma.

This page intentionally left blank

Geotechnical Aspects of Underground Construction in Soft Ground – Viggiani (ed)
© 2012 Taylor & Francis Group, London, ISBN 978-0-415-68367-8

Design methods and predictive tools for deep excavations and bored tunnels

L. Callisto
University of Rome 'La Sapienza', Rome, Italy

ABSTRACT: Papers in the present session deal with the design of geotechnical systems. Among the Authors' struggles to perform reliable predictions of real structures, it is instructive to discern two distinct strategies: (a) gaining on previous experience, and (b) decoupling. This general report on TS5 briefly illustrates the implementation of these strategies, making specific reference to some of the papers included this session.

1 OVERVIEW

A total of twenty papers belong to this session, with topics about equally distributed between open excavations and tunnelling. The Authors' affiliation is predominantly academic (50%), but with a fair share of people coming from industry (35%), and with some co-operation between industry and academia (15%).

The present session focuses on design methods, that is, most of the papers deal with real geotechnical structures. Hence, on the one hand the papers present only a limited number of advanced, sophisticated calculations; and on the other hand the Authors devote specific efforts in order to get reliable predictions on the behaviour of the structures.

This general report goes concisely through some of the papers, emphasising the basic strategies that the Authors employed in their struggle to get reliable predictions. In this sense, it is instructive to see that most of the papers basically implement either of the two following strategies:

– adapt previous experience to the present situation (gaining from previous experience);
– break up complicated problems into a number of simpler problems (decoupling).

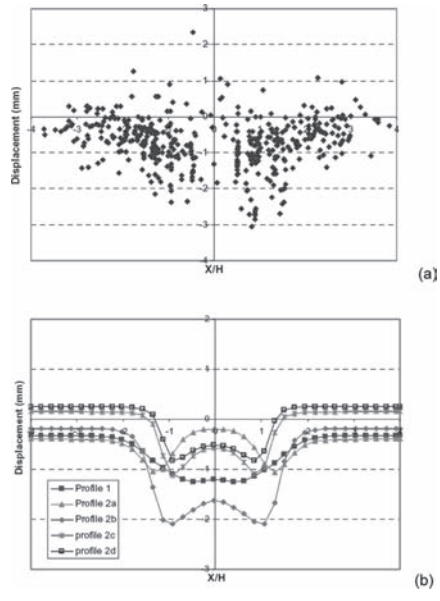

Figure 1. Data used by Boubu et al. (2011) for training and validation of the neural network (a); and vertical settlements obtained considering different soil profiles (b).

2 GAINING FROM PREVIOUS EXPERIENCE

Boubu et al. (2011) present calculations of the settlements produced by the excavation of a subway tunnel in Tolouse (Figure 1.a), using a neural network scheme. The network was trained on 60% of the measurements, while the remaining 40% was used for validation. It is apparent that this predictiton method relies heavily on the experience obtained within the same project. After a process of successive elimination, the Authors singled out the factors that influence more its predictive abilities (Figure 1.b). These factors turned out to be five TMB operational parameters, and the soil profile, intended here as a mere sequence of different layers, that is, a sort of geological profile.

Fillibeck & Vogt (2011) develop a number of site-specific correlations between the observed volume loss and the tunnelling methods used in Munich. Figure 2 shows one these correlations for

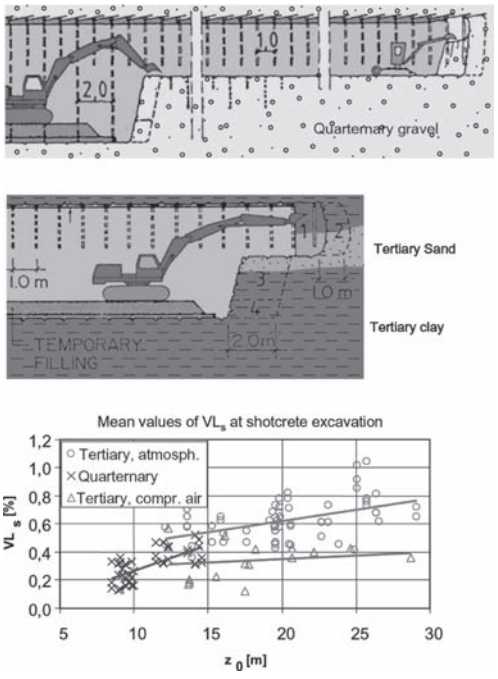

Figure 2. Site-specific correlation fond by Fillibeck & Vogt (2011) between volume loss and (i) excavation technology; (ii) gelology.

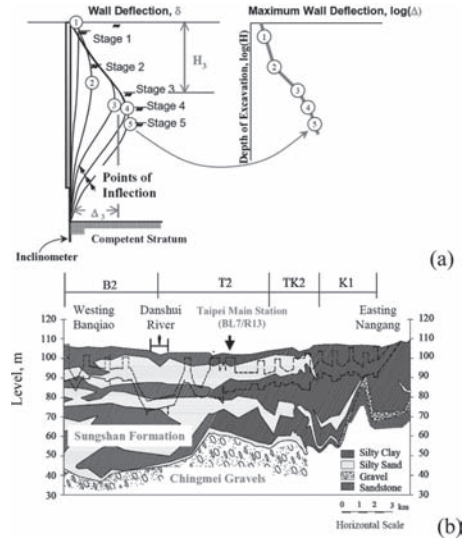

Figure 3. Definition of wall deflection path (a), and geological section at Taipei (b) (after Hwang & Moh 2011).

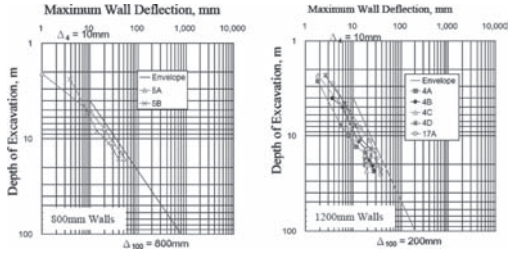

Figure 4. Wall deflection paths for deep excavation in Taipei, grouped according to the thickness of the retaining wall (after Hwang & Moh 2011).

shotcrete-supported headings. The correlations hinge on technological details and on the geologic origin of the soils encountered, and seem to leave the soil mechanics completely out of the picture.

Hwang & Moh (2011) use wall deflection paths to represent the observed behaviour of deep excavations in Taipei. Wall deflection paths represent the lateral walls displacements as a function of the excavated depts., in a log-log scale (Figure 3). Also in this case, the soil properties influence the curves only through the local geologic profile; hence, it appears that past experience may help only for excavations carried out in a similar geological context. On the other hand, the construction sequence is not taken into account (and one has to argue that the excavations in Taiped have all followed the same construction scheme) while a surprisingly large emphasis is given to the bending stiffness of the wall, as data are grouped according to the wall thickness (Figure 4). But bending stiffness may have a dominant role only in the cases of wall toes embedded in a very stiff layer. In any other case, horizontal displacements will have a rigid-body component that is essentially independent on the thickness of the wall.

Festa et al. (2011) develop a kinematic analysis of the progressive position of a TBM shield used for excavating a specific tunnel. This analysis is used to evaluate the amount of the soil displaced inward by the shield, and the geometrical distribution of the gap that forms between the shield and the excavated sol, and that has to be grouted (Figure 5). According to the Authors, this information is to be included in a prospective detailed numerical analysis of the excavation process.

Svoboda & Mašín (2011) use the displacements induced by an exploratory tunnel (which is in fact the top heading of a larger tunnel) to optimize the input data of a numerical calculation of the larger tunnel. The numerical analyses employ a hypoplastic soil model, that is calibrated on the results of laboratory tests carried out on undisturbed samples. Then, based on the displacements measured during the construction of the exploratory tunnel (Figure 6), an optimization procedure

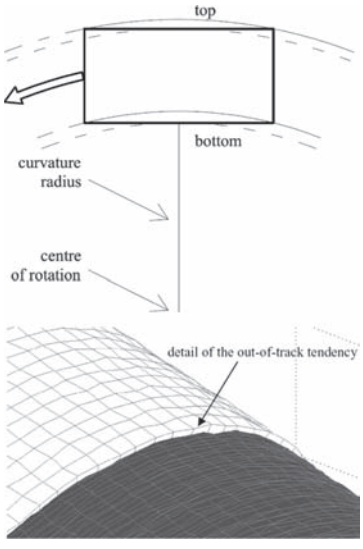

Figure 5. Kinematic analysis of a TBM shield (after Festa et al. 2011).

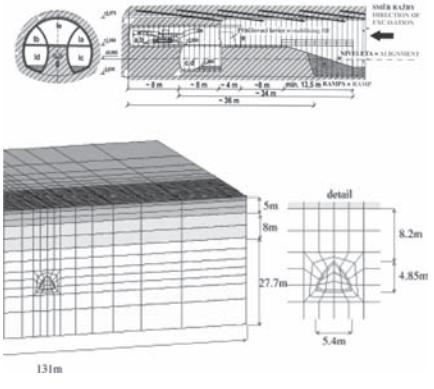

Figure 6. Simulation of the excavation of the exploratory tunnel (after Svoboda & Mašín 2011).

is carried out searching for the optimum values of the earth coefficient at rest K_0 and of the soil stiffness parameter r, that provide the best fit between the measurements and the calculation (that for the present purpose are carried out in plane strain conditions). The optimized quantities are then used for a three-dimensional simulation of the excavation of the entire tunnel (Figure 7). The vertical displacements computed at the ground surface match quite closely the measurements, while the agreement is less satisfactory for the displacements at deeper locations.

The present work uses the experience gained in the first part of the project to calibrate a sound

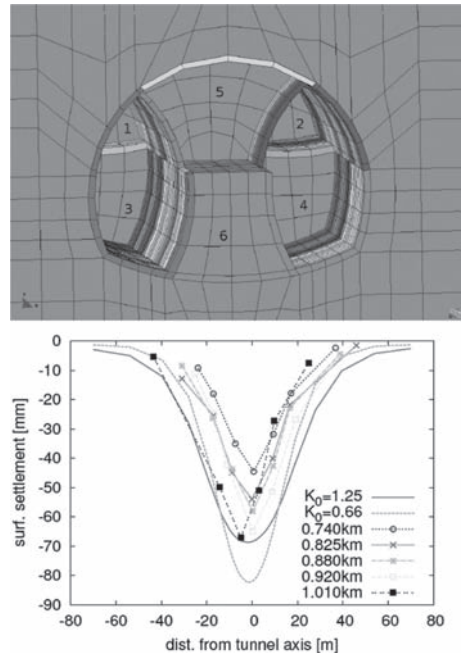

Figure 7. Three-dimensional analysis of the entire tunnel (after Svoboda & Mašín 2011).

soil constitutive model which in turn is used for predictions; it shows effectively that empiricism does not implies necessarily to neglect the fundamental mechanics of the problem.

3 DECOUPLING

Two papers in the present session address the problem of evaluating the effects induced by tunnelling of pre-existing foundation piles.

In the Amsterdam TC28 conference, Surjadinata et al. (2006) developed a decoupled procedure in which the tunnel-induced displacements are evaluated in the free-field first, via a fully elastic three-dimensional FEM analysis, and then these free-field displacements are fed into a BEM program that studies the soil-structure interaction. Now, the same group of Authors (Surjadinata et al. 2011) use the same method to develop design charts, presented in a non-dimensional form (e.g. Figure 8), that allow the evaluation of the pile displacement and internal forces, starting from the volume loss, the problem geometry, and the soil-pile reative stiffness.

A very similar decoupled approach is presented by Basile (2011): free-field displacements, computed with any available method, can be inserted into a

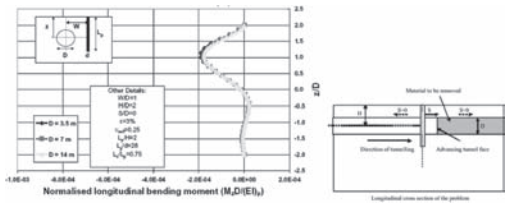

Figure 8. Design chart for the evaluation of the longitudinal bending moment in a foundation pile, induced by tunnelling (after Surjadinata et al. 2011).

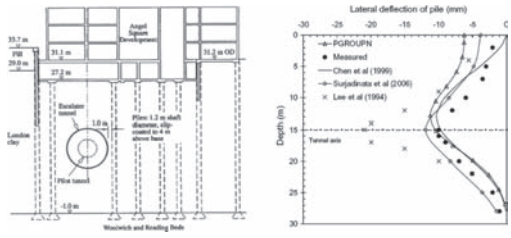

Figure 9. Comparison of the lateral deflection of a foundation pile computed by different authors for the case study of the Angel escalator tunnel (after Basile 2011).

BEM calculation to study the soil-pile interaction. The specific procedure presented by the Author includes local non-linearity at the soil-pile contact and can deal with pile groups connected by a rigid or flexible cap.

Interestingly, the two papers use, among others, the same case study to test the models, namely the construction of the escalator tunnel for the Angel tube station in London. Figure 9 shows the good comparison between the measured pile deflection and the predictions obtained with the two methods.

A two-step decoupled approach is also used by Gaspari et al. (2011) in a very different problem, dealing with the evaluation of the internal forces induced in the lining of a vertical shaft by an earthquake. The maximum shear strain γ_{max} induced by the earthquake in the free-field is evaluated first, using the maximum particle velocity prescribed by the Eurocode 8 design spectra. Then, this maximum shear strain is converted into displacements that in turn are applied statically to the boundaries of a plane-strain finite-element mesh, to study the soil-structure interaction and evaluate the internal forces in the lining (Figure 10).

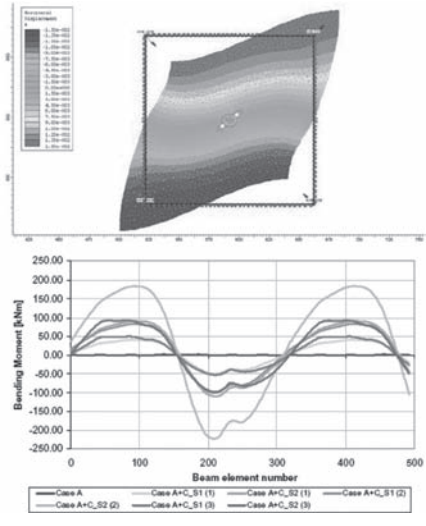

Figure 10. Free-field maximum shear strain applied to the mesh boundaries, and ensuing bending moments in the shaft lining (after Gaspari et al. 2011).

Motoi (2011) uses a decoupled approach to evaluate the ground movements induced by an excavation. In a first step, the horizontal displacements of the retaining wall are computed using the subgrade reaction methods. As reported by Motoi (2011), Kono & Shigheno (2011), and Sakamoto e Katsura (2011) in their respective papers in this session, general wisdom in Japan seems to indicate a strong reliability of the subgrade reaction method in evaluating the behaviour of a deep excavation. However, in other parts of the world this view is not shared at all, mostly due to the difficulties in the selection of the subgrade coefficients. The papers above mentioned provide sparse and contrasting information to that effect.

In Motoi (2011), once the horizontal wall displacements are calculated, they are imposed to the lateral boundary of a finite element mesh, in order to compute the vertical displacements below

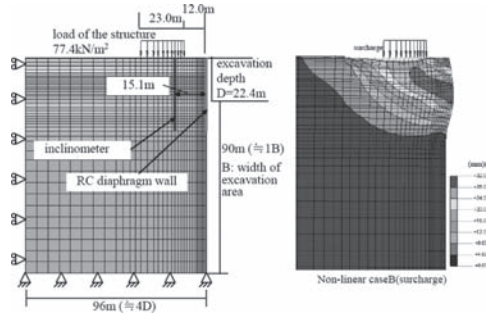

Figure 11. Numerical analysis presented by Motoi (2011), in which the horizontal displacements of the retaining wall computed with a subgrade reaction analysis are imposed to the right-hand side of the mesh boundary.

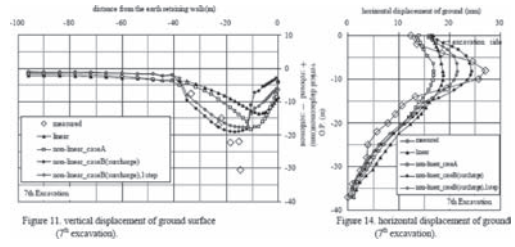

Figure 12. Comparison between computed and measurement displacement (after Motoi 2011).

a pre-existing structure and the horizontal displacements in the ground at a distance from the excavation (Figure 11). The agreement between the computed and measured displacements is good (Figure 12), although the paper fails to clarify whether this is an actual prediction or rather a back-analysis.

4 CONCLUSIONS

Most of the papers presented to this session rely on previous experience, that is to empiricism, in order to predict with some confidence the behaviour of the structures. This is not surprising, as geotechnical engineering is strongly rooted with experimental observation and field measurements. However, in several papers to this session empiricism was used in a manner that is somewhat disappointing, as it tends to bypass soil mechanics: decisions are made by considering geology alone (meaning here a mere qualitative description of the nature of soil) and by choosing an appropriate technology. Unfortunately, this practice implies a loss of generality and, more importantly, does not lead to any insight into the behaviour of the structures.

In general, any comparison between predictions and observation is an iterative task, implying successive modifications and refinements to the predictive analyses. Moreover, a large part of the prediction methods that were employed in the present papers imply some decoupling; and, in principle, decoupling implies iteration. Although iterations are seldom performed in the actual use of decoupled calculations, it would be good practice to indicate how the accuracy of a decoupled calculation would be improved by successive iterations: this would improve the analyst's control of the whole computation process and help to get a better grasp on the analysis procedures.

REFERENCES

Basile F. 2011. Pile-group response due to tunnelling. Proceedings of 7th International Conference of TC28: Geotechnical aspects of underground construction in soft soils. Roma.

Boubou R., Emerialut F. & Kastner R. 2011. Prediction of surface settlements induced by TBM using Artificial Neural Networks method. *Proceedings of 7th International Conference of TC28: Geotechnical aspects of underground construction in soft soils*. Roma.

Festa D., Broere W., v.d. Woude S., & Bosch J.W. 2011. Tunnel-boring process in urban environment. Modeling for reliability: a kinematic study. *Proceedings of 7th International Conference of TC28: Geotechnical aspects of underground construction in soft soils*. Roma.

Fillibeck J. & Vogt N. 2011. Prediction of Tunnel-Induced Settlements in Soft Ground. Proceedings of 7th International Conference of TC28: Geotechnical aspects of underground construction in soft soils. Roma.

Gaspari G.M., Quaglio G. & Floria V. 2011. A simplified numerical method for design of tunnels under seismic conditions. Example: Istanbul Metro design, Kadikoy-Kartal Line. *Proceedings of 7th International Conference of TC28: Geotechnical aspects of underground construction in soft soils*. Roma.

Hwang R.N. & Moh Z.C. 2011. Performance of deep excavations in the Taipei Basin. Proceedings of 7th International Conference of TC28: Geotechnical aspects of underground construction in soft soils. Roma.

Kono T. & Shigeno Y. 2011. FEM Analyses on Deep Excavations in Soft Clay of Earth Retaining Structure. Proceedings of 7th International Conference of TC28: Geotechnical aspects of underground construction in soft soils. Roma.

Motoi Y. 2011. Prediction Method of the Displacement of Surrounding Ground during Excavation. Proceedings of 7th International Conference of TC28: Geotechnical aspects of underground construction in soft soils. Roma.

Sakamoto T. & Katsura Y. 2011. A nonlinear soil spring model considering ground stress and strain change during excavation. *Proceedings of 7th International Conference of TC28: Geotechnical aspects of underground construction in soft soils*. Roma.

Surjadinata J.Q., Hull T.S. & Carter J.P. 2011. Effects of Tunnelling on a Single Pile: Three-Dimensional Design Tool. *Proceedings of 7th International Conference of TC28: Geotechnical aspects of underground construction in soft soils*. Roma.

Surjadinata, J.Q., Carter, J.P., Hull, T.S., Poulos, H.G. 2005. Analysis of effects of tunneling on single piles. *Proceedings of 7th International Conference of TC28: Geotechnical aspects of underground construction in soft soils*. The Netherlands. 665–671.

Svoboda T. & Mašín D. 2011. 3D simulations of a NATM tunnel in stiff clays with soil parameters optimised using monitoring data from exploratory adit. *Proceedings of 7th International Conference of TC28: Geotechnical aspects of underground construction in soft soils*. Roma.

This page intentionally left blank

Construction, design, and measured performance of bored tunnels

This page intentionally left blank

Geotechnical Aspects of Underground Construction in Soft Ground – Viggiani (ed)

Application of the image and laser sensors based tunnel scanning system

M. Sagong & T.H. Koh
Korea Railroad Research Institute, Uiwang, South Korea

B.S. Chun, B.H. Lee & Y.S. Byun
Hanyang University, Seoul, South Korea

ABSTRACT: Degradation of tunnel concrete liner requires routine and repetitive inspection to increase the life cycle of the structures. The tunnel inspection task, however, is labor intensive and time consuming process. Hence a computer based inspection system needs to be developed. In this paper, applicability of a tunnel scanner based upon a laser and an image scanning system, called as opto-laser tunnel scanner, is discussed. The image scanner can capture detailed surface features of tunnel liner such as micro cracks and spall, and laser scanner can reproduce geometric characteristics of a tunnel liner. Both types of data set have their own application. In addition the combined data set show three dimensional features of tunnel liner. This application will extend the data usage so it can be applicable for tunnel management.

1 INTRODUCTION

Most tunnel concrete liners installed as a structural element to support tunnel loads undergo degradation process which causes loss of the material strength and increase of permeability mainly produced by generation of various types cracks. In consequence a routine and repetitive inspection is required to provide timely maintenance to increase the life cycle of the structure.

Previously, the tunnel inspection was mainly conducted by human, hence it took long time and efforts. Recently with aid of computers and IT technology, vision or laser based systems have been developed (Asakura and Kojima, 2003, Yu et al. 2007, Yoon et al. 2009). The vision based system uses Charge-Coupled Device (CCD) cameras or video camera to capture the surface images of concrete liner. From the image, location, shape and size of the cracks are found. Likewise, a laser based system uses laser sensor to measure distance from the sensor to a target. From the scanning process the spinning mirror mounted at the front of the sensor deflects the laser rays to a circumferential direction, and the sensor measures returned laser rays. This measurement includes the geometric and radiometric features of a tunnel. The geometric feature of a tunnel represents three dimensional characteristics of the tunnel, which represents dimensions and shapes of the tunnel and attachment at the concrete liner. The radiometric features represent surface characteristics of the concrete liner for example, wetness of the tunnel liner and shape, size and distribution of surface crack. A successful application of the synthesized radiometric and geometric data set has been shown to delineate the surface cracks and spalls of a concrete liner (Yoon et al. 2009). The combined image and laser based system has advantages, such as acquisition of image and laser data sets, which allowing the identification of dimensional and surface features. Hence the system is more versatile and has wide applicability. This paper discusses about the development of the synthesized image and laser scanning system, and shows system configuration, optimization and data display. In this paper the synthesized image and laser scanning system is named as an opto-laser scanning system.

2 SYSTEM CONFIGURATION

2.1 *Laser scanner*

The main physical components of the opto-laser tunnel scanning system are as follows: laser scanners, image acquisition system, illumination, and Rail Guided Vehicle (RGV). A laser scanner set is composed of high speed Laser Range Finder (LRF) and line scanner (see Fig. 1).

The role of LRF is measurement of a distance from the sensor to a target. The range of the LRF used for the system is 16 m and sampling rate is 200 k/sec. An emitted laser ray is deflected while the laser rays pass through the line scanner, which includes a rotating mirror, a motor and an encoder. The stationary type laser scanner

has a scanning profile in a single plane like in Figure 2.

Since the RGV moves the laser scanner moves along the axis of a tunnel. Consequence, the moving profile of laser rays is shown in Figure 3.

Three set of laser scanner units are installed on the opto-laser scanner. The system configuration is shown in Figure 4.

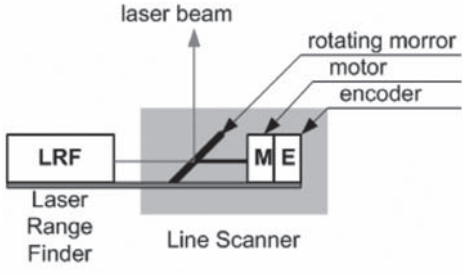

Figure 1. Constituent of a unit laser scanner.

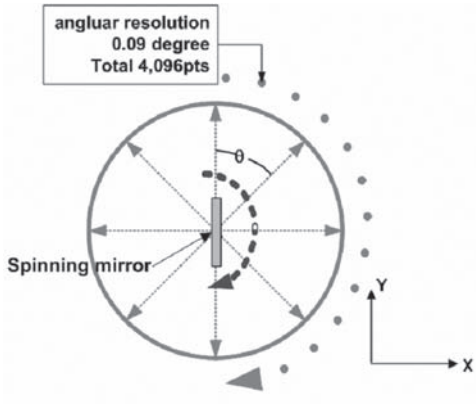

Figure 2. Laser rays profile of a single plane.

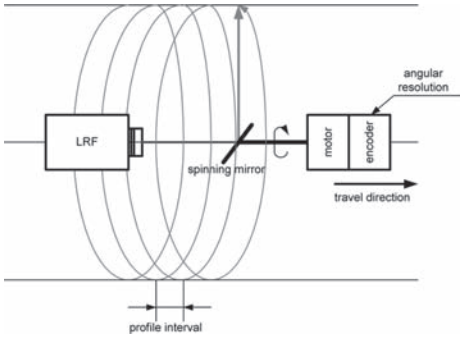

Figure 3. Helical profile of laser rays while traveling of RGV.

2.2 *Image acquisition system*

Like laser scanner, multiple channels of image acquisition system is installed for the opto-laser scanner. Three Charge Couple Device (CCD) and illumination are integrated. The effective picture element of the used CCD camera is 768(H) × 494(V).

A sufficient quantity and constant intensity of light is important for high quality image. The opto-laser scanner uses 250 W HID lamp. The CCD camera and ramp installed are shown in Figure 5.

2.3 *Rail Guided Vehicle (RGV)*

A locomotive type RGV was developed and the structure of RGV was designed to install the laser scanner, CCD camera and illumination. The RGV developed has 5 modules: laser scanner array, CCD camera array, control, battery, and power. Laser scanner and CCD camera array modules are main parts for data acquisition. In addition, the rest modules are quite important for accurate data acquisition. The control module executes overall control of RGV, and data management. The power module consists of RGV frame, DC motor, chain gear, bearing house, wheel shafts and wheel. The equally distributed data acquisition depends on traveling speed of RGV.

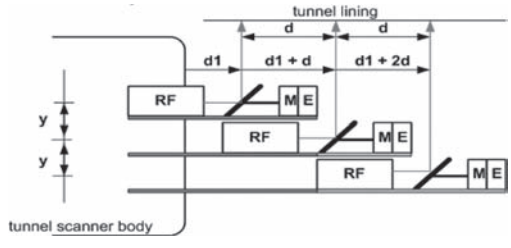

Figure 4. Multi laser scanner system configuration.

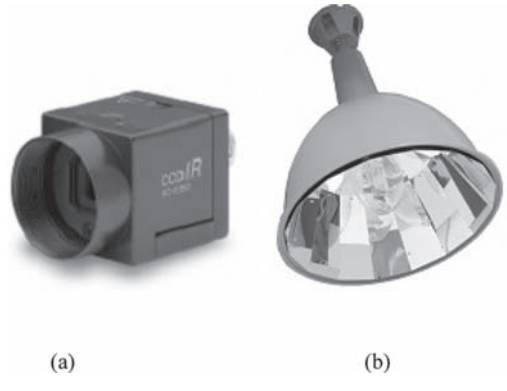

Figure 5. CCD camera (a) and illumination (b) installed for opto-laser tunnel scanner.

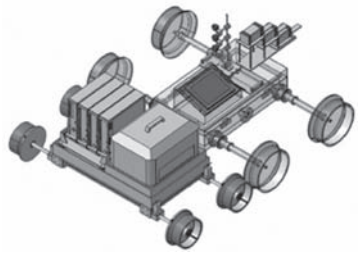

Figure 6. Three dimensional model of RGV.

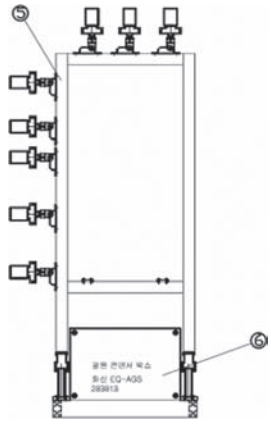

Figure 7. The main frame for cameras.

Hence assuring constant speed of RGV is quite crucial for the acquisition of high quality data set. A current generator was installed on the RGV to provide the required electric power for traveling of RGV and operating of the laser scanners and CCD cameras. The overall shape of RGV is shown in Figure 6.

The area covered by CCD camera depends on the distance between a camera and target. Due to the capacity of the camera, the covered area of a camera is limited and depends on the required resolution of an image. The opto-laser scanner can host 8 cameras and each camera can adjust their shooting angle toward the target. The main frame for the cameras was attached to the RGV and shown in Figure 7.

3 DATA ACQUISITION AND CORRECTION

3.1 *Development of digital filter for laser scanner*

An array of laser scanner acquires geometric and radiometric data which require correction process to increase the accuracy and resolution of the data. The sources producing low resolution data set of laser scanner are as follows: angular resolution of encoder in line scanner, laser spot size, edge effect, and interfering radiation. As the spot size of laser signal is smaller and the angular resolution is higher, higher resolution of laser data set can be achieved. The spot size and angular resolution depend on the capacity of laser sensor and line scanner.

The edge effect is another problem that deteriorates the resolution of laser scanning data. Once the laser ray hits the edge of a target, the reflected signal from the edge will be scattered and this process produces wrong point or artifact, which distorts realistic dimension of the target. Therefore, a digital filter is required to reduce the edge effect.

Finally, the radiation interfering is produced by the ambient light. The ambient light must be checked and laser signal must be modified to minimize the radiation interfering. A digital filter was developed to handle the edge effect and radiation interfering.

The digital filter developed to increase the resolution of laser data set uses a mixed criterion of range and ambient light intensity data. In a given range, the measure data should be in a limited range of light intensity. Therefore, with mixture of range and light intensity interval, a sufficient amount of noise points were eliminated. At the second stage, another digital filter was used. The filter used backscattered intensity values of laser rays. The outliers, the data points of unusual radiometric values, were eliminated from the normal distribution of intensity value. Figure 8 shows a raw data set and the digital filter processed data set.

3.2 *Panoramic image generation*

The arrays of CCD camera with macro lens capture surface images of tunnel liner. The opto-laser tunnel scanning system employs relatively small size main frame and small numbers of cameras and illumination compared to an ordinary vision based tunnel scanning system. The ordinary vision based tunnel scanning system uses almost the same size and shape of frame with a tunnel to install the CCD camera or camcorder and illumination. Under this configuration of camera, the Field Of View (FOV) of each camera is short and this condition requires large number of cameras. Hence at least one or two hours are required for setup. However, the permitted time for a railway tunnel inspection at most is three or four hours at night in Korea. Therefore, a rapid installation of components is important function which is required in the field.

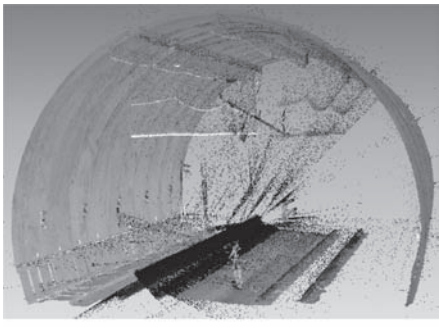

(a)

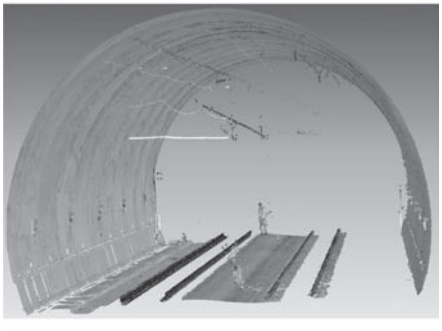

(b)

Figure 8. Laser scanning data set. A raw data set (a) digital filter processed data set (b).

The capture image undergoes panoramic image generation and image processing to obtain high quality images Since the concrete liner surface is not flat, the pixels will distort, near the edge. Therefore the zone of non-distorted image segment needs to be defined. From the continuously capture images, an edge or singular point is determined and the point is used as a reference point to calculate the amount of shift or travel for each images. Based upon the calculated pixel, an effective image segment is determined for each image. A panoramic image is generated from the merge of the effective image segments which was collected from the continuously capture images (see Fig. 9).

Figure 10 shows a merged image representing the surface features of concrete liners. In order to obtain high resolution images, several steps of digital image process were conducted. Initially, bright compensation process was conducted. Bright compensation process eliminates the bright difference generated by the various target distance from the sensor. Bright compensation process uses image histogram. The range, distribution and centroid of image histogram were adjusted to display images with relatively similar brightness.

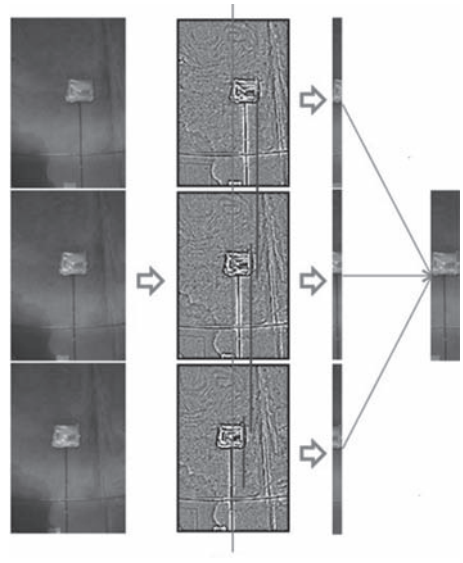

Figure 9. Merge process of image segment.

Figure 10. Panoramic image merged from image segments.

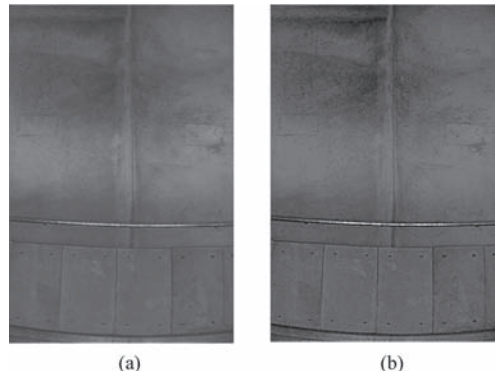

(a) (b)

Figure 11. A comparison between original (a) and processed (b) images.

The contrast compensation process employs various filters such as layer blending, gradient map, Gaussian blur. Figure 11 shows original and processed images.

The merge and generation of panoramic image were conducted after enhancement of image quality.

4 MAPPING OF IMAGE AND LASER DATA

The merit of the use of laser and image data is that the two data sets can be used for different purposes. Image data can be used of identification of surface texture and condition and laser data can be applicable for geometric investigation of structures. In addition, an integration of these two different features of data produces another way of application. Mapping of laser and image data produces three dimensional image which reproduces realist condition of tunnel. This kind of mapped data has more versatile application for tunnel inspection and maintenance. Figures 12 and 13 show merged panoramic image and mapped image.

The mapped image detail displays surface characteristics of concrete liner. The process of mapping follows i) edge detection ii) thining iii) key point extraction and iv) key point matching.

Figure 12. Panoramic image.

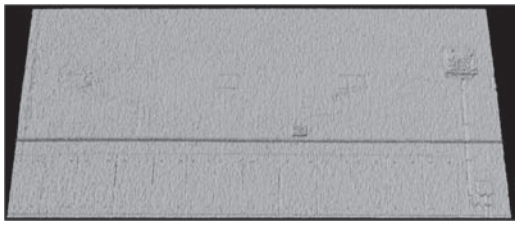

Figure 13. Mapped image.

5 CONCLUSIONS

The developed IT and computer technologies are getting applied to the labor intensive tunnel inspection. Hence an automation of the inspection process will reduce the cost and time in near future. In this paper, a system configuration and data processing for tunnel scanner employing image and laser scanners was discussed. The integrated system captures surface image of tunnel liners and geometric features of the structure. The optimized vision system developed was intended to reduce the install time and number of CCD cameras and illumination. The capture image undergoes digital image process such as bright and contrast compensation. In addition, the effective image segment is collected to generate the merged image. These processes produce high resolution image that can be used to define surface characteristics of concrete liner. The digital filter was developed to eliminate outliers of laser data set. The filter employs the use of ambient light intensity, range, and backscattered intensity. The mixed used of three parameters shows successful elimination of outliers.

The developed laser and image scanning systems were mounted on a RGV. While RGV travels, laser and image scanners continuously scan the internal features of a tunnel. The scanned data successfully represents surface characteristics of concrete liner and dimension of the tunnel. In addition, the mapped data displays realistic three dimensional features of a tunnel. The merged data represent extended application of the opto-laser tunnel scanner.

Further study needs to automatically identify the cracks and classified surface characteristics such as leakage and spalls.

REFERENCES

Asakura T, Kojima Y. 2003. Tunnel maintenance in Japan. *Tunnelling and Underground Space Technology*. 18: 161–191.

Yu SN, Jang JH, Han CS. 2007. Auto inspection system using a mobile robot for detecting concrete cracks in a tunnel. Automation in Construction 16: 255–261.

Yoon, Jong-Suk, Sagong, Myung, Lee J.S., Lee, Kyu-sung. Feature extraction of a concrete tunnel liner from 3D laser scanning data. NDE&E International 42: 97–105.

This page intentionally left blank

Geotechnical Aspects of Underground Construction in Soft Ground – Viggiani (ed)
© 2012 Taylor & Francis Group, London, ISBN 978-0-415-68367-8

Manipulations of the sticky clays regarding EPB tunnel driving

G. Spagnoli
Department of Engineering Geology and Hydrogeology, RWTH Aachen University, Aachen, Germany

M. Feinendegen
Chair of Geotechnical Engineering, RWTH Aachen University, Aachen, Germany

R. Ernst
Herrenknecht AG, Schwanau, Germany

M. Weh
Marti Tunnelbau AG, Bern, Switzerland

ABSTRACT: During mechanical tunnel driving with Earth Pressure Balanced (EPB) Shields, clogging between the excavated material and metallic parts of the machine can lead to technical and economical problems. Mainly responsible for such issues are the clayey materials. The research described in the following deals with the study of the clogging causes. Besides, investigations of electro-chemo-mechanical manipulations of the properties of clays are performed. Clayey materials were mixed with different electrolytes or subjected to an electrical field and the variations of their properties were measured. Information from these clay manipulations is coupled with the pioneer cone pull-out tests developed to detect and quantify the stickiness. Besides, the effective improvements of the geotechnical properties of the excavated materials will be tested by means of in situ experiments. Together with Herrenknecht AG a device was designed and developed to scale up the laboratory findings in order to analyze the effects of reducing adhesion simulating a tunnel driving through sticky clay formations.

1 INTRODUCTION

Earth Pressure Balance (EPB) tunneling machines are commonly used for the construction of tunnels in soft soils ranging from coarse sands and gravels to stiff clays. These machines use the excavated soil in a pressurized head chamber to apply a support pressure to the tunnel face during excavation. The number of tunnel projects excavated by means of TBM EPB technique is constantly increasing (e.g. the Heinenoord tunnel in the Netherlands, Katzenberg tunnel in Germany, Madrid MetroSur in Spain, Roma 4 Venti in Italy). In fact, the use of such technology improves the productivity of the job site and sometimes the application of TBM is the only alternative, especially for large traffic and supply tunnels, due to their high performance.

However, during the excavation of tunnels it is possible to encounter several problems due to the clogging between TBM and excavated materials. This may cause great difficulties in its excavation, transport and reuse, as well as in the course of the construction progress. Delays problems might therefore be caused. In addition, these can lead to hostilities between awarding authorities and executing companies. According to Thewes & Burger (2005), the economy of a tunnelling project can depended very much on the clogging potential of the encountered material. The advance rate in clay can be as low as 1/10 of the regular progress in granular soils. In fact, it has been calculated that from an economic point of view, the clogging of TBM is not desired.

Responsible for clogging are mainly adhesion processes that occur at the interfaces and at the surfaces of the clay minerals and tools (Spagnoli et al. 2010a). For instance, according to Thewes (1999), Feng (2004) and Weh et al. (2009), clays which leads to clogging problems are high cohesive with high liquid limits and a high plasticity index. Hence, these types of soils tend to become very sticky on contact with water, due to the swelling effect of clay particles. Several solutions are present on the market but not always their performances are satisfactory. Besides, not always the chemo-mechanical properties of clays are well understood. The clogging problem, therefore, remains an important issue during the tunnel constructions. Clogging can constrain mechanical tunnelling through to a complete standstill.

A clogging risk is always given when water comes into contact with a soil prone to clog. Therefore, according to Weh et al. (2009) one has to distinguish between two cases. The case 1 is the case of a young geological soil. With increasing load during the geological time, the density of soils increases and so the water content and clogging risk decrease. For case 2 there are contemporaneously, during the mechanical heading, soils prone to clog and water from adjacent excavating geological formation. When both are mixed in the excavation chamber, it could happen that a critical consistency will reached and therefore also the clogging. According to Weh et al. (2009) the soils prone to clog are, before the excavation, xeric. That means with high density and high consistency.

Soils with higher consistency have a huge water demand. The water demand is dependent on the consistency of the slurry. Besides, during the mechanical heading, the mixing of water with excavated materials lead to a cycle where with increased clogging, the tunneling advance decreases. With addition of excavated material in the mixing chamber, the ratio water/soil excavated decreases. That leads to a worse tunnelling advance. The consistency in the slurry increases with time, but only because the slurry is not in equilibrium in the excavation chamber. It means that parts of not degraded soils swim in a slurry. These not degraded parts have a tendency to adsorb water from the slurry. The slurry is becoming, therefore, increasingly homogenous and stiffer as function of time. According to Weh et al. (2009), the cyclic change from tunnel advance and standstill is also problematic. In fact during standstills, water flows in the excavation chamber. Water is gathering at the basis of the excavation chamber. This water then has to be transported together with the excavated materials. The restart of the tunnel heading after a standstill leads to a mixing of mountain water and excavated material. Thereby, the consistency of the material which is originally not critical is changed to a critical consistency, due to the mixture with water and this leads to a clogging (Fig. 1).

Starting from this information systematic laboratory tests have been conducted in order to understand which the minerals that cause clogging are. Besides, a new test device has been developed to investigate and classify different soils and rocks as until now no suitable test procedure or classification scheme for the clogging potential is available. Finally, based on electro-chemo-mechanical theories, new manipulation methods have been studied on clays and have been coupled with the cone pull-out tests to measure the variation of clogging of the fine-grained materials.

2 THE INFLUENCING PARAMETERS

The most important parameters which influence the clogging are:

- the grain size;
- the mineralogy;
- the water content;
- the chemistry and pH of water.

It is clear that the mineralogy has a strong influence on the determination of Atterberg limit. Atterberg limits are important since they are of vital importance to decide the water content which the excavated materials have to have in the mixing chamber. Mineralogy, geotechnical properties of the excavated soils and the availability and quantity of water seem to play an important role for the clogging potential (Weh et al. 2009).

Mineralogical investigation on clay samples from tunnelling projects with clogging problems showed the clays which might lead to more problematic tunnel driving (Fig. 2). From this figure it is clear that smectite is present as clay fraction with high amount. However, due to the low number of tunnel data, no statistical interpretation is possible.

Besides mineralogy, also the geotechnical properties of the excavated soils and the availability of water seem to play an important role for the clogging potential. In Figure 3 values for the local water inflow at the face, the relative amount of sticking of excavated material to the cutting wheel as well as the contact force of the cutter head are given for an approximately 3 km long tunnel part. Moreover, the respective geology is plotted in the background.

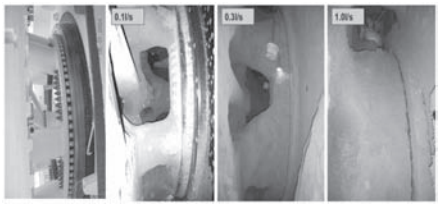

Figure 1. Influence of the water inflow on the clogging of excavation chamber (after Weh et al. 2009).

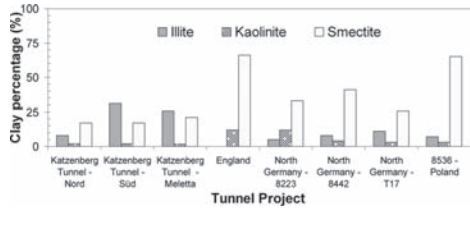

Figure 2. Clay mineralogical analysis through XRD measurement on clay samples of tunnel projects.

The chart shows, that the clogging of the cutter head is strongly related to the water inflow at the face which is directly linked to the respective geology. Another fact is that the sticking of excavated material to the cutting tools leads to an increasing contact force of the cutter head, when regarding the respective geology. The needed energy and the corresponding construction costs increase. It seems, therefore, that the data generated by tunnel driving with TBM (penetration, thrust forces, pressures of annular grouting etc.) are crucial information for the interpretation and prediction of advance rates and potential troubles.

Moreover, also pH variations of the mountain water can dramatically change the geotechnical properties of clays (Palomino & Santamarina 2005; Gajo & Maines 2007).

According to Jancsecz (1991) adhesion is highly dependent on simple soil mechanical parameter as water content, undrained shear resistance, liquid limit and plasticity index (Fig. 4). Therefore, it is highly probable that the modification of these parameters could reduce the adhesive behaviour of the excavated materials. From all this information, an adequate investigation of the excavated material and the chemistry of the ground water might help to predict and reduce the clogging during tunnel excavation.

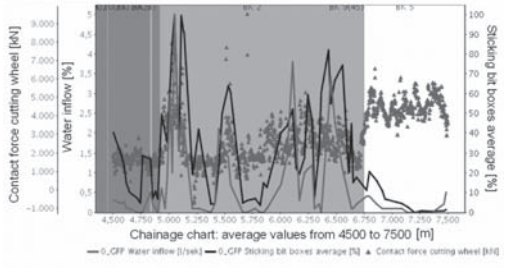

Figure 3. Graphical multi-axes evaluation of TBM and geological/geotechnical data.

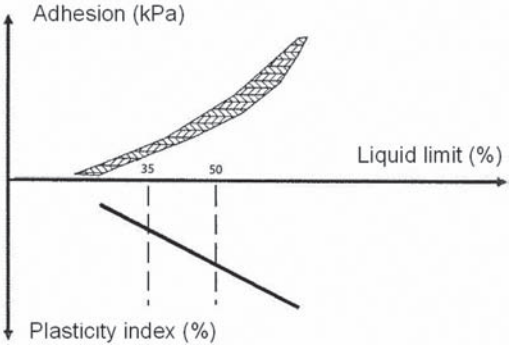

Figure 4. Correlation between adhesion and soil mechanical parameter (after Jancsecz 1991).

3 CLOGGING MEASUREMENTS

3.1 *The cone pull-out test*

For a better identification and quantification of the mechanisms affecting the clogging behaviour on a laboratory scale, the so called "cone pull-out test" has been developed (Feinendegen et al. 2010). The sample material is compacted in a standard proctor device, a steel cone is inserted into a pre-drilled cone-shaped cavity and loaded for 10 minutes with the magnitude of the applied load between 3.8 kN/m² and 189 kN/m² depending on the consistency. The load is then taken off and the specimen is placed in a test stand where the cone is pulled out with a rate of 5 mm/min. The tensile forces and the displacements are recorded. Different clay types with varying mineralogy and plasticity have been tested up to now in a number of test series with different cones and soil consistencies. Table 1 shows the relevant properties of some selected clays.

In the main experiments four different clays were examined: clay 13 from Westerwald (Germany); clay 14, the extremely plastic known as Ypresian or London Clay and clay 15, Boom Clay both from Belgium and clay 16, which represents a pure sodium smectite from India. In Figure 5 (left) the curves of the pull energy over the consistency are shown for these four clays, whereas in Figure 5 (right) the corresponding adherences are plotted. It can easily be seen, that the (quantitative)

Table 1. Physical characteristics of the tested clays.

Clay	13	14	15	16
Plasticty %	21	129	50	385
Liquid limit %	49	159	72	455
Loss on ign %	3.9	2.6	4.9	n.d.
Fine content %	59	33	49	86
Smectite %	2	35	17.5	100
Kaolinite %	65	36	39	–
Illite %	12	7	20	–

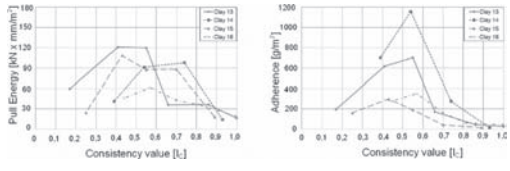

Figure 5. Pull energy over consistency (left) and Adherence over consistency (right).

correlation of these curves is not always as good as in the preliminary tests, but the (qualitative) shape is still somehow similar. Nevertheless, from Figure 5 (right) a direct comparison of the four soils can be drawn. Clay 14, the Ypresian Clay, shows a characteristic steep developing with a very high maximum of adherence (1150 g/m²) at a consistency of IC = 0.54. The curves for clay 15, the Boom Clay and the pure smectite (clay 16) are more even with considerably lower adherences of 275 g/m² and 350 g/m² respectively. Finally, for Clay 13 from the Westerwald the maximum value of 700 g/m² lies in between, but the curve is a bit irregular.

3.2 *Evaluation of the clogging potential*

Based on the results obtained so far, a draft of a classification scheme to quantify the clogging potential of different fine-grained soils has been developed (Fig. 6). Classes of high, medium and low clogging potential are assigned to the diagram with the adherences derived from the cone pull-out tests plotted over the consistency. One can directly identify the very high risk of clogging for clay 14. In particular, the sharp increase of the curve up to the maximum of 1150 g/m² is a strong indication for problems to be expected. Also Clay 13 with a maximum adherence of 700 g/m² will lead to extensive clogging. But also for the two other clays noteworthy adherences have to be reckoned with. In this connection it should be mentioned, that all clays presented here were deliberately chosen as sticky clays. Other samples were examined that showed adherences of less than 100 g/m² and can thus be defined as "not prone to clogging". However, the ranges of high, medium and low clogging potential are up to now defined arbitrarily. There is still a strong need for a verification by the EPB tunneling praxis.

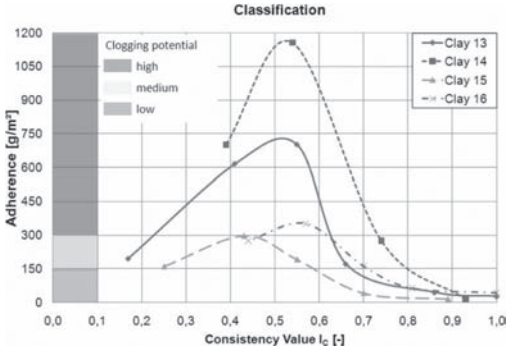

Figure 6. Draft of a classification scheme.

4 ELECTRO-CHEMO-MECHANICAL MANIPULATIONS OF CLAYS

The mechanical behaviour of soils and particularly of fine-grained soils (e.g. clays) is intimately related with the chemical properties of the medium and this relationship has been denoted as "chemical-mechanical coupling", which refers to the changes in mechanical properties of the soil in a medium subjected to chemical changes (and viceversa) (Santamarina et al. 2002). Among these chemical parameters, for instance, the dielectric constant (ε) and the electrolyte concentration (n_0) of the pore fluids both influence greatly the geotechnical behaviour of the clays (Mitchell and Soga 2005). Besides, another variable which has to be taken into account is the pH of the fluids. Since it is very likely to found situations where the environmental pH conditions change (e.g. leakage of acid mine waters and oils from storage facilities, variation of the groundwater chemistry), and considering that such new established conditions might lead to significant variation in the geotechnical properties of clayey materials, the investigation of the influence of pH and salt concentration changes on mechanical properties of clays is very important in the geoengineering field.

This phenomenon plays an important role for the engineering response of the material. Numerous authors have already dealt with and analyzed the problem (e.g. Mesri & Olson 1970; Olson 1974; Di Maio 1996; Kaya & Fang 2000, Anandarajah & Zhao 2000; Sridharan 2002). The influence of the dielectric constant, the electrolyte concentration and pH values of pore fluids plays an important role, particularly in the case of 2:1 expanding clays such as smectite. Kaolinite (1:1 clay) and illite (2:1 non-expanding clay) do not respond in the same way. In fact, they have a very thin Diffuse Double Layer (DDL) expansion (Sridharan et al. 1988; Gajo & Maines 2007) due to the negligible isomorphic substitution. Increasing the salt concentration (or decreasing the dielectric constant) the DDL thickness decreases (Verwey & Overbeek 1948), leading to smaller particle distance. Besides, for the following discussion, it will be assumed that the DDL theory is applicable. Clay particles systems are frequently conceptualized as a series of parallel clay particles. The Poisson-Boltzmann equation (Mitchell & Soga 2005) for a single particle can be integrated to obtain the mid-plane electrolyte concentration and potential between two clay particles. An approximate indication of the influences of particle spacing and pore fluid chemistry can be seen in terms of thickness of DDL as given by:

$$\frac{1}{\kappa} = \left(\frac{\varepsilon_0 \varepsilon R T}{2 n_0 e^2 v^2} \right)^{\frac{1}{2}} \quad (1)$$

where $1/\kappa$ is the DDL thickness (in nm), T is the absolute temperature given in K, n_0 the ionic concentration in the bulk solution in mol/l, ε_0 and ε are the electric permittivity of vacuum and the relative dielectric constant of the pore fluid, respectively, whereas v^2 is the valence of the prevailing cation. The constants are the elementary charge ($e = 1.602 \cdot 10^{-19}$ C) and the gas constant ($R = 8.3145$ J/mol·K) (Israelachvili 1991). However, the variation of liquid limit for kaolinite for different dielectric constant or electrolyte concentration is almost negligible if compared with the variation which occurs for smectite (Fig. 7).

The difference in chemo-mechanical behaviour for kaolinite and smectite is probably due to the existence of two different mechanisms governing the liquid limit of soils, taking into account the clay mineralogy and the pore medium chemistry. One mechanism might be controlled by the thickness of diffuse double layer which governs the liquid limit. Sridharan & Venkatappa Rao (1975) stated that the liquid limit of soils is mainly due to the diffuse double layer held water. The most important conclusions, concerning the structure of the double layer as function of the electrolyte concentration (and/or dielectric constant) of the fluid is that the extension of the double layer in solution decreases with increasing electrolyte concentration (or decreasing dielectric constant) as shown by equation 1.

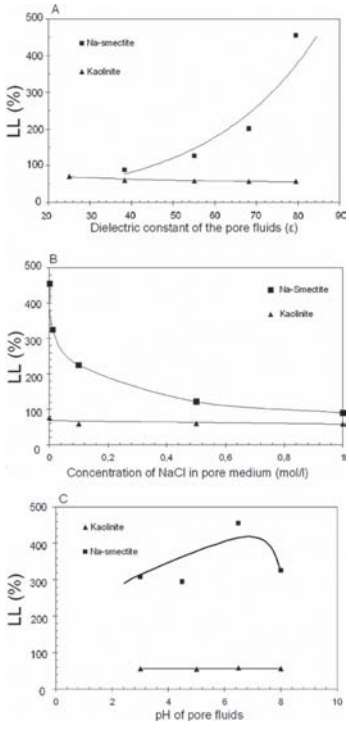

Figure 7. Variation of the liquid limit for smectite and kaolinite for (A) different dielectric constant, (B) electrolyte concentration or pH values (C) of pore fluids.

Several vane shear tests and direct shear tests showed the influence of the pore fluid compositions on the mechanical behaviour of clays. Spagnoli et al. (2010b) showed the impact of the pore fluids compositions on different types of smectites (i.e. calcium and sodium) on the undrained shear strength (Fig. 8).

Regarding kaolinite the variations of mechanical properties is different for that for smectite. The results for Kaolinite for different consistencies show that Kaolinite does not experience any relevant change in the shearing behaviour. The variations of shear stress are negligible. It seems, in fact, that the shearing behaviour of Kaolinite is controlled mainly by pure physical contact on the interparticle level. From the results obtained, it is possible to state that the mechanical behaviour of Kaolinite is not dependent on the chemistry of pore fluids. Therefore, the results agree with those of Olson (1974) and Di Maio (1996). However the pH value causes a strong increase in undrained and drained shear strength (Fig. 9).

However, an acid or alkaline environment seems to lead to a stiffness of the materials. That could be due to the dissolution of Al of the clay structure for high (or low) pH which acts as coagulant. Potentiometric acid-base titrations till pH 3 and 8, measurements of dissolved Al in the extracts, coupled with geochemical calculations, were consistent with the theoretical assumption and reinforced the idea that the release of Al plays a key role in the undrained shear strength behaviour of clays when experience acidification.

Following the assumption stated by equation 1 and by using the cone-pull out test, Na-smectite was mixed with water and 1 mol/l NaCl for different consistencies (0.55, 0.65, 0.7, and 0.85) to observe the variation of the clogging potential of this particularly clay. Fig. 10 clearly shows that the clay mixed with the electrolyte does not stick anymore to the cone. In fact, the increased internal shear strength of the clay, if mixed with a fluid with higher electrolyte concentration, leads to a general drop of the stickiness of the material.

Also by using an electric charge, clogging could be decreased. By applying an electric charge to the steel parts, water can be transported through the clay by electro-osmosis to the interface between the clay and the steel. This creates a film of water at the clay-steel interface and therefore reduces the adherence.

Experiments with the cone pull-out test were performed. Smectite was compacted in a proctor top for different consistencies (0.85, 0.70, 0.55 und 0.4).

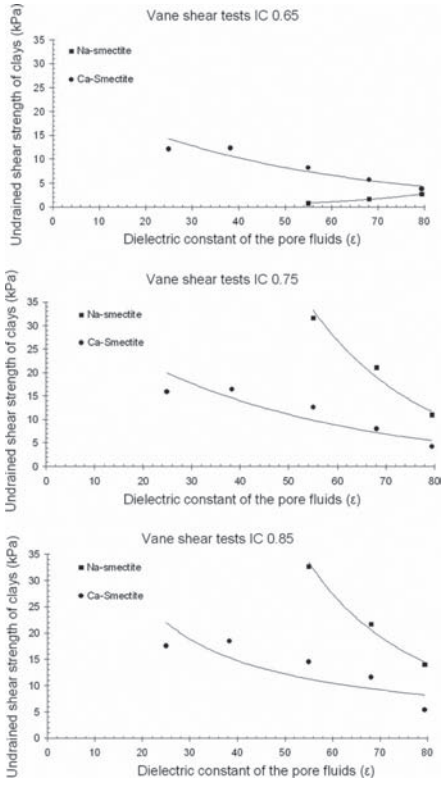

Figure 8. Effect of the dielectric constant on the undrained shear strength under different consistency conditions for Na and Ca smectite (after Spagnoli et al. 2010b).

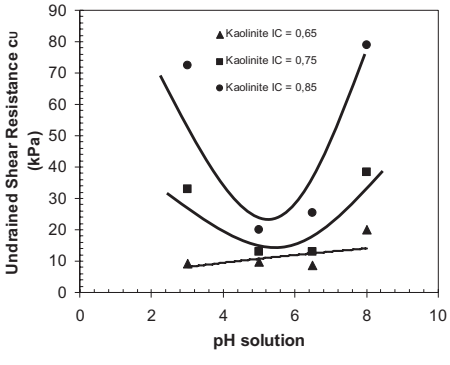

Figure 9. Variation of the undrained shear strength for kaolinite with different pH values of pore fluids.

Then the cone was gently put on the clay surface for 10 min and used as cathode while the structure of proctor pot was the anode. A potential of 2.5 V (33 V/m) was used in all tests for 10 min by using DC. After this time it was pulled out with a rate of 5 mm/min. Figure 11 shows the results.

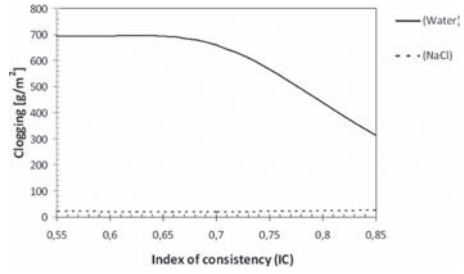

Figure 10. Variation of the clogging for Na-smectite mixed with water and 1 mol/l NaCl.

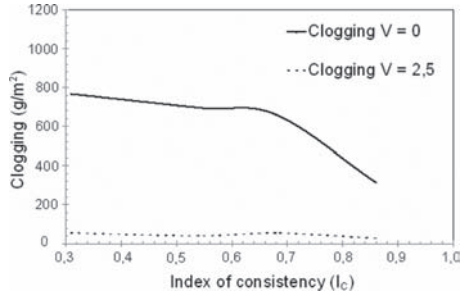

Figure 11. Clogging for Na-smectite without and with the application of an electrical field.

From Figure 12 it is clear that the water film, created by the electro-osmosis, acted as a "protection" to the sticky materials.

The use, however, of DC, could be a disadvantage. Extended electrical laboratory investigation was performed by using AC. Not only current intensity but also water flow depend on the electric impedance of the Electrode-Soil System (ERS impedance), i.e. the current intensity depends on soil resistivity and on the Electrode-Soil Contact (ERC) impedance. It has been shown that for DC measurements the contact impedance is often crucial for the system impedance whereas for high frequencies (e.g. 10 kHz) the influence of the contact impedance is of minor importance. Electrical Impedance Spectroscopy (IS) measurements were carried out (two electrode) to study the properties of the Electrode-Soil System (ERS) and especially the influence of the contact impedance on the ERS impedance. IS measurements on pre-loaded and non-loaded samples, simulating the conditions of the tilted plate tests, were performed in the frequency range from 1 Hz to 1 MHz using the IAI impedance analyzer PSM1735.

Figure 13 shows that AC signals are more effective in reducing adherence than DC signals for smectite. With AC generally lower field strengths are needed to reduce the adherence time.

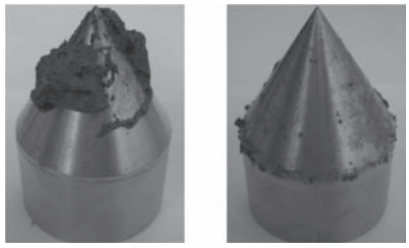

Figure 12. Left the Na-smectite tested with an IC = 0.4 with no application of electric field and right the same material mixed with the same consistency but with an applied voltage of 33 V/m.

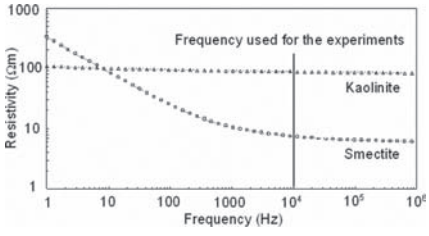

Figure 13. Resistivity of the electrode-soil system versus frequency obtained by IS measurements for smectite.

Besides, application of electro-osmosis during real tunnel heading could lead to the applicative problems. By applying a negative charge to the steel surface of the TBM, this steel surface is protected from corrosion. However the anode will corrode faster compared to an uncharged surface. The anode will not only wear out faster; a rusted anode will also have a lower conductivity and as a result the amount of water transported by electro-osmosis will be lower.

To generate electro-osmotic flow voltages which will electrolyze water are used. Therefore hydrogen and oxygen gas will develop as can be observed from the half reactions for water electrolysis.

At the anode: $2H_2O - 4e^- \rightarrow O_2\,(g) + 4H^+$
At the cathode: $2H_2O + 2e^- \rightarrow H_2\,(g) + 2OH^-$

The oxygen developed at the anode will probably not cause problems. However the hydrogen gas is flammable, and if mixed with oxygen at the right concentration it can explode. When an electric current passes through a clay mass, the clay mass is heated and the temperature will rise. Because the specific resistance of clay is many times larger than that of steel, the heat development in the clay is many times larger than in the steel electrodes.

Also the influence of the electrical current and possible produced magnetic fields on computers and electrical machines inside the TBM is not exactly known.

5 MANIPULATION OF CLAYS IN SITU

To transfer and prove the results of the new standardized adhesion laboratory test and to verify new manipulation techniques, a Clogging Test System (CloggTS) will be developed (Fig. 14). It is designed to support the geotechnical soft ground evaluation and conditioning related to clogging affinity in early project phases. The test also aims at coming closer to some geological-geotechnical aspects and to the reality of TBM layout with respect to material excavation and conveying processes in EPB-TBM. It is important to construct a robust, effective and economic clogging test system adapted to multiple use and to log those operational TBM data relevant for detecting clogging. Among those are visual notes, advance rate, face contact force of the cutting tool, torque of cutting and conveying tools, cutting tool revolution (rpm), temperature, and if so, the amount of additives given into the system. It is planned to vary operational data during testing. The CloggTS will enable a systematic and complex investigation of clogging and soft ground material conditioning. This includes the detection of index properties and other characteristics of the ground and additives. Besides classical parameters also parameters relevant to clogging like ground water saturation, slake durability, adhesion stress, ζ-potential, clay mineralogy, void ratio, swelling potential or Cation Exchange Capacity (CEC) are involved. Undisturbed geomaterial samples will be taken, if possible.

By this, further geological/geotechnical ground characteristics that may be of importance for the adhesion/clogging propensity can be involved. Among those are low-scale geological interbedding and fissuring (e.g. fissured clays), ground water saturation, anisotropic ground properties and mixed tunnel face conditions. Main issue of the CloggTS is to assess the transferability of medium-scale test results to TBM projects and to evaluate the efficiency and applicability of chemical or physical conditioning (clay surface manipulation) of soft ground materials regarding technical, operational and environmental aspects as well as the reuse of the excavated material.

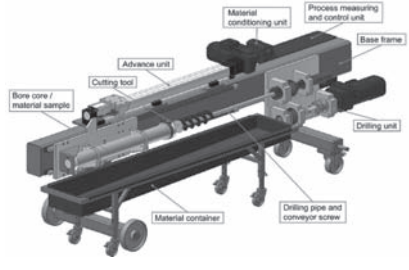

Figure 14. Clogging test system (prototype).

6 CONCLUSIONS

The clogging of the excavated materials is highly complex due to the different variables which came into play. The evident parameters (clay) mineralogy and particle size of the excavated material, in particular the significant influence of the water content and/or water inflow and the resulting (change of) consistency of the material are extremely important data to be identified.

The cone pull-out test is a first approach to understand the clogging properties of excavated materials. From such data a first interpretation will help the construction phases in situ. Electro-chemo-mechanical manipulations based on empirical models shows that the clays do not responds in the same manner. While with kaolinite the DDL model does not work, smectite shows strong variation in chemo-mechanical properties. Finally, the different factors affecting the clogging propensity that have been identified so far will be studied in a TBM-like medium-scale test. The respective test setup is currently in the concept state.

ACKNOWLEDGMENT

The authors would like to thank the BMBF/DFG "Geotechnologien" program (pub. no. 1550) for the financial support, which made this research possible.

REFERENCES

Anandarajah, A. & Zhao, D. 2000: Triaxial behavior of kaolinite in different pore fluids, *Journal of the Geotechnical Engineering Division*, ASCE, 126(2): 148–155.

Di Maio, C. 1996. Exposure of bentonite to salt solution: osmotic and mechanical effects, *Géotechnique*, 46(4): 695–707.

Feinendegen, M., Ziegler, M., Spagnoli, G., Fernández-Steeger, T., Stanjek, H. 2010. A new laboratory test to evaluate the problem of clogging in mechanical tunnel driving with EPB-shields. In: *Proc. EUROCK 2010*, Lausanne, Switzerland, Taylor & Francis Group, London.

Feng, Q.L. 2004. Soil conditioning for modern EPBM drives. *Tunnels and Tunnelling International*, 18–20.

Gajo, A. & Maines, M. 2007. Mechanical effects of aqueous solutions of inorganic acids and bases on a natural active clay, *Géotechnique*, 57(8): 687–699.

Israelachvili, J. 1991. *Intermolecular and surface forces*, Academic Press.

Jancsecz, S. 1991. Definition geotechnischer Parameter für den Einsatz von Schild Vortriebsmaschinen mit suspensionsgestützter Orstbrust, *Forschung + Praxis*, 34: 34–60.

Kaya, A. & Fang, H.S. 2000. The effect of organic fluids on the physicochemical parameters of the Fine-Grained Soils, *Canadian Geotechnical Journal*, 37(5): 943–950.

Mesri, G. & Olson, R.E. 1970. Shear strength of montmorillonite. *Géotechnique,* 20(3): 261–270.

Mitchell, JK, & Soga, K 2005. *Fundamentals of Soil Behavior*. John Wiley and Sons.

Olson, R.E. 1974. Shearing strengths of kaolinite, illite and montmorillonite. *Journal of the Geotechnical Engineering Division*, ASCE, 100(11): 1215–1229.

Palomino, A.M. & Santamrina, J.C 2005. Fabric map for kaolinite: Effect of pH and ionic concentration on behavior. *Clays and Clay minerals*, 53(3): 211–223.

Santamarina, J.C., Klein, K., Palomino, A. & Guimaraes, M. 2002. Micro-Scale Aspects of Chemical-Mechanical Coupling—Interparticle Forces And Fabric. In *Chemical Behaviour: Chemo-Mechanical Coupling from Nano-Structure to Engineering Applications*, Edts., C. Di Maio, T. Hueckel and B. Loret, June, Maratea, Balkema, Rotterdam, pp. 47–64.

Spagnoli, G., Fernández-Steeger, T., Azzam, R. Feinendegen, M., Neher, H.P. & Stanjek, H. 2010a. Investigation of adherence behaviour and related effects on different scales in mechanical tunnel driving. In: *Proc. Underground Construction Prague 2010, Transport and City Tunnels*, ITA-AITES, 14–16. June 2010, Prague, Czech Republic, 692–699.

Spagnoli, G., Fernández-Steeger, T., Feinendegen, M., Stanjek, H. & Azzam R. 2010b. The influence of the dielectric constant and electrolyte concentration of the pore fluids on the undrained shear strength of smectite. *Soils and Foundations*, 50(5): 757–763.

Sridharan, A. & Venkatappa, Rao G. 1975. Mechanism controlling the liquid limit of clays, Proc. *Istanbul Conference on Soil Mechanics and Foundation Engineering*, 1, 75–87.

Sridharan, A, Rao, S.M. and Murthy N.S. (1988): Liquid limit of kaolinitic soils, *Géotechnique*, 38(2): 191–198.

Sridharan, A. 2002. Engineering behaviour of clays: Influence of mineralogy. In *Chemical Behaviour: Chemo-Mechanical Coupling from Nano-Structure to Engineering Applications*, Edts., C. Di Maio, T. Hueckel and B. Loret, June, Maratea, Balkema, Rotterdam, pp. 3–27.

Thewes, M. 1999. *Adhäsion von Tonböden beim Tunnelvortrieb mit Flüssigkteinsschilden*. PhD thesis, University of Wuppertal, Institute of Soil Mechanics and Foundation Engineering, 21.

Thewes, M. & Burger, W. 2005. Clogging of TBM drives in clay—identification and mitigation of risks. In Erdem & Solak (eds) *Underground Space USE: Analysis of the Past and Lessons for the Future*, 737–742.

Verwey, E.J.W. & Overbeek, J.T.G. 1948. *Theory of the stability of lyophobic colloids*. Elsevier.

Weh, M., Ziegler, M. & Zwick, O. 2009. Verklebungen bei EPB-Vortrieben in wechselndem Baugrund: Eintrittsbedingungen und Gegenmaßnahmen. In *Tunnel—Räume für zukunftssichere Mobilität*. 185–189, STUVA-Tagung 2009, Hamburg. Gütersloh: Bauverlag.

Geotechnical Aspects of Underground Construction in Soft Ground – Viggiani (ed)
© 2012 Taylor & Francis Group, London, ISBN 978-0-415-68367-8

The effects of anisotropy and of unhomogeneity of stress state on the lining of road tunnel in a Flysch formation

V.M. Santoro
IGeS, Rome, Italy

ABSTRACT: For the implementation of a road in Fortore Valley, Campobasso, Italy, the excavation of a 2000 metres long tunnel is in progress in a Flysch geological formation. The construction is based on a traditional technique of full excavated polycentric invert segmented section with primary lining of steel ribs, steel mesh and shotcrete. The swelling phenomena following the excavation compelled the designer to propose the stabilization of the face core through synthetic nailing, and a forepoling along a splayed surface. In order to contrast the settlements of the steel ribs due to swelling, prestressed tie backs and foundation micropiles were designed at the rib toes. The tie-backs are equipped with a special improving system, the TFEG device. Monitoring results of the deflection of the contour of the excavated section showed anisotropy of the behaviour of the formation due to the slope effect. Numerical analyses for the simulation of the constructive process confirmed the field results.

1 INTRODUCTION

1.1 *The road tunnel*

The cross section of the tunnel consists of a free area of around 80 square meters with a full excavated section of 112 square meters.

The first 200 meter were excavated into the weathered terms of the clay formation of Toppo Capuana Marls, a swelling structured clay layer.

The construction of the tunnel is based on traditional technique of full excavated polycentric invert segmented section, with primary lining of steel ribs, steel mesh and shotcrete.

In particular, the primary lining consists in two ribs IPE 180 positioned at intervals of 1 meter with a layer of shotcrete reinforced by welded steel mesh.

The project provides individual fields of excavation 9 meters long; the inverted segment of the concrete polycentric is build about 20 meters far from the face core, while the polycentric formwork is achieved far about 60 meters.

Stabilization of the face core was performed through synthetic nailing, whilst a 15 meters forepoling along a splayed surface allowed a safe advance of 9 meters.

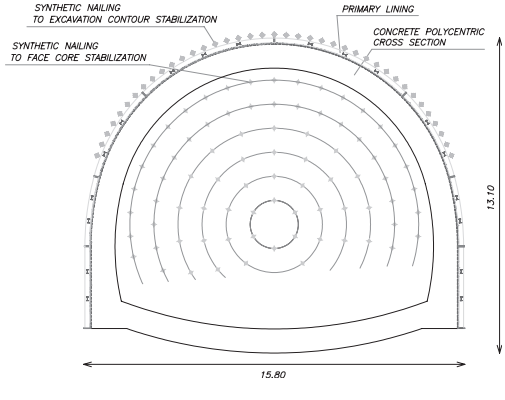

Figure 1. Cross section of tunnel.

1.2 *Geological features of the site*

The geological set up of area is characterized by a broad syncline with axis in direction N-S formed by two principal flyschoid geological units. The older is originated in Serravalliano-Tortoniano age and consists in marly-clay-limestone; the latest formation, referred to the Toppo Capuana clayey units, involves a big part of the S. Croce tunnel, and consists mainly of blue-grey marly clays and clayey marls.

Moreover, the upper part of the formation, whose thickness is limited (generally less than 10 metres), is characterized by a medium degree of cracking and deterioration.

The distribution of major lithologies is conditioned by a structural setting characterized by folds in the Apennines convergence, complicated by tectonic slivers.

The involved area of the tunnel is not affected by a significant groundwater flow in relation to low permeability of the outcropping geological units.

1.3 *Geotechnical feature of the model*

Three different geotechnical units were taken into account, based on the following average mechanical parameters:

Unit A
$\gamma = 18.5$ kN/m^3 $\Phi' = 19°$ $c' = 0$ kPa $E = 10$ MPa

Unit B
$\gamma = 20.5$ kN/m^3 $\Phi' = 22°$ $c' = 25$ kPa $E = 30$ MPa

Unit C
$\gamma = 20.5$ kN/m^3 $\Phi' = 22°$ $c' = 50$ kPa $E = 80$ MPa

1.4 *Behavior after excavation and stabilization measures*

Some cross sections have been instrumented for the measurement of convergence and settlement of rib toes.

The results show that the excavation of the individual fields causes significant phenomena of relaxation and swelling of the contour of excavation, that produced heavy convergence rate and settlement of the rib toes, as plotted in Figures 3 and 4.

Has been observed like the left downhill toe of the ribs have higher value of settlement than the right toe for every field of excavation. Also the value of settlement incremented when the excavation progress was faster.

When it was seen that large displacements coccurred there were adopted some additional measures like micropiles for the foundation of the ribs and prestressed horizontal tie-backs.

The stabilisation measures were dimensioned following the traditional Observational Method.

Monitoring results of the strain state of the excavated section showed anisotropy of the

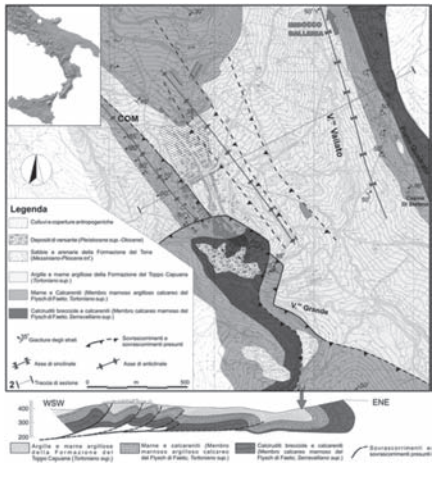

Figure 2. Geological map of the area.

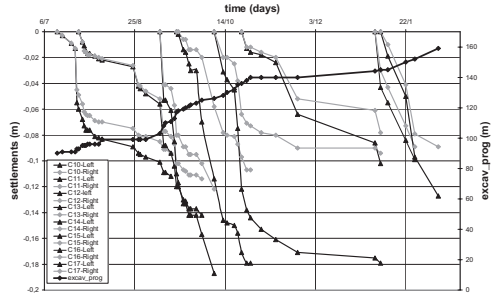

Figure 3. Vertical settlements in right and left rib toes for every excavation field.

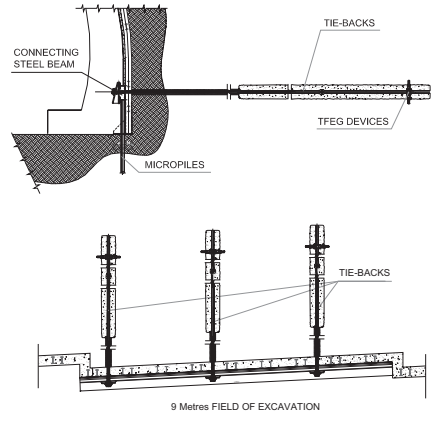

Figure 4. On progress stabilization measures.

behaviour of the formation due to the slope effect, when cover heights are about 20–30 meters. In fact, as shown by the plots, the downhill rib settlement is always higher than the correspondent on the uphill side, due to the upper anisotropy rate of the stress state.

Every excavation fields presents three tie-backs for a total length of 15 meters (free length of 8 meters and fixed length of 7 meters) and a variable numbers of micropiles (from 3 to 7 elements as a function of monitoring) for a length of 12 meters.

The micropiles are designed for a drilling diameter of 160 mm with steel pipe reinforcement of 101.6 mm.

The prestressed tie backs were equipped with innovative improvement system (TFEG devices that will be presented in chapter 4) that allowed the reduction of both the length of drilling, and of the time needed for pre-tensioning the rod.

The efficiency of stabilization measures consisted in a reduction of the settlements of rib toes and the stemming of collapse event at the boundary of the excavation.

In particular the measures produced a rapid decrease of the closure convergence and stabilization of the settlements.

2 ANALYSIS OF EFFECTS OF EXCAVATION

2.1 *FEM modeling*

Some numerical FEM non linear analyses were developed in order to evaluate the effects of the excavation and the subsequent deformation of the primary lining.

The analyses were conducted using the Plaxis code, using the soil stress-strain criterion of Mohr-Coulomb.

The model considered the effects of relaxation at the face core of the tunnel, that is a reduction of 30% of the original stress state during the transitional phase between the excavation and the building of the reinforcement of the lining.

The analyzed cross-section here under is located at 140 m far from the tunnel entrance section, that matches with the worst condition as for the angle of the slope and the cover height of the excavation. The critical location is also confirmed by the results of the monitoring that show the highest values of the settlement of the rib toes.

2.2 *Analysis of results without any reinforcements*

The analysis of horizontal deformation arrows displays that the excavation produces important deformational phenomena that involves great portion of the soil body. This portion has asymmetric frustum of cone form due to the slope effect, like in Figure 6.

In particular it can be clearly seen that the depression induced by excavation is very asymmetrical.

The principal stress directions are modified because of the combination of the effects of excavation stress disturb and of the slope.

This effects generate anisotropic and not homogeneous stress-strain field like in Figure 7.

Also the analysis of displacements in the primary lining shows that the excavation causes trends to deform towards downhill, as confirmed by plotted strains.

2.3 *Results of FEM analysis with reinforcement elements*

Subsequent analysis was performed by inserting the elements of stabilization.

The effects of the micropiles and tie-backs looks clear observing the trend of displacement of lining, in which the patterns of horizontal and vertical settlements is heavily reduced, especially in the area of the rib toes.

The upper values of displacement of primary lining is about few centimetres, that are close to the results of the monitoring after the installation of the elements.

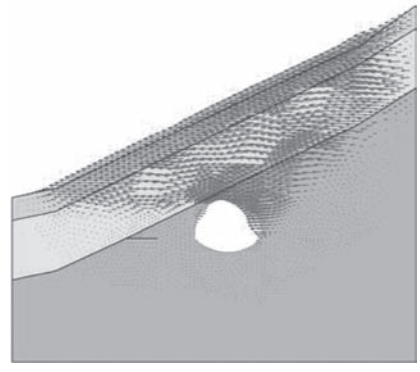

Figure 5. Horizontal displacements.

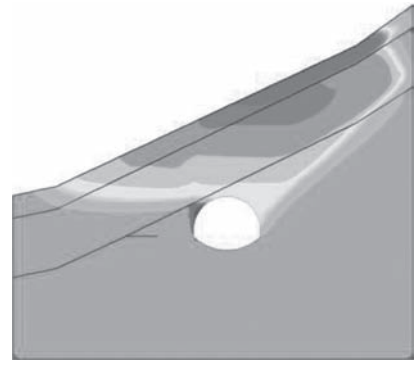

Figure 6. Horizontal displacements.

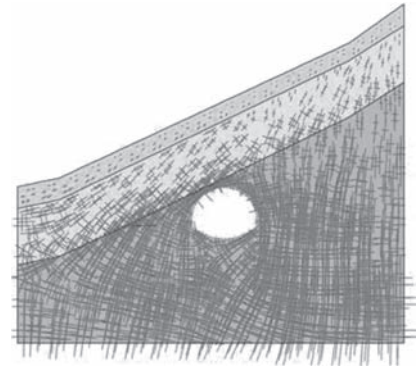

Figure 7. Anisotropy of principal stress direction.

The pattern of axial force and bending moment showed a marked asymmetry. The left part of the lining is stressed by higher values of axial force according to the stress-strain behaviour and to the local anisotropy stress rate of the rock mass. The trend of strain due to the slope effects causes increase of bending moment value in the right toe of the lining. The maximum value of axial force in the lining is about 1500 kN, and the value of bending moment is about 71 kNm per longitudinal unit length.

The two micropiles at the toes of the ribs are also stressed in an asymmetrical way, as can be observed through the horizontal and vertical displacement pattern (Fig. 11). Horizontal displacements are more severe in the uphill right foot of the rib, while

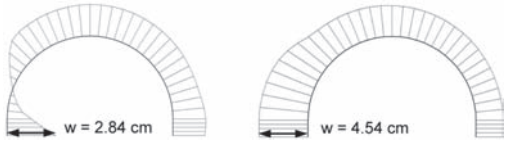

Figure 8. a) Horizontal displacements of primary lining without reinforcement at the rib toes with extreme value; b) Vertical settlements.

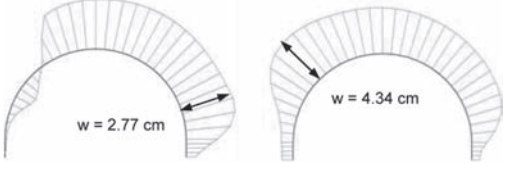

Figure 9. a) Horizontal displacements of primary lining; b) Vertical settlements.

Figure 10. a) Axial force on primary lining; b) Bending moment.

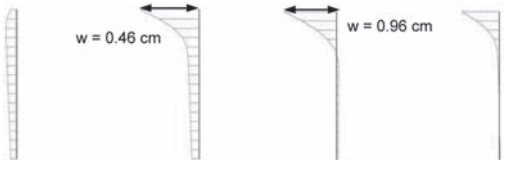

Figure 11. a) Horizontal displacements in micropiles with extreme value; b) Vertical settlements in micropiles.

Figure 12. Horizontal displacement in tie-backs.

the vertical displacements was higher in downhill left side.

In accord with the evidence of displacements, the analysis of stress state of the micropile foundation put in evidence that, in terms of axial force, was more stressed the downhill left elements, that reach the value of 837 kN while the right side element reaches the value of 630 kN.

In fact in left downhill side of the tunnel a collapse event occurred to the connecting horizontal steel beam, due to the high shear-torsional effect caused by the eccentricity between the micropiles reactions and the axial force of primary lining. The collapse involved the web of the steel beam, that was punching off by the steel pipe of a micropile.

In terms of bending moments the highest values on micropiles were detected on right hand side of the tunnel, due to the large amount of horizontal displacement.

The acting shear force reaches the value of 40 kN and the bending moment the value of 7,5 kNm.

The reactions on tie-backs look consistent with the general behaviour of the model. In fact, these elements are stressed by incremental tension forces equal to 275 kN for the element in right side and 45 kN for the element in left side. This is a confirmation of the slope effect and of the consequent anisotropy and unhomogeneity of in situ stress state.

The collapse event occurred on the ties connecting steel beam during the works can be reasonably justified taking into account the higher value of the overall complex bending moment acting on the right uphill side.

3 DESIGN APPLICATIONS OF RESULTS

3.1 *Analysis of connecting beam stress state*

Collapse events allowed to perform back-analysis of the stress levels and of the forces involved into the tunnel excavation. It was analyzed the stress state of the steel beam connecting the tie-back and micropile heads with the primary lining.

This study looks forward to comparing the values obtained by FEM analysis with the ones obtained by an independent back analysis of plastic deformations of the beams. The yielding

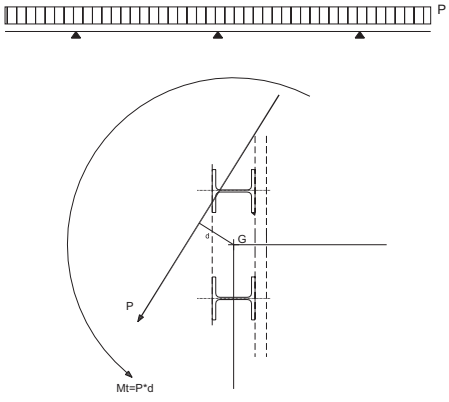

Figure 13. a) Model of connecting beam stress; b) Cross section.

of steel beam is generated by the combination of shear stresses and bending-torsional stresses.

The FEM analysis also allows the evaluation of the distribution of the reaction of tie-backs and micropiles, moreover for the upward side, where the anisotropy effects caused the anticipated yielding of the structure. It was obtained for vertical reaction of the single micropile the value of 837 kN and for the reaction of tie back with TFEG system the value of 275 kN.

An independent back-analysis is carried out starting from the yielding state in the web of the beam and supposing a simplified static condition based on the Saint-Venant model. Taking into account the eccentricity of the vertical forces transmitted by the ribs of the primary lining, considering the same inclination of the resultant of the reaction of the tie backs and of the micropiles, the condition of yielded of the steel beam section leads to the value of 299 kN in tie-back and to the value of 788 kN for micropile. These values look like very close to those obtained from FEM analysis.

4 USE OF TFEG AS IMPROVEMENT DEVICE OF TIE-BACKS FIXED LENGTH

4.1 *The system*

The method TFEG—acronym for Thriving Friction by Extruded Gear—allows to improve the capacity to transfer of the load from foundation piles of small, middle or large diameter, or from tie-backs or anchorages into the soil.

The improvement sorts out through the extrusion of metallic spikes into the soil, preventively set up along the micropile steel tube or connected to the steel reinforcement of the element of foundation. The TFEG system, responds to the need of

Figure 14. Tie-back equipped with TFEG.

increasing the efficiency of loads transfer or to reduce the entity of the settlements required for the mobilization of the strength at the base of the pile or tie rods.

The function of the system for tie-backs is to increase the shaft strength against the pull-out and, at same time, to reduce the lengths of drilling foundation.

In tie-backs application this solution allows to speed up the activation of the tensile pre-stressing load of the anchor whenever the time factor plays a very important role before the extension process of the plastic zone into the soil or the rock mass.

4.2 *TFEG in prestressed tie-backs*

In order to preliminarily evaluate the contribution of the TFEG device to the overall tensile strength, a simplified model was developed.

The failure strength of TFEG system depends on the failure mechanism. Two general failure behavior can be looked over.

The first one is related to the collapse of the soil around the TFEG's spike surface, sorting out in a local failure pattern: LFM—Local Failure Model.

On the opposite, whenever the contribution to the bearing capacity of the different adjacent spikes match cross each other, an overall failure surface would involve the soil around the foundation length of the tie back along a potential cylindrical surface—CFAp—Cylindrical Failure Approach.

LFM is formed in soft soils, where the available shear strength leads to the development of a local failure surface around the spike.

Base hypotheses of the approach result in general conservative. In fact, the slip lines of the collapse pattern stop at the centre of the fixed length and all the 3-d effects of the failure model are neglected.

Furthermore, the compaction effects of the penetration into the soil of the TFEG and the consequent increase of soil friction are not taken into account.

CFAp mechanism, on the contrary, is more favorable for stiffer and more resistant soils, for which the failure surface diameter can reach up to the external diameter of the exploded TFEG system.

Figure 15. a) LFM collapse mechanism; b) CFAp collapse mechanism.

The transition from LFM to CFAp depends on the development of global failure surfaces, then by the mechanical properties of the soil and by the geometry of the TFEG.

The firmer the soil, the higher its shear strength, and the wider the TFEG geometry, the higher the probability of triggering of the three-dimensional effect arc or vault between the tips extruded, and the probability that the CFAp patterns sparks out.

A simple analytical approach is available for the LFM failure pattern. It is based on the hypothesis to consider the shaft of the deep element as a rigid body, and the single TFEG extruded spike like a shallow foundation independent from the context, whose surface is equal to the horizontal projection of the piston. The cross dimension of the equivalent shallow foundation is assumed as the average diameter of the TFEG.

It is worth comparing the extreme tensile load of a traditional tieback with the correspondent of a TFEG equipped tieback.

Considering the ultimate tensile load of traditional tie back in homogeneous cohesive soil characterized by undrained cohesion c_u you can consider:

$$R_u = \pi D\, l_u\, \alpha c_u \tag{1}$$

where R_u = extreme tensile load in tieback; D = diameter of perforation; l_u = fixed anchor length without TFEG; α = reductive coefficient of undrained cohesion.

Expressing the value of undrained cohesion by in situ CPT data leads to:

$$R_u = \pi D\, l_u\, \alpha \frac{R_p}{n} \tag{2}$$

where R_p=Cone penetration strength, n=coefficient depending by OCR of the clayey soil.

For the improved tie-back element, the ultimate tensile load can be expressed, in the LFM pattern, as the sum of the strength of a traditional tie-back and the increment strength offered by the TFEG element:

$$R_t = R_u + F_t \tag{3}$$

where F_t = increase of tensile load by TFEG with LFM approach.

The second term can be express as follows:

$$R_t = \pi D\, l_t\, \alpha \frac{R_p}{n} + n_p\, A_{T1}\, R_p \tag{4}$$

where l_t = fixed anchor length with TFEG; n_p = number of TFEG elements; A_{T1} = strength area of single TFEG element.

The efficiency of the system E can be shown as the ratio between the strength of tfegged and untfegged element:

$$E = \frac{R_t}{R_u} = \frac{l_t}{l_u} + \frac{n_p\, A_{T1}}{\pi D\, l_u \dfrac{\alpha}{n}} \tag{5}$$

It is interesting to observe that the efficiency of the system depend on the soil mechanical parameters, only by the n and α coefficient.

In the case of $E = 1$, it is possible to evaluate the reduction of fixed anchor length as:

$$r_l = \frac{l_u - l_t}{l_u} \tag{6}$$

and, after some transformations, to evaluate the area of TFEG system requested to reduce the fixed anchor length from l_u to l_t ensuring the same value of extreme tensile force:

$$n_p A_{T1} = r_l \pi D l_u \frac{\alpha}{n} \tag{7}$$

This expression shows that in LFM conditions the TFEG required area is higher when higher is the diameter and fixed anchor length. It also shows that if α coefficient increases—less undisturbing drilling conditions—the TFEG area increases too; on the contrary if n coefficient increases—higher soil OCR—the TFEG area decreases.

Defining the ratio between the total TFEG spikes area and the untfegged tie-back shaft surface as the surface improvement coefficient—SIC -, it is possible to write:

$$SIC = \frac{n_p\, A_{T1}}{\pi D l_u} = r_l \frac{\alpha}{n} \tag{8}$$

The expression provides the percentage rate of the required TFEG section to get the same strength as for the utfegged element of length l_u. The relation results in design charts as the one shown in Fig. 16 that allows the fast pre-dimensioning of the system.

In CFAp approach, when the collapse happens over the cylindrical surface with diameter D_t,

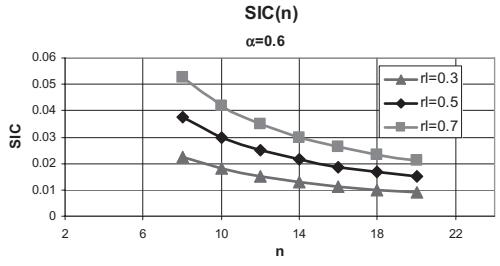

Figure 16. Chart for TFEG pre-dimensioning.

envelope of the extruded TFEG spike, R_t can be expressed by:

$$R_t = \pi D_t \, l_t \, c_u \tag{9}$$

Even in this case, imposing the efficiency of the system equal to 1, $-R_t = R_u-$, leads to:

$$\pi D_t \, l_t \, c_u = \pi D \, l_u \, \alpha c_u \tag{10}$$

then

$$\frac{D_t}{D} = \frac{\alpha}{1 - r_l} \tag{11}$$

this value couldn't be lower than 1. The ratio D_t/D is called *DIC* (Diameter Improvement Coefficient).

Imposing that $DIC > 1$:

$$r_l > 1 - \alpha \tag{12}$$

This fact allows to conclude that although the diameter of the cylinder is so small, a great reduction of the fixed length is always obtained.

If the (11) is express in this form:

$$r_l = \frac{1 - \alpha}{DIC} \tag{13}$$

it is possible observe that, being the value of *DIC* near to 2–3, the r_l value (length reduction) is included between 70%–90%.

5 CONCLUSION

The case history of an excavation of a large tunnel in flysch structurally complex formations, in heavily tectonized geological area, with a high propensity to swell was presented. Instability of deformation related to the post-excavation relaxation required the adoption of reinforcing elements at the foot of the primary lining through the implementation of micropiles and tie-backs.

By carrying out a FEM analysis it was possible to enlight the influence of stress-state in soil mass for the evaluation of the stress on the reinforcement elements. The value of axial force on micropiles and on tie-backs were compared with the value obtained from a back-analysis based on an plastic condition in the connecting beam. The results of the two analysis were approximately fit back.

The tie-backs were equipped with a special improving system, the TFEG.

This device was used to improve the efficiency of tieback fixed length and to produce the quick mobilization of the effect of anchoring and therefore the application of pre-stressing load in real time.

A sensitive increase of the strength was observed comparing traditional tie back with a element with the same characteristics but equipped with TFEG device. It was also proposed a simplified method for a first evaluation of the contribution of the TFEG system to the overall bearing capacity.

ACKNOWLEDGEMENTS

Special thanks to Nicola Maione, inventor of the TFEG system and to Simone Polito contributed to the set up and the run of the numerical model of the reported case history.

REFERENCES

AGI Associazione geotecnica italiana, 1985. Geotechnical engineering in Italy. *Published on the occasion of the ISSMFE Golden Jubilee*.

Santoro, V.M. & Maione, N. 2007. The TFEG Method for the improvement of deep foundations predictions and performances for micropiles. *XXIII Convegno nazionale di geotecnica - Abano Terme 2007.*

Santoro, V.M. & Maione, N. 2010. L'uso del TFEG per la stabilizzazione del rivestimento di prima fase di una galleria in una formazione flishoide con eterogeneità e anisotropia della stato tensionale. In *Gallerie e grandi opere in sotterraneo N. 94 Giugno 2010.*

Viggiani, C. 1999. Fondazioni. *Hevelius Edizioni.*

This page intentionally left blank

Geotechnical Aspects of Underground Construction in Soft Ground – Viggiani (ed)
© 2012 Taylor & Francis Group, London, ISBN 978-0-415-68367-8

Foam conditioning in EPB tunnelling

M. Thewes & C. Budach
Institute for Tunnelling and Construction Management, Ruhr-Universität Bochum, Germany

A. Bezuijen
Deltares, Delft, The Netherlands

ABSTRACT: Earth-Pressure-Balance (EPB) shields are the most common type of tunnel boring machine in soft ground. Due to recent advances in soil conditioning, EPB-shields have been also successfully applied in coarse-grained soils by using foams as conditioning agents for soft ground, to realize a homogenous support pressure and to ensure low water permeability in water bearing grounds. Until now recommendations for the use of foam conditioning with EPB-shields are based on experiences from job sites.

To come up with a knowledge-based approach for dimensioning foam conditioning applications, different research projects have been carried out and are ongoing in Delft and Bochum and will be described in this paper. A laboratory scale test set-up was used that allowed mixing of foam with soil under pressurized conditions and various test series with foam and soil-foam mixtures were performed. Properties of conditioned soil, like behaviour of flow, stability and water permeability, were tested and analyzed. The research helps to understand the main mechanism of soil conditioning with foam for EPB tunneling. A new recommendation for laboratory practice for foam production and soil-foam-mixtures is given. Apart from the foaming agent, also the foam generator has a significant influence on the quality of the foam.

1 INTRODUCTION

In mechanised tunnelling with active face support, the earth pressure balance shields have a dominating market share worldwide, with hydro/slurry shields far behind. This is due to operational and economical advantages of EPB-shields, although the slurry shield can achieve more precise face support (Thewes 2007). According to measurements performed during drilling of the Botlek Rail Tunnel, the fase support can be variable both along the vertical and the horizontal direction (Bezuijen et al, 2005, Bezuijen and Talmon, 2005).

Earth pressure balance shields in closed mode make use of the excavated material to support the face. Conditioning of the excavated material is often necessary to process the soil to support medium.

For fine grained clayey soils it is often necessary to reduce stickiness, clogging by providing some lubrification (Merrit 2004). For these soils water, polymer or bentonite suspensions are often used as conditioning agents. Thewes and Burger (2003) note that foam can be used with sticky clays to reduce the consequences of clogging.

In coarse- and mixed-grained sandy soil by contrast, it is necessary to increase the porosity until a value above the maximum porosity of that soil and to reduce the permeability of the mixture. Because of the foam, earth pressure shields can also be used in coarse-grained soils, where shield machines with slurry face support were used some years ago (Maidl 1995).

This paper will concentrate on soil conditioning with foam for sandy soil.

2 TECHNIQUE FOR SOIL CONDITIONING AND THEIR GOALS

2.1 *Technique for soil conditioning*

In order to produce foam, water and foaming agent (surfactant) are mixed in defined proportions in a turbulent environment to make a surfactant solution. The surfactant concentration (c_f) describes the percentage by mass of surfactant (Q_f) in the solution (Q_L) (water and surfactant) and ranges according to application between 1.5 and 5%. Alternatively to the mass proportions, the volume flows can also be considered with no further conversion factors, because the densities of water and surfactant are approximately equal (Table 1, Eq. 1).

The surfactant solution is fed together with a stream of compressed air through a foam generator,

Table 1. Overview of important foam parameter for soil conditioning (for parameters see text).

Equation	Calculation
1	$c_f = \frac{Q_f}{Q_l}$
2	$FER = \frac{Q_F}{Q_L}$
3	$FIR = \frac{Q_F}{Q_S} = \frac{Q_F}{v \cdot A_S}$

which contains turbulators. The whirling and turbulent flow through the turbulators causes the surfactant solution to foam. The volumetric relationship between the foam flow (Q_F) under support pressure conditions and the supply of surfactant solution (Q_L) is described by the Foam Expansion Ratio (*FER*) (Table 1, Eq. 2). Typical values for *FER* are between 10 and 25.

The foam is introduced into the existing support medium in the excavation chamber through openings in the bulkhead and cutter head. It is also possible to feed foam into the screw conveyor.

The ratio of the volume flows of the injected foam (Q_F) and the excavated soil (Q_S) is described as Foam Injection Ratio (*FIR*) and can be calculated depending on the advance rate (v) and the face area (A_s) (Table 1, Eq. 3). The volume flows of the individual foam ingredients can also be calculated depending on the advance rate Various parameters for soil conditioning with EPB shields were analysed in Thewes and Budach (2010 b).

2.2 *Goals of soil conditioning*

For coarse- and mixed-grained soils, the objectives of conditioning with foam result from the required characteristics of the support medium:

- Suitable flowing behaviour of the support medium to ensure sufficient flow of material in the excavation chamber and the screw conveyor,
- Support of the entire face with nearly homogeneous material to transfer the support pressure to the surrounding ground,
- Reduction of the water permeability, so that water flow during excavation hardly influences the porosity of the mixture. For example too much water flow into the soil mixture in the screw conveyor may lead to a sand-water mixture that flows easily through the conveyer, so that the necessary pressure difference cannot be maintained. The increase of the compressibility of the support medium, in order to dampen volume and support pressure fluctuations in the excavation chamber caused by the process,
- Reduction of the internal friction of the support medium, in order to reduce the drive torque and thus the energy consumption of the cutterhead and screw conveyor and also to reduce wear on the cutting tools and other mechanical components.

Table 2. Overview of desired properties of support media of EPB-shields (Thewes and Budach 2010 a).

Parameter	Value
Permeability	$k_f < 10^{-5}$ m/s
Consistency for material flow	$0{,}40 < I_C < 0{,}75$
Consistency for sufficient pressure gradient in screw conveyor	$0{,}60 < I_C < 0{,}70$
Compressibility	Depending on geological properties of soil and on dimensions of shield machines
Consistency and plasticity for low stickiness	$I_C < 0{,}50$ and/or $I_P < 20\%$

k = water permeability [m/s], see DIN 18130, T1; $I_C = (w–w_p)/I_p$ consistency index of clay [–], see DIN 18122, T1; $I_P = (w_l–w_p)$ plasticity index of clay [–], see DIN 18122, T1; w = water content of clay [–]; w_l = water content of clay at liquid limit [–]; w_p = water content of clay at plastic limit [–].

To use an EPB-shield without soil conditioning, the soil should have properties as listed in Table 2, using the Atterberg limits (w_l and w_p) of the soil. These are based on results of published experience for drilling in clayey soils.

3 OVERVIEW OF PREVIOUS WORK

Guidelines for foam injection ratios based on experience from job sites were published by EFNARC (2005). The *FIR* values shown in Table 3 can be correlated to the porosity of various soil types.

To compare *FIR* and porosity, an overview of porosities of chosen soils is given in Table 4. The indicated bandwidth of typical foam injection ratios, however, is larger than the bandwidth of the porosities and this results in a high level of uncertainty for any prognosis of the foam consumption of a planned tunnel drive with an EPB-shield. Maidl (1995) describes the calculation of the necessary *FIR* depending on the maximum porosity of the soil. The volume of injected foam should be at least so large that the sum of the volumes of fine material, remaining water, air bubbles and

Table 3. Recommended foam injection ratio for various soils (EFNARC 2005).

Soil	*FIR* [%]
Sandy clay—silt	40–60
Sand—clayey silt	20–40
Sand	30–40
Clayey gravels*	25–50
Sandy gravels*	30–60

*High stability and anti-segregation properties needed to develop and maintain a cohesive soil as impermeable as possible.

Table 4. Overview of porosity of chosen soil types with medium and high density, see Hiltmann (1998).

Soil	Porosity n
Sand	0.30–0.40
Silt	0.37–0.45
Clay	0.42–0.58

foam is equal to the porosity of the coarse content of the soil in loose bedding.

Bezuijen (2002) has quantified how the permeability of the soil influences the necessary amount of foam to be injected. However, likely also other mechanisms (for example the size of the foam bubbles compared to the size of the pores) play a role.

During tunnelling often a higher *FIR* is required than the expected *FIR* and therefore the recommendation has to be checked based on experiences on comparable soils.

The properties of the produced foam are important for the conditioning of coarse-grained soil in order to ensure foam of constant quality and to achieve reproducible results. Important factors influencing the foam quality are the type of foaming agent and its concentration in the foaming liquid, the Foam Expansion Rate (*FER*), the volume percentage of foam in the soil (*FIR*), the type of foam generator used and the level of counterpressure. Until now, only few scientific studies were conducted to examine the influences of the listed factors for producing foam for soil conditioning (Maidl 1995, Quebaud et al. 1998, Merrit 2004).

Maidl presented grain size distributions of soils where and EPB with foam can be used. Due to technical progress, it is possible now to use EPB for soils with coarser grains than recommended by Maidl. Quebaud et al. investigated the some physical properties of foam with and without polymer additives and suggested that the 'slump' (shortly described in section 4.2) of a foam-sand mixture should be between the 100 and 150 mm. Merrit investigated the efficiency of foam injection in stiff London clay and found that up to a *FIR* of 60% most of the water was absorbed by the clay, breaking down the foam. Adding polymer was more effective.

So far, no detailed recommendations for foam production in laboratories for simulation soil conditioning in EPB tunneling were given. In lab tests foam typically is produced at flow rates much lower than on an EPB machine. Due to different principles of foam production most of the results are not comparable with results of real-scale foam production.

A variety of experimental studies were conducted by different researchers about the conditioning of coarse-grained soil with foam (Maidl 1995, Quebaud et al. 1995, Merrit 2004, Borghi 2006, and Peila 2009). Here, the foams were produced at atmospheric conditions, then mixed with different types of soil and placed in a pressure tank. The conditioned soil was pressurised and extracted with a screw conveyor to characterise the pressure gradient and the material flow in the screw conveyor. With this experimental setup it is difficult to simulate the closed mode of an EPB-Shield because the foam-soil-mix, when being produced at atmospheric pressure, will undergo significant changes of plasticity and permeability upon pressurization. Bezuijen and Schaminée (2001) performed model experiments in which the foam was created with a 'TBM' foam gun under a pressure of 1 bar above the atmospheric pressure. However, they used only two foam agents each with its own foam gun and performed a limited number of tests.

Therefore, further research on foams and foam-soil-mixes are advised to gather new information about their quality. They are also necessary to set up improved guidelines for foam conditioning for upcoming projects.

4 METHODS TO DETERMINE THE QUALITY OF FOAMS AND SOIL-FOAM-MIXTURES

4.1 *Methods to determine the quality of foams*

At present, there is no standardized method for determining the quality of foam for EPB-shields neither on shield machines nor in laboratories. For foams to be used with an EPB-shield, the following requirements can be defined. The foam should

- have a constant and uniform density, which means that liquid and air are completely mixed and that all parts of the produced foam have the same properties,
- be stable for the duration of stay in the excavation chamber and
- have a homogenous structure of bubble size.

To determine the foam parameters, the following test methods can be used. The focus of these methods is the determination of parameters in laboratories, but the methods can also be adapted for shield machines.

The density of the foam is measured to determine the volumetric content of liquid and air and to control the *FER*. The density is determined by the weight of the foam by known volume. According to EFNARC (2005) the drainage time is evaluated to get information on stability and drainage performance of foam. Therefore a funnel with a sieve is used and the time period is measure, for draining the liquid of the foam. The size of the foam bubbles can be measured by microscope to control its homogeneity (Pena 2007).

4.2 *Methods to determine the quality of soil-foam-mixtures*

So far, there are also no standardised test methods available to determine the quality of conditioned soil, the foam-soil-mix. Some requirements regarding unconditioned soil with a high content of fines are presented in Table 2. Since these requirements cannot be fulfilled by a coarse-grained soil, a range of test methods has been developed to determine additional properties of coarse foam-soil-mixes as support medium. The parameters that can be used to describe these additional properties are:

- density of the support medium to determine the distribution of support pressure across the tunnel face
- workability, relative yield stress and the relative viscosity of the support medium
- permeability to allow for conclusions regarding the range of applicability of EPB-shields and to determine the water flow from the tunnel face
- compressibility of the support medium to evaluate the sensitivity towards variations in volumetric flow
- stability of the support medium against unmixing, especially during halt of cutterhead rotation

A method to measure the density in the field through the bulkhead is described by Bezuijen et al. (2005). The density of the soil-foam-mixture can be measured by determining its weight and volume. The workability (deformability) can be determined by using the slump test as an index test. Here, soil is filled into a special cone, which then is lifted. By measuring the height of the soil-foam-mixture before and after lifting the cone it is possible to determine the slump. The test procedure follows ASTM C143 (1999). The water permeability can be measured by determination of the volume flow of water that flows through a sample of soil-foam-mixture according to DIN 18130. For the measurement of the compressibility of the soil-foam-mixture it is placed in a transparent cylinder and after applying different pressures the volume is measured. The stability of the media can be described by measuring its volume over time.

5 RESULTS OF EXPERIMENTAL RESEARCH ON FOAMS AND SOIL-FOAM-MIXTURES

5.1 *Results of test with foams*

At Ruhr-University Bochum's tunnelling laboratory a series of experiments regarding the production of foam was conducted, introducing a wide variation of process parameters. The following parameters were varied during the tests:

- flow rate of foam
- type of foam gun
- level of counter pressure
- length of conveying system
- type of conditioning agent
- concentration of conditioning agent c_f
- Foam Expansion Ratio (*FER*)

An industrial foam generator was installed, which allows for flow rates similar to real projects with EPB-shields, so that foam can be produced under realistic conditions. With this foam generator, as shown in Figure 1, the production parameters, such as the flow rates of air and liquid, the usage of a pressure tank or the length of the piping system can be varied. Three types of foam guns with different mechanical inserts for the creation of turbulences were used during the tests.

Numerous different qualities of foam have been produced and their properties were characterized. As selected result the mass of the drained liquid

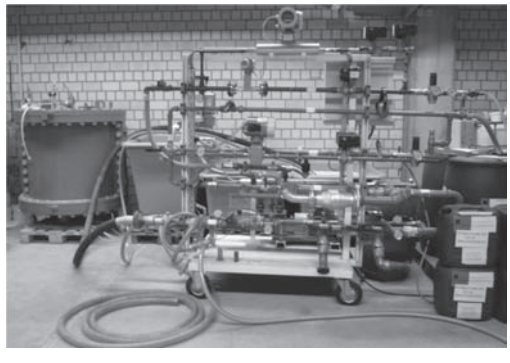

Figure 1. Foam generator of the Institute for Tunnelling and Construction Management at Ruhr-University Bochum, Germany (Thewes et al. 2010).

from the foam is shown as a function of time. Results of the tests showed, that the drained liquid mass from various foams strongly depends on the choice of foaming product and of the foam generator. For the tests four different foaming products and two different foam generators were used to produce foam under atmospheric pressure. The *FER* of the foam was 15 and c_f = 3%. 80 g of each foam was placed in a filter funnel with a diameter of approximately 13 cm and porosity 1 (maximum 100–160 µm). Figure 2 shows a filter funnel to determine the drain liquid from the foam.

In Figure 3 the thin lines show the drainage times of foams produced with Foam Generator 1 (FG1), and the thick lines show the drainage times of foams produced with FG2. Product 1 and Foam generator 2, compared with foams from other combinations of products and foam generators, has the highest drainage time of almost 1200 seconds for 40 g of drained liquid and also more or less constant increase of the drained liquid.

The combination of product 1 and foam lance 2 shows an almost ten times longer drainage time than product 4 and foam lance 1 for 40 g of drained mass. The first combination therefore results in a more durable foam.

Since in the filter funnel the hydraulic gradient is approximately 1, the results can be used to determine the permeability of the foam itself. The most impermeable foam (the combination Product 1—FG2) has a permeability of $2.7*10^{-6}$ m/s, the most permeable (Product 4—FG1) a permeability $2.5*10^{-5}$ m/s. So there is nearly a factor of 10 difference. For Product 1, changing the foam gun only from FG1 to FG2 leads to a 2.7 times lower permeability. For Product 4 this is a factor of 1.9.

The most likely explanation for the differences found between the two foaming generators is that FG2 generates finer foam bubbles, resulting in a lower permeability for the water between the foam bubbles.

Figure 2. Filter funnel for determination of drain time.

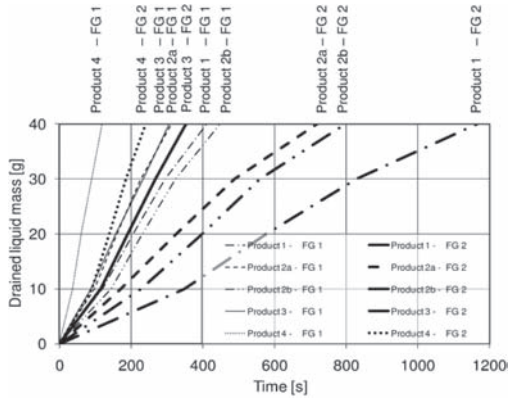

Figure 3. Drainage times from different foaming products and different foam generators.

Further research is necessary how the foam stability as found in these laboratory tests relates to the quality of the foam necessary in a TBM. From the tests described by Bezuijen et al. (1999), it appeared that without drainage a sand-water-foam mixture can be remarkable stable. In a foam mixture without soil and without drainage the air bubbles will move upwards due to the buoyancy forces. However, with soil, the upward directed movement of the air bubbles is hampered by the soil particles resulting in a more stable mixture. The question to be answered in further research is how the stability of a foam-water-air mixture is influenced by the shear stresses that are exerted on it in the mixing chamber and in the screw conveyor.

The results of the tests on foam have shown that there is a great influence of the input parameters on the foam production on the properties of the resulting foam. To the authors knowledge, the influence of the foam gun has not been reported before. The properties of foam during lab testing should be characterized with foam generators, which use a principle similar to that on Earth Pressure Balance Shields.

5.2 *Results of test on soil-foam-mixtures*

Different soil-foam-mixtures with a variation of the injection ratio *FIR* have been tested. As a selected result, the slump test of mixtures with increasing injection ratio is shown. Sand with a grain size diameter between 0.2 and 0.6 mm was used with a water content of 10%. The foam parameters were c_f = 3% and *FER* = 15. Initial tests showed that there is a high influence of the mixing time on the density of the soil-foam-mixture. For comparable results the soil was always mixed with foam within a gravity mixer for 30 seconds. During laboratory

testing it is of importance to add the necessary amount of foam immediately after production to the soil to keep the influence of the time-dependent change of foam properties to a minimum.

Figure 4 shows the results of the slump test with increasing foam injection ratio. With increasing *FIR* the slump value will also increase. On job sites values of the slump tests can range between 5 or 25 cm (Vinai 2006). Normally, slump values between 10 and 20 cm are within the range of the practical use of the conditioned material. For these values a *FIR* of round 10 and 20% can be determined with the performed tests.

The results of the tests on conditioned soil in laboratory under atmospheric condition show that the *FIR* in Sand 0.2–0.6 mm was lower than the recommendend *FIR* of EFNARC. Due to the water content of w = 10% the water will fill the pores and the required volume of foam is lower, but due to the water, the permeability of the mixture will be higher.

Normally a foam expansions ratio of around 15 is recommended for injection in sand. Due to the presence of pore water the effective *FER* in the mixture can be much lower. For a *FER* which is much larger than 1 and saturated soil. The effective FER_s of the mixture is not determined by the original *FER*, but by the amount of foam injected, resulting in the relation (Bezuijen, 2002):

$$FER_s = \frac{FIR}{n} \tag{1}$$

where *n* is the porosity of the soil. This means that when foam is injected with a *FER* of 15 in saturated sand with a porosity of 40% and the amount of foam injected is 40% of the soil volume (thus *FIR* is 0.4) then the effective *FER* (FER_s) in saturated sand is only one. Consequently the muck will be very wet.

Bezuijen et al. (1999) have shown experimentally that consequently the permeability of a saturated sample injected with foam can be 50 times higher than for a sample that is unsaturated before the foam injection.

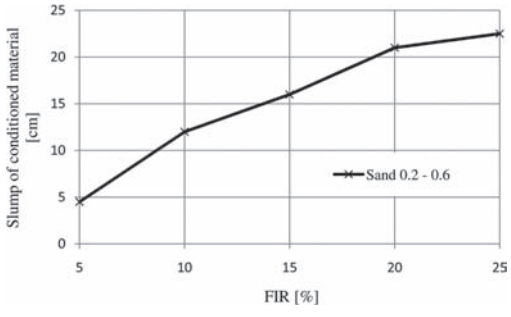

Figure 4. Slump of a soil-foam mixture with increasing *FIR*.

6 RECOMMENDATIONS FOR PRACTICE

6.1 *Recommendations for foam production*

From the results of the tests on realistically produced foams, various influences on the investigated properties, which are shown in Table 5, can be determined depending on the production parameters. Mainly, the choice of foam generator and the conditioning agent have great influence on the drainage time and the bubble size of the foam. For the investigation under support pressure, the pressure was increased up to 1.5 bar relative excess pressure. This showed that the excess pressure has only a slight influence on the density, but a large influence on drainage time. The bubble size of the foam, which is related to drainage time, so far could not be determined under pressure because no suitable method of optical measurement is available.

Results as described in this paper indicate that a smaller bubble size leads to a longer drainage time and consequently to more stable foam. However, it is likely that the bubbles need a minimum dimension. When the bubbles size becomes too small it is possible that the bubbles migrate

Table 5. Overview of qualitative influence of different parameters on the quality of foam.

		Influence on		
		Density	Drainage time	Bubble size
Type of foam gun		o	++	++
Volume flow of foam Q_F	FG1/FG2	+/o	+/+	+/+
Pumping pressure	FG1/FG2	o/o	+/+	o/o
Length of pumping line	FG1/FG2	o/o	o/o	o/o
Conditioning agent	FG1/FG2	o/o	++/++	++/++
Surfactant concentration c_f	FG1/FG2	o/o	o/+	+/+
Foam expansion ratio *FER*	FG1/FG2	+/o	+/+	+/+
Back-pressure p_{supp}	FG1/FG2	o/o	++/+	x/x

FG1 = foam gun 1; FG2 = foam gun 2; o = no or little influence; + = medium influence; ++ = great influence; x = not determined.

Table 6. Overview of qualitative influence of different parameters on the quality of soil-foam mixtures.

	Influence on			
	Density	Flow behaviour	Water permeability	Compression
Foam	o	+	++	o
FIR	++	++	+	++
FER	o	++	++	+
Grading curve	++	++	++	+

o = no or little influence; + = medium influence; ++ = great influence.

though the pores of the not yet excavated soil and that would prevent an effective 'plastering' of the face, which may lead to instability. This aspect will be subject of further research.

6.2 *Recommendation for soil-foam-mixtures*

Based on the results of the tests, the influence on the essential parameters of the support media can be derived (Table 6). Regarding individual test results, reference is made to Thewes (2010). Apparently the properties of the support media depend greatly on the properties of the soil. In addition, the water permeability of the support media can be strongly influences by the type of the foam; the density,

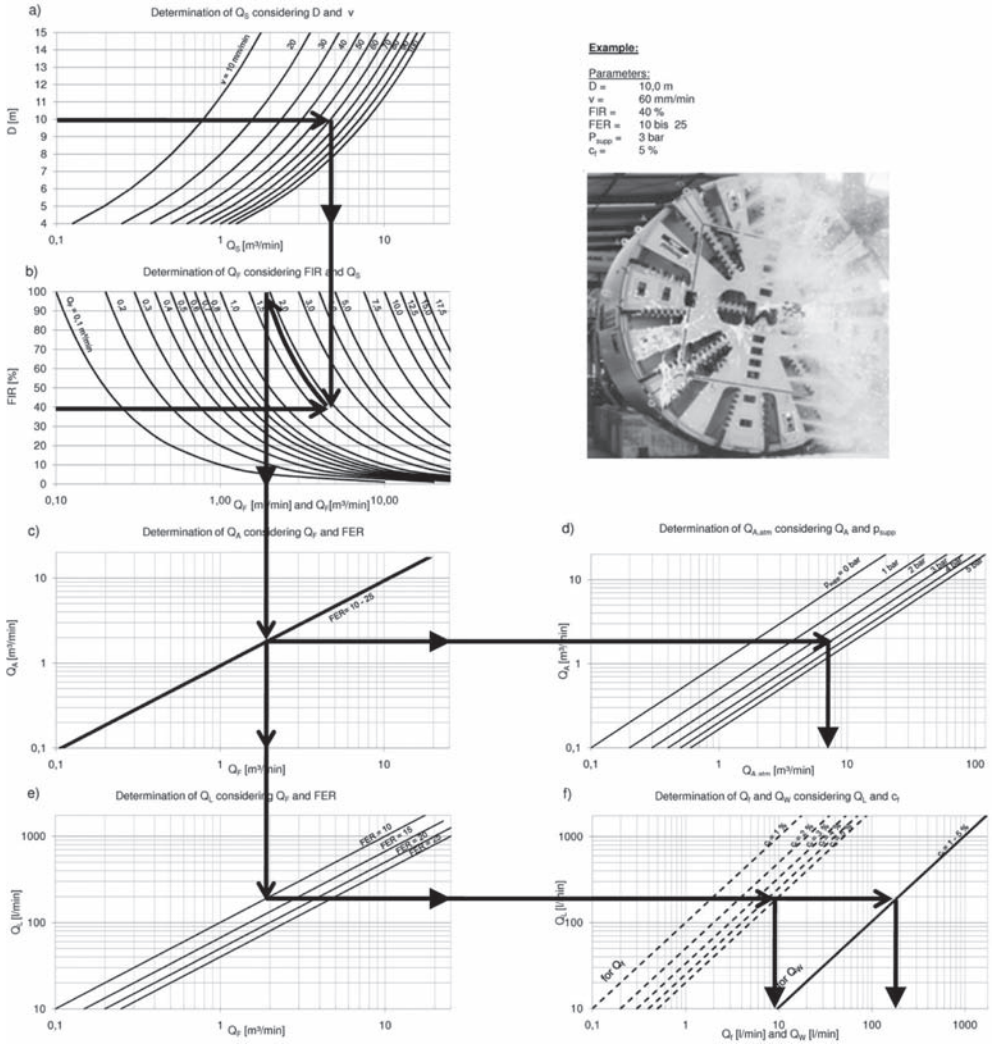

Figure 5. Graph for determination of production parameters of foam production (Budach 2010).

the flow behavior and the compressibility by the *FIR* and the flow behaviour and water permeability by the *FER*.

For the dimensioning of foam generators and for checking volume flows during tunnelling a graph was developed by Budach (2010) (see Fig. 5, at the end of the paper).

The volume flow of the soil Q_S can be calculated depending on the shield diameter D and the advance speed v, see part a) of the graph. For example, an EPB-Shield with a diameter of 10.0 m and an expected advance speed of 60 mm/min results in the volume flow of the soil Q_S, here 4.7 m³/min.

The required volume flow of the foam under support pressure conditions depending on the volume flow of the soil Q_S and the *FIR* can be determined in part b) of the graph. The required volume flow of foam Q_F can be calculated by getting the intersection of the vertical line of Q_S and the horizontal line of *FIR*. The value can be read at the top of the diagram. Therefore a parallel line to the plotted lines will be drawn and the intersection at the top will be determined. In the example, the volume flow of the foam Q_F is 1.9 m³/min.

A vertical line of the value of Q_F will be extended in part c) of the graph for determine the volume flow of the air under support pressure Q_A. This line will cross the plotted line of the *FER*. A horizontal line will be drawn through this point to the right side. The volume flow of the air under support pressure Q_A can be determined to 1.7 m³/min.

The volume flow of the air under atmospheric condition $Q_{A,atm}$ depends on the support pressure p_{supp} and Q_A. The horizontal line of part c) will be extended in part d) and will cross the line with the expected support pressure. The value of $Q_{A,atm}$ can be determined by draw a vertical line and cross the horizontal axis at the bottom of that part. The value for $Q_{A,atm}$ is 6.8 m³/min.

The volume flow of the liquid Q_L can be determined in part e) of the graph. The drawn line of the lowest *FER* is necessary for the identification of Q_L. This line and the extended vertical line of Q_F will be crossed and a horizontal line will be plotted in this part. The volume flow of the liquid can be read at the right side of the graph. The value of Q_L is 190 l/min in this example.

This value is necessary for the determination of the volume flow of surfactant Q_f and the volume flow of water Q_w. Both depend on the concentration of c_f. For determination of Q_f the horizontal line will be crossed with the line with the highest value of c_f. A vertical line will be drawn through this point and at the bottom of the diagram the volume flow of the surfactant Q_f can be determined. This procedure is also necessary for the determination of Q_W. The values are 9.5 l/min for Q_f and 190 l/min for Q_W.

This example does not take into account pore water and pore water flow. As mentioned pore water decreases the effective *FER* and pore water flow may lead to a loss of foam volume (the water in the foam flows into the soil due to the higher pressure in the foam than in the surrounding pore water). Bezuijen (2002) presents equations how pore water and pore water flow influences the amount of foam to be injected and the effective *FER* (the foam expansion ratio when the pore water is taken into account, thus the ratio between the volume of air and the volume of the water in the pores with added the volume of pore water).

7 CONCLUSION

Recent experimental research on the foam conditioning during EPB tunnelling has focused on the production of the foam itself as well as the foam-soil-mix resulting from soil conditioning. Regarding the foam produced for lab tests it has become clear that the foam generator has a rather significant influence on the foam quality. It is therefore important to calibrate a scaled down foam production unit used in a laboratory so that foam it produces will be comparable to foam produced at real scale, or to use a real scale generator. Further it is important to frequently check the foam which is produced during a tunnel drive regarding its quality parameters.

Besides the type of mechanical foam production equipment, also the type of foaming agent has a strong influence on the quality of the foam and thus on the effectiveness of the conditioning process.

The research presented here has shown that foam bubbles of a smaller size lead to a more stable foam. In future research it will be investigated whether there are limits to this conclusion, for example because very small bubble may possibly migrate through the pores of unexcavated sandy soil.

The amount of pore water and pore water flow under influence of the applied pressures in an EPB have a significant influence on the foam behaviour and therefore the stability of the EPB tunnelling process when drilling in sand.

REFERENCES

ASTM C143/C 143M—00 2003, Standard test method for Slump of Hydraulic-Cement Concrete.

Bezuijen A., Joustra J.F.W., Talmon A.M., Grote B. 2005, Pressure gradients and muck properties at the face of an EPB, *5th. Int. symposium on Geotch. Aspects of Underground Construction in Soft Ground*, Amsterdam.

Bezuijen A., Talmon A.M. 2005, Pressure gradients, *Tunnels & Tunnelling Int.*, 14–17.

Bezuijen, A. 2002, The influence of permeability on the properties of a foam mixture in a TBM, 4th Int. Symp. on Geotechnical Aspects of Underground Construction in Soft Ground—IS Toulouse 2002.

Bezuijen, A., & P.E.L. Schaminée 2001, Simulation of the EPB-shield TBM in model tests with foam as additive, Proc. *Int. Symp. on Modern Tunneling Science and Techn. Kyoto*.

Borghi, F. 2006, *Soil conditioning for pipe-jacking and tunnelling*, PhD. Thesis, Geotechnical Engineering Group, University of Cambridge.

Budach, C. 2010, Neue Untersuchungen zur Konditionierung von Lockergesteinen bei Erddruckschilden, *50 Jahre STUVA 1960–2010: Vergangenheit trifft Zukunft*, 252–261, Gütersloh: Bauverlag.

DIN 18122, T1 Juli 1997, Zustandsgrenzen (Konsistenzgrenzen), Bestimmung der Fließ- und Ausrollgrenzen.

DIN 18130, T1 Mai 1998, Baugrund, Untersuchung von Bodenproben: Bestimmung des Wasserdurchlässigkeitsbeiwertes, Teil 1: Laborversuche.

EFNARC (ed.) 2005, Specification and guidelines for the use of specialist products for mechanised tunnelling (TBM) in soft ground and hard rock.

Hiltmann, W., Stribrny, B., Baermann, A. 1998, Handbuch zur Erkundung des Untergrundes von Deponien und Altlasten, Bundesanstalt für Geowissenschaften und Rohstoffe, *Bd.5: Tonmineralogie und Bodenphysik*.

Maidl, U. 1995, Erweiterung der Einsatzbereiche der Erddruckschilde durch Bodenkonditionierung mit Schaum (The extension of the scope of application of shield machines through soil conditioning with foam), PhD. Thesis, Ruhr-Universität Bochum.

Merrit, A. 2004, *Conditioning of clay soils for tunneling machine screw conveyors*, PhD. Thesis, Geotechnical Engineering Group, University of Cambridge.

Peila, D., Oggeri, C., Borio, L. 2009, Using the Slump Test to Assess the Behavior of Conditioned Soil for EPB Tunneling, *Environmental & Engineering Geoscience*, Vol. XV, No. 3, 167–174.

Pena, M. 2007, Foam as a Soil Conditioner in Tunnelling: Physical and Mechanical Properties of Conditioned Sands, PhD. Thesis, Oxford.

Quebaud, S., Sinai, M. & Henry, J.P. 1998, Use of chemical foam for improvements in drilling by earth-pressure balance shields in granular soils *Tunnelling and Underground Space Technology*, Vol. 13, No. 2, 173–180.

Thewes, M. 2007, TBM Tunnelling Challenges—Redefining the State-of-the-Art, Keynote lecture at the 2007 ITA World Tunnel Congress, Prague, *Tunel*, Vol. 16, 13–21.

Thewes, M., Budach, C. 2010 a, Schildvortrieb mit Erddruckschilden: Möglichkeit und Grenzen der Konditionierung des Stützmediums, *Tagungsband des 7. Kolloquium 'Bauen in Boden und Fels'*, Technische Akademie Esslingen, 26.-27.01.2010, ISBN 3-924813-81-7, 171–183.

Thewes, M., Budach, C., 2010 b, Konditionierung von Lockergesteinen bei Erddruckschilden, *Geomechanics and Tunnelling*, No. 3, 256–267.

Thewes, M., Budach, C., Galli, M., 2010, Laboruntersuchungen von verschiedenen konditionierten Lockergesteinsböden für Tunnelvortriebe mit Erddruckschildmaschinen, *Tunnel*, Nr. 6, 21–30.

Thewes, M., Burger, W., 2003, Verklebungen beim Schildvortrieb on Tonformationen—Erkennen und Begrenzen technischer und vertraglicher Risiken (Sticking during shield tunnelling in clay formations—the recognition and limitation of technical and contractual risks). STUVA Tagung 2003 in Dortmund. *Forschung + Praxis 40*, 182–187, Gütersloh: Bertelsmann.

Vinai, R., A contribution to the study of soil conditioning techniques for EPB TBM applications in cohesionless soils, PhD thesis, Politecnico di Turino, Italy, 2006.

Wilms, J., 1995, *Zum Einfluss der Eigenschaften des Stützmediums aus das Verschleißverhalten eines Erddruckschildes*, Mitteilungen aus dem Fachgebiet Baubetrieb und Bauwirtschaft, Heft 12, Universität Essen.

This page intentionally left blank

Geotechnical Aspects of Underground Construction in Soft Ground – Viggiani (ed)
© 2012 Taylor & Francis Group, London, ISBN 978-0-415-68367-8

High-resolution multichannel seismic survey for the excavation of the new headrace tunnel for the Crevola Toce III hydropower scheme in the Ossola Valley, Italy

M. Sapigni
ENEL Produzione S.p.A., Venezia-Mestre, Italy

A.M. Baldi, F. Bianchi & J. De Luca
S.G.G. S.r.l., Siena, Italy

ABSTRACT: A high-resolution seismic survey was conducted for the excavation of the new headrace tunnel for the Crevola Toce III hydropower scheme in an area located between the valleys of the Toce and Diveria rivers. From the geological point of view, the area of the headrace tunnel, 9,2 km long, entirely involves lithotypes belonging to the lower Pennidic Units. In particular the bedrock is composed of a series of gneissic crystalline nappes (Valgrande, Antigorio and Verampio) interlayered by metasediment units (Teggiolo and Baceno) originally corresponding to the triassic-cretaceous sedimentary cover of the crystalline crust. The tunnel path runs mainly through the Antigorio gneiss, but the detailed analysis of the preliminary studies identified a series of geomechanical issues that the tunneling will face through the Baceno metasediments, approximately in the chainage range 6,200–6,700. The metasediments have an average thickness around 70 meters and a general low inclination toward SE; they are composed of a lower gypsum-anhydrite layer locally with micaceous content, fractured marbles and calcschists, and at least two cohesionless sugary carbonate horizons with characteristics of soil. To better define this complex geologic structure, intersected also by a Deep-Seated Gravitational Slope Deformation (DSGSD) with a thickness of 180–260 meters, high resolution seismic reflection and refraction profiles were executed parallel and perpendicular to the tunnel axis, together with VSP and down hole seismic test into geomechanical holes about 400 meters deep drilled near the alignment. In particular, a seismic reflection and refraction line of about 3,000 meters was realized along the tunnel axis. The interpretation of the seismic data through the reflection method, the tomography refraction technique and the tomographic inelastic attenuation processing then allowed geological modelling of the examined area, highlighting the blanket of the DSGSD, its sliding plane, the series of metasediments below, the trends of the basement and also a determination of the geophysics and geomechanics profile along the axis of the tunnel. Based on this data, it was possible to evaluate different tunnel paths aiming to minimize the tunnel length crossing the very poor quality metasedimentary rocks.

Keywords: DSGSD, tunnel, seismic reflection, VSP, seismic refraction, inelastic attenuation, tomography.

1 INTRODUCTION

Seismic reflection data, until recently, has seldom been used for landslide investigations due to the complexity of the internal structure and the relatively rough terrain of landslides. Seismic refraction has been the preferred method in order to supplement geotechnical investigations of landslides consisting of trenching and drilling. However, seismic refraction methods are limited when investigating complex geologic structures with interbedded low- and high-velocity layers.

This study presents the results of a multidisciplinary investigation, centred around seismic reflection profiling, for a new diversion tunnel that will be excavated through a repetition of metamorphic crystalline and sedimentary rocks underlying a prehistoric Deep Seated Gravitational Slope Deformation.

Since the crossing of the metasediments is technically difficult and high risk, a second, more extensive geophysical survey was undertaken with the aim to reconstruct the 3D orientation and thickness of the metasedimentary horizon and the DSGSD basal surface. This would help minimize the tunnel length crossing the very poor quality metasedimentary rocks and maximize the tunnel separation from the overlying deep seated landslide.

2 GEOLOGICAL SETTING

The diversion tunnel layout crosses the deepest part of the Penninic Units traditionally assigned to the ancient northern european margin overthrusted by the oceanic crust and the southern austroalpine margin during the continental collision of the alpine orogenesis. The present-day deep topographic erosion allows us to have a glimpse onto the structure of the Lepontine nappes, tectonic units formed by flat recumbent folds consisting of orthogneissic cores with discontinuous micaschistic and paragneissic outer zones overlaying mesozoic metasediements (Schmidt & Preiswerk 1905; Castiglioni 1958; Milnes et al 1981; Steck, A. 2008). The latter are composed of calcschists, dolomitic and calcitic marbles, quartzites and discontinuous gypsum and anhydritic horizons. This petrographic and rheologic sandwich is the result of many deformative phases the most important of which sliced and thrusted the former continental mainly granitic crust onto the sedimentary cover with displacements of tens of kilometres (Maxelon & Mancktelow; 2005). The amphibolitic metamorphic conditions achieved during the main deformation phase allowed the mineralogical transformations that gave place to the pervasive axial plane foliation forming the present-day schistosity and most prominent weakness planes of the rock mass. Successive slightly or non metamorphic folding events gave the nappe pile its present dominant structure visible along the Antigorio valley with a flat lying attitude in its central part, around the so-called Verampio window, passing to a steep southward inclination near Crevoladossola (Mancktelow N. 1985; Grasemann B., Manktelow N.; 1993) (Fig. 1). The N-S cross section shows the geologic structure of the mountain ridge and the trace of the diversion tunnel. The main feature is represented by the thick, late Variscan (ca. 340 Ma), Antigorio unit composed of a monotonous leucocratic orthogneiss that only rarely shows any structural or petrographic diversity (Bigioggero et al 1977). To the north it overlays the deepest alpine unit corresponding to the equally late variscan Verampio granitic gneiss and its country rock represented by the garnet-rich Baceno micaschists. Interlayered between these two big tectonic units is located the most important permeable unit (Baceno metasediments) which has been well defined after the drilling of three deep boreholes. It has an average thickness around 70 meters and is composed of a lower gypsum-anhydrite layer, at least two cohesionless sugary carbonate horizons, dolomitic marbles and calcschists.

The mountain ridge is cross-cut by many brittle faults arranged in two main sets oriented NW-SE and ENE-WSW. They are the product of the brittle last exhumation phase of the Lepontine dome along the Simplon Fault (Bistacchi & Massironi 2000; Grosjean et al 2004; Zwingmann & Mancktelow, 2004; Campani et al, 2010).

Detailed geological mapping, boreholes and an initial geophysical survey allowed to identify the huge deep seated landslide (DSGSD) (Agliardi et al., 2001) in the northern part of the section that might be genetically linked to the underlying weak metasedimentary horizon. This landslide has a thickness ranging from 180 to 250 m and, under 50–60 m of glacial deposits, it is mainly composed of weak to very weak, degraded Antigorio gneiss. In its northern half the lowermost portion has almost completely involved the metasedimentary layer (Fig. 2).

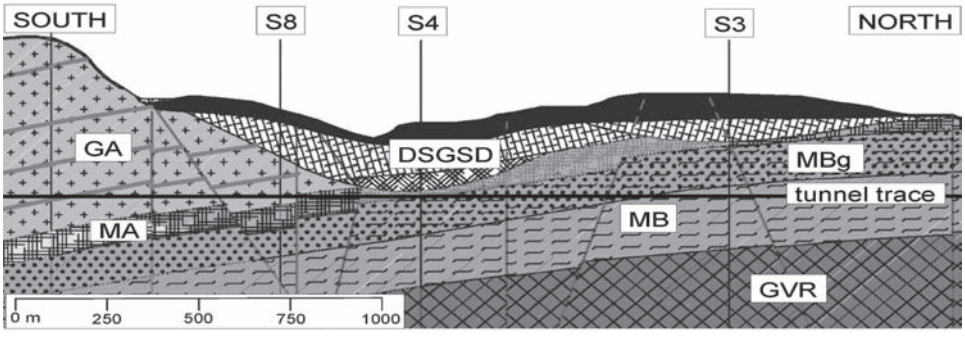

Figure 1. Geological cross section corresponding to the northern half of the diversion tunnel trace. This interpretation was done before the main geophysical survey was performed DSGSD: Deep Seated Gravitational Slope Deformation (involved terrains: black: moraine deposits,light hatch: Antigorio gneiss; heavy hatch: metasediments); GA: Antigorio gneiss; MA: metasediments; MBg: garnet-rich Baceno micaschists; MB: garnet-poor Baceno micaschists; GVR: Verampio gneiss. The location of the three boreholes are also indicated.

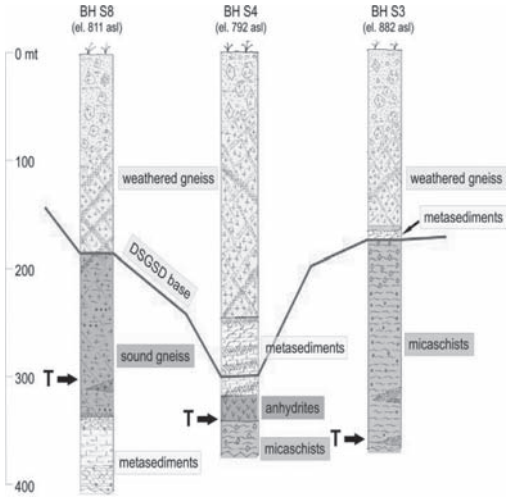

Figure 2. Schematic representation (not to scale) of the main geological units crossed by the boreholes. The horizontal distance between the soundings are: 1,0 km from S3 to S4 and 0,4 km from S4 to S8. T: tunnel elevation.

3 GEOPHYSICAL SURVEY

The principal scope of the geophysical survey was to model the geological structure of the sub-soil in the area between tunnel chainages 4 + 600 and 7 + 600. In this sector, geological and stratigraphic factors had previously not permitted a sufficiently detailed geological modelling.

The geophysical prospecting consisted of the following activities (Fig. 3):

- Seismic reflection profiles (coverage 30 sites over) 6,195 m length;
- Seismic refraction profiles using tomographic method 6,110 m length;
- VSP (Vertical Seismic Profiling) seismic probing in geognostic surveys 525 m length;
- Electrical tomography profiles 1,200 m length.

Seismic reflection profiles were obtained using a nominal coverage of 30 sites, with 120 groups of simultaneously active geophones (4 per group) situated at a distance of 5 metres from each other. Blasting gelatin was used for energization in shafts located at 20 metre intervals.

To record seismic refraction profiles, 120 simultaneously active geophones were utilised and distributed across the soil at a distance of 10 metres from each other. Blasting gelatin was again used for energization in shafts located at 30 metre intervals.

Seismic probing using the V.S.P. method (Vertical Seismic Profiling) was carried out using a chain of 24 geophones at 5 metre intervals, with 2.5 m recording intervals in order to obtain a nominal coverage of 3,000%. With the same scope, seismic velocity measurements were also taken during the surveys, allowing for accurate seismic velocity values to be attributed to the various lithotypes covered by the surveys.

For the analysis of seismic reflection data, the following process was adopted:

Phase 1: Pre-processing

a) Conversation of format
b) Geometry *input*
c) *Trace killing*

Phase 2: Shot data processing

a) RMS *gain*
b) Spectral analysis
c) Band pass pre-filtering
d) Resampling
e) Band pass filtering
f) *Exponential* gain
g) *Mixing*
h) "*Spiking*" deconvolution
i) AGC *gain*
j) *Muting*
k) Band pass filtering
l) *Sorting*

Phase 3: CDP data processing

a) *Pre-stack phase*
   - Aerated static corrections
   - Analysis of velocity every 10 C.D.P.
   - *Normal Moveout* correction
   - Residual static corrections
b) *Stack*
   - C.D.P. summation (stacking)
   - Reduction to common datum
   - RMS *gain*
c) *Post-stack phase*
   - Migration
   - *Mixing*

Phase 4: Complex attributes

Final migrated sections were used to determine complex trace attributes, including instantaneous phase, amplitude envelope and instantaneous frequency (Fig. 4). These parameters are capable of increasing the data's vertical resolution, is particularly the geometrical structure of the reflectors with the instantaneous phase, and variations of signal characteristics on the same reflection with amplitude envelope and instantaneous frequency.

Initially a spectral analysis of the complete set of seismic refraction data was performed in order to verify the frequency distribution of the seismic signal.

The signal was predominantly concentrated at a frequency between 20 and 200 Hz. These values were specified for the band pass filters, to improve the quality and legibility of the seismic data, especially

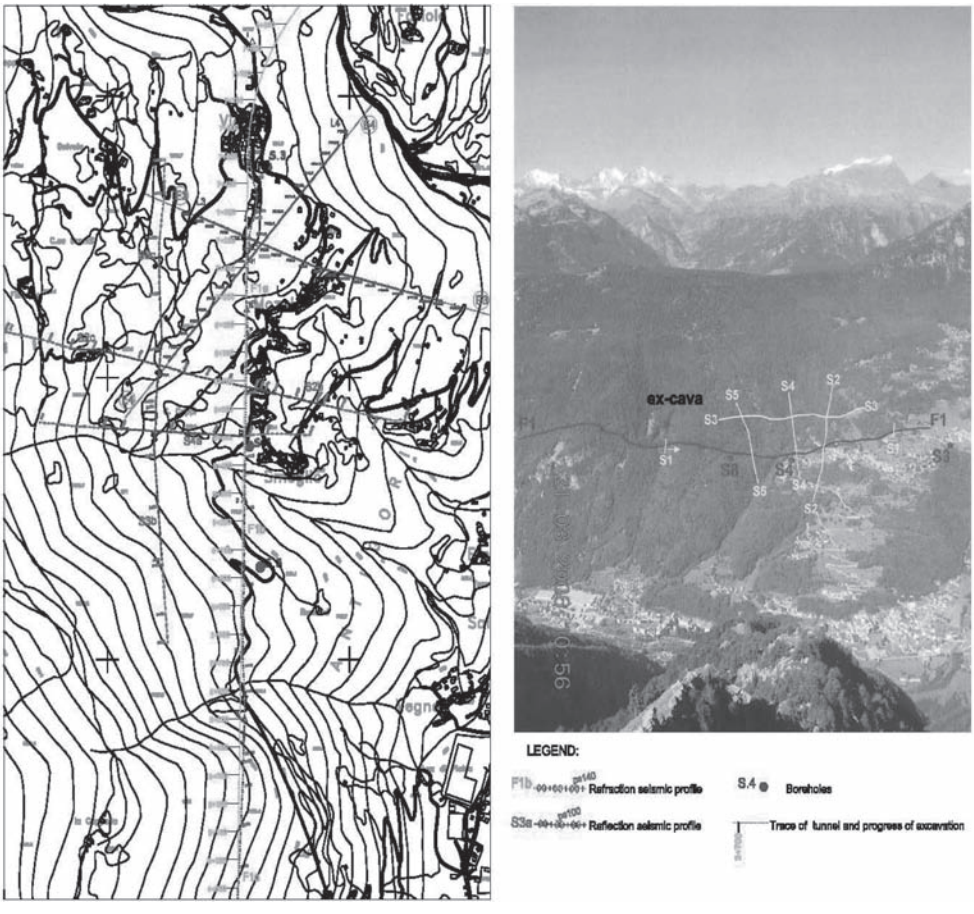

Figure 3. Map and photo of the study area with position of the investigations.

the data derived from distant energization. The tomographic interpretation of seis-mic profiles was carried out using a programme which subdivided the space into 5 m long cells (Fig. 6). Dromocrone graphs for single profiles were interpreted using the G.R.M. method (Generalised Reciprocal Method), used for "reciprocal times", based on the notion of the delay time of the recorded seismic impulses under the geophones. Such method is characterised by a discrete resolution capacity, and has also proven to be capable of significantly reducing ambiguity caused by the presence of low and/or hidden velocity layers (Fig. 5).

VSPs were obtained at zero offset and proved to be strongly influenced by consistent noise of high amplitude, linked to vertical oscillations of the water column in the surveyed hole. These were most likely associated with the small diameter of the surveyed completion tubing, inside which the chain of geophones acts as a piston. These events and any corresponding events with opposing motion were entirely removed during processing in order to highlight primary reflections, or rather upgoing and even downgoing event types.

4 RESULTS

Using the results of all the seismic profiles made it possible rebuild a 3D geological model of the subsoil. The following maps were prepared to show the geological—geophysical—geomechanical section along the tunnel alignment:

- tectonic model for the area: the fault pattern was developed in two different versions. In the first, fault correlation follows only geophysical and interpretative criteria and is controlled by the planimetric layout of the profiles. In the second version the fault pattern has been modified to better integrate with regional geology.

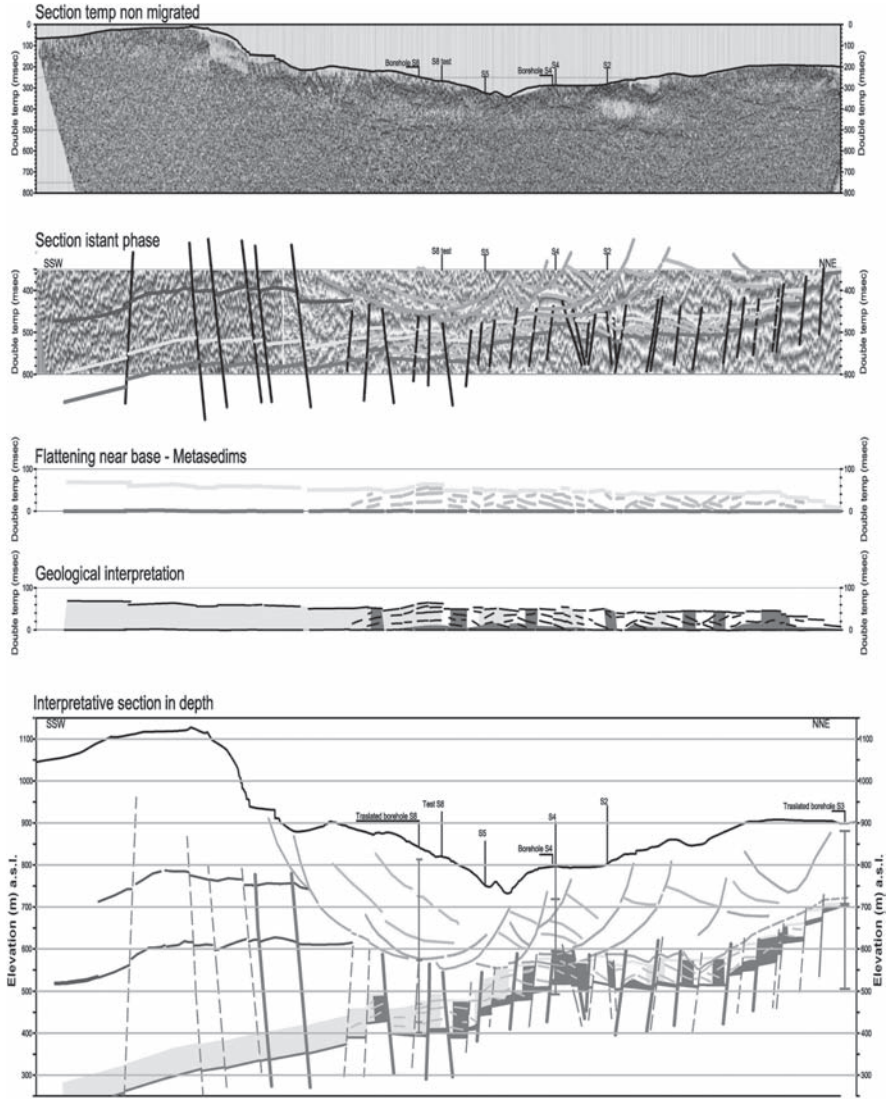

Figure 4. Reflection seismic profile n°1.

- DSGSD bed: stratigraphic results of the three deep seismic surveys carried out using survey adjustment.
- Topographic map of metasedimentary sequence top surface: created using seismic profiles with samples taken at 10 metre intervals.
- Map of the basement top surface: for this plot samples were taken every 10 metres on the seismic profiles. The development of this surface was correlated by a slight emergence in the northern zone, located at 770 m above sea level, showing that the base dips to the south-east. Over the axis of the tunnel approximately two kilometres toward the south, the altitude is approximately 225 m above sea level.
- thickness map of metasedimentary sequence: Samples were taken every 10 metres on the seismic lines. Thickness trends reveal a maximum in the north-western zones, of 125 m and minimum values across the eastern area; the minimum thickness is at deep seismic survey S3.
- Map of compression wave velocity (Vp): seismic velocity values were obtained at the tunnel elevation of 510 m above sea level. These values were attributed to the different cells in the tomographic interpretation, and an isoline map

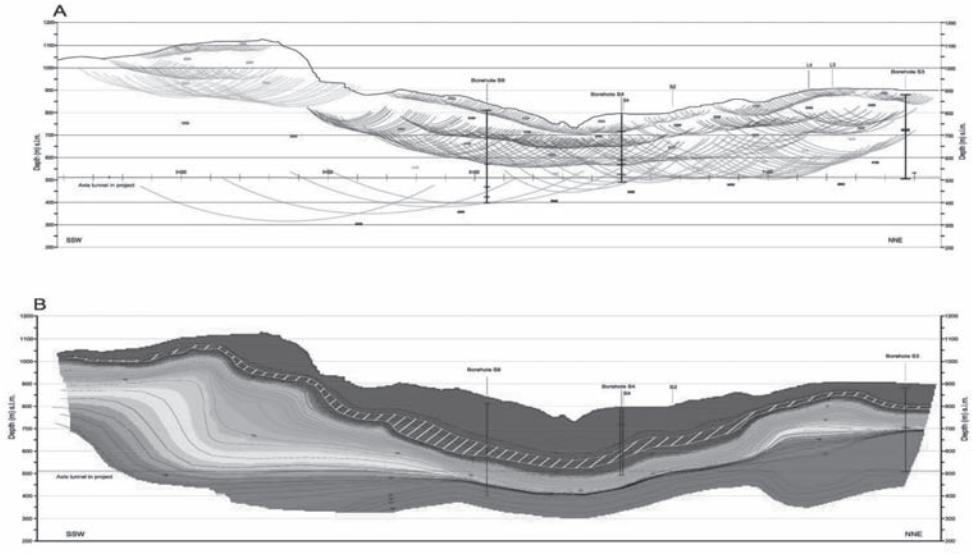

Figure 5. Rifraction seismic profile n°1: A Interpretative Section GRM: B Anaelastic attenuation elaboration.

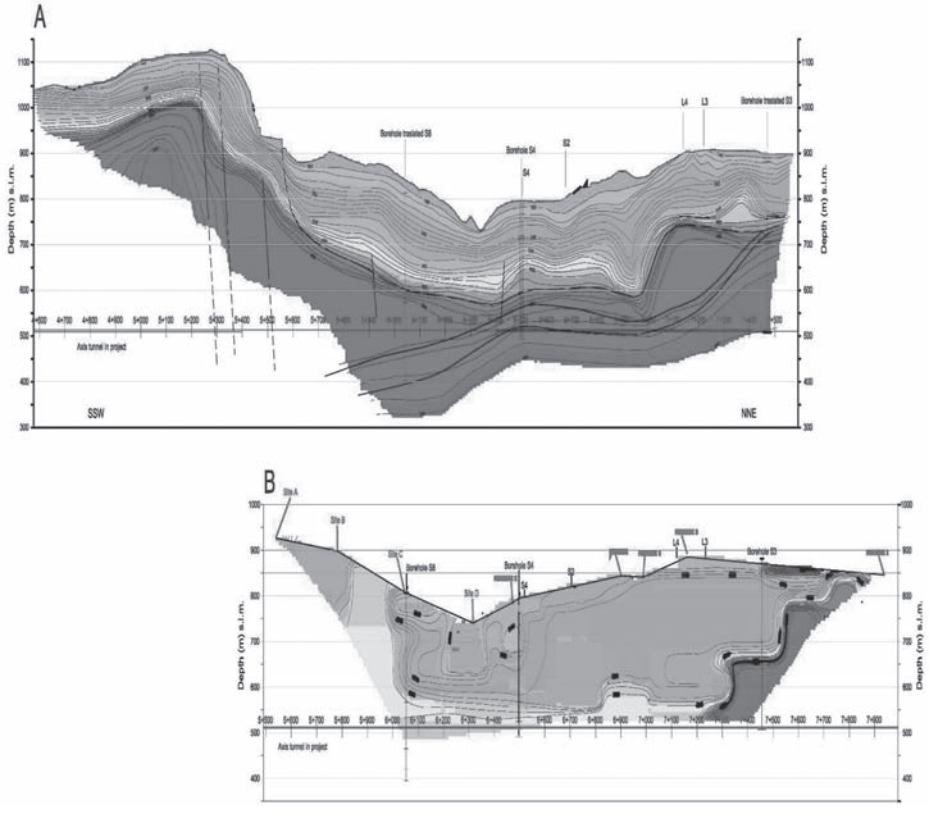

Figure 6. Tomographic analysis of seismic profile 1 integrated with the velocity data of the boreholes (A); Seismic tomography section only from boreholes (B).

was been published. This map shows a rather constant value of Vp to the west of the tunnel, whilst revealing decreasing values of Vp towards the east (towards the valley).

- map of stack seismic velocity: using interval velocity determined on seismic reflection profiles at 510 m above sea level, seismic velocity values were obtained which do not correspond with values obtained using seismic refraction. However the values provide a comprehensive understanding of the resistance characteristics of the rock. Interval velocity is calculated using the Dix formula (Baldi et al 2009). The map reveals a more jagged trend with respect to the previous data, with a lower limit of generally 4,000 m/sec, and some circular and concentric shaped zones showing generally lower values (lower than 4,000 m/sec).

Based on the 3D model, a geological profile of the tunnel was published (Fig. 7), indicating:

a) The DSGSD cover occupies a significant part of the upper central zone of the section. Discontinuities and/or secondary slip surfaces have been highlighted within it;
b) The lower DSGSD earth flow (or "bed") generally affects the "Gneiss di Antigorio" (GA) and also the metasedimentary sequence over a 200 metre thickness. In any case, this surface never reaches or comes close to the altitude of the tunnel;
c) In the "Gneiss di Antigorio" various discontinuities have been revealed;
d) The "metasedimentary sequence" shows a regular pattern although affected by a system of faults, each of which has been assigned an increasing number from south to north, for the purposes of representation and description;
e) The lithotypes pertaining to the "metasedimentary sequence" have been subdivided into different groups where possible, and in particular:
   - *Mma: altered marble;*
   - *Mmp: prevalent marble;*
   - *Me: evaporitic lithotypes in banks and lenses*, present exclusively at the base of the sequence;
f) The base is constituted by the "Micascisti di Baceno" (MB) and is affected by the same system of faults which affects the metasedimentary sequence.

The lower part of the figure from top to bottom shows the following elements:

a) Thickness of the tunnel cover, expressed in metres;
b) Layout of geological structure at the tunnel crown (514.8 m above sea level) and invert (510.0 m above sea level), each for a stretch of 50 metres;

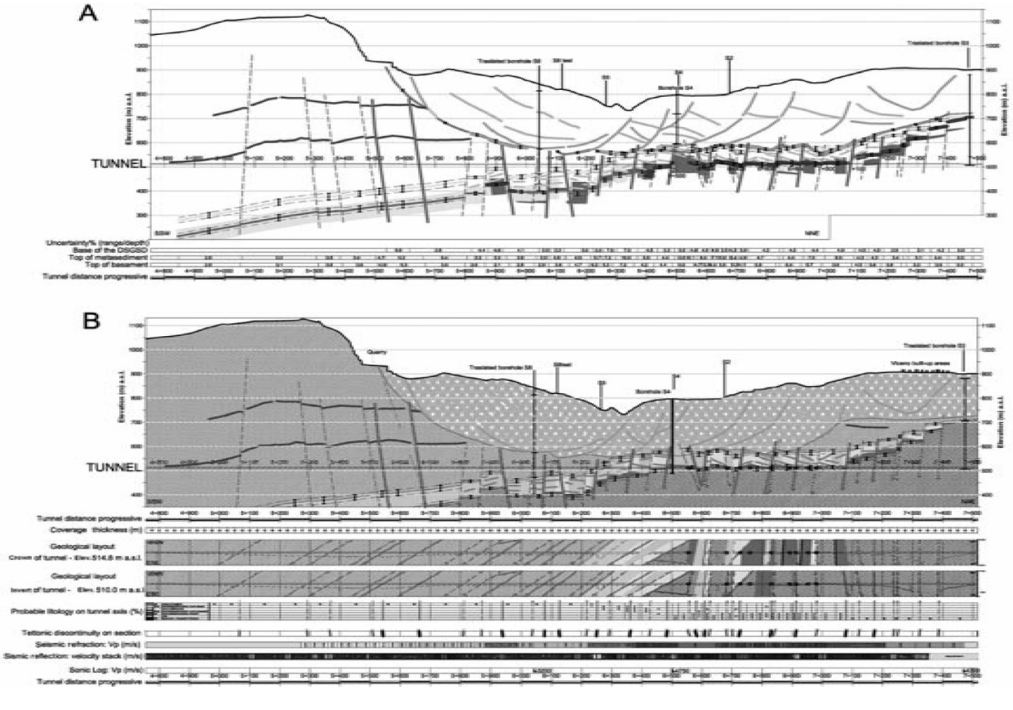

Figure 7. Geophysical (A) and geological-structural (B) models of the tunnel profile.

c) on each side. In these sections the following elements have been reported:
   - Faults are defined as either definite or indefinite with an indication of the lower area;
   - The most probable lithology and the subdivision of various lithotypes for the metasedimentary sequence where possible.

d) The probable lithology on the tunnel axis. Homogenous stretches have been identified, often marked out by faults. Each of these units has been assigned a probability expressed as a percentage, in relation to the possibility that the stretches will be revealed whether independently or associated, at the excavation face. Two sub-units have been derived from the geological interpretation of seismic reflection parameters (interval velocity and complex attributes), defined as mixed and undifferentiated marble.

e) The tectonic discontinuities identified in the section have been defined as either definite or indefinite. Depending on the intensity of the seismic signal and its inclination, each discontinuity has been placed into a geometrical band of uncertainty with a probability range expressed as a percentage between 0 and 100. The dimensions of these bands range between 5, 10 and 15 m.

f) Seismic velocity Vp expressed in m/sec with velocity values accurately measured at of 10 meter intervals and ranging from a minimum of 4,580 to a maximum of 6,990 m/sec.

g) Seismic stacking velocity obtained from seismic reflection, again expressed in m/sec measured at 10 meter intervals and ranging from a minimum of 3,250 to a maximum of 4,870 m/sec.

h) Sonic velocity values, in m/sec, recorded during the three deep geognostic surveys.

Finally in order to simplify the geological model, axonometric reconstruction projections were also prepared (Fig. 8).

In Figure 9 is depicted the three-dimensional geological model based on the high resolution seismic lines and boreholes.

In Figure 9A the top and bottom surfaces of the metasediments are reproduced. In the northern section the top of the basement is constructed by contour lines with an elevation greater than the elevation of the diversion tunnel (510 m a.s.l.). These contour lines highlight the area where the tunnel would always lie below the metasediments, i.e. inside the basement of the Baceno micaschist. The layout of the basement top was also correlated to the same rocks out cropping along Alfenza Creek around 770 m asl and the evidence of an older geoelectric survey (E4 on the map).

In the southern section, the top of the metasediments is reproduced by contour lines below 510 m asl where the tunnel would be excavated in Antigorio gneiss.

The central section of the geological model is horizontal 510 m a.s.l. and corresponds to the tunnel stretch crossing the metasediments. This zone between the basement top and the gneiss base has a mean NE-SW strike in accordance with the general geological setting and a dip toward SE.

In Figure 9B is reproduced the base surface of the DSGSD (Deep Seated Gravitational Slope Deformation). The contours suggest a general sliding direction toward SE.

In Figure 9A are also reported 4 alternative tunnel alignments which maintain the minimum curvature radius of 500 m, minimize the metasediment crossing length, localize the entrance and exit from the metasediments where the gradient of

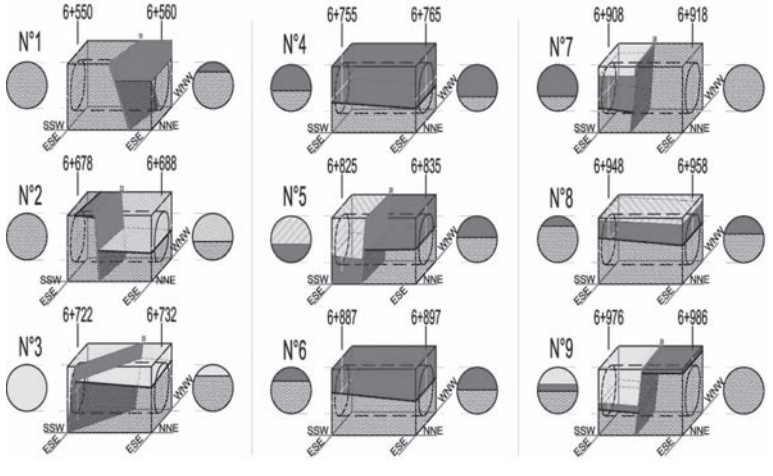

Figure 8. Axonometric projections.

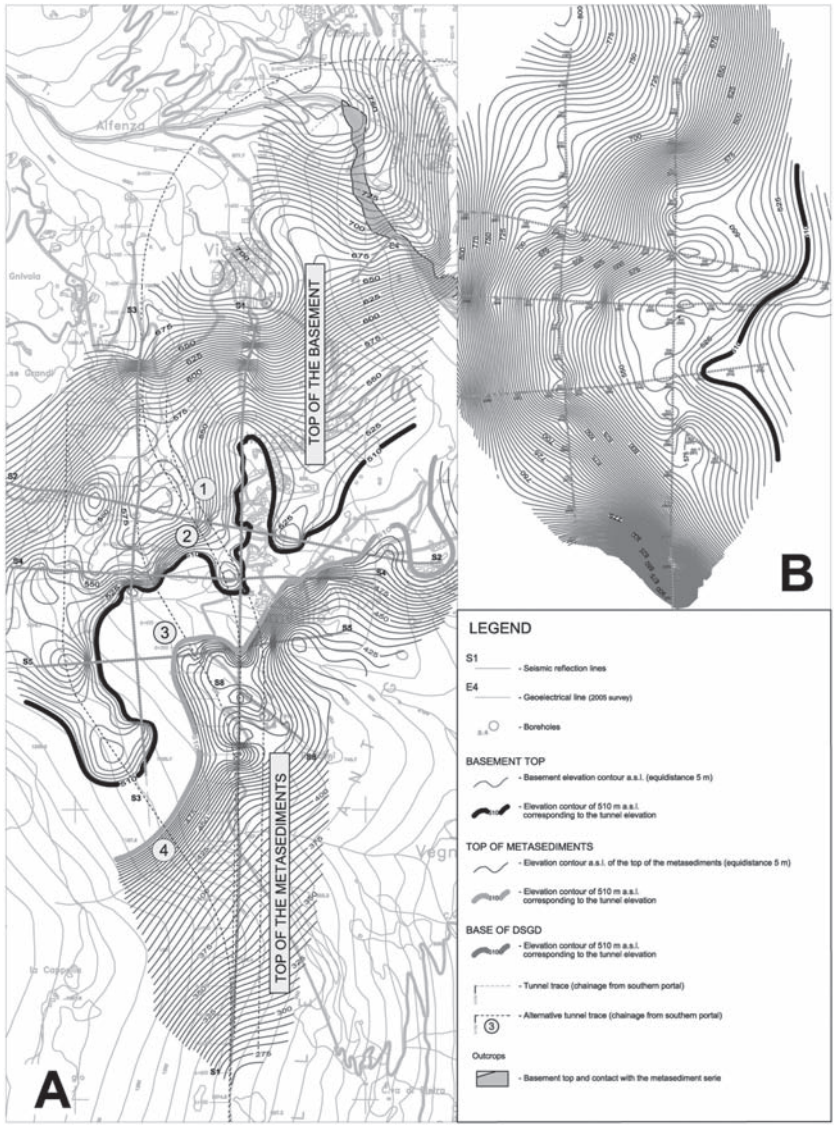

Figure 9. Three-dimensional geological model of the diversion tunnel northern sector. A: Top of basement and metasediment surfaces respectively above and below the tunnel elevation of 510 m a.s.l. Four alternative tunnel traces are indicated. B: map of the DSGSD base highlighting the 510 m a.s.l. contour.

the contact is higher and maximize the separation from the base of the DSGSD.

5 CONCLUSIONS

The geophysical prospecting investigations enabled building a 3D geological model in the area intended for excavation for a future hydraulic tunnel. The model allowed for the different geological units to be positioned in space according to probabilistic and statistical criteria at the various levels along the tunnel excavation. Certain critical situations which will be revealed as tunnelling progresses, were also defined and described.

The model also allowed for various alternate tunnel configurations to be reviewed, which would redacte the length of the critical section of the excavation in the altered lithotypes keeping the tunnel elevation the same.

An analysis of seismic velocities, obtained from both refraction and reflection profiles made it possible to correlate to geomechanical characteristics of the rocks. This will allow for further assessment during the actual excavation, in order to reduce uncertainties, which any tunnel excavation in complex geological conditions would entail.

REFERENCES

Agliardi F., Crosta G., Zanchi A. 2001. Structural constraints on deep-seated slope deformation kinematics. *Engeneering Geology* 59: 83–102.

Badley P. 1988. Practical Seismic Interpretation, P.P.

Baldi A.M., Bianchi F 1999. Sperimentazione della tecnica di rilievo sismico a riflessione T.S.P. per l'esplorazione sull'avanzamento delle gallerie. Atti XX Convegno Nazionale di Geotecnica: "Sviluppi nell'esecuzione e nell'impiego delle Indagini Geotecniche"- Associazione Geotecnica Italiana—Parma .

Baldi A.M., Bianchi F., Boerio V., Francia S., Giorgi F. 2001. New layout of A1 Florence—Bologna highway: integrated seismic rerflection survey and tomographic inversion to perform structural geological modelling along the main tunnel route, Atti Congresso "ITA 2001 Word Tunnel Congress: Progress in tunnelling after 2000", Milano 2001. Ed. Patron, Bologna vol. I, 147–156.

Baldi A.M., Bianchi F., Boerio V., Francia S., Giorgi F. 2001. Construction of third lame aloug the A1 highway across hilly Florence outskirts: geophysical investigation at tunnel routes, Atti Congresso "ITA 2001 Word Tunnel Congress: Progress in tunnelling after 2000", Milano 2001, Ed. Patron Bologna vol. I, 157–167.

Baldi A.M., Bianchi F., Giorgi F., De Marco M., Locatelli E., Ferrari F. 2006. The reconstruct of the geologic section of motorway tunnels with seismic survey: "Connecting road from A4 to Valtrompia" Lumezzane—Brescia. Atti del Congresso "Fifteenth international symposium on Mine Planning & Equipment Selection", Torino. Vol. 1 525–530.

Baldi A.M, Fuoco S., De Luca J. 2006. Application of new seismic methodologies for the solution of geomechanic problems connected to the excavation of tunnels. Atti: fifteenth international symposium on Mine Planning & Equipment Selection. Torino. Vol. 1 531–536.

Baldi A.M., Fuoco S., Cucino P., Nucolussi Paolaz P. 2007. Lo scavo della galleria stradale di Martignano (Trento): previsioni e riscontri, il ruolo delle indagini geofisiche. Atti XXII Convegno Nazionale di Geotecnica ad Abano "Previsioni e controllo del comportamento delle opere". Pàtron Editore, Bologna, 123–130.

Baldi A.M., Ceveneini G., Gambassi R., Notari D. 2009. The processing of interval seismic velocities has allowed, by bulding a statistical-neural, to predefine the time for excavation of gallery with TBM. Atti del workshop in geofisica tenutosi a Rovereto il 25 – 26 giugno 2009: "Nuove frontiere per la geofisica applicata".—Rovereto Ed. Osiride.

Bigioggero B., Boriani A., Origoni Giobbi E. 1977. Microstructure and mineralogy of an Orthogneiss (Antigorio Gneiss—Lepontine Alps). *Rendiconti Società Italiana di Mineralogia e Petrologia* 33:99–108.

Bistacchi A., Massironi M. 2000. Post-nappe brittle tectonics and kinematic evolution of the north-western Alps: an integrated approach. Tectonophysics 327: 267–292.

Bringiotti M. 1996, Guida al Tunnelling. L'arte e la tecnica, Edizioni PEI.

Campani M., Mancktelow N., Seward D., Rolland Y., Müller W., Guerra I. 2010. Geochronological evidence for continuous exhumation through the ductile-brittle transition along a crustal-scale low-angle normal fault: Simplon Fault Zone, central Alps. *Tectonics* 29, TC3002, doi:10.1029/2009TC002582.

Cardarelli E., Bernabini M., De Nardisd R. 1995. Some consideration in travel time tomograpphy in shallow seismic survey. Extended Abstract 57th Conference of EAEG in Glasgow.

Cardarelli E., 2003. Ray Tracing applied to travel time seismic tomography (Theory and examples) Bollettino di geofisica Teorica ed Applicata. Vol. 44 281–305.

Cardarelli E., 2008. Modelling—2D complex anomalies by seismic tomography, (detection and delineation of anomalies with sharp boundaries). Bollettino di geofisica teorica ed Applicata Vol. 49 n. 2 pp. 265–277.

Castiglioni G. 1958. Studio geologico e morfologico del territorio di Baceno e Premia (Val d'Ossola—Alpi Lepontine). *Memorie degli Istituti di Geologia e Mineralogia dell'Università di Padova* XX: 2–82.

Couvreur J.F., Thimus J.F. 1996. Creep and ultrasonic waves. Symposium "Eurock 96" Torino. 41–47.

Feroci M., Orlando L., Balia R.,Bosman C., Cardarelli E., Deidda G., Some considerations on shallow seismic reflection surveys 2000 Journal of Applied Geophysics 45 127–139.

Geophysical Service Inc. 1980. Course of instruction in the geophysics of seismic data processing, Dallas, Texas.

Grasemann B. & Mancktelow N. 1993. Two-dimensional thermal modelling of normal faulting: the Simplon Fault Zone, Central Alps, Switzerland. *Tectonophysics* 225: 155–165.

Grosjean G., Sue C., Burkhard M. 2004. Late Neogene extension in the vicinity of the Simplon fault zone (central Alps, Switzerland). *Eclogae geol. Helv.* 97: 33–46.

Hope V.S., 1993. Application of seismic trasmission tomography in civil engineering. PhD. Dissertation University of Surrey USA.

Hope V.S., Clayton C.R.I., Barla G. 1996. Class "A" predictions of the locations of major rock discontinuities at a storage cavern site, using seismic tomography. Symposium "Eurock 96" Torino. 925–932.

Kaus A., Wolf Boening & Partner GbR 2008. BEAM-Real Time Ground Prediction while Tunnel-Drivage.

Kneib G. 1999. Automatic seismic prediction ahead of the tunnel bore machine, Atti dell'EAGE 61st Conference and Technical Exhibition—Helsinki, Finland, 7–11 June. 4–45.

Mancktelow N.S. 1985. The Simplon line: a major displacement zone in the western Lepontine Alps. *Eclogae Geologicae Helvetiae* 78: 73–96.

Maxelon M. & Mancktelow N.S. 2005. Three-dimensional geometry and tectonostratigraphy of the Pennine zone, Central Alps, Switzerland and Northern Italy. *Earth-Science Reviews* 71: 171–227.

Milnes A.G., Greller M., Müller R. 1981. Sequence and style of major post-nappe structures, Simplon-Pennine Alps. *Journal of Sructural Geology* 3: 411–420.

Mora, P., 1989 Inversion = migration + tomography: Geophysics, 54, 1575–1586.

Schmidt C. & Preiswerk H. 1905. Geologische Karte der Simplongruppe. *Beiträge zur Geologischen Karte der Schweiz,* [N.F.] 26, Spezialkarte No. 48.

Steck A. 2008. Tectonics of the Simplon massif and Lepontine gneiss dome: deformation structures due to collision between the underthrusting European plate and the Adriatic indenter. *Swiss Journal of Geoscience* 101: 515–546.

Sattel G., Frey P., Amberg R. 1992. Prediction ahead of the tunnel face by seismic methods-pilot project in Centovalli Tunnel, Locarno, Switzerland. First Break, January 92, vol. 10.

Sheriff R.E., Geldart L.P. 1976. Structural Interpretation of Seismic Data: Am. Assoc. Of Pet. Geol. Ed. Course note ser. 23.

Tarantola, A., 1988, Theoretical background for the inversion of seismic waveforms, including elasticity and attenuation: in Scattering anda Attenuation of Seismic Waves, Birkhaeuser, Basel.

Zwingmann H. & Mancktelow N. 2004. Timing of Alpine fault gauges. *Earth and Planetary Science Letters* 223: 415–425.

This page intentionally left blank

Geotechnical Aspects of Underground Construction in Soft Ground – Viggiani (ed)
© 2012 Taylor & Francis Group, London, ISBN 978-0-415-68367-8

Geotechnical instrumentation data management

John L. Gilby P. Eng.
Golder Associates Ltd., Mississauga, Ontario, Canada

Monica Socol
Golder Associates Ltd., Mississauga, Ontario, Canada

ABSTRACT: In response to the need for effective and timely management of information and monitoring data, this paper introduces two complimentary applications that have been developed for tunneling projects to manage geotechnical information. They have been successfully used on a tunneling project in Italy and are now being used on two major tunneling projects in Canada as well as other smaller projects.

A Geo-Engineering Content Management System (GECMS) has been developed. A one-stop web portal designed to aid project designers, construction and monitoring crews to manage all geo-engineering and related documentation, instrument monitoring data and spatial data both historically or generated during a project.

Monitoring is a key part of any excavation and one of the major concerns is timely management of the instrumentation data to verify design parameters as development proceeds. As technology is ever changing, data is collected automatically and more frequently, new techniques are needed to manage the data, this is where the Geotechnical Instrumentation Data Interpretation and Evaluation (GIDIE) application has been implemented.

1 INTRODUCTION

Effective and timely management of information and monitoring data is a key part of any geotechnical excavation project. As technology is ever changing and now that data is collected automatically and more frequently, new techniques are needed to manage the volume of data generated. Recognizing these needs Golder has developed tools to make this possible through a content management system (GECMS—Geo Engineering Content Management System) and Instrumentation Data Management and Monitoring application (GIDIE—Geotechnical Instrumentation Date Interpretation and Evaluation). Both of these applications are web based and available to those who have security rights; they complement each other and can be implemented either together or independently. GIDIE has been successfully implemented on a recently completed tunneling project in Italy, and through experience with this project both applications have been upgraded to be more efficient.

The collection and management of monitoring data has changed significantly over the years, the author has been working with instrumentation and monitoring programs for over 35 years and through this experience has lead the development of these applications.

2 THE NEED FOR DATA MANAGEMENT

The experience of 35 years of collecting and analyzing geotechnical data, where through the years data has been collected manually by collecting and plotting by hand on graph paper; to automated collection and plotting using handheld devices; to spreadsheets; and now to databases and web delivery show how technological changes can help in analyzing data in a timely manner (Gilby, Yuen & Aston, 1988). Through each of these stages, the volume of data has increased and the need to manage it more effectively and efficiently has become more evident.

As technology changes have allowed for more data to be collected, management has become more difficult and although computer speeds have increased significantly the large volumes of data collected have meant that the analysis does not necessarily become any easier (Borgonovo et al., 2007).

The data management techniques described in this paper were devised from experience and the application has been developed with the following needs:

- A flexible efficient database for holding data through user configuration;
- Access to data from anywhere there is an internet connection to allows for interrogation of

readings in the event of alarms and to allow viewing by users with rights to the data;
– Ease of use and quick access to tools, graphs and reports;
– Flexibility to evaluate, accept and reject data based on prescribed conditions;
– Consistent and flexible reporting tools including text and charting, including personalized needs; and
– Import and export of data to allow for further processing.

3 CONTENT MANAGEMENT (GECMS)

3.1 *Features*

The Geo Engineering Content Management System (GECMS) Web Portal provides the user with single sign-on to multiple components tightly integrated together:

– A powerful Document Management System that enables the user to upload and share all the project related documents, and to publish the documents for authorized use through a robust revision and approval process.
– Multiple ways of searching for documents:
  • Spatial Map search: where the user identifies a location on the map and is provided with the list of documents the user has permissions to read, linked to the location selected. From this list, the user can click on a document and see it on-line in the browser.

Figure 1. GECMS web portal.

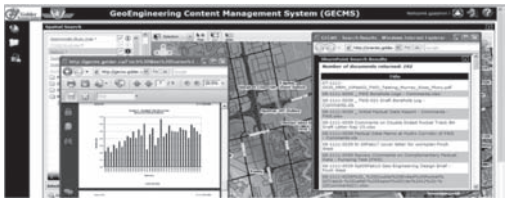

Figure 2. Saptial map search.

Figure 3. Tabular search.

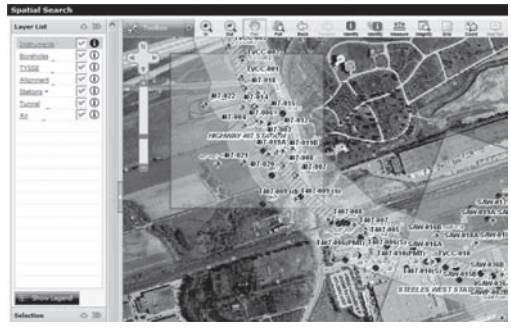

Figure 4. Spatial data viewer.

• Tabular Search: when the user knows more details about a specific document he is searching for (i.e. part or full title, author, creation date, etc.), the user can enter the searching criteria in a form and is provided with the list of documents he has permissions to read, that match the searching. Again, just one more click and the desired document is displayed in the browser.
• Spatial data viewer—GIS query, viewing and mapping tool displaying Geo-engineering spatial data such as boreholes, infrastructure and topographic data, and also all the monitoring instruments.
• Instrumentation Data Management and Monitoring tool (GIDIE).

3.2 *GECMS document workflows*

There are two main document workflows in GECMS: Document Publishing and Document searching.

– GECMS enables various document management roles contributing to document workflows within GECMS. GECMS Administrator—administers the site.

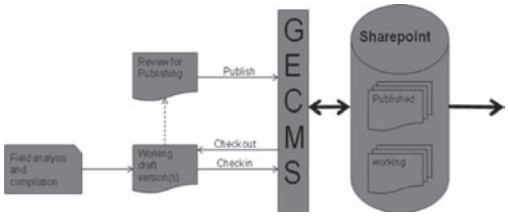

Figure 5. GECMS document workflow.

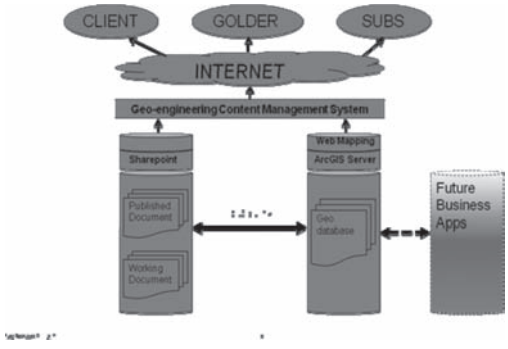

Figure 6. GECMS workflow.

- Publisher—publishes draft documents into published documents.
- Contributor—creates, loads and edits documents in working draft folders.
- Viewer—view only of published documents.

In some projects spatial data is updated on a regular basis and would go through a similar publishing process.

3.3 *Benefits of GECMS on large geotechnical projects*

There are many benefits to implementing a content management system especially on a large geotechnical project that combines a high volume of information with many disconnected users of the information. The major benefits that can be realized are:

- Project spatial data managed in one central location;
- Project documents managed in one central location;
- Enables limited and secure access to documents;
- Enables version control of documents;
- Links project documents to spatial locations to enable spatial searching;
- More than one document can be linked to one spatial feature;
- Collaborative document sharing and development; and
- Can integrate spatial and document management with other databases such as EquIS, gINT and acQuire.

4 INSTRUMENTATION DATA MANAGEMENT (GIDIE)

4.1 *Features*

Based on experience we developed a series of features to be included in the monitoring application. The key to the application is a robust and well thought out data model and much time has been spent on this. The database has been developed in SQL Server. The tables in the database are configured to allow input of the following:

- Project or section data;
- Administration and user information to allow for secure access;
- Instrumentation information;
- Device information (in this case the differentiation between instrument and device is for example that a 4 point extensometer would be an instrument and each anchor would be the device); and
- Formulae for calculation of reduced/engineering values.

Each of the above has sufficient fields to define the use completely as follows:

- Information to allow the database administrator to configure and administer the users and their permissions;
- Definition of the project and/or sections;
- Web Portal Application look-and-feel customization per project and/or section;
- Instrument details showing the devices within the instrument, its location, etc.;
- Serial numbers of devices;
- Calibration constants, which can change with time if re-calibration is necessary;
- The number of devices in the instrument;
- Formulae required to reduce the data from raw readings if necessary;
- Flags to show whether processing is required or not;
- Alert and alarm levels, and the action to be taken if there is an exceedence; and
- The type of report and chart required (whether 1 device per plot or multiple devices per plot). Most plots are time against some reading; however there are special needs for example inclinometers and plotting tunnel advance against readings.

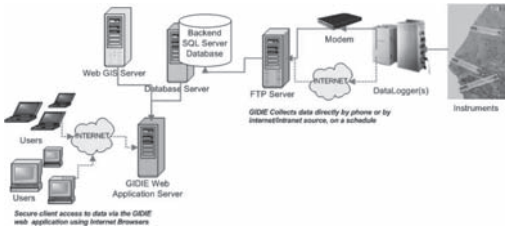

Figure 7. Integrated application of GIDIE.

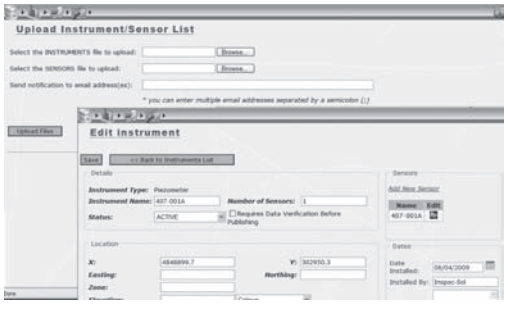

Figure 8. Instrument upload.

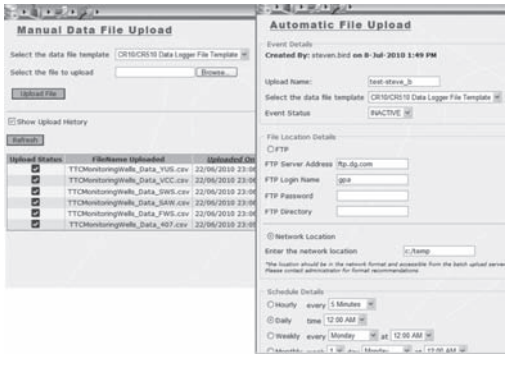

Figure 9. Manual data upload.

The flexibility of the system allows users with administration rights to define new instruments that may not be currently supported or even developed. In some cases it may however be necessary to add features to this to allow some new instruments to be included.

During the development of the application and in response to stakeholders, a number of instruments have been incorporated and as more are requested, the specifics of these instruments and sensors will be programmed into the application. Currently the application supports the following instruments and charting types:

Figure 10. Reports.

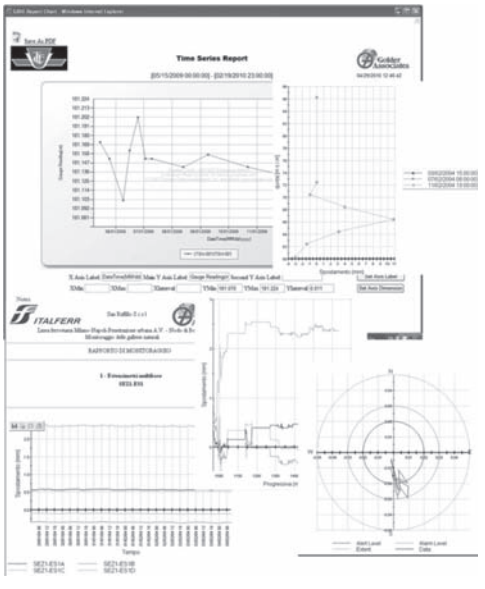

Figure 11. Custom graphing and reporting.

- Vibrating wire instruments (strain gauges, extensometers, piezometers, pressure cells, jointmeters, etc.);
- In place inclinometers (vw and servo acc.);
- Manual inclinometers;
- Electolevels;
- Topographical instruments;
- Hydraulic instruments (load cells, etc.); and
- TBM/tunnel/excavation/construction advance.
- User definable instruments and devices that have similar features to the supported ones (new devices may need additional programming before completely supported—ongoing support);
- Charting supports:
  - Single instrument (time v reading);
  - Multiple devices in one instrument (time v reading);

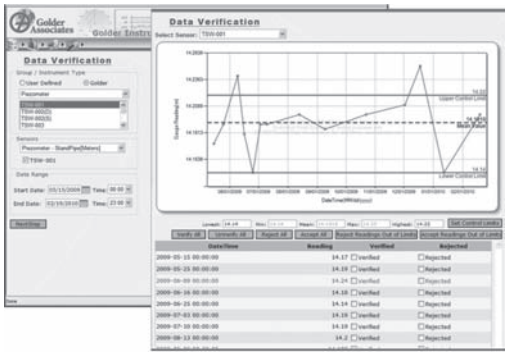

Figure 12. Data verification.

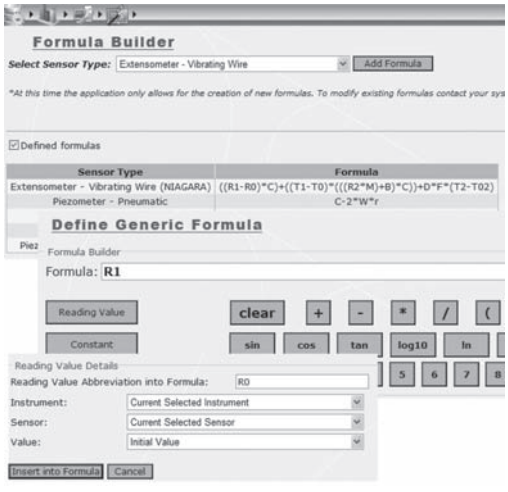

Figure 13. Formula builder.

- Inclinometer plots;
- Polar plots;
- Combination plots; and
- Tunnel-settlement plots (plotting instruments referenced to the tunnel location).

4.2 *Application*

GIDIE is a powerful Instrumentation Data Management and Monitoring tool that is tightly integrated as a module with the spatial and document management system components from the Web Portal but can also be used as its own application. The following shows a schematic example of how the data flows from the instrument to the users' computer via communication and the database.

Following are a series of screen shots of the application and its features:

- Instruments and Devices are easy to be defined in the system either manually or through automatic upload of a list of instruments/devices.
- Calibration information can be entered at any time an instrument needs to be calibrated; updated formulas would be applied automatically to calculate the corrected values.
- Data from instrumentation can be loaded automatically through various communications methods as well as manually in near real time and is available for immediate analysis.
- Quick Access to Flexible Reports and Graphs for one or multiple instruments—allows for creation of reports real-time or batch mode at predefined times (the reports can be sent by email to various stakeholders in .pdf or .csv format).
- Various graphical methods of presenting the data including batch printing of custom charts.
- Data export for usage and integration with other applications (export in .csv format).
- Data Verification—allow the user to visualize the data and reject the erroneous values.
- Formula builder to calculate reduced readings from raw data—automatically integrated in the data upload process.
- Multiple levels of security in accessing the instrumentation data:
  - Reader (who can only view reports for specific instruments)
  - Writer (who can upload data either manually or automatic; or verify the correctness data)
  - Power User (who can also enter new instruments/devices; change calibration details).

4.3 *Integration of GIDIE into GECMS*

When GECMS is used as a portal entry to GIDIE, tools providing interface, mapping and document management are managed through GECMS. The following GIDIE information items can be stored and managed in GECMS:

- Instrument locations
- Instrument specifications
- Instrument Calibrations
- Instrument installation report
- Monitoring reports (manual or scheduled).

5 CASE STUDY—TORONTO YORK SPADINA SUBWAY EXTENSION

5.1 *Background*

- 8.6 km long extension of the Spadina Subway line from Downsview to the City of Vaughan in York Region.

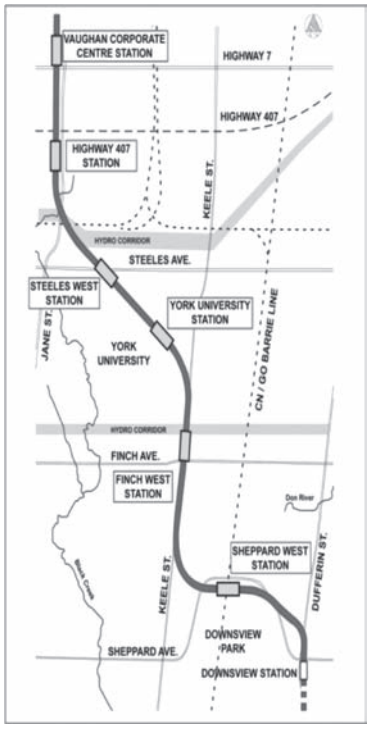

Figure 14. Toronto transit commission TYSSE project.

- First subway line crossing the City of Toronto boundaries
- Funded by three levels of government:
  - The Government of Canada
  - The Province of Ontario
  - The City of Toronto and The Regional Municipality of York
- Cost: $2.6 billion.

5.2 *The need for GECMS*

- One of the primary concerns was document management
- Documents to be stored at one location
- Documents to be easily sharable among stakeholders or contractors working at the same project location performing differing but dependent tasks
- Add spatial element to the document management.

5.3 *Golder's role*

- Golder has been retained by the TTC as the Principal Geo-engineering Engineering Consultant for the TYSSE project.
- Golder's primary role is management of subsurface risks and the development work including the following:
  - Oversight role on geo-engineering works;
  - Site investigation standards and minimum investigation requirements;
  - Review of the Geotechnical sections of the design manual;
  - An overall strategy for managing soil and groundwater; and
  - Review of the data obtained from the construction instrumentation program.
- One of Golder's key deliverables is to develop and maintain a Geo-engineering Content Management System (GECMS).
- GECMS is designed to manage all geo-engineering and related documentation and spatial data both historically or generated by this project.
- Golder has successfully integrated these web mapping, document management and instrumentation data components into a one-stop web portal to aid stakeholders, project designers and construction contractors.

6 BUSINESS CHALLENGES OF WEB DEVELOPMENT

As GECMS is a web deployed application, accessible from anywhere in the world by many user groups with differing business environments, many business challenges arise. The following are some of the business challenges and the mitigating measures taken to overcome each.

- Many sub contractor (multi-agency) teams managing a variety of inter-related geotechnical and geo-environmental tasks:
  - Management of document security—limited sharing of working drafts.
  - Manage document versioning workflow—from working draft to publish.
- Spatial data currency—constant updates:
  - Establishment of spatial data workflow ensuring timely and quality updates.
  - TTC base updates workflow.
  - Station and tunnel alignment updates workflow.
  - Borehole location updates workflow.
- A variety of internal office automation environments, internet connection speeds and browser versions:
  - Provision of additional training and support.
  - Test on many environments to ensure minimum functions.
- A variety levels of computer savvy amongst users:
  - Provision of well documented system.
  - User training.

- Train the trainer.
- Additional training for administration staff.
- Provision of additional support.

7 CONCLUSIONS

The GECMS/GIDIE application has been developed to automate and simplify data collection and interpretation from documentation and instrumentation systems. Over the years there have been a variety of methods of collecting and reducing such data that have been time consuming and once the interpretation has been made, the excavation has often past and the data is of less use. By incorporating this system into a near real-time web based application, data can be evaluated much quicker for contractors and designers to evaluate the safe working and to verify design parameters.

This application has been used on a number of monitoring programs with the major ones being tunnel development in Italy as well as current tunneling projects in Toronto and Ottawa, Canada.

REFERENCES

Borgonovo, G., Locatelli, L., Perolo, M., & Ramelli, E. (Golder Associates) and Marchionni, V. (S. Ruffilo), 2007. *Progressing Monitoring of Tunnel under Railway Embankment.*

Gilby, J.L. & Yuen, C.M.K (Golder Associates) and Aston, T.R.C. (CANMET). 1988. *Geotechnical monitoring of tunnel boring machine drivages at the Donkin-Morien Mine, Nova Scotia*. CIM Bulletin.

This page intentionally left blank

Geotechnical Aspects of Underground Construction in Soft Ground – Viggiani (ed)
© 2012 Taylor & Francis Group, London, ISBN 978-0-415-68367-8

Design and construction of a sewer tunnel in difficult site conditions

P. Croce
University of Cassino, Italy

S. Di Maio, G. Speciale & L. Cassibba
Sering Ingegneria s.r.l., Italy

ABSTRACT: The paper deals with a sewer tunnel, recently excavated in the city of Palermo. The tunnel layout is close to existing urban facilities and residential buildings. The geotechnical profile is quite variable and the soil cover ranges between 7 and 9 m. The groundwater level is located at mid height between the invert arch and the vault of the tunnel. Excavation support was granted by means of the canopy technique, employing micropiles and jet grouting. A detailed monitoring program was also organized and tunnel construction was followed step by step allowing for proper design changes, according to the subsoil conditions met during excavation. The case history is reported by describing the tunnel layout, the geotechnical profile and the monitoring plan. Recorded settlements of the existing structures are analyzed, considering the influence of the geotechnical properties of the subsoil as well as the peculiar construction sequence of tunnelling.

1 INTRODUCTION

Tunnel construction in urban areas is generally a very difficult task for several typical reasons that may be listed as follows:

i. the presence of weak soils (including made land), characterized by low shear strength, which may compromise the stability of the underground excavation
ii. the occurrence of seeping water, coming from local aquifers or water lines leakage, which may induce soil piping along the cavity
iii. the excavation process which generates soil deformations that may induce excessive settlements of adjacent or overlying buildings
iv. the crossing of other underground facilities which may interfere with digging activities.

It is well known that tunneling through weak soils may result in face and vault instability, unless proper soil support is provided during excavation. This goal can be reached either by using a TBM or by installing a set of reinforcing elements, forming a sort of canopy along the cavity contour and behind its face.

However, the use of a TBM becomes technically and economically feasible only for long tunnels with ample curvature radii, circular cross section and constant diameter.

On the contrary, the canopy technique can be readily used for short tunnels, non circular cross sections and abrupt changes of direction. The canopy technique can also be customized in order to account for variable soil properties, by making proper use of the different soil reinforcing techniques. Design features can also be modified in real time to meet unforeseen situations, such as unexpected soil conditions, undetected underground facilities or excessive surface settlements, as it frequently happens in urban areas. In such cases, it may be appropriate to apply the observational method (Nicholson et al., 1999; Patel et al., 2007; Croce, 2010) in which the design is reviewed during construction as allowed by the Eurocode EC7.

In the following, the typical features of the canopy technique are first recalled, considering the available soil reinforcing methods and their implementation in the tunneling procedure. This technique was successfully employed in order to excavate a sewer tunnel, built in difficult site conditions in the city of Palermo.

The case history is then reported in some detail by describing the tunnel layout, the geotechnical profile, the design features and the monitoring plan. Finally, recorded settlements of the existing structures are analyzed, considering the influence of the geotechnical properties of the subsoil as well as the peculiar construction sequence of tunneling.

2 CANOPY TECHNIQUE

The canopy technique is based on the use of soil reinforcing methods which provide stability of the tunnel contour during excavation. Such canopy is

obtained by means of steel micropiles and/or jet grouting columns which are installed in advance with respect to excavation. Moreover, for very weak soils, the stability of the tunnel face may be granted by diffused reinforcement of the soil behind the face, which can be pursued either by jet grouting treatments or by the insertion of fibreglass elements (bars or tubes).

During excavation, the face reinforcing components are removed together with the soil, while the contour elements are progressively supported by setting up steel ribs and shotcrete in order to complete the provisional lining of the tunnel. The final lining, made of reinforced concrete, can then be installed at a later and more convenient time.

In principle, each reinforcement technique is best suited for particular soil types and seepage conditions. Jet grouting treatments are generally preferred for sandy soils, providing larger columns which can be set aside forming a sort of supporting arch (Fig. 1A). The latter can provide also waterproofing, when properly dimensioned, if pore water pressures are not too high.

However, for fine grained materials jet grouting is not very effective and so for clayey soils it is usually more convenient to choose micropiles (Fig. 1B). In particular, steel micropiles are used for the tunnel contour while fibreglass bars or tubes are employed for the face reinforcement, since they can be easily truncated during excavation. Finally, in difficult cases or doubtful soil conditions, it may be useful to combine jet grouting and micropiles in order to form a sort of reinforced jet column.

Whatever method of soil reinforcement is chosen, the canopy technique is characterized by a construction sequence which proceeds by subsequent spans, as depicted in Figure 2. The span length is usually comprised between 6 and 10 m. For each span

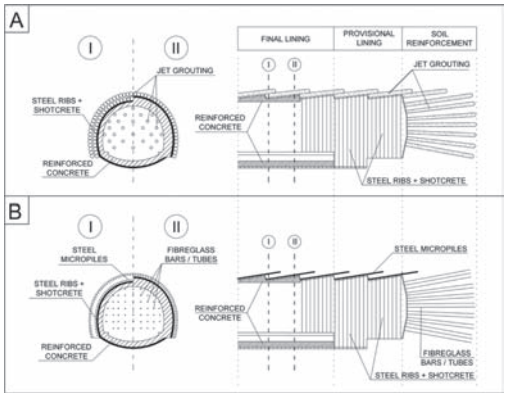

Figure 1. Schematic drawings of the canopy technique: A—reinforcement by jet grouting columns, B—reinforcement by steel micropiles and fibreglass bars or tubes.

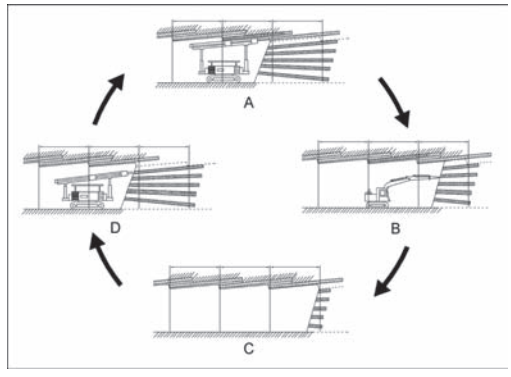

Figure 2. Tunnelling sequence by the canopy technique: A—reinforcement of tunnel contour by jet grouting and/or steel micropiles, B—excavation, C—excavation completed, D—face reinforcement by jet grouting and/or fiberglass bars or tubes (optional).

there are two main construction phases: treatment along the tunnel contour (Fig. 2A) and soil digging (Fig. 2B). After the excavation is completed (Fig. 2C) it is possible to consolidate the tunnel face (Fig. 2D) when this treatment is needed.

3 TUNNEL DESIGN

The sewer tunnel, which is still under construction in the city of Palermo, is almost 5 km long and is characterized by frequent changes of cross section and abrupt variations of direction, in order to meet peculiar hydraulic requirements and to conform to the urban features of the city. The tunnel stretch considered in the present paper is about 350 m long and is located downtown Palermo under a busy street, named "Corso Re Ruggero" (Fig. 3). This street is bordered on one side by a subway line which was previously built by cut and cover.

Therefore, on this side, the tunnel runs along a sheet pile wall (Fig. 4). On the opposite side of the tunnel, three different conditions are met. Along the first half of the tunnel stretch, there are some residential buildings (Fig. 4a) of various dimensions and characteristics, such as masonry and reinforced concrete. They are all placed on shallow foundations, with the exception of one single edifice founded on reinforced concrete piles.

In the second half of the tunnel stretch the street is bordered by an old masonry retaining wall, standing over a city park (Fig. 4b). Another relevant structure is the subway ticket office, which is connected to the subway line through a pedestrian underpass (Fig. 4c). This particular situation is met in the middle point of the tunnel stretch.

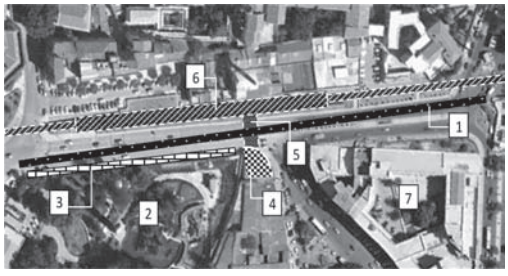

Figure 3. Plan view. 1) Tunnel layout 2) Park 3) Retaining wall 4) Subway Ticket Office 5) Pedestrian underpass 6) Subway line 7) Buildings.

For each span the cross section of the excavation ranges between the following values: width 5.10–5.40 m, height 5.40–6.00 m. The soil cover, taken as the distance between ground level and tunnel crown, is comprised between 7 m and 9 m.

The tunnel intersects different geologic formations. At the bottom, just below the invert arch, there is a continuous thick stratum of dense silty sands. On top of this stratum there are several layers of calcarenitic rocks, characterized by a very variable degree of cementation. The overall thickness of the calcarenitic layers ranges between 3 and 11 m. Moreover, the continuity of the calcarenitic formation is interrupted by alluvial sediments deposited by the ancient river Kemonia which bordered the city of Palermo many centuries ago. The grain size distribution of these alluvial soils is reported on Figure.5.

Finally, on top of the natural soils, there are relevant layers of made land i.e. materials of anthropic origin (bricks, pottery, fragments, transported soil, etc.). The groundwater level is located at the depth of 10 m, practically at mid height between the invert arch and the vault of the tunnel.

Several continuous borings were performed, at the design stage, providing the elements for drawing the geotechnical profile along the tunnel. However, due to the remarkable lithological variability of the subsoil, it was not possible to detect the contact between the alluvial materials and the calcarenitic formation.

Moreover only few undisturbed samples of calcarenite were retrieved, since these materials are very fragile and are thus subjected to extensive breakage during mechanical boring. However, it was well known that the degree of cementation of the calcarenites is very variable, generally low, and some times negligible due to their peculiar petrographical features (Canzoneri et al., 2002).

Design was thus accomplished by dimensioning three types of canopies, and each type of canopy was associated to a typical stratigraphical sequence (Fig. 6). In particular, steel micropiles

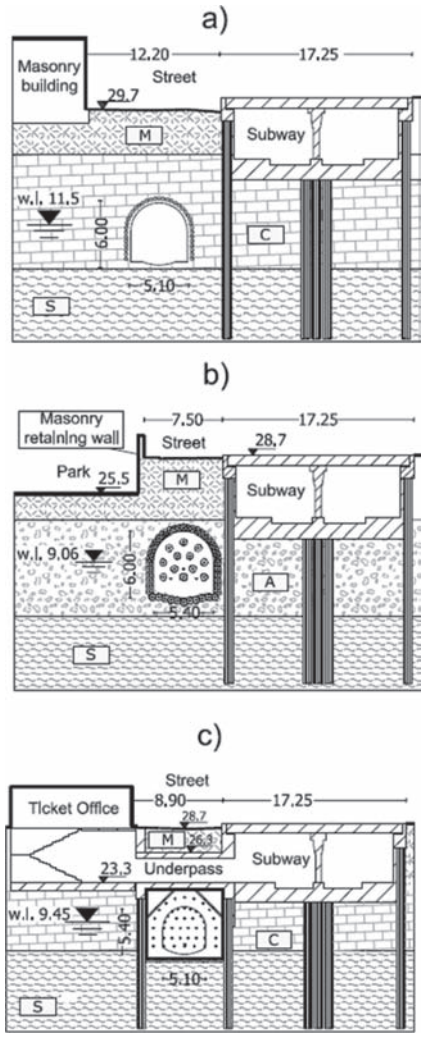

Figure 4. Typical cross sections: a) Micropiles Canopy b) Jet grouting Canopy c) Steel frame. (M made land; C calcarenites; A alluvial soils; S silty sands; W.L. water level).

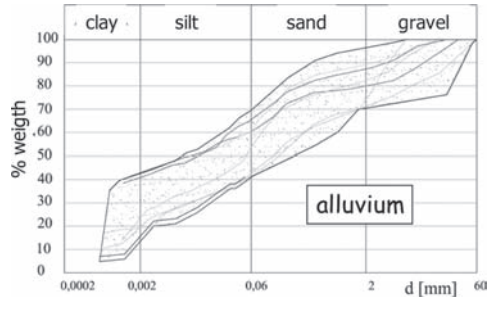

Figure 5. Grain size distribution of the alluvial soils.

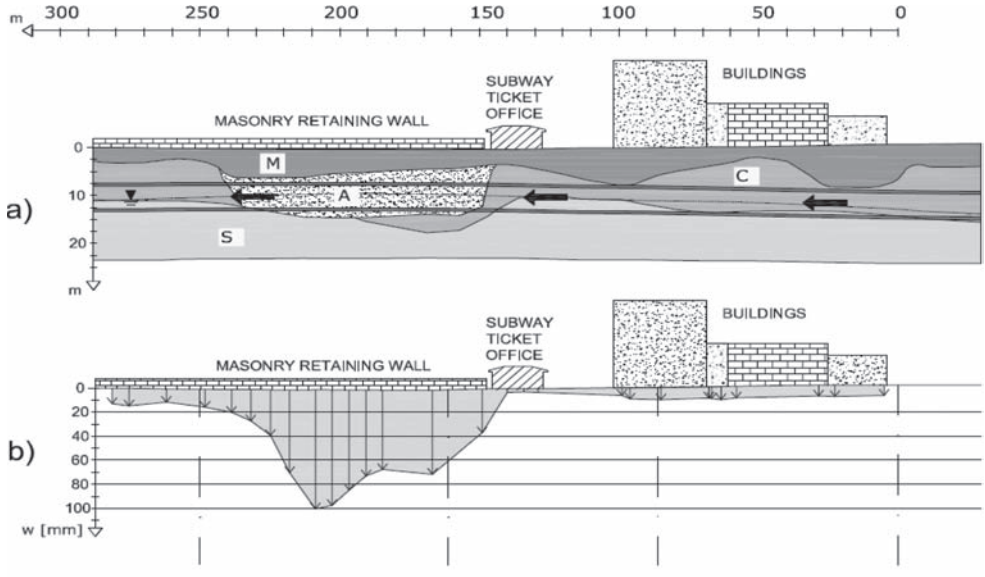

c)

1.a	2	1.b	1.a	CANOPY TYPE
22 STEEL MICROPILES (d=0,06m)	23 REINFORCED JET COLUMNS (d=0,6m)	22 STEEL MICROPILES (d=0,06m)	22 STEEL MICROPILES (d=0,06m)	VAULT
———	12 REINFORCED JET COLUMNS (d=0,6m)	10 STEEL MICROPILES (d=0,06m)	———	PILLARS
———	15 REINFORCED JET COLUMNS (d=0,6m)	———	———	INVERT
———	12 REINFORCED JET COLUMNS (d=0,6m)	22 FIBREGLASS MICROPILES (d=0,06m)	———	FACE
3 HORIZONTAL DRAINS (d=0,09m)	3 HORIZONTAL DRAINS (d=0,09m)	3 HORIZONTAL DRAINS (d=0,09m)	3 HORIZONTAL DRAINS (d=0,09m)	DRAINAGE

Figure 6. Tunnel Construction: a) Geotechnical Profile; b) Final settlements; c) Canopy Types (M made land; C calcarenites; A alluvial soils; S silty sands).

were prescribed for supporting the vault in the calcarenitic formation, considering that the cover was mainly composed by made land (canopy type 1.a). The micropiles were extended down along the tunnel pillars, where it was expected to intercept the dense silty sands (canopy type 1.b). Jet grouting was prescribed instead for the alluvial soils of river Kemonia (canopy type 2). Horizontal drains were prescribed for all the tunnel spans. A special steel frame was devised for crossing the pedestrian underpass, where excavation was essentially supported by the pre-existing reinforced concrete slab and piles (see Fig. 4c).

4 CONSTRUCTION AND MONITORING

Tunnel excavation was recently completed, under "Corso Re Ruggero", but the final concrete lining has not yet been cast in place at the time of writing. During excavation a detailed monitoring program was carried on and the tunnelling process was followed step by step for each construction span, having an average length of 9 m.

This observational procedure allowed for proper design implementation of the design canopies, according to the subsoil conditions met during excavation. In particular, the following monitoring activities were carried on:

i. lithological observation of the excavation face and evaluation of water drainage
ii. sub-horizontal borings to check subsoil conditions for subsequent spans
iii. deformation measurements of the provisional lining by means of convergence bolts
iv. deformation measurements of the steel ribs by strain gauges
v. direct stress measurements on the steel ribs by means of load cells
vi. topographical observations of the ground surface and of the existing buildings
vii. inclinometric, assestimetric and piezometric measurements from vertical borings.

All the above measurements provided useful contribution for checking the design and for prescribing the most appropriate solutions for each excavation span, according to the principles of the Observational Method. However, in practice, lithological and topographical observations proved to be the most valuable means for construction control (Leta et al., 2007). A typical stratigraphical condition observed on site is shown by a picture taken at the tunnel face (Fig. 7).

Topographical data were retrieved and processed in real time, allowing for continuous checking of surface settlements. However, measurements of bench marks placed on the road surface were affected by traffic disturbance which induced excessive scattering. On the contrary, continuous settlement data were recorded from the bench marks placed on the existing buildings and on the masonry retaining wall located along the park. These data provided the most useful mean for monitoring the near by structures.

The final settlements, measured after tunnelling completion, reached quite different values (Fig. 5b), corresponding to the various subsoil conditions (Fig. 5a) and canopy types (Fig. 5c).

Buildings settlements were always less than 10 mm and did not cause any problem to the existing structures. This behaviour was related to the over all stiffness of the calcarenitic layers. On the other hand, the settlements of the retaining wall reached a maximum value of 100 mm causing relevant tilting towards the park. Such larger settlements were associated to the lower stiffness of the alluvial soils of river Kemonia and to a higher percentage of ground volume loss.

The same data were later analysed in order to investigate the effects of tunnelling in more detail.

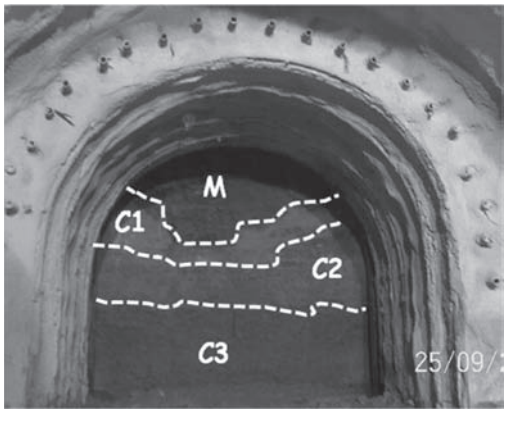

Figure 7. Lithological observation of excavation face: M made land; C1 slightly cemented calcarenite; C2 weakly cemented calcarenite; C3 cemented calcarenite.

For such purpose the settlements recorded at the bench marks have been plotted versus distance y from the tunnel face at the time of recording. Such distance was taken along the horizontal, with reference to the orthogonal projection of the bench mark on the tunnel axis.

Figure 8a shows the settlements measured by the bench mark which experienced the maximum final settlement. This bench mark, labelled by number 8.3, was placed on the previously mentioned masonry retaining wall located between the street and the park. The plot points out that settlement is produced not only by excavation of the span located directly under the check point but also by excavation of the preceding and of the following spans. It can also be appreciated that, when excavation is approaching the bench mark (i.e. negative distance on plot) the settlement proceeds not only during excavation but also when the tunnel face is immobile (dotted lines between excavation spans). A similar behaviour was observed for all bench marks.

However, if these discontinuities are disregarded, the measured settlements can still be interpolated by a Gauss cumulate probability curve (Fig. 8b) as first suggested by Peck (1969) and later confirmed by several authors (e.g. O'Really and New, 1982; Nyren et al. 2001). Moreover, if the settlements S recorded at each bench mark are scaled

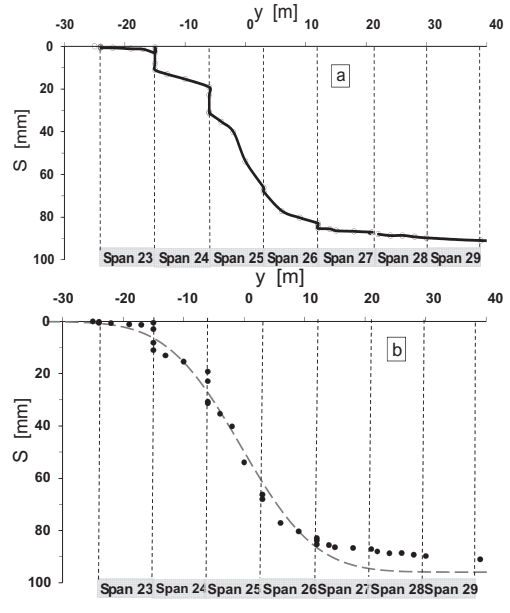

Figure 8. Surface Settlements (S) vs. Distance (y) from excavation face as recorded at bench mark 8.3 (under retaining wall). a) Settlement progress b) Data interpolation by cumulate probability curve.

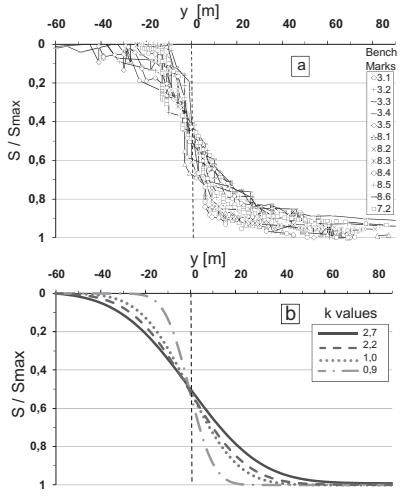

Figure 9. Settlements ratios for all bench marks. a) Recorded data b) Average settlement ratios (k = 2.7—building settlements on calcarenite; k = 2.2—retaining wall settlements on calcarenite; k = 1.0—under pass settlements on steel frame; k = 0.9—retaining wall settlements on alluvial soils).

with respect to their maximum value S_{max}, then all the data can be grouped in a single plot as reported on Figure 9a.

The parameter k was estimated for each bench mark according to the well known relation

$$\frac{S}{S_{max}} = \frac{1}{kH\sqrt{2\pi}} \int_{-\infty}^{y} e^{\frac{-y^2}{2(kH)^2}} dy \qquad (1)$$

The k values, obtained by numerical best fitting of the recorded data, are reported on Table 1 together with the maximum settlement S_{max} and the depth H of the tunnel centre line.

Clearly, the results are scattered because of the variable conditions encountered along the tunnel stretch. However these data can be further analysed by considering four different combinations of structures and subsoil characteristics, listed as they were met during tunnelling:

1. buildings on calcarenite (canopy 1.a/1.b)
2. underpass on calcarenite (steel frame)
3. retaining wall on alluvial soils (canopy 2)
4. retaining wall on calcarenite (canopy 1.a).

Table 1. Settlements data.

Bench mark	S_{max} (mm)	H (m)	k	Soil type	Canopy type	Existing structures	k	S_{max} (mm)
1,2	3,5	11,7	4,3	Calcarenite	1.a	Buildings	2,7	7,7
2,1	3,5	11,7	3,9					
2,2	3,9	11,7	4,5					
2,3	9,4	11,2	2,9					
3,1	10,6	11,2	2,3					
3,2	9,9	11,2	2,2					
3,3	9,7	11,2	2,0					
3,4	9,9	10,6	1,4					
3,5	9,4	9,6	2,2		1.b			
4,1	6,9	9,6	1,3					
4,2	2,6	10,0	0,8		Steel frame	Underpass	1,0	2,5
4,3	2,2	9,9	1,2					
4,4	2,6	9,9	1,1					
7,2	70,3	9,7	1,1	Alluvium	2	Retaining wall	0,9	64,0
7,3	67,6	9,8	1,0					
8,1	71,3	9,7	0,9					
8,2	83,4	9,7	0,8					
8,3	95,9	9,7	0,8					
8,4	99,2	9,7	0,9					
8,5	68,2	9,8	0,8					
8,6	39,2	9,8	0,9					
8,7	26,3	9,8	0,8					
8,8	19,0	9,8	0,9					
8,9	15,5	9,9	2,8	Calc.	1.a		2,2	12,9
8,10	11,0	10,0	1,4					
8,11	13,0	10,2	1,0					
8,12	12,2	10,3	3,6					

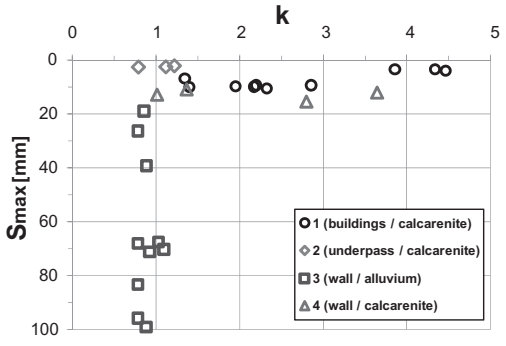

Figure 10. Maximum settlements and k values for different combinations of structures and subsoil characteristics.

For each of the above groups, average values of S_{max} and k are reported in Table 1 and average settlement trends are drawn in Figure 9b. Moreover S_{max} values are plotted versus k values in Figure 10, in order to provide a general picture of the observed settlements.

By comparing data groups 3 and 4, the influence of subsoil properties can be singled out. In fact, in these two cases, the influence of the masonry wall (see Fig. 4b) is equal and probably very limited due to its poor rigidity. It is thus confirmed that the amount of settlement is mostly related to the subsoil stiffness, higher for calcarenites and lower for alluvial soils, even though relevant data scattering is observed particularly for the alluvial soils. Some scattering is also observed for buildings settlements on calcarenite (data group 1) due to their variable structural and foundation features (Standing, 2006; van Tol, 2006). However, in the average, buildings settlements are smaller than those of the masonry wall on calcarenite. This difference can be attributed to their higher structural rigidity and also to their larger distance from the tunnel axis (see Fig. 4a). The underpass settlements are even smaller due to the very high rigidity of this piled structure (see Fig. 4c).

Finally from Figure 9b it can be seen that the settlement curves are steeper for the alluvial soils with respect to the calcarenitic formation. It also appears that the higher rigidity of the buildings, compared to that of the masonry wall, provides a more elongated shape to the length-settlement curves.

5 CONCLUSIONS

The project of a shallow sewer tunnel in difficult site conditions has been successfully accomplished by means of the canopy technique, making proper use of different soil improvement methods: steel and fibreglass micropiles, jet grouting, horizontal drains. In particular, design was carried on by dimensioning three different types of canopies, each one associated to a typical stratigraphical sequence.

During excavation a detailed monitoring program was organized and the tunnelling process was followed step by step for each construction span. This observational procedure allowed for proper implementation of the design canopies according to the subsoil conditions met during excavation.

Settlement recording was the most effective means for monitoring the near by structures in real time and provided also useful data for investigating the effects of tunnelling afterwards. It was found that the final settlements measured after tunnel completion reached very different values, corresponding to the various subsoil conditions and canopy types.

It was also observed that settlements are produced not only by excavation of the span located directly under the check point but also by excavation of the preceding and of the following spans. In addition it was appreciated that settlements proceed not only during excavation but also when the tunnel face is immobile. However, by careful processing of all the settlement data, it was observed that the relation between settlement ratio and distance from the tunnel face still follows, with acceptable approximation, the typical shape of a Gauss cumulate probability curve as repeatedly observed for TBM tunnelling.

Clearly, more observations are needed in order to gain a better understanding of movements induced by canopy technique tunnelling In fact only few cases on this topic have been published so far (e.g. Croce et al. 2004, Russo & Modoni, 2006). Some new settlement data gained by other case histories of canopy tunnelling are going to be reported in the near future (Croce et al., 2011).

REFERENCES

Canzoneri V., Giammarinaro M.S., Gugliuzza G., & Vallone P. 2002. "Area urbana palermitana: analisi delle proprietà geotecniche dei terreni supportata da tecnologia GIS". *Atti del XXI Convegno Nazionale di Geotecnica*, L'Aquila 2002.

Croce, P. 2010. Application of the Observational Method in Urban Tunnelling. *14th Danube-European Conference on Geotechnical Engineering.* 2–4 June, Bratislava, Slovak Republic.

Croce P., Modoni G. & Russo G. 2004. Jet-grouting performance in tunnelling. *Geosupport 2004.* J.P. Turner & P.W. Mayne eds. ASCE Geotechnical Special Publication No. 124. pp. 910–922.

Croce P., Russo G. & Spacagna R.L. 2011. Settlements induced by tunneling in clay shales. *XV European Conference on Soil Mechanics and Geotechnical Engineering.* Athens. September 12–15.

Leta M., Barba D., Canzoneri V., & Giammarinaro M.S. 2007. Public works: an important resource to upgrade territorial knowledge. *VI Forum Geoitalia.* Rimini 2007.

Patel D., Nicholson D., Huybrechts N., & Maertens J. 2007. The observational Method in Geotechnics. Proceedings of XIV European Conference on Soil Mechanics and Geotechnical Engineering: Geotechnical engineering in urban environments, Madrid. vol. 2.

Nicholson D., Tse C., & Penny C. 1999. Observational Method in ground engineering—principles and applications. *Report 185.* CIRIA. London.

Nyren R.J., Standing J.R., & Burland J.B. 2001. Surface displacements at St James's Park greenfield reference site above twin tunnels through the London Clay. *Case studies from construction of the Jubilee Line Extension.* London. Thomas Telford. Pp. 387–400.

O'Really M.P., & New B.M. 1982. Settlements above tunnels in the United Kingdom—their magnitude and prediction. *Tunnelling '82*. London. IMM, pp. 173–181.

Peck, R.B. 1969. Deep excavation and tunneling in soft ground, *Proceeedings of VII ICSMFE,* Mexico City. State of the art volume. pp. 225–290.

Russo G., & Modoni G. 2006. Monitoring results of a tunnel excavation in an urban area. *Geotechnical Aspects of Underground Construction in Soft Ground.* Bakker et al. eds. Taylor and Francis. London.

Standing J.R. 2006. Monitoring ground and structural response to underground construction works. *Geotechnical Aspects of Underground Construction in Soft Ground.* Bakker et al. eds. Taylor and Francis. London. pp. 67–79.

van Tol A.F. 2006. The effects of tunnelling on existing structures. *Geotechnical Aspects of Underground Construction in Soft Ground.* Bakker et al. eds. Taylor and Francis. London. pp. 31–41.

Viggiani G., & Soccodato F.M. 2004. Predicting tunnelling induced displacements and associated damage to structure. *Rivista Italiana di Geotecnica XXXVIII, n. 4,* pp. 11–25.

Geotechnical Aspects of Underground Construction in Soft Ground – Viggiani (ed)
© 2012 Taylor & Francis Group, London, ISBN 978-0-415-68367-8

Prediction and performance of a ground freezing application to the rehabilitation works of an existing tunnel

A. Pigorini, A. Sciotti & G. Zoppo
Italferr, Italy

G. Calabresi
Geotechnical Consultant, Italy

ABSTRACT: The Cassia-Monte Mario railway tunnel, which runs through a hill in the northern part of Rome (Italy), has required invert demolition and reconstruction. The tunnel crosses heterogeneous sandy and silty soils below the water table. In order to prevent the ingress of water, the ground freezing technique was applied. The paper describes the design predictions based on simplified thermal analyses, laboratory tests and real-scale trial fields which were performed to integrate and validate the design predictions. Field tests were supported by automatic monitoring system implemented to measure the temperatures in the ground and deformation effects induced by freezing on the lining. The paper focuses on the role played by field tests which gave a decisive contribution to the correct and effective planning of the execution phase. This allowed to reach a better insight into the application of the ground freezing for underground works.

1 INTRODUCTION

In the last years ground freezing application to tunnelling is largely spreading in Italy in response to problems due to groundwater conditions: frozen soil provides a strong watertight barrier allowing the excavation to safely proceed (e.g. Colombo *et al*. 2009).

Recent developments in ground freezing techniques have indeed resulted in more efficient and cost-effective freezing systems that can compete with other ground improvement techniques. However, the design of a freeze system is still challenging as it involves the prediction of freezing process and soil response: real-scale trial fields are required to integrate and validate the design predictions and to accurately plan the construction stages.

In this paper the ground freezing application to rehabilitation works of an existing tunnel is described and the role of trial fields in the design and execution stage is highlighted.

2 THE CASSIA-MONTE MARIO TUNNEL

The Cassia-Monte Mario tunnel belongs to the double track railway line forming the Northern Railway Belt of the city of Rome (Italy). The 8.8 m internal diameter tunnel, which has a length of 4.4 km, crosses the Monte Mario hill, made up of cohesive and granular deposits of Plio-Pleistocene age below groundwater table. The maximum overburden is 75 m. The excavation of the tunnel began in 1944 and was carried out quite irregularly, with many interruptions and breaks, until 1984. The long construction history was indeed characterized by many problems due to difficult soil and groundwater conditions: various instability phenomena occurred in the southern section (km 21.100 ÷ km 21.700), which also produced significant effects on the surface. To overcome this situation, a 150 m long pilot tunnel was built to carry out ground improvement works prior to excavation. Extensive cement and silicate injections were also performed from ground surface.

In recent times (2004) the tunnel required rehabilitation works aimed at strengthening the original structure (particularly the invert), controlling the water leakage and enlarging the tunnel clearance profile. During the execution of the invert reconstruction, a serious disruption took place: a sudden ingress of water and, then, water and soil occurred from the invert excavation. The water inflow (up to 100 l/s) could not be stopped easily and the tunnel was flooded. The amount of mud which accumulated into the tunnel was about 5000 m^3. Despite the significant overburden (60 m) (Fig. 1), the event had repercussions on the surface with settlements up to several hundreds of millimetres.

After this event the suspension of works was imposed and a detailed geotechnical study was carried out to identify the most appropriate design solution to continue invert reconstruction.

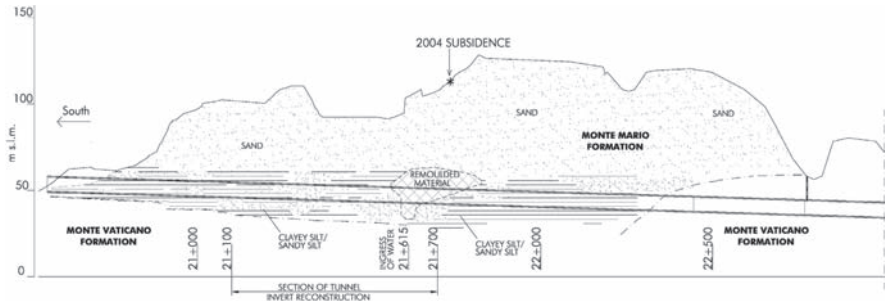

Figure 1. The schematic geotechnical profile along the Cassia-Monte Mario tunnel where the Monte Mario Formation is crossed.

3 THE GEOTECHNICAL CONTEXT

The geological profile along the tunnel route consists of a marine deposit of stiff overconsolidated clay of Pliocene age (Monte Vaticano Formation), overlain by a Pleistocene deposit of clayey silt and sandy silt (Monte Mario Formation), with sandy interbeddings, becoming medium dense sand in the upper part.

Along the stretch which has been characterized by instability phenomena during the construction, the tunnel crosses the Monte Mario Formation (Fig. 1).

Soil properties have been investigated by means of numerous geotechnical surveys which were carried out both from the ground surface and from within the tunnel.

The soil at the tunnel level is characterized by a silt content between 40÷50%, while the sand fraction can vary between 30÷48% and the clay between 13÷22%. The Liquid and Plastic limits are respectively equal to 26% and 18%. The natural water content at the tunnel depth has an average value of 20%. Strength parameters are typical of fine dense granular soils: $c' = 40 \div 50$ kPa, $\omega' = 34°$ for a range of confinement pressure between 200 and 600 kPa, with the high value of cohesion mostly related to the mutual interlocking of the grains.

Geotechnical investigation also revealed that the ground around the tunnel where the inflow of water occurred is loosened and remoulded with high water content.

The average horizontal permeability determined by Lefranc tests is about 5×10^{-5} m/s. Vertical permeability measured by means of laboratory test varies between 1.2×10^{-8} and 9×10^{-9} m/s. The high anisotropy of permeability has to be correlated to the frequent sandy interbeddings.

Piezometers installed in boreholes drilled from within the tunnel and from the ground surface showed piezometric levels increasing in the stretch between km 21.100 and km 21.700 and reaching the maximum value of 20 m above the tunnel invert. The piezometric measurements often show significant variations at short distances but no particular variations over time have been identified.

It is reasonable to assume that the extensive ground improvement works, carried out during the tunnel excavation to counteract the difficult soil conditions, modified the original soil structure and properties, particularly creating unpredictable groundwater flow-paths.

In some cases, during geotechnical investigations, small cavities, probably related to previous boreholes, have been identified.

As a consequence, the soil permeability and groundwater flow-paths represented the main uncertainty the ground freezing design had to face with.

4 THE DESIGN OF THE GROUND FREEZING APPLICATION

4.1 *Design criteria*

To resume works in safety, it was necessary to ensure the water-tightness and improved strength of the soil around the tunnel invert. At the initial design stage, jet grouting and artificial ground freezing seemed to be the suitable methods to meet these requirements.

Considering the heterogeneity of the subsoil and the necessity of realizing a continuous water cut-off, the effectiveness of jet grouting seemed to be low and ground freezing was selected as the most appropriate solution.

Artificial ground freezing is normally realized through the circulation of a refrigerant fluid into freeze pipes, installed in the soil, to extract heat from the ground until the temperature falls below the groundwater freezing point. In this case, the indirect method (brine method) was adopted as freezing technique (Harris 1995; Andersland & Ladanyi 2004).

This method requires the use of an industrial refrigeration plant, from which the refrigerant liquid (a water solution of calcium chloride $CaCl_2$ brine, whose operational temperature is generally in the range from −18°C to −30°C) is delivered to freeze pipes drilled in the ground. A freeze pipe consists of two concentric tubes: the refrigerant fluid enters into the open-ended inner tube and flows through the annulus between the two tubes, drawing heat from the ground. The outer tube is connected to the return lines so that the brine is sent back to the plant, where it is cooled and delivered again to the freeze pipes.

Adopting the ground freezing, the tunnel invert reconstruction has required the preliminary freezing of an arch of soil around the invert and side walls by an array of freeze pipes drilled from the tunnel and, then, the removal of the pipes to proceed with the excavation and cast of the new invert.

The frozen soil arch around the tunnel was aimed at temporarily preventing the ingress of water and improving strength and deformation properties of the soil. As the excavation took place when pipes were dismantled, the freezing system was designed to ensure the maintenance of the above requirements until the completion of the new invert.

4.2 *Design predictions*

The prediction of the real ground behaviour during and after the freezing process was an hard task to tackle, due to the uncertainties about the changes which the soil around the tunnel has suffered in the long history of instabilities and ground improvements. As a consequence, real-scale trial fields were considered a necessary step in the design stage.

The design analyses first focused on the evaluation of geometrical features and mechanical properties of the frozen soil required to ensure water-tightness and stability at the bottom of the excavation.

These design requirements were evaluated by means of 2D numerical analyses based on the finite element method. The analyses were carried out reproducing the initial tunnel conditions by the back-analysis of lining stress measurements and then simulating the preliminary stage of the ground improvement and invert excavation. The results indicated that a 3 m thick arch of frozen soil was necessary below the invert and around the lower part of the side walls (Fig. 2). Lining displacements induced by excavation are about 20 mm (Fig. 2).

Parametric analyses were performed progressively decreasing strength and stiffness of the frozen soil; the results showed that an average compressive strength of about 1.5 MPa was required to allow the construction safely proceeds.

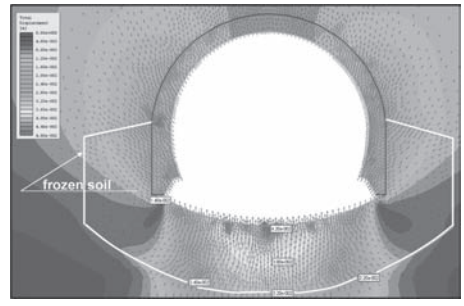

Figure 2. Displacements field induced by invert excavation with the protective arch of frozen soil.

Laboratory tests under temperature and strain rate controlled conditions were performed to measure strength and stiffness properties of the Monte Mario silt in the frozen condition. Uniaxial compressive tests were carried out on samples frozen at the temperatures of −5°C, −10°C and −15°C, imposing a strain rate of 1%/min (Sayles *et al*., 1987) The results showed that the average short-term compressive strength of the frozen soil ranges from 3.5 MPa (−5°C) to 7 MPa (−15°C) and the initial modulus from 120 MPa (−5°C) to 600 MPa (−15°C). Experimental tests performed on similar soils (e.g. Lunardi *et al*. 2001) indicated that long term uniaxial compressive strength can decrease almost to 40% of the short term value, considering a free standing time of the frozen soil of about 7 days.

Hence, on the basis of the numerical analyses and laboratory tests results, the mechanical properties shown by the soil at the temperature T = −5°C were set as the minimum design requirements for the arch of frozen soil. As a consequence, the temperature T = −5°C was identified as the maximum temperature that could be accepted during the thawing process, after the removal of the freeze pipes, until the completion of the new invert.

To predict the rate of freezing, thermal computations were carried out by means of a simplified model (Sanger & Sayles 1979). According to this model, the freezing process develops in three stages: at first, the frozen soil columns grow from separate freeze pipes; then, the separate frozen soil columns merge to form a continuous wall and, finally, two separate rows of frozen columns merge to form a thicker wall of frozen soil.

The model has been applied to predict the time required for the formation of the frozen columns (stage 1) and the time required for the formation of the frozen wall (stage 2). In the first stage the

temperature field around a freeze pipe, in the frozen region, was determined according the Fourier heat flow equation, assuming a steady-state condition:

$$\frac{d^2T}{dr^2} + \frac{1}{r}\frac{dT}{dr} = 0 \quad (1)$$

where T = temperature at the distance r. The time required to freeze the column to a radius R was thus obtained from the following:

$$t_I = \frac{R^2 L_I}{4K_1 T_s} \cdot \left[2\ln\left(\frac{R}{r_o}\right) - 1 + \frac{C_1 T_s}{L_I} \right] \quad (2)$$

where R = radius to the interface frozen-unfrozen soil, r_0 = radius of the freeze pipe, T_s = difference between the temperature at the freeze pipe and the freezing point of water, K_1 = thermal conductivity of the frozen soil, C_1 = frozen soil specific heat, L_I = a function of the latent heat of fusion of the soil water and unfrozen soil specific heat.

Due to the soil heterogeneity, the prediction of the freezing time was carried out considering different scenarios characterized by variations in soil particle size: clay, silt, and sand. In Table 1 the main physical and thermal properties used in the analyses are indicated.

Assuming a temperature of the brine of –28°C the time for the closure of the frozen columns (with a spacing of 1 m) was in the range between 20 days (sand) and 30 days (clay).

The role played by the brine temperature was also investigated: Figure 3 shows the growth of the frozen column in a silty soil, assuming different freeze pipe temperatures.

The freezing time predictions by the simplified model are indeed conservative, nevertheless they gave useful information to plan the freeze pipes lay out and construction stages to be validated by the field tests (see § 5).

Table 1. Main physical and thermal parameters.

Parameter		Sand	Silt	Clay
Dry specific weight	kN/m³	15.90	15.89	15.87
Water content	%	25.20	25.50	25.80
Saturation degree	–	1.0	1.0	1.0
Frozen soil specific heat	kJ/m³ K	2.19	2.195	2.20
Unfrozen soil specific heat	kJ/m³ K	3.061	3.067	3.072
Frozen soil conductivity	kJ/hmK	12.50	10.60	8.70
Unfrozen soil conductivity	kJ/hmK	7.10	6.00	4.90

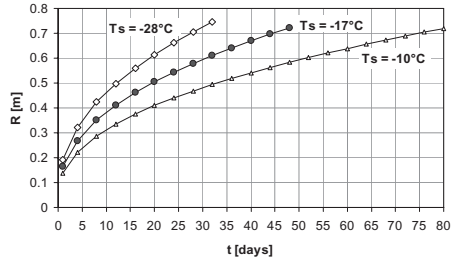

Figure 3. Variation of the radius of the frozen column (isotherm T = 0°C) over time for different values of the freeze pipe temperature, considering the properties of a silty soil.

Considering that the excavation works required the dismantling of the freeze pipes, i.e. these works took place during the thawing process, the estimation of the rate of thawing was the crucial aspect of the design. It had indeed a strong influence on the definition of the construction stages and temperature at which the excavation could start (target temperature, T_o).

Experimental tests on the real site appeared to be the most reliable way for accurately evaluating those aspects and validate the preliminary assumption of a target temperature $T_o = -10$°C.

Finally, one of the major concern in the design stage was the evaluation of the expansion of the ground due to freezing and the possible effects on tunnel lining. Because of the uncertainties about soil properties and structural behaviour of the tunnel, it was decided to address this issue in the trial field, implementing an accurate system to monitor lining displacements.

5 TRIAL FIELD

5.1 *Geometrical layout*

The trial field was realized inside the tunnel for a length of 48 m. Freeze pipes were installed with a spacing of 1 × 1 m, in a radial arrangement to freeze a 3 m thick soil body below the tunnel invert and around the side walls up to a height of about 2.5 m (Fig. 4). The pipes spacing varies from 1.20 m at the top to 1.35 m at the bottom.

The length of the pipes is in the range from 4.0 m to 4.8 m. The upper section of the pipes, drilled through the existing invert, was insulated to delimitate the target frozen zone of the tube. The total volume of frozen soil was 2640 m³.

The field test length was subdivided into 4 sections with a length of 12 m each. Each section was equipped with 210 freeze pipes, for the total number of 840 pipes in the trial field.

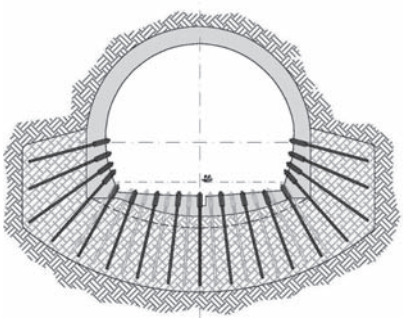

Figure 4. Freeze pipes lay out in the tunnel cross-section.

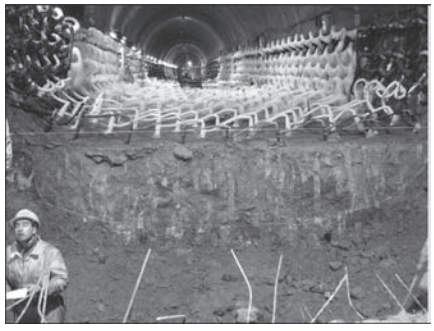

Figure 5. The excavation of the existing invert.

All pipe installations were realized using a preventer system to rapidly close the hole in case of uncontrolled flows of water and/or soil.

The freezing ground application was preceded by injections of water-cement mixtures to reduce the soil permeability and to contrast possible preferential pathways of water especially in the area affected by the water inflow.

5.2 *The refrigeration system*

The refrigeration plant was located inside the tunnel and connected through pipes to the cooling towers realized at the south portal. A freeze plant with a capacity of 500 kW was used. The freeze plant was designed for simultaneously freezing a tunnel length of 48 m. The designed brine supply temperature was –28°C. The delivery system was planned and realized in order to separately feed each row of freeze pipes and to disconnect the pipes installed at the invert, while feeding the pipes at the side walls.

5.3 *The monitoring system*

The monitoring system was developed to be simple and robust in order to work in the complex conditions of a tunnel under construction.

The temperature monitoring system was composed of temperature sensors and data loggers for the automatic data acquisition and recording, allowing real time data processing to control both the freezing and thawing process.

Temperature measurement tubes were installed at well defined distance from the freeze pipes for a total number of 19 for each section: 11 in the invert and 8 at the side walls. Each tube was equipped with 3 sensors, placed at a depth of 0.5 m (upper sensor), 1.5 m (intermediate sensor), 2.5 m (lower sensor) from the top of the tube. The total number of sensors is 57 for each section and 228 in the trial field. The temperature measurement tubes at the side walls were maintained active also during the demolition and reconstruction works to control the thawing process. Temperature sensors were also installed along the delivery system to check the brine temperature.

Monitoring of the tunnel lining behaviour was carried out to control possible movements induced by freezing and thawing as well by excavation. Monitoring program included 3D geodetic optical levelling and invar tape to measure tunnel lining diametrical distortion (convergence). Moreover invar tape was used to monitor side walls movements, verifying possible compressions or extensions.

Ground surface and subsurface movements were also controlled respectively by optical levelling and borehole inclinometers and extensometers.

5.4 *Construction stages*

The sequence of construction stages was the following:

1. freezing of the four 12 m long sections,
2. removal of the freeze pipes only in section n°1 when the target temperature T_o = –10°C was measured below the invert and at the side walls,
3. demolition and reconstruction of the invert in section n°1 working for successive stages with a length of 4 m,
4. removal of the freeze pipes in section n°2 when the target temperature T_o = –10°C was measured in the frozen soil body,
5. demolition and reconstruction of the invert in section n°2 working for stages with a length of 4 m, and this cycle was repeated for section n°3 and n°4.

During the excavation works the actual shape and structural features of the existing invert were discovered: the invert is characterized by a marked and abrupt reduction of the cross-section size at the side walls connection. In some cases the lack of any structural continuity between the invert and side walls was found out.

5.5 *The monitoring results*

During the trial field 840 freeze pipes were simultaneously active and 228 thermometric sensors were installed in the ground recording data every 8 hours. Monitoring data were an invaluable aid to analyze the freezing process and to define the critical design parameters.

The freezing process is well described by the temperature data plotted versus time. Figure 6 shows the typical measured trend recorded by the sensors below the invert: an initial rapid decrease of temperature is followed by a slowdown trend approaching the freezing point of groundwater. Then, the temperature starts decreasing again but slower than in the previous phase.

At the beginning of the process the freezing rate is in the range 1.3°C/day ÷ 1.7°C/day, decreasing to 0.6 ÷ 0.8°C/day after the freezing point.

During the experimental test, the temperature of the brine flowing into the freeze pipes did not reach the operative value $T = -28$°C, also because of the unsatisfactory insulation of the feeding system. Even if the average brine temperature was $T = -17$°C, the thermal condition $T = 0$°C was attained in about 25 days, while the target temperature $T_o = -10$°C was reached in about 45 days.

Temperature measurements in the ground below the invert were generally homogeneous, while the temperature data in the ground at the side walls were more scattered, showing a coefficient of variation always greater than 0.3 (Fig. 7).

The spatial distribution of the temperature was characterized by a decreasing gradient along the axis of the temperature tubes, due to the radial arrangement of the freeze pipes that caused an increase of the sensor-freeze pipe distance from the

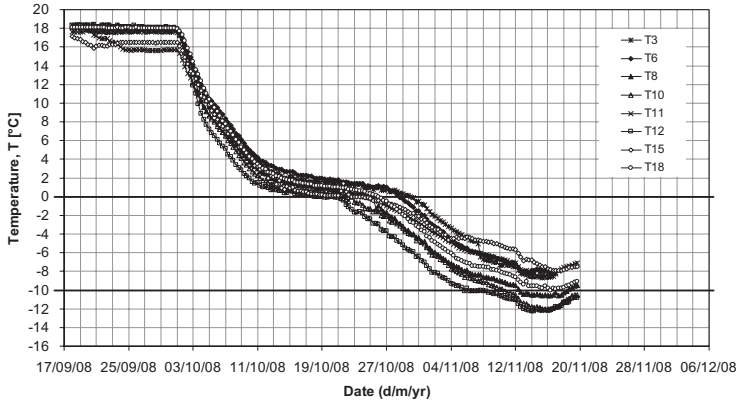

Figure 6. Variation of temperature with time during ground freezing. Data from intermediate sensors below the invert in section n°1.

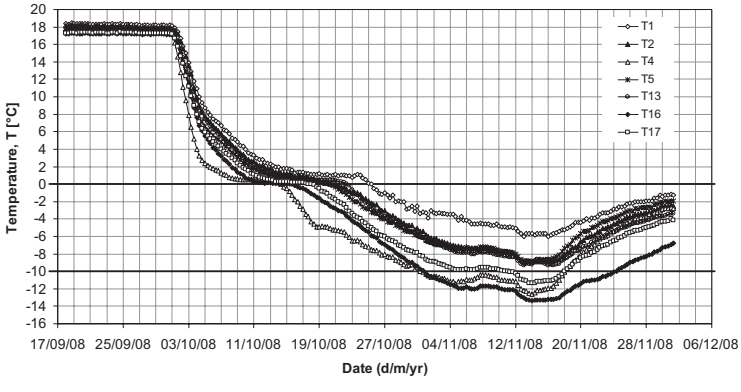

Figure 7. Variation of temperature with time during ground freezing. Data from intermediate sensors at the side walls in section n°1.

top to the bottom. As a consequence, the upper thermometers, that were located closer to the freeze pipes, recorded an apparent faster cooling than the lower sensors. The decreasing radial gradient was in the range between 1.6°C/m and 2.8°C/m.

A different response has been noticed between the sensors installed below soil invert and those installed at the side walls. As a rule, comparing sensors with the same distance from the freezing pipes, the temperatures measured at a given time below the invert were higher than temperatures measured at side walls. The maximum measured difference was 2.7°C.

The thawing process has been monitored for more than 2 weeks for each section. A non linear variation of temperature with time was measured and a faster heat of the ground was observed in the upper sensors (Fig. 8).

Considering a period of time of 7 days the rate of thawing varies in the range from 0.36°C/day to 0.58°C/day with an average value of 0.4°C/day for the sensors below the invert. For the sensors at the side walls the rate varies from 0.38°C/day to 0.81°C/day with an average value of 0.6°C/day.

The freezing process produced slight effects on the tunnel: in sections n°2, 3 and 4 an average convergence of 4 mm was measured (Fig. 9). A different behaviour was observed in section n°1, where outward 6 mm displacements of the side walls were recorded.

Movements associated to the excavation stage were more significant; the data were also analysed considering the effect produced by the excavation of the adjacent section (Fig. 9).

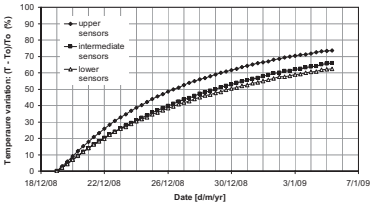

Figure 8. Temperature variations measured in the ground at the side walls during the thawing process. The variation is expressed as a percentage of the temperature to at the beginning of the thawing process.

5.6 *Field trial results*

The field experimental evidences validated the designed freezing system and helped in defining the time schedule of works and planning the construction site activities.

On the basis of the measured freezing rate, even considering the real brine temperature, the soil response appeared more similar to a sand behaviour, according to the simplified model used in the design stage.

Moreover, two operative temperatures were defined to guide the construction stage. Trial field demonstrated that the demolition and invert reconstruction of a 12 m long section could be completed in a week. Considering that the maximum acceptable average temperature of the thawing phase was calculated to be $T = -5$°C, and the maximum measured rate of thawing was 0.6°C/day, the target temperature at which excavation could start was set $T_o = -10$°C. Thus the design preliminary assumption was confirmed.

However, the dependence of the temperature measurements on the sensor-freeze pipes distance and the different response between invert sensors and side walls sensors highlighted the necessity of a careful analysis of monitoring data. Thus, a procedure for the target temperature evaluation was developed.

This procedure defined the target temperature as the average value $T_o = -10$°C measured in the frozen soil, considering separately data from the side walls sensors and invert sensors; moreover various controls of the quality and representativeness of the data were required (e.g. the coefficient of variation). Additional requirements (e.g. the

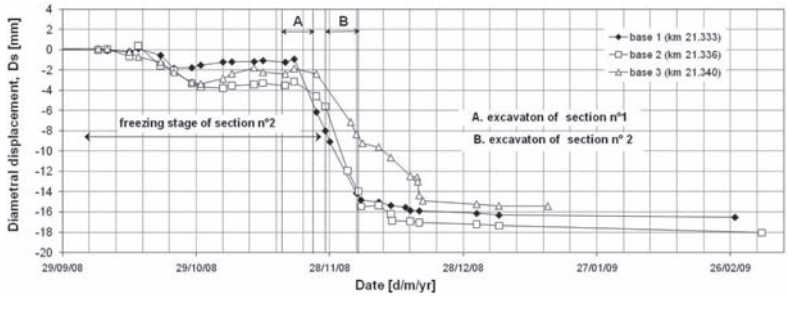

Figure 9. Lining displacements measured during the freezing and excavation stages in tunnel section n°2. (Negative values indicate convergence).

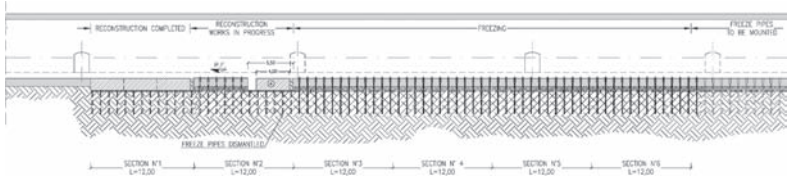

Figure 10. The sequence of tunnel invert reconstruction.

average temperature for each temperature tube $T \leq -7.5°C$) were also implemented to ensure about local fails in the formation of the frozen soil.

6 CONSTRUCTION PHASE

The invert reconstruction was carried out for a total tunnel length of 325 m, according to the cyclic sequence that was tested in the trial field (Fig. 10):

1. freezing of four sections in advance,
2. removal of the freeze pipes in the first section when the target temperature in the frozen soil was reached according to the procedure above described,
3. freezing of the fifth section, in order to provide a length of 48 m of freezing soil in advance,
4. demolition and reconstruction of the invert of the first section, advancing for stages with a length of 4 m each.

All the execution stages have been carried out with the constant control of thermal conditions and lining deformations.

The procedure for the target temperature evaluation has proved to be a useful tool for a rapid data analysis to control the thermal requirements for excavation.

Monitoring of the temperatures demonstrated that the thermal condition $T = 0°C$ was reached between 16 and 20 days.

Monitoring of the movements inside the tunnel during the freezing stage confirmed that in most cases the tunnel underwent a convergence of some millimetres (2÷5 mm). Outward movements of the side walls have also been recorded. Side walls generally suffered slight extensions. The different pattern of deformation appears indeed to be related to the effectiveness of the structural continuity between the old invert and side walls (e.g. Fig. 5). During the excavation stage the average measured convergence was about 14 mm.

Long term monitoring ensured about the stabilization of induced movements (e.g. Fig. 9) and proved the end of thawing process. In situ investigations (cone penetration tests) were carried out before and after the freezing process: the results demonstrated that mechanical properties were not affected by artificial freezing.

7 CONCLUSIONS

The design of the ground freezing application to the Cassia-Monte Mario tunnel was a challenging task, as it required the prediction of the behaviour of a soil which has suffered modifications from its natural state in the long history of tunnel instabilities and ground improvements. The structural behaviour of the existing lining was also not easily to predict because of the different methods of tunnel execution which were adopted over time.

In this complicated context, real-scale trial fields were an important step of the design stage, giving a deeper insight into the temperature field in the frozen soil body, the rate of freezing and thawing and the associated volume changes. An effective planning of the execution was carried out on the basis of the field testing and the invert reconstruction was successfully completed.

Long term monitoring and in situ tests have allowed to verify the complete exhaustion of the freezing process without any adverse consequences on the existing lining and on the ground surface.

REFERENCES

Andersland, O.B. & Ladanyi, B. 2004. *Frozen Ground Engineering*. Second Edition, John Wiley & Sons, Inc.

Colombo, G., Cavagna, B., Cassani, G. & Manassero V. 2009. La tecnica del congelamento artificiale del terreno per lo scavo delle gallerie di stazione della metropolitana di Napoli. *Gallerie e grandi opere sotterranee*, 89: 23–34.

Harris, J.S. 1995. *Ground freezing in Practice*. Thomas Telford.

Lunardi, P., Leoni, F. & Valente, A. 2001. Full scale test of grouting and freezing for new extension of Rome underground, line B1. In *Progress in tunnelling after 2000. Proc. AITES-ITA World Tunnel Congress, Milano, 10–13 June 2001.* Bologna: Patron.

Sanger, F.J. & Sayles, F.H. 1979. Thermal and rheological computations for artificially frozen ground construction. *Engineering Geology*, 13: 311–337.

Sayles, F.H., Baker, T.H.W., Gallavres, F., Jessberger, H.L., Kinosita, S., Sadovskiy, A.V., Sego, D., Vyalov, S.S. 1987. Classification and laboratory testing of artificially frozen ground. *Journal of Cold Regions Engineering*, 1: 22–48.

Geotechnical Aspects of Underground Construction in Soft Ground – Viggiani (ed)
© 2012 Taylor & Francis Group, London, ISBN 978-0-415-68367-8

Flow around a TBM: A Comparison of analytical and numerical models

A. Bezuijen
Deltares, Delft, The Netherlands

F. Nagel
Zerna Ingenieure, Bochum, Germany

G. Meschke
Ruhr University Bochum, Germany

ABSTRACT: The flow of bentonite and grout around a TBM influences the settlement trough that is created during TBM tunneling. Not taking into account this flow, leads to a calculated settlement trough that is too deep. Two calculation methods have been developed: a 1-D analytical model taking into account the basic aspects of this flow and assuming flow in only one direction and a 3-D numerical model, which also assumes flow in one direction, but considers the calculated width and spatial distribution of the steering gap using a hybrid Finite Element—Finite Difference model. The paper describes briefly both models (making reference to more elaborate descriptions) and compares the results of both models. It will be discussed what are the limits of the analytical model and where the numerical model has to be used.

1 INTRODUCTION

Nowadays TBM tunneling, especially in cities, has very strict requirements on the allowed settlement. Decreasing the average settlement and the maximum settlement in a tunnel project requires craftsmanship of the operators of the TBM, but also requires improved understanding of the processes that are of importance during tunnelling.

The research to improve the understanding of the tunnelling process follows generally 2 paths. One path was to simulate the tunneling process more and more accurate in numerical programs (Dijk, van & Kaalberg, 1998, Kasper & Meschke, 2004, Möller & Vermeer, 2008). With this research it is possible to improve our understanding of the tunnelling process because it is possible to study the interaction between various mechanisms, more than it is possible without these numerical programs. The other path is to study the individual mechanisms that occur during tunnelling. The basic idea here is that it is not the interaction between various mechanisms that hamper our understanding of the tunnelling process, but that not all mechanisms itself are sufficiently understood. For this second path usually model tests are performed (Merritt & Mair, 2006), field tests are analysed (Bezuijen & Talmon, 2008, Bezuijen et al. 2004) or simple models are proposed (Bezuijen, 2009).

Both these research paths are combined in this paper that presents results of research on the influence of grout and bentonite flow around the TBM on the settlement through. A simple calculation model (Bezuijen, 2009) is implemented in a 3-D FEM program (Nagel, 2009) and the results of the calculation model itself are compared with the results of the numerical program. This allows investigating where the interaction between the models becomes important.

The results of the 1-D calculation model have already be compared with the results of a 2-D numerical model (Bezuijen & Bakker, 2008), but here the TBM was not included in the model and it was only investigated what deformation would occur when the soil around a tunnel is pressurized with a liquid.

2 FLOW AROUND A TBM

A TBM is slightly tapered allowing it to maneuver in the soil, see for an example Figure 1. The drawing in this figure is not to scale because then the difference in diameter would not be distinguishable.

The cross-sectional area at the back is approximately 0.5 to 1% smaller than the cross-sectional area at the front (the actual value differs for each

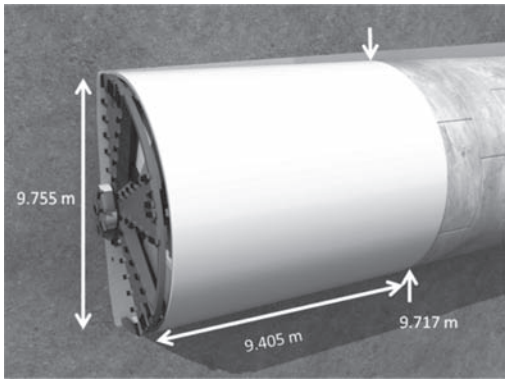

Figure 1. Dimensions of the TBM for the Botlek Rail Tunnel in the Netherlands (drawing not to scale).

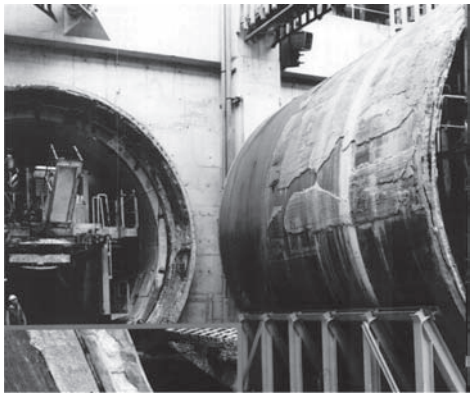

Figure 2. 2nd Heinenoord Tunnel, the Netherlands. Grout on the TBM shield after drilling of the first tube.

TBM and also depends on whether over-cutters are used during drilling). Until recently, most calculation models developed to describe the tunneling process of a TBM (Dijk van & Kaalberg, 1998, and Meschke and Kasper, 2004) assume that the soil stays in contact with the TBM over the entire shield. This means that, neglecting the soil dilatancy, the settlement trough caused by the passage of the TBM must be 0.5 to 1%. However, it was found (Bezuijen and Talmon, 2008), that in several cases the total measured settlement trough after passage of the TBM and the consolidation of the tail void grout is smaller than 0.5 to 1%. In some cases even a negative volume loss was reached.

Information from the field also showed that the assumption of the TBM shield staying always in contact with the soil is not correct. When the TBM that was used during the construction of the 2nd Heinenoord Tunnel in the Netherlands had finished the first tube and was turned to start the 2nd one, it appeared that there was grout on the shield, see Figure 2. indicating that grout can flow from the tail void along the shield.

Furthermore, measurements at the Botlek Rail Tunnel showed that the pressures measured at the tunnel face are quite comparable with the pressures measured on the shield 2.8 m from the tunnel face. This also indicates that there exists a communication between the process fluids along the shield for at least 2.8 m (Nagel et al. 2009).

3 MODELLING

3.1 *General*

Assuming that there is a gap between the TBM shield and the soil, this gap must be filled with grout, injected at the tail void, or with bentonite from the front (in case of a slurry shield TBM). The flow process, and the resulting pressure distribution was described in an analytical 1-D model by Bezuijen (2007). The principles of this model were used to enhance a 3-D FEM model to take into account a flow of process fluids within those parts of the TBM shield which are not in full contact with the soil (Nagel, 2009).

3.2 *1-D analytical model*

To model the soil deformation accurately, it is necessary to model the flow around the TBM and around the lining. The interaction between TBM, tunnel lining and the surrounding soil is governed by bentonite slurry that is injected at the tunnel face and grout that is injected in the tail void. Due to overcutting, bentonite slurry will flow along the shield skin of the TBM and the tapered shield will also lead to a grout flow along the shield skin from the tail of the TBM (Bezuijen, 2007). Possible distributions of bentonite slurry and grout are shown in Figure 3 and described below.

1. Grout flows from the tail to the tunnel face and bentonite flows from the tunnel face to the tail (this situation can only occur when there is some volume loss in the joint between the TBM and the soil, for example due to grout bleeding or penetration of bentonite into the soil). In this situation, the lowest pressure will be present where the bentonite and grout meet.
2. Bentonite flows backwards to the tail and pushes the grout out of the joint between the TBM and the soil. The pressure will be highest at the tunnel face and will decrease towards the tail. This cannot be a continuous situation, but can occur temporarily.

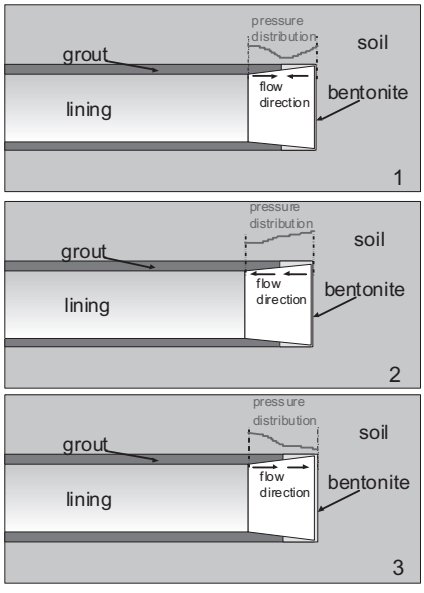

Figure 3. Possible flow directions and sketched pressure distributions along the TBM. The third situation is worked out quantitatively.

3. Grout flows to the tunnel face and pushes bentonite towards the tunnel face. The pressure is highest at the tail close to the grout injection points, and will decrease in the direction of the tunnel face. This can be a continuous situation and will be worked out further.

Assume a TBM with a small change in diameter (diameter decrease from front to back). The TBM is boring in soil that is assumed to be linearly elastic with a shear modulus G. Assume that the soil around the shield is in contact with the shield skin. This leads to a decrease in soil stresses around the TBM from the tunnel face towards the tail. A simple approach is to ignore the influence of gravity and assume a tunnel that is positioned perfectly symmetrically in the borehole. In such a situation and for linear elastic soil behaviour, the relationship between deformation and stress reduction can be written as (Verruijt, 1993):

$$\Delta\sigma = 2\frac{\Delta r}{r}G \tag{1}$$

where $\Delta\sigma$ is the change in pressure, Δr the change in radius, r the radius of the tunnel and the grout, and G the shear modulus of the soil around the tunnel.

Calculating the pressure from front to tail of the TBM (without the influence of grout or bentonite flow) will lead to an ongoing pressure reduction. However, grout is injected at the tail of the TBM. If this is injected at a pressure higher than the pressure calculated using Eq. (1), the soil will be pushed from the TBM and the situation shown in Figure 4 will occur. The grout will flow in the joint between the soil and the TBM, which will lead to a pressure drop in the grout. The pressure is highest in the tail and decreases when flowing through the joint in the direction of the TBM's tunnel face. This pressure drop is determined by the yield stress in the grout and the width of the joint. Assuming that most flow-induced friction will develop between the soil and the grout and also assuming that the grout behaves as a Bingham liquid, the pressure drop can be written as:

$$\Delta P = \frac{\Delta x}{s}\left(\tau_\gamma + \eta\frac{dv}{dy}\right) \tag{2}$$

In (2), ΔP is the change in pressure due to the flow, Δx a length increment along the TBM, s the joint width between the tunnel and the soil, τ_γ the shear stress of the grout around the TBM, η the dynamic viscosity, and dv/dy the velocity gradient in the flowing liquid perpendicular to the joint. In Bezuijen et al. (2004) the measured yield strength of grout was assumed to be 1500 Pa, the dynamic viscosity is 50 Pa.s, and the drilling speed was less than 1 mm/s. To influence the soil deformation, the joint width between the TBM and the soil must be in the order of centimeters (because the tapering is in order of centimetres, see Figure 1), which means that dv/dy is in the order of 0.1 1/s. Viscous forces can be ignored in such a situation, because the second term on the right hand side of Equation (2) is much smaller than the first.

Using these equations and the known shape of the tunnel, it is possible to calculate the joint width that can be expected and the distance the grout in the tunnel flows over the TBM shield.

The following calculation procedure is used: the soil around the tunnel is assumed to behave as independent slices with a thickness Δx, see Figure 4. Knowing the geometry of the tunnel, the grouting pressure, the soil pressure and the elastic

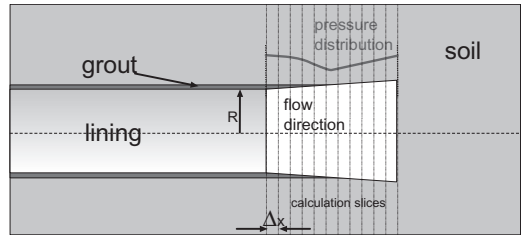

Figure 4. Idealised sketch of a TBM and lining in grout (picture not to scale).

properties of the soil, the joint width at the tail of the TBM can be calculated using Equation (1). This joint width can be used to calculate the pressure drop caused by grout flow towards the front of the TBM over the distance Δx using Equation (2). The resulting pressure (the original grouting pressure minus the pressure drop) is used to calculate the deformation and joint width of the next slice, and so on. For each calculation, a check is made whether the calculated joint width is still positive. If this is not the case, the soil is in contact with the TBM and the pressure is calculated from Equation (1) using the actual diameter of the TBM for that slice.

The same procedure can be applied for the bentonite flow when the bentonite around the shield is pushed to the front by the grout. Only the yield stress of the bentonite will be different from the yield stress of the grout and the pressure at the front is known and the pressure at the boundary between the grout and bentonite (somewhere on the shield) has to be calculated. In the program the pressure distribution of the grout is calculated from the tail to the front as well as the pressure of the bentonite from the front to the tail. It is assumed that there is bentonite when the calculated bentonite pressure is higher than the calculated grout pressure and that there is grout at the locations where the calculated grout pressure is the higher one; see also Bezuijen, 2009.

3.3 *Numerical model*

The analytical formulas for computation of the flow of grout and bentonite within the steering gap as presented in Equation (2) and used for the 1-D analytical model are implemented within a FE-model recently developed for the transient, process-oriented numerical simulation of the shield supported tunnel advance in partially and fully saturated soft soil (see Nagel et al. 2010) This simulation model allows to analyze the shield supported tunnel construction as a time variant process taking into account the TBM, the surrounding soil and the tunnel tube as separate components (see Figure 5).

The tunnel advance is simulated in a sequence of excavation and down-time steps by elongation of the hydraulic jack elements and step-wise activation and deactivation of soil, grouting mortar and lining elements. The TBM is modeled as a three dimensional deformable body connected via frictional contact to the surrounding underground and by the hydraulic jacks to the lining tube. Its conical geometry as well as a possible overcutting is taken into account. For description of the surrounding underground a CamClay-type model known as the CAS-model is used (Nagel and Meschke, 2010; Yu, 1998).

To consider within this model for an inflow of bentonite and grout into the steering gap a consecutive algorithm is applied: on the one hand side the *Finite Difference Method* (FDM) is applied to compute the pressure distribution within the steering gap based on the differential relationship given in Equation (2) (see Figure 6); on the other hand side a modified contact algorithm is introduced to take into account the effects of a pressurized liquid film between the two contact surfaces.

By application of the FDM, the pressure distribution within the steering gap is computed before each time step for simulation of TBM advance according to the actual gap width and

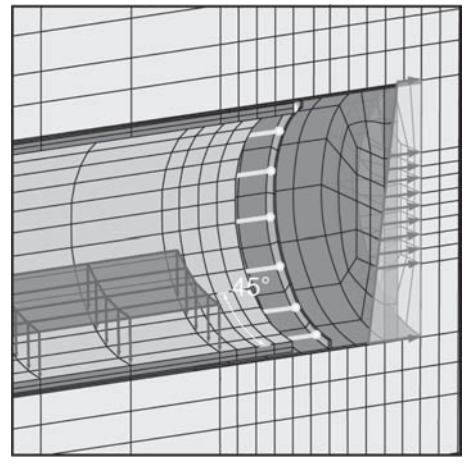

Figure 5. FE-model for simulation of TBM advance including TBM, lining tube and soil.

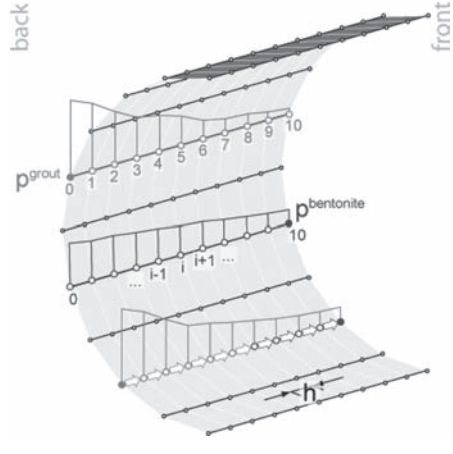

Figure 6. FDM mesh for computation of fluid pressures within steering gap.

gap distribution. Subsequently, advance of the TBM is simulated taking into account the so-obtained pressure distribution along the shield skin by application of the modified contact algorithm. Using this scheme, the pressure distribution within the gap is evaluated explicitly and held constant during the time step whereas the coupling of this fluid pressure onto the soil displacements is computed implicitly.

For the computation of the flow of the process liquids around the TBM only the third of the scenarios presented in Figure 3 is considered. To compute the pressure distribution Equation (2) is evaluated separately for both the face support and the tail void grout considering the grouting pressure at the tail as a boundary condition for the flow of the grouting mortar and the face pressure at the front end of the TBM as a boundary condition for the flow of the support medium. The FDM mesh applied to solve Equation (2) is assumed as a set of parallel lines distributed uniformly around the shield skin at constant distances (see Figure 6).

To model contact between the deformable TBM and the surrounding soil via the shield skin a surface-to-surface contact algorithm is employed. For consideration of a pressurized liquid between the two contact surfaces the contact normal force t_N acting on both contact surfaces is modified as the liquid pressure acts on both surfaces if the gap is not closed.

If the gap is opened (i.e. $s > 0$), the pressure transmitted by the liquid onto the surfaces is expressed by equivalent forces in the direction of the outward normal of the soil element facets. Thus, the normal contact force t_N is given by

$$t_N = \begin{cases} p_{liquid} & p_{liquid} \geq \langle \lambda_N + \varepsilon_N s \rangle \\ \langle \lambda_N + \varepsilon_N s \rangle & otherwise \end{cases} \quad (3)$$

Expression of the contact normal force by Equation (3) is equivalent to separation of the soil from the shield skin if the liquid pressure exceeds the normal contact force between TBM and soil.

4 COMPARISON OF RESULTS

To be able to compare the results of both models it is necessary to determine a shear modulus from the model parameters of the CAS-model used within the numerical simulation. The constitutive law in the numerical model uses a stress dependent bulk modulus (K):

$$K = \frac{\mu p'}{\kappa} \quad (4)$$

where $\mu = 1 + e$ with e the void ratio p' the volumetric effective stress and k is the slope of the URL. The relation between K and the shear modulus G can be written as:

$$G = \frac{3K(1-2\nu)'}{2(1+\nu)} \quad (5)$$

where ν is the Poisson ratio. The bulk modulus of the soil close to the TBM will be determined by the pressure loading of the grout at the tail and the pressure of the bentonite at the front. To calculate G the mean pressure was determined (270 kPa) and this value was used to calculate K and G. The other parameters of the CAS-model are assumed as: $\nu = 0.3$, $\kappa = 0.01$ and $\lambda = 0.05$. Using these parameters it was found that G was 15 MPa for the soft soil case and 30 MPa in the stiff soil case. It should be mentioned that for a tunnel in sand both values would represent 'soft soil', but here the definition given by Nagel et al. 2010 is used for consistency.

Some of the situations simulated by Nagel et al. 2010 were also simulated with the analytical model. However, in this case the only situation that can be compared is the situation where a constant pressure around the TBM is assumed, since the analytical model is a 1-D model. Consequently, for the analytical model, the shape of the gap will differ from the shape in a field situation where the pressure is a function of the height. Only the soft soil situation was simulated by Nagel in case there was 0.025 cm overcutting. Therefore only the soft soil simulations were used in the analytical model calculations.

The results are presented in Figure 7 and Figure 8.

The parameters used in the analytical model are presented in Table 1.

The analytical model presents only one value for the gap, since it is a 1-D model. The value found for the tail is in reasonable agreement in both models, when comparing the result of the analytical model with the average gap in the numerical model, see also Table 1. However, for the other locations (on the middle and at the front of the TBM) the agreement is less good. This is caused by the boundary conditions. Without overcutting it is assumed that there is no possibility for the bentonite to flow around the TBM, only grout can flow from the tail to the front. This results in a situation where at most locations the calculated pressure is lower than the soil pressure and thus the soil stays in contact with the shield skin. The analytical model works with only one soil pressure (the vertical soil pressure), Consequently, the horizontal stress in the soil is overestimated. The numerical model, which calculates both horizontal and vertical stresses shows that there is still a gap.

In the situation with overcutting the analytical model predicts that directly behind the cutting

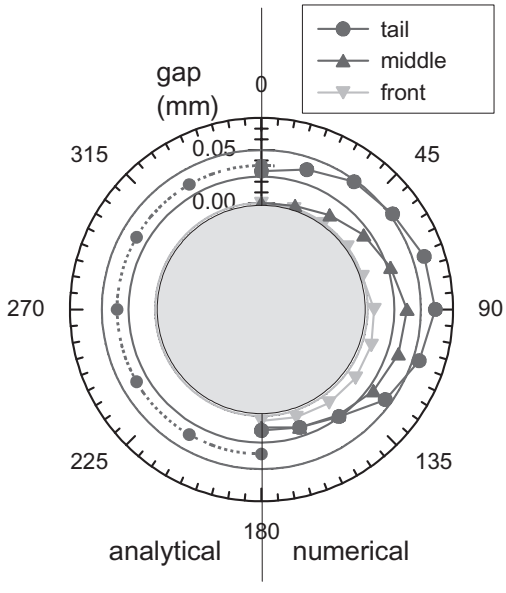

Figure 7. Gap width calculated with the numerical (right) and the analytical model (left) compared. The analytical model resulted in no gap width for the middle and front position, no overcutting, soft soil. The drawn circles over 360 deg show the theoretical opening without soil deformation.

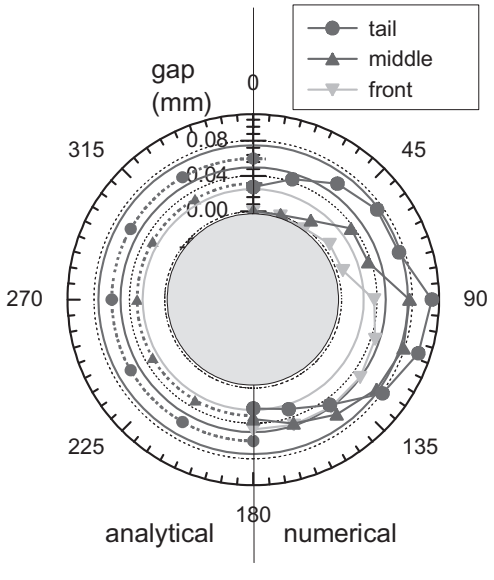

Figure 8. Gap width calculated with the numerical (right) and the analytical model (left) compared. The analytical model resulted in no gap width for the front position, 0.025 m overcutting, soft soil. The drawn circles over 360 deg show the theoretical opening without soil deformation.

Table 1. Results of the analytical and numerical models: calculated volume loss and gap width at the tail of the TBM.

	Numerical		Analytical	
Situation	ΔV %	Gap mm	ΔV %	Gap mm
Without overcutting	0.29	41	0.57	36
0.025 m overcutting	0.45	60	0.45	63

wheel the soil collapses on the TBM. This makes the calculation of the bentonite pressures along the TBM a bit arbitrary and so the gap width. In the calculation shown in Figure 8 a minimum gap width of 0.01 m at the front is assumed.

The way to calculate the pressure distribution and the corresponding gap width is the same in both methods. What is different is that a stress dependent soil model is used in the numerical model and that the position of the TBM is a result of the equilibrium forces acting on the shield skin, whereas in the analytical solution it is assumed that the TBM is in the middle of the hole. The stress dependent soil model will result in a lower Young's modulus when the stresses are lower and therefore more deformation can be expected at lower stresses.

Comparing the calculated volume loss and the average gap as calculated with both models, it appears that the volume loss is overestimated in the analytical model for the situation without overcutting. The result with overcutting shows an almost perfect agreement. As can be seen from Figure 8, this agreement is valid for the average value of the gap, not for the gap at each position. The numerical solution shows a smaller diameter vertically and a larger diameter horizontally.

5 CONCLUSIONS

The results of a 1-D analytical model for the flow of viscous process fluids along the shield skin are compared with the results of a 3-D finite element program for TBM tunneling enhanced by a contact model for the soil-TBM-interface considering fluid flow. It appeared that the 1-D analytical model is able to show the principle of what can be expected when the gap between the TBM shield and the soil is not closed. The model also shows why this gap is not closed in most cases during drilling. The 3-D numerical model goes much further. It takes into account the stress dependent behavior of the soil, the vertical gradient in the pressure (which cannot be neglected, Nagel, 2009) and the position of

the TBM with respect to the hole that is drilled by the TBM.

It should be realized that the present study constitutes a comparison between calculation models only and that validation by means of measurements is needed. A first verification was possible, using the results of the Botlek Rail Tunnel (Nagel et al. 2009), however, here the instruments were not placed at the ideal positions for verification of the theory.

The inflow of process fluids into the steering gap of the TBM reduces friction and leaves more space for the TBM to move with respect to the just drilled hole. The pressure distribution around the TBM depends on the TBM position with respect to the excavated hole, which itself is influenced by various factors such as the soil stiffness, the overcut, the steering trajectory and others. On the other hand, the fluid pressure has an influence on the gap width and the distribution of the gap around the shield. To fully account for these rather complex spatio-temporal interactions during tunnel construction, the 3D numerical simulation model for TBM advance enhanced by a contact model for the fluid flow along the shield seems to be a suitable tool.

The difference in resulting settlement trough and volume loss as found with both models, taking or not taking into account the influence of the bentonite and grout flow around the TBM, shows that the flow around the TBM becomes certainly important when volume losses become less than 1% as is nowadays the case. A better understanding of the flow pressures around the TBM and the resulting soil deformations is therefore necessary to further minimize volume losses.

REFERENCES

Bezuijen, A., 2009. The inuence of grout and bentonite slurry on the process of TBM tunnelling. Geomechanics and Tunnelling 2 (3), 294–303.

Bezuijen, A., Talmon A.M., 2008, Processes around a TBM. Proceeding 6th Int. Symposium on Underground Construction in soft Ground, Shanghai. 3–13.

Bezuijen, A., 2007. Bentonite and grout flow around a TBM. Tunnels & Tunnelling International (June), 39–42.

Bezuijen A., Talmon A.M., Kaalberg F.J. and Plugge R. 2004 Field measurements of grout pressures during tunneling of the Sophia Rail tunnel. *Soils and Foundations vol, 44, No 1, 41–50, February.*

Dijk B.F.J., van & Kaalberg F.J., 1998, 3-D geotechnical model for the North/Southline in Amsterdam. In Application of Numerical Methods to Geotechnical Problems, Cividini A (ed.). Proc. 4th European Conference on Numerical Methods in Geotechnical Engineering, Udine, Springer: Wien, pp. 739–749.

Kasper, T., Meschke, G., 2004. A 3D finite element simulation model for TBM tunnelling in soft ground. International Journal for Numerical and Analytical Methods in Geomechanics 28 (14), 1441–1460.

Merritt, A.S & Mair R.J., 2006. Mechanics of tunnelling machine screw conveyors: model tests. *Geotechnique 56, issue 9, November, 605–615.*

Möller, S., Vermeer, P., 2008. On numerical simulation of tunnel installation. Tunnelling and Underground Space Technology 23 (4), 461–475.

Nagel, F., 2009, Numerical modelling of partially saturated soil and simulation of shield supported tunnel advance, PhD Thesis, Ruhr-Universität Bochum, Germany.

Nagel, F., Bezuijen, A., Stascheit, J., Meschke, G., 2009. Measurements and simulations of uid and ground pressures around a TBM. In: Meschke, G., Beer, G., Eberhardsteiner, J., Hartmann, D., Thewes, M. (Eds.), Proceedings of the 2. International Conference on Computational Methods in Tunnelling (*EURO*: TUN 2009). Vol. 1. Bochum, Germany, pp. 61–70.

Nagel, F., Meschke, G., 2010. An elasto-plastic three phase model for partially saturated soil for the finite element simulation of compressed air support in tunnelling. International Journal for Numerical and Analytical Methods in Geomechanics 34 (6), 605–625.

Nagel, F., Stascheit, J., Meschke, G., Process-oriented numerical simulation of shield-supported tunnelling in soft soils. Geomechanics and Tunnelling, 3, 2010, 268–282.

Verruijt A., 1993, *Soil Dynamics*, Delft University of Technology, b28.

Yu, H., 1998. CASM: A unified state parameter model for clay and sand. International Journal for Numerical and Analytical Methods in Geomechanics 22, 621–653.

This page intentionally left blank

Geotechnical Aspects of Underground Construction in Soft Ground – Viggiani (ed)
© 2012 Taylor & Francis Group, London, ISBN 978-0-415-68367-8

Design of jet-grouting for tunnel waterproofing

Marcos Arroyo & Antonio Gens
Departament of Geotechnical Engineering and Geosciences, UPC, Barcelona, Spain

Paolo Croce & Giuseppe Modoni
University of Cassino, Italy

ABSTRACT: A case history in Barcelona is described where a tunnel was excavated by traditional methods below an active railway line through a formation with lenses of water-bearing granular material. To avoid the possibility of sudden collapses a massive jet-grout treatment was applied. The treatment took several forms. Subvertical double and triple-fluid injection was applied whenever possible. Sub-horizontal monofluid canopies and slabs executed from within the tunnel were however required in zones where no vertical access was possible. This communication focuses on the later type of treatments and gives an overview of the design tools that were applied. These comprised the execution of several large trial fields and the systematic application of a probabilistic framework for design.

1 INTRODUCTION

It is a common paradox that surface transport infrastructures are usually more needed where there is less space available for them. Underground developments are then inevitable, be that by means of tunnels and excavations, or through refurbishment and adaptation of existing infrastructures, requiring new foundations and/or extensions. Wherever urban infrastructure construction activities take place there is a large likelihood that one form or another of ground improvement would be required. Ground improvement allows construction to proceed where otherwise it would be impossible, because some relevant required soil property (strength, stiffness, permeability) is missing.

Jet grouting is a technique where a high-pressure injection of mortar, with or without other accompanying fluids (water, air), impacts the ground in a borehole. In most cases the original ground is thus eroded, mixed with the mortar and, in fluid form, partly evacuated to the surface (resulting on what is called "spoil"). The remaining soil-cement mixture sets "in situ", resulting on a stiffer, stronger, more impermeable and less ductile material than the original soil. The injection equipment is displaced along the borehole, thus creating a body of treated soil of columnar shape. Several such injections are combined to create the desired shape of treated soil: slabs, arches and walls are common examples.

The basic reasons for jet-grout success are clear: of all the means of ground injection, jet is not only the fastest procedure, but is also the only one suitable for all improvement purposes (strengthening, stiffening, impermeabilization). In tunnelling operations jet grouting has the added attractive of access versatility: treatments can be executed from within the tunnel, from the surface of the ground or, eventually, from a side shaft.

This paper describes a case history in Barcelona where a variety of jet-grout treatments were performed to help drive a tunnel through water-bearing sediments under an active railway line. After giving the geotechnical background of the problem as well as a brief account of the construction procedures applied, the paper focuses on the design tools employed. Several results from large-scale "in situ" tests are described; afterwards an example of a probabilistic approach employed in design is outlined. Finally a brief summary of the observed treatment outcomes is also given.

2 PROJECT DESCRIPTION

2.1 *Location*

The new High Speed Railway Link between Madrid and Barcelona was open to traffic in February 2007. The Southern entry of the new line into the city of Barcelona follows the trace of the historical railway entrance, heading towards Sants railway station (Fig. 1). This railway entrance crosses the city of Hospitalet de Llobregat, just south of Barcelona. Hospitalet is currently involved in a major urban redesign operation in which the suppression of the railway barrier plays a major role. For this reason

Figure 1. Plan view of the High Speed Railway Link south entrance to Barcelona.

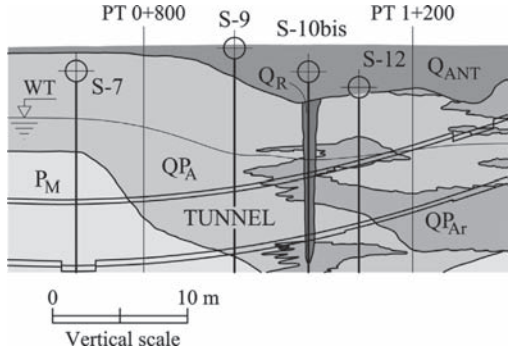

Figure 2. Geotechnical profile alongside the central part of the tunnel. P_M stiff tertiary marl; QP_A medium stiff clay-dominated quaternary deposits; QP_{Ar} sand-dominated quaternary deposits; Q_R gravel-dominated quaternary deposits; Q_{ANT} made ground. Spacing amongst vertical reference lines 20 m; spacing amongst horizontal reference lines 2 m.

the design of the new high speed link located it below ground well before its arrival at Sants.

In plan, the new link follows closely the current tracks, so much that the final 2 km stretch (marked IV in Fig. 1), had to be excavated just below them. The railway line south of Sants is the main medium and long-distance line out of Barcelona, doubling also as a very busy commuter line. Therefore only limited railway traffic restrictions were possible and the new entry had to be built below the still active old lines.

2.2 *Ground conditions*

The tunnel is located on the alluvial plain of Barcelona. The western limit of this geomorphological unit is given by the Collserola mountain range, whereas the southern and northern limits are given by the deltaic systems of two river mouths (Llobregat and Besos, respectively). The alluvial plain is formed by Quaternary deposits overlying a Tertiary substratum. The main unit of the Quaternary deposits in the tunnel area is a brown red clay that includes some carbonated levels and thin sand layers (QP_A in Fig. 2). This unit is crossed by a network of paleochannels, fossilized remains of a network draining the nearby Collserola range into the Mediterranean. These paleochannels are formed by sands and gravels with a variable clay matrix (QP_{Ar}). Younger, recently active brook deposits are also crossed by the tunnel trace (Q_R). The Tertiary deposits, mostly from Pliocene and Miocene age, are formed by some ochre sands and clays (PA) and blue-grey marine marly clays (P_M). The water table in the area is generally located between 10 and 15 m depth.

2.3 *General tunneling concept*

The main tunnel section had nearly 110 m^2. The longitudinal profile was established to pass below several underground road passages and a tube line that marked its lowest point. The tunnel cover varied between a minimum of 6 m and a maximum of 25 m. In the situation just described the main construction priority was to avoid any risk of sudden ground collapse, however minor. On the other hand, and thanks to an active ballast maintenance program, slowly induced excavation settlement could be easily compensated.

EPB tunnelling is generally the favoured urban tunnelling choice when soft soils are present on a tunnel trace. However, for relatively short tunnels or when access shafts for an EPB are not easily located, traditionally mined excavation might offer an interesting and robust alternative. These two circumstances were present at the tunnel here described. A partitioned section procedure, known as the traditional Madrid or Belgian Method, was then selected as the basic excavation procedure for the tunnel. It is worth mentioning, however, that this method is relatively slow, with median advance rates of 30 m/month per excavation front (Sacyr 2008). To comply with a tight construction schedule this required the execution of 2 intermediate deep access ramps and 3 further deep shafts to open intermediate excavation fronts.

The first 800 m of the tunnel were located either above the water table or within the impermeable, homogeneous PM layer. There, the Belgian method, with occasional forepoling help, was successfully applied (for details, see Deu et al. 2007). The last 600 m of the tunnel were again located mostly

above the water table, and a similar construction procedure was applied.

However, in the approximately 400 m corresponding to the central and deepest part of the tunnel, the presence of erratic channels of quaternary deposits with a large granular fraction (QP_{Ar}, Q_R) was coincident with a water table well above the tunnel crown (Fig. 2). There were also close precedents showing that running ground conditions at the tunnel face were a distinct possibility. This was a major cause for concern, and thus there was some consensus that even the small partitioned and braced excavation fronts allowed by the Belgian method did not offer enough guarantee against that kind of failure. Therefore in that part of the tunnel a different construction procedure, relying on a systematic use of jet-grout, was envisaged.

2.4 *Jet-grouting treatments*

Jet-grout was selected as the soil improvement tool that was best suited to avoid the possibility of ground flows towards the excavation. The main function of the treatment was then one of impermeabilization around the tunnel; the natural soil had more than adequate resistance and stiffness to span the tunnel section without excessive deformations (Table 1).

Two types of treatments were applied. In locations where access above the treated zone was possible, vertical or subvertical columns were employed. For this type of treatments powerful two- and three-fluid means of jet injection could be applied, since the spoil might be evacuated from the surface and the geometry of a newly executed column was not unstable. The typical design column diameter for the vertical columns was 2.5 m. The layout included full face sections, where the whole tunnel face was covered by the treatment (Fig. 3a) and sections where the columns where only surrounding the tunnel (Fig. 3b). The purpose of the full face sections was to create longitudinally isolated excavation zones, so as to minimize the extension of hypothetic failures.

Table 1. Geotechnical parameters; average values in parentheses.

Material	Fines %	w %	N_{SPT}	S_u kPa	E MPa
Q_{ANT}	80-9 (50)	(15.1)	(5)	–	7.5
Q_R	86-14 (43)	(16.1)	(48)	–	22.5
QP_A	99-50 (80)	(18.4)	(24)	(100)	22.5
QP_{Ar}	80-5 (30)	(14.5)	(31)	–	40
P_M	23-99 (95)	(20.8)	(34)	(150)	42

However, there were some zones within the treated tunnel section where surface access above the tunnel was impossible. In these zones the excavation was partitioned between heading and bench (Fig. 4). Treatment of the heading created a soil chamber by covering the full section perimeter and closing the full tunnel face ahead of the excavation using sub-horizontal columns. From within the excavated heading followed a full treatment of the bench with subvertical columns. Executing the injection from within the tunnel itself only allowed for single-fluid injection and relatively small diameter columns (around 0.5 to 1 m, see below for details).

These zones executed from within the tunnel were the most critical, both because the treatment execution was particularly risky and because the required number of columns made the procedure very slow. A number of special measures were then taken to guarantee a successful outcome, both at the design stage and at the execution stage. While this paper focuses on design, it is worth mentioning, amongst the execution-related aspects, the

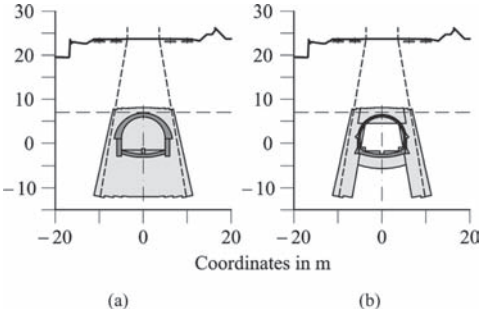

Figure 3. Typical treatment configurations where surface access was available.

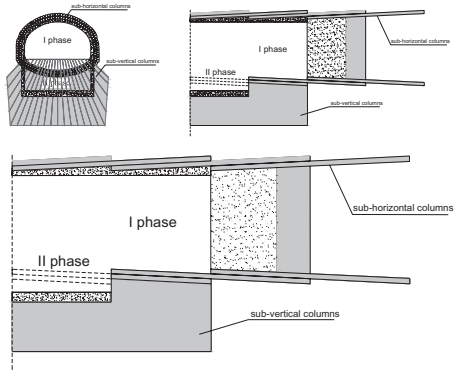

Figure 4. Typical configuration for treatment from within the tunnel (transverse and longitudinal sections).

systematic application of a manually controlled blow-out preventer (Guatteri et al. 2009), a tool that helped to avoid instabilities with the sub-horizontal injections.

3 JET-GROUT DESIGN TOOLS

3.1 *General approach*

The development of jet-grout has been technologically driven, with the relevant science lagging behind. As a result the design, implementation and control of jet-grout treatments has developed on a heuristic basis, lead by practitioners and real-life experience applications. Although this approach has been successful in most cases, a number of high-profile construction problems can be traced to ineffective jet-grout treatments, for instance the Souterrain tram tunnel in The Hague (NL) (van Tol 2004), the Les Cretes tunnel of the Aosta highway in Italy (Croce et al. 2004) and the Kaoshiung Mass Rapid Transport tunnel, in Taiwan (Ishihara 2008).

The effectiveness of jet grouting treatments is dictated by the interaction between technological factors and natural soil properties, the role of which cannot yet be predicted with sufficient accuracy but needs to be evaluated by means of experimental investigations. To prove the efficiency of treatments, execution of preliminary field trials is in fact required by current standards (e.g. ENV 12716 1997). In design cases where the treatment should provide watertightness, continuity of treatment is the most fundamental aspect. Field trials should then focus on the cross sectional dimensions and on the required spacing of contiguous columns supposed to overlap.

Concerning the former point it is worth reminding that, for a given set of injection parameters, column diameters are strongly influenced by natural soil properties and that inhomogeneous subsoil conditions turn into irregularities of column shape and discontinuity of the waterproofing barriers (e.g. Croce & Modoni 2005). With regard to the second aspect, even if a direction is specified for columns axes, deviations are possible depending on how accurately the position and inclination of injection tools is controlled. Generally, even when low tolerances are prescribed, unpredictable misalignments occur, particularly for longer columns, due to the self weight of perforation bars or to inaccurate driving of the supporting arms.

Bearing in mind these goals, different field trials were specifically devised in the presented work, some to find relations between column diameters and treatment parameters, others to quantify the effects of imperfect drilling operations.

All the information collected in the trials was then fed into probabilistic design models to explicitly take into account the inherent variability of the method and deal economically with the uncertainty of the treatment outcomes.

3.2 *Vertical column trials*

A first field trial was located within one of the intermediate deep access ramps to the tunnel. The ramp itself was roughly at the middle of the stretch were the treatment was required, however, specific stratigraphy at the ramp site was dominated by the more clayey quaternary levels (QP_A).

Two parallel rows of ten vertical columns each (identified as A and B in Fig. 5) were injected for a length of about 15 m starting at 2 m below the surface. Four columns of each group (A1, A8, A9, A10 and B1, B8, B9, B10) were positioned with spacing larger than the expected diameter (0.5 m) to provide data in diameter variability and material properties. The other six were intended to overlap being injected with variable axes span (0.30 m for A2, A3, A4 and B2, B3, B4 columns, 0.45 m for A5, A6, A7 and B5, B6, B7).

All columns were executed with a single-fluid system, like the one to be applied later within the tunnel. Columns A and B shared some injection parameters like nozzle diameter (3 mm) and rotation velocity (12 rpm). However, they did differ in several parameters (Table 2): withdrawal

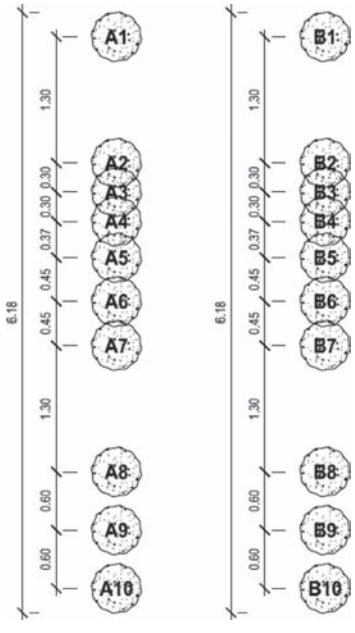

Figure 5. Plan view: vertical column trials.

Table 2. Injection parameters of vertical trial columns.

Column type	v (cm/min)	p (bar)	V_0 (m/s)	ρ (t/m^3)	W/C
A	37	350	200	1.59	1/1.2
B	35	400	212	1.52	1/1

speed, v; injection pressure, p (and, consequently, nozzle velocity, V_0); water/cement ratio, W/C (and, consequently, grout density, ρ).

The treatment parameters for both columns had been initially proposed by the contractor, whose experience-based average diameter estimate for both types of treatment was equal to 50 cm.

It seemed clear, however, that other predictive approaches to estimate column diameter were also worth trying. For instance, the treatment input energy per unit length could be computed following Croce & Flora (2000) as

$$E_n = \frac{8\rho V_0^3}{\pi \mathrm{v} \mathrm{d}^2} \quad (1)$$

In the case of the vertical trial columns type A columns had $E_n = 7.36$ MJ/m, whereas type B columns had $E_n = 9.06$ MJ/m. It was then expected that type B columns would result in higher column diameters and, because of their higher W/C ratio, in smaller strengths.

Several treatment outcomes were measured in the field trial. On the one hand, continuous rotary coring of four columns provided samples at every meter on which to measure strength (unconfined compression, q_u), stiffness (on-sample deformation measurements, E_{50}) and density of the treated material. On the other hand the top four meters of all the trial columns were examined while excavating the station access ramp and cross sectional dimensions were taken by measuring the length of cemented soils samples cored by horizontal drilling. A summary of the results obtained through these measurements is included in Table 3.

The average diameter of columns B was higher than the average diameter of columns A, in agreement with the computed energy input (1). The strength of columns B was less than that of columns A, again as expected from the W/C relation. Strength variability was higher than geometric variability. The latter was also easily quantified by means of the distributions of column diameters (Fig. 6).

It was made clear that, while detrimental for the mechanical properties of the treated soils, a larger amount of water in the injected mix enhanced the erosive action of the jet and resulted in larger column diameters. For the case here contemplated the reduction in strength was immaterial, whereas the increase in diameter was clearly beneficial.

Table 3. Measured treatment outcomes on vertical trial columns.

Column type	$\bar{D}$ (m)	COV (D)	q_u (MPa)	COV (q_u)	E_{50}/q_u
A	0.38	0.14	11.6	0.26	573
B	0.48	0.12	7.9	0.38	576

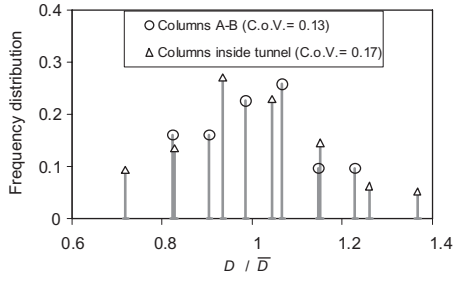

Figure 6. Distributions of column diameters measured at the vertical field trials.

A second consequence of this first field trial was to show the benefits that might follow from a rational approach to diameter prediction. A more elaborated predictive formula, following from Modoni et al. (2006), was then proposed and validated with a later round of single-column field trials. It is not possible here to give a detailed account of this latter round of single-column trials. However, it is worth mentioning that the sub-horizontal columns that were finally adopted as a basis for the treatment execution were injected with larger nozzle diameter (3.5 millimeters), with higher water-cement ratio (1.5/1), and with a lower lifting speed (20 cm/min) than those originally proposed.

3.3 *Full-scale heading trial*

A second, more ambitious, field trial took place to test the execution of the treatment conceived for the heading section of the tunnel. An almost full-scale (80%) heading section was built with a similar geometry and procedure as that intended in the tunnel (Fig. 4) from a dedicated 15 m deep excavation.

For reasons of space availability the trial took place at some 8 km to the south of the tunnel location. This meant that instead of on the Barcelona alluvial plain the trial was fully within the Llobregat delta plain. The geotechnics of the Llobregat delta are rather different from that of

the alluvial plain, with a medium dense sand layer overlaying a soft sandy and clayey silt and water table close to the surface (e.g. Gens et al. 2011). The trial heading section was mostly performed within the silt layers and had 9 m soil cover above the crown, mostly in sands. The geotechnical conditions for the jet-grout execution at the trial site were then clearly unfavorable when compared to those prevailing at the tunnel site. However, it was felt execution under such conditions will clearly prove the potential and/or show the limitations of the proposed construction technique.

The tunnel contour canopy consisted of two concentric rows of 151 diverging columns, 12 m long and with 0.50 m expected diameters, injected after initial perforation of a previously created thick jet grouting supporting wall. A 3 m thick plug was created at the deeper end of the tunnel, made of 174 columns of 0.80 m diameter, located on six concentric circles with 0.50 increasingly larger radii.

A net of vibrating wire piezometers and settlement plates was installed above and around the trial tunnel for monitoring purposes. Treatment execution parameters were continuously recorded and, in several instances, measurements of column axis inclination were also performed.

Here only a few results from this trial will be commented; some results can also be found in Guattieri et al. (2007). During jet injection asymmetrical settlements and heave were recorded at ground level (about 20 millimetres maximum settlement on one side and 10 mm heave on the other side, Fig. 7). These movements were likely related to a pressure build-up induced by injection. However, water pressure measurements were almost constant in all the piezometers.

While this outcome was hardly welcome, it was not very discouraging. On the one hand, settlement issues were of limited concern (although the possibility of brusque jet-induced motion limited the temporal window for treatment in certain cases). On the other hand, the construction of the railway tunnel had to be performed at considerably larger depths below a thicker soil cover. Even in the absence of a detailed model, it was clear that the movements that were induced at the trial were well above those to be expected on site.

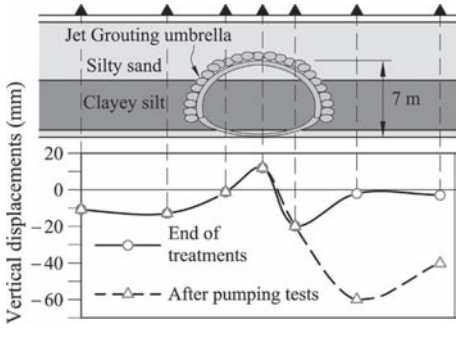

Figure 7. Profile of settlements at ground level induced by execution of treatments and extraction of water from the tunnel chamber.

After conclusion of treatments, a test on the waterproofing capacity of the jet grouted soil was performed, by inserting a number of pipes at the front of the tunnel and by extracting, with a vacuum pump, the water present in the inner chamber. Pumping lasted two days and the amount of water extracted was well below the estimated soil water content (less than 5%). The poor response of the pipes was likely due to clogging of the pipe protective filters by silt particles. During this test, a sudden drop of water head was measured in a piezometer located on the right side of the tunnel. Moreover, this was immediately followed by a funnel shaped collapse that emerged at the ground surface in a position close to the contact of the canopy and the extreme plug of the tunnel (see settlement profile of Fig. 6).

Explanation for this result can be found in the consolidation of soil inside the tunnel chamber activated by the extraction of water and by the lack of bending capacity of jet grouting. It is worth mentioning that jet grouting columns were not reinforced and that collapse occurred at the attachment of columns to the end plug, i.e. where the flexural moment reaches its maximum values. The amount of consolidation settlement to be expected at the tunnel site was much less and therefore it was concluded that passive (i.e. without pumping) dewatering of the soil chamber could be applied safely at the tunnel.

Also particularly interesting are the measurements of column axes inclination, which are rather infrequently performed in jet grouting treatments within tunnels. These were measured using one inclinometer mounted on the injection mast (Jean Lutz 2006). The two components Δy and Δz of deviation from the theoretical axis direction, plotted for five different columns in Figure 8, show that there is a common systematic downward trend. Deviations increase significantly with column length, and their absolute values are non-negligible.

The deviations could be explained as a result of the bending of perforation bars due to their self weight (which, for the measured columns, was also increased by the inclinometer). Partial compensation can be provided by an initial upward inclination of the perforation axis, as shown by column S01-15E.

Again, and despite is large magnitude, this systematic deviation was not a major cause

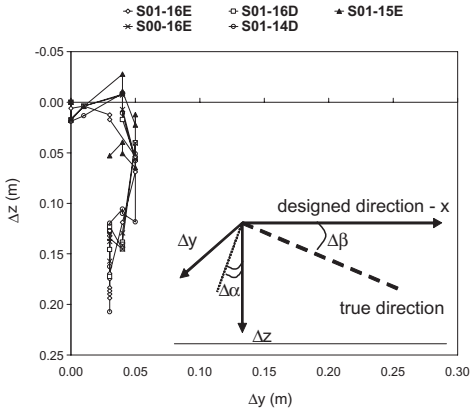

Figure 8. Deviation of column axes from their theoretical position (deviation projected on a plane orthogonal to column axis).

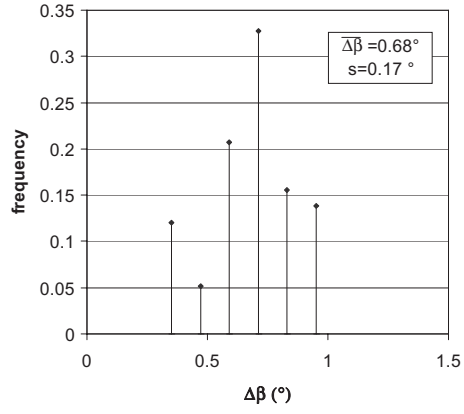

Figure 9. Frequency distribution of the inclination deviation angles Δβ.

for concern. The continuity of a jet grouting canopy is not particularly sensitive to systematic deviations. On the other hand a random scattering of column directions would be very detrimental for the same objective. The deviation data were analyzed to quantify the random scatter in direction. The average direction of columns was calculated and the two angles (azimuth Δα and divergence Δβ) expressing the deviation of columns axes from this mean trend were evaluated. The plot in Figure 9 shows that a bell shaped frequency distribution can be clearly inferred for the divergence angle Δβ, while Figure 10 shows that the distribution of azimuth angle Δα is approximately uniform.

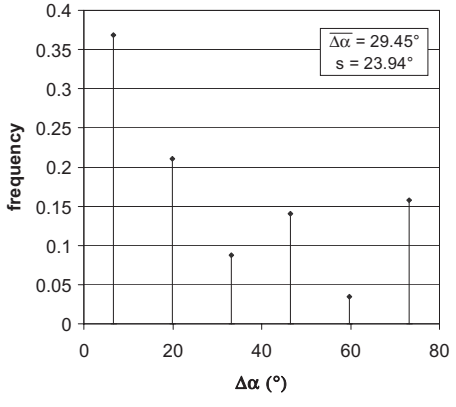

Figure 10. Frequency distribution of the azimuth deviation angles Δα.

3.4 *Probabilistic approach*

The continuity of different jet grouting structures (canopies, plugs and vertical walls) was routinely analyzed during the project by developing probabilistic methods specifically customized for each structure. An analysis developed for the perimetral canopies of a tunnel heading (Fig. 4) is here reported to illustrate these calculations.

The probabilistic analysis of this structure was performed selecting two sections, at the extremes of the overlap section between two consecutive canopies (see Fig. 11a). Based on the field trial results as well as on later quality assurance measurements, a probabilistic distribution was assigned to column diameters and column axes deviation. In particular, a Gaussian distribution has been considered for column diameters with a mean value equal to 0.75 m and a coefficient of variation equal to 0.17. This value of average diameter has been chosen as equal to the minimum value estimated with the adopted set of injection

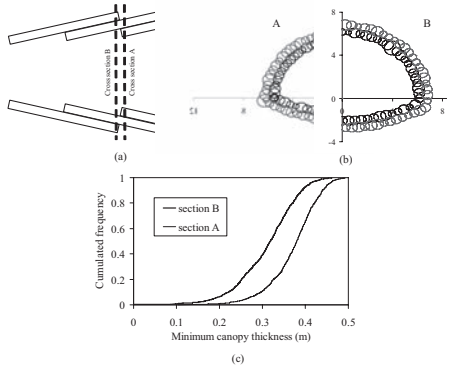

Figure 11. Probabilistic analysis of the continuity of tunnel canopy (a. longitudinal section; b. example of cross section simulation; c. cumulated frequency distributions of the minimum thickness of the canopy).

parameters for sandy soils, considering these latter as the most critical in case of piping.

Random divergence of column axes from their designed position has been modelled by considering angles $\Delta\alpha$ and $\Delta\beta$ respectively distributed with uniform and Gaussian laws. For the latter a nil average value and a standard deviation of 0.68° were assigned.

A Monte Carlo simulation technique was applied, generating one thousand cross sections consistently with the adopted probabilistic distributions (one example of simulation result is reported in Fig. 11b). The minimum canopy thickness was then calculated in each case to obtain a statistical sample of this simulation outcome. The cumulative frequency distribution of this variable (Fig. 11c) represents the discontinuity hazard of this particular structure.

4 JET GROUT PERFORMANCE

The field trials and probabilistic methods described above were useful to generate confidence on the construction team about the issue of one construction operation that was initially perceived as extremely risky. About 100 m of the main tunnel and access galleries were thus treated in full section or just at the bench from within the tunnel. The advance was performed without any incident.

However, and despite the optimization allowed by the probabilistic design, the complexity of the subterranean treatments still resulted in very slow excavation procedure, with median advance rates below 1 m/day. An effort was then made to allow even some partial surface access above most of the treated tunnel length and therefore vertically executed treatments were applied in most of the treated section. Lacking time to perform the same extensive trials that preceded the subhorizontal treatments, the uncertainty on the jet grouting outcomes for vertical treatments was higher, particularly for column diameter. Hence ancillary pumping to lower the water pressure on the treatment walls was introduced as an auxiliary measure to increase the safety of excavation. The combination of partial pumping and vertical jet-grout chambers was successful in that the tunnel was excavated without incidents at a median advance rate two to three times higher than that allowed by subhorizontal treatment.

5 CONCLUSION

The reported case history has proved that the design of jet grout structures can largely benefit from a rational approach that includes experimentally based uncertainty within a probabilistic framework. The measurements taken and observation made at the field trials in this project contain useful information for future designs in similar conditions.

ACKNOWLEDGEMENTS

The authors acknowledge the opportunity given by ADIF to participate in the studies described in this work. The contribution of the Spanish Ministry of Science through research grant BIA2008-06537 is also gratefully acknowledged.

REFERENCES

Croce P. & Flora A. 2000. Analysis of single fluid jet-grouting. *Geotechnique* 50 (6): 739–748.

Croce P. & Modoni G. 2005. Design of Jet Grouting Cut-offs. *Ground Improvement* 10 (1): 1–9.

Croce P., Modoni G. & Russo G. 2004. Jet grouting performance in tunneling. *ASCE Geosupport 2004, Orlando, February 4–7, 2004*.

Deu, A., Arroyo, M., Gens, A. & Alonso, E. 2007. Tunnelling under an active railway line on Barcelona soft soils in *Tunnels, drivers of change ITA international conference, Madrid November 2007*, 858–869. AETOS.

ENV 12716. 2001. Execution of special geotechnical works: jet grouting. *European Committee for Standardization*.

Guatteri, G., Koshima, A., Lopes, R, Ravaglia, A. & Pieroni, M.R. 2009. Historical cases and use of horizontal jet grouting solutions with 360° distribution and frontal septum to consolidate very weak and saturated soils. In Ng, Huang & Liu (eds) *6th International Symposium Geotechnical Aspects of Underground Construction in Soft Ground—Taylor & Francis Group, London.*

Gens, A., Di Mariano, A. & Yubero, T. 2011. EPB tunneling in deltaic deposits: observations of ground movements. In *7th International Symposium Geotechnical Aspects of Underground Construction in Soft Ground* (this conference).

Ishihara, K. & Lee, W.F. 2008. Forensic diagnosis for site-specific ground conditions in deep excavations of subway constructions. In Huang & Mayne (eds) *Geotechnical and geophysical site characterization*, 31–59.

Jean Lutz S.A. 2006. TIGOR, Instrumented rod for the drilling deviation measurement, Technical sheet.

Modoni G., Croce P. & Mongiovì L. 2006. Theoretical modelling of jet grouting. *Géotechnique*, 56 (5): 335–347.

SACYR 2009. High Speed railway line Madrid-Barcelona-French frontier. Stretch La Torrassa—Sants. SACYR.

van Tol, F. 2004. Lessons learned from jet grouting at a tunnel project in the Hague. In A Dhouib, Magnan et Mestat (Eds.), *ASEP-GI 2004* (321–331). Paris: LCPC.

Geotechnical Aspects of Underground Construction in Soft Ground – Viggiani (ed)
© 2012 Taylor & Francis Group, London, ISBN 978-0-415-68367-8

Modelling a deep tunnel excavation in a low-porosity tectonised clay

D. Boldini
University of Bologna, Bologna, Italy

A. Graziani
University Roma Tre, Rome, Italy

ABSTRACT: The design of excavation in clayey soils is usually based on the hypothesis that the material displays undrained behaviour during construction. In the case of a deep tunnel, the high stress relief induced by excavation is associated to the development of a wide plastic zone where pore pressure may significantly decrease up to reach negative values in a wide area surrounding the tunnel walls. This type of hydro-mechanical behaviour, however, hardly applies to pervasively fissured scaly-clays, which can exhibit a macroscopic opening of fissures during stress release, resulting in a loss of saturation. In the paper, the stress-strain behaviour observed during construction of a large-diameter tunnel in scaly clays at depth as high as 400 m is reviewed. Different modelling approaches both for the short- and long-term conditions are investigated, ranging from a roughly simplified dry-medium model to a two-phase model with a coupling between permeability and plastic deformation.

1 INTRODUCTION

The hydro-mechanical behaviour of clayey soils and rocks can vary notably as a function of percentage and type of clay minerals, water content and possible presence of a fissure network, often caused by tectonic events.

In this respect, a useful classification is that proposed by the Comité Français de Méchanique des Roches (2000), which distinguishes between "plastic" and "rigid" clays:

- plastic, soil-like, clay formations generally are found at depths lower than 350 m and are characterised by a Young's modulus $E' < 500$ MPa and by a water content $w > 10\%$;
- stiff, rock-like, argillaceous formations (indicated with several geologic terms, such as marls, argillites, claystone, shales, argillaceous schist, etc.) are those characterised by a Young's modulus $E' > 2000$ MPa and by a water content $w < 10\%$.

This classification may also orientate the choice of the modelling approach. The main alternative, at least in the context of simple models suited to practical engineering applications, is between the "one-phase" and the "two-phases" approach. The first one, generally associated to visco-elastic or visco-plastic constitutive laws (e.g., Boidy *et al.* 2002, Boldini *et al.* 2004a, Debernardi & Barla 2009), is preferred for the stiff, rock-like, clays. The second one, in which time-dependent deformations are only due to consolidation phenomena (e.g., Gäber & Labiouse 2003, Carranza-Torres & Zhao 2009) is the classical approach for plastic clays. A combined approach (i.e viscous behaviour coupled to consolidation phenomena) was sometimes adopted (e.g., Bonini *et al.* 2009) although in this case greater difficulties arise in the estimation, at the field scale, of the many parameters which control hydro-mechanical and viscous behaviour.

This paper focuses on the response of "rigid" clays to tunnel excavation. Therefore, the discussed topics are mainly of interests for tunnelling in argillaceous rocks, such as argillites, mudstones and schist, frequently characterised by a scaly structure.

A common question the study should likely contribute to answer is: when is the rough hypothesis of "dry medium" actually acceptable for tunnel design in low-porosity argillaceous formations?

A further question is: which is the impact of the fissure network, on the hydro-mechanical response in the short- and long-term?

The influence of fissure opening as a consequence of the unloading process due to tunnel excavation is investigated in this paper by different phenomenological approaches which can be easily implemented in numerical Finite Element or Finite Difference models.

The proposed modelling approaches assume different limit behaviours of the plastic annulus around the tunnel, substantially controlled by the effect of fissure opening, which may cause loss of saturation, in the short-term, and a general increase in permeability, in the long-term.

The application of the proposed models will be discussed with reference to the case of the Raticosa tunnel, excavated in a scaly clay formation of central Italy (Boldini *et al.* 2004b).

2 MODELLING APPROACHES

Static analysis of geotechnical structures in low-permeability grounds is frequently carried out for two idealised situations: the short-term conditions ($t = 0$), characterised by the undrained behaviour of the porous medium, and the long-term conditions ($t = \infty$), in which a stationary pore pressure distribution is reached.

In Appendix, some useful analytical solutions for the two aforementioned limit conditions are summarised.

The excess pore pressures Δp generated by tunnel excavation and the new boundary conditions imposed at the tunnel wall (i.e., by a pervious or impervious lining) initiate a time-dependent groundwater flow until the final stationary pore pressure distribution is established. During the transitory phase (consolidation process) an increase in the loading applied on the lining generally occurs.

For tunnelling in clay formations, it is routinely assumed that ideal undrained conditions hold during the excavation stages. However, the interaction between pore water and soil skeleton exhibits unconventional features in fissured or tectonised formations of very low porosity (Gasc-Barbier *et al.* 1999), where the available free water can be rather limited and fissure opening due to stress relief favours desaturation.

In the following, specific modelling approaches are presented in order to appreciate the influence of fracture opening. The mechanical behaviour of the ground is simply modelled as an ideal elasto-plastic medium, characterised by the Mohr-Coulomb strength criterion.

Four different hypotheses were formulated in order to evaluate the hydro-mechanical response in the short-term (Fig. 1):

- Model 1: conventional undrained behaviour;
- Model 2: undrained behaviour with tensile strength of water equal to zero;
- Model 3: undrained behaviour with pore pressure set equal to zero in ground zones as plastic deformation develops;
- Model 4: dry-medium behaviour.

Model 1 and Model 4 can be seen as two limit behaviours, which encompass the real hydro-mechanical response during tunnel excavation.

Model 3 assumes that the pore pressure suddenly drops to zero in the elasto-plastic region due to the opening of fissures during unloading.

For the long-term situations two possible hypotheses were considered. The first assumes that plastic deformations do not change permeability inside the plastic annulus around the tunnel (i.e., $k_{el} = k_{pl}$). In the calculations, this hypothesis was associated to short-term Models 1, 2 and 4. The second assumption represents the limit case of a plastic annulus characterised by infinite permeability with respect to the undisturbed ground in the elastic zone, as a consequence of fissure opening (i.e., $k_{el}/k_{pl} = 0$). It was associated to Model 3.

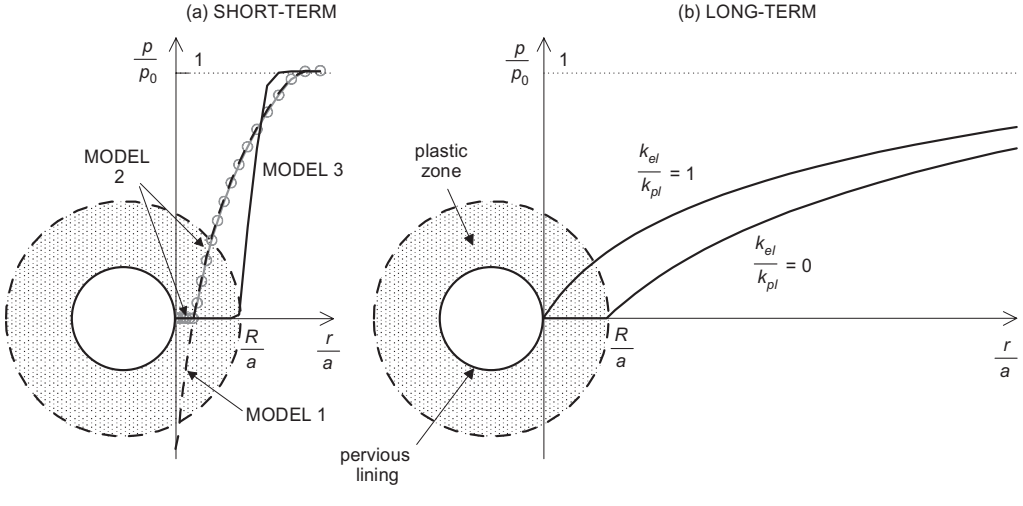

Figure 1. Possible schemes of pore-pressure distribution for short- (a) and long-term situation (b). a is the tunnel radius, R the plastic radius and p_0 the undisturbed in situ pore pressure.

3 RATICOSA TUNNEL

The Raticosa tunnel is one of the several tunnels realised for the new Bologna-Florence high-speed railway line (Italy). The tunnel, having an overburden of up to 500 m, is located in the Apennine chain and crosses a tectonized clay-shale formation called Chaotic Complex for about 4.5 km (Fig. 2).

The chaotic structure of such formation is the result of tectonic actions from Miocene-Pliocene to Plio-Pleistocene. The Chaotic Complex is mainly composed by a pelitic matrix with dispersed and disaggregated lithic components. The matrix is formed by an assemblage of clay scales of the size of millimetres to centimetres whose surfaces are curved, smooth and at times striated. Mineral composition, obtained by X-ray diffraction, was found to be very variable. Deeper samples are characterised by a lower phyllo-sillicate content (25%–30%), which increases to 40%–50% for the shallower samples. Smectite is generally present in small proportion in the form of alternating illite-smectite layers.

The tunnel (diameter D = 14 m) was full-face excavated with an hydraulic hammer. Due to the poor mechanical properties and to the expected heavy squeezing conditions, full face-excavation required face reinforcement using fibre-glass dowels (35–80 dowels, 20–24 m in length, installed every 10–12 m of tunnel advance). A closed-ring primary lining, consisting of a shotcrete layer (thickness 0.25–0.30 m) and steel sets (2 IPN220 including an arched strut in the invert), was applied at each round of excavation (length 1.0–1.2 m). The final lining, made of reinforced concrete (invert and sidewalls) and plain concrete (vault), was completed at a maximum distance from the face of 2D.

3.1 *Laboratory testing*

The clayey formation is characterised by a very low natural water content and can be identified, according to the classification of the Comité Français de Méchanique des Roches (2000), as a stiff, indurated clay.

A summary of the physical and index properties (Boldini *et al.* 2004b) measured on specimen and block samples taken at depths ranging from 175 and 520 m is given in Table 1, although it should be reminded that the geotechnical characterisation of structurally complex formations presents many uncertainties.

An indirect indication of the tendency to dilation and loosening during unloading of the scaly structure of such formation is provided by the value of saturation degree measured in laboratory specimen, generally appreciably lower than unity (Table 1).

Figure 3 shows the results of one-dimensional Huder-Amberg test obtained for a sample trimmed from a block recovered from the tunnel face at a depth of 430 m. The test procedure is similar to the conventional oedometer compression test, the only difference being that the first loading, unloading and reloading stages are performed without adding water in the apparatus. The first loading-unloading cycle (point C) seems sufficient to recover an approximately undisturbed initial state, characterised by high saturation degrees and, possibly, closed fissures.

Table 1. Index and physical properties of the tectonised clays at a depth ranging from 175 to 520 m (Boldini *et al.* 2004b).

Unit weight of total volume γ (kN/m^3)	20.8–24.1
Unit weight of solid γ_s (kN/m^3)	26.7–27.3
Natural water content w (%)	2.4–9.4
Liquid limit w_L (%)	30–41
Plastic limit w_P (%)	16–20
Saturation degree S_r (%)	48–94
Clay fraction (%)	3–20
Permeability k (m/s)	$<10^{-11}$

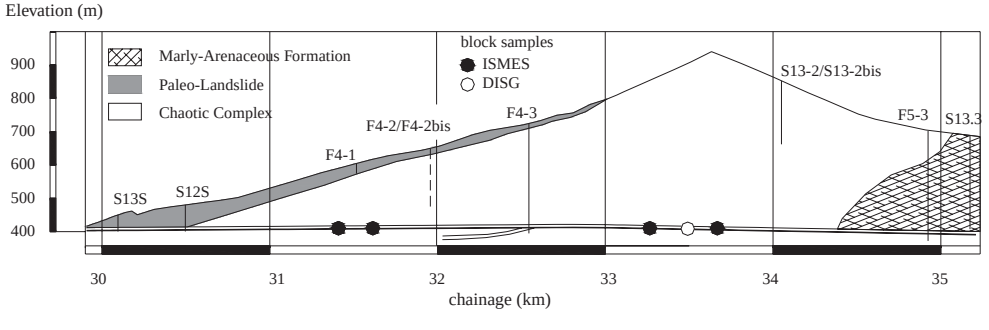

Figure 2. Geological profile along the Raticosa tunnel (Boldini et al. 2004b).

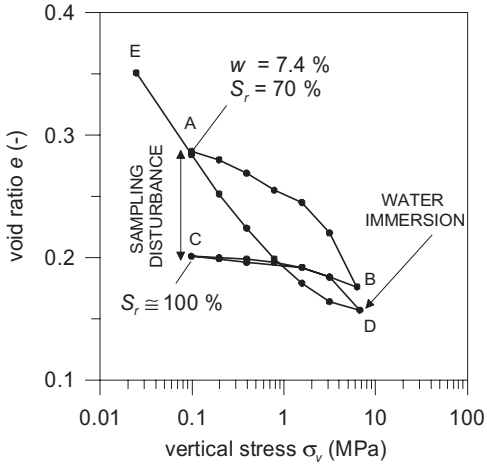

Figure 3. Results of a Huder-Amberg test performed on a sample taken at the tunnel face at the depth of 430 m (Boldini *et al.* 2004b).

Swelling after water immersion (point D) was negligible, thus, it can be argued that the swelling pressure is lower than the applied stress $\sigma_{v,D}$, which in turn was set approximately equal to the vertical lithostatic stress at the sample depth, under the assumption of pore pressure $p_0 = 0$ (hypothesis of dry-medium). On the base of the previous experimental results, the hypothesis of fully saturation and hydrostatic pore pressure distribution cannot be rejected. Therefore, it represents one of the possible scenarios considered in the following numerical investigations.

3.2 *Monitoring data*

At present, no reliable information is available on water table position and pore pressure distribution inside the Chaotic Complex. 14 vibrating wire piezometres, installed during tunnel excavation up to a distance of 15 m from the tunnel wall, have not given so far significant measurements of pore pressure. This evidence can be reasonably explained as an effect of the scaly structure of the formation, characterised by fissures that can be easily sheared and opened by the unloading caused by tunnel excavation.

The whole construction process was performed under the continuous control of a monitoring system, mainly based on the geodetic survey of tunnel wall displacements ("convergence" measurements) and on deformation measurements carried out by a sliding micrometer along pipes installed from the face in the direction of the tunnel axis ("extrusion" measurements).

In this study, attention was focused only on convergence measurements since they can be easily compared with the displacements of the tunnel cross-section predicted by plane strain models.

Figure 4 shows two examples of convergence measurements along the horizontal diameter as a function of the distance x of the monitoring section from the tunnel face. These data refer to monitoring sections at depths ranging from 325 to 375 m.

The convergence measurements were interpolated by empirical laws in order to evaluate separately evaluating the two contributions of face advance and time.

The "instantaneous" diametric convergence of the tunnel at great distance from the face, C_∞, which also includes the displacement C_0 occurred before the zero reading, is obtained by the well-known relationship of Panet & Guenot (1982):

$$C(x) = C_f + (C_\infty - C_f)\left[1 - \left(\frac{0.84R}{x + 0.84R}\right)^2\right] \qquad (1)$$

where C_f is the convergence of the diameter at the face and R is the plastic radius (Fig. 1). For an elastic medium, C_f is equal to $0.27 \cdot C_\infty$ but the same relationship approximately holds also for an elasto-plastic medium, if C_∞ is properly evaluated.

Data fitting was performed by adopting the procedure described in Graziani *et al.* (2005) which consists in assuming relationship (1) as a shape function and in estimating the section-specific C_∞ value on the basis of the first two measurements of convergence. Adopting a plastic radius R equal to twice the tunnel radius, the estimated total horizontal convergence resulted to be within the interval 0.06–0.18 m for all the available monitoring sections at depths ranging from 325 to 375 m.

Most of the monitoring sections exhibit some amount of time-dependent deformations, as demonstrated by convergence measurements that go on increasing even after the face effect is exhausted (practically, for $x > 2a$, having indicated with a the tunnel radius, and time $t > 7$ days) (Fig. 5).

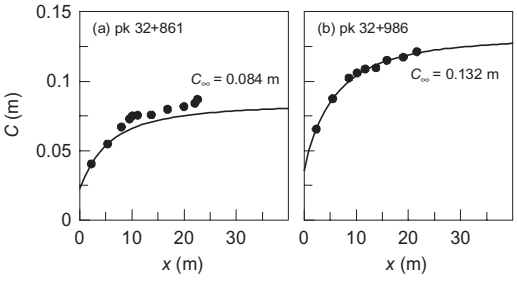

Figure 4. Measured diametric convergences versus face distance and their interpolation by Panet & Gunet (1982) empirical law.

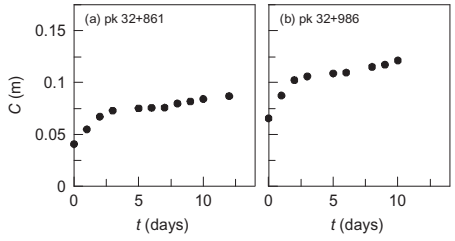

Figure 5. Measured diametric convergences versus time.

4 NUMERICAL MODEL

The numerical model considers a circular tunnel (radius $a = 7$ m) at a depth of 350 m, assuming an isotropic state of initial stress ($S_0 = 8.05$ MPa at the depth of the tunnel axis). The mechanical parameters required for the assumed ideal elasto-plastic model are: Young's modulus $E' = 2000$ MPa, Poisson's ratio $\nu' = 0.3$, cohesion $c' = 200$ kPa, friction angle $\varphi' = 15°$; the dilatancy angle ψ is 0° or 5°.

Plane-strain numerical analyses were performed by the finite difference code FLAC (ITASCA 2005), adopting a coupled solution scheme. A fully axisymmetric model, which implies that gravity is disregarded, was preferred in order to make the numerical model as much as possible comparable to the analytical solutions. The grid represents a quarter of tunnel, with the interval (a, r_{max}) of the calculation domain subdivided into 60 elements (Fig. 6). At the external boundary ($r_{max} = 20\ a$) stress conditions corresponding to the lithostatic situation were applied.

The main differences between the analytical and numerical approaches stem from the limited extent of the grid (r_{max}) and the imposed boundary conditions for $r = r_{max}$.

The analysis of data from the monitoring sections indicates a radial convergence (i.e., half of the diametric convergence C) of the tunnel before support installation in the range 20–30 mm and a total measured increment of radial convergence approximately equal to 30 mm.

Values of convergences in agreement with such measurements can be obtained in the numerical models by assuming a relaxation factor $\lambda = 0.5$ at the time of support activation (general reference about the definition and use of the relaxation factor can be found, e.g., in Panet & Guenot 1982). More precisely, the relief ($\lambda = 0.5$) was calibrated with reference to the case of Model 3, which can be considered the most realistic, as discussed in the following.

The same stress relief is used in Figure 7 to find the starting point of the support curve when applying the Characteristic Curves method.

Considering the short-term characteristic curve of the tunnel represented in Figure 7, the 30 mm increment in convergence undergone by the support is compatible with an overall stiffness of the support system $K_l = \Delta q/\Delta u_a = 100$ MPa/m. Again, this back-calculated stiffness corresponds to an equivalent Young's modulus of 16 GPa, for a lining thickness of 0.3 m, as assumed for the beam elements utilised to model the lining.

The effect of face reinforcement was not considered in the model, but its potential influence on wall convergence arises implicitly from the calibration of the stress relief by the monitoring data.

Figure 7 also shows the long-term characteristic curve for the perfectly pervious tunnel, calculated by the analytical solution (Eq. (A7) reported in Appendix).

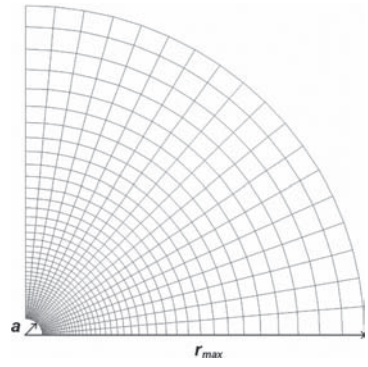

Figure 6. Mesh employed in the numerical analyses.

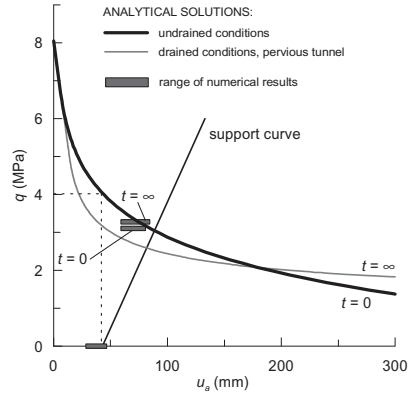

Figure 7. Characteristic curves for the tunnel in drained and undrained conditions and for the lining; the range of numerical results for different models is also indicated.

5 RESULTS

The distribution of pore pressure obtained by the different modelling approaches are reported

in Figure 8a, which refers to the short-term equilibrium conditions after lining installation. The conventional undrained analysis with a small dilatancy angle (Model 1b, $\psi = 5°$) is the only case in which negative pore pressures develop around the tunnel. Looking at the pore pressure profiles, the limit of the plastic zone can be identified as the point where pore pressure starts to decrease from the undisturbed value p_0. It can be noticed that the extent of the plastic zone is smaller for Model 3, in which pore pressure is set equal to zero as soon as plastic strains develop.

Figure 8b shows the long-term profiles of pore pressure, according to the two possible idealised steady-state situations, previously defined. The striking difference between the two pore pressure profiles can be roughly viewed as a "shift" of the curve from the tunnel wall to the limit of the plastic annulus.

Figure 9 illustrates the increment in displacement for three characteristic phases of tunnel life, namely, before and after lining installation, in the short-term, and at the end of the consolidation process.

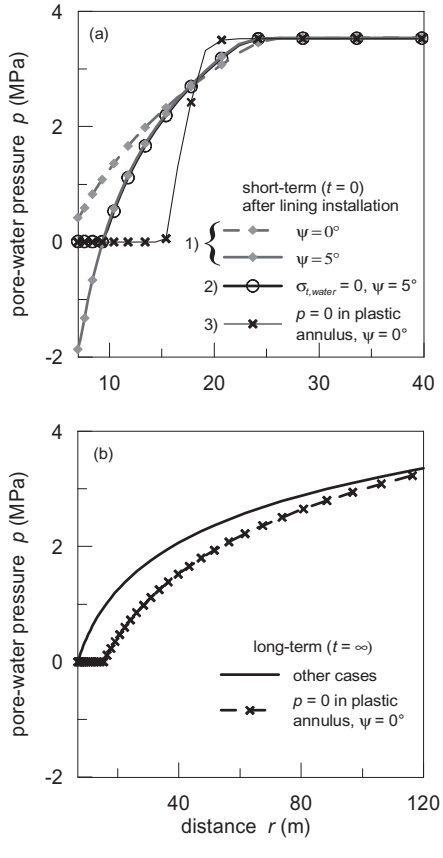

Figure 8. Pore-pressure distribution around the tunnel in the short- (a) and long-term (b), for Model 1, 2 and 3.

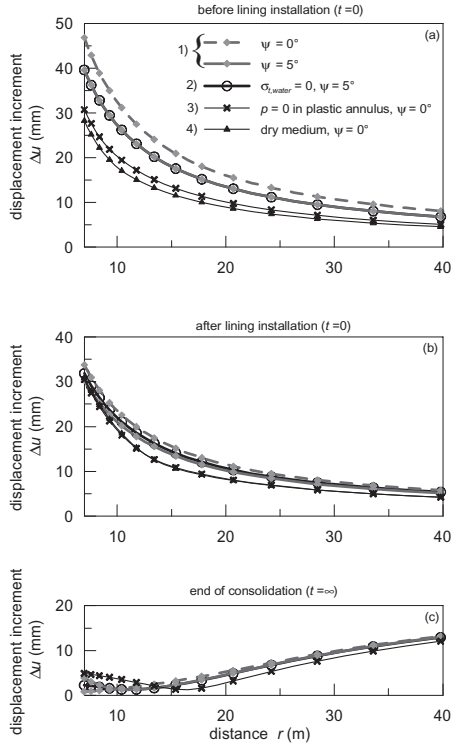

Figure 9. Distribution of displacement increment around the tunnel occurred before (a) and after the lining installation (b) and at the end of the consolidation process (c).

The increment in tunnel convergence before lining installation (Fig. 9a) is significantly different for the various models: maximum and minimum values are obtained for the conventional undrained analysis (Model 1) and the dry medium analysis (Model 4), respectively. A modest dilatancy angle (Model 1b) tends to reduce the displacement. Moreover, Model 1b and Model 2 give the same results, indicating that negative pore pressures are not yet present, while they develop due to the second phase of stress relief, i.e., after placement of the lining (Fig. 9b).

The different ways of modelling solid-water interaction, in the short-term, seem to have a negligible influence on the increase in displacement after lining installation (Fig. 9b), and consequently on the support load. At this stage, the calculated total diametric convergence varies between 120 and 150 mm, thus resulting slightly larger than the "instantaneous" closure obtained from monitoring data.

The displacement increments due to consolidation predicted by the different models are comparable far from the tunnel wall, while, although being modest, differ significantly near the excavation

(Fig. 9c). The calculated increment in radial convergence ranges between 1 and 5 mm. This means that the ratio between the time-dependent closure and the "instantaneous" closure is less than 10%, a value significantly lower than those obtained from the regression analysis of monitoring data (around 27%). It can be therefore argued that most of time-dependent deformation is of viscous nature and, therefore, that pore pressure equalization plays a minor role.

Finally, a comparison in terms of convergence and lining load between the various numerical predictions and the analytical characteristic curves is shown in Figure 7, for the three main steps of calculation (i.e., before lining installation, after lining installation in the short-term and at the end of the consolidation process). The long-term analytical (i.e., uncoupled) solution gives erroneous predictions, as generally occurs for the case of pervious lining (Graziani & Ribacchi 2001).

6 CONCLUSIONS

The paper analyses specific issues concerning the hydro-mechanical response of fissured argillaceous rocks to tunnelling. The study started from the case-history of a deep tunnel excavated in a highly tectonized clay formation (Raticosa tunnel, Italy). A common problem in this kind of structurally-complex formations is the difficulty in obtaining reliable measurements of pore pressure and, thus, the uncertainty in formulating the most appropriate model of solid skeleton-pore water interaction.

A wide range of conceptual models for the short-term behaviour were compared, ranging from the conventional undrained response to models specifically formulated for stiff fissured clays, for which the development of negative pore pressure during unloading stress paths may be limited as a consequence of shearing and opening of fissures. The limit case of a fully dry medium was also considered.

For the long-term situation, two idealised cases were considered, depending of the permeability of the plastic annulus around the tunnel, which can be assumed either equal to that of the undisturbed ground or infinite, again as a consequence of fissure opening.

It was found that the different models predict significantly different convergences of the tunnel wall in the situation before lining installation, but have only a modest influence on support loads. Even the simplest model of fully dry-medium could provide a satisfactory estimate of the short- and long-term load on the lining.

Since the proposed models encompass a very wide range of possible hydro-mechanical responses, they could represent an useful tool to asses the impact of uncertainties about the real behaviour of complex geo-materials, particularly in the preliminary design of deep tunnels.

For the case of Raticosa tunnel, increment in tunnel closure due to consolidation processes, as predicted by the proposed models, represent only a part of the measured time-dependent increment. Most of the delayed convergence seems to be caused by viscous deformation of the rock.

7 APPENDIX

All the analytical solutions herein considered refer to a cylindrical borehole in an infinite medium.

7.1 *Short-term conditions*

A simple analytical solution (Salençon 1959) for the undrained situation is based on the following hypotheses: circular tunnel of radius a, ideal elasto-plastic medium and axisymmetry conditions with isotropic in situ total stress S_0 and uniform pore water pressure p_0.

The undrained behaviour of the porous medium is obtained by considering a null volumetric deformation and a purely cohesive shear strength, equal to c_u. The plastic radius R (distance of the outer boundary of the plastic zone from the tunnel axis) and the radial displacement u are given by the following expressions:

$$\frac{R}{a} = \exp\frac{\mathrm{OF}-1}{2} \quad \text{with} \quad \mathrm{OF} = \frac{S_0 - q}{c_u} \tag{A1}$$

$$\frac{u(r)}{a} = u_a \cdot \frac{1}{r} = \frac{c_u}{2G}\exp(\mathrm{OF}-1)\cdot\frac{a}{r} \tag{A2}$$

G is the shear elastic modulus, q the tunnel support pressure and, OF the so called Overload Factor.

In the plastic annulus around the tunnel, σ_r and σ_θ, the total radial and the circumferential stress, are obtained by equilibrium and plasticity conditions:

$$\sigma_r = q + 2c_u \ln\frac{r}{a} \qquad \sigma_\theta = q + 2c_u\left(1 + \ln\frac{r}{a}\right) \tag{A3a,b}$$

The excess pore pressure Δp must be equal to the variation of the total mean stress; hence, the distribution of Δp around the opening is given by:

$$\begin{aligned} &\Delta p = p - p_0 = -S_0 + q + c_u\left(1 + 2\ln\frac{r}{a}\right) \text{ for } \mathrm{r} \le \mathrm{R} \\ &\Delta p = 0 \text{ for } \mathrm{r} > \mathrm{R} \end{aligned} \tag{A4}$$

Finally, given all the aforementioned hypotheses, the undrained cohesion c_u can be expressed as a

function of the drained strength parameters c_u, c', φ':

$$c_u = (S_0 - p_0)\ \sin\varphi' + c'\cos\varphi' \qquad \text{(A5)}$$

7.2 *Long-term conditions*

Regarding the long-term conditions ($t = \infty$), Lembo-Fazio and Ribacchi (1984) proposed to evaluate the state of stress and deformation around deep tunnels assuming that a stationary radial flow establishes inside an annular zone spanning from the tunnel wall to a radius r_0, which represents the limit of the zone influenced by seepage (i.e., $p = p_0$ for $r \geq r_0$). The corresponding pore pressure distribution is:

$$p(r) = p_a + (p_0 - p_a)\ \ln\left(\frac{r}{a}\right) \Big/ \ln\left(\frac{r_0}{a}\right) \qquad \text{(A6)}$$

where p_a is the value of pore pressure at the tunnel wall.

The general solution for stresses and displacements around the tunnel is described in Lembo-Fazio and Ribacchi (1984); afterward, it was applied by Graziani and Ribacchi (2001) to the case of uncompressible fluid and elasto-plastic solid skeleton. For an ideal plastic medium with a Mohr-Coulomb strength criterion (cohesion c', friction angle φ', dilation angle ψ'), it is given by Eq. (A7).

p_R is the value of pore water pressure at the plastic radius R; G and ν' are the usual elastic constants; h is a parameter which takes the influence of the pore pressure gradient into account; N and K are, respectively, the triaxial and dilatancy factors.

$$\begin{aligned}\frac{u}{a}\cdot 2G = &\left[\begin{matrix}(S_0 - p_0)\sin\varphi' + \\ (p_0 - p_R)\dfrac{1-2\nu'+\sin\varphi'}{2(1-\nu')}\end{matrix}\right]\frac{(R/a)^{K+1}}{(r/a)^K} \\ &+\left[\begin{matrix}(S_0 - p_0 + c'\cdot\cot g\varphi')(1-2\nu') - \\ h\dfrac{1+NK-\nu'(K+1)(N+1)}{K+1}\end{matrix}\right] \\ &\cdot\left[\frac{(R/a)^{K+1}}{(r/a)^K} - (r/a)\right] + \\ &-\left[\begin{matrix}(q - p_0 + c'\cdot\cot g\varphi' - h) \\ \dfrac{1+NK-\nu'(K+1)(N+1)}{K+1}\end{matrix}\right] \\ &\cdot\left[\frac{(R/a)^{K+1}}{(r/a)^K} - (r/a)^N\right]\end{aligned} \qquad \text{(A7)}$$

$$\frac{R}{a} = \left\{\frac{(1-\sin\varphi')\cdot\left[\begin{matrix}S_0 - p_R - \dfrac{(1-2\nu')}{2(1-\nu')} \\ \times(p_0 - p_R) + c'\cdot\cot g\varphi'\end{matrix}\right] - h}{q - p_a + c'\cdot\cot g\varphi' - h}\right\}^{\frac{1}{N-1}} \qquad \text{(A8)}$$

$$h = \frac{p_0 - p_a}{(N-1)\cdot\ln(r_0/a)}, \quad N = \frac{1+\sin\varphi'}{1-\sin\varphi'}, \quad K = \frac{1+\sin\psi'}{1-\sin\psi'} \qquad \text{(A9a,b,c)}$$

REFERENCES

Boidy, E., Bouvard, A. & Pellet, F. 2002. Back analysis of time-dependent behaviour of a test gallery in claystone. *Tunn. Undergr. Sp. Tech.* 17: 415–424.

Boldini, D., Lackner, R. & Mang, H.A. 2004a. Influence of face reinforcement and shotcrete support on static conditions of deep tunnels: a thermo-chemo-mechanical study. *Rivista Italiana di Geotecnica* 4: 52–69.

Boldini, D., Graziani, A. & Ribacchi, R. 2004b. Raticosa tunnel, Italy: characterization of tectonized clay-shale and analysis of monitoring data and face stability. *Soils and Foundations* 44: 59–71.

Bonini, M., Debernardi, D., Barla, M. & Barla, G. 2009. The mechanical behaviour of clay shales and implications on the design of tunnels. *Rock Mech. Rock. Engng*. 42(2): 361–388.

Carranza-Torres, C. & Zhao, J. 2009. Analytical and numerical study of the effect of water pressure on the mechanical response of cylindrical lined tunnels in elastic and elasto-plastic porous media. *Int. J. Rock Mech. Min. Sci.* 46: 531–547.

Comité Français de Méchanique des Roches 2000. *Manuel de méchanique des roches. Tome 1: Fondaments. Roches Argileuses.* Paris: Les Presses de l'Ecole des Mines.

Debernardi, D. & Barla, G. 2009. New viscoplastic model for design analysis of tunnels in squeezing conditions. *Rock Mech. Rock. Engng.* 42(2): 259–288.

Gasc-Barbier, M., Ghoreychi, M. & Tessier, D. 1999. Comportament mécanique de roches argileuses profondes: incidence de la texture. *Proc. 9th ISRM Congr., Paris*, 595–600.

Gäber, R. & Labiouse, V. 2003. Influence of pore water on the design of deep galleries in low permeability rocks. *Proc., 10th ISRM Congr., Johannesburg*, 347–350.

Graziani, A., Boldini, D. & Ribacchi, R. 2005. Practical estimate of deformations, loads and stress relief factors for deep tunnel supported by shotcrete. *Rock Mechanics and Rock Engineering* 38: 345–372.

Graziani, A. & Ribacchi, R. 2001. Short- and long-term load conditions for tunnels in low permeability ground in the framework of the convergence-confinement method. *Proc. Intern. Symp., Kyoto,* 83–88.

ITASCA 2005. *FLAC, User's Manual, Version 5.0*. Itasca Consulting Group Inc., Minneapolis, Minnesota.

Lembo-Fazio, A. & Ribacchi, R. 1984. Influence of seepage on tunnel stability. *Proc., Int. Conf. on Design and Performance of Underground Excavations, Cambridge*, 173–181.

Panet, M. & Guenot, A. 1982. Analysis of convergence behind the face of a tunnel. *Proc., Tunneling 82, Brighton*, 197–204.

Salençon, J. 1969. Contraction quasi-statique d'une cavité à symmétrie sphérique ou cylindrique dans un milieu éleastoplastique. *Ann. Ponts et Chaussées* 4: 231–236.

Geotechnical Aspects of Underground Construction in Soft Ground – Viggiani (ed)
© 2012 Taylor & Francis Group, London, ISBN 978-0-415-68367-8

Micro-measurement and monitoring system for ageing underground infrastructure (Underground M3)

K. Soga
University of Cambridge, Cambridge, UK

A. Ledesma
Universitat Politècnica de Catalunya, Barcelona, Spain

A. Roncaglia
CNR, Bologna, Italy

I. Vaníček
Czech Technical University in Prague, Prague, Czech Republic

ABSTRACT: Advances in the development of computer vision, miniature Micro-Electro-Mechanical Systems (MEMS) and Wireless Sensor Network (WSN) offer intriguing possibilities that can radically alter the paradigms underlying existing methods of condition assessment and monitoring of ageing civil engineering infrastructure. This paper describes some of the outcomes of the European Science Foundation project "Micro-Measurement and Monitoring System for Ageing Underground Infrastructures (Underground M3)". The main aim of the project was to develop a system that uses a tiered approach to monitor the degree and rate of tunnel deterioration. The system comprises of (1) Tier 1: Micro-detection using advances in computer vision and (2) Tier 2: Micro-monitoring and communication using advances in MEMS and WSN. These potentially low-cost technologies will be able to reduce costs associated with end-of-life structures, which is essential to the viability of rehabilitation, repair and reuse. The paper describes the actual deployment and testing of these innovative monitoring tools in tunnels of London Underground, Prague Metro and Barcelona Metro.

1 INTRODUCTION

Deterioration of ageing civil engineering infrastructure and the associated increase in the proportion of budgets spent on maintenance present significant challenges to our society. Dense spatial and temporal information, integrated with appropriate data analytical tools, is required to assess and reduce the likelihood of, or improve the efficient response to failures of key elements of critical infrastructure resulting from degradation, overload, or disasters due to natural and/or man-made causes. The maintenance, refurbishment and safe operation of ageing infrastructure under severe financial constraints forces civil engineers to strive for technological advances which will allow them to sense, monitor and better understand the behaviour of their engineering systems under both normal and extreme operating conditions.

Nowhere is this more apparent than in large-scale critical systems such as the networks of tunnels that lie beneath our cities. Some of this infrastructure was constructed more than half a century ago and there is widespread evidence of deterioration. Old tunnels are in particular vulnerable to adjacent ground disturbance, for instance piling and deep excavations.

At the moment, network wide monitoring is prohibitively expensive and very limited in terms of obtaining the necessary data for quick assessment, especially in the case of emergencies due to natural or deliberately caused disasters. Advances in the development of computer vision and Micro-Electro-Mechanical Systems (MEMS) offer intriguing possibilities that can radically alter the paradigms under-lying existing methods of condition assessment and monitoring. Future monitoring systems will undoubtedly comprise Wireless Sensor Networks (WSN) and will be designed around the capabilities of autonomous nodes. Each node in the network will integrate specific sensing capabilities with communication, data processing and power supply.

This paper presents an overview of a European collaborative project "Micro-Measurement and Monitoring System for Ageing Underground

Infrastructures (Underground M3)" funded by the EUROCORES Smart Structural Systems Technologies (S3T) Programme of the European Science Foundation. The main aim of the project was to develop a system that uses a tiered approach to monitor the degree and rate of tunnel deterioration. The system comprises of (1) Tier 1: Micro-detection using advances in computer vision and (2) Tier 2: Micro-monitoring and communication using advances in MEMS and WSN. The paper describes the innovative monitoring tools developed in this project.

2 CONDITIONS OF AGEING TUNNELS

One of the main features of the project is the participations of underground railway owners and maintenance operators. The monitoring system developed for this project have been tested at three metro systems in Europe; Prague Metro, London Underground and Barcelona Metro.

London Underground Ltd (LUL) has 402 km of railway lines. Approximately 45% of this (181 km) are underground tunnels and many of them are 75–100 years old. 80% of the tunnels are made of cast-iron. Deterioration of the linings and change in earth pressures with time are concerns because these are associated with the decrease in the clearance between the tunnel linings and the trains, affecting the train operation.

The Barcelona Metro was founded in 1924. It currently has nine metro lines; six are operated by Ferrocarril Metropolità de Barcelona and three are operated by Ferrocarrils de la Generalitat de Catalunya. The network has a length of 124 km with 164 stations. Most of the tunnels are constructed by the cut-and-cover method and use masonry, steel, plain concrete, reinforced concrete, and diaphragm walls depending on the time of construction. More recent tunnels are made by shield machines. The concerns of the tunnel operators are wet areas, oxidation of reinforcement, and cracks and fissures.

Prague Metro has three lines and consists of about 60 km of tracks running mostly underground and 57 stations. It is about 30 years old and is mostly Russian-built. In August 2002, the metro suffered flooding that occurred in Central Europe. 19 stations were flooded and several building movements have been attributed to this event. The long term effects of the damages caused by flooding are one of the major concerns of the underground operator.

At present the tunnels of the three metro systems are monitored if a specific problem has arisen in which case a system can be retrofitted before repair and strengthening work is undertaken so that the effectiveness of the refit can be examined. The current employable technologies for the assessment of such infrastructure range from network-wide visual inspection to surveying and deployment of instruments for monitoring performance at critical sections (or response to adjacent construction). These technologies have evolved with the maintenance needs, but three general limitations remain.

- High cost of equipment and data processing limits usage and/or constrains the scope and frequency of sampling and inspection.
- Measurement techniques that interfere with vehicle movements in tunnels are seriously discouraged, while direct access is very difficult. There is also a need to conduct quick inspection check as maintenance crews are moving.
- New technologies are needed for specific classes of problems, e.g. monitoring of joint rotations in tunnel lining.

This Underground M3 project comprises an integrated research program to evaluate and develop prototype monitoring systems for condition assessment of ageing underground infrastructure. The main aim is to develop a system that uses a tied approach to monitor the degree and rate of deterioration. The system comprises of (1) Tier 1: Micro-detection and (2) Tier 2: Micro-monitoring and communication.

3 TIER 1: MICRO-DETECTION

For maintenance works of underground structures, visual inspection is a common practice for detecting and monitoring anomalies such as cracks, spalling and staining. Photographs and videos are commonly used as a mean of recording anomalies, although over years, image collections become large and difficult to organize and browse. Improving the ways that an image database is accessed and visualized are expected to result in a substantial progress in the effectiveness of monitoring, in particular of remote monitoring, like shaft inspection, where inspectors cannot easily access the inspection site.

One way to assist inspectors in organising a large collection of images and examining the tunnel surface is providing them with automatic tools that combine a large number of pictures into a single high-quality wide-angle composite view. This process is commonly referred to as image mosaicing. There are many image stitching software packages, such as Microsoft Image Composite Editor (ICE) and Autopano, the vast majority of which rely on a number of strong assumptions on the camera motion or on the scene geometry to be strictly true. In fact, these packages are genuinely designed for

generating panoramas, and they require images to be captured by a camera roughly rotating about its optical centre, or by capturing the plane at "infinity" (i.e. the scenes where all objects are distant and there is little or no parallax). The images from typical underground structure inspection do not meet such requirements and these packages fail to generate good mosaics, as shown in Figure 1 (Top).

A new computer vision system has been developed in this project to perform mosaicing of images captured inside a tunnel from a standard digital camera or videos. It can simultaneously cope with free camera motion and the more complex geometry of the scene. In the proposed system, starting from a set of pictures from a section of the tunnel linings, first the approximate 3D geometry of the scene and consequently warp each frame are recovered in order to generate a set of pictures that can be stitched together using any standard mosaicing technique. In fact, for images captured inside a tunnel, this warping procedure can be imagined as prompting pictures of a tunnel that has been flattened, or unrolled onto a plane (see Fig. 1 (bottom)). In order to do this, the system obtains the sparse 3D reconstruction of the tunnel using Structure from Motion (SfM) (Snavely et al., 2005) from the input images.

A sparse 3D model, i.e. a 3D point cloud, can be recovered from digital photographs, together with the camera poses, i.e. translations and rotations with respect to a given reference frame. The reconstruction procedure is composed of two modules: point track generation; and multiple view geometry estimation.

In the first module, interest points are extracted from each input image and matched across multiple frames in order to obtain a set of points that consistently appear in multiple images as shown in Figure 2. The 2D coordinates of such points are collected and concatenated forming 2D trajectories over the multiple frames. Success at this stage relies on the robustness of the extraction and matching scheme of the interest points.

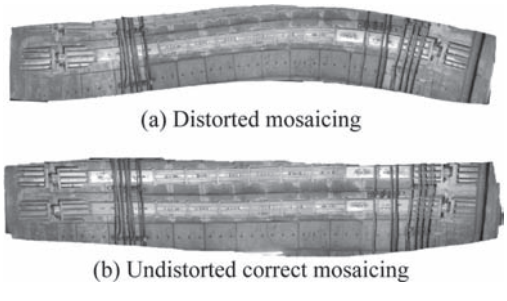

(a) Distorted mosaicing

(b) Undistorted correct mosaicing

Figure 1. Image mosaicing of the London Underground tunnel image sequences.

Figure 2. Keypoint matching.

An interest point is an image point whose neighbourhood (i.e. an image patch centred at that point) displays distinctive features that are stable under perturbations arising from some degree of perspective transformations, illumination variations and noise such that the same interest points can be extracted with high degree of reproducibility. This invariance allows key points to be matched across multiple images. The Scale Invariant Transform Features (SIFT) is an example of stable image feature (Lowe, 2004). Interest points are detected in scale-space, and are assigned descriptors that summarize their appearance by the orientation histogram of the intensity gradients within a patch, thus achieving invariance to scale, orientation, affine distortion, and partial invariance to illumination changes.

The second module is classically formulated as a large-scale optimization problem (see Zisseman and Hartley (1999) for a detailed explanation of multiple view geometry). The output from the first module is used to initialize the optimizer, estimating the sparse point cloud and camera poses using overlapping triplets of images. The estimation is then refined by Bundle Adjustment (BA) (Lourakis and Argyros, 2004). The BA algorithm iteratively adjusts the positions of the 3D coordinates and the camera poses to minimize the sum of the distances between the reprojections of the reconstructed 3D points through the estimated cameras, and the interest points 2D coordinates. Figure 3 shows a sparse 3D reconstruction of three tunnels.

Cylinders are surface of zero Gaussian curvature, so it is possible to define a local isometry for flattening the curved surface onto a plane (Chaiyasarn et al., 2009). Moreover, given the constraints on the image collection process, cameras are located inside the cylinder and each ray intersects the surface in only a single visible point, defining for each image a one-to-one mapping between image samples and points on the surface. These facts allow us to define a warping that produces the flattened versions of the input images (see Fig. 4).

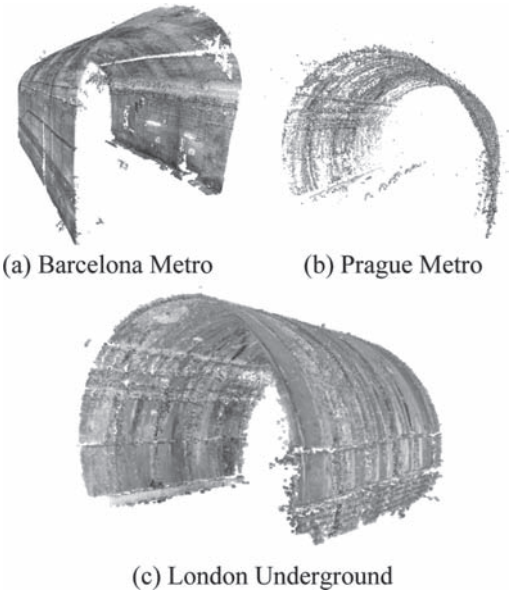

Figure 3. Sparse 3D reconstruction of three tunnels.

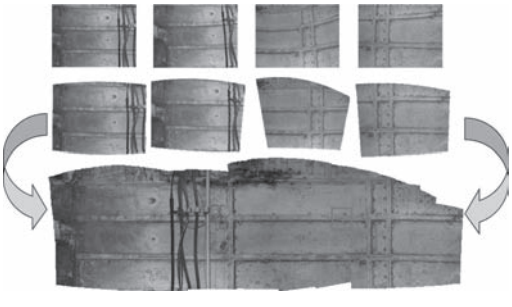

Figure 4. Creating an undistorted mosaiced image.

Figure 1 shows qualitative comparison between the mosaic images from the homography-based method and the proposed method. Perspective distortion is clearly removed in the result. An example of a larger composite image is shown in Figure 5. With this system it is possible to identify regions of change in images of the same scene taken at different times since the images have spatial coordinates assigned. This is much needed for inspection since engineers will be able to assess the deterioration rate of a structure and then devise regime for repair. The prototype of the system including the software and the apparatus for acquiring images is currently being developed so that it can be practically adopted in the underground structure inspection procedure.

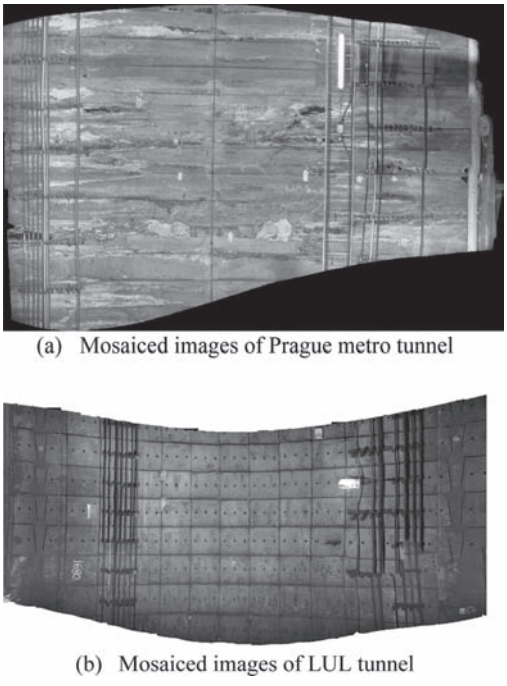

Figure 5. Undistorted mosaic images of tunnels.

4 TIER 2: MICRO-MONITORING AND COMMUNICATION

4.1 *Micro Electro Mechanical Systems (MEMS)*

Once significant anomalies or cracks are detected in a Tier 1 assessment using computer vision techniques, there is a need for more intensive monitoring. This will be a Tier 2 targeted micro-monitoring process. It is proposed that the solution for underground infra-structure monitoring is the use of low cost sensors of a distributed nature.

Micro Electro Mechanical Systems or MEMS are small integrated devices or systems that combine electrical and mechanical components varied in size from micrometers to millimeters, which can merge the function of computation and communication with sensing and actuation to produce a system of miniature dimensions. MEMS extend the fabrication techniques for semiconductor industry to include mechanical elements and the inherently small size of MEMS enables high level integration of micromachined components or structures to realize multiple functions or capabilities on the same silicon chip for greater utility. The majority of the MEMS applications in civil infrastructure monitoring act as sensors, which have emerged as a high sensitive monitoring candidate for structural

control and assessment, health monitoring, damage repair and system preservation of civil infrastructure. MEMS sensors will offer major advantages in terms of smaller size, lower power consumption, more sensitive to input variations, cheaper cost due to mass production and less invasive than larger devices, and extend the performance and lifetimes over conventional systems. A range of MEMS sensors is now available in civil applications, which can measure acceleration, inclination, temperature and pressure. In this project, potentially low-cost MEMS strain or displacement sensors were developed.

An example of MEMS resonant strain sensors that were developed for the project is shown in Figure 6. The basic principle of this MEM strain sensor is to couple the strains axially onto a vibrating beam, similar to the conventional vibrating wire strain gauges. The figure shows Double-Ended Tuning Fork (DETF) parallel-plate resonators with reduced coupling gaps (<1 μm) (Ferri et al., 2010). The added strain energy in the beam shifts its resonant frequency. The strain can be inferred by monitoring the shift in resonant frequency.

The small size of MEMS enables them to be used in situations where conventionally sized components are not applicable. Another advantage is their low power requirement (e.g. 500 micro watts to 40 milli watts). Due to the economies of scale achievable with conventional chip manufacturing processes, they can be produced at relatively low cost.

The fabrication process of the strain sensor has been previous reported in Ferri et al., (2008). The process is starting from silicon on insulator substrates. The silicon device layer is heavily doped and annealed in order to obtain a low sheet resistance. On the substrate, a low temperature oxide layer is then deposed by Chemical Vapour Deposition (CVD) and patterned by Reactive Ion Etching (RIE). A CVD polycrystalline silicon layer is then deposited and completely oxidized to shrink the gaps patterned on the initial oxide later. The deep RIE is then utilized to patent the reduced gap oxide mask on the silicon device layer with reduced line widths. The process is ended by an isotropic wet etching in buffered oxide etch.

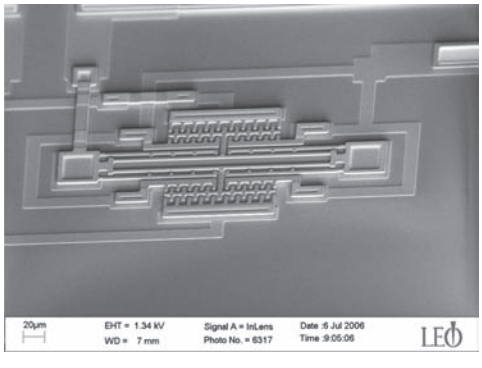

Figure 6. Double-Ended Tuning Fork (DETF) parallel-plate resonators.

Mechanical modeling of the MEMS sensor has also been performed as shown in Figure 7 to estimate the sensitivity of the system. Since the resonant MEMS sensors are operated through a self-sustained electrostatic actuation using an electronic oscillation loop, no static bias current is needed for their operation and the dynamic power requirements can be comparatively small.

As part of this project, a prototype MEMS crackmeter was developed with a thin steel strip fixed across a crack or joints on the tunnel, onto which a multi-directional MEMS strain sensor is soldered (Fig. 8) (Ferri et al., 2009, 2010a). The MEMS devices are bonded to a thin steel bar by epoxy glue, packaged in vacuum and tested by applying strain to the bar, showing good tolerances to packaging parasitics, measurement reversibility, and strain sensitivity of 10 Hz/με. The steel strip is equipped by a nut which allows for changing the unstrained length of the strain sensor. This crackmeter will be deployed at a section in Prague Metro in the near future. We plan to report the performance of the developed MEMS in the future.

4.2 *Wireless sensor network*

The use of wireless sensor technology, which transmits the sensor data using radio, allows a rapid deployment due to elimination of some of the cabling and thus has significant potential benefits for underground monitoring. Combined with MEMS sensors, there is the opportunity for significant overall cost savings for large scale monitoring (Hoult et al., 2009; Stajano et al., 2010).

A prototype WSN system developed in this project was recently installed at a section of London Underground, Prague Metro and Barcelona

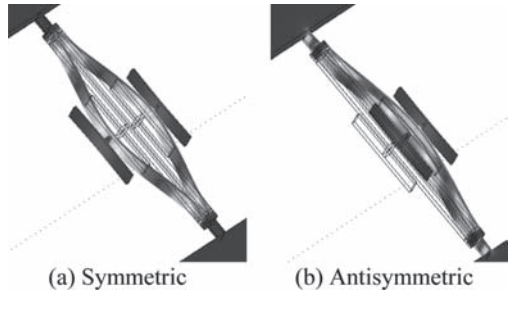

Figure 7. Mechanical modeling of the MEMS sensor.

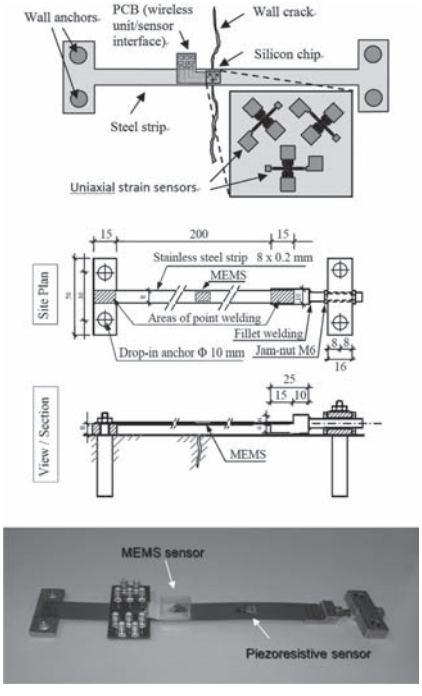

Figure 8. MEMS crackmeter.

Metro (see Fig. 9). It consisted of several WSN motes and a gateway, which were manufactured by Cross-bow Technology Inc. They were packaged and installed in such a way that they can survive for long-term monitoring (see Fig. 10). The effective mote-to-mote range was found to be approximately 15 meters and the layout installed included both star and mesh topologies as illustrated in Figure 8. Further details of the deployments can be found in Bennett et al., (2010a, b).

A limited number of motes were used in this trial so that it has predictable network topology to assess the performance of the WSN system. The gateway was connected to the internet via a router and GPRS. The system is currently tested to identify deployment and operational challenges in using sensor networks for monitoring and management of ageing underground infrastructure.

The WSN hardware that is used in this research has processing capabilities to prompt the development of computationally demanding signal processing algorithms which would allow adaptive data collection and local processing of data for the extraction of failure signals. The availability of more computationally powerful platforms also allows common implementation of various data collection scenarios, in-network processing and compression algorithms.

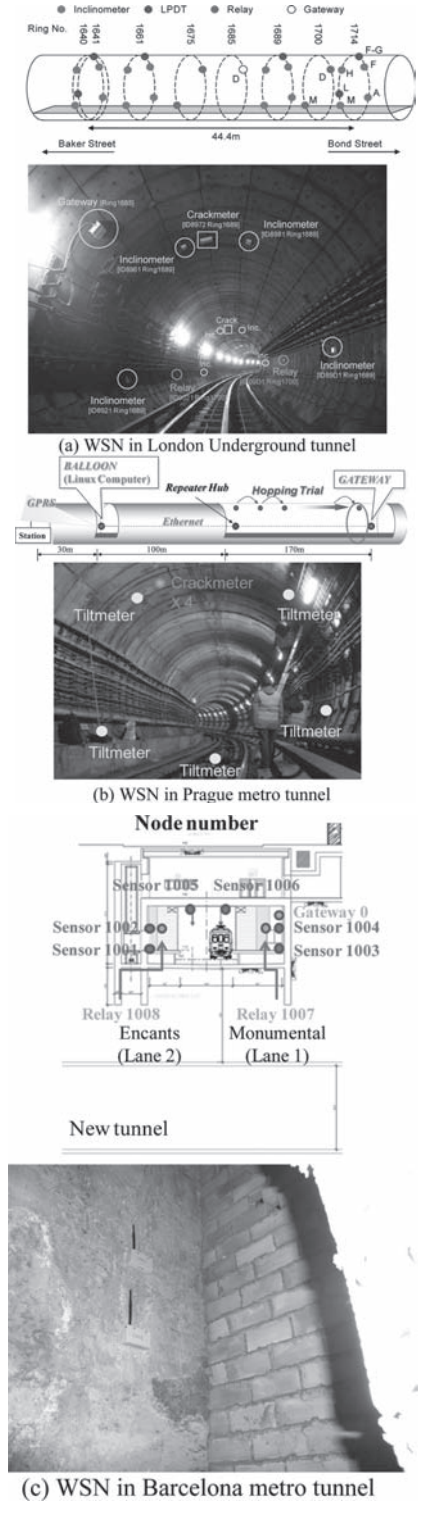

Figure 9. WSN deployment in three tunnels.

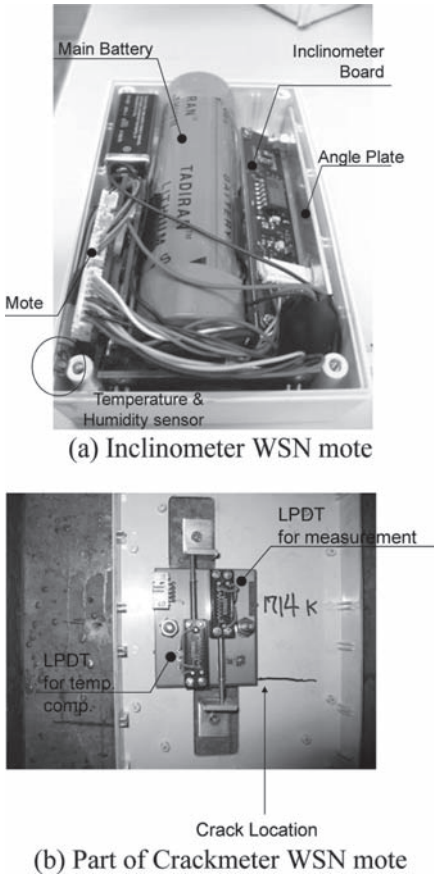

Figure 10. WSN motes.

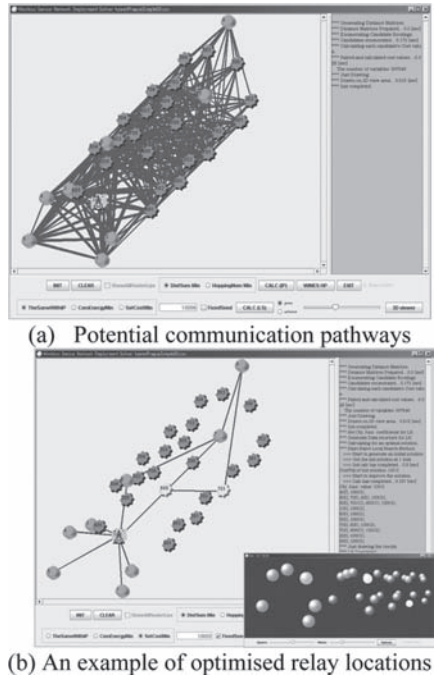

Figure 11. WSN deployment tool.

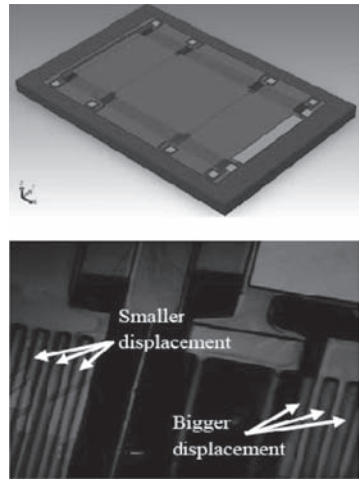

Figure 12. An example of MEM power harvester developed in this project (Wong et al., 2009).

As the size of a WSN increases, an effective deployment is essential as there is limited engineering hours to install it in a real operational underground railway system. The installation has to be done as fast as possible, but the established communication network needs to be robust and redundant. In this project WSN deployment tools were developed for system configuration and management, for data collection and visualization and for in-situ debugging.

Figure 11 shows one of such tools, in which the locations of relay motes are optimized by considering communicable distance, reliability, robustness and data transmit capacity. Figure 11(a) illustrates possible communication paths for potential positions of relay motes at the Prague metro site, whereas Figure 11(b) shows the relay mote locations that are optimized for minimum communication distances using a heuristics based optimization method. For each sensor, there are at least two non-overlapped routes to the gateway and the data flow quantity (throughput) does not exceed the upper bound set beforehand. It is also possible to apply other objective functions such as minimizing the setting cost, the hopping number (the transfer number) for each route, the energy consumption, or combinations of these. Further details can be found in Hirai and Soga (2010).

Since underground infrastructure may not be frequently accessible, the developed system also needs to employ low power consumption in conjunction with the ability to harvest power from its immediate environment. The project also investigated the possibility of developing an energy harvesting unit that will power the MEMS sensors and the WSN system. An example of the developed MEM power harvesters is shown in Figure 12 (Wong et al., 2009). This solution is practical as the sensors are used for long-term monitoring and as a result measurements are not required to be made frequently. It is envisaged to use the energy available in the surrounding environment. For underground railways, the obvious choice is harnessing energy from pressure fluctuations while the trains are running. But other possibilities are currently being assessed.

5 CONCLUSIONS

In this project a new monitoring system was developed. The vision of the Underground M3 project is effective monitoring of ageing underground infrastructure using computer vision techniques and the widespread installation of miniature, low-cost, low-power wireless sensors on key components of the infrastructure. These sensors will be multiply redundant through overlapping networks and provide substantial on-board processing capabilities to reduce the volume of data transmitted to base stations. The sensors have the potential to be built into an economically viable generic WSN monitoring system providing key decision support capabilities to the system managers. The challenges of this project have been therefore to validate the capability of the recently developed computer vision techniques in the underground environments and to demonstrate how large numbers of small, low-cost sensors can be employed and integrated into large-scale engineering systems in order to improve performance and extend the lifetime while continuously evaluating and managing uncertainties and risks.

ACKNOWLEDGEMENTS

The authors would like to thank the ESF/EPSRC for their financial support of this research (EP/E003338/1 "Micro-Measurement and Monitoring System for Ageing Underground Infrastructures (Underground M3)").

REFERENCES

Bennett, P.J., Kobayashi, Y., Soga, K. and Wright, P. (2010): "Wireless Sensor Network for Monitoring of Underground Tunnel," Proceedings of ICE, Geotechnical Engineering, Vol. 163, No. GE3, pp. 147–156.

Bennett, P.J., Soga, K., Wassell, I.J., Fidler, P., Abe, K., Kobayashi, Y. and Vanicek, M. (2010): "Wireless Sensor Networks for Underground Railway Applications: Case studies in Prague and London," Smart Structures and Systems, Vol. 6, No. 5–6, pp. 619–639.

Chaiyasarn, K., Kim, T-K., Viola, F., Cipolla, R. and Soga, K. (2009): "Image Mosaicing via Quadratic Surface Estimation with Priors for Tunnel Inspection," 2009 IEEE International Conference on Image Processing. Egypt.

Ferri, M., Mancarella, F., Roncaglia, A., Ransley, J., Yan, J. and Seshia, A.A. (2008): Fabrication of DETF sensors in SOI technology with submicron air gaps using a maskless line narrowing technique', Proceedings of IEEE Sensors (2008), 1131–1134.

Ferri, M., Mancarella, F., Yan, J., Lee, J.E.-Y., Seshia, A.A. Zalesky, J., Soga, K. and Roncaglia, A. (2009): Design and Prototyping of a MEMS-based Crackmeter for Structural Monitoring, Proceedings of the 15th International conference on solid-state sensors, actuators and Microsystems, 315–318.

Ferri, M., Mancarella, F., Seshia, A., Ransley, J., Soga, K., Zalesky, J. and Roncaglia A., (2010a): "Development of MEMS strain sensors for crack monitoring in ageing civil infrastructures", Smart Structures and Systems, Vol. 6, No. 4, pp. 225–238.

Ferri, M., Mancarella, F., Belsito, L., Roncaglia, A., Yan, J., Seshia, A., Soga, K., and Zalesky, J. (2010b): Strain sensing on steel surfaces using vacuum packaged MEMS resonators, Eurosensor (2010).

Hirai, C. and Soga, K. "An Experimental Model of Relay Deployment Planning Tool for a Wireless Sensor Network System to Monitor Civil Engineering Structures", Proceedings of the Ninth IASTED International Conference on Parallel and Distributed Computing and Networks (PDCN 2010), February 16–18, 2010, Innsbruck, Austria, pp. 164–171.

Hoult, N.A., Bennnet, P.J., Stoianov, I., Maksimović, C., Middleton, C.R., Graham, N.J.G. and Soga, K. (2009): "Wireless Sensor Networks: creating 'Smart Infrastructure'," Proceedings of ICE, Civil Engineering, Vol. 162, August 2009, pp. 136–143.

Lourakis, M. and Argyros, A. (2004): The design and implementation of a generic sparse bundle adjustment software package based on Levenberg-Marquardt, Technical Report, http://www.ics.forth.gr/~lourakis/sba/.

Lowe, D.G. (2004): Distinctive Image Features from Scales-Invariant Keypoints, IJCV 60, 2:91–110.

Snavely, N., Seitz, S. and Szeliski, R. (2005): Photo Tourism: Exploring Photo Collections in 3D, Proc. of SIGGRAPH (2005), 835–846.

Stajano, F., Hoult, N., Wassell, I., Bennett, P.J., Middleton, C.R. and Soga, K. (2010): "Smart Bridges, Smart Tunnels: Transforming Wireless Sensor Networks from Research Prototypes into Robust Engineering Infrastructure," Ad Hoc Networks, Vol. 8, No. 8, November 2010, pp. 872–888.

Wong, Z. and Yan, J. and Soga, K. and Seshia, A.A. "Dynamic mechanical amplifier in MEMS power harvesting", POWERMEMS 2009 Workshop, Washington, D.C. USA, December 1–4, 2009.

Zisserman, A. and Hartley, R. (1999): Multiple View Geometry in Computer Vision, Cambridge University Press, Cambridge, 1999.

Geotechnical Aspects of Underground Construction in Soft Ground – Viggiani (ed)
© 2012 Taylor & Francis Group, London, ISBN 978-0-415-68367-8

Settlement monitoring and tunnelling process adaptation—case of South Toulon tunnel

J.P. Janin, D. Daniel & R. Kastner
LGCIE, INSA de Lyon, Lyon, France

F. Emeriault
Grenoble-INP,UJF-Grenoble 1, CNRS UMR 5521, 3SR Lab, Grenoble, France

A. Guilloux & H. Lebissonnais
TERRASOL, Montreuil, France

ABSTRACT: The construction of urban shallow tunnel induces deformations of soil that spread from the cavity and towards the surface forming a settlement trough. In urban zones, it is essential to control the volume and shape of the settlement depression in order to avoid damages on neighbouring buildings. This paper presents the case of the South Toulon tunnel, realized by a full-face excavation with soil reinforcement ahead of the face by a pipe umbrella and face bolting. This project shows how it is possible to regulate the tunnelling process (reinforcement and lining adjustments) by mainly considering the monitoring and the prediction of surface settlements. For this purpose a simple analytical equation, describing the development of surface settlements on the tunnel axis against the tunnel face progress, has been used. Some examples of this approach will be presented.

1 INTRODUCTION

The excavation of a tunnel produces a disequilibrium of the initial stress field in the ground mass, inducing soil deformation and settlements. Deformations of soil are triggered in the core ahead the tunnel face, and are later increased by the convergence of the excavated cavity. In urban areas, it is essential to control and minimize the settlements due to tunnelling in order to avoid damage on neighbouring buildings and other service networks. Therefore, predicting surface settlements becomes one of the most important key tasks in tunnelling process. For this purpose, some authors, as Dubois & Jassionnesse (1997), Serratrice (2002) etc, proposed different equations to model the progression of settlements on the tunnel axis for the 1st tube of the Toulon tunnel.

This paper reports data from the particular case study of the South Toulon tunnel. During its excavation, surface settlements are continuously monitored by automatic stations with a high frequency. The analysis of the measured movements shows that the development of surface settlements on the tunnel axis can be represented by a simple analytical equation based on few parameters. The adjustment of these parameters on the settlements observed ahead of the tunnel face leads generally to a quite accurate prediction of the settlement evolution with the tunnel progress and in particular its final stabilized value. This permits to continuously adapt the tunnelling process in order to avoid building damage and to optimize economically the pre-reinforcement.

Firstly, the principal characteristics of the South Toulon tunnel will be presented. Then, the study will focus on the method used to analyze and predict the ground displacements in order to optimize the tunnel progress. Some examples of this approach will be described as well.

2 SOUTH TOULON TUNNEL

The South Toulon tunnel will connect motorways A50 and A57 from Nice to Marseille (Fig. 1). It is parallel to the North tunnel previously built between 1994 and 2000. It has a 120 m^2 section and is 1820 m long. It is realized in an urban area with a limited overburden (about 35 m maximum). The tunnel construction presents many difficulties starting from the characteristics of crossed soils.

2.1 *Geology and geotechnical context*

One of the most important difficulties of this project is the Toulon geology. In fact, it is very heterogeneous at the tunnel face scale (Fig. 2) and

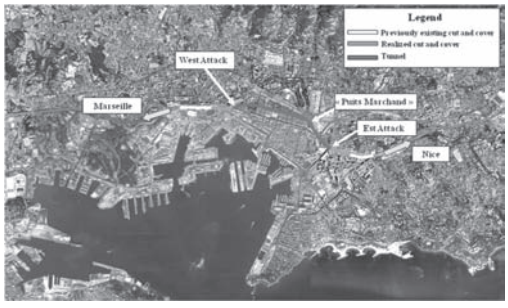

Figure 1. South Toulon tunnel location.

Figure 2. A South Toulon tunnel face.

along the tunnel layout. Thus, several geological and geotechnical investigations (sample and destructive drillings, pressuremeter tests ...) were performed. Such studies identified more than ten different soil types: altered and fractured quartzophyllites, Permian claystone, Gypsum, Trias limestone, Breccia, etc. Besides, the geological formations are often characterized by a thrust phenomenon.

Due to the geological heterogeneity and to the difficulty to make tests on undisturbed samples, the geotechnical model is not easy to define. For instance, for the quartzophyllites, only the Young modulus could be found from a statistic analysis of the pressuremeter tests. A value of 120 MPa is used in the preliminary project.

As a consequence of this high geological incertitude, horizontal drillings are done from the tunnel face during the tunnel progress as well. In addition, the geologists control and analyse the tunnel face after each excavation step before shotcreting.

2.2 *Excavation method*

Because of the high geology variation and in order to control the surface settlements, the ground mass ahead of the tunnel face was reinforced by a pipe umbrella and face bolting with different densities. Figure 3 shows one of the most common reinforcement profile used in the project. The Table 1 summarises the principle characteristics of reinforcement bolts (average values). In fact, density, length and renewal vary continuously depending on soil conditions and settlements previsions.

Face Bolts Fibre glass/Steel 18 0 4.5/9.

The excavation progresses generally by 1.5 m steps. After each step, one HEB 180 rib is installed and the unsupported soil is lined with shotcrete.

The tunnel invert (HEB 220) is realized either immediately or with a delay depending on ground deformations.

This excavation procedure is based on the so-called "ADECO-RS" method developed by Lunardi (2008). Lunardi understood that protecting and improving the strength and stiffness of the ground ahead of the tunnel face allows realizing full face excavations of tunnels even under difficult ground conditions. This methodology permits to increase tunnel stability and to reduce tunnel deformations and surface settlements in case of shallow tunnels.

In Lunardi's theory, the function of the prereinforcements ahead of the face is to prevent the loosening of the soil and is defined as "conservation" interventions. He describes two mechanisms of "conservation":

– Protective conservation: the reinforcements have to channel the stresses around the advance core in order to maintain the natural strength and deformation characteristics. In the case of Toulon tunnel, this role is played by the pipe umbrella.
– Reinforcement conservation: the reinforcements improve directly the natural strength and stiffness of ground in the core ahead of the tunnel face. Horizontal fibre-glass bolts are used for

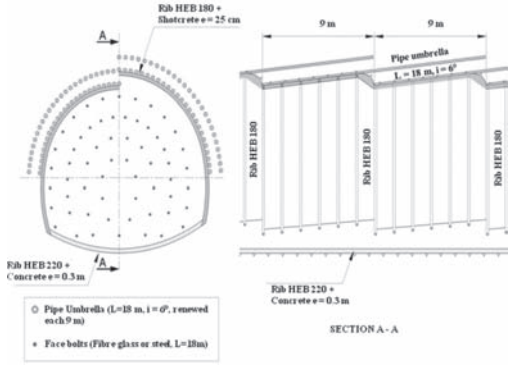

Figure 3. A common reinforcement profile of South Toulon tunnel.

Table 1. Reinforcement characteristics.

Reinforcement type	Material	Length (m)	Inclination (°)	Renewal (m)
Pipe umbrella	Steel	18	6/14	9
Face bolts	Fibre glass/steel	18	0	4.5/9

this purpose and they are one of the keys to the success of this technology. In fact they present high axial strength but they can be cut easily during the excavation.

The "ADECO-RS" approach can be summarized in two steps: a design stage and a construction one. The first phase consists in a geological and geotechnical analysis of the ground through which the tunnel passes and in the tunnel division into sections with uniform stress-strain behaviour. For each section, thresholds levels of deformations can be chosen depending mainly on the overburden, the geology and the buildings resistance, which are previously investigated. Then, considering such previsions, the type of reinforcement to apply has to be chosen. In the second step (the construction stage) stabilization works are set up based on design predictions. During the following phase, the continuous monitoring of the displacements in the tunnel and at the ground surface is essential (see Fig. 4).

The observed ground response is compared to the predicted one and necessary adaptations (on lining and prereinforcements) are done to guarantee the excavation stability and limit the surface settlements.

In the last twenty years, several examples have proved the validity of this approach: Rome-Florence rail line (1985), San Vitale tunnel (Italy, 1991), Tartaiguille tunnel in TGV rail line (France, 1998).

2.3 *Automatic system for settlement measurements*

Because of the complexity of the Toulon geology and the high urbanization above the tunnel layout, an automatic system of settlement measurements has been set up by SOLDATA. These measures are added to a regular control of tunnel displacements (convergence and face extrusion).

The principal objectives of such monitoring are the followings:

- to guarantee the short term tunnel stability and therefore the workers security;
- to verify the impact of excavation on buildings and to avoid damage;
- to assure the long term stability and serviceability of the tunnel.

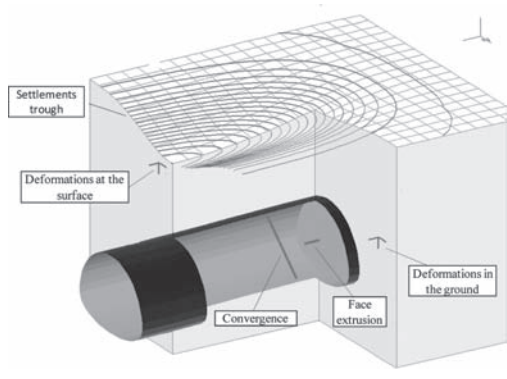

Figure 4. Ground deformations and surface settlements during the excavation of a shallow tunnel.

The settlements monitoring system consists in automatic stations that measure the ground surface and building displacements with a high frequency. A transverse profile is defined every 9 m along the whole tunnel layout. There are two different approaches (see Fig. 5). In order to measure the ground settlement, the automatic stations record the vertical movement of points positioned on a virtual horizontal grid without the need for targets. Thanks to these measures, the ground subsidence profiles can be plotted and the differential settlements, which cause the building structure damages, can be calculated. These data are collected once per day (CENTAURE system). The same stations can point at prism targets, fixed on buildings, and they record their movements in X, Y, Z directions. In this case the measure is recorded every two hours (CYCLOPE system). Table 2 summarises the different characteristics of the two measurement systems.

In order to avoid systematic errors, the total stations are regularly calibrated against prism targets considered fixed because far from the influence zone of excavation progress.

All data are immediately centralized in a geographical information system and recorded in a pc database. The database contains also tunnel displacements measures and other important information, such as geological tunnel face surveys, piezometric measurements and tunnel work timing.

Figure 5. CYCLOP and CENTAURE measurement systems (SOLDATA).

Table 2. Characteristics of the automatic measurement systems.

System	Measure directions	Frequency	Precision
CENTAURE	Z	1 measure/ day	+/– 0.5 mm
CYCLOP	X, Y, Z	1 measure/ 2 hours	+/– 0.5 mm

Thanks to a remote access, the project team can connect onto the site and observe the monitored data from their offices. Moreover, in order to facilitate the analysis of the measured movements, automatic curves are generated and available on the webpage. As far as the works security is concerned, two types of alarms can be automatically generated: in situ alarms (emergency lights and sirens) and e-mails sent to project participants. Thus, in case of unforeseen events, rapid action can be taken.

In Toulon project, the adjustment of the tunnel process is based mainly on the prevision of surface settlements development on the tunnel axis. The following section describes such methodology.

3 REAL TIME PREDICTION METHOD

The settlement trough caused by the tunnel excavation is tridimensional. The traditional methods of settlements previsions are based on the study of surface subsidence in a transverse section perpendicular to the tunnel axis. During the Toulon tunnel works progress, this analysis is regularly made, especially when the excavation concerns an urbanized zone. Nevertheless, the prereinforcement and lining adjustment are essentially based on the settlements previsions carried out from the movements observed ahead of the tunnel face. For this purpose, it is essential to find a formulation describing the development of surface settlements on the tunnel axis with accuracy.

3.1 *Models describing the settlements on the tunnel axis*

Figure 6 shows the settlements of three surface points directly above the tunnel axis against their distance from the tunnel face. The curves were done when the tunnel face was located at chainage PM 1081. The surface point PM 1095 is, in this example, 14 m ahead of the tunnel face and it settles down by 10 mm already. The point PM 1075 is 6 m behind the tunnel face with 25 mm of settlement. Finally, the movement of the point PM 1018, 63 m behind the tunnel face, is stabilized. The graph shows that more than 40% of surface displacements can take place ahead of the tunnel face. The curves evolve thanks to the new measures arriving with the tunnel face progress.

In order to make settlement previsions, it is necessary to find an equation that is able to describe the developments of surface settlements on the tunnel axis. Afterwards, the prediction method consists in calibrating the parameters of the model on the first settlements observed ahead of the tunnel face. This optimization can be repeated each time new data are collected. The final settlement prevision becomes therefore more and more accurate with the tunnel progress.

A normal exponential equation was used in some tunnel construction sites in order to describe the trend of settlements along the tunnel axis.

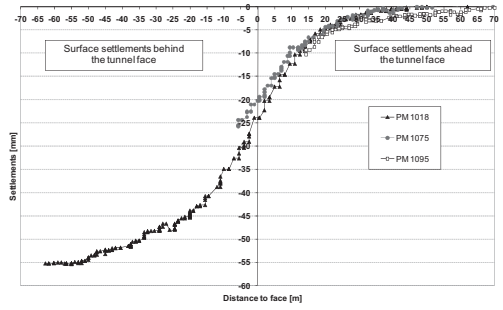

Figure 6. Settlements of three surface points caused by the excavation advancement.

Grasso & Pelizza (1994) analysed the settlements measured during the construction of Doria tunnel, in the Voltri railway layout. They concluded that it is possible to represent the settlements evolution against the distance from the tunnel face with an exponential equation depending on the tunnel overburden.

Dubois & Jassionnesse (1997) analysed the in-situ measurements of North Toulon excavation. Based on the Sagaseta (1987) method, they suggested that the settlement of a surface point, caused by the excavation of a section of the tunnel (source), is proportionally controlled by the displacements at the source and inversely proportional to the square of the distance between the point and the source.

Serratice & Magnan (2002) studied the settlements evolution (S) against the distance from the point considered to the tunnel face (x) in a section of the North Toulon tunnel. Starting from the Loganathan & Poulos (1998) approach, they proposed the following semi-empirical equations:

$$S(x) = 0 \quad \text{for } x > x_0 \tag{1}$$

$$S(x) = S_0 \cdot \left[1 - \exp\left(-A \cdot X^2\right) / \left(1 + X^2\right)\right] \quad \text{for } x < x_0 \tag{2}$$

with

$$A = \frac{a \cdot H^2}{\left(R + H\right)^2}, \quad X^2 = \frac{\left(x - x_0\right)^2}{H^2} \tag{3, 4}$$

In the previous equations, x_0 is the distance of the point at ground surface ahead of the tunnel face where the settlements start to appear. S_0 is the maximum settlement expected and R and H are respectively the tunnel radius and the tunnel depth. Finally, they calibrated the a parameter ($a = 0.25$). This model has the advantage to have only two unknown parameters, S_0 and x_0.

Bourgeois (2002) carried out three dimensional finite element analyses using the CESAR-LCPC code to simulate the North Toulon tunnel excavation. The following equations were suggested in order to represent the numerical results:

$$S(x) = S_f \cdot \left[1 - th(x/D_+)\right] \quad \text{for } x > 0 \tag{5}$$

$$S(x) = S_0 \cdot \left[1 + \left(S_f/S_0 - 1\right) \cdot \exp(x/D_-)\right] \quad \text{for } x < 0 \tag{6}$$

with

$$D_- = D_+ \cdot (S_0/S_f - 1) \tag{7}$$

In this case, S_f, S_0, D_+ represent respectively the settlement at ground surface directly above the tunnel face, the expected final settlement and the extent of the settlement trough ahead the face.

The Serratrice-Magnan and Bourgeois models were tested on the settlements trend on the tunnel axis, measured during the South Toulon tunnel excavation (see Fig. 7).

Nevertheless, another model is analysed as well. It is an empirical model based on the optimisation of exponential equations on in situ settlements measured in different projects, such as the Jubilée Line in London. The equation is the following (8):

$$S(x) = 0.5 \cdot S_0 \cdot \left\{1 - th\left[\left(\frac{k}{i}\right) \cdot x\right]\right\} \tag{8}$$

where

- S_0 is the estimated final settlement;
- the ratio k/i regulates the curve shape;
- i is the parameter used in the normal probability Gaussian function to describe the shape of the settlement trough in a transverse section (it correspond to the standard deviation and represents the distance from the point of inflexion of the settlement trough to the tunnel axis);
- k is a dimensionless parameter;
- x is the distance, at a given moment, between the point considered and the tunnel face.

In order to obtain a better approximation with the South Toulon data, the previous expression is modified, introducing an additional parameter a. It is a translational parameter that permits to modify the ratio S_{face}/S_0. Therefore, the equation becomes (9):

$$S(x) = 0.5 \cdot S_0 \cdot \left\{1 - th\left[\left(\frac{k}{i}\right) \cdot \left(x + a\right)\right]\right\} \tag{9}$$

The optimization by the least square method of three different models on stabilized points

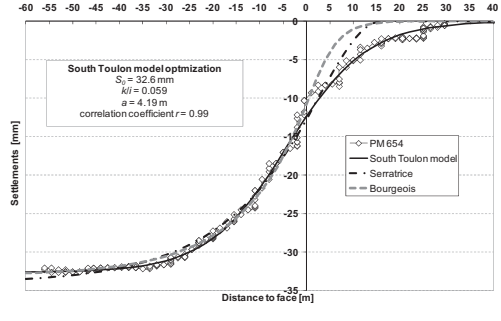

Figure 7. Optimization of three models on an example of South Toulon tunnel in situ settlement measurements.

shows that the modified approach proposed in Eq. 9 gives the best results in the particular case of the South Toulon tunnel. Therefore, it has been chosen to make the final settlement predictions.

In fact, as shown in the example on Figure 7, with both Serratrice-Magnan and Bourgeois models, it is possible to obtain a good approximation of the settlements progression behind the tunnel face ($x < 0$). Nevertheless, they are not able to represent the settlements ahead of the tunnel face ($x > 0$). On the other hand, the modified approach leads to a rather accurate estimation of the whole settlement evolution with the tunnel advance, by an adjustment of the 3 free parameters (S_0, ratio k/i and a) on the settlements observed ahead the tunnel face (Fig. 7).

3.2 *South Toulon tunnel settlement thresholds*

In the South Toulon tunnel project, the tunnel layout is divided in different sectors, each one characterized by three threshold levels (vigilance, anomaly and alert). These thresholds are related to the final absolute and differential surface settlements and depend mainly on the overburden, the geology and the buildings resistance.

In addition to the settlements predictions, the modified approach is also used, for each sector, to draw the three curves corresponding to the three settlement thresholds. In this case the S_0 parameter is imposed while the other two parameters (k/i and a) are chosen in order to fit the curve on the settlement trends of the sector concerned.

The real time comparison of the predicted settlement curves with the 3 threshold curves corresponding to the sector is the basic element of the adjustment of tunnel process.

In fact, the project contract imposes the following conditions:

- if the settlement prediction curves are above the vigilance threshold one, a reduction of the prereinforcement is recommended;
- if the settlement previsions exceed the anomaly curve and come close to the alert one, it is necessary to change the tunnel process, increasing for instance the prereinforcement, in order to limit further settlements and stay close to the anomaly threshold.

In order to economically optimize the works progress and, at the same time, to avoid building damages, the tunneling process has to be continuously adapted fitting the settlement evolutions on the anomaly curve. An example of this approach is presented in the following section.

3.3 *Example of tunneling process adaptation on settlements prediction*

Figure 8 shows the study on the settlements evolutions of a Toulon sector realized when the tunnel face was at point of advancement (PM) 820. This zone is characterized by the quartzophyllites.

The points at PM 766, 782, 802 started their settlement ($x > 0$) with a worrying trends next to the alert curve.

Besides, during the excavation from the PM 758 to PM 792, tunnel face instabilities often occurred. For all these reasons, in accordance with the project contract, the following modifications of the tunneling process were applied:

- the umbrella pipes were increased from 21 to 33 unit and their inclination moved from 14° to 6°;
- the face bolting was improved with 15 short autodrilling bolts, 9 m of length, grouted with resin;
- the face tunnel excavation was divided in 5 different steps in order to limit the instabilities.

These operations permitted to decrease the face tunnel instabilities but also to ameliorate the surface settlements evolution. In fact, the settlements trends of the analyzed points (PM 766, 782, 802) returned, in the left part of the graph, toward an acceptable tendency between the vigilance and anomaly thresholds curves.

After having passed this critical zone, the ground conditions improved. The settlements trends of the points above and ahead the tunnel face (PM 811, PM 818 and PM 829) ameliorated as well. As shown in the Figure 8, the prediction curve for these points, done when the tunnel face was at PM 820, led to a final settlement above the vigilance threshold. Therefore, the team project decided to modify once more the tunneling process in order to economically optimize the prereinforcement. The umbrella pipes were substituted with autodrilling bolts having a smaller inertia. In addition, the

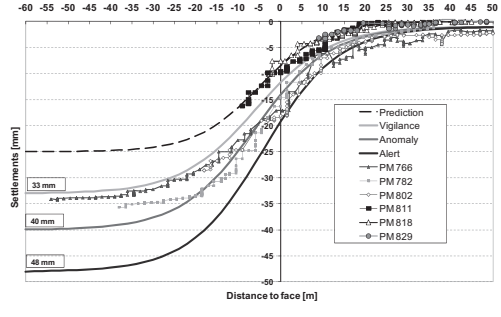

Figure 8. Example of tunnelling process adaptation on settlements predictions.

face bolting was lightened and the rib invert was suppressed.

3.4 *Surface settlements analysis in the transverse sections*

During the South Toulon tunnel excavation, in addition to the analysis of settlement evolution at ground surface directly above the tunnel axis, the trends of the surface subsidence in transverse sections have also been considered. Numerous studies (Peck 1969, Schmidt 1969, Attewell & Farmer 1974, Atkinson & Potts 1977, etc.) proved that the settlements (S) can be described with a good approximation using a normal probability Gaussian function (equation 10).

$$S(x) = S_{max} \exp\left(\frac{-x^2}{2i^2}\right) \tag{10}$$

where

S_{max}: maximum ground surface settlement above the tunnel axis;

x: horizontal distance to the tunnel axis;

i: standard deviation corresponding to the distance between the point of inflexion of the settlement trough and the tunnel axis.

It is very important to estimate the position of the point of inflexion. The i value identifies the area in which the settlements curve presents a curvature change and the slope (β) of the subsidence profile is maximum. Besides, it separates two zone of the soil: an extension zone over the convex parts of the settlement trough and a compression zone over the concave parts. The building is subject to different solicitations depending on its position in the above mentioned zones.

Different authors studied the effects of differential settlements on the buildings. The researches of Skepmton & MacDonald (1956), based on the observation of 98 buildings, showed that, to induce damage in the concrete structures, it is necessary to reach a value of β equal to 1/150. More cautious allowable values are proposed in Eurocode 7: β equal to 1/500 for framed structures in reinforced plugged concrete and 1/200 for open frames. These values were suggested by Polschin & Tokar (1957).

Figure 9 shows the example of the analysis of the movements measured in the Chalucet street, perpendicular to the Toulon tunnel axis. This zone is characterized by the quartzophyllites. The two different monitoring systems were available in this street. There were ground surface points on the street (CENTAURE) and targets points installed on the buildings (CYCLOP).

The optimization with the least squares method of the parameters of Peck's approach for the transverse trough has been conducted on both sets of values. In the Figure 9, the different buildings (C35, C60, etc...) are also shown with their respective positions relative to the tunnel axis. In both cases, the values of i are the same. With this value, it is possible to locate the two points of inflection of the settlement trough and compare them with the buildings position. The result is that, in the given example, the most critical consequences could appear at the contact between buildings C34 and C33 on the north side and between C60 and C59 on the south side of the tunnel layout. Nevertheless, in this case the maximum slope at inflexion point was low (1 mm/m) and no damage appeared in the buildings.

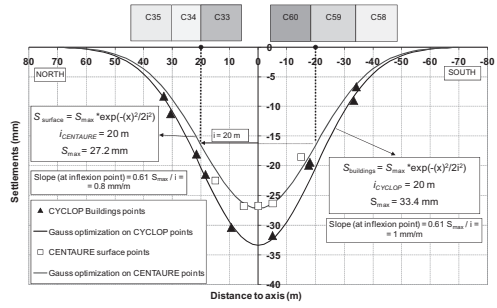

Figure 9. Gauss optimizations on transversal settlement measures.

Even if the buildings seem to follow the ground subsidence profile, the two optimizations diverge when getting close to the tunnel axis. The absolute settlements measured on the buildings are larger than those observed on the ground surface. This gap increases especially after the inflexion point. This phenomenon is probably caused by the weight and the low stiffness of the buildings.

3.5 *Differential settlements predictions*

As shown in the previous paragraph, it is essential to study the development of both differential and absolute settlements in order to avoid buildings damage. The differential settlement of a building is the ratio between the settlements difference of two target prisms fixed on its structure and the horizontal distance between them. The building size and position with respect to the settlement profile and its structure characteristics determine its differential settlement. As for absolute settlements, the project contract imposes three threshold levels of final differential settlements for each sector of Toulon layout. Therefore, it was necessary to elaborate a prediction method for this kind of settlements, as well.

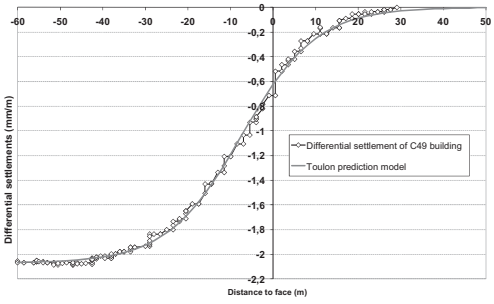

Figure 10. Model prediction of differential settlements.

The proposed approach for the prevision of absolute settlements on Toulon tunnel axis was tested on the differential settlements. The study revealed that it is possible to use the same model for the absolute settlements prediction.

As shown in the example below (Fig. 10), it is satisfying to substitute S_0 with the maximum predicted differential settlement ($S_{diff\ max}$) in the equation (9). The prevision method is the same of this for absolute settlements. The model is adapted on the first differential settlement observed ahead of the tunnel face. It is eventually optimized as soon as new measures are obtained. The final differential settlement prevision, which becomes more and more accurate with the tunnel progress, is compared with the project thresholds values. Therefore, different decisions can be taken in order to fulfil the project contract conditions.

4 CONCLUSION

During the excavation of urban deep tunnels, it is essential to control and reduce the settlements in order to avoid buildings damage. This paper proposes a method of settlements prediction based on a simple analytical equation. This equation has been validated by analysing the surface settlement caused by the excavation of the South Toulon Tunnel. The examples shown in this study prove that this model can be applied to both absolute and differential settlement previsions. The proposed equation proved to be a useful tool for the observational method during tunnel excavation. In fact, through this model, it is possible to continuously adjust the tunnelling process just by comparing the predicted settlements to the threshold values imposed by the project contract.

It could be interesting to test this equation on other tunnel projects in order to validate it. Besides, this could permit to find a relation between the model parameters (k/i and a) and the project features, such as the soil and the prereinforcement characteristics.

REFERENCES

Atkinson, J.H. & Potts D.M.1977. Subsidence above Shallow Tunnels. *Journal of Geotechnical Engineering,* Vol. 103: 307–325.

Attewell, P.B & Farmer I.W. 1974. Ground deformation resulting from shield tunnelling in London clay. *Canadian Geotechnical Journal*, Vol. 11: 380–396.

Bourgeois, E. 2002. Analyse numérique tridimensionnelle des tassements provoqués par le creusement d'un tunnel par la technique du prédécoupage mécanique – Application à la traversée souterraine de Toulon. *Bulletin des laboratoires des Ponts et Chaussées,* Vol. 237: 37–57.

Dubois, P. & Jassionnesse, C. 1997. The Toulon underground tunnel crossing. First feedback analysis carried out using on-site measurements. *Tunnel for people, Conference of the International Tunneling Association:* 157–162.

Grasso, P., Brino, L., Rabajoli, G., Astore, G., Pelizza, S. 1994. Metodologia per la previsione ed il controllo delle subsidenze. Un'applicazione: La Bretella di Voltri. *Gallerie e grandi opere sotterranee*, Vol. 43: 12–25.

Loganathan, N. & Poulos, H.G. 1998. Analytical prediction for tunnelling-induced ground movements in clays. *J. Geotech. Geoenviron. Eng.*, Vol. 124(9): 846–856.

Lunardi, P. (ed) 2008. Design and construction of tunnels–Analysis of controlled deformation in rocks and soils (ADECO-RS). Berlin: Springer.

Peck, R.B. 1969. Deep excavation and tunnelling in soft ground. *7th ICSMFE State of the art Volume:* 225–290.

Polschin, D.E. & Tokar, R.A. 1957. Maximum allowable non uniform settlements of structure. *Proc 4th Int. Conf. on Soil Mech. and Found.*, Vol 1: 402–405.

Sagaseta, C. 1987. Evaluation of surface movements above tunnels. A new approach. *Colloque Interaction Sols Structures:* 445–452.

Schmidt, B. 1969. Settlements and ground movements associated with tunneling in soil. *PhD thesis.* University of Illinois.

Serratrice, J.F. & Magnan, J.P. 2002. Analyse des tassements de surface pendant le creusement du tunnel nord de la traversée Souterraine de Toulon, *Bulletin des laboratoires des Ponts et Chaussées,* Vol. 237: 5–36.

Skempton, A.W. & MacDonald, D.H. 1956. Allowable settlement of buildings. *Proc. of Institute of Civil Engineering*, Part III, Vol. 5: 727–768.

Geotechnical Aspects of Underground Construction in Soft Ground – Viggiani (ed)
© 2012 Taylor & Francis Group, London, ISBN 978-0-415-68367-8

Backcalculation of internal forces in the segmental lining of a tunnel: The experience of Line 1 in Naples

E. Bilotta & G. Russo
University of Napoli Federico II, Naples, Italy

ABSTRACT: The prediction of the internal forces in the segmental lining of a bored tunnel is a rather complex task as they are significantly influenced by even apparently minor details of the installation process. Typically experimental researches on the performance of tunnel linings are based on monitoring the strains in the structural elements which are subsequently converted into forces. This last passage is not at all straightforward and the paper will deal with some of the difficulties encountered in carrying out such step for the data provided by a case history in Napoli. The twin tunnels of Line 1 Underground Extension in Napoli (Italy) were bored by EPB shields and lined with pre-cast reinforced concrete segments. Vibrating wire gauges were embedded in the segments of four lining rings and the strain values were recorded since the segments were concreted in the manufacturer's factory, during their installation in the tunnel and for several months afterwards. The back-calculated values of hoop forces and bending moments in the instrumented rings of the tunnel lining are reported and discussed in the paper.

1 INTRODUCTION

The design of a segmental lining for a tunnel excavated by a tunnelling machine usually requires consideration of the whole process of production and assembly of the segments as well as of the serviceability stage of the lining. Nevertheless, the common design practice assumes that the load history during installation does not influence the internal forces in the serviceability stage and that the former internal forces do not exceed the latter (Blom, 2002).

As the assembly of the lining is generally neglected in the design stage, an ideal situation is assumed as initial condition for conventional calculation, which is probably not realistic. Deformation and even cracking of the lining are sometimes observed during the installation stage, denoting a significant stress level in the lining, which is usually neglected in design calculations (Bakker and Bezuijen, 2009).

Monitoring the strains in a segmental lining during the whole construction process and later, during the lifetime of a tunnel, is therefore useful to gain a deeper knowledge of its real performance. Usually internal average forces are deduced by local strains measurements, even if such passage is not at all straightforward.

Accordingly, during the construction of an underground railway in Naples (Italy) the segments of four rings were instrumented to measure their strain history.

2 GROUND CONDITIONS

The twin circular tunnels of Naples Underground Line 1 extension were constructed at variable depth (maximum depth 45 m bgl) in various ground conditions.

A 1 km long initial stretch of the two tunnels was bored through alluvial sands and silty sands, below the groundwater table, starting from a shaft at about 17 m below the ground level. In this initial stretch the tunnels did not underpass any significant building. After this initial part the line enter into the Neapolitan Yellow Tuff, which is a soft rock usually underlying layers of sandy soils (Fig. 1). Both site and laboratory investigations were carried at the design stage. A limited overview of the average values of the deduced physical and mechanical properties of the sand is proposed in Table 1.

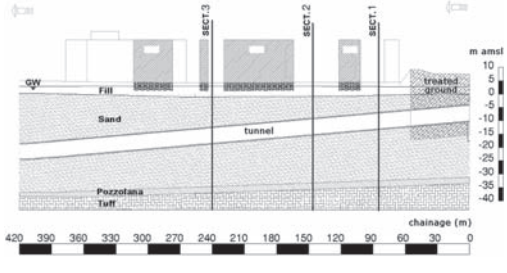

Figure 1. Ground conditions.

Table 1. Average values of geotechnical parameters for sand.

Dry unit weight, γ_d [kN/m^3]	15
Saturated unit weight, γ_{sat} [kN/m^3]	19
Permeability, k [m/s]	10^{-6}–10^{-7}
Cohesion, c' [kPa]	0
Friction angle, ϕ'	38°
Small strain shear modulus, G_o [MPa]	10 + 5z
Earth pressure coefficient, K_o	0.4–0.5

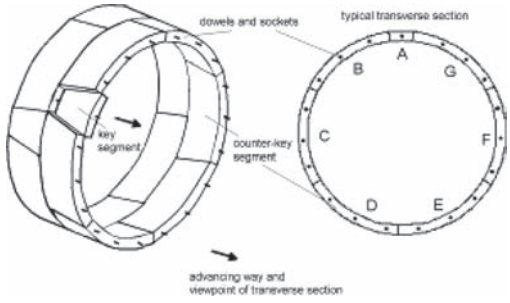

Figure 2. Sketch of the lining.

3 INSTRUMENTED LINING

The tunnels were bored by using two earth pressure balanced shields (D = 6.75 m) and installing a precast reinforced concrete segmental lining (5.85 m ID, 6.45 m OD). Each ring of lining consisted of seven segments, assembled as shown in Figure 2.

A system of sockets and plastic dowels was used along the transverse joints (i.e. between rings) to guarantee accurate positioning of the segments. The dowels had also a static role providing temporary support of the segments during ring completion and definitive link between adjacent rings. The segments were not connected along the longitudinal joints (i.e. in the same ring) where they were only provided with neoprene waterproof gaskets. These gaskets were eventually compressed when the key segment was fitted into place or later when the assembled ring was pushed out the shield and exposed to grouting and external soil pressure. The water tightness of the lining rely obviously upon such a compression.

The EPB machine advancement in the soil is granted by 19 hydraulic jacks separated in 7 groups which provide the needed reaction pushing against the rings already installed. Such longitudinal forces may get to very high values and represent a very important source of both strains and stresses in the lining as it will be shown in the following sections. The position of the jacks along the ring is shown in Figure 2. The experimental program concerning the observation of internal forces in the lining was based on the adoption of strain gauges in four independent rings of the lining. Vibrating wire gauges were embedded in the precast segments of the monitored rings. Two couples of gauges along the circumferential direction (1–2 and 3–4) were deployed in each segment except the key and a single gauge was installed perpendicularly (5), as schematically shown in Figure 3, where a picture of the steel cage of the instrumented segment is shown.

Hence, the strain values were measured since the segments were concreted, during their installation in the tunnel and for a long time afterwards. A total

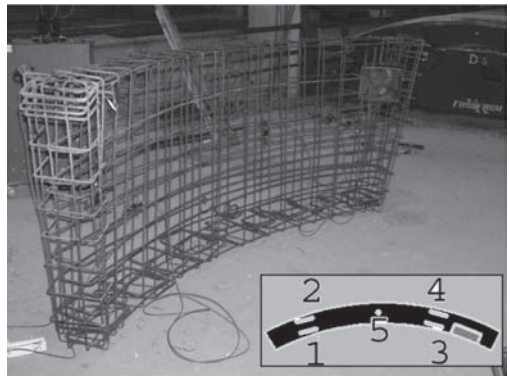

Figure 3. Layout of the vibrating wire gauges in a lining segment.

of 12 measurements of bending and hoop strain (gauges 1–2 and 3–4) and 6 measurements of longitudinal normal strain (gauges 5) were available for each instrumented ring. Each instrumented lining segment was individually tested before installation to check the measured strains with those computed under known load conditions (Bilotta et al., 2005). The locations of the two instrumented rings for each tunnel are shown in Figure 4 and described in Table 2.

The segments of the instrumented rings 3 and 4, both belonging to the north tunnel, which was excavated later than the south tunnel, were equipped with radio loggers. These enabled wireless data transfer during the segment lifetime including the assembly stage, when all the external cables had to be disconnected.

4 THERMAL EFFECTS ON VIBRATING WIRE GAUGES

The vibrating wire gauges are based on the principle that if the tensile stress in the wire increases,

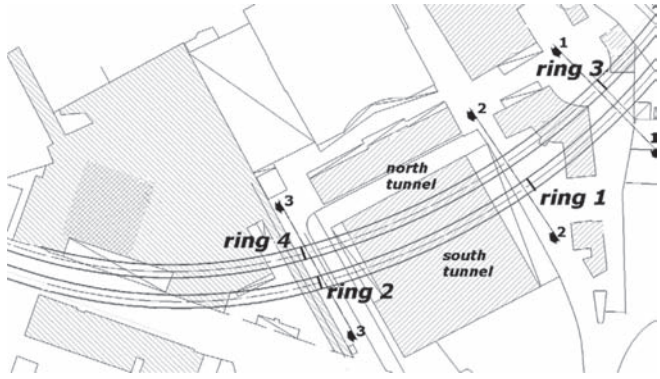

Figure 4. Plan view of the tunnels with the position of the instrumented rings.

Table 2. Position of the instrumented rings of lining.

Instrumented ring #	Monitoring section	Tunnel	Chainage (m)	Axis depth (m)
1	2	South	146	16
2	3	South	245	19.5
3	1	North	86	14
4	3	North	245	19.5

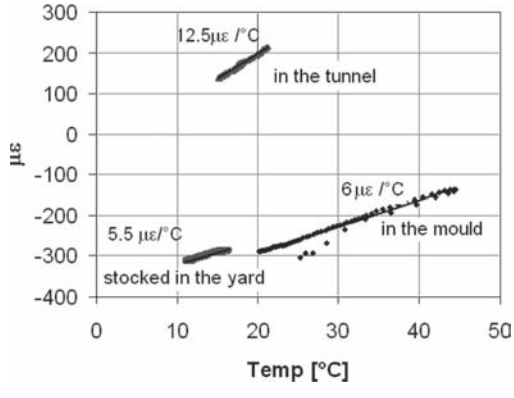

Figure 5. Strains *vs* temperature at various stages of the segment life (longitudinal gauge).

its resonance frequency increases as well. As this frequency can be measured by exciting the wire with an electric pulse, the gauge is in fact a stress indicator. Such a measurement is potentially self-compensated for temperature, provided that the thermal expansion coefficient of the structural element to which the gauge is linked is the same of the wire. However, if the strain of the structural element is the target quantity to know, a correction of the vibrating wire measurement may be needed, depending on how the structural element is constrained at the boundaries when the temperature change occurs (Russo, 2005). For this purpose temperature measurements are systematically recorded by thermocouple sensors embedded in the vibrating wire gauges.

The instrumented concrete segments were exposed to thermal changes both during the installation, mainly because of the grout reactions at the shield tail, and later on, when even the small seasonal temperature changes in the tunnel can introduce significant spurious effects on overall small strain changes (typically few tens of microstrains).

Due to the difference of the thermal expansion coefficient of the concrete segment and the steel wire (≈4–5 με per °C), an "apparent" compression of about 6 με per °C of thermal change was often measured at constant external loads. For very constrained conditions (i.e. for longitudinal gauges in the tunnel) such a compression increased up to 12 με per °C, which has to be interpreted as wire detensioning between "fixed" ends as far as temperature increases. For instance in Figure 5 the "apparent" compression of a longitudinal gauge is shown at three different stages of its life, corresponding to different degrees of restraint of the

concrete segment in which it was installed: when the segment was concreted in the mould (hydration heat), when it was stocked in the manufacturer yard (daily and seasonal temperature changes) and when it was installed in the tunnel (seasonal temperature changes). In the following sections the strains measurements were always purged by temperature effects.

5 STRAIN HISTORY

A data logger embedded in each instrumented segment allowed the measurements to be taken with a constant pre-set frequency. Wireless technology used only for the loggers embedded in the segments of the instrumented rings 3 and 4 allowed the data to be recorded at any wished time with out-of-sequence scanning. Such a feature was particularly useful to manually control the strain measurements during the assembly of segments inside the shield and throughout the following tunnelling operations. For the limited space of the paper just an example of measurements taken during installation is given in Figure 6 with reference to the haunch segment D of the ring 3, which is numbered as 70 in the construction sequence of the north tunnel.

The strain values shown in the figure were zeroed before the segment was erected and corrected for temperature, as it increased of about 10°C around the ring due to the heat developed by grouting hydration reaction occurring at the shield tail. The measurements plotted against the time in the figure refer to the assembly of ring 70 and cover also the installation of the subsequent rings from 71 to 74, including the drilling periods in-between (see the arrows). When the TBM advanced for the excavation, it applied through the jacks a significant thrust on the assembled ring. As shown in the figure, the jack forces acting on the segment D induced a high longitudinal compression (Fig. 6b) and a decompression in the circumferential direction (Fig. 6a). Such a Poisson effect was rather evident in the initial stages reported in the figure as the ring was nearly free to expand inside the shield. As far as the instrumented ring approached the shield tail, compressive circumferential strains prevailed over the Poisson effect (Fig. 6a). The latter almost disappeared once the ring left the shield tail and was radially loaded by the backfill grout first and by the earth and water pressure later.

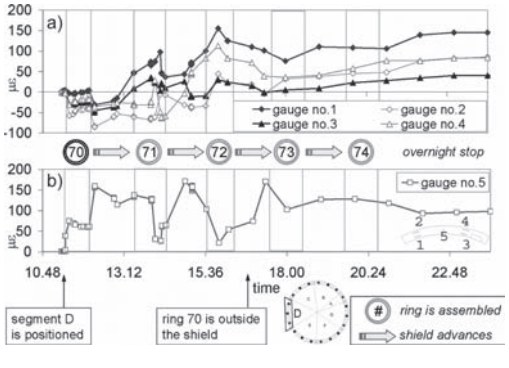

Figure 6. Typical strains measured during installation: (a) circumferential; (b) longitudinal.

It is evident that before being loaded by the surrounding ground the segments underwent a complex strain history due to the ring assembly. The magnitude of the overall measured strains as shown in the figure is not that large, hence the need to apply temperature corrections on the gauge readings. During the installation of the instrumented ring the geometry of the structural system changes and, particularly, both the loading system and the degree of restraint of each single segment change. Even for such reasons the back-calculation of average internal forces in the final lining starting from strain measurements may present some difficulties. This issue will be discussed in the next section.

6 INTERNAL FORCES

Usually internal bending moments and hoop forces in the sections of a lining are simply obtained using the beam theory starting from the strains measured along the circumferential direction only, i.e. neglecting the coupling between such strains and the rather large longitudinal forces applied by the hydraulic jacks due to Poisson effect. Obviously in a point of an elastic three dimensional body subjected to a general state of stress the strain along one direction depends on the values of three principal normal stresses acting in the same point. As demonstrated by Blom (2002) in a similar problem, concerning a full segmental lining tested in a laboratory, the coupling with the third principal direction of the problem—i.e. the radial direction—can be neglected. Accordingly, the diagram of the normal circumferential stresses in concrete, σ_c, was assumed as linear and defined through the two values, acting along the fibers of gauges nos. 1 (or 3) and 2 (or 4):

$$\sigma_{c,1} = \frac{E_c}{\left(1-\nu_c^2\right)}\left(\varepsilon_1 + \nu\varepsilon_L\right) \tag{1a}$$

$$\sigma_{c,2} = \frac{E_c}{\left(1-\nu_c^2\right)}\left(\varepsilon_2 + \nu\varepsilon_L\right) \tag{1b}$$

where ε_1 and ε_2 are the strains measured by the circumferential (or transversal) gauges nos. 1 (or 3) and 2 (or 4) and ε_L should be the longitudinal strain measured at the same location of the gauges 1 and 2 (or 3 and 4).

In this case this last strain was not directly measured. Blom (2002) analysing by FEM a single segment of the lining subjected to three-point load representing the jack forces showed that (Fig. 7):

a. the longitudinal strain is maximum along the direction of the point load;
b. in the mid transverse section of the segment the longitudinal strain decreases almost to zero at the centre between two subsequent forces.

Being the geometry of the segments and of the point load very similar but not exactly the same to that analysed by Blom, it was decided to adopt two different and extreme assumptions when using the equations 1a) and 1b):

1. the longitudinal strain ε_L was assumed equal to the value measured by the longitudinal gauge no. 5, ε_5—i.e. maximum value (hyp. 1);
2. the longitudinal strain ε_L was assumed equal to zero—i.e. approximately the minimum value calculated by Blom (2002) or, in other words, the assumption correspond to neglect the coupling Poisson's effect (hyp. 2)

In the application of the equations 1a) and 1b) the Young's modulus was assumed equal to $E_c = 30$ GPa while the Poisson's ratio, ν_c, was assumed equal to 0.2. Furthermore a tensile strength of the concrete has been considered in the back-calculations as the stress corresponding to –100 με. Passing from circumferential strains to bending and hoop forces the contribution of the steel cage bars was calculated from the values of strain in the concrete measured at the gauges (assumed equal to the strain of the corresponding steel bar) and using $E_s = 210$ GPa.

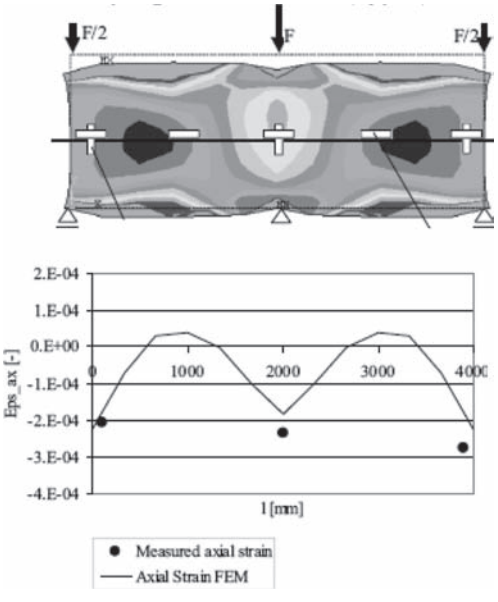

Figure 7. FEM calculations of longitudinal strains in a segment subjected to three-point load (after Blom, 2002).

The amount of data available for the four instrumented rings even in the long term is noticeable and a more extensive and detailed report will be published elsewhere. It was decided to dedicate this paper only to show and discuss, for all the four instrumented rings, the significant effects of different assumptions and procedures when deriving internal forces.

For such a reason the strains measured and adopted for internal forces back-calculations refer only to a single date approximately corresponding to the full completion of the tunnel stretch, that is about 5 to 7 months after the ring installation. Therefore the external loads on the ring can be surely considered as completely developed. Available long term measurements show some minor creep effects which will not be discussed here.

The values of the strains are the increments from the initial condition assumed as that one just preceding the segments erection in the shield. The measurements were also corrected for temperature effects, as briefly discussed at §4.

The back-calculated values of hoop force, N, and bending moment, M, are plotted as grey or white diamonds in Figure 8 versus the angle θ measured along the ring no. 1 counterclockwise from the hauch (at the tunnel axis level). The grey diamonds ('exp 1') correspond to the previously discussed hypothesis 1 while the white diamonds ('exp 2') correspond to the hypothesis 2.

The trend of the experimentally derived internal forces is not significantly affected by the two different assumptions. It can be noted a very high value of hoop force N (Fig. 8a) at least in one point and many points where the hoop force is very low or even null. Rather low values of bending moments were generally back-calculated along the ring with most of the values falling in the range of ±50 kNm (Fig. 8b).

Even being the trend rather similar the two different hypotheses on the coupling of the longitudinal and circumferential strains produce along the ring differences between the deduced internal forces as high as 30–40%.

In the same Figure 8, two different theoretical calculations are also shown for comparison. Such calculations were performed assuming a bedded

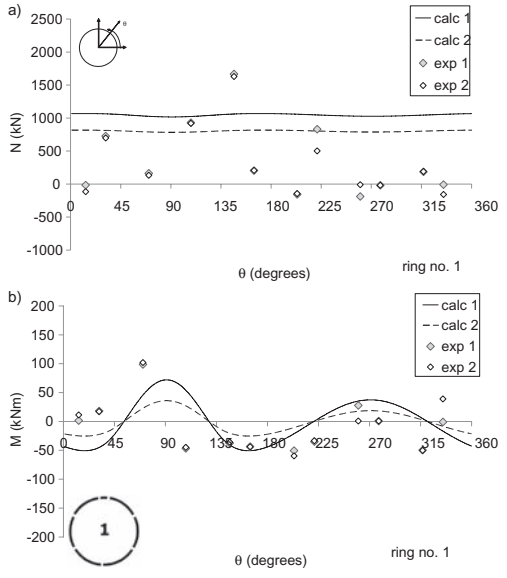

Figure 8. Hoop force N (a) and bending moment M (b) in ring no. 1—Back-calculation and theoretical predictions.

ring model for shallow tunnels, that is without tension bedding at crown (Schulze & Duddeck, 1964). An equivalent elastic Young's modulus for soil, E_s, over the likely range of shear strain around the tunnel (10^{-2} % and 10^{-1} %), was assumed as corresponding to $E_s = 40$ MPa.

As the lining ring is made of segments, a reduced flexural stiffness was assumed for the equivalent structural section of the ring, estimated in about one half of the full value for the single segment, according to widely used expressions depending on the number of segments and the geometry of the longitudinal joints (e.g. Muir Wood, 1975; AFTES, 2001).

Constant hydrostatic pressure, u, and an anisotropic ($K_0 = 0.5$) distribution of effective stress, $\sigma'(\theta)$, were assumed around the tunnel lining. The latter can be defined according to a deconfinement ratio, λ, as:

$$\sigma'(\theta) = (1-\lambda) \cdot \sigma_o'(\theta) \qquad (2)$$

where $\sigma_o'(\theta)$ is the initial litostatic stress.

The deconfinement ratio λ at the TBM's tail is a function of the shield geometry, of the applied earth pressures at the shield face and of backfill grout pressure at its tail. Considering the values of the face and backfill pressures measured during the excavation, in the calculations with the theoretical model λ was assumed as ranging between 0 ('calc 1') and 0.5 ('calc 2'). Full bond was assumed between the ground and the lining, although the real behaviour would be dependent on a complex interaction between the soil, the pre-cast concrete segments and the backfill grout.

Figure 8a shows that both the theoretical predictions are not able to reproduce in detail the backcalculated values of hoop forces, their variation along θ and, particularly, the extremely low values almost everywhere along the invert. On the other hand, the prediction of bending moments (Fig. 8b) is more satisfactory since both their magnitude and their distribution along the ring show a better agreement with the experimental results.

Similar plots are shown in the following Figures 9, 10 and 11 for rings nos. 2, 3 and 4 respectively.

The back-calculated values of hoop forces in ring no. 2 (Fig. 9a) are very high, even when compared with the upper values obtained by theoretical calculations—i.e. with $\lambda = 0$ ('calc 1').

As shown in Table 2 the section 2 is deeper than the section 1 the depth difference being only about 20%. The locally deduced values of hoop forces starting from the measured strains in the lining have an average value along the full lining which is between two and three times that corresponding to the ring 1. Of course higher values of the backfill grout pressures around the ring 2 might have occurred and partially explain such differences. Unfortunately the grout pressure data are not available in all the instrumented rings thus it is

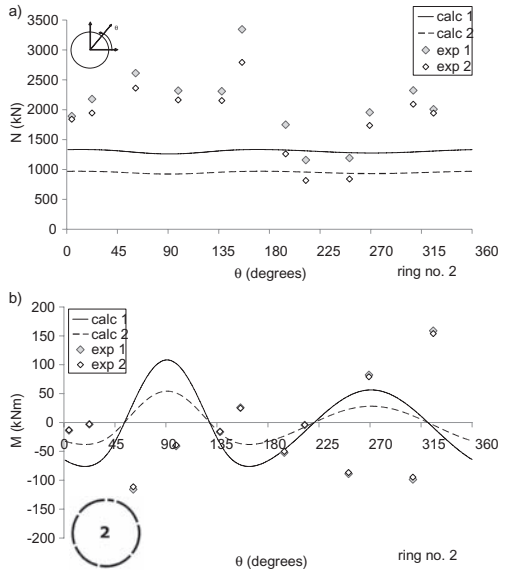

Figure 9. Hoop force N (a) and bending moment M (b) in ring no. 2—Back-calculation and theoretical predictions.

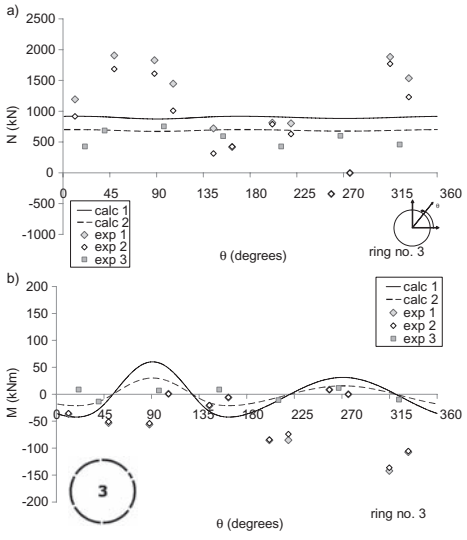

Figure 10. Hoop force N (a) and bending moment M (b) in ring no. 3—Back-calculations and theoretical predictions.

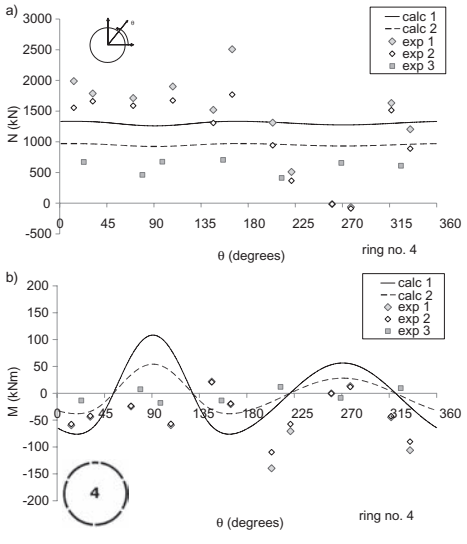

Figure 11. Hoop force N (a) and bending moment M (b) in ring no. 4—Back-calculations and theoretical predictions.

not possible to discuss on the influence of such a factor. On the other hand the back-calculated experimental bending moments in the same ring (Fig. 9b) are in better agreement with the theoretical calculations at least in terms of their magnitude, In such a case most of the experimental values fall in the range ± 100 kNm. As for ring 1, however the experimental values and calculations show rather different distribution along the lining.

In Figure 10a and 11a the back-calculated values of hoop forces in rings no. 3 and no. 4 are finally reported; the bending moments in the same rings are plotted in Figure 10b and 11b.

For such rings a further procedure for the back calculations of hoop forces and bending moment was added ('exp 3').

The new procedure aimed to derive the values of the internal forces at the interface between each couple of adjacent segments, instead of those acting in the section where the vibrating wire gauges were installed.

As discussed in section 5, the measurements during the installation showed that significant strains arose in the segments during the assembly process and before the ring left the shield. Detailed informations on such preliminary strains are available only for rings 3 and 4 which were equipped with radio loggers.

In order to explicitly consider such stage in the back-calculations, the boundary value problem of assembling a ring of the lining must be faced and solved. In such a problem only a vector of five strains at five points per segment is known at each stage, while the loading vector has a variable number of components as the assembly process proceed (jack thrusts, eccentric forces acting along the longitudinal joints, shear forces transmitted through the dowels along the transverse joints, backfill grout pressure around the ring) with the most of these components substantially unknown. Thanks to the wireless logging system installed in the segments of the two rings no. 3 and no. 4, the strains measurements were taken at the most significant stages of the installation, enabling at least to establish a clear link between measured strain vectors and geometric partial configuration of the assembling ring. The numerical problem was then solved by Pepe (2008) which reports the results for the two rings. Further details on the procedure may be found in that work.

The results of such incremental back-calculation, considering each stage of the assembly process, are shown in Figures 10 and 11 with grey squares ('exp 3'). The same procedure also enabled the back-calculation of the internal forces which stemmed in the lining from the assembly process, on the basis of the strains measured in the lining when the ring was assembled inside the shield. Although for space limit reasons further details on the procedure are not provided, it is worthy mentioning that, at the end of the assembly of the instrumented ring, the internal forces in the lining were highly variable, resulting very high inside each segment and practically null at

the interface between each couple of adjacent segment.

Such a result of not having any significant interaction between each couple of adjacent segments when the ring is completed could be determined at the design stage by prescribing the tolerances to be allowed between the segments during their assembly in the shield. Furthermore, although the mechanical tolerances can be strictly prescribed during the prefabrication of the segments, those involved with their assembly are usually entirely managed by the operators of the TBM during the construction process. As stated by Blom (2002), and confirmed by the Authors' experience, in this kind of lining the segments are generally installed in place rather smoothly, i.e. without generating significant interaction forces between pairs of adjacent segments. Only the key segment, which is also the final one, may be forced in the tight gap left to complete the ring: in such a case, the operator increases the jack thrust out of the ordinary, causing even evident damages (visible cracks) to the adjacent segments.

The values of the forces at the interface between adjacent segments plotted in the Figure 10 and 11 ('exp 3') only arised as a result first of the interaction between the rings deforming outside the shield and the instrumented ring inside the shield and later as the influence of the interaction between the same ring and the external soil with the interposed backfill grout. In the Figures 10 and 11 also the two sets of experimental back-calculated internal forces labelled 'exp 1' and 'exp 2' are reported. They were obtained with the same procedure described for the ring 1 and 2. With reference to these first two sets the same comments already reported for the ring no. 2 are possible. The two extreme hypotheses on the value of the longitudinal strain along the segment lead to quite different values of hoop forces, the difference being as high as 30–40%. The differences on the bending moments are less significant but not at all negligible. In both cases the average hoop force along the lining is much higher than that predicted by the theoretical calculations while a better agreement can be found for the bending moment. On the other hand the internal forces derived at the interface between the segments with the third back-calculation procedure ('exp 3') using the same measured strains show less scatter along the lining, and, above all, exhibit an average value which is significantly lower than the calculated values.

The Authors believe that the somewhat discouraging picture described until now with:

i. very large differences between the forces derived by different procedures applied to the back-calculations starting from the same experimental strain data;

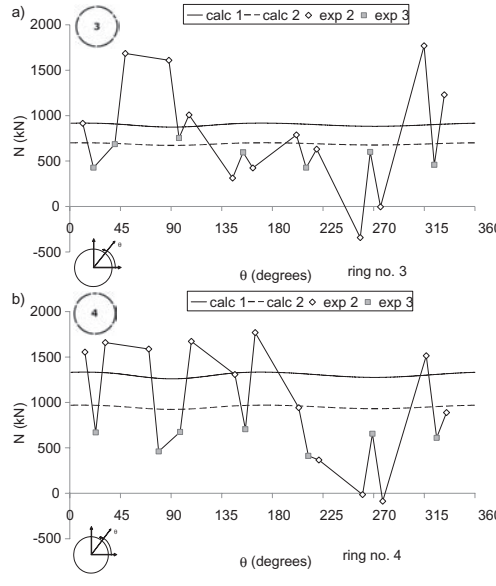

Figure 12. Hoop forces along the lining of the ring no. 3 and no. 4.

ii. theoretical calculations which do not show a true satisfactory agreement with none of the experimentally derived distribution of internal forces;

can largely change if simply the set labelled as 'exp 1' (or 'exp 2') on one side and the set labelled as 'exp 3' on the other side are considered together and not as alternative. In such a case for instance, for the ring 3 and 4 the hoop forces derived by the known strains could be represented as in Figure 12.

The figure shows that hoop forces are highly variable along the lining or, better, inside each segment the lining is made of. The theoretical calculations carried out with simple methods fail in predicting such a high variability being completely neglected the assembly stage; on the other hand the average value of the hoop forces produced by the theoretical calculations are indeed in good agreement with the average experimental value of the hoop forces along the lining if the overall experimental distribution reported in Figure 12 is considered.

7 CONCLUSIONS.

The paper reports the results of the back-analysis of the strains measured in four instrumented rings of the segmental lining of the two tunnels of the Line 1 Underground Extension in Napoli (Italy). The main issues related to the instrumentation, the

data processing and the back-calculations procedures were discussed.

The segmental nature of the lining and the relative assembly process was shown to be responsible of highly variable distribution of the internal forces in the lining. Without taking into account both these aspects neither the internal forces derived by the strains measurements nor the theoretical predictions can be considered as reliable and realistic.

The fundamental role played by the innovative technology of the wireless logging in two out of the four instrumented rings was shown: this technology allowed a clear correspondence to be established between real time logged data and geometrical configurations of the lining segments, during the quick assembly process when no wire connections were allowed for.

The observed high variability of strains and stresses in these lining types suggest also the use of a higher number of strain gauges within an instrumented section, with more gauges dedicated to the measurements of longitudinal strains.

Furthermore, should the distribution of internal forces like those reported in Figure 12 be confirmed by further experimental or numerical investigations, the ordinary methods adopted for the calculations of the forces in the lining at the design stage should be largely revised.

REFERENCES

AFTES (2002). Recommendations on the convergence-confinement method. Tunnels et ouvrages souterrains (174): 414–424.

Bakker K.J. and Bezuijen A. (2009). Ten years of bored tunnels in The Netherlands: Part II, structural issues. Geotechnical Aspects of Underground Construction in Soft Ground—Ng, Huang & Liu (eds). Taylor & Francis Group, London. 249–254.

Bilotta E., Russo G., Viggiani C. (2005). Ground movements and lining strains during an underground tunnel construction in cohesionless soil in Naples. Proc. Int. Geotechnical Conf. on Soil-Structure Interaction: Calculation Methods and Engineering Practice, St. Petersburg, Russia, V.M. Ulitsky (ed.), ASV Publishers, Saint Petersburg-Moscow, Vol. 1, pp. 59–64.

Blom, C.B.M. (2002). Design philosophy of concrete linings for tunnels in soft soils. PhD Thesis, Technical University of Delft. DUP Science. Delft, The Netherlands.

Muir Wood, A.M. (1975). The circular tunnel in elastic ground. Géotechinque 25(1):115–127.

Pepe, G. (2008). Rivestimenti di gallerie in conci prefabbricati: sperimentazione e analisi. PhD Thesis, University Federico II of Naples (in Italian).

Russo, G. (2005). Some considerations from the strain measurements in the precast RC lining of the tunnels of Line 1 Extension in Naples. Workshop on Excavation in urban areas of historical and archaeological interest. Naples, 15–17 December 2005. http://www.geotecnica.unina.it/British-CRUI%20 WS2005/russo.pdf.

Schulze, H. and Duddeck, H. (1964). Spannungen in schildvorgetriebenen Tunneln. Beton- und Stahlbetonbau 59(8): 169–175.

This page intentionally left blank

Geotechnical Aspects of Underground Construction in Soft Ground – Viggiani (ed)
© 2012 Taylor & Francis Group, London, ISBN 978-0-415-68367-8

Backanalysis of measured movements in ageing tunnels

C. de Santos, A. Ledesma & A. Gens
Technical University of Catalunya, UPC, Barcelona, SPAIN

ABSTRACT: The paper describes a procedure to perform backanalysis in a systematic manner in the context of ageing tunnels. Basically the input data include information on relative displacements or deformations of specific points in the lining of a tunnel exhibiting long term movements and the objective of the procedure is to identify a set of parameters that characterize the surrounding soil and the lining properties. Any damage in the infraestructure should give a change in those parameters identified. The analysis should be able to obtain useful information for the manager of the tunnel, in terms of maintenance, repair of some sections, warning in case of danger, etc. The paper presents the basic theory of parameter identification and an application to the backanalysis of a tunnel section from London Underground, where some measurements of rotation of lining segments are available.

Keywords: Inverse analysis, tunnels, ageing.

1 INTRODUCTION

The work presented in this paper has been developed in the context of the European Science Foundation Project "Micro-Measurement and Monitoring System for Ageing Underground Infrastructures". The research project focus on the monitoring of the deterioration of underground structures by means of new technologies based on wireless sensor networks, including computer vision and miniature electromechanical sensors. Ageing of tunnels is observed as a deterioration of the lining in most cases. Opening of cracks, strains or relative displacements or rotations between two points constitute typically the main variables that can be measured on the lining surface. Other basic measurements like pore water pressures in the surrounding soil or absolute displacements could be considered as well in further developments.

All the data provided by these sensors must be gathered and stored in a comprehensive database. Due to the large amount of data involved, a postprocessor is required, in order to provide to the manager responsible for the maintenance a first insight into the overall behaviour of the infrastructure.

After identifying the most critical sections, it is necessary to perform a more sophisticated analysis in order to relate the damage with a cause. If the reason for that damage is not found out, it will be difficult to make appropriate decisions. This is often a difficult task due to the nature of the failure modes, involving complicated interactions between the underground structures and the adjacent ground. Therefore, it is necessary to analyze the mechanical response of the underground structure and the surrounding soil. There are several commercial codes based on the finite element method that can assist in that task. They usually solve the problem in a direct manner; that is, given a particular geometry and a set of parameters, they predict the stresses and strains of the structure. However, in this case field measurements constitute the input data, and the manager of the system would expect an assessment of the integrity and properties of the materials involved. This is in fact an inverse problem, in which mechanical parameters are estimated from measurements as strains or relative displacements.

The estimation of soil and rock parameters based on field instrumentation data is a traditional and a common procedure in Geomechanics. However, the use of optimization techniques to perform backanalysis in a more systematic manner is a relatively recent development (Gioda & Sakurai, 1987). From a mathematical point of view, the identification of parameters results in a minimization problem. Nowadays, the use of system identification and optimization techniques allows the performance of this type of analyses in a more rational and objective manner. Examples of backanalysis in the context of tunnel excavation problems are described in Ledesma et al (1996, 1997) and Gens et al (1988, 1996) among others. In those works, a maximum likelihood approach is presented to estimate the required parameters. The main difficulty when estimating parameters is that several combinations of them may give similar results in terms of measurement variables and therefore the solution is not unique. Because of that, part of

the research in this field has been devoted to the improvement of the optimization process itself. A recent example of identification in Geomechanical problems using genetic algorithms has been presented by Levasseur et al (2008).

This paper presents an example of backanalysis performed using field data from an old tunnel in the context of the research project mentioned above. First, a basic theory about parameter identification is presented. Then, a real case involving a tunnel section in London Underground is described. In this case, ageing is due to consolidation and drainage of the surrounding soil. The Ko parameter and the stiffness of the joints between lining segments have been identified. In fact, both parameters are very difficult to measure and this type of techniques could be very useful in practice.

2 BACKANALYSIS PROCEDURE

It is assumed that a fixed and deterministic model relates a set of variables x and a set of parameters p. Some of the variables x are measured and form the vector of measurements x^*. The best parameters are those that minimize the difference between measured and computed variables. A simple procedure to establish that, is defining the so called "objective function", F:

$$F = \sum_{i=1}^{m} (x_i^* - x_i)^2 \quad (1)$$

where m is the number of measurements. F represents the error between the measurements and the same variables computed with the model, computed using a least squares criterion. Expression (1) can be generalized when measurements are not independent or have different errors (Ledesma et al, 1996). Note that F is a function of the parameters, as x = M(p), where M represents the model. Minimizing F will provide with the set of parameters that best simulate the measurements obtained.

It should be pointed out that F depends in a nonlinear manner on the parameters. The model M is usually represented by a Finite Element analysis. Even when a linear law is used, the objective function, F, is nonlinear with respect to the parameters p. That makes difficult to find the minimum of F. When only one or two parameters are identified, a simple inspection of the values of F may be enough to estimate the minimum. This has been the case in the example described in this paper. Moreover, the plot of the objective function is useful to understand the sensitivity of measurements to the parameters considered in the analysis. However, if more than two parameters are involved, then it is more convenient to use any suitable minimization algorithm.

In general it is necessary to choose between methods that only need evaluations of the function and methods that also require computations of the derivative of that function. Algorithms using the derivative of the objective function are expected to be more powerful than those using only the values of the function itself, but they may be generally more time consuming. A combination of both approaches can be also a good strategy in complex problems.

3 APPLICATION TO AGEING TUNNELS IN LONDON

3.1 *Site description*

The application of the backanalysis procedure outlined above refers to a particular section in the Northbound tunnel of the Jubilee Line, between Baker Street and Bond Street in London Underground, built in the seventies using a shield.

In the simulation, both tunnels have been taken into account, although only measurements from the Northbound tunnel have been considered in the backanalysis procedure. This is because ageing on those tunnels is apparently due to the consolidation and drainage of the surrounding soil (Shin et al., 2002) and, therefore, both tunnels must be considered in the geometry for the analysis.

The Northbound tunnel has a diameter of about 4 m and was excavated mainly in London clay. Lining is made of 22 concrete segments in most of the tunnel. Ring 960 was surveyed and it has been considered as the "section analysis" in this work.

Some ageing effects have been detected in this section including rotations between segments and loss of circularity. The geotechnical profile includes the following layers, from top to bottom (Fig. 1):

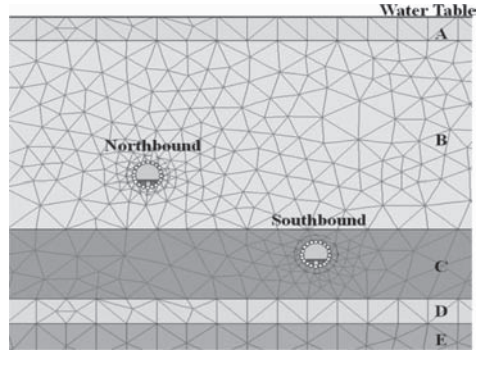

Figure 1. Geotechnical profile. See text for soil description.

– 4 m of gravel and coarse material (Layer A)
– 31.5 m of London Clay (Layer B)
– 11.5 m of red clays from the Lambeth Group (Layer C)
– 4 m of a carbonate sand (Layer D)
– Chalk as base rock (Layer E).

Table 1 presents a summary of the main parameters required in the hydro-mechanical analysis performed. They have been obtained from different sources: Tube Lines (2004, 2006a, b), Koungelis & Augarde (2004), Addenbrooke & Potts (2001), Shin et al (2002) and Wongsaroj et al (2007).

3.2 *Measurements available*

Figure 2 presents a picture of the tunnel in the area of interest, and Figure 3 shows a sketch of the cross section including the slab for the tracks and labels for the segment joints: A–N. The segments have the following properties (Tube Lines, 2006a):

– EA = 2,520E06 kN/m.
– EI = 5927,04 kNm²/m.
– Segment thickness d = 0,168 m.
– Poisson's Ratio ν = 0,2.

where E is the Young modulus, A the cross section area and I the inertia. Measurements available refer to the rotation between segments due to the movements of the lining. Probably the initial shape of the lining when constructed was not circular (Lyons, 1979) but it is difficult to distinguish between original imperfections and movements produced along time, as only one set of displacements has been measured and compared with the theoretical circular shape.

The measurements available give the rotation between two contiguous segments, ϕ, as depicted in Figure 4. That rotation originates a displacement of the contact point between segments, which is known as "eccentricity" ("c" in Figure 4). Values of "c" for all the joints indicated in figure 3 (A–N) have been used as main data in the identification process.

3.3 *Identification of parameters*

The direct problem has been analyzed by using the Finite Element Code "Plaxis" (version 8 in 2D). Figure 1 shows the finite element mesh used in the simulations. As this analysis is focused on the inverse problem, a simple constitutive law was selected for the direct problem. In this case, an elastic—perfect plastic law based on Mohr-Coulomb and available in Plaxis was used. First, the initial stresses are generated assuming a Ko parameter in advance. Then the tunnel is excavated, installing the lining and computing for equilibrium after release of the initial stresses. We have used an additional contraction loss of the lining corresponding to a volume loss of 1.4%, in order to take into account the effect of the shield (gaps, open excavation, installation of segments, etc), just during construction. That value is just an estimation based on experience. After that state, drainage is allowed, and a fully drained analysis is performed, keeping constant the water table and the hydraulic conditions in the geometry. Future improvements of the model will include the consideration of the actual groundwater history in the zone.

For the inverse problem we have considered the Ko parameter of London clay and the stiffness of the joints as the main parameters to be identified. On the one hand, the stiffness of the segment joints with respect to rotation is a difficult parameter to know in advance and therefore a backanalysis constitutes the only manner to obtain a consistent value. On the other hand, the Ko parameter, although well known for London clay, has an important influence on the deformed shape of the linings.

Table 1. Parameters considered.

Parameters	Gravel	London clay	Lambeth group (clay)	Lambeth group (sand)	Chalk
Dry soil weight γ_{Dry} (kN/m³)	17	18	18	17	18
Sat soil weight γ_{Sat} (kN/m³)	20	20	20	20	20
Permeability K_x (m/day)	1	1E-05	1E-05	0,5	1E-05
Permeability K_y (m/day)	1	5E-04	5E-04	0,5	5E-04
Young's modulus E (kN/m²)	5280	20000 + 3200 z	200000	30000	20000000
Poisson's ratio ν	0,32	0,2	0,2	0,3	0,2
Cohesion c′ (kN/m²)	–	15	15	–	400
Friction angle φ′	35	25	27	34	40
Effect stress ratio K_0	0,5	Variable	1	1	1

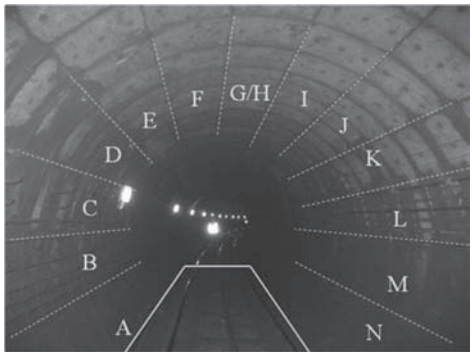

Figure 2. Picture of the tunnel.

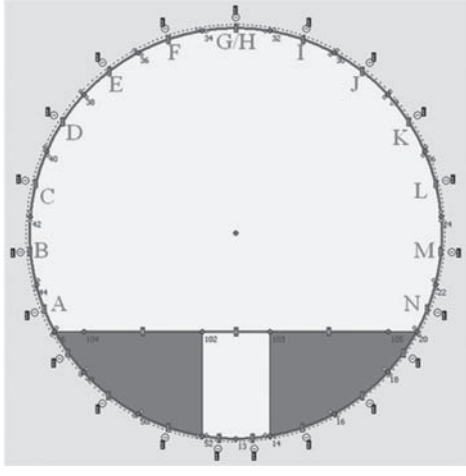

Figure 3. Cross section of the tunnel.

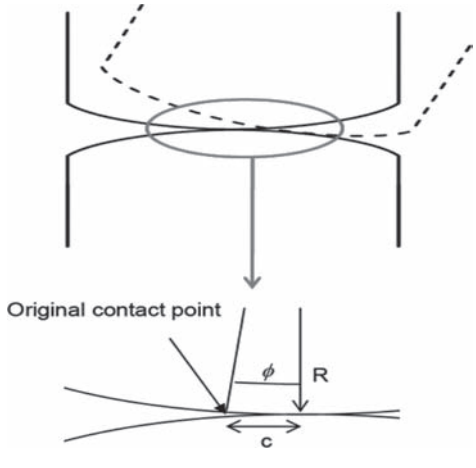

Figure 4. Rotation between two segments ($c = R\phi$).

The objective function adopted for this case, F, had the following expression:

$$F(Ko,Cr) = \sum_{jo\,\mathrm{int}\,A-B}^{jo\,\mathrm{int}\,M-N} \left(\frac{x^*}{d} - \frac{x_{Plaxis}}{d} \right)^2 \qquad (2)$$

where x_{plaxis} refers to the eccentricity values obtained from the direct analysis using Plaxis and x^* corresponds to the measured eccentricities ("c" in figure 4). Also, "d" is the segment thickness (used to make the error dimensionless) and Cr the joint stiffness for rotation.

A first analysis was carried out considering a fixed value of Ko and identifying the minimum of "F" with respect Cr. The range of stiffness studied was between 0 (free joint) and 10^7 kNm/rad/m which corresponds to a rigid joint for all practical purposes. Values of Ko were 0.5, 1, 1.5 and 2. In this case, "F" depends on one variable only, and it is easy to plot the objective function and to obtain the minimum by simple inspection. Figures 5–8 present the objective function depending on Cr, for the different values of constant Ko adopted. Note that all of them show a minimum for Cr values close to 10000 kNm/rad/m. In fact, for greater values of Cr, the objective function does not show important changes, suggesting that after that value, joints are stiff enough and the problem becomes not sensitive to any further change. It should be pointed out also that the effect of Ko seems to be less important than expected, as all figures show a similar pattern. Thus segment rotations are not too sensitive to changes in Ko.

A second analysis was performed considering both, Cr and Ko, as parameters to be identified. In this case several combinations of Cr and Ko were used to solve the direct problem, and then the objective function (2) was computed. In this manner it was possible to plot that function and to obtain the minimum by direct inspection also. That is, a minimization algorithm was not required in this problem. Figure 9 presents that function for

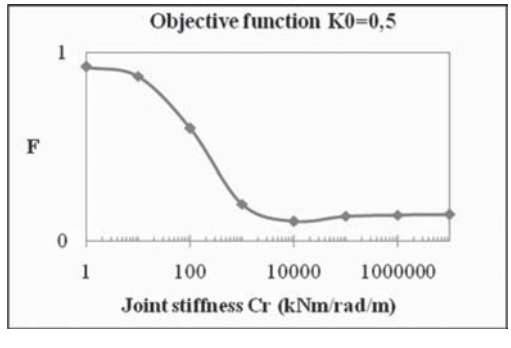

Figure 5. Objective function ($K_0 = 0,5$).

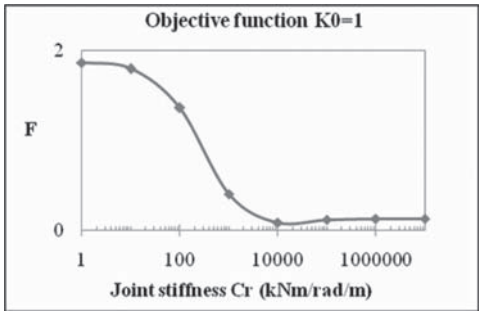

Figure 6. Objective function (K_0 = 1).

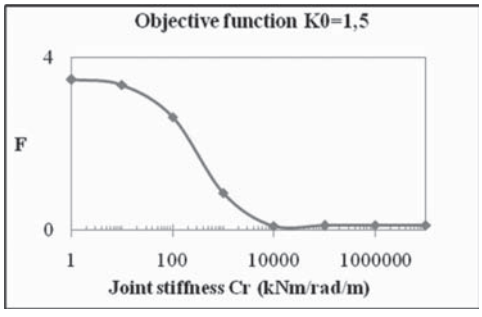

Figure 7. Objective function (K_0 = 1,5).

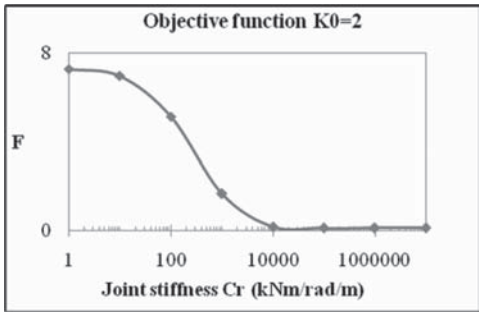

Figure 8. Objective function (K_0 = 2).

this case. Obviously the result should be similar to that obtained in the first series of analyses. Now the minimum is found for a value of Cr close to 10000 kNm/rad/m and a value of Ko = 1.5. This value for the earth pressure coefficient at rest is quite common in many Finite Element analyses involving London clay. Therefore, this result is consistent with the previous experience available. For the joint stiffness, however, the previous knowledge is scarce, and the value obtained constitutes a good estimation to be considered in further finite element analyses.

Figure 10 shows a comparison between measured eccentricities (average values over 6 rings) and the computed ones using the parameters identified (Ko and Cr). Despite the discrepancies, the model captures the main trends of the measurements. However, there are some simple expressions (3) to determine the stiffness of the joints between lining segments (Blom, 2002).

$$Cr = \frac{bl^2 Ec}{12} \tag{3}$$

where *Cr* is the stiffness of the joint, *b* is the width of the ring, *l* is the contact length between lining segments and *Ec* is the elasticity modulus of concrete. This expression shows the importance of the contact between segments, related to the quality of construction. Every segment was built one by one and every contact length could be different. For this reason it was considered the case where all stiffness of joints are independent. Table 2 shows the joint stiffness values and the contact length for every joint computed using (3), whereas Figure 11 shows a comparison between measured eccentricities in one ring and the computed ones using the values from Table 2 with Ko = 1.5. To check the values which were used in this part of the analysis it was assumed a maximum stiffness joint value of *Cr* = 35280 kNm/rad/m, which corresponds to the values from expression (3) with *l* = 168 mm (segment thickness). Most of the joints fulfilled this restriction except joints K–L, L–M and M–N.

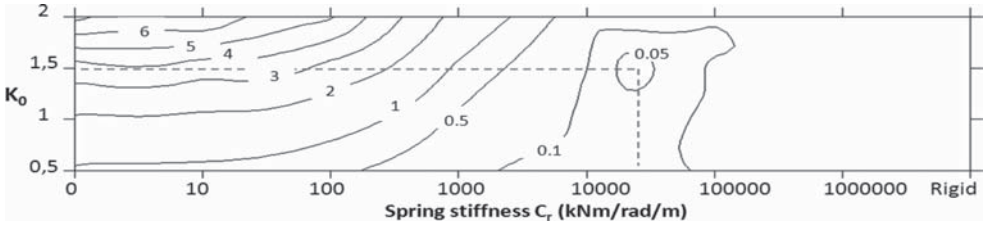

Figure 9. Objective function F(Cr, K_0).

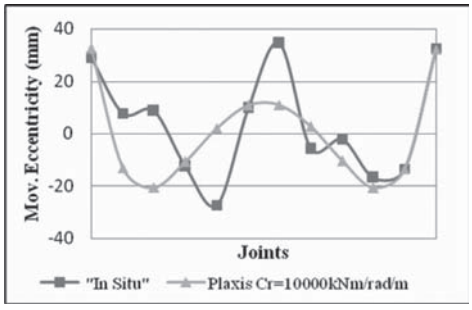

Figure 10. Comparison between measured eccentricities and the computed ones using the parameters identified (Ko and Cr).

Table 2. Joint stiff values and contact length for each joint.

Joint	Cr (kNm/rad/m)	L (m)
A–B	8800	0,084
B–C	19000	0,123
C–D	15000	0,109
D–E	20000	0,126
E–F	7000	0,075
F–G/H	3200	0,060
G/H–I	8200	0,081
I–J	10000	0,089
J–K	12000	0,098
K–L	Rigid	–
L–M	Rigid	–
M–N	Rigid	–

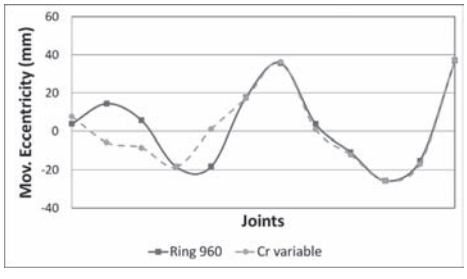

Figure 11. Comparison between measured eccentricities and the computed ones using the parameters identified (Ko and Cr variable).

4 CONCLUSIONS

The paper presents an example of estimation of parameters from measurements from the lining of ageing tunnels. This process is expected to be performed in an automatic manner in order to assess the evolution of the lining of tunnels undergoing deterioration. Inverse problem techniques can be used in this process as they have proven to be efficient in Geomechanical problems. The identification of Ko and the joint stiffness of a segmental lining has been performed from measurements of rotations between segments in a real case involving a tunnel in London Underground. Joint stiffness is particularly difficult to measure in practice and may be related to lining deterioration. In this respect, a systematic application of the identification of parameters techniques, constitute a useful tool for the safety assessment of old tunnels.

ACKNOWLEDGEMENTS

The work described in this paper has been carried out under the framework of the European Science Foundation Project "Micro-Measurement and Monitoring System for Ageing Underground Infrastructures". Also, the Spanish Research Agency has funded this research (codes BIA2006-27031-E and BIA2008-06537) and therefore, both institutions are acknowledged with thanks. The authors also gratefully acknowledge the information and assistance provided by Mr. Peter Wright (Tube Lines, London) and London Underground Ltd.

REFERENCES

Addenbrooke, T.I., Potts, D.M. (2001). Twin Tunnel Interaction: Surface and Subsurface Effects. The International Journal of Geomechanics. 1(2): 249–271.

Blom, C.B.M (2002). Design philosophy of concrete linings of tunnels in soft soils. PhD thesis. Civil Engineering Department of Delft University of Technology.

Gens, A., Ledesma, A., Alonso, E.E. (1988). Back analysis using prior information—Application to the staged excavation of a cavern in rock. Numerical Methods in Geomechanics, Swoboda ed., Innsbruck, Balkema, p. 2009–2016.

Gens, A., Ledesma, A., Alonso, E.E. (1996). Estimation of parameters in Geotechnical Backanalysis—II. Application to a tunnel excavation problem. Computers and Geotechnics, 18:29–46.

Gioda, G., Sakurai, S. (1987). Back analysis procedures for the interpretation of field measurements in Geomechanics. Int. J. for Numerical Analyt. Methods Geomech., 11:555–583.

Koungelis, D.K., Augarde, C.E. (2004). Interaction between multiple tunnels in soft ground. Proc.18th Australasian Conference on the Mechanics of Structures and Materials, Perth, Australia, Taylor and Francis. 2:1031–1036.

Ledesma, A., Gens, A., Alonso, E.E. (1996). Estimation of parameters in Geotechnical Backanalysis—I. Maximum Likelihood Approach. Computers and Geotechnics, 18:1–27.

Ledesma, A., Romero, E. (1997). Systematic backanalysis in tunnel excavation problems as a monitoring technique. Proc. 14th Int. Conf. Soil Mech. Found. Engng. Hamburg, Balkema, 3, p. 1425–1428.

Levasseur, S., Malécot, Y., Boulon, M., Flavigny, E. (2008). Soil parameter identification using a genetic algorithm. Int. J. for Num. Analyt. Methods Geomechanics. 32(2):189–213.

Lyons, A.C. (1979). Construction from Baker Street to Bond Street exclusive and from Admiralty Arch to Aldwych. Proc. Instn Civ. Engrs, 1:375–394.

Shin, J.H., Addenbrooke, T.I., Potts, D.M. (2002). A numerical study of the effect of roundwater movement on long-term tunnel behavior. Géotechnique, 52(6):391–403.

Tube Lines (2004). Characterisation of London Clay. Internal Report: GCG-L001-N416-DTAAWP2-TUN-RPT-00001.London.

Tube Lines (2006a). Deep Tunnel Assessment Report in accordance with LUL Engineering Standard E3322, A2 October 2000. Internal Report: TLL-F042-N416-DTATT408-TUN-RPT-00001. London.

Tube Lines (2006b). Development of Assessment Criteria for Expanded Concrete Linings. Internal Report: TLL-L001-N416-DTAAWP2-TUN-RPT-00004. London.

Wongsaroj, J., Soga, K., Mair, R.J. (2007). Modelling of long-term ground response to tunneling under St James's Park, London. Géotechnique. 57(1):75–90.

This page intentionally left blank

Geotechnical Aspects of Underground Construction in Soft Ground – Viggiani (ed)
© 2012 Taylor & Francis Group, London, ISBN 978-0-415-68367-8

Modelling and monitoring of a urban underground excavation

A. Cantone
Department of Civil Engineering, II University of Naples, Italy

R. Fico
Structural & Geotechnical Designer Collaborator, Naples, Italy

F. Cavuoto
Structural & Geotechnical Designer, Naples, Italy

A. Mandolini
Department of Civil Engineering, II University of Naples, Italy

ABSTRACT: The highly urbanization of the area where Montesanto Station (Naples, Italy) is located and the need to guarantee the transportation service to travellers during the works gave birth to the plan of the combined use of 3D numerical analyses and the real time monitoring of significant parameters (displacements, strain, stresses and temperature) to confirm the set of design criteria assumed and calibrate the design parameters affecting the problem faced. The 3D analyses simulated the step by step excavation predicting the stress-strain behaviour; hence the comparison of the analytical predictions with the corresponding values derived through the monitoring (238 points being monitored) allowed to calibrate the model as the excavation advanced, thus refining the analysis itself and improving the safety level.

1 INTRODUCTION

The Montesanto Station of Cumana Railway Line, owned by S.E.P.S.A. ("Limited Public Service Company"), is located in the very historical hearth of Naples (Italy) and can be deemed a critical junction of the city transportation network, given the closeness both to the Montesanto Station of the cable railway line and to the Montesanto Station of Metro Line 2, a few meters far on the West side (see Fig. 1).

Since 2004 expansion works are in progress at the Station in order to build, what is more, a pedestrian tunnel providing an alternative exit to travellers from the two lines currently in service (Cumana and Circumflegrea Lines). The highly urbanization of the area where the opera is located, the nature of soils crossed, and mostly the need to guarantee the transportation service to travellers during the works, gave birth to the plan of different measures to protect the existing tunnels and to soil improvements in the excavation area.

The design of the technical interventions that could minimize the effects of the excavation on the existing tunnels was carried out by means of both 2D and 3D numerical analyses. In order to control the proper execution of the ongoing works and to verify the adequacy of the design solutions adopted, an intensive monitoring activity was planned under the supervision of the Civil Engineering Department (DIC) of the Second University of Naples: a monitoring system based on the observation method was thus contrived;

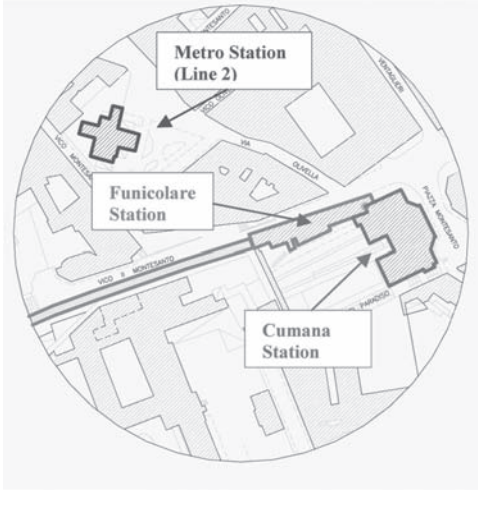

Figure 1. Location of Montesanto Station.

starting from the data collected through the monitoring (sidewalls displacements, stress state in the liners, etc), the numerical model selected for the design analyses was controlled or calibrated, if necessary; in the latter case, a new verification of the design solutions adopted would have been achieved and more appropriate auxiliary solutions would have been set.

2 DESCRIPTION OF THE OPERA & WORK CHRONOLOGY

The 40 m long, 7 m large pedestrian tunnel will be perpendicular to the two upper tunnels in service (see Fig. 2a); the distance between the upper rails and the design tunnel crown will be of just 3.5 m (see Fig. 2b); the connection of the pedestrian tunnel with the station outside will be guaranteed by escalators, therefore a 30° sloped 8 m diameter tunnel has been already constructed (see Fig. 2c), turning into a big service tunnel (11 m diameter) when going down at the design tunnel depth.

The intervention area soil, upper than the water table, is rather heterogeneous: the descending tunnel housing the escalators and the big connection service tunnel lie within a region made of Neapolitan yellow tuff, whereas the tunnel to build will lie in pyroclastic sand (except for a short first portion). The excavation, carried out by employing the traditional technique (by cutting and temporary supporting with steel arches and shotcrete, before the permanent concrete casting) will be executed after the accomplishment of different soil improvements: a ring of sub-horizontal metallic pipes in the crown (7° sloped, 10 m long), 5.5 m overlapped with those installed in the previous step; the excavation ground will be improved by glass-reinforced plastic nailing (20 mm diameter, 12 m long); jet-grouting sub-horizontal columns will support the pre-support bases. Moreover, consolidation interventions have been already executed to sustain the top tunnels sidewalls, by means of 10 m long micro-piles; a 0.60 m deep parterre on piles has been also constructed to sustain the rails.

The excavation of the descending tunnel started on Oct. 4, 2005 and was completed by Sept. 2006 (see Fig. 3), whereas the big service tunnel was completed by Dec. 2006. In the early 2007 the first connection portion with Metro Line 1 was built; the concrete casting of the as built tunnels was carried out before the excavation of the pedestrian tunnel. However, many works slowdowns occurred mainly due to the complexity of the specific yard position.

In April 2008 the construction of the pedestrian tunnel below the two railways started. According to the design, 7 advancement steps had to be performed: a first 6 m advancing step, five further 4.5 m steps, and a final 6 m step. At each step, before cutting and placing the pre-support liner, the soil improvements were accomplished, while the permanent reinforced concrete liner was planned to be cast in place backwards after reaching the dig bottom, in order to speed up the advancement, given the reduced room available.

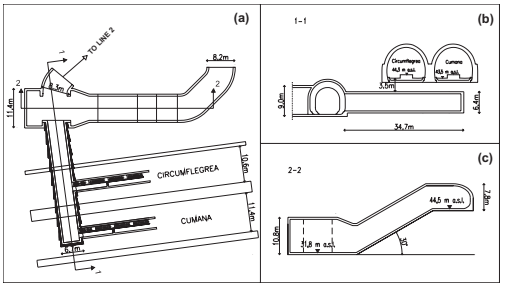

Figure 2. Pedestrian tunnel views: (a) plan; (b) section 1-1; (c) section 2-2.

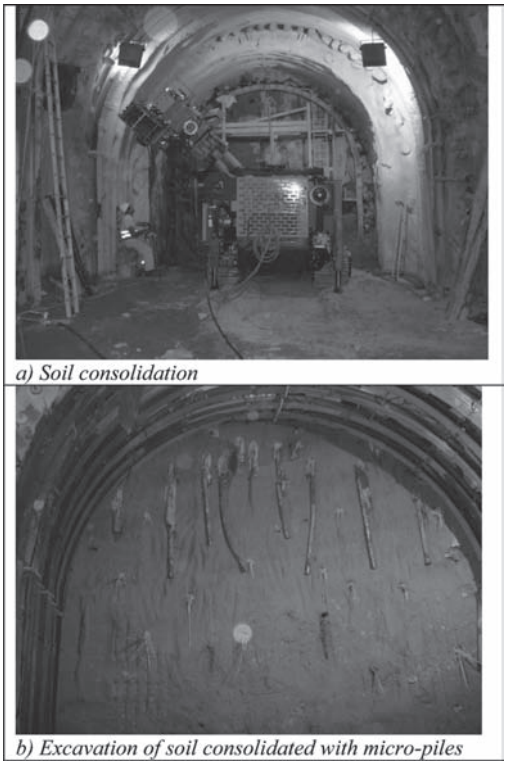

Figure 3. Tunnel excavation snapshots.

The last excavation step was completed at Dic 1, 2008. The activities were very complex, due to both the reduced room available (Fig. 3a) and the need to manually carry out the cutting of the sub-vertical micro-piles consolidating the ground from the sidewalls and the foundation slab of the upper tunnels, where these were interfering with the excavation front (Fig. 3b).

3 ANALYSIS

The numerical analyses were based on both two-dimensional and three-dimensional simulations, performed by means of *Plaxis2D* software and *FLAC3D* software, respectively; given the complexity and the significance of the project, the two-dimensional-based design assumptions were confirmed and refined with the 3D analyses. In particular, the *FLAC3D* is an explicit finite-difference program for engineering mechanics computation that can simulate the behavior of three-dimensional structures built of soil, rock or other materials that undergo plastic flow when their yield limits are reached. The full dynamic equations of motion are used, even when modelling systems are essentially static; this enables *FLAC3D* to follow physically unstable processes without numerical distress.

The model assumed in the *FLAC3D* is constituted by a $72 \times 40 \times 50$ m^3 parallelepiped, having 8 different solid groups, each with different and specific mechanical properties (see Fig. 4); besides the modelling of the different types of soil and the structural elements of the existing tunnels (*tuff*), the step by step soil improvements foregoing the tunnel excavation have been integrated as well. All the mentioned groups are characterized by the Mohr-Coulomb constitutive model.

Several parametric analyses were performed in order to weigh the main variables affecting the simulation; in particular, the elastic modulus of the pyroclastic sand E_s was assessed; the geotechnical investigation lead to assume a value of E_s ranging between 50 and 100 MPa; within this range the displacement derived with the analyses varied of about 5 mm, whereas for $E_s > 100$ MPa the displacement variation highly reduced.

The results that were finally accounted for correspond to $E_s = 100$ MPa, considered the most reliable value according to the experimental campaign previously performed; the displacement of the four sidewalls relating to the Circumflegrea and the Cumana Lines tunnels were thus derived, together with the corresponding stresses; moreover, a further inspection was provided by the stress analysis of the temporary support of the design tunnel.

The displacements of the most relevant points on the existing tunnels (corresponding to some of the points monitored, see next section) were derived for each of the 7 advancing steps;

Table 1 reports the vertical (w) and the horizontal (u) components of the estimated displacements relating to the four sidewalls of the two existing tunnels caused by the excavation occurring beneath (the values are ordered by following the excavation advancement direction).

Table 1. Displacement of sidewalls relating to the existing tunnels: Circumflegrea (Circ.) and Cumana (Cum.)

		Circ.		Cum.		Circ.		Cum.	
		w (mm)				u (mm)			
Step	d (m)	1	2	3	4	1	2	3	4
0	0	0	0	0	0	0	0	0	0
1	6,0	17,6	12,9	13,0	14,9	4,2	5,4	3,9	6,3
2	10,5	21,4	13,0	13,1	15,0	4,7	5,4	3,9	6,4
3	15,0	21,6	13,6	13,5	15,0	4,8	5,7	3,6	6,6
4	19,5	21,6	17,2	15,4	15,3	4,6	6,1	2,7	6,8
5	24,0	21,7	19,5	19,6	15,6	4,8	5,3	2,7	6,8
6	28,5	21,7	19,9	20,5	15,6	5,0	5,0	3,1	6,8
7	34,5	21,8	20,0	20,5	18,8	5,0	5,0	3,0	7,5

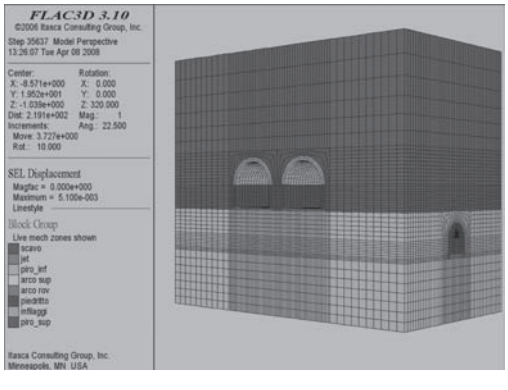

Figure 4. *FLAC3D* model view.

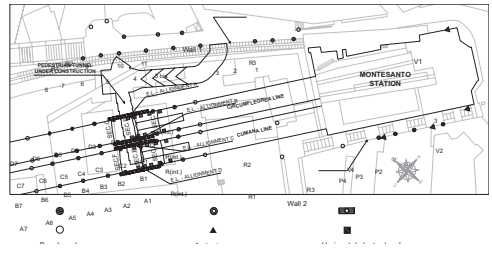

Figure 5. Monitoring system scheme.

4 MONITORING AND CONTROL PLAN

The monitoring and control plan (see Fig. 5) is given by two independent measurement systems, one automatic the other manual.

The automatic system provides the control of vibrations, movements and stresses variations induced in the liners by the excavation operations: the first is based on the use of 4 speedometers laid on structures placed both outside and inside the station; the second is based on the employment of 56 electro-levels (36 horizontal and 20 vertical) to control the sidewalls movements, placed on a 18 m long line along the new tunnel axis; the third system is based on the use of load cells inserted within the existing tunnels liners and on vibrating wire gauges installed on both the tension and the compression sides of the pre-support steel arches of the pedestrian tunnel. In particular, to control the stress state of the existing tunnels liners, 4 monitoring sections are identified, two for each tunnel, each one having 5 load cells; as for the control of the stress state in the pre-support liner of the pedestrian tunnel, five sections were instrumented, each one having 6 control points, with a total of 12 gauges per section liner.

In February 2007 two cracks-gauges were installed as well, in order to monitor the opening over time of a crack occurred on Vicereale Wall, retaining the cable railway line.

All sensors installed converge into automatic switchboards that record the data at time intervals scheduled depending on the excavation operations and via modem transfer them to the Administration, to Building Contractor Bureau, and to the DIC.

The manual system is given by a network of benchmarks and optical surveys: 40 measurement benchmarks and 13 reference benchmarks, controlled by means of topographic levelling, have been installed to monitor the displacements of both the existing tunnels sidewalls and the structures nearby the station (a residential building and the Wall 1, see Fig. 5); plus, 34 optical surveys, inspected by employing a total station, have been placed in order to gather the convergence measurements in the tunnel and to monitor a supporting wall that will be directly influenced by the work in progress activities ("Paradise Stairs" supporting wall).

The monitoring plan is completed by the temperature control on site by means of thermal sensors properly placed. The total number of points under control is 239 (see Fig. 5).

5 MEASURES

The most significant displacement measures gathered relate to the cable railway restraint wall and to the first sidewall of the Circumflegrea Line. Figure 6 reports the displacements observed along this wall from the 29th of June 2006 (zero value) to the 29th of January 2009 (last available scanning); vertical dot-dashed lines point out the most significant dates of the excavation history.

All the benchmarks had vertical displacements, with a maximum value of 24 mm at benchmark # 6. The deformed shape of the wall clearly shows a sagging zone and a hogging zone. The maximum angular distortion recorded ($\beta_{max} = 7.1 \times 10^{-4}$) is lower than the threshold prescribed in the scientific literature to avoid the structural damage of the type of structure investigated ($8 \times 10^{-4} < \beta_{adm} < 3 \times 10^{-3}$, Day 2000).

Figure 7 depicts the displacements gauged on the 1st Circumflegrea sidewall so far, confirming that the automatic and manual control systems are in good agreement.

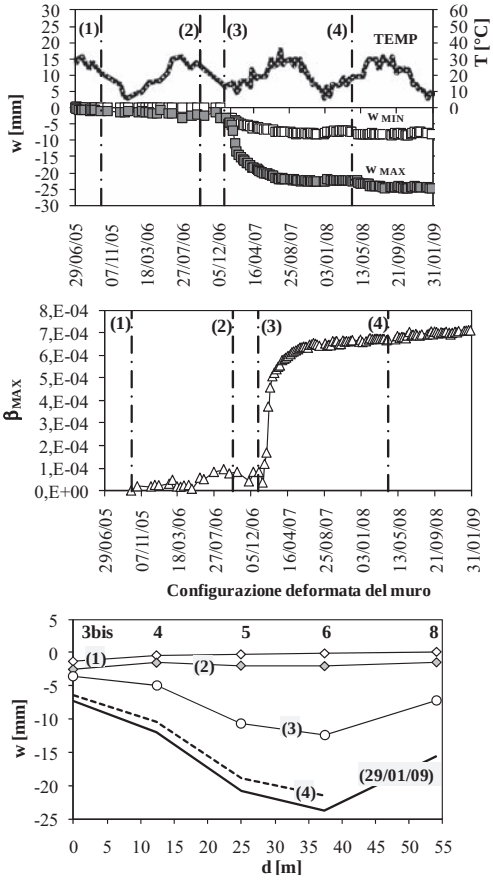

Figure 6. Time evolution of displacements (1) work start; (2) completion of descending tunnel; (3) completion of service tunnel; (4) pedestrian tunnel excavation start.

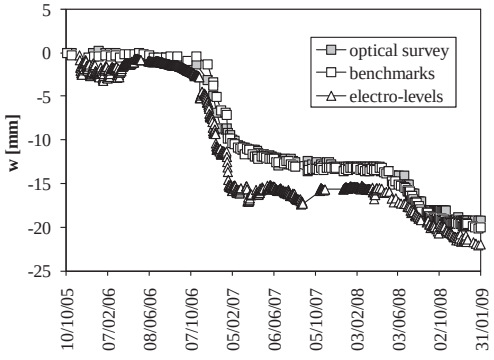

Figure 7. Displacements of 1st sidewall.

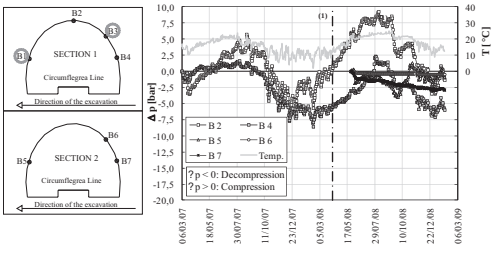

Figure 8. P and T data of Circumflegrea. (1) 1st breakthrough start.

As for the accuracy of the tunnels displacements measured, the scientific literature does not give specific indications, despite the existence of case studies relating to tunnels interested by new forthcoming tunnel excavations. Nevertheless, it is certainly possible to set a displacement threshold related to the structural safety of the two tunnels in service.

For this purpose it was necessary to know the mechanical and geometrical characteristics of the existing tunnels liners, and to assess the initial stress state. Hence, two different experimental campaigns were performed along with time (June '05 and February '07), made of coring, single and double jack tests carried out on specimens taken within the intervention area soil.

The tunnels liners were found to be made of piperno masonry, red bricks masonry and variable thickness concrete strata. The single jack tests allowed measuring the service stresses, ranging between 0.35 and 2.40 MPa; the double jack tests showed an ultimate stress value higher than 3.50 MPa. The displacement scannings were aided by stress scannings given by load cells installed on two sections of the Circumflegrea tunnel astride the tunnel to build (the 1st in March '07, and the 2nd in June '08); the pressure variations are reported in Figure 8, together with the temperature variations. The maximum compression value (~9,3 bar) was detected on cell B2 during the 3rd excavation step. It can be observed that the pressure variations seem to be strongly influenced by the temperature variations.

6 COMPARISON OF THEORETICAL AND EXPERIMENTAL RESULTS

The calibration of numerical analyses carried out to predict the displacements expected after each excavation step, strictly depended on the mechanical parameters initially based on the experimental test results; afterwards, with the measures progressively gathered in terms of sidewalls displacements, existing and as built liners stresses, a further calibration of such parameters could be performed in the pipeline.

After the completion of the fifth excavation step, the comparison between the analytical and measured displacement values could be performed, as shown in Figure 9a (the zero displacement value refers to the construction of the pedestrian tunnel below the two railways).

It is clear that the expected displacements overestimate the values measured; it is believed that such disagreement is due to three main factors:

- the uncertainty related to the assessment of the Elastic modulus, E_s;
- the model did not take into account the aforementioned reinforcement of the upper sidewalls;
- the simulation of the progressive excavation determines displacement values that do not take into account the time dependence; this implies that the displacements expected involve delayed adjustment phenomena (due to the viscosity behaviour of soil) that might occur along with time.

After the completion of the (last) seventh excavation step, the comparison between analytical and measured displacement values gave the two curves shown in Figure 9b; a slight approach of the measured displacements trend with respect to the theoretical values can be observed, related to the first three sidewalls which were more influenced by the excavation steps 5 to 7.

Finally, the comparison of analytical versus displacement values measured after one year from the excavation completion was performed, as depicted in Figure 9c; a further approach between the two curves is observed.

It is clear from Figure 9c that the expected soil sinking still overestimate the corresponding measured values, but at a lower rate with respect to Figure 9b: this confirms that time plays a significant role in this process; it is believed that a

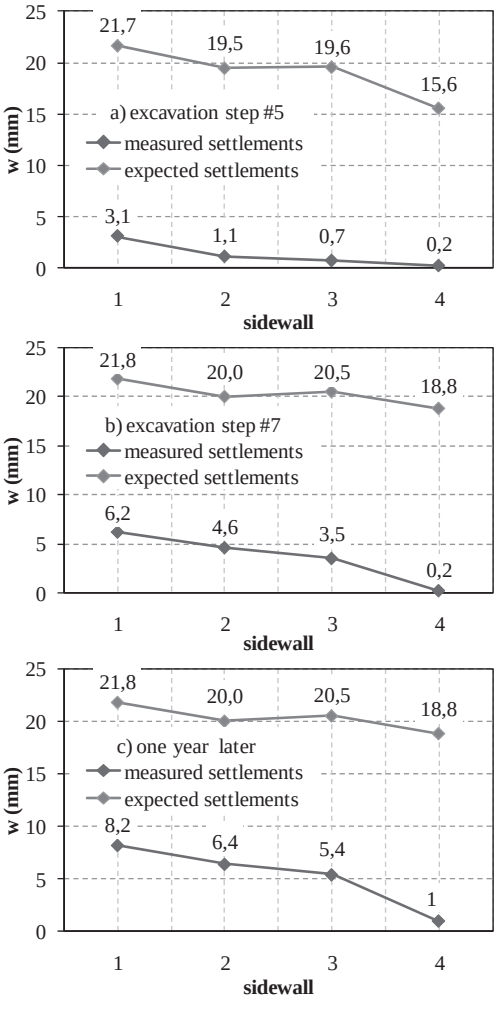

Figure 9. Comparison between theoretical and measured vertical displacements.

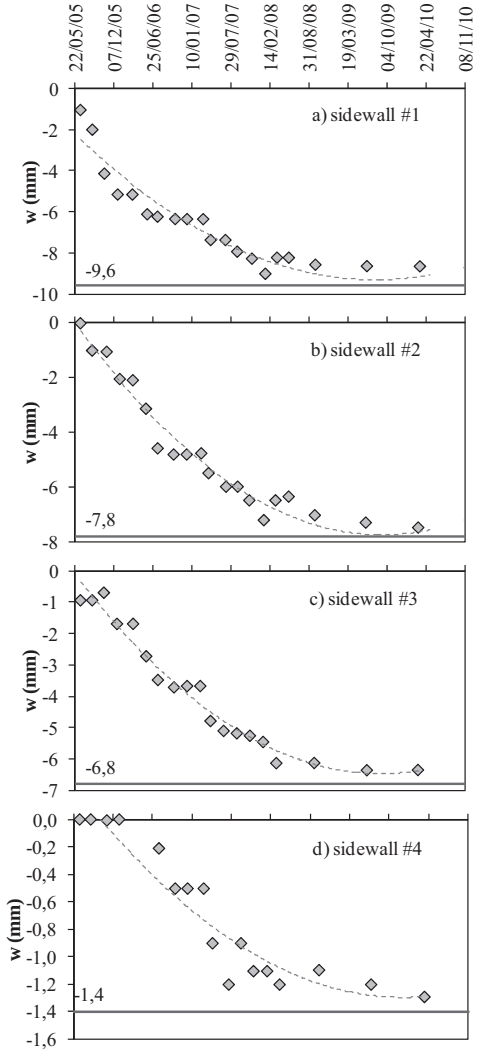

Figure 10. Displacements vs time behaviour.

further approach will be acquired between the two trend lines along with time.

This is confirmed by displacements-to-time trend of Sidewall 1 (see Fig. 10a), Sidewall 2 (see Fig. 10b), Sidewall 3 (see Fig. 10c), and Sidewall 4 (see Fig. 10d): the sinking trend lines have been extrapolated up to one year after the last measuring; the trend along with time goes to an horizontal asymptotic value, corresponding to the occurred settlement process, still ongoing at the present data.

It can be concluded that the expected values have to be deemed an upper bound for the measured data.

Nevertheless, the trend of analytical versus measured displacement curves confirms that the model approach fits the effective general behaviour of the complex space investigated.

The stability verification of the 3D model corresponding to the displacements derived was supported by the verification of the stress levels of the existing liners; in particular, the maximum differential vertical displacements observed between the adjacent sidewalls after the 5th and the 7th advancing simulated step was derived between the two sidewalls of Circumflegrea tunnel; the maximum compressive stress value derived on the relevant *tuff* liner was found to be 3.5 MPa, which is lower than the ultimate value derived from the experimental testing. Figures 11a and b illustrate the stress state just discussed.

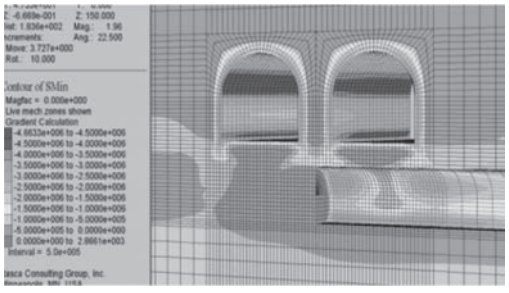

Figure 11a. Maximum compressive stresses of liners (excavation step #5).

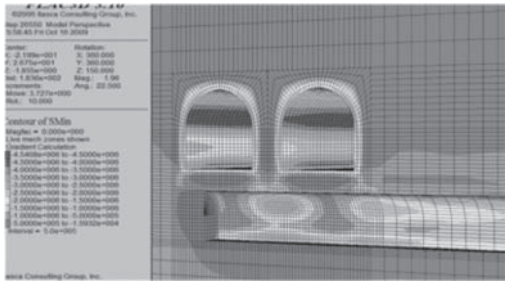

Figure 11b. Maximum compressive stresses of liners (excavation step #7).

7 CONCLUSIONS

In the present paper the main issues related to the accomplishment of underground structures in deeply urbanized and highly historical and monumental areas has been illustrated.

With reference to the new pedestrian tunnel serving the Montesanto Station, it has been shown how an integrated approach between 3D numerical analyses and real time monitoring of significant parameters as displacements, strain, stresses and temperature can confirm the set of design criteria assumed for the specific project, and in the meantime can refine their use by extending its application field through the proper calibration of the manifold parameters involved in the definition of complex works interacting with earthy materials which behavior is very unclear and thus needing deep investigations to support the design.

ACKNOWLEDGMENTS

The work presented herein is part of the research agreement between Ferrosud 2 S.C.R.L. and the II University of Naples.

Special acknowledgments go to Mr. A. Allagrande from S.E.P.S.A., Mr. S. Buttarelli, Mr. P. Guarino and Mr. L.Murena from Ferrosud 2, and to Mr. L. Campobasso, project manager.

REFERENCES

R.W. Day—Geotechnical Engineer's Portable Handbook—New York, 2000—McGraw Hill.

Itasca Consulting Group, Inc. 2006. FLAC3D—Fast Lagrangian Analysis of Continua in 3 Dimensions, Ver. 3.1 User's Guide. Minneapolis: Itasca.

This page intentionally left blank

Geotechnical Aspects of Underground Construction in Soft Ground – Viggiani (ed)
© 2012 Taylor & Francis Group, London, ISBN 978-0-415-68367-8

The Line 3 of the Metro of Cairo

Paolo Patrizi
SYSTRA, Paris, France

ABSTRACT: A consortium of major French contractors is currently realizing the works for Line 3 of the Underground of Cairo (Cairo is the first African city to have an Underground, back in the eighties). The line is divided into 4 phases, phase 1 (4.2 km) under construction, phase 2 (6.5 km) works to start soon, phase 3 (16.6 km) under design and phase 4 (12 km) still to be designed. This 40 km new line will connect western Cairo (left bank of the river Nile) to Cairo Business District on the right bank downtown and Cairo Airport on the east of the city. Ground conditions are made by a layer of clay/silt (up to 10 m) overlying a sandy silt layer and sand from 20 m up to 90 m and more. Ground water table is a couple of meters below street level. 1 km before the end of phase 1 a major collapse occurred in the slurry TBM, whose causes are yet to be understood. TBM recovery is being carried out through a shaft that is being excavated 3 m in front of the collapse point. Its diaphragm walls have been driven DOWN to a clay layer underlying the sand level to guarantee for watertightness (over 90 m panel depth). Ground freezing is then carried out to reach the shield, that is going to be extracted from the shaft, allowing the tunnel lining to be completed. The remaining tunnel of phase 1, as well as the beginning of phase 2 and the whole of phase 3 are going to be excavated with a new slurry machine that is expected to arrive to Cairo to complete the works.

1 INTRODUCTION

1.1 *Metro in cairo*

Cairo is the first African city to have an Underground metro line, Line 1, which construction dates back to the 80s. Line 2 followed shortly thereafter, and was completed in the early 2000s. Line 3 is now under construction, with a contract dated 2007.

With its huge traffic demand of 66.000 PPHPD (Passengers Per Hour Per Direction), its construction and operation are actually very challenging.

Trains are 145 m long and call for a station of similar length, and this brings all the stations to be box shaped, with a length of 150 m and a variable width, based on the traffic demand.

The Line 3 is divided into 4 design-construction stages, awarded to French Consultant Systra (Design) and to French-Egyptian Contractor ML3 (Vinci-Bouygues-Colas-Orascom). It is shown in green on the Figure 1 (Lines 1 and 2 are shown in black). In fact Systra was involved in Cairo transport Master Plan as early as the 60s, and French contractors work on Metro construction from the very beginning, showing a high reciprocal commitment between France and Egypt.

Line 3 is Y-shaped and its total length is to be approximately 40 km.

Demand is slightly unbalanced on the two branches (North and South, on the Eastern edge of the line), and this means that on 3 trains, 1 will be directed to the Southern (Mohandessin) Branch, while 2 are sent to the Northern (Imbaba) branch. The Workshop and Siding Area is located on the edge of the Northern track, with an area of 40 Hectares approximately (80 trains will be parked there).

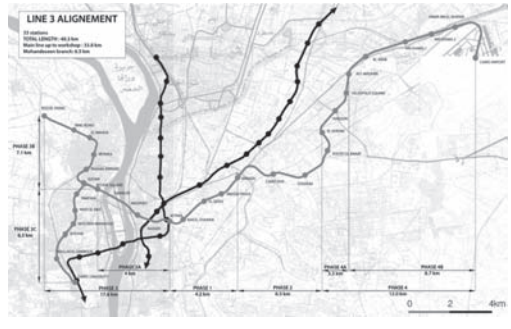

Figure 1. Cairo metro lines—lines 1 and 2 (existing) in black and line 3 (under construction) in green.

1.2 *Geology outlook*

The following summarizes the general subsurface soil layering along the Metro route. The city of Cairo occupies the area of the alluvial valley of the river Nile. Before construction of the High Dam in Assouan in 1971, the river was free to flood all the area between the rocky formations of the

Mokattam hills on the East, and the area of the pyramids in Giza, on the West.

Phases 1 and 2 occupy the eastern edge of the Nile Alluvial Valley, with water table depth ranging from 2 to 10 m, and phase 4 gets in the Mokattam hill, with more rocky layers than previously.

The entire region of Phase 3 lies within the flood plain of the Nile, which at Cairo has a width of about 12 km extending from the Citadel at Gabal El-Mokattam to the Giza Pyramids Plateau, with a ground elevation generally ranging between 17 and 22 m above sea level. The geological units are mainly Nile sediments and the setting within local regions is affected by the changes in the Nile course that occurred throughout history.

Fill: A top fill layer of various depths is encountered in mostly all borings. The constituents of the fill layer vary with depth and location but it is generally characterized by the presence of bricks, pottery, concrete and limestone pieces mixed with sand, silty sands, and clays. The depth of the fill layer ranges between 1 m and 10 m from ground surface. The larger depths are mainly in the region around Attaba area. Smaller depths are encountered as we head towards Cairo Airport. Layers are as follows.

Upper sand: A sand layer generally follows the top fill layer along the metro route. The sand is of medium to fine grain size and sometimes mixed with gravel, especially around Heliopolis area till Abbasia. The sand lies in a medium to very dense condition. It thickness range between zero and 13.0 m.

Clay: Layers of stiff to very stiff silty clay, mixed sometimes with gravel or sand, appear generally after the previously described layers. The sequence of these layers is generally consistent throughout the metro route. The thickness of the clay layer varies between zero and 15.0 m in average. The layer generally appears under water table, except in the areas near Cairo airport such as Omar Ibn El-Khatab region.

Lower sand: Layers of generally very dense fine to medium grained sand always appear following all the above layers and extend to the end of the boreholes. The layer also appeared alternatively with clay layers around the area of the river Nile near 26th of July Street and Zamalek.

Gravel: Occasionally, a layer of gravel, mostly mixed with sand, of a thickness ranges between 4.0 m and 13.0 m appears from depths ranges between 5.0 m and 10.0 m. The presence of this layer is verified in the area from Heliopolis to El Geish.

Ground water: Ground water depth ranges between 2.0 m and 20.0 m below existing ground surface along most of the line. However, no ground water table is encountered in the areas of Cairo Airport.

2 CONSTRUCTION OF LINE 3—PHASE 1

A preliminary design for the whole line was carried out in 2000–2002 by Consultant SYSTRA. After a few years' stop of construction activities in Cairo, works started in 2007 with the development of the Basic Design and the actual start of construction activities for Phase 1. Phase 1 is actually the central part of the line, and it was decided to start with the construction of the northern edge station, named "Abbasia" that is also the TBM launching site.

2.1 *Construction method*

The construction is based on a simple scheme, in which all the stations are built with diaphragm wall support and heavy civil works completed before the station's crossing by the TBM. The tunnel is one double track tunnel Ø8.35 internal/9.15 m external, as was the case for Line 2.

2.1.1 *Stations*

The construction sequence is generally "top down", with all the intermediate slabs cast while driving down the excavation, the slabs also serving as props to the diaphragm walls.

However, once the perimetral D-walls are executed, an injected plug will need to be realized to enable excavation below the water table.

According to the available data, the hydraulic conductivity of the geotechnical units is 3.0×10^{-4} m/s for the Lower Sand and 3.0×10^{-5} m/s for the Upper Sand. The high value of the hydraulic conductivity combined with the position of the water table lead to a preliminarily estimate of the average water inflow of 2.000 l/s for each station (7.200 m^3/h).

Pumping a flow of water of the order of 2.000 l/s during the excavation of the stations has been disregarded because of possible detrimental effects on the surrounding buildings, as well as logistic problems. Before starting the excavation, a bottom plug is created at the bottom of the D-walls to enable excavation under the water table with the use of dewatering wells inside the station box, that are deeper than the final excavation level.

In practice, permeability is the key parameter for the choice of permeation grout. The soil voids determine whether the grout flows freely or is obstructed by filtration. As a general guide, it is difficult to permeate soils with a permeability of

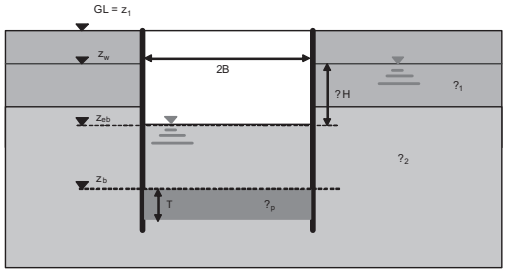

Figure 2. Typical section of stations, with plug injected at the toe of the D Walls.

Figure 3. A view of Attaba station with temporary props.

less than 1.0×10^{-5} m/s using cement-bentonite grouts.

Such grouts are generally used in a pre-injection phase to fill large voids. Chemical grouts can be used to permeate fine-grained soils as they can penetrate finer voids than even the finest particulate cement grouts.

In fact, the plug is not designed to be a watertight plug, but rather a treatment in which the permeability of the ground is reduced to a value that would reduce the gradient of water pressures within its thickness.

The simple rule that has been used up to now is given by the need to reduce to 1/3 such gradient. For example, if the water pressure to be counterbalanced is 30 m (3 bars), then a thickness of 10 m is required for the plug. Verification of the uplift of the plug also has to be carried out. In usual conditions, the soil left in place between the bottom of the excavation and the base of the plug would need to have a thickness roughly half that of the water pressure to be balanced (eg 30 m thickness for 3 bars of water).

The plug is created with low pressure permeation grouting (bentonite-cement + silicates gel). Then, the efficiency of the plug can be checked with a pumping test, with actual inflows to be compared to theoretical values.

Excavation can start, with conventional top-down techniques, up to the bottom of the base raft, with all the intermediate slabs being cast while proceeding with the excavation. Before reaching the final excavation level and casting the raft, one or two levels of struts are installed, in order to continue the excavation up to the final level.

Once the bottom raft is cast, then the TBM can pass through the station. In some cases, a complete top down technique could be used, and the slabs were all cast while driving down the excavation.

2.1.2 *Tunnels*

In proximity of the Nile alluvial valley, for phases 1 and 3, the tunnels are excavated with a Slurry TBM, while the rest, phases 2 and 4 will be excavated with an EPB machine. Up to the 3rd September 2009, all the slurry Tunnels were due to be excavated by the same "Cleopatra" machine which was also used for the construction of Line 2 in the nineties contemporary to Rome's "prolungamento Linea A" and the road tunnel "Al Azhar", in central Cairo.

With Slurry TBMs, the face pressure is kept by a circuit of bentonite, with "clean" bentonite being brought to the face and "heavy" bentonite, (bentonite + muck) extracted from the face and sent to a recycling plant to the surface. The face pressure of the bentonite is adjusted through an air bubble, whose pressure is controlled by the pilot.

One special mention is given by the so-called "bell" method, that is used in Cairo for the machine to break-in and break-out from the stations. This is an alternate solution to the case in which a curtain of soil treatment (generally Jet Grouting) is created adjacent to the station box.

The "bell" method consist in putting in place a steel cylinder as shown on the following sketch, that would enable the annular gap between the bell and the tailskin, with convenient (gasket + seal), to hold the pressure.

A simplified sketch explaining the principles governing the Bell system shown on Figure 4.

The actual steel bell is shown on Figure 5.

This method can be used for both Break-ins and Break-outs, and its interest is in that it reduces the high cost and complications connected to the usual Jet Grouting plugs that need available space and site occupation for a considerable time above the station/tunnel connection.

2.1.3 *The collpase*

The 3rd September 2009, while the TBM was driving on the before-last section between El Guesh

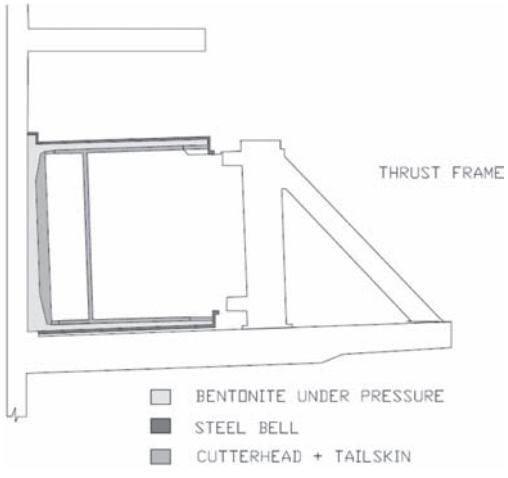

Figure 4. The Bell—principle sketch.

Figure 5. The bell for break in and break out.

and Bab El Shaaria, a sinkhole took place during excavation of the tunnel, and the crew was obliged to abandon the machine in place. Fortunately, no injured were recorded, but the project took a serious stop in its construction, as the tunnel was flooded with mud.

A 3 m thick wall was constructed 200 m behind the cutterhead, water was pumped in the empty tunnel and brought in equilibrium with the ground water table (roughly 2.bars) to stabilize water and soil movements, while a rescue shaft was constructed from the street with the D walls, located 2 m in plan in front of the stuck machine, and ground treatment with injections was initiated from the street level to compact the soil layers around the collapse area.

Ground freezing was selected as the option to recover the TBM, with 2 rows of 30 m long freezing pipes to be fed with brine to be drilled all around the shield. It is interesting to observe the increased performances of freezing plants in the last 10 years, with brine temperature being today as low as −30°C, while only −23°C were reached back in 1999. Figure 7 shows a section of the shaft, and of the freezing pipes.

To avoid having to realize the bottom plug, it was decided to drive the D-walls where driven down to a clay layer some 95 m deep from the street level (compared to the level of the TBM to be rescued of −30 m). Figure 8 shows the freezing pipes once they were drilled from the Rescue Shaft.

Brine circulation was started in the beginning of April, and temperature measurement pipes allowed to check the drop of the surrounding temperatures.

Such pipes were both parallel to the freezing pipes and perpendicular pipes, drilled from the surface. These permit to follow the thickness of the ice wall.

To gain information about the actual configuration of the collapsed area from the inside, a team

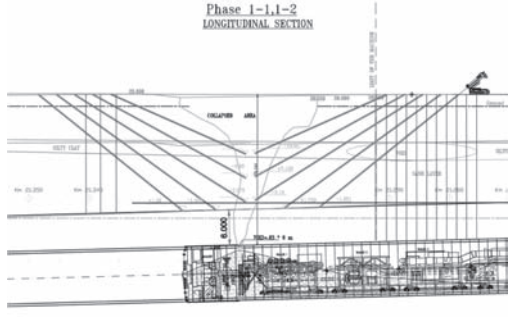

Figure 6. Compaction grouting above the collapse area.

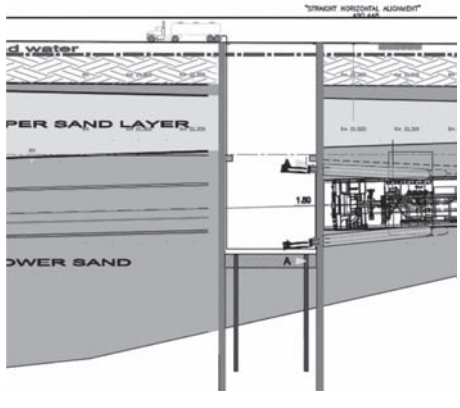

Figure 7. The collapse recovery shaft.

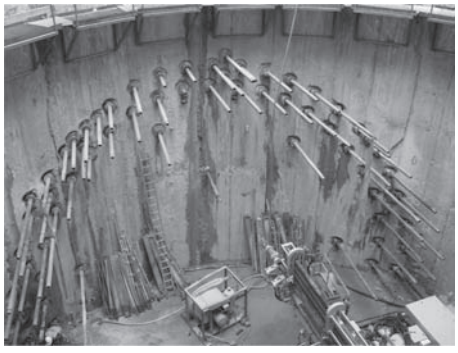

Figure 8. Freezing pipes layout.

Figure 10. Backup trailers from the tunnel.

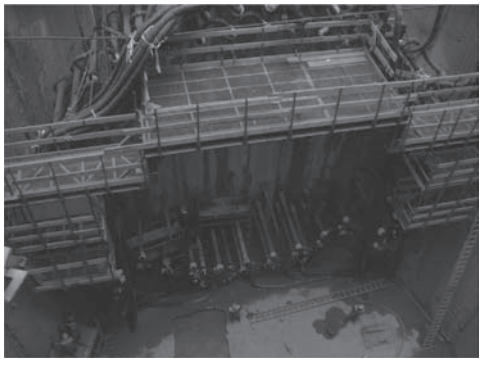

Figure 9. Freezing pipes feeding.

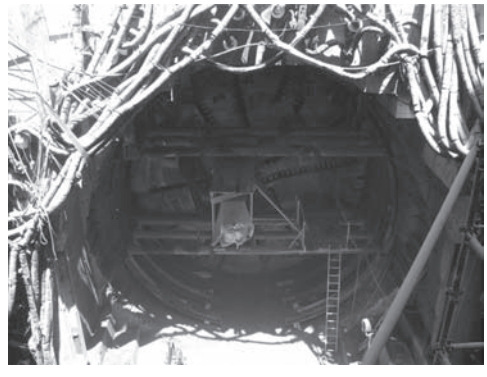

Figure 11. Access to the cutterhead.

of divers was sent to the plugged TBM, from a Man Lock on the 3 m wall. They could observe the lining up to the collapsed area, whose integrity is essential to ensure the effectiveness of the Ground Freezing, and put in place a few additional temperature monitoring points.

Closure of the ice-wall was observed 4 weeks after start, with a sharp increase of the water pressure inside the tunnel due to ice expansion. The tunnel was dewatered in 3 steps with 24 hours stops between the steps, to ensure no leakage.

Tunnel was then made accessible with demolition of the 3 m wall, and it was possible to get to the TBM backup trailers, as seen in Figure 10.

At the same time, on the other side of the machine, demolition of the wall of the Rescue Shaft was executed ads access to the cutter head was made possible.

Recovery has been completed in January 2011.

During the recovery, a new Slurry TBM was brought to Cairo to finish up the works for phase 1 and continue on phase 2 and phase 3. It started at the opposite edge of Phase 1, in the Station of Attaba, heading eastward towards the rescue Shaft where the old TBM was being recovered.

The rescue shaft was reached by the new slurry machine in December 2010, thus phase 1 tunnels were completed, then the TBM was brought to Abbasia station to start phase 2 tunneling.

3 DESIGN OF LINE 3—PHASE 3

Phase 3 is the Western Edge of Line 3. It starts in the same station of Attaba, downtown, and drives westwards. The tunnel is obviously the same that was described for phase 1 and it will be excavated with the same Slurry Machine that was described for phase 1.

For the stations, the same design principles of Phases 1 and 2 have been kept here, trying to keep all the stations with the typical "box" shape, with no "mining" techniques.

The typical stations used in the design of Cairo Metro are the usual rectangular box shape, whose length is going to be of 150 m and whose minimum

width is 21 m and is generally adjusted to traffic demand of each station.

The main critical points of the line are be described hereafter.

3.1 *Underpass of line 2*

Attaba square is already the location of one Line 2 station, whose layout is perpendicular to Line 3. Line 3 underpasses Line 2 right after Attaba station, with one very critical design challenge. It is required for the plan alignment of Line 3 to turn a tight curve to the left to be able to reach the following (Nasser) station, and at the same time it is essential for the profile to dip down, maximizing the cover between Line 2 existing tunnel and the new Line 3 tunnel. The vertical and plan transition curves, cannot be superimposed and because of this is it was not possible to guarantee a sufficient distance between the two tunnels. Specific compensation grouting and/or Jet Grouting interventions are planned to reduce the risk of movements in the Line 2 tunnel that will be closed to traffic during a few days for the crossing to happen with no risk to the metro users.

Compensation grouting, as shown on Figure 12 has been selected among the mitigation measures.

3.2 *Station nasser*

The first station, called Nasser is probably the most difficult of the whole line because of the huge

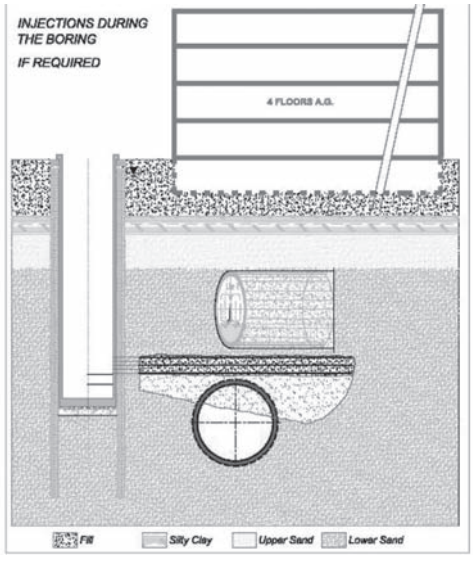

Figure 12. Compensation grouting during line 2 crossing.

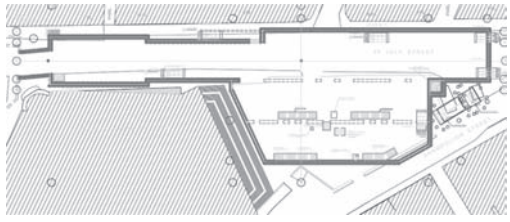

Figure 13. Nasser station.

traffic demand (it is a correspondence station with Line 1) together with a very small space available. The Traffic demand is estimated to be of 25.000 exiting passengers in the peak hour and this brings the platforms to be at least 5 m wide.

It is important to note that because of the depth of the Line 2 Tunnel crossing, and the maximum slope of 4% for the ramps, the station will need to be a deep station, with 4 levels (1 Ticket Level, 2 Intermediate Levels and 1 Platform Level, plus the Underplatform). This brings the rail level to be 30 m from street level.

The designers studied all possibilities, to avoid demolition of existing buildings and found that the only possible solution would be to bring the D walls very close to the existing building, leaving a very tiny space for utilities and residents during the works. An alternative would have been the excavation of the accesses to the platform using traditional "mining" techniques with ground strengthening by jet grouting or ground freezing. However, because of the lack of experience in these grounds in Cairo, with cohesionless material and very high water table, it was decided to avoid the construction of tunnels beneath the existing buildings, which are old, with poor foundations and with very little information available. Diaphragm walls layout is shown on Figure 13 (total length of the station is 200 m).

One particular aspect of Nasser station is a tunnel to connect the two paid areas (thus with a deep tunnel to be constructed with traditional techniques). The following picture shows the final configuration of the pedestrian tunnel and the metro tunnel (deeper).

A section is shown on Figure 14.

One fundamental design parameter is the order of construction of these two tunnels. The TBM tunnel will probably be constructed first because it lies on the critical path in the overall construction programme and any delay on it will be reflected by a delay on the final construction schedule.

3.3 *Underpass of the 25th July flyover*

The 25th July flyover was built in the eighties to give a breath to the continuously increasing traffic

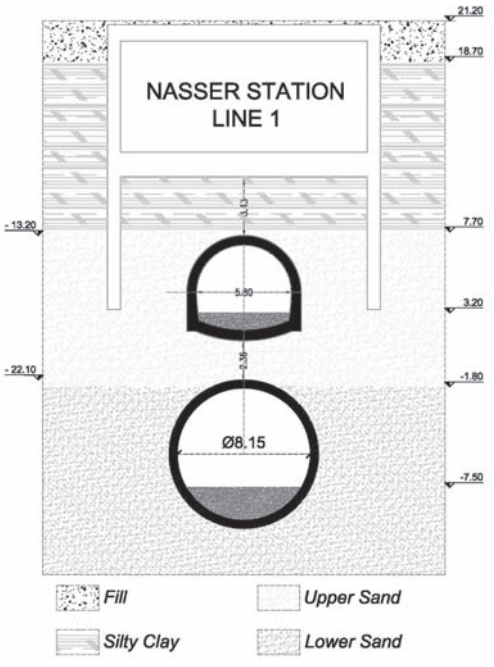

Figure 14. Line tunnel and pedestrian tunnel for connection with line 1 in Nasser.

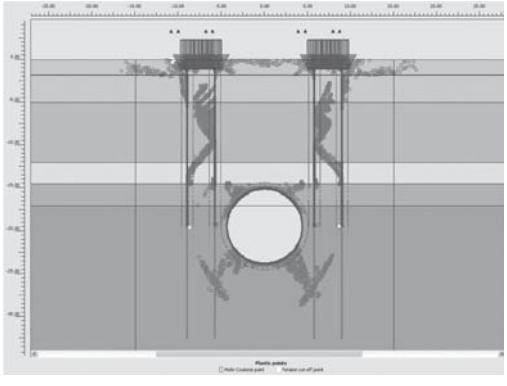

Figure 15. FEM results of TBM crossing the flyover.

demand in Cairo, and allow rapid connection from downtown to the new Easter areas of the city.

Drawings of the foundation pile caps were readily made available by Cairo Authorities, but nothing is known, at present, about the depth of the piles. Finite Element analyses show that, as could be expected given the fact that they essentially work with base resistance, stability of the piles is affected if the tunnel is driven below their base, close to their influence area.

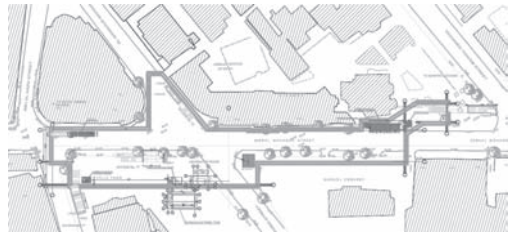

Figure 16. Zamalek station.

Due to the lack of reliable data on pile length, stability of the viaduct will need to be closely monitored during construction of the tunnel, possibly with traffic closure.

3.4 *Nile crossing*

The TBM tunnel will pass twice beneath the Nile River, before and after Zamalek area.

The position of the tunnel with respect to the river bed has been evaluated on the basis of preliminary bathymetric survey of the river bed.

A sufficient tunnel overburden (at least 1 diameter) is guaranteed when tunnelling beneath the Nile River. No major problems are foreseen if tunnelling in controlled conditions, with pressurized tunnel face within the prescribed operational values.

3.5 *Zamalek station*

The Third Station along the Line in Phase 3 is on the island of Zamalek, in between the two Nile crossings above.

Again, because of the depth of the Nile crossing, and the maximum slope of 4% for the ramps, the station will need to have 4 levels (1 Ticket Level, 2 Intermediate Levels and 1 Platform Level, plus the Underplatform. This brings the rail level to be just below 30 m from street level.

Again, the lack of space is the major design constraint, but the small passengers number of 5.000 exiting passengers in the peak hour made it possible to design a station between D Walls with minimal expropriations.

3.6 *Buildings underpass*

In order to roughly estimate the risk of damage for each building, and consequently the need of soil treatment the following Rankin's damage criteria (Rankin W.J., 1988, Ground movements resulting from urban tunnelling: Predictions and Effects) are used. This table is commonly used for preliminary damage characterisation. The threshold values indicated in the table do not consider the conservation

conditions and the existing state of cracking of the building, i.e., it is assumed that the building is in a perfect state of conservation. A factor of safety of 2 can be considered on these values to take into consideration the lack of knowledge (at this stage of the design) in Cairo of the real conditions of the buildings along the alignment.

Soil treatments were then decided based on the expected settlements.

4 CONCLUSIONS

The construction of a new Metro line in an old city as Cairo, where modern activities overly several millenaries of history, requires careful design and construction. These included the used for a pressurized TBM for tunnel excavation. Elaborate ground treatment technologies were also implemented by the Contractor after the occurrence of a collapse that caused the machine to be blocked underground.

Geotechnical Aspects of Underground Construction in Soft Ground – Viggiani (ed)
© 2012 Taylor & Francis Group, London, ISBN 978-0-415-68367-8

Methods of monitoring of metro lining in Prague

M. Vaníček, S. Chamra, D. Jirásko, J. Macháček, I. Vaníček & J. Záleský
Czech Technical University in Prague, Prague, Czech Republic

A. Hada, K. Chaiyasarn & K. Soga
University of Cambridge, Cambridge, UK

ABSTRACT: There are several reasons for monitoring of underground structures and they have already been discussed many times, e.g. from the view of ageing or state after accidental event like flooding of Prague metro in 2002. Monitoring of Prague metro is realized in the framework of international research project sponsored by ESF-S3T. The monitoring methods used in Prague are either classical one or new or developing one. The reason for different monitoring methods is the different precision of each method and also for cross-checking between them and their evaluation. Namely we use convergence, tiltmetres, crackmetres, geophysical methods, laser scanning, computer vision and finally installation of MEMS monitoring devices. In the paper more details of each method and obtained results will be presented. The monitoring methods are complemented by wireless data collection and transfer for real-time monitoring.

1 INTRODUCTION

Ageing of structures represents a general problem and have a little bit different undertone for individual types of structures. At present day there are millions of civil engineering and building structures, where design serviceable life is usually defined in the range of 70–120 years. However at the same time we are speaking about structures, mainly underground one, for which serviceable life should be much longer.

Underground structures have specific properties, they are much less accessible and relevant state verification is more complicated. For the majority of the underground structures the dome-shaped roof is composed by concrete lining. The basic manifestation of changes on such structures is directly connected with deformation—of all profile, in local cracks or micro cracks on the concrete surface. The chemical degradation of the surface is another manifestation.

International research project was established to study the effects of tunnel lining ageing and to suggest the monitoring options to predict the lining deterioration in order to determine the optimized plan of care (repair, refurbishment, reconstruction). Within this international project 3 metro systems were included in the monitoring trial—Prague, London and Barcelona. The main manifestation of the tunnel lining deterioration is its deformation in time.

Changes in deformation can be observed by different methods in accordance with length of sector or according to demanded preciseness. Generally it is valid that for longer sectors the methods with lower preciseness are used, as are able to inform about prevailing character of deformation, about deformation development in longer time interval. They can be used also for the evaluation of abrupt changes in loading. Therefore the following methods and experiences with them are described in more details:

- Conventional monitoring using convergence tape measurements, tilt plates measurements and crackmeters measurements—determination of deformation in time for one selected profile.
- Vibrations monitoring using geophysical type of measurements by geophones—determination of relative deterioration of individual lining segments, where geophones are installed.
- 3D laser scanning measurements for determination of exact shape of lining and its possible movement in time, which seems to be very useful for longer sectors.
- Photographic methods based on comparison of pictures (camera) or picture sequences (video—camera) inscribed as "Computer Vision", where pictures taken in the different time periods are compared, whereas cannot be taken from the same position. The methods are proposed for sectors with the length of order m or tens of m.

– Novelty methods enabling very precise measurement, whether for observation of the deformation of the whole tunnel profile or for deformation in micro scale, capable to measure the deformation changes in the order of 1×10^{-4} mm (MEMS systems—micro electrical mechanical systems), which are able to observe the development of deformation of microcracks in time.

A great attention is devoted not only to the deformation measurement but also to the data recording, see Vaníček et al. (2008). It is not only the question of frequency of individual measurements but first of all of question of transfer of measured values to the place of destination. Direct measurement on the place where measuring devices are located is the up to now the simplest method, but it is necessary to perform it during night time when the metro system is closed. Second phase is continual collection of data with the help of data-logger and with subsequent transfer to the laptop after a certain time period during the night site visit. Another possibility is to use wired connection of sensors to the central, which is situated nearby and accessible from the metro station. Wireless technology represented last advanced phase, when measured values are collected by wireless network directly in the tunnel and subsequently send again with wireless technology to the server for further processing and evaluation. This system allows for continuous control of measured data on a computer.

2 MONITORING SITES

For Prague metro monitoring several possible monitoring locations were identified during initial site walkovers through metro tunnels. The locations were suggested not only by the project team but also by the metro operating company "Prague transport company" based on their long-term visual inspection and experience. Also some members of the project team were participating on inspections of Prague metro tunnels after theirs flooding in August 2002 (Vaníček et al. (2007)). The experience from inspections was also accounted for during the walkovers and site identification.

As a result of the site identification a decision was made on selection of 2 main sites for monitoring in the frame of our project.

2.1 *Monitoring profile 1*

The first site, which was instrumented in December 2006 by first set of conventional and geophysical monitoring equipment, is located on line C in between the stations "Nádraží Holešovice" and "Vltavská" on track 2 chainage 18 + 275 km. This

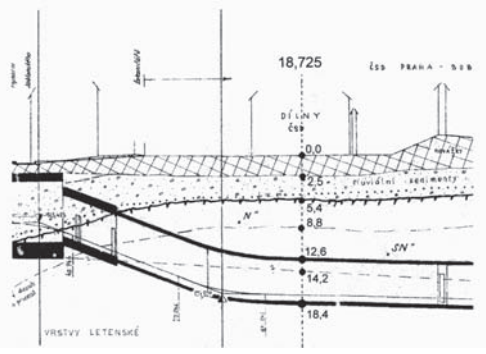

Figure 1. Long section through metro tunnel in monitoring profile 1.
Geological conditions
0.0–2.5 made ground
2.5–5.4 sandy (silty-sandy) gravel
5.4–8.8 Letenské schists—highly weathered ("N")
8.8–14.2 Letenské schists—weathered ("SN")
>14.2 Letenské schists—unweatherd
top lining face ~ 12.6 m; bottom lining face ~ 18.4 m.

site was continuously amended by additional monitoring equipment.

The tunnel in this section was constructed using so called the "Prague" ring tunnelling method with lining from precast reinforced concrete segments. This monitoring profile is situated about 12.6 m below surface (see Fig. 1). On the lining there are visible network fine and thick cracks. Based on verbal information somewhere in this section there was most probably large overdig.

The bedrock rocks are formed of ordovic Letenské layers within flysch formation. This is characterised by interlaying of weaker rocks (clayey-silty schists, siltstones) with hard to very hard rocks (quartzite, silicious sandstones, silicious gray wackes).

2.2 *Monitoring profile 2*

The second site, which was instrumented in December 2008 by first set of geophysical monitoring equipment, is located on line A in between the stations "Staroměstská" and "Můstek" on track 1 chainage 19 + 467 km.

Tunnel lining is composed of mass press concrete of 345 mm inn thickness, which was made by mechanised shield TŠčB-3. In the lining there are visible several types of failures. Based on available information there was large overdig in the area under the church of St. Havel, where the whole shield train supposed to stop for 4 days. In the section between the stations "Staroměstská" and "Můstek" strengthening of overburden was

performed by injection wells and infill grouting of caverns opened during tunnelling.

The bedrock rocks are formed of highly tectonically cracked Zahořanské, Bohdalecké and Dobrotivské layers composed mostly from clayey schists. Dividing line of these layers is located approximately at the chainage 19 + 463 km. Through selected section (about km 19 + 450) is passing one of the main tectonic lines of Barrandien—so called "Prague fault" of 20 m in width. We assume that in this section micro-seismic movements could manifest as a reaction on seismic events from either Krušné Mountains or further away European sites.

3 CONVENTIONAL MONITORING

Conventional monitoring was divided into two main stages with respect to the selected section, see Fig. 2:

- In the first stage it was portable tiltmeter and deployment of tilt plates, convergence measurements by tape in between installed convergence bolts for measurements of overall section deformation together with lining and air temperatures;
- In the second stage monitoring of cracks behaviour by crackmeters with logging of data using data-loggers;

Convergence monitoring was used for checking of the global deformation of the tunnel test section in time. The measured deformations were in the range of tenths of millimetre in the monitoring period of three years. Distance measurement between individual points is performed by convergence tape with precision of 0.01 mm and repeatability of 0.05 mm. For measuring of lining tilting system from Slope Indicator company is used. This system is composed of set-in probe, reading unit and bronze tilt plates. Measurement range is ±53° from vertical with precision of 8 arc seconds, i.e. 0.04 mm/m. Tilt plates close to the tunnel crown indicated long-term symmetric inclination changes almost related to the lining temperature variations, Fig. 3. The other plates, by tunnel invert and one close to the rail, indicated similar range of inclination changes but not directly related to variations of the temperature. Comparison of tilt and convergence lined out that nodal/fixed points of the lining are perhaps close to the convergence bolts and the significant deformations are inclination changes mostly affected by temperature, Záleský, J. et al (2008).

Conventional methods of monitoring proved that selected profile even showing some marks of deterioration is stable and measured deformations are in acceptable range showing long-term cyclic behaviour. However pointed out on significant thermal sensitivity of the concrete tunnel lining which can result in faster deterioration of it, especially in case of evidence of active crack system (Bubeníček et al, 2008).

Crack monitoring indicated cracks activity less than 0.1 mm range of deformation, Figure 4.

Figure 2. View of the test section 1, direction Vltavská station (tilt plates and convergence bolts are presented by yellow circles and cracked lining segment by red ellipse where crackmeters, geophones and inclinometers are installed).

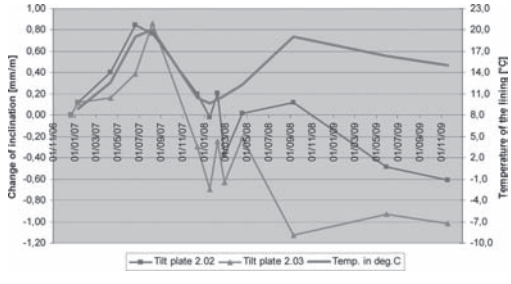

Figure 3. Results of tilt changes monitoring—plates parallel to the tunnel crown.

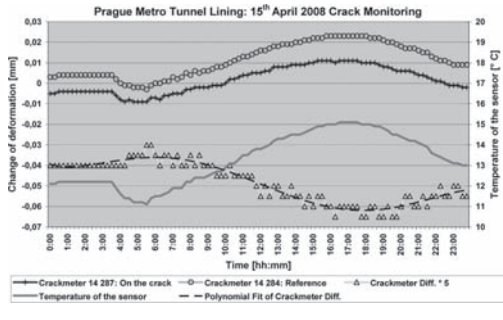

Figure 4. Selected results of crack monitoring in tunnel section in km 18 + 725.

There is selected a day snap (mid-April 2008) with high temperature variation. Thermal compensation of gathered displacement data is necessary. The best way of compensation is an application of reference crack sensors. This is precisely, what is done in the test section, namely with respect to the future installation of newly developed MEMS sensors by our international partner in the project—CNR Bologna. The crack activity as "Crackmeter Difference" is presented in the Figures 4. The compensated crack activity is 5 times overscaled in the Figure showing closure of the crack with increasing temperature, as expected.

4 VIBRATIONS MONITORING

Initially two alternatives of geophysical monitoring were installed in the monitoring profile 1. The first method is an analysis of time-development frequency spectra of the structure vibrations under the traffic loads. Seismic velocity sampling is the second method and is based on the measurement of elastic wave velocity passing through the tunnel lining. The first method is using MEMS geophones embedded into concrete lining. Always 2 geophones are embedded, one in cracked section of lining and second in visually intact part of lining.

Before installing of crackmeters in the monitoring profile 1 the second method was capable of visualising the cracks in the tunnel lining segment. Unfortunately the stiffness and wave velocity propagation of the crackmeters affected the results of this method and was afterwards discontinued and never installed in the monitoring profile 2.

The first method proved itself nicely as it is capable of showing not only changing behaviour of tunnel segmental lining on climatic changes (mainly temperature) but as a side effect also technical conditions of the individual axles of train undercarriages.

The measurements with first monitoring method are affected by several aspects. The aspects on which the monitoring is corrected for are:

- Temperature;
- Humidity;
- Train units weight (i.e. peak and off peak periods);
- Induced noise on long cables through tunnel;
- Train speed.

The measured raw data from monitored profile 2 for the first geophysical method are presented for a monitoring period between December 2008 and 2009 on Figure 5.

The results of monitoring corrected for the main aspects in the order as above are showed on Figure 6.

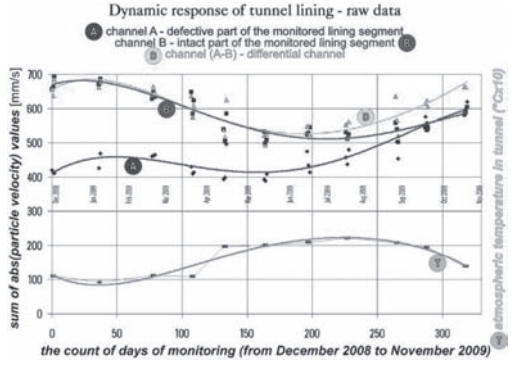

Figure 5. Monitored raw data from dynamic response of tunnel lining at monitoring profile 2 (Můstek).

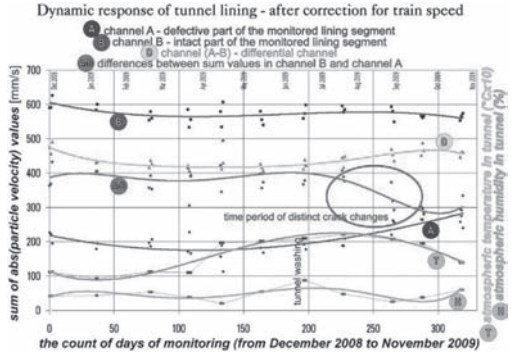

Figure 6. Monitored data from dynamic response of tunnel lining at monitored profile 2 (Můstek) after correction.

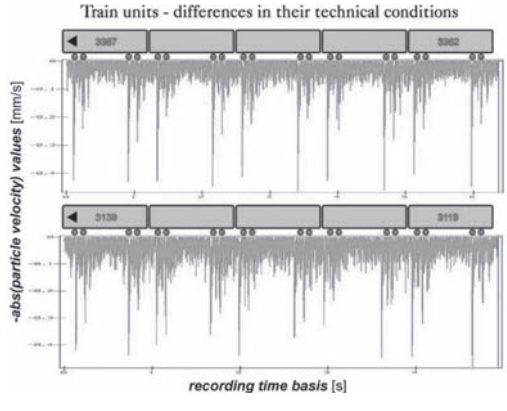

Figure 7. Monitored data as response to train passage.

When placing the train units above the monitored data, it is clearly visible location of train undercarriage axles (see Figure 7) and also any irregularities indicating some defects on axles (see Figure 8).

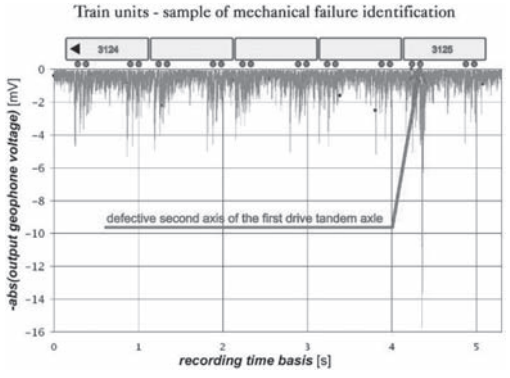

Figure 8. Indication on axle defect from monitored data.

Figure 9. Laser scanner Leica HDS3000 in the Prague metro tunnel close to Můstek station (Pospíšil, J. et al, 2007).

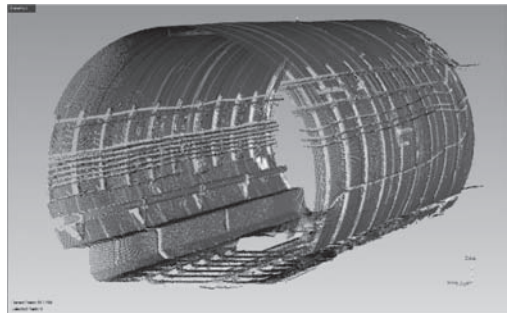

Figure 10. View of cloud of measured points by Leica HDS3000 (Koska, B., 2008).

5 3D LASER SCANNING

3D laser scanning of tunnels is using for determining tunnel shape (geometry) already for some time, but mainly for old tunnels before their refurbishment. Our addition to the concept of 3D laser scanning of tunnels includes the options for determination of proper shape of tunnel just after construction, in order to check the quality of construction works and baseline for future monitoring and numerical modelling. When the tunnel is rescanned by the end of guarantee period, it can be checked on the predicted tunnel deformation in this period and on possible warranties. In long-term monitoring it is possible to check again the time dependent convergence of tunnel. This measurement can determine relatively large change in deformation—in the order of centimetres.

Another use of the 3D laser scanning can be the base for computer vision monitoring (see next chapter) in terms of 3d mapping of lining photos.

We used this monitoring technique at our monitoring profile 2 (Můstek)—Figure 9. Some results from initial 3D laser scan are presented on Figure 10.

6 COMPUTER VISION

This approach to monitoring is based on nowadays availability of the digital photos comparison. Currently it is possible to compare two photos of the same object even when they are not taken from the same spot and determine the differences between them. Based on this assumption a system that is capable of comparing the photos of tunnel lining from different time spots and determines the differences between them is currently being finalized. In the near future it will be possible to automatically determine the features on the lining, if it is a lining defect or not.

The first step in this task is to map the taken photos of the lining onto 3D space (Chaiyasarn et al. (2009)). Within this step first of all it is necessary to stitch the taken photos together. Stitching of photos for tunnel lining shows several problems, mainly cylindrical shape of the photographed object from different angles and distances (see Figure 11). These photos are having serious deformations on their edges and hence there are problems in theirs stitching along the overlaps. Assuming a cylindrical shape of the lining it is possible to use mathematical transformations that could eliminate such distortions of the photos edges and allow for stitching and mapping the photos onto 3D space (see Figure 12). This solution works fine for concrete lining that is in general flat, while for cast-iron lining with ribs does not work at all and following approach has to be applied.

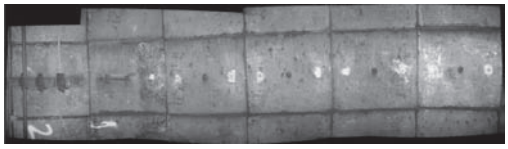

Figure 11. Automatic stitching of tunnel lining photos excluding the knowledge about its geometry.

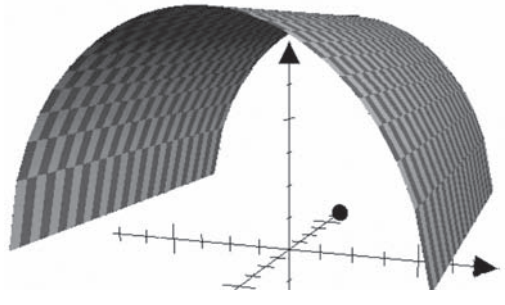

Figure 12. Scheme of the surface for lining photos mapping—additional information.

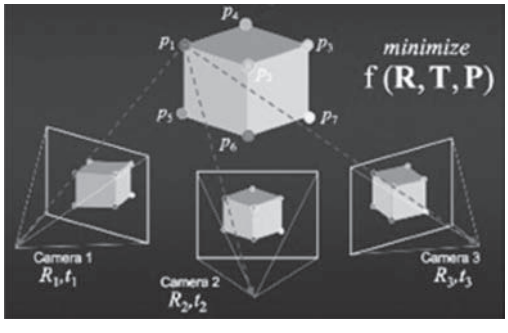

Figure 13. Proposed procedure for structured lining photographing and for determining the special localization of photographed object.

In this approach it is required for positioning individual points from digital photo into space to perform complicated mathematical transformations over several photos at once. From this it is obvious that we need several photos of the same object from different views. Using this approach it does not matter the angle and distance of the camera from the lining even on the contrary it is a requirement for proper spatial location of each photo. Suggested way of taking photos for proper spatial location is shown on Figure 13. These days we are also checking the option of combining this approach with 3D laser scanning of the tunnel lining that can provide the 3D model and later to map the photos on it, which we believe can significantly simplify the creation of the primary special lining model.

Once the selected part of the tunnel lining will be either way spatially modelled and primary photos placed on this model then it will be possible to easily place new photos and compare them in time.

7 MICRO-MONITORING

In order to be able to monitor in micro level development of micro cracks, it is necessary to use specialised equipment. This MEMS equipment was developed in the frame of our international project by colleagues from CNR in Bologna. MEMS sensors are very small (sub millimetre scale), hence they are very power consumption effective and could be used for long-term monitoring. The advantage of these MEMS sensors is their precision in the range of.

In order to connect such devices to the tunnel lining, several alternatives have been checked. Unfortunately direct gluing on tunnel lining is not possible as the device was introducing a stiffening effect, hence it was finally decided to connect the MEMS sensor onto a thin (0.25 mm) steel flat bar (see Figure 14), which will be anchored to the tunnel lining.

Produced and calibrated MEMS strain sensor (see Figure 15) is going to be shortly installed in our monitoring profile 1 just underneath the existing crackmeters.

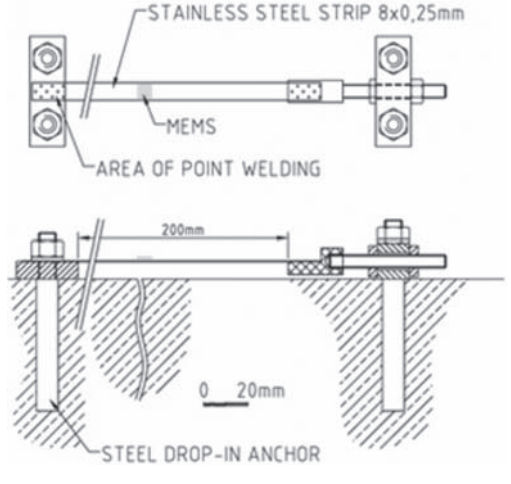

Figure 14. Design of MEMS crackmeter for tunnel lining.

Figure 15. Prototype of MEMS based crackmeter.

8 WIRELESS DATA COLLECTION AND TRANSFER

In order to be able to monitor the behaviour of tunnel lining almost instantly, it is necessary to provide a data collection network that has virtually no maintenance and high speed of installation. These criteria are met by wireless sensor network for data collection and by mobile phone modem for data transfer from tunnel.

Wired connection is very difficult, as usually a lot of very long cables are required and there is a huge problem to get them from tunnel through sealing profile (doors). This is issue is known to us here in Prague, as we using this approach for geophysical monitoring.

For wireless sensor network it is essential to be reliable, hence redundant and robust. In terms of redundancy we specified need for 2 independent paths from sensor to network gateway, where the data are collected. In Prague we adopted a simplified approach to provide redundant system—between gateway and monitoring profile we placed every 20 m set of 2 relay motes on each side of the tunnel top above the train running profile. Where 20 m distance was determined by simple trial in tunnel. And defines the shortest distance on which the motes can communicate between each other without any interruption in the tunnel, if they are place just on the lining on the same side of the straight tunnel.

The monitoring profile 1 was instrumented by WSN in September 2008. As the monitoring profile is about 300 m from the nearest station, where mobile phone signal is available, we installed the system "brain"—Balloon mini computer with GPRS modem about 30 m from station platform into the tunnel—Figure 16. WSN gateway (Figure 17) was installed about 100 m further down the tunnel with a connection to Balloon via Ethernet cable. Both Balloon and gateway are also connected to mains power supply. From gateway to actual monitoring profile there is 170 m distance which is "hopped" by 8 pairs of relay motes.

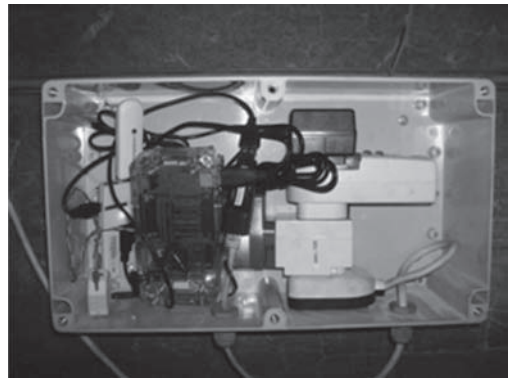

Figure 16. Central point of sensor network in tunnel—mini PC Balloon managing the wireless network and connecting to the internet.

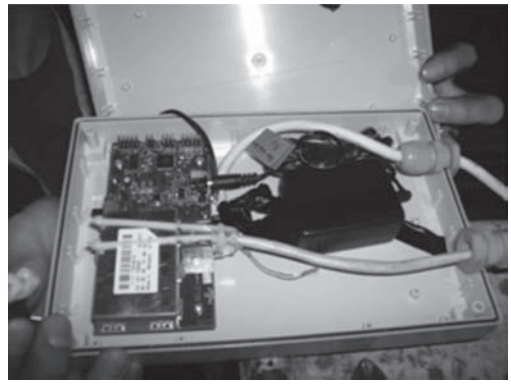

Figure 17. Wireless sensor network gateway connected with central point via Ethernet cable.

The actual monitoring profile was instrumented in parallel to conventional monitoring by WSN tiltmeters (5×) and crackmeters (2 pairs), see Figure 18.

The measurements are taken every 8 minutes. The frequency of measurements was decided from an analysis of energy consumption of the WSN. And the selected frequency was found as most energy efficient. Quicker readings would consume more energy, while longer periods would not save almost anything as there is certain overhead required for WSN to keep alive.

Output from the monitoring is presented for simple visualization in a form of website. Where data from 1 particular date are shown, examples of which are presented on Figure 19 (temperature

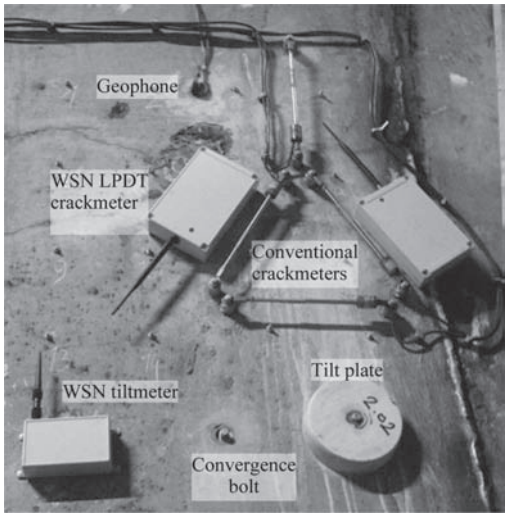

Figure 18. Photo of the instrumented profile showing all monitoring elements—convergence bolt, tilt plate, Geokon crackmeters, geophone, wireless crakmeters and wireless tiltmeter.

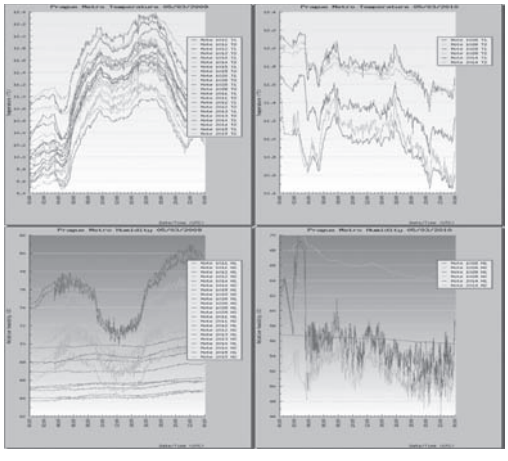

Figure 19. Output from monitoring on the web for temperature and humidity on 5th March 2009 and 2010.

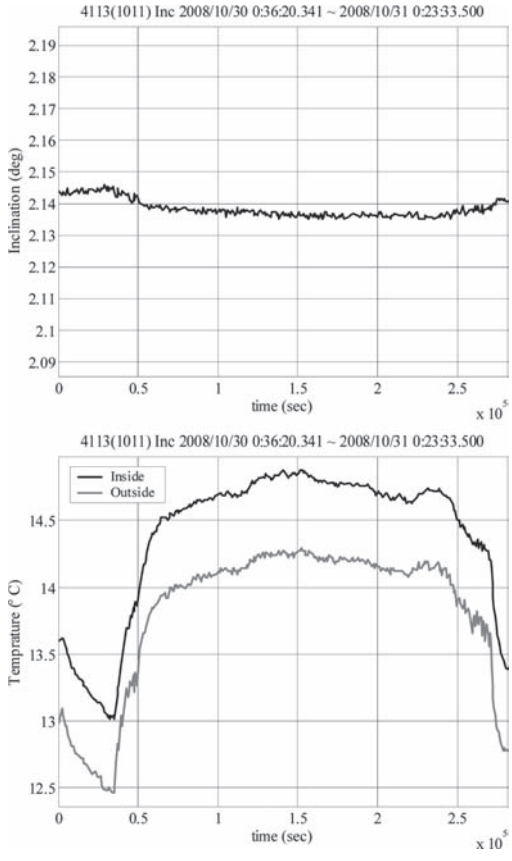

Figure 20. Detailed output for Inclinometer 1011 on 30th October 2008—clear indication of lining rotation as response to temperature changes.

and humidity for 5th March 2009 and 2010). The presentation of crackmeters and inclinometers readings are almost straight lines, hence detailed analysis per sensor is required and results are shown on Figure 20 for inclinometer 1011.

The system of WSN proved very reliable in Prague, even some back analysis presented by Bennett et al. (2010) indicated that relay motes of WSN could be spaced even double the distance as installed now.

The GPRS data transfer from Balloon PC seems to be reasonably reliable and the scheduled frequency data transfer from tunnel to the university server of 30 minutes is working well. If there is a connection problem, the data are collected at Balloon and transferred later.

On the monitoring profile 2 the WSN crackmeters and inclinometers together with the whole network were installed in December 2010.

9 CONCLUSIONS

All the mentioned monitoring methods are providing clear indication of the lining behaviour. It was indicated what monitoring method is useful for what type of application. Computer vision methods are useful for routine maintenance walkovers, laser scanning for proper geometry determination and comparison with numerical modelling and to show long-term creep type of movements in the range of

centimetres. The other direct methods either conventional or MEMS/WSN based are used for monitoring of potentially sensitive and already disturbed linings with mainly visible cracks, they are very sensitive but localized. The presented geophysical method can indicate deterioration of concrete lining even before any visible signs, therefore this method is very promising and also we found that have side effects that are of high interest for metro transport company in the determination of technical state of undercarriage axles. And they already proposed further closer cooperation in this matter.

Wireless sensor networks prove very reliable and can be used for almost on-line monitoring and if connected with allowable limits, it can automatically warn the infrastructure owner about potential problem.

ACKNOWLEDGEMENTS

The authors thank to the Grant Agency of the Czech Republic for allowing them, in the framework of the grant project GA 103/09/1600 "Research of monitoring methods for micro-deformation of (metro) tunnel lining", to prepare and publish this paper, which is part of the international research project—Eurocores Programme—Smart Structural Technologies (S3T) "Micro-Measurement and Monitoring System for Ageing Underground Infrastructures (Underground M3)".

REFERENCES

Bennett, P.J., Soga, K., Wassell, I.J., Fidler, P., Abe, K., Kobayashi, Y. and Vaníček, M. (2010): "Wireless Sensor Networks for Underground Railway Applications: Case studies in Prague and London," Smart Structures and Systems, Vol. 6, No. 5–6, pp. 619–639.

Bubeníček, M., Chamra, S., Macháček, J., Pruška, J., Vaníček, I., Vaníček, M., Záleský, J.: On-line Monitoring for Verification of Tunnel Lining Condition. In: The Present and Future of Modern Transport. CTU Prague, 2008, pp. 23–24.

Chaiyasarn, K., Kim,T-K., Viola, F., Cipolla, R. and Soga, K. (2009): "Image Mosaicing via Quadratic Surface Estimation with Priors for Tunnel Inspection," 2009 IEEE International Conference on Image Processing. Egypt.

Ferri, M., Mancarella, F., Seshia, A., Ransley, J., Soga, K., Záleský, J. and Roncaglia A., (2010a): "Development of MEMS strain sensors for crack monitoring in ageing civil infrastructures", Smart Structures and Systems, Vol. 6, No. 4, pp. 225–238.

Vaníček, I., Chamra, S., Macháček, J., Pruška, J., Vaníček, M., Záleský, J.: Ageing of underground structures—Prague metro, ČVUT Praha, 2008, 172 p, ISBN: 978-80-01-04251-9.

Vaníček, I., Záleský, J., Chamra, S., Vaníček, M. and Macháček, J., 2007. Methods of quality checking of the Prague Metro tunnel lining after flooding. Proc. XIVth ECSMGE Madrid. Cuéllar, V. et al (eds). Millpress, Rotterdam, Vol. 2, pp. 1033–1038.

Záleský, J., Bubeníček, M., Ferri, M., Roncaglia, A. Monitoring of the Prague metro tunnel lining. In: II. Conf. EuroEngGeo. Madrid, 2008, CD, 5p.

This page intentionally left blank

Geotechnical Aspects of Underground Construction in Soft Ground – Viggiani (ed)
© 2012 Taylor & Francis Group, London, ISBN 978-0-415-68367-8

Two adjacent railway tunnels underneath the historic city of Mainz

H. Quick, J. Michael & S. Meissner
Ingenieure und Geologen GmbH, Darmstadt, Germany

U. Arslan
Technische Universität Darmstadt, Germany

ABSTRACT: Different challenging tunnel projects in the downtown area of the city of Mainz in Germany are presented. These tunnels run parallel in a distance of 4 m to max. 50 m. The tunnels were built in soft soil conditions consisting of filling, clay and marl layers of the Tertiary. The paper presents the different construction techniques, the calculation methods for the two tunnels as well as the results of measurements for the New Tunnel Mainz. The experience for the construction of this tunnel and the results of the measurements were the basis for the chosen construction and calculation method for the rehabilitation of the Old Tunnel Mainz, which is currently under construction.

1 INTRODUCTION

The New Tunnel Mainz had been constructed in the years 1998 to 2001 directly adjacent to the existing Old Tunnel Mainz. This old tunnel built in 1884 is currently being rehabilitated, converted and enlarged during the next years. Due to the small overburden of both tunnels and sensitive structures on the ground surface challenging and unique tunnelling techniques were chosen to guarantee the stability and serviceability of the tunnels and of sensitive structures. In addition calculation methods and results from geotechnical measurements are presented in the following. The situation of the tunnels is shown in figure 1.

2 GROUND CONDITIONS

The geological condition is mainly characterized by the tertiary strata (Miocene) of the Mainzer Basin. The Tertiary strata sequence consists of an alternating sequence of marly clays, chalk marl, sandy silts (hydrobia silts, hydrobia oyster shells) and sands in an alternating sequence with chalkstone banks (fig. 2). The chalkstone banks are partly compact/massive to weathered. The consistency of the in-situ ground is stiff to semi-solid, turning into soft/paste-like if water intrudes. The groundwater can be found up to the level of the floor/upper edge of track; otherwise there is only local stratum water of little importance.

3 OLD TUNNEL MAINZ

3.1 *Construction*

The Old Tunnel Mainz was erected in the years 1881 until 1884 as one continuous double track tunnel. The tunnel has an horseshoe shape and the lining consist of sandstone with a thickness of approx. 0.9 m. The German core center tunneling technique was used to built the Old Tunnel Mainz with an overall length of 1200 m. The German core center technique (fig. 3) uses partial drivings, mostly sidewall drivings. Due to the bad condition of the tunnel, especially the masonry and to improve the smoke venting system, a 300 m long and up to 26 m deep open cut was built in the early 30ies of the last century, which divides the tunnel nowadays into the Tunnel Mainz Central Station and the Tunnel Mainz south (fig. 1/2).

The Old Tunnel Mainz consists of the following structures:

- Tunnel Central Station: 663 m
- Open cut: 300 m
- Tunnel Mainz South: 246 m

4 CONSTRUCTION OF THE NEW TUNNEL

4.1 *Construction techniques*

Parallel to the existing Old Tunnel Mainz, the New Tunnel Mainz was built in the years 1998 to 2000.

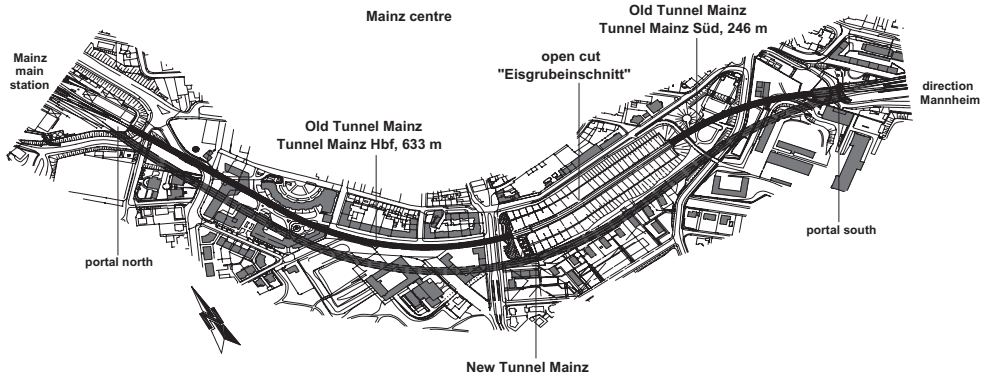

Figure 1. Plan view tunnel situation (Quick et al. 2001).

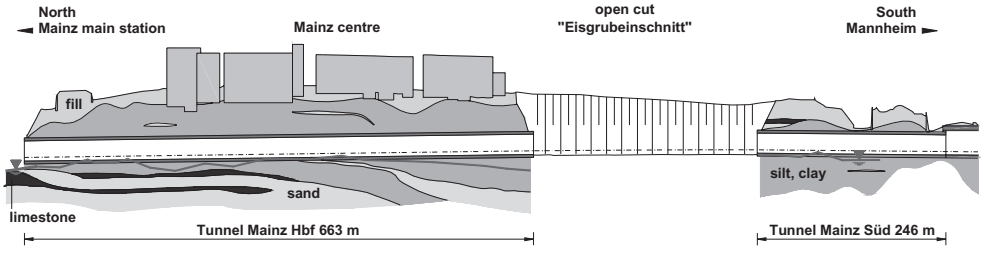

Figure 2. Geotechnical longitudinal section—Old Tunnel Mainz.

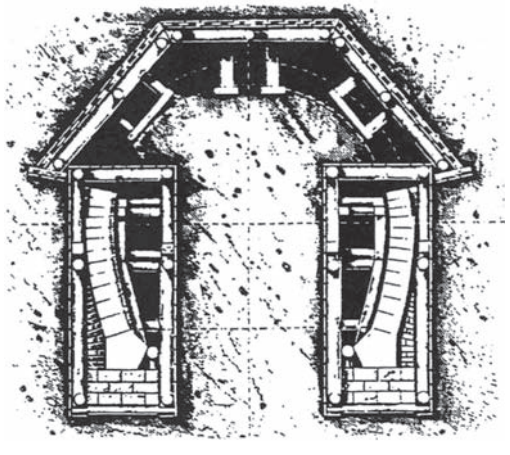

Figure 3. German core centre technique—Old Tunnel Mainz (Maidl 2004).

The new 1250 m long double track railway tunnel with a low overburden of 10 m to 23 m runs under buildings including a hotel with basements up to 10 m under ground level. Moreover, there are old (Roman) underground hollow spaces (gallery systems) to be undercrossed.

The clearance between the Old Tunnel Mainz and the new one varies between 4 m and 50 m (fig. 4).

Regarding ground conditions, existing settlement-sensitive structures and the possible influence on the Old Tunnel Mainz the excavation of the New Tunnel Mainz had to be carried out only with little deformation. Hence, an universal shotcrete tunnelling method with side wall drifts followed by the excavation of the calotte and core/bench was chosen as construction method (fig. 5).

The distance between the side wall faces and the final lining (ring closure) was limited to less than 100 m and in particularly sensitive parts to 50 m. The distance between the calotte face and the ring closure of the preliminary support was restricted to 30 m. Apart from the usual measurements in tunnelling additional securing measures were applied in areas of settlement-sensitive structures. They are as follows:

– Horizontally injected steel pipe roof shelter (strengthening of the longitudinal rock bearing arch) (fig. 5). The roof shelter is placed in the upper area of the face. The length of the drilling is 20.5 m. The minimum overlapping to the next roof shelter is 3 m. The advantage of

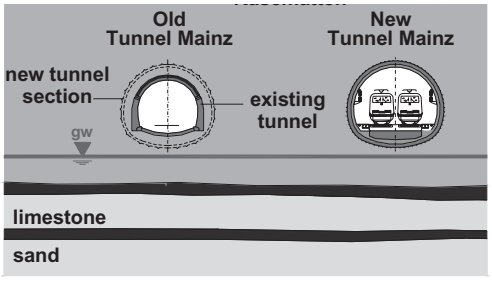

Figure 4. Geological cross section.

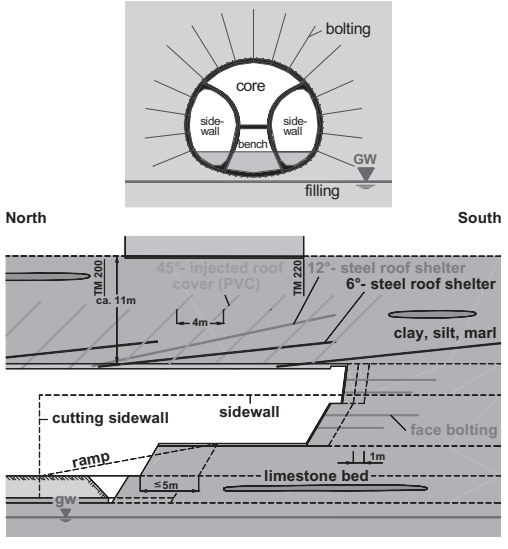

Figure 5. Undercrossing of a hotel; driving concept and securing measures (Steiger et al. 1999).

this technique is quite very obvious; a widening of the roof area to place the drillings is not necessary.

– In order to prevent any dilatational effect above the tunnel roof, 45 degree inclined, grouted PVC-fans are installed in continuous distances of about 5 m.
– Injections from the ground surface, pre-installed injection systems under the foundation of buildings as well as systematic face boltings within the tunnel are applied additionally in order to minimize deformations. All these measures together in connection with prior determined combinations of available measures were the basis of a successful driving with little deformations under settlement-sensitive structures.

4.2 *Calculation method*

For proof of the stability and serviceability 2D- and 3D-numerical calculation were carried out by means of the Finite-Element-Method with the program Abaqus (figs 7, 8). Continuum elements were used for the soil, where as beam elements for the lining. For the realistic simulation of the soil an elastoplastic soil behaviour was chosen (Quick et al. 2001). The modified Drucker-Prager material law with cap was implemented. The yield surface of this elastoplastic model is not constant in the principal stress space. It can expand due to plastic straining. Furthermore it distinguishes between different stiffness for loading, unloading resp. reloading.

For the calculation of the preceding deformations as well as to account for three dimensional arching effects around the unsupported tunnel the alpha-method was applied (fig. 6). The principle of this method is to reduce the stiffness of the finite elements which are to be removed in the next calculation step. The reduction causes changes in the initial stress field and therefore leads to preceding deformation. In case of the sidewall and calotte drivings the factor is set to 0.5. This assumption which controls mainly the preceding deformations was verified by measurements (fig. 11). In any case the evaluation of the factor α is difficult and is mostly based on experience.

The 3D-finite element model was created by extruding the 2D-mesh. Under respect of the construction procedure the length was chosen to 100 m (fig. 8).

4.3 *Monitoring*

Regarding the extraordinary situation to undercross several settlement-sensitive structures with only low overburden in soft ground an extensive geotechnical monitoring program had been carried out. At the surface the deformations due to tunnelling are measured in close distances by levelling as well as deformation monitoring systems, working on the principle of corresponding tubes. Figure 9 shows the measured surface settlements

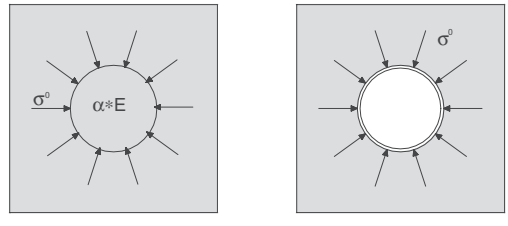

Figure 6. Principle of the alpha-method (Quick et al. 2001).

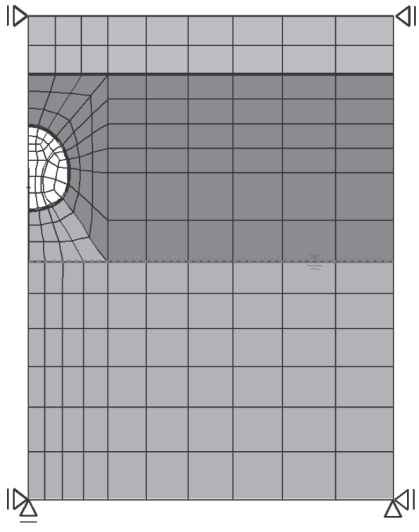

Figure 7. 2D-finite element mesh of the New Tunnel **M**ainz.

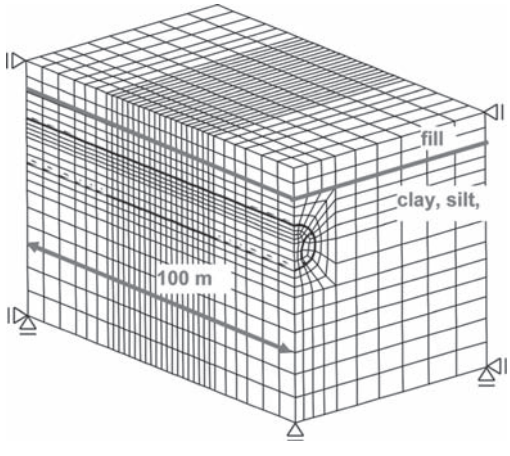

Figure 8. 3D-finite elements mesh of the New Tunnel Mainz.

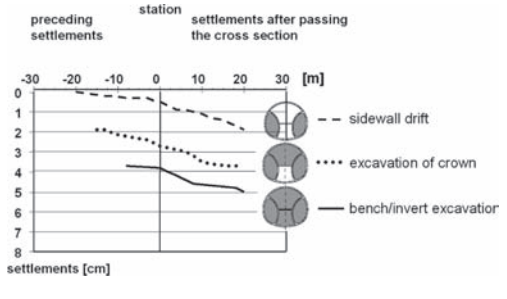

Figure 9. Measured surface settlements due to drivings (TM 117).

due to the driving at station TM 117. The surface settlement adds up to 5 cm. The settlements measured at the ground surface along the tunnel (fig. 10) were in most areas between 1.5 cm and 2.5 cm in average; at the very beginning of the driving additional securing measures—as described prior—have not been applied; the settlements at surface reached up to unacceptable 11 cm.

Figure 10 shows the surface settlements under respect of the different drivings (sidewall drift, excavation of crown etc.) at station TM 117. This station is close to the portal north (fig. 1). Most of the measured surface settlements are related to excavation of the sidewall drifts and the crown, while only a smaller amount of settlements arise from the bench/invert excavation.

Figure 11 shows the comparison between the measured roof displacements of the tunnel and the calculated roof displacements at station TM 117. The results of the 2D-caluclation show a good correspondence with measurements regarding the

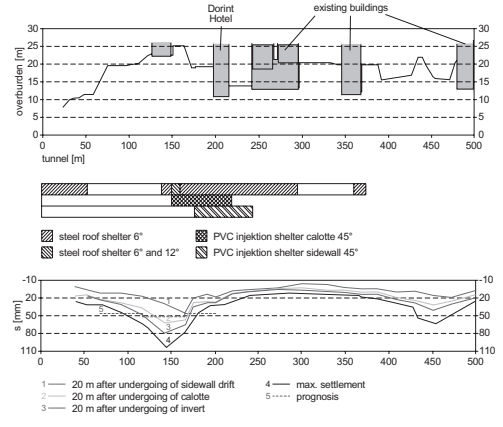

Figure 10. Surface settlement at surface due to tunneling.

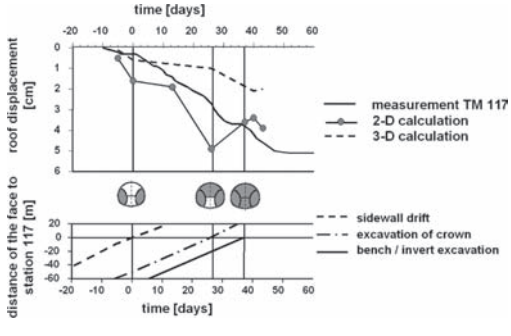

Figure 11. Comparison of measurements and calculations (roof displacements).

preceding displacement as well as the displacements due to the excavation of the sidewall drifts and the crown. However the calculated heave of the roof due to the excavation of the bench/invert does neither match the measurement nor the expected ground behaviour (fig. 11). For such soft soil conditions it is therefore in some cases necessary to increase the reloading-stiffness of the finite elements below the tunnel, in order to reduce the calculated heaving of the tunnel.

5 REHABILITATION OF THE OLD TUNNEL

5.1 *Construction technique*

Theure rehabilitation and enlargement of the Old Tunnel Mainz is going to be done under respect of the experiences of the New Tunnel Mainz. The partial loose ground (old back filling) around the Old Tunnel is improved by injections. In the first step the old filling around the tunnel is injected. Voids will be filled, improved by injections (bulk filling). For this 10 drillings up to a length of 2.5 m in a longitudinal distance of 1.5 m are carried out (fig. 12).

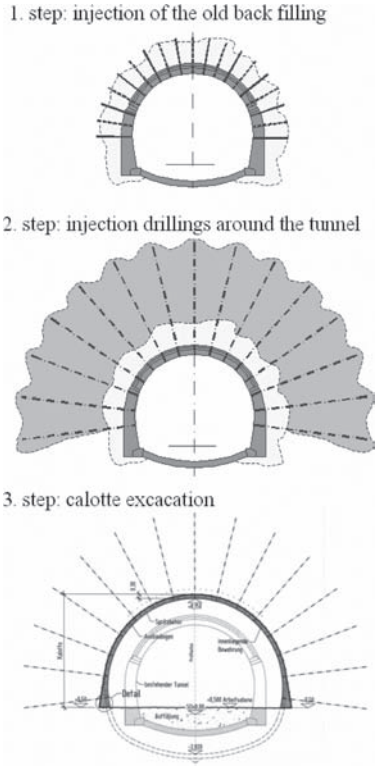

Figure 12. Tunnelling technique—Old Tunnel Mainz.

In the second step up to 8.5 m long injection drillings around the tunnel to activate a support ring are drilled. These two ground improvement steps are done under protection of the existing Old Tunnel. Subsequently the calotte driving in shotcrete method with an additional forepiles takes places. For the stability of the preliminary lining of shotcrete with a thickness of 0.30 m a widening of the calotte footing was established. In the final construction step the invert is excavated and the preliminary ring closure is achieved.

The distance between the face of the calotte driving and the preliminary ring closure with shotcrete is limited to less than 12 m.

5.2 *Calculation method*

For the design and the proof of the serviceability of the tunnel and the mentioned structures 2D- and 3D-numerical calculation are carried out with the program Plaxis. The numerical calculations regard all construction phases as well as the former excavation of the Old Tunnel Mainz and the New Tunnel Mainz. In order to create realistic results the material law of Hardening Soil with a yield surface, which is not fixed in the principal stress space is used. The yield surface expands due to plastic straining. In addition the material law can distinguish between different stiffness for loading and unloading resp. re-loading.

To account for the three dimensional arching effect of the unsupported enlargement of the Old Tunnel Mainz the beta-method is applied under respect of the used calculation program. The principle of this method is described in 3 steps (fig. 13):

1. Generation of the initial stress field $-\sigma^o$.
2. De-activation (excavation) of the tunnel clusters without activation of the tunnel lining and generation of (1-beta) reduced forces, which can be done by a reduction of the ultimate level of the full calculation step.
3. Activation of the tunnel lining.

The beta-value was obtained by an iterative back analysis of the New Tunnel Mainz. The predicted surface settlements of the 2D calculation for the ground surface amount to approx. 2 cm (fig. 14).

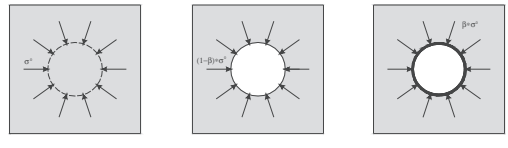

Figure 13. Principle of the beta-method.

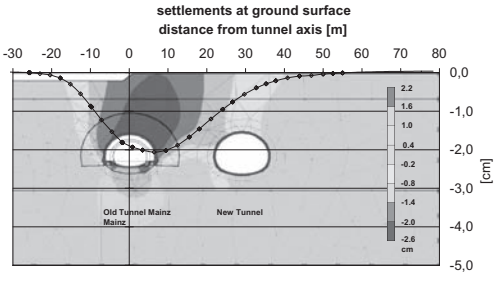

Figure 14. Calculation results—Old Tunnel Mainz.

5.3 *Monitoring*

The rehabilitation of the Old Tunnel Mainz is accompanied by an extensive monitoring program within the tunnel and on ground surface. For a quick interpretation of the data three levels of settlement limits for different areas under respect of the overburden and the existing structure were defined. On the basis of pre-defined measures such as an additional temporary shotcrete invert settlements can be slowed down and reduced to guarantee the stability of the existing structures.

6 CONCLUSION

The presented tunnels in the inner city of Mainz in soft soil conditions show a variety of different measures in the ground for the drivings in order to meet the requirements of the serviceability of existing buildings. 2D or 3D calculations were carried out to predict the displacements. It is shown that the evaluation of the input parameters and the calculation methods is complicated but decisive for the calculated results. Hence, every tunnelling project must be accompanied by an intelligent monitoring program to observe the impact on the environment due to the drivings and to ensure the stability and serviceability of the tunnel and neighboring structures as well as to generate data for possible back-analysis in order to improve the calculated results and to verify the assumptions. The paper shows also numerical approaches with different material laws and calculation methods. These different approaches can all lead to tolerable results, if methods are used properly and the input parameters are evaluated appropriately.

REFERENCES

Emeriault, F., Bonnet-Eymard, T. & Kastner, R. 2005. *Movements induced on existing masonry buildings by the excavation of a station of Toulouse subway line B*—5th international symposium, Amsterdam, Geotechnical Aspects of Underground Construction in Soft Ground. June 2005.

Kovacevic, N., Edmonds, H.E., Mair, R.J. & Higgins, K.G. 1996. *Numerical modelling of the NATM and compensation grouting trials at Redcross Way*—Geotechnical Aspects of Underground Construction in Soft Ground, Rotterdam, 1996.

Maidl, B. 2004. *Handbuch des Tunnel- und Stollenbaus*. 3. Auflage. Verlag Glückauf GmbH, Essen.

Quick, H., Michael, J., Schöttner V., Arslan, U., Katzenbach, R. 2000. *Tunnelling and Deep Excavation in Soft Ground*—GeoEng2000, Melbourne, 19.–24. November 2000.

Quick, H., Michael, J., Arslan, U. 2001. *About the effect of preliminary measures on ground movements due to tunnelling*—Response of Building to Excavation-Induced Ground Movements, London, 17.–18. July 2001.

Steiger, H., Theissen-Wenzel, C., Quick, H. 1999. *Neuer Mainzer Tunnel—Behandlung geotechnischer Grenzfälle in der Planung und Ausführung*—Vorträge zum 6. Darmstädter Geotechnik-Kolloquium, Darmstadt, 11. März 1999, Mitteilungen des Institutes und der Versuchsanstalt für Geotechnik der Technischen Universität Darmstadt, Heft Nr. 44.

Geotechnical Aspects of Underground Construction in Soft Ground – Viggiani (ed)
© 2012 Taylor & Francis Group, London, ISBN 978-0-415-68367-8

Aicha-Mauls on the Brenner Base Tunnel—status of the works and results

H. Quick & J. Michael
Ingenieure und Geologen GmbH, Darmstadt, Germany

K. Bergmeister
BBT-SE

E. Facchin
BBT-SE

ABSTRACT: The Brenner Base Tunnel is an indispensable element of the trans-border European priority scheme TEN Project No. 1 comprising a roughly 2,200 km long high-speed railway route between Berlin/Germany and Palermo/Italy. According to the latest planning the Brenner Base Tunnel will be 55 km long (fig. 1), including the directly following deviation tunnel of Innsbruck the entire tunnel construction will be 62,7 km long and hence the longest tunnel of the world. The concept of the tunnel comprises a maximum velocity of 250 km/h for the railway traffic. In the year 2007 the construction of the investigation tunnels Aicha and Mauls had begun; their construction is an integral part of the safety, maintenance and dewatering concept. The experience and results of their drivings and related monitoring of the rock and the rock mass behavior are crucial information for the latter design and construction of the main tunnels. Analogous to the system applied at the Gotthard Base Tunnel the Brenner Base Tunnel will consist of 2 single-tracked tunnels running parallel in a clearance of about 70 m. Between them runs a smaller exploration tunnel. Each 333 m rescue and service galleries will connect the main tunnel tubes (Figure 1).

1 PROJECT DESCRIPTION

The Brenner Base Tunnel is an essential link in the altogether 2,200 km high-speed rail route Berlin-Munich-Verona-Bologna-Palermo. The planned Brenner Base Tunnel is 55 km long, or including the underground line to bypass Innsbruck 62.7 km long. The tunnel is designed for rail traffic with a maximum speed of 250 km/h.

Work was started on the two investigation tunnels at Aicha and Mauls in Italy in 2007, the construction of these being an essential part of the rescue, maintenance and drainage concepts for the Brenner Base Tunnel as well as serving to investigate the geotechnical and tunnelling conditions of the future main tunnel. The Brenner Base Tunnel will consist of a system with two single-track tunnel bores (Figure 1), similarly to the Gotthard Base Tunnel. Beneath the two main tunnels, a smaller investigation tunnel is provided and pedestrian cross-passages will be constructed at regular intervals of 333 m between the two bores.

2 GEOLOGICAL AND TECTONIC OVERVIEW

The Aicha and Mauls tunnels will pass through the tectonic unit of the Brixener granite, which belongs to the South Alpine unit. This unit contains these lithologies: granite, granodiorite, aplitic and pegmatitic veins. The Brixener granite (Figure 2) is a non-metamorphic tectonic unit, strongly deformed during the Alpine orogeny. The result of this deformation was to form a multitude of brittle joints and faults. The northernmost part of the project area, where the intermediate starting cut at Mauls and the last kilometres of the Aicha investigation tunnel are situated, lies within the area of the Periadriatic Seam. The Periadriatic Seam represents geologically the northern border of the South Alpine unit and is a dominant, predominantly west-east striking fault system characterised by brittle fracture.

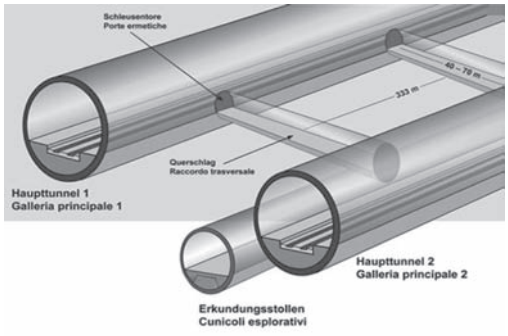

Figure 1. Concept of Brenner Base Tunnel.

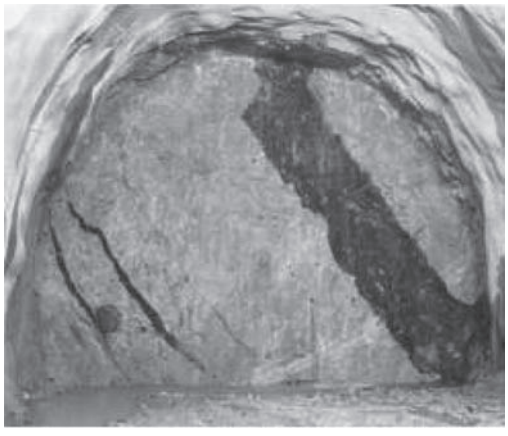

Figure 2. Brixener granite with basalt vein.

3 MAULS ADIT

The Mauls adit will be used for material deliveries during the construction of the main bores of the base tunnel and after their completion will guarantee access for maintenance and rescue sorties. The 1,767 m long adit has a slope of 9% and an excavation cross-section of 92 m^2. On a second axis, the Mauls investigation tunnel ("Periadriat-ica" axis) will be constructed with a length of about 0.5 km toward the Aicha investigation tunnel and the dismantling chamber of the Aicha TBM drive will also be constructed. These tunnels were conventionally excavated in a single-stage with shotcrete lining. The tunnelling work in Mauls was completed at the end of October 2009 and the Periadriatic Seam section at the end of March 2010. The average advance rate was 5.85 and 5.21 m/d (net) respectively.

4 AICHA INVESTIGATION TUNNEL

Tunnelling work has been underway at Aicha since December 2007. The first 150 m were excavated by conventional drill and blast and then continued as planned with a tunnel boring machine (TBM) followed by segment lining to the intended end of the tunnel after 10.418 km. The excavated diameter of the double shield TBM is 6.3 m. The annular gap between segment and rock, which is specified with different type classes for the various structural loadings (overburden pressure, faults, water pressure), will be filled with gravel. The current net advance rate is about 16 m/d.

5 GEOTECHNICAL MEASUREMENT EQUIPMENT

Geotechnical measurement equipment is being installed a regular intervals in the mountain and in the form of measurement segments, from which the stress and strain alterations can be queried digitally over WLAN (Aicha Tunnel) or manually (Mauls Tunnel). The data is entered into the database (2doc) by the site supervision staff and evaluated with regard to the geological-tectonic situation at the face, the results of geophysical advance investigations of the measuring instruments installed in boreholes and the machine and the machine parameters. The data and the relevant graphical evaluations are available online at all times for the project parties. In addition, the site supervision staff produces daily, weekly and monthly geological-hydrogeological and geotechnical reports, in which the investigation results are displayed as a whole and evaluated with regard to the prognosis of rock behaviour and structural basics.

When fault zones or significant new discoveries regarding the rock/groundwater conditions are encountered, the site supervision, after discussion with the client, can order the installation of additional geotechnical measuring equipment. Table 1 shows the instrumentation installed in the two tunnels so far.

Near each of the portals at Aicha and Mauls, an inclinometer and a groundwater level gauge were installed. During the drives, surface levelling was carried out in these areas.

5.1 *Conventional advance*

During tunnelling work at the Mules intermediate starting point, the TBM dismantling chamber and the "Periadriatic Seam" section, the geotechnical measurement instrumentation was supplemented

Table 1. Overview of amount and kind of geotechnical and hydrological measurement devices.

Geotechnical-hydrogeological measurement equipment *Geotechnische-hydrogeologische messeinrichtung*	Number (as of 31/05/2010) *Anzahl (Stand 31.05.2010)*		
	Aicha tunnel	Mauls adit	Periadriatic seam tunnel
Inclinometer *Inklinometer*	1	–	–
Groundwater quantity (portal) *Grundwassermessstelle (Portal)*	1	–	–
Surface leveling *Oberfldchennivellement*	1	1	–
Rock thermometer recording *Felsthermometrische Erhebung*	30	14	6
Magnetic extensometer *Magnetextensometer*	5	–	–
Five-point extensometer *Mehrfachstangenextensometer (5 fach)*	–	–	4
Measurement segment cross-section: (each 4 pairs of strain gauges/2 pairs of strain gauges) *Messtubbingquerschnitt (a 4 Paar Dehnungsmessgeber/a 2 Paar Dehnungsmessgeber)*	34/4	–	–
Measurement section, conventional excavation, with: Pair of strain gauges (CV) Pressure cell in rock (CP) Pressure cell in lining segment (CR) *Messquerschnitt konventioneller Vortrieb mit Dehnungsaufnehmerpaar (CV) Druckmessgeber im Gebirge (CP) Druckmessgeber im Ausbaubogen (CR)*	–	5X(5CV + 3CP) and 2X(3CV + 3CP + 5CR)	1X(5CV + 3CP)
Discharge measurement in tunnel/portal *Schiittungsmessung (im Tunnel/Portal)*	4/1	1/1	–
Piezometer in tunnel/portal *Piezometer (im Tunnel/Portal)*	7/1	1	–
Convergence survey section *Konvergenzmessquerschnitte*	46	63	16
Face deformation measurement (current/no longer current) *Ortsbrustverschiebungsmessungen (aktuell/nicht mehr aktuell)*	–	1/6	1/3

by the installation of thermometer and multiple extensometer and vibration measurements were carried out.

5.1.1 *Convergence measurement cross-sections*
Five surveying pins with removable reflex targets were installed at each survey cross-section. The survey pins were additionally equipped with protection against blasting in order to be able to perform a measurement soon after detonation. On average, convergence survey cross-sections were set up every 27.5 m; the targets were surveyed geodetically (3D). The maximum deformations (in this case convergences) were less than 4 mm for the entire period of measurement.

5.1.2 *Measurement of face deformation*
Whenever tunnelling was stopped for any length of time, nine reflex targets were installed in the face and surveyed geodetically (3D). The maximum horizontal deformation was less than 3 mm.

5.1.3 *Thermometer recording*
The rock temperature is monitored using altogether 14 resistance temperature sensors and three thermistors, which are each installed about 2 m deep in the rock. At the end of the drive toward the Periadriatic Seam, three thermistors were installed at depths of 0.5, 3 and 30 m. The rock temperature in the Mauls adit rises from 14 °C near the portal with 100 m overburden to 26 °C under an overburden of 1,210 m (Figure 3). In the Aicha Tunnel, the measured temperatures under overburden depths of 400 to about 1,200 m remain fairly constant at 20 to 22 °C.

5.1.4 *Strain gauges and pressure cells*
Main survey cross-sections were set up at 8 places along the Mauls adit. These cross-sections vary according to the type of layout and the number of instruments. A main survey cross-section normally consists of three pressure cells in the rock (crown, both spring lines) and five strain gauges

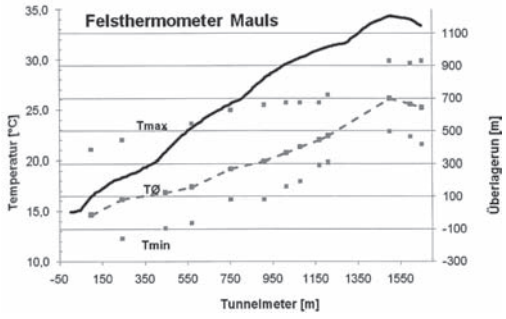

Figure 3. Results of the thermometer data at Mauls.

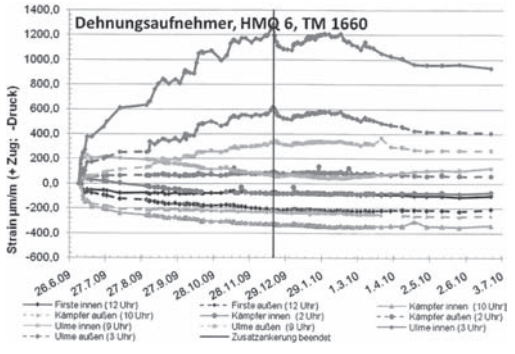

Figure 4. Graph of the strain measurements at main tunnel survey section 6, Mauls Tunnel Geological cross section.

(crown, both spring lines and both sides), which are installed in pairs in the shotcrete lining.

At the TBM dismantling chamber, the lining is additionally supported with steel arches. This is due to the greater cross-section required and the relatively short separation of the two later main tunnel bores. In this area, a main survey cross-section consists of three pressure cells in the rock (crown, left- and right-hand spring lines), six pressure pads on or in the steel arch and three strain gauges, which are installed in pairs in the shotcrete lining.

The measured data is not only recorded for the design of the planned main tunnel, but is also evaluated in the course of the tunnel advance with regard to the current stability of the tunnel and the lining. The main survey cross-section 6, which was installed at the start of July 2009, can serve as an example: a clear and continuous increase of the stresses (strains) was recorded in the right side of the shotcrete lining (Figure 4).

Neither the data from the convergence measurement cross-sections nor the evaluation of the geological conditions recorded during the advance could deliver any conclusions about the reasons for this increased stress. In the middle of October 2009, with the measured values continuing to rise, the first fine cracks were noticed in the shotcrete lining. Additional anchoring (12 Swellex, L = 5 m) only achieved a slowing ot the increasing strain, and only pattern bolting (1 m × 1 m) in a section of altogether 10 m long prevented a further increase of stress and stopped the progressive crack formation.

5.1.5 *Multiple extensometer*

At the end of the drive toward the Periadriatic Seam, the last main survey cross-section was set up near the face. The instrumentation included, in addition to the pressure cells and the strain gauges, four five-point extensometers. These measure the radial deformation at a distance of 1.5, 3.5, 4.5, 10.5 and 15 m from the side of the tunnel. In combination with the strain gauges and the pressure gauges in their immediate vicinity, these can be used to analyse deformations and stress transfers in the rock mass, above all in relation to further advance toward the Periadriatic Seam.

The survey cross-section installed at the end of the "Periadriatica" drive is equipped with a data logger, which records data from all the instrumentation installed at the section. The measured values are recorded and read out at fixed intervals.

5.2 *Mechanical advance*

Measurement segments, magnetic extensometers, rock thermometers and pore water pressure gauges were installed in the Aicha investigation tunnel. Four pairs of vibrating wire strain gauges are cast into the segments tan-gentially. Advance drilling, reflection seismic and geo-electrical measurements were undertaken to investigate ahead of the advance. The results were used to develop prognoses for the rock conditions ahead of the machine and risk management. The prognoses were compared and validated against the TBM parameters and the face images.

5.2.1 *Magnetic extensometer*

At four cross-sections, magnetic extensometers were installed with depths of up to 12 m and spacing between 0.8 and 2 m radially in the crown and spring line areas. These were installed using a radial drill behind the shield tail of the TBM so that stress transfers after excavation were taken into account. The maximum deformations measured were less than 1.5 mm/m.

5.2.2 *Measurement segments*

Instrumented segments are currently installed at 34 cross-sections. The eight strain gauges per measurement segment cross-section are each installed in pairs in the segments at the spring line and the crown.

The tangential arrangement of the strain gauges can measure positive and negative strains in the segment ring. These are read manually as long as the segment is within the TBM and after that by WLAN. The recorded values (us, Hz) are converted to stresses and provide useful information about the stress distribution and any relevant alterations in the stress distribution in the segment ring. At the same time, the client undertakes the back-calculation of the lining design for use for the planned main tunnel.

5.2.3 *Geodetic measurements*
In areas where significant strains were measured in the segments, removable reflex targets were installed and surveyed geodetically (3D) to check the deformation of the tunnel lining.

5.2.4 *WLAN query system*
The instrumentation (thermometer, measurement segments and piezometers) was equipped with a WLAN query system after leaving the backup. The measured values from each sensor were transmitted by radio to gateways.

The gateways are equipped with a data logger, which saves the received data at configurable times (twice a day). The data at the gateways can be read and further processed by special software at any time. In addition, it is possible using a radio-logger to control the sensors singly with a code at the location and read the data directly. At the moment, the gateways are connected with the glass fibre cables used to transmit all TBM data to the site management offices. This makes it possible to view and graphically process the data at and time.

5.2.5 *Hydrological measurements*
At locations with large water ingress, seven vibrating wire pore water pressure sensors were installed at a depth of 11 to 15 m in the tunnel side wall. The discharge is recorded at five positions in the tunnel with a measurement weir via data logger. The discharge at the portal is detected and recorded by a laser. The forecast short-term discharges were mostly not reached during the excavation.

At the moment, the discharge at the portal is about 55 l/s (forecast 200°l/s).The chosen arrangement of the various data loggers for discharge measurements in the tunnel and the measurement of the total discharge at the portal enable the observation of water ingress into the tunnel for individual sections. The maximum recorded water pressure in the tunnel is 2.1 bar.

5.2.6 *Rock behaviour*
To describe the variety of geological conditions, project-specific rock mass behaviour types based on the OGG guideline [1] were defined and assigned to each section [2] [3] [4]. During the tunnelling work, these forecasts were compared with the actually encountered rock classes (RMR according to Bieniawski) and the rock behaviour. After about 8,300 m had been driven, there was a good agreement with the forecast; the tendency is (excepting the problems described in the next section) slightly more favourable rock conditions (Table 2). In addition to the geological recording of the face, windows are provided in the segments for visual checking and recording of the rock in-situ.

6 FAILURE EVENT IN THE AICHA TUNNEL

After faults belonging to the Periadriatic Seam, running mostly across the direction of the tunnel, had been bored through as planned, a progressive failure of the segments occurred at the left side of the tunnel at 6.150 over a length of about 100 m, starting in the already lined tunnel and extending forward until the TBM was jammed (Figure 5).

Table 2. Comparison between the prognosis of rock classes and types of rock behaviour with the results of the investigation tunnel Aicha.

Prognosis				Actual	
Station (m) from, to	Rock type	Rock class (Bieniawski)	Rock behaviour type	Rock class (Bieniawski)	Rock behaviour type
0–70	GB-G-D-20 L	IV	undefined	III–IV	GVT1
70–2,340	GB-G-20 L	II–III	GVT2	I–III	GVT1
2,340–3,790	GB-G-19 L	III	GVT2	I–IV	GVT1
3,790–6,000	GB-G-19 K	II–III	GVT 2/5	I–V	GVT 1, seldom GVT 2
6,000–9,517	GB-G-181	II–III	GVT 2/5	I–IV	GVT 1, seldom GVT 2
9,517–10,408	GB-G-18H	II–III	undefined	not yet driven	not yet driven
Faults	GB-NE	I–V	GVT 3	III–V	GVT 2
Faults	GB-EW	I–V	GVT 3	III–V	GVT 2

Figure 5. Failure in the Aicha Tunnel, breakage of the left-hand shotcrete lining.

The failure occurred in an area, which had been defined as unfaulted or weakly faulted in both the advance investigations and the geological and rock mechanical face records. The geophysical process used was reflection seismic measurements performed every 150 m to investigate the geological-tectonic conditions in advance. This was supplemented with drillings ahead of the machine, which were however only undertaken when they fitted with construction logistics and during stoppages.

The data from the measurement segment installed at TM 6099 shows strain increases within 24 hours of (converted) up to 10 MPa (tension stress at inner strain gauge, compression at outer) in the left side wall (Figure 6).

After the failure, extensive additional investigation measures (radial core drilling, advance drilling) were carried out, and monitoring systems (automatic crack width sensors) were installed. Figure 7 shows the investigation measures and the installed measurement equipment.

The direct investigations carried out in the left-hand side and crown (20 m long core drillings) show that there is, an almost vertical fault zone running nearly parallel very close to the side of the tunnel (Figure 8). This could not be recognized from the tunnel itself.

For the determination of the structural loading, 3D-FE calculations were carried out (Figure 9),

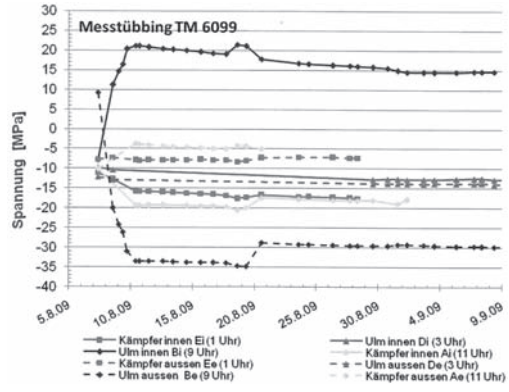

Figure 6. Data from the measurement segment at TM 6099.

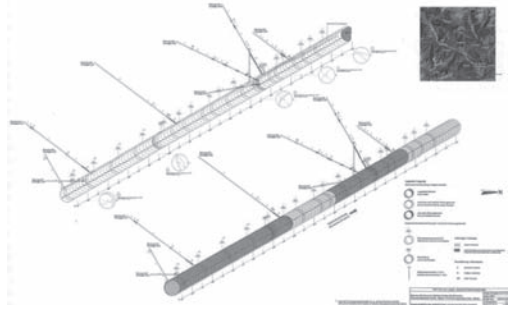

Figure 7. Overview of instrumentation and core drillings at TM 6150.

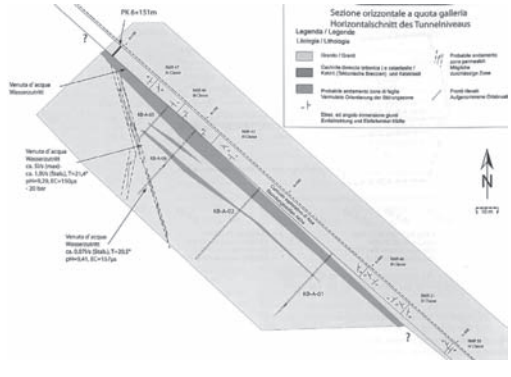

Figure 8. Plan of investigated fault zone and water ingress at TM 6000 to 6150.

in which the measured deformations and stresses were back-calculated in parameter studies and limit state analysis and the appropriate combinations of values were determined [7] [8].

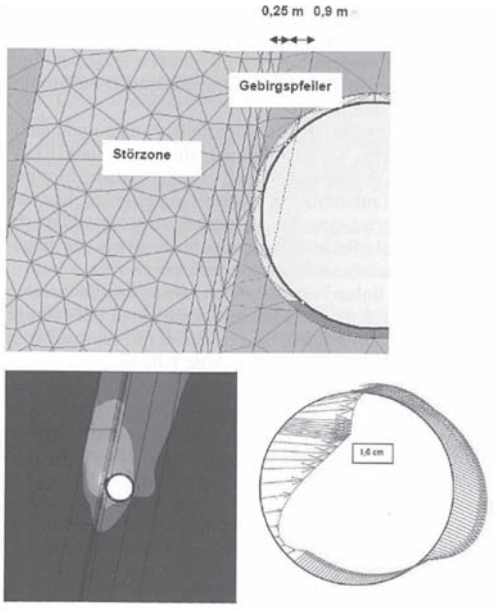

Figure 9. Calculation model and results of the 3D-FE calculations.

These were put into practice in further work on the verification of structural stability and the design of the lining.

The investigation works specified to clarify the cause and the subsequent repair caused a stoppage of one month. In parallel, an extended risk management scheme was produced to lay down fixed rules for the type and extent of measures and risk management functions for the remaining tunnelling work. The use of differently reinforced segments (types L to XXP) is also based on the experience gained in the tunnel and subsequent measurement data.

7 RISK MANAGEMENT

After the failure, the original procedure and extent of measures for risk management were widened. For the mechanical tunnel drive, at least two risk evaluations were undertaken every day by the site supervision.

The risk evaluation includes the assessment of the forecast and encountered geological situation (rock mechanics inventory of the face, interface properties, assignment of the rock class according to Bieniawski, description of hydrogeological indicators, analysis of the muck etc.) and the assessment and interpretation of the geo-technical data, the assessment and interpretation of the geophysical advance investigations and the current TBM parameters like penetration index, thrust force, revolution speed, torque, including control of the volume of annular gap filling.

Based on the risk evaluation, the previously fixed measures or packages of measures are applied. These include not only tunnelling measures but also decisions about lining and advance investigation:

- reduction of the advance rate,
- less thrust force,
- installation of segments of different thickness (Figure 10),
- use of additional strengthening measures (installation of steel ribs),
- installation of instrumentation (measurement segments),
- increasing the frequency of geological and rock mechanics investigations,
- drilling advance holes and recording of drilling parameters,
- geophysical down-hole investigations with radar.

In addition, hydrogeological evidence is kept and rock thermometers are installed according to risk class in addition t the planned instrumentation.

The penetration index (thrust force per mm penetration) has proved useful as an aid to risk evaluation (B). Particularly on account of the tendency to agree with the qualitative ups and downs of rock

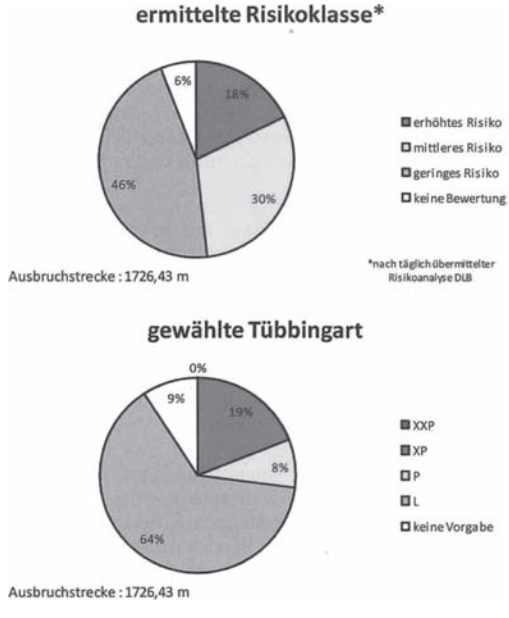

Figure 10. Risk class and segment types.

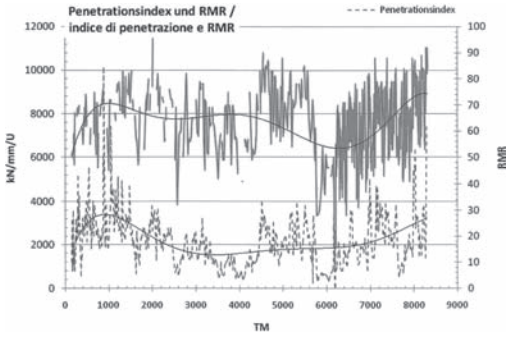

Figure 11. Penetration index as an aid to risk evaluation.

quality (measured by RMR values), the measures were selected and applied according to the risk management.

8 OUTLOOK

Tunnelling work in Aicha was completed in October 2010. The construction of the investigation tunnel by conventional and mechanical methods and the installed and interpreted instrumentation has provided valuable knowledge for the planning of the main tunnel bores.

REFERENCES

[1] Bundesgesetz liber die Vergabe von Auftragen (Austrian law governing the award of contracts) *(BVergG 2002)—BG-Bl. I, Nr., 99/2002*, Nationalrat der Bundesrepublik Oster-reich.

[2] Brandner, R., Reiter, F. & Tochterle, A.: *Geologische Prog-nose des Brenner Basistunnels—ein Uberblick (Geological forecasts of the Brenner Base Tunnel - an overview)*. BBT-Symposium. Innsbruck, 2005.

[3] John, M., Reiter, F., Skuk, St. & Venturini, G.*: Geotechni-sche Aspekte fur den Bau des Brenner Basistunnels (Geotech-nical aspects for the construction of the Brenner Base Tunnel)*. BBT-Symposium. Innsbruck, 2005.

[4] Facchin, E: *Brenner Base Tunnel: The first construction site from Aica to Mules.* BBT-Symposium Innsbruck, 2010.

[5] Bergmeister, K.: *Brenner Basis Tunnel: Aktueller Stand (Brenner Base Tunnel: current situation)*. Tunnel 1/2010.

[6] Quick, H. et al. (2009): *Monitoring at the exploration tunnels Aicha-Mauls, Preliminary results.* Turin, 2009.

[7] Barla, G.: *Esame delle condizioni interazione tra ammasso roccioso e rivestimento in conci al la progressiva PK 6+100.* Unpublished report, 2009.

[8] Prof. Dipl.-Ing. H. Quick—Ingenieure und Geologen GmbH: *Numerische Simulation/Rüickrechnung Schadens-ereignis Bereich TM 6120–6140 im Erkundungsstollen Aicha (Numerical studies/back calculation of the failure at TM 6120–6140 in the Aicha investigation tunnel*. Unpublished report, 2009.

Geotechnical Aspects of Underground Construction in Soft Ground – Viggiani (ed)
© 2012 Taylor & Francis Group, London, ISBN 978-0-415-68367-8

A new tunnel bored in alluvial soft soil under the Malaga Airport

C.S. Oteo
Construction Technology Department, Universidade da Coruña, Spain

J. García Pérez
Aeropuertos Españoles y Navegaciòn Aérea, Spain

H. Moreno
ACCIONA-SAND, Spain

P. de La Fuente
Universidad Politécnica de Madrid, Spain

J. Oteo Escobar
Europea de Ingenieria y Servicios S.A., Madrid, Spain

ABSTRACT: Due to the Extension of Malaga Airport, it became necessary to route the Malaga-Fuengirola railway line underground, creating two subterranean stations and more than 2 Km of tunnel. Although the tunnel end could be resolved using continuous slurry trench walls, the presence of the River Guadalhorce has led to the problem being resolved by executing the tunnel using a tunnel boring machine of ∅ 9.40 m to excavate through the sediments of that river (soft clay, loose sand, etc., with a very high water table). The article describes the works, with the most important landmarks (zones with scarce coverage, pass under the existing railway, emergency shaft, etc.), as well as the treatment of the land that it was necessary to perform. It also describes the auscultation carried out and comparison of its results with the forecasts of movements previously performed, with a code of finite elements.

1 ANTECEDENTS

The Malaga-Fuengirola railway line is a sole electrified track, with double track in some of the stations. There are two fundamental aspects that make action on the line necessary: at the time, a study was carried out of the need to double the line due to increased demand, and to increase the facilities at Malaga Airport. At the same time, the extension of the airport runways made it necessary to route line underground, with it passing under the River Guadalhorce, near that Airport. Those underground routing works consisted of execution of a corridor for double track with a total length of approximately 4,000 metres, from the exit of Los Prados station, at Km. 4 + 355 of the present track, to the exit of the present Airport–Traveller Terminal station (Km. 8 + 347). The feature of that corridor is that it runs underground for practically the whole route.

These underground routing works have been co-financed by AENA and the present Directorate General of Railway Infrastructures of The Ministry of Development.

2 DESCRIPTION OF THE SOLUTION PREPARED

The stretch forming the object of this article includes the following functional elements (Fig. 1):

- Guadalhorce Station (Km. 0 + 735 – Km. 0 + 931).
- Airport Station (Km. 2 + 870 – Km. 3 + 110).
- Initial Pumping Shaft (Km. 0 + 420).
- Emergency Exit, Ventilation Shaft and Pumping Shaft (Km. 1 + 892).

The stretch forming the object of the project had four construction types applied to the underground routing of the railway line, that were:.

a) Section with embankment and/or open cast excavation. b) Open cast section between conventional walls. c) Open cast section between slurry trench walls with an upper and lower slab (width between walls of 9.40 to 10.34 m). d) Tunnel excavated by tunnel boring machine (E.P.B. type, with an exterior diameter of 9.40 m; stretch length: 1,971.55 m).

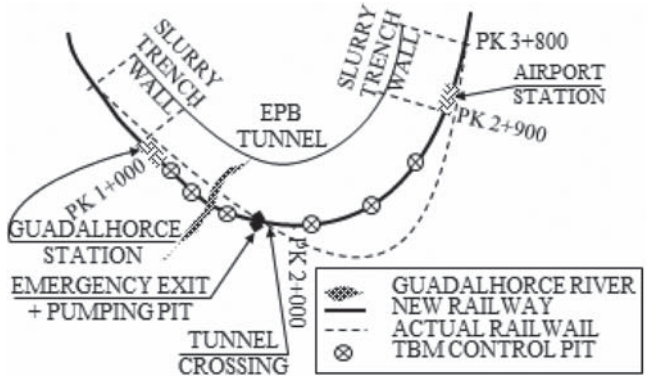

Figure 1. Zone Plant.

Figure 1 shows the schematic ground plan of the works with the most outstanding elements.

3 GEOLOGY AND GEOTECHNIQUE

The airport zone and the railway route of the Malaga-Fuengirola line affected by the Project are located in the lower part of the River Guadalhorce Basin, in the municipal district of Malaga. The route is fully located in the fluvial facies and interior estuary of the river Guadalhorce. These materials are flanked by the hills of Malaga, that constitute the main source areas of the materials. The sedimentary basin of the lower Guadalhorce is enclosed by Pliocene materials, their edges and the border faults of the mountain ranges. As these reliefs are relatively near and as a consequence of the isostatic and climatic readjustment movements, the fluvial deposits associated with the river Guadalhoce have quite considerable thicknesses, with the detritic facies of the banks characterized by a gradual transition from coarse to fine materials, at the edge of the basin.

As stated in the Project, the geological site conditions were strongly affected by the presence of the sea; due to the interaction with the sea, continious material readjustments occurred at the site of the Project. This fact, along with the fluvial dynamic, meant that the co-relation between sedimentary deposits is highly complex and the resulting morphologies have scarce lateral continuity. The alluvial soil of the Guadalhorce is highly heterogeneous detritic sequences of gravels, sands, silts and clay, with lens of organic silts and grey clay associated with the early mouth of the estuary and the abandonment of old canals. That is to say, there are alternating coarse and fine materials, with loose density and soft consistence, respectively.

The planned route runs from its start to Km. 2 + 300 somewhat perpendicular to the present course of the river, then gradually turning to run parallel to it, from Km. 2 + 700 to the end. There is a great variation in horizons on the alluvial plains, the following having been distinguished: a) Anthropic fills (R). b) Quarternary fine sediments (clay and muds, QM). c) Fine to coarse sand with pebbles (Qs). d) Quaternary gravel (QG). e) Quaternary grey and greenish clay (Qc). f) Pliocene clay (PC). g) Partially cemented gravel (PGC). h) Pliocene brown marly clay (PCM), the near sustratum. The last three horizons are Pliocenic and, thus, more competent. Table 1 summarises the main geotechnical properties of that ground assumed for the analytical analysis deduced from laboratory tests, S.P.T. an pressiometric tests and the engineering personal experience in the zone and Figure 2 shows a schematic geotechnical section through the tunnel development.

4 TUNNEL BETWEEN SCREEN WALLS

The underground stretch, as has already been stated, has a length of 3925 m. The solution adopted alternates between use of the tunnel boring machine between Km. 0 + 930 and Km. 2 + 800, continuous slurry trench walls, both on corbel as well as *in situ* top slab, and the corbel walls.

The solution adopted in this case is that of continuous reinforced concrete walls, either corbelled or strutted horizontally by top slabs and invert.

These continuous diaphragms have thicknesses of 1.00 m and 1.20 m, with embedding between 12 and 18 m under the excavation level, due to the low consistency of the ground. Their calculation was performed using the RIDO french numerical program. One must state that, with regard to

Table 1. Summary of geotechnical properties for diaphragm walls analysis.

Ground	Units	Dry bulk density (t/m³)	Water content (%)	% Fine content (**)	Cohesion (t/m²)	Friction angle (º)	Horizontal reaction modulus (t/m³)
Clays long term location	QM	1.63	27	80–95	2.0	28	1000
	Qc						
	Qcs						
	Pc						
	Pcs						
Clays short term location	QM	1.63	27	80–95	4.0 (2.0) (*)	22 (28)	1000 (2500)
	Qc						
	Qcs						
Sand	Qs	1.80	15	30	0.0 (0)	33 (33)	1200 (4000)
	Ps						
Gravel	QG	1.91	6	11	0.0 (0)	36 (36)	1800 (1800)
	PG						
Fillings	R	1.7	12	VAR	0.0 (0)	26 (25)	250 (250)
Pliocene	Pc	1.9	10	40	4.0 (2.0)	22 (28)	1000 (2500)
	Pcs						

(*) Final parameters
(**)% through nº 200 sieve ASTM

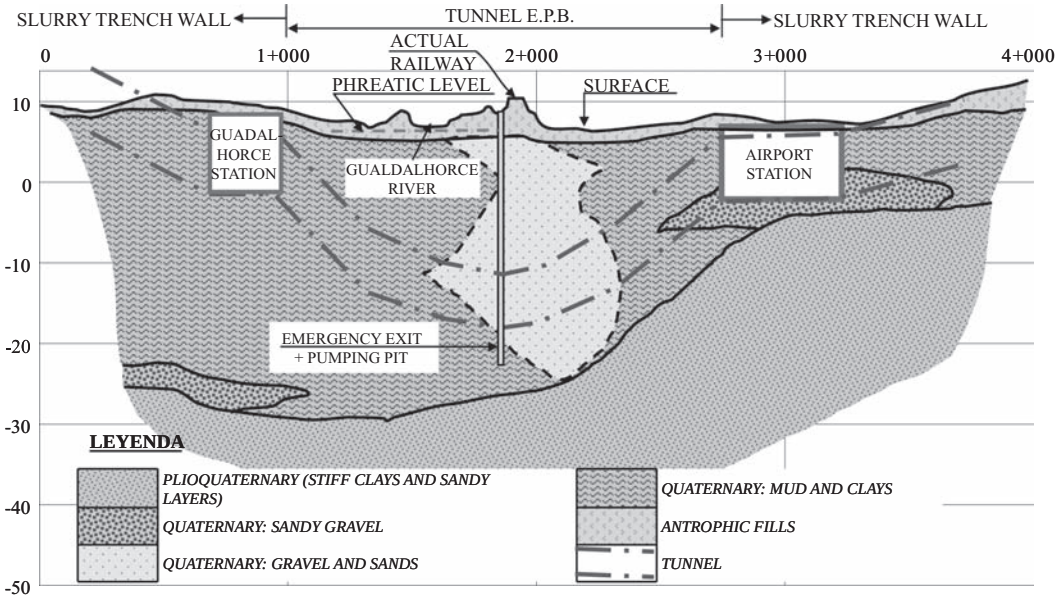

Figure 2. Schematic geotechnical profile of the area.

the definition of the invert, (1.0 to 1.20 m thick), according to the span and depth, with a V shape.

5 GUADALHORCE STATION

The Guadalhorce station and the entrance shaft used for the tunnel boring machine (adjoining the previous one) have a length of 197 m and are located between Km. 0 + 733 and Km. 0 + 930, placing the tunnel boring entrance shaft at the end, between Km. 0 + 835 and Km. 0 + 930. The shaft was formed using continuous slurry trench walls of reinforced concrete, (thicknesses of 1.00 m and 1.20 m). The diaphragm walls were strutted horizontally using reinforced concrete slabs and crossbeams.

The level of intermediate strutting of the tunnel boring machine cutting face shaft is 7.50 m above the floor level. The crossbeams, with a section of 2.2 × 2.0 m, were planned in reinforced concrete (5 intermediate side walls), defining four intermediate openings and two ends (Figure 3).

During the planned excavation of the entrance shaft for the tunnel boring machine, the installed instrumentation detected excessive displacements in the walls (nearly 90 mm horizontal displacement) with settlements of about 50 mm in a building near to the works (Fig. 3).

New tests (dynamic penetrometers) allowed a new ground profile to be defined, with a greater level of fillings (3 m more thickness). The project had already been calculated with some short term shear strength parameters (initial parameters of Table 1) that gave less thrust and deformations than those that had been measured at the field (Fig. 3). Recalculation with the another's geotechnical parameters (Table 1 final parameters defined by local experience deduced from actual works at the Málaga Underground) allowed better reproduction of what had happened (Fig. 3). These assumed measures were as follows:

- Provisional metallic shoring up of the "in situ" wall (7 circular profiles (∅ 610 mm, e = 12.5 mm).
- Execution of Jet-Grouting columns at the foot of the walls to avoid displacement obtain its foot, that was excessive according to the available measurements.
- Execution of a concrete invert for improved reinforcement of the screen wall in the definitive phase.
- Shotcrete treatment of the walls intrados—on steel mesh—to guarantee long term durability due to the excess displacement being equivalent to fissuring of the concrete (more cover).

Based on the experience obtained from excavation of the start shaft for the tunnel boring

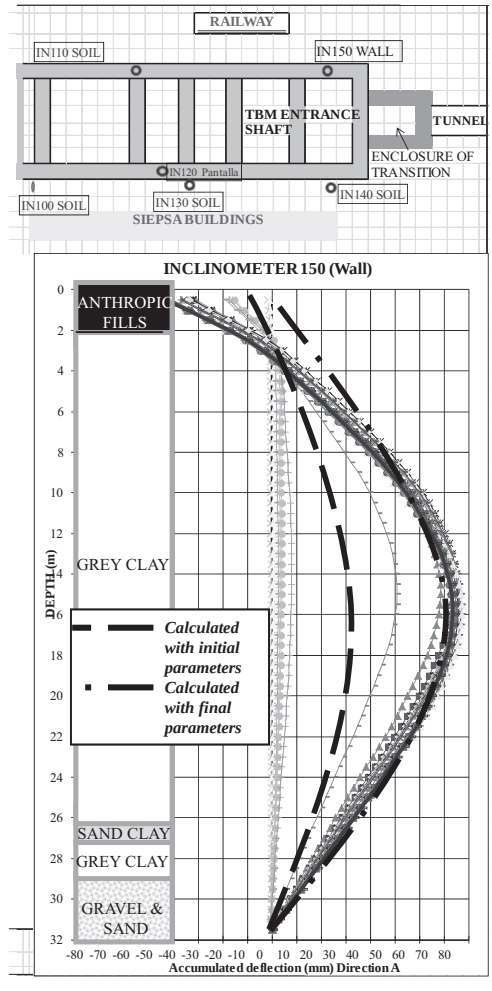

Figure 3. Deformation data shown by the inclinometer IN 150, situated near the entrance shaft.

machine, in order to apply it to excavation of the line tunnel and with new stretch data provided by the excavations carried out, a new process of the line tunnel construction was proposed in the initial zone. The aim of this was to limit the excessive movements of the walls.

Following the previous study, it was recommended to adopt a new excavation construction process for the continious walls by using provisional metallic shoring (HEB-300/2.5 m profiles) located at 4.00 m above the maximum excavation, to limit and control the screen deformations.

Within the line tunnel in the initial zone, special attention was paid to Km. 0 + 500, due to the nearness of several existing silos to the tunnel. After carrying out the relevant study, in addition to provisional metallic shoring of the line tunnel,

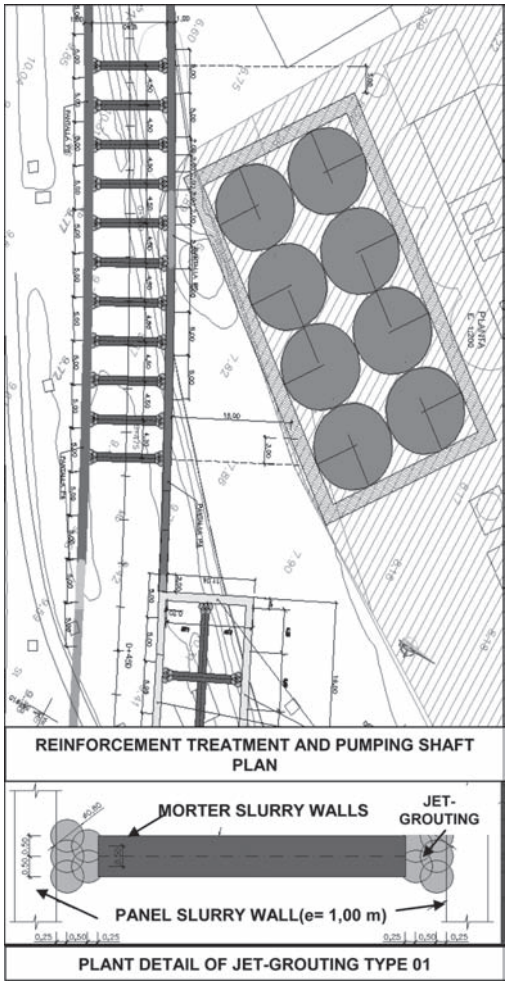

Figure 4. Ground plan of the silos and props at the foot of the screen walls of the line tunnel and initial pumping shaft.

it was recommended to provide props at the foot of the diaphragm by performing Jet-grouting and mortar set screens under the excavation (Figure 4). The results obtained were satisfactory and the silo settlement less than 3 mm.

6 TUNNEL WITH T.B.M

6.1 *General aspects*

As already mentioned, most of the tunnel was excavated using an E.P.B. tunnel boring machine of ∅ 9.40 m, with reinforced concrete segments 32 cm thick. The excavation was performed fully in soft clay with sand and loose quaternary gravel,

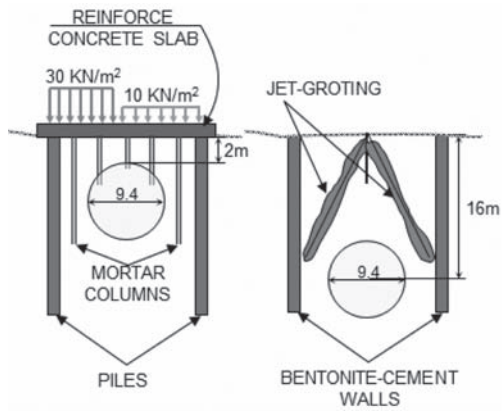

Figure 5. a) Initial treatment (T-3). b) Tent shaped treatment (T-6).

sometimes with scarce top cover. Mainly for that reason apart (from passing under the actual railway to be replaced) diverse ground treatments were designed, in order to assure the stability of the works (and reduce the surface movements, as appropriate).

The following is a brief list and description of the most important treatments performed (not including the "start" shaft of the E.P.B. and other specific cases).

6.2 *Initial stretch and Crossing of the Azucarera-Intelhorce road (T-3 and T-4)*

Due to the quantity of existing utilities affected in the area where the tunnel boring machine crossed the Azucarera-Intelhorce road (as soon as the tunnel with the E.P.B. commenced), a pile founded concrete slab 1 m thick was laid, on which to fasten the utilities affected and thus prevent the excavation becoming unstable, given the scarce existing top cover (3 m). In order to improve the ground conditions after the tunnel boring machine passed through, injections were executed every 4.5 m to fill the gaps under that slab. The gantry crane was installed on that slab to stock and supply segments (Fig. 5a).

6.3 *Stretch between Km. 1 + 202 and Km. 1 + 290 (T-6)*

On this stretch, there is a level of quaternary gravel with the groundwater table (GWT) at the tunnel crown level. The fine content of this material is very low, #0.080, lower than 20%. Due to the lack of fine particles in this material at the tunnel crown, it was foreseen that chimneys might possibly form

due to instability of the crown, as happened on one occasion. In order to avoid or limit formation of such chimneys, it was decided to treat the gravel in the tunnel crown zone by columns of jet—grouting laid out in a canadian tent shape (Fig. 6b). It was also decided to eliminate possible water flows by forming sealed enclosures made of bentonite—cement walls. In order to avoid specific instability and these being dragged, a transversal screen of mortar piles was made at the centre of each one of those enclosures, and after the tunnel boring machine passed through, a draining ditch was dug in each one of those enclosures.

6.4 *Inspection tasks (T-7)*

In order to inspect and review the machinery and repair it when necessary, it was decided to establish inspection shafts, every 300 metres, also taking advantage of the emergency exit at Km. 1 + 870 as an inspection shaft (7 inspection shafts). These inspection shafts (that are 15 m wide and 4 m long), except for that located at Km 1 + 100, are made as a sealed enclosure of weak block concrete inside by mortar piles (3 rows of ∅ 850 mm). In same cases (Km. 1 + 100) the piles were of the secant type, given the presence of sand and gravel.

6.5 *Emergency exit (T-8)*

Two sealed enclosures were made in this zone using weak concrete slurry trench walls with a thickness of 1.20 m in order to be able to eliminate the thrust of the water to be extracted by pumps from the actual sealed enclosure and facilitate construction of the connections between the tunnel and exit shaft. Moreover, in order to join the tunnel emergency exit, prior to its construction, a treatment was carried out from the surface based on micro-cement injections, limited in turn with a jet grouting screen. Finally, in order to facilitate excavation of the exit shaft and improve the behaviour of the screens, a jet-grouting plug was made under the invert level if the enclosure could not be exhausted (finally, that background treatment was necessary, Figure 6).

6.6 *Passage under the railway (T-9)*

The crossing with the existing railway on the surface takes place toward halfway through the tunnel, where the crown of the tunnel is at a depth of 20 metres. The ground is formed by quaternary sand with punctual alternating gravel, with the water table located about 3–4 metres from the surface. In order to avoid subsidence problems in the train track due to the tunnel boring machine passing under it, the decision was made to from a "canadian tent" using jet-grouting columns, reinforcing the railway side

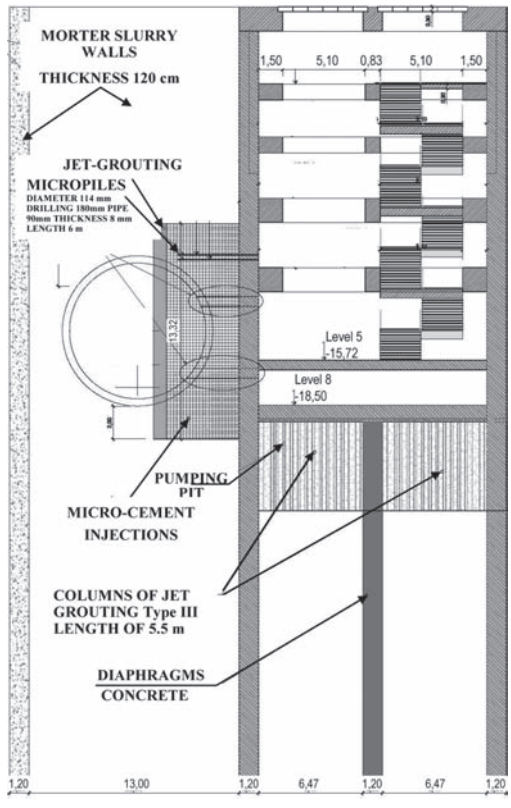

Figure 6. Transversal section of the emergency exit with treatment.

with a double jet grouting line (similar to T-6 treatment, Fig. 5b).

6.7 *Arrival at the airport station (T-10 and T-11)*

Preloading of the future airport runways was to be carried out in this zone, that runs from Km. 2 + 040 to 2 + 885. The height of the preloading would be double that of the final filling. The tunnel was not built until all the consolidation subsidence had taken place, to avoid excessive deformation to the tunnel once it was built. (Fig. 7, treatment T-10).

Apart from that issue, the natural ground cover above the crown is scarce, sometimes even less than a half diameter. In order to avoid stability problems, all the preloading was left to treatment T-10, until the tunnel had been built, not being withdrawn until afterward, so that, in order to accelerate that consolidation, wick drains were placed from km. 2 + 040 to 2 + 680. The total lining above the tunnel at the moment of it being built, natural ground plus filling with preloading, was at least 1 diameter. In the area where the cover was less, the

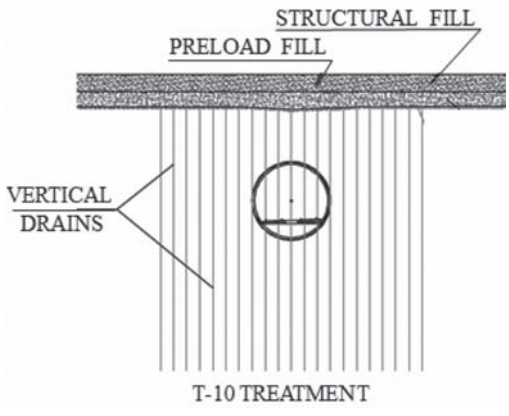

Figure 7. Treatment under the airport pavement.

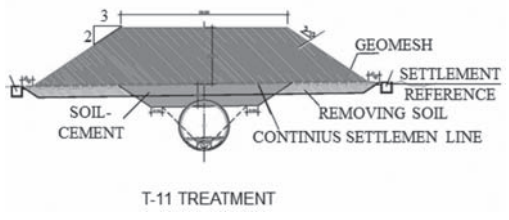

Figure 8. Treatments under runways.

preloading was increased until it reached that figure (from Km 2 + 680 to 2 + 885), being performed with the same material and degree of compacting as the rest of the filling, slope 3H/2V and a crown width of 30 metres.

In some zones, the natural ground was reinforced with a layer 4 metres thick of ground stabilised with cement, (Fig. 8, treatment T-11).

7 RESULTS OBTAINED

7.1 *Instrumentation*

Diverse types of instrumentation has been installed along the works:

a) Into the slurry trench walls: Inclinometers. b) On tunnel segments: Cells to measure the total pressure on the lining and stresses originated on the tunnel segments. c) In the ground: Instrumentation to measure the settlement and horizontal movements, that might affect near infrastructures (buildings, utilities, etc.)

Inclinometers, total pressure cells, vibrating cord extensometers, levelling markers, rod extensometers, piezometers, electro-levels, etc., were used for that purpose.

The most conflictive points of the stretch, as already remarked in point 6, that were performed by tunnel boring machine, were studied using the PLAXIS two-dimensional finite elements code, in order to estimate: a) Maximum axial thrust on the segments. b) Maximum bending moment on the segments. c) Vertical and horizontal movements in the ground. d) Thrusts on the slab and supporting piles (initial stretch).

7.2 *Results obtained in different points from the tunnel*

7.2.1 *Initial zone and Azucarera-Intelhorce road crossing (T-3 and T-4)*

Given the high number of interferences and due to the movements calculated in the project for this zone being very high (settlement at the crown estimated at 128 mm.), a finite element model was prepared in PLAXIS to estimate the settlements, taking the treatment to be performed into account. The calculation model took (drained stress hardening soil model, with the unload modulus 2,5 times the load modulus, with $K_0 = 0,6$, the profile of Fig. 2 and the shear strength properties from Table 1) into account the two hypotheses that could be raised according to the value assigned to the stress relaxation of the ground coefficient (α) in this soft soil, applying α values of 0.2 and 0.3. The maximum values estimated were about 25% of the design one, about 10–25 mm above the crown; the results measured after excavation of the tunnel (measured immediate settlement) perfectly fitted the models and, more specifically, that obtained using the highest ground relaxation value, that means that the soft ground has an immediate stress relaxation of about 30% (Fig. 9).

7.2.2 *Zone between Km. 1 + 202 and Km. 1 + 290 (T-6)*

Due to the lack of fine materials and the heterogeneity of the gravel in this area, the results obtained were according to the time, there being immediate settlement according to the PLAXIS

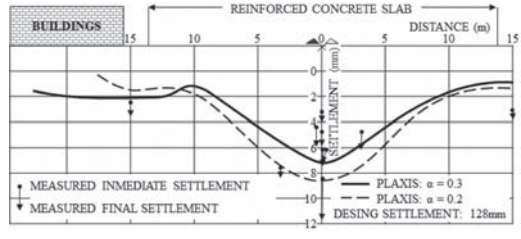

Figure 9. Comparison between theoretical analysis and the measured settlement induced by tunnel excavation (T-3).

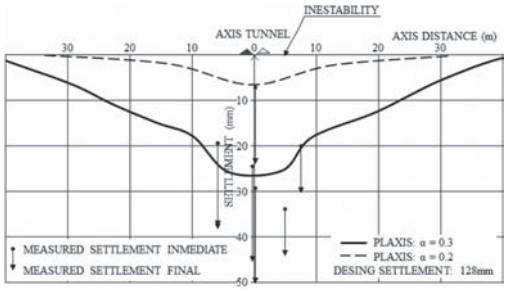

Figure 10. Treatment T-6: theoretical and field behaviour, in this zone a superficial instability has been originated.

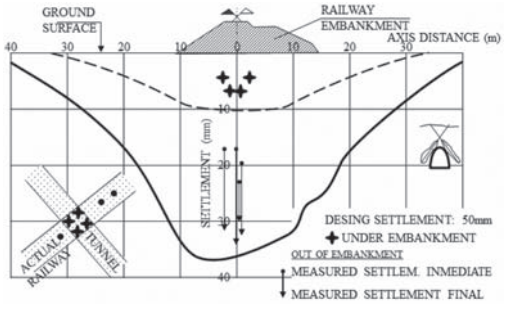

Figure 11. Crossing under actual railway: theoretical and measured settlements.

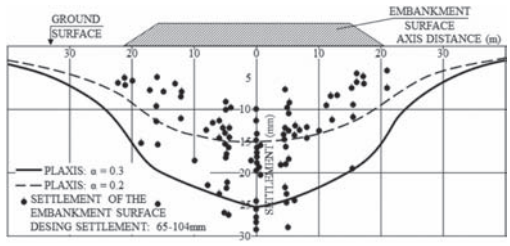

Figure 12. Treatment T-10 tunnel crown depth about 10–12 m.

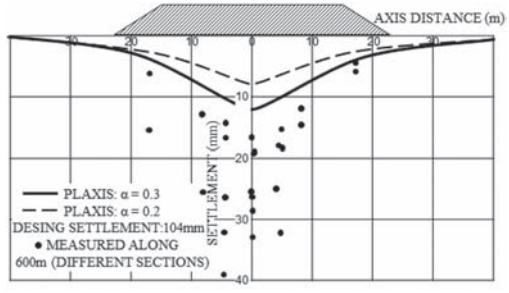

Figure 13. Treatment T-11. The measured settlements including part of the soil consolidation under the surface preload.

model calculating that by greater release of those tensions or ground accommodation, that settlement would gradually increase, between 30 and 40%, observing that they stabilise after 28–35 days after the excavation, always taking into account that they never reach even 50% of the design settlement (about 10 cm, Fig. 10).

7.2.3 *Crossing under the railway (T-9)*

The crossing under the existing railway was a delicate point, due to trains continually passing overhead, but the settlement caused in the railway track was about 4–6 mm, being lower than the model estimates. The railway platform was also monitored, there being somewhat greater settlement, of about 20 mm (Fig. 11). The different measured procedure to justify, in our opinion, these discrepancies.

7.2.4 *Arrival at airport station (T-10 and T-11)*

The last models studied were highly difficult to define, due to the variability of the soil conditions in the cross section that might exist due to there being different thicknesses in each level of the treatments. The results of calculation sections chosen (Figs. 12 and 13) are similar to the results obtained and, in both cases, they were about 15–25 mm.

7.2.5 *Summary of the obtained results*

In the initial project, evaluation was carried out of the maximum subsidence originated by the tunnel boring machine, by the Sagaseta & Oteo Method (1974 and Oteo and Sageseta, 1982), using average bulk deformation modulus, (Fig. 14): interval of 1 to 3, without taking treatments into account. The cover above the tunnel crown is also shown in this figure. Settlement between 15 and 45 cm was foreseen, without a clear degree of certainty. However, it was possible to reproduce the ground treatment in each case using the PLAXIS Code, obtaining settlement figures from 10 to 40 mm, fairly similar to those really measured. In zones without treatments, settlement reached 20 cm.

As may be appreciated from observation of Figure 14, the degree of approximation was fairly satisfactory.

ACKNOWLEDGEMENTS

The authors of this article wish to express their thanks to AENA and the Directorate General of Railway Infrastructures for permission to publish these results, especially to Manuel Sáez (Director

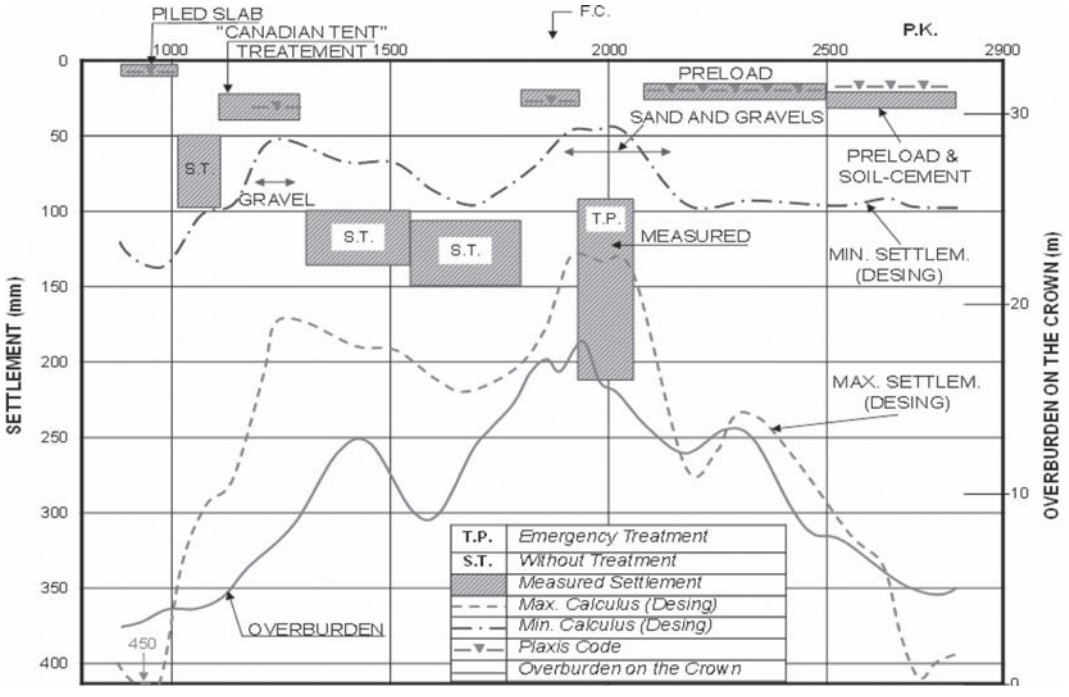

Figure 14. Comparison of the subsidence foreseen and measured.

of the Malaga Plan) and Antonio Gutiérrez (Gen. Dir. of Railway Infrastructures). They would also like to thank Fernando Correchel, (AENA), the consortium UTE NUEVA PISTA, the consortium UTE ATCV, the companies Rodio-Kronsa, SITE, Terratest and Tecnasol (who performed the ground treatment), INMATEINSA (that was in charge of the instrumentation), for all the collaboration provided. A special mention goes to AEPO.

REFERENCES

Oteo, C. & Sagaseta, C. 1982 Predictions of settlements due to underground openings. *Int. Symp. on Numerical Models in Geomechanics. Dugar, Pyer and Studer eds. Zurich. pp. 653–59.*

Sagaseta, C. & Oteo, C. 1974. Análisis de la subsidencia originada por la excavación de túneles. *1er Simposio Nacional sobre Túneles, Madrid, Vol. 1.*

This page intentionally left blank

Geotechnical Aspects of Underground Construction in Soft Ground – Viggiani (ed)
© 2012 Taylor & Francis Group, London, ISBN 978-0-415-68367-8

Analysis of convergence data and 3D numerical modelling of tunnels excavated in fine-grained soils

P. Perazzelli & T. Rotonda
Department of Structural and Geotechnical Engineering, Sapienza University, Rome, Italy

D. Boldini
Department of Civil, Environmental and Material Engineering, University of Bologna, Bologna, Italy

A.M. Ajmone-Cat
Astaldi S.p.A., Rome, Italy

P.M. Gianvecchio
CO.MERI S.p.A., Rome, Italy

ABSTRACT: This paper focuses on the convergence measurements of twin motorway tunnels under excavation in a Pliocene formation in the South of Italy. The tunnels are driven full face, with a cross-section of 120 m^2, by means of a conventional excavation method, up to a maximum depth of 120 m. The primary lining is an open arch made up of shotcrete and steel sets; the definitive lining consists of concrete cast in three different stages. Convergence measurements were analyzed on the basis of the curve-fitting technique proposed by Sulem et al. (1987). Then, the influence on tunnel deformation of overburden and lining construction sequence is investigated. Finally, the role of the primary and final linings in reducing tunnel convergence is investigated by means of a three-dimensional stress-strain analysis, performed with FLAC3D code.

1 INTRODUCTION

Modern tunnelling methods include ground displacement monitoring as an essential part of the construction: it allows confirmation of design assumptions and provides a basis for changes in the excavation sequence and support methods. The paper presents convergence measurements carried out at two parallel motorway tunnels under excavation in a fine-grained formation in the South of Italy.

Convergence measurements were analyzed accordingly to the model proposed by Sulem et al. (1987), which relates tunnel displacements to both face distance and time-dependent behaviour of the soil. The influence of the lining construction sequence, as well as that of tunnel overburden, are discussed. Three-dimensional numerical stress analyses, using the FLAC3D code, are also presented, in order to investigate the role of different primary support systems and the construction sequence of final lining on the tunnel deformation.

2 SANTA MARIA TUNNELS

The Santa Maria twin tunnels are part of the new motorway route 'SS 106 Jonica', under construction on behalf of ANAS S.p.A.. The motorway crosses the South of Italy running along the Jonic Sea, between the towns of Taranto and Reggio Calabria. The tunnels take the name from the Santa Maria hill, in the Catanzaro countryside, through which they are excavated.

The tunnels, which are currently under construction, are 1.3 km long. They are identified as "North tunnel", which runs towards Taranto, and "South tunnel", which runs towards Reggio Calabria.

The twin tunnels are excavated in a Pliocene formation, mostly consisting of silty clay. They are driven full face using a conventional excavation method, up to a maximum depth of 120 m. The tunnel diameter is about 13.0 m, which corresponds to a cross-section of 120 m^2, and the minimum clearance between the tunnels is 20 m.

An open primary lining made up of shotcrete and steel sets has been adopted. The concrete final lining has been cast in three different stages, i.e. the sidewall, invert and vault of the tunnel section.

Careful monitoring is being carried out in order to ensure compliance with construction quality requirements, verify design assumptions and adapt primary lining. Regular measurement of tunnel displacements is carried out. In a few sections along the tunnel extension also the load in the lining is monitored.

2.1 *Geological and geotechnical outlines*

The Santa Maria hill is formed by two Pliocene formations (Fig. 1). In the upper part of the hill there is a formation denominated 'Asa', composed of alternating layers of sandstones (decameter thickness) and loose sand (centimetric thickness). At the bottom of the hill there is a lithological unit denominated 'Ags', composed of alternating levels of gray blue silty clay (multidecameter), crossed locally by layers of sand and silt, and of decameter levels of silty-sandy clay.

The tunnels are mainly excavated through the Ags formation. During the design stage, geotechnical investigations were carried out only in areas near the tunnel entrance and in areas subject to higher overburdens. During the excavation, samples have been also collected from the tunnel face, in order to improve the knowledge of soil properties at the tunnel depth.

Along the entire route, the tunnels pass through a fine-grained soil with a high percentage of silt (on average up to 50%) and a variable percentage of clay and sand. In some limited areas the percentage of the sand increases up to 40% (Fig. 2).

A summary of the physical and mechanical properties of the soil sampled at the tunnel face is shown in Table 1. No significant variations are recorded between the two tunnels. Plastic and liquid limits vary in the intervals, respectively, 20–25% and 30–50% (Fig. 3). Values of water content, in the interval between 20 and 30%, are close to the plastic limit. Using Casagrande's classification, the fine fraction of the soil sampled can be classified as an inorganic clay of medium plasticity.

Compressibility was investigated in the laboratory by means of oedometer compression tests: compressibility and swelling indexes exhibit values in the intervals, respectively, 0.06–0.12 and 0.020–0.055.

Triaxial, as well as direct shear tests, were also carried out. Very high scattered values of strength parameters were obtained along the tunnels: the peak cohesion varies in the interval 20–50 kPa, while the peak friction angle varies in the interval 25°–35°. The larger values of friction angle, associated to the lower values of cohesion, were obtained for samples with a higher percentage of sand.

Limited data is available on the water table level and on pore pressure distribution in the excavated

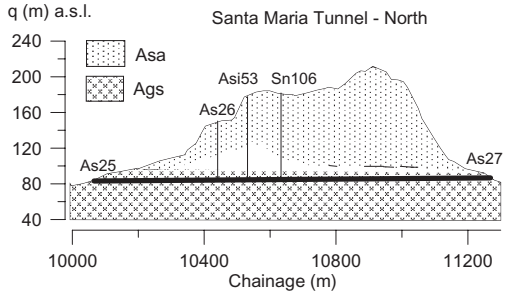

Figure 1. Schematic geological profile of the Santa Maria tunnel (North) (the thick line represents the tunnel). Vertical boreholes are also shown.

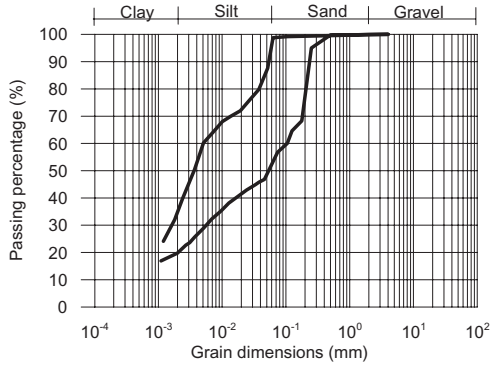

Figure 2. Two limit grain-size distributions of soil samples collected at the tunnel face.

Table 1. Properties of the soil.

Properties	Min-Max
Total unit weigth γ(kN/m^3)	20.8–21.4
Dry unit weigth γ_d (kN/m^3)	17.2–19.3
Solid unit weigth γ_s (kN/m^3)	26.4–26.5
Void index e	0.39–0.56
Natural water content w (%)	21–32
Liquid limit w_l (%)	30–50
Plastic limit w_p (%)	18–25
Saturation degree S_r (%)	91–99
Clay fraction CF (%)	13–41
Compression index C_c	0.06–0.12
Swelling index C_s	0.02–0.055
Peak cohesion c'_p (kPa)	18–51
Peak friction angle φ'_p (°)	25–35

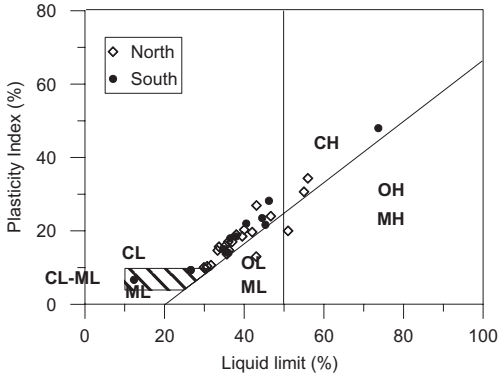

Figure 3. Casagrande's classification of the soil.

formations. In the design stage water table was assumed to be close to the bottom of Asa formation, i.e. at about 20 m above the tunnel crown. The hydraulic conductivity estimated from oedometer compression tests was shown to be very low, varying in the interval 10^{-11}–10^{-10} m/s.

The high percentage of silt and the high disturbance of samples taken at the tunnel face, did not allow in oedometer compression tests a reasonable estimation of the preconsolidation pressure, therefore the overconsolidation ratio is not directly known.

3 DESIGN AND CONSTRUCTION

The design of the tunnels was based on the observational ADECO-RS approach (Lunardi 2000). Different typology of primary linings were applied to specific geotechnical conditions; the effectiveness of the adopted solution are checked by comparing the monitored convergences to predetermined reference values.

Figure 4 shows the typical cross-section of the tunnel with the primary lining consisting of an open ring of shotcrete (thickness of 0.20–0.30 m) and steel sets (2 coupled bars among the types IPN 160–180–220). The unsupported span has a length of up to 1.0–1.2 m for the more ordinary excavation sections (section area of 120 m^2), while it decreases up to 0.75 m in the case of larger excavation sections (section area of 180 m^2), planned as security stop areas.

Face reinforcement consists of 18 m long fiberglass bolts, installed every 10–12 m of face advancement, thus resulting in a overlap of 6 m. In some cases face bolting, with a maximum density of 1 bolts/m^2, is adopted.

The concrete final support (thickness of 0.8–1.0 m) is cast in three separate stages, the cast

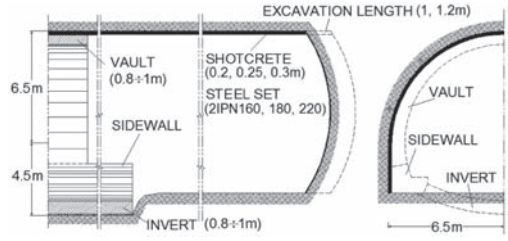

Figure 4. Typical cross—and longitudinal section of the tunnel.

length being typically 6–12 m. Firstly, concrete at the sidewall (Fig. 4) is constructed at a maximum distance from the face of 24–30 m; then, the invert is cast typically 6–12 m behind the sidewall; finally, the arch lining is closed by the vault, generally 60–70 m from the face.

The advance rate of the tunnel is between 1.5 and 3.0 m/day.

4 ANALYSIS OF CONVERGENCE MEASUREMENTS

The construction process is monitored mainly through the geodetic survey of displacements at the tunnel wall. Monitoring sections include 5 targets installed according to a typical scheme: three at the top-heading and two at each sidewall.

A monitoring section is installed every excavation cycle, i.e. 12 ÷ 18 m; they should be placed no more than 1 m from the face. Monitoring is interrupted when the permanent concrete lining is cast.

For shorter distances from the face, i.e. less than 15 m (almost 1 tunnel diameter), one measurement per day is carried out, while for longer distances, the frequency decreases to 2 or less measurements per week.

4.1 *Data convergence interpretation*

The interpretation of convergence data was based on the regression model proposed by Sulem et al. (1987). The model supposes that the tunnel closure C is influenced both by the face distance and time dependent behaviour of the soil:

$$C(x,t) = C_{\infty}\left\{1-\left[\frac{X}{x+X}\right]^2\right\}\left\{1+m\left[1-\left(\frac{T}{t+T}\right)^n\right]\right\} \quad (1)$$

where x is the distance of the monitoring section from the face and t is the time elapsed since the face crossed the control section. The parameter C_{∞} represents the closure corresponding to an infinite advancement rate; the parameter X corresponds to

the face effect (it is related to the plastic radius R); parameters m, T and n describes the time effect; the quantity $C(1+m)$ represents the closure at infinite distance and time.

The measured convergence is a fraction of the actual total closure; it generally depends on the face distance x_0 at the "zero" reading and on the time t_0 elapsed since the face crossed the monitoring section until the "zero" reading:

$$\Delta C(x_i,t_i) = C(x_i,t_i) - C(x_0,t_0) \qquad i = 1,k \qquad (2)$$

Solving the non linear equation (1) on the basis of the collected data $\Delta C_i(x_i,t_i)$, for example by means of a minimum squares regression technique, allows the estimation of the regression parameters.

As suggested by various authors (Sulem et al. 1987, Boldini et al. 2002), the parameter n was fixed at the value of 0.3 in order to reduce the ill-conditioning of the set of k equations (2).

In the regressions analysis convergence data collected during sidewall and invert installations were not considered. In this way the influence of invert excavation and variation of stiffness support on the regression results are minimized.

In Figure 5 three examples of convergence fitting of the L_1 control length are represented. The regression model is shown to be able to fit the measurements corresponding to different excavation sequences. Moreover the increase in convergence during breaks in excavation is also accurately matched by the model.

Parameters determined by the regression analysis of convergence measurements from the control length L_1 are reported in Figure 6 as a function of the tunnel chainage. The magnitude of the parameter C_∞ is often lower than 0.150 m, corresponding to an average deformation nearly 1% (L_1 = 14 m); it increases as the tunnel proceeds, probably due to the related overburden increment. The length X varies between 5 and 15 m, and it is frequently close to 6.5 m, i.e. equal to the tunnel radius. The characteristic time T is widely scattered in the range 1–35 days. The non-dimensional parameter m also shows a large range of variation, between 0 and 4.

From these results it seems inadequate to define a single behaviour model in term of convergence, representative of all conditions encountered. On the other hand the regression model makes it possible to estimate the tunnel closure before the "zero" reading $C(x_0, t_0)$, allowing the comparison of measurements collected in different monitoring stations.

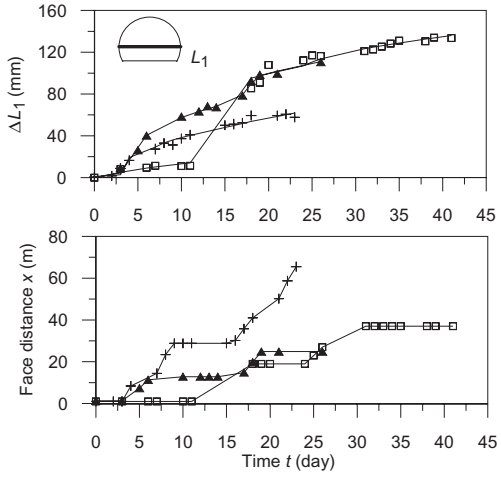

Figure 5. Examples of curve fitting (continuous line) of convergence measurements ΔL_1 (symbols) with time (on the top) at three monitoring sections. At the bottom the distance of the monitoring section from tunnel face versus time is shown.

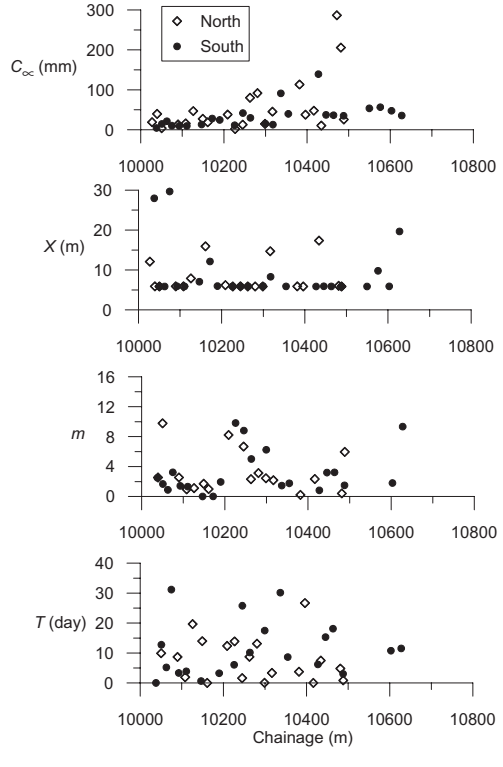

Figure 6. Regression parameters from eq. (1) obtained from the convergence data of the horizontal control length L_1 for both North and South tunnels.

4.2 *The influence of the sequential installation of definitive lining*

The construction sequence of the various structural elements of the final lining is relevant in the development of the convergence.

Figures 7a and 7b illustrate, as an example for three monitoring sections, the measured closure of the horizontal control length L_1 with time in relation to the history of the distance of the monitoring section from the face. The distance of the sidewall and the invert installation from the section itself is also shown (Figs. 7c, and 7d, respectively). The installation of the final support elements at the sidewall (i.e. distance equal to zero in Fig. 7c) causes the closure of L_1 to end, even if the arch of the primary support is not closed at the foot.

The measurements of the oblique tunnel convergences also show the same behaviour as the horizontal convergence. However, the vertical displacement at the crown continues to increase overtime until reaching an asymptotic value.

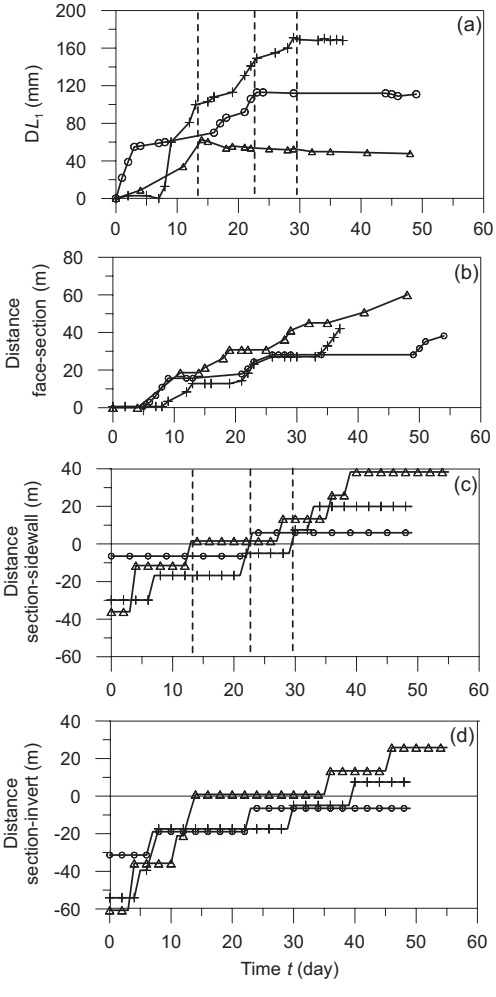

Figure 7. Time histories of: a) the measured convergence of the horizontal closure L_1; b), c) and d) the progression of the face, sidewall and invert concrete, respectively, with reference to the control section position. The vertical lines refers to the time of casting of the sidewall.

4.3 *Comparison of data at different monitoring sections*

Generally, there are many factors that affect tunnel convergence: geometry and depth of tunnel; geotechnical properties and hydraulic conditions; the characteristics of primary and definitive supports; excavation sequence, especially in the case of twin tunnels.

Comparison of monitored data was carried out without taking into account the variability of the mechanical properties and hydraulic condition of the soil encountered by the tunnel. Differences in the primary support and in the sequence of installation of final lining were also assumed as negligible.

The comparison focused on the influence of the tunnel depth and distinguished the data from the two tunnels, with the aim of assessing eventual interaction effects.

In order to evaluate a dissymmetry of the tunnel deformation, the convergence from two oblique control lengths, ΔL_2 and ΔL_3 (Fig. 8), was considered. In Figure 8 such measurements, normalized

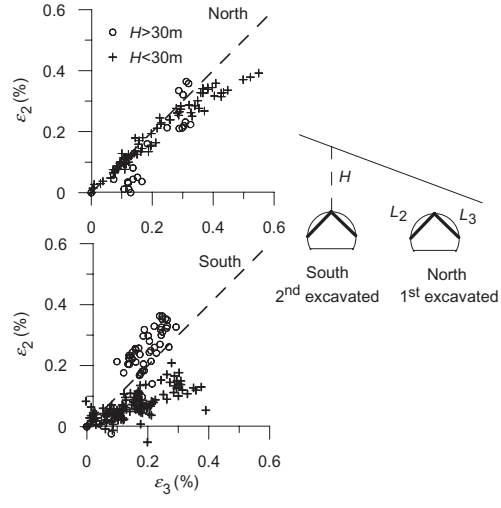

Figure 8. Comparison between the deformations of oblique control lengths for both tunnels. A different symbol is used to distinguish between data recorded at tunnel sections below and above 30 m of overburden.

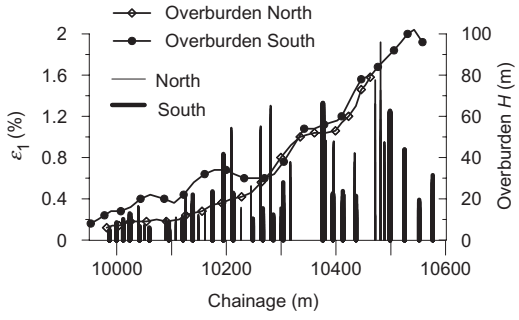

Figure 9. Deformation of the horizontal control length (bars) and overburden (symbols) along both the tunnel axes.

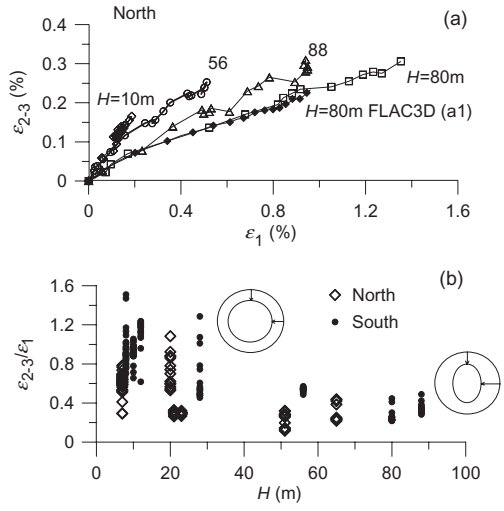

Figure 10. (a) Mean deformation ε_{2-3} of the two oblique control lengths against the horizontal deformation ε_1 from several monitoring sections (open symbols) and from FLAC3D analyses (full symbols) at different overburden H. (b) Ratio between measured deformations of oblique and horizontal control lengths related to overburden H.

to the initial basis length ($L_2 = L_3 = 9$ m) and indicated as ε_2 and ε_3, are plotted for several monitoring sections. If tunnel cover H is high (>30 m), an almost symmetric shape of tunnel closure is displayed in both tunnels, even though data are largely scattered. On the other hand, at lower tunnel cover ($H < 30$ m) the convergence of the control length ΔL_3 is always larger than ΔL_2.

The dissymmetry in the tunnel closure could be ascribed to the rotation of the original principal stresses due to the slope or to the sequence of tunnel excavation. As the dissymmetry in the closure at the lower cover ($H < 30$ m) is negligible in the North tunnel (firstly excavated) and more marked in the South tunnel (later excavated), it suggests a higher influence of the sequence of tunnel excavation.

In Figure 9 the deformation of the horizontal closure, indicated as ε_1, as well as the overburden H, are represented as a function of the tunnel chainage. Deformation values from the North and South tunnels are quite similar. The horizontal closure, even though very scattered, reasonably increases with the overburden. The average increment of ε_1 with overburden is 0.018%/m, corresponding to a horizontal closure increase of 0.0025 m per 1 m of overburden.

It should be noted that in the larger excavation section (180 m^2), the deformation of the horizontal convergence is very similar to that of the ordinary section.

Comparison between ε_1 and the average value of ε_2 and ε_3, for several monitoring sections of the North tunnel is shown in Figure 10a. Convergence increases during the excavation, maintaining a constant ratio, which differs with depth. Figure 10b shows the correlation between depth and ratio of oblique to horizontal closure deformations, which can be considered as a measure of the oval shape. At lower overburden this ratio differs significantly, with an average closer to 1.0, while at larger overburden ($H > 40$ m) it decreases significantly. The tunnel deformation at lower depth maintains a homothetic shape, while at larger depth an oval-shaped closure, with the maximum closure in the horizontal direction, occurs. This evidence could be related to the incomplete closure of the primary support.

5 STRESS-STRAIN NUMERICAL ANALYSIS

Convergence measurements showed that the installation distance of the primary lining strongly affect the tunnel behaviour. Moreover, placement of the lining at the sidewall (also without invert) seems to have a key role in reducing tunnel displacement (Fig. 7).

In order to better understand these phenomena, comparative stress analyses, simulating the sequence of lining installation, were carried out. Analyses were performed with the commercial finite difference code FLAC3D (Itasca 2006) in the three dimensional domain.

5.1 *Numerical models*

The analyses were performed maintaining constant the tunnel overburden (H = 80 m) and soil properties.

The soil was modeled as an elastic perfectly plastic material, obeying the Mohr-Coulomb yielding criterion. Cohesion and friction angle were assumed equal to $c' = 30$ kPa and $\varphi' = 30°$, respectively. A non associated plasticity flow rule, characterized by the null value for the dilation angle ψ' was considered. As soil stiffness was not directly investigated, reasonable values for the elastic constant were assumed, i.e. $E' = 400$ MPa and $\nu' = 0.3$. The coefficient of earth pressure at rest K_0 was chosen equal to 1, a typical value for deep tunnels.

The analyses were performed in undrained conditions in the effective stress domain. According to the design assumptions, water table was fixed at 20 m above the tunnel crown.

The soil and water properties used in the analyses are summarized in Table 2.

Due to the symmetry in the vertical plane of the tunnel axis, only one half of the entire domain was modeled. The calculation mesh, consisting of 271680 nodes and 260967 zones, is reported in Figure 11. The component of displacement perpendicular to the vertical boundary planes was restrained. All components of the displacement were restrained at the bottom of the model.

The excavation process was simulated by applying the following procedure: for each excavation step, equal to 1 m, a set of soil elements are changed into null elements; the excavated soil slice remains unsupported while the primary lining is installed 1 m behind. The primary lining consists of shotcrete, modeled as elastic shells, and steel sets, modeled as elastic beam elements. The lining elements were considered perfectly adhered to the soil.

In order to take into account the maturation process of shotcrete, its Young modulus E_s was increased during face advancement, while a constant value of the Poisson ratio of 0.25 was assumed. An empirical relationship (Chang 1994, Graziani et al. 2005) was assumed to describe the dependence of E_s on time:

$$\frac{E_s(t)}{E_{s,28}} = c_1 \exp\left(\frac{c_2}{t^{c_3}}\right) \tag{3}$$

where c_1, c_2 and c_3 are equal, respectively, to 1.062, –0.446, 0.6 and the Young modulus at 28 days of maturation was fixed at 20 GPa.

The beam elements consisted of two coupled IPN standard steel beams (Tab. 3).

Three different types of primary linings were considered, i.e. minimum, average and maximum stiffness, as proposed in the design (Tab. 3).

The permanent lining elements considered in the analysis were sidewall and invert concrete, while the vault element was not included. The structural elements were modeled through elastic brick elements, characterized by Young modulus and Poisson ratio equal to 25 GPa and 0.25, respectively. A perfect adherence of the structural elements to the soil was assumed.

Sidewall and invert elements were installed every 6 m, as in the actual construction. Two different installation distances from the face were considered: 12 and 24 m (corresponding to minimum distances from the face of 6 and 18 m after the casting, respectively). Two hypotheses of installations were investigated: installation of concrete at the sidewall only (cases a2, a3 in Tab. 3) and installation of both sidewall and invert (cases a4, a5 in

Table 2. Relevant parameters adopted in the numerical analyses.

Soil	
Dry unit weigth γ_d (kN/m^3)	18
Porosity n	0.35
Young modulus E' (Mpa)	400
Poisson ratio ν	0.3
Friction angle φ' (°)	30
Cohesion c' (kPa)	30
Dilation angle Ψ' (°)	0
Water	
Unit weigth γ_w (KN/m^3)	10
Bulk modulus K_w (Gpa)	2
Maximum suction s (kPa)	200
Initial State	
Height of water table on the tunnel crown h_w (m)	20
Coefficient of earth pressure at rest K_0	1

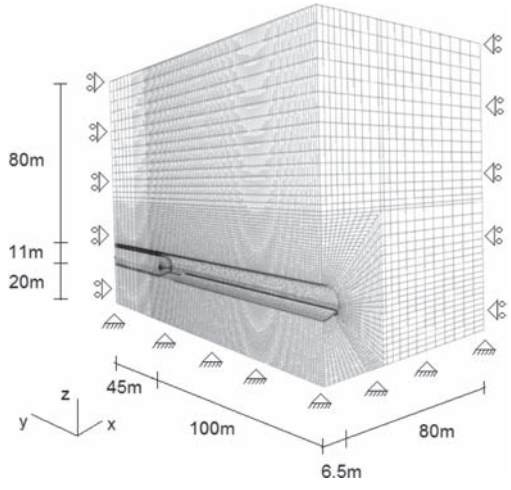

Figure 11. Calculation mesh including boundary constraints.

Table 3. Lining characteristics adopted for the various analyses.

Primary lining	(min)*	(average)	(max)*
Shotcrete thick. (m)	0.2	0.25	0.3
Steel sets	2IPN160	2IPN180	2IPN180
Definitive lining			
Installation length (m)		6	
Maximum installation distance (m) for:			

	(a1)	(a2)	(a3)	(a4)	(a5)
Sidewall	∞	12	24	12	24
Invert	∞	∞	∞	12	24
Vault	∞	∞	∞	∞	∞

*primary linings investigated only in the condition (a3)

Tab. 3). The case of definitive lining installed at infinite distance was also investigated (case a1 in Tab. 3).

5.2 *Results*

The L_1 horizontal convergence and the vertical displacement at the crown from the analyses are reported in Figure 12. The installation of sidewall and invert concrete at long distances from the face (a1) and at the maximum distance of 24 m (a5) gives a horizontal deformation ε_1 between 0.7% (a5) and 1% (a1), comparable with the monitoring data at similar overburden (Fig. 9).

Also the deformation ε_{2-3} from numerical analyses shows a good agreement with the measured values (Fig. 10a). Furthermore the analyses provide a ratio $\varepsilon_{2-3}/\varepsilon_1$ varying from 0.28 (a5) to 0.25 (a1), consistent with the non homothetic tunnel deformation measured at higher overburdens (Fig. 10b).

The behaviour of tunnel deformation when only sidewall concrete is installed (a1, a2 and a3) is also qualitatively confirmed by the numerical investigations. Figure 12a shows that, at the installation distance of 24 m (a3), horizontal convergence stops increasing when the sidewall concrete reaches the reference section, at 18 m (i.e. minimum installation distance for this case). Figure 12b, on the contrary, shows that the vertical displacement at the crown is still increasing at the same distance, attaining a final value only at a larger face distance (24 m). The noticeable effect of sidewall casting is confirmed by comparing the maximum values of displacements obtained at different installation distances (a1, a2 and a3). Even though the sidewall is installed at 24 m (almost 2 times tunnel diameter) from the face (case a3), convergence strongly reduces with respect to the infinite installation distance (case a1) (Fig. 12).

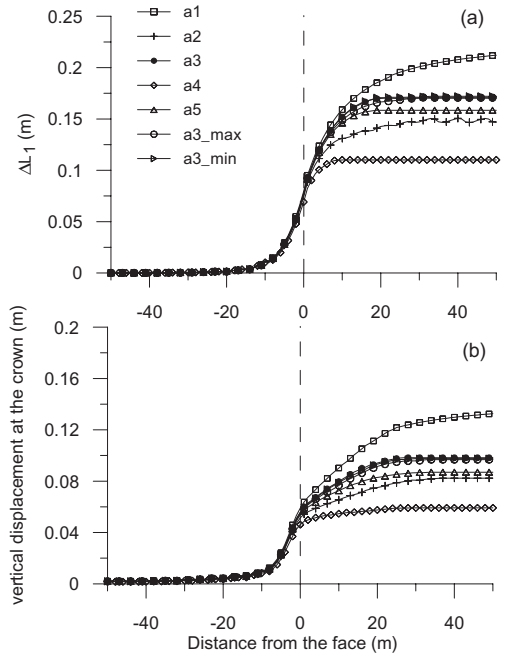

Figure 12. (a) Shortening of the horizontal control length L_1 and (b) vertical displacement at the crown resulting from the numerical stress analyses.

Figure 12 also shows that, for both the horizontal convergence and the vertical displacement at the crown, there are no significant differences if sidewall is cast alone (a3) or together with the invert (a5), when the installation distance is longer than 24 m. At shorter installation distance (12 m), the placement of the sidewall alone (a2) and with the invert (a4) produces different results: the invert installation shows a sharp reduction in the increase of convergence as the face advances.

The role of invert installation can reasonably be assumed: closure of primary lining with the invert strongly increases the overall lining stiffness. On the contrary, the important increase in stiffness following the sidewall installation is less apparent.

The influence of the installation of primary linings with different stiffnesses (minimum, average and maximum), in the hypothesis that only the sidewall is cast at the distance of 24 m (a3), is also shown in Figure 12. In these analyses, at least for the investigated soil properties and tunnel depth, results show that in order to reduce tunnel convergences it is not possible to separate the effects of an increase in the primary lining stiffness, from those of a reduction in the distance between the primary and definitive linings.

6 CONCLUSIONS

In this paper monitoring data from two tunnels excavated in a fine-grained formation are analysed and compared with the results of 3D numerical simulations.

The regression model of Sulem et al. (1987) proved to be a reliable instrument in the comparison of convergence data measured at different face distances and relative to different excavation sequences.

The detailed analysis of the convergence measurements of the two tunnels suggested some evidence from the interaction between lining and soil. Analyses showed that tunnel overburden, as well as the different components of the definitive lining (at sidewall and invert), clearly affect the intensity of tunnel deformation. At the higher depth the tunnel shape does not depend on the overburden: the higher horizontal closure is presumed to be influenced by the low stiffness of the primary lining, working as an open arch. The concrete at the sidewall increases the stiffness at the foot of the primary lining, so reducing the effects of punching.

Horizontal and vertical displacements from 3D numerical analyses were in accordance with the monitoring data.

The numerical stress analyses highlighted (in accordance with the monitoring data) the relevant role of the installation distance of the different structural elements of the linings.

Results from convergence measurements suggest that the effects of the excavation sequence between the two tunnels requires further analyses.

ACKNOWLEDGEMENT

The contribution of ANAS S.p.A. (the developer of the motorway route) and Astaldi S.p.A. (the main contractor) to the promotion of scientific knowledge is greatly appreciated. Thanks to Astaldi S.p.A. are also due for allowing site access and their financial contribution to this research.

REFERENCES

Boldini, D., Graziani, A. & Ribacchi, R. 2005. Raticosa tunnel, Italy: characterization of tectonized clay-shale and analysis of monitoring data and face stability. *Soils and Foundations* 44(1): 59–71.

Chang, Y. 1994. Tunnel support with shotcrete in weak rock—A rock mechanics study. Ph.D. Thesis, Division of Soil and Rock Mechanics, Royal Institute of Technology, Stockholm, Sweden.

Graziani, A., Boldini, D. & Ribacchi, R. 2005. Practical estimate of deformations, loads and stress relief factors for deep tunnels supported by shotcrete. *Rock Mech. Rock Engng.* 35(5): 345–372.

Itasca 2006. *Flac3D, Vers. 3.1*. Minneapolis

Lunardi, P. 2000. The design and construction of tunnels using the approach based on the analysis of controlled deformation in rocks and soils. *Tunnels & Tunnelling International* 5: 3–29.

Sulem, J., Panet, M. & Guenot, A. 1987. Closure analysis in deep tunnels. *Int. J. Rock Mech. Min. Sci. & Geomech. Abstr.* 24(3): 145–154.

This page intentionally left blank

Geotechnical Aspects of Underground Construction in Soft Ground – Viggiani (ed)
© 2012 Taylor & Francis Group, London, ISBN 978-0-415-68367-8

Back-fill grout with two component mix in EPB tunneling to minimize surface settlements: Rome Metro—Line C case history

S. Pelizza & D. Peila
DITAG, Politecnico di Torino, Torino, Italy

R. Sorge & F. Cignitti
Metro C S.c.p.a. (Astaldi S.p.a.), Rome, Italy

ABSTRACT: The instantaneous filling of the annulus created behind the segment lining at the end of the tail shield during TBM advance is an operation of paramount importance. Its main goal is to minimize displacements around the tunnel and induced surface settlements due to lost volume at the tail shield. For correctly achieving these goals, the simultaneous back-filling system and the injected material should satisfy technical, operational and performance characteristics. The two-component injection system for back-filling while excavating with shielded TBMs is progressively replacing the traditional use of cementitious mortars.

In the paper different systems of back-filling grout and in particular the two-component system are analyzed and discussed together with a description of the Rome Metro (Line C) case history where this type of back-filling was widely applied.

1 INTRODUCTION

The instantaneous filling of the "annulus" created behind the segment lining at the end of the tail shield during TBM advance (Fig. 1) is an operation of paramount importance. Its main goal is to minimize displacements around the tunnel and induced surface settlements due to lost volume at the tail shield [1, 2, 3]. The management and control of settlements induced by the construction of tunnels in urban areas is very important since they can damage nearby the buildings. Furthermore, the back-filling operation must [1, 4, 5, 6, 7, 8, 9, 12]:

- lock the segmental lining into the right position, avoiding movement owing to both segmental self-weight and the thrust forces and hoop stresses generated by the TBM;
- bear the loads transmitted by the TBM back-up weight;
- ensure a uniform, homogeneous and immediate contact between ground and lining;
- avoid puncture loads by ensuring the application of symmetrical and homogeneous loading along the lining;
- complement the waterproofing of the tunnel with the concrete lining and gasketry (i.e. if the lining has cracks due to wrong installation, back-fill grout should help mitigate any water inflow).

For correctly achieving the above goals, the simultaneous back-filling system and the injected material should satisfy the following technical, operational and performance characteristics:

- the back-filling should ideally be instantaneous in order to avoid the presence of voids in the "annulus" while advancing with the TBM. For this reason, back-filling is typically carried out through pipes inserted inside the TBM tail skin, uniformly distributed around the tail skin (Fig. 1);
- the "annulus" must be regularly and completely filled so that the lining is fully linked to the surrounding ground (the system becomes monolithic);
- the reliability of the system must be guaranteed in terms of transportability of the mix. The grout must be designed to avoid choking off the injection pipes, segregating in pumps and bleeding, in conjunction with the time the grout is being transported and distance from batching to injection;
- the injected material has to gel very quickly after injection (which is carried out progressively with generation of the "annulus") but without choking the injection pipes and nozzles (especially the ones for the accelerator admixture). The injection must always be carried out until either achieving the maximum pressure that is a function of the TBM face pressure or the theoretical volume);

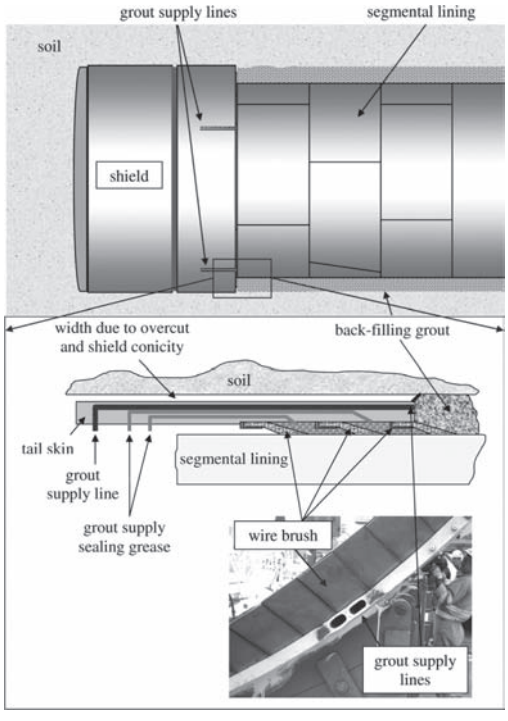

Figure 1. Scheme of grouting through the tailskin.

- the injection can be re-started and integrated with any previously injected material at any time;
- the injected material should be homogeneous in respect to physical characteristics and mechanical behavior throughout the "annulus";
- the injected material must not be able to be washed out by ground water.

2 TYPE OF MATERIAL FOR BACK-FILLING

Injected materials can have different characteristics and mechanical behavior. Different backfill types require different equipment as summarized in Table 1 following the classification proposed by Thewes and Budach [9] following the scheme proposed by EFNARC [6]. Generally speaking the three main types of injected materials are inert mix, cement mix and two component mix. The main properties of these mixes are reported below.

2.1 *Inert mix*

Inert mix is based on sand transported in water with other constituents, such as filler, fly ash, etc.

Table 1. Main properties of the segmental lining.

Tunnel outside diameter	6400 mm
Tunnel inner diameter	5800 mm
Segment lining thickness	300 mm
Minimum curvature radius	210 m
Segment lining length	1400 mm
Numbers of segments for each ring	7 (6 + key segment)

In a rock mass it is possible to use a simple mix of sand and gravel (pea gravel) just to fill the annulus void. Generally speaking it is a cheap system. The absence of cement avoids the risk of clogging the pipes due to premature setting [6, 7].

The sand has to be properly selected/graded and mixed: size and type anomalies significantly increase the possibility of an irregular and heterogeneous filling leading to pipe clogging.

As the sand cannot be pumped readily, it must be injected behind the tail skin through the segments. Typically this is carried out through either 1 or 2 propriety grout sockets cast into the segments. This has a counter effect of possibly adding to potential weak points from a waterproofing perspective.

Setting is very retarded (or it never occurs) and the final strength is very low. The inert mix is often chosen by French designers and contractors, as briefly described by the Working Group n.4 of the AFTES [10]: "The control of the injected material and of its hardening during the production and injection are really complex, and the progressive renunciation of the cement mix is in favor of products with postponed grip (pozzolanic reaction) and poor compression strength. This product is injected directly and continously through the pipes placed in the thickness of the tail behind the last ring in the annular space directly behind this one".

2.2 *Cementitious mix*

Cementitious mix is constituted by water, cement, bentonite and chemical admixtures (also named mortar) necessary to modify the water/binder ratio and the initial and final setting times. It is an active mix with a very high fluidity. It has to be easily pumpable, and is usually retarded (some hours) to avoid risks of choking the delivery pipes during transportation and injection.

The presence of cement helps develop mechanical strength, which can reach high values (15–20 MPa at 28 days, even if it is not really necessary for good back-filling). Also this type of mix is very negatively influenced by variations in its ingredients, which can lead to choking the pipes. The mix should be injected as close to the face as

possible to provide rapid support to the segment ring. Injection through the tail skin into the "annulus" can cause serious problems with choking. The high frequency of choking of grout supply lines involves discontinuity in the back-filling operation. This creates voids and joints that do not allow the grout to completely fill the annulus thus not performing the design requirements.

Thewes and Budach [7] and EFNARC [6] have described these types of mortar in reduced active systems. Reduced active systems have a fraction of cement usually varying between 50 kg/m^3 and 100 kg/m^3 while in active systems the binder component develops full hydration with a cement content of over 200 kg/m^3.

2.3 *Two-component mix*

Two-component mix is typically a super fluid mortar, stabilized in order to guarantee its workability for a long time, usually at least 72 hours (from batching to transport and injection) to which an accelerator admixture is added at the injection point into the "annulus".

The mix gels a few seconds after the addition of the accelerator (Fig. 2), normally 10–12 seconds, during which the TBM advances approximately 10–15 mm. The gel exhibits a thixotropic consistency and starts developing mechanical strength almost instantaneously (weak but sufficient for the purpose: 50 kPa at 1 hour is typical).

The main characteristic of the two-component mix is the quick development of its mechanical properties thus permitting the best filling of the void.

This system is injected under pressure throughout the "annulus" and is able to penetrate into any voids present. Also it can penetrate into the surrounding ground (depending on its permeability).

Furthermore, the retarding agent has a plasticizing effect and is able to inhibit the mortar from setting thereby guaranteeing its workability up to 72 hours after batching. This facilitates stockpiling grout in mixer-containers that are bigger than the theoretical volume of material to be injected per ring. This is useful in avoiding one of the most common mistakes, that is, batching and stockpiling only the theoretical amount and not more. If eventually a bigger void is found that needs to be filled, you could leave the crown unsupported for too long, leading to potentially serious consequences.

The accelerator admixture is based on sodium silicate. Its addition to the fluid mortar leads to an almost immediate gel formation which starts developing mechanical strength. Such gels are homogeneous and therefore avoid point loading of the segments.

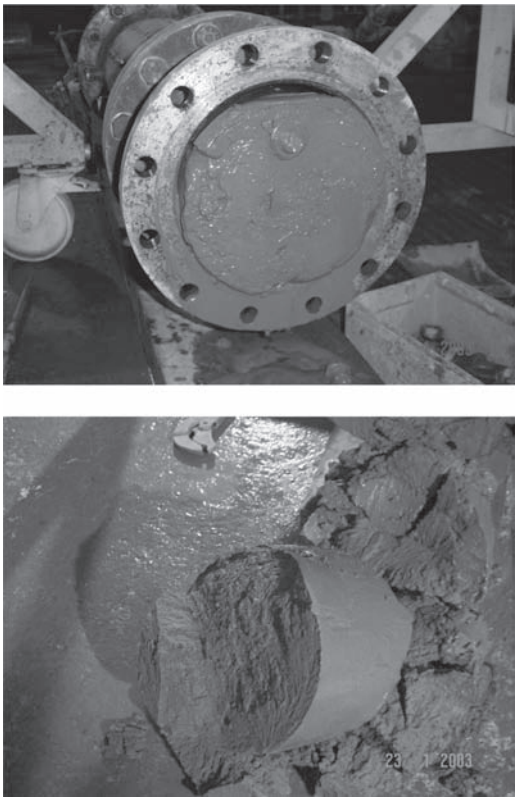

Figure 2. Photographs of the two component mix after gelling.

The constituents of two-component back-fill grout are sourced from "industrial" production and so should be perfectly controlled. This guarantees its regularity with obvious advantages in the consistent quality of fresh and hardened mixes. No constituent should exhibit variable characteristics (such as sand).

Using a proper mix-design and specifically designed equipment the risks of blockage can be minimized. Some problems can arise with the nozzle of the accelerator line blocking. This can normally be attributed to an improper cleaning regime or simple wear and tear of the injection outlet mechanism.

The bentonite significantly increases the homogeneity and impermeability of the hardened mix. Furthermore, it minimizes the bleeding, helps in achieving a thixotropic consistency when the flow stops because the "annulus" is full and so helps in the gelling process, conferring greater impermeability to the system (less than 10^{-8} m/s).

3 PERFORMANCE ANALYSIS OF THE TWO-COMPONENT SYSTEM

3.1 *Creation of an annular incompressible bubble*

The injected material for a two-component system is an ultra-fluid slurry which, due to addition of an accelerator admixture just before its injection, gets a thixotropic consistency in a few seconds. As it is made up of a huge amount of water (approximately 800 litres per cubic meter of material), it is an incompressible fluid, just like water.

The consequence of this is that the annulus void created behind the TBM tail skin is a closed annular bubble, filled instant per instant, with an uncompressible fluid.

Therefore, every movement of the surrounding ground which tends to enter in the bubble or any movement of the concrete lining which tends to reduce the bubble volume, instantaneously leads to the creation of a reaction-pressure inside the fluid, uniform throughout the volume and around all the surfaces of the volume, avoiding any deformation.

Therefore the incompressible zone of gel perfectly confines the concrete rings already installed and the new concrete ring which has to be installed.

So this can be carried out the following conditions must be achieved:

- the injected material must remain incompressible;
- the fluid must not escape from the annulus void:
  - it must not permeate through the surrounding ground (this is avoided by the ground water that exerts a hydrostatic pressure on the injected material);
  - it must not escape through the space between the tail and the tunnel face, which is avoided by a correct balance between the tunnel face pressure and the injection pressure (which must be approx. 0.2 bar higher, not more);
- if the surrounding ground is in poor condition, it tends to squeeze towards the annulus. It cannot be allowed to move with excessive pressure, otherwise the force required to advance the machine would increase too much. This has to be balanced and controlled with equilibrium between the pressure in the excavation chamber and the injection pressure. This can be aided by lubrication of the extrados of the tail skin with a bentonite slurry. Bentonite slurry injection should take place exactly where the tail is blocked and bears on the ground, i.e. behind the invert of the lining and in the rear part of the tail;
- the segment ring just installed must not be deformed (i.e., without ovalization) due to its own weight, which could lead to an anomalous installation of the rings or too low a pressure on the upper segments;
- the gel must not be leached by the underground water.

From the above, it is evident that it is necessary to inject a fluid that does not harden instantaneously, but that becomes a gel quickly and progressively without avoiding the formation of an incompressible annulus at constant volume.

The long term mechanical strength of the backfill material does not have any meaning, because it does not give any structural contribution to bearing the hydrostatic and geostatic loads (these are completely supported by the concrete lining), but the gel has to be as homogeneous as possible to mitigate the external punching loads.

To achieve this goal the gel must not decompose after its injection: its durability must guarantee that the incompressible annular filling is maintained permanently.

Therefore attention should be paid to the behavior of the injected material in the early stages (from the first seconds to some hours), which includes the installation and the injection of segment rings. It is evident that the existence of a closed incompressible annulus is the most efficient and important factor.

3.2 *Durability*

The durability of the gel which totally fills the annular void is guaranteed in the normal humidity conditions of the ground (even more so when the tunnel is drilled under the water table). During the construction of many Metro Lines in Singapore the authors understand that since the two-component system has started to be used, more than ten years ago, there has only been positive indication of grout durability. Comprehensive proof of grout behavior for the future does not exist, but the gel must have two features which indicate its durability:

- the undeformability: this parameter immediately appears as the most significant, as the gel is made up principally of water. If the water is not lost (by evaporation or filtration), the material will remain stable for ever. It is therefore essential that the host ground maintains its natural humidity;
- the technical impermeability of the ground (10^{-8} m/sec). This is the physical parameter that favors the creation of the situation described above.

Both these characteristics can be measured in the laboratory and can be assumed as indicators of durability.

3.3 *Consistency and compression strength of the hardened mix*

An important consideration from the above is that, when a super-fluid two-component mix is used, the early stage mechanical strength is more important than the latter stage strnght. The concrete lining, not the back-filling grout, must bear the applied long term hydrostatic and geostatic pressures.

It is in the first hours (8 rather than 24 when the TBM advances regularly) that the gel must fill every void in the "annulus" (and eventually in the surrounding ground) and protect the segment lining. This is achieved by the high fluidity of the injected material and its rapid gel setting time. Furthermore the gel must hold the ring in its built position (avoiding the formation of punching loads) and at the same time avoiding the last installed rings deforming due to the TBM thrust and cutting wheel rotation.

It is of paramount importance that the mix creates a gel after a few seconds and an incompressible annulus is generated: therefore the gel set must be tested (at 0.5 and 8 hour stages) to confirm that the strength is suitable, for example with a pocket penetrometer. The selection of the half hour test time can be adjusted to suit the time taken to build one ring. The first test time should be long enough for the grout to achieve a strength adeguate to avoid the lining floating around in the grout.

Tests after 24 hours are only suitable to check that the gel does not decompose, but increases its strength over time in order to allow the extraction of cores through the segments. This may be useful to directly check the effective total filling of the "annulus".

Testing of compressive strength on cores extracted in situ (even if the coring can partially disturb the sample) is the most reliable method because the material is injected in the "annulus" at pressure and remains there in environmentally natural conditions.

4 TWO COMPONENT MIX. EXAMPLE OF APPLICATIONS—ROME METRO—LINE C (ITALY)

The tunnels of Metro Line C are under construction in Rome using four EPB machines and will constitute the third line of Rome metro.

Metro C S.c.p.a. is the General Contractor for the engineering and construction, formed by Astaldi S.p.a. (leader of the joint venture), Vianini Lavori, Ansaldo STS, Cooperativa Muratori e Braccianti di Carpi and Consorzio Cooperative Costruzioni.

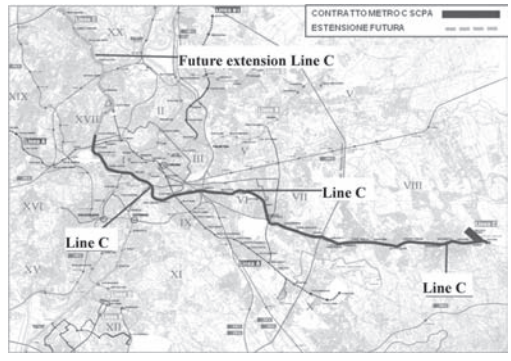

Figure 3. General layout of Line C and interconnections with other Rome Metro lines (A and B).

The layout of the Line (Fig. 3) is 25 km long (18 km underground) with 29 stations. It crosses Rome from south-east to north-west.

Line C will have three connections with the others two existing metro lines, the A Line (in San Giovanni and Ottaviano stations) and the B Line (in Fori Imperiali-Colosseo station).

Presently Line C has been built in the first sections called T7, T6A, T5 e T4, between the Montecompatri-Pantano station (south-east) and the San Giovanni station, for a lenght of about 18.5 km of which 10 km are underground with 22 stations.

The Line C will be operated driverless with a Total Automation System. The Central Direction of Operations is located at Graniti train depot (at the south-east end of the line) and the stations will contain automatic doors synchronized with the train's doors.

When operating this metro line will have the largest passenger transport in Europe with a maximum capacity of 24000 passengers/hour in each direction. Each direction is managed with a single tunnel with 5.8 m inner diameter and with a lining thickness of 0.30 m. The segmental lining is universal (Fig. 4, Tab 1).

The main geological formations encountered by the tunnels are volcanic soils with properties ranging from loose soils to soft rocks (Fig. 5 and Tab. 2). All the tunnels are below water table, which can be higher than 15 m over the tunnel crown.

Four EPB machines were used for the construction of the tunnels with an excavation diameter of 6.71 m (Fig. 6 and Fig. 7). Since the lining has an outer diameter of 6.40 m, the thickness of the backfilling annulus is about 150 mm.

Backfilling was carried out with a two component mix. This mix was studied by Metro C

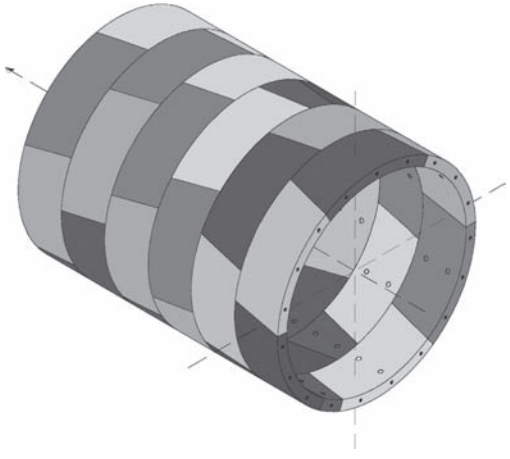

Figure 4. Segment lining scheme.

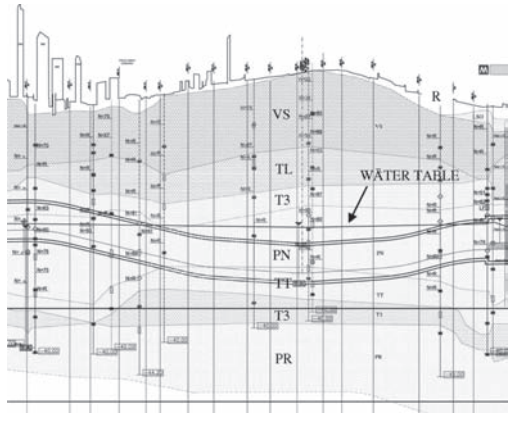

Figure 5. Example of a stretch of the geological profile between stations of Torre Spaccata and Giglioli. The figure highlights the variability of the encountered soils.

Table 2. Main geotechnical properties of the soils.

Gelogical formation	γ [kN/m^3]	φ' [°]	c' [kPa]	E [MPa]	k [m/s]
Antropic soils (R)	17.0	25	10	35	1E^{-5}
Recent alluvial soil (LSO)	18.5	27	20	70	1E^{-6}
Villa Senni Tuff (VS)	17.5	30	25	100	1E^{-6}
Lionato Tuff (TL)	17.5	35	300	300	5E^{-6}
Pyroclastic soil (TT)	17.0	33	10	100	1E^{-7}–1E^{-6}
Black pozzolane (PN)	17.0	35	10	130	5E^{-6}
Red pozzolane (PR)	17.0	35	10	130	5E^{-6}

Key: γ: soil density; φ': drained friction angle; c': drained cohesion; E: deformation modulus; k: permeability coefficient.

Figure 6. Photographs of the first EPB machine used for the excavation of the tunnels.

Figure 7. Photographs of the second EPB machine used for the excavation of the tunnels.

using special tests and research carried out by the Department of Land Environment and Geoengineering of Politecnico di Torino.

The first mix component is an ultra-fluid mortar, with the following characteristics:

- it is stable and does not cause separation of water and solid contents, despite the very high water/binder ratio. This is important to avoid clogging in the injection lines, especiallly during long breaks, and to allow the transportation of the mortar over long distances.
- It is able to guarantee the workability for at least 72 hours after batching. Immediately before

Table 3. Two component mix adopted in Metro C Line in Rome (values per m^3 of hardened material).

Water	770–820 kg
Bentonite	30–60 kg
Cement	310–350 kg
Retarding agent	3–7 l
Accelerator admixture	50–100 l

injection, the mortar is admixed with an accelerator, based on modified sodium silicate, which leads to an almost immediate creation of a thixotropic gel. The gel is able to completely fill in the annular space around the concrete lining (as proved by the several core samples extracted through the segments) and to improve the waterproofing features of the tunnel (the permeability coefficient of the hardened material is comparable to that of a clay).

The ingredients of the two-component mix are reported in Table 3.

The right dosage of each ingredient depends on several factors, such as the desired pumpability. For example, in those machines where the mix is pumped from the batching plant directly to the TBM, the material must have good pumpability properties and the bleeding must be a minimum, therefore the percentage of bentonite is increased. The project requirements for the development of mechanical strength only deal with the very-early and early stage (up to 24 hours), when the TBM tail passes over and the back-filling material gets in contact with the surrounding ground.

For later stages, the requirement only concerns the durability of the hardened material (ensured by the natural moisture of the ground) and its impermeability.

The accelerator admixture is based on sodium silicate enriched SiO_2 and characterized by an optimal ratio SiO_2/Na_2O. The SiO_2 content improves the strength and durability properties of the hardened mix. The main properties of the mix are: gel time: 5–15 s; uniaxial compression strength after 1 h: ≥50 kPa; after 8 h: ≥100 kPa; after 24 h: ≥450 kPa and permeability coefficient: $\leq 1{,}0 \times 10{-}8$ m/s.

Many tests, also required in the tender documents, were carried out to check both the quality of the hardened mix and the thickness of the annulus. Special attention was given to checking the complete filling of the annulus gap, particularly over the crown of the segment lining.

These investigations were developed using georadar tests (Fig. 8, Fig. 9 and Fig. 10), direct core drilling of the lining and the backfilling (Fig. 11) and visual check where the tunnel was successively

Figure 8. Execution of Georadar Tests above the machine backup.

Figure 9. Example of transverse section that was investigated with georadar.

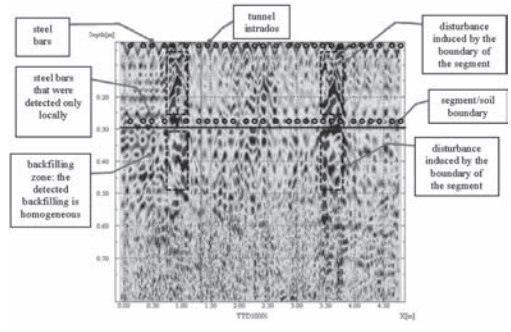

Figure 10. Example of the result of the georadar investigation along an arch as indicated in Fig. 9.

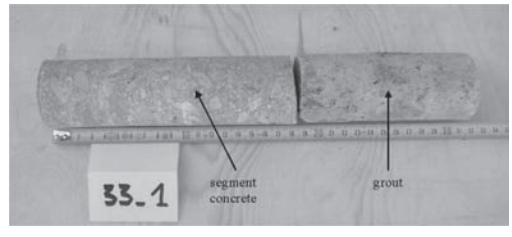

Figure 11. Photograph of a core sample of the lining and of the back-filling grout.

Figure 12. Photographs of the hardened back-filling at the contact between the station diaphram walls and the tunnel.

Figure 13. Detail of the tunnel crown in Fig. 12.

demolished in the station areas (between the diaphram walls where the tunnel were excavated before by the machine) (Fig. 12 and Fig. 13).

The investigations showed good backfilling along the whole line. An other indirect check of the quality of backfilling (both of the operation of injection and of the type of mix used) was provided by the displacement monitoring around the tunnel and on the ground surface. The surface settlements along 8 km of excavated tunnel were generally smaller than one order of magnitude less than the values forecasted in the design stage.

With reference to the strength properties of the hardened mix the carried out tests have shown the following average values of monoaxial compressive strength: 0.05 MPa at 1 hour, 0.01 MPa at 8 hour and 4.5 MPa at 24 hours. After longer hardening time the specific tests requested by the client have provided values of uniaxial compressive strength bigger than 5 MPa after 180 curing days.

5 CONCLUSIONS

The two-component injection system for backfilling while excavating with face pressure applied by shielded TBMs is progressively replacing the traditional use of cementitious mortars. There are two main reasons for this: it reduces the risks of blocking pipes and pumps (common when pumping cementitious systems) and guarantees complete filling of the annular void created after the TBM tail passage, thus avoiding surrounding ground movements. The main features of such a material are: super-fluid initial consistency, creation of a gel a few seconds after the injection, compressive strengths ranging approx. 0.1 to 1 MPa. The goal of the back-filling is effectively carried out in the first minutes after injection, therefore it is important to focus the attention on the last 2–3 installed rings and not more.

Consequently, and according to international experience, it is important to verify that the mix actually gels quickly, in order to homogeneously confine the segment ring.

As it is impossible to verify all this inside the "annulus", it is necessary to prepare and test samples in the laboratory, determine the consistency achieved by the gel in the first few hours and later. Investigating the latter stages is meaningless, because the gel mechanical strength does not influence the structural behaviour of the tunnel lining if the "annulus" is completely filled in.

The example application of Rome metro-Line C clearly shows the advantages of back-filling using ultra-fluid two-component mixes, activated with an accelerator. This type of fluid is able to completely fill the annulus due to the fluidity of the mix and speed of hardening (a thixotropic gel is formed in a few seconds) thus permitting correct management and control of surface settlements that are important when tunneling in urban areas.

REFERENCES

[1] Guglielmetti, V., Mahtab, A. & Xu, S. 2007. Mechanised tunnelling in urban area. Taylor & Francis. London.

[2] Maidl, B., Herrenknecht, M. & Anheuser, L. 1995. Mechanised Shield Tunnelling. Ernst&Sohn. Berlin.

[3] Vinai, R., Oggeri, C. & Peila, D. 2007. Soil conditioning of sand for EPB applications: A laboratory research. Tunnelling and Underground Space Technology 23(3) 308–317.

[4] Vinai, R., Borio, L., Peila, D., Oggeri, C. & Pelizza, S. 2008. Soil conditioning for EPBMs. Tunnels and Tunnelling International December 25–27.

[5] Wittke, W., Erichsen, c: & Gattermann J. 2006. Stability Analysis and Design for Mechanized Tunnelling. WBI, Felsbau GmbH. Aachen.
[6] EFNARC 2005. Specification and guidelines for the use of specialist products for Mechanized Tunnelling (TBM) in Soft Ground and Hard Rock. www.efnarc.org.
[7] Japan Society for Civil Engineering 2006. Standard Specification for tunneling. Tokio, p. 172.
[8] Bappler, K. 2008. Entwicklung eines Zweikomponenten-Verpressystems fur Ringspaltverpressung beim Schildvortrieb. Taschenbuch fur den Tunnelbau. Verlag Gluckauf GmbH. Essen, pp. 263–304.
[9] Thewes, M. & Budach, C. 2009. Grouting of the annular gap in shield tunnelling—An important factor for minimisation of settlements and production performance. ITA-AITES World Tunnel Congress 2009 "Safe Tunnelling for the City and Environment". Budapest.
[10] AFTES, (French National Tunnelling Association) 2005. Recommandations sur les techniques d'excavation mécanisée. Recommandations de l'AFTES sur le tunneliers et voussoirs 1. Paris.
[11] Tomoya Iijima & Al. 2009. Excavation management with use of shield machine in rapidly changing soil condition. ITA-AITES World Tunnel Congress 2009 "Safe Tunnelling for the City and Environment". Budapest.
[12] Pelizza, S., Peila, D., Borio, L., Dal Negro, E., Schulkins, R. & Boscaro, A. 2010. Analysis of the performance of two component back-filling grout in tunnel boring machines operating under face pressure, In ITA-AITES World Tunnel Congress 2010, *Tunnel Vision Towards 2020*. Vancouver (CA).

This page intentionally left blank

Geotechnical Aspects of Underground Construction in Soft Ground – Viggiani (ed)
© 2012 Taylor & Francis Group, London, ISBN 978-0-415-68367-8

Deep excavation of Malatesta Station in Rome: Design, construction and measures

E. Romani & R. Sorge
Metro C S.c.p.A., Roma, Italy

G. Guiducci, A. Lucarelli & G. Furlani
Studio Sintesi, Rimini, Italy

ABSTRACT: Malatesta station is one of the new Rome urban subway line stations. Its construction required deep excavations in urban area, under high water pressures.

Site stratigraphy is characterized by the superimposition of pyroclastic soils, having different cementation degrees, and Tevere's alluvional soils. The stratigraphic column base in composed by Monte Vaticano Pliocenic Clays and Pleistocene marine Clays, which are typical Rome bedrock.

The excavation deepness, the presence of nearby buildings and the high water thrust obliged to use top-down excavation method and to install a controlled dewatering system.

Numerical analysis using FEM were performed and the computation results were compared with the corresponding field measures results. A wide monitoring activity has been carried out: settlement control has been successful and wall movements have been typically small to moderate.

1 INTRODUCTION

The new urban subway line in Rome is called Metro Line C and it is realized by General Contractor Metro C S.c.p.a. This subway line connects the south-east suburb area to north-west suburb area and it has been developed with regards to the historic and urban importance of the area it crosses.

The Malatesta Station is located in a highly urbanized area along the Stretch T4, only few hundred meters far from the homonymous starting shaft of tunnel boring machines (TBM Malatesta Shaft). For this reason, the geometry of the station box has been performed both contemplating the "void" crossing and "full" crossing of tunnel boring machines.

The station has been constructed with top-down construction method and excavations have been realized between diaphragm walls. The geometrical characteristics of main structural elements are summarized in Table 1.

Table 1. Geometrical characteristics of main structural elements.

Lateral Diaphragm walls:	280 cm × 100 cm
Central Diaphragm walls:	250 cm × 80 cm
Roof slab level (70 cm thick):	+30.40; +31.20 m ASL
Concourse level (50 cm thick):	+24.10; +24.60 m ASL
Ticket hall level (50 cm thick):	+20.00 m ASL
Base slab level (150 cm thick):	+11.90 m ASL

2 GROUND CONDITIONS

The ground conditions at Malatesta Station of Line C from the various phases of ground investigations are presented in section in Figure 1.

Figure 2 shows the location of the most relevant boreholes considered.

They indicate that the ground generally comprises made ground (R), composed by sandy–silty matrix mainly of pyroclastic nature up to 6 m thick, over recent alluvional deposits (LSO), which are predominantly silty-sandy material with organic content either dispersed or present in lenses, that have total thickness of 9 m (Fosso dell'Acqua Bullicante).

Above these strata, the Inferior Tuff Complex consists of a stratification of granular sized non cohesive pyroclastic material to high cementation layers (T1 and T2) and fine ash sized to granular sized pyroclastic material with very stiff layers and layers of yellow Tuff of variable cementation (TA).

At the bottom of pyroclastic strata, there is a sedimentary fluvio-lacustrine pre-volcanic complex

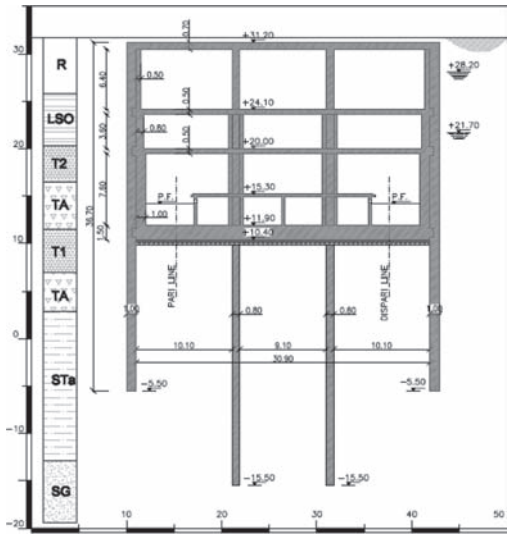

Figure 1. Cross-section.

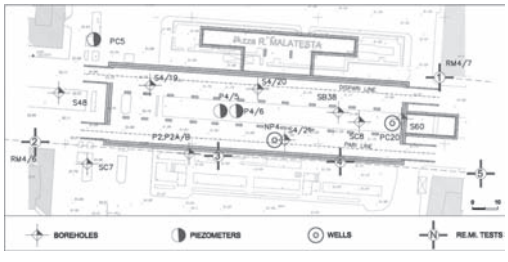

Figure 2. Plan.

(PaleoTevere Unit 2), including these geological units:

– clayey sandy silt (STa) with carbonate concretions and localised levels of travertine concretion, up to 7÷12 m thick;
– medium to coarse sand with gravel and lenses of silty sand and clayey and sandy silt (SG) with maximum thickness of 7 m.

The bedrock of the Rome area is composed by the Monte Vaticano Pliocenic clays and the Pleistocene marine (APL). At Malatesta Station, the top level of APL layer has been defined with some boreholes (S4-19, S4-20 and S4-21) at the level of −30 m ASL.

Only a brief summary of geotechnical parameters relating to the station design are presented below.

The design parameters have considered all the available data, including results from in-situ tests (CPT, SPT, Lefranc permeability tests and RE.MI seismic tests) as well as laboratory tests (including particle size distribution tests, Atterberg limit tests, unconsolidated undrained triaxial tests and quick undrained tests).

Table 2. Geotechnical design parameters.

Layer	γ (kN/m^3)	Φ (°)	c' (kPa)	c_u (kPa)	K (m/sec)
R	17	28	10		1 E-5
LSO	17	30	20		1 E-5
TA	17	32	30	60	1 E-6
T1/T2	17	35	25÷40		3 E-5
STa	18.5	24	25	230	1 E-9
SG	19	35	5		1 E-5

The observations about the groundwater level have considered all the available data, including the ancient ground water control (may 2000-feb. 2001 and gen-may 2002) and the systematic measurements started after the ground investigation campaign in 2006–2007, with installation of new piezometers.

The ground water measurements confirm the existing piezometric data along the stretch T4 and suggest that the water level in the area of Malatesta Station is at +26 m to +27 m ASL.

The Casagrande Cells located in sand and gravel layer (SG) indicate the water level at +21 m to +21,5 m ASL.

3 STATION EXCAVATIONS

In order to reduce the interferences with the surface road network and minimize soil movements, the station was built with top-down construction method.

Figures 3 through 4 show construction photographs from two top-down excavation phases.

The sequence construction begins with the realization of diaphragm walls, 100 cm thick, along the box perimeter with length of 119 m and width of 33 m. The diaphragm walls have a total length of

Figure 3. Roof opening and first floor slab.

Figure 4. Excavation under third floor slab.

36 m and they extend more than 10 m into clayey layers of the almost impermeable stratum called STa, providing both the temporary and permanent earth pressure support for excavation. Than it is realized a double alignment of central diaphragm walls, 80 cm tick, with the aim to support the intermediate slab floors during provisional phase.

This is followed by excavation to just below the roof slab level of the underground structure, with the retaining walls supporting the soil at the sides. The roof slab is then constructed and connected to lateral diaphragm walls, providing a massive support across the excavation. Access openings on the roof slab are provided so that works thereafter could proceed downwards to the base slab level of the underground structure and the site area could reduce to the central part of Malatesta Square.

The depth of diaphragm walls was designed such that the full water pressure on the bottom of the soil between the diaphragm walls could be resisted by the weight of the soil (uplift), however the dewatering wells have to be installed in order to facility the operations of works machines.

A number of 6 drilled wells with diameter of 400 mm are installed along the double alignment of central diaphragm walls; they reach a depth of 6.5 m below the formation level, providing safety conditions to place the base slab, and during maximum digging they pump 7.22 l/sec

Upon completion of second floor slab, provisional steel struts (see Fig. 5) are installed at level of +15.00 m ASL, providing safety conditions to reach the final excavation level, and a different procedure for excavating is adopted. Longitudinal sectors, 12 m width and 5 m deep, have been excavated with progressive construction of the base slab.

The advantage of trench sectioning is it allows to avoid uplift and instability of formation level before base slab placing.

Actually all these phases are fully completed, the base slab is placed and the intermediate steel struts are removed. Dewatering system is still active and it will be turned off when the interior lining will be cast. Figure 6 shows a construction photograph of Breaktrough TBM.

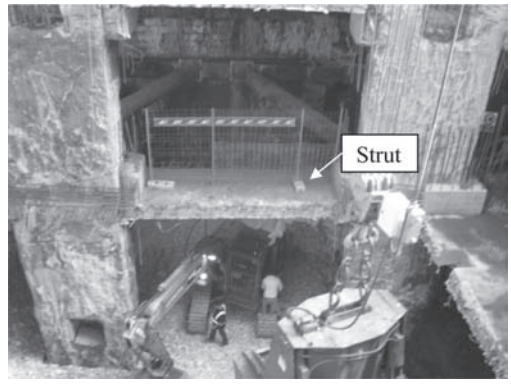

Figure 5. Excavation under third floor slab.

Figure 6. Breaktrough TBM.

4 MONITORING SYSTEM

A wide monitoring activity has been carried out in order to verify the stability of supporting structures during construction and also the design assumptions to allow adjustment and optimization of the constructed processes.

For these reasons, the monitoring system has interested different topics:

- Water-table monitoring, by means piezometers installed outside the excavation (Casagrande cells) and inside excavation (electric piezometers under final excavation level);
- Ground movement monitoring, by means of several in-place inclinometers, multi-base assestimeters and precise levelling points;
- Building movement monitoring, by means of automated total stations to give real-time three dimensional displacements and remotely logged biaxial electrolevel tiltmeters;
- Structures monitoring, by means of inclinometers for measurement of horizontal displacements,

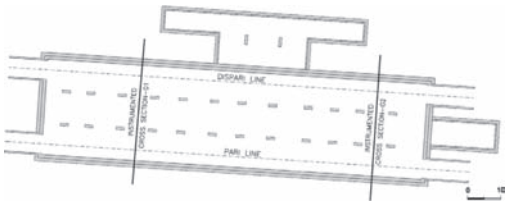

Figure 7. Plan view with position of monitoring instruments.

extensometers for the determination of the stress-strain of the structures and strain gauges load cells on steel struts.

The following Figure 7 shows the position of control sections (named section 1 and 2) and two inclinometers inside the diaphragm elements for horizontal displacement control (named IN03P and IN04P).

The Figure 8 shows the instrumented section 1.

The monitoring design has fixed threshold and limiting values for all the used instruments, which may trigger responses ranging from more frequent readings to modifications of construction procedures and, in the extreme, to implementation of a specified contingency plan.

The Figure 9 shows water levels measured during excavation phases. The external piezometers (Casagrande cells) have been placed around the initial external water table (≈ +25 m ASL) with a drop around 1 m up to 2–3 m for the shallowest piezometers. The internal piezometers (electric type) have measured a level around final excavation level, thus with a pseudo-hydrostatic gradient.

The Figure 10 shows load profile of steel struts, measured by strain gauges load cells.

5 NUMERICAL ANALYSIS

5.1 *General aspects and objectives*

Several numerical analysis, using finite elements method, have been performed in order to model the behavior of the supporting structures and the effects of the excavation.

Initially, a simplified and conservative 3D-FEM model ("elasto-plastic springs") has been used to design the structural elements. Then, more complex 2D and 3D-FEM models have been performed in order to analyze the detailed aspects:

- verify predicted effects induced in the neighboring buildings and understand the observed behavior of the supporting structures and ground movement;
- sensitivity analysis of the results about geotechnical parameters variability and different hydraulic conditions;
- stability analysis;
- analysis of three-dimensional excavation of the last step (from +15 m ASL to +10 m ASL), that has been described before, and consists of trench sectioning.

The last aspect has requested a full three-dimensional FEM model in order to evaluate the advantage due to the excavation procedure adopted.

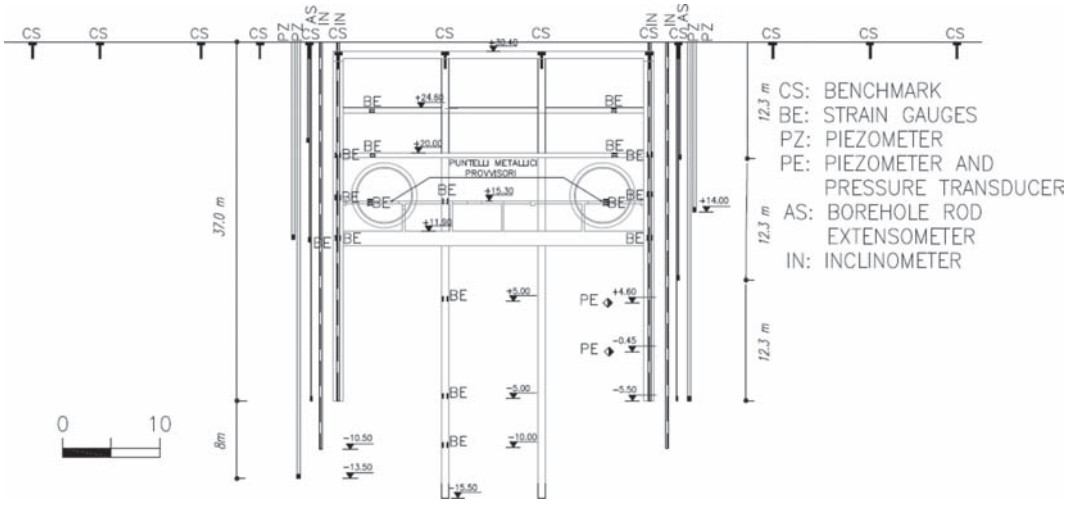

Figure 8. Instrumented section 1.

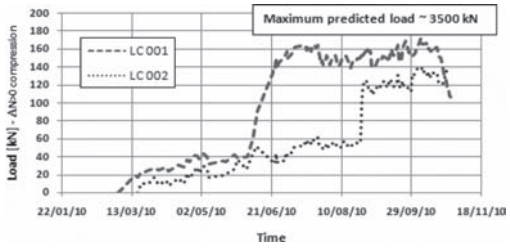

Figure 9. Internal Piezometric level during time excavation.

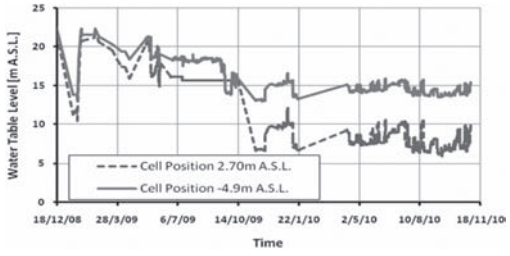

Figure 10. Load profile of steel struts during excavation from level +15 m ASL to +10 m ASL.

5.2 *3D-FEM model: description and main results*

The 3D finite element analysis has been performed using Plaxis 3D Foundation.

A soil model section of 260 m × 180 m × 40 m (L × B × H) has been adopted. Horizontal displacements on model's vertical boundaries have been restrained, while all displacements have been restrained on the bottom boundary. The structures have been modeled with plate elements (horizontal floor slabs and vertical diaphragm walls) connected to the surrounding soil by interface elements having a frictional strength that is 2/3 of soil strength. All structural elements have been modeled using linear elastic property of the concrete.

Variable mesh size has been applied to soil layers and structures of the station to save computation time. Mesh has been refined inside and around the excavation volume and then expanded by going to the boundary. The total number of triangular elements is about 11000, with about 33000 nodes. A fully meshed Plaxis 3D is showed in Figure 11.

The Hardening Soil small model, abbreviated as HSS small model, has been selected for design. This constitutive model is a powerful tool especially for excavation problems. The main design geotechnical parameters are shows in Table 3.

The model involves frictional hardening characteristics to model plastic shear strain in deviatoric loading, and cap hardening characteristics to model plastic volumetric strain in primary compression.

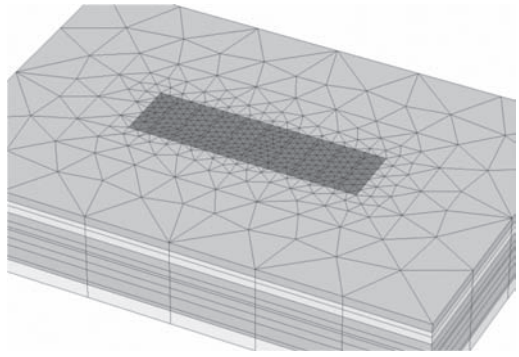

Figure 11. Meshed 3D Plaxis model.

Failure is defined by means of the Mohr-Coulomb failure criterion (strength parameters ϕ', c').

Moreover, this model incorporates strain dependent stiffness moduli, simulating the different reaction of soils to small strains and large strains.

Soil stiffness is therefore modeled with "large strain parameter" (Poisson's ratio ν; E_{ur}, E_{50}, E_{oed} that describe the unloading–reloading stiffness and primary compression stiffness) and low strain parameters (G_0 and $\gamma_{0.7}$, that are shear modulus at small strains and the shear strain at which the secant shear modulus value is reduced to 70% of its initial value). The $\gamma_{0.7}$ has been estimated following the suggestion in the Plaxis manual as:

$$\gamma_{0.7} = \frac{1}{9 \cdot Go} \cdot \left[2 \cdot c' \cdot (1 + \cos 2\varphi') - \sigma'_1 \cdot (1 + ko) \cdot \sin 2\varphi' \right] \quad (1)$$

where ko is the coefficient of lateral earth pressure at rest and σ'_1 is the effective vertical stress.

Therefore the operative shear modulus G is a function of shear strain γ and stress level by the following expression:

$$G = \frac{G_o}{\left(1 + a \gamma / \gamma_{0.7}\right)} \quad (2)$$

Table 3. Main input parameters of HS small model.

Layer	γ (kN/m³)	φ' (°)	c' (kPa)	G_0 (MPa)	E_{ur} (MPa)	E_{50} (MPa)
R	17	28	10	85	45	15
LSO	17	30	20	85	45	15
TA	17	32	30	280	145	48
T1/T2	17	35	30	850	440	147
STa	18.5	24	25	200	105	35
SG	19	35	5	750	390	130

The shear modulus at small strains (G_0) has been calculated using shear wave velocity measures ($G_0 = \rho \cdot Vs^2$). As said before, the HS small model also requires the definition of the unloading/reloading Young's modulus (E_{ur}). In this case E_{ur} has been set equal to 1/5 of small strain Young's modulus ($E_0 \approx 2.6 \cdot G_0$), that is a value that in previous experiences of the Authors has given good accordance between analyses and site monitoring measures. Finally, as suggested in the PLAXIS manual, has been set $E_{50} = E_{ur}/3$ and $E_{oed} \cong E_{50}$.

The analysis have simulated the main stages of construction and excavation.

- Geostatic initialization using the ko procedure; activation of all the plate elements (diaphragms) and their interfaces;
- Sequential excavation phases up to +15 m ASL (subway platform level) with construction of the internal contrast floor at levels +31.0 m (roof slab), +24.1 m and +20.0 m ASL.
- Installation of provisional steel struts (+15 m ASL) and excavation up to formation level (+10 m ASL) proceeding by through partial longitudinal sectors, 12 m width; this excavation phase has been divided into 9 consecutive steps. Figure 12 shows the configuration of the model in an intermediate excavation stage. The model also considers the stabilizing effect of the base slab that is executed before of the next excavation stage.
- Completion of the excavation (and base slab) and removal of the provisional steel struts.

The FEM model led to quantify the stabilizing confinement effect due to the methodology excavation through partial longitudinal sectors. An medium increase of about 50% is observed for the effective vertical stress acting along the diaphragm wall below the final excavation level, where acting the passive resistance (Figure 1313). Therefore, in order to take into account this phenomena in the simplified 1d-FEM analysis, an equivalent surcharge has been applied on the final excavation level during the last phase.

Figure 14 shows the 3D deformation of retaining walls after completion of excavation and base slab construction.

Figure 15 shows the distribution of the vertical bending moment (M): the maximum value is ±800 kNm/m, in good agreement with the simplified 1D and 2D FEM models.

As shown in Figure 16, the predicted ground settlements fit the field measurements quite well for instrumented section 1, but higher values were measured for section 2 without any damage.

Figure 17 shows the comparison of measured wall horizontal displacements and those predicted using the 3D FEM model. Measures and numerical analyses results agree well in the upper part of the wall, while in the lower (inside ground) part of the wall FEM analyses are still conservative and predict horizontal displacements are higher than the measured ones.

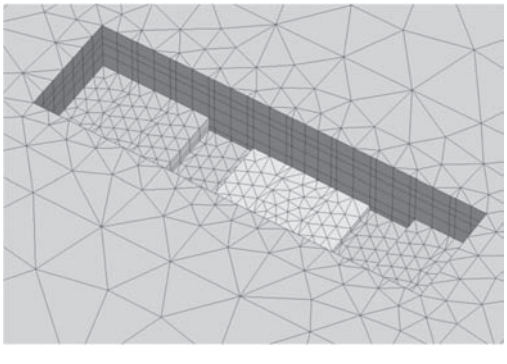

Figure 12. Intermediate longitudinal stage excavation (the view of internal structural floor is disabled).

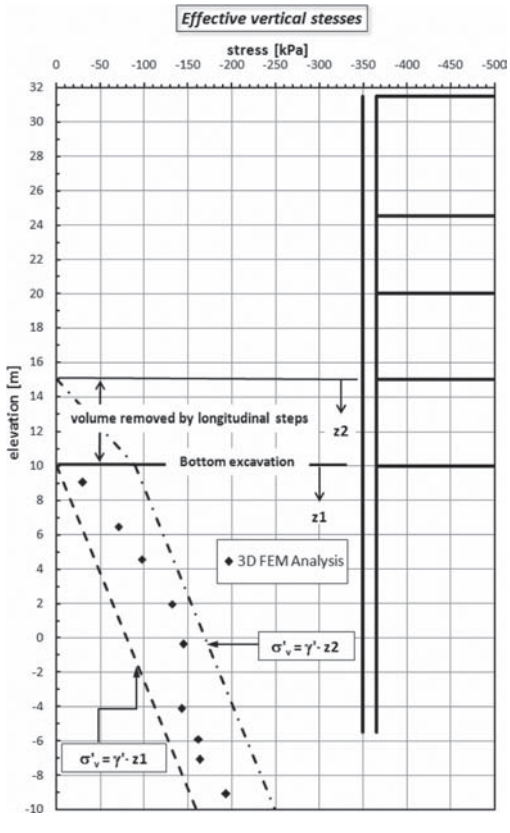

Figure 13. Effective vertical stress below final excavation level.

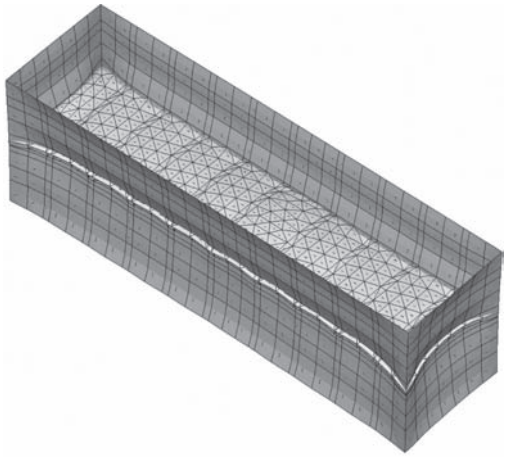

Figure 14. Deformed mesh structures (amplified × 400 times).

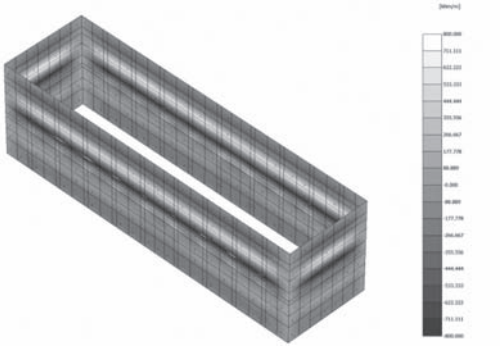

Figure 15. Vertical bending moment (Mmax ±800 kN m/m).

6 CONCLUSIONS AND MONITORING CONSIDERATIONS

Monitoring measures have been obtained over all the period of construction works, highlighting that:

- The perimeter diaphragm walls, embedded into a stratum with low permeability, allows a good separation between water level outside the station box (not significantly affected either by the excavation or by the dewatering process) and water level inside the station box (almost coincident with final excavation level);
- The measured deformations of the supporting structures are less than the predicted deformations, with shear state correlated to allowable stress.

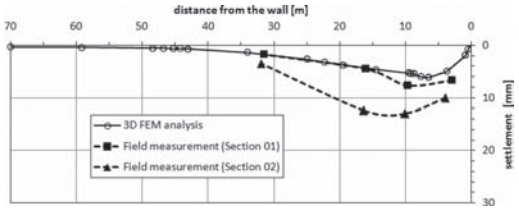

Figure 16. Prediction and monitoring of settlements.

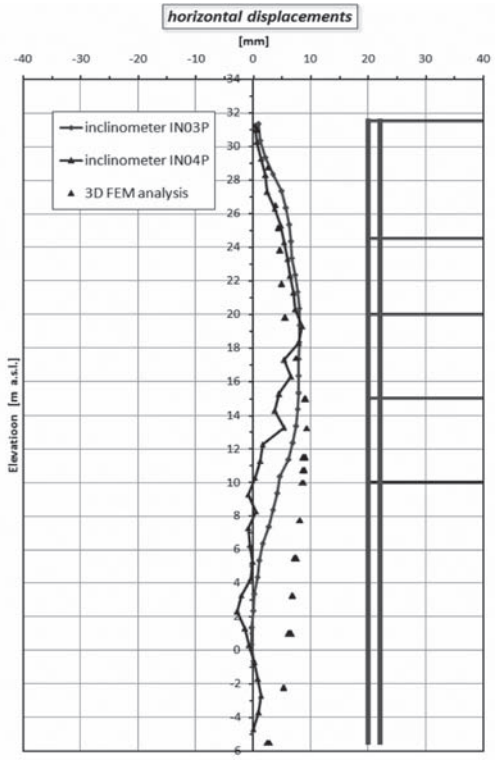

Figure 17. Prediction and monitoring of horizontal displacements with depth.

It has to be underlined that building monitoring showed maximum settlement of 6÷10 mm and maximum horizontal displacements of 10÷13 mm, without any damage. During monitoring activity it has been observed a high dependence of measures with temperature variation, both in short time and seasonal fluctuation. Therefore measures have been corrected by the influence of external temperature.

Also in the case of Malatesta Station the good monitoring program and the critical comparison of monitoring measures with design predictions provided key information that lead to a safe and successful construction.

REFERENCES

Benz, T. et al. 2009. "*A small-strain overlay model*." International Journal for Numerical and Ana-lytical Methods in Geomechanics, 33, 25–44.

Burland, J.B. 1965. "*The yielding and dilation of clay*." Geotech-nique, 15, 211–214.

Calvello, M. & Finno, R. 2004. "*Selecting parameters to optimize in model calibration by inverse analysis*." Computer and Geotechnics, 31, 410–424.

Chang, C.S. & Abas, M.H.B. 1980. "*Deformation analysis for braced excavation in clay*." Proceedings of the Symposium on Limit Equilibrium, Plasticity and Generalized Stress Strain Ap-plications in Geotechnical Engineering, ASCE, Hollywood, Florida, 205–225.

Duncan, J.M. & Chang, C.Y. 1970. "*Nonlinear analysis of stress and strain in soils.*" Journal of the Soil Mechanics and Founda-tions Division, ASCE, 96, 637–659.

Hashash, Y.M.A. & Whittle, A.J. 1996. "*Ground movement prediction for deep excavations in soft clay*." Journal of Geo-technical Engineering, ASCE, 122, 474–486.

Hsieh, P.G. et al. 2008. *"Basal heave analysis of excavations with consideration of anisotropic undrained strength of clay."* Canadian Geotechnical Journal, 45, 788–799.

Hsieh, P.G. et al. 2010. "*Use of the total stress undrained model to the analysis of deep excavation*." Proceed-ings of the 17th Southeast Asian Geotechnocal Conference, Taipei, Taiwan.

Ou, C.Y. 2006. *Deep Excavation: Theory and Practice*. Taylor and Francis, Netherlands.

Ou, C.Y. & Lai, C.H. 1994, *"Finite element analysis of deep excavation in layered sandy and clayey soil deposits." Canadian Geotechnical Journal, 31, 204–214*.

Ou, C.Y. et al. 2000. *"Building response and ground movements induced by a deep excavation."* Geo-technique, 50, 209–220.

Ou, C.Y. et al. 1998. "*Performance of dia-phragm wall constructed using top-down method.*" Journal of Geotechnical Engineering and Geoenvironmental Engineering, 124, 798–808.

Ou, C.Y. et al. 2000, *Three-dimensional deformation behavior of the TNEC excavation case history,* Canadian Geotechnical Journal, 37, 438–448.

Ou, C.Y. et al. 2010, *"Evaluation of clay constitutive models for analysis of deep excavation under undrained conditions."* Journal of GeoEngineering, 5, 9–20

Pestana, J.M. & Whittle, A.J. 1999. "*Formulation of a unified constitutive model for clays and sands.*" International Journal for Numerical and Analytical Methods in Geomechanics, 23, 1215–1243.

Plaxis bv, Delft, Netherlands 2007. "3D Foundation version 2. User's Manual." Part 3: Material Models Manual & Part 4: Scientific Manual.

Prevost, J.H. 1979. "*Undrained shear tests on clay.*" Journal of the Geotechnical Engineering Division, ASCE, 105, 49–64.

Schanz, T. et al. 1999. "*The hardening soil model: Formulation and verification.*" Beyond 2000 in Com-putational Geotechnics—10 years PLAXIS. Balkema, Rotterdam.

Schofield, A. & Wroth, P. 1968. *Critical State Soil Mechanics*, McGraw-Hill, London.

Geotechnical Aspects of Underground Construction in Soft Ground – Viggiani (ed)
© 2012 Taylor & Francis Group, London, ISBN 978-0-415-68367-8

Line C in Rome: Remote monitoring system

R. Sorge
Metro C, Rome, Italy

S. Moretti & O. Tripoli
IMG Srl, Rome, Italy

ABSTRACT: The complexity and dimensions of the design of Rome's Line C underground and the variety of interferences between construction and territory required the development of an automatic and remote controlled monitoring system. The monitoring system used, involves a great quantity of instruments and guarantees real time data management, publication and evaluation; the system collects, processes, and delivers data, to the appropriate agencies involved in the construction, and it also provides a historical overview during all the building phase.

1 LINE C—ROME UNDERGROUND

1.1 *Introduction*

Rome's Line C subway, under construction by General Contractor Metro C S.c.p.A. since 2007, is a fully automated underground railway line characterized by an automatic train control system; The trains are "driverless" and platform doors will slide open simultaneously with those of the train on arrival, increasing station safety and improving service quality.

The line, with its 30 stations, crosses the Capital from the south-east side (Pantano) to the north-west area (Farnesina), stretching over a distance of 28,2 km. The construction of Line C will almost double the area covered by the current underground network and it represents one of the most important works ever built in an urban context.

The main characteristic of the stations is the length of the platforms, 110 m long in order to accommodate the purposely planned and constructed trains, made up of 6 cars for a total length of 107 m. The train has a maximum transportation capacity of 24.000 passengers per hour in each direction, and a maximum frequency of 3 minutes during rush hours.

The eastern part of the line, 8,7 km long, emerges onto the surface just outside the "highway ring" (G.R.A.) until Pantano, running along the Casilina state road, on the existing path of the Rome-Pantano railroad. Along this section of the line there are 11stations, of which 10 existing that will be adapted to subway standards.

The Line C Depot/Workshop, situated in Graniti on an area of 22 hectares, is the operating and technological core of the new line. This area will be used to house the complete rolling stock fleet of line C and the Operation Head Office, located in a dedicated building, will be responsible for remote train steering and control.

The main part of the line runs inside the "highway ring" (G.R.A.) for approximately 18,5 km, and is characterized by two single railroad tunnels, with a distance between centre lines variable between 18 and 40 meters.

Each tunnel has a diameter of 6,70 m. In order to avoid interference with archaeological findings, which in some downtown areas are located up to 16–18 meters from the surface, and at the same time limit the effects of settlements due to excavation, the tunnels run between 20 meters and 35 meters under ground level.

This route is expected to have:

- 11 deep "box shaped" stations, with few exceptions, made with the "bottom-up" method; stations are on average 20 m deep below the water table;
- 8 special box shaped shafts, including 3 for TBM erection and dismantling and 5 for the implementation track junctions;
- 11 circular vent shafts, for line ventilation and water collection, located in the lower points of the line;
- 4 blind-hole tunnels of about 180 m length for turnout tracks;
- 900 m of platform tunnels built by TBM tunnel enlargement. Due to territorial interferences, it was not possible to position all station platforms inside "box shaped" stations.

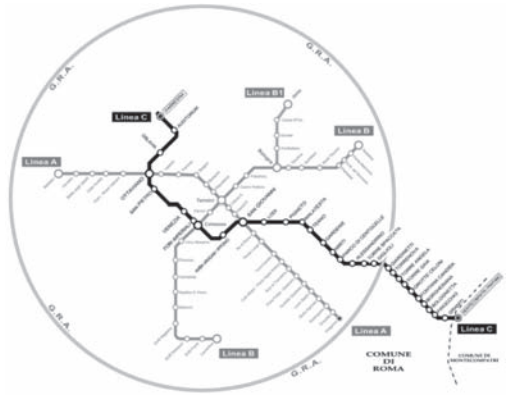

Figure 1. Subway network.

Figure 2. Subway train.

The main characteristics of Line C are:

	Length (km)	Tunnels (km)	Stations (n°)	Shafts (n°)
Pantano—Farnesina	28,2	39,0	30	38
1st functional phase (in execution):				
Open air line	8,7		11	
Underground line	**9,8**	**19,6**	**11**	**19**

1.2 *Execution of works*

From 2007, after a complex campaign of archaeological and geotechnical surveys, along the First Functional Route from San Giovanni to Pantano, more than 14,000 m of tunnels (external diameter 6,40 m and internal diameter 5,80 m) have been constructed, 37 work sites have been opened and 3 base camps are currently active.

As of June 2010 work completion is more than 60%.

In the Graniti site the construction of the Depot/workshop is almost complete and the first trains have arrived and are ready to start the tests of functionality and interface between the systems.

Figure 3. Line C Depot/Workshop in Graniti area.

Figure 4. TBM across the Station.

The main issues faced during the execution of the works have been those linked to archeology and to the interaction with the urban context. The urban context is characterized by not only the pre-existing buildings but also by the historical-monumental sites, by the underground facilities, and by the underground caves that characterize most of the underground path.

Overall, the works of Line C, are characterized by the following quantities:

- deep excavation 4,500,000cu.m.
- concrete 1,600,000cu.m.
- steel 280,00t
- rails 7,400t
- copper 150t
- cables 110 km
- pre-cast tunnel lining segments 25,000

Moreover Metro C has acquired 4 Herrenknecht TBMs, and has ordered from Ansaldo Breda a fleet of 30 trains (length 107 m), each consisting of 6 cars, available form 2010 at the Graniti workshop.

1.3 *The monitoring of the activities as a priority*

The concurrence of all the processes mentioned above, located in different sites at the same time,

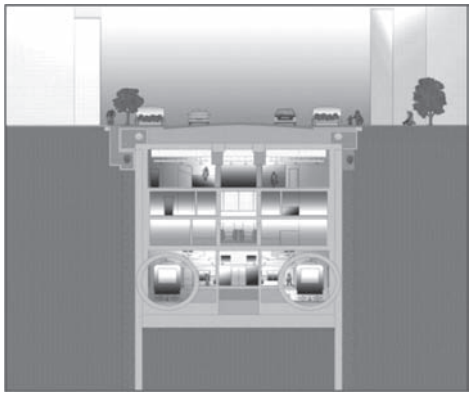

Figure 5. Box shaped station.

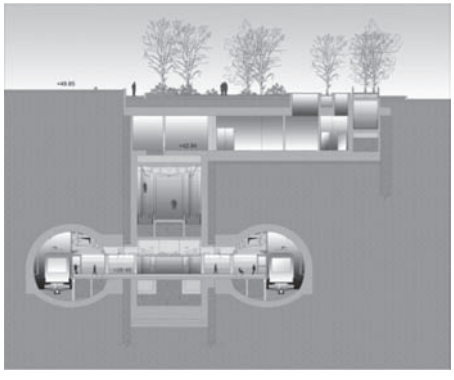

Figure 6. Station built by widening TBM tunnel.

mostly all underground and in urban areas with distinctive characteristics of historical and archaeological sites, requires the establishment and development of a complex automatic monitoring system, able to check the compliance between existing building, environmental situations and design assumptions and prevent unchecked negative developments regarding the safety of buildings, staff and the urban context, by fostering the necessary remedies.

The overall goal of monitoring while constructing is, not only verifying the compliance between the actual behavior of the land, facilities and environment and what was expected, but also taking care of the safety of workers and residents, and the maintenance of existing buildings: buildings, sewers, water and gas mains, etc.

It is therefore necessary that the monitoring has the following features and requirements:

- complete information;
- reliability of the system (of the component as well as of the entire structure) and counter checks of the required precision;
- well-timed information related to activities in progress;
- minimization of human error;
- flexibility in the system's usage, interpretation and adaptability.

The system must also be usable in real time by numerous people, from different institutions, in total security.

In fact, this system should be configured so that it can simultaneously handle a large number of instrumental groups, about 933, including:

Stations and shafts:	90 geotechnical sections
Along the TBM line:	60 geotechnical sections
	198 topographical sections
	60 instrumental rings
Ordinary buildings:	329
Sensitive buildings:	196

The monitoring tools for this configuration are about 20,000, divided as follows:

Table 1. Monitoring instrumentation.

Type	Quantity
Basic devices	
Triaxial accelerometer	4
Fixed extensometer	15
Strain gauge	5.192
Levelling pin	3.335
Load cell	83
Wall clinometer	457
Sliding deformeter	10
Rod Extensometer	173
Inclinometer	283
Prism	6.514
Crackmeter	4
Casagrande Piezometer	396
Electrical piezometer	127
*Automated systems**	
Pressure sensor (piezometer)	372
In place inclinometer sensor (inclinometer)	1.415
Displacement sensor (rod extensometer)	519
DAU (Data Acquisition Unit)	177
RTS (Robotized Total Station)	185

*232 km of cables are provided for measuring and centralization of control systems.

This complex and articulated configuration of instruments needs a system able to handle a large amount of data, in order to ensure a smooth flow of information starting from the instrument and reaching the planning area, the construction area, the works manager, the board of testing and clients.

The work flow has to allow ongoing verification of the compliance of design parameters, especially in case of pre-arranged events as "expected trend" or exceeded thresholds, and process with reliability a large amount of information coming daily from the instruments. This is impossible with the traditional monitoring systems.

It is also necessary to handle a great amount of documents such as monitoring reports, history and development of all the instrumental measurements and data consultation, visualization and storage.

In fact, during the first 3 years of construction the monitoring system processed more than 60 million records concerning geotechnical data and 40 million records regarding topographical data.

In order to fulfill the requirements and cover the needs described above, considering the enormity and simultaneity of works, the main goal was to characterize the monitoring system with a widespread presence of automatic processes, in order to allow quick scalability, independence from human factors and, at the same time, highlight in advance among a huge amount of information trends which are critical compared to expected values.

2 ARCHITECTURE OF THE MONITORING SYSTEM AND ITS PERFORMANCE

2.1 *Scenario analysis*

During the analysis for the definition of the requirements for a monitoring system which could satisfy the previously discussed objectives, a number of peculiar elements were highlighted:

- great variety of installation sites;
- great variety in the characteristics of monitoring instruments;
- simultaneous operations;
- great amount of data;
- long operating lifetime of the system.

The installation sites include: tunnels, station sites, civic buildings, residential buildings, monuments and architectural works along the Line C route, urban streets, highways, light railways and railroad hubs.

The long list of instrument types and the differences in their characteristics (e.g. sensors with manual reading or automatic and remote instruments), needed to be handled with a versatile system, able to take into account new instruments not foreseen within the initial design.

Works involve different and parallel decisional structures. Sites and their management structure are coordinated by the engineering office which modulates the monitoring architecture according to site phases. These structures are spatially distributed (de-localized) and mutually independent from each other, relatively speaking. The overall system also needs to address people with different specializations. A unifying system, in terms of monitoring data handling and distribution, was required.

Information concerning the amount of data analyzed during the first three years of operation, efficiently show the volume and complexity of the system being developed. A constant flow of data that keeps increasing on one hand shouldn't hamper works with false alarms, on the other hand has to guarantee a strict control for the safety of the work environment, of pre-existing structures and of citizens.

2.2 *System architecture*

The system implemented to answer the requirements of the above-described scenario is made of well-defined elements summarized as follows:

- basic devices (with manual or automatic reading);
- automatic and remote systems;
- Data Processing System, DPS;
- Data Dissemination System, SDD.

In order to assure adequate frequency of sampling and at the same time minimize human intervention, the design of the monitoring system provided, at the executive level, Smart Automated Systems. These are implemented by DAU (Data Acquisition Units) (Fig. 7), which are remotely programmable according to control needs.

Very high precision RTS's (Robotized Total Stations) are instead used for topographical checks

Figure 7. DAU (Data Acquisition Unit).

Figura 8. RTS (Robotized Total Station).

(Fig. 8). While the first ones can guarantee constant readings of nearly all of the geotechnical and structural monitoring instruments, the second ones can guarantee cycles of geodetic readings both within a station work site and along the TBM excavations, following it step-by-step along the line galleries.

A quick response and access to data can be guaranteed by an innovative computer-based system, a hardware/software platform which can handle an increased number of data, response times and workload. Quick response time includes the entire monitoring management process: from data acquisition to its availability to system users—designers, people in charge of the site, Construction Management and General Supervision—by giving clearly readable layouts available in light and well-known digital formats (PDF, Excel and so on) ready for printing and presentation.

All this is made possible by a software environment that includes webGIS components and automatic procedures for data acquisition and processing. By enabling the remote management of the monitoring network, it minimizes the time gap between data acquisition and processing and its availability.

2.3 *DPS, Data Processing System*

The DPS, Data Processing System, is the core of the entire system. It is composed of specialized operators, dedicated software and hardware and a complex data transfer network based on wired and wireless (UMTS or Radiomodem) links.

Its innovative design required the development of software applications which could:

- acquire measurements;
- automatically process data;
- perform validation checks;
- generate automatic warnings when pre-defined attention and alert thresholds are exceeded;
- automatically archive documents;
- distribute the data using the DDS, a dedicated web-based platform with webGIS components.

The automatic routines that perform these tasks are specific for each instrument and for every kind of data exchange (manual or automatic). They are designed to minimize human errors through data entry forms (for those kind of instruments wich are not automatic neither do not support remote control), and to minimize the risk of data loss or data mix-ups, which is very serious if connected to false alarms or, worse, to missed alarms.

In detail, the DPS:

- provides the tools necessary to manage the data monitoring of Rome's Line C subway in specific routes, meeting the requirements of high speed processing, validation and distribution of data and emergency management;
- collects and organizes data coming from the instruments;
- analyzes and validates data imported from remote-controlled, automated and manual instruments, through automatic routines that prevent transcription errors; analyzes data identifying instrumental errors and exceeding of the thresholds of attention and alarm;
- produces reports and statistics;
- produces updated maps;
- manages the SSAT** and SSAL**;
- stores data;
- has an interface dedicated to the publication of data via the Web called SDD, Data Distribution System.

The DPS works by applying a series of standard operating procedures (SOP), which regulate the flow of information and the data output (graphs and tables). These procedures have the task of minimizing the error introduced.

The DPS manages data from the instrument to the final storage. The path of the data is illustrated in the figure below:

The first area, A, manages the acquisition of data: in field personnel and automated systems (remote-controlled or not) collect data in formats and ways compatible with the following (B) procedures for processing and storage. The data transfer routine check the consistency of the data before their storage.

The final area, C, is responsible for data processing and data validation, for charts elaboration and layouts development according to design changes during construction.

**Superamento Soglia di Attenzione e Superamento Soglia di Allarme (that is: exceeding of the alert threshold and exceeding of alarm thresholds).

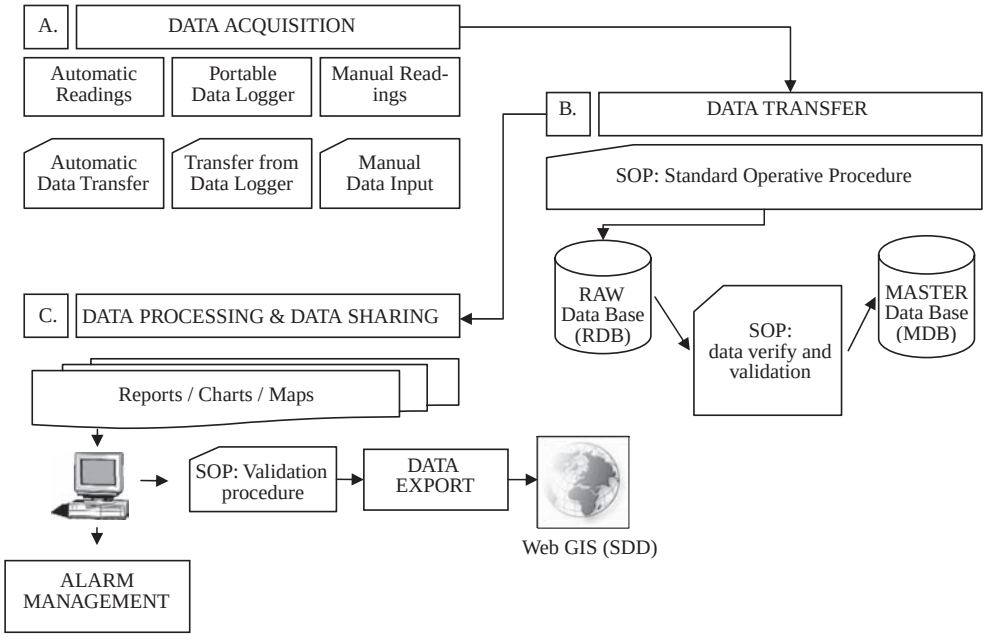

Figure 9. DPS Data flow chart.

Operators use the DPS data transfer routine to transfer the information from monitoring tools to dedicated databases. The system is structured to handle all the instruments during the different stages of processing. Some instruments, however, do not support remote control or support remote control only in some phases, because of design requirements. Data from these instruments require intermediate steps such as field reading operations, transcription and manual data entry in the database. For these data too entry forms allow you to minimize errors.

The following images in Figure 10 show some of the forms of computer data management tools developed for the different sectors of line C (T3, T4, T5, T6a, T7) and for Graniti Depot.

2.4 *Alert thresholds and Alarm thresholds*

To allow the monitoring staff and users to distinguish, in the continuous flow of data, sensitive information, a key role is played by the Alert Thresholds (SAT) and the Alarm Thresholds (SAL). They allow to focus on critical aspects of design, abnormal behaviors, especially on their evolution when corrective action is taken.

- Event SSAT (Alert threshold exceeded)
- Event SSAT (Alarm threshold exceeded)

The procedures to be undertaken once the event SSAT (or the next SSAL) occurs are clear, defining timing and participation and communication mechanisms. The reporting is gradually available on the platform, SDD, until the critical event is solved.

Figure 11 shows the flow chart which describes the procedures adopted in the case of SSAT and SSAL.

Until now, during processing, there were 9 SSAL events and 39 SSAT events, all settled and solved (Resolved planning corrective procedures with redefinition of the new SAT/SAL).

2.5 *SDD (Data Dissemination System)*

The SDD is a web-based application which enables access to monitoring data from any location. The application core has been developed using standard languages, like PHP (on the server-side) and JS (on the client-side), while complex and multi-layered maps and other innovative location-based functions are managed by integrating UMN Map Server with the rest of the system (UMN Map Server, now a project by the Open Source Geospatial Foundation, was originally developed by the University of Minnesota).

A minimalistic design approach ensured that the user interface is fast and efficient and at the same time clean and multi-browser compatible, despite the typical shortcomings of web-distributed applications.

All the data are stored in a MySQL-based relational database synchronized by a replication mechanism with a subset of the main DPS database.

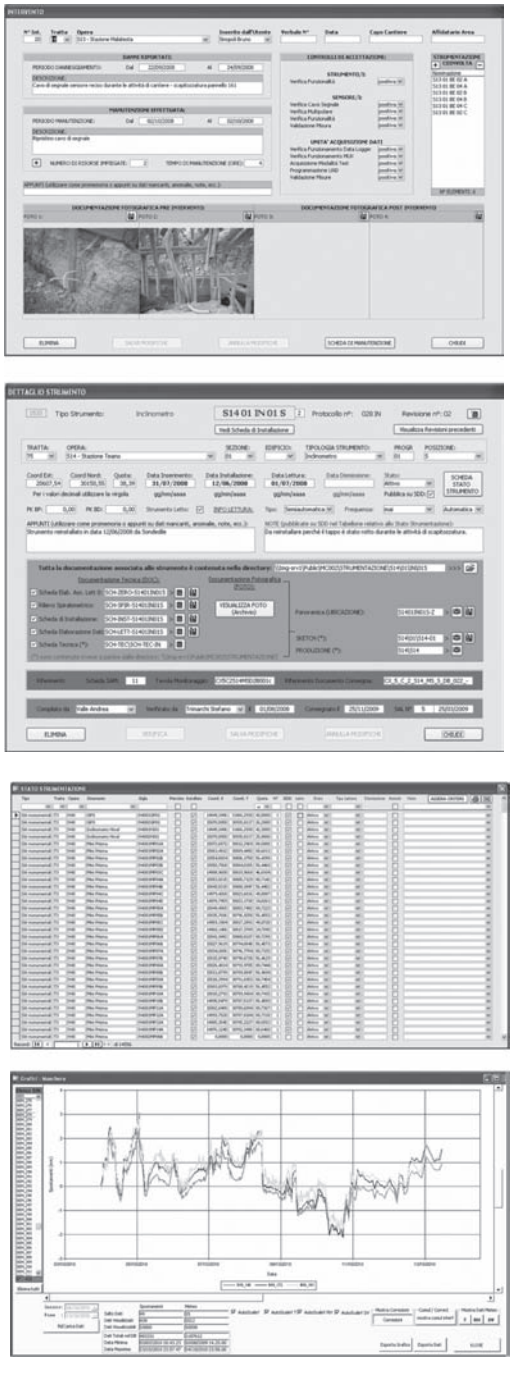

Figure 10. DPS. Examples of informatic tools.

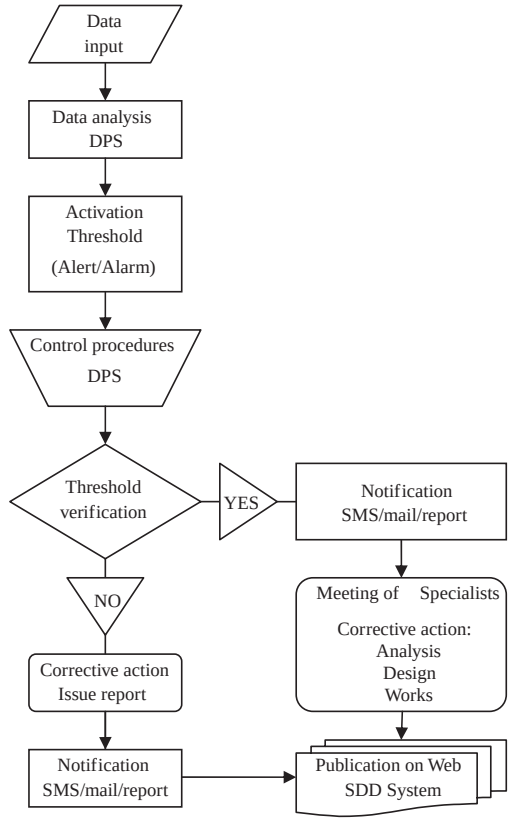

Figure 11. Management of SSAT/SSAL. Procedure chart.

The design and development of the SDD is successfully based on open-source products and technologies. The result is a stable, fast and easy to upgrade application, adjustable and scalable to other monitoring contexts.

In order to create a modular, extensible and flexible system, it was decided to provide two types of user interfaces: map priority views (Fig. 12) and data priorities views (research papers, warning event handling).

The map priority view offers the possibility to search for tools and monitored objects by exploring the area with typical Web-GIS interface (similar to the widespread regional consultation systems such as Google Maps), which are selected by the instruments, sensors (individuals or groups) or monitored elements (e.g. buildings or sections of monitoring) with the selection cursor that changes depending on the context. By selecting an entity on a map, you can get a list of documents (spreadsheets and data processing, installation sheets) associated with it (Fig. 13).

For monitoring purposes, the SDD is provided by a data form which allows the user to access the numerical data database via the web, making them exportable in standard formats (xls, csv,

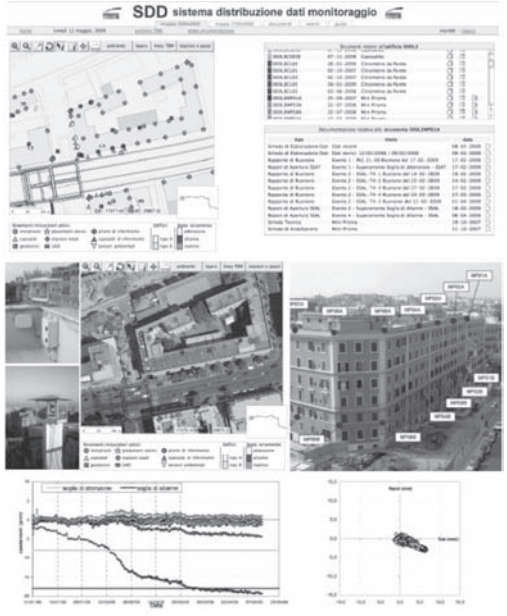

Figure 12. SDD. Example of priority map wiew.

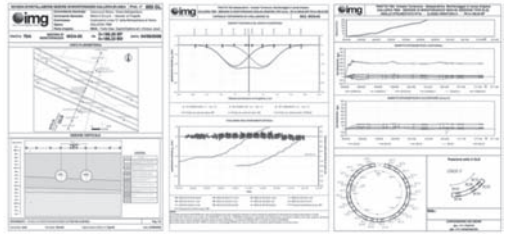

Figure 13. SDD. Example of monitoring layouts.

Figure 14. SDD. Example of settlement analysis (subsidence & displacement vectors).

Figure 15. Monumental sites. Monitoring tower for the Basilica Maxentius.

dat) and displayed in graphical format directly into the web browser, for capillary remote controls, by the designers, building site, the Construction Management, the General Supervision and Commissioning.

The DPS and SDD server, hosted in two servers houses, also provide backup and disaster recovery.

The evolution of the DPS-SDD is developed together with the design requirements. The peculiarities of some portions of the track and, in particular, the crossing of the historical and monumental area of the city from San Giovanni district to the right bank of the Tiber River, required the addition of functional tools such as data module and modules which allow the synoptic representation of events.

Among the many tools available, the modules for the settlements due to excavation and movement, allow you to view changes in the statistical distribution of horizontal and vertical alignment of data, directly on the map, making it easier and more immediate to understand the areal development of a phenomenon, and the evaluation of the adequacy of the readings between nearby points.

3 CONCLUSION

Automation, remote monitoring tools and data distribution via the web were the winning choices. The possibility of data projection during decision-making meetings has undoubtedly improved the time needed to prepare them. No paper, no plotter to work on, no volume to browse or design plan to roll on the meeting table. It is estimated that on a daily average basis about

Figure 16. Basilica Maxentius. Particular of geodetic prism.

Figure 17. Particular of monitoring tower of Basilica Maxentius.

80,000 monitoring records are analyzed, while the SDD platform is powered by over 1300 report data, excluding the supplementary documentation (technical data sheets and installation tools, graphics, production, etc.).

The overview of project-data-territory is available 24/7 from any position, with a computer connected to the Internet.

The entire monitoring system described above has been extensively tested on the works of the T4 to T7 sectors of the line and can be considered fully efficient and capable of being interfaced with ease with all the monitoring equipment already in use. In addition, from May 2009 a pre-trial monitoring phase on some buildings of special architectural and historical value on the portion T3 of the line (Palazzo Venezia, the Vittoriano and the Basilica Maxentius) is in progress.

In particular, the Basilica Maxentius is constantly monitored by an integrated system consisting of modern geodetic monitoring equipment: Leica TCA 2003 robotic total stations, GPS sensors, ground radar interferometer IBIS-L, in addition to constant monitoring by SAR Interferometry System.

The preliminary monitoring of the section T3 of the line has the following objectives: to define the deformation behavior of the structures in undisturbed conditions, to test equipment such as innovative monitoring instruments such as Ground Based Radar Interferometry (Gb-InSAR from earth surface) and to provide for these usage protocols and how to manage data from DPS and the SDD.

After the two-year planned preliminary monitoring, the DPS and SDD management system will be able to integrate and automatically manage the data collected, whether they come from the most traditional instruments, or from those of last generation, This feature makes it one of the most advanced and complete monitoring system for the control of major projects in urban areas.

This page intentionally left blank

Physical and numerical modelling of deep excavations and bored tunnels

This page intentionally left blank

Geotechnical Aspects of Underground Construction in Soft Ground – Viggiani (ed)
© 2012 Taylor & Francis Group, London, ISBN 978-0-415-68367-8

Review of Newtonian and non-Newtonian fluids behaviour in the context of grouts

Sina Kazemian
University Putra Malaysia, Serdang, Malaysia

Arun Prasad
Banaras Hindu University, Varanasi, India

Bujang B. K. Huat
University Putra Malaysia, Serdang, Malaysia

ABSTRACT: The objective of this review is to elucidate the rheological behavior of cement based grout. Rheology of grouts is a way of describing its properties without paying any attention to whether it is a homogenous grout or a mixture of grains in a grout. Cement grout based rheology is characterized by at least two parameters; yield stress and plastic viscosity. The rheological models are used to describe the relationship between shear stress and shear rate. The Newtonian fluids are true fluids that tend to exhibit constant viscosity at all shear rates. A non-Newtonian fluid is a fluid for which the relationship τ/γ' is not a constant. Pseudo-plasticity or shear thinning is the most common type of time-independent and non-Newtonian fluid behavior observed. It is characterized by an apparent viscosity which decreases with an increasing shear rate. Many mathematical models for fluids behavior have been proposed to model the shear thinning characteristics. These models are based on curve fitting method that gives empirical relationships for the shear stress vs. shear rate curves. Some models are based on the statistical mechanics. The Bingham model does not give an exact description of the behavior of a cement based grout even if the geometry is defined, but there are other models and the selection of model should be done carefully based on the requirement.

1 INTRODUCTION

1.1 *Rheology and viscosity of fluids*

Rheology can be defined as the study of the change in the form and flow of the matter. The scope of rheology includes elasticity, viscosity, and plasticity. Rheology of grouts is a way of describing its properties without paying any attention to whether it is a homogenous grout or a mixture of grains in a grout (Eklund, 2005). It is normally applied to fluid materials (or materials that exhibit a time dependent response to stress). It can also be defined as the study of the flow of the grout flows, before the setting point is reached. This is crucial due to the fact that the grout must be placed by some kind of mechanical process like, pumping into the prepared forms. Cement grout based rheology is characterized by at least two parameters: yield stress and plastic viscosity. In a similar way, an elastic solid is characterized by two parameters: Young's modulus and Poisson's ratio (Bentz *et al*., 2006).

Brookfield Engineering Labs Inc. (2010a) emphasized that by measuring the rheology parameters of fluids much useful behavioral and predictive information can be obtained. These include quality control, chemical, mechanical, and thermal treatments, effects of additives on the curing reaction, and direct assessment of the process ability. Furthermore, the rheological measurements may also be used as an indicator of micro structural changes occurring in hydration of the cement-based grout or the investigation of the effect of admixtures, and the development of cementitious systems that are easily pumped or placed (Struble and Ji, 2001).

Hånsson (1993) stated that the rheological behavior of a cement-based grout is difficult to define because of the concentration and characteristics of the particles as well as the suspension medium. The rheological behavior is influenced by the chemical reactions in progress during the hydration of the cement and the thixotropy is dominant at short cycle times. The rheological models are used to describe the relationship between shear stress and shear rate. Syrjålå (1996) stated that there was no general rheological constitutive model

available that time for non-newtonian fluids. Most commonly used time independent models in suspension rheology are: Newton model, Bingham model, power law model, modified power law model, and Casson model.

Brookfield engineering labs inc. (2010a) defined that the viscosity is the measure of the internal friction of a fluid. This friction becomes apparent when a layer of fluid moves in relation to another. By increasing the friction, a greater amount of force is required to for this movement, which is called shear. The shearing occurs whenever the fluid is physically moved or distributed, as in pouring, spreading, spraying, mixing, etc. It should be mentioned that highly viscous fluids, therefore, require more force to move than less viscous materials.

Consider two parallel flat areas of fluid of the same size A which are separated by a distance dx (Fig. 1). If the plates are moving in the same direction at different velocities V_1 and V_2, then the force required to maintain the speed is proportional to the difference in speed through the liquid, or the velocity gradient (Equation 1).

$$F/A = \eta\, dy/dx \tag{1}$$

where η is the viscosity of the fluid.

The shear rate describes the shearing which the liquid experiences. In other words, the velocity gradient, dy/dx, which is a measure of the change in speed at which the intermediate layers move with respect to each other is called the shear rate ($\dot{\gamma}$) and its unit of measure is the reciprocal second (s^{-1}). The term F/A indicates the force per unit area and is the shearing action or shear stress (τ). The unit of measurement of shear stress is dynes per square centimeter (dynes/cm^2) or Newton per square meter (N/m^2). According to the above statement, viscosity can be defined as shear stress over shear rate:

$$\eta = \tau / \dot{\gamma} \tag{2}$$

The most commonly used unit for viscosity is poise. A fluid with a shear stress of 1 dyne/cm^2 which produces a shear rate of 1 s^{-1}, has viscosity of 1 poise or 100 centi-poise. In the SI system, the unit of measurement of viscosity is Pa·s or mPa·s. One Pa·s is equal to 10 poise, and the smaller unit is one mPa·s which is equal to 1 cpoise.

2 NEWTONIAN AND NON-NEWTONIAN FLUIDS

The Newtonian fluids are true fluids that tend to exhibit constant viscosity at all shear rates (Karol, 2003; Krizek and Pepper, 2004). The relationship between the shear stress (τ) and the shear rate ($\dot{\gamma}$) is a straight line for the Newtonian fluids, and the viscosity of the fluid remains constant as the shear rate is varied (Fig. 2). Taylor (1997) showed that the fluids of simple and stable molecular structure generally obey the Newtonian law, like water and thin motor oils.

In practice, at a given temperature, the viscosity of a Newtonian fluid will remain constant regardless of which viscometer model, spindle or speed is used to measure it (Brookfield Engineering Labs Inc., 2010a).

A non-Newtonian fluid is a fluid for which the relationship $\tau/\dot{\gamma}$ is not a constant. In other words, when the shear rate is varied, the shear stress doesn't vary in the same proportion (or even necessarily in the same direction). Thus, the variation of shear strength causes to change the viscosity of such fluids. This is also called the "apparent viscosity" of the fluid. It is accurate only when the experimental parameters are provided and are also adhered to. Non-Newtonian fluids can be explained as fluids consisting of a mixture of molecules with different shapes and sizes. As they pass by each other, as happens during a flow, their size, shape, and cohesiveness will determine how much force is required to move them (Brookfield Engineering Labs Inc., 2010a).

Chhabra and Richardson (2008) defined the non-Newtonian fluid as one whose flow curve (shear stress versus shear rate) is either nonlinear or does not pass through the origin, i.e. where the apparent viscosity (ratio of shear stress to shear rate) is not constant at a given temperature and pressure but is dependent on the flow conditions such as flow geometry, shear rate, etc. Such materi-

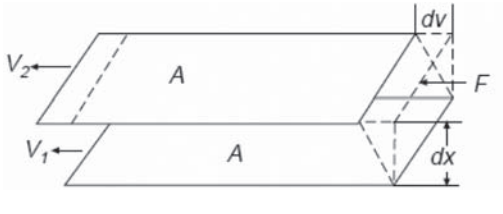

Figure 1. The definition of viscosity (after Brookfield Engineering Labs Inc., 2010a).

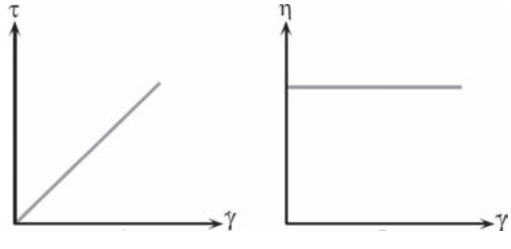

Figure 2. Newtonian fluids behaviour.

als can be conveniently categorized into three general classes:

1. Fluids, for which the rate of shear at any point can be determined only by the value of the shear stress at that point at that instant. These fluids are also known as purely viscous, time independent, inelastic or generalized Newtonian fluids.
2. Fluids, for which the relation between shear stress and shear rate depends on the duration of shearing and their kinematic history, in addition to the above conditions. These fluids are called time-dependent fluids.
3. Substances showing the characteristics of both, ideal fluids and elastic solids, and also showing partial elastic recovery after deformation are classified as visco-elastic fluids.

2.1 *Psedo-plastic fluids*

Pseudo-plasticity or shear-thinning is the most common type of time-independent and non-Newtonian fluid behavior observed. This is also characterized by an apparent viscosity that decreases with an increasing shear rate (Figure 3). Examples of the pseudo-plastic fluids are paints and emulsions.

Brookfield Engineering Labs Inc. (2010a) emphasized that in pseudo plastic fluids, the moment the spindle is turned, the structure of molecules of the fluid will be temporarily changed. This will lead to the molecule formation orientated more parallel to the spindle surface. Hence, the slowing down of the spindle rotation will decrease the change in the structure of the molecule. Faster the rotation of the spindle, the more the structure is destroyed; and the lesser of the structure of molecules will slide in together. Hence, the lower the viscosity will be.

2.2 *Dilatant fluids*

Dilatant fluids are similar to pseudo-plastic systems in that their apparent viscosity increases with increasing shear rate and they are time-independent fluids; thus these fluids are also called shear-thickening fluids (Figure 4).

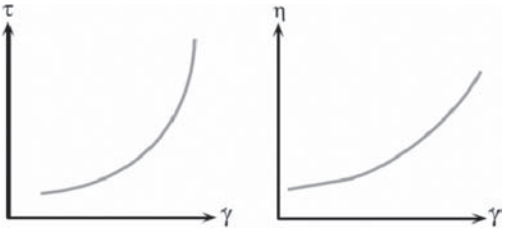

Figure 4. Dilatant fluids behavior.

This type of fluid behavior is normally observed in concentrated suspensions; such as sand/water mixtures, slurries of clay, compounds of candy, china clay, titanium dioxide, and corn flour in water (Griskey *et al*., 1985; Metzner and Whitlock, 1958). Chhabra and Richardson (2008), and Goddard and Bashir (1990) explained this kind of fluid behavior as follows: the voids are minimum at rest and the liquid present in the suspension is sufficient to fill all the voids. At low shear rates, the liquid is able to lubricate the movement of each particle. Thus, the resulting stresses are therefore small. On the other hand, the material expands or dilates slightly at high shear rates so that there is no longer sufficient liquid to fill the increased voids. This prevents the direct solid–solid contacts resulting in increased friction and higher shear stresses (as shown schematically in Figure 5).

2.3 *Viscoplastic (plastic fluids)*

This type of fluid (which is time-independent) behaves as a solid under static conditions. As shown in Figure 6, a certain amount of stress must be applied to the fluid before any flow is induced, known as the yield stress (f′). Conversely, when the externally applied stress is smaller than the yield stress, such a material will deform elastically. Once the magnitude of the external stress has exceeded the value of the yield stress, the flow curve may be linear or non-linear but will not pass through the origin (Chhabra and Richardson, 2008; Uhlherr *et al*., 2005).

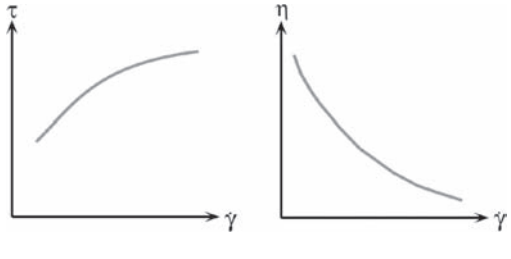

Figure 3. Pseudo-plastic fluids behaviour.

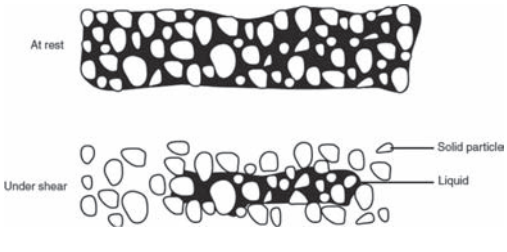

Figure 5. Schematic representation of dilatant behavior (after, Chhabra and Richardson, 2008).

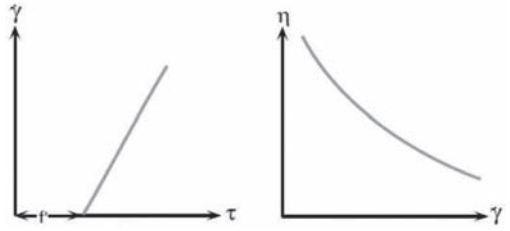

Figure 6. Plastic fluids behaviour.

However, the structure breaks down, at a stress level higher than f′, and the substance behaves like a viscous material, like Tomato ketchup.

2.4 *Thixotropic fluids*

In practice, apparent viscosity in some fluids may depend on the rate of shear and also the time for which the fluid has been subjected to shearing (Chhabra, 2010). The viscosities of time dependent fluids gradually decrease/increase as the internal structures present are progressively broken down or linked up. The rate of change of viscosity with time approaches zero or increases as the number of such structural linkages, capable of being broken down, reduce or increase; like bentonite-water suspensions, red mud suspensions (waste stream from aluminum industry), cement paste, and crude oils (Chhabra, 2010; Chhabra and Richardson, 2008; Nguyen and Uhlherr, 1983).

Thixotropic fluid is a category of time-depended fluid. Nguyen and Uhlherr (1983) explained thixotropic fluids as materials when sheared at a constant rate, their apparent viscosity (or the corresponding shear stress) decreases with the time of shearing (Figure 7 (a)), such as red mud suspension containing solids.

Figures 7 (b) and (c) show the hysteresis loops of thixotropic fluids. A hysteresis loop of thixotropic fluid can be defined as the flow curve obtained from an experiment in which if the shear rate is gradually increased at a constant rate from zero to some maximum value and then decreased at the same rate to zero again. Chhabra (2010) concluded that the rate of increase or decrease of shear rate, the duration of shearing, and the past kinematic history of the sample will decide the shape, height, and the enclosed area of the hysteresis loop. The larger the enclosed area, stronger is the time-dependent behavior of the materials. Thus, no hysteresis loop is observed for time-independent fluids, *i.e.* the enclosed area of the loop is zero. Struble and Ji (2001) observed the behavior of cement grout to be similar to thixotropic fluids and it is shown in Figure 8. The rheological parameters of

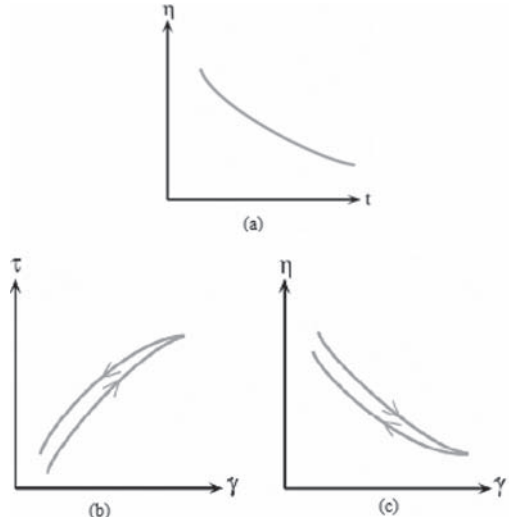

Figure 7. Thixotropic fluids behaviour.

grouts influence the course of the grouting. Eriksson (1998) illustrated different examples showing how the viscosity and yield value changed the spreading of the grout in a defined geometry. Håkansson (1993) stated that the rheology changes in grouts depend on the w/c ratio and the specific surface of the grout.

2.5 *Rheopexy or negative thixotropy fluids*

The second category of time-depended fluids is rheopexy or negative thixotropy fluids. The fluids for which their apparent viscosities increase with time of shearing are said to display rheopexy or negative thixotropy (Figure 9). Figures 9 (b) and (c) show the hysteresis loops of rheopexy fluids. In these cases, they are inverted, as compared with thixotropic fluids. In this type of fluid, the structure builds up by shear is applied and will break down when the material is at rest. In other words, in contrast to thixotropic fluids, the external shear encourages the build-up of structure in this case (Chhabra, 2010; Chhabra and Richardson, 2008). Both thixotropy and rheopexy behavior, Brookfield Engineering Labs Inc. (2010a) emphasized, can occur together with any of the previously mentioned flow behaviors.

Freundlich and Juliusburger (1935), Keller and Keller Jr (1990), Pradipasena and Rha (1977), Steg and Katz (1965), and Tanner (2000) have reported similar behavior of rheopexy fluids with suspensions of aqueous gypsum paste, saturated polyester, protein solutions, coal-water slurries, and ammonium oleate and colloidal suspensions of vanadium pentoxide.

3 MATHEMATICAL MODELS FOR FLUID BEHAVIOR

A review of the literature shows a number of mathematical models have been proposed for the behavior of the fluid to model the shear-thinning characteristics. Many of these methods attempt at curve fitting, giving empirical relationships for the shear stress or apparent viscosity-shear rate curves; while, other methods are based on the theory in the statistical mechanics (Bird *et al*., 1987; Chhabra and Richardson, 2008).

As mentioned earlier, non-Newtonian fluids show a nonlinear stress-rate relationship which can be represented using an equation. However, the coefficients of a model, in some cases, can be used to predict the behavior of a fluid under the conditions of use. On the other hand, linear relationship is shown by Newtonian fluids which can be defined by a proportional response in the shear stress for a corresponding change in the shear rate (Brookfield Engineering Labs Inc., 2010a). Some of the more widely used models include Newton, Bingham, Casson, NCA/CMA Casson, Power Law, and Herschel Bulkley and their descriptions are shown in Table 1.

The grouts behavior has been modeled with Bingham model by Wallner (1976), Håkansson (1993), and Amadei and Savage (2001). Håkansson (1993) stated, "The Bingham model does not give an exact description of the behavior of a cement based grout even if the geometry is defined but laboratory tests show that the deviation is small".

4 CONCLUSIONS

Cement grout based rheology is characterized by at least two parameters: yield stress and plastic viscosity. The rheological measurements may be used as an indicator of micro structural changes occurring in hydration of the cement-based grout or the investigation of the effect of admixtures, and the development of cementitious systems. The rheological models are used to describe the relationship between shear stress and shear rate. The behavior of cement-sodium silicate system grout with kaolinite was investigated with the Bingham model using Brookfield viscometer. The Bingham model does not give an exact description of the behavior of a cement based grout even if the geometry is defined. However, careful consideration should be taken by any perspective researcher to choose the rheometric model to characterize the cement grout.

Table 1. Mathematical models for fluids behaviour

Model	Equation	Description
Newton	$\tau = \dot{\gamma}$	Linear (water)
Bingham	$\tau = \tau_0 + \eta\dot{\gamma}$	Yield linear
Casson	$\sqrt{\tau} = \sqrt{\tau_0} + \sqrt{\eta\dot{\gamma}}$	Linear between the square root of shear stress and the square root of the shear rate
NCA/CMA Casson	$(1+a)\sqrt{\tau} = 2\sqrt{\tau_0} + (1+a)\sqrt{\eta\dot{\gamma}}$	
Power law	$\tau = k\dot{\gamma}^n$	Pseudoplastic
Herschel Bulkley	$\tau = \tau_0 + k\dot{\gamma}^n$	

REFERENCES

Ajlouni, M.A. 2000. Geotechnical Properties of Peat and Related Engineering Problems. *PhD Thesis*, University of Illinois at Urbana-Champaign, USA

Alwi, A. 2007. Ground Improvement on Malaysian Peat Soils Using Stabilized Peat-Column Techniques. *PhD Thesis*, University of Malaya, Kuala Lumpur, Malaysia.

Amadei, B. & Savage, W.Z. 2001. An Analytical Solution for Transient Flow of Bingham Viscoplastic Materials in Rock Fractures. *Int. J. Rock Mech, & Min. Sci.,* Vol. 38, pp 285–296.

Bentz, D.P., Garboczi, E.J., Bullard, J.W., Ferraris, C., Martys, N. & Stutzman, P.E. 2006. *Virtual Testing of Cement and Concrete*. In Significance of Tests and Properties of Concrete and Concrete-Making Material. (Lamond J.F. and Pielert, J.H. (ed.)), ASTM International, West Conshohocken, PA, USA.

Bird, R.B., Armstrong, R.C. & Hassager, O. 1987. *Dynamics of Polymeric Liquids. Fluid Dynamics*. 2nd ed., Vol. 1, *Wiley Interscience*, New York, USA.

Brookfield Engineering Labs Inc. 2008. Viscometers, Rheometers & Texture Analyzers for Laboratory and Process Applications. *Brookfield Eng. Labs*, pp 4–35.

Brookfield Engineering Labs Inc. 2010a. More Solutions to Sticky Problems: A Guide to Getting More from Your Brookfield Viscometer. *Bull. Brookfield Eng. Labs,* pp 1–53.

Brookfield Engineering Labs Inc. 2010b. Brookfield DV–II+ Pro. *Brookfield Eng. Labs,* Manual No. M/03-165-C0508, pp 3–71.

Chhabra, R.P. & Richardson, J.F. 2008). *Non-Newtonian Flow and Applied Rheology*. 2nd ed., *Butterworth-Heinemann*, Oxford, UK.

Edil, T.B. 2003. Recent Advanced in Geotechnical Characterization and Construction over Peat and Organic Soils. *In Proceeding of 2nd Int. Conf. on Advances in Soft Soil Eng. and Tech*., ed. Huat et al., Putrajaya, Malaysia.

Edil, T.B. & Wang, X. 2000. Shear Strength and K0 of Peats and Organic Soils. *Geotechnics of high water content materials, ASTM STP 1374*, West Conshohocken, Pa., USA, pp 209–225.

Eklund, T. 2005. Penetrability Due To Filtration Tendency of Cement Based Grouts. *PhD Thesis*, Dept. of Soil and Rock Mechanics, Royal Institute of Technology, Stockholm.

Eriksson, M. 1998. Mechanisms that Control the Spreading of Grout in Jointed Rock. *ARD-98-15, SKB*, Stockholm, Sweden.

Freundlich, H. & Juliusburger, F. 1935. Thixotropy, Influenced by the Orientation of Anisometric Particles in Sols and Suspensions. *Trans. Faraday Soc.,* Vol. 31, pp 920–921.

Goddard, J.D. & Bashir, Y. 1990. *Recent Developments in Structured Continua II*. Longman, London, UK.

Griskey, R.G., Nechrebecki, D.G., Notheis, P.J. & Balmer, R.T. 1985. Rheological and Pipeline Flow Behaviour of Corn Starch Dispersions. *J. Rheology,* Vol. 29, pp 349–360.

Håkansson, U. 1993. Rheology of Fresh Cement-Based Grouts. *PhD Thesis*, Dept. of Soil and Rock Mechanics, Royal Institute of Technology, Stockholm.

Karol, R. H. 2003. *Chemical Grouting and Soil Stabilization*. 3rd ed., Marcel Dekker Inc., New Jersy, USA.

Keller, D.S. & Keller, Jr, D.V. 1990. An Investigation of the Shear Thickening and Behavior of Concentrated Coal-Water Dispersions. *J. Rheol.,* Vol. 34, pp 1267–1291.

Krizek, R.J. & Pepper, S.F. 2004. Slurries in Geotechnical Engineering. *Texas A&M University, Texas*, USA.

Metzner, A.B. & Whitlock, M. 1958. Flow Behavior of Concentrated (Dilatant) Suspensions. *Trans. Soc. Rheology*, Vol. 2, pp 239–254.

Nguyen, Q.D. & Uhlherr, P.H.T. 1983. Thixotropic Behavior of Concentrated Red Mud Suspensions. *Proc. 3rd Nat. Conf. on Rheol,* Melbourne, Australia, pp 63.

Pradipasena, P. & Rha, C. 1977. Pseudo plastic and Rheopectic Properties of Globular Protein (β Lacto globulin) Solution. *J. Texture Studies,* Vol. 8, pp 311–325.

Puppala, A.J., Pokala, S.P., Intharasombat, N. & Williammee, R. 2007. Effects of Organic Matter on Physical, Strength, and Volume Change Properties of Compost Amended Expansive Clay. *Journal of Geotechnical and Geoenvironmental Engineering*, ASCE, U.S.A., Vol. 133, No. 11, pp 1449–1461.

Steg, I. & Katz, D. 1965. Rheopexy in Some Polar Fluids and in Their Concentrated Solutions in Slightly Polar Solvents. *J. Appl Polym Sci,* Vol. 9, pp 3177–3193.

Struble, L.J. & Ji, X. 2001. Rheology – In Handbook of Analytical Techniques in Concrete Science and Technology. Ramachandran V.S. and Beaudoin J.J. (ed.), *William Andrew Publishing*, New York, USA.

Syrjålå, S. 1996. Numerical Study of Heat Transfer Behaviour of Power-law Non-Newtonian Fluids in Rectangular Channels. *PhD Thesis*, Technical Research Centre of Finland, VTT Chemical Technology, Espoo, Finland. ISBN 951-38-4950-3.

Tanner, R.I. 2000. *Engineering Rheology*. 2nd ed. Oxford University Press, London, UK.

Taylor, H.F.W. 1997. *Cement Chemistry*. 2nd ed., Thomas Telford Publishing, London, UK.

Uhlherr, P.H.T., Guo, J., Zhang, X-M., Zhou, J.Z.Q. & Tiu, C. 2005. The Shear-Induced Solid-Liquid Transition in Yield Stress Materials. *J.* Non-Newtonian *Fluid Mech.* Vol. 125, pp 101–119.

Wallner, M. 1976. Propagation of Sedimentation Stable Cement Pastes in Jointed Rock. *Rock Mechanics and Waterways Construction*, University of Aachen, Germany.

Geotechnical Aspects of Underground Construction in Soft Ground – Viggiani (ed)
© 2012 Taylor & Francis Group, London, ISBN 978-0-415-68367-8

Stability of cohesive-frictional soils with square underground openings

K. Yamamoto
Department of Ocean Civil Engineering, Kagoshima University, Kagoshima, Japan

A.V. Lyamin, D.W. Wilson, A.J. Abbo & S.W. Sloan
Centre for Geotechnical and Materials Modelling, University of Newcastle, NSW, Australia

ABSTRACT: Stability of foundations laying on cohesive-frictional soils with multiple underground openings (tunnels) of square shape has been analyzed under plane strain conditions. Soil domain was loaded with a uniform surface pressure and a series of tunnel size to depth ratios as well as center-to-center distances have been considered. Rigorous lower and upper bound solutions were obtained by applying numerical limit analysis and presented in the form of dimensionless stability charts for the case of dual tunnel. For comparison purposes several rigid block upper bound mechanisms have been also developed and the obtained values of collapse loads were tested against the results of limit analysis computations.

1 INTRODUCTION

Rapid increase in the volume of constructions in densely populated urban areas brings the task of accurate estimation of the stability of soils with multiple underground openings to the priority list of geotechnical engineers. On the other hand it appears that there is no generally accepted design or analysis method available to assess the stability of the structures resting on a stratum with shallow underground openings of square or rectangular cross-section. The efficient utilization of underground space dictates that the non-circular openings and tunnels should be preferred in the design as quadrilateral objects like trains and buildings are usually used there. Furthermore, large size non-circular tunnels are quickly becoming a widespread building technology by virtue of the development of advanced tunneling machines. The merits of the construction of non-circular underground openings compared to circular ones would be the reduction of the area of excavated section, the reduction of the surplus soils, thus diminished environmental issues, and the reduction of rented space for the construction of tunnels. Although the top, bottom, right and left spaces of circular tunnels are usually useless, circular tunnels have been predominantly used so far since their construction is easier from the standpoint of excavation and maintenance of the heading.

In practice, it is often the case that the construction of dual square tunnels is a better alternative to a single large square tunnel as in terms of construction cost, as from utilization point of view. In this paper, the ultimate bearing capacity and failure mechanisms of cohesive-frictional soils with dual square tunnels have been theoretically and numerically investigated assuming plane strain conditions. In contrast to the case of a single tunnel, the center-to-center distance of dual tunnels appears as an important factor influencing the stability of the whole system. Drained loading conditions are considered, the internal tunnel pressure is set to zero, and a continuous load is applied to the ground surface. Both smooth and rough interface conditions between the loading and soils are modelled. For a series of tunnel size to depth ratios and material properties, rigorous lower and upper bound solutions for the ultimate bearing capacity of the considered soil mass are obtained by applying advanced limit analysis techniques (Lyamin & Sloan 2002, Krabbenhøft et al. 2005). For practical convenience the results are presented in the form of dimensionless stability charts, with the actual bearing capacities being closely bracketed from above and below. The results of numerical limit analyses are verified through the comparison with the upper bound collapse loads obtained using rigid block mechanisms specifically developed for modeling the collapse of dual square tunnels.

The application of numerical limit analysis to the stability of shallow tunnels has been pioneered by Sloan and Assadi who investigated the undrained stability of a plane strain square tunnel in a cohesive soil (Assadi & Sloan, 1991) and the stability of square and circular tunnels in cohesive soil with shear strength varying linearly with depth (Sloan & Assadi, 1991, 1992) using linear programming techniques. The stability of the tunnel was described conveniently by two load parameters

$(\sigma_s - \sigma_t)/c_{u0}$ and $\gamma D/c_{u0}$. Lyamin & Sloan (2000, 2001) considered stability of plane strain circular and square tunnels in cohesive-frictional soil. The nonlinear programming technique was applied which vastly reduced the CPU time required and also allowed to increase the number of finite elements employed for the analyses, thus resulting in very accurate solutions. The drained stability of the tunnel was described by the load parameter σ_t/c'. Wilson et al. (2008) investigated the undrained stability of dual square tunnels using numerical limit analysis and rigid block upper bound methods. Stability charts were generated for a variety of tunnel depths, material properties and inter-shaft distances. Recently, Yamamoto et al. (2010a) initiated investigation on the ultimate bearing capacity and the failure mechanism of cohesive-frictional soils with a shallow square tunnel. Several rigid block mechanisms were developed and the obtained upper bounds of collapse loads were compared with the results of numerical limit analysis to verify the validity of both approaches. This paper extends the above mentioned research to the case of dual square tunnels.

2 PROBLEM DESCRIPTION

The problem description is given in Figure 1. The ground is modelled as a uniform Mohr-Coulomb material with a cohesion c', friction angle ϕ' and unit weight γ, assuming drained loading conditions. The tunnel is of dimension B, depth H and the center-to-center distance S. The internal tunnel pressure is set to zero ($\sigma_t = 0$). The ultimate bearing capacity of cohesive-frictional soils with the inclusion of dual square tunnels is described conveniently by the dimensionless load parameter σ_s/c' which is a function of $\phi', \gamma B/c', H/B, S/B$ and L/B, as shown in Eq. (1).

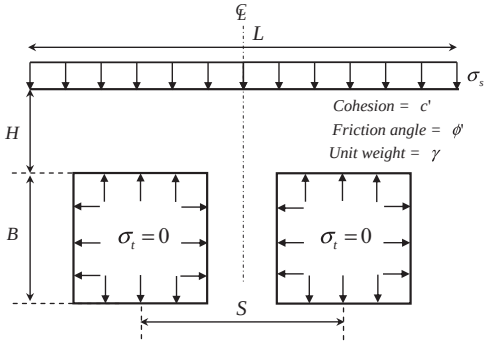

Figure 1. Plane strain dual square tunnels in cohesive-frictional soil.

$$\sigma_s/c' = f(\phi', \gamma B/c', H/B, S/B, L/B) \quad (1)$$

As continuous loading is applied to the ground surface the L/B parameter is eliminated from equation (1). Formulating the problem in this manner permits a compact set of stability charts to be constructed, which are useful for design purposes. The problem parameters considered in this paper are $H/B = 1.0$–5.0, $\phi' = 0^\circ - 20^\circ$ and $\gamma B/c' = 0 - 3$. Both smooth and rough interface conditions between the loading and soil are considered.

3 NUMERICAL LIMIT ANALYSIS

Limit analysis utilizes the power of lower and upper bound theorems of plasticity theory to provide rigorous bounds on collapse loads from both below and above. The theorems themselves are based on the principle of maximum energy dissipation, which is valid for soils following an associated flow rule. The use of finite element discretization of the soil combined with mathematical optimization to maximize the lower bound and minimize the upper bound has now made it possible to handle efficiently the problems with complex geometries and loading conditions. The formulations of numerical limit analysis used in this paper originate from those given by Sloan (1988, 1989) and Sloan & Kleeman (1995) who employed active set linear programming and discontinuous stress and velocity fields to solve variety of stability problems. Since then, numerical limit analysis has evolved significantly and the computational tools used for this study are those described in Lyamin & Sloan (2002) and Krabbenhøft et al. (2005).

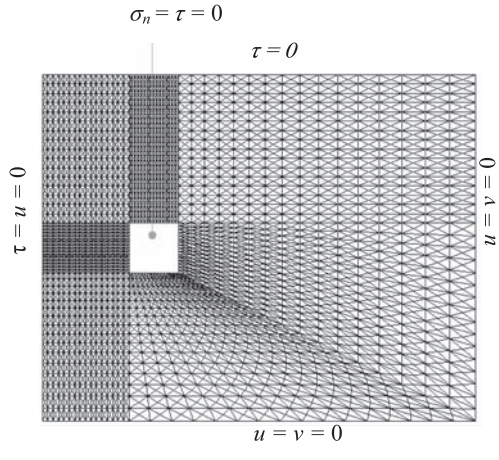

Figure 2. Finite element mesh for H/B = 3 and S/B = 4.5 showing boundary conditions for numerical limit analysis.

Figure 2 show the lower bound and upper bound half-mesh for $H/B = 3$ and $S/B = 4.5$ with smooth interfaces. The mesh is symmetric, and similar meshes are used for both lower and upper bound analyses. Typical lower/upper bound mesh has 7168 triangular elements and 10640 stress/velocity discontinuities. In the lower bound analysis, extension elements are included along the soil domain boundaries to represent a semi-infinite material. The loading is modelled as an infinite width loading, thus it is applied to the whole extend of the surface of soil domain. Careful mesh refinement around the tunnel is required to get accurate solutions. The mesh is particularly dense around the tunnel and is smoothly connected from the tunnel face toward the boundary.

4 UPPER BOUND RIGID BLOCK ANALYSIS

Together with numerical limit analysis techniques the semi-analytical rigid block methods were employed in this study to find the upper bound solutions for considered problem. The solutions obtained provide an additional check on the finite element analysis results and the mechanisms developed will be able to serve as simple design tools for practicing engineers. Three types of rigid block mechanisms were constructed as shown in Figure 3. In this Figure, A_i is the area of the rigid block; V_i is the kinematically admissible velocity of block i; V_{ij} is the velocity jump along discontinuity and l_{ij} is the length of the discontinuity itself between blocks i and j; α, β and δ are the angular parameters which determine the geometry of the rigid block mechanisms for mechanism 1 (γ is dependent parameter for mechanism 1); ϕ' is the dilatancy angle. Mechanism 1 is a simple roof and left (one) side collapse mechanism suitable for shallow tunnels and the mechanisms 2–3 are more complex, roof and both sides collapse mechanisms. The total numbers of angular parameters of mechanisms 1–3 are 3, 7 and 8, respectively. The soil mass was assumed to be governed by Mohr-Coulomb failure criterion and an associated flow rule. The geometry of the blocks is allowed to vary while being constrained such that their areas and boundary segments lengths stay positive. The details of rigid block analysis can be found in Chen (1975).

The minimum upper bound solution for each mechanism was obtained by optimizing its geometry using the Hooke & Jeeves algorithm with discrete steps (Bunday, 1984). This method works by performing two different types of searches, an exploratory search and a pattern search. The rigid block analyses are extremely quick taking of the

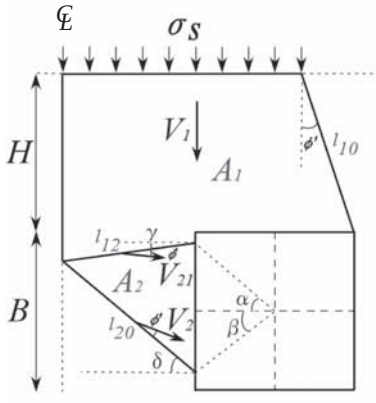

(a) mechanism 1

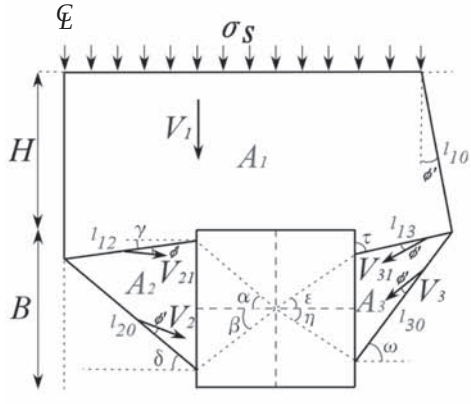

(b) mechanism 2

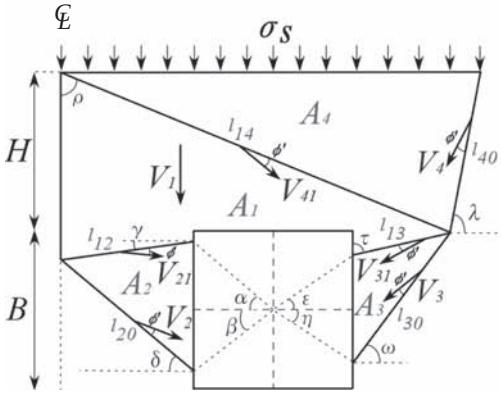

(c) mechanism 3

Figure 3. Upper bound rigid block mechanisms for dual square tunnels.

order of just one second. Provided an appropriate mechanism is chosen, this technique gives a fairly accurate upper bound estimate which can be used to check the finite element solutions and does not require significant computational efforts.

5 RESULTS AND DISCUSSION

Figures 4–6a, b, c show the plastic zones, power dissipations and rigid block mechanisms for dual square tunnels. The plastic zones and power dissipations are obtained from the numerical lower and upper bound limit analyses, respectively, and shown by grey shading. The dimensionless load parameter σ_s / c' obtained from all of the methods used is included in each figure. It can be observed from Figures 4a, b that for the case of shallow depth, small friction angles and close center-to-center spacing between the tunnels, the collapse mechanism consists of two distinctive zones. Firstly, the wall separating the tunnels is collapsing by virtue of classical "cross" shaped slip surface. Secondly, the failure zone extends to the ground surface from the outside top corners of the tunnels. As can be noticed from Figure 4c the failure mechanism of the rigid block techniques agree well with those observed in the plastic zones and power dissipations (Figs. 4a, b). Moreover, in this case, the upper bound solution from the rigid block technique is superior to the solution obtained by numerical limit analysis. For the case of moderate depth, small friction angles and moderate center-to-center spacing presented in Figures 5a, b, the collapse mechanism enlargers forming the dual slip band between the tunnels and extending now to the ground surface from both lower and upper corners on the outside of the tunnels. The ultimate bearing capacity in this case is high than that shown in Figure 4, due to increase of H/B and S/B. The upper bound solution (Fig. 5c) obtained from the rigid block technique is also in good agreement with that from the numerical limit analysis (Fig. 5b). Figure 6 shows the case of deep depth, small friction angles and moderate center-to-center distance between the tunnels. In this case, two failure areas join each other, forming continuous collapse mechanism which encompasses the entire tunnel. Not surprisingly, the rigid block results (Fig. 6c) tend to be larger than the results of numerical limit analysis (Fig. 6b) as it becomes harder to provide accurate solutions due to increased depth and moderate center-to-center distance. Concluding the discussion on the collapse patterns presented in Figures 4–6, it can be stated that when H/B and S/B increases the failure mechanism slowly extends vertically and transversely, and shows the multiple modes to eventually encompass the entire tunnel. The S/B parameter plays, therefore, a key in the ongoing failure pattern and the increase in bearing capacity due to the effect of interaction.

Of the several rigid block mechanisms developed in this study (Figure 3), the best upper bound solutions were almost always obtained from mechanisms 1 and 3, which consist of three and eight angular parameters, respectively. In general, mechanism 1 is suitable for the cases of shallow tunnels with low friction angles and mechanism 3 for the case of deeper tunnels, high friction angles and wider center-to-center distance. In general for the cases of shallow tunnels, small friction angles and close center-to-center spacing between the tunnels the upper bound solutions obtained from the rigid block and numerical limit analyses are in good agreement (Figs. 4–5b, c), with the rigid block results tending to be larger than the limit analysis when H/B or ϕ' or S/B increases. This is due to the assumption that failure mechanism extends from the ground surface into the depth with the inclination angle equal to the friction angle ϕ'. Also, tunnels with a deeper and wider center-to-center spacing have a more complex collapse pattern, therefore, the simple rigid block mechanisms proposed in this study are generally less accurate for such configurations. Furthermore, it is more difficult to propose an efficient rigid block mechanism in the case of cohesive-frictional soils than in the case of purely cohesive material. As shown in Figure 6, the collapse mechanism for deeper tunnels is quite wide at the surface as well as it extends further around the bottom of the tunnel. Even using mechanism 3, the feasible solutions could not be easily obtained for high values of H/B, ϕ' or S/B.

Figures 7–8 show the comparison of stability numbers obtained from both numerical limit and rigid block analyses for smooth interface conditions. The lower and upper bound solutions of the limit analysis for each $\gamma B / c'$ are plotted using broken and solid lines, respectively. It can be observed from Figures 7–8 that for all considered cases the stability numbers decrease when $\gamma B / c'$ increases and the ultimate bearing capacity increases monotonically with the increase of S/B, except for the cases of close proximity, $S/B \leq 2.0$ (Fig. 8a) and $S/B \leq 3.0$ (Fig. 8b). For the cases of 1) $H/B = 1$ and $\phi' = 10^\circ$, $S/B \leq 3.5$, 2) $H/B = 1$ and $\phi' = 20^\circ$, $S/B \leq 2.5$, 3) $H/B = 3$ and $\phi' = 10^\circ$, $S/B \leq 4.5$ and 4) $H/B = 4$ and $\phi' = 10^\circ$, $S/B \leq 4.0$, it is found that the upper bound solutions from the rigid block method have relatively good agreement with those obtained from the numerical limit analysis. But, with an increase of S/B the accuracy of considered rigid block mechanisms becomes poor. In most cases of $\gamma B / c' = 3$ (Fig. 8a, b), feasible solutions could not be obtained because the tunnel collapses under soil self weight. It is important to mention

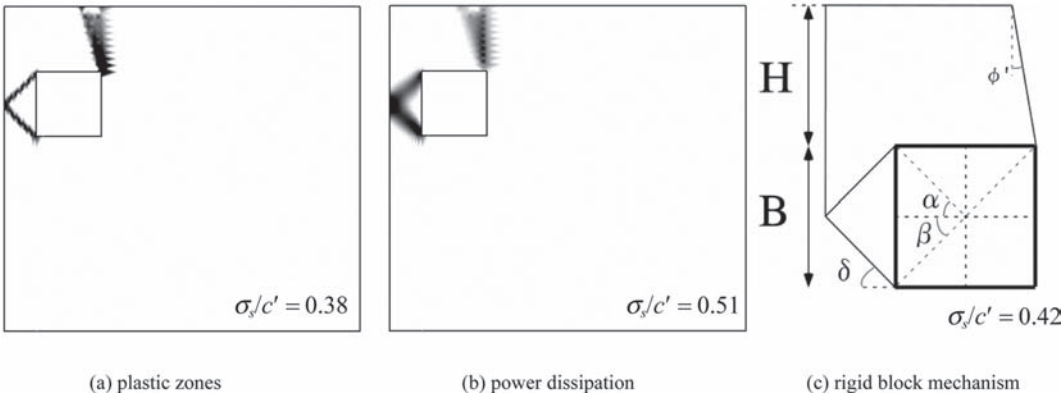

Figure 4. Comparison of numerical limit analysis with rigid block mechanism (H/B=1, ϕ' = 10°, $\gamma B/c'$ = 1, S/B = 2.0, smooth interface).

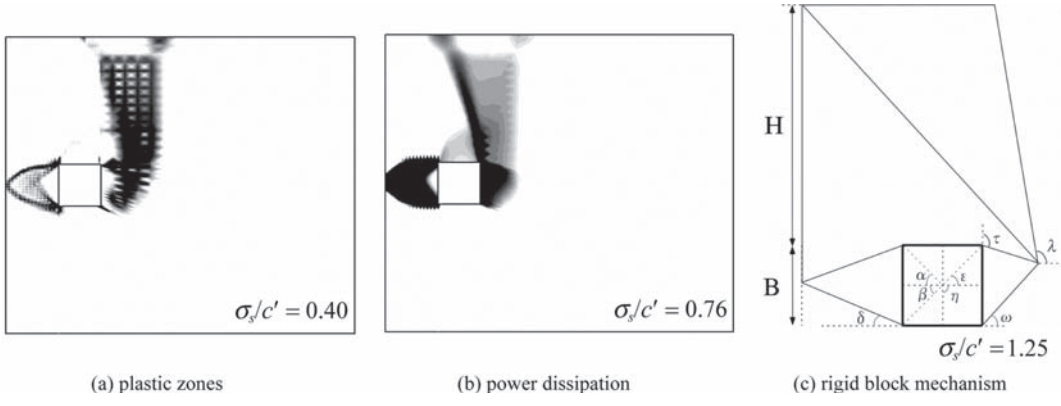

Figure 5. Comparison of numerical limit analysis with rigid block mechanism (H/B = 3, ϕ' = 10°, $\gamma B/c'$ = 1, S/B = 3.5, smooth interface).

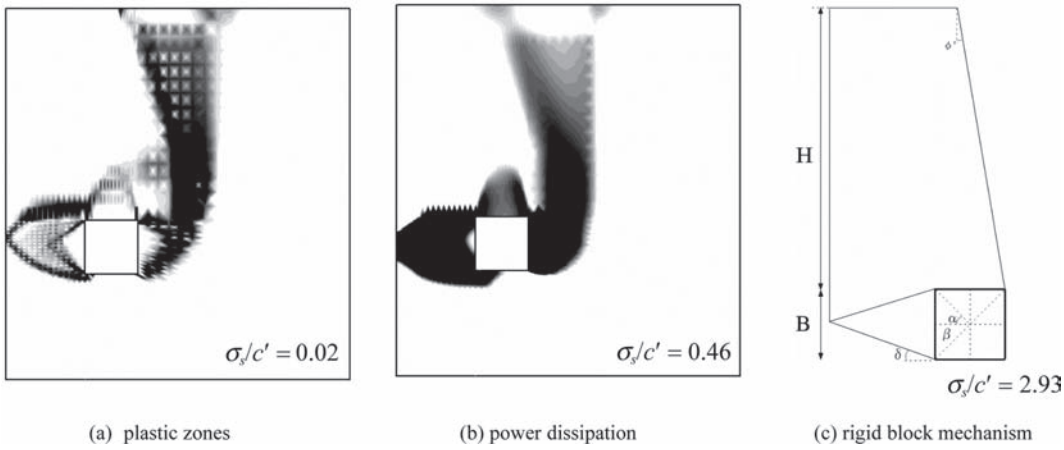

Figure 6. Comparison of numerical limit analysis with rigid block mechanism (H/B = 4, ϕ' = 10°, $\gamma B/c'$ = 1, S/B = 4.0, smooth interface).

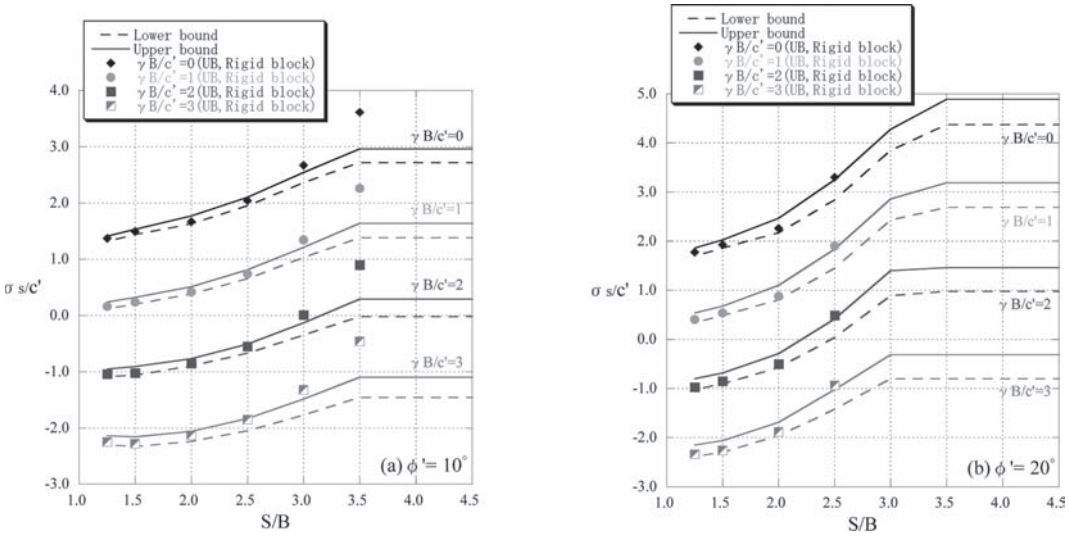

Figure 7. Stability bounds for dual square tunnels (H/B = 1, ϕ' = 10°, 20°, smooth interface).

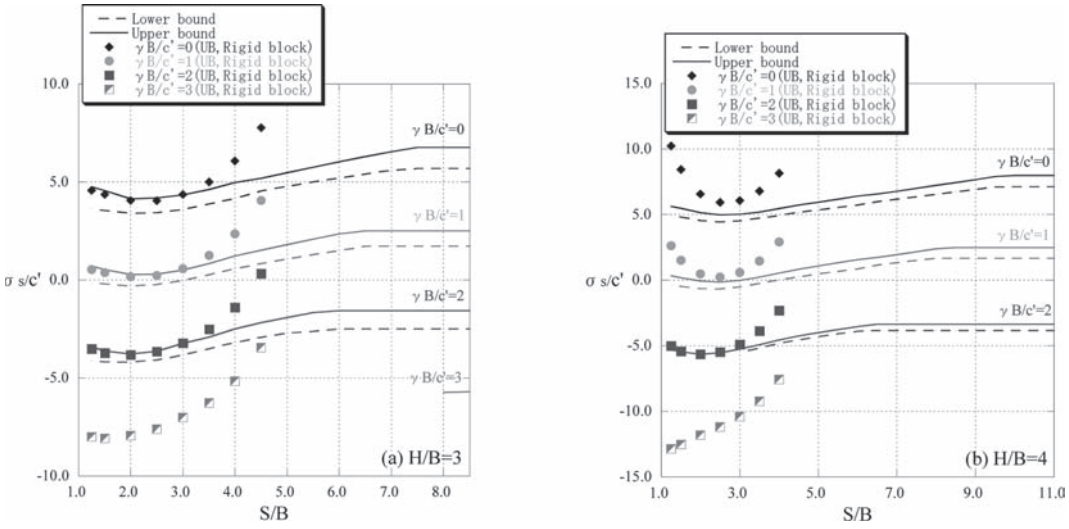

Figure 8. Stability bounds for dual square tunnels (H/B = 3,4, ϕ' = 10°, smooth interface).

the sign convention used for stability numbers presentation. A positive value of stability number implies that a compressive normal stress can be applied to the ground surface up to this value, while a negative stability number means that we can only apply a tensile normal stress to the soil surface (no bearing capacity in normal sense). The negative range of stability numbers is likely to be of less practical interest than the positive one. When S/B increases further, the lower and upper bound limit analysis solutions tend to stay constant after a certain value of S/B has been reached (e.g. $S/B = 3.5$ for $\gamma B/c' = 0-3$ (Fig.7a)). The plots of plastic zones and power dissipations show no interaction between dual square tunnels at these points and after that the failure mechanism becomes that of two individual single tunnels. Thus, such points are regarded as the no interaction points for dual square tun nels and this information would be important for engineering practice. The no interaction spacing decreases when $\gamma B/c'$ increases for each H/B and ϕ'. Comparing to the case of dual circular tunnels (Yamamoto et al., 2010b), it can be mentioned that the bearing capacity of

cohesive-frictional soils with dual square tunnels is obviously smaller due to the singular points (corners) of non-smooth tunnel shape.

6 CONCLUSIONS

The stability problem of soil domains under continuous uniform surface load with the inclusion of dual square tunnels has been investigated analytically and numerically under plane strain conditions. The results of conducted analyses have been presented in the form of dimensionless stability charts. Several rigid block mechanisms have been developed to check the validity of the numerical limit analysis and serve as a handy practical means as well. Comparison of upper bound solutions obtained from the rigid block analysis with those of the numerical limit analysis shows good agreement when H/B, ϕ' and S/B are small. In general, the accuracy of the rigid block technique for dual square tunnels was found to be better than that for dual circular tunnels.

For the cases of deeper and closely spaced tunnels, it has been observed that the bearing capacity exhibits a slight decrease due to the interaction between the tunnels. This interaction tends to disappear when the center-to-center distance exceeds a certain value (no interaction point). As expected, bearing capacity of soils with dual square tunnels has been found to be inferior comparing to case of dual circular tunnels. For future work, it is proposed to develop suitable for practical use rigid block mechanisms which are efficient also for high frictional angles and moderate center-to-center distance.

REFERENCES

Assadi, A. & Sloan, S.W. 1991. Undrained stability of shallow square tunnel. *Journal of Geotechnical Engineering*, ASCE, **117**(8): 1152–1173.

Bunday, B.D. 1984. Basic optimisation methods. Edward Arnold.

Chen, W.F. 1975. Limit analysis and soil plasticity. Elsevier, Amsterdam.

Krabbenhøft, K., Lyamin, A.V., Hjiaj, M. & Sloan, S.W. 2005. A new discontinuous upper bound limit analysis formulation. *International Journal for Numerical Methods in Engineering*, 63: 1069–1088.

Lyamin, A.V. & Sloan, S.W. 2000. Stability of a plane strain circular tunnel in a cohesive-frictional soil. In D.W. Smith & J.P. Carter (eds), *Developments in theoretical geomechanics*, Balkema, Rotterdam, 139–153.

Lyamin, A.V., Jack, D.L., & Sloan, S.W. 2001. Collapse analysis of square tunnels in cohesive-frictional soils. In S. Valliappan & N. Khalili (eds), *Proc. of the First Asian-Pacific Congress on Computational Mechanics*, Sydney, 20–23 November 2001. Elsevier, 405–414.

Lyamin, A.V. & Sloan, S.W. 2002. Lower bound limit analysis using non-linear programming. *Int. J. Numer. Meth. Engng.*, 55: 573–611.

Sloan, S.W. 1988. Lower bound limit analysis using finite elements and linear programming. *Int. J. Numer. Analyt. Meth. Geomech.*, 12: 61–77.

Sloan, S.W. 1989. Upper bound limit analysis using finite elements and linear programming. *Int. J. Numer. Analyt. Meth. Geomech.*, 13: 263–282.

Sloan, S.W. & Assadi, A. 1991. Undrained stability of a square tunnel in a soil whose strength increases linearly with depth. *Computers and Geotechnics*, 12: 321–346.

Sloan, S.W. & Assadi, A. 1992. Stability of shallow tunnels in soft ground. In G.T. Houlsby & A.N. Schofield (eds), *Predictive soil mechanics*, Thomas Telford, London, 644–663.

Sloan, S.W. & Kleeman, P.W. 1995. Upper bound limit analysis using discontinuous velocity fields. *Comp. Methods in Appl. Mech. and Engng.*, 127: 293–314.

Wilson, D.W., Abbo, A.J., Sloan, S.W. & Lyamin, A.V. 2008. Undrained stability of dual square tunnels. In D.N. Singh (ed.), *Proc. of the 12th Int. Conf. of Int. Assoc. for Comp. Methods and Advances in Geomechanics (IACMAG)*, Goa, India.

Yamamoto, K., Lyamin, A.V., Wilson, D.W., Abbo, A.J. & Sloan, S.W. 2010a. Bearing capacity analysis of cohesive-frictional soils with a shallow square tunnel. In John Chien-Chung. Li & Meei-Ling. Lin (eds), *Proc. of 17th Southeast Asian Geotechnical Conference*, Taipei, 10–13 May 2010. Taiwan Geotechnical Society, 219–222.

Yamamoto, K., Lyamin, A.V., Wilson, D.W., Abbo, A.J. & Sloan, S.W. 2010b. Bearing capacity analysis of cohesive- frictional soils with dual circular tunnel. In R. Kastner & S. Aversa (eds), *Proc. of 7th Int. Sym. on Geotechnical Aspects of Underground Construction in Soft Ground*, Roma, 16–18 May 2011. CRC Press, submitted.

This page intentionally left blank

Geotechnical Aspects of Underground Construction in Soft Ground – Viggiani (ed)
© 2012 Taylor & Francis Group, London, ISBN 978-0-415-68367-8

Bearing capacity analysis of cohesive-frictional soils with dual circular tunnels

K. Yamamoto
Department of Ocean Civil Engineering, Kagoshima University, Kagoshima, Japan

A.V. Lyamin, D.W. Wilson, A.J. Abbo & S.W. Sloan
Centre for Geotechnical and Materials Modelling, University of Newcastle, NSW, Australia

ABSTRACT: The ultimate bearing capacity and the failure mechanism of cohesive-frictional soils with the inclusion of dual circular tunnels have been theoretically and numerically investigated assuming plane strain conditions. Unlike the case of a single tunnel, the center-to-center distance appears as a new problem parameter, which plays a key role in tunnel stability. A continuous loading is applied to the ground surface. For a series of tunnel diameter to depth ratios and material properties, rigorous lower and upper bound solutions for the ultimate bearing capacity of the considered soil mass are obtained by applying recently developed numerical limit analysis. For practical suitability the results are presented in the form of dimensionless stability charts. As an additional check and also a handy practical means, upper bound rigid block mechanisms for dual circular tunnels have been developed and the predicted collapse loads compared with the results from numerical limit analysis.

1 INTRODUCTION

The accurate assessment of the stability of foundations above shallow tunnels is a very important task due to the increasing demand on construction of buildings and tunnels in urban areas. Unfortunately, no generally accepted design or analysis method is available at the moment to evaluate the ultimate bearing capacity of cohesive-frictional soils with shallow tunnel inclusions. The design of tunnels for roads and railways often utilize separate tunnels to carry traffic in opposite directions. Also, in the expansion of underground transportation systems new tunnels have recently been designed and then constructed near existing tunnels. In practice, it is often seen that the construction of dual circular tunnels is a better option than a single large circular tunnel.

In this paper, the ultimate bearing capacity and failure mechanisms of cohesive-frictional soils with dual circular tunnels have been theoretically and numerically investigated assuming plane strain conditions. Compared to the case of a single circular tunnel, the effect of center-to-center distance on dual circular tunnels is naturally a key factor. In addition, it is assumed that the problem of interaction between dual tunnels is more complex due to the geometry of the tunnels and the properties of the lining and surrounding soils. Drained loading conditions are considered, the internal tunnel pressure is set to zero, and a continuous load is applied to the ground surface. Both smooth and rough interface conditions between the loading and soil are modelled. For a series of tunnel diameter to depth ratios and material properties, rigorous lower and upper bound solutions for the ultimate bearing capacity of the considered soil mass are obtained by applying recently developed numerical limit analysis techniques (Lyamin & Sloan 2002, Krabbenhøft *et al*. 2005). For practical suitability the results are presented in the form of dimensionless stability charts, with the actual bearing capacities being closely bracketed from above and below. As a validation of the results and also as a convenient practical calculation, upper bound rigid block mechanisms for dual circular tunnels have been developed and the obtained values of collapse loads are compared with the results of the numerical limit analysis.

The application of computational limit analysis to the stability of shallow tunnels has been pioneered by Sloan & Assadi (1992) who investigated the stability of a plane strain tunnel in a cohesive soil with shear strength varying linearly with depth using linear programming techniques. The stability of the tunnel was described conveniently by two load parameters $(\sigma_s - \sigma_t)/c_{u0}$ and $\gamma D/c_{u0}$. Lyamin & Sloan (2000) considered the stability of a plane strain circular tunnel in a cohesive-frictional soil. The nonlinear programming technique

was applied which allowed a vast shortening of the computational time as well as increasing the number of finite elements, thus resulting in very accurate solutions. The drained stability of the tunnel was described by the load parameters σ_t / c'. In addition, Wilson *et al*. (2008) investigated the undrained stability of dual square tunnels using numerical limit analysis and rigid block upper bound methods. Stability charts were generated for a variety of tunnel depths, material properties and inter-shaft distances. Recently, Yamamoto *et al*. (2009) initiated investigation of the ultimate bearing capacity and the failure mechanism of cohesive-frictional soils with a shallow circular tunnel. The upper bound rigid block mechanisms were also developed and the computed collapse loads compared with the results of numerical limit analysis. This paper presents the extension of this research to dual circular tunnels.

2 PROBLEM DESCRIPTION

The dual circular tunnel problem to be considered is presented in Figure 1. The ground is modelled as a uniform Mohr-Coulomb material with a cohesion c', friction angle ϕ' and unit weight γ, assuming drained loading conditions. The tunnel is of diameter D, depth H and the center-to-center distance S, and the internal tunnel pressure is set to zero ($\sigma_t = 0$). The ultimate bearing capacity of cohesive-frictional soils with the inclusion of dual circular tunnels is described conveniently by the dimensionless load parameter σ_s / c' which is a function of ϕ', $\gamma D / c'$, H/D, S/D and L/D, as shown in Eq. (1).

$$\sigma_s / c' = f(\phi', \gamma D / c', H / D, S / D, L / D) \tag{1}$$

As continuous loading is applied to the ground surface the L/D parameter may be eliminated from equation (1). Formulating the problem in this manner permits a compact set of stability charts to be constructed using the 4 remaining dimensionless parameters. The range of parameters considered in this paper are $H/D = 1$–5, $\phi' = 0^\circ$–20, $\gamma D / c' = 0$–3 and tunnel spacing $S/D = 0$–11. Both smooth and rough interface conditions between the loading and soil are considered.

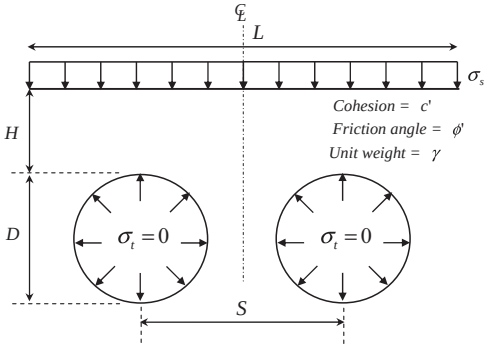

Figure 1. Plane strain dual circular tunnels in cohesive-frictional soil.

3 NUMERICAL LIMIT ANALYSIS

Limit analysis utilizes the power of lower and upper bound theorems of plasticity theory to provide rigorous bounds on collapse loads from both below and above. The theorems themselves are based on the principle of maximum power dissipation, which is valid for soil following an associated flow rule. The use of finite element discretization of the soil combined with mathematical optimization to maximize lower bound and minimize upper bound has now made it possible to handle routine problems with complex geometries and loading conditions. The formulations of numerical limit analysis used in this paper originate from those given by Sloan (1988, 1989) and Sloan & Kleeman (1995) who employed active set linear programming and discontinuous stress and velocity fields to solve variety of stability problems. Since then, numerical limit analysis has evolved significantly and the techniques used in this paper are those described in Lyamin & Sloan (2002) and Krabbenhøft *et al*. (2005).

Figure 2 show the lower bound and upper bound half-mesh for H/D = 1 and S/D = 2 with smooth interfaces. The mesh is symmetric, and

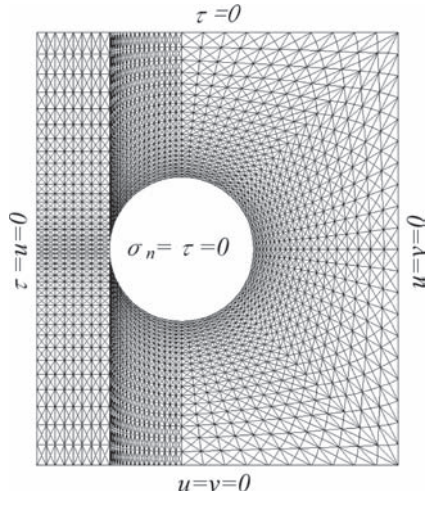

Figure 2. Finite element mesh for H/D = 1 and S/D = 2 showing boundary conditions for numerical limit analysis.

similar meshes are used for lower and upper bound analyses. Typical lower/upper bound mesh has 7680 triangular elements and 11412 stress/velocity discontinuities. In the lower bound analysis, extension elements are included along the soil domain boundaries to represent a semi-infinite material. When the width of loading, L, equals $2H + D + S$ in Fig. 2, the loading is regarded as the infinite width loading, because the whole failure mechanism is included within the domain. Careful mesh refinement around the tunnel is required to get accurate solutions. The mesh is particularly dense around the tunnel and is smoothly connected from the tunnel face toward the boundary.

4 UPPER BOUND RIGID BLOCK ANALYSIS

Semi-analytical rigid block methods were used in this study to find the upper bound solutions for the problems considered. These solutions provide an additional check on the finite element limit analysis results and will be able to also serve as simple design tools for practicing engineers. Three types of rigid block mechanisms were constructed as shown in Figure 3. In this Figure, A_i is the area of the rigid block; V_i is the kinematically admissible velocity of block i; V_{ij} is the velocity jump along the discontinuity between blocks i and j; l_{ij} is the length of the discontinuity between blocks i and j; α, β, γ, δ, ε, λ and ω are the angular parameters which determine the geometry of the rigid block mechanisms for mechanism 1 (θ is dependent parameter for mechanism 1); ϕ' is the dilatancy angle. Mechanism 1 is a simple roof and side collapse mechanism typically suitable for shallow tunnels, while mechanisms 2 and 3 are more complex and are characterized by collapse of both the roof and side of the tunnel. The total numbers of unknown angular parameters in each of the mechanisms are 7, 8 and 12 respectively. The behavior of the soil mass was assumed to be governed by Mohr-Coulomb failure criterion and an associated flow rule. The geometry of the blocks is allowed to vary while being constrained such that their areas and boundary segments lengths stay positive. The details of rigid block analysis can be found in Chen (1975).

The minimum upper bound solution for each mechanism was obtained by optimizing its geometry using the Hooke & Jeeves algorithm with discrete steps (Bunday, 1984). This method works by performing two different types of searches, an exploratory search and a pattern search. The rigid block analyses are extremely quick taking of the order of just one second. Provided an appropriate mechanism is chosen, this technique gives a fairly accurate upper bound estimate which can be used

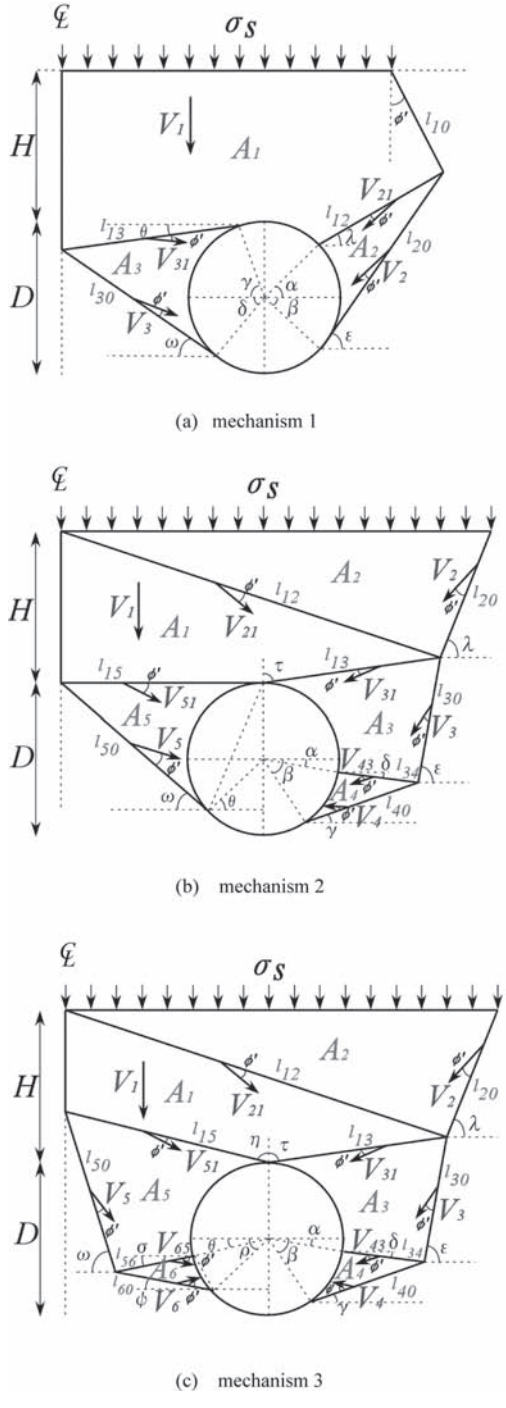

Figure 3. Upper bound rigid block mechanisms for dual circular tunnels.

to check the finite element solutions and does not require significant computational efforts.

5 RESULTS AND DISCUSSION

Figures 4–6 show the plastic zones (a), power dissipations (b) and rigid block mechanisms (c) for the dual circular tunnels. The plastic zones and power dissipations are obtained from the numerical lower and upper bound limit analyses and the rigid block mechanism is obtained from the upper bound rigid block analysis. The intensity of plastic zones and power dissipations are shown by the color shading. The dimensionless load parameter σ_s / c' of the lower and upper bound solutions obtained from the numerical limit and rigid block analyses is included in each figure. It is found from Figures 4a and 4b that for tunnels of a relatively shallow depth, small that for tunnels of a relatively shallow depth, small friction angles and close center-to-center spacing, a small slip surface originates between dual circular tunnels and a large slip surface originates at top on the outside of the tunnels. The large slip surface curves toward the ground surface. As can be seen from these figures the failure mechanisms of the rigid block technique agree well with those observed in the plastic zones and power dissipations. For the case of moderate depth, small friction angles and close center-to-center spacing presented in Figures 5a and 5b, a small slip surface between dual circular tunnels enlarges to cover the top and bottom of the tunnel and the large slip surface originates around the outer side of the pair of tunnels. The ultimate bearing capacity in this case is higher than that shown in Figure 4 due to increase of H/D and S/D. The upper bound solutions (Figs. 4–5c) obtained from the rigid block technique are in good agreement with those from the numerical limit analysis (Figs. 4–5b). Figure 6 shows the case of deep depth, small friction angles and moderate center-to-center distance. The slip surface between dual circular tunnels enlarges to encompass the entire tunnel and the large slip surface originates around the bottom of the tunnel. It is observed from Figures 6a and 6b that the plastic zones have developed around the entire tunnel. In this case, the rigid block results (Fig. 6c) tend to be larger than the results of numerical limit analysis (Fig. 6b) due to the deep depth and moderate center-to-center distance.

When H/D and S/D increase, as shown in Figures 4–6, the failure mechanism slowly extends vertically and transversely to eventually encompass the entire tunnel. These deeper and wider collapse mechanisms are more complex than those for shallow and narrow ones. The rigorous lower and upper bound solutions bracket the true ultimate bearing capacity quite accurately for the case of small frictional angles. It is found from Figures 4–6 that the S/D parameter has a key role for the pattern of failure mechanism and the increase of bearing capacity due to the effect of interaction. Of the several developed rigid block mechanisms shown in Figure 3, the best upper bound solutions were almost always obtained from mechanisms 1 and 3, which consist of three and six rigid blocks. In general, mechanism 1 is suitable for the cases of shallow tunnels with low friction angles and mechanism 3 for the case of deeper tunnels and high friction angles. In the case of moderate ϕ' and H/D, when S/D is increased, the best upper bound solutions started to be produced from mechanism 3. For the case of $\phi' = 20^\circ$, all the best upper bound solutions were obtained from mechanism 3. Additionally, the upper bound solutions obtained from the rigid block and numerical limit analyses are in good agreement (Figs. 4–5b, c), with the rigid block results tending to be larger than the limit analysis ones when H/D or ϕ' or S/D increases. This is due to the assumption that failure mechanism extends from the ground surface into the soil mass with the inclination angle equal to the friction angle ϕ'. Also, tunnels with a deeper and wider center-to-center configuration have a more complex collapse pattern, therefore, the simple rigid block mechanisms proposed in this study are generally less accurate for deeper and moderate distance tunnels than for shallow and close distance ones. Furthermore, it is more difficult to propose an efficient rigid block mechanism in the case of cohesive-frictional soils than in the case of purely cohesive material. As shown in Figure 6, the collapse mechanism for deeper and moderate distance tunnels is quite wide at the surface as well as it extends further around the bottom of the tunnel. Even using mechanism 3, the feasible solutions could not be easily obtained for high values of H/D or ϕ' or S/D.

Figures 7–8 shows the comparison of stability numbers obtained from both numerical limit and rigid block analyses. The interface condition is smooth. The lower and upper bound solutions of the numerical limit analysis for each $\gamma D / c'$ are plotted using broken and solid lines, respectively. As a general trend for all considered cases it can be observed from Figures 7 and 8 that stability numbers decrease when $\gamma D / c'$ increases. It is found that the ultimate bearing capacity increases monotonically with the increase of S/D, except for the cases of close proximity, $S/D \le 2.0$ (Fig. 8a) and $S/D \le 3.0$ (Fig. 8b). For the cases of 1) $H/D = 1$ and $\phi' = 10^\circ$, $S/D \le 3.0$, 2) $H/D = 1$ and $\phi' = 20^\circ$, $S/D \le 2.0$, 3) $H/D = 3$ and $\phi' = 10^\circ$, $S/D \le 4.0$ and 4) $H/D = 4$ and $\phi' = 10^\circ$, $S/D \le 3.5$, it is found that the upper bound solutions from the rigid block method have relatively good agreement with those

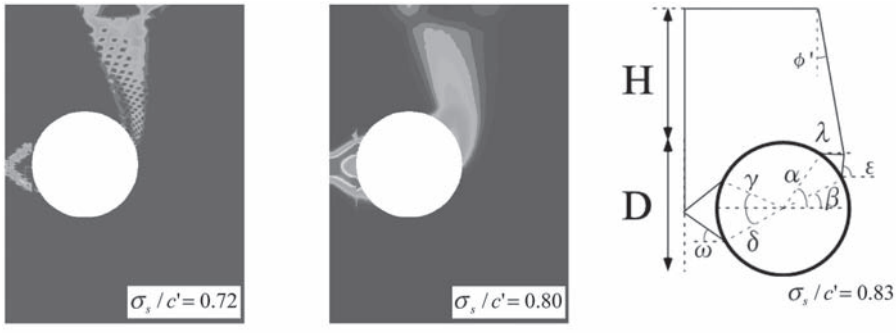

(a) plastic zones (b) power dissipation (c) rigid block mechanism

Figure 4. Comparison of numerical limit analysis with rigid block mechanism ($H/D = 1$, $\phi' = 10°$, $\gamma D/c' = 1$, $S/D = 1.5$, smooth interface).

(a) plastic zones (b) power dissipation (c) rigid block mechanism

Figure 5. Comparison of numerical limit analysis with rigid block mechanism ($H/D = 3$, $\phi' = 10°$, $\gamma D/c' = 1$, $S/D = 2.0$, smooth interface).

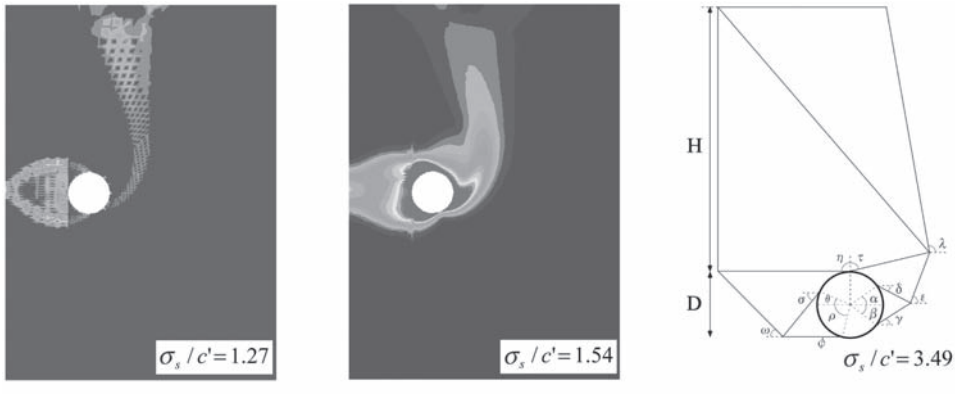

(a) plastic zones (b) power dissipation (c) rigid block mechanism

Figure 6. Comparison of numerical limit analysis with rigid block mechanism ($H/D = 4$, $\phi' = 10°$, $\gamma D/c' = 1$, $S/D = 4.0$, smooth interface).

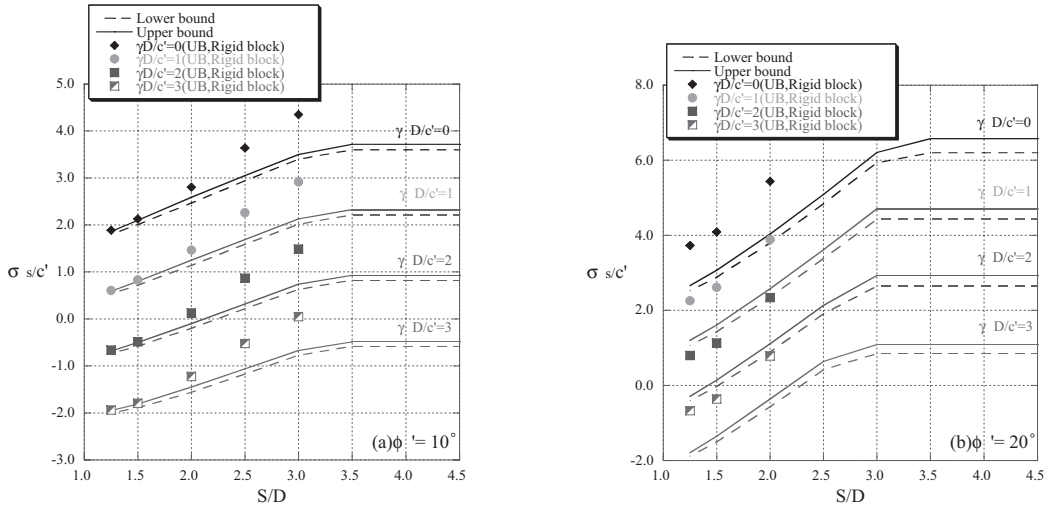

Figure 7. Stability bounds for dual circular tunnels (H/D=1, ϕ' = 10°, 20°, smooth interface).

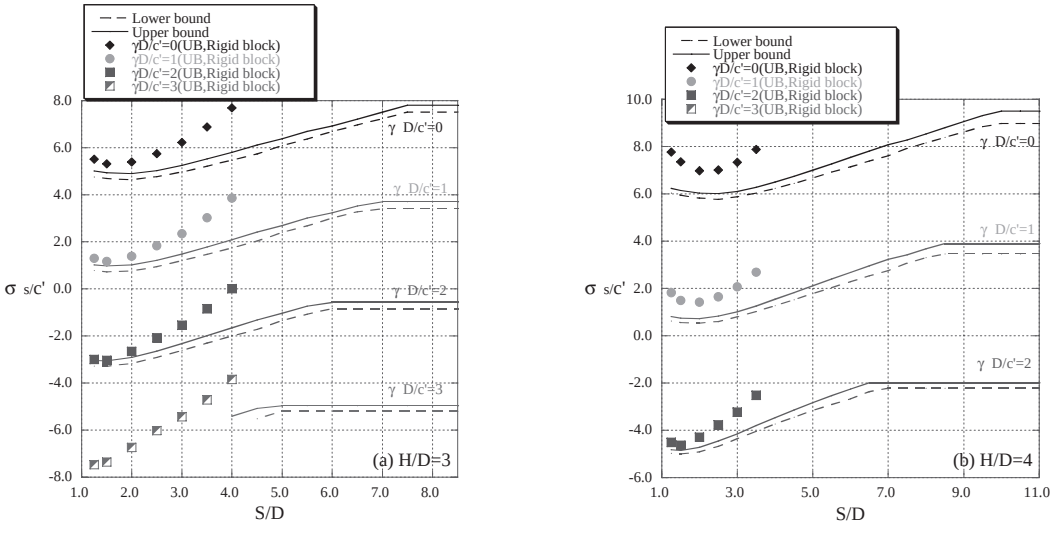

Figure 8. Stability bounds for dual circular tunnels (H/D =3,4, ϕ' = 10°, smooth interface).

obtained from the numerical limit analysis. But, with the increase of S/D the accuracy of considered rigid block mechanisms becomes poor. In most cases of $\gamma D / c' = 3$, $S / D \le 4.5$ (Fig. 8a) and $\gamma D / c' = 3$ (Fig. 8b), the feasible solutions from the rigid block and numerical limit analyses could not be obtained because the tunnel collapses under soil self weight. It is important to mention the sign convention used for stability numbers presentation. A positive value of stability number implies that a compressive normal stress can be applied to the ground surface up to this value, while a negative stability number means that we can only apply a tensile normal stress to the soil surface (no bearing capacity in normal sense). The negative range of stability numbers is likely to be of less practical interest than the positive ones. When S/D increases further, the lower and upper bound solutions of the numerical limit analysis tend to become constant at certain point, e.g. at $S / D = 3.5$ for $\gamma D / c' = 0 - 3$ (Fig.7a). The plots of plastic zones and power dissipations show no interaction between dual

circular tunnels at such points and after that the failure mechanism becomes that of two individual single tunnels failing independently. Thus, these points are regarded as the no interaction points for dual circular tunnels and this information would be important for engineering practice. Also, it is found that the no interaction points decreases when $\gamma D / c'$ increases for each H/D and ϕ'.

6 CONCLUSIONS

The ultimate bearing capacity and the failure mechanisms of cohesive-frictional soils with the inclusion of dual circular tunnels have been investigated and rigorous bounds on the stability numbers computed assuming plane strain conditions. The results of these analyses have been presented in the form of dimensionless stability charts. As an additional check of the validity of the numerical limit analysis several rigid block mechanisms for dual circular tunnels have been developed. Comparison of upper bound solutions obtained from the rigid block analysis with those of the numerical limit analysis shows good agreement when H/D, ϕ' and S/D are small.

For the cases in which the dual tunnels are deeper and in close proximity, it has been confirmed that the bearing capacity exhibits a slight decrease due to the interaction between pair of circular tunnels. Also, the interaction tends to disappear when the center-to-center distance exceeds a certain value (no interaction point). For future work, it is proposed to develop suitable for practical use rigid block mechanisms which are efficient also for high frictional angles and moderate center-to-center distance.

REFERENCES

Bunday, B.D. 1984. Basic optimisation methods. Edward Arnold.

Chen, W.F. 1975. Limit analysis and soil plasticity. Elsevier, Amsterdam.

Krabbenhøft, K., Lyamin, A.V., Hjiaj, M. & Sloan, S.W. 2005. A new discontinuous upper bound limit analysis formulation. *International Journal for Numerical Methods in Engineering*, 63: 1069–1088.

Lyamin, A.V. & Sloan, S.W. 2000. Stability of a plane strain circular tunnel in a cohesive-frictional soil. In D.W. Smith & J.P. Carter (eds), *Developments in theoretical geomechanics*, Balkema, Rotterdam, 139–153.

Lyamin, A.V. & Sloan, S.W. 2002. Lower bound limit analysis using non-linear programming. *Int. J. Numer. Meth. Engng.*, 55: 573–611.

Sloan, S.W. 1988. Lower bound limit analysis using finite elements and linear programming. *Int. J. Numer. Analyt. Meth. Geomech.*, 12: 61–77.

Sloan, S.W. 1989. Upper bound limit analysis using finite elements and linear programming. *Int. J. Numer. Analyt. Meth. Geomech.*, 13: 263–282.

Sloan, S.W. & Assadi, A. 1992. Stability of shallow tunnels in soft ground. In G.T. Houlsby & A.N. Schofield (eds), *Predictive soil mechanics*, Thomas Telford, London, 644–663.

Sloan, S.W. & Kleeman, P.W. 1995. Upper bound limit analysis using discontinuous velocity fields. *Comp. Methods in Appl. Mech. and Engng.*, 127: 293–314.

Wilson, D.W., Abbo, A.J., Sloan, S.W. & Lyamin, A.V. 2008. Undrained stability of dual square tunnels. In D.N. Singh (ed.), *Proc. of the 12th Int. Conf. of Int. Assoc. for Comp. Methods and Advances in Geomechanics (IACMAG)*, Goa, India.

Yamamoto, K., Lyamin, A.V., Wilson, D.W., Abbo, A.J. & Sloan, S.W. 2009. Limit analysis of shallow tunnels in cohesive frictional soils. In G. Meschke, G. Beer, J. Eberhardsteiner, D. Hartmann & M. Thewes (eds), *Proc. of 2nd Int. Conf. on Comp. Methods in Tunnelling*; *EURO:TUN 2009*, Bochum, 817–824.

This page intentionally left blank

Geotechnical Aspects of Underground Construction in Soft Ground – Viggiani (ed)
© 2012 Taylor & Francis Group, London, ISBN 978-0-415-68367-8

Centrifuge modelling of the response of buildings to tunnelling

R.P. Farrell
Laing O'Rourke (formerly University of Cambridge), UK

R.J. Mair
Department of Engineering, University of Cambridge, UK

ABSTRACT: Understanding how buildings respond to tunnelling induced ground movements is an area of great importance for many urban tunnelling projects. Testing described in this paper aims to investigate soil structure interaction effects by observing the response of elastic and non elastic beams of varying stiffness and geometry to tunnelling, using the 8 m diameter beam centrifuge at Cambridge University. Soil and structure displacements are extensively monitored through a photo imaging technique which enables a detailed analysis of the interaction mechanisms. Results demonstrate that buildings can significantly modify greenfield ground movements in both the vertical and horizontal planes. The magnitude of the modification is shown to be strongly dependent on the relative building stiffness. It is also shown that negligible horizontal strains are transferred into the model buildings. This can have significant implications for commonly adopted damage assessment methods.

1 INTRODUCTION

While relatively accurate predictions of the greenfield ground movements, in both the vertical and horizontal planes, can be made (Mair & Taylor, 1997), the presence of a structure alters these movements in what is termed soil-structure interaction. The estimation of the risk of damage to buildings, however, typically involves assuming that the structure deforms according to the greenfield ground movements. Estimates of the damage using this assumption can therefore be highly conservative.

Potts & Addenbrooke (1997) conducted a parametric finite element analysis investigating the response of buildings to tunnelling. Two parameters were defined to explain the modification to the settlement and axial response of buildings; these were the relative bending stiffness (ρ^*) and the relative axial stiffness (α^*). ρ^* and α^* were later modified by Franzius et al (2006), the former to be dimensionless. Expressions for ρ^*_{mod} and α^*_{mod} are presented in Equations 1 and 2 respectively:

$$\rho^*_{\text{mod}} = \frac{EI}{E_s B^2 z_0 L} \tag{1}$$

$$\alpha^*_{\text{mod}} = \frac{EA}{E_s BL} \tag{2}$$

where EI and EA are the bending stiffness and the axial stiffness of the structure respectively. E_s is the secant stiffness of the soil at 0.01% axial strain, at a depth of $z = z_0/2$. B is the building width and L is the length parallel to the tunnel heading. Dimensions are illustrated in Figure 1.

Settlement distortions to buildings are typically measured in both hogging and sagging modes of deformation using the deflection ratio (Δ/L or DR, defined in Figure 1). The hogging and sagging regions are partitioned by the point of inflexion (i) of the settlement trough. Potts and Addenbrooke (1997) quantified the modification to settlement distortions in terms of the ratio of the measured deflection ratio to the equivalent greenfield value, as presented in Equation 3. This ratio is given the term 'modification factor' (M^{DRhog} and M^{DRsag}).

$$M^{DR} = \frac{DR^{str}}{DR^{GF}} \tag{3}$$

Where DR^{GF} is the greenfield deflection ratio and DR^{str} is the deflection ratio displayed by the building; both are defined separately in hogging and sagging.

Modification factors to the greenfield settlement distortions are highly dependent on ρ^*_{mod} (Franzius et al., 2006). Similarly, the modification to tensile and compressive horizontal strains, in the hogging and sagging regions respectively, are highly dependent on α^*_{mod} (Franzius et al., 2006).

This paper presents the results of a series of centrifuge tests in which model aluminium, masonry

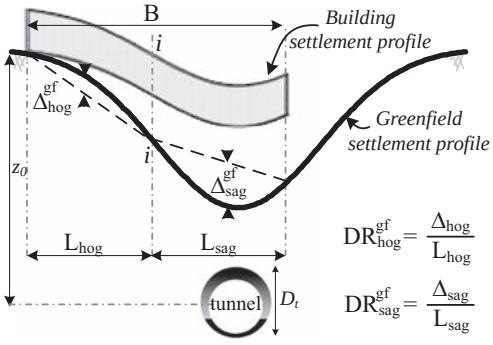

Figure 1. Influence of soil-structure interaction on settlement distortions.

and micro-concrete beam structures of varying stiffness and geometry are subjected to tunnelling induced ground movements. A greenfield test was also carried out, the results of which are used to quantify the modification to greenfield distortions that the various buildings display.

2 EXPERIMENTAL SETUP

2.1 *Centrifuge package and model design*

A series of centrifuge tests were carried out on the 8 m diameter centrifuge at the University of Cambridge to investigate the response of buildings to tunnelling in sands. Figure 2 shows the package used for this series of tests.

Centrifuge tests were carried out under plane strain conditions at 75 g. Using common scaling laws (Taylor, 1995), the model was designed to represent a 6.15 m diameter (D) tunnel with cover (C) of 8.25 m (at prototype scale), in fraction E silica sand. Model dimensions are shown in Figure 3.

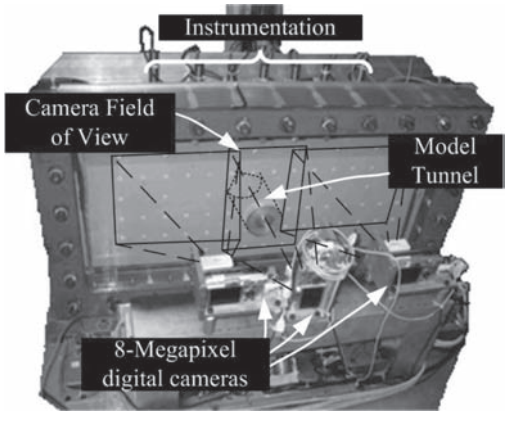

Figure 2. Centrifuge model package.

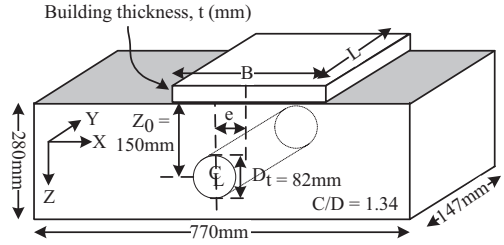

Figure 3. Model dimensions (in model scale).

Sand was poured into the model using an automatic sand pourer which enables a high level of repeatability between tests to be achieved. The model was poured with the Perspex face down and with the model tunnel in place, allowing for a uniform distribution of sand throughout the entire model. Relative sand density was 90% for this series of tests.

The model tunnel was formed using a brass mandrill with an outer latex rubber lining. The resulting annulus between the two is filled with water until an 82 mm diameter cylinder is obtained. This model tunnel is then placed in a recess in the front Perspex face and the back aluminium plate to achieve plane strain conditions.

During the test, volume losses are imposed by withdrawing the fluid from the tunnel using a piston and motor driven actuator system. This system is calibrated to withdraw the water at a controlled rate. The volume loss is determined from the ratio of the volume of fluid withdrawn to the volume of the tunnel. This method allows the volume loss to be accurately determined throughout the test.

To avoid volume changes in the tunnel as the model spins up to 75 g, due to remaining air in the system, the tunnel-piston system is connected to a fixed head of water in a standpipe at the back of the model. The resulting pressure head at the tunnel axis corresponds to the vertical total stress at the tunnel axis. The connection to the standpipe is controlled remotely using a solenoid valve and is opened during spin-up, and closed again once the model reaches 75 g, before initiating volume losses.

The face of the package was formed from Perspex to allow the use of particle image velocimetry (PIV) (White et al, 2003) to measure soil displacements. This technique uses digital imaging to track the movements of patches of pixels throughout the test. As PIV tracks the inherent soil texture, intrusive markers are not required. For this purpose, three 8 megapixel cameras were mounted on the front of the package (see Figure 2). Volume losses were induced in 0.1% increments and digital photos taken at each increment. This allows the measured displacements to be related to a specific volume loss.

2.2 *Modelling of buildings*

Two different types of building were considered in this research, namely fully elastic beam structures and beam structures capable of cracking.

Fully elastic structures used in this series of tests were constructed from aluminium beams (E = 70GPa) of varying thickness. The width of each aluminium beam was kept constant throughout the test series (B = 400 mm) and each structure was placed symmetrically about the tunnel axis. In each case plane strain conditions were present. A rough interface was modelled by gluing fraction E sand to the base of the structure. Geometric and structural properties for each of the 4 no. aluminium beams tested (STR-1 to STR-4) are given in Table 1.

Beam buildings capable of cracking were modelled using micro concrete and masonry with cement based mortar. Micro concrete mixes were formed from Orindary Portland Cement (OPC) and various grades of relatively fine sand (fraction C, D and E represent 45%, 30% and 25% of the aggregate mix respectively). The stiffness of the mix at various water-cement ratios (w/c) was calibrated using point load tests on sacrificial model beams. This also allowed for the effect of time on the mix strength to be assessed. The Young's modulus (E) of the micro-concrete mix at the w/c ratio of 0.8, used in test MCS-1, was estimated as 4 GPa at the time of testing.

Figure 4. Model aluminium beam building (STR-2) with strain gauges.

Masonry buildings were modelled using 1/12th scale model bricks with an OPC based mortar. Plaster of Paris was added to the mortar to reduce the ductility and model the characteristics of real masonry more accurately. Point load tests on sample masonry walls indicated a Young's modulus (E) of 1.5–2GPa for the 2 no. masonry buildings modelled in this series of tests, MAS-1 (see Figure 5a) and MAS-2L. A further masonry building, termed MAS-2R, was modelling using 1/50th scale model bricks with an elastic silica gel mortar (see Figure 5b) to simulate a beam with a very low bending and axial stiffness. Geometric and structural properties for each of beams tested are given in Table 1.

Prototype scale axial (EA) and bending (EI) stiffness values modelled are comparable with values from similar centrifuge studies and from estimates of the stiffness of actual structures from case studies (see Figure 6). The influence of building weight was not investigated in this test series. Model structures were also fitted with strain gauges to measure the bending and horizontal strains at various locations. An indication of the contact stress between buildings and the soil was obtained from Earth

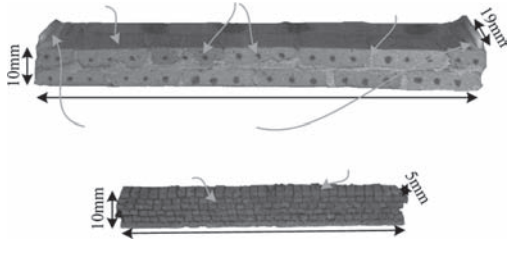

Figure 5. Model masonry buildings with (a) cement based mortar and (b) silica gel mortar.

Table 1. Test series details.

Test Name	Material	Model scale B (mm)	e†1 (mm)	t (mm)	L (mm)	EI (kNm²/m)	EA (kN/m)	Prototype scale EI (kNm²/m)	EA (kN/m)
GF-1	Greenfield—no building								
STR-1	Aluminium	400	0	1.6	145	2.4×10^{-2}	1.1×10^{5}	1×10^{2}	8.4×10^{6}
STR-2	Aluminium	400	0	5	145	7.3×10^{-1}	3.5×10^{5}	3.1×10^{5}	2.6×10^{4}
STR-3	Aluminium	400	0	10	145	5.8×10^{0}	7×10^{5}	2.5×10^{6}	5.3×10^{7}
STR-4	Aluminium	400	0	20	145	4.7×10^{1}	1.4×10^{6}	2.0×10^{7}	1.0×10^{8}
MCS-1	Micro-concrete	400	0	5	145	4.1×10^{-2}	2.0×10^{4}	1.8×10^{4}	1.5×10^{6}
MAS-1	Masonry	115	–67	10	18	1.6×10^{-1}	2.0×10^{4}	7.1×10^{4}	1.5×10^{6}
MAS-2	(a)Masonry†2	195	–45	10	18	1.25×10^{-1}	1.5×10^{4}	5.4×10^{4}	1.1×10^{6}
MAS-2	(b)Masonry†2	75	120	10	5	1.25×10^{-2}	1.5×10^{3}	5.4×10^{3}	1.1×10^{5}

†1where, e is the eccentricity of the building measured as the distance from the mid-point of the building to the tunnel centreline.

†2 two buildings were tested in MAS-2. Building (a), MAS-2L, was located to the left of the tunnel and building (b), MAS-2R, was located to the right hand side of the tunnel.

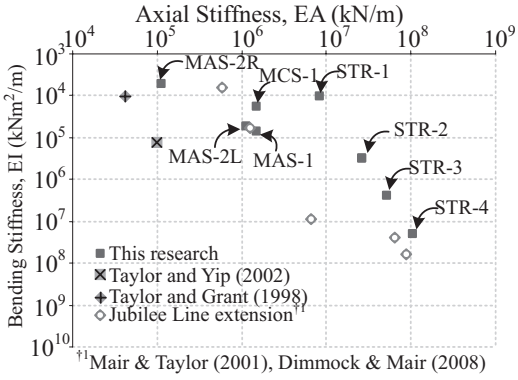

Figure 6. Bending and axial stiffness of real structures.

Pressure Cells (EPC's) which were glued to the underside of model buildings.

Similar modelling techniques have been adopted by Taylor & Grant (1998) and Marshall (2009) in centrifuge modelling of the response to tunnelling of structures and pipelines respectively.

3 BUILDING SETTLEMENT RESPONSE

3.1 *Building settlements*

The settlement profiles of the aluminium beam buildings, STR-1 to STR-4, at 2% volume loss are illustrated in Figure 7. The greenfield settlement profile (GF-1) is also shown for reference STR-1 is seen to behave fully flexibly with regions of hogging and sagging evident, while STR-4 demonstrates the most rigid response. Therefore, depending on a building's stiffness, or more specifically ρ^*_{mod}, the settlement response can be fully flexible, fully rigid or somewhere in between. Clearly a more rigid response implies correspondingly smaller distortions and consequently, less damage. This highlights the potential conservativeness of assuming the building to follow the greenfield settlement.

The settlement profiles of the micro concrete and masonry buildings in tests MCS-1, MAS-1 and MAS-2, at 2% volume loss, are illustrated in Figure 8a-c respectively. Similar to STR-1, building MCS-1 is seen to respond relatively flexibly with regions of hogging and sagging evident. MAS-1 on the other hand was observed to behave relatively rigidly and simply tilted. The response of MAS-2L was found to be relatively flexible with both hogging and sagging modes of deformation observable, although the response is significantly influenced by the development of a crack above the tunnel centreline. Scatter in the settlement data for MAS-2R is observed, although the response appears to be

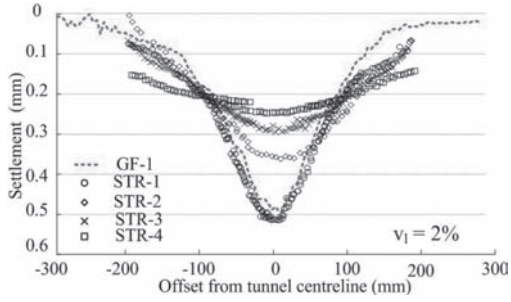

Figure 7. Surface settlement profile for structures STR-1 to STR-4.

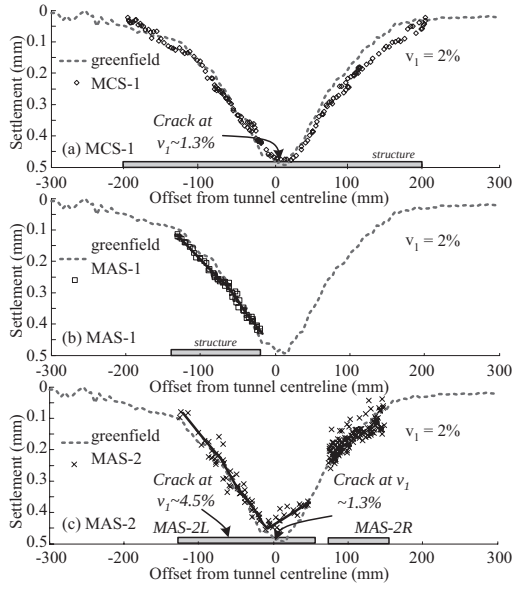

Figure 8. Building settlements compared with greenfield settlements in tests MCS-1, MAS-1 and MAS-2.

relatively flexible. Cracking and damage to buildings is discussed further in Section 5.

3.2 *Building embedment*

The settlement response of STR-4 clearly indicates that the edges of the building settle more than the greenfield trough and embed into the soil (see Figure 7). Above the tunnel centreline however, building settlements are substantially less than greenfield values, suggesting the formation of a gap between the soil and the building. The development of a gap beneath buildings STR-2 to STR-4 has been confirmed from PIV measurements (Farrell, 2010).

The formation of a gap beneath more rigid buildings is important as it results in a redistribution of the building weight away from the tunnel centreline. This trend is also evident for building MAS-1 (see Figure 8b) where building settlements

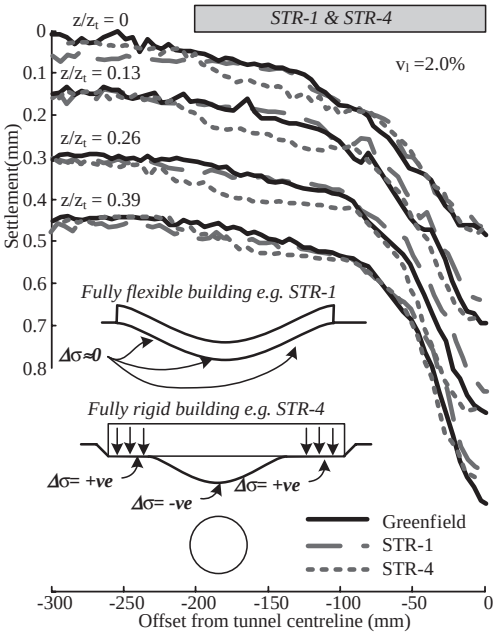

Figure 9. Settlement of soil beneath flexible and rigid buildings (STR-1 & STR-4) compared with greenfield settlements.

at the trough shoulders (~x = –80 mm) are larger than the greenfield settlements.

Figure 9 illustrates the effect of building embedment on the underlying soil through comparison of soil settlements at various depths beneath the rigid STR-4 with those beneath the flexible STR-1. The greenfield settlement profile is also shown for reference. Soil settlements beneath the flexible STR-1 are seen to agree well with greenfield values at all depths. Soil settlements beneath the rigid STR-4 however are seen to be larger than the greenfield values in the region of $-200 < x < -90$ mm, highlighting this embedment effect. The influence of this embedment beneath STR-4 is seen to extend to a depth of roughly $z/z_0 = 0.26$. This depth of influence is likely to be dependent not only on ρ^*_{mod}, but also on the building weight, as heavier buildings will redistribute more weight and cause larger settlements. Observations of building weight redistribution have been confirmed from EPC's located along the base of model buildings.

3.3 *Modification to settlement distortions*

The observed relationship between modification factors to the settlement distortions and the relative building stiffness (ρ^*_{mod}) is shown in Figure 10a and 10b for hogging and sagging distortions respectively. Design curves proposed by Franzius

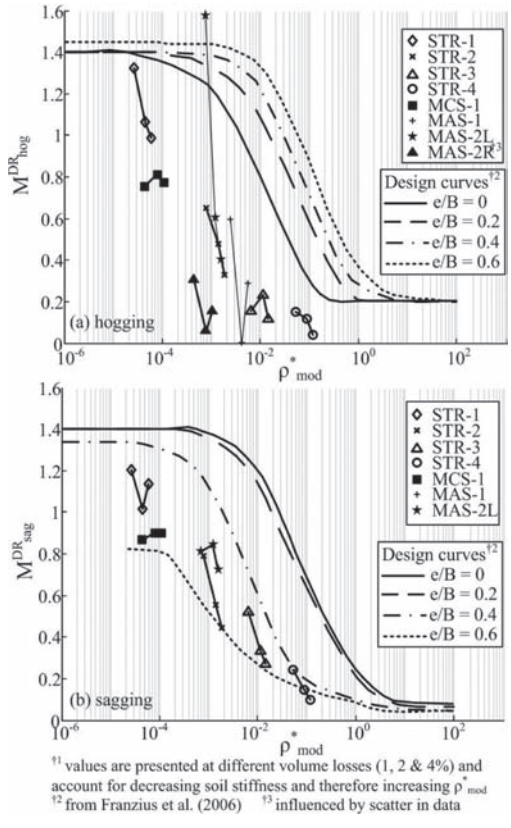

Figure 10. Modification factors in (a) hogging (b) sagging (from Franzius et al., 2006).

et al. (2006) are also shown. Measured modification factors are presented at volume losses of 1, 2 and 4% and account for the change in the soil stiffness on ρ^*_{mod}. An interesting observation is that for the very flexible STR-1, modification factors greater than unity are observed. This is consistent with observations from finite element analyses (Franzius et al, 2006) and indicates that the distortions are larger than the greenfield values. This is likely to result from the influence of horizontal shear stresses acting at the base of the building to increase the curvature.

The relationship between ρ^*_{mod} and M^{DR} is seen to be highly non-linear in both hogging and sagging which again is in agreement with observations from finite element analyses. This highly non-linear relationship is highlighted by the decrease in M^{DR} for the elastic beams (STR-1 to STR-4) as volume losses increase. This decrease in M^{DR} arises as volume losses increase soil strains which reduces the soil stiffness and increases ρ^*_{mod} which results in an increasingly rigid response. This trend is not as

evident for non elastic buildings, as cracking simultaneously reduces the building stiffness and ρ^*_{mod}.

While the agreement between the design lines and the measured M^{DR} values is relatively poor, the design lines do represent an upper bound to the modification factors, as was their intended purpose. Scatter in the modification factors—as exemplified by MAS-2L in hogging—results from the limit of the precision (0.02 mm) of PIV and the ensuing errors in estimating the deflection ratio.

4 BUILDING HORIZONTAL RESPONSE

4.1 *Horizontal displacements*

Figure 11a–c shows the horizontal displacement profile of buildings STR-4, MAS-1 and MAS-2 respectively, at 2% volume loss. Greenfield horizontal displacements are also illustrated for reference. It can be observed that STR-4 displayed negligible horizontal displacements and significantly modified the greenfield settlement profile. All buildings placed symmetrically about the tunnel centreline displayed similar behaviour.

Building MAS-1 on the other displays a net horizontal displacement which is roughly equal to the maximum greenfield horizontal displacement indicating that the ground laterally displaces the building. Differential horizontal displacements and hence horizontal strains, however, remain negligible.

A net horizontal displacement of building MAS-2L (see Figure 11c) is also observed, although the magnitude of this displacement is less than the maximum greenfield displacement. Differential horizontal displacements or horizontal strains are difficult to identify due to scatter in the data but are significantly smaller than the greenfield strains.

Horizontal displacements of building, MAS-2R are seen to agree reasonably well with the greenfield values. Despite scatter in the data differential horizontal displacements and hence horizontal strains can be observed. Horizontal strains are discussed further in Section 4.2.

Surface horizontal displacements, measured directly beneath model buildings STR-4, MAS-1 and MAS-2L at 2% volume loss, are illustrated in Figure 12a–c respectively. Greenfield horizontal displacements are also illustrated for reference. Displacements beneath STR-4 agree well with the greenfield values close to the tunnel centreline ($x > -50$ mm). Towards the edge of the building ($x < -100$ mm) friction reduces the horizontal soil displacements, indicating that where a gap does not form, horizontal soil displacements are negligible. All buildings located symmetrically about the tunnel centreline had a similar effect on the underlying soil.

The horizontal displacement of MAS-1 on the other hand is seen to cause an increase in the soil displacements towards the edge of the building

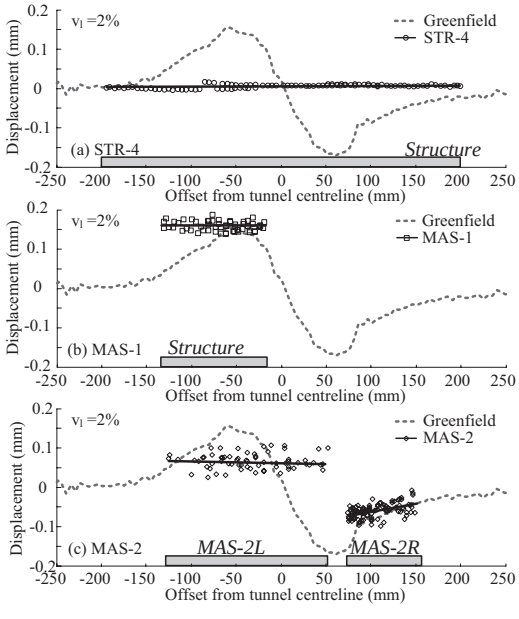

Figure 11. Horizontal displacement profile for model buildings in tests (a) STR-4, (b) MAS-1 and (c) MAS-2.

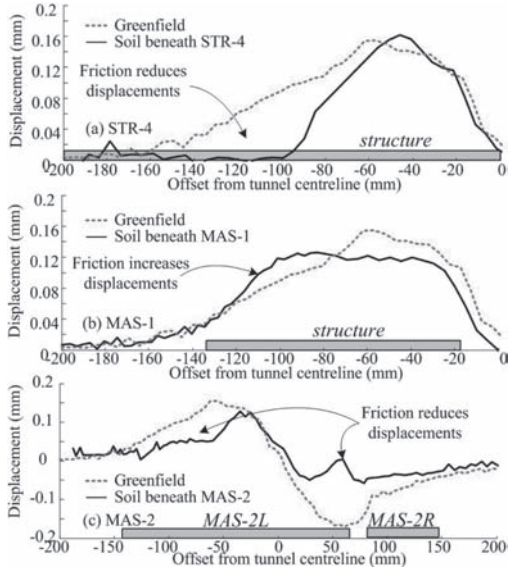

Figure 12. Horizontal displacement profile for soil beneath model buildings in tests (a) STR-4, (b) MAS-1 and (c) MAS-2.

(x < −80 mm). This also results from friction at the soil structure interface.

Similar to STR-4, MAS-2L can be seen to restrain horizontal displacements towards its edges. This is particularly evident towards the right hand side of the building (x ~ 50 mm) where large greenfield horizontal displacements (~0.2 mm) are reduced to zero. Relatively good agreement between measured horizontal displacements and greenfield displacements close to the tunnel centreline, indicate that friction in this region is significantly lower than at the edges.

4.2 *Modification to horizontal strains*

Figure 13 shows the horizontal displacements of the buildings and soil surface in test MAS-2 at a volume loss of 2%. Greenfield horizontal displacements are presented for reference. Horizontal strains, estimated from the slope of a straight line fitted to the horizontal displacements, are also indicated. Average greenfield horizontal strains across building MAS-2L are estimated as roughly 0.125%, where compression is positive. Although there is some scatter in the data, horizontal strains within MAS-2L are substantially smaller, at roughly 0.014%.This implies that strains within the building are roughly 10% of the greenfield values.

Horizontal strains within MAS-2R, however, are evident from the differential horizontal displacements and are roughly 30% of the average greenfield horizontal strain. The prototype scale axial stiffness (EA) of this building however is extremely low, due to the silica gel mortar and is equivalent to only a 4 mm thick reinforced concrete slab (for E = 27GPa). Horizontal strains within the aluminium beams tested were also found to be negligible relative to greenfield strains, as illustrated in Figure 14, for building STR-3. Similar conclusions of negligible horizontal strains being induced in buildings with continuous footings have been reached by Viggiani and Standing (2001), Mair (2003) and Dimmock & Mair (2008).

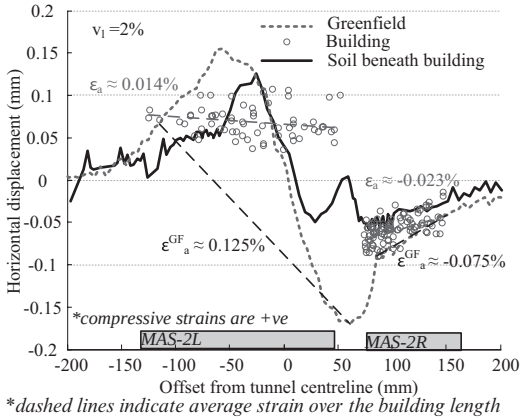

dashed lines indicate average strain over the building length

Figure 13. Estimation of horizontal strains from measured horizontal displacements of buildings in test MAS-2 and from greenfield measurements.

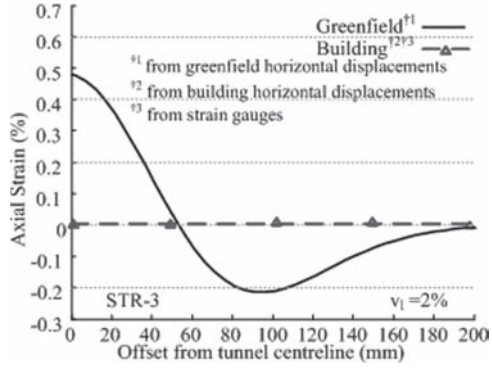

Figure 14. Measured horizontal strain in building STR-3 compared with greenfield horizontal strains.

5 DAMAGE

The development of cracks in the non elastic model buildings has been identified through an analysis of the incremental settlement profiles. Observations were later verified through visual inspection of the models. Strains at which cracking occurs have been estimated from differentiation of the settlement profile and where possible, from strain gauges.

Observed cracking in the masonry building MAS-2L is illustrated in Figure 15. Cracking in the sagging region of the trough occurred at 1.1–1.5% volume loss and at a strain of roughly 350 με. This crack developed at the base of the model, where bending induced tensile strains are largest. Cracking in the hogging region of the trough occurred at 4–5% volume loss (350–500 με) and emanated from the top of the model, again where bending induced tensile strains are largest. Cracking in building MCS-1 was also observed in the sagging region, at a volume loss of 1.3% (roughly 180 με).

A damage category chart for buildings in hogging and with an L/H ratio of 4, corresponding to STR-4, is presented in Figure 16. This chart has been developed using simple beam theory proposed by Burland and Wroth. (1974) and assuming limiting tensile strains for different damage categories as proposed by Boscardin and Cording (1989). Categories of damage, ranging from 0–5, have been defined by Burland et al. (1977) and represent an escalation from negligible damage to severe structural damage.

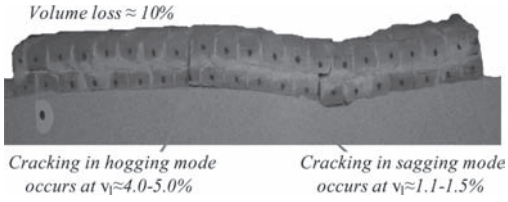

Figure 15. Observed cracking of building MAS-2 L.

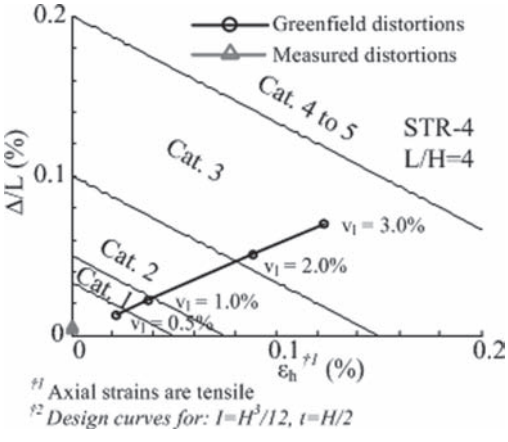

Figure 16. Damage category chart for STR-4 (L/H = 4) in hogging with greenfield and measured building distortions.

It can be observed from Figure 16 that superimposing greenfield distortions onto building STR-4 would result in category 3 level of damage, at a volume loss of 3%. However, as the building behaved rigidly and simply embedded into the soil, settlement distortions were negligible. Combined with the negligible horizontal strains, the revised risk damage can be estimated as 'negligible'. This highlights the conservativeness of assuming buildings to deform according to the greenfield distortions (both vertical and horizontal).

6 CONCLUSIONS

The response of elastic buildings and buildings capable of cracking to tunnelling induced ground movements has been investigated using centrifuge modelling. The following conclusions can be made:

1. The modification to settlement distortions is a function of both the building and soil stiffness. Results presented in this paper indicate that this relationship is highly non-linear. This agrees with finite element data in the literature (e.g. Franzius et al., 2006)
2. Buildings that respond rigidly to tunnelling do so by redistributing their weight. This can cause buildings to embed into the soil in certain places. This agrees with observations from field studies (Farrell et al., 2011).
3. Horizontal strains transferred into model buildings were generally negligible, as is often observed in the field (Mair, 2003). The exception to this was a highly flexible building which had a prototype scale axial stiffness equivalent to that of only a 4 mm reinforced concrete slab. Nevertheless, horizontal strains within this building were still less than 30% of the greenfield strains.
4. Estimating the risk of damage to buildings by superimposing greenfield distortions can be highly conservative due to the influence of the soil-structure interaction on the settlement and particularly the horizontal building distortions. Centrifuge test results have shown that this interaction can be roughly quantified from empirical relationships, such as those proposed by Franzius et al. (2006)

ACKNOWLEDGEMENTS

The authors would like to thank the EPSRC and the Cambridge European Trust for funding this research.

REFERENCES

Boscardin, M.D. & Cording, E.J. (1989). Building response to excavation-induced settlement. *ASCE Journal of Geotechnical Engineering,* 115, pages 1–21.

Burland, J.B., Broms, B.B. & De Mello, V.F.B. (1977). Behaviour of foundations and structures. *Proceedings of the 9th International Conference on Soil Mechanics and Foundations Engineering*, volume 2, pages 495–546. Tokyo.

Burland, J.B. and C.P. Wroth (1974). Settlement of buildings and associated damage. *Settlement of Structures*, Cambridge, pages 611–654. Pentech Press, London, Cambridge.

Dimmock, P.S. and R.J. Mair (2008). Effect of building stiffness on tunnelling-induced ground movement. *Tunnelling and Underground Space Technology*, 23, no. 4, pages 438–450.

Farrell, R.P., Mair, R.J., Sciotti, A., Pigorini, A. & Ricci, M. (2011). The response of buildings to tunnelling: a case study. *Geotechnical Aspects of Underground Construction in Soft Ground.* Unpublished. Rome. Balkema.

Franzius, J.N., Potts, D.M. & Burland, J.B. (2006). The response of surface structures to tunnel construction. *Proceedings of the Institution of Civil Engineering—Geotechnical Engineering*, 159, no. 1, pages 3–17.

Mair, R.J (2003). Research on tunnelling-induced ground movements and their effects on buildings—lessons from the Jubilee Line Extension. *Response of buildings*

to excavation induced ground movements. Proceedings of the international conference, pages 3–26, CIRIA SP199.

Mair, R.J., Taylor, R.N. & Burland, J.B. (1996). Prediction of ground movements and assessment of risk of building damage due to bored tunnelling. *Geotechnical Aspects of Underground Construction in soft ground*, pages 713–718. Balkema, London.

Mair, R.J. & Taylor, R.N. (2001). Settlement predictions for Neptune, Murdoch and Clegg Houses and adjacent masonry walls. Building Response to tunnelling–Case studies from construction of the Jubilee Line Extension, London. Vol. 1: Projects and Methods. In Burland J.B., Standing J.R., and Jardine F.M., (eds) *CIRIA SP200*, pages 217–228. London: Thomas Telford.

Marshall, A.M. (2009). Tunnelling in sand and its effect on pipelines and piles. *Ph.D. thesis*, Cambridge University, UK.

Potts. D.M. & Addenbrooke, T.I. (1997). A structures influence on tunnelling induced ground movements. *Proc. Inst. Civ. Engrs. Geotechnical Engineering*, Vol. 125, pages 109–125.

Taylor, R.N. (1995). Geotechnical Centrifuge Technology. London: Blackie Academic and Professional.

Taylor, R.N. & Grant R.J. (1998). Centrifuge modelling of the influence of surface structures on tunnelling induced ground movements. In Negro Jr & Ferreira (eds). *Tunnels and Metropolises.* Pages 261–265. Rotterdam: Balkema.

Viggiani, G. & Standing, J.R. (2001). The Treasury. *In:* Burland, J.B., Standing, J.R. & Jardine, F.M. (eds.) *Building response to tunnelling: case studies from construction of the Jubilee Line Extension, London*, pages 351–366. London, volume 2. CIRIA and Thomas Telford.

White, D.J., Take, W.A. & Bolton, M.D. (2003). Soil deformation measurement using particle image velocimetry (PIV) and photogrammetry. *Geotechnique*, Vol. 53(7), pages 619–631.

This page intentionally left blank

Geotechnical Aspects of Underground Construction in Soft Ground – Viggiani (ed)
© 2012 Taylor & Francis Group, London, ISBN 978-0-415-68367-8

Tunnelling-induced deformation on a masonry structure: A numerical approach

A. Amorosi
Department of Hydraulic Engineering and Chemistry, Technical University of Bari, Bari, Italy

D. Boldini
Department of Civil, Environmental and Material Engineering, University of Bologna, Bologna, Italy

G. de Felice & M. Malena
Department of Structures, University Roma Tre, Rome, Italy

ABSTRACT: In this paper the analysis of a possible damage mechanism induced by shallow tunnelling to an ideal masonry structure is carried out using a numerical approach based on 2D FE analyses. The masonry structure is modelled adopting an advanced constitutive model which was specifically implemented in a commercial finite element code. The masonry structure, schematised as a block structure with periodic texture, is regarded at a macroscopic scale as a homogenized anisotropic media. The macroscopic model is shown to retain memory of the mechanical characteristics of the joints and of the shape of the blocks (de Felice *et al.*, 2010). The overall mechanical properties display anisotropy and singularities in the yield surface, arising from the discrete nature of the block structure and the geometrical arrangement of the units. The soil, a medium consistency clayey material, is modelled by means of a simple linear elastic-perfectly plastic model. The numerical analyses were performed assuming, as a first simplified step, plane strain and plane stress conditions for the soil and the masonry structure, respectively. The investigation provides preliminary insights into the soil-tunnel-structure interaction by taking into account different values of volume loss, with reference to a typical wall-type masonry structure.

1 INTRODUCTION

Numerical predictions of free-field settlements induced by tunnelling in fine grained soils are influenced by different factors, which include 2D or 3D geometrical discretisation, correct representation of the construction stages, assumed state of the soil, drainage conditions, numerical techniques and constitutive hypotheses. Adding a pre-existing surface structure renders the above prediction more complex, the results being also dependent on the geometry, weight, stiffness and strength of the structure.

Nonetheless, one of the key problem in modern civil engineering is exactly that of predicting the response—and minimise the related damage—of surface structures interacting with underground infrastructures in urban areas. As such, the aforementioned analyses might represent a central ingredient in a modern strategy of tunnel design.

Different approaches characterised by increasing levels of complexity can be adopted in the analyses, including empirically-based free-field analytical predictions, simplified 2D numerical analyses based on schematic assumptions for both the soil and the surface structure, up to complex 3D simulations accounting for the non-linear and irreversible behaviour of the soil and, more rarely, of the structure.

In this paper we summarise some preliminary results of a multi-disciplinary research program aimed at combining the advances in geotechnical and structural engineering with reference to the numerical analyses of tunnel excavations interacting with masonry surface structures. The long term objective of the research is that of providing an insight into the damage patterns of ancient masonry structures interacting with underground constructions, by means of up to date constitutive models and numerical FE tools.

In this paper the results of 2D FE simulations of the excavation of an ideal shallow tunnel in a medium consistency clayey soil are presented, first with reference to free-field conditions and then assuming the pre-existence of a surface masonry wall. The analyses are aimed at establishing the role of the masonry structure on the resulting surface settlement profile and at investigating the evolution of the plastic strain accumulation into the wall.

Major emphasis is given here to the effects of the advanced constitutive model assumed for the masonry, while a more conventional hypothesis is considered for the soil.

2 CONSTITUTIVE MODELS

The constitutive models for soil and masonry are formulated in the framework of classical rate-independent plasticity.

2.1 *Soil model*

A linear elastic-perfectly plastic constitutive model was selected for the soil, characterised by a Mohr-Coulomb yield criterion and a null dilatancy angle.

These relatively simple constitutive assumptions will be removed in the next steps of the research in order to simulate better the mechanical response of soil in this class of boundary value problems.

2.2 *Masonry model*

A linear elastic-perfectly plastic constitutive model was selected for masonry too, where however anisotropy in both elastic properties and strength envelop are taken into account.

The model is formulated in the framework of homogenization theory of periodic media, referring to a block masonry structure, consisting of a periodic pattern of elastic blocks with cohesive and frictional joints. In such a case, a closed-form approximated expression for the elastic strain energy is provided in de Felice *et al.* (2009) that takes the following form:

$$W(\boldsymbol{\varepsilon}^e) = \frac{1}{2}\left(\frac{E_x}{1-\nu_{xz}\nu_{zx}}\left(\varepsilon^e_{xx}\right)^2 + \frac{E_z}{1-\nu_{xz}\nu_{zx}}\left(\varepsilon^e_{zz}\right)^2\right) + \\ + \frac{1}{2}\left(\frac{2\nu_{xz}E_z}{1-\nu_{xz}\nu_{zx}}\varepsilon^e_{xx}\varepsilon^e_{zz} + 4G\left(\varepsilon^e_{xz}\right)^2\right) \tag{1}$$

where x and z are the horizontal and vertical direction, respectively. The coefficients in (1) depend on the elastic Lamè coefficients of the blocks (λ'_b, μ_b) and the normal K_n and tangential K_t stiffness of the joints, as well as on the height a and width b of the blocks as follows:

$$\frac{1}{E_x} = \frac{4a}{4abK_n + b^2K_t} + \frac{1}{4\mu_b} + \frac{1}{4(\lambda'_b + \mu_b)} \tag{2}$$

$$\frac{1}{E_z} = \frac{1}{aK_n} + \frac{1}{4\mu_b} + \frac{1}{4(\lambda'_b + \mu_b)} \tag{3}$$

$$\frac{1}{G} = \frac{1}{aK_t} + \frac{4a}{4abK_t + b^2K_n} + \frac{1}{\mu_b} \tag{4}$$

$$\frac{\nu_{xz}}{E_x} = \frac{\nu_{zx}}{E_z} = \frac{\lambda'_b}{4\mu_b(\lambda'_b + \mu_b)} \tag{5}$$

The elastic domain is defined in the context of multi-surface perfect plasticity as:

$$E_\sigma = \left\{\boldsymbol{\sigma} \mid f^\alpha(\boldsymbol{\sigma}) := \mathbf{n}^\alpha : \boldsymbol{\sigma} - c^\alpha \le 0 \ \ \forall \ \ \alpha \in [1,..,m]\right\} \tag{6}$$

where $f^\alpha(\boldsymbol{\sigma})$ are m independent planes, intersecting in a non smooth way, which define the yield surface. The expression for the yield surface of block masonry is provided in de Buhan and de Felice (1997) on the basis of the yield design homogenisation method. In particular, if the blocks are assumed as infinitely resistant bodies and the joints as frictional interfaces, with cohesion c and friction angle ϕ, the yield surface comprises $m = 4$ planes which can be written in terms of stress components in the Oxz reference adopted for the joints as follows:

$$\begin{aligned} f^1 &:= \mu\sigma_{xx} + tg(\varphi)\sigma_{zz} + (1 + tg(\varphi)\mu)\sigma_{xz} \\ &\quad -c - c\mu / tg(\varphi) \le 0 \\ f^2 &:= \mu\sigma_{xx} + tg(\varphi)\sigma_{zz} - (1 + tg(\varphi)\mu)\sigma_{xz} \\ &\quad -c - c\mu / tg(\varphi) \le 0 \\ f^3 &:= \sigma_{zz} + 1/tg(\varphi)\sigma_{xz} - c/tg(\varphi) \le 0 \\ f^4 &:= \sigma_{zz} - 1/tg(\varphi)\sigma_{xz} - c/tg(\varphi) \le 0 \end{aligned} \tag{7}$$

where $\mu = 2a/b$ is the aspect ratio height-to-width of the blocks.

The evolution of plastic strain $\boldsymbol{\varepsilon}^p$ is controlled by the associated flow rule expressed as proposed by Koiter (1960):

$$\dot{\boldsymbol{\varepsilon}}^p = \sum_{\alpha=1}^{m} \dot{\gamma}^\alpha \frac{\partial f^\alpha(\boldsymbol{\sigma})}{\partial \boldsymbol{\sigma}} \tag{8}$$

where $\dot{\gamma}^\alpha$ are the m multipliers, subjected to the Kuhn-Tucker conditions for $\alpha \in [1,..,m]$:

$$\dot{\gamma}^\alpha \ge 0 \quad f^\alpha(\boldsymbol{\sigma}) \le 0 \quad \dot{\gamma}^\alpha f^\alpha(\boldsymbol{\sigma}) \equiv 0 \tag{9}$$

and to the consistency condition $\dot{\gamma}^\alpha \dot{f}^\alpha(\boldsymbol{\sigma}) \equiv 0$ (the summation convention is not enforced).

The assumption of associated flow rule may be not completely satisfactory in the case of block structures, since the blocks may slide with no dilation, giving rise to a non associated flow rule at the macroscopic scale; on the structural viewpoint, this assumption may lead to an overestimate of the ultimate load as clearly pointed out in Drucker (1954). On the other hand, such a hypothesis allowed the model to be integrated at the Gauss point level

by means of a very efficient numerical procedure based on quadratic minimisation (see Goldfard and Idnani 1983 for details).

3 NUMERICAL ANALYSES

3.1 *Geometry, boundary and initial conditions, modelling of the excavation*

The geometry of the numerical model is shown in Figure 1. The coordinate system is defined such that x is the distance from the tunnel axis in the horizontal direction and z is the depth below the ground surface.

The tunnel is located at a depth of $z_0 = 20$ m and is characterised by a diameter $D = 10$ m. It is excavated in a homogeneous layer of medium consistency clay with the ground water level coincident to the ground surface. The assumed value of K_0 is 0.593. All the simulations of the excavation process are performed in undrained conditions.

The masonry structure represents a typical ancient wall characterised by a width of 40 m, an height of 5 m and a thickness of 1 m. The principal plane of the structure is parallel to the tunnel section. The offset distance between the centre of the wall and the tunnel centre line, i.e. its eccentricity, is equal to 20 m: its right corner has the same x-coordinate as the tunnel axis.

The numerical study is performed by the Finite Element Program Abaqus. The mesh is composed by 8-node quadrangular plane strain elements for the soil and 4-node quadrangular plane stress elements for the masonry. This latter assumption is considered necessary when modelling the problem in 2D, as plane strain elements, if assumed for the wall, would induce a non realistic enhancement of its stiffness.

The excavation of the tunnel was simulated by de-activating the soil elements inside the tunnel section, by replacing these elements with equivalent nodal forces at the tunnel boundaries and by progressively reducing these nodal forces to simulate the tunnel face advancement. Prior to these stages, activation of gravity was reproduced.

In the numerical analyses the reduction of the nodal forces was performed by imposing decrements equal to 5% or smaller near failure conditions.

3.2 *Soil and masonry parameters*

The mechanical parameters adopted for the masonry structure in the numerical simulation are: $\gamma = 15$ kN/m^3, $a = 8$ cm, $b = 32$ cm, $E_b = 3.18$ GPa, $\nu_b = 0.23$, $K_n = 3060$ MN/m^3, $K_t = 1280$ MN/m^3 $c = 5$ kPa and $\phi = 31°$. E_b and ν_b indicate the Young modulus and the Poisson ratio, respectively.

The soil parameters are indicated in Figure 1.

4 NUMERICAL RESULTS

4.1 *Numerical results: Free-field analysis*

Figure 2 shows the values of volume loss obtained for increasing percentage of unloading in the two analyses. In both cases the curves indicate an initial linear trend, followed by a non-linear one for unloading larger than about 20%. The collapse of the tunnel is achieved for unloading in excess of 55% in the free-field analysis and of 43% in the analysis with the masonry structure.

Figure 3 shows the free-field surface settlements for values of the volume loss, V_L, equal to 0.68% and 2.28%. The first value is considered typical for a good performing EPB excavation while the

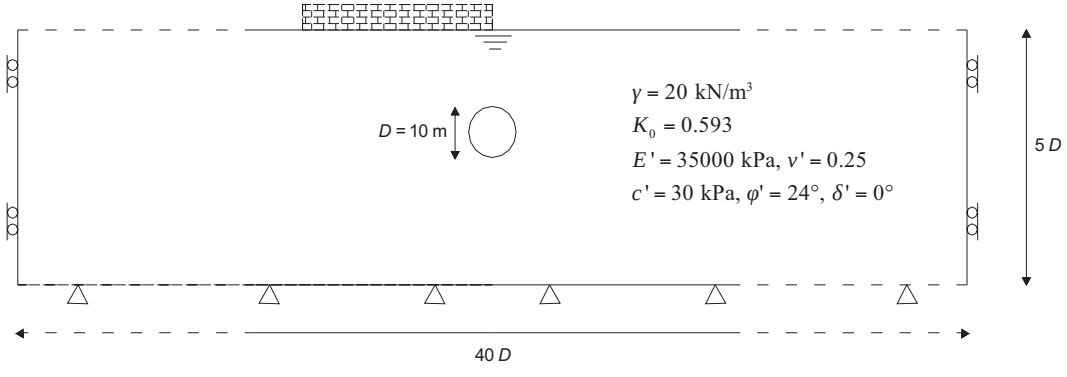

Figure 1. Geometry of the problem and soil parameters adopted in the numerical analyses.

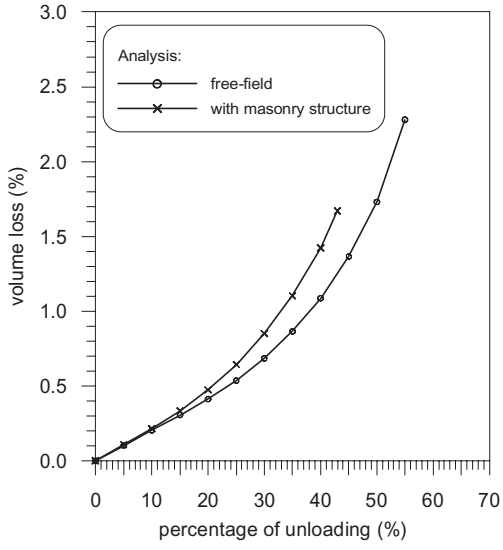

Figure 2. Volume loss against percentage of unloading.

second is closer to the failure conditions for the problem under study. A volume loss of 0.68% is obtained in the free-field analysis applying an unload of the nodal forces equal to 30%. The corresponding percentage of unloading to achieve a volume loss of 2.28% is equal to 55%.

The maximum settlement calculated in the numerical analysis for a volume loss of 0.68% underestimates those predicted by the Gaussian distributions (Peck 1969) for parameters $K = 0.6$ and $K = 0.7$. In addition, the settlements predicted by the numerical analyses produce wider subsidence profiles as compared to those associated with the Gaussian distributions.

As expected, the accordance between the numerical results and the empirical predictions improves in the case of $V_L = 2.28\%$, given the larger amount of plastic behaviour involved: the resulting maximum surface settlement is close to the one estimated by the Gaussian distribution for $K = 0.7$. The comparison between the profiles of the empirical and numerical solutions shows that these latter produce narrower subsidence profiles but non-zero values of the settlements far from the tunnel axis of symmetry.

4.2 *Numerical results: Analysis with masonry structure*

Figure 4 shows the deformed mesh for the stages of gravity application, excavation and application of equivalent nodal forces and for different percentage of forces unloading (the magnification factor of the deformed mesh is the same in all figures). The results of the free-field analysis are reported on the left column while those relative to the analysis with the masonry structure are illustrated in the right one.

The activation of gravity was performed by a sequential activation of soil gravity first, followed by that of the structure. At the end of the stage, the structure is inflected symmetrically with respect to its centre.

The stage where the soil and water in the tunnel are de-activated and substituted with equivalent nodal forces does not produce significant mesh deformation, as expected.

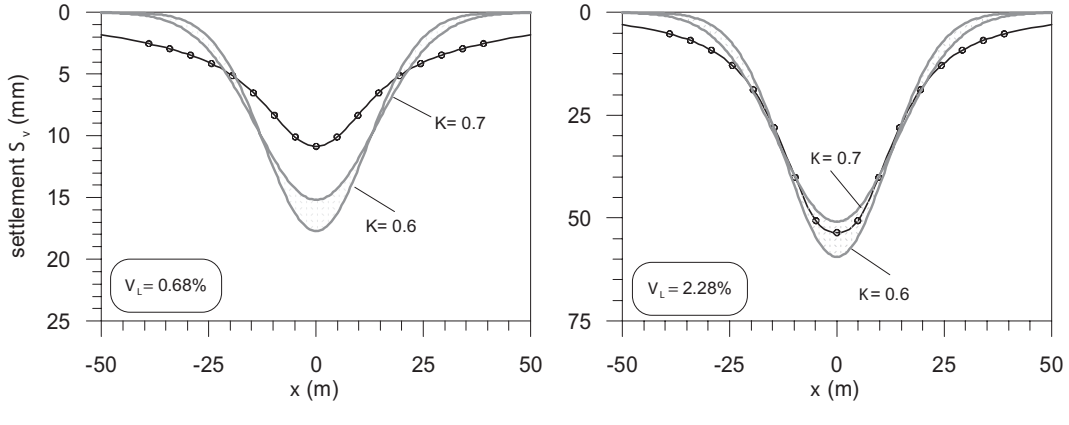

Figure 3. Net vertical settlement for a volume loss of 0.68% (on the left) and 2.28% (on the right) for the free-field analysis and comparison with empirical solutions.

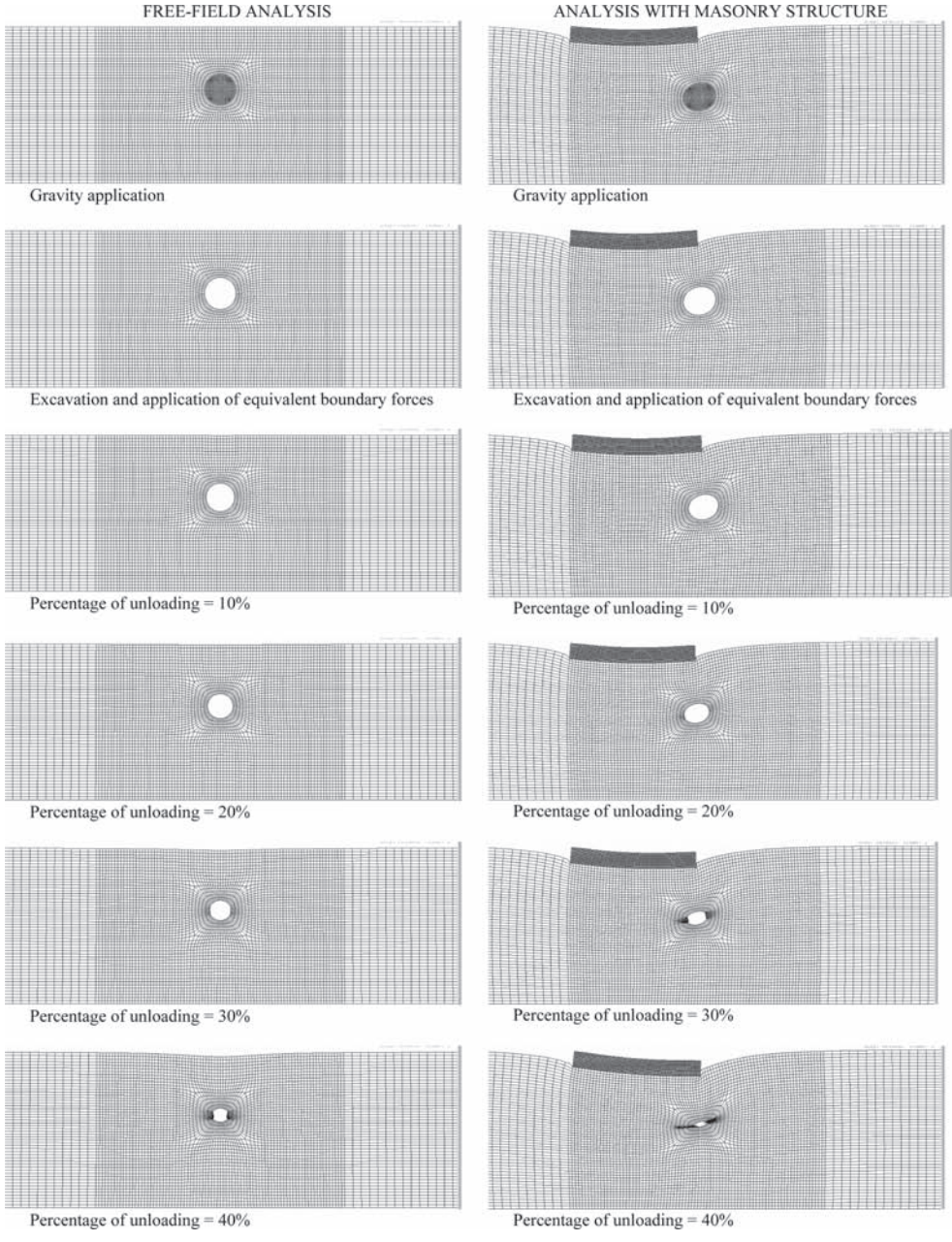

Figure 4. Deformed mesh for different percentage of unloading in free-field analysis (on the left) and in analysis with masonry structure (on the right).

In the free-field analysis, the increasing percentage of nodal forces unloading leads to a progressive deepening of the subsidence profile, which is symmetric with respect to the tunnel axis. Also, due to the relatively low value of K_0, the tunnel section deforms into an ellipse characterised by a horizontal maximum axis. Figure 5 plots the deformed mesh for this analysis at a percentage of unloading of 55%, right before the collapse.

The corresponding analysis with the masonry structure displays a completely different pattern for tunnel and soil deformation, largely influenced

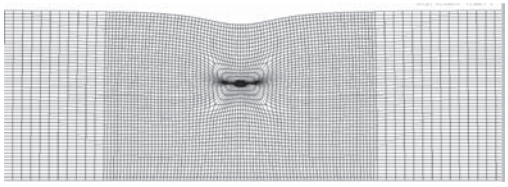

Figure 5. Deformed mesh for a percentage of unloading of 55% in free-field analysis.

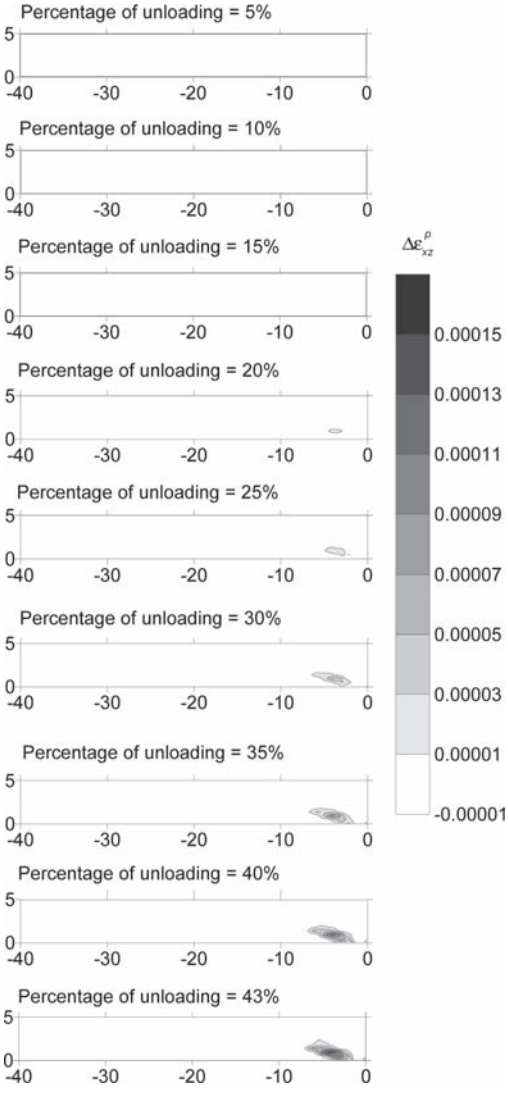

Figure 6. Increment in shear plastic strain in the masonry structure for different percentage of unloading.

by the pre-existing deformation distribution due to the gravity application. In this case, the tunnel section assumes an elliptical shape characterised by a diagonal orientation of the axes. As a consequence of tunnel excavation, the structure shows a displacement pattern characterised by the superposition of a prevailing rigid rotation towards the tunnel centre and a shear driven deformation concentrated in its right end side.

Figure 6 shows in detail the accumulation of plastic shear strain within the masonry structure. In the figure, the incremental plastic strains are evaluated with reference to the stage of gravity application in the structure. For increasing percentage of unloading, the incremental plastic strain tend to concentrate on the right end side of the masonry wall, consistently with the above discussed displacement pattern of the structure.

Figure 7 shows the net vertical displacements (i.e. calculated with reference to the stage of deactivation of the tunnel elements and application of equivalent boundary forces) for the free-field analysis (on the left) and for the analysis with the masonry structure (on the right). The main features of the free-field analysis results were already discussed with reference to Figure 3. The presence of the masonry structure significantly modifies the distribution of vertical displacement both in terms of shape and intensity. The presence of the structure produces a sharp modification of the underneath subsidence profile, leading to a downward bended curvature. Moreover, comparing the results of the two analyses at corresponding percentages of unloading shows that the one with the structure is characterised by larger settlements, not only beneath the structure but also for $x > 0$: this should be related to weight of the wall. Finally, at $x = 0$ the vertical displacement profile is characterised by a strong discontinuity, caused by the marked difference in stiffness between the soil and the wall.

5 CONCLUSIONS

The paper describes some preliminary results of an ongoing research dedicated to the analysis of the interaction between the excavation of shallow tunnels in urban areas and the pre-existing ancient masonry structures located at the surface.

The study, conducted with the Finite Element code Abaqus, was performed in 2D conditions assuming plane strain and plane stress conditions for the soil and the structure, respectively. As such, the analysed problem is that of an ideal tunnel excavated under a masonry structure, this latter being characterised by its principal plane oriented perpendicularly to the tunnel axis.

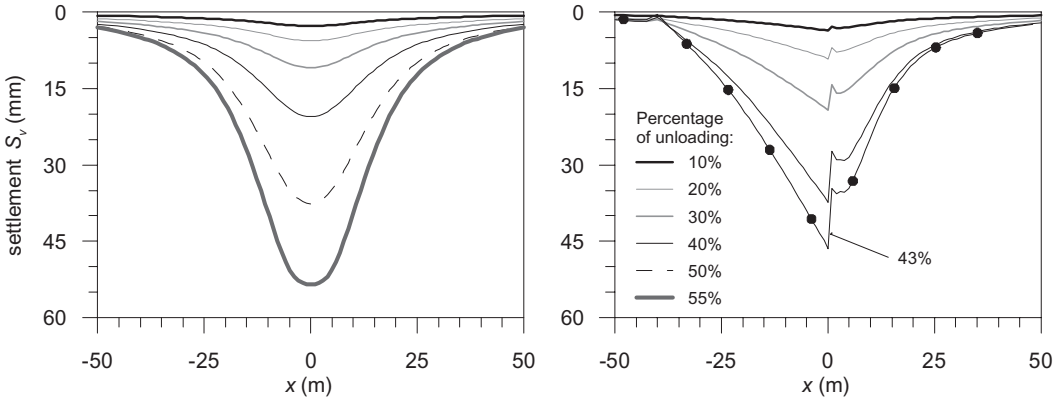

Figure 7. Comparison of net vertical settlement for free-field analysis (on the left) and analysis with masonry structure (on the right) for different percentage of unloading.

The modelled structure represents an ancient masonry wall, schematised as a block structure with periodic texture. Its continuum behaviour at the macro-scale (i.e. at the scale of the analysis) was derived by means of a homogenisation procedure based on relatively simple assumption at the local scale (i.e. at the scale of blocks and joints). The resulting model is characterised by a non-linear anisotropic mechanical response. The soil, a medium consistency clay, was modelled by a simple elasto-plastic constitutive assumption.

The numerical results were able to capture the main features of the soil-structure interaction, including the modifications in the subsidence profile and the related deformative pattern in the structure. In particular, due to the eccentricity of the wall with respect to the tunnel centre, plastic strain tend to accumulate in the right end side of the masonry structure, which is closer to the excavated zone.

The presence of the structure enhances the excavation-induced settlements and accelerates the collapse process, as compared to what predicted in free-field conditions.

The next steps in the research activity will be addressed to the following points:

– a 3D schematisation of the problem will be implemented in order to account for different tunnel-wall relative positions and to improve the simulation of tunnel excavation and the associated subsidence phenomena;
– the soil will be modelled with an advanced constitutive model, capable of describing the early irreversible and highly non-linear behaviour of natural soils, so as to improve the prediction of tunnelling-induced displacements;
– a non-associate flow rule will be included in the formulation of the masonry constitutive model to avoid the overestimation of its collapse load. Moreover, a complete multi-scale approach will be implemented in order to localize the plastic strain calculated at the macro-scale—in the homogenised medium—into the corresponding relative displacements at the scale of blocks and joints. This will allow a more direct evaluation of the damage associated to tunnel excavation.

ACKNOWLEDGEMENT

Thanks are due to Mr. Marco Ferrandino for the help provided during the final computational stage.

REFERENCES

de Buhan, P. & de Felice, G. 1997. A homogenisation approach to the ultimate strength of brick masonry. *J. Mech. Phys. Solids* 45(7): 1085–1104.

de Felice, G., Amorosi, A. & Malena, M. 2009. Elasto-plastic analysis of block structures through a homogenization method. *International Journal for Numerical and Analytical Methods in Geomechanics* 34: 221–247.

Drucker, D.C. 1954. Coulomb friction, plasticity and limit loads. *ASME J. Appl. Mech.* 21: 71–74.

Goldfard, D. & Idnani, A. 1983. A numerical stable dual method for solving strictly convex quadratic programs. *Mathematical Programming* 27: 1–33.

Koiter, W.T. 1960. General theorems for elastic–plastic solids. In N. Sneddon and R Hill (eds), *Progress in Solids Mechanics*: 165–221. Amsterdam: North–Holland.

Peck, R.B. 1969. Deep excavations and tunneling in soft ground. 7th int. Conference on Soil Mechanics and Foundation Engineering, State of the art volume, *Proc. Int. Symp.*: 225–290.

This page intentionally left blank

Geotechnical Aspects of Underground Construction in Soft Ground – Viggiani (ed)
© 2012 Taylor & Francis Group, London, ISBN 978-0-415-68367-8

The dynamic behavior of shield circular tunnels and surrounding granular soils during earthquakes

M. Hatambeigi
Tarbiat Mo'alem University, Tehran, Iran

Y. Pashang Pisheh
Amirkabir University of Technology, Tehran, Iran

M. Pashang Pisheh
Islamic Azad University, Yazd, Iran

ABSTRACT: In this paper, the seismic behavior of shield circular tunnels and surrounding granular soils during earthquake excitations is investigated. In order to perform this study, a 2D dynamic Finite Element model was established applying the FEM. Moreover, to determine the influence of the surrounding soil and concrete lining characteristics, a parametric study was carried out on the essential parameters of the soil and the concrete lining. It has been shown that the ground surface settlements and the peak point of the tunnel deformations decrease with the increase of the soil stiffness, cohesion, and damping ratio. Furthermore, an increase of the concrete lining thickness will decrease the settlement of the upper soil mass and the tunnel lining deformation, whereas it will increase the magnitude of the internal forces of the lining elements.

1 INTRODUCTION

In recent years, the ever-increasing growth of the cities and consequently development of the transportation and communication routes like the subway and other underground structures has lead to especial and extensive studies regarding underground spaces. In addition to the existing problems in analysis and design of the tunnels under static loadings, evidences about the damages of such structures during earthquakes duly reminds the necessity of investigating the dynamic behavior of such underground structures. Figure 1 shows the damaged conditions observed at the Uonuma tunnel in Japan during the 2004 Mid Niigata earthquake, in which the concrete lining was broken to fall off to a track (Shimizu & Suzuki 2007).

Hence nowadays, in addition to considering the static conditions in the design of the section and lining of tunnels, identifying the factors involved in the seismic response of such structures and their influence on the structural specifications of the tunnels is of special importance (Goodman 1989, Kirzhner & Rosenhouse 2000).

In the present study, with making use of Finite Element Method, the seismic behavior of a tunnel with 8 meters diameter during an earthquake in plane strain conditions is investigated and then, the influence of such loading conditions on the resulting stresses and deformations has been analyzed. Finally, through changing some of the essential specifications of the existing soil and concrete lining of the tunnel, the effects of those parameters are assessed.

2 THE NUMERICAL MODELING

In order to perform the current study, a two-dimensional Finite Element model was prepared to simulate the static and dynamic behavior of circular shield tunnels. The corresponding numerical model contains an 8-meter-diameter tunnel centered at 12 m depth of a sandy soil with medium density. To generate the model, after excavation of the corresponding tunnel and installation of the tunnel lining, the volume loss has been simulated by applying the contraction to the tunnel lining. This contraction was defined in the staged construction calculation in the magnitude of 2 percent. Figure 2 illustrates the Finite Element mesh and the position of the mentioned tunnel section.

The materials chosen for modeling the soil layer and tunnel lining were considered as sandy soil and normal structural concrete. The strength and behavioral properties of the soil used in the analyses have

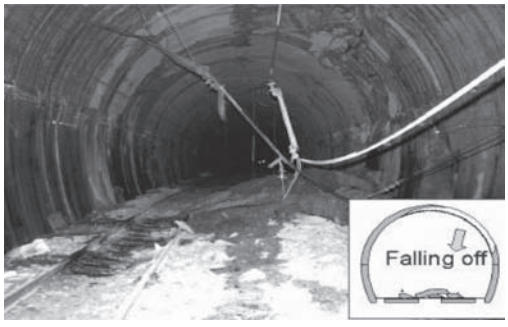

Figure 1. Damage of the Uonuma tunnel.

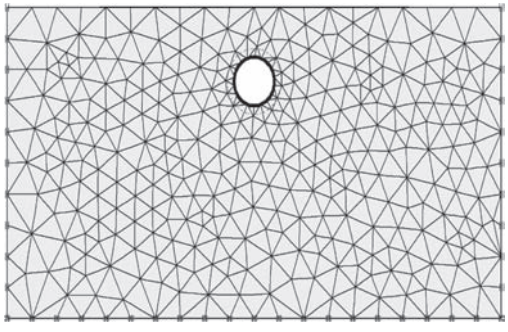

Figure 2. Finite Element model used in the static and dynamic analyses.

Table 1. Mechanical properties of the sandy soil layer material.

γ_{dry}	E_{static}	$E_{dynamic}$	Φ	C	Ψ
kN/m^3	MPa	MPa	deg	kPa	deg
17	30	90	35	0	5

γ_{dry} is the dry unit weight, E is the module of elasticity, Φ is the internal friction angle, C is the cohesion parameter, and Ψ is the dilation angle.

Table 2. Dimentional and mechanical properties of the concrete lining.

t	$E_{Concrete}$	EA	EI
mm	GPa	kN/m	kN.m^2/m
200	20	4E + 6	1.33E + 4

t is the concrete lining thickness, E is the concrete Young modulus, A is the area, and I is the moment of inertia of the concrete element section.

been assigned as the medium density sandy soil. In addition, modeling the stress-strain behavior of the surrounding sandy soil was carried out with simulating this material as an Elasto-Plastic material with a Mohr-Coulomb criterion and a non-associated flow rule. This constitutive model is a conventional model commonly used to represent the stress-strain behavior and corresponding shear failure in soils and rocks. Simulation of concrete lining behavior in analyses was made considering Elastic model as well. The mechanical properties of the granular soil used in the analyses as well as the behavioral and dimensional properties of the concrete lining elements are represented in Tables 1, 2 respectively.

3 STATIC ANALYSES

At first, it is necessary that the initial vertical and horizontal stresses in different points of the model be calculated and attributed to the model as the existing initial conditions. These conditions are presented taking into account the specific weight of the materials and applying the lateral coefficient of earth pressure at-rest (K_0). Then, considering the excavation and construction steps, the stress and deformation values at the end of each stage have been calculated; the results of which have been given in Figures 3–5.

As it can be seen in Figure 3, excavation of the tunnel in the depth of the 12 m will result in some settlement in the ground surface and the tunnel vertex. Diagrams of the axial forces and the resulting bending moment created in the tunnel lining due to the static overburden pressure have been shown in Figure 5.

4 SIMULATION OF THE EARTHQUAKE GROUND MOTION

In order to perform the dynamic analyses of the model, the ground acceleration time history of El-Centro earthquake (1940) was employed. The simulated horizontal acceleration time history is presented in Figure 6. As it can be seen, the peak

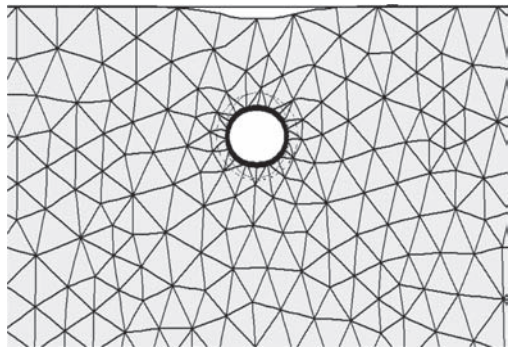

Figure 3. The close view of the resulted deformations after the excavation of the tunnel and installation the tunnel lining (Maximum settlement of the peak point of the tunnel: 24 mm).

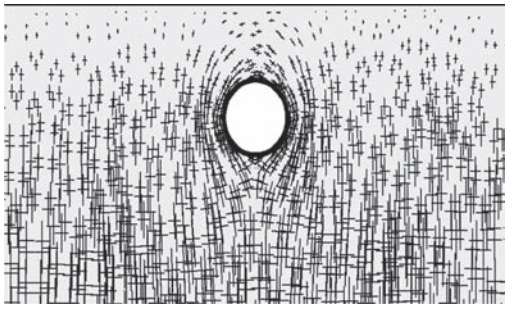

Figure 4. Stress vectors after the excavation of the tunnel and installation the tunnel lining.

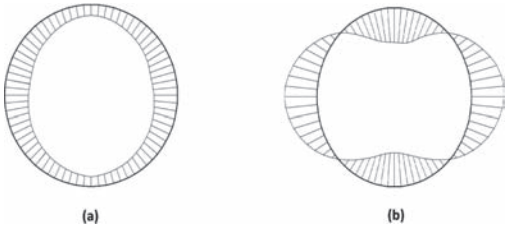

Figure 5. Diagrams of (a): Axial force and (b): Bending moment in the tunnel concrete lining due to the overburden loads (Maximum axial compressive force: 115.3 kN/m and Maximum bending moment: 44.2 kN.m/m).

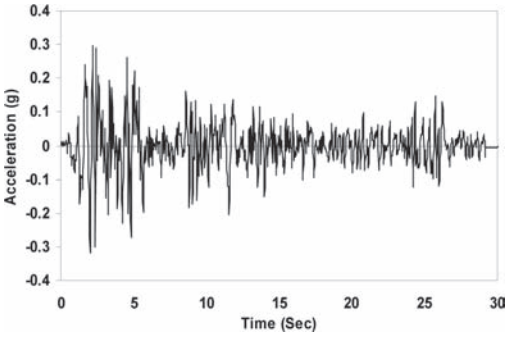

Figure 6. Horizontal acceleration time history based on El-Centro earthquake.

horizontal component of the ground accelerations is 0.319 g.

To apply the earthquake excitation, the input ground motion at the basement of the model was defined by means of the dynamic multipliers provided in the corresponding Finite Element program. These multipliers are a set of scaling factors on the prescribed unit displacement applied on the bottom of the model to produce the actual dynamic load magnitudes such as displacements, velocities, and accelerations (Richart & Woods 1970). Therefore, the applied loading will result in deformations

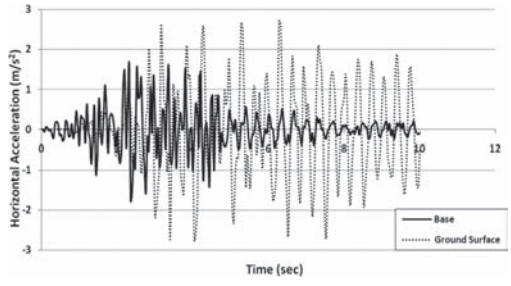

Figure 7. Time-horizontal acceleration curves at the basement of the model and ground surface.

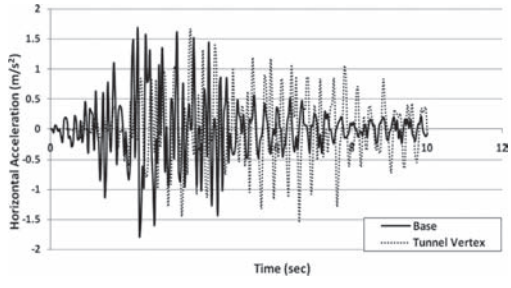

Figure 8. Time-horizontal acceleration curves at the basement of the model and top point of the tunnel.

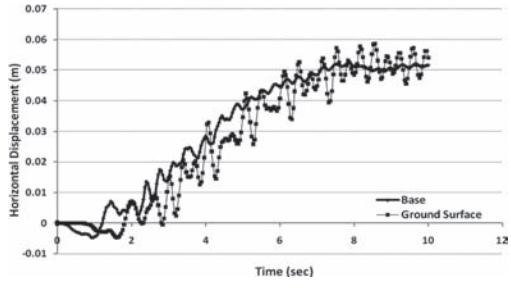

Figure 9. Time-horizontal displacement curves at the basement of the model and ground surface.

in the soil materials as well as in the tunnel lining. Figures 7–10 show respectively time-acceleration and time-displacement curves created during the dynamic analyses of the corresponding model at the basement, ground surface, and the tunnel vertex. As it can be seen in Figures 7, 8, the peak accelerations at the top of the model are much larger than the basement accelerations from the earthquake itself. Moreover, considering Figures 9, 10, it could be concluded that, due to the residual deformations resulting from the nature of geomaterials, the values of the settlements will not fall back into the condition before applying the dynamic loads. In other words, consideration of the curves shows

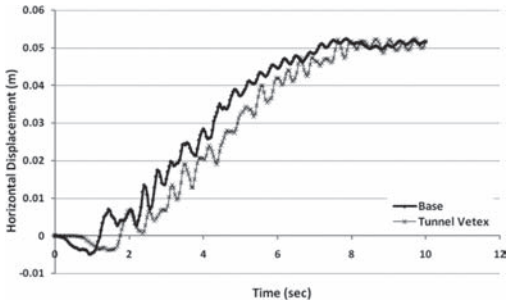

Figure 10. Time-horizontal displacement curves at the basement of the model and top point of the tunnel.

Table 3. The stiffness parameters of the sand materials used in the studies.

Material type		E_{sta} MPa	G_{sta} MPa	E_{dyn} MPa	G_{dyn} MPa	V_s m/s	V_p m/s
Sand	(type1)	30	11.5	90	34.6	141	264
Sand	(type2)	40	15.4	110	42.3	156	292
Sand	(type3)	50	19.2	140	53.8	176	329

E is the Young modulus, G is the shear modulus, and V is the wave velocity in the soil material.

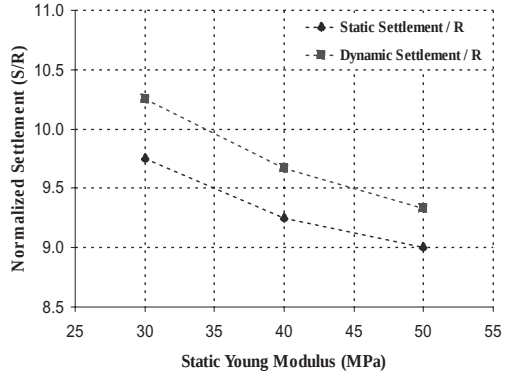

Figure 11. The effect of the soil material stiffness on the normalized settlement of the tunnel lining.

that at the end of each cycle, the displacement values of the desired points are increased to some extent and the point will not return to the situation before that cycle. In fact, some residual deformation will remain in the desired point.

5 PARAMETRIC STUDIES

In this section, various studies have been performed to investigate the effect of the surrounding soil and tunnel lining properties on the underground structure response during El-Centro earthquake excitation. It must be noted that, throughout this series of analyses, the soil and the tunnel lining structure specifications have been considered as equal to the same parameters presented already in Tables 1, 2. In other words, in any one of the cases, only the effect of the particular parameter on the analysis results has been assessed through changing the corresponding parameter and maintaining other parameters constant.

5.1 *The effect of the soil material stiffness on the tunnel response*

By changing the soil material stiffness parameter, elasticity modulus, around the tunnel and consequently changing the shear modulus as well, the effect of this parameter on the deformation of the upper soil layer as well as the settlements and internal forces created in the tunnel lining has been investigated. The elasticity modulus of the sand material used for static and dynamic analyses performed in this stage of the studies has been given in Table 3 (Kramer 1995, Das 2002).

Figure 11 shows the effect of the soil Young modulus on the maximum values of the settlements appeared in the peak point of the tunnel, normalized to the radius of the tunnel. As it is observed, increasing the stiffness of the soil material around the tunnel, the settlement occurred at the peak point of the tunnel is decreased. Furthermore, considering Figures 12, 13 showing the material stiffness changes effect on the internal forces magnitudes induced in the tunnel lining, it can be inferred that increasing the Young modulus of the soil material, the maximum axial force and bending moment produced in the concrete tunnel lining are decreased in both static and dynamic conditions.

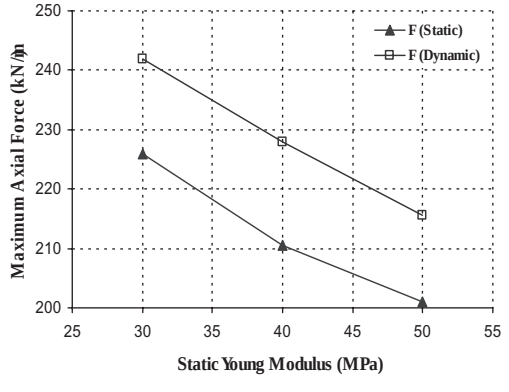

Figure 12. The effect of the soil material stiffness on the magnitude of the axial force of the tunnel lining.

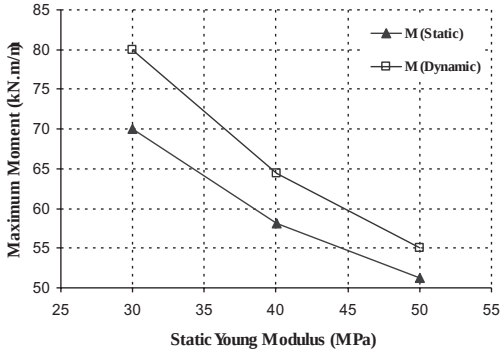

Figure 13. The effect of the soil material stiffness on the magnitude of the bending moment of the tunnel lining.

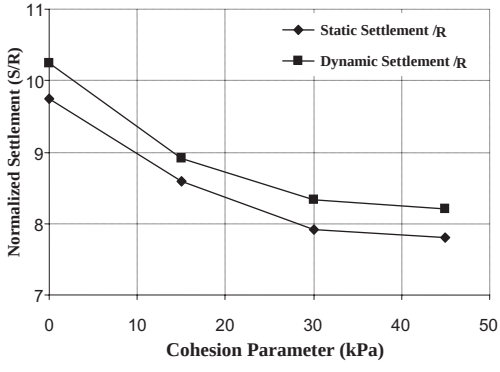

Figure 14. The effect of the soil cohesion on the normalized settlements of the tunnel lining.

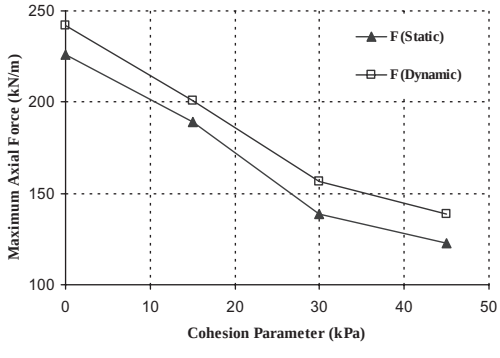

Figure 15. The effect of the soil cohesion on the axial force of the tunnel lining structure.

5.2 *The effect of the soil cohesion parameter on the tunnel response*

In order to investigate the soil shear strength parameter's effect on the settlements and internal forces created in the tunnel lining, the soil cohesion parameter effect has been studied through taking into account of the cohesionless sandy soil material as well as the mixed materials in the desired numerical model. Figures 14–16 demonstrate the settlement variations of the peak point of the tunnel and the internal forces created in the tunnel lining in accordance with the cohesion changes of the surrounding soil. As it is shown, increasing the soil cohesion parameter magnitude, the settlement level of the peak point of the tunnel is decreased; the effect of which could be more obviously seen in low cohesions. Moreover, it can be observed that by the increase of this parameter, the maximum value of the axial forces and the bending moment created in the concrete lining structure will decrease in the static and dynamic analyses of the corresponding numerical model.

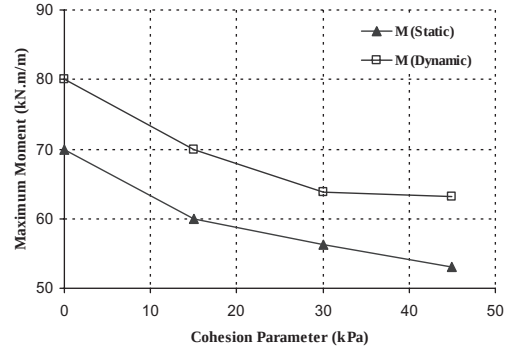

Figure 16. The effect of the soil cohesion on the bending moment of the tunnel lining structure.

5.3 *The effect of the soil material damping on the tunnel behavior*

In this series of analyses, the physical damping resulted from viscous effects existing in the materials has been considered in the model using the Rayleigh damping. The relation of this kind of damping is of matrix type in which a damping matrix (C) with its matrix components of mass (M) and stiffness (K) is used as follows:

$$C = \alpha M + \beta K \tag{1}$$

Where α and β are the mass and stiffness damping ratio constant respectively.

So in analyses made in this stage, attempt has been made to study the material damping changes effects on the deformations and internal forces created in the model, considering sandy materials with different damping ratios. It must be noted that, the dynamic analyses made in this part of the study contain three values of Rayleigh damping ratios as follows:

1 Without material damping: $\alpha = 0.0$ & $\beta = 0.0$
2 $\alpha = 0.001$ & $\beta = 0.05$
3 $\alpha = 0.01$ & $\beta = 0.1$

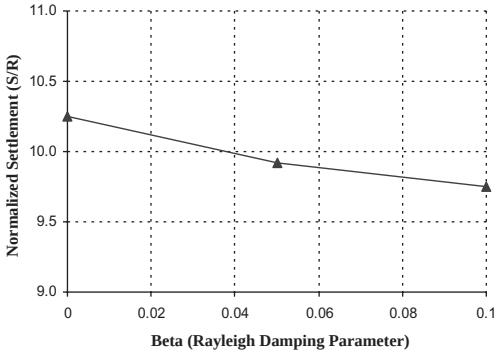

Figure 17. The effect of soil damping on the normalized settlements of the tunnel lining.

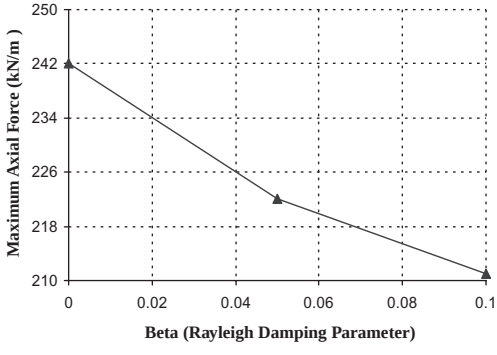

Figure 18. The effect of soil damping on the axial force of the tunnel lining.

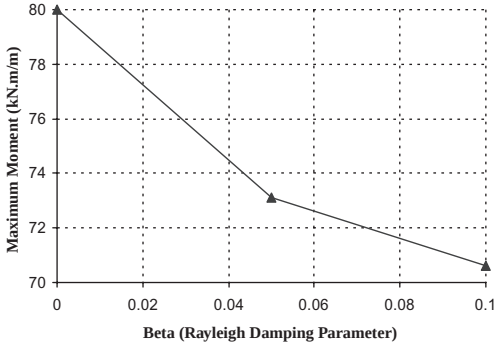

Figure 19. The effect of soil damping on the bending moment of the tunnel lining.

The corresponding analyses results have been illustrated in Figures 17–19. As it is observed, increasing the damping values of the sandy materials around the tunnel, in addition to the decrease in the settlement of the peak point of the tunnel, the internal forces values formed in the concrete lining are also decreased.

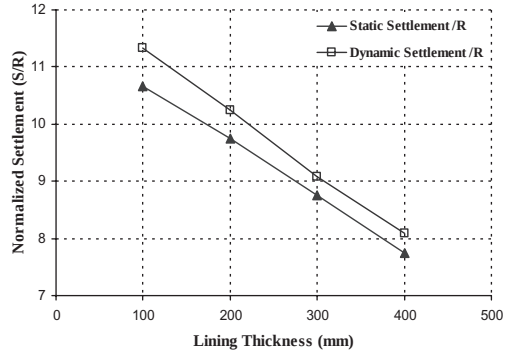

Figure 20. The effect of the lining thickness on the normalized settlements of the tunnel lining.

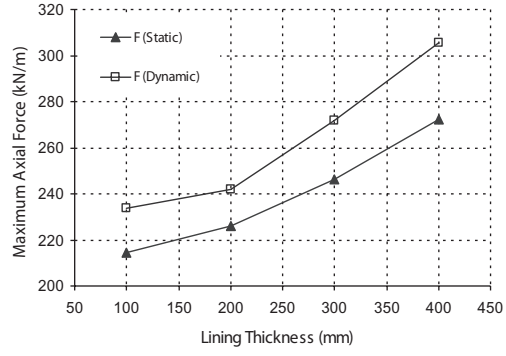

Figure 21. The effect of the lining thickness on the axial force of the tunnel lining.

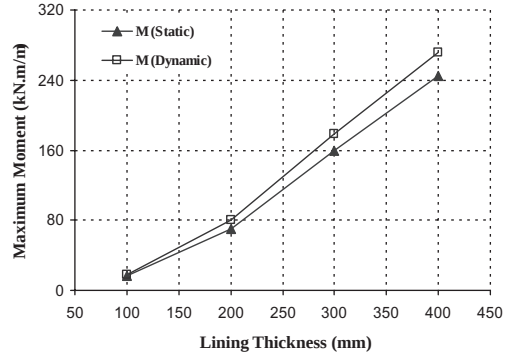

Figure 22. The effect of the lining thickness on the bending moment of the tunnel lining.

5.4 *The effect of the concrete lining thickness on the tunnel response*

In this section, the effect of the lining thickness on the deformations and internal forces appeared in the concrete lining of the underground structure has been investigated. Figure 20 shows the settlement changes

of the peak point of the tunnel with the various thickness of the tunnel lining. As it can be noticed, by the increase in the thickness of the tunnel lining, the vertical settlement of the tunnel vertex is decreased. Moreover, considering Figures 21, 22 reveal that by the increase of the tunnel lining thickness and thereby its stiffness, the maximum absolute values of the axial force and the bending moment increase in both static and dynamic analyses.

6 CONCLUSIONS

In this study, the static and dynamic behavior of an underground structure with circular section during a known earthquake has been investigated. Taking notice of the analyses made, the following can be summarized as the main results of the research:

- During application of the earthquake loading on the base of the model, the maximum accelerations induced at the top of the model get much larger than the accelerations from the earthquake itself. Moreover, due to formation of the residual deformations caused by the soil nature, the occurred settlements values do not fall back into the situation before earthquake excitation. In other words, at the end of each cycle, the displacement value of the location is increased and it will not return back to the situation before that cycle.
- By increasing the elasticity modulus and cohesion parameter value of the soil materials around the tunnel, the settlements, the maximum axial forces, and the bending moment created in the tunnel lining decrease in static and dynamic conditions.
- Increasing the damping magnitude of the soil materials around the tunnel, in addition to the decrease in the settlement in different points of the tunnel, the internal forces values formed in the concrete lining of the tunnel are also decreased.
- By increasing the thickness of the concrete lining of the tunnel and thereby its stiffness, the settlement occurred in the soil and tunnel lining is decreased; meanwhile, the maximum absolute value of the axial force and bending moment in both static and dynamic analyses of the model is increased.

REFRENCES

Das, B.M. 2002. *Principles of Soil Dynamics*. Boston: PWS-Kent Publishing Co.

Goodman, R.E. 1989. *Introduction to Rock Mechanics*. Berkeley: John Wiley & Sons.

Kirzhner F. & Rosenhouse G. 2000. Numerical Analysis of Tunnel Dynamic Response to Earth Motions. *Tunneling and Underground Space Technology* 15 (3): 249–258.

Kramer, S.L. 1995. *Geotechnical Earthquake Engineering*. Upper Saddle River, New Jersey: Prentice Hall Inc.

Richart, F.E. & Woods, R.D. 1970. *Vibrations of Soils and Foundations*. Englewood Cliffs, New Jersey: Prentice-Hall Inc.

Shimizu, M. & Suzuki, T. 2007. Historical damages of tunnels in Japan and case studies of damaged railway tunnels in the Mid Niigata Prefecture Earthquake. *Underground space-The 4th Dimension of Metropolises: Proceeding of the world tunnel congress 2007 and 33rd ITA/AITES annual general assembly, Prague, May 2007*: 1937–1943.

This page intentionally left blank

Geotechnical Aspects of Underground Construction in Soft Ground – Viggiani (ed)
© 2012 Taylor & Francis Group, London, ISBN 978-0-415-68367-8

An investigation into Inclined Struts method as a type of shoring

A. Fakher
Associate Professor, Faculty of Civil Engineering, University of Tehran, Tehran, Iran

S. Sadeghian
Faculty of Civil Engineering, University of Tehran, Tehran, Iran

ABSTRACT: Underpinning and shoring are two conventional forms of temporary supports given to the buildings next to excavations. "Inclined Struts", as a type of retaining structure which can be used to support buildings next to excavations, can be categorized as underpinning and shoring. In this method, some inclined struts connect the bottom of the excavation to the footing of adjacent buildings. Despite the excessive use of the inclined struts in years, they have been poorly investigated. Herein, the most prevalent construction use of the "Inclined Struts" are simulated using 3 dimensional FDM and the excavation-induced displacements of buildings caused in each method are compared. The presented paper is in the continuation of a previous two dimensional study undertaken by the authors. The current study indicates that excavation-induced displacements of buildings considerably depend on the sequences of excavations. In case an excavation is done in three suggested stages, the least excavation-induced displacement will occur. Indeed, the excavation is firstly done up to the final desired depth but a premital soil margin is remained next to the wall of the excavation. Afterwards, struts are installed and finally the excavation is completed. This paper also discusses the number, position and sequences of installation of struts which results in the least excavation-induced displacements.

1 INTRODUCTION

Excavation-induced displacement caused by underground construction is of great importance in planning the excavations. Particularly, in urban areas it would be impossible to estimate how much of allowable displacement of structures has been done before starting the excavation construction. During excavation and support of open-cuts, changes in the state of stress in the ground mass around the excavation and loss of ground is inevitable. Due to the changes in stress and the ground losses, vertical and horizontal ground movements occurs in the surrounding of excavation, which consequently results in rotation, deformation, and possibly some levels of damages in buildings and facilities next to excavation.

Shoring and underpinning are two frequently-used methods in all over the world. Shoring is a form of temporary support which can be given to existing buildings adjacent to excavation to avoid damage to neighbouring structures. Similarly, underpinning is another temporary support for existing buildings next to excavations. Generally, the main object of underpinning works is to transfer the load carried by a foundation from its existing bearing level to a new level at a lower depth.

"Inclined Struts Method" as a type of retaining system, which can be categorized as a type of shoring or underpinning, is widely used in Iran. Despite the excessive use of "Inclined Strut" method, adequate researches have not been conducted about it. Besides, International references have not adequately point out to this method. Moreover, there are not adequate international resources concerning the mechanism of shoring and underpinning.

Conventionally, there are some differences in using inclines strut in excavation next to buildings. These differences are in the number as well as order of excavation's stages. The aim of this paper is to introduce different construction methods and then compare them to find out the method which leads to the least excavation-induced displacements.

The presented three dimensional study of inclined struts is in the continuation of a previously published research on two dimensional numerical study of inclined struts (Sadeghian & Fakher, 2010).

2 THE USE OF INCLINED STRUT IN EXCAVATION

2.1 *Inclined struts in literature*

Inclined Strut can be considered as shoring or underpinning depending on load transfer mechanism. Shoring is a form of temporary support given to excavations or buildings next to excavations to

prevent excessive deformation of excavation wall or building next to excavation. There are three basic systems of shoring, used to support existing structures next to an excavation named:

I. Dead shoring
II. Raking shoring
III. And Flying shoring

Dead shoring system is used to carry vertical loadings from building next to excavation to the bottom of excavation. In Dead Shoring a vertical support usually installed under the foundation of existing structures. In this type of shoring a measure should be applied to excavate the soil beneath some of the foundations of the buildingBut raking shoring system is used to support a combination of vertical and horizontal loadings. Flying shoring system could be considered as an alternative to raking shoring to give a clear working space at ground level. (Chudley & Greeno, 2006)

Underpinning is another kind of temporary support for buildings next to excavations. Underpinning caries a part of the foundation load to a lower depth where can be the bottom of the excavation. (Chudley & Greeno, 2006)

The use of Inclined Struts method is a traditional method widely used to support buildings next to not very deep excavations. In this method, wooden or steel "struts" are used to connect the foundation of adjacent building to the bottom of excavation (as shown in Fig. 1), so Inclined Struts can be categorized as raking shoring method or underpinning.

Previous studies regarding inclined struts, tried to find the best place for inclined strut to be connected to the building next to excavation. In fact, they used two dimensional analysis and simulated excavation configurations shown in Figure 1. As can be seen in Figure 1, struts were assumed to connect the bottom of the excavation to the first floor, the wall or the foundation of the adjacent building, or they were assumed to connect two adjacent footing of neighboring buildings (Sadeghian & Fakher, 2010). These studies concluded that Configuration shown as Figure 1-b results in the least excavation-induced displacement and in this respect it is advisable to connect the bottom of the excavation to the foundation of neighboring building in case inclined struts applied as retaining system to support building next to excavation.

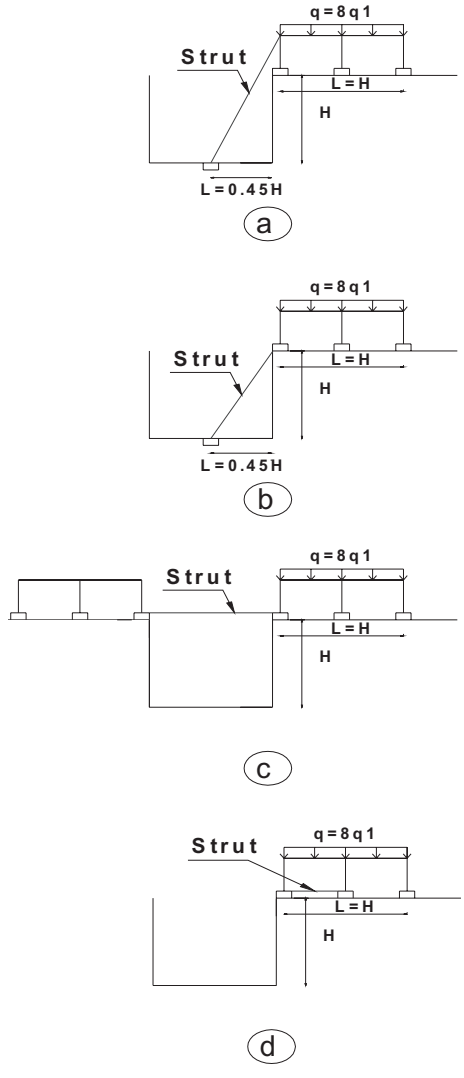

Figure 1. Common configurations of excavation procedure used in traditional shoring method which are investigated in previous studies. (a) Inclined struts connected to the first floor. (b) Inclined struts connected to the footing. (c) flying shoring. (d) Two adjacent footing of neighbouring building are fully connected. (Sadeghian & Fakher, 2010).

2.2 *Combination of vertical and horizontal displacement to assess damages*

To assess damages occurred in buildings next to excavations both vertical and horizontal displacements should be considered. Firstly, settlement damage to masonry buildings was addressed by Burland and Wroth (1974) and Burland *et al.* (1977), who introduced a damage classification system. Later, Boscardin and Cording (1989) illustrated the importance of horizontal displacement in initiating damage. Figure 2 illustrates the combination of angular distortion; define in this case as the maximum change in slope angle of the "beam" or "wall", and horizontal strain. Damage categories were based on the criteria suggested by Skempton and Macdonald (1956) and work of the

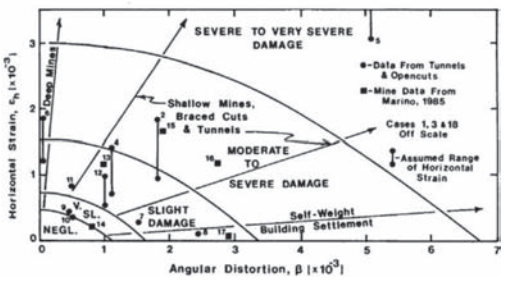

Figure 2. Relationship between angular distortion, horizontal strain, and damage category Boscardin and Cording (1989).

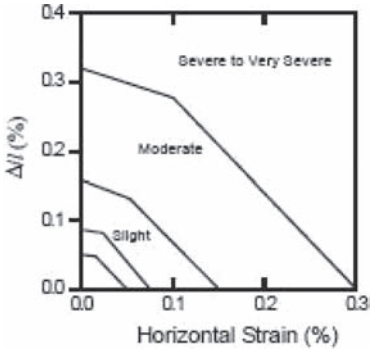

Figure 3. Relationships between damage category, horizontal strain and deflection ratio (Δ/L) which is defined as maximum deflection between the beam deflection line and the straight line between the two end points (chord) divided by the chord length, Burland (1995).

U.K. National Coal Board (1975). Figure 2 was derived for building with length (L) to height (H) ratio of 1 in terms of horizontal strain and angular distortion (β). In fact, angular distortion is the maximum change in slope along the beam or the slope at the supports.

A later modification of the critical strain approach by Burland (1995) induced lateral strain based on the work of Boscardin and Cording (1989) and adapted different values of critical strain to reflect different damage categories, as illustrated in Figure 3. However this approach was limited to the case of $L/H = 1$.

2.3 *Governing mechanism*

As proposed by the authors (Sadeghian & Fakher, 2010) predominant mechanisms of Inclined Struts to support buildings next to excavation are as follows:

a. Due to the excavation, the bearing capacity of the foundations next to it reduces. Using inclined struts, a portion of building loads conveys to the bottom of the excavation. So inclined struts conveniently compensate the bearing capacity reduction.
b. Inclined and horizontal Struts restrain the excavation-induced horizontal displacement and also tensile strain in buildings next to excavation. Therefore, it reduces the damage of the building as Boscardin and Cording (1989) presented a graph, shown in Fig. 6, which shows the importance of horizontal displacement.

3 NUMERICAL ANALYSIS

Conventionally, if inclined struts is used to support the building next to excavation, excavation will be done in several stages. To find the best construction method in terms of the number of stages in which full excavation should be divided as well as the order of chosen stages, numerical analysis are used in the present study. A number of most common configurations of construction methods regarding applying inclined struts to support buildings next to excavation, are modelled using three dimensional Fast Lagrangian Analysis of Continua, FLAC (Itasca, 2002).The results are compared and ones which leads to the least excavation-induced deformation introduces.

3.1 *Numerical simulation and input data*

The inclined struts and adjoining building are modelled using beams (a type of structural element in FLAC). Mohr-Coulomb constitutive model has been chosen for soil elements. The parameters of soil and structural elements have been shown in Table 1.

Table.1. The parameters of soil and structural elements used in numerical modelling.

Parameters	Units	Amount
Moment Interia	m^4	4.80E-05
Beam cross section	m^2	4.80E-03
ν	–	0.35
γ_{soil}	kN/m^3	20
H	m	8
E_{steel}	kN/m^2	2.0E+08
E_{soil}	kN/m^2	8.0E+04
C	kN/m^2	20
ϕ	–	35

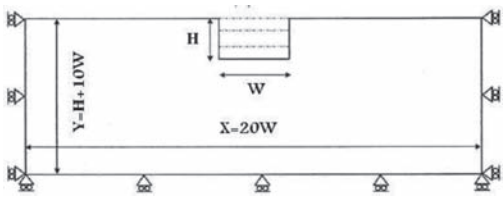

Figure 4. Boundary condition of the numerical model.

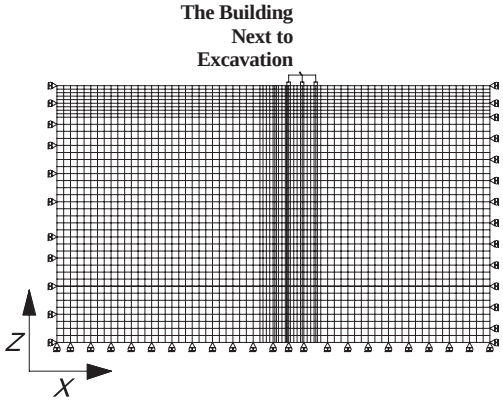

Figure 5. Discretisation of the medium for modelling.

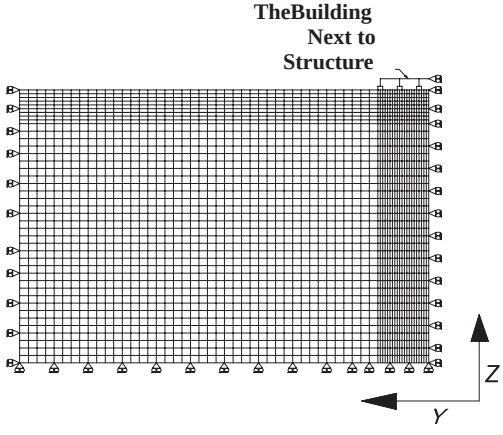

Figure 6. Discretisation of the medium for modelling.

To minimize boundary effects, the vertical boundary at the far ends is set 80 m away (almost 10 times of excavation's width) from the centre of excavation, (Fig.4). It, therefore, is assumed to be free in vertical direction and restricted in horizontal direction. The bottom horizontal boundary is restricted in the both horizontal and vertical directions. The boundary condition and the discretization of the medium for modelling have been shown in Figures 4 to 6.

3.2 *Modeling Stages*

Firstly, the *in-situ* horizontal and vertical stresses are generated. Initial *in-situ* horizontal and vertical stresses are as follows:

$$\sigma_y = \gamma h$$

$$\sigma_x = K_0 \sigma_y$$

where γ is the soil density, K_0 is the coefficient of earth pressure at-rest, and σ_v and σ_h are the vertical and horizontal initial stresses at depth of h respectively.

Secondly, it is assumed that an eight-floor building with 5 and 2 spams in y and x direction respectively has been located next to the excavation. The depth of modelled excavation (H) is considered to be 8 m since it is a typical depth when the traditional Inclined Struts method is used.

The width of excavation (W) and also the width of neighbouring building (L) are assumed equal to 8 m in the models as a number of researchers consider H/L and H/W equal to one in their studies. (e.g., Burland & Wroth, (1974)).

Thirdly, excavation stages are modelled according to common excavation procedures. Boundaries between the stages are modelled by geometry lines and on the basis of considered order for excavating as described later in this paper. Restrained areas in geometry lines are omitted, according to the desired excavation stages. It is assumed that the underground water level is low enough that total stress analysis can be conveniently applied.

3.3 *Modeling different configuration*

As it has been mentioned here before, the inclined struts are supposed to connect the foundation of adjacent building to the bottom of the excavation. Conventionally, full excavation is done in several stages. Various construction procedures associated with inclined struts method are commonly as follows:

Procedure (1)
According to this procedure, the excavation is done in merely one stage. Afterwards, inclined struts are installed. In fact it is the easiest way of installation method of inclined struts.

Procedure (2)
In this procedure, excavation is divided into two main stages. The boundary of these two stages has been shown by a boundary line in Figure. 7. The soil in the further part of the excavation area from the neighboring structure (named V0 in Figure. 7) is firstly removed. Then the soil margin, remaining

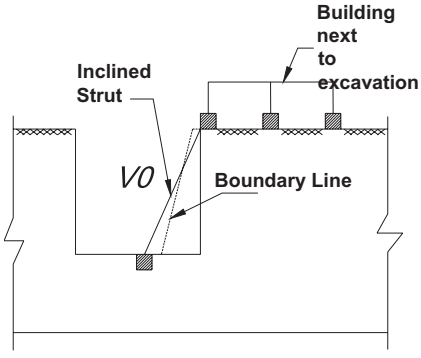

Figure 7. Cross section of excavation stages and strut installation in various procedures studied.

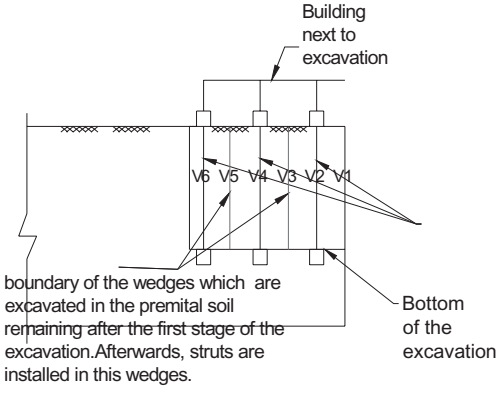

Figure 8. The longitudinal cross section of studied excavation and consequence of strut installation in procedures (1) to (4).

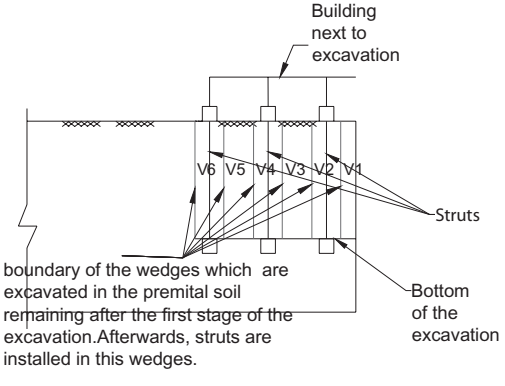

Figure 9. The longitudinal cross section of studied excavation and consequence of strut installation in procedures (5) and (6).

in front of the foundation of neighboring structure and placed in areas called V2, V4, and V6 are excavated and simultaneously inclined struts are installed and connect the foundations to the bottom of excavation. Finally, excavation is completed and the soil in areas named V1, V3, and V5 are removed.

Procedure (3)
Similar to first procedure, soil in area V0 (Fig. 7) is removed. Then, the soil margin which is remained in front of the foundation and situated in areas named V2 and V6 are replaced by inclined struts, connecting foundation of neighboring structure to the bottom of excavation. Next, the soil which is remained in V4 is removed and an inclined strut is installed, instead. Finally, the soil situated between inclined struts is removed. (Fig. 8)

Procedure (4)
Similar to No. 2 and 3 procedures, soil in V0 is removed. As shown in Figure. 7. Then, the soil placed in front of foundation (between boundary lines as shown in Figure. 8) and placed in V4 is removed and replaced with an inclined strut. Afterwards, the soil margin in area V2 and V6 are replaced by inclined struts. Finally, the remained soil is removed. (Fig. 8)

Procedure (5)
Similar to the rest procedures (except procedure No 1), the soil in V0 is removed as shown in Figure. 7. Then, the soil in V1 and V3 in Figure. 9 are replaced with inclined struts. Next, the soil margin in V2 is removed and inclined struts are installed.

Procedure (6)
It is exactly the same as No. 5 but after excavating V0 (Fig.7), the premital soil in V2 (Fig. 8) is removed and an inclined strut which connect the foundation of adjacent building to the bottom of the excavation is installed. Next, the soil in V3 and V1 is replaced with inclined struts as can be noticed in Figure. 9

3.4 *Analysis result*

Excavation-induced displacements in ground next to excavation as well as the wall of the excavation caused by different excavation procedures are compared in Figures 10 and 11.

As it can be seen in Figures 10 and 11, No. 1 procedure leads to the greatest excavation-induced displacements. Therefore, doing excavation in one stage, results in the highest level of damage in neighboring building although it is the easiest procedure in using inclined struts. Other procedures contribute to almost the same excavation-induced

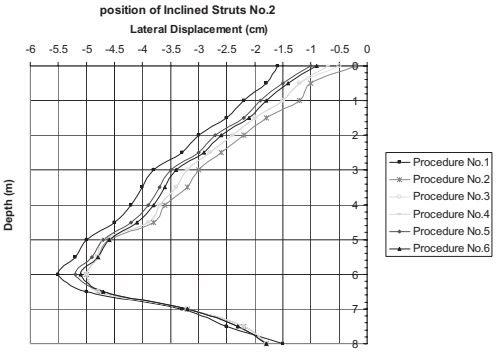

Figure 10. Lateral displacement caused by mentioned procedures.

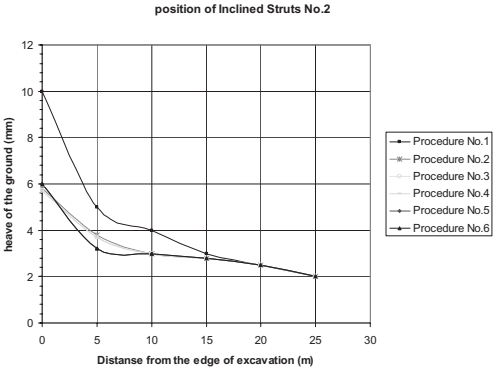

Figure 11. Displacement of the adjacent ground caused by mentioned procedures.

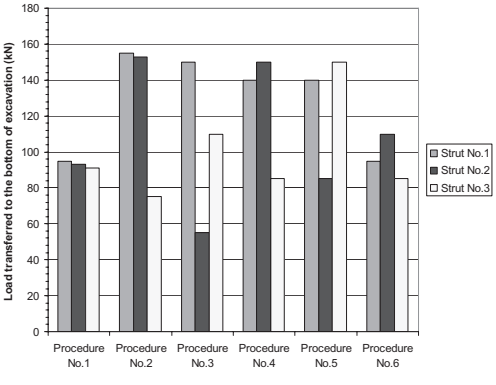

Figure 12. Load transferred to the bottom of the excavation in different procedures.

displacements. However, more detailed studies, reveals that Procedure No. 2, 3 and 4 leads to the least displacements in comparison with Procedures No. 5 and 6. However, there are not to much difference between the displacement rendered by Procedure 2, 3 and 4. this may reveals the fact that the order of stages do not affect the excavation-induced displacement considerably. The little difference between displacement associated with procedures No. 5 and 6 confirm this fact, as well. On the other hand it can be concluded that the width of the wedge play an important role in the excavation-induced displacement. The later conclusion inferred from the different displacement caused by procedure No. 2, 3 and 4 compared with procedure No. 5 and 6. (Fig. 10 and 11)

Moreover, Figure 12 compares the amount of the load which is transferred to the bottom of the excavation via inclined struts. Considering the mechanism of inclined strut which is discussed previously, one of the main objects of inclined is to transfer a portion of load of the adjacent building's foundation from its bearing level to the bottom of the excavation. Therefore, it can be noticed from Figure 12 that procedure No. 1 is not work efficiently in comparison with other methods. Although, No. 2 and 3 seems slightly more efficient in this regard, there are not considerable differences between the rest procedures.

4 CONCLUSION

The presented 3D study confirms the results of previously published 2D studies (Sadeghian & Fakher, 2010). In addition, the following conclusions are suggested base on the presented research.

a. To minimize excavation induced displacement, it is essential that a premital soil margin of excavation to be left before the installation of inclined struts. It means, the excavation of the premital margin should be done after the installation of inclined struts.
b. The sequence struts installation has not any considerable effects on excavation induced displacement. However, the simultaneous installation of struts could minimize displacement.
c. To install each inclined struts, the above mentioned perimital soil margin should be excavated in a very narrow trench perpendicular to the excavation wall. The width of this trench plays an important role on the amount of displacements and should be minimized.

REFERENCES

Boscardin, M.D. and Cording, E.G. (1989), "Building Response to Excavation-Induced Settlement", Journal of Geotechnical Engineering, Vol. 115, No. 1, pp. 1–21.

Burland, J.B. and Wroth, C.P. (1974), "Settlement of Buildings and Associated Damage" SOA Review,

Conf. Settlement of Structures, Cambridge, Pentech Press, London, pp. 611–654.
Burland, J.B., Broms, B.B., and DEMello, V.F.B. (1977), "Behaviur of foundations and structures", State-of-the-Art Report. Proc, 9th Int. Conf. on Soil Mech. And Found. Engr., 2, Tokyo, Japan, pp. 495–546.
Burland, J.B. (1995), "Assessment of Risk of Damage to Buidings due to tunnelling and Excavations", Invited Special Lecture to IS-Tokyo", 95:1st.
Chudley, R. and Greeno, R. (2006), "Building Construction Handbook", Technology and Engineering, pp. 728.
Itasca (2002a (, "Fast Lagrangian Analysis of Continuain 2 Dimensions – FLAC2D "Second Revision, April.
National Coal Board (1975), "Subsidence Engineers Handbook", National Coal Board Production Dept., London, England.
Sadeghia, S. and Fakher, F. (2010), "An Investigation into a Shoring Method to Support Buildings Adjacent to Excavations", *The 17th Southeast Asian Geotechnical Conference, Taipei, Taiwan,* pp. 207–210.
Skempton, A.W. and Macdonald, D.H. (1956), "The Allowable Settlement of Buildings", Proc. Inst. Of Civ. Engrs., Part 3, 5, pp. 727–784.

This page intentionally left blank

Geotechnical Aspects of Underground Construction in Soft Ground – Viggiani (ed)

Understanding ground deformation mechanisms during multi-propped excavation in soft clay

S.Y. Lam, S.K. Haigh & M.D. Bolton
University of Cambridge, UK

ABSTRACT: To maximize the utility of high land cost in urban development, underground space is commonly exploited, both to reduce the load acting on the ground and to increase the space available. The execution of underground constructions requires the use of appropriate retaining wall and bracing systems. Inadequate support systems have always been a major concern, as any excessive ground movement induced during excavation could cause damage to neighboring structures, resulting in delays, disputes and cost overruns. Experimental findings on the effect of wall stiffness, depth of the stiff stratum away from the wall toe and wall toe fixity condition are presented and discussed.

1 INTRODUCTION

To better understanding on the effects of excavation on the movement of the surrounding ground, the direct method is to carry out physical tests and observe them. Centrifuge model tests of deep excavations in slightly over-consolidated soft clay have been carried out using a newly developed testing system, in which the construction sequence of a multi-propped wall for deep excavation can be properly simulated in flight.

2 CENTRIFUGE TESTING

2.1 *Experimental testing programme and setup*

Figure 1 shows the experimental setup of the present study. The rectangular model container is made of aluminum alloy with internal dimensions 790 mm in length, 180 mm in width and 470 mm in depth. The front face of the container consists of a Perspex window, which enables the whole testing process to be monitored by cameras mounted in front. As an increase in soil self-weight leads to an increase in excess pore pressure, the model ground first had to undergo about 5 hours of reconsolidation until at least 90% of the consequential consolidation was achieved. The degree of consolidation was monitored by judging whether pore pressure transducer (PPT) readings were approaching their hydrostatic state. The excavation was then started. The in-flight excavator operated at a rate of 10 mm/s horizontally and with 4 mm vertical increments (Lam et al., 2010). In order to achieve realistic quasi-undrained responses, the excavation process should be finished within a reasonably short period of time. Figure 4 shows the progress of excavation in all tests. Excavation to an excavation depth of 5.5 m finished within 30–40 minutes (72–96 days at prototype scale), which is similar to the typical rate of excavation in the field. Table 1 summarizes the objectives and test descriptions of the test programme.

2.2 *Prop installation and gate system*

Instrumentation comprising of pore pressure transducers in the soil, earth pressure cells on the retaining wall, bending moment strain gauges on the wall, load cells on the props and linear variable transformers for displacement measurements were installed. Digital cameras were mounted in front of the Perspex window for particle image Velocimetry (PIV) purposes (White and Take, 2002) and LED arrays were situated to illuminate the clay cross-section without causing glare, or shadows. In this paper, only pore pressure and PIV data was discussed.

The vertical plane through the center of an excavation could be regarded as a plane of symmetry. A "gate wall" (as shown in Figure 1) aimed to represent this plane of symmetry, so that only one side of the excavation needed to be modeled. A prop installation sub-system was designed to provide in-flight support, initially to the gate wall and ultimately to the retaining wall, during the experiment. Three pairs of cylinders were mounted on a rigid support frame and positioned at 0 mm, 36 mm and 72 mm below the initial clay surface. Props were driven via pistons in the cylinders which were actuated through a hydraulic/pneumatic control system.

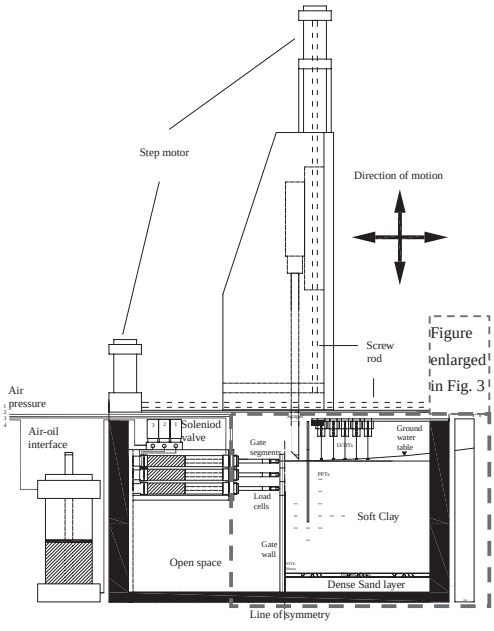

Figure 1. Schematic diagram of experimental setup with in-flight excavator.

Backward pressure inlets were connected to a compressed air source for retreating the cylinders. Forward pressure inlets were connected to an oil pressure reservoir so that they could provide a similar propping force at each excavation level. Each level of props was controlled individually through solenoid valves. The oil supply manifold was connected to an air-oil interface through a needle valve which was used to control the rate of advance of each pair of props, in sequence. Compressed air acting on the front face of the pistons was transmitted from an external compressor and regulator, and was supplied to the centrifuge through a pneumatic coupling. Before the experiment, the system was saturated with hydraulic oil. The prop stiffness was obtained by conducting axial-load displacement tests in a loading rig. The target stiffness of a fully-saturated prop was found to be about 1.66 kN/mm.

Figure 2 shows the gate system. At the start of the experiment, three pairs of sacrificial gates, each 36 mm high, sat on the top of the gate wall. They acted as a support to retain the soil to be excavated. The gates were temporarily supported by the pairs of cylinders throughout the initial reconsolidation stage before excavation. The forces required to support the gate segments were monitored by axial load cells attached at the end of each prop. Figure 2 shows the sequence of the first excavation stage. At the start of excavation, the first pair of cylinders was retracted so that the first layer of gates was in an unstable condition and was easily knocked down by the scraper of the in-flight excavator. The in-flight excavator then makes a 4 mm cut into the soil, which was scraped off into the open space inside the cylinder support system. The scraper then returned to its initial position and made another 4 mm cut, repeating until the excavation level reached the top of the second level of gates. At that moment, the first level of props was pressurized again to support the retaining wall. The prop force required could be adjusted by looking at the readings given by the prop load cells. This completed the first stage of excavation. As the scraper was specially made in an inverted T-shape, it could continue scraping below the first pair of props. The second and third stages of excavation could therefore proceed by repeating the same steps carried out for the first level.

2.3 *Preparation of model ground*

A base layer of fine Fraction E sand was formed by pluviation using an automatic pouring machine (Madabhushi *et al*., 2006). A constant fall-height of 600 mm was used to achieve a uniform layer with a relative density above 95% and a dry unit weight of 16.0 kN/m^3. Saturation of the sand was effected by connecting the bottom drainage hole to a standpipe filled with water. Since one of the objectives of these particular tests was to monitor excavation in soft clay and to compare different bracing schemes, lightly over-consolidated kaolin clay was used in the models. Clay powder was mixed with water to about twice the liquid limit (i.e. 120% moisture content), the mixing taking place under vacuum for at least two hours. The clay slurry was carefully poured on the bearing layer.

Table 1. A summary of centrifuge testing programme.

Test		Objective	D (mm)	Prop stiffness (kN/mm)	System stiffness $EI_{wall}/\gamma_w s^4$	Toe fixity
1	Floating rigid wall with stiff props	Baseline	300	1.66	2860	Free
2	Floating flexible wall with stiff props	Wall stiffness	300	1.66	106	Free
3	Fixed-base flexible wall with base slab	Fixed wall toe	300	1.66	106	Fixed
4	Fixed-base flexible wall in shallow clay	Clay thickness	160	1.66	106	Free

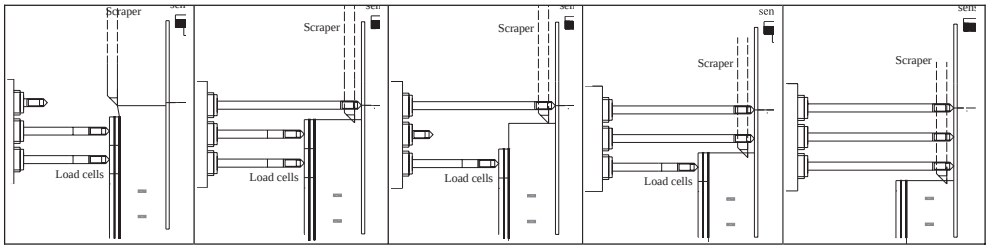

Figure 2. Modeling sequences of excavation.

The container was placed in a hydraulic press, and pressure was applied to the clay in six loading steps (to 2 kPa, 5 kPa, 10 kPa, 20 kPa, 40 kPa and 80 kPa, and 160 kPa).The final pressure of 160 kPa was intended to achieve an estimated c_u of 25 kPa for the clay at mid-depth in the centrifuge model when it had swollen back into equilibrium at 60 g.

When the settlement of the clay in the press became steady under 80 kPa, the clay was unloaded. Nine PPTs were inserted through pre-drilled openings in the back wall of the container. PPTs were installed through 90 mm long holes augured horizontally into the clay using a hand drill. The final locations of the PPTs are shown in Figure 3. After installation, loading was brought back to 80 kPa. After equilibration, the consolidation pressure was further increased to 160 kPa. After settlement was steady, the pressure was reduced again to 80 kPa and the clay was allowed to swell into equilibrium. Removal of this final pressure was known to be possible without drawing air into the clay.

The loading plate was removed. After trimming the clay surface, the resulting clay thickness was 295 mm. The front wall of the model container was then removed. The clay and base layer were then removed from that half of the package that would contain the cylinder support system. The retaining wall, in the particular test to be described here, is made of either a 2 mm or a 6 mm thick aluminum alloy plate with an equivalent stiffness (EI) of 10.4 MNm/m^2 or 280.8 MNm/m^2 at prototype scale, respectively. These walls simulate a sheet pile wall (US steel, PDA-27) and a 0.9 m thick diaphragm wall in the field. Greased wiper seals were used to prevent water from seeping past the sides of the wall and to ensure a free sliding condition with minimal friction. The wall was installed at a depth of 160 mm (equivalent to 10.6 m prototype). A set of vertical guides and a cutter were used to dig a trench with the same thickness as the wall. The wall was then pushed into the trench using a vertical guide. With the clay cross-section uppermost, grains of black-dyed fraction E sand were blown onto the clay to provide PIV texture. Lubricant was then applied to the Perspex window to reduce

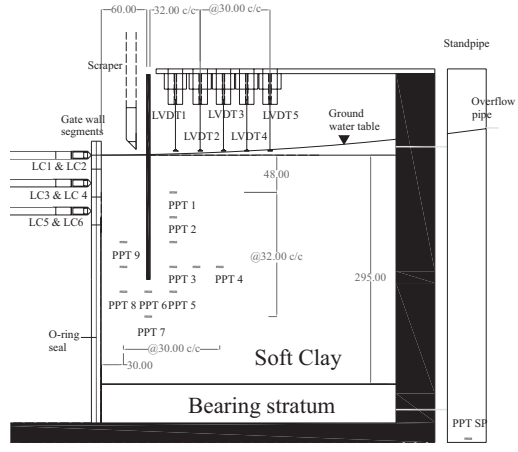

Figure 3. Positions of instruments on model package.

friction against the soil cross-section. The Perspex window was then bolted to the main body of the container. LVDTs were assembled at 30 mm spacing intervals from the wall to measure the soil settlement profile. Finally, the water table in the clay was to be maintained at the ground surface by permitting overflow from a stand pipe which would be supplied continuously throughout the experiment. Two 8 megapixels cameras took pictures throughout the experiment with the provision of suitable lighting. The detailed locations of the instrumentation are shown in Figure 3.

2.4 *Excavation test procedure*

The in-flight excavator was bolted above the model container, and the integrated assembly was transferred onto the centrifuge swing platform. This was fixed to the torsion-bar catches which permit the package to rotate into a fixed-end condition at a centrifuge acceleration of about 10 g. The model was then brought to its scale acceleration of 60 g. There are three test phases for a typical centrifuge test of deep excavation–reconsolidation, in-flight

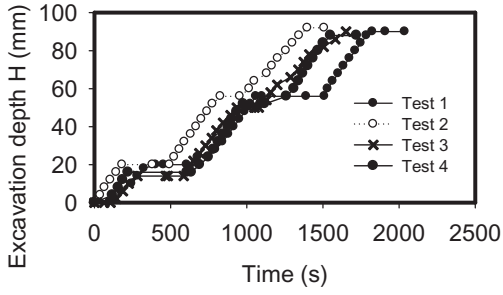

Figure 4. Progress of excavations.

excavation, and long-term equilibration. In this paper, only results on the excavation phase are presented.

As an increase in soil self-weight leads to an increase in excess pore pressure, the model ground first had to undergo about 5 hours of reconsolidation until at least 90% of the consequential consolidation was achieved. The degree of consolidation was monitored by judging whether pore pressure transducer (PPT) readings were approaching their hydrostatic state.

The excavation was then started. The in-flight excavator operated at a rate of 10 mm/s horizontally and with 4 mm vertical increments. In order to ensure that realistic quasi-undrained responses were observed, the excavation process should be finished within a reasonably short period of time. Figure 4 shows the progress of excavation in all tests. Excavation to an excavation depth of 5.5 m finished within 30–40 minutes (72–96 days at prototype scale), which is similar to the rate of excavation in the field.

Following excavation, the test was allowed to continue and excess pore pressures that had been generated by excavation were observed to dissipate as long term deformations were monitored.

3 RESULTS AND DISCUSSIONS

3.1 *Pore pressure behavior during excavation*

As the excavation proceeds, the ground water level in front of the wall was lowered simultaneously. The bottom drainage layer was connected to a standpipe which maintains a hydrostatic water pressure measured from soil surface at the back of the wall throughout each test. Water flow through the sides of the wall was prevented by greased seals. Under such condition, downward seepage at the backside of the wall and upward seepage in front of the wall in long terms should be expected.

Figure 5(a) shows the variation of pore water pressure during excavation using a 0.9 m thick diaphragm wall in Test 1. In front of the wall, there was a negative pore pressure built-up (PPT 9 and PPT 8) due to the reduction in total mean stresses during excavation. The magnitude of the negative pore pressures was smaller than the effective over-burden pressure lost in excavation. This is owing to the fact that the negative pore pressure were cancelled out by the positive pore pressures generated by shear deformation of clay. On the other hand, the change in pore pressure measured at the back of the retaining wall (PPT 1, PPT 2 and PPT 3) was relatively small because the stiff prop supports limited lateral wall deformation and thus limited reduction in lateral horizontal stress.

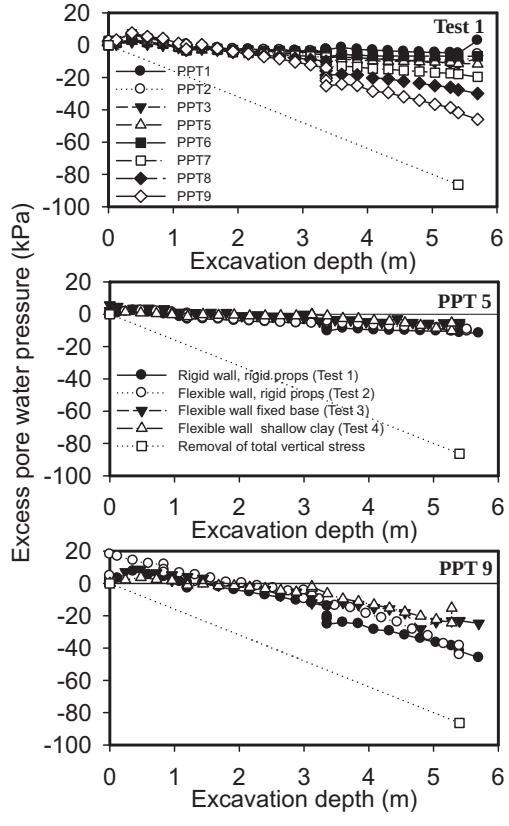

Figure 5. Variation of water pressure (a) for Test 1 (PPT 1–9) (b) at bottom of excavation site (PPT9) for tests (c) at mid-depth of wall on retained side (PPT5) for all tests.

Comparison of variation of pore water pressure underneath the excavation (PPT 9) for different centrifuge tests is made in Figure 5(b). The removal of over-burden stress is plotted on the same graph for comparison. As described earlier, the negative pore pressure by removal of the over-burden stress is cancelled out by the generation of positive excess pore pressure by shear deformation of clay. The decrease

in rate of pore pressure reduction for Test 2, 3 and 4 is ascribed to more extensive excavation induced shear strain induced by flexible wall bulging and thus generation of positive excess pore water pressure. On the other hand, a similar comparison carried out for pore water pressure below the wall toe on the retained side (PPT5) (Figure 5(c)) shows very similar rate of development of excess pore pressure for all cases. The influence of vertical over-burden stress removal is cancelled out by the shear induced positive excessive fluid pressure in a similar order of magnitude for all tests.

3.2 *Ground settlement and wall deflection*

The characteristics of wall deflection and ground settlement profile during undrained excavation is a vital parameter for assessing potential damages to neighbouring structures and buried services. In an ideal excavation process, the support level is installed at an early stage in order to minimize cantilever movement of the wall. However, this may not be always possible in practice due to a variety of site constraints and construction sequences. In the present studies, the excavation procedures initiated with a cantilever stage of excavation, which was then followed by singly propped and finally multi-propped excavation. Ground movements were captured by the PIV technique. Results of ground settlement profile at some discrete measurement point away from the retaining wall monitored by LVDTs are also included for comparisons for Test 2. In general, the results obtained by LVDTs and the PIV technique are comparable, which ensures that the model is testing under plane strain condition properly.

Figure 6 shows the development of lateral wall displacement and ground settlement of a deep excavation using flexible wall (Test 2). Consistent with results shown by previous researchers (Powrie, 1986), rotation of wall about the wall toe was observed in the cantilever excavation stage. Maximum incremental cantilever wall deflection of about 10 mm was observed at the wall crest in prototype scale (0.167 mm in model scale), which is equivalent to 0.2% of average engineering shear strain in the 45 degree triangular zone behind the wall according to Osman and Bolton (2004).

Considering the incremental deformations of a multi-propped wall supporting a deep excavation in soft, undrained clay, at each stage of excavation the incremental displacement profile of the ground and the wall below the lowest prop was assumed to be a cosine function by O'Rourke(1993) as

$$\delta w = \frac{\delta w_{\max}}{2}\left(1-\cos(\frac{2\pi y}{\lambda})\right) \quad (1)$$

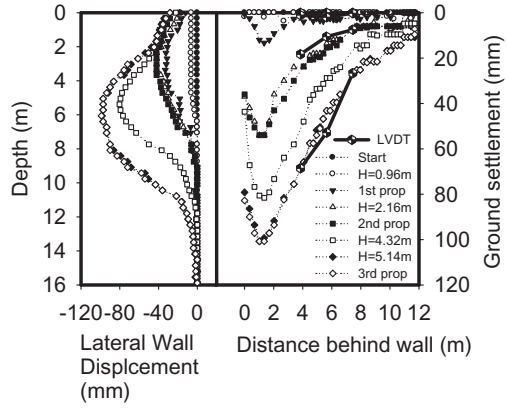

Figure 6. Development of wall deformation and ground settlement with progress of excavation (Test 2).

where δw is the incremental wall displacement at any distance y below the lowest support, δw_{max} is its maximum value, and λ is the wavelength of the deformation, regarded as proportional to the length s of the wall below the lowest level of current support $\lambda = \alpha s$.

O'Rourke (1993) defined the wavelength of the deformation as the distance from the lowest support level to the fixed base of the wall. Osman and Bolton (2006) suggested a definition for the wavelength of the deformation based on wall end fixity. For walls embedded into a stiff layer beneath the soft clay, such that the wall tip is fully fixed in position and direction, the wavelength was set equal to the wall length ($\alpha = 1$). For short walls embedded in deep soft clay, the maximum wall displacement occurs at the tip of the wall so the wavelength was taken as twice the projecting wall length ($\alpha = 2$). Intermediate cases were described as restrained-end walls ($1 < \alpha < 2$). For the excavation in deep soft clay layer, the α value is found to be 1.3–1.5. It should be noted that this value would be a function of soil-wall relative stiffness.

The settlement tough occurs at some distance away from the wall, which is slightly different from the triangular tough pattern observed by Powrie (1986). The subsequent stages of excavation involve deep-seated soil flow mechanism and bulging of the retaining wall below the lowest level of struts. The maximum incremental lateral wall displacement for the second and the third stages were 30 mm and 90 mm (0.5 mm and 1.5 mm in model scale), respectively. These movements were equivalent to about 0.6% and 1.5% of average incremental engineering shear strain, respectively, within the deformation zone according to Bolton et al. (2008).

These findings once again showed the importance of small strain stiffness of over-consolidated soil on analyzing multi-propped excavation problem. The development of settlement toughs is complicated by the superposition of deep settlement tough near the wall. This observation is consistent with the general observation given by Clough and O'Rourke (1990) that the settlement tough of a multi-propped excavation is bounded by a trapezoidal zone extended up to 2 times the maximum excavation depth. It is also noted that the areas underneath the two curves are roughly equal, consistent with zero volumetric strain in undrained conditions.

3.3 *Effect of wall stiffness*

Clough et al. (1989) proposed a semi-empirical procedure for estimating movement at excavations in clay in which the maximum lateral wall movement; δ_{hm} is evaluated relative to factor of safety (FS) and system stiffness, which is defined as follows:

$$System\ stiffness\ (\eta) = EI/\gamma_w h^4 \tag{3}$$

where EI is the flexure rigidity per unit width of the retaining wall, γ_w the unit weight of water and h the average support spacing.

It should be emphasized that FS is used as an index parameter. The system stiffness is defined as a function of the wall flexural stiffness, average vertical separation of supports, and unit weight of water, which is used as a normalizing parameter.

As a result, it is very interesting to know if the normalized wall deformation would change by varying system stiffness and keeping other parameters unchanged in a centrifuge test. The wall deformation profile is shown in Figure 7.

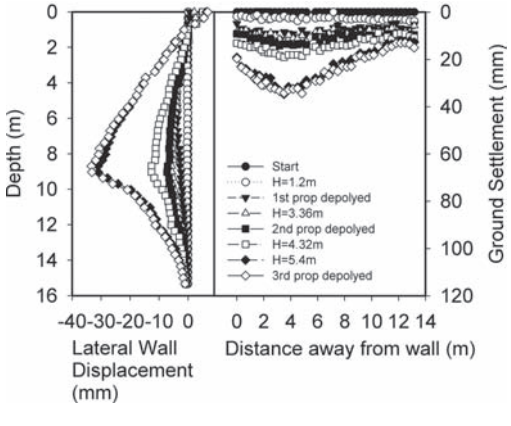

Figure 7. Development of wall deformation and ground settlement with progress of excavation (Test 1).

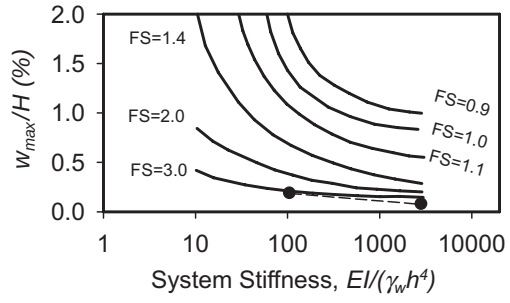

Figure 8. Variation of wall deformation with system stiffness following Clough et al. (1989).

The wall thickness of rigid retaining wall is 3 times that of its flexible counterpart. Since the moment of inertia I term is proportional to cubic of the thickness of wall, the system stiffness differed by a factor of 27. Figure 8 shows δ_{hm} plotted relative to system stiffness for various FS. The factor of safety for the present excavation geometry and soil profile is calculated by the following expression.

$$FS = \frac{(N_c)(c_u)}{H\left(\gamma - \frac{2}{\sqrt{2}}\frac{c_u}{B}\right)} = \frac{(6)(27)}{5.4\left(16 - \frac{2}{\sqrt{2}}\frac{27}{12}\right)} = 2.34 \tag{4}$$

The system stiffness of the rigid wall is calculated to be 2850 whereas that of the flexible wall is 106. The black circles in Figure 8 show the results of the present study. This slight underestimation of wall deformation indicates that system stiffness might be a good measure for quantifying performance of wall deformation for excavation cases. However, the use of factor of safety to quantify wall deformation ignores small strain non-linear stiffness of the soil and also the incremental nature of the construction.

3.4 *Effect of depth to stiff bearing stratum*

Mana and Clough (1981) presented parametric studies on the effect of depth to the bearing stratum on maximum lateral wall displacement for fixed base wall. Results showed that movements increase with excavation width and depth to the bearing stratum. The magnitude of lateral wall displacement increases by a factor of 1.5 when the depth to the stiff layer doubles. However, soils are considered to be elastic which implies that the local development of plastic strain is not possible and over-prediction of soil movements. Jen (1998) investigated into the same issue again with a more sophisticated numerical constitutive model i.e. the MIT-E3 model. Parametric studies

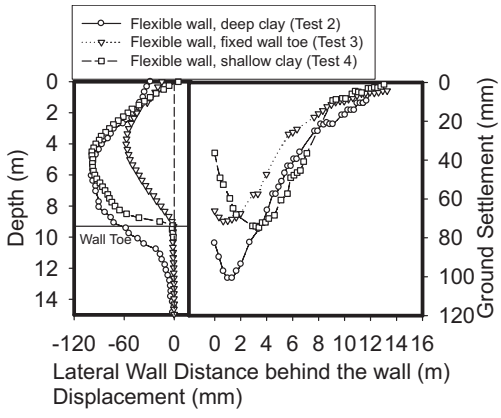

Figure 9. Wall deflection and ground settlement profile for excavation using flexible wall (Test 2, 3 and 4).

on the effect of depth to the hard stratum on lateral wall displacement for excavation using floating wall were carried out. Results show that the depth of end stratum only affects wall deflection below the excavation level, especially the wall toe. On the other hand, shallower clay would have a stronger impact on the distribution of far-field ground settlement. As the location of the rigid base become shallower, the trail of the settlement trough tapers off much more rapidly. The distance for the tapering off is roughly equal to the depth of stiff stratum.

Figure 9 shows the final wall displacement and ground settlement profiles of excavation in shallow clay (Test 4). Since the wall toe is not fixed to the base, wall toe rotation and wall bulging movement are the major deformation mode shape. The lateral wall deformation mode shape is very much similar to that of Test 2 except that the length of the bulge is limited to the depth of stiff layer. The evolution of the soil displacement mechanism is illustrated in Figure 10 for different stages of excavation. The introduction of the first pair of pre-loaded props induces much inward displacement at the wall crest (as shown in Figure 10(a)). The deformation mechanism changed to a free bulging mode which is equivalent to loading a simply supported beam being held vertically. It is the stage that much wall rotation can be developed since there is no moment restraint for props at the wall crest (as shown in Figure 10(b)). After the introduction of the second props, the wall length below the lowest prop is bending moment restrained at the prop location. As an effect, not much wall rotation at the lowest prop location could be observed for excavation stage 3 (Figure 10(c)). The maximum lateral wall displacement for the second and the third stages

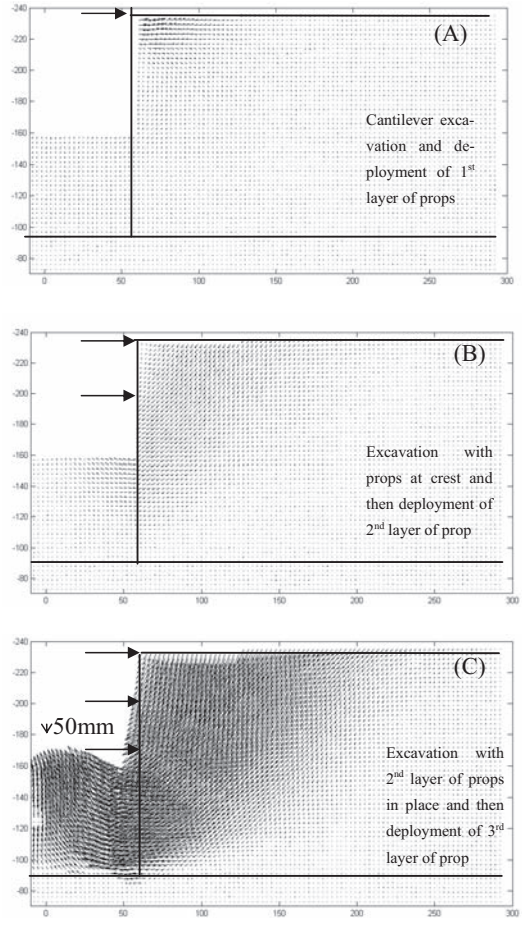

Figure 10. Incremental displacements for different stage of excavation for Test 4.

were 45 mm and 100 mm, respectively. These movements were equivalent to about 0.9% and 2% of average overall engineering shear strain, respectively, within the deformation zone according to Bolton et al. (2008).

Compared with the deformation mechanism of excavation test in deep soft clay, two major observations are spotted. Firstly, the amount of maximum wall displacement is not affected by the depth to the stiff stratum. The difference in the two tests is within 10%. This is comparable to the observation by numerical simulated result by Jen (1998) suggesting that the maximum wall movement would differ only by 20% when the depth of stiff layer increase from 5 m to over 50 m below wall toe. Secondly, the settlement profile of the present test does show a much rapid tapering off as the distance get further away from wall. This observation echoes the results simulated by FEA by Jen (1998).

This implies that an engineer who wants to control the extent of excavation induced movement can consider fixing wall toe with ground improvement methods.

3.5 *Effect of wall toe fixity conditions*

For deep excavation in soft ground, the maximum wall deflection of the retaining wall usually occurs at the final excavation level. To limit wall deflection at this level, ground improvement techniques (e.g. Jet-grouting) are usually employed prior to an excavation. A common approach is to improve the entire soil layer within the excavation zone below the excavation level to fix the wall toe. In the present study, a centrifuge test (Test 3) is carried out to understand how an infinitely stiff fixed base slab layer at the wall toe would affect the deformation mechanism.

Figure 9 shows the effectiveness of a fixed based wall for controlling the lateral wall displacement and ground settlement of excavations. Since the wall toe is fixed to the base, only wall bulging movement is allowed as the deformation mode shape. The lateral wall deformation mode shape is very much similar to that of Test 2 except the fact that a bending moment restraint is being imposed at the wall toe. The maximum lateral wall displacement for the second and the third stages were 40 mm and 65 mm, respectively. These movements were equivalent to about 0.8% and 1.3% of average overall engineering shear strain, respectively, within the deformation zone. In effect, the wall toe fixity restraint controlled lateral soil deformation below final excavation level and the extent of the soil settlement tough away from the wall.

Following Clough et al. (1989) approach, the incremental wall displacement can be generally represented by a normalized wall displacement and depth below lowest prop relationship normalized with wavelength of deformation (Eq.2) shown in Figure 11. Results show that the normalized curves for both floating and fixed base wall broadly follow the cosine curve. The assumed deformation mode shape is proven to be a good representation of a typical wall bulging displacement profile below the lowest prop for multi-prop deep excavation stages.

4 CONCLUDING REMARKS

Maximum lateral wall displacement of a floating support system is a function of the flexural stiffness of the retaining wall. Tripling the thickness of the floating wall reduces maximum wall displacement by 65%, which might not be considered as an economical approach. The depth to the stiff stratum away from the wall toe of a floating flexible wall system does not have a significant effect on maximum wall displacement for floating walls. The wall toe fixity condition is critical in controlling soil deformation below final excavation level and the extent of development of ground surface settlement away from the wall. Should stringent criteria for controlling ground movement during deep basement construction be applied, designers by all means have to restrict wall toe movement either by introducing a base grout or keying the wall toe into a stiff stratum.

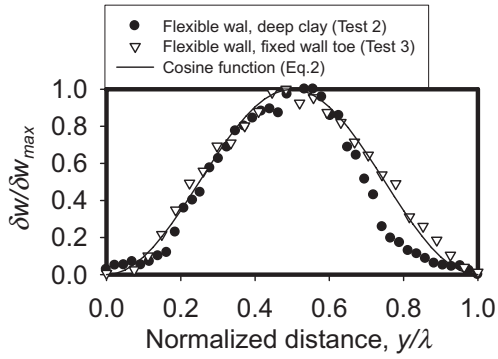

Figure 11. Variation of normalized incremental displacement with distance below the lowest prop.

ACKNOWLEDGEMENTS

The authors would like to acknowledge Mr. John Chandler, Mr. Richard Adams, Mr. Kristian Pether and Mr. Chris McGinnie, the technicians of the Schofield Center, University of Cambridge for their dedication to the project.

REFERENCES

Bolton, M.D., Lam, S.Y. & Osman, A.S. (2008). Supporting excavations in clay-from analysis to decision-making. Special Lecture, *6th International Symposium of Geotechnical Aspects of Underground Construction in Soft Ground.* April, Shanghai.

Clough, G.W. & O'Rourke, T. D., (1990). Construction induced movements of in situ walls. In Proc. Design and performance of earth retaining structure, ASCE Special conference, Ithaca, New York, pp 439–470.

Clough, G.W. & Smith, E.W. and Sweeney, B.P.(1989) Movement control of excavation support system by iterative design. *Foundation Engineering Current Principles and Practices*, Vol.2 ASCE, New York, NY, 1989, pp 869–882.

Jen, L. C. (1998). The design and performance of deep excavation in clay. *Ph.D thesis*, MIT.

Lam, S.Y., Elshafie, M.Z.E.B., Haigh, S.K. & Bolton, M.D. (2010). Development of a new apparatus for modeling deep excavation related problems in geotechnical centrifuge. *ASTM Geotechnical Testing Journal*. (in Press)

Madabhushi, S.P.G., Houghton N.E., & Haigh S.K. (2006). A new automatic sand pourer for model preparation at University of Cambridge. Proc. *ICP-MG'2006,* Hong Kong, pp 217–222.

Mana, A.I. & Clough, G.W. (1981). Prediction of movements for braced cuts in clay. ASCE *Soil Mechanics and Foundations Division Journal,* 107(6): 759–777.

Osman, A.S. & Bolton, M.D. (2004). A new design method for retaining walls in clay, *Canadian Geotechnical Journal*, 41(3): 453–469.

Osman, A.S. & Bolton, M.D. (2006). Ground movement predictions for braced excavations in undrained clay. *J. Geotech. & Geoenvir. Engrg.,* ASCE, Vol. 132, No. 4, April 1, 2006.

O'Rourke, T.D. (1993). Base stability and ground movement prediction for excavations in soft clay. *Retaining structures,* Thomas Telford, London, 131–139.

Powrie, W. (1986). The behaviour of diaphragm walls in clay *Phd thesis*, University of Cambridge.

White, D.J. & Take, W.A. (2002). GeoPIV: Particle image velocimetry (PIV) software for use in geotechnical testing, *Technical Report CUED/D-SOILS/TR322*, October 2002, University of Cambridge.

This page intentionally left blank

Geotechnical Aspects of Underground Construction in Soft Ground – Viggiani (ed)

Face stability control for EPB tunnels in a non homogeneous till formation with highly permeable layers

A. Graziani & A. Lembo-Fazio
University Roma Tre, Rome, Italy

M. Moccichino & P. Romualdi
SELI S.p.A., Rome, Italy

ABSTRACT: Glacial till section of the Canada Line EPB tunnels in Vancouver experienced some disruption during the excavation, owing to the presence of soft layers of loose sand with abundant water recharge, which gave origin to difficult conditions of mixed face. A careful adaptation of the muck conditioning system was required in order to obtain a low permeability and a regular distribution of pressure inside the excavation chamber. The influence of muck permeability on face stability was investigated by 3D Finite Difference models. Conventional analyses, in which the pore pressure distribution at face is a-priori assumed, were initially performed. A modelling approach in which also the conditioned soil inside the excavation chamber and the screw conveyor is represented was then explored. It was demonstrated that a muck permeability at least equal to the in-situ permeability of the soft ground layer is sufficient to virtually eliminate the drawdown effect associated to the excavation advance.

1 INTRODUCTION

This paper analyzes face stability problems in EPB tunnels on the base of the experience acquired during the excavation of a stretch of Canada Line in Vancouver, BC, Canada. The problems at hand encompass possible technological solutions as well as geotechnical modeling issues for a typical case of mixed face, owing to the presence of a soft layer of higher permeability.

Technical issues mainly concern the research of optimal parameters for muck conditioning in order to properly transfer face support pressure and avoid water loss through the screw conveyor. Past experiences and field testing of muck properties and pressure distribution (Bezuijen & Schaminee, 2001, Bezuijen et al., 2005, Hashimoto et al., 2009) represented the base for the experimental investigations carried out at the construction site.

Insight into the behavior of conditioned soil inside a system as complex as an EPB machine was also provided by scale model tests (Merrit & Mair, 2006, Vinai et al., 2008).

The modeling approaches applied in this paper belong to the category of 3D numerical models for seepage-mechanical analysis. In this framework, the collapse mechanism of the tunnel face has been investigated by a progressive reduction of the support pressure. The results can be compared to the limit equilibrium method (Anagnostou & Kovari, 1996).

2 CASE STUDY

2.1 *Canada Line in Vancouver*

The Canada Line is a rapid transit system recently completed in Vancouver for the 2010 Winter Olympics. The bored tunnel section consists of 2.45 km of twin bored tunnels and 3 stations. The tunnels were driven with a 6 m diameter Earth Pressure Balance Tunnel Boring Machine (EPBM) and lined with 250 mm thick, 5.3 m diameter, 1.4m length precast concrete segments. Unforeseen difficulties occurred while boring the 750 m stretch through glacial and interglacial deposits of sand, silt, and clay with granitic boulders.

The bored tunnels pass under a lateral branch of the Vancouver bay (False Creek) and the Downtown area (Fig. 1).

Sloping down (5.5%) the alignment reaches its first lower spot roughly in the middle of False Creek. Hence, it commences to rise, reaching False Creek's North shore and then smoothly arrives in Yaletown Station. The tunnels continue along Davie Street on a northwesterly bearing to the point where, just under the Brava Towers buildings, they curve right through 90 degrees onto a northeasterly bearing.

Approximately in the middle of the False Creek, the geology changes turning from sandstone into the overlying glacial deposits (till). Midway through the curve on Brava Towers, the tunnels turn back into sandstone bedrock.

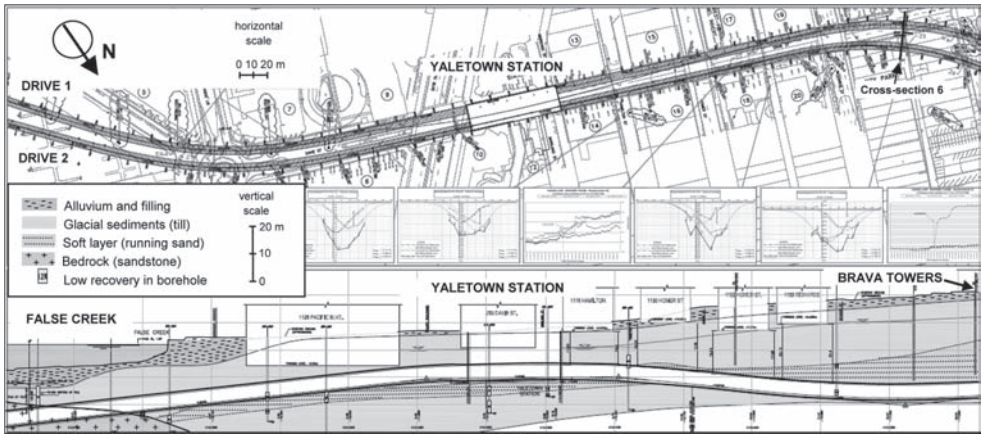

Figure 1. Plan of Canada Line from False Creek to Brava Towers and geological profile along tunnel alignment (ratio of vertical to horizontal scale, 1:2).

2.2 *Geological situation and geotechnical investigations*

The Early Tertiary sandstones and siltstones are massive and jointing is poorly developed or absent.

The till consists of a clay-silt-sand matrix with gravel and very strong cobbles and boulders up to several meters in diameter.

During the Quaternary Period, within the last 1 million years, the Vancouver area was intermittently covered by thick ice of glaciers. The ice sculpted the landscape and deposited a variety of glacial and non-glacial sediments which include thick complex units of glacial till and stratified drift deposited beneath, and at the margins of the ice.

The more difficult geomechanical conditions correspond to a situation frequently faced while boring from False Creek to Brava Towers, which was characterized by the presence of significantly continuous layers of high permeability loose sand.

Evidence of the wide spread and continuity of such a soft inclusion with abundant water recharge was obtained during the drillings for the pile sheet of Yaletown Station.

Sonic drillings, vertical profiles of grain size distribution and borehole tests (pressuremeter, SPT and hydraulic conductivity testing) gave further indications about the geotechnical properties (Table 1) and the typical thickness of the soft inclusions, which could thereafter soundly be represented as a continuous layer. Where this layer intersects the tunnel section, a typical case of mixed face conditions occurs.

Table 1. Geotechnical properties of soils.

	Strong till	Weak till	Silt	Sand
Unit weight, γ (kN/m^3)	21.5	21.5		
Porosity, n (-)	0.3	0.3		
Shear modulus, G (MPa)	170	60		
Elastic modulus, E'(MPa)	425	150	65	
Cohesion, c′ (kPa)	100	25		30
Friction angle, φ′ (°)	40	38		32
Undrained cohesion, c_u (kPa)	800	200		
Permeability, k (m/s)	10^{-8}–10^{-7}	10^{-8}–10^{-7}		10^{-5}

3 PROBLEMS DURING EXCAVATION AND ADOPTED SOLUTIONS

3.1 *Drive 1*

The EPBM started boring the Outbound tunnel (Drive 1) from S-E. Favourable conditions of strong impermeable till lasted for approximately 300m to just beyond Yaletown Station. Regular cutting head inspections and tool changes could be made in normal (atmospheric) conditions. Surface and building settlements were limited to 1 or 2mm with minimum cover of 12 m to the crown of the tunnel and water table approximately 8m below surface. A face support pressure of approximately 1 bar was maintained throughout.

After Yaletown, the muck was noted to contain increasingly higher proportions of wet sand and silt. The next intervention revealed a layer of wet sand within a stronger till matrix that could not be supported in normal atmospheric conditions due to the mobilization of groundwater.

In this area, there was more than 20 m head of water above the crown. At this stage the face support pressure was increased to prevent the possibility of over excavation. Pressing forward, the penetration rate continued to decrease with increased thrust and it became clear that the cutting tools were at the end of their useful life.

In these conditions. After approximately twenty advances in extremely poor ground conditions of silt and sand, where face interventions were not possible even with compressed air, the ground conditions became better with the volume of water decreasing significantly. Throughout the soil section, the ground was conditioned with foam to work the muck into a low-permeability paste to properly transfer face support pressure.

However, this conditioning was less than ideal and the material would flow through the screw conveyor if not mechanically managed by partial closure of the guillotine door. There was significant concern that the machine could become immobilized as it entered the soil/sandstone interface under Brava Tower, where further problems such as nested boulders or inclusions of poor ground were expected.

The decision on how to continue the drive under the highest risk section was based on a number of factors: (i) the settlement readings in all buildings along this section had remained very low (less than 4 mm); (ii) analysis of the Brava Tower structure showed that with a settlement of 9 mm of an individual footing, the stresses in the structure would increase only by 10%; (iii) experience had shown that adequate ground control (low loss of ground) could be achieved even with worn cutting tools.

Considering all facts, a calculated risk was taken to continue the drive. The TBM under passed the building (34 advances) in less than 5 days with the penetration rates reducing from 50 to 30 mm/min. The maximum settlement experienced at any footing was 6 mm (Fig. 2).

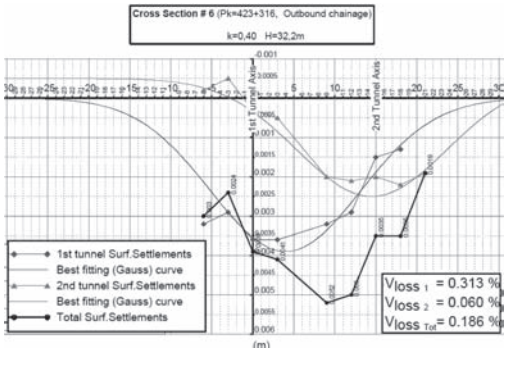

Figure 2. Example of surface settlements measured during tunnel excavation (Cross section #6).

3.2 *Design upgrade and experimental section*

The results achieved during Drive 1 provided the basis for improvements for Drive 2. In particular, several mitigation measures were taken, such as:

1. Tunnel separation increased by 1 diameter (from 12 m to 18 m) underneath the Brava Towers.
2. Use of cutting tools with a mixed-face configuration (ripper teeth and cutters).
3. Automatic grout line cleaning and polymer injection added to the original conditioning system.
4. Additional 24-hour monitoring (surface, buildings, and extensometers) for critical sections.
5. Locating maintenance areas based on the Drive 1 records, where safe and "open face" cutting head maintenance might be possible.
6. Specialized crew for hyperbaric intervention continuously available on site.

In the critical section, beyond Yaletown station, the principal criterion used for the EPB pressure calculation was to counter balance the water table pressure and add 20 kPa as a safety buffer. The pressure was progressively raised from 150 kPa to 200 kPa, reaching a maximum of 220 kPa near Brava Towers.

In addition, an experimental section was successfully driven with high face support pressures (up to 2 bar) before approaching the station to check the TBM performance and determine the appropriate soil conditioning parameters.

Variations of water flow, foaming agent and polymer concentration were investigated through slump tests, permeability tests, and visual inspections of the muck.

Slump tests did not depend on excavation pressure while muck density recorded 13 to 15 kN/m^3 values. High EPB pressure required high surfactant percentage (TA, 1.0–1.2%), low water flow in the excavation chamber and high Foam Injection Rate (FIR, 110–140).

Eventually, the selected conditioning parameters granted reaching a permeability of the excavation spoil ranging from 10^{-9} to 10^{-8} m/s, producing a pulpy and water-tight paste (slump, 15–20 cm).

3.3 *Drive 2*

Excavation reached smoothly the Yaletown Station box, which provided the opportunity to fully refurbish the cuttinghead.

At the first maintenance area 70m from the station, the sand layer was found to be approximately 2 m deep and half way up the face with hard till (with boulders) above.

Excavation continued as planned even into a unforeseen full face of sand. Unlike the first drive, the high operating pressures could be maintained and the ground was properly conditioned using only foam. The assumptions about a short

section of "good" ground for the second maintenance area proved to be correct too.

The third maintenance area, shortly before the alignment entered the footprint of the Brava Towers, was again planned adjacent to a very short section of "good" ground experienced in Drive 1. The 2 hour intervention at this location began with a steady flow of water coming from the sand layer that started to cause sloughing of the ground above the crown of the machine. The intervention was abandoned but revealed that the cutting tools were in relatively good condition. The construction team made the decision to complete the drive without further planned stops, until the TBM was fully into the sandstone.

The machine advanced at an average of 12 rings per day (17m), at 2.2 bar face support pressure at the top of the cutting chamber and 2.7 bar at inlet to screw conveyor.

4 HYDRO-MECHANICAL MODEL

4.1 *General features*

Although it is likely that more than a single layer exists, possibly with additional minor inclusions and lenses of limited extent, to keep the model as simple as possible a unique layer was considered. The thickness of the soft layer was fixed equal to 1.5 m, that is D/4 (where D is the tunnel diameter, equal to 6 m), while its position within the face was varied.

On the basis of the baseline geotechnical characterization and the additional investigations carried out during tunnel construction (Table 1), the two materials which compose the calculation model were given the parameters listed in Table 2. The parameters of the till formation represent the average properties of an ideal medium formed by randomly alternated strata of weak and strong till.

Table 2. Model parameters.

	1) Till formation	2) Sandy layer
Bulk unit weight, γ (kN/m^3)	21.5	21.5
Porosity, n (-)	0.3	0.3
Shear modulus, G (MPa)	120	24
Elastic modulus, E' (MPa)	300	60
Poisson ratio, ν' (-)	0.25	0.25
Cohesion, c' (kPa)	20	0
Friction angle, φ' (°)	40	30
Dilation angle, ψ (°)	0	0
Permeability, k (m/s)	10^{-8}	10^{-6}

The material model assumed in the following analyses is the linear elastic perfectly plastic model with Mohr-Coulomb strength criterion. The behaviour of the water-saturated porous medium during excavation advance was represented by a two-phase approach. Only the drained elastic moduli and the drained strength parameters are therefore required, while the undrained behaviour is governed by the water bulk modulus ($K_w = 2$ GPa), porosity and the solid skeleton bulk modulus.

The initial stress conditions in the soil mass were obtained by assuming a unit weight of the rock mass of $\gamma = 21.5$ kN/m^3 and a coefficient of lateral pressure at rest $K_0 = 0.5$. Pore pressures have a hydrostatic distribution.

The tunnel reaches its section of minimum overburden (about 15 m) at the chainage of Yaletown Station, whilst the maximum overburden (about 30 m) corresponds to the under passing of Brava Tower, near the end of the soil section of the tunnel. The model (Figure 3), refers to the section of minimum overburden, with the undisturbed water table at 6 m depth from the ground surface. The grid represents a half of a single tunnel, with the face located midway of the longitudinal length of the grid.

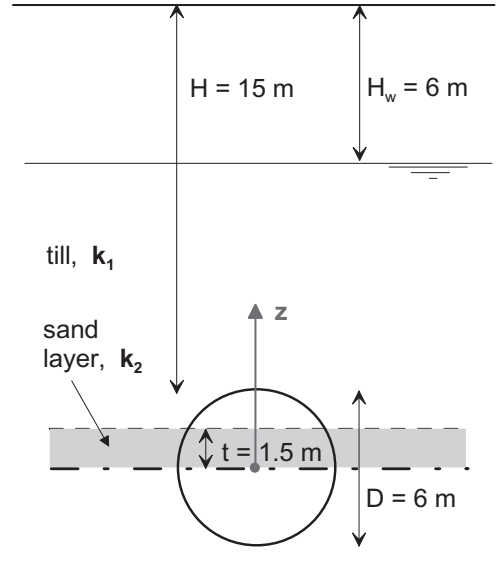

Figure 3. Typical cross-section of tunnel with the sand layer positioned in the first upper half the face.

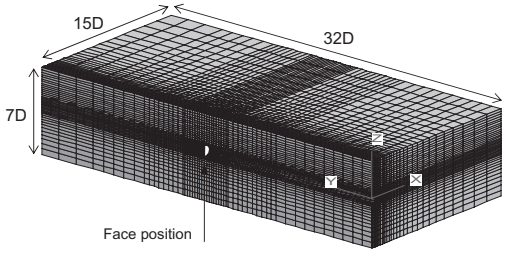

Figure 4. General layout of the 3D model grid.

4.2 *Preliminary analyses of face stability*

The gradual increase in ground deformation and loads on the EPB shield during tunnel excavation is associated with the stress redistribution taking place in the vicinity of the advancing face and with the consolidation process in the ground surrounding the tunnel. Time-dependent consolidation processes are particularly relevant for tunnelling through water-bearing, low-permeability ground.

Around the EPB shield, plastic deformation and remoulding of the saturated ground also occur. In a low-permeability ground, the water content cannot change immediately after excavation. Instead, excess pore pressures develop, which dissipate over the time. In case of non-hydrostatic in situ stress ($K_0 \neq 1$), pore pressure change along the tunnel wall can be negative as well positive.

Stability analyses are frequently carried out for two idealised situations: the short-term conditions ($t = 0$), characterised by the undrained behaviour of the porous medium, and the long-term conditions ($t = \infty$), in which a stationary pore pressure distribution is reached.

In any case, tunnel excavation causes a transient seepage flow process. If the excavation proceeds slowly or the permeability is relatively high, the conditions can also be practically drained since the short term. More in general, the hydro-mechanical response at the tunnel face is governed by the ratio of excavation rate v_a to ground permeability k (Anagnostou 1995).

In case of layered ground, the situation becomes even more complex, because the characteristic times for pore pressure equalization can be very different for materials of markedly different permeability.

The proposed modelling approach is based on the application of three-dimensional (3D) Finite Difference Models (Flac3D, Itasca 2006), which can achieve a realistic prediction of ground response at the face as well as of ground loads acting on the TBM (Graziani et al. 2007). An uncoupled calculation scheme was adopted, therefore, each hydro-mechanical analysis is split in two phases, seepage analysis and mechanical equilibrium.

For the preliminary set of analyses, the following assumptions were made in order to simplify the model, aimed at the assessment of the face stability: i) lining is perfectly rigid and installed before any deformation of the tunnel walls, ii) both lining and EPB shield represent impermeable boundaries so as flow is directed only towards the face, iii) the excavation camber is not included in the model, thus the boundary conditions applied to the face consist of fixed distributions of pore pressure as well as of effective stress, with given vertical gradients.

Two limit cases were considered for groundwater flow boundary conditions. Case A) represents the situation of maximum drainage at the tunnel face (pore pressure p = 0), corresponding to very high permeability of the spoil-water mixture inside the excavation chamber (i.e., totally unsatisfactory conditioning). Case B) represents the optimal situation, where the undisturbed hydrostatic pore pressure distribution is fully preserved, thanks to a sufficiently low permeability of the conditioned soil inside the excavation chamber, which therefore acts as an ideally impermeable barrier.

For case A), the time-dependent pore pressure distribution is calculated for increasing flow time.

Further assumptions were required to define the shape of the total pressure profile applied to the face. Again, two possible schematizations were considered: (1), a linear distribution characterized by a vertical gradient $\gamma_f = 10$ kN/m^3; (2), a uniform distribution. In either case, the variable chosen as control parameter is the total pressure (σ_{T0}) applied at the centre of the tunnel face.

There is no simple relation between the vertical gradient γ_f and the density of the muck inside the excavation chamber. Many factors, such as the water content, the foaming additives and the rotation speed of the cutting head can affect the vertical pressure gradient (Bezuijen et al. 2005). The assumed γ_f value was estimated from the average readings of pressure gauges at different positions inside the excavation chamber.

The limit support pressure at the face was calculated by the progressive reduction in the effective stress applied to the face. A safety factor can also be defined, e.g., as the ratio between the actual/design total pressure to the collapse limit pressure.

In a first set of analyses the position of the sand layer was considered fixed (base of the layer at z = 0, as in Figure 3), while boundary conditions at the face were varied (Table 3).

Table 3. Preliminary analyses without modeling of the EPBM.

	Permeability		Face conditions		
Case	k_1 (m/s)	k_2 (m/s)	Total pressure	Pore pressure	Analysis
A1	10^{-8}	10^{-6}	linear	A) p = 0	Flow + Mech
A1U	– *	10^{-6}	linear	A) p = 0	Flow + Mech
A2	10^{-8}	10^{-6}	uniform	A) p = 0	Flow + Mech
B1	10^{-8}	10^{-6}	linear	B) undisturbed	Mech only
B2	10^{-8}	10^{-6}	uniform	B) undisturbed	Mech only

*undrained

For the situation of "maximum drainage" at the face (case A), the time required to attain steady-state flow was found to be about 3 hours (Fig. 6). Hence, considering the typical excavation rates, it is reasonable to assume that the excavation devel-

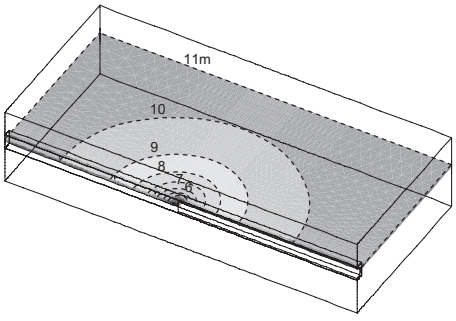

Figure 5. Analysis A1. Pore pressure distribution (interval 1 m) within the sand layer (plane z = 1 m).

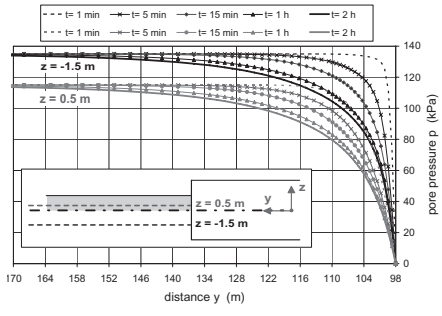

Figure 6. Analysis A1. Isochrones of pore pressure in front of the face along two lines in the plane x = 0.

ops in drained conditions, at least for what concerns the behaviour of the soft layer of higher permeability.

Therefore, a simplified modelling approach was also considered, in which the flow domain is limited to the high permeability layer, while the surrounding till formation is assumed to display a fully undrained response (analysis A1U, Table 3).

The deformation response of the tunnel face (Fig. 7) to the progressive decrease in support pressure, up to the limit of collapse, is monitored by the "characteristic curve" of the face: i.e., y-displacement ("face extrusion") vs total pressure σ_{T0} (Fig. 8). Collapse occurs essentially as squeezing deformation of the sand layer, which also induces local tensile failure in the overlying till (Fig. 7).

The main findings of the first set of analyses are hereafter summarized.

In case of fully drainage (p = 0), the distance of influence of the face on flow conditions is about 6D, i.e., at greater distances the reduction in pore pressure is less than 5% (Fig. 5 and 6). This situation represents the worst case scenario for the assessment of the impact of the excavation process (excessive drawdown of water table, risk of large settlements). On the other hand, this case corresponds to minimum demand of total pressure to stabilize the face (σ_{T0} = 20 k Pa, Figure 8).

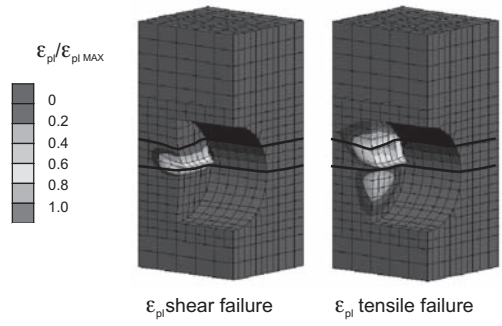

Figure 7. Collapse mechanism of the tunnel face. Plastic shear and tensile deformations for analysis A1.

In case of no disturbance of the initial hydrostatic pore pressures, the minimum total pressure necessary for face stability corresponds to σ_{T0} = 120 kPa, which indicates that almost the whole amount of pressure is required to counterbalance the water pressure.

The influence of the vertical gradient γ_f of face pressure seems modest, at least within the limits posed by the accuracy (±5 kPa) in the determination of the collapse load (Fig. 8). This result can be explained considering the small thickness of the low strength layer with respect to the tunnel diameter. The response of the face to unloading is therefore markedly different, and more advantageous, from the case of homogeneous soil.

The influence of the position of the high permeability layer inside the face was then investigated. Four different situations were analyzed, corresponding to a relative elevation z of the base of the layer, with respect to the tunnel axis, of –3, –1.5, 0 and 1.5 m.

The position of the soft layer within the tunnel face has a limited but yet significant influence on the minimum pressure necessary to avoid instability. Figure 9 show the situation in terms of average pressure σ_{T0} as a function of layer position: the

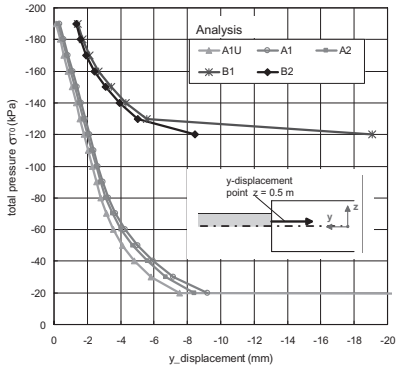

Figure 8. Extrusion displacement of the sand layer as a function of the total support pressure.

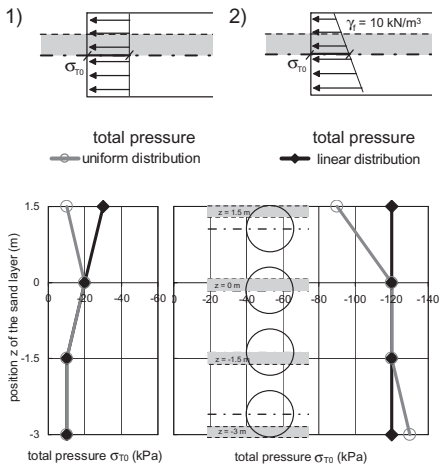

Figure 9. Minimum required support pressure σ_{T0} for different position of the sand layer and total pressure distribution.

maximum variation in σ_{T0} is of about 20 kPa. A less important variation would be obtained if the pressure value at the middle of the soft layer were considered instead of the pressure σ_{T0} at the centre of the tunnel face.

In conclusion, the amount of pore pressure reduction inside the excavation chamber, with respect to the undisturbed ground, proved to be the parameter which mostly affects the required support pressure. In fact, the difference in total support pressure between the limit cases A and B is very large. Moreover, intermediate situations, i.e. a partial drainage of the face, are equally possible.

The fundamental question therefore arises of how the pore pressure at the face can be properly estimated on the base of the relevant properties of the conditioned soil and EPB operation mode. To this purpose, the results of the experimental testing program on the conditioned soil could be instrumental.

4.3 *Analyses with explicit modeling of EPBM*

A possible refinement of the previous analyses is the capability of modeling also the conditioned soil inside the excavation chamber and the screw conveyor. This approach eliminates the need of an a-priori assumed distribution of pore pressure over the tunnel face but require an appropriate assessment of the permeability of conditioned and fully remoulded soil inside the machine. In fact the flow domain also includes, although with an idealized geometry, the aforementioned parts of the EPBM (Fig. 10).

Following the same approach of the analysis "without EPBM", a two-phase model has been adopted for the conditioned soil as well as for the natural soil surrounding the tunnel. The flow process and thus the pore pressure distribution was analyzed for increasing times (transient flow) up to obtain the steady state flow conditions. The key parameter is the permeability (k_{EPB}) of the conditioned soil inside the EPB, which determines not only the time required to reach stationary flow but also the relative head loss inside the EPB with respect to the decrease in hydraulic head in the surrounding ground.

Again, the analysis has been split down in two phases: the "flow" calculation, up to steady state, and then the "mechanical" phase, in which a progressive decrease in total stress applied to the face has been performed.

Valuable and explicatory results have been obtained carrying out the analyses described in Table 4, in which it is assumed $k_{EPB} = 10^{-6}$ or 10^{-5} m/s.

The main findings of these analyses are the following.

Most of the head loss occurs along the screw conveyor. The steady-state flow, established approximately after 4 hours, is characterized by a linear decrease in pore pressure from the inlet point to the discharge opening. This result, quite obvious from a theoretical standpoint, given the constant cross-section of the screw conveyor, should be only tentatively accepted owing to the oversimplified modelling. It is therefore essential that the

Table 4. Analyses including the EPBM conditioned soil.

	Permeability			Face conditions		
Case	k_1 (m/s)	k_2 (m/s)	k_{EPB} (m/s)	Total pressure	Pore pressure	Analysis
C2	10^{-8}	10^{-6}	10^{-6}	linear	–	Flow + Mech
C2U	– *	10^{-6}	10^{-6}	linear	–	Flow + Mech
C3	10^{-8}	10^{-6}	10^{-5}	linear	–	Flow + Mech

*undrained

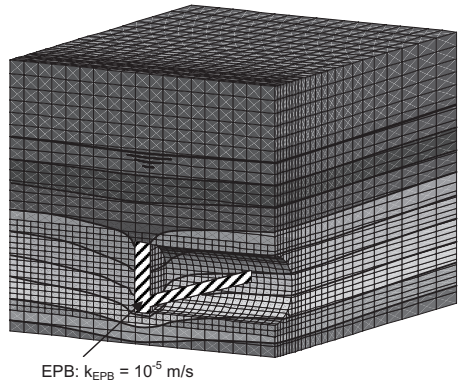

Figure 10. Analysis C3. Steady-state pore pressure contours (interval 20 kPa) in the model with EPB.

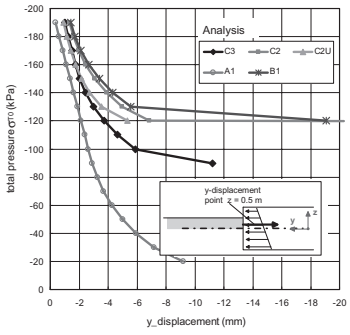

Figure 11. Comparison of characteristic curves of the face for different analyses.

linear distribution of pore pressure was confirmed by measurements performed in scale model tests (Merrit & Mair 2006).

It is sufficient to guarantee a muck permeability k_{EPB} as low as 10^{-6} m/s, that is, equal to the assumed in-situ permeability of the sand layer, in order to virtually eliminate the drawdown effect associated to the excavation advance. In fact, in this case, groundwater conditions stay undisturbed and most of the head loss develops inside the screw conveyor. From a mechanical point of view, the total pressure required for face stability equals that obtained in the previous analysis with "no drainage" hypothesis (Fig. 11).

If the permeability of the conditioned muck is increased to 10^{-5} m/s, steady-state pore pressure at face decrease significantly below the original undisturbed value ($\sigma_{T0} = 90$ instead of 120 kPa). Correspondingly, the "characteristic curve" of the face (i.e., extrusion displacement of the sand layer vs total pressure) indicates a stiffer behaviour than the previous case and a limit pressure of 90 kPa instead of 120 kPa.

The "characteristic curve" of the face shows that under the ordinary support pressure of 150 kPa the displacement at the centre point of the soft layer is as low as 3 mm.

Similar results, in terms of pore pressure as well as of face displacement, can be obtained also by a more fast calculation in which only the high permeability layer is represented by a two-phase approach whilst the surrounding low permeability till behaves as an "undrained" medium (analysis C2U).

5 CONCLUSIONS

Typical conditions of mixed face with layered ground of different strength and permeability have been considered.

A modeling approach which includes also the conditioned soil of the EPB in the seepage analysis has been proposed. In this way, a direct link can be established between conditioned soil properties and ground response during EPB boring.

Minimum support pressures required for face stability were calculated for different permeability of the conditioned soil, position of the sand layer and total pressure distribution over the face.

The main finding of this study is that a permeability of the conditioned soil inside the EPB shield less or equal to the permeability of the more permeable layer (10^{-6} m/s) can virtually eliminate the drawdown of the groundwater table.

In situ measurements of spoil permeability, as it flows off from the screw conveyor, have indicated values as low as 10^{-8} m/s, when the material exhibits a well homogenized texture and a low water content (i.e., optimum conditioning). Much higher values of permeability were obtained for disaggregated muck, which, in this case, was flowing discontinuously from the screw conveyor.

Data reported in the technical literature, mainly coming from EPB excavations in fine sand and silt, indicates muck permeability generally higher, in the range 10^{-6}–10^{-5} m/s (Bezuijen et al. 2005). In this case, a partial drainage of the face occurs. The influence of this less favorable conditions on face stability could also be investigated by the proposed model.

REFERENCES

Anagnostou G. 1995. The influence of tunnel excavation on the idraulic head. *Int. J. Num. Anal. Meth. Geomech*., 19, 725–746.

Anagnostou G. & Kovari K. 1996. Face stability conditions with Earth-Pressure-Balanced shields. *Tunnelling and Underground Space Technology*, 11, 165–173.

Bezuijen A. & Schaminee 2001. Simulation of the EPB-shield TBM in model tests with foam as additive. *Int. Symp. Modern Tunneling Science And Technology*, Kyoto, Adachi Et Al. (eds), 935–940.

Bezuijen A., Talmon A.M., Joustra J.F.W. Grote B. 2005. Pressure gradients and muck properties at the face of an EPB. *Int. Symp. Geotechnical Aspects Of Underground Construction In Soft Ground*, Amsterdam, Bakker et al. (eds), 195–201.

Graziani A., Capata A. Romualdi P. 2007. Analysis of rock-TBM-lining interaction in squeezing rock. *Felsbau*, 25, 6, 22–31.

Hashimoto, T., Ye, G.L., Nagaya, J., Konda, T. & Ma, X.F. 2009. Study on earth pressure acting upon shield tunnellining in clayey and sandy grounds based on field monitoring. *Int. Symp. Geotechnical Aspects of Underground Construction in Soft Ground,* Shanghai, Ng et al. (eds), 307–312.

Itasca 2006. Flac 3D, User's Manual, Ver. 3.1.

Merrit A.S. & Mair R.J. 2006. Mechanics of tunnelling machine screw conveyors: model tests. *Geotechnique*, 56, 9, 605–615.

Vinai R., Oggeri C., Peila D. 2008. Soil conditioning of sand for EPB applications: a laboratory research. *Tunnelling And Underground Space Technology*, 23, 308–317.

Geotechnical Aspects of Underground Construction in Soft Ground – Viggiani (ed)
© 2012 Taylor & Francis Group, London, ISBN 978-0-415-68367-8

Numerical simulation of long-term twin-tunnel behaviour at St James's park

R.G. Laver
AECOM, Hong Kong

K. Soga
Department of Engineering, University of Cambridge, Cambridge, UK

ABSTRACT: The twin-tunnel construction of the Jubilee Line Extension tunnels beneath St James's Park was simulated using coupled-consolidation finite-element analyses. The effect of defining different permeabilities for the final consolidation stage was investigated, and the performance of a fissure softening model was also evaluated. The analyses suggested an unexpectedly high permeability anisotropy for soil around the tunnel crown, possibly due to stress-induced permeability changes, or low-permeability laminations. Also, the permeability profile and lining conductivity were found to differ between the tunnels. Inclusion of the fissure model gave a narrower settlement trough, more alike that in the field, by preferentially softening simple shear behaviour. Long-term settlements at the site continue to increase at an unexpectedly high rate, suggesting the possibility of creep or unexpected soil softening during excavation.

1 INTRODUCTION

The impact of long-term changes after tunnel construction has attracted increasing interest. At the surface, continuing movements after excavation can cause further damage to buildings (Harris 2002), whilst below the surface, lining distortion and degradation is presenting a safety hazard for ageing metro systems. An understanding of the long-term behaviour of tunnels is urgently needed before these problems can be mitigated effectively.

Wongsaroj (2005) conducted a parametric study to investigate factors influencing the long-term behaviour of a single tunnel, through a series of coupled stress–pore pressure finite-element analyses.

To validate his analyses, he simulated the construction of the Jubilee Line Extension (JLE) twin tunnels beneath St James's Park, London, (1995–1996) and compared results to the monitoring data reported by Nyren (1998). To validate the long-term response, the resulting consolidation period was also simulated.

However, Wongsaroj executed only single-tunnel analyses, so that each tunnel was excavated in greenfield initial conditions; twin-tunnel interaction was therefore not accounted for.

This paper presents the simulation of twin-tunnel construction at St James's Park using coupled finite-element analyses, to account for interaction between the tunnels.

The simulation served to validate a parametric study investigating the long-term behaviour of twin tunnels; this study is described in Laver (2010).

The analyses also provided an opportunity to trial a new fissure model, outlined in Laver & Soga (2011). The fissure model was developed in response to two key observations from recent laboratory test data on London Clay (Hight et al. 2007): softening on fissures in triaxial extension tests, and softer behaviour for torsional shearing modes in the Hollow Cylinder Apparatus (HCA).

The twin-tunnel simulation of St James's Park also enabled the effect of different permeabilities to be assessed.

During the consolidation stage following construction of the first tunnel, Wongsaroj (2005) trialled different distributions of soil and lining permeability to match settlements and pore pressures in the field. To do this, he assigned different permeabilities to different strata, and also varied the permeability around the lining circumference.

Initially, the best-fitting soil and lining permeabilities found by Wongsaroj were applied in the twin-tunnel analyses of St James's Park. However, this resulted in poor replication of the final consolidation period—after construction of both tunnels—a period which Wongsaroj did not simulate. Four further combinations of soil and lining permeability were therefore trialled to match the field data better.

2 SITE DESCRIPTION

The Jubilee Line Extension beneath St James's Park consisted of two tunnels; one running westbound, and the other eastbound. More details about the site and monitoring can be found in Nyren (1998).

2.1 *Construction*

The twin 4.85 m-diameter running tunnels were excavated using backhoes in open-face shields, leading to volume losses of 3.3% and 2.9% respectively for westbound and eastbound tunnels.

The instrumentation was installed along a plane perpendicular to the tunnels; Figure 1 illustrates the instrumented section in elevation.

At 31 m depth, the advancement of the deeper westbound tunnel past the instrument plane was followed 256 days later by the 21 m-deep eastbound tunnel. Being diagonally juxtaposed in elevation, the tunnels were separated by 21.5 m in plan. Unlike its perpendicular crossing with the eastbound tunnel, the instrument plane intersected the westbound tunnel at an angle of around 80.

The lining was erected from unbolted concrete segments, which were expanded against the soil by inserting wedge-shaped key segments at knee level.

2.2 *Instrumentation*

The instrumentation included 24 Surface Monitoring Points (SMPs), providing 3-D surface displacements. Subsurface horizontal and vertical displacements were monitored by nine electrolevel inclinometer holes and eleven extensometer arrays. Five piezometers installed above the tunnels and four spade cells at eastbound tunnel axis level gave pore pressures and horizontal stresses.

2.3 *Geology & hydrogeology*

Topsoil and sandy man-made fill (Made Ground) at the site is underlain by sandy Alluvium and coarse to fine flint gravel (Terrace Gravel) to around 6–8 m Below Ground Level (BGL). Beneath this, London Clay extends to over 40 m depth, successively giving way to the Lambeth Group, Thanet Sands and Chalk bedrock.

Two aquifers persist across London: a deep aquifer in the Thanet Sands and Chalk below the London Clay and Lambeth Group, and a perched aquifer in the Terrace Gravels, recharged by precipitation and from the river Thames.

The pore pressure profile shown in Figure 2 nearby the site indicated a water table rising to about 5 m BGL. However, the sub-hydrostatic pore pressures towards the base of the London Clay indicated slight underdrainage from the deeper aquifer below.

Water strikes in several boreholes suggested the presence of water in claystone and sand partings.

3 ANALYSIS DETAILS

3.1 *Modelling procedures*

Twin-tunnel construction was simulated using the finite-element package ABAQUS. The simulation was divided into four stages: (i) westbound tunnel excavation, (ii) consolidation during the rest period, (iii) eastbound tunnel excavation, and (iv) consolidation until steady-state.

The two excavation stages were modelled with 3-D meshes for accurate replication of the excavation process. The mesh used is pictured in Figure 3. The lateral boundaries were located sufficiently distant to make boundary effects negligible. Data

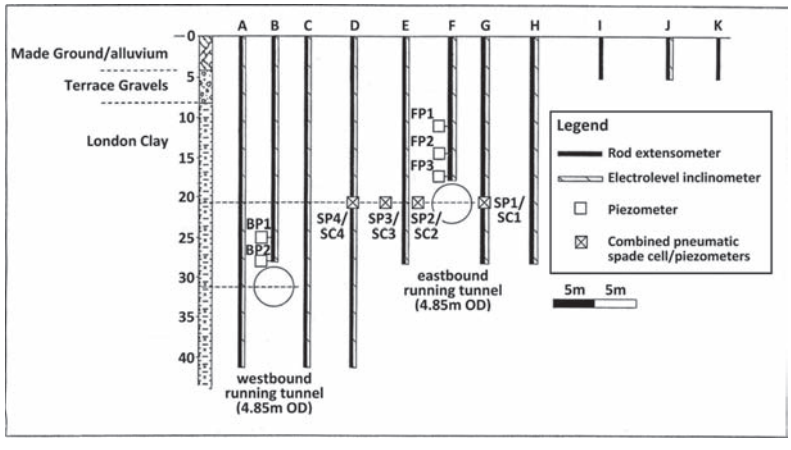

Figure 1. Elevation of instrumentation layout at St James's Park (after Nyren, 1998).

was extracted at a plane through which the tunnel was excavated, representing the instrument plane at St James's Park.

The two consolidation stages were modelled with 2-D meshes to reduce computational time. The 2-D meshes were defined with the same geometry as the instrument plane of the 3-D meshes.

By the end of each excavation analysis, a plane-strain condition had been reached on the instrument plane of the 3-D mesh. All data on the plane necessary to continue the analysis was then mapped to the 2-D mesh to model the ensuing consolidation during the rest period. Similarly, at the end of this stage, which lasted 256 days, data from the 2-D mesh was mapped onto the entire length of the 3-D mesh ready to model the eastbound excavation.

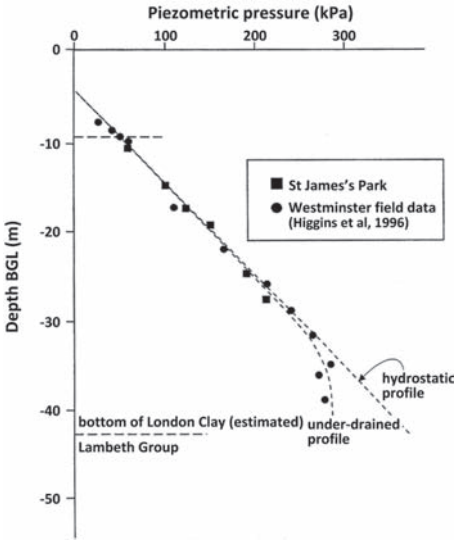

Figure 2. Pore pressure profile at St James's Park (after Nyren, 1998).

Excavation was progressed by removing soil elements and activating lining elements in 2 m lengths. A 6 m unsupported length for the tunnel heading was assumed, to match field observations (Nyren 1998). The speed of excavation simulated the rate of advance at St James's Park, progressing at 1.6 m per hour.

A linear elastic model was applied to the tunnel lining to model concrete, with $E = 28$GPa, $\upsilon = 0.15$ and $\rho = 2400$ kg m^{-3}, and the actual lining thickness of 0.2 m was adopted.

To reduce computational time, 8-node linear elements were mainly used, with 20-node reduced-integration quadratic elements only in a region immediately surrounding the tunnel, for a smoother pore pressure response. The tunnel lining was modelled with 8-node quadratic continuum shell elements. The lining and soil elements shared the same nodes at the tunnel boundary, thus simulating no-slip contact.

All analyses restricted out-of-plane displacements on the vertical boundaries, whilst displacements at the model base were fixed. Pore pressures were maintained at the ground surface and base of the model to locate the water table at 5 m below the ground surface, defining +50 kPa at the base to impart slight under-drainage to the hydrostatic profile. During the consolidation stages, a drainage-only seepage condition was applied around the tunnel boundary so that pore fluid could flow only into the tunnel, rather than out of it.

3.2 *Constitutive model*

Figure 3 illustrates the representative soil profile—the same used by Wongsaroj (2005)—derived by extrapolating borehole logs from ground investigations (Nyren 1998, Standing & Burland 1999). The stratum 'Made Ground' also includes the underlying Alluvium too.

The constitutive model formulated by Wongsaroj (2005) was adopted to model all soil strata. Building upon a critical-state foundation,

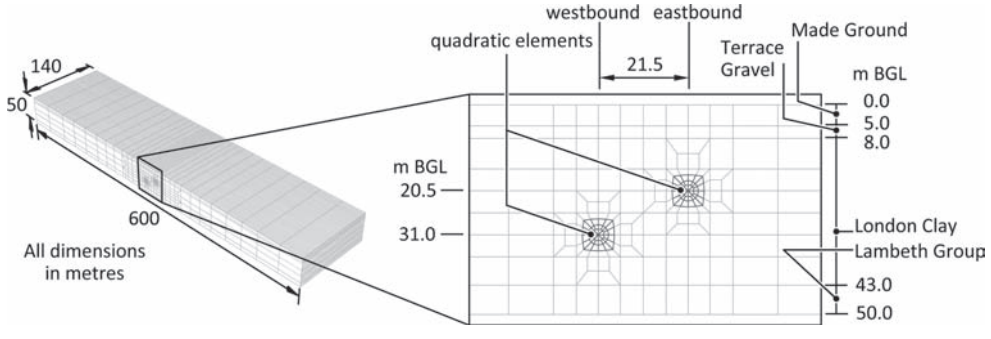

Figure 3. Geometry of 3-D mesh for twin-tunnel analyses.

Wongsaroj incorporated features from previous constitutive models.

The Modified Cam Clay (MCC) yield surface (Wheeler 1997) was adopted, allowing strength anisotropy to be modelled by rotating the yield surface. The equation of its axis is given by $s_{ij} = p' \beta_{ij}$, such that the tensor β_{ij} describes the rotation. The yield surface grows according to the plastic volumetric strain increment $d\varepsilon_v^p$:

$$dp'_0 = \frac{1+e}{e(\rho_c - \rho_r)} p'_0 \, d\varepsilon_v^p \tag{1}$$

where ρ_c as the gradient of the normal compression line, ρ_r that of the swelling line, p'_0 the intercept of the initial yield surface with the hydrostatic axis and e is the void ratio.

Wongsaroj combined elastic and plastic behaviour within the yield surface by implementing the sub-load surface of Hashiguchi & Chen (1998). This surface is geometrically similar to the yield surface, but scaled down by a factor R so that it passes through the current stress point. Its growth is related to its relative size, such that dR is a function of R:

$$dR = u_1 \left(\frac{1}{R^m} - 1 \right) \left\| d\varepsilon^p \right\| \tag{2}$$

where $d\varepsilon^p$ is the plastic strain increment, and u_1 and m are material constants.

Failure in the π-plane followed that proposed by Matsuoka & Nakai (1985).

Wongsaroj adopted a cross-anisotropic elastic stiffness matrix. Small-strain stiffness degrades as formulated in the MIT-S1 model of Pestana (1994). Formulated in log e–log p' space, the swelling gradient ρ_r degrades according to:

$$\rho_r = \frac{1 + \omega_s \xi_s}{C_b} \left(\frac{p'}{p_a} \right)^{\frac{1}{2}} + D\left(1 - \xi^r\right) \tag{3}$$

The constant p_a is the atmospheric pressure, whilst C_b, ω_s, D and r are material constants. The variables ξ and ξ_s are dimensionless distances in stress space since the last stress reversal, defined along the hydrostatic axis and in the deviatoric plane respectively.

The dimensionless distances ξ and ξ_s are reset and the initial stiffness is restored when the stress reverses. A stress reversal is defined according to Pestana (1994), by the scalar product of the current strain increment vector with the vector of accumulated strains since the last reversal. Thus, a negative product defines a change in strain direction.

The soil parameters applied to each stratum are summarised in Table 1. The initial preconsolidation pressure p'_0 varied linearly with depth: varying from 1000 kPa at the surface to 1080 kPa at 8 m depth, then increasing stepwise to 3000 kPa before increasing to 3420 kPa at 50 m depth. A bulk unit weight of 20 kN m^{-3} was applied to all strata. The derivation of these parameters is detailed in Laver (2010).

3.3 *Fissure softening model*

For London Clay, fissure softening was trialled by incorporating a fissure model into the constitutive model formulated by Wongsaroj (2005).

The fissure model assumes that fissures only exist on sub-horizontal and sub-vertical planes, within an inclination of ±16° from the horizontal and vertical directions respectively. Fissures in London Clay have been observed to pre-dominate at these orientations (Skempton et al. 1969).

Softening on these fissures is initiated when a critical friction angle of 11.5° is exceeded on these planes. Softening is implemented by applying a reduction factor to all components of the elastic stiffness matrix isotropically. The reduction factor ramps gradually down from unity to a minimum value as the friction angle rises above the critical value; the range over which this happens was set as 1.5°.

The minimum value of reduction factor, ζ_{min}, is dependent upon the element size to correctly account for the localisation of softening. The relation is given by:

Table 1. Soil parameters applied to strata.

	Stratum			
Parameter	Made ground	Terrace gravel	London clay	Lambeth roup
v_{vh}	0.2	0.2	0.015	0.2
v_{hv}	0.2	0.2	0.04	0.2
v_{hh}	0.2	0.2	0.12	0.2
G_{hh}/G_{vh}	1	1	1.5	1
C_b	100	400	300	900
ω_s	15	15	10	50
ρ_c	0.2476	0.556	0.3	0.37
D	0	0	0.05	0.05
r	0	0	2	2
u_1	100	100	300	100
m	0.1	0.1	0.05	0.1
M	0.984	1.418	0.814	1.07
β_{vv}	0	0	0.1	0
β_{hh}	0	0	–0.05	0
e_0	0.65	0.5	0.7	0.65
K_0	0.6	0.4	1.2	1.2

$$\zeta_{\min} = \frac{1}{1 + \dfrac{f_{\text{fiss min}}}{C_{\text{el}}}} \tag{4}$$

where C_{el} is a characteristic element length. The fissure property $f_{fiss\ min}$ was set as 3.6, determined by fitting to laboratory tests (Laver & Soga 2011).

3.4 *Analyses performed*

Six analyses were performed to investigate the effect of fissure softening and the choice of soil and lining permeabilities. In all analyses, Wongsaroj's soil and lining permeabilities were applied during the rest period between westbound and eastbound excavations.

Alternative permeabilities were only trialled in the final consolidation phase to avoid modelling the computationally expensive eastbound excavation for each trial. The six analyses were:

1. **MODFW** adopts Wongsaroj's constitutive model with fissure softening incorporated, and his choice of soil and lining permeabilities. His soil permeability profile is presented in Figure 4 and is detailed in Table 2, whilst his lining conductivity is represented by the westbound tunnel in Figure 5. The units of London Clay in Table 2 were located from borehole data collected at St James's Park by Standing & Burland (1999).
2. **MODFS1** same as MODFW, but with both kv and kh for Unit A3ii (20.5 m–28 m BGL) halved during the final consolidation.
3. **MODFS2** same as MODFS1, but with both kv and kh for Unit B2 (8 m–20.5 m BGL) reduced tenfold during the final consolidation.
4. **MODFS3** same as MODFS1, but with only k_v for Unit B2 reduced tenfold during the final consolidation.

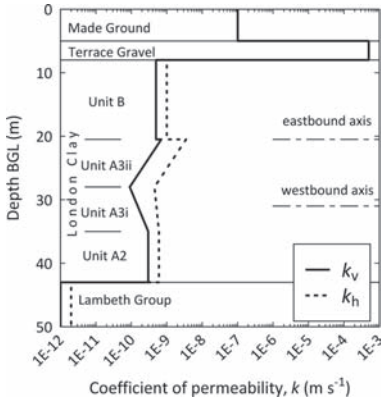

Figure 4. Permeability profile for analyses MODFU & MODFW.

Table 2. Permeability profile for analyses MODFU & MODFW.

	Depth	k_v	k_h
Stratum	m	m s^{-1}	m s^{-1}
Made ground	0–5	5×10^{-7}	5×10^{-7}
Terrace gravel	5–8	1×10^{-4}	1×10^{-4}
London clay			
Unit B2	8–20.5	5×10^{-10}	1×10^{-9}
Unit A3ii	20.5–28	7×10^{-10} to 9×10^{-11}	3.5×10^{-10} to 4.5×10^{-10}
Unit A3i	28–35	9×10^{-11} to 3×10^{-10}	4.5×10^{-10} to 6×10^{-11}
Unit A2	35–43	3×10^{-10}	6×10^{-10}
Lambeth group	43–50	5×10^{-12}	1×10^{-12}

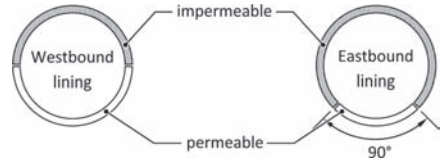

Figure 5. Lining permeabilities for analysis MODFT.

5. **MODFT** same as MODFW, but with the permeable region below the tunnel axis reduced for the eastbound tunnel, as shown in Figure 5.
6. **MODUT** adopts the same permeabilities as MODFT, but with Wongsaroj's unmodified constitutive model.

In trials MODFS1–3, soil permeabilities were rede-fined for the final consolidation stage, so that these trials were not entirely realistic. These trials were conducted purely to investigate the effect of permeability during final consolidation.

4 RESULTS AND DISCUSSION

4.1 *Effect of permeability*

Figures 6 and 7 show vertical displacements due to consolidation and pore pressures around the eastbound tunnel 371 days after its completion. The figures highlight the inadequacy of Wongsaroj's permeabilities (MODFW) to simulate the final consolidation stage:

(i) consolidation below axis level is overestimated by 25%, (ii) slight swelling above the tunnel is not replicated, and (iii) pore pressures above the crown recover to significantly lower values than in the field.

The analyses trialling alternative permeabilities sought to improve the replication. Trials MODFS1

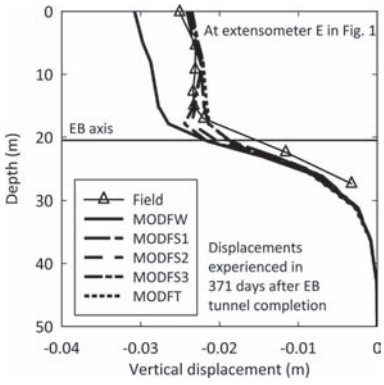

Figure 6. Profiles of vertical displacements adjacent to eastbound tunnel developed in first 371 days after its completion.

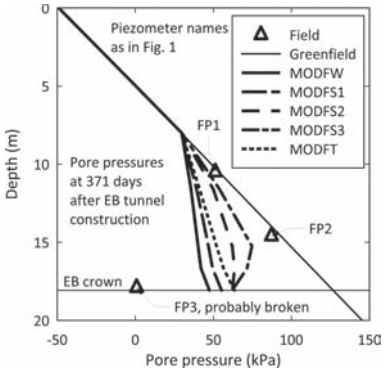

Figure 7. Pore pressure profiles at centreline of eastbound tunnel 371 days after its completion.

and MODFT both successfully reduced the consolidation below the springline to a realistic level. Both trials achieved this by reducing tunnel inflow below axis level in two different ways: MODFS1 reduced the permeability of the stratum encompassing the lower half of the tunnel (Unit A3ii), whilst MODFT reduced the conductivity of the lining itself below the spring-line. The fact that adjusting either the soil or the lining conductivity gave the same improvement highlights the uncertainty associated with backanalysing permeability values from field data.

However, both trials failed to replicate the swelling region above the crown and the recovery of pore pressures here. To overcome this, trials MODFS2 and MODFS3 reduced the permeability of the stratum encompassing the upper half of the tunnel (Unit B2). Trial MODFS2 maintained the same ratio between vertical and horizontal permeabilities, whilst trial MODFS3 reduced only the vertical permeability, giving $k_h/k_v = 20$.

Figure 6 shows that both trials reproduced the swelling zone above the crown. However, trial MODFS3 fitted the recovery of pore pressures significantly better in Figure 7.

The horizontal permeability (10^{-10} m s^{-1}) adopted for MODFS2 is still realistic, and within the range for Unit B2 (Hight et al. 2007). However, the permeability anisotropy ratio in trial MODFS3 is unexpectedly high for London Clay; two possible explanations for this are:

- Unit B2 may have a high in-situ anisotropy due to laminations. Nyren (1998) reported that clay-stone bands were encountered in 75% of boreholes sunk around St James's Park. The clay-stone would be less permeable than the surrounding clay, and would reduce the vertical permeability, whilst maintaining the horizontal permeability.
- The permeability of Unit B2 might have evolved due to tunnelling stress changes. The extension stress path above the crown might have closed vertical flow paths, but opened horizontal ones. Similar swelling and pore pressure recovery was also observed above the westbound tunnel crown (Nyren 1998)—founded instead in Unit A3i—suggesting stress-related permeability change to be the primary cause, rather than laminations in the strata.

Also, the need to modify soil permeabilities to match the field data for the final consolidation phase suggests that the permeability profile varies transversely between the two tunnels.

4.2 *Performance of fissure model*

Figure 8 compares normalised settlement troughs from trials MODUT and MODFT to assess the performance of the fissure model in replicating

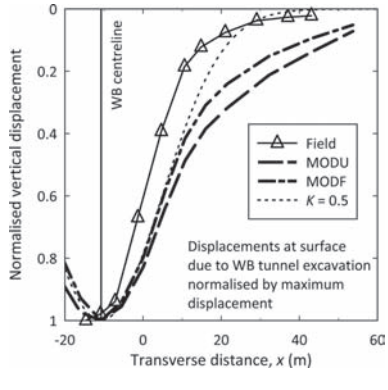

Figure 8. Surface settlement troughs due to westbound tunnel excavation.

the westbound tunnel excavation. Trials MODUT and MODFT both adopt the lining permeabilities shown in Figure 5; this improved the modelling of consolidation below the eastbound tunnel without the need to redefine soil permeabilities for the final consolidation.

The figure shows that both trials produce significantly wider troughs than those in the field, even though the trough at St James's Park is unusually narrow—with $K = 0.35$ (Nyren 1998) instead of $K = 0.5$, as expected for clay (Mair et al. 1993).

Despite this, comparison of trials MODUT and MODFT demonstrates that fissure softening helped to simulate a narrower trough. This is because the fissure model preferentially softened behaviour in simple shear compared with other shearing modes.

Figure 9 identifies different shearing modes during tunnel excavation, showing that simple shear modes are active between the tunnel and the ground surface. Softer behaviour in these modes for trial MODFT reduced the spread of settlement, resulting in a narrower trough.

The fissure model provides a realistic method to make the trough narrower for fissured clays like London Clay, even though the trough is still too wide. However, narrower troughs are also observed for un-fissured clays in the field, e.g. Guedes de Melo & Santos Pereira (2000).

For unfissured clays, an alternative to simulating softer shear behaviour without invoking fissure softening would be to apply the tangential stress rate (Hashiguchi & Tsutsumi 2001). Here, plastic strains evolve according to the component of the stress increment tangential to the yield surface, in addition to the normal component. However, the implementation is currently limited to isotropic elasticity; generalisation to anisotropic elasticity would render it practically useful for modelling clays in large-scale numerical analyses.

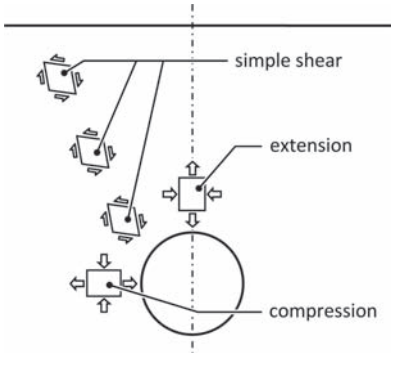

Figure 9. Shearing modes induced by tunnel excavation.

4.3 *Replication of long-term settlements*

Figures 10 and 11 present the long-term settlements developed since completion of the eastbound tunnel, showing variation with time and settlement troughs respectively.

Figure 10 shows that predicted settlement rates agree well with the field data in the first few years. After this however, settlement in the field continues to develop at an appreciable rate, showing little signs of decaying, even after 10 years.

This could be due to the overestimation of coefficient of consolidation c_v in the field; also presented on Figure 10 is an analysis adopting back-analysed values of stiffness and permeability; the stiffness parameter C_b for London Clay was reduced from 300 to 100, whilst both horizontal and vertical permeabilities of Unit A3ii—encompassing the permeable portion of the eastbound lining—were

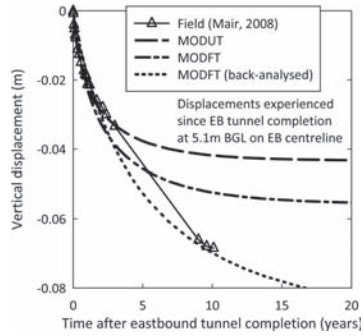

Figure 10. Development of long-term settlement with time after eastbound tunnel completion.

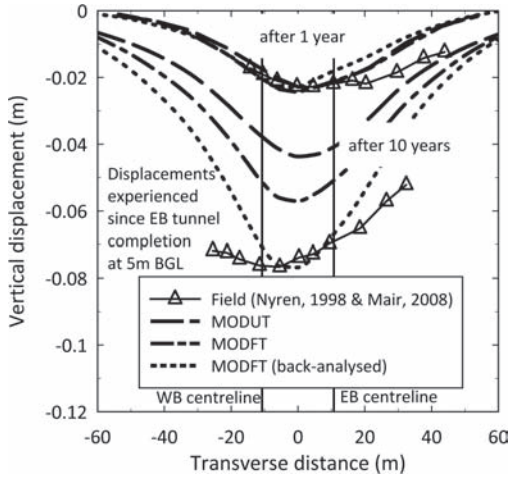

Figure 11. Long-term settlement troughs after eastbound tunnel completion.

halved. This demonstrates that the field data can be fitted by reducing c_v; whether the back-analysed stiffness and permeability are realistic for the site remains to be ascertained. It should also be noted that the back-analysed plot does not represent a realistic simulation: the stiffness and permeability were only modified in the final consolidation stage; the plot is therefore only demonstrative.

In Figure 11, simulated trough widths are roughly similar to those in the field; differences can be attributed to transverse variation in the permeability profile.

5 CONCLUSIONS

This paper presented the simulation of the JLE twin-tunnel construction below St James's Park using coupled-consolidation finite-element analyses.

The analyses investigated the effect of defining different soil and lining permeabilities on the final consolidation phase. A different soil permeability profile best-matched the consolidation stage after eastbound excavation than that after the west-bound one, highlighting a transverse variation of permeability in the field.

Defining a high degree of permeability anisotropy for the stratum encompassing the eastbound tunnel crown resulted in a more realistic pore pressure response. In the field, the high anisotropy might either be due to stress-induced permeability changes or to the presence of claystone laminations. These findings highlight the need for more data on field permeabilities, particularly on how permeability evolves with stress change. The findings also highlight the sensitivity of long-term behaviour to both soil and lining permeabilities.

The analyses also assessed the performance of the fissure model in simulating tunnel excavation. The analysis incorporating the fissure model successfully produced a narrower settlement trough—more alike that in the field—by preferentially softening behaviour in simple shear. The fissure model therefore provides a realistic method of replicating a narrow settlement trough in fissured clays. For unfissured clays, similar behaviour might be achievable by incorporating the tangential stress rate (Hashiguchi & Tsutsumi 2001).

The simulations highlighted that settlements in the field continue to develop at an unexpectedly high rate, which can be attributed to an overestimation of stiffness and permeability in the field.

REFERENCES

Guedes de Melo, P.F.M. & C. Santos Pereira (2000). The role of k_0 value in numerical analysis of shallow tunnels. In Kusakabe, Fujita, and Miyazaki (Eds.), *Proc. Int. Symp. Geotech. Aspects of Underground Construction in Soft Ground*, Rot-terdam, pp. 379–384. Balkema.

Harris, D.I. (2002). Long term settlement following tunnelling in overconsolidated London Clay. In *Proc. 3rd Int. Symp. Geotech. Aspects of Underground Construction in Soft Ground*, Toulouse, pp. 393–398.

Hashiguchi, K. & Z.P. Chen (1998). Elastoplastic constitutive equation of soils with the subloading surface and the rotational hardening. *Int. J. Numer. Anal. Methods in Geomechanics 22*, 197–227.

Hashiguchi, K. & S. Tsutsumi (2001). Elastoplastic constitutive equation with tangential stress rate effect. *Int. J. Plast. 17*, 117–145.

Hight, D.W., A. Gasparre, S. Nishimura, N.A. Minh, R.J. Jardine, & M.R. Coop (2007). Characteristics of the Lon-don Clay from the Terminal 5 site at Heathrow Airport. *Géotechnique 57* (1), 3–18.

Laver, R.G. (2010). *Long-term behaviour of twin tunnels in clay*. Ph. D. thesis, University of Cambridge.

Laver, R.G. & K. Soga (2011). Performance of two constitutive models for fissures in clay. In *Int. Symp. on Deformation Characteristics of Geomaterials*, Seoul, Korea. in press.

Mair, R.J., R.N. Taylor, & A. Bracegirdle (1993). Subsurface settlement profiles above tunnels in clays. *Géotechnique 43* (2), 315–320.

Matsuoka, H. & T. Nakai (1985). Relationship among Tresca, Mises, Mohr-Coulomb and Matsuoka-Nakai failure criteria. *Soils & Foundations 25*(4), 123–128.

Nyren, R.J. (1998). *Field measurements above twin tunnels in clay*. Ph. D. thesis, Imperial College of Science, Technology & Medicine, London.

Pestana, J.M. (1994). *A unified constitutive model for clays and sands*. Ph. D. thesis, Massachusetts Institute of Technology, Boston.

Skempton, A.W., R.L. Schuster, & D.J. Petley (1969). Joints and fissures in London Clay at Wraysbury and Edgware. *Géotechnique 19* (2), 205–217.

Standing, J.R. & J.B. Burland (1999). Report on ground characterisation to explain tunnelling volume losses in the West-minster area. Internal report, Imperial College of Science, Technology & Medicine, London.

Wheeler, S.J. (1997). A rotational hardening elasto-plastic model for clays. In *Proc. 14th Int. Conf. Soil Mech. & Foundation Engng.*, Volume 1, Hamburg, pp. 431–434.

Wongsaroj, J. (2005). Three-dimensional finite element analysis of short and long-term ground response to open-face tunnelling in stiff clay. Ph. D. thesis, University of Cambridge.

Geotechnical Aspects of Underground Construction in Soft Ground – Viggiani (ed)
© 2012 Taylor & Francis Group, London, ISBN 978-0-415-68367-8

The efficiency of compensation grouting in sands

K. Soga
University of Cambridge, Cambridge, UK

A. Bezuijen
Deltares/Delft University of Technology, Delft, The Netherlands

K. Eisa
Atkins Ltd., London, UK

ABSTRACT: Physical model experiments on compensation grouting in sands were performed in two different setups (Cambridge and Delft). The effect of water-cement (w/c) ratio, bentonite content (b.c.) and injection rate on compensation efficiency was investigated. Results show a considerable drop in compensation efficiency resulted from reducing the soil density. Injection in dense sand (R.D. = 93%) resulted in efficiencies between 40–90%, whereas injection in medium-dense sand (R.D. = 60–75%) yielded in reduced efficiencies between 10–40%. When the w/c ratio increased from 0.5 to 1.5 for a given density (R.D. = 93%) and the b.c. of 4%, the compensation efficiency value decreased. Typical efficiencies were between 60% and 40–50% for w/c ratios of 0.5 and 1.5, respectively. The values of compensation and grout efficiencies were almost equal, suggesting that pressure filtration happens mainly during injection. Increasing the b.c. improved the compensation efficiency. When a higher b.c. of 12% to 14% was used, typical compensation efficiencies in dense sand were 78 and 90% for w/c ratios of 1.5 and 1.8 respectively.

1 INTRODUCTION

When an underground excavation takes place, as in tunnel boring, stress relief occurs in the surrounding soil with a tendency of the soil to move towards the opening produced by the excavation. This causes serious movements to the structures above the ground, which may result in severe damage. In compensation grouting, the grout material is injected between the structures and the excavated area to compensate for the volume loss and therefore counteract the resulting settlement (Mair and Hight, 1994).

The success of any compensation grouting project is assessed by whether the observed settlements were corrected or not and how much grout had to be injected to achieve that target. Soga et al. (1999) defined grout efficiency, η, as the ratio of the increase in soil volume of a volume element local to grout injection points, V_E, to the injected volume of grout, V_{inj} as shown in Figure 1.

Under ideal conditions, the volume increase should be equal to the volume injected, giving a grout efficiency of 1. However, this is not the case in practice. The resulting volume increase is always less than the volume of injected grout due to the fluid being "squeezed" out of the grout mix (pressure filtration) and the grout escaping from the designated area by migration along fractures or existing zones of weakness in the soil. Even when a good ground response is achieved immediately after injection, the grout efficiency tends to decrease with time due to continuing pressure filtration and/or dissipation of positive excess pore pressures in the case of clayey soils (Soga et al., 2004).

Furthermore, compensation efficiency, ζ, is defined as the ratio of the volume of the surface heave created by grouting, V_{SH}, to the injected volume of grout (V_{inj}). This efficiency is affected, in addition to local losses, by the far-field geometry of the site. Figure 1 shows the difference between grout and compensation efficiencies as well as some of the boundary conditions that might affect the latter.

Compensation efficiencies of 3–22% are reported for compensation grouting in the field (Chambosse and Otterbein, 2001; Au et al., 2003). Somewhat higher values, 30–50%, in stiff London Clay (Mair, 2003). Soga et al. (2004) performed grout in the laboratory on clay specimens prepared at different overconsolidation ratios ranging from 1 to 10. For highly overconsolidated clay the compensation efficiency was close to 1 irrespective of grout spacing and injection sequence. For normally consolidated and lightly overconsolidated clays the

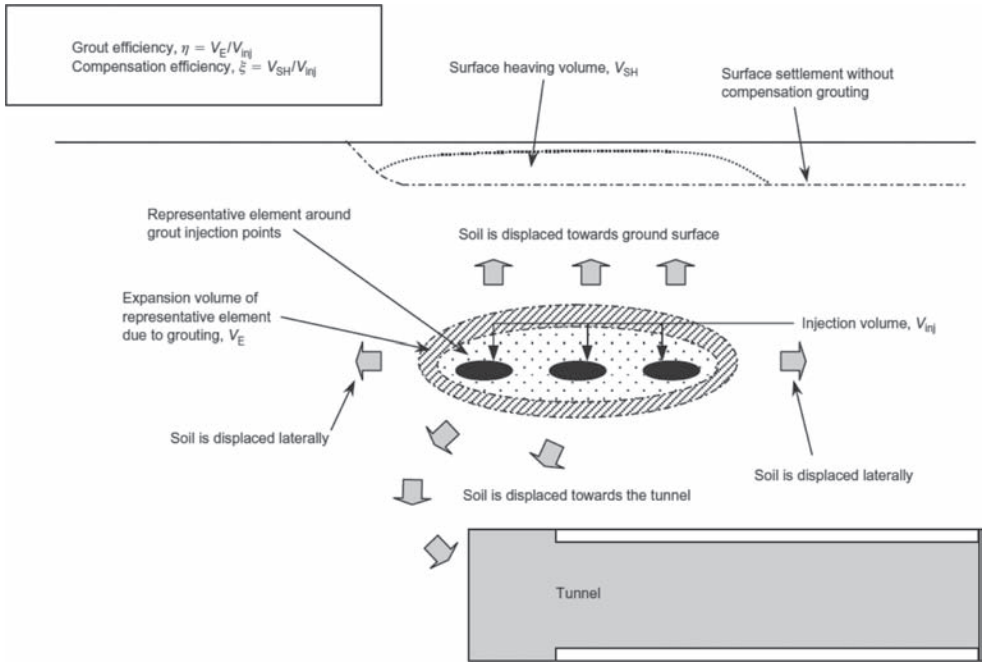

Figure 1. Grout efficiency and compensation efficiency in compensation grouting (after Soga et al., 2004).

grout efficiency increased when the separation in space and time between the injections was reduced (sometimes a negative efficiency). A finite element study of the laboratory experiments (Au et al., 2003) confirmed a mechanism that the grout efficiency of normally consolidated and lightly overconsolidated clays can reduce dramatically with time, owing to (a) soil contraction by extensive shearing during the injection, and (b) soil compression by the ultimate increase in mean effective pressure around the injection point caused by the injection pressure locked in when the grout solidified. For heavily overconsolidated clays, the pore water migrated from the positive excess pore pressure zone around the injection point to the negative zone some distance away from the injection point, during the consolidation stage. Soil compression near the injection point and swelling at some distance away from the injection point resulted in a negligible overall consolidation effect for heavily overconsolidated clays.

There is limited study on compensation grouting in sands and its efficiency. In this study, physical model experiments of compensation grouting in sands were performed in two different setups (Cambridge and Delft). One of the objectives of the experiments was to evaluate the compensation efficiency of cement bentonite grouting in sand. The results of the experiments are presented in this paper.

2 EXPERIMENTAL SET-UP

2.1 *Cambridge set-up*

The Cambridge experimental setup is shown in Figure 2. A steel consolidometer tub of 850 mm in internal diameter and 400 mm in height was used as the model container. To apply confining pressure on the large cross-sectional area of the tub, a latex air bag was fixed to the inner side of the tub cover. In all experiments reported in this paper, a confining pressure of 100 kPa was applied.

An open-ended injection tube was used for grout injection. The zinc-plated steel tube had an outer diameter of 14.5 mm, an inner diameter of 12.5 mm and a total length of 550 mm. The injection tube was inserted approximately at the middle of the sample height with a slope of 1:60 downwards. Cling film was wrapped around at the end of the tube in order to prevent sand from entering. Grout injection was conducted using a progressive helical cavity pump, which is capable of producing a continuous, uniform flow of grout (0.2 to 3.33 litre/min). A pressure transducer was connected to the end of the injection tube, about 250 mm outside the tub to measure the injection pressure.

Injection tests were conducted in Leighton Buzzard fraction D clean silica sand (particle size 150~300 μm, $e_{max} = 0.988$ and $e_{min} = 0.585$, $k = 5 \times 10^{-4}$ m/s at 93% relative density). The sand

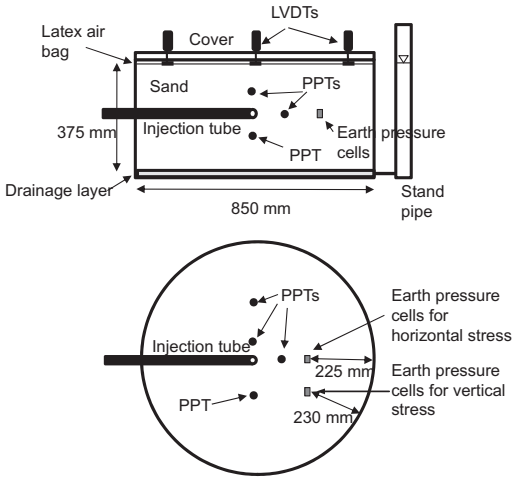

Figure 2. Cambridge set-up.

was poured in the tub in dry condition using a computer-controlled sand hopper. After sand pouring finished, the pores were filled with carbon dioxide and the water table was raised from the bottom in order to saturate the sample. For all the tests, the relative density was 93%. Free drainage at the bottom of the model was allowed through a drainage layer that consisted of 6 mm clean gravel covered with a sheet of geotextile.

The model was instrumented with miniature pore pressure transducers (PPTs, Druck PDCR81), earth pressure cells (EPCs) and linear variable differential transducers (LVDTs) as shown in Figure 2. Holes were made in the air bag to install LVDTs so that the sample surface movement during injection could be monitored. In the current experiments, the pore pressure change was very small because the sand had a relatively large permeability.

Further details of the experimental system can be found in Eisa (2008).

2.2 *Delft set-up*

The Delft experimental setup is shown in Figure 3. Grout injection tests were conducted in a cylindrical steel container of a 900 mm diameter and a changeable height (600 mm or 830 mm). A PVC plate rested on the top of the saturated sand sample, tightly sealing it off from an upper water chamber by means of rubber O-rings. Confinement was applied by means of pressurising this water chamber using compressed air. Air pressure was applied through a glass cylinder that also showed the change in water level resulting from soil heave. This change was measured during the experiment with a differential pressure transducer. In order to raise the K_0 to a value closer to 1, the sand model was "over-consolidated" by applying a confining pressure of 300 kPa at the beginning and then the confinement was reduced to 100 kPa before the grout injection.

A simplified model of the tube à manchette (TAM) ran across the diameter of the cylindrical container as shown in Fig. 3. The tube had an internal diameter of 22 mm, with four 7 mm holes at the middle, equally spaced around the perimeter. A rubber sleeve covered the holes and two rings, one on each side, were used to prevent the injected grout from flowing along the tube. The injection tube position was fixed at 360 mm above the bottom of the container. Grout injection was performed using a plunger pump and an injection rate up to 10 litre/minute. Four pore pressure transducers and two total stress cells were placed around the injection point.

Baskarp sand (particle size 90~200 μm, $e_{max} = 0.88$, $e_{min} = 0.52$, $k = 8 \times 10^{-5}$ m/s at e_{min}) was used in the Delft tests. The sand was wet-pluviated into water inside the model container. Two pumps were used to circulate sand around in a storage tank filled with water and a third one was used to pump the sand into the sample container. This sample preparation technique produced samples of

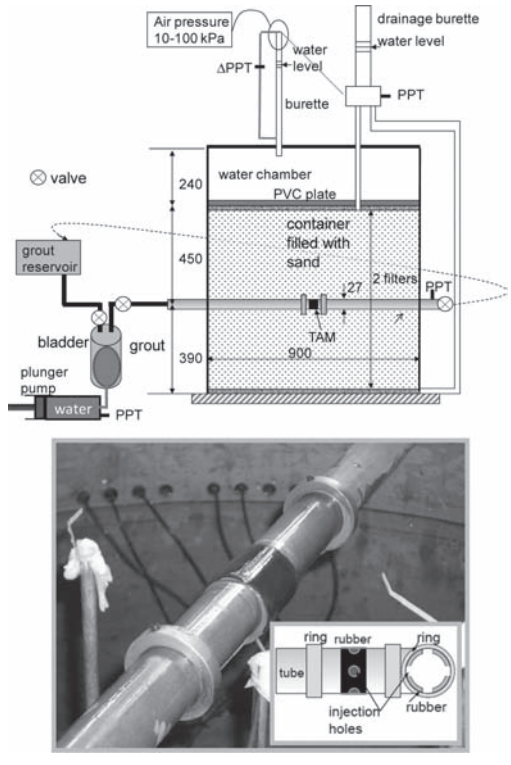

Figure 3. Delft Setup.

about 10% relative density. The loose sand model was then densified to required relative densities (60% or 70%) by dropping the whole container over a height of 25 mm as many times as required. At the end of the densification stage, the sample was trimmed to the desired height and the actual relative density was checked by means of weight and volume measurements. The model had a double drainage system.

Further details of the experimental system can be found in Sanders (2007) and Rietdijk et al. (2010).

2.3 *Testing programme*

Using the two experimental setups, 28 successful grout injection tests were performed for the conditions described above (see Table 1). The tests investigated the effect of water-cement (w/c) ratio, bentonite content (b.c.) and injection rate on soil-grout interaction. Only selected data will be presented in this paper to report the effect of these parameters on grouting behaviour in sandy soils. Further details can be found in Kleinlugtenbelt (2005), Sanders (2007) and Eisa (2008).

Ordinary Portland cement (OPC)-bentonite mixtures were used. The OPC used at Cambridge (Rugby by Rugby Cement and Blue Circle-ProCem by Lafarge Cement) conform to the British/European Standard BS EN 197–1-CEM I and have a density in the range of 2800–3200 kg/m^3 and a mean particle size of 5–30 μm. The OPC used at Delft (Lengfurt CEM I, 42.5R) develops strength more rapidly than the other types used. However, this has no effect on the results of the grout injection tests since all the processes that are of interest to this study take place during and shortly after injection before cement hardens.

The tested grouts had w/c ratios ranging from 0.5 to 200. In the Cambridge mixes, sodium bentonite (GWB Wyoming, Steetley Bentonite & Absorbents) was used. The b.c. was varied as 0.4%, 4% and 8% by weight of mixing water. For the Delft tests, sodium-activated bentonite (Colclay D90, Ankerpoort NV) was used. The b.c. was varied as 4% and 7% by weight of mixing water.

The method of grout mixing is very important because different mechanical properties could be obtained by using different mixing methods even with the same grout constituents. A high-shear roller mixer (R14 Roller Mixer by Colcrete Eurodrill company (Cambridge) and T50 basic Ultra Turrax by IKA Laboratory (Delft)) were used. They operate on the principle of the colloidal mill and wets or hydrates each particle of powder by an intensive shearing action, which results in complete dispersion by mechanical means. Before mixing, bentonite was hydrated using de-aired water and left for 24 hours. De-aired water was used for mixing so as to reduce the possibility of having air bubbles in the injection system. OPC was then gradually added to the pre-hydrated bentonite while being mixed. The time needed for this process varied depending on the amount of the cement and the bentonite to be introduced, but it was kept constant for similar mixes.

Table 1. Testing programme.

Set up	w/c	Bentonite %	Injection rate (l/min)	Injection volume (l)
Cambridge	0.5	0.4	0.385	0.98
(14 tests)	–5.0	–8	–3.33	–1.38
Delft	1.0	4	2	0.67
(14 tests)	–200	–7	–10	–1.0

3 TEST RESULTS

3.1 *Cambridge tests*

The surface heave of the soil sample during injection was measured by means of 5 LVDTs. Using these point-measurements, the heaving profile along the diameter of the soil sample could be drawn. A curve-fitting technique has to be used in order to calculate the heaved volume and consequently the compensation efficiency.

For most of the Cambridge tests, the heaving profile was found to have a maximum value directly above the initial location of the injection point; with lower values recorded towards the sides of the soil samples. This suggests that the heaving profile could be approximated by a Gaussian distribution. Taking the point of injection as the origin, heaving at any point, h, is then given as:

$$h = h_{\max} e^{-0.5(x/i)^2}$$

Where: h_{max} is the maximum heave above the injection point, x is the distance from the origin to the point at which heaving is required, and i is the standard deviation or the distance from the origin to the point of inflection.

The Gaussian distributions obtained for several Cambridge tests using the Least-squares method are shown in Figure 4, along with the point-measurements of the actual heaving at the end of injection. Although further experimental investigation is needed to verify the applicability of Gaussian distribution to approximate the ground displacement profile by a point source, a reasonably good fitting was obtained in most of the tests, with the exception of tests using grouts of w/c = 5.0. Fracture grouting was experienced in these cases and the

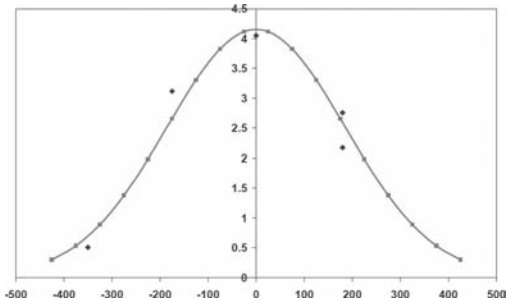

Figure 4. Examples of LVDT readings and the fitted Gaussian curve (scale in mm).

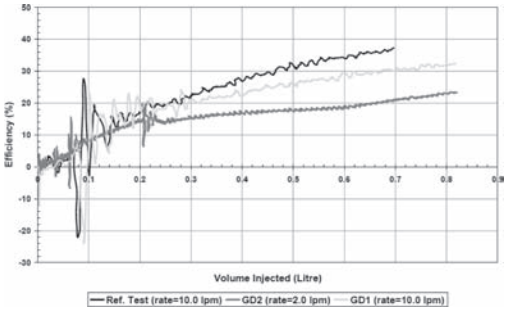

Figure 5. Change in compensation efficiency with injection volume.

heaving patterns were affected by the non-uniform movement of grout inside the soil model. Based on the fitted Gaussian distributions, the total heaved volume from each test was calculated.

The grout efficiency for the different injection tests was calculated as the ratio between the volume of the hardened grout (24 hours after the injection test) and the injected grout volume. Water displacement was used to obtain the volume of the hardened grout. The grout material was left submerged into water for 2–3 minutes for any voids to be filled before it was dipped into a container filled with water and the displaced volume was measured. The end w/c ratio was calculated assuming that the difference between the injected and the hardened grout volumes is solely due to the loss of water by pressure filtration. The volume of the hardened grout was not measured for some of the tests because they yielded sand fracturing or due to experimental difficulties.

3.2 *Delft tests*

Heaving of soil sample was continuously measured during injection in the GeoDelft setup. This was done by means of a differential pressure transducer that measures the pressure at the base of a glass cylinder filled with water and connected to the compressed air supply system. As a result, it is possible to plot the change in compensation efficiency as the injection progresses. Figure 5 shows the change in efficiency for different injection tests. The unexpected surges in efficiency in some of the tests resulted from the readings of heaved volume being affected by some air bubbles in the measuring glass cylinder.

In general, the compensation efficiencies for almost all the GeoDelft tests were lower than the values of the Cambridge tests because of the lower relative density of the soil samples (R.D = 70%, compared to 93% in the Cambridge tests). The grout efficiency was not measured in this series of tests.

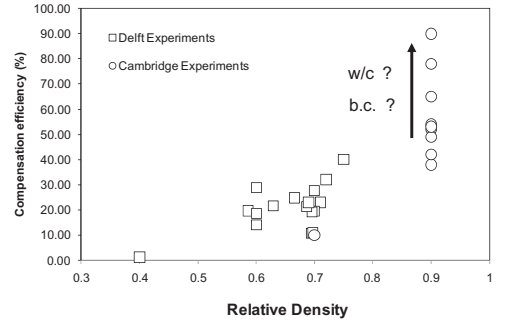

Figure 6. Effect of relative density on compensation efficiency. The arrows next to w/c and b.c. show that the compensation efficiency increases with decrease in w/c and increase in b.c.

3.3 *Effect of soil density*

A considerable drop in compensation efficiency resulted from reducing the soil density as shown in Fig. 7. Injection in dense sand (R.D = 93%) resulted in efficiencies between 40–90%, whereas injection in medium-dense sand (R.D = 60–75%) yielded in reduced efficiencies between 10–40%. The variation for a given density is due to differences in water-to-cement ratio and bentonite content, which will be discussed in later sections. One injection test was performed in a soil model with R.D. = 40%. In this case, the compensation efficiency was close to zero percent.

When grout was injected in medium-dense or loose sand, soil had to be compacted before any heaving would occur, whereas the response of dense soil was much quicker. This may explain why in practice a pre-conditioning stage, in which a grout mix is injected to compact soil, is usually performed prior to the commencement of compensation grouting.

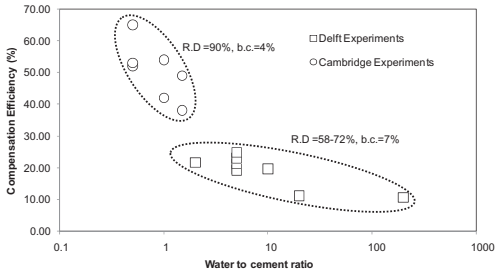

Figure 7. Effect of water-to-cement ratio on compensation efficiency.

3.4 *Effect of w/c ratio*

Figure 7 shows the effect of w/c ratio for a given soil density of R.D. = 93% (Cambridge experiments). Only the data with a bentonite content of 4% is presented (the effect of benonite content is presented later). For grout mixes of the low w/c ratio of 0.5, typical grout and compensation efficiencies were around 60%. As shown in Figure 8, most of the grout remained close to the injection point, creating a reasonably regular shape of hardened material due to the limited amount of free water in the grout mix. Therefore, no significant change in compensation efficiency with the injection rate is to be expected.

When the w/c ratio increased from 0.5 to 1.5, the compensation efficiency value decreased. As shown in Figure 7, typical efficiencies were between 45–55% and 40–50% for w/c ratios of 1.0 and 1.5, respectively. There was some influence of the injection rate on the efficiency. With more free water in the mix, faster injection allows less time for pressure filtration to take place during injection and so the loss in injected volume becomes less. Furthermore, fingering starts to take place when mixes of moderate w/c ratios are injected faster. This causes the grout to cover a larger area, but the shape of the hardened material becomes thinner, as shown in Figure 9. The difference in efficiency due to the change in injection rate was about 11–12%.

Figure 10 shows a comparison between the compensation efficiencies and the grout efficiency for experiments using grouts with w/c ratio ranging from 0.5 to 1.5. As described before, compensation efficiencies are calculated at the end of injection, whereas grout efficiencies are based on the volume of the hardened grout 24 hours later. The values of compensation and grout efficiencies were almost equal, which suggests that pressure filtration happens mainly during injection. In the dense sand (RD = 93%) there will be hardly further densification during the injection and since the container prevents lateral deformation all grout volume present after injection results in the same volume

Figure 8. Hardened grout for w/c = 0.5 and b.c. = 4%.

(a) Slow injection 0.385 l/min

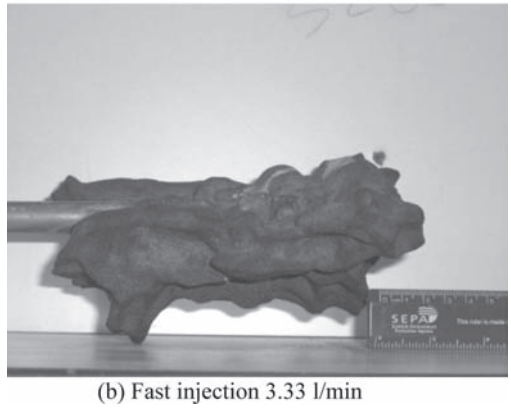

(b) Fast injection 3.33 l/min

Figure 9. Hardened grout for w/c = 1.5 and b.c. = 4%.

of heave. At lower relative densities of the sand the compensation efficiency will be less than the grout efficiency due to densification of the sand.

With the Cambridge set-up, it was not possible to calculate the efficiency for grouts with very high w/c ratios, since the injected grout spread unevenly

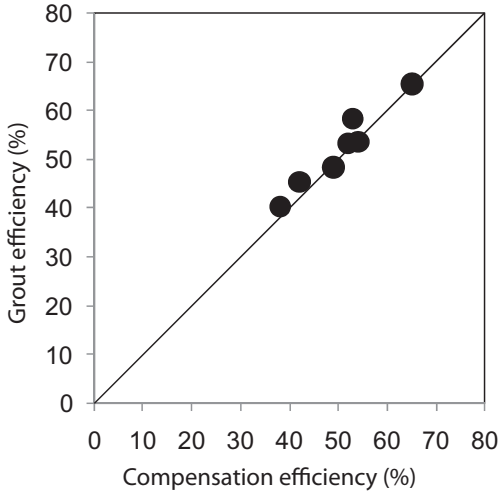

Figure 10. Comparison between grout efficiency and compensation efficiency from the experiments using grout with w/c = 0.5 to 1.5.

within the soil and it was not possible to compute the heaved volume accurately, as discussed before.

On the other hand, it was possible to evaluate the compensation efficiency using the Delft setup irrespective of hardened grout shapes. Experiments performed in medium dense sand (R.D. = 58–72%) resulted in efficiencies of between 10–30%. It was found that the efficiency decreased with the water-to-cement ratio as shown in Figure 7. The effect of injection rate becomes more evident for the high w/c ratio of 5.0. The grout tends to spread more for a faster injection rate as shown in Figure 11. The compensation efficiency was 23% when the injection rate was 2.00 litre/minute, where it increased to 32–37% when the injection rate was 10.00 litre/minute. With more free water in the mix, faster injection allowed less time for volume loss by pressure filtration and so, higher efficiencies were achieved.

For a grout with a WCR of 2 and 8% of betonite (percentages given by weight), the volume of solids is only 20% of the total volume. Assuming a porosity between the solids of 40%, the total volume of solids and pores is 33% of the total volume. This means that the loss of water can already have a large influence on the efficiency as defined above.

3.5 *Effect of bentonite content*

The change in bentonite content had an influence on the compensation efficiency as shown in Fig. 12. For tests with grout of w/c = 1.5 (injection rate = 3.33 litre/minute), increasing the bentonite content from 4% to 8% improved the compensation

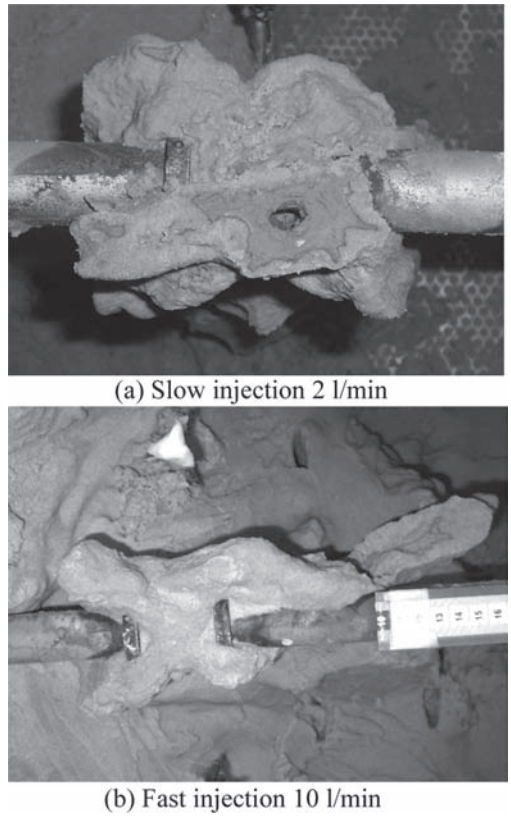

Figure 11. Hardened grout for w/c = 5.0 and b.c. = 7%.

efficiency by about 30%. When a higher bentonite content of 12% and 14% were (??) used, typical compensation efficiencies were 78 and 90% for w/c ratios of 1.5 and 1.8 respectively. This is attributed to the influence of bentonite content on pressure filtration.

The substantially high efficiency of 90% was the result of sand fracturing, as the accompanying

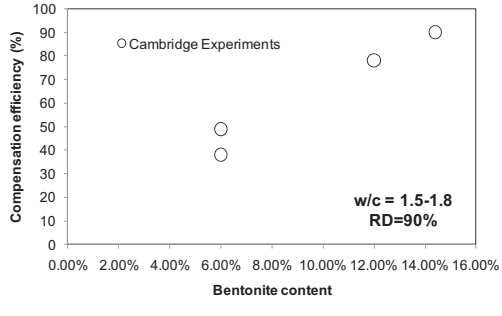

Figure 12. Effect of bentonite content on compensation efficiency from the tests using grout of w/c = 1.5 to 1.8.

formation of a low permeability particle accumulation around the fractures would limit the occurrence of pressure filtration.

4 CONCLUSIONS

Physical model experiments on compensation grouting in sands were performed in two different setups (Cambridge and Delft). Although there were difference in the way soil heave was measured in the two setups used, different approaches were adopted to assess the compensation efficiency of the grouting tests by the end of injection. Nonetheless, a reasonable agreement was found between the results obtained from the two setups.

The effect of water-cement (w/c) ratio, bentonite content (b.c.) and injection rate on compensation efficiency was investigated. Results show that a considerable drop in compensation efficiency resulted from reducing the soil density. Injection in dense sand (R.D = 93%) resulted in efficiencies between 40–90%, whereas injection in medium-dense sand (R.D = 60–75%) yielded in reduced efficiencies between 10–40%. When an injection test was performed in a soil model with R.D. = 40%, the compensation efficiency was close to zero percent (Kleinlugtenbelt, 2005).

When the w/c ratio increased from 0.5 to 1.5 (a bentonite content of 4%) for a given density (R.D. = 93%), the compensation efficiency value decreased. Typical efficiencies were between 60% and 40–50% for w/c ratios of 0.5 and 1.5, respectively. Using the Cambridge set-up, it was possible to compare the compensation efficiency to the grout efficiency. The values of compensation and grout efficiencies were almost equal, suggesting that pressure filtration happens mainly during injection and sideways deformation is negligible.

A similar finding was made when the w/c ratio was varied from 2 to 200 using the Delft setup. Experiments performed in medium dense sand (R.D. = 58–72%) resulted in decrease in compensation efficiency from 30% to 10% when the w/c ratio increased from 2 to 200.

Increasing the bentonite content improved the compensation efficiency. When a higher bentonite content of 12% to 14% was used in dense sand, typical compensation efficiencies were 78 and 90% for w/c ratios of 1.5 and 1.8 respectively. The higher content of fine particles led to a considerable reduction in pressure filtration, which is in agreement with the literature review (Rawlings et al., 2000 and Bruce et al., 1997). Consequently, more fingering took place and a significant improvement in efficiency was achieved.

REFERENCES

Au, S.K.A., Soga, K., Jafari, M.R., Bolton, M.D. and Komiya, K. (2003): "Factors affecting long-term efficiency of compensation grouting in clays," *Journal of Geotechnical and Geoenvironmental Engineering, ASCE, Vol. 129, No. 3*, pp. 254–262.

Bruce, D.A.; Littlejohn, G.S. and Naudts, A.M.C. (1997), Grouting Materials for Ground Treatment: A Practitioner's Guide, Grouting: Compaction, Remediation and Testing, *Geotechnical Special Publication No. 66, ASCE, New York, USA*, pp. 306–334.

Chambosse and Otterbein, (2001) State of compensation grouting in Germany. *Proc. XVth Int. Conf. on Soil Mechanics & foundation Eng.*, Turkey, Istanul. 1511–1514.

Eisa, K. (2008) Compensation Grouting in Sand, PhD dissertation, University of Cambridge.

Kleinlugtenbelt, R. (2005), *Compensation Grouting, Laboratory Tests in Sand*, MSc thesis, Delft University of Technology, the Netherlands.

Mair, R.J. (2004), Research on tunnelling-induced ground movements and their effects on buildings—Lessons from the Jubilee Line Extension. *Response of buildings to excavation-induced ground movements,* Jardine F.M. (ed.) CIRIA Special publication 201, ISBN 0860175774. pp. 3–26.

Mair, R.J. and Hight, D.W. (1994), Compensation Grouting, *World Tunnelling*, November, pp. 361–367.

Rawlings, C.G., Hellawell, E.E. and Kilkenney, M.W. (2000), *Grouting for Ground Engineering,* CIRIA, The Basingstoke Press, Hampshire, UK.

Rietdijk, J., Schenkeveld, F.M., Schaminée, P.E.L., Bezuijen, A. 2010. The drizzle Method for Sand Sample Preparation. *Proceedings of the International Conference on Physical Modelling in Geotechnics 2010 (ICPMG 2010)* 267–272.

Sanders, M.P.M. (2007), *Hydraulic Fracture Grouting, Laboratory Tests in Sand,* MSc thesis, Delft University of Technology, the Netherlands.

Soga, K., Bolton, M.D., Au, S.K.A., Komiya, K., Hamelin, J.P., Van Cotthem, A., Buchet, G. and Michel, J.P. (1999), Development of Compensation Grouting Modelling and Control System, *Proceedings of the 3rd International Symposium on Geotechnical. Aspects of Underground Construction in Soft Ground, Tokyo*, Balkema, Rotterdam, the Netherlands, pp. 425–430.

Soga, K., Au, S.K.A., Jafari, M.R. and Bolton, M.D. (2004), Laboratory Investigation of Multiple Grout Injections into Clay*, Geotechnique, Vol. 54, No. 2*, pp. 81–90.

Geotechnical Aspects of Underground Construction in Soft Ground – Viggiani (ed)
© 2012 Taylor & Francis Group, London, ISBN 978-0-415-68367-8

Tunneling in stratified soft ground: Experimental study on 1g EPBS reduced scale model

N. Berthoz, D. Branque, H. Wong & G. Généreux
Université de Lyon, Ecole Nationale des Travaux Publics de l'Etat, Département Génie civil et Bâtiment, FRE CNRS 3237, Vaulx-en-Velin, France

D. Subrin & E. Humbert
Centre d'Etudes des Tunnels, Avenue François Mitterrand, Bron cedex, France

ABSTRACT: This paper presents several results concerning soft ground tunneling with Earth Pressure Balanced Shield (EPBS), obtained on reduced scale model. Under the condition of "equilibrium rate tunneling", surface settlements and arching effects around the TBM are analyzed in homogeneous and stratified soils, with a particular attention on the influences of face pressure and soil mass configuration. Failure mechanisms by face collapse, observed in homogeneous pure frictional and frictional-cohesive materials as well as stratified soils (cases of two and three-layered soils), are then presented.

1 INTRODUCTION

Estimation of critical tunnel face pressures required in low resistance soils as well as forecasting surface settlements for pressurized shield tunneling has been the subject of different experimental works using 1g or centrifuged physical laboratory models (Meguid & al, 2008). Note that most of these studies were conducted on homogeneous soils.

However, stratified soil layers with different mechanical properties are frequently encountered in practice (Chu & al, 2007). To date, only a few studies using centrifuged reduced scale model and with "pressurized air bags" were reported on stratified soils (Hagiwara & al, 1999; Caporaletti & al, 2008).

The "Département Génie Civil et Bâtiment" of ENTPE has developed an original reduced scale model of EPBS. It is able to recreate, under normal gravity, the different phases of excavation process. The objective is to analyze in order to better understand the mechanisms involved for this excavation method, to provide assistance to steering on site, to develop theoretical and numerical tools of tunnel design. Different tests, firstly performed on homogeneous pure frictional (Branque & al, 2002) and frictional-cohesive materials (Doan, 2007), are then extended to stratified soils so as to get closer to the prevailing conditions on site.

This paper presents the main results obtained for these materials. Regarding the equilibrium rate tunneling (rate minimizing ground deformations), the influences of face pressure and soil mass configuration on surface settlements and arching effects around the TBM are studied. Failure mechanisms by face collapse, exhibited on reduced scale model in two and three-layered soils, are then analyzed and compared to those observed in homogeneous soils.

2 THE ENTPE EPBS MODEL

2.1 *Description of the experimental setup*

The ENTPE EPBS model (geometric scale between 1/4 and 1/20) allows to reproduce the main features of this excavation method: excavation of soil by the cutter head (diameter: 0,55 m), face confinement by excavated material contained in the working chamber, immediate radial confinement by the cylindrical steel shield tail (Cf. Figure 1). Note that an uniform surcharge q may be applied on ground surface by means of air chambers.

The EPBS model features an extensive instrumentation very similar to real TBM's: measures of the torques on the cutting wheel and screw conveyor, the axial thrust exerted by the cylinder, the pressures in the working chamber, the mass of material discharged and the shield penetration speed. It also offers the ability to monitor extensively the soil mass with surface and internal displacement sensors (type LVDT) and internal total stress sensors (Entran EPN50 and Kyowa BE2KC).

During the tests, the TBM penetrates into the ground through a circular hole on the container wall. Maximum penetration is 1m. Tests are composed of two phases: an equilibrium rate tunneling is carried out during the first 95 centimeters of excavation,

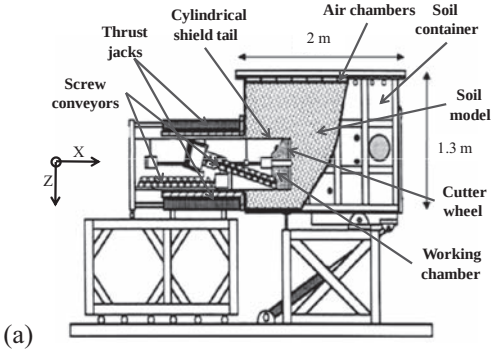

(a)

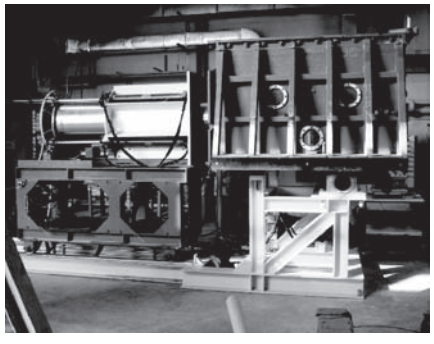

(b)

Figure 1. Sectional diagram (a) and photography (b) of EPBS model of ENTPE.

followed by an over-extraction (under-extraction) period, source of a lack (excess) of confinement of the working face, and leading the soil mass to failure.

2.2 *Soil models and configurations studied*

Soil mass models are prepared from Hostun S28 dry sand (purely frictional) or slightly wet (frictional-cohesive). For this second case, the cohesion depends on water content and density of the sand.

Soil models and the mode of preparation (poured at zero height for purely frictional material and layer-by-layer compaction for frictional cohesive material) have been identified taking into account the similitude conditions (partial similitude defined by Mandel (1962) and described in Doan (2007)).

Due to the low level of stresses prevailing in the reduced scale model, soil mass is prepared in a loose state so as to approach the ideal similitude on the volumetric behavior (Scott, 1989). Density and water content are controlled during soil mass confection.

Two types of stratification were analyzed (Figure 2): two-layered soil (self-stable frictional cohesive layer just underneath the tunnel axis and purely frictional above) and three-layered soil (same configuration as for the two-layered soil but with an additional layer of frictional-cohesive soil at the limit of stability above the crown).

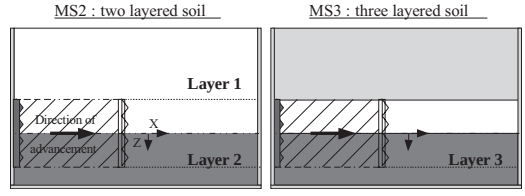

Figure 2. Longitudinal section of stratified soils.

Table 1. Mechanical characteristics of soils models.

Test		γ (kN/m³)	Dr (%)	E_t (MPa)	c′ (kPa)	φ′ (°)	ψ′ (°)	q (kPa)
MC3		13.20	0.7	10	2.5	36	5	0
MC4		13.15	0.7	10	1.5	36	5	0
MC5		13.05	0.6	10	0.5	36	5	0
MC6		13.05	0.6	10	0.5	36	5	50
MC7		13.05	0.6	10	0.5	36	5	50
MC8		13.05	0.6	10	0.5	36	5	0
MF11		13.70	0.2	5	0	39	2	0
MF13		13.70	0.2	5	0	39	2	0
MS2	1	13.25	0.0	5	0	39	2	0
	2	13.30	0.7	10	3	36	5	0
MS3	1	13.20	0.7	10	0.5	36	5	0
	2	13.25	0.0	5	0	39	2	0
	3	13.30	0.7	10	3	36	5	0

Mechanical characteristics (total weight γ, relative density Dr, apparent cohesion c′, friction angle φ′ and dilatancy angle ψ′) of different homogeneous and stratified soil masses studied in this paper are given in Table 1. These mechanical characteristics have been obtained with triaxial, trench stability and Casagrande shear tests.

3 SURFACE SETTLEMENTS

Under equilibrium rate tunneling, the vertical displacements measured at the ground surface reveal a stationary behavior. Hence, the longitudinal settlement profiles relative to the reference frame attached to the shield is independent of the position of the latter (Berthoz & al, 2010).

Figure 3 summarizes for all tests carried out under ideal tunneling rate the contours of longitudinal settlement profiles. These are inferred from stationary behavior described above.

Note firstly that only 30 to 60% of settlement measured at 1D at the rear of the working face are observed before passage of the shield and may be related to volume losses occurring at the front (compressive action of the cutting wheel, lack of front pressure…), the remainder being generated behind the face by shearing along the cylindrical shield tail (no overcut).

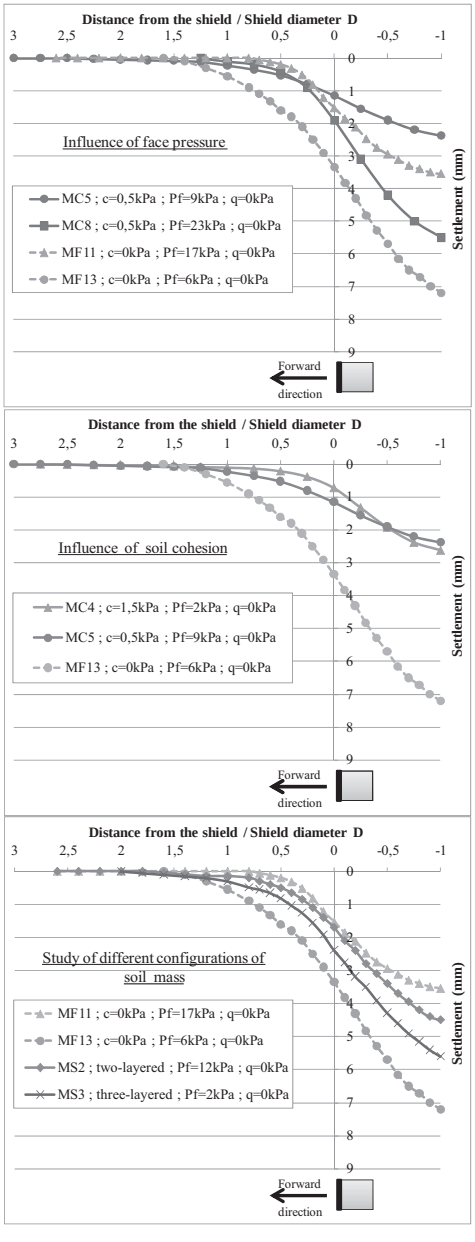

Figure 3. Contours of longitudinal settlements profiles inferred from stationary behavior in equilibrium rate tunneling.

Also, note that the magnitude of settlements observed on the reduced scale model (several mm) is consistent but relatively large compared to those that can be measured in situ (several cm), taking into account the scale ratio. Recall that our objective was to control them under different conditions.

Concerning influences of average face pressure (Pf) and soil cohesion on ground settlements, results of analyses show that the settlements generated in front of the working face decrease as the conditions of stability of the soil mass improve: increase of the face pressure or of the soil cohesion. It seems however that an important face pressure tends to amplify settlements behind the shield (test MC8 in relation to MC5). This result, consistent with those observed in extreme regime of under-extraction (Subrin & al, 2009), is explained by the appearance of horizontal tensile stresses in the ground above the shield.

In terms of stratified soils, the comparison between the results of tests MS2, MF11 and MF13 tends to show the lack of influence of the frictional-cohesive layer located underneath the tunnel axis. Given their regularity, it seems that the difference of the settlements observed during these three tests can be essentially attributed to the difference of the applied face pressures.. However, the stabilizing effect of a frictional-cohesive cover is undeniable as far as the settlements measured during test MS3 (three-layered soil) are of similar magnitudes as those observed in two-layered soil (test MS2) although face pressure was much lower.

4 LONGITUDINAL ARCHING EFFECT

Figure 4 shows the evolution of vertical stress measured along tunnel axis, at 0.2D above tunnel crown, during a phase of equilibrium rate tunneling. These measures reflect a stationary behavior characterized by a slight increase approaching the shield, followed by a strong decrease, even cancelling completely the vertical stress at the shield passage. Then it rises again to a value which can be sometimes higher than its initial value. This stress evolution during shield advancement explains by the existence of a longitudinal arching effect, already partially observed on a centrifuged model (Nomoto & al, 1999).

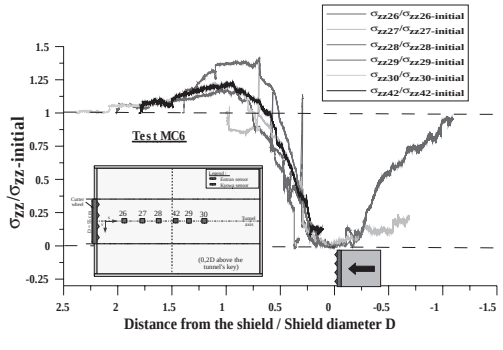

Figure 4. Stationary profile of stress measures 0.2D above the tunnel crown.

Figure 5 assembles contours of vertical stress profiles measured in the longitudinal direction, at 0.2D above the tunnel crown. These contours, deduced from the stationary behavior, show a slight shift (about 0.2D) of a lightened zone (due to arching effects) at the rear of the working face, indepedently of the tests conditions.

Moreover, in homogeneous purely frictional and frictional-cohesive grounds (figures 6a and 6b), a decrease of face pressure (relative to the initial horizontal stress at tunnel axis σ_{h0}) tends to generate higher displacements (Cf. paragraphs 3), thus mobilizing higher shear stresses, causing an enlargement of the lightened zone and a dicrease in the magnitude of load transfer to both sides of it.

Tests carried out also highlight the large increase of the extension of the lightened zone and the stronger decrease in the magnitude of load transferred to both sides of it, when soil cohesion increases. This observation, made for homogeneous soils, is in line with the increased ability to mobilize shear stresses with a higher cohesion.

This behavior is confirmed by tests performed in stratified soils. Indeed, case of three-layered soil (two-layered soil respectively), made with a frictional-cohesive overburden (purely frictional respectively) is similar to the frictional-cohesive (purely frictional respectively) homogeneous case.

5 FACE COLLAPSE

5.1 *Homogeneous soils*

In our tests, face collapse is obtained by a voluntary excessive discharge of the ground contained in the working chamber (over extraction rate). For frictional-cohesive materials, a failure mechanism in rigid blocks is observed, as evidence by the sudden nature of internal displacements measured close to the working face (Figure 6). Cutting the soil masses post-test showed that this failure block interfered with all the working face, and stretched up to 0.3D at the shield front and 0.1D above the crown, for tests performed with a cohesion of 0.5kPa (Figure 6 et Figure 8a). Note that this

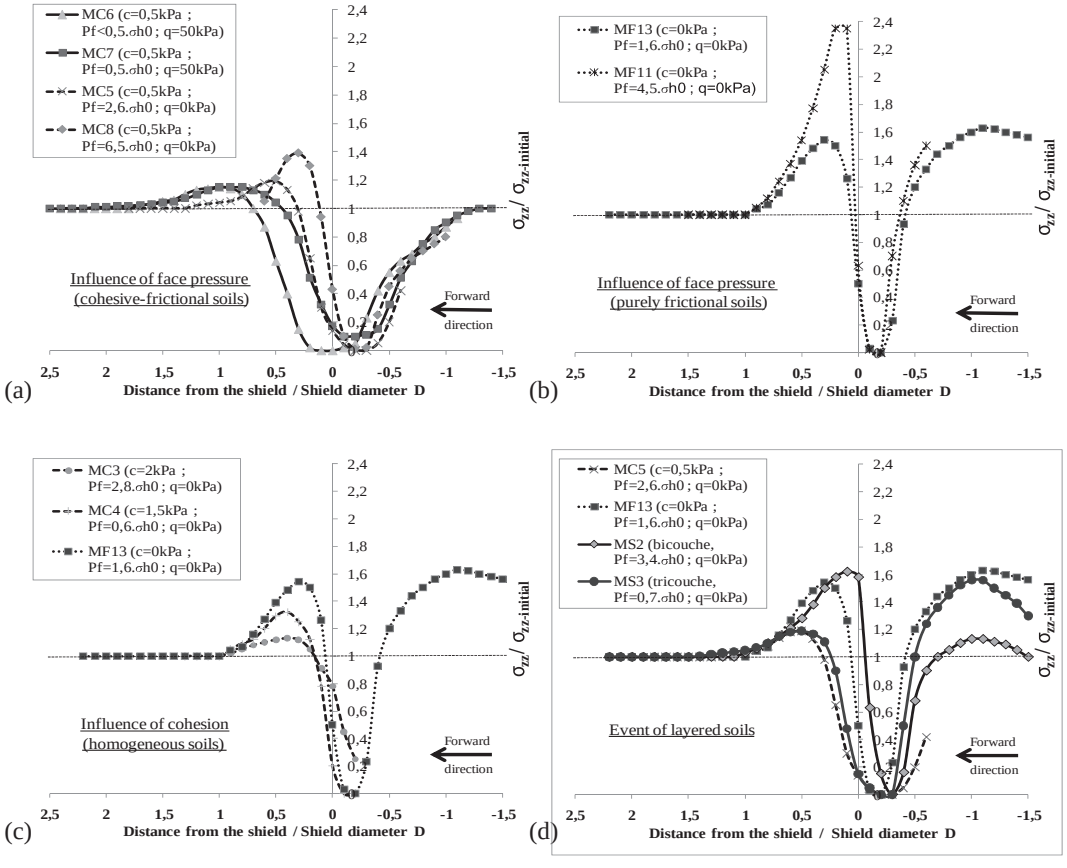

Figure 5. Contours of vertical stress profiles in equilibrium rate tunneling.

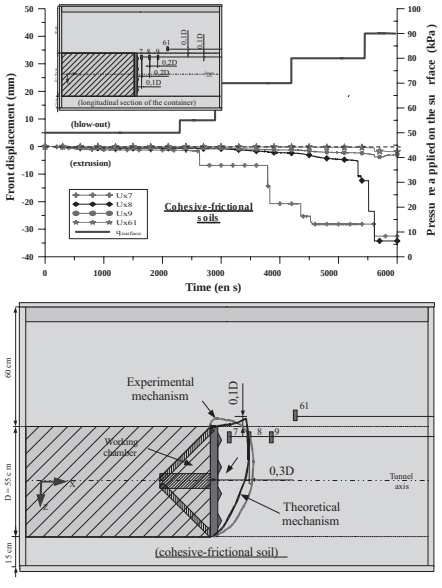

Figure 6. Main displacements and face collapse mechanism in homogeneous frictional-cohesive material.

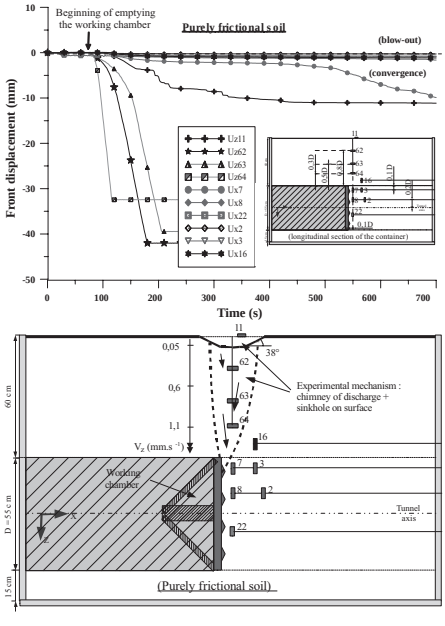

Figure 7. Main displacements and face collapse mechanism in homogeneous purely frictional material.

experimentally observed mechanism as well as the limit frontal pressures are in agreement with current theoretical approaches (Subrin & al, 2009).

In purely frictional soils, a chimney of discharge directly above the shield is observed. It is characterized by progressively increasing horizontal and vertical displacements (Figure 7) when the shield approaches. A circular sinkhole is generated at the ground surface (Figure 8b). Note that this flow originates near the crown and remains much localized as evidenced by the absence of displacements measured by frontal horizontal sensors. Note also that the vertical velocity of discharge decreases when approaching the surface, in accordance with the lateral extension of the void generated.

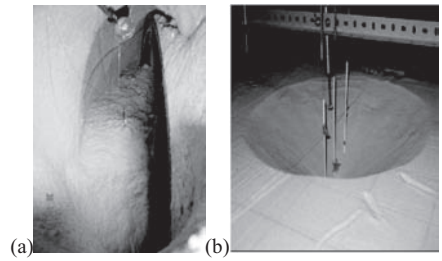

Figure 8. Photographs of face collapse mechanisms in frictional-cohesive (a) and purely frictional (b) soils.

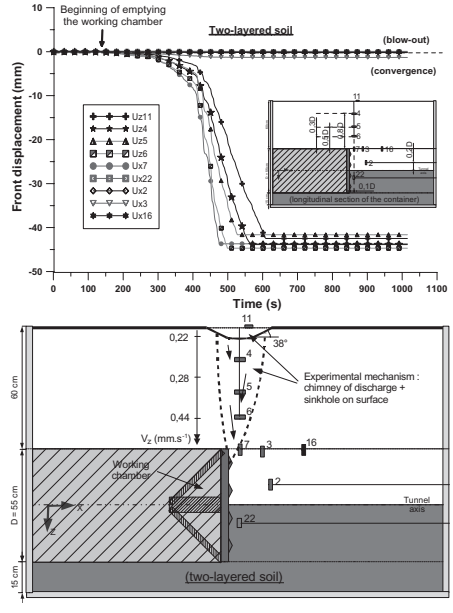

Figure 9. Main displacements and face collapse mechanism in two-layered soil.

5.2 *Stratified soils*

Failure mechanism observed in two-layered soil is very similar to that seen in homogeneous purely frictional soil, as evidenced by front displacements measured. The existence of cohesion or not underneath the tunnel axis does not alter significantly

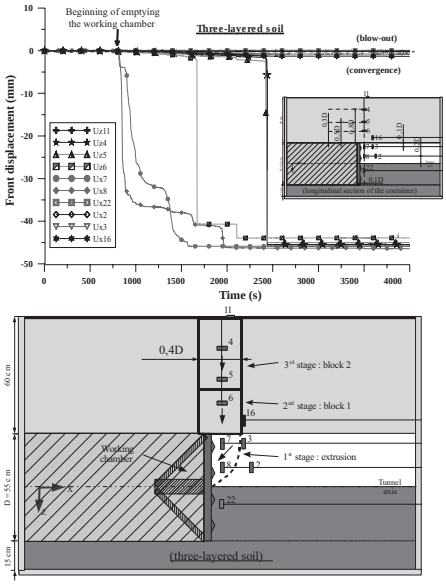

Figure 10. Main displacements and face collapse mechanism in three-layered soil.

the geometry of failure mechanism. However, it is interesting to note that vertical velocities v_z are lower in two-layered soil than in purely frictional soil, the rotation speed of screw conveyor being identical. The increase of cohesion of the material stirred in the working chamber thus limits strongly its ability to be extracted.

The test performed with a three-layered soil mass reveals an original face collapse mechanism, which is significantly different from homogeneous purely frictional and frictional-cohesive cases. This failure takes place in three phases as evidenced by displacement measurements (Figure 10). Firstly, flow of the purely frictional layer, located at the upper part of the working face, takes place, according to failure mechanisms commonly observed in these soils. The important decompression generated at the tunnel crown then causes a failure by blocks in the frictional-cohesive layer, the latter being at limiting stability. The last failure zone, a cylinder of diameter 0.4D off-centred at 0.1D front of the shield, is different from that observed in homogeneous frictional-cohesive soil, in accordance with the difference of loadings. Indeed, the flow occurring in purely frictional layer leads more to a "trap-door" type of loading than simply an insufficient face pressure.

6 CONCLUSION

Several results concerning tunneling in soft ground obtained from an EPBS reduced-scale physical model were presented in this paper.

For equilibrium-rate tunneling, influences of face pressure and soil mass configuration (value of cohesion, soil stratification) on surface settlements, tunnel crown displacements and longitudinal arching effects were analyzed.

Face collapse mechanisms in homogeneous purely frictional and frictional-cohesive soils were then described, followed by two mechanisms in stratified (two-layered and three-layered) soils. The first of these revealed the weak influence of a cohesive layer underneath the tunnel axis, except the ability to extract the material stirred in the working chamber. Finally, an original mechanism was exhibited in three-layered soils.

REFERENCES

Berthoz, N., Branque, D., Wong, H., & Subrin, D. 2010. Evolution des champs de contraintes et déplacements autour d'un tunnelier à front pressurisé, *Actes des Journées Nationales de Géotechnique et de Géologie de l'Ingénieur,* Grenoble, France, 779–786.

Branque, D., Subrin, D., & Boutin, D., 2002, Etude sur modèle réduit du creusement des tunnels par la méthode du bouclier à pression de terre. *Proceedings of the 3rd International Symposium on Underground Construction in soft ground, International Society for Soil Mechanics and Geotechnical Engineering,* Toulouse, France, 43–48.

Caporaletti, P., Burghignoli, A., Scarpelli, G., & Taylor, R.N. 2008. Assessment of tunnel stability in layered ground, *Geotechnical Aspects of Underground Construction in Soft Ground, Proceedings of the 6th International Symposium,* Shanghai, China, 627–633.

Doan, H.V. 2007. Creusement des tunnels en terrain meuble: étude expérimentale sur modèle réduit de tunnelier à pression de terre en sol cohérent frottant, *thèse de doctorat de l'ENTPE / INSA Lyon.*

Hagiwara, T., Grant, R.J., Calvello, M., & Taylor, R.N. 1999, The effect of overlying strata on the distribution of ground movements induced by tunneling in clay. *Soils and Foundation,* 39 (3), 63–73.

Mandel, J. 1962. Essais sur modèle réduits en mécanique des terrains. Etude des conditions de similitude, *Revue d'industrie minérale*, No. 9, 611–620.

Meguid M.A., Saada.O., Nunes M.A., & Mattar J. 2008. Physical modeling of tunnels in soft ground: A review, *Tunneling and Underground Space Technology*, n°23, pp 185–198.

Nomoto T., Imamura S., Hagiwara T., Kusakabe O., & Fujii N. 1999. Shield Tunnel Construction in Centrifuge, *Journal of geotechnical and geoenvironmental engineering*, vol 125, n°4, 289–300.

Scott, R.F. 1989. Essais en centrifugeuse et technique de la modélisation, *Revue française de géotechnique,* No. 48, 15–34.

Subrin, D., Branque, D., Berthoz, N., & Wong, H. 2009. Kinematic 3D approaches to evaluate TBM face stability: comparison with experimental laboratory observations, *Proceedings of the 2nd International Conference on computational Methods in Tunneling,* Bochum, Germany, 801–808.

Geotechnical Aspects of Underground Construction in Soft Ground – Viggiani (ed)
© 2012 Taylor & Francis Group, London, ISBN 978-0-415-68367-8

Effects of the excavation procedure on the stability of diaphragm wall panels

D. L'Amante & A. Flora
Department of Hydraulic, Geotechnical and Environmental Engineering, University of Napoli Federico II, Napoli, Italy

ABSTRACT: The stability of panels during construction must be always considered in the design of diaphragm walls. The classical 2D methods to evaluate the maximum depth of excavation of a trench with or without slurry are too conservative for panels, because of the unrealistic geometrical simplification. Trying to back analyze a failure observed in Napoli during the excavation of a panel in a weakly cemented soil without slurry support, it was found that the position of the operating machine on the edge of the panel is likely to have played a role in the mechanism. Therefore, 2D and 3D FEM parametric numerical analysis have been carried out, to consider some relevant aspects that are generally neglected at the design stage, such as the real 3D geometry of the panels and the position of the operating machine. By comparing the FEM results with available 2D and 3D analytical solutions, it is found that the machine can play both a positive and a negative role on the stability of the panel, depending on its position.

1 INTRODUCTION

Deep excavations in urban area have to be realized minimizing the effects on the environment of all the working activities. The first to be considered is the construction of the retaining structure itself, both in terms of displacements of the soil and stability of the excavation (typically a panel). The panel can be realized with or without the use of stabilizing slurries, depending on soil physical and mechanical properties.

Adopting a limit equilibrium method (LEM), analytical solutions originally developed for trenches considering slurry pressure (Nash and Jones, 1963, Morghenstain and Thamasseb, 1965) are often used for stability calculations. In the case of a self sustaining material with no slurry, a simple solution is available considering the soil as a perfectly plastic material. In fact, the static and kinematic theorems state that the critical height h_c (*i.e.* the one corresponding to failure) is:

$$\frac{2c}{\gamma}\sqrt{K_p} \le h_c \le \frac{4c}{\gamma}\sqrt{K_p} \tag{1}$$

where $K_p = \tan^2(45 + \varphi/2)$ is the passive coefficient of earth pressure.

For panels, which have a length of no more than a few meters, all these solutions result into an overconservative value of h_c because they refer to unrealistic plain strain (2D) conditions. More complex 3D LEM solutions can be used to take in account in a simple way the real geometry of the problem, even though all of them introduce arbitrary assumptions concerning the shape of the failure surface (Piaskowski & Kowalewski 1965, Fig. 1, Washbourne 1984, Fig. 2, Fox 2004 Fig. 3)

Since in 3D models the stabilizing forces increase with depth more rapidly than the destabilizing ones, the factor of safety may increase with depth, contrarily to what happens in the 2D models (Fig. 4). In this paper, the solutions of these 3D models are not reported for the sake of brevity. In the following, however, the solution by Fox (2004) (formally very long) will be used.

Nowadays, 2D and 3D numerical analyses are easily carried out to evaluate the stability of a panel, and are a reliable alternative to more traditional LEM formulas Lachler *et al.* (2007) and Brzakala and Gorska (2008) show a comparison between the factor of safety (3D) computed by LEM and FEM for slurry panels in cohesionless soils. In both cases the difference between the safety factors FS computed by LEM and by FEM is less than 25% of the largest value.

Lachler *et al.* (2007) also observe that FS decreases until a certain depth, after which it remains constant: for excavations deeper than this limit depth, the sliding wedge does not start at the bottom of the panel.

This paper reports the results of 2D and 3D FEM analyses, initially carried out to interpret a failure mechanism observed on a site by the authors and shortly recalled in the following. The

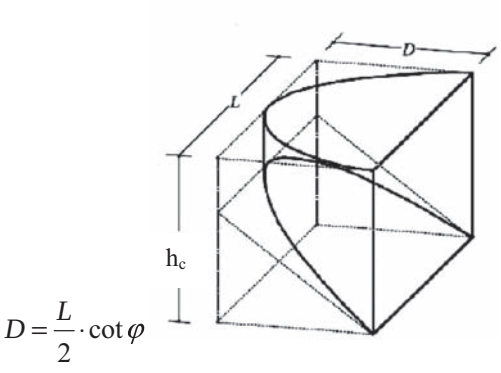

Figure 1. Unstable wedge (Piaskowski & Kowalewski, 1965) behind a panel having length L.

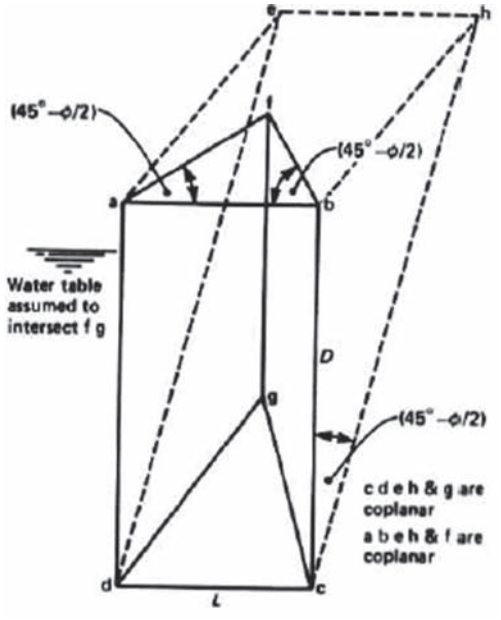

Figure 2. Unstable wedge behind a panel (Washbourne, 1984).

failure mechanism pertained to a panel excavated in a pyroclastic silty sand which, as shown in the next section, was expected to be stable considering the value of its critical height h_c calculated using LEM 3D formulas.

2 THE CASE HISTORY OF A PANEL COLLAPSED DURING CONSTRUCTION

For the construction of an underground parking lot in Napoli to be excavated in unsaturated pyroclastic silty sands (pozzolana), a sustaining

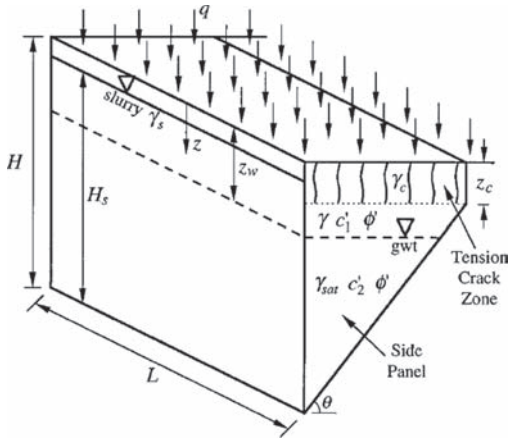

Figure 3. Unstable wedge behind a panel (Fox, 2004).

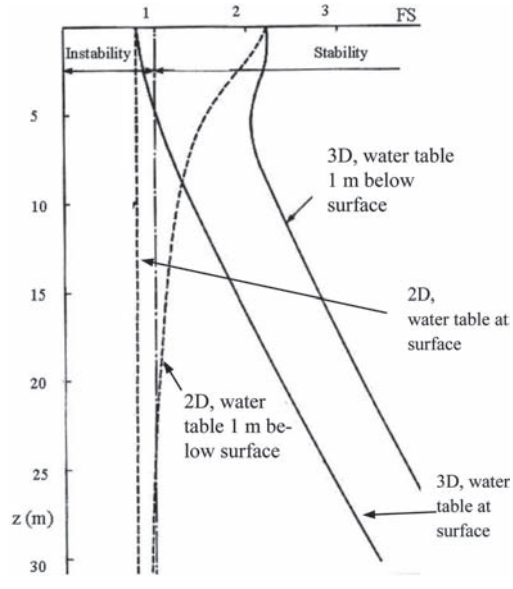

Figure 4. Safety factor FS versus depth for a 3D LEM solution (Washbourne, 1984).

structure consisting of a reinforced concrete diaphragm wall had to be realized. The wall is made of adjacent rectangular panels, 25 m deep and with a cross section of 6×0.6 m^2. For the unsaturated pozzolana, the geotechnical characterization reported an apparent cohesion $c = 10 \div 15$ kPa and a friction angle $\varphi = 35°$, being $\gamma = 12$ kN/m^3. These values are typical for simplified total stress analyses in these Neapolitan unsaturated materials. The designer decided to excavate the panels with no slurry support, assuming that soil cohesion was sufficient for stability, even though no stability calculation was included in the design report. Indeed, the application of the solution by Fox (2004) (Fig. 5) shows

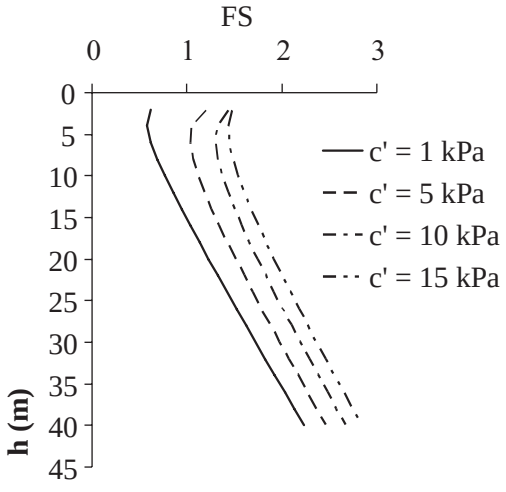

Figure 5. FS versus depth for different values of cohesion calculated using the solution by Fox (2004).

that for 10 kPa < c < 15 kPa, the excavation should be always stable, with a safety factor increasing with depth for z larger than about 6 m.

Unexpectedly, one of the first panels to be realized collapsed during the excavation (Fig. 6) at a depth of about 11 m, with a steep failure surface closed at middle depth of the panel under construction. The only difference with the other few panels previously realized without any problem was the position of the operating machine (Fig. 7), in this case placed on the longer side of the cross section of the panel. A numerical analysis was therefore planned to see if the position of the operating machine could be the factor explaining the observed failure mechanism, as described in the following section. However, before realizing the subsequent panels, ground improvement of the first few meters along the perimeter of the panels to be excavated was carried out. No other accident happened and the diaphragm wall was successfully completed.

3 NUMERICAL ANALYSES

The parametric numerical analyses were carried out with Plaxis 2D and Plaxis 3D Foundation. Four 2D and thirty-two 3D analyses have been carried out changing soil cohesion, panels dimensions and position of the operating machine. Three different positions of the operating machine have been considered in the 3D analyses: no machine (*absent load*), machine operating on the short side (*positive load*), machine operating on the long side (*negative load*). The first case is certainly unrealistic but is the one typically considered in both LEM and FEM solutions. The other two cases (positive and

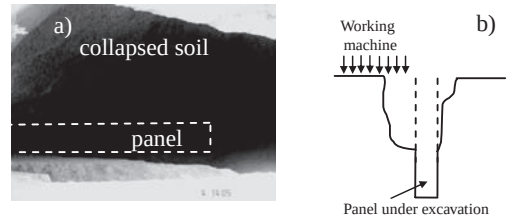

Figure 6. Collapsed panel. a) picture of the failure surface; b) sketch of the observed failure mechanism.

Figure 7. Pictures from the site in Napoli: different positions of the operating machine during panel excavation: a) on the long side; b) on the short side.

negative position of the machine) refer to positions that are both possible on site, as reported in the previous section.

In the calculations, the machine load is applied to the soil by a couple of belts. For each position, a different symmetry is adopted to prepare the mesh (Fig. 8). In 2D analyses, no machine load at ground level was considered.

Excavation has been simulated removing the soil in the panel by steps of 1 m, until the soil eventually collapse at a critical depth h_c.

For 3D analyses, in the case of absent load (double symmetry), the mesh is 100 m deep and 50×50 m^2 large, being composed by about 23000 wedge elements (Fig. 9). In the case of positive or negative load (simple symmetry) the volume of the mesh and the number of the elements is doubled. The 2D mesh is 100 m deep and 50 m large, composed by about 8000 triangular elements. All the meshes are finer around the panel.

The soil has been modeled using the Hardening Soil Model (HSM); the most relevant parameters for the mechanisms under study are reported in Tab. 1, with values of the cohesion between 1 and 15 kPa. The chosen values are typical of an uncemented unsaturated pozzolana.

Table 1. Main parameters of the soil in the FEM analyses.

γ_{sat} [kN/m^3]	ϕ' [°]	c′ [kPa]	Dilation angle, ψ [°]	K_0
12	35	1, 5, 10, 15, 20	5	0,9

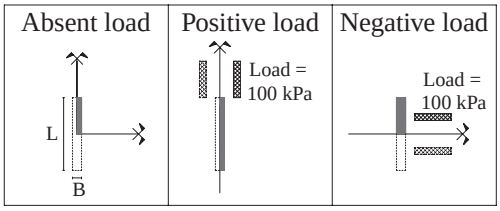

Figure 8. Position of the belt of the operating machine respect the panel and considered symmetry.

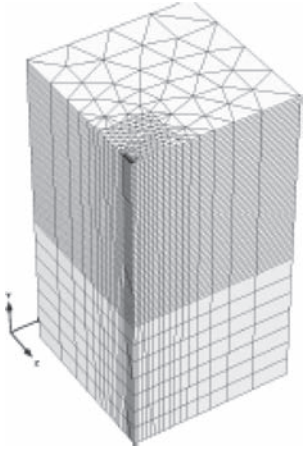

Figure 9. 3D mesh for the case of absent load.

4 ANALYSES OF RESULTS

Soil was assumed to collapse when the numerical analyses did not converge. With Plaxis, the sliding surface can be identified using several variables (shear strain, incremental shear strain, relative shear stress, plastic points). All of them were taken into account in this work. Tab. 2 reports a summary of the results obtained with 3D analyses. In the table, L and B and respectively the length and the width of the panel (Fig. 8).

In Fig. 10 some the 3D sliding surfaces for different values of cohesion in absence of load are shown for the case of panels having a cross section of 8×1 m^2. The horizontal cross section of these failure surfaces is approximately an arch of circumference having the side of the panel as a chord. The vertical section orthogonal to the long side of the panel shows the well known fact that these surfaces become steeper as cohesion increases; for $c' = 15$ kPa, the failure surface is mostly vertical (Fig. 10). For $c' = 20$ kPa, the analyses were stopped at a depth of excavation of 56 m without reaching failure.

For low values of the cohesion, the load of the operating machine plays a relevant role, influencing the value of the critical height h_c as well as the failure mechanism, which is deeply modified by the machine and resembles that typical of a foundation limit load failure (Figs. 11 and 12). For higher values of cohesion, the slip surface does not include the operating machine if the load is in a positive position.

Tab. 2 shows that, for conditions similar to those pertaining to the site in which the failure was observed and a negative position of the operating machine, the critical height h_c has values between 3 m and 26 m for cohesions in the range $5 \text{ kPa} < c < 10$ kPa, considering a panel having $L = 6$ m and $B = 1$ m. Even though this value of B is larger than the one on site, when the machine is on the long side of the excavation and the failure mechanism does not include the short side, the value of B is not very relevant. For the same panel, the cases of absent or positive load correspond to larger values of h_c. The depth of failure observed on site is consistent with the results of the analyses considering the operating machine in a negative position, thus confirming the relevance of this apparently minor load on the overall stability of the panel under excavation.

The results of 2D analyses are summarized in Tab. 3; in the table, both the critical excavation depth h_c and the depth of the bottom of the slip surface are reported. These results, as most of the 3D ones, show that the slip surface does not start from the bottom of the excavation (as supposed by LEM) but 1 or 2 meters above, consistently with the evidence recorded on site in Napoli (see previous section).

Table 2. 3D analyses carried out and resulted h_c.

B (m)	L (m)	Position	c′ (kPa)	h_c (m)
0,4	6	absent	10	33
0,4	8	absent	1–5–10–15	8–12–19–34
0,4	10	absent	10	15
0,4	12	absent	10	13
1	6	absent	5–10	14–32
1	8	absent	1–5-10–15	5–10–18–34
1	10	absent	10	14
1	12	absent	10	12
0,4	6	positive	10	33
0,4	8	positive	10	19
0,4	10	positive	10	14
0,4	12	positive	10	12
1	6	positive	5–10	13–36
1	8	positive	1–5–10–15	2–4–18–38
1	10	positive	10	14
1	12	positive	10	13
1	6	negative	5–10	3–26
1	8	negative	1–5–10–15	2–2–4–33
1	10	negative	10	3
1	12	negative	10	3

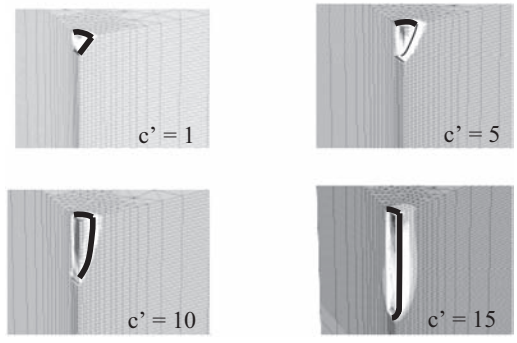

Figure 10. Sliding surface for different values of cohesion (incremental shear strain shadings, light color corresponds to the maximum value).

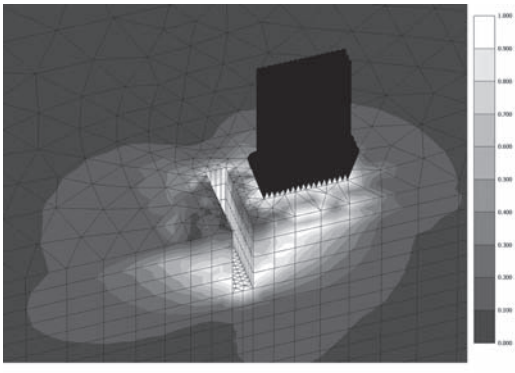

Figure 11. Unstable soil in the case of load in a negative position (τ/τ_{max} shading, light color correspond to the maximum value of relative shear stress) for $c' = 10$ kPa, L = 8 m, B = 1 m.

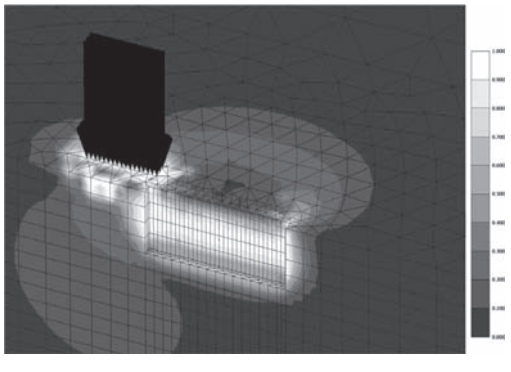

Figure 12. Unstable soil in the case of load in a positive position (τ/τ_{max} shading, light color correspond to the maximum value of relative shear stress) for $c' = 5$ kPa, L = 8 m, B = 1 m.

Table 3. 2D analyses carried out and resulted h_c.

c′ (kPa)	1	5	10	15
h_c (m)	3	3	4	6
depth of failure mechanism (m)	1.7	2.7	3.7	5

Table 4. FS calculated with the formula of Fox (2004) for the critical heights h_c.

c′ (kPa)	h_c (m) (3D FEM)	FS (FOX, 2004)
1	5	0.60
5	10	1.12
10	18	1.66
15	34	2.55

In Tab. 4 the 3D results for the cases of absent load are summarized along with the extension D (see Fig. 1) of the failure surface at ground level calculated with some 3D LEM formulas and estimated in the numerical analyses. The value of D calculate with the approach of Washborne (1984) is the closest to FEM solutions; the solution by Piaskowski and Kowalewski (1965) overestimates D, while the one by Fox (2004) overestimates D for the deepest critical heights and underestimates it for the lowest ones.

In Fig. 13 the value of h_c calculated with 3D FEM is plotted versus c′ for different positions of the load (considering a panel having a cross section of 8×1 m^2). In the same figure, the values of h_c calculated by 2D LEM (Eq. 1) and 2D FEM are also reported. In the case of absence of load, h_c computed by FEM 3D is always larger than the one by 2D LEM and 2D FEM, and rapidly increases with c′.

Generally speaking, 2D and 3D FEM analyses give values of h_c smaller than the correspondent LEM, except for the case of a very low value of cohesion ($c' = 1$ kPa). Fig. 13 also shows that, for 3D FEM analyses, for small values of cohesion the maximum value of h_c corresponds to the case of absence of load; somehow unexpectedly, on the contrary, for high values of the cohesion the machine may have a positive effect, the deepest possible excavation (largest value of h_c) corresponding to the case of operating machine on the short side of the panel (load in a positive position).

This can be physically explained by looking to the failure surface: for low values of cohesion (see Figs. 11 and 12) its position is influenced by the machine, which is all included in the unstable wedge of soil. When the cohesion is high, the much steeper failure surface has a position unaffected by the operating machine; in the case of positive

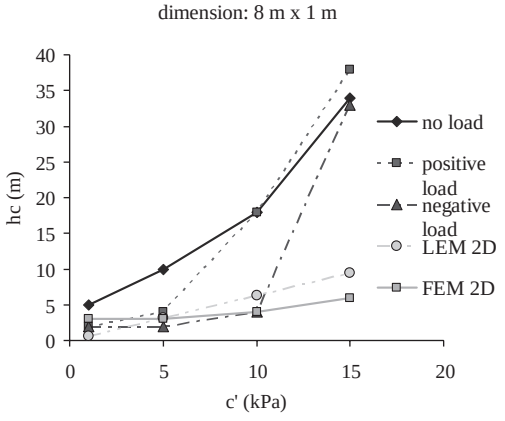

Figure 13. Value of h_C versus c′ and the position of the load.

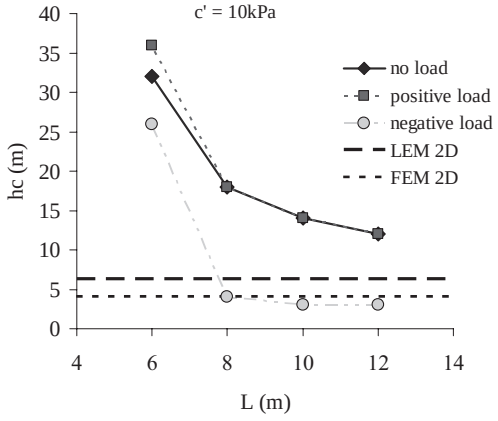

Figure 14. Value of h_c versus panel length L.

Table 5. Results for absent load: h_c calculated by 3D FEM; D by 3D LEM and 3D FEM.

L (m)	B (m)	c′ (kPa)	h_c (m)	H* (m)	D (m)	$D_{Washbourne}$ (m)	$D_{Piaskowski}$ (m)	D_{Fox} (m)
6	0,4	10	33	32	2	2,59	4,29	6,10
8	0,4	1	8	6	3,2	2,59	5,72	1,25
8	0,4	5	12	9	4,3	3,46	5,72	2,89
8	0,4	10	19	16	4,8	3,46	5,72	4,65
8	0,4	15	34	32	2,2	3,46	5,72	7,32
10	0,4	10	15	12,5	5	4,32	7,15	4,09
12	0,4	10	13	11	5,2	4,75	8,57	3,76
6	1	10	32	31	2	2,59	4,29	6,01
8	1	1	5	3	2	1,30	5,72	0,96
8	1	5	10	8,5	4	3,46	5,72	2,58
8	1	10	18	16	4,4	3,46	5,72	4,50
8	1	15	34	32	2,5	3,46	5,72	7,07
10	1	10	14	12	4,9	4,32	7,15	3,90
12	1	10	12	9,5	5,1	4,10	8,57	3,55

*depth of the slip surface.

load, the machine placed on the short side of the panel has the beneficial effect of increasing the mean stress within the soil, thus resulting into an increase of the critical height.

Fig. 14 reports the value of h_c versus panel length L for the different positions of the load, in the case of c′ = 10 kPa and B = 1 m. As expected, h_c decreases as L increases. In the case of negative load, for L > 8 m h_c becomes smaller than that calculated in 2D conditions. The cases with no load or with the load in a positive position have more or less the same h_c, the largest values pertaining to the latter case for the lower values of L.

In the case of load in negative position, h_c is always lower than in the other cases. For L higher than 10 m, h_c does not change. This is because

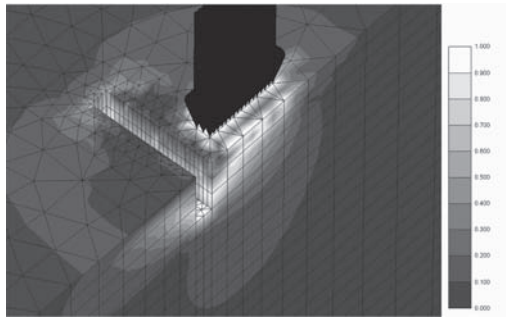

Figure 15. Unstable soil in the case of load in a negative position (τ/τ_{max} shading, light color correspond to the maximum value of relative shear stress), for c′ = 10 kPa, L = 12 m, B = 1 m.

as the length of the panel becomes large enough, the failure surface closes around the machine (Fig. 15), again resembling a foundation limit load mechanism, being unaffected by the remaining part of the panel, that therefore plays no role in the mechanism.

5 CONCLUSIONS

The stability of panels is a key issue in the design of diaphragm walls. A somehow unexpected failure mechanism observed on site by the authors during panel excavation with no slurry support in a weakly cemented material could be explained by taking into account the weight of the operating machine. To confirm this hypothesis and to analyze the effect the this usually neglected load has on the stability of panels excavated in soils with a small cohesion, 3D numerical analyses were carried out, comparing the results with some of the available analytical solutions.

It was found that 2D solutions (LEM or FEM) are usually conservative, unless an operating machine on the long side of the panel is considered. In this case, as the panel gets longer or the cohesion gets smaller, 3D FEM solutions give values of h_c lower than any 2D calculation. In most cases, the operating machine on the short side of the panel under excavation has a positive effect.

REFERENCE

Brzakala, W. & Gorska K. 2008. On Stability Analysis of Slurry–Wall Trenches. *Plaxis Bulletin 24*.

Fox, P.J. 2004. Analitical solution for stability of slurry trench. *Journal of Geotechnical and Geoenvironmental Engineering*: 749–757.

Lächler, A.; Vermeer P.A. & Wehnert, M. 2007. Assessment of diaphragm wall stability and deformation. *Proceedings of the 14th European Conference on Soil Mechanics and Geotechnical Engineering, Vol. 2, Madrid, Spain*: 1055–1060.

Morgenstern, N. R. & Amir-Tahmasseb I. 1965. The stability of slurry trenches in cohesionless soils. *Geotechnique* 15, n 4: 387–395.

Nash, J.K.T. & Jones, G.K. 1963. The support of trenches using fluid mud. *Grouts and Drilling Muds in Engineering Practice, London*: 177–180.

Piaskowski, A. & Kowalewski, Z. 1965. Application of tixotropic clay suspensions for stability of vertical sides of deep trenches without strutting. *6th Int. Conf. SMFE, Montreal.* Vol.III: 526–529.

Washbourne, J. 1984. The three dimensional stability analysis of diaphragm wall excavation. *Ground Engineering* 17(4): 24–29.

This page intentionally left blank

Geotechnical Aspects of Underground Construction in Soft Ground – Viggiani (ed)
© 2012 Taylor & Francis Group, London, ISBN 978-0-415-68367-8

Water table lowering effects on excavations

N.P. Raposo
Instituto Politécnico de Viseu, Viseu, Portugal

A. Topa Gomes
Faculdade de Engenharia da Universidade do Porto, Porto, Portugal

ABSTRACT: Excavations in granite residual soil, at Porto, tend to be performed lowering the water table. This operation can be performed either previously or during the excavation works. In any case, for practical purposes, it is commonly assumed that the non saturated condition creates an increase in both the resistance and the stiffness of the soil and hence it is safe to model the excavation as a soil with effective stresses equal to the total stresses. Nevertheless the above referred, considering that the water table is already at the bottom of the excavation, and hence not modeling the lowering operation, versus modeling the water table lowering conduces to significant differences in the behavior of the excavation, particularly by changing the at rest condition, which is a fundamental parameter in the design of retaining structures. The present paper discusses the strategy to model this operation and the differences in the results, both in the ground and in the retaining structure, as a consequence of the adopted strategy. In the final part of the paper attention will be given to the main aspects that are not covered by a non saturated model, presenting clues for further developments or strategies to take into consideration the problem with simplified models.

1 INTRODUCTION

The dominant geotechnical materials in the city of Porto are granites which may present significant weathering depths, reaching more than 20 m of residual soils. Although being a soil-like material, granite residual soils tend to exhibit certain stiffness gain when the water table is lowered. On the other hand, the practical advantages of working without water and the gains produced by the non saturated condition, both in strength and stiffness, encourage the systematic lowering of the water table. Recently, during the construction of Porto Light Rail Metro, 11 underground stations were constructed, all associated with the drawdown of the water table.

In any case the topic is far from being completely understood. This paper presents a numerical study in which several strategies to model the water table lowering are adopted and its implications on the displacements and forces of the structural elements are analyzed.

2 DESCRIPTION OF THE MODEL

2.1 *Brief description of Porto Granite Residual Soils*

Granite residual soils cover a large area of the northern part of Portugal, being the material predominant at most superficial horizons in the city of Porto. These soils, well characterized by Viana da Fonseca (1996, 2008) and Topa Gomes et al. (2008) are saprolitic materials, preserving the natural fabric of the original rock, with less than 10% clay, around 20% silt and almost 70% sand. A small percentage of gravel also appears. Figure 1 presents a typical range of granulometric curves for these soils. The soil may exhibit, in certain cases, some plasticity.

Recent studies have shown that non saturated conditions have decisive influence on both, stiffness and strength. Regarding strength, experimental results conduced to a friction angle with respect to suction of 14° (Topa Gomes, 2009) and hence an equivalent cohesion for the classic Mohr-Coulomb failure criteria may be obtained by the following equation:

$$c' = c'_{sat} + (u_a - u_w)\tan(14^\circ) \quad (1)$$

where c'_{sat} = saturated effective cohesion and $(u_a - u_w)$ = matric suction.

Concerning the soil stiffness, triaxial tests under non saturated conditions showed an increase in the Young modulus in accordance with equation (2):

$$E/E_{sat} = 1 + 0.078\,(u_a - u_w) \quad (2)$$

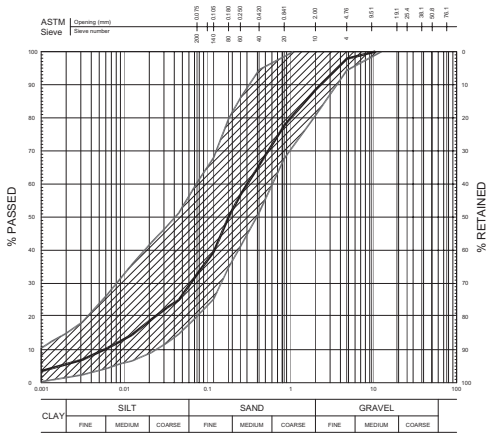

Figure 1. Typical granulometric curves for Porto Granite Residual soil.

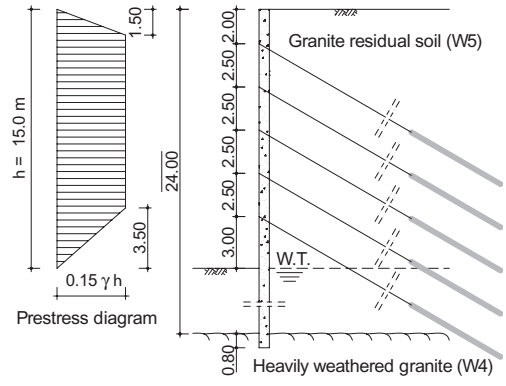

Figure 2. Geometry of the excavation and ground anchors presstress diagram.

where E = unsaturated soil stiffness and E_{sat} = saturated soil stiffness.

2.2 *Excavation and retaining wall characteristics*

The excavation considered on this study is a typical example of what is commonly executed in Porto. As shown in Figure 2, it is a 15 m depth and 30 m wide excavation, performed in moderated to highly decomposed granitic materials. The length of the excavation was considered long enough so the tridimensional effects were negligible. This last consideration allows the use of a plane strain model.

Regarding the soil of the excavation site, two distinct soil strata were considered: the most superficial layer is a granite residual soil (W5) with 24 m thickness; bellow, there is a heavily weathered granite (W4).

The wall retaining the excavation is formed by concrete piles with 0.60 m diameter and 0.80 m distance between axes. The piles length was considered with 24.8 m which means they penetrate the lower stratum of heavily weathered granite (W4) about 0.80 m. Considering a value of 30 GPa for the concrete Young modulus, a flexural stiffness of 160,000 kNm²/m is obtained.

To simulate the contact between the piles and the soil in a realistic way, interface elements with two thirds of the soil strength were used.

Supporting the wall there is a grid of anchors, spaced 2.5 m and 3.0 m in the vertical and horizontal directions, respectively. Altogether there are five levels of anchors. The anchor rod was considered to have 4 cm² of cross section and a stiffness value of 200 GPa. The anchors have a free length of 10 m and a grout body with 6.0 m. The tilt angle of 30º is common to all anchors. The prestress force was established according to the diagram in Figure 2, derived from Terzaghi & Peck diagrams for granular materials (Terzaghi & Peck 1967).

The trapezoidal shape of the diagram is a direct consequence of the vertical spacing of the anchors (2 m from the surface to the first level of anchors and 3 m from the fifth level to the excavation base) and the fact that the force in every anchors was set to the same value. In each anchor a prestress force of 390 kN is applied.

The water table was assumed to be coincident with the surface before the excavation works had begun. Prior to excavation works, it was lowered 15.0 m, up to the maximum excavation depth.

Apart from the initial consideration, described in the next item, the phreatic level is kept unchanged during all construction phases.

2.3 *Numerical model*

PLAXIS was elected as the numerical code to be used in this study, partly because of its user friendly interface, but mostly because it's one of the most used software in earth retaining structures design. Taking in consideration that this study tries to reproduce the design environment, in its entire vicissitudes, no other software seemed plausible. Besides, the hardening soil constitutive model, included in PLAXIS, proved to be particularly suitable to model the granite residual soil behavior (Raposo 2007), mainly because of its ability for considering different stiffness values according to the stress path followed.

An excavation such as the ones modeled in this paper is composed of several phases. The simulation of the excavation phases begins with the execution of the piles, followed by the first excavation step of 2.5 m height (0.5 m bellow the first level of anchors). The next phase corresponds to the

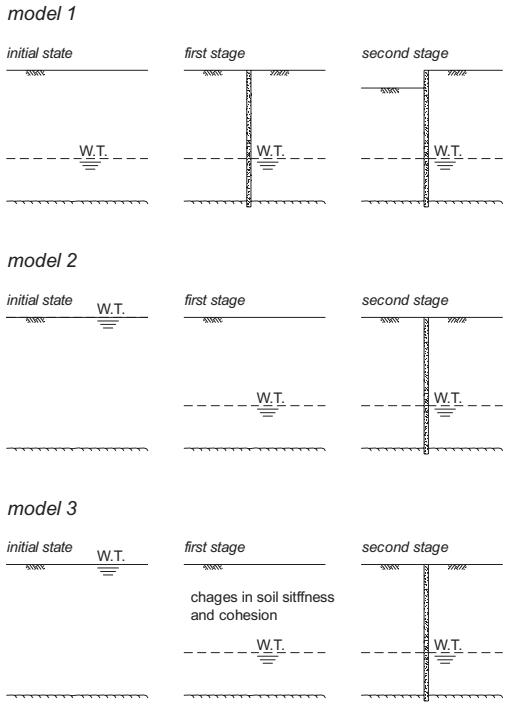

Figure 3. Schematic representation of the calculation models.

placement of the ground anchors and the application of the prestress forces. Successive excavation steps and prestress phases are made until the final depth of 15 m is reached.

To study the effect of the water table variations and modeling options on the soil's behavior around the excavation, three different calculation models were created, according to the most commonly used approaches to this problem. Figure 3 shows the first stages of each numerical model, highlighting the differences among them.

In model 1 the water table lowering is not included in the calculations. Right from the first calculation step the water table is admitted to be at the base of the excavation. This is probably the most common approach designers use to model excavations, having in simplicity its principal advantage. It will serve as reference for the other models.

In model 2 the water table lowering is explicitly considered. In the first calculation step, before the execution of the wall, the water table is lowered 15 m, from the surface up to the maximum excavation depth.

In model 3, besides the considerations regarding the water table lowering, identical to those in the previous model, the effects of suction on soil

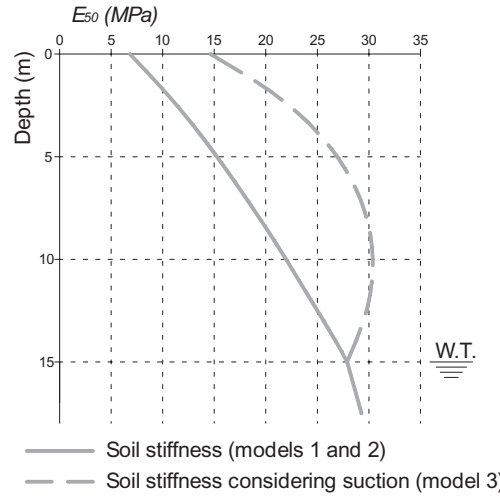

Figure 4. Effects of suction in soil stiffness.

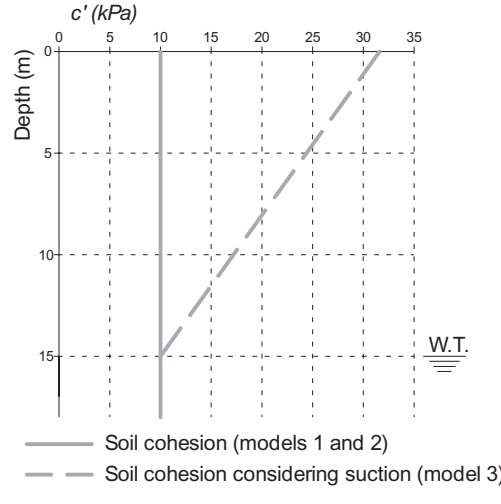

Figure 5. Effects of suction in soil cohesion.

stiffness and strength (cohesion) are considered according to equations (1) and (2).

Figures 4 and 5 compare the soil stiffness and cohesion considered in each numerical model.

The soil mass around the excavation was modeled using two different constitutive models. The upper layer of granite residual soil was modeled using the hardening soil model. To model the lower level, the heavily weathered granite (W4), an elastic perfectly plastic model was used. The decision to use a simpler model in the lower stratum was taken for simplicity purposes. Taking into account the low shear stress and the small strains in this region, it didn't seem necessary to use a more sophisticated

constitutive model. Furthermore, the strength and stiffness of the material at this depth is quite high when compared to the upper soil, in which would be expected significant strain levels.

Although the use of only two different layers might seem insufficient to adequately represent the behavior of the ground around an excavation in this type of soil, it must be made notice that the used constitutive models allow the variation of soil properties with depth, namely the stiffness parameters and the cohesion, as shown in Figure 4 and Figure 5. Using the hardening soil constitutive model, the soil stiffness becomes dependent of the confining stress σ'_3, according to the equation:

$$E = E^{ref}\left(\frac{c'\cos\phi' + \sigma'_3\sin\phi'}{c'\cos\phi' + p'^{ref}\sin\phi'}\right)^m \quad (3)$$

were E^{ref} = the reference stiffness determined from triaxial tests at a confining stress p'^{ref}; c' = effective cohesion; ϕ' = friction angle; and m = stress dependency stiffness parameter.

In model 3, to assign different stiffness and cohesions due to suction, the upper layer of residual soil was divided in several layers with 2.5 m thickness.

The model was truncated at a depth of 39 m, 15 m bellow the transition of the two soil layers described above. At this depth the displacements are small enough to be considered null. Similarly, at a distance of 75 m away from the wall, corresponding to five times the excavation depth, the horizontal displacements were considered negligible and thus horizontal fixities were used (Wood 2004).

Tables 1 and 2 include the soil parameters considered in all the calculations.

Table 1. Soil parameters.

	Granite residual Soil (W5)	Heavily weathered granite (W4)
	Hardening soil model	Elastic perfectly plastic model
Unsaturated weight	19 kN/m³	22 kN/m³
Saturated weight	20 kN/m³	23 kN/m³
Effective cohesion	10 kPa(1)	100 kPa
Friction angle	33º	42º
Dilatancy angle	11º	12º
Soil stiffness	25 MPa(1) (2)	400 MPa
Poisson coefficient	0.26	0.2
Pressure coef. at rest	0.5	0.33

(1) This is the base value. In some cases it is changed due to suction according to equation (2)
(2) This value corresponds to the secant young's modulus (for primary loading) at 50% strength, derived from triaxial tests with the reference confining pressure of 100 kPa.

Table 2. Hardening model soil advanced parameters(1)

	Granite residual Soil (W5)
	Hardening soil model
Soil stiffness for unloading and reloading	75 MPa
Oedometric soil stiffness	25 MPa
Stress dependency stiffness parameter	0.7
Failure ratio	0.9

(1) Details about these parameters can be found in Brinkgreve et al. (1989)

Table 3. Results summary—maximum values.

	Calculation model		
	Model 1	Model 2	Model 3
Bending moments (kNm/m)	212.4	210.9	195.7
Wall horizontal disp. (mm)	36.2	36.2	28.5
Surface settlements (mm)	15.2	81.1	64.8

3 RESULTS

3.1 *Global analysis of the results*

The results that were considered to be the most important are the maximum bending moment in the wall, the horizontal wall movements and surface settlements. Table 3 summarizes the results obtained in the three models after the final excavation stage, allowing a first glance at the outcome.

Aiming for a better comprehension of the differences between the models, the next two Figures can help to understand the phenomenon. In Figure 6 the earth pressure coefficient is displayed. This coefficient is obtained dividing the effective horizontal stress by the effective vertical stress. It corresponds, in all models, to the earth pressure coefficient after the groundwater changes, just prior to the first excavation stage.

It is perceptible that the groundwater table lowering almost does not change the K_0 value, proving that, from a numerical point of view, models 1 and 2 are very similar. Model 3 will be different from the previous as different strength as stiffness properties are assigned to the materials, as a consequence of the non saturated condition.

Figure 7 presents the earth pressure coefficient, K, at the end of the excavation. It is clear that models 1 and 2 are almost coincident whereas model 3 presents smaller values for K, in the excavation height. These values were determined on a vertical plane 5 m away from the wall.

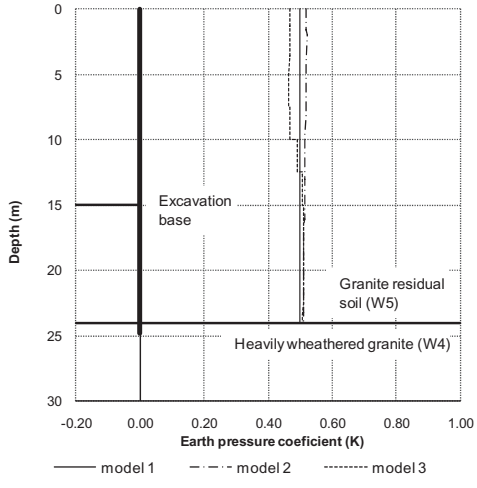

Figure 6. Earth pressure coefficient after the uniform lowering of the water table.

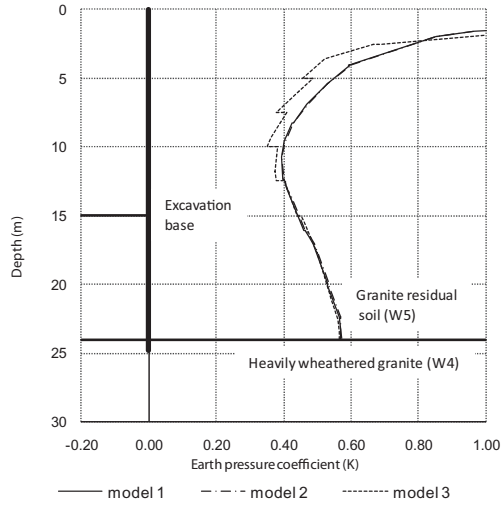

Figure 7. Earth pressure coefficient after the completion of the excavation, on the active side, through a vertical plane 5 m away from the wall.

Model 3 presents smaller values for K as a consequence of the increased cohesion for the soil, which allows smaller values for the horizontal effective stress without violating the adopted Mohr-Coulomb failure criteria.

In the uppermost 2.5 m, K tends to grow rapidly as the vertical effective stress tends to zero. As a consequence the values were truncated at a maximum of 1.0.

Regarding model 3, it must be made notice of the sudden variations of the earth pressure coefficient at depths 5 m, 7.5 m, 10 m, 12.5 m and 15 m. These jumps are caused by the methodology followed to introduce the suction in this model. They correspond to the transition between layers of soil with different stiffness and cohesion, so it can be stated that this is a numerical haziness, without much effect on the quality of the results.

Figure 8 shows the horizontal effective stress on the active side, measured on a plane 5 m away from the wall, the same plane used for Figure 7. The differences between model 3 and the remaining are relevant. The cause to that disparity seems to be the soil improvement caused by suction. This can explain the bigger differences felt near the surface, since the suction grows from the water table, at 15 m depth, up to the surface. Taking this explanation into account it should be no surprise that the bigger discrepancy from model 3 to models 1 and 2 are located in the first few meters.

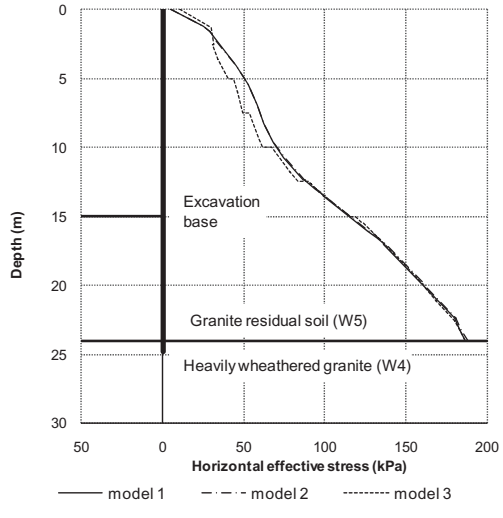

Figure 8. Horizontal effective stress on the active side, after the completion of the excavation, through a vertical plane 5 m away from the wall.

3.2 *Bending moments*

The effects of the water table variations on the wall bending moments can be observed in Figures 9 and 10. Regarding the bending moments at the last stage, Figure 9 shows a significant variation according to how the groundwater level changes were considered in the calculations. Although the results of excavations model 1 and model 2 are quite similar, in model 3 the bending moments diagram is shifted to the right, resulting on higher negative moments in the first half of the excavation height, and lower positive moments in the proximity of the excavation base. Despite the mentioned differences, the maximum bending moment sit's

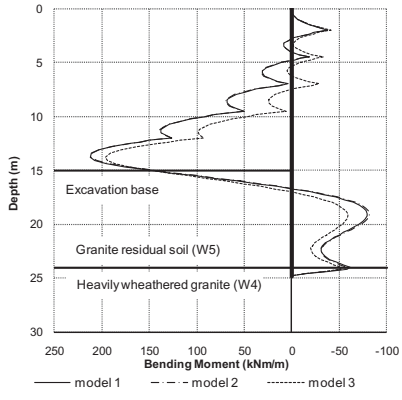

Figure 9. Bending moments after the last excavation stage.

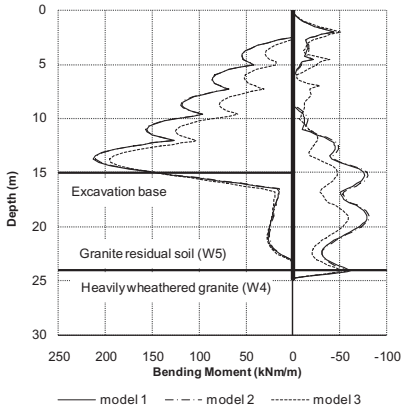

Figure 10. Bending moments envelope after the last excavation stage.

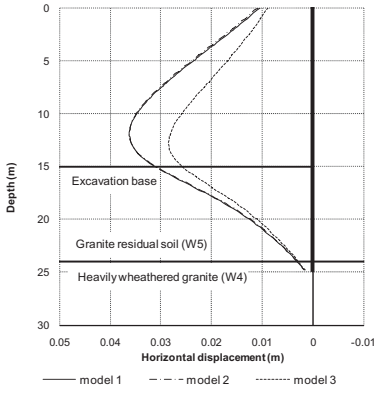

Figure 11. Wall displacements after the last excavation stage.

around 210 kNm/m, with variations between the three models not exceeding 8%.

Figure 10, presenting the bending moments envelope, conduces to similar conclusions as Figure 9. There are important differences in the upper part of the excavation but, near the bottom of the excavation and bellow, the results of the several calculations tend to agree with each other. In both Figures it can be noticed a significant difference between the calculations, which should not be too worrying, considering that the bending moments in this region are far from the maximum values.

The comparison between Figures 9 and 10 shows that the maximum bending moments are obtained after the last excavation step. In all the three models the maximum bending moment is located somewhere between 1.0 m and 1.5 m above the base of the excavation.

3.3 *Wall displacements*

In Figure 11 are displayed the wall displacements after the end of all the excavation works. As exposed in the previous sections, the distinct strategies to lower the water table in models 1 and 2 didn't produce relevant differences in the *in situ* stresses. Naturally, the wall displacements are very much similar.

The introduction of the suction effects, in model 3 results in lower wall displacements. Taking model 1 as reference, the horizontal movement was reduced 21%. The main reasons to this reduction are the increase of the soil stiffness and strength caused by the matric suction.

3.4 *Surface displacements*

The correct modeling of the groundwater in an excavation has capital importance regarding the surface settlements. Taking a close look at Figure 12 it can be verified that the consideration of a first stage, in which the groundwater is lowered, produces important vertical settlements. In model 2, a total maximum settlement of 81 mm was predicted, about 5 times larger than the value obtained in the reference calculation, model 1, where no groundwater level change was considered. In model 3, the consideration of matric suction and its effects over the soil strength and stiffness, reduces the total settlement when compared to model 2, but the total value remains high.

Since the surface settlements appear to be very dependent on the first stage, where the groundwater table is lowered, a detailed analysis of these movements was performed.

In model 1, as the water table lowering wasn't modeled, the settlements due to this process were

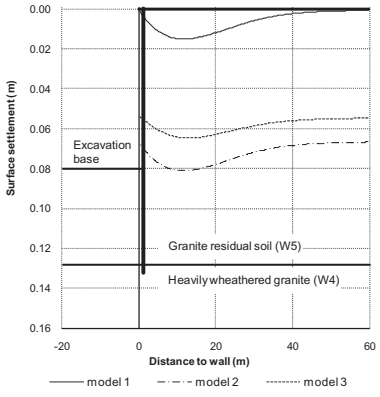

Figure 12. Surface settlement after the last excavation stage.

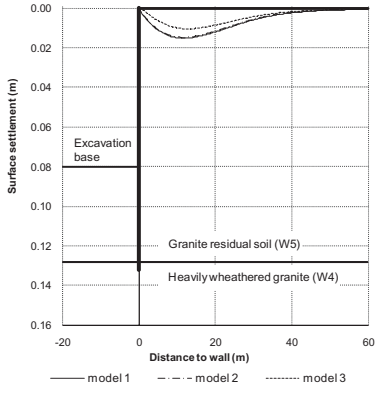

Figure 13. Surface settlement due to the excavation and presstress phases.

necessarily zero. In model 2 these uniform settlements reached a total value of 66.3 mm, while in model 3 they were 54.3 mm.

Figure 13 represents the settlements obtained after the water table lowering operation, this means, the total settlements subtracted by the ones produced during the water table variation. For comparison purposes the scale of the Figure was kept the same as in Figure 12. This Figure shows a quite similar behavior in all the three models. Nevertheless, the values obtained on model 3 are about 30% smaller than the ones in models 1 and 2. These differences are justified by the soil properties improvement caused by matric suction.

4 CONCLUSIONS

The comparison between models 1 and 2 shows that the groundwater variations, prior to the excavation, have no appreciable effects on wall forces and deflections. Even though, the groundwater lowering has an undeniable importance when referring to the surface settlements. This parameter has shown responsibility for approximately 80% of the surface settlement, in models 2 and 3. This scenario gains even more relevance in cases where the groundwater table profile, after drainage, is not uniform.

The consideration of a non saturated soil condition is crucial. Model 3 showed that the use of a simple model to reproduce the effects of soil suction resulted in the improvement of the retaining wall performance, reducing bending moments by 8%, whereas wall deflections and surface settlements were reduced more than 20%.

Given the importance of the simulation of the unsaturated soil behavior, confirmed by the values above, the design of such excavations should comprise a fully coupled hydro mechanical analysis. For such analysis it is fundamental to perform a set of *in situ* tests allowing the evaluation of soil stiffness variations with suction, mainly as a consequence of water table fluctuations.

ACKNOWLEDGMENTS

The authors would like to acknowledge Instituto Politécnico de Viseu and Centro de Estudos da Construção-FEUP by the financial support.

REFERENCES

Brinkgreve, R.B.J, Broere, W. & Waterman, D. 2004. *PLAXIS: Finite Element Code for Soil and Rock Analyses (2D - Version 8)*. Delft: Plaxis bv.

Raposo, N.P. 2007. *Pré-dimensionamento de Estruturas de Contenção Ancoradas.* MSc thesis Porto: Faculdade de Engenharia da Universidade do Porto. (in Portuguese).

Terzaghi, K. & Peck, R.B. 1967. *Soil Mechanics in Engineering Practice,* 2nd Edition. New York John Wiley & Sons.

Topa Gomes, A. 2009. *Elliptical shafts by the Sequential Excavation Method. The example of Metro do Porto*. PhD thesis. Porto: Faculdade de Engenharia da Universidade do Porto. (in Portuguese).

Viana da Fonseca, A. 1996. *Geomecânica dos solos residuais do granito do Porto. Critérios para o dimensionamento de fundações*. PhD thesis. Porto: Faculdade de Engenharia da Universidade do Porto. (in Portuguese).

Viana da Fonseca A. & Coutinho, R.Q. 2008. *Characterization of residual soils*. Keynote paper—In 3rd International Conference on Site Characterization. Taiwan—1–4 April 2008.

Wood, A.T. 2004. *Geotechnical Modeling*. New York: Spon Press.

This page intentionally left blank

Geotechnical Aspects of Underground Construction in Soft Ground – Viggiani (ed)
© 2012 Taylor & Francis Group, London, ISBN 978-0-415-68367-8

Influence of leakage on tunnel behavior in soft soils

D.M. Zhang & H.W. Huang
Department of Geotechnical Engineering, Tongji University, Shanghai, China

Z.Y. Fan
Shanghai Municipal Engineering Design General Institute, Shanghai, China

ABSTRACT: The effect of tunnel leakage on tunnel behavior was studied by small scale model tests in terms of the tunnel settlement as well as lining moment. Both the finite permeable and impermeable water inflow regimes of tunnel lining were considered in the model tests. The influence of tunnel leakage was revealed by the development of tunnel settlement and lining moment with time. The tunnel settlement increases with time when the tunnel is permeable, while the tunnel is lifted when the tunnel is impermeable. The magnitude of tunnel settlement depends on the quantity of tunnel leakage. Longitudinal differential settlements usually arise from tunnel leakage. The lining moments increase with time at tunnel crown and invert when the tunnel is permeable, but the variation of lining moment can be neglected when the tunnel is impermeable.

1 INTRODUCTION

Tunnel leakage has been one of the most problematic technical difficulties widely existing in operating tunnels especially in soft soils as shown in Figure 1. Its unfavorable influence on tunnel structures, waterproofing of joints and normal running of a tunnel has required more attention than ever. The leakage of tunnel usually results in the post-construction settlements of the tunnel (Mair, 2008; Zhang *et al.*, 2005; Shin *et al*., 2002; O'Reilly *et al.*, 1991). The influence of leakage on the tunnel has been studied mainly using numerical modeling method due to the large timescale of field-based research. This difficulty seriously limits the field monitoring data to be obtained to present the relationship between tunnel permeability and settlements of tunnels and soils. Therefore, the numerical modeling method has been a most powerful way to study the effect of water inflow on the tunnels and soils. O'Reilly *et al*. (1991) firstly introduced the definition of relative permeability of tunnel lining and soils to study the influence of tunnel leakage. The relative permeability was originally presented as the ratio of the lining permeability k_l to the soil permeability k_s. The relative permeability of tunnel lining and soils was extensively employed in numerical modeling to simulate the inflow effect of groundwater on the settlement of tunnel and soils (Zhang *et al.* 2005; Shin *et al*. 2002). Later, Wongsaroj (2005) expressed the relative permeability as a dimensionless number RP defined as $(k_l/k_s)\cdot(C/t_L)$, where C is the clay cover above the tunnel crown, t_L is the thickness of the tunnel lining.

In addition to the numerical modeling method, some analytical solutions are also found in the literature. Carter *et al.* (1982) studied the evolution of stress and settlement of soils around tunnel face with time considering two types of drainage conditions of the tunnel lining, one was fully permeable and the other was impermeable. Later, the time-dependent behavior of soils and the stiffness of lining were taken into account by Carter *et al*. (1983, 1984) to perfect their study described in Carter *et al.* (1982). Based on the studies of Carter *et al*. (1982, 1983, 1984), Li *et al*. (1999) studied the long-term behavior of tunnels considering the finite permeability of tunnel.

All the research found in the technical literature has proved that the relative permeability was the most important factor which controls the behavior of tunnels and surrounding soils when tunnel leakage happened. However, the tunnel lining permeability k_l used in relative permeability was considered to be uniform along the tunnel, which is not always the reality for tunnels with precast segments. Most of the tunnels in soft soils contain the longitudinal and circumferential joints and hand holes. Most of the leakage happened through the joints and hand holes shown in Figure 1 in Shanghai, China. Therefore, the permeability of tunnel lining is not uniform along the tunnel, but it was really difficult to simulate the actual state of tunnel leakage in both numerical modeling and analytical solutions. Considering the limitation of field-based database, the small scale model tests were performed to study the influence of the tunnel leakage on the tunnel and soils.

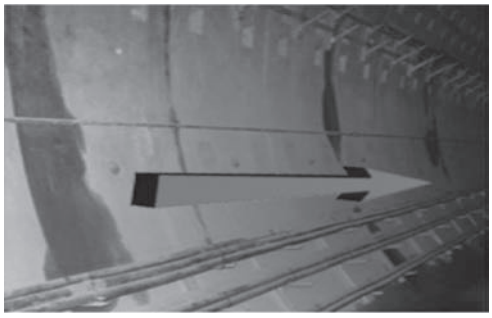

Figure 1. Leakage of shield tunnel in soft soils.

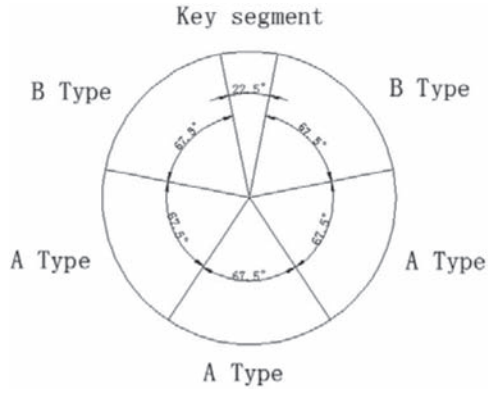

Figure 2. The partitioning of the tunnel segments.

2 TUNNEL MODEL

The tunnel model was designed with the prototype of Shanghai metro tunnel. The prototype tunnel is 6.2 meter and 5.5 meter in external and internal diameter respectively. The thickness of the segment is 0.35 meter. The width of the segment is 1 meter. The tunnel ring was installed by 6 segments namely 1 piece of key segment, 2 pieces of B type segment and 3 pieces of A type segment. The assembly of the tunnel segments was shown in Figure 2. The segments were connected by steel bolts.

The tunnel model was made of high density polyethylene (hdpe) and consists of 6 segments. The segments of tunnel model were cut from the hdpe tube with the division proportion shown in Figure 2. The analogous theory was applied and the similarity scale between practice and model was taken as 38.75 considering the diameter modulus. Both the geometric and stiffness similarity were considered in the tunnel model. The similarity scales were shown in Table 1 and the parameters of model and prototype tunnels were listed in Table 2. The coefficient of stiffness is defined as the ratio between tunnel stiffness with joints and stiffness without joints. The equivalent stiffness of tunnel with joints was applied.

The steel bolts were modeled by screw. The number and size of screw were determined based on the coefficient of stiffness ratio. The segments were staggered installed in the model tunnel. The key segment staggered 22.5° in two rings. Every two rings were a staggered circle. The tunnel model comprised of 50 rings. The tunnel model is shown in Figure 3.

The model test was carried out in a steel container. The steel container is 1.5 meter long, 0.8 meter wide and 0.9 meter high. Six taps were set in two rows at the side of the container. The transparent hose was connected to the taps, so the variation of the water level could be detected from the transparent hose just with rules.

Table 1. The similarity scales between practice and model.

Geometric ratio	Elastic modulus ratio	Coefficient of stiffness ratio	Concentrated load ratio
38.75	29.36	1137.7	44085.88

Table 2. The parameters of model and prototype tunnels.

	External Diameter	Segment thickness	Segment width	Elastic modulus
	m	m	m	MPa
Prototype	6.2	0.35	1	3.45×10^4
Model	0.16	0.0095	0.258	1175

Figure 3. The assembly of the tunnel segments.

3 PROCEDURE OF MODEL TEST

3.1 *Monitoring devices*

The water level, the lining stress as well as the settlements of the tunnel were monitored during the model test. The water level could be detected through the transparent hose with rulers shown in Figure 4. The stress of lining was measured by strain gauges. The strain gauges were set on two rings of No. 26 and No. 37. The tunnel model was numbered from No. 1 to No. 50 from one end to the other. The distribution of strain gauges on each ring is shown in Figure 5.

The neutral axis of the lining during bending was supposed to coincide with the central line of the thickness along width direction. So the bending moment and the hoop thrust of the lining could be derived using Equation 1 and Equation 2.

$$M = \frac{(\varepsilon_1 - \varepsilon_2)EI}{t} \tag{1}$$

$$N = \frac{(\varepsilon_1 - \varepsilon_2)EA}{2} \tag{2}$$

Where, ε_1 and ε_2 are the compression and extension strain measured during the model tests, E is the elastic modulus of the segment concrete, I is the moment of inertia of the segment, t is the thickness of the segment, A is the area and could be calculated by the thickness times the width of the segment.

The settlement of the tunnel was measured by the dial indicator at ring No. 5, No. 12, No. 19, No. 26, No. 33, No. 40, No. 46, so totally 7 settlement monitoring points were set along the tunnel. The settlement was measured at the crown of the tunnel. A settlement transmission device had to be designed because the tunnel model was embedded in the soil and its settlement could not be monitored directly. The transmission device contains a steel bar and a steel tube. The steel bar was used to transmit the settlement. One end of the steel bar was perpendicularly connected to the crown of the tunnel model and the dial indicator was put on the other end. The steel bar should be strong enough and not to deform during the settlement transmission. The steel bar was protected by the steel tube not to be affected by the surrounding soils.

3.2 *Procedure of the model test*

Two types of model tests were performed in terms of the permeability of the tunnel. One was finite permeable test, the other was impermeable test. In impermeable test, the tunnel joints were sealed by epoxy resin, while the tunnel joints were not sealed and kept as the original state in the finite permeable test. In both tests, the two ends of the tunnel were sealed to stop the inflow from the ends.

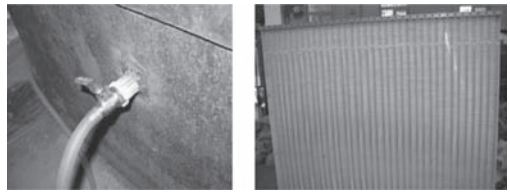

Figure 4. The water level measuring device.

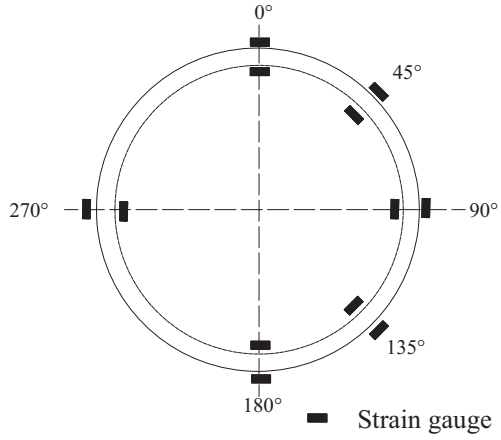

Figure 5. The distribution of stain gauges.

The sand was chosen as the soil medium in the model test to save testing time. The model test in the clay medium will be performed later. The permeability of the sand is larger than 10^{-5} m/s. The procedure of the tests is described in the following.

Step 1. The sand was laid layer upon layer in the steel container. The thickness of each layer was kept less than 5 cm to guarantee the density of the sand.

Step 2. The tunnel model was taken his place when the sand was laid until 48 cm thick from the bottom.

Step 3. The settlement transmission device was set on the crown of the tunnel perpendicularly.

Step 4. The sand was laid again over the tunnel with the same way as in step 1. The total thickness of the laid sand was 24 cm in this step.

Step 5. The verticality of the settlement transmission device was checked. Besides, it was ensured that the steel bar didn't nestle up to the steel tube.

Step 6. The dial indicators as well as data taker were finally installed.

The water was not recharged during both test, so the drawdown of water level was considered. The ongoing model test was shown in Figure 6.

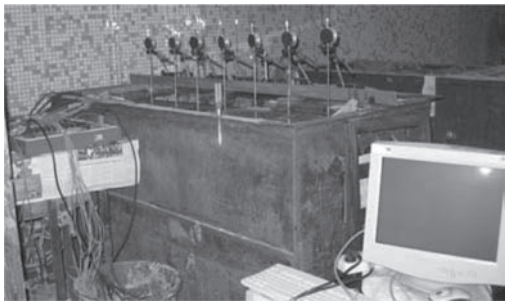

Figure 6. The ongoing model test.

4 EXPERIMENTAL RESULTS AND ANALYSIS

4.1 *The development of tunnel settlement in finite impermeable test*

The evolution of tunnel settlements with time and water drawdown was shown in Figure 7–13. The water level was computed from the container bottom.

The initial water level in the test was 84 cm and the final water level was 63 cm. The tunnel leakage could be presented by the water level drawdown because the leakage from the tunnel joints was the only cause for water drawdown. The sand was used in the model test, so the tunnel leakage could be the main contribution to the tunnel settlement. The figures showed that the tunnel settlement is proportional to the water drawdown. The final settlements at Ring No. 5, Ring No. 12, Ring No. 19, Ring No. 26, Ring No. 33, Ring No. 40 and Ring No. 46 were 0.62 mm, 0.48 mm, 0.41 mm, 0.37 mm, 0.42 mm, 0.43 mm and 0.53 mm respectively. During the model test, more bubbles were found near the two ends of the tunnel model. This means that the leakage near the two ends was much more serious. Apparently, the leakage not only results in the tunnel settlement but also the differential settlement and in turn the differential settlement will accelerate the tunnel leakage. The differential settlement was shown in Figure 14. However, the relationship between the water level change and equivalent permeability of tunnel was not calculated.

4.2 *The development of tunnel settlement in impermeable test*

The tunnel joints were all sealed with epoxy resin to stop the water inflow. The typical tunnel settlements in the impermeable test were shown in Figure 15–21.

The behavior of tunnel under impermeable condition could be presented by Figure 15–21. Under impermeable condition, the tunnel experienced a certain heave at the beginning of the test due to the buoyancy produced when the water was injected into the test container. After about 30 hours, the heave of the tunnel reached the equilibrium and no settlement was developed thereafter because of the impermeability of the tunnel. It was found that the tunnel around Ring No. 46 exhibited a different behavior from the other parts of the tunnel. The settlement instead of heave was measured at Ring No. 46 because of the slight leakage there. The water level was not affected by the slight leakage around the Ring No. 46. The water level was kept as a constant during the model test.

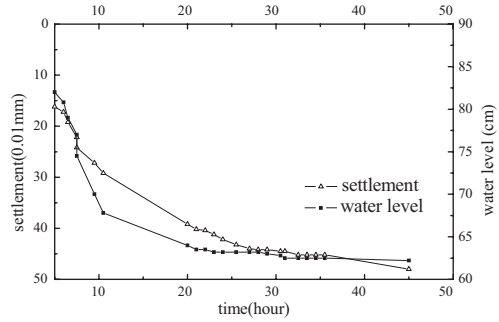

Figure 7. Development of tunnel settlement with time and water drawdown at Ring No. 5 in finite permeable test.

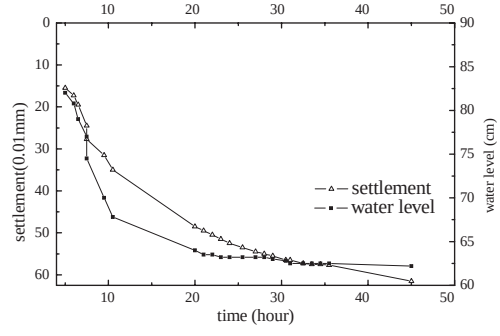

Figure 8. Development of tunnel settlement with time and water drawdown at Ring No. 12 in finite permeable test.

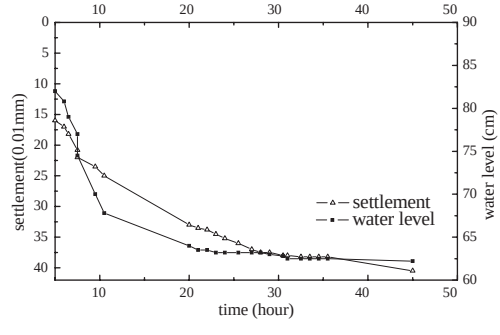

Figure 9. Development of tunnel settlement with time and water drawdown at Ring No. 19 in finite permeable test.

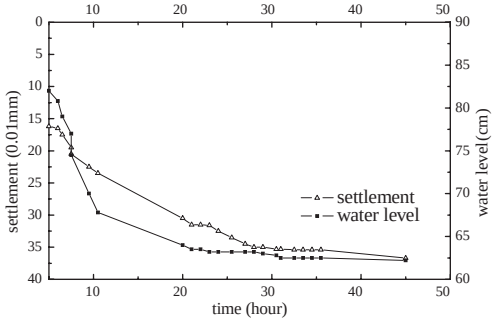

Figure 10. Development of tunnel settlement with time and water drawdown at Ring No. 26 in finite permeable test.

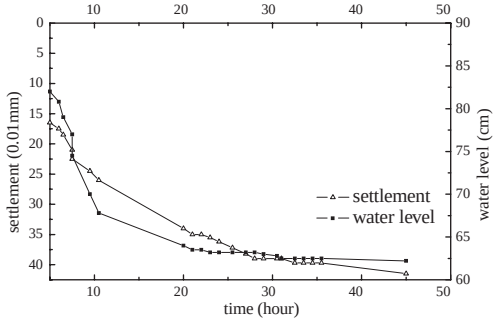

Figure 11. Development of tunnel settlement with time and water drawdown at Ring No. 33 in finite permeable test.

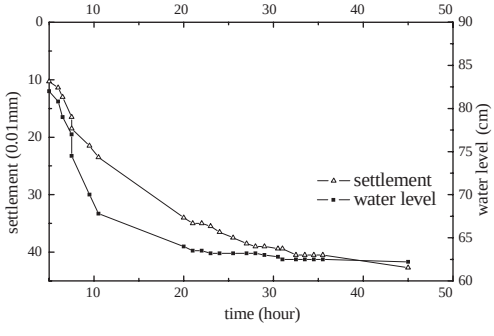

Figure 12. Development of tunnel settlement with time and water drawdown at Ring No. 40 in finite permeable test.

The influence of leakage on tunnel settlement could be revealed by the comparison on the evolutions of tunnel settlement under finite permeable and impermeable conditions. Improving the waterproof capacity of tunnel joints is an effective way to reduce the unfavorable influence of tunnel leakage.

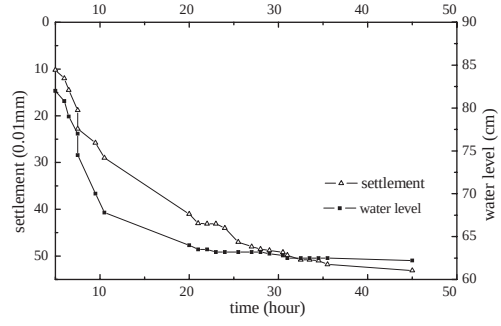

Figure 13. Development of tunnel settlement with time and water drawdown at Ring No. 46 in finite permeable test.

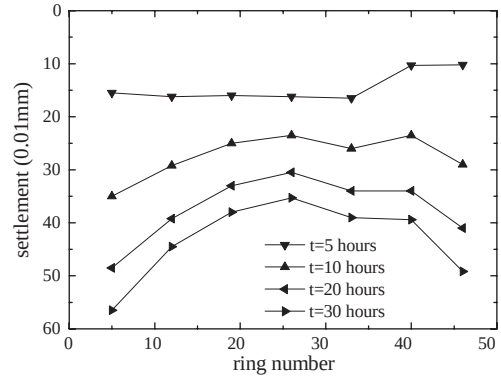

Figure 14. The differential settlement due to leakage in finite permeable test.

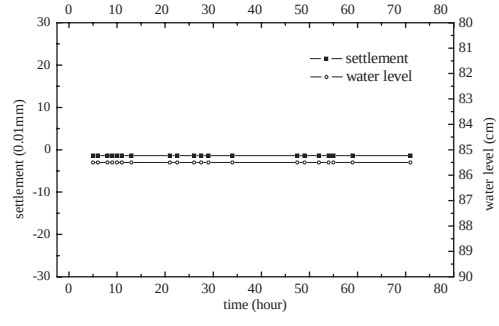

Figure 15. Development of tunnel settlement with time and water drawdown at Ring No. 5 in impermeable test.

4.3 *The development of lining moment in finite permeable test*

The moment of tunnel lining was obtained through the strain gauges and derived from Equation 1. The hoop thrust was not discussed in this paper considering its minor influence on the performance of tunnel lining. However, the strain gauges

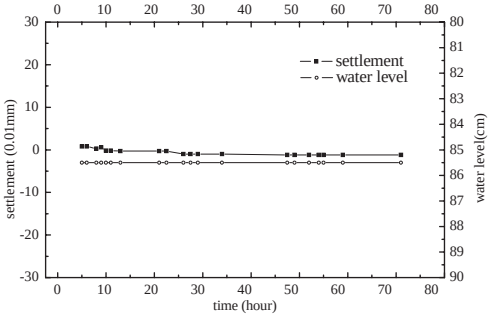

Figure 16. Development of tunnel settlement with time and water drawdown at Ring No. 12 in impermeable test.

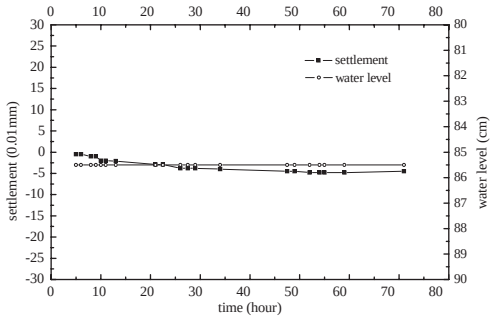

Figure 17. Development of tunnel settlement with time and water drawdown at Ring No. 19 in impermeable test.

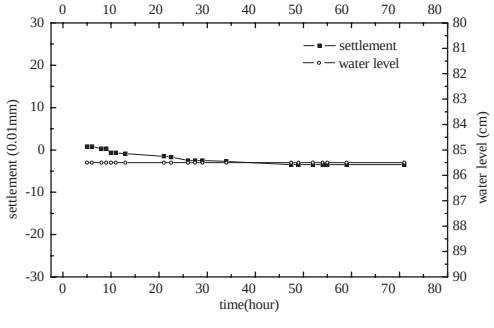

Figure 18. Development of tunnel settlement with time and water drawdown at Ring No. 26 in impermeable test.

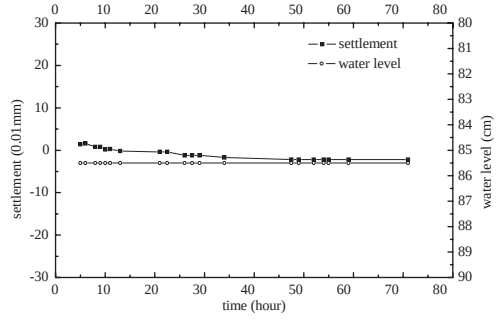

Figure 19. Development of tunnel settlement with time and water drawdown at Ring No. 33 in impermeable test.

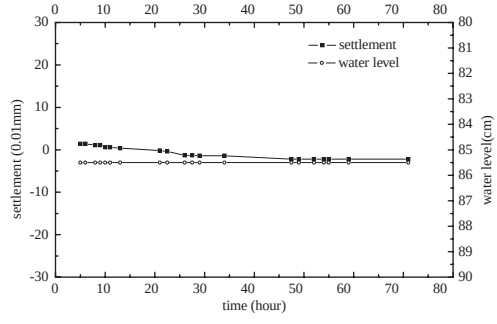

Figure 20. Development of tunnel settlement with time and water drawdown at Ring No. 40 in impermeable test.

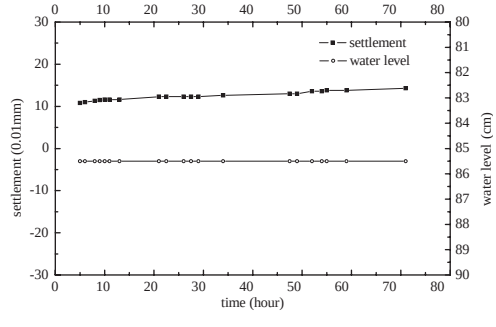

Figure 21. Development of tunnel settlement with time and water drawdown at Ring No. 46 in impermeable test.

at the positions of 45°,135° and 270° of the tunnel circumference were destroyed during the test. Therefore, the influence of tunnel leakage on the inner force of tunnel was presented by the variation of moment calculated at the position of 0°, 90° and 180° of tunnel circumference. The evolutions of the moment with time at Ring No. 26 and No. 37 were illustrated in Figure 22–23 respectively. The water level change could be referred in Figure 7–13.

Both Figure 22 and Figure 23 demonstrated that the tunnel leakage resulted in the significant increase of lining moment at tunnel crown and invert. However, the lining moment at the spring line did not change much. The moments at the crown and invert of Ring No. 26 increased from 47.1 N*mm to

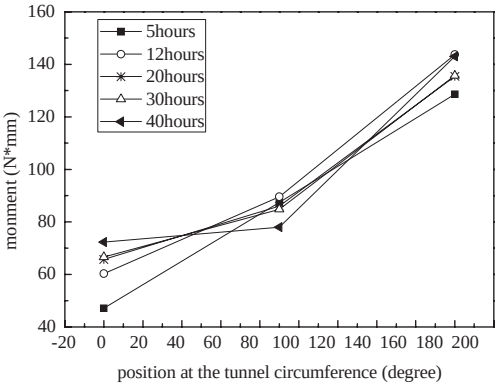

Figure 22. Variation of lining moment at Ring No. 26 in finite permeable test.

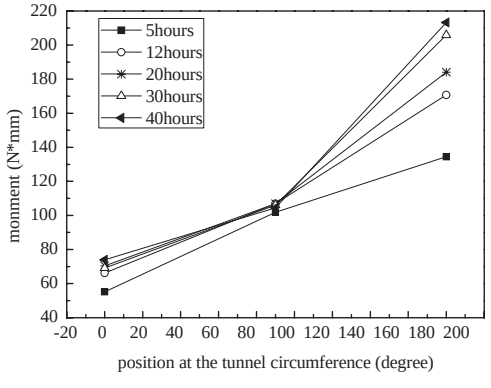

Figure 23. Variation of tunnel moment at Ring No. 37 in finite permeable test.

72.3 N*mm and from 128.6 N*mm to 143 N*mm when water level was dropped from 83 cm to 63 cm. More than 50% have been increased during the leakage period at the crown of the tunnel. While at Ring No. 37, the increase of moment at the tunnel invert is much more remarkable than that at the tunnel crown. The increase of lining moment at the tunnel crown and invert reached 34% and 59% respectively at Ring No. 37. Considering the measure errors during the test, it was hard to conclude the influence of tunnel leakage on the moment development at the tunnel crown and invert. However, one thing was clear that the tunnel leakage resulted in more increase of lining moment at the tunnel crown and invert rather than at the spring line of the tunnel.

Besides, it was found that the lining moment increase more quickly at the beginning of the test. The reason was the water level dropped quickly during this period and the water drawdown reached 18 cm, while the total drawdown of the water was 21 cm during the test. From this point of view, the variation of lining moment is proportional to the magnitude of drawdown of the water.

Additionally, the figures showed that the influence of tunnel leakage on the lining moment is more notable at Ring No. 37 than that at Ring No. 26. This could be explained when referring Figure 14 where the tunnel settlement was bigger at Ring No. 37 than that at Ring No. 26. This phenomenon revealed that the more serious the leakage, the more significant effect would have in terms of the tunnel settlement and lining moment.

4.4 *The development of lining moment in impermeable test*

The development of lining moment with time in impermeable test was presented in Figure 24–25.

Apparently, the lining moment in impermeable test did not change as much as that in finite

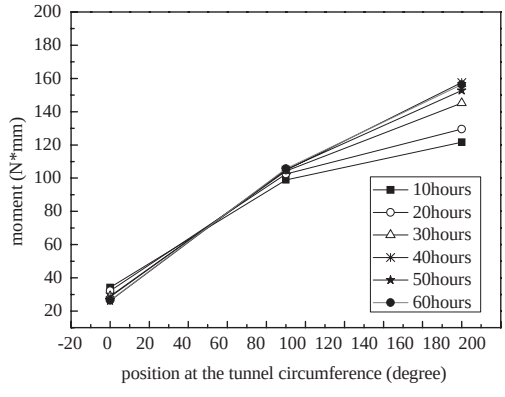

Figure 24. Variation of lining moment at Ring No. 26 in impermeable test.

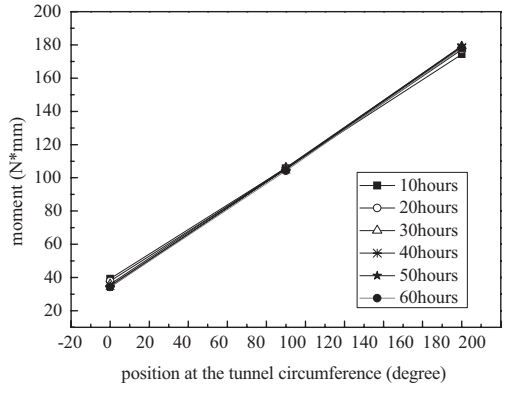

Figure 25. Variation of lining moment at Ring No. 37 in impermeable test.

permeable test. Theoretically, the inner force of tunnel lining should be kept as constant because the load exerted on the tunnel did not change at all during impermeable test. However, the moment at the tunnel invert of Ring No. 26 was scatted.

Although the lining moment did not increase under impermeable conditions, the lining moment at the spring line was higher in impermeable test than that in finite permeable test due to the larger buoyancy in former case.

5 CONCLUSIONS

Both finite permeable and impermeable small scale model tests were carried out with the prototype of Shanghai metro tunnel. The influence of tunnel leakage on the tunnel performance was studied in terms of the tunnel settlement and lining moment as well. The following was revealed from the tests:

a. The tunnel settlement increases continually with time when the tunnel lining is finite permeable. In contrast, the tunnel is lifted with time when the tunnel lining is fully impermeable and then reaches an equilibrium state. This is in accordance with the numerical modeling results of Mair (2008) where it was found that the long-term surface settlement increases with time when the tunnel is permeable and reduces with time when the tunnel is impermeable.
b. The tunnel leakage not only results in the tunnel settlement but also the longitudinal differential settlement. The longitudinal differential settlement leads to the opening of the circumferential joints of the tunnel. Consequently, it will accelerate the leakage of the tunnel. From this point of view, it is an effective way to improve the waterproof capacity of the tunnel joints to reduce the long-term settlement of tunnel and tunnel leakage as well.
c. The lining moments at the tunnel crown and invert increase with time when the tunnel is permeable. However, the variation of lining moment at the spring line of the tunnel could be ignored. The results from permeable test show that the more serious the tunnel leakage, the more increase of the lining moment at the tunnel crown and invert. In contrast, the lining moment does not have significant change all along the tunnel circumference. But the moment at the spring line is higher when tunnel is impermeable than that when tunnel is permeable.
d. The small scale model test is verified to be a useful way to study the behavior of tunnel with permeable and impermeable inflow regimes of tunnel lining. However, there is a big risk to monitor the inner force of the tunnel with strain gauges. Besides, the quantity of water inflow through each joint is difficult to measure and then it is not easy to build the quantitative relationship between tunnel leakage and settlement and inner force variation of the tunnel.

ACKNOWLEDGEMENTS

The financial supports from National Natural Science Foundation of China (50608058) and Hitech Research and Development Program (863 Program) of China (2006AA11Z118) are highly acknowledged.

REFERENCES

Carter, J.P. & Booker, J.R. 1982. Elastic consolidation around a deep circular tunnel. *International Journal of Solids and Structures* 18 (12): 1059–1074.

Carter, J.P. & Booker, J.R. 1983. Creep and consolidation around circular openings in infinite media. *International Journal of Solids and Structures* 19 (8): 663–675.

Carter, J.P. & Booker, J.R. 1984. Elastic consolidation around a lined circular tunnel. *International Journal of Solids and Structures* 20 (6): 589–608.

Li, X. 1999. Stress and displacement fields around a deep circular tunnel with partial sealing. *Computers and Geotech-nics* 24 (2): 125–140.

Mair, R.J. 2008. Tunnelling and geotechnics: new horizons. *Geotechnique* 58(9): 695–736.

O'Reilly, M.P., Mair, R.J. & Alderman, G.H., 1991. Long-term settlements over tunnels: an eleven-year study at Grimsby. P*roceedings of Conference Tunneling, London, Institution of Mining and Metallurgy*: 55–64.

Shin, J.H., Addenbrooke, T.L. & Potts, D.M. 2002. A numerical study of the effect of groundwater movement on long-term tunnel behavior. *Geotechnique* 52(6): 391–403.

Wongsaroj, J. 2005. Three-dimensional finite element analysis of short- and long-term ground response to open face tunnelling stiff clay. *PhD Thesis.* Cambridge University.

Zhang, D.M., Huang, H.W. & Yang, J. 2005. Influence of partial drainage of linings on long-term surface settlement over tunnels in soft soils. *Chinese Journal of Geotechnical Engineering* 27(12): 130–1436.

Geotechnical Aspects of Underground Construction in Soft Ground – Viggiani (ed)
© 2012 Taylor & Francis Group, London, ISBN 978-0-415-68367-8

Effect of soil stratification on pipe behaviour due to tunnelling-induced ground movements based on the displacement controlled method

Z.G. Zhang
Department of Civil Engineering, Shanghai University, Shanghai, P.R. China
Department of Geotechnical Engineering, Tongji University, Shanghai, P.R. China
Shanghai Institute of Applied Mathematics and Mechanics, Shanghai, P.R. China

M.S. Huang
Department of Geotechnical Engineering, Tongji University, Shanghai, P.R. China

M.X. Zhang
Department of Civil Engineering, Shanghai University, Shanghai, P.R. China

W.D. Wang
East China Architecture Design Institute, Shanghai, P.R. China

ABSTRACT: The available theoretical predictions for the pipe behaviour due to tunnelling-induced ground movements are usually based on the assumptions that the ground is homogeneous. Actually, effects of soil stratification should be taken into account. This paper presents displacement controlled method to analyze the pipe behaviour due to tunnelling-induced ground movements by the means of layered half space model, which can solve the problem subjected to homogeneous soil as well as multi-layered non-homogeneous soils. The accuracy of the proposed solutions is verified by the centrifuge test data and the results from displacement controlled finite element numerical analysis. In addition, the difference between homogeneous and non-homogeneous layered soils is also studied to estimate the pipe behaviour. The results discussed in this paper indicate that the soil non-homogeneity, neglected in previous solutions, has a significant influence on the existing pipe behavior induced by adjacent tunnelling in multi-layered soils.

1 INTRODUCTION

Underground construction, including tunnelling, causes both vertical and lateral ground movements. For existing buried structures, such as pipes, the ground movements induced by tunnelling may cause reduction in bearing capacity of the structures as well as the development of additional settlements, and lateral movements. Accurate prediction of tunnelling effects on existing buried pipes poses a major challenge during design and practice in the urban geotechnical environments.

The conventional approach for solving the above mentioned problem utilizes the numerical simulation method, such as the finite element method (e.g., Yamaguchi et al., 1998; Addenbrooke and Potts, 2001; Chehade and Shahrour, 2008). Tunnelling in the finite element models is usually simulated by applying forces corresponding to a fraction of the initial stress-state, to the nodes on the tunnel boundary. This method, designated here as the force controlled method (i.e., FCM), has the advantage of being able to take full account of the nonlinear interaction between the existing pipes and its surrounding soil, and to consider the complicated process of tunnelling. However, the FCM will lead to long CPU times since the simulation of the process may be slow. And it is difficult to reflect visually the arbitrary ground loss, which is the main cause for the deformation behavior of existing pipes induced by tunnelling. In order to overcome those disadvantages, the displacement controlled method (i.e., DCM) is applied in this study. In the DCM, the effect of tunnelling is simulated by prescribing displacements up to nodes around the tunnel rather than by adding forces.

Recently some attempts have been made to develop displacement controlled methods to analyze the pipe deformation behaviour due to adjacent tunnelling, all of which are based on the Winkler model or the homogeneous half space model. The conventional approach for obtaining a solution for

this problem utilizes the Winkler model such as that proposed by Attewell et al. (1986). The Winkler model has the advantage of simplicity for the complex tunnel-soil-pipe interaction through a single degree of freedom load-displacement relation. However, the Winkler model can not take account of the soil continuum. Klar et al. (2005) obtained a closed form solution for the Winkler model, and suggested a more rigorous solution based on the homogeneous half space model. In this study, the green-field soil settlements are described by a Gaussian curve. Vorster et al. (2005) utilized the boundary integral method to formulate a design method for estimating the effect of tunnelling on buried pipes. They took advantage of the explicitly defined green-field settlements and introduced a modified Gaussian curve which allows the practitioner more freedom in fitting green-field settlement data relatively to the commonly used Gaussian curve. It is worth noting that all of the above solutions are based on the assumption that the ground is homogeneous and the effects of soil stratification should be taken into account.

In the current research, the displacement controlled method is presented to evaluate the effects of soil stratification on pipe behaviour due to tunnelling-induced ground movements. The fundamental solution for the layered soils is obtained by applying the double Laplace transform and transfer matrix method based on the layered half space model. In order to simulate the real non-uniform soil deformation behaviour at the tunnel opening, the displacement controlled pattern proposed by Loganathan and Poulos (1998) is applied to describe green-field soil settlements.

2 LAYERED HALF SPACE MODEL

As shown in Figure 1, the layered half space model is built in a Cartesian coordinate system, and the arbitrary load is concentrated at a point (x_0,y_0,h_{m1}) in the m th layer (assuming the load surface is considered as an artificial interface). The arbitrary load can be decomposed into the three components $P(x,y_0,h_{m1})$, $R(x_0,y_0,h_{m1})$, and $Q(x_0,y_0,h_{m1})$ along the x, y, z direction, respectively. The key assumptions involved in the derivation are: (1) The layered soils consist of n parallel, elastic isotropic layers lying on a homogeneous elastic half space, where n is an integer and satisfies $n \geq 1$; (2) The i th layer occupies a layer region $h_{i-1} \leq z \leq h_i$ of thickness Δh_i, ($\Delta h_i = h_i - h_{i-1}$), Young's modulus E_i and Poisson's ratio μ_i, where $i = 1, 2, ...,$ or n, and h_0 is defined by the value of zero; (3) the stresses and the displacements located at the each interface between two connected layers are completely continuous; (4) The boundary surface $z = 0$ is considered as traction free.

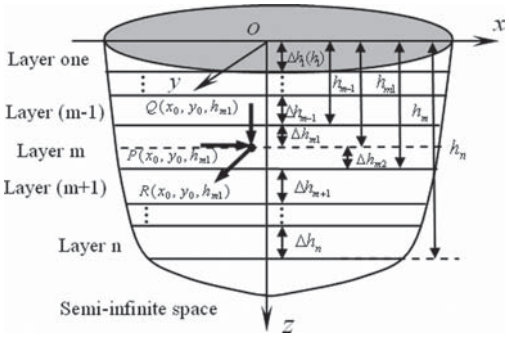

Figure 1. Layered half space model.

Considering a traction free condition at the ground surface of the layered system, it can be expressed as follows:

$$\tau_{zx}(x,y,0) = \tau_{zy}(x,y,0) = \sigma_z(x,y,0) = 0 \tag{1}$$

On the other hand, for a fixed boundary condition at the bottom of the layered system (h_n approaches ∞), it can be expressed as follows:

$$u(x,y,h_n) = v(x,y,h_n) = w(x,y,h_n) = 0 \tag{2}$$

According to assumption 3, the continuity conditions at the interfaces of the n-layered system (including the load surface) can be obtained:

$$u(x,y,h_i^+) = u(x,y,h_{i-1}^-) \tag{3a}$$

$$v(x,y,h_i^+) = v(x,y,h_{i-1}^-) \tag{3b}$$

$$w(x,y,h_i^+) = w(x,y,h_{i-1}^-) \tag{3c}$$

$$\tau_{zx}(x,y,h_i^+) = \tau_{zx}(x,y,h_{i-1}^-) - p(x,y,h_{m1})g(z) \tag{3d}$$

$$\tau_{zy}(x,y,h_i^+) = \tau_{zy}(x,y,h_{i-1}^-) - r(x,y,h_{m1})g(z) \tag{3e}$$

$$\sigma_z(x,y,h_i^+) = \sigma_z(x,y,h_{i-1}^-) - q(x,y,h_{m1})g(z) \tag{3f}$$

where h_i is the distance from the bottom of the i th layer to the surface of the first layer ($i = 2, 3, \cdots,$ or n); the superscripts "+" and "−" denote the values of the functions just on upper and lower interface boundary of the i th layer; $p(x,y,h_{m1})$, $r(x,y,h_{m1})$, and $q(x,y,h_{m1})$ denotes the surface density distribution of the point load $P(x_0,y_0,h_{m1})$, $R(x_0,y_0,h_{m1})$, and $Q(x_0,y_0,h_{m1})$, respectively, i.e.,

$$p(x,y,h_{m1}) = P(x_0,y_0,h_{m1})\delta(x-x_0,y-y_0) \tag{4a}$$

$$r(x,y,h_{m1}) = R(x_0,y_0,h_{m1})\delta(x-x_0,y-y_0) \tag{4b}$$

$$q(x,y,h_{m1}) = Q(x_0,y_0,h_{m1})\delta(x-x_0,y-y_0) \tag{4c}$$

with $\delta(x-x_0, y-y_0)$ is the Dirac singularity function; and g(z) is a term to judge whether the arbitrary load existed at the artificial interface or not, i.e.,

$$g(z)=\begin{cases}1 & z=h_{m1}\\ 0 & z\neq h_{m1}\end{cases} \tag{5}$$

In order to reduce the partial differential equation into the algebraic equation, the double Laplace integral transform will be applied to the state variables:

$$\overline{f}(\xi,\eta,z)=\int_0^\infty\int_0^\infty f(x,y,z)e^{-(\xi x+\eta y)}dxdy \tag{6}$$

where ξ, η are the integration parameters for the Laplace transform.

The inverse double Laplace transform can be expressed as follows:

$$f(x,y,z)=-\frac{1}{4\pi^2}\int_{\beta-i\infty}^{\beta+i\infty}\int_{\beta-i\infty}^{\beta+i\infty}\overline{f}(\xi,\eta,z)e^{\xi x+\eta y}d\xi d\eta \tag{7}$$

Using the double Laplace integral transform for the continuity conditions in Eqs.(3a)–(3f) and the transfer matrix method, the equations governing the relations between the six variables at two boundary surfaces $z=0$ and $z=h_n$ can be expressed as follows:

$$\overline{G}(\xi,\eta,h_n^-)=[F_1]\overline{G}(\xi,\eta,0)-[F_2]\{Q\} \tag{8}$$

where $\overline{G}(\xi,\eta,0)$ is the state variable vector located at the surface $z=0$ in the transform domain, i.e.,

$$\overline{G}(\xi,\eta,0)=[\overline{u}(\xi,\eta,0)\quad \overline{v}(\xi,\eta,0)\quad \overline{w}(\xi,\eta,0)\quad \overline{\tau}_{zx}(\xi,\eta,0)\quad \overline{\tau}_{zy}(\xi,\eta,0)\quad \overline{\sigma}_z(\xi,\eta,0)]^{\mathrm{T}}$$

and the elements of $\overline{G}(\xi,\eta,h_n^-)$ are the analogous with the ones of $\overline{G}(\xi,\eta,0)$; $[F_1]$ is the global transfer matrix from the first layer to the n th layer; $[F_2]$ is the local transfer matrix from the m th layer to the n th layer; $\{\overline{Q}\}$ is the load vector in the transform domain, i.e.,

$$[F_1]=\Phi(\xi,\eta,\Delta h_n)\Phi(\xi,\eta,\Delta h_{n-1})\cdots\Phi(\xi,\eta,\Delta h_1) \tag{9a}$$

$$[F_2]=\Phi(\xi,\eta,\Delta h_n)\Phi(\xi,\eta,\Delta h_{n-1})\cdots\Phi(\xi,\eta,\Delta h_{m2}) \tag{9b}$$

$$\{Q\}=[0\quad 0\quad 0\quad \overline{p}(x,y,h_{m1})\quad \overline{r}(x,y,h_{m1})\quad \overline{q}(x,y,h_{m1})]^{\mathrm{T}}$$

in which Δh_i is the thickness of the i th layer with $\Delta h_1=h_1$, $\Delta h_i=h_i-h_{i-1}$(i = 2, 3, ···, or n), and $\Delta h_{m2}=h_m-h_{m1}$; $\Phi(\xi,\eta,z)$ is called the transfer matrix, and $\Phi(\xi,\eta,z)=\exp[zA(\xi,\eta)]$, i.e.,

$$A(\xi,\eta)=\begin{bmatrix}0 & 0 & -\xi & \frac{1}{G} & 0 & 0\\ 0 & 0 & -\eta & 0 & \frac{1}{G} & 0\\ \frac{\mu}{\mu-1}\xi & \frac{\mu}{\mu-1}\eta & 0 & 0 & 0 & \frac{1-2\mu}{2G(1-\mu)}\\ \frac{2G}{\mu-1}\xi^2-G\eta^2 & \frac{G(1+\mu)}{\mu-1}\xi\eta & 0 & 0 & 0 & \frac{\mu}{\mu-1}\xi\\ \frac{G(1+\mu)}{\mu-1}\xi\eta & \frac{2G}{\mu-1}\eta^2-G\xi^2 & 0 & 0 & 0 & \frac{\mu}{\mu-1}\eta\\ 0 & 0 & 0 & -\xi & -\eta & 0\end{bmatrix}$$

By applying the two boundary conditions of Eqs.(1) and (2), the $\overline{G}(\xi,\eta,0)$ and $\overline{G}(\xi,\eta,h_n^-)$ in Eq. (8) can be determined analytically.

For a given depth z in the i th layer above the horizontal plane on which the load acts (including just on the plane, i.e., $z\le h_{m1}$), the stresses and displacements in the transform domain can be expressed as follows:

$$\overline{G}(\xi,\eta,z)=[S]\overline{G}(\xi,\eta,0) \tag{10}$$

where

$$[S]=\Phi(\xi,\eta,z-h_{i-1})\Phi(\xi,\eta,\Delta h_{i-1})\cdots\Phi(\xi,\eta,\Delta h_1) \tag{11}$$

For a given depth z in the i th layer below the horizontal plane on which the load acts (i.e., $z>h_{m1}$), the stresses and displacements in the transform domain can be expressed as follows:

$$\overline{G}(\xi,\eta,z)=[S_1]\overline{G}(\xi,\eta,h_n^-) \tag{12}$$

where

$$[S_1]=\Phi(\xi,\eta,z-h_i)\Phi(\xi,\eta,-\Delta h_{i+1})\cdots\Phi(\xi,\eta,-\Delta h_n) \tag{13}$$

Applying the inverse double Laplace transform of Eq. (7) into the solution $\overline{G}(\xi,\eta,z)$ in Eqs.(10) and (12), the elastic solution for stresses and displacements in the multi-layered soils subjected to the vertical load can be obtained. For the special case $P(x_0,y_0,h_{m1})=1$, $R(x_0,y_0,h_{m1})=1$, and $Q(x_0,y_0,h_{m1})=1$, the solution is the fundamental solution for the multi-layered soils subjected to the arbitrary unit point load.

3 DISPLACEMENT CONTROLLED METHOD

Figure 2 shows a schematic diagram of the problem, in which an existing pipe is buried in layered elastic soils. The key assumptions of the computing model are: (1) The existing pipe remains in contact with the surrounding soils; (2) The existing pipe is elastic, homogeneous, and continuous; (3) The presence of the existing pipe does not affect the

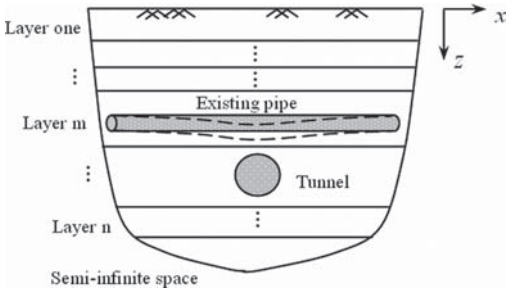

Figure 2. Effects of soil stratification on pipe behaviour due to tunnelling.

tunnel; (4) The soil response to loads, at the pipe level, is not aware of the tunnel; (5) The green-field soil settlements are calculated by analytical solutions proposed by Loganathan and Poulos (1998).

Assumption 3 simply means that the tunnel exhibits the same behavior as it would if there was no pipe. This is an essential assumption in the formulation allowing for decoupling of tunnel behavior in the solution of the pipe response, through the use of a green-field settlement trough. Assumption 4 means that the soils exhibit the same resistance (stiffness) to movement at the pipe level, whether the tunnel exists or not. This assumption allows the use of the fundamental solution for a vertical load in the layered half space model. Assumption 5 shows how to describe the green-field settlement profile at the level of the existing pipe.

Following the above-mentioned assumptions, the pipe behavior is represented by:

$$[K_b]\{u_b\} = \{F_b\} \tag{14}$$

where $[K_b]$ is the stiffness matrix of the tunnel composed of standard beam elements, $\{u_b\}$ is the displacement vector, $\{F_b\}$ is the force vector representing soil loads acting on the beam elements.

The soil continuous displacement at the arbitrary point i can be represented:

$$u_{si} = \sum_{j=1}^{n} R_j \delta_{ij} \tag{15}$$

where R_j is the tunnel force acting on the point j of the soil medium; δ_{ij} is the soil continuous displacement at point i due to the unit load at point j, and it is calculated by the fundamental solution for the layered half space system.

The summation in Eq. (15) can also be written as follows:

$$u_{si} = R_i \delta_{ii} + \sum_{j=1, j\neq i}^{n} R_j \delta_{ij} \tag{16}$$

where the first term of the right side is defined herein as the local displacement due to its own load. The second term is additional continuous displacement at that point due to forces acting at different points. δ_{ii} is the displacement of the singularity point. Such displacement is taken as the average displacement around the circumference of the pipe.

In order to consider the adjacent tunnelling, Eq. (16) can further be decomposed as follows:

$$u_{si} = R_i \delta_{ii} + \sum_{\substack{j=first\ pipe\ node \\ j\neq i}}^{last\ pipe\ node} R_j \delta_{ij} + u_{si}^f \tag{17}$$

where the second term of the right side is additional displacement of the point i due to forces resulting from soil-pipe interaction. The third term is additional displacement due to the existence of tunnel. By assumptions 5, u^f_{si} is defined as the green-field settlement profile at pipe level, and is calculated by the method proposed by Loganathan and Poulos (1998).

The static equilibrium condition and the displacement compatibility relation are required. They can be expressed as follows:

$$F_{bi} = -R_i \tag{18}$$

$$u_{si} = u_{bi} = R_i \delta_{ii} + \sum_{\substack{j=first\ pipe\ node \\ j\neq i}}^{last\ pipe\ node} R_j \delta_{ij} + u_{si}^f \tag{19}$$

By introducing Eqs.(18) and (19) in to Eq. (14), the deformation behavior of the existing pipe due to tunnelling can be obtained:

$$([K_b] + [K_s] + [K_s][\lambda_s][K_b])\{u_b\} = [K_s]\{u_s^f\} \tag{20}$$

where $[K_s]$ is the local soil stiffness matrix, which only takes consideration of the effect of the singularity point, i.e.,

$$[K_s]_{ij} = \begin{cases} \dfrac{1}{\delta_{ii}} & i = j \\ 0 & i \neq j \end{cases} \tag{21}$$

and $[\lambda_s]$ is the soil flexibility matrix, which doesn't take consideration of the effect of the singularity point, i.e.,

$$[\lambda_s]_{ij} = \begin{cases} \delta_{ij} & i \neq j \\ 0 & i = j \end{cases} \tag{22}$$

in which δ_{ii} and δ_{ij} can be calculated by the inverse transform of Eqs. (10) and (12).

It is worth mentioning that omitting $[K_s][\lambda_s][K_b]$ in the above equation will result in a Winkler model. That means the soil reaction acting on the existing tunnel is not affected by the soil response at different locations along the tunnel. So the term $[K_s][\lambda_s][K_b]$ can thus be regarded as an additional term considering the continuous effects. However, because the components of $[K_s]$ are different from those which are constructed by commonly used subgrade coefficients, such as proposed by Vesic (1961), the solution obtained by omitting this term may not be the Winkler solution.

4 APPLICATION EXAMPLES

By the approach discussed above, the computer program has been written for estimating the existing pipe behavior in the homogeneous soil and layered soils.

4.1 *Example for homogeneous soil*

Vorster (2005) carried out the centrifuge model tests to estimate the effects of tunnelling on existing pipe. The tests were conducted in Leighton Buzzard Fraction E silica sand under 75 g acceleration. In prototype scale, one set of the tests represented a 4.5 m diameter tunnel with a depth of 11.25 m, and running transversely beneath a pipe with the outer diameter 1.2 m and wall thickness 0.15 m (EI = 203.86 MN • m^2) buried at a depth of 4.2 m. And the equivalent average ground loss ratio was set at 0.3%, 1% and 2%, respectively.

The description and analysis of centrifuge model tests is also with prototype scale. In the analysis, the soils are divided into forty layers and each has the same elastic parameters. The thickness of each layer is 1 m. Figures 3 and 4 show calculated pipe vertical displacements and bending moments estimated from the proposed method, together with the observations from centrifuge tests.

From the above figures, it can be seen that the calculated pipe vertical displacements and bending moments are in general consistent with the observed shapes, though there are slightly differences between the two results. When the ground loss ratio is small (e.g., $\varepsilon \leq 1\%$), there is a good agreement between the observed and calculated profiles of the pipe vertical displacements and bending moments in magnitude and shape. However, the difference between the observed and calculated results of the pipe vertical displacement and bending moment profile increases as the ground loss ratio increases. In addition, the difference between the calculated values and observed results in the vicinity of the tunnel (e.g., the range of $x = \pm 5$ m) is obviously. The reason may be that the soil nonlinear effects induced by tunnelling are highly when compared with the difference in the field far away from the tunnel and with the difference of the less ground loss ratio.

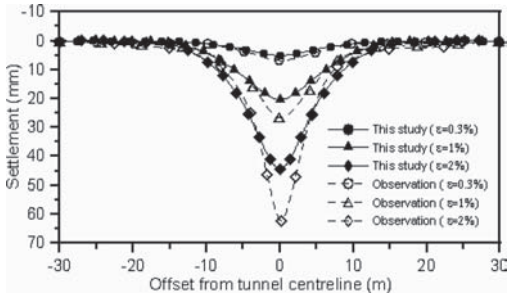

Figure 3. Comparisons of pipe vertical displacement.

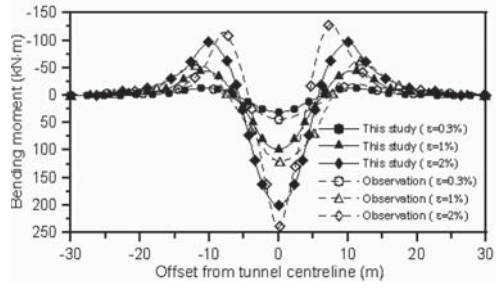

Figure 4. Comparisons of pipe bending moment.

4.2 *Example for layered soils*

In order to study the effects of the layered complexity on the accuracy of the proposed method, the tunnelling-induced ground movements in five layered soils are analyzed. The first layer is 2.8 m, the Young's modulus is 2.53 MPa, the Poisson's ratio is 0.33; the second layer is 5.2 m, the Young's modulus is 7.44 MPa, the Poisson's ratio is 0.32; the third layer is 12 m, the Young's modulus is 13.16 MPa, the Poisson's ratio is 0.3; the forth layer is 12.1 m, the Young's modulus is 22.3 MPa, the Poisson's ratio is 0.3; the five layer is 20.3 m, the Young's modulus is 50.7 MPa, the Poisson's ratio is 0.2.The outer diameter and inner diameter of an existing tunnel ($EI = 3.09 \times 10^7$ kN • m^2) are 6.2 m and 5.5 m, respectively. It is buried at a depth of 13.3 m. A newly-built tunnel with the outer diameter 6.4 m and axis depth 25 m is running transversely beneath the existing tunnel. The equivalent average ground loss ratio is 2.02%.

In order to compare with the displacement controlled solutions, the finite element numerical analysis is conducted based on the large-scale

commercial software. Figure 5 shows the 2-D mesh used in the analysis. There are 5120 elements and 5190 nodes. A displacement controlled finite element model (i.e., DCFEM) proposed by Cheng et al. (2007) is adopted in this study. In this model, the effect of tunnelling is simulated by prescribing displacements to nodes around the tunnel opening rather than by prescribing forces, which is similar to non-uniform oval-shaped ground deformation pattern by Loganathan and Poulos (1998).

Figure 6 show computed green-field soil settlement profiles based on the DCFEM and closed form solutions by Loganathan and Poulos (1998). The numerical results are close to analytical results. Although the maximum settlement from numerical analysis is slightly over analytical results, the difference between the two calculated results in the far field is negligible. Figures 7 and 8 show the existing tunnel settlement and bending moment results using the proposed solutions under the condition of the homogeneous soil and layered soils, and their comparisons with those presented by DCFEM. The elastic parameters of the homogeneous soil are calculated by the means of weighted average method proposed by Poulos and Davis (1980).

As shown in figures 7 and 8, the proposed results based on realistic layered soils provide a reasonably good match with the computed results by DCFEM. However, the proposed results based on homogeneous soil show a poor agreement with DCFEM. The reasons for the slightly differences

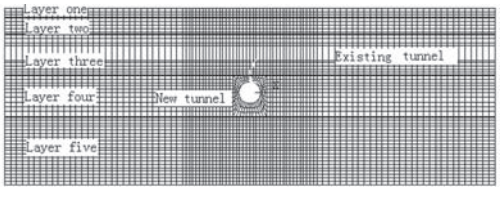

Figure 5. Finite element mesh for five layered soils.

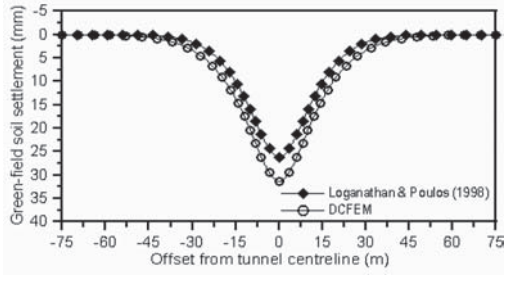

Figure 6. Comparisons of green-field soil settlement.

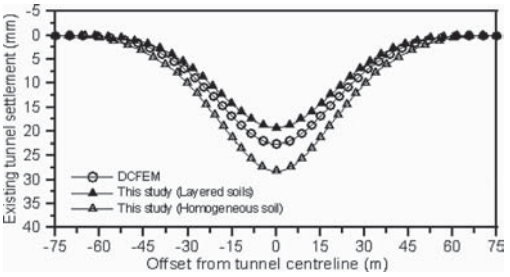

Figure 7. Comparisons of existing tunnel settlement.

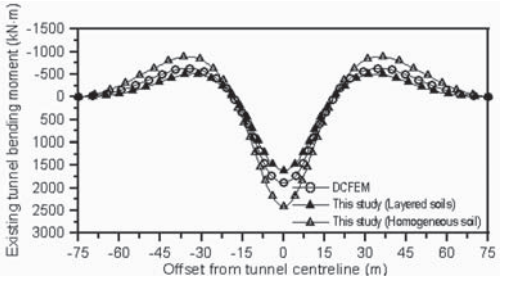

Figure 8. Comparisons of existing tunnel bending moment.

between the proposed results for layered soils and DCFEM may be partially that the different approach for the green-field soil settlements. That is to say, the proposed results of the existing tunnel deformation will more approach the DCFEM analysis results as if the green-field soil settlements by other method more approach those through DCFEM.

From the above-mentioned analysis, it is shown that the proposed method is a valid approach with higher precision in assessing the existing tunnel behavior in non-homogeneous layered soils. Moreover, as to the layered soils where the difference of elastic parameters among successive layers is large, the error obtained via the weighted average method based on homogeneous half space model is not negligible.

5 CONCLUSION

An efficient and practical displacement controlled method to predict the effects of soil stratification on pipe behaviour due to tunnelling-induced ground movements has been suggested. The fundamental solution for layered soils is obtained by applying the double Laplace transform and transfer matrix method based on the layered half space model. Then the existing pipe is regarded as the Euler-Bernoulli beam. Composing green-field soil

settlements caused by the adjacent tunnelling to the existing pipe, the displacements and internal forces from the displacement controlled solution equation are obtained.

The results discussed in this paper indicate that the proposed method provides reliable estimates for the pipe behaviour due to tunnelling-induced ground movements in multi-layered soils. Moreover, it has been demonstrated that as for the layered soils where the differences of elastic parameters among successive layers are large, the error is not negligible, which is obtained employing average elastic parameters based on homogeneous soil converted from layered soils. It should be noted that the major limitation of the proposed method stems from the simplified assumptions of linearity and elasticity. However, it appears to be useful for a preliminary design of tunnels to predict the tunnelling-induced pipe deformation, specially considering that the small ground loss can be obtained though the strict operation and the modern technique.

ACKNOWLEDGEMENTS

The authors acknowledge the financial support provided by China Postdoctoral Science Foundation under research grant No. 20100470677 and by the National Science Fund of China for Distinguished Young Scholars under research grant No. 50825803 and by the research fund for the Doctoral Program of Higher Education of China under research grant No. 20070247066, and wish to express their sincere gratitude to Dr. Klar Assaf at Univ. of Cambridge (Technion-Churchill college exchange postdoctoral researcher) for his insightful suggestion.

REFERENCES

Addenbrooke, T.I. & Potts, D.M. 2001. Twin tunnel interaction: surface and subsurface effects. *International Journal of Geomechanics*, ASCE, 1(2): 249–271.

Attewell, P.B., Yeates, J. & Selby, A.R. 1986. Soil movements induced by tunneling and their effects on pipelines and structures. *London: Blackie & Son Ltd.*: 122–145.

Chehade, F.H. & Shahrour, I. 2008. Numerical analysis of the interaction between twin-tunnels: influence of the relative position and construction procedure. *Tunnelling and Underground Space technology*, 23(2): 210–214.

Cheng, C.Y., Dasari, G.R., Chow, Y.K. & Leung C.F. 2007. Finite element analysis of tunnel-soil-pile interaction using displacement controlled model. *Tunnelling and Underground Space Technology*, 22(4): 450–466.

Klar, A., Vorster, T.E.B., Soga, K. & Mair R.J. 2005. Soil-pipe interaction due to tunnelling: comparison between Winkler and elastic continuum solutions. *Geotechnique*, 55(6): 461–466.

Loganathan, N. & Poulos, H.G. 1998. Analytical prediction for tunneling-induced ground movements in clays. *Journal of Geotechnical and geoenvironmental engineering,* ASCE, 124(9): 846–856.

Poulos, H.G. & Davis, E.H. 1980. Pile foundation analysis and design. *New York: Wiley,* 93–100.

Vesic, A.B. 1961. Bending of beams resting on isotropic elastic solids. *Journal of Engineering Mechanics,* ASCE, 87(2): 35–53.

Vorster, T.E.B. 2005. The effect of tunnelling on buried pipes. *Ph.D. Thesis, U.K.: University of Cambridge.*

Vorster, T.E.B., Klar, A., Soga, K. & Mair R.J. 2005. Estimating the effects of tunneling on existing pipelines. *Journal of Geotechnical and geoenvironmental engineering,* ASCE, 131(11): 1399–1410.

Yamaguchi, I., Yamazaki, I. & Kiritani, Y. 1998. Study of ground-tunnel interactions of four shield tunnels driven in close proximity, in relation to design and construction of parallel shield tunnels. *Tunnelling and Underground Space technology*, 13(3): 289–304.

This page intentionally left blank

Geotechnical Aspects of Underground Construction in Soft Ground – Viggiani (ed)
© 2012 Taylor & Francis Group, London, ISBN 978-0-415-68367-8

Influence of overcut length on jack force and acting earth pressure during pipe jacking

A. Asanprakit, M. Sugimoto & J. Chen
Nagaoka University of Technology, Nagaoka, Niigata, Japan

ABSTRACT: Pipe jacking method pushes a tunnelling machine through concrete pipes ahead of the jacks. The main factors influencing jack force is the friction resistance between pipes and ground. To reduce the resistance, the overcutting between pipes and the surrounding soil is carried out. So far, most of the analytical or empirical models estimating jack force do not consider the overcutting area, then the pipe behavior is not still clarified well. To overcome this problem, the new analysis model, called as the stack pipe model, has been developed by using the full ground spring model that can take overcutting effect into consideration. This study aims to make clear the influence of the overcut length on jack force and earth pressure acting on pipes by parameter studies. As a result, it was found that jack force and acting earth pressure on pipes are greatly influenced by the overcut length.

1 INTRODUCTION

Pipe jacking method is an economically rational and environmentally safe technique for installing underground pipelines. Hydraulic jacks are used to push pipes and TBM through the ground from a launching shaft at the same time as excavation is taking place with the TBM. The main factor influencing jack force is the frictional resistance between pipes and ground. To reduce the friction resistance, the excavation radius by a TBM is larger than the outer radius of the pipes, that is, the over-cutting area between pipes and ground exists, which is a significant factor giving influence to jack force.

It is important to calculate the jack force accurately to design a jacking pipe safely and economically. Prediction models on jack force based on some analytical and empirical approaches were proposed (Atalah et al. 1994; Japan Sewage Association 2000; Phelipot et al. 2001). However, most of the models estimating jack force do not consider the over-cutting area, then the pipe behavior is not still clarified. To overcome this problem, the new analysis model, called as the stack pipe model, has been developed by using the full ground spring model that can take over-cutting into consideration (Sugimoto & Asanprakit 2010). This analysis model has been validated using ideal data and site measured data in the previous research.

The main objective of this paper is to make clear the influence of the overcut length on jack force and earth pressure acting on pipes by parameter studies using the above-mentioned stack pipe model. Subsequently, the simulation results are examined from the viewpoint of geometric conditions and mechanics. Finally, the influence of overcut length on jack force and pipe behavior is discussed.

2 STACK PIPE MODEL

2.1 *FEM analysis model*

The FEM software package DIANA was used for the analysis. The pipe surface was modeled by a four-node quadrilateral isoparametric curved shell element. A total of 32 divisions and eight divisions were generated in a circular and an axial direction, respectively, to configure a pipe shape. The ground was represented by 2-node translation spring elements called "ground spring", which is attached perpendicularly to the pipe axis between each node of the pipe surface and initial excavation surface. Moreover, the cushion material inserted between the pipes and the machine connection between the pipe and machine were also modeled by 2-node translation spring elements in the axial, radial, and tangential directions. The former and later spring elements are called "joint spring" and "machine connection spring", respectively. The frictional resistance around the pipe during jacking is a dynamic friction, and it does not depend on the relative displacement in the axial direction between the pipe and the ground. The friction between the pipe and the ground was accomplished by a Mohr-Coulomb friction interface element. Fig. 1 shows a FEM model for pipe jacking analysis, where L is the absolute pipe length and t_a is the cushion thickness.

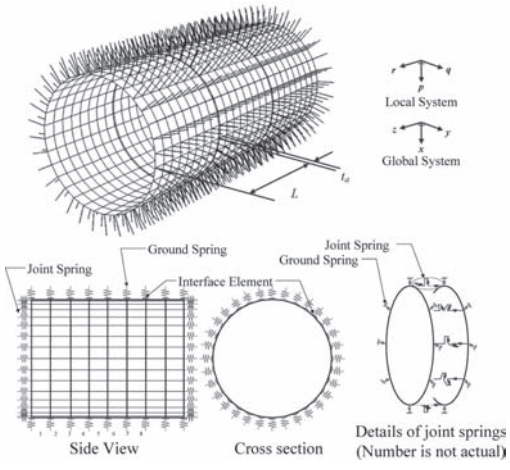

Figure 1. 3D finite element model.

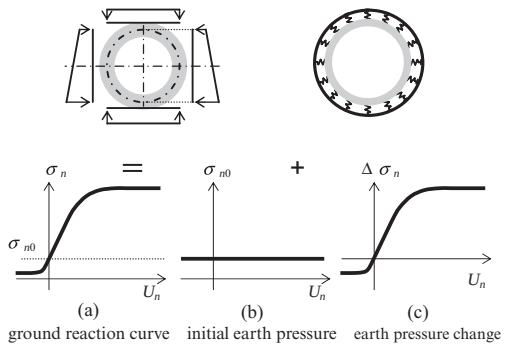

Figure 2. Interaction model between ground and pipe.

2.2 *Ground spring model*

In the ground spring, the ground reaction curve shown in Fig. 2 was adopted as the interaction model between the ground and the pipe. In the figure, U_n is the length of the perpendicular line from the initial excavation surface to the pipe surface (+: outward), and σ_n is the normal earth pressure acting on the pipe. σ_n is composed of the constant initial earth pressure due to overburden load σ_{n0}, and the earth pressure change $\Delta\sigma_n$, which depends on U_n. In the analysis, σ_{n0} is introduced by a pre-stress force in the ground spring before analysis. $\Delta\sigma_n$ is generated as a result of the analysis. In addition, σ_n is the total earth pressure for the Total Stress Analysis, and the effective earth pressure for the Effective Stress Analysis. By using this ground spring model, it is not necessary to carry out an initial stress analysis as a general finite element analysis. Furthermore, a rigid body displacement of the pipe in the transverse direction can be allowed.

The nonlinear ground reaction curve developed in the kinematic shield model (Sugimoto & Sramoon 2002), as shown in Fig. 3, was adopted to represent the ground reaction curve in Fig. 2(a). The relationship of the coefficient of earth pressure in the vertical and horizontal directions, K_v and K_h, and the distance from the initial tunnel surface to the pipe, U_n, (+: outward of tunnel) can be represented by

$$K_h(U_n) = \begin{cases} (K_{h0} - K_{h\min})\tanh\left(\dfrac{a_h U_n}{K_{h0} - K_{h\min}}\right) + K_{h0} & (for\ U_n \le 0) \\ (K_{h0} - K_{h\max})\tanh\left(\dfrac{a_h U_n}{K_{h0} - K_{h\max}}\right) + K_{h0} & (for\ U_n \ge 0) \end{cases} \quad (1)$$

$$K_v(U_n) = \begin{cases} (K_{v0} - K_{v\min})\tanh\left(\dfrac{a_v U_n}{K_{v0} - K_{v\min}}\right) + K_{v0} & (\text{for } U_n \le 0) \\ (K_{v0} - K_{v\max})\tanh\left(\dfrac{a_v U_n}{K_{v0} - K_{v\max}}\right) + K_{v0} & (\text{for } U_n \ge 0) \end{cases} \quad (2)$$

where K_{h0} is the coefficient of earth pressure at rest; K_{v0} is the initial coefficient of vertical earth pressure normally equal to 1; subscripts max and min indicate the upper and lower limit of the coefficient of earth pressure, respectively; and a_h and a_v are the gradient slope of function K_h and K_v at $U_n = 0$, respectively. Moreover, the coefficient of earth pressure in any direction, K_θ, can be interpolated as

$$K_\theta(U_n, \theta) = K_v(U_n)\cos^2\theta + K_h(U_n)\sin^2\theta \quad (3)$$

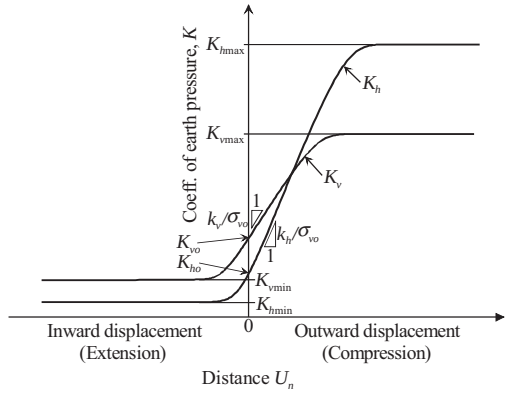

Figure 3. Ground reaction curve.

where θ is the angle from the downward vertical direction. Finally, the earth pressure normal to pipe surface, σ_n, can be estimated from

$$\sigma_n = K_\theta(U_n, \theta)\sigma_{v0} \quad (4)$$

3 ANALYSIS CONDITIONS

In this study, three analysis cases with changed overcut length of 0.005, 0.010, 0.015 m, respectively, were adopted to examine the pipeline behavior.

All analysis cases were carried out in a single layer of sandy ground, which total unit weight is 20 kN/m^3 and the groundwater level is 0.50 m below the ground surface, as shown in Fig. 4. As shown in Fig. 5, the tunnel is 20.12 m long, which is composed of the straight alignment and a rightward curved alignment with a radius of 50 m. The beginning point of curve (*BC*) and the end point of curve (*EC*) are located at the distance of 75.63 m and 84.35 m, respectively. The coefficient of vertical subgrade reaction k_v was assumed to be equal to k_h. Table 1 shows the detailed values for the tunnel, pipe, and ground properties.

The cushion material and the watertight rubber ring are placed within the collar of the pipe. The characteristics of the joint spring in the axial direction and radial and circumferential directions were set by the cushion material specification (Sekisui Plastic Co., Ltd. 2004), as shown in Fig. 6 and Table 2.

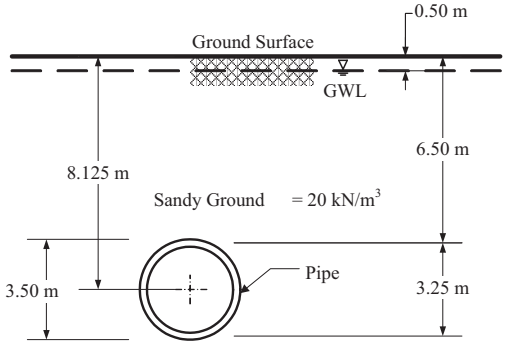

Figure 4. Geological profile.

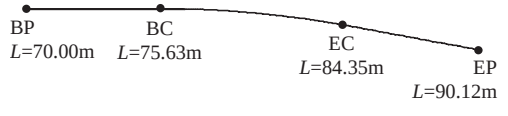

Figure 5. Horizontal alignment.

Table 1. Analysis conditions.

Item	Parameter	Value
Tunnel	Horizontal curve radius (rightward)	50 m
	Rotation angle of the curve	10 degree
	Vertical slope gradient	0.0%
	Tunnelling depth	6.50 m
	Groundwater level	0.50 m
	Overcut length	0.005, 0.010, 0.015 m
Pipe	Inner radius of pipe	1.500 m
	Length of pipe	0.80 m
	Pipe thickness	0.25 m
	Cushion thickness	0.04 m
	Class of cushion material	FJ2.0
	Cushion position	90 degree
	Young's Modulus of pipe	3.6×10^7 kN/m^2
	Poisson ratio	0.17
	Concrete density	24 kN/m^3
Ground	Effective Overburden Pressure at spring line	86.25 kPa
	Hydrostatic pressure at spring line	76.25 kPa
	Dynamic friction coefficient	0.1
	Dynamic adhesion	0.0 kN/m^2
	Coeff. of earth pressure $K_{h\min}$	0.01
	K_{h0}	0.50
	$K_{h\max}$	5.00
	$K_{v\min}$	0.01
	K_{v0}	1.00
	$K_{v\max}$	5.00
	Coeff. of subgrade reaction k_h	15000 kN/m^3
	k_v	15000 kN/m^3

Table 2. Spring constant of joint spring.

Direction	Disp. (m)	Spring constant (kN/m/each)
Axial dir. with cushion		4222500
	–0.020	242679
	–0.016	72589
	–0.012	31107
	–0.004	124464
	–0.002	580750
	0.000	0.71
Axial dir. without cushion		7.143E + 06
	–0.040	0.71
Radial, circumferential dir.		3.125E + 06
	–0.045	2.792E + 05
	0.045	3.125E + 06

The stiffness constant in the radial direction of the interface element was set so that 1 mm relative displacement generates 100 MPa stress to fix the ground spring on the pipe surface. The stiffness constant in the tangential direction of the

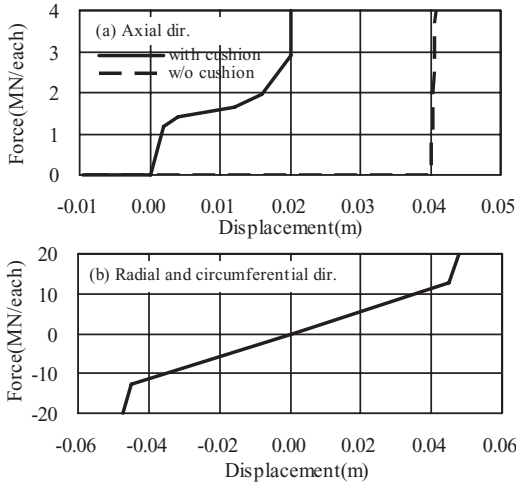

Figure 6. Characteristics of joint spring.

Table 3. Properties of the interface element.

Properties	Value
Stiffness constant in normal dir. (kN/m^3)	1.00E + 08
Stiffness constant in tangential dir. (kN/m^3)	3333
Frictional constant	0.1
Adhesion (kN/m^2)	0.0

Table 4. Spring constant of the machine connection spring.

Direction	Properties	Value
Axial dir.	Spring constant (kN/m)	3005.61
	Pre-stress force for all (kN)	1017.43
Radial dir.	Spring constant (kN/m)	1.0
Circumferential dir.	Spring constant (kN/m)	1.0

interface element was set to be equivalent to the tangential spring with 1/3 spring constant of the ground spring (Railway Technical Research Institute 1997). Table 3 shows the properties of the interface element.

Usually, the face pressure is on the compressive side from the earth pressure at rest. Then the spring constant of the machine connection springs in the axial direction was set, as shown in Table 4, taking account of the ground properties and the number of machine connection springs.

4 SIMULATION RESULTS

By changing the overcut length U_{n0} a mong 0.005, 0.010, and 0.015 m, the contour maps of the gap from the initial tunnel surface to the pipe periphery U_n (+: outward of tunnel) and the normal earth pressure σ_n around the pipe periphery during jacking are shown in Fig. 7 and Fig. 8, respectively. Note that the pipe periphery is unfolded as a flat plate, that is, the vertical axis shows the circumference of the pipe, while the horizontal axis shows the distance. The vertical lines in both figures represent the end of each pipe. In addition, the jack force is shown in Table 5.

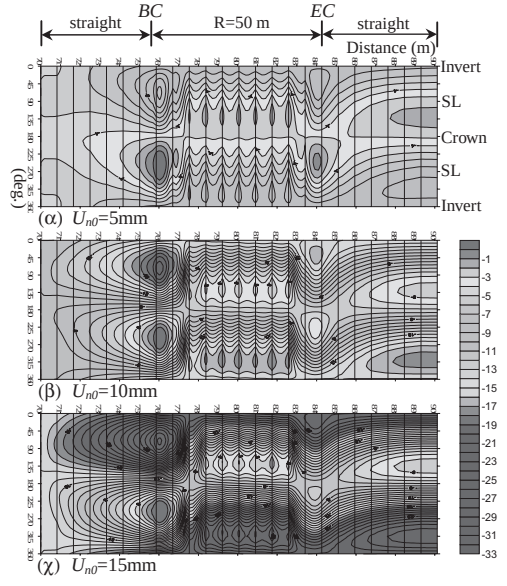

Figure 7. U_n distribution around pipe (mm).

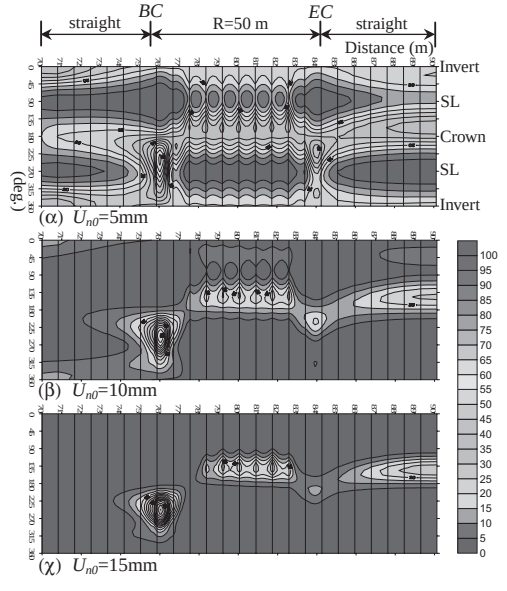

Figure 8. σ_n distribution around pipe (kN/m^2).

Table 5. Jack force and resistance.

Overcut length m	Jack force F_J kN	Resistance at face F_f kN	Resistance around pipe periphery F_R kN	F_R/L kN/m	F_R/A kN/m^2
0.005	1457	1143	314	16.37	1.60
0.010	1265	1145	120	6.25	0.61
0.015	1227	1148	79	4.13	0.40

From Fig. 7 and Fig. 8, the followings are found:

1. U_n has a negative sign in the whole area due to the over excavation.
2. Along the pipeline, U_n on the top is larger than U_n at the bottom. It means that the pipeline moves upward to the tunnel crown due to the over excavation and the buoyancy force.
3. At the rear end of the first pipe, U_n is close to the values of over excavation due to the fixed boundary condition in the transverse direction.
4. U_n is larger at the left spring line along the straight and curved alignments and at the right spring line around *BC* and *EC*. These come from the bending stiffness at the joint due to the cushion material and the magnitude of the jack force. This behavior is reasonable from the viewpoint of geometric condition.
5. On the curved alignment, U_n is larger at both ends of the pipe on the convex side and at the center of the pipe on the concave side. This is also reasonable from the viewpoint of geometric conditions.
6. σ_n at the top and bottom is larger than σ_n at the spring line. This results from $K_{h0} = 0.5$.
7. σ_n distribution agrees with the U_n distribution. σ_n is less than the initial overburden pressure σ_{n0} because of $U_n < 0$.

Comparing the results in Fig. 6, Fig. 7 and Table 5, the influence of overcut length U_{n0} are found as follows:

1. The larger the overcut length U_{n0} is, the larger U_n at the top is. At the same time, U_n at other positions become smaller. This comes from that the pipeline was moved upward due to the buoyancy force when U_{n0} increased. Relatively U_n at other positions decreased due to geometric conditions.
2. With the increase of the overcut length U_{n0}, the area of earth pressure which closed to 0 increased, too.
3. The jack force F_J and the friction resistance F_J around pipe decrease with the increase of the overcut length U_{n0}. This is because the over cutting significantly reduces the contact between pipe and ground.

5 CONCLUSIONS

The parametric study focused on overcut length was carried out using the stack pipe model. The simulation results were examined from the viewpoint of geometric conditions and mechanics. As a result, it was confirmed that the proposed analysis model can express the gap between initial excavated surface and pipes, the earth pressure acting on pipe surface, the jack force, and the frictional resistance around pipe surface reasonably. In addition, it was found that jack force and acting earth pressure on pipes are greatly influenced by the overcut length.

REFERENCES

Atalah, A.L., Bennett, D. & Iseley, T. 1994. Estimating the required jacking force. *Proc., North American No-Dig 94*, NASTT, Dallas, Paper D2.

Japan Sewage Association. 2000. *Guideline for sewage pipe-jacking*, JSA, Tokyo. (in Japanese)

Phelipot, A., Pellet-Beaucour, A.-L. & Kastner, R. 2001. Calculation method of soil-pipe frictional resistance during microtunnelling operations. *Tunnelling and Underground Space Technology* 17(1): 83–97.

Railway Technical Research Institute. 1997. *Design standard and commentary of railway structure for shield tunnels in urban areas*, Maruzen, Tokyo. (in Japanese)

Sekisui Plastic Co., Ltd. 2004. *Thrust transmission material catalog*, Sekisui Plastic Co., Ltd., Tokyo. (in Japanese)

Sugimoto, M. & Asanprakit, A. 2010. Stack pipe model for pipe jacking method. *Journal of Construction Engineering and Management* 136(6): 683–692.

This page intentionally left blank

Geotechnical Aspects of Underground Construction in Soft Ground – Viggiani (ed)
© 2012 Taylor & Francis Group, London, ISBN 978-0-415-68367-8

Assessment of building damage induced by excavation using plate analogy

E. Namazi
Steel Technology Centre, Universiti Teknologi Malaysia, Johor Darul Ta'zim, Malaysia

H. Mohamad
Faculty of Civil Engineering, Universiti Teknologi Malaysia, Johor, Malaysia

ABSTRACT: Prediction of building tolerance to excavation-induced ground displacements is a major concern in underground construction in urban areas. Currently the limiting tensile strain procedure is the most commonly used method for predicting building damage. In this method, it is assumed that the onset of cracking is associated with the average tensile strain within the structure. Linear-elastic deep beams are used to simulate individual walls of the building. Due to the two-dimensional nature of the method, the walls are taken to be perpendicular to the excavation axis and the effects of warping and twisting of the building are ignored. In this paper, the whole building is assumed to behave like a simply supported rectangular elastic plate which is uniformly loaded. The third-order plate theory of Levinson is used to obtain the deflection of the plate in terms of bending and diagonal strains. By simple superposition, the effect of twist and horizontal displacement on the tensile strain in the building is included. The exact elasticity solution for homogenous plate subjected to tensional loading is used to obtain the tensile strain in the twisted plate.

1 INTRODUCTION

When a tunnel is driven in soils underlying crowded urban environments, the response of nearby surface structure is a major concern. Over the past decades, efforts have been made to assess the impact of excavations-induced ground movements on buildings damage based on empirical and analytical methods. The earliest method based on empirical models used numerous case studies to establish correlations between distortion parameters and the corresponding damage limits (*e.g.* Skempton and MacDonald, 1956; Polshin and Tolkar, 1957; Bjerrum, 1963; Charles and Skinner, 2004 and Michalak, 2009).

The building damage assessment using the analytical approach was first proposed by Burland and Worth (1974) and Burland *et al.*, (1977). They idealized the building as a simply-supported elastic deep-beam subjected to a point load at the centre. They introduced the concept of limiting tensile strain to study the onset of cracking for beams undergoing sagging and hogging modes of deformation.

Boscarding and Cording (1989), Burland (1997) and Mair *et al.* (1996) later connected the concept of limiting tensile strain and linear-elastic deep beam theory to define the criteria of damage based on distortion parameters including angular distortion or deflection ratio and horizontal strain.

Whenever a building is positioned above the excavating tunnel, the building must be examined for cracks running both normal to and in the plane of the tunnel axis. In the classical two-dimensional (2D) deep beam theory, only the transverse section of the building to the tunnel axis is considered. A building which is narrow in the direction orthogonal to the tunnel axis may not experience serious cracking parallel to the tunnel centre line, but a building that is long both parallel to, and transverse to, the tunnel centre line may experience cracking in the two orthogonal directions (Attewell 1978).

Buildings however do not generally lie exactly perpendicular to the tunnel centre line. When the tunnel is constructed obliquely underneath the existing structure, the building is subjected to three-dimensional (3D) modes of deformation such as twisting or warping. In this case, the 2D deep beam theory is insufficient to be used for risk assessment of building damage induced by tunnelling.

In this paper, the whole building is idealized like a simply supported rectangular elastic plate with a uniformly distributed load. The third-order plate theory of Levinson is used to obtain the deflection of the plate in terms of diagonal and bending strains. By simple superposition method, the effect of twist and horizontal displacement on the tensile strain in the building is included. The criterion of

the limiting tensile strain that relates to the onset of visible cracking in structures is used to classify the damage in terms of deflection ratio, horizontal strain and twist.

2 DISTORTION PARAMETERS

This paper contains the standard terms used in association with building distortion analysis. These terminologies are defined as below:

- *Horizontal strain or lateral distortion*, ε_h, is the difference in horizontal displacements between two discrete points over their distance.
- *Deflection ratio,* Δ/L, is the most meaningful distortion parameter in the context of cracking walls. The deflection ratio is defined as the relative deflection, Δ, divided by the distance between the two reference points, L, where the relative deflection is the maximum displacement of the settlement profile of a structure relative to the straight line connecting two settlement reference points, as shown in Figure 1.
- *Angular distortion* or *relative rotation,* β, is defined as the differential settlement between two points divided by the distance between them, less the tilt, where tilt is defined as the rigid body rotation of whole structure (Figure 1).

The following term is used to account the three dimensional mode of deformation.

- *Twist*, θ (Figure 2): If a linearly varying displacement is assumed on the edges of the plate and on any lines parallel to these edges, then the twist (the angle of twist per unit length) can be calculated from the differential settlement of the corners. For instance the twist around the length of the plate is (Franzius, 2004):

$$\theta_{ab} = \frac{\frac{S_3 - S_4}{a} - \frac{S_2 - S_1}{a}}{b} \tag{1}$$

Where a, and b are the dimensions of the plate; S_1, S_2, S_3 and S_4 are the settlements at points *1*, *2*, *3* and *4* respectively.

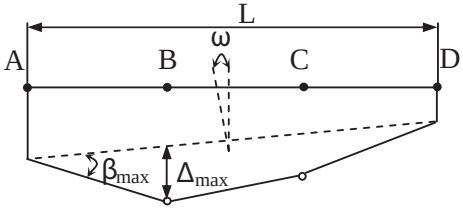

Figure 1. Building and ground movement parameters.

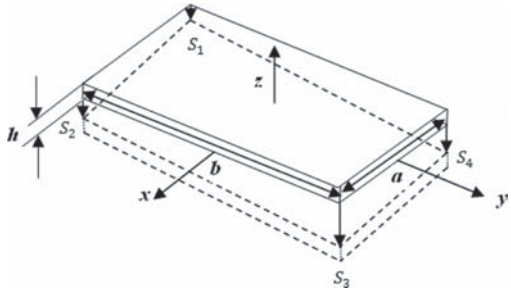

Figure 2. Twist.

3 DEEP BEAM ANALOGY

The analogy between a building and a simple idealised deep beam employed by Burland and Worth (1974) is shown in Figure 3. The analogue of the building is a simply-supported elastic deep-beam of length L and height H. There are two bending and shear modes of deformation due to loading. Both bending and shearing modes of deformation must be considered simultaneously.

The total deflection of the beam Δ at the middle of the span is given by first-order beam theory of Timoshenko (1957) in both shear and bending as:

$$\Delta = \frac{PL^3}{48EI} + \alpha\frac{PL}{4GA} \tag{2}$$

where, P = point load; E = Young's modulus;
G = shear modulus; A = area of the beam;
I = second moment of area;
and α = shear correction factor.

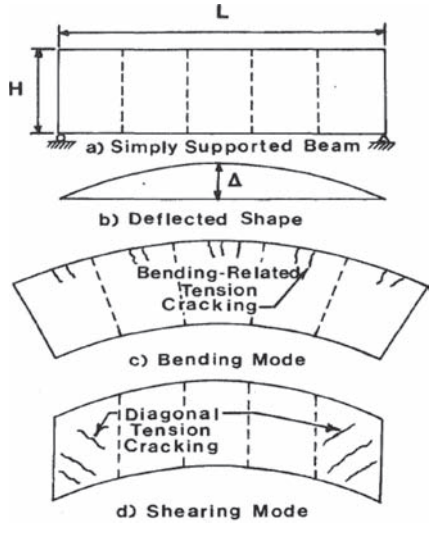

Figure 3. Simple deep beam in bending and shearing modes of deformation (Burland and Wroth, 1974).

The first part and second part of Equation 2 shows the deflection due to bending moment and shearing force respectively. The deflection due to shearing force strongly depends on the shear cortion factor α which was taken as 1.5 (Burland and Wroth, 1974). A shear correction factor of 1.2 derived from the exact theory of elasticity and the method of virtual work respectively was used by Netzel (2009), instead of the simplified shear factor of 1.5.

Burland and Worth (1974) calculated maximum bending and diagonal tensile strains in the beam for a given deflected shape of the building to find out which type is critical. They rewrite the maximum deflection ratio of a loaded beam (Equation 2) in terms of maximum extreme fibre $\varepsilon_{b,\max}$ and diagonal $\varepsilon_{d,\max}$ strains as follow

$$\frac{\Delta}{L} = \left(\frac{L}{12t} + \frac{3I}{2tLH} . \frac{E}{G} \right) \varepsilon_{b,\max} \tag{3}$$

and

$$\frac{\Delta}{L} = \left(1 + \frac{HL^2}{18I} . \frac{G}{E} \right) \varepsilon_{d,\max} \tag{4}$$

where t is distance from the neutral surface. It is recognised that foundations of many buildings restrain the above structures to deformation. Thus in this circumstance it is more realistic to consider the neutral surface at the bottom. Burland and Worth (1974) showed the hogging with neutral axis in the bottom of the beam is far more damaging than sagging with neutral axis in the middle of the beam.

The calculated maximum diagonal tensile strain and bending tensile strain from the above equations are compared with different limiting tensile strain values given in Table 1 to indicate the different category of the damage.

The approach described above so far only dealt with risk of building damages due to the vertical displacements. Boscarding and Cording (1989) include horizontal tensile strain in the above analysis using simple superposition to consider the role of horizontal displacement induced by adjacent excavation.

Table 1. Relationship between limiting tensile strain and category of damage (after Boscarding and Cording, 1989).

Category of damage	Normal degree of severity	Limiting tensile strain (ε_{lim})(%)
0	Negligible	0–0.05
1	Very slight	0.05–0.075
2	Slight	0.075–0.15
3	Moderate	0.15–0.3
4 to 5	Severe to very severe	>0.3

4 THICK PLATE MODEL

The concept of critical tensile strain in conjunction with simple elastic thick plate theory are used to obtain a criteria for the onset of visible cracking based on deflection, horizontal strain and twist. In the current study, the whole building is idealized as a rectangular thick plate of a uniformly distributed load with length b, width a and thickness h which is simply supported on all edges (see Figure 4).

The third-order plate theory of Levinson (1980) is used to obtain the deflection of the plate by analytical solutions. This theory does not require the shear correction factor in contrast to first-order beam theory of Timoshenko.

In the third-order plate theory, the displacement field includes horizontal displacement u in x-direction, horizontal displacement v in y-direction, vertical displacement w in z-direction and tranversal rotations normal to about the y-axes, ϕ_y and x-axes, ϕ_x. These displacements are called the gene-ralized displacements. The displacements in the x and y directions are obtained by calculating the displacement in z direction and rotations of transverse normal to both x and y directions (Reddy 2007). Cooke & Levinson (1983) used Levy's solution to give the expression for displacement in z direction (total deflection) and rotations about the y and x axes of a rectangular plate simply-supported plate on all edges, i.e. $x = 0$, $x = a$ and $y = \pm b/2$ as:

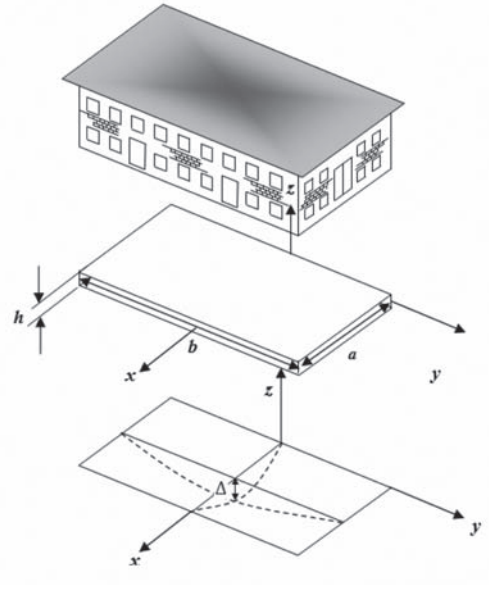

Figure 4. Thick plate model.

$$w = \sum_{m=1}^{\infty} f_m(y)\sin\frac{m\pi x}{a} \tag{5}$$

$$\varphi_x = \sum_{m=1}^{\infty} g_m(y)\cos\frac{m\pi x}{a} \tag{6}$$

$$\varphi_y = \sum_{m=1}^{\infty} h_m(y)\sin\frac{m\pi x}{a} \tag{7}$$

where $f_m(y)$, $g_m(y)$ and $h_m(y)$ are arbitrary functions of the distance to the centre of the plate in the longitudinal direction y which can be obtained from boundary conditions. The series from Equations 5 to 7 converge rapidly, and a satisfactory approximation is obtained by taking only the first term of the series, which in the case of simply-supported plate gives

$$w(x,y) = \left(\begin{array}{l} A_1\cosh\dfrac{\pi y}{a} + B_1 y\sinh\dfrac{\pi y}{a} + \\ \left(\dfrac{4P}{aD}\right)(1+\zeta_1)\left(\dfrac{a}{\pi}\right)^5 \end{array}\right)\sin\frac{\pi x}{a} \tag{8}$$

$$\varphi_x = \left(\begin{array}{l} -\dfrac{4P}{aD}(1-\varepsilon_1)\left(\dfrac{a}{\pi}\right)^4 + E_1\cosh\dfrac{\pi y}{a} - \\ B_1\dfrac{\pi y}{a}\sinh\dfrac{\pi y}{a} \end{array}\right)\cos\frac{\pi x}{a} \tag{9}$$

$$\varphi_y = \left(\left(E_1 - B_1\right)\sinh\frac{\pi y}{a} - B_1\cosh\frac{\pi y}{a}\right)\sin\frac{\pi x}{a} \tag{10}$$

where D is flexural rigidity of the plate and A_1, B_1, E_1, ξ_1, ε_1 are constants obtained as

$$D = \frac{Eh^3}{12(1-\upsilon^2)} \tag{11}$$

$$A_1 = -\frac{P}{D\cosh\beta_1}\left(\frac{a}{\pi}\right)^4\left(\frac{4(1+\xi_1)}{\pi} + \frac{b}{a}\tanh\beta_1\right) \tag{12}$$

$$B_1 = \frac{2P}{aD\cosh\beta_1}\left(\frac{a}{\pi}\right)^4 \tag{13}$$

$$E_1 = \frac{P}{aD\cosh\beta_1}\left(\frac{a}{\pi}\right)^4\left(4(1-\varepsilon_1) + \pi\left(\frac{b}{a}\right)\tanh\beta_1\right) \tag{14}$$

$$\xi_1 = \frac{6D}{5Gh}\left(\frac{\pi}{a}\right)^2 \tag{15}$$

$$\varepsilon_1 = \frac{3D}{10Gh}\left(\frac{\pi}{a}\right)^2 \tag{16}$$

$$\beta_1 = \frac{\pi b}{2a} \tag{17}$$

The maximum central deflection Δ is obtained by substituting the $x = a/2$ and $y = 0$ in Equation 8 which gives:

$$\Delta = \delta_1\frac{P}{D}a^4 \tag{18}$$

where δ_1 is numerical factor depending on the dimension ratios of b/a, h/a and mechanical properties of the plate. The quantity δ_1 can be obtained as:

$$\delta_1 = \frac{4}{\pi^5} + \frac{4}{5\pi^3(1-\upsilon)}\left(\frac{h}{a}\right)^2 - \frac{4}{\pi^5\cosh\dfrac{\pi b}{2a}} - \frac{4}{5\pi^3(1-\upsilon)\cosh\dfrac{\pi b}{2a}}\left(\frac{h}{a}\right)^2 - \frac{b}{a}\frac{\tanh\dfrac{\pi b}{2a}}{\pi^4\cosh\dfrac{\pi b}{2a}} \tag{19}$$

where υ is the Poisson's ratio.

The investigation in the accuracy of the two-dimensional deep beam theory as opposed to the plate theory is discussed with reference to Figure 5. A dimensionless deflection ratio $(\Delta/a)/(Pa^3/D)$ of various plate sizes b/a are plotted against the height ratio h/a. In general, as the ratio b/a increases, the maximum ratio of deflection $(\Delta/a)/(Pa^3/D)$ approaches to the value calculated for a uniformly loaded beam, *i.e.* by making $b/a = \infty$. For instance, when $b/a = 2$, the difference between $(\Delta/a)/(Pa^3/D)$ for the beam and plate at $h/a = 0.4$ is about 25%. When $b/a = 3$, this difference decreases to around 9%. It may be concluded from this comparison that for $b/a > 3$ the deflection due to pure bending obtained by a plate can be replaced by those for a beam without substantial error.

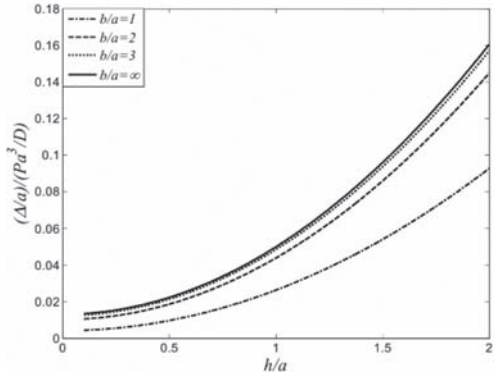

Figure 5. Comparison between maximum ratio of deflection for beam and plate.

Using the Von Kárma´n equations (Clive and Irving, 1973) the nonlinear strains associated with the displacement field are obtained. When the neutral surface is in the middle, the bending and shear strain in the plate may be written in terms of maximum deflection ratio as Equations 20 and 21 respectively. It was noted that in the old buildings, the foundation may be separated by a damp-proof course and the floors and roofs which are joined to the walls are restrained by floor and roof beams (Boone, 2001). Taking into account of these factors the neutral surface is considered to remain in the mid-plane of the plate.

$$\varepsilon^{d}_{b,\max} = \frac{\delta_2}{\delta_1}\frac{\Delta}{a} \tag{20}$$

$$\gamma^{d}_{\max} = \frac{\delta_3}{\delta_1}\frac{\Delta}{a} \tag{21}$$

where $\varepsilon^{d}_{b,\max}$ is maximum bending strain induced by plate deflection, $\gamma^{d}_{\max}$ is maximum shear strain induced by plate deflection, δ_2, δ_3 are numerical factors depending on the dimension ratios of the plate b/a, h/a and mechanical properties of the plate. These factors can be obtained as

$$\delta_2 = \left(\frac{h}{a}\right)\frac{2}{\pi^3} + \left(\frac{h}{a}\right)^3 \frac{1}{15\pi(1-\upsilon)} - \frac{1}{\cosh\dfrac{\pi b}{2a}} \times \left(\left(\frac{h}{a}\right)\frac{2}{\pi^3} + \left(\frac{h}{a}\right)^3 \frac{1}{15\pi(1-\upsilon)} - \left(\frac{h}{a}\right)\left(\frac{b}{a}\right)\frac{\tanh\dfrac{\pi b}{2a}}{2\pi^2} \right) \tag{22}$$

$$\delta_3 = \frac{1}{\pi^2(1-\upsilon)}\left(\frac{h}{a}\right)^2 \left(1 - \frac{1}{\cosh\dfrac{\pi b}{2a}}\right) \tag{23}$$

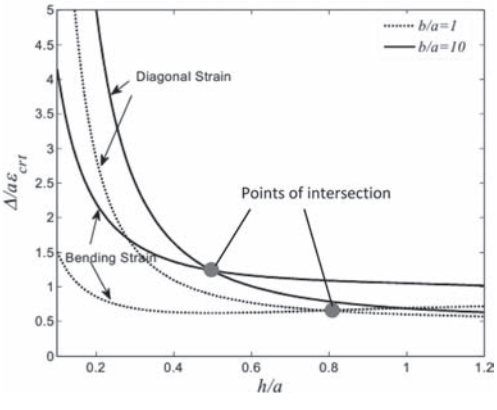

Figure 6. Relationship between $\Delta/(a\varepsilon_{crt})$ and h/a for different value of b/a.

For a given value of deflection ratio, the critical value of tensile strain ε_{crt} is obtained by choosing the highest value between Equations 20 and 21.

Equations 20 and 21 are plotted in Figure 6 to show when plate is flexing in both bending and shear. Figure 6 shows the relationship between normalised deflection ratio $\Delta/(a\varepsilon_{crt})$ and height ratio h/a for rectangular dimension of b/a equal to 1 and 10. The full and broken lines are the equivalent expressions for $b/a = 10$ and $b/a = 1$ respectively. It is evident that, for a given value of critical tensile strain, the criteria for initial cracking are sensitive to both building dimension ratios of h/a and b/a.

The full lines of $b/a = 10$ in Figure 6 would indicate building dimension that is close to the 2D deep beam theory. The intersection between the two lines denote the point when bending or diagonal strains becomes critical. It can be seen here that bending strain is critical when the height ratio h/a is less than 0.5. However, the plate theory demonstrates that when the building has a square dimension ($b/a = 1$), the critical strain due to bending has now been extended for buildings with height ratio $h/a < 0.8$. It can be concluded that the critical intersection point changes according to the dimension ratio of a building and not fixed as oppose to the deep beam theory.

4.1 *Influence of twist displacement on the tensile strain*

Case records show that when a building oriented at a significant skew to the axis of tunnel, measurable building twisting occurs (Geilen & Taylor, 2001a,b; Withers, 2001; Standing *et al*, 2003). The damage recorded in some of these cases ascribed to the twisting displacement of the structure. In order to consider the twisting effects, the additional shear and bending strains arising from twist displacement must be calculated. In this case, the concept of limiting tensile strain is applied to the twisted plate of a rectangular cross section.

When a plate is twisted, two mode of displacements are induced in the plate: (i) the displacement corresponding to the rotation of the cross sections of the plate and (ii) the displacement corresponding to warping of the cross section. For rectangular cross section of the plate with a high value of a/h, Lekhnitskii (1981) gives the expression for maximum shearing strain by seeking the warping function and applying the strain-displacement relations

$$\gamma^{t}_{\max} = \frac{8\theta h}{\pi^2} = \frac{8\varphi}{\pi^2}\frac{h}{a} \tag{24}$$

where $\gamma^{t}_{\max}$ is the maximum shear strain induced by twisting, ϕ is the angle of twist, and θ is the twist

(the angle of twist per unit length) which can be calculated from the differential settlement of the four corners.

In addition to the shear strain, the twist causes additional bending strain ε_b^t to the building, *i.e.* the distance between two longitudinal cross sections of the building changes. In this circumstance, the external walls in the building expand against the compressive internal (*i.e.* central) walls. This is shown in Figure 7. The strain distribution of the twisted plate indicates tensile strain occurs in the most remote fibre and compressive strain at the centre of the plate. Maximum bending tensilestrain $\varepsilon_{b,\max}^t$ in the remote fibre is

$$\varepsilon_{b,\max}^t = \frac{\theta^3 b^3}{24} = \frac{\varphi^3}{24}\left(\frac{b}{a}\right)^3 \tag{25}$$

And the maximum compressive strain $\varepsilon_{b,\min}^t$ at the centre is

$$\varepsilon_{b,\min}^t = -\frac{\theta^2 b^2}{24} = -\frac{\varphi_2}{24}\left(\frac{b}{a}\right)^2 \tag{26}$$

4.2 *Overall strain in simple thick plate*

For a building to settle under its own weight (*i.e.* without horizontal strain), the maximum bending and shear strain induced by deflection and twist are added together. The maximum tensile strain is the one that is greater of maximum bending tensile strain and diagonal tensile strain. When the building is distorted due to ground settlement induced by underground excavation, the horizontal strain component must also be included. In this circumstance the overall bending strain includes strains caused by deflection (Eq. 20), twist (Eq. 25) and horizontal displacement is obtained by simple superposition principle.

$$\begin{aligned}\varepsilon_{br} &= \varepsilon_h + \varepsilon_{b,\max}^d + \varepsilon_{b,\max}^t \\ &= \varepsilon_h + \frac{\delta_2}{\delta_1}\frac{\Delta}{a} + \frac{\varphi^3}{24}\left(\frac{b}{a}\right)^3\end{aligned} \tag{27}$$

For the case of shearing mode of deformation, the resultant diagonal tensile strain ε_{dr} can be evaluated using Mohr's circle of strain. From Equations 21, 24 and horizontal strain the value of ε_{dr} is given by:

$$\varepsilon_{dr} = \varepsilon_h\left(\frac{1-\upsilon}{2}\right) + \sqrt{\left(\varepsilon_h^2\left(\frac{1+\upsilon}{2}\right)^2 + \frac{1}{4}\left(\frac{8\varphi h}{\pi^2 a} + \frac{\delta_3}{\delta_1}\frac{\Delta}{a}\right)^2\right)} \tag{28}$$

The critical tensile strain $\varepsilon_{\text{crit}}$ has two diagonal and bending tensile strain components in two perpendicular directions. To evaluate the damage potential in buildings, the maximum value of tensile strains

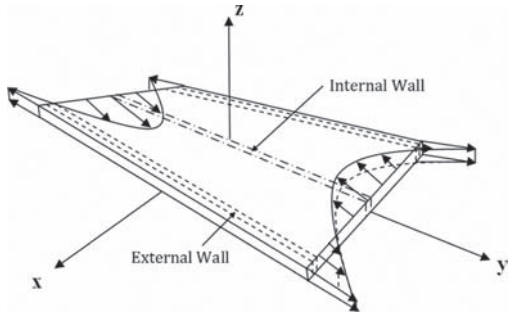

Figure 7. Axial strain distribution due to twist.

obtained by Equations 27 and 28 can be used in conjunction with Table 1.

Equation 27 shows the overall bending strains are sensitive to twist and rectangular ratio *b*/*a* whereas Equation 28 shows the overall diagonal strains are sensitive to twist and height ratio *h*/*a*. This means, in tall buildings (high ratio of *h*/*a*) twist causes more diagonal strain whereas in t e long buildings (high ratio of *b*/*a*) twist causes more bending strain. Moreover, as shown previously in Figure 6, twist changes the height ratio *h*/*a* to ascertain which type of bending and diagonal tensile strain is critical.

5 CONCLUSIONS

The criterion of critical tensile strain that relates the onset of cracking in a structure is used in prediction of damage to structures induced by ground settlement. In this study, the building is idealised as a rectangular thick plate with a uniformly distributed load and simply supported on all edges. The plate theory enables the determination of maximum tensile strain in the structure caused by twist displacement, deflection and horizontal displacement. The 3D plate theory is considered to be a more realistic approach in contrast to the deep beam theory as the latter assumes buildings only positioned perpendicular to the excavations. Moreover, by using the higher-order plate theory, the method requires no shear correction factor.

The study shows when the building deforms due to ground settlement, twist deformation can reduce the building's tolerance to deflection and horizontal displacement. In short, the strains caused by twist should be included to predict the building damage.

The twist increases the bending and diagonal strain in the structures. The investigation shows twist causes more diagonal strain than bending strain for tall buildings in contrast to long buildings where twist causes more bending strain.

The comparison between thick plate and deep beam theories shows for a building with dimension

ratio $b/a > 3$ under pure bending, the rectangular plate can sufficiently be replaced by the uniformly-distributed loaded beam to obtain the maximum tensile strain without substantial error. The study illustrated for a given value of critical strain ε_{crit}, the criteria for initial cracking are sensitive to the plate shape, b/a. Moreover, the twist also alters the h/a to ascertain which diagonal and bending tensile strains is critical.

Although the approach provides the analytical framework for three dimensional building damage assessment, it is clear that field data with measurements of twist displacement, horizontal displacement and deflection are required to verify the approach. Currently the authors have concentrated the effort to collect the well documented case histories to check the accuracy of the method proposed.

It must be emphasised that buildings are invariably of quite complex shape. Such complexity cannot accommodate in any analytical solution like simple thick plate. Hence this relatively simple method is considered as a preliminary investigation. The plate model requires only additional information of settlements at four corners of the building to account the building twist deformation. In order to increase the accuracy, detailed evaluation includes consideration of particular features of building and excavation accompanied by engineering judgment are necessary.

ACKNOWLEDGEMENT

This research is funded by the Ministry of Higher Education, Malaysia under the Fundamental Research Grant Scheme (FRGS UTM-Vot. 78618).

REFERENCES

Attewell, P. 1978. Ground movements caused by tunnelling in soil. In J. D. Gedds, Proc. of large ground movements and structures. Cardiff:812–948. Penthec Press, Cardiff. London.

Bjerrum, L. 1963. Discussion session IV. *Proc, European Conf. on Soil Mech. and Found. Engr.,* II; 135–137 Wiesbaden, Germany.

Boone, S.J. 2001. Assessing construction and settlement-induced building damage: a return to fundamental principles. *Proceeding, underground construction, Institution of Mining and metallurgy*: 559–570, London.

Boscardin, M.D. & Cording, J.C. 1989. Response to excavation-induced Settlement. *Journal of Geotechnical Engineering*, Vol. 115, 1–21.

Burland, J.B. & Wroth, C.P. 1974. Settlement of buildings and associated damage. *proc. Conference .settlement of structures*:611–654. Pentech Press, London.

Burland, J.B., Broms, B.B., de Mello, V.F.B. 1977. Behavior of foundations and structures. *State-of-the-Art Report. Proc, 9th lnt'l. Conf. on Soil Mech. and Found. Engr*., II, Tokyo, Japan, 495–546.

Burland, J.B. 1997. Assessment of risk of damage to buildings due to tunnelling and excavation. *Earthquake geotechnical engineering,* Idhihara, Belkema, Roterdam. 1189–1201.

Charles, J.A. & Skinner, H.D. 2004. Settlement and tilt of low-rise building. Geotechnical Engineering 157. 65–75.

Clive L.D. & Irving H.S. 1973. Solid Mechanics: A Variational Approach. *McGraw-Hill Inc*.,US.

Cooke, D.W. & Levinson, M. 1983. Thick Rectangular Plates—II: The Generalized L´evy Solution *Int. J. Mech. Sci*., 25, 207–215.

Franzius, J.N. 2004. Behaviour of building due to tunnel induced subsidence. *Ph.D. thesis*. Imperial College of Science, Technology and Medicine, London.

Geilen, T. & Taylor, G.R.T. 2001a. Telephone house, London bridge street. Chapter 33 of:Burland, J.B., Standing, J.R. & Jardine, F.M. *Building response to tunneling*. Vol. 2.

Geilen, T. & Taylor, G.R.T. 2001b. The BT building, London Bridge Street. Chapter 34 of:Burland, J.B., Standing, J.R. & Jardine, F.M. *Building response to tunneling*. Vol. 2.

Leknitskii, S.C. 1981. Theory of Elasticity of an Anisotropic Body, pp. 280–287. Mir, Moscow.

Levinson, M., 1980. An accurate simple theory of statics and dynamics of elastic plates. Mech. Res. Commun. 7, 340–350.

Mair, R.J., Taylor, R.N. & Burland, J.B. 1996. Prediction of ground movements and assessment of risk of building damage due to bored tunnelling. Pages 713–718 of: *Proc. of the International Symposium on Geotechnical Aspects of Underground Construction in Soft Ground*:713–718. Rotterdam: Balkema.

Michalak. H. 2009. Selected problems of designing and constructing underground garages in intensively urbanised areas. In Madryas, C., Przybyla, B., Szot, A, *Underground Infrastructure of Urban Areas*:193–201. Taylor & Francis Group, London, UK.

Netzel, H. 2009. Building response due to ground movements. *Ios press publisher*, Amsterdam.

Polshin, D.E. & Tolkar, R.A. 1957. Maximum allowable non-uniform settlement of structures. *Proc, 4th Int. Conf. on Soil Mech. and Found. Engr., 1*: 402–405 London, England.

Skempton, A.W. & MacDonald, D.H. 1956. The allowable settlement of buildings. *Proc, Inst, of Civ. Engrs., Part Iii, 5*: 727–784.

Standing, J.R., Gras, M., Taylor, G.R., Gupta, S.C. & Burland, J.B. 2003. The response of building in park place to underground excavation and compensation grouting: a case study from the Jubilee line London. In F.M. Jardine, *response of building to excavation induced ground movement. Proceedings of the international conference*. 2001. Imperial College, London, UK.

Timoshenko, S. 1957. Strength of Materials—Part 1*, D. Van Nostrand Co. Inc.*,London, England.

Timoshenko, S. 1971. Mechanics of Materials. *Van Nostrand Reinhold Company.*

Withers, A.D. 2001. Surface displacement at three surface reference sites above twin tunnels through the Lambeth Group. Chapter 37 of:Burland, J.B., Standing, J.R. & Jardine, F.M. *Building response to tunneling*. Vol. 2.

This page intentionally left blank

Geotechnical Aspects of Underground Construction in Soft Ground – Viggiani (ed)

Comparing the limit equilibrium method and the numerical stress analysis method of tunnel face stability assessment

P. Perazzelli
Department of Struct. and Geotech. Eng., Sapienza University, Rome, Italy

G. Anagnostou
ETH Zurich, Switzerland

ABSTRACT: The aim of this work is to compare two approaches for evaluating the stability of a tunnel face that is reinforced by bolts: the limit equilibrium method of Anagnostou & Serafeimidis (2007) and the numerical stress analysis method. The comparative calculations have been carried out in respect of a dry cohesive—frictional soil. The numerical solutions were obtained by employing the finite difference code FLAC3D assuming an elastic, perfectly plastic material obeying the Mohr-Coulomb yield criterion. The paper starts with the relatively simple case of an unreinforced tunnel face, comparing the model predictions concerning the necessary support pressure and discussing the influence of tunnel shape, in situ stress and dilatancy. The calculations show that the limit equilibrium method and the numerical stress analysis method provide results which are close to those obtained by other existing analysis methods. The second part of the paper investigates the reinforcing effect of the bolts. The numerical stress analysis method shows clearly that shear failure of the soil around the bolts governs the bolt-soil interaction ahead of the face, suggesting that the bond strength (i.e. the resistance of the interface between grouted bolt and soil) to be used in the limit equilibrium methods should take due account of the shear resistance of the ground and thus the normal stresses prevailing in the core ahead of the face. As shown in the paper, this can be done reasonably well by means of a simplified procedure.

1 INTRODUCTION

When tunnelling through low strength ground the stability of the excavation face is a major concern for the geotechnical engineer. In mechanized tunnelling, closed shields are applied for stabilizing the face. In conventional tunnelling, several techniques could be applied: ground reinforcement of the excavation face by bolts, partial excavation, ground improvement by grouting or artificial freezing. Face reinforcement is a popular solution because of its relatively low cost, its great flexibility and its adaptability to local geological conditions. The bolts are installed on the face with a distribution that depends on the stratigraphy and quality of the encountered ground and are removed as the excavation advances. Fiberglass bolts are often employed because–besides having a high tensile strength–they exhibit brittle behaviour, which is favourable for the excavation process.

Many researchers have studied the stabilizing effect of face bolts through spatial numerical stress analyses. Peila (1994) performed 3D FEM computations which illustrated that reinforcement reduces the deformations and the plastic zone in the core ahead of the face, while the installation of a lining limits the plastic zone and the radial displacements around the tunnel. Ng & Lee (2002) performed parametric 3D FEM analyses to study the influence of the axial stiffness of the bolts with respect both to the stability of the tunnel heading and surface settlement in stiff clay. Yoo & Shin (2003) studied the effect of several reinforcing parameters (spacing, length and axial stiffness) on stability, both for cohesive and cohesive-frictional soil and for different cover-to-diameter ratios. Dias & Kastner (2005) investigated–by means of 3D finite difference analyses–the behaviour of a reinforced face of a deep tunnel in soft rock for different bolt spacings and different assumptions concerning the interface between the grouted bolt and the surrounding soil (perfect adherence or finite bond strength). Furthermore, they compared the numerical results obtained from a model that took account of each bolt individually with the results of simplified numerical analyses, where the effect of bolting is taken into account either by introducing an equivalent face support pressure or by increasing the cohesion of the core. Kavvadas and Prountzopoulos (2009) performed 3D FEM analyses in order to

find out the optimum bolt length and the equivalent face support pressure for different soil shear strength parameters and cover-to-diameter ratios.

For practical engineering purposes, a 3D numerical stress analysis is a heavy and time consuming method. It is also an unnecessarily complex way (actually a long way round) if it is only the stability of the face (but not the deformations of the ground) that is concerned. Simpler approaches, like the limit equilibrium methods (Cornejo,1989; Anagnostou & Kovári, 1994; Broere, 1998; Anagnostou & Serafeimidis, 2007), or methods based on plasticity theorems (Leca & Dormieux, 1990, Mandel & Halphen, 1974; Caquot & Kerisel, 1956) are typically used for this purpose. These methods take into account the reinforcing effect of the bolts either by introducing support forces or by assuming a higher cohesion for the ground.

The present paper investigates the stability of the reinforced tunnel face in cohesive-frictional soils by means of 3D numerical stress analyses. More specifically, for a given soil friction angle, tunnel geometry and depth of cover, the minimum soil cohesion needed for equilibrium is calculated numerically for different bolting densities and compared with the results obtained by the limit equilibrium method of Anagnostou & Serafeimidis (2007). The investigation consists of two phases: (i) in the first phase, the comparison is performed in terms of the face support pressure at limit equilibrium, i.e. by means of a simplified numerical model that does not consider any bolt individually; (ii) the satisfactory results of the first phase encouraged the Authors to continue the comparative analyses with a complex model of reinforcement, which takes account of individual bolts and their interaction with the surrounding soil.

2 INVESTIGATED PROBLEM

We consider a square, 100 m^2 big tunnel face excavated through homogeneous soil at a depth of 23 m (Fig. 1). The choice of the unusual square shape is due to the aim of the work: the comparison between the numerical analysis and the limit equilibrium method of Anagnostou & Serafeimidis (2007), which is based upon the simplified model of a rectangular face. However, in order to investigate whether the assumption concerning the face shape affects the results of the stability analysis significantly, numerical calculations were carried-out also for a more realistic geometry (Fig. 1).

A low-strength, cohesive-frictional ground and dry conditions are considered. All calculations were carried-out for a friction angle φ' of 25°, a unit weight γ of 17 kN/m^2 and cohesion values c' between 0 and 15 kPa. Specifically for the stress analysis, assumptions have to be made concerning

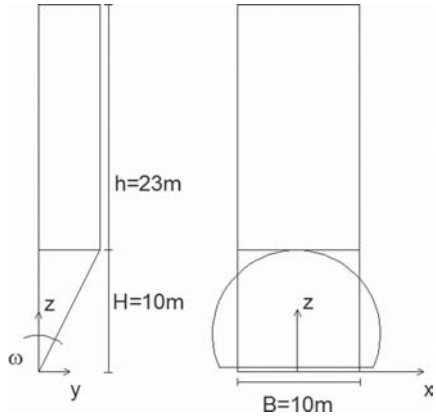

Figure 1. Failure mechanism with square face after Anagnostou & Serafeimidis (2007) and non-square face of equivalent area.

the initial stress field and the deformability of the ground. The parameters can be found in Table 1. The influence of the angle of dilatancy ψ and of the coefficient of earth pressure at rest k_0 was numerically investigated only for the simplified numerical model, which considers a face support pressure instead of the individual bolts.

3 LIMIT EQUILIBRIUM METHOD

The computational method of Anagnostou & Serafeimidis (2007) is based upon a failure mechanism that consists of a wedge and the overlying prism (Fig. 1). The critical inclination ω of the inclined slip plane is determined iteratively so that it maximizes the support requirements. The method represents an improvement of the model of Anagnostou & Kovári (1994) in that it eliminates the need for an *a priori* assumption of the distribution of the vertical stress σ_z in the wedge and offers the possibility of analyzing a layered ground with an arbitrary distribution of reinforcement.

The stabilizing effect of the bolts is considered as a support pressure s given by:

$$s = n \cdot min[Fz,\ max(\pi d\tau_m\, a,\ Fp),\ \pi d\tau_m\,(L'\text{-}a)], \qquad (1)$$

Where n denotes the reinforcement density (e.g., number of bolts per sqm), F_z is the tensile strength of the bolt, τ_m *is* the bond strength at the soil–grout interface, d is the grouted borehole diameter, a is the bond length inside the wedge and L' denotes the actual bolt length. Note that the bond lengths a and $(L'\text{-}a)$ vary over the height of the wedge and, moreover, they depend also on the specific mechanism considered, i.e. on the angle ω. Consequently,

Table 1. Geotechnical parameters of the investigated problem.

Soil	
Unit weigth γ[kN/m^3]	17
Young modulus E' [MPa]	400
Poisson ratio ν	0.3
Friction angle φ' [°]	25
Cohesion c' [kPa]	0–15
Dilatation angle ψ' [°]	0 or 10*
Initial State	
Litostatic stress distribution	
Coefficient of earth pressure at rest k_0	0.57 or 0.70*

*used only in the analysis of the unreinforced face

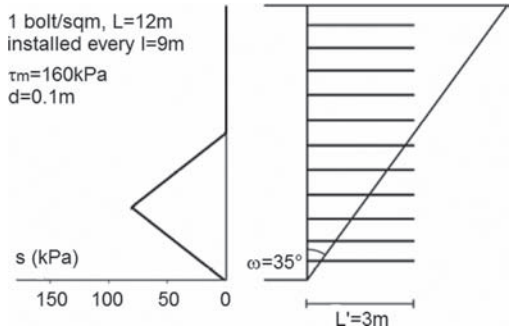

Figure 2. Example of support pressure distribution in the limit equilibrium method of Anagnostou & Serafeimidis (2007).

the support force offered by the reinforcement will not be uniformly distributed even in the case of constant bolt spacing (Fig. 2).

In the present paper, the method is employed firstly assuming that the support pressure s is uniform, i.e. without considering the reinforcement peculiarities (Section 4). Subsequently, in the calculations considering a reinforcement, the needed bolting density is determined as a function of the soil cohesion for fixed values of the parameters d, L' and τ_m (Section 5).

4 STRESS ANALYSIS OF THE UNREINFORCED TUNNEL FACE

4.1 *Numerical model*

The stress analyses were performed by the 3D finite difference code FLAC3D Vers. 4.1. The ground is modeled as an elastic, perfectly plastic material obeying the Mohr-Coulomb yielding criterion and a non-associated plasticity flow rule. The relevant geotechnical parameters are reported in Table 1; two values of the coefficient of earth pressure at rest k_0, 0.57 and 0.7, are considered.

Due to the vertical symmetry plane, only one half of the entire domain needs to be discretised. Figure 3 shows the dimensions of the computational domain, which consists approximately of 75000 nodes and 69000 zones. The displacements of the vertical model boundaries parallel and perpendicular to the tunnel axis are fixed in the direction x and y, respectively. All displacement components are fixed at the bottom model boundary.

In order to avoid rather secondary effects and to focus directly to the tunnel face behavior, the details of the excavation and support sequence are not simulated. Instead a simplified excavation scheme is adopted, where the position of the tunnel face remains fix in the model and the excavation

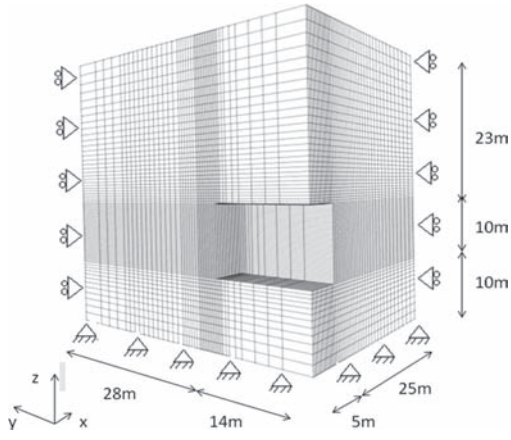

Figure 3. Computational domain and boundary conditions.

process is simulated by a gradual reduction of the longitudinal stress acting on the face. The tunnel support is considered rigid and extends up to the face. The analysis consists of the following steps: (i) initialization of the in situ stress, considering a lithostatic distribution; (ii) removal of the brick elements representing the excavated tunnel volume, fixing of the grid-points on the tunnel boundaries and calculation of the reaction grid-point forces; (iii) replacement of the restraint conditions for the grid-points on the face by support forces equal to the reactions; (iv) gradual reduction of the support forces at the face grid-points, equivalent to a reduction of the original horizontal stress by a factor, which is constant along the face.

4.2 *Face stability criterion*

The common way to investigate the face stability is to evaluate the relation between the longitudinal

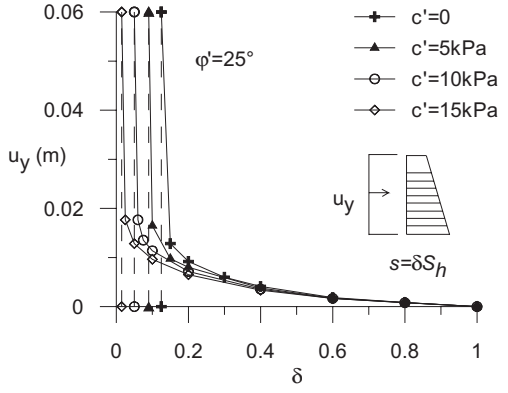

Figure 4. Longitudinal displacement at the center of the face as a function of the normalized support pressure (square tunnel face, $k_0 = 0.57$, $\psi = 0$).

displacement of a control point of the face (here, the center of the face) and the applied support pressure normalized by the initial horizontal stress (Vermeer & Ruse, 2001). The instability is represented by the asymptotic increase of the displacement to infinity, when the face support pressure approaches the limit value.

Figure 4 shows examples of this relation for a particular parameter set. The left end of each curve indicates the minimum pressure, for which equilibrium was achieved, and represents an upper bound of the limit pressure. The vertical dashed lines show the values of the face support pressures, for which an equilibrium was *not* found, and indicate a lower bound of the limit pressure. As the difference between two bounds is very small, the limit support pressure s_{lim} was calculated as the mean value of the two bounds.

4.3 *Results*

Table 2 contains the results of all performed calculations, while Figure 5 shows the relationship between the limit support pressure and the cohesion according to the results of the numerical analyses under different assumptions concerning k_0-value, dilatancy angle ψ and face shape (single marked points). The diagram includes for the purpose of comparison the numerical results of Vermeer & Ruse (2001), which concern a circular face of equivalent area, and the results of the limit equilibrium analyses after Anagnostou & Serafeimidis (2007) and Anagnostou & Kovári (1996) for coefficients of lateral stress λ of 0.80 or 1. Our numerical results are close to those of Vermeer & Ruse (2001) and confirm their conclusion, that the influence of k_0-value on the limit support pressure is negligible. A higher dilatancy angle increases only slightly

Table 2. Stress analysis results for unreinforced face.

Geom*	ψ [°]	k_o [-]	c' [kPa]	δ_{equil} [-]	$\delta_{non\text{-}equil}$ [-]	s_{lim}** [kPa]
Q	0	0.57	0	0.150	0.1250	37.80
Q	0	0.70	0	0.125	0.1000	37.49
Q	10	0.57	0	0.125	0.1000	30.93
C	0	0.57	0	0.125	0.1000	31.65
Q	0	0.57	5	0.100	0.0900	26.12
Q	0	0.70	5	0.080	0.0600	23.32
Q	10	0.57	5	0.080	0.0600	19.25
C	0	0.57	5	0.090	0.0800	23.91
Q	0	0.57	10	0.060	0.0500	15.12
Q	0	0.70	10	0.050	0.0250	12.50
Q	10	0.57	10	0.050	0.0250	10.31
C	0	0.57	10	0.050	0.0400	12.66
Q	0	0.57	15	0.025	0.0150	5.50
Q	0	0.70	15	0.025	0.0125	6.25
Q	10	0.57	15	0.025	0.0125	5.15
C	0	0.57	15	0.010	0.0050	2.11

*Q = square face; C = sub-circular face (Fig. 1)

**Mean value along the face obtained from $s_{lim} = \delta S_h$, where S_h is the initial horizontal stress at the center of the face

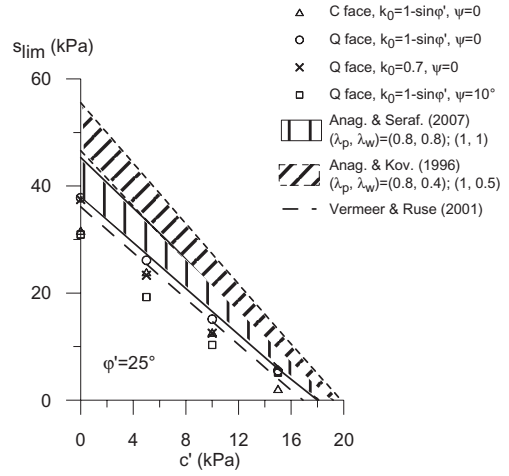

Figure 5. Limit support pressure s_{lim} as a function of the soil cohesion for $\phi' = 25°$ according to different methods.

face stability. The differences between the square and the other, more realistic tunnel shapes are very small. The limit equilibrium method of Anagnostou & Kovári (1996) overestimates the necessary support pressure. The limit equilibrium method of Anagnostou & Serafeimidis (2007) gives results very close to those of the stress analysis particularly for $\lambda = 1$, i.e. for the value proposed by Terzaghi and Jelinek (1954). The value of $\lambda = 0.8$ (suggested

by the model tests of Melix, 1987, and adopted by Anagnostou and Kovári, 1996, for elaborating design nomograms) is on the safe side.

Figure 6 compares the limit support pressures obtained by several methods for the case of a cohesionless soil. For lower values of friction angle ($\varphi' = 20$–$25°$), the solution of Anagnostou & Serafeimidis (2007) is located between the lower bound solution of Leca & Dormieux (1990) and upper bound solutions of Mandel & Halphen (1974) and Caquot & Kerisel (1956). The predictions of Anagnostou & Kovári (1996) are close to the upper bound solutions. At higher values of the friction angle, the differences between all these methods became negligible and the model predictions are close to experimental results (centrifuge modeling). The results of the FLAC3D calculation of Figure 5 are closer to the solution of Vermeer & Ruse (2001) and Leca & Dormieux (1990).

In conclusion, in the simpler case of an unreinforced face, the results obtained after Anagnostou & Serafeimidis (2007) are absolutely close to the predictions of stress analysis and comparable with other existing methods.

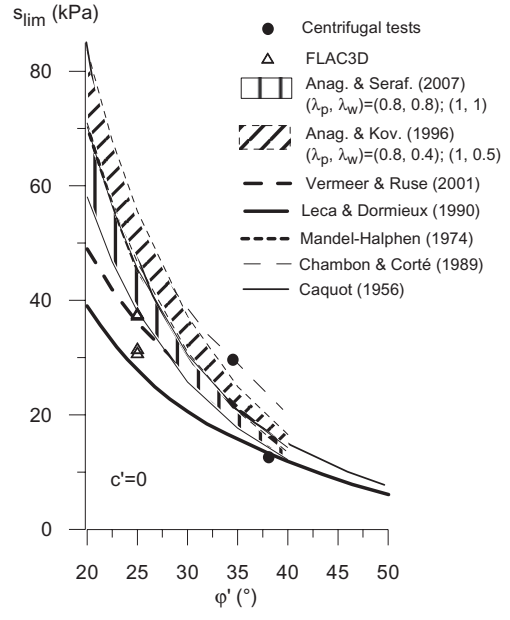

Figure 6. Limit support pressure s_{lim} as a function of the soil friction angle for $c' = 0$ according to different methods (diagram after Ribacchi 1993).

5 STRESS ANALYSIS OF THE REINFORCED TUNNEL FACE

5.1 *Computational model*

The numerical analysis of the reinforced face was performed for the same geometrical and geotechnical parameters as in the last Section (Table 1). On account of the main objective of the present work (the comparison with the limit equilibrium method) and also of the small effect of face geometry, only the square face was investigated.

The bolts were modeled individually using the "cable" element in the FLAC3D code. This structural element behaves like an elastic, perfectly plastic material that may yield in tension but cannot resist a bending moment. The assumed Young modulus E_b and cross-sectional area A_b of the cable elements (Table 3) are typical for fiberglass pipes. The tensile strength of the cable was taken infinite, i.e. bond failure is the only failure mechanism considered. The reason for this modeling decision is that we want to focus to the effect of the grouted bolt—soil interface.

Since the cable elements are fully grouted, the force developing along its length is the response to relative motion between the cable and the grid. The numerical formulation of the interface between the structural element and the grid, which represents conceptually the interface between soil and grouted bolt, is incorporated in the numerical formulation of the structural element. The code allows for an elasto-plastic interface model defined by the stiffness K_{int}, perimeter p_{int} and shear strength parameters c_{int} and φ_{int}. The present work assumes practically rigid-plastic interface behavior, i.e. a high value of the interface stiffness K_{int} (Table 3). Concerning the bond strength the assumption was made that it depends on the confining stress according to Mohr-Coulomb criterion with strength parameters equal to those of the soil ("stress-dependent bond strength"). For the purpose of comparison (Section 5.2), also a simplified model ("constant bond strength") considering a shear resistance of $\tau_m = 160$ kPa was considered (Table 3). Such a

Table 3. Parameter values of the grouted bolt model.

Cable elements			
Length	L' [m]	7	
Area	A_b [m^2]	0.00785	
Young modulus	E_b [GPa]	20	
Interface cable-grid			
Borehole diameter	d [m]	0.1	
Shear stiffnes	K_{int} [GPa]	10	
Strength	$\tau_m = \sigma tan\varphi_{int} + c_{int}$	(i)*	(ii)
	c_{int} [kPa]	160	c'
	φ_{int} [°]	0	$\varphi' = 25°$

*Only in Section 5.2

value corresponds to the bond strength of a loose to medium dense sand at a depth of more than 4 m (Ostermayer, 1991).

The bolt length L' is taken equal to 0.7 H, i.e. 7 m. (This value is, for example, equal to the minimum length of initially 12 m long bolts overlapping by 5 m.) The bolts are horizontal and uniformly distributed on the face on a rectangular grid. Four different bolting patterns were investigated, consisting of 3×6, 5×10, 6×12 or 7×14 bolts in the modeled half face and corresponding to bolt densities n of 0.36, 1, 1.44 and 1,96 m^{-2}, respectively.

In order to simulate better the behavior of the soil between the bolts in the case of high bolting density, a finer mesh is adopted than in the numerical model for the unreinforced face (Fig. 3): the size of the square brick elements, which discretize the face, is here 0.125 m instead of 0.25 m in the previous mesh. The excavation process was simulated as described in Section 4.1.

For each bolting pattern the face stability was investigated for a series of closely spaced cohesion values in order to determine an upper and a lower bound of the minimum cohesion needed for stability for the given bolting pattern (Table 4). The limit cohesion c'_{lim} was taken as the mean value of these bounds (last column of Table 4). The black circular markers in Figure 10 show the relationship between limit cohesion c'_{lim} and bolt density n calculated in this way. They will be compared to the limit equilibrium predictions in Section 5.3. But before doing this the issue of bolt—soil interface modeling will be addressed.

5.2 *On the assumption about the bond strength*

This section compares the results obtained when assuming a stress-dependent bond strength with the results for a constant bond strength considering the case of a face reinforcement by 6×12 bolts (bolt density n = 1.44 m^{-2}). The two analyses provide close values of limit soil cohesion: c'_{lim} = 6–8 kPa in the case of a constant bond strength τ_m of 160 kPa and 8–10 kPa in the case of a stress-dependent bond strength. As can be seen from Figure 7, however, relevant differences exist concerning the soil—bolt interaction close to limit equilibrium.

In the case of a constant bond strength (τ_m = 160 kPa, c' = 8 kPa), the contour lines of longitudinal displacement and the extrusion profile show clearly big gradients in the vicinity of the bolts (Fig. 7a). At the grout–soil interface the soil displacement is practically zero because the shear stress does not reach the bond strength of 160 kPa and a perfect adherence is preserved at

Table 4. Stress analysis results for reinforced face (stress-dependent bond strength).

n [bolts/m^2]	c'_{equil} [kPa]	$c'_{non\text{-}equil}$ [kPa]	c'_{lim} [kPa]
0.36	14	12	13
1.00	12	10	11
1.44	10	8	9
1.96	7	5	6

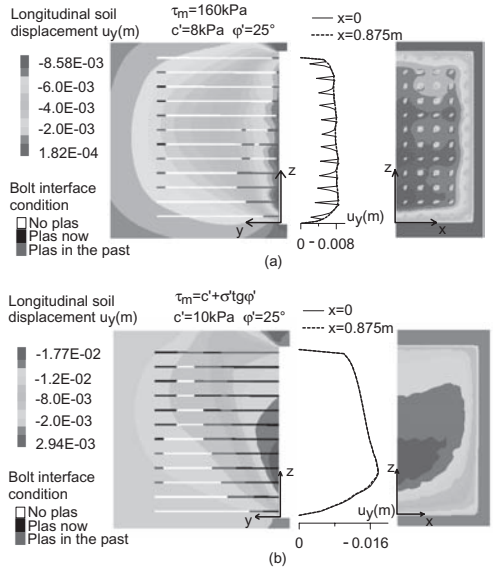

Figure 7. Extrusion profiles of the face, contour lines of the soil longitudinal displacement and bolt interface condition for the upper bound of the limit cohesion (i.e., for the minimum considered cohesion satisfying equilibrium): (a) constant bond strength τ_m = 160 kPa (results for c' = 8 kPa and n = 1.44 bolts/m^2); (b) stress-dependent bond strength $\tau_m = \sigma \tan\varphi' + c'$ (results for c' = 10 kPa and n = 1.44 bolts/m^2).

the interface, while the surrounding soil fails. So, shear failure occurs not exactly at the interface (this is not possible due to the assumed high bond strength) but within the soil close to the interface. The soil flows around the grouted bolt, thus "by-passing" the constraint imposed by the assumed high bond strength.

In the case of the stress-dependent bond strength, shear failure occurs at the grout—soil interface resulting in a discontinuity of the displacements of soil and bolts, in a smooth extrusion profile and in larger longitudinal displacements (Fig. 7b). The bond failure observed in this case is due to the low bond strength in the ground close

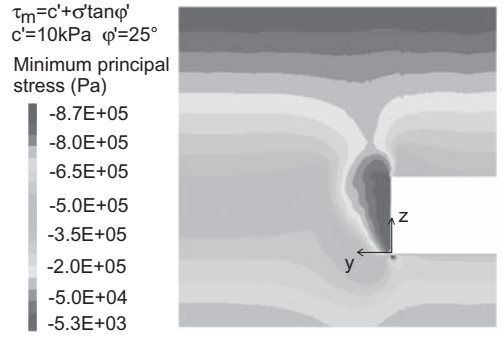

Figure 8. Contour lines of the minimum principal stress (compressive stresses are negative) in the vertical symmetry plane for the upper bound of the limit cohesion (i.e., for the minimum considered cohesion satisfying equilibrium) assuming a stress-dependent bond strength τ_m of $\sigma \tan\varphi' + c'$ ($n = 1.44$ bolts/m^2).

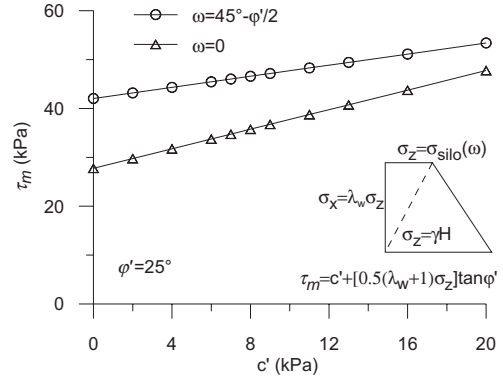

Figure 9. Bond strength τ_m determined based upon the shear strength parameters of the soil and assuming a trapezoidal confining stress distribution according to Anagnostou & Kovári (1994).

to the face: The bond strength is low overthere because it depends on the confining stress, which decreases strongly in the vicinity of the face due to the soil plastification associated with the axial stress release (Fig. 8).

These results indicate that the simplifying assumption of a constant bond strength (which is often made in limit equilibrium analyses) should take due account of the strength parameters of the soil and of the stress level in the core ahead of the face.

5.3 *Comparison with limit equilibrium method*

The lowest curve in Figure 10 shows the necessary bolt density n as a function of the soil cohesion according to the limit equilibrium method of Anagnostou & Serafeimidis (2007) and assuming a constant bond strength τ_m of 160 kPa. The numerical stress analyses (black markers) lead to considerably higher reinforcement densities than predicted by the limit equilibrium method. This is true not only for the stress-dependent bond strength FLAC3D model (black circles), but also for the numerical model assuming a constant bond strength (single triangle) of 160 kPa—the same value as in the limit equilibrium analysis. The reason is that in the stress analysis the soil flows around the grouted bolt irrespectively of the practically perfect bond that was assumed specifically for the grout–soil interface (see last Section). The significant overestimation of the reinforcing effect of the bolts is due to the assumed bond strength τ_m, which as discussed in last section, is not consistent with the resistance of the surrounding soil to shearing. The bond strength in a cohesive—frictional material should consider the shear strength parameters of the soil and the confining stress on the bolts as the later influences the frictional resistance.

A consistent assumption about the confining stress (and finally about the bond strength τ_m) can be made by considering the stress distribution in the ground within the wedge. Following Anagnostou & Kovári (1994), we assume that the ratio λ_w of the horizontal to the vertical stress σ_x/σ_z is constant, while the vertical stress σ_z changes linearly from γH in the tunnel floor to the silo pressure at the top of the wedge (see inset of Fig. 9). The confining stress needed for the calculation of the bond strength is taken equal to the mean stress $0.5(1 + \lambda_w)\sigma_z$. For simplicity, a constant bond strength is assumed in the limit equilibrium analysis based upon the average vertical stress, i.e. the stress σ_z in the centre of the face. As suggested by Anagnostou and Kovári (1994) and as assumed also for the computation of the nomograms of Anagnostou and Serafeimidis (2007), the value of λ_w is taken equal to 0.4, i.e. half as high as the value used for calculating the silo pressure from the overlying prism ($\lambda_p = 0.8$).

Figure 9 shows the computed bond strength τ_m as a function of the soil cohesion c' for two values of the angle ω (The angle ω plays a role because it affects the silo pressure and thus the confining stress and the frictional resistance.) The bond strength values calculated in this manner are by a factor of 4 to 5 lower than the initially assumed value of 160 kPa and, combined with the nomograms of Anagnostou & Serafeimidis (2007), lead to bolt density predictions which are very close to the stress analysis results (Fig. 10).

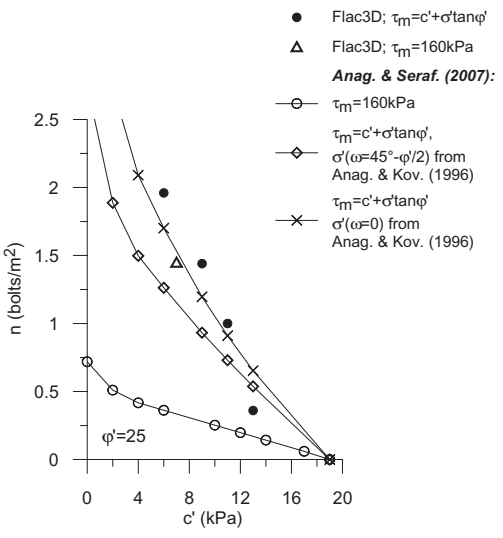

Figure 10. Necessary bolt density as a function of soil cohesion $\varphi' = 25°$ according to stress analysis with a stress-dependent bond strength and after Anagnostou & Serafeimidis (2007) under different assumptions concerning the bond strength.

6 CONCLUSIONS

The limit equilibrium analysis after Anagnostou & Serafeimidis (2007) and the numerical stress analysis with the finite difference code FLAC3D provide very close predictions about the stability of an unreinforced tunnel face in dry cohesive frictional soil. The predictions are also absolutely comparable to the predictions obtained by other methods reported in the literature.

The numerical results confirmed that the effects of the lateral earth pressure coefficient, of the dilatancy angle and of the face shape (square, circular, sub-circular) are not important.

In the particular geotechnical and geometrical conditions investigated, the stress analysis of the reinforced face, with modeling of the individual bolts, shows clearly that the failure of the soil around the bolts limits the shear stress developing at the interface bolt—soil and, therefore, the reinforcing effect. For this reason, the bond strength used in the limit equilibrium analyses should consider the shear strength parameters of the ground and the confining stress in the core ahead of the face. Adopting a bond strength based upon the stress distribution after Anagnostou & Kovári (1994) represents a consistent approach and leads to limit equilibrium results which agree very well with the numerical results.

REFERENCES

Anagnostou, G. & Serafeimidis, K. (2007). The dimensioning of tunnel face reinforcement. ITA-AITES World Tunnel Congress "Underground Space–the 4th Dimension of Metropolises", Prague.

Anagnostou, G. & Kovári, K. (1994). The face stability of slurry-shield driven tunnels. *Tunnelling and Underground Space Technology*, 9 (2), 165–174.

Anagnostou, G. & Kovári, K. (1996). Face stability conditions with Earth Pressure Balanced shields. *Tunnelling and Underground Space Technology*, 11 (2), 165–173.

Broere, W. (1998). Face Stability Calculation for a Slurry Shield in Heterogeneous Soft Soils. *Tunnels and Metropolises*, Sao Paolo, Brazil, 1998, pp. 215–218.

Caquot, A. & Kerisel, J. (1956). Traité de mecanique des sols. Gauthier Villars, Paris.

Cornejo, L. (1989). Instability at the face: its repercussions for tunnelling technology. Tunnels and Tunnelling. April, No.21:69–74.

Dias, D. & Kastner, R. (2005). Modélisation numérique de l'apport du renforcement par boulonnage du front de taille des tunnels. Can. Geotech. J. 42 (6): 1656–1674.

Leca, E. & Dormieux, L. (1990). Upper and lower bound solutions for the face stability of shallow circular tunnels in frictional material. Geotechnique, 40, 581–606.

Mandel, J. & Halphen, B. (1974). Stabilité d'une cavitè sphérique souterraine. 3rd Congr. ISRM, 2B, 1028–1032.

Melix, P. 1987. Modellversuche und Berechnungen zur Standsicherheit oberflächennaher Tunnel. *Veröff. des Inst. für Boden- und Felsmechanik der Univ. Fridericiana in Karlsruhe*, 103 (in German).

Ng, CWW, & Lee, GTK (2002). A three-dimensional parametric study of the use of soil nails for stabilising tunnel faces. Computers and Geotechnics. Vol. 29, Issue 8, 673–697.

Ostermayer, H. (1991). Verpreßanker. In *Grundbau-Taschenbuch* 4. Auflage Teil 2. Herausgeber: U. Smoltczyk, Berlin: Ernst & Sohn.

Kavvadas, M. & Prountzopoulos, G. (2009). 3D Analyses of Tunnel Face Reinforcement using Fibreglass Nails. Eur:Tun 2009 Conference. Bochum.

Peila, D. (1994). A theoretical study of reinforcement influence on the stability of a tunnel face. Geotechnical and Geological Engineering, Vol. 12, Num. 3, 145–168.

Ribacchi, R. (1993). Recenti orientamenti nella progettazione statica delle gallerie. 23rd Convegno Nazionale di Geotecnica–Opere in sotterraneo. Rimini.

Terzaghi, K. & Jelinek, R. 1954. *Theoretische Bodenmechanik*, p. 505. Berlin a.o.: Springer-Verlag (in German).

Vermeer, P.A., Ruse, N. & Marcher, T., 2002. Tunnel heading stability in drained ground. Felsbau 20 (6), 8–18.

Yoo, C. & Shin, HK. (2003). Deformation behavior of tunnel face reinforced with longitudinal pipes-laboratory and numerical investigation. Tunnelling and Underground Space Technology. Vol. 18, Issue 4, 303–319.

Geotechnical Aspects of Underground Construction in Soft Ground – Viggiani (ed)

An analytical method to control tunnel lining settlements

A.D. Garini
Consulting Engineer, Cicagna, Italy

ABSTRACT: A method to control tunnel lining settlements, particularly indicated in urban areas for soft soils and shallow bored tunnels, is presented. The method is based on the classical strength of material virtual works theorem and uses both the displacements and the forces forms. It is noticeable that this approach also permits to follow analytically the internal forces behaviour along the multi supported circular lining beam. Moreover the method, from this point of view, overwhelms the known F.E.M. hyper-static reaction method as this latter requires the definition of the loads acting on the supports. In fact this analytical solution analogously to the static and seismic methods recently illustrated by the author for flexible anchored retaining walls permits to impose the internally calculated support reactions to eliminate or limit the settlements, so rendering about neutral the underground tunnel intervention on the urban environment, by an opportune choice of tensioned anchors.

1 INTRODUCTION

1.1 *Underground urban environment*

Underground works in soft soils urban areas are undoubtedly a very difficult environment for the engineers to dominate a design process and, besides the important dig-related aspects of preserving underground services, the main problem is the settlement controlled operations, because even displacements of few millimetres may damage important monuments or produce considerable buildings economic losses.

On the other hand, nowadays there are numerous techniques to face these difficulties; besides the traditional temporary interventions such as bolts, centres, shotcrete and jet-grouted umbrellas, it is now possible to use closed shield tunnelling with TBM/EPBS machines and especially the compensation grouting techniques, either by soil fracture, for fine grained soils, or by compaction grouting for granular soils, all of which effective in terms of the hole stiffness reinforcement while the engineering analysis is faced via a continuum stress-strain behaviour with as output the tunnel convergences.

1.2 *Technical approach*

In this paper, considering whatever intervention technique, we are focusing on pre-stressed anchors to limit the tunnel convergence, immediately after having bored the tunnel. In the paper a strength of materials analytic approach is proposed to avoid important settlements of the tunnel ring and so of the surrounding soil and building environment. This approach suggests containing the radial reactions of an arch with pre-stressed anchors so imposing in those points even no settlements at all.

The main related phenomenological aspects are the viscous–plastic soil deformations behaviour, which may be encountered in squeezing soils or similar soils, that in general produce long term—movements.

To focus on the maximum dimensions of the phenomenon, in case of middle squeezing poor rock overburden of about 330 m they experienced convergences of up to 2 m in the very noticeable case of the Saint Martin la Porte access adit linked to the 53 km long Lyon–Turin Base Tunnel (Russo *et al*. 2009).

This entails that, in case of more limited dimensions of the phenomenon, like shallower soil overburden, as in urban areas, the settlement problems on the definitive lining may be a complex and complicated matter to deal with.

This new analytical procedure is similar to that proposed for the case of multi–anchored vertical walls in multilayered soils as Garini (2008) has provided as a consequence of the analytical method with the limit equilibrium approach to calculate these kinds of walls, the possibility to control the lateral settlement behaviour by imposing the right reaction force by the anchorages.

Indeed for tunnel calculation too exist numerical methods such that of hyper-static reactions or other more complex that has the limit of not having the tie-back force as a calculated reaction (Oreste, 2002). Actually, in this case these forces can be deduced from the convergence-confinement method, but with this method, suitable for deep

tunnels, it's impossible to consider a precise particular load distribution on the lining circle.

Moreover, if one considers a particular load distribution the approach presented in this paper has shown to be fit even in seismic areas, for vertical walls (Garini, 2009), and so with an opportune choice of the seismic loads, may applied also for circular tunnels.

2 THE METHOD: CIRCULAR ARCHES MULTI-SUPPORTS SYSTEM

2.1 *Strength of materials approach*

As known from the strength of materials, a system of beams can be solved via the theorem of virtual works either in the form of the forces through a compatibility equation or in the form of the displacements as an equilibrium equation.

So if we consider an entire circular arch of 180° we can divide it in several little arches, each of them with a centre angle less than 90°.

Once the external load combination of each arch *ij* between node *i* and node *j* is known, it is possible to calculate the entire arch internal forces M_{io}, T_{io} and N_{io} for node *i* (and the same can be done for node *j*) via the forces method for the particular external loads.

In the same way it is automatically possible to know the little arch internal forces, angular, tangential and radial displacements via the forces method for a single node *j* rotation φ_j or a single node *j* tangential displacement w_j or at last for a node *j* single radial displacement v_j.

Finally, for a generic double clamped circular truss with *n* intermediate hinged supports, in a particular node *i* there is only the influence of nodes $i-1$ and $i+1$ and so, in the node *i* where the internal force R_i is present, the equilibrium can be imposed, expressed by the equation (Baldacci, 1979):

$$R_i = R_{io} + \sum_{j=1}^{n} R_{ij}\,\xi_j \tag{1}$$

For *n* intermediate hinged supports, there are $n + 2$ total supports and a double clamped arch will have $n + 3$ hyper-static degrees.

In practice, a double clamped arch with *n* hinged intermediate supports will have *n* unknown rotations and a system of *n* equations with *n* unknown rotations will have to be solved.

Notice only that we need to have a method to evaluate the internal forces in isostatic arches (*e.g.* cantilever arches).

Solving the linear system expressed by equation (1) will bring to the total knowledge of the internal forces and especially of the reactions of the supports that are the pre-tension forces to give to the tie back anchor strands.

2.2 *Isostatic little arches calculation method*

In general we have a little circular arch with a central angle $\underline{\beta}$, less than 90° with a $q_x(x)$ and $q_y(y)$ load distributed respectively along the horizontal *x* and vertical *y* dimensions, but directly applied on the circular arch at the point (x, y) of central angle β; hence $x = R\,(1 - \cos(\beta))$, and $y = R \sin(\beta)$, and the single distributed load contributions can be added in function of β, as β varies.

So, according to the Taylor series $dx = -\sin(\beta)\,dl$ and $dy = \cos(\underline{\beta})\,dl$ we'll have a radial and tangential distributed load of this type:

$$q_r = -(\sin(\beta))^2\, q_x + (\cos(\beta))^2\, q_y \tag{2}$$

$$q_t = -\sin(\beta)\cos(\beta)\, q_x - \cos(\beta)\sin(\beta)\, q_y \tag{3}$$

where β is the central angle in the load application point, and regarding the distributed load q_t positive when in compression, and the radial load q_r positive when centripetal.

The shear forces can be evaluated, analogously to the rectilinear beams, for an arch of central angle $\underline{\beta}$, considering the various contributions of $q_r(\beta)$ and $q_t(\beta)$, as β varies, eventually making an integral operation on β (Fig. 1).

It follows that:

$$T(\underline{\beta}) = H_0 \cos(\underline{\beta}) - V_0 \sin(\underline{\beta}) + \int_0^{\underline{\beta}} [q_r(\beta)\cos(\underline{\beta} - \beta) + q_t(\beta)\sin(\underline{\beta} - \beta)]\, R\, d\beta \tag{4}$$

where R is the little arch radius and we apply the ordinary beam sign convention namely T and H_0 are positive when we begin the calculation from the left end of the beam (arch in this case) and this is acted upon by an upward force.

In the same manner the normal force can be expressed as:

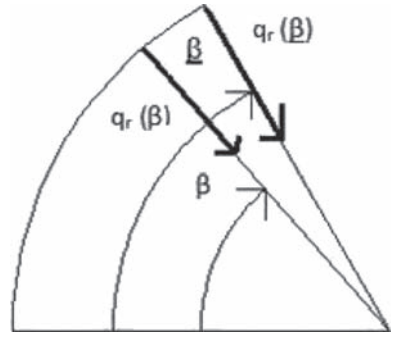

Figure 1. Evaluation of the q_r contributions to Shear Force as β varies for an arch of central angle $\underline{\beta}$. Analogous considerations are done for the q_t contributions and hence for the Normal Force.

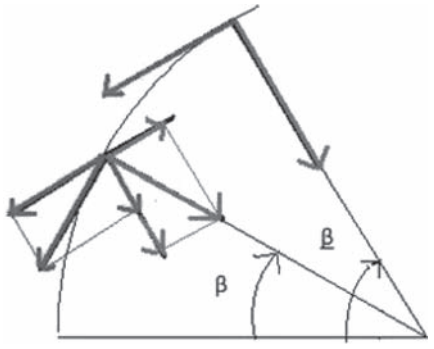

Figure 2. Evaluation of normal and shear forces contributions to the bending moment as β varies for an arch of central angle β̲. Notice that T is here drawn negative according to the ordinary beam left end conventions, while N is positive as in traction.

$$N(\beta) = H_0 \sin(\beta) + V_0 \cos(\beta) - \int_0^{\beta} [q_r(\beta) \sin(\beta - \beta) - q_t(\beta) \cos(\beta - \beta)] R \, d\beta \quad (5)$$

Here also, as in ordinary convention rules, V_0 and N are positive when in traction.

Finally (see Fig. 2), the bending moment can be expressed as:

$$M(\beta) = M_0 + H_0 R \sin(\beta) - V_0 R (1 - \cos(\beta)) + \int_0^{\beta} [T(\beta) \cos(\beta - \beta) - N(\beta) \sin(\beta - \beta)] R \sin(\beta - \beta) \, d\beta + \int_0^{\beta} [N(\beta) \cos(\beta - \beta) + T(\beta) \sin(\beta - \beta)] \times R [1 - \cos(\beta - \beta)] \, d\beta \quad (6)$$

Obviously H_0,V_0 and M_0 are the reaction forces in the cantilever clamp, namely for β = 0 and T(β), N(β) must be calculated in Eqs. 4 and 5 respectively with the position T(β) = T(β̲, β) = T(β, ζ) and N (β) = N(β̲, β) = N(β, ζ), where ζ is the integrand variable. Finally as usual M is regarded as positive when is tending the intrados fibres.

3 SETTLEMENT PRONE URBAN SOFT SOILS ENVIROMENTS APPLICATION EXAMPLES

3.1 *Compensation grouting approach and its limits*

Compensation grouting (Essler *et al*., 2000) either the Soil Fracture Grouting (Soilfrac) process in fine grained soils or the Compaction Grouting process in granular soils are nowadays used in these urban soft soil environments.

Compaction grouting has however the limit of high pressure of injection, that permits its application only in close proximity to the tunnel face (Essler *et al*., 2000).

Actually, soil fracture, as the grouting injection propagate as much as greater is the overburden, that in general is heterogeneous, does not permit to know exactly the mechanical properties of the new *in situ* realized material and so any FEM analysis to model the soil improvement will result in a lack of good numerical quantitative reliability for the long term settlement to precisely figure out.

3.2 *Analytical controlled settlement approach application example*

When on the other hand we apply the method herein presented, the design features, instead of longitudinal and transverse grouting height, taking in account the urbanized complex environment close to probable building piled foundations, are thought in terms of lining thickness and pre–stressed anchoring distances.

We can now suppose to have the situation depicted in Figure 3 with the load q = 150 KN/m^2, representative of an average urban subsoil, where we focus on the upper semi circle of the tunnel lining, that for sub–urban areas purposes is of greater concern. Besides we consider the upper semicircle divided in 3 equal arches, so each with centre angle of 60 degrees.

Just for sake of simplicity we will use the noticeable elastic weight strength of materials formulas to figure out the rotations in nodes 2 and 3, by the artifice to consider the parabolic arch equivalent to the particular 60 degree circular arch, imposing the point passage for the keystone and the imposts, or in a simpler way by considering the rise of f = R(1 – √3/2) = 6 m × 0.13397 = 5.866 m with reference to the arch chord l_{chord} = R.

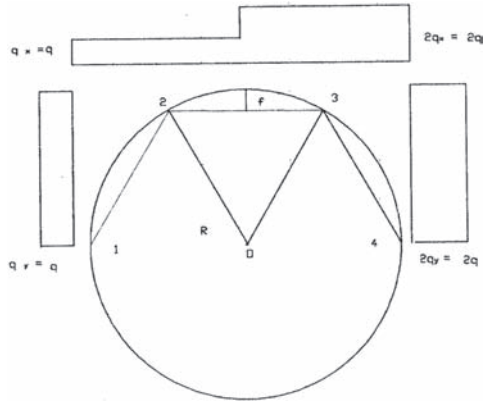

Figure 3. Tunnel of radius R = 6 m in which are imposed no convergences at all in the node 2 and 3 by the application of two pre stressed tie back in the nodes 2 and 3, while, in this example, in the nodes 1 and 4 invert arch is supposed sufficiently stiff and the building loads sufficiently reduced to avoid significant convergences.

So it is:

$$M_2 = M_{2C}^{o} + 4/G\varphi_2 + 2/G\varphi_3 + M_{2L}^{o} + 4/G\varphi_2 \quad (7)$$

$$M_3 = M_{3C}^{o} + 4/G\varphi_3 + 2/G\varphi_2 + M_{3L}^{o} + 4/G\varphi_3 \quad (8)$$

where $G = l_{chord}/EJ = R/EJ = 5.86$ E-6 $(KNm)^{-1}$ for $h_{lining} = 0.7$ m, is the beam elastic weight and:

$$M_{2C}^{o} = + q\, l_{chord}^2/192\,(3 + 11\upsilon)/(1 + \upsilon) - 2\, q\, l_{chord}^2/192\,(3 - 5\upsilon)/(1 + \upsilon) + 51/280\, q\, f^2 - 38/280\, q\, f^2 = 200.600\ KNm \quad (9)$$

and:

$$M_{3C}^{o} = q\, l_{chord}^2/192\,(3 - 5\upsilon)/(1 + \upsilon) - 2\, q\, l_{chord}^2/192 \times (3 + 11\upsilon)/(1 + \upsilon) + 19/280\, q\, f^2 - 102/280\, q\, f^2 = -393.582\ KNm \quad (10)$$

for the central arch (suffix C), and $\upsilon = 45/(4\ f^2)$ $J/A(=45\ h^2/(48\ f^2)$ for a rectangular lining section per unit length), while:

$$M_{2L}^{o} = - q\, l_{chord}^2/12\, \upsilon/(1+ \upsilon) = -186.983\ KNm \quad (11)$$

$$M_{3L}^{o} = + q\, l_{chord}^2/6\, \upsilon/(1+ \upsilon) = +373.967\ KNm \quad (12)$$

for the lateral arches (suffix L).

So, solving the linear system with 2 equations and 2 unknowns, we have:

$\varphi_2 = -0.0000145$ rad; and $\varphi_3 = 0.000018$ rad;

hence the vertical forces V are:

$$V_2 = V_2^{o} - 6/(G\, l_{chord})(2\varphi_2 + \varphi_3) \quad (13)$$

$$V_3 = V_3^{o} - 6/(G\, l_{chord})(2\varphi_3 + \varphi_2) \quad (14)$$

where:

$$V_2^{o} = V_{2C}^{o} + V_{2L}^{o} = (13 + 6)\, q\, l_{chord}^2/32 + q\, l_{chord}^2/4 + q\, f^2/(4\, l_{chord}) - q\, l_{chord}^2/[(8\ f) \times (1 + \upsilon)]\,(\sqrt{3}/2) = 4135.247\ KN/m \quad (15)$$

$$V_3^{o} = V_{3C}^{o} + V_{3L}^{o} = (26 + 3)\, q\, l_{chord}^2/32 + q\, l_{chord}^2/2 - q\, f^2/(4\, l_{chord}) - q\, l_{chord}^2/[(4\ f) \times (1 + \upsilon)]\,(\sqrt{3}/2) = 6739.628\ KN/m \quad (16)$$

While, if we suppose $EA = \infty$, we have the horizontal forces Z:

$$Z_2 = Z_2^{o} = Z_{2C}^{o} + Z_{2L}^{o} = 3\, q\, l_{chord}^2/[(16\ f) \times (1 + \upsilon)] + (11 + 6)/14\, q\, f - q\, l_{chord}\,(\sqrt{3}/4) - q\, l_{chord}^2/[(16\ f)\,(1 + \upsilon)] = 247.499\ KN/m \quad (17)$$

$$Z_3 = Z_3^{o} = Z_{3C}^{o} + Z_{3L}^{o} = 3\, q\, l_{chord}^2/[(16\ f) \times (1 + \upsilon)] + (3 + 22)/14\, q\, f - q\, l_{chord}\,(\sqrt{3}/2) - q\, l_{chord}^2/[(8\ f)\,(1 + \upsilon)] = -318.709\ KN/m \quad (18)$$

And, finally, the reaction forces, that will equal the tie- back pre - stressed forces are:

$$R_2 = (\sqrt{Z_2^2 + V_2^2}) = 4144.513\ KN/m \quad (19)$$

$$R_3 = (\sqrt{Z_3^2 + V_3^2}) = 6743.495\ KN/m \quad (20)$$

These reactions will permit to have, once the tunnel loads be correctly evaluated, for any long term condition, to have no settlement at all in the nodes 2 and 3, whilst a good choice of the lining section will give a limited flexural displacement according to the above shown elastic line equation. In this way it is possible to limit the typical trough like cross surface settlement feature due to the tunnel boring (Essler et al. 2000).

From this example is evident that to have no settlement at all, the tie-back forces are huge and so a correct design process must consider the use of multi–anchoring points along with a design controlled convergence threshold.

The alternative solution of a protective compensation grouting canopy could not be cost effective while could be less reliable from a stress-strain modelling point of view.

Indeed this example has been developed using most important parabolic arch beam particular loading cases noticeable formulas.

If we have to consider a generic load distribution we would develop the force method as follow, according to the sketch depicted in Figure 4, to find out T_2, N_2 and T_3, N_3 and as above calculate R_2 and R_3:

$$\eta_1 = \eta_{10} + \eta_{11}\, X_1 + \eta_{12}\, X_2 + \eta_{13}\, X_3 \quad (21)$$

$$\eta_2 = \eta_{20} + \eta_{21}\, X_1 + \eta_{22}\, X_2 + \eta_{23}\, X_3 \quad (22)$$

$$\eta_3 = \eta_{30} + \eta_{31}\, X_1 + \eta_{32}\, X_2 + \eta_{33}\, X_3 \quad (23)$$

where obviously:

$$\eta_{i0} = \int_l (N_0 N_i/EA + T_0 T_i/GK + M_0 M_i/EJ)\, dl \quad (24)$$

$$\eta_{ij} = \int_l (N_i N_j/EA + T_i T_j/GK + M_i M_j/EJ)\, dl \quad (25)$$

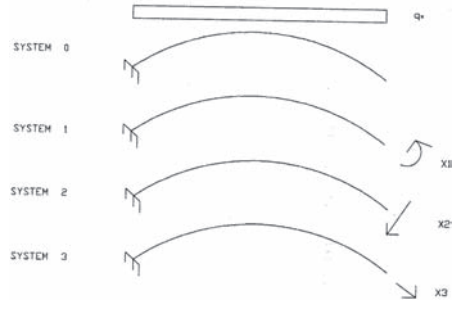

Figure 4. Typical example to calculate a generic circular arch internal forces distribution by the virtual works theorem in the forces form.

Of course equations (24) and (25) must be used along with equations (4), (5) and (6).

Solving the system in X_1, X_2, and X_3, permits to figure out node *i* internal forces for the displacement to use as perfect or sinking clamp values:

$$N_i = N_o + \sum_{j=1}^{3} N_j X_j \ (i = 2 \text{ or } 3) \quad (26)$$

$$T_i = T_o + \sum_{j=1}^{3} T_j X_j \ (i = 2 \text{ or } 3) \quad (27)$$

$$M_i = M_o + \sum_{j=1}^{3} M_j X_j \ (i = 2 \text{ or } 3) \quad (28)$$

4 CONCLUSIONS

An analytical approach, particularly suitable for shallow soft soils, to calculate multi-supported circular arches using known theories of strength of materials, but also implementing the basic isostatic little arches analytical solution has been illustrated.

This methodology is particularly versatile for sub soils, which tend to behave with viscous and even squeezing constitutive laws so for the long term settlement behaviour that typically shows a transverse trough like settlement feature, when the tunnel had been bored without an alternative technique like compensation grouting, that anyway is not easy to contain costs, to control the geo mechanical reliability, and the operative construction aspects.

This method also permits as in other analogue calculations for vertical multi-anchored walls, developed by the author, to calculate the generally non radial supports reactions, imposing certain maximum supports convergences or no supports settlements at all by figuring out the pre-stressed tie back forces.

Only notice that, as a consequence, the maximum convergence, for a particular truss length, will depend from the number of intermediate supports and on the lining flexural rigidity and especially can be calculated on a target base, so deciding the maximum allowable convergence.

REFERENCES

Baldacci, R. 1983. *Scienza delle Costruzioni.* Torino: UTET, vol. 2.

Essler, R.D. & Droof E.R., Falk E., 2000. Compensation Grouting Concept, Theory and Practice. *Advances in Grouting and Ground Modification—Geotechnical Special Publication No 104,* Denver, Colorado: ASCE.

Garini, A.D. 2008. An analytical calculation of multianchored walls and some consequences. *Proceedings of the Second BGA International Conference on Foundations, ICOF 2008*. Dundee: IHS BRE Press.

Garini, A.D. 2009. A dynamic load calculation for multianchored flexible walls. *Performance Based Design in Earthquake Geotechnical Engineering—from Case Histories to Practice*. London: Taylor & Francis Group

Oreste, P. 2002. The convergence-confinement method: roles and limits in modern geotechnical tunnel design. *Gallerie:* Bologna. P atron Editore, 24 (66): 44–50.

Russo, G. & Repetto L., Piraud J., Laviguerie R. 2009. Back—analysis of the extreme squeezing conditions in the ecxploratory adit to the Lyon-Turin base tunnel. *Proceedings of the 3rd CANUS Rock Mechanics Symposium* Toronto: Ed. M. Diederichs and G. Grasselli.

This page intentionally left blank

Geotechnical Aspects of Underground Construction in Soft Ground – Viggiani (ed)
© 2012 Taylor & Francis Group, London, ISBN 978-0-415-68367-8

Interaction between tunnelling and bridge foundation—3D numerical investigation

C. Yoo & S.J. Wu
Sungkyunkwan University, Suwon, Korea

ABSTRACT: This paper presents the results of three-dimensional numerical investigation on the interaction between conventional tunnelling and a pile supported bridge. A hypothetical tunnelling condition under an existing pile supported bridge was first developed with due consideration of urban tunnelling situation. Various components of the bridge including piers, piles, and pile caps are realistically modeled. Also included in the model is the pile-ground interface to simulate possible slip between the piles and the ground during tunnelling. The results of the analysis indicate that during tunnel driving, piles directly above the tunnel experience significant loss of their supporting capacity due to downward settlements of piles relative to surrounding soil. Piles further away from the tunnel however tend to experience increases in the pile load. Practical implications of the findings are discussed.

1 INSTRUCTIONS

Due to continued urban population growth, there has been a pressing need for expansion of infrastructures for transportation. Going underground has become a viable option for expansion of transportation due largely to environmental consideration. During urban tunnelling, there are many cases where a tunnel is constructed under existing pile-supported buildings or a bridge. As typical urban tunnelling situations involve unfavorable ground conditions, the effect of tunnelling on any existing structures is considered of prime design and construction issues.

There have been a number of studies concerning tunnelling under an existing pile(s) (Vermeer and Bonier 1991, Chen et al. 1999, Lee and Ng 2005, Lee and Jacobsz 2006, Lee and Yoo 2006, Cheng et al. 2007). Although these previous studies have identified important governing mechanism relevant for the effect of tunnelling on an existing pile(s), most of the studies are based on idealized tunnelling situations or simplified plane strain approximations.

In this paper, the results of a three-dimensional numerical investigation into the conventional tunnelling under an existing pile supported bridge are presented, aiming at identifying the fundamental governing mechanism of the effect of tunnelling on the stability of the bridge, in terms of settlements and load carrying capacity of piles. A hypothetical tunnelling situation was developed and a three-dimensional finite element model was constructed in order to attain meaningful results that can be extended to similar tunnelling works in urban environment. A particular attention was paid to the modelling of the pile-ground interface so as to allow for realistic simulation of the soil-structure interaction. The following sections present the tunnelling and site conditions, the 3D finite-element model, and finally, practical implications of the findings.

2 TUNNELLING CONDITION AND FINITE ELEMENT MODELING

2.1 *Tunnelling condition*

A hypothetical tunnelling condition in which the tunnel is excavated under a four lane roadway bridge is considered as shown in Figure 1. For simplicity, it was assumed that the direction of tunnel driving is perpendicular to the axis of the bridge. A typical tunnel cross section in urban tunnelling was considered in this investigation. The tunnel has a maximum height and width (D) of 8.0 m and 11.0 m, respectively, giving the net excavation area of approximately 87 m^2.

It was assumed that the tunnelling is performed in a multi-layered ground consisting of a 14 m thick decomposed granitic soil with a thickness ranging 8.0~12.5 m below which a solid granitic rock layer is followed. No groundwater table is assumed to exist. In terms of the primary support pattern, the tunnel was assumed to be supported by a 200 mm thick shotcrete layer with a typical bench-cut excavation method. No rock bolts are considered in this study to simplify the model.

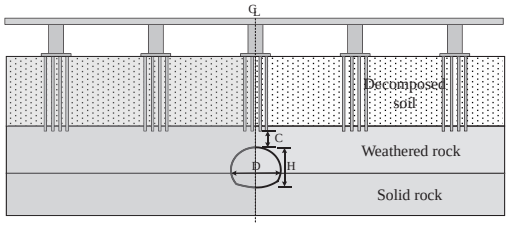

Figure 1. Schematic view of tunnelling condition.

The bridge is supported by piers having 20 m center-to-center spacing, each of which has a 1.5 m × 3.0 m cross section with eight, 15 m long, 0.5 m diameter steel piles, installed at 1.5 m centre-to-centre spacing. The clearance between the tunnel crown and the pile tip (C) is 1.5 m.

2.2 *Finite element modeling*

A three-dimensional (3D) finite element model was adopted in this study with due consideration of the three-dimensional nature of the tunnel-bridge geometry and the excavation condition. The analysis was carried out using a commercial finite element package Abaqus (Abaqus, Inc. 2007).

On account of the symmetry about the tunnel centerline, only 1/2 of the entire domain was included in the model. Figure 2 shows the finite element model, consisting of nearly 141,000 three-dimensional elements with over 218,000 nodes. In the analysis, the components of bridge structure, i.e., pier, pile cap, and piles, were explicitly modelled including the pile-soil interface. The bridge deck, however, was not included in the model but replaced with an equivalent surcharge corresponding to the body weight of the bridge deck.

The eight-node linear displacement elements with reduced integration (C3D8R) were used to discretize the ground and the piles while the linear quadrilateral shell elements (S4R) were used for the shotcrete lining. The pile-soil interface behavior was modeled using the contact pairs with appropriate frictional property. In terms of displacement boundary condition, the degree of freedom perpendicular to the vertical boundaries was restrained while pinned support was assumed at the bottom boundary.

The ground was assumed to be an elastic-plastic material obeying the Mohr-Coulomb failure criterion together with the non-associated flow rule by Davis (1968). The structural members of the bridge as well as the shotcrete lining were assumed to be an elastic material having Young's moduli of 23 GPa and 10 GPa, respectively, with a Poisson's ratio of 0.25. Table 1 summarizes the geotechnical properties of the ground.

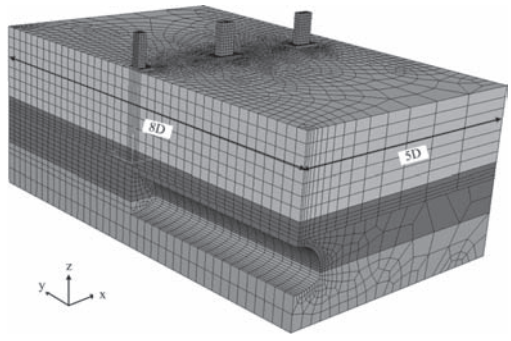

Figure 2. 3D finite element model.

Table 1. Material properties for soil and rock layers.

	Decomposed granitic soil	Weathered granite rock	Solid granite rock
γ [a] (kN/m^3)	21	25	25
c′ [b] (kPa)	20	50	450
ϕ' [c] (deg)	33	35	45
E [d] (MPa)	60	200	1000
K_o [e]	0.5	0.5	1.0
v [f]	0.30	0.25	0.25

[a]γ = total unit weight; [b]c′ = cohesion; [c]ϕ' = internal friction angle; [d]E = deformation modulus; [e]K_o = lateral earth pressure coefficient; [f]v = Poisson's ratio

3 BRIDGE RESPONSE TO TUNNELLING

3.1 *General*

The bridge response to tunnelling was examined using the results from the 3D FE analysis such as progressive changes of pile settlement and load. Figure 3 depicts the symbols used for the piles.

3.2 *Pile tip settlement and load*

The progressive development of pile tip settlements with the tunnel advancement for piles CP1, CP4, and CP6 are shown in Figure 4. As seen in Figure 4, the pile tip settlement S_v for CP1 starts to develop when the tunnel heading arrives at 2.0D away from the pile location. The pile tip settlement then increases approximately to $0.06\%D$ when the tunnel heading arrives immediately below the pile. Note that the pile settlement of $0.06\%D$ amounts to 50% of its final value, suggesting that any unprotected pile can experience 50% of its final settlement before the passage of tunnel heading. Further advancement of the tunnel heading rapidly increases the pile tip settlement until the tunnel heading reaches approximately 1.0D beyond the pile CP1. Due to remoteness of the piles CP4

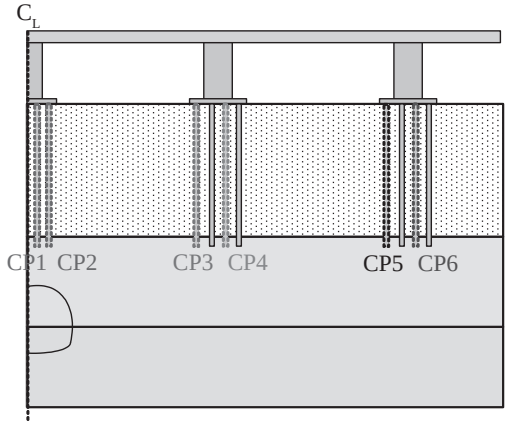

Figure 3. Notations used for piles.

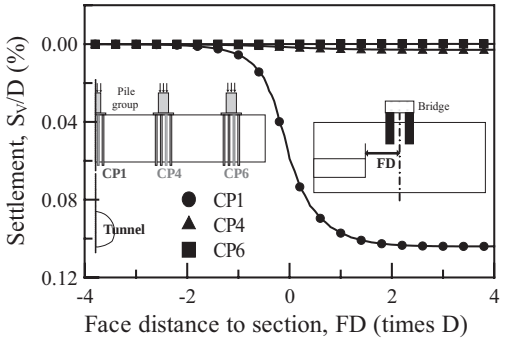

Figure 4. Progress development of pile tip settlements.

and CP6 from the tunnel, the pile tip settlements are negligible, i.e., less than $0.002\%D$.

Progressive changes in the pile tip load (ΔP_{tip}) with the tunnel advancement are shown in Figure 5. In this figure, the positive sign of ΔP_{tip} indicates an increase in ΔP_{tip} whereas the negative sign indicates a decrease in ΔP_{tip}. As expected, pile CP1 experiences significant changes during the tunnel advancement. For example, it is seen that the pile tip load gradually increases by 50 kN, or 24.5% from its initial load of 204 kN, until the tunnel heading reaches approximately −1.0D away from CP1. A sudden decrease in pile load then follows as the tunnel advancement is continued until the tunnel heading reaches immediately below the pile tip, resulting in a maximum decrease of 300 kN, or 147% of the initial value. No significant variation in ΔP_{tip} is seen after the passage of the tunnel heading beyond the pile CP1. The decrease in the pile load is in essence an indication that the pile loses its load supporting capacity during the tunnel advancement caused by the pile settlement

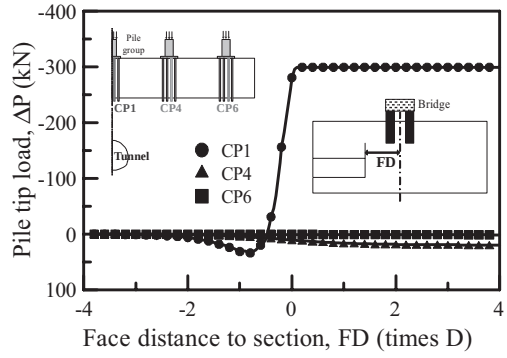

Figure 5. Progress development of pile tip load.

as observed in Figure 4. Of interest trend is that most of the pile tip load reduction is completed before the tunnel heading passes the pile, implying the most critical stage being just before the tunnel passage in view of the bridge stability.

Piles CP4 and CP6, located further from the tunnel laterally, however show increases in ΔP_{tip}, although the magnitudes are not as significant, i.e., less than 50 kN. The increases in the pile load for CP4 and CP6 are likely caused by the downdrag of the surrounding soil as will be further discussed later in the section. The trends shown here are in good agreement with those reported by Yoo and Kim (2008) in which the performance of multi-faced tunnelling under a pile-supported building in water bearing soft ground is investigated.

3.3 *Pile axial load and relative settlement*

Figure 6 illustrates the changes in the axial pile load (ΔP) at various stages of tunnel excavation for piles CP1, CP4, and CP6. As shown for CP1, the axial load tends to decrease during the tunnel advancement, resulting in a maximum decrease as great as 500 kN, or 125% from the initial value, when the tunnel heading arrives 2.0D away from the pile. For CP4 and CP6, the axial loads along the pile shaft tend to increase somewhat, although the magnitudes of the increase are only minimal, i.e., less than 50 kN. As noted by Yoo and Kim (2008), for similar tunnelling situations considered in this study, whether or not pile load increases or decreases fully depends on the lateral location of a pile relative to the tunnel being considered. For example, a decrease in pile load is expected for piles located directly above the tunnel while a slight increase in the pile load should be expected for piles located laterally some distance away from the tunnel.

Normalized relative settlements (S_v/D) of the piles with respect to surround soil are shown in

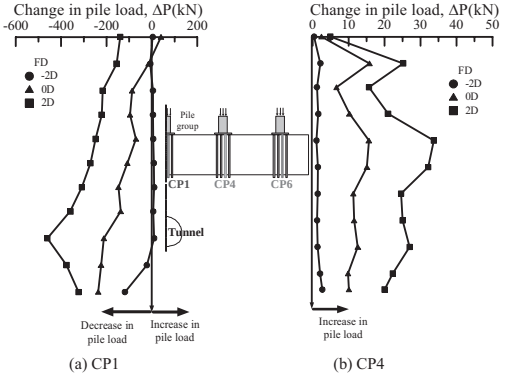

Figure 6. Change in pile axial load during tunnel advancement.

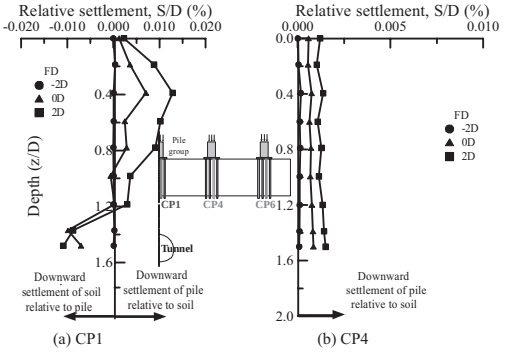

Figure 7. Relative settlement between piles and soil during tunnel advancement.

Figure 7 for various tunnelling stages. Note that a downward settlement of surround soil relative to pile is denoted by a negative S_v/D whereas the opposite sign i.e., positive, indicates that a pile settles more than surrounding soil. In terms of the pile load development, a negative S_v/D induces a negative skin friction (NSF) along the pile shaft while a positive S_v/D results in a positive skin friction (PSF) as indicated by Lee and Ng (2005). As shown in Figure 7(a) for pile CP1, negative as well as positive relative settlements are appeared to develop along the pile with a neutral point at the lower 1/4 of the pile length. For example, positive relative settlements, as great as $S_v/D = 0.013\%$, are developed in the upper 3/4 portion while negative relative settlements, as great as $S_v/D = 0.013\%$, are developed in the lower 1/4 portion of the shaft. In pile CP4, only positive relative settlements are developed but with 1/10 order of the magnitudes compared to CP1.

4 CONCLUSIONS

The results of a three-dimensional numerical investigation into the conventional tunnelling under an existing pile supported bridge are presented in this paper, aiming at identifying the fundamental governing mechanism of the effect of tunnelling on the stability of the bridge, in terms of settlements and load carrying capacity of piles. A hypothetical tunnelling situation was developed and a three-dimensional finite element analysis was carried out.

The results of the analysis indicate that during tunnel driving, piles directly above the tunnel experience significant loss of load due to downward settlements of piles relative to surrounding soil. Piles further away from the tunnel however tend to experience increases in the pile load. Also shown is that the most critical stage is just before the tunnel passage in view of the bridge stability as most of the pile tip load reduction is completed before the tunnel heading passes the pile.

REFERENCES

Abaqus Inc. 2007. ABAQUS user's manual, version 6.7. Abaqus, Inc., Pawtucket, Providence, R.I.

Chen, L.T., Poulos, H.G. & Loganathan, N. 1999. Pile Responses Caused by Tunnelling. *Journal of Geotechnical and Geoenvironmental Engineering*, 125(3): 207–215.

Cheng, C.Y., Dasari, G.R., Leung, C.F., Chow, Y.K. & Rosser, H.B. 2007. Finite element analysis of tunnel-soil-pile interaction using displacement controlled model. *Tunnelling and Underground Space Technology*, 22(5): 450–466.

Davis, E.H. 1968. Theories of plasticity and the failure of soil masses. Soil mechanics: Selected topics, Butterworth's London, U.K., pp. 341–380.

Lee, G.T.K. & Ng, C.W.W. 2005. Effects of Advancing Open Face Tunnelling on an Existing Loaded Pile. *Journal of Geotechnical and Geoenvironmental Engineering*, 131(2): 193–201.

Lee, C.J. & Jacobsz, S.W. 2006. The influence of Tunnelling on Adjacent Piled Foundations. *Tunnelling and Underground Space Technology*, 21(3–4): pp. 430.

Lee, Y. & Yoo, C. 2006. Behavior of a Bored Tunnel adjacent to a Line of Loaded Piles. *Tunnelling and Underground Space Technology*, 21(3–4): pp. 370.

Vermeer, P.A. & Bonnier, P.G. 1991. Pile settlements due to tunnelling. In Proceedings of the 10th European Conference on Soil Mechanics and Foundation Engineering, 2, Florence, Italy, Balkema, Rotterdam, The Netherlands, pp. 869–872.

Yoo, C & Kim, S.B. 2008. Three-dimensional numerical investigation of multi-faced tunnelling in water-bearing soft ground. *Canadian Geotechnical Journal*, 45(10): 1467–1486.

Geotechnical Aspects of Underground Construction in Soft Ground – Viggiani (ed)
© 2012 Taylor & Francis Group, London, ISBN 978-0-415-68367-8

Numerical analysis of precast tunnel segmental lining supported by full-scale experimental tests

F. Cignitti & R. Sorge
Metro C S.c.p.a. (Astaldi S.p.a.), Rome, Italy

A. Meda, F. Nerilli & Z. Rinaldi
University of Rome "Tor Vergata", Rome, Italy

ABSTRACT: The behavior of precast tunnel segments, subjected to the Tunnel Boring Machine (TBM) thrust is analyzed in the paper, with particular reference to the case of the Rome Metro C line. Firstly a proper finite element (FE) code is applied with the aim of evaluating the load related to the first crack formation, and the evolution of the crack opening. The obtained results are validated through full-scale tests, developed in the Material and Structure Laboratory of the Rome University "Tor Vergata", on actual segments. A suitable system and set-up has been realized in order to re-create the in appropriate way the in-situ load conditions.

1 INTRODUCTION

The tunnel construction by adopting a Tunnel Boring Machine (TBM) is nowadays the most extensively adopted system. The tunnel lining is usually made with precast segments in reinforced concrete, loaded by two kinds of actions. The first one occurs in the construction phase (i.e. demoulding, handling and TBM thrust) and the second one is given by the soil pressure that causes stresses on the lining ring.

Nevertheless, for this kind of structures, the construction phase is often the most severe condition. In particular, the effects of the TBM thrust on the segments can lead to a severe stress field on the element, with subsequent cracks that can jeopardize the structural durability. For this reason, the structural design requires a similar attention with respect to the geotechnical design.

In order to study the problem of the TBM thrust effect on the precast segment, a numerical study, combined with an extensive experimental campaign, has been carried out. It has to be remarked that in the simple design procedure the actions transmitted by the TBM are considered as single point load acting on the segment circumferential side. This model is far away with respect to the actual field condition, mainly for two reasons: (a) the action is not properly a point load, but the dimensions of the usually adopted thrusting shoes allow a distributed pressure and (b) more loads (thrusting shoes) are present on the segment, and their relatively small spacing implies a reciprocal interaction and does not allow to consider the situation of a single load. For this reason a numerical modeling, by means of a proper finite element (FE) code (DIANA, Manie & Kikstra; 2008) has been carried out with the aim of simulating, as deeper as possible, the actual actions on the segment. Furthermore, the adopted FE code allows modeling the concrete cracking phenomena and predicting the crack opening. This aspect is very important because in this kind of structures the crack opening limit has to be fulfilled (Burgers et al., 2007).

Due to the complexity of the problem, the study was integrated with a series of full-scale experimental tests with a specifically designed system able to reproduce the TBM thrust on the element. The results of the experimental tests, carried out in the first research phase, were used for validating the numerical model, which can be considered a valuable tool for the precast segment design.

The case study herein analyzed refers to the tunnel lining of the Rome Metro C line.

2 PRESENTATION OF THE PROBLEM

During the excavation process, the TBM machine uses the already placed lining for contrasting the advancing thrust. The lining is made with reinforced concrete precast segments, combined as in Figure 1.

The TBM acts on the lining by means of several hydraulic jacks whose force is applied on the segments with steel shoes. In a traditional set-up,

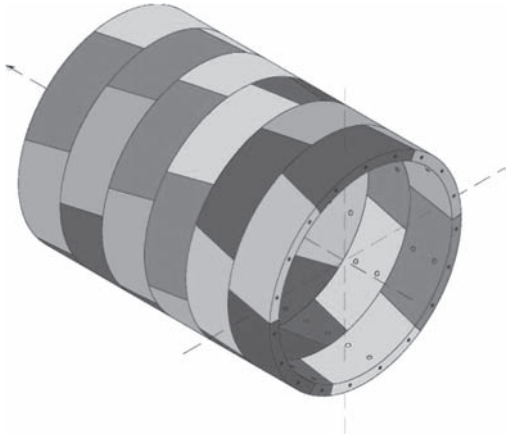

Figure 1. Segmental lining scheme.

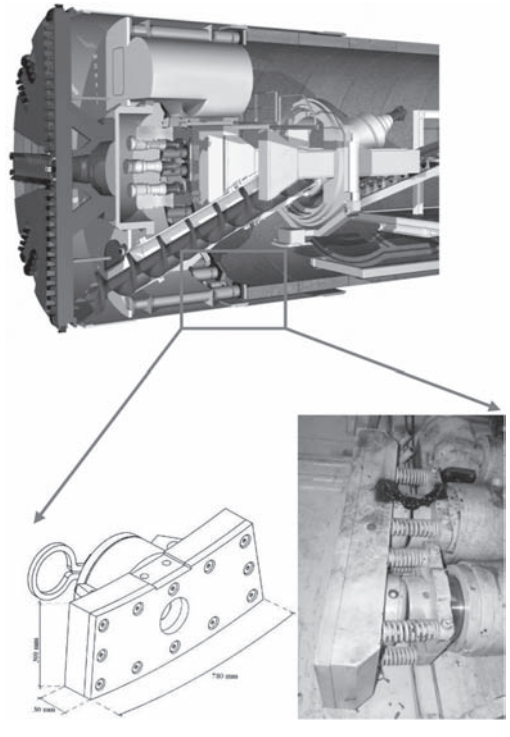

Figure 2. Transversal section of TBM with shoe detailing.

two jacks act on a single shoe. Between the steel shoes and the segment, a Teflon layer, having a thickness of 30 mm, is present. The shoe surface is shown in Figure 2.

With reference to segment type D of the ring (Figure 3, Figure 4), three shoes act on the elements. The distance between the shoes centroids is equal to 1000 mm while the free space between them is

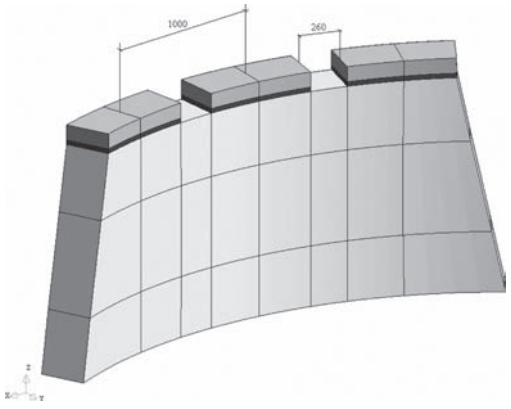

Figure 3. Segment geometry.

260 mm (Figure 3). The segment has a thickness of 300 mm, an average length of 1400 mm and a width of 300 mm.

3 FE MODELING

Aim of the study is to investigate the possible cracking phenomena due to the TBM thrust action. The precast segment is so modeled by adopting a non-linear fracture mechanic approach for the concrete.

The development of crack patterns is studied by means of the smeared crack approach, combined to the "total strain rotating crack" model (Rots, 1988). With this approach the stress–strain relationship is evaluated in the principal directions of the strain vector. A crack is initiated when the principal tensile stress exceeds the value of the tensile strength and its direction is perpendicular to the direction of the principal tensile stress. The effect of the cracking is spread over the area that belongs to an integration point of the mesh. When cracking starts, the principal stress follows a tension-softening stress-strain diagram, which is characterized by three material parameters: tensile strength, fracture energy, shape of the softening diagram. An additional parameter, which is very important for this approach, is the crack band width over which the crack is smeared out, related to the size of the finite element mesh (Figure 5). The value of this parameter, that can affect the analysis outcome, has been accurately chosen, with a parametric enquire, in order to optimize the convergence of the model, independently of the results of the experimental tests.

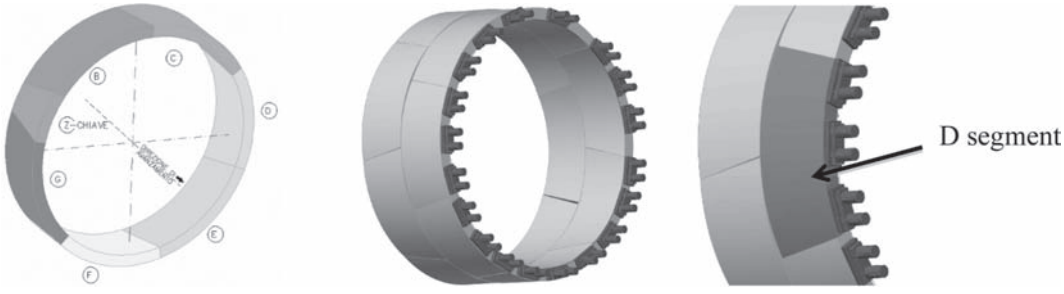

Figure 4. Segment D.

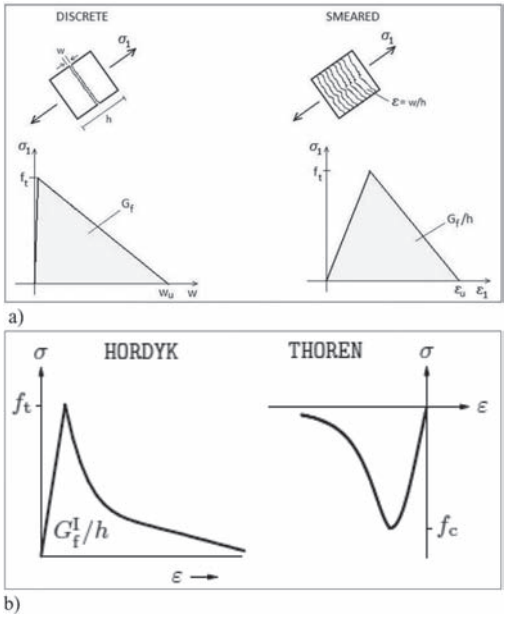

Figure 5. a) Smeared crack approach, b) constitutive relationships of concrete in tension and compression.

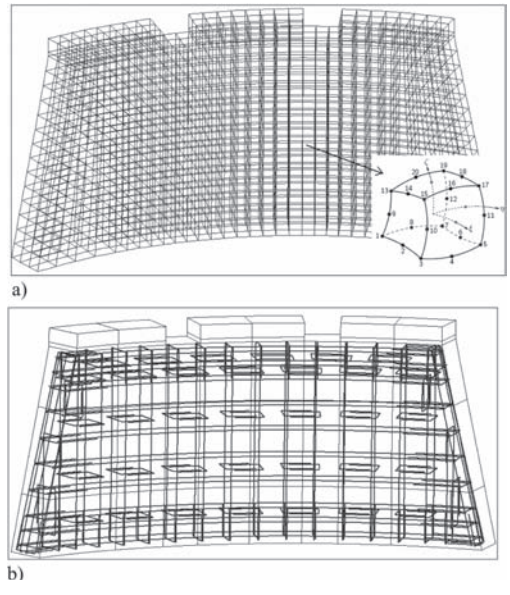

Figure 6. a) Element mesh, b) Reinforcement modeling.

Table 1. Mechanical material properties.

Material	E MPa	ν –	f_c MPa	f_t MPa	G_f N/m
Concrete	41658	0.2	84	4.6	150
Steel(shoes)	210000	0.15	–	–	–
Steel(bar)	210000	0.15	–	–	–
Teflon	600	0.46	–	–	–

The nonlinear tension softening suggested by Corneliuson et al. (1986), usually named "Hordijk relationship", is adopted for plain concrete, as shown in Figure 5. The fracture energy, G_f, is determined with reference to the MC1990 (1993). The compressive behavior of the concrete is approached by the curve proposed by Thorenfeld at al. (1997), whose parameters have been assigned on the basis of the actual concrete compression strength.

The Finite Element 3D mesh was composed by adopting 20 nodes prismatic elements having a side dimension about 60 mm (Figure 6a).

Due to the low stresses acting on the reinforcement, the steel was considered with an elastic behavior. The reinforcement bars were modeled with discrete element embedded to the concrete mesh (Figure 6b).

The concrete properties have been derived by uni-axial compression and tensile tests carried out on cores drilled by the segment used for the experimental validation, described in the following.

The main properties of the modeled materials are summarized in Table 1.

The boundary conditions adopted for the segment was chosen in order to restrain the vertical displacement at the segment base, considering a

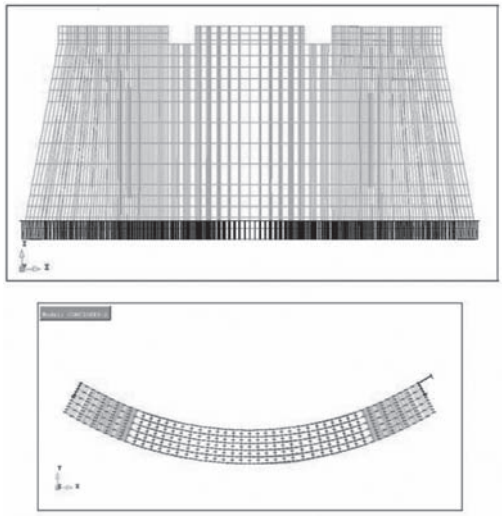

Figure 7. Boundary conditions.

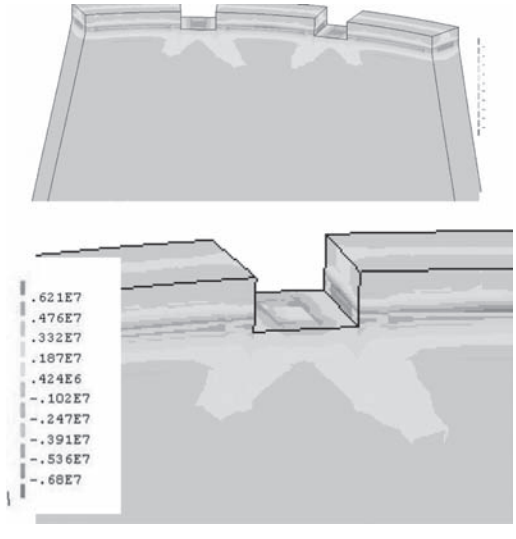

Figure 8. Stress distribution.

Figure 9. First crack location, between the shoes.

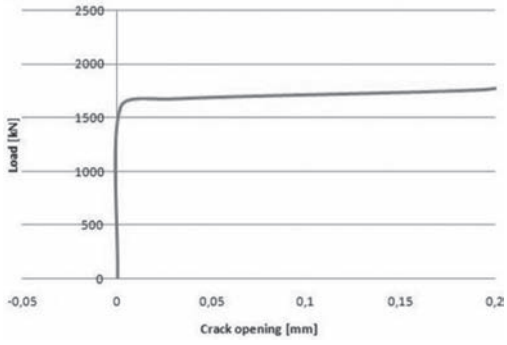

Figure 10. Numerical Load (one shoe)—crack opening.

rigid contact between the segment and the already placed lining, having infinite stiffness (Figure 7). Furthermore, constrains were placed in order to link the torsion segment displacement.

The incremental analysis, needed with this kind of model, was carried out by increasing the shoes load pressure. In this way it was possible to increment the load on the shoes maintaining a stable behavior.

4 NUMERICAL FE RESULTS

Firstly, the results of the analysis at a load level smaller than the cracking one is presented. Figure 8 shows the principle stress distribution pattern in the segment. It can be noticed that tensile stresses are present in the zones between the shoes and in a limited region at the segment base. It is evident that the stress distribution is far away with respect to the situation exhibited when a point load is considered: the maximum stresses are not located under the acting load (shoes) but under the unloaded surface between the shoes.

Figure 9 refers to the loading step related to the cracking onset. It can be noticed that the first crack occurred in the zone between the shoes in correspondence of a load level about 1596 kN for each shoes (total load of 4788 kN). The crack stabilized (at this load level) at an initial opening value equal to 0.00148 mm.

Figure 10 shows the evolution of the maximum crack opening by increasing the load level. It can be noticed that, starting from an opening, equal to 0.00148 mm, the crack opening evolves up to about 0.2 mm in correspondence to a load level equal to 1932 kN for each shoes. The evolution of the crack opening can be followed thanks to the adopted model for the concrete under tension.

In fact, if a simple brittle relationship is adopted for modeling the tensile behavior of the concrete

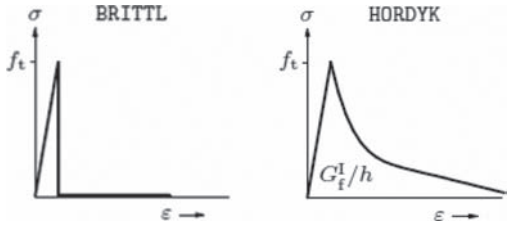

Figure 11. Tensile concrete model: Comparison between brittle and Hordijk models.

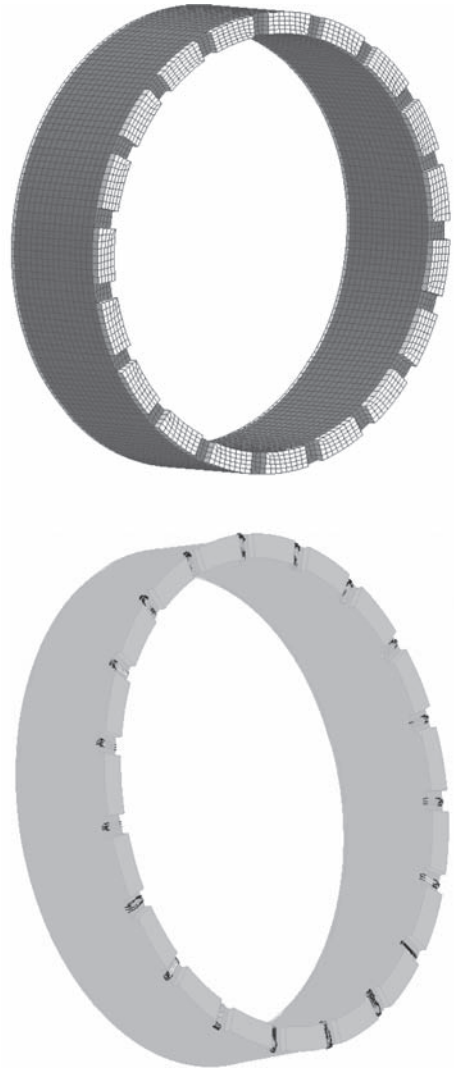

Figure 12. Complete ring model.

(Figure 11), the crack opening measured at the first cracking stage results equal to 0.25 mm. Nevertheless, it is worth noting that the load level related to the first cracking, obtained with a brittle model for the concrete, results equal to 1596 kN, i.e. equal to the one obtained with the smeared crack model.

In order to verify the behavior of the overall lining and not only to limit the analysis to a single segment, a model of the complete ring (Figure 12) has been developed. In this case it was not considered the presence of the steel reinforcement, because the main aim of this analysis was only to compare the load level related to the first cracking.

The first cracking of the complete ring model occurs at a load level (on a single shoe) of about 1512 kN very close to what obtained on the single segment (1596 kN). It has to be remarked that the first cracking load in the single segment results the same for the model with and without reinforcement.

5 EXPERIMENTAL VALIDATION

In order to validate the numerical model, an extensive experimental campaign has been set up. Aim of the tests was to reproduce the in situ TBM thrust on a single precast segment.

A suitable testing system has been designed in order to perform full-scale tests, by applying thrust on the segment up to 4000 kN on a single shoe, with up to three shoes on a single segment. The testing system is illustrated in Figure 13. Two hydraulic jacks act on every steel shoe. A close ring frame is adopted for every jacket, having a maximum loading capacity of 2000 kN. The total loading capacity of the system is equal to 12000 kN.

The precast segment is placed on a RC beam having a cross section of 800×800 mm, internal to the close ring frames. In order to obtain a uniform support a 25 mm thick steel plate is placed between the segment and the RC beam (Figure 13).

A hydraulic control system has been adopted with the aim of applying the loads similarly to what happens with the TBM. In particular it was possible to control the load on a single jacket and, with ad hoc valves, it was possible to maintain constant the oil pressure in the circuit.

The loads applied on the segment were measured by means of three inductive load pressures, each for every couple of jackets. The vertical displacements of the steel shoes were measured with potentiometer wire transducers, placed on the front side (intrados) and on the rear side (extrados) of the segment (Figure 14). Furthermore, two LVDTs were adopted for measuring the crack opening between the steel shoes (Figure 14).

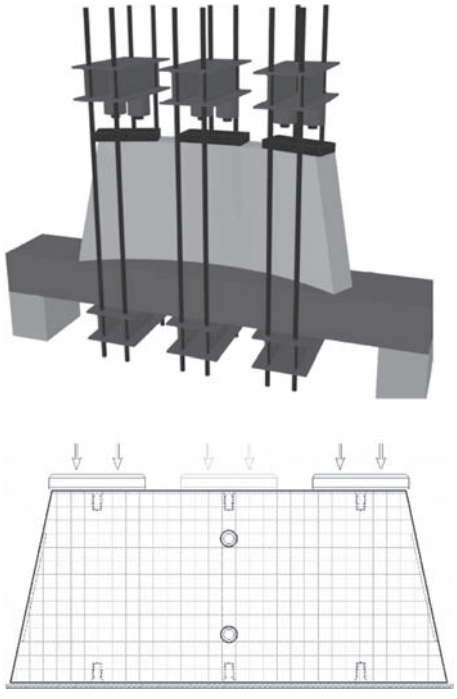

Figure 13. Test set-up.

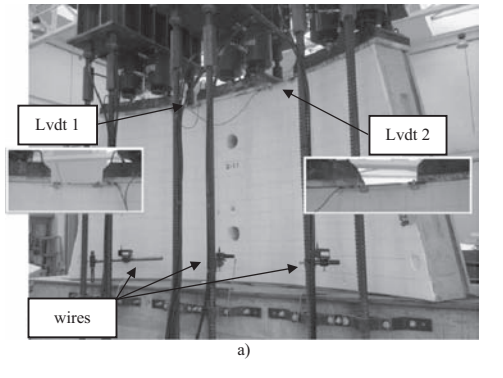

a)

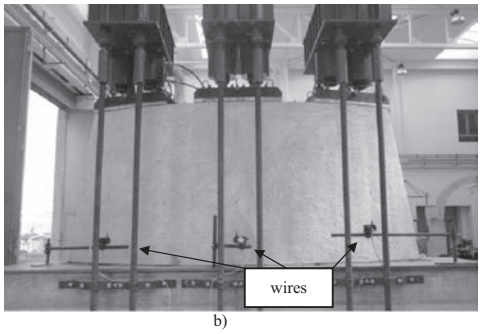

b)

Figure 14. Test set-up—Instrumentation; a) intrados, b) extrados.

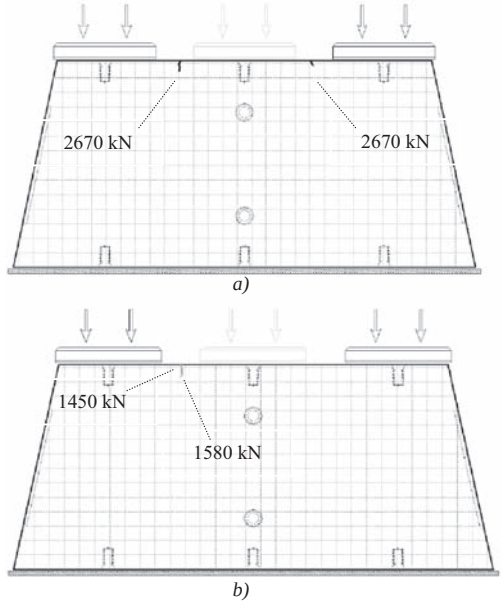

Figure 15. Experimental test: crack pattern.

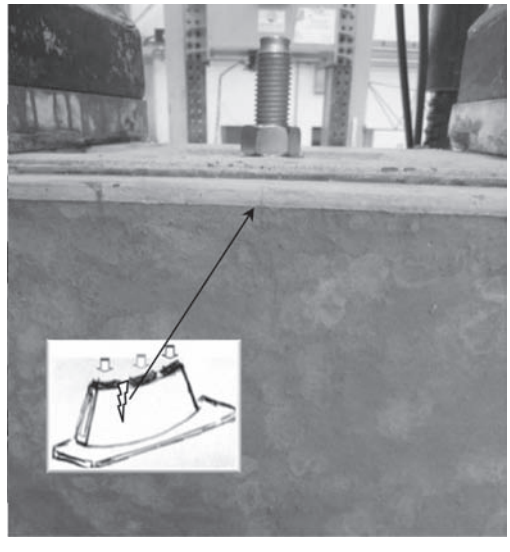

Figure 16. First crack.

Figure 15 shows the crack pattern evolution for different load levels in a tested segment.

It can be noticed that the crack onset is in accordance with the numerical forecast. As a matter of fact the first crack opens on the extrados side for a load level of about 1500 kN, for each shoe, and it is located between the load shoes.

A detail of the first crack is highlighted in Figure 16.

6 CONCLUDING REMARKS

The results of both numerical and experimental analyses on tunnel precast reinforced concrete segments subjected to TBM thrusts, allow drawing the following remarks:

- numerical FE analyses, can simulate the actual behavior of the segment, with reference to the crack onset and opening, provided that a correct model is adopted for the tensile response of the concrete. As a matter of fact, both the load related to the first crack and the opening crack evolution are caught by the numerical model;
- for the analyzed case, loaded by three couple of jacks, the cracks appear between the load shoes and not under them; this aspect should be taken suitably into account in the design phase;
- the analysis of a single segment appears to be representative of the entire ring.

ACKNOWLEDGEMENT

The authors are grateful to Eng. Angelo Caratelli, for his irreplaceable work during the experimental tests.

REFERENCES

Burgers R., Walraven J., Plizzari, G.A. & Tiberti, G., (2007): "Structural behaviour of SFRC tunnel segments during TBM operations", in World Tunnel Congress ITA-AITES 2007, Praga, pp. 1461–1467.

Cornelissen, H.A.W., Hordijk, D.A. & Reinhardt, H.W. 1986. Experimental determination of crack softening characteristics of normal weight and lightweight concrete, Heron 31, 2, 1986.

Manie, J. & Kikstra, W.P. 2008. Analysis Procedures, DIANA – Finite Element Analysis. User's manual release 9.3. Delft: TNO DIANA BV.

MC1990. Comité Euro-International du Béton. 1993. CEB-FIP Model Code.

Rots, J.C. 1988. Computational modeling of concrete fracture, Doctoral Thesis, Delft University of Technology.

Thorenfeldt, E., Tomaszewicz, A. & Jensen, J.J. 1987. Mechanical properties of high-strength concrete and applications in design. In Proc. Symp. Utilization of High-Strength Concrete. (Stavanger, Norway).

This page intentionally left blank

Geotechnical Aspects of Underground Construction in Soft Ground – Viggiani (ed)
© 2012 Taylor & Francis Group, London, ISBN 978-0-415-68367-8

The ground movement simulator: An interesting facility for the study of the behavior of buildings submitted to ground subsidence

M. Caudron, M. Al Heib & B. Hor
National Institute for Industrial Facilities and Risks (INERIS), Verneuil en Halatte, France

F. Emeriault
CNRS UMR 5521, 3SR Lab, Grenoble, France

ABSTRACT: Soil subsidence of various extend and amplitude can result from the failure of underground cavities, whether natural (for example caused by the dissolution of rocks by underground water flow) or man-made (such as mines and quarries). The impact of the movements of the ground on existing structures (houses, buildings, bridges, etc…) is generally dramatic. A large small-scale physical model is developed in order to improve our understanding of the behaviour of the building subjected to ground subsidence or collapse. We focus on the soil-structure interaction and on the mitigation techniques allowing reducing the vulnerability of the stakes.

1 INTRODUCTION

INERIS is working for many years on the "ground movements" risk caused by underground cavities (mines, quarries and tunnels). Several research tasks are followed concerning the stability of the cavities, the prediction of the ground movements reaching the ground surface, the behaviour of the building subjected to this hazard and mitigation techniques.

A large small-scale physical model is developed in order to improve our understanding of the behaviour of the building subjected to ground subsidence or collapse. We focus on the soil-structure interaction and on the mitigation techniques allowing reducing the vulnerability of the stakes.

This article is composed in a first part on the presentation of the physical model, the measurement facilities and the basic hypothesis. Secondly a corresponding building model is detailed. We develop then two similar tests, the first one presenting the case of a ground subsidence in greenfield condition while the second one uses the building model: a slab with his loading. We detail the influence of the position of the structure with respect to the cavity.

2 BIBLIOGRAPHY

2.1 *Mining subsidence & soil-structure interaction*

The subsidence is generally caused by convergence or collapse of anthropic or natural underground cavities. This phenomenon can be very prejudicial for the structures and infrastructures on the surface and for the population. Empirical rules exist for the estimation of the building damages caused by such ground movements (…). But they are limited by the context of their definition. There is very few relationships to determine the damages caused to a building by ground movements and taking into account the soil-structure interactions. These are mainly based on numerical studies (Potts & Addenbrook 1997, Dimmock & Mair 2008, Deck & Anirudth 2010).

Several research projects are focused on the study of the ground-structure interactions phenomena under the effect of the soil movements (Standing 2008, Lee et al. 2007, Sung et al. 2006, Abbass 2004, Deck 2002, Burd et al. 2000, Nakai et al. 1997).

While previous works (Caudron 2007) had allowed shedding some light on the interest of taking into account the soil-structure interaction, this paper will focus on the conception of a new small-scale physical model intended for the study of mining subsidence and the consequences on building on the ground surface. Previously, a bidimensionnal small-scale physical model was used (Caudron et al. 2006). However, the 2D nature of this model was a too important limit for the expected results preventing any transposal to the reality.

2.2 *Physical model for mining subsidence*

Very few physical models have been used to study the effects of ground movements caused by the mining process or by the collapse of old mine or quarries. We can mention a block caving small-scale

physical model: Castro et al. (2007) and Trueman et al. (2008). This model is dedicated to the study of block caving exploitation method and not to the ground movement rising to the surface. Few models are focusing on the phenomena corresponding to the formation of a subsidence trough. Genis et al. (2008) studied the effect of an earthquake on the stability of an old coal mine located in Japan. They showed that depending on the geometry, the failure may happen in the pillars or at the mine ceiling. Dyne (1998) conceived a model, trap door type, in order to represent the happening of sinkholes in an ancient coal mine in Pennsylvania. The model was a very simple one with a trap door of four different widths and a single layer of sand as overburden.

Ren et al. (2010) achieved several tests with 1 g smal-scale physical model concerning subsidence characters of ground and wall rock due to underground mining. Few details are reported in literature on the parameters and the hypothesis to model it.

For these different works, none consider the potential damages caused by the rising subsidence on the surrounding buildings.

On this particular subject, several small-scale physical models have been realized in the field of tunnels. For example, Nakai et al. (1997) and Shahin et al. (2004) use a bidimensionnal physical model for the study of the influence of the position and nature of the foundation of a building subjected to settlements caused by a tunnel boring.

Tests have been performed in the context of EU research project "QUAKER" to study the influence of several buildings, considering different geometries, weight and foundation systems, on the path followed by a fault activated by the Kocaeli earthquake (Bransby et al. 2008a and 2008b). Very interesting results are obtained, showing a more or less important bifurcation of the fault when a building is located close the path obtained in Greenfield condition. The bifurcation can even become very important in the case of heavy building or when a deep foundation system is used.

3 THE APPARATUS

3.1 *Hypothesis and conception*

The first part of the hypothesis comes from the rules of similarity. It is very difficult, if not impossible to achieve a perfect similarity with a small-scale model. As we are not using a centrifuge, the gravity in the model will be normal gravity. Results would be only qualitative one and not quantitative.

The geometry scale factor may range up to 1/50. With a size of 2 m by 3 m in the horizontal plan for a thickness up to 1 m, we would be able to represent a soil block as large as 100 m by 150 m with a height of 50 m. With the 1 g gravity, the main consequence is that for high scale factor values, the difference between the achieved values of stresses and the normally scaled ones become very large and might cause some important differences.

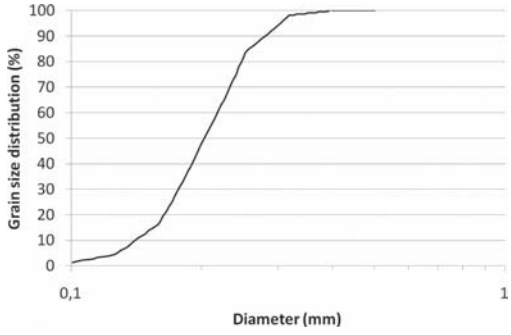

Figure 1. Grain size distribution of the Fontainebleau sand.

To take into account the high magnitude of subsidence, mines and quarries as cavities being at the origin of the ground movements caused by their collapse, the maximal depth of 50 m may appear like a serious limit for this model. However, we choose not to model the cavity itself but only the equivalent void raising to the ground surface. This is achieved by the use of electric jacks with a vertical moving trap-door. The apparatus is designed to be equipped with 48 jacks at most, in a configuration of 6 rows of 8.

The model is still being in an early stage of development, only one jack is installed. The cross-section of the actuator is limited to 250×250 mm², corresponding to up to 12.5×12.5 m². The apparatus is indeed limited to localized phenomena: sinkhole or collapse/subsidence of small-extent. When more jacks would be installed, various shapes of collapse/subsidence would be able to be modeled.

Up to 48 jacks may be installed on the apparatus. The purpose is to be able to model, for example, a chosen area from a subsidence trough observed in a mining basin and then to study the effects of this particular trough on the buildings and the protection potential of several mitigation techniques.

3.2 *Material*

The soil used is the Fontainebleau sand, category N34. The grain size distribution and the mechanical properties are reported in Figure 1 and Table 1 respectively.

3.3 *Monitoring*

Measurement of surface displacements is achieved by the mean of stereo digital imagery. This allows

Table 1. Mechanical characteristics of the sand.

	Density	E (MPa)	φ (°)	c (kPa)
Sand	1.6	5–20	35–37	0–2

monitoring the whole top surface of the ground and more especially where ground movements happen. A commercial product is chosen, Vic3D from Limess Gmbh, being very effective in the task of computing the movements with the grains of sand showing very low contrast on the photos.

Two cameras, 4 MP each, are used. They allow a maximal frequency capture of 8 images/second at full resolution, with the possibility to reach 30 images/second with a 1 MP resolution. They have to be calibrated before the start of a test by the use of a test pattern. A good calibration allows obtaining very precise measurements with an error of 1/100 of a pixel in good conditions: that's 10 μm when 1 pixel is equal to 1 mm. In the tests presented later in this paper, we have a ratio close to 2 pixels per millimeter. But, due to the nature of the sand, constituted of small particles and so not a continuous media, the corresponding maximal error is around 0.10 pixel giving 0.05 mm: this is quite a good performance (White et al. 2003).

One disadvantage of this method of monitoring is the huge volume of data created by a single test. With a volume of 8 Mo per capture (two images of 4 Mo each) and considering the full speed frequency of capture, it represents near 2 Go of raw data to be stored each minute. For a full test and with the exploitation files for the digital correlation process, this corresponds to a total between 30 and 40 Go.

3.4 *The building model*

A building model corresponding to an individual house had to be created to be used in the tests in order to study the effects of the soil-structure interactions during the happening of a subsidence trough and after what the effects of this ground movement on the structure.

Geometry was chosen for this building. Inspired from the database existing on the building damaged by mine subsidence in the east of France, like Lorraine basin, a house is considered, whose characteristics are shown in Figure 2 (Deck et al. 2003).

While it is not possible to make in a direct way a 3D realistic small-scale model of this structure, we have to simplify it. For the first campaign of tests, we chose to consider only an elastic behavior and to use an equivalent slab. The followed process to simplify the building and to obtain the small-scale model is presented on Figure 2.

Three steps compose it: first, the equivalent slab is determined such as the bending stiffness and the

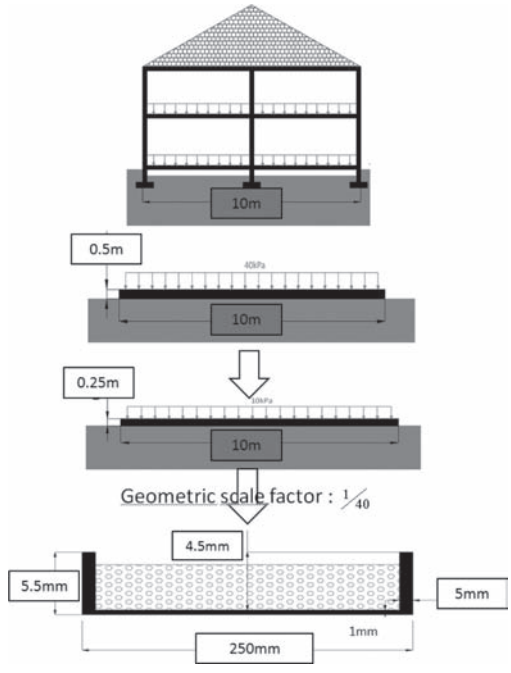

Figure 2. Simplification procedure of the 3D building to an equivalent small-scale slab.

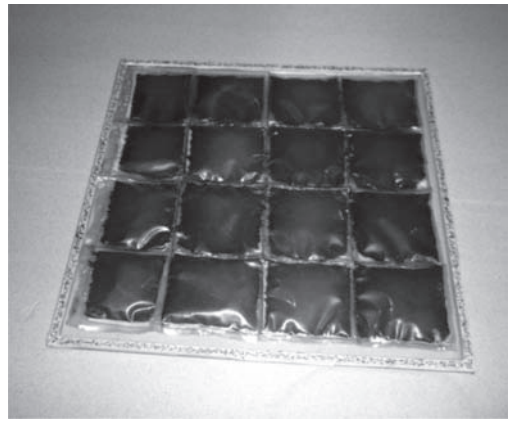

Figure 3. The resulting small-scale structure model composed of a hollow slab and small bags of lead powder representing the load.

axial stiffness of this slab are quite equivalent to the 3D structure. Then we choose to reduce the stiffness, in both directions, in order to exacerbate the strains in the structure. Both stiffnesses are approximately halved. From this very simple structure at prototype scale, a small scale model is conceived by applying the scale factors.

As shown on Figure 3, two parts are used for the structure model. The first one is a hollow slab

while the second one is composed of lead powder in a plastic bag. This allows the model to present a stiffness and a stress transmitted to the ground equivalent to the prototype's ones.

This small scale model is laying on the ground without taking into account any foundation parts. This is limiting the interaction between the soil and the structure. However, this procedure makes it very simple to reproduce on several tests. The next small-scale building model should emphasize a foundation system so as to respect a configuration closer from the reality.

3.5 *Achievement of a test*

The sand is manually put in the apparatus by layers if 15 cm thick. Each layer is compacted by a compacting tool equipped with 15 cm long needles in order to ensure a certain level of density, repeatable for each different test. This is repeated until the total height of the soil layer is reached, in our case, 30 cm. Afterwards a 130 cm wide rule is used to obtain the right level on the whole ground surface.

A snapshot is then taken by both cameras to insure that the ground surface is flat enough with a difference less than 5 mm in altitude between the points the highest and the lowest. The building model is then placed delicately on the ground surface, its position depending from the modeled case (see part 4 of this paper).

The acquisition by the two cameras is then started with a frequency of 0.5 Hz. The motion program of the jack is launched at the same time a snapshot is taken by the camera. The jack is moved down at a speed of 0.125 mm/second for a total of 30 mm.

At the end of the test, the displacements of the ground and the structure are computed by the DIC program.

4 RESULTS OF THE TESTS CAMPAIGN

This campaign is dedicated to the study of the influence of the building position relative to a subsidence trough. After the presentation of the reference result, the subsidence trough in greenfield condition, the results from the parametric study are presented.

4.1 *Greenfield condition*

Four identical tests were performed in order to ensure a good level of repeatability. As shown on Figure 4, the greenfield trough is symmetric. The average global characteristics are summarized in Table 2, which S_{max}, i, R_{max}, α and ε_h are respectively

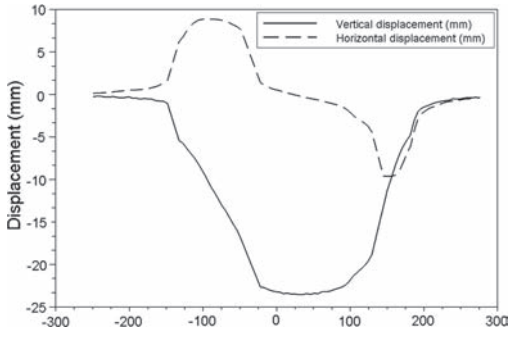

Figure 4. Displacements in Greenfield condition.

Table 2. Geometric characteristics of the surface ground displacement.

Characteristics	Average
S_{max}	96 cm
i	4 m
R_{max}	44 cm
α	21.6%
ε_h	–10.5%

the maximum settlement, the distance to the point of inflexion, the maximal horizontal displacement, the maximal slope and the maximal horizontal strain). The indicated values are in prototype scale (1/40 geometric scale). Differences from one test to another are not very important, but cannot be neglected; it is less than 15% of variation.

4.2 *Parametric study*

Three positions are used for the building model. They are defined with respect to the main component of the subsidence trough. Position n°1 is where the slope is the greatest, position n°2 correspond to the building being on the extension area and position n°3 puts the building completely in the compression area. Figure 5 presents these three different positions. Three particular axes are then defined for the exploitation of the results. They are chosen so that they go from the center of the building to the center of the subsidence trough.

Four tests are performed for each position of the building, as for the greenfield condition. Results are then presented for two points of view. First the displacement measured at ground surface will be compared in order to identify the effect of the building on the ground behavior. Secondly some light will be shed on the strains in the building model.

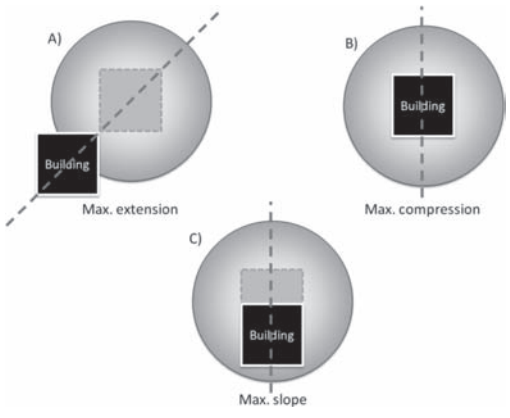

Figure 5. Building position for the parametric study.

4.2.1 *Ground behavior*

The building engenders some important differences in the soil displacement at ground surface. The trough, formerly symmetric in greenfield condition, shows clearly some dissymmetry. However, the building being in B position, centered in the subsidence trough, does not break the symmetry. Two examples of ground displacement curves are shown on Figure 6, corresponding to the axis plotted for the positions A & C of the building.

It appears that the soil movements are reduced due to the effect of the soil-structure interaction. Different areas may be distinguished, depending on the relative displacement of the ground to the building model. In the center part of the trough, the ground falls off the building due to a more important displacement, while on the other side of the building, its rotation causes another detachment.

4.2.2 *Consequences on the building*

The optical measurement setting allows catching the movements and the strains of the building. Those measures are synthesized in Table 3 concerning the main strain modes for a building. It can be seen that the measured strains are very small. Several reasons are identified:

- The elastic behavior chosen for the building model;
- The fact that the building is just laying on the ground surface;
- The stiffness of the building being too important.

The soil-structure interaction is thus clearly identifiable: the behavior of the soil is modified in an important manner due to the presence of the building, and consequently the strains measured in the structure are different from those calculated using the ground displacement in Greenfield condition.

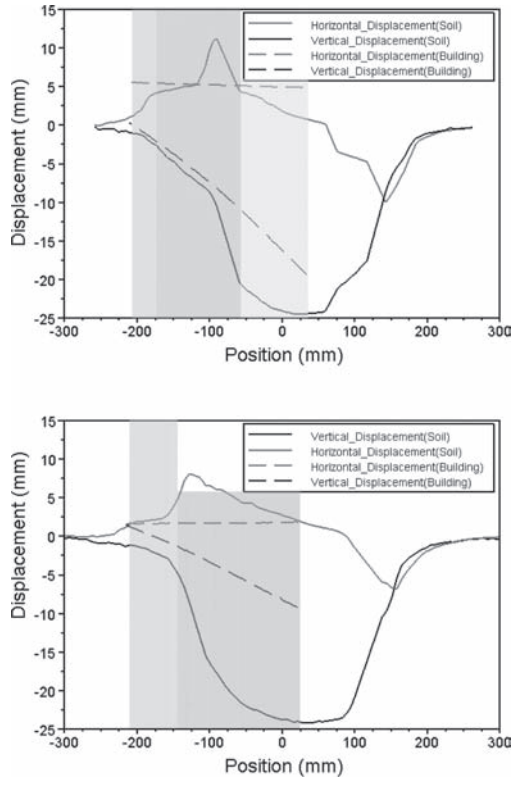

Figure 6. Behavior of the ground for two different positions of the building (top: pos. A; down: pos. C).

Table 3. Comparison between the strains determined in greenfield and ISS conditions.

Case	Horiz. strain	Bending radius	Slope
	(%)	(m)	(%)
Greenfield (pos. A)	–5	–	21.6
ISS (pos. A)	–0.21	–	6.4
Greenfield (pos. C)	–10.5	–1.67	21.6
ISS (pos. C)	–0.24	–9.42	11.1

5 CONCLUSIONS AND PROSPECTS

This study presents a new apparatus allowing to model ground movements caused by the collapse of underground cavities. A simple structure model, conceived in order to stand for a personal housing, is used with two purposes: observe the evolution of the ground movements in presence of the building and its behavior; highlight the importance of the soil-structure interaction.

As a conclusion for this study, we would like to emphasize the fact that these tests represent the

first step of a more global research for the consequences of ground movements on building, by taking into account the soil-structure interactions. It was established than the soil-structure phenomenon must not be neglected and that it depends greatly of the relative position of the building in the subsidence trough.

Still, many technical improvements must be brought to the small-scale physical model. The initial state of the sandy soil must be clarified and several jacks will be set up to increase the variety of subsidence trough geometry that the apparatus is able to achieve.

However, in parallel, the structure model should be improved in order to represent in a more realistic way a building. The main points are the design of the foundation system and of the upper part of the structure. Afterwards a new test campaign may be set up with the final objectives to study the performance of mitigation techniques.

ACKNOWLEDGEMENT

The authors would like to thank the French Ministry for Environment, Sustainable Development and the Sea for the partial founding of this research program.

BIBLIOGRAPHY

Abbass-Fayad, A. 2004. Modélisation numérique et analytique de la montée de cloche des carrières à faible profondeur. Etude de l'interaction sol-structure due aux mouvements du terrain induits par des fontis. *Institut National Polytechnique de Lorraine. PhD Thesis*.

Burd H.J., Houlby G., Augarde C., Liu G. 2000. Modelling tunneling-induced settlement of masonry building. *Proc. Inst. Civ. Eng. Geotech. Engng*, 143:17–29

Bransby M., Davies M. and Nahas A. 2008. Centrifuge modelling of normal fault-foundation interaction. *Bull. Earthquake Eng*. 6:585–605.

Bransby M., Davies M., Nahas A. and Nagaoka S. 2008. Centrifuge modelling of reverse fault-foundation interaction. *Bull. Earthquake Eng*. 6:607–628.

Castro R, Trueman R, Halim A. 2007. A study of isolated draw zones in block caving mines by means of a large 3D physical model. *Int J Rock Mech Min Sci 2007*;44:860–70.

Caudron M., Emeriault F., Kastner R. & Al Heib M. 2006a. Sinkhole and soil-structure interactions: Development of an experimental model. *Int. Conf. on Physical Modeling in Geotechnics, Hong-Kong*, 04–06 Aug. 2006, pp 1261–1267.

Caudron M., Emeriault F. & Al Heib M. 2007. Contribution of the experimental and numerical modeling to the understanding of the soil-structure interaction during the event of a sinkhole. *ECSMGE 2007, Madrid*.

Deck O., Al Heib M., and Homand F. 2003. Taking the soil-structure interaction into account in assessing the loading of a structure in a mining area. *Engineering Structure* 25:435–448.

Deck O. and Anirudth 2010. Numerical study of the soil-structure interaction within mining subsidence areas. Computers and Geotechnics. Article in Presse.

Dimmock P. and Mair R. 2008. Effect of building stiffness on tunnelling-induced ground movement. *Tunnelling and Underground Space Technology* 23 (2008) 438–450.

Dyne L. 1998. The prediction and occurence of chimney subsidence in southwestern Pennsylvania. *Master Thesis from Virginia Polytechnic Institute and State Faculty*.

Genis M. & Aydan O. 2008. Assessment of dynamic response and stability of an abandoned room and pillar underground lignite mine. *12th IACMAG, Goa, India*, pp 3899–3906.

Lee, Y. & Bassett, R. 2007. Influence zones for 2D pile-soil-tunnelling interaction based on model test and numerical analysis. *Tunnelling and Underground Space Technology*, 22, 325–342.

Nakai, T.; Xu, L. & Yamazaki, H. 1997. 3D and 2D model tests and numerical analyses of settlements and earth pressures due to tunnel excavation. *Soils and Foundations*, 37, 31–42.

Potts D. and Addenbrook T. 1997. A structure's influence on tunnelling induced ground movements. *Proc. Inst. Civ. Eng. Geotech. Eng*. 125 (2), 109–125.

Ren W., Guo C., Peng Z. and Wang Y. 2010. Model experimental research on deformation and subsidence characteristics of ground and wall rock due to mining under thick overlying terrane. *Int. J. Rock Mec. & Mining Sc*. 47 (2010) 614–624.

Shahin, H., Nakai, T. Hinokio, M. Kurimoto, T. and Sada, T. 2004. Influence of surface loads and construction sequence on ground response due to tunnelling. *Soils and Foundations*, 44:71–84.

Standing J. 2008. Impact of underground works on existing infrastructure. *Post-Mining'08, Nancy (France)*. Invited Lecture.

Sung, E.; Shahin, H.; Nakai, T.; Hinokio, M. & Makoto, Y. 2006. Ground behavior due to tunnel excavation with existing foundation. *Soils and Foundations,* 2:189–207.

Trueman R., Castro R, & Halim A. 2008. Study of multiple draw-zone interaction in block caving mines y means of a large 3D physical model. *Int. J. of Rock Mechanics and Mining Sciences* 45 (2008) 1044–1051.

White D., Take W. and Bolton M. 2003. Soil de formation measurement using particle image velocimetry (PIV) and photogrammetry. *Geotechnique*, 53:619–631.

Geotechnical Aspects of Underground Construction in Soft Ground – Viggiani (ed)
© 2012 Taylor & Francis Group, London, ISBN 978-0-415-68367-8

Experimental and numerical study of grout injections in silty soils

L. Masini & S. Rampello
"Sapienza", University of Rome, Italy

G.M.B. Viggiani
"Tor vergata", University of Rome, Italy

K. Soga
University of Cambridge, Cambridge, UK

ABSTRACT: Compensation grouting is increasingly employed as a mitigation technique of settlements induced by tunnelling and its effectiveness both in clayey and sandy soils is reported in a wide number of case histories. However, the results are highly dependent on grout properties, injection characteristics and soil properties. An experimental study was conducted to investigate the parameters that control grout injections in silty soils. The results from one injection test in a large sample of silty soil show that the compensation efficiency, defined as the ratio of the volume of heave obtained at ground surface and the injected grout volume, is much lower than one and tends to decrease with time, while the initial volume of grout lost due to pressure filtration is small. Finally, results from finite elements back analyses of the laboratory test show that a good agreement with the experimental data can be obtained if the development of large strains is taken into account.

1 INTRODUCTION

Compensation grouting has become a widely used technique to protect existing structures from excessive settlement induced by tunnelling carried out in densely built urban areas. Figure 1 shows a scheme of application of compensation grouting to compensate for tunnelling induced settlements. Basically, grout is injected in the zone between the tunnel crown and the foundations of the structure to compensate for the stress relief due to the excavation process (Mair & Hight 1994). The injection is carried out through sleeved tubes (*tubes à manchette*) which can be installed from a vertical shaft in a fan shaped array.

The effectiveness of compensation grouting can be quantified using the compensation efficiency ξ, defined as the ratio of the volume of heave obtained at ground surface, V_{SH}, and the injected grout volume, V_{inj} (Au *et al*. 2002):

$$\xi = V_{SH}/V_{inj}$$

Ideally, if soil deformation due to the injection process occurred in undrained conditions, ξ would be equal to one, as the volume of injected grout would produce the same amount of heave at ground surface. In practice V_{SH} is always less than V_{inj} ($\xi < 1$) because of volume loss due to several reason. In normally consolidated clayey soils it has been shown (Au 2001, Au *et al*. 2003) that ξ decreases with time due to soil consolidation, as positive excess pore water pressure is induced during the injection process. Long term efficiency could even reach negative values, *i.e.* grout injections could produce long term settlements rather than heave.

In sandy soils, the experimental findings (McKinley 1993, McKinley & Bolton 1999, Sanders 2007, Bezuijen *et al*. 2007, Eisa 2008) show that the injection pressure causes a mixture of water and finer particle to filtrate from the grout body into the adjacent sand pores. Compensation efficiency reduces as pressure filtration occurs. The amount of fluid lost by pressure filtration depends on the grout water-cement ratio and bentonite content, and on the injection rate. Eisa (2008) has shown that fast injections of grout with relatively high bentonite content and water-cement ratio result in low volumes lost by pressure filtration and high compensation efficiencies.

This study focuses on grout injections in silty soils. To this aim, laboratory grout injections tests

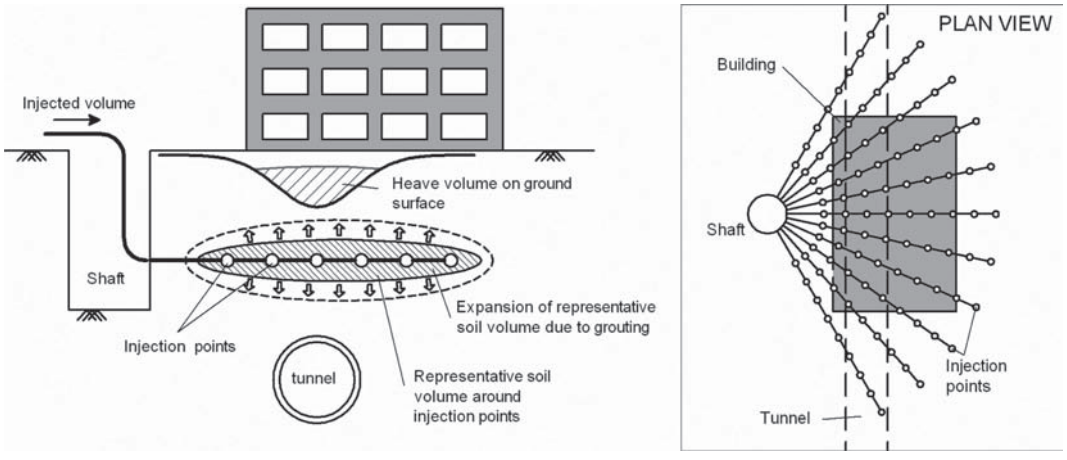

Figure 1. Schematic field layout of grout injection to compensate for tunneling induced settlement.

were preformed in a large sample of normally consolidated silty soil. The injection pressure, the sample surface displacements, the volume of fluid drained from the sample, and the stresses and pore water pressures at different locations in the sample were measured during and after the tests. In the following, the results of the tests are first illustrated and then compared to the experimental findings obtained for grout injections in clayey and sandy soils.

Finite-element analyses were also conducted to simulate the grout injection test. The results of these analyses are compared with the experimental data in terms of ground surface displacement, excess pore water pressure and stress changes. The analyses were carried out assuming large strains.

2 EXPERIMENTAL WORK

2.1 *Testing apparatus and methods*

The laboratory investigation was conducted at the Schofield Centre of the University of Cambridge (UK). The experimental setup used for the grout injection test is shown in Figure 2. A cylindrical steel tub with an internal diameter of 850 mm and a height of 400 mm is used to contain the sample. Drainage of fluid from the sample is allowed from the base of the tub through a drainage layer, consisting of sand, gravel, geotextile, and filter paper. A confining pressure is applied to the top of the sample by inflating with pressurised air a rubber bag fixed to the inner side of the tub cover. An open-ended metallic tube (inner diameter 7.5 mm, external diameter 12.5 mm) was used to inject the

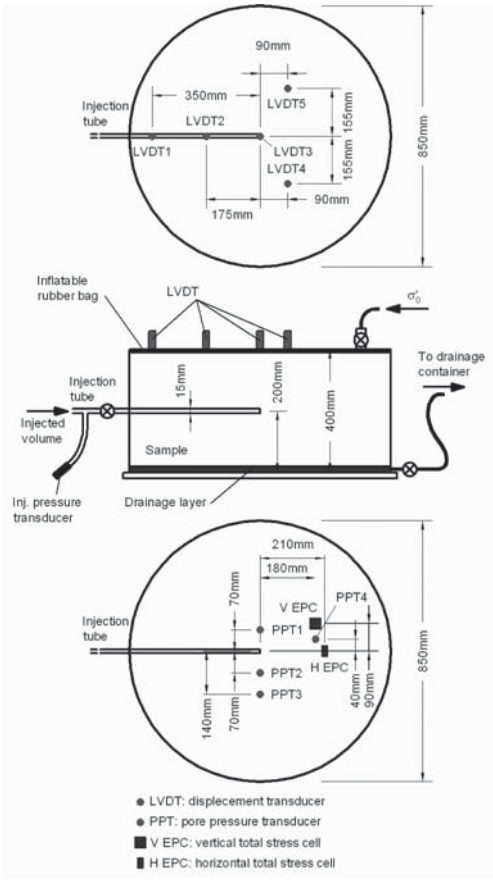

Figure 2. Experimental setup and instruments location.

grout. The injection point is located approximately at the centre of the sample. Grout is injected using a progressive helical cavity pump. Five displacement transducers (LVDTs), located in the positions shown in Figure 2, are used to measure the displacements at the sample surface during and after the injection. The spindle of each LVDT passes through a hole in the cover of the tub and rests on a thin latex membrane sealed on the sample surface to prevent water from leaking out. The rubber bag used to apply the confining pressure is sealed around the five LVDTs spindle holes. Two earth pressure transducers (EPCs) for the horizontal and vertical total stress and four pore water pressure transducers (PPTs) are installed inside the tub at the level of the injection point and at different distances from it. A pressure transducer (PT) installed along the injection tube, just outside the tub, measures the injection pressure.

The grout injection test was performed in a large sample of silica flour.

Table 1 lists the physical properties of type 3045/300 silica flour ($D_{10} = 7\,\mu m$, $D_{50} = 16\,\mu m$) which was used in the experiment (Silva 2005). The sample was prepared from a slurry with a water content of 58%, or twice the liquid limit. The slurry was poured into the tub and vibrated, and then allowed to sediment under its own weight overnight. Finally, the slurry was consolidated to the confining pressure chosen for the test (100 kPa in this case). After the test, measurements of void ratio made on the soil extracted from two boreholes located away from the injection body showed a good homogeneity of the sample, with an average void ratio of 0.83.

Grout is a mixture of water, cement and bentonite. Before the test, the bentonite was allowed to hydrate for 24 hours, and then mixed with cement using a high shear mixer. A total volume of 1000 cm^3 of grout was injected at a constant rate of 47.8 cm^3/s under a confining pressure σ_{conf} = 100 kPa, applied at the top of the sample. A relatively fluid grout was injected (water cement ratio $a/c = 1.8$), with a bentonite content equal to 8% of the weight of water.

For ease of reference, Table 2 summarises all the main parameters of the test; further experimental details can be found in (Au 2009 and Masini 2010).

Table 1. Physical properties of silica flour (Silva 2005).

Specific gravity of soil particles	G_S	2.652
Liquid limit	w_L	29%
Plastic limit	w_P	27%
Plasticity index	I_P	2%
Minimum void ratio	e_{min}	0.72
Maximum void ratio	e_{max}	1.83

Table 2. Parameters of the injection test.

Sample void ratio	e_0	0.83
Confining pressure	σ_{conf}	100 kPa
Injection rate	v_{inj}	47.8 cm^3/s
Injected volume	V_{inj}	1000 cm^3
Grout water-cement ratio	a/c	1.8
Grout bentonite-water ratio	b/a	8%

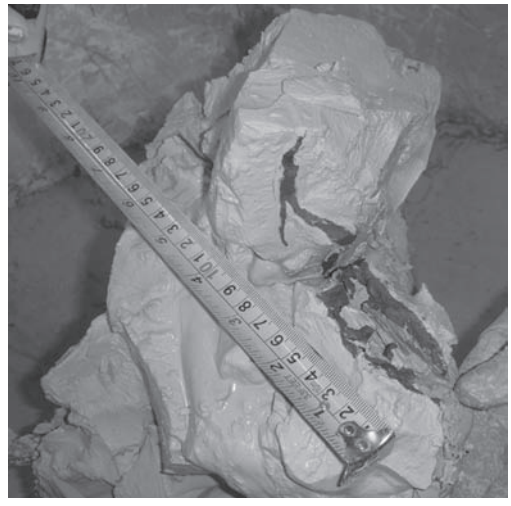

Figure 3. Grout injection in silt.

2.2 *Results*

Figure 3 shows the exhumed injection body 24 h after the test; a narrow fracture was observed to develop almost vertically from the injection point. Propagation of grout within the soil is influenced by the stress state in the soil. In fact, it has been found that fracture orientation is parallel to the major principal stress, in this case the vertical one (Jaworski *et al*. 1981, Mori & Tamura 1987, Mhach 1991, Murdoch 1993, Yanagisawa & Ali 1994).

Previous experimental findings (Sanders 2007, Eisa 2008) show that high viscosity grouts propagate close and uniformly around the injection point, while low viscosity grouts result in soil fracturing. Since grout viscosity increases with the volume of grout fluid lost by pressure filtration, the way grout propagates within soil is affected by pressure filtration. This feature can hardly be applied to clayey soil, as their low permeability permits only a very slow filtration to take place from the injection body.

Figure 4 shows the grout body from a test carried out using the same experimental setup, with the same grout and injection parameters listed in Table 2, but in dense sand (Eisa 2008, Masini 2010). In dense sand (relative density of 90%),

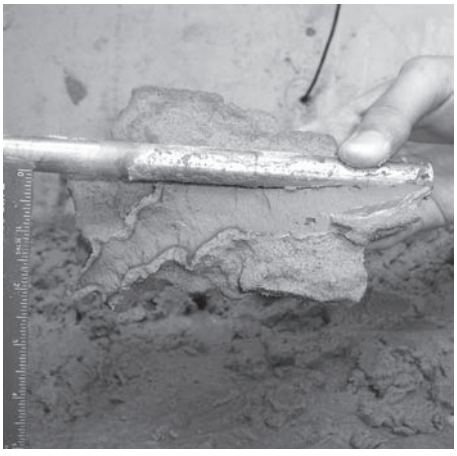

Figure 4. Grout injection in sand (Gafar 2008, Masini 2010).

grout viscosity increased significantly during the injection process because of pressure filtration, causing thick fractures into the soil. Conversely, in silty soil, the volume of grout fluid lost by pressure filtration during the injection process was negligible (see Figure 5) and grout viscosity was low enough to create narrow fractures. Similar findings have been obtained in clayey soils (Au 2001).

Figure 6 shows the displacement contours and profiles at the top of the sample measured at the end of the injection process. Positive displacements indicate heave. The compensation efficiency ξ was estimated from the ratio of heave to injected volumes.

The maximum heave ($w = 2.36$ mm) was obtained above the injection points. Major displacements were also observed along the injection tube due to some grout propagation just underneath the injection tube. This zone, indeed, is the most affected by the presence of the injection tube during sample preparation. This aspect together with the development of vertical fractures and the possible presence of some air bubbles in the system, resulted in low compensation efficiency ($\xi = 26\%$).

Figure 7 shows time variation of compensation efficiency ξ and the results obtained by Au (2001) injecting different fluids (grout with different water-cement ratio, epoxy resin and water) in normally consolidated (OCR = 1) samples of kaolin. Compensation efficiency decreases with time due to dissipation of the positive excess pore water pressure induced during injection, as shown in Figure 8. The long-term efficiency in silt ($\xi = 13\%$, $t = 12000$ s) was half the value at the end of injection process ($\xi = 26\%$), whereas large negative long-term values of ξ were obtained in clay, meaning that injections eventually caused settlement rather than heave. Therefore, even if compensation efficiency sensibly

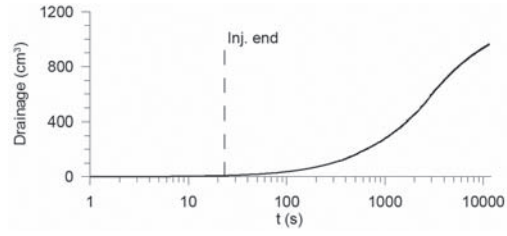

Figure 5. Volume of fluid drained from the sample.

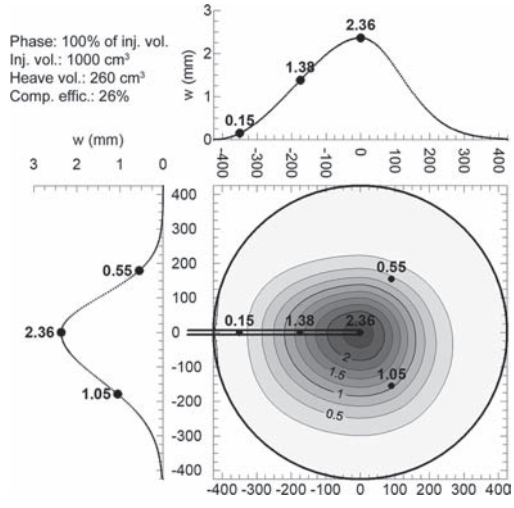

Figure 6. Displacement isolines (mm) and profiles at the top of the sample, obtained at the end of the injection process.

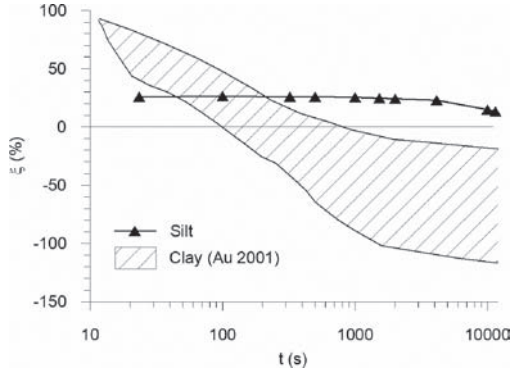

Figure 7. Time variation of compensation efficiency in normally consolidated (OCR = 1) samples of silt and clay (Au 2001).

decreases with time because of consolidation, it can be thought that long-term efficiency in normally consolidated silty soils is still positive, unlike what is observed for clayey soils.

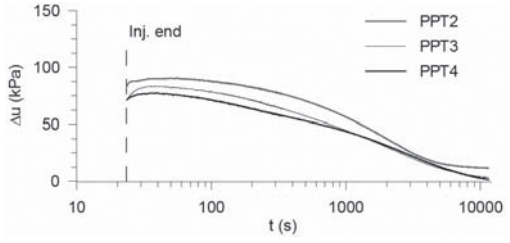

Figure 8. Excess pore water pressure measured after injection.

3 NUMERICAL SIMULATION

A numerical simulation of the injection test was carried out using the finite element method. The propagation of grout into the soil is a very difficult phenomenon to model, therefore a simple cavity expansion is introduced here to model the injection process. The study aims to asses whether it is possible to use a simple model to reproduce the effects induced by grout injections in terms of displacements, stress state and pore water pressure changes.

The axisymmetric model used for the numerical investigation of the injection test is shown in Figure 9. The mesh has a radius of 425 mm and a height of 360 mm reproducing the size of the tub used in the experiments. The initial radius of the injection cavity was taken to be equal to the radius of the injection tube (6 mm). The injection point is located at the centre of the axis of symmetry. Displacements at the base were fully constrained, while only vertical displacements were allowed along the left boundary. The interface between the soil and the container at the right boundary was modelled as an interface with reduced strength and stiffness parameters. Interface displacements are fully constrained at the right boundary.

The water head was located at the upper boundary and hydraulic flow was allowed through the lower boundary only. A 100 kPa confining pressure was applied to the upper boundary.

The injection body was modelled as a non-porous linear elastic material, with the same unit weight γ and Poisson's ratio ν of the soil, while the Young's modulus was chosen in order to optimise the calculation process, as preliminary analyses showed that the mechanical behaviour of the grout only affects the calculation time.

The mechanical behaviour of the soil was described by an elastic-plastic model with isotropic deviatoric hardening (*Hardening Soil*, HS, Schanz *et al*. 1999), implemented in the finite element code PLAXIS used for the analyses. The model is capable of reproducing soil non-linearity due to the occurrence of plastic strains from the beginning of the loading process. The elastic behaviour is defined by isotropic elasticity through a stress-dependent Young's modulus:

$$E' = E^{\text{ref}} \left(\frac{c' \cdot \cot \varphi' + \sigma_3'}{c' \cdot \cot \varphi' + p^{\text{ref}}} \right)^{\text{m}} \tag{1}$$

where σ'_3 is the minimum principal effective stress, c' is the cohesion, φ' is the angle of shearing resistance, $p^{\text{ref}} = 100$ kPa is a reference pressure; E^{ref} and m are model parameters.

The model has two yield surfaces, f_s and f_v, with independent isotropic hardening depending on deviatoric plastic strain γ^{p} and on volumetric plastic strains $\varepsilon^{\text{p}}_{\text{v}}$, respectively. Figure 10 shows the shape of the yield surfaces and schematically indicates their evolution.

The deviatoric hardening rule is related to parameter E'_{50}, while the volumetric one is controlled by parameter E'_{oed}. Both of them are given by expressions similar to Eq.(1) but, in contrast to E', they are not used within a concept of elasticity. The flow rule is associated for states lying on the surface f_v, while a non-associated flow rule is used for states on the surface f_s.

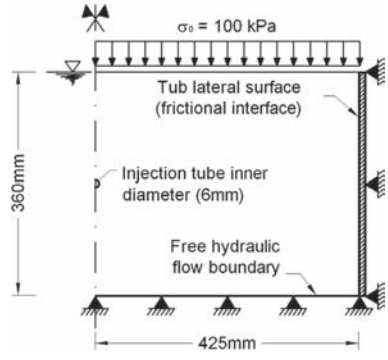

Figure 9. Finite element model for grout injection test simulation.

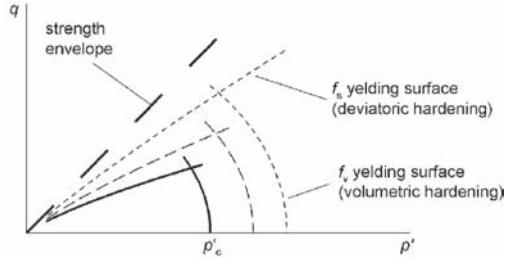

Figure 10. Yied surfaces of the Hardening Soil model and their evolution.

A feature of HS model is that under monotonic loading it can account for non-linear stress-strain behaviour, and for the occurrence of irreversible strains from the beginning of the loading process; this implies that for undrained conditions an increase of deviatoric stress q produces excess pore water pressure.

A dilatancy cut-off was introduced defining a state of density where dilatancy ends after extensive shearing. To this aim, an initial void ratio e_{init}, and a maximum void ratio e_{max} were specified. Starting from e_{init}, volume changes result in a state of maximum void e_{max}, at which the mobilised dilatancy angle ψ is set to zero.

Soil parameters were calibrated using the results of standard drained triaxial tests (TX-CID) carried out by Silva (2005) on reconstituted samples of silica flour, normally consolidated at p'_0 = 50, 100 and 200 kPa.

Since E' represents the tangent initial Young's modulus of the stress-strain curve, it has been related to the shear modulus at small strains G_0. Specifically, E'^{ref} and m were estimated from the relationship proposed by Silva (2005):

$$\frac{G}{p_a} = 300\left(\frac{p'}{p_a}\right)^{\frac{2}{3}} \tag{2}$$

where p_a is the atmospheric pressure. The remaining model parameters were calibrated best-fitting the TX-CID tests results.

Figure 11 shows the comparison between model simulations and tests results. A fair agreement between experimental data and model prediction can be obtained using the values listed in Table 3. The value of e_{init} was obtained by averaging the values of void ratio at the beginning of the deviatoric phase in the TX-CID tests. The coefficient of earth pressure at rest K_0 was estimated from:

$$K_0 = (1-\sin\varphi')\cdot OCR^{\sin\varphi'}$$

Figure 12 shows a comparison between Eq.(2) and HS model prediction (Eq.(1)), computed using the values in Table 3. A fair agreement is obtained for p' > 100 kPa.

In order to account for the different densities of triaxial test samples ($D_{R,1}$ = 100%) and the injection test sample ($D_{R,2}$ = 90%), the strength and stiffness parameters in Table 3 were corrected according to Bolton (1986):

$$\begin{aligned} &\varphi' - \varphi'_{cv} = 3DI \\ &DI = D_R\left(10 - \ln p'_f\right) - 1 \end{aligned} \tag{3}$$

where DI is a dilatancy index empirically related to the relative density D_R and to the mean effective stress at failure p'_f. Since φ'_{cv} is a state parameter, the relationship between the peak angle of shearing resistance and the relative density is obtained from Eq.(3), assuming a constant value of φ'_{cv}:

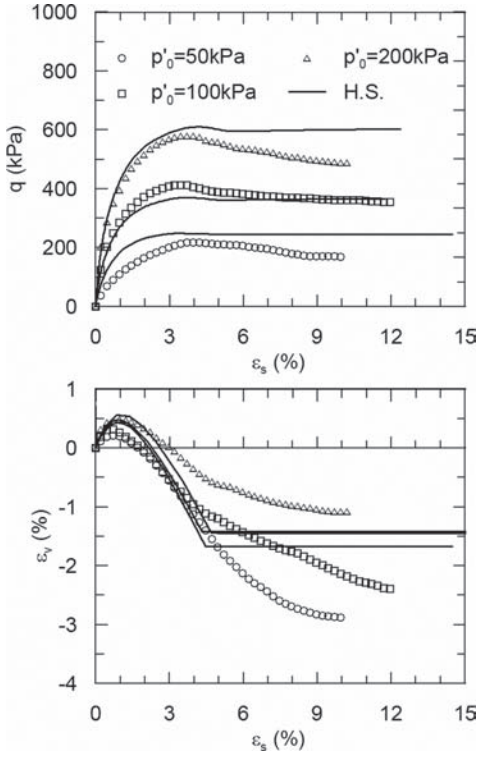

Figure 11. Comparison between TX-CID tests results and model simulation.

Table 3. Soil parameters for TX-CID tests F.E. simulation.

γ	19 kN/m^3
φ'	32.8°
c'	35 kPa
e_{init}	0.653
e_{max}	0.675
ψ	20°
ν	0.2
K_0	0.458
OCR	1
E'^{ref}	86,400 kPa
m	0.705
E'^{ref}_{50}	40,000 kPa
E'^{ref}_{oed}	22,000 kPa

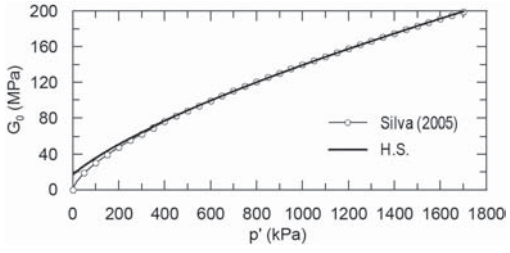

Figure 12. Comparison between Eq.(2) obtained by Silva (2005) and HS model prediction, Eq.(1).

$$\varphi'_1 - \varphi'_2 = 3(DI_1 - DI_2) \tag{4}$$

where the subscripts indicate that parameters are related to the two relative densities $D_{R,1}$ and $D_{R,2}$.

As Eq.(3) was proposed for purely frictional soils, values of φ'_1 = 38.1° and c'_1 = 0 kPa were obtained from TX-CID tests results. From Eq.(4), assuming p'_f = 237.8 kPa, it follows that φ'_2 = 37.08° and c'_2 = 0 kPa. The dilatancy angle ψ was set to zero since the initial void ratio of the injection test is higher than e_{max}. Finally, the stiffness parameters E'^{ref}, $E'_{50}{}^{ref}$ and $E'_{oed}{}^{ref}$ were scaled by the factor

$$\mu = \frac{q_{f,1}}{q_{f,2}} = \frac{M(\varphi'_1) + q_0(\varphi'_1, c'_1)}{M(\varphi'_2) + q_0(\varphi'_2, c'_2)} \tag{5}$$

where:

$$M = \frac{6\sin\varphi'}{3-\sin\varphi'}$$
$$q_0 = \frac{6c'\cos\varphi'}{3-\sin\varphi'} \tag{6}$$

For φ'_1=32.8°, c'_1=35 kPa, φ'_2=37.08°, c'_2=0 kPa, the following values were obtained: μ = 1.353, $E'_{50}{}^{ref}$ = 63,850 kPa, $E'_{50}{}^{ref}$ = 29,560 kPa and $E'_{oed}{}^{ref}$ = 16,258 kPa.

Soil parameters used for the analyses are listed in Table 4.

As the volume of fluid drained from the sample during the test was negligible, it was assumed that the injection process resulted mainly in distortional strains, with small volume change. Hence, the analyses were carried out assuming undrained conditions.

The injection process was simulated by sequential volume expansions of the grout body. Since the experimental results showed values of compensation efficiency lower than 100% (ideal undrained conditions), the calculations were carried out applying to the grout body a volume expansion equal to the heave volume obtained at the sample surface from LVDTs readings. The analyses were carried out in terms of effective stresses, removing the hypothesis of small strains. Thus, mesh nodes coordinates were updated after each calculation step, thus allowing for the development of large strains.

Figure 13 shows the displacement profile at the upper boundary (sample surface) and the LVDT readings at the end of the injection process. The maximum heave obtained from the numerical model is sensibly larger than the experimental value and major displacements are developed near the injection body. This may be due to the vertical fracture which developed up to the top of the sample and may have spread the heave profile. In addition, a zone close around the injection body was observed to occur, where the distortional strains induced by volume expansion were very high (ε_s > 100%). Outside this zone, numerical model prediction and experimental data are in a closer agreement.

Similar features can be observed from the excess pore water pressure and stress variations profiles obtained at the injection point level, as shown in

Table 4. Hardening soil parameters for F.E. simulation of the injection test.

γ	19 kN/m^3
φ'	37.08°
c'	0 kPa
ψ	0°
ν	0.2
K_0	0.397
OCR	1
E'^{ref}	63,850 kPa
m	0.705
$E'_{50}{}^{ref}$	29,560 kPa
$E'_{oed}{}^{ref}$	16,258 kPa

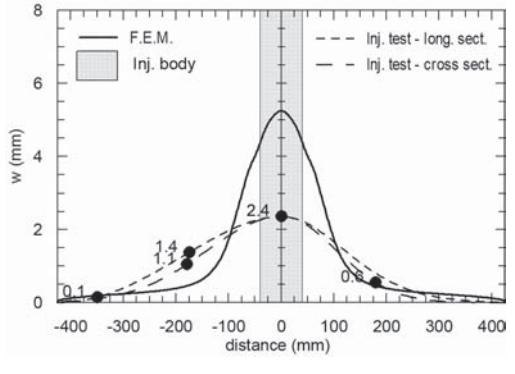

Figure 13. Surface displacements at the end of the injection.

Figure 14 and Figure 15. Within the zone of large strains, the numerical solution is not plotted since it is not accurate due to highly irregular trends. The computed excess pore water pressure and stress variations are larger than the experimental data

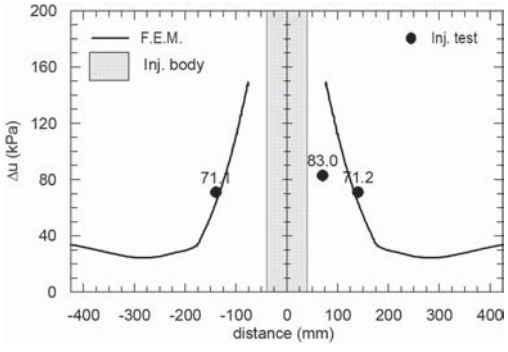

Figure 14. Excess pore pressure profile at the injection tube level, at the end of the injection.

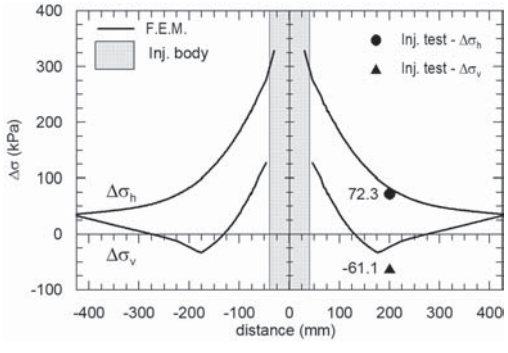

Figure 15. Stresses variation profile at the injection tube level.

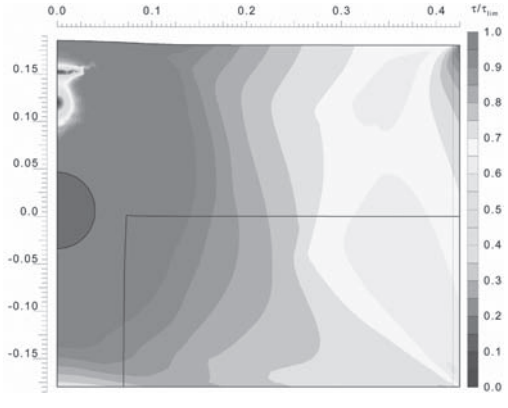

Figure 16. Mobilized shear strength contours at the end of the injection.

within a distance of about three times the injection body radius, with high gradients in the area closer to the injection body. However, a good prediction can be still obtained at greater distances.

Figure 16 shows the τ/τ_{lim} contours at the injection end. The grout expansion caused the complete mobilization of the shear stress in a large area around the injection body. The numerical results clearly show that the injection process involves the attainment of soil strength, with the development of large plastic strains.

4 CONCLUSION

The main features of grout injection in silty soil were investigated performing a laboratory injection test in a large reconstituted sample of silica flour. The experimental results show that, differently from what was observed in sandy soils, pressure filtration is negligible during the injection process, so that it does not affect grout propagation into the soil. On the other hand, it was confirmed that grout tends to develop into the soil parallel to the major principal stress.

The injection resulted in a low compensation efficiency (ξ = 26%). In addiction, data showed that the efficiency reduces with time for a normally consolidated sample, but less dramatically than what was found for clayey soils.

The injection process in silty soil was studied through a finite element analysis, simulating a cavity expansion. Specifically, the injection process was simulated by applying volume expansions to the grout body equal to the heave volume measured during the test at the top of the sample. In the analyses, the development of large strains was accounted for updating the mesh nodes coordinates after each calculation stage. The numerical results showed that the injection process induces large distortional strains in a zone around the injection body where the soil strength is fully mobilized and where displacements, excess pore water pressure and stress variations were sensibly higher than those measured. However, a satisfactory agreement with the experimental data can be achieved outside this zone, which extends about three times the radius of the injected body.

Even if the complex soil-grout interaction mechanism was not simulated, the results suggest that the effects of grout injections can be studied with simple models in term of stress changes and excess pore water pressure induced into the soil.

Although this study identifies some aspects of grout injections in silty soils, the interpretation of the test is limited by the scale of the laboratory tests. Further investigations are necessary to examine the applicability of the findings to the field scale conditions.

REFERENCES

Au, S.K.A. 2001. Fundamental Study Of Compensation Grouting In Clay. Ph.D. Thesis, University Of Cambridge. Cambridge, UK.

Au, S.K.A., Bolton, M.D. & Soga, K. 2002. Effect Of Multiple Injection On Long Term Compensation Grouting—Laboratory And Numerical Studies. *Proc. Geotechnical Aspects Of Underground Construction in Soft Ground*: 657–662. Lyon. Spécifique.

Au, S.K.A., Soga, K., Jafari, M.R., Bolton, M.D. & Komiya, K. 2003. Factors Affecting Long-Term Efficiency of Compensation Grouting In Clays. *ASCE, Journal Of Geotechnical And Geoenvironmental Engineering* 129(3): 254–262.

Au, W. 2009. An Experimental Study of Compensation Grouting in Silt, M.Phil. Thesis, University of Cambridge. Cambridge, UK.

Bezuijen, A., Sanders, M.P.M., Hamer, D.A. & Van Tol, A.F. 2007. Laboratory Tests on Compensation Grouting, The Influence Of Grout Bleeding. *Proc. 33rd Ita-Aites World Tunnel Congress*, *Prague.* Rotterdam: Balkema.

Bolton, M.D. 1986. The Strength and Dilatancy of Sand. *Géotechnique* 36(1): 65–78.

Eisa, K. 2008. Compensation Grouting In Sand. Ph.D. Thesis, University of Cambridge. Cambridge, UK.

Jaworski, G.W., Seed, H.B. & Duncan, J.M. 1981. Laboratory Study of Hydraulic Fracturing. *Asce, Journal Of Geotechnical And Geoenvironmental Engineering* 107(6): 713–732.

Mair, R.J. & Hight D.W. 1994. Compensation Grouting. *World Tunnelling:* 361–367.

Masini, L. 2010. Studio sperimentale della tecnica delle iniezioni di compensazione in terreni sabbiosi e limosi. Ph.D. Thesis, "Sapienza", University of Rome. Rome, Italy.

McKinley, J.D. 1993. Grouted Ground Anchors and the Soil Mechanics Aspects of Cement Grouting. Ph.D. Thesis, University Of Cambridge. Cambridge, UK.

McKinley, J.D. & Bolton, M.D. 1999. A Geotechnical Description of Fresh Cement Grout, Filtration and Consolidation Behaviour. *Magazine of Concrete Research* 51(5): 295–307.

Mhach, H.K. 1991. An Experimental Study of Hydraulic Fracture and Erosion. Ph.D. Thesis, City University. London, UK.

Mori, A. & Tamura, M. 1987. Hydrofracturing Pressure of Cohesive Soil. *Soils and Foundations* 27(1): 14–22.

Murdoch, L.C. 1993. Hydraulic Fracturing Of Soil During Laboratory Experiments—Part 1–3. *Géotechnique* 43(2): 255–287.

Sanders, M.P.M. 2007. Hydraulic Fracture Grouting, Laboratory Tests in Sand. M.Sc. Thesis, Delft University of Technology. Delft, the Netherlands.

Schanz, T., Vermeer, P. & Bonnier, P. 1999. Formulation and Verification of the Hardening-Soil Model. *Proc. Plaxis Symposium Beyond 2000 in Computational Geotechnics:* 281–296. Amsterdam, the Netherlands.

Silva, M.F. 2005. Numerical and Physical Models of Rate Effects in Soil Penetration. M.Sc. Thesis, University Of Cambridge. Cambridge, UK.

Yanagisawa, E. & Ali, K. 1994. Two Dimensional Study of Hydraulic Fracturing Criteria in Cohesive Soils. *Soils And Foundation* 34(1): 1–9.

This page intentionally left blank

Geotechnical Aspects of Underground Construction in Soft Ground – Viggiani (ed)
© 2012 Taylor & Francis Group, London, ISBN 978-0-415-68367-8

3D finite element analysis of deep excavations with cross-walls

S. Rampello & S. Salvatori
"Sapienza", University of Rome, Italy

ABSTRACT: Ground movements induced by deep open excavations retained by diaphragm walls may be substantially reduced using sacrificial cross-walls installed as props between the retaining walls. In this paper, a 3D finite element study is presented in which the retaining walls and the cross-walls are modelled using brick elements and accounting for the interfaces between the panels of diaphragm walls and of cross-walls. Influence of cross-walls spacing and length in reducing the horizontal deflection of diaphragm walls and the ground settlements behind the excavation is evaluated. Companion plane strain analyses, in which an homogeneous equivalent medium is considered in between the retaining walls, are also presented to assess the capability of 2D analyses to predict the performance of deep excavations in which cross-walls are used as a mitigation measure to reduce wall deflections and ground movements.

1 INTRODUCTION

Constructions of deep box excavation in soft ground generally result in ground movements that can induce significant damage to adjacent buildings and services. To reduce their impact, box excavations are usually retained by stiff diaphragm walls and props installed as the excavation progresses. However, vertical stress relief associated to excavation induces surface settlements even when the retaining walls are prevented from moving horizontally and deep-seated inward displacements of the walls that cannot be controlled by the props that are installed within the excavation itself (Burland et al., 1979).

To minimise the impact of deep excavations in urban areas, inward displacements of diaphragm walls and surface settlements around excavations may be reduced installing an internal support system below the formation level, prior to excavation. Such a system of deep in situ props may be constituted by tunnelled struts (Stevens et al., 1977; Bailey et al., 1999), ground treatment methods such as jet mechanical mixing (Osborne et al., 2009) and jet grouting, used to replace the soil below the final excavation level, or sacrificial cross-walls (Hsiung et al., 2001; Ou et al., 2006; Hsieh et al., 2008). Cross-walls can be formed by jet grouted columns or unreinforced panels installed with diaphragm walling equipment. They are installed between the perimeter diaphragm walls before the start of excavation and are excavated out with the soil down to the depth of the final excavation level. At the end of the excavation sequence, the only portion of the cross-walls remaining to resist to the horizontal deflection of the diaphragm walls is that eventually extending below the bottom of excavation.

In recent years, cross-walls have been often used in deep excavations in urban Taiwan area to reduce diaphragm wall deflections and associated ground movements. Well documented case histories permitted to assess the effectiveness of cross-walls in reducing excavation-induced displacements (Hsiung et al., 2001; Ou et al., 2006), provided that the joints between the perimeter diaphragm walls and the cross-walls are well constructed (Hsieh et al., 2008). The beneficial effects were evaluated by comparing horizontal wall deflections monitored at locations affected by the presence of cross-walls with those measured at sites with no special support (Hsiung et al., 2001) or computed under plane strain conditions assuming no cross-walls (Ou et al., 2011).

Effectiveness of cross-walls in reducing wall deflections and ground movements has been recently studied by Merrit et al. (2010) via 3D finite element analyses in which the retaining walls and the props were represented by shell elements and the cross-walls by membrane elements; specifically, influence of horizontal axial stiffness of cross-walls relative to that of perimeter retaining walls was assessed.

This paper deals with a 3D finite element study of deep excavations in which the diaphragm walls and the cross-walls are modelled using brick elements and the contacts between the corresponding panels are represented by interface elements.

Excavations were modelled without cross-walls and with cross-walls of different length, installed at different spacing. To assess the capability of 2D analyses to predict the performance of deep excavations with sacrificial cross-walls, plane strain analyses were also carried out in which an equivalent material is used to represent the soil and the cross-walls within the excavation.

2 PROBLEM DESCRIPTION

2.1 *Soil profile and constitutive model*

Ground conditions adopted in the analyses are representative of those encountered in the historical centre of Rome, close to the Tiber river. The soil profile shown in Figure 1 consists of medium dense gravelly Made Ground, with an average thickness of 9 m, overlying recent alluvial deposits of Pleistocene age. They consist of slightly overconsolidated clayey silt, about 6 m in thickness, medium dense silty sand, 15 m thick, normally consolidated silty clay, 27 m in thickness and sandy gravel, of 6 to 8 m thick. The gravel is underlain by a thick layer of stiff and overconsolidated silty clay of Pliocene age.

Figure 1 show typical profiles of tip resistance q_c measured by CPTU tests and of small-strain shear modulus G_0 as obtained by Cross Hole tests. The profile of pore water pressure was observed to be hydrostatic with hydraulic head at about the bottom of the Made Ground.

The mechanical behaviour of all soils was described using an elastic-plastic rate independent model with isotropic hardening (*Hardening Soil*, *HS*; Schanz et al. 1999), available in the model library of the code Plaxis. The model is capable of reproducing soil non-linearity due to the occurrence of plastic strains from the beginning of the loading process.

The elastic behaviour is defined by isotropic elasticity through a stress-dependent Young's modulus:

$$E' = E^{\text{ref}} \left(\frac{c' \cdot \cot \varphi' + \sigma_3'}{c' \cdot \cot \varphi' + p^{\text{ref}}} \right)^{\text{m}} \quad (1)$$

where σ'_3 is the minimum principal effective stress, c' is the cohesion, φ' is the angle of shearing resistance and p^{ref} = 100 kPa is a reference pressure; E^{ref} and m are model parameters.

The model has two yield surfaces, f_s and f_v, with independent isotropic hardening depending on deviatoric plastic strain γ^p and on volumetric plastic strain ε^p_v, respectively. The deviatoric hardening rule is related to parameter E'_{50}, while the volumetric one is controlled by parameter E'_{oed}. Both of them are given by expressions similar to Eq. (1) but, in contrast to E', they are not used within a concept of elasticity. The flow rule is associated for states lying on the surface f_v, while a non-associated flow rule is used for states on the surface f_s.

Under monotonic loading, *HS* model can account for non-linear stress–strain behaviour, with tangent initial modulus equal to E', and for the occurrence of irreversible strains from the beginning of the loading process. Upon unloading, the model assumes elastic behaviour with Young's modulus E', thus reproducing a significant change in stiffness.

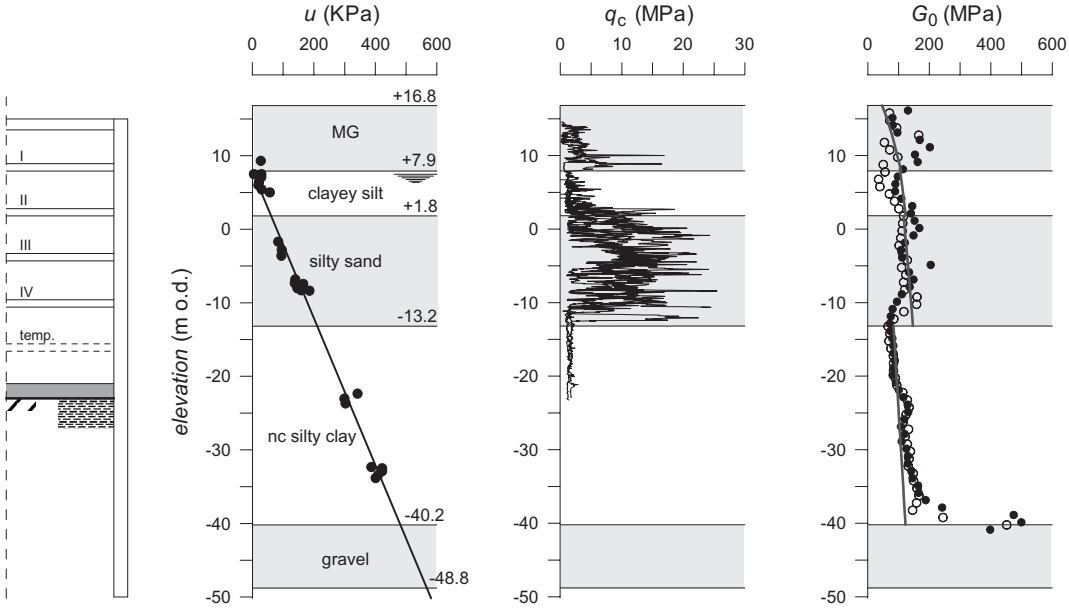

Figure 1. Vertical section of the excavation with soil profile.

Since E' represents the tangent initial Young's modulus of the stress-strain curve, it has been related to the shear modulus at small strains G_0 obtained from Cross Hole tests. In particular, values of E^{ref} and m were obtained by best fitting the cross-hole test results using Eq. (1) and assuming $\nu' = 0.2$. The continuous line in Figure 1 represents the prediction of G_0 obtained with the values of c', φ', E^{ref} and m reported in Table 1. Specifically, the values of σ'_3 needed for computing E' were obtained using the values of the coefficient of earth pressure at rest K_0 listed in the table.

It is worth mentioning that OCR has to be regarded as a Yield Stress Ratio (YSR) defined in the framework of strain hardening plasticity, so that values of $OCR > 1$ can be specified also for geologically normally consolidated soil layers exhibiting a yield stress larger than the in situ stress; this was the case for the granular soils such as the made ground and the layers of sand and gravel.

Stiffness decay with shear strain was described using ratios of $E^{ref}/E^{ref}_{50} = 15$ for the normally consolidated silty clay, 20 for the stiff over-consolidated clay deposit and 10 for the remaining soil layers; $E^{ref}_{50}/E^{ref}_{oed} = 1$ and an angle of dilatancy at failure $\psi = 0$ were adopted for all soils; these values provided a satisfactory fitting with the stress-strain curves observed in the triaxial tests.

Analyses were carried out in terms of effective stresses modelling the clay layers as undrained and the other soils as drained.

Table 1. Soil properties.

Soil	γ (kN/m^3)	c' (kPa)	φ' (°)	OCR	K_0	E^{ref} (MPa)	m
MG	18.5	15	29	2.0	0.52	280	0.6
Silt	19.0	24	26	2.4	0.83	220	0.7
Sand	19.0	–	31	5	0.49	270	0.5
nc clay	18.6	24	25	1.1	0.60	120	0.9
Gravel	19.0	–	35	5	0.43	2100	0.5
oc clay	20.0	30	28	2.5	0.82	450	0.8

2.2 *Excavation model and structural properties*

The excavation consists of an elongated box with a length (66.8 m) to width (33.6 m) ratio of about 2 and a depth of about 40 m. Dimensions of the box excavation are typical of planned metro stations in the historical centre of Rome. The excavation is retained by diaphragm walls and by horizontal propping levels installed during the top down excavation sequence.

In the analyses the excavation was carried out in twelve stages, with seven levels of props constructed as excavation progresses. The wall behaves as an embedded cantilever up to the excavation level at +7.9 m o.d. (8.9 m depth), at which the first propping level is installed. The sequence of excavation and propping then continues to the final excavation level at –23 m o.d. (40 m depth). Figure 2 depicts schematically the final stages of excavation; 6 to 6.4 m of soil were excavated after the construction of each propping level constituted by the floor slabs, with the exception of temporary steel props installed at stage 9 at an elevation of –16.6 m o.d..

The perimeter retaining walls reach the deep layer of stiff clay, to prevent from uplift the excavation

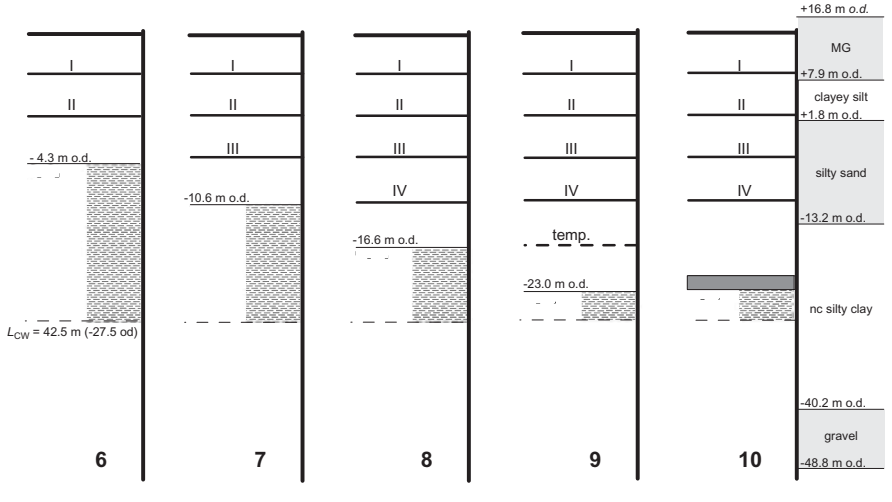

Figure 2. Excavation stages; cross-wall length $L_{cw} = 42.5$ m.

bottom and to minimise water flow within the excavation; they are assumed to be formed from reinforced concrete for a length of 55 m and from unreinforced concrete for the final portion, 10 m long.

Diaphragm wall panels, as well as cross-wall panels, were assumed to be 1.5 m thick and 2.8 m wide. Three lengths were considered for the sacrificial cross-walls: L_{cw} = 38 m that is equal to the maximum depth of excavation (–23 m o.d.); L_{cw} = 42.5 m and 47.0 m, for which the cross-wall toe is installed 4.5 and 9.0 m below the final excavation level (–27.5 m o.d. and –32.0 m o.d.), respectively.

Three values of cross-wall spacing were also assumed in the analyses (Fig. 3): s = 8.4, 11.2 and 22.4 m, with two, three and seven panels of diaphragm walls included in between the cross-walls. The ratio between the area occupied by the cross-walls and that of the soil within the excavation was A_{cw}/A_{soil} = 21.7, 15,4 and 7.2%, in the three cases.

Using symmetry, a portion of the box was considered in the analyses extending between the centre line of adjacent cross-walls as shown in the plan view of Figure 4 for a cross-wall spacing s = 8.4 m, so that a current central portion of the box excavation was modelled.

The 3D finite element mesh extends to about 100 m behind the diaphragm walls, that is 2.5 times the excavation depth, and up to the excavation centre line in front of it. Its height is about 2 times the final excavation depth (76.8 m). A 3D view of the domain analysed for cross-wall spacing s = 11.2 m is shown in Figure 5, without the soil inside the excavation.

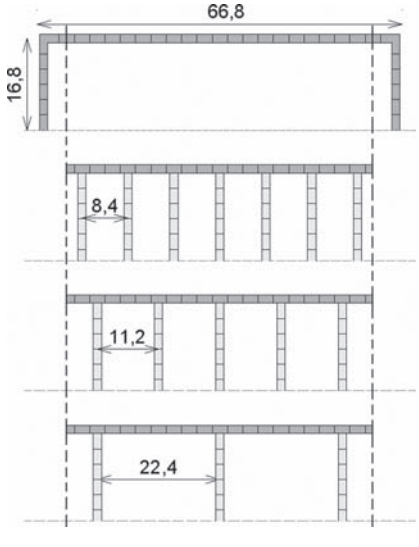

Figure 3. Analysed schemes of cross-walls systems.

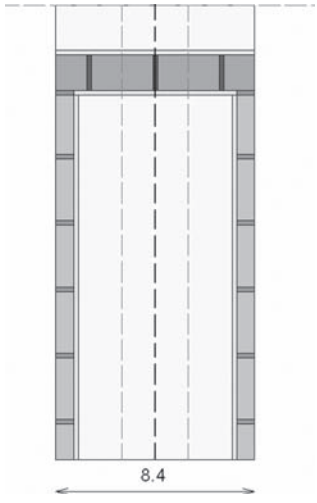

Figure 4. Plan view of the analysed domain for cross-wall spacing s = 8.4 m.

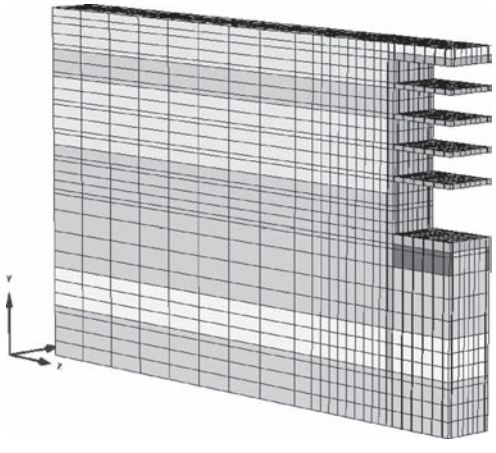

Figure 5. 3D view of the analysed domain for cross-wall spacing s = 11.2 m.

Both soil and structural elements were discretised with 15-noded linear strain wedges; 10240, 14144 and 37056 elements were used for the three values of cross-wall spacing.

All the structural elements were modelled as linear elastic materials with a Poisson coefficient $\nu' = 0.15$. The unit weight was $\gamma = 24$ and 25 kN/m^3 for unreinforced and reinforced concrete.

Cross-wall panels were assumed to be formed from unreinforced concrete of strength (and stiffness) lower than that of perimeter diaphragm walls; specifically, the cross-walls Young's modulus was 60% of that of diaphragm walls, $E_{cw} = 0.6\ E_{dw}$.

Stiffness of the floors of the box construction, acting as propping levels, was reduced to account for the presence of the lift and stair openings, also used to extract the soil during excavation; openings area was assumed to be 40% of the floor area in total.

Floor slabs were connected to the diaphragm walls through linear elastic interface elements, 0.2 m thick, with a stiffness reduced by about an order of magnitude to minimise the transmission of bending moment to the retaining wall ($E = 1.8$ GPa).

Table 2 summarises the properties of structural elements.

The temporary steel props installed at the elevation of −16.6 m o.d. were also modelled using brick elements, assuming a Young's modulus of 3 GPa to represent tubular steel props.

Soil–structure interfaces were modelled using finite elements 0.2 m thick (Fig. 4). The same constitutive model adopted for the soils was used, but with reduced strength and stiffness parameters (Table 3). Specifically, a reduction factor R_{int} was used for c' and tan φ', while the reduction was equal to R_{int}^2 for the Young's modulus.

Stiffness profile of soil–structure interfaces, and the stiffness decay with shear strain were described using the same values of m, E^{ref}/E^{ref}_{50}, $E^{ref}_{50}/E^{ref}_{oed}$ and ψ adopted for the soils.

The contacts between diaphragm wall panels and cross-wall panels, as well as the contacts between cross-walls and diaphragm walls were also modelled through finite elements, 0.2 m thick. The mechanical behaviour of these elements was described using a linear elastic—perfectly plastic Mohr—Coulomb model. The shear strength between the panels was characterised by negligible coesion, $c = 2$ kPa, a friction angle $\varphi = 35°$ and a dilatancy angle at failure $\psi = 10°$, while the stiffness was equal to that of the corresponding panels: $E = 36$ GPa for contacts between panels of diaphragm walls and $E = 22$ GPa for contacts between panels of cross-walls and between diaphragm walls and cross-walls.

Table 2. Stiffness of structural elements.

	f_{ck} (MPa)	Reduction	E' (GPa)
Reinforced perimeter wall	32	–	36.0
Unreinforced perimeter wall	12	–	22.0
Cross wall	12	–	22.0
Floor propping level	32	0.6	21.6
Bottom slab	32	–	36

Table 3. Soil–structure interface properties.

Soil	R_{int}	c'_{int} (kPa)	φ'_{int} (°)	E^{ref}_{int} (MPa)
Made ground	0.7	10.5	20	137
Clayey silt	0.7	16.8	18	108
Silty sand	0.7	–	22	132
nc silty clay	0.7	16.8	18	59
Gravel	1.0	–	35	210
oc silty clay	0.8	24	22	288

3 ANALYSIS RESULTS

3.1 *Three-dimensional finite element analyses*

Refinement of 3D meshes was evaluated through preliminary analyses carried under plane strain conditions (without cross-walls) using the 2D and the 3D suites of the code Plaxis. Soil and structural elements were discretised with 15-noded 3rd order strain triangles in the 2D model and with 15-noded linear strain wedges in the 3D model. Refinement of 3D meshes was assumed satisfying when differences of computed wall deflections were lower than 5% for all stages of excavation.

The results of 3D finite element analyses were examined to evaluate the effects of cross-walls spacing and length on the horizontal deflections of the perimeter diaphragm walls and the ground settlements behind the excavation. Both of them are in the following referred to the middle section between the cross-walls (dashed line in Fig. 4).

Figure 6 compares profiles of horizontal wall deflections computed for excavation to 40 m depth (stage 9), without cross-walls and with cross-walls of varying length, installed at different spacing. Table 4 summarises the computed values of maximum wall deflections.

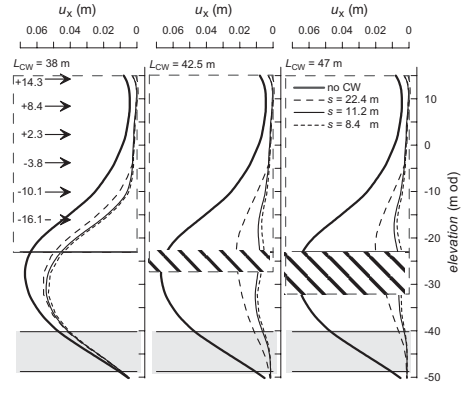

Figure 6. Effects of cross-walls spacing and length on wall deflections.

Table 4. Maximum wall deflections.

	No CW	s = 8.4 m	s = 11.2 m	s = 22.4 m
L_{cw} m	u_x mm	u_x mm	u_x mm	u_x mm
38.0	67.2	53.2	54.3	56.0
42.5		9.5	10.7	22.1
47.0		7.2	8.9	20.3

In all cases, the horizontal wall displacements are strongly reduced throughout the excavation depth, while a different behaviour is observed below the bottom of excavation depending on cross-walls length. For values of L_{cw} = 38 m, equal to the maximum excavated depth, a slight influence of cross-walls spacing is observed on the displacement profiles and the maximum wall deflection is about 20% lower than that computed without cross-walls. When cross-walls are prolonged below the final excavation level, horizontal deflections strongly reduce also below the formation level and the influence of cross-walls spacing becomes more evident. For a cross-walls length L_{cw} = 42.5 m (4.5 m depth below the excavation bottom) the maximum wall deflection reduces of about 85% using a cross-wall spacing s = 8.4–11.2 m and of about 67% using s = 22.4 m. A further increase in cross-walls length, L_{cw} = 47 m, (9.0 m depth below the excavation bottom) provides a further reduction of maximum wall displacement (≅ 90% for s = 8.4–1.2 m and 70% for s = 22.4 m), although the benefit of increasing L_{cw} reduces for higher cross-walls spacings. Limited extension of cross-walls length below the final excavation level then produces a significant reduction of wall deflections along the embedded portion of the retaining walls.

Figure 7 shows variation of horizontal deflections along the diaphragm wall at –19 m o.d., 3 m below the temporary propping level and at the excavation level (–23 m o.d.) for the case of L_{cw} = 42.5 m. Wall displacements smoothly increase with distance from cross-walls with negligible relative displacements between the panels of the diaphragm walls.

Sufficient connection between wall panels was then provided by the strength properties assumed for the interface elements and by the contribution of both the temporary props and the soil below the excavation level. Similar trends were computed from additional analyses in which the friction and the dilatancy angles were reduced to 30° and 5°, respectively.

Figure 8 shows the displacement field computed without cross-walls and with cross-walls of different length installed at spacing s = 11.2 m; the

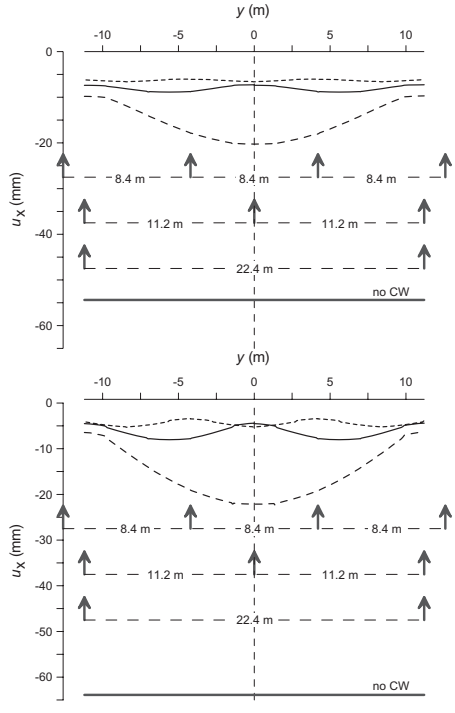

Figure 7. Maximum horizontal deflections of perimeter diaphragm walls with varying cross-wall spacing: a) –19 m o.d; b) –23 m o.d.

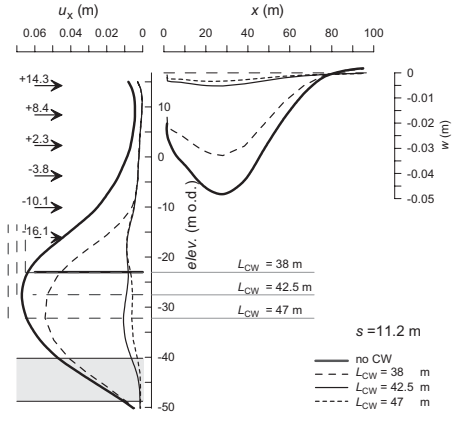

Figure 8. Effect of cross-wall length on displacement field at constant cross-wall spacing s = 11.2 m.

results refer to the final excavation level at –23 m o.d. (40 m depth). Both wall deflections and ground surface settlement profile behind the excavation are for the mid-section in between the cross-walls. Table 5 reports the maximum surface

Table 5. Maximum surface settlements.

	No CW	L_{cw} = 38.0 m	L_{cw} = 42.5 m	L_{cw} = 47.0 m
w_{max} (mm)	48.2	32.9	5.2	3.4

settlements, obtained at a distance of about 30 m from the wall.

Consistently with reduction of wall deflections, cross-walls also reduce substantially the magnitude of surface settlements. Specifically, benefit increases with cross-walls length, settlement reduction varying from about 32% for L_{cw} = 38 m to about 90% for L_{cw} = 42.5–47 m. Surface settlements also reduce with decreasing cross-walls spacing although limited benefit is obtained for $s < 11.2$ m.

3.2 *Plane strain finite element analyses*

To evaluate the capability of predicting the performance of deep excavations with sacrificial cross-walls assuming plane strain conditions, comparison 2D finite element analyses were finally carried out.

In the analyses, the soil and the cross-walls within the excavation were modelled as an equivalent homogenous material with linear elastic behaviour, while the interface between the equivalent material and the diaphragm walls was described using a linear elastic—perfectly plastic Mohr—Coulomb model.

Properties of the equivalent homogeneous material were obtained averaging the soil and the cross-walls properties, weighted on the corresponding dimensions occupied in plan. The equivalent Young's modulus was for example evaluated using the relationship:

$$E_{eq} = \frac{E_{cw} \cdot t + E_s \cdot (s - t)}{s} \quad (2)$$

where t and s are the cross-walls thickness and spacing and E_{cw} and E_s are the cross-walls and soil Young's moduli.

Preliminarily to this, average soil properties were evaluated for the soil layers included throughout the cross-walls length, considering the layers thickness as a weighting factor. Due to the assumed linear elastic behaviour, soil stiffness was computed using the values of E'_{50} at the mid point of each layer, that can be thought to be representative of stiffness at average strain levels, rather than using the values of E' that were linked to the small-strain shear modulus G_0. Similar values of average soil properties were obtained for the different cross-walls lengths, so that the following quantities were assumed: $\gamma = 18.8$ kN/m^3, $E' = 22$ MPa, $c' = 14$ kPa and $\varphi' = 28°$.

The unit weight and the stiffness of equivalent material were slightly affected by cross-walls length as well, so that a single value of γ_{eq} and E_{eq}' were assumed for each cross-walls spacing (Table 6).

Strength parameters of interfaces elements between the equivalent material and the diaphragm walls were obtained using relationships similar to Eq. (2) for c_{eq} and tan φ_{eq} and a reduction factor $R_{int} = 0.7$. Again, similar values were obtained irrespective of cross-walls length and spacing thus assuming $c_{int} = 9$ kPa and $\varphi_{int} = 21°$. Stiffness of interface elements was instead obtained multiplying the values of E_{eq} in Table 6 for the reduction factor $R_{int}^2 = 0.49$.

Figure 9 compares profiles of wall deflections computed for stage 9, when the final excavation level is reached, under 2D and 3D conditions; results refer to cross-walls length L_{cw} = 42.5 m (–27.5 m o.d.).

For values of $s = 8.4$ and 11.2 m, the plane strain analyses, in which the cross-walls and the soil within the excavation are described by an equivalent material, provide a fair estimate of wall deflections along the excavated depth, while horizontal wall displacements are overestimated below the final excavation levels, when assuming plane strain conditions.

Specifically, maximum wall displacements computed in the 2D analyses are of about 2 times greater than those computed in the 3D analyses and occur at higher depths. Significant differences in the deflection profiles are instead observed for $s = 22.4$ m, for which the three-dimensional pattern of behaviour is more relevant.

Similarly to the results obtained for the wall deflections, plane strain analyses also provide an overestimate of ground surface settlement profiles behind the wall, as shown in Figure 10 for L_{cw} = 42.5 m; again, for $s = 8.4$ and 11.2 m maximum settlements computed under 2D conditions are about 2 times greater than the ones computed under 3D conditions.

Then, plane strain analyses in which an equivalent material was used to represent the soil and the cross-walls within the excavation provided an overestimate of wall deflections and ground movements. However, significant differences in

Table 6. Young's moduli of the equivalent material.

	s = 8.4 m	s = 11.2 m	s = 22.4 m
E_{eq}´(MPa)	3950	2965	1494
γ_{eq} (kN/m^3)	19.7	19.5	19.1

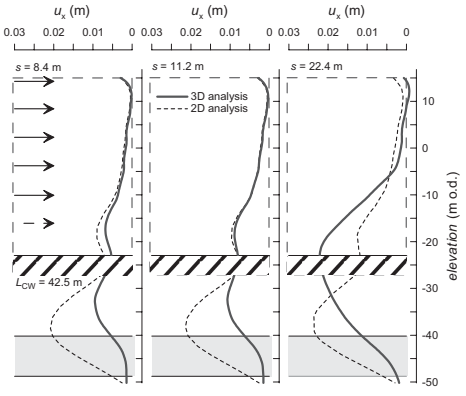

Figure 9. Horizontal displacement of the diaphragm walls computed by 3D and 2D finite element analyses.

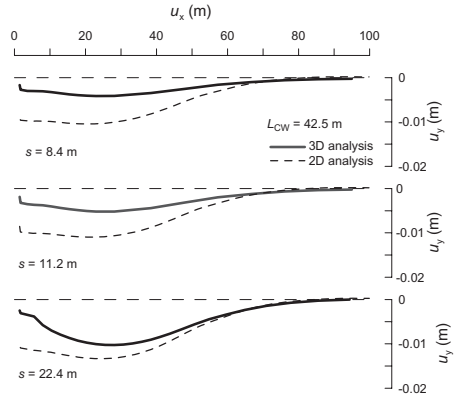

Figure 10. Surface settlement profiles computed by 3D and 2D analyses: L_{cw} = 42.5 m, s = 11.2 m.

profiles of wall deflections were obtained from 2D and 3D analyses when cross-walls spacing was increased to s = 22.4, due to the increasing influence of the 3D displacement field.

4 CONCLUSIONS

3D finite element analyses of deep excavations with sacrificial cross-walls were carried out to assess the effectiveness of cross-walls as a mitigation measure for reducing the horizontal deflections of diaphragm walls and the ground settlements around the excavation. In the analyses, a portion of the box excavation was modelled extending between the centre line of two adjacent cross-walls. Both soil and structural elements, including the cross-walls, were described by 15-noded linear strain wedges, using interface elements to model the soil–structure contacts and the contacts between the structural elements, such as those between the panels of diaphragm walls and of cross-walls.

Specifically, the analyses were performed to investigate the effects of cross-walls length and spacing on the ground movements induced by the excavation, considering a soil profile typical of central Rome.

The results show that sacrificial cross-walls permit to reduce substantially the diaphragm wall deflections and the ground surface settlements behind the perimeter diaphragm walls. Ground movement reduces further prolonging the cross-walls below the final excavation depth and reducing cross-wall spacing. However, a reducing benefit was observed for values of cross-walls embedded length greater than 4.5 m and for cross-walls spacing lower than 11.2 m.

Comparison 2D analyses were also carried out to evaluate the capability of predicting the performance of a deep excavation in which cross-walls are used as a mitigation measure to reduce ground movements. In the analyses, an equivalent material was modelled to represent the cross-walls and the soil within the excavation. For cross-wall spacing s = 8.4 and 11.2 m., a fair agreement was obtained for wall displacements computed throughout the excavated depth, while an overestimate was obtained for wall deflections computed below the excavation bottom and for the ground surface settlement profiles behind the excavation. On the other side, profiles of wall deflections computed by 2D and 3D analyses differed substantially for s = 22.4 m, for which the 3D patterns of behaviour strongly affect the computed displacement field.

ACKNOWLEDGEMENTS

The Authors wish to thank Mrs F. Buono and Dr G. Landi for useful information on soil data and Prof. L. Callisto for fruitful discussions and suggestions.

REFERENCES

Bailey R.P., Harris D.I. and Jenkings M.M. (1999). Design and construction of Westminster station on the Jubilee Line Extension. *Proc. Instn Civ. Engrs Civ. Engng Jubilee Line Extension*, 132: 36–46.

Burland J.B., Simpson B. and St John H.D. (1979). Movements around excavations in London Clay. *Proc. 7th ECSMFE*, Brighton, 1: 13–29.

Hsieh H.S., Lu Y.C. and Lin T.M. (2008) Effects of joint details on the behaviour of cross walls. *Journal of Geo Engineering*, 3 (2): 55–60.

Hsiung B.C.B., Nash D.F.T., Cheng K.H., Huang C.C. and Hwang, R.N.H. (2001). The effectiveness of jet-grout slabs and cross-walls in restricting wall movements in deep excavations. *Proc. 14th Southeast Asia Geotech. Engng Conference*, Hong Kong, China.

Merritt A.S., Menkiti C.O., Harris D.I., Zdravkovic L., Potts D.M. and Mair R.J. (2010). 3D finite element analysis of a diaphragm wall excavation with sacrificial crosswalls. *In Geotechnical Challenges in Megacities, GeoMos2010, Int. Geotech. Conf.*, Moscow, Russia.

Osborne N.H., Ng C.C. and Cheah C.K. (2009). The benefits of hybrid ground treatment in significantly reducing wall movements: A Singapore case history. *In Geotechnical aspects of underground construction in soft ground*. Ng, Huang & Liu (eds), Taylor & Francis Group, London, 447–453.

Ou C.Y., Hsieh P.G. and Lin Y.L. (2011) Performance of excavation with cross walls. *Journal of Geotechnical and Geoenvironmental Engineering*, ASCE, 137 (1), 94–104.

Ou C.Y., Lin Y.L. and Hsieh P.G. (2006). Case records of an excavation with cross walls and buttress walls. *Journal of Geo Engineering*, 1 (2): 79–86.

Schanz, T., Vermeer, P., Bonnier, P. 1999. Formulation and Verification of the Hardening-Soil Model. *Proc. Plaxis Symposium Beyond 2000 in Computational Geotechnics*, Amsterdam, the Netherlands, 281–296.

Stevens A., Corbett B.O. and Steele A.J. (1977). Barbican Arts Centre: the design and construction of the substructure. *The Structural Engineer*, 55 (11): 473–485.

This page intentionally left blank

Geotechnical Aspects of Underground Construction in Soft Ground – Viggiani (ed)
© 2012 Taylor & Francis Group, London, ISBN 978-0-415-68367-8

A 3D numerical study of deep excavations in clayey soils

E. Erbì & F.M. Soccodato
Department of GeoEngineering and Environmental Technologies, University of Cagliari, Italy

ABSTRACT: In this paper the results of a number of three-dimensional (3D) numerical analyses of deep excavations in a clayey soils are presented and discussed. The parametric study involved different geometries, with varying plan dimensions and depths of excavation. The analyses were carried out using a non linear, plasticity hardening soil model. The attention is focused on horizontal displacements (wall deflections) as well as on vertical displacements (settlement profiles behind wall). Two-dimensional (2D) plane strain numerical analyses were also carried out in order to compare results and to highlight 3D effects on predicted displacement fields. The results confirmed that, especially for excavations characterized by relatively low length to excavation depth or length to width ratios, 3D effects play a significant role in reducing the displacements obtained from 2D plane strain analyses.

1 INTRODUCTION

The evaluation of horizontal displacements of walls supporting deep excavations is a key-step in the subsequent estimation of ground movements. Frequently, deflections (and their maximum values) are evaluated following semi-empirical approaches (Clough & O'Rourke 1990, Mana & Clough 1981), or by carrying out one-dimensional (*Winkler* methods) or two-dimensional (2D) plane strain numerical analyses. In the first case, the effects of geometry, sequences of excavation, stiffness of wall and props are not explicitly taken into account, as the approach is based on a large collection of measured data. In the second case, representative numerical analyses must be based on adequate modelling of soil behaviour and, also, of the sequence of excavation and support installation. However, it is well known that three-dimensional (3D) effects related to the geometry (height, width and length) of the excavation can affect induced ground movements.

In fact, a number of studies based on the results of 3D numerical analyses allowed to highlight the effects of excavation geometry (e.g., Ou *et al.,* 1996, Zdravkovic *et al.,* 2005, Finno *et al.,* 2007). All these studies, although based on different soil and structural models, try to explain observed performances by comparing results obtained from 2D and 3D analyses.

With reference to the maximum horizontal deflections of the wall, Ou *et al.* (1996) suggested typical trends of a Plane Strain Ratio, defined as the movement computed by 3D analyses divided by that computed by a 2D plane strain simulation, as a function of the width to length (B/L) ratio and of the distance from the corner of excavation. Finno *et al.* (2007) carried out a large number of parametric 3D numerical analyses of supported excavations; they used a slightly different definition of the Plane Strain Ratio *PSR*, in this case defined as the maximum movement in the centre of the excavation wall computed by 3D analyses divided by that computed by a 2D plane strain simulation. Finno *et al.* (2007) showed that *PSR* in mainly influenced by the geometry, *i.e.*: length to excavation height (L/H_e) ratio and width to length (B/L) ratio, by the stiffness of supporting system and by the factor of safety against basal heave.

The results of these studies may be used to estimate the maximum deflection of the wall in order to evaluate, by following semi-empirical approaches such as that proposed by Ou & Hsieh (1998), settlement profiles behind wall. Distributions of ground movements parallel to the sides of the excavation may be finally estimated using semi-empirical procedures, such as that proposed by Fuentes & Devriendt (2010) or that based on the use of a complementary error function (Robosky & Finno, 2006).

This paper presents the main results of a number of 3D numerical analyses of supported deep excavations in clayey soils. The geometry of the parametric study, the soil profile and the modelling approaches are described in the following section; successively, the numerical results are presented and discussed.

2 LAYOUT OF NUMERICAL ANALYSES

Figure 1 shows a cross-section of the problem under consideration.

The soil profile is typical of the historical and central area of Rome. The top layer is made ground (*MG*), 10 m in thickness, mainly coarse grained; buried remains of ancient structures are also found in this layer. Soft silty clay (*Ag*) are found underneath, down to a depth of 60 m. Finally, a layer of sand and gravel (*GS*), a few meters thick, covers the stiff and overconsolidated clayey deposit (*Apl*) which represents the geological base formation of the Roman area. The pore water pressure distribution is almost hydrostatic, with a piezometric level located 10 m below ground level. Tip resistance q_C and small strain shear modulus G_0 profiles as obtained from cone penetration and cross-hole seismic tests are also shown in Figure 1.

The excavation height H_e ranges between 16 and 28 m (H_e = 16, 20, 24 and 28 m), with a fixed total height of the retaining structure H equal to 40 m. Thus, the ratio H / H_e is in the range 1.5 ÷ 2.5, which is typical of supported excavation in soft clayey soils. In plan, a total of 4 geometries were considered: 2 square (with $B = L$ = 20 and 40 m) and 2 rectangular (with B = 20 m and L = 40 and 80 m).

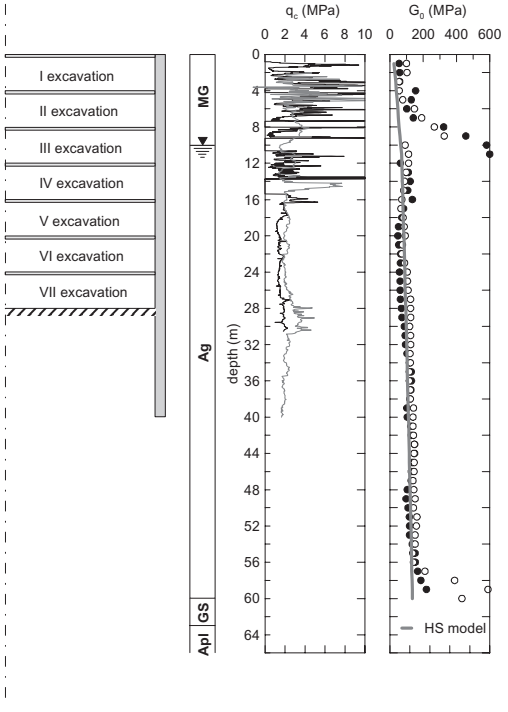

Figure 1. Cross-section of the problem and soil profile.

The numerical analyses were carried out using the commercial finite elements codes *PLAXIS 3D Foundation*. Figure 2 shows a view of a typical 3D mesh adopted. Symmetry allows to model only one quarter of the problem. Due to the high stiffness characterizing the *GS* and *Apl* layers, the bottom boundary of the mesh was located at a depth of 60 m; the mesh extends behind the wall at least 5 times the excavation height in order to minimize border effects (Robosky 2005, Ou & Shiau, 1998). Displacements were restrained in all directions along the bottom boundary, and in the out of plane direction on vertical lateral boundaries.

The mechanical behaviour of soils was modelled using the *Hardening Soil* model (Schanz *et al.*, 1999). This is an elasto-plastic soil model with stress-dependent stiffness, characterised by both deviatoric and volumetric hardening. Tables 1 and 2 report the constitutive soil parameters adopted in the analyses. Calibration of model parameters follows from the geotechnical characterization of the site (Rampello, 2011). In particular, the elastic stiffness E_{ur} was set equal to the small strain

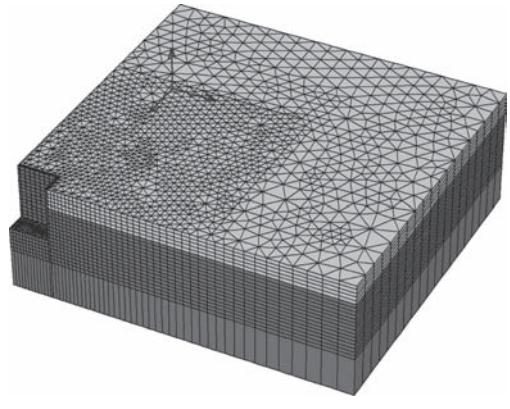

Figure 2. Typical 3D mesh.

Table 1. Hardening Soil model: general parameters.

Soil	γ (kN/m³)	c' (kPa)	φ' (°)	OCR (–)	K_0 (–)	ν' (–)
MG	18.5	15	28	2.0	0.50	0.2
Ag	18.2	20	25	1.3	0.58	0.2

Table 2. Hardening Soil model: stiffness parameters.

Soil	E_{ur}^{ref} (MPa)	m (–)	$E_{ur}^{ref}/E_{50}^{ref}$ (–)	$E_{oed}^{ref}/E_{50}^{ref}$ (–)
MG	240	0.8	10.0	1.0
Ag	160	0.7	10.0	1.0

stiffness as obtained from seismic *in situ* tests and laboratory resonant column and bender elements tests. Thus, high values of E_{ur}/E_{50} and E_{ur}/E_{oed} ratios (E_{50} and E_{oed} being the stiffness in primary (virgin) deviatoric and isotropic loading, respectively) were adopted in order to match the marked non-linearity of soils observed in laboratory tests. Dilatancy was set equal to zero.

The analyses were carried out in terms of effective stresses, under undrained conditions for the clayey layer *Ag*. The retaining structure was considered to be a reinforced concrete (r.c.) diaphragm wall. Isotropic, elastic solid elements were used to model each single panel (sectional area: 2.4×1.0 m, Young modulus $E = 30$ GPa, Poisson ratio $\nu = 0.15$). In order to capture the influence of joints between panels, which give rise to an 'anisotropic' behaviour of walls, thin solid elements (10 cm in thickness) with reduced elasto-plastic mechanical properties were introduced to simulate the panel to panel contact.

The contact (interface) between wall and soils was also modelled with thin, solid elements (10 cm in thickness), characterised by the same constitutive model adopted for soils; stiffness and strength properties of these elements were set equal to 70% of the values corresponding to adjacent intact soils.

A *Top-Down* type construction sequence was assumed. Continuous r.c. floor slabs, 0.20 m thick and with a vertical spacing of 4.0 m, were modelled with anisotropic (membrane-like) shell elements.

Figure 3 shows two detailed views of the mesh with included wall and slab elements.

The steps of the numerical analyses were as follows:.

1. initial conditions (geostatic stresses);
2. activation of walls (wished in place);
3. excavation of 4 m;
4. installation of floor slab at previous elevation;
5. repetition of steps 3) and 4) until H_e is reached.

Two-dimensional, plane strain numerical analyses, with $B = 20$ and $B = 40$ m, were carried out with the same code, using the same soil and structural models adopted for the full 3D analyses.

3 ANALISYS OF RESULTS

Figure 4 shows a typical result obtained from the numerical analyses with $B = 20$ m, reporting wall deflections u and settlements behind wall at ground level w with reference to the symmetry section (at a distance from the corner $d = L/2$). For direct comparison, the results of the corresponding 2D plane strain analysis are also shown in the figure.

The shapes of wall deflections and of settlement profiles are very similar to those observed and reported in the literature for deep and multi-propped excavations in soft clayey soils.

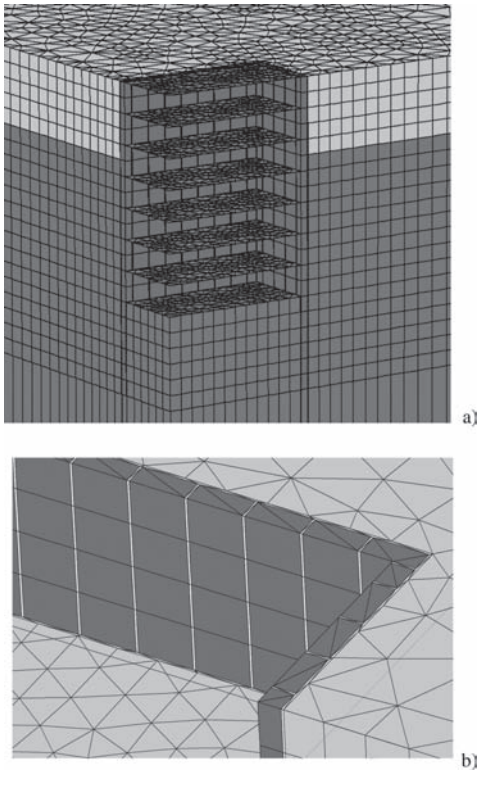

Figure 3. Details of the 3D mesh: a) walls and slabs; b) panel interfaces.

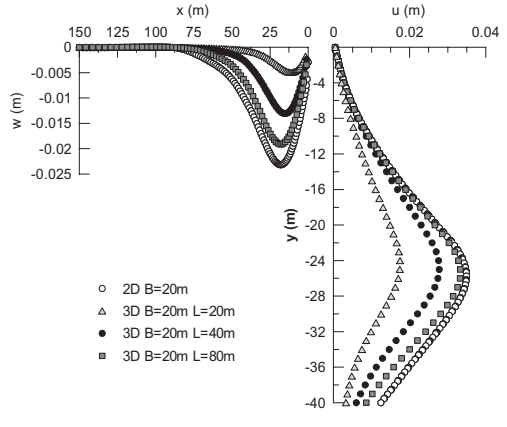

Figure 4. Settlement profiles and wall deflections obtained from numerical analyses (symmetry section; $H_e = 28$ m).

In fact, maximum deflections u_{max} occur at a depth close to excavation bottom and the maximum settlement w_{max} at some distance from wall position.

The different analyses, for a given excavation depth, showed deflection profiles very similar in shape, u_{max} occurring at the same depth; on the other hand, the distance from wall at which w_{max} appears decreases with increasing 3D geometry effects. With decreasing L, wall deflections are lower and settlement profiles are progressively narrower than those related to the corresponding 2D analysis.

Distributions of maximum wall deflection in the direction parallel to the wall are plotted in Figure 5 for two excavation depths. According to Ou *et al.* (1996), a distance of at least 20 m from corner seems to be necessary in order to reach an almost stationary value of u_{max}. Furthermore, the numerical results confirm that the 'anisotropic' modelling of the retaining structure (interfaces between adjacent panels) gives rise to non zero, even though relatively low, deflections at the corner of excavation (Zdravkovic *et al.,* 2005).

PSR is plotted as a function of L/H_e and of L/B in Figure 6. Open symbols refer to *PSR* associated to short sides (SS) of excavation. It may be noted that, according to Finno *et al.* (2007) and Ou *et al.* (1996), *PSR* increases with L/H_e and L/B, and decreases with increasing H_e. For all the 3D geometries considered, 2D maximum deflections were reached only for the excavation characterized by the maximum length (L = 80 m). The results obtained in this study fall in the range defined by the bounding curves suggested by Finno *et al.* (2007). For a given L/H_e ratio, average values of *PSR* decrease with decreasing side length. For $L/B \leq 1$ (and L = 20 m) 2D axisymmetric analyses with anisotropic wall properties should yield results closer to those obtained from 3D analyses (Zdravkovic *et al.,* 2005).

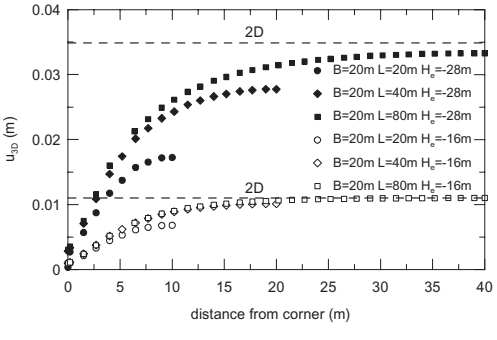

Figure 5. Distribution of maximum deflections along wall.

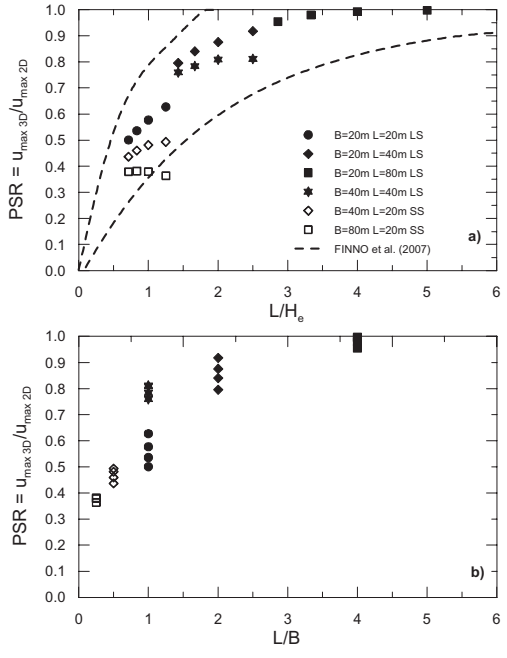

Figure 6. Plane strain ratios plotted as a function of: a) length to height of excavation ratio; b) length to width ratio.

Figure 7 shows the relation between maximum deflections and maximum settlements, normalised by excavation height, as obtained from numerical analyses. For L > 20 m, maximum normalised deflections range between 0.05 and 0.15%, values which are near the minimum values observed for deep excavations in clayey soil reported in literature (Long 2001, Moormann 2004). Figure 7 indicates that all the 2D analyses showed comparable and the highest normalized w_{max} to u_{max} ratios, ranging between 0.5 to 0.75: with increasing 3D effects, for a given H_e, the corresponding w_{max} to u_{max} ratios are progressively reducing.

These values are somewhat lower than the observed performances reported in literature, which suggests, for deep excavations in soft clayey soils, $w_{max} = u_{max}$ (Ou & Hsieh 1998, Long 2001). Finally, it may be also be noted the significant differences in w_{max} to u_{max} ratios between the 3D and the 2D analysis of the smallest squared excavation ($L = B = 20$ m).

The wall deflections already shown in Figure 4 are re-plotted in Figure 8, each profile being normalised by its maximum value. Shapes look similar, but it can be noted that, with increasing 3D effects, normalised deflections are significantly lower below excavation level and only just a little bit higher above.

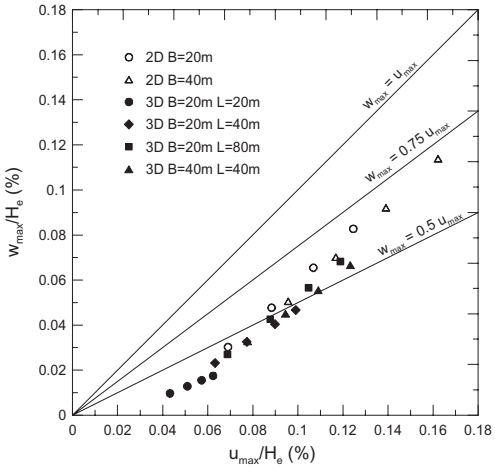

Figure 7. Normalised trends of maximum ground settlements versus maximum wall deflections.

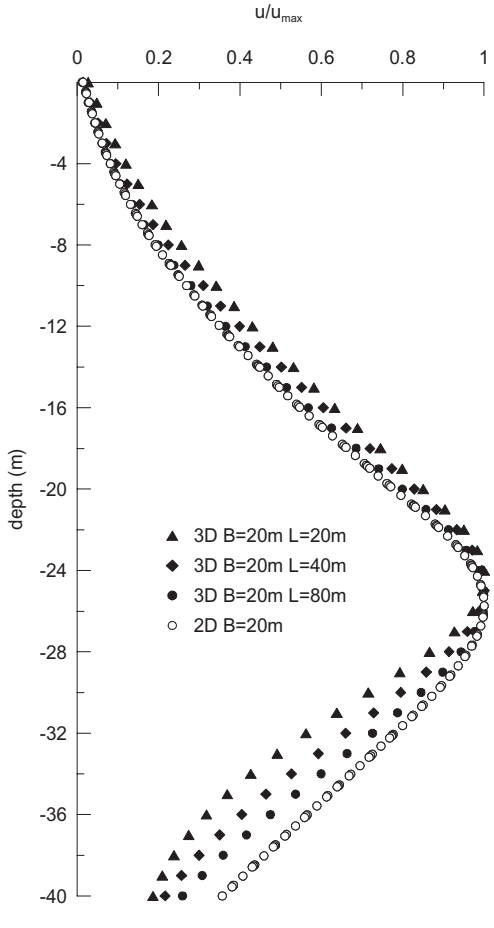

Figure 8. Normalized deflections (H_e = 28 m).

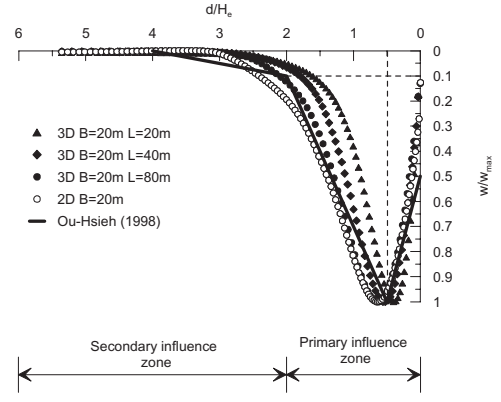

Figure 9. Normalized ground settlement profiles (H_e = 28 m).

Figure 9 reports normalised ground settlement profiles behind wall. Settlements and distances from wall position already shown in Figure 4 are normalised by excavation height and maximum settlement, respectively. It may be observed that, for all the analyses carried out, settlement profiles are in a nice agreement with the normalized shape proposed by Ou & Hsieh (1998) and based on a number of observed performances. This occurrence, which is not very common to be obtained from numerical analyses, can be attributed to the marked non-linearity that characterises the constitutive soil model used with the adopted selection of model parameters.

Figure 9 also shows that increasing 3D effects give rise to settlement profiles progressively narrower than those related to 2D conditions. This result is consistent with data shown in Figure 8: clearly, shapes of deflections and of ground settlement profiles are closely linked each other. Furthermore, the results indicate that the extension of ground settlement profiles is primarily related to deep (below excavation level) movements of the wall.

4 CONCLUSION

In this paper the results of a 3D numerical study of deep excavations in soft clayey soils have been presented and discussed.

The analyses were carried out using an advanced soil model capable to reproduce the significant non-linearity which characterises soil behaviour. The parametric study involved different lengths of excavation sides, considering square and rectangular excavations, and different excavation heights.

Thin solid elements with reduced mechanical properties were used to model the panel to panel and the panel to soil contacts.

2D plane strain numerical analyses were also carried out, with the same soil and structural models, in order to highlight 3D effects on wall and on ground movements.

The results obtained in this study appear to confirm some of the main findings reported in literature. More in detail:

- the ratio of maximum horizontal deflection obtained from the 3D and from the corresponding 2D plane strain analysis (*PSR*) tends to unity when L/H_e is greater than 4.0;
- for a given length to width ratio, *PSR* decreases with increasing excavation height;
- for squared excavations, or for $L/B < 1$, *PSR* are relatively low: 2D axisymmetric analyses with anisotropic wall properties should yield results closer to those obtained from 3D analyses;
- a distance from the corner greater than 20 m seems to be necessary to reach a stationary value of the maximum deflection;
- shapes of wall deflections are similar with varying L/B and L/H_e ratios. However, with increasing 3D effects the relative (normalized) amount of deep movements decreases;
- shapes of ground settlements profiles obtained behind the wall were in fair agreement with those obtained by well-established semi-empirical methods. This occurrence underlines the importance of the use of appropriate (highly nonlinear) constitutive soil models in this kind of analyses.

REFERENCES

Clough, G.W. & O'Rourke, T.D. (1990). Construction-induced movements of in situ walls. In Proc. Design and Performance of Earth Retaining Structures, Ithaca, N.Y. ASCE SP 25, 439–470.

Finno, R.J., Blackburn, J.T. & Roboski, J.F. (2007). Three-Dimensional Effects for supported excavations in *clay. Journal of Geotechnical and Geoenviromental Engineering* **133** (1): 30–36.

Finno, R.J. & Roboski, J.F. (2006). Distributions of ground movements parallel to deep excavations in clay. *Canadian Geotechnical Journal*, **43**: 43–58.

Finno, R.J. & Roboski, J.F. (2005). Three-Dimensional responses of a Tied-Back Excavation through clay. *Journal of Geotechnical and Geoenviromental Engineering*. **131** (3): 273–282.

Fuentes, R. & Devriend, M. (2010). Ground movements around corners of excavation:empirical calculation method. *Journal of Geotechnical and Geoenviromental Engineering*. **136** (10): 1414–1424.

Leung, H.Y. & Charles, W.W. (2007). Wall and Ground Movements associated with deep excavations supported by cast in situ wall in mixed gorund conditons. *Journal of Geotechnical and Geoenviromental Engineering*, **133** (2): 129–143.

Lin, D.G. & Woo, S.M. (2007). Three dimensional analyses of deep excavation in Taipei 101 construction project. *Journal of GeoEngineering*, **2** (1): 29–41.

Mana, A.I. & Clough, G.W. (1981). Prediction of movements for braced cuts in *clay. Journal Geotechnical Engineering Division ASCE,* **107** (6): 759–777.

Moormann, C. (2004). Analysis of wall and ground movements due to deep excavations in soft soil based on a new worldwide database. *Soils and Foundations*, **44** (1): 87–98.

Ou, C.Y. & Hsieh, P.G. (1998). Shape of ground surface settlement profiles caused by excavation. *Canadian Geotechnical Journal*, **35**: 1004–1017.

Ou, C.Y. & Shiau, B.Y (1998). Analysis of the corner effect on excavation behaviors. Canadian Geotechnical Journal, **35**: 532–540.

Ou, C.Y., Chiou, D.C. & Wu, T.S. (1996). Three-Dimensional finite element analysis of deep excavations. *Journal of Geotechnical Engineering*, **122** (5): 337–345.

Ou, C.Y., Hsieh, P.G. & Chiou, D.C. (1993). Characteristics of ground surface settlement during excavation. *Canadian Geotechnical Journal*, **30**: 758–767.

Rampello, S. (2011). Personal communication.

Schanz, T., Vermeer, P.A. & Bonnier, P.G. (1999). Formulation and verification of the Hardening-Soil Model. In: R.B.J. Brinkgreve, Beyond 2000 in Computational Geotechnics. Balkema, Rotterdam: 281–290.

Wang, J.H., Xu, Z.H. & Wang, W.D. (2010). Wall and ground movements due to deep excavations in Shanghai soft soils. *Journal of Geotechnical and Geoenviromental Engineering*, **136** (7): 985–994.

Zdravkovic, L., Potts, D.M. & St Jhon, H.D. (2005). Modelling of 3D excavation in finite element analysis. *Géotechnique*, **55** (7): 497–513.

Construction, design, and measured performance of deep excavations

This page intentionally left blank

Geotechnical Aspects of Underground Construction in Soft Ground – Viggiani (ed)
© 2012 Taylor & Francis Group, London, ISBN 978-0-415-68367-8

Interaction of retaining structure with adjacent building: Multi-stage numerical analysis

E.M. Comodromos & M.C. Papadopoulou
University of Thessaly, Greece

ABSTRACT: Large settlements induced to a multi-store building at the initiation of the construction of a diaphragm wall led to a demand of re-dimensioning the initial retaining measures. To achieve this target a multi-stage numerical analysis was carried out including the simulation of excavation using bentonite slurry and concreting stages. Appropriate pre-supporting measures were defined based on an iterative process in order to meet the demands of acceptable level of settlements. A steel tube curtain was applied to minimize the stress release due to unfavorable pressure differentiation. The instrumentation during construction and the comparison of the numerical prediction with the in situ measurements were quite helpful during the application of the proposed design.

1 INTRODUCTION

The demolition of an old building for the construction of a multi-store building with a 4-level underground parking provoked large settlements on an adjacent building. The aim of the present paper is to investigate the interaction between the retaining structures, consisting of a diaphragm wall combined with steel struts, and the adjacent building and to design the appropriate measures that will minimize the effects during the diaphragm construction.

The project is located in Thessaloniki, at the sea-front Nikis Av., and the excavation of 20.00 m width and 25.0 m length extends to the depth of 12.0 m. For the construction of the 4-level underground parking, the construction of a reinforced concrete diaphragm wall was predicted, while the excavation was planned in stages with the installation of steel struts accordingly.

It is widely accepted that underground constructions and retaining structures installation in urban environment with neighbouring buildings can cause disturbance of the foundation conditions of the latter. The consequences are more severe the poorer the subsoil conditions are. In the case of soft soil formations with low shear strength parameters and high compressibility, stress release can be observed underneath the adjacent buildings, resulting in unacceptable values of differential settlements.

As far as the case under investigation is concerned, large settlements and rotations were observed on the adjacent building when demolishing the old one and its foundation. This was the reason that led to the decision of underpinning the foundation of the adjacent building using jet grouting, prior to the construction of the diaphragm wall. The conditions were so poor that soil was unable to undertake the stresses temporarily caused at the soil pile boundary before grout hardening, resulting in the increase of settlement and rotation of the adjacent building.

For the surveillance of the movements of the adjacent building several inspection points were installed at different periods of time and at various levels, including the top of the building as well as the common boundary of the two buildings. Displacement measurements recorded every day showed that further measures should be taken in order to prevent soil movement and limit stress release under the foundation during the construction of the diaphragm wall (before the hardening of the concrete).

2 SUPPORTING METHOD

2.1 *Selection of supporting measures*

In order to carry the lateral pressure and prevent soil movement under the adjacent building, it was decided to assemble a steel tube curtain at the common boundary of the two buildings. The selected method has sufficient strength and stiffness to sustain the lateral pressures with the minimum disturbance, since the steel tubes will be installed by rotating and cutting soil. Furthermore, the characteristics of these elements are guaranteed by the manufacturer and thus the risk of construction defects is eliminated. A bitumen coat was also proposed in case further reduce of lateral friction

was needed. As far as the implementation of the proposed method is concerned, it is rather simple, owing to the equipment commonly used to perform boreholes. Its main disadvantage, in comparison with other methods, is additional time and higher cost demands.

2.2 *Method description—construction stages*

The sequence of the supporting measures installation initially involved the placement of the steel tubes at the common boundary with the adjacent building, as illustrated in Figure 1. The heads of the steel tubes were fixed in a a reinforced concrete beam as shown in the figure. The excavation of the diaphragm wall was carried out in segments of 2.80 m.

During excavation procedure, bentonite slurry completely filled the diaphragm shaft, while the lifting of the excavator head was accomplished very slowly in order to avoid soil boiling on the excavation sides. At every segment concreting was poured from the bottom of the excavation using a tube. The same procedure was followed for the next 2.80 m segment of the diaphragm wall. Measurements of displacements were acquired and evaluated on a continuous basis to minimize the risk of deteriorating the situation.

When the construction of the diaphragm was completed, the excavation took place in stages. Each stage included, apart from the excavation to a certain level, the installation of steel tube struts (final design of excavation and retaining procedure carried out by the constructor). Displacements measurements were still recorded for every excavation phase until the basement slab is constructed.

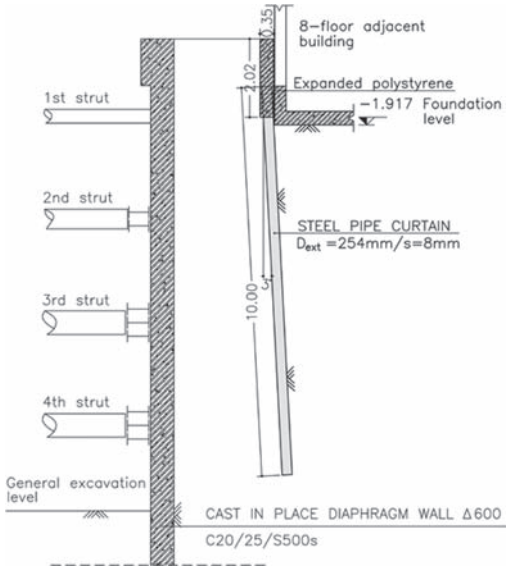

Figure 1. Supporting measures cross section.

3 NUMERICAL ANALYSIS

3.1 *Soil profile*

The results of a geotechnical investigation carried out in the site have been evaluated, along with the results of a geotechnical survey conducted for the construction needs of a nearby building.

The subsoil in the area of the project initially consists of depositions, down to the depth of 7.20 m, composed of silty sand with gravel, which is characterized by a low shear strength with practically zero cohesion. The layer of depositions is underlain by the sea-bed consisting of loose silty sand with shells and organics, with a thickness of 2.60 m. The third soil formation encountered is a cohesive layer, with shear strength parameters increasing with depth. In general, the subsoil in the area of the project is very compressible with relatively low shear strength down to a depth of 10.00 m. According to EN 1998-1:2003 it is classified to S2 soil category which includes deposits of liquefiable soils, of sensitive clays, or any other soil profile not included in types A–E or *S*1 and requires special studies. Table 1 presents the main soil properties of each soil layer, adopted for the numerical analysis and derived from geotechnical investigation and evaluation of in-situ and laboratory tests.

3.2 *Simulation procedure*

The numerical simulation of the excavation procedure was performed using the finite difference code FLAC (ver. 5.0). At the bottom level of the computational domain all movements were restrained, whereas at the lateral exterior sides lateral movements perpendicular to the boundary were restricted. Table 1 summarizes the properties of the soil layers, while the elastic-plastic Mohr-Coulomb constitutive model was used to simulate the behaviour of the soil. It is noted, however, that in case of unloading the deformations moduli presented in Table 1 are 10 times higher.

The analysis was two dimensional (plain strain conditions), while in reality triaxial conditions at the corners of the excavation are more favorable (Moormann and Katzenbach R., 2002). The number of soil elements was 6960, while 125 beam elements were used to simulate the adjacent building (115 elements) and the steel tubes (10 elements). Beam elements were considered as linear elastic and their rigidity has been accordingly modified for the 2-D analysis

Table 1. Effective shear strength parameters and deformations moduli used in the analysis for the profile sublayers.

	Layer FILL	Layer S	Layer M	Layer C	Layer C1	Layer S1	Layer C2
Depth (m)	0.0–7.0	7.0–10.0	10.0–13.0	13.0–17.0	17.0–22.0	22.0–25.0	>25.0
Unit weight γ(kN/m^3)	19.4	16.5	15.8	21.1	21.5	21.1	21.3
Bulk modulus b (MPa)	7.42	5.00	2.50	5.00	8.33	16.70	25.00
Shear modulus s (MPa)	3.42	2.31	1.15	2.31	3.85	7.69	11.5
Cohesion c (kPa)	3	1	2	5	10	0	30
Angle of friction ϕ (°)	30	30	20	32	28	38	35

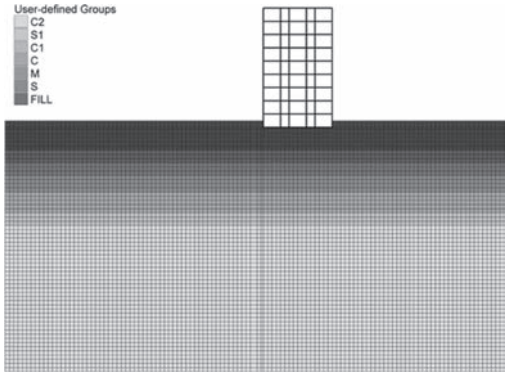

Figure 2. Finite difference mesh.

(divided by spacing). Figure 2 illustrates the mesh used together with soil stratification adopted.

The groundwater level was found at the depth of 1.50 m and therefore the appropriate hydrostatic pressure is allowed for in the analysis. No drainage have been taken into account.

The numerical analysis included all construction stages. More specifically, the first step corresponded to the initialization of the stress field (Stage 0), while the next stage includes the adjacent building allowing for its loads (Stage 1). The next stages, Stages 2–4, simulated the excavation of the diaphragm down to the depth of 2.0, 5.0 and 22.0 m, respectively). The simulation allowed for the bentonite slurry action, whereas the presence of the steel tubes was evaluated by solving the same problem twice, with and without activating the steel tube elements.

The analysis which incorporated the pre-supporting measures was followed by excavation stages to the final excavation level, according to the final design of excavation and retaining procedure. Thus the first excavation stage was simulated by removing soil elements down to the depth where the first strut was to be placed (Stage 5). Four excavation stages followed (Stages 6 to 9) until the level of −11.84 m, including the installation of a tube strut in each stage, at the appropriate levels so as not to impede the construction of the slabs of the building. In order to limit soil spreading underneath the adjacent building during excavation phases, it was found from a preliminary analysis, that the struts must be prestressed at 500 kN each.

3.3 *Numerical analysis results*

The cinematic field and the settlements of the adjacent building after the excavation of the diaphragm until the depth of 5.0 m are illustrated in Figure 3. The presence of the bentonite slurry was incorporated in the analysis, and the steel tubes were also activated. In Figure 4 horizontal displacements of the adjacent building and bending moments at steel tubes are presented for the same stage. The horizontal displacement at the top of the building equals to 1.8 mm while the maximum settlement is 0.56 mm.

Next construction stage (Stage 4), simulating 22.0 m diaphragm excavation, led to displacements and moments illustrated in Figures 5 and 6. The horizontal displacement at the top and the settlement reaches 22.2 mm and 17.9 mm respectively. The pre-supporting tubes' maximum moment is 42.8 kNm/m and determined the required section.

In the case where the steel tubes were not activated (no pre-supporting measures taken), the corresponding displacements for Stages 3 and 4 are presented in Figures 7 and 8 respectively.

Without the implementation of the pre-supporting measures, the lateral displacement at the top of the building is already 12.2 mm at Stage 3, while the settlement is 5.9 mm. Excavating 22.0 m of the diaphragm without the installation of the tube curtain (Fig. 8) leads to a horizontal displacement of 42.7 mm and a settlement of 34.6 mm.

When comparing the results of the two analyses, with and without the steel tubes, it is realized that the application of the proposed pre-supporting measures prior to the diaphragm construction contributes considerably to stress reduce limitation under the adjacent building, minimizing its settlement to acceptable limits.

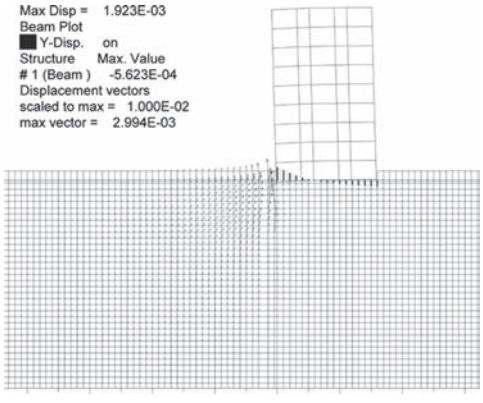

Figure 3. Displacement field and settlements of the adjacent building, Stage 3.

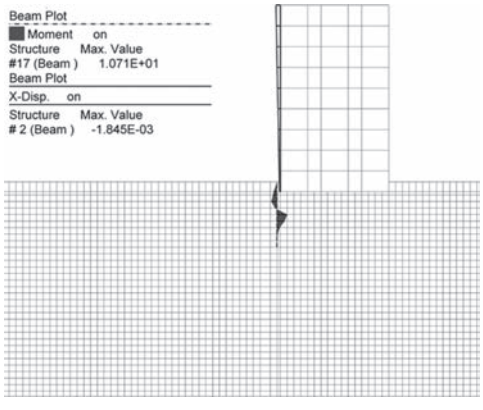

Figure 4. Horizontal displacements of the adjacent building and bending moments at steel tubes, Stage 3.

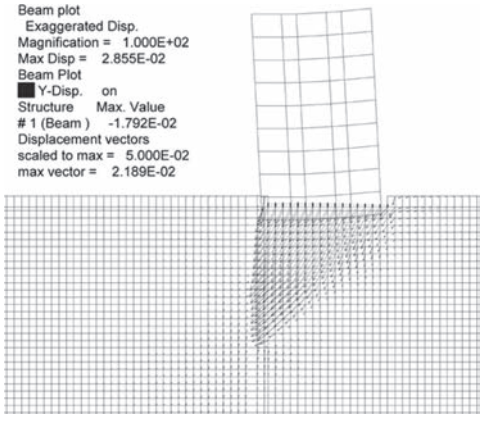

Figure 5. Displacement field and settlements of the adjacent building, Stage 4.

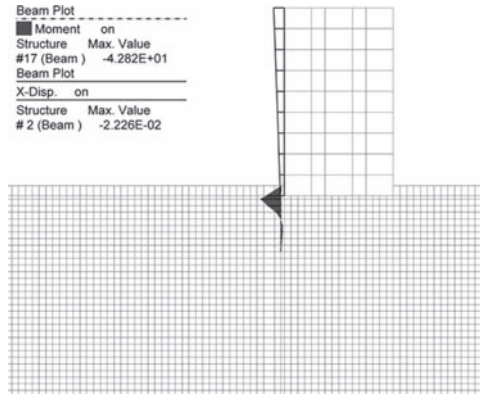

Figure 6. Horizontal displacements of the adjacent building and steel tubes' bending moments, Stage 4.

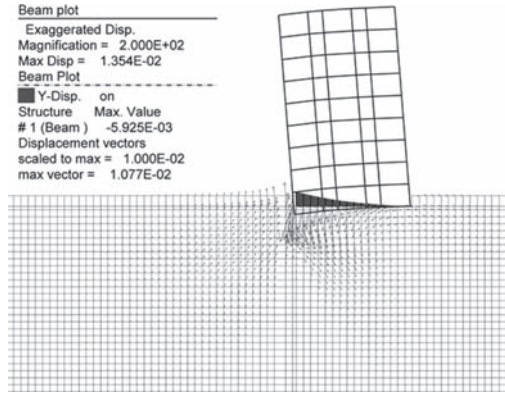

Figure 7. Displacement field and settlements of the adjacent building, without pre-supporting, Stage 3.

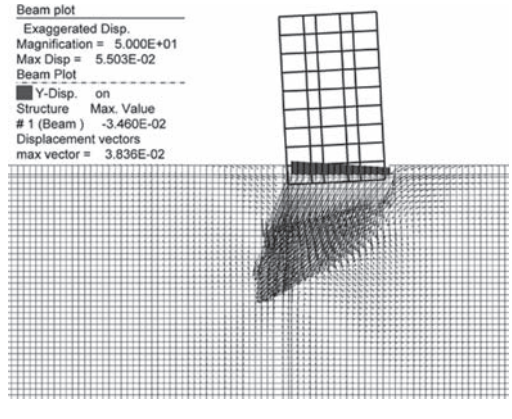

Figure 8. Displacement field and settlements of the adjacent building, without pre-supporting, Stage 4.

The settlement provoked by the diaphragm construction is of the order of 18 mm, given the installation of the tube curtain precedes the diaphragm excavation. Provided that the recorded settlement before the elaboration of the present analysis was approximately 25 mm, the total anticipated settlement by the end of the diaphragm construction will be of the order of 43 mm.

The maximum values of tube bending moments are summarized in Table 2, where maximum displacements are presented as well for both cases (with and without tube curtain installation).

The results of the final stage of the analysis (Stage 9) are illustrated in Figure 9. More specifically, the figure depicts the isovalues of horizontal displacements of the soil, the horizontal displacements of the adjacent building, the bending moments of the diaphragm and the axial forces of the prestressed struts. It is realized that the final horizontal displacement at the top of the adjacent building, after the final excavation stage down to the foundation level was 7.7 mm. It is also worth mentioning that the aforementioned value is achieved only in case of adequately prestressed struts (in fact precompressed) and that in case of no prestressing imposed, displacements would exceed the acceptable limits. The latter was validated after a series of analyses which determined the precompression force as well.

Table 2. Horizontal displacements and settlements of the adjacent building with and without steel tubes diaphragm during excavation and bending moments of tubes for all excavation stages.

Stage	Max. horizontal displacement without pre-supporting (cm)	Max. settlement without pre-supporting (cm)	Max. horizontal displacement with pre-supporting (cm)	Max. settlement with pre-supporting (cm)	Max. tube bending moment (kN.m/m)
2	0.0	0.0	0.0	0.0	7.2
3	1.2	0.6	0.0	0.0	10.7
4	**4.3**	**3.5**	**2.2**	**1.8**	**42.8**

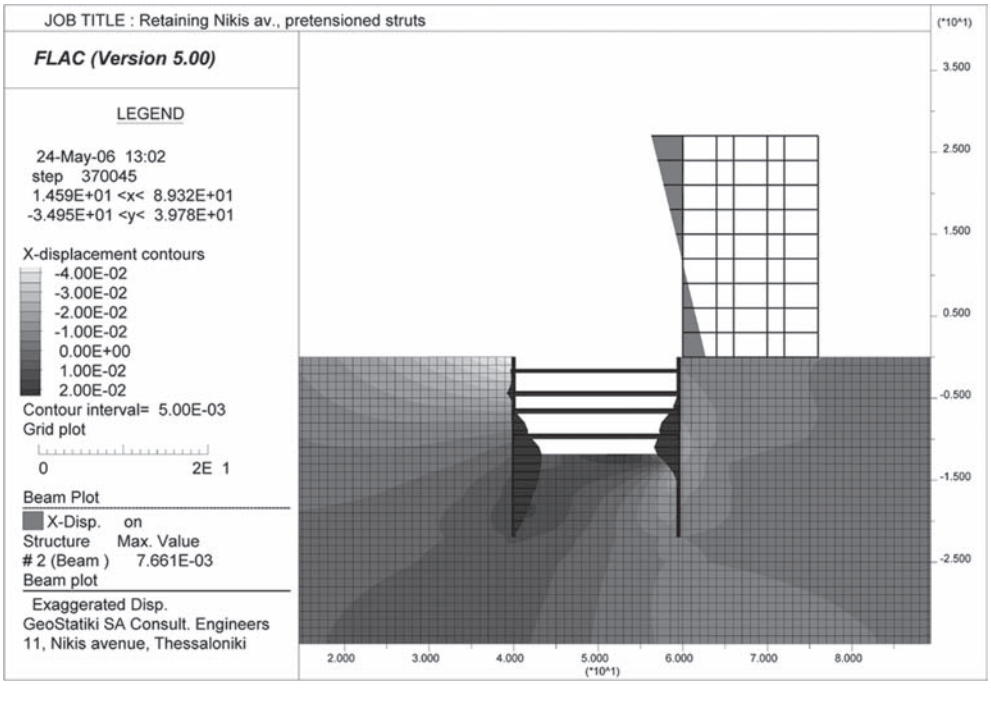

Figure 9. Horizontal displacements of the adjacent building, diaphragm bending moments and struts' axial forces, Stage 9.

4 DESIGN OF STEEL TUBES

The problem presented has been numerically solved within the notion of soil—structure interaction, the implementation of which does not include the use of safety factors. Consequently, for the design of the structural elements (steel tubes in this case), forces and moments from the numerical analysis must be multiplied by a general factor of safety. Given that steel quality is St 37, for permanent use of the steel tubes, the allowable stress is taken equal to σ_s = 161 MPa (DIN 17100). The required moment of resistance for the tubes' section, W_{req}, is calculated using Equation 1:

$$W_{req} = \frac{M_{\max}}{\sigma_s} * F \quad (1)$$

where F = the factor of safety and $M_{\max}$ = the maximum bending moment developed along tubes (see Table 2).

Tubes of with 254 mm external diameter and a thickness of 8 mm were applied, with moment of resistance $W \approx 368.65$ cm^3.

5 COMPARISON OF IN-SITU MEASUREMENTS AND NUMERICAL RESULTS

During the construction of the projects measurements of displacements were continually taken at several points of the adjacent building, as the final design specified. It is noteworthy that the recorded horizontal displacement at the top of the adjacent building after the construction of the diaphragm was 20 mm, which is practically equal to the numerically estimated (22.2 mm).

The prestressed struts enabled the excavation to the final depth, limiting the displacements to acceptable values. The struts' disposition after the final excavation stage is shown in Figure 10.

Figure 10. Disposition of retaining measures after the final excavation stage.

6 CONCLUSIONS

With the aim to solve the problem of minimizing the effects of stress reduce under an adjacent building during the construction of the retaining elements of a four level basement at a seaside area in Thessaloniki, a numerical analysis was carried out. Large settlements had already been observed when demolishing the old building. The application of jet grouting was not effective and further settlements and rotation of the adjacent building were observed. It was therefore considered that the construction of the diaphragm wall using bentonite slurry would further enlarge the effect due to the fact of unfavorable pressure differentiation at the upper part of the excavation where lateral pressure underneath the foundation of the adjacent building would be higher than that of the bentonite slurry.

It was therefore decided to assemble a steel tube curtain to carry the lateral pressure and prevent soil movement under the foundation. To achieve this target a multi-stage numerical analysis was carried out including the installation of the tube curtain, the simulation of excavation and soil replacement by bentonite slurry. An iterative process of analysis has permitted an effective design for both the length and the section of the tubes. The analysis was then extended to the construction of the diaphragm wall, the excavation in stages and the installation of steel struts accordingly. In order to maintain lateral displacement to an acceptable limit and at the same time sustain the development of bending moment below the diaphragm wall capacity an iterative process of analysis was also carried out.

The horizontal displacement at the top of the adjacent building was recorded when the diaphragm started using a gauge dial at the boundary with the next building founded on piles. By the construction of the diaphragm it was 20 mm, which is practically equal to the numerically estimated (22.2 mm).

REFERENCES

Geognossi S.A. 2005. Geotechnical investigation—study for the construction of a new building at Nikis Av. & C. Dil str. Thessaloniki.

Geostatiki S.A. 2006. Pre-supporting measures study for the retaining measures construction of a new building at Nikis Av. & C. Dil str. Thessaloniki.

Itasca Consulting Group Inc. FLAC: Fast Lagrangian Analysis of Continua. User's Manuals version 5.0.

Moormann, C.T. & Katzenbach, R. 2002. Three-dimensional effects of deep excavations with rectangular shape. In Proc. *2nd Soil-Structure Interaction in Urban Civil Engineering*: 135–142. Zurich.

Themeliodomi S.A. 2005. Final study for excavations, pumping and retaining measures of a new 8-floor building with a 4 level basement at Nikis Av. & C. Dil str. Thessaloniki.

Geotechnical Aspects of Underground Construction in Soft Ground – Viggiani (ed)

Effect of pressurized grouting on anchor behavior in residual soils

Tae-Sub Kim
Shinwha Soil Tech. Co., Ltd., Seoul, Korea

Bo-Kyoung Sim
Hyundai Eng. and Const. Co., Ltd., Seoul, Korea

Jong-Sun Kim
Korea University Seoul, Korea

Seok-Won Lee
Konkok University Seoul, Korea

In-Mo Lee
Korea University Seoul, Korea

ABSTRACT: The purpose of this study is to figure out the effect of pressurized grouting on diameter enlargement and pullout resistance of the compression ground anchor installed in decomposed residual soils. The laboratory chamber tests were carried out for 3-types of soils which are abundant in Korean peninsula. These tests simulate the real construction process of a ground anchor with pressurized grouting. Experimental results showed that grout permeation effect into the ground through porous media has to be taken into account when estimating the anchor diameter, if the permeability of the ground is larger than 10^{-3} cm/sec. A series of in-situ anchor pullout tests was executed in 3 different sites which represent 3 types of residual soils used in laboratory chamber tests. Results of in-situ tests showed that the effect of the pressurized grouting is more prominent in a softer ground with smaller SPT-N value. Based on experimental results, a new equation to estimate the pullout resistance as a function of the SPT-N value was proposed which might be applicable to decomposed residual soils.

1 INSTRUCTION

Various types of ground anchors are frequently used in earth-retaining structures such as a retaining wall, a slope, and tieback during excavation. In designing the compression ground anchor, the pullout resistance is a key parameter which varies subject to the installation method, soil dilation, roughness of anchor surface, shear strength of the soil, group effect, grout injection method, and so on.

Regarding the effect of pressurized grouting on pullout resistance in a ground anchor, Hobst & Zajic (1983) carried out laboratory pullout tests on the ground anchor and showed a significant increase in pullout resistance due to the pressurized grouting. Kleyner et al. (1993) discussed the effect of grout pressure on the capacity of bore-injected piles and anchors. Recently, Yin et al. (2008) investigated the increase of pullout resistance in a soil nailing system caused by pressurized grouting through the laboratory pullout tests. Even though some previous studies have applied the cavity expansion theory to the analysis on the enlargement of the anchor body diameter due to pressurized grouting, the penetration (permeation) characteristics of the cement grout have not been properly taken into consideration in their studies.

This paper evaluates the effect of pressurized grouting on pullout resistance of a compression ground anchor according to the soil types by performing both the pilot-scale laboratory chamber tests and field tests. Not only the cavity expansion theory but also the grout penetration theory are adopted in this study and are compared with experimental test results to investigate the effect of pressurized grouting on the enlargement of the anchor body diameter. Based on field ground anchor pullout tests, a new equation to estimate the pullout resistance proposed, which might be applicable to decomposed residual soils.

2 THEORIES UTILIZED FOR PRESSURIZED GROUTING

2.1 *Cavity expansion theory*

In this study, the cavity expansion theory based on the equations of elasto-plastic analysis by Yu & Houlsby (1991) is modified to be more suitable for analyzing the pressurized grouting.

The pressurized ground anchor is generally constructed by a continuous process of drilling and grout injection into a borehole under pressure. During drilling, the plastic zone is developed around a circular borehole leading to inward displacement in the stress state of $\sigma_r < \sigma_\theta$, where σ_r and σ_θ are stresses in the radial and tangential directions, respectively. This stress condition can be defined as an active loading condition. When pressurized grouting is performed, σ_r increases while σ_θ decreases in the plastic zone. Hence, the stress state moves towards an isotropic stress state, $\sigma_r = \sigma_\theta$, through a stress reversal, and then perhaps moves to another yield state where $\sigma_r > \sigma_\theta$. This stress condition can be defined as a passive loading condition. In this paper, the equations for a passive loading condition will be shown.

Figure 1 shows a borehole of radius a in an infinite soil mass. The borehole is subjected to an internal pressure, p_i, which simulates a pressurized grouting and initial in-situ isotropic stress, σ_0^∞. For the elastic region, $r \geq b$, the radial and tangential stresses can be derived by the Kirsh solution as follows:

$$\sigma_r = \sigma_0^\infty \left(1 - \frac{a^2}{r^2}\right) + p_i \left(\frac{a^2}{r^2}\right) \tag{1}$$

$$\sigma_\theta = \sigma_0^\infty \left(1 + \frac{a^2}{r^2}\right) - p_i \left(\frac{a^2}{r^2}\right) \tag{2}$$

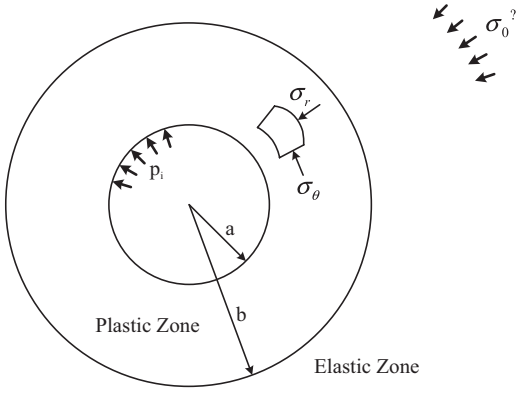

Figure 1. Elastic and plastic regions.

For a passive loading condition, the radial and tangential stresses in the plastic region ($a \leq r \leq b$) can be obtained as follows:

$$\sigma_r = \left(p_i + \frac{\sigma_c}{k-1}\right)\left(\frac{r}{a}\right)^{\frac{1}{k}-1} - \frac{\sigma_c}{k-1} \tag{3}$$

$$\sigma_\theta = -\frac{1}{k}\sigma_c + \frac{1}{k}\left[\left(p_i + \frac{\sigma_c}{k-1}\right)\left(\frac{r}{a}\right)^{\frac{1}{k}-1} - \frac{\sigma_c}{k-1}\right] \tag{4}$$

where $k = \tan^2\left(45 + \frac{\phi}{2}\right)$; and

$$\sigma_c = 2c\tan\left(45 + \frac{\phi}{2}\right) \tag{5}$$

The radius b for the passive loading condition can be obtained as follows:

$$b = a\left[\left(\frac{2\sigma_0^\infty - \frac{\sigma_c}{k}}{\frac{1}{k}+1} + \frac{\sigma_c}{k-1}\right)\frac{1}{p_i + \frac{\sigma_c}{k-1}}\right]^{\frac{1}{\frac{1}{k}-1}} \tag{6}$$

The radial displacement of a borehole can be obtained based on the elasto-plastic theory. The radial displacement at the borehole wall, $r = a$ under a passive loading condition can be expressed as Eq. (7):

$$u_r = \frac{1}{2G}a^{-\frac{1}{k_\psi}}\left[C(1-2\nu)\left(b^{\frac{1}{k_\psi}+1} - a^{\frac{1}{k_\psi}+1}\right) - D\left(b^{\frac{1}{k_\psi}-1} - a^{\frac{1}{k_\psi}-1}\right)\right] + u_{r(r=b)}\left(\frac{b}{a}\right)^{\frac{1}{k_\psi}} \tag{7}$$

$$C = \frac{(\sigma_h - \sigma_{r(r=b)})b^2 - (\sigma_h - p_i)a^2}{b^2 - a^2}; \quad \text{and } D = \frac{a^2b^2(a_{r(r=b)} - p_i)}{b^2 - a^2}; \tag{8}$$

where G indicates the shear modulus, ν is the Poisson's ratio, k_ψ is the dilation angle.

Therefore, Eq. (7) makes it possible to estimate the radial displacement of a borehole caused by pressurized grouting and to evaluate the enlargement of the anchor body diameter.

2.2 *Permeation characteristics of pressurized grouting*

The permeation (penetrability) of cement grout is affected subject to the grain size distribution of base soils and cement, the concentration and viscosity of grout suspensions, the pore size of base soils, injection pressure, and the permeability of base soils. Moreover, the viscosity of grout suspension varies with time caused by chemical reactions that occur when the grout suspension moves through pores in the soil matrix. The increased viscosity of grout suspension causes a reduction in the permeability of grout through the soil matrix. Kim et al. (2009) studied the permeation characteristics of cement grout based on spherical coordinates. This paper utilized the solution proposed by Kim et al. (2009) to estimate the permeation distance of cement grout for the pressurized grouting of the grout anchor.

3 LABORATORY CHAMBER TESTS

3.1 *Experimental set-up*

Pilot-scale chamber tests were performed in order to investigate the effect of pressurized grouting on ground anchor. Figure 2 shows the chamber and apparatus set-up with full instrumentation. The chamber consisted of a cylindrical tank with an inside diameter of 600 mm and a height of 300 mm. Two earth pressure cells and two Linear Variable Differential Transducers (LVDTs) were installed to measure the earth pressure and displacement of the borehole caused by pressurized grouting, respectively. In addition, three pore water pressure transducers were mounted inside the borehole to measure the changes of the excess pore water pressure inside the grout with time. The grout injection equipment consisted of a packing device installed on the upper cap of the chamber and injection tank, being designed to discharge the inside grout to the outside soil by air pressure.

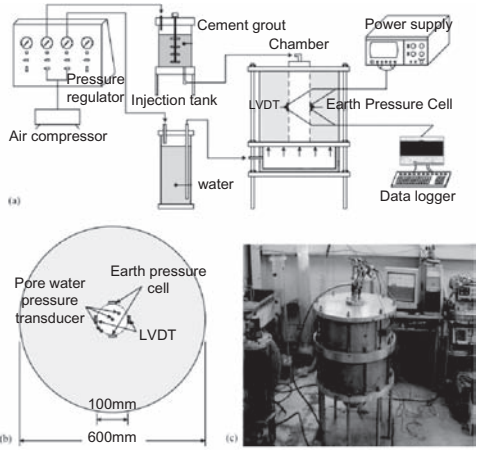

Figure 2. Experimental set-up for pilot-scale chamber test: (a) test set up with full instrumentation; (b) cross section of the chamber; and (c) photo of the chamber test in progress.

The soil samples for the chamber tests were collected from the areas of Jong-am Dong (Sample A), Jeon-nong Dong (Sample B), and Gong-duk Dong (Sample C) where the field tests were scheduled to be conducted. Soil properties of each sample were measured and summarized in Table 1. The injected grout suspension was prepared by mixing Portland cement with water to the ratio of 50%. The cement grout properties are summarized in Table 2. The viscosity change in grout suspension used in this study was measured by using a viscometer before injection. Figure 3 shows the viscosity of grout suspension with time and the relationship between grout viscosity and time is presented by the solid line. This curve is needed for the step wise numerical model shown in the next section (Kim et al. 2009).

The procedure for the chamber test was as follows. A soil specimen of 17.7 kN/m^3 unit weight was created by compaction, and LVDTs and earth pressure cells were installed to measure the expansion of the borehole and the pressure variation of the surrounding soil resulted from the grout injection. The drilling process was simulated by extracting a 100 mm diameter pipe after compaction which had been inserted during compaction. The vertical confining pressure of 88.5 kPa was applied to simulate an in-situ stress condition at a ground depth of 5.0 m. Subsequently, pressurized grouting was applied to three samples with the pressures of 196 kPa, 294 kPa, and 392 kPa, respectively.

3.2 *Penetration of cement grout into the soil*

The grout was injected for 1000 sec into the borehole. The amount of grout particles deposited in the soil matrix according to the distance from the injection hole was evaluated by using the step wise numerical model proposed by Kim et al. (2009) and is shown in Figure 4.

Even if the grout particles penetrate into the neighboring ground due to pressurized grouting, it does not necessarily confirm that the entire boundary in the neighboring ground is considered as the anchor body. Therefore, a certain criterion is required for the judgment of the boundary of an enlarged anchor body caused by the penetration of cement grout. For this purpose, the mixed soil-cement samples according to the mass of grout particles deposited per unit volume were prepared and uniaxial compression tests for each sample were

Table 1. Soil properties used in chamber test.

	Jong-am Dong (Sample A)	Jeon-nong Dong (Sample B)	Gong-duk Dong (Sample C)
Specific gravity, Gs	2.60	2.64	2.64
Friction angle, ϕ [deg]	32.74	34.41	31.67
Dilation angle, K [deg]	4.60	6.10	0.00
Cohesion, C [kPa]	20.47	25.57	25.51
Elastic modulus, E [MPa]	40.08	82.83	78.64
Poisson's ratio, kψ	0.400	0.394	0.407
Coefficient of permeability, k [cm/sec]	3.38×10^{-3}	2.21×10^{-4}	4.36×10^{-5}
Mean of pore radius lognormal distribution, m	–2.3055	–2.5859	–2.4487
Standard deviation of pore radius lognormal distribution, b	1.4097	1.2690	1.1071

Table 2. Cement grout properties used in chamber test.

Water-cement	50%
Initial concentration of grout	1.2 g/cm^3
Specific gravity of grout particle	3.0 g/cm^3
Average size of grout particle	0.011 mm

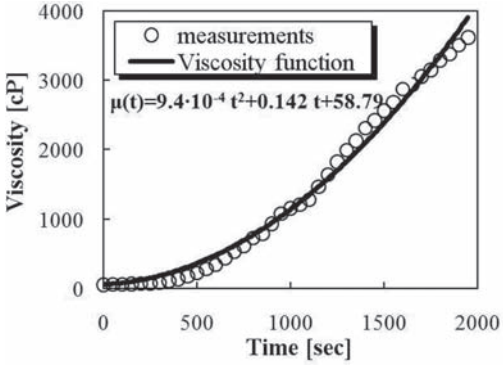

Figure 3. Change of grout viscosity with time.

carried out to evaluate the uniaxial compression strength. The results of uniaxial compression tests are shown in Figure 5. The criterion defined the mass of grout particles deposited per unit volume, $\sigma = 0.20$ g/cm^3, in which the sample shows a solid state, to judge the boundary of the anchor body of the ground anchor caused by the penetration of cement grout.

3.3 *Enlargement of anchor body diameter*

Table 3 shows the results of the enlargement of the anchor body diameter after 1000 sec pressurized grouting. The results were obtained from both the laboratory chamber tests and theoretical analyses.

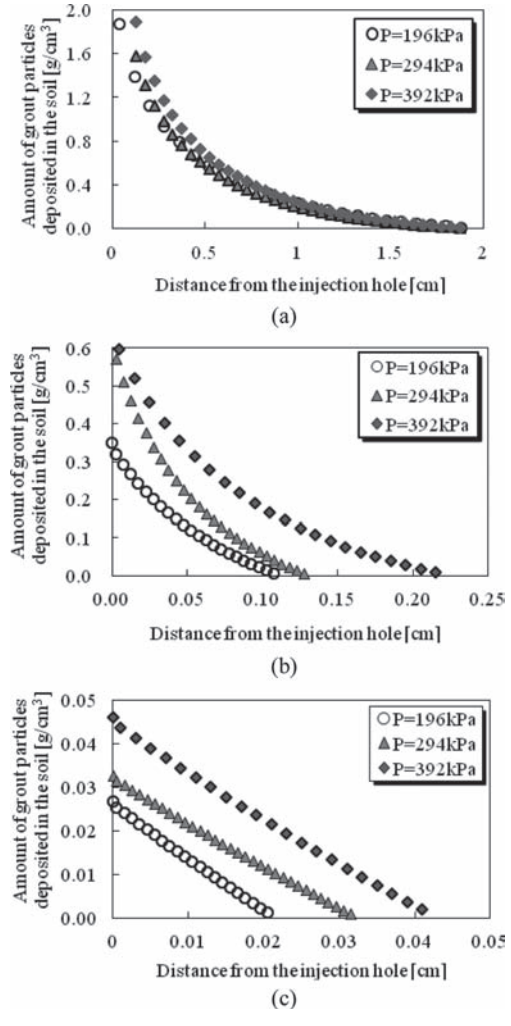

Figure 4. Amount of deposited particles with distance: (a) Jong-am Dong (sample A); (b) Jeon-nong Dong (sample B); and (c) Gong-duk Dong (sample C).

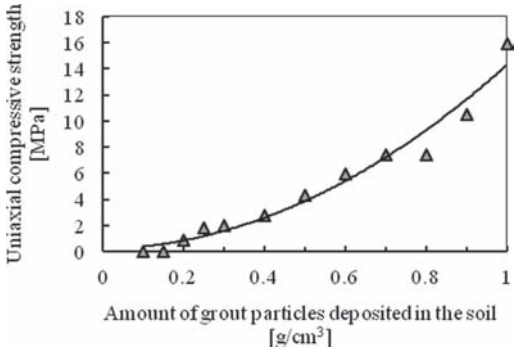

Figure 5. Result of uniaxial compression strength with amount of grout particles deposited.

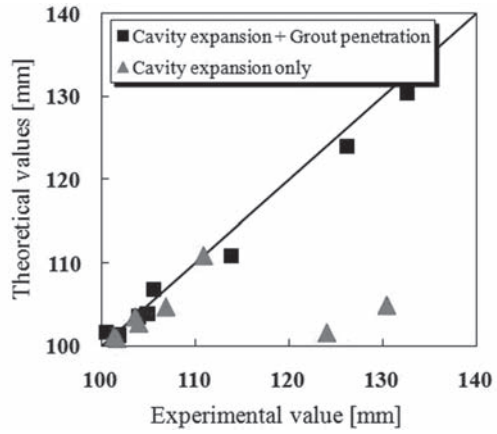

Figure 6. Comparison between test result and theoretical value of the enlargement of anchor body diameter.

Table 3. Results of enlargement of anchor body diameter.

	Results from theoretical analysis					Lab. test
	k [cm/sec]	Injection pressure [kPa]	Cavity expansion theory[1] [mm]	Grout penetration[2] [mm]	Cavity+ penetration[3] [mm]	Chamber test result[4)] [mm]
Sample A	3.38×10^{-3}	196	101.61	122.40	124.01	126.20
		294	104.91	125.50	130.41	132.41
Sample B	2.21×10^{-4}	196	100.94	100.65	101.59	100.48
		294	102.76	101.15	103.91	104.87
		392	104.72	102.10	106.82	105.54
Sample C	4.36×10^{-5}	196	101.27	–	101.27	101.87
		294	103.53	–	103.53	103.97
		294	102.76	–	110.80	113.87

1) Diameter obtained from cavity expansion theory only by using Equation (15) + 100 mm (borehole diameter); 2) Diameter obtained from grout penetration theory only by using step wise numerical analysis + 100 mm (borehole diameter); 3) Summation of cavity expansion and grout penetration ($^{(1)+2)}$ –100 mm (borehole diameter)); 4) Results from laboratory chamber tests.

The 4th, 5th, 6th and 7th columns indicate the final diameters of the anchor body evaluated from the cavity expansion theory (Eq. (7)) only, from the grout penetration theory proposed by Kim et al. (2009), from the summation of cavity expansion result and grout penetration result, and from the laboratory chamber tests, respectively. The comparison between the experimental test results (7th column) and the theoretical values (4th and 6th columns, respectively) is shown in Figure 6. The enlargement of the anchor body diameter estimated from the summation of the cavity expansion theory and grout penetration (6th column) matches well with that obtained from experiments. However, in the case where the ground has a larger permeability as noted in sample A, the evaluation of enlargement by adopting only the cavity expansion theory (4th column) can lead to underestimation. It can be concluded that the enlargement of the anchor body diameter caused by pressurized grouting must be estimated by combining the cavity expansion theory and the grout penetration theory, if the coefficient of permeability is larger than approximately 10^{-3} cm/sec.

4 FIELD TEST OF PRESSURIZED GROUTING GROUND ANCHOR

4.1 *Test method*

Field tests to measure the pullout resistance of the ground anchor, to identify the enlargement of the

ground anchor body due to pressurized grouting were carried out 22 times in 5 phases as shown in Table 4. Field tests were conducted in the areas where the soil samples for laboratory chamber tests were collected. The physical properties were obtained through the in-situ and laboratory tests and their results are shown in Table 5. Herein, the SPT-N_{60} values representing each ground were shown after being calibrated based on 60% energy efficiency in a standard penetration test.

The procedure for the installation of the pressurized grouting ground anchor is shown in Figure 7, in which the assembled tendons were inserted into the inside of a casing after drilling with double casing, and a cement grout with a 50% water-cement ratio was then injected into the borehole through pressurized grouting. Pressure was applied on the head of the casing immediately after the casing was pulled up to the top of the bonded length. To measure the pullout resistance in an installed ground anchor, curing was applied for three days after construction and pullout tests were then performed. Since the purpose of this study is to compare the pullout resistances of pressurized grouting

Table 4. Field test results.

Site	Soil type	Average SPT-N60	Permeability [cm/sec]	Test case	Injection pressure [kPa]	Pullout resistance [kN]	Diameter of anchor body [mm]
Jong-am Dong (1st phase)*1	Silty sand	8	6.15×10^{-3}	A-1	100	445.1	168.1
				A-2	100	551.0	162.7
				A-3	100	572.0	163.1
				A-4	100	403.0	162.2
				A-5	–	297.0	143.8
Jeon-nong Dong (2nd phase)*2	Decomposed residual soil	21	1.37×10^{-4}	B-1	–	325.7	156.0
				B-2	220	386.5	164.0
				B-3	250	447.9	165.6
				B-4	250	470.8	164.0
Gong-duk Dong (3th phase)*2	Decomposed residual soil	66	1.20×10^{-4}	C-1	–	503.7	140.3
				C-2	196	470.4	142.3
				C-3	157	477.3	141.6
Ga-jwa Dong 1 (4th phase)*2	Decomposed residual soil	15	5.27×10^{-4}	D-1	–	170.4	–
				D-2	–	176.5	136.1
				D-3	196	302.1	–
				D-4	294	272.6	143.2
Ga-jwa Dong 2 (5th phase)*2	Decomposed residual soil	15	5.27×10^{-4}	D-5	220	238.8	–
				D-6	250	103.9	–
				D-7	230	405.0	–
				D-8	200	114.2	–
				D-9	280	394.6	–
				D-10	230	207.7	–

*1) l = 6 m ; *2) l = 5 m.

Table 5. Properties of field soil.

	Jong-am Dong (Sample A-F)	Jeon-nong Dong (Sample B-F)	Gong-duk Dong (Sample C-F)	Ga-jwa Dong (Sample D-F)
SPT-N60 value	8	21	66	15
Friction angle, ϕ [deg]	32.74	34.41	32.49	27.84
Cohesion, C [kPa]	20.47	25.57	25.51	4.90
Elastic modulus, E [MPa]	40.08	82.83	87.64	–
Poisson's ratio, kψ	0.4000	0.394	0.407	–
Coefficient of permeability, k [cm/sec]	6.15×10^{-3}	1.37×10^{-4}	1.20×10^{-4}	5.27×10^{-4}

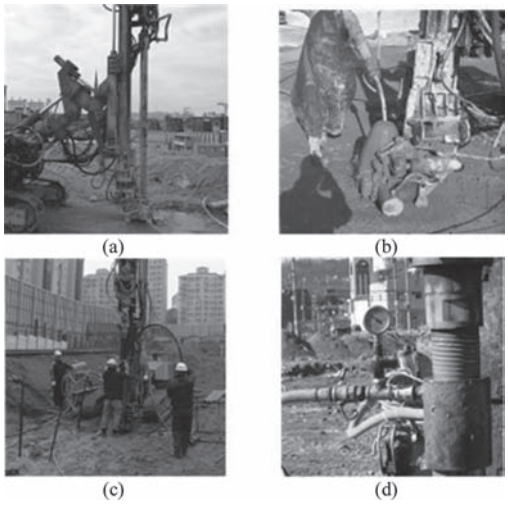

Figure 7. Procedure for installation of pressurized grouting ground anchor: (a) drilling with double casing; (b) gravitational grouting; (c) insert tendons into the borehole; and (d) pressurized grouting.

with those of non-pressurized grouting and at the same time to evaluate the decrease in pullout resistance caused by the group effect, the ultimate pullout resistance of the ground anchor is defined as the maximum load at which the pullout displacement occurs continuously with no increase in the load. After the pullout test, the anchor body was dug out and investigated to measure the enlarged diameter of the anchor body.

4.2 *Effect of the pressurized grouting on ground anchor*

The field ground characteristics, grout injection pressure, ultimate pullout resistance and enlarged diameter of the anchor body obtained from a series of field tests are summarized in Table 4. In the case where pressurized grouting is performed, other than the case of non-pressurized grouting, the ultimate pullout resistance was found to increase by 1.66 times for silty sand and 1.47 times for decomposed residual soil ($N_{60} < 50$) on average, which proved that the injection of pressurized grouting is beneficial to raise the ultimate pullout resistance of a ground anchor.

Figure 8 shows the relationships between (a) pullout resistance vs SPT-N_{60}; (b) pullout resistance vs permeability; (c) diameter of anchor body vs SPT-N_{60}; and the field test result vs theoretical value. Herein, the ratio of pullout resistance means the ratio of pullout resistance of the pressurized grouting ground anchor to

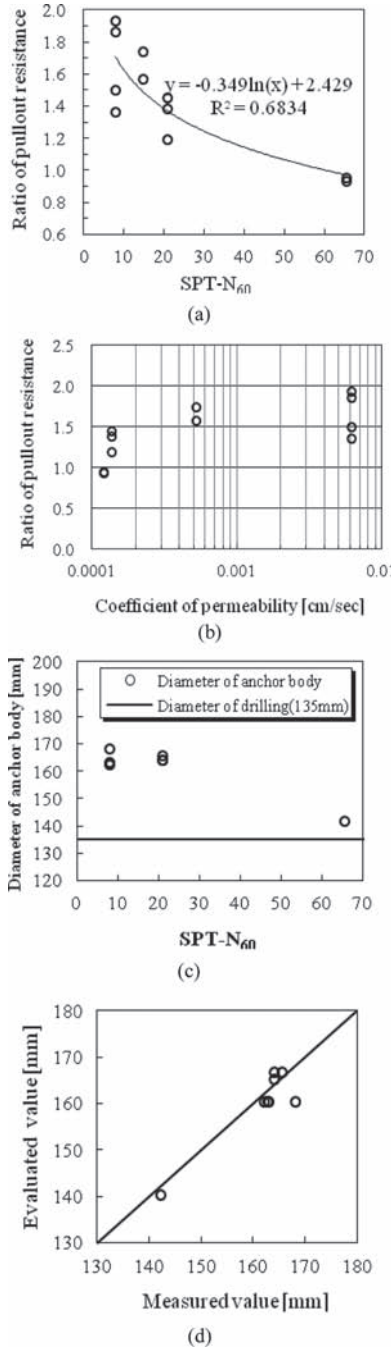

Figure 8. Field test results: (a) effect of pressurized grouting on pullout resistance according to SPT-N_{60} value; (b) effect of pressurized grouting on pullout resistance according to permeability; (c) enlargement of anchor body diameter according to SPT-N_{60} value; and (d) comparison of the enlargement of anchor body diameter between test result and theoretical value.

that of the non-pressurized ground anchor. When the pressurization was applied as can be seen in Figure 8(a) in comparison with non-pressurization, the field test results demonstrated that the ultimate pullout resistance for the case of decomposed residual soil whose SPT-N_{60} value was below 50 is increased by 1.19–1.74 times. However, the value for decomposed residual soil with an SPT-N_{60} value of more than 50 is increased by 0.93–0.95 times with little expectation of increasing pullout resistance due to pressurized grouting. As shown in Figure 8(b), it was found that a larger permeability in the ground corresponded to a higher effect in pullout resistance due to pressurized grouting. It was identified that the diameter of the ground anchor body in the case of performed pressurized grouting, exhibited a diameter larger than the drilled diameter as shown in Figure 8(c) when the ground has low SPT-N_{60} values. The enlargement of anchor body diameters estimated theoretically from the combination of the cavity expansion theory and the grout penetration theory matched reasonably well with the results obtained from field tests as shown in Figure 8(d).

5 CONCLUSIONS

The results of this study can be summarized as follows:

1. It was found that the grout penetration theory should be considered along with the cavity expansion theory in evaluating the enlargement of the anchor body diameter caused by pressurized grouting, if the permeability of the ground is larger than 10^{-3} cm/sec.
2. When the pressurization is applied to the compression anchor, the ultimate pullout resistance for the case of decomposed residual soil whose SPT-N_{60} value is below 50 should be increased by 1.19–1.74 times. However, the value for decomposed residual soil with an SPT-N_{60} value of more than 50 should be increased by 0.93–0.95 times with little expectation of increasing pullout resistance due to pressurized grouting. In addition, it is found that a larger permeability in the ground corresponds to a higher effect in pullout resistance due to pressurized grouting.

REFERENCES

Hobst, I.L. & Zajic, I.J. 1983. Anchoring in rock and soil. Amsterdam: 2nd Ed., Elsevier Scientific Publishers.

Kim, J.S., Lee, I.M., Jang, J.H., and Choi, H.S. 2009. Groutability of cement-based grout with consideration of viscosity and filtration phenomenon. *International Journal for Numerical and Analytical Methods in Geomechanics* 33(16): 1771–1797.

Kleyner, I.M., Krizek, R.J., and Pepper, S.F. 1993. Influence of grout pressure on capacity of bore-injected piles and anchors. *Proc., of the International Conference on Grouting in Rock and Concrete*, Salzburg, Austria: 159–165.

Yin, J.H., Su, L.J., Cheung, R.W.M., Shiu, Y.K., and Tang, C. 2008. The influence of grouting pressure on the pullout resistance of soil nail in compacted completely decomposed granite fill. *Geotechnique* 59(2): 103–113.

Yu, H.S. & Houlsby, G.T. 1991. Finite cavity expansion in dilatants soils: loading analysis. *Geotechnique* 41(2): 173–183.

Geotechnical Aspects of Underground Construction in Soft Ground – Viggiani (ed)
© 2012 Taylor & Francis Group, London, ISBN 978-0-415-68367-8

Design and construction of anchored diaphragm walls and dewatering system for the excavation of a two-level basement car park at the Al Ghazala Hotel Intercontinental in Tripoli—Libya

C. Asioli, M. Agostini & T. Minotti
Trevi S.p.A., Italy

ABSTRACT: This paper covers the adopted design criteria and the main results obtained in the design of the multi-anchored diaphragm wall and the dewatering system for the excavation of a two level basement car park at the Al Ghazala Hotel Intercontinental in Tripoli, Libya. The following design aspects are particularly highlighted: site geotechnical conditions and adopted design geotechnical parameters, preliminary design carried out to check the conceptual design and to choose the most economic solution, final construction design of diaphragm walls, anchors and dewatering system. Moreover, construction aspects concerning diaphragm walls, ground anchors and dewatering wells are also illustrated.

1 INTRODUCTION

From July 2007 until March 2008 TREVI S.p.A. was engaged in the design and construction of anchored diaphragm walls and dewatering systems for the excavation of a two-level basement car park at Al Ghazala Hotel Intercontinental in Tripoli, Libya.

The investor of the project was MAGNA PROPERTIES GROUP Ltd.—Libya and the Main Contractor was MAN ENTERPRISE S.A.L.. Design and construction management was performed by DAR ALHANDASAH Engineering.

Currently, the basement is completed and the building is under construction.

Figure 1. The site.

2 PROJECT DESCRIPTION

The project's location is in the town centre of Tripoli, Libya, approximately 150 m from the Mediterranean coast, near Al Ghazala round about.

The project dealt with a prestigious, multi-use development in the bay area of Tripoli overlooking the Mediterranean Sea. The development includes a two-level basement car-park, which is extending across the whole area of the site.

The site area had an almost flat shape of approximately 195 m × 70 m and the ground levels varied from 3.4 to 7.0 m from mean sea level.

For the raft foundation construction it was necessary to excavate the area down to –5.0 ÷ –8.0 m elevation. The excavation depth, measured from the ground level, is in the range of 8.3 ÷ 12.0 m.

Temporary support of the soil was achieved by multilevel anchored diaphragm walls.

The diaphragm wall, 600 and 800 mm thick, with a depth up to 18 meters, provided a continuous temporary structure to prevent soil collapse and water inflow during the digging works. The excavation was carried out by using a cable suspended, hydraulically operated clamshell. Two/three anchors' levels with 3 and 4 strands were adopted.

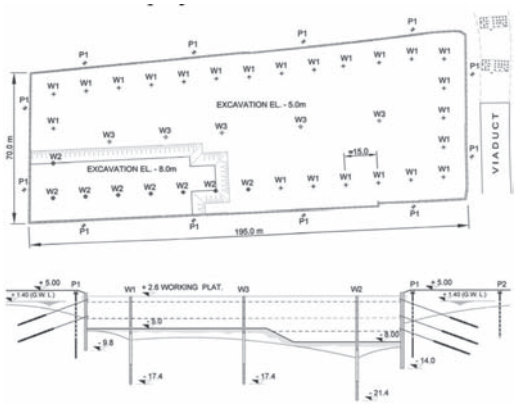

Figure 2. General layout and typical section.

For the deepest level, in order to avoid high inlet water flows through the wall, a preventer device was applied directly to the anchorage reservation installed in the diaphragm wall.

In order to control ground water level, 31 wells with a length of 20 ÷ 24 m were installed inside the excavation area 10 m far from the diaphragm walls. Longitudinal wells spacing was approximately 15 m. 5 additional wells were installed in the middle of the excavation area and were also utilized to check the groundwater level during dewatering stages. All the wells had a drilling diameter of 800 mm with an internal 355 mm diameter steel casing and a slotted length of 7 m.

Submersible pumps having discharge capability between 90 to 420 l/min with a minimum prevalence of 25 m were installed inside the wells.

Figure 2 shows the general layout and the typical section of the project.

3 GROUND CONDITIONS

The soil investigation, carried out by Al-Tamier Engineering Consulting Bureau, was carried out in three phases from June 2005 to October 2006. It comprised a total of 14 boreholes drilled to depths varying from 24 m to 55 m.

Standard Penetration Tests (SPT) were carried out in coarse grained deposits and in fine grained or completely weathered rock. Coring rock samples, where rock strata were encountered, were retrieved using Double Tube Core Barrel. Upon completion of boreholes, standpipes and piezometers were installed to monitor the ground water table. Rising head tests were performed into eight boreholes using a submersible pump and three pumping tests were also carried out into two boreholes after enlarging the borehole diameter. Physical, mechanical and chemical laboratory tests were carried out on soil samples and intact cylindrical rock core specimens taken from the boreholes.

The subsoil conditions encountered in the drilled boreholes indicated that in the first 3.0 m the subsoil consisted of dark brown to grey sands with some silts and some gravels, followed by a 27.0 m thick layer of light brown fine sands with some silts and some gravels (Pleistocene aged Gargaresh Formation). Thin layers of highly weathered limestone with roughly a 0.5 m thickness were encountered during the drilling. At a depth of 14.5 ÷ 15.5 m, the sand became cemented with very high SPT values.

This layer is followed by a layer of rounded boulders and fine sands whose thickness varied from 2.0 m to 4.0 m.

Finally a layer of slightly to highly weathered limestone, calcarenite and claystone (Middle Miocene Al Khums Formation), which continued till the end of boring, was encountered at a depth of about 35.0 m.

Ground water table is approximately +1.4 m from mean sea level.

Soil is mostly fine to medium sand (63%) with gravel (17%) and silt (20%). Prevalence of non plastic material is also confirmed by Atterberg Limits.

Relative density (Dr%) was evaluated from SPT test by means of the Skempton (1986) correlation for NC fine sands, angle of internal friction has been assumed according to Schmertmann (1977) suggestion, and elastic modulus was estimated according to D'Apollonia (1970) for NC fine sands.

Back analyses of pumping tests were carried out using the well theory of free aquifer, in order to estimate the average soil permeability.

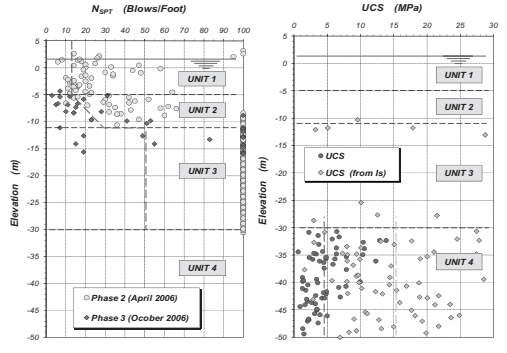

Figure 3. SPT values and UCS resistance.

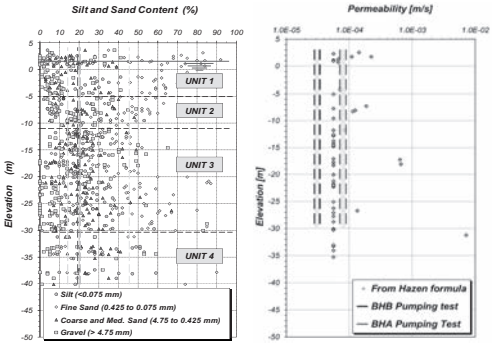

Figure 4. Fine content distribution and permeability.

Soil permeability was in the range of 7.1 ÷ 8.9 10^{-5} m/s for test A and in the range of 2.8 ÷ 3.4 10^{-5} m/s for test B. Figure 4 shows permeability values estimated by sieve analysis, using Hazen formula, and by pumping tests.

In summary, the design soil stratigraphy and the geotechnical design parameters adopted in the calculation were:

Unit 1: from ground level to –5.0 m, sand with silt and gravel. ($\gamma_n = 18.5$ kN/m³, $\varphi' = 30°$, $E_{50} = 5.5$ MPa; $E_{ur} = 14$ MPa; $k_h = 1.0 \times 10^{-4}$ m/s).
Unit 2: from –5.0 to –11.0 m, fine to medium dense sand. ($\gamma_n = 19.0$ kN/m³, $\varphi' = 33°$, $E_{50} = 13$ MPa; $E_{ur} = 32.5$ MPa; $k_h = 1.0 \times 10^{-4}$ m/s).
Unit 3: from –11.0 m o –30 m, very dense/cemented sand. ($\gamma_n = 20.0$ kN/m³, $\varphi' \geq 35°$, $E_{50} = 24.7$ MPa; $E_{ur} = 62$ MPa; $k_h = 6.0 \times 10^{-5}$ m/s).
Unit 4: below –30 m, weathered limestone ($k_h = 1.0 \times 10^{-5}$ m/s). This unit has been considered only for dewatering analysis.

4 PRELIMINARY ANALYSIS

In order to evaluate the dewatering effects on the adjacent structures, select the wells position and check the wall's dimension quoted in the conceptual design, a preliminary calculation was carried out.

In order to take into account all the aspects involved with the dewatering system and with the excavation phases (settlement of the adjacent building, position and number of wells, stresses on the diaphragm wall and anchors, bottom excavation stability, global stability, etc.) a FEM analysis has been carried out using Plaxis® code.

A Hardening Soil Model, with a different stiffness for primary loading or unloading-reloading stress paths, was adopted to schematize soil layers.

The three following different models were analyzed, with different pumps position and wall embedded length, to find out the most economic solution.

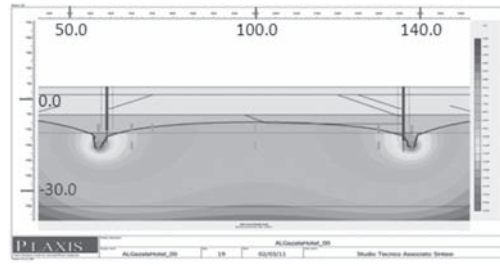

Figure 5. Model A—G.W. Head (Red = –15 m; Blue = 3 m).

Model A: dewatering by external deep wells; wall embedment length 5 m.
Model B: dewatering by internal deep wells; wall embedment length 5 m.
Model C: dewatering by internal deep wells; wall embedment length 9 m.

Figure 5 shows the position of the water level after the water table lowering in the Model A (by external wells). In order to maintain the water table inside the excavation area below the final excavation level, the required pumping rate was 80 m³/day/m and the outside water table was lowered to –13.0 m elevation.

The maximum vertical settlements were in the range of 26 ÷ 30 mm with a very wide influence area.

In models B and C, adopting three internal wells, the external water table was lowered to a –5.0 m elevation and the maximum vertical settlements were in the range of 20 ÷ 24 mm.

Required pumping rates, to maintain the water table below the final excavation level, were respectively equal to 45 and 35 m³/day/m.

The 4 m more diaphragm wall length of model C didn't bring big advantages, hence the inside position of the wells and the diaphragm wall embedment length of 5 m were chosen (model B) in order to have a smaller water discharge and keep the external water level as high as possible.

Wall thickness of 600 and 800 mm and anchor levels quoted in the Conceptual Design were confirmed by the preliminary analysis.

5 DIAPHRAGM WALLS' FINAL DESIGN

Due to different external surcharges and geometries, six different sections were analyzed in order to achieve the most economic solution for the retaining wall. The deepest section geometry (type 2) is illustrated in Figure 6.

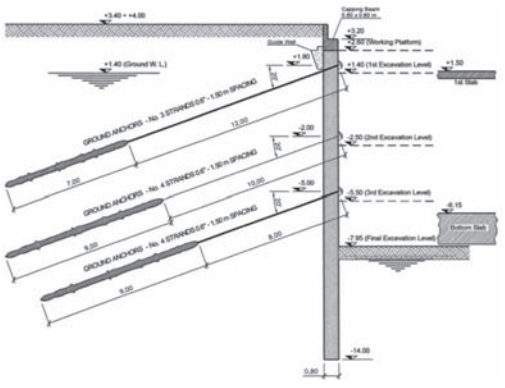

Figure 6. Section type 2.

5.1 *Method of analysis*

In order to evaluate stresses in the diaphragm wall and anchors, the computed program PARATIE v.6.2 (distributed by Harpaceas®), which gives reliable results despite its simple use, has been utilized.

The program takes into account the soil-structure interaction and is able to follow the diaphragm walls' behavior during all execution phases.

Diaphragm wall is modeled by means of a one-dimensional linear elastic finite element with a bending stiffness "EJ" (beam element); the behavior of soil is taken into account by elasto–plastic springs, jointed to the nodes of the beam element, having a stiffness "k" proportional to the soil's in-situ stiffness. Moreover, the code allows to model support structural elements like anchors and props, as elastic springs with an axial stiffness "EA".

The soil-structure interaction problem is solved adopting the Winkler's model which subdivides the soil into independent strata.

The elasto-plastic constitutive law used to model the behavior of the soil is defined by the active and passive pressure coefficient. When the analysis starts, the soil is in geostatic conditions i.e. the ratio σ'_h/σ'_v is equal to k_0 and the soil behaves elastically until the ratio σ'_h/σ'_v is in the range (k_a, k_p), when the ratio σ'_h/σ'_v reaches the limit value k_a or k_p stresses are set to active or passive pressure.

5.2 *Calculation phases*

According to construction sequences the following calculation phases have been considered:

1. Excavation up to elevation +1.4 m;
2. Installation and tensioning of the first anchor's level;
3. First dewatering stage (internal water level at –3.0 m) and excavation up to elevation –2.5 m;
4. Installation and tensioning of the second anchor's level;
5. Second dewatering stage (internal water level at –6.0 m) and excavation up to elevation –5.5 m;
6. Installation and tensioning of the third anchor's level;
7. Third dewatering stage (internal water level at –8.5 m) and excavation down to elevation –8.0 m;
8. Construction of the bottom slab;
9. Detensioning of the third and second level of anchors;
10. Construction of the top slab;
11. Detensioning of the first level of anchors;

Soil stiffness parameters have been calibrated on FEM results and are illustrated below:

- Unit 1: $E_{vc} = 37$ MPa, $E_{ur} = 93$ MPa;
- Unit 2: $E_{vc} = 40\ [(\sigma'_v/100)]^1$ MPa, $E_{ur} = 2.5\ E_{vc}$;
- Unit 3: $E_{vc} = 71\ [(\sigma'_v/100)]^1$ MPa, $E_{ur} = 2.5\ E_{vc}$;

To take into account the worse hydraulic condition, a hydrostatic water pressure distribution on the faces of the wall has been considered, adopting the original external water level and assuming that the internal water level would be 50 cm below the excavation level.

5.3 *Results*

Structural calculation of the steel reinforcement was performed according to Eurocode EC2 "Design of concrete structures", considering a minimum value of 1.5 for the partial safety factor on load (γ_L).

Since such factoring is incompatible with wall-ground interaction analysis as it introduces artificial yielding in the ground springs, design stresses were calculated applying the safety factor directly to the characteristic stresses.

Anchors bond length, executed with I.G.U. method (single stage grouting at low pressure), was calculated according to the well-known Bustamante-Doix proposal considering an ultimate adhesion between foundation and soil equal to 240 kPa.

Allowable capacity of temporary anchors was evaluated assuming a safety factor equal to 2.0.

As far as the deepest section's results are concerned, the PARATIE program has been compared to results from PLAXIS calculation. Figure 7 shows good agreement between the bending moment evaluated with the two different analyses.

5.4 *Global stability*

Global stability analysis has been conducted via c'/φ' reduction procedure available in Plaxis. The program reduces soil resistance parameters until failure is reached.

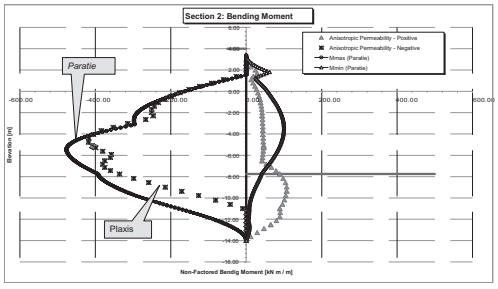

Figure 7. Results comparison.

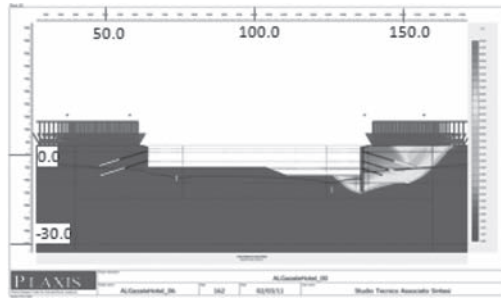

Figure 8. Failure mechanism for section 2. (Displacement label: Red = 10 m; Blue = 0 m).

Therefore the safety factor is:

$$FS = c'_{design} / c'_{failure} = \tan \cdot (\varphi'_{design}) / \tan (\varphi'_{failure})$$

The minimum safety factors obtained were 1.68 for the deepest section (type 2) and 1.55 for section 1.

Figure 8 shows the collapse mechanism in correspondence of the final excavation level, considering anisotropic condition for soil permeability.

6 DESIGN OF THE DEWATERING SYSTEM

Dewatering analysis was carried out by Plaxis® considering an isotropic soil permeability ($k_h = k_v$) which maximizes the water discharge quantity.

Pumping wells were located inside the excavation area in two lines, approximately 10 m far from diaphragm walls. Pumps elevation has been considered at the middle depth of the slotted length of wells: pump #1 (left side) was at –10 m and pump #2 (right side) was at –14.5 m.

Dewatering simulation was executed by an iterative calculation, changing the water discharge until the piezometric level inside the excavation area was 50 cm below the excavation level. In this way it was possible to find out the global water discharge necessary to lower the water for each dewatering stage.

Figure 9 shows flow field for the final dewatering stage.

At the final excavation depth, the maximum water discharge was 27 m³/day/m for the pump #2, close to the deepest section, and 16 m³/day/m for the pump #1 located where the maximum excavation reached –5.0 m. Considering the perimeter of the rectangle containing all wells, the total water discharge for the whole area has been estimated as follows:

$$Qt = 16 \times 350 \text{ m} + 27 \times 100 \text{ m} = 8300 \text{ m}^3/\text{day}.$$

Assuming a factor of safety equal to 1.5, the pumping system was dimensioned for 12500 m³/day.

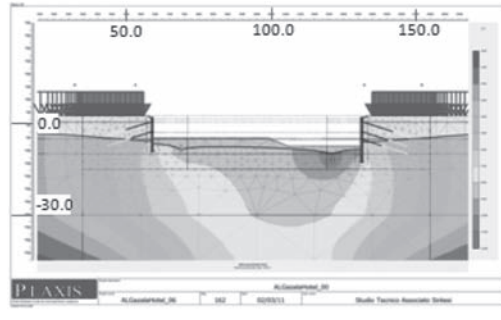

Figure 9. Piezometric head at final dewatering stage. (Red = –12.0; Blue = 0.0 m).

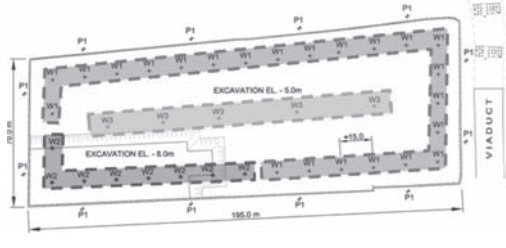

Figure 10. Wells distribution.

A total of 31 main wells were adopted, plus 5 additional wells, positioned in the middle of the excavation area, to be activated only in case of necessity.

Inside each well, a D = 355 mm steel pipe having a screen length of 7 m was positioned for pump installation. A maximum slot size equal to 2 mm with a 10% minimum slotted surface has been adopted.

Six inches submersible pumps, having a working discharge capability between 130 to 600 m³/day (90 to 420 l/min) with a minimum prevalence of

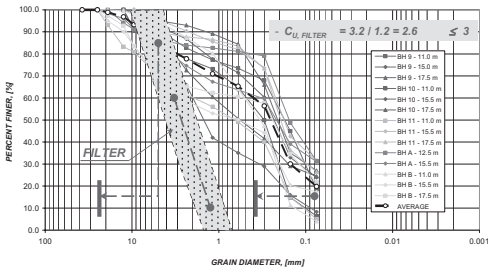

Figure 11. Grain size distribution of the filter.

25 m were selected. In order to monitor the ground water level outside the excavation area, 13 standpipes were installed all around the diaphragm wall perimeter.

6.1 *Filter material*

Filter grain size distribution has been designed according to U.S. Corps of Engineers (1955) "Drainage and Erosion Control" and Ciria report C515 "Groundwater Control—Design and Practice".

In particular, the following criteria were adopted:

- The D_{15} size of the filter should not be 5 times greater than the D_{85} size of the natural soil surrounding the filter (to prevent movement of fines from the aquifer).
- The D_{15} size of the filter should not be 4 times less than the D_{15} size of the protected material (filter more permeable than the aquifer).
- The maximum size of the filter particles (D_{100}) should not be bigger than 9.5 mm.
- Uniformity coefficient of the filter ($C_U = D_{60}/D_{10}$) should be less than 3 (to minimize risk of segregation during placement).

Figure 11 shows the adopted filter grain size distribution, evaluated by taking into account the average grain size distribution of the natural soil in correspondence of the slot part of the pipe.

7 CONSTRUCTION

7.1 *Diaphragm walls*

The diaphragm wall excavation was carried out by using a SOILMEC BH-12 hydraulically operated clamshell, suspended from a Link-Belt 318 crane. A service crane having a lifting capacity of 55 tons was adopted for cage installation and concreting. The trench stability during excavation was assured by the presence of stable bentonite suspension.

Figure 12. Soilmec BH12 clamshell.

Figure 13. Stop-end extraction by hydraulic jacks.

Figure 14. Anchors executions.

After completion of primary panels excavation and before steel cage installation, two steel sheet piles (stop ends) were installed at both ends of the trench. The stop ends were extracted after the concrete pouring, in order to create a non linear

contact with the concrete of the secondary panels and increase the shear resistance of the joint.

33% of regular panels and all irregular ones (corners and multiple panels) were tested for integrity using cross-hole sonic test. For each panel, 4 sonic pipes were installed with the steel cage.

7.2 *Anchors*

Temporary anchors were constructed in compliance with the European code EN 1537—"Execution of special geotechnical work—Ground Anchors".

Two Soilmec SM 405/8 drilling rigs equipped with a mast extension able to reduce the rods handling operations were utilized. The cased rotary drilling method was adopted to prevent soil collapse of the sandy soil.

For the deepest anchor level, in order to avoid high inlet water flows through the wall, a "preventer" device was applied directly to the anchorage reservation connected to the steel cage during the diaphragm wall execution.

Anchors were injected in a single stage at low pressure (max net pressure 5 ÷ 6 bar) using a dedicated grouting pipe right after the completion of the installation. The drilling fluid was displaced by the grouting pumped from the tip of the anchor.

Anchors' pre-stressing was carried out by single unit hydraulic jacks fed by a hydraulic power pack unit.

During stressing operations, the behavior of all anchors was tested up to 1.2 times the design load in order to compare it with the theoretical design behavior.

The effective free length (L_{ef}) had to be between the following limits:

$$0.9 \times L_{free} \leq L_{ef} \leq L_{free} + 0.5\ L_{bond}$$

Figure 15 shows some examples of the acceptance test.

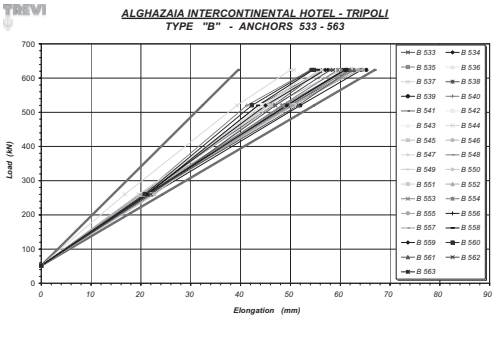

Figure 15. Examples of the acceptance test.

Figure 16. Situation before pumps activation.

Figure 17. Situation after pumps activation.

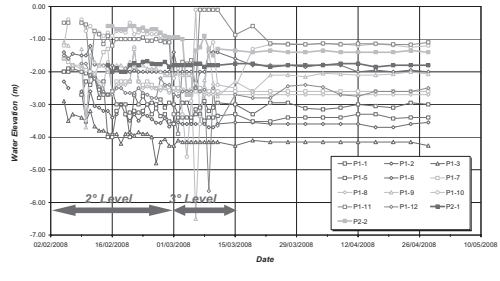

Figure 18. Water level monitoring.

7.3 *Dewatering*

Drilling of wells was executed without bentonite suspension, after all the surrounding diaphragm walls were completed. A temporary 800 mm casing, was installed by means of a Soilmec R50 hydraulic rotary rig. After each hole was drilled to its full length, it was flushed out with clean water to remove any loose material. The well screen and casing were then installed. The filter material was eventually introduced by gravity feed down the outer annulus. The temporary casing was removed as the filter sand was placed.

The well was then developed by airlift for a 1 hour minimum time or until the discharge water was free from drilling mud and/or fines. Admissible sand content after well development should be less than 100 p.p.m.

A 6" diameter electric submersible pump (type Lowara 6Z611/5 and 6Z621/2) suspended by means of a support rope, was installed in each well with the pump inlet located towards the base of the well.

The discharge's main take-off was installed around the excavation area by Main Contractors with take offs at each well location; the take-off was to be fitted with a non return valve.

Water discharge was managed by Main Contractor.

An average of approximately 10000 m^3 of water per day has been discharged for one year. Sedimentation tank was not necessary.

13 observation standpipes were installed for monitoring drawdown water levels outside the area. Records for a 3 month period, in correspondence of the soil mass excavation phases and anchors execution, show a water lowering just outside the diaphragm wall, varying from 2.5 to 5.5 m compared with the natural level.

When the construction basement was completed, approximately one year after pumps installation (February 2008–March 2009), pumps were extracted and wells were grouted by cement mortar.

7.4 *Production*

A total of 7250 m^2 of diaphragm walls was completed with a single equipment in 66 working days (11 weeks), from October to December 2007, with an average production of 110 m^2 per day and a peak of 200 m^2 per day.

After diaphragm walls' completion, 36 wells were executed in 15 working days.

The soil mass excavation of approximately 150000 m^3 and the simultaneous installation of 575 anchors (10200 m) were completed in 66 working days, from January to March 2008, using two drilling rigs with an average production of 26 anchors per week per rig.

8 CONCLUSIONS

This was a real "Teamwork Project". All parties involved did their best, bearing in mind the benefits for the Project.

Since the design stage, up to the completion of the soil mass excavation, all issues have been approached and rapidly resolved with the involvement of the Engineer, the Main Contractor, the Foundations Specialist and the Designer.

A remarkable time-saving result has been achieved during the anchors construction phase because the excellent cooperation between the Main Contractor, who was in charge of the soil mass excavation, and the Specialized Contractor avoided any loss of time.

The strong links between the dewatering system and the diaphragm walls design gave us the opportunity to provide to the Engineer with the overall project design.

ACKNOWLEDGEMENTS

The authors wish to thank the professional team of MAN Enterprise S.A.L., DAR Al-Handasah Engineering and our Consultant firm Studio Sintesi for their cooperation to the design and construction of the project, specifically:

Mr. Antoine Fakhry (MAN Country Manager)
Mr. Bassam El Amil (MAN site Manager)
Mr. Hatem El Gamal (DAR site Engineer)
Mr. Augusto Lucarelli (Studio Sintesi)

Special thanks to Mrs Silvia Bertozzi for her valuable support in preparing a more comprehensible English version of the text.

Geotechnical Aspects of Underground Construction in Soft Ground – Viggiani (ed)
© 2012 Taylor & Francis Group, London, ISBN 978-0-415-68367-8

Underground car parks in Italian urban areas: Not an easy task!

G. Pagotto, P. Silvi & F. Casadei
Trevi SpA, Cesena, Italy

ABSTRACT: TREVI SpA has been involved for over 15 years in the field of underground car parks construction in Italian urban areas, offering a turn-key product named TreviPark. It is a cylindrical automated underground silo. This experience offered a comprehensive view about several aspects to be faced in order to come out with the final product. Among these aspects, we mention: human relations with job site neighbours, relations with the ancient heritage such as underground archaeological finding, the impact with the existing underground utilities, monitoring of the neighbouring pre-existing structures before, during and after the construction stage, relevant aspects of the design (soil investigation, loading, modelling of anticipated construction tolerances, impact on local hydrology and deformations behind the retaining wall), technological features in order to meet the design requirements like drilling verticality, walls and basement's waterproofing.

This paper would like to offer an overview of these aspects by focusing on some of them.

1 INTRODUCTION

For over 15 years, Trevi SpA, a worldwide leader in the field of special foundations, has been offering the private and public sector a mechanised, automatic, fully secure and unmanned underground car park that is commercially known as TreviPark (see Fig. 1). Civil and also mechanical components of the car park are designed, manufactured and installed by the Trevi Group; particularly the mechanisation is a Soilmec SpA product. The reduced sizes of the entry and exit bays (without entry ramps) make TreviPark's environmental impact negligible, the surrounding area may be maintained in its original conditions and urban facilities may be enhanced. The system can be successfully introduced and integrated into all urban environments, both historical and modern. All TreviParks are connected to a dedicated Control Centre that operates 24 hours a day, giving instructions to the client, operating thanks to a remote control system on the software which manages the electro-mechanical unit and by coordinating emergency reparations and maintenance systems.

The product is attractive because of its efficiency and pleasantness, and the experience gained over these years in the acquisition, management and construction stages allow us to emphasize some aspects that are usually underestimated and could be a real surprise for the Contractor, especially when operating in Italian urban areas. In the following paragraphs some of these aspects will be shortly described.

Figure 1. TreviPark construction sequence: secant piles retaining wall and excavation, placing of prefabricated internal structures, installation of car lift and final urban facilities.

2 DEALING WITH NEIGHBOURS

In order to successfully execute an underground car park, it might be useful to involve and make sensitive the public opinion to not only the

advantages deriving from the execution of the intervention, but also to the performance of the various site activity phases. In agreement with what usually happens in other European countries, also in Italy, for the execution of some underground car parks, it has been possible to achieve a remarkable result by regularly informing the citizens about the works' progress, with forecasts about the final date of the works, the problems which had to be faced and solved and the various activities in progress (this is possible through press releases and other media, but also through illustrative panels placed outside the site). Citizens can be also invited, upon previous agreements, to visit the site so that they can personally realize what's going on and how works are carried out. Some sections of the fence around the site might be left open in order to allow residents and citizens to follow, day by day, the trend and the progress of the works.

The Italian law offers the residents living close to the car park a whole series of advantages in order to purchase or use the built car stalls, but despite these opportunities, in many occasions and especially in the starting phases, residents are likely to obstruct the execution of this type of works because they fear a consistent impact on the pre-existing physical and cultural structures, both during the execution and their following running. Districts' committees are then established and they can delay the issuing of the authorizations by the relevant Departments (it usually takes 3 ÷ 6 months but even 1 ÷ 2 years can be required). Anyway, our experience has shown, in many cases, that, once works were completed, those who were contrary to the project, realized then how good the initiative was and they even bought the built car stalls.

3 MONITORING OF EXISTING STRUCTURES

Before the site setting up for the car park execution, status surveys (legalized certificates) are usually carried out with regard to the buildings close to the car park to be constructed. This is in order to highlight their structural conditions at the time of the survey, that is, before the start of the works by means of photographs, assessments and measurements of the buildings' fissuring status, etc… .

At the same time, bench marks are installed for the topographic measurements to be performed in the most significant points of the buildings surrounding the areas interested by the car park construction. Level measurements are made and repeated along a significant time period (at least 6 months) before the works' start, in order to set the reference value and check that no deforming phenomena are in progress and also check the effect of the weather changes on the movements of the buildings and the optical measurements.

During the execution phases of the work, topographic measurements are carried out with variable frequencies per each type of phase. Warning threshold values are defined as adequate whenever they are exceeded and works in progress are to be interrupted in order to study the phenomena in progress and decide on the actions to undertake (i.e. the Aposa torrent, Via Finelli, Bologna).

These topographic readings are usually prolonged also after the completion of the car park, with a monthly frequency and for at least one year.

In some cases, in order to reassure the residents, and before starting the works, some dynamic monitoring surveys have been carried out in some buildings. In this way it was possible to detect the effects of environmental vibrations of the cars' traffic with no works in progress, 24 hours a day. Then, data were compared with the vibrations produced in the site, especially during the most critical phases of the car park construction (excavation, laying of the reinforcement cage, concreting, etc…). Results have highlighted that in the examined sites (i.e. Via D'Azeglio, Bologna) the vibrations induced by the works were of minor entity (maximum peak particle velocity ppv_max = 0.46 mm/sec), comparable to those of the normal environmental noise (ppv_max = 0.22 mm/sec), and, anyhow, within the limits set by the rules as per the type of controlled buildings (threshold for damage ppv = 3.0 mm/sec).

4 ANCIENT HERITAGE

In addition to the possible presence of architectonic, monumental and landscape limitations on the surface, there is a further element which must not be neglected, and precisely, the presence of archaeological finding in the underground.

By archaeological finding we mean any kind of finding linked to the past, also relating to not very long ago, on whose destiny the Department of Archaeological Heritage ruling on the area must decide, with reference to periods before the middle age, or the Department of Architectonic and Monumental Heritage for earlier ages. Since Italian cities are mainly historical cities which changed over the time due to subsequent stratifications, it's very common to find historical finding whenever the ancient part of the city is excavated.

Sometimes small and removable findings of minor importance are encountered, but it might happen to find more valuable remains: in this case the relevant Department will stop the works for a more or less long time (i.e. in Piazza Fabbri, Cesena, Figure 2,

Figure 2. Archaeological campaign at Fabbri square in Cesena (detail of a Roman mosaic 1st cent. A.D.).

for 6 months and in via d'Azeglio, Bologna, for 2 years) in order to ascertain, through an excavation campaign made by qualified personnel, the entity and the consistence of the findings, and then assess their destination.

In order to assess and estimate the costs involved by the archaeological risks, it is advisable to carry out preliminary archaeological surveys on the chosen area; these are carried out both on the basis of the documents and information available and by means of aimed core sampling (through drill holes) of underground materials, with following examination on the nature and the origin of the extracted fragments by specialized laboratories.

The mostly adopted solution consists in the execution of preliminary archaeological excavations, each on 10–20% of the intervention surface and for a depth that is at least equal to that assessed with regard to the most ancient traces, to be performed in some sampling points of the intervention area.

5 PRELIMINARY WORKS/EXISTING UTILITIES

One of the most demanding preliminary works in the execution of underground car parks is the determination and the re-location of the underground utilities sometimes intensively located under the city centres.

The time planning and the economic evaluation of the interventions are particularly difficult (i.e. Largo Pizzetti, Rome, the re-location of underground utilities required 8 months and 350.000€).

As for the determination, it is not always possible to get exhaustive and complete information, sometimes due to the lack of updated technical documents. As a matter of fact, while some institutions have already a complete set of documents, mainly on computer formats, for others it is necessary to patiently carry out researches in registers and also explorative core borings on the site are often required.

It should be also taken into account that the shifting is not easy for all utilities; in case of telephone systems, video-heating systems or sewerage manifolds with remarkable size, the deviation and the services' restoration costs involved can be sometimes so high to become, de facto, economic insurmountable obstacles for the execution of an underground car park.

If the car park must be executed in areas that are more sensible than others to the emission of dusts and noises, for example close to hospitals and schools, special precautions must be taken in order to fall within acceptable disturbance values as per regulations.

In order to mitigate the acoustic impact of the site, some provisions can be adopted, such as the fencing of the excavation area with elements characterized by high sound-absorbing features (with a full and continuous wall) and the same execution of the excavations is performed with methods suitable for exploiting, as adequately as possible, the requirements of sound waves' and vibrations' absorption by the ground and it will be possible to intervene on the noise produced by the used equipment by increasing their soundproofing. Moreover, excavation works, which are the noisiest phase, could be performed according to time schedules agreed with the municipal administrations and the district councils. In extreme cases, and for very limited periods, extensions to the noisy limits can be asked, and these will be issued by the Municipality upon previous agreement by the Supervising Authorities (i.e. via Finelli and via D'Azeglio in Bologna).

In order to contain the spreading of the air-dispersed dusts, efficacious measurements might be adopted, such as the use of dust-preventive cloth assembled on the trucks destined to the transport of inert matters and excavated materials and also the frequent wetting of the loading/unloading areas and access ways to the site—in order to maintain a condition of constant moisture of the materials which are likely to release dusts in their dry status.

During the site phase, it might be necessary to interrupt all or some parts of the traffic flows around the area interested by the intervention. These measures will have to be adopted for the strictly necessary period, envisaging all necessary requirements so that the works can be accomplished in quick times, with no interruptions, in order to limit to the minimum the traffic discomforts.

6 SOIL INVESTIGATION

Geological and Geotechnical investigations are the first steps in order to prepare the geotechnical model through which underground structures will be analysed. One of the main difficulties arising at this stage is the superposition of competences between the Geologist and the Designer. The conflict between geological and geotechnical reports must be avoided, particularly as far as soil properties are concerned, since these data must be evaluated by the Designer who chooses the foundation type. Unfortunately, the soil investigation is often performed by the Owner before appointing the Designer and this might imply additional soil investigations.

The new national technical code for the constructions (NTC) edited on 2008, considers the whole Italian country as a seismic land with different earthquake characteristics according to the geographic position and the local soil seismic behaviour. Soil classification is in function of the shear wave velocity parameter evaluated from ground level down to a 30 m depth. This means that the soil involved by the underground structures must be investigated for at least 30 m and, in any case, for such a depth where mechanical and hydraulic variations in the ground conditions may be anticipated.

Standard in-situ and laboratory tests are employed to evaluate static strength and deformation characteristics (un-drained and drained). In addition, some more sophisticated tests to define the dynamic behaviour of the soil, such as seismic cone penetration tests or down-the-hole tests in boreholes (field) and cyclic triaxial tests (laboratory), have to be carried out.

It is better to perform drilling for tests outside the footprint of the car park. In case some drillings must be performed in the area to be excavated, attention must be paid to the holes' sealing in order to prevent incoming water from flowing through a preferential path.

7 LOADS AND MODELLING

In most cases it is difficult to know the loading system from the surrounding existing buildings. Many times, these car parks are placed in down town areas and the plans of the buildings are often missed. Thus, information such as foundation type, foundation base elevation and characteristics of the foundation material are often not available. This leads to the subsequent need for foundations' core borings in order to take samples and complete surveys of the structure in order to have enough information (weights and plan distribution of loads) to complete the calculation model. These operations may be performed only with the authorization of the adjacent buildings' owner.

The calculation model must simulate all actions on the structure, from the natural loading (earth and water pressures, earthquake, etc.) to external overloads (buildings, traffic, etc.), internal reactions (capping beam, ring beams/wall, bottom slab, etc.). Interference might occur in case of multi car park systems (several shafts at reduced spacing) or other underground structures (metro). Possible anomalies on the theoretical cylinder shape within the construction tolerances have to be considered.

The vertically symmetric shape of the retaining wall shows several particularly favourable aspects:

- the circular shape under a more or less uniform radial loading (water and earth pressures) induces prevalent compression hoop stresses on the section which allow the use of high compression/low tension resistance materials like the concrete.
- the tendency to ovalization of the circular shape is opposed by the passive earth pressure; hence, it can be said that the system is self-centring.
- in case of loss of reaction at the diaphragm wall toe, the cylinder shape is self standing.

The most unfavourable loading conditions are usually due to un-symmetric actions such as localised overloads (adjacent buildings, operating equipment, etc), inclined ground level, seismic actions, etc... Figure 3 shows an example of the worst loading conditions matched with a localised shape anomaly. It is a plane view of ¼ of the retaining wall.

The plane q pressure distribution on the car park shaft, due to a localised overload, is simulated by a sinusoidal equation, Equation 1, where q' is the value of maximum pressure.

$$q = q' \times \cos(2 \times \alpha) \quad (45° \le \alpha \le 90°) \tag{1}$$

The pressure q may be constant or variable on vertical direction.

The simplest way to simulate the seismic effects is to use an equivalent static loading q_{eq} according to the Mononobe (1929) and Okabe (1926) or Wood (1973) proposal and to consider a variable

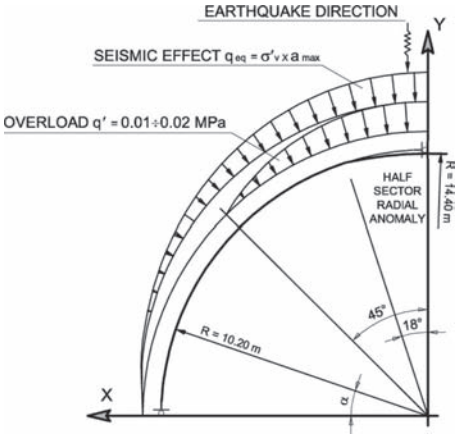

Figure 3. Example of loading condition on ¼ of the shaft—plan view.

loading distribution on the plane like that given by Equation 2:

$$q = q_{eq} \times \sin\alpha \quad (0° \le \alpha \le 90°) \tag{2}$$

Where $q_{eq} = \sigma_v \times a_{\max}$ = seismic horizontal pressure; σ'_v = effective vertical stress and $a_{\max}$ = maximum horizontal ground acceleration.

The anomaly, with respect to the perfect cylinder shape, is simulated on an angle of 36°, with a vertical deviation of about 1%.

With regard to the interference between two or more shafts, the study performed by Alessi et al. (1993) summarised in Figure 4 is interesting.

The graph shows the variation of the normalised radial soil rigidity around a shaft k_α/k_t versus the normalised free distance between shafts $\xi = x/R$.

Where k_t refers to the soil rigidity in case of a single shaft given by Equation 3:

$$k_t = E_t / \left[R \times (1 + \nu_t) \right] \tag{3}$$

While E_t = Young modulus of soil; R = radius of shaft; ν_t = Poison coefficient of soil; k_α = radial soil rigidity at a given α angle accounting for shafts interference; k_0 = radial soil rigidity at $\alpha = 0°$ (minimum distance between shafts); k_{180} = radial soil rigidity at $\alpha = 180°$ (on the opposite side of the shaft); x = minimum free distance between shafts' and s = thickness of the retaining wall.

It can be seen that while the k_{180}/k_t parameter is practically independent by the distance of shafts and about equal to 1, the k_0/k_t ratio rises slowly from big spacing up to about $x = 0.5 \times R$, having then a sharp increase when the shafts become more and more close till a theoretical infinite rigidity when the shafts are in contact.

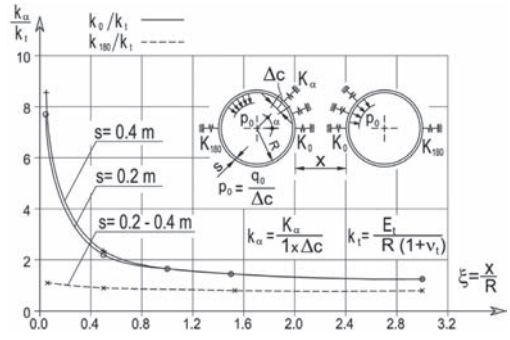

Figure 4. k_α/k_t versus $\xi = x/R$ graph.

The new code for construction (NTC-08) require realistic simulation of the events hitting the structure, considering the complexity of model and loading conditions; this calls for the adoption of powerful calculation tools like 2D and 3D Finite Element Methods.

8 HYDROLOGY

The construction of underground car parks may change the local hydrology. A row of narrow-spaced underground shafts may create a barrier to the natural flow of the water in the ground, especially if a high hydraulic gradient is present. The effect is to induce an increase in the ground water level upstream the shafts and a decrease downstream. In order to avoid such a problem and to maintain the original hydraulic conditions, draining trenches may be envisaged between each shaft to increase the permeability locally.

Under seismic conditions, Westergaard (1933) approach may be used to evaluate the hydraulic thrust against the retaining wall.

9 DEFORMATIONS BEHIND RETAINING WALL

Either during the construction of the retaining wall, or during the excavation inside the shaft and after, under service conditions, deformations will be induced in the ground space around the car park. The high rigidity of the circular shape is such to guarantee very small deformations behind the retaining wall. Anyhow, if the existing structures (buildings) are very close to the shaft and are ancient and heavy, and the foundations are insufficient and/or deteriorated, some preliminary works may be required in order to increase the safety level of the work. In case it is necessary to

increase the local stability (single panel excavation stability) during the construction of the retaining wall, a reticulate micropile wall (at least No. 2 rows of micropiles inclined on opposite directions parallel to the retaining wall) may be envisaged between the existing foundations and the single panel borings. If the real capacity of the existing foundations is close to the loading system, an adequate safety condition must be reached before the construction of the car park starts. The increase in the foundation capacity may be obtained through one of the following methods: by increasing the dimensions and strength of the existing foundations, by increasing the capacity thanks to deep foundations like micropiles or by improving the characteristics of the natural soil. In all cases it is a further problem.

10 AS-BUILT SHAFT CHECK VERSUS EXCAVATION

In order to take advantage of the cylindrical shape effect, it is fundamental to control the as-built retaining wall during the stage of soil excavation from the shaft and to check that the deviations measured on site are within the construction tolerances considered in the design.

Here below, there's an example of procedure that checks the construction tolerance of the cylinder retaining wall performed by secant piles. The control is focused on verifying two types of anomalies that will be solved in different ways: a local and an extended anomaly. The control is performed at pre-defined elevations, frequency increased with depth and amount of anomalies noticed. At each control elevation, the position of each pile is measured, supplying a set of data per pile that includes: radius r_i, radial deviation Δr_i and tangential deviation Δt_i. Radii are placed on a bar chart as shown on Figure 5, theoretical and average values are drawn, but more than anything else, it is important to control the running curvature along the perimeter to emphasise the presence of local or extended anomalies.

The following relationship is used, Equation 4:

$$c_i = r_{i+1}\cos(360/n) - 2r_i + r_{i-1}\cos(360/n) \qquad (4)$$

Local anomalies are further examined through the comparison of measured radial and tangential deviations and the envelope of admissible deviations as shown in Figure 6. If the actual position of the pile falls out from the referenced envelope, it has to be repaired (above ground water level: by local demolition and reconstruction; below ground water: several techniques may be used in order to reinstall the correct cylinder shape).

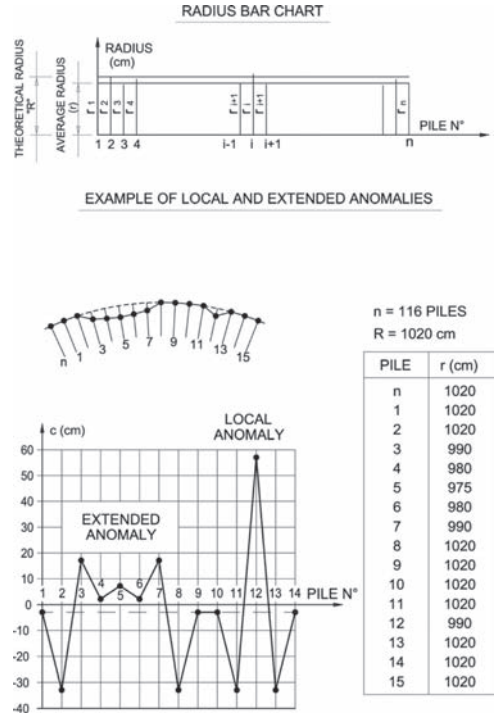

PILE	r (cm)
n	1020
1	1020
2	1020
3	990
4	980
5	975
6	980
7	990
8	1020
9	1020
10	1020
11	1020
12	990
13	1020
14	1020
15	1020

Figure 5. Example of local and extended anomaly detection.

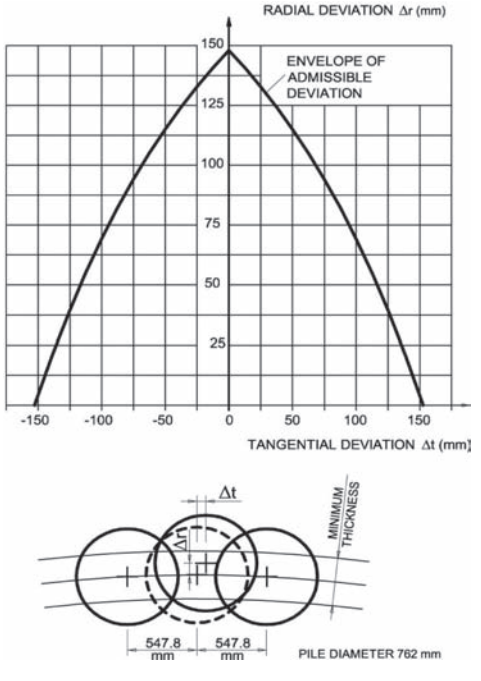

Figure 6. Example of local anomaly evaluation.

Extended anomalies usually call for much heavier corrective operations. The re-profiling of the internal surface of the shaft through a ring wall/beam could be a solution.

11 WALLS AND BASEMENT'S WATER-PROOFING

When the car park is constructed on a site where the soil profile is described as cohesion-less and highly permeable and the excavation will go deeper than the water table, great attention has to be paid in order to guarantee the waterproofing of the side retaining wall and the excavation bottom.

According to the cylinder shape of the shaft, no particular joints are usually necessary in order to avoid water incoming from the side because of the horizontal hoop pressure between adjacent elements that seal the wall.

The target to make the bottom of the excavation impervious is much more difficult and expensive. If the soil profile is such that, by increasing the depth of the retaining wall more than what it is strictly required by structural/stability reasons, it is then possible to fix the base of the wall inside a natural impervious soil layer, and at a reasonable cost, this condition is absolutely desirable. Otherwise an artificial bottom plug has to be constructed at such a depth to balance the underwater pressure with respect to the stabilising weight of the soil on the top. Injections and jet-grouting techniques are usually employed. But the most important and difficult aspect of this work is the check of the imperviousness of the plug and, in case, the definition of faulty positions in order to repair them, and this control has to be performed before the excavation stage.

Once there were techniques that required an hydraulic gradient to be established between the inside and the outside the shaft, but now a new technique developed by Texplor does not need any variation in the hydraulic natural equilibrium and is able to give a clear picture of the position of the existing faults either on the side or on the bottom of the shaft. The system works on the principle that the electric current flows easily where water is present, so, by inducing an electric field into the ground and by measuring the passage of current standing from the working platform, it can supply the position of the faults, if any.

12 SHAFT: TECHNOLOGICAL IMPLEMENTATION

The complex logistics of the underground car park construction (narrow spaces, pre-existing buildings nearby the excavations, restrictions as far as noise, vibration and environmental pollution are concerned and reduced time schedule) require the adoption of innovative technologies and equipments in terms of production, quality of the product and reduced environmental impact.

Implementing the well known Continuous Flight Auger (CFA) technique for the pile construction, the Cased Auger Piles (CAP) and the Cased Secant Pile (CSP) technologies were developed. A continuous flight auger is housed inside a casing on the piling equipment. Auger and casing are driven by two independent rotaries. They penetrate simultaneously in the ground during the excavation stage; then the auger is extracted while pumping the concrete and later the casing is withdrawn and reinforcements may be placed using a vibrator, if required. The side wall of the car park shaft is obtained through primary and secondary secant piles at a given spacing in order to get the required overlapping. For this application, special guide walls are requested to guarantee the correct plan position of the piles and the guide of the casing at ground level (see Fig. 7).

The main advantages of the CSP technique are:

- piles are constructed without using drilling fluids, in any kind of soil, above and below ground water table, thus the removed soil is at its natural state and may be disposed with no problem, at low cost;
- the casing gives high rigidity to the excavation system, minimizing the verticality tolerance. Vertical deviations in the range of 0.5%–0.7% were measured for the cased length of the piles;
- the drilling system allows the piles to cross very hard materials (from weak to medium rock, low reinforced concrete slab, masonry wall, etc.);
- the jobsite installation plant is minimised both with regard to space and time;
- noise, vibration and impact shocks are reduced to a minimum;

Figure 7. Guide walls and SoilMec equipment for CSP retaining wall construction.

– the casing allows the piles to be constructed nearby existing foundations, hence avoiding stresses' reductions during the drilling stage and with a minimum disturbance during the construction of the whole shaft.

SoilMec SpA of Trevi Group, a mechanical world leader in the construction of rigs for the execution of geotechnical works, have developed a range of equipments particularly dedicated to the execution of CSP in function of the geometric features of piles (diameter, cased length, total length, etc) and geotechnical characteristics of soils (www.soilmec.it).

13 CONCLUSIONS

The aim of this paper is to emphasize some aspects in the car park project that could be underestimated by the Contractor. Authors believe that the following themes may not be disregarded, especially if the job site is placed in the down town of Italian cities.

– As far as the success of car park construction is concerned, the establishment of good public relations with local authorities and people living nearby the area involved by the car park is extremely important;
– Taking into consideration the ancient history of Italian towns, any excavation in the down town has a high probability to encounter underground archaeological findings, with a consequent forced shifting of the time construction schedule;
– Preliminary works may be very time- and money-consuming, particularly the detection and re-location of existing utilities could be so difficult that the Contractor or the Owner might abandon the project;
– Environmental requirements about noise, vibrations and air-dispersed dust as well as local traffic interruption must be carefully planned;
– Monitoring plays an important role for quite all works in civil engineering, but this is particularly true when the behaviour of the structure depends on its shape (arc effect), and the impact on the neighbouring pre-existing buildings may be extremely remarkable;
– Finally, the new Italian technical code for the constructions (NTC) edited in 2008 requires realistic simulations of soil-structure interactions as well as loading conditions (seismic actions), therefore modelling and analyses of theoretical and as-built conditions must be performed using somewhat sophisticated calculation tools.

ACKNOWLEDGEMENTS

The Authors wish to express their appreciation to Mrs Valentina Guidi for her valuable support in preparing a comprehensible English version of the text.

REFERENCES

Alessi, R. Merli, M. Pagotto, G. and Paviani, A. 1993. Analisi di alcune problematiche connesse alla realizzazione di strutture cilindriche interrate, isolate o a gruppi, ad asse verticale. AGI, XVIII Convegno Nazionale di Geotecnica, Rimini, volume I, pp 3–12 (in Italian).

Mononobe, N. 1929. Earthquake-proof construction of masonry dam. Proc. World Engineering Conference, volume 9, p. 275.

New Italian technical code for the constructions. Norme tecniche per le costruzioni. D.M. 14/01/2008 (in Italian).

Okabe, S. 1926. General theory of earth pressure. Journal Japanese Society of Civil Engineering, volume 12, n. 1.

Westergaard, H.M. 1933. Water pressures on dams during earthquakes. Trans. ASCE, volume 98.

Wood, J.H. 1973. Earthquake-induced soil pressure on structures. Report No. EERL 73-05, California Institute of Technology, Pasadena, CA, pp. 311.

Geotechnical Aspects of Underground Construction in Soft Ground – Viggiani (ed)
© 2012 Taylor & Francis Group, London, ISBN 978-0-415-68367-8

Recent uses of directional drilling technology in the construction field

D. Vanni & M. Siepi
TREVI SpA, Cesena, Italy

M. Croce
Agenzia Governativa per la Bonifica di Discariche Pubbliche Manfredonia, Italy

F. Melli & V. Specchio
SOGESID SpA, Italy

ABSTRACT: The increasing complexity of the modern projects requires a never ending process of innovation in the construction technologies. In fact, the constant need to improve the transportation networks in especially congested urban areas, entails the need of accurate technologies to cope with the increasing depth of excavation for underground structures. The improvement of the efficiency becomes therefore essential, to save time and money. As a result, the need to control the excavation process has become a must in most of the technologies involved in these projects. In recent years the use of the hydromill turned out to be fairly ordinary for the excavation of the deep shafts, where the compliance of tight tolerances is of paramount importance. The same tight tolerance is now required also for sub-horizontal drilling, when special technologies are used for drilling long holes. For this reason, the use of the HDD technology (Horizontal Directional Drilling) has been recently introduced also in geotechnical works. The paper summarizes some of these applications in recent projects of TREVI, as curvilinear holes necessary for the compensation grouting in Bologna High Speed Railway, or the installation of pilot holes for the construction of cut-off walls in the rehabilitation of dams in New Zealand and in United States. Then, the paper describes the latest application of this technology for the execution of long holes required for the sealing of the bottom in a dumping area in Manfredonia, Italy.

1 FOREWORD

The use of directional drilling has been for long time a privileged area for the oil industry, for the execution of "Christmas tree" wells to maximize the productivity from a single well neck.

Then, the gained experience was used to develop "river crossing" methods, especially for the installation of pipelines and underservices in crowded areas and/or difficult conditions. In turn, the same experience was then used for the so called trenchless market, where the Horizontal Directional Drilling (HDD in short) was used for the installation of pipelines in urban areas to avoid the open cut excavation for the installation of pipelines (Fig. 1).

In the present days the market of construction is becoming more and more competitive, and there is an increasing demand for high quality work, where this can lead to a reductions in the costs. It is a fact that by increasing the quality control, the "safety factor" can be reduced, as there are reliable measurements. As the Directional Drilling allows to measure and control every single hole, therefore the overdesign can be reduced to a minimum.

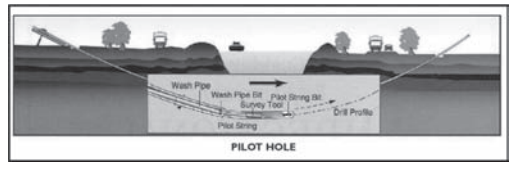

Figure 1. River crossing technology (typical).

The present paper describes the original application of the Directional Drilling in different projects for various purposes, demonstrating the big potential of this technology in the construction field.

2 PREVIOUS GEOTECHNICAL APPLICATIONS OF DIRECTIONAL DRILLING

TREVI introduced the use of the Directional drilling in first years of 2000 in a large project of

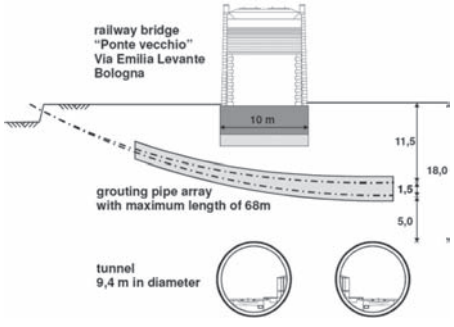

Figure 2. Via emilia bridge—compensation grouting.

the metro in Naples (line 1 Dante-Garibaldi) for three different stations. About 30,000 m boreholes in excess of 50 metres were successfully drilled for the installation of freezing pipes and thermometric probes. The selection of the directional drilling was dictated by the need to precisely install the freezing pipes with an accuracy of few centimetres.

The holes were drilled starting from shafts as deep as 40 m, with a water counter head of up to 30 m. The depth, the congested milieu, the presence of vehicles traffic and of the railway line added difficulty to the guidance system. In order to overcome the problem, after many tests, a new method making use of a micro-coil was invented and successfully used throughout the rest of the project.

In the same years, the directional drilling was used in two projects of compensation grouting in Bologna. The compensation grouting was necessary to concurrently control the settlements created under two brick bridges by the excavation of the TBM for the high speed railway passing underneath the existing common railway (Fig. 2). Since the congestion in the area and the tight schedule did not allow the original plan to excavate a shaft and drill the boreholes for the compensation grouting in a fan shape layer, it was proposed and agreed to drill the holes from the surface, therefore minimizing the impact to the existing activities in the vicinity.

Two layer of sub-horizontal holes were drilled for the installation of sleeved steel pipes at a depth of approximately 15 metre under road level. The hole were up to 65 metre long.

Both projects were successfully completed.

3 DIRECTIONAL DRILLING USED FOR REPARATION OF TOW DAMS

3.1 *Arapuni dam: a 95 metre deep cut-off wall*

In 2005 TREVI was invited to participate a tender for the reparation of the Arapuni dam in New Zealand. The 60 metre high, gravity concrete dam owned by Mighty River Power suffered since the beginning of seepage problems, due to a series of vertical fractures under in the dam foundation, with the presence of highly erodible joint infill that is vulnerable to piping erosion. This combined with nearlake pressure in areas under the dam due to open fractures in the ignimbrite rock foundation pose a risk of a major leak under the dam.

An extensive programme of investigative core drilling and detailed foundation mapping was completed to determine the extent and nature of the fissure systems. The investigation findings allowed partial cut-offs to be designed to specifically target each of four sets of identified vertical fractures.

Considering the difficulty of the job, the Client decided to form an Alliance with the Contractor.

The closed collaboration of the Alliance (Owner and Contractor) and the Designer (Damwatch of Wellington, NZ) allowed to select a method which suites the requirement of complete the project maintaining the reservoir fully operational.

Construction of the four overlapping bored pile walls consisted of 400 mm diameter holes drilled at 350 mm centres. The 95 m deep holes from the dam crest extend through the concrete dam and 40 to 60 m into the vertically jointed ignimbrite (Fig. 3).

In order to form a continuous wall with such tight tolerances, TREVI proposed to use an innovative method involving the use of directional drilling to form pilot holes, to be further reamed out to the design diameter. The pilot holes were drilled using a mud motor, followed by a patented special reverse circulation drilling system.

3.2 *Wolf Creek Dam: 1000 holes for 85 metre deep cut-off walls*

In 2008 the US Army Corps of the Engineers issued the tender for the installation of a 24-in thick (60 cm), 274 ft deep (84 metre) concrete positive cut off wall to stop the seepage under the Wolf Creek Dam, in Jamestown, KY.

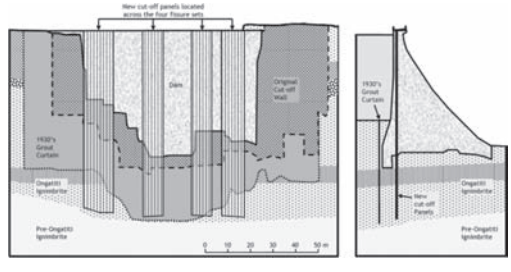

Figure 3. Arapuni cut-off wall (view and cross section).

The dam, built in the late 40's, is formed of a concrete section and an earth section, and suffered since the its birth of seepage under its foundation. The dolomitic karstic limestone is crossed by a large system of fissures and caves, and the danger of piping was underestimated at the time of construction.

After several sinkholes appeared downstream, the dam was repaired in the late 70's, by installing a positive cut off wall of secant piles.

However, in the time the instrumentation showed signs of distress, with high piezometric levels, and the COE decided to install a second cut-off wall upstream of the previous one.

The tight specification of the job, with a maximum deviation from verticality of 6 inches (150 mm) were judged suitable for the directional drilling, to duplicate the success of New Zealand.

It was therefore decided to install secant piles using reverse circulation to follow the pilot holes drilled with the directional drilling. The selected method allows to systematically control the deviation within the tolerances of the project.

The project will involve drilling up to 1000 holes, and its completion is due in 2013.

4 CONTAINEMENT OF TWO POLLUTED AREA IN MANFREDONIA, ITALY

In the hills close to the city of Manfredonia, in Apulia, southern Italy, it was discovered that two dumping sites needed to go under an important retrofitting work.

The two sites, called Conte di Troia and Pariti I-RSU (Fig. 4), were used in the past years to dispose industrial and urban wastes, backfilling the excavation of exploited calcarenite quarries and then capped.

The area is located on a gently sloping hill, and the two sites are separated by a gully called "Vallone di Mezzanotte", which originated from the Karstic—erosive activity on the bedrock (calcarenite and calcilutites limestone).

The uniaxial compressive strength ranges from 5 to 10 MPa for the calcareniti and 25 to 30 MPa for the calcilutites. Both rocks are deeply fractured. The water table is at the sea level, 50 m below the surface dump area.

Several campaign of soil investigation, together with environmental and hydro-geologic studies allowed to discover that no protection sheet was installed at the base of the dumping areas.

Particularly, in 2009, some samples have been collected from the base of the waste, and analyzed in laboratory. The result was that the fractured calcarenite at the base (Figs. 5 and 6) is sometimes clean and sometimes contaminated for few meters

Figure 4. Location of the two areas.

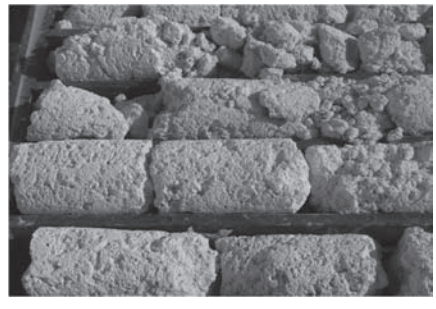

Figure 5. The calcarenite at the base of Conte di Troia.

Figure 6. Borehole camera in corings, with evident fractures.

under the waste bottom, but there is no leachate. It has been supposed that the leachate generated from the drained water migrates to the below water table through the biggest fissures so that it cannot accumulate.

Therefore, to comply with the directive CEE 91/156, the installation of a containment is required to avoid hazards to the environment and to the water system. The project is under a dedicated Government Agency (Ufficio del Commissario Delegato per la bonifica di discariche pubbliche di Manfredonia OPCM n.3836/09).

The Conte di Troia disposal area has a total surface of 25.454 m^2, and a perimeter of 780 m. The volume of the waste material is 140.000 m^3, and its maximum thickness is 16 m.

The surface of Pariti I-RSU is 19.600 m^2, and a perimeter of 660 m. The volume is 260.000 m^3, and its maximum thickness is 25 m (Fig. 7).

A first hypothesis was the removal of the wastes and the temporary relocation of the waste in a close by area, to allow the installation of the impermeable membrane to contain the waste as per the current regulation.

However, due to excess of time needed and the great volume of waste of uncertain nature to be moved (with all the related environmental risks) it was decided to design a solution of an in-situ containment. So a second project was designed with vertical impervious diaphragm walls on the perimeter and a grouted bottom plug carried out with a huge quantity (up to 25,000 holes for approximately 500,000 lm of drilling) of vertical boreholes crossing the total waste area to reach the calcarenite below to be treated.

But, obviously, also this second solution was affected by time and environmental risk problems. So the final designers (Sviluppo Italia and Sintesi) selected a very innovative solution foreseeing that the impervious bottom slab should be created by grouting the rock underneath the volume of the waste (as found by the soil investigation) by means of a double layer of sub horizontal curved directional drillings (Fig. 8).

The perimeters of the area should be contained in the same way by installing a cut-off wall with a triple row of sub-vertical holes.

In 2010 the public tender has been awarded to an ATI leaded by Cons. Coop. Costruzioni—Mucafer) with Trevi as specialist Sub-Contractor.

The works started immediately after the award, and involved several rigs and plants to cope with a tight schedule.

The bottom slabs of the two areas will be formed by a total of 565 holes, equal to 58,380 linear metre.

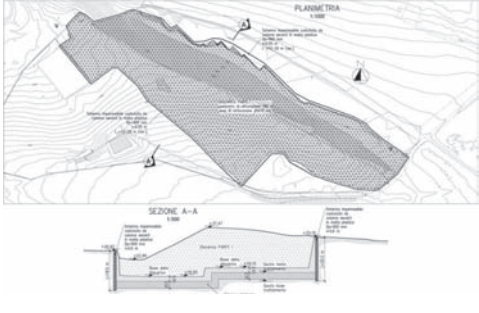

Figure 7. Pariti I-RSU, plan and cross section.

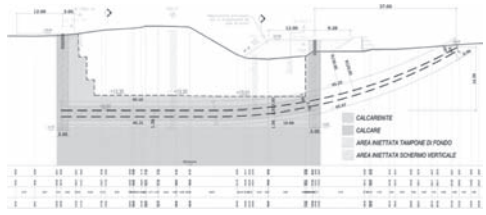

Figure 8. Bottom slab created by directional drilling.

Figure 9. Panoramic view of Conte di Troia site.

The average length is 103 m with a maximum of 150 m.

The holes are drilled using a surface magnetic guidance method. The system allows to calculate the position of the drilling tool by creating artificial magnetic fields at the surface. The strength and direction of the generated field are detected by the instrumentation equipping the drill string, and transmitted in real time to the steering engineer. Every single hole shall be planned in advance, and the spatial coordinates of the various surveys shall be compared to the theoretical position to decide the need of a correction. The accuracy requested is plus/minus 30 cm.

Due to the extremely high grade of fracturation of the rock, a downstage grouting method is required in some zones. The holes are drilled until the circulation of the holes can be efficiently maintained. As soon as the flushing of the cuttings cannot be granted, the hole is stopped and grouted. After hardening, the hole is re-drilled.

The procedure is repeated until reaching the design length. Special expansive cement mixture are used to prevent over-grouting due to the highly permeable rock due to the fissures, or to the possibility that the grout by-passes into the waste mass.

The first stage of rough injection, is followed by a second stage aiming to improve the waterproofing of the main fissures and to treat the smallest ones.

To this purpose MPSP (Multiple Packer Sleeved Pipe System) formed by 2″ steel tubes are inserted

Figure 10. Rigs drilling for grouting.

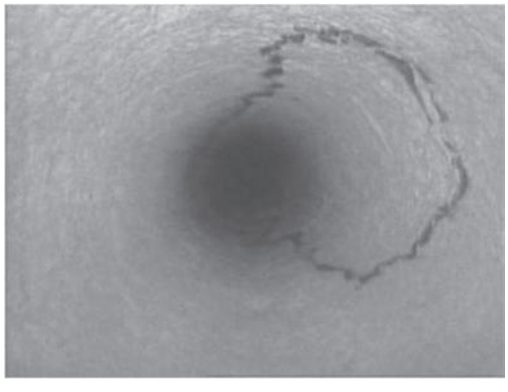

Figure 11. Fractures grouted (borehole camera).

in the boreholes and grouted with high penetration cement and silica mixes.

The result obtained is checked both with permeability test (Lugeon test) and systematic use through of borehole camera inspections. Figure 10 shows efficaciously the good result obtained with fissures completely grouted with cement (grey) and silica (white) mix.

The work is planned to be mostly completed at the end of 2010.

5 CONCLUSIONS

The technology of directional drilling has recently been successfully used for a number of challenging projects in a variety of conditions.

The flexibility of the system allowed to find a solution to difficult geotechnical problems where accuracy is a paramount, proving once more that the merging of the knowledge from one sector to other can be beneficial.

Particularly the Manfredonia dumps case is an original and innovative example of how to solve the problem to isolate a contaminated area with reasonable cost and without touching the waste mass.

REFERENCES

Amos P, Bruce D.A, Lucchi M, Newson T, Wharmby N, Design And Construction Of Seepage Cut-Off Walls Under A Concrete Dam In New Zealand With A Full Reservoir *American Society of Dam Safety Officials (ASDSO) Conference Austin Texas, USA, September 2007.*

Amos P, Bruce D, Lucchi M, Watkins N, Wharmby N, Design And Construction Of Deep Secant Pile Seepage Cut-Off Walls Under The Arapuni Dam In New Zealand*, US Society of Dams Conference Portland Oregon USA, April 2008.*

Amos P: Construction of Seepage Cutoff Walls under a Concrete Dam in New Zealand with a Full Reservoir, *Dam Safety Association of Turkey, First National Symposium and Exposition on Dam Safety, 2007*.

Amos P, Fletcher A, Lucchi M, Wharmby N: Prevention of Foundation Piping at Arapuni Dam using Discrete Cutoff Walls, *New Zealand Geotechnical Society 2008 Geotechnical Symposium, September 2008*.

Amos P, Watkins N, Lucchi M, Wharmby N: Extending Deep Cut-off Wall Technology—Construction of Seepage Cut-off Walls under Arapuni Dam in New Zealand with a Full Reservoir, *New Zealand Society of Large Dams (NZSOLD) and Australian Committee of Large Dams (ANCOLD) Conference Queenstown New Zealand, November 2007.*

Kummerer C, Thurner R, Siepi M, 2007. Compensation grouting for limiting settlements of two railway bridges induced by a twin-tunnel excavation. *ECSMGE_ Madrid 2007*.

Minguez F, Gregory A, Guglielmetti V 2005. Best practice in EPB management. In *Tunnel & Tunnelling international, November 2005*: 21–25.

Riley G, Arapuni task a world first: An international alliance undertakes dam-engineering work that is "pushing the envelope of existing technologies". *Contractor Vol. 31 No. 3 April 2007, Auckland, New Zealand.*

Vanni D, Cribari F, Siepi M, 2004. Utilizzo delle per-forazioni direzionate (HDD) per interventi di conge-lamento e compensation grouting. *Convegno SO-CIETÀ ITALIANA GALLERIE (SIG), "Le gallerie nelle grandi opere di comunicazione e di servizio", SAIE 13 ottobre 2004, Bologna, Italia.*

Vanni D, Cribari F, Siepi M, 2006. Soil freezing under a volcano; il congelamento del terreno sotto un vul-cano; l'esperienza delle perforazioni teleguidata per appli-cazioni profonde in piazza Garibaldi a Napoli. *10th International conference on piling and deep foundations, 2006, Amsterdam, Netherlands.*

Wharmby N, Lucchi N, Newson T, Amos P, Arapuni Dam Foundation Enhancement Works, Australia and New Zealand Joint Geotechnical Conference, Brisbane Australia, October 2007.

This page intentionally left blank

Geotechnical Aspects of Underground Construction in Soft Ground – Viggiani (ed)

Leak detection in complex underground structures using an innovative geophysical method

D. Vanni
Trevi SpA, Cesena, Italy

E. Geutebrück
Texplor Exploration & Environmental Technology GmbH, Potsdam, Germany

ABSTRACT: An increasing number of underground structures for transportation and buildings in urban areas often require deep excavations under the groundwater table. Surely the main problem connected is the final test of the water tightness of the resulting structure, *i.e.* of the diaphragm wall and of the plugs. Texplor's ECR®/EFT® technology is able to obtain quickly a reliable detection of potential leaks and to perform the quality control of horizontal and vertical cut-offs also in very complex and deep structures like metro tunnels or building pits, even before excavation. Further advantages are the non-destructive measurements from the surface, the flexible spacing of measuring grids, which can be easily adjusted according to each project and virtually no depth limit for the practical investigation. This paper describes the application of the technology in two building pits in Florence and Cremona in Northern Italy, which were carried out in accordance with RCT, a company of Trevi Group.

1 OVERVIEW ON THE TECHNOLOGIES

The ECR/EFT/FGM leak detection technologies were developed and patented by Texplor GmbH and are used for the leak investigation of:

- Deep foundations: diaphragm and sheet pile walls
- grouting areas
- reinforced concrete constructions
- gel-sealed basements
- underwater bottom slabs
- natural and artificial water retaining horizons
- geomembrane sealings

Leaks in sealing constructions are detected quickly and reliably with these methods. Leak areas are identified and displayed on a ground map. Horizontal and vertical sealings can be investigated either by temporary surveys or by stationary installations for long-term control. Groundwater movements are not necessary for the investigations.

1.1 *ECR®-multisensor leakage detection technology*

The method ECR is based on the physical principle that the groundwater flow in a porous subsurface medium ensures an electric flow by ion transport and creates a measurable electric field in the area.

If a leakage exists in a construction surrounded by groundwater, a natural or artificially enhanced local groundwater movement can be expected in the leakage area. This local groundwater stream is moving through the leakage and creates an electric field by this movement (known in physics as streaming potential), which is superimposed on the existing natural background field and, therefore, is a *detectable anomaly*.

For the accurate detection of these electrical fields caused by groundwater, a multichannel high speed–high resolution telemetric sensor system is in use. Depending on the size of the investigation area, several hundred non-polarizable, high-sensitive sensors form a grid or, in general, one array. A telemetric data recording system ensures fast and reliable data acquisition of the whole sensor array at the same time (see Fig. 1).

Hence, natural groundwater streams can be located and outlined in any underground sealing construction, dam or basin or natural geological seals by measuring the potential streaming anomalies. The results of the measurements are analyzed and displayed in maps (see Fig. 2).

1.2 *EFT®-active leakage detection technology in combination with ECR®*

EFT technology introduces an artificial electric field into the ground around a sealing system which is forced into the sealing construction to create a mechanical movement of ions. These movements of ions through the untight locations in the sealing

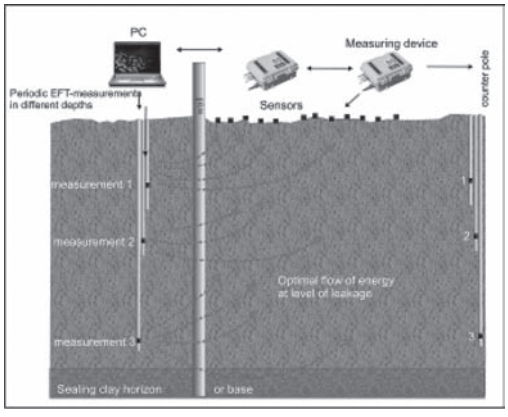

Figure 1. Schematics of ECR®/RFT® leak detection system.

Figure 2. Display of results.

system create an intensified ion flow which can be detected by the ECR sensor system on the surface.

The created positive ions clash against the grains and take the water particles with them. This mechanical impact is very small with respect to natural groundwater flow, but is still present. This principle is based on the relation V = IR (V = voltage, I = current, R = resistance). EFT is based on this effect.

Normally, if the current changes, the voltage also changes immediately. If the current is doubled, the current flow results in a doubling of the voltage and also of the resistance. In case a hole is present, a small flow is running without considerable resistance through the hole. As the electric flow increases, the mechanical resistance increases near the hole. Both electric and mechanical blockages take place in the vicinity of the hole. This increase in resistivity leads to the fact that the relation between flow (I) and tension (V) at a certain moment is no longer linear. The flow is no longer undisturbed and the sensor above the position, where this electrical anomaly is observed, indicates the location of the hole. An electrode in one or more observation wells induces an electrical field in the subsurface outside the building pit. This electrical field is forced through the outside sealing structure into the pit by a counter pole (see Fig. 1). On its way through the sealing structure, the induced current follows the least resistive path towards the second pole, which in most cases, is through water and the openings in the sealing construction. Therefore, the electrical potential field changes significantly at an opening, compared to the field in the rest of the construction. The areas of leakages are characterized by an increased local energy flow which can be detected and outlined by the surface sensor grid. Furthermore, the increased energy flow creates a structure at the leakage location, which is characteristic for the type of leakage (joint, underpass a wall, hole in a wall, hole in a bottom plug etc.). To avoid any disturbance by electrical noise in an industrial area, a reference is introduced, thus allowing this very accurate measurement also in highly noisy areas like railway stations, industrial buildings etc. (References: Admiraal & Geutebrück 2007; Brouwer & Veldhuizen, 2011; Geutebrück, 1997; Geutebrück, Hofmann & Ottomann 2001).

1.3 *Implementation*

The Texplor methods ECR and EFT and the combination of both methods FGM, a self-developed telemetric data recording system, are carried out to investigate all kinds of vertical and horizontal natural or artificial sealing system. The measurements are non-destructively carried out at surface level and/or in boreholes (with small sensors). The telemetric data recording system (FGM) ensures fast and reliable data acquisition of the whole sensor-array at the same time (see Fig. 3).

Figure 3. Telemetric data recording system (FGM).

Non-polarizable, high-sensitive sensors are placed on the surface of the investigated area in a pre-designed grid. Texplor uses special sensors, which are very stable against natural and artificial disturbances. The sensors are placed in measuring grids with flexible spacing on the surface of the measuring area which can be easily adjusted according to each project. The type of soil between source and sensor influences the detected electric field. Sandy subsoil (relatively low conductivity) behaves differently to a peat or clay layer (relatively higher conductivity). Therefore, we have to observe that the measured absolute potential can be different, depending on the soil type. As a consequence, zero reference measurements are carried out by both EFT and ECR methods. Because of that, it is possible to measure differences, as a result of which the properties of the ground between source and receiver can be neglected. The results of measurements are analyzed and displayed in maps.

The ECR technology was employed in many projects in Italy, Germany, Austria and Ireland and lately also in China.

This paper describes two projects carried out in Florence and Cremona by TEXPLOR in cooperation with RCT and Trevi. RCT is the commercial partner in Italy for TEXPLOR.

2 CASE HISTORY: BUILDING PIT IN FLORENCE

The building pit in Florence, central Italy, is located on the former FIAT company premises and covers an area of about 12,000 m^2. The entire perimeter of the pit is surrounded by streets and old buildings (see Fig. 4).

2.1 *General description*

In order to build a three-floor underground parking, under the new structures, a total of 11,500 m^2 diaphragm walls with an average depth of 26 m are installed to form the walls of the underground structure, which is excavated to a depth of 15 m. The entire area is divided into five sectors by means of self-hardening slurry walls. In three of the sectors, a 2.5 m thick jet grouted bottom plug with watertightness purposes is formed by means of 2.0 m diameter columns. Other structural works performed as foundations are *"barrettes"*, piles, micropiles and anchors (see Fig. 5).

Soil conditions are described as a succession of different layers in recent alluvium (bottom to top): Group GP, composed by gravel and cemented sandy gravel, and Group SS, composed by silty sand, silt and silty clay in the bottom part of the area to be excavated. There is a single level of water table in the backfill (–5 m from the street level). Due to the cemented layers, foundation technologies are modified, preferring piles to the single foundations *"barrettes"*. Moreover, thanks to the presence of a clayey thick layer in the central part of the area, the bottom plug is substituted with a deepening of the outer structures.

2.2 *Leak detection*

The target of this investigation was a quality control of the present status of the sealing construction of three measuring areas consisting of:

– diaphragm and self hardening slurry walls;
– jet-grouting bottom plug.

with the following types of possible failures:

1. Open joints at the diaphragm elements;
2. "Windows" in the diaphragm elements;
3. Open contact between jet-grouting bottom plug and diaphragm walls;
4. "Holes" in jet-grouting bottom plug;
5. Connection of the extension to the clay horizon;

Figure 4. Plan view of florence site.

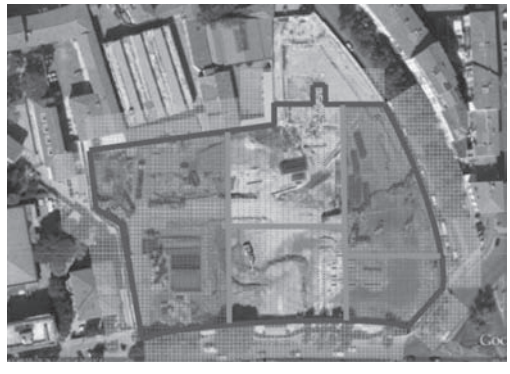

Figure 5. Sketch of works.

6. Investigation of the natural clay horizon for "holes";
7. "Windows" in the self hardening slurry walls;
8. Open contact between injected jet-grouting bottom plug and self hardening slurry walls;
9. Connection between piles or *barrettes* and clay horizon.

The prerequisites for a leak detection measurement are the installation of wells inside and outside at different depths. The surface must be smooth and may not dry up and must be watered in warm or hot weather conditions. Texplor technologies were employed to investigate three different areas for a total surface of about 5500 m^2.

Subsequently the measurements of area Z3 are described. To investigate the sealing construction, an array of approx. 200 sensors was positioned in area Z3. A cross-section of the investigated area is shown in Figure 6.

The general areal sensor-array had a distance of 4×4 m for the investigation of the natural clay layer-area; in the diaphragm wall areas a more tight sensor grid of 2×2 m was installed for a better evaluation of local events like joint leakages, for example. The sensor grid is shown in Figure 7.

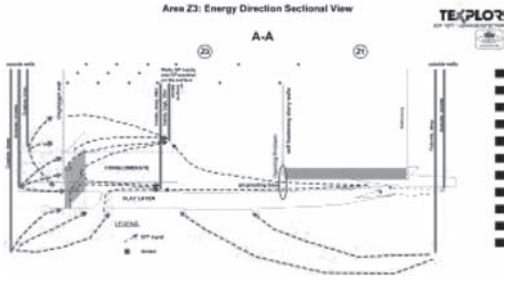

Figure 6. Sectional view of sealing construction and outside well situation for wall extension and clay layer investigation.

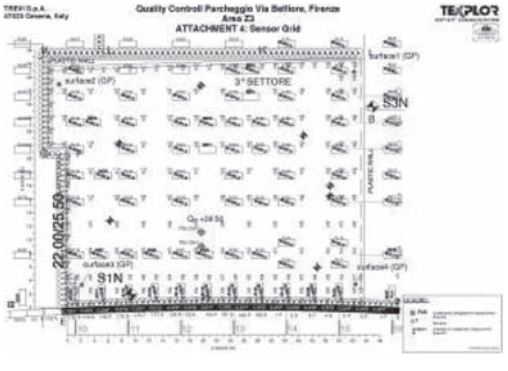

Figure 7. Sensor grid in Z3 area.

The general surface (street) levels are around El. 43.0 m above sea level. At the time of the measurement, the excavated surface of the Z3 pit-area had an elevation of approx. 39.6 m. The bottom of the jet grouting Z1 and Z2 was approx. El. 13.0 m. In the Z3 area, additional columns were installed to extend the diaphragm walls' base from El. 14.0 m to 7.0 m. For the active measurements with EFT tracers, 14 wells in the outside of the Z3 area were geometrically positioned. The geometry is necessary to provide special directional views on the different wall sections. Each geometrical location for EFT tracer input consists of 2 or 3 wells with different depths. For the investigation of the walls and plastic walls, well depths between 15 and 18 m were used. For the investigation of the natural clay layer, well depths between 42 and 46 m were used.

During the first step, base-measurements were performed to collect the natural existing electrochemical field at site, no active energy was induced during these measurements into the ground. These data were collected as baseline data and compared with the following active data, where EFT-energy was directionally forced from the outside wells into the pit to detect locations where the energy (and also groundwater) can pass through the sealing construction. During the second step, an active ECR/EFT measurement was performed to visualize the leakage situation by observing and locating any enhanced energy flow through the sealing structure. Multiple geometries were used with different wells to induce energy in the subsoil and force it into the pit construction. Basically for each investigation of a special wall area and the neighboring bottom plug area, three various deep wells outside of the pit were strategically used to induce the electrical EFT-tracer into the subsurface. To cover the complete Z3 area, four different geographic points inside the pit (on the surface of excavation level) and 2 wells inside Area Z3 were used for the counter pole positions.

The results of the leakage detection measurements in the Z3 area were shown in different maps in which the position of all leakage anomalies through the walls or below the walls are displayed in blue color on the base map. In Figure 8 the results of the investigation of the clay horizon including the wall extensions below a depth of –25 m are displayed.

Figure 9 shows the results of the investigation of the walls and extension from surface level to –25 m. After having finished the measurements, the data are analyzed and interpreted so that the results are already available directly at the site. Hence, the necessary and targeted sanitation works can start immediately afterwards.

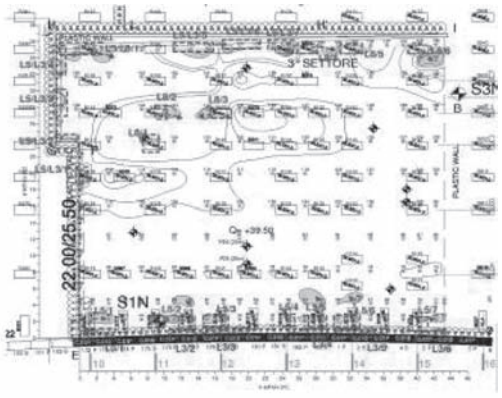

Figure 8. Map of leakages below –25 meters—clay horizon including wall extension.

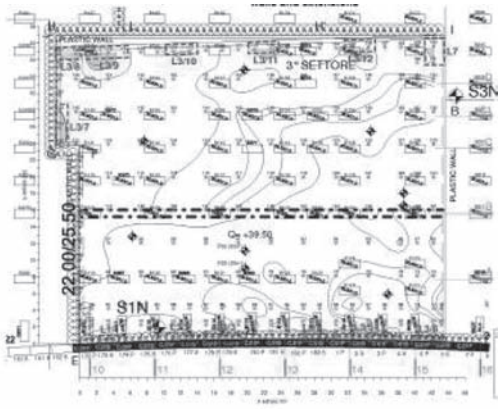

Figure 9. Map of leakages from surface to –25 m through walls and jet grouting extensions.

3 CASE HISTORY: BUILDING PIT IN CREMONA

A new underground public parking area is about to be built in the centre of Cremona, northern Italy. A 43.0 × 74.0 m area has to be excavated for a depth of 14.0 m, in order to create the pit for a four floors underground parking.

3.1 *General description*

A continuous diaphragm wall with a maximum depth of 26 m is built to protect the pit that has to be excavated. The diaphragm walls are embedded in a natural silty clayey bottom plug. The excavation of the pit highlighted some leakages through joints between diaphragm walls. These leakages are not admissible, due to the short distance between pit and existing buildings. The client asked Trevi Group to find an efficient method for assessing the extent of leakages so as to design any possible corrective actions (see Fig. 10).

The soil conditions are a succession of backfill (up to 8.0 m thick) of anthropic nature, recent alluvium (sandy and clayey sand with some gravelly layer from –8.0 to –24.0 m from working level) and a succession of silty sand and sandy silts up to –28.0 m in the bottom part of the area to be excavated.

3.2 *Leak detection*

The aim of the complete diaphragm wall area's investigation was to detect any leakage in:

- the joints of the wall segments;
- the diaphragm wall segment body itself;
- the sealing contact between the segment and the clay.

The investigation was performed in 2 areas having different depths—shallow (street level to approx.—10 m depth) and deep (approx.—10 m down to end depth of diaphragm segments—26 m) in order to estimate the depth development of the detected leakages. Texplor technologies were employed to investigate different areas for a total amount of about 4400 m^2.

As for Florence, during the first step, base-measurements were performed to collect the natural baseline electrochemical field at site. During the second step, an active ECR/EFT-measurement was performed to visualize the leakage situation by observing and locating any enhanced energy flow through the sealing construction.

To investigate the sealing construction, a quantity of approx. 370 sensors was positioned, with an array of 2 × 2 m along the walls, for getting complete information on the tightness situation.

Figure 10. View on the job site.

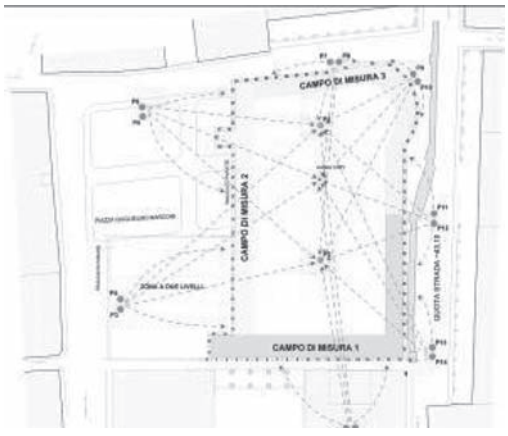

Figure 11. Detailed energy directions.

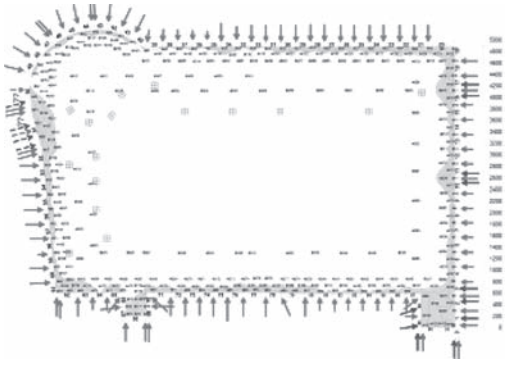

Figure 12. Map of leakages below –20 m—clayey horizon.

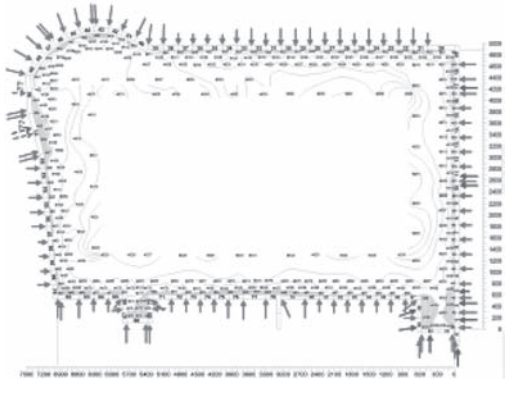

Figure 13. Map of leakages from surface to –20 m through diaphragm walls.

EFT-tracer injection was performed from 14 wells positioned outside, 2 wells inside were drilled for positioning antipoles, 42 different energy arrays combined with 75 measuring cycles were performed, for a total amount of over 3500 single measurements (see Fig. 11).

The results of the ECR/EFT-leakage detection measurements were shown in different maps in which the position of all leakage anomalies through the walls or below the walls are displayed in blue color on the base map. Figure 12 shows the results of the investigation of the clayey horizon below a depth of –20 m.

In Figure 13 the results of the investigation of the walls and extension from surface level to –20 m are shown.

4 CONCLUSIONS

The Texplor ECR and EFT technologies and the combination of both methods were developed for the quality control of any kind of artificial or natural impermeabilization systems.

Clients receive a base map of the construction with colored areas (points of energy paths through sealing construction) indicating the leakage locations and a description of the constructional reasons and size of leakage. The leakages where energy can migrate through the walls' joints or bottom plugs are colored in blue.

The above-described technologies allow to detect the points from where water flows through the structures and to work out any possible corrective actions.

Finally, listed hereunder are the main key points of the described technologies:

- Quality control of horizontal and vertical sealing-systems
- Fast and reliable detection of leakages
- Non-destructive areal surveys, flexible measuring grid, high sensor density
- Immediate control of renovation procedures
- Pumping of groundwater is not necessary
- Single investigations or stationary installations for long-term control
- Leakage areas are localised, identified and spatially displayed in a base map
- Thanks to the fact that works are carried out by measuring minimum potential differences (mV) and minimum currents (mA), currents are prevented from being affected or absorbed by any underground conductive object
- When using the Texplor method, data interpretation cannot be disregarded. Despite a rigorous quality control on the equipment's operation

and on data acquisition, the detection of permeation or weak areas—and most of all the causes—(presence of a hole; lack of connection between vertical works and bottom plug, etc. …) require the interpretation of a technician, who will investigate the anomaly's geometry.

REFERENCES

Admiraal, B.J. & Geutebrück, E. 2007. Dichtheitsüberprüfung von HDI-Sandwichwänden beim Bau einer U-Bahnstation unter dem Zentralbahnhof Amsterdam, *Tagungsband Geotechnik*, Wien.

Brouwer, R., Veldhuizen, F. 2011. Lekdetectie bij bouwputten toepassing van de elektrische potentiaalmethode, *Geotechniek* 3/2011, p. 260–265.

Geutebrück, E. 1997: Geophysikalische Qualitätskontrolle von Dichtwänden und Dichtsohlen*, Tagungsband Österreichische Geotechniktagung*, Wien.

Geutebrück, E., Hofmann, R. & Ottomann, A. 2001. Geotechnische Erkundungen und Qualitätssicherungen im Grundbau, *Konferenzbericht des 1. Siegener Symposium*, Universität Siegen, Institut für Geotechnik, Siegen.

This page intentionally left blank

Geotechnical Aspects of Underground Construction in Soft Ground – Viggiani (ed)
© 2012 Taylor & Francis Group, London, ISBN 978-0-415-68367-8

Construction of a large underground parking in Bari downtown

R. Granata & F. Gioia
Trevi S.p.A., Italy

V. Cotecchia
Emeritus Professor, Bari Politechnical University, Italy

ABSTRACT: The paper deals with the investigation, treatment and monitoring activities performed to allow the construction of a large underground parking in Bari downtown. The construction of parking, which has three floors underground, required the excavation of a basin a 13 m deep, 7 m of which under the water-table natural level. Furthermore, the perimeter of the structure is very close to the historical buildings facing on the Square. To allow the excavation and construction activities in safe and dry condition, grouting treatment were designed and performed, to create a bottom plug under the entire area, and an impervious and firm curtain along the perimeter. The excavation was successfully completed, in safe and dry condition, the residual water inflow being less than 4 l/s over a total wet surface of about 10,000 m^2.

1 INTRODUCTION

The underground parking built at Cesare Battisti Square, in the Bari Downtown (Fig. 1), is a complex structure, because the urban context and the special geomechanical and hydrologic condition. The structure is 156 m long and 45 m wide. With an area of about 7000 m^2 it covers almost entirely the Cesare Battisti Square.

The building includes three floors underground. The construction required the digging of about 85,000 m^3 of rock, with an excavation 13 m deep over an area of about 7040 m^2.

At Cesare Battisti Square, the ground level is approximately 5 m above the sea level, while the groundwater table is 0.5 m a.s.l. Thus the excavation had to be carried out 7 m under the natural water-table level.

Figure 1. Map of Bari Downtown and Location of the Cesare Battisti Square (A = construction Site, Google Map 2010).

These circumstances, and the presence of historical buildings in the immediate boundary of the construction site, required a very accurate study of the geotechnical and hydrogeological issues, and the analysis of the interference between site conditions and new structures.

Thereafter, to allow the excavation and the construction activities in safe and dry condition, the design required the construction of a bottom plug under the entire excavation area, an impervious curtain along the perimeter, and the strengthening of the excavation walls.

2 GEO-HYDROLOGICAL CONDITION

2.1 *Geological condition*

At site, the ground and road level is 4 to 6 m a.s.l. The southern part of the construction area was covered by debris of bioclastic deposits (Tirrenian age), overlaying the Cretaceous bedrock ("Bari Limestone"), which outcrops in the northern portion.

The Cretaceous bedrock is thousands of meters thick. It is composed of a sequence of limestone, dolomitic limestone and dolomite. The thickness of the layers, measured in situ by coring, ranges from a few centimeters to 70 cm.

Overall, the Mesozoic Carbonate Sequence endured tectonic activities that produced mild folding and created fractures, mostly sub-vertical, crossing the limestone-dolomite strata. This condition triggered the karst phenomena, at site

resulting in frequent small cavities and open joints. Voids and joints are partially filled with the "Terra Rossa", the typical red clay derived from the residual dissolution of the limestone.

The fractured limestone houses the aquifer, where the groundwater flows primarily through the fractures and open joints. The permeability of this aquifer is generally estimated in 10^{-3} to 10^{-4} m/s.

The water table is characterized by a low hydraulic gradient, the groundwater flowing from the inland to the sea. The freshwater aquifer stands on the sea water. The transition zone between fresh and salty water has thickness and position variable as function of the piezometric load and aquifer peculiarity (Cotecchia, 1977).

The Cesare Battisti Square is located about 750 m from the sea coast, and the tidal fluctuations influence the piezometric level of the groundwater table. At site, the hydraulic gradient values vary daily on regular basis, ranging between 0.016% and 0.068%; and the transition zone is located between –24 and –30 m a.s.l.

2.2 *Hydrogeological condition*

An extensive investigation program was carried out, both in the project area and neighborhood, to acquire hydrogeological information about the aquifer behavior in the area interested by the construction works.

The data obtained from 58 piezometers, distributed on the downtown area, were carefully analyzed. Likewise, tests were carried out to investigate the chemical-physical characteristic of the groundwater.

To measure the actual hydraulic conductivity of the aquifer at site, three boreholes were drilled at Cesare Battisti Square. Tests were carried out by pumping water from the three wells, under various flow-rate steps, up to a max of 9 l/s. During all the tests, the water level unchanged, both in the well and in the surrounding piezometres. These results confirmed the high permeability of the rock mass at site, and the estimated values of 10^{-3} to 10^{-4} m/s.

The results obtained from site investigation and tests allowed the construction of a conceptual model of the aquifer: This was utilized in the numerical analysis of filtration phenomena performed by finite element method, with the computer code SUTRA (Satured-Unsatured-TRAnsport), version 2D3D.1, a computer program that simulates fluid movement and the transport of either energy or dissolved substances in a subsurface environment.

degree An accurate study was performed to assess the effects related with the construction of the underground car-park, and namely to evaluate how the creation of an underground impervious "box" may affect the groundwater levels, both in the short and long period.

The analysis evaluated in few centimeters the changes of the upstream water-table level, and demonstrates that this negligible value does not affect the natural groundwater flow, neither the equilibrium between groundwater and seawater, and the safety of the next structures. The results obtained from the calculation and analysis are discussed in detail in Cotecchia et al. (2007) and Cotecchia & Scuro (2010).

2.3 *Geomechanic characteristics*

In the initial phase of the works, a detailed exploratory campaign was carried out to define the geological profile and the mechanical characteristics of the rock layers at site. Ten boreholes were drilled along the perimeter and within the construction area.

The boreholes were drilled by continuous coring, to a depth of 25 m. The recovered coring and RQD values showed the presence of a limestone with marked stratification, and joint spacing in the order of decimeters. At site, the limestone is thoroughly fractured and characterized by small karst, locally filled with red clays (see photos in Fig. 2 and the typical lithological profile in Fig. 3).

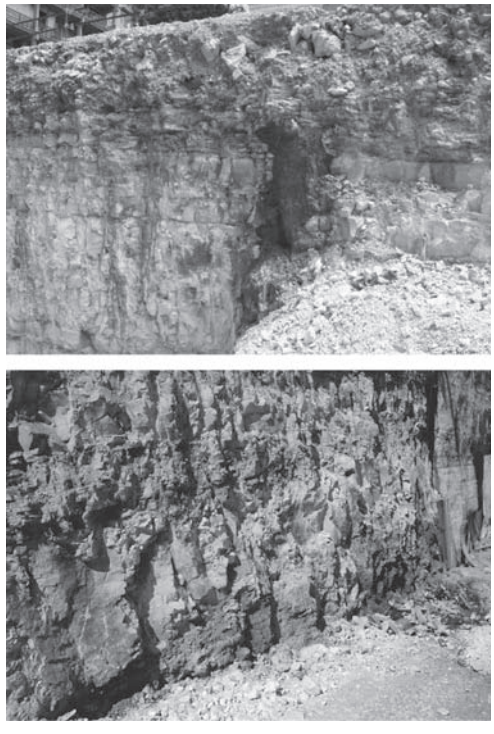

Figure 2. Photos of limestone at site.

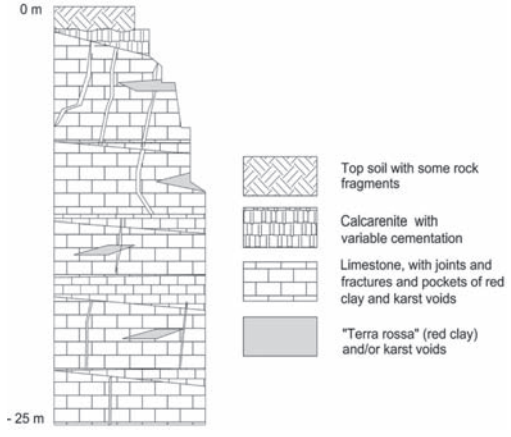

Figure 3. Typical lithological profile at site.

On the base of this data, the limestone was classified as heterogeneous and anisotropic rock.

Nevertheless, as described by Cotecchia & Tafuni (2007), considering the frequency of these discontinuities and based on the rock-mechanics knowledge, it was possible to define the geomechanical behavior of a rock mass "equivalent" to that actually existing at site. This rock mass was assumed be characterized by parameters ranging between the A and B types described in Table 1. The paper (Cotecchia & Tafuni, 2007) explains the geotechnical and structural analysis that were implemented to estimate the stability of the excavation (base and side walls) during the construction phase, and the global stability of the structure, once the construction is completed.

3 PROJECT DEFINITION

This underground parking is a complex structure, because the urban context and the site peculiar geomechanical and hydrological condition. As anticipated, the construction required the digging of about 85,000 m^3 of rock, within an excavation 13 m deep, and 7 m under the water-table natural level.

Table 1. Estimated geomechanical parameters for limestone. (Cotecchia & Tafuni, 2007).

	γ (kN/m^3)	c' (kPa)	ϕ' (°)	E' (kPa)	σT (kPa)	ν (–)
Fractured Rock—A	24	150	32	3.00 E06	20	0.3
Fractured Rock—B	25	200	40	5.00 E06	100	0.3

To allow the execution of these excavation activities in dry and safe condition, special grouting treatments were designed, to consolidate and seal the fissures and the cavities in the rock mass surrounding the structure.

Namely, these works were devoted to minimize the seepage water into the excavation, and to ensure the stability of the excavation walls on which are founded the nearby historic buildings.

The goal of this treatment is essentially provisional, fulfilling both static and hydraulic functions during the excavation and construction works. Once the structure construction is completed, the hydraulic and static stability is assured by the reinforced-concrete structure itself, calculated and planned on purpose: the hydraulic stability of the whole structure is guaranteed by its own weight, while the stability of the rock side walls is ensured by the reinforced concrete walls built onto the rock and counteracted by the horizontal structures (Fig. 4).

To study the stability of the side walls during the transitional stage, numerical analysis were carried out with the finite element method, utilizing the computer code Plaxis 2D (Tafuni & Cotecchia, 2007).

The analysis were performed in the bi-dimensional condition, on the cross section of the structure (Fig. 5). The rock mass was considered as a solid elastic—entirely plastic, adopting the geotechnical parameters of Table 1. The model took into account the filtration due to the lowering of the groundwater level to the bottom of excavation.

The analysis results gave a safety factor F = 1.75; this taking into account the seismic

Figure 4. Final assonometry of the underground parking (Cotecchia e Tafuni, 2007).

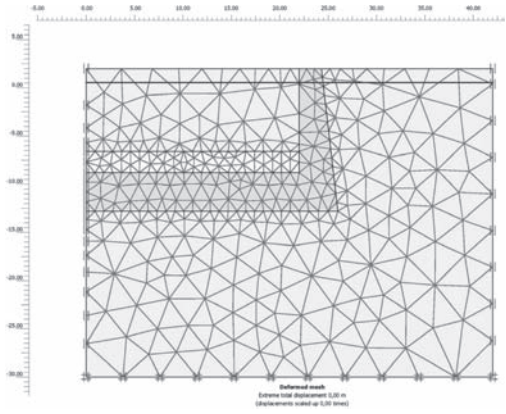

Figure 5. Stability tests carried out by FEM method (Plaxis 2D). Discretisation model adopted in the calculation.

actions implemented with pseudo-static method, using the horizontal coefficients of seismic intensity kh = 0.075 and the vertical coefficient kv = kh/2, as required by the Technical Code (Cotecchia & Tafuni, 2007).

Depth and thickness of the bottom plug have been designed in order to guarantee the stability against the uplift during the transient phase, namely when the excavation phase has been completed but the reinforced concrete structure is not built yet (Fig. 6).

The grouting treatment was designed to create a bottom plug under the base of the excavation, and a vertical cut-off along the side walls at the perimeter. Along the perimeter, the grouting treatment was also aimed to consolidate the rocky side walls, in order to ensure the stability of the excavation against the hydraulic pressure resulting from the high water-table level outside the digging area.

Therefore, boreholes were drilled and grouted over the entire area, to create a bottom plug 4 m thick, whose top end is located 2.2 m under base of the excavation. On the perimeter, along the designed excavation wall, the grouting was performed on the whole excavation depth, from the grade to the base of the bottom plug. The foundation plan geometry and sections are illustrated in the drawings of Figures 7 and 8.

Finally, to allow a better control of possible residual water inflow during the excavation phase, the area (7040 m^2) was subdivided in three portions, by means of two internal separation walls. These cutoff walls were obtained by grouting two rows of boreholes on the entire length, from the bottom plug to the working platform.

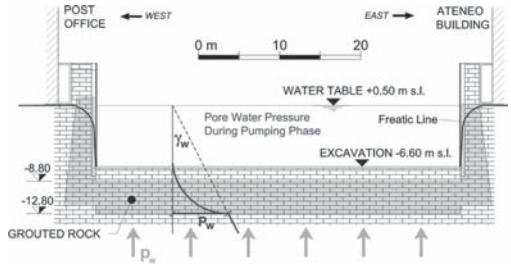

Figure 6. Hydraulic stability scheme.

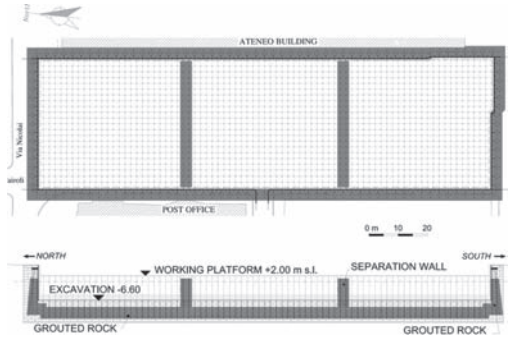

Figure 7. Parking foundation. plan geometry and longitudinal section.

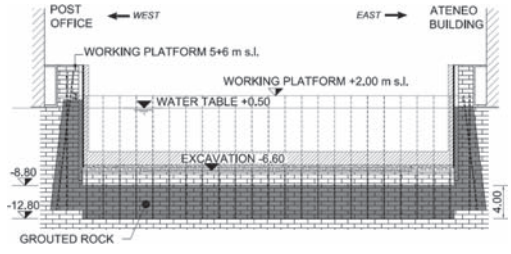

Figure 8. Parking foundation. cross Section.

4 EXECUTION OF GROUTING WORKS

4.1 *Grout mixes*

Three different kinds of mixes were grouted at site. The compositions and the main characteristics of the utilized mixes are listed in Table 2.

As a rule, the Mix A was injected in the Primary and Secondary holes. This mix is stable against the decantation, and is characterized by a fair viscosity. It can permeate joints and fissures having relatively wide opening (millimeters). Once in place, it adequately fills and seals the voids.

The Grout B (Mistra Mix) is very stable against both decantation and filtration under pressure.

Table 2. Composition and main characteristics of grout mixes.

Grout mix type	Type A standard	Type B mistra	Type C exp. grout
Composition kg/m³			
Cement (§)	425	365	785
Bentonite	13	18	16
Water	850	867	628
Admixture	–	(*)	(#)
Characteristics			
Density (g/cm³)	1.29–1.31	1.25–1.27	1.40–1.45
Marsh Viscosity (l/s)	35–40	31–35	
Bleeding	2–4%	≤1%	
Volume yield			160–170%
(§) Cement CEM-IVA-32.5	(*) Mistra admixture (#) Expansion agent		

As well, it is characterized by low viscosity and cohesion. These features allow the permeation of fine fissures, over relatively long paths (De Paoli et al., 1992). As a result, this grout can permeate and seal the fissures left untreated by the Standard Mix. Generally, the Mix B was grouted in the Tertiary and Quaternary holes.

The "Expanded Mix" (also known as "*coulis mousse*") is a "Low Mobility Grout", characterized by high viscosity and volumetric yield. Once in place the mix swells, filling large voids and cavity, if any. This type of grout was utilized in the northern part of the site (see Fig. 13 in the following), where the exploratory holes discovered a very weathered and fractured rock with voids (decimeters). This Mix C was grouted in a preliminary phase, in the very first Primary Holes. It was useful to decrease the volume to be grouted, avoiding dispersion of mixes out of the area to be treated.

All the grouts were prepared in the mixing plant installed at site. According to the good grouting practice, routine controls included density, viscosity and bleeding tests, carried out at least twice per shift on the grouts sampled at the mixing plant. In addition, specimens were prepared and delivered to the specialized laboratory, to be tested for strength (UCS) and permeability (k) after 28 days of curing. As an average, the following values were measured:

Mix A: UCS ≅ 1.3 MPa, $k \cong 4 \times 10^{-9}$ m/s
Mix B: UCS ≅ 1.1 MPa, $k \cong 1 \times 10^{-9}$ m/s
Mix C: UCS ≅ 1.0 MPa

4.2 *Grouting method, pattern, and sequence*

The consolidation and waterproofing treatment was realized by permeation grouting, utilizing the MPSP—Multi Packer Sleeved Pipes—method (Bruce & Gallavresi, 1988).

The method consists in subdividing the hole by permanent packers, creating sections (2–4 m long) to be grouted individually. The permanent packers ("bags") are installed on a pipe equipped with sleeved valves, and the pipe is inserted in the hole already drilled to the full depth. Once in place, the bags are inflated with a suitable water cement grout.

Thereafter the grouting treatment can start. Using a small double-packer, lowered into the pipe, the grout is injected through one of the valves in the section confined by the bags.

The general grouting pattern and spacing adopted at site is shown in Figure 9. At first, was completed the consolidation and waterproofing of the rock at the perimeter (boreholes X, Y, Z), thereafter the waterproofing of the bottom plug.

In general, the boreholes were drilled by the roto-percussion system, with down the hole hammer and temporary casing.

To allow the gradual sealing of the gaps, and the evaluation of the progressive effect of the treatment, the injections were performed in a sequence of primary, secondary, tertiary (and quaternary) holes, drilled and grouted with the splitting spacing system.

As a good practice, no drilling activity was performed within a radius of at least 6 m from the hole ready to be grouted, or under grouting.

All the grout activities were performed according with the Standard EN 12715, with the procedure described in the following

4.3 *Drilling and grouting of holes on the perimeter*

The grouting holes were drilled from the existing road level (El. +4 ÷ 6 m s.l.) to the base of the

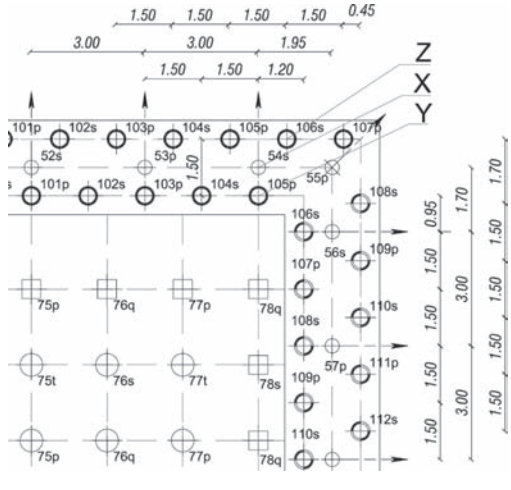

Figure 9. Grouting holes—pattern and spacing.

bottom plug (El.–12.0 m). The grouting-hole mesh included three parallel rows: two rows (Z and Y) of vertical holes 1.5-m spaced, one row (X) of holes 3-m spaced and slightly inclined (7°) (see Figs. 9 and 10.

Each grout hole was subdivided in 6 stages by MPSP packers. Each stage was individually grouted, with the specific criteria designed as function of depth, sequence and spacing. In general, the parameters values were within the following limits: V_{max} = 250 ÷ 500 l/m, P_{max} 8–18 bar, P_{min} 6–11 bar.

Once started, the grouting each stage was continued without interruption, until the refusal criteria were reached, i.e. the max grout take V_{max} and the minimum pressure P_{min}, or the refusal pressure P_{max}.

Where in the first pass the V_{max} was injected without reaching the P_{min}, within 24 hours the grouting was resumed injecting additional grout, until the required P_{min} was obtained.

Figure 10. Drilling of the boreholes on the perimeter.

Figure 11. Grouting on the perimeter, to create an impervious grout curtain and to consolidate the walls of the designed excavation.

Locally, where drilling founded large pocket of red clay, steel micropiles were installed to strengthen the excavation side walls (Fe510 steel pipe, 88.9 mm in diameter, 10 mm thick).

4.4 *Grouting of bottom plug*

Before starting the drilling activity, excavation and earth movement were completed to lower the working platform from approx El +5 m to +2 m s.l.

The grouting holes were located on a square pattern, with a final distribution of 1 hole each 4 m^2 (see Figs. 9 and 12).

The holes were drilled to the final depth (El.–12.8 m, i.e. the designed base of the grouted bottom plug), and grouted only in the deepest 4 meters. Each hole was divided in two stages, clogged at top by the MPSP permanent packer.

As anticipated, in the northern portion of the site (characterized by extremely weathered and fractured rock), the very first Primary Holes were pre-grouted with the Expanding Mix.

Afterward, the treatment was carried out by drilling and grouting a sequence of Primary, Secondary and Tertiary-Quaternary holes, positioned with the splitting spacing method.

The grouting was performed implementing the design parameter, without interruption until the refusal criteria were reached (V_{max} = 400 l/m, P_{max} = 19 bar). Where the V_{max} was injected without reaching the designed P_{min} = 10 bar in the first pass, the grouting was resumed within 24 hours, injecting additional grout until the required P_{min} was obtained.

4.5 *Grout take and final pressure*

During the injection phase, the grouting parameters for each section were carefully monitored and

Figure 12. Drilling and grouting of the boreholes under the entire area to create a bottom plug.

recorded. Once the grouting of a series of holes (in a stretch of the area) was completed, the analysis of the actual grout-take and pressure behavior was performed. On the basis of the results achieved, it was decided how to proceed in the adjacent holes, adjusting the type of grout and grouting parameters.

Figure 13 graphically illustrates the grout-take value recorded for each hole, and expressed in terms of liter per meter (l/m) of grouted length.

Considering the hole spacing and the grouted thickness, the volume of mixes injected can be formulated as percentage of grout-take referred to the volume of treated soil/rock.

The bottom-plug holes (square pattern, 2 m spacing) were grouted over a length of 4 m. The holes on the perimeters (triangular-irregular pattern, 3.0 ÷ 1.5 m spacing) were grouted over a length of 12.5 m.

In average, the resulting percentage of grout-take is 15–20% of the grouted rock volume. This value is close to the expected one, and comparable to those recorded in other similar projects completed in the neighborhood (Andidero building on Perotti Waterfront, Teatro Petruzzelli, and others).

As said, the grouting pressure had to reach a certain minimum value, before considering completed the grouting of the hole. Thus, for almost all the holes, the grouting was continued until this minimum value was obtained. About the 20% of the sections reached the refusal pressure (P_{max}) in the first pass. Most of the other boreholes reached the designed value of minimum pressure (P_{min}) in the first or in the second pass.

5 VERIFICATION WATER TEST

After the grouting activity completion, before starting the excavation phase, site water tests were performed, to check the treatment results and measure the residual permeability. Twelve boreholes were drilled within the area, to test the bottom plug; 16 boreholes were drilled along the perimeter, to test the lateral grout curtain (see Fig. 14).

To avoid the punching of the bottom plug, the drilling was always stopped at least 1 m above the base of the treatment. The tests were carried out utilizing a packer to confine the portion of rock to be tested. The tests were performed under low pressure, to avoid the risk of hydrofracturing. The test in the bottom plug involved the entire treated length. The borehole in the lateral curtain was tested in three stages.

The permeability test results are summarized in Table 3, and detailed in the diagrams of Figures 15 and 16.

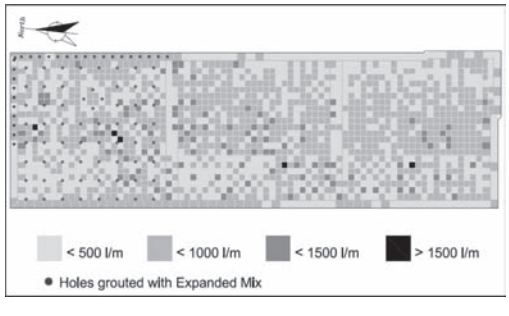

Figure 13. Hole grout takes.

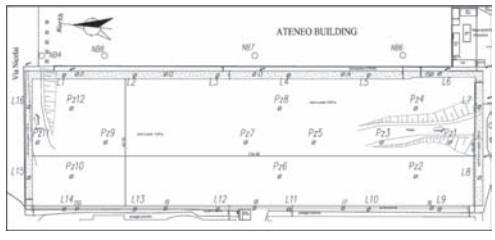

Figure 14. Location of piezometers and testing boreholes.

Table 3. Summary of the water test results, after grouting.

Permeability, average values (m/s) after grouting				
	North side	East side	West side	South side
Grout curtain				
El. +0 to –2 m s.l.	2.5E-07	3.5E-07	2.8E-07	3.1E-07
El. –3 to –5 m s.l.	1.8E-07	5.6E-07	2.6E-07	2.5E-07
El. –6 to –8 m s.l.	2.1E-07	3.3E-07	2.9E-07	9.6E-07
	North sector	Central sector		South sector
Bottom plug				
El. –10 –12 m s.l.	4.6E-07	6.4E-07		1.8E-07

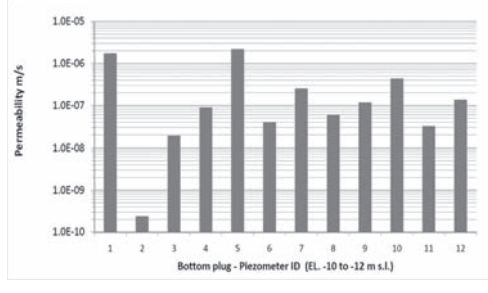

Figure 15. Results of water test after grouting—bottom plug.

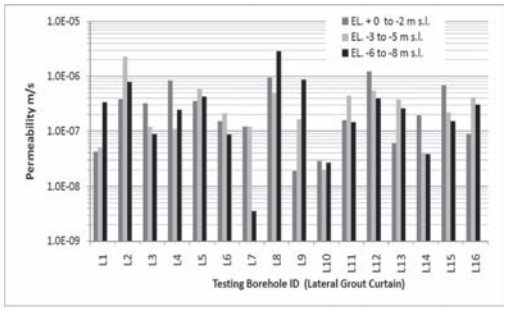

Figure 16. Grout curtain at the perimeter: results of water test, after completion of treatment.

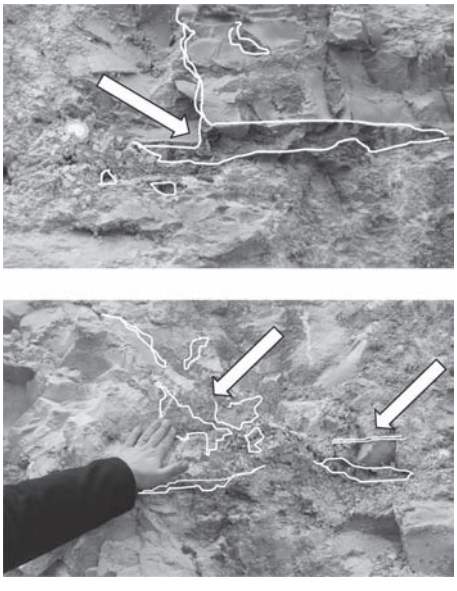

Figure 17. Excavation works, after the grouting treatment. The arrows point to the treatment.

Figure 18. Excavation works, after the grouting treatment performed to consolidate and waterproof the foundation rock.

As shown, these values are very smaller than those recorded before the treatment, the final average permeability being less than 4×10^{-7} m/s.

6 CONCLUSIONS

Preliminary site investigation and accurate geomechanical and hydrogeological analysis were performed to evaluate the site condition.

The grouting works were started on April 2006, and completed on April 2007. After that, the construction works were suspended, due to administrative matter.

The activities were resumed during the 2009 spring. Coring drillings and site water tests were performed, to measure the residual permeability and check the quality of the treated rock, providing very good results. Thereafter, the construction of the underground parking R.C. structure started with the excavation works. During the digging of the 80,000 m^3 of rock, the nearby historical buildings were continuously monitored.

The excavation activity was successfully completed (2009 spring) in safe and dry condition, the residual water inflow being less than 4 l/s over a total wet surface of about 10,000 m^2 (Figures 17 and 18).

REFERENCES

Bruce, D.A., Gallavresi, F., 1988. The MPSP System: A New Method of Grouting Difficult Rock Formations — *"1988 ASCE Conference"*, Nashville, May 1988.

Cotecchia, V., 1977. Studi e ricerche sulle acque sotterranee e sull'intrusione marina in Puglia (Penisola Salentina). *Quaderni dell'Istituto di Ricerca sulle acque, n. 20,* Lithoprint, Roma 1977.

Cotecchia, V., Scuro, M., Barbone, G., 2007. Condizioni di impatto idrogeologico della falda acquifera sottostante alla città di Bari prodotto dalla realizzazione di un parcheggio sotterraneo in piazza Cesare Battisti. *Proc. "Giornata in Ricordo di Renato Ribacchi, Associazione Geotecnica Italiana", Roma, December, 12th, 2007, pages 257–269.* Pàtron Editore.

Cotecchia, V., Scuro, M., 2010. "Protrait of a coastal karst aquifer: the city of Bari". *AQUA mundi, Journal of water science, vol. 1, Issue 2, December 2010, Am 02201.*

Cotecchia, V. & Tafuni, N., 2007. La progettazione geotecnica di un grande parcheggio interrato nell'acquifero calcareo del centro urbano della città di Bari. *Proc. "Giornata in Ricordo di Renato Ribacchi, Associazione Geotecnica Italiana", Roma, December 2006, pages 245–256.* Pàtron Editore.

De Paoli, B., Bosco, B., Granata, R., Bruce, D.A., 1992. "Fundamental Observations on Cement Based Grouts (1): Traditional Materials", *Proc. ASCE "Grouting, Soil Improvement and Geosynthetics", New Orleans, Louisiana, February 25–28, 1992, pages 474–485.*

European Standard, 2000. "EN 12715:2000. Execution of special geotechnical work. Grouting"—*Publisher BSI (English version) September 2000, 56 pages.*

US Geological Survey, "SUTRA (Satured-Unsatured Transport) Code, Version 2.0 [2D3D.1], *Virginia USA, September 2003.*

Winston, R.B. and Voss, C.I., 2003, SutraGUI, a graphical-user interface for SUTRA, a model for ground-water flow with solute or energy transport: *U.S. Geological Survey Open-File Report 03-285, 114 pages.*

This page intentionally left blank

Geotechnical Aspects of Underground Construction in Soft Ground – Viggiani (ed)

Seepage experiences for deep urban excavation at the TBM Malatesta shaft, Rome

A. Capata & V. Capata
S.G.S. Studio Geotecnico Strutturale, Rome, Italy

ABSTRACT: The control of water pressure and seepage in a deep urban excavation, in elevated hydraulic heads conditions, has represented and continues to represent one of the main problems for the realization of the new C Line Subway stations in Rome. The subway line, which extends from the city center to the suburban southeast, is characterized mainly by pyroclastic materials over Pleistocene deposits. Dewatering systems for the C Line Stations have been implemented in order to lower the water level below the final excavation level, without appreciable repercussions on the external diaphragm walls. On the basis of carried out experience, this paper will describes and explains the results of the dewatering system that has been designed and executed for controlling the water underpressure and management of the seepage process in deep open pits subjected to elevated hydraulic heads.

1 INTRODUCTION

The realization of a deep excavation in a high hydraulic head condition, in absence of waterproofing treatment at the base, usually needs dewatering systems to control the piezometric condition and, more generically, is employed for lowering the water table within the diaphragm walls. This is a particularly sensitive aspect in the excavation of the new C Line Subway in Rome, where on account of the high density of archaeological remains, the subway stations are at an average depth of 25 meters below ground level. The stations are also characterized by elevated hydraulic loads. The purpose of this paper is to explains the dewatering system used for the TBM Malatesta Shaft, describing the monitoring devices that have been predisposed and the results that have been achieved by the dewatering system during the testing phases. The final section of the paper will cover another dewatering case that will arise in due course along the line, underlining the results and the differences in relation to the first case.

2 GEOLOGICAL PROFILE

The C line stations interest a large area characterized by the volcanic products of the Albani Hills, which represent the majority of excavated materials. The geological longitudinal profile of the TBM Malatesta Shaft, is represented in Figure 1 and synthesized below. The upper layer is constituted by backfill (R) which is so rich in archaeological remains that it has conditioned the construction sites. This is a heterogeneous material of a pyroclastic nature of a silt-sandy granulometry thickened by gravels. Below this there is an upper volcanic complex which extends over almost the entire line until to the bottom excavation. The pyroclastic formation is classified as Villa Senni Tuff (VS), Lionato Tuff (TL), Muddy Tuff (TT) and Black/Red Pozzolanas (PN & PR). These materials are of a sand-gravelly or slime-sandy granulometry, strongly cemented (TL) in parts. These are the main formations that interest the excavations of the stations. The pozzolana deposit in particular is chiefly concerned by the dewatering process on account of its elevated thickness. The Lower Tuff complex (TA, T1, T2) lies immediately above the Pleistocene deposits. The layer of Clayed Tuff (TA) is composed slime-sandy grain material of a good consistency. These layers run between hard tuff T1, T2 strata, which are sand-gravelly and subordinately slime-sandy in grain and size. Locally these layers can be of a rock consistency. Although strongly cemented at intervals, these rock layers are in a highly fractured condition (es. T1). Still further below are the Pleistocene layers (ST/STa, AR and SG). The first of these layers is made up of slime and sand (STa/ST) of average to elevated consistency. The intermediary layer is generally constituted by clays and lake slimes (AR).

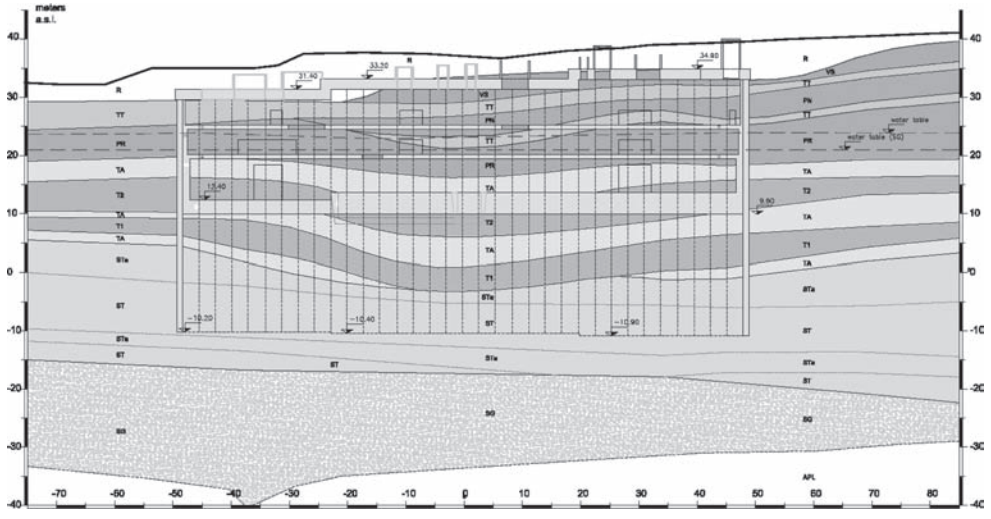

Figure 1. Geological profile of TBM Malatesta Shaft.

Table 1. Geotechnical design parameters of the strata.

Layer	W (%)	γ (kN/m^3)	W_L (%)	I_P (%)	K (m/sec)
R	25	17	n.d.-46	n.p.-12	1 E-5
VS	45	17	n.d.	n.p.	1 E-6
TT	42	17.5	38	7	5 E-6
PN	35	17.5	n.d	n.p.	1 E-5
PR	37	17	n.d.	n.p.	1 E-5
TA	52	17	42-n.d.	8-n.p.	5 E-5
T1-T2	40	17	n.d.	n.p.	5 E-5
ST	28	18.5	28	6	8 E-6
STa	38	18	58	30	1 E-7
SG	–	20	–	–	1 E-4

The lower stratum is characterized generally by gravels in a sandy matrix, with few silty elements that has originated from the Paleotevere deposit (SG). This layer contains the main acquifer of the city of Rome, which in turn is sustained by an underlying basal formation of Pliocene Clays (APL).

Table 1 illustrates the geotechnical layout parameters of the various strata.

3 GENERAL HYDRAULIC CONDITION

In general terms the hydraulic situation of the area of Rome can be broken down into four main geological complexes: 1) the backfill complex, 2) the alluvial deposit complex, 3) the volcanic deposit complex and 4) the Pleistocene deposit complex, at whose base there is an impermeable substratum of Pliocene clay (bedrock). The main aquifer is located in the Pleistocene sediments and above the volcanic deposits. The drainage channels are constituted by the Tiber and the Aniene rivers and theirs affluents.

The C line runs mainly along the left bank of the Tiber, from the Albani Hills southeast to northwest. An acquifer in the superficial alluvial deposits, located in the central zone of the C line, is regulated by the water table of the river and has the tendency to disappear together with the alluvial deposits (Ventriglia, 2002).

4 SEEPAGE PROCESS: DESIGN ASPECTS

The design of the depths, diameters and distance between the wells is based on the interpretation of the permeability and punctual dewatering tests along the line (AGI, 1977) as well as on calculations of the volume of dewatering and the piezometric condition imposed by the drainage.

The calculation of the distance and depth of the wells refers to a hydraulic scheme that calculates the seepage process, cautiously imagined according to a minimum path directed from the base (water supply) to the top.

A budget for the in/out water volume through the excavation base was calculated, balancing out the two flows—the first from the outside inwards and the second from the inside, receiving and processing the volume of water from the first flow.

The seepage process around every drainage point was therefore assimilated to that of a well like that in Figures 2 and 3.

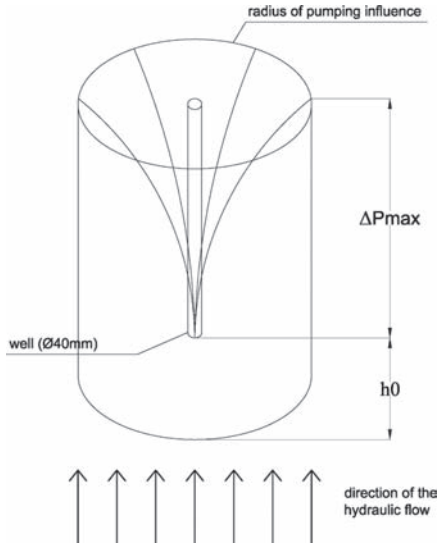

Figure 2. Design sketch of hydraulic flow during the pumping.

The following equation regulates the two flows:

$$\frac{\pi x R^2}{L} \cdot (\Delta H - \Delta P_m) \cdot K1 = \frac{2\pi \cdot K2 \cdot 2 \cdot D \cdot \Delta P_m \cdot G}{\ln\left(R/Ro\right)} \quad (1)$$

so the maximum overpressure value can be defined as:

$$\Delta P_m = \frac{\Delta H \cdot R^2 \cdot \ln\left(R/Ro\right) \cdot K1/K2}{R^2 \cdot \ln\left(R/Ro\right) \cdot K1/K2 + 4 \cdot D \cdot L \cdot G} \quad (2)$$

where:

- $K1$ is the permeability of outside strata;
- $K2$ is the average permeability of the strata under the bottom excavation;
- L is the seepage path, equal to h_0;
- $\Delta P_m = \Delta P_{max}/2$ unknown is the average hydraulic pressure;
- R is the distance between the wells;
- Ro is the radius of the well, equal to 20 cm;
- $\Delta H = H - h_0$ is the hydraulic head;
- G represents the degree of well penetration in the aquifer;
- D is the drainage thickness of the well.

To vary of the distance R between the wells, the underpressure ΔPm is drawn, compatible with the stability conditions that we want to reach and the flow Q for the single well. The dewatering efficiency has been studied

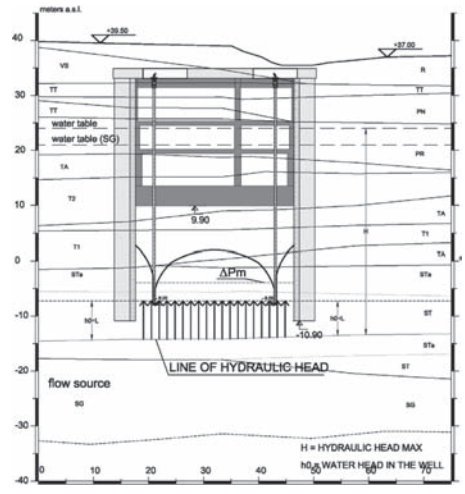

Figure 3. Scheme of seepage flow.

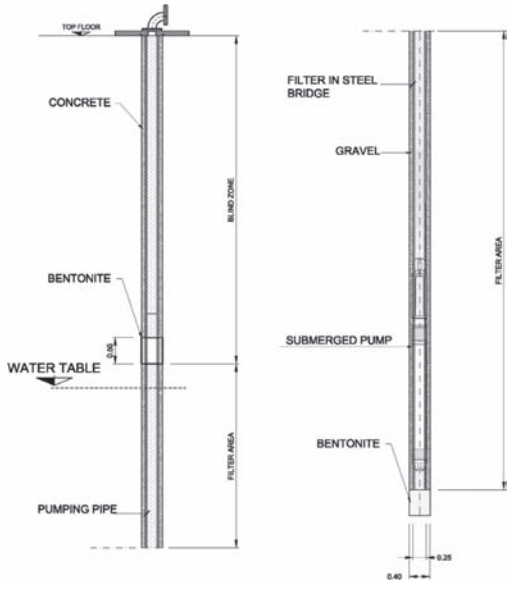

Figure 4. Schematization of the well.

through the Forchheimer's (1930) and Dachler's (1936) solutions in order to provide the real lowering phreatic level inside the open pit.

5 DEWATERING SYSTEM DESIGN

The dewatering system is made up of a total of 12 wells. The wells (Ø400 mm) are deep around the base of the diaphragm walls, inside the ST layer

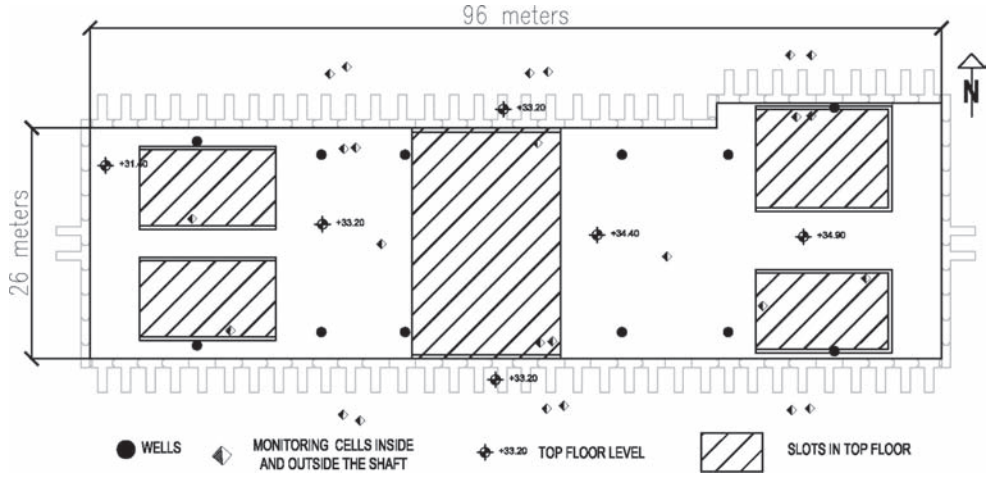

Figure 5. Monitoring plan of TBM Malatesta Shaft.

Figure 6. Picture of pumping system of the Mirti Station: flow meter and pipes.

(–8.0 m a.s.l.) with a drainage window of 32 meters over a total depth of 40 meters. The dewatering interests both the volcanic and Pleistocene complexes, leaving out the SG layer. The wells have been equipped with a submerged 5.0 kW (7.5 HP) pump. The executive scheme is as illustrated in the following figure.

Before the beginning of excavation, the system has been tested.

During the dewatering test, the piezometric level was monitored by 25 piezometric cells: 12 Casagrande cells, located outside the perimeter of diaphragm walls and 13 Vibrating Wire cells, located under the bottom excavation inside the perimeter of the diaphragm walls.

In the Figures 5 and 6 it has been represented a monitoring devices planning in the TBM Malatesta Shaft and an example of the pumping system equipped for dewatering.

6 THE TBM MALATESTA SHAFT DEWATERING TEST: EXPERIMENTAL RESULTS AND DESIGN VALUES

The TBM Malatesta Shaft has been already completed in order to begin work on the four TBM tunnel excavations. It has an area of around 2500 m^2 and was built with T section diaphragm walls. The length of the diaphragm walls varies between 40 and 44 meters. The elevation of the bottom floor is +9.90 m a.s.l., or around 25 meters from ground level, for a maximum hydraulic head of 14–15 meters (water table at 24 m a.s.l.). As can be deduced in Figures 3 and 7, the calculated hydraulic flow is directed upwards by the excavation at the base and fed by the SG deep formation. The Inferior Tuffs complex has been pierced completely and the diaphragm walls are driven into the sand-silty ST/STa layer.

The dewatering system was tested in September 2008. It confirmed the presence of two different water tables, the uppermost at an elevation of +24.00 m a.s.l. and the principal water table at an elevation of +22.00 m a.s.l., separated by the silty (STa) layer. The most external wells in proximity to the angles of the shaft showed a smaller efficiency in comparison to the more central ones, with a greater dewatering area available. Overall the dewatering test produced positive results, with a lowering of the inside piezometric level beneath the bottom of excavation of over 15 meters in relation to the initial water table

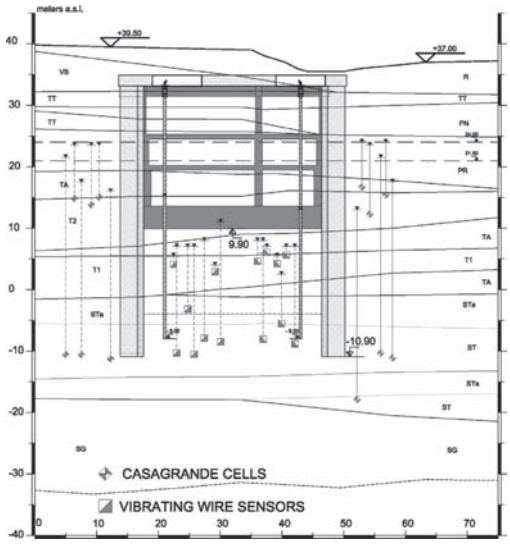

Figure 7. Monitoring section of the TBM Malatesta Shaft.

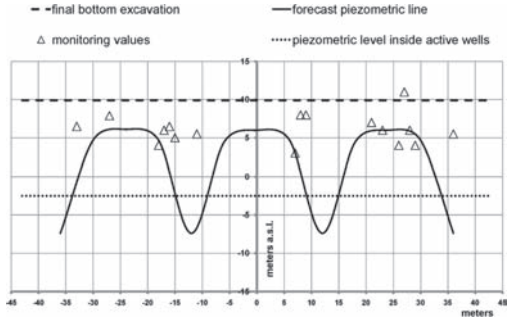

Figure 8. Comparison between piezometric forecast line (4 wells) and experimental measures.

Figure 9. Example of the cavity in the T1 stratum during the excavation of Malatesta Station, about 25 meters under the water table.

(Figs. 7, 8 and 10). The recovery of the inside groundwater, measured in the 24 hours that followed the switching off of the system, underlined the substantial impermeability of the lower layers and the waterproofing of the diaphragm walls. In fact, after one day of recovery, the water table stood at an average of 15 m a.s.l., or 9 meters under the initial levels, with a slow tendency to rise. The outside piezometers located nearest to the diaphragm walls attested to the absence of repercussions on the upper phreatic level. The deep water table measured a lowering of piezometric levels of 6–7 meters in relation to the initial water table. This trend further confirmed the impermeability of the silty layer, highlighting the existence of a clear hydraulic separation between the two water tables. The calculated piezometric condition was confirmed by the values indicated on the monitoring piezometers placed within the shaft.

The global flow that resulted varied from around 700 m^3/day with 8 active wells to around 800 m^3/day with 12. The flow values on each single well were about equal to 1.0 l t/sec against a value of 1.4 lt/sec calculated during the design phase, or around 960 m^3/day with 8 active wells.

7 ANOTHER SEEPAGE CASE ALONG THE LINE

This paper has illustrated the results of dewatering tests performed before the beginning of the excavations for the TBM Malatesta Shaft. The shaft has since been completed without any problems.

The seepage calculations were confirmed by the experimental tests performed. They also underlined the possibility of checking piezometric conditions in the presence of elevated hydraulic loads. In this case the study of the seepage processes in the sand-gravelly SG layer confirmed the basin of feeding and therefore the one-dimensional hydraulic flow directed upwards by the lower section. The high permeability of the fracturing hard tuff layers was exceeded, deepening the diaphragm walls until the upper layer of the Pleistocene formation. This layer has a variable permeability according to the size of the silty part but with a behavior that is well known and comparable to that of a saturated porous medium. Unfortunately this Tuff complex has not been closed by diaphragm walls in some stations. The flow recorded in these cases was much more during the dewatering tests.

For example, the Gardenie Station stands around 1200 meters away from the TBM Malatesta Shaft, with about 19 meters of hydraulic head

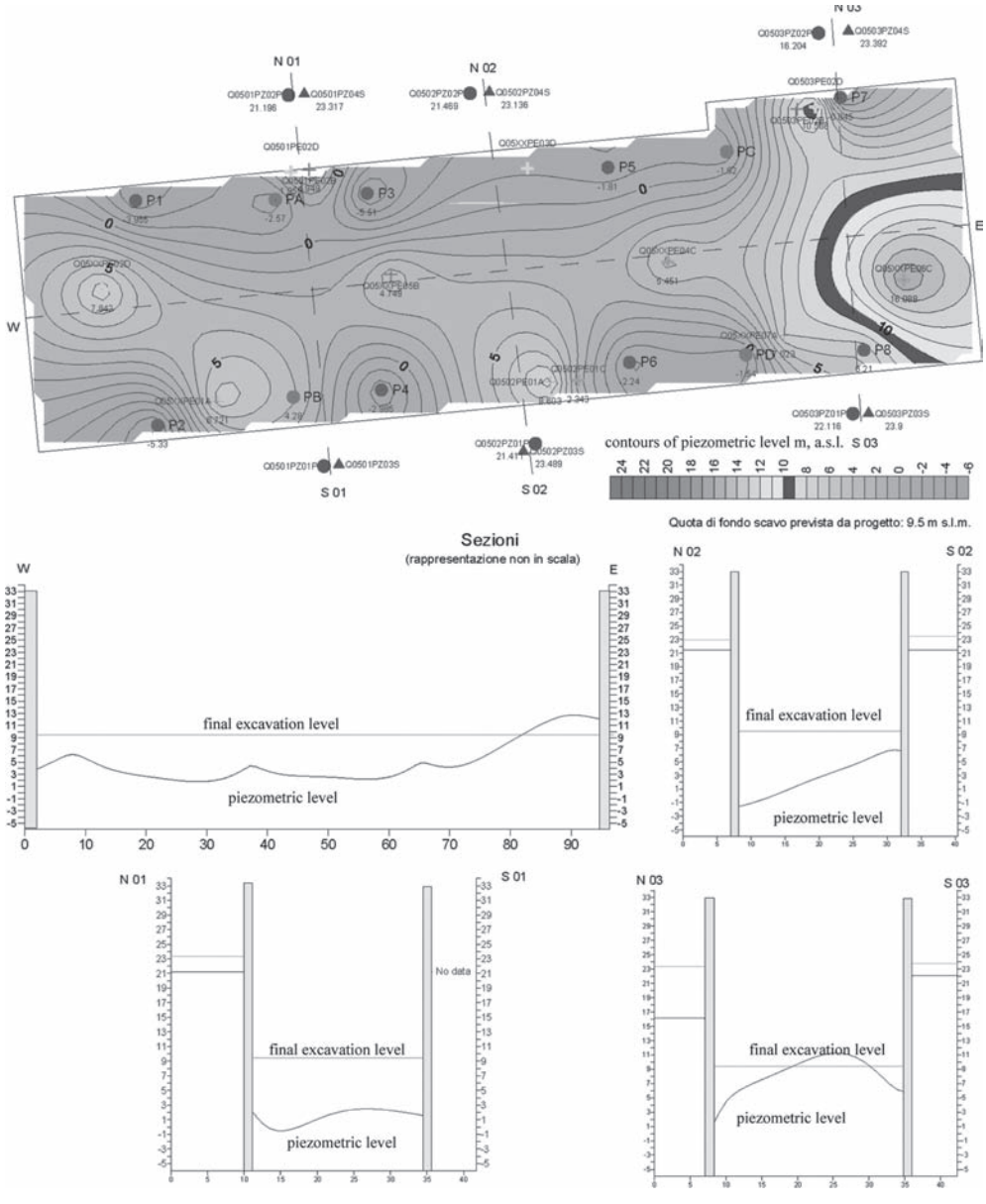

Figure 10. Lowering piezometric contours planning inside the TBM Malatesta Shaft and longitudinal/transversal dewatering sections during the test (IMG, 2008).

on bottom excavation and its dewatering system reached the lower tuff layers.

In this case the flow was about 6000 m^3/day (1st testing, Fig. 11—Geoslope, 2002). A bottom plug was therefore made for reducing the permeability of the hard tuff layer, located under the base of the excavation. The ground treatment with cement injections considerably reduced the permeability of the tuff, saturating the fractures and existing hollows (Fig. 9) in the several hard layers and recreating the characteristics of a medium akin to that of a traditional saturated porous mean. The global flow after the realization of the bottom plug was around 3500 m^3/day (2nd testing), allowing for the lowering of piezometric inside level down to the base of the excavation.

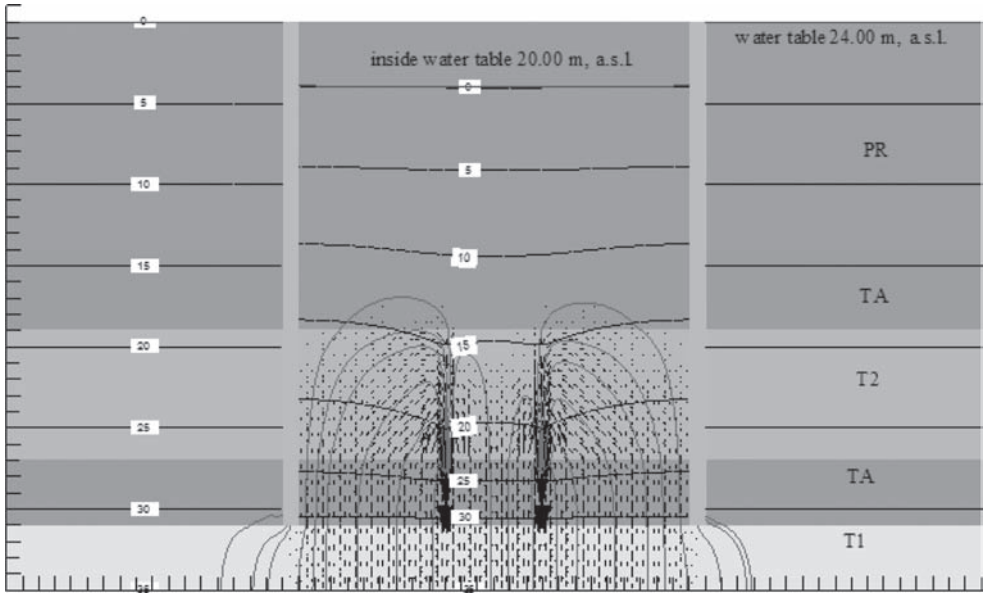

Figure 11. Groundwater back-analysis simulation of dewatering test in Gardenie Station without the bottom plug: hydraulic flow and piezometric contours.

When these hard layers are intercepted and confined by diaphragm walls, as in the TBM Malatesta Shaft, their flow contribution is therefore secondary because they are no longer fed. Alternatively, the hydraulic flow is preponderant and does not allow the attainment of the required hydraulic conditions.

8 CONCLUSIONS

The control of the seepage process is usually the major design aspect in underground construction with important hydraulic loads realized without a bottom plug. Piezometric conditions management is therefore the geotechnical aspect of greatest importance for the completion of the C Line Subway in Rome, in view of the considerable dewatering flows. The excavation of the Roman pyroclastic formation, on account of the well known difficulties of hydraulic behavior forecasting, was certainly the most difficult aspect of all.

The several punctual tests also recorded a discreet flow in these kinds of soil (around 5 lt/sec) but could not register a different hydraulic behavior from the traditional methods notoriously based on bi-dimensional seepage paths in aquifers confined beneath. Only when the hydraulic flow through mostly altered tuff layers (like T1) was interrupted by diaphragm walls or by a bottom plug execution, the seepage flow was limited.

REFERENCES

AGI (1977) "Recommendations planning and execution of the geotechnical investigations", AGI, June 1977.
Dachler, R. (1936) "Grundwasserstromung", Julius Springler, Vienna.
Forchheimer P. (1930) "Hydraulik", 3rd edn. Teubner, Leipzig.
Geoslope User's guide—Geostudio (2002) v5.11, Geo-Slope int. Ltd. Calgary, Canada 2002.
IMG (2008) "Dewatering testing report of TBM Malatesta Shaft", IMG, C Line consultant for monitoring
Ventriglia U. (2002) "Geology of the City of Rome" published by the Geological Survey and Soil—Province of Rome.

This page intentionally left blank

Geotechnical Aspects of Underground Construction in Soft Ground – Viggiani (ed)
© 2012 Taylor & Francis Group, London, ISBN 978-0-415-68367-8

Spatial effects on excavations in deep soft lacustrine clay

P. Becker
University of Strathclyde, Glasgow, Scotland

G. Berhane
Ed. Zueblin AG, Stuttgart, Germany

H.-G. Kempfert
University of Kassel, Germany

ABSTRACT: A case history of a deep excavation in Constance near the lake Constance north of the German Alps is presented in this paper. The excavation was 90 m long, 17.5 to 22.5 m wide and 6 m deep. The underground condition in Constance and the surroundings is known of a deep and soft deposit of lacustrine clay. The spatial effects on the excavation, specially the effects of the construction steps on the deformation behaviour as well as the mobilization of each support element, has been studied by means of back analyses using the Finite Element Method (FEM) with 2D-models. The computed results are compared with the measured data from the project with respect to the time dependency of the soil-structure-interaction and deformation behaviour. For this purpose, additional pore pressure sensors were installed to record the development of excess pore pressure corresponding to different construction stages. Finally, recommendations on numerical modelling of excavations in soft soils are presented, and mobilization factors for support elements and the stress path dependant stiffness of soft soils are described.

1 INTRODUCTION

Prediction of deformations resulted from excavations in soft soils is generally performed using the Finite Element Method (FEM) and with the application of advanced constitutive soil models. A reliable estimation of deformations in advance of the project is generally not possible due to the variety of factors on soil-structure-interaction (see Becker 2009). Rather the FEM is applied at excavations in soft soils for more than three decades in conjunction with the observation method. The numerical calculation leads with variations of the material parameters to both alarm and limit values of deformations and forces, taking into account a realistic modelling of the boundary value problem.

The time-dependent material behaviour and the characteristic stress paths in excavations, which differ from those of standard laboratory tests, require a high degree of experience of the geotechnical engineer for estimating the material parameters. If there are no appropriate laboratory test results and calibration of measuring results in the planning phase is not yet possible, uncertainties regarding the numerical deformation prediction increase significantly and hamper as well the design of structures and the optimization of the construction process. In the following numerical analysis of a case study, the stress-strain behaviour of soft soils depending on stress-paths due to the excavation process is considered using a commercially available FE-Program and advanced constitutive soil models.

2 GENERAL DESCRIPTION OF THE EXCAVATION SITE

2.1 *Support system and construction stages*

The case history is located in southern Germany at Lake Constance. The construction work for the 5-storey building with a length of 87.5 m and a width between 17.5 and 22.5 m began in the summer of 2007. A site plan of the excavation is shown in Figure 1.

The excavation is 5.90 m deep and it is supported by a secant bored pile wall. The piles have a diameter D = 1.07 m and a pile length l = 10.5 m. The bored pile wall was reinforced by a concrete beam wale at the top all around, which gives the wall additional strength in the longitudinal direction of the excavation pit previous to the installation of the struts.

The construction sequence is shown in Figure 2. The excavation was conducted in slices from a preliminary excavation level at depth of –1.50 m

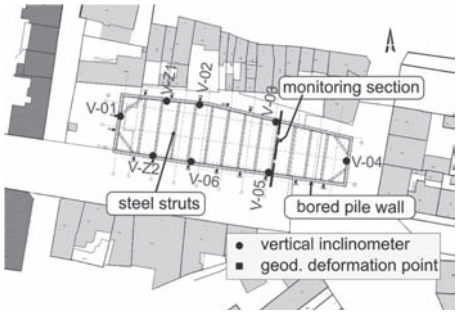

Figure 1. Site plan with monitoring section.

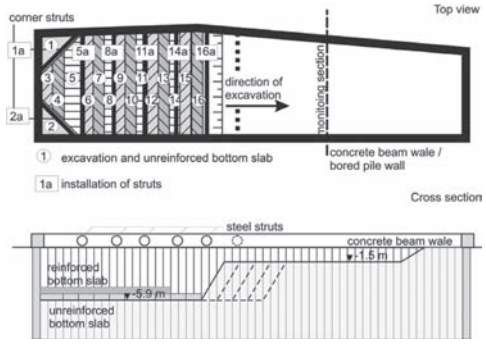

Figure 2. Top view and cross section of the excavation site with idealized construction stages.

below the surface. The excavation was started at the two Western corners making use of the spatial support of bored pile wall and upper concrete beam wale. Immediately after the excavation a triangular-shaped unreinforced bottom slab (d = 50 cm) was placed. Diagonal steel tube struts with a diameter D = 80 cm were installed afterwards at the corners. Thereafter, the excavation proceeded with a sloped trench of 2 m width and immediate placement of unreinforced bottom slabs in daily time basis. With the progress of the excavation and reaching the entire excavation width, the first steel tube strut with a diameter D = 76 cm was installed (step 5a in Fig. 2).

After each further excavation in slices over the entire width of the excavation, unreinforced bottom slabs were placed and the struts installed at a centre to centre distance of 6.9 m. Finally, a reinforced bottom slab was casted on the top of the unreinforced bottom slab (Fig. 2).

2.2 *Underground condition*

The soil investigation was conducted using bore holes and cone penetration tests. Additional information on the underground was also available from previous excavation sites in direct surrounding, see for e.g. Becker et al. (2008) and Kempfert & Gebreselassie (2006).

The ground consists of 5 layers (Fig. 3). The upper most layer is 2.0 m thick fill material. Beneath the fill is a 10.0 to 26.0 m thick soft lacustrine clay deposit which is divided into 2 layers. The upper lacustrine clay has predominantly soft consistency whereas the lower lacustrine clay has a soft to stiff consistency due its sand and gravel contents. Beneath the lacustrine clay layers is a 7.0 to 10.0 m thick transient layer with predominantly sand and silt content and a variable content of gravel particles. From a depth of −19 m in the west and −37 m in the east downwards, the underground is dominated by a ground moraine.

2.3 *Monitoring*

The excavation was accompanied by the observation method. In particular seven vertical inclinometers and twenty geodetic deformation points were installed (Fig. 1). Moreover, pore pressure transducers were installed into at a specified monitoring section (Fig. 1). In Figure 4 is the layout of the pore pressure transducers in the monitoring section shown. For more details about the instrumentation refer to Becker (2009).

2.4 *Measurement results*

The measurement results are discussed for the monitoring section defined in Figure 1. Due to the limitation of the length of this paper, the measurements results are shown in section 4 of this paper in connection with numerical analysis results. For more information refer to Becker (2009).

The time dependant and spatial influence of slice wise excavation on the horizontal wall displacements at the upper concrete beam wale is identified by the evaluation of the geodetic deformation measurements (Fig. 11). At measuring point 3301 the first deformations were recorded 20 days prior to the execution of the corresponding excavation slice on 02.11.2007.

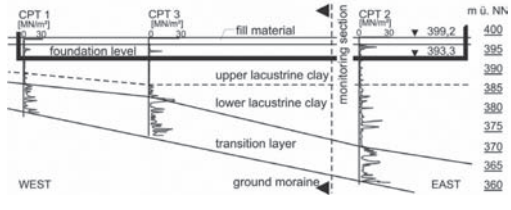

Figure 3. Underground condition in West–East cross section.

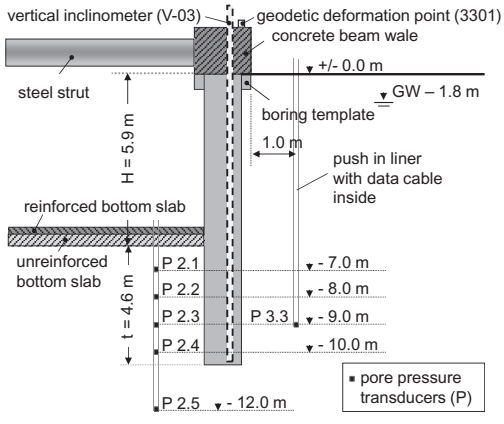

Figure 4. Monitoring section through bored pile wall showing pore pressure transducers, vertical inclinometer and geodetic deformation point.

The vertical inclinometer measurements at the monitoring section are shown in Figure 10. In the left chart are the measurements from the southern bored pile wall (V-06 and V-05) and in the right chart are from the northern side (V-02 and V-03). The horizontal displacements on the southern side (V-06 and V-05) show a uniform distribution with maximum values of 9 mm at the wall head and 12.5 mm to 14 mm at the wall toe. The deformation of the opposite northern side (V-02 and V-03), however, vary between 5 mm and 11 mm at the wall head and between 7.5 and 17 mm at the wall toe. The maximum displacement ratio $u_h/H = 0.25\%$ is very moderate and it is support system dependant. For further deformation measurements, see Becker (2009).

The time-dependent development of excess pore pressure is shown in Figure 12. The excavation of the slice at the location of the monitoring section was done on 02.11.2007. As a result of the stress relief due to the excavation, an excess pore pressure change of 48 kN/m^2 occurred at all measuring points in front of the wall toe. Influence of wall deformation on excess pore pressure was not observed. Afterwards, a slight increase of excess pore pressure was observed due to the consolidation process. The installation of the reinforced bottom slab resulted in a sudden increase of the excess pore pressure by an amount of 10 kN/m^2.

3 SPATIAL EFFECTS ON STIFFNESS OF SOFT SOILS

3.1 *Stress path dependant stiffness*

It is well known that the stiffness of soils is dependent on the applied stress path, e.g. primary loading and un-/reloading, see also Parry (1995), Gebreselassie (2003) and Powrie et al. (1998). Furthermore, the dependency of the stiffness of soft soils on stress paths due to excavation is investigated by Becker (2009). The stiffness of the soil from stress path tests differs significantly from standard laboratory tests. Figure 5 shows idealized stress paths in excavations, which were analysed for soft soils. The stress path D (TSP-D) is typical for stress condition in the centre direct below the excavation bottom. The influence of horizontal stresses due to wall deformations increases with approaching the retaining structure and the stress path turns anticlockwise and corresponds to the stress path TSP-F.

A summary of the stiffness ratios of the secant modulus E_{50} for soft lacustrine clays are shown in Table 1.

3.2 *Numerical modelling of stress-strain behaviour of soft soils*

Characteristic stress path zones (SPZ) in excavations in soft soils for different construction phases

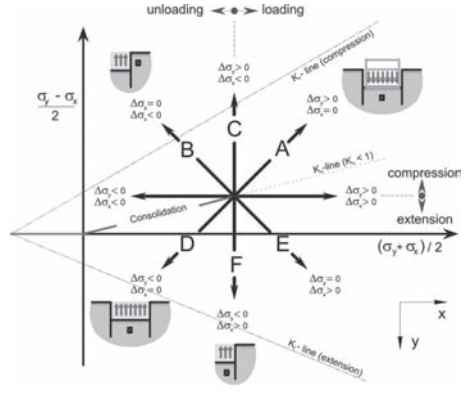

Figure 5. Idealized stress paths for triaxial tests.

Table 1. Influence of stress paths on stiffness of soft lacustrine clays, after Becker (2009).

	$f_{TSP} = E_{50,TSP-i}/E_{50,TSP-A}$			
Stress path	Lacustrine clay[1]	Lacustrine clay[2]	Kaolin	Average
TSP-A	1.0	1.0	1.0	1.0
TSP-B	9.0	5.1	1.2	5.1
TSP-D	7.8	1.3	3.4	4.2
TSP-E	5.3	2.9	3.2	3.8
TSP-F	8.7	4.2	–	6.5

[1]from this case history; [2]from a different case history (to be published soon).

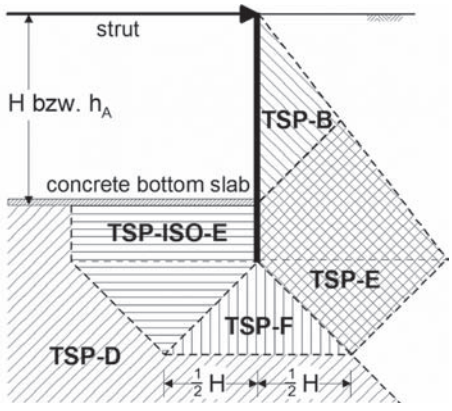

Figure 6. Characteristic stress path zones (SPZ).

have been identified as a result of a numerical parameter study by Becker (2009). In Figure 6 is the SPZ together with the corresponding total stress paths depending on the construction stage and the resulting soil structure interaction shown for a retaining wall with support at the top with strut and at the bottom with concrete bottom slab. For additional SPZ's at different construction phases see Becker (2009).

4 NUMERICAL BACK ANALYSIS

4.1 *General*

The 2D numerical analysis was performed for the monitoring section indicated in Figure 1. The spatial influences of soil structure interaction on the deformation behaviour, e.g. slice wise excavation, installation of supporting bottom slab and steel struts, are considered in the analysis using an idealized modelling of the construction progress. The time-dependent behaviour was considered with the help of an undrained analysis using a coupled consolidation analysis which take into account the actual construction periods.

The numerical calculation was made using the FEM program PLAXIS v9. The elasto plastic Hardening Soil model (HS) and also the Hardening Soil Small model (HSS) were applied as constitutive soil models. For detailed information's about the soil models see Schanz (1998), Brinkgreve et al. (2004, 2008) and Benz (2007).

4.2 *FE model geometry and idealisation of spatial effects*

At the monitoring section is the excavation width B = 21.4 m and the excavation depth H = 5.9 m. The FE model has a width of 2.5.B = 54.5 m on both sides of the excavation and has a height of 50 m (Fig. 7).

The constructive elements were modelled with both continuum and structural elements. The bored pile wall was idealized as linear elastic continuum elements. Additionally a linear elastic beam is arranged at the axis of the bored pile wall, which was used for estimating the section forces. The bending stiffness of the beam element did not affect the bored pile wall stiffness, because of $EI_{Beam} \approx 0$. The section forces of the beam element are then be multiplied with an adjustment factor f depending on the stiffness ratio according to Equation 1.

The unreinforced and the reinforced bottom slabs with thickness d = 0.75 m and d = 0.80 m respectively are discretised using continuum elements. The upper concrete beam wale was idealised with an additional load which is equal to its weight. The supporting effect of the concrete beam wale was idealised using different activation stages of the upper steel struts (see also section 4.3).

$$f = \frac{EI_{continuum} + EI_{Beam}}{EI_{Beam}} \tag{1}$$

4.3 *Calculation phases*

The real construction process of the excavation at the monitoring section has been distributed to a longer period to take account of temporal effects on the stress deformation behaviour and was related to excess pore pressure measurements.

The main difficulty in a 2D analysis is to model the spatial effects of the supporting structures. For this case study, this is the slice wise construction of the bottom slab and the installation of the steel struts. These effects were examined separately in a numerical analysis. Figure 8 shows the idealized

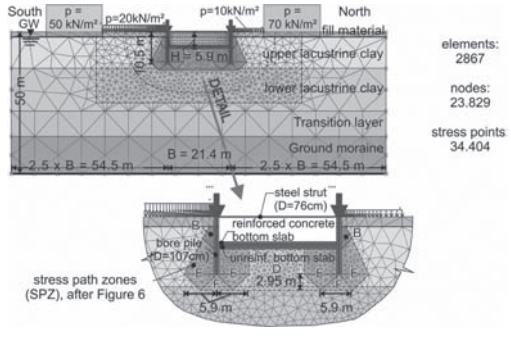

Figure 7. FE geometry model with characteristic Stress Path Zones (SPZ) in detail.

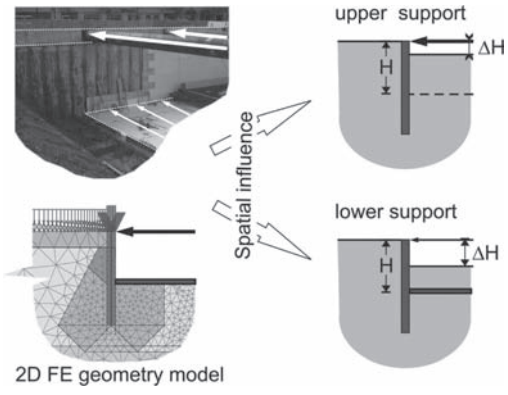

Figure 8. Idealization of spatial effects considering upper and lower support of the retaining wall.

model which take into account the upper and lower supporting structures.

The spatial effect of the steel struts in conjunction with the bending stiffness of the upper concrete beam wale was analysed using a mobilisation factor f_{mob} according to Equation 2 and Figure 8. Here, ΔH is the excavation depth before the installation of the support element and H is the full excavation depth.

The spatial effect of the bottom slab in conjunction with the slice wise excavation and the remaining support from the soil, which is still to be excavated, was also analysed using the mobilisation factor f_{mob}.

$$f_{mob} = \frac{\Delta H}{H} \tag{2}$$

The calculation phases are summarized in Table 2. For all calculation steps a groundwater flow calculation was carried out with a water table at a depth of −1.8 m behind the wall and at the bottom of excavation within the excavation. The above mentioned spatial effects were considered at the calculation phases 04 and 07. This changed the calculation phase in a purely plastic calculation and soil excavation was controlled by the program's internal factor m_{stage}, which reduces the stiffness of the excavation area, see also Schikora & Fink (1982) and Lackner (2008). The partial excavation depth H_i can be approximately determined using Equation 3. The subsequent calculation step was performed using a coupled consolidation analysis taking into account the conceptual construction period of the previous step, where the partial calculation step ($m_{stage} < 1.0$) has been completed.

$$H_i = m_{stage} \cdot \Delta H \tag{3}$$

Table 2. Calculation phases.

Phase	Type	Description	Time [d]
00	P	Initial stress (K_0-procedure)	
01	P	Activation of surcharge load	
02	C	Installation of bored pile wall (whished-in-place)	10
03	C	Activation of upper concrete beam (additional load)	5
04	C[1]	1st excavation step −1.0 m	5
05	P	Installation of upper struts	
06	C	2nd excavation step −2.0 m	4
07	C[1]	3rd excavation step −5.9 m	11
08	P	Installation of lower concrete slap	
09	C	Consolidation	9
10	P	Construction of reinforced concrete slap	10
11	C	Consolidation (min pore pressure)	

N.B.: P—plastic calculation; C—plastic consolidation with coupled consolidation analysis; [1]Calculation with m_{stage} 1.0 plastic (P) and following phase was plastic consolidation (C).

4.4 *Material parameters*

The material parameters for the relevant upper lacustrine clay layer were determined from laboratory tests (Becker 2009). The parameters of the remaining soil layers were adopted from geotechnical reports and verified by parameters from adjacent projects. The additional Hardening Soil Small (HSS) model parameters were estimated based on Benz's (2007) empirical correlations. In Table 3 are the material parameters for the HS model and in Table 4 for HSS model.

The material parameters of the structural elements are indicated in Table 5 and of the continuum elements in Table 6.

Taking into account the stress path dependent stiffness in the characteristic stress path zones (SPZ) according to Table 1 the modified stiffness are summarized in Table 7. Here, the stiffness was increased with the stiffness ratios f_{TSP} from the average values for each stress path zone respectively.

4.5 *Comparison with measurement results*

Before the comparison of the numerical calculations with the measurement results the spatial influence of the supporting elements and the stress path dependant stiffness is discussed. The results of variation of the mobilisation factor $f_{mob,F}$ which represents the idealisation of the supporting bottom slab are presented exemplary. The mobilisation factor for the upper steel strut is kept constant with $f_{mob,K} = 0.017$ throughout this analysis.

Table 3. Soil parameters for the HS-model.

Soil layer	γ_{sat} [kN/m³]		γ_{unsat} [kN/m³]		$k_x = k_y$ [m/d]	
a) Unit weight and permeability						
Fill material	20.0		20.0		8.64E-2	
Upper lacustrine clay	19.0		19.0		8.64E-4	
Lower lacustrine clay	19.0		19.0		8.64E-4	
Transition layer	20.0		20.0		8.60E-4	
Ground moraine	22.0		22.0		8.60E-4	
	E_{50}^{ref} [MN/m²]	G_0^{ref} do.	E_{ur}^{ref} do.	p^{ref} do.	v_{ur} [–]	m [–]
b) Stiffness parameters						
Fill material	3.0	3.0	12.0	0.1	0.2	0.60
Upper lacustrine clay	5.9	4.5	19.0	0.1	0.2	0.90
Lower lacustrine clay	6.0	5.5	24.0	0.1	0.2	0.90
Transition layer	8.0	8.0	32.0	0.1	0.2	0.80
Ground moraine	30.0	30.0	120.0	0.1	0.2	0.75
	c′ [kN/m²]	φ′ [°]		ψ′ [°]		Rf [–]
c) Shear strength parameters						
Fill material	0.01	27.5		0.0	0.90	
Upper lacustrine clay	0.01	27.5		0.0	0.90	
Lower lacustrine clay	0.01	25.0		0.0	0.90	
Transition layer	0.01	27.5		0.0	0.90	
Ground moraine	10.00	27.5		0.0	0.90	

Table 4. Additional soil parameters for the HSS-model.

Soil layer	G_0^{ref} [MN/m²]	$\gamma_{0.7}$ [–]
Fill material	35.0	4.2E-04
Upper lacustrine clay	33.0	3.0E-04
Lower lacustrine clay	55.0	2.0E-04
Transition layer	60.0	2.4E-04
Ground moraine	140.0	1.0E-04

Table 5. Material properties of the structural elements.

Structural element	EA [kN/m]	EI [kNm²/m]	w [kN/m/m]	ν [–]
Steel strut (D = 76.2 cm)	7.088E05	5.011E04	0.27	0.3
Bored pile	0.01	0.01	0	0

Table 6. Material properties of the continuum elements.

Continuum element (non-porous)	γ kN/m³	$k_x = k_y$ m/d	ν	E_{ref} MN/m²
Unreinforced bottom slab (d = 0,50 m)	23.0	0	0.20	2.5E04
Reinforced bottom slab (d = 0,80 m)	25.0	0	0.20	3.2E04
Bored piles (D = 1,50 m)	25.0	0	0.20	2.5E04

Table 7. Modified stress path dependant stiffness.

SPZ	f_{TSP}	E_{50}^{ref} [MN/m²]	E_{ur}^{ref} [MN/m²]	G_0^{ref} [MN/m²]	$\gamma_{0,7}$ [–]
B	5.1	16.23	48.80	48.80	3.0E-04
D	4.2	13.40	40.20	40.20	3.6E-04
E	3.8	12.12	36.36	36.36	4.0E-04
F	6.5	20.74	62.21	62.21	2.4E-04

The spatial effects of installing the bottom slab at different mobilisation factors on the wall deformation are shown in Figure 9. The computation results using the HS-model (standard) confirm the difficulties of prediction of the deformations in excavation in soft soils. Here, the material parameters are taken from standard triaxial tests and the excavation depths are modelled with realistic assumptions. Similar results had been achieved for the HSS model. In this case, the calculated deformations can only

approach the measurement results if one assumes an excavation level at –2.25 m, i.e. $f_{mob,F} = 0.38$. This excavation depth seems to be rather unrealistic in view of the construction process. In addition, a very high sensitivity to the displacements at the wall toe was observed for both soil models due to the low stiffness in the area of the wall toe.

By taking into account the modified stiffness in characteristic Stress Path Zones (SPZ) the above mentioned sensitivity disappeared. The calculated deformation with the HS-model could approach the measurement results only at a very low mobilisation factor with $f_{mob,F} = 0.38$, which results in an overestimation of the displacements at the head of the wall by 33%. For the HSS-model the best match was found with a mobilisation of the bottom slab from an excavation depth –3.95 m to –4.45 m ($f_{mob,F} = 0.67$ to 0.75). In another comparative calculation, which is not shown here, and that enabled the head reinforcement after an excavation of –0.50 m ($f_{mob,K} = 0{,}085$), no effect on the displacements was found at the toe of the wall, but a corresponding reduction in wall displacements at the head of the wall was observed.

In the following the numerical results using the HSS-model with stress path dependant stiffness in characteristic stress path zones and using the optimized mobilization factors of $f_{mob,K} = 1/6$ and $f_{mob,F} = 2 / 3$ are presented. The mobilisation factors correspond to an excavation depth at - 1.0 m for activating the steel strut and an excavation depth at - 3.95 m for activating the bottom slab.

In Figure 11 the measured wall deformations are compared to the numerical results. With the identified mobilization factors and the modified stress path dependant stiffness, the deformation behaviour can be described very well as expected. In particular a good match between measured and computed toe and head displacements was achieved. The comparison of the numerical results with the results of the vertical inclinometer V-03 on the northern side of the monitoring section can be neglected, because there was some problems in the orientation of this inclinometer. On the other hand, there is a good agreement with the nearby inclinometer V-02.

The spatial effects on the deformation behaviour of excavations in soft soils could be identified for the conducted optimized calculation with modified stress path dependant stiffness and an optimised and realistic idealisation of the excavation steps. Furthermore, the time dependant effects had been analysed as shown in the following figures. The displacements at the head of the wall depending on the construction progress are shown in Figure 11. The numerical results confirm the time dependant increase of the wall head deformations at the measuring point 3301 due to the application of coupled consolidation analysis. In particular the time dependant increase of horizontal displacements after the excavation the slice (02.11.2007) along the monitoring section could be captured after some selected idealisations had been made. In addition, computation results using the HS-model are shown in Figure 11, which takes into account the modified stiffness. After the installation of the steel strut support the results were overrated with the HS-model and could not be approximated afterwards.

The measured time-dependent excess pore pressure development shown in Figure 12 can be described well by the numerical analysis. The calculated excess pore pressure varies depending on the position (Fig. 4), whereas the measurement results describe a uniform pore water pressure $\Delta u \approx -48$ kN/m². The measured pore water pressure matches the corresponding effective stress due to the vertical stress relief.

The subsequent consolidation is accelerated considerably by reloading the underground due to the unreinforced bottom slab and in particular the reinforced bottom slab.

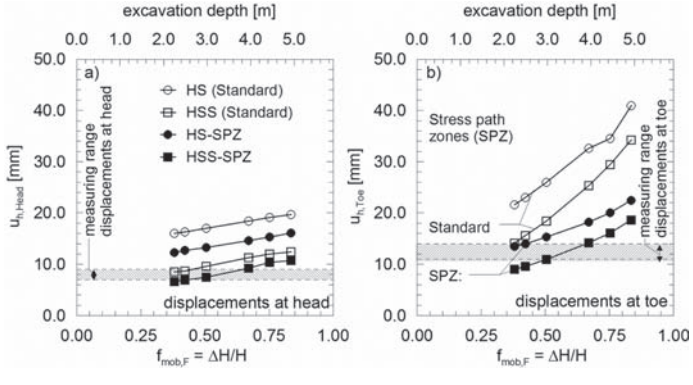

Figure 9. Influence of the mobilisation factor $f_{mob,F}$ on horizontal displacements at the top (a) and the bottom (b) of the bored pile wall.

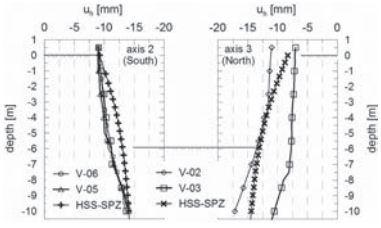

Figure 10. Comparison of calculated horizontal wall displacements with measurement results.

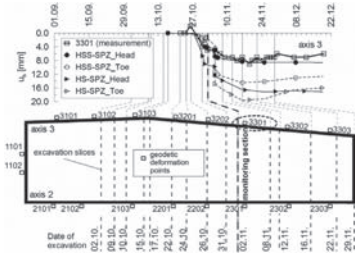

Figure 11. Comparison of calculated horizontal displacements at upper concrete beam wale with measurement results.

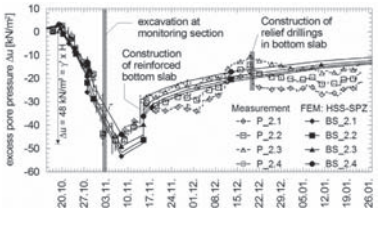

Figure 12. Comparison of calculated excess pore pressures with measurement results.

5 CONCLUSION

The described case study shows very clearly the benefits of a stiff retaining wall in combination with an upper concrete beam wale that can be placed in advance of the excavation. The measurement results inside and outside the excavation area are well below commonly expected values in excavation in soft soils. Although the relevant upper lacustrine clay layer stiffness for this project are slightly higher than in the neighbouring case studies, the selected excavation procedure has prove to be a very good solution for the succesfully completion of excavations in soft soils.

The numerical analysis of the case study confirms the need to take into account the stress path dependent material parameters in the calculation of excavations in soft soils. It was shown that without such optimization technique a successful deformation prediction taking into account a realistic construction process is not possible, neither with Hardening Soil model nor with the Hardening Soil Small model is possible. Taking into account the stress path dependent stiffness in characteristic stress path zones (Becker 2009) resulted in a significant improvement of the numerical prediction of deformations.

The spatial influence of soil-structure interaction designated for this project is considered successfully by idealisation of the upper steel struts and the slice wise excavation and placement of the lower bottom slab with mobilization factors in a two-dimensional numerical analysis. An optimized deformation prediction can be achieved with this method which takes into account the stress path dependent stiffness behaviour when using soil models with isotropic material properties. Application of the Hardening Soil Small model led to a good match with the measurement results.

REFERENCES

Becker, P. 2009. Zeit- und spannungspfadabhängiges Verformungsverhalten bei Baugruben in weichen Böden. Schriftenreihe Geotechnik, Heft 22, Universität Kassel.

Becker, P.; Gebreselassie, B. & Kempfert, H.-G. 2008. Back analysis of a deep excavation in soft lacustrine clays. *6th International Conference on Case Histories in Geotechnical Engineering*. Arlington, Virginia, USA 2008 (Paper 5.17; CD-ROM).

Benz, T. 2007. *Small strain stiffness of soils and its numerical consequences.* Universität Stuttgart. Mitteilung des Institutes für Geotechnik, Heft 55.

Brinkgreve, R.B.J.; Broere, W. & Waterman, D. 2004: *Plaxis—Finite Element Code for Soil and Rock Analyses*. Rotterdam.

Brinkgreve, R.B.J.; Broere, W. & Waterman, D. 2004. *Plaxis—Manual*.

Gebreselassie, B. 2003. Experimental, Analytical and Numerical Investigations of Excavations in Normally Consolidated Soft Soils. Schriftenreihe Geotechnik, Universität Kassel, Heft 14.

Kempfert, H.-G. & Gebreselassie, B. 2006. *Excavations and Foundations in Soft Soils*. Springer Verlag, Berlin.

Lackner, C. 2008. Numerical Simulation of Geosynthetic Reinforced Embankments. *Proc. of the 19th European Young Geotechnical Engineers Conference,* Győr, Hungary, pp. 207–215.

Parry, R.H.G. 1995. *Mohr Circles, Stress Paths and Geotechnics*. E & FN Spon, London.

Powrie, W.; Pantelidou, H. & Stallebrass, S.E. 1998. Soil stiffness in stress paths relevant to diaphragm walls in clay. *Géotechnique 48*, No. 4, pp. 483–494.

Schanz, T. 1998. *Zur Modellierung des mechanischen Verhaltens von Reibungsmaterialien.* Universität Stuttgart, Mitteilung des Inst. f. Geotechnik, Heft 45.

Schikora, K. & Fink, T. 1982. Berechnungsmethoden moderner bergmännischer Bauweisen beim U-Bahn-Bau. *Bauingenieur 57*, S. 193–198.

Geotechnical Aspects of Underground Construction in Soft Ground – Viggiani (ed)
© 2012 Taylor & Francis Group, London, ISBN 978-0-415-68367-8

Detection of imperfections in diaphragm walls with geophysical measurements

R. Spruit
Rotterdam Public Works, Engineering Department, Rotterdam, The Netherlands
TU Delft, Delft, The Netherlands

V. Hopman
Deltares, Delft, The Netherlands

A.F. van Tol
Deltares, Delft, The Netherlands
TU Delft, Delft, The Netherlands

ABSTRACT: After calamities with leaking diaphragm walls in Amsterdam and Rotterdam the caution to use diaphragm walls in deep excavations in the Netherlands increased. In densely populated areas the risk of unanticipated and uncontrollable leakage and the following subsidence is not acceptable. In autumn 2009 a joint research project was initiated at Rotterdam Public Works and TU-Delft aiming at development of a system of measurements and interpretation to detect zones in the diaphragm wall with high risk of leakage. The research started with a series of in-situ tests. Four types of measurements (distributed temperature during pouring and hydration of the concrete, natural gamma radiation, cross hole seismic and direct resistivity between the rebars and a conductivity CPT) were executed on 5 test panels and 2 laboratory size blocks. In this paper the results from the measurements are presented. Preliminary conclusions on how to set up a survey are drawn. An outlook into the further progress of the research will be given.

1 INTRODUCTION

Traditionally, diaphragm walls were considered a safe and proven technology for constructing the wall of a deep excavation. Due to recent uncontrollable leakages occurring in metro building projects in Amsterdam and Rotterdam (Netherlands), the risk profile of the diaphragm wall has changed.

As there is a clear need to reduce the uncertainty of the quality of in-situ formed construction elements, a research has been started to determine if areas with a high risk of leakage can be detected before excavation takes place. From December 2009 till May 2010, instrumentation and testing took place on site and on laboratory scale.

Like in borehole geophysics, it was assumed that the combination of several tests will lead to a reliable conclusion. Therefore, four different measurements were carried out.

2 TEST LOCATION

Underneath the 'Kruisplein' in the center of Rotterdam a 6 stores underground parking facility is being constructed. Diaphragm walls to a depth of 40 m minus surface level (at which level a clayey layer with high hydraulic resistivity is present) will ensure a robust and watertight ground retaining construction.

Several measures to improve the quality of the diaphragm walls were included in the contract. To reduce the uncertainty of the final build quality, the hydraulic resistance of the wall is also tested by lowering the water table inside the building pit.

Still, in case of bentonite inclusions in the joints between the diaphragm wall panels, potential weak spots in the wall will not be found in the pumping test, as the bentonite inclusion has a high hydraulic resistance and will therefore prevent water inflow through the diaphragm walls. During excavation however, the bentonite inclusions may become instable, due to the change in horizontal ground and water pressure. After gradual degradation of the bentonite inclusion a sudden major leak can occur, resulting in large volumes of water and (possibly) sand flowing into the building pit. If transport of sand occurs, subsidence outside the building pit will occur, causing damage in case of to neighboring buildings and infrastructure.

It was therefore thought worthwhile to investigate the possibilities to detect bentonite inclusions prior to excavation. Measurements on site and on laboratory scale were performed.

3 DESCRIPTION OF THE TESTS AND RESULTS

3.1 *Temperature*

During fabrication of a diaphragm wall panel the volume in the excavated trench is being replaced several times. After reaching the final depth with the excavator the excavation bentonite has to be replaced by fresh (lighter) bentonite which in the next stage has to be replaced by concrete. Each material has a specific temperature when entering the trench. By using a vertically positioned distributed temperature measurement, it is possible to keep track of the different materials in the trench. The temperature has been measured with optical fibers (Del Grosso et al. 2001). With a Sensornet Oryx DTS (Sensornet 2009), the temperature distribution along the fiber could be measured. The temperature accuracy is around 0.01 °C whereas the accuracy of the position of the measurements is 1 m. The fibers were positioned as indicated in Figure 1.

As it is assumed that most problems occur around the joints, the temperature sensors were positioned as close to the joint as possible. One fiber was attached to the rubber joint profile, another fiber was connected to the rebar grid and finally a fiber was lowered into the joint area using a metal weight at the bottom end of the fiber.

The temperature measurements started after the reinforcement cages were positioned and continued until one week after the concrete was poured into the trench. Every 20 minutes a measurement cycle was performed, clearly showing the rising concrete level in the trench because the temperature of the concrete was with 17 °C higher than the temperature of the bentonite with 13 °C (Fig. 5).

During curing of the concrete the temperature rose in 55 hours from 15 °C to 35 °C (Fig. 2).

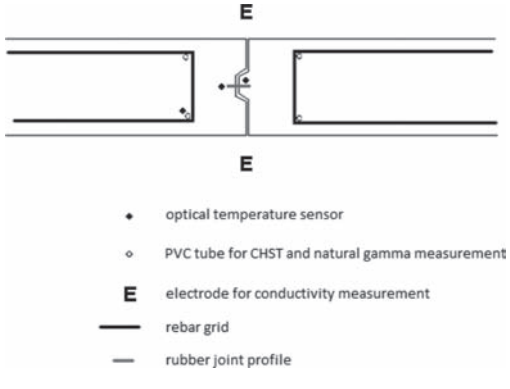

Figure 1. Top view of the location of the sensors around a diaphragm wall joint.

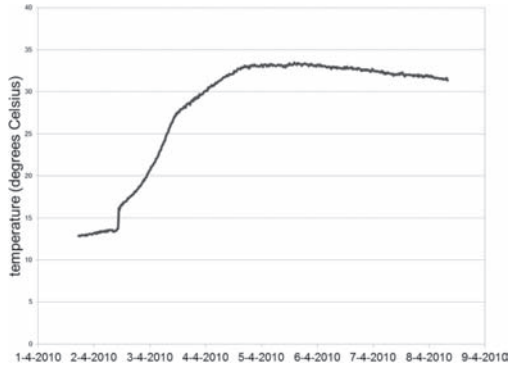

Figure 2. Temperature development in the next joint.

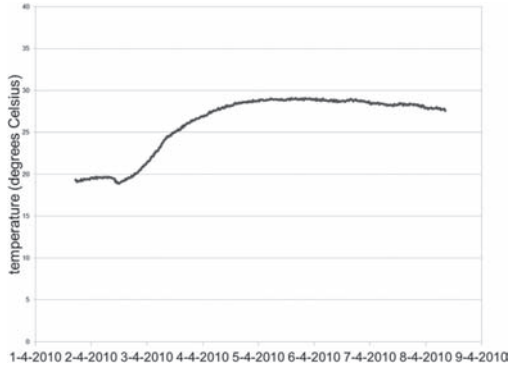

Figure 3. Temperature development in the previous joint.

Figure 3 shows that along the joint with the previous panel (previous joint, concrete 1 week old), the temperature of the bentonite in the joint is around 20 °C. When the concrete level approaches, a slight drop of around 1 °C–2 °C occurs, possibly indicating stirring of the bentonite and/or replacement of bentonite for concrete. When this drop in temperature consistently occurs along the vertical profile of the wall, it seems plausible that (almost) no bentonite has stayed behind in the joint.

In Figure 4 at sensorposition 88, all subsequent temperature measurements show 19 °C, possibly indicating an area where bentonite stayed behind in the joint.

On the sensor along the next joint, the steady change from bentonite temperature to concrete temperature indicates a decent joint. This is illustrated in Figure 5.

At position 110 in Figure 5, a slight delay in the concrete pouring process can be seen. As each line indicates a measurement 20 minutes later, the 2 almost identical measurements at position

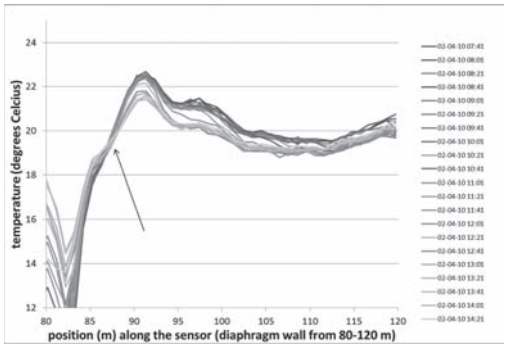

Figure 4. Temperature graph in the previous joint.

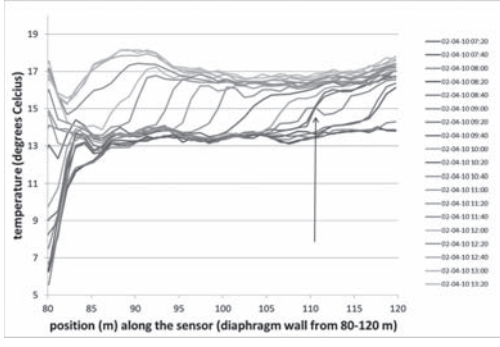

Figure 5. Temperature profile during concreting.

110 indicate a stop of 20 minutes during the concrete pouring.

In the laboratory test, the temperature measurements were less convincing, partly due to the more rapid pouring of the concrete (the laboratory block was only 2*2*1 m^3 instead of 42*6*1.2 m^3) and partly because of the spatial resolution of the temperature measurement of 1 m.

3.2 *Natural gamma radiation*

Normally, clay minerals tend to have a higher natural radioactivity than the ingredients of concrete. It was therefore assumed that areas with high amounts of bentonite remaining in the trench after the pouring of concrete might be detected by measuring the natural radioactivity. Using a gamma ray detector, the radiation along the joint was measured, using the PVC tubes indicated in Figure 1.

Unfortunately, the natural radioactivity of the concrete came out to be higher than the radioactivity of the bentonite. Even with a gamma spectrometer no detectable differentiation between bentonite and concrete could be made.

Table 1. Radioactivity of concrete and bentonite as determined using samples originating from the site.

Specimen	^{40}K (Bq/kg)	^{232}Th (Bq/kg)	^{238}U (Bq/kg)
Concrete	215	20	30
Bentonite (dry)	160	12	15
Bentonite (wet)	107	9	7

As it will be almost impossible to detect a small amount of material in the joint with a relatively low radioactivity when the majority of the material has a relatively high radioactivity, this detection method can only be used if the concrete mixture consists of especially selected materials with low radioactivity.

3.3 *Cross-hole seismic tomography (CHST)*

The speed of sound in a solid medium is depending on the density and the shear stiffness. Because concrete and bentonite have a different density and shear stiffness, it must be possible to discriminate between concrete and bentonite using an acoustic signal. By attaching PVC tubes on the rebar cages on both sides of the joint (Fig. 1), it is possible to send an acoustic signal across the joint.

This method is already commercially available for testing the integrity of large diameter bored piles (Amir et al. 2008). In the test we used the CHUM equipment of PileTest (PileTest 2009).

In advance it was unknown what influence the joint would have on the signal transmission as there is little experience in similar situations.

In literature (Likins et al. 2004, Amir et al. 2008) different opinions on the tube material to be used were found. For robustness and better bonding with the concrete, steel tubes should be chosen. In PVC tubes the signal seems to contain less noise. Debonding of the PVC tubes from concrete seems unlikely when the tubes are filled with water (Likins et al. 2004).

As the reinforcement cages were not prepared for the tubes, they had to be retrofitted. PVC tubes are much easier to handle than steel ones. Therefore 14 out of the 16 tubes we chosen PVC, the 2 remaining ones were chosen steel, making it possible to compare the different materials.

The measurements on site could be performed very fast especially considering the 42 m wall depth. Within 30 minutes all 6 cross-hole combinations could be measured. This is the time needed for the simple 'horizontal' measurement in which both source and receiver are on the same level and are pulled up simultaneously. Theoretically it is

also possible to vary the source/receiver position in such a way that 2D tomography is performed. In the signal there was generally no hint for the need of this extra measurement density.

Only in one joint an anomaly was found. At the depth at which this anomaly was found, clayey layers are expected outside the excavation. Therefore no further measures are taken to prevent leakage as the soil itself functions as a barrier. As excavation is still in progress no verification of the size of the anomaly can be made yet.

In Figure 6 the anomaly at 8–9 m minus surface level can clearly be seen. The upper 4 m consists of low grade concrete due to pollution with bentonite.

From the laboratory tests (Fig. 8) a first indication of the anomaly size can be deducted. The test blocks were poured in a normal formwork with a steel joint profile as the lower boundary of the formwork. After curing of the first half, the block was inverted, an anomaly was sculptured in the joint area, the formwork was attached again and the upper block was poured. Instrumentation was set up similar to the in-situ tests.

A typical CHUM graph from the test blocks is shown in Figure 7. The known anomaly is present from 0.1 m to 1 m and varies in thickness from 0 to 0.3 m.

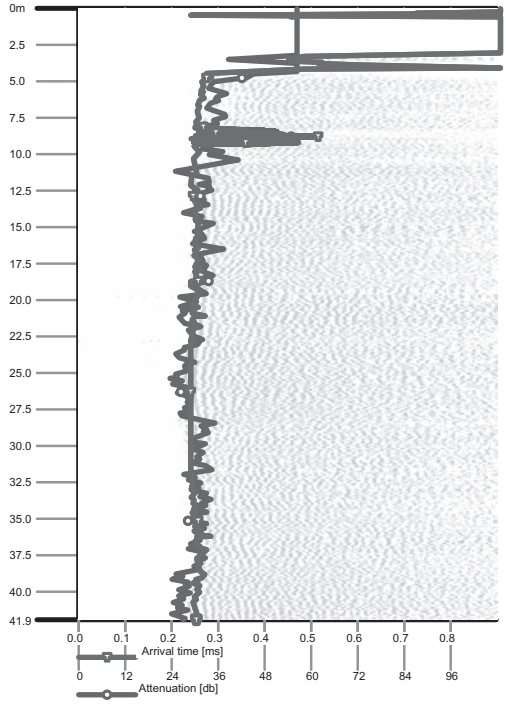

Figure 6. Cross-hole seismic profile.

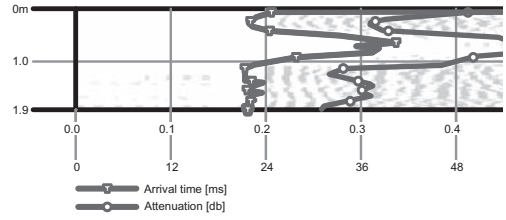

Figure 7. Typical CHST profile of the laboratory block, straight across the joint.

Figure 8. Laboratory block.

The average (from two test blocks) extra arrival time for a joint contaminated with 0.3 m bentonite is straight across the joint 0.23 ms and 0.35 ms diagonally across the joint. Because the 'straight' signal can partly bypass the inclusion, the expected extra travel time will be around 0.1 ms per 0.1 m bentonite inclusion.

The average damping of the signal is 20 dB for a joint with 0.3 m bentonite. 7 dB damping per 0.1 m bentonite is expected.

The anomaly found in the in-situ profile of Figure 6 shows 0.25 ms extra arrival time combined with 24 dB damping. If the laboratory samples

prove to be representative, the size of the anomaly could be in the order of 0.25 m (based upon arrival time) and 0.35 m (based upon damping). When we combine the extra arrival time with the damping, we expect around 0.3 m of bentonite in the joint. In October the excavation will reach the anomaly. As the anomaly was only found in the cross section of the side to be excavated, we expect to get an in-situ confirmation of the laboratory tests.

3.4 *Resistivity*

Based on the principle that solid concrete has a high electrical resistivity (compared to soil), it is expected that an imperfection in the joint could be made visible in an electrical resistivity measurement along the joint (Hwang et al. 2007). For this measurement a reference electrode (steel rod) was pressed into the soil with a CPT truck outside the building pit. With a resistivity cone attached to the CPT truck, an electrode was gradually pressed into the soil inside the building pit.

The local electrical soil resistivity was measured with the CPT cone (CONE in Fig. 9), the electrical resistivity from the cone to the reference electrode outside the building pit was measured (REF in Fig. 9) as well as the resistivity between the cone and the rebar grids on both sides of the joint (RBG_N, RBG_S in Fig. 9).

The resistivity profile was measured at the same joint as the CHST profile of Figure 6 in which an anomaly was detected at 8 to 9 m minus reference level. In Figure 9, at the same depth, there is a 30% (relative to the average 1 MOhm resistance) decrease of the resistivity over the diaphragm wall (REF in Fig. 9). The resistivity from the cone to the rebar grid north of the joint (RBG_N in Fig. 9) also shows a slight dip in resistivity. It can therefore be concluded that there probably indeed is an anomaly at this depth, only occurring in the panel north of the joint. The anomaly probably reaches to 1/3 of the wall thickness, based upon a decrease of the resistivity of 30%.

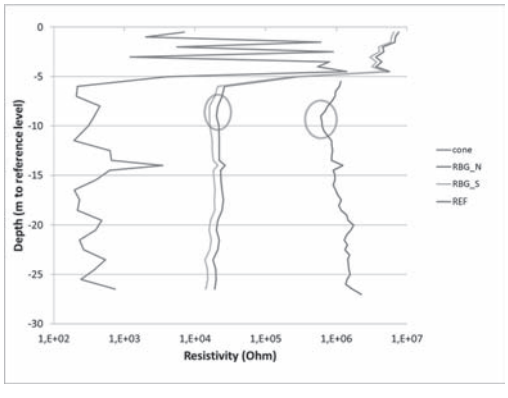

Figure 9. Resistivity profile.

3.5 *Interpretation*

When the information of the resistivity measurement is combined with the CHST profiles of the same joint, which show only defects in one profiles out of six it is concluded that:

- there will probably be a defect on the side of the excavation with rough dimensions of 1 m high, 0.3 m wide at the maximum (from CHST measurements).
- the defect will probably extend 0.4 m into the wall (1/3 of 1.2 m) and will be only present in the panel north of the joint (from resistivity measurements).
- the temperature measurements of this specific joint (Fig. 4) do not clearly show a drop in temperature during the pouring of the concrete, especially at the depth of the anomaly found in figure 6 which is an extra indication that a bentonite inclusion could be present.

4 CONCLUSIONS

The measurements performed on the 'Kruisplein' location in Rotterdam as well as in the laboratory generally improved our understanding of the concrete pouring process of diaphragm walls.

The natural gamma radiation measurement did not function as intended as a result of the high natural radioactivity of the concrete. In case the ingredients of the concrete are screened on low radioactivity, this method could be useful.

The temperature measurements might be used to monitor the efficiency of the refreshing of the bentonite mixture prior to the concrete pouring. During the pouring of the concrete, the process in which the bentonite is replaced by concrete can be monitored. With the distributed temperature measurement it is already in the production stage possible to indicate areas that have a higher chance of showing defects.

The CHST measurements proved to provide detailed information about the quality of the joint. Using the first reference information of the laboratory blocks, it is possible to estimate the volume of the anomaly that was found in the test area. Exposing this anomaly later in the project during excavation of the building pit will provide additional reference material.

The resistivity measurements proved to be useful for investigating the depth into the wall of an anomaly and helped indicating on which side of the joint the anomaly is located.

Further investigation of the temperature measurements will focus on the best location and interval (in time) for the measurements to be performed.

Further investigation on the CHST method will focus on the change in signal (frequency domain) during passage of the joint. The change in stiffness from concrete to the material in the joint might be visible as a change in the characteristics of the signal, providing extra information about the contents of the joint material. Also additional reference measurements will be performed.

Further investigation of the resistivity measurement will focus on the improvement of the measurement setup, as to reduce operating time in the field and at the same time improving resolution.

ACKNOWLEDGEMENTS

The tests were cofounded by the Municipality of Rotterdam and the contractor Besix/Franki. Some of the measurements were sponsored by Deltares, Medusa Exploration, Gemeentewerken Rotterdam-VLG, Fugro and Brem.

REFERENCES

Amir, J.M. & Amir, E.I. 2008. Capabilities and Limitations of Cross Hole Ultrasonic Testing of Piles; http://www.piletest.com/papers/IFCEE2009.Capabilities_and_Limitations_of_Cross_Hole_Ultrasonic_Testing_of_Piles.pdf.

Del Grosso, A. & Inaudi, D. 2001. Monitoring of Bridges and Concrete Structures with Fibre Optic Sensors in Europe; http://195.186.87.221/Bibliography/PDF/C92.pdf.

Hwang, R.N. & Ishihara, K. & Lee, W.F. 2007. Forensic Studies for Failure in Construction of An Underground Station of the Kaohsiung MRT System; http://civil.iisc.ernet.in/~gls/Courses_files/FORENSIC%20GEOTECHNICAL%20ENGINEERING.pdf.

Likins, G. & Webster, S. & Saavedra, M. 2004. Evaluation of defects and tomography for CSL; http://www.pile.com/reference/stresswave2004/SW2004-046-Eval_of_Defects_and_Tomography_for_CSL.pdf.

PileTest 2009. http://www.piletest.com/show.asp?page=chum.

Sensornet 2009. http://www.sensornet.co.uk/news/product-literature/.

Geotechnical Aspects of Underground Construction in Soft Ground – Viggiani (ed)
© 2012 Taylor & Francis Group, London, ISBN 978-0-415-68367-8

An integrated monitoring and risk management system for civil construction works

E.P.T. Smits
Rotterdam Public Works, Rotterdam, The Netherlands

ABSTRACT: The Rotterdam Randstad Rail project comprises building of a bored tunnel and the rebuilding of an underground station from two-track single platform to three-track, two platform configuration, suitable for a light-rail transportation system. Obviously, the building process in the centre of Rotterdam has to meet all kinds of terms and conditions; one major design condition is that public transport in the station is not to be affected during building activities. It was therefore concluded that the technical complexity of the project and the financial control required a risk management system. Risk control by means of monitoring was the heart of the risk management system. The environment, in the broadest sense, has been made key issue for set-up of the monitoring program and selecting monitoring parameters. Consequently, the requirements made by the environment are the boundary conditions for the construction process. This strategy led to a change of view of the role monitoring should play in a construction process and now is the working standard in Rotterdam projects.

1 INTRODUCTION

Randstad Rail is a light-rail connection between the cities of Rotterdam and The Hague. The connection concerns partly existing track and partly a new line. The new part runs by urban area and is approximately 3 km long, of which 2 km is carried out by means of tunnel boring techniques. It is the first bored tunnel in an urban area in the Netherlands. In the centre of Rotterdam the new line connects with an existing line. For this, the existing head station is extended from a two-track single platform to a continuing triple-track layout with two platforms. Important design condition was that the underground railway transport cannot be interrupted during the building process.

Rotterdam public works has looked after both the whole design and the process to the invitation to tender and has been actively involved during construction works.

The demands made on the project ask for technical excellence and a complicated phasing. This entails a high risk profile. To prevent quality loss and damage during construction works and to mitigate financial and time-risks, monitoring and risk control has been explicitly used in the project.

The choice for the parameters and the role which monitoring eventually played at project control and how this led to a new look on the setup of a monitoring plan and its integration in the project is the subject of this paper.

2 PROJECT DESCRIPTION

2.1 *Technical description*

The project consists of the following components:

- Conventional tunnel, constructed using the cut and cover technique, with a length of 0,7 km. Conventional tunnelling has been adopted on spots where ground cover is insufficient for the construction of a bored tunnel. Start and reception shaft pits were delimited with diaphragm walls with a thickness of 1,2 m, reaching a depth of 40 m below ground level.
- Bored tunnel, length 2,3 km. The bored tunnel consists of two tubes with an inner diameter of 6,3 m. For the passage of the holocene soft soils, where tunnel support was insufficient, ground improvement, like MIP, jet-grouting and ground replacement, was used on a large scale.
- A new underground station (20 m depth) with an identical way of construction as was used for the start and reception shaft.
- The reconstruction of an existing underground station. For this reconstruction a building pit was created around the existing station, using diaphragm walls. On the location where the subway tube cuts the building pit the ground was frozen in order to create a watertight wall.

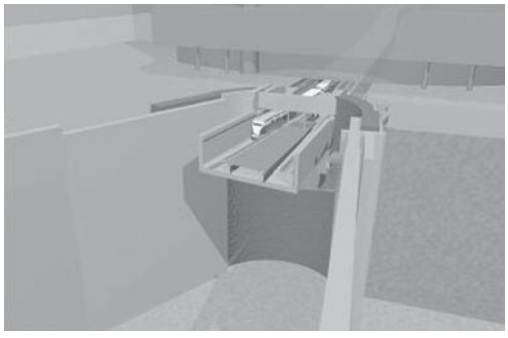

Figure 1. Cross-section of the old station, diaphragm walls and frozen soil for the new station.

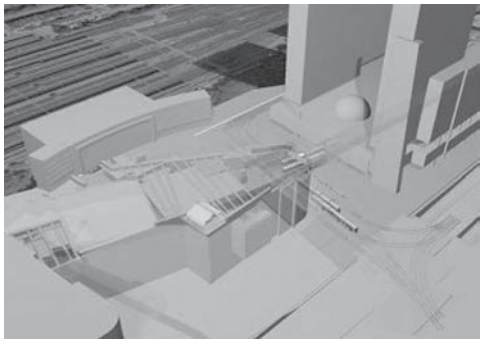

Figure 2. 3D birds-eye view of the position of the old station within the building pit.

2.2 *Project surroundings*

The line crosses several infrastructures, such as the railway track Rotterdam—Utrecht, the 6-lane motorway A20 and the 13 tracks of Rotterdam Centraal Station. It passes at a short distance from houses from the 1930s. The underground station to be reconstructed was built in the 1960s and consists of submerged caissons.

The physical surroundings, like adjacent building and infrastructure, dictated in an important degree the way the construction process has been carried out. Regarding infrastructure, demands were made with regard to both safety and functionality. For adjacent buildings, the acceptable soil deformation was determined by the capacity of the buildings foundations to deal with the loads originating from soil movement.

Accessibility of the train station, traveller security and the fact that the public transport was not to be affected in any way constricted the way the project was build.

Apart from the physical demands made by the surroundings the implementation of a monitoring system is also determined by legal provisions particularly with regard to noise, vibration and spills.

Figure 3. Location of bored tunnel under 13 railway tracks of Rotterdam Central Station.

2.3 *Financials*

The project is financed by a number of agencies of which the central government was one. The project received a one-off contribution from the central government in which the repurchase of all the identified risks were included.

On the condition that proactive risk management would by applied during construction, the project got a considerable discount on the insurance fee.

So, a thorough risk identification is not only important with regards to technical control but contributes substantially to financial feasibility.

The total investment costs are M€ 500.

3 RISK MANAGEMENT AND SURROUNDINGS

Something, which is justified form a technical point of view is not necessarily justified from a social point of view. This consideration forms the base of the centrality of the (social) surroundings, as defined above, in establishing the monitoring programme. The responsibility with regards to the surroundings which the government has during the realisation of large inner city projects, the empowerment of the inhabitants and the claim culture of the society means that project limits do not end with the building pit walls but extend into the "surroundings". This means that a definition of the "surroundings", plays an important role in making a risk management and monitoring programme.

For the monitoring programme risk control (for "whom" are you taking the measurements, what is part of your "surroundings") has been linked to technical monitoring ("what" are you going to do).

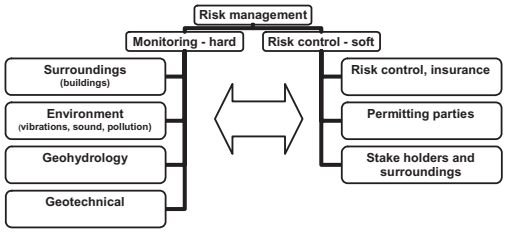

Figure 4. Risk control and monitoring.

By application of account management the project benefits for different stakeholders have been determined and it was determined what, from the stakeholders point of view, made the project a success.

In the preliminary phase a long list with risks was drawn which also contributed to the choice for the monitoring programme, the hazard levels and the frequency of the measurements. For instance:

- For the railway track crossing, lengthy discussions took place with the permitting party about the allowable track deformations. The technical specifications of the monitoring system, hazard levels, and alarm procedure is based upon the discussions. The frequency of the measurements of track deformation is adjusted to the influence of the construction works. During TBM passage a measurement was taken every 15 minutes, whereas during other works a measurement a week was sufficient. Risk control carried out for the track owner led to a tailor made monitoring- and alarm system. This considerably facilitated authorisation of the track crossing.
- For the buildings alongside the bored tunnel the acceptable relative distortion for the 1930's brick buildings was calculated. The location of the monitoring points was chosen in such a way that the results could be easily translated into relative distortion. Because the chance of damage is actively diminished insurance fee was reduced.
- For the reconstruction of the underground subway station stress changes in the subsoil (due to pit digging, change in groundwater levels, ground freezing *etc*.), can cause differential displacements between the old caissons. The displacements are registered on the joints of the caissons. The displacements are a measurement for the displacement of the tracks in the caissons. A fully automated measuring system is incorporated in the tunnel which sends an SMS in case a hazard level is exceeded. Hazard levels and alarm procedure have been setup together with the track owner.

4 MONITORING

Monitoring goes beyond taking measurements. In the perception of the Rotterdam Municipality monitoring comprises taking measurements, testing whether or not the hazard levels have been reached and subsequently decide if the mitigating measure has to be implemented.

4.1 *Monitoring program*

The monitoring program was designed by the Rotterdam Municipality. The measurements are carried out by the contractor. The responsibility for the control of the construction process lies with the contractor, measurements and construction process become this way directly coupled.

Most of the monitoring programme was rather conventional (settlement gauges, inclinometers), only for the measurements on the railway tracks a fully automated system was operational which kept track of some 1200 measuring points.

4.2 *Testing of hazard levels*

In the contract the obligation has been incorporated that the contractor must test the results with regard to the hazard levels and at imminent overshooting must alarm the client. Alarming is done using SMS. For the graphical registration of all measurements an internet application is used.

The S- and I-hazard level are defined as follows:

- The S-level is a value at which raised alertness is necessary and at which mitigating measures can be taken to prevent exceeding of the I-level.
- The I-level is the level above which the damage and calamity chance is unacceptable.

The spacing which is kept between S- and I-level is coordinated on the time which it takes to implement a mitigating measure.

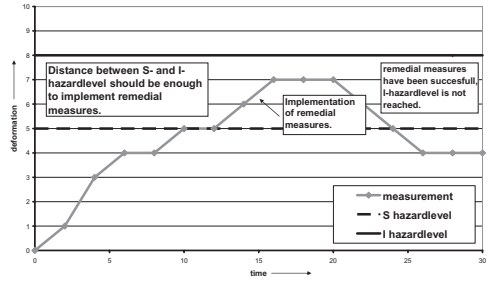

Figure 5. Principle of determining S- and I-hazard level.

4.3 *Mitigating measures*

The way in which monitoring in Rotterdam is now done marks a clear transition form reactive to proactive approach.

The clear choice for S- and I-level actually enforces the undertaking of action when a S-level is exceeded, without having to think what and when to do next. A couple of examples:

- Exceeding the S-level of railway track means that the track owner is informed directly. He decides about the severity of the situation and calls, when necessary, for action. The frequency of measurement is increased and the work process is modified in such a way that deformations come to a halt.
- Exceeding the S-level of a pipe means that steel tension is calculated, when necessary the pipe is raised and replaced in the ground.
- In case of large deformations within buildings there are basic foundation reparation plans ready. For instance the use of ground improvement in the foundation layers, installing jacks to lift the building or, in a worst case situation, installing a complete new foundation. When the S-level is exceeded these are elaborated upon.

By incorporating testing and control within the ideas of monitoring Rotterdam has obliged itself to a proactive approach. What this means for the organisation is subject of the next chapter.

5 ORGANISATION AND RISK MANAGEMENT TEAM

In the organisation a risk and quality management team is created which carries out actively risk management. The team consists of specialists (soil mechanicians, geo-hydrologists, environmental specialists, *etc*.). Their task is to signal risks on the basis of the monitoring results, write a report, propose mitigating measures and make sure someone is responsible for the risk.

Keeping track of the risk and the implementation of mitigating measures is done on a monthly basis, in the presence of all who are responsible for the risk and the project manager.

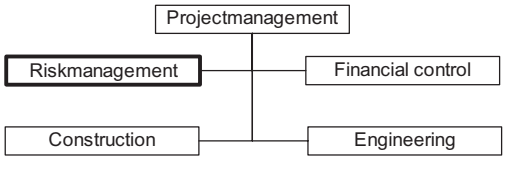

Figure 6. Position of risk management in the project organisation.

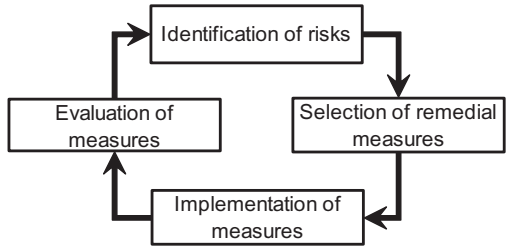

Figure 7. Risk management cycle.

Once every trimester the team reports to the project manager. In the report the original list of risks is updated, the mitigating measures are evaluated and new risks appear. By giving the risk and quality management team a clear position in the project organisation and by clearly delineating the responsibilities it proved actually to be possible to act proactive.

In the trimester report a financial chapter is included in which the budget is compared with the necessary financial reserve for identified risks and costs for implemented mitigating measures. More about this in the next chapter.

6 FINANCIAL CONTROL

Extra project costs arise as a consequence of:

- Scope broadening.
- Omissions and defects in the original plan.
- Risks.

All works not included in the original contract have been labelled according to the above partitioning. The constituent was responsible for financing scope broadenings, for omissions/defects and risks a separate budget was available. How the budget available for risks is calculated is explained in this section.

6.1 *Risk budget*

In the preliminary phase a long list with possible risks was identified. Each risk has been given a possibility (percentage) and, in case the risk should occur the costs for reparation or mitigation have been determined. Using Monte Carlo analysis it was statistically determined how much budget was necessary to be sure that the budget would cover the risk associated costs in 95% of the cases.

Each trimester the list with risks was updated. Risks disappear because of work progress or because of the implementation of mitigating measures. New insights or a change in working method can incorporate new risks. Based upon the

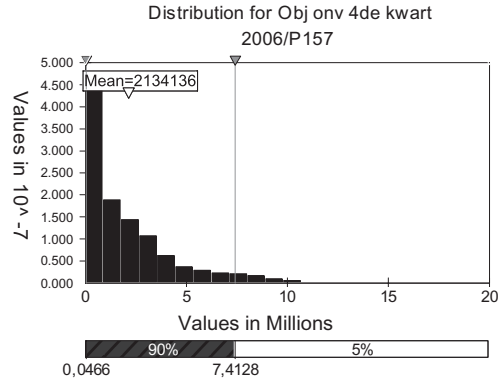

Figure 8. Monte Carlo calculation of necessary reserve for identified risks.

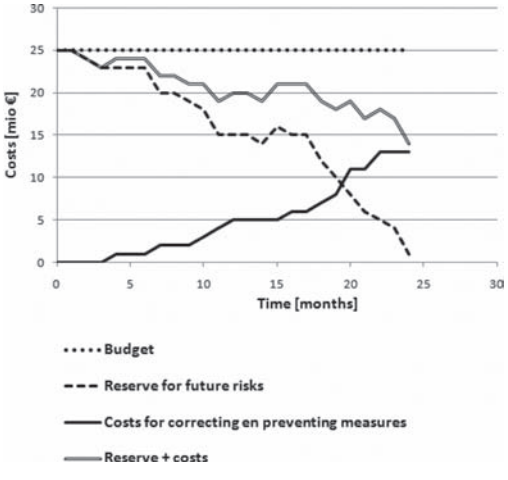

Figure 9. Development of risk related costs.

updated list the necessary risk budget is calculated. As the project progresses the necessary reserve for future risks generally diminishes.

At the same time the original budget is used to finance preventing and correcting measures.

By comparing the sum of costs and reserve with the original budget the financial reserves in the project become clear.

7 CONCLUSIONS

From the Randstad Rail project we have learned that a fully integrated risk and monitoring system contributes to project control. It was also recognised that in nowadays complex society a risk management and monitoring system makes a project more easy to accept for those who live or work next to the construction works.

Lessons learned in the Randstad Rail project with regards to monitoring and risk management have now made the four steps used in the process the standard for Rotterdam civil construction works. To summarise:

1. Determine project surroundings and the demands they put upon the project itself. Acknowledge the success factors of the stakeholders and make them a part of the risk management.
2. Draw the technical outline of the monitoring programme and make the contractor responsible for the measurements. Determine both S- and I-hazard level for each monitoring instrument, taking into account the safety and structural demands made by the "surroundings".
3. Determine, in the preliminary phase of the work, which mitigating measures to take, when a S- or I-level is exceeded (proactive approach). Give a risk- and quality management team a place in the organisation, directly linked to the project manager. Make the team responsible for risk identification, on a cyclic base, and implementation of mitigating measures.
4. Since there is a large financial component in risk management, link the financial and risk control to each other to get a better idea of the development of risk related costs. Also, to make sure that there is a budget to finance mitigating measures, whenever necessary.

This page intentionally left blank

Geotechnical Aspects of Underground Construction in Soft Ground – Viggiani (ed)
© 2012 Taylor & Francis Group, London, ISBN 978-0-415-68367-8

The study of displacements of diaphragm walls built in Warsaw Quaternary soils

A. Siemińska-Lewandowska & M. Mitew-Czajewska
Warsaw University of Technology, Warsaw, Poland

U. Tomczak
Soletanche Polska Sp. z o.o., Warsaw, Poland

ABSTRACT: In the paper 18 cases of deep excavations executed in Quarternary soils (silty sands, silty clays, clayey sands and Pliocene clays) in Warsaw are presented. All of the cases were executed in urban areas that is why excavation walls were protected by means of diaphragm walls and measurements of displacements of these walls were performed. The results of measurements and geotechnical conditions, support systems (anchors, struts, slabs) as well as methods of construction (open excavation or top and down method) are presented. Final conclusions concerning the displacements of diaphragm walls executed in Warsaw Quaternary soils are given.

1 INTRODUCTION

Over the last few years, in Poland a lot of deep excavations are being built especially in big cities. Road and metro tunnels as well as deep underground car parks (2–5 levels) under office and housing buildings are a common issue nowadays. Theses excavations are typically protected by means of soldier pile walls, sheet pile walls, continuous bored piling or most often by diaphragm walls. In order to ensure the safety of surrounding structures displacements of excavation walls, ground surface and building settlements as well as the heave of the bottom of excavation are measured during excavation. In Warsaw, 10 to 20 m deep excavations are built mostly in soft soils—Tertiary and Quaternary deposits—with very high water level behind the wall. Difficulties with proper assessment of design parameters of these soils cause problems with precise theoretical assessment of deep excavation walls displacements values. The estimation of theses displacements is necessary for proper risk evaluation of excavation walling and surrounding structures. From the other hand wide database of real displacements values gives opportunity to asses mechanical parameters of surrounding soil body using the method of back analysis.

18 cases of deep excavations executed in Warsaw were analysed. In all cases the excavations were protected by means of diaphragm walls, but different wall support methods were used. In the paper, 3 chosen cases, representing typical construction stages when using anchors, struts or top and down method of construction, were described. Geotechnical conditions below the bottom of excavation and measurements results (maximum and minimum wall displacements) were presented and discussed, Tomczak (2010).

2 GEOTECHNICAL CONDITIONS

In Warsaw region, in general, differential Quaternary overburden (1–100 m thickness)—mostly glacial deposits—covers a layer of Tertiary clays. The processes of soil erosion connected with forming the river net as well as a glacitectonic deformation effects in this region appeared in geological past. The decompression, erosion and weathering processes followed. As a result of these processes the soil body, especially Tertiary soils in Warsaw are non-homogenous with discontinuities and contain lots of lenses of different lithology often with water under high pressure. Therefore it is difficult to properly asses design parameters of theses soils.

In order to determine mechanical parameters of soils, especially the deformation modulus, in-situ and laboratory tests are usually carried out. In situ tests such as e.g.: Dynamic Probing Light (DPL), Cone Penetration Tests (CPTU), pressuremeter tests and geophysical technique—vertical electrical sounding VET or laboratory tests, e.g.: triaxial

shear test CIU, consolidometer tests CRL, bender elements test (undrained, isotropic loads), etc. All these methods of determination of soil parameters give a very wide range of its values. The ranges of values of typical Warsaw soil parameters, specified basing on 18 excavation cases, are given in Table 1.

Proper evaluation of mechanical soil parameters is a main issue in the displacements approach to the static analysis of diaphragm walls. Siemińska-Lewandowska (2001, 2006) states that calculation values of soil parameters are frequently underestimated, especially values of modulus of elasticity E_0. It is estimated that over half of deep excavation walls in Poland are designed and constructed using geological and engineering documentation drawn up based on results of simple drilling and dynamic probing, Wysokiński et al. (1999). Only macroscopic assessment of type of soil and its state is performed during surveys. Results are then used to determine values of geotechnical parameters of soil (e.g. c, φ, M, E) based on a number of simplified charts and tables included in applicable standards and in literature, Wiłun (2001). E_0 modulus value, however, is not constant for a soil and it changes with variation of axial deformation ε_1 and effective average stress p'. Physical non-linearity is very strong for small deformations, Burland (1989), Gryczmański (1995). Deformations of diaphragm walls calculated using the finite element method under the assumption of linear soil elasticity are much larger than observed in reality and measured with inclinometers or using precise geodesic leveling methods. The best method of the E_0 modulus value assessment is to derive it from back analysis based on in-situ displacements measurements, Mitew-Czajewska (2005). Back analysis may be performed if a large number of measurement data is available. The data base created basing on the in-situ measurements in Warsaw, described below, will be used in the back analysis for the estimation of soil parameters, especially the E_0 modulus value. Future analysis of diaphragm walls using finite elements method (and Mohr-Coulomb or other constitutive soil models) may be based on these parameters.

Table 1. Geotechnical parameters of typical soil layers.

No	Name	IL/ID (°)	ϕ (°)	c (kPa)	E_o (MPa)
1.	Clay (I)	0	11–13	55–60	16–22
2.	Sandy clay (Gp)	0.3–0.2	16–18	28–31	22–28
3.	Sandy clay (Gp)	0.1–0.0	20–25	35–50	36–67
4.	Fine sand (Pd)	0.5–0.6	30–31	0	46–55
5.	Fine sand (Pd)	0.7–0.8	31–33	0	65–66
6.	Medium sand (Ps)	0.45	33	0	73
7.	Medium sand (Ps)	0.7–0.8	34–35	0	80–111
8.	Gravel (Po)	0.45–0.5	38	0	129–154

3 CASE STUDIES

In the paper, 3 typical methods of construction of deep excavations protected by diaphragm walls are presented—anchored walls, strutted walls and top and down method.

3.1 *Anchored diaphragm wall*

The method of anchored diaphragm wall is described basing on an example case—the construction of underground car park of "Canal+" building in Warsaw (Fig. 1). Typical cross section is shown on Figure 2.

In that case the stability of the diaphragm wall has been provided by one level of ground anchors at –3,0 m below ground level (b.g.l.). There were two designed capacities of anchors—560 kN and 750 kN. Anchors were made of high tensile strength steel wires (Rv = 1260 MPa). Total anchor length was 17 m, in which 9 m was the anchor grouted body.

Designed construction stages were as follows:

1. Soil levelling, forming of the working platform;
2. Execution of guide walls;
3. Execution of diaphragm walls;
4. Execution of the reinforced concrete capping beam;
5. Excavation—3,5 m b.g.l.;
6. Forming and stressing of ground anchors at –3,0 b.g.l.;
7. Final excavation, max. –11,70 m b.g.l.;
8. Execution of foundation slab;
9. Execution of all underground slabs;

Figure 1. Construction site "Canal+".

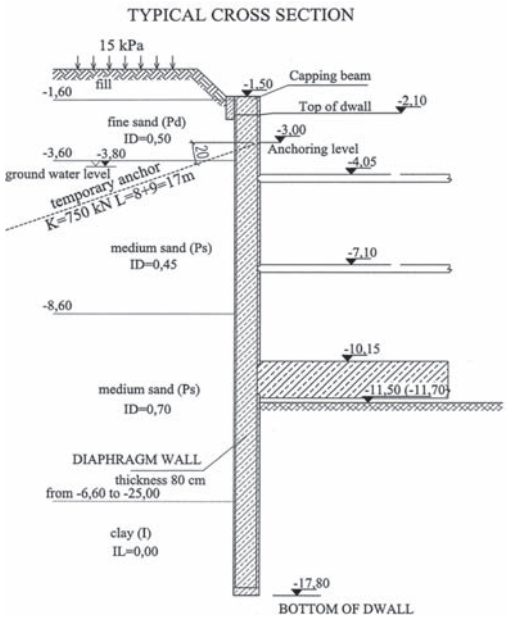

Figure 2. Typical cross-section of anchored diaphragm wall.

10. Cutting off anchors after the foundation slab and slabs reached 100% of its designed strength;
11. Execution of the remaining structure.

Geotechnical conditions:
1–2 m thick layer of uncontrolled fills covers 6–18 m thick layer of Pleistocene non-cohesive soils (fine, medium sands and gravel) under-lied by Tertiary clays.
Ground water level occurs at 2,7–3,5 m b.g.l.

3.2 *Strutted diaphragm wall*

The method of strutted diaphragm walls is one of the most commonly used methods of excavation support. This method is described basing on an example case—the construction of underground car park of "Equator 2" office building in Warsaw. Typical cross section is shown on Figure 3.

Designed construction stages were as follows:

1. Soil levelling, forming of the working platform;
2. Execution of guide walls;
3. Execution of diaphragm walls;
4. Execution of the reinforced concrete capping beam;
5. Excavation—5,65 m b.g.l.;
6. Installation of struts—5,15 b.g.l.;
7. Final excavation, max. –11,00 m b.g.l.;
8. Execution of foundation slab;
9. Execution of "–1" slab at –6,675 m m b.g.l.;

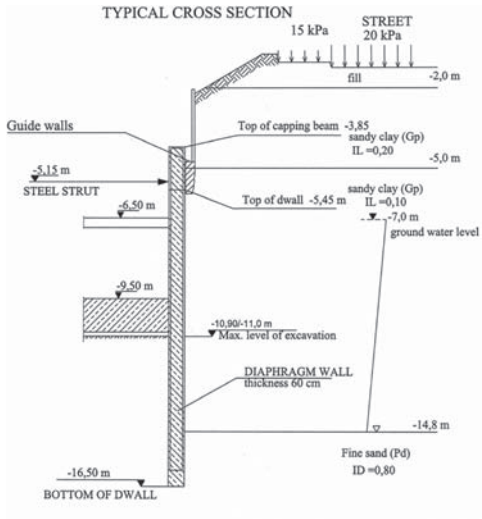

Figure 3. Typical cross-section of strutted diaphragm wall.

10. Dismantling of struts after the foundation slab and the "-1" slab reached 100% of its designed strength;
11. Execution of the remaining structure.

Geotechnical conditions:
2 m thick layer of fills covers Quaternary deposits: 3–12 m thick layer of sandy clays under-lied by fine and medium dense sands.
Ground water level stabilises at –7 m b.g.l.

3.3 *Top and down method*

The top and down method, using basement slabs to successively prop diaphragm walls, is used to restrict horizontal wall displacements and vertical settlements behind the wall, Puller (1996). The minimisation of soil movement is obtained due to regular propping of the diaphragm wall by all underground slabs, considerable elastic stiffness of slabs and the avoidance of displacements occurring during re-propping. The top and down method is therefore used in urban areas, close to existing structures and buildings. This method is described basing on an example case—the construction of 5 storey, underground car park of an office high-rise building at Prosta street in Warsaw (Fig. 4). Typical cross section is shown on Figure 5.

Designed construction stages were as follows:

1. Soil levelling, forming of the working platform;
2. Execution of guide walls at –2,0 m b.g.l. and –2,5 m b.g.l. (for barrettes);
3. Execution of diaphragm walls and barrettes;
4. Execution of the reinforced concrete capping beam;

Figure 4. Construction site at Prosta St.

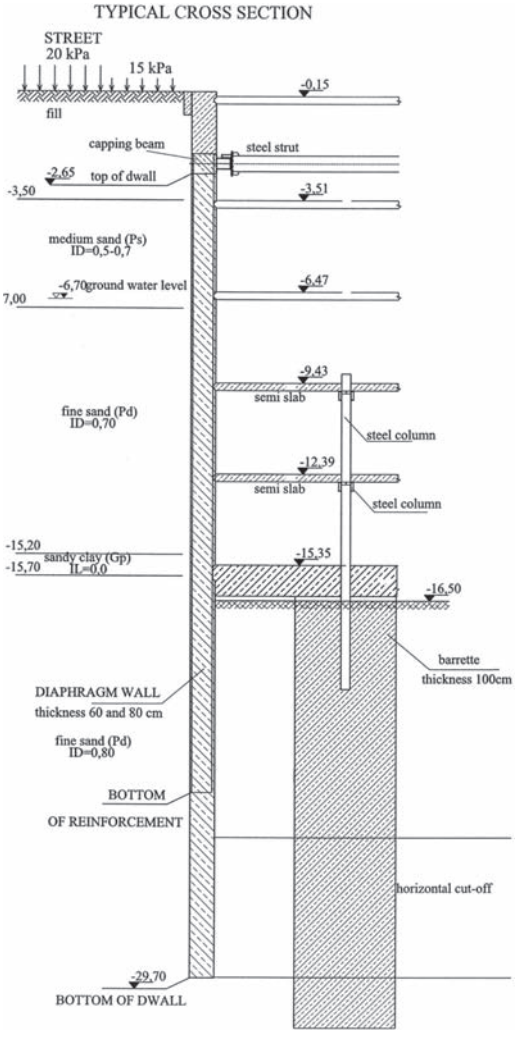

Figure 5. Typical cross-section in top and down method.

5. Excavation—3,0 m b.g.l.;
6. Execution of water cut-off barrier and installation of dewatering systems;
7. Installation of struts—2,40 b.g.l.;
8. Excavation –9,70 m b.g.l. (below the bottom of "–4" slab);
9. Execution of "–4" slab (top level of the slab –9,43 m b.g.l.);
10. Excavation –12,65 m b.g.l. (below the bottom of "–5" slab);
11. Execution of "–5" slab (top level of the slab –12,39 m b.g.l.)
12. Final excavation, max. –16,50 m b.g.l.;
13. Execution of foundation slab;
14. Execution of local excavations below lift shafts execution of the foundation slab in theses areas;
15. Execution of the remaining structure.

Geotechnical conditions:
A 3–5 m thick layer of fills covers Quaternary fluvio-glacial deposits—medium and fine, mostly dense sands, in which cohesive, 0,5 to 5 m thick, interbedding of sandy clays could be found.
Ground water level occurs at –6,7 m b.g.l.

4 RESULTS OF MEASUREMENTS AND DISCUSSION

In all cases, measurements of horizontal displacements of diaphragm walls were performed in all

Table 2. Horizontal displacements of diaphragm wall.

Retaining system	Horizontal displacements				
	min. (mm)	max. (mm)	min. (%H)	max. (%H)	average (%H)
Anchors					
Case 1	1.9	15.8	0.02	0.14	0.08
Case 2	1.6	7.7	0.02	0.07	0.04
Case 3	0.6	7.9	0.01	0.10	0.05
Case 4	7.9	23.0	0.09	0.26	0.18
Case 5	0.3	3.0	0.00	0.03	0.01
Case 6	1.3	5.3	0.01	0.05	0.03
Case 7	0.0	2.6	0.00	0.02	0.01
Case 8	0.7	5.8	0.01	0.05	0.03
Struts					
Case 1	1.8	11.6	0.02	0.14	0.08
Case 2	3.6	10.1	0.05	0.14	0.10
Case 3	0.1	8.3	0.00	0.11	0.05
Case 4	2.9	12.0	0.02	0.10	0.06
Case 5	2.0	11.7	0.02	0.09	0.06
Top and down method					
Case 1	0.5	1.7	0.00	0.02	0.01
Case 2	8.0	24.0	0.07	0.20	0.13
Case 3	3.0	16.5	0.02	0.10	0.06
Case 4	4.0	14.8	0.03	0.12	0.08
Case 5	0.4	11.7	0.00	0.14	0.07

Table 3. Summary of structure details and geotechnical conditions below the excavation.

Retaining system	D. Wall thickness (m)	Depth of exc. (H) (m)	DW Depth below excavation level (m)	Geotechnical conditions below excavation (m)
Anchors				
Case 1	0.8	11.50	6.05	Clay I*
Case 2	0.6	10.55	5.80	Sandy clay Gp*
Case 3	0.6	8.05	4.00	Sandy clay Gp*
Case 4	0.6	8.70	3.80–4.80	Clay I*
Case 5	0.6	11.03	4.00	Sandy clay Gp*
Case 6	0.6	10.71	3.00–3.50	Sandy clay Gp*
Case 7	0.6	10.65	3.10–3.60	Sandy clay Gp*
Case 8	0.6	11.00	4.20	Sandy clay Gp*
Struts				
Case 1	0.6	8.15	3.55–4.05	Fine sand Pd
Case 2	0.6	7.15	3.55	Sandy clay Gp*
Case 3	0.6	7.85	3.45	Sandy clay Gp*
Case 4	0.6	11.70	4.00–4.90	Sandy clay Gp*
Case 5	0.8	12.40	5.50–6.10	Fine sand Pd
Top and down method				
Case 1	0.6	10.68	5.00	Fine sand Pd
Case 2	0.6	12.20	4.35–4.85	Sandy clay Gp*
Case 3	0.8	16.50	12.20	Fine sand Pd
Case 4	0.8	12.30	5.10–6.30	Sandy clay Gp*
Case 5	0.6	8.60	4.0	Sandy clay Gp*

*cohesive soil.

construction stages. Benchmarks were located on capping beams, at the top of diaphragm walls. The measurements were made using precise geodesic leveling method (angle-linear method) by means of Leica TPS1200+ appliance.

Maximum and minimum horizontal displacements of diaphragm walls measured during excavation in all cases are presented in Table 2. Column 4 of Table 2 shows displacements in relation with excavation depth.

Additionally—the thickness of diaphragm wall, the depth of the excavation, the depth of the wall below the final excavation level, method of excavation support as well as geotechnical conditions below the excavation are given in the Table 3.

There were: 8 anchored, 5 strutted and 5 top and down cases analysed. In all cases excavations and diaphragm walls were executed in Quaternary soils.

In all cases, there was constant quality of work control performed during construction in accordance with International Standards (ISO).

5 CONCLUSIONS

Taking into account all analyzed cases the general conclusion may be derived that in case of 7–12 m deep excavations executed in Warsaw the horizontal displacements do not exceed 0,2% of the excavation depth (H).

It was observed that when cohesive soils occur below the bottom of excavation the displacements range from 0,01 to 0,26% of excavation depth. In case of non-cohesive soils the range is 0,0 to 0,14% of the excavation depth.

When analyzing the horizontal displacements of the diaphragm wall in relation to the method of excavation support it may be stated that:

- in case of anchored excavations average horizontal displacement is up to 0,18% of excavation depth (H),
- for strutted (propped) excavations average horizontal displacement is from 0,05 to 0,10% of excavation depth (H),
- when using top & down method the average horizontal displacements is up to 0,08% of the excavation depth (H).

REFERENCES

Burland J.B. 1989. Small is beautiful—the stiffness of soils at small strains. 9th Bjerrum Memorial Lecture. Canadian Geotechnical Journal. 26(4): 499–516.

Dybicz R. 2010. The analysis of soil-structure interaction based on in situ measurements. Doctoral thesis. Oficyna Wydawnicza Politechniki Warszawskiej (in Polish).
Gryczmański M. 1995. The introduction to the description of elasto-plastic soil models. KILiW PAN. IPPT PAN. Studia z Zakresu inżynierii 40. 156. (in Polish).
Mitew-Czajewska M. 2005. In situ measurements and numerical analysis of displacements of diaphragm walls. Doctoral thesis. Wydawnictwa Politechniki Warszawskiej. (in Polish).
Mitew-Czajewska M. & Siemińska-Lewandowska A. 2010. *In situ* geotechnical surveys and static analysis of deep excavations. Poznań University of Life Sciences Press.
Polish code PN-83/B-03010. Retaining structures. Static calculations and design. (in Polish).
Polish code PN-81/B-03020. Construction soils. Shallow foundations. Static calculations and design. (in Polish).
Puller M. 1996. Deep excavations. A practical manual. Thomas Telford Publishing.
Siemińska–Lewandowska, A. 2001. The displacements of anchored diaphragm walls. Oficyna Wydawnicza Politechniki Warszawskiej. (in Polish).
Siemińska–Lewandowska, A. 2006. The design of deep excavation walls—theory and practice. Wydawnictwa XXIX Zimowej Szkoły Mechaniki Górotworu i Geoinżynierii. Geotechnika i Budownictwo Specjalne. KGBiG AGH Kraków: 329–344. (in Polish).
Technical design of diaphragm walls for office building Equator II at Al. Jerozlimskie St. in Warsaw. Soletanche Polska Sp. z o.o. (in Polish).
Technical design of diaphragm walls for office-housing building at Prosta St. in Warsaw. Soletanche Polska Sp. z o.o. (in Polish).
Technical design of diaphragm walls for office building Canal + at Sikorskiego St. in Warsaw. Soletanche Polska Sp. z o.o. (in Polish).
Tomczak U. 2010. The monitoring of diaphragm walls. (in polish).
Wiłun Z. 2001. Basics of geotechnics. Wydawnictwa Komunikacji i Łączności. Edition V. (in Polish).
Wysokiński L. & Kotlicki W. & Motak E. 1999. Geotechnical issues during construction in urban areas. Inżynieria i budownictwo 10/1999. 579–583. (in Polish).

Geotechnical Aspects of Underground Construction in Soft Ground – Viggiani (ed)
© 2012 Taylor & Francis Group, London, ISBN 978-0-415-68367-8

Design control and monitoring of a jet grouted excavation bottom plug

N. Eramo & G. Modoni
University of Cassino, Cassino, Italy

M. Arroyo Alvarez de Toledo
Universidad Politécnica de Catalunya, Barcelona, Spain

ABSTRACT: Jet grouting is adopted in different geotechnical conditions to ensure provisional earth retaining and waterproofing functions in excavations. Despite careful theoretical models available to predict the mechanical response of these structures, design is often carried out without adequate control, i.e. by assuming ideal effectiveness of ground improvement. On the contrary, adverse effects have been documented by past experiences which can be traced back to erroneous prediction of treatments effects, inaccurate control of the execution or to unexpected responses of the surrounding environment. All these uncertainties, which are critical when working in urban areas, can be minimized by detailed preliminary field trials, accurate treatment execution control and a prompt monitoring of the surrounding area. The present paper illustrates these issues with a description of the design and execution of a massive jet grouting bottom plug forming the base of a large excavation for a tube station. The results of preliminary field trials are summarized to directly compare the effectiveness of different injection systems and introduced in statistical design analyses of the jet grouted structure. A detailed investigation of the surface movements induced by injections is also reported. To this aim, the evolution of displacements recorded around trial columns and on the area surrounding the excavation is mapped to evaluate the effects of the different adopted injection techniques.

1 INTRODUCTION

Jet grouting is adopted in a variety of geometrical configurations to ensure provisional or final earth retaining and waterproofing functions at the bottom and walls of excavations (e.g. Balossi Restelli et al., 1986; Santoro & Bianco, 1995; Sondermann & Toth, 2001; Miyasaka et al., 1992). The basic solution consists in a continuous impervious barrier formed with assemblies of overlapped columns. Another important requirement is the resistance against buoyancy, usually provided by self weight and/or internal strength of the foundation system. This function can be satisfied by creating massive cemented soil portions (plugs) of overlapped columns.

Regardless the analysis method applied, the successful performance of these structures is strongly influenced by the cemented soil geometry and materials properties. In particular, since waterproofing is due to the interpenetration of adjacent columns (Croce et al., 2006), discontinuous barriers may result from perforation deviations or by overestimation of columns diameter. Also prediction of the resistance against uplift forces becomes worthless if inexact determination is made of unit weight or shear strength of cemented soil.

All these properties, dependent on the interaction between injected fluids and original soil, cannot be precisely controlled by simply tuning the injection parameters and thus represent the most significant source of uncertainty in the calculation. Different approaches are promoted by different standards to govern uncertainty in the design and to properly define a treatment. The Japanese code (JJGA, 2005) deterministically provides diameter, unit weight and strength of columns for different jet grouting systems (double or triple fluid) and undisturbed soil properties (N_{SPT} values); uncertainty is then managed with global safety factors fixed for various types of structures. On the contrary European standard (ENV 12716, 2001) and US guidelines (G.I. ASCE, 2009) do not suggest typical values for jet grouting properties but stress on the role of preliminary field trials and Quality Control—Quality Assurance tests for their quantification. In particular the ENV 12716 standard insists on the assessment of variability of jet grouting properties and on its influence on the performance of structures. Following this second approach a procedure for the design of jet grouted bottom plugs is herein applied to the excavation of a railway station near Barcelona. Properties of columns determined by field trial investigations are statistically analyzed and introduced in the

assessment of the continuity and resistance against buoyancy forces of the bottom plug. Results of field trial experiments and monitoring of the effects on the surrounding environment are also discussed in relation with different adopted injection techniques.

2 THE CASE STUDY

The excavation considered in the present study (Fig. 1) is aimed to host a station along a new subway line in Barcelona.

It extends over a sub rectangular plan arrangement having a total length of 107.4 m, a width ranging from 17.2 m (in the middle part) to 29.1 m (in the left part), and a maximum depth of 18.7 m below the ground level, this latter positioned 4.7 m a.s.l. In order to minimise the disturbance at the upper road level, the excavation has been performed with a cut and cover method, briefly summarised in the following steps:

- Excavation for about 2.5 m depth below the ground surface and execution, all along the side of station and descending ramps, of reinforced concrete diaphragm walls (1.2 m thick and 20 m deep);
- Execution of a jet grouting bottom plug (with thickness variable between 8 and 10 m) extended for about 3 m out of the side walls in order to anchor their foot and to increase resistance against buoyancy;
- Excavation by TBM of a 8.43 m large tunnel throughout the station;
- Cast of beams and slabs on the roof of the station, cover with soil and excavation down to the lower level (3.3 m b.s.l.);
- Cast of beams and slabs, excavation to the next level (11.47 m b.s.l.) and demolition of the tunnel shield;
- Cast of the lowest slab and fill by concrete of the gap from the jet grouted plug.

Walls of piles and micropiles, extending at depths larger than the jet grouting plug, were created in the

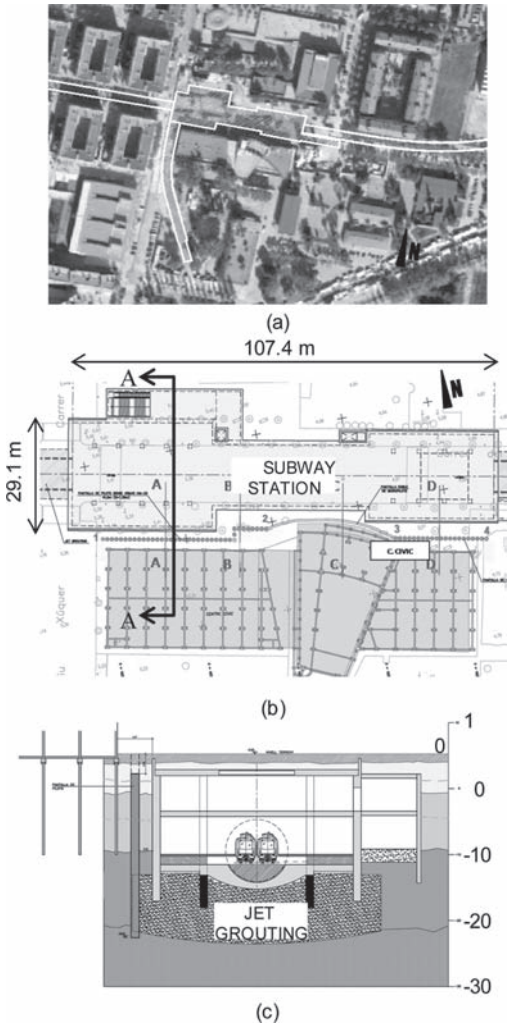

Figure 1. Location of the station and nearby buildings in the urban texture (a), plan map (b) and cross section A-A (c).

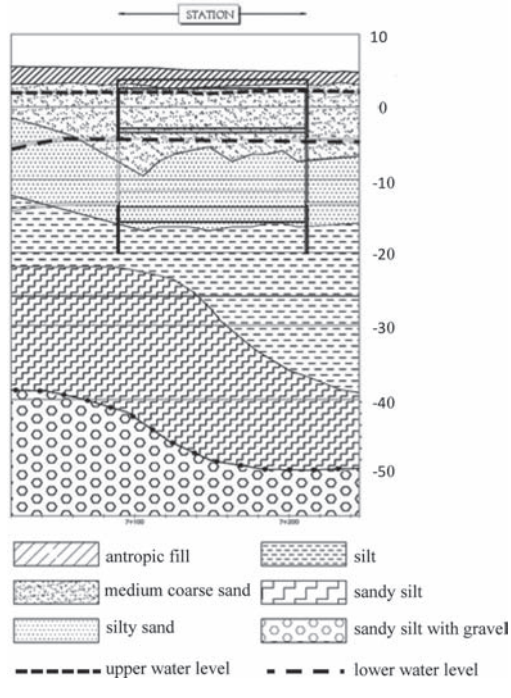

Figure 2. Schematic subsoil profile around the station.

southern part of the station to prevent settlements induced by excavation on the nearby building.

The composition and the geotechnical characteristics of the subsoil have been obtained from two different experimental campaigns carried out at different design stages. The combination of both investigation results gives the profile reported in Figure 2, showing an alternation of different alluvial soil layers.

Two different water bearing strata, separated by silty materials, have been identified by piezometers located at different plan positions and depths. Figure 1 shows the waterproofing and the uplift resisting functions of the jet grouting plug, whose depth was limited to avoid influence on the water circulation of the upper acquifer.

3 FIELD TRIAL INVESTIGATION

Before execution of treatments different field trials were performed with the following purposes:

- Recognition, from a comparison of different systems and sets of injection parameters, of the most effective solution to ensure the required characteristics of columns;
- Definition of quality control/assurance and monitoring plan to be implemented in the construction process;
- Check of possible undesired effects produced by the execution of treatments.

With reference to the first goal, the properties of cemented soil columns listed in Table 1 were established by the designer to satisfy functionality of the plug. Moreover continuity had to be warranted by overlapping of columns. All these standards formed a benchmark for the experimental activities carried out before and during the construction of the plug.

In the preliminary stage, verification of these requirements was accomplished by injecting several triplets of columns with different systems (double and triple fluid), injection parameters and procedures, and monitor nozzle configuration (Fig. 3.a). In particular three sets of columns (groups A, C and D) were injected with double fluid systems, one (G) with triple fluid system and the other three (B, E and F) with Sanella method (Sanella, 2007). This latter procedure, described in Fig. 3.b consists in the injection of the upper column section (1/3 of columns length in group B and E, 2/3 in group F) with water and of the lower section (2/3 of columns length in group B and E, 1/3 in group F) with grout. This procedure is aimed to fill the upper part of columns with returning spoil (Fig. 3.b). The columns axes, located at the corner of a triangle, were distanced accordingly with the

	Double fluid			Sanella method			Triple fluid
Parameter	A	C	D	B	E	F	G
Nozzles diameter, d (mm)	4.5	6	Upper=3.8 Lower=5	4.5	Upper=5 Lower=3.8	4.5	
Number of nozzles	2	1	2	2	2	2	
Grout pressure (bar)	350	400	375	350	400	380	150
Air pressure (bar)	10	10	10	10	10	10	>8
Water pressure (bar)	-	-	-	350	300	380	575
Uplift speed (sec/cm)	28”/ 6cm	33”/ 4cm	55.5”/ 6cm	32”/ 6cm	55.5”/ 6cm	60”/ 6cm	60”/ 6cm
Water cement ratio by weight W/C	1.1/1	1/1	1/1	1.1/1	1/1	1/1	1/1
Expected column diameter (m)	2.0	2.5	2.5	2.0	2.5	3.0	4.3
Columns mesh (m x m)	1.58x1.38	2.05 x 1.78	2.05 x 1.78	1.58 x 1.38	2.05 x 1.78	2.46 x 2.13	3 x 3.5

(a)

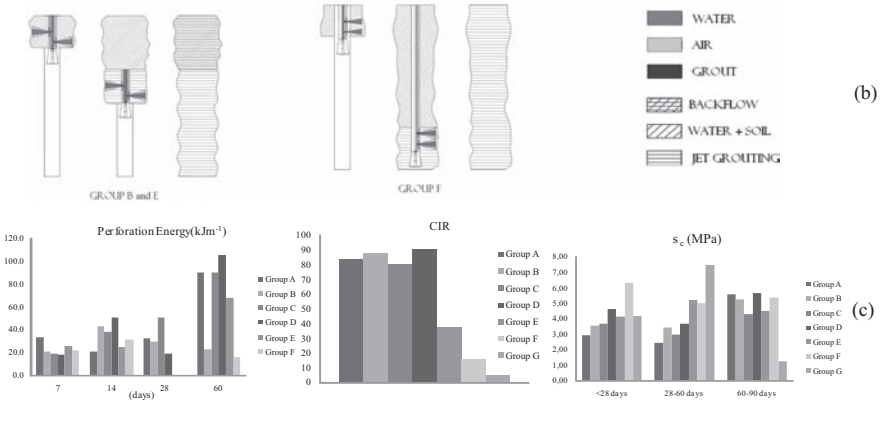

(b)

(c)

Figure 3. Selected results from jet grouting field trial (a) list of adopted injection parameters and techniques; (b) Sanella method injection procedures; (c) measured parameters.

expected diameter in order to produce overlapping of columns. The best solution was then chosen based on a comparative analysis of the following tests results (Fig. 3.c):

– Instrumented drilling performed in the centre of each triplet at different time after injection;
– Continuous rotary boring in the centre of triplets and at different distances from columns centre with evaluation of core improvement rate (Yoshitake et al., 2003);
– Laboratory tests (uniaxial compression, density, Young's modulus, permeability) on samples cored from columns.

These indexes have been also adopted as a routine control to check the effectiveness of jet grouting during the execution of treatments. Based on these results the set of injection parameters listed with letter D in Figure 3.a has been selected as the most effective for the bottom plug injection.

For this column type, the frequency distributions reported in Figure 4.a and 4.b have been obtained for the unit weight γ and the uniaxial compressive strength σ_c of cemented soil. A Gaussian function can be fitted to both plots: the median values and the standard deviations are respectively 16.0 kN/m^3 and 1.21 kN/m^3 for the unit weight, 6.481 MPa and 3.37 MPa for the uniaxial compressive strength. Note that his variability includes that due to the variation of soil types within the treated volume.

Another field trial test consisted in the measurement of the perforation deviations. Inclinations measured on 44 columns provide the

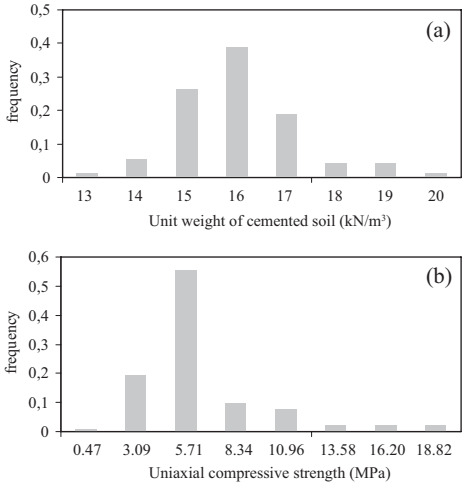

Figure 4. Frequency distributions of unit weight γ and uniaxial compressive strength σ_c of cemented soil.

Table 1. Required properties of cemented soil.

Property	Unit	Accepted value
Uniaxial compressive strength	MPa	>3,5
Traction resistance	MPa	>0,6
Young's modulus	GPa	1 < E < 4
Density	kN/m^3	>16
Permeability	cm/s	10^{-7}

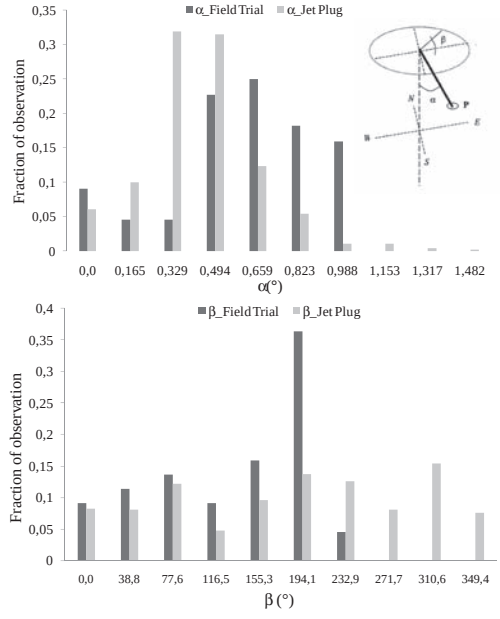

Figure 5. Statistical deviation of columns axes from vertical direction during field trial and routine quality control tests.

frequency distributions reported in Figure 5 for the α and β angles quantifying the deviation from verticality.

These plots show relatively small angles α (indicating the deviation from the ideal vertical direction), with a median value of 0.37° and a standard deviation of 0,16° and an almost flat distribution of the azimuth angle β. Similar distributions have been also retrieved by tests performed during routine control of the production columns.

4 PROBABILISTIC ANALYSES

The continuity and the resistance of the bottom plug are here evaluated with probabilistic calculations based on statistic derived from the

results previously shown. With regard to the imperviousness of the barrier, a check has been made on the probability that continuous holes could cross the whole plug. To this aim the geometry of several columns triplets is simulated with a Monte Carlo technique by assigning a normal distribution to the angle α, and a uniform distribution to β. Mean and variance of α are taken from the previous statistical analyses (Fig. 5). The columns diameters D at different depths have been calculated by assuming a normal distribution with mean value equal to the design assumption (2500 mm). It is worth recalling that column diameters cannot be measured at such big depth and that this assumption is based on the continuity of drilling energy profile measured during tests. The coefficients of variation have been assumed between 0.05 and 0.2 (direct measurement performed in a site close to this station provided a value of 0.13).

By repeating this numerical experiment for one thousand triplets of columns, a frequency distribution of the minimum holes dimensions can be derived. The values correspondent to a cumulated probability of 5%, reported in Figure 6 as functions of the columns axes distance at ground level, shows that gap dimension reduces with variability of columns diameter CV(D), and that is nil for the assigned axis span at ground level (2.0 m).

The functionality of the plug has been verified by a numerical simulation of the construction process using a two dimensional FEM code (Brinkgrave & Vermeer, 2000). The properties of original soil layers have been calculated from the results of in situ and laboratory tests, the stiffness of cemented soil has been estimated by laboratory tests under the assumption of a linear elastic perfectly plastic behaviour (Mohr Coulomb constitutive model). If the experimentally determined average unit weight (16 kN/m^3) is assigned to the whole jet grouted plug, the ratio between the self weight of the structure and the resultant buoyancy force becomes equal to 1.91.

To evaluate failure likelihood, the maximum tangential stress τ_{max} and the correspondent normal

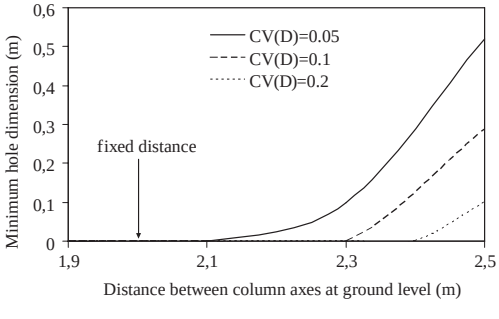

Figure 6. Probabilistic assessment of plug continuity.

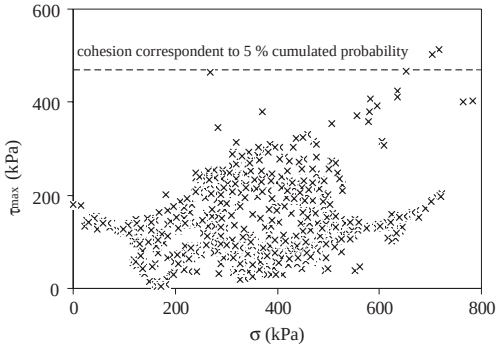

Figure 7. Stress state tolerability of the bottom plug.

stress σ have been computed from the stress tensor in all calculation points of the plug and compared with failure envelopes obtained from laboratory tests (Fig. 7). For simplicity a purely cohesive resistance has been assigned to the cemented soil with limit tangential stress calculated as half of the uniaxial compressive strength σ_c. Variability of this latter (Fig. 4.b) is considered by adopting a normal distribution and by reporting in Figure 7 the envelope correspondent to an accepted probability of failure equal to 5%. The plot shows that only two τ_{max} values are located above the assumed envelope, while all other points fall in the safe region. It must however highlighted that this result becomes fully satisfactory when considering the positive effect of confining stress on the cemented soil resistance, which has been neglected in this analysis.

5 GROUND SURFACE MOVEMENTS

Both the execution of a massive jet grouting treatment and the subsequent excavation were expected to produce movements of the nearby ground. Concerning jet grouting, significant uplifts have been recorded by previous studies (e.g. Russo and Modoni, 2005) when repeated injections are performed close to each other. To deal with these effects, a detailed monitoring plan was implemented in the present case. Settlements induced by columns injection were initially observed in field trial experiments using four benchmarks at different distances from the centre of columns triplets; a topographic observation network was subsequently installed on the ground and buildings surrounding the station to observe the effects produced by current operations.

The movements induced by the different injection systems described in Figure 3 on a benchmark located at 3.75 m distance from the centre of column triplets are reported in Figure 8.a. The plot shows

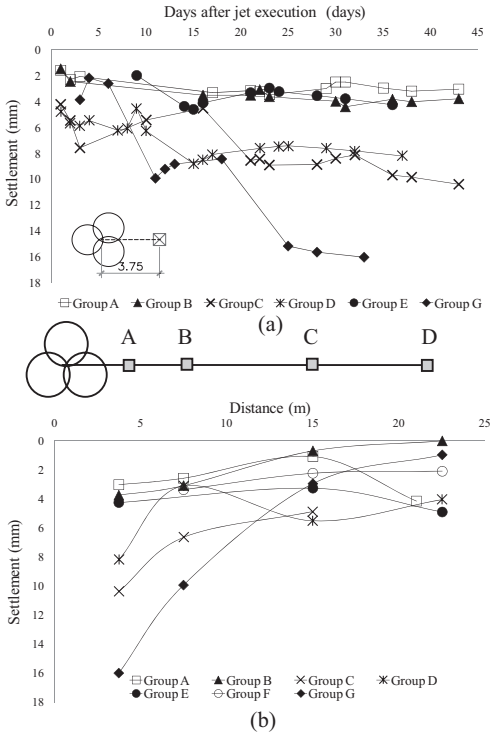

Figure 8. Ground settlements induced by different injection systems (a) instrumentation's setup; (b) settlements profile; (c) time evolution.

a progressive increase of downward settlements for all cases, beginning soon after injection and proceeding with a faster rate in a period of about two weeks. The comparison among the different results leads to the following considerations:

– Settlements induced with triple fluid are from two to six times larger than those produced by double fluid systems;
– With regard to double fluid, larger final settlements (8–10 mm) are obtained near columns injected with C and D systems, these latter presenting a rod lifting speed lower than adopted for system A (it is worth noting that grout in systems B, E and F is injected only in a portion of column length).

The profiles of maximum settlements recorded on the benchmarks located at different distances (Fig. 8.b) show a common concave shape attenuating with distances and reaching a maximum near the centre of columns triplets. Based on these results it is not possible to give a conclusive assertion about the mechanisms involved in the movements. However, it is interesting to observe the relation existing between maximum measured settlements and total amount of injected cement among the different columns triplets (Fig. 9). This result suggests as possible explanation the lack of support given by fresh grout-soil mix on the surrounding soil (C, D and G are arguably the larger columns) and/or the consolidation induced by the considerable heat developed during the cement hydration process.

Settlements induced by the injection of the excavation plug have been continuously monitored with high precision optical levelling on a grid of 35 benchmarks located all around the station (Fig. 10).

By interpolating these data with a geostatistical technique (Kriging), two settlement maps have been created describing the situation before and after the execution of the jet grouting treatments. From these two maps (Fig. 10.a and 10.b) it is seen that the most subsiding area (the largest settlements at the end treatments are about 55 mm) is located near the south west border of the station, close to the ramp accessing to the construction site. In particular, by observing the time evolution on different benchmarks (Fig. 10.c) it is seen that less than 20 mm are induced by the construction of diaphragm walls, built for the accessing ramp and the station, while the remaining part (about 35 mm) has occurred during and after the execution of jet grouting treatments. It is also worth observing that triple fluid injections (with the set of parameters indicated with G in Fig. 3) were attempted in this area to increase the speed of operations and that this system was discarded after observing the sudden increase of settlement rates on closer benchmarks (point 1 in Fig. 10.a and corresponding curve in Fig. 10.c).

It can be concluded that, up to the end of the process, when the subsidence rate becomes negligible, jet grouting operations have produced overall downward settlements of about 40 mm near the south-east border of the station, where a larger part of treatments performed with double and

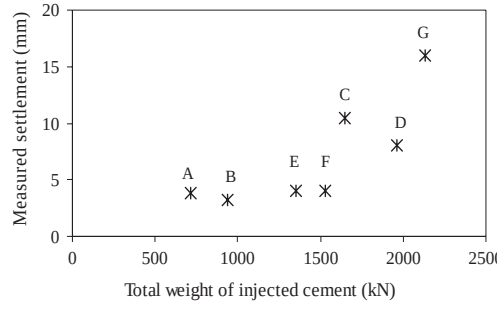

Figure 9. Relation between measured settlements and injected amount of cement.

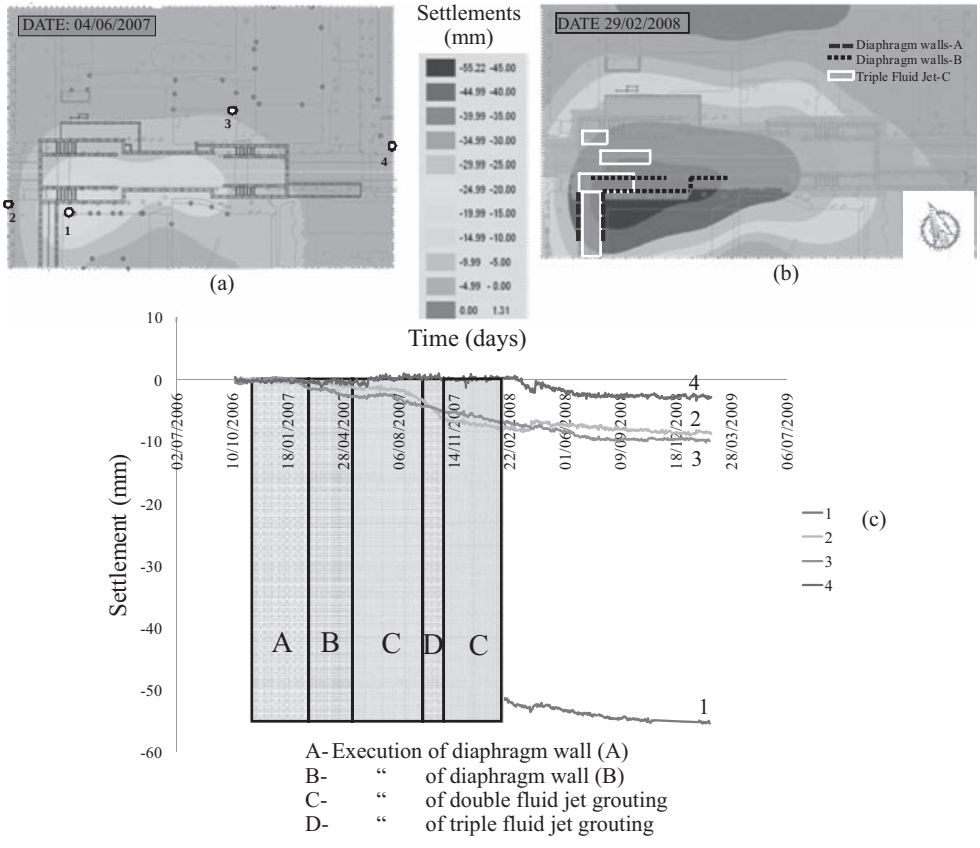

Figure 10. Contour of settlements before (a) at after (b) jet grouting treatments and settlement evolution on different benchmarks (c).

triple fluid are concentrated. Displacements in the outer zones are in the range of few millimetres.

6 CONCLUSIONS

The procedure described by the European Standard ENV12716 (2001) "Execution of special geotechnical works: jet grouting" has been herein illustrated with the analysis of an excavation bottom plug created with jet grouting. In particular, the Standard recommends to prove by preliminary field experiments the effectiveness of the adopted injection system, to verify the execution of treatments with an accurate control plan and to monitor possible undesired effects on the surrounding environment. With reference to the former aspect a comparison has been established among different injection systems. The selection of the optimum injection technique was based on different tests (drilling energy per unit length, sample recovery index; uniaxial compressive strength) all providing satisfactory results for the chosen system. The results obtained by preliminary field tests were then used to perform a probabilistic prediction of the functionality of the jet grouting plug (continuity and stress compatibility). With reference to the effects on the surrounding environment, particular attention has been paid to the movements induced at road level by execution of treatments, initially observed during field trial investigations and monitored during construction of the plug. Contrarily with former studies, the results obtained in the present case have shown a non negligible pattern of downward settlements induced by injections. Movements become particularly relevant for those systems injecting a big amount of cement. The importance of field measurements and their introduction in the design have been clearly demonstrated in this work both to optimise the solution (a reduction of the amount and the quality of cement could be assumed) and to minimise the undesired effects (by considering injection techniques providing lower settlements).

Too often essential operational details of jet grouting treatments are left to the criteria of operators. The advantage of applying an objective procedure for the design and the control of jet grouting treatments are clear. On the one hand it will support design decisions with data specifically obtained in the same conditions of the final work, on the other hand it provides a rational frame to advance towards more effective treatments. This article illustrates how this procedure can be established.

REFERENCES

Balossi Restelli A., Colombo A., Gervaso F., Lunardi P. (1986) "Tecnologie speciali per il preconsolidamento di scavi nelle alluvioni di Milano in occasione della costruzione della linea 3 della Metropolitana", Congresso Int. "Grandi Opere Sotterranee", Firenze, 8–11 giugno.

Brinkgreve R.B.J., Vermeer P.A., (2000), Plaxis Manual, version 7.2., A.A. Balkema Rotterdam, Delft, the Nederlands.

Croce, P., Modoni G., Palmisano, F., (2006) Progetto di fondazioni a pozzo realizzate con la tecnica del jet grouting. Convegno Nazionale dei Ricercatori di Ingegneria Geotecnica, Bari, settembre 2006.

ENV 12716 (2001). "Execution of special geotechnical works: jet grouting", European Committee for Standardization.

Geo Institute of ASCE, Grouting Committee, (2009), Jet grouting Guideline, American Society of Civil Engineers, 29 pages.

Japanese Jet Grouting Association, (2005). "Jet Grouting Technology—JSG method, Column Jet Grouting method". Technical Information, 13th edition (English translation), October 2005, 80 pages.

Myasaka G., Sasaki Y., Nagata T., Shibazaki M., Yoda M., (1992) "Jet Grouting for a Self-standing Wall". Grouting, Soil Improvement and Geosynthetics, ASCE Geotech. Special Publ. n. 30, vol. 1.

Russo G., Modoni G. (2005). Monitoring results of a tunnel excavation in urban area. 5th Intern. Symposium of the Technical Committee TC28, Geotechnical Aspects of Underground Construction in Soft Ground, June 15–17, Amsterdam (ISBN 9780415391245).

Sanella A. (2007). Soil improvement process using jet grouting. European Patent EP 1 795 655 A1.

Santoro V.M., Bianco B., (1995) "Realizzazione di una struttura in gettiniezione per il sostegno di uno scavo in depositi piroclastici. Controllo di qualità in corso d'opera." Associazione Geotecnica Italiana -XIX Congresso Nazionale di Geotecnica, Pavia, 19–21 settembre.

Sondermann W.,Tòth P.S., 2001, "State of the art of the jet grouting Shown on different application", Atti del IV Int. Conf on Ground Improvement, Helsinki Giugno 7–9.

Yoshitake I., Mitsui T., Yoshikawa T., Ikeda A., Nakagawa K., 2003. "An Evaluation Method of Ground Improvement by Jet-Grouting", Proceedings of JSCE (Japan Society of Civil Engineers), volume n.735, pp. 215–220.

Geotechnical Aspects of Underground Construction in Soft Ground – Viggiani (ed)
© 2012 Taylor & Francis Group, London, ISBN 978-0-415-68367-8

Dewatering tests results for underground C Line stations construction

Massimo Grisolia & Giuseppe Iorio
Department of Civil, Architectural and Environmental Engineering, University of Rome "Sapienza", Italy

Antonio Zechini
RomaMetropolitane S.r.l., Rome, Italy

ABSTRACT: The new C Line of Rome Underground -T4, T5 and T6A lots- mainly runs into volcanic deposits deriving from the Colli Albani apparatus, widely extended in south-eastern areas of Rome. The local hydrogeological framework is very complex due to the large variations of permeability in function of granulometry, cementation processes and secondary fracturing of pyroclastic strata. The bottom of the excavation of the underground stations lies 25/30 meters below the groundwater level. In order to allow dry conditions and to prevent bottom heave during excavation, the groundwater level is lowered by deep wells systems. Some dewatering field tests showed how the local stratigraphy strongly affects the dewatering efficiency. Steady state filtration FEM analyses allowed to compare permeability of soil with Lefranc in situ tests results and to verify the efficiency of grouted plugs.

1 INTRODUCTION

The new C Line of Rome Underground runs NW to SE across the city centre, with a total length of more than 25 km and 30 stations. At present, the T4, T5 and T6 A lots, about 10 km twin running tunnels and eleven stations, are in advanced working state of progress.

Due to the presence of a densely built urban environment, the selected solution for the construction of the stations consists of a "cut and cover" excavation retained by multi-propped diaphragm walls to minimise settlements and prevent damage to the structures.

The excavation depth of the stations are about 25 to 30 m, with a maximum of 20–25 m below the water table. In order to assure dry conditions and hydraulic heave stability, deep wells systems have been designed to lower groundwater level and piezometric head during excavation.

Dewatering systems have been preliminary tested by long term pumping field tests.

The paper shows the result of numerical analyses carried out to interpret dewatering field tests made for three different stations of T5 lot, namely Teano, Mirti and Gardenie.

2 HYDRO GEOLOGICAL AND GEOTECHNICAL CONDITIONS

The geological sequence along the new C Line under construction consists of a base deposit of stiff overconsolidated clay of Pliocene age (APL unit) covered by a layer of fluvio-palustrine very dense sandy gravels of Pleistocene age (SG) followed by either medium stiff clayey silts and dense sandy silts (Paleotevere units AR, ST) (Figs. 1 and 2).

These deposits are covered by a Middle to Upper Pleistocene piroclastics volcanic soils deriving from the Colli Albani apparatus, widely extended into the southeast of Rome.

The pyroclastic sequence, linked to the past explosive volcanic activities, is characterized by old altered tuffs (lithoid and pseudo-lithoid tuff T1-T2 and clayely tuff TA), "pozzolane" (Pozzolane Rosse PR and Pozzolane Nere PN) and lithoid tuff (Tufo Lionato). Frequent and relatively deep ancient ditches filled by alluvial silty-clayey and sandy deposits (Alluvioni dei fossi unit, LSO) cut into the pyroclastic deposits.

A layer of made ground (R) of varying thickness covers the stratigraphic sequence and the natural soil profile everywhere.

The local hydrogeological framework is very complex and characterized by a double groundwater system. The upper main aquifer is mainly represented by the "pozzolane sequences" (PR/PN). The lower aquifer consists of the Pleistocene deposits (SG) which overlain Pliocene marine claystone bedrock (APL). The pyroclastic deposits (pozzolane, lithoid and pseudo-lithoid tuff and clayely tuff) show large variations in permeability in function of primary porosity, compaction processes, sealing, and secondary fracturing. Permeability

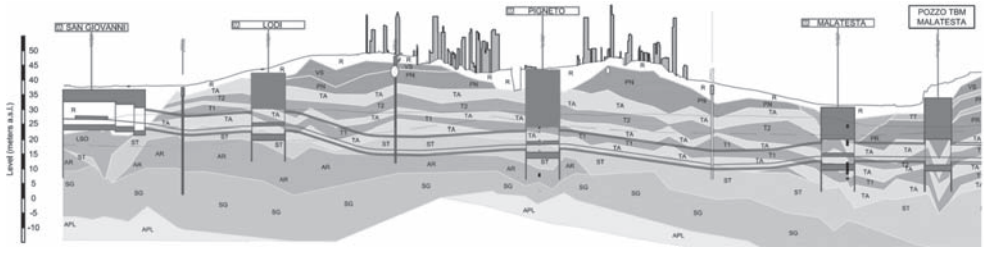

Figure 1. Geological profile from S. Giovanni to Malatesta stations (adapted from Metro C, Progetto costruttivo).

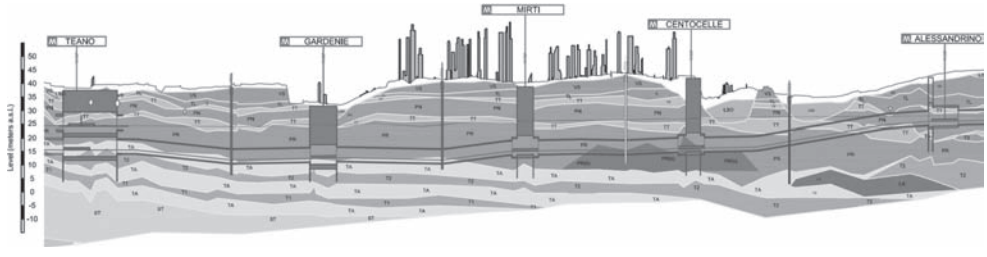

Figure 2. Geological profile from Teano to Alessandrino stations (adapted from Metro C, Progetto costruttivo).

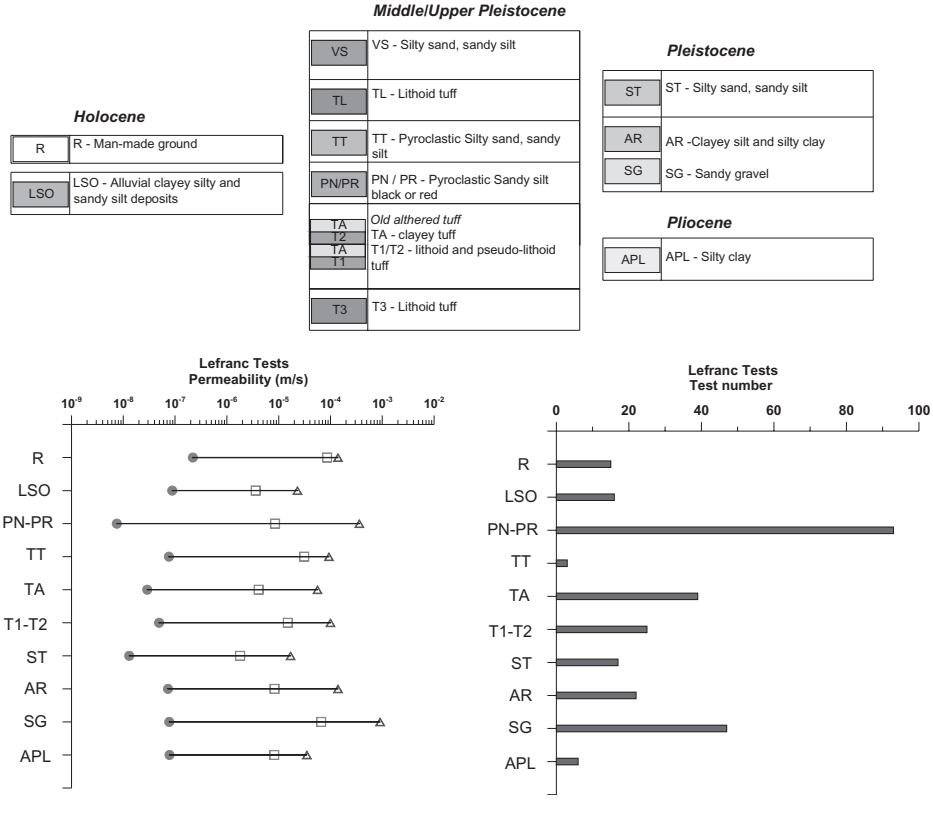

Figure 3. Lefranc permeability tests results.

values for each soils type have been determined by Lefranc tests at variable head (Fig. 3) and by some preliminary pumping tests. Lefranc tests indicated a wide range of permeability, with values from $7.5 \cdot 10^{-9}$ m/s up to $3.6 \cdot 10^{-4}$ m/s for pozzolane PR/PN, $4.9 \cdot 10^{-8}$ m/s to $1.0 \cdot 10^{-4}$ m/s for the lithoid and pseudo-lithoid tuff (T1-T2), and $1.3 \cdot 10^{-8}$ m/s to $1.7 \cdot 10^{-5}$ m/s for the Pleistocene deposits ST.

3 GEOTECHNICAL AND ENVIRONMENTAL CONDITIONS

The construction of C Line stations requires deep excavations under high hydraulic head. The main geotechnical and environmental problems related to the water seepage are connected with:

1. lowering the groundwater level in order to allow the excavation in dry conditions;
2. stability of the bottom line during excavation;
3. seepage effect on the stability of diaphragm walls;
4. ground settlements induced by water table lowering.

3.1 *Dewatering field tests*

Dewatering field tests were systematically carried out, consisting of:

– step drawdown and constant rate discharge tests (24h) carried out in the first installed well;
– long term (8–21 day) dewatering test by pumping all the wells installed into each station.

Monitoring activities included the measurements of daily pumping rate and the hydraulic head for each well. Measurements were taken inside the stations by electrical piezometers and outside by Casagrande piezometers installed along the perimeter of excavation. The instruments layout is schematically shown in Figure 4.

4 DEWATERING FIELD TEST RESULTS

The results of the dewatering field tests, in terms of total pumping rate, drawdown achieved and pore pressure distribution inside the excavation areas, are presented for three deep stations (Teano, Mirti and Gardenie.

4.1.1 *Teano station*

The excavation consists of an elongated box about 140 m long and from 14 to 28 m wide which accommodates the station and the "Manufatto Diramazione C1". The maximum excavation depth is about 29 m from the ground level. Natural groundwater level was 14 m above the bottom of the excavation. Dewatering system was constituted by n. 12, 400 mm diameter wells penetrated 26 m into the volcanics deposits ("TA" and "T1-T2") with slotted screen extending from the water table surface (assumed +23.5 m O.D.) to the bottom (Figure 4a). The total pumping rate was approximately 17 l/s and the established pore water pressure distribution inside the ground allowed dry conditions during excavation. Side effects on external water table were very limited (maximum lowering of 0.20 m).

4.1.2 *Mirti station*

The station consists of a rectangular box retained by diaphragm walls 65 m long and 37 m wide. The maximum excavation depth is about 34 m from the ground surface. In this case the required drawdown of the water table in the volcanic soils is about 18 m. The dewatering system consists of 14 400 mm diameter wells placed inside the station box, pumping from the volcanics complex "TA" and "T1-T2", (Fig. 4b). During long term tests the achieved drawdown was enough to allow dry conditions during excavation. The total pumping rate, approximately 70 1/s, was much more than design prevision, and a water pressure distribution with depth, different from an hydrostatic trend (Fig. 4b) was observed. The lowering of external water table in the volcanic deposits was quite limited (0.7 m).

4.1.3 *Gardenie station*

The station, retained by diaphragm walls, is about 114 m long and 28 m wide. The maximum excavation depth is about 27 m from the ground level. Dewatering system was constituted by 14 400 mm diameter wells penetrated 34 m into the volcanic deposits "TA" and "T1-T2" (Fig. 4c). During long term tests the water table drawdown was only of about 2.0–6.0 m at a total pumping rate of approximately 70 1/s. The external groundwater level lowering was about of 1.0 m.

5 SEEPAGE FLOW ANALYSIS

Although the geological pattern of the three sites were similar, the performances of the dewatering tests were very different.

In the case of Teano station, water flow mainly derived from the deeper aquifer located in ST (Fig. 5). The upper volcanic deposits (PR) and fluvio-palustrine (ST) were not acting as a single hydrogeological unit since the piezometric level recorded in ST stratum was around 12–14 m lower than the level measured into the upper volcanic deposits. The low value of pumping rate (<1.0 l/s for each well) indicates that the deeper aquifer is fed by sandy gravels of Pleistocene deposits (SG),

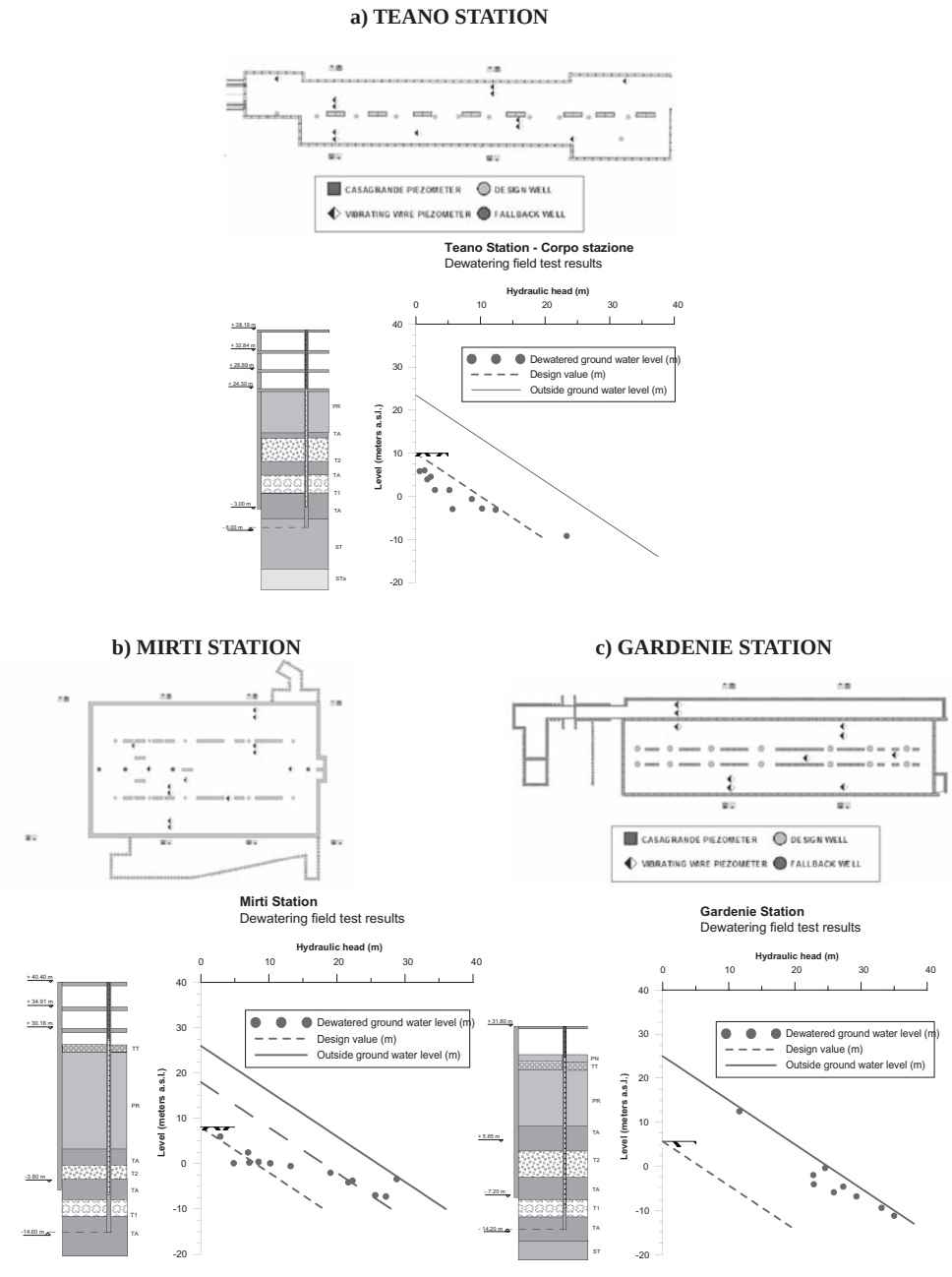

Figure 4. Teano, Mirti and Gardenie Station—Planimetry of well and piezometer arrangement during dewatering field test (Courtesy of Metro C S.p.A.) and pore pressure during dewatering field test.

and it is semi-confined by the low permeable altered pseudo-lithoid tuff (T2) and clayey tuff (TA) layers. The hydraulic disconnection between ST and overlying pozzolane PR caused no relevant effects on shallow aquifer.

Into Gardenie and Mirti stations, the hydraulic seepage scheme was very different from Teano configuration and far from design forecasts. In Mirti station, seepage flow is mainly horizontal and derives from the aquifer located in old altered tuffs

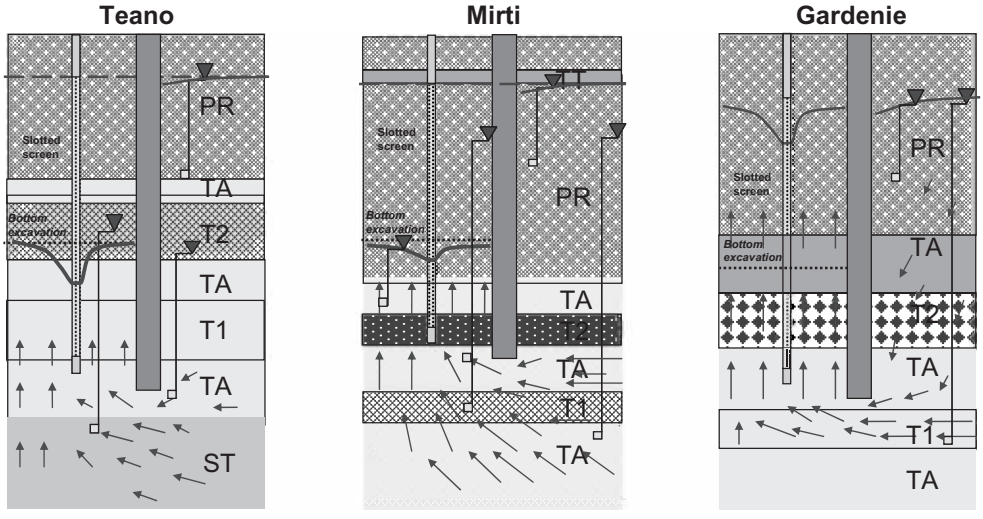

Figure 5. Teano, Mirti and Gardenie: different seepage flow.

TA-T1 characterised by high permeability. The overlying low permeability pseudo-lithoid tuff T2, in which piezometric pressure drop is concentrated, determines an hydraulic disconnection between TA and overlying pozzolane PR. As for Teano Station, no significant effects on shallow aquifer located in the overlying pozzolane PR was recorded.

At Gardenie station, seepage flow derives directly from the shallow aquifer located in volcanic deposits. Piezometric measures in the upper level of the old altered tuffs TA indicates a similar piezometric level as in the overlying pozzolane PR. Continuous pumping modified the shallow aquifer located in the PR pozzolane PR.

When the flow of water occurs upwards from the Pleistocene deposits (ST), the pumping rates were low (Teano, Q < 1.0 l/s for each well). When the seepage flow directly derives from the shallow aquifer located in volcanic deposits the quantity and velocity of water dramatically increases.

6 GROUTED BOTTOM PLUGS

In the case of Mirti and Gardenie stations, the quantity of pumped water was quite greater than the design assessments. To reduce the local permeability of granular and fractured tuffs and minimise the groundwater inflow, an horizontal grout curtain was realised by a Multiple-Packer Sleeved Pipe (MPSP) injection system. Preliminary pumping tests showed how much the grout injections reduced the water inflow. Figure 6 shows the profile of the hydraulic head obtained from the piezometers measurements at the intermediate excavation phase of October 2010.

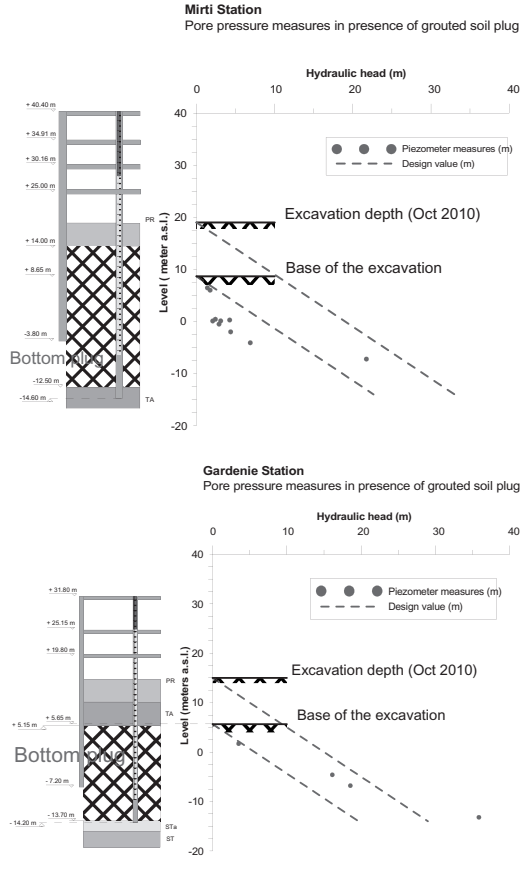

Figure 6. Mirti and Gardenie: pore pressure measures in presence of the grouted bottom plug.

In Mirti station the total pumping rate (approximately 8 l/s) ensure safe and workable conditions throughout constructions phases. External water table lowering in the volcanic deposits are quite limited and less than 0.3 m.

In Gardenie station the mean total pumping rate is approximately 40 l/s and significantly lower than that measured at the initial conditions (>70 l/s). The leakage through the grout plug allows excavation to proceed in dry conditions. Pore water pressure distribution inside the excavation is in line with the design forecasts. The effects on the external water table lowering in the volcanic deposits are quite limited (≈0.8 m).

7 NUMERICAL ANALYSES

A series of simplified two-dimensional steady state flow FEM analyses using PLAXFLOW v1.6 code were carried out, in order to define mean permeability of volcanic deposits in Teano, Mirti and Gardenie stations. Permeability values were routinely calibrated to obtain pore water pressure distributions similar to those measured. To simulate dewatering, it was necessary to define a geological cross section, physical properties of soils and hydraulic boundary conditions. The reference stratigraphies of every stations were chosen similar to those already showed in Figure 4. In the analysis it was assumed an isotropic and constant value of permeability k for each stratum. Diaphragm walls were simulated with "*screen elements*" across which flow does not occur.

To calibrate the permeability for each soil layers it was necessary to force a specified outflow for each well. This was defined by an equivalent discharge flow rate q^- per unit width determined by

$$q^-\left(\text{litres/s}\right) = \frac{Q_m}{n_{dr} \cdot a_l \cdot \left(B \cdot L\right)_{station}}$$

Where Q_m is the steady state global mean pumping rate on entire station, B and L are the characteristics dimensions of the station and a_l is the number of wells on the station alignment.

Once defined the mean permeability of volcanic deposits k_{ft}, in the cases of Mirti and Gardenie stations it was possible to deduce the loss of permeability of grouted soils k_{grout} after the treatment expressed by a "*Reduction Permeability Factor*" F_R:

$$F_R = \frac{k_{ft}}{k_{grout}}$$

7.1 *Analysis results*

Pore water pressure distributions obtained with FEM filtration analyses inside the excavation are shown in Figure 7.

In Table 1 are presented the permeability values obtained by finite element analyses calibrated on pumping tests. For each station the main k values for each soil layer are compared with the range of value obtained by in situ Lefranc tests (Fig. 3).

Analyses results indicate a wide range of permeability values for the same soil in the different stations: from $1.0 \cdot 10^{-6}$ m/s to $5.0 \cdot 10^{-5}$ m/s for pozzolane PR/PN, $1.0 \cdot 10^{-7}$ m/s to $5.0 \cdot 10^{-3}$ m/s for the lithoid and pseudo-lithoid tuff (T1-T2), and $2.4 \cdot 10^{-6}$ m/s to $5.0 \cdot 10^{-4}$ m/s for clayey tuff (TA).

Great discrepancy appears between such results and Lefranc in situ tests mainly for the lithoid and pseudo-lithoid tuff (T1-T2) and clayey tuff (TA). In particular, from Gardenie station tests: layers T1-T2: k_{ft} = $5.0 \cdot 10^{-3}$ m/s; Lefranc range: from $4.2 \cdot 10^{-7}$ m/s to $9.5 \cdot 10^{-4}$ m/s; layer

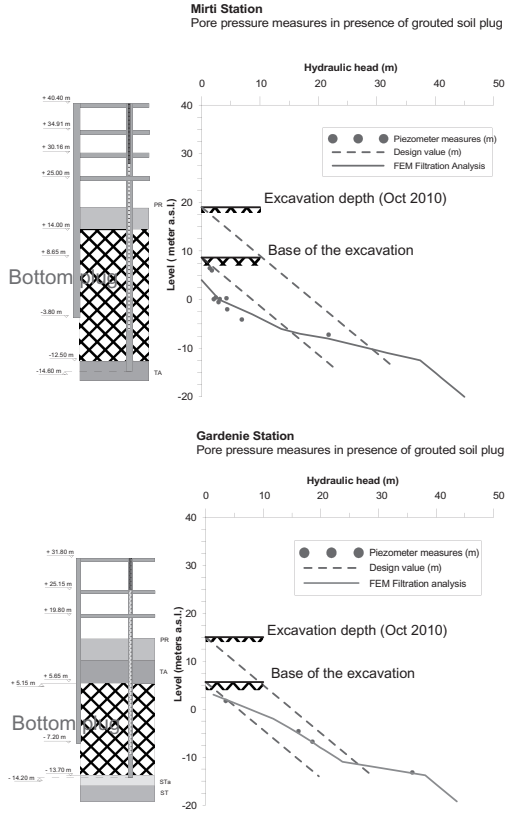

Figure 7. Mirti and Gardenie: pore pressure distribution inside the excavation obtained from numerical analyses.

Table 1. Permeability reduction factor values calculated in back analyses.

Layer	Permeability lefranc tests Range (m/s) From	To	Permeability FEM analysis field tests (m/s)	Reduction permeability factor
Teano station				
PR	5,80E-07	6,30E-05	5,00E-06	
TA	3,00E-06	2,80E-04	3,00E-04	
T2	6,00E-08	3,70E-04	9,00E-04	
TA	3,00E-06	2,80E-04	5,00E-05	
T1	6,00E-08	3,70E-04	8,50E-06	
TA	3,00E-06	2,80E-04	2,40E-06	
ST	–	–	2,00E-05	
STa	–	–	5,00E-08	
Mirti station				
PR	5,20E-08	8,30E-05	1,00E-06	–
PR	5,20E-08	8,30E-05	1,00E-06	1
TA	2,90E-08	2,80E-04	1,00E-04	10
T2	2,90E-08	1,30E-05	3,00E-07	1
TA	2,90E-08	2,80E-04	5,00E-04	300
T1	2,90E-08	1,30E-05	5,00E-05	20
TA	2,90E-08	2,80E-04	5,00E-04	250
Gardenie station				
PR	2,10E-07	4,50E-05	5,00E-05	–
TA	1,40E-06	2,10E-04	5,00E-04	–
TA	1,40E-06	2,10E-04	5,00E-04	5
T2	4,20E-07	9,50E-04	5,00E-03	700
TA	1,40E-06	2,10E-04	9,00E-05	5
T1	4,20E-07	9,50E-04	5,00E-03	700
TA	1,40E-06	2,10E-04	5,00E-04	2000

TA: $k_{ft} = 9.0 \cdot 10^{-5} \div 5.0 \cdot 10^{-4}$ m/s; Lefranc range: from $1.4 \cdot 10^{-6}$ m/s to $2.1 \cdot 10^{-4}$ m/s. From Mirti station tests: layer TA: $k_{ft} = 1.0 \cdot 10^{-4} \div 5.0 \cdot 10^{-4}$ m/s; Lefranc range: from $2.9 \cdot 10^{-8}$ m/s to $2.8 \cdot 10^{-4}$ m/s.

Grouting with MPSP system reduced the permeability of almost two-three order of magnitude mainly for very fractured lithoid tuffs (T1-T2, Gardenie) and very coarse clayey tuff (TA, Mirti and Gardenie). The efficiency of this consolidation techniques appears lower in presence of lithoid tuffs (T2, at Mirti station) and fine grained clayey tuff.

8 CONCLUSIONS

The monitoring of dewatering field tests was useful to better understand the groundwater flow in a typical complex geological sequence of Rome subsoil.

Numerical FEM analyses calibrated on pumping tests results allowed to estimate the average permeability values of pyroclastic deposits better than classic Lefranc variable head tests results.

In pyroclastic soils, Lefranc tests, performed on a limited section of the boreholes, may be not significant due to local variation of the geotechnical properties.

MPSP grouting system was appropriate to control permeability of soils for complex fractured lithoid tuffs and coarse clayey tuffs strata.

REFERENCES

Cashman, P.M. & Preene, M.. *Groundwater Lowering in Construction. A practical guide*. Taylor & Francis Group ISBN 0-419-21110-1.

Corazza, A., Giordano, G. & De Rita, D. 2006. Hydrogeology of the city of Rome. In Heiken (eds), *Tuffs—their proprierties, uses, hydrology and resources*. Geological Society of America Special Paper 408: 113–118.

Iorio G. (2010). Problematiche geotecniche connesse con la realizzazione di stazioni metropolitane. PhD Thesis, Sapienza University of Rome (in italian).

Linney, L.F. & Withers, A.D. 1998. *Dewatering the Thanet beds in SE London: three case histories*. Quarterly Journal of Engineering Geology, 31: 115–122.

Metro C. Progetto costruttivo—Metropolitana di Roma Linea C—Tratte T4-T5.

This page intentionally left blank

Geotechnical Aspects of Underground Construction in Soft Ground – Viggiani (ed)
© 2012 Taylor & Francis Group, London, ISBN 978-0-415-68367-8

Evaluation of negative skin friction on sheet pile walls at the Rio Grande dry dock, Brazil

C.M. Santana, F.A.B. Danziger, F.R. Lopes & L.B. Becker
Federal University of Rio de Janeiro, Rio de Janeiro, Brazil

R.J.L. Pereira
Petrobras, Rio de Janeiro, Brazil

ABSTRACT: This paper describes numerical analyses to evaluate the negative skin friction on the sheet pile walls of the Rio Grande dry dock, in the State of Rio Grande do Sul, Brazil. The walls support an excavation about 350 m × 133 m in plan, 17 m deep, and also serve as foundations for a very heavy mobile crane. The analyses were carried out with a finite element code (Plaxis 2D), considering plane strain condition, a reasonable assumption considering the length of the excavation. The various construction phases were simulated to evaluate the influence of negative skin friction in each of them. Axial forces in the sheet pile walls, induced by negative skin friction, reached 620 kN/m in the final phase, which includes storage on the ground surface.

1 INTRODUCTION

1.1 *Main characteristics of the project*

The Rio Grande dry dock aimed at the construction and repair of vessels of PETROBRAS, the Brazilian State Oil Company. Situated in the city of Rio Grande, in the State of Rio Grande do Sul, Brazil, the construction of the dry dock required an excavation about 350 m long, 133 m wide and 17 m deep. Sheet pile walls were used in most of the project, although diaphragm walls were also used. Four levels of prestressed anchors were used. Figure 1 shows the dry dock after the construction of the bottom slab.

The sheet pile walls have variable length of embedment. However, in most cases walls with short and discontinuous length of embedment, as shown in Figures 2 and 3, were used. A concrete beam with height of 3.3 m was constructed at the top of the sheet pile walls. The wall was designed to allow the traveling of a mobile crane almost 100 m high, weight of 32 MN and load capacity of 6 MN.

During the operation of the dry dock the area next to their walls will be subjected to loads from storage of materials and equipment. The design of

Figure 1. The Rio Grande dry dock (with mobile door).

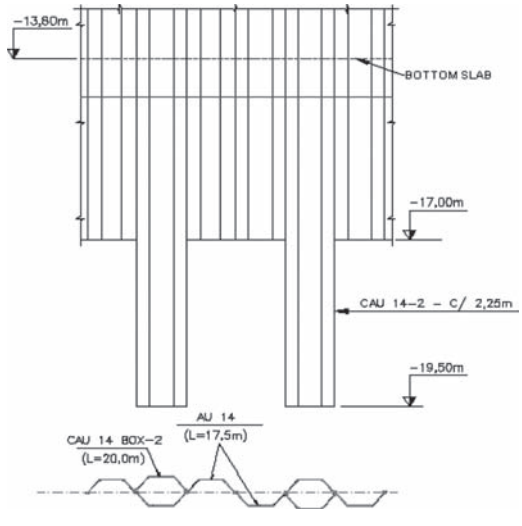

Figure 2. Typical elevation of the wall.

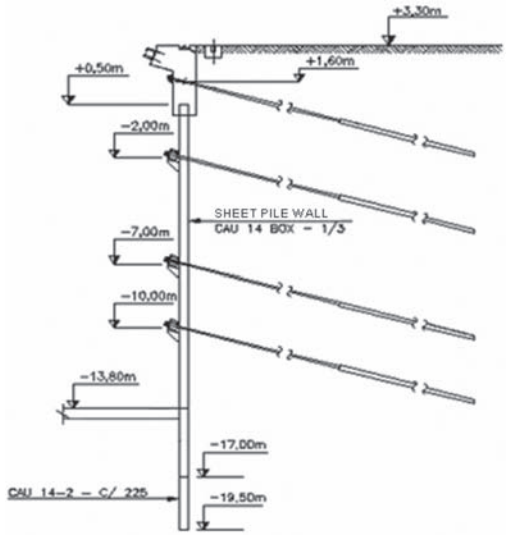

Figure 3. Cross section of wall A.

wall "A", *e.g.*, provides load of 30 kPa until 10 m away from the wall, followed by 100 kPa until a distance of 60 m from the wall. Moreover, a mobile crane will travel on the wall "A", with vertical and horizontal design loads of 873 kN/m and 87.3 kN/m, respectively.

The bottom slab has variable thickness, 1.54 m at the borders and 0.60 m in the center. Approximately 4,000 steel I piles about 30 m long were used as foundations for the slab. The piles will be subjected to uplift loads due to the water, and also to compression loads in some parts of the slab when ships are under construction.

A number of problems occurred during construction and COPPE/Federal University of Rio de Janeiro was commissioned by PETROBRAS to assist it both in the design check and in the construction.

1.2 *Construction of Wall "A"*

After an unsuccessful trial of driving the sheet piles through dense superficial sand layers, an excavation was made, then the walls were installed inside of it. The excavation was supported by bentonite slurry, later filled with a mixture of bentonite slurry and cement.

The lowering of the water table was performed both internally and externally to the walls. However, the system did not succeeded in lowering the external water table below elevation –7.0 m.

The four anchor levels were constructed as the excavation was proceeding, as shown in Figure 3. The anchors were pre-stressed immediately after execution, except those at the first level, which were pre-stressed after the third level.

Figure 4. Execution of a partial excavation.

When the excavation reached elevation –13 m, *i.e.*, about 1 m of the bottom slab, the walls suffered significant displacements. The contractor then decided to construct berms next to the walls, about 15 m width and 3.5 m height.

Only the central part of the excavation proceeded until the bottom slab level, and pile driving started. The bottom slab was then constructed. In this meantime, a number of solutions were studied to allow the excavation close to the walls. It has been suggested by the contractor to make excavations with a limited width of 6.6 m (partial excavations). The suggested width was checked using the 3-D code Plaxis, but the corresponding analysis is outside the scope of the present paper. After a partial excavation, the wall was supported by a temporary metal structure, and then the bottom slab was completed. More than one partial excavation could be executed simultaneously, provided that at least a distance of 19.8 m (width of three partial excavations) was kept between partial excavations. Figure 4 shows the execution of a partial excavation.

After the completion of the bottom slab, the lowering of the water table was switched off, and a water pressure of 150 kPa acted on the slab.

2 NEGATIVE SKIN FRICTION

The phenomenon of negative skin friction on piles is well known (*e.g.*, Zeevaert, 1959; Johannessen and Bjerrum, 1965; Bjerrum *et al.*, 1969; Endo *et al.*, 1969; Fellenius, 1972; Fellenius, 1984; Combarieu, 1985). However, earth retaining walls, underground structures (*e.g.*, basements) and sheet-pile walls can also be subjected to negative skin friction, provided there is a relative move-

ment between the structure and the surrounding soil. This relative movement occurs when the settlement of the structure is limited (by a somewhat rigid foundation) and the external soil settles in consequence of: i) embankment placed on soft soil, ii) lowering of water table, iii) surcharges placed on the ground surface. In retaining structures used in connection with excavations there is an additional cause of negative skin friction, which is the vertical movement of the soil during the excavation procedure, downward on the external side of excavation and upward internally.

In the case of the Rio Grande dry dock the following characteristics were important in the generation of negative skin friction on the sheet pile wall:

- Lowering of the water table during excavation, inducing settlements in the clayey layers behind the sheet pile wall.
- Construction of four anchors levels during excavation, which restricted the movements on the walls.
- Connection of the bottom slab to the wall at the end of the excavation, which caused significant restriction in the movement of the walls.
- Surcharges to be applied adjacent to the walls (on ground level), which would cause significant settlements in the soil.

Furthermore, the process of excavation inside the dock caused relative soil movements, which were downward in external side of excavation and upward in the internal side.

According to Fellenius (1984), relative movement between piles and soil of a few milimeters is sufficient to mobilize the negative skin friction. According to Bjerrum and Johannessen (1965), the negative skin friction load is proportional to the normal effective stress of the soil at the interface with the pile. However, the stress state in this region is very complex, since it is influenced by displacements of soil and pile. Such complex situation can only be analysed by numerical methods.

3 ANALYSIS PERFORMED

3.1 *Analysis methodology*

Analysis of the variation of axial load in the various construction phases were performed in wall "A" of the Rio Grande dry dock using a computer code based on Finite Elements Method, Plaxis 2D v.8. A plane strain condition was assumed, which is justified by the ratio between length and height of the wall (126.0 m: 22.8 m). Figure 5 shows the geometry considered in the numerical analysis.

In order to simulate the length of embedment of the sheet pile wall, which has variable length,

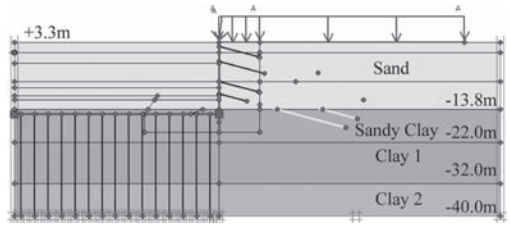

Figure 5. Geometry considered in the analysis.

an equivalent stiffness was calculated, since a plane strain condition was considered. Another simplification adopted in the analysis was that the corrugated shape of sheet pile walls was not considered. Due to this shape each meter of sheet pile wall has a developed length of around 1.22 m. Thus the real negative skin friction is expected to be something between the estimated values and 1.22 times these values. It is expected that some kind of plugging would occur, and the real value would be closer to the estimated value, but this subject deserves more research.

Variations in the thickness of bottom slab were considered using plate elements with variable stiffness.

Piles were represented as linear elements with equivalent axial stiffness to that obtained in load tests of piles under axial tensile loads and similar loading level, carried out at the Rio Grande dry dock. These elements have been considered having no bending stiffness and not transmitting load to the soil along its length. It is noteworthy that the piles in the dry dock will be subjected, predominantly, to tensile loads.

Anchors were represented as linear elements, with separation between free length (not transferring load to the soil) and anchored length (transferring load to the soil). Design load of each anchor level was activated at the proper phase. In following phases the axial load was allowed to vary as a consequence of deformations.

As the negative skin friction increases during consolidation, the behavior of the soil was assumed drained. The upper sand layer was considered as a linear elastic perfectly plastic material, obeying the Mohr-Coulomb failure criterion. The clay layers were considered as materials with behavior based on the Cam-Clay modified model and with OCR equal to 1.5, according to laboratory and in situ testing. A transfer friction factor between soil and structure (interface factor) equal to 1.0 was adopted.

Table 1 shows the main parameters of strength and deformability of the soil layers adopted in the analysis, which were based on laboratory and field testing and correlations available in the literature.

Table 1. Soil parameters.

Material	ϕ' (°)	c (kPa)	E (MPa)	C_C/C_S	e_0	ν
Sand	45.0	1.0	100	–	–	0.35
Sandy clay	22.6	13.6	–	1.400/ 0.080	1.43	0.20
Clay 1	26.0	1.0	–	0.340/ 0.037	1.46	0.15
Clay 2	26.0	1.0	–	0.565/ 0.079	2.10	0.15

ϕ' = friction angle; c = reference cohesion; E = reference Young´s modulus; C_C = compression index; C_S = swell index; e_0 = initial void ratio; ν = Poisson's ratio.

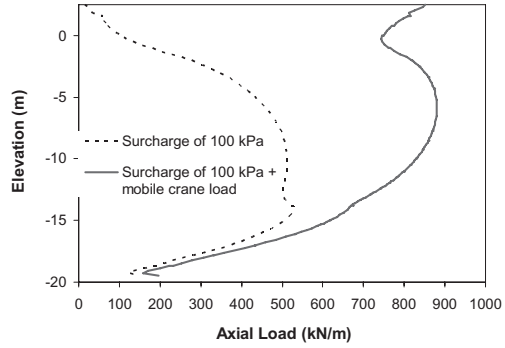

Figure 6. Axial load in the wall in case 1.

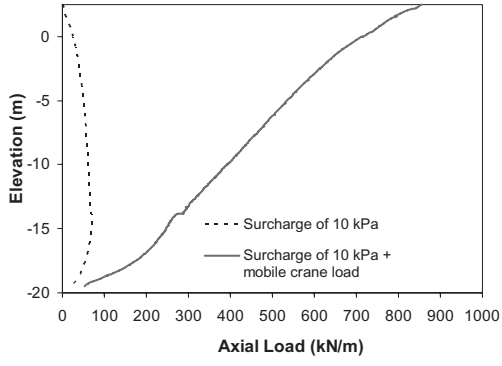

Figure 7. Axial load in the wall in case 2.

3.2 *Parametric analysis*

A parametric analysis was performed with the aim of studying, even in a simplified way, the effect of simultaneous action of: i) surcharge on the ground level adjacent to the wall and ii) the load of the mobile crane on the wall. These two actions produce opposing effects on the walls, as far as the relative displacement of the wall and the soil is concerned. In fact, the surcharge generates settlements in the soil behind the wall, inducing negative skin friction. The second action produces settlements in the wall, mobilizing positive skin friction.

The analysis was performed without simulation of the excavation and therefore without considering the presence of anchors, bottom slab and metal piles. The load on ground level was applied on both sides of the wall. Two cases were simulated: case 1: surcharge of 100 kPa; case 2: surcharge of 10 kPa. In both cases it has been assumed that the negative skin friction was mobilized before the action of the crane load.

Figures 6 and 7 show the results of these simulations. It may be noted that, before applying the loading of the mobile crane, the axial load increases until a certain depth and then decreases again, and this depth represents the so-called neutral plane (*e.g.,* Endo *et al.,* 1969; Fellenius, 1984; Combarieu, 1985).

Both numerical simulations (cases 1 and 2) show mobilization of negative skin friction along most of the wall when the surcharge is applied on the ground level. In both cases the neutral plane is about the elevation -14 m.

In case 1 it can be observed (Figure 6) that the axial load generated by the negative skin friction is not fully added to the vertical loading from the mobile crane (873 kN/m). This is because the loading of the mobile crane causes settlements on the wall, which demobilize part of the negative skin friction. Due to the deformability of the wall, this effect is more important in its upper part, since the magnitude of settlements on the wall decreases with depth.

In case 2 the negative skin friction is completely demobilized when the load of the mobile crane is applied (Figure 7). In fact, the loading of the mobile crane causes an increase of the settlements on the wall, which completely demobilizes the negative skin friction. As the negative skin friction initially mobilized in case 2 was lower than in case 1, the magnitude of the increase of settlements on the wall was able to reverse the "sign" of the friction mobilized.

In Figures 6 and 7 a change in the behavior of the axial load at around elevation –14 m can be noticed, which is a consequence of the differences in the compressibility and the earth pressure coefficient of the layers of sand and sandy clay.

3.3 *Case of wall "A"*

The phases of construction and operation of wall "A" were simulated with the code Plaxis 2D.

Figure 8 shows the geometry after the last phase. Table 2 shows the phases included in the simulation and the values of maximum axial load on the wall in each phase. It should be noted that the value of maximum axial load includes the effects of negative skin friction, the vertical component of the load of the anchors and the load of the mobile crane (only at phase 13). Phases 1 until 11 are sequential. Phases 12 and 13 are exclusive, and both start from phase 11.

In the analysis performed it was not possible to simulate the excavation of the berm in partial excavation. To minimize this shortcoming, the excavation of the berm and the connection between bottom slab and wall was considered simultaneously.

In Table 2 a positive sign of maximum axial load indicates compression and negative sign indicates tension.

At the end of Phase 2, the wall is under tension as a result of the expansion of the soil inside the dock, induced by the excavation to elevation 0.0 m. However, at the end of Phase 3 the wall is under compression.

As the walls were represented by elements of plate with zero thickness and weight, it can be assumed that the axial loads are due to the vertical components of loads of the anchors and the negative skin friction. The negative skin friction is a consequence of soil movements induced by the surcharge on the ground level and also by the excavation process.

Subtracting from the maximum axial load obtained at the end of Phase 12 the vertical component of the load of the anchors, a value of maximum negative skin friction of 622 kN/m is obtained. Subtracting from the maximum axial load at the end of Phase 13 both the vertical component of the load of the anchors and the vertical component of the load of the mobile crane, a maximum negative skin friction value of 619 kN/m is obtained. This indicates that in this case the loading of the mobile crane was not enough to demobilize the negative skin friction significantly, which can be attributed to the high stiffness of the piled bottom slab, restricting the settlements on the wall.

Figure 9 shows the axial load diagram of the wall "A" at the end of Phase 13. The horizontal sections

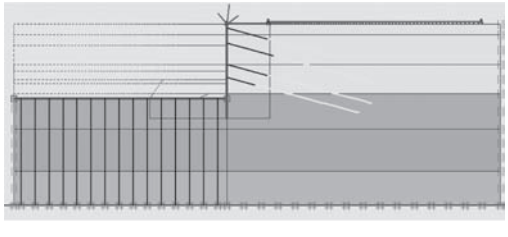

Figure 8. Model analyzed at phase 13.

Table 2. Maximum axial load in each phase.

Phase	Maximum axial load (kN/m)
1. Installation of the wall.	0
2. Excavation until elevation 0.0 m and construction of the first anchor line (no loaded).	–150
3. Lowering of water table until elevation –3.5 m, excavation until elevation –2.5 m and construction of the second anchor line.	165
4. Lowering of internal water table until elevation –8.5 m and external until elevation –7.0 m, excavation until elevation –7.0 m and construction of the third anchor line.	484
5. Prestressing first anchor line.	466
6. Lowering of internal water table until elevation –11.5 m, excavation until elevation –10.5 m and construction of the fourth anchor line.	537
7. Lowering of internal water table until elevation –15.0 m.	504
8. Excavation until elevation –15.0 m without remove berms.	559
9. Lowering of external water table until elevation –15.0 m.	583
10. Excavation of the berms and construction of bottom slab.	827
11. Elevation of external water table until elevation –0.0 m.	199
12. Surcharge on ground level with 30 kPa until 10 m away from the wall and 100 kPa until a distance of 60 m from the wall.	932
13. Surcharge on ground level with 30 kPa until 10 m away from the wall and 100 kPa until a distance of 60 m from the wall and loading of mobile crane.	1800

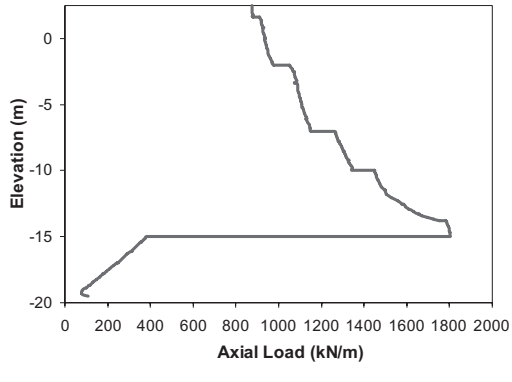

Figure 9. Axial load on wall "A" at the end of phase 13.

of this chart represent the vertical components of the loads in the four anchor levels and the load transferred in the connection between the bottom slab and the wall.

As mentioned before, as a consequence of the corrugated shape of the sheet pile wall, the value of the expected maximum axial load is expected to be something between the estimated values and 1.22 times these values. It is expected that some kind of plugging would occur, and the real value would be closer to the estimated value, but this subject deserves more research.

4 CONCLUSIONS

Numerical simulations performed with the code Plaxis 2D estimated significant values of negative skin friction on wall "A" during operational phases of the Rio Grande dry dock (about 620 kN/m). The negative skin friction acting on that wall is the result of the construction procedure (the process of excavation and lowering of the water table) and surcharges on the ground level adjacent to the wall.

The parametric study showed that in some cases loading on top of the wall can reduce or reverse the negative skin friction. However, this effect was not significant in the case of Rio Grande dry dock, which has a high stiffness of the piled bottom slab that was connected to sheet pile wall, reducing the settlements induced by the passage of the mobile crane.

REFERENCES

Bjerrum, L., Johannessen, I.J., and Eide, O. 1969. Reduction of negative skin friction on steel piles to rock, *Proceedings, 7th. ICSMFE, México*, vol. 2, pp. 27–34.

Combarieu, O. 1985. Frottement négatif sur les pieux, Laboratoire Central des Ponts et Chaussées, Rapport de Recherche no. 136.

Endo, M., Minou, A., Kawasaki, T., and Shibata, T. (1969). Negative skin friction acting on steel pipe pile in clay, *Proceedings*, *7th. ICSMFE, México*, vol. 2, pp. 85–92.

Fellenius, B.H. 1972. Downdrag on piles due to negative skin friction, *Canadian Geotechnical Journal,* vol. 9, no. 4, pp. 323–337.

Fellenius, B.H. 1984. Negative skin friction and settlement of piles, Proceedings, 2nd International Seminar—Pile Foundations, Nanyang Technological Institute, Singapore.

Johannessen, I.J. and Bjerrum, L. 1965. Measurement of the compression of a steel pile to rock due to settlement of the surrounding clay, *Proceedings. 6th ICSMFE, Montreal*, vol. 2, pp. 261–264.

Zeevaert, L. 1959. Reduction of point bearing capacity because of negative friction. *Proceedings, 1st Pan American Conference on Soil Mechanics and Foundation Engineering,* vol. 3, pp. 1145–1152.

Geotechnical Aspects of Underground Construction in Soft Ground – Viggiani (ed)
© 2012 Taylor & Francis Group, London, ISBN 978-0-415-68367-8

Challenging demands on the geotechnical design and first monitoring results of the T185 in Frankfurt

S. Meissner, H. Quick & J. Michael
Ingenieure und Geologen GmbH, Germany

U. Arslan
Institut für Werkstoffe und Mechanik im Bauwesen, TU Darmstadt, Germany

ABSTRACT: The foundation system for the high-rise building TOWER185 is an excellent example to show the specific considerations undertaken to design the building pit and the piled-raft foundation. On the basis of experiences made during the past 20 years in the design, the construction and the back-analysis of the load-settlement behavior of numerous high-rise buildings in Frankfurt and consequently the well known soil and groundwater conditions, a realistic soil-structure-interaction-behavior in combination with numerical methods could be applied to design an optimized foundation system for the TOWER185. Since the center of area does not correspond to the center of mass certain considerations had to be taken into account in order to reduce the tilting of the tower and to guarantee the serviceability.

1 GROUND INVESTIGATIONS

The ground investigations are essential preliminary to the construction of high-rise buildings. The objectives of a ground investigation are to obtain reliable information to generate an economic and appropriate design, to evaluate all conditions associated with the ground and the groundwater as well as to meet the requirement for the tendering, the construction, the time and the cost schedule. The results and the interpretation of the investigations are crucial factors for the stability and serviceability of the structure. Especially when designing high-rise buildings the ground and groundwater conditions as well as all relevant geological data must be investigated in detail. The ground conditions have to be worked out by a geotechnical engineer. The investigation can consist of:

- Direct investigations (drillings, trial pits)
- Geophysical methods (crosshole seismic)
- Field and laboratory tests (geotechnical / geothermal)
- Load tests (plate or pile)

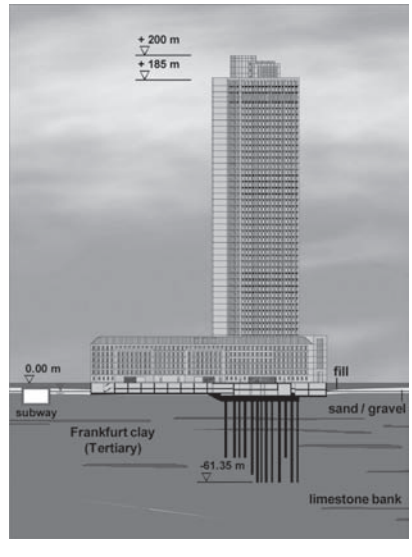

Figure 1. Ground model.

In order to evaluate the ground conditions within the area of the project T185 properly, 11 boreholes with length up to 110 m were interpreted. The ground encountered consists of Quaternary sands down to 5 m below the surface followed by the so called Frankfurt clay which was formed 2 to 10 million years ago as a result of the sedimentation in the Tertiary sea in the Mainz basin (Fig. 1). This clay includes limestone banks and layers of calcareous sand. The clay is geologically overconsolidated through older, already eroded sediments. Therefore, the subsoil is highly horizontally stressed.

The first groundwater level in the Quaternary sands is approximately 3 m below ground surface. The second groundwater level is perched and circulates in the fissured limestone banks and sand lenses. The energy level of the perched

groundwater level in the Tertiary reaches the level of the Quaternary groundwater level.

2 PIT CONSTRUCTION

Due to the above mentioned ground conditions, the influence on adjacent structures (subway, buildings etc.) and the presence of ground/groundwater contaminations in some areas, the lowering of the groundwater tables had to be prevented. This could be achieved by applying an impermeable retaining wall around the excavation area. In order to reduce the energy level in the Tertiary sediments it is necessary to install pressure relief wells distributed over the pit area. The length of these relief wells is governed by the uplift situation of the excavation level.

The retaining wall consists of secant pile walls as well as of diaphragm walls (Fig. 2). To optimize construction time the excavation area was divided into two areas. The excavation level within the tower area is 85.75 mNN (–11.5 m) and for the low-rise complex 90.0 mNN (–7.0 m). The areas are divided by a diaphragm wall without reinforcement. By means of the pit division the two areas were treated accordingly regarding the length of the retaining walls, dewatering situation and excavation process, which led to optimization in terms of buildings costs and construction time. The bottom of the retaining wall for the tower area reaches down to 75.50 mNN (–21.5 m) respectively down to 85.5 mNN (–11.5 m) for the low-rise complex (Fig. 3).

The serviceability of the adjacent subway and the sewage channel directly next to the retaining wall had to be guaranteed at all times. Since a conventional anchoring system could not be applied, the retaining wall was supported by struts with temporary pressure cells to pre-stress the retaining wall and additional piles with anchoring system (Fig. 3). In order to prove the serviceability of the adjacent subway plane numerical simulations were carried out. The construction phases were simulated in detail. The calculated deformations are presented in Figure 4. In consequence of the high-qualified construction works in this cross section the monitored deformations added up only to 0.5 cm and were in good agreement with the calculated deformations.

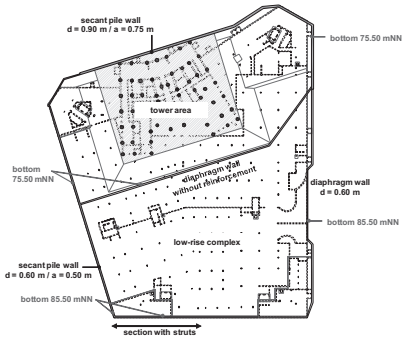

Figure 3. Layout plan building pit.

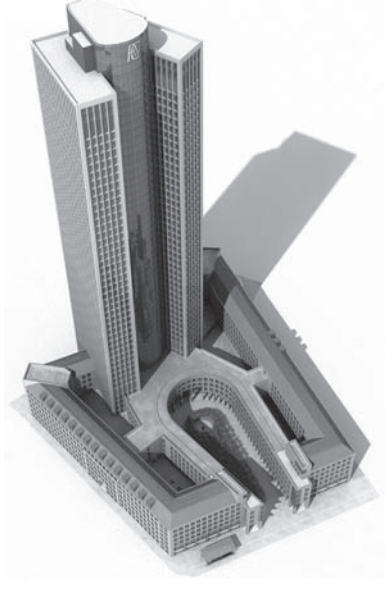

Figure 2. Animation picture.

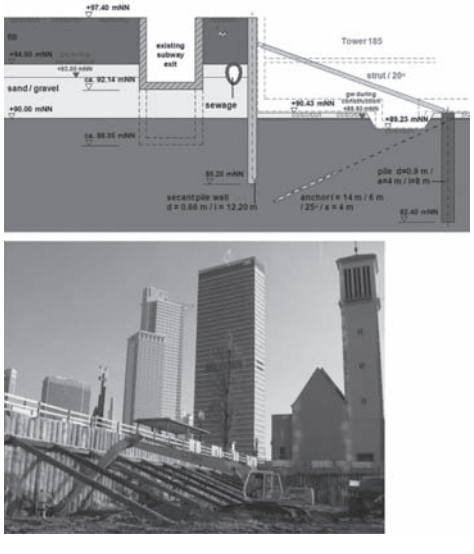

Figure 4. Building pit—cross section subway.

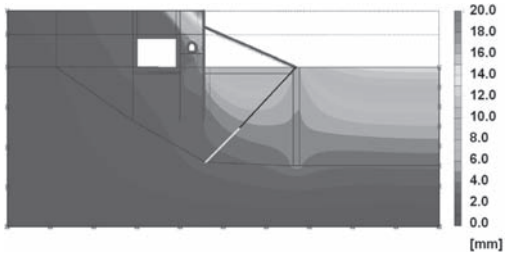

Figure 5. Building pit—Numerical simulation.

3 FOUNDATION SYSTEM

Design of a foundation has to satisfy always the following conditions:

- Factor of safety against failure of the foundation and of the supporting soil has to be adequate at Ultimate Limit State (ULS)
- Settlement of the foundation, as a whole and in particular differential settlements under working loads, should not be so large as to affect the serviceability of the structure at Serviceability Limit State (SLS)
- Safety and stability of nearby buildings and services must not be put at risk at Ultimate Limit State (ULS)/Serviceability Limit State (SLS)

With increasing height of buildings respectively increasing loads a raft foundation is not suitable to transfer the loads properly into the ground. Therefore a pile foundation is often used. The main function of a pile foundation is to transfer all loads by piles to a lower level of the ground which is capable of sustaining the load with an adequate factor of safety (ULS).

In addition to the often used raft or pile foundation, the innovative piled-raft foundation is nowadays often used to transfer the loads into the ground. In comparison to a pile foundation, in the piled-raft foundation, both the piles and the raft transfer the loads into the ground. The loads are transferred by skin friction and end (toe) bearing as well as contact pressures of the raft with the ground (bearing pressure). The piles are used up to their ultimate bearing capacity (load level) which is higher than the allowable design value for a comparable single pile. The piled-raft foundation represents a complex foundation system, which requires a qualified understanding of the soil-structure interactions.

The task for the geotechnical engineer is to evaluate by means of numerical calculations the load distribution between the piles and the raft as well as the pile stiffness parameter and the subgrade modulus. The distribution of the total load between the raft and the piles is described by the coefficient of the piled-raft foundation.

The piled-raft foundations system can lead to the following advantages in comparison to a raft or pile foundation:

- Reduction of settlements and differential settlements of structures
- Reduction of tilt in consideration of eccentric loading or inhomogeneous soil conditions
- In case of hybrid foundation it is possible to avoid joints in the raft
- Reduction of number of piles and pile length in comparison to a pile foundation
- Reduction of forces, stresses within the raft in case of an optimal position of the piles

In case of the high-rise building T185 various three-dimensional numerical simulations with the Finite-Element-Method were carried out in order to obtain an optimized foundation design. The following geotechnical idealizations were considered for the mesh generation:

- Tower area: modeling under consideration of the symmetries (raft: 3.5 m)
- Location of the piles
- Piles with diameter of 1.5 m (piles are modeled quadratically with the same skin area)
- Relevant areas of the connected low-rise buildings (raft thickness: 0.9 m)

The three-dimensional numerical model consists of continuum wedge elements with 15 nodes and 6 integration points for each element. Simulations with the Finite-Element-Method are always based on material laws. A material law can be depicted as the mathematical relation between stress and strain. A number of material laws for soil mechanical applications are available. The appropriate law has to be used in respect of the particular problem and the scientific objective. In this case the elastoplastic Hardening Soil model was used. The yield surface of the Hardening Soil model consists of two parts in the principal stress space (conus and cap). They can expand due to plastic straining. Furthermore it is distinguished between different stiffness of the material for loading, unloading and reloading. The deformation behavior can be simulated with a hyperbolic relationship between the vertical strain and the deviator stress. Both the shear conus and the yield cap have the hexagonal shape of the classical Mohr-Coulomb failure surface. The cap expands as a function of the pre-consolidation stress. The Hardening soil model involves six parameters.

Due to the eccentric loading situation of the overall system various numerical simulations were carried out to find the optimal pile length and to minimize the tilting of the tower. Piles within the core of the tower area as well as at one edge of the tower had to be longer ($l = 50$ m). The calculated settlements under serviceability loads add up to nearly 10 cm (Figs. 6 and 7).

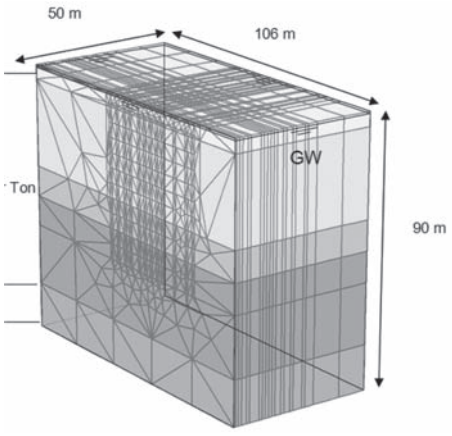

Figure 6. Numerical model.

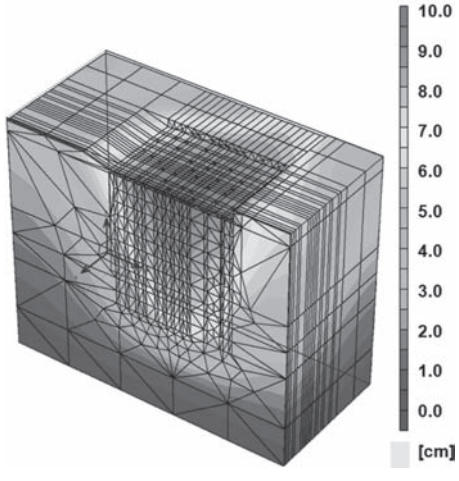

Figure 7. Calculated settlements.

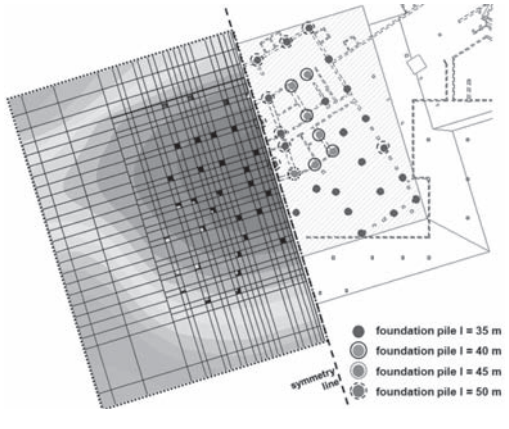

Figure 8. Settlement plot (layout) and pile layout plan.

4 MONITORING PROGRAM (OBSERVATIONAL METHOD)

A monitoring program to proof the quality of the foundation system is always recommended, so for the aforementioned high-rise buildings on a piled-raft foundation. With help of the program it is possible to compare the prognosis with the in-situ behavior of the foundation. The monitoring program must be worked out by a geotechnical expert in consideration of the foundation system, ground conditions, loading, construction phases, etc. The geotechnical expert has also to interpret all data obtained by the program. A typical monitoring program should consist of pile load cells, earth pressure cells, porewater pressure cells, extensometers and geodetical (gauging) bolts. The data can be collected for decisive construction phase or continuously.

In case of the T185 the monitoring program consists of 3 instrumented piles with load cells, 9 earth pressure cells, 2 porewater pressure cells underneath the tower raft and 20 geodetical (gauging) bolts on the raft.

5 MONITORING RESULTS

5.1 *Building pit*

The geodetical measurements of the retaining wall showed a maximal head displacement of 23 mm within the tower area and 15 mm within the low-rise area. Within the section with struts the displacements added up to only 5 mm. The adjacent subway construction showed displacement of smaller than 3 mm. All measured results were within the prognosis.

While dewatering works were carried out, the withdrawn amount of (ground)water was documented as well as 12 groundwater standpipes within the area of the pit. Figure 9 shows that ca.

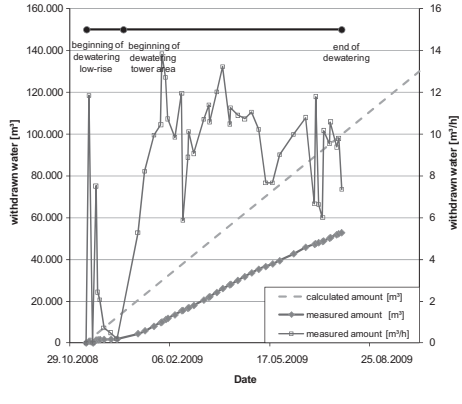

Figure 9. Dewatering: calculated/measured comparison.

53.000 m³ of (ground)water has been withdrawn. This is approximately 40% of the calculated amount. The groundwater standpipes showed nearly no influecne due to the lowering of the groundwater within the pit.

5.2 *Foundation*

Figures 9 and 10 illustrate the so far measured settlements of the construction. These results show a good correspondence with the calculated settlements. The maximum settlements so far add up to 4.1 cm. The calculated settlement for the final state is around 10 cm.

Figure 10. Measured settlements (09.07.2010).

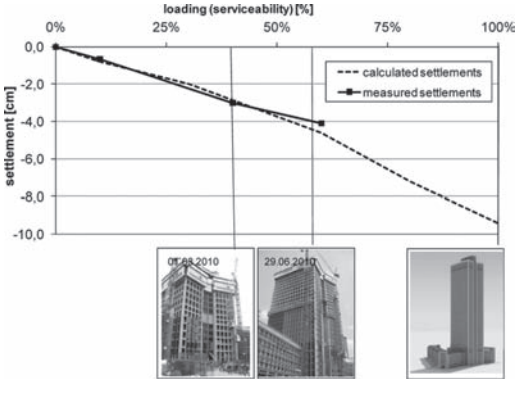

Figure 11. Settlement behavior: calculated/measured settlement.

6 CONCLUSIONS

On the basis of an extensive ground investigation and a detailed description of the ground, the foundation of high-rise buildings can be planned in an economic and safe manner. The choice of the adequate building pit and foundations system is often depending on the proof of the serviceability of the high-rise building and/or neighboring structures.

The conventional design of a pile foundation assumes that the load acting on the piles must be carried by the piles alone with a margin of safety against failure. This approach can be considered as conservative especially when piles are acting mainly as friction piles.

Where friction piles are primarily used to reduce settlements (satisfy the serviceability) and where an adequate factor of safety against failure is provided, the innovative piled-raft foundation has been put forward in the past. The essence of the piled-raft foundation is to employ piles so that settlements are reduced to an acceptable amount. The successful design and construction has been verified by many structures including many high-rise buildings.

Based on the theoretical knowledge and a qualified understanding of the soil-structure interaction numerical simulations can be used especially to optimize buildings pits and foundation systems and to evaluate deformations of the structure and neighboring structures.

By carrying out a monitoring system it is possible to verify the assumptions made and to improve the design methods for future projects.

REFERENCES

Arslan, U., Zimmer, C., Quick, H., Meißner, S. 2006. *Monitoring und Qualitätssicherung in der geotechnischen Ingenieurpraxis*, "Sicherheitsgewinn durch Monitoring?", Festschrift zum 65. Geburtstag von Univ. Prof. Dr.-Ing. Peter Grübl. Wilhelm Ernst und Sohn 2006.

Burland, J.B. 2004. *Interaction between structural and geotechnical engineer*, Imperial College London, Joint Structural Division Annual Seminar 2004.

Hanisch, J. et al. 2001. *Richtlinie für den Entwurf, die Bemessung und den Bau von Kombinierten Pfahl-Plattengründungen (KPP)* (KPP-Richtlinie).

Quick, H., Meissner, S., Keiper, K., Arslan, U. 2005. *Complex foundation design in inhomogeneous ground conditions for a (high) rise building in Frankfurt*, Germany—16th International Conference on Soil Mechanics and Geotechnical Engineering, Osaka, 12.-16.09.2005.

Quick, H., Michael, J., Meissner, S., Arslan, U. 2007. *Deep foundations and geothermal energy—a multi-purpose solution*—8th International Conference on Multi-purpose High-Rise Towers and Tall Buildings, Abu Dhabi, 10.12.2007.

Schanz, T., Vermeer, P.A., Bonnier, P.G. *The hardening soil model: Formulation and verification*. Beyond 2000 in Computational Geotechnics 1999.

This page intentionally left blank

Geotechnical Aspects of Underground Construction in Soft Ground – Viggiani (ed)
© 2012 Taylor & Francis Group, London, ISBN 978-0-415-68367-8

Geotechnical design of a railway tunnel and an underground station supporting the new city hall, Delft, The Netherlands

M.J.C. Everaars, E. Kwast & C.M. Meulblok
Grontmij Netherlands BV, De Bilt, The Netherlands

S. Delfgaauw
ProRail BV, Witteveen+Bos Consulting Engineers BV, Utrecht, The Netherlands

H. Mortier
Combination Crommelijn, Construction Company CFE NV, Dordrecht, The Netherlands

ABSTRACT: The Delft railway tunnel project comprises of the design and construction of a 2.4 km long, four track railway tunnel, an underground railway station and an underground parking in the historic city centre of Delft. Monuments and historical buildings are supported by shallow foundations very close to the excavations. The lowest excavation level is about 10 m below the ground surface. The ground water level is 1.5 m below ground surface. The cut-and-cover tunnel is retained by diaphragm walls in order to minimise ground deformations and to allow construction of buildings on top of the tunnel.

After construction of the railway tunnel and removal of the existing railway viaduct, 37 hectares of reclaimed public surface can be redeveloped. Public space in the city centre of delft is scarce. Therefore several new buildings will be located on top of the tunnel. One of those buildings, a new 5 story high city hall, will be constructed on top of the proposed underground railway station. Here the diaphragm walls have a combined function; retaining soil and ground water and supporting high structural loads from the city hall. Loads from the superstructure are concentrated into columns with centre-to-centre spacing of 8.1 m. These columns are placed on top of the diaphragm walls. Minimising differential settlement is the critical structural requirement for the city hall and the tunnel. This could be achieved by assessment of required wall stiffness and tip levels using load spread models, and if necessary the application of base and shaft injection. The moment the tunnel is in exploitation the frame of the city hall is constructed.

This publication discusses the general outline of the railway tunnel project around and below the new city hall. It explains the geotechnical engineering and construction of the retaining and supporting function of the railway tunnel wall while facing the challenges of the Dutch soft delta soils.

1 DELFT RAILWAY TUNNEL

1.1 *Introduction*

For traffic volume and environmental reasons, the city council of Delft and the Dutch railway organization ProRail BV decided to initiate the construction of a railway tunnel through the City. The tunnel project comprises of the design and construction of a 2.4 km long four track double railway tunnel, an underground station and an underground parking. The construction of the tunnel will be mainly retained by a cut-and-cover (top-down) technique using diaphragm walls. The contract is assigned to the contractor Combination "CrommeLijn" (CCL), a co-operation between CFE NV, Mobilis BV TBI infra and Dura Vermeer Group BV. In the Design & Construct contract the engineering consultant Grontmij Netherlands BV is responsible for the engineering. In June 2008 Grontmij started the final design. The construction started in August 2009. The project is expected to be completed in 2017.

This paper discusses the developments around the future underground railway station (Fig. 1).

1.2 *Redevelopment of urban areas*

After construction of the tunnel and removal of the existing railway viaduct, almost 37 hectares of reclaimed city ground can be redeveloped (Delfgaauw et al., 2010). According to the plan of the Catalan architect Joan Busquets the area will have a complete makeover. New condos with almost 1,500 apartments will be built and an extensive public transport branch point consisting of an underground railway station and a bus and tram

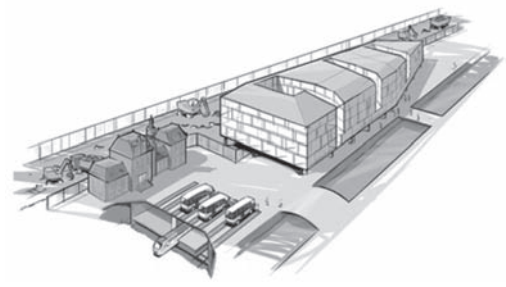

Figure 1. City hall located on top of railway tunnel.

Figure 2. Artist impression city hall, Delft, The Netherlands.

platform will be realised. A new city hall, designed by the Delft architects of Mecanoo, will be built on top of the tunnel (Fig. 2). This paper addresses the highly interactive design of this complex part of the tunnel project.

1.3 *Shallow sub/surface strata*

The shallow sub-surface strata in the western part of The Netherlands can be characterized by almost 20 m of soft soil of Holocene origin underlain by medium to dense sands of Pleistocene origin. North of the tunnel area a factory is situated that extracts large amounts of brackish groundwater from the Pleistocene sands. The drawdown results in low pore pressures in the Pleistocene sands, an advantage during construction as it reduces the risk of up-lift of the bottom of the excavation. With limited measures deep excavations can be achieved although the final tunnel construction is designed to retain higher upward water pressures in case the extraction ends.

2 ORGANISATION AND CONTRACT

The project outlined above involves complex developments of infrastructure and urban regeneration. Apart from the clients it has many stakeholders, from owners of local stores to inhabitants, local authorities, and transport companies.

The project organisation is typical for large public works. The main client consists of a co-operation of ProRail and the city council of Delft. The clients contracted the combination DRB (DHV, Railinfra Solutions and Benthem Crouwel Architects) for preliminary design. Extensive risk assessments regarding safety and legal aspects were performed, as this is the first project in the Netherlands where large buildings are supported by and integrated with a railway tunnel. After proving the technical, financial and legal feasibility, the preliminary design was back-translated to functional specifications in a D&C contract that was awarded to CCL.

Mecanoo and ABT are designers of the city hall, which will be tendered in a separate contract. All designing parties work closely together with the contractor, the client and its advisor DRB in so-called interface meetings to integrate their partial designs.

3 CONSTRUCTION

3.1 *Main design choices*

The main design challenges are:

- Differential settlements and settlements of the tunnel due to the loads of the city hall need to be limited because of serviceability of the rail tracks, leakage of the tunnel structure itself and the stability of the city hall.
- The presence of the historical station building, supported by a shallow foundation close to the excavation.
- The limited available space.

Diaphragm walls and barrettes were selected as main foundation elements because of their stiffness in both horizontal and vertical directions and the construction method leads to minimal deformation of nearby buildings, e.g. the historical railway station.

3.2 *Construction sequence*

The building pit for the underground station comprises three boxes (northern, central and southern), separated by watertight sheet pile walls. This subdivision is implemented to allow for staged construction dictated by the interfaces with existing nearby structures and the construction itself. Below the layout of the railway station is described from north to south.

3.2.1 *Northern part*

The northern part of the railway station has two representative sections (Fig. 3). One section has a

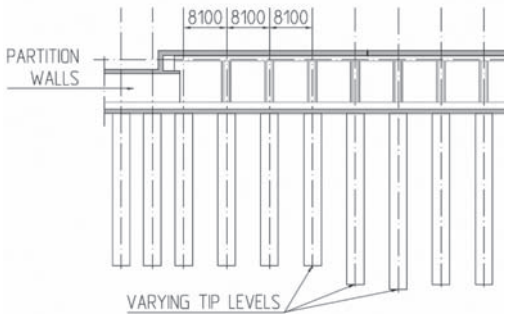

Figure 3. Longitudinal cross section northern part.

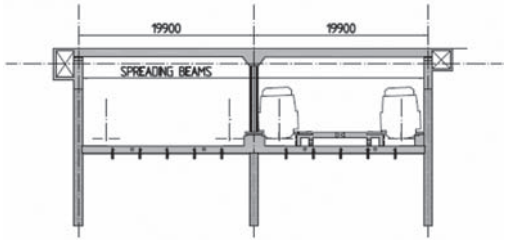

Figure 4. Cross section northern part.

lower roof and as a consequence an earth cover of several metres. The second section has a 2.7 m higher roof. Between both sections a solid concrete beam crosses (Fig. 4) the station transversally from one outer diaphragm wall to the other outer diaphragm wall. The span is approximately 40 m. The excavation depth is 10 m. To reduce the necessary dimensions of this beam, it is supported by the tunnel partition walls. This means that the generally applied top-down construction sequence had to be altered to a bottom-up sequence in the lower northern section in order to finish the supporting walls and transversal beam before the roof could be concreted. Moreover, the process of staged dewatering, as is applied in other tunnel sections, was changed to a complete draw down to the base floor level. To avoid a too high quantity of dewatering, the necessity of compartment walls was obvious.

In the second section, with the high roof, central columns with longitudinal spacings of 8.1 m support the roof, while at the far ends the roof slab is fixed to the outer diaphragm walls. As the high structural column loads of the city hall have to be supported by the diaphragm walls and the central columns, measures had to be taken to limit possible differential settlements. Due to the great variation of concentrated vertical structural loads

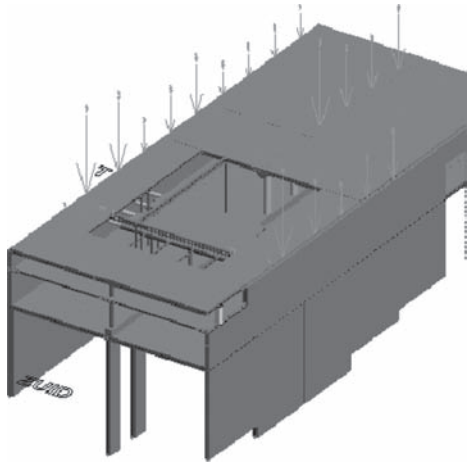

Figure 5. Structural model northern part.

(4 MN to 28 MN), large, solid spreading beams had to be casted on top of the outer diaphragm walls. Conservatively, the load spread through the joints of diaphragm wall panels by mobilisation of side friction was not taken into account. Load spread could be achieved with beam heights of approximately 3.0 m. Below the central columns, barrettes were applied with varying tip levels to achieve the required bearing capacity and stiffness. Iterative structural and geotechnical design (Fig. 5) was required with regard to scenarios with upper bound ($\sqrt{2}.k_{mean}$, kN/m) and lower bound ($\sqrt{2}/k_{mean}$, kN/m) vertical stiffness characteristics.

The section with the high roof was constructed top-down. After installation of the diaphragm walls and barrettes, the spreading beams are casted after partial removal of the top section of the diaphragm walls. Reinforcement of the concrete spreading beams is connected to the reinforcement cages of the diaphragm walls. Before covering the tunnel section with the concrete roof, anchor piles are installed which counterbalance uplift below the future tunnel floor.

3.2.2 *Central part*

The central part of the underground railway station is characterised by two important aspects. At one side there is the historical building of the old railway station that needs to be preserved. It is located at no more than 3.0 m distance from the outer diaphragm wall. On the opposite side, the future ground surface level is equal to the intermediate floor level of the underground railway station, about 3.0 m below the tunnel roof slab. This asymmetrical load situation had to be addressed in both design and construction (Fig. 6).

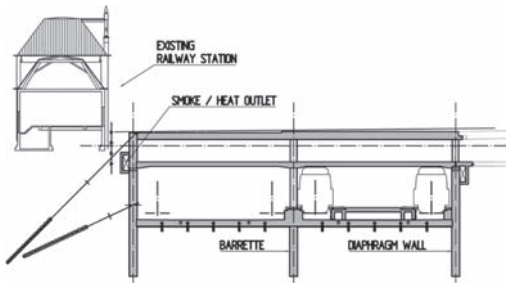

Figure 6. Cross section central part.

In order to reduce the deformations of the historical railway station, the allowable horizontal diaphragm wall deflection (1/100 of the excavated height) that was stipulated for the northern and southern part has to be limited. Therefore the diaphragm walls will be installed with smaller panel widths of 3.8 m in comparison with panel widths of 7.3 m as applied elsewhere. By doing this, the expected horizontal ground deformations during the bentonite phase of the diaphragm wall excavations will be reduced. Furthermore, pre-stressed grout anchors are applied to support the wall between the intermediate floor and base floor. After installation of the outer diaphragm walls and barrettes, the diaphragm wall near the historical railway station will be anchored at its top level. After excavation to the intermediate floor level, anchor piles will be installed and the intermediate floor is cast. The next stage is the installation of pre-stressed grout anchors at a level between the intermediate floor and the tunnel floor. The last stage comprises of casting the roof slab and supporting columns. Now, the pre-stressed grout anchors can be relieved and removed.

3.2.3 *Southern part*

The southern part is also subdivided into a high and a low section (Fig. 7). The higher section will be constructed top-down and the lower section bottom-up.

The construction sequence of the low section was introduced to facilitate casting of five partition walls. At the extremity of this section however, a length of 14.0 m of the roof slab is cast using the top-down method, as this slab temporary supports a compartment sheet pile wall. The reinforcement in the connection roof/diaphragm wall was designed taking into account the self weight of the slab and supports by the partition walls (top-down).

The high roof slab settlement which takes place during top-down construction requires compensation. Before placement of fill on top

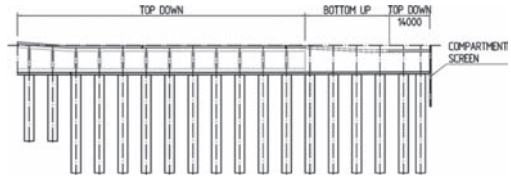

Figure 7. Longitudinal cross section southern part.

of the roof, the slab will be jacked up to reduce bending moments and shear forces at the slab/diaphragm wall connections. Reaction force is obtained from the partition walls.

3.3 *Definition of concrete mixture*

In the southern part, the bending moments in the connection diaphragm wall/roof slab are very high. Required spacing of vertical rebars in the diaphragm wall did not meet the Dutch code (NEN-EN1538, 2000). During the design process, it became apparent that geohydrological conditions were different than originally anticipated for. This resulted in even higher bending moments. As the required reinforcement could not be applied, a test programme was executed to find the optimal concrete mixture and the required casting method to assure a satisfactory result. The test was performed in shallow diaphragm wall shaped excavations (Fig. 8) which included representative reinforcement. Four different concrete mixtures and/or casting methods were applied to investigate the replacement of bentoniet by concrete in the dense reinforcement cages. After hardening, core samples were collected for testing concrete quality and concrete distribution between the rebars and couplings. A concrete mixture with aggregate size 4/16 without any treatment after pouring (i.e. vibration, poking, etc.) proved to be the best option.

3.4 *Barrettes*

At midspan the tunnel roof is support by a row of columns with spacings of 8.1 m. These columns have longitudinal concrete beams above and below. The lower beam, being part of the tunnel floor, is supported by barrettes instead of a continuous diaphragm wall. As it would be too expensive to cast barrettes up to roof level and shorten them afterwards down to tunnel floor level, temporary steel columns were applied in this section. The barrettes were equipped with reinforcement cages which reach up to the future tunnel floor level. Before installation, the reinforcement cages and steel profiles were welded together at ground surface. The reinforcement was lowered into the trench.

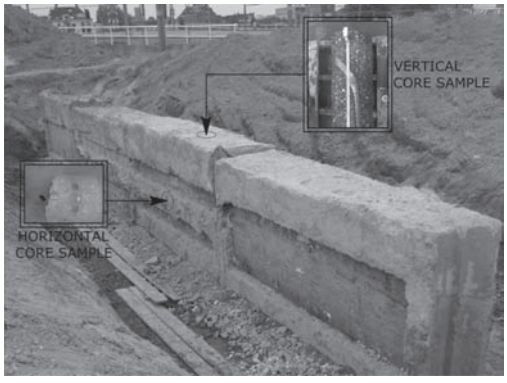

Figure 8. Concrete mixture test.

Finally, the barrettes were casted to future tunnel floor level, and after sufficient hardening, the section between future floor level and ground surface was back-filled with gravel. The steel profiles could be used to support the roof during top-down construction. The gravel can easily be removed during the excavation. After the floor is cast, a formwork can be placed around the steel profiles to give the columns a concrete look.

4 ENGINEERING DIAPHRAGM WALLS

4.1 *Combined function diaphragm walls*

The diaphragm walls below the city hall have combined functions. They retain ground and groundwater pressures and they support the city hall located on top of the tunnel. In accordance with CUR166 (2005) interaction of the vertical and horizontal wall stability should be analysed where vertical loads are substantial (over 12.5 kN/m^2). In this case loads from the city hall are over 50 kN/m^2.

The CUR166 (2005) is a leading handbook for civil engineers. The user is guided through design and construction aspects of soil and ground water retaining constructions. The handbook will become part of the Dutch national annex to Eurocode 7.

The horizontal stability of the propped diaphragm walls was assessed using the computer program MSheet (Delft Geosystems, The Netherlands) based on the Winkler theory of beams with elastic-plastic spring behaviour. Separately, assessment of the vertical stability of the diaphragm walls were performed in accordance with the Dutch standard for compression piles NEN6740 (2006) and NEN6743-1 (2006) applying the computer program MFoundation (Delft Geosystems, The Netherlands). Pile design was based on the Dutch q_c-method and took account of stress reduction by trench excavation and a complex geo-hydrological profile. The described design routine proved to be very practical. However to verify the results of the separate assessment of horizontal and vertical stability, a finite element study was performed using Plaxis 2D.

4.1.1 *Horizontal stability*

According to design approach B outlined in CUR166 (2005) a finite element study (FEM) was performed using representative ground parameters, groundwater levels and geometry in the different construction stages. The hardening soil model was applied with parameters such as c′, φ′, $E'_{50;ref}$, $E'_{oed;ref}$ and $E'_{ur;ref}$. For critical construction stages separate calculation steps were added in the FEM using design parameters. To obtain maximum displacements, forces and bending moments, drained soil behaviour was applied to the model. In the FEM the direction of the friction angle (δ, °) at the concrete wall and soil interface is automatically determined for vertical loading of the wall.

In the elasto-plastic spring model the approach is different. The model uses parameters such as c′, φ′, δ′ and k_h. k_h (kN/m^3) is the horizontal subgrade reaction. In the final construction stage the diaphragm wall is vertically loaded up to 1.9 MN/m'. The balance of vertical forces has to be achieved by rotating the wall friction angle bottom-up, from tip level to about the excavation level, at the active side of the retaining wall. Results of both calculations are given in Table 1. The presented case has diaphragm wall tip levels of NAP –23.5 m penetrating 5 m into dense to medium dense Pleistocene sand.

The verification results for horizontal stability of the retaining walls show that:

- The calculated maximum bending moments (ULS) in FEM and the spring model are comparable, but appear in different construction stages.
- Introduction of vertical loads increases maximum bending moments in the retaining wall.

Table 1. Calculation results FEM 2D and Spring Model.

	FEM 2D	Spring model
Construction stage	$M_{max;ULS}$ [kNm/m']	$M_{max;ULS}$ [kNm/m']
Maximum excavation level	1,010	1,356
Completion tunnel	1,154	993
Vertical load from superstructure	1,308	989

$M_{max;ULS}$, Maximum bending moment in diaphragm wall (ultimate limit state).

– In the spring model no clear increase is observed of the maximum bending moment between completion of the tunnel and application of vertical load on the retaining wall.

This practical design approach was maintained. However a second order bending moment was added to the results of the final spring model construction stage. This additional moment was calculated using the maximum deflection of the retaining wall from the spring model calculation and the introduced vertical load from the superstructure. For the case presented in Table 1 this was 135 kNm/m' (0.07 m × 1,9 MN/m'). The results from the FEM and the spring model become comparable, 1,308 kNm/m' versus 1,154 kNm/m'.

4.1.2 *Vertical stability*

To verify the design approach comparison is made between results of FEM analyses, results of spring model analyses and results of the Dutch q_c-method in the ULS.

In the FEM and the spring model wall friction was mobilised over the wall length including the Holocene soil layers. The q_c-based method took account of wall friction from the top of the deep Pleistocene sands. In the FEM and the spring model the wall friction is assessed using the slip-method while the Dutch q_c-method relates wall friction to q_c using empirical pile constants ($\alpha_p = 0.5$, $\alpha_s = 0.006$ and $s = 0.63$ according to NEN6743-1 (2006)). End bearing of the spring model was also based on the q_c-method, where in the FEM the end bearing was assessed by multiplication of effective stress below the tip of the diaphragm wall (including the effective weight of the wall) with the tip surface. A summary of calculation results is presented in Table 2.

The conclusions drawn from the verification of the design approach for vertical stability are as follows:

– Total wall friction assessed with the FEM and the spring model is comparable.
– Wall friction in the Pleistocene sands assessed with the spring model and the q_c-based model are equal.
– End bearing assessed with the FEM is underrated because the vertical balance in reached at a limited vertical deformation of 40 mm ($0.03D_{eq}$) in ULS. According to NEN6743 (2006) the maximum deformation in ULS is 0.1 to $0.2D_{eq}$.
– Assessment of vertical stability using the Dutch q_c-method separate from horizontal stability is possible. However, wall friction in the Holocene soil layers is neglected.

Table 2. Comparison of bearing capacities (ULS) of different models.

Model	$F_{shaft;d}$ [kN/m'] H	P	$F_{tip;d}$ [kN/m']	F_d [kN/m']
FEM	360	310	1,260	1,930
Spring model	200	470	1,520	2,190
Dutch q_c based method	–	480	1,520	2,000

$F_{shaft;d}$, ULS shaft resistance; $F_{tip;d}$, ULS end bearing; F_d, ULS total bearing capacity; H/P, Holocene/Pleistocene.

4.2 *Vertical support and deformations*

The city hall columns are supported by the outer diaphragm tunnel walls and the barrettes at the centre of the tunnel. Strict differential settlement criteria were prescribed in the tunnel contract to assure the structural integrity of the city hall. In transverse direction differential settlement between adjacent structural columns has to be reduced to <20 mm (Fig. 9) and in longitudinal direction to <15 mm (Fig. 10). Maximum absolute vertical column settlement has to be limited to 30 mm.

According to the Dutch standard NEN6743-1 (2006), the load-settlement behaviour is a function of the ratio of load and resistance. Load-settlement

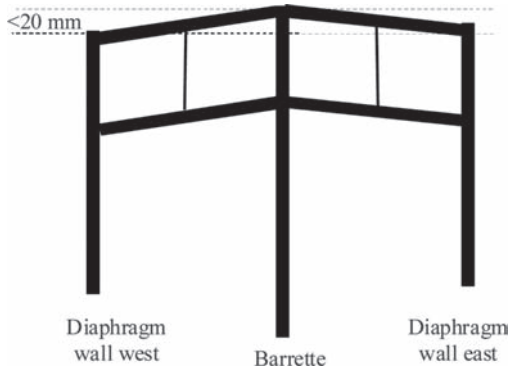

Figure 9. Transversal differential settlement.

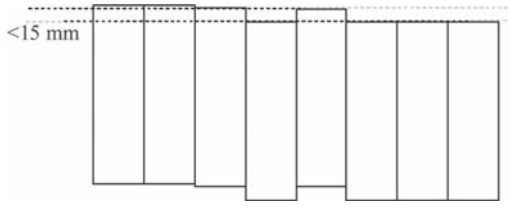

Figure 10. Longitudinal differential settlement.

behaviour of diaphragm walls and barrettes is assumed to be comparable to that of bored piles.

To control (differential) settlement three possible options were considered:

1. Post base and shaft grout injection. Application of this technique increases pile stiffness as well as the bearing capacity. The technique has not widely been applied to improve the performance of diaphragm walls and barrettes. The effect of post injection for this project could only be verified by load tests.
2. Spreading beam on top of the diaphragm walls and barrettes for steady load distribution at tip level.
3. Varying tip levels to control vertical stiffness.

A combination of options 2 and 3 was selected. A feasibility study indicated that the increase of tip levels by about 7 m is equivalent to the application of shaft and base injection. In addition, prediction of performance of diaphragm walls after injection is subject to uncertainties (Hamza & Ibrahim., 2000).

A summary of the calculation results is as follows. City hall column settlements between 5 mm and 25 mm were assessed. The maximum column loads of up to 28 MN per barrette (L/W is 3.3 m/1.0 m) requires tip levels of 46.5 m below ground surface which is comparable to Thasnanipan et al. (2001).

Because of the high ground water levels impermeable retaining walls are required. Vertical loading conditions however result in irregular settlements of the diaphragm wall panels. The spreading beam contributes to reduce differential vertical settlements of neighbouring panels to <5 mm. Joints between diaphragm wall panels have limited differential settlement capacity to a maximum vector deformation of 25 mm. Therefore, measures such as post joint injection are available for instant use during construction.

5 RISK EVALUATION

5.1 *General*

The design process and the construction of the tunnel are based on the method of systems engineering (Everaars et al., 2010). SE translates abstract top-requirements into more practical requirements.

The design process produced additional requirements which were introduced in SE. Specifications are systematically evaluated and broken down further into practical requirements for construction. Critical requirements for design and construction of the city hall tunnel section are outlined in the sections below.

Parallel to design of the Delft railway tunnel an expert panel produced a state of the art report on design and construction of diaphragm walls (CUR231, 2010). Best practices and main risks regarding diaphragm wall supported excavations were addressed.

5.2 *Engineering*

Interaction of structural loads, soil properties and foundation stiffness were very sensitive when calculating differential settlement. Therefore extensive SI was performed to derive soil profiles and soil parameters. Additional SI was performed to mark out a clay layer thinning below the city hall.

Structural engineers and geotechnical specialists combined forces during an iterative design approach, while project management focussed on coordinating with the external structural engineers for the city hall superstructure.

5.3 *Construction*

In order to reduce failure risk, additional measures, such as monitoring, tests and adjustments of construction methods are taken.

5.3.1 *Monitoring and testing*

In order to validate the applied design methodology, monitoring instruments are attached to some cross sections before the start of construction. Inclinometers are installed at close distances to the diaphragm wall and at one location directly inside the diaphragm wall. A series of settlement markers up to a distance of 25 m of the diaphragm wall is installed to monitor horizontal and vertical ground deformations. Monitoring data enables verification of design models.

As recent experiences learned that failures of diaphragm wall trenches were often caused by joint anomalies (bentonite inclusions), sonic logging equipment was installed at panel joints close to existing (historical) buildings. The equipment comprises four watertight HDPE tubes (two at both sides of the joint), fixed to the reinforcement cage. After concrete hardening, sonic logging is performed by lowering transmitters and receivers at opposite sides of the diaphragm wall for joint inspection.

5.3.2 *Adjusted construction methods*

During the design process and construction preparation measures were proposed to control risks. In some cases the design was adjusted. Below two examples are given.

Initially, a short sheet pile wall was anticipated for at a minimum distance from the façade of the historical railway station to improve trench stability.

The idea was that this sheet pile wall, which is necessary to construct the heat/smoke outlet conducts between the façade and the future tunnel, would reduce the required bentonite level in the stable diaphragm wall trench. Analyses, including introduction of stabilised soils between sheet pile wall and diaphragm wall, however resulted in low safety factors. For this reason high bentonite levels were required and installation of the sheet pile wall was scheduled after concrete hardening of the diaphragm wall.

Pre-stressed grout anchors in the central section of the railway station were originally planned to pass through metal tubes incorporated in the reinforcement cages. As these tubes should form an important rheological obstacle during the concreting of the diaphragm walls, this concept was left. The lower grout anchors with spacing of 1.9 m (two per panel) will now pass through drilled holes. Those holes will be cored during excavation. To avoid drilling through reinforcement special cages were designed. The holes for the top anchors, with spacing of 3.8 m (one per panel) could pass through the diaphragm wall in the unreinforced central zone. This zone is where the concrete is tremied.

5.3.3 *Diaphragm wall joints*

The tunnel design addressed risks related to the required impermeability of diaphragm wall joint (analyses of horizontal and vertical stiffness and the introduction of a spreading beam). Quality control of underground works is difficult and no proven in-situ test is available to investigate joint quality. For this reason extensive monitoring will be performed during the excavations. After detection of leakages immediate post joint grout injection will be applied.

5.4 *Project management*

When working on a project with different parties and different contracts, proper communication is indispensable. In this project this is achieved by intensive interface management. Ideally, discussions lead to solutions that are favourable for all parties involved. In some occasions, decisions have to be made for the benefit of the project as a whole. The Client's Change Control Board decides in cases were contract changes are required to improve the overall design or to minimise risks, such as:

- Contractually, the designers of the city hall had to take measures to reduce train induced vibrations. However, it proved impossible to incorporate this in their concept and it was decided to take measures underneath the railway tracks.
- It was decided to transfer parts of the scope of the city hall (an underground bicycle park directly adjacent to the tunnel) to the tunnel contract, in order to minimise construction, logistic and planning risks.

6 CONCLUSION

Application of diaphragm walls in the cut and cover tunnel reduces ground deformations and therefore minimises settlement of nearby buildings. The relatively high bearing capacity of diaphragm walls creates opportunities to build on top of the tunnel.

A new city hall will be constructed directly on top of the railway tunnel over a length of 130 m. Limiting (differential) settlement of the diaphragm walls was the critical structural requirement here. Load-settlement behaviour is controlled by using spreading beams and variation of diaphragm wall tip levels.

In consequence of construction on top of the tunnel, the diaphragm walls below have two interacting functions. They retain ground and ground water and they provide vertical support. A FEM analysis has proven that assessment of horizontal and vertical stability can be performed separately.

REFERENCES

CUR166 2005. Retaining walls, 4th print, Part 1 en 2, CUR, Gouda, October 2005.

CUR231 2010. Handbook diaphragm walls, Foundation CURNET, Gouda, September 2010.

Delfgaauw, S., Mortier, H., Jonker, J. and Mastbroek, H. 2010. Four-track railway tunnel re-unifies the city of Delft in The Netherlands, ITA-AITES World Tunnelling Congress, Vancouver, Canada, May 2010.

Everaars, M.J.C, Kwast, E. and Meulblok, M. 2010. Risk management in the geotechnical design process of a railway tunnel in urban environment, Delft, The Netherlands, Proc. 11th International Conference Geotechnical Chalenges in Urban Regeneration, DFI-EFFC, London, United Kingdom, May 2010.

Hamza, M. and Ibrahim, M.H. 2000. Base and shaft grouted large diameter pile and barrettes load tests, Developments in Geotechnical Engineering, Bangkok, Thailand, November 2000.

NEN6740 2006. Geotechnics—TGB 1990—Basic requirements and loads, September 2006.

NEN6743-1 2006. Geotechnics—Calculation method for bearing capacity of pile foundations—Compression piles, November 2006.

NEN-EN1538 2000. Execution of special geotechnical work—Diaphragm walls, February 2000.

Thasnanipan, N., Maung, A.U., Aye, Z.Z. and Tanseng, P. 2001. Record load test on large barrette and its performance in the layered soils of Bangkok, 5th International Conference on Deep Foundation Practice, Singapore, April 2001.

Geotechnical Aspects of Underground Construction in Soft Ground – Viggiani (ed)

CSM-cutter soil mixing—worldwide experiences of a young soil mixing method in soft soils

F.-W. Gerressen & Thomas Vohs
BAUER Maschinen, Schrobenhausen, Germany

ABSTRACT: The CSM method of deep mixing has been in operation now for nearly seven years. In many applications so far in already fifteen countries all over the world, the method has given excellent results both technical and economical. Its use has been extended to replace many Jet grouting and other conventional deep soil mixing projects as well as plastic diaphragm walls, sheet piles and other cut-off walls on prestigious projects. The paper will show a range of applications executed all over the world in soft soils.

1 INTRODUCTION

BAUER Maschinen GmbH developed the CSM technique in 2003 by drawing on the experience gained in the production and deployment of diaphragm wall cutters in the construction of cut-off and diaphragm retaining walls.

2 CONSTRUCTION PRINCIPLE

The CSM System differs essentially from traditional techniques in that the in situ mixing of the existing soil with self-hardening slurry is performed by mixing tools rotating about horizontal axis rather than the traditional vertical axis. The in-situ soil mixed with self-hardening slurry produces a wall construction material that takes on the role of a cut-off and/or structural retaining wall.

The cement and bentonite content and the water/cement ratios of the mixing slurry are determined by the strength and/or permeability requirements of the project and the properties of the soil being mixed. In general, for a stronger wall, cement content is increased and water/cement ratio is lowered. Typically, sandy soils will require a larger amount of bentonite in the slurry than clays. At some clay sites where enhanced resistance to permeability is not required, acceptable fluidization of the soil can be achieved without the use of bentonite.

A typical construction sequence is as follows:

a. Construction of a good sized open guide trench for retaining excess slurry.
b. Fluidization of the soil mass during penetration to the final depth as an appropriate slurry is simultaneously introduced. Depending on the prevailing conditions, either bentonite slurry is added to the mixing and fluidization process or cement slurry is introduced into the soil during penetration. The volume of slurry injected is determined by the rate of cutter penetration.
c. During withdrawal, the precise volume of slurry required for producing the final wall construction material is injected.
d. A continuous wall is formed by the construction of individual panels in an alternating sequence of overlapping primary and secondary panels. Secondary panels can be constructed immediately after completion of primary panels, i.e. "wet-into-wet". The cutter technology does, however, also enable cutting into panels that have already hardened, i.e. "hard-into-hard".
e. To utilize the wall as a structural retaining wall, steel columns (IPB sections) are inserted into the freshly mixed wall panels.

In mixing applications less than 15 m deep in relatively soft ground, a one phase mixing procedure may be used. In the one phase procedure, the final slurry product consists of cement and water or a cement, bentonite and water mixture, which is injected on both the down stroke and the upstroke of the machine. Advantages of this procedure include the additional mixing of the cement and the soil and the simplicity of only having one slurry mix.

When mixing deeper panels or penetrating difficult (slow) to mix soils or rock, a two phase system is used. Instead of using self-hardening slurry from the beginning onward as in a one-phase system, just bentonite slurry is used on the down stroke. Once the final depth is achieved, the cement slurry is introduced and mixed on the upstroke. This method prevents the mixing tool from being

trapped in the panel if the panel construction time exceeds the initial set time for the cement slurry.

The size of individual panels is determined by the type and size of equipment being deployed. Panels can be constructed in lengths ranging from 2.4 m to 2.8 m and wall thicknesses of 0.55 m to 1.2 m.

3 EQUIPMENT

The most important elements of the CSM unit are the cutter gear drives. They are driven by hydraulic motors which are located in a water-tight housing. The slurry is introduced into the soil directly between the mixing wheels. During construction, the counter-rotating mixing wheels and vertically mounted plates are effectively acting like a forced action mixer. Because of this mixing principle, CSM is suitable for mixing cohesive soils. For loosening and mixing the soil different types of mixing wheels were developed.

The mixing unit (Fig. 1) is either mounted on a guided Kelly bar or on a wire rope-suspended cutter frame equipped with special steering devices. The standard set-up is the "Kelly-guided" setup, capable of reaching depths up to 43 m (Fig. 2).

"Rope-suspended" systems are particularly suited for construction of deep soil mix walls. The greatest depth to date at which a wire rope-suspended unit has successfully installed a soil mix wall to date is 60 m, using a compact unit called QuattroCutter (Fig. 3).

Both systems must be accompanied by an intensive quality assurance programme. All process-specific production and plant-specific operating data are visualised throughout the construction phase and stored for subsequent documentation and evaluation. Information presented includes penetration rates, alignment, and slurry injection rates and volumes (Fig. 4).

Figure 1. Mixing wheels and housing for hydraulic gear drives.

Figure 2. Kelly-guided CSM unit, USA.

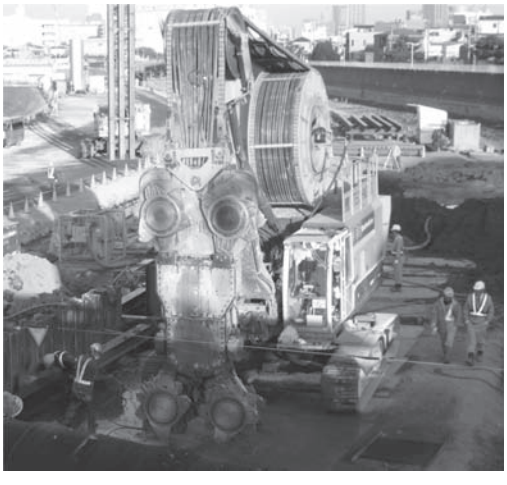

Figure 3. Wire rope-suspended CSM unit, QuattroCutter, Japan.

Figure 4. Rig operator's on-board computer screen.

4 COMPARISON WITH OTHER TECHNIQUES

The CSM process has significant advantages over conventional techniques like e.g. secant pile walls or sheet piling walls. These are:

- The existing soil is utilised as construction material.
- Very little spoil material is generated; this renders the technique particularly suited for work on contaminated sites.
- CSM is an ideal alternative to the traditional "Berlin wall" system, which is better known as soldier beam wall with timber lagging, for the use in high groundwater conditions, or to sheet pile walls in soil formations unsuitable for pile driving or in close proximity to vibration-sensitive buildings.
- CSM is a vibration free method.
- No delivery of ready mixed concrete is necessary.

In comparison to traditional deep soil mixing methods CSM has the following advantages:

- A high degree of verticality of wall panels is achieved by the counter-rotating cutter wheels.
- The cutter principle ensures construction of clean and trouble-free joints even between wall panels of different construction age e.g. after weekend breaks or prolonged stoppages on site.
- Harder soil formations can be easily penetrated, broken down and mixed by using the cutter wheels as cutting and mixing tool.
- Homogenise the cohesive soils and self harden slurry through horizontal mixing.
- In relation to small base units, high daily output and high panel depth may be achieved.

5 APPLICATIONS IN SOFT SOILS

5.1 *Retaining walls*

The CSM system is very commonly used to construct water-tight soldier beam retaining wall system for excavation pits especially near sensitive inner-city building where vibration free system are essential. It provides an alternative solution to conventional methods such as secant pile walls and/or sheet piles

An example for an excavation pit shows a jobsite executed in Osaka, Japan (Fig. 6) for the construction of the new Hanjin Expressway. Soil conditions are shown in Figure 5.

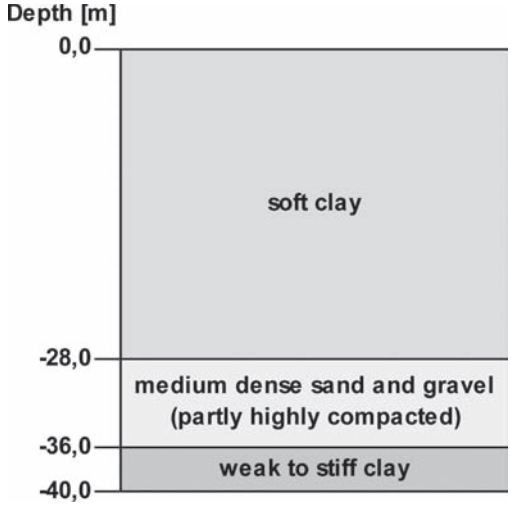

Figure 5. Soil conditions Hanjin Expressway, Osaka, Japan.

Figure 6. Wire rope-suspended CSM unit, QuattroCutter Osaka, Japan.

The CSM panel was socked for 1.5 to 2 meters into the clay layer under the sand layer. The wall was 0.55 meter wide and extended to approximately 38 m deep; the excavation depth was 13 m deep. Steel beam sections were inserted into the fresh mixed panels and extended to a depth of 18 m. The wall functioned as a cut-off-wall beyond the tip of the steel section. Due to the relatively long production time associated with the high depth of the panel, the two phase system was selected. The BAUER QuattroCutter was used to execute the task. The QuattroCutter is made of a frame combining two BCM 5 mixing heads; one at the bottom and one at the top of the frame. The arrangement of two mixing heads ensures an intensive and homogeneous mixing as well as a high directional accuracy for high depth.

Another example for a retaining wall in soft soils was done in Meise, Belgium (Fig. 8). An excavation pit for building a storage basin for rain and used water was executed. Soil conditions are represented in Figure 7.

The retaining wall had a width of 0.55 meters and about 13 m deep. One of the main reasons the CSM method was chosen is the nearness of the surrounding houses. Therefore a vibration free method had to be used. The 1-Phase system and a BAUER MBG 24 were used for the execution of the jobsite. Figure 8 shows the Kelly guided CSM unit and the tight space at the jobsite.

Figure 8. MBG 24 with Kelly guided SCM mixing head, executing a retaining wall, Meise, Belgium.

5.2 *Foundations*

On several building projects CSM panels were used as foundation elements. Apart from the main advantages of the CSM process, such as the use of the existing subsoil as construction material and the minimized spoil removal, a further advantage results from the fact that the same equipment can be deployed to construct first the retaining wall for the excavation and then the foundation elements. The system can be used for single elements as well as for strip foundations or it's possible to construct the foundation elements concurrently with the retaining wall and connect with each other in such a way that the retaining wall is subsequently also capable of carrying vertical loads.

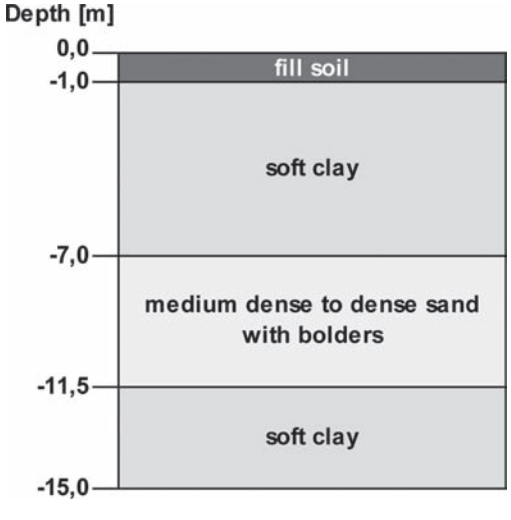

Figure 7. Soil conditions, Meise, Belgium.

For a project in Vittorio Veneto, Italy, where a new sport hall building was being constructed, the CSM panels, 7 meter deep, were reinforced with tension bars HEA120 which were used as uplift anchors to tie-down a raft foundation in adverse groundwater conditions (Fig. 9). The soil was mainly soft silt. Additionally a 9.5 m, back-anchored and reinforced CSM retaining wall was executed for a 4.5 meter excavation pit.

5.3 *Soil improvement*

Soil improvement can be another application for the use of CSM system.

One of the largest CSM projects ever constructed was for ground improvement purpose. It was part of

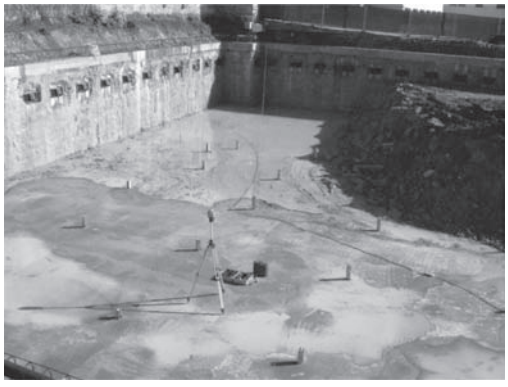

Figure 9. CSM Wall and CSM panels with tension bars used as uplift anchors, Vittorio Veneto, Italy.

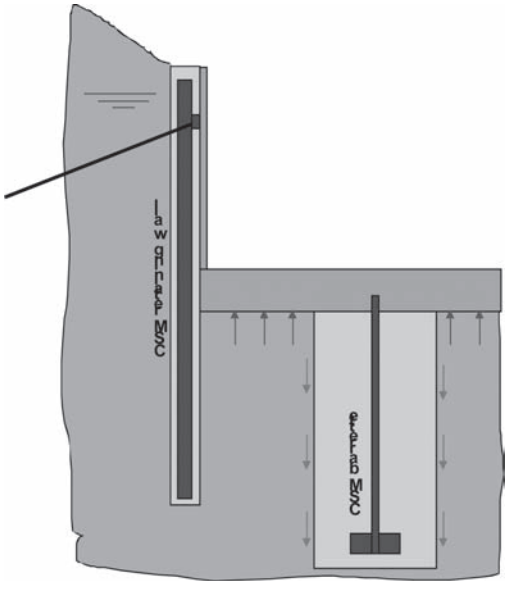

Figure 10. CSM panels (barrettes) reinforced with tension bars and back anchored CSM wall, Vittorio Veneto, Italy.

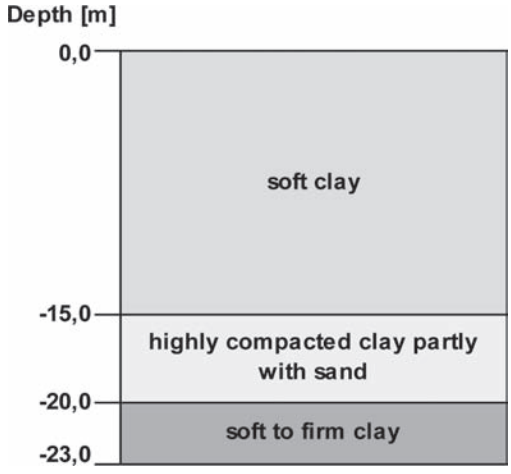

Figure 11. Soil conditions, Bologna, Italy.

Figure 12. Soil improvement, Bologna, Italy.

the new main station in the city centre of Bologna, Italy. The foundation of the new station will be supported on diaphragm walls extended to a depth of 23 meter. The subsurface soil consisted mainly of medium to soft clay (Fig. 11) and needed to be stabilized with a CSM wall before the diaphragm walls execution, to prevent settings of the buildings and the old main station located nearby.

Two BAUER BG 28 and one RTG RG 25 S with BCM cutters used on the jobsite. Each of these three BAUER units is supposed to produce about 25.000 m² (total 75.000 m²) of CSM-wall with a tolerance in deviation of less then 0.5% per meter. The CSM-wall itself was also 23 meter deep and 0.8 meter wide. The required 28 days of the CSM-wall compressive strength was 1.6 MPa. Therefore a two phase system is used. Tests prior to the execution indicated that the requested deviation and strength of the CSM-wall could be achieved.

Figure 13. BAUER SideCutter, Japan.

The BAUER units were showing a remarkable performance in this difficult soil conditions. The average production rate was about 15–20 m² per hour.

Further more soil stabilization has been used for liquefaction mitigation or slope stabilization in single cases in Canada, Italy and Portugal.

6 SUMMARY AND OUTLOOK

The described examples have demonstrated that this young construction technique, which combines the advantages of the cutter and the soil mixing technique, has been successfully established in the market all over the world even in very traditional soil mixing markets like Japan. The technique offers a great diversity of possible applications, such as cut-off walls, structural retaining walls, foundation elements and numerous others.

The capacity to reach big depths offers an enormous potential for the construction of deep walls especially for cut-off walls for dams or the en-capsulation of contaminated sites.

The demand of reaching big depth in combination with limited space ends up with the latest development of a rope-suspended unit, a so called SideCutter. The SideCutter has the ability to turn just the cutting head without turning the upper carrier (Fig. 13).

REFERENCES

Fiorotto, R., Stötzer, E., Schöpf, M., Brunner, W. CSM Cutter Soil Mixing—An innovation in Soil Mixing for creating cut-off and retaining walls. *International Conference on Deep Mixing* 2005.

F.-W. Gerressen, M. Schöpf, E. Stötzer. CSM-Cutter Soil Mixing—Worldwide experiences of a young soil mixing method. *Deep Mixing 2009 Okinawa Symposium,* 2009.

E. Stötzer, W. Brunner, R. Fiorotto, F.-W. Gerressen, M. Schöpf. CSM Cutter Soil Mixing—A New Technique for the Construction of subterranean walls—Initial experiences Gained on completed projects. *10th international Conference on Piling an Deep Foundations*, (534), 7 p. 2006.

F.-W. Gerressen, M. Schöpf, E. Stötzer. Venedig macht dicht—Das CSM Verfahren Cutter Soil Mixing als Teil des Hochwasserschutzkonzeptes MOSE *6. Kolloqium Bauen in Boden und Fels,* (591), 6p. 2008 (Germany).

Geotechnical Aspects of Underground Construction in Soft Ground – Viggiani (ed)
© 2012 Taylor & Francis Group, London, ISBN 978-0-415-68367-8

The construction of deep excavation ditch in weak soil in St. Petersburg

R. Mangushev
St. Petersburg State Civil Engineering University, St. Petersburg, Russia

E. Lashkova & V. Smolenkov
Company "Geoizol", St. Petersburg, Russia

A. Osokin
Company "Geostroy", St. Petersburg, Russia

ABSTRACT: The information about the engineering- geological conditions in the central part of St. Petersburg which are characterized by deep thickness of weak water saturated soil is given. Three buildings with large underground space constructed in St. Petersburg are considered as examples. The depth of each space exceeds 12 m and required the usage of modern and nonstandard construction and technological methods for protection of the ditch walls. The wall protection was done by sheet piles, by "Wall in ground" method, and "jet grouting". The soil excavation was carried out by traditional method or "Top–down" method. The basic constructive schemes and technological methods of ditch excavation, test results of deformation of the protection walls during excavation of the ditch and the settlements of the neighboring buildings are given.

1 INTRODUCTION

The development of the modern City is not possible without the development of underground space. But the construction conditions in St. Petersburg are much more complicated than in any other region of the country. Mainly this is explained by specific geological conditions—the central part of the City is located on weak, water saturated thixotropic soil, which change their properties depending on the effect of different forces—natural and technogenic. Most of the buildings which were constructed in 18–19 centuries or beginning and middle of 20-th century have cracks and damages of the bearing structures and require the reinforcement of their base and foundations (Mangushev, 2004).

Any additional settlement of such buildings during ditch excavation by traditional method (pile sheet wall, soil excavation, lowering of ground waters by open excavation and etc) may cause unpredictable result.

The construction in St. Petersburg require high professionalism starting with projecting work when you choose the method of supporting the wall of the ditch and the technology of the future work. The availability of the modern equipment for underground work and qualified personnel is of great importance. The examples of the construction of three modern buildings with large underground space in St. Petersburg are given in the present article.

2 FIVE LEVEL UNDERGROUND PARKING ON KOMENDANTSKAYA SQUARE

In 2006 the company "GEOIZOL" made the project and started construction of the circular 5 level underground parking on Komendantskaya Square. The depth reached 19,5 m and the diameter 78 m. The general cross section is shown in Figure 1.

The main problems which appeared during the construction were the absence of the experience in the construction of such types of buildings

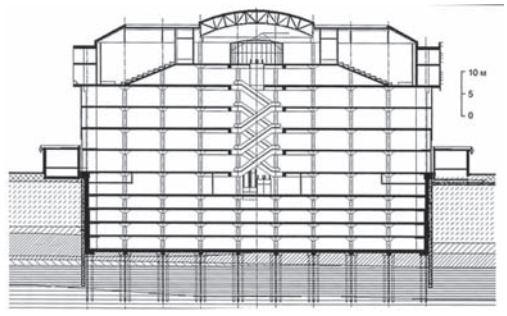

Figure 1. The general cross section of the building.

in St. Petersburg and complicated geological conditions (thixotropic soil in the upper part of the geological section, high level of ground waters and presence of big boulders).

Since the parking with such spacious underground room was constructed in newly developing region it was possible to dispose it at the distance of 100 m from the nearest buildings. This allowed to ignore the effect of the parking on neighboring buildings.

The technical solution of the erection of the underground part of the building suggested:

1. Initial trench made by "wall in ground" method 24 m deep and 0,8 m wide which was filled cement-clay solution (Fig. 2a) The ground was excavated by portions 3,3 m long each.
2. Immersion of the metal semicircular sheet pile into the trench and its subsequent concreting (Fig. 2b). Sheet pile served as a reinforcing element and additional seal.
3. Erection of monolith concrete beams which served as stiffening ribs and excavation of the ditch by portions while making monolith walls and parts of beam ceiling (Fig. 3).
4. The erection of 290 anchor borrow concrete piles 12 m long section 250 mm and concreting the reinforced concrete plate on the level—18 m (Fig. 4).

There were no influx of the water from outside of the wall since the "wall in the ground" reached the dense undisturbed Cambrian clay.

In order to avoid the floating up of the bottom of the structure under the pressure of hydrostatic force, the reinforcement of anchor borrow concrete piles was connected with the reinforcement of the lower plate. This allowed to make united anchor system.

The horizontal movement of the circular walls during the ditch excavation was checked with the help of inclinometers. Inclinometers were immersed into the earlier installed plastic tubes along the whole height of the "Wall in ground".

Figure 2. Initial trench made by "Wall in ground" method (a) and sheet pile immersion (b).

Figure 3. The beams, parts of ceiling and excavation of the ditch level by level.

Figure 4. Anchor piles and monolith reinforced concrete bottom plate.

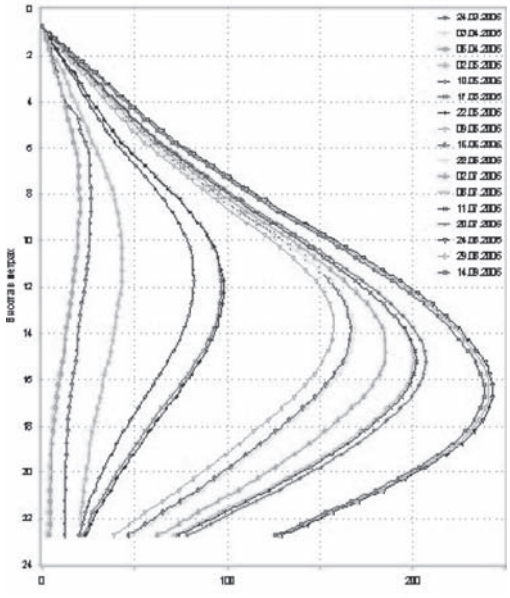

Figure 5. The horizontal movement of walls of underground structure within certain period of time.

Figure 6. General view of the building with 4 level parking.

The horizontal movement of walls of underground structure during excavation within certain period of time is shown in diagram (Fig. 5).

The maximal measured movement of the wall into the ditch was 250 mm and happened at the depth of 15 meters. A t the end of 2008 the building was put into operation (Fig. 6).

3 THE UNDERGROUND PART IN STOCKMANN TRADE CENTER

In 2007 the construction of the new Stockmann Trade Center was started in the center of the city on the corner of Nevskii Prospect. and Vosstania str. The building has 3–4 level underground space 15 meters deep in the form of trapezium (the base is 60 m the height of one of the sides 130 m) (Fig. 7).

On 2 sides of the construction site there were neighboring buildings. As a protective structure of the underground part the initial project suggested the metal sheet pile Larcen V 25 m long which was immersed by vibro immerser of high frequency.

The experience received in St. Petersburg showed that this method of immersing the sheet pile into unstable soil could result in the settlement of the neighboring buildings and exceed the allowed value. That is why foundations of the buildings along Nevskii Prospect were reinforced by piles "Titan" prior the excavation of the ditch. The piles were tested against 70 ton vertical loading.

Since the Client failed to agree with the owner of the building along Vosstania str. upon the foundation reinforcement of his building, it was necessary to make the protection wall along one of the sides of the ditch as "wall in ground" instead of pile sheet. Figure 8 (Smolenkov, 2009).

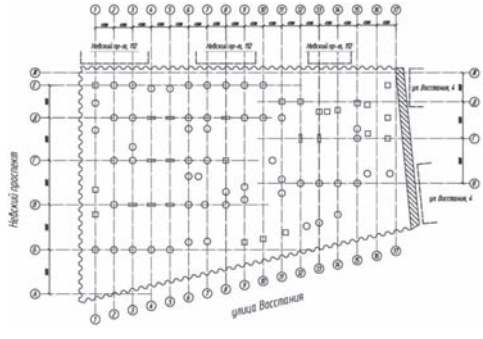

Figure 7. Scheme of the underground part of the Trade Center.

Figure 8. "Wall in ground" along one of the sides of the ditch.

Figure 9. Excavation of the soil under the ceiling.

Though the stiff sheet pile was used along three sides and "wall in ground" along the forth side, the stiffness of the structure was not sufficient due to the weak soil in the construction site. The deformation of the sheet pile below the bottom of the ditch could occur.

In order to avoid the damaging effect of the new building on the old neighboring buildings and metro station the engineers suggested to fix the lower part of the sheet pile at the depth 17–20 m by making the soil diaphragm by jet technology (Broid, 2004).

Further development of the underground space was done by Top-Down method. Some new technical solutions were applied: borrow piles-columns reinforced by steel tube and special metal profile and also borrow piles of standard diameter and with expansion in the lower part up to 1300 mm which supported the ceiling. The length of the piles was 40,8 m.

The ceilings which were put on the ground and under which the soil was later excavated through technological apertures, served as strut elements for protecting the structure. (Fig. 9).

After finishing the ceiling on the ground level the construction of the overground elements—columns, walls, ceilings of the upper floors—was started.

All the works on the ground level and further construction of the over ground level did not cause any serious additional settlements of the neighboring buildings, their foundations were earlier reinforced by piles "Titan". But the building which was not reinforced in its foundation, received deformation of the bearing structures and required the restoration.

4 THE ERECTION OF THE UNDERGROUND PART IN THE TRADE CENTER IN LIGOVSKII PROSPECT

In 2006 the territory which earlier was intended for the construction of the railway station was bought by another Company. The plans were changed and it was decided to construct there a trade Center with underground 3 level parking. The third level must have independent entrance from Ligovskii prospect which was not possible due to several reasons and as a result it was decided to have 2 levels.

The ground characteristics in the construction site are typical for the central part of St. Petersburg—glacial moren deposits, laid below weak water saturated sea, lake and lake glacial-deposite. are located on the depth 25 m.

Since the destination of the building changed, the construction scheme was changed. It became necessary to evaluate the bearing capacity of the existing piles which were erected earlier. For this purpose the ditch was excavated and piles were tested under the loading 3000 kN.

785 piles with diameter 550 mm were added to the existing piles using DDS method and 6 of them were tested under static loading (Mangushev et al., 2010).

The test results showed the growth of the bearing capacity of the piles erected earlier—the settlement of the pile was less than 30 mm under the loading 3000 kN.

When the work started again at the construction site at the end of 2006 there was already sheet pile along the perimeter of the construction site immersed to the depth of 11 m. The preliminary calculations showed that the stability of the pile sheet protection was not provided after the excavation newly projected ditch 8,5 m deep.

Different variants were checked and finally semicircular pile sheet 21 m long was chosen.

The calculations made by different experts showed that the stability of the pile sheet can be provided on condition of certain sequence of work done while excavation of the ditch.

According to the calculations made in the computer programmer "Steel Wall", during the last period of ditch excavation the deformation of the sheet pile when 2 levels of struts were made, should be equal to 34 mm and maximal value of the bending moment 303,0 kN, coefficient of the stability 1,94 (Fig. 10).

The technology of ditch excavation included the excavation of its central part and making slopes of the pile sheet wall on the projected mark and the erection of the monolith reinforce concrete plate in the center, followed by erection of strut in the form of metal beams between reinforce concrete plate and sheet pile protection. (Fig. 11).

It was suggested to make ditch excavation part by part in the area of location of metal beams and after that to make final concreting of monolith plate and walls of the underground part, after that the struts were dissembled. All the work was done

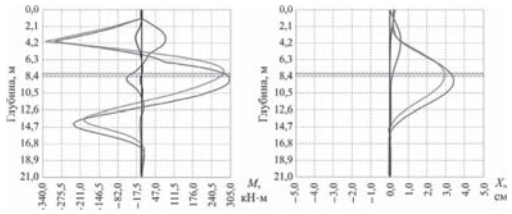

Figure 10. Calculated value of the moment M and movement X at different stages of the ditch excavations.

Figure 11. View of struts in the ditch.

Figure 12. The construction of the underground part of the Trade Center at Ligovskii prospect.

very close to the existing rail way and the building of the railway station.

The further construction of the underground part of the building was done by open technology under the protection of the sheet pile and walls in the underground part (Fig. 12). At present time the construction of the building is successfully finished.

5 CONCLUSIONS

The considered examples of these civil buildings in St. Petersburg with large underground space showed that it was possible to make the deep large ditches in soft soil on the condition of proper selection of the rigidity of the protection structure. The choice of these structures is determined by calculations and organizing the test sites.

REFERENCES

Broid I.I. 2004. Jet grouting technology, ASV, M, 448 pp.

Mangushev R.A. 2004. The analysis of the constructions of the bases of old buildings in the Centre of St. Petersburg. «Soil mechanic and Foundations», No 5, M, p.13–16.

Mangushev R.A., Ershov A.V., Osokin A.I. 2010, Newpile technologies. SPBGASU—ASV, Sankt-Peterburg-Moskow, 160 pp.

Smolenkov V.Ju. 2009. *Company* "GEOIZOL" experience constructions of the underground objects in St. Petersburg. "Building construction", No 2, p.43–45.

This page intentionally left blank

Geotechnical Aspects of Underground Construction in Soft Ground – Viggiani (ed)
© 2012 Taylor & Francis Group, London, ISBN 978-0-415-68367-8

Effect of staged dewatering and excavation on the heave of soil beneath deep excavation

G. Zheng
Key Laboratory of Coastal Civil Engineering Structure and Safty, Ministry of Education, China
Department of Civil Engineering, Tianjin University, Tianjin, China

Z. Li
Tianjin Infrastructure Investment and Construction Company, Tianjin, China

ABSTRACT: Deep excavation in soft ground can induce significant heave of soil beneath the bottom of excavation. Field measurement of a staged excavation project using top-down method was carried and shown that vertical displacement of uplift pile supporting permanent column is large. For staged dewatering and excavation, dewatering at each stage can increase the relief of effective stress of each stage of excavation compared with staged excavation without dewatering, so the effect of staged dewatering on the behavior of soil need to be investigated. Triaxial tests were performed to simulate the process of staged dewatering and staged excavation. Test results show that dewatering can reduce the final amount of heave of bottom of excavation. Soil located at different location relative to the excavation is subjected to different stress path. This leads to that larger heave of bottom of excavation close to diaphragm wall compared with that close to center of excavation. The effect of dewatering must be taken into account when predicting heave induced by deep excavation in soft ground.

1 INTRODUCTION

Dewatering is necessary to lower the ground water table below bottom of deep excavation in soft ground. For deep excavation using bottom-up method, multi-level struts or slabs are needed to maintain the stability and to reduce the internal forces and deformation of diaphragm wall. In such case, the whole construction activities include staged dewatering and excavation. At each stage, dewatering is first performed to lower the ground water table down to 0.5 m~1 m below the bottom of the following subsequent stage of excavation, then the soil to be excavated at the subsequent stage of excavation is removed. Step by step, the subsequent staged dewatering and excavation can commence until the final bottom of excavation is reached.

Deep excavation in soft ground can induce significant heave of bottom of excavation and consequently cause vertical displacement of pile supporting permanent column and sometimes diaphragm wall when top-down method is employed. Furthermore, heave of soil beneath bottom of excavation can induce tensile force in pile. The uneven upward displacement between piles and that between piles and diaphragm wall can induce additional internal force in the slabs and columns. Besides, when there is existing tunnel located under the excavation, the heave of soil can cause the upward movement of tunnel. Thus, the effect of soil heave on the underground structures must be limited to prevent causing any damage to underground structure, or negative effect on the serviceability of underground structure.

The heave of the bottom of excavation has long being paid attention to since 1950s. Stanley (1956) reported that large heave of bottom of excavation can occur for deep excavation without dewatering, however, the heave of excavation bottom can be greatly reduced by dewatering before excavation commence. Burland (1979) has investigated soil movements around excavations in London clay. Buford (1988) reported the heave of tunnels beneath an excavation in London due to the heave of overlying soil. The maximum heave measured was about 20–30 mm after excavation activities in 1957 and this upward displacement still continued and maximum magnitude reached about 50 mm in 1986. Lo & Ramsay (1991) proposed the methodology to deal with the "construction over tunnels" problem by a case record of excavation above subway tunnels in Toronto. Zheng et al. (2010) carried centrifuge tests to investigate the effect of overlying on tunnel linings.

The heave of soil beneath the bottom of excavation can induce the upward movement of pile. Consequently, tension force is generated in the pile body (Iwasaki et al. 1994). The heave induced

tension may be influenced by the excavation depth, pile length and soil modulus (Lee et al. 2001, Poulos & Davis 1980, Huang et al. 2007.). Zheng et al. (2010) carried centrifuge tests on the effect of deep excavation on the capacity of smooth single pile in sand and indicated that the pile's vertical capacity is reduced by up to 20%, i.e., the capacity of the pile loaded after excavation is only 80% of that of the pile loaded on the ground surface, as in a conventional loading test.

Although the heave of bottom of excavation and its effect on underground structure has been investigated and a lot of papers regarding this issue have been published, however, the behavior of soil inside the excavation during staged dewatering and excavation has not been paid much attention. This paper presents the triaxial tests and field measurements performed by the authors to investigate the effect of staged dewatering and excavation on the behavior of soil beneath the bottom of staged excavation, and on the upward displace of piles supporting permanent columns when top-down method is employed.

2 FIELD MEASUREMENTS

A deep excavation project located in Tianjin, China using top-down method was monitored. The depth of excavation is 25.8 m with 3 levels of slab, which are supported by permanent columns, as shown in Figure 1. The permanent columns are plunged 2.5 m into the piles.

The diaphragm wall is 48 m deep with 1.2 m width. The diameter of bored pile is 2.2 m and the

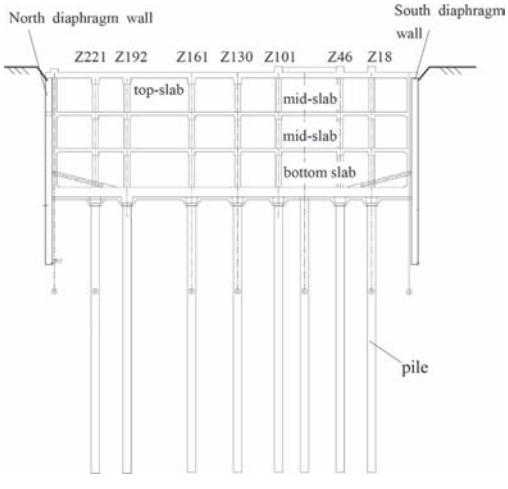

Figure 1. Profile of excavation using top-down method.

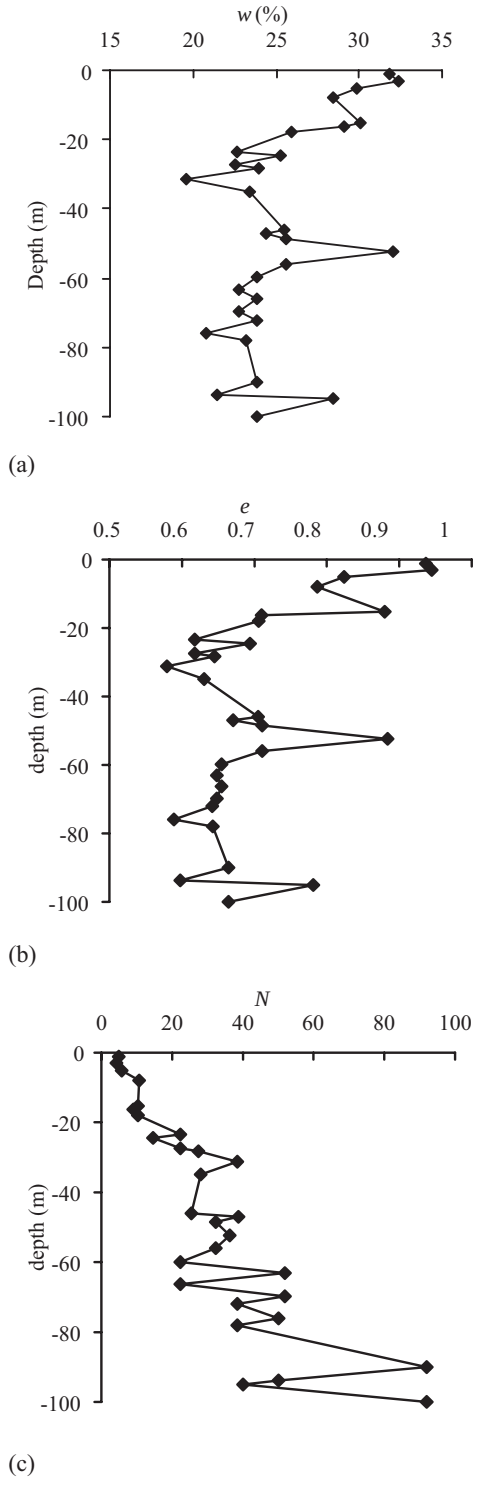

Figure 2. Soil parameters distribution along depth: (a) water content; (b) void ratio; (c) blow count of SPT.

length is 55 m. The permanent column is steel pipe. The depth of roof slab is 3 m below ground surface, the 1st mid-slab is 6.2 m below the top slab, and the 2nd mid-slab is 6.6 m below the 1st mid-slab. After the depth of 25.8 m is reached, the bottom slab is constructed and then dewatering is terminated.

The ground is mainly comprised of silty clay and silt, underlain by sand layers 80 m below ground surface. The main parameters of soil are shown in Figure 2.

Staged construction is adopted during the whole excavation process. Dewatering, excavation and construction of slab are performed subsequently at each stage. Dewatering is performed by deep wells with depth of 40 m and spacing of 15 m inside the diaphragm. The diameter of deep well is 273.6 mm.

During the staged excavation, the vertical movement of roof slab corresponding with the location of permanent columns and diaphragm wall was monitored, as shown in Figure 3. In the figure, SE denotes staged excavation and MS is mid-slab in Figure 1. The measured vertical displacement of roof slab at the locations of permanent columns can be roughly regarded as the displacement of piles if the compression of permanent columns is neglected.

It can be seen from Figure 3 that the heave of piles increased faster at the 1st stage and 2nd stage of excavation but increased much slower at the 3rd stage of excavation. That there are more loads applied to top of piles due to mid-slabs construction may be part of the reasons. However, there is one more important reason that leads to the smaller increase of heave of piles at the 3rd stage. Due to the dewatering before each stage of excavation, the ground water table was lowered from its original level, 1 m below ground surface, down to 1 m below bottom of the final excavation stage, the effective stress of soil below the lowered ground water table was increased and can thus be preloaded. Moreover, the soil beneath the bottom of excavation became over-consolidated and the degree of over consolation of soil remained became larger and larger with the further going of staged excavation.

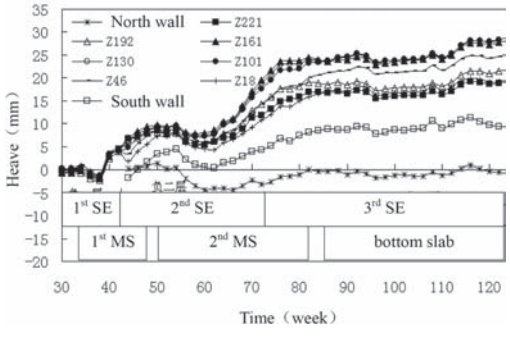

Figure 3. Heave of diaphragm wall and piles.

3 TRIAXIAL TESTS

3.1 *Stress change during staged excavation*

In order to investigate the effect of staged dewatering and excavation on the soil behavior beneath the bottom of excavation, triaxial tests were performed to simulate the stress path that the soil below the bottom of excavation was subjected to during staged dewatering and excavation. Three typical location of soil located at the bottom of final stage of excavation are considered, as shown in Figure 4. The depth of excavation is 30 m and there are totally 3 stages of excavation. When dewatering is considered, each stage of dewatering is followed by the staged excavation. The ground water table is assumed to be lowered to the same level with that of the bottom of each excavation. The process of staged dewatering and excavation is shown in Table 1.

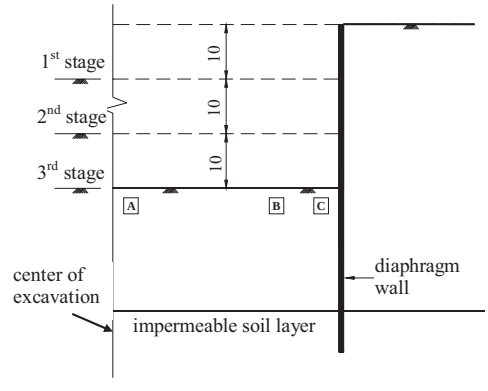

Figure 4. Schematic geometry of staged excavation (unit: m).

Table 1. Staged excavation simulation without dewatering.

Construction stages	Construction activities
Initial state	–
1st stage dewatering	Ground water table –10 m
1st stage excavation	Depth of excavation –10 m
2nd stage dewatering	Ground water table –20 m
2nd stage excavation	Depth of excavation –20 m
3rd stage dewatering	Ground water table –30 m
3rd stage excavation	Depth of excavation –30 m

In Figure 4, location A is near the excavation center line, location C is near the diaphragm wall and location B is somewhere between location A and location C. By assuming the width of excavation is infinitely large, and the process of excavation is fast enough to be regarded as undrained condition, the total vertical stress change at location A due to the staged excavation without dewatering is shown in Figure 5.

However, for deep excavation in soft ground, the soil to be excavated is subjected to staged dewatering and excavation. In this paper, the process of staged dewatering is assumed to be drained condition. If the change of unit weight of soil due to dewatering is neglected, the total vertical stress change during the whole process of staged dewatering and excavation can be easily obtained.

Similarly, by assuming the width of excavation is infinitely large, and the process of excavation is fast enough to be regarded as undrained condition, the total vertical stress change at location A due to the staged excavation with staged dewatering is shown in Figure 6a.

After the 1st stage of excavation, the soil beneath the bottom of the 1st excavation has become over-consolidated. The degree of over-consolidation of soil will increase with the further stage of excavation. Since the process of each stage of excavation is assumed to be undrained, negative pore water pressure in soil over-consolidated beneath the bottom of excavation is generated due to overlying excavation, as shown in Figure 6b.

The vertical effective stress at each stage of dewatering and excavation is shown in Figure 6c. Each stage of dewatering can increase the vertical effective stress. Consequently, the stress relief at each excavation is increased.

3.2 *Triaxial tests*

Triaxial tests were performed to simulate the stress path of soil located at the three typical locations shown in Figure 1. The soil physical characteristics are shown in Table 2.

At each stage of excavation, the soil at location A, B and C are subjected to vertical stress relief. By taking the lateral stress coefficient at rest as 0.5 and assuming that the width of excavation is infinitely large, the UU in Table 3, i.e. the ratio of

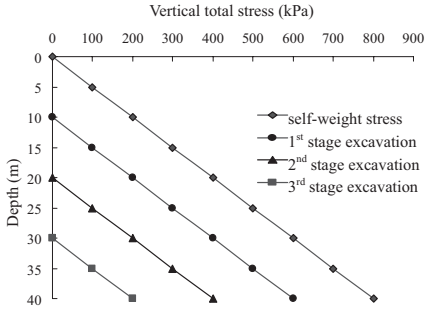

Figure 5. Changes of total vertical stress near the excavation center without dewatering.

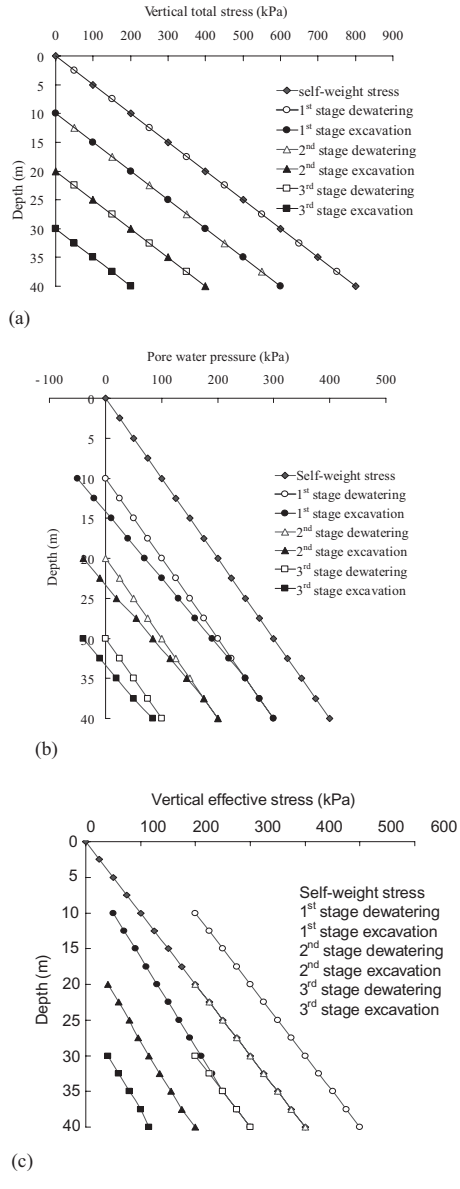

Figure 6. Stress and pore water pressure change due to overlying staged dewatering and excavation: (a) vertical total stress; (b) pore water pressure; (c) vertical effective stress.

Table 2. Physical characteristics of silty clay.

Water content w /%	Void ration e	Unit weight γ/kN/m^3	Index of plasticity I_p
25.3	0.694	20.1	12.8

Table 3. Stress paths of triaxial tests without dewatering.

	Without dewatering		
Stage	UU = 2	UU = 4	UU = ∞
1. Initial state	300/150	300/150	300/150
2. 1st stage excavation	200/100	200/125	200/150
3. 2nd stage excavation	100/50	100/100	100/150
4. 3rd stage excavation	0/0	0/75	0/150

Table 4. Stress paths of triaxial tests with dewatering.

	Staged excavation and dewatering		
Stage	UU = 2(*)	UU = 4(*)	UU = ∞(*)
1. Initial state	300/150	300/150	300/150
2. 1st stage dewatering	400/200	400/200	400/200
3. 1st stage excavation	200/100	200/150	200/200
4. 2nd stage dewatering	300/150	300/200	300/250
5. 2nd stage excavation	100/50	100/150	100/250
6. 3rd stage dewatering	200/100	200/250	200/300
7. 3rd stage excavation	0/0	0/200	0/300

vertical effective stress relief to horizontal effective stress relief of soil at location A can be taken as 2. While UU at location C can be taken as UU = ∞ by assuming that the horizontal stress loss due to excavation can be fully compensated by passive earth pressure. The UU of soil at location B is between that of soil at location A and location C and is simply taken as 4.

The stress path of soil specimens in triaxial tests for excavation without dewatering is shown in Table 3, the stress path of soil specimens in triaxial tests to simulate staged dewatering and excavation is shown in Table 4. In Table 3, taken UU = 2 as an example, the initial vertical effect stress at location A is 300 kPa by taking the effective unit weight of soil as 10 kN/m^3, and correspondingly, the initial horizontal effective stress at location A is 150 kPa. Thus the initial effective stress state of soil at location A can be expressed as 300/150.

3.3 *Soil behavior during excavation*

The axial strain ε_a change with the increase of major stress deviation $\Delta(\sigma_v - \sigma_h)$ for stress path shown in Table 3 is shown in Figure 7.

The relationship between axial strain ε_a and major stress deviation $\Delta(\sigma_v - \sigma_h)$ in Figure 7 can be expressed as:

$$(\sigma_{vc} - \sigma_{hc}) - (\sigma_v - \sigma_h) = \frac{\varepsilon_a}{a + b\varepsilon_a} \quad (1)$$

where σ_{vc} and σ_{hc} are the vertical and horizontal consolidation pressure before shearing when the specimen was subjected K_0 consolation. For soil specimen subjected to triaxial tension, the vertical

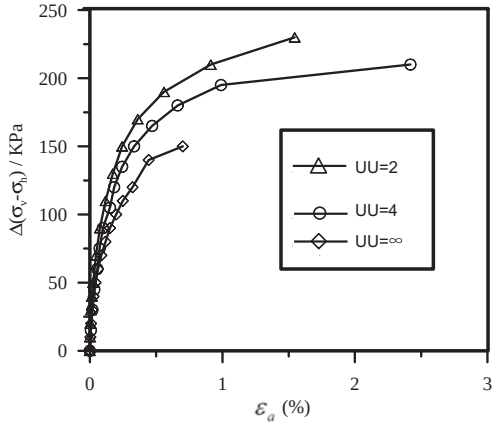

Figure 7. Stress increment-strain curves under different unloading paths without dewatering.

stress σ_v became the minor principal stress and the horizontal stress σ_h became the major principal stress. Therefore, the relationship between axial strain ε_a and major stress deviation $\Delta(\sigma_v - \sigma_h)$ was shown in Figure 8. In Figure 8, $\Delta(\sigma_v - \sigma_h)$ is normalized by $\dfrac{\varepsilon_a}{(\sigma_{vc} - \sigma_{hc}) - (\sigma_v - \sigma_h)} \Big/ \text{MPa}^{-}$.

From Equation (1) and Figure 5 the Initial tangent unloading modulus can be obtained, as shown in Table 5.

The Initial tangent unloading modulus of soil subjected the stress path shown in Table 4 can be obtained as well by the same way, as shown in Table 6.

By comparing the initial tangent unloading modulus of soil in table 5 and table 6, it can be seen that staged dewatering can significantly reduce the

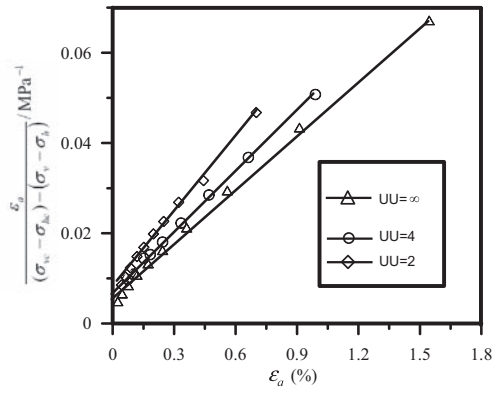

Figure 8. Hyperbolic stress-strain curve fittings under different unloading paths.

Table 5. Initial tangent unloading modulus (MPa) of soil without dewatering.

	Stress path		
Stage	UU = 2	UU = 4	UU = ∞
1st stage excavation	129.8	140.8	175.4
2nd stage excavation	50.1	57.8	52.1
3rd stage excavation	22.8	Failure	Failure

Table 6. Initial tangent unloading modulus () of soil with dewatering.

	Stress path		
Stage	UU = 2(*)	UU = 4(*)	UU = ∞(*)
1st stage excavation	212.8	312.5	400.0
2nd stage excavation	111.1	188.67	137.2
3rd stage excavation	74.6	Failure	Failure

soil compressibility and consequently reduce the heave of soil beneath the bottom of excavation.

It can also be seen from Figure 5, Table 5 and Table 6 that the soil sample experienced the stress path UU = ∝(*), i.e. the stress path of soil located at location C close to diaphragm, as shown in Figure 5, yielded the largest extension, while the soil sample experienced the stress path UU = 2(*), i.e. the stress path of soil located at A close to center line, produced the least extension. To a certain extent, this can illustrate that the heave of bottom of excavation near diaphragm wall is often larger than that near the center of excavation.

4 CONCLUSIONS

By conducting triaxial tests and field measurements, the following conclusions can be drawn:

1. Staged excavation and dewatering can induce the over-consolidation of soil beneath the bottom of excavation. The degree of over consolation of soil remained became larger and larger with the further going of staged excavation.
2. Compared with excavation without dewatering, staged dewatering can reduce the compressibility of soil below the bottom of excavation, consequently, the total amount of heave is reduced.
3. The soil located at different location relative to the excavation is subjected to different stress path. Larger heave of bottom of excavation close to diaphragm can occur compared with that close to center of excavation.
4. The effect of staged dewatering on the soil behavior can't be neglected when predicting the displacement of underground structure during excavation.

ACKNOWLEDGMENTS

This research was supported by the National Basic Research Program of China ("973 Program") (Grand no: 2010CB732106) and national Natural Science Foundation of China (Grant no. 50878144).

REFERENCES

Burland, J.B. 1979. Movements around excavations in London clay[J]. *Geotechnique,* 29 (1): 13–29.

Burford, D. 1998. Heave of tunnels beneath the Shell Centre, London, 1956–1986[J]. *Geotechnique,* 38(1): 155–157.

Burland, J.B., Simpson, B., St John, H.D. 1979. "Movements around excavations in London clay." *Proceedings of the 7th European Conference in Soil Mechanics and Foundation Engineering*, Brighton, U.K. 1, 15–19.

Huang, M.S, Ren, Q., Wang, W.D., Chen, Z. 2007. Analysis for ultimate uplift capacity of tension pile under deep excavation[J]. *Chinese Journal of Geotechnical Engineering*, 4(11): 1689–1695. (in Chinese).

Iwasaki, Y., Watanabe, H., Fukuda, M., Hirata, A., Hori, Y. 1994. Construction control for underpinning piles and their behavior during excavation[J]. *Geotechnique*, 44(4): 681–689.

Lee, C.J., Al-Tabbaa, A., Bolton, M.D. 2001. Development of tensile force in piles in swelling ground." *Proceedings of the Third International Conference on Soft Soil*, Hong Kong, 345–350.

Lo, K.Y. and Ramsay, J.A. 1991. The effect of construction on existing subway tunnels-a case study from Toronto[J]. *Tunnels and Deep Space*, 6(3): 287–297.

Poulos, H.G., and Davis, E.H. 1980. *Pile foundation analysis and design*, John Wiley & Sons,Inc., Toronto.

Stanley S. 1956. The elastic heave of the bottom of excavation[J]. *Geotechnique,* 9(2): 62–70.

Zheng G., Wei S.W., Peng S.Y., Diao Y., C.W.W. Ng. Centrifuge modeling of the influence of basement excavation on existing tunnels. *Physical Modelling in Geotechnics. Springman,* Laue & Seward (eds) . 2010 Taylor & Francis Group, London. pp:523–527.

Zheng G., Peng S.Y., Diao Y., C.W.W. Ng. In-flight investigation of excavation effects on smooth single piles. *Physical Modelling in Geotechnics. Springman*, Laue & Seward (eds) . 2010 Taylor & Francis Group, London. pp:847–852.

This page intentionally left blank

Geotechnical Aspects of Underground Construction in Soft Ground – Viggiani (ed)
© 2012 Taylor & Francis Group, London, ISBN 978-0-415-68367-8

Design and construction of deep excavations in Shanghai

W.D. Wang & Z.H. Xu
Department of Underground Structure & Geotechnical Engineering, East China Architectural Design & Research Institute Co., Ltd., China

ABSTRACT: Numerous deep excavations have been carried out in Shanghai for constructing high-rise buildings, subway transportation networks and other underground structures in the past two decades. There is significant advancement in design and construction practice of deep excavations in Shanghai. This paper presents the current status of design and construction practice adopted. Firstly, geological and geotechnical conditions are presented. Secondly, commonly used deep excavation support systems are introduced. Then, a few cases which are benchmarks of deep excavations are presented. These include the largest deep excavation, the deepest excavation, the largest circular excavation, the basement excavation for the tallest building in china, and the largest excavation constructed by top-down method in Shanghai. Finally, concept of performance-based design, criteria of deformation control, and measures in mitigating the impact of deep excavations on adjacent structures and properties are introduced. These measures include top-down method, reinforcement of soils inside the excavation, zoned excavation, and "Time and Space Effect" excavation method.

1 INTRODUCTION

Shanghai is the largest city in China with a population of about 20 million. It is also the financial and commercial center of this country. It has become one of the most energetic municipalities in the world. With the rapid economic growth in the past two decades, the city has achieved drastic economic and social reforms with construction industry playing an important role. A large number of high-rise buildings, subway transportation networks and other underground structures have been built in Shanghai during the past two decades. Figure 1 shows a bird view of a corner of the city showing numerous skyscrapers. Figure 2 shows the map of the Shanghai metro network in operation. Up to now, there have been 11 lines and 280 stations put into operation. The operation length of the Shanghai rail transit network is about 420 km and it has become the longest rail transit network in the world. Most of these construction involved deep excavations. As a result, there is significant advancement in design and construction practice of underground works. Presented herein is the current status of design and construction of deep excavations in Shanghai.

Figure 1. A bird view of a corner of the Shanghai city showing numerous skyscrapers (from http://bbs.home.news.cn/).

Figure 2. Map of the Shanghai metro network in operation (http://www.shmetro.com).

2 GEOLOGICAL AND GEOTECHNICAL CONDITIONS

Shanghai is washed by the East China Sea on the east and Hangzhou Bay on the south. North of the city, the Yangtze River pours into the East China Sea. The 'shallow soils', from ground surface to a depth of about 135 m, were deposited during the Quaternary period (SCMC, 1997). These shallow soils have important significance to engineering activities. Figure 3 shows a typical soil profile in Shanghai and the geotechnical parameters of the soil. It should be noted that compressibility modulus $E_{s0.1\sim0.2}$ was obtained by oedometer tests at stresses ranging from 100 kPa to 200 kPa while undrained shear strength s_u was obtained from in situ vane shear tests.

The top layer is artificial fill with a thickness of less than 2 m. The second layer is yellowish dark brown inorganic clay, with low to medium plasticity and medium compressibility. This layer has a lower water content and void ratio and a higher undrained shear strength than the underlain soft clay. The second layer is lightly overconsolidated, perhaps due to climate effect such as evaporation. The third layer is very soft silty clay with a thickness of about 7 m. It is in a medium plastic and high compressible state. Mean value of water content of this layer is about 46% and the mean s_u value is about 28 kPa. The horizontal permeability coefficient of this layer is the order of 10^{-6} m/s. The fourth layer is 7 m thick very soft clay, which contains mica, organic matter, and silty sand. It has the largest void ratio and compressibility, but has the lowest coefficient of permeability (the order of 10^{-8} m/s) among the 'shallow soils'. The mean value of s_u of this layer is about 37 kPa. Sensitivity values of both the third and fourth layer soils are larger than 5. The fifth layer is grayish silty caly with a thickness of about 10 m. It is low to medium plastic with medium to high compressibility. Mean value of s_u of this layer is about 75 kPa. The sixth layer is dark green stiff clay with a thickness of 4 m. It is overconsolidated with an OCR of about 2.0 and low to medium plastic. SPT N value of this layer ranges from 18 to 30. The seventh layer is silty sand with a thickness of about 15 m. SPT N value of this layer ranges from 28 to 70. Coefficient of permeability of this layer is the order of 10^{-5} m/s. The groundwater table is generally 0.5 m below the ground surface.

3 DEEP EXCAVATION SUPPORT SYSTEM

3.1 *Retaining wall*

Support systems for deep excavations consist of three main components, namely, retaining walls, lateral support system and vertical support system. For retaining walls, six types of walls are commonly used in Shanghai.

The first kind of retaining wall is diaphragm wall which has relatively high stiffness and provides effective water tightness. As its cost is quite high, it is usually used in project with more than three levels of basements. In most cases, diaphragm wall is adopted as retaining wall as well as outside wall of basement. The most commonly

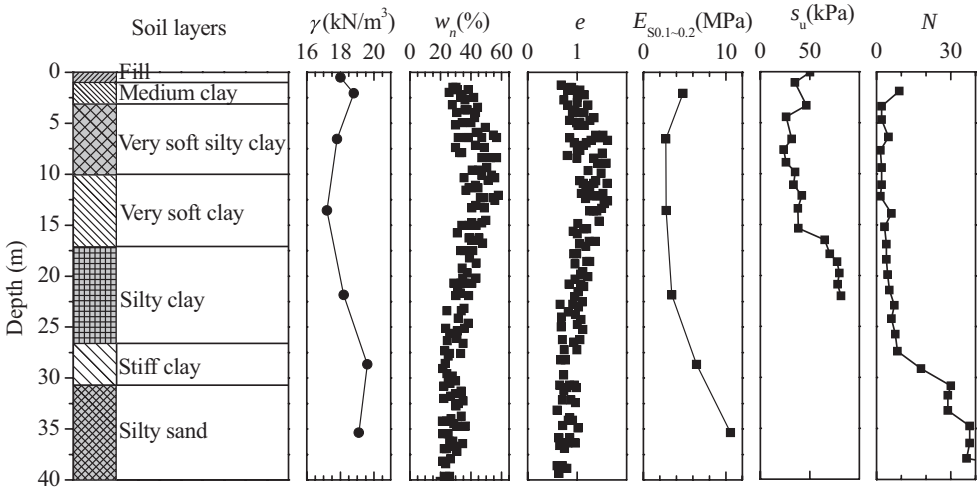

Note: γ = unit weight, w_n = water content, e = void ratio, $E_{s0.1\sim0.2}$ = compressibility modulus, s_u = undrained shear strength, N = SPT N value

Figure 3. Typical soil profile and geotechnical parameters in Shanghai soft ground.

used wall thicknesses are 800 mm, 1000 mm, and 1200 mm. In order to guarantee water-tightness at the joints of wall panels, high pressure rotary jet grouting piles are usually used at the back of wall, while RC pilasters are used in front of the wall (see Fig. 4(a)).

The second kind of retaining wall is contiguous pile wall (see Figure 4(b)) which is usually adopted as temporary wall in Shanghai. The gap between two bored piles typically ranges from 150 mm to 200 mm. Deep soil mixing columns, constructed at the back of contiguous pile walls, are used as waterproof curtains. The cost of this kind of retaining wall is lower and construction speed is higher comparing with diaphragm wall.

The third type of retaining wall is compound deep soil mixing wall which is formed by deep soil mixing columns and the steel H-beams inserted inside the deep soil mixing wall (see Figure 4(c)). In this kind of wall, the deep soil mixing columns are used as waterproof curtains, while steel H-beams are used to bear bending moments. The deep soil mixing columns, with commonly used diameters of 650 mm, 850 mm and 1000 mm, are usually performed by machine with three shafts of augers and mixing paddles in Shanghai. In order to form continuous waterproof curtains, the deep soil mixing columns are constructed by overlapping adjacent soil mix elements. After finishing the construction of the underground structure, the steel H-beams can be pulled out and can be reused in other projects. The soil mix method can be very effective at providing stiff and waterproof retaining systems. However, it is rather limited to medium and large-scale projects because of high mobilization costs.

The fourth type of retaining wall is the deep soil mixing wall (see Figure 4(d)) which has enjoyed success and popularity since the 1990s. According to the experience in Shanghai, thickness of the cross section of a deep soil mixing wall ranges from 0.7 to 1.0 times the excavation depth, while the penetration depth of the wall range from 1.0 to 1.4 times the excavation depth. As the cross section of a deep soil mixing wall is very thick, it performs like a gravity wall. Excavations supported by deep soil mixing walls are usually excavated without struts. Wang et al (2010) collected 34 excavations supported by deep soil mixing walls in Shanghai. They found that maximum lateral displacements of the wall range from 0.3%H to 2.4%H with an average value of 0.91%H, where H is the excavation depth.

The fifth type of wall is compound soil nail wall (see Figure 4(e)) which is a combination of single or double rows of deep soil mixing columns with soil nails. Deep soil mixing columns is also used as waterproof curtain. Distance of soil nails range from 0.8 m to 1.0 m, while length of the soil nails ranges from 1.5H to 2.5H. Cost of compound soil nail wall can be very competitive. As a result, it has been developed quickly in recent years.

Other uncommonly used retaining walls include sheet pile wall and secant pile wall. Sheet pile walls were popular in the 1980s in Shanghai. Due to some severe problems such as nose pollution and effect of vibration on nearby building during installation, and large displacement during excavation,

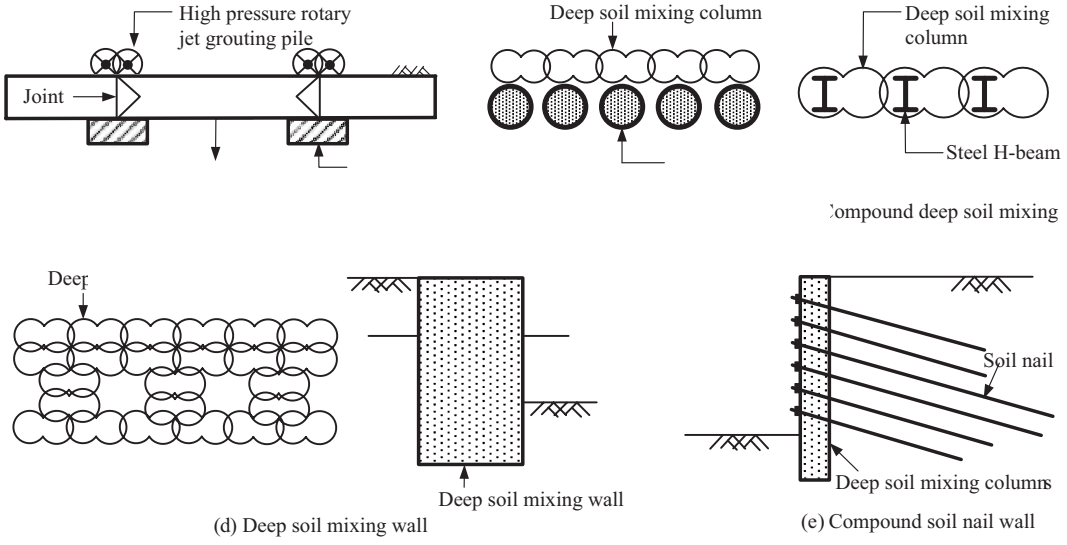

(d) Deep soil mixing wall (e) Compound soil nail wall

Figure 4. Sketch maps of different type of commonly used retaining walls in Shanghai.

sheet pile walls are now seldom adopted in deep excavations in this region.

A database of 304 deep excavation case histories in Shanghai was set up. The number of excavations retained by diaphragm walls, contiguous pile walls, compound deep soil mixing walls, compound soil nail walls, deep soil mixing walls, and sheet pile walls are 128, 78, 30, 23, 34, and 11, respectively. Figure 5 depicts the excavation depth distribution of different types of retaining wall. It shows that diaphragm walls are the most frequently used retaining walls. It is frequently adopted in 10 m to 25 m deep excavations and the maximum excavation depth reaches 41.2 m. Contiguous pile walls are frequently used in excavations with depth of 5 m to 15 m. Compound deep soil mixing walls are frequently used in excavations with depth of 5 m to 10 m and there is a trend to be used in much deeper excavations. Compound soil nail walls and deep soil mixing walls are generally used in excavations with depth less than 8 m. Sheet pile walls are generally adopted in 6 m to 9 m deep excavations. However, it has been rarely used since the 1990s. Excavation depth distributions in Figure 5 can be used as a guide in selecting supporting system according to excavation depth.

3.2 *Lateral support system*

Due to the poor ground condition, it is considered that anchors are not very applicable in Shanghai. As a result, temporary steel and Reinforced Concrete (RC) struts as well as slabs of the underground structure are used as lateral support system. Steel tubes and H-beams are frequently used steel struts. Commonly used diameter of steel tubes is 609 mm with thickness of 10 mm, 12 mm, or 14 mm. While the H700 × 300 and H500 × 300 are frequently used H-beams. Steel struts are generally arranged orthogonally, as shown in Figure 6(a) and Figure 6(b). For excavations with depth less than 7 m, sometimes inclined struts with one end supported on the bottom slab are used, as shown in Figure 6(c). For narrow excavations (such as subway stations) retained by diaphragm walls, steel struts without wale (see Figure 6(d)) are used to accelerate construction speed. Steel struts are generally preloaded and sometimes they are reloaded during the excavation procedure when stress lost is severe. Steel struts are rather limited to irregular excavations. Moreover, it is not suitable for large-scale projects because that it is difficult to guarantee the installation quality and control deformation of the excavation.

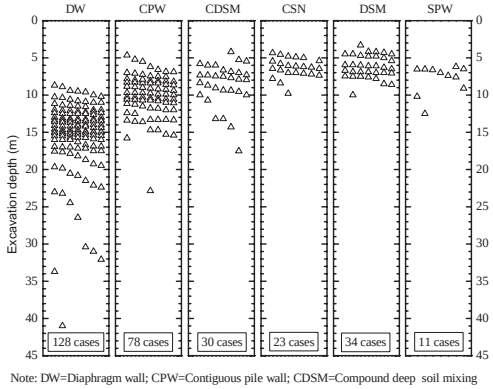

Note: DW=Diaphragm wall; CPW=Contiguous pile wall; CDSM=Compound deep soil mixing wall; CSN=Compound soil nail wall; DSM=Deep soil mixing wall; SPW=Sheet pile wall

Figure 5. Excavation depth distribution of different types of retaining wall.

RC struts, which have good integrity and quite high stiffness, are suitable for most excavations especially for irregular and large-scale excavations. RC struts can be arranged orthogonally (see Figure 6(e)) or formed by truss system (see Figure 6(f)). In order to gain large working space, sometimes RC ring struts (see Figure 6(g)) are used. In some cases, a combination of steel and RC struts is adopted (see Figure 6(h)). In this kind of strut system, the first level struts are RC struts while the following level struts are steel struts. This combination is benefit to deformation control because it can take the advantages of good integrity and quite high stiffness of the RC struts and quick installation of the steel struts. Temporary RC struts are not benefit to environment protection as they have to be demolished after the construction of underground structure. However, due to low cost of labor in China and its reliability in deformation control, RC struts are still the most popular struts form in Shanghai.

When environmental protection is extremely strict or working space and construction time is limited or excavations are very large, the top-down method is used. On this occasion, retaining walls are supported by permanent concrete floor slabs of underground structure (see Figure 6(i)). Design and construction of top-down method are quite complicated. Though thousand of deep excavations have been constructed in the past two decades in Shanghai, only about 30 of them were constructed by top-down method. However, there is a trend of increase of adopting this method.

3.3 *Vertical support system*

Lateral support system is propped by vertical support system. Vertical support system is composed of steel lattice column and bored pile. Steel lattice column, which is erected in the bored pile, is usually made up of four pieces of hot-rolling equilateral angle steel welded with tie plates, as

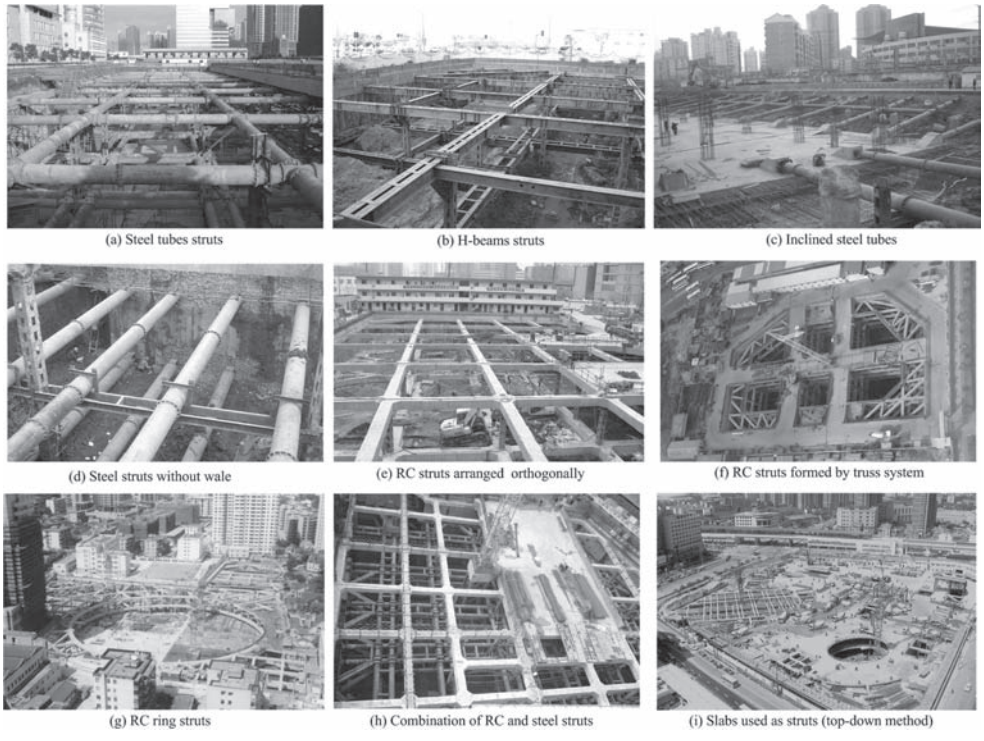

Figure 6. Types of lateral support system commonly used in Shanghai.

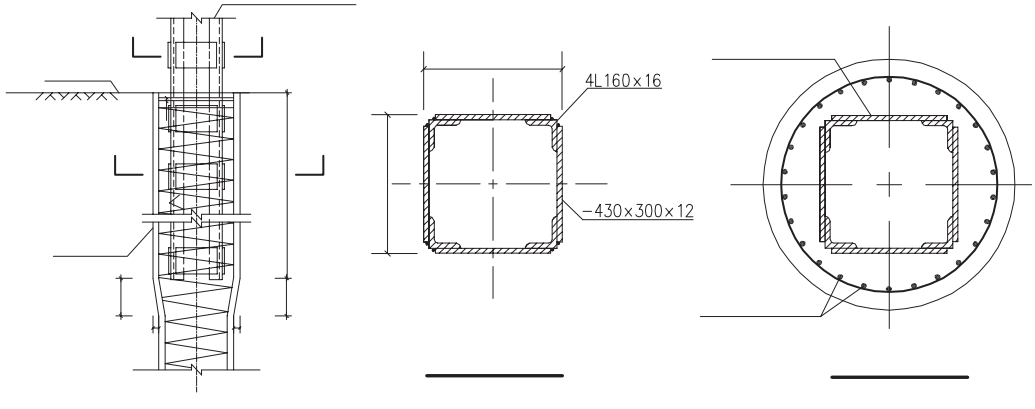

Figure 7. Steel lattice column erected in bored pile to form vertical support system.

shown in Figure 7. Commonly used section of the steel lattice column is 460 mm × 460 mm. Sometimes the diameter of bored pile is expanded in the range of about 3 m at the top of pile to facilitate the penetration of steel lattice column (see Figure 7).

For top-down method, steel lattice columns (see Figure 8(a)) or steel tubes (see Figure 8(b)) filled with concrete, are used as vertical support system during the excavation stage. They will finally be encased in concrete to be transferred into permanent columns of underground structure (see Figure 8(c)). Perpendicularity of less than 1/250 is required for the installation precision of the steel lattice columns and steel tubes in top-down method (SCMC, 2010).

(a) Steel lattice column used in top-down method during excavation stage

(b) Steel tubes used in top-down method during excavation stage

(c) Steel tubes encased in concrete to be transferred into permanent columns in top-down method

Figure 8. Steel lattice column and steel tubes used in top-down method.

4 BENCHMARKS OF DEEP EXCAVATIONS IN SHANGHAI

4.1 *The largest deep excavation*

The Shanghai Hongqiao Comprehensive Transportation Hub (SHCTH) is the biggest modern city comprehensive transportation engineering in China. It is a comprehensive transportation center including the new Western Terminal, the Eastern Metro Station, the Eastern Traffic Square, the Maglev Station, the High-Speed Railway Station, the Western Metro Station, and the Western Traffic Square. The project involves ultra-large and deep excavations. The excavation area of the project was about 580,000 m^2, and the excavation depth ranged from 9 m to 29 m. It is so far the largest deep excavation in Shanghai. A combined supporting system was adopted according to the characteristics of the excavation. Sloped excavation and deep soil mixing walls (with a thickness of 5.7 m and depth of 13 m) were used for the shallow excavation area, while 800 mm thick diaphragm walls which were braced by two levels of RC struts was adopted for the deep excavation area. Figure 9 shows a sectional view of typical supporting system adopted in this project. Figure 10 shows a photo of the construction site when the soil was cut to the final elevation. The excavation was completed in 2009 and the whole SHCTH project was put into service in March, 2010. Despite the poor ground condition and long time construction, deflections of the deep soil mixing walls were generally less than 74 mm while deflections of the diaphragm walls were generally less than 55 mm. The combined supporting system was proved to be quite successful for this ultra-large and deep excavation.

4.2 *The deepest excavation (Tang and Zhu, 2009)*

The remediation project of the collapsed tunnel of Metro Line 4 is so far the deepest excavation in Shanghai. The length of the shield tunnel between the South Pudong Road Station and Nanpu Bridge Station was 2000 m, among which 440 m was under the Huangpu River. The tunnel collapsed due to quick sand caused by the construction of the passage of the air shafts on July 1, 2003. The collapse caused large ground settlements and many adjacent buildings had to be disposalled. It was decided to conduct the remediation at the original place using cut-and-cover method. The remediation was divided into three parts, namely, the east part, the middle part, and the west part, as shown in Figure 11. The lengths of the three parts were 174 m, 62.5 m and 28 m, respectively. The maximum excavation depth was 41 m. The excavation was retained by 1.2 m thick diaphragm wall with a depth of 65.5 m. The diaphragm walls, which were penetrated into the second sand layer (usually adopted as bearing layer for piles of super high-rise buildings), were the deepest walls in Shanghai. As the diaphragm walls were extremely deep and there were so many obstacles caused by the collapse, construction of the diaphragm wall was a great challenge. The diaphragm walls were supported by 9 levels of RC struts. In order to improve the properties of the collapsed soils inside and outside of the excavation, triplex pipe jet grouting with a maximum depth of 50 m was adopted to strengthen the soils. Dewatering was conducted in the excavation by wells with depth of 60 m to satisfy the requirement of safety against confined water upheaving. The remediation commenced in August, 2004 and it was completed in the first half of the year 2007. Figure 12 shows a photo of the construction site. Maximum lateral displacement of the diaphragm wall was 48 mm.

4.3 *The largest circular excavation*

The Shanghai 500 kV World Expo Underground Transmission and Substation (SWEUTS) project is located in the center district of the city. It is an important attached project of the 2010 Shanghai World Expo. Completion of the project will make it one of the largest and most advanced underground

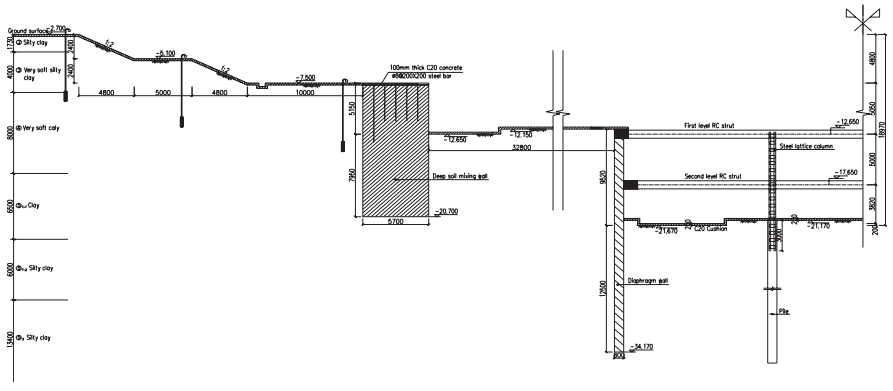

Figure 9. Sectional view of the typical supporting system adopted in the SHCTH project.

Figure 10. A photo of the construction site when the soil was cut to the final elevation.

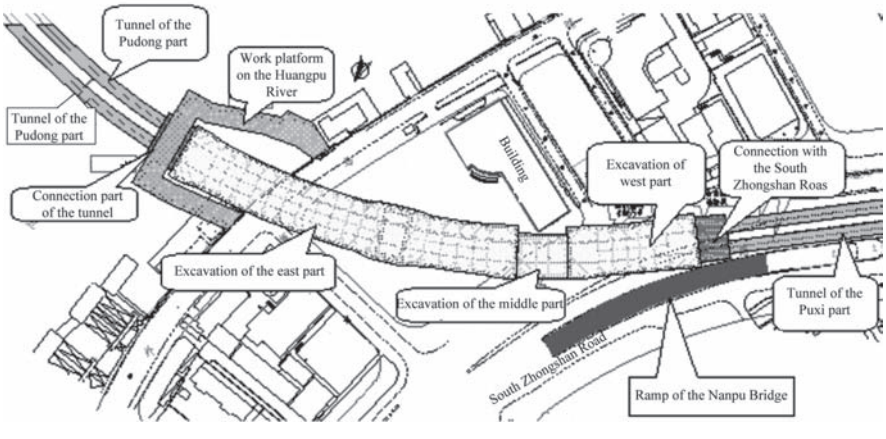

Figure 11. Plane view of the remediation project of the collapsed tunnel of Metro Line 4 (according to Tang and Zhu, 2009).

Figure 12. A photo of the construction site (from http://www.51xuewen.com/group/287/topic_11354.htm).

substations in the world. The project, constructed to a depth of 34 m below the ground surface has a diameter of 130 m. It is so far the largest and deepest circular excavation in Shanghai. It is also one of the largest circular deep excavations in the world. The project was constructed by top-down method. The ring was made of 80 panels of diaphragm walls of 1.2 m in thickness with their toes embedded in relatively competent stratum. The 57.5-meter long diaphragm walls were installed to the silty clay and silty sand interbedded strata through the firm sand soil layers with SPT N value of 28 to 50. The firm sandy soil layers had brought great difficulties to the installation of the diaphragm walls. To ensure quality and speed of diaphragm wall installation, the sectors of wall trenches in soft soils (above the sand soil layer) were excavated by conventional clamshell grabs while the deep sectors in the firm sandy soil layers and the silty clay and silty sand interbedded strata were formed by trench cutting machines. The diaphragm walls were braced at the floor levels by the four basement slabs. In order to reduce the spacing of the lateral struts and further restricting wall movements, temporary ring RC strut frame systems were installed between the slabs in the first, second and fourth level basement. Steel tubes with diameter of 550 mm and thickness of 16 mm, filled with Grade 60 concrete at the same position of the permanent columns were erected in bored piles to support the underground structure that was constructed from the top level downward at the excavation stage. The steel tubes would finally be encased in concrete to be transferred into permanent columns. Figure 13 shows a sectional view of the supporting system. Figure 14 shows photos of the construction site. It cost about three years to construct the project and it was put into service in 2009. Monitored results showed that maximum deflections of the diaphragm walls were less than 49 mm.

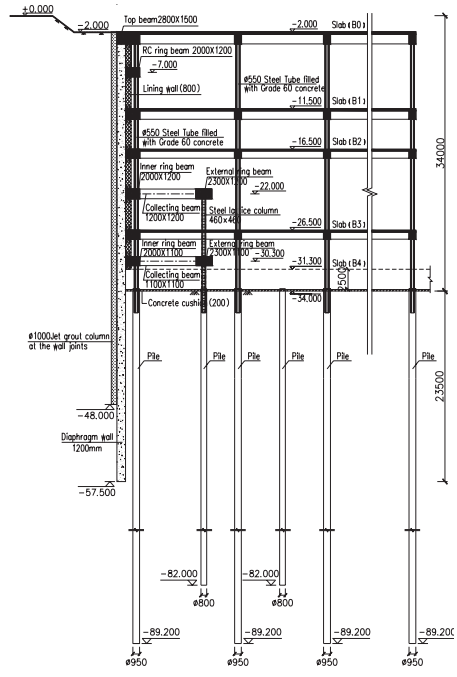

Figure 13. Sectional view of the supporting system of the SWEUTS project.

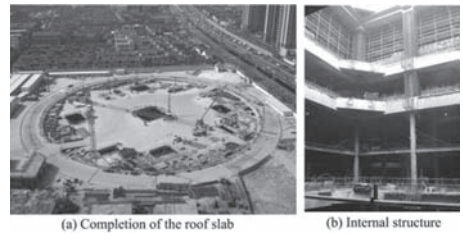

Figure 14. Photos of the construction site of the SWEUTS project.

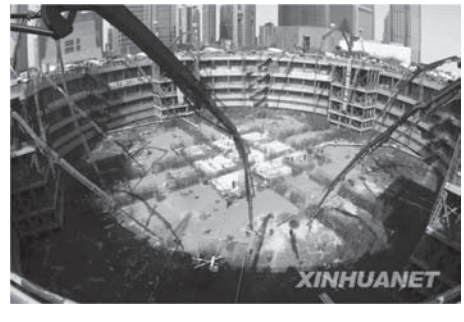

Figure 15. A photo showing pouring concrete of the bottom slab of the tower block of the Shanghai tower (from http://news.xinhuanet.com/photo).

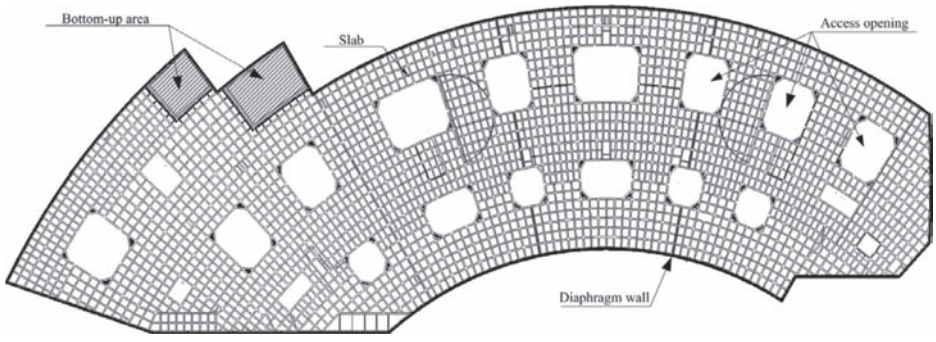

Figure 16. Plan view of the structure of the roof slab and distribution of access openings.

4.4 *Basement excavation for the tallest building in China*

Being the tallest building under construction in China at this moment for its height of 632 m, the Shanghai Tower deserves a space herein. The five-level basement of the project is one of the deepest building basements in Shanghai. Excavation area of the project is 34960 m^2. Excavation depth of the tower block is 31.2 m while that of the podium block is 26.7 m. It is decided to excavate the tower block by bottom-up method and excavate the podium block by top-down method. This united method was also used in the excavation of the basement of the Shanghai World Financial Center (Chu et al, 2005) which is now the tallest building in service (construction completed in 2008) in China with a height of 492 m. The tower block of the Shanghai Tower is firstly excavated and the podium block will be excavated after the B0 slab of the tower block is completed. The tower block is retained by 1.2 m thick circular diaphragm walls with depth of 50 m. The external diameter of the circular diaphragm wall is 123.4 m. Six levels of RC ring beams are constructed inside the wall to reinforce the diaphragm walls for reducing wall deflections. The 6 m thick mat of the tower block is supported on bored piles of 1.0 m in diameter to a maximum depth of 88 m from ground surface. Excavation of the tower block was completed in February, 2010 while construction of the basement was completed in September, 2010. Figure 15 gives a photo showing pouring concrete of the bottom slab of the tower block. Wall deflections observed were 76.5 mm or less (Jia et al, 2010). Excavation of the podium block will commence soon.

4.5 *Largest excavation constructed by top-down method*

The excavation of the North Square of Shanghai South Railway Station (NSSSRS) is so far the largest deep excavation constructed by top-down method. The NSSSRS was a two stories underground structure with an excavation area of 40000 m^2 and depth of 12.5 m. The excavation was retained by 800 mm thick diaphragm walls with depth of about 27.5 m. The walls were supported by the slabs of the underground structure. In order to accelerate the cut and transportation of soils for this ultra large excavation, large size access openings were set in the slabs. The area of the largest access opening was about 700 m^2, while that of others ranges from 400 m^2 to 500 m^2. The areas of these access openings were much larger than those in conventional projects constructed by top-down method. Figure 16 shows the distribution of the access openings in the roof slab. Diaphragm wall deflections observed were 41 mm or less.

5 DEFORMATION CONTROL OF DEEP EXCAVATIONS

5.1 *Concept of performance-based design*

In the 1980s, environment protection problem was not very severe as excavation depth was generally quite shallow. Sheet pile walls and bored pile walls were commonly used to retain the soils. In those days, these retaining walls were generally designed in consideration of their structural capacity and the stability of the ground below the final excavation depth without due consideration given to their lateral deformations. Since the early 1990s, excavations have tended to go not only deeper and deeper but also larger and larger. Meanwhile, deep excavations are often constructed in close proximity to existing structures and properties including buildings, subway stations, metro tunnels, embankments and underground pipelines. As people have become more and more aware of their own rights and the government has recognized the importance of sustaining the safety of public facilities such as subway

Table 1. Protection grade of deep excavations (according to SCMC, 2010).

Environmental conditions	Distance of the structure or properties from the excavation (s)	Protection grade
Heritage buildings, factory buildings with precision instruments and machines, important buildings with shallow foundations or short pile foundations, metro lines, flood control walls, very important services such as water mains and gas mains	$s \leq H$	I
	$H < s \leq 2H$	II
	$2H < s \leq 4H$	III
Common building with shallow foundations or short pile foundations, important services such as water supply pipes, gas pipes, and sewage pipes	$s \leq H$	II
	$H < s \leq 2H$	III

Note: H is the excavation depth.

Table 2. Control criteria for protection environment (SCMC, 2010).

Protection grade	Maximum allowable displacement of wall	Maximum allowable ground settlement
I	0.18%H	0.14%H
II	0.3%H	0.25%H
III	0.7%H	0.55%H

stations and tunnels, protection of adjacent properties has become serious concern for deep excavations. In order to protect the adjacent buildings and properties, the concept of performance-based design, instead of capacity-based design, has been adopted in deep excavations since the 1990's. The purpose of performance-based design is to limit wall displacement and hence ground movements behind walls to fulfill the requirement of deformation control of adjacent properties.

Performance of deep excavations is governed by many factors (Manna and Clough, 1981) such as construction conditions (including soil properties, ground water, existing structures and properties, transient surcharge loads during and after construction), design parameters (including stiffness of the wall, stiffness of supports, support spacing, and depth and with of excavation), and construction parameters (including method and sequence of construction, and during of construction). It is difficult to evaluate the performance of deep excavations and its impact on adjacent structures and properties considering all of these factors. As a result, predicting the magnitude of ground movement and deformation of adjacent structures and properties is still the most challenging task facing the engineers involved in the design and construction of a deep excavation in urban environment.

As ground movements can not be predicted accurately (Gaba et al, 2003), case history data provide a useful guide when making prediction for new deep excavations or setting up criteria of deformation control in comparable conditions. To avoid damage to adjacent structures and properties, three different protection grades (see Table 1) was setup for deep excavations according to the local code of Shanghai (SCMC, 2010). Each grade is defined depending on the importance of the environmental condition and the distance of the structure or properties from the excavation. In order to setup criteria of deformation control of deep excavations, a large number of case histories of deep excavations were collected. They were then classified according to the protection grades defined by Table 1. Maximum lateral displacements of wall were analyzed for each protection grade. The mean value of the maximum lateral displacement of wall was considered as the allowable lateral displacement of wall for each protection grade. Allowable ground surface settlement for each protection grade was obtained by 0.8 times the maximum allowable lateral displacement of wall according to the statistical relationship between maximum ground settlement and maximum lateral displacement of wall. Criteria of deformation control of deep excavations were then obtained, as shown in Table 2. Control criteria listed in Table 2 can be used as a guide in the design of deep excavation. According to the experience in Shanghai, normal operating of the adjacent structures and properties will not be likely affected according to the control criteria listed in Table 2, as long as the excavations are constructed with normal construction activities.

5.2 *Deformation control method*

5.2.1 *Using top-down method*

Top-down method provides a stiff support system for the retaining wall. Therefore, top-down method is more effective in deformation control than bottom-up method. Study conducted by Wang et al (2010) shows that average value of maximum deformation of 32 excavations constructed by

top-down method in Shanghai is 0.27%H, which is much smaller than the average value of 0.4%H for 200 excavations constructed by bottom-up method (see Figure 17). Top-down method is consequently a good choice to minimize ground movements for deep excavation adjacent to sensitive environment.

Figure 18 shows the plane view of the construction site of the Xingye Building which located in the old city zone of Shanghai. The building has 19 floors above ground and three floors under ground. Excavation depth of the west side of the building was 14.4 m while that of the east side was 12.4 m. The excavation site was adjacent to 15 buildings, among which 8 (Building A to Building H) were heritage buildings with shallow foundations or strip foundations with short wooden piles. The minimum distance between the excavation and the heritage buildings was about 4.2 m. Meanwhile, many old pipelines were distributed under the Hankou Road and the Sichuan Road. Environmental protection was extremely strict in this project. Top-down method was adopted in order to protect the adjacent buildings and services. The excavation was retained by 1.0 m thick diaphragm walls on the west and south sides, and by 0.8 m thick diaphragm walls on the north and east sides. The diaphragm walls were supported by three levels of slabs of the permanent substructure. Monitored results showed that the maximum lateral displacement of the wall was 37.9 mm and the maximum ground settlement was 22.4 mm. Figure 19 shows a 3D settlement distribution of Building A at the final excavation stage. The maximum settlement of Building A was 27.2 mm. Building A was a RC frame structure. According to empirical limitation criteria proposed by Polshin and Tokar (1957), limiting distortion of the cracking of infill of RC frame structure was 1/500. The maxi-mum angular distortion of Building A was about 1/780, which was smaller than 1/500. As a result, no further development of the original old cracks of Building A was observed. Top-down method was very effective in deformation control in this project and the normal use of the adjacent buildings and services was not affected by the excavation.

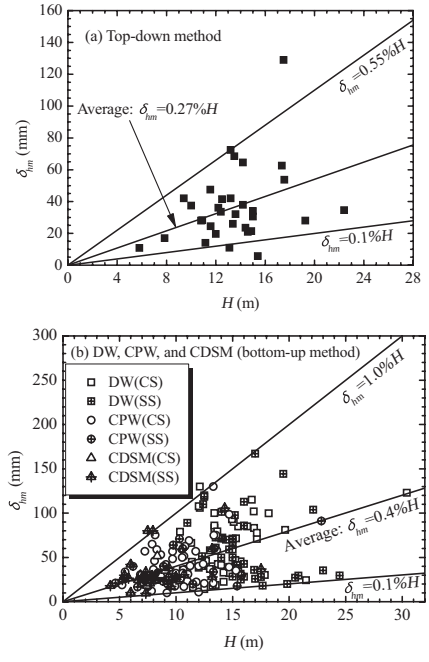

Figure 17. Maximum lateral displacement of wall δ_{hm} versus excavation depth H (Wang et al, 2010).

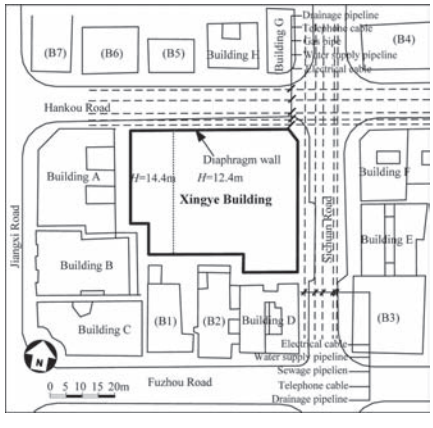

Figure 18. Plane view of the construction site of the Xingye Building.

5.2.2 *Reinforcement of soils inside the excavation*

In order to increase the strength of soft soils and thus reduce the deformation of the soils during

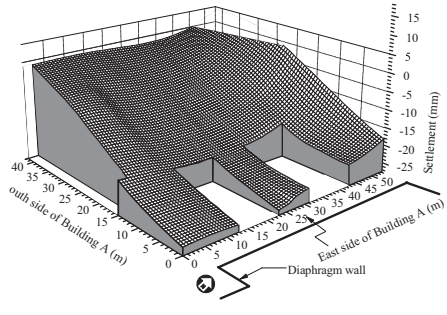

Figure 19. 3D settlement distribution of Building A at the final excavation stage.

excavation to protect the adjacent structures and properties, reinforcement of soils inside the excavation is widely used in Shanghai. The soils inside the excavation may be reinforced by deep mixing method (using double shaft machine or triple shaft machine) or jet grouting method. For deep soil mixing columns formed by double shaft machine, dosage of cement is generally required not less than 13% with a water-cement ratio of 0.45 to 0.6. The unconfined compressive strength (UCS) of the deep soil mixing columns is required not lower than 0.6 MPa after cured for 28 days. For deep soil mixing columns formed by triple shaft machine, dosage of cement is generally required not less than 20% with a water-cement ratio of 1.5 to 2.0. The UCS of these deep soil mixing columns is required not lower than 0.8 MPa after cured for 28 days. While for columns formed by jet grouting method, dosage of cement is generally required not less than 25% with a water-cement ratio of 0.8 to 1.5. The UCS of the columns is required not lower than 1.0 MPa after cured for 28 days. The layout of the reinforcement depends on the construction features and stratum conditions. Figure 20 shows the commonly used layouts of the reinforcement of soils inside the excavation.

The Nanjing West Road Block project located in the central district of Shanghai city. The excavation depth of the podium and tower part was 14.2 m and 15.5 m, respectively. On the south side of the excavation, the No.2 subway tunnels which were laid about 8.5 m below the ground surface were only about 10.2 m away from the excavation (see Figure 21). The excavation was divided into two zones, namely, Zone I and Zone II. Zone I was retained by 0.8 m thick diaphragm wall which were supported by three levels of RC struts. Excavation of Zone I started after the finish of the construction of Zone I. Zone II was retained by 1.0 m thick "T" type diaphragm wall with a depth of 42 m on the south side. The "T" type diaphragm walls were supported by RC struts at the first level and three levels of steel struts. In order to reduce the effect of excavation on the tunnels, shirt-edge type soil reinforcement was adopted on the south side of the excavation. The soils inside the excavation were reinforced by deep soil mixing columns formed by triple shaft machine. The diameter of the columns was 650 mm. The width of the reinforcement ranged from 10 m to 15 m. The reinforcement started from the elevation of –5.400 m while ended at the elevation of –20.600 m, as shown in Figure 22. Dosage of the cement above and below the final excavation depth was 10% and 20%, respectively. Deep soil mixing columns were also used to reinforce the trench of the "T" type diaphragm walls. It was proved that the reinforcement of the soils inside the excavation was effective. Figure 23 show the lateral displacement of the diaphragm wall on the south side of the excavation. The maximum lateral displacement was only 21.8 mm. The maximum displacement of the tunnels was less than 5.0 mm. The metro in operation was successfully preserved.

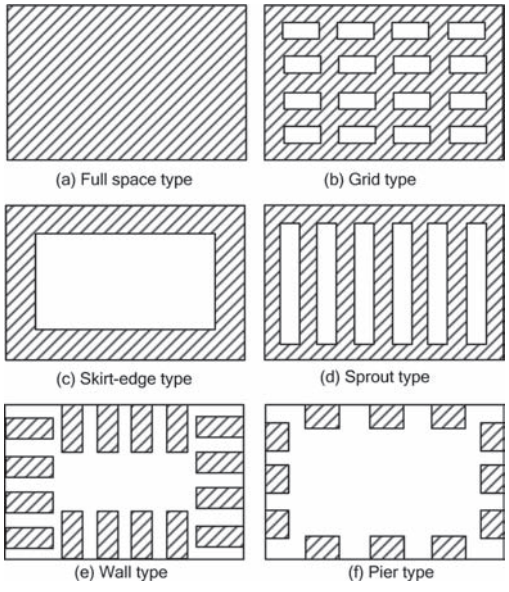

Figure 20. Layouts of the reinforcement of soils inside the excavation.

5.2.3 *Zoned excavation*

Zoned excavation method is sometime used for excavation with very strict environmental protection requirement. In this method, the excavation is divided into a relatively big pit and a small pit. The small pit is just adjacent to the structures or properties which need careful protection. The big pit and the small pit are separated by temporary walls such as diaphragm walls and contiguous pile walls. The big pit is firstly excavated. The excavation of the big pit will have a very limited effect on the structures and properties adjacent to the small pit as the separation walls and the soils in the small pit form a barrier to the structures and properties. The small pit will then be excavated after the construction of the underground structure of the big excavation zone is finished. The excavation of the soil and installation of struts can be very quick as the area of the small pit is small. Previous study shows that the creep property of soft soils in shanghai (Huang and Gao, 2005) plays a critical role in soil deformation in deep excavations. Therefore, quick excavation of the soils will shorten the elapsed time of construction and this will be very effective in

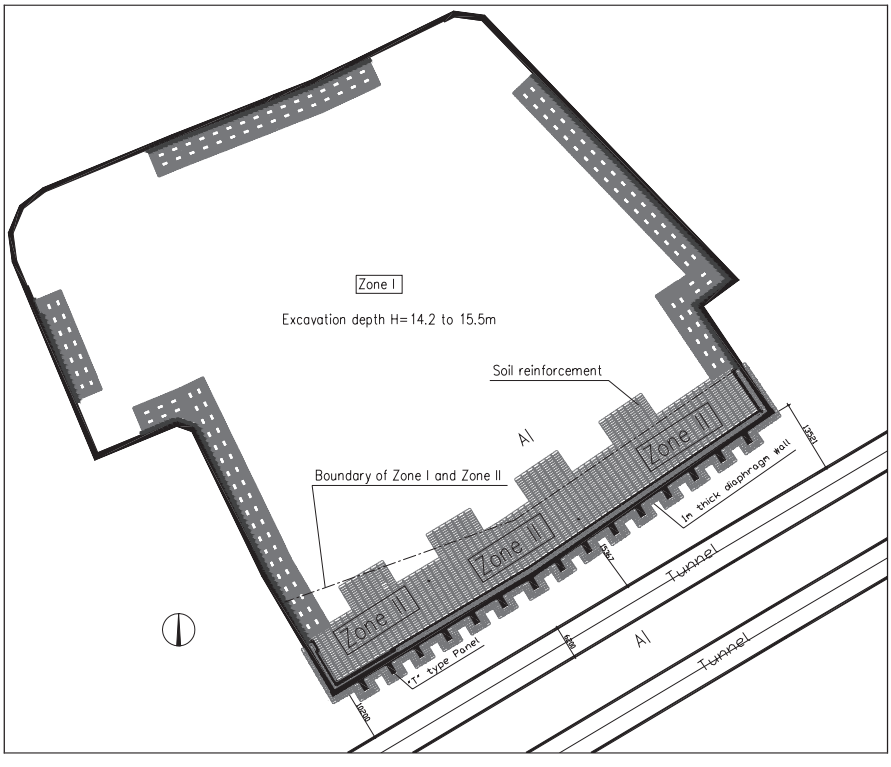

Figure 21. Layout of the reinforcement of the excavation of the Nanjing West Road Block project.

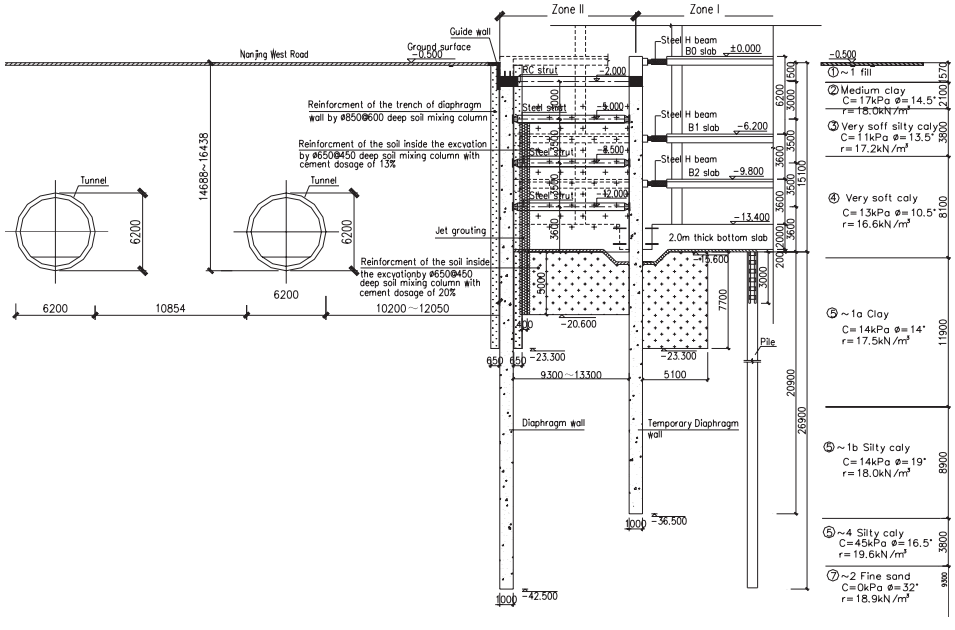

Figure 22. Sectional view of the excavation.

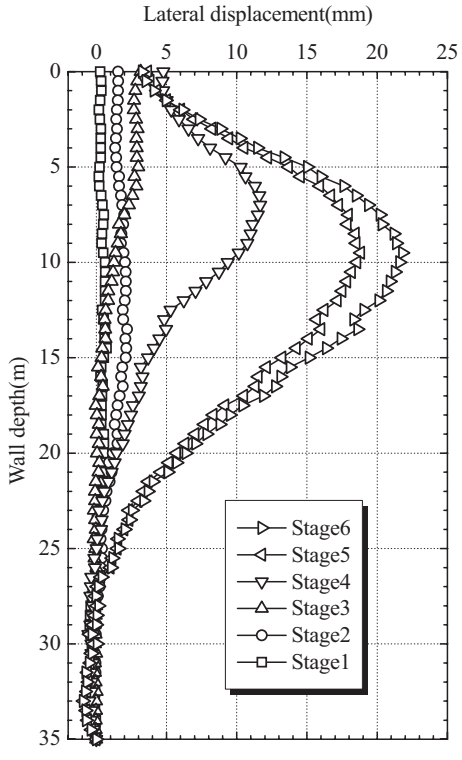

Figure 23. Lateral displacement of wall.

reducing the impact of the excavation on the adjacent structures and properties.

The Shanghai Shengda Center project was adjacent to the No. 4 metro and No. 2 metro. The No. 4 metro tunnels which were laid 16 m below the ground surface are only about 6 m away from the excavation. The excavation depth of the project ranged form 17.15 m to 22.15 m. In order to protect the tunnels of the No.4 metro, the excavation was divided into two zones, namely, Zone I and Zone II, as shown in Figure 24. Zone I and Zone II was separated by 1.0 m thick temporary diaphragm wall with a depth of about 41 m. The Excavation of Zone I was retained by 1.2 m thick diaphragm wall on the north side and 1.0 m thick diaphragm wall on the east side. The diaphragm walls of Zone I were retained by five levels of RC struts. The excavation of Zone II was retained by 1.0 m thick diaphragm walls. The diaphragm walls of Zone II were retained by the first level RC struts and four levels of steel struts below. Zone I was firstly excavated. Excavation of Zone II commenced after the construction of the underground structure of Zone I finished. Figure 25 shows a sectional view of the retaining system of the excavation. Figure 26(a) shows the lateral displacement of the inclinometer installed at monitored point Q16 (see Figure 25) in the diaphragm wall in Zone I. The maximum lateral displacement was 32.8 mm. Figure 26(b) shows the lateral displacement of the inclinometer

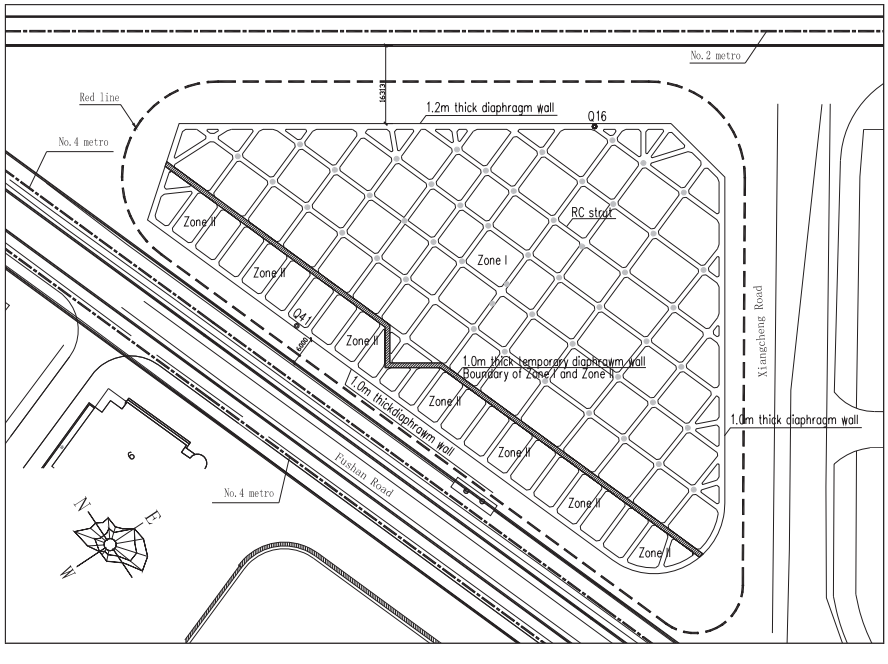

Figure 24. Plane view of the construction site of the Shanghai Shengda Center.

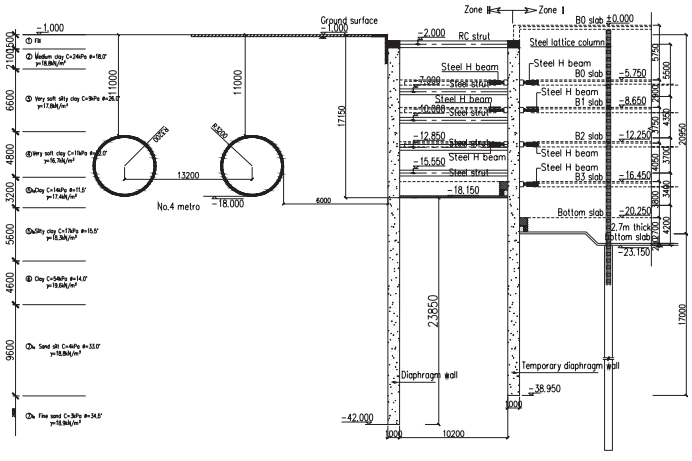

Figure 25. Sectional view of the retaining system of the Shanghai Shengda Center.

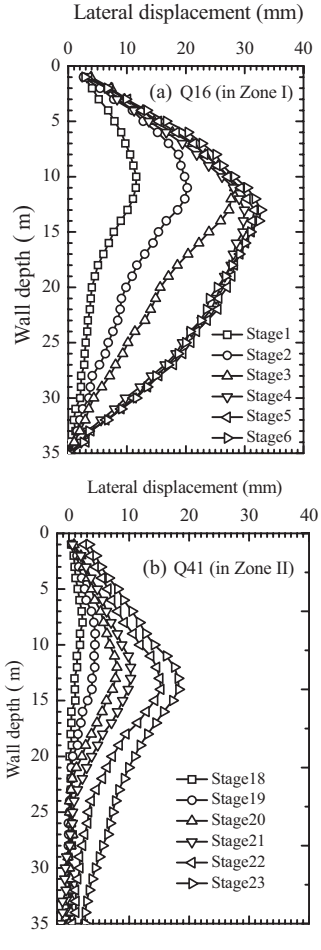

Figure 26. Lateral displacement of diaphragm wall.

installed at monitored point Q41 (see Figure 25) in the diaphragm wall in Zone II. The maximum lateral displacement was only 18.3 mm. It is obvious that deformation of Zone II was much smaller than that of Zone I. Monitored results also show that the maximum settlement of the tunnels of No.4 metro was about 5.2 mm. The normal operation of the tunnels was not affected by the excavation.

5.2.4 *"Time and space effect" excavation method*

The deformation of retaining structure and soils mass around the excavation relates to many important factors such as the volume of excavation, duration without struts due to creep effect, and sequence of the excavation. Liu et al. (1999) suggested excavation procedure taking into account the rational planning and sequence of the excavation, including the lifts, plots, symmetry, time, and bracing. This so called "Time and Space Effect" excavation method is an empirical method developed in Shanghai. Engineering practice has proved that this excavation method is efficient for deformation control of deep excavations in Shanghai soft soil.

The Shanghai Square project (Liu and Wang, 2009) consisted two parts, namely, the north part and the south part. The north part had 34 floors above ground and three floors under ground. Excavation area of the north part was 9656 m^2 and the excavation depth ranged from 15.1 m to 16.0 m. The No.1 metro tunnels were only about 2.6 m away from the excavation on the south side. The excavation was retained by 0.8 m thick diaphragm walls with depth ranging from 25.2 m to 28.2 m. The diaphragm walls were supported by 4 levels of RC struts. "Time and Space Effect" excavation method was adopted in this project.

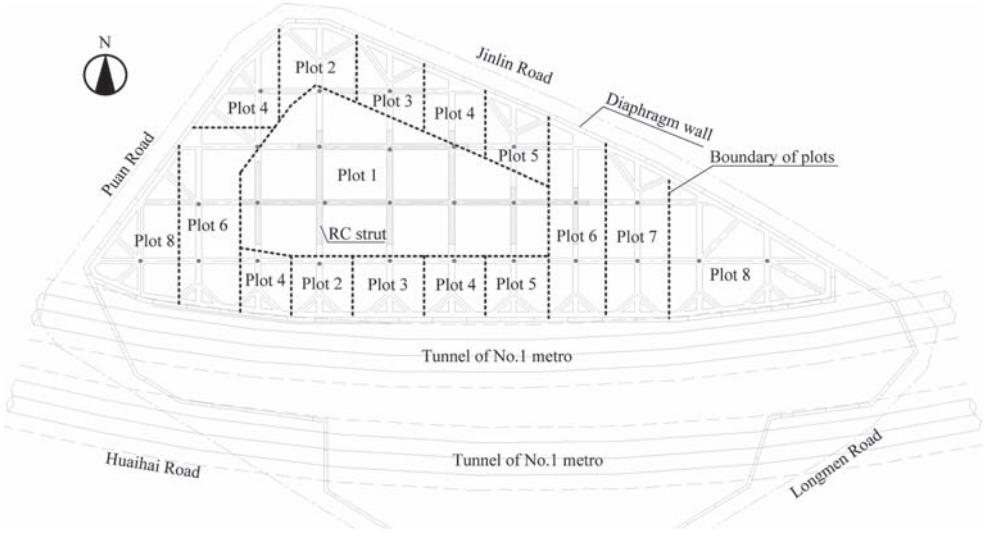

Figure 27. Plane view of the plots of the excavation of the Shanghai Square project (according to Liu and Wang, 2009).

The north part was excavated in five lifts. In each lift, the excavation was divided into 8 plots, as shown in Figure 27. The steps in the excavation procedure were as follows: (1) excavating the soil in Plot 1; (2) pouring the RC struts corresponding to the unloading space; (3) excavating the soil in Plot 2 ~ Plot 8 sequentially and promptly installing the corresponding struts in turn; and (4) continuing steps 1–3 for the second, third, fourth, and fifth lifts until the design depth of the excavation was achieved. It was required that the above excavation procedure should be strictly observed and over cut of the soil should be avoided. Moreover, RC struts should be poured in 48 hours after the soil was excavated. Monitored data showed that the maximum lateral displacement of the diaphragm wall was 28.2 m. Maximum lateral displacement and maximum settlement of the tunnel were 13.1 mm and 14.1 mm, respectively.

6 SUMMARY AND CONCLUSION

Numerous deep excavations have been carried out in Shanghai for constructing high-rise buildings, subway transportation networks and other underground structures in the past two decades. There is significant advancement in design and construction practice of deep excavations in Shanghai. The successful completion of the introduced cases which are benchmarks of deep excavations is an index of the technology level and the quality of the local construction industry.

For deep excavations adjacent to complex environment conditions, performance-based design is an essential concept for engineering practice so that the surrounding structures and properties can be protected effectively. Three different protection grades and corresponding deformation control criteria were setup for deep excavations according to the local experience. These can be used as a guide in the design and construction of deep excavations. Top-down method, reinforcement of soils inside the excavation, zoned excavation, "Time and Space Effect" excavation method are effective measures in mitigating the impact of deep excavations on adjacent structures and properties. However, due to limitations in the state of current knowledge in soil mechanics, the complex nature of soil behavior, and complex mechanism of soil-structure interaction, quantitative prediction of the effect of these methods is still very difficult and it needs further investigation. Therefore, use of instrumentations to monitor the performance of excavations and the surrounding structures and properties should be considered as an essential element of the total technique.

ACKNOWLEDGEMENTS

The authors wish to gratefully acknowledge the financial supports from the Science and Technology Commission of Shanghai Municipality (No. 08201200901).

REFERENCES

Chu, W.H., Huang, Y.J., and Zhang, X.H. (2005). Case study on construction monitoring for tower part of Shanghai World Financial Center. *Chinese Journal of Underground Space and Engineering*, 1(4): 627–633. (in Chinese).

Gaba, A.R., Simpson, B., Powrie, W. & Beadman, D.R. 2003. *Embedded retaining walls: guidance for economic design*, CIRIA C580 Report. London: CIRIA.

Huang S.M., and Gao D.Z. edit. (2005). *Foundation and Underground Engineering in Soft Ground*. 2nd edition, China Architecture and Building Press, Beijing. (in Chinese).

Jia, J., Xie, X.L., Zhai, J.Q., Liu C.P., and Zhang, Y. (2010). Safety and stability control of circular foundation pit of Shanghai Tower. *Chinese Journal of Geotechnical Engineering*, 32(S1): 370–376. (in Chinese).

Liu G.B., and Wang W.D. edit. (2009). *Excavation Engineering Manual*. 2nd edition, China Architecture and Building Press, Beijing. (in Chinese).

Liu, J.H., Liu, G.B., and Fan, Y.Q. (1999). Theory and pratice of "Time and Space Effect" in deep excavations in soft soils. *Underground Engineering and Tunnels*, No. 3, pp. 7–12. (in Chinese).

Mana A.I., and Clough G.W. (1981). Prediction of movements for braced cuts in clay. *Journal of the Geotechnical Engineering Division*, ASCE, 107(6): 759–777.

Polshin D.E., and Tokar, R.A. (1957). Maximum allowable non-uniform settlement of structures. *Proceedings of the 4th International Conference on Soil Mechanics and Foundation Engineering*, London, England, Vol. 1, pp. 402–405.

Shanghai Construction and Management Commission (SCMC) (1997). *Code for Investigation of Geotechnical Engineering (DGJ08-37-2002)*, shanghai (in Chinese).

Shanghai Construction and Management Commission (SCMC) (2010). Technical Code for Deep Excavations (DG/TJ08-61-2010), Shanghai (in Chinese).

Tang J., and Zhu W.J. (2009). Application of information technology in the Remediation Project of the Collapsed Tunnel of Metro Line 4. *Shanghai Construction Technology*, (2): 15–18 (in Chinese).

Wang J.H., Xu Z.H., and Wang W.D. (2010). Wall and ground movements due to deep excavations in Shanghai soft soils, *Journal of Geotechnical and Geoenvironmental Engineering*, 136(7): 985–994.

This page intentionally left blank

Geotechnical Aspects of Underground Construction in Soft Ground – Viggiani (ed)
© 2012 Taylor & Francis Group, London, ISBN 978-0-415-68367-8

3-D finite element modeling and construction aspects for vertical shafts in Metro C Rome

G. Furlani, G. Guiducci & A. Lucarelli
Studio Sintesi, Rimini, Italy

A. Carrettucci & R. Sorge
Metro C S.c.p.A., Roma, Italy

ABSTRACT: On October 2009 the two TBM used to excavate T5 Stretch of new Rome Metro C subway line reached the reception shaft 5.4, where the machines have been uplifted for maintenance activity. After a brief description of general geotechnical site conditions, this paper discusses the main geotechnical aspects of the shafts project and illustrates some of the numerical analyses that were carried out during design activities. Moreover the main construction solutions adopted have been described as well as the related monitoring controls carried out during construction.

1 INTRODUCTION

Two circular vertical shafts for the extraction of Metro C TBM have been excavated in Piazza S. Felice, Rome. The inner shaft diameter is 15.7 m while the distance between shafts axis is 21.3 m. In the final layout the two structures will be connected by technical rooms and will work as ventilation chimneys.

As reported in Figure 1, the maximum depth excavation is about 45 m from the ground level, and, as the external water table is approximately 24 m above the bottom of the excavation. The excavation is protected by 56 m deep diaphragm walls, which are 1.0 m thick.

The shafts are located in a densely urbanized area; therefore specific design choices have been adopted in order to minimize the disturbance on the surrounding soil and existing structures.

The circular diaphragm walls have been excavated using hydraulic cutter in order to obtain waterproof joints and good static collaboration between the elements. The inner soil below the shaft bottom was treated by cement injections with the aim to reduce ground permeability and control the water seepage from the bottom; this method has been preferred to jet grouting because of soil marked heterogeneity as cemented and lithoid layers alternates loose silty sandy layers. The bottom plug is shaped as an inverted arch in order to optimize the reaction to uplift (and save materials and money).

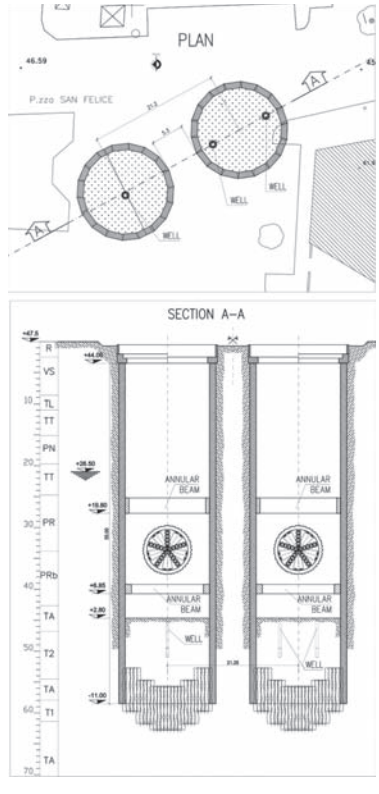

Figure 1. Vertical section: shafts geometry and soil profile.

2 GEOTECHNICAL CONDITIONS

The subsoil of the area was explored by geotechnical site investigations; Near the shaft two 65 m long boring have been carried out.

The ground surface is almost flat with an altitude of +47.5 m a.s.l.. Below the fill R, the subsoil profile, as shown in Figure 1, consists of typical roman volcanic formations which are characterized by altered tuffs (VS, TL,TT, TA), black-red silty sand pyroclastic materials (PN, PR) and lithoid tuff (T1, T2). The design properties of the various geotechnical units are summarized in Table 1. The most challenging site condition is the high variability of soil cementing: different degrees of cementation have been found along the excavation, from unbounded to well-cemented sand (unit PN, TT, PR) up to fissured soft rock (unit PRb. TA, T1 and T2). Figures 2 and 3 show an example of the marked variability of volcanic materials found at various depths.

Piezometric measurements have shown that the water table maximum level is +26.5 m a.s.l., which means about 21 m from the ground level.

Permeability distribution is quite complex and in situ Lefranc tests data have shown great dispersion. In the cemented tufs the permeability is linked to the type and distribution of fractures,

Table 1. Soil properties used in design.

	γ	c'	φ'	Go
Units	kN/m^3	kPa	deg	MPa
VS	17.0	10	33	390
TL	17.0	25	35	840
TT	17.0	15	34	450
PN	19.0	10	35	480
PR	18.0	10	35	570
PRb	20.0	300	35	660
TA	17.5	30	35	300
T1-T2	17.5	40 ÷ 300	35	930

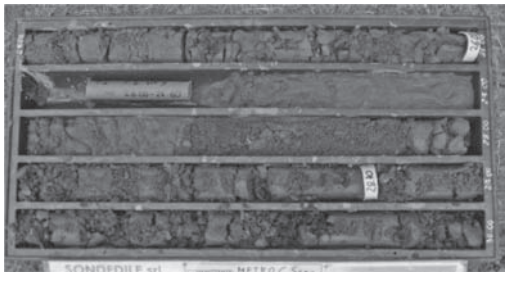

Figure 2. Red-pyroclastic soil (PR) from 25 m to 30 m depth.

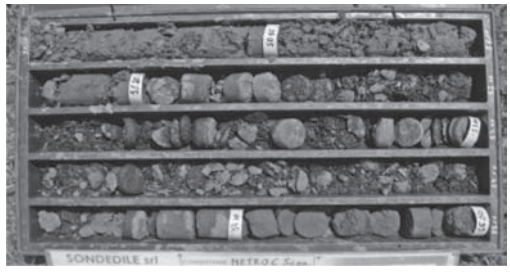

Figure 3. Cemented tuff from 55 m to 60 m depth.

in the silty sand and altered tuffs it depends on the clayey content (see Figs. 1–3). The total available experimental data and experiences in similar conditions leads to a medium-high permeability values (average 10^{-5} with minimum of 10^{-4} m/s).

3 THREE DIMENSIONAL ANALYSIS

3.1 *Critical aspects and objectives*

The behavior of the structures and the effects of the excavation have been analyzed using a numerical finite element model.

Since the two dimensional modeling (plane or axial-symmetry condition) is inadequate for the markedly three-dimensional geometry of the problem, a complete 3D fem model has been used to investigate all critical aspects of soil-structure interaction and construction phases and in particular:

- mutual interaction between the two shafts (the inter-axis distance is about 21 m and the minimum spacing are about 5 m);
- additional effects of asymmetrical earth pressure (i.e. treatment of the soil around the hole of TBM, loads of the surrounding buildings foundation);
- redistribution of the vertical and circumferential stresses on the wall after the local demolition to allow TBM entrance;
- analysis of seismic conditions using pseudo-static method.

The structural shell is made of adjacent panels without reinforcement passing through the vertical joints. For this reason, design prescription has fixed to to 4 MPa the maximum horizontal compressive stresses, calculated on the contact area of the joint reduced by the error of vertical construction of the diaphragms.

3.2 *The numerical models*

In order to predict the interaction between the shafts and the surrounding soil, a 3D finite element

analysis has been performed, using the commercial code "Plaxis 3D Foundation".

Numerical model section dimensions are 150 m × 120 m × 180 m (L × B × H). Horizontal displacements on model's vertical boundaries have been restrained, while all displacements have been restrained on the bottom boundary. The structures have been modeled with plate elements (vertical diaphragm walls) connected to the surrounding soil by interface elements having a frictional strength that is 66% of soil strength. Solid elements have been used to model the inner annular beams contrast, which have been activated during the excavation. All structural element have been modeled using linear elastic property of the concrete.

Varied mesh size have been applied to soil layers and structures of the shafts to save computation time. Mesh has been refined inside and around the shafts and then expanded by going to the boundary. The total number of elements is about 28000, with about 80600 nodes. A fully meshed Plaxis 3d is showed in Figure 4.

Figure 5 shows a close up on the structural plate and annular contrast beam. To ease the reading of the output solicitations, a low stiffness beam element has been inserted in the middle of the cluster representing shafts' structures. Axial and Flexural stiffness of the beam element is about 1/1000 of panel's stiffness in order to avoid excessive increase of total stiffness. Therefore the output internal forces of these elements had to be multiplied $\times 1 \cdot 10^{+3}$.

A simplified axial symmetry model has also been analyzed, in order to have a benchmark of the results obtained with 3D fem modeling. It also led to a better investigate some design aspects as seepage and stability analysis of the soil below the bottom excavation.

The mesh of the axial symmetric model is shown in Figure 6. The section clearly shows the bottom plug made of cement injection and shaped as an inverted arch.

The Hardening Soil small model' for 'Hardening Soil model with small-strain stiffness (Benz et al., 2009), has been selected for design. This constitutive model is a powerful tool especially for excavation problems. The main design geotechnical parameters are shown in Table 3.

The model involves frictional hardening characteristics to model plastic shear strain in deviatoric loading, and cap hardening characteristics to model plastic volumetric strain in primary compression. Failure is defined by means of the Mohr-Coulomb failure criterion (strength parameters φ', c').

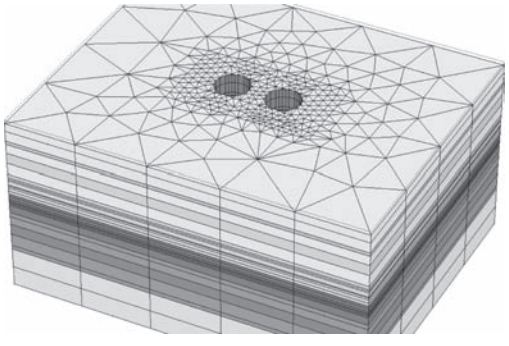

Figure 4. Meshed 3d plaxis model.

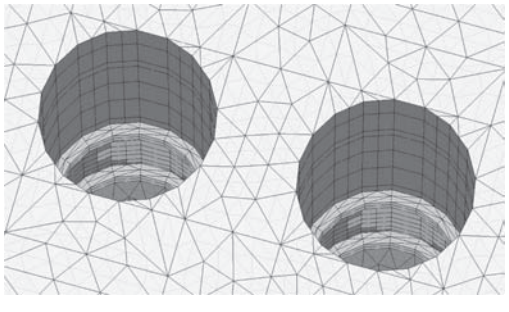

Figure 5. Detail meshing of the structural elements (diaphragm walls and contrast beams).

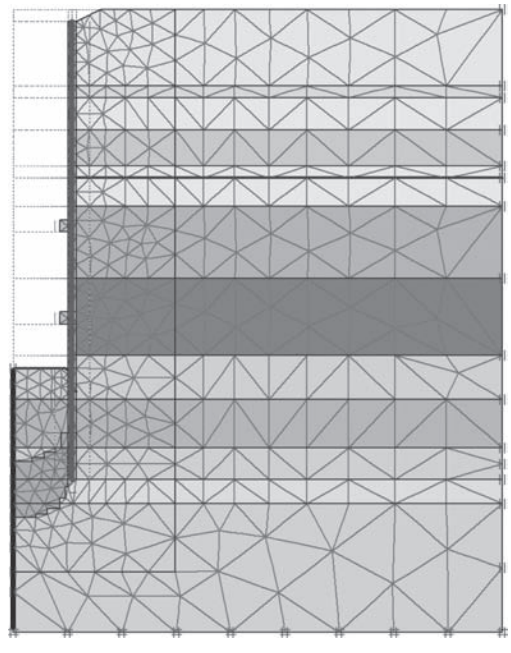

Figure 6. Meshed 2d plaxis model (axial-symmetric).

Moreover, this model incorporates strain dependent stiffness moduli, simulating the different reaction of soils to small strains and large strains.

Soil stiffness is therefore modeled with "large strain parameter" (Poisson modulus ν, E_{ur}, E_{50}, E_{oed} that describe the unloading–reloading stiffness and primary compression stiffness) and low strain parameters (G_0 and $\gamma_{0.7}$, that are shear modulus at small strains and the shear strain at which the secant shear modulus value is reduced to 70% of its initial value). The $\gamma_{0.7}$ was estimated following the suggestion in the Plaxis manual as:

$$\gamma_{0.7} = \frac{1}{9 \cdot Go} \cdot \left[2 \cdot c' \cdot (1 + \cos 2\varphi') - \sigma'_1 \cdot (1 + ko) \cdot \sin 2\varphi'\right] \quad (1)$$

where *ko* is the coefficient of lateral earth pressure at rest and σ'_1 is the effective vertical stress.

Therefore the operative shear modulus G is a function of shear strain γ and stress level by the following expression:

$$G = \frac{G_o}{\left\{1 + a \left/ \gamma_{0.7}\right.\right\}} \quad (2)$$

S_{small} strains shear modulus at (G_0) has been calculated using shear wave velocity measures ($G_0 = \rho \cdot Vs^2$). As said before, the HS_{small} also requires the definition of the unloading/reloading Young's modulus (E_{ur}). In this case E_{ur} has been set equal to 1/5 of small strain Young modulus ($E_0 \approx 2.6 \cdot G_0$), that is a value that in previous experiences of the Authors has given good accordance between analyses and site monitoring measures. Finally, as suggested in the PLAXIS manual, $E_{50} = E_{ur}/3$ *and* $E_{oed} \approx E_{50}$ have been set.

The analysis have simulated the main stages of construction and excavation:

- geostatic initialization; activation of all the plate elements (diaphragms) and their interfaces;
- simulation of soil improvement, modifying the geotechnical parameters in the volume of soil affected by the treatment (TBM breakthrough and bottom barrier for the seepage control);
- sequential excavation phases up to +7 m a.s.l. with construction of the two beams annular contrast at +21 m a.s.l. and +7.6 a.s.l. (above and under the tunnel crossing);
- demolition of the two openings for the TBM;
- excavation to maximum depth (+2.8 m a.s.l.).

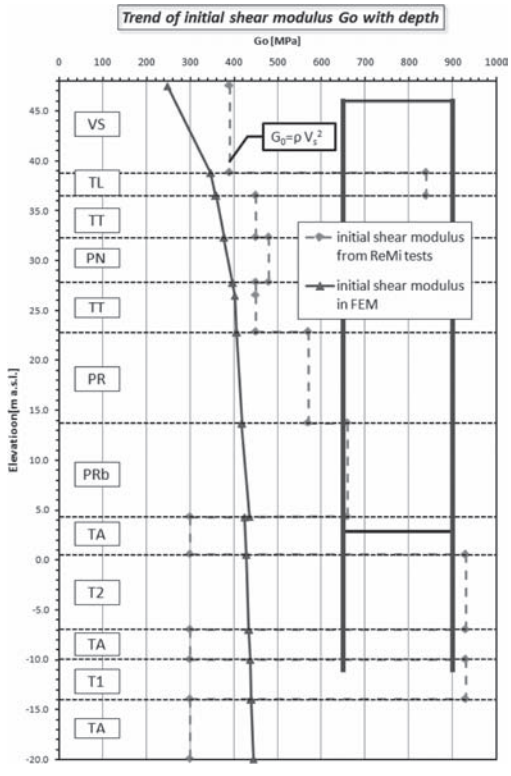

Figure 7. Shear dynamic modulus (G_0) vs depth.

3.3 *Main results of the analysis*

Figure 8 shows the 3D deformation of retaining walls after demolition of openings TBM (amplified 1500 times).

The maximum displacement is about 2.4 mm; the deformed mesh highlights that the most stressed panel is located to the sides of the opening, due to the lack of mutual lateral support following the demolitions. It is also evident the confinement effect offered by the annular beams, placed immediately above and below the TBM aperture.

The demolition of the opening leads to a redistribution of vertical and horizontal stresses with compression lines which tend to concentrate on the sides, above and below the hole. The following Figures 9 and 10 show the distribution of the vertical bending moment (M) and horizontal axial stresses (H), respectively. Figure 11 shows the axial stress obtained in the most stressed annular beam, which are all in compression.

As discussed above, the maximum vertical moment is reached in the panels located on the sides of the holes (about 300 kN m/m, medium value determined on the width of the panel);

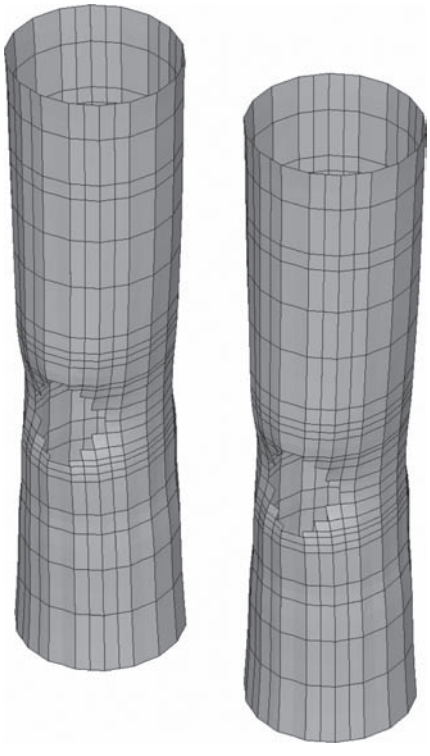

Figure 8. Deformed mesh structures (amplified × 1500 times).

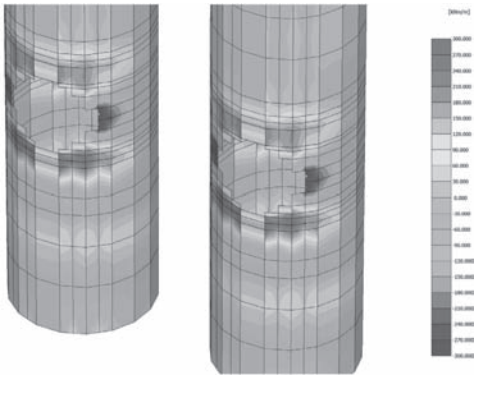

Figure 9. Vertical bending moment (M_{max} ≈ 300 kN m/m).

therefore for these zones an integrative reinforced steel gage has been adopted.

The maximum horizontal compression is approximately 4000 kN/m, and is reached at the base of the TBM hole where the annular contrast beam is located. The stress distribution decreases

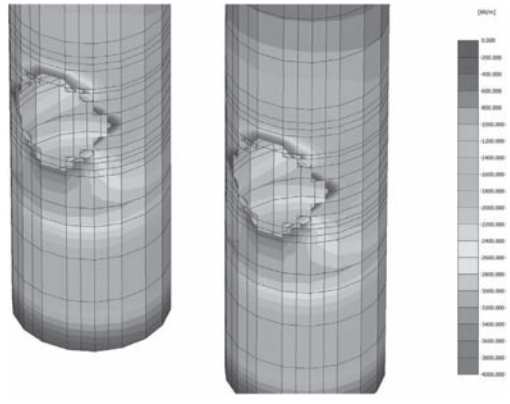

Figure 10. Horizontal axial stresses (H_{max} ≈ 4000 kN/m).

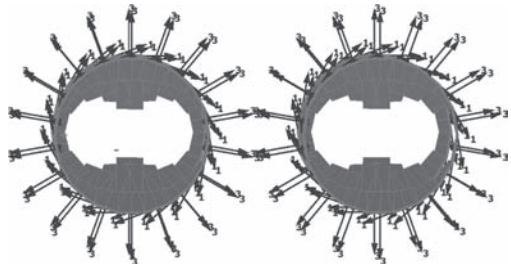

Figure 11. Axial force in the annular beam (N_{max} ≈ 2120 kN, N_{min} ≈ 480 kN).

far away from the openings where the distribution tends to be uniform. The maximum values reached in the diaphragm walls below the contrast beam is about 2800–3000 kN/m, in perfect agreement with the value obtained with the 2D axial-symmetric model (= 2820 kN/m, reached around the bottom excavation).

In order to limit the stress on the contact vertical joints between the panels (<4.0 MPa), an executive vertical tolerance < 0.3% has been prescribed.

4 CONSTRUCTION ASPECTS AND MONITORING

4.1 *Diaphragm walls*

The circular diaphragm walls have been excavated using hydraulic cutter in order to obtain a good control of the verticality, waterproof joints and a good static collaboration between the panels forming eighteen panels (nine primary and nine secondary panels) located with a inner diameter of 13.7 m. Each panel has been excavated with

a nominal width of 2.8 m and an overlap of 30–380 mm between the primary and secondary panel (see Fig. 12). This allowed a better control of panel verticality. Maximum deviations have therefore been very small (less than 0.1%, see Fig. 13).

4.2 *Groundwater control*

One of the most critical aspects of the project concerns the control of groundwater seepage from the base of the excavation, powered by a hydraulic head of about +24 m. Permeability distribution is quite complex and in situ Lefranc tests have shown great data dispersion. As it was expected, water flow analysis have shown that the water seepage phenomena is governed by the vertical permeability of soil located below the bottom of excavation: in the cemented tuffs (T2) the permeability is linked to the type and distribution of fractures, in the altered tuffs (TA) it depends on the clayey content (see Figs 1–3). The total available experimental data and experiences in similar conditions leads to a medium-high permeability values (average 10^{-5} with minimum of 10^{-4} m/s).

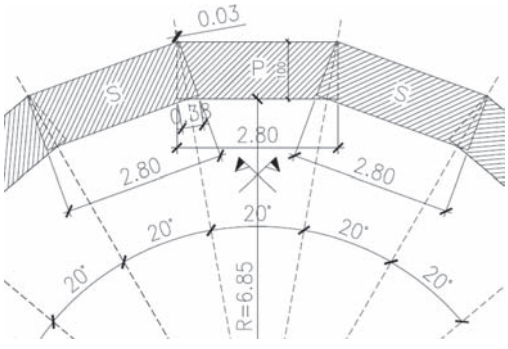

Figure 12. Plan disposition of the diaphragm panels.

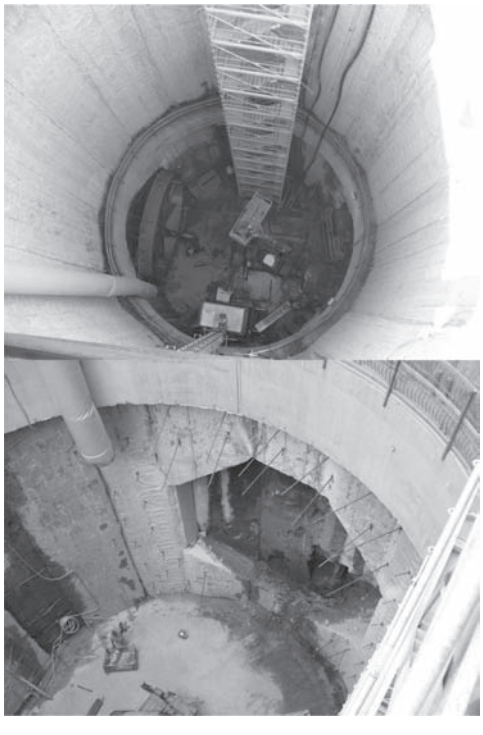

Figure 13. Internal view after excavation.

In order to reduce soil permeability and control the vertical water seepage from the bottom, the inner soil below the shaft bottom was treated by cement injections. The treated volume is 7 m thick and shaped like inverted arch in order to optimize the uplift global resistance (see Fig. 1).

The adopted technique, named MPSP (Multi Packer Sleeved Pipe, see also Bruce et al., 2009), owes much to the principle of the classical manchette system. Also in this case grout is injected in the surrounding rock through the ports of a plastic tube placed in a predrilled hole, but no sleeved grout is used.

The sleeved pvc tube (diameter 50 mm) has been retained and centered in each borehole (diameter 100 mm) by two collars-fabric bags inflated in situ with cement grout. These collars has been placed along each grout pipe in order to isolate two grouting stages, 3.5 m long each (see Fig. 14). The holes are located on the vertices of an equilateral triangle mesh with 2.2 m long side (primaries holes). Secondary holes are located in intermediate position to intensify the treatment. In final layout hole spacing is 1.1 m.

Grouting has been executed in standard "tube a machette" procedure, starting from the bottom part via the double packer, using stable cement-bentonite mixes of water cement ratio 1 (by weight) and 2% bentonite. The grouting parameters have been chosen to respect target volumes (maximum 250–300 lt/m to prevent potentially waste of grout) and target pressures (maximum 25–30 bar).

The inside pumping tests performed before starting the excavations have allowed an experimental verification of the executed treatment. The tests have been performed pumping water from inside the shafts with continuous measurement of flow discharge and levels of internal and external electric piezometers.

Two tests were carried out working separately on the two shafts; similar results have been obtained in both cases. In the graph of Figure 15 are showed the experimental data measured during the test

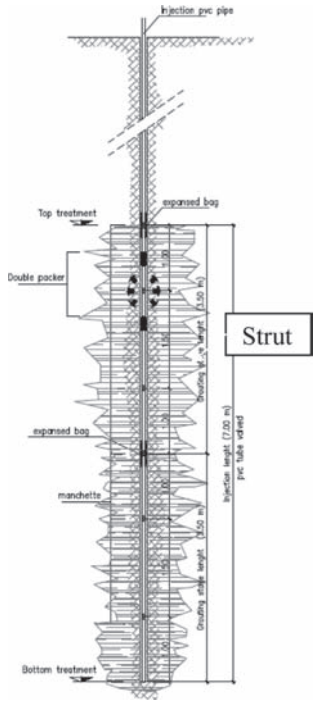

Figure 14. MPSP system.

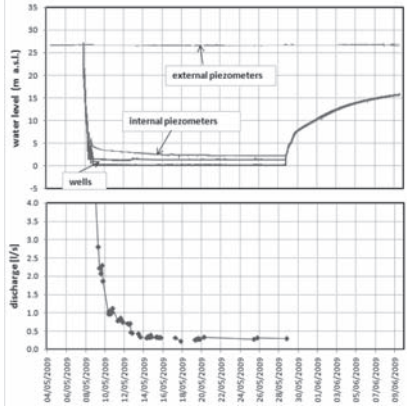

Figure 15. Pumping test: outflow pumping and piezometric levels measured vs time.

conducted into the shaft B.D.. As shown in the figure the test is divided into two phases:

– in the first phase the internal pumping was activated in order to empty the shaft and maintain the internal water level constant around +0.0 m a.s.l. until stabilization of the discharge flow; the balance was achieved after about 500 hours by pumping approximately 0.3 l/s (same value for both wells);
– the second phase is a recovery test without pumping: there was a recovery of only 65–70% of the initial hydraulic head after 200–300 hours.

The external piezometers have shown a negligible drop (less than 0.1 m).

Assuming mono-dimensional seepage, the back-analysis lead to a equivalent permeability of the injected volume of $4 \cdot 10^{-7}$ m/s, which is a drastic reduction of the values of natural soils (average 10^{-5} m/s, with maximum of 10^{-4} m/s). The small discharge measured (25–30 m^3/day) was confirmed during the excavation, without perceptible effect on the external water table.

4.3 *Monitoring system*

A wide monitoring activity has been carried out in order to verify design assumptions, to optimize and adjust construction process and to control the stability and serviceability of supporting structures.

For these reasons, the monitoring system dealt with many aspects, and mainly:

– Water-table monitoring, by means piezometers installed outside and inside excavation (Casagrande and electric cells respectively): no relevant effects was observed on the external piezometers during shaft excavation (see also paragraph 4.2); a drop around –4.5 m was measured during TBM reception phase, followed by immediate recovery (see Fig. 16).
– Diaphragm horizontal displacements monitoring, by means of inclinometers. As shown in Figure 17, the values measured are negligible and comparable to the instrument accuracy.
– Building movement monitoring, by means of automated total stations. The history of vertical settlements measured for the nearest building (that is about 10 m far from the shaft) is shown in Figure 18: the totality of the displacements (≈10 mm) were measured during ground improvement works that were needed for the TBM reception phase; no relevant movements was observed during shaft excavation and reception phases.

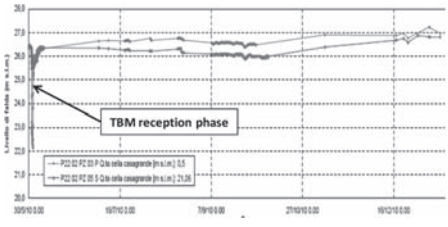

Figure 16. External piezometrics level monitoring.

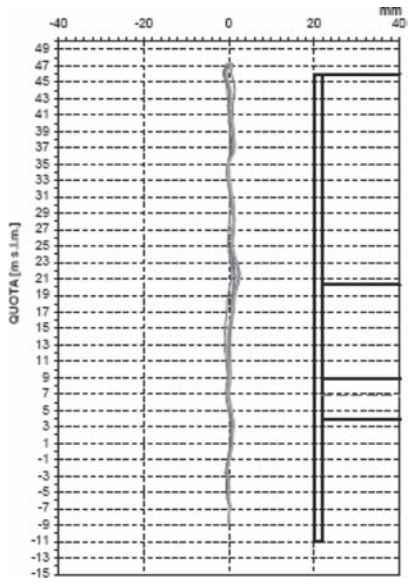

Figure 17. Horizontal displacements measured along the diaphragm by inclinometer.

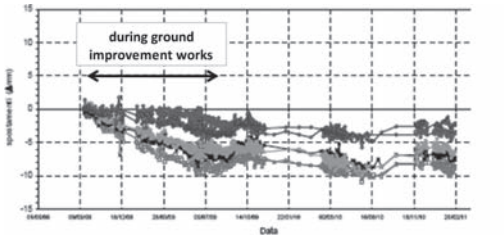

Figure 18. Vertical displacements of the building 1403.

5 REMARKS

The design, construction and monitoring of 5.4 shaft of new Rome Metro C subway line have been described in this note.

Design analyses, needed to investigate all critical aspects of soil-structure interaction and construction phases, have been performed using a complete 3D Finite Element Model, since plane strain hypothesis us inadequate for the markedly three-dimensional geometry of the problem.

Analyses have outlined the most stressed panels and stress redistribution around TBM holes in the shafts.

One of the most critical aspects of the project concerns the control of groundwater seepage from the base of the excavation. In order to reduce soil permeability, the inner soil below the shaft bottom was treated by cement injections. The adopted technique, named MPSP (Multi Packer Sleeved Pipe), led to a drastic reduction of the permeability of the natural soil: a small water discharge has been pumped during the excavation, without perceptible effect on the external water table.

A wide monitoring activity has been carried out in order to verify the behavior of the soil-structure system during construction and also to verify the design assumptions adopted. As predicted by design analyses, no relevant effects were observed during excavation of the shaft. The major effects observed were due to TBM work activities, ground improvement and reception phases.

REFERENCES

Benz, T. et al. 2009. "*A small-strain overlay model*." International Journal for Numerical and Analytical Methods in Geomechanics, 33, 25–44.

Bruce, D.A. et al. 2009. "*The MPSP system: a new method of grouting difficult rock formations*." ASCE Conference, May 1988, Nashville, TN.

Plaxis bv, Delft, Netherlands 2007. "3D Foundation version 2. User's Manual." Part 3: Material Models Manual & Part 4: Scientific Manual.

Geotechnical Aspects of Underground Construction in Soft Ground – Viggiani (ed)
© 2012 Taylor & Francis Group, London, ISBN 978-0-415-68367-8

Effect of cement on tropical peat stabilized by deep mixing method

Sina Kazemian
University Putra Malaysia, Serdang, Malaysia

Arun Prasad
Banaras Hindu University, Varanasi, India

Bujang B.K. Huat
University Putra Malaysia, Serdang, Malaysia

ABSTRACT: Peats show high compressibility and low shear strength and hence are problematic in geotechnical engineering context. Cement is widely used for the stabilization of peat by Deep Mixing Method (DMM). This paper presents the results of the model study of the compressibility properties of peat stabilized with columns formed by DMM. Consoilidation and Scanning Electron Microscopy (SEM) were performed on peat samples stabilized with cement treated columns. The results showed that the compressibility behaviour of peats can be improved significantly by installing columns of peat stabilized with cement. The amount of cement used was observed to influence the engineering behaviour of treated tropical peats. Sapric peat showed a better response compared with hemic and fibrous peats.

1 INTRODUCTION

Deep mixing method is a widely used method for stabilizing organic soils. This method, originally developed in Sweden and Japan more than thirty years ago, is becoming well established in an increasing number of countries. Originally lime was the only binder used, but cement has been widely used since the mid 1980s, with considerably higher strength achieved (Åhnberg et al., 1995). The introduction of cement has made it possible to stabilize "problematic soils" with high organic contents and high water:soil ratios (Åhnberg, 2006; Janz and Johansson, 2002). Comprehensive trials and field works have been carried out where cement, and cement with different industrial binders have shown to improve the mechanical properties (shear strength and compressibility) of organic soils and peats (Axelsson et al., 2002; EuroSoilStab, 2002; Hebib and Farrell, 2003; Moore, 1989). Since peat already has a high water content, the required water for soil-cement reaction comes from it. Therefore, Dry Mixing Method (DMM) and Dry Jet Mixing (DJM) methods are effective for peat stabilization instead of wet mixing method (Yang et al., 1998). Berry (1983) reported that the consolidation process is complicated by the occurrence of secondary compression which appears to extend indefinitely.

In this paper, an attempt has been made to evaluate the effects of using cement by DMM method on the compressibility of tropical peats by forming stabilized cement columns and performing SEM test on treated tropical peats. This model study was initiated in order to evaluate the influence of dry cement to stabilize peats, in terms of a reduction in compressibility by performing Rowe cell tests.

2 MATERIALS AND METHODOLOGY

2.1 *Materials*

Peat was collected from various locations near Kuala Lumpur, Malaysia to have all the three varieties: fibrous, hemic and sapric peats. The physico-chemical properties of fibrous, hemic and sapric peats are presented in Table 1. Ordinary Portland cement (hereinafter called cement), used in this study as a binding agent, was obtained locally.

Table 1. Physico-chemical characteristics of untreated peats.

Parameters	Fibrous peat	Hemic peat	Sapric peat
Moisture content [%]	506.5	324.6	188.2
Specific gravity	1.26	1.302	1.42
Organic content [%]	94.23	81.3	75.31
Fiber content [%]	79.1	53.2	31.3
Bulk unit weight [kN/m^3]	9.86	10.3	11.1
pH	3.8	4.81	5.97

2.2 *Methodology*

2.2.1 *Sample preparation*

A suitable auger was designed and fabricated to collect undisturbed peat samples as per BS 1377-1 (BS, 1990). Once in the laboratory, the top cover on the cylindrical tube was opened to extract the sample. The auger enables the extraction of samples 150 mm in diameter and 230 mm in height. The top and bottom of the specimen was trimmed carefully and quickly to minimize any change in the water content of the soil sample (Figure 1(a)). According to BS 1377-8 (1990) and BS 1377-6 (1990), the height (H) of the specimen was 37.5 mm for the consolidation test.

In order to evaluate the compressibility of peat reinforced by stabilized cement column, samples of peat with cement column were prepared by inserting a PVC tube in the center of the specimen and extracting soil from within the tube. Next, the extracted peat, at its natural water content, was thoroughly homogenized by household mixer and then cement was added to it at a typical dose rate of 200 kg/m^3 (Axelsson et al., 2002). The stabilized cement columns in the composite peat samples were prepared with cement:peat ratio of 50:50, 70:30, 80:20 and 90:10 (Table 2).

The cement-peat mixture, mixing thoroughly for five minutes, was replaced back in PVC tube, and the tube was finally withdrawn forming the stabilized cement column (Figure 1 (b)). Care was taken to replace back the peat-cement mixture as soon as possible, but not later than 30 minutes; as this was the initial setting time of cement. The columns formed in peat were of diameters (R) 37.5 mm

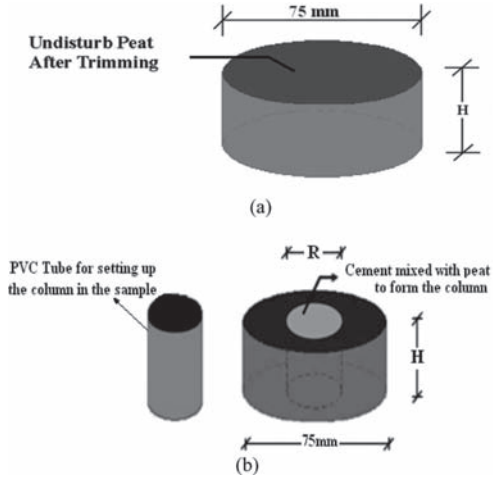

Figure 1. Sample preparation (a) cylindrical test specimen from the undisturbed soil sample after trimming and (b) method used to set up cement column in specimen.

Table 2. Various quantities of cement used in cement stabilized columns.

Samples	Condition
Control sample	Untreated peat
Sample I	Peat = 50%; cement = 50%
Sample II	Peat = 30%; cement = 70%
Sample III	Peat = 20%; cement = 80%
Sample IV	Peat = 10%; cement = 90%

(column-area ratio = 25%). The samples were then cured for 28 days in a soaking basin before performing consolidation tests (Rowe cell).

Holm (2000) presented several case histories of deep mixing and the typical column-area ratios (cement column area to treated peat area) being used in practice are between 5–35%. In this study, the cement column diameter was 37.5 mm and the column-area ratio was 25%.

2.3 *Experimental methods*

Physical properties of peat and treated peat columns with different cement ratio were determined and are mentioned in Table 1. The compressibility characteristics of peats determined are: (i) Compression index (C_c), and (ii) Coefficient of secondary compression (C_α).

3 RESULTS AND DISCUSSION

3.1 *Compressibility characteristics of cement columns of stabilized tropical peat*

The compressibility characteristics of peats with cement stabilized column were studied by Rowe cell for pressures of 50, 100, 200, and 300 kPa. The compression index (C_c) of fibrous, hemic and sapric peats for pressures of 50 kPa is shown in Figure 2(a). As expected, the C_c for peats decreased with an increase in the cement content. The C_c for untreated fibrous peat with a column-area ratio of 25% was 1.68 and it decreased to 1.03 with 90% cement. Similarly, the C_c for untreated hemic and sapric peats with a column area ratio of 25% were lower at 1.27 and 1.16 respectively and they decreased to 0.72 and 0.547 respectively.

The nature of curves of C_c for fibrous, hemic and sapric peats for consolidation pressures of 100, 200 and 300 kPa were similar to those for 50 kPa. This is due to the fact that the cement particles bind together the soil particles causing an increase in shear strength and a decrease in compressibility. Fibrous peat shows a higher reduction in C_c compared with hemic and sapric

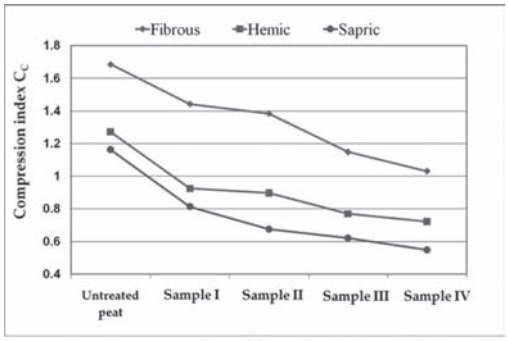

(a)

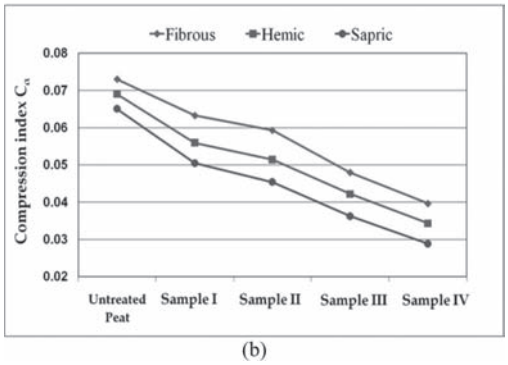

(b)

Figure 2. Consolidation results: (a) Compression index (Cc), and (b) Secondary compression index (Cα) of treated fibrous, hemic and sapric peats at 50 kPa consolidation pressure.

peats. The reasons for this behavior are higher void ratio and nature of fibres in fibrous peat that allow for higher compression and bending.

The secondary compression index (C_α) was evaluated for different peat samples and are presented in Figure 2(b) for a consolidation pressure of 50 kPa. It was observed that C_α decreases with an increase in cement content for all; fibrous, hemic and sapric peats.

The C_α of untreated fibrous peat with a column area ratio of 25% was 0.073 and as expected, it decreased to 0.040 with 90% cement. Similarly, the C_α of untreated hemic and sapric peats were 0.069 and 0.065 respectively, which is lower than that of fibrous peat. They decreased to 0.034 and 0.028 for hemic and sapric peat respectively with 90% cement. However, it agrees well with the findings reported in the literature (Holm, 2000; Kazemian et al., 2009; Mesri and Castro, 1987).

The nature of curves of C_α for fibrous, hemic and sapric peats at a consolidation pressures of 100, 200 and 300 kPa were observed to be similar to those at 50 kPa. The compressibility of peats stabilized with cement treated columns decreased with an increasing cement amount. This is quite obvious as the mass of binder is increasing per unit volume of the peat; cement increases the strength and transforms peat into a stiffer state as mentioned earlier. The effect of cement on compressibility parameters of sapric peat is higher among others as stated above as well.

The above findings are justified for the fact that when water comes in contact with cement, three reactions take place: (i) cement reacting with water called hydration, (ii) pozzolanic reactions between calcium hydroxide [$Ca(OH)_2$] from burnt cement and pozzolanic minerals in the soil, and (iii) ion exchange between calcium ions (from cement) with ions present in the colloids of peats, which leads to an improvement in the strength of the treated soil strength. Cement initiates chemical reaction with water (called hydration) and tricalcium silicate (C_3S) and dicalcium silicate (C_2S) (from cement) are mixed with water, calcium ions are quickly released into the solution with the formation of hydroxide ions. When the concentration of calcium and hydroxide ions reaches a certain threshold value, calcium hydroxides crystallizes out of solutions and finally leads to the production of calcium silicate hydrate (C–S–H) and thus, bonding the particles and increasing the shear strength (Janz and Johansson, 2002).

3.2 *Microstructural study of treated tropical peat*

Figure 3 shows the different effects of cement ratios on treated fibrous peat. The amount of fibrous-acicular C–S–H gel in sample I (with 50% cement) was much less than in sample IV (with 90% cement), proving the effect of cement on cementation and pozzolanic reactions. Furthermore, there were few spherical C–S–H particles or other types of C–S–H morphologies of cementation in treated fibrous peat with 50% cement (sample I) that exhibited nominal hydration, and more C–S–H gel was produced in treated fibrous with 90% cement (sample IV) [Figures 3(a) and 3(c)]. The SEM results were consistent with the Rowe cells results, such that at low cement ratios, the compressibility parameter of the treated fibrous peat was low because of the lower production of C–S–H gel.

Figures 3(b) and 3(d) show the SEM micrograph of treated sapric peat cured in distilled water. It was observed that the amount of C–S–H gel in treated sapric peat with 90% cement (sample IV) was much higher than in compare with sapric treated with 50% cement (sample I). Furthermore, it was observed [Figures 3(b) and 3(d)] that abundant massive and spherical or coralloid aggregations of C–S–H gels were produced in treated sapric peat with 90% cement (sample IV) in comparison with treated sapric peat with 50% cement (sample I).

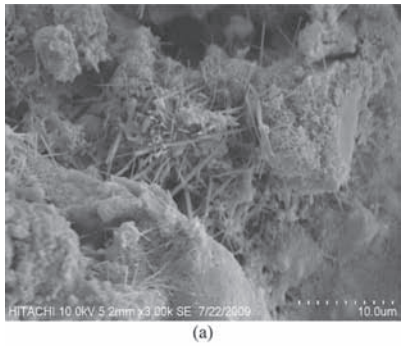

(a)

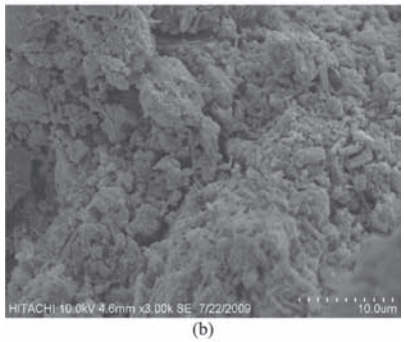

(b)

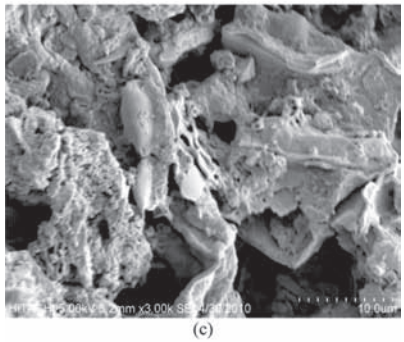

(c)

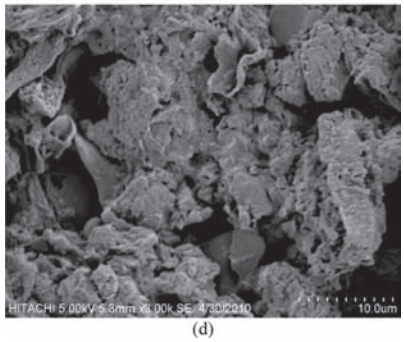

(d)

Figure 3. (a) Fibrous peat treated with 90% cement (sample IV); (b) Fibrous peat treated with 90% cement (sample IV); (c) Fibrous peat treated with 50% cement (sample I); (d) Fibrous peat treated with 50% cement (sample II).

This implies that the effect of cement on sapric the same fibrous cause to decrease the compressibility parameters of treated peat. In addition, by comparison of Figures 3(b) and 3(d), it is cleared that the effect of cement of sapric is much higher than fabrious which has been explained before. These findings are consistent with the findings presented in the literature (Hebib and Farrell, 2003), who reported that cement decreases the compressibility of tropical fibrous peat and that this will be more effective when sapric peat are treated by cement.

4 CONCLUSIONS

The following conclusions can be drawn from this study:

1. The compressibility parameters (C_c and C_α) decrease with an increase in the cement content. This is due to the fact that the hardened soil-cement matrix formed due to the hydration reaction, pozzolanic reaction, and cation exchanges that take place when cement comes in contact with water.
2. The production of C–S–H gels is the maximum in sapric peat. This is because as the mass of binder is increasing per unit volume of peat; cement increases the strength and transforms peat into a stiffer state.
3. Fibrous peat shows a higher reduction in C_c compared with hemic and sapric peats. The reason for this behavior is the presence of higher voids and the nature of fibers that allow higher compression and bending.
4. The effect of cement is the maximum on sapric peat.

REFERENCES

Åhnberg, H. 2006. Swedish Deep Stabilization Research Center, Linköping, Sweden, Report No. 16.

Åhnberg, H., Johansson, S.E., Retelius, A., Ljungkrantz, C., Holmqvist, L. & och Holm, G. 1995. en Kemisk-Ffysikalisk Studie av Stabiliserings Effekter, *Rapport No 48*, *Statens Geotekniska Institut*, Linkoping.

American Society for Testing and Materials. 1982. *Annual Book of ASTM Standards*. Philadelphia, PA. USA.

Axelsson, K, Johansson, S.E. & Anderson, R. 2002. Swedish Deep Stabilization Research Centre, Report No. 3.

Berry, P.L. 1983. Quarterly Journal of Engineering Geology 16: 103–112.

BSI British Standards. 1990. *BS 1377: Part 2, 3, 6 and 8*.

EuroSoilStab. 2002. European Commission, CT97-0351, Project No. BE 96-3177, p. 15–60.

Hebib, S. & Farrell, E.R. 2003. *Canadian Geotechnical Journal* 40(1): 107–120.

Holm, G. 2000. Geotechnical Special Publication No. 112, ASCE, Reston, VA, US.

Janz, M. & Johansson, S.E. 2002. Swedish Deep Stabilization Research Centre, Report No. 9.

Kazemian, S., Prasad, A., Ghiasi, V. & Huat, B.B.K. 2009. *In* C.F. Leung, J. Chu, & R.F. Shen, *Ground Improvement Technologies and Case Histories (ISGI09),* Singapore. p. 533–541.

Mesri, G. & Castro, A. 1987. *Journal of Geotechnical Engineering* 113(3): 230–247.

Moore, P.D. (1989). International Journal of Coal Geology 12: 89–103.

Yang, S.D., Yagihashi, J.N. & Yoshizawa, S.S. 1998. *Geotechnical Special Publication No. 81*, ASCE, Reston, VA, US.

This page intentionally left blank

Design methods and predictive tools for deep excavations and bored tunnels

This page intentionally left blank

Geotechnical Aspects of Underground Construction in Soft Ground – Viggiani (ed)
© 2012 Taylor & Francis Group, London, ISBN 978-0-415-68367-8

Effects of tunnelling on a single pile: Three-dimensional design tool

J.Q. Surjadinata & T.S. Hull
GHD-Geotechnics, Sydney, Australia

J.P. Carter
University of Newcastle, Newcastle, Australia

ABSTRACT: In most tunnelling projects in urban areas, a preliminary assessment is often required of the impact of a tunnel excavation on foundations adjacent to the tunnel. Despite the significant recent advances in computer hardware and commercial software, a full 3-D analysis is still relatively costly, especially if it is to be employed as a preliminary assessment tool to ascertain the impact of tunnel excavation on existing foundations. This paper provides a convenient and cost-effective design tool, in the form of design charts, that will allow an economical preliminary assessment of the 3-D effects of tunnelling on a single pile. The method adopted to develop these design charts will be briefly described and their use in practice will be illustrated by application of the design charts to several published case histories.

1 INTRODUCTION

Recently there has been an increasing interest in adopting three-dimensional (3-D) numerical analysis to assist in the design and planning of tunnelling projects. This is partly driven by the increasing accessibility of high-powered computing hardware and the convenience offered by modern CAD-based commercial software, which together enable ease of input and output of the often complex 3-D geometry involved in a tunnelling problem.

In tunnelling projects in urban areas, a preliminary assessment is often required of the impact of a tunnel excavation on foundations adjacent to the tunnel. The 3-D geometry of the tunnel and the adjacent foundations commonly found in urban areas may prohibit the use of a conventional plane strain approximation of the problem. In particular, for a tunnel excavation next to existing pile foundations there is increasingly a need for full 3-D analysis.

Despite recent significant advances in computer hardware and commercial software, full 3-D analysis is still relatively costly when employed as a preliminary assessment tool to ascertain the impact of tunnel excavation on existing pile foundations. A cost effective and convenient alternative for preliminary assessment are design chart solutions that can provide a first-order elastic prediction of the pile response due to adjacent tunnel excavation.

Currently, there is only the published design chart of Loganathan et al. (2001) which provides a plane strain solution of pile response to tunnel excavation. However, due to the plane strain nature and the limited pile-tunnel arrangements considered in the Loganathan solution, a 3-D solution that takes into account a larger range of pile and tunnel arrangements would be useful.

Surjadinata (2009) conducted a study of the 3-D response of a pile due to tunnelling. Part of the outcome consisted of 3-D design charts for the response of a single pile due to tunnelling.

This paper provides a brief description of the method adopted by Surjadinata (2009) to develop the 3-D design charts. Their use in practice is then illustrated by application of the design charts to two published case histories.

2 TUNNELLING INDUCED PILE RESPONSE

The design charts were based on an extensive 3-D parametric study of the tunnelling-induced response of a single (wished-in-place) elastic pile, assuming a homogenous isotropic linear elastic soil. To overcome the need to perform full 3-D analysis for every case in the study, the efficient combined Finite-and-Boundary-Element Analysis (FAB) method was employed. The method is based on two stages of analysis. The first stage is to predict the elastic free-field soil displacement induced by a tunnel excavation. This displacement is then used as input to a special boundary element analysis (Hull, 1998) of an elastic pile to obtain the response of the pile. This method has been verified against several existing case studies ranging from existing numerical predictions to

back analyses of measured pile response. Further details of the FAB method and the verification of the FAB method can be found in Surjadinata *et al*. (2005, 2006).

It was shown that the maximum elastic pile response due to tunnelling is primarily dependant on the following parameters:

- Ground loss (ε)
- Diameter of the tunnel (D)
- Normalised tunnel depth (H/D)
- Normalised pile length (L_p/H)
- Normalised pile distance (W/D)
- Pile stiffness relative to the soil (L_c/L_p)
- Pile slenderness ratio (L_p/d)
- Position of tunnel face relative to the pile axis (S)

where L_c is the corresponding effective pile length. (Further details of L_c can be found below).

The definition of ground loss (ε) adopted is the reduction in volume of a circular tunnel, expressed as a percentage of the initial excavated tunnel volume.

The geometrical representation of the parameters above, with the exception of L_c, can be found in Figure 1 and a comment on the significance of each parameter is provided below.

From the parametric study it was found that the magnitude of the lateral and vertical responses of the pile attain a maximum value at the plane strain condition (S→∞). As the tunnel passes the pile, S = 0, the magnitude of the longitudinal response of the pile attains its maximum value. These maximum responses are presented for the three non-dimensional tunnel depths investigated in this study, i.e., H/D=2, 3 and 5. These normalised depths will be referred to as "shallow", "intermediate" and "deep", respectively. The magnitudes of the responses are considered for three different pile lengths relative to the tunnel depth (L_p/H = 0.5, 1 and 2). The three pile lengths will be referred to as "short", "intermediate" and "long".

The parameter L_c is the effective or critical length of the pile. L_c is used in this study to define the pile to soil relative stiffness and it is normalised with pile length (L_p). Parameter L_c/L_p is essentially K_R from Poulos and Davis (1980). Detailed explanation of L_c can be found in Poulos (1982) and Hull (1987).

For completeness, the equations for L_c suggested by Hull (1987) are adopted for this study:

$$L_{cB} = \pi\sqrt{2}\left(\frac{(EI)_p}{E_s}\right)^{\frac{1}{4}} \quad (1)$$

$$L_{cA} = \sqrt{\frac{\pi(EA)_p}{E_s}} \quad (2)$$

where L_{cB} = the effective pile length for bending in the lateral and longitudinal directions, L_{cA} = the effective pile length for axial load, $(EI)_p$ = pile bending stiffness, $(EA)_p$ = pile axial stiffness, and E_s = the appropriate soil Young's modulus.

The individual relationships of the parameters listed above (W/D, L_c/L_p, and L_p/d) with the magnitudes of the maximum pile responses in 3 directions, i.e., lateral displacement (U_{xmax}), vertical displacement (U_{ymax}), longitudinal displacement (U_{zmax}), lateral bending moment (M_{xmax}), longitudinal bending moment (M_{zmax}), and axial force (F_{ymax}) were discussed in Surjadinata (2009) and will not be repeated here. Using these relationships, it is possible to generate a system of design charts that provides the maximum magnitude of an elastic pile response due to tunnelling.

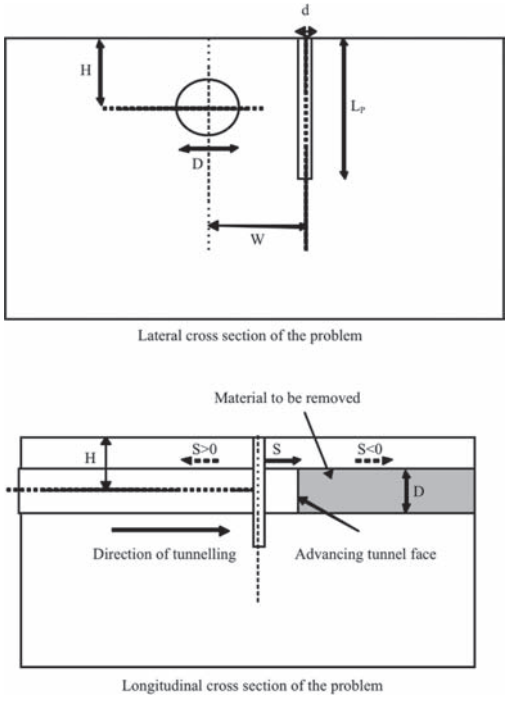

Figure 1. Problem geometry.

3 CREATION OF DESIGN CHARTS

The minimum number of charts required to summarise a particular maximum pile response (e.g., M_{xmax}) is three. These three charts make up a set and are referred to as a "3-chart design set". Each set will correspond to a particular pile response, and a particular pile length (L_p/H = 0.5, 1 or 2).

This means for each pile length, six different 3-chart sets provide the 3-D maximum pile responses. The complete 18 design chart sets are provided in Surjadinata (2009) and interpolation between these charts enables typical pile-tunnel geometries to be evaluated. For illustration purposes, only 2 sets (i.e., U_{xmax} and M_{xmax} for $L_p/H = 2$) will be presented and they can be found in Figures 4 and 7, respectively.

In an elastic analysis, the pile responses due to tunnelling are proportional to the ground loss (ε) and therefore all maximum pile responses will be normalised against ε.

A brief summary of the creation and features of each chart in the 3-chart design set is provided below.

3.1 *Results of 3-D study*

Based on the parametric study, Figure 2 shows the normalised 3-D pile displacement profiles for a pile adjacent to a tunnel. Each displacement profile in a chart corresponds to a different tunnel diameter (D). This figure shows that the pile displacements in three directions can be normalised by D. Note that the normalised vertical displacement in Figure 2(b) is for a different tunnel-pile arrangement than that corresponding to the normalised horizontal displacement, in order to illustrate that the normalisation is valid for any tunnel-pile arrangement. Note that z is the vertical position measured from the tunnel axis, upwards is positive.

Figure 3 shows the normalised pile bending moments and axial force for a pile adjacent to a tunnel. Figures 3(a) and (c) show that the pile bending moment in the lateral and longitudinal directions can be conveniently normalised against $(EI)_p/D$. Figure 3(b) shows that the axial force induced in the pile can be normalised against $(EA)_pL_p/D$.

3.2 *"Reference" chart*

Using the normalisation procedures described above, the first chart in the 3-chart set, referred to as a "reference" chart was created. An example of a reference chart is the first (top) chart in Figures 4 and 7.

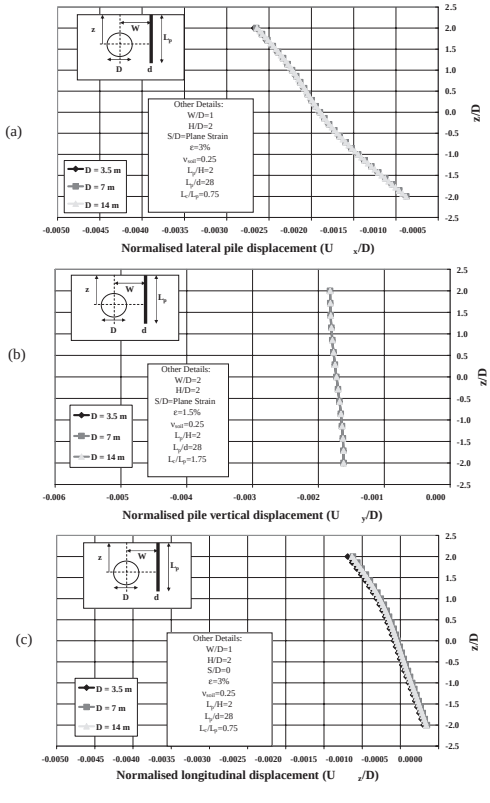

Figure 2. Normalised pile displacement profiles.

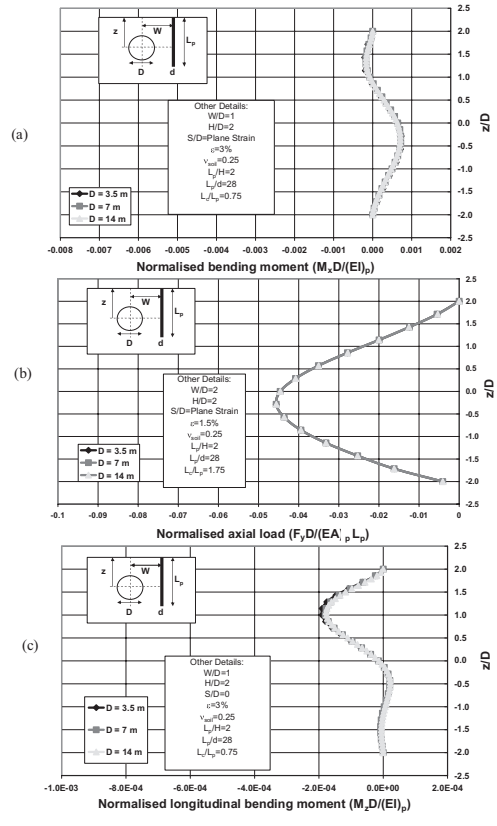

Figure 3. Normalised axial force and bending moment.

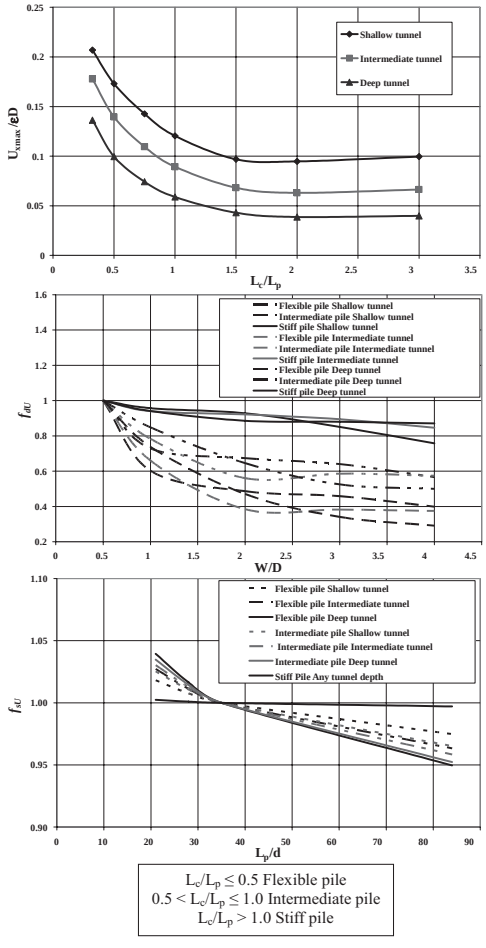

Figure 4. Maximum lateral displacement design charts set for $L_p/H = 2$ (Long pile).

In each "reference" chart there are three curves that correspond to a maximum pile response for the three tunnel depths considered (shallow, intermediate and deep). For each pile response, the "reference" chart shows the normalised maximum pile response plotted against L_c/L_p.

In all of the "reference" charts in this study, parameters W/D and L_p/d are kept constant (W/D = 0.5 and $L_p/d = 35$). To take into account other values of W/D and L_p/d, correction factors are applied to the normalised pile responses obtained from the "reference" charts. These correction factors are denoted as f_d and f_s, and they take into account other values of W/D and L_p/d, respectively. The charts that provide the values of f_d and f_s are called auxiliary charts.

The correction factors employ a second letter in the subscript: U indicates displacement, M indicates bending moment and F indicates axial force. Hence, f_{dU} is for displacement, f_{dM} is for bending moment, and f_{dF} is for axial force.

3.3 *First auxiliary chart*

The first auxiliary chart contains the correction factor f_d plotted against the pile distance ratio (W/D), with values of f_d provided for the three pile stiffnesses (flexible, intermediate and stiff) and the three tunnel depths (shallow, intermediate and deep). An example of this chart is the second (middle) chart in Figures 4 and 7.

3.4 *Second auxiliary chart*

The second auxiliary chart contains the correction factor f_s plotted against the pile slenderness ratio (L_p/d). Similar to f_d, values of f_s are provided for the three pile stiffness values and the three tunnel depths. An example of this chart is the third (bottom) chart presented in Figures 4 and 7.

4 LIMIT OF APPLICATION

The application of the proposed design charts is limited to L_c/L_p values presented in the "reference" charts. Specifically, it is not recommended to extrapolate the values of the design charts for cases with L_c/L_p below 0.3 or beyond 3.

5 DESIGN CHARTS GUIDE

In order to use the design charts to obtain the magnitude of the maximum pile response, the steps to be taken are:

1. Establish the values of L_p/H, ground loss (ε in %), the diameter of tunnel (D), L_c/L_p, W/D and L_p/d.
2. Choose the figure (3-chart set) that corresponds to the pile response in question and the value of L_p/H determined in step 1.
3. From the reference chart in the set, read the normalised magnitude of the maximum pile response (at W/D = 0.5 and $L_p/d = 35$).
4. From the auxiliary charts read off the multiplication factors f_d and f_s that take into account the different values of W/D and L_p/d.
5. The magnitude of the maximum pile response can be found by the following equations:

$$U_{x,y\,or\,zmax} = U^* \times \varepsilon D \times f_{dU} \times f_{sU} \quad (3)$$

$$M_{x\,or\,zmax} = M^* \times \varepsilon \times \frac{(EI)_p}{D} \times f_{dM} \times f_{sM} \quad (4)$$

$$F_{ymax} = F^* \times \varepsilon \times (EA)_p \times \frac{L_p}{D} \times f_{dF} \times f_{sF} \quad (5)$$

where U* = normalised displacement value (read from the relevant reference chart), M* = normalised bending moment value (read from the relevant reference chart), F* = normalised axial force value (read from the relevant reference chart), f_{dU}/f_{dM}/f_{dF} = correction factors obtained from the first auxiliary chart in the design chart set and f_{sU}/f_{sM}/f_{sF} = correction factors obtained from the second auxiliary chart in the design chart set.

6 APPLICATION OF DESIGN CHARTS

Due to space limitations, only estimates of the full-scale measurements of lateral pile response due to tunnelling will be shown below. Application of the design charts for pile response in the other directions can be found in Surjadinata (2009).

There appear to be only two detailed full-scale measurements of lateral pile response due to tunnelling reported in the literature (Lee et al., 1994 and Pang et al., 2006) prior to 2009. These cases are used to illustrate the level of agreement between the predictions from the design charts, the full-scale measurements in the field and also the numerical predictions presented in the published case studies.

6.1 *Angel underground station in London—background*

The first field case was published by Lee et al. (1994) with data obtained during the construction of a tunnel for the Angel Underground Station in London. The excavation of the tunnel involved two construction steps. Firstly, a pilot tunnel with a diameter of 4.5 m was excavated and this was followed by enlargement of the pilot tunnel to a diameter of 8.25 m. The tunnel centre line is 15 m from the surface. Mair (1993) reported that the ground loss for the pilot tunnel was estimated to be 1.5% and that an additional ground loss of 0.5% occurred due to the pilot tunnel enlargement. The soil profile reported by Lee et al. (1994) shows linearly increasing undrained shear strength from about 50 kPa at the surface to approximately 220 kPa at 30 m depth. An average undrained shear strength (s_u) of 135 kPa was assumed, which is typically associated with a soil Young's modulus of approximately 54 MPa (400 s_u). This value of soil modulus was adopted for the design chart-based prediction and that of Loganathan (1999).

The pile of interest was located 5.7 m away from the tunnel axis with a length of 28 m and a diameter of 1.2 m. Inclinometers were installed within the pile to measure its lateral deflection (U_{xmax}). A cross-sectional view of this case history can be found in Figure 5.

6.2 *Angel underground station in London—analysis*

The step-by-step calculation of U_{xmax}, using the proposed design charts, is as follows:

1. Pilot tunnel contribution
   L_p/H = 1.86 (adopt L_p/H = 2 chart set)
   H/D = 3.33 (Intermediate tunnel)
   εD = 1.5% × 4.5 m = 0.0675 m
   W/D = 1.267
   L_c/L_p = 0.452 (Flexible pile)
   L_p/d = 23.33
   U^* = 0.18 (Figure 4—Reference chart)
   f_{dU} = 0.55 (Figure 4—Auxiliary chart 1)
   f_{sU} = 1.02 (Figure 4—Auxiliary chart 2)

   $$U_{xmax} = U^* \times \varepsilon \times D \times f_{dU} \times f_{sU}$$
   $$U_{xmax} = 0.18 \times 0.00675 \times 0.55 \times 1.02$$
   $$U_{xmax} = 0.0068 \text{ m} = 6.8 \text{ mm}$$

2. Tunnel enlargement contribution
   L_p/H = 1.86 (adopt L_p/H = 2 chart set)
   H/D = 1.82 (Shallow tunnel)
   εD = 0.5% × 8.25 m = 0.04125 m
   W/D = 0.69
   L_c/L_p = 0.452 (Flexible pile)
   L_p/d = 23.33
   U^* = 0.21 (Figure 4—Reference chart)
   f_{dU} = 0.78 (Figure 4—Auxiliary chart 1)
   f_{sU} = 1.02 (Figure 4—Auxiliary chart 2)

   $$U_{xmax} = U^* \times \varepsilon \times D \times f_{dU} \times f_{sU}$$
   $$U_{xmax} = 0.21 \times 0.04125 \times 0.78 \times 1.02$$
   $$U_{xmax} = 0.0069 \text{ m} = 6.9 \text{ mm}$$

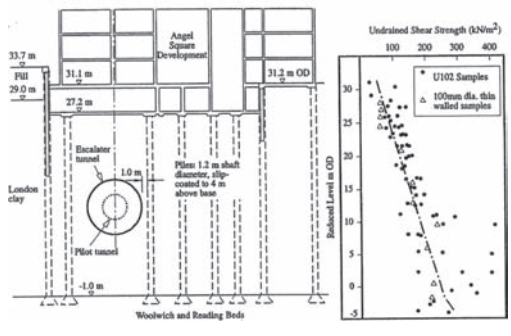

Figure 5. Cross-sectional view of Angel underground station case study (after Lee et al., 1994).

The final U_{xmax} prediction is obtained by superposition of the two separate analyses described above:

$U_{xmax} = 6.8 + 6.9$ mm $= 13.7$ mm

6.3 *Angel underground station in London—discussion*

Lee et al. (1994) reported that a maximum lateral deflection (U_{xmax}) of the pile of 10 mm was measured at the depth of the tunnel axis. They also provided a plane strain FEM prediction which indicated that U_{xmax} at this depth would have been 20 mm. Loganathan's (1999) design charts predict the position of U_{xmax} to be slightly above the depth of the tunnel axis with a magnitude of 11.9 mm.

The prediction obtained from the proposed design charts is therefore conservative and differs by 13% from the prediction based on the Loganathan (1999) design charts. This is considered reasonable agreement between the proposed design charts and the existing solution.

The difference between the prediction of the design charts and the measured lateral pile displacement (Lee et al., 1994) is relatively small at 3.7 mm, suggesting that as a first-order approximation the proposed design charts are capable of providing reasonable predictions of the pile response in this case.

6.4 *MRT north-east line C704 in Singapore—background*

The second field case was published by Pang et al. (2006) with data obtained during the construction of twin parallel tunnels (North-bound and South-bound) for the MRT (Mass Rapid Transport) North East line C704 in Singapore. Both tunnels were excavated at a depth of 21 m by EPB (Earth Pressure Balance) machines, each 6.5 m in diameter. The pile group was situated between the twin tunnels. Each pile has a diameter of 1.2 m and a Young's modulus of 28 GPa was used to represent the pile stiffness. The geometry of this problem, including sectional and plan views of the pile group, is shown in Figure 6. Further details of this problem can be found in Pang et al. (2006).

The pile group of interest reported by Pang et al. (2005 & 2006) is Pier 20. This pier rests upon a group of four piles, as can be seen in Figure 6. The pile in this group used for comparison purposes was designated P1 by Pang et al. (2005 & 2006) and its position can be seen in Figure 6. It is located very close to the South-bound tunnel with only 1.6 m clear distance between the side of the tunnel and the side of the pile. The clear distance

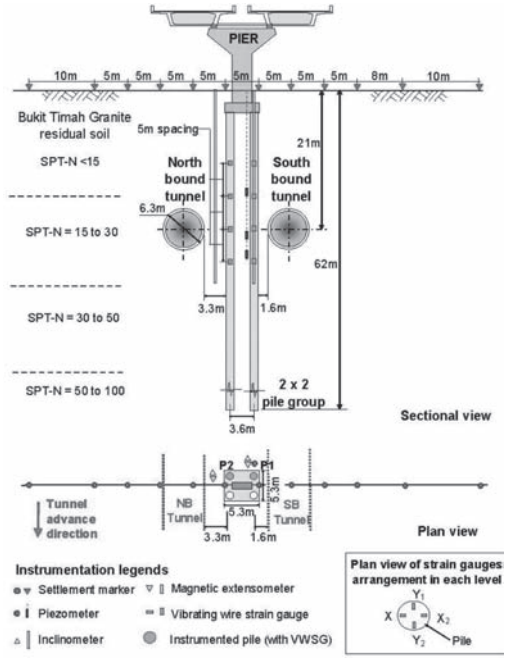

Figure 6. Geometry of MRT N-E line C704 Singapore (after Pang et al., 2006).

between the side of the North-bound tunnel and the side of pile P1 is 6.9 m. The measured ground loss ε from the South-bound tunnel is 1.38%.

Pang et al. (2005) also provided a non-linear 3-D FEM prediction of the maximum response of pile P1. For the FEM analysis, Pang et al. (2005) adopted a multi-layered soil model with a strain dependant Modified Cam Clay formulation developed by Dasari (1996). In this formulation, prior to yielding, the soil stiffness varies with strain.

Pang et al. (2006) note that the pile is mainly embedded in completely weathered (residual soil) Bukit Timah granite. For the predictions using the proposed design charts, it was assumed that the residual soil is uniform with a stiffness of 8.25 MPa (Hefny et al., 2004).

6.5 *MRT north-east line C704 in Singapore—analysis*

Pang et al. (2006 & 2005) provided measurements and FEM predictions of the maximum responses of pile P1. They are the induced lateral and longitudinal bending moments (M_{xmax} & M_{zmax}) and the induced axial force (F_{ymax}). Due to space constraints, only the measurement of maximum lateral bending moment (M_{xmax}) will be compared against the prediction obtained using the proposed design charts.

Note that the measured pile responses are due to ground loss from the South-bound tunnel only.

The step-by-step calculation of the maximum lateral bending moment using the chart solutions is as follows:

South-bound tunnel contribution

L_p/H = 2.9 (adopt L_p/H = 2 chart, see note below)

H/D = 3.23 (Intermediate tunnel)

ε/D = 1.38%/6.5 m = 0.002123 m^{-1}

$(EI)_p$ = 28000 MPa × 0.10178 m^4 = 2850.0 M Nm^2

W/D = 0.838

L_c/L_p = 0.316 (Flexible pile)

L_p/d = 50.8

M^* = 0.29 (Fig. 7)

f_{dM} = 0.46 (Fig. 7)

f_{sM} = 0.95 (Fig. 7)

$$M_{xmax} = M^* \times (EI)_p \times \frac{\varepsilon}{D} \times f_{dM} \times f_{sM}$$

$$M_{xmax} = 0.29 \times 2850 \times 0.002123 \times 0.45 \times 0.95$$

$$M_{xmax} = 0.75 \text{ MNm}$$

Note that the pile length for this case is beyond $L_p/H = 2$ and the design chart for $L_p/H = 2$ was used in the calculation above. This serves as an illustration that for any pile length (L_p/H) beyond 2, the design chart set for $L_p/H = 2$ is the applicable design chart set. The reason is that the maximum portion of pile length that is significantly affected by the tunnel's presence appears to be limited to twice the depth of the tunnel (2H), as observed in Surjadinata (2009).

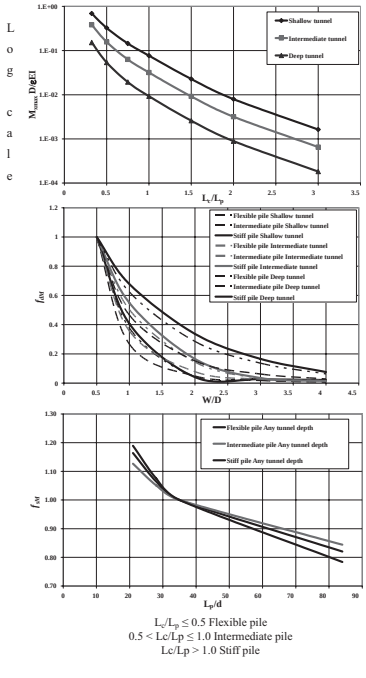

Figure 7. Maximum lateral bending moment design charts set for Lp/H = 2 (Long pile).

6.6 *MRT north-east line C704 in Singapore—discussion*

The measured value of M_{xmax} of pile P1 at the tunnel axis level reported by Pang et al. (2006) was 0.403 MNm and the prediction using the proposed design charts solution is 0.75 MNm. The difference between the measured M_{xmax} and the prediction from the design charts is expected since there are two fundamental differences between the assumed model and reality.

The first difference is due to the fact that the measured value of M_{xmax} is for a pile within a pile group, while the design charts were created for a free-standing single pile. Since the stiffness of a pile connected to the other piles in the group by a (relatively) rigid pile cap might be expected to be higher than a free-standing pile, it is expected that the measured pile response will be lower than the prediction obtained from the proposed design charts. Hence, the values of M_{xmax} predicted for a pile in a group are expected to be less than those of a single free standing pile.

The second difference is that the measured M_{xmax} is for a pile embedded in a layer of soil of increasing stiffness with depth, while the proposed design charts were created for a pile embedded in elastic soil with uniform stiffness. Generally in this case, elastic analysis will provide a conservative prediction of M_{xmax}.

Hence, it is expected that the measured maximum responses of pile P1 will be less than the corresponding predictions from the proposed design charts.

The 3-D non-linear elastoplastic FEM prediction of M_{xmax} reported by Pang et al. (2005) for the same pile (P1) at the level of tunnel axis is 0.6 MNm and, as shown above, the prediction using the proposed design charts solution is 0.75 MNm.

This difference is expected due to the fact that the FEM approach modelled features such as the rigidity of the pile group, layered soil, non-linear elastoplastic soil model and the details of the rate of tunnel advancement, while the design chart solution is for a single pile within a uniform linear elastic soil.

Despite these differences, the proposed design charts provide a reasonable and conservative first order prediction of M_{xmax}, relative to both the measured value and the non-linear FEM prediction.

As further indication of the agreement between the chart prediction and the measured data, though not presented in detail here, employing the charts gave predictions of M_{zmax} = 0.17 MNm and F_{ymax} = 4.05 MN in comparison with the measured

values of M_{zmax} = 0.16 MNm and F_{ymax} = 3.4 MN presented in Pang et al. (2006). Complete comparison of Pang et al. data and predictions obtained using the proposed design charts can be found in Surjadinata (2009).

7 ADVANTAGES OF THE DESIGN CHARTS

The main advantage of the proposed design chart system is that it will allow predictions of the pile responses to be made with little cost (in time and effort) relative to existing numerical methods. Given the reasonable degree of agreement with both existing solutions and field measurements of pile response, the proposed design charts should allow cost-effective first-order predictions to be made with some confidence.

Furthermore, if a more refined estimate of the maximum pile behaviour is needed, the first-order estimates from the proposed design charts can be used as a "point of reference" for a more sophisticated numerical analysis.

Another advantage of the proposed design charts relative to other methods published to date is their ability to predict the maximum pile response in the third (longitudinal) direction. To the best knowledge of the authors there are no other published design charts that are able to provide predictions of this type.

Due to all of these advantages, it is therefore considered that the proposed design chart solutions can be comfortably adopted as a preliminary 3-D design tool.

8 SUMMARY

A brief summary of the generation and organisation of design charts for singles piles subjected to the effects of tunnelling was presented. This was followed by a step-by-step guide to using the proposed design charts and a discussion on the limitations of the design charts. Then the application of the proposed design charts to two well-known cases studies was presented in order to illustrate the degree of agreement between the predictions from the design charts, other theoretical methods (FE and other design charts) and measured pile responses. The application of the design charts in these cases indicated that they provide reasonable and conservative predictions.

It is concluded that given the advantages of the design charts solutions, they can reasonably be adopted as a preliminary 3-D design tool.

As additional full scale data become available, more comparisons of the design chart results will be possible and this should allow a better (and more complete) assessment of their predictive capabilities.

REFERENCES

Dasari, G.R. (1996). Modelling the variation of soil stiffness during sequential construction. *PhD thesis*, Cambridge University.

Hefny, A.M. and Lo, K.Y. (1999). Analytical solutions for stresses and displacement around tunnels driven in cross-anisotropic rocks. *Int. J. Numer. Anal. Meth. Geomech*., 23, pp 161–177.

Hull, T.S. (1987). The behaviour of laterally loaded piles. *PhD Thesis*, Department of Civil Engineering, The University of Sydney.

Hull, T.S. (1998). Manual for computer program PALLAS. Centre for Geotechnical Research, The University of Sydney.

Lee, R.G., Turner, A.J. and Whitworth, L.J. (1994). Deformations caused by tunnelling beneath a piled structure. *Proc. XIII Int. Conf. Soil mechanics and Foundation Engineering*, New Delhi, India, pp 873–878.

Loganathan, N. (1999). Effect of tunnelling adjacent to pile foundations. *Ph.D Thesis*, Department of Civil Engineering, The University of Sydney, Australia.

Loganathan, N., Poulos, H.G. and Xu, K.J. (2001). Ground and pile-group responses due to tunnelling. *Soils and Foundations*, 41(1), pp 57–67.

Mair, R.J. (1993). Developments in geotechnical engineering research: application to tunnels and deep excavations Unwin memorial Lecture 1992. *Proc. Instn. Civ. Engrs*, 93, pp 27–41.

Pang, C.H., Yong, K.Y. and Chow, Y.K. (2005). Three-dimensional numerical simulation of tunnel advancement on adjacent pile foundation, *Proceedings of the 31st ITA-AITES World Tunnel Congress*, 7–12 May 2005, Istanbul, Turkey.

Pang, C.H., Yong, K.Y., Chow, Y.K. and Wang, J. (2006). The response of pile foundations subjected to shield tunnelling, *Proceedings of the 5th International Conference of TC28 of the ISSMGE*, Netherlands, pp 737–743.

Poulos, H.G. (1982). "Developments in the analysis of static and cyclic lateral response of piles." *Proc., 4th Int. Conf. on Numerical Methods in Geomechanics*, Canada, 1117–1135.

Poulos, H.G. and Davis, E.H. (1980). Pile Foundation Analysis and Design, New York, John Wiley & Son.

Surjadinata, J.Q., Carter, J.P., Hull, T.S., Poulos, H.G. (2005). Analysis of effects of tunneling on single piles. *Proceedings of 5th International Conference of TC28 of the ISSMGE,* Netherlands, pp 665–671.

Surjadinata, J.Q., Carter, J.P., Hull, T.S., Poulos, H.G. (2006). Combined Finite-and-Boundary-Element analysis of the effects of tunneling on single piles. *International Journal of Geomechanics*, Vol 6 No. 5, pp 374–377.

Surjadinata, J.Q. (2009). The Influence of tunneling on single piles. *Ph.D Thesis*, Department of Civil Engineering, The University of Sydney, Australia.

Geotechnical Aspects of Underground Construction in Soft Ground – Viggiani (ed)
© 2012 Taylor & Francis Group, London, ISBN 978-0-415-68367-8

Prediction method of the displacement of surrounding ground during excavation

Y. Motoi
Obayashi Corporation, Tokyo, Japan

ABSTRACT: Excavation works cause the displacement of surrounding ground and structures. This paper shows a method to predict of the displacement by using the Winkler model analysis method together with Finite Element Method (FEM). This method takes into consideration the nonlinearity of soil properties. In this paper, this method is applied to an excavation work. The result of comparison of analysis results and measured data shows that this method is effective for prediction of displacement of surrounding ground.

1 INTRODUCTION

Excavation works cause the displacement of surrounding ground and structures. This paper shows a method to predict of the displacement by using the Winkler model analysis method together with Finite Element Method (FEM).

By the general finite element method, it is difficult to predict the displacement of earth retaining walls during excavation compared with Winkler model analysis. This paper shows a method to predict the displacement of the surrounding ground by defining the results of Winkler analysis, prediction accuracy of the displacement is high, as boundary condition to the wall position of the Finite Element Method (FEM). This method is called "forced displacement method".

In forced displacement method, generally the soil properties are treated as linear elastic materials in FEM. This paper shows a method to treat the soil properties as non-linear materials in forced displacement method. The surrounding ground has non-linear properties that hardness changes depending on distortion.

This paper presents a case study applied forced displacement method to an excavation work near to a railroad. This case study compares the result of non-linear analysis with linear analysis.

2 GEOLOGICAL OUTLINE

Figure 1 shows geological outline and the section for analysis. From the surface of the ground to

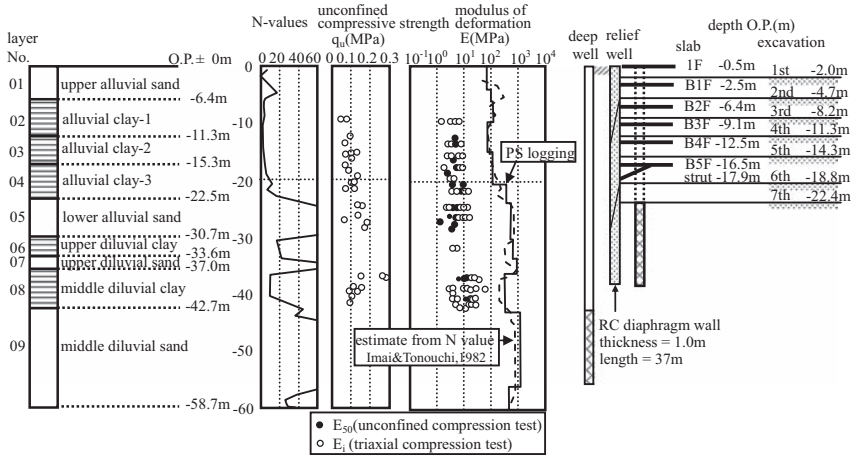

Figure 1. Geological outline and the section for analysis.

Table 1. Soil properties.

Layer no.	Soil	Bottom depth OP—m	γ_t kN/m^3	ν	V_s m/sec	E_{ps} kN/m^2	c kN/m^2	ϕ deg	k_h*B kN/m^2
01	Sand	6.4	16.7	0.33	130	76,000	0	20	2280
02	Clay	11.3	15.7	0.499	130	76,000	25	15	2280
03	Clay	15.3	15.7	0.499	150	101,000	37	15	3030
04	Clay	22.5	15.7	0.499	270	327,000	60	10	9810
05	Sand	30.7	18.6	0.33	320	518,000	0	45	15540
06	Clay	33.6	16.2	0.499	240	266,000	166	10	7980
07	Sand	37.0	18.6	0.33	320	518,000	0	40	518000
08	Clay	42.7	16.2	0.499	240	266,000	↑ for Winkler analysis		
09	Sand	58.7	19.6	0.33	460	1,126,000			

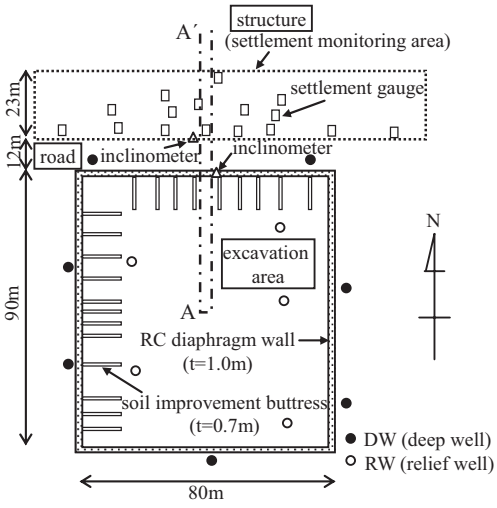

Figure 2. Plan of the excavation and measurement points.

about O.P. (Osaka pale) –22.5 m, alluvial soft clay accumulates, and the N-value is 0–1. Alluvial sand accumulates from O.P.–22.5 m to –30.7 m. Firm diluvial clay and sand underlie the alluvial sand.

Table 1 shows soil properties. Modulus of deformation, E_{ps}, of each layer is estimated form the results of PS logging carried out at a site nearby.

3 OUTLINE OF THE EXCAVATION WORK AND THE MEASUREMENT

3.1 *Excavation work*

Figure 2 shows the plan of the excavation area and measurement points. The plane size of the site is about 80 m × 90 m, and the excavation depth is 22.4 m.

The excavation method is inverted construction method. RC diaphragm walls of thickness 1.0 m is installed to O.P.–37.0 m as earth retaining walls (Fig. 1).

3.2 *Measurement*

There is a structure (a railroad viaduct) in the north side of the site (Fig. 2). Between the site and the structure, there is a road of 12 m in width.

Settlement of ground surface under the viaduct are measured with settlement gauges. Horizontal displacement of ground in the distance of 15.1 m from the earth retaining walls are measured with inclinometer.

4 OUTLINE OF FEM ANALYSIS

4.1 *FEM analysis model*

Figure 3 shows 2-Dimension FEM model. The displacement of the results of Winkler analysis are defined as boundary condition to the RC diaphragm wall position of the FEM model.

Only the ground of the back side of earth retaining walls is modeled and influence of load of building and removed soil in excavation area is ignored.

The analysis domain of the back ground is 96 m. This is equivalent to about 4 times of the excavation depth. The analysis domain of the depth direction is 90 m from the final excavation level. This is approximately equal to excavation width.

As for the boundary condition of the back end, the vertical direction is free, and the horizontal direction is fixed. As for the boundary condition of the bottom of the FEM model, the vertical direction and the horizontal direction are fixed. The load of the structure 77.4 kN/m^2 acts on the ranges from distance 12.0 m to 35.0 m from the earth retaining walls.

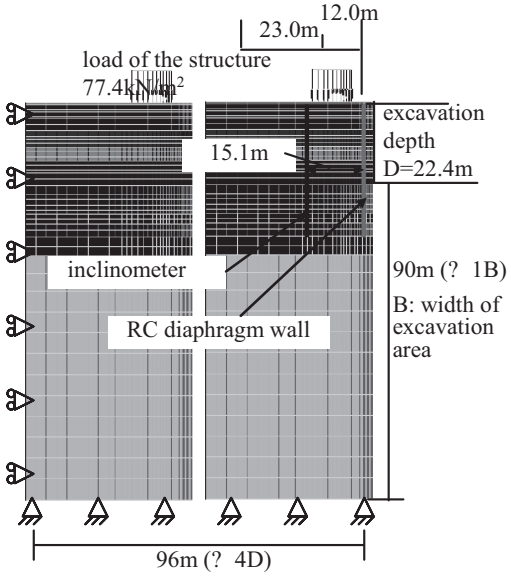

Figure 3. 2-dimension FEM model.

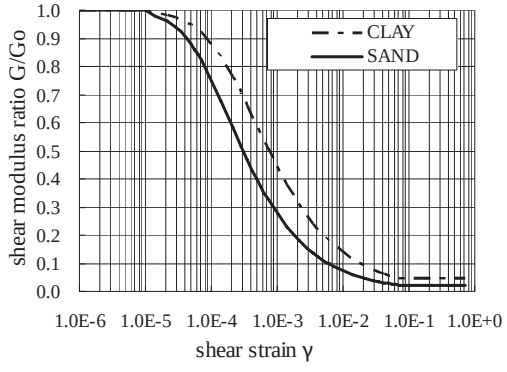

Figure 4. G/Go-γ curves of soil.

4.2 *Soil materials*

The soil is modeled as two-dimensional plane distortion element. The soil properties is set by two ways, one is treated as linear elasticity and the other is non-linear elasto-plastic body.

By the linear elastic analysis, modulus of deformation and Poisson's ratio are evaluated in E_{ps}, ν shown to Table 1 each.

In the non-linear analysis, modulus of deformation is estimated as shear modulus ratio concerning shear strain shown to Figure 4. In analysis, it is similar to multi-linear this curve. Initial modulus of deformation and Poisson's ratio of this case are evaluated in E_{ps}, ν shown to Table 1 each. Analysis errors occur so that modulus of deformation changes with the change of the distortion in the non-linear analysis. Each analysis step is divided into 100 smaller steps to reduce this analysis errors.

4.3 *Evaluation of load of the structure*

Load of the structure acted on the back side as shown in Figure 3. To confirm the influence of the difference in handling of the load, three cases of following analyses were carried out.

Linear case: Soil properties are linear. Structure load is not considered.
Non-linear case A: Soil properties are non-linear. Structure load is not considered.
Non-linear case B: Soil properties are non-linear. Stress distortion state by the load is considered.

In non-linear case B, structure load acts in analysis step1, and modulus of deformation is reduced depending on the distortion of each soil element. Displacement of the soil is returned to beginning in analysis step 2. Modulus of deformation reduced in step1 is inherited on this occasion. The displacement of the results of Winkler analysis are defined as boundary condition to the RC diaphragm wall position of the FEM model in analysis step 3 (Fig. 5).

4.4 *Forced displacement*

Figure 6 shows forced displacement to the RC diaphragm wall position analyzed by Winkler method. Soil properties for Winkler method are in Table 1 and lateral earth pressure are shown in Figure 6.

Measured displacement of the RC diaphragm walls by inclinometer are shown in Figure 7. The analysis value almost accords with measurement value except displacement of the top of the wall from 5th to 7th excavation. The maximum displacement of 7th excavation is about 30 mm. It occurs at depth form O.P.–14 m to –15 m.

5 FEM ANALYSIS RESULTS

5.1 *FEM analysis results*

Figure 8 shows examples of the FEM analysis results. This figure shows the composition of the displacement of vertical direction and horizontal direction of final excavation step (7th excavation). The maximum of ground displacement in the linear and non-linear case A analysis appears close to the wall and the displacement becomes smaller as to leave from the wall.

In non-linear case B, because of the surcharge, displacement of viaduct area is large. This analysis

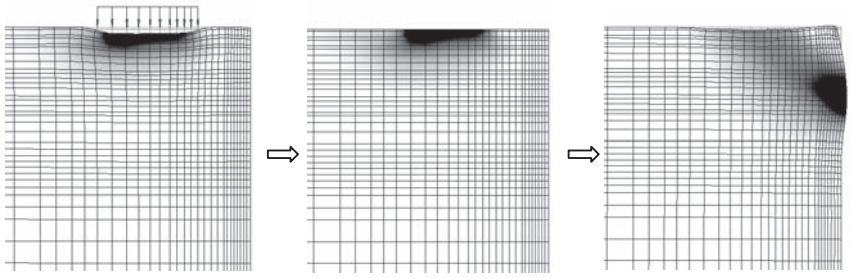

step1: Structure load acts and modulus of deformation is reduced depending on the distortion of each soil element.

step2: Displacement of the soil is returned to beginning. Modulus of deformation reduced in step1 is inherited on this occasion.

step3: The displacement of the results of Winkler analysis are defined as boundary condition to the RC diaphragm wall position.

Figure 5. Analysis step of non-linear case B.

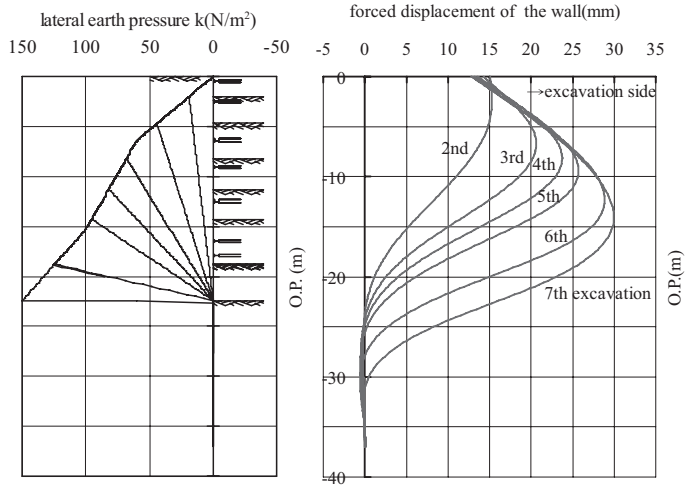

Figure 6. Forced displacement analyzed by Winkler method.

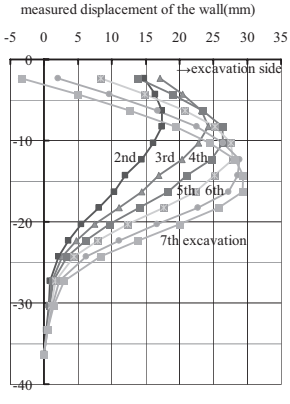

Figure 7. Measured displacement of the wall.

result shows the influence of the hardness reduction that occurred by analysis step 1. The conventional forced displacement method cannot consider the influence of such local ground hardness reduction, because the method treats the ground as linear.

5.2 *Vertical displacement of ground surface*

Figures 9–11 show the vertical displacement of ground surface in FEM analyses with measured data. Results of step 2, 4, 7 are shown as representative.

The analysis results of settlement of linear and non-linear case A which do not consider influence of load of the structure show the peak at a position from about 5 m to 10 m from the wall and it gets smaller gently depending on the distance

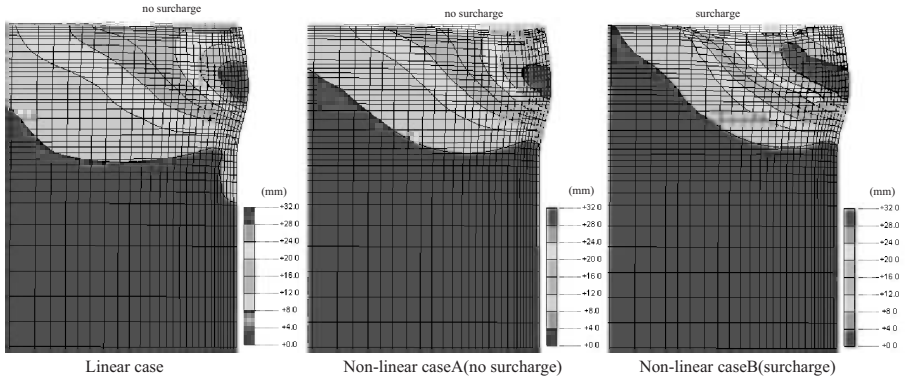

Figure 8. Composition of the displacement of vertical and horizontal direction of FEM analysis.

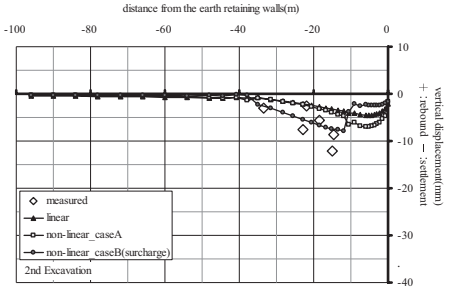

Figure 9. Vertical displacement of ground surface.

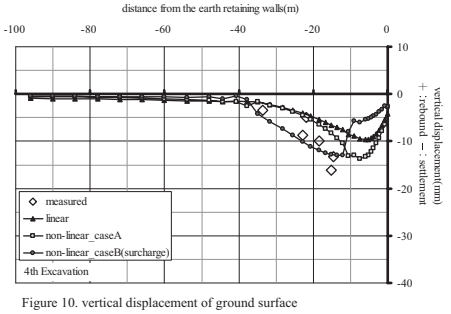

Figure 10. vertical displacement of ground surface

Figure 10. Vertical displacement of ground surface.

from the wall. On the other hand, according to the measurement data, the large settlement occurs under the viaduct. Although the difference of the local maximum is large, the analysis result of non-linear case B shows the tendency of the measurement data.

This result shows that this method is effective as prediction technique of settlement of the surrounding ground.

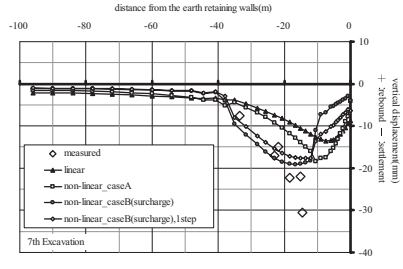

Figure 11. Vertical displacement of ground surface.

5.3 *Horizontal displacement of ground*

Figures 12–14 show the horizontal displacement of ground at the position that was 15.1 m away from earth retaining walls in FEM analyses with measured data. Results of step 2, 4, 7 are shown as representative.

The measurement data of the horizontal displacement of the ground 15.1 m away from the wall shows the maximum at depth from O.P.–6 m to –10 m. Analysis results of non-linear case B accord with this tendency best. In addition, the analysis result of non-linear case A is small in comparison with it of linear. This relation is reverse in the case of settlement of ground surface.

The ratios with the measurement data of the maximum of analysis results through all steps are 69–90% in linear, 63–78% in non-linear case A, and 90–116% in non-linear case B. This result shows that this method is effective as prediction technique of horizontal displacement of the ground.

5.4 *Influence on analysis result by excavation process*

Figures 11 and 14 show the results that defined forced displacement as boundary condition of FEM of the last (7th) excavation by one step in

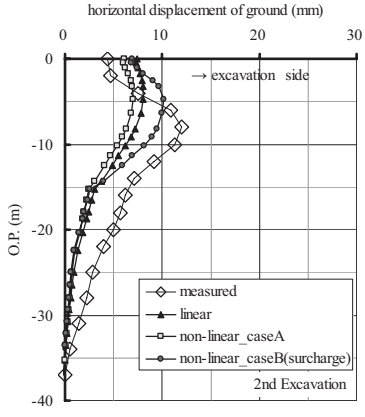

Figure 12. Horizontal displacement of ground.

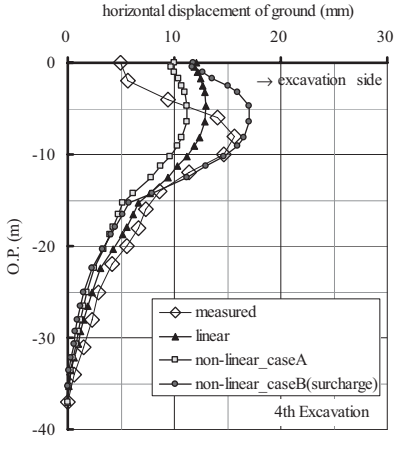

Figure 13. Horizontal displacement of ground.

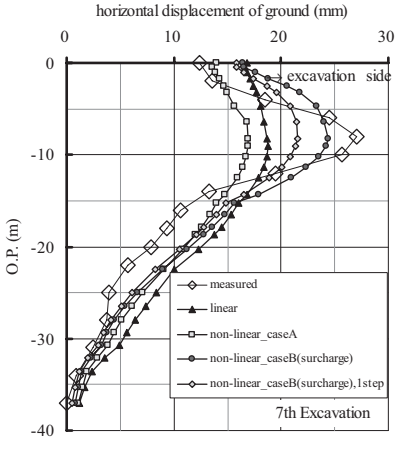

Figure 14. Horizontal displacement of ground.

defiance of the excavation process. The purpose of this examination is to confirm the influence of excavation process for analysis result.

The settlement and the horizontal displacement of the ground show the distribution that resembled the analysis result that considered the excavation process, but these maximums are about 10% smaller than them. This result suggests that prediction precision improves by considering excavation process.

6 CONCLUSIONS

This paper showed a method to predict of the displacement by using the Winkler model analysis method together with FEM. This method is called "forced displacement method".

In forced displacement method, generally the soil properties are treated as linear elastic materials in FEM. This paper presented a method to treat the soil properties as non-linear materials in forced displacement method and results of case study applied this method to an excavation work near viaduct of railroad.

According to the measurement data, the large settlement occurred under the viaduct. Although the difference of the local maximum was large, the analysis result of non-linear case B (stress distortion state by the load is considered) showed the tendency of the measurement data.

The measurement data of the horizontal displacement of the ground 15.1 m away from the wall showed the maximum at depth from O.P.−6 m to −10 m. Analysis results of non-linear case B accorded with this tendency best.

The result of comparison of analysis results and measured data showed that this non-linear method is effective for prediction of displacement of surrounding ground. In addition, prediction precision improves by considering excavation process.

On the other hand, a prediction by this analysis is difficult when large ground displacement occurs locally. This is the part needing the improvement of this method of analysis.

REFERENCES

Architectural Institute of Japan 2002. Recommendation for design and construction practice of earth retaining for excavation, pp. 228–237(in Japanese).

Aoki M. et al. 2000. Evaluation Methods of Surface Settlement of Retained Side Ground Based on Measured Earth Retaining Wall Displacement(Part1), Summaries of Technical Papers of Annual Meeting A.I.J, pp. 537–538 (in Japanese).

Ministry of Land, Infrastructure and Transport 2001. Notification No. 387 (in Japanese).

Ueno T. et al. 1993. An example of Excavation Work of large-scale building, The Foundation Engineering & Equipment,Vol. 21, No. 7, pp. 97–101 (in Japanese).

Geotechnical Aspects of Underground Construction in Soft Ground – Viggiani (ed)
© 2012 Taylor & Francis Group, London, ISBN 978-0-415-68367-8

Numerical modeling of diaphragm wall behavior in Bangkok soil using hardening soil model

N. Phien-wej & M. Humza
Asian Institute of Technology, Bangkok, Thailand

Z. Zaw Aye
Seafco Public Company Limited, Bangkok, Thailand

ABSTRACT: A numerical study was performed incorporating the Hardening Soil model to examine its applicability in capturing the diaphragm wall behavior in Bangkok subsoils. The model was first calibrated for a well monitored excavation case in Bangkok. Then it was applied for three other cases for verification. The predicted wall and ground movement behavior compares reasonably with observed behavior, suggesting advantage of the soil model for application in Bangkok subsoils. Empirical correlations are proposed for estimating the Hardening Soil model parameters from undrained shear strength of soft clays and from SPT 'N' values for stiff to hard clays and sand of Bangkok subsoils.

1 INTRODUCTION

Diaphragm walls have been widely used as primary and permanent structural elements for supporting deep excavations in urban area of Bangkok. Due to the complex nature of the soil structure interaction, a realistic soil constitutive model is crucial in order to estimate the behavior and magnitudes of wall and ground movements.

Soil response to loading is nonlinear, inelastic and highly dependent on the magnitude of stress. This behavior has a significant influence on the stresses and displacements developed within the reinforced structure. The constitutive model commonly used to investigate performance of braced excavations in Bangkok is the linear-elastic perfectly plastic Mohr Coulomb yield criterion. It popularity continues although it does not always give a good fit for both magnitude and pattern for ground movements (Phienwej & Photayanuvat 1998, Hooi 2003). In general, its use leads to settlement troughs shallower and wider than those actually observed (Addenbrooke et al. 1997, Masin & Herle 2005) and it underestimates bending moments in diaphragm wall (Ng et al. 2005). It is, therefore, suggested to use a soil model that considers non-linear stress strain behavior, unloading stiffness, stress-dependent stiffness, hardening, and dilatancy.

In this study, two constitutive models were used in comparative analysis of deep excavations in Bangkok subsoils, i.e. the linear-elastic perfectly Mohr Coulomb model and the Hardening Soil model.

2 SUBSOIL PROFILE

Bangkok is situated on the flat topography of Bangkok Plain. Subsoils consist of a thick marine soft silty clay layer of 12–15 m in thickness. It is underlain by alternating layers of alluvial stiff to hard clay and dense to very dense sand to gravel. The soft clay which is well known as "Bangkok soft clay" has high water content (70–120%), high plasticity, low strength and high compressibility. (Phienwej et al 2007).The typical subsoil profile with geotechnical properties is given in Figure 1.

3 SELECTED ANALYSIS CASES

Four completed excavation cases are chosen for the comparative analysis made in this study.

3.1 *MRT Silom station*

Silom Station involved the deepest excavation made in the construction of first Bangkok underground MRT project of 20 km long rail length. The stacked-platform station has four levels of floor slab. The station was constructed underneath a road overpass bridge of which the piled foundation needed to be underpinned for the station construction. The first excavation depth was 6.45 m for casting of the roof slab and it was deepened to the final excavation depth of 32.55 m. A dense sand layer of the first Bangkok Sand was encountered from depth of 8.5 m above the final excavation level. Hence, the excavation required dewatering.

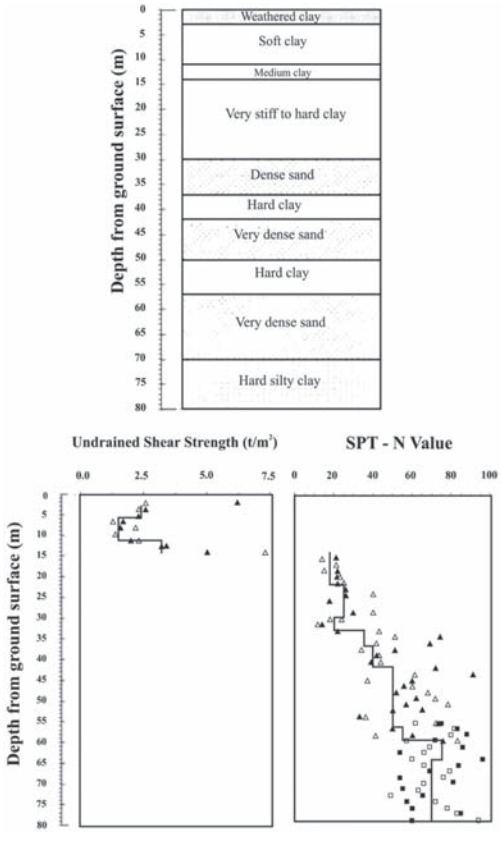

Figure 1. Typical Bangkok subsoils profile (Wonglert et al. 2008).

The diaphragm wall was toed into the Second sand layer at 46.5 m depth. The excavation was made by the top-down construction method utilizing concrete floor slabs as wall bracing.

3.2 *MRT Thiam Ruam Mit station*

Thiam Ruam Mit station is located beneath the carriageway of a wide city road. This station forms an interchange station and it has three levels i.e. platform, concourse and retail levels constructed within a diaphragm wall box. The station was constructed using the top down technique. Piles or barrettes and preformed columns were installed along the center of the station to provide mid span support to the slabs. The maximum excavation depth was 17.5 m and the toe of the diaphragm wall was at 22 m depth.

3.3 *Central Hospital of Bangkok*

Central Hospital is located in the old commercial area of Bangkok. The project included the construction of four level basements and one multipurpose recreational area. The main feature of the project was the split floor levels and a temporary steel transfer beam was used to transfer the load from north to south diaphragm walls. Maximum excavation depth was 20 m.

3.4 *Bangkok City hall car park*

The excavation was for construction of two-level underground car park, located in front of Bangkok City Hall in the area of the historical sector of the city. This construction site was surrounded by numbers of sensitive structures that posed many constraints, which called for the need of careful consideration in establishing design criteria and procedures of excavation (Thasnanipan et al, 2004). Diaphragm walls were founded at 16 m below ground level for the excavation depth of 6.6 m. Barrettes having same toe depth as bored piles were installed at 8 m spacing along with diaphragm wall panels.

Value engineering option and observational method were applied in this project. Phase 1 works comprised excavation to 2.2 m depth and with temporary struts installed at 1.8 m. The second stage of excavation involved excavation to 6.6 m depth with toe soil berms. A major modification was made during the course of the excavation involving replacing of cross-lot struts by inclined rakers for the north wall and removal of soil berm at east and west diaphragm walls.

4 FINITE ELEMENT ANALYSIS

Plane strain finite element analysis was made using PLAXIS version 8.5 software to simulate the selected excavation cases. The FEM mesh is made of 15-node triangular elements and has width 7 times the excavation width and depth 2.5 times the maximum excavation depth (e.g. for a case of excavation depth of 30 m and half width of 15 m, the mesh is 80 m deep and 105 wide). The undrained analysis using effective strength parameters of the Bangkok stratified subsoils. The effective frictional angles used are 23 degrees for soft clay, medium stiff clay and stiff clay, 27 degrees for silty clay and 36 degrees. A range of small cohesion is used for clayey soil layers. The input strength parameters are in accordance with the test results of the comprehensive geotechnical program made in the First Bangkok underground MRT project (Phienwej and Photayanuvat, 1998). The drawdown condition of Bangkok groundwater in the subsoils due to past deep well pumping was considered in the analysis. The drawdown is 22 m in the first sand layer.

5 CONSTITUTIVE MODELS

The Mohr Coulomb (MC) model and Hardening Soil (HS) model in PLAXIS code are used in the analysis in order to compare the prediction results of wall and ground movements so that assessment could be made on the better constitutive model for use in future deep excavations in Bangkok subsoils.

The MC model in PLAXIS adopts the linear elastic perfectly plastic constitutive law. It requires five parameters, i.e. E and ν for linear elastic behavior and c and φ for yield function and ψ as dilation angle for plastic deformation behavior. The HS considers non-linear stress strain behavior of soil according to the hyperbolic model and allows for shear and compression hardening (Schanz & Vermeer 1997). Total strains are calculated by stress dependent moduli, different for loading and unloading. Input parameters of the model consists of the strength parameters φ, c, and dilation angle ψ. Soil stiffness is defined by parameters E_{50}^{ref} and E_{ur}^{ref} (unloading-reloading modulus) for shear behavior and E_{oed}^{ref} for volumetric behavior.

Schanz & Vermeer (1997) reported that E_{50}^{ref} of sandy soils showed relationship with 1-D modulus E_{oed}^{ref}. Hence, if data on the oedometer modulus is given, it can be used to estimate the triaxial modulus. Generally, it is suggested that E_{50}^{ref} be equal to E_{oed}^{ref} whereas $E_{ur}^{ref} = 3E_{50}^{ref}$. This empirical relationship is adopted in the initial step of analysis in this study.

6 MODEL PARAMETERS

6.1 *Mohr Coulomb model parameters*

The model has been widely used in both research study and design practice in related to Bangkok soils and the characteristics and values of soil property parameters are well established. The stiffness parameters used in Silom and TRM stations of Bangkok Underground MRT project are adopted from the result of back-calculation study Hooi (2003).The suggested undrained soil modulus values of the soils are as follows:

Soft and Medium Clay:	$E_u = 500\ C'_u$
First Stiff Clay:	$E_u = 700\ N_{60}$
Clayey Sand:	$E_u = 900\ N_{60}$
Second Hard Clay:	$E_u = 1600\ N_{60}$
Third Hard Clay:	$E_u = 2500\ N_{60}$

where, E_u (kN/m^2) = undrained Young modulus, C'_u = corrected field vane shear strength of clay and N_{60} = corrected SPT 'N' values.

For Central Hospital and BMA project, the stiffness parameters were derived from the soil test data. Undrained shear strength of soft and medium clay was obtained from unconfined compressive strength. For stiff clay layers, the stiffness parameters were based on SPT 'N' values. For sand layers, it was estimated from E'/N relationship given by Burland and Burbidge (1985).

6.2 *Hardening soil model parameters*

Two sets of HS soil parameters were used in the initial run for purpose of calibration. The first set used E_{oed}^{ref} values in accordance with past laboratory oedometer test results on Bangkok soils (STS 2006). Then E_{50}^{ref} was assumed to have the same value as E_{oed}^{ref} and $E_{ur}^{ref} = 3E_{50}^{ref}$. For the second set, the parameters were derived from the MC parameter values by setting E_{50} of HS model at the midpoint of each layer to the E_{ref} of the Mohr-Coulomb model and deriving E_{50}^{ref} using Equation 1. E_{oed}^{ref} and E_{ur}^{ref} are assumed to be equal to E_{50}^{ref} and $3E_{50}^{ref}$ respectively.

$$E_{50} = E_{50}^{ref}\left[\frac{c\cos\varphi - \sigma'_3\sin\varphi}{c\cos\varphi + p^{ref}\sin\varphi}\right]^m \quad (1)$$

7 HS MODEL CALIBRATION

For calibration, the predicted lateral displacement behavior of diaphragm wall by HS model is compared with the observed data of Silom Station using both sets of parameter as discussed above. Figure 2 compares the observed and pre-

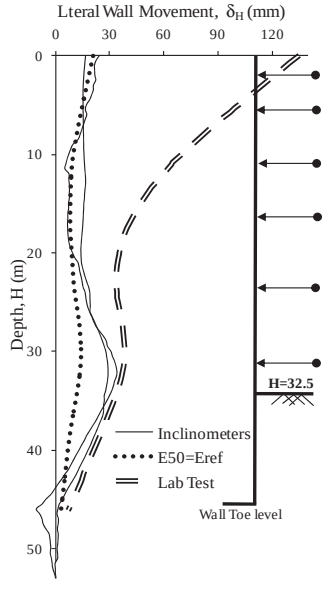

Figure 2. Predicted lateral ground movements using two sets of parameters of HS model.

dicted lateral ground movements at the wall for the last stage of excavation (32.5 m depth). The maximum lateral movement as predicted by using the parameters determined from laboratory test results is 136.5 mm. It grossly over-predicts the actual behavior, particularly at shallow depths. On the other hand, the second set of parameters gives reasonable prediction for early excavation stages (shallower excavation depths). However, it shows underestimation of the magnitude of ground movement at deeper depths in the sand layer, including the base level and below.

8 PREDICTED PERFORMANCE

To investigate the suitability of the HS model parameters for Bangkok subsoils, analysis of diaphragm wall behavior of Silom Station excavation was performed for comparative study of observed values of lateral ground movements and predicted values using adjusted parameters of HS model in comparison of the MC model prediction suggested by Hooi (2003).

The predicted ground movements are primarily influenced by soil stratigraphy and soil model parameters used. In this step, HS soil parameters of clayey soil layers are iteratively adjusted until the calculated results show reasonable agreement with the observed data. Then obtained HS model parameter values are compared with the MC model parameters of each of the soil layers. The back-calculated HS stiffness parameters of Silom Station excavation is summarized in Table 1.

8.1 *Lateral ground movement*

Figure 3 illustrates the comparison between observed and predicted lateral ground movements by using the MC and HS models. At the base excavation, inclinometers indicate slightly larger bulges than the predictions by both models. Generally, the HS model shows a better prediction than the MC model. The prediction by the former compares reasonably well with the observed magnitude and pattern.

The magnitude of the deflection predicted by MC model is overestimated near the base level. This is due to the fact that a stiffer unloading modulus is considered in the analysis by HS model.

8.2 *Bending moment*

It has been reported by previous researchers that the bending moment in the wall predicted by analysis using the HS model is comparatively higher than those obtained using the MC model. The finding in this study for Bangkok subsoil is in line with it.

Figure 4 shows the predicted bending moments by both models. The pattern and point of inflexion as predicted by both models are similar. The magnitude of maximum positive as well as negative bending moment as generated by HS model is slightly higher than that of the MC model.

8.3 *Ground surface settlement*

Figure 5 shows comparison between the observed and predicted surface settlements. As expected, the surface settlement trough predicted by the HS model

Table 1. Stiffness parameters in analysis of Silom station.

				Mohr coulomb parameters	Hardening soil parameters	
	Depth	SPT	Su	E'	E_{50}^{ref}	E_{ur}^{ref}
Soil layer	m	N60	kPa	MPa	MPa	MPa
Made ground	0–2			10.8	5.0	25
Soft clay1	2–7		17	8.3	4.2	33.6
Soft clay2	7–10		17–22	8.3–11.3	5.8	46.4
Medium clay	10–15		35	18.3	9.2	73.6
Stiff clay	15–19	15	75	38.3	10.2	102
Clayey sand	19–20	10		36.6	9.3	27.9
Silty clay	20–24	17		61.7	15.6	46.8
Silty sand1	24–27	27		88.4	27.0	81
Silty sand2	27–33	40		170	40.0	120
Silty sand3	33–37	26		83.5	26.0	78
Hard clay	37–45	16		90.5	17.0	170
2nd sand	45–67	48		230	36.0	108
2nd hard clay	67–80	22		217	23.9	239

Note: $E_{oed}^{ref} = E_{50}^{ref}$.

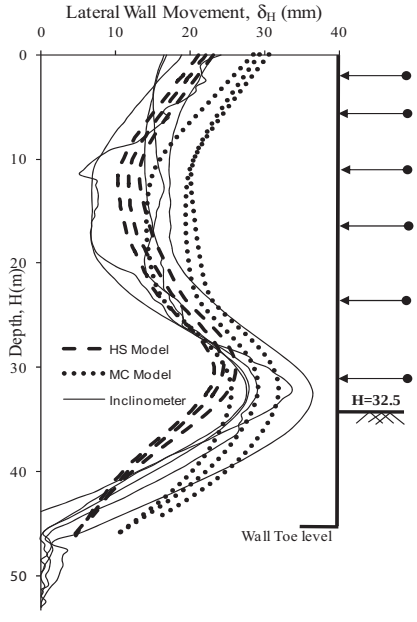

Figure 3. Observed and predicted lateral ground movements–Silom station.

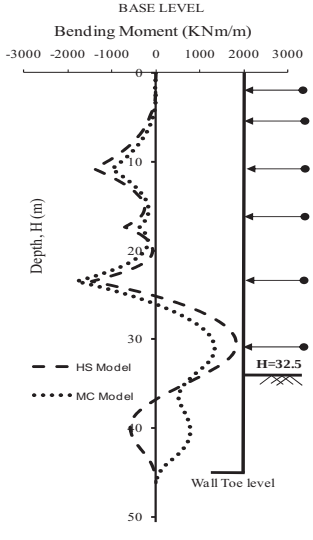

Figure 4. Predicted bending moments in D wall—Silom Station.

is much better than MC model prediction. It agrees very well with the observed settlement profile indicating the suitability of HS model in predicting the surface settlement trough whereas, the MC model predicts a much wider settlement trough. This is due to the fact that a more realistic difference in the unloading/loading stiffnesses used in the HS model.

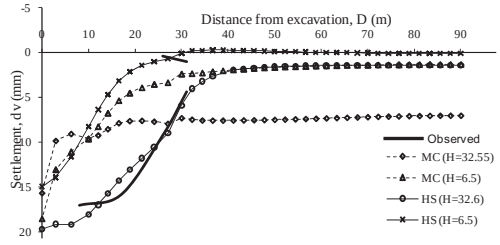

Figure 5. Observed vs. predicted surface settlement—Silom station.

Table 2. Correlations of hardening soil model parameters.

Soil description	E_{50}^{ref} (kN/m^2)	E_{ur}^{ref} (kN/m^2)	m (–)
Made ground	5000–7000	5 E_{50}^{ref}	0.5
Soft and medium clay	250 S_u	8 to 10 E_{50}^{ref}	1.0
Stiff clay	700 N_{60}	10 E_{50}^{ref}	0.85
Clayey sand & silty/sandy clay	900 N_{60}	3 E_{50}^{ref}	0.85
Medium to dense sand	750 N	3 E_{50}^{ref}	0.8
Dense to very dense sand	1000 N	3 E_{50}^{ref}	0.5
Hard clay	1100 N_{60}	10 E_{50}^{ref}	0.8
Dark grey clay	2500 N_{60}	10 E_{50}^{ref}	0.8

9 EMPIRICAL DETERMINATION OF HS MODEL PARAMETERS

An attempt is made to establish empirical correlation between stiffness parameters of HS model parameters of Bangkok subsoils with common investigation soil properties, i.e. undrained shear strength S_u for soft and medium stiff clays and SPT "N" values for stiff clay and sand. The correlations are determined from the results of the calibration analysis of Silom Station described above. The values of stiffness parameters of HS model simulation that yield closest fit to the observed data are compared with the corresponding MC model parameters (Hooi, 2003). The derived correlations are given in Table 2.

10 MODEL VERIFICATION

For verification on the suitability of the HS model and the suggested empirical correlations of stiffness

parameters for Bangkok soil, FEM analysis of three other excavation cases mentioned earlier are made.

10.1 *Thiam Ruam Mit station*

Figure 6a shows the observed lateral wall displacements of Thiam Ruam Mit Station excavation and the comparison with predictions using the MC and HS models. Inclinometers which were installed in south side of the station excavation showed wall movements in the braced mode. However, the third inclinometer showed the cantilever mode indicating difference in lateral restraints at ground level.

Both models predict the cantilever mode of wall deflection until the 3rd excavation level. The MC model over-predicts the wall deflection by 25% in the cantilever mode and almost by the same level at the toe of wall. The settlement trough predicted by HS model is shallower than that predicted by MC model and observation (Fig. 7a).

Figure 8a shows the comparison of the predicted bending moments. The profile of bending moments as predicted by HS model is higher than the MC model in the final stage of excavation.

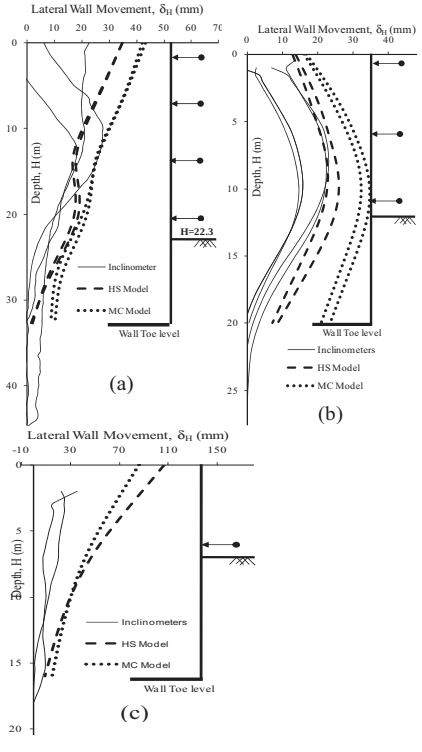

Figure 6. Predicted and observed lateral wall movements (a) Thiam Ruam Mit station; (b) Central Hospital; (c) BMA Car Park.

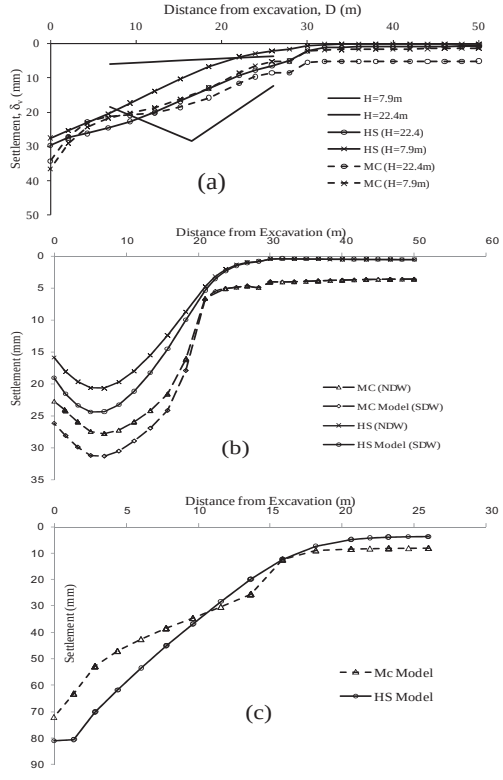

Figure 7. Predicted Settlement troughs (a) Thiam Ruam Mit station; (b) Central Hospital; (c) BMA Car Park.

10.2 *Central Hospital project*

Figure 6b shows comparison of the predicted and observed wall deflection. The observed wall movements are of the typical braced mode. The difference in deflections of two inclinometers is due to the difference between the excavation levels of north south wall. In this excavation case, the prediction by MC model using the empirical parameters grossly overestimates the values at all depths. On the other hand the prediction by HS model is quite reasonable. On the ground surface settlement, the observed settlement trough is not available for this case. HS model predicts shallower but narrower settlement trough as compared to the MC model, although the shapes of the trough are similar (Fig. 7b).

Both models predicted pretty much similar bending moments in the wall (Fig. 8b).

10.3 *Bangkok City hall car park excavation*

Figure 6c show lateral wall movement of the excavation (BMA Car Park).The mode of movement is of cantilever mode. In this case the predictions by both MC and HS models yield much

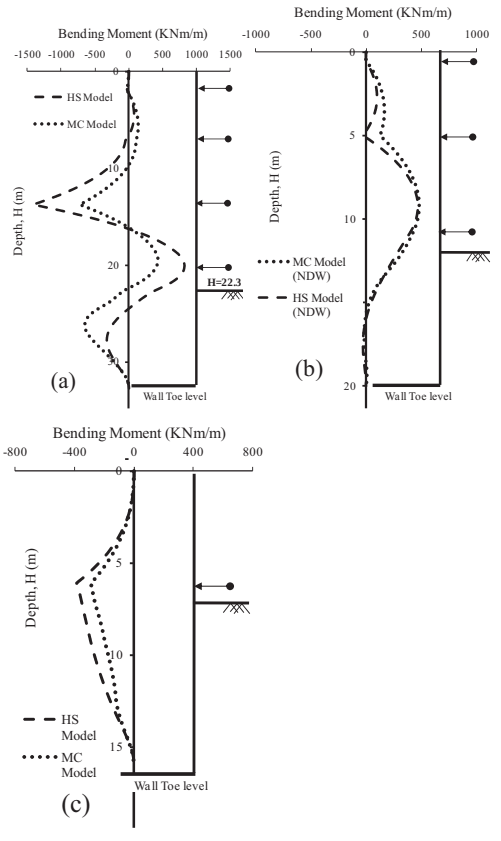

Figure 8. The Predicted bending moments (a) Thiam Ruam Mit station; (b) Central Hospital; (c) BMA Car Park.

over-prediction as compared to the observation and both are of the cantilever mode. The excavation in this project was only 6.6 m deep soft clay layer thus the cantilever mode still dictates the wall response. It appears that there is no advantage to use HS model in this type of excavation.

The predicted ground settlements and bending moment in the wall and are shown in Figures 7c and 8c, respectively. The predicted ground settlement troughs of the two models are not so different.

11 CONCLUSIONS

A numerical study is performed to appraise the validity of the Hardening Soil model for excavation in Bangkok subsoils. The following points can be concluded:

- The direct input of stiffness parameters derived from the lab test results showed erroneous wall movement predictions.
- The predicted deflection behavior of diaphragm wall shows good agreement with observed behavior by using the proposed empirical correlations in all cases except for the one with shallow excavation in the soft clay.
- The lateral deflection estimated by Hardening Soil model is smaller than that of the Mohr Coulomb model, resulted from higher unloading/reloading stiffness used.
- The Mohr Coulomb model overestimates wall toe movement as compared to Hardening Soil Model up to 50%.
- Settlement trough predicted by the Hardening Soil model is more realistic than that given by the Mohr Coulomb model.
- The wall bending moment estimated by Hardening Soil model are higher than that of Mohr coulomb model.
- The derived empirical correlations for estimating of Hardening Soil model stiffness parameters of Bangkok subsoils appear to be quite reasonable based on the verification results of few instrumented cases. However, further verification investigation is recommended.

ACKNOWLEGEMENTS

The authors would like to thanks PLAXIS b.v. for granting a license of PLAXIS software for educational use to Asian Institute of Technology for which the second author used to conduct MS thesis research on the topic. He thanks Seafco Public Company for giving him a scholarship for master degree study.

REFERENCES

Addenbrooke, T.I., Potts, D.M. & Puzrin, A.M. 1997. The influence of pre-failure soil stiffness on the numerical analysis of tunnel construction. *Geotechnique* 47 (3): 693–712.

Brinkgreve, R.B.J., 2002, PLAXIS Version 8 Material Models Manual, Delft University of Technology & PLAXIS b.v., The Netherlands.

Burland, J.B. & Burbidge M.C. 1985. Settlement of foundations on sand and gravel. *Institution of civil engineering; Proc.,* 78:1325–1381.

Hooi, K.Y. 2003. Ground Movements Associated with Station Excavations of the First Bangkok MRT Subway, *M. Eng Thesis*, Asian Institute of Technology, Bangkok.

Liao, S.S.C. & Whitman, R.V. 1986. Overburden Correction Factors for SPT in Sand. *Journal of Geotechnical Engineering* 112(3): 373–377.

Mair, R.J. & Taylor, R.N. 1996. Geotechnical Aspects of Underground Construction in Soft Ground. *Geotechnical Aspects of Underground Construction in Soft Ground; Proc. Intern. Symp., 15–17 April 1996.* London, U.K.

Masin, D. & Herle, I. 2005. Numerical Analysis of a Tunnel in London Clay using Different Constitutive Models. *The 5th international symposium TC28 geotechnical aspects of underground construction in soft ground*; *Proc*., Amsterdam, The Netherlands: 595–600.

Ng, C.W.W. & Lings, M.L. 1995. Effects of Modeling Soil Nonlinearity and Wall Installation on Back Analysis of Deep Excavation in Stiff Clay. *Journal of Geotechnical Engineering* 121(10): 687–695.

Phienwej, N. & Photayanuvat, C. 1998. Geotechnical Aspects of the First Underground MRT Project in Bangkok. *The Second Asia Tunneling Summit*; *Proc.,* Kuala Lumpur, Malaysia.

Phienwej N., Sirivachiraporn A., Suwansawat S. & Aye, Z.A. 2007. Ground movements associated with the underground excavations of the first Bangkok MRT Line.*16th Southeast Asian Geotechnical Conference*; Proc. 8–11 May. Subang Jaya, Malaysia.

Schanz, T. & Vermeer, P.A. 1997. On the Stiffness of Sands. *Prefailure Deformation Behaiour of Geometricals; Proc. Symp.,* London: ICE.

Schanz, T., Vermeer, P.A., & Bonnier, P.G. 1999. The Hardening Soil Model: Formulation and Verification. *International Symposium Beyond 2000 in Computational Geotechnics—10 Years of PLAXIS International; Proc.* Amsterdam, Netherlands, pp. 281–296.

Stroud, M.A. & Butler, F.G. 1975. The Standard Penetration Tests and the engineering properties of glacial materials. Symposium on Engineering Behaviour of Glacial Materials; Proc. University of Birmingham. England.

STS instruments company 2006. Soil report of Suvarnabhumi Airport project, Bangkok.

Thasnanipan, N., Aye, Z.Z. & Submaneewong, C. 2004. Construction of Diaphragm Wall Support Underground Car Park in Historical Area of Bangkok. *Fifth International Conference on Case Histories in Geotechnical Engineering; Proc.,*13–17 April 2004. New York.

Wonglert, A., Jongpradist, P. & Kalasin, T. 2008. Wall Movement Analysis of Deep Excavation in Bangkok Subsoil considering Small Strain Stiffness. *Journal of Research in Engineering and Technology* 5(4): 393–405.

Geotechnical Aspects of Underground Construction in Soft Ground – Viggiani (ed)

A nonlinear soil spring model considering ground stress and strain change during excavation

T. Sakamoto & Y. Katsura
Institute of technology, Shimizu Corporation, Tokyo, Japan

ABSTRACT: In practical designs, Winkler model is used to evaluate retaining wall behaviors during excavation. Soil spring coefficients have to be properly assigned in simulating retaining wall behaviors accurately. Soil spring properties are often represented by bilinear curves considering stiffness and ultimate ground reaction based on ground surveys. The stiffness of the soil spring is usually unchanged throughout the analysis. However, it is rational that the soil spring coefficients can be changed depending on ground stress and strain change during excavation. In this paper a simple nonlinear soil spring model is proposed considering ground stress and strain change during excavation. At an 11 m excavation site of Holocene clay ground in Tokyo-Bay area, retaining wall behaviors were observed. Analytical results by the proposed model showed excellent agreements with the observed results, which indicates that the proposed model, although it is simple, is promising for simulating retaining wall behaviors in a fairly reliable manner. In order to simulate retaining wall behaviors at different excavation stages, it is necessary to evaluate soil springs by using changes in soil stress and strain.

1 INTRODUCTION

Winkler modeling is usually used to calculate retaining wall deformation in Japan. Winkler model uses an elastic beam to express a retaining wall and assumes external pressure acting at the ground side and lateral ground reaction on the excavation side. Lateral ground reaction on the excavation side is calculated by use of soil springs at different depths. The method of setting soil springs is important in this case. A commonly used soil spring setting method is to assume that ground consists of elastic and plastic regions (bilinear model) and soil springs in the elastic region are constant (Architectural Institute of Japan, 2002). This method, however, ignores the nonlinearity of soil and in many cases unable to simulate retaining wall behaviors. As a result of various studies on soil spring setting based on observed retaining wall displacements, therefore, other methods have been reported. They include the method of reducing soil springs by use of vertical effective stress at each stage of excavation (Motoi, 2009) and the method of reducing soil springs on the basis of the $G/G_0 - \gamma$ relationship (Terada, 2005). A problem of the method by Motoi (2009) is that soil springs are calculated by use of post-excavation vertical effective stress, and changes in strain are ignored. A problem of the method Terada (2005) is that although changes in effective stress and strain are taken into consideration, the $G/G_0 - \gamma$ relationship under effective stress is used regardless of the excavation stage. This study, therefore, proposes a soil spring determination method that takes into consideration changes in soil stress and strain in the Winkler model. Finally, this study also verifies the validity of the proposed soil spring determination method on the basis of observed retaining wall displacements during excavation.

2 SOIL SPRING DETERMINATION METHOD CONSIDERING SOIL STRESS AND STRAIN

Figure 1 shows the basic concept of the Winkler model. The basic equation for the beam–spring model is as follows:

$$EI\frac{d^4y}{dx^4} + p_h \cdot B = w \cdot B \tag{1}$$

where EI is the flexural stiffness of the retaining wall (kN · m^2), y is displacement (m), x is depth (m), p_h is lateral subgrade reaction on the excavation side (kN/m^2), w is external force behind the retaining wall (kN/m^2) and B is a reference width (m). In Eq. (1), the subgrade reaction p_h on the excavation side equals the difference between the lateral pressure on the excavation side and the equilibrium lateral pressure, and the external pressure w behind the retaining wall equals the difference between the lateral pressure behind the retaining wall and the equilibrium lateral pressure. This paper proposes a

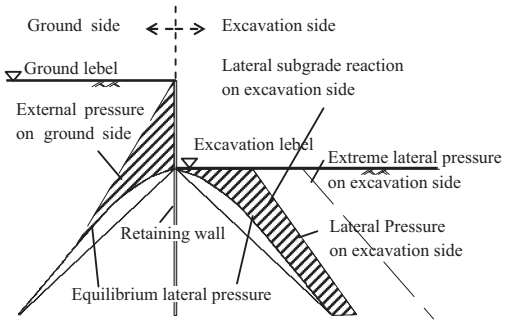

Figure 1. Basic concept of Winkler model.

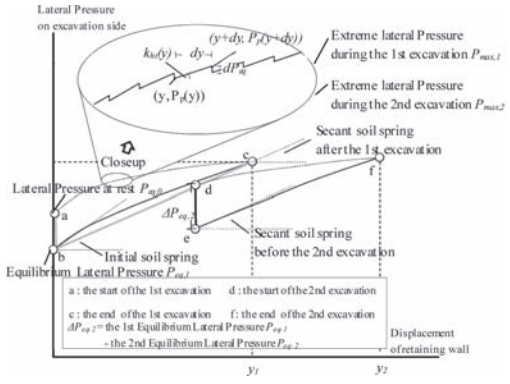

Figure 2. Relationship between retaining wall displacement and the lateral pressure on the excavation side.

soil spring evaluation method for the calculation of the lateral ground reaction on the excavation side. Figure 2 shows the relationship between retaining wall displacement and the lateral pressure on the excavation side. This study does not take into account the decrease in the lateral pressure behind the retaining wall (Katsura, 1996). Changes in the lateral pressure on the excavation side due to excavation during the process from the beginning of excavation until after the first excavation (path a→c) can be expressed as

$$p_{p,1} = p_{eq,0} - \int_{p_{eq,1}}^{p_{eq,0}} dp_{eq} + \int_0^{y_1} k_{ht}(y)dy \qquad (2)$$

where $p_{p,1}$ is the lateral pressure on the excavation side the end of the first excavation (kN/m^2), $p_{eq,0}$ is lateral pressure on the excavation side at the start of excavation (kN/m^2), $p_{eq,1}$ is equilibrium lateral pressure after the first excavation (kN/m^2), y_1 is retaining wall displacement at the end of the first excavation (m) and $k_{ht}(y)$ is tangential soil spring at any depth on the excavation side (kN/m^2/m). Path a→c consists of path a→b and path b→c. The second term of the right-hand side of Eq. (2) corresponds to the changes in the lateral pressure on the excavation side on path a→b, and the third term corresponds to changes in the lateral pressure on the excavation side on path b→c. If $k_{ht}(y)$ is assumed to be constant, then the results will be identical to the results obtained by the conventional method (Architectural Institute of Japan, 2002) shown with the gray lines in Fig. 1. It is thought likely, however, that as in the case of decreases in soil stiffness in the vertical direction due to excavation and structural construction (Tamaoki et al., 1993), soil stiffness in the lateral direction also decreases because of decreases in overburden pressure and increases in soil strain. This indicates that a function capable of expressing nonlinearity should be used for the tangential soil spring on the excavation side, $k_{ht}(y)$. In this study, it is assumed that the tangential soil spring on the excavation side, $k_{ht}(y)$, in the displacement–lateral pressure relationship can be expressed by a hyperbola, and the tangential soil spring on the excavation side, $k_{ht}(y)$, on path b→c is expressed as

$$k_{ht}(y) = \frac{k_{h0}}{\{1 + k_{h0} \cdot y / (p_{\max,1} - p_{eq,1})\}^2} \qquad (3)$$

where k_{h0} is the initial soil spring at any depth (kN/m^2/m), and $p_{max,1}$ is the extreme lateral pressure on the excavation side (kN/m^2) during the first excavation. To obtain the hyperbola, the initial soil spring k_{h0} is determined according to soil survey results, and the extreme lateral pressure is calculated from the Rankine–Resal formula. The brace preload path is assumed to be path c→d on the assumption that the post-excavation secant soil spring is maintained. To determine the soil spring during the second excavation, it is assumed that the initial soil spring at the start of excavation is the same as the secant soil spring after the first excavation, and Eq. (3) is applied by defining the point (e) at which the second excavation is started as the origin. By doing this, the soil spring that takes into consideration the changes in ground stress and strain at each stage of excavation can be evaluated easily.

3 EVALUATION OF SOIL PROPERTIES

3.1 *Initial stiffness evaluation method*

Stiffness against elastic deformation amounting to about 0.001% or less of strain can be determined by the shear wave velocity *Vs* obtained through seismic velocity logging. Hence, the initial stiffness k_{h0} can be expressed (Japan Society of Civil Engineers, 1996) as

$$k_{h0} = (10/3) \cdot E_0 \cdot (10B_H/3)^{(-3/4)} \quad (4)$$

$$E_0 = 2(1+\nu) \cdot \rho_t Vs^2 \quad (5)$$

where B_H is a reference width (=10 m), ν is Poisson's ratio and ρ is the wet density of soil (g/cm^3).

3.2 *Equilibrium lateral pressure evaluation method*

Many studies have shown that equilibrium lateral pressure resulting from excavation-induced overburden pressure removal remains (Mayne et al., 1982). In this study, the equilibrium earth pressure coefficient $K_{eq,n}$ during the n-th excavation is modeled (Fig. 3) on the basis of the results of the laboratory K_0 tests on Toyoura standard sand specimens reported by Uchiyama et al., (1997) and is expressed as

$$K_{eq,n} = \beta + \frac{\sigma_{1,0}}{\sigma_{1,n}} \cdot (-\alpha\beta + K_0) \quad \left(\frac{\sigma_{1,n}}{\sigma_{1,0}} < \alpha\right) \quad (6)$$

$$K_{eq,n} = \frac{\sigma_{3,0}}{\sigma_{1,n}} \quad \left(\frac{\sigma_{1,n}}{\sigma_{1,0}} \geq \alpha\right) \quad (7)$$

where K_0 is the coefficient of earth pressure at rest at the start of excavation, $\sigma_{1,0}$ is vertical effective stress at the start of excavation (kN/m^2), $\sigma_{1,n}$ is vertical effective stress after the n-th excavation (kN/m^2), α (=0.8) and β (=0.175) are constants determined by test results and $\sigma_{3,0}$ is lateral effective stress at the start of excavation for foundation (kN/m^2). The earth pressure at rest is unknown after constructing retaining wall, so it is assumed that the soil at this site is normal consolidated. The coefficient of earth pressure at rest, K_0, for sand and clay is calculated, respectively, as follows:

Sand (Jaky's formula): $K_0 = 1 - \sin\phi$ (8)

Clay (Alpan, 1987): $K_0 = 0.19 + 0.233 I_p$ (9)

where ϕ is the internal friction angle and I_p is the plasticity index.

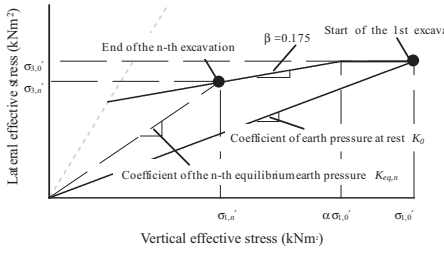

Figure 3. Model of equilibrium earth pressure coefficient $K_{eq,n}$ during the n-th excavation.

4 OBSERVED RESULTS-BASED VALIDATION OF THE PROPOSED METHOD

4.1 *Overview of construction work and analysis*

The construction site considered in this study is located at Holocene clay ground in Tokyo Bay area. Figure 4 gives an overview of the excavation and retaining wall construction site. Figure 5 summarizes geological and analytical information. The soil properties were determined according to soil survey results. The internal friction angles φ of the sand layers were

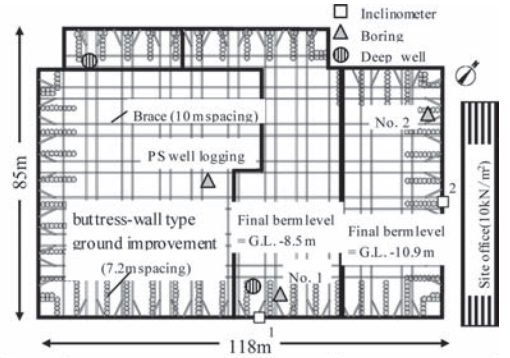

Inclinometer	Soil mixing wall			Brace (mm)
	Beam(mm)	Spacing(mm)	Foot level(m)	
1	H-450×200×9×14	900	G.L.-17	1st : 2H-350×350×12×19
2	H-500×200×10×16	600	G.L.-19	2nd: 2H-400×400×13×21

Figure 4. Overview of the excavation and retaining wall construction site.

	Depth (G.L.-m)	Type	N-value	γ_t (kN/m3)	C (kN/m2)	φ(°)	V_s(m/s) Natural	V_s(m/s) Improved	Initial soil spring
Layer 1	3	Filled	3	18	10	0	130	0	21200
Layer 2	5.7	Filled	2.3	18	10	0	180	400	73700
Layer 3	6.4	Sand	3	18	0	23	180	400	73700
Layer 4	7.6	Sand	6	18	0	26	180	400	73700
Layer 5	10.9	Clay	2	16	35	0	160	400	70300
Layer 6	18	Clay	0.8	18	70	0	160	400	70300

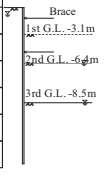

(a)Inclinometer 1

	Depth (G.L.-m)	Type	N-value	γ_t (kN/m3)	C (kN/m2)	φ(°)	V_s(m/s) Natural	V_s(m/s) Improved	Initial soil spring
Layer 1	3	Filled	7.5	18	10	0	130	0	21200
Layer 2	5.7	Filled	1.7	18	10	0	180	400	73700
Layer 3	6.4	Sand	5	18	0	25	180	400	73700
Layer 4	7.6	Sand	12	18	0	30	180	400	73700
Layer 5	10.9	Clay	1.5	16	35	0	160	400	67400
Layer 6	16.7	Clay	0.5	18	50	0	160	400	70300
Layer 7	20	Clay	1	16	75	0	150	400	64700

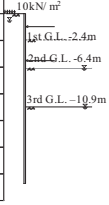

(b) Inclinometer 2

Figure 5. Geological and analytical information.

calculated from SPT N-values by using Osaki's formula ($\varphi = \sqrt{20N + 15}$). The shear wave velocity Vs in the natural ground was evaluated through PS well logging. The shear wave velocity Vs in buttress-wall type ground improvement method was evaluated in terms of the Vs–q_u relationship (Asaka et al., 2003) of the in-situ soil on the basis of the unconfined compressive strength of in-situ core samples. The soil on the excavation side is reinforced by the buttress-wall type ground improvement method, it is necessary to evaluate soil springs for composite ground. The initial stiffnesses k_{h0} of the natural ground and the improved ground were determined from their Vs values, and the initial stiffness k_{h0} of the composite ground was evaluated on the basis of the improved area ratio α (=20%) of the improved ground relative to the natural ground. This analysis assumes that the pressure on the ground side is constant. The lateral pressure at the ground side and the extreme lateral pressure on the excavation side are calculated by using the Rankine–Resal formula. On the basis of measurement results, pore water pressure at the ground side was assumed to be statically distributed from G.L. −1 m, regardless of the progress of excavation. Pore water pressure on the excavation side was assumed, in view of the progress of excavation, to be statically distributed from the bottom of the excavation. For the first excavation and the second excavation, however, static distribution of water pressure from the bottom of the central excavation at the preceding stage was assumed.

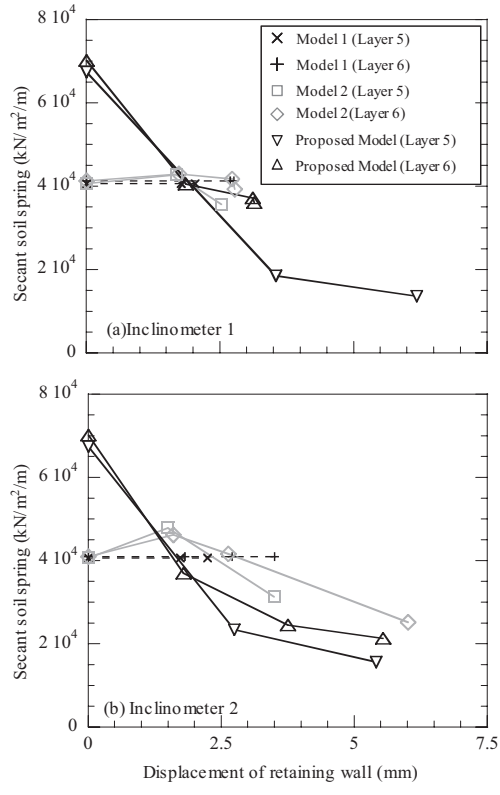

Figure 6. Relationship between secant soil spring and retaining wall deformation for Layers 5 & 6.

4.2 *Analytical results*

Figure 6 shows the relationship of a commonly used soil spring (Model 1), a soil spring reduced by use of vertical effective stress (Model 2) and the proposed soil spring (Proposed Model) with retaining wall deformation for Layers 5 and 6. Figure 7 shows the relationship of the stiffness reduction ratio of the soil spring relative to the pre-excavation soil spring for Layers 5 and 6 with retaining wall deformation. The soil spring of Model 1 was calculated from the following equations:

Sand in natural ground: $k_{h0,\ in\text{-}situ} = 1000 \cdot N$ (10)

Clay in natural ground: $k_{h0,\ in\text{-}situ} = 100 \cdot C$ (11)

Improved soil: $k_{h0,\ buttress} = 100 \cdot (q_u/2)$ (12)

Soil spring for composite ground:

$$k_{h0,\ composite} = (1 - \alpha)\ k_{h0,\ in\text{-}situ} + \alpha \cdot k_{h0,\ buttress} \quad (13)$$

where N is the SPT N-value of natural ground, C is the cohesion of natural ground, q_u is the strength of buttress-wall type ground improvement core sample (kN/m²), $k_{h0,in\text{-}situ}$ is the soil spring for natural ground, $k_{h0,buttress}$ is the soil spring for buttress-wall type ground improvement, $k_{h0,composite}$ is the soil spring for composite ground and α is the improved area ratio of buttress-wall type ground improvement.

The soil spring of Model 2 was calculated from the following equation:

$$k_{h,\ composite,\ n} = k_{h0,\ composite} \cdot (\sigma'_{1,n}/\sigma'_{1,0})^{0.5} \quad (14)$$

where $k_{h,composite,n}$ is the soil spring during the n-th excavation, $k_{h0,composite}$ is the initial soil spring prior to excavation, $\sigma'_{1,n}$ is vertical effective stress after the n-th excavation and $\sigma'_{1,0}$ is vertical effective stress prior to excavation.

The pre-excavation soil spring of the proposed model is greater than those of Model 1 and Model 2. The reason is that the proposed model evaluates the soil properties in terms of strains of the order of 0.001% or less by using shear wave velocity. The soil spring of the proposed model becomes smaller as retaining wall deformation increases. In contrast, the soil spring of Model 2

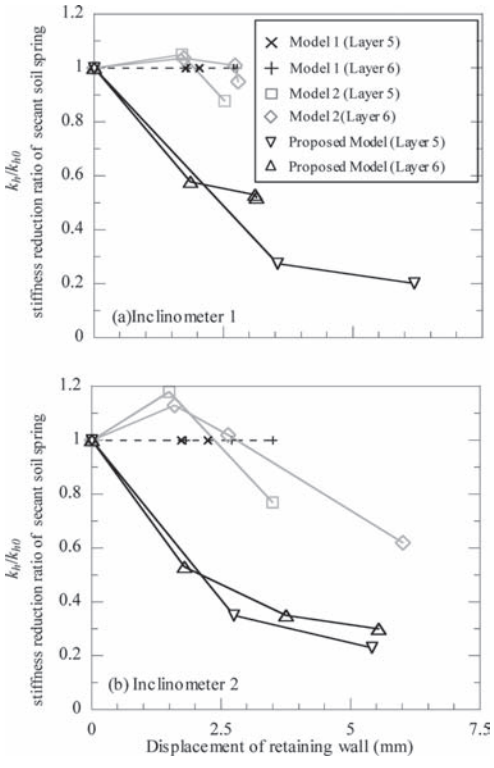

Figure 7. Relationship between stiffness reduction of secant soil spring and retaining wall deformation for Layers 5 & 6.

during the first excavation becomes greater than the initial soil spring. After that, the soil spring becomes smaller as retaining wall deformation increases. The reason why the soil spring of Model 2 during the first excavation becomes greater than the initial soil spring is that the influence of the increase in vertical effective stress due to the lowering of the groundwater level is greater than the influence of the decrease in vertical effective stress due to excavation. The soil spring reduction r atio of Model 2 is greater than that of the proposed model. The reason for this is that the proposed model evaluates the soil spring by using changes in ground stress and strain, while Model 2 evaluates the soil spring solely in terms of changes in ground stress.

Figure 8 shows observed retaining wall deformations and analytical results. The calculated values obtained from Model 1 are smaller than the measured values. This is because the soil spring is overestimated. The calculated values for the first excavation obtained from Model 2 are similar to those obtained from Model 1 and are smaller than the measured values.

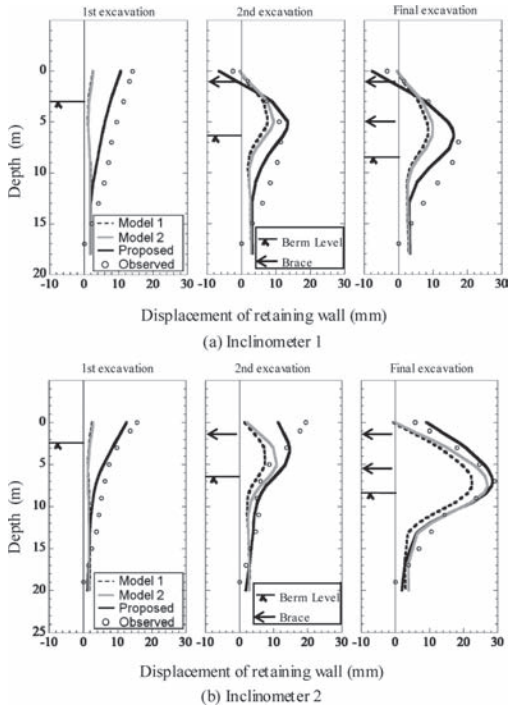

Figure 8. Observed retaining wall deformations and analytical results.

This is because the soil spring is overestimated. The calculated values for the first excavation obtained from Model 2 are similar to those obtained from Model 1 and are smaller than the measured values.

The calculated values for the second and third excavations are smaller than the measured values obtained from Inclinometer 1 and show fair agreement with the measured values obtained from Inclinometer 2. The calculated values obtained from the proposed model are highly consistent with the measured values obtained from the two inclinometers (1 and 2) for the process from the first excavation to the third excavation. This indicates that in order to simulate retaining wall displacement at different stages of excavation, it is important to evaluate soil springs by using changes in soil stress and strain.

5 CONCLUSION

A soil spring determination method that takes into consideration soil stress and strain changes in a beam–spring model has been proposed. While retaining wall deformation throughout the excavation process cannot be explained in the

conventional method, the proposed method has made it possible to explain observed retaining wall displacements at different excavation stages with good accuracy. In order to simulate retaining wall behaviors at different excavation stages, it is necessary to evaluate soil springs by using changes in soil stress and strain.

REFERENCES

Alpan, I. (1967): The empirical evaluation of the coefficient K0 and K0, R, Soils and Foundations, Vol. 7, No.1, pp. 31–40.

Architectural Institute of Japan (2002): Recommendation for Design and Construction Practice of Earth Retaining for Excavation. (in Japanese).

Asaka, Y., Katsura, Y. (2003): Relationship between shear wave velocity and unconfined compression strength of soil cement, of technical papers of Annual Meeting Architectural Institute of Japan. B-1, Structures I, pp. 443–444. (in Japanese).

Japan Society of Civil Engineers (1996): Standard specifications for tunneling for cut-and-cover tunnels, pp. 133–136.

Katsura, Y. (1996). Study on evaluation method of lateral pressure acting on retaining wall during excavation. PhD Thesis, Hokkaido University, Japan, pp. 36–45. (in Japanese).

Mayne, P.W. and Kulhawy, F.H. (1982): K0-OCR relationships in soil, Journal of Geotechnical Engineering, Vol. 108 (GT6), pp. 851–872.

Motoi, Y. (2009): Design value of earth retaining walls by the Winklerian model with springs on the both sides of the wall, Journal of structural and construction engineering, AIJ, No. 641, pp. 1345–1351.(in Japanese).

Tamaoki, K., Katsura, Y., Kishida, S. (1993):Young's moduli of bearing strata estimated from vertical deformation during excavation and construction, Journal of structural and construction engineering, AIJ, No. 446, pp. 73–80.(in Japanese).

Terada, K. (2005): A Method for Calculating the Rebound of Ground and the Displacement of Earth Retaining in Excavation Construction, Soil mechanics and foundation engineering, The Japanese Geotechnical Society, 53(7), pp. 14–16. (in Japanese).

Uchiyama, N., Katsura, Y. (1997): Lateral Pressure remained after Excavation, Proceedings of the 32nd Japan National Conference of geotechnical engineering, Vol. 2, pp. 1689–1690. (in Japanese).

Geotechnical Aspects of Underground Construction in Soft Ground – Viggiani (ed)
© 2012 Taylor & Francis Group, London, ISBN 978-0-415-68367-8

How to analyse walls for deep excavations

A. Hettler
University of Sciences and Technology of Dortmund, Germany

T. Schanz
Ruhr-Universität Bochum, Germany

ABSTRACT: The paper gives a survey how to analyse walls for deep excavations according to the rules of the German committees for excavations (EAB) and for numerical calculations in geotechnics (AK 1.6). In most cases relevant in engineering practice it is sufficient to use a classical linear elastic beam model. This can be improved introducing a subgrade reaction at the foot of the wall. For complex systems—this means for example complex in geometry and/or initial and boundary conditions—the finite element method is recommended to be used. The paper closes with open questions and gives some ideas for future research, for example how to perform a full design with FE-method and how to take into account different stages of construction processes.

1 INTRODUCTION

During the last years the investigation of serviceability limit states has gained more and more importance. Especially in the case of inner city excavations adjacent to buildings the admissible deformations are often very small. Therefore the engineers have to select carefully the design tools. High demands in design do not implicate automatically finite-element-calculations. Depending on the boundary conditions also classical models may be sufficient or even equivalent.

Additional difficulties may rise in combination with so called deep excavations. Deep may not be defined only by the geometrical depth. Deep can be understood by the degree of technical difficulties in design. This may include for example the geometrical depth, soil conditions, magnitude of water pressure, groundwater conditions and the condition of adjacent buildings. It is supposed that a precise definition of a deep excavation is difficult to be found but in a qualitative sense an approach for practical purposes is possible. For example in Berlin sand and groundwater conditions an excavation of more than 20 meters deepth may be called a deep excavation. For the soft clay at the lake of Konstanz a depth of more than 5 to 6 meters can already cause extreme difficulties in the construction process. For details, see Hettler (2010).

The aim of the paper is to give a survey about the calculation methods which are used in German practice and which are compatible with Eurocode 7. Mainly three models are used:

- the classical beam model
- the beam model combined with subgrade reaction at the foot of the wall
- finite-element-analysis

It is also intended to initiate a discussion and to compare the different methods in different countries within Europe.

2 SAFETY CONCEPT

Eurocode 7 admits three ways to investigate safety. In Germany procedure 2* was introduced. This means the following steps:

- design of the structural system
- determination of characteristic loads and calculation of characteristic effects
- determination of design values for effects by multiplying the characteristic values with the partial safety factors
- investigation that the design values of effects are smaller or equal to the design values of resistences.

It is believed that the calculation with characteristic values is advantageous, especialy for nonlinear systems. In such cases it may happen that the calculations for example with design values for φ and c lead to unrealistic results and the interpretation of the results may be difficult. Only for linear elastic systems calculations with design values for loads and resistences are mathematically equivalent. Then the

user can decide whether to calculate with characteristic or design values. Sometimes it is easier to find the minimum dimensions by applying design loads. For details, see Hettler (2009) or Weißenbach and Hettler (2010). See also the discussion in section 5.

3 CLASSICAL BEAM MODEL

According to the German recommendations for excavations (EAB, 2006, 2008) the following simplifications are assumed when investigating the limit state:

- The static system is an elastic beam with unyielding supports.
- Each step in the construction process is analysed separately, neglecting previous steps.

The earth support may be classified into the following systems:

- A free earth support, which is fixed at the toe with a force $C_{h,k} = 0$ and where the resultant of the soil reactions $\sigma_{h,k}$ is the supporting force $B_{h,k}$ (Fig. 1a). The embedded length is t_0.
- A partly fixed earth support with length t_1' (Fig. 1b).
- A fixed earth support with length t_1 and the boundary condition $M_c = 0$ and a vertical tangent at the support (Fig. 1c).

The extra length Δt_1 in Figure 1b and c is necessary to transfer the support forces $C_{h,k}$ to the soil as proposed by Blum. For details, see Weißenbach, Hettler, Simpson (2003) or Hettler and Weißenbach (2010).

A particular feature in German design of excavations is how to calculate the earth pressure.

In a first step a triangular distribution according the Rankine's theory is assumed. Then following Weißenbach's proposals it is redistributed, as shown by the example in Figure. 2.

The German recommendations for excavations (EAB) propose different earth pressure figures, depending for example on the stiffness of the wall, the stiffness of the props and the number of props. For details, see EAB (2008).

For investigating serviceability limit states the beam model has to be improved:

- The supports may be assumed as elastic springs.
- The predeformations before installing the next prop are taken into account and added up during the installation process.

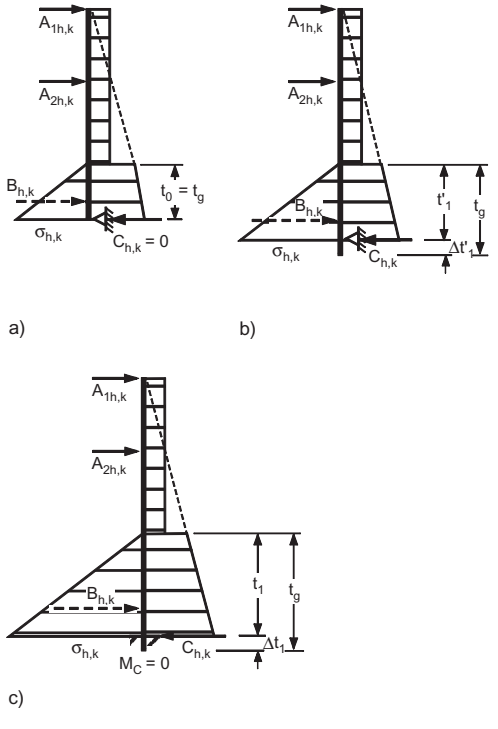

Figure 1. a) Elastic beam with free earth support b) partly fixed earth support c) fixed earth support.

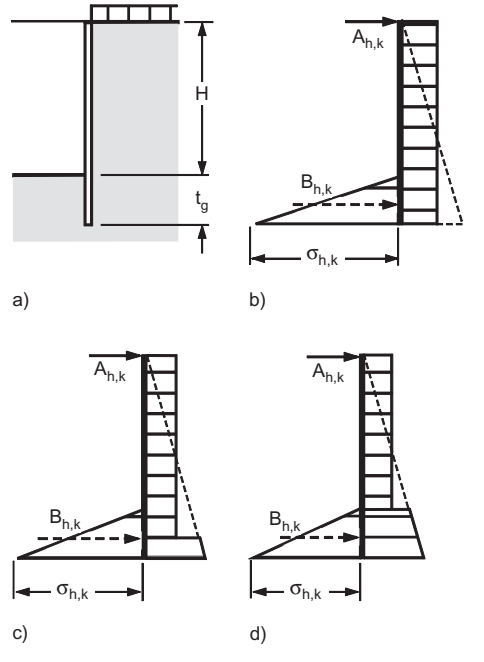

Figure 2. Excavation wall with free earth and propped at the top a) statical system, b) redistribution of the classical earth pressure up to the toe of the wall c) up to the gravity center of the supporting force $B_{h,k}$ d) up to the bottom of the excavation.

– Subgrade reaction is used for the earth support, see section 4.

In very simple cases the improved beam model may also be sufficient to estimate roughly the deformations adjacent to the wall and not only for the wall itself. But generally if the deformations in the surrounding have to be investigated numerical methods are recommended, see section 5.

4 CALCULATIONS USING SUBGRADE REACTION

The non yielding earth supports in section 3 lead to a contradiction between the earth pressure distribution and the displacements at the embedded part of the wall. These deficencies can be avoided by models using a subgrade reaction. Following the German recommendations for excavations the preloading by the weight of the excavation can be taken into account as illustrated in Figure. 3. As initial stress state the earth pressure at rest $e_{0g,k}$ is assumed, calculated for the original ground surface. For physical reasons the horizontal stress may not surpass the passive earth pressure $e_{ph,k}$. A subgrade reaction is only admitted in the embedded part t_B in Figure. 3. A further limitation is that the sum of the initial stress and the stress from subgrade reaction may not surpass the passive earth pressure.

The difficulty is how to determine the subgrade reaction modulus. During the last years the EAB-committee has evaluated a number of field cases and proposed a range of values for the subgrade reaction modulus, which will be published in the next time. Furthermore nonlinear mobilisation curves may be used as proposed for example by Besler (1998) or Vogt (1984) and which give very reasonable results (Hettler et al. (2005), Hettler & Maier (2004). In practice it may be helpful to determine the subgrade reaction modulus by a finite-element analysis for one case and to use it afterwards in design for other load cases. By this way much time can be economised without really loosing accuracy.

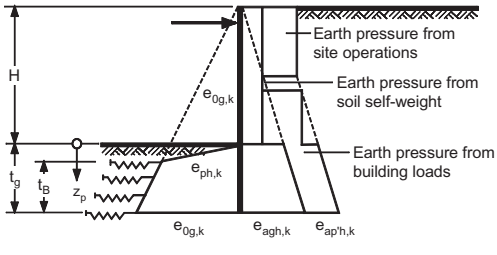

Figure 3. Load model for subgrade reaction in sand.

5 FINITE-ELEMENT ANALYSIS

In Schanz (2006a, 2006b) the current German status of application of numerical methods to calculate retaining walls is documented. By illustrative practical examples it is shown following the recommendations the numerical results regarding global stability are comparable to those using classical approaches. Stability in the numerical approach is defined as the ratio of the actual system resistance related to the system resistance at failure. For situations where the system resistance is determined just by the strength of the soil this approach (phi-c-reduction) is resulting in the classical Fellenius definition. It is equivalent to the definition of factors of partly safety (GZ 1C) following DIN 1054:2005-01. In practice additional structural elements (the wall itself, anchors, struts & nails) contribute to the system resistance. Therefore their resistance considering relevant failure modes (see Fig. 7) must be taken into account in the determination of global safety. A straight forward concept includes the reduction of characteristic resistance of structural elements (loading capacity of anchors, maximum bending moments of the wall) simultaneously to the soil strength. During reduction different levels of safety for the soil and these structural elements must be carefully considered.

6 DEFORMATIONS INDUCED BY CONSTRUCTION PROCESSES

Modern commercial finite-element software allows for taking into account a stepwise construction procedure. This may be called a staged construction analysis. Modelling the construction process itself is up to now rather reserved to scientific investigations for special cases. But there is still a gap in modelling the effects of constructing for example vibrated piles, so called RI-piles (RI = german abbreviation for vibrated and grouted) or anchors. In those cases the deformations from the construction processes may be the dominant factor as the following example may show.

Deep excavations in Berlin were often constructed by installing under water a concrete bottom slab which was anchored to resist against uplift. In the case of the Debis excavation at Potsdamer Platz the horizontal displacements of the wall caused during the installation of the so called RI-piles were 4 times higher than predicted by a classical analysis (Triantafyllidis, 1998).

After the final excavation under water the maximum deformation in the cross section MV 1 and MV 2 was about 10 to 12 mm (see phase 2 in Fig. 4b and c). It increased to about 38 to 58 mm

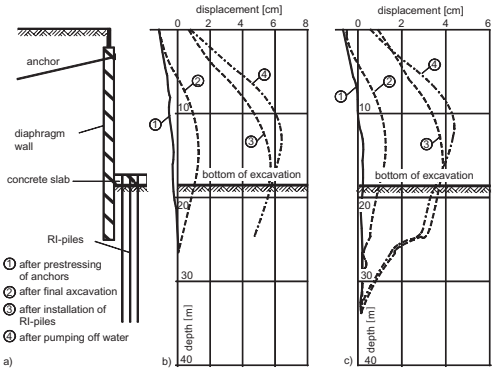

Figure 4. Debis-excavation at Potsdamer Platz: a) cross section of excavation b) displacements in cross section MV 1 c) displacements in cross section MV 2.

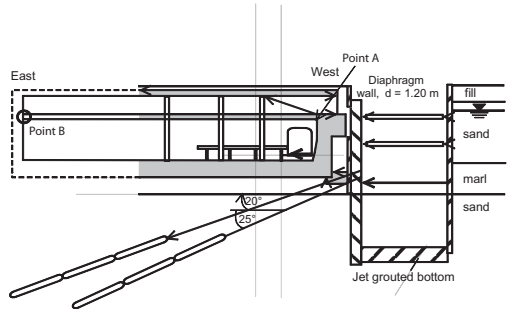

Figure 5. Cross section of city railway station and excavation wall at Potsdamer Platz in Berlin.

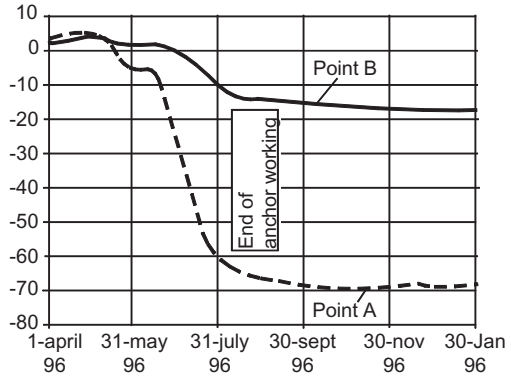

Figure 6. Settlements at points A and B of city railway station at Potsdamer Platz in Berlin caused by installation of grouted anchors.

in phase 3 when the RI-piles were constructed. Pumping off the water in phase 4 caused only a relatively small additional displacement of 10 mm to 12 mm. The maximum difference of about 20 mm in cross sections MV 1 and MV 2, where the geological conditions are quite similar, can be explained by the time sequence and the geometrical arrangement of the piling works. Obviously the embedment at the foot of the wall reduced and at the same time pore water pressure increased. For details see Triantafyllidis (2000).

The installation of grouted anchors may also cause damages in adjacent buildings particularly for multilevel anchored walls showing high density of anchor placement. Boring against groundwater with a hydraulic head is judged as specially unfavorable effect. Constructing the excavation walls for the long distance train station Potsdamer Platz in Berlin two rows of anchors had to be built very close under the tunnel and the station for the city railway, see Figure 5.

Although the material transport was carefully controlled during drilling settlements of the city railway tunnel were observed up to 7 cm, see Figure 6. For details see Borchert (2008).

7 FURTHER REMARKS ON FEM-ANALYSIS

Closely related to the definition of global safety as discussed above is the identification of the relevant reason for failure including the failure kinematics. Using the extended features of FE-analysis it must be asked which reason for failure is relevant and which different failure mechanisms must be analyzed. This important topic is studied in detail by Grabe et al. (2008) for sheet pile walls applying a so called "plastic-plastic-approach". In order to trigger the occurrence of plastic hinges they analyzed six different causes, among others the reduction of the strength of the wall, lowering the groundwater table and an increase of the specific gravity. Theoretically all possible causes must be considered, as for example some more are shown in Figure 7, in order to determine the minimum of safety. For example in Figure 7f, using FE-analysis, an increase of the vertical force P might result in rather large deformations. These deformations might change the direction of the action from $+2/3\varphi$ to $-2/3\varphi$. Therefore the earth pressure increases, the anchor might fail and/or the wall might fail before the wall sinks vertically. For further details, see Hettler and Schanz (2008).

The described task is not unique in the frame of application of FE-analysis, but also included when applying classical methods. In the frame of classical methods only a limited number of different causes for failure are analyzed. Based on long

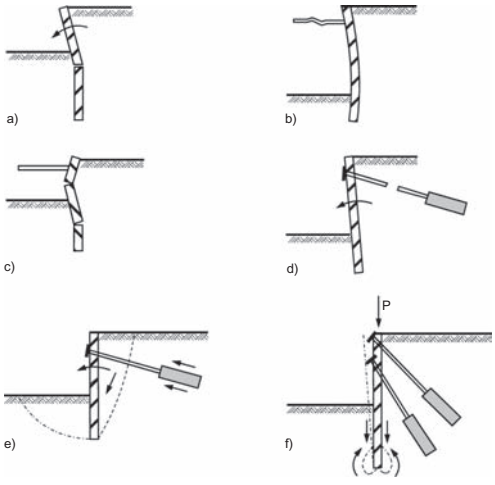

Figure 7. Examples showing effects producing failure and failure mechanisms.

term experience this decision seems to be sufficient. Brinch Hansen and Lundgren (1960) concluded, based on their work on anchored sheet pile walls: One might think, that comparable to the procedure to determine cause for failure in the soil the task must be extended to the global system including structural elements. Different from considering all possible cause it seems sufficient to study a limited number of causes to derive a safe construction.

Different from the calculation of wall deformations by using FE analysis the decision on the appropriate constitutive model is of less importance when performing stability analysis. For practical cases it can be shown that simple ideal-elastic-ideal-plastic models using the same failure criterion result in the same global safety as more complex models considering for example isotropic strain hardening. It can be concluded that the detailed stress path influenced by the individual soil models is of minor importance compared to the definition of the ultimate condition.

REFERENCES

Besler, D., 1998. Wirklichkeitsnahe Erfassung der Fußauflagerung und des Verformungsverhaltens von gestützten Baugrubenwänden. Schriftenreihe des Lehrstuhls Baugrund-Grundbau der Universität Dortmund, Heft 22.

Borchert, K. 2008. Innerstädtische Baugruben, Erfahrung zur Verformungen und Dichtigkeit, Bauen in Boden und Fels, Esslingen, Technische Akademie.

Brinch Hansen, B. Lundgren, H. 1960. Hauptprobleme der Bodenmechanik, Berlin, Springer-Verlag.

EAB 2008, Recommendations on Excavations, 2nd English Edition, Ernst & Sohn.

Empfehlungen des Arbeitskreises Baugruben (EAB), 2006. 4. Auflage, Berlin, Verlag Ernst und Sohn.

Grabe, J., Schürmann, B., Katzmann, A. 2008. Zur plastischen Berechnung von Baugrubenwänden, Bundesanstalt für Wasserbau, Kolloquium "Anwendung der Finite-Elemente-Methode" Karlsruhe, BAW.

Hettler, A. 2009. Einbindetiefen und Schnittgrößen bei gestützten Wänden mit beliebiger Fußauflagerung. Bautechnik, Heft 9, pp. 542–546.

Hettler, A. 2010. Bodenmechanische Herausforderungen bei tiefen Baugruben. RUB RuhrGeo Tag, Schriftenreihe des Lehrstuhls für Grundbau Boden- und Felsmechanik, Heft 43, Ruhr-Universität Bochum.

Hettler, A., Borchert, K. 2010. Herstellungsbedingte Verformungen bei tiefen Baugruben. Baugrundtagung 2010, München Deutsche Gesellschaft für Geotechnik.

Hettler A., Gutjahr, St. Vega-Ortiz, S. 2005. Nichtlinearer Bettungsansatz von Besler bei Baugrubenwänden, Bautechnik 82 (2005), Heft 9, pp. 593–604.

Hettler, A., Maier, T. 2004. Verschiebungen des Bodenauflagers bei Baugruben auf der Grundlage der Mobilisierungsfunktion von Besler. Bautechnik 81, Heft 5, pp. 323–336.

Hettler, A., Schanz, T. 2008. Zur Anwendung der Finite-Elemente-Methode bei Baugrubenwänden. Bautechnik 85, Heft 9, pp. 603–615.

Hettler, A., Triantafyllidis, Th. 2009. Deformations of deep excavation walls by construction process. 17th ICSMGE Tagung (DGGT), Alexandria, 5.9.-9.9.09.

Schanz, T. 2006a. Aktuelle Entwicklungen bei Standsicherheits- und Verformungsberechnungen in der Geotechnik. Geotechnik 29 (1), pp. 13–27.

Schanz, T. 2006b. Standsicherheitsberechnungen von Baugruben—Berechnungsbeispiele, Geotechnik, 29 (4), pp 359–368.

Triantafyllidis, T. 1998. Neue Erkenntnisse aus Messungen an tiefen Baugruben am Potsdamer Platz in Berlin, Bautechnik 75, pp. 133–154.

Triantafyllidis, T. 2000. Ein einfaches Modell zur Abschätzung von Setzungen bei der Herstellung von Rüttelinjektionspfählen, Bautechnik 77, pp. 161–168.

Vogt N. 1984. Erdwiderstandsermittlung bei monotonen und wiederholten Wandbewegungen in Sand. Baugrundinstitut Stuttgart, Mitteilung 22. Stuttgart.

Weissenbach, A., Hettler, A., Simpson, B. 2003. Stability of excavations. Geotechnical Engineering Handbook. Vol. 3, Ernst & Sohn, Berlin.

Weißenbach, A., Hettler, A. 2010. Baugruben—Berechnungsverfahren, Ernst & Sohn.

This page intentionally left blank

Geotechnical Aspects of Underground Construction in Soft Ground – Viggiani (ed)

Prediction of tunnel-induced settlements in soft ground

J. Fillibeck & N. Vogt
Zentrum Geotechnik, Technical University of Munich, Germany

ABSTRACT: Tunneling in soft ground always leads to stress redistribution and displacements in the surrounding soil. Therefore, when planning shallow tunnels in areas sensitive to settlements, the prediction of the deformations above the tunnel is very important. In order to describe tunnel-induced settlement troughs, the Gaussian distribution function is most commonly used. Its input parameters are the point of inflection i and the volume of the settlement trough, described by the so called volume loss VL_s. These two parameters have to be defined in order to be able to predict a settlement trough which is close to that in situ. In the literature, the results of settlement measurements are frequently presented, however the results are mostly not comparable due to different boundary conditions. Therefore, the range of published settlement troughs vary widely and there are very few as well as inaccurate datainformation concerning the size of the parameters i und VL_s. In this paper the empirical prediction-method of Fillibeck is introduced to determine the parameters i und VL_s which was deduced from more than 350 carefully selected and proved measurement results as well as accompanying 2D- and 3D- FE-calculations using advanced constitutive models.

1 INTRODUCTION

Nowadays the realistic prediction of tunnel-induced settlements in urban areas is very important, in order to gain the acceptance of the population for a tunneling project. In this case numerical analyses as well as empirical procedures are suitable. The inputs of such empirical procedures are derived from earlier tunneling projects. The empirical methods mostly use the function of Gaussian distribution function to describe the settlement trough. The input parameters are the point of inflection i and the volume of the settlement trough, described by the so called volume loss VL_s or otherwise abbreviated VL in the literature.

In this paper an empirical method is introduced to predict i and VL_s for shotcrete or shield excavation which was deduced from a large number of carefully selected and proved measurement results. For shotcrete excavations more than 200 measured sections of the Munich subway as well as 50 further measured sections under other geological conditions as well as more than 100 measuring sections for shield excavation could be considered. With the help of these measurements as well as 2D- and 3D- FE-back analysis using advanced constitutive models, the influence of the following parameters was determined:

- geological situation
- tunnel depth
- size of the excavation
- soil stiffness

Because of the large number of comparable measurements, it was possible to describe the size of the settlement trough in relation to the probability of occurrence. So the probability of falling below or exceeding the maximum settlement, tangent inclination or deflection ratio can be predicted.

The evaluations shown are the results of research performed in the context of a Habilitation at the Zentrum Geotechnik of the TU München (Fillibeck (2010)). There the evaluations are described and proven in detail.

2 DESCRIBING THE SETTLEMENT TROUGH

2.1 *Mathematical description of the settlement trough*

The settlement trough across the heading is considered. As comparisons showed, the settlement trough can be described suitably by the Gaussian distribution (Schmidt (1969); Peck (1969)). The settlement s(x) at the point x and the volume of the total settlement trough V_s at the ground level per meter heading are defined by 2 parameters being; the maximum settlement s_{max} as well as the distance of the point of inflection of the Gauss function from the tunnel axis I (Equation 1 and Fig. 1).

$$s(x) = s_{max} \cdot e^{-\frac{x^2}{2 \cdot i^2}} \quad (1)$$

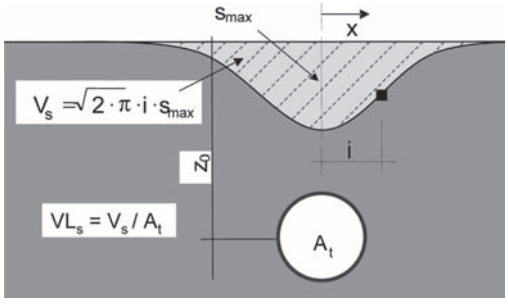

Figure 1. Definitions pertaining to the settlement trough.

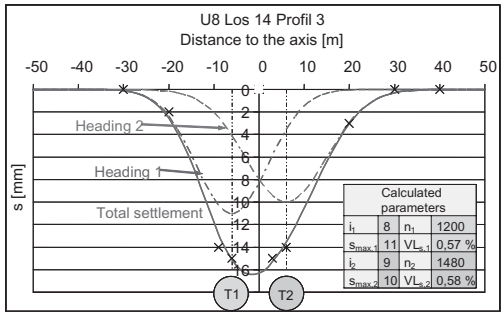

Figure 2. Analysis of a total settlement trough.

According to the Gauss function the point of inflection corresponds to the standard deviation.

The calculation of the volume of the settlement trough per meter heading V_s can be calculated by means of Figure 1.

If one defines the volume loss VL_s as the ratio between the cross-section of the settlement trough V_s and that of the tunnel A_t, then the unknown s_{max} can be expressed alternatively in terms of VL_s (Equation 2). Subsequently, VL_s as it is commonly termed in the literature, is used instead of s_{max} next to i, as a second parameter for the description of the settlement trough.

$$s_{max} = VL_s \cdot \frac{A_t}{\sqrt{2 \cdot \pi} \cdot i} \quad (2)$$

2.2 *Determination of VL_s and i from the results of measurement*

In the case of parallel tunnel headings, the total settlement trough results from the sum of the two settlement troughs of the single tunnels. Thus, the total settlement trough is described by 4 parameters $VL_{s,1}$, $VL_{s,2}$, i_1 and i_2.

Figure 2 exemplarily shows the analysis of the two shotcrete-headings of the U8 subway, Lot 14 in Munich, with the two single settlement troughs, the total settlement trough (addition of the single settlement troughs) and the corresponding measured values (crosses). According to the principle of the least squared smallest error squares, the total settlement trough was determined by mathematical variation of the 4 first unknown parameters, so that the total settlement trough matched the measured values (mathematical optimization) the best. Hence the parameters $VL_{s,1}$, $VL_{s,2}$, i_1 and i_2 were derived.

3 GENERAL DATA FOR THE ANALYSIS OF THE SHOTCRETE HEADINGS

The majority of the analyses of the shotcrete headings are based on measurements done in Munich. According to the heading methods performed on the Munich subsoil, a distinction has to be made between headings in the quarternary gravel and those of the predominantly fine-grained, tertiary soils.

Figure 3 shows exemplarily a quarternary heading above groundwater. The top heading is initially excavated with a total cross section of about 35 m² to 42 m². The large supporting core for the working face stabilization as well as the use of spiling or lagging sheets in the crown, are salient. Very coarse grained gravels are injected in advance as required.

The tertiary heading is affected by the adjacent water pressure of the tertiary sand layers within the tertiary clays and silts. If the sand layers can be dewatered, an atmospheric heading is possible. In Munich top headings with short reaching heads predominate (Fig. 4).

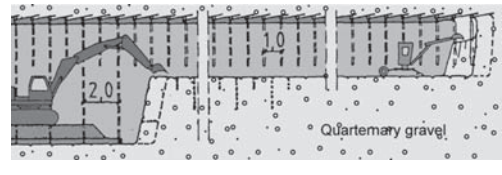

Figure 3. Top heading in the quarternary gravel.

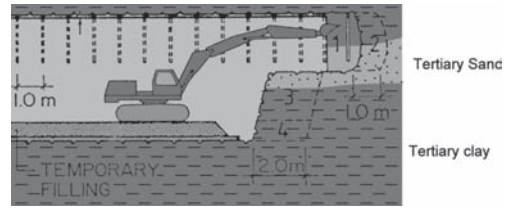

Figure 4. Heading in the tertiary.

If the sand layers cannot be dewatered, the possibility of a heading with the help of compressed-air support exists, where the air pressure must be maintained at a higher level than the maximum water pressure. To make sure that the excess air pressure does not become too high, it can be expedient to decrease the water pressure in the relevant sand layers by means of dewatering.

The analyses usually include two parallel tunnel tubes, whereby it was differentiated between synchronous and offset synchronous headings (4). Offset synchronous headings are characterized by a minimum distance of 25 m between the working faces of the respective tunnel tubes in heading direction.

The distance between both tunnel tubes (soil pillar) is an important parameter governing the settlements in parallel headings. The relationship between width of the soil pillar and tunnel diameter d is named ratio (a/d). By analyzing the shotcrete headings, the results show that the tunnel tubes influence each other and the settlement troughs increase if:

– a/d < 0,3 for the offset synchronous and synchronous headings or
– 1 < a/d < 0,3 and tunnel depth z_0 > 12 m for synchronous headings.

Therefore, these headings were not taken into consideration in the following analysis.

Likewise, settlements resulting from dewatering during the tertiary heading were not considered, since the dewatering caused very wide and flat settlement troughs (widths > 200 m). Thus, no damage potential results from the dewatering because of the very small settlement differences (Fillibeck & Zaunseder (2008)).

4 EQUATIONS FOR THE DETERMINATION OF THE VOLUME LOSS

4.1 *Volume loss for shotcrete excavations*

In the following analysis it was distinguished between:

– atmospheric shotcrete excavations in fine grained soils,
– atmospheric shotcrete excavations in coarse grained soils and
– shotcrete excavations with compressed air support.

Initially, the various results of measurements for the Munich subway (~35–42 m²) were evaluated. Thereby the volume loss was determined, according to the geological situation and the tunnel depth z_0. Figure 5 shows exemplarily the volume loss for atmospheric shotcrete excavations in the fine-grained tertiary soil.

The average volume loss can be described well by the regression lines shown in Figure 5. However, in practice it is also of interest to determine the settlement trough with higher confidence intervals or with lower probability of occurrence. For this the confidence interval of the measured values has to be determined. In Figure 5 the results for the upper confidence intervals of 90% and 99% are shown. They can also be described by a linear regression. A confidence interval of 99% means for example, that the probability of occurrence of a volume loss lying above the linear regression value amounts to 1%. Thus, the required volume can be determined as a function of the selected confidence interval.

In Figure 6 the measured volume loss with the regression lines (mean values) of the 3 shotcrete excavation methods are summarized.

The volume loss of the atmospheric shotcrete excavation is about twice as large as the shotcrete excavation with compressed air support. The compressed air supports the working face and the tunnel wall, so that altogether smaller settlements arise.

Subsequently, the evaluations were supplemented by measurements conducted in 50 further

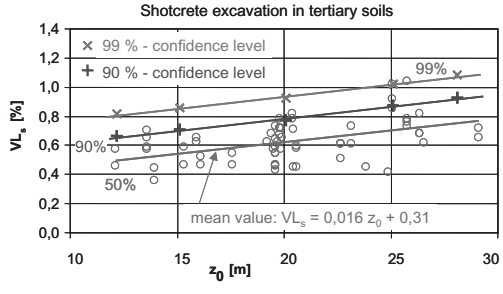

Figure 5. Vl_s at atmospheric shotcrete excavations in the tertiary soils.

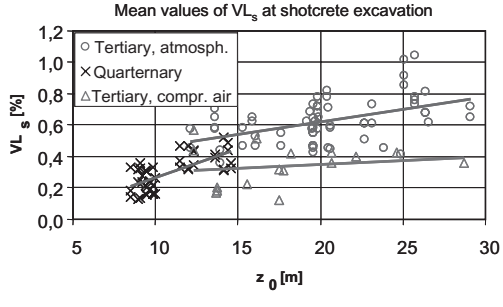

Figure 6. Volume loss of the different shotcrete excavation methods.

shotcrete excavations under other ground conditions. As it is shown on the basis of the evaluations and also on the comparison with FE-analyses, it can be assumed in good approximation that the size of the settlement trough is inversely proportional to the soil stiffness. This was considered in the equations to determine the volume loss. They are presented in Table 1 with confidence intervals of 50% (average value) and 99%.

As a result, the modulus $E_{100,ref}$ corresponds to the stiffness of the adjacent soil in MN/m² at a reference normal stress of 100 kN/m².

4.2 *Volume loss of very large cross sections driven in several shotcrete-sections*

Very large cross sections cannot be driven in one heading, as the working face is liable to fail. Therefore, they are subdivided into several headings. Hence, the question arises as to whether the given equations can also be used for these very large cross sections. This was examined with the help of 4 very large shotcrete excavations, to which extensive measurement results were available.

The following results are presented using the example of the "Theresienwiese" Station (Fig. 7) of the subway U5/9 in Munich. This atmospheric shotcrete excavation with a break out section of about 180 m² was carried out in 1979 in the tertiary clays. The whole cross section was divided into 5 headings, divided into top heading, bench and invert. For the empirical calculations each top heading, bench and invert were regarded as individual headings.

Initially, the settlement troughs of the partial headings were determined according to Equations 1 and 2, considering a volume loss with a 50% probability of occurrence according to

Table 1. VL_s at a confidence interval of 50% und 99%.

$VL_{s,50\%}$	$VL_{s,99\%}$
Atmospheric shotcrete excavation in gravel	
$(0{,}037 \cdot z_0 - 0{,}10) \cdot \frac{120}{E_{100,ref}}$	$(0{,}037 \cdot z_0 + 0{,}09) \cdot \frac{120}{E_{100,ref}}$
Atmospheric shotcrete excavation in fine-grained soil	
$(0{,}016 \cdot z_0 + 0{,}31) \cdot \frac{100}{E_{100,ref}}$	$(0{,}016 \cdot z_0 + 0{,}61) \cdot \frac{100}{E_{100,ref}}$
Shotcrete excavation with compressed air support	
$(0{,}005 \cdot z_0 + 0{,}26) \cdot \frac{100}{E_{100,ref}}$	$(0{,}005 \cdot z_0 + 0{,}57) \cdot \frac{100}{E_{100,ref}}$

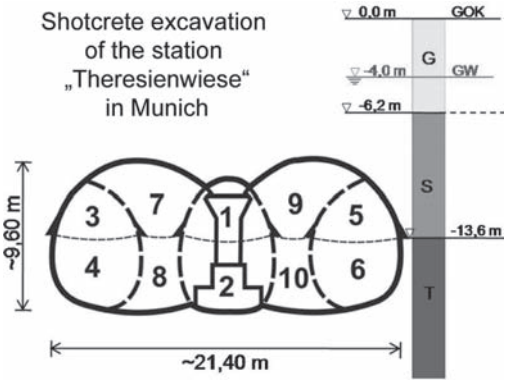

Figure 7. Excavation work at the station Theresienwiese of the U5/9 in Munich.

Table 1 and the point of inflection i corresponding to Section 5.

These settlement troughs were referred to the tunnel axis and subsequently superimposed, resulting in the total settlement trough shown in black in Figure 10.

The measured results agree very well with the settlement trough determined by the empirical method. This was also the case with the 3 other cross sections examined. Thus, the total settlement trough of a cross section, which is driven in several partial headings, can be determined by superimposing the single settlement troughs of the individual headings using the volume loss for the corresponding partial cross sections. The same applies to parallel tunnel headings (see Section 3). This is however not valid if the partial cross sections affect each other during heading, for example at synchronous headings with a pillar ratio a/d less than 0,3, see Section 3.

4.3 *Volume loss for shield tunneling*

In the following only shield tunneling methods with face support (hydraulic, earth pressure and compressed air shield tunneling) were considered, since these apply to settlement-endangered areas in granular soil.

For the investigations of the volume loss with shield tunneling, over 100 measured cross-sections of current construction measures could be evaluated. Excavations prior to 1995 were not considered, since in the past few years the mechanical engineering has substantially improved, so that fewer settlements have been reported in the past few years (see above).

The following results are valid in granular soil, however not in soils with less than a soft consistency, very loose density or structure-sensitivity. This classification is necessary, since for exam-

ple the dynamic demands of the tunnel boring machines can lead to relevant additional settlements. This cannot be documented with the procedure described herein.

According to evaluations the volume loss tends to be smallest with hydraulic shield driving, however the difference to those with compressed air or earth pressure support is very small. Beyond that, no clear differences were observed with different subsoil and supporting pressures. Therefore, all the different tunnel driving methods were regarded as being independent of the subsoil and the supporting pressures.

Figure 9 illustrates the volume loss as a function of A_t/z_0. As the regression (power function) shows, the volume loss decreases with the A_t/z_0.

In order to once again be able to indicate the volume loss as a function of the confidence interval, the examined range was divided into 3 sections. For each section the confidence interval was determined and then approximated by means of a balance function for the total range. In Figure 9 the curves and equations for the determination of the volume loss for a confidence interval of 50% and 99% are shown.

For future practice it is of substantial importance that in the cross sections examined here from the recent past the volume loss consistently lies below 0.5% and thus clearly under the value of 2.0%, indicated frequently in publications on shield driving.

Recently, the technique of the tunnel boring machines has improved in important settlement-relevant sectors (for example by grouting the gap behind the shield tail and by keeping the supporting pressure constant). Therefore, with newer shield headings, smaller settlements result and thus smaller maximum volume losses can be assumed. Due to inevitable fluctuations, it however is suggested that no volume loss smaller 0.25% be considered for the settlement prediction, as would result from large A_t/z_0-values.

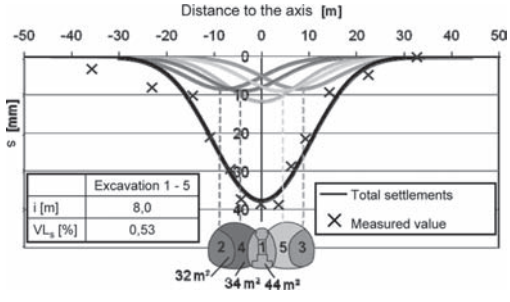

Figure 8. Comparison of measured results and eempirical correlation.

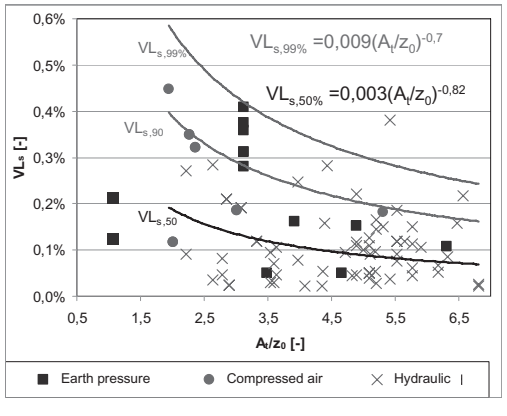

Figure 9. Volume loss with shield tunneling.

5 DETERMINATION OF THE POINT OF INFLECTION

In the following, the results of the Munich headings are initially presented again. As already recognized in other publications, the point of inflection i depends particularly on the geological conditions (grain size distribution, density and consistency) and on the tunnel depth.

Therefore, the quarternary and tertiary layers of the Munich subsoil are regarded separately, depending on the tunnel depth.

Figure 10 shows the point of inflection in the quaternary gravel i_G in relation to the tunnel depth z_0. As to be expected, i_G increases with z_0. It can be described by means of the regression line given in Equation 3.

$$i_G = 0{,}57 \cdot z_0 \tag{3}$$

The determination of the point of inflection in the tertiary layers beneath the quarternary layers

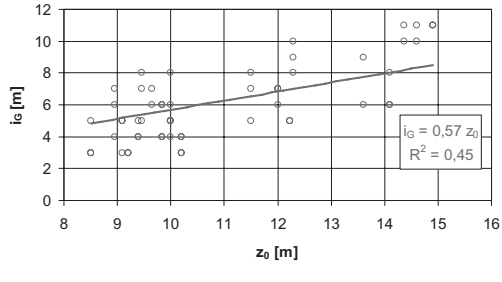

Figure 10. Point of inflection i_G in the quarternary gravel.

is somewhat more complicated, since it concerns a multi-layer system (see also New & O'Reilly (1991)). The point of inflection of the total settlement trough i_{ges} consists of individual contributions of the respective layers. This is shown in Figure 11, where i_G, i_S, i_{CL} and i_S are the points of inflection of the respective layers and $z_0 - d_{CL}$ is the thickness of the gravel and sand layer.

Assuming that i_G and i_S of the quaternary gravels and tertiary sands are approximately alike with equivalent layer thicknesses (they possess similar stiffness and strength) and that i_G is determined by Equation 3, the point of inflection of the fine grained tertiary soil layers i_{CL} can be determined. This is illustrated in Figure 12, a plot of i_{CL} against the layer thickness d_{CL}.

The expected linear dependence on z_0 is also obtained here. The point of inflection i_{ges} of the multi-layer system can be determined by means of the following equation:

$$i_{ges} = 0{,}82 \cdot d_{CL} + 0{,}57 \cdot (z_0 - d_{CL}) \quad (4)$$

Equations (3) and (4) are valid for underground conditions comparable to those in Munich. These are medium dense to dense gravels or sands and clays and silts of firm to stiff consistency respectively.

The evaluation of excavations subject other underground conditions show that also the consistency and the density exert a certain influence. With increasing consistency and density the point of inflection exhibits a corresponding increase.

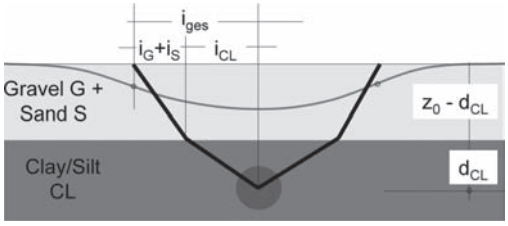

Figure 11. Point of inflection i_{ges} in layered soils.

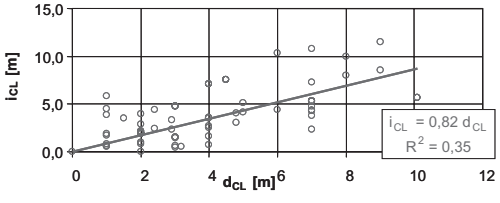

Figure 12. Point of inflection i_{CL} of the finegrained tertiary clays and silts.

Table 2. Points of inflection for different adjacent soils.

		i [m]
Gravel/sand	Loose—medium dense	0,25 to 0,5 · z_0
	Medium dense—dense	0,4 to 0,6 · z_0
Clay/silt	Soft—semisolid	0,3 to 0,6 · z_0
	Semisolid—solid	0,5 to 0,9 · z_0

By taking the available evaluations into consideration as well as published data, for example Mair & Taylor (1997) and Tan & Ranjith (2003), which are based again on different excavation evaluations, the following ranges of points of inflection may be proposed.

Since the results of the evaluations and the available published data were scattered, a bandwidth of points of inflection are indicated for the given ranges of the density or consistency. Thus, a small point of inflection can be assigned to a low density/consistency and a higher point of inflection to a higher density/consistency.

With the choice of a suitable point of inflection i it must be considered that with decreasing i the maximum tangent inclinations, strains and curvatures increase, with the result that—depending upon the location of the building with respect to the tunnel—the damage potential rises. However, the damage potential also increases with the volume loss. In order not to calculate an unrealistically high damage potential, two limit cases are suggested: Case 1 considers a high volume loss ($VL_{s,99\%}$) and a mean point of inflection and Case 2 a medium volume loss ($VL_{s,50\%}$) and a small point of inflection (according to a small density/consistency).

6 SUMMARY

With the empirical method presented herein, maximum settlement troughs resulting from shotcrete or shield tunneling can be predicted. The input parameters required to describe the transverse settlement trough by means of the Gauss function assumed here, are the point of inflection i as well as the volume loss VL_s.

The point of inflection i is a measure of the width of the settlement trough. The volume loss VL_s, which is defined as the ratio of the volume of the settlement trough per m heading to the tunnel cross section, corresponds to the magnitude of the settlement trough. Based on the results of measurements and taking the data of other publications into consideration, detailed proposals could be made for the choice of VL_s und i as a function of

the heading depth, the geology and the soil stiffness. Due to the multiplicity of the available measurements it was furthermore possible to specify the volume loss as a function of the probability of occurrence.

It is clear that not all possible boundary conditions can be considered with the empirical procedure presented here. But even if this succeeded, it is in the nature of the things that the settlements are subject to a certain scatter. Thus it is not possible to calculate a "true" settlement trough in advance but, at best a prediction depending on the probability of occurrence can be made. The described procedure, which is based on a very large number of comparable measurements and experiences, could be of great help and provide a possible solution. Alternative computations, which are usually implemented by means of finite element analyses, also require the estimation and/or variation of different inputs, if no regional experience with comparable tunnel headings is available. Experience shows, that this often leads to larger and frequently non realistic ranges of differently large settlement troughs, which can hardly be evaluated with accuracy. In this case, the determination of the settlement trough with the finite element method does not exhibit substantial advantages in relation to the simple empirical procedure presented here.

REFERENCES

Fillibeck, J. & Zaunseder, M. 2008. Risiko von Setzungsschäden beim U-Bahn-Bau—Auswertung und Prognose von Setzungen. In: 7. Geotechnik-Tag in München, Titel: Risiko und Sicherheit in der Geotechnik.

Fillibeck, J. 2010. Prognose von Setzungen beim Lockergesteinsvortrieb—Empirische und numerische Verfahren. Habilitationsschrift am Zentrum Geotechnik der TU München. Eingereicht 09/2010.

Franzius, J.N. 2003. Behaviour of buildings due to tunnel induced subsidence. PhD thesis, Imperial College, University of London.

Mair, R.J. & Taylor, R.N. 1997. Theme lecture: Bored tunneling in the urban environment. 14th International Conference Soil Mechanics and Foundation Engineering. Hamburg, S. 2353–2384.

New, B.M. & O'Reilly, M.P. 1991. Tunneling induced ground movements: Predicting their magnitudes and effects. Ground Movement and Structures, ed. J.D. Geddes, S. 671–697.

Peck, R.B. 1969. Deep excavations and tunneling in soft ground. Proc. 7th International Conference Soil Mechanics and Foundation Engineering, Mexico City (1969). State of the Art Volume, S. 225–290.

Schmidt, B. 1969. Settlements and ground movements associated with tunneling in soils, PhD Thesis, University of Illinois, Urbana.

Tan, W.L. & Ranjith, P.G. 2003. Parameters and Considerations in Soft Ground Tunneling. http://www.ejge.com/2003/Ppr0344/Abs0344.htm.

This page intentionally left blank

Geotechnical Aspects of Underground Construction in Soft Ground – Viggiani (ed)
© 2012 Taylor & Francis Group, London, ISBN 978-0-415-68367-8

Strains and failure characteristics of pyroclastic materials in deep excavation

Alessandro Lombardi & Aldo Capata
S.G.S. Studio Geotecnico Strutturale, Rome, Italy

ABSTRACT: This paper presents the results of investigations (substantially on site) for the determination of the failure and deformability characteristics of pyroclastic soils interested by the Centocelle Park station excavation (underground Line "C" in Rome). For a correct estimation of the mechanical characteristics of the different formations, two type of investigations were carried out, both of a traditional kind (pressuremeter tests, SPT, direct shear tests) and seismic tests. The most representative aspects of the constitutive model and the mechanical behavior of the soil at the small strains characteristic of the open pit excavation are described shortly and the results of the performed tests and the criteria of choice of the design deformability parameters are illustrated. Finally, from the monitoring data obtained during the excavation of the station, similarities and differences of measured diaphragm wall displacements, compared to prediction obtained by finite element models are shown.

1 INTRODUCTION

This paper illustrates the results of the geognostic investigation made for the Centocelle Park station design (subway line C in Rome), in order to determine the deformability parameters of pyroclastic soils interested by the excavation. The *in-situ* investigation, consisting of seismic tests (RE.MI. Refraction Microtremor), permitted an estimate of the elastic modulus at small strains (from 0.01% to 0.1%) that are usually reached in the open pit station (in this case approximatively 27 meters). A comparison was made between the results obtained from traditional investigations (pressuremeter tests and, only for lithoid soils, unconfined compression tests) and those obtained from the seismic investigation. The analysis of the behavior of the deep excavations under working conditions is subordinate to the knowledge of the elastic modulus at small deformations (G_0 or E_0). The numerous researches made on the behavior of soils at small strains (Rampello & Silvestri, 1993; Stokoe *et al.*, 1995), have shown that the G_0 modulus can be taken as a "state parameter", like the initial voids ratio e_0, the earth pressure coefficient at rest K_0 or the effective vertical lithostatic stress σ'_{v0} (Ghionna *et al.*, 2006). For these reasons, in the design practice, there is a need to define the shear modulus G_0 variation with depth for all layers interested by excavation. The nature of this "fundamental" parameter is better defined by the relation between G_0 and propagation speed of shear waves provided by the elastic theory:

$$G_0 = \rho \cdot V_s^2 \qquad (1)$$

in which ρ is the soil density. Equation (1) allows conversion of data obtained by RE.MI., *i.e.* shear wave velocity, to the stiffness parameter of reference.

From these considerations and from the results of the seismic investigation, a numeric simulation of the excavation was made in order to verify the stress-strain behavior of the soil-structure complex and for comparison with results obtained by measurement carried out during the excavation phases.

2 PYROCLASTIC MATERIALS INTERESTED BY THE EXCAVATION OF CENTOCELLE PARK STATION

2.1 *Geological profile*

From a geologic point of view, the area interested by the Centocelle Park station building is covered by alluvial backfill underlain by the products of the *Colli Albani* volcanic apparatus and the *Sabatino* volcano that are very common in the east and south-east part of Rome.

The soil succession includes typical Roman Pozzolanas, largely in banks of weakly bonded material, to the extent than they can be classified as incoherent. In some places these are also facies with considerable bonding (soft rock behavior). Finally, there are successions made up of by frequent interbedding of incoherent materials and other materials with various bonding degrees.

The whole thickness of Volcanites is represented by:

– *The Superior Complex of Colli Albani volcanic products*, composed by altered pyroclastics materials called Villa Senni Tuff (VS) deposited on top the Lionato Tuff (TL) and finally over the Black (PN) and Red Pozzolanas (PR).
– *The Inferior Tuffs Complex* are composed by a succession of lithoids (T1-T2-T2*) and incoherent layers (TA). In general, at the top of Inferior Tuffs, there are layers of altered pyroclastics materials called "Terrosi Tuffs" (TT). The geotechnical profile of the station is represented in Figure 1.

2.2 *Strain characteristics of pyroclastic soil*

The RE.MI. tests performed permitted to define shear wave velocity profiles and therefore G_0 profiles similar to that shown in Figure 2. Such profiles underline in enough detail the stiffness variations of the different soil layers.

Below the backfill layer (R) an increase of V_S can be seen which is due to the presence of Lionato Tuff (TL). The behavior of this layer will not be analyzed, in view of its reduced thickness and the absence of continuity along the station. The values of shear wave velocity, V_S, and of G_0 and E_0 moduli at small strain are presented in Table 1, together with the geotechnical design parameters.

The most important soil layers for the design of retaining structures are the so called *Pozzolanas*. *Black Pozzolanas* (PN) are made up of incoherent to pseudo-coherent fine grain pyroclastic material and an ash–cinders matrix, that is blackish-grey and sometimes purplish in color, that can have a low bonding degree.

Red Pozzolanas (PR), under the PN layer, are characterized instead by their purplish red color, and a much coarse matrix.

The good geotechnical characteristics of such layer have been confirmed by the numerous SPT tests concluded at refusal. The direct shear tests gave friction angles larger than 35° and very dispersed cohesions around an average value of 10.3 kPa (Figs. 3 and 4). The average value of the G_0 modulus is equal to 440 MPa for the PN layer and to 580 MPa for the PR layer. The pressuremeter modulus provided results equal to E_m = 88 MPa (PN) and to 70 MPa (PR). In order to carry out a comparison between the elastic modulus of the pressumeter tests and the static modulus inferred from the RE.MI. tests, we have used the correlation proposed by Rzhevsky and Novik (1971): $E_0 = 8.3 \cdot E_{static} + 0.97$ in which E_0 represents the elastic modulus at a small strain obtained by the RE.MI. tests. The comparison between the modulus obtained from pressuremeter tests is shown in Figure 8, which illustrates that for the pozzolanas and altered tuffs layers, the values of the static modulus E obtained from RE.MI. tests are lower than those obtained from pressuremeter tests over almost the whole interval of depth analyzed.

During investigation in the station area, a highly cemented layer was found (indicated as PRb) which confers the characteristics of a lithoid tuff to the material (Fig. 7).

The RE.MI. profile confirms a stiffness increase between +10.00 and +3.00 m a.s.l. up to values around 880 MPa, comparable with those of Lionato Tuff and of the unaltered Inferiors Tuffs (T1-T2). The high bonding degree in the basal portion of the bed of pozzolanas (PRb)

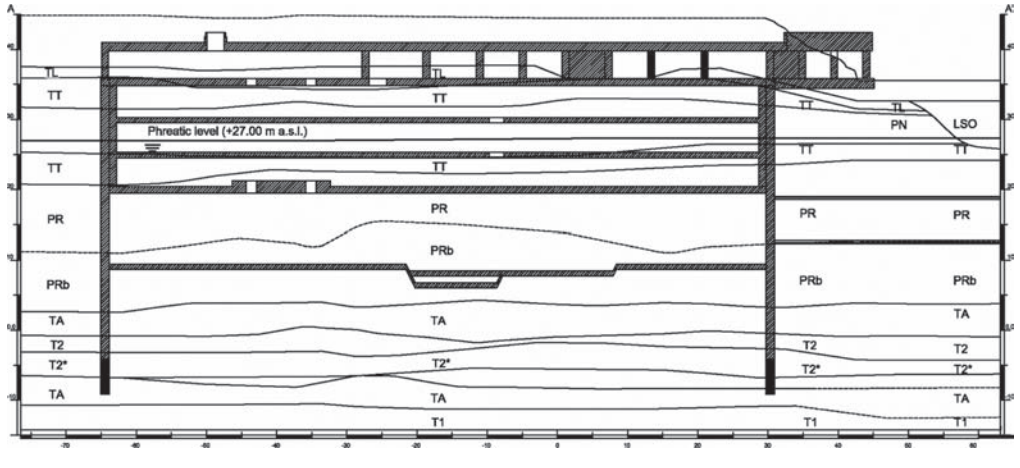

Figure 1. Geological profile of Centocelle Park station.

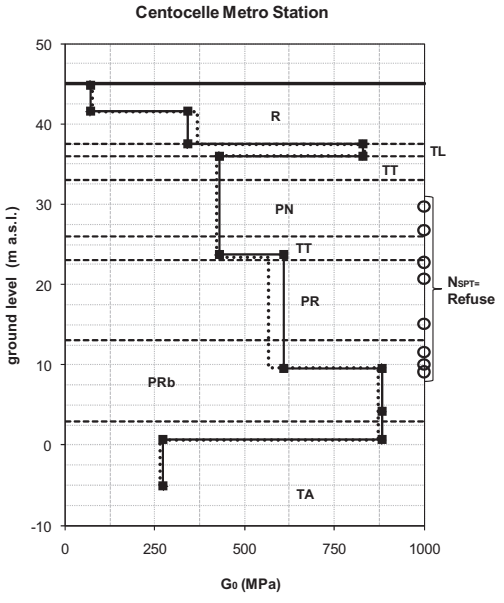

Figure 2. G_0 modulus profile from RE.MI. tests.

Table 1. Geotechnical parameters of the Centocelle Park station soil layers.

	ρ	V_S	G_0	E_0	c′	φ′
Layer	Mg/m³	m/s	MPa	MPa	kPa	degrees
R (backfill)	1.70	330	185	407	10	25
TL	1.75	690	832	1830	25	35
TT	1.70	500	425	935	25	34
PN	1.75	500	438	963	5	35
TT	1.70	500	425	935	25	34
PR	1.85	560	580	1276	5	35
PRb	1.90	680	879	1933	300	35
TA	1.75	391	268	589	30	35
T2	1.75	–	–	–	40	35
T2*	2.00	–	–	–	300	35

was confirmed by numerous uniaxial compression tests in which it was possible to obtain resistances variables between 4.5 and 33.7 MPa with an average value of 18.6 MPa. From tests with measurement of deformations, an average tangent Young's modulus $E_{t,50}$ of 12 GPa was obtained. To perform a comparison between modulus values G_0 obtained by geophysical tests on site, initial tangent modulus (E_{ti}) where deduced through stress-strain curves, obtaining the results given in Table 2.

The stress-strain curves show a progressive increase of the tangent elastic modulus for small deformations (Figs. 5 and 6). This behavior is probably due to the progressive closing of macropores and partly due to the unreliability of measurements in the initial part of stress-strain curve. It is nonetheless worth observing that this behavior does not depend on the type of measurement of deformations (strain gauges or displacements transducers). The elastic modulus values obtained by laboratory tests are obviously larger than those obtained through the measure of V_s, that characterize the

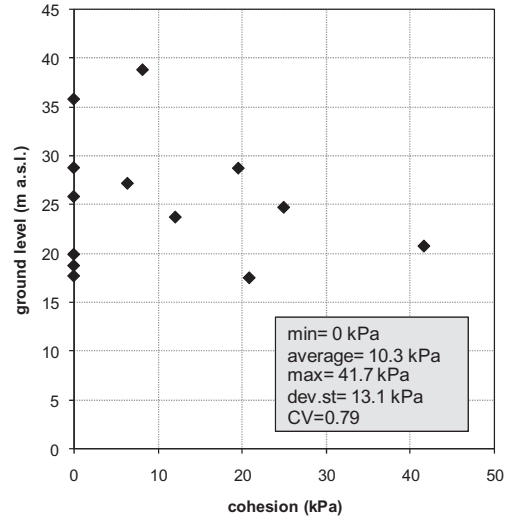

Figure 3. Cohesion versus ground depth (m a.s.l.) for Pozzolana layers (PN-PR layers).

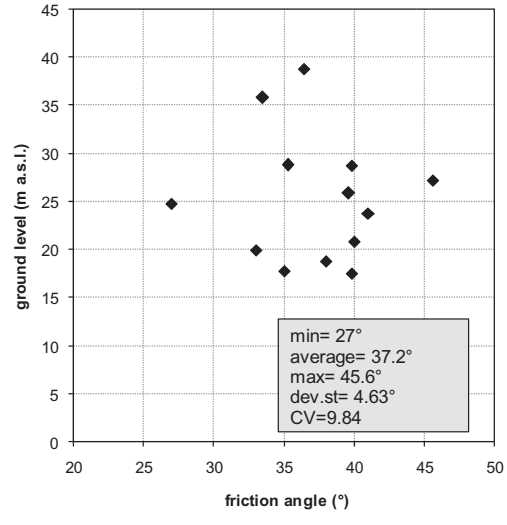

Figure 4. Friction angle versus depth (m a.s.l.) for Pozzolana layers (PN-PR layers).

Table 2. Summary of results of uniaxial compression tests on PRb specimens.

Parameter	Average	Min	Max	St. dev.	CV
σ_f (MPa)	18.50	4.50	33.71	6.75	2.74
$E_{t,50\%}$	12044	4360	25660	4769	2.53
$E_{s,50\%}$	11570	5390	18960	3350	3.45
E_{ti}	8197	2500	16667	3886	2.11
G_0	3726	1136	7576	1766	2.11

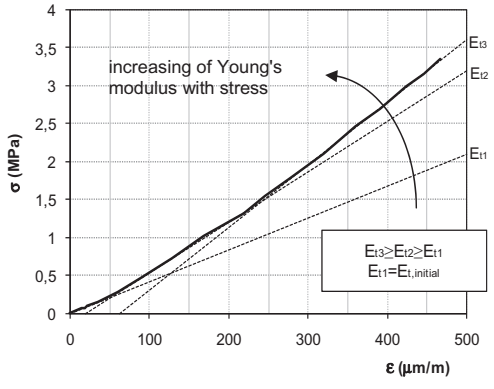

Figure 5. Progressive stiffening of PRb specimens.

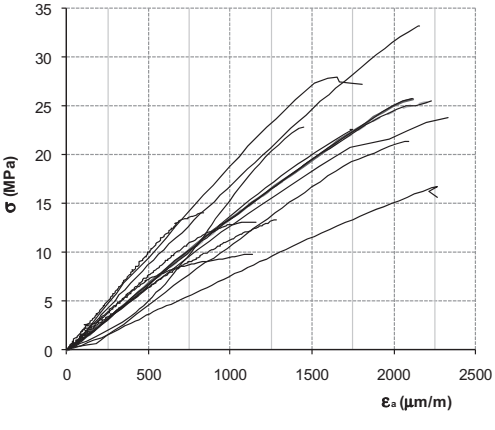

Figure 6. Some stress-strain curves from unconfined compression tests on bonded Pozzolanas (PRb) layer.

soil at the deposit-scale: detected differences on the average value of shear modulus, allow an estimation of its reduction in of to 75% from the deposit-scale to rock material (specimen-scale). This stiffness reduction is probably overestimated given the unreliability of RE.MI. tests for depths up to 40 m, and it does not appear justified, due to the relative structural homogeneity of deposit on studying.

3 PREDICTION OF BEHAVIOR OF EXCAVATION AND COMPARISON WITH MONITORING MEASURES

3.1 *Description of the station*

The station is made up of a deep structure excavated between a 1.20 m thick diaphragm wall. In order to realize the station diaphragm walls has been necessary to perform a preliminary excavation of a maximum height equal to 8.50 m, sustained by a cantilevered retaining wall (piles of diameter equal to 1.20 m, distance 1.40 m).

The project (Figs. 9 and 10) foresees a maximum excavation of around 27.00 m with conventional top-down method, sustained by a diaphragm wall (length equal to 45.00 m) realized with hydromill, without steel reinforcement for the last 5 m with the sole the function of allowing the execution of a waterproof layer made up of a cement injection to hydraulically insulate the station.

For the top-down phases only two slabs will be realized (top slab and slab at +20.05 m a.s.l. level) up to the attainment of the maximum excavation depth (+8.70 m a.s.l.), while the structure is expected to be completed with cast concrete slabs (two mezzanine slabs and mat foundation slab), which together with the concrete inner wall will resist both the hydrostatic pressure and the remaining earth pressure. It is worth highlighting that it was possible to reach maximum excavation depth with just two slabs on account of the favorable effect of reduced earth pressure due to presence of PRb layer, characterized by a pseudo-lithoid behavior.

Figure 7. Specimen of cemented Pozzolana (PRb).

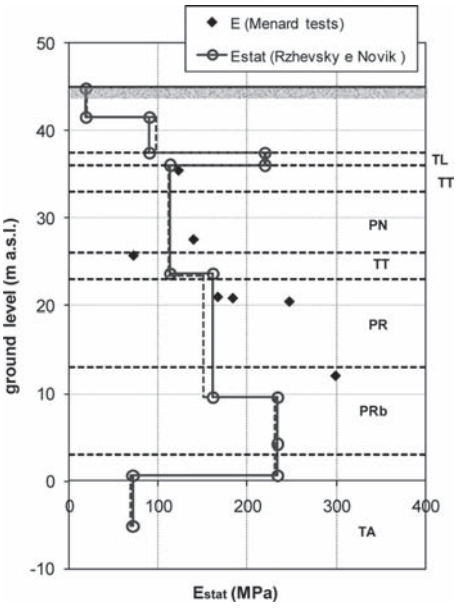

Figure 8. Comparison between "static" modulus determined from RE.MI. (with Rzhevsky and Novik relationship) and pressumeter tests.

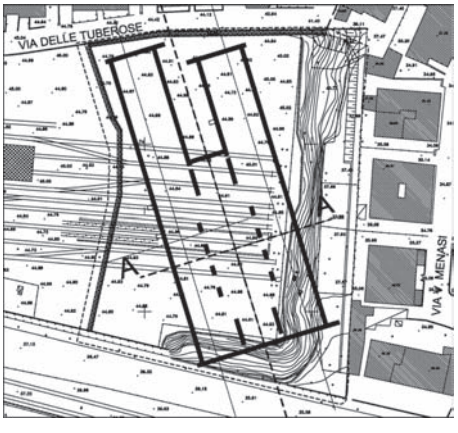

Figure 9. Planimetric view of station (in evidence the calculation section analyzed).

The main geometric characteristics of the structures of the station are summarized below:

- L = 45 m (diaphragm-wall length);
- s = 1.20 m (diaphragm-wall thickness);
- s = 1.00 m (slab thickness (top down phases));
- l = 38.70 m (station width).
- z_e = 27.10 m (maximum excavation depth);
- EJ = 4855918 kN/m^2/m (diaphragm-wall stiffness).

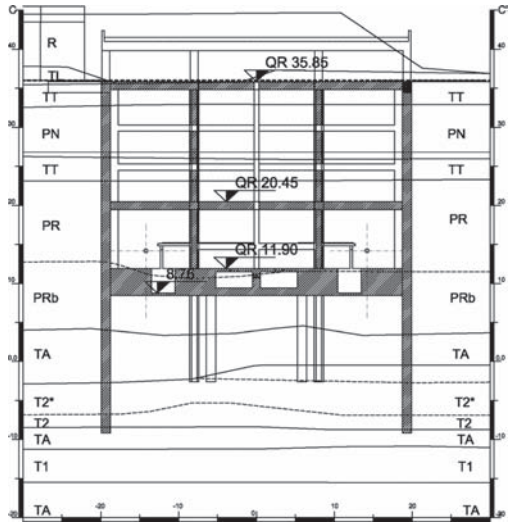

Figure 10. Geotechnical cross section of Centocelle Park station.

3.2 *Structural and geotechnical model*

Below is a description of the geotechnical and structural model. From ground level, the soil layers interested by the excavation are shown in Table 3.

The analysis for the prediction of soil-structure behavior was carried out through the finite elements code PLAXIS version 9.0, in drained conditions (phreatic level at 27.00 m a.s.l.). At the edges of the model the following boundary conditions apply: free upper surface, null horizontal displacement on lateral surfaces and null horizontal and vertical displacement on lower surface.

3.3 *FEM analysis constitutive law*

Soil behavior was represented by an elastic-plastic constitutive law with strain hardening. In particular the *Hardening Soil Model with Small Strain Stiffness* (HSSmall) (Benz, 2006) was used. This model represents an evolution of the Hardening Soil Model (HS) (Schanz *et al*. 1999), which contemplates a hyperbolic stress-strain relation.

The behavior in the elastic field is defined by the elastic Young's modulus E', which depends on the effective stress state with equation:

$$E' = E^{ref}\left(\frac{c'\cdot\cot\varphi' + \sigma'_3}{c'\cdot\cot\varphi' + p_{ref}}\right)^m \quad (2)$$

in which p_{ref} = 100 kPa is a reference pressure, E^{ref} is the Young's modulus for $\sigma'_3 = p_{ref}$, σ'_3 is the principal effective minimum stress and *m* is an non dimensional

Table 3. Geotechnical parameters of the Centocelle Park station layers.

Layer	γ kN/m^3	z_{sup} m a.s.l	z_{inf} m a.s.l.	c' kPa	φ' degrees	G_0 MPa
R (backfill)	17	44.00	36.00	10	25	185
TT	17	36.00	33.00	25	34	425
PN	17.5	33.00	26.00	5	35	438
TT	17	26.00	23.00	25	34	425
PR	18.5	23.00	13.00	5	35	580
PRb	19	13.00	3.00	300	35	879
TA	17.5	3.00	0.00	30	35	268
T2	17.5	0.00	–4.15	30	35	879

coefficient, varying between 0.2 and 1 according to the grain size of the material. The hardening parameter is a function of plastic shear strains through parameter E_{50} and of plastic volumetric strain through the parameter E_{oed}. The modulus E_{50} and E_{oed} vary with stress state through relations formally similar to equation (2). For the unloading and re-loading phases, the model provides an elastic behavior with a reference modulus linked to the first unloading modulus according to the following equation:

$$E_{ur} = E_{ur}^{ref} \left(\frac{c' \cdot \cot\varphi' + \sigma'_3}{c' \cdot \cot\varphi' + p_{ref}} \right)^m \quad (3)$$

in which $E_{ur}^{ref} = 1 \div 3\ E_{50}^{ref}$. The range of deformations for which a soil actually gives an elastic response, with an almost total recovery of the applied deformation, is very limited. This aspect of soil behavior is highlighted by the characteristic "S" shaped curve of shear modulus reduction with shear strain amplitude (Atkinson & Sallfors, 1991).

The *HSSmall* model can take into account real soil stiffness in small deformations and its dependence on the level of deformations achieved by introducing two additional parameters: G_o^{ref} e $\gamma_{0.7}$. The first parameter represents soil stiffness for reduced levels of deformation ($\varepsilon < 10^{-6}$), while the second is the shear strain for which the secant shear modulus is reduced to 70% of the value of G_o. The G_o and $\gamma_{0.7}$ parameters essentially depend from the stress state and from the relative density (void index) of the soil. The dependence of G_o by the stress state is represented by the law:

$$G_0 = G_{0ref} \left[\frac{\left(c' \cos\varphi' - \sigma'_{min} \sin\varphi'\right)}{\left(c' \cos\varphi' + p_{ref} \sin\varphi'\right)} \right]^m \quad (4)$$

similar to that one used for E_{50} and E_{ur}. The deformation $\gamma_{0.7}$ is assumed to be independent on the average of the stress state and equal to:

$$\gamma_{0.7} = \frac{1}{9(G_{O,ref})} \cdot \left[\left(2c'(1+\cos(2\varphi')) - \sigma'_1 (1+K_O)\sin(2\varphi')\right) \right] \quad (5)$$

Similarly, operative values of modulus during loading and unloading (E_{ur}^{ref}), defined earlier, can be deduced by first calculating elastic modulus value for small deformation, according to the well-known elasticity relation and by dividing the obtained value for a k coefficient derived from the graphic correlation represented in Figure 11 (Alpan, 1970).

During simulation of the excavation of the Centocelle Park station, the G_0 modulus was deduced by interpretation of the RE.MI tests, while the E_{50}^{ref} was deduced by dividing by 3 the E_{ur}^{ref} modulus obtained using the Alpan correlation. Alternatively it would have been possible to follow the procedure suggested by Callisto *et al.* (2007), which involves comparing the elastic modulus values at small deformation obtained by geophysical tests (for example Cross-Hole), with those obtained by simulation of triaxial tests to determinate the reductive factor in order to pass from the E_0 to the E_{50}^{ref}.

3.4 *Monitoring instrumentation*

The horizontal displacements of the diaphragm wall during construction were measured using inclinometer tubes cast into the diaphragm wall. Figure 12 illustrates the monitoring section under examination, in which it is possible to recognize the inclinometers placed within the diaphragm-walls.

3.5 *Analysis results and comparisons with monitoring measures*

The results of the geotechnical analysis are presented below as:

1. horizontal displacements of diaphragm wall;
2. mobilized strength;

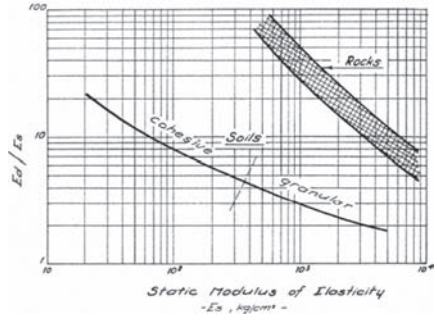

Figure 11. Graphic correlation between values of dynamic modulus at small strain (E0 = Ed) and the static unloading-reloading modulus ($E_{u,rref} \sim E_s$) (Alpan 1970).

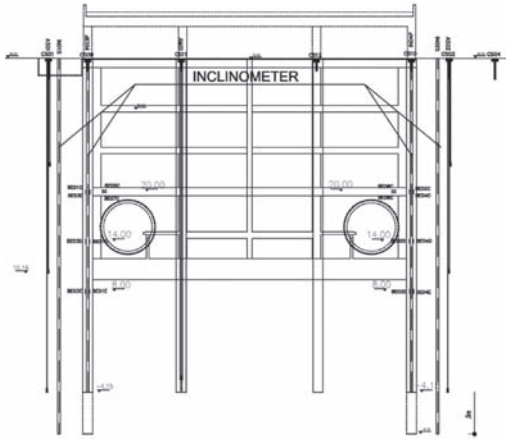

Figure 12. Monitoring cross section.

In the results below, the left diaphragm is located near the cantilevered retaining wall (piles Ø 1200 mm). All curves of Figure 13 refer to the final excavation phase (+8.70 m a.s.l.).

The finite element model (curves with continuous lines) shows displacements that are generally higher than those measured (curves with dotted lines), and approximately of the same magnitude for the diaphragm-walls (left and right side).

The measured displacements (for left and right diaphragm wall) are virtually identical for the first six meters of depth. They than differ with a maximum deviation of about 9 mm. From the middle of the PRb layer (+8.00 m a.s.l.) the displacements have the same value.

The calculated displacements agree with those measured on the right diaphragm wall, and the maximum difference (only for the upper part, up to +23.00 m a.s.l.) is equal to about 5 mm. Compared with the measured displacements on left diaphragm wall they are lower than those calculated for the entire excavation height.

In Figure 14, the contours of mobilized shear strength, defined by ratio τ/τ_{max} between the maximum shear stress acting on one point and the corresponding available strength, highlight areas in which the ratio is equal to around 1 (soil near to failure conditions). These areas are located between the slab at +20.05 m a.s.l. and the mat foundation slab, at an excavation depth where the PR-PN layer is reached.

In order to find the best set of parameters to approximate the measured displacements on left the diaphragm wall, it was therefore considered more appropriate not to increase the values of the G_0 modulus for layers (PN and PR), but to instead amplify the cohesion value of the PN and PR layers.

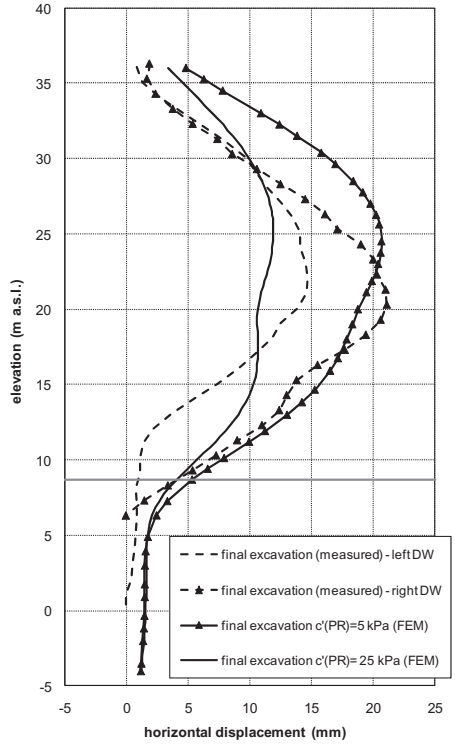

Figure 13. Comparison between lateral diaphragm-wall displacements: measured values and FEM results.

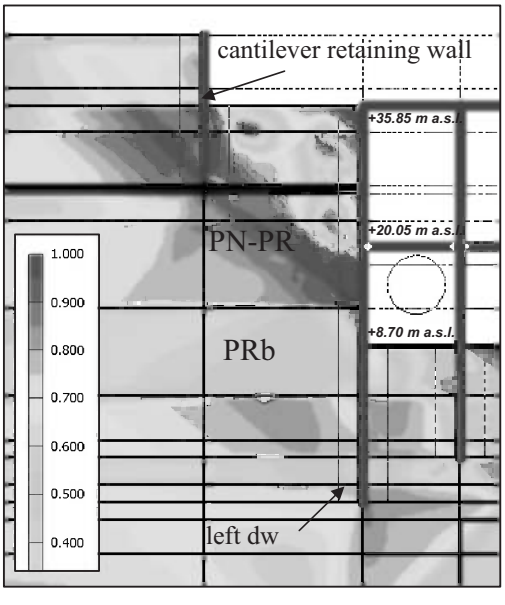

Figure 14. Contours of mobilized strength: design cohesion value of PN/PR layers equal to 5 kPa.

The new cohesion value (c′ = 25 kPa) was chosen by observing laboratory results of tests made on Pozzolanas of the closest stations along Line C (Alessandrino, Mirti and Gardenie stations).

With a higher of cohesion value, the calculated displacements decrease, although the shape of the curve is not exactly the same as that measured. In particular the measured displacements decrease much faster in the lower part of excavation height.

The shape of the curve remains roughly unchanged also increasing Young's modulus of the PRb layer.

This result suggests that displacements on the left diaphragm wall were affected, by more favorable geotechnical conditions (higher values of stiffness and/or cohesion, bonding degree) and by the actual realization sequence of the mat slab foundation: it is possible that the concrete cast of the mat foundation slab on the left side was carried out with excavation samples of small amplitude. The difference between the values of displacement calculated and measured in the first meters of excavation can partly be attributed to the occurrence, on the top slab, of slightly different load conditions from the assumed load design: in this case, the negative (earth side) bending moment acting on the top structural node, may, in fact, have limited the deformation on the excavation side.

4 CONCLUSIONS

The geotechnical investigations performed, have revealed some peculiarities of behavior of pyroclastic soils in the area interesting from excavation of Centocelle Park Station. The good geotechnical characteristics of Pozzolana layer (PN and PR) have been confirmed by the numerous SPT tests concluded with refusal and high values of friction angle measured by direct shear test. The cohesion values are, instead, very dispersed. The PRb layer showed substantially a soft-rock behavior, with a progressive hardening with increase of applied load. This behavior, probably due to the progressive closing of macropores, could result in part from the unreliability of measure in the initial part of stress-strain curve.

The results of numerical analysis, as horizontal displacements, are in substantial agreement with that measured for the right diaphragm-wall, while the displacements measured on left diaphragm wall are lower than those calculated for any excavation height. This anomaly could be attributed to the fact that on the left side the cohesion value of the layers PN-PR is higher than assumed in the calculations, probably because the disturbance on samples during taking and testing. This also proves that the negative effects due to a difficult sampling, leads to a wrong evaluation of the bonding degree of this material. Numerical analysis with a cohesion value c′ (PN-PR) = 25 kPa, provided displacement values closer to those measured on left diaphragm-wall, but with different shape: the measured displacements decrease much faster in the lower part of excavation height. The different sequence of realization of mat foundation slab (concrete cast with samples excavation of small amplitude) may have further reduced the displacements.

REFERENCES

Alpan I. (1970). The geotechnical properties of soils. *Earth-Science Reviews* 6:5–49.

Atkinson J.H., and Sallfors G. (1991). Experimental determination of soil properties. *In Proc. 10th ECSMFE, Florence, Vol. 3, 915–956, 1991.*

Benz T. (2006). Small-Strain Stiffness of Soils and its Numerical Consequences. *PhD Thesis Stuttgart University*.

Brinkgreve R.B.J. (2008). PLAXIS 2D, Reference Manual, Version 9.0 PLAXIS b.v..

Callisto L., Rampello S., Calabresi G.. (2007). Scelta delle modalità costruttive e previsione del comportamento di uno scavo profondo a pianta circolare. *XXIII Convegno Nazionale di Geotecnica:* 169–176. Padova-Abano Terme 16–18 Maggio 2007

Ghionna, V.N., Mortara, G., Porcino D. (2006). Caratterizzazione e modellazione dei terreni per la previsione del comportamento delle opere geotecniche. *XXIII Convegno Nazionale di Geotecnica:* 11–44. Padova-Abano Terme 16–18 Maggio 2007.

Rampello S., Silvestri F. (1993). The stress-strain behavior of natural and reconstituted samples of two overconsolidated clays. *Proc. 1st Int. Symp. on Geotechnical Engineering of Hard Soils—Soft Rocks: 769–778*. Athens 1993, Balkema, Rotterdam, 1.

Rzhevsky V., Novik G., 1971. The Physics of Rocks. Moscow, MIR Publishers.

Schanz T., Vermeer P.A., Bonnier P.G. (1999). The Hardenimg soil model: Formulation and verification. *Beyond 2000 in Computational Geotechnics—10 Years of PLAXIS.* Balkema, Rotterdam, ISBN 90 5809 040 X.

Stokoe K.H. II, Hwang S.K., Lee J.H.K. Andrus R.D., (1995). Effects of various parameters on the stiffness and damping of soils at small to medium strains. *Proc. Advances in the Art of Testing Soils under cyclic loading conditions, ASCE, Convention*, Detroit.

Geotechnical Aspects of Underground Construction in Soft Ground – Viggiani (ed)
© 2012 Taylor & Francis Group, London, ISBN 978-0-415-68367-8

Simplified numerical method for tunnel design under seismic condition: Some examples about Istanbul Metro design, Kadikoy-Kartal Line

Giuseppe Maria Gaspari, Giovanni Quaglio & Vincenza Floria
Geodata Engineering SpA, Torino, Italy

ABSTRACT: Historically, underground facilities have experienced a lower rate of damage than surface structures. Nevertheless, some underground structures registered significant damages in recent large earthquakes; the resultant database which can be found in literature, together with the quite slight overburden of many stretches of the Istanbul new metro line, required a particular care on the verification of the vulnerability of the underground structures under severe seismic events.

This article describes briefly the main assessments on the approaches used by engineers in quantifying the seismic effect on an underground structure, both referring to deterministic either probabilistic methods. However, this study has the goal to propose a method that could be as more consistent as possible with the common procedures nowadays adopted to evaluate the effect of seismic motion on tunnels. In particular, as the complex geometry of most of the cross sections in Istanbul Metro underground structures is not simple enough to make proper use of the closed form solutions, a numerical method is recognized as the only one to assist the design process. However, a simple yet rational method of analysis for evaluating the ovaling effect was preferred than a complete coupled analysis, with an application of the time dependent acceleration spectrum, because the large number of different structures and geological conditions required to optimize the time cost of the procedure.

1 INTRODUCTION

Historical data usually report that underground facilities experienced a lower rate of damage than surface structures, thus leading to the assumption that tunnels, particularly the ones which lie deeper, can be affected by very little damage during a seismic shake, due to their vibration mode which is very close in terms of amplitude and frequency to that of the surrounding ground.

Nevertheless, some underground structures registered significant damages in recent large earthquake; the resultant database which can be found in literature, together with the quite slight overburden that many stretches of long underground structures can have, require a particular care on the verification of the vulnerability of the underground structures under severe seismic events.

2 ASSESSMENTS ON TUNNELS SEISMIC DESIGN

It is not common practice to consider seismic actions in tunneling project; usually only for very shallow (overburden minor than 6 m) underground structures the seismic actions are considered when performing the structural design. However, due to the high seismicity level of certain areas, as for instance the case of the densely urbanized area of Istanbul as showed in Figure 1, it is a requirement of the Municipality that all the final linings have to be designed to resist the seismic loads.

2.1 *Tunnels induced effects by earthquakes*

Tunnels and underground structures are usually affected by earthquakes in terms of transient ground motion and permanent ground deformation, which take place due to the shaking. As for transient

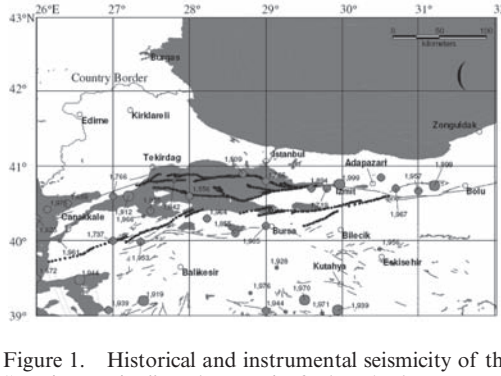

Figure 1. Historical and instrumental seismicity of the "Straits Region" and tectonic faults [Ambraseys and Finkel, 1991].

ground motion, it must be considered that especially velocity pulses of strong motion can develop shear and tensile strain that need to be checked against the strength of the tunnel and immersed tube. The principal types of transient ground motion are due to travelling body (P and S) waves and surface waves, especially Rayleigh waves in large sedimentary basins (Fig. 2). The principal causes of permanent ground displacement are faulting, tectonic uplift and subsidence, liquefaction and densification of loose granular deposits.

Tunnels and underground structures are mostly affected by ground settlement due to liquefaction, while lifelines crossing a fault plane subjected to normal faults promote tension. As a consequence, a tunnel crossing a lateral spread or landslide perpendicular to the general direction of soil movement is subjected to bending strain and extension. Transient ground motion induces relatively small levels of strain and deformation than the permanent ground deformations, so that they are usually not considered in the design process and in verifications.

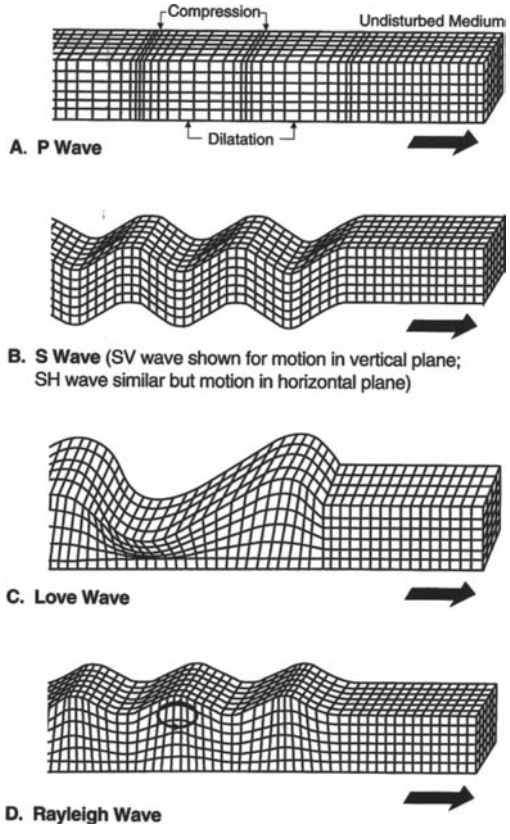

Figure 2. Ground response to seismic waves [Bolt, 1978].

The ground strain and the curvature due to wave propagation influence the response of the tunnels. The motion of the soil particle depends on the type of waves, but can always be resolved into a longitudinal and transverse component with respect to the tunnel and immersed tube axis. The propagation velocity of the body and surface waves along the alignment (apparent velocity of propagation) and the peak ground velocity are the two important parameters that control wavelength and amplitude. The maximum ground curvature will be equal to the second derivative of the transverse displacement with respect to distance and is controlled by the peak ground acceleration, transversal to the direction of wave propagation, and by the apparent velocity of propagation.

The main assumption which is widely accepted is that the response of the buried tunnels in earthquakes follows closely the deformation imposed on by the soil media. For small to moderate ground motion the tunnel strain can be taken equal to the ground strain. However, for large ground motion the tunnel or immersed tube strain is limited by the slippage that occurs at the pipe-soil interface.

2.2 *Seismic design criteria for tunnels*

Several studies documented earthquake damages to underground facilities: as an instance, Sharma and Judd (1991) collected qualitative data for 192 reported observations while Power et al. (1998) provided an extensive database with 217 case histories. Thus, in recent years, the earthquake resistant design criteria have been revised to incorporate performance-based design both for building and non-building structures. NEHRP (2003) Recommended Provisions presents criteria for the design and construction of new structures subject to earthquake ground motions in order to minimize the hazard to life and to increase the expected performance of structures having a substantial public hazard due to occupancy or use. For essential facilities, damage limitation criteria are stricter in order to better provide for continued functioning of the facility.

Depending on the performance criteria, limited structural and non-structural damage can be expected as a result of the "design ground motions". For ground motions in excess of the design levels, the intent of the Provisions is for the structure to have a very low likelihood of collapse. In order to provide for a uniform margin against collapse at the design ground motion, the ground motion hazards are defined in terms of Maximum Considered Earthquake (MCE) ground motion, described, statistically, at a probability of exceedance of 2 percent in 50 years (meaning a return period of about 2500 years). In regions where the seismic hazard

is typically controlled by large-magnitude events occurring on a limited number of well-defined fault systems (such as the Marmara Region) it is considered more appropriate to directly determine maximum considered earthquake ground motions based on the characteristic earthquakes of these defined faults and to compute the ground motion parameters through deterministic procedures.

2.3 *Applicability of current codes to underground constructions*

Although the current codes for the earthquake resistant design of transportation lifelines are not specifically applicable to the subway systems, their field of application can be extended to the evaluation of the risk basis for the assessment of design basis ground motion. In this respect, the dimensioning of the final lining of all the underground structures of Istanbul Metro project was done in conformity with the Eurocode 8 [CEN, 1994], that is often in strong agreement with the Japanese Code [JRA, 1996] and the USA Codes [AASHTO, 1996].

In all these codes, during "strong shaking", "some" degree of damage is allowed. The definition of "some" degree of damage generally implies flexural yielding, provided that no collapse takes place. Japanese Code expects elastic performance under the design earthquake, which may have a return period in the order of 75 years. A ductility check on this design is then made assuming a much larger earthquake with a return period of about 500 years. The Eurocode stipulates that the function shall be maintained, with appropriate reliability, after the design seismic event, which corresponds to a 475-year return period earthquake for bridges of average importance. Furthermore, in AASHTO Code the definition of "strong shaking" is already taken into account for the design earthquake with a 475 year return period. Although AASHTO does not explicitly require a two-level design, the new Caltrans/Applied Technology Council Criteria [Buckle, 1996] specify design for the "Functional Evaluation Earthquake" and the "Safety Evaluation Earthquake" corresponding, respectively to 100 and 1000 year return periods. Caltrans code essentially follows the ATC-32 [Improved Seismic Design Criteria for California Bridges, ATC 1996]. Finally, AGI Guidelines for geotechnical aspects of seismic design also mention (Silvestri and Simonelli, 2005) two levels (L1 and L2) for the definition of the design earthquake ground motions, respectively for probability of exceedence of 50% and 10% of the reference lifetime.

So that a second level of ground motion was considered, identifying a return period of about 2500 years as the strongest event ever happened in the region of the Straits.

3 ISTANBUL METRO SEISMIC DESIGN ASSUMPTIONS

For the seismic design of the Kadikoy-Kartal Mass Transportation Route two levels of ground motion were considered for earthquake resistance design purposes and will be presented in this chapter.

3.1 *Functional evaluation earthquake ground motion (S1)*

This ground motion refers to earthquakes that can reasonably affect the transportation route at any location during its lifetime. Considering the seismicity of the region and the importance of the tunnels, it will be prudent to assign a 50% probability of exceedance in 50 years. This ground motion level will also be checked with deterministic median (50 percentile) ground motions that would result from a Mw = 7.5 scenario earthquake occurring on the Main Marmara Fault, and the larger of the two assessments will be selected. Under exposure to this ground motion the transportation system will be fully operational (essentially linearly elastic performance).

3.2 *Safety evaluation earthquake ground motion (S2)*

This ground motion can be assessed either deterministically or probabilistically. The probabilistic ground motion for the safety evaluation typically has a long return period (approximately 2500 years), which corresponds to 2% probability of exceedance during 50 years. This level of ground motion is associated with the Maximum Credible Earthquake (MCE) is defined as the largest earthquake, that is capable of occurring along an earthquake fault, based on current geologic information, which is quite similar, if not identical to the NEHRP (2003) definition. Under Safety Evaluation Earthquake only repairable damage with no danger to life is allowed.

3.3 *Expected performance levels under design ground motions*

The performance levels expected under S1 and S2 ground motions are defined below:

	Expected performance	
Earthquake level	Functionality	Damage
S1	Continuous	Minimal
S2	Limited	Considerable

"Continuous Functionality" performance criterion refers to the uninterrupted service of the

structure immediately after an earthquake. On the other hand the "Limited Functionality" performance criterion will guarantee only limited use a few days after an earthquake. Full functionality is aimed to be obtained in at least a few months. The "Minimal" damage criterion refers to the nearly linearly-elastic response. To meet the performance criteria required under the S1 earthquake the "Response Modification Factor" should not exceed 2 [Caltrans, 1999]. The "Repairable" Damages should be repaired with minimum effects on functionality. The "Considerable" damages should not cause total collapse and loss of life.

These S1 and S2 levels of ground motion were originally quantified in frequency domain using the standardized response spectral shape of NEHRP, 2003 or IBC, 2006 in terms of the short-period (0.2 s) and 1 s-period spectral amplitudes at NEHRP B/C site class boundary. The site dependent spectra was then generated using the NEHRP Site Class definitions and the associated spectral site amplification factors [refer to *"Preliminary determination of the design basis ground motions for the Istanbul Kadikoy—Kartal railed mass transport system"*, Bogazici University, Kandilli Observatiry and Earthquake Research institute Department of Earthquake Engineering].

3.4 *Ground deformation approach*

The general procedure for seismic design of tunnel structures is based primarily on the ground deformation approach. During earthquakes, tunnel structures are assumed to move together with the surrounding soil media. The structures, therefore, are designed to accommodate the deformations imposed by the ground. However, the effects of soil structure interaction can play an important role in the seismic response of tunnel or over buried structures, particularly when the structure is surrounded by soft media (such as the case for an immersed tunnel) and therefore should be considered in the analysis. Furthermore, for tunnel structures with considerable structural discontinuities (such as joints between tunnel segments and between the tunnel and the station structure) detailed evaluations have to be given to the effects of these discontinuities on the earthquake resistance of the tunnel.

3.4.1 *Spatially varying ground motion time histories*

Due to the length of the structures, the effect of spatial variations of ground motions is an important factor to be considered for the proposed tunnel structures. The wave-passage effect results from different arrivals of seismic waves at different parts of the structure and can be taken into account by assuming a time lag of the ground motion time histories between any two locations along the tunnel alignment.

3.4.2 *Ground failure*

Stability of ground surrounding the tunnel structures shall be considered in the design. The surrounding ground includes natural and backfill earth mass located within a zone that may influence the performance of the tunnel during and after earthquakes. For the Kadikoy-Kartal Mass transportation Route, the ground failure as a result of seismic shaking may include liquefaction and slope stability (landslides occurrence was often verified with pseudo-static methods).

3.4.3 *Site response analysis*

In all cases the earthquake excitation can be represented by a vertically propagating horizontally polarized shear wave incident from the engineering bedrock (NEHRP B/C boundary).

An underground tunnel structure undergoes three primary modes of deformation during seismic shaking (Fig. 3):

- ovaling deformation;
- axial deformation;
- curvature deformation.

The ovaling deformation is caused primarily by seismic waves propagating perpendicular to the tunnel longitudinal axis. The axial and curvature deformations are induced by components of seismic waves that propagate along the longitudinal axis and/or by spatially varying ground motions resulting from local soil/site effects. Wave propagation strain tend to be most pronounced at the junctions of dissimilar buried structures (such as tunnel connecting with a building) or at the interfaces of different geological materials (such as passing from rock to soft soil).

The approach used to examine the effect of the seismic actions on the tunnel stability is the free-field

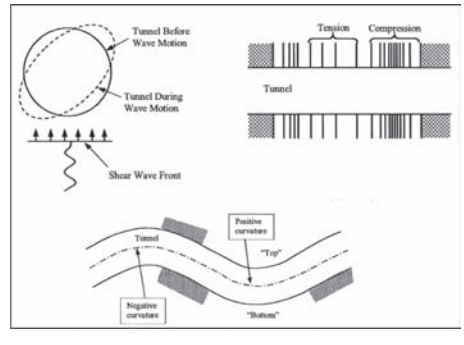

Figure 3. Primary deformation modes of tunnels due to seismic shaking [Owen and Scholl, 1981].

shear deformation method [Wang, 1993, Power et al. 1998; Hashash et al. 2001], which assumes that the deformation of the structure should conform to the deformation of the soil in the free-field under the design earthquakes (S1 and S2).

3.5 *Application of the free-field shear deformation method*

The methodology of the seismic design has to incorporate the additional loading imposed by ground shaking and deformation. In general seismic design, loads for tunnel are characterized in terms of the deformations and strain imposed on the structure by the surrounding ground based on their interaction.

To describe the procedure used to compute deformations and forces induced by this interaction, two design approaches have been introduced:

- Free-field deformation approach [Wang 1996; Power et al. 1998; Hashash et al. 2001]
- Soil–structure interaction approach

In free-field deformation approach, the ground deformation caused by seismic waves is assumed to occur in the absence of structure or excavation. These deformations ignore the interaction between the underground structure and the surrounding ground, but can provide a first-order estimate of the anticipated deformation of the structure. The closed form elastic solution results in combined axial and curvature deformations, assuming the tunnel as an elastic beam and maximum strain at critical incidence angle. The advantages and disadvantages of this method have been reported by Wang (1993).

The presence of an underground structure modifies the free-field ground deformations; so a method based on soil-structure interaction is required. This solution uses the beam-on-elastic foundation approach that is used to model (quasi-static) soil-structure interaction effects. Under seismic loading, the cross-section of a tunnel experiences axial bending and shear-strain due to free-field axial, curvature,

The closed form solutions for estimating ground-structure interaction for tunnels are generally based on the assumptions that:

- The shape of the tunnel is circular,
- The ground is an infinite, elastic, homogeneous, isotropic medium,
- The circular lining is generally an elastic, thin walled tube under plane strain conditions,
- Full-slip or no-slip conditions exist along the interface between the ground and the lining,
- Loading conditions are to be simulated as external loading (overpressure loading) or excavation loading.

3.6 *Evaluation of the maximum shear deformation in free field conditions*

As could be evaluated in previous paragraph, there are some limitations in the application of the free-field method, related to the complex geometry of tunnel sections. This section is deputed to describe the approach adopted for the simulation of the seismic effects taking the advantage of using numerical analysis in order to overcome the listed limitations.

The applied methodology foresees the application of a deformation to the ground so as to deform the underground structures and to obtain the stresses acting in the final lining in case of a seismic event.

As for the aforementioned approach, from the value of the short period spectral acceleration S_S (according to the mentioned Seismic Report of Bogazici University) it is possible to get the Pick Ground Acceleration (PGA, here a_{gR}) by the equation (1):

$$a_{gR} = 40\%\ S_s \tag{1}$$

which assumes that the deformation of the structure should conform to the deformation of the soil in the free-field under the design earthquakes (S1 and S2).

The design basis ground motion parameters to be used in the earthquake resistant design of the tunnels will be stipulated as follow:

- the S_s values used into the analyses for the S1 (Functional Evaluation) Level earthquake were obtained from "S_S deterministic Median" values for each borehole or station location.
- The S_S values used into the analyses for the S2 (Safety Evaluation) Level earthquake were obtained from "S_S—2475 years" values for each borehole or station location.

The site-specific Pick-Ground-Acceleration ($a_{max,s}$) is given by equation (2), where S is the soil factor, defined in terms of the ground type [EC 8]:

$$a_{\max,s} = S \cdot a_{gR} \tag{2}$$

The value of S, suggested in Eurocode 8, is based on the types of elastic response spectra and its values are recorded in specific depending on the earthquake moment magnitude scale: $M_w < 5.5$ or $M_w > 5.5$.

In order to consider the depth of the tunnels, a simplified procedure [Hashash et al. 2001] was considered to define the pick acceleration at the depth of the tunnel $a_{z,max}$: it consists in the determination of a reduction coefficient C for the peak acceleration on the surface depending on the depth of the tunnel (Table 1) as for equation (3):

$$a_{z,\max} = C \cdot a_{\max,s} \tag{3}$$

where $a_{z,max}$ is the pick acceleration at the depth of the tunnel.

Table 1. Ratios of ground motion (C) at depth to motion at ground surface [Power et al. 1996].

Tunnel depth (m)	Ratio of ground motion at tunnel depth to motion at ground surface
≤6	1.0
6–15	0.9
15–30	0.8
>30	0.7

The value of $a_{z,max}$ is used to determine the γ_{max} (maximum shear deformation in free-field condition) from the peak ground velocity V_s, which is a function of earthquake magnitude and distance from the seismic source, as shown in equations (4) and (5):

$$\gamma_{\max} = \frac{V_s}{C_s} \tag{4}$$

$$V_s = k \cdot a_{z,\max} \tag{5}$$

where k is the ratio of peak ground velocity to peak ground acceleration; C_s is the apparent propagation velocity of S-wave and it was assumed (along the entire alignment) equal to 2 km/s, according with the prescription given by Prof. Dr. Mustafa Erdik.

The apparent propagation velocity of S-wave (C_s), in fact, is not necessarily equal to the real propagation velocity; in fact, several authors [O'Rourke & Liu, 1999; Power et al. 1996; Paolucci & Pitilakis, 2007] have suggested values between 1 and 5 km/s.

The value of γ_{max} corresponds to the maximum horizontal displacement imposed in the numerical model, calculated as per equation (6).

$$\Delta x_{\max} = \gamma_{\max}\left(\frac{h_{\mathrm{mod}}}{2}\right) \tag{6}$$

The horizontal displacement Δx_{max} is obtained applying to the sides of the model punctual forces in order to generate a pure shear deformation of the entire model (Fig. 4) and consequently the ovaling effect of the excavation boundary, as shown in Figure 5. Results will be deeply discussed in following paragraphs, but it is already possible to appreciate how the deformed shape is similar to the theoretical approach shown in Figure 7.

Through this methodology, it was possible to obtain the stresses, due to the ovaling deformations, acting in the underground final structures for the cases of the design earthquakes. In order to verify also axial and curvature deformation (usually these effects are secondary in respect of the ovaling ones), it was accepted to use the analytical closed-form solution [Barla et al. 2008]. The estimated deformations allowed to define the thickness of the movement joints with the specific function to absorb the seismic deformations (Fig. 6).

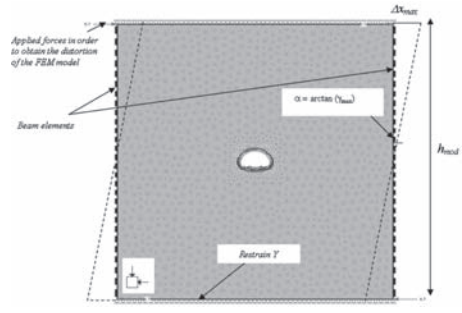

Figure 4. Numerical model for the application of the free-field shear deformations method.

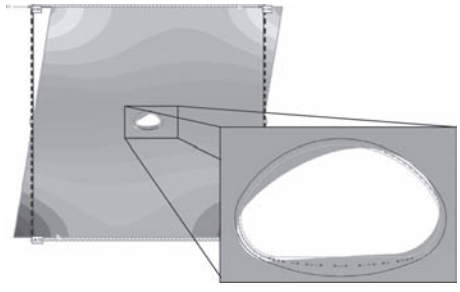

Figure 5. Ovaling effect of the excavation boundary.

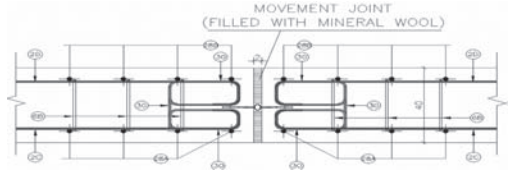

Figure 6. A typical movement joint, filled with mineral wool, between final lining blocks.

3.7 *FEM analysis of the ovaling phenomenon*

A series of computational analyses using finite element code (Phase2—v6, RocScience) were performed in order to verify the proposed procedure in the previous section and to properly calibrate the model, so to get same results for a circular shaped tunnel as from simplified methods with closed form solutions [Barla et al. 1986; Wang, 1993; Bobet, 2003; Corigliano et al. 2008].

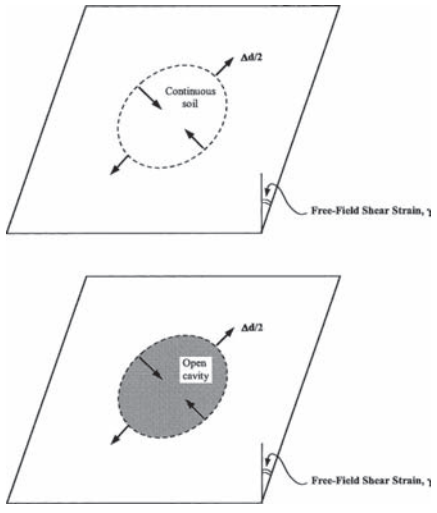

Figure 7. Free-field shear distortion of perforated and non-perforated ground, circular shape [Wang, 1993].

The assumptions made for these analyses include the following:

- Plane strain model with no gravity loading was performed.
- No water pressure and no flow boundary conditions were assumed in the model.
- Seismic shear wave loading is simulated by pure shear conditions, through a "trial & error procedure", by applying horizontal line-forces to the upper and lower external boundaries of the model, thus checking whether the obtained horizontal displacement Δx_{max} was the desired one or further analyses are required to achieve it.

The Authors verified that the direct application of the displacement field to the mesh rather than a force distribution could not allow a proper evaluation of the real effects in terms of stresses on the tunnel lining.

- In order to make possible the rigid distortion of the model and to create a pure shear condition, high strength liners were modeled at the vertical external borders and a hinge was created on both sides at an height of h/2. Hinges were introduced in order to create a proper restraint that can avoid numerical errors due to eventual fictitious horizontal translations.
- As the geometry of the cross sections (particularly of the switches, exemplified in this article) is not regular, no advantage of the anti-symmetric loading conditions could be taken, thus the entire lining/ground system was analyzed.
- Lining was modeled by a series of continuous flexural beam elements of linear elasticity through the "Equivalent Axis Beam Method". The hypothesis of an elastic dominion for the structure even in the case of the S2 seismic condition is a conservative way to take into account the difficult evaluation of the activation and evolution of plastic hinges.
- Due to its high stiffness, subsoil layers were modeled as a linear elastic homogeneous and isotropic material.
- No-slip condition along the lining-ground interface is assumed as it is recognized the most suitable for rock formations and for a proper simulation of waterproofing.
- Mechanical parameters implemented in the model were derived directly from the information given by field tests and laboratory studies on the specimens taken from the borehole: unfortunately, specific values from dynamic tests could be obtained along the whole alignment, thus a number of correlations found in literature were considered and compared: as for the elastic modulus, Stacy correlation was adopted, a ratio $E_{dyn}/E_{static} = 2$ was used, with: E_{dyn} = dynamic modulus of the equivalent material used for numerical analyses and E_{static} = elastic Young modulus measured with site testing (pressuremeter) on the rock mass.

3.8 *Dimensioning and verifications of the final lining*

The numerical analyses have been chosen to dimension the final lining in static and seismic conditions with and without water pressure.

In order to verify the final lining under static and seismic load conditions (with and without water pressure) different loading combinations have been investigated through FEM and structural numerical simulations, with the hyperstatic reaction method.

Three typologies of numerical analyses have been performed, as shown in Table 2. It must be

Table 2. Numerical analysis typologies.

Analysis	Description	Induced stresses
A	FEM analysis in static condition without water pressure	S(g)
B	FEM analysis in static condition with water pressure	S(g) + S(w)
C	Pseudo-static FEM Analysis (free field method—ovaling effect) without water pressure	ΔS(g)

S(g): Stress function of the field stress; S(w): Stress function of the water pressure; ΔS(g): Increase of stress function of the field stress.

underlined that analysis C has been carried out with two different seismic conditions (called S1 and S2).

Table 3 shows the six different loading combinations based on the previously mentioned analysis. In the seismic conditions, the internal forces obtained from A (or B) simulations have been summed to the internal forces obtained from C + S1 (or C + S2) analysis, as for the common known method of superposition of the effects of the actions.

The structural verifications are performed according to EN 1992 [Eurocode 2] for Ultimate Limit State (U.L.S.) and Serviceability Limit State (S.L.S.), except for the seismic case in which this last one is not required. The structural analyses were performed in order to demonstrate the final lining adequateness in terms of geometry, thickness and reinforcement.

3.8.1 *Structural verification for ultimate limit state (U.L.S.)*

As for the U.L.S. verifications, for the final lining verification α, that is a factor taking into account for the effects of long duration loads, is considered equal to 0.85 [EC2, paragraph 3.1.6].

The magnitudes of the bending moment, axial force, and the shear force were determined by numerical analysis after applying the pounded water load in order to simulate the long term conditions. The axial force, bending moment and shear force values, which were obtained directly from the numerical analyses, were multiplied by a factor γ_G, as shown in equations (7):

$$N_d = \gamma_G \cdot N_k \quad M_d = \gamma_G \cdot M_k \quad V_d = \gamma_G \cdot V_k \tag{7}$$

For the bending moment—axial force verification, the resistance envelope for the final lining is obtained according with formulations (8) and (9):

$$f_{cd} = \frac{\alpha \cdot 083 \cdot R_{ck}}{\gamma_c} = \frac{\alpha \cdot f_{ck}}{\gamma_c} \tag{8}$$

$$f_{yd} = \frac{f_{yk}}{\gamma_s} \tag{9}$$

where:
γ_c is a resistance reduction factor for the concrete
γ_s is a resistance reduction factor for the steel

The factors for actions and resistance depending on the condition considered: Static, Seismic S1 or Seismic S2.

Refer to Table 4 in order to review a summary of the considered input data for the S.L.U. verifications and all the corresponding adopted coefficients.

3.8.2 *Structural verification for serviceability limit state (S.L.S.)*

For the S.L.S., the structural analyses consist in verifying that the width of the crack w is less than 0.3 mm. In the same way the maximum stress

Table 3. Loading combinations.

	Static condition	Seismic condition S1	Seismic condition S2
Dry condition	A	A + C_S1	A + C_S2
Saturated conditions	B	B + C_S1	B + C_S2

Table 4. Summary of the considered input data and factors for the ultimate limit state verifications.

	Bending moment—axial force verification			Shear force verification		
		Seismic condition			Seismic condition	
	Static condition	S1 PGA_475	S2 PGA_2475	Static condition	S1 PGA_475	S2 PGA_2475
γ_G	1.35	1.0	1.0	1.35	1.0	1.0
γ_c	1.5	1.5	1.0	1.5	1.5	1.0
γ_s	1.15	1.15	1.0	1.15	1.15	1.0

PGA_475 = peak ground acceleration refers to average return period of 475 years; PGA_2475 = peak ground acceleration refers to average return period of 2475 years; γG = amplification factor of loads [EC1, paragraph 9.4.3]; γc = resistance reduction factor for the concrete [EC2, paragraph 2.4.2.4]; γs = resistance reduction factor for the steel [EC2, paragraph 2.4.2.4].

must be always lower than the allowable stress for concrete and steel.

In detail, the maximum compressive stress for the concrete and for the steel is obtained as:

$f_{c,SLS} = 0.6 \cdot f_{ck}$ [EC2, paragraph 7.2]
$f_{y,SLS} = 0.8 \cdot f_{yk}$ [EC2, paragraph 7.2]

For the seismic condition, the S.L.S. verification is not required, so that it will not be shown in this article, but it was necessary to verify the Static conditions of the final lining.

4 APPLICATION CASE: SHAFT S12

This chapter deals with the case study of Shaft S12, one of the biggest shafts of the entire line Kadikoy-Kartal of Istanbul Metro. Its function is double, both for temporary access for workers and equipment in the tunnels and for definitive holding of the lifts and ventilation to access Kucukyali Station. Because of this reason, a proper evaluation and dimensioning of the final lining was necessary to be delivered to the Engineer, including seismic verifications as for the aforementioned concern to this load condition by the Municipal Authority.

Despite the irregular geometry, showed in Figure 8 in an axonometric view corresponding to the interception with the running tunnel (section A2.2), it was chosen as typological by the Authors, because it is really representative of the typical condition of the underground structures in Istanbul, where the highly urbanized context, summed to geological and hydro-geological difficulties, produces necessarily the need for an integrated design, able to answer to every problem and to modify itself elastically.

4.1 *Construction sequences for final lining*

The main construction sequences of the shaft final lining are summarized as:

- intersection tunnel—shaft: invert water proofing;
- intersection between running tunnel and shaft: invert reinforced concrete cast in place;
- shaft: invert reinforced concrete cast in place;
- intersection between running tunnel and shaft: sidewalls and crown water proofing;
- intersection tunnel—shaft: sidewalls and crown reinforced concrete cast in place;
- shaft: water proofing;
- shaft: final lining cast in place.

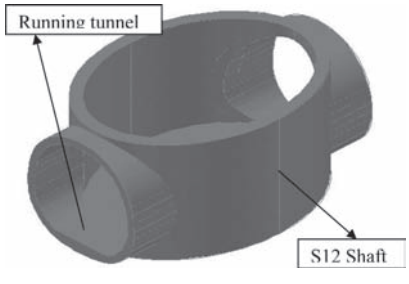

Figure 8. 3D view of Shaft S12 intercepting running tunnel.

4.2 *Static analyses*

The static study of the shafts was achieved with 2D elastic-plastic FEM analyses. In particular, the maximum loaded horizontal section was analyzed.

The 2D, elastic-plastic, plane strain FEM analyses were performed with the following stages:

1. Initial homogeneous and isotropic field stress.
2. Simulation of the face excavation through a reduction of the Young modulus according to the "Stiffness reduction method";
3. Installation of the primary support (shotcrete and rock bolts);
4. Removal of the primary rock support system and simulation of the final lining;
5. Reduction of the ground cohesion and stiffness by as much as 50% (in order to consider the long term geomechanical characteristics reduction). In the circular shaft an additional load equal to the 10% of the pressure on the final lining has been added in order to simulate an anisotropic load condition.

4.3 *Pseudo-static analyses*

The passage of earthquake waves through the soil/rock causes four distinct deformations patterns of the shaft opening. These are: (1) longitudinal or axial strain which are uniform over the sections, (2) shear strain acting on horizontal sections of the shaft, (3) flexural strain resulting from bending of the shaft and (4) hoop strain arising either from the influence of axial strain as described by Poisson's ratio or from ovaling deformations (see Fig. 9).

Two main assumptions have been considered in the seismic design of shafts:

1. the shaft lining deforms in accordance with the surrounding ground;
2. compression (P) and shear (S_H and S_V) waves are assumed to propagate in a direction parallel to the axis of the shaft.

Based on these considerations, on the geomechanical parameters and on the specific construction procedures, the most impacting effects on the final lining of the shaft are due to the free-field shear strain acting on the horizontal sections creating ovaling deformations on the final lining.

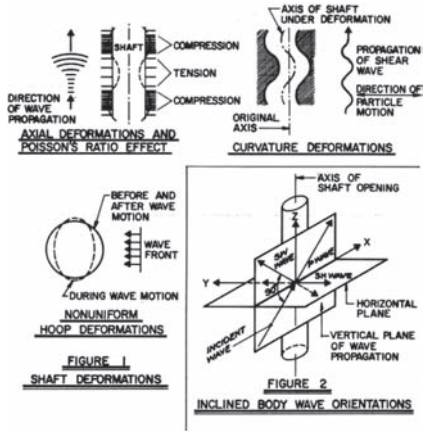

Figure 9. Seismic waves and consequences on vertical shafts.

4.4 *Seismic analyses model*

For Shaft S12 final structures a seismic resistant design was performed, giving to the structures the requested safety requirements. Referring to the methodology illustrated in Section 3, the data characterizing the seismic design are reported in following table:

Earthquake level	S1	S2
S_s [g]	0.607	1.357
a_{gr} [g]	0.243	0.543
$a_{max,s}$ [g]	0.243	0.543
a_z [g]	0.194	0.434
V_s [m/s]	0.188	0.421
C_s [m/s]	2000	2000
γ_{max} [–]	0.0000942	0.000211
Δ_{xmax} [m]	0.0066	0.0147

Many numerical analyses were carried out in order to verify and compare the stresses, normal forces and bending moments acting in the shaft final lining according with the seismic design. Three main models were selected in order to check the opportunity of adopting the aforementioned method and all of them had the same exact dimensions and mesh refinement as the FEM static model showed in Figures 10 & 11.

The adopted methods only differ for the way the deformation defined in Section 3 is applied to the model. They can be summarized as following:

1. Δ_{xmax} direct application on the top and bottom of the model to the extreme nodes (Fig. 12);
2. pure shear deformation of the model obtained through vertices displacement imposition (Fig. 13);

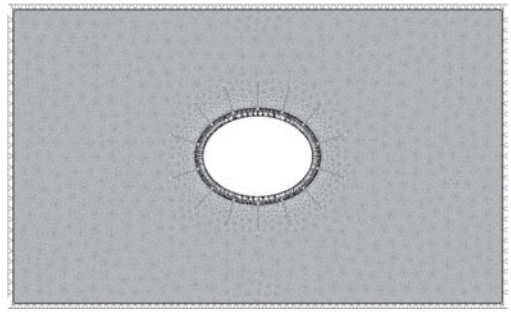

Figure 10. FEM numerical model for static analysis.

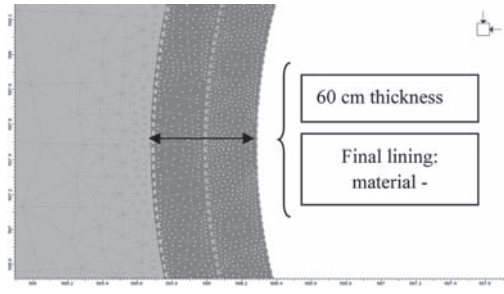

Figure 11. Detail of the mesh refinement in the Phase2 model.

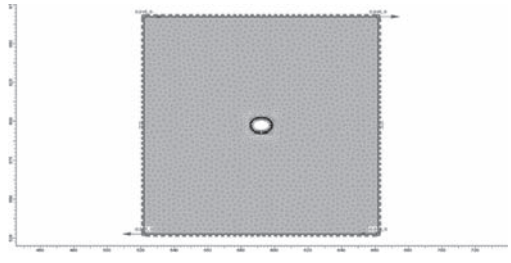

Figure 12. Numerical analysis through method 1.

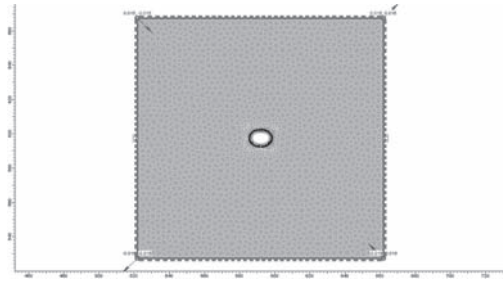

Figure 13. Numerical analysis through method 2.

3. iterative process to determine the external forces to be applied to the external boundaries in order to obtain the prescribed horizontal displacement.

This last one will be demonstrated in following chapter as the most appropriate one from an engineering point of view.

4.5 *Seismic analyses results*

In subsequent figures the results of numerical analysis are shown, in order to compare the three methods: as previously anticipated, the third method is the most suitable, as the displacements are not excessively affected by secondary motions which are not proper of a pure shear (as shown in Fig. 14).

Furthermore, respect to the second method, the lower values of normal forces registered and contemporary similar results in terms of bending moments, lead to the conclusion that the verification would generally be on the side of safety in the third method, so that this one was adopted for dimensioning steel bars. In details, Figure 16 represents axial force (N)—positive values correspond to compressive forces-, bending moment (M) and shear forces (V) in the final lining for the static case (without water—as instances—A), while Figures 17–19 for both seismic case S1 and S2, and comparing the three methods for the three defined parameters. Those last figures show the results of the analyses combined as superposition of effect of the seismic with the static stresses (always with no presence of water). It can be noticed how the effects of an earthquake with a larger time of occurrence can be almost the double in terms of forces and moments.

4.6 *Final lining dimensioning*

All the load combinations (static and seismic, with and without water load) were verified and the reinforced concrete was dimensioned according with

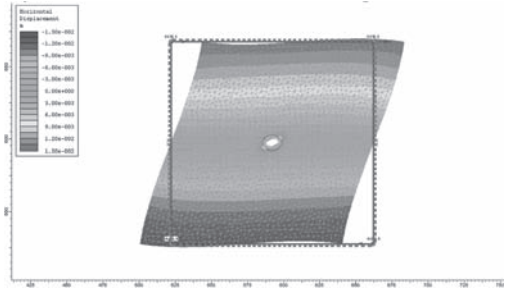

Figure 14. Results in terms of horizontal displacements in deformed shape with method 1.

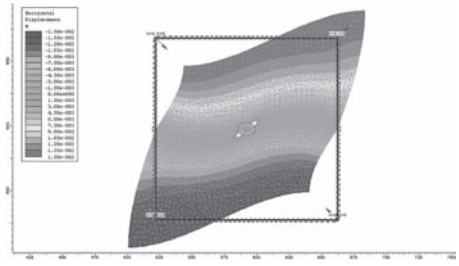

Figure 15. Results in terms of horizontal displacements in deformed shape with method 2.

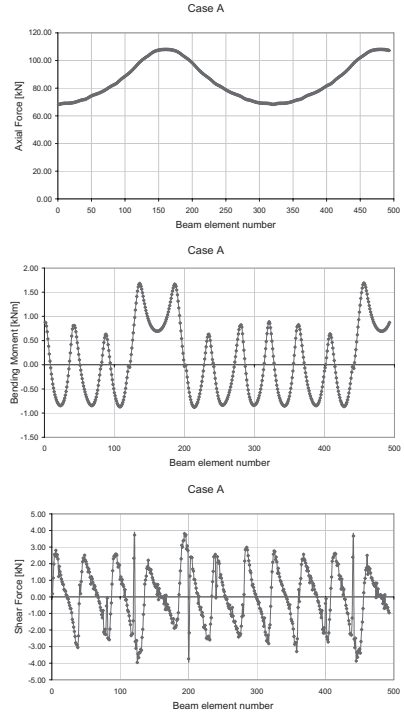

Figure 16. Static results as for Normal Forces, Bending Moments and Shear Forces for case A in shaft S12.

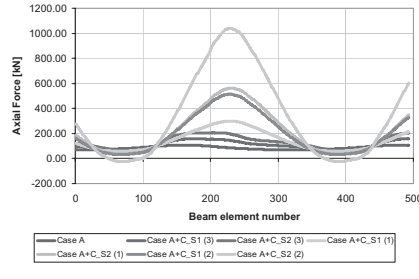

Figure 17. Comparison between static and seismic results as for Normal Forces obtained with the three applied methodologies.

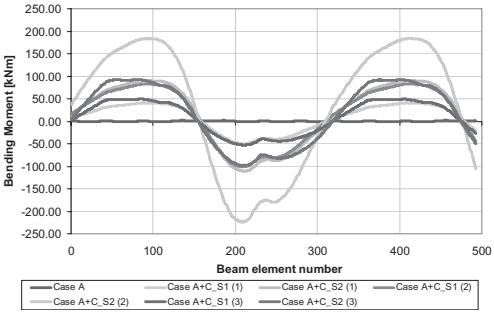

Figure 18. Comparison between static and seismic results as for Bending Moments obtained with the three applied methods.

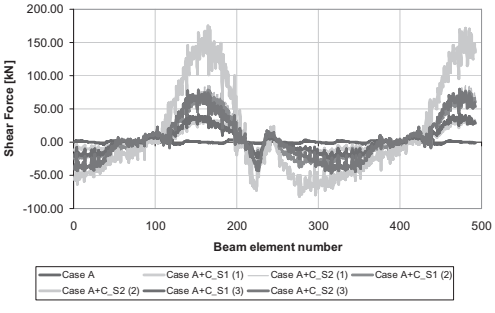

Figure 19. Comparison between static and seismic results as for Shear Forces obtained with the three applied methodologies.

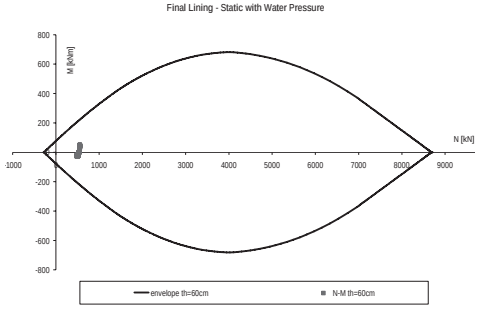

Figure 20. ULS—MN verification for final lining—static case.

the prescription given by Eurocodes and Turkish Standards. Figures 20–22 finally, only present examples of the ULS verification of the final lining of the shaft, joining together all the different beams in which the lining was modeled. In those cases water was taken into account.

In conclusion, according to the contents of the article, in the last presented figures there is only the "axial-force/bending moment" verifications

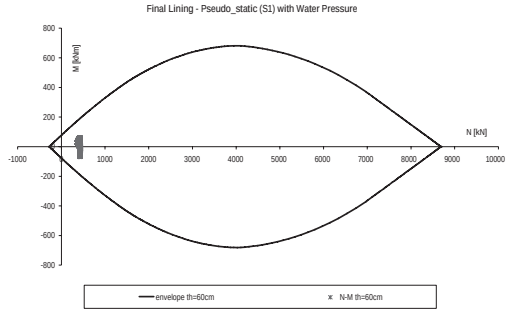

Figure 21. ULS—MN verification for final lining—seismic S1 case with the same reinforcement dimensioned for static case.

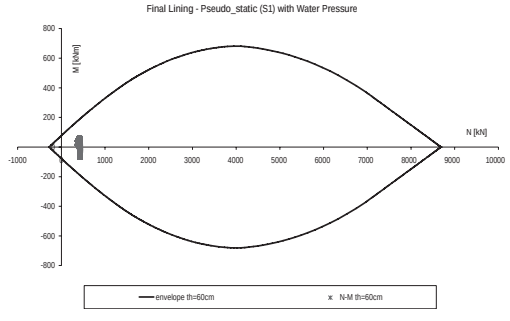

Figure 22. ULS—MN verification for final lining—seismic S1 case with the same reinforcement dimensioned for static case.

carried out for the load combination with water pressure, in both the seismic cases S1 and S2. As for the "shear verification", instead, the maximum shear force between the static and seismic conditions had been verified in each section of the final lining. From the result of structural analyses it is possible to define the quantity of reinforcing steel for the concrete sections of the final lining.

5 FUTURE DEVELOPMENTS

One possible development of the proposed method is to dispose three-dimensional modeling in order to take into account the effect of geological discontinuities along the tunnel longitudinal direction which can affect the stress and deformation in the lining.

In fact, just a simple difference in the value of the deformation modulus of the ground could sensibly change the seismic wave velocity in different stretches of the tunnel alignment. This would cause, in reference with the previously reported

formulas, a differential shear deformation expected in consecutive blocks of the lining, thus causing an increase of stress on the concrete related to differential movements of successive portions of the lining.

Usually this effect is avoided through the design of appropriate structural and movement joints, very often filled with very deformable but impermeable material (such as fiberglass wool or similar), that allow a massive reduction of the stresses if they are properly conceived and installed at the correct distance one from the others.

Nevertheless, it is important to verify that each block is not affected by those differential shear and torsional deformations, but this would require an accurate knowledge of the geology at each meter of the alignment in order to make effective the three-dimensional analyses.

6 CONCLUSIONS

Istanbul Metro has been a successful experience of design-construction of large-scale infrastructure projects in a complex and dense urban context. The challenge of a seismic-resistant design was obliged by the specific critical location of the city, located in proximity of active faults.

In the past, seismic design of tunnel structures received considerably less attention than that of surface structures, perhaps because of the conception about the safety of most underground structures.

Despite this understanding, in the last few years, increasing interest is given to the seismic effect of underground structures, but a significant disparity exists among engineers in design philosophy, loading criteria and methods of analysis. The hope is that of coming as soon as possible to a codification of this subject as well as it have been happening in the field of the seismic effects on over surface structures.

REFERENCES

AMBRASEYS N.N. and FINKEL C.F. (1991)—*Long-term seismicity of Istanbul and of the Marmara Sea region*. Terra Nova, III, 527–539.

BARLA G., BARLA M., PERINO A., PRINIRPITO M. (2008)—*Soluzioni analitiche e numeriche nella progettazione sismica delle opere in sotterraneo*. Proceedings of the XII MIR, pp 335–357, Torino.

BUCKLE I. A. (1996)—*Overview of Seismic Design Methods for Bridges in Different Countries and Future Directions*. Paper No. 2113, 11 WCEE, Acapulco, Mexico.

HASHAHSH Y.M.A., HOOK J.J., SCHMIDT B., YAO J.I.C., (2001)—*Seismic design and Analysis of underground structure*. Tunnelling and Underground space Technology, Vol. XVI, No.4, pp147–293, San Francisco, CA, USA.

KAWASHIMA K., (2000)—*Seismic Design of Underground Structures in Soft Ground*. Geotechnical Aspects of Underground Construction in Soft Ground: Proceedings of International Symposium on Geotechnical Aspects of Underground Construction in Soft Ground, IS-Tokyo'99, Japan, 19–21 July 1996, Balkema, Netherlands.

PAOLUCCI R., PITIKALIS K., (2007)—*Seismic risk assessment of underground structures under transient ground deformation*. In Pitikalis, K. (editor). Earthquake Geotechnical Engineering. Chapter 18, pp 433–459. Springer-Vienna.

POWER M.S., ROSIDI D., KANESHIRO J., (1996)—*Strawman: screening, evaluation, and retrofit design of tunnels. Report Draft.* Vol. III, National Center for Earthquake Engineering Research, Buffalo, New York.

WANG J.N., (1993) - *Seismic design of tunnel—A simple state of the art design approach*. Parson Brinckerhoff Quade & Douglas, Inc., New York, Monograph 7.

This page intentionally left blank

Geotechnical Aspects of Underground Construction in Soft Ground – Viggiani (ed)
© 2012 Taylor & Francis Group, London, ISBN 978-0-415-68367-8

FEM analyses of deep excavations and earth retaining structures in soft clay

Takao Kono & Yoshimasa Shigeno
Takenaka Corporation, Chiba, Japan

ABSTRACT: In recent years, an increasing amount of excavation work has come close to adjacent structures. To reduce the effects of excavations on adjacent structures, it is becoming increasingly important to predict the displacement of earth retaining walls and the retained soil movement. 2D finite element analyses were performed to simulate the behavior of an earth retaining wall. In this FEM simulation, a Mohr-Coulomb failure model was adopted to consider soil stiffness dependence on shear strain. The influence of the initial Young's modulus and the soil stiffness dependence on confining pressure were examined. FEM calculation results were compared with the monitoring results of excavations in soft clay. Excavation depth was 17.0 m and the retaining wall was soil-cement with H-section steel. Excavation was done using a total of four levels of RC slab struts and the top down method. A good agreement was found with displacements of the retaining wall between the calculation results and observation datas using the deformation modulus at small strain E_o estimated from the results of PS logging. The analysis was effective in predicting the vertical displacement of the retained soil.

1 INTRODUCTION

Recently, excavations that are adjacent to railways and the roads have been increasing in cities. In the adjacent excavations, it is important to control the influence on the adjacent structures as much as possible. It is becoming increasingly important to estimate not only the lateral displacement of earth retaining walls but also the movement of the ground behind the retaining walls.

There are two basic approaches to predict the ground movements caused by excavation. Peck (1969), Aoki et al. (2000) and Moorman (2004) proposed prediction of settlement behind retaining walls based on measurement results. Roscoe (1970) and Aoki et al. (1990) proposed prediction forms of settlement assuming a slip surface behind the retaining wall. The method based on actual measurement results is a simple empirical method, and effective to understand the amount of settlement qualitatively. However, it is difficult to evaluate the influence on the adjacent structure accurately by this method. Moreover, if structures exist behind a retaining wall, it is very difficult to define a slip surface in the soil, so the method of defining a slip surface in soil is not suitable for displacement forecasts of the adjacent structure.

In recent years, FEM analyses are used to estimate the displacement of the adjacent structure. In the FEM analysis, there are two methods for analyzing. One is a step by step analysis, and another is applying displacements as a boundary condition. In Japan, to predict the behavior of adjacent structures, the FEM analysis applying displacement is generally used (AIJ 2006). With the FEM analysis applying displacement, the prediction accuracy is high because it uses lateral displacement of the wall calculated by beam-spring analysis. However, the influence of the adjacent structure cannot be considered when only the wall displacement is calculated (AIJ 2006).

In this paper, a step by step FEM analysis is performed to predict the wall displacement and ground movement due to excavation in soft ground. In the analysis, the elasto-plastic Mohr-Coulomb failure model is used to examine the influence of the constitutive model. Moreover, to examine the influence of the deformation modulus used for the analysis, the deformation modulus is set from V_S derived from *PS* logging or *N* value and cohesion *c*.

2 OVERVIEW OF EXCAVATIONS AND GROUND CONDITIONS

2.1 *Excavations*

Figures 1 and 2 shows a plan and section of the excavation and soil profile of the project. The building had multiple basements, and was eight stories above ground. The project excavation covered an area of 135 m × 50 m, at a depth of GL – 17.0 m. There were office buildings and shore protection next to the retaining wall, so the wall displacement caused by excavation had to be strictly controlled.

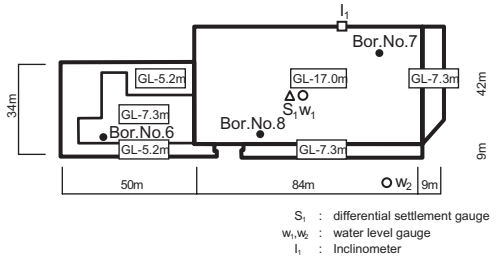

Figure 1. Plan of excavation.

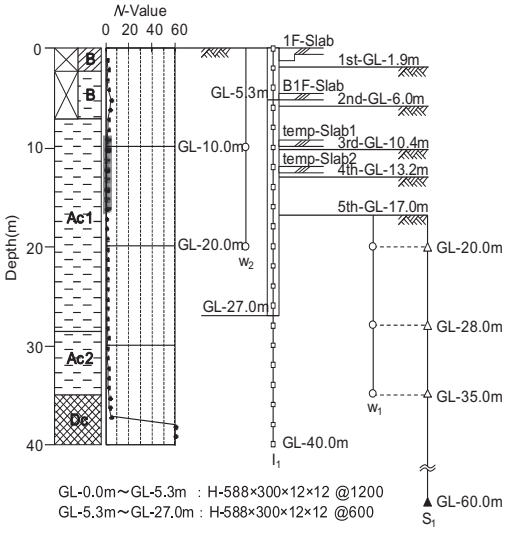

Figure 2. Section of excavation.

Excavation was done using a total of four levels of supporting struts, including two basement floors and two temporary RC slabs. The top down method was used to build these supports.

The retaining wall comprised soil cement up to 28 m, reinforced with H-section steel (H588 × 300) of 27 m length. The pitch of the H-section steel down to GL – 5 m was 1200 mm, because the lateral pressure that acted on the wall was lower close to ground level, and from GL – 5 m to GL – 27 m was 600 mm. Ground water was pumped from dewatering wells.

Table 1 shows the excavation monitoring equipment and instrument locations are shown Figures 1 and 2. The lateral displacement of the retaining wall, the water pressure that acts on the wall, the vertical displacement of the ground and water pressure in the ground were measured. Because the retaining wall was not embedded in stiff ground, the retaining wall toe was assumed to move into the excavation (Tanaka, 1994). Therefore, the bottom

Table 1. Monitoring instruments.

Items	Equipment	Measurement depth
Lateral displacement of the wall	Inclinometer	GL – 0 m–GL – 40 m (@2.0 m)
Water pressure on the wall	Water-level gauge	GL – 10 m, –20 m
Vertical displacement of the ground	Differential settlement gauge	GL – 20 m, –28 m, –35 m
Water pressure in the ground	Water-level gauge	GL – 20 m, –28 m, –35 m

of the inclinometer was embedded in the mudstone by about 5 m. Because this project involved deep excavation into soft clay there was a risk of base heave. Therefore, vertical heave was measured in the center of the excavation. It was assumed at GL-60 m in the mudstone there was zero vertical displacement. The lateral displacement of, and the water pressure on the retaining wall were measured from the completion of retaining wall construction to the completion of the excavation. The vertical displacement and water pressure in the ground were measured from the second excavation to the end of the excavation work.

2.2 *Ground condition*

The project location was at the mouth of the Katabira River and the east side of the East Japan Railway Company's Yokohama Station. The site was reclaimed prior to the 1930's. The Soil profile at the site is shown in Figure 3. To the south of the site, alluvial sand exists between the soft clay and mudstone. Soft clay layers extend from the ground surface to a depth of about 35 m. The thickness of the soft clay layer is almost constant across the site.

Soil properties are shown in Table 2 and Figure 4. Natural water content w_n of the soft clay ranged 70% to 100%, and was close to the liquid limit. The values of on drained shear strength were ranged 40 kpa to 70 kpa. Shear wave velocities were in the range to 100 m/s to 120 m/s in the soft clay layer and 460 m/s to 610 m/s in the mudstone. The groundwater level was 1.6 m below ground level and was GL-4.1 m in the mudstone layer.

3 MEASURED RESULTS

3.1 *Lateral displacement of retaining wall*

Figure 5 shows the lateral displacement of the retaining wall. Lateral displacement gradually increased

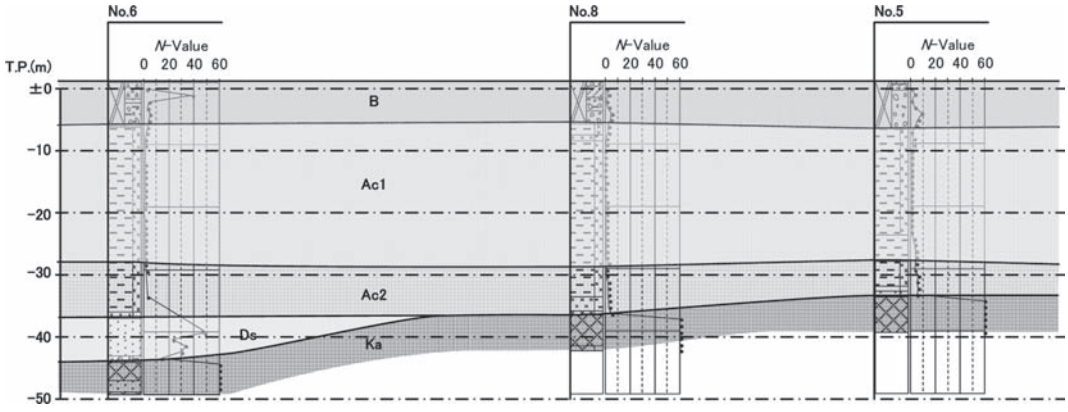

Figure 3. Soil profile.

Table 2. Soil properties.

Soil layer	w_n (%)	γ (g/m^3)	c (kN/m^2)	V_s (m/sec)
Fill (B)	–	1.70	–	160
Clay (Ac1)	70	1.57	45	100
Clay (Ac2)	90	1.45	65	120
Sand (Ds)	–	1.82	–	460
Clay (Ka)	–	1.90	–	610

during excavation, reaching its maximum near the base of the excavation. The lateral displacement of the earth retaining wall was up to 90 mm at the final excavation stage. The lateral displacement of the toe of the retaining wall (GL – 26 m) was lessthan 50 mm.

3.2 *Water pressure*

Figure 6(a) shows the water pressure that acted on the retaining wall and Figure 6(b) shows the water pressures below the base of the excavation. The water pressure that acts on the back of the retaining wall hardly changed over the excavation period. On the other hand, water pressure below the base of the excavation decreased as the excavation progressed. During excavation, the ground water was pumped from deep wells, so water pressures inside the excavation changed. Water pressures inside the excavation were not able to be measured because of equipnent problems after the fourth excavation.

3.3 *Vertical heave of excavation*

Figure 7 shows the vertical displacement of the center of the excavation over time. Vertical displacement gradually increased during excavation, and was upto 45 mm at the final excavation stage. Large displacement was measured near the excavation base at GL-20 m and GL-28 m in the final excavation stage. Vertical displacement increased rapidly in the initiation phase of the final excavation. However, it was judged that it was not heaving because the increase in displacement was gradual afterwards. The depth distribution of the vertical displacement at each excavation stage is shown in Figure 8. The vertical displacement in the excavation bottom was about 45 mm. However, the vertical displacement in the very stiff mudstone was about 2 mm.

4 OUTLINE OF FEM ANALYSIS

4.1 *Mesh and analysis condition*

The FEM analysis was carried out in the two dimensional plane strain condition and total stress analysis was adopted. The FEM mesh is shown in Figure 9. The width of the mesh was assumed to be 101 m, and the distance from the retaining wall to the mesh boundary was assumed to be 80 m, which was near 5 times in depth of excavation (17 m). The depth of the mesh was assumed to be GL – 60 m, equal to the depth of the base of the differential settlement gauge. The analysis steps are shown in Table 3. An initial stress was analyzed to create self weight and 11steps were analyzed to the final excavation depth following the retaining wall, excavation struts installation procedure.

In this analysis, the coefficient of earth pressure at rest K_o was assumed to be 1.0 in the initial stress analysis, based on measured results showing K_o ranged 0.9 to 1.0 (Kanaya et al., 1973, Kuroyanagi et al., 1977) in soft clay. Moreover, the building self weight at each excavation stage was considered as

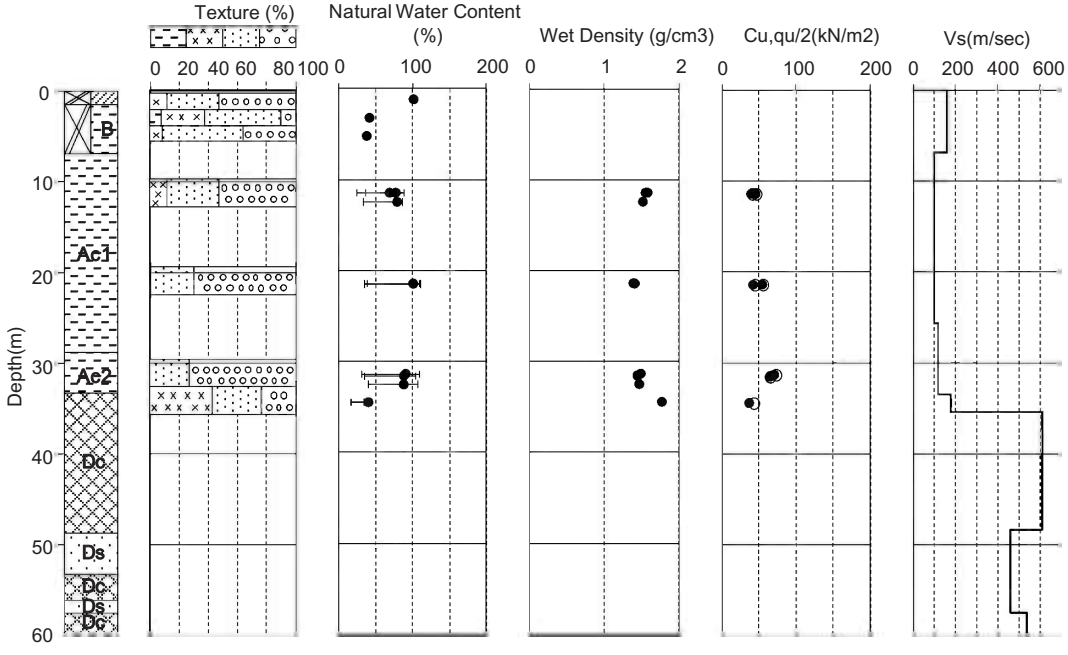

Figure 4. Soil properties.

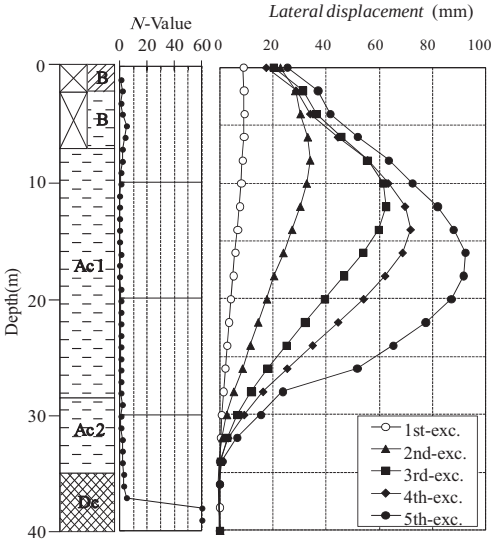

Figure 5. Lateral displacement of earth retaining wall.

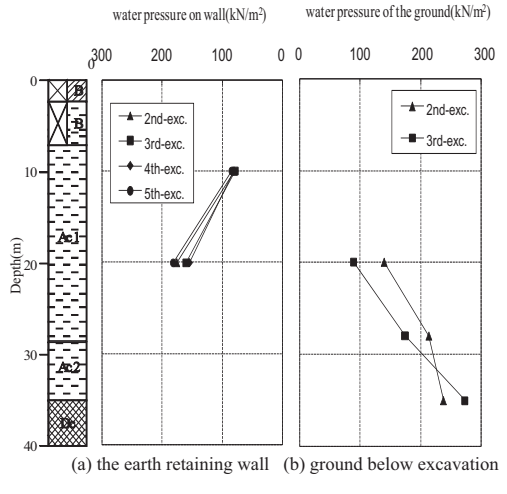

Figure 6. Water pressure.

a vertical load, because the top down method was adopted in construction (see Table 4). The building self weight was applied at the depth of 2/3 of the length of the bored piles (AIJ, 2000) as a uniform load.

4.2 *Numerical model and soil parameters*

In the excavation analysis, unloading caused by excavation and loading caused by the building self weight and the preload to the retaining wall are caused at the same time. In this analysis, the Mohr-Coulomb failure model (Hashiguchi, 2009, Shigeno, 2010) was adopted to predict the lateral deformation of the retaining wall and the vertical

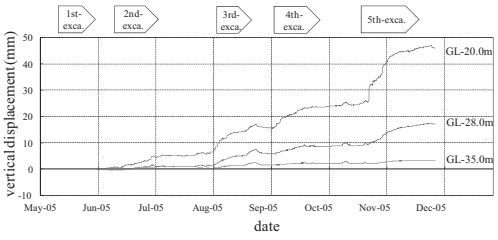

Figure 7. Relation between pate vertical displacement and time.

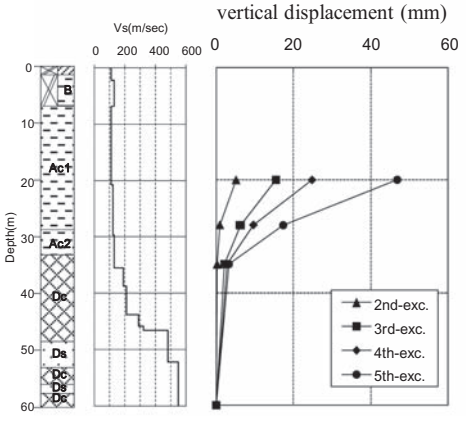

Figure 8. Depth distribution of vertical displacement.

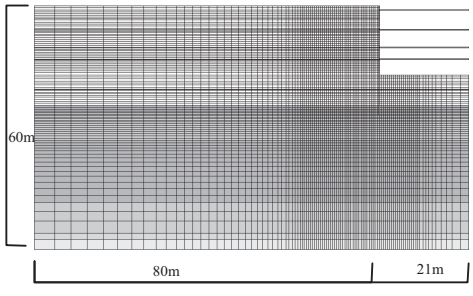

Figure 9. FEM analysis mesh.

displacement of the excavation base. The stress and strain relations in the Mohr-Coulomb model are shown in Equation 1 and 2 below:

$$\dot{\sigma} = E\dot{\varepsilon} - \Lambda E\frac{\partial f}{\partial \sigma} \qquad \Lambda = \frac{\dfrac{\partial f}{\partial \sigma}E\dot{\varepsilon}}{UC\left\|\dfrac{\partial f}{\partial \sigma}\right\| + \dfrac{\partial f}{\partial \sigma}E\dfrac{\partial f}{\partial \sigma}} \tag{1}$$

Table 3. Analysis steps.

Step	Construction condition	Remarks
Step 1	Initial stress	$K_o = 1.0$
Step 2	Installation of the wall	
Step 3	1st excavation	GL – 1.9 m
Step 4	Installation of 1st layer struts	GL – 1.0 m
Step 5	2nd excavation	GL – 6.0 m
Step 6	Installation of 2nd layer struts	GL – 5.9 m
Step 7	3rd excavation	GL – 10.4 m
Step 8	Installation of 3rd layer struts	GL – 10.3 m
Step 9	4th excavation	GL – 13.2 m
Step 10	Installation of 4th layer struts	GL – 13.1 m
Step 11	5th excavation	GL – 17.0 m

Table 4. Building self weights.

Step	Excavation condition	Constructed floor	Weights (kN/m^2)
Step 3	1st excavation	–	0.0
Step 5	2nd excavation	1st floor	10.0
Step 7	3rd excavation	1st, B1 floors 2nd floor	27.0
Step 9	4th excavation	1st, B1, tem. 1 floors 2nd–6th floors	62.0
Step 11	5th excavation	1st, B1, temp.1, 2 floors 2nd–7th floors	74.0

$$U = m\cot\left(\frac{\pi}{2}\frac{\langle R - R_e\rangle}{1 - R_e}\right) \tag{2}$$

where C = cohesion; R = ratio to yielding surface of Tresca ($0 < R < 1$); R_e = ratio in elasticity limit; and m = Model parameter.

Moreover, the change in the soil stiffness as a function of confining pressure is given by Equation 3 below:

$$E = E_o\left(\frac{\sigma_m}{\sigma_{mo}}\right)^{0.5} \tag{3}$$

where E_o = Initial deformation modulus; σ_{mo} = Initial confining pressure; and σ_m = Confining pressure.

Soil stiffness and soil strength parameters used for the analysis are shown in Tables 5 and 6 respectively. The small strain deformation modulus E_o was derived from V_S from *PS* logging and used for the Mohr-Coulomb model. The deformation modulus E_{50} was obtained from *N*-values

Table 5. Soil stiffness parameters.

Soil layer	Bottom depth (m)	*N*-Value	E_o (MN/m²)	E_{50} (MN/m²)
Fill	7.8	4	124.0	4.2
A-Clay1	24.5	1	45.7	8.8
A-Clay2	33.2	5	61.7	15.3
D-Clay1	48.4	99	2020.0	378.0
D-Sand1	53.0	141	1090.0	395.0
D-Clay2	56.0	102	1150.0	378.0
D-Sand1	57.5	144	1090.0	403.0
D-Clay3	60.0	97	1580.0	378.0

Table 6. Soil strength parameters.

Soil layer	Bottom depth (m)	γ (kN/m³)	c (kN/m²)	υ	m
Fill	7.8	17.0	20.0	0.4	2000
A-Clay1	24.5	14.0	42.0	0.4	50
A-Clay2	33.2	15.0	73.0	0.4	50
D-Clay1	48.4	19.0	1800.0	0.4	65
D-Sand1	53.0	19.5	300.0	0.3	90
D-Clay2	56.0	19.0	1800.0	0.4	65
D-Sand1	57.5	19.5	300.0	0.3	90
D-Clay3	60.0	19.0	1800.0	0.4	65

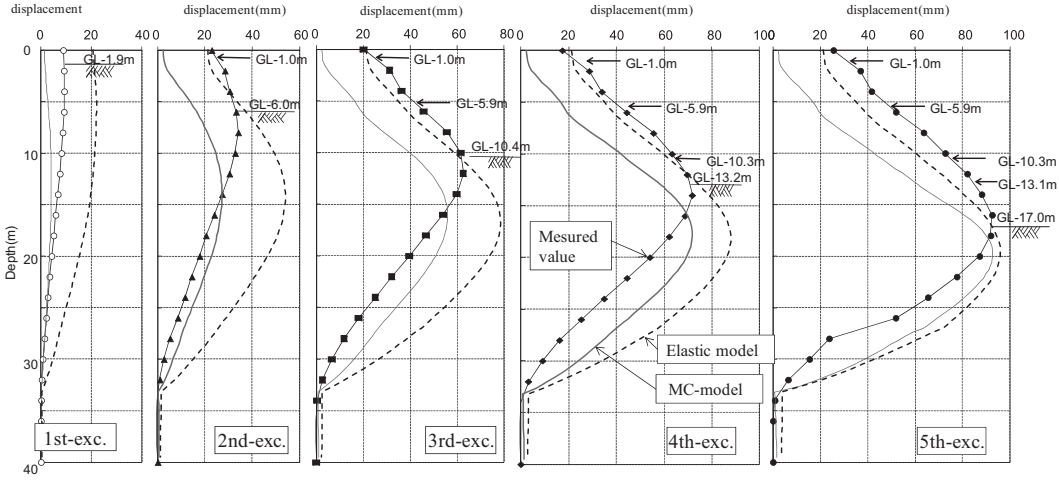

Figure 10. Comparison between analytical and measured value (lateral displacement).

or cohesion *c* and used for elasticity analysis. The retaining wall and struts were modeled with as beams.

5 ANALYSIS RESULTS

5.1 *Lateral displacement of retaining wall*

Figure 10 shows a comparison between the analytical values obtained with the FEM analysis and actual measured values. The analytical values showed good agreement with the measured values at each stage of excavation though some distribution shapes were different. Displacement below the wall also corresponds well.

The result of the elastic analysis using E_{50} in Table 5 is shown in Figure10. The analyzed value is much higher than the measured value in the early excavation stages. However, the analytical value corresponds to the actual measurement value comparatively well in the fifth excavation stage. It was thought that the stiffness has not decreased much because the excavation unloading is small in the early stages of the excavation. This leads us to conclude that to forecast the retaining wall displacement in each excavation stage, it is necessary to evaluate the soil stiffness corresponding to the amount of excavation unloading.

5.2 *Vertical displacement of excavation base*

The lateral distribution of the vertical displacement of the excavation base is shown in Figure 11. The depth distribution of the vertical displacement in the centre of the site is shown in Figure 12. The analytical values showed reasonable agreement with the measured values at each stage of excavation.

The result of the elasticity analysis using E_{50} in Table.5 is shown in Figure11. The analytical value is much larger than the actual measurement

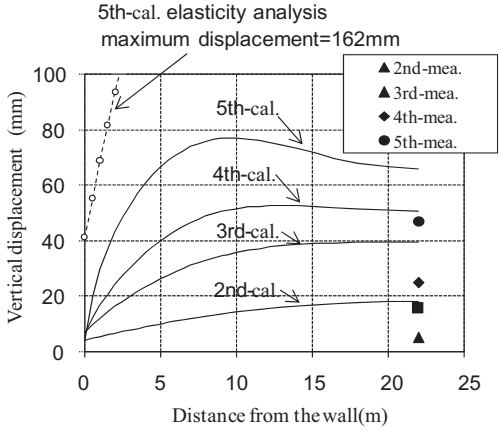

Figure 11. Comparison between analytical and measured value (vertical displacement away from wall).

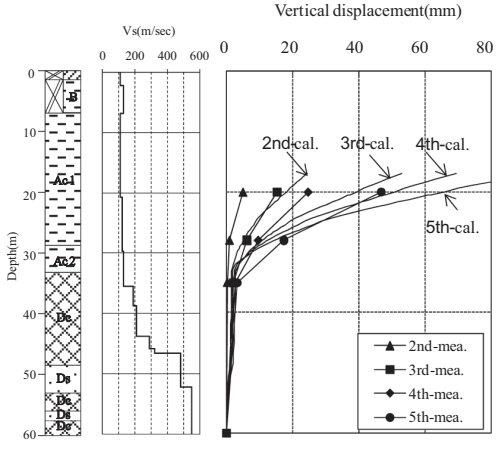

Figure 12. Comparison between analytical and measured value (vertical displacement with depth).

value, because a reducing shiffness E was used in the analysis. It is important to adopt an appropriate soil stiffness considering the stress strain conditions to predict the vertical displacement appropriately.

6 CONCLUSIONS

The lateral displacement of the retaining wall and the vertical displacement of soil in soft clay were evaluated by FEM analysis. In the FEM analysis, the deformation modulus at small strain E_o and Mohr-Coulomb model was adopted. The following conclusions were mode:

1. The analytical values of maximum lateral displacement of the retaining wall showed good agreement with the measured values at each stage of excavation.
2. The analytical values of vertical displacement of soil showed reasonable agreement with the measured values at each stage of excavation.
3. An elastic analysis was executed for comparison. The analytical value was much higher than the actual measurement value at the end of excavation.
4. The vertical displacement of the ground was over predicted by the elastic analysis.
5. It is necessary to evaluate the soil deformation modulus appropriately to forecast lateral and vertical displacements. It is concluded that the Mohr-Coulomb model and deformation modulus at small strain E_o are suitable for excavation analysis.

REFERENCES

AIJ 2000. Recommendations for Design of Building Foundation, pp. 230–232 (in Japanese).

Aoki M. et al. 2000. Evaluation Methods of Surface Settlement of Retained Side Ground Based on Measured Earth Retaining Wall Displacement (Part 1, Part 2), Summaries of Technical Papers of Annual Meeting A.I.J, pp. 537–540 (in Japanese).

Christian Moormann 2004. Analysis of Wall and Ground Movement due to Deep Excavations in Soft Soil Based on a New Worldwide Database, Soils and Foundations, Vol. 44, No. 1, pp. 87–98.

Hashguchi 2009. Elastoplasticity theory, Springer.

Kanaya Y. et al. 1973. Measurement results of Lateral Earth Pressure on RC earth retaining wall, Proc. of 7the Japan National conf. on SMFE, 499–502 (in Japanese).

Kuroyanagi M. and Inoue Y. 1975. Measurement results of Lateral Displacement and Lateral Earth Pressure on RC earth retaining wall in Soft Ground, Proc. of 9th Japan National conf. on SMFE, 785–788 (in Japanese).

Peck, R.B. 1969. Deep Excavation and Tunneling in Soft Ground. Proc. 7th International Conference on Soil Mechanics and Foundation Engineering, Mexico, State-of-the-art Vol. 7, pp. 225–290.

Roscoe 1970. The Influence of Strains in Soil Mechanics, Geotechnique, Volume 20, Issue 2, 129–170.

Shigeno Y. et al. 2010. Rebound and Settlement Analysis of the Building using Three-dimensional elasto-plastic FEM, Summaries of Technical Papers of Annual Meeting A.I.J, pp. 681–682 (in Japanese).

Tanaka H. 1994. Behavior of A Braced Excavation in Soft Clay and The Undrained Shear Strength For Passive Earth Pressure, Soils and Foundations, Vol. 34, No. 1, pp. 53–64.

This page intentionally left blank

Geotechnical Aspects of Underground Construction in Soft Ground – Viggiani (ed)
© 2012 Taylor & Francis Group, London, ISBN 978-0-415-68367-8

The influence of jet-grout constitutive modelling in excavation analyses

M. Ciantia
Dipartimento di Ingegnieria Strutturale, Politecnico di Milano, Italy

M. Arroyo
Department of Geotechnical Engineering and Geosciences, UPC, Barcelona, Spain

R. Castellanza
Dipartimento di Ingegnieria Strutturale, Politecnico di Milano, Italy

A. Gens
Department of Geotechnical Engineering and Geosciences, UPC, Barcelona, Spain

ABSTRACT: A bonded elasto-plastic soil model is employed to characterize cement-treated clay in the finite element analysis of an excavation on soft clay supported with a soil-cement slab at the bottom. The soft clay is calibrated to represent the behaviour of Bangkok soft clay. A parametric study is run for a series of materials characterised by increasing cement content in the clay-cement mixture. The different mixtures are indirectly specified by means of their unconfined compressive strength. A similar parametric analysis is run in parallel using a linear elastic-perfectly plastic model for the clay-cement. Results from both series of analysis are compared highlighting the differences in predicted behaviour of the retaining wall and the excavation stability.

1 INTRODUCTION

Jet-grouted slabs are often employed in deep excavations in soft soils to reduce wall displacements and/or impermeabilize the excavation bottom (Eramo et al. 2011; Bitetti, 2007; Shirlaw, 2005). The slab has a structural role and its geometry and resistance need to be specified. While some simple design rules are available (JJGA, 2005; Shirlaw, 2005) a more in-depth analysis is sometimes necessary. A numerical simulation might be employed for the purpose, particularly if the movement of the retaining wall is required for design. The mechanical behaviour of the treated soil bodies is generally represented with simple models, typically the elastic perfectly plastic Mohr Coulomb model (e.g. Ho & Hu, 2006). One characteristic that is poorly represented by that type of models is brittleness of mechanical response, a basic trait of cemented geomaterials both natural and artificial.

On the other hand, brittleness is well captured by elasto-plastic bonded soil models (Gens & Nova, 1993). Bonded soil models have already shown their value with very diverse natural materials, from soft rocks like calcarenite (Lagioia & Nova, 1995) to very soft Holocene structured clays (Rouainia & Wood, 2000; Arroyo et al. 2008). Despite some early examples (Di Prisco et al., 1992), the application of bonded soil models to cement-improved soils has received somewhat less attention until very recently (Ciantia, 2009; Horpibulsuk et al., 2010).

One important obstacle to the practical application of bonded soil models is that they appear hard to calibrate. Nevertheless it is shown here that measuring porosity and unconfined compressive strength of the soil-cement and having knowledge of the amount of cement in the mixture is enough to initialize the main state variables of a bonded elasto-plastic model. Most of the other model parameters can be obtained from reconstituted samples of the treated soil.

A finite element model of a deep underwater excavation in clay partially sustained with a soil-cement slab is here employed as a trial case to study the influence in the excavation response of modelling the slab with a simple or a more refined constitutive model. The same measured properties of the slab are always assumed (unconfined compressive strength, porosity, cement content), but they are interpreted differently to initialize the different constitutive models being compared. We thus explore if the micro brittle response of the bonded model has consequences at the engineering scale.

2 BONDED SOIL MODEL

The bonded elasto-plastic model here employed is based on the CASM (Clay and Sand Model) developed by Yu (1998). The original CASM has been here both extended, (by introducing a new adimensional scalar history variable, *b,* representing "bonding") and modified (by using a different plastic potential formulation from that originally proposed).

The way the bonding variable enters the model follows closely the original proposal of Gens & Nova (1993). The yield surface is assumed to enlarge with increasing amount of bonding in the soil. Figure 1 shows the normal consolidation lines and yield surfaces for both unbonded and bonded materials with various amounts of bonding.

The yield surface can be expressed as follows:

$$f = \left(\frac{\sqrt{3}J}{M_\theta (p + p_t)} \right)^n + \frac{1}{\ln r} \ln \frac{(p + p_t)}{p_t + p_c} = 0 \tag{1}$$

Where, as in the following, all the stresses are assumed effective. To obtain the behaviour shown in Figure 1,

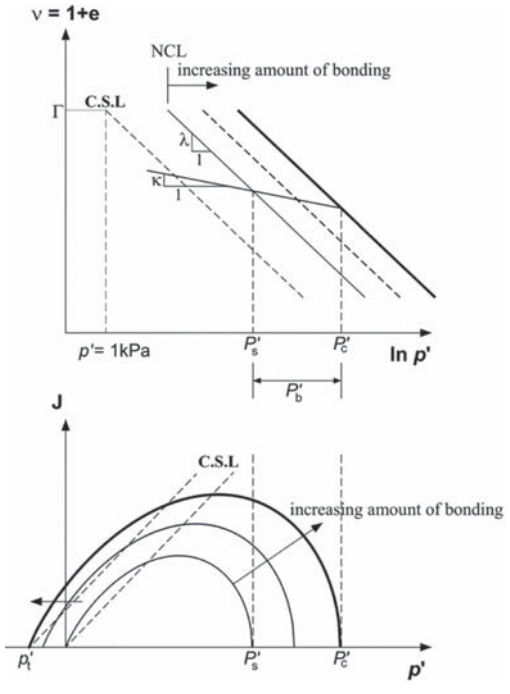

Figure 1. The normal consolidation lines (NCL), critical state lines (CSL) and yield surfaces for both unbonded and bonded materials.

$$\begin{aligned} p_c &= p_s (1 + b) \\ p_t &= p_s (\alpha_t b) \end{aligned} \tag{2}$$

p_s is the preconsolidation pressure of the unbonded reference material. p_c controls the yielding of the bonded soil in isotropic compression and p_t the cohesion and tensile strength of the material; α_t is a parameter. The unbonded behaviour is recovered when b goes to zero.

In CASM the parameters n and r control the shape of the yield surface. M_θ is expressed as a function of Lode's angle θ, and determines the shape of the failure surface in the deviatoric plane, following a proposal by Sheng et al. (2000).

The plastic potential function has a similar form to the yield surface. One extra adjustment parameter, m, is introduced to allow the possibility of non-associated behaviour:

$$g = \left(\frac{m\sqrt{3}J}{M_\theta (p + p_t)} \right)^n + \frac{1}{\ln r} \ln \frac{(p + p_t)}{p_t + p_c} = 0 \tag{3}$$

A classic volumetric hardening law is here employed for the unbonded material.

$$\frac{dp_s}{p_s} = \frac{d\varepsilon_v^p}{\lambda^* - \kappa^*} \tag{4}$$

λ^* and κ^* are the compression parameters of the reconstituted clay, but referred to ε_v:ln p space.

Bonding (b) decreases exponentially with a plastic strain damage measure (h):

$$\begin{aligned} b &= b_0 e^{-h} \\ dh &= h_1 \left| \mathrm{d}\varepsilon_v^p \right| + h_2 \left| \mathrm{d}\varepsilon_s^p \right| \end{aligned} \tag{5}$$

h_1 and h_2 are material parameters (greater than zero) defining the degradation rate. Further discussion of the CASM bonded model formulation and an example of its performance can be found at Gonzalez et al. (2009).

3 CALIBRATION PROCEDURE

3.1 *State variables*

Apart from the current stress state, the model includes two state variables: p_s and b. The calibration procedure for these state variables builds upon experimental work done on cement-mixed Bangkok clay by Bergado and co-authors (Lorenzo & Bergado, 2004; Horpibulsuk et al., 2004; Lorenzo & Bergado, 2006; Bergado et al, 2006). These authors

work with controlled mixtures of reconstituted Bangkok clay and cement slurry, formed and cured in the laboratory.

Cement content on the mixture is specified by A_w, the ratio between cement weight and dry soil weight. It has been observed that the mechanical behaviour of the mixture is controlled by the ratio between current void ratio and cement content (e_{0t}/A_w). This mixing ratio accounts for the effects of initial clay water content, slurry water/cement ratio, slurry/clay mixing ratio and, because of using the current void ratio, curing time. Different combinations of these variables that result in the same mixture ratio (e_{0t}/A_w) show the same mechanical response.

Bergado and co-authors repeatedly proved the quantitative usefulness of that measure, obtaining good correlations with unconfined compressive strength, (Lorenzo & Bergado, 2004), oedometric yield points, (Horpibulsuk et al., 2004), peak resistance on undrained triaxial tests (Lorenzo & Bergado, 2006) and yield points on constant stress ratio drained triaxial tests (Bergado et al, 2006). For instance, in this latter case, they proposed the following empirical relation for the intersection of the yield surface of the mixture and the isotropic axis (units of measure kPa)

$$p_c = 0.49\left(\frac{e_{0t}}{A_w}\right)^2 - 31.9\left(\frac{e_{0t}}{A_w}\right) + 733 \tag{6}$$

In the relation above we have employed deliberately the symbol p_c to evidence the direct connection between this empirical relation and the model presented in the previous section. The particular formulation employed in (6) has some drawbacks and, to obtain a better fit to a wider range of experiments, can be advantageously substituted (Ciantia, 2009) by the following expression

$$p_c = F\left(\frac{e_{0t}}{A_w}\right) = k_1 e^{-k_2\left(\frac{e_{0t}}{A_w}\right)} + k_3 \tag{7}$$

where k_1, k_2 and k_3 are constants, taking the values 1188 [kPa], 0.046 [–] and 4 [kPa], respectively. Whatever the precise shape employed for the function F in (7) it follows from (2) that

$$b = \frac{F\left(e_{0t}/A_w\right)}{p_s} - 1 \tag{8}$$

On the other hand, p_s, the preconsolidation pressure of the unbonded reference material can be easily related to the current void ratio e_{0t} (Figure 1)

$$p_s = \exp\left(\frac{N - (1+e_{0t}) - \kappa \ln\left(p_{0t}\right)}{\lambda - \kappa}\right) \tag{9}$$

Where p_{0t} is the current isotropic stress of the material (i.e. the stress concomitant with e_{0t}) and N is the ICL value at the reference pressure (p_a, here equal to 1 kPa).

Therefore, using equations (7) to (9) it is possible to initialize the model state variables (p_c, p_s) if the current void ratio and cement content of the mixture is known. Since the latter might not be always available, advantage might be taken of the good correlation that exists between unconfined compressive strength, q_u and mixture ratio. For instance, for cement-mixed Bangkok clay (Lorenzo & Bergado, 2004)

$$\left(\frac{q_u}{p_a}\right) = 10.33 e^{-0.046\left(\frac{e_{0t}}{A_w}\right)} \tag{10}$$

3.2 *Parameters of the reference material*

There are 8 parameters in the model that describe the mechanical response of the reference material (Table 1). Reconstituted Bangkok clay is assumed here as reference for the cement-treated Bangkok clay. While the geotechnical characteristics of the natural Bangkok clay have been object of much research (e.g. Balasubramaniam et al. 1978; Shibuya & Tamrakar 2003) the same does not apply to the reconstituted material. As many other soft clays, Bangkok clay is naturally endowed with a certain amount of structure and therefore its response is not always representative of that of the same material reconstituted. This made difficult the ideal approach to calibration of these parameters, which is by examining tests on the reference material only. Actually, it was only for the critical state friction angle (and hence for M) that such approach was possible (with data from Kamei et al. 2004).

Two alternative approaches were then employed. On the one hand, the classical Burland (1990) correlation between plasticity and reconstituted compressibility was used to obtain estimates of the relevant parameters (λ, N).

On the other hand, several aspects of the response of the reference material are predicted by the model to remain unaltered in the cement-mixed material. These aspects include the shape of the yield surface (controlled by parameters n and r), the degree of non-associativeness (controlled by parameter m) or the elastic response, (controlled by parameters κ and υ). Therefore such parameters can be also

Table 1. Parameters of the reference material.

N	λ	κ	M	n	r	m	ν
4	0.262	0.04	1.2	2	1.5	1.7	0.25

identified by observations on the improved material and that was the approach followed here. The resulting parameter set is collected in Table 1. More details about the calibration procedure are given by Ciantia (2009).

3.3 *Parameters of the cemented material*

The model parameters controlling behaviour of the cemented material are only three: the traction intercept parameter, α_t (eq. 2) and the degradation rate parameters, h_1 and h_2 (eq. 5). The value of α_t was estimated at 0.3 based on the yield surfaces reported by Bergado et al (2006). The value of the ratio h_1/h_2 was assumed equal to 3, following results for naturally cemented clay from Callisto & Rampello (2004).

The parameter controlling bond degradation rate, h_1, was obtained from simulations of oedometer tests for a single mixture (A_w = 10%). As already observed by Arroyo et al (2008) for Bothkennar clay, it appeared that the h_1 parameter that best suited the experiments was variable with the initial bonding of the material, b_0. The following dependency was then established

$$h_1 = 0.83\ln(b_0) + 1.77 \tag{11}$$

This result points to a shortcoming of the Gens & Nova bond evolution rule (5), which is unable to accommodate the high sensitivity of bond degradation rate to initial bonding. Alternative rules, with higher order dependency on initial bonding have been formulated, for instance, by Lagioia & Nova (1997).

3.4 *Illustrative results*

The model thus calibrated was verified against an extended database of oedometric tests and triaxial CIU tests on various mixtures of clay-cement (Ciantia, 2009). One example of the simulation results obtained is illustrated in Figure 2, where the stress-paths predicted for several undrained triaxial tests are displayed alongside the experimental results. It can be seen that the model has the potential to at least partly represent the "snap-back" traces that are typical of these softening materials. It is worth mentioning that, if the same tests are run using an elastic-perfectly plastic model such as the MC model, no such snap-back behaviour is observed and the stress path traces remain at their peak.

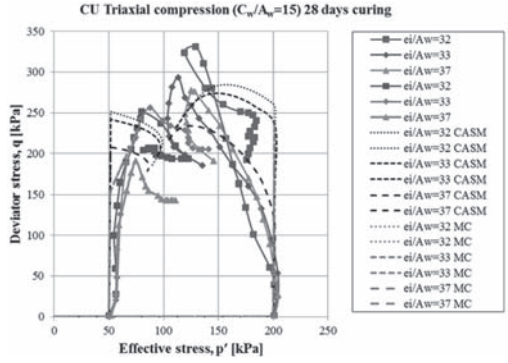

Figure 2. Simulation of undrained triaxial compression tests on cement-improved Bangkok clay. Experimental results from Lorenzo & Bergado (2006).

4 APPLICATION TO EXCAVATIONS

4.1 *Numerical implementation*

The bonded soil model described above was imple-mented in the finite element code PLAXIS Version 8, which has a facility to implement user-defined (UD) soil models.

4.2 *Description of the case*

In practice, jet grout slabs are not common in Bangkok, possibly because deep excavations penetrate below the clay level into stiffer layers (Phienwej, 2009). An artificial case (Figure 3) was then built into a finite element model with the specific purpose of exploring the sensitivity of the analysis to the material characterization of the treated soil.

The case built had three layers of clay with normally consolidated clay below excavation level, an overconsolidated layer on the surface (labelled 3 in the figure, OCR = 3) and an intermediate medium-consolidated layer (labelled 4 in the figure, OCR = 2). All these clay layers were modelled using the bonded CASM model presented in section 2, but with no bonding (i.e. initializing b = 0). The model parameters in all layers were those previously established for the reconstituted Bangkok clay (Table 1). The stress state was initialized with the Plaxis in-built K_0 procedure.

A thick (1 m) concrete (E = 30 MPa) retaining wall was supported at 0.5 m below its head by a rigid strut (400 kN/m/m) and at its bottom by a 3 m thick layer of cement treated clay. The excavation maximum depth was set at 11 m. The excavation process is simulated as a sequence of uniform excavation steps, of 1 m depth each. The strut is activated after the first excavation step. All the simulations assumed undrained behaviour of all the soil layers involved (including the clay-cement).

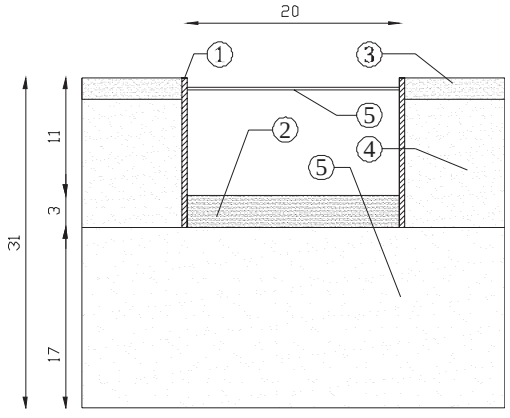

Figure 3. Schematic of the case analyzed.

4.3 *Parametric analysis*

A parametric analysis was performed employing two variables. The first was the constitutive model describing the behaviour of the clay-cement, which could be either a linear elastic-perfectly plastic model with Mohr-Coulomb yield (MC) or that described in the previous sections (bonded CASM). The other parameter was the unconfined compressive strength (UCS, q_u) of the clay-cement.

When the clay-cement was modeled using the MC model the only state variable of the material was stress. The initial stress of the slab was assumed isotropic and equal to the initial vertical stress. Four values of unconfined compressive strength were chosen for the parametric analysis (Table 2). Friction and dilatancy were neglected and strength was given by cohesion equal to half the UCS. Following common engineering practice for these materials, the Young's modulus was taken to be directly proportional to the UCS. The constant of proportionality assumed here was equal to 250, which is within the range found in the literature for jet-grout (e.g. Fang et al., 2006).

When the clay-cement mixture was modelled using the bonded CASM model a larger number of state variables required initialization. Clay-cement mixtures with the same UCS as in the previous case were the objective. To achieve that it was first necessary to make some assumptions about the initial clay water content (120% typical of Bangkok clay, Balasubramaniam et al., 1978), the water/cement (W/C) ratio in the slurry mixed with the clay (chosen as 1) and the curing time before the mixture attained the specified UCS (90 days, to allow for a fast but realistic construction schedule). Then, four values of cement content A_w were specified to attain the objective UCS. Note that the after curing void ratio value, e_{0t}, (which is the initial void ratio for the simulation) it is fixed once the previous mixture parameters have been specified. This was made following empirically-based expressions describing clay-cement mixture curing given by Lorenzo & Bergado (2006). Clearly, if a real case was to be simulated using this procedure, such an indirect evaluation of the soil-cement void ratio could be advantageously substituted by direct measurements on representative clay-cement field samples.

The main mixture properties corresponding to the different cases are collected in Table 3 below. Note that of all the mixture cement contents tabulated only the larger one (60%) is characteristic of jet-grouted mixtures, whereas the others are well below the typical range and more akin to those observed in deep soil mixing treatments.

Once the mixture properties are specified the state variables can be initialized using equations (6) to (8) above. The results obtained for the cases here analyzed are shown in Table 4.

Table 2. Variable parameters of MC model simulations.

Unconfined compressive strength q_u	Cohesion c	Young's modulus E
kPa	kPa	MPa
62	31	15.5
250	125	62.5
637	318	159
814	407	203

Table 3. Mixture properties for CASM model simulations.

Unconfined compressive strength q_u	Cement content by dry weight A_w	Initial void ratio e_{0t}	Mixture ratio e_{0t}/A_w
kPa	%	–	–
814	60	3.28	5.47
637	30	3.24	10.8
250	10	3.12	31.16
100	6	3.08	51.48

Table 4. Initial state variables of CASM model simulations.

Unconfined compressive strength q_u	b	p_s	p_c
kPa	–	kPa	kPa
814	6777	0.14	927
637	4386	0.17	727
250	991	0.29	287
100	211	0.34	116

4.4 *Simulation results*

Only a few simulation results will be presented here. In Figure 4 the movements in a point located at the contact between the soil-cement slab and the retaining wall are represented for the four cases computed using the MC model, against the excavation stage. As a reference the results obtained in a simulation where no slab of soil-cement is present are also included in the graph. Figure 5 represents the same results but now for the cases computed using the bonded CASM model.

A first distinction can be made between those cases where the simulation attained the end of the excavation and those where it did not achieve the final excavation stage because of a numerical lack of convergence that is indicative of failure. Failure happened only for two cases: that without soil improvement and that where the soil improvement was smaller (A_w = 5%; UCS = 62 kPa). It is interesting, however, to note that a stable support is attained even for a relatively low-strength mixture (A_w = 10%; UCS = 250 kPa).

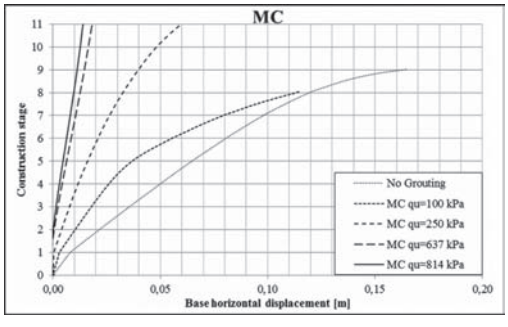

Figure 4. Horizontal displacement at the monitoring point vs excavation stage. Jet-grout slab modelled using MC.

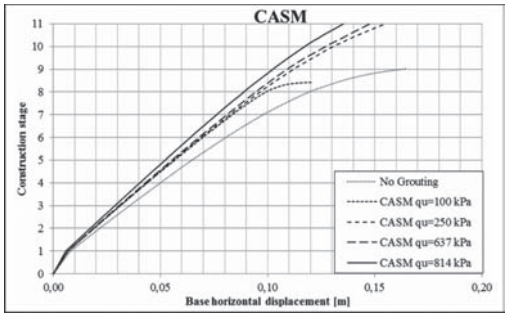

Figure 5. Horizontal displacement at the monitoring point vs excavation stage. Jet-grout slab modelled using CASM.

These results were true both for the simulations run using MC and for those run with the bonded CASM. Hence, from the point of view of predicting structure failure in absolute terms it was indifferent which constitutive model was employed. Note, however, that failure was attained for the cemented case (q_u = 62 kPa) at displacements much closer to the stable cases when using CASM than when using MC. This is an indication of structural brittleness, the kind of behaviour that would complicate the use of excavation monitoring as a preventive tool.

The choice of constitutive model for the clay-cement had also some important consequences for the stable cases. Displacements of the wall monitoring point were between 3 and 10 times higher when the improved soil slab was modeled using the bonded CASM than when it was modeled using the MC model.

It is also clear that the amount of displacement predicted by the bonded CASM was far less sensitive to the UCS of the mixture. Going from a q_u of 250 kPa to one of 814 kPa (or from a cement content of 5% to one of 60%) did only improve marginally the wall movement (Figure 5). When the clay-cement was modeled with the MC model, the stiffness of the structural response was clearly improved with increased UCS (Figure 4).

Similar observations can be made if the movement of the whole wall is considered. For the CASM model cases (Figure 6) the improved slab stiffness is always well below that of the head strut support, and an inverted cantilevered profile develops for all cases. For the MC model cases (Figure 7) there is a clear transition between low-motion and

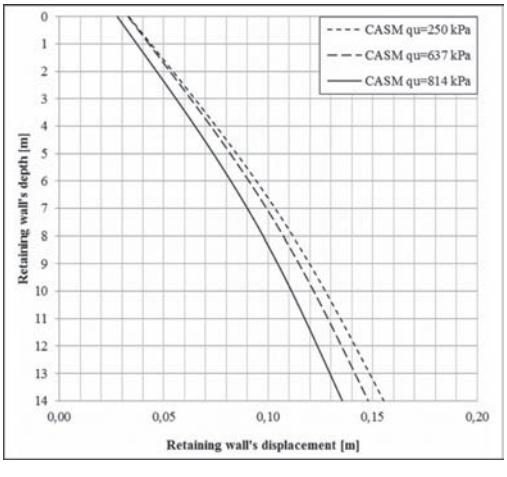

Figure 6. Horizontal displacement of the retaining wall vs depth. Jet-grout slab modelled using CASM.

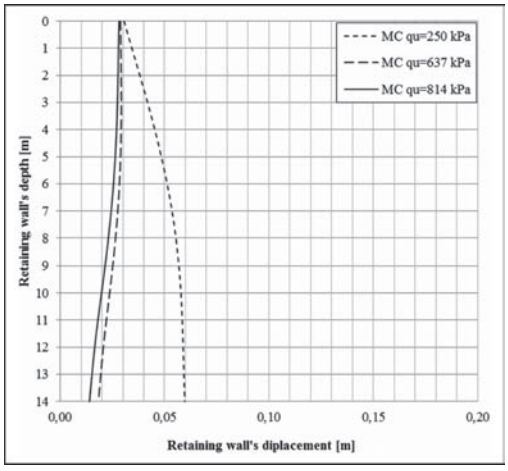

Figure 7. Horizontal displacement of the retaining wall vs depth. Jet-grout slab modelled using MC.

higher-motion cases in the strength range explored. It is clear that, for the higher strength cases, the wall movements predicted with the CASM model would have more serious implications in a real case, were the excavation is often surrounded by sensitive structures.

5 CONCLUSIONS

There are still some uncertain areas in the application of models such as the bonded CASM to real structures. The main one is that the laboratory behaviour that has been matched by the model corresponds to mixtures of relatively low-cement content cured at low pressures. It is unclear if the behaviour of field mixtures, cured under stress and, at least for most jet-grouted cases, generally containing higher cement contents than those explored here would be equally matched by the model.

However, from the results presented in this paper it can be already concluded that the use of an advanced constitutive model like the bonded CASM model will not be indifferent for the design of clay cement slabs supporting retaining walls. It appears that, for the same UCS, far larger movements might be predicted for the structure. Also, when failure appears, it happens in a more sudden manner. These results suggest that caution should be exercised if a simplified approach is used as a base for design.

Finally, it should be emphasized that the use of a model such as the bonded CASM would shifts the design emphasis from one based on the measurement of brittle material outcomes (like UCS) to one based on specified mixture properties (like cement content). Such an approach would clearly simplify control and field quality assessment procedures.

ACKNOWLEDGEMENTS

We are grateful to Nubia Gonzalez, from UPC, who provided the Plaxis subroutine coding the cemented CASM model and solved many numerical doubts. The support of the Spanish Ministry of Science through research grant BIA2008–06537 is also gratefully acknowledged.

REFERENCES

Arroyo, M., González, N., Butlanska, J., Gens, A. & Dalton, C. (2008) SBPM testing in Bothkennar clay: structure effects, *Geotechnical and Geophysical Site Characterization–Huang & Mayne (eds)* Taylor & Francis Group, London, 456–462.

Balasubramaniam, A.S., Hwang, Z.M., Uddin, W., Chaudhry, A.R. & Li, Y.G. (1978) Critical state parameters and peak stress envelopes for Bangkok clays, *Quarterly J. of Eng. Geol. and Hydrogeology*, 11, 219–232.

Bergado D.T., Taechakumthorn C., Lorenzo G.A. & Abuel-Naga H.M. (2006). Stress deformation behavior under anisotropic drained triaxial consolidation of cement treated soft Bankok clay, *Soils and Foundations*, Vol. 46, No. 5, 629–637.

Bitetti, B. (2007) Monitoraggio dei lavori di costruzione della linea B1 della metropolitana di Roma, *Incontro annuale dei Ricercatori di Geotecnica, IARG 2007,* Salerno, 4–6 Luglio 2007.

Burland, J.B. (1990) On the compressibility and shear strength of natural clays, Geotechnique 40:33, 329–378.

Callisto L. & Rampello, S. (2004) An interpretation of structural degradation for three natural clays. Can. Geotech. J. 41: 392–407.

Ciantia, M.O. (2009) *Modellazione del comportamento meccanico di terreni fini trattati con cemento*, Tesi di Laurea, Facolta di Ingegnieria, Politecnico di Milano.

Di Prisco C., Matiotti R., Nova R., (1992). A mathematical model of grouted sand allowing for strength degradation, *Numerical Models in Geomechanics*, 25–35.

Eramo, N., Modoni, G. & Arroyo, M (2011) Design, control and monitoring of a jet grouted excavation bottom plug, *7th International Symposium on Geotechnical Aspects of Underground Construction in Soft Ground.*

Fang, YS, Kao, CC, Chou, J, Chain, KF, Wang, DR & Lin, CT (2006) Jet grouting with the superjet-midi method, *Ground Improvement*, 10,2, 69–76.

Gens A., Nova R. (1993). Conceptual bases for a constitutive model for bonded soils and weak rocks, *Geotechnical Engineering of hard soils-soft rocks*, 485–494.

Gonzalez, N., Arroyo, M. & Gens, A. (2009) Identification of bonded clay parameters in SBPM tests: a numerical study, *Soils and Foundations* 49, 3, 329–340.

Ho, C.E. & Hu, S. (2006) Numerical analysis of jet grout elements for braced excavation in soft clay, ASCE Geocongress 2006 Geotechnical Engineering in the Information Technology Age, (doi 10.1061/40803(187)260).

Horpibulsuk, S., Liu, M.D., Liyaparathina, D.S. & Suebsuk, J. (2010) Behaviour of cemented clay simulated via the theoretical framework of the Structured Cam Clay model, Computers & Geotechnics, 37, 1–9.

Horpibulsuk S., Bergado D.T., Lorenzo G.A. (2004). Compressibility of cement-admixed clays at high water content, Geotechnique 53, No. 2, 151–154.

JJGA (Japan Jet Grout Association) (2005) Jet Grouting Technology (JSG method, Column Jet Grout method) Technical Information. 13th Edition (October 2005). Unofficial translation by T. Inui, K. Soga, H. Ji & Y. Ando.

Kamei, T., Tanaka, M. & Hayashi, S. (2004) Comparison of shear characteristics of undisturbed and remoulded Bangkok clay, Mem. Fac. Sci. Eng. Shimane Univ., 38, pp. 1–7.

Lagioia R. & Nova R., (1995) An experimental and theoretical study of the behaviour of a calcarenite in triaxial compression, *Géotechnique*, 45, 4, 633–648.

Lorenzo G.A., Bergado D.T. (2004). Fundamental parameters of cement-admixed clay—New approach, *Journal of geotechnical and geoenviromental engineering ASCE*, 1042–1050.

Lorenzo G.A., Bergado D.T. (2006). Fundamental characteristics of cement-admixed clay in deep mixing, Journal of materials in civil engineering, ASCE, 161–174.

Phienwej, N. (2009) Ground movements in station excavations of Bangkok first MRT, *Geotechnical Aspects of Underground Construction in Soft Ground-Ng, Huang & Liu (eds)* Taylor & Francis, 181–186.

Porbaha A., Raybaut J.L., Nicholson P. (2001). State of the art in construction aspects of deep mixing technology, Ground improvement, 3, 132–140.

Rouainia, M. & Wood, D.M. (2000) A kinematic hardening constitutive model for natural clays with loss of structure, *Géotechnique*, 50, 2, 153–164.

Sheng D, Sloan S.W. & Yu, H.S. (2000). Aspects of finite element implementation of critical state models. *Computational Mechanics* 26, 185–196.

Shirlaw, J.N. (2004) Jet grouting soft clays for tunnelling and deep excavations–design and construction issues, in Johnsen, Byle & Bruce (Eds), *Grouting and Ground Treatment: Proceedings of the Third International Conference*, February 10–12, 2003, New Orleans, Louisiana, ASCE.

Shibuya S., Tamrakar S.B. (2003). Engineering properties of Bangkok clay, Characterisation and Engineering Properties of Natural Soils—Tan et al. (Eds.) Sweets & Zeitlinger, Lisse, 645–692.

Yu, H.S. (1998). CASM: A unified state parameter model for clay and sand. *International Journal of Numerical and Analytical Methods in Geomechanics*, No. 22, 621–653.

Geotechnical Aspects of Underground Construction in Soft Ground – Viggiani (ed)

Pile-group response due to tunnelling

F. Basile
Geomarc Ltd, Messina, Italy

ABSTRACT: The paper describes an efficient and practical method of analysis for estimating the deformation and load distribution of existing pile foundations during the tunnelling process. The method involves two separate steps: (1) estimate of the free-field ground movements caused by the tunnel excavation, and (2) analysis of the pile group subjected to the computed free-field ground movements. The first step may be carried out using alternative procedures, ranging from empirical methods to 3D numerical analyses. The second step is performed by PGROUPN, a computer program for pile-group analysis based on a non-linear boundary element solution. Validity of the approach is illustrated through comparison with alternative numerical solutions and field measurements. The results indicate that the method is capable of generating reasonable predictions of pile response for many cases of practical interest, thus offering substantial cost savings over a complete 3D analysis of tunnel-soil-pile interaction.

1 INTRODUCTION

One of the major concerns that arise from tunnelling in urban environments is the assessment of the likely impact on existing structures. The effects can be even more pronounced in the case of piled structures, as tunnelling could potentially be carried out very close to piles. In such cases, a proper assessment of the deformations, forces and moments generated in the existing piles by the tunnelling-induced ground movements becomes crucial.

Current analysis methods to assess the impact of tunnelling on existing pile foundations may be broadly classified into two categories:

a. Simplified two-stage approaches involving initial separation of the soil and the pile so that the soil movements are first computed and then imposed on the piles;
b. Complete (or coupled) numerical analyses involving simultaneous modelling of the pile, the soil and the tunnel excavation.

The latter category is generally based on three-dimensional finite element (FEM) or finite difference (FDM) analyses which provide a complete solution for the behaviour of both the soil and the pile (*e.g.* Mroueh & Shahrour 2002). While such solutions are the most powerful numerical tool currently available, they are very expensive in terms of data preparation (pre- and post-processing) and computational times. The cost of such analyses may become prohibitively high if non-linear soil behaviour and complicated construction sequences are to be taken into account. Apart from the computational requirements, complete 3D numerical analyses are complex to use for design purposes, particularly when non-linear behaviour is to be considered. Major difficulties are related to the construction and interpretation of a 3D model (modelling errors are easily overlooked), the high mesh dependency, the uncertain in assigning mechanical properties to the pile-soil interface elements, the interaction with adjacent structures, and the modelling of the excavation sequence. Thus, a complete 3D analysis is more suited to obtaining benchmark solutions (against which simpler analyses can be checked) or to obtaining a final design solution for major projects, rather than as a practical tool for less demanding problems or in the preliminary design stages (in which multiple tunnel configurations and scenarios have to be examined).

In order to overcome the above shortcomings, simplified approaches have emerged (*e.g.* Chen *et al.* 1999, Xu & Poulos 2001, Loganathan *et al.* 2001, Kitiyodom *et al.* 2005, Surjadinata *et al.* 2006). Such approaches are based on a two-stage analysis:

1. evaluation of the free-field ground movements caused by the tunnel excavation;
2. analysis of the piles subjected to the computed free-field ground movements.

1.1 *Estimation of soil movements*

Estimation of tunnelling-induced ground movements can be carried out using alternative procedures, namely, empirical methods, analytical expressions, and numerical analyses. Each method has its own strengths and weaknesses.

Empirical methods are based on a Gaussian error function (Peck 1969, Mair *et al*. 1996) and are widely employed in engineering practice. The main limitations are related to their applicability to different tunnel geometries, ground conditions and construction techniques, and in the limited information they provide about the horizontal movements and subsurface settlements.

In the light of the above limitations, a number of closed-form analytical solutions have been proposed (Sagaseta 1987, Verruijt & Booker 1996). In particular, the analytical expressions developed by Loganathan & Poulos (1998) for the estimation of the surface settlements, subsurface settlements and horizontal movements have the advantage to take into account the various construction methods and the non-linear ground movements (due to oval-shaped gap) around the tunnel-soil interface. Such expressions allow rapid estimation of the ground deformations by using a simple soil parameter, the Poisson's ratio, and their applicability has been successfully verified through comparison with a number of case histories.

While empirical and analytical methods provide a simple and practical means of estimating tunnelling-induced ground movements, numerical analyses (generally based on FEM or FDM) provide the most powerful tool to carry out such predictions because of their ability to consider the ground heterogeneity, soil nonlinearity, advanced soil models, 3D effects, complex foundation and tunnel geometries, the interaction with surrounding structures, and the excavation method and sequence. However, even though favourable comparisons with measured ground movements have been reported (*e.g*. Lee *et al*. 1994, Surjadinata *et al*. 2006), finite element models are often known to over-predict the width and to under-predict the gradient of the settlement trough (*e.g.* Chen *et al*. 1999, Pound 2003). To obtain better predictions, it is often necessary to use advanced soil models and to carefully select the corresponding model parameters. Moreover, the designer should bear in mind the complexity and high computational costs involved, particularly if non-linear soil behaviour and 3D effects have to be taken into account.

1.2 *Analysis of pile response*

The second step of the procedure is usually carried out by a boundary element (BEM) analysis of the single pile or the pile group subjected to the vertical and lateral tunnelling-induced soil movements evaluated using any of the methods described above. Current analysis methods are mainly restricted to purely elastic analyses or to single isolated piles (*e.g*. Chen *et al*. 1999, Xu & Poulos 2001, Kitiyodom *et al.* 2005). It is indeed generally assumed that group interaction effects are beneficial to the pile response as compared to single isolated piles, *i.e.* group effects lead to a reduction of the deformations, forces and moments induced in the piles.

2 PGROUPN ANALYSIS

The proposed analysis is based on the two-step approach described above and is carried out within PGROUPN (Basile 2003, 2010a), a completely general computer program for pile-group analysis employing a boundary element (BEM) formulation. The originality of the analysis lies in its ability to model both the effects of group interaction and soil nonlinearity at the pile-soil interface.

Use of a non-linear soil model is of basic importance in design as it avoids exaggeration of stresses at pile group corners (a common limitation of purely linear models), thereby reducing consequent high loads and moments. Benefits of this include an improved understanding of pile group behaviour and thus more effective design techniques. The analysis involves negligible computational costs (both in terms of data preparation and computer execution times) and is widely adopted in pile design through the software Repute (Bond & Basile, 2010).

In this paper, the PGROUPN analysis, originally developed for direct applied loading at the pile cap level, has been extended to deal with externally imposed ground movements in both the vertical and lateral directions. It is noted that the extended analysis may be employed not only in the tunnelling case described herein but in many circumstances in which pile foundations are subjected to "passive" loadings arising from vertical and/or horizontal movements of the surrounding ground. Examples include slope movement, excavation, consolidation of clay, swelling or shrinking of an expansive clay, cavity development, construction of adjacent piles or buildings, and kinematic effects induced by earthquakes (Basile 2010b).

A description of the theoretical formulation of the PGROUPN analysis for the case of direct applied ("active") loading has been presented elsewhere (Basile 2003). The modelling of the pile-soil interaction problem in "active" and "passive" piles is quite similar and hence only a brief description of the passive case is given below. The program makes use of the traditional Mindlin solution to perform a *complete* analysis of the group (*i.e.* the simultaneous influence of all the elements of all the piles within the group is considered), thereby overcoming the limitations of interaction factor and Winkler models.

The analysis employs a sub-structuring technique in which the piles and the surrounding soil

are considered separately and then compatibility and equilibrium conditions at the pile-soil interface are imposed.

2.1 *Soil domain*

The soil displacements, arising both from the stresses caused by pile-soil interaction and the external source of ground movement, may be expressed as:

$$\{u_s\} = [G_s]\{t_s\} + \{u_e\} \quad (1)$$

where u_s are the soil displacements, t_s are the soil stresses, G_s is the soil flexibility matrix obtained from Mindlin's (1936) solution, and u_e are the external soil movements. It is noted that Mindlin's solution is strictly applicable to homogeneous soil conditions. In practice, however, this limitation is not strictly adhered to, and the influence of soil non-homogeneity is often approximated using the average value of soil modulus at the influencing and influenced pile nodes.

2.2 *Pile domain*

If the piles are assumed to act as simple beam-columns which are fixed at their heads to the pile cap, the pile displacements may be written as:

$$\{u_p\} = [G_p]\{t_p\} \quad (2)$$

where u_p are the pile displacements, t_p are the pile stresses, and G_p is a matrix of coefficients obtained from the elementary (Bernoulli-Euler) beam theory.

2.3 *Limiting stress and non-linear soil behaviour*

It is essential to ensure that the stress state at the pile-soil interface does not violate the yield criteria. This can be achieved by specifying the limiting stress at the pile-soil interface using the classical equations (refer to Basile, 2003). Non-linear response of the soil is modelled by assuming that the soil Young's modulus varies with the stress level at the pile-soil interface according to the common hyperbolic stress-strain law:

$$E_{tan} = E_i \left(1 - \frac{R_f t}{t_{lim}}\right)^2 \quad (3)$$

where E_{tan} is the tangent soil modulus, E_i is the initial tangent soil modulus, R_f is the hyperbolic curve-fitting constant, t is the pile-soil stress and t_{lim} is the limiting value of pile-soil stress. Thus, the soil and pile equations described above for the linear response are solved incrementally using the modified values of soil Young's modulus of Equation 3, while enforcing the conditions of yield, equilibrium and compatibility at the pile-soil interface.

3 NUMERICAL RESULTS

Validity of the approach is verified through comparison with published results from alternative numerical analyses. Attention will be focused on the effects of group interaction and soil nonlinearity.

3.1 *Comparison with Kitiyodom et al. (2005)*

The accuracy of the PGROUPN analysis is assessed for the case of an existing single pile adjacent to a tunnel under construction, as illustrated in Figure 1.

The free-field tunnelling-induced soil movement profiles to be input into the pile analysis have been calculated using the analytical expressions of Loganathan & Poulos (1998), as shown in Figure 1. It can be seen that the soil movements increase with increasing ground loss ratio (ε), as expected. The vertical ground movements increase gradually with depth to a maximum located near the tunnel crown (at 17 m depth). Below this level, the vertical ground movements decrease rapidly while the lateral ground movements become dominant. Below the tunnel

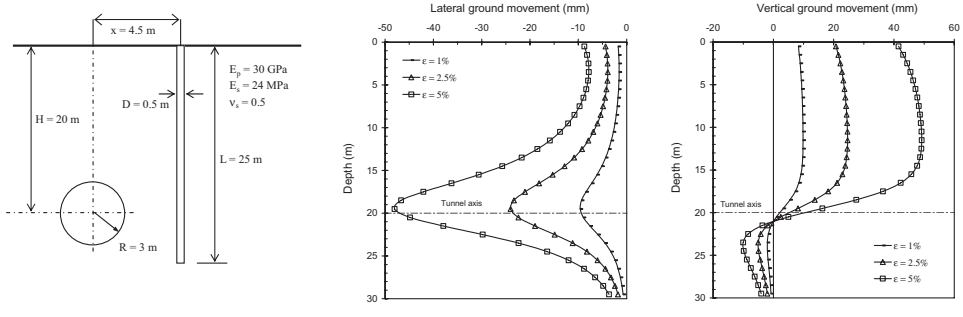

Figure 1. Single-pile problem analysed and computed free-field ground movements.

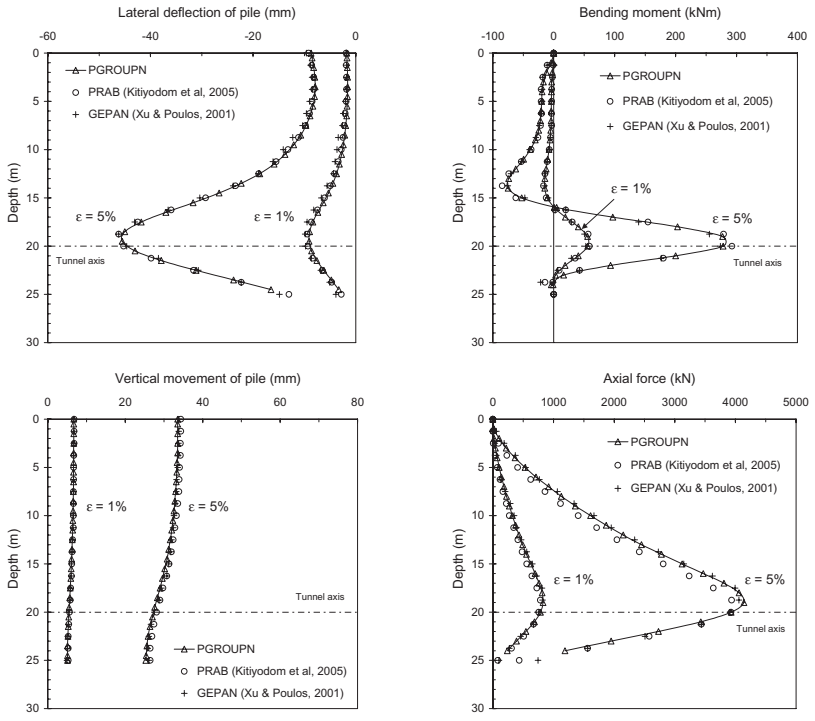

Figure 2. Comparison of single-pile response.

invert (at 23 m depth), both vertical and lateral ground movements quickly decrease with depth.

Figure 2 compares the (elastic) pile response calculated with PGROUPN with that predicted by alternative numerical approaches. The computer program PRAB (Kitiyodom *et al*. 2005) is based on a hybrid model which combines a load-transfer analysis for single-pile response with a Mindlin-based BEM analysis to evaluate pile-soil-pile interaction. A more rigorous boundary element analysis is performed by the code GEPAN (Xu & Poulos 2001) in which the cylindrical elements at the pile-soil interface are in turn divided into partly cylindrical or annular sub-elements. Both programs are however restricted to the linear elastic range.

An excellent agreement between analyses is observed in Figure 2. The lateral pile deflections are very similar to the soil deflections (reflecting the relatively small lateral stiffness of the pile), with the maximum value occurring just above the tunnel axis level. The bending moment profile has a double curvature, with the maximum also occurring just above the tunnel axis level. The pile settlements are relatively uniform along the entire shaft (reflecting the relatively large axial stiffness of the pile), with the pile-head settlement which is less than the maximum vertical soil movement. Compressive axial force (*i.e.* a drag force) is induced in the pile due to the downward vertical ground movements in the upper portion of the pile (*i.e.* above approximately the tunnel axis). Such downward vertical ground movements also result in negative skin friction in the upper portion of the pile. In the lower portion of the pile (*i.e.* below approximately the tunnel axis), a decrease of the compressive axial force is noted, due to the upward movement of the soil in this zone. The maximum axial force is observed in the section located just above the tunnel axis level. Finally, as expected, larger movements, forces and moments are developed with increasing ε, thus emphasising the importance of minimising ground loss during tunnel excavation.

The effects of group interaction in the linear elastic range are examined for the problem illustrated in Figure 3, where an existing fixed-head 2×2 pile group is located in proximity of a tunnel under construction. The tunnelling-induced ground movements have again been estimated using the solutions of Loganathan & Poulos (1998) for a ground loss ratio of 1%. The pile cap is considered to be fully rigid and free-standing, *i.e.* no interaction between the cap and the ground is considered. This is a reasonable assumption for this type of problems, as shown by Mroueh & Shahrour (2002).

Figures 4–5 compare the pile-group response obtained from PGROUPN, PRAB and GEPAN

(as reported by Loganathan *et al.* 2001), showing a favourable agreement between analyses. Both the front-pile and the back-pile results are shown in the figures. As expected, the deformations, axial force and bending moment of the front pile (closer to tunnel) are higher than for the back pile.

In order to compare the pile behaviours both as single isolated pile and within the group, the figures also show the responses of identical single piles located at an equal horizontal distance from the tunnel centreline (*i.e.* x = 4.5, 6.9 m). It is observed that the lateral deformation and bending moment profiles for single piles are similar to those of the corresponding piles in the group (except for a difference in bending moment near the pile-head due to the fixity condition). The maximum bending moment occurs in the front pile at about the tunnel axis level and is 14% lower than that of the corresponding single pile, whereas the maximum bending moment in the back pile is 23% higher than that of the corresponding single pile.

Pile-to-pile interaction effects appear to be more significant in the evaluation of the pile settlement and axial force profiles. In particular, the effects of group interaction lead to a reduction of the maximum axial force of 27% in the front pile and of 48% in the back pile, as compared to the corresponding single pile (*i.e.* a beneficial effect). The above results demonstrate the importance of considering pile-to-pile interaction effects in order to obtain a more realistic prediction of pile-group behaviour.

A practical feature of the proposed approach is that the tunnelling-induced ground movements to be input into the pile-group analysis can be calculated using any suitable method. For example, the PGROUPN boundary element analysis may be used in combination with a separate 3D finite element or finite difference analysis, with the free-field ground movements predicted by FEM (or FDM) and the pile-group response to these ground movements predicted by PGROUPN. This allows the adoption of a more powerful tool for the prediction of the free-field ground movements as compared to available analytical solutions, thereby

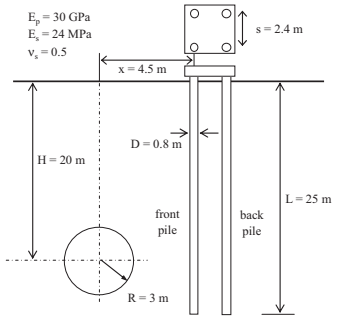

Figure 3. Pile-group problem analysed.

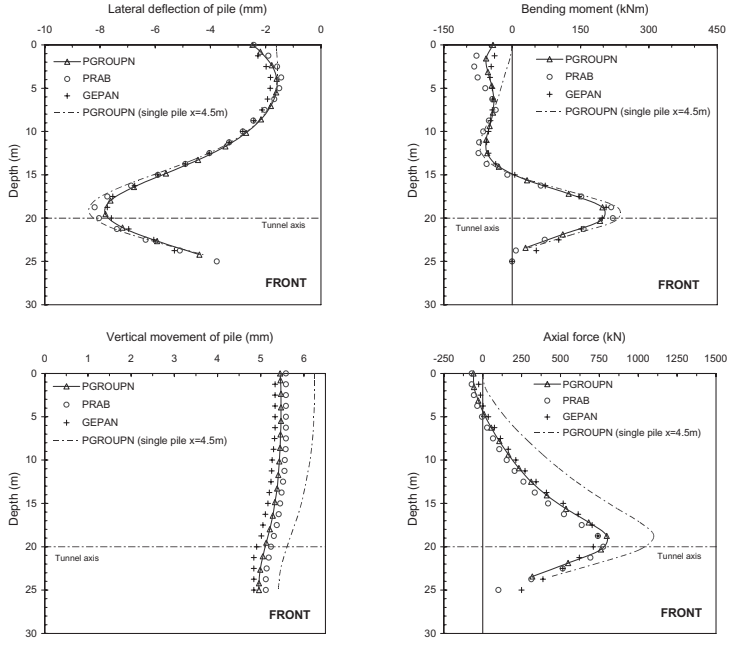

Figure 4. Comparison of pile-group response for front pile.

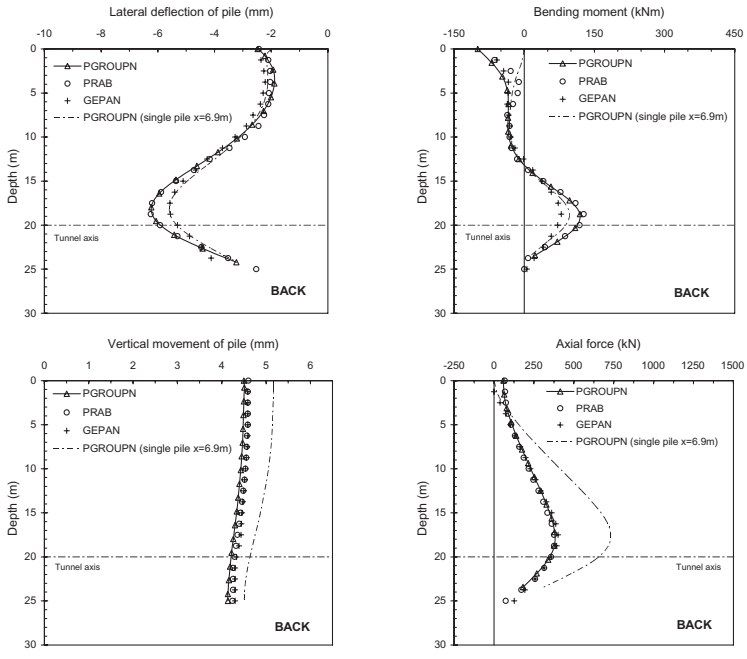

Figure 5. Comparison of pile-group response for back pile.

enabling consideration of such aspects as the ground heterogeneity, soil nonlinearity, advanced soil models, 3D effects, complex tunnel geometries, and the excavation sequence.

The combined approach therefore provides a practical compromise for many design situations, overcoming the need for a complete 3D FEM/FDM analysis of tunnel-soil-pile interaction which is limited by the high computational costs and complexity involved, particularly if non-linear soil behaviour and complicated construction sequences are to be taken into account. As reported by Surjadinata *et al.* (2006), the execution time of a boundary element analysis is a mere fraction (approximately 1/1000th) of the time needed for a complete 3D finite element analysis. A key advantage of the combined approach is that only a single 3D FEM/FDM analysis for each tunnel configuration is required, independent of the multitude of configurations of pile foundations that may be of interest. The free-field tunnelling-induced ground movements generated by the FEM/FDM analysis are then input into a number of separate and inexpensive PGROUPN analyses of the existing pile foundations. The combined approach therefore has the potential to generate economical predictions for many practical cases, enabling engineers to investigate many more cases than are viable at present by a complete 3D FEM or FDM analysis and allowing parametric studies to be readily performed.

In order to illustrate an application of the combined approach, the 2×2 pile group of Figure 3 has been analysed using the free-field tunnelling-induced ground movements computed by the finite difference program FLAC3D (Itasca 2002) for a computed ground loss ratio of 4.69%, as reported in Figure 6. The ground movements calculated by the analytical expressions of Loganathan & Poulos (1998) are also shown in the figure; these will be used as input into the PGROUPN and PRAB analyses.

Figure 7 compares the front-pile response obtained from PGROUPN, PRAB and a complete FLAC3D analysis of the tunnel-soil-pile problem, as reported by Kitiyodom *et al.* (2005). It is observed that, although the shape of the deformation, axial force and bending moment profiles are similar, the maximum values predicted by PGROUPN (and PRAB) are higher than those predicted by FLAC3D.

Similar findings were reported by Loganathan *et al.* (2001) based on a comparison between FLAC3D and a boundary element analysis (similar to PGROUPN). Finally, it is noted that a closer agreement with FLAC3D is obtained using a combined approach in which the free-field ground movements from FLAC3D are input into the PGROUPN analysis.

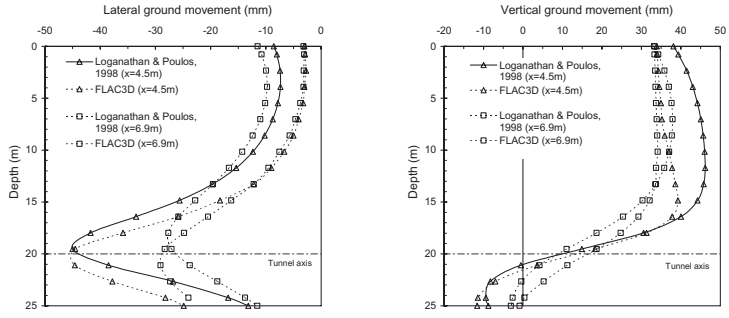

Figure 6. Comparison of computed free-field ground movements.

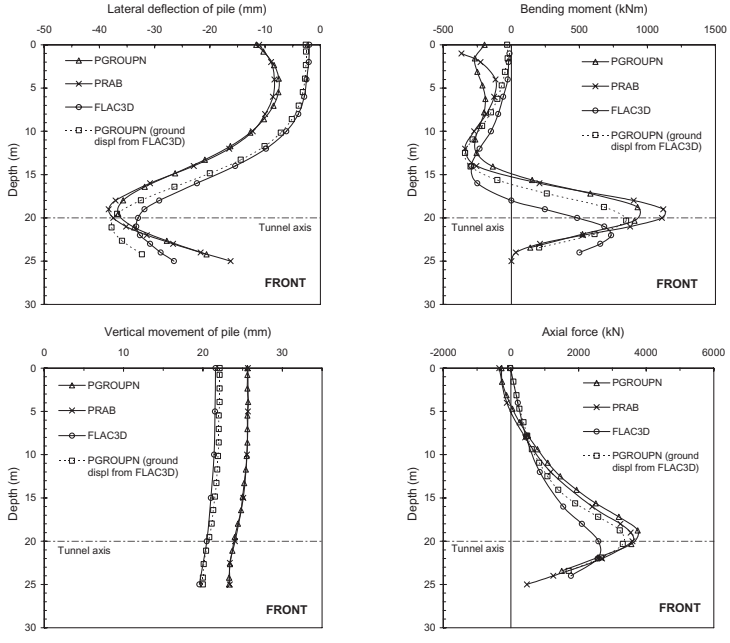

Figure 7. Comparison of pile-group response for front pile.

3.2 *Comparison with Chen et al. (1999)*

The effects of non-linear soil behaviour at the pile-soil interface are examined for the single-pile problem analysed in the linear elastic range in Figures 1–2. The input data and free-field ground movements due to tunnelling are those shown in Figure 1, while the additional parameter required for the non-linear analysis is the soil undrained shear strength (C_u) of 60 kPa, resulting in a limiting skin friction of 48 kPa, and limiting end-bearing and lateral pile-soil pressures both equal to 540 kPa.

In order to directly compare the results with the boundary element solution of Chen *et al.* (1999), which adopts an elastic-perfectly plastic interface model, the PGROUPN analyses have been carried out using zero values for R_f in Equation 3. Such an assumption implies that the effects of soil nonlinearity are only caused by plastic yielding at the pile-soil interface, while the dependence of soil stiffness on the stress level is disregarded.

Figure 8 shows a favourable agreement between the pile responses predicted by Chen *et al.* (1999) and PGROUPN for two ground loss ratios (ε) of 1% (a common design value) and 5% (an extreme value). It is crucial to observe the difference in pile response between the non-linear analyses of Figure 8 and the preceding linear analyses of Figure 2. The lateral deformation and bending moment profiles are nearly identical for both the linear and non-linear analyses, thereby indicating that

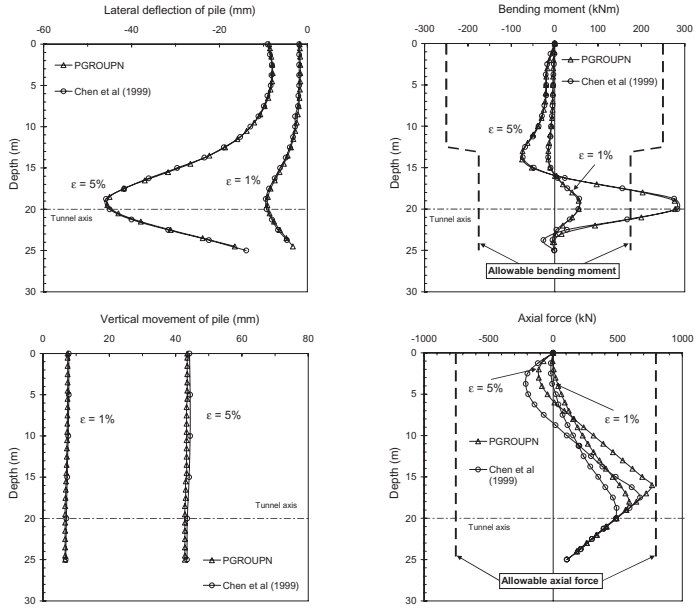

Figure 8. Comparison of single-pile response.

the limiting lateral pile-soil pressures were never reached along the pile.

However, the effects of soil nonlinearity play a significant role in the evaluation of the axial response (in particular the axial force distribution); for the case of $\varepsilon = 5\%$, the limiting skin friction is nearly fully mobilised along the pile, thereby causing slippage at the pile-soil interface. Soil nonlinearity effects lead to a reduction of the maximum axial force of 29% for $\varepsilon = 1\%$ and of 82% for $\varepsilon = 5\%$, as compared to the corresponding linear analysis. If a non-linear soil model with stress-dependent soil stiffness (*i.e.* with not zero values of R_f in Equ. 3), such reductions of maximum axial force would become even more significant, specifically 43% for $\varepsilon = 1\%$ and 83% for $\varepsilon = 5\%$. It may also be observed that, in the non-linear analysis, both compressive and tensile axial forces are induced in the pile, with the compressive force in this case being larger. The above results demonstrate the importance of considering non-linear soil behaviour in order to obtain a more realistic and, in this case, economical prediction of pile behaviour.

With regard to the pile capacities, these have been estimated by Chen *et al.* (1999) using the traditional global factor-of-safety approach, *i.e.* an allowable axial pile capacity of 796 kN for compression and 754 kN for tension, and an allowable bending moment of 250 kNm in the top half of the pile and 175 kNm in the bottom half. It is noted that both the developed axial forces and bending moments are considerable, especially considering that they are solely induced by tunnelling without taking into account those induced by other type of loading at the pile-head (*e.g.* from the superstructure). In fact, the maximum axial force and bending moment reach the allowable values for the 5% ground loss ratio.

In order to assess both the effects of pile-to-pile interaction and soil nonlinearity, the single-pile problem analysed in Figure 8 is extended to the case of a fixed-head 3×3 pile group. The piles have a centre-to-centre spacing of three pile diameters and the tunnelling-induced ground movements have been derived from the analytical solutions of Loganathan & Poulos (1998) for a ground loss ratio of 1%.

Figure 9 reports the PGROUPN predictions of bending moment and axial force for Pile 1, *i.e.* the most heavily loaded pile in the group. The predictions for an identical single pile located at an equal horizontal distance from the tunnel (*i.e.* x = 4.5 m) are also shown for comparison. There are no differences in the bending moment profiles between linear and non-linear analyses for both the single pile and the pile in the group. However, as already noted in the comparison of Figure 4, group effects lead to a reduction of the maximum bending moment of 15% in Pile 1 as compared to the single isolated pile.

As previously observed, the effects of soil nonlinearity and group interaction play a more significant role in the evaluation of the axial force distribution, leading to a substantial reduction of the maximum values obtained from a linear analysis of the single isolated pile.

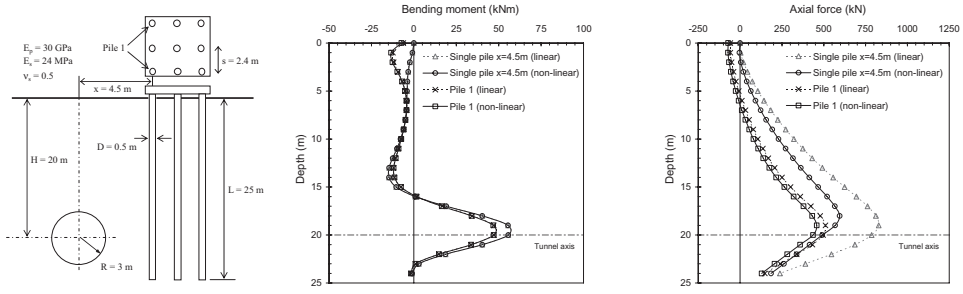

Figure 9. Pile-group problem analysed and PGROUPN predictions.

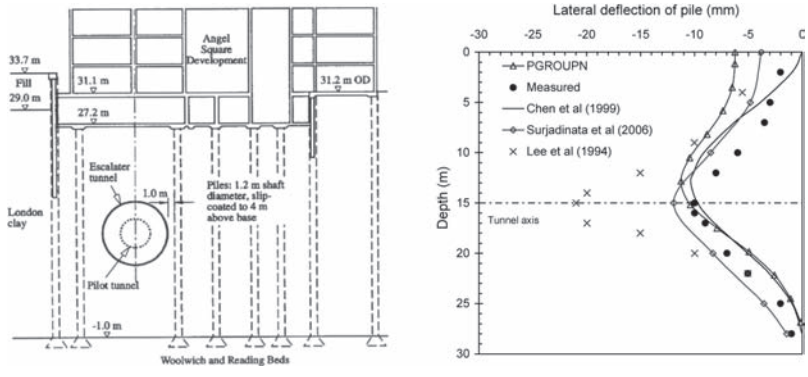

Figure 10. Case history analysed and comparison of pile deflections.

4 CASE HISTORY

Validity of the approach is assessed through comparison with a case history reported by Lee *et al.* (1994) in which the lateral pile displacements were measured. The tunnel was excavated for the Angel Underground Station in London and involved two construction stages, *i.e.* a pilot tunnel of 4.5 m diameter, followed by an enlargement to 8.25 m diameter. Measured pile deflections were reported for a pile that had a diameter of 1.2 m and was located 5.7 m away from the tunnel. At the pile location, the depth of the tunnel axis level was approximately 15 m. Measured ground loss ratios were 1.5% for the pilot tunnel and 0.5% for the tunnel enlargement. The existing pile foundations were embedded in 28 m of London Clay underlain by the Woolwich and Reading beds. Ground investigation data showed that the average undrained shear strength of the London Clay increased linearly from about 50 kPa at the top to about 220 kPa at the bottom. To ensure consistency between analyses, the soil stiffness is derived from the correlation $E_s/C_u = 400$, the pile Young's modulus is 35 GPa, and the pile is analysed as a single fixed-head pile. The free-field tunnelling-induced ground movements are estimated by applying the solutions of Loganathan & Poulos (1998) to each construction stage, with the final ground response obtained by superposition.

Figure 10 shows a comparison of the pile lateral deflections, including the results from the two-stage approaches of Chen *et al.* (1999), based on BEM, and of Surjadinata *et al.* (2006), which adopts a combined 3D FEM-BEM approach. Also shown are the predictions from a complete 2D FEM analysis by Lee *et al.* (1994). A favourable agreement between profiles is found, except for a general over-prediction of the finite element analysis. The above results lend further confidence in the application of simplified two-stage approaches in design.

5 CONCLUSIONS

A practical method of analysis for estimating the deformations, loads and moments induced on existing pile foundations during the tunnelling excavation has been suggested. The method is based on a two-stage approach: (1) estimate of the free-field tunnelling-induced ground movements, and (2) analysis of the pile group subjected to the computed

free-field ground movements. The first step may be carried out using alternative procedures, ranging from empirical methods and closed-form analytical solutions to 3D numerical analyses. The second step is performed by PGROUPN, a computer program for pile-group analysis based on a non-linear boundary element solution. Validity of the approach has been assessed by comparison with alternative numerical solutions and a published case history. Based on the results presented in the paper, a number of considerations may be made:

- The proposed approach is capable of generating reasonable predictions of pile-group response for many design cases, thus offering a practical compromise between the limitations of current analysis methods (mainly restricted to the linear elastic range or to single-pile response) and the complexity and time-consuming nature of complete 3D analyses of tunnel-soil-pile interaction. Due to the negligible computational costs (both in terms of data preparation and computer execution times), a large number of cases can be analysed efficiently, enabling parametric studies to be readily performed.
- Group interaction effects have an influence on the pile-group deformations and load distribution. In particular, the effects of pile-to-pile interaction lead to a reduction (*i.e.* a beneficial effect) of the maximum values of bending moment and, especially, axial force in the most heavily loaded pile of the group, as compared to a single isolated pile located at an equal horizontal distance from the tunnel centerline.
- Soil nonlinearity effects generate a significant reduction of the maximum axial force in the pile, as compared to a linear elastic analysis, thereby allowing a more realistic and economical prediction of pile-group response.
- The general characteristics of tunnelling-induced pile behaviour predicted by two-stage analyses are found to be similar to those from complete 3D analyses of tunnel-soil-pile interaction, with the two-stage analyses generally over-predicting the maximum values of pile displacements, forces and moments (*i.e.* on the conservative side).
- Two-stage combined approaches, in which the free-field ground movements are predicted by a rigorous FEM or FDM analysis and the pile-group response is predicted by a relatively simple BEM analysis (such as PGROUPN), have the potential to generate economical predictions for many cases of practical interest, thus representing a major saving over the cost of conducting a complete 3D FEM or FDM analysis.

REFERENCES

Basile, F. 2003. Analysis and design of pile groups. In John W. Bull (ed.), *Numerical Analysis and Modelling in Geomechanics*, Spon Press, Chapter 10: 278–315.

Basile, F. 2010a. Torsional response of pile groups. Proc. 11th DFI & EFFC Int. Conf. on Geotechnical Challenges in Urban Regeneration, London: 13p.

Basile, F. 2010b. Pseudostatic analysis of pile groups under earthquake loading. *Proc. 14th Danube-European Conf. on Geot. Engineering "From Research to Design in European Practice"*, Bratislava, Slovakia: 19p.

Bond, A.J. & Basile, F. 2010. *Repute 2.0, Software for pile design.* Reference Manual, Geocentrix Ltd, UK: 49p.

Chen, L.T., Poulos, H.G. & Loganathan, N. 1999. Pile responses caused by tunnelling. *ASCE J. Geotech. and Geo–environmental Engng*. 125 (3): 207–215.

Itasca 2002. *FLAC3D User's Guide*. Itasca Consulting Group.

Kitiyodom, P., Matsumoto, T. & Kawaguchi, K. 2005. A simplified analysis method for piled raft foundations subjected to ground movements. *Int. J. Numer. Anal. Meth. Geomech. 2*9: 1485–1507.

Lee, R.G., Turner, A.J. & Whitworth, L.J. 1994. Deformations caused by tunnelling beneath a piled structure. *Proc. XIII Int. Conf. ICSMFE*, New Delhi: 873–878.

Loganathan, N., Poulos, H.G. & Xu, K.J. 2001. Ground and pile-group responses due to tunneling. *Soils and Foundations* 41 (1): 57–67.

Mair, R.J. Taylor, R.N. & Burland, J.B. 1996. Prediction of ground movements and assessment of risk of building damage due to bored tunnelling. *Proc. Int. Symp. on Geotechnical Aspects of Underground Construction in Soft Ground*, Mair & Taylor (eds), London: 713–718.

Mroueh, H. & Shahrour, I. 2002. Three–dimensional finite element analysis of the interaction between tunneling and pile foundations. *Int. J. Numer. Anal. Meth. Geomech. 2*6: 217–230.

Peck, R. 1969. Deep Excavations and Tunneling in Soft Ground, State of the Art Report. *Proc. 7th Int. Conf. ICS-MFE*, Vol. III, Mexico: 225–281.

Pound, C. 2003. Session 1: Prediction of damage to buildings and other structures from tunnelling. *Proc. Int. Conf. on Response of buildings to excavation-induced ground movements*. CIRIA Special Publication SP201, London: 27–34.

Sagaseta, C. 1987. Analysis of undrained soil deformation due to ground loss. *Geotechnique* 37 (3): 301–320.

Surjadinata, J., Carter, J.P., Hull T.S. & Poulos, H.G. 2006. Analysis of Effects of Tunnelling on Single Piles. *Proc. 5th Int. Symp. Geotech. Aspects of Underground Construction in Soft Ground*, Amsterdam, 15–17 June 2005, Edited by Kwast *et al.*: 665–671.

Verruijt, A. & Booker, J.R. 1996. Surface settlement due to deformation of a tunnel in an elastic half plane. *Geotechnique* 46 (4): 753–756.

Xu, K.J. & Poulos, H.G. 2001. 3-D Elastic analysis of vertical piles subjected to passive loadings. *Computers and Geote-chnics* 28: 349–375.

Geotechnical Aspects of Underground Construction in Soft Ground – Viggiani (ed)
© 2012 Taylor & Francis Group, London, ISBN 978-0-415-68367-8

Prediction of surface settlements induced by TBM using Artificial Neural Networks method

R. Boubou
Lyon University, INSA—Lyon, LGCIE, France

F. Emeriault
Grenoble INP, Laboratoire 3SR, CNRS, Grenoble, France

R. Kastner
Lyon University, INSA—Lyon, LGCIE, France

ABSTRACT: This paper presents a methodology to correlate ground surface movements and TBM operation parameters based on Artificial Neural Networks. The methodology is applied to the vertical ground surface movements obtained on Contract 2 (4.7 km long) of the subway line B tunnel of Toulouse (France) excavated with an Earth Pressure Balanced TBM. The determination of the most influential TBM operation parameters is based on an elimination procedure. The employed ANN allowed also to study the effect of different types of soil on ground movements.

1 INTRODUCTION

Tunnels built in urban zones are generally, for economic reasons shallow tunnels. The construction of this kind of tunnels can not be realized without having an impact on the existing buildings. The use of new construction methods such as shield Tunnel Boring Machine (TBM) enables to control ground deformations and to guarantee stability in variable geological contexts. In order to ensure an optimal performance of the TBM, it is necessary to identify well the role of its different operation parameters which control the displacements created during different excavation phases. Theses displacements are transmitted towards surface and the resulting ground settlements can affect the nearby constructions. The reduction of ground displacements requires a good knowledge of the TBM operation parameters which are indeed related to many other elements such as the nature and the mechanical characteristics of the excavated soils, the tunnel dimensions, its depth and the performance of excavation ensured by the TBM.

According to the observations carried out on various building sites, the description of settlements has been until recently mainly based on geological and geometrical parameters (Peck 1969). Comprehensive numerical and analytical analysis (Vanoudheusden 2006, Kasper & Meschke 2006) are still time consuming methods and alternative approaches are required to correlate ground movements to TBM operation parameters. In addition, these methods have for the moment considered only simple parameters of the ground-machine interaction. The pressures applied by the TBM during the various phases of confinement (Oota et al. 2006) and annular void grouting (Komiya et al. 2001) are thus generally regarded as the most influential factors on ground displacements. Other TBM operation parameters have also been studied such as the TBM advance rate (Melis et al. 1997), the jack thrusts (Matsushita et al. 1995) and the parameters of TBM deviations during its advance (Vanoudheusden 2006).

Recent studies showed that the artificial neural network (Shahin et al. 2004, Jaksa et al. 2008) can be employed successfully for the prediction of settlements induced by tunnelling (Neaupane & Adhikari 2006, Yoo & Kim 2007). Compared to the usual design methods, they allow analyzing a larger quantity of data by integrating more complicated nonlinear combinations (Kim et al. 2001). The excavation parameters, particularly those of TBM operation, are more easily analyzed with ANN (Javadis 2006, Santos & Celestino 2008). This approach is less severe on the consideration of the geological conditions for settlements prediction; it does not require an identification of the soils' constitutive laws and parameters to represent the variability of the ground (Yoo et al. 2009).

The aim of this paper is to propose and evaluate a methodology based on the ANN to predict

vertical ground surface movements, taking into account TBM operation parameters and other geological (nature and thickness of the different soil layers concerned by the tunnel excavation) and geometrical parameters (diameter and depth of the tunnel). The methodology is applied to the particular case study of Contract 2 of Toulouse subway line B tunnel (France). This 4.7 km long tunnel has been excavated by an Earth Pressure Balanced machine (EPB) in the highly overconsolidated Toulouse "molasses". Then, a procedure of successive elimination is proposed to identify the most influential TBM operation parameters affecting settlements. Concerning the geological parameters, the effect of different types of soil on the form and the amplitude of displacements will also be analyzed.

2 CASE STUDY: TOULOUSE SUBWAY LINE B TUNNEL

The 12.6 km long subway line B of Toulouse has been realized with three different pressurized-face TBM techniques: earth pressure balanced TBMs for contracts 2 and 5; slurry shield machine for contract 4; and contract 3 was realized by a compressed air TBM. The tunnels run through the Toulouse "molasses" (hard sandy clay with pockets and lenses of very dense sand). Geotechnical investigations have shown that in these formations, K_0 is greater than 1, generally close to 1.7 (Vanoudheusden 2006). This molasses are covered by alluvia formations and made ground. The excavated diameter is 7.8 m for Contract 2 with a cover ranging from 1.2 to 2.8 diameters. The water table is mostly found 4 m below ground level.

The research project METROTOUL (2002–2005) has been initiated to collect and analyze the results of the different monitoring devices installed during the excavation of the tunnel as well as several of its 21stations (Vanoudheusden 2006).

2.1 *Geological database*

The geology has been determined by more than 300 boreholes drilled within 30 to 50 m from the tunnel axis and through all the soil layers of interest to the project (Antea et al. 2000). On the average, one investigation point was installed every 63 m along the tunnel drive.

For the analysis presented in this paper, the geological data of Contract 2 containing nature and thickness of each soil layer were collected from the boreholes carried out on this contract. The different soil layers are distributed in five categories: Cover (alluvium or fill), Clay, Sandy clay, Sand and "Hard" conglomerate.

The thickness of each type of soil was calculated between the level of the tunnel axis and the ground surface. Statistical analysis is carried out to determine the most frequent geological profiles (Table 1). For this statistical analysis, the thickness of each soil layer is normalized to the tunnel axis depth.

Table 1. Most frequent geological profiles found in the boreholes of Contract 2.

Profile	Cover %	Clay %	Sandy clay %	Sand %	Hard %	Frequency %
1	25	3	45	22	5	12.63
2a	30	40	20	0	10	8.42
2b	30	40	30	0	0	8.42
2c	40	30	30	0	0	8.42
2d	42	26	26	6	0	8.42

Only 95 boreholes were considered in this analysis (the closest boreholes to the 95 transverse settlement profiles containing at least 3 levelling points). The main five geological profiles which represent almost half of the cases found along Contract 2 will be employed in the analysis.

2.2 *In-situ measurements*

The vertical ground surface movements were monitored during the different tunnelling phases by precise levelling of transverse profiles installed every 30 m along the tunnel drive. Each profile consists of at least 5 points located on pavement or on the nearby buildings. Unfortunately, the number of monitoring points close to the tunnel axis is very small (precise levelling is a manual operation and therefore, for safety reasons, only a few points were installed in the middle of streets or boulevards when the tunnel alignment was following them). For the analysis presented in this paper, only points located on buildings are employed, considering that the corresponding movements appeared to be more accurate than those of points installed on the pavement. Based on the small observed amplitudes of displacements and their fast stabilization, only short-term movements (compiled between –20 m and +50 m after the TBM passage) are considered in this analysis. Figure 1 shows the measured ground displacements represented in a cross section according to X/H, with X the horizontal distance of the levelling point from the tunnel axis and H is the depth of the tunnel axis in the corresponding cross section.

It should be mentioned that the data presented were collected along the Contract 2 (4.7 km) where the variation of the TBM operation parameters along it, can affect the form and amplitude of the displacement trough and which explains the observed variation of displacements with X/H. At the ends of the settlement trough (±4X/H), the

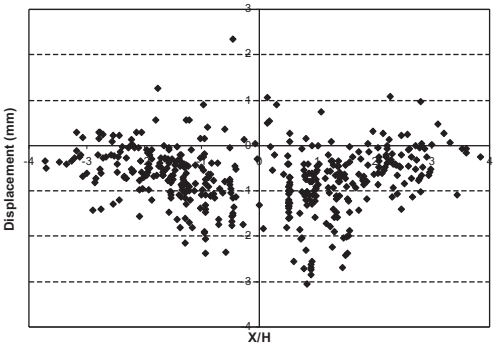

Figure 1. Ground surface displacements measured along Contract 2, represented in cross section.

small movements can be related to the uncertainty of measurements which can thus be estimated at approximately ±0.5 mm. The simulation of such small displacements is one of the difficulties of this analysis, especially with the measured accuracy of about 0.5 mm.

More than 150 TBM operation parameters were recorded on Contract 2. In a first analysis, the following 10 main parameters have been selected by Vanoudheusden (2006): TBM advance rate, hydraulic pressure used for the cutting wheel, confining pressure at the tunnel face, annular void grouting pressure and volume of grout, total jack thrust, time required for the excavation and installation of one tunnel lining ring, horizontal and vertical guidance parameters *Diffdh* and *Diffdv* (which represent change in horizontal and vertical TBM divergence from the design alignment) and total work required for one ring excavation.

3 GROUND SURFACE DISPLACEMENTS PREDICTION

An ANN methodology was used to determine correlation between ground displacements and TBM parameters. The analyzed TBM operation parameters were selected by a preliminary analysis [Boubou *et al*. (2009)] carried out on this contract which did not consider the geological variability along the tunnel drive. The elimination procedure (section 4) used to determine the most influential TBM operation parameters showed that the best description of the observed ground displacements is obtained with the following 7 parameters: TBM advance rate, confining pressure at the tunnel face, vertical guidance parameters *Diffdv*, total jack thrust, the volume of injected grout, hydraulic pressure used for the cutting wheel, and the time required for the excavation and installation of one tunnel lining ring.

In this study, these 7 parameters are employed as the ANN inputs in addition to 5 other parameters representing the geology (thickness H_i of each type of soil). A last parameter [exp $(-X^2/H^2)$] which represents the horizontal distance between the levelling point and the tunnel axis normalised by the tunnel depth was added to the ANN inputs. This parameter was used in order to privilege the data that are close to the tunnel axis (which are of small quantity) by considering an exponential form of X/H.

Out of the 432 available levelling points (Fig. 1), the points that do not belong to a transverse profile of at least 3 points and up to 5 points have been discarded. Thus only 95 levelling points have been considered and their corresponding data have been associated to local geology resulting from the analysis of the closest boreholes.

The optimized ANN geometry is then the following: 13 inputs, two hidden layers with 7 neurons in each one, one output. An optimal number of 6000 calculation cycles was used to perform the ANN training, where 60% (57 values) of data have been used for the actual training and the remaining 40% (38 values) for the validation step. The ANN performance is evaluated by the Root Mean Square Error (RMSE) of the validation step given by Equation 1:

$$RMSE\ \% = \frac{\sqrt{\frac{\sum (S^2 - C^2)}{N}}}{\sqrt{\frac{\sum S^2}{N}}} \quad (1)$$

where S is the measured value of the displacement; C is the value of the displacement computed by the ANN; and N is the number of considered points for the validation set of data. This definition implies that RMSE should be as low as possible.

The first calculation yields value for RMSE equal to 13.13% at the validation step (Fig. 2). The histogram of the differences between calculated and the corresponding measured displacements showed a Gaussian distribution with 76.3% of the differences smaller than 0.75 mm (Fig. 3).

Calculated settlement trough was drawn in a cross section for the set of mean values of TBM parameters by varying X/H between –4 and +4. Considering the five main geological profiles, Figure 4 shows that the shape of the settlement trough is strongly influenced by the geological conditions. Profile 1 having 22% of sand gave a true settlement trough without the heave behaviour that is observed in some case close to the trough centre. On the other hand, the presence of 10% of conglomerate in the profile 2a induces the smallest settlement at the tunnel axis of all five geological

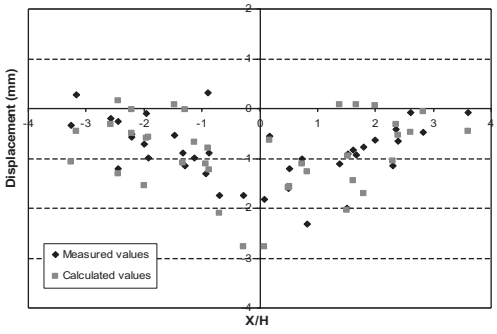

Figure 2. Calculated against measured displacements (validation step).

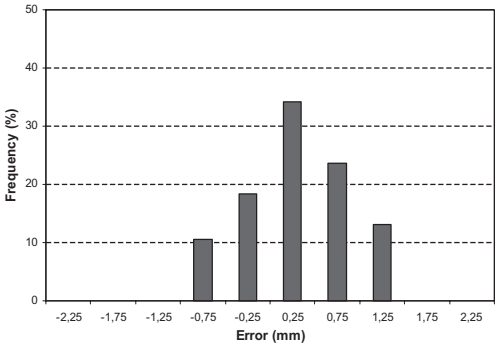

Figure 3. Histogram of the differences between measured and calculated displacements.

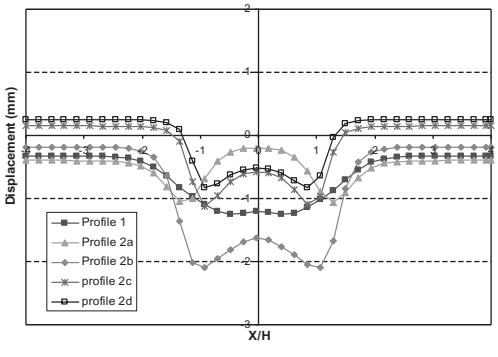

Figure 4. Displacement troughs traced for the principal geological profiles of Contract 2.

profiles. The predicted heave in the trough centre is relatively more important for the profiles 2a, 2b and 2c having an important existence of clayey soil. This behaviour has been observed on all the contracts of Toulouse subway line B and numerical simulation has shown that it can be explained by the highly overconsolidated character of the soil

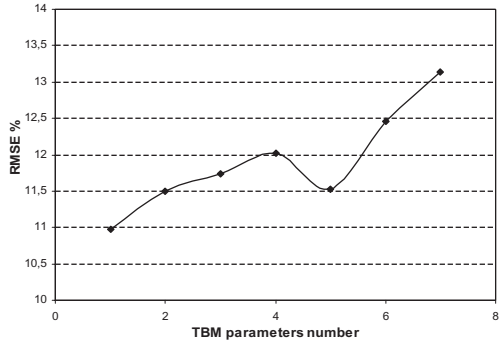

Figure 5. Evolution of RMSE value according to the number of TBM operation parameters employed in the analysis.

(in particular the clayey molasses) and the corresponding value of K_0.

In order to classify the TBM operation parameters according to their influences on displacements prediction, a procedure of successive elimination of parameters (Boubou et al. 2009) has been applied to the 7 parameters used in this analysis.

4 TBM PARAMETERS ELIMINATION PROCEDURE

The principle of this procedure is that at each step, the parameter that degrades the least the RMSE value when it is not considered in the ANN calculation will be eliminated. It has been noticed that the elimination of some parameters can even improve the RMSE value. The successive elimination of the parameters decreased the value of RMSE up to 5 parameters when this value starts to increase again (Fig. 5). Thereafter the value of RMSE starts to degrade, which is related to an insufficient number of parameters employed in the analysis (conclusion also confirmed by the histogram of the error distribution).

The optimal number of parameters is then 5 parameters, the classification of these parameters according to their importance is presented in Table 2.

The analysis carried out after the elimination of the two least influent parameters (P_1 and P_2) reduces the RMSE value to 11.5%. In this case (calculation with 11 parameters) 81.6% of the points present a difference between predicted and observed displacement smaller than 0.75 mm, compared to 76.3% in the initial case with 13 parameters (Fig. 6).

It can be concluded that the ANN is well adapted to the description of ground surface vertical movements and correlation with TBM parameters. The

Table 2. Classification of TBM parameters according to their relative increasing importance.

N	Parameter
1	Time required for one tunnel ring realisation
2	Hydraulic pressure used for the cutting wheel
3	*Diffdv*—vertical guidance parameter
4	TBM Advance rate
5	Confining pressure
6	Volume of injected grout
7	Total jacks thrust

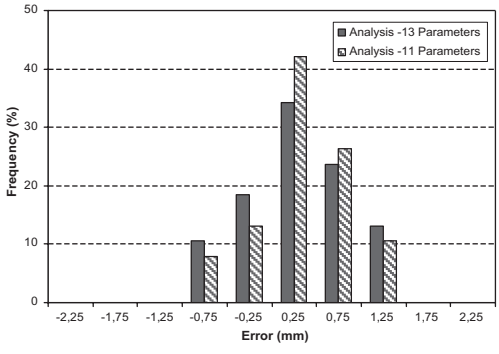

Figure 6. Error distribution histogram for two cases with 11 and 13 parameters employed in the analysis.

proposed methodology is based on both TBM operation parameters and geological data without defining any correlation between ground surface displacements and the employed data. The ANN is based on the training examples in order to calculate the required displacement. Using an optimal number of TBM operation parameters improves the prediction results. A parametric study will thus be required in order to better interpret and physically estimate the influence of each parameter on the results. Concerning the geological data, the role of each geological profile will be presented in the following section.

5 EFFECT OF THE GEOLOGY ON GROUND SURFACE DISPLACEMENTS PREDICTION

In this analysis, the percentages of each type of soil will be varied around the percentages of one of the reference profiles (profile 2c in Table 1). Table 3 presents the different cases considered in the analyses based on the ANN with the 5 optimal TBM operation parameters.

For example, to study the effect of sand on ground displacements, three profiles were proposed

Table 3. Different geological profiles considered.

Profile	Cover %	Clay %	Sandy clay %	Sand %	Hard %
3	40	25	25	10	0
4	40	20	20	20	0
5	40	10	10	40	0
6	40	20	40	0	0
7	40	40	20	0	0
8	40	30	25	0	5
9	40	30	20	0	10
10	40	20	25	0	15

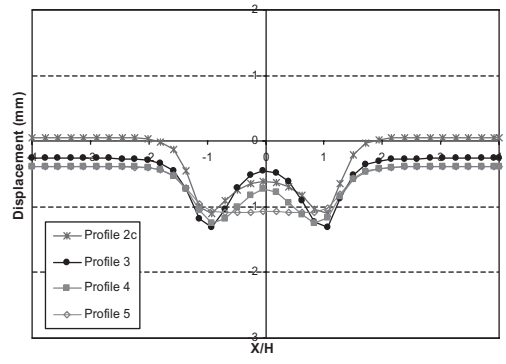

Figure 7. Effect of the sand percentage on the shape of the displacement trough.

(3, 4 and 5). The analysis shows that the observed heave behavior close to the tunnel axis is mainly related to the existence of the clayey soil.

The increase of the sand percentage (which is made by reducing the clay and the sandy clay percentages) in the suggested profiles 3, 4 and 5 gives a deeper settlement trough with a reduction in the observed heave close to the tunnel axis (Fig. 7). A settlement trough without the heave behavior is even obtained with the profile 5 (having 40% of sand and 10% of clay).

In a second step, the clay percentage was varied in the two profiles 6 and 7, the variation being made by varying the sandy clay percentage. Figure 8 shows that the increase in the clay percentage from 20 to 40% gives a deeper displacement trough with a more important heave effect close to the tunnel axis.

On the other hand, the increase of the percentage of conglomerate in the profiles 8, 9 and 10 (Fig. 9) induces a reduction in the maximum settlement at the tunnel axis and lessens the heave.

In conclusion, the higher percentages of the two types of soil "sand" and "hard" lessens heave effect close to the tunnel axis. The presence of clayey soil

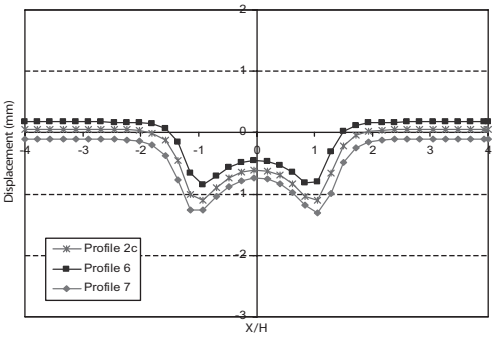

Figure 8. Effect of the clayey soil percentage on the shape of the displacement trough.

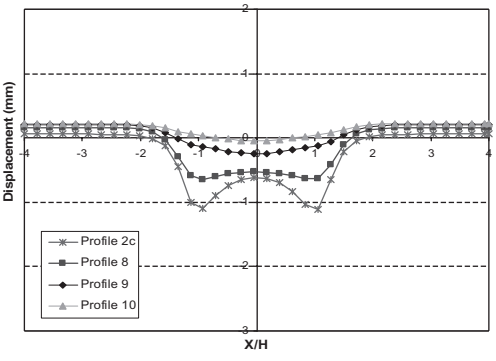

Figure 9. Effect of the hard soil percentage on the shape of the displacement trough.

gives a deeper displacement trough with heave close to the tunnel axis. It is recalled that this heave behavior has been explained by the overconsolidated character of ground particularly in the case of clayey profiles (Vanoudheusden 2006).

6 CONCLUSION

Ground movements induced by tunnelling and their correlation with TBM operation parameters and the surrounding geology were analysed using a methodology based on the artificial neural networks. Data of the Toulouse subway line B tunnel were employed to evaluate the ability of the suggested methodology to describe accurately the observed movements. The elimination procedure provided the five most influential TBM operation parameters on the ground surface settlements. Thus it is possible to analyse with the trained network the effect of the thickness of each type of soil on the shape and the amplitude of settlements. For example, the important presence of sand induces an increase in settlement whereas that of clay induces a modification of the shape of the settlement trough (with possible heave in the vicinity of the trough centre). The presented analysis showed that, based on the available excavation data, artificial neural networks can be a useful tool to predict the displacements induced by the TBM. It must be stressed that the proposed methodology does not require any a priori assumption on the shape of the settlement trough or on the relations between settlements and TBM operation parameters. The results obtained are acceptable even when in the considered case study the measured displacements are relatively small compared to the measurement accuracy. This type of analysis can be employed to determine, on a specific case, the required phenomenon or features to take into account in complex numerical models at a design phase. The developed methodology should be applied in the analysis of other cases of tunnel excavations in other geological contexts and/or with other types of TBM.

REFERENCES

Antea—Temsol—Cebtp – 2Gh, Ligne B – Reconnaissance géologique, géotechnique et hydrogéologique, rapport de synthèse B1998-0101-M, 1998, Document B-AVP-ANT-RA-715-LB-00 0.

Boubou, R., Emeriault, F. & Kastner, R. 2009. Prediction of surface settlements induced by tunnel boring machines using artificial neural networks method. In *2nd International Conference on Computational Methods in Tunnelling-EURO:TUN 200; Bochum*: 627–632.

Jaksa, M.B., Maier, H.R. & Shahin, M.A. 2008. Future challenges for artificial neural network modelling in geotechnical engineering. In *12th International Congress of IACMAG*; Goa, India: 1710–1719.

Javadis, A.A. 2006. Estimation of air losses in compressed air tunneling using neural network. *Tunnelling and Underground Space Technology*, vol. 21: 9–20.

Kasper, T. & Meschke, G. 2006. A numerical study of the effect of soil and grout material properties and cover depth in shield tunnelling. *Computers and Geotechnics*, vol. 33: 234–247.

Kim, C.Y., Bae, G.J., Hong, S.W., Park, C.H., Moon, H.K. & Shin, H.S. 2001. Neural network based prediction of ground surface settlements due to tunnelling. *Computers and Geotechnics*, vol. 28: 517–547.

Komiya, K., Soga, K., Agaki, H., Jafari, M.R. & Bolton, M.D. 2001. Soil consolidation associated with grouting during shield tunneling in soft clayey ground. *Géotechnique*, vol. 51, n°10: 835–846.

Matsushita, Y., Iwasaki, Y., Hashimoto, T. & Imanishi, H. 1994. Behaviour of subway tunnel driven by large slurry shield. In *Geotechnical aspects of underground Construction in Soft Ground*; 1994: 253–256.

Melis, M., Arnaiz, M., Oteo, C.S. & Mendana, F. 1997. Ground displacements in Madrid soils due to tunnel

excavation with earth pressure TBM. In *Int. Conf. Soil Mech. and Foundation Engineering*; Hamburg: 1433–1436.

Neaupane, K.M. & Adhikari, N.R. 2006. Prediction of tunneling-induced ground movement with the multi-layer perceptron. *Tunnelling & Undergr. Space Tech.*, vol. 21: 151–159.

Oota, H., Nishizawa, K., Hashimoto, T. & Nagaya, J. 2006. Prediction of shield tunnelling influences on ground deformation based on the construction process. In *Geotechnical aspects of underground construction in soft ground;* Amsterdam: 275–281.

Peck, R.B. 1969. Deep excavations and tunneling in soft ground. State-of-the-Art report. In *7th International Conference on Soil Mechanics and Foundation Engineering; Proc. vol. 3, Mexico, 1969:* 225–290.

Santos, Jr. O.J. & Celestino, T.B. 2008. Artificial neural networks analysis of Sao Paulo subway tunnel settlement data. *Tunnelling & Undergr. Space Tech.*, vol. 23: 481–491.

Shahin, M.A., Maier, H.R. & Jaksa, M.B. 2004. Data division for developing neural networks applied to geotechnical engineering. *Journal of Computing in Civil Engineering*, Vol. 18, n°2: 105–114.

Vanoudheusden, E. 2006. *Impact de la construction des tunnels urbains sur les mouvements de sol et le bâti existant, Incidence du mode de pressurisation du front*. PhD thesis, INSA of Lyon: 294 p.

Yoo, C. & Kim, J-M. 2007. Tunneling performance prediction using an integrated GIS and neural network. *Computers and Geotechnics*, vol. 34: 19–30.

Yoo, C., Kim, S.B. & Jung, H.S. 2009. Prediction of ground settlement during tunnelling in water bearing ground. In Hamza et al. (eds), *17th Int. Conf. Soil Mech. & Geotechnical Eng.*; Alexandria, Egypt: 1953–1956.

This page intentionally left blank

Geotechnical Aspects of Underground Construction in Soft Ground – Viggiani (ed)
© 2012 Taylor & Francis Group, London, ISBN 978-0-415-68367-8

Durability of calcarenitic hypogea in the underground cultural heritage of Palermo (Sicily)

M. Zimbardo, L. Ercoli & N. Nocilla
Dipartimento di Ingegneria Strutturale, Aerospaziale e Geotecnica, Università di Palermo, Italy

ABSTRACT: The paper deals with the stability conditions of hypogea, several hundred m^2 wide, dating from the Punic period to the XIX century, dug out of the calcarenitic table that makes up the bedrock of the Plain of Palermo in the Fossa della Garofala. This work concerns the influence that the shape of the hypogea and the characteristics of the lithotypes wields on the instability and decay phenomena taking place, by mean of laboratory tests on the calcarenite and parametric numerical models. The comparison between the numerical models and the actual instability phenomena validated the use of the empirical formula of Hoeck to the mechanical characterization of complex structured rock-mass in soft rock.

1 INTRODUCTION

Fossa della Garofala is the last part of the Conca d'Oro landscape, now totally immersed in the urban area, in which the geological and geomorphological values are compounded by cultural values that cover a span of history from the Punic period to the XIX century.

In a city where, as everywhere densely urbanized, it is almost impossible to read the features of the original environment, this area provides a rare synthesis of natural and anthropogenic environment of great cultural interest. Fossa della Garofala is a narrow valley carved by the stream Kemonia, not far from the nucleus of the Punic town of Palermo (Fig. 1).

Calcarenitic outcrops and the large supply of underground water since ancient times represented a resource for human activities, the first traces of which go back to proto age.

The systematic attendance of places was encouraged certainly by very striking undermining the foot of the slopes, which led to the formation of grottoes used as a shelter from since antiquity until the last war.

2 GEOLOGY AND MORPHOLOGY

Most of the calcarenitic bedrock of the Palermo Plain probably formed during the Sicilian Age in coastal and shallow sea environment; the last trasgressive cycle in the Palermo Plain is represented by the post-Tyrrhenian marine deposits found at an elevation of 21 m above sea level in the Papireto depression, near the Fossa della Garofala.

The neo-tectonic and climatic events that have occurred since the Pleistocene Epoch, from the alternating marine/continental phases to the final emersion are clearly visible on the rocky walls of the Fossa della Garofala. The valley profile, 1.8 km long, develops between 70 m and 30 m above sea level with a mean slope of 2%, which was carved out by the Kemonia creek on the calcarenitic table. The Kemonia flows between the two faults that are the boundaries of the Monreale graben, and reveals how tectonics exerted a strong control over the subterranean and superficial hydrography of the Plain of Palermo.

The calcarenitic body shows both the last marine sedimentation processes during interglacial periods both the erosion processes of the valleys during the continental phases, due to glaciations.

The most important aspect of the continentality phases is to be found in the valley's morphology. In fact, the deep incision of the valley, in respect of the Kemonia's small watershed, can be seen as the combined effect of the lowering of the sea level during glacial periods and the progressive neotectonic upgrowing of the ground at a rate of about 20 cm/1000y.

The valley's first erosion phenomena were triggered during the Middle Pleistocene when a sharp reduction in environmental temperature was coupled with intense tectonic lifting which caused the emergence of a vast area of the Plain. At the beginning of the Upper Pleistocene, the progressive heating of the climate caused another marine ingression that was, however, mitigated by slow tectonic lifting and a temporary interruption of erosion processes.

These latter started again with great intensity at the beginning of the Wurm glaciation, at which

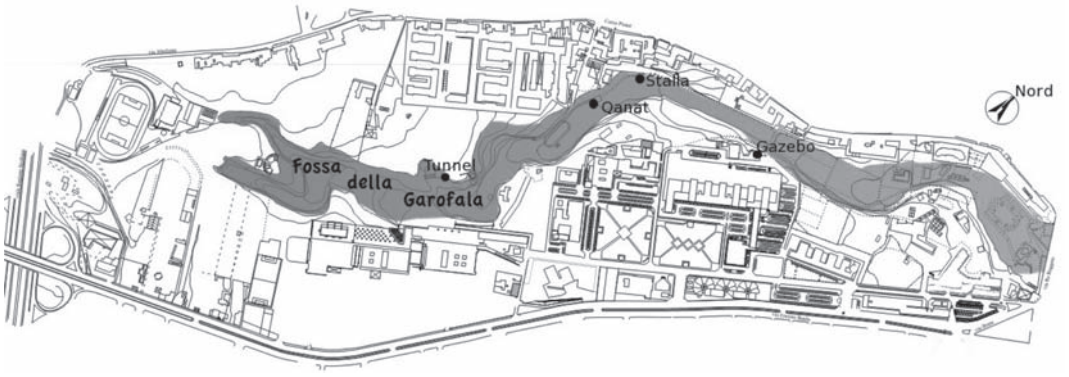

Figure 1. Map of the Fossa della Garofala.

time both sea level and the depth of the valley were at their minimum. The erosion of the valley continued until five centuries ago as the Arab geographer Ibn Hawqual reports. Evidence of the Kemonia's geomorphologic history are the sub-vertical rocky walls of the valley that were cut by the flow of water, the shallow subsurface flow that feeds a rich riparian embankment and several grottoes that were.

3 CULTURAL HERITAGE

The first signs of human activity are of protohistoric age, as witnessed by the oven tomb found on the extreme southern edge of the Fossa and by another similar cavity, presumably of the same age, found a little further north on a big rocky outcrop.

The erosion at the base of the escarpments, which caused the formation of large grottoes, certainly encouraged the inhabitants to adapt these grottoes (Fig. 2a), a couple of metres high, about four metres deep and about ten metres long, to their own needs.

A curve tunnel branches off from inside one of these grottoes, that is partially enclosed by a wall, and penetrates deep into the rock, towards west (Fig. 2b).

To the north along the flanks of the valley, there are many deep hypogea.

Three of these hypogea are of particular importance. "Gazebo" hypogeum (Fig. 2c), so-called because the part in the open air houses a cast iron structure covering a circular tank. The shape of this tank could be compatible with an ancient system for retting plant fibres. Prince d'Aci used it as a fish tank, during the time of Prince d'Aumale it was reused as a covered dung pit (Biuso 1881).

The Gazebo hypogeum has a polygonal plain, about 400 m^2; it is enclosed on all sides by vertical rock walls, onto which five rectangular rooms open up. These rooms also have a rectangular plain or are L-shaped; the bottoms and walls waterproofed demonstrate that they were used as covered water tanks. There are two accesses to the hypogeum: an arch dug out of the rock and a curvilinear gallery, the cross section of which looks like the mouth of a furnace. Next to this is a very big hypogeum, that looks in plan like mesh, made up of a gallery from where other short galleries branch out. At the end of such galleries there is a shelf-like niche (Fig. 3b).

The hypogeum "Stalla" (Fig. 2e), so-called because it was last used as a stable (Biuso 1881), has only one room and is about 230 m^2 in size. The flat roof, that juts out for a width of about 8 m, is supported by pillars made of calcarenite ashlar blocks.

The same sort of stonework encloses the room, that is accessible through an ancient, pointed arch portal; it receives light through two windows of the same shape (Fig. 3a). There are traces of persistent water percolation on the walls: the back wall, shaped to fit a semi-circular niche (Fig. 2f) brings to mind the artificial Arab waterfalls of Arab-Norman buildings here the rock wall, is encrusted with carbonate concretions that indicate the presence of a now dried up spring. The shape of this hypogeum, with its semi-circular niche and its side tanks, makes you think it was used either for religious purposes or for retting papyrus fibres.

4 MACRO AND MICROTEXTURE OF THE ROCK

The rocky walls of the Fossa are made up of yellow bio-calcarenite, rich in macro-fossils concentrated in "nests" and sometimes in levels, konwn in the geotechnical literature as Nodular Calcarenite (CN), one of the main rock types, by extension

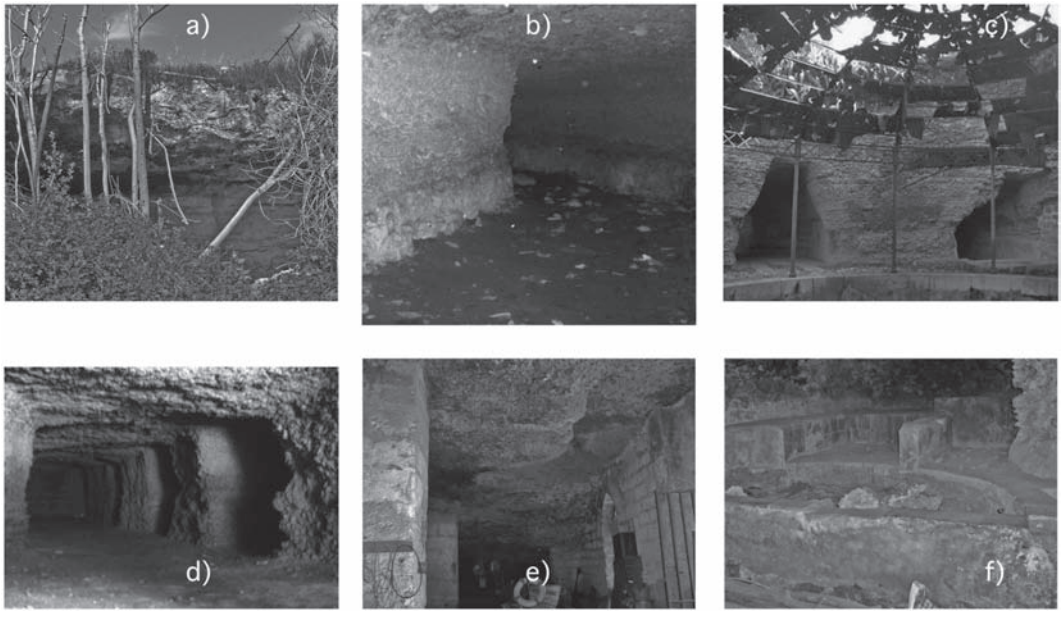

Figure 2. Hypogea in the Fossa della Garofala a) grotto; b) tunnel; c) Gazebo; d) "mesh" tunnels; e) Stalla; f) nichel.

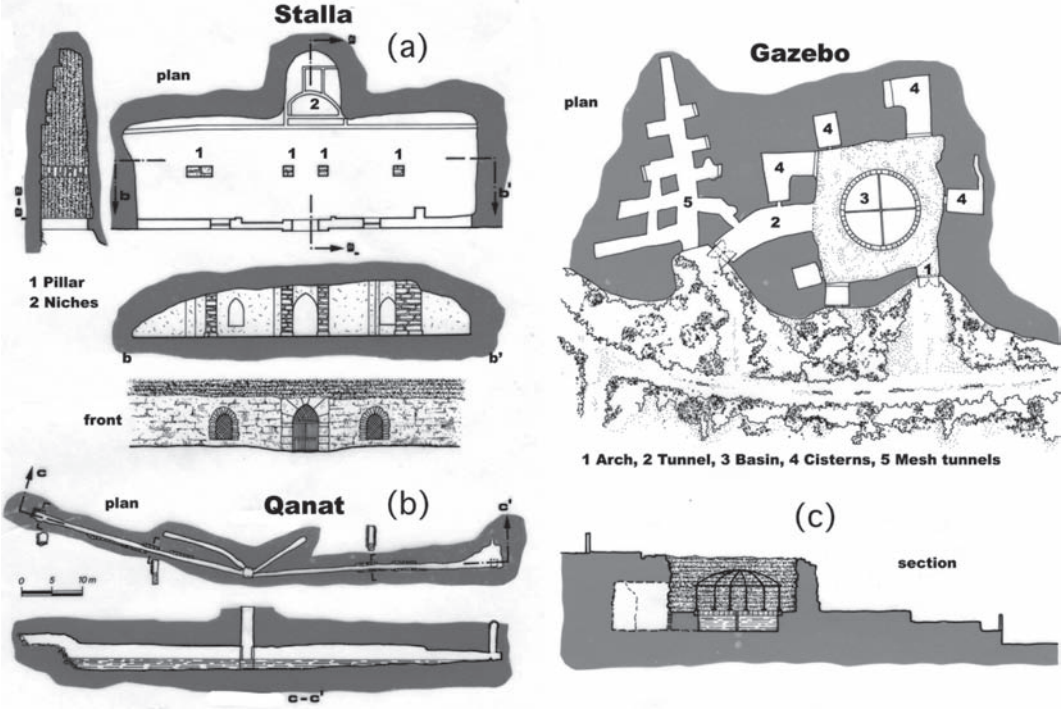

Figure 3. Plans and sections of the main Hypogea a) Stalla; b) Qanat; c) Gazebo and "mesh" tunnels.

and thickness, of calcarenitic Palermo formation (Nocilla et al. 2005).

The walls have a carious aspect to be referred to the presence of strongly cemented and welded nodules, while the inter-nodular spaces are filled with the same incoherent arenaceous material, that has often been removed by floating processes.

Two different levels can be recognised in terms of macro-structure: the lower one has sub-horizontal stratification, highlighted by selective erosion phenomena which gives it a strato-nodular layered texture. Localised structures, caused by currents, are concentrated near the contact with the upper one. This latter shows a chaotic distribution of the pseudo-nodules which indicates more variable deposition conditions (Fig. 4).

The selective erosion that has affected the calcarenitic deposit after emergence resulted in a progressive differentiation of levels with different degrees of cementation.

The nodules, centimeter in size, consist of sandstone clasts linked by sparitic cementation. They form a continuous but irregular level that assumes shapes and forms like animal figures, called "kindchen".

The banks with a nodular structure are frequently defined at the base and at the roof by thin layers of rock with texture more uniform and cementation more continuous; on the surfaces of these layers a thin coating of loose sand is present (Fig. 5).

Thin sections show that the rock is a biocalcarenite containing fragments of red algae, foraminifera and fragments of mollusc shells.

The rare lithic clasts are carbonate and sometime quartz. The particle size varies within the different depositional levels from very fine to medium-fine.

The grains are welded by a thin sparitic patina in the porous areas, spare calcite fills almost completely the intergranular voids in the nodules.

In the single layer, the nodules are "welded" together in points or in reduced areas of contact; similar "welding", less frequent and however with non-uniform distribution, can be seen, sometimes, in a vertical direction between nodules of adjacent layers.

Water seepage through the rock mass, particularly intense during the wet season, induces dissolution processes of the thin patina of sparite that wraps the grains; the weakly cemented areolae disaggregate: so that even unnoticeable flows cause the progressive removal of silt and fine sand, enhancing nodular structure of the rock.

The frame of the nodules within the banks, made therefore to the scale of decimeters, has been expressed in terms of packing density (PD) (Kahn 1956). Measurements provides average values of 50% (Fig. 6).

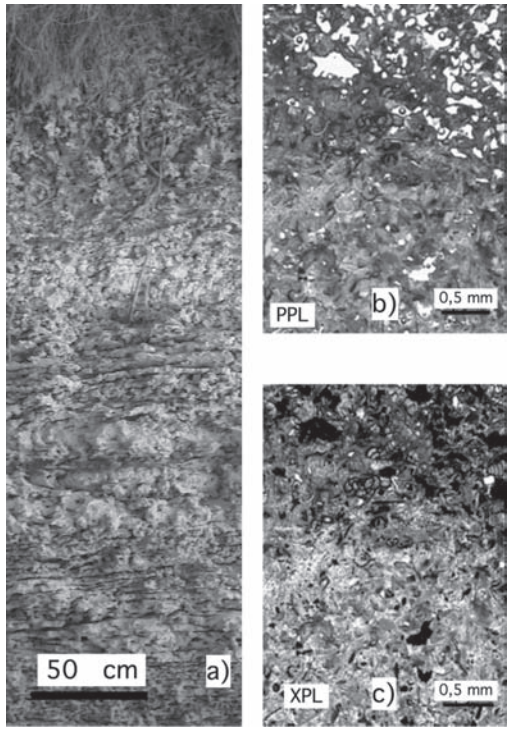

Figure 4. Structure of the rock-mass: a) microtexture of the calcarenite: b) thin section in plane polarized light c) thin section in crossed polarized light.

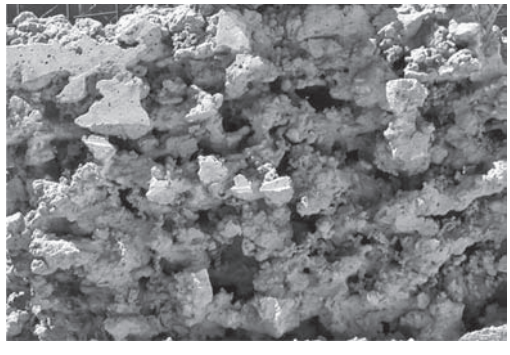

Figure 5. Locked nodules.

5 MECHANICAL CHARACTERIZATION

The mechanical characterization has been carried on both on single nodules both on strato-nodular samples. The weight per unit of volume of the rock varies between 17 e 22 kN/m^3, depending to the ratio, in the range 45%–60%, between the volume of the nodules and the total volume.

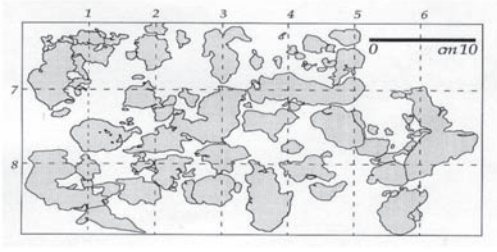

Figure 6. Measurement of packing density (PD) of the nodules.

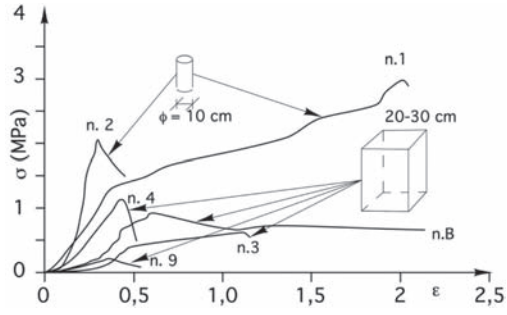

Figure 7. Uniaxial compression tests.

The strength of nodules has been obtained by point load tests, that give values of the uniaxial strength between 1 and 30 MPa ($\sigma_{fmean} \approx 10$ MPa).

The strength of the nodular bank was instead measured by uniaxial compression tests (Fig. 7) on cylindrical samples (10 cm diameter) and on roughly cubic blocks, with side ranging from 20 to 30 cm, shaped by mean of a bandsaw. Unlike the nodules, the uniaxial compression tests on the aggregate made of welded nodules and interlocked sands give values of σ_f considerably lower, ranging from 0.2 to 3 MPa; tests evidence a large scale effect.

This effect significantly influences the tangent modulus, that ranges between 50 and 1200 MPa.

The results of uniaxial compression tests (Fig.8) show that the values differ even an order of magnitude.

Consequently, at the scale of the rock-mass, the rock is classified as "very poor".

The heavily different mechanical behaviour of the strato nodular samples in respect to a single nodule causes the difficulty of reaching a reliable geotechnical modeling of the rock-mass.

As shear strength parameters were adopted the following values (Zimbardo 2009):

$c' = 500$ kN/m^2; $\varphi' = 33°$.

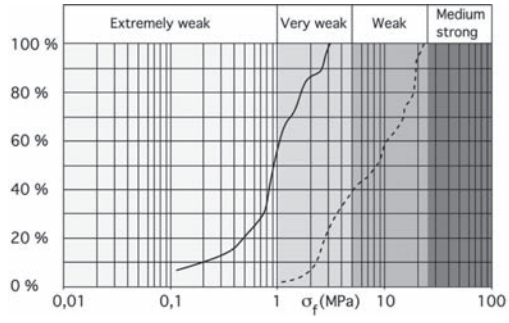

Figure 8. σ_f values distribution curve obtained by mean of uniaxial compressive tests on strato nodular samples and by mean of point load tests on the nodules.

In consideration of the scale effect and of the deformation characteristics, we have used too, the empirical method of Hoek, evaluating the GSI index.

The classification introduced by Hoek (1994), for very poor rock-mass made of sparsely interconnected elements (angular or sub angular) with surfaces of the individual elements little or very altered, indicates GSI values between 15 and 30.

The empirical formula relating the deformability modulus to GSI index, proposed by Hoek & Diederichs (2006) provides the following range of values:

$10 \div 86$ MPa

which may be considered acceptable according to the results of tests on samples of higher dimension.

6 DESCRIPTION OF THE INSTABILITY PHENOMENA

In the grottoes and in the hypogea, collapse occur from tunnel roofs and new fractures appear on the walls rock that separate the cavities.

At the bottom of the covered tanks in fact it's possible to see a growing accumulation of blocks and sand coming from the roof of the cavity, where fresh falls of slabs are evident (Figs 9a, b).

The most significant collapse occurred after the 2002 earthquake, these collapse in fact have caused a dangerous reducing of the roof thickness.

On rock diaphragm and sidewalls, irregular fractures very persistent, that divide the rock-mass in large blocks with a predominant vertical development, are present.

A thick natural vegetation (Celtis australis, Ailantus altissima, Rhamnus alaternus) in recent decades has grown to the crowning of the sub vertical walls that surround the hypogea or which are

Figure 9. Rock mass decay phenomena: a) fall of slabs b) development of cracks c) fall due to the pull out of the roots.

the sides of the valley. Both to the wedge effect of the roots, both the effect "sail" that the wind exerts on the foliage (Brown & Sheu 1975), (Nocilla 1999), caused significant collapse especially on the vertical walls of the valley (Fig. 9c).

7 ANALYSIS OF INSTABILITY PHENOMENA

The study of onset conditions of the instability phenomena was analyzed using a finite element program that allows stress-strain analysis at different, even in parametric terms, boundary conditions.

The analyses performed by varying the Poisson's coefficient between 0.2 and 0.4 show a modest influence of this parameter.

The following analyses were developed varying the E modulus value between 40 MPa, that is the mean value suggested by the elaboration proposed by Hoek, and 1000 MPa, that is close both to the maximum value determined by laboratory tests, both to the values given in the literature on the basis of back-analysis of vertical displacements of buildings in the Palermo calcarenite (Valore 1999).

The deformation values in the roof obtained assuming the minimum E value are comparable with those deduced from the measurements with the laser scanner; these latter, infact, evidence the misshapen of the roof in respect to original planarity of the strata.

For example, referring to a cavity 2 m large, for E = 40 MPa, in dry conditions the maximum vertical displacement of the roof is equal to 3.1 cm (Fig.10a), and it assumes values of 3.5 cm in presence of saturated soil. In the case of a larger span (3 m), e.g the "L-shaped" tank (Fig. 9a), the increasing of the deformation is noticeable: in dry condition it reaches the value 9,5 cm, in saturated condition 10,6 cm (Fig. 10b). The numerical analyses for the saturated condition are carried out in terms of effective stress. In this condition (S = 1) the phreatic level has been assumed at the ground level.

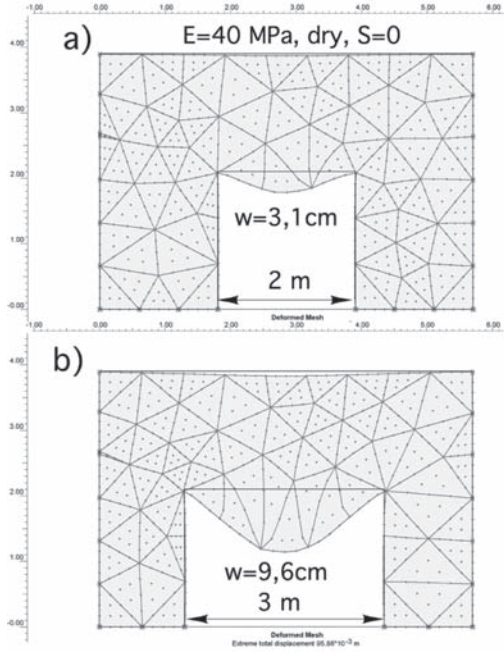

Figur 10. Displacements: E = 40 MPa, dry condition a) span 2 m, b) span 3 m.

For E = 1000 MPa the displacement in the roof is 0,12–0,14 cm respectively in dry and wet conditions(Fig. 11a). The same low values (0,38–0,42 cm respectively in dry and wet conditions) are obtained also considering the larger cavity (Fig.11b).

For the nodular calcarenite, the deformability characteristics of the rock-mass are, hence, properly indicated by the empirical formula of Hoek, and they are also close to the results obtained by laboratory tests on samples of larger size.

Shear stresses which would justify the failure events can only be obtained by considering larger spans or the pressure due to root systems.

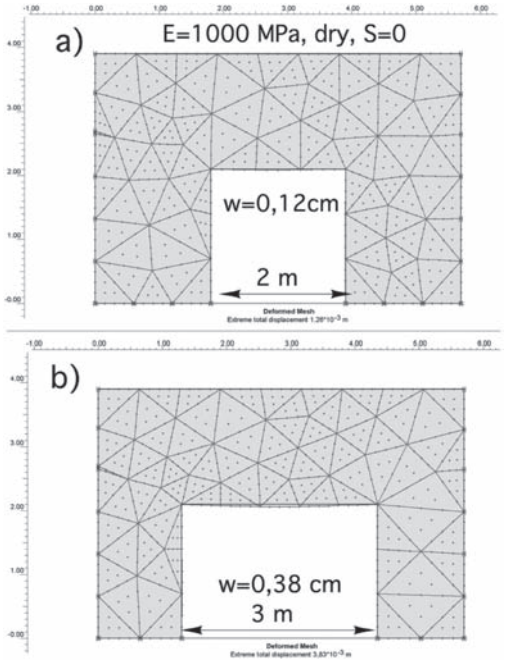

Figure 11. Displacements: E = 1000 MPa, dry condition a) span 2 m, b) span 3 m.

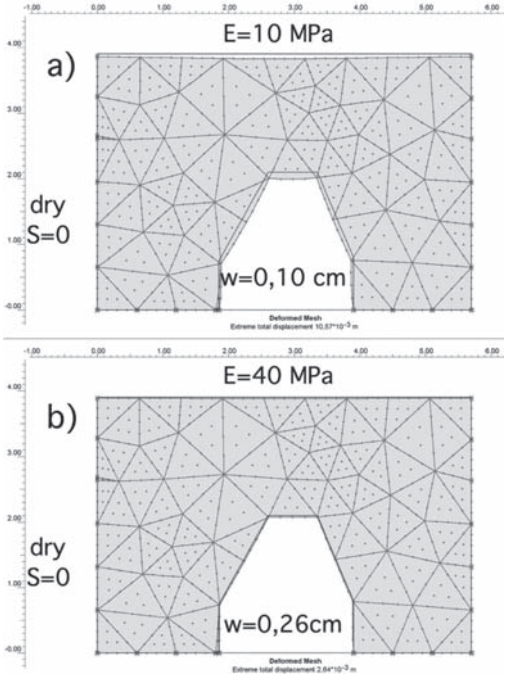

Figure 12. Displacements: a) E = 10 MPa, b) E = 40 MPa

As it is not known the intensity of the stress induced by the roots, the pressures were considered as uniformly distributed on the single layer surface and with the maximum value of 1 kPa: roof shear stresses of 0.2 MPa–0.4 MPa are achieved; these values are close to failure condition.

Some further analysis, assuming cusped shape (2–3 m large) provide deformations characterized by negligible vertical displacements, both in the case of E = 40 MPa, both for very high values of deformability (E = 10 MPa), that could be assumed merely in the case of a complete decay of rock mechanical charactericstics (Figs 12a, b).

The analysis and the surveys indicate the possibility of:

- detachment of slabs from the roof, making even more small thickness of the vault (e.g. slab fallen in the underground tank to the left of the access tunnel to "Gazebo");
- enlargement of fractures at first hidden or a little open, as in the small tank on the right side and in the rock architrave of "the arch entrance";
- neoformation of persistent fractures, such as in rock walls and in the arch of the entrance.

On the contrary no cracks neither slab falls are present on the vaults of the curved tunnel in plan, that in section have "cuspide shape", that is a typical shape used in Sicily from very ancient time (VI century B.C.) in the exploitation of weak rock masses (e.g. Hear of Dyonisus in Syracuse).

8 CONCLUSIONS

The structure of the rock mass, characterized by irregularly alternated nodular calcarenite banks and continuous layers of weakly cemented sands, plays an important role on the stability. In fact the rock-mass is like a sequence of flat subhorizontal plates.

In the interlayers it is possible the development of significant action of the roots of such magnitude as to give rise stresses and strains that lead damage failure.

The variability of the micro and macro texture characteristics of the rock generates an extremely complex structure, whose mechanical characterization was achieved in laboratory with uniaxial compression tests. For the characterization of the rock-mass it was necessary to refer to the Hoek empirical method.

The modeling has given values of deformation of the roof comparable with the deformed shapes of non collapsed vaults measured with a laser scanner.

The analysis also highlighted the influence of the saturation conditions of rock and subsequent

filtration processes. These processes not only lead an increment of the deformation in the roofs, but also lead the constant and continuous decay of the mechanical characteristics due to the corrosion of the weld between the nodules and due to the progressive removal of the grains of silt from the internodular voids and from sandy laminations.

REFERENCES

Biuso, S. 1881. Planimetria del parco di S.A.R. del Duca di Aumale. *Mappa acquerellata.* Archivio della Facoltà di Agraria Università di Palermo.

Brown, C.B. & Sheu, M.S. 1975. Effects of deforestation on slope *J. Geotech. Eng. Div*, ASCE, 101,GT2.

Hoek, E. 1994. Strengt of rock and rock masses *ISRM News Journal* 2, 4–16.

Hoek, E. & Diederichs, M.S. 2006 Empirical estimation of rock mass modulus *Int. J. Rock Mech. & Min. Sci.* 34 (8), 1165–1186.

Kahn, J.S. 1956. The analysis and distribution of the properties of packing in sand-size sediments part 1: on the measurement of packing in sandstones. *Journal of geology*, 64: 385–395.

Nocilla, N. 1999. Instabilità parietali e compatibilità ambientale. *AMBIENTE 2000*, 48.

Nocilla, N., Zimbardo, M. & Evangelista, A. & Ramondini, M. 2005. Caratterizzazione geotecnica di tipiche rocce tenere di Palermo. *Incontro Annuale dei Ricercatori di Geotecnica* Ancona.

Valore, C. 1999. Additional contribution to report nr 2: The role of calcarenites in the urbanization of Palermo. *Proc. 2nd Int. Symp. On Hard Soils—Soft Rocks*. Naples, 12–14 Oct. Balkema, Rotterdam, 3, 1269–1281.

Zimbardo, M., Ercoli, L. & Nocilla, N. 2008. Problemi di conservazione delle camere ipogee in calcarenite nella Fossa della Garofala (Palermo) *DIA.CO.MA. ST* Belvedere di San Leucio.

Zimbardo, M. 2009. Comportamento meccanico di rocce tenere: le calcareniti di Palermo e Marsala. *Tesi di dottorato in Ingegneria delle Costruzioni XXII ciclo* Napoli.

Geotechnical Aspects of Underground Construction in Soft Ground – Viggiani (ed)
© 2012 Taylor & Francis Group, London, ISBN 978-0-415-68367-8

Deep excavation in Bulgaria—comparison of measured and computed performance

A.E. Totsev
University in Sofia (UACEG), Bulgaria

ABSTRACT: This paper presents a comparison between the results of field monitoring during the construction of a bored pile wall anchored at level 4 with results computed by the finite element analysis (FEM) using the Mohr-Coulomb model and Hardening Soil model (PLAXIS Software). Field monitoring was carried out to measure wall displacement and anchor forces by using inclinometer measurement, geodetic surveying and resistance strain gauge measurement.

1 INTRODUCTION

A 14 m deep excavation for underground garages was planned during the construction of a new office-and-apartment centre in the town of Stara Zagora, Bulgaria. The southern and eastern sides of the excavation are situated next to a 9- and 5-storey building, respectively. The northern and eastern borders are the main streets in the city. Instruments for monitoring activities were concentrated in the northern side, next to Tsar Kaloyan St., where the excavation depth was 14.3 m (Fig. 2). There were no buildings or machines during the excavation works in that area. As a results, the interpretation of the experimental data was not affected by uncertainties associated to the presence of buildings.

Inclinometer measurement in the pile construction, geodetic surveying and resistance strain gauge measurement in the anchors and piles were made during all excavation stages. The results present the variation in the anchor forces, bending forces in the pile, lateral movements and elastic line of the wall. These data are used for comparison with the calculation results by applying different constitutive models.

2 SUPPORT CONSTRUCTION

The excavation was protected by bored pile walls supported by four levels of anchors (Fig. 1). The exact depth of the excavation is 14.30 m. The wall is made of drilled piles with a diameter of 0.40 m (Fig. 1). The piles are 13.00 m long with a 3.00 m embedded length. The pile spacing is 1.50 m. The anchors are 15 m long with force at installation zero. The diameter is 0.15 m. The anchor inclination is 15°–20°. A wooden plank is placed between the piles and in front of the soil. Above the pile head 4.30 m of the excavation is supported with soil nails, a steel net and shotcrete (Fig. 1). The reinforcing mesh is held in place with 2.0 m–2.5 m long soil nails. Shotcrete with a 3–5 cm thickness is designed to "close" the system. The construction of the retaining wall can be divided into the following separate phases (Fig. 2):

- Stage I: Excavation up to 2.00 m. Shotcrete with soil nails and reinforcing net;
- Stage II: Excavation up to 4.30 m. Shotcrete with soil nails and reinforcing net; Drilling and concreting the piles;
- Stage III: Excavation up to 5.30 m. Drilling and concreting the anchors—Level 1;
- Stage IV: Excavation up to 7.30 m. Drilling and concreting the anchors—Level 2;
- Stage V: Excavation up to 10.30 m. Drilling and concreting the anchors—Level 3;
- Stage VI: Excavation up to 12.30 m. Drilling and concreting the anchors—Level 4;
- Stage VII: Excavation up to 14.30 m.

3 FIELD MONITORING

The measurements made during excavation are used to describe the construction behaviour and consist of: 1. Anchor force measurement; 2. Lateral wall displacement measurement; 3. Pile elastic line determination; 4. Pile force measurement. Two different approaches based on the resistance strain gauge measurement are used for anchor force determination. An inclinometer was installed within a pile allowing for measurements

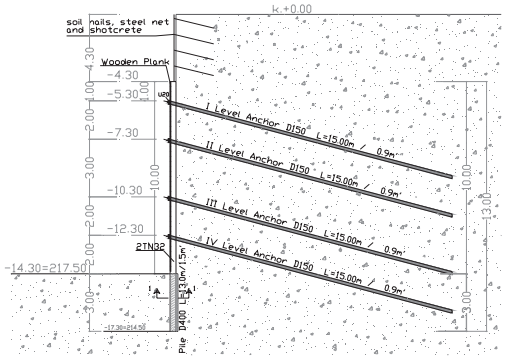

Figure 1. Cross section of excavation. Construction stage.

Figure 2. Northern part of the excavation.

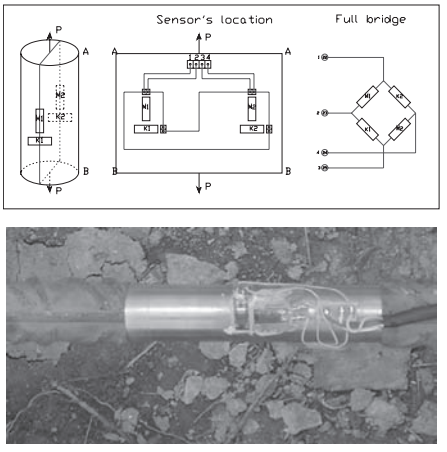

Figure 3. Anchor force measurement: design and arrangement.

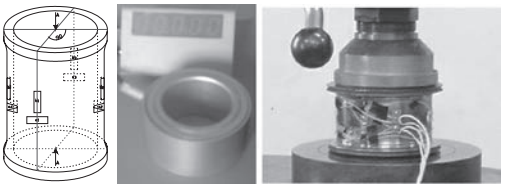

Figure 4. Dynamometer: design and arrangement.

of wall deflections. Additionally, the lateral wall displacement is determined by using geodetically gauging points.

3.1 *Anchor force measurement*

3.1.1 *Sensor bar*

Four strain gauges, two measuring and two compensating, connected in a full Wheatstone bridge were placed on the anchor bar (Fig. 3). The measurement technique used for the resistance strain implementation is Hottinger Baldwin Messtechnik-vd 73002. Two anchors on both sides of the inclinometer pile were investigated. The quality of the measuring system was laboratory tested before the field test realization. The results yielded a less than 2% error.

3.1.2 *Dynamometer*

A dynamometer was designed along with the sensor bar for the anchor force measurement. The same idea was implemented in manufacturing the dynamometer. Eight strain gauges (4 measuring and 4 compensating) connected in a full Wheatstone bridge were placed on the four main axes of a 5.5 cm high steel ring. The external and internal diameters of the ring are 10.5 cm and 7 cm (Fig. 4). Before using the dynamometer it was laboratory tested on 20t and 30t presses and the resultant deflections were less than 0.5% of the range (30t).

3.1.3 *Anchor forces*

The final values for the anchor forces determined after estimation of the available results are presented in Table. 1. The results for the different construction stages are summarised in Fig. 6.

3.2 *Bending moment measurement*

Foil strain gauges were also placed along the reinforcement length (2T-profile) to determine the pile forces using the same arrangement as that for the anchors (Fig. 5)

In view of protecting the individual gauging points from external effects, they were coated with strain gauge varnish, mastic, silicon and protective foil.

The measurement of the relative linear deformations was performed by resistance strain gauges based on the tensoeffect (the property of some materials to change proportionally their electric resistance under the action of the element deformation). The final values for the bending moments in the pile are presented in Table. 2. The results for the different construction stages are summarised in Fig. 6.

Table 1. Anchor forces [kNm].

	Anchor			
Stage	No1	No2	No3	No4
No1	–	–	–	–
No2	–	–	–	–
No3	–	–	–	–
No4	43.17	–	–	–
No5	80.22	94.21	–	–
No6	75.77	82.24	112.46	–
No7	80.44	95.64	138.22	124.70

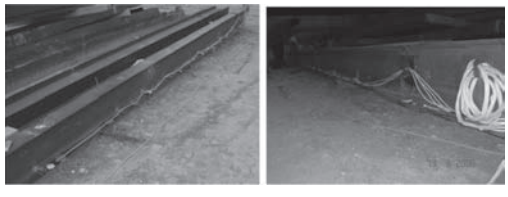

Figure 5. Bending moment measurement.

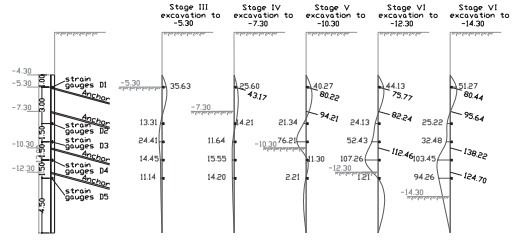

Figure 6. Anchor forces and bending moments in the pile measured at different stages.

Table 2. Bending moments [kNm].

	Level				
Stage	D1	D2	D3	D4	D5
No1	–	–	–	–	–
No2	–	–	–	–	–
No3	–35.63	13.31	24.41	14.45	11.14
No4	–25.60	+14.21	11.64	15.55	14.20
No5	–40.27	21.34	76.21	–11.30	2.21
No6	–44.13	24.13	52.43	107.26	1.21
No7	–51.27	25.22	32.48	103.45	94.26

3.3 *Wall displacement measurement*

The lateral displacements at the pile and anchor heads were measured by using geodetically gauging points and measurement devices SOKKIA-330R-Fine AVG with expected accuracy of 5/10 mm and by building an inclinometer tube in a pile. The most interesting points are at the pile and anchor heads. Detailed measurements describe the exact deformation (move) of the wall during the construction period. The results for five stages (Stage III—Stage VII) are summarized in Table. 3 and Fig. 7.

4 SOIL PARAMETERS

The soil properties used in the analysis were taken from a site investigation carried out in September 2007 together with additional in-situ testing performed in April 2008. The soil consists of five soil layers. Clay formations with organic substances and gravel mixed with ceramic debris and artificial embankments outcrop on the surface. That first layer is 3.00 m thick. Immediately under the embankment opens up a layer of gravel-interspersed compact clay loam, light brown in color. Its thickness varies within 3.30–4.10 m (Layer 2). Layer 3 is granite gneiss, broken, highly weathered, argillized, friable and yellowish-brown. That layer occurs under Layer 2 to the end of the investigated depth. Layer 4 consists of loams, friable and in some places calcareous, light gray and yellow, which occurs at depths of approx. 9.70–10.40 m.

In certain places Layer 3 is interrupted by interlayers of yellow, plastic loam—Layer 5. These clayey interlayers of 0.60–1.00 m thickness alternate with granite gneisses. The excavation design was performed taking into account the continuous water pumping and a dry foundation pit.

The strength parameters used in Mohr-Coulomb and Hardening Soil model analyses for the different soil layers are summarized in Table 4.

Table 3. Wall displacement [mm].

	Level				
Stage	GGP 1	GGP 2	GGP 3	GGP 4	GGP 5
No1	–	–	–	–	–
No2	0	–	–	–	–
No3	1.4	0	–	–	–
No4	3.9	1.9	0	–	–
No5	7.7	4.1	2.8	0	–
No6	9.1	5.7	7.6	2.7	0
No7	11.4	7.2	8.4	4.1	2.9

Table 4. Soil parameters used in FE analysis.

Soil layer	Soil parameters γ, *[kN/m³]*	E, *[kN/m²]*	c, *[kN/m²]*	φ, *[°]*
No1 (0–3.0 m)	21.0	5500	10	20
No2 (3.0–6.8 m)	20.8	7000	25	25.3
No3 (6.8–30.0 m)	24.1	19000	16	25
No4 (9.7–10.4 m)	20.7	19000	8	20
No5 (16.7–17.1 m) (18.9–19.5 m) (19.9–20.5 m)	21.1	16000	18	21

5 NUMERICAL ANALYSIS

5.1 *Basic assumptions*

The analysis using the FEM is further presented for the different construction stages and compared with the final measurement data. Several parameters enter the analysis of a sheet pile wall. The issue of determining the soil parameters as a function of field measurement and numerical analysis comparison will not be discussed. The example will be calculated by means of a FEM analysis using one of the most widely used software in design practice, PLAXIS with two possibilities for soil model idealization: the Mohr-Coulomb model and the Hardening Soil model The idea in this analysis is based on the following prerequisites:

I. Calculation of the different construction stages with PLAXIS using the Mohr-Coulomb model and modeling anchors as "fixed-end anchor" elements or an inclined pile using beam elements;
II. Calculation of the different construction stages with PLAXIS using the Hardening Soil model and modeling anchors as "fixed-end anchor" elements or an inclined pile using beam elements;
III. Comparison and discussion of the results

5.2 *FE-Modeling*

The excavation was modelled by the FEM programme PLAXIS. The analysis took into account all the stages of the excavation. The finite element mesh used in the plane strain calculation is shown in Fig. 8. The bored pile wall was schematized as a beam element. The anchors were simulated by PLAXIS "fixed-end anchor" elements (Fig. 8a). That means elastic springs of a given axial stiffness with one fixed (no displacement) end and the other movable end connected to the pile wall by a given longitudinal distance from the wall. The anchors were also simulated as an inclined pile using beam elements (Fig. 8b). The soil behaviour was simulated

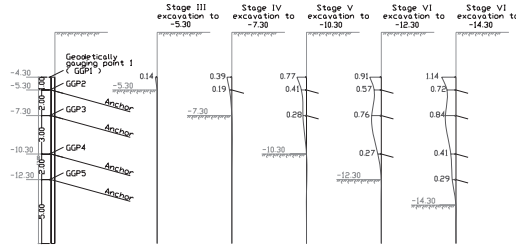

Figure 7. Wall displacement results.

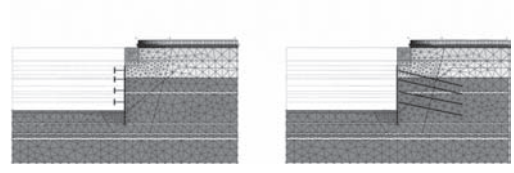

Figure 8. FE Model: a) "fixed-end anchor"; b) plate elements.

Table 5. Calculation and field monitoring results—M, Q, δ.

Combination	parameters M_{max}, *[kNm]*	δ_{ph}, *[mm]*	δ_{max}, *[mm]*
MC.FA.CS3	24.57	0.799	2.60
MC.PE.CS3	24.57	0.799	2.60
HS.FA.CS3	34.46	0.717	2.41
HS.PE.CS3	34.46	0.717	2.41
FMR.CS3	*40.20*	*1.40*	*1.40*
MC.FA.CS4	33.23	1.010	4.450
MC.PE.CS4	27.13	14.88	14.88
HS.FA.CS4	29.59	0.980	4.500
HS.PE.CS4	20.47	9.170	9.170
FMR.CS4	*35.30*	*3.900*	*3.900*
MC.FA.CS5	86.46	0.980	12.39
MC.PE.CS5	96.97	29.73	33.18
HS.FA.CS5	80.66	1.070	9.460
HS.PE.CS5	96.60	21.65	24.92
FMR.CS5	*76.70*	*7.700*	*7.700*
MC.FA.CS6	84.53	1.200	16.92
MC.PE.CS6	118.68	52.97	62.68
HS.FA.CS6	66.33	1.18	12.70
HS.PE.CS6	109.88	48.37	57.66
FMR.CS6	*107.30*	*9.100*	*9.100*
MC.FA.CS7	88.07	1.470	21.11
MC.PE.CS7	154.95	101.3	109.5
HS.FA.CS7	70.50	1.61	16.4
HS.PE.CS7	141.43	99.50	110.61
FMR.CS7	*109.40*	*11.4*	*11.4*

*HS – Hardening Soil Model; MC – Mohr-Coulomb model; FA – fixed-end anchor; PE – anchor as a plate element; CS – construction stage; FMR – field monitoring results; δ_{ph} – horizontal displacement in pile head.

using the Mohr-Coulomb model and the Hardening Soil model of the PLAXIS code. The selection of the soil properties used in the calculation was based on the results of the geotechnical investigation performed at the site.

6 COMPARISON AND ANALYSIS OF THE RESULTS

In this study of the performance of an anchored pile wall founded in Stara Zagora an interesting correlation was obtained between the field measurements and final element analysis based on the Mohr-Coulomb model and Hardening soil model. Although no soil characteristics were changed, the comparison with the results of monitoring activities lead to the following conclusions:

- The most accurate solution as compared with the experimentally determined values is obtained for the bending moments in the beam.

Table 6. Calculation and field monitoring results—anchor forces.

	parameters			
Combination	A_1,*[kN]*	A_2,*[kN]*	A_3,*[kN]*	A_4,*[kN]*
MC.FA.CS3	–	–	–	–
MC.PE.CS3	–	–	–	–
HS.FA.CS3	–	–	–	–
HS.PE.CS3	–	–	–	–
FMR.CS3	–	–	–	–
MC.FA.CS4	89.87	–	–	–
MC.PE.CS4	81.71	–	–	–
HS.FA.CS4	91.28	–	–	–
HS.PE.CS4	77.80	–	–	–
FMR.CS4	*43.17*	–	–	–
MC.FA.CS5	69.86	226.8	–	–
MC.PE.CS5	97.78	84.25	–	–
HS.FA.CS5	93.45	235.50	–	–
HS.PE.CS5	96.02	105.03	–	–
FMR.CS5	*80.22*	*94.21*	–	–
MC.FA.CS6	73.78	208.0	244.2	–
MC.PE.CS6	90.94	97.39	118.37	–
HS.FA.CS6	103.7	254.4	314.7	–
HS.PE.CS6	107.9	131.7	143.4	–
FMR.CS6	*75.77*	*82.24*	*112.46*	–
MC.FA.CS7	83.12	219.1	227.1	304.3
MC.PE.CS7	100.2	105.8	140.96	168.38
HS.FA.CS7	115.8	279.96	373.4	358.4
HS.PE.CS7	139.5	156.5	220.9	198.95
FMR.CS7	*80.44*	*95.64*	*138.22*	*124.70*

*HS – Hardening Soil Model; MC – Mohr-Coulomb model; FA – fixed-end anchor; PE – anchor as a plate element; CS – construction stage; FMR – field monitoring results.

  The difference in the maximum values for the different computational schemes varies within ± (26–28)%. The method of modeling the anchorage bearing has a basic effect on the value of the bending moments.
- Regarding the displacements in the pile head, the selected soil model and to a higher degree, the method of supporting (anchor modeling) is of particular significance. The results concerning the maximum displacements in modeling the anchor as a "fixed-end anchor" approximate considerably the experimentally determined displacements. The differences are negligible within several mm and not exceeding 60%. In modeling the anchors as plate elements the differences reach and exceed 600%.
- It should be noted that the experimentally obtained deformed line for the pile differs considerably from that obtained by computational methods. The latter is mostly valid for the final construction stage CS7.
- When comparing the experimentally obtained values for the anchor forces with the computational ones it can be seen that the differences reach and exceed 200% depending on the computational schemes adopted. In the anchored bored pile wall the forces, regardless of the computational scheme used, have similar values whereas with increasing the number of anchor series, the adopted computational model influences highly the forces obtained. Results closest to the experimentally ones are obtained when using the Mohr-Coulomb model and modeling anchors as plate elements. The differences in that case (with some exceptions) are about 9–12%. Unfortunately, it is this computational combination that yields the most inaccurate results with respect to the wall displacements and maximum bending moment redimensioned by 42%.

The difference between the measured and calculated wall displacement can be explained by the assumed increase in the stiffness modulus (about 2–2.5 times). Some authors recommend such a reduction [Ilov] taking into account the three-dimensional soil behavior.

7 CONCLUSION

The requirements for accuracy in designing excavation projects in city areas call for comprehensive analytical models like the Finite Element Method to be put into practice. Another analytical model widely used in Bulgarian practice is the Subgrade Reaction Method. A basic conclusion drawn from the investigation carried out is that there is no computational model or scheme, even in the most recent software products, which

can reflect accurately the actual behavior of the structure. From a designer's point of view, avoiding accidents means building up excess reserves and raising the degree of safety. A literature survey [von Wolffersdorff] confirms the dispersion of the results using different calculation models even for relatively simple excavation cases. As demonstrated in the example above, the estimation of the results complies with the full numerical analysis, soil parameters interpretation and the most important field monitoring. Numerical back analysis can be performed for reducing the input soil parameters as a result of detailed measurement of the construction behavior during the different construction stages [Totsev, Vogt&Totsev]. Similar timely exercised control can prevent accidents or reduce the construction price by specifying the primary project.

REFERENCES

Ilov G., 2009, *Soil Mechanics*, ERA.

Totsev A., 2006, *Numerical and experimental investigation of diaphragm walls*, PhD Dissertation.

Vogt N., A. Totsev, 2006, *Back-analysis of collapsed excavation*, Стронтелiство 2: 2–9.

von Wolffersdorff P., 1994, *Feldversucht an einer Spundwand in Sandboden: Versuchsergebnisse und Prognosen*, Geotechnik 17: 73–83.

von Wolffersdorff P. & Mayer P., 1996, *Gebrauchstauglichkeitsnachweise für Stützkonstruktionen*, Geotechnik 19: 291–300.

Geotechnical Aspects of Underground Construction in Soft Ground – Viggiani (ed)
© 2012 Taylor & Francis Group, London, ISBN 978-0-415-68367-8

Tunnel-boring process in urban environment: Modeling for reliability—a kinematic study

D. Festa, W. Broere, S.v.d. Woude & J.W. Bosch
Delft University of Technology, The Netherlands

ABSTRACT: Research in tunneling often focuses on the interaction between the TBM and the lining or the TBM and the environment. Little attention has been given to the interaction between the surrounding soil and the grouting process on one hand and the driving characteristics on the other hand. This interaction is influenced by, amongst others, the machine features, the tunnel alignment and the choices of the TBM operators. Although a huge amount of data is automatically collected by the TBM during operations, this data is not directly related to soil properties. A kinematic analysis of the TBM, based on monitoring data of the Hubertus Tunnel is used to show how the interaction between the machine and the surroundings varies from one side to the other of the TBM. This implies that different processes are likely to occur in different positions around the shield. These processes are subject of further study.

1 INTRODUCTION

The increasing use of Tunnel Boring Machines (TBMs) in urban areas, close to historic buildings sensitive to settlements and near to pile foundations, leads to larger technical and operational challenges for these projects.

This has inspired research into the interaction between the TBM, the built up environment and the newly erected lining.

Little attention has been given to the interaction between the soil and the grouting process versus the driving characteristics of the TBM, even though this paper will show that this interaction is significant and can in turn influence the settlements that occur or the extent to which pile foundations are influenced. This paper will present the first results of a research project that aims to improve the understanding and control of the tunneling process in built-up environments.

The overall advancing process of a TBM involves multiple operations and physical processes. Accordingly it has been decided to carry out distinct analyses, investigating the unknown processes one by one, such as to gain a structured knowledge of the overall tunneling process based on a thorough understanding of the separate underlying processes.

Since the kinematic behavior of the TBM appeared of primary interest, this paper will focus on this subject.

1.1 *Reference project*

The kinematic model will be validated by monitoring data collected at the Hubertus Tunnel project in The Hague, The Netherlands. Most of the considerations referred in this paper have therefore been derived from this project, as the full set of monitoring data was available.

2 PRINCIPLES OF GEOMETRY AND KINEMATICS

When a rectangular plane section is driven along a circular path of constant curvature, this motion can be described by a centre of rotation, a curvature and the relative position between the curvature radius and the rectangle.

Different configurations would lead to different descriptions of the motion of the TBM. This is illustrated in the following figures. In Figure 1 the centre

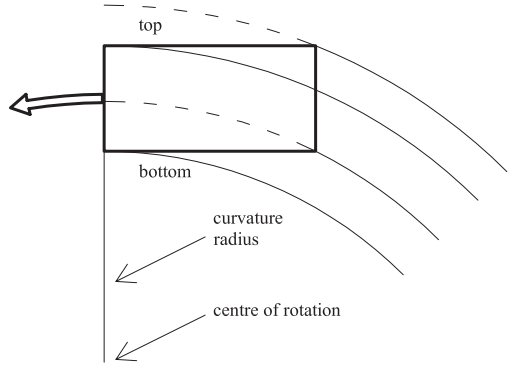

Figure 1. Centre of rotation connected to bottom-left edge.

of rotation is connected to the bottom-left corner of the rectangle; in Figure 2 to the bottom-right.

In both cases the size of the rectangle, the curvature of the trajectory and the angle between the radius and the longitudinal axis of the rectangle (assumed perpendicular to each other, in this example) are the same.

When we focus on the interaction between the top side of the rectangle and the trajectories drawn by its top edges, the first set-up (Fig. 1) shows that the trajectory of the top-left corner is internal to that of the top-right one, while the second set-up (Fig. 2) shows a reversed situation.

This means that, whilst a pure rotation takes place, in the first case the top side must "displace" the surrounding soil, whilst in the second case the surrounding soil can relax after the TBM has passed (assuming any kind of elastic soil behavior).

Finally, an intermediate configuration (Fig. 3) having the centre of rotation connected to the mid point of the bottom side leads to a mixed behavior where at the top side first a phase of relaxation (from the top-left edge to the mid point) and then a recompression (from the mid point to the top-right edge) of the pre-relaxed surrounding soil occurs.

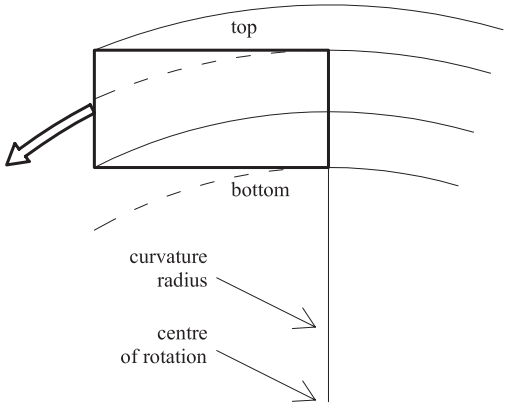

Figure 2. Centre of rotation connected to bottom-right edge.

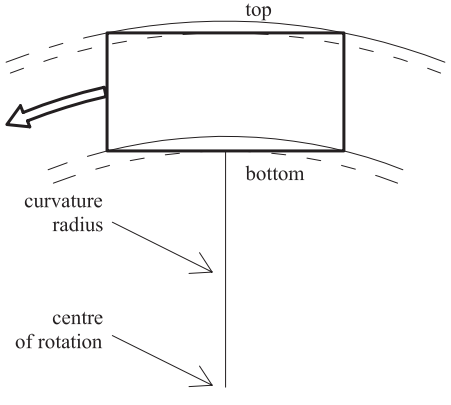

Figure 3. Centre of rotation connected to bottom-centre.

On the bottom side first a phase of compression (from the bottom-left edge to the mid point) and then a phase of relaxation (from the mid point to the bottom-right edge) occur.

Also notice that in this last configuration the trajectories of the top and bottom edges are superimposed.

The configuration depicted in Figure 3 seems most likely and adheres closely to general expectation of how a TBM behaves.

The exactness of this description will be discussed in Paragraph 3, when a comparison with monitoring data is made. However, the three different configurations show that the method of steering and the centre of rotation of the TBM do strongly influence the interaction with the surrounding soil, as well as the forces and moments acting on the machine.

2.1 *Shield positioning systems*

The positioning and guidance system of a TBM is provided through a series of measuring devices and reference points installed both inside the shield and along the concrete lining already in place.

A laser receiving box is connected to the shield and located in the upper part of it, around halfway of the shield length. The receiver is equipped with two target plates to determine the jaw of the TBM and two inclinometers to determine its roll and pitch.

These devices provide the position of the machine and its orientation in space.

Information is collected and recorded at a variable time interval, usually 5–6 seconds long.

The driving system is based on two imaginary (calculated) points inside the shield which follow the designed tunnel alignment. Both lay along the longitudinal axis of the shield: the first one (front) is positioned at the front face of the shield and the second one (rear) at an intermediate position between the front and the rear section, and generally does not coincide with the rear section.

Following Figure 4 provides a plot of the scheme described.

The overall purpose of the monitoring system is to provide to the TBM operators information on the actual position of the two (calculated) points versus their optimal position corresponding to each advance of the machine. Other derived values are also provided (e.g. tendencies, pitch, roll, jaw).

Comparing this steering system with the three configurations assumed in the previous section we

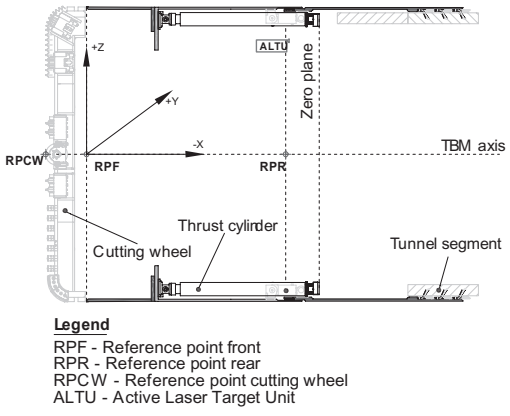

Figure 4. Shield positioning system.

notice that the real situation is actually intermediate between the first (Fig. 1) and the third (Fig. 3).

Therefore peculiarities of both schemes may appear. Cycles of compression and relaxation around the shield occur, as two points on the machine axis follow the same trajectory. Furthermore sideslip of the machine tail can be expected as the second reference point is positioned ahead of the machine tail.

In addition, although machine drivers constantly strive to follow the design alignment with both target points, sometimes this is not possible as this would require excessive driving forces, paired with the risk to damage the equipment and the already placed concrete lining. In those cases it is preferable to keep a slightly skewed orientation of the machine when this involves smaller driving forces. From time to time the skewing required differs in direction and amount.

The understanding and modeling of these driving configurations may also be considered the goal of the present research.

2.2 *Monitored data and models*

All models and matching results presented in this paper are strictly derived from the monitored data. Only a necessary filtering activity has been carried out wherever needed and in case of unlikely physical configurations.

During the modeling phase the interpretation of data and results has been strictly avoided such as to escape from any conditioning to the model.

3 THE HUBERTUS TUNNEL

3.1 *Main features*

The Hubertus Tunnel consists of two parallel tubes long 1666.70 m and 1653.48 m. The Hydroshield is 10,235 mm long, at front has diameter of the shield of 10,510 mm and at rear of 10,490 mm, i.e. the shield has a tapering of 10 mm (in radius). Furthermore a standard overcutting of 10 mm (in radius) is present.

The machine tail void grouting system consists of six injection openings distributed along the circumference. Of these only four (the upper ones) were used during the operations.

The final concrete lining is made from 2000 mm long rings with an external diameter of 10,200 mm. The theoretical tail void thickness is therefore 165 mm.

Figure 5 shows an overview of the design alignment, with the smallest horizontal curvature radius of 550 m. The deepest point of the tunnel axis is located at 27.73 m below surface. The tunnel is located in dune sand consisting of well packed silty sands and sandy silts with some clay.

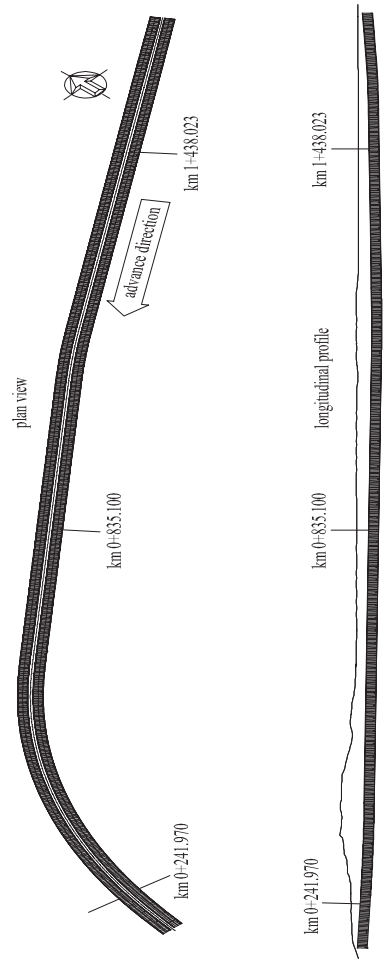

Figure 5. Hubertustunnel project: designed alignments.

4 THE KINEMATIC MODEL

4.1 *Motivation*

The kinematic behavior of the TBM was selected as the first sub-process to study as this is of direct interest to the TBM operators (as it is common to follow the design alignment with the least diversion possible).

A kinematic model could help to understand unpredictable reactions of the TBM encountered especially during the initial phase of the boring operations and could be used to improve operational control of the TBM.

The kinematic model can also be considered the first step towards a full model predicting changes in the stress distribution around the tunnel and anticipating strains and settlements.

Such a model, including processes such as grouting and the interaction with surrounding soil, is the desired result of the full research program.

4.2 *Development*

The advancement of the shield has been measured and recorded for both tubes.

This has been reported as the horizontal and vertical deviations from the theoretical alignment of the front and back target plates of the positioning system.

As the average time interval between two measurements is around 5 to 6 seconds, the advance between two adjacent readings is in the order of few mm.

According to the monitored advance, taking into account the deviations from the optimal aligning, the tracks of the excavation wheel and of the shield tail have been calculated with the use of MATLAB.

At this stage of the research the shield tail has been assumed non-deformable. This condition, more or less realistic according to soil conditions and shield features, will be reconsidered in the future.

The resulting model allows displaying the TBM shield in any advance position along the alignment. In addition, thorough the comparison of the shield skin with the mentioned tracks, the amount of interaction of the TBM with soil, in distinct positions around the shield, is visualized.

4.3 *Results*

Some specific results from the model will be discussed.

The first section of interest is encountered at km 1 + 438.023 of the south tube, where the shield is located in a straight downward position. Here the analysis shows where at that location the profile of the shield was inside the track of the excavation wheel or (partially) skewed outside.

Taking two cross sections of the shield, one horizontal and one vertical, we can visualize the amount of compression or relaxation and the amount of interaction at the left, top, right and bottom sides of the shield as shown in Figure 6.

The sign convention is as follows: the gap with a distance between track and shield skin is positive when the shield moves inside the track of the excavation wheel and negative when outside.

If the gap is positive we assume the soil around the shield is relaxed, when it is negative, we assume the shield skin is displacing the surrounding soil.

From Figure 6 one can observe that the shield was driving horizontally skewed towards the right hand side, since the gap on the left side was of 45 mm, whilst on the right side a negative gap (soil displaced), although very limited, was present.

From the vertical point of view, the machine presents a downward pitch (vertical skewing) more emphasized than required by the downward trend of the trajectory (1% in this position). Therefore the machine shows here what we could refer as a sinking tendency in its front part, and a buoyant tendency in its rear section. At the bottom-side the shield tail has a gap width of 60 mm and the soil is relaxed, while the top-side has a negative gap width of 23 mm and the soil is displaced.

Another section of interest is encountered at km 0 + 835.100 of the south tube, where the shield is located in a straight upward position (0.8%).

From Figure 7 one can observe that the shield was driving horizontally straight (left and right side lines are almost superimposed, and the gap at the tail almost coincides with the standard one of 20 mm, obtainable combining overcut and tapering effects), but with an upward pitch (vertical skewing) more emphasized than required by the upward trend of the trajectory. At the bottom-side the shield tail has

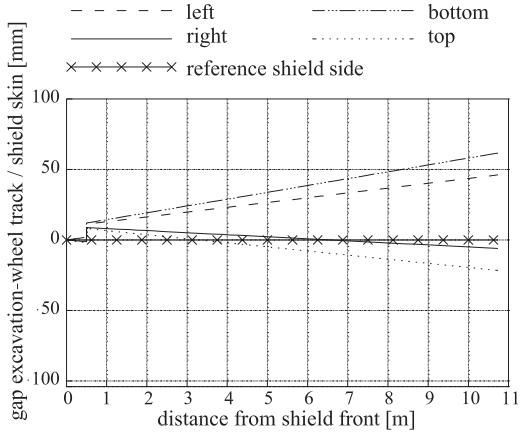

Figure 6. South tube—km 1 + 438.023.

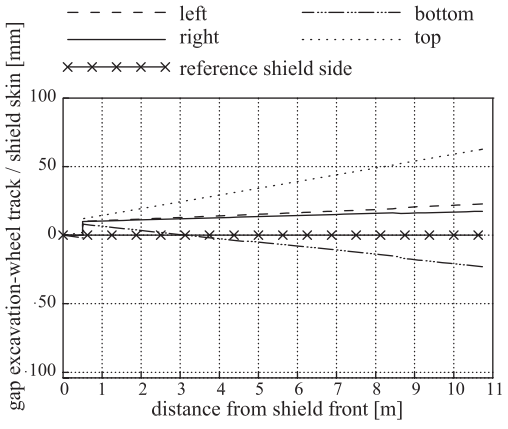

Figure 7. South tube—km 0 + 835.100.

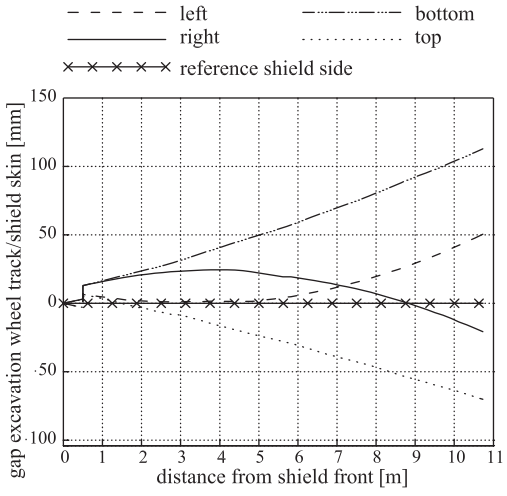

Figure 8. South tube—km 0 + 241.970.

therefore a negative gap width of 25 mm and the soil is displaced, while the top-side has a positive gap width of 60 mm and the soil is relaxed.

It is interesting to compare this last case to that shown in Figure 6. Focusing on the vertical behavior of the shield, we observe a reversed situation between top and bottom sides in the two cases, both from the qualitative (sign of the gap) and quantitative (width of gaps) point of view.

In other words the shield seems to emphasize the vertical trend of the trajectory both when in downward and upward direction.

At km 0 + 241.970, where the trajectory has a horizontal curvature radius of 550.00 m (leftward) and an upward steepness of about 4%, the shield shows a gap width on the right hand side of 20 mm (Fig. 8). The complementary effect can be seen at the left hand side where the tail gap thickness is 50 mm, therefore larger than the standard one of 20 mm (when combining the overcut and tapering effects).

From the vertical point of view the shield has a negative gap width of 70 mm at the top side, with a positive gap width increasing to 110 mm at the bottom side (Fig. 7).

The curved trends of the left and right side lines deserve additional explanations.

In contrast to the two previous cases, the TBM is in a horizontal leftward curve. Therefore the track of the excavation wheel is also curved.

As depicted in Figure 3, at the top side, the gap goes from zero at the front, to a maximum in the mid section, and then comes back to zero at the tail. If we assume for the top-right edge to protrude outside the track of the excavation wheel, also a zone of compression can be expected, depicted by a negative tail in the line representing the gap width at the right side of the shield. This behavior can clearly be seen in the "right" line of Figure 8.

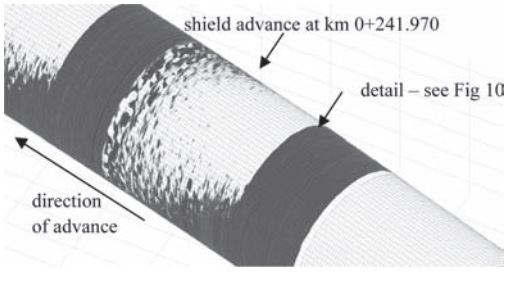

Figure 9. 3D view of the shield at km 0 + 241.970.

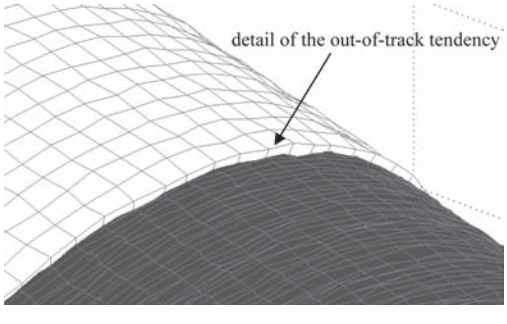

Figure 10. Detail of the out-of-track at the top side at km 0 + 241.970.

The theoretical size of the gap width at the top side (negative in this case, therefore with displaced soil) is also visualized in Figures 9 and 10, as a 3D model.

The shield skin is depicted in white, the track of the excavation wheel in grey. Where white is visible,

this means that the shield skin is out-of-track in that sector and displaces the soil outwards.

This happens anytime the shield-tail protrudes outside the tube excavated by the excavation wheel.

5 CONCLUSIONS

5.1 *Summary and highlights*

The results of a kinematic analysis carried out on the monitoring data obtained at the Hubertus Tunnel project in The Netherlands have been presented.

The study of the kinematic behavior of a TBM shield is the first step towards the construction of a full numerical model predicting changes in the stress distribution around the tunnel.

Results show that also in standard driving conditions, the interaction of the shield with its surrounding and the extent to which soil is displaced or relaxed can significantly change from one side to the other of the TBM. This means that different physical processes (e.g. soil compression/relaxation, grout flow around the shield, shield-tail deformation) are likely to occur in distinct positions around the shield, therefore influencing its own equilibrium.

At this stage the shield tail has been simplified as non deformable.

A more complete set of results, broader than the selection presented in this paper, shows that in different positions along the alignment, although with similar curvature and steepness, the behavior of the shield differs. A number of factors can contribute to this effect, including varied soil conditions and varied maneuvering.

More research is still needed to understand and model how a certain TBM behavior is determined by a specific set of environmental and operational circumstances.

5.2 *Forthcoming research*

A next step would be to take the gap width derived with the present model into account in an analysis of the tail void grouting process.

From the model presented, it is possible to retrieve the size of the gap created by the advancement of the shield and its spatial distribution around the TBM. This could be used to establish a correlation between the *theoretical grouting need*, and the amounts of grout actually injected during the boring process.

ACKNOWLEDGEMENTS

The permission of the "Projectorganisatie Hubertustunnel" to use the data and the support of J.F.W. Joustra in actually providing the data is gratefully acknowledged.

REFERENCES

Bezuijen, A. et al. 2004. Field measurements of grout pressures during tunneling of the Sophia rail tunnel. *Soils and foundations, Vol. 44, No. 1: 39–48.* Japanese Geotechnical Society.

Bezuijen, A. & Talmon, A.M. 2006. Grout pressures around a tunnel lining, influence of grout consolidation and loading on lining. *Tunneling. A decade of progress*: 77–82. Leiden: Taylor & Francis/Balkema.

Bezuijen, A. & Talmon, A.M. 2009. Processes around a TBM. *Geotechnical aspects of underground construction in soft ground*: 3–13. Leiden: CRC Press/Balkema.

Hashimoto, T. et al. 2009. Study on earth pressure acting upon shield tunnel lining in clayey and sandy grounds based on field monitoring. *Geotechnical aspects of underground construction in soft ground*: 307–312. Leiden: CRC Press/Balkema.

Maidl, B. et al. 1996. *Mechanised Shield Tunneling.* Berlin: Ernst & Sohn Verlag.

Nagel, F.J. 2009. *Numerical modeling of partially saturated soil and simulation of shield supported tunnel advance. PhD thesis report.* Bochum: Institute for Structural Mechanics, Ruhr-University Bochum.

Talmon, A.M. et al. 2001. Grout pressures around a tunnel lining. *Tunneling. A decade of progress*: 77–82. Leiden: Taylor & Francis/Balkema.

Geotechnical Aspects of Underground Construction in Soft Ground – Viggiani (ed)
© 2012 Taylor & Francis Group, London, ISBN 978-0-415-68367-8

Mechanical analysis of jet grouted supporting structures

A. Flora, S. Lirer & G.P. Lignola
University of Naples "Federico II", Italy

G. Modoni
University of Cassino, Italy

ABSTRACT: Due to the well known defects of jet grouting columns (diameter, position), the real shape of supporting structures made of overlapped elements, as shafts or tunnel canopies, is often far from being geometrically regular, and defects have to be taken into account. The design of such structures cannot be but probabilistic or semi-probabilistic, because it may hide unforeseen risks if a deterministic approach is adopted. As a consequence, this is the typical case in which sophisticated numerical analyses may just give the illusion of being refined, if possible defects are not correctly taken into account. In the paper, the results obtained in previous works by the authors adopting such an approach with reference to shafts and tunnel canopies are summarized. Even though these approaches represent a progress in the design of jet grouted supporting structures, they do not take into account soil-structure interaction and the truly three-dimensional behaviour of these structures. In the paper, it is shown that soil-structure interaction strongly reduces stresses in the jet grouted soil, and discontinuities can be accepted in the structure without necessarily implying structural failure as long as they keep smaller of a given limit value. These improvements are a first step towards a less conservative design procedure of jet grouted structures.

1 INTRODUCTION

The use of jet-grouting with earth supporting functions has greatly increased in recent years. At the design stage, however, there is still a relevant degree of uncertainty, mainly due to the lack of reliable methods for predicting the diameter and the position of the columns, as well as the mechanical properties of the cemented soil (soilcrete), all varying along columns axis due to a number of reasons. As a matter of fact, these defects make jet grouted columns far from being perfectly cylindrical, homogeneous bodies. It follows that, most times, jet grouting is designed on the basis of subjective rules of thumb, subsequently refined on site by means of trial and error tests (trial fields). In order to improve the reliability of design analyses, two complementary research efforts are needed: on one hand, field trials must be carefully analysed to find the relevance of columns defects in the largest possible variety of subsoil conditions and jet grouting technology; on the other hand, more satisfactory design methods taking into account the intrinsic variability of jet columns must be conceived. This paper focuses on this second aspect, with reference to the particular case of provisional support in tunnelling (open structure, Fig. 1.a) or in shafts (closed structure, Fig. 1.b), realized in cohesionless soils (ideal for jet grouting effectiveness) or at the most soft clays. These structures have the common property that the supporting action is committed to the arching effects given by overlapping of columns. Considering the potentially dramatic effect of defective, not interpenetrated columns, design analyses must necessarily combine careful prediction of columns properties and mechanical schematisation.

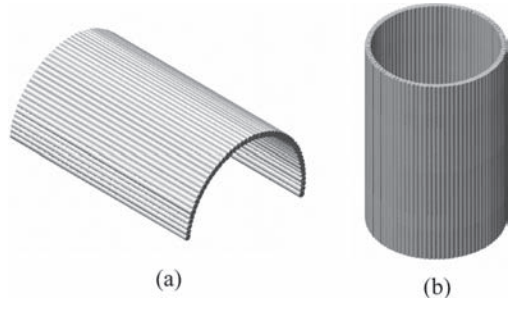

Figure 1. Typical jet-grouted supporting structures for tunnels (a) and shafts (b).

In previous papers, (e.g. Lignola et al. 2008, Flora et al. 2007, Croce et al.; 2006; Croce et al. 2008) the authors have suggested to simulate geometrical and mechanical defects of columns by means of probabilistic models to be calibrated with

statistical analyses of the results of available field trials. These models have been then introduced into mechanical analyses, carried with different approaches, to take into account defects into the design of jet grouted structures. The first part of this paper is devoted to a brief summary of this activity with reference to the above mentioned supporting structures (Fig. 1); in the second, the limits of the proposed predictive methods are highlighted, and possible improvements suggested. These latter have been commented by reporting the results of preliminary analyses.

2 PROPERTIES OF COLUMNS

Regardless of accurate control in the execution of treatments, jet grouting columns are generally acknowledged to be far from being cylindrical and homogenous bodies. The main reasons for such discrepancy are related to soil properties and defects in jet grouting execution. The previous is relevant as subsoil conditions may sharply vary even within a few meters: this frequent heterogeneity of soils in grading and stress history results into very different (and variable) values of undisturbed soil mechanical parameters, say stiffness and strength. Then, extremely variable interactive mechanisms with the injected fluids take place, with the result that the dimensions and mechanical properties of the cemented soil can be largely variable along the axis of each single column.

Furthermore, although particularly sensitive instrumentations are now available to control the initial positioning and alignment of the perforation equipment, errors must be expected, and deviations from the prescribed direction systematically take place due to some deformation of the battery of rods.

These problems may sum up, possibly becoming critical for the jet grouted supporting structures: for shafts, mostly in the case of a considerable length of the columns; for tunnels, due to the fact that sub-horizontal columns deviate more from their ideal axis (Croce et al. 2008). In order to evaluate the implications of these defects on the performance of the supporting structures it is convenient to distinguish geometrical and mechanical variables and to derive their typical variation from statistical inferences of the results collected from field investigations.

2.1 *Geometrical properties*

From the available documented site tests, it can be generally seen that the diameters of columns are randomly scattered around their mean value with symmetric bell shaped frequency distributions (Croce et al., 2004). According to this result, a Gauss probability function, customised to the particular case by an average value and a coefficient of variation CV(d), can be conveniently adopted to simulate diameters variability. Although mean values and standard deviations should be evaluated by performing specific field trials in the same conditions (subsoil and injection techniques) of the studied case, their values can be preliminarily estimated on the bases on published evidences (e.g. Croce et al., 2006) for the different soil types (Table 1). The table shows that both the mean values and the coefficients of variation generally increase as the soil gets coarser, and as a consequence larger columns with larger variability must be expected for coarser soils.

Misalignment of columns from their prescribed directions can be defined by the statistical distributions of α and β, respectively representing (see Fig. 2) for a vertical column the angle formed by the axis with the assigned direction and the orientation with reference to a fixed plan direction (azimuth).

Neglecting deviations induced by systematic factors, not meaningful on the relative alignment of columns and thus on the continuity of structures,

Table 1. Diameters of columns for different original soil types and injection systems (modified after Croce et al., 2004).

Soil	Average diameter D_{col} (m)			Coefficients of variation CV (D_{col})
	Single fluid	Double fluid	Triple fluid	
Gravely	0.7–1.1	1.0–1.5	2.0–2.4	0.05–0.25
Sandy	0.5–1	0.7–1.5	1.2–2.0	0.02–0.10
Silty clayey	0.4–0.6	0.6–0.9	1.0–1.5	0.02–0.05

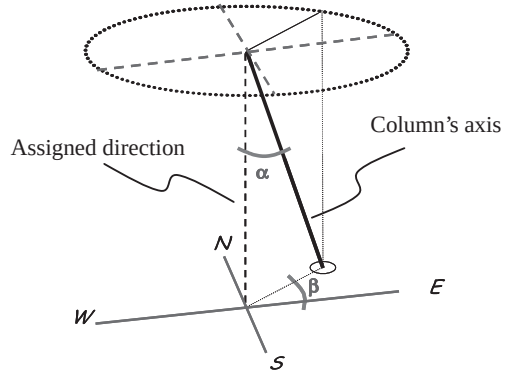

Figure 2. Definition of column deviation from its prescribed direction.

Table 2. Soilcrete uniaxial compressive strength for different treated soils (modified after Bell, 1993).

Uniaxial compressive strength	Clay	Silt	Sand	Gravel
Average value, $\bar{\sigma}_{lim}$ (MPa)	0,5 ÷ 3	5 ÷ 25	4 ÷ 18	5 ÷ 30
Coefficient of variation, CV (σ_{lim})	0,02 ÷ 0,05		0,02 ÷ 0,1	0,05 ÷ 0,15

and focusing only on the random component, a uniform distribution between 0° and 180° and a Gauss probability function around zero can be respectively assumed for the angles β and α. The standard deviation of α does not depend on the soil type, being strongly related to the robustness of drilling equipment and to the operators' ability. Values in the range of 0.5–1° have been typically recorded in monitored systems.

2.2 *Mechanical properties*

Jet grouted soil is generally assumed to behave as a low quality concrete and, similarly to this material, its resistance is defined in terms of uniaxial compressive strength σ_{lim}. Variation of this latter may in principle occur along vertical and radial directions within the column's body. However published data (Croce et al., 2004) have shown that, apart from a slight increase with depth, uniform random scattering is usually observed on σ_{lim} values. The asymmetric frequency distribution derived from statistical analyses of these data suggests, together with the logical consideration that σ_{lim} cannot assume negative values, to simulate variability with a log-normal probability function to (Croce et al. 2004). Parameters of this distribution can be related to the mean and the standard deviation of data and should be again derived from specific field. However, preliminary structural analyses can be performed based on the indicative values given in Table 2. These values show that larger and more variable σ_{lim} must be expected on coarser soils.

3 BIDIMENSIONAL ANALYSES

From a mechanical viewpoint the supporting structures shown in Fig.1 can be imagined as assemblies of interconnected longitudinal (columns) and cross sectional (arches formed by overlapped columns) elements. Under simplified assumptions (linear response of these elements and surrounding soil thrusts independent on deformation, i.e. no soil structure interaction), the distribution of forces between columns and arches can be calculated combining equilibrium and consistence via the well known differential equation:

$$W\frac{d^4v}{dz^4} + K \cdot v = p_e - p_i \quad (1)$$

where z is the longitudinal coordinate, *v* the displacement in the cross sectional plane, W the flexural stiffness of the columns, K the compressive stiffness of cross sectional arches, p_e and p_i respectively the external and internal stresses given by the soil (the internal ones being progressively removed as the soil is excavated within the shaft). For instance, Figure 3 reports bending moments on columns calculated for the case of a 21 m long vertical shaft (D_{shaft} = 12 m, 63 columns having D_{col} = 0.6 m). The solution has been obtained for an inner excavation of 15 m, considering the two cases of perfect columns, mutually overlapped over the whole length, and of a lack of continuity in the horizontal arch at 15 m depth (obtained by imposing K = 0 for z = 15 m). The difference between the two curves is very large, showing an increase of moments up to 23 times due to the missed overlapping of columns just at one depth.

The example reported in Figure 3 shows the importance of assessing continuity and stress tolerability in the cross sectional elements of curved jet grouted structures. The following paragraphs report two bi-dimensional analyses developed for the supporting structures shown in Figure 1, probabilistically taking into account the defects of columns.

3.1 *Tunnel's canopies*

Jet-grouted canopies (often also called umbrella) are often used for tunnel temporary support. Such

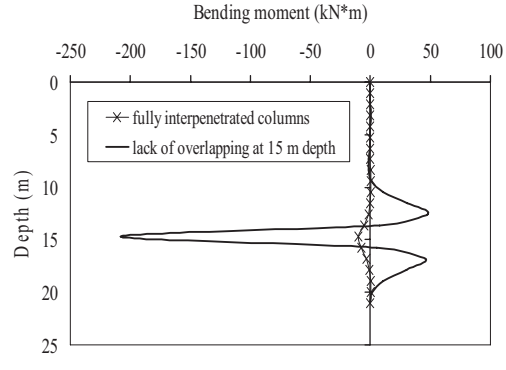

Figure 3. Bending moment profiles on columns for perfect and defective walls.

a jet grouting structure is a sequence of partially overlapped vaults, each having the shape of a frustum of cone with the length and opening angle the operators wish to use.

In the hypothesis that the jet grouted vault has no resistance in the longitudinal direction, the jet grouted umbrella works as far as the single columns are overlapped by a thickness sufficient to ensure arching support. In the ideal situation of perfectly oriented cylindrical columns, such a thickness depends only on columns diameter, soil properties and depth from ground level. In practice, columns overlapping and therefore arch thickness strongly depend on columns defects, and the overall structural performance must be considered by taking into account the possible variations of both diameter and axis inclination.

The combination of these defects gives rise to a much more irregular shape, which by no means is a regular frustum of cone, with cross-sections like the one reported in Figure 4. A random variation of the overlapping thickness is expected, and overlapping decreases along the span more dramatically then it would in the ideal case of columns having no defects. There is a critical length of the span after which structural continuity is difficult to obtain.

Once probabilistic distribution laws of statistical variables (geometrical and mechanical properties of the columns) are given, it is possible to explore different scenarios by Monte Carlo Method simulations (Lignola et al., 2008).

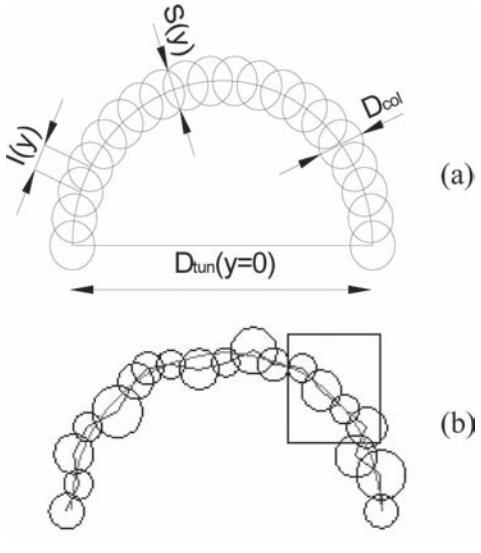

Figure 4. Typical jet-grouted umbrella cross section: a) with cylindrical columns (D_{col} = cost); b) with irregular columns.

In Figure 5 the simple case of an imperfect jet-grouted umbrella (D_{col} = 0.6 m) as a support of a shallow tunnel having D_{tun} (y = 0) = 8 m is reported.

The initial overlapping between adjacent columns (at the beginning of the span y = 0) is 80% of the column diameter. Due to variations in position and diameter of the columns, the geometric shapes generated by Monte Carlo simulations are *imperfect*, and therefore have in each cross section ($0 < y < y_{max}$) neither semi-circular shape nor constant overlapping thickness (S(y) in Fig. 4). In this example, the rather irregular shape is assumed to be represented by an equivalent semi-circular arch having a cross sectional constant thickness $S_{5\%}$ (the value lower than 95% of all obtained thicknesses).

As expected, the lack of overlapping is basically governed by defects in the position of the columns' axis (represented by the standard deviation of angular deviations $\sigma(\alpha)$), while the variation of column diameter (represented by the coefficient of variation of column's diameter CV_d) plays a minor role. This simple approach is attractive and can be easily implemented along with a simple structural model to check arch performance (Flora et al., 2007), in the hypothesis that jet grouted columns have no longitudinal flexural capacity; as a consequence equilibrium in the jet grouted umbrella is possible only if transversal arches are complete and able to carry the design loads. In such a way, a complex 3D problem is converted into a much simpler 2D problem.

Even though this simple approach allows to perform risk evaluations, the structure with defects may have an irregular axis that makes the real structure far from the perfect arch, with the consequence of possible unexpected flexural moments that cannot be considered by the described approach (equivalent ideal arch).

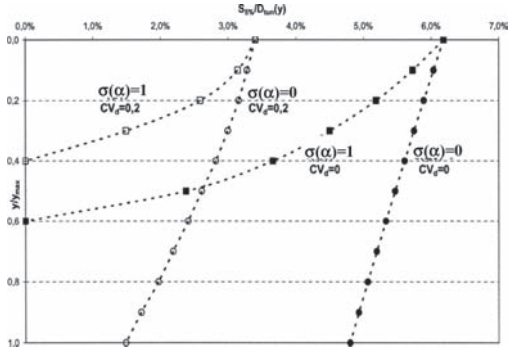

Figure 5. Design charts for sand: the normalized value $S_{5\%}/D_{tun(y)}$, versus the normalized y/y_{max}.

Lignola et al. (2009), therefore, have developed a simple numerical code able to analyse the behaviour of irregular arches taking into account defects both in dimensions and position of each single column, i.e. studying each cross section as it comes out from a random probabilistic generation. Irregular arches may be generated for instance with a Monte Carlo procedure, considering the statistical parameters of defects and modeled as assemblies of mono-dimensional beam elements able to develop bending moments, axial forces, and shear forces. The behavior of individual elements is characterized by the element's stiffness relation with constant cross section having an height equal to the overlapping thickness. Then, the global stiffness matrix, needed to get the exact solution of the structural problem, is obtained by assembling each single element local matrix. This stiffness method allows in fact to account for real structures with defects, far from being a perfect arch. Frictional hinges are considered as external constraints at the base of the curved open structure. External loads can be applied considering any wished stress redistribution caused by the complex 3D effects of tunnel excavation. In the program, vertical loads are introduced as a function of an equivalent depth z, and horizontal loads are considered proportional to the vertical ones via a coefficient K. The results obtained with this code show the significant role played by the irregular shape of cross sectional elements given by defective columns.

Both the proposed approaches allow to plan the number of jet grouted columns to be used and their initial overlapping, also in multilayered layouts to be adopted with a given level of confidence once stability of the jet grouted supporting structure, and the tunnel average diameter is given.

3.2 *Shafts*

The influence of columns defects on circular excavation shafts has been evaluated with a similar probabilistic analysis (Croce et al., 2006, Fusco, 2009). A shaft of diameter D_{shaft} formed by a single crown of identical overlapped columns having diameter D_{col}, mutual span i and uniaxial compressive strength σ_{lim}, can be preliminarly studied as a cylindrical tube inserted into a homogeneous soil. Under these ideal conditions (perfect cylinder, no defects), the limit depth where the soil confining action produces collapse of the cemented soil (z_{lim}), can be easily calculated by the following equation (Croce et al., 2006):

$$z_{lim} = \frac{2\sigma_{lim}\sqrt{D_{col}^{\ 2} - i^2}}{K_0 \cdot \gamma \cdot D_{shaft}} \qquad (2)$$

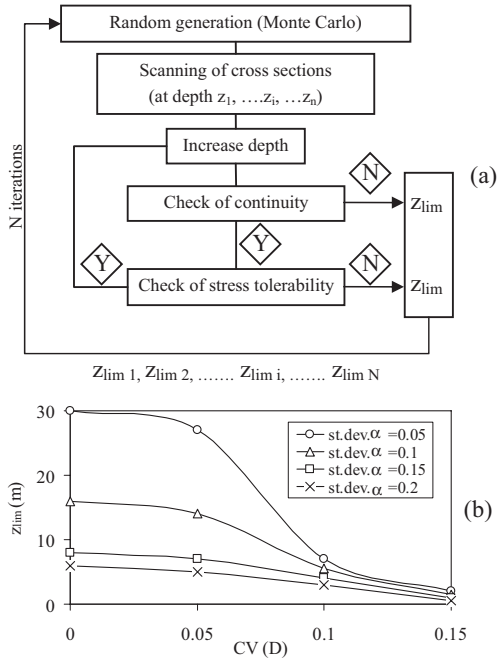

Figure 6. Calculation process for a vertical jet grouted shaft (a) and sample of results with CV(σ_{lim} = 0.2)(b).

By considering defects in both diameter and axis position, a solution can be obtained using the calculation process described in Figure 6.a. A non cylindrical shaft is generated with Monte Carlo simulation technique, where the geometrical and mechanical properties of columns are simulated with the probabilistic models introduced in the second paragraph. z_{lim} is then defined at the first depth where at least one between continuity or stress tolerability conditions is not fulfilled.

The big influence of variability of columns properties can be seen in Figure 6.b, where the limit depth corresponding to 5% accepted probability of failure is calculated (D_{shaft} = 12 m, 63 columns having D_{col} = 0.6 m, γ = 20 kN/m^3, K_o = 0.5, σ_{lim} = 13 MPa).

4 IMPROVEMENTS OF DESIGN METHODS

The results obtained in all the previously described analyses show that, independently on the considered case and regardless of the adopted probabilistic procedure, very large thicknesses are generally required to guarantee integrity of the jet grouted structures; in some case, the values could be too large to be realistic.

This result is significantly affected by the very conservative assumptions made in previous calculations. In particular, collapse of structures has been referred only to continuity or stress tolerability of cross sections, while nil contribution has been considered from the longitudinal flexural resistance of columns. Even assuming nil tensile strength of soilcrete, a significant improvement to the flexural resistance of columns may on the contrary derive from the longitudinal compressive stresses and/or from the possible insertion of reinforcements. Furthermore, nil interaction was assumed between supporting structures and surrounding soil (applied forces independent on displacements), while this effect could in principle produce a reduction on the assumed thrusts. Finally, it is worth considering the fully three dimensional nature of the studied problem, with its implications on the supporting structure and the surrounding soil. In the next paragraphs, the relevance of these factors on the results of calculations is singularly considered.

4.1 *Soil structure interaction*

Soil-structure interaction may influence the stress state in the structure to a great extent, its relevance depending on soil-structure relative stiffness. The use of the stiffness method previously described with reference to tunnels, for instance, allows to simply take into account the interaction between the jet-grouted structure and the surrounding soil through a number of independent Winkler type springs. Then, the stresses acting on the structure change along the loading process because of structure's deformation. Inward movements release the springs and decrease the horizontal stress component (active path), while outward movements have the opposite effect (horizontal stress increase, passive path).

For example, the non dimensional deformed shape $w(\eta)$ in the local coordinate system of an element loaded by a transverse unit displacement is given by:

$$w(\eta) = 2x^3/L^3 - 3x^2/L^2 + 1/w(\eta) \tag{3}$$

Because of this displacement field, the independent springs load the element with a pressure $p(\eta) = \kappa \cdot w(\eta)$, giving rise to an additional displacement field, $w'(\eta)$, according to equation:

$$w'(\eta) = \frac{\kappa L^4}{EI}\left(\frac{x^7}{420L^7} - \frac{x^6}{120L^6} + \frac{x^4}{24L^4} - \frac{13x^3}{210L^3} + \frac{11x^2}{420L^2}\right) \tag{4}$$

where κ is the interaction parameter. A possible expression of this parameter is:

$$\kappa = a \cdot S \cdot \left(\frac{E_{soil}}{D_{tun/shaft}}\right) \tag{5}$$

being S and $D_{tun/shaft}$ respectively the structural thickness and the diameter of either the tunnel or the shaft, and E_{soil} the soil stiffness.

Soil stiffness is a nonlinear function and depends on the sign of the displacement function. To avoid an iterative approach, an elastic formulation can be adopted for the Winkler springs with a constant stiffness κ. In Figure 7, for instance, the results of a calculation carried out with the code developed by Lignola et al. (2009) considering also Soils Structure Interaction (SSI) is reported (assuming a = 2) to show how relevant it can be. Since inward movements reduce the stresses applied on the arch the structure with SSI is in a much safer structural condition.

The subgrade reaction factors κ given by eq. 5 have been compared with those obtained by a linear interpolation of the relations found with two dimensional FEM simulations (Plaxis 2D, Brinkgreve & Vermeer, 2000) between normal stresses and displacements at the contour of a semicircular canopies. To this aim a parametric variation has been assigned to the cover (2.5 ÷ 10 m), the diameters (5 ÷ 10 m) and the wall thicknesses (0.6 ÷ 1 m) of the canopy and to the stiffness of cemented soil (2 ÷ 8 GPa). The non linear soil response has been simulated with an elasto-plastic, double hardening surface model (Schanz, 1998) by considering different stiffness parameters ($E_{50\%} = 40 \div 238$ MPa). The comparison reported in Figure 8.a for two positions A and B (respectively at the top and the base of the crown). on the arch-soil interface is not particularly satisfactory due to the large spread of results,

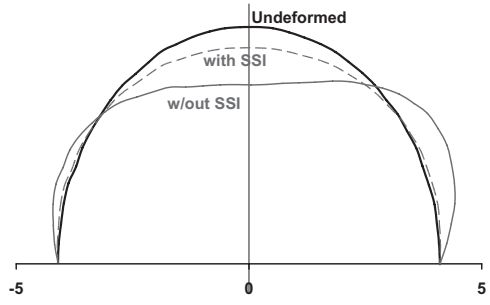

Figure 7. Effect of soil-structure interaction in terms of displacements in the arch (cross section of a jet-grouted canopy (after Lignola et al., 2009).

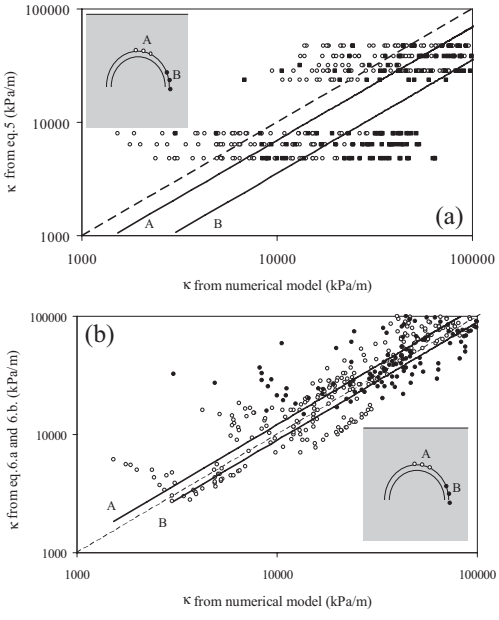

Figure 8. Subgrade reaction factors obtained from simplified relations (a. with eq.5; b. with eqs. 6.a and b) compared with those obtained by the numerical model.

indicating that the value of κ given by eq. (5) may be oversimplified, or at least unable to catch the different soil response for stress release (active) and stress increase (passive) paths.

An improvement (see Fig. 8.b) in the interpretation of numerical results can be obtained separating the two kinds of paths (in this case defined for active and passive points respectively from the results in point A and B) introducing the following two empirical regression curves:

$$\kappa = 0.2 \frac{\left(E_{jet} \cdot s_{jet}\right)^{0.36} \cdot E_s \cdot z^{0.86}}{D^2} \quad (6.a)$$

$$\kappa = 0.32 \frac{\left(E_{jet} \cdot s_{jet}\right)^{0.43} \cdot E_s^{0.57} \cdot z^{0.5}}{D} \quad (6.b)$$

A positive effect of soil structure interaction on the horizontal displacements and stresses of columns has also been shown on jet-grouted shafts by Fusco (2009) (Fig. 9).

It must be however pointed out that, due to the larger stiffness of closed rings compared with tunnel canopies, the advantage of considering SSI is not particularly relevant. Therefore, in an attempt to reduce complexity of structural analyses, SSI could be conveniently avoided unless very slender

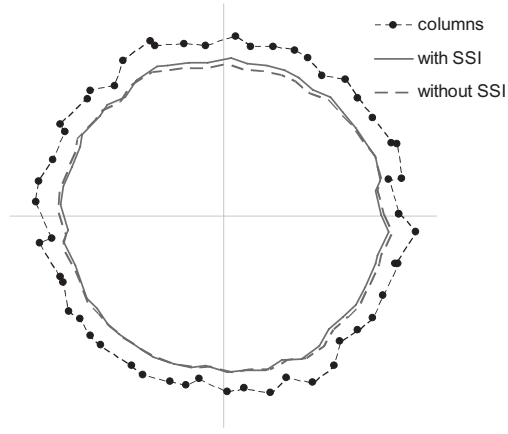

Figure 9. Effect of soil-structure interaction in terms of displacements in the cross section of a jet-grouted shaft: D_{shaft} = 10 m; D_{col} = 1 m; σ_{lim} = 10 MPa (Fusco, 2009).

shaft sections are considered (but this latter case is in contrast with the above discussed need of reducing defects).

4.2 *Three dimensional (3D) response*

By analysing structural performance, it is found for both tunnels and shafts that the lack of overlapping is the most probable failure mechanism. In Figure 10, for example, the results of a case study of jet-grouted canopies are shown (Lignola et al., 2009). In the figure, the upper bar represent the percentage of arches that fail (that is the probability of failure P_f) for the given cross section/arch of the umbrella, while the lower bar represents the percentage of the three expected failure modes (soilcrete failure, stability failure and no columns overlapping). Starting from the 8th arch, P_f reaches 100% and the corresponding most probable failure mechanism is always the lack of overlapping.

This depends on the fact that, in these 2D analyses, the lack of continuity (i.e. no overlapping between at least two adjacent columns) is considered as a condition sufficient to attain arch failure. This is certainly very conservative, as the 3D jet grouted structure (either open or closed) may have the ability to carry soil loads even if in a small portion it is not continuous. The question is: how small should this portion be? How can we take into account the existence of structural discontinuities from a structural viewpoint? The questions are worth being considered and deserve an answer.

From a theoretical point of view, the structural analysis of geometric discontinuities (in the following briefly called 'holes') is very complex. Holes in

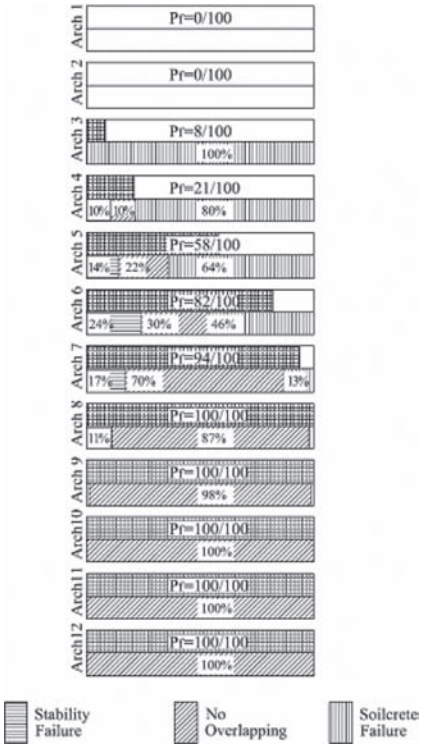

Figure 10. Probability of failure for arches forming an umbrella (D_{tun} = 8 m; D_{col} = 0.6 m) with defects in sand soil with CV_d = 0.10 and $\sigma(\alpha)$ = 0.5. Effect of Soil-Structure Interaction (SSI). (Lignola et al., 2009).

the structure cause a local increase in the intensity of the stresses, depending on the dimension and shape of the hole itself. A proper analysis should include the real geometry of the hole, which the case of defected jet grouted structures is strictly related to the statistical parameters adopted for the analysis.

Figure 11, for instance, shows typical maps of holes on the lateral surface of a shaft, as numerically calculated using two different sets of statistical parameters of the columns geometrical properties (CV_d = 0.1 in both cases; $\sigma(\alpha)$ = 0.5° and 1° respectively) using the extension to shafts of the code developed by Lignola et al. (2009) previously described. These maps show, as expected, that the amount of holes increases with depth, and that most of them are connected. However, some are not, specially in the upper part of the shaft.

To estimate the maximum allowable dimensions of the hole in the case of the shaft, the stress increase within the structure around the hole has been calculated via the simplified analytical

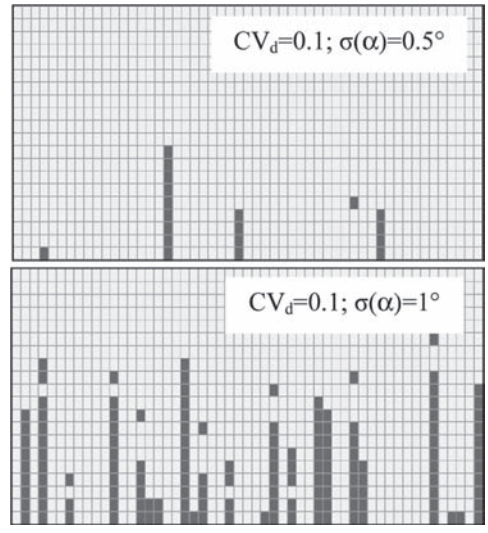

Figure 11. Maps of holes on the lateral surface of a shaft, for different angular deviations (D_{shaft} = 10 m; D_{col} = 1 m; σ_{lim} = 10 MPa).

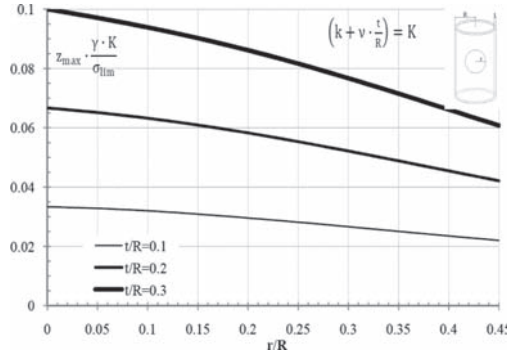

Figure 12. Design chart for maximum radius of critical holes at depth lower than z_{max}.

method suggested by Young and Budynas (2002) (see Appendix A). The structural safety is analysed by verifying that $\sigma_1 K_t \le \sigma_{lim}$, being σ_1 the maximum compressive stress within the jet grouted structure (see Appendix A). By manipulating this structural condition, a simple relation can be found:

$$z \cdot \frac{\gamma \cdot K}{\sigma_{lim}} \le \frac{t}{R \cdot K_t} \qquad (7)$$

being $K = k + \nu \cdot t/R$. In this relation, the radius r of the hole is included in the expression of K_t (Appendix A). Eq. (7) allows to plot the design chart shown in Figure 12, in which z_{max} is the

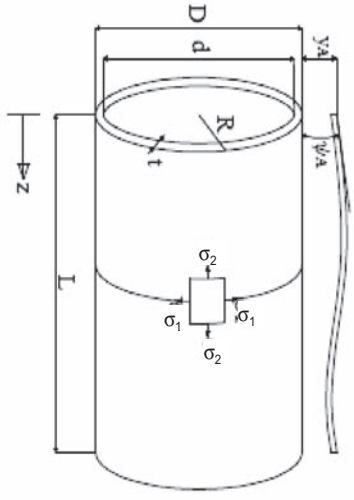

Figure 13. Scheme of a cylindrical shaft.

maximum depth at which a hole having radius r still complies safety conditions. For a given geometry of structure and defects, the deeper is the location or the lower is cemented material strength, the smaller is the maximum hole radius r that complies with structural safety.

By using the chart reported in Figure 12 it can be easily seen that, if the jet grouted soil has fair strength, holes of dimensions of a meter or so do not necessarily imply structural failure, even at considerable depths. Even though the chart refers to circular holes, it suggests that the assumption that arches (for tunnels) and rings (for shafts) have to be continuous in the cross section to avoid failure may be too strong. Further research is needed and is currently under course to extend and confirm this result.

5 CONCLUSIONS

Jet grouted supporting structures are unavoidably affected by defects. By using a simple probabilistic or semi probabilistic approach, structural performance can be assessed with a given level of confidence. This probabilistic approach is rational and cost effective if compared with a deterministic one. Yet, the approaches suggested by the authors in the past, briefly recalled in the paper, may still result into massive structures with large thicknesses under typical soil loads. In this paper, it is argued that the reason why of this conservativeness in results is the inability of the original approach to take into account some relevant aspects, namely Soil-Structure Interaction (SSI) and the truly 3D behaviour of tunnel canopies and shafts.

By introducing SSI into a numerical code developed by some of the authors (Lignola et al., 2009) it was shown that the stresses within the jet grouted structure strongly reduce, and a less conservative design can be obtained. A simplified approach is also suggested to take into account the existence of structural discontinuities ('holes') without necessarily implying structural failure. So doing, the three dimensional ability of the structure to carry loads can be considered, and less conservative design attempted.

APPENDIX A

Young and Budynas (2002) propose a formula to evaluate the increase of stresses around a circular hole of radius r on the wall of a cylindrical shaft (having thickness t and external radius R, Fig. 13) via the use of a stress multiplier, called stress concentration factor K_t.

The formula can be applied if $t/R > 0.1$ and $r/R < 0.45$. The intensity factor is then calculated as:

$$K_t = C_1 + C_2\left(\frac{r}{R}\right) + C_3\left(\frac{r}{R}\right)^2 + C_4\left(\frac{r}{R}\right)^3 \tag{8}$$

where the parameters C1, C2, C3 and C4 are:

$$C_1 = 3.000$$

$$C_2 = 2.773 + 1.529\left(1 - \frac{t}{R}\right) - 4.379\left(1 - \frac{t}{R}\right)^2$$

$$C_3 = -0.421 - 12.782\left(1 - \frac{t}{R}\right) + 22.781\left(1 - \frac{t}{R}\right)^2$$

$$C_4 = 16.841 + 16.678\left(1 - \frac{t}{R}\right) - 40.007\left(1 - \frac{t}{R}\right)^2$$

In the case of loads linearly increasing with depth z, the vertical and horizontal normal stresses (σ_1 and σ_2 in Fig. 13) within the jet grouted structure can be calculated as:

$$\sigma_2 = \gamma \cdot z \tag{9}$$

$$\sigma_1 = \gamma \cdot z \cdot \left(\frac{K_0 \cdot R}{t} + \nu\right) \tag{10}$$

where the horizontal stress in practical cases is always larger than the vertical one.

REFERENCES

Bell A.L., (1993). Jet Grouting. In Ground Improvement, M.P. Moseley Editor, Blackie, pp. 149–174.

Brinkgreve R.B.J. and Vermeer P.A., (2000). Plaxis Manual, version 7.2. A.A. Balkema Rotterdam, Delft, the Nederlands.

Croce P., Flora A., Modoni G., (2004). Jet grouting: design, execution and control (in Italian). Hevelius editore, Benevento.

Croce P., Modoni G. and Palmisano, F., (2006). Design of jet grouted shafts for foundation (in Italian). National Conference of Researchers of Geotechnical Engineering (CNRIG), Bari (Italy), pp. 327–339.

Croce P., Modoni G., Russo G., (2008). Observations on the use of stabilisation techniques for tunnelling in granular soils (in Italian), Proc. of the Conf. in Memory of Prof. Renato Ribacchi, Associazione Geotecnica Italiana, Patron editore, pp. 271–280.

Flora A., G.P. Lignola, G. Manfredi, (2007). A semi-probabilistic approach to the design of jet grouted umbrellas in tunnelling. Ground Improvement, Vol. 11, No. 4, 207–217, Thomas Telford Ed.

Fusco A., (2009). Probabilistic analysis of the behavior of jet-grouted shaft (in Italian). Master Thesis University of Naples "Federico II".

Lignola G.P., A. Flora, G. Manfredi (2008). A Simple Method for the Design of Jet Grouted Umbrellas in Tunneling. Journal of Geotechnical and Geoenvironmental Engineering (ASCE), vol. 134, No. 12, pp. 1778–1790.

Lignola G.P., Flora A. and Manfredi G., (2009). Effect Of Defects on Structural Safety of Jet Grouted Umbrellas In Tunneling. 10th International Conference on Structural Safety and Reliability (ICOSSAR). Osaka (Giappone), pp. 3404–3411.

Schanz T., (1998). Zur Modellierung des Mechanischen Verhaltens von Reibungmaterialen (in German), Habilitation Thesis, Stuttgart University.

Young W.C & Budynas R.G., (2002). Roark's Formulas for stress and strain. Mc Graw Hill Ed.

Geotechnical Aspects of Underground Construction in Soft Ground – Viggiani (ed)
© 2012 Taylor & Francis Group, London, ISBN 978-0-415-68367-8

3D simulations of a NATM tunnel in stiff clays with soil parameters optimised using monitoring data from exploratory adit

T. Svoboda & D. Mašín
Charles University in Prague, Czech Republic

ABSTRACT: The paper demonstrates the application of a hypoplastic model in class A predictions of a NATM tunnel in an urban environment. The tunnel, excavated in a stiff clay, is 14 m wide with 6 m to 21 m of overburden thickness. The constitutive model was calibrated using laboratory data (oedometric and triaxial tests) and the parameters were optimised using monitoring data from an exploratory drift. Based on the optimised data set, the future tunnel was simulated. After the tunnel excavation, it could be concluded that the model predicted correctly surface settlements, surface horizontal displacements, and the distribution of vertical displacements with depth. It overpredicted horizontal displacements in the vicinity of the tunnel.

1 INTRODUCTION

The main issue of tunnelling in urban environment, typically characterised by a low overburden thickness and presence of surface infrastructure, is the control of settlements induced by tunnel excavation. The first step in the design of any protective measure reducing the tunnel impact on surrounding buildings is an accurate prediction of the tunnelling-induced displacement field.

The present paper demonstrates the application of an advanced constitutive model (Mašín in 2005) in predictions of a complex tunnelling problem in urban environment. The goal was to provide class A predictions of the displacement field induced by a 14 m wide road tunnel in stiff clay, with an overburden of 6 m to 21 m. The parameters of the constitutive model were calibrated on laboratory data and optimised using monitoring data from an exploratory drift. The drift was located in top heading of the future tunnel. Based on the optimised data set, class A predictions of the displacement field induced by the tunnel were performed in 2008 and early 2009. In November 2009, the full profile of the tunnel passed the simulated cross-section, which allowed us to compare the predictions with the data from the geotechnical monitoring.

2 KRÁLOVO POLE TUNNELS

The Královo Pole tunnels (often referred to as Do-brovského tunnels) form a part of the northern section of the ring road of Brno town in the Czech Republic. The tunnels consist of two parallel tubes with a separation distance of about 70 m and lengths of approximately 1250 m. The tunnel cross-section height and width are about 12 m and 14 m respectively, and the overburden thickness varies from 6 m to 21 m. The tunnels are driven in a developed urban environment (see Fig. 1). The displacement field induced by the tunnel excavation was thus an important issue the designers had to cope with.

The geological sequence in the area is shown in Fig. 2. From the stratigraphical point of view, the area is formed by Miocene marine deposits of the Carpathian fore-trough, the thickness of which reaches several hundreds meters in this location (Pavlík et al. 2004). The top part of the overburden consists of anthropogenic materials. The natural Quaternary cover consists of loess loam and clayey loam with the thickness of 3 to 10 m. The base of the Quaternary cover is formed by a discontinuous layer of fluvial sandy gravel, often with a loamy admixture. The majority of the tunnel is driven through the Tertiary calcareous silty clay. The clays are of stiff to very stiff consistency and high plasticity.

Before the Královo Pole project, there was only little experience with the response of the Brno clay to tunnelling. In order to clarify the geological conditions of the site, and in order to study the mechanical response of the Brno clay, a comprehensive geotechnical site investigation programme was designed, the crucial part of it being an excavation of three exploratory drifts. The drifts were triangular in cross section with the side-length of 5 m and were designed to form parts of the top headings of the future tunnels (Fig. 3). The total

Figure 1. Temporary portals of the Kralovo Pole tunnels (Horák 2009).

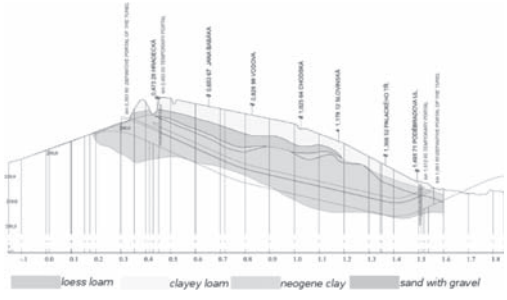

Figure 2. Longitudinal geological cross-section along the tunnels (Pavlík et al. 2004).

Figure 3. Exploratory drifts situated in the top headings of the future Královo Pole tunnels.

length of the three drifts was over 2000 m. For technological reasons, they were not driven along the complete length of the future tunnels.

The tunnels were driven by the New Austrian Tunneling Method (NATM), with sub-division of the face into six separate headings (Fig. 4). The face subdivision, and the relatively complicated excavation sequence, were adopted in order to

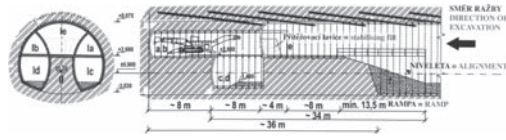

Figure 4. Sketch of the excavation sequence of the tunnel (Horák 2009).

minimise the surface settlements imposed by the tunnel.

3 LABORATORY EXPERIMENTS AND CONSTITUTIVE MODEL CALIBRATION

The behaviour of loess loams and sandy gravels was found not to influence significantly the predicted tunnel performance (Svoboda et al. 2010), the laboratory experiments thus focused on the behaviour of Brno clay. Triaxial CIUP tests and oedometric tests were performed in order to calibrate the selected constitutive model. The triaxial specimens were equipped with submersible local LVDT axial strain transducers in order to evaluate the soil stiffness in the small strain range. In addition, one specimen was equipped with bender elements to measure the soil stiffness in the very small strain range by means of propagation of shear waves. Oedometric tests have been performed on undisturbed and reconstituted specimens. The specimens were loaded up to axial pressures of 13 MPa in order to find the position of the normal compression line and in order to evaluate the apparent overconsolidation ratio, which is also used for estimation of the coefficient of earth pressure at rest K_0.

The mechanical behaviour of the Brno clay was simulated using the hypoplastic model for clays (Mašín 2005) enhanced by the concept of intergranular strains (Niemunis and Herle 1997). This model was selected to represent the advanced constitutive models, which are capable of predicting the nonlinear soil behaviour, with high stiffness at very small strains and a nonlinear decrease of stiffness with increasing strain level. The implementation of the model into various finite element programs (such as Plaxis, ABAQUS, Tochnog Professional) is freely available on the internet (Gudehus et al. 2008).

For details of the model calibration, see Svoboda et al. (2010). The parameters of the model are summarised in Table 1.

4 SIMULATION OF THE EXPLORATORY DRIFT

The finite element predictions of the exploratory drift and of the whole tunnel were performed using software Tochnog Professional. The geometry of the exploratory drift and the finite element mesh

Table 1. Brno clay parameters of the clay hypoplastic model.

φ_c	λ*	κ*	N	r
19.9°	0.128	0.01	1.506	0.45
m_R	m_T	R	β_r	χ
16.75	16.75	0.0001	0.2	0.8

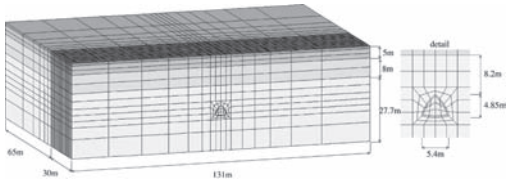

Figure 5. Finite element mesh used in the analyses of the exploratory drift.

consisting of 4680 8-noded brick elements are shown in Fig. 5. The evaluated cross-section corresponded to the front boundary of the finite element model. It was checked that no additional displacements at the evaluated cross-section were caused by the further advance of the drift face. Steady state conditions were thus reached. The mesh density was selected to be approximately the same for the drift and full tunnel simulations (Sec. 5). The analyses were performed as undrained using penalty approach with bulk modulus of water equal to $K_w = 100$ MPa. This procedure is described in Mašín (2009). No interface elements have been used between the tunnel lining and the soil; therefore sliding of the lining with respect to soil has not been allowed which is a reasonable assumption for shotcrete lining. On the vertical sides of the mesh, normal horizontal movements have been restrained, whereas the base has been fixed in all directions.

The bottom 27.7 m thick stratum represent the Brno clay and it has been simulated using the hypoplas-tic model with parameters from Tab. 1. The overlying layers of loams and gravels were simulated using the Mohr-Coulomb model with the parameters obtained during the site investigation (Pavlík and Rupp 2003) (Table 2). The shotcrete lining was simulated using continuum elements in the 3D model. Its was modelled by a linear elasticity with time dependent stiffness calculated using an empirical relationship (Oreste 2003)

$$E = E_f \left(1 - e^{-\alpha t / t_r}\right) \tag{1}$$

where E_f is the final Young modulus, α is a parameter and $t_r = 1$ day is the reference time. The same parameters as the ones adopted by Mašín (2009)

Table 2. Mohr-Coulomb model parameters of the layers overlying the Brno clay strata.

	φ [°]	c [MPa]	ψ [°]	E [MPa]	v [-]
Backfill	20	10	4	10	0.35
Loess	28	2	2	45	0.4
Sandy gravel	30	5	8	60	0.35

were used in the simulations (E_f = 14:5 GPa and α = 0.14). The simulated excavation sequence represented the one adopted on the site. An excavation step of 1.2 m was followed by the lining installation.

The initial conditions of the simulation consisted of the determination of vertical stresses, the void ratio and the coefficient of earth pressure at rest K_0. The vertical stress was calculated from the unit weight of soil: $\gamma = 18.8$ kN/m^3 for clay, 19.5 kN/m^3 for secondary loess and 19.6 kN/m^3 for sandy gravels. Water table corresponded to the Brno clay—sandy gravel interface. The initial void ratio of the Brno clay $e = 0.83$ was derived from the undisturbed samples from both boreholes.

Because no reliable *in-situ* measurements of K_0 were available in the Brno clay massif, two extreme values of K_0 were considered in the analyses. First, the value of K_0 was determined from Mayne and Kulhawy (1982) empirical relationship:

$$K_0 = (1 - \sin\varphi_c) OCR^{\sin\varphi_c} \tag{2}$$

The overconsolidation stress of 1800 kPa was estimated on the basis of the oedometer tests on the undisturbed Brno clay samples, with the corresponding overconsolidation ratio (OCR) of 6.5, leading to $K_0 = 1.25$. The calculation of K_0 according to Eq. (2) assumes that the apparent soil overconsolidation was caused by the actual soil unloading resulting from the erosion of overlying geological layers. Creep represents the second possible interpretation of the measured overconsolidation. This interpretation would lead to the K_0 value calculated from the Jáky (1948) relationship:

$$K_0 = 1 - \sin\varphi_c \tag{3}$$

leading to $K_0 = 0.66$. K_0 of the layers overlying Brno clay was always calculated from (3) using the friction angles from Tab. 2.

The procedure of the analyses was as follows. First, the drift was simulated using the 3D finite element method. The next step was optimisation of the model parameters to account for inaccuracies of the description of soil massif based on small-size laboratory specimens. As

the optimisation was CPU demanding and not feasible in 3D, an equivalent 2D model to the presented 3D model was developed. After the optimization stage, the drift was simulated in 3D using the optimised parameter set. The 2D model was based on the load reduction method (Schikora and Fink 1982). The load reduction factor λ^d was calculated to ensure that the 3D analyses and the equivalent 2D analyses predicted as closely as possible the surface settlement troughs. The actual factors λ^d for the drift simulations were $\lambda^d = 0.50$ (for $K_0 = 1.25$) and $\lambda^d = 0.53$ (for $K_0 = 0.66$). The adequacy of the 2D representation had been demonstrated in a separate paper (Svoboda and Mašín 2010). The 3D and equivalent 2D models gave comparable predictions of the displacement fields, apart from the displacements in the very close vicinity of the tunnels.

4.1 *Optimisation of the model parameters*

In geotechnical practice, a common problem is that due to the size effects, sampling disturbance and limitations of experimental devices laboratory specimens do not represent the behaviour of the soil massif with sufficient accuracy. For this reason, the soil parameters calibrated by means of laboratory experiments have been corrected using an inverse analysis of the exploratory drift. The corrected parameters were then used for the class A predictions of the deformations due to the tunnel.

In the optimisation stage we focused on the shear stiffness. Namely, the parameter r controlling the large-strain shear stiffness as well as the small-strain shear stiffness was optimised. As the value of K_0 has also remarkable influence on the results, all the simulations were performed with two extreme K_0 values (as explained above). The inverse analysis has been performed using the software UCODE. In the inverse analysis, the parameter values are automatically adjusted until the model's computed results match the observed behaviour of the system (Finno and Calvello 2005). In the analyses, results of the simulations were compared with the measurement of the vertical displacements at several locations. Three locations were at the surface, where the vertical displacements were measured by means of geodetic survey. The fourth monitoring point was located just above the drift crown and it was monitored by means of an extensometer. The differences between the simulation and the monitoring data were expressed in terms of an objective function $S(b)$ (Finno and Calvello 2005) which takes the form:

$$S(b) = \left[y - y'(b) \right]^T \omega \left[y - y'(b) \right] \tag{4}$$

Table 3. Original and optimised values of the parameter r.

Parameter set	r
Original param.	0.45
Optimised r, $K_0 = 1.25$	0.51
Optimised r, $K_0 = 0.66$	0.49

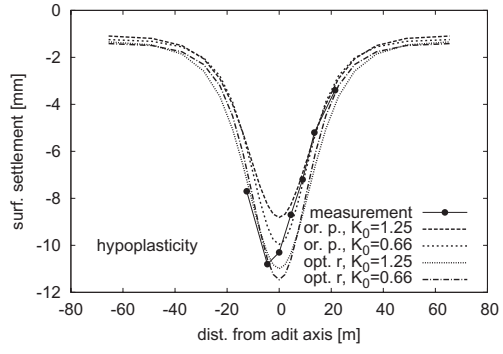

Figure 6. Surface settlement troughs due to exploratory drift predicted with the original parameter set ("or. p.") and with optimized value of the parameter r ("opt. r").

Where b is a vector containing the values of parameters, y is a vector of observations, $y'(b)$ is a vector of the computed values corresponding to the observations and ω is the weight matrix. The weight matrix evaluates the significance of each measurement.

Typically, the weight of each observation is taken as the inverse of its error variance (Finno and Calvello 2005). In the present case, with a low number of observations, however, each of the four observations is given the same weight equal to unity. UCODE performs the optimisation using by means of minimization of the objective function $S(b)$ using the modified Gauss-Newton method.

The surface settlement troughs predicted with the original and optimised parameter sets, compared with the monitoring data, are shown in Fig. 6. Clearly, the model predicts reasonably both the settlement trough shape and magnitude already with the original parameter set. The optimisation procedure leads to a slight increase of the parameter r (Tab. 3) and a further improvement in predictions.

5 3D SIMULATIONS OF THE KRÁLOVO POLE TUNNELS

As the last step in the investigation, the whole tunnel was simulated in 3D with the optimised parameter set. The results represent class A predictions,

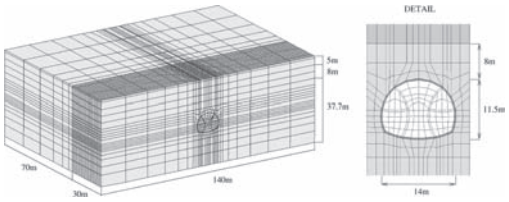

Figure 7. Finite element mesh used in the analyses of the whole tunnel.

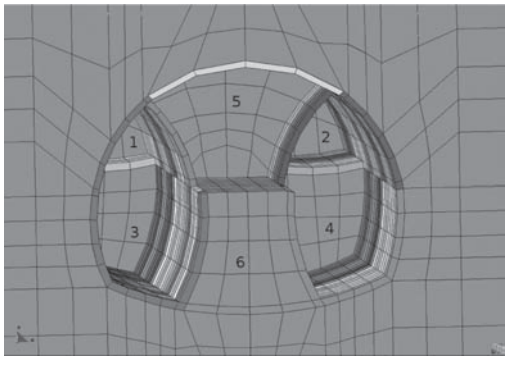

Figure 8. The excavation sequence as represented by the model.

as they were performed in the period 2008 to early 2009, and thus before the tunnel excavation passed the simulated cross-section (November 2009).

In 3D, the finite element mesh consisting of 18 352 8-noded elements was used. The mesh and the modeled geometry are shown in Fig. 7. As in the case of the drift simulations, the evaluated cross-section was located at the front tunnel boundary. Steady-state conditions with no additional displacements with further advance of the tunnel face were reached. Other details of the analyses (drainage conditions, boundary conditions) were the same as in the exploratory drift simulations (Sec. 4). The tunnel lining was modelled using continuum elements with the thickness of 0.35 m as a linear elastic material with time dependent stiffness (as in the case of the exploratory drift). A 100 meters long simulated portion of the tunnel corresponded to the tunnel chainage 0.790–0.890 km (Fig. 2). The models considered the complex excavation sequence with the tunnel face subdivided into 6 segments (Figure 8). The excavation was performed in steps 1 to 6 (Fig. 8) with an unsupported span of 1.2 m. A constant distance of 8 m was kept between the individual faces, except the distance between the top heading and the bottom, which was 16 m.

The surface settlement troughs for both K_0 values are presented in Figure 9a. Due to the scatter of

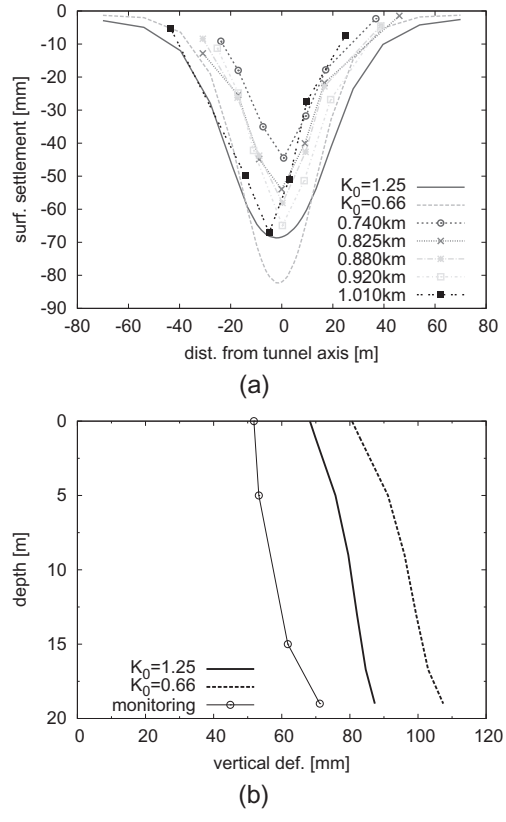

Figure 9. Surface settlement trough (a) and extensometer measurements (b). Class A predictions compared with the monitoring data.

the monitoring data, several measurements at the chainages close to the simulated cross-section are presented. The agreement between the simulated and measured settlements is very good. The settlement magnitude is better predicted represented by the simulation with the higher K_0, while the trough shape is better predicted by the low K_0. Both predictions are on the safe side of the monitoring data (displacements are slightly overpredicted).

Figure 9b shows measurements of an extensometer located above the tunnel crown. The difference between the monitoring data and the simulations is approximately constant with depth, and corresponds to the slight overestimation of the surface settlements in Fig. 9a. Fig. 9b thus indicates that the hypoplastic model predicted correctly also the distribution of vertical displacements with depth, not only surface settlements.

Although the model predicted correctly the vertical displacement field, it significantly overestimated horizontal displacements in a vicinity of the tunnel in the tunnel depth. This is demonstrated

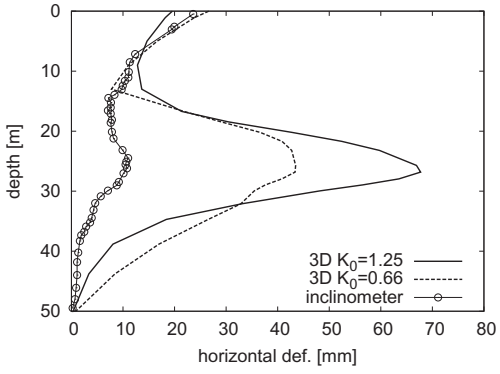

Figure 10. Inclinometric measurement, inclinometer located 3 m from the tunnel side.

in Fig. 10, showing the inclinometric measurements from an inclinometer located 3 m from the tunnel side. One of the possible reasons for this discrepancy is an absence of the small-strain stiffness anisotropy in the hypoplastic model. A similar problem was pointed out by Mašín (2009), who concluded that incorporation of the small-strain stiffness anisotropy into the hypoplastic model would improve the predicted shape of the settlement trough. This indicates a direction for the future development of the hypoplastic model. It is, however, necessary to stress out that although the horizontal displacements were overpredicted in the tunnel depth, their magnitude in the vicinity of the surface was predicted correctly. the correct predictions of the surface displacements are important in estimating the damage to the surrounding buildings.

6 CONCLUSIONS

It was shown that the application of an advanced soil constitutive model, in combination with quality experimental data and 3D finite element analysis, may lead to accurate forward predictions of the displacement field induced by a tunnel with low overburden thickness. The hypoplastic model for clays enhanced by the intergranular strain concept gave accurate predictions of the surface settlement, surface horizontal displacements, and the distribution of vertical displacements with depths. For both K_0 values adopted the model overpredicted the horizontal displacements in the vicinity of the tunnel.

ACKNOWLEDGEMENT

The authors greatly appreciate the financial support by the research grants GACR P105/11/1884, GACR 103/09/1262, GAUK 134907 and MSM0021620855.

REFERENCES

Finno, R.J. & M. Calvello (2005). Supported excavations: Observational method and inverse modelling. *Journal of Geotechnical and Geoenvironmental Engineering ASCE 131*(7), 826–836.

Gudehus, G., A. Amorosi, A. Gens, I. Herle, D. Kolymbas, D. Mašín, D. MuirWood, R. Nova, A. Niemunis, M. Pastor, C. Tamagnini, & G. Viggiani (2008). The soilmodels. info project. *International Journal for Numerical and Analytical Methods in Geomechanics 32*(12), 1571–1572.

Horák, V. (2009). Kralovo pole tunnel in Brno from designer point of view. *Tunel 18*(1), 67–72.

Jáky, J. (1948). Pressures in silos. In *Proc. 2nd Int. Conf. Soil Mechanics*, Volume 1, pp. 103–107. Rotterdam.

Mašín, D. (2005). A hypoplastic constitutive model for clays. *International Journal for Numerical and Analytical Methods in Geomechanics 29*(4), 311–336.

Mašín, D. (2009). 3D modelling of a NATM tunnel in high K_0 clay using two different constitutive models. *Journal of Geotechnical and Geoenvironmental Engineering ASCE 135*(9), 1326–1335.

Mayne, P.W. & F.H. Kulhawy (1982). K_0-OCR relationships in soil. In *Proc. ASCE J. Geotech. Eng. Div.*, Volume 108, pp. 851–872.

Niemunis, A. & I. Herle (1997). Hypoplastic model for cohesionless soils with elastic strain range. *Mechanics of Cohesive-Frictional Materials 2*, 279–299.

Oreste, P.P. (2003). A procedure for determining the reaction curve of shotcrete lining considering transient conditions. *Rock Mechanics and Rock Engineering 36*(3), 209–236.

Pavlík, J., L. Klímek, & D. Rupp (2004). Geotechnical exploration for the Dobrovského tunnel, the most significant structure on the large city ring road in Brno. *Tunel 13*(2), 2–12.

Pavlík, J. & D. Rupp (2003). The large city ring road Brno, section I/42 Dobrovského A, exploratory adits (in Czech). Technical report, Geotechnical site investigation, Geotest Brno.

Schikora, K. & T. Fink (1982). Berechnungsmethoden moderner bergmäannischer Bauweisen beim U-Bahn-Bau. *Bauingenieur 57*, 193–198.

Svoboda, T. & D. Mašín (2010). Convergence-confinement method for simulating NATM tunnels evaluated by comparison with full 3D simulations. In J. Zlámal, A. Butovič, and M. Hilar (Eds.), *Proc. International Conference Underground Constructions Prague 2010—Transport and City Tunnels, Prague, Czech Rep.*, pp. 795–801.

Svoboda, T., D. Mašín, & J. Boháč (2010). Class A predictions of a NATM tunnel in stiff clay. *Computers and Geotechnics 37*(6), 817–825.

Geotechnical Aspects of Underground Construction in Soft Ground – Viggiani (ed)
© 2012 Taylor & Francis Group, London, ISBN 978-0-415-68367-8

Numerical analysis of 20.5 m deep excavation with anchored diaphragm wall

J. Josifovski, S. Gjorgjevski & M. Jovanovski
Faculty of Civil Engineering-Skopje, University Ss. Cyril and Methodius, R. Macedonia

ABSTRACT: The deep excavation in built-up urban areas surrounded by high-rise buildings with deep basements makes this engineering problem quite formidable. Such a project for construction of eight storey administrative-residential building located in the city centre of Tirana, Albania is described in this paper. It anticipates a 20.5 m deep excavation surrounded by six and eight storey buildings with basements. To ensure an undisturbed excavation of 27.7 × 36.9 m pit a multi anchored diaphragm wall has to be constructed. The finite element method has been used to check the stability, calculate the system and determine the internal forces, displacements, support reactions under earth and water pressure. The proposed model had been able to give realistic estimation of the excavation soil behaviour which was proved during the process of construction.

1 INTRODUCTION

The excavation of 27.7 × 36.9 m pit is necessary for construction of eight storey administrative-residential building in the city centre of Tirana. The structure has six underground storeys with bottom floor as a basement, next 3 floors as parking lots while the top 2 floors are shopping and administrative premises. All together sums up to a depth of 20.5 m, see Figure 1.

The excavation is secured by diaphragm wall with thickness $t = 0.8$ m, length $L = 129.2$ m and height $H = 25$ m which has only a temporal character. The reinforced concrete wall is constructed out of segments with 2.7 m width. The supporting structure represents a multi anchored diaphragm wall with height of 20.5 m plus additional 4.5 m depth bellow the pit. The supports are pre-stress anchors introducing additional stabilizing forces in the system. Depending on the requirements anchor type TTS15 with 5, 6 and 7 cables has been employed. Every cable is comprised out of 7 wires ϕ5 mm with total diameter of 15 mm. The horizontal anchor spacing is $L_s = 2.7$ m and vertical is $h_s = 3$ m. The anchors are positioned with inclination of 15 degrees to the horizontal and varying length.

2 CONSTRUCTION PROCEDURE

The excavation had been performed according to carefully devised procedure. To ensure a safe excavation of the pit, first a diaphragm wall has to be constructed. Specialized machines were employed to excavate the wall. After positioning of reinforcement a continuous concrete pour through fixed pipes has been executed is 25 m deep. The construction of the diaphragm wall enabled the next phase, namely the excavation of the pit. The excavation and positioning of the anchors has been performed in six continuous phases which are described in Table 1 with respect to the excavation depth h.

Parallel to the excavation a dewatering of the pit had been performed using pumps with sufficient capacity and number. The anchoring is performed in counter-clockwise direction with rotational drilling and piping (130–180 mm). Next the grouting if the anchors is performed using a cement injection mass with 3% bentonit. After reaching the hardening condition of the injection mass the pre-tensioning of the anchors can start. Before proceeding with the excavation of the next phase the anchors from the previous have to been finished. To ensure that design values of the anchor forces are properly introduced it is necessary that 10% of anchors fulfil the acceptance test.

3 GROUND CONDITIONS

The boreholes gave a clear picture of the ground profile which is comprised out of 10 almost horizontal layers. The ground conditions in this project were defined according to data obtained from the field investigations and laboratory tests.

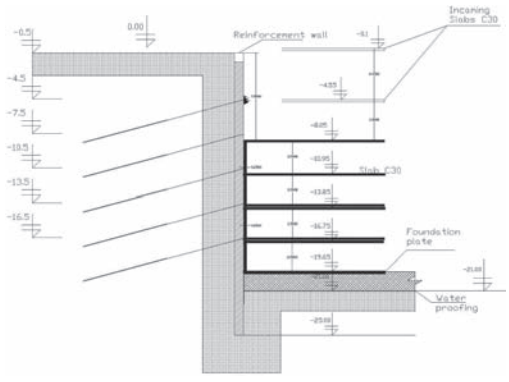

Figure 1. Multi anchored diaphragm wall section AA(left) protecting the excavation.

Table 1. Excavation phases.

Phase	1	2	3	4	5	6
h (m)	–4.0	–8.0	–11.5	–14.5	–17.5	–20.5

Table 2. Soil properties.

Type	h (m)	γ (kN/m^3)	ν (/)	M_v (MPa)	c (kPa)	ϕ (^{0})
N	1.0	17.0	0.3	3	5	18
CI	3.4	19.3	0.3	10	30	18
ML	5.9	19.1	0.31	8	10	20
GW	6.8	19.0	0.34	11	25	18
ML	14.5	19.6	0.32	11	15	21
CL	16.0	19.6	0.30	12	5	24
CL	17.5	20.0	0.28	18	45	25
M	20.0	22.0	0.27	25	150	30
M	24.0	24.0	0.26	45	200	32
M	40.0	24.0	0.26	55	250	34

In the numerical model the soil had been represented by the following material parameters: γ as a unit weight, ν as a Poisson's ratio, M_v as a compression modulus, strength parameters c as cohesion and ϕ as angle of internal friction. They are presented in Table 2 for every lithological unit with respect to the depth h.

The top layer (N) is a man-made embankment brownish silty clay containing pieces of bricks and roots with a thickness of 0.7 m; layer (CI) is silty clay mixture with yellow colour medium dense with average thickness of 2.4 m; layer (ML) is clayly silt predominate brown colour medium-dense with thickness from 2.0 to 2.5 m; layer (GW) is sandy gravel with local presence of claylike matrix with thickness of 0.5 m to 0.7 m; layer (CL) is composed of silty clay mixtures medium low dense yellow colour encountered at 4.5 up to 9 m depth; layers (M) are Neogene's deposits composed by claylike Marls to highly weathered alveoli. The underground water is present on 4 to 5 m below ground surface in layers (ML) and (GW) while top and bottom layers are with low permeability and relatively dry.

4 NUMERICAL ANALYSIS

In order to obtain a realistic behaviour of the deep excavation supported by a diaphragm wall the problem has been analysed with the finite element method. The computer program Plaxis which is specialized for geotechnical engineering has been used in combination with some analytical solutions. The program enables simple but efficient spatial modelling of different structural elements and accurate material definition.

The ground stress-strain state during excavation is calculated on a two-dimensional plane-strain finite element model. The soil is discretized as elastoplastic material using a Mohr-Coulomb definition vis-a-vis the reinforced concrete wall as a linear material. The spatial discretization had been varied depending on the situation and detailing level but in general triangular plane elements with 15 nodes had been used. The structural elements were modelled using three node beam elements.

4.1 *Excavation*

Since there is a difference in the ground and loading conditions on the construction site it was decided that all four sides of the pit has to be analysed. The excavation pit from three sides is surrounded by buildings with basements, thus different structural solutions of the anchored diaphragm wall are necessary. They are distinguished by the wall section name e.g. AA or BB followed by subscripts 'l' or 'r' for left and right side. The stage construction has been simulated in six continuous phases, hence the initial phase calculates the initial ground stresses with constructed diaphragm wall. The excavation scenario from Table 1 is illustratively presented in Figure 2.

First, a finite element analysis with fix-end anchors has been performed to determine the characteristic force for every phase in different level. The results for both wall sections left to right are presented in Table 3 through Table 6.

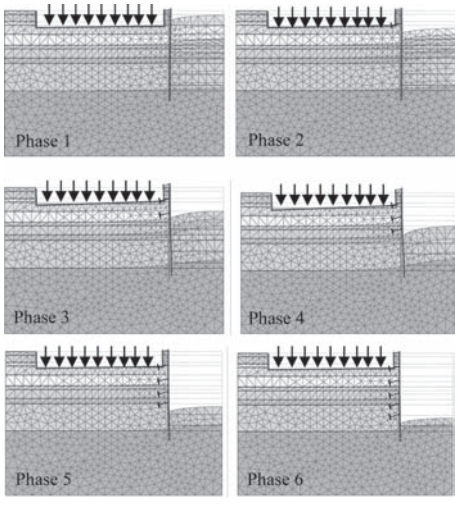

Figure 2. Deformed finite element mesh of wall section AA_i for construction phase (1–6).

Table 3. Characteristic phase anchor force in wall section AA_l.

	P_k (kN/m)				
Level (m)	Ph.2	Ph.3	Ph.4	Ph.5	Ph.6
–4.0	240.3	146.2	155.1	158.0	164.7
–8.0		541.8	493.6	491.2	492.2
–11.5			401.2	422.4	417.2
–14.5				401.2	502.5
–17.5					470.5

Table 4. Characteristic phase anchor force in wall section AA_r.

	P_k (kN/m)				
Level (m)	Ph.2	Ph.3	Ph.4	Ph.5	Ph.6
–4.0	194.7	79.4	80.6	79.6	87.9
–8.0		501.7	449.2	448.4	451.6
–11.5			372.8	385.3	381.1
–14.5				382.4	428.4
–17.5					401.1

The calculation of the required anchor forces is performed with respect to the overall stability in every phase of excavation.

4.2 *Anchors*

The anchor lock-off force P_0 has been determined according to EN 1537 as.

$$P_0 = 0.60 P_{tk} \quad (1)$$

Table 5. Characteristic phase anchor force in wall section BB_l.

	P_k (kN/m′)				
Level (m)	Ph.2	Ph.3	Ph.4	Ph.5	Ph.6
–4.0	–	–	–	–	–
–10.5		134.0	26.0	34.4	42.8
–11.5			495.9	480.0	467.1
–14.5				355.4	372.0
–17.5					361.2

Table 6. Characteristic phase anchor force in wall section BB_r.

	P_k (kN/m′)				
Level (m)	Ph.2	Ph.3	Ph.4	Ph.5	Ph.6
–4.0	199.4	87.8	92.6	93.5	99.8
–8.0		533.3	479.5	479.8	482.6
–11.5			396.7	404.0	400.0
–14.5				432.3	474.2
–17.5					459.5

Table 7. Lock-off tendon force.

Anchor type	P_0 (kN)	P_0/L_a (kN/m)
4TTS15	840	311
5TTS15	1050	389
6TTS15	1260	467
7TTS15	1470	544

where P_{tk} is the characteristic load capacity of tendon. In the case of TTS15, $P_{tk} = 350$ kN, which leads to 210 kN as loading capacity per anchor thread. The total tendon force is assumed to be N (number of cables) times the thread force, see Table 7.

According these values adequate anchor types have been assumed which fulfil minimum required force P_k for different sections of the wall, see in Table 8 through Table 11.

4.3 *Anchor grouted body*

A special attention had been given to the calculation of a single anchor following the classical solution after P. Lendi, see Figure 5.

The grouted body of the anchor is positioned in the layer (M)—Marls (below depth 10.5 m) with

Table 8. Anchors in wall section AA_l.

Level (m)	Anchor type	P_0 (kN/m)	P_0 (kN)
–4.0	4TTS15	311	840
–8.0	7TTS15	544	1470
–11.5	6TTS15	467	1260
–14.5	7TTS15	544	1440
–17.5	6TTS15	467	1260

Table 9. Anchors in section AA_r.

Level (m)	Anchor type	P_0 (kN/m)	P_0 (kN)
–4.0	4TTS15	311	840
–8.0	7TTS15	544	1470
–11.5	5TTS15	389	1050
–14.5	6TTS15	467	1260
–17.5	6TTS15	467	1260

Table 10. Anchors in wall section BB_l.

Level (m)	Anchor type	P_0 (kN/m)	P_0 (kN)
–4.0	–	–	–
–10.5	4TTS15	311	840
–11.5	6TTS15	467	1260
–14.5	5TTS15	389	1050
–17.5	5TTS15	389	1050

Table 11. Anchors in wall section BB_r.

Level (m)	Anchor type	P_0 (kN/m)	P_0 (kN)
–4.0	4TTS15	311	840
–8.0	7TTS15	544	1470
–11.5	6TTS15	467	1260
–14.5	6TTS15	467	1260
–17.5	6TTS15	467	1260

anchor bond length at L_b = 15 m. The calculation determines many important parameters e.g. design resistant anchor force $R_d = R_k / \gamma_R$ of where γ_R is a partial factor of anchor resistance, see Table 12.

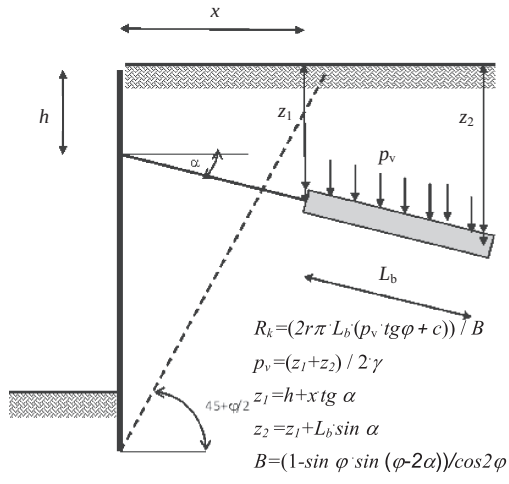

Figure 5. Ground anchor.

Table 12. Soil and anchor properties.

Cohesion	c	150	kPa
Internal friction	ϕ	30°	0.523
Unit weight	γ	19.2	kN/m^3
Height	H	11.5	m
Distance	x	10.0	m
Bond length	L_b	15.0	m
Angle to horizontal	α	15°	0.262
Width	B	1.3	m
Start depth	z_1	14.18	m
End depth	z_2	18.06	m
Earth pressure	p_v	309.52	kPa
Resistance force	R_k	2323.44	kN
Partial factor	γ_R	1.35	/
Design resistant force	R_d	1721.06	kN

A more comprehensive analysis with greater detailing and application of so-called node-to-node anchors has been performed next, see Figure 6.

Using this type of anchors, comprised of tendon and grouted body, should help to obtain more realistic picture of the stress distribution of the anchors in the soil. In this model the anchors have been pre-stressed with the determined lock-off force from Table 4. The program calculates the problem which to a solution of the displacements, see Figure 7.

The maximal displacements in the soil are in the layer GW close to the grouted bodies between the second and third anchor. The displacements are around 4 cm with no implications on the stability of the wall.

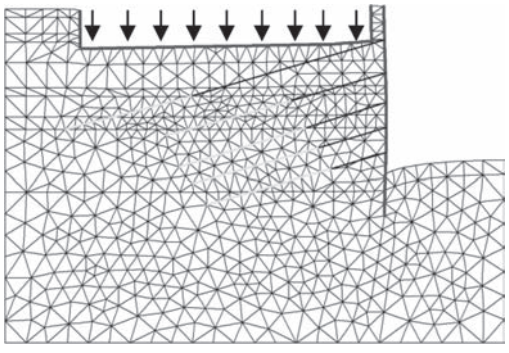

Figure 6. Deformed finite element mesh of wall section AA_l (phase: 6).

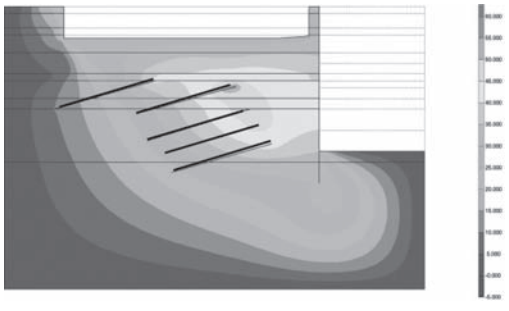

Figure 7. Horizontal displacements of wall section AA_l (phase 6: shadings).

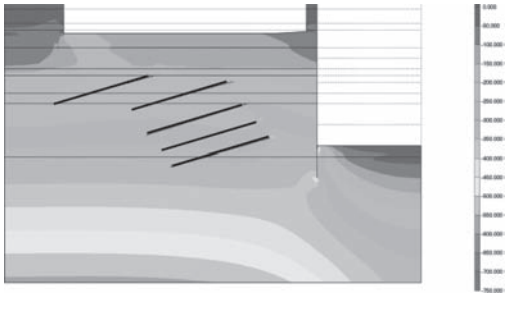

Figure 8. Effective stresses of wall section AA_l (phase 6: mean shadings).

The soil displacements are result of the stress distribution in the ground, therefore the effective mean stresses is presented in Figure 8.

Slight stress concentration can be seen in the toe of the diaphragm wall which is not significant for the stability. In the soil next to the wall the stress ranges from 150–400 kPa.

Moreover, this calculation can be used to confirm the assumptions made with the analytical solution. Hence, the built-up force in the anchor can be evaluated through a force-displacement relation, see Figure 9.

The ordinate *Sum-Mstage* represents the percentage of the applied anchor force while u_t is the total anchor displacement. At design resistant force P = 1720 kN (or *Sum-Mstage* = 1) the displacement is slightly below 4 cm (in a strain range below 0.3%). The anchors free length L_f is variable depending on the level as it is shown in Table 13.

4.4 *Diaphragm wall*

Beside the soil stress and deformation these analysis also determines the forces and bending moments inside the structural elements. They are presented as cumulatively as envelopes covering all phases of construction. Internal forces and moments of wall section AA_l are presented in Figure 10.

The maximal registered values are: bending moment 388.0 kNm/m, axial force –1370 kN/m and shear force 503.5 kN/m.

Similarly the internal forces and moment for wall section AA_r are presented in Figure 11.

The maximal bending moment is M_{max} = 309.4 kNm/m while maximal internal forces are N_{max} = –1090 kN/m and Q_{max} = 401.2 kN/m.

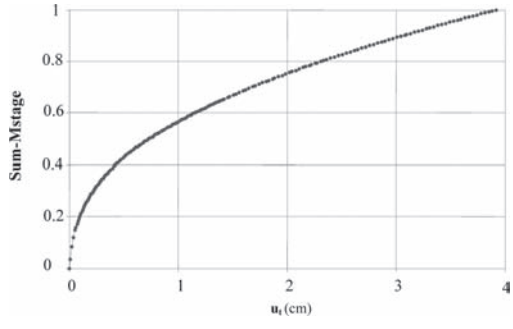

Figure 9. Force-displacement curve of test anchor.

Table 13. Anchors types with total length.

Level (m)	AA_r	AA_l	BB_r	BB_l	$L = L_f + L_b$ (m)
–4.0	4TTS15	4TTS15	4TTS15	–	24.5 + 15
–8.0	7TTS15	7TTS15	7TTS15	–	12.5 + 15
–10.5	–	–	–	4TTS15	11.0 + 15
–11.5	5TTS15	6TTS15	6TTS15	7TTS15	10.5 + 15
–14.5	6TTS15	7TTS15	6TTS15	5TTS15	8.5 + 15
–17.5	6TTS15	6TTS15	6TTS15	5TTS15	7.0 + 15

The envelopes for wall section BB_l are presented in Figure 12.

The maximal bending moment in section BB_l is 641.4 kNm/m, maximal axial force is –743.5 kN/m and maximal shear force is 372.8 kN/m.

Next, envelopes for wall section BB_r are presented in Figure 13.

The maximal bending moment is 416.9 kNm/m, maximal axial force is –1170 kN/m and maximal shear force is 466.5 kN/m.

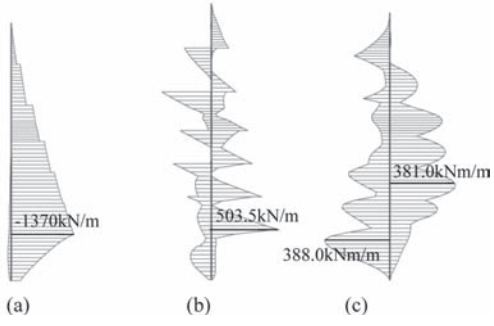

Figure 10. Envelops wall section AA_l: (a) Axial force N, (b) Shear force Q and (c) Bending moment M.

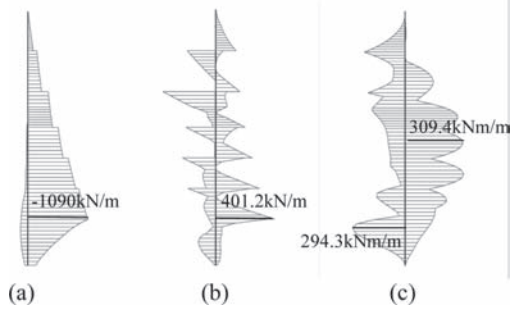

Figure 11. Envelopes in wall section AA_r: (a) Axial forces N, (b) Shear force Q and (c) Bending moment M.

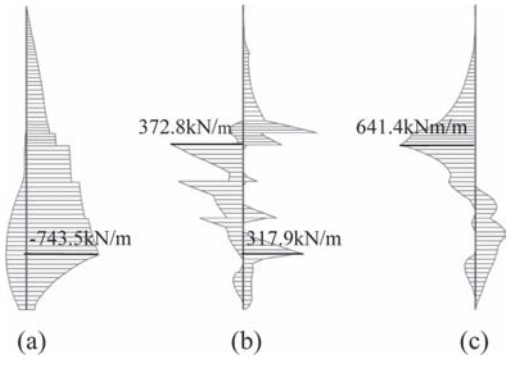

Figure 12. Envelopes in wall section BB_l: (a) Axial force N, (b) Shear force Q and (c) Bending moment M.

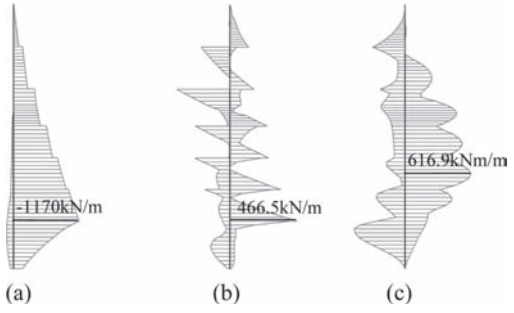

Figure 13. Envelopes in wall section BB_r: (a) Axial force N, (b) Shear force Q and (c) Bending moment M.

Table 14. Maximal internal wall forces and bending moments.

Internal q. vs. wall section	N_{max} (kN/m)	Q_{max} (kN/m)	M_{max} (kNm/m)
AA_l	–1370.0	503.5	388.0
AA_r	–1090.0	401.2	309.4
BB_l	–743.5	372.8	641.4
BB_r	–1170.0	466.5	416.9

Although there are certain differences in the supporting system e.g. anchor force and ground conditions it can be still concluded that there is no large variance in the results. An optimal distribution of the internal forces and moments is obtained which only speaks in favour of the proposed solution, see Table 14.

The wall in section BB_l has the unfavorable load combination due to lowered position of the first row of anchors.

According to these results a design of the reinforced concrete sections of the diaphragm wall had been made according to EN 1992 using the recommended partial factors.

5 CONCLUSIONS

The problem of deep excavation in highly urbanized area such as the city centre of Tirana has proved to be quite formidable engineering task. In particular the greater depth and the built-up surrounding make it especially difficult. In this project a multi anchored diaphragm wall has been used as support to a 20.5 m excavation pit. The paper presents an insight in the process of numerical modelling offering some conclusive discussions.

Several types of analyses had been performed with different level of detailing to help for more

Figure 14. Deep excavation pit with multi anchored diaphragm wall in Tirana.

realistic to simulation of the deep excavation process. Some difficulties of not quite precise regulative were encountered but they were overcome by additional investigations. The proposed numerical model has been able precisely to describe the effects of the anchoring and excavation. The technical solution of multi anchored diaphragm wall had been proved during the actual construction of the wall and excavation of the pit as very effective. At all time the diaphragm wall deflections had been measured. The recordings had confirmed all predictions made in this analysis. The construction had started in September 2009 and finished in March 2010, see Figure 14.

REFERENCES

German Society for Geotechnics (Deutsche Gesellschaft fur Geotechnik e. V.) 2003. Recommendations on Excavations, Ernst & Sohn Verlag fur Architektur und technische Wissenschaften GmbH & Co. KG, Berlin, ISBN 3-433-01712-3.

Kempfert, H.G. & Gebreselassie, B. 2006. Excavations and Foundations in Soft Soils, Springer-Verlag Berlin Heidelberg, ISBN 540-32894-7.

Potts, D.M. & Zdravkovic, L. 1999. Finite element analysis in geotechnical engineering: theory. Imperial College of Science, Technology and Medicine, Thomas Telford Publishing, Thomas Telford Ltd, ISBN 0-7277-2783-4.

Potts, D.M. & Zdravkovic, L. 2001. Finite element analysis in geotechnical engineering: application. Imperial College of Science, Technology and Medicine, Thomas Telford Publishing, Thomas Telford Ltd, ISBN 0-7277-2753-2.

EN 1997–1:1994 Eurocode 7: Geotechnical design—General rules

pr EN 446 Grout for prestressing tendons—Grouting procedures.

This page intentionally left blank

Geotechnical Aspects of Underground Construction in Soft Ground – Viggiani (ed)
© 2012 Taylor & Francis Group, London, ISBN 978-0-415-68367-8

Performance of deep excavations in the Taipei Basin

Richard N. Hwang & Z.C. Moh
Moh and Associates, Inc., Taipei, Taiwan

ABSTRACT: The concept of wall deflection path and reference envelope is introduced herein for evaluating the performance of diaphragm walls. It has been found that, at a given site, wall deflection paths, which are plots of maximum wall deflections versus depths of excavation, converge to a narrow band as excavation goes beyond a depth of 10 m or so. The envelope of a family of wall deflection paths, i.e., the so-called reference envelope, characterizes performance of diaphragm walls with a specific set of ground conditions. Based on the data obtained for deep excavations carried out in recent years, reference envelopes are established for the T2, TK2 and K1 Geological Zones of the Taipei Basin and they can be used to evaluate the performance of individual walls. Furthermore, back analyses are performed to calibrate the soil parameters to be adopted in the numerical analyses.

1 INTRODUCTION

Because of the presence of a thick layer of young sediments to a depth of, up to, 60 m in the Taipei Basin, diaphragm walls are normally required for excavations exceeding 8 m in depth. An enormous quantity of field data have been collected in recent years and the performance of diaphragm walls in deep excavations has been analyzed systematically.

The performance of diaphragm walls will be most conveniently evaluated by studying the so-called wall deflection paths which are plots of maximum wall deflections versus depths of excavation in a logarithmic scale. Wall deflection paths at a certain site tend to converge to a narrow band as the excavation goes beyond a depth of 10 m or so. The envelope of a family of wall deflection paths thus characterizes the performance of retaining systems with similar configurations for excavations with similar ground conditions. Based on the data obtained, the so-called reference envelopes have been established for the T2, TK2 and the K1 Zones in the Taipei Basin (Moh & Hwang, 2005; Hwang & Moh, 2007).

The performance of diaphragm walls in the excavation for constructing Sandao Temple Station of the Taipei Metro is evaluated herein to illustrate the application of wall deflection paths and reference envelopes. Furthermore, back analyses are performed to calibrate the soil parameters to be adopted in the numerical analyses.

2 GEOLOGY OF THE TAIPEI BASIN

At the top of the Taipei Basin is the so-called Sungshan Formation of, up to, 60 m in thickness underlain by the Chingmei Gravels. Figures 1 and 2 show the north-south and east-west geological sections, respectively, of the basin. As can be noted, the Sungshan Formation comprises an alternation of silty clay and silty sand sublayers and the six-sublayer sequence is most evident in the central city area where the Taipei Main Station (BL7/R13 Station of the Taipei Metro) is located. Toward the east and the north, the sandy sublayers diminish and clayey sublayers become dominating; and toward the west and the south, the stratigraphy of sublayers becomes rather complicated with silty sand and silty clay seams interbedded in these sublayers. Based on the information obtained in recent years, Lee (1996) proposed to divide the Basin into 22 geological zones as depicted in Figure 3 which is adopted herein for categorizing ground conditions.

Figure 4 shows the typical CPT profiles obtained in the T2 Zone. As can be noted that the six-sublayer sequence in the Sungshan Formation is clearly identifiable. The various soil sublayers can better be identified in the porewater pressure profile than tip resistance or local friction. In short, Sublayers I, III and V consist primarily of silty sands and Sublayers II, IV and VI consist primarily of silty clays. The sandy sublayers, i.e., Sublayers I, III and V, thin out toward the east and the north of the basin and become unidentifiable in the K1 Zone as can be noted in Figures 1 and 2. TK2 Zone is a transition between T2 and K1 Zones.

3 WALL DEFLECTION PATHS AND REFERENCE ENVELOPES

A large quantity of field data have been collected in recent years and it is therefore possible to conduct systematic analyses on the performance of retaining

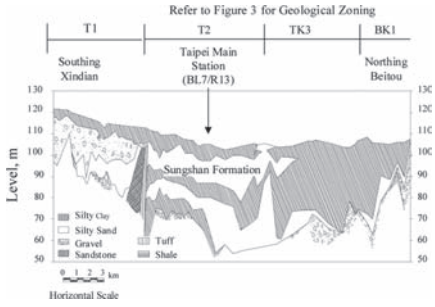

Figure 1. North-south geological section of the Taipei Basin.

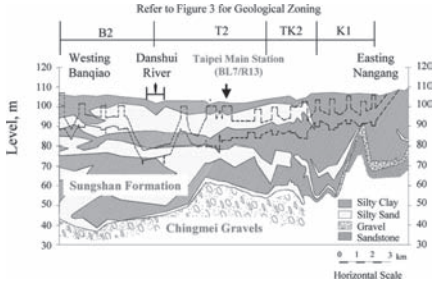

Figure 2. East-west geological section of the Taipei Basin.

systems. As illustrated in Figure 5(b), the maximum deflections in the deflection profiles in each stage are plotted versus depths of excavations in a log-log scale and such a plot is designated as "wall deflection path" (Moh & Hwang, 2005; Hwang, et al. 2006; Hwang, et al. 2007). The envelope, designated as "reference envelope" herein, of a family of wall deflection paths can be considered as a site characteristic curve for diaphragm walls and can be used for evaluating the performance of individual walls. Reference envelopes are defined by:

a. wall deflections for shallow excavations, represented by deflections at depths of excavation up to 4 m, i.e., Δ_4,
b. wall deflections projected to a depth of excavation of 100 m, i.e., Δ_{100}.

The depth of 4 m is chosen because the first digs are usually within 4 m and the depth of 100 m is chosen for convenience because Microsoft Excel only plots full log-cycles. Furthermore, the extension of reference envelopes to this depth amplifies the differences in reference envelopes among various cases and makes it easier to study the effects of various factors affecting the performance of walls.

The deflection paths for diaphragm walls with thicknesses of 600 mm, 800 mm, 1000 mm, and 1200 mm for excavations in the T2 Zone are shown

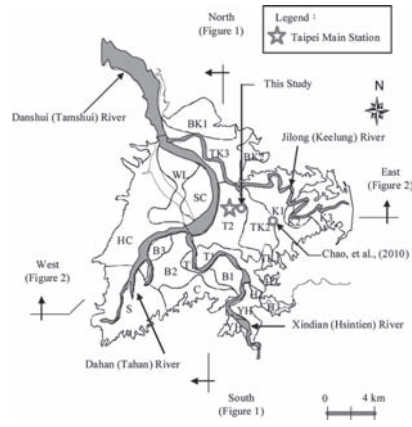

Figure 3. Geological zoning map of the Taipei Basin (Lee, 1996).

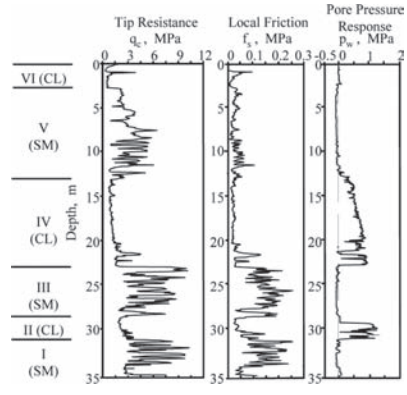

Figure 4. Typical results of CPT tests in the T2 Zone.

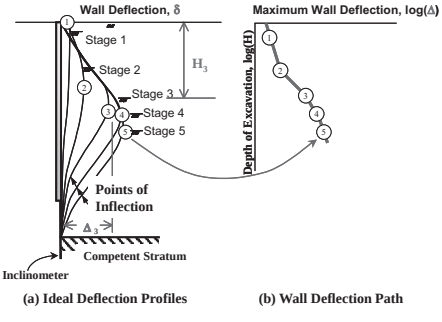

Figure 5. Ideal wall deflection profiles and wall deflection path.

in Figures 6 to 9. Individual inclinometers are identified by suffixes such as A, B, C, etc, affixed to the site numbers. Also shown in the figure are the reference envelopes which are the envelopes of respective deflection paths.

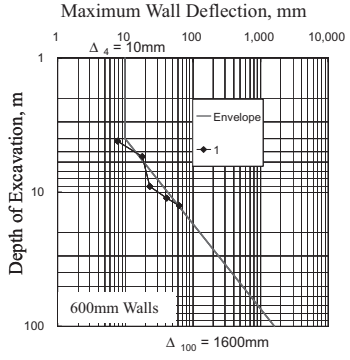

Figure 6. Wall deflection paths and reference envelopes for 600 mm walls in the T2 Zone.

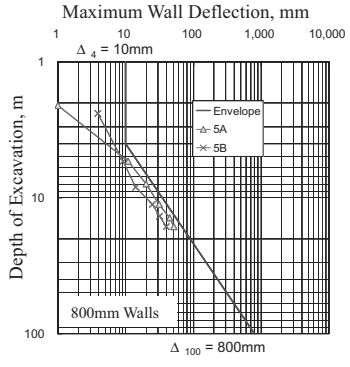

Figure 7. Wall deflection paths and reference envelopes for 800 mm walls in the T2 Zone.

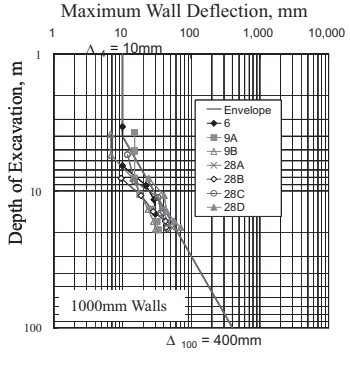

Figure 8. Wall deflection paths and reference envelopes for 1000 mm walls in the T2 Zone.

There are numerous ways to draw reference envelopes based on the data presented and the decisions are inevitably subjective. The reference envelopes shown in Figures 6 to 9 were so drawn that, as shown in Table 1, deflections for depths

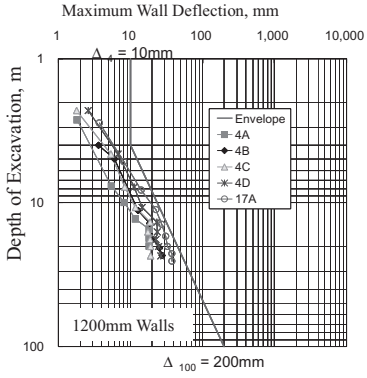

Figure 9. Wall deflection paths and reference envelopes for 1200 mm walls in the T2 Zone.

Table 1. Comparison of reference envelopes for the T2, TK2 and K1 Zones.

Wall thickness, mm	Δ_4, mm			Δ_{100}, mm		
	T2	TK2	K1	T2	TK2	K1
600	10	12		1,600	1600	
700		12			1200	
800	10	12	30	800	800	800
900		12	30		600	600
1000	10*		30	400*		400
1200	10			200		

* for the case of interest

of excavation of 4 m or less, i.e., Δ_4, remain to be the same regardless of wall thickness while wall deflections for depths of excavation of 100 m, i.e., Δ_{100} decrease by a factor of 2 as wall thickness increases from 600 mm to 800 mm, from 800 mm to 1000 mm, and from 1000 mm to 1200 mm.

To illustrate the application of the concept of wall deflection path in evaluating the performance of diaphragm walls, the performance of diaphragm wall during excavation for constructing Shandao Temple Station (BL8 Station) of the Taipei Metro is studied herein. Figure 10 shows the layout of the station and the cut-and-cover tunnels connected to the east end of the station. The station is located in the T2 Zone and, as shown in Figure 11, the six-sublayer sequence is clearly identifiable.

Inclinometers were installed in 5 sections for monitoring wall deflections as shown in Figure 10. The readings obtained for Section B, for example, are shown in Figure 12. As can be noted, significant outward wall movements were reported for both Inclinometers SID-7 and SID-11 which stopped at the same depth as the toe of diaphragm walls. Such outward wall movements were not reasonable

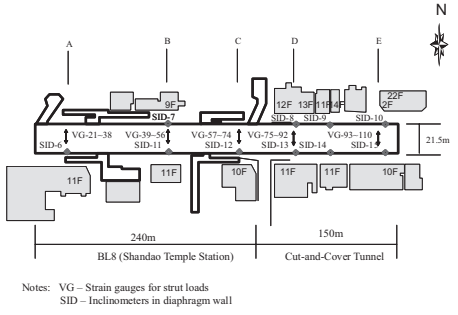

Figure 10. Layout of Shandao Temple Station and locations of instrumented sections.

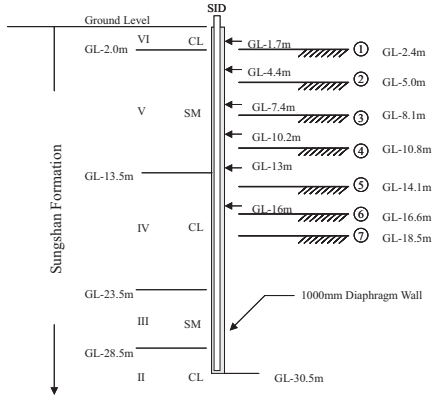

Figure 11. Ground conditions and excavation scheme.

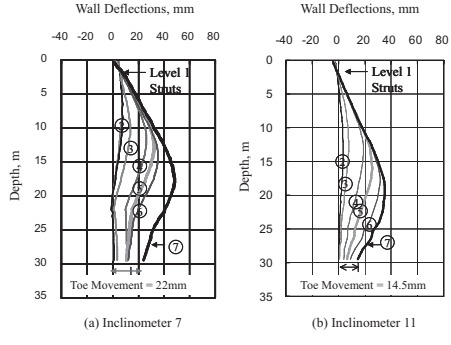

Figure 12. Inclinometer readings before correction.

because they imply significant elongation of struts. They were obviously caused by the movements at the toes which were assumed to be fixed in computing wall deflections. As depicted in Figure 5, the subsequent wall movements at the each strut level should be very small once the struts at this level is preloaded. Inclinometer readings can thus be corrected accordingly (Hwang, et al. 2007). The readings duly corrected by taking the end points of Level 1 struts as reference points are shown in Figure 13 and the toe movements were found to be 22 mm for Inclinometer 7 and 14.5 mm for Inclinometer 11.

The hypothesis that wall movements at the two ends are minimum once struts are preloaded has been verified by studying the changes in strut loads in the case of interest (Hwang, et al. 2007). Figure 14 shows the strut loads recorded at the upper 4 levels by strain gauges in Section B. Take Level 1 for example, the maximum increase in loads was 23.3 tonnes after preloading, corresponding to a shortening of the strut of only 1.4 mm for a cross-sectional area of 173.9 cm^2 and a length of 21.5 m, assuming an E value of 200,000 N/mm^2. Wall movements at the two ends of the strut would only be a half of this magnitude. Wall movements of such small magnitudes are indeed negligible for practical purposes.

The toe movements for all the inclinometers computed by following the same procedure are plotted versus depth of excavation in Figure 15. The final toe movements varied from 5 mm to 31 mm. The movements of Inclinometers SID-10 and SID-15 were smaller than those of others because these two inclinometers were very close to the eastern wall which helped to reduce wall movements. Although Inclinometer SID-6 was located at the west end of the excavation, grouting was once carried out to

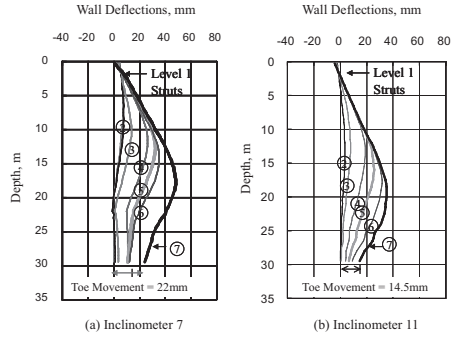

Figure 13. Inclinometer readings after correction.

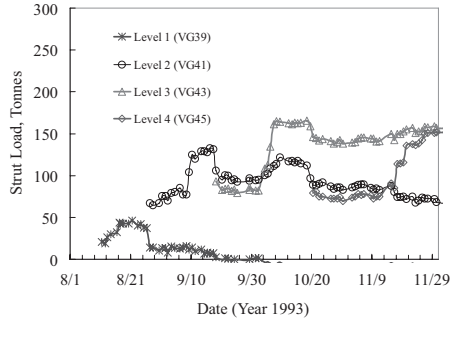

Figure 14. Strut loads in Section B.

stop leakage on the diaphragm wall at this location and presumably increased the movement at the toe.

The final wall deflections, with the toe movements duly accounted for, for the northern and the southern walls are shown in Figures 16 and 17 respectively.

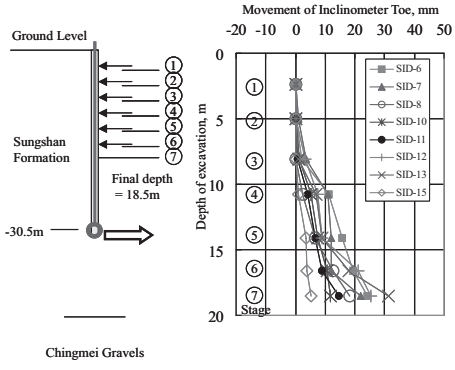

Figure 15. Progressive toe movements of inclinometers.

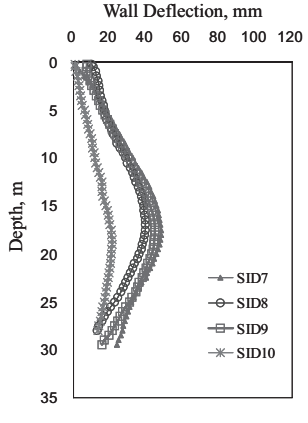

Figure 16. Final deflections of the northern wall.

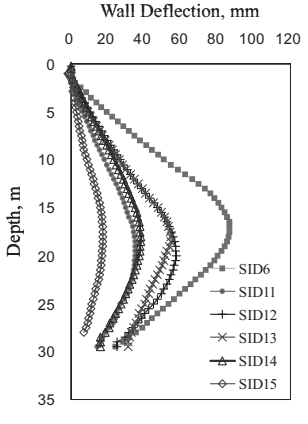

Figure 17. Final deflections of the southern wall.

Even with SID-6, SID-10 and SID-15 excluded, the readings for other inclinometers are far from being consistent. The maximum deflections varied from 35.2 mm (SID-11) to 57.6 mm (SID-12).

4 BACK ANALYSES

The purpose of back analyses is to calibrate soil parameters to be used in numerical analyses for predicting the performance of future excavations in similar ground conditions by comparing the results obtained with the observations. The cases chosen for calibration must be compatible with the numerical schemes adopted for the calibration to be meaningful. However, with the diversity in the observed wall deflections as depicted in Figures 16 and 17, the key question to ask is "Which curve is representative of the case studied?".

Back analyses nowadays are most commonly conducted by performing two-dimensional finite element analyses and so are predictions of performance of excavations. In theses analyses, structures adjacent to the excavations are normally ignored except for research purposes. Therefore, the observed wall deflections chosen should be free of the influences of adjacent structures for the comparison to be fair.

In well developed cities in which deep excavations are normally carried out, there are always tall buildings with deep basements along major roads. Besides, there are also likely large underground structures, such as culverts, subways, underpasses, etc. These structures inevitably affect the performance of walls during excavations. Therefore, the wall deflections to be adopted for calibration must be selected with care.

Since the presence of adjacent underground structures can only reduce wall deflections, the envelope of a family of wall deflection paths would approach to the path representing the behavior of walls free of the influences of adjacent structures as more and more cases are included. Therefore, the reference envelope would be more appropriate than individual wall deflection curves, or individual wall deflection paths, to be used as the basis for comparison in back analyses.

In the case of interest, there are many highrise buildings varying from 9 to 22 stories in height right next to these two walls as depicted in Figure 10. There are presumably deep basements under these buildings as well. These basement together with the retaining walls which were left in place after construction provided much resistance to ground movements and hence reduced wall deflections during excavation for constructing the station. The situation is further complicated by the presence of auxiliary facilities, such as entrances/exits,

ventilation shafts, etc. as depicted in Figure 10, which also tended to reduce wall deflections. This well explains why the wall deflection paths shown in Figures 18 an 19 are below the reference envelope established for the T2 Zone, refer to Figure 8, with the only exception of SID-6 of which the readings were affected by grouting. It thus becomes clear that none of the wall deflection curves shown in Figures 16 and 17, and nor of the wall deflection paths shown in Figures 18 and 19, represents the true behavior of walls in free-field excavations.

The reference envelopes proposed in Figures 6 to 9 were established based on the observations made in many excavations in the T2 Zone. They were established with duly consideration given to walls in different geological zones, refer to Table 1. For the reasons given above, the envelope shown in Figure 8 is the envelope for walls of 1 m in thickness and is the one to be adopted in back analyses.

The computer program PLAXIS V8, released by PLAXIS BV of Amsterdam, the Netherlands

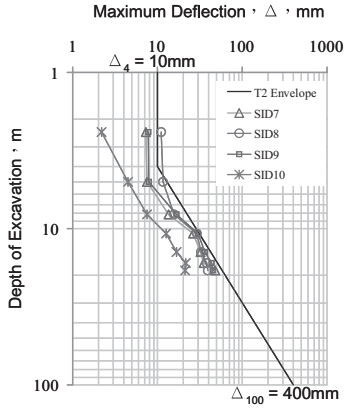

Figure 18. Deflection paths for the northern wall.

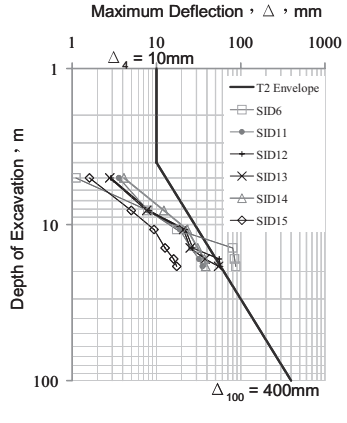

Figure 19. Deflection paths for the southern wall.

(PLAXIS, 2002), was used and the mesh adopted in the back analyses is shown in Figure 20. The soil properties are given in Table 2. As a first attempt, the Young's moduli were determined as follows:

for clayey soils

$$E = 800\ Su \quad (1)$$

in which Su = undrained shearing strength, and for sandy soils

$$E = 4000\ N\ (kPa) \quad (2)$$

where N = blow counts in standard penetration tests. For the purpose of illustration, the readings obtained by Inclinometer SID-12 which gave larger wall deflections than others are chosen for comparison. The wall deflections obtained in the last 3 stages of excavation are compared with the results of the analyses in Figure 21. The toe movements obtained from the analyses are in a fair agreement with what was observed after correction were made. However, the maximum wall deflections appear to have been under-estimated in the back analyses.

The wall deflection path obtained in the back analyses is compared with the reference envelope for 1 m walls in the T2 Zone, i.e., the one shown in Figure 8, in Figure 22. It can be represented by

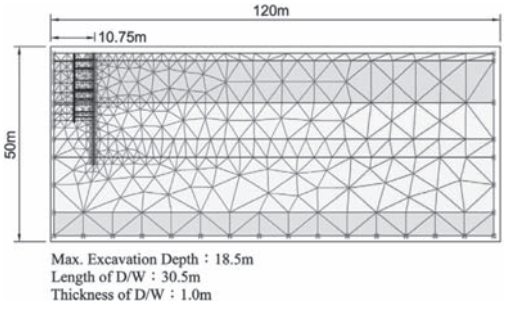

Figure 20. Finite element model adopted in PLAXIS analyses.

Table 2. Soil properties adopted in PLAXIS analyses.

Depth (m)	Soil type	γ_t (kN/m^3)	N	S_u (kPa)	c′ (kPa)	Φ′ (deg)	E (MN/m^2)	ν
0–2	CL	18.6	3	20	0	30	16	0.45
2–13.5	SM	18.4	8	–	0	33	32	0.35
13.5–23.5	CL	18.8	6	40	0	32	32	0.45
23.5–28.5	SM	19.3	18	–	0	32	72	0.35
28.5–43.5	CL	19.4	17	80	0	33	64	0.40
43.5–50	SM	21.6	30	–	0	35	120	0.30

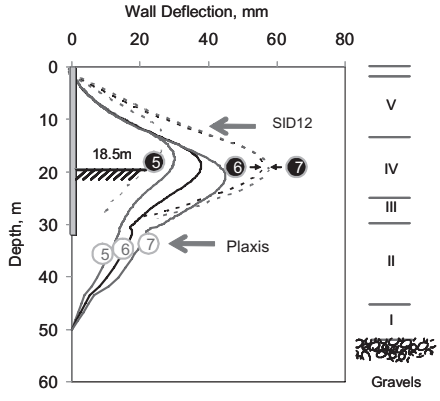

Figure 21. Comparison of wall deflections obtained in back analyses with corrected inclinometer readings.

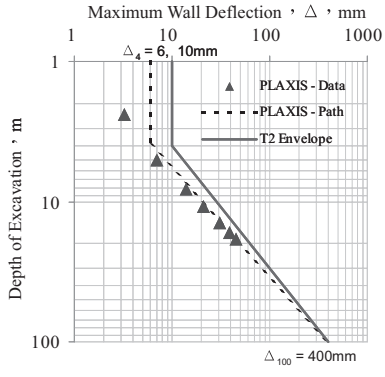

Figure 22. Comparison of wall deflections path obtained in back analyses with the reference envelope for the T2 Zone.

Δ_4 = 6 mm, Δ_{100} = 400 mm. The Δ_{100} value obtained is the same as that for the reference envelope shown in Figure 8 but the Δ_4 value is only 60% of that for this reference envelope.

Figure 23 shows the results of finite element analyses using PLAXIS in a previous study carried out for an excavation for Kaohsiung Metro (Hsiung and Hwang, 2009). A Δ_4 of 13 mm was obtained In Set A analyses in which soil moduli were obtained as follows:

$$E = 500\ Su \quad (3)$$

and, for sandy soils

$$E = 2000\ N\ (kPa) \quad (4)$$

In Set B analysis, the Young's moduli of soils were halves of what were used in Set A analyses

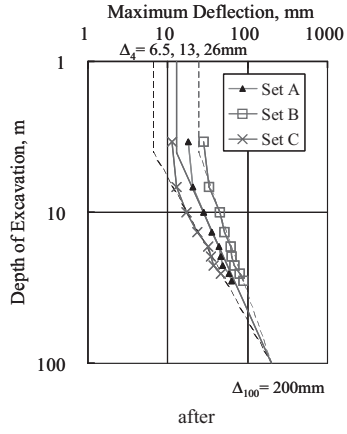

Figure 23. Influence of Young's moduli on wall deflections paths (Hsiung and Hwang, 2009).

and the Δ_4 was doubled to 26 mm. In Set C analysis, the Young's moduli were twice what were used in Set A analyses and the Δ_4 were halved to 6.5 mm. It becomes evident that the Δ_4 values are inversely proportional to the soil moduli. The changes in soil moduli, however, did not affect the Δ_{100} value.

In the case of interest, the soil moduli appear to have been over-estimated so the Δ_4 value obtained was smaller than what it should be. The computed wall deflection path would well match the reference envelope if soil moduli were reduced to 60% of the values given in Equations 1 and 2. That means, It then appears, Equations (3) and (4) would be suitable for the soils in the Sungshan formation.

To verify whether Equations (3) and (4) can indeed be used for soils in other geological zones in the basin, the results of a previous study conducted by Chao, et al., (2010) are referred to herein. Finite element analyses were performed using PLAXIS for an excavation carried out at a site which is right at the boundary between TK2 and K1 Zones as shown in Figure 3. As shown in Figure 2, sandy soils are absent at the TK2/K1 boundary and the ground is dominated by clayey soils. This greatly reduces the complicity of the problem. Equation (3) was adopted for the clayey soils and the wall deflection path obtained is shown in Figure 24. Although the Δ_{100} value obtained, i.e., 300 mm, is slightly smaller than that for walls of 1 m in thickness, the wall deflection path obtained in the range of excavation depths of 10 m to 30 m which is of primary interest falls in-between the reference envelopes for the TK2 and the K1 Zones as expected. It is thus concluded that Equation 3 can indeed be used for clayey soils in back analyses.

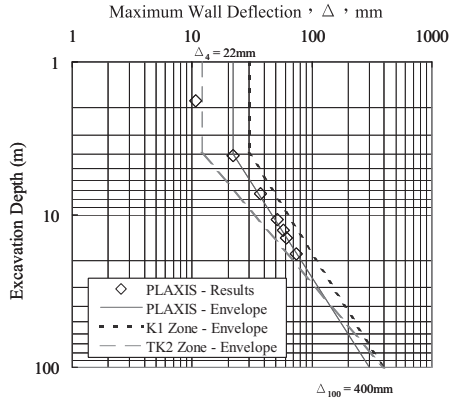

Figure 24. Wall deflections path for clayey soils (Chao, et al., 2010).

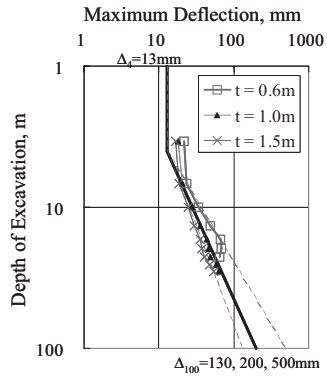

Figure 25. Influence of wall stiffness on deflection paths (Hsiung and Hwang, 2009).

Regarding Equation (4), more analyses are desired to be conducted for excavations at sites where sandy soils dominate before its applicability can be generalized.

The results of PLAXIS analyses depicted in Figure 23 confirm that Δ_{100} values are rather insensitive to soil moduli. Therefore, the adoption of the same Δ_{100} values for T2, TK2 and K1 Zones appears to be valid. On the other hand, it is interesting to note that the Δ_4 values are insensitive to wall stiffness as depicted in Figure 25 (Hsiung & Hwang, 2009). In the first stage of excavation, walls behave as cantilevers offer little resistance to ground movements because of the great depths of soft deposits.

5 CONCLUDING REMARKS

Inclinometer readings should be interpreted with care. Readings can be calibrated to account for toe movements by assuming wall movements at the first strut level are insignificant once struts at this level are installed and preloaded.

Performance of diaphragm walls can be evaluated by studying their wall deflection paths. Wall deflection paths are linear in the range of 10 m to 20 m, if plotted in a log scale, for excavations in thick soft sediments.

Reference envelopes of a family of wall deflection paths can be defined by Δ_4 and Δ_{100}. The Δ_4 values are insensitive to the stiffness of walls and the Δ_{100} values are a function of the stiffness of walls.

Wall deflection paths of individual walls can be compared with reference envelopes for studying the influences of various factors on wall deflections.

Instead of individual walls, reference envelopes should be used for calibrating soil parameters to be used in back analyses.

In back analyses and in analyses for predicting wall deflections, the Young's moduli for clayey soils can be estimated by assuming E = 500 Su. For sandy soils, E moduli equal to 2000 N (in kPa) appear to be reasonable, however, more case studies are required for confirmation.

REFERENCES

Chao, H.C., Chang, J.F. & Hwang, R.N. (2010). Evaluation of performance of diaphragm walls in deep Excavations by using deflection path method, *Proc., 17th Southeast Asian Geotechnical Conference*, Taipei, Taiwan, vol I, pp. 390–393.

Lee, S.H. (1996). Engineering Geological Zonation for the Taipei City, *Sino-Geotechnics*, vol. 54, April, pp. 25–34 (in Chinese).

Hsiung, B.C. & Hwang, R.N. (2009). Evaluating performance of diaphragm walls by wall deflection path, *Special Issue on Excavation and Tunneling in Geotechnical Engineering Journal of SEAGS*, pp. 81–90.

Hwang, R.N. & Moh, Z.C. (2007). Deflection paths and reference envelopes for diaphragm walls in the Taipei Basin, *J. of GeoEngineering*, v2, no. 1, April, Taipei, Taiwan, pp. 1–12.

Hwang, R.N., Moh, Z.C. & Kao, C.C. (2006). Design and construction of deep excavations in Taiwan, *Seminar on "The State-of-the-Practice of Geotechnical Engineering in Taiwan and Hong Kong"*, 20 January, Hong Kong.

Hwang, R.N., Moh, Z.C. & Wang, C.H. (2007). Toe movements of diaphragm walls and correction of inclinometer readings, *J. of GeoEngineering*, v2, no. 2, August, Taipei, Taiwan pp. 61–72.

Moh, Z.C. & Hwang, R.N. (2005). Geotechnical considerations in the design and construction of subways in urban areas, *Seminar on Recent Developments on Mitigation of Natural Disasters, Urban Transportation and Construction Industry*, 30 November–2 December, Jakarta Indonesia.

PLAXIS (2002). *Reference Manual*, PLAXIS BV, Amsterdam, the Netherlands.

Geotechnical Aspects of Underground Construction in Soft Ground – Viggiani (ed)
© 2012 Taylor & Francis Group, London, ISBN 978-0-415-68367-8

Geotechnical issues related to dry maintenance of open cut excavations below groundwater table in soft soils: Reliability of a simplified calculation model

F. Carnevale, R. Gallotti, F. Caneparo & P. Pampanin
Technital S.p.A., Milano, Italy

ABSTRACT: The construction of the so-called "Passante di Mestre" contemplated the realization of long stretches in cut section standing under the groundwater table. It was therefore necessary to foresee an accurate control of the water table level during the whole construction process, with a specific and careful attention on the subsidence effects of the existing nearby buildings. As the area of interest stretched for 4 Km, it was necessary to have a model as much versatile and consequently simplified as physically possible. The model was based on the considerations by Mansur & Kaufman, with the application of the superimposition. The validity of such simplified approach has been verified through a finite element model. Based on a results comparison, it was possible to assess how the simplified prevision method could catch with an acceptable degree of approximation the dewatering mechanism and its effects in the system.

1 INTRODUCTION

The Mestre connection is the bypass of the urban stretch of highway A4, see Figure 1.

The typical cross section is 32.5 m wide. The layout develops with 9 stretches in cut section, 8 artificial tunnels and 4 viaducts.

This paper focuses on the geotechnical issues faced along the stretch between Salzano and Martellago, where the road was built for about 4 Km on cut section standing below groundwater level.

Two are the main geotechnical aspects dealt with during design and herein discussed: the maintenance of a dewatered open cut excavation and the monitoring of subsidence effects on adjacent building caused by the type and method of excavation.

2 GEOTECHNICAL SOIL CHARACTERIZATION

Along the layout, 7 boreholes and 24 cone penetration tests with piezocone (CPTU) were carried out. The boreholes allowed for the definition of the soil stratigraphy while the CPT tests were used to define the resistance and deformability parameters, together with the permeability characteristics of the cohesive soils through the dissipation tests.

Figure 2 shows a stratigraphic cross section representative of the whole project area.
The average stratigraphy and the project geotechnical characterization are presented herein after.

DESIGN STRATIGRAPHY

Elevation m from sea level	Layer	Notes
10.00÷2.00	IV	Superficial layer. Alternation of sandy and cohesive layers, sand and fill
2.00÷0.00	I_A	Silty Sand
0.00÷-6.00	III	Alternation of sandy and cohesive layers
-6.00÷-8.00	II	Clayey silt/ Silty clay with sand
-8.00÷-12.00	I_B	Silty Sand
-12.00÷-22.00	V	Alternation of sandy and cohesive layers

GEOTECHNICAL CHARACTERIZATION

Layer	γ (kN/m³)	OCR (-)	DR (%)	c_v (m²/s)	c_u (kPa)	c' (kPa)	ϕ' (°)	E_{oed} (MPa)	G_{max} (MPa)	M_c (MPa)	M_r (MPa)	ν (-)	k_0 (-)
IV	18.5	3	-	1E-6	0	0	36	15	50	2	10	0.35	0.5
IA	19.5	-	75	-	0	0	40	15	50	-	-	0.33	0.5
III	19.5	2	-	2E-6	50	0	32	15	80	-	-	0.35	0.5
II	19	2	-	2E-6	100	5	30	15	80	-	-	0.35	0.5
IB	19.5	-	75	-	0	0	38	30	200	-	-	0.33	0.5
V	19	2	-	1E-6	80	5	32	20	80	10	32	0.33	0.5

The groundwater table along the layout ranged between 1 and 1.5 m below the ground level. The design of the pumping system has been carried out based on the permeability of the depositional levels as reported in Table1.

3 WORK SCHEDULE AND RELATED GEOTECHNICAL ISSUES

The work schedule required the execution and maintenance of excavations under the groundwater table. Figure 3 shows a cross section aligned to the road layout, indicating the ground, the groundwater and the excavation levels. The more pervious layers are highlighted in grey.

The method of excavation and the pumping system design were defined based on this scenario.

Figure 1. Layout (taken from www.wikipedia.it).

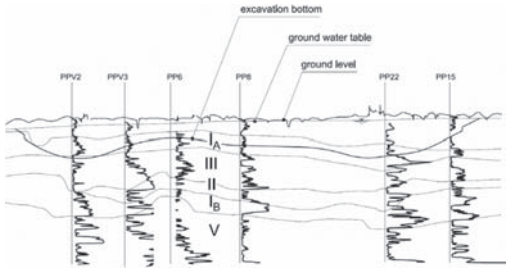

Figure 2. Stratigraphic cross section along the layout.

Table 1. Depositional levels and permeability coefficients.

Depositional levels	Description	Permeability (m/s)	
		Kx	Kz
IA/IB	Silty sand	1E-5	1E-5
II	Clayey silt/Silty clay with sand	1E-8	1E-8
III	Alternation of sandy and cohesive layers	1E-6	5E-7
IV	Superficial layer. Alternation of sandy and cohesive layers, sand and fill	1E-7	1E-7
V	Alternation of sandy and cohesive layers	1E-7	5E-8

The excavations were kept dry through a system of active wells, installed at the slopes toe, which controlled the piezometric level in the deep permeable layer IB so to ensure stability of the excavation grade against hydraulic uplift.

Since the excavation grade was usually below the top of the first permeable level, water can infiltrate into the excavation sideways, therefore a passive well system was foreseen in order to avoid this phenomenon.

In Figure 4 the described wells layout is shown according to the medium stratigraphy.

The hydraulic drawdown necessary to keep dry the excavation could have sensible impacts at a distance from the excavation itself.

This aspect is crucial considering the nearby buildings, since the variation of the soil pore pressure could induce settlements on the structures.

It was evaluated that the area affected by the drawdown keeps within 50 m from the slope edge. Figure 5 indicates an example of existing buildings adjacent to the excavation.

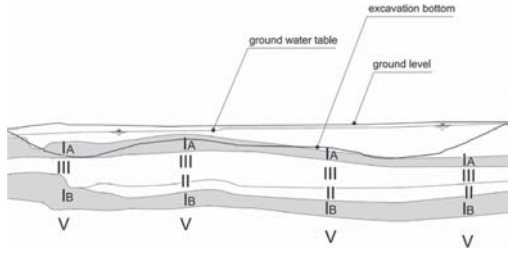

Figure 3. Excavation layout in relation to the stratigraphy and to the groundwater level.

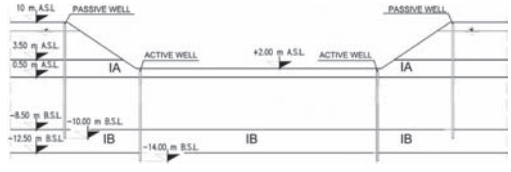

Figure 4. Typical wells layout.

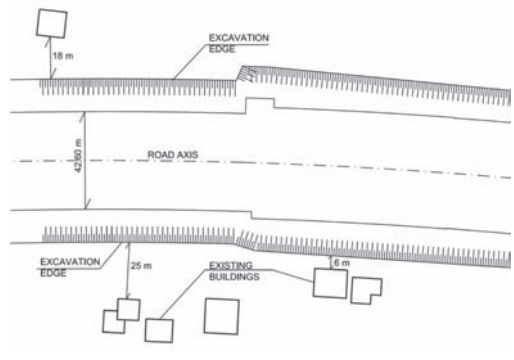

Figure 5. Plan of buildings nearby the excavation.

4 MONITORING SYSTEMS

Given the geotechnical issues to be faced, a coupled monitoring system was set up to control the piezometric level and the actual settlement development on nearby buildings.

Figure 6 shows a typical cross section with the piezometers locations for groundwater control. Two different piezometers typologies were adopted: deep piezometers and superficial piezometers for the control respectively of the piezometric level in layer IB and IA. Additional piezometers were installed nearby the buildings subjected to topographical monitoring so to allow for the correlation of the piezometric drawdown with the potential measured settlements.

The buildings topographic monitoring was composed of a system of benchmarks positioned in correspondence to the horizontal structural elements.

Differential settlements and the consequent angular distortions β, which express the damage of the building according to its structural typology, were obtained through the altimetric displacements of benchmarks themselves.

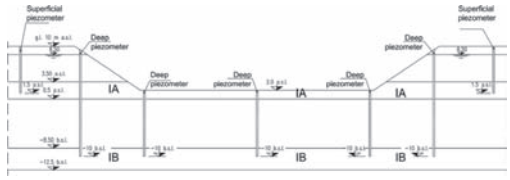

Figure 6. Piezometers location for the monitoring programme.

5 DRY EXCAVATION MAINTAINANCE

5.1 *Constructive scheme*

Wells spacing was set at 12 m. The open cut advancement module was 96 m long, equal to the distance of 4 construction joints for the structure, as illustrated in Figure 7.

In correspondence to the initial, central and final sections of the module, sections of measurement were placed, consisting of 5 deep piezometers, DP, and 2 superficial, SP.

Therefore the construction of the pumping system followed in several phases.

Phase 1: the active wells, the deep and superficial piezometers are installed.

Phase 2: the wells are activated and the piezometers are monitored up to the achievement of the system equilibrium according to the lowering estimations of the wells dynamic level and especially of the piezometers level.

Phase 3: the first excavation phase is executed up to the first advancement module of 24 m, joint I of Figure 7.

Phase 4: the bedding layer is placed up to the first subunit and the second subunit, joint II, is excavated.

Phase 5: the structural slab is completed up to first subunit so to guarantee the hydraulic stability, the bedding layer is executed up to the second subunit and the excavation proceeds up to the third subunit, joint III.

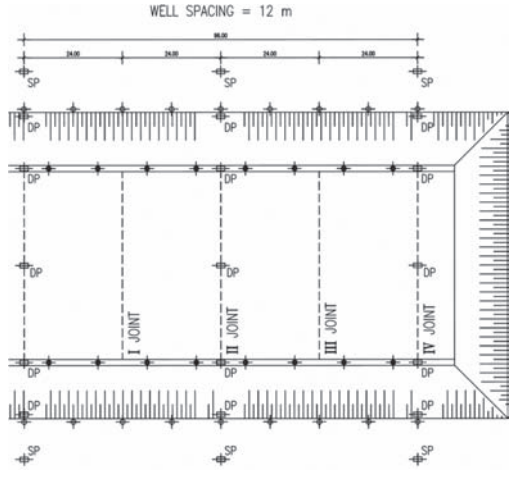

Figure 7. Wells system advancement module.

Phase 6: the wells system is activated and the following module, that is the following 96 m, is monitored and the structure completed up to the first subunit. The slab is constructed up to the second subunit to prevent hydraulic uplift. The bedding is executed up to the third subunit. The following module is monitored until the steady-state conditions reached. The excavation proceeds up to the fourth subunit, joint IV.

Phase 7: the bedding is executed up to the fourth subunit, the hydraulic stability is reached up to the third subunit and the excavation proceeds up to the first subunit of the following module.

Phase 8: the structure up to joint IV of the first advancement module is completed in order to achieve hydraulic stability. The slab up to the first subunit of the second advancement module is poured. The excavation up to the second subunit of the second advancement module is realized.

Phase 9: The wells of the first advancement module are switched off and the construction proceeds with the following module following the same sequence with bedding up to the first subunit and excavation up to the second subunit.

5.2 *Wells system design*

Once the piezometric drawdown required for uplift stability was defined, the scope of the design was to evaluate the dynamic water levels within the project area, the consequent required wells discharge and the expected drawdown in corresponce to the monitoring points.

As the monitored layout stretched for about 4 km, a simple and versatile calculation scheme was necessary. For this reason an Excel spreadsheet was created by implementing Mansur & Kaufman theory for confined aquifers, like layers IA and IB. Such model is versatile and adaptable to the stratigraphic and geometric changes along the 4 km layout, but on the other hand it simplifies the problem. The simplified Excel program was therefore validated through a 3D finite elements model implemented in Feflow and representing a single advancement module for the same stratigraphic conditions, geometric wells configuration and piezometric monitored verticals. The implemented geometry is that reported in Figure 4 and Figure 6.

5.3 *Simplified calculation model*

Since the scheme is 3D, the simplified model proposed by Mansur & Kaufman (1962) was adopted, considering that the wells system pumps water only from the deep permeable layer IB.

The wells system can work in two ways:

– constant discharge
– constant dynamic level

Since in practice it is easier to regulate the pump discharge than to maintain a constant dynamic water level, in the model a constant dynamic level in the wells was maintained.

Given a system with n wells the drawdown at the ith wells is evaluated as the sum of the effects of all the wells in the system.

In the present case, the aquifers are confined and the lowering inside well "i" is equal to:

$$H - h_{wi} = \frac{1}{2 \cdot \pi \cdot k \cdot D} \cdot \left(Q_{wi} \cdot \ln\left(\frac{R}{r_{wi}} \right) + \sum_{j=1}^{n-1} Q_{wj} \cdot \ln\left(\frac{R}{r_{j,i}} \right) \right) \quad (1)$$

Being:
H = undisturbed groundwater level;
h_{wi} = water level inside well i;
k = aquifer coefficient of permeability;
D = aquifer thickness;
Q_{wi} = well discharge;
R = well influence radius;
r_{wi} = radius of ith well;
$r_{j,i}$ = distance of each well from ith well or from jth point.

In a generic point "i" within the system, the drawdown is given by the sum of the drawdown induced by the other wells, that is:

$$H - h_i = \frac{1}{2 \cdot \pi \cdot k \cdot D} \cdot \sum_{i=1}^{n} Q_{wi} \cdot \ln\left(\frac{R}{r_i} \right) \quad (2)$$

If there were n wells and m control points the solver would be formed by $n + m$ equations in $n + m$ unknowns, which are the drawdown values in the wells or in the control points.

Being:

$\overline{\delta} = [\delta_1, ..., \delta_i, ..., \delta_N]$ the vector containing the drawdown in the n wells;

$\overline{Q} = [Q_1, ..., Q_i, ..., Q_N]$ the vector of the pumped discharges in the n wells;

$$\overline{\overline{D}} = \begin{bmatrix} \frac{1}{2\pi kD}\ln\left(\frac{R_1}{r_{1,1}}\right) & \dots & \dots & \frac{1}{2\pi kD}\ln\left(\frac{R_1}{r_{1,N}}\right) \\ \dots & \frac{1}{2\pi kD}\ln\left(\frac{R_2}{r_{2,2}}\right) & \dots & \dots \\ \dots & \dots & \dots & \dots \\ \dots & \dots & \dots & \frac{1}{2\pi kD}\ln\left(\frac{R_N}{r_{N,N}}\right) \end{bmatrix}$$

the matrix with the distances within the wells, the resolution system is the following:

$$\overline{Q} \cdot \overline{\overline{D}} = \overline{\delta} \quad (3)$$

Choosing instead in this case to fix the wells dynamic level, the corresponding discharge to be pumped out is given by:

$$\overline{Q} = \overline{\delta} \cdot \left(\overline{\overline{D}} \right)^{-1} \quad (4)$$

Once the discharge to be pumped from each well is determined, the system made of n+m equations can be solved, obtaining the m drawdowns in the m corresponding control points.

In this way, fixing the wells dynamic level, obtaining the discharges to be pumped from Equation (4), the drawdown induced by the n wells can be calculated in each defined control point using Equation (3).

5.4 *Finite element model*

The finite element model was implemented in the code FEFLOW 5.3 (2008).

The model was developed re-creating the advancement module 96 m long and 40 m wide. The geometry was extended for about 500 m from each side and up to a depth of 80 m.

In this way, it was possible to apply a potential boundary condition correspondent to the undisturbed groundwater level (8.5 m a.s.l.). The soil was modelled with 3D elements.

The following conditions were imposed to the aquifer: undisturbed groundwater level at the model boundaries, 8.5 m a.s.l, and in correspondence to the active wells at the toe of the slope a 10 m drawdown, that is –1.5 m b.s.l.; the wells are made of a permeable stretch only next to layer IB, as in the simplified model.

Based on the applied boundary conditions the following results were obtained and analyzed: pumped discharge from each active well located at the toe of the slope; total head at the top of layer IB next to the deep piezometers; total head at the top of layer IA next to superficial piezometers; total head at the top of layer IB. Figure 8 shows a 3D view of the finite element model and the mesh representing the wells and the excavation area.

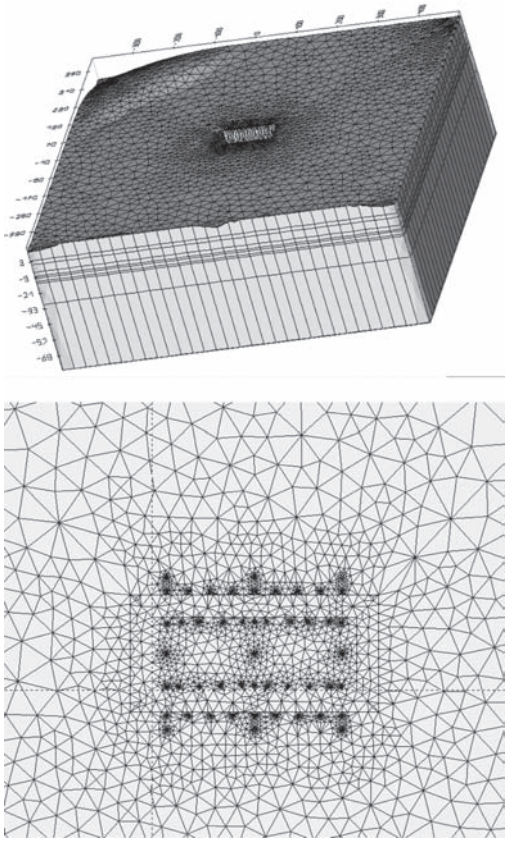

Figure 8. 3D FEM Modeling.

5.5 *Simplified model validation*

The comparison between FEM model results and those obtained from the simplified model herein is presented.

The common data input for the two calculation models were the stratigraphy, as already discussed, and the imposed dynamic level in the active wells, where a 10 m drawdown imposed in respect to the undisturbed groundwater level.

The comparison between the two calculation tools was done firstly in respect to the drawdown values at the piezometers location, both for the deep "DP" and the shallow "SP" ones. The results are given in Table 2 with reference to the names introduced in Figure 9.

A further comparison was done on the total discharge pumped out from the active wells.

The total pumped discharge calculated with Feflow is 2 l/s while the simplified model calculation provided 2.6 l/s. The two fold comparison suggests that the two models are in good agreement. Generally, the simplified model tends to predict fairly lower drawdown values compared to the ones obtained from the FE model. The gap between the results seems anyway acceptable and, from a qualitative standpoint, the use of the simplified brings to a reasonably more conservative well system design.

Based on the results obtained and considering the lower computational complexity, coupled with shorter calculation time, the simplified model seems therefore suitable for well system design in engineering practice.

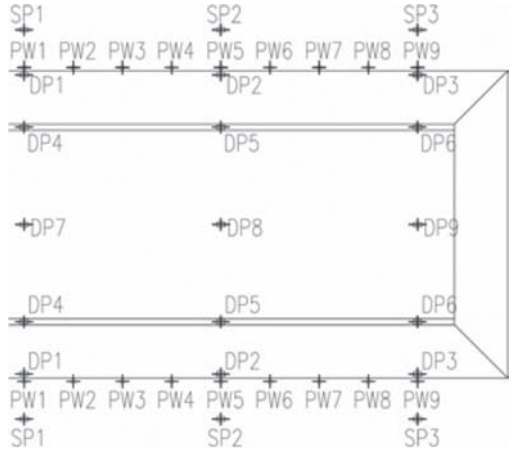

Figure 9. Observation points for piezometric lowerings calculation: "DP" = deep piezometer, "SP" = shallow piezometer.

Table 2. Results comparison between FEM and simplified model calculation.

Observation point	Calculated drawdown (m)	
	Feflow	Simplified model
SP1	5.94	5
SP2	6.75	6.03
SP3	5.9	5
PW1	6.34	4.7
PW2	6.84	5.64
PW3	7	6.41
PW4	7.25	6.82
PW5	7.3	7.03
PW6	7.27	7.09
PW7	7.19	7.03
PW8	6.72	6.82
PW9	6.3	6.41
DP1	6.48	8.55
DP2	7.6	8.68
DP3	6.58	8.55
DP4	7.37	7.8
DP5	8.90	8.67
DP6	7.23	8.68
DP7	7.28	7
DP8	8.73	8.88
DP9	7.17	7

6 INDUCED SUBSIDENCE NEXT TO THE EXCAVATION AREA

The wells system lowers the groundwater level inside the excavation perimeter, with obvious effects in the nearby external area. This can cause a subsidence settlement due to the increase of the effective stresses in the permeable layers and also in part of the cohesive levels.

The reduction of the hydrostatic head in the two permeable layers has been evaluated up to a distance of 50 m from the wells axes; at greater distances, the dewatering effect was considered negligible.

With the aim of assessing the effects of dewatering on the areas outside the excavation, settlements were computed at a distance of 25 and 50 m from the active wells position. The analysis was run in two scenarios:

- Pore pressure reduction within the sandy layers with no consolidation in the clay layers (short term conditions);
- Pore pressure reduction within sandy layer and consolidation of the clay layers (long term conditions).

The results are presented in Table 3.

Assuming that the maximum differential settlement could be 50% of the total value and considering the most frequent dimensions of the existing buildings along the layout, the following values of angular distortion have been calculated:

Table 3. Calculated settlements.

Distance (m)	Settlements (mm)	
	Short term	Long term
25	11	46
50	4.5	20

Table 4. Calculated distortions.

Distance (m)	Maximum distortion		
	Maximum differential settlement (mm)	Reference distance (m)	Distortion
25	23	5	1/200
50	10	5	1/500

According to the structural typology of the existing buildings, typically realized in masonry or in reinforced concrete frames, the maximum tolerable angular distortion has been establish between 1/250 and 1/150. In general it can be observed that within 25 m from the wells axes the evaluated distortion is next to the limit conditions.

Beyond 50 m instead the settlements induced by the subsidence are totally allowable.

Based on this results, during the whole construction period a mitigation system was foreseen for the buildings within 30 m from the active wells axes.

7 SYSTEMS OF SUBSIDENCE MITIGATION

The remediation measure was aimed to minimize the subsidence by limiting the water level variation close to the buildings.

Re-injection wells were therefore placed between the working area and the buildings. These wells were built as vertical drains and were all connected with a top trench where the water table was kept at the undisturbed level. The efficiency check of the system was accomplished in the buildings between progressive 2+247.5 and progressive 2+297.5, see Figure 5. Figure 10 shows a typical cross section next to the buildings illustrating the position of the re-injection wells system with respect to the active wells and to the excavation.

Through simplified Mansur & Kaufman model it was verified that the presence of 10 m spacing

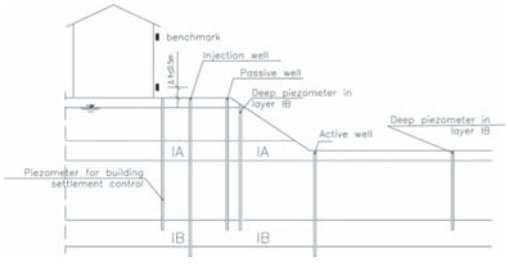

Figure 10. Section next to the buildings nearest to the excavation showing the measures for the mitigation of subsidence effects.

re-injection wells was enough to maintain the groundwater level constant while the pumping system was working.

8 CONCLUSIONS

Presently, the construction works along the whole road development have been completed and the highway road connection is now in service. The dewatering system turned out to be adequately designed and no particular problems were encountered during construction. The mitigation system composed of passive wells proved as well to be efficient in minimizing the effect of pumping.

All the pumped discharges and the piezometric measured levels resulted in good agreement with the mathematical modeling calculation.

The simplified model was able to foresee the actual behaviour of the pumping system inside and outside the excavation area. Its particular versatility proved to be successful being able to adapt to all geometric and stratigraphic configurations along the project development.

This simplified prevision model, validated with a finite element model, proved to be a reliable alternative to more complex computation tool.

From the application point of view it can be said that the simplified model, implementing Mansur & Kaufman theory, proved to be very efficient and entirely respondent to the design needs.

REFERENCES

FeFlow (Finite Element Flow) 5.3 (2008) developed by WASY GmbH.

Mansur C. I. & Kaufman R.I. 1962. Dewatering. *Chapter 3 in Foundation Engineering* edited by G.A. Leonards. Mc-Graw-Hill Company, New York.

This page intentionally left blank

Ground movements, interaction with existing structures and mitigation measures

This page intentionally left blank

Geotechnical Aspects of Underground Construction in Soft Ground – Viggiani (ed)
© 2012 Taylor & Francis Group, London, ISBN 978-0-415-68367-8

Compensation grouting: Mechanisms determining the shape of the grout body

A. Bezuijen & A.F. van Tol
Deltares/Delft University of Technology, The Netherlands

ABSTRACT: The shape of the grout body as a function of the grout properties is studied in a number of laboratory tests. This paper describes a calculation model, derived with the results of these tests that describe the mechanisms determining the grout shape in the soil during compensation grouting. It is shown that when grout is injected in a permeable soil, the permeability of the grout filter cake, the injection pressure and the amount of solids in the grout influence the shape of the grout body created in the soil. Furthermore the installation procedure of the TAM's is of importance. The model presents a relation between the injection pressure and the shape (thickness versus length) of the grout body. For the usual cement bentonite grout, high injection pressures necessarily lead to irregular shaped grout bodies, which have more resemblance with the shape of potatoes than with fractures. Consequences for practical application will be discussed.

1 INTRODUCTION

Compensation grouting is used regularly to compensate the settlements that may occur during underground construction. The method is still rather empirical: Grout is injected and the movement of buildings is monitored. The shape of the grout body created is generally not known. This shape is of importance to predict the extent of the area were heave is created. The empirical procedure can lead to surprises, such as an amount of heave that is less than expected or heave at a different location from where the grout was injected (Paans 2002).

A research programme was performed to investigate the mechanisms that are of importance for compensation grouting in sand (Bezuijen 2010). This research programme was performed at Deltares and Delft University in collaboration with the University of Cambridge (Eisa 2008). Laboratory tests were performed and field measurements were analysed in this programme. Laboratory tests were performed with different set-ups, both in Cambridge and in Delft. A researcher from Cambridge did experiments with the set-up in Delft and in Cambridge to investigate whether differences in results were the result of different set-ups or different researchers.

While other papers (Gafar et al. 2008, Bezuijen et al. 2010) describe the experiments and the results, this paper concentrates on the mechanisms that determine the shape of the grout body when injected in sand. It describes the mechanisms that create a fracture in sand and how these determine the shape of the fracture.

It will be described what mechanism is responsible for a fracture in sand and how the grout properties and injection pressure determine the filter cake and what the influence is of the filter cake on the fracture behaviour. The thickness of the filter cake gives a minimum width of the fracture and using the cavity expansion theory, it is possible to relate the width of the fracture with the injection pressure. The combination of these results leads to a formula that relates the shape of the fracture to the grout properties and the sand parameters.

2 FRACTURE MECHANISM

Assume a cylindrical cavity in soil. Grout injection will imply a pressure loading on this cavity. In case of a continuum situation with purely radial loading, this will lead to a cavity expansion as described in literature (see for example Luger & Hergarden 1988). However, sand grains do not form a perfect continuum, there are always some irregularities between the grains, see Figure 1.

Furthermore, the pressure of the injected fluid will lead to an increased radial stress and a decreased tangential stress (σ_θ in Figure 1) around the cavity. Since the fluid pressure in the cavity will be the same in all directions, the fluid pressure that is equal to the radial stress will exceed the tangential stress in the soil and push the grains apart at an irregularity to start a fracture. This mechanism

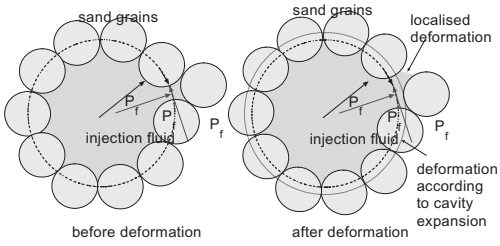

Figure 1. Sketch showing possible deformation modes of the injection hole. In reality there will be more grains around the injection hole. The figure illustrates the principle only.

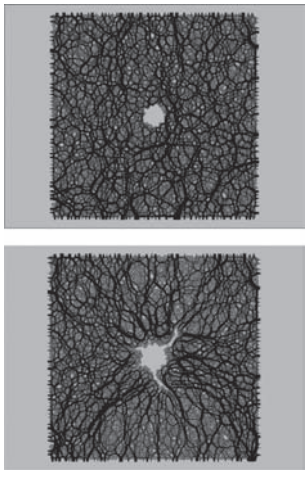

Figure 2. Results of DEM fracture calculations (Pruiksma 2002).

was also found in DEM calculations that include the influence of fluid flow (Pruiksma 2002), See Figure 2.

The figure shows the stress transmission through the grains before (with a low pressure in the cavity) and during fracturing (with a much higher pressure in the cavity). Note that the original stress distribution has changed quite a lot due to the increased pressure in the cavity.

From these results, we concluded that the original K_0 (the ratio between horizontal and vertical stress) may have only a limited influence on the fracture direction, because the pressure distribution is changed before a fracture occurs, as appears from analysing the calculation results shown in Figure 2.

3 GROUT PROPERTIES

When grout is injected in sand, as is done during compensation grouting, the grout will have a much higher pore pressure than the surrounding sand.

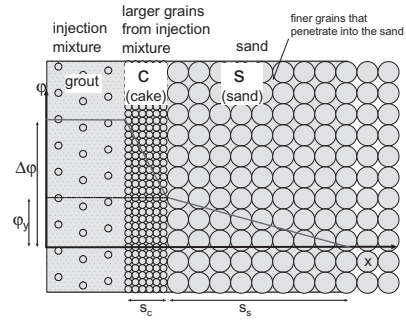

Figure 3. Plastering that can occur during pressure infiltration due to larger grains in the mixture that cannot penetrate into the sand and sketch of the pressure distribution over the injection liquid.

As a consequence, the sand will react as a filter and liquid and fine particles will be pressed from the grout into the sand, a process called pressure filtration. This process reduces the water content in the grout and leads to a filter cake, see Figure 3. S_c in this figure is the thickness of the filter cake and S_s is the thickness of the infiltrated zone in the sand. $\Delta\varphi$ and φ_y indicate the pressure drop over the filter cake and infiltrated zone respectively. The thickness of the filter cake is a function of the pressure difference (or difference in piezometric head $\Delta\varphi$) over the filter cake, the porosity of the filter cake and the permeability of the filter cake.

For a constant injection pressure, this can be written as (McKinley and Bolton 1999):

$$S_C = \sqrt{2k_c \frac{1-n_i}{n_i - n_e} \Delta\varphi t} \qquad (1)$$

Where k_c is the permeability of the filter cake, n_i is the initial porosity of the grout, n_e the porosity of the cake and t is time.

The thickness of the filter cake has two consequences:

- when the filter cake is thicker than half the grain diameter, it will fill the irregular surface between the grains, see Figure 1. The situation that will occur is sketched in Figure 4.
- a thicker filter cake is only possible in wider fractures. The filter cake has to fit within the fracture.

4 WIDTH OF FRACTURES

The width of the fractures as a function of the injection pressure of the grout can be calculated using numerical methods. However, here an analytical method is used, based on cavity expansion.

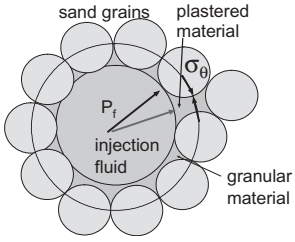

Figure 4. Cavity and plastering.

This method will be less accurate then a suitable numerical method, but the advantage is that a closed form formulation can be reached that links the relevant parameters in one formula, as will be shown in the next section.

The formula as derived by Luger and Hergarden (1988) is used to describe the relation between the diameter increase of the cavity and the cavity pressure. This equation takes into account large strains, but does not take into account the influence of dilatancy, leading to:

$$p' = (p'_f + c.\cot\phi)\left[\frac{1-(R_0/R_p)^2}{Q_1}\right]^{\left\{\frac{\sin\phi}{1+\sin\phi}\right\}} - c.\cot\phi \qquad (2)$$

with:

$$Q_1 = \frac{\sigma'_0 \sin\phi + c.\cos\phi}{G} \qquad (3)$$

p' the effective pressure in the bore hole,
p'_f $= \sigma'_0 (1+sin\phi) + c.cos\phi$ the pressure where plastic deformation in the soil starts,
σ'_0 the effective stress around the hole before pressurising,
c the cohesion of the material,
R_0 the original radius of the bore hole,
R_p the radius after pressurisation,
G $= E/(2(1+\nu))$ the shear modulus,
E Young's modulus,
ν the Poisson ratio,
ϕ the friction angle.

To come from this formula to a relation that describes the width of a fracture, it is assumed that the stress distribution at some distance of a fracture can be approximated with the stress distribution of a larger imaginary cavity, see Figure 5. This assumption is, to some extent, supported by the results of FEM calculations (Bezuijen 2010).

As a first approximation and disregarding dilatancy in the sand, the volume increase in the fracture must also lead to the same volume increase in the imaginary larger cavity. Using cavity expansion theory, it is possible to calculate the pressure needed to achieve this volume increase at the border of the

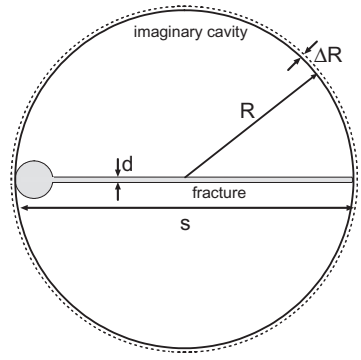

Figure 5. Fracture and imaginary cavity to calculate the injection pressure, see text.

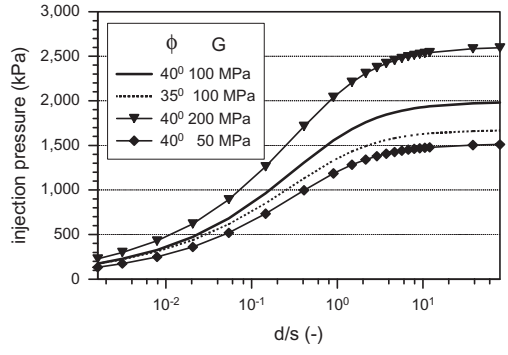

Figure 6. Theoretical relation between fracture shape and injection pressure using cavity expansion theory for different values of the friction angle (ϕ) and the shear modulus (G).

imaginary cavity. Since plastic deformation close to the cavity is limited (Bezuijen 2010), the pressure at the border of the imaginary cavity will be comparable to the pressure in the fracture and it is therefore possible to estimate the fracture pressure.

For the two-dimensional case (with a fracture plane perpendicular to the plane shown in Figure 5) it can be derived that

$$\frac{R+\Delta R}{R} = \sqrt{1+\frac{4}{\pi}\frac{d}{s}} \qquad (4)$$

The parameters for this equation are defined in Figure 5. Combination of this equation and Eq. (2), leads to a relation between *d*/*s* and the injection pressure shown in Figure 6.

The relation presented in Figure 6 will not be valid for values of d/s larger than 1. However, the relation is also shown for large values of d/s, so that the figure reaches the limiting cavity expansion pressure. From this figure, it can be concluded that, if the limiting cavity expansion pressure in

the soil and the injection pressure is known, it is possible to estimate the width-length ratio for the fractures. This width-length ratio will increase for higher injection pressures. Thus when during compensation grouting the injection pressure is close to the limiting cavity expansion pressure, there will be no real fractures, and the length and width of the grout body will be comparable.

5 FRACTURE WIDTH AND FILTER CAKE

Combination of Eq. (4) in Eq. (2), assuming that the cohesion can be neglected (as is normally the case in sand) and that d/s is much less then 1, it is possible to simplify the relation for the injection pressure to:

$$P' = P'_f \left[\frac{4d}{\pi s} \frac{1}{Q_1} \right]^{\left(\frac{\sin\phi}{1-\sin\phi} \right)} \tag{5}$$

In practical applications of compensation grouting the mixture has a WCR (water/cement ratio, by weight) of 2 or less. For such mixtures the pressure infiltration (see Figure 3, finer grout particles leaking into the sand) has limited influence on the pressures and the plastering or pressure filtration as described with Eq. (1) dominates the process. The filtration will lead to a reduction of the thickness of the fracture and for the fracture to remain open, the thickness has to be larger than 2 times the thickness of the filter cake that has formed in the filtration process, see Figure 7.

Neglecting the volume of the water that filtrated from the fracture and assuming a constant fracture thickness, the relation between the volume injected into the fracture (Q) and its thickness (d), length (s) and its width (w) can be written as:

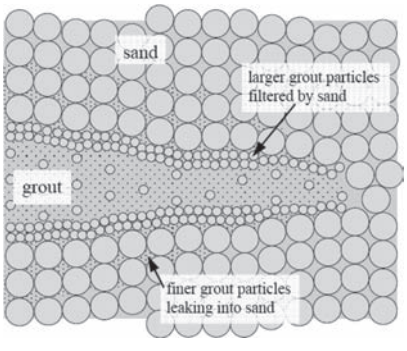

Figure 7. Sketch of the formation of a filter cake (the larger grout particles filtered by the sand). (Gafar et al. 2008).

$$Q = sdwt \tag{6}$$

Combination of Eq. (1) and Eq. (6) with the condition that the thickness of fracture has to be larger than 2 times the filter cake leads to:

$$\frac{d}{s} > \frac{8wk_c}{Q} \frac{1-n_i}{n_i-n_e} \frac{P_{ext}}{\gamma_w} \tag{7}$$

In this equation the difference in piezometric head ($\Delta\phi$) between the pore water in the sand and the injected grout as given in Eq.(1) is now written as a pressure difference (P_{ext}) using:

$$P_{ext} = \gamma_w \Delta\phi \tag{8}$$

Eq. (5) can be used for the injection pressure in Eq. (7) leading with Eq. (3) with c = 0 to:

$$\frac{d}{s} > \left[\frac{8wk_c}{Q} \frac{1-n_i}{n_i-n_e} \frac{\sigma'_0}{\gamma_w} (1+\sin\phi) \right]^{(1+\sin\phi)} \cdot \left(\frac{4G}{\pi\sigma'_0 \sin\phi} \right)^{\sin\phi} \tag{9}$$

This formula is of interest, since it relates the width of the fractures to soil parameters. Some approximations and simplifications were necessary to derive this formula but it shows how parameters are related. The formula shows that a higher injection rate per unit width of the fracture leads to lower values of d/s and thus to thinner fractures. Higher effective stress in the soil and/or a higher stiffness of the soil leads to higher values of d/s and thus shorter thicker fractures.

Note that, according to this model, the pressure drop due to the viscosity and/or the yield stress of the grout does not have an influence on the shape of the fracture. In classical fracture theory as developed for the fracturing of rock these are important parameters. However, the fractures in sand are so wide that the pressure drop due to yield stresses or viscous forces in the grout can be neglected (Bezuijen 2010).

6 CALCULATION RESULTS

The consequence of Eq. (9) is that the fracture shape depends on the soil properties and the filtration properties. The equation is shown graphically in Figure 8. It presents the calculated d/s and the injection pressure (P_{ext}) for different values of the permeability of the grout cake and the shear modulus of the soil. The calculations were run for the parameters presented in Table 1.

Experiments (Bezuijen et al. 2009) have shown that the permeability of the grout filter cake can vary over orders of magnitude. The plot shows that this will lead to a variation of the injection pressure (P_{ext}) with the same magnitude as the variation

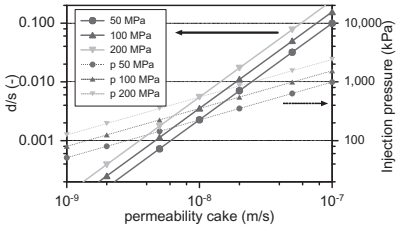

Figure 8. Calculated values for d/s and P_{ext} for various cake permeabilities and shear moduli, see also text.

Table 1. Parameters used in d/s calculation.

Parameter	Value	Dimension
injection rate	10	l/min
Width of fracture	0.5	m
n_i	0.84	–
n_e	0.45	–
confining stress	100	kPa
Friction angle	40	degr.

in the permeability and to a variation of the d/s values that is even more then the variation in the permeability of the filter cake. In reality the variations are a bit smaller, because at very low values of d/s the pressure losses due to the yield stress of the grout and its viscosity cannot be neglected anymore. However, the conclusion remains the same: the necessary injection pressure to create a fracture is not only determined by the soil properties and the effective stress in the soil, but also by the grout properties.

7 EXPERIMENTAL VERIFICATION

Tests were performed in a pressurized container at 100 kPa effective stress and approximately 10 kPa of pore pressure. A sketch of the container with its dimensions is shown in Figure 9. The sand used was Baskarp sand with a d_{50} of 135 µm. The sand was wet pluviated and densified to a relative density of 65%. The method used, is described by Rietdijk et al. (2010) and results in homogeneous sand samples. The sand was pre-stressed to 300 kPa before the test. The idea was to increase the horizontal stress as could also be the case during pre-grouting. This procedure however, was only partly successful.

Three test series where performed with these set-up, more details can be found in Bezuijen et al. (2010) and Bezuijen (2010).

Experiments in this set-up by Sanders (2007) show the relation between the injection pressure and the shape of the fractures. See Figure 10 and Figure 11.

The results of these tests show that, in agreement with the model developed, in most tests a larger injection pressure corresponds with shorter and thicker fractures. Only Test 10 is an exception, probably due to a sand sample with a bit lower relative density.

The results of the calculation model have also been checked quantitatively with results of model tests.

This comparison appeared rather difficult, since only tests with a limited pressure infiltration zone (see Figure 3) could be used. Only four suitable tests could be selected from the model tests series performed in Delft (Bezuijen 2010). Since only the shear modulus of the sand was not known, this value was used as a fit parameter. For one of the tests the value

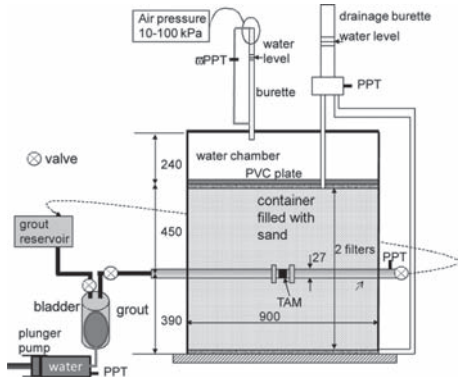

Figure 9. Set-up of the experiments. Note that changes in pore volume and sand volume can be measured as changes in the water levels.

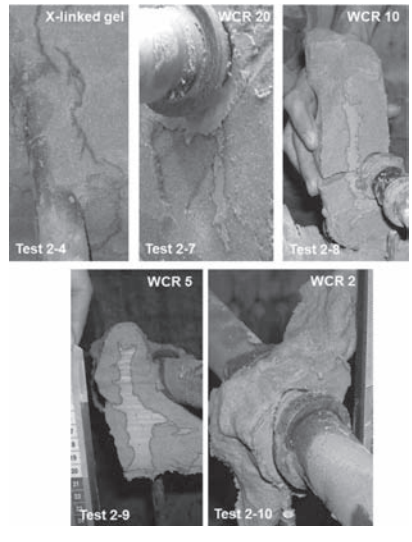

Figure 10. Shape of fractures for increasing cement content. The tube in the figures is the injection tube, see Figure 9.

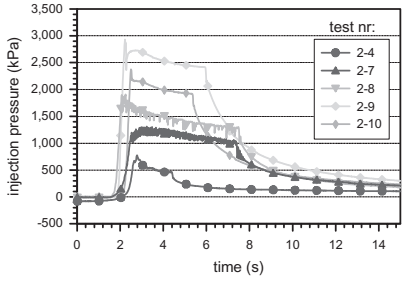

Figure 11. Injection pressures in various tests, 1st setup, 2nd series.

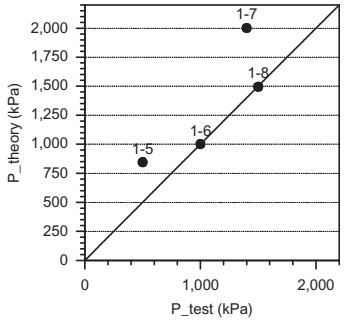

Figure 12. Calculated maximum pressures compared with measurements, calculation fitted for Test 1–8.

of the shear modulus in the calculation was adapted in a way that the calculated injection pressure corresponded with the measured one. The sand preparation procedure was the same for all tests selected and therefore it was assumed that also the shear modulus was the same for all tests. The parameters from Table 2 were used in all tests and furthermore for each test the values presented in Table 3 were used to calculate the injection pressure. These results were compared with the measured values—see Figure 12—and although quite different confining stresses were applied and the permeability of the grout cake (which was measured for each experiment) also varied quite significantly, there was reasonable agreement. More information about the tests can be found in Kleinlugtentbelt (2005).

From the comparison with tests results it can be concluded that there is qualitative agreement found with the tests of Sanders (for these tests the model could not be compared quantitatively, because there was too much pressure infiltration during these tests with high WCR values) and reasonable quantitative agreement with the tests of Kleinlugtenbelt.

8 FIELD TESTS

When the first results of the model tests, described briefly in the section above became available,

Table 2. Parameters with constant values in the calculations.

Parameter	Value	Dimension
shear modulus	125	MPa
injection speed	10	l/min
width of fracture	0.5	m
Friction angle	40	deg.

Table 3. Parameters used to calculate injection pressures.

No	n_e (–)	n_i (–)	Permeab. gr. cake (m/s)	Conf. stress (kPa)	Pressure Calc. (kPa)	Pressure measured (kPa)
1–5	0.53	0.74	9.6*10–8	24	500	845
1–6	0.55	0.77	4.7*10–8	50	1000	1000
1–7	0.55	0.77	4.7*10–8	100	1400	2002
1–8	0.59	0.8	2.7*10–8	116	1500	1500 (fit)

these were compared with the results of field measurements. It appeared that the injection pressures in the model were often higher than the injection pressures reported in the field. The injection pressures reported from field tests are not very accurate, since normally the pressure is measured at the injection pump and not at the nozzle. Measurements at the Amsterdam North/South line have shown that there can be 7.5 bar pressure difference between the pressure at the pump and the pressure at the nozzle (Kleinlugtenbelt 2009). Furthermore, there is a huge variation in measured injection pressures.

Literature (Chambosse & Otterbein 2001) describes that the injection pressure increases during a compensation grouting campaign. The idea is that, during the initial injections, horizontal pressure is still relatively low; the grout fractures may extend in a vertical direction. However, after a number of injections, horizontal pressure rises and the principal direction of the fractures will be horizontal. The higher horizontal pressure and the hardened grout around the injection sleeves lead to higher injection pressures.

This theory was tested using the injection data from a compensation grouting project in Amsterdam, Vijzelgracht. A few sleeves were selected in which quite a number (50–70) of injections were performed. The injection pressure measured at the end of the injection was plotted for each of these injections. The results are shown in Figure 13.

The figure shows that the injection pressure may indeed tend to increase when the number of injections through the same sleeve increases, but the tendency is rather weak. The scatter for the subsequent injections is much larger. It is possible that an injection pressure of more than 34 bar is followed by much lower injection pressures slightly higher than 5 bar.

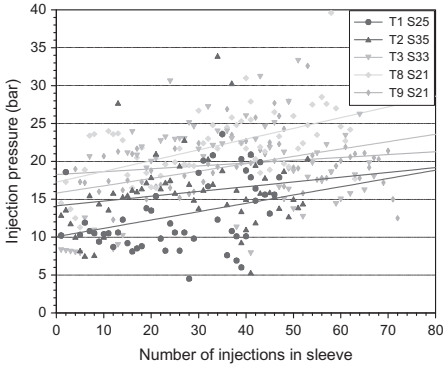

Figure 13. Pressure measured at the end of the injection for subsequent injections in one sleeve. The legend presents the tube number (T) and the sleeve number (S) for which the pressures are given.

This result means that the relation between the number of the injections in the sleeve and the injection pressure, and therefore the relationship between the amount of grout injected and the injection pressure (because 25 litres were injected in all the injections shown), is not as straightforward as is sometimes assumed. A possible cause is that the injections in various sleeves of one TAM interact with each other. The injection at one point probably sometimes creates a low stress situation around another injection point, resulting in lower injection pressures when that other injection point is used.

The model tests described above have been performed at a comparable stress level than the field injections. In the model tests with grout the injection pressures varied between 12 and 29 bar, see Figure 11. The grout used in the field test makes a rather permeable cake compared to the grout used in the model tests. This means that, according to the calculation model presented, the injection pressure in the field should be higher and it should be certainly higher when we take into account that there is a pressure loss in the injection tube of several bars in the field test. Comparing the pressures shown in Figure 11 and Figure 13 it appeared that in most cases the pressures in the model test are higher than the pressures found during first injection in the field. It is therefore likely that the stress situation around the TAM (Tubes à Manchettes, the injection tubes) is different in the field and in the model. One explanation is already mentioned above: the influence due to interaction. The injection at one location leads to higher stresses there, but since the sum of the vertical stresses has to remain the same, this implies that the vertical stresses elsewhere decrease. Another reason is the consolidation of the sleeve grout, as will be explained below.

9 INFLUENCE OF SLEEVE GROUT

Model tests as well as calculation models on soil fracturing as occurs during compensation grouting normally do not take into account the installation of the TAMs. It is assumed that the installation has no influence on the surrounding soil and that the stress distribution has not changed due to the installation. For the model tests described above this is also more or less the case, but not for a field project.

The installation procedure in the field is sketched in Figure 14. The figures show an artist impression of a cross-section through a TAM and the soil during installation. First the TAM is installed by pressing it, together with a protective casing into the soil horizontally. Bentonite slurry is sometimes used to lubricate the casing. After installation, sleeve grout is injected between TAM and the casing to prevent soil settlement and after that the casing is retracted. The retraction and the consolidation of the grout will lead to unloading of the surrounding soil. In the next stage a packer is installed and the grout is injected.

The unloading of the soil just around the sleeve grout leads to lower soil pressures and consequently, according to be calculation model described before, to lower injection pressures and lower values of d/s thus thinner and longer fractures.

To check this the model set-up shown in Figure 9 was adapted to incorporate the installation procedure (Bezuijen et al. 2010). It appeared that introducing the installation procedure in the test, led to

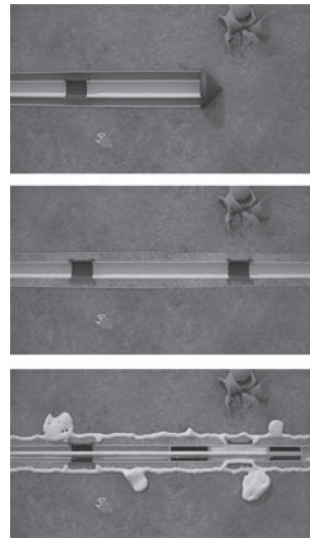

Figure 14. Three stages during compensation grouting: the installation of the TAM (inner tube) with a casing to protect the rubber sleeves (top), the retraction of the casing after injection of sleeve grout (middle) and the injection of grout (bottom).

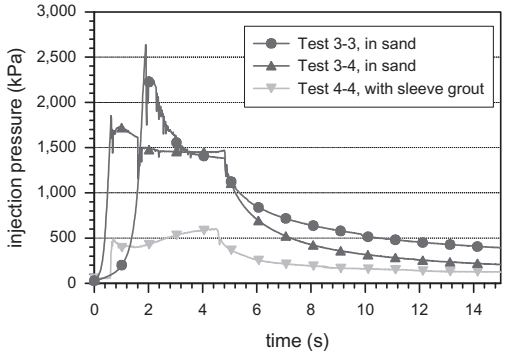

Figure 15. Difference in injection pressure for laboratory tests with (sleeve grout) and without (in sand) simulation of the installation procedure.

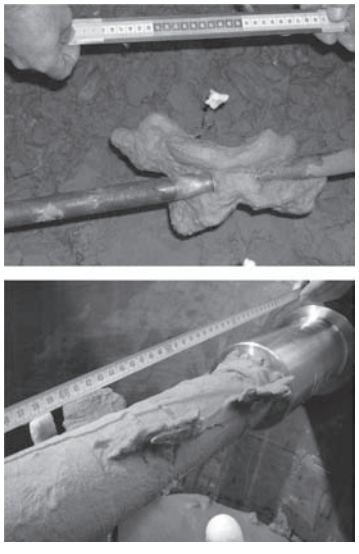

Figure 16. Difference in fracture shape for laboratory tests with (bottom) and without (top) simulation of the installation procedure.

lower injection pressures and thinner fractures, see Figure 15 and Figure 16).

10 CONCLUSIONS

A calculation model has been developed that describes the influence of the filter cake formation on the fracture shape for compensation grouting in sand. For the situation with limited pressure infiltration into the sand, this model describes the relation between the grout and soil properties and the shape of the fractures. The model is in agreement with measurements in laboratory set simulating compensation grouting in sand. It shows that high injection pressures (close to the cavity expansion theory in sand) will lead to relatively short and thick fractures.

With the results of the calculation model, it is likely to assume that the fluctuations in the injection pressures measured in the field are at least partly caused by stress differences caused by the successive injections. The influence of the sleeve grout is explained.

REFERENCES

Bezuijen, A.,Tol, A.F. van & Sanders, M.P.M 2010. Compensation grouting research, the influence of the physical model. *Proceedings of the International Conference on Physical Modelling in Geotechnics 2010 (ICPMG 2010)*.1309–1314

Bezuijen, A. 2010. Compensation and corrective grouting in sand, *Experiments and modelling. Phd-Thesis.* Delft University of technology.

Bezuijen, A., Sanders M.P.M. & Hamer D. Den 2009. "Parameters that influence the pressure filtration characteristics of bentonite grouts" *Géotechnique,* Vol 59, Isue 8, 717–721.

Chambosse, G. & Otterbein, R. 2001. State of the art of compensation grouting in Germany. *Proc. XVth Int. Conf. on Soil Mechanics & Foundation Engineering*, Turkey, Istanbul. 1511–1514

Eisa K. 2008. *Compensation grouting in sand*. Phd-Thesis, University Cambridge, November.

Gafar, K., Soga, K., Bezuijen, A., Sanders, M.P.M. & Tol, A.F. van 2008. "Fracturing of sand in compensation grouting." *Proc. 6th Int. Symposium on Geotch. Aspects of Underground Construction in Soft Ground, Shanghai. 281–286*

Kleinlugtenbelt, R. 2009, Pressure drop in packer system, internal report.

Kleinlugtenbelt, R. 2005. *Compensation grouting, laboratory tests in sand*. MSc thesis. Delft University of Technology.

Luger, H.L. & Hergarden, H.J.A.M. 1988. "Directional Drilling in soft soil, influence of mud pressures." *Proc. No-Dig, Int. Soc. Trenchless Technology*, 155–161

McKinly, J.D. & Bolton, M.D. 1999. "A geotechnical description o fresh cement grout — filtration and consolidataoin behaviour". *Magazine of concrete research* **51**, vol. 5 October, 295–307.

Paans, W.J.M. 2002. "The influence zone and effectiveness of fracture grouting on piled foundations" MSc thesis TU Delft. April.

Pruiksma, J. 2002, *"Hydraulic fracturing with the distict element method"*. DelFrac Report, GeoDelft CO386730/12 V3.0.

Rietdijk, J., Schenkeveld, F.M., Schaminée, P.E.L., & Bezuijen, A. 2010. The drizzle Method for Sand Sample Preparation. *Proceedings of the International Conference on Physical Modelling in Geotechnics 2010 (ICPMG 2010)* 267–272.

Sanders, M.P.M 2007. *Hydraulic fracture grouting, laboratory tests in sand*. MSc thesis. Delft University of Technology.

Geotechnical Aspects of Underground Construction in Soft Ground – Viggiani (ed)
© 2012 Taylor & Francis Group, London, ISBN 978-0-415-68367-8

Analysis of ground movements induced by tunnels in sand based on contract CR3 in Kaohsiung Metro

B.C.B. Hsiung
National Kaohsiung University of Applied Sciences, Kaohsiung, Taiwan

ABSTRACT: In this paper, ground movements induced by shield- machine bored tunnels in sand were explored. The main ground condition on site consists of silty sand with high groundwater table. Observations show the accumulated maximum surface settlement caused by tunnel construction reached up to 3.5 to 27.0 mm at the end. Back analyses of transverse surface settlement using some empirical methods were delivered to determine two parameters, width parameter *K* and volume loss *V*. It was found that *K* is in the range of 0.35 to 0.51, no matter 1st or 2nd drive tunnel. While, *V* varies from 0.20% to 1.05% for the 1st drive tunnel and 0.18% to 1.27% for the 2nd drive tunnel so no large difference is seen. Finally, numerical analyses were carried out and results were compared with observations in order to determine a parameter V_L which is ratio of convergence area of tunnel. It was recommended that V_L in general is in the range of 0.5% to 1.0% based on results of this study.

1 INTRODUCTION

Due to fast development of urban areas, the shield-machine bored tunnels are widely applied for use of underground utilities, such as water and power supply, metro and common conduits. However, additional ground movements may be induced by construction of underground structures which may lead to damage of structures and should be well- predicted.

Several studies have been conducted to evaluate the magnitude of ground and structure settlements induced by shield tunnelling but most of them were based on cases in clay (Peck, 1969, Attewell & Farmer, 1974, Mair *et al*., 1981, O'Reilly & New, 1982, Rowe & Kack, 1983, Clough & Leca, 1993, Lake *et al.*, 1996 and Sigl & Atzl, 1999) and the study of performances of shield- machine bored tunnel in sand is comparatively limited.

Ground movements induced by shield tunnelling in silty sand with high groundwater level is examined in this paper. Moreover, a back analysis of field observed data using an empirical method is undertaken in order to interpret two parameters, width factor *K* and volume loss *V*. Finally, a numerical analysis is delivered and results from numerical analysis and observations are compared.

2 PROJECT BACKGROUND

Kaohsiung is the political and economical centre in southern Taiwan and the city began to design its new metro system in the 90's and construction commenced in 2002.

Data taken from Contract CR3 of Kaohsiung Metro Project, Taiwan were used for this study. Contract CR3 is located at ChienJian and Lingya District of Kaohsiung City and it also has three cut-cover stations (R7, R8 and R9) and four single-line twin- bored tunnels (LUR15, LUR16, LUR17 and LUR18) with three cross- passages. Figure 1 presents the network of Kaohsiung metro and the location of CR3. For the purposes of this paper, only the construction of the tunnels is considered, and station construction is not included.

As stated above, there are four tunnels at CR3. The track alignment mainly went alone Chung-Shan Road, one of main roads in north- south

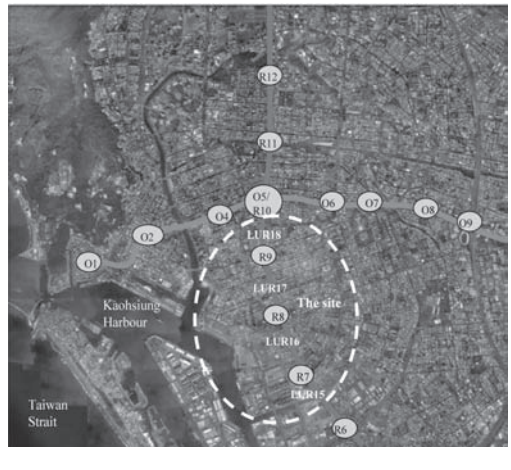

Figure 1. The location of site.

direction of Kaohsiung City. Two tunnels (up-line and down- line) run parallel at the same depth. The depth of centre of tunnels varies from 13 m to 20 m below surface level and centre to centre distance of twin tunnels is in the range of 16.5 to 19.0 m.

For CR3, two Earth- Pressure- Balance (EPB) machines (refer to Fig. 2) are used for construction of tunnels and the construction sequence of these tunnels is indicated in Figure 3. The diameter of the machine was 6.3 m and the outer and inner diameter of tunnel lining was 6.16 m and 5.60 m, respectively The rings were 1.2 m wide reinforced concrete and each ring consisted of six segments, one K-type segment, two B-type segments and three A-type segments.

Kaohsiuung City is located at southwest coast of Taiwan and the geological formations have been developed in either late Tertiary or Quaternary. Figure 4 presents geology of Kaohsiung City. In the city, it is seen that the ground mainly consists of alluvial material, such as sand, silt and clay.

Figure 2. EPB shield machine used for Contract CR3.

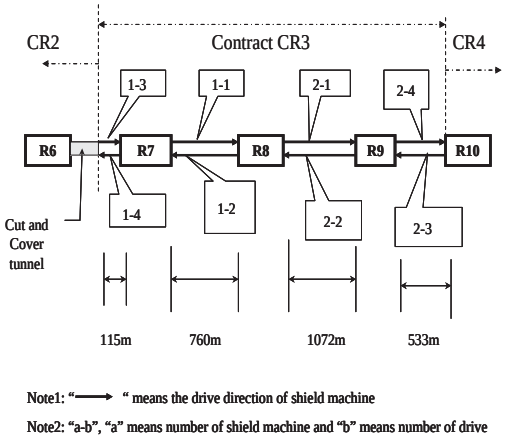

Figure 3. Construction sequences of tunnels at CR3.

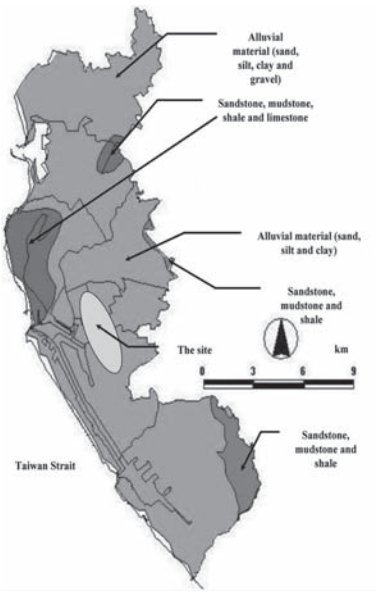

Figure 4. Geology of Kaohsiung city.

Table 1. Brief description of ground strata at LUR15.

Layer	Description of ground	Depth	γ_t (kN/m^3)	Average SPT- N value
I	Silty sand with clay, sily clay and sandy silt	Surface to 12.9 m below; groundwater level observed at 2.9 m below ground level	20.0	13
II	Soft silty clay with clayey silt	In the range of 12.9 m to 14.6 m below the ground surface	19.1	13
III	Silty sand occasionally with sandy silt	In the range of 14.6 m to 26.0 m below the ground surface	19.8	16
IV	Firm clay	Beneath 26.0 m below the ground surface	20.2	20

Some field investigations were delivered at CR3 and it was found that the main soil stratum at CR3 consists of very thick silty sand, occasionally with sandy silt and clay. Tables 1–3 present brief

Table 2. Brief description of ground strata at LUR16.

Layer	Description of ground	Depth	γ_t (kN/m^3)	Average SPT- N value
I	Gray silty sand. Backfill materials are observed on surface occasionally	Surface to 13.8 m below; groundwater level observed at 2.5 m below ground level	19.9	10
II	Soft silty clay	In the range of 13.8 m to 15.5 m below the ground surface	19.4	9
III	Gray silty sand	In the range of 15.5 m to 23.3 m below the ground surface	19.8	16
IV	Gray silty sand	Beneath 23.3 m below the ground surface	19.5	18

Table 3. Brief description of ground strata at LUR17.

Layer	Description of ground	Depth	γ_t (kN/m^3)	Average SPT- N value
I	Yellow and grey silty sand. Backfill materials and silty clay are observed on surface occasionally	Surface to 8.3 m below; ground-water level observed at 1.5 m below ground level	19.7	17
II	Gray silty sand occa-sionally with silty clay and sandy silt	In the range of 8.3 m to 21.9 m below the ground surface	19.8	13
III	Gray silty sand	Beneath 21.9 m below the ground surface	19.6	17

descriptions of ground strata at LUR15, LUR16 and LUR17. The SPT- N value varies between 9 and 20 and total unit weight of soil at CR3 is in the range of 18.4–20.2 kN/m^3. The groundwater level is high, approximately at surface to 3.0 m below surface level and remains in the same hydrostatic condition as prior to tunnel construction.

3 EVALUATION OF GROUND MOVEMENTS AND VOLUME LOSS RATE

For CR3, instruments installed on site include bench marks for surface level, tiltmeters, crack gauges, extensometers, observation wells and inclinometers.

In this paper, only the surface settlement measurement is addressed. Selected time history of surface settlement measured exactly above the centre of tunnel from LUR15, LUR16 and LUR17 were shown in Figures 5–7. From these figures, it was indicated that the settlement mainly occurred immediately after passing of head and 3.5 to 18.2 mm of surface settlement was induced when driving the 1st tunnel. The adjacent second drive might cause further settlement and the maximum accumulated surface settlement varied from 3.5 to 27.0 mm. Ground reached fully stable at

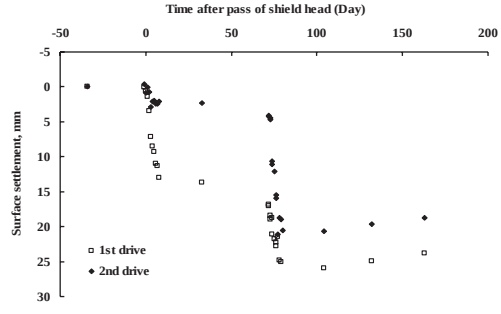

Figure 5. Time history of settlements measured at LUR15.

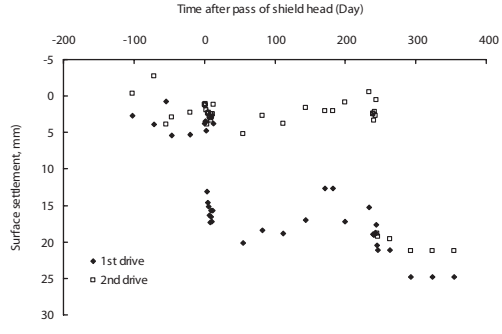

Figure 6. Time history of settlements measured at LUR16.

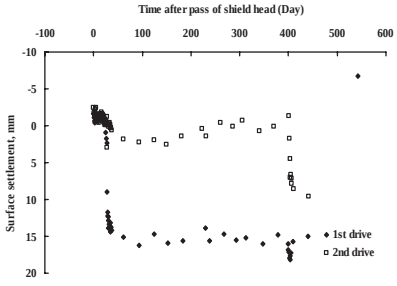

Figure 7. Time history of settlements measured at LUR17.

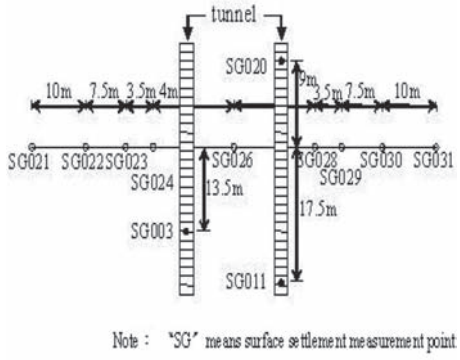

Figure 8. Survey array for surface settlement measurement.

approximately 20–40 days after passing of shield head and no consolidation settlement was seen. It is seen that the ground slightly heaves several days after passing of the shield at LUR16 and LUR17 and this might be connected with additional grouting from inside the segment.

In order to determine the transverse surface settlement trough induced by construction of the tunnel, several survey arrays on ground level were installed perpendicular to the tunnel, as shown in Figure 8. "SG" on Figure 8 means the locations of surface settlement points. In this paper, seven selected sections (LUR15-1 at LUR15; LUR16-1 at LUR16; LUR17-1, LUR17-2, LUR17-3, LUR17-4 and LUR17-5 at LUR15) were chosen for further analyses. Back analyses were undertaken based on the method suggested by Peck (1969) and O'Reily & New (1982) in order to obtain two parameters, width factor K and volume loss rate V.

Peck (1969) concluded that transverse surface settlement trough induced by a circular bored tunnel could be simulated by the use of a normal distribution curve. Therefore, the volume loss rate V is determined by

$$V = \frac{\delta_{\max} i}{0.126 R^2} \tag{1}$$

In which $\delta_{\max}$ is the maximum surface settlement and R is radius of tunnel. i is defined by

$$i = KZ_0 \tag{2}$$

Where Z_0 is the depth of tunnel.

To carry out the transverse surface settlement analysis, settlement trough induced by each tunnel has to be interpreted from field observations individually. Table 4 presents the interpreted δ_{max} from each section and it is in the range of 3.5 to 24.5 mm.

Tables 5 and 6 present the results by the use of empirical methods suggested by Peck (1969) and O'Reily & New (1982). It is seen that K is in the range of 0.35 to 0.51 for both of 1st drive and 2nd drive tunnel. V varies from 0.20% to 1.05% for the 1st drive tunnel and 0.18% to 1.27% for the 2nd drive tunnel. Both of them are close. Hsiung & Lu (2008)

Table 4. Interpreted δ_{max} at LUR15, LUR16 and LUR17.

Name of section	Up- track or Down- track tunnel	Number of drive at the section	δ_{max} (mm)
LUR15-1	Down- track	2nd	18.8
	Up- track	1st	13.7
LUR16-1	Up- track	1st	24.5
	Down- track	2nd	17.3
LUR17-1	Up- track	1st	16.2
	Down- track	2nd	15.0
LUR17-2	Up- track	1st	4.3
	Down- track	2nd	10.2
LUR17-3	Up- track	1st	3.5
	Down- track	2nd	7.8
LUR17-4	Up- track	1st	6.4
	Down- track	2nd	9.4
LUR17-5	Up- track	1st	6.8
	Down- track	2nd	3.5

Table 5. Interpreted K and V for 1st drive tunnel.

Name of section	K	V (%)
LUR15-1	0.35	0.82
LUR16-1	0.43	1.05
LUR17-1	0.47	0.72
LUR17-2	0.57	0.45
LUR17-3	0.46	0.20
LUR17-4	0.40	0.30
LUR17-5	0.51	0.43

Table 6. Interpreted K and V for 2nd drive tunnel.

Name of section	K	V (%)
LUR15-1	0.42	1.27
LUR16-1	0.46	1.21
LUR17-1	0.51	0.52
LUR17-2	0.46	0.42
LUR17-3	0.47	0.41
LUR17-4	0.56	0.46
LUR17-5	0.34	0.18

and Hsiung (2010) undertook similar works for other tunnels in Kaohsiung metro and it was found that V of CR3 is comparatively higher. The difference might be connected with ground treatment and performance of machine and workmanship.

4 NUMERICAL ANALYSIS

Considering the rate and capability of development of computer software, commercial computer software is commonly used nowadays to simulate surface settlement induced by shielding tunnels. Studies using numerical simulation for ground movement predictions have been delivered by Sagaseta (1987), Addenbrooke & Potts (1996), Inokuma & Fujimoto (1996), Melis *et al.* (2002), Cooper *et al.* (2002) and Pound & Beverage (2003). However, most of studies stated above aim to evaluate induced movements of tunnels in clay, not in sand. Therefore, a study is carried out to evaluate ground deformations induced by bored tunnels in sand using observed data of CR3 and computer software PLAXIS (PLAXIS BV, 2002) in this paper.

Similar to works completed using empirical methods, the same seven sections were selected for numerical analyses. A schematic drawing of the mesh is shown in Figure 9. For analyses of a shallow tunnel, Chen *et al.* (1997) suggested that the vertical boundary should be placed at least eight times the tunnel diameter from centre of tunnel so the vertical boundary of the mesh was set at 55.0–60.0 m away from centerline between two tunnels. In addition, the horizontal boundary was put at approximately 31.9–55.0 m below surface level based on deepest borehole.

An elastic- perfect plastic "Mohr- Coulomb (MC)"model was taken to simulate soil behaviour. Tables 7–9 present soil parameters selected for analyses. In these tables, ϕ is the effective friction angle of the soil, γ_t is the total unit weight and c' indicates the cohesion of the soil. For definition of parameters used, the physical characteristics of the soil (such as total unit weight) were measured in the laboratory, ϕ ıs given by CECI (2000) from interpretation of SPT- N value since results

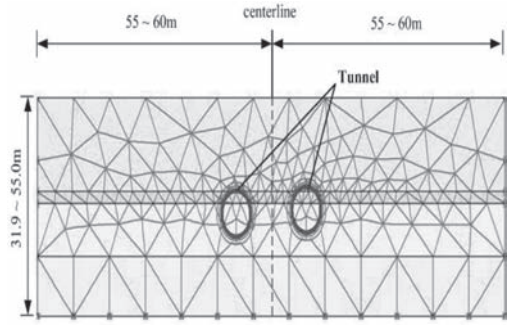

Figure 9. Schematic drawing of analytical mesh.

Table 7. Simplified soil parameters used for analyses at LUR15.

Soil type (from surface)	Thickness (m)	ϕ (degree)	γ_t (kN/m^3)	C′ (kPa)
Silty sand	12.9	30	20.0	0
Soft clay	1.7	32	29.1	0
Silty sand	11.4	33	19.8	0
Firm clay	29.0	0	20.2	160

Table 8. Simplified soil parameters used for analyses at LUR16.

Soil type (from surface)	Thickness (m)	ϕ (degree)	γ_t (kN/m^3)	C′ (kPa)
Silty sand	13.8	34	19.9	0
Soft clay	1.7	30	19.4	0
Silty sand	7.8	33	19.8	0
Silty sand	8.8	33	19.5	0

Table 9. Simplified soil parameters used for analyses at LUR17.

Soil type (from surface)	Thickness (m)	ϕ (degree)	γ_t (kN/m^3)	C′ (kPa)
Silty sand	8.3	36	19.7	0
Silty sand	13.6	36	19.8	0
Silty sand	10.0	31	19.6	0

from triaxial consolidated drained/undrained tests were not available. At last, based on previous studies in areas nearby (Hsiung & Hwang, 2009), the recommended elastic stiffness of soil (E) was interpreted.

After boring the tunnel, tunnel reinforcement concrete segments were used to construct tunnel lining and these segments were simulated by the use of plate elements.

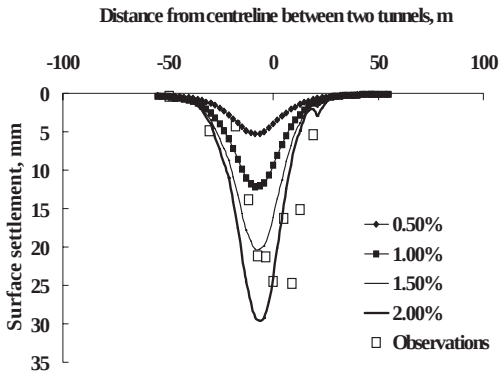

Figure 10. Comparison of results of numerical analysis and observations for up- track tunnel at LUR16.

Except soils and tunnel segments, the actual groundwater level seasonally varies from surface to 3.0 m below surface level so it was assumed to be on surface level in the analyses.

An additional parameter V_L has to be used for the simulation of tunnel-induced surface settlement using PLAXIS and it means the ratio of convergence area of tunnel to the whole area of tunnel. In this paper, V_L was assumed to be 0.5%, 1.0%, 1.5% and 2.0%.

Considering analytical results and observations taken from the site, it is seen that interpreted V_L at up- track tunnel of LUR16 is even greater than 1.5% accompanied with observations from the site, as indicated in Figure 10. V_L determined from rest of tunnels is smaller, in the range of 0.5% to 1.0%. Since up- track tunnel of LUR16 is a tunnel constructed by the 1st drive of machine, it is suspected that larger ground movement and V_L are thus induced.

5 CONCLUSIONS

In this paper, the ground movements induced by bored tunnels in sand were studied and it could be concluded at first that the maximum accumulated surface settlement reached up to 3.5 to 27.0 mm. Ground reached fully stable condition at approximately 20–40 days after passing of shield head and no consolidation settlement was seen.

Secondly, back analyses of transverse surface settlement trough by the use of some empirical methods were delivered in order to interpret two parameters, width parameter K and volume loss rate V. Based on results of this paper, K is in the range of 0.35 to 0.51 for both of 1st drive and 2nd drive tunnel. In contrast, V varies from 0.20% to 1.05% for the 1st drive tunnel and 0.18% to 1.27% for the 2nd drive tunnel. There is no large difference for K and V values determined from the 1st and 2nd drive tunnel. However, V is comparatively higher than other cases having similar conditions and this might be connected with ground treatment and performance of machine and workmanship.

Finally, numerical analyses were carried out and results were compared with observations in order to determine a parameter V_L. It was recommended that V_L in general is in the range of 0.5% to 1.0%.

ACKNOWLEDGEMENT

The author would like to thank for Kaohsiung metro Contract CR3 Pan Asia- Far East- Gesaki Joint Venture for providing field data needed for the paper. Assistances from Mr. Kuo, Edward and Mr. Lin, Jason of National Kaohsiung University of Applied Sciences, Kaohsiung, Taiwan for paper preparation are appreciated also.

REFERENCE

Addenbrooke, T.I., Potts, D.M. 1996, Twin tunnel construction: ground movements and lining behaviour, Proceedings, International Symposium Geotechnical Aspects of Underground Construction in Soft Ground, London, pp. 441–446.

Attewell, P.B. and Famer, I.W. 1974, Ground deformations resulting from shield tunneling in London clay, Canadian Geotechnical Journal, Vol. 11, pp. 380–395.

CECI, 2002, Structure protection evaluation report in Contract CR2 of Kaohsiung Metro Systems (in Chinese).

Chen, Y.C., Lai, J.H., Hwang, R.N. and Lin, G.J. 1997, Measured and analysis of the pore pressure changes induced by shield tunneling, Sino- Geotechnique, Vol. 60, pp. 97–107 (in Chinese).

Cooper, M.L., Chapman, D.N., Rogers, C.D.F., and Chan. A.H.C. 2002, Movements in the Piccadilly Line tunnels due to the Heathrow Express construction, Geotechnique, Vol. 52, No. 4, pp. 243–257.

Hsiung, B.C.B and Lu, K.L. 2008, Case record: A bored tunnel on Kaohsiung Rapid Transit System, Contract CR2, Journal of GeoEngineering, Vol. 3, No. 1, pp. 33–40.

Hsiung, B.C.B. and Hwang, R.N. 2009, Deflection path of deep excavations in soft ground, Geotechnical Engineering Journal, Southeast Asia Geotechnical Engineering Society, Special issue on deep excavations and tunnelling in soft ground, Volume 40, Issue 2, June, p. 81–90.

Hsiung, B.C.B. 2010, The case record of bored tunnels in sand based on the Kaohsiung mass rapid transit system project, Contract CO2, Journal of GeoEngineering (under review).

Inokuma, A. and Fujimoto, A. 1996, An improvement of FEM analysis in ground settlement prediction in shielding tunneling, Proceedings, International Symposium Geotechnical Aspects of Underground Construction in Soft Ground, London.

Mair, R.J., Gunn, M.J. and O'Reilly, M.P. 1981, Ground movements around shallow tunnels in soft clays, Proceedings, 10th International Conference on Soil and Foundation Engineering, pp. 323–328.

Melis, M., Medina, L. And Rodriguez, J.M. 2002, Prediction and analysis of subsidence induced by shield tunneling in the Madrid Metro extension, Canadian Geotechnical Journal, No. 39, pp. 1273–1287.

O'Reilly, M.P. and New, B.M. 1982, Settlements above tunnels in the U.K.- their magnitude and prediction, Tunneling '82, pp. 173–181.

Peck, R.B. 1969, Deep excavations and tunneling in soft ground, Proceedings, 7th International Conference on Soil Mechanics and Foundation Engineering, Mexico City, State-of-the-Art volume, pp. 225–290.

Pound, C. and Beveridge, J.P. 2003, Recent experiences of the prediction of tunneling induced ground movements, FLAC and Numerical Modeling in Geomechanics, edited by Brummers et al., pp. 161–167.

Rowe, R.K. and Kack, G.J. 1983, A theoretical examination of the settlements induced by tunneling: Four case histories, Canadian Geotechnical Journal, Vol. 20, pp. 299–314.

Sagaseta, C. 1987, Analysis of undrained soil deformation due to ground loss, Geotechnique, Vol. 37, No 3, pp. 301–323.

Sigl, O. and Atzl, G. 1999, Design of bored tunnel lining for Singapore MRT North East Line C706, Tunnelling and Underground Space Technology, Vol. 14, No. 4, pp. 481–490.

This page intentionally left blank

Geotechnical Aspects of Underground Construction in Soft Ground – Viggiani (ed)
© 2012 Taylor & Francis Group, London, ISBN 978-0-415-68367-8

The response of buildings to tunnelling: A case study

R.P. Farrell
Laing O'Rourke, Dartford, UK (formerly University of Cambridge)

R.J. Mair
Department of Engineering, University of Cambridge, UK

A. Sciotti, A. Pigorini & M. Ricci
Italferr, Italy

ABSTRACT: The response of buildings to tunnelling induced ground movements is an area of great importance for many urban tunnelling projects. This paper presents the response of two buildings to the construction of a 12 m diameter sprayed concrete lining (SCL) tunnel with face reinforcement, in Italy. Soil and structure displacements were monitored through extensive instrumentation. The settlement response of the two buildings was found to differ significantly, demonstrating both flexible and rigid response mechanisms. Comparison of the building settlement profiles with greenfield settlements enables the soil structure interaction to be quantified. Encouraging agreement between the modification to the greenfield settlement profile displayed by buildings and estimates made from existing predictive tools is observed. Potential issues for infrastructure connected to buildings, arising from the embedment of rigid buildings into the soil, are also highlighted.

1 INTRODUCTION

The estimation of the risk of damage to buildings typically involves assuming that the structure deforms according to the vertical and horizontal greenfield ground movements. While the greenfield ground movements are relatively well understood, due to extensive field measurements and centrifuge studies (Mair & Taylor, 1997), the presence of a structure alters these movements in what is termed the soil-structure interaction. The modification to these ground movements can result in smaller distortions and levels of damage to overlying structures than may have been predicted.

Potts & Addenbrooke (1997) conducted a parametric finite element analysis on the problem illustrated in Figure 1, to investigate the response of buildings to tunnelling. Two parameters were defined to explain the modification to the settlement and axial response of buildings; these were the relative bending stiffness (ρ^*) and the relative axial stiffness (α^*). ρ^* and α^* were later modified by Franzius et al (2006), the former to be dimensionless as well as the latter. Expressions for ρ^*_{mod} and α^*_{mod} are presented in Equations 1 and 2 respectively:

$$\rho^*_{mod} = \frac{EI}{E_s B^2 z_0 L} \tag{1}$$

$$\alpha^*_{mod} = \frac{EA}{E_s BL} \tag{2}$$

where EI and EA are the bending stiffness and the axial stiffness of the structure respectively. E_s is the secant stiffness of the soil at 0.01% axial strain, at a depth of $z = z_0/2$. B is the building width and L is the length parallel to the tunnel heading. Dimensions are illustrated in Figure 1.

Settlement distortions to buildings are typically measured in both hogging and sagging modes of deformation using the deflection ratio (Δ/L or DR, defined in Figure 1). Note that the hogging and sagging regions are partitioned by the point of inflexion (i) of the settlement trough. Potts and Addenbrooke (1997) quantified the modification to settlement distortions in terms of the ratio of the measured deflection ratio to the equivalent greenfield value, as presented in Equation 3. This ratio is given the term 'modification factor' (M^{DRhog} and M^{DRsag}).

$$M^{DR} = \frac{DR^{str}}{DR^{GF}} \tag{3}$$

where DR^{GF} is the greenfield deflection ratio and DR^{str} is the deflection ratio displayed by the building; both are defined separately in hogging and sagging.

Modification factors to the greenfield settlement distortions are highly dependent on ρ^*_{mod} (Franzius et al., 2006). Similarly, the modification to tensile and compressive horizontal strains, in the hogging and sagging regions respectively, are highly dependent on α^*_{mod} (Franzius et al., 2006).

This paper discusses mechanisms governing the soil-structure interaction based on observations of the response of two buildings to the construction of a 12 m diameter tunnel in Quaternary fluvial deposits. The tunnel was constructed with an open face using a temporary sprayed concrete lining, commonly known as the SCL(sprayed concrete lining) method. Reinforcement of the tunnel face and above the crown was also carried out prior to excavation and installation of the permanent concrete lining.

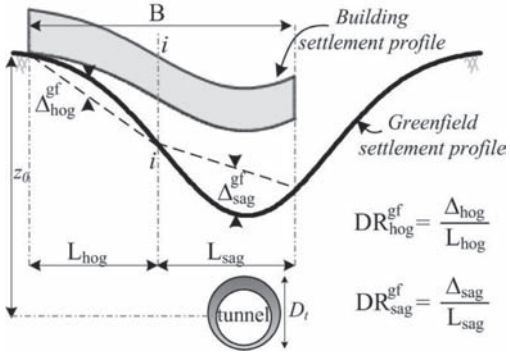

Figure 1. Influence of soil-structure interaction on settlement distortions.

2 PROJECT OVERVIEW

2.1 *Tunnelling works*

A 12 m diameter tunnel was constructed beneath two buildings using the SCL method and extensive protective measures. The tunnel axis is located at 20.95 mAD and ground level varies from 44.3 to 46.2 mAD giving a minimum depth of cover (C) of roughly 17.3 m. A plan of the site is presented in Figure 2. Construction was carried out from east to west in 6 m stages, with the exception of the first stage, which was 12 m in length.

2.2 *Buildings and instrumentation*

Two buildings overlie the excavation, both of which have been constructed with load bearing masonry walls on strip footings with reinforced concrete floor slabs. The building to the west of the site, building 107, is a 5 storey commercial structure. The building to the east of the site, building 106, is a two storey commercial structure. Both buildings lie transverse to the tunnel axis, and the eccentricity, defined as the distance from the midpoint of the building to the tunnel centreline, is roughly 8.7 m ($e/B = 0.23$). An aerial view of the site is presented in Figure 3.

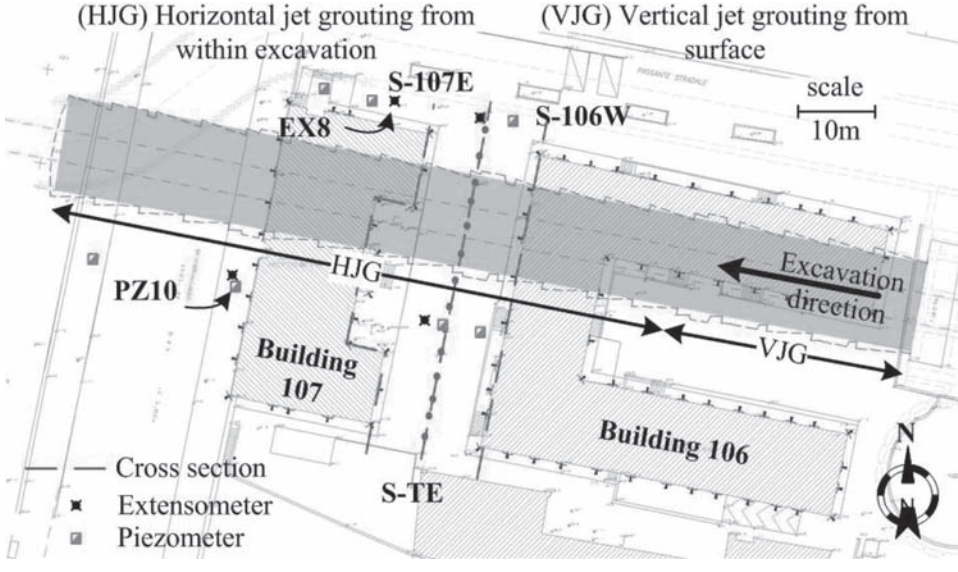

Figure 2. Site plan.

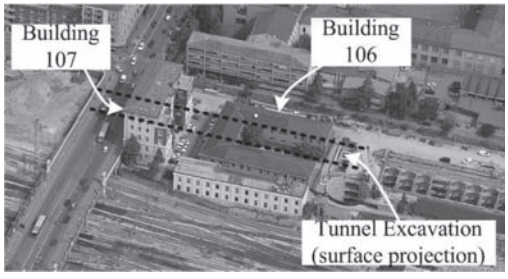

Figure 3. Aerial view of site.

Reflective prisms, placed at first floor level around the perimeter of the building facades, allowed building settlements to be measured. Ground settlements between the two buildings were measured using BRE type settlement studs. Subsurface settlements were obtained from extensometers at 1 m intervals to a depth of 40 m. Pore pressures were measured using Casagrande piezometers and piezocells, at locations indicated in Figure 2. Piezometer response zones are indicated in Figure 6.

2.3 *Protective measures*

Extensive protective measures were adopted to maintain stability of the tunnel excavation and to reduce ground movements. In total, over 2,000 vertical jet grout columns were installed over the initial 33 m of the excavation (see Figure 2), vertical jet grouting was carried out from the surface to form a reinforced soil/grout canopy around the tunnel. Subsequent further reinforcement of the soil directly above the crown and into the face was carried out prior to tunnelling using horizontal jet grouting, as indicated in Figure 4. Horizontal jet grouting was initially carried out from the excavation from which construction of the tunnel was started and was later conducted from within the tunnel. Grout was injected using a single fluid system at a pressure of 400 bar.

Subsequently, due to operational constraints, the ground ahead of the tunnel crown and ahead of the tunnel face was reinforced using 500 mm diameter horizontal columns, without vertical jet grouting, as illustrated in Figure 5. These columns were formed by horizontal jet grouting from within the tunnel and were 20 m in length into the face and 14 m in length above the crown. The minimum distance between the tunnel face and the end of these columns was 8 m and 14 m for the columns ahead of the tunnel crown and ahead of the face, respectively. Regions in which horizontal jet grouting alone was conducted from within the tunnel excavation are indicated in Figure 2.

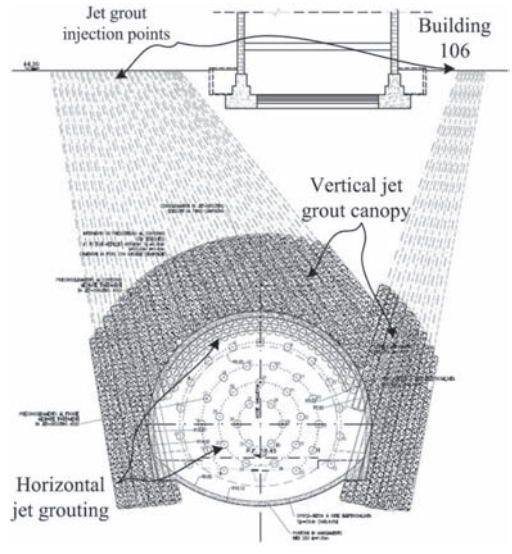

Figure 4. Vertical jet grouting.

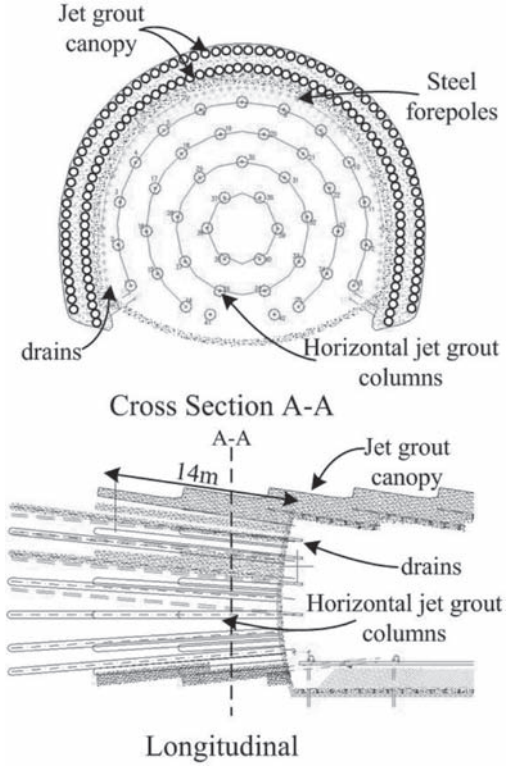

Figure 5. Horizontal jet grouting.

The number of horizontal jet grout columns installed into the tunnel face was reduced over the course of the project. Where this was the case, additional fibreglass face anchors and drains were installed into the face instead. Fibreglass face anchors were 20 m in length and were easily dug out during the excavation. The face anchors were later altered to allow for compensation grouting through *tubes á manchette* (TAM's).

2.4 *Ground conditions*

The site geology consists of lightly over-consolidated fluvial deposits from the Quaternary period. Ground conditions, illustrated in Figure 6, are highly stratified with layers of silty clays and clayey silts, termed the T1 formation, interbedded with lenses of sandy silt and silty sands, termed the T2 formation. These descriptions have been confirmed from particle size distribution tests. Casagrande plasticity charts classify the T1 formation as a medium to high plasticity clay.

The water table was found to lie 5 m below ground level (~39 mAD) although under-drainage from an underlying gravel layer means that conditions are not hydrostatic. The permeability of the T2 formation beneath the tunnel invert was estimated from in-situ permeability tests to lie between 10^{-6} to 10^{-7} m/s. The high fines content of the T1 formation (72–99%) indicates a very low permeability and this is consistent with the observed lack of water inflows at the tunnel face throughout construction.

Results from 6no. CPT tests indicate that the undrained shear strength (c_u) at the tunnel axis to be around 120 kPa. SPT and undrained unconsolidated (UU) triaxial tests indicate lower strengths of around 80 kPa, although this may be due to sample disturbance.

Correlations proposed by Duncan and Buchignani (1976) are used to estimate the undrained soil stiffness (E_u) from the undrained shear strength taking $E_u = 600\ c_u$, for $I_p = 30\%$. Based on these correlations E_u at a depth of $z = z_0/2$ is estimated to be about 90 MPa.

3 GREENFIELD RESPONSE

3.1 *Vertical settlement profile*

For the purpose of investigating greenfield ground movements, cross section S-TE (see Figure 2) is analysed as it is the least influenced by the adjacent buildings. This section is located on tarmac. Figure 7 shows the settlement profile along section S-TE at various stages during the excavation. Gaussian curves fitted to the settlement data are also illustrated. Settlements can be seen to increase as the tunnel face proceeds towards the cross section. As the tunnel face passes beyond section S-TE ($d > 0$) the contribution of further construction to the maximum settlement (196 mm) can be seen to be relatively small, indicating that most of the settlement occurs ahead of the tunnel face.

Gaussian curves fitted to the settlement data—obtained using a non linear least squares regression analysis—gave R^2 values in excess of 0.975 indicating a relatively good fit to the settlement data, as illustrated in Figure 7. This is consistent with other field observations (e.g. Peck, 1969; O'Reilly and New, 1982).

The trough width parameter, K, defined as $K = i/z_0$, was found to increase from 0.45 to 0.55 as the excavation passed beyond section S-TE ($d > 0$). This agrees well with a value of 0.5 often observed for tunnelling in clays (O'Reilly & New, 1982; Mair and Taylor, 1997). The increase in K with time may be attributed to consolidation of the T1 formation.

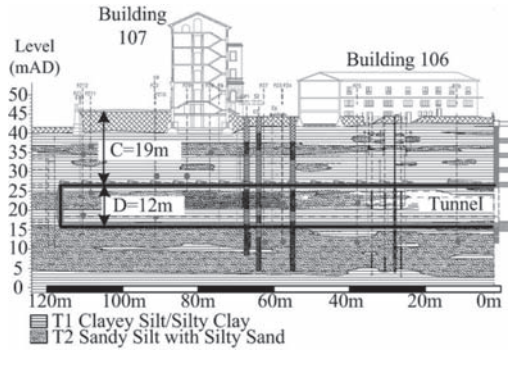

Figure 6. Elevation of site and stratigraphy.

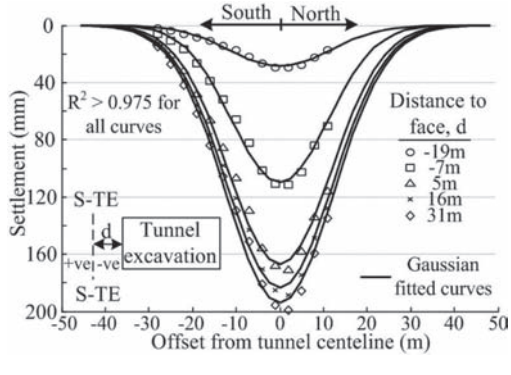

Figure 7. Greenfield surface settlement profile at section S-TE.

3.2 *Volume losses*

The variation in the normalised surface settlement trough volume (v_s) with distance from the excavation face (d), is illustrated in Figure 8 for the greenfield cross section S-TE, where v_s is the volume of the settlement trough expressed as a percentage of the cross sectional tunnel area.

It can be seen that when the excavation is directly beneath section S-TE ($d = 0$), v_s equals 3.2%. This is seen to increase to 5.1% when the excavation face is 28 m ($2.3D_t$) beyond S-TE. Assuming negligible contraction or dilation of the soil and ignoring consolidation effects, the volume loss resulting from the tunnel construction can be estimated as about 5%. Bearing in mind typical volume losses for open face tunnelling in stiff clay are in the range 1.0–2.0% (Mair & Taylor, 1997), this is a large volume loss for an urban tunnelling project.

4 CAUSES OF VOLUME LOSSES

Despite the extensive protective measures adopted during this project, large volume losses have been observed, particularly where horizontal jet grouting was carried out from within the tunnel excavation alone, as was the case beneath section S-TE.

Figure 9 shows the settlement response of the western façade of building 107 at the tunnel centreline (x = 0) against time during stages 12 and 13 of the excavation (indicated on inset). The change in pore pressure (ΔU) against time, measured just below the tunnel axis (28 mbgl) from piezometer PZ10, is also shown. Pore pressure changes relate to the measurements at the time of installation of the piezometer. This occurred when the perpendicular distance from the tunnel face to the piezometer was around 20 m. The jet grouting is observed to cause a large increase in pore pressure which is consistent with an undrained response of the ground, as highlighted by Mair and Taylor (1993).

Interestingly, a large increase in the settlement is observed during the jet grouting in stage 12 while the tunnel excavation itself causes only a slight increase in the settlement rate. Subsequent jet grouting during stage 13 is observed to coincide with further increasing settlements of building 107. Again the excavation of section 13 does not appear to have a significant impact on the rate of settlements. In total, up to 70% of the building settlements occurred during phases of horizontal jet grouting. Consolidation and the tunnel excavation itself also contributed to the settlements. In effect the protective measures adopted, although necessary for tunnel stability, contributed significantly to the observed settlements.

5 BUILDING DETAILS

The bending stiffness (EI) of buildings 106 and 107 has been estimated by summing the individual stiffness of each structural component, including walls, slabs and footings, as indicated by Equation 4. As the buildings are constructed from load bearing masonry it is assumed that shear transfer between the walls and slabs is negligible. Consequently, the

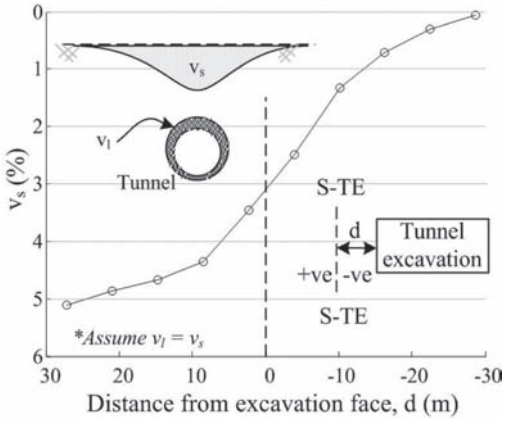

Figure 8. Variation in normalised trough volume at section S-TE against distance from the excavation face.

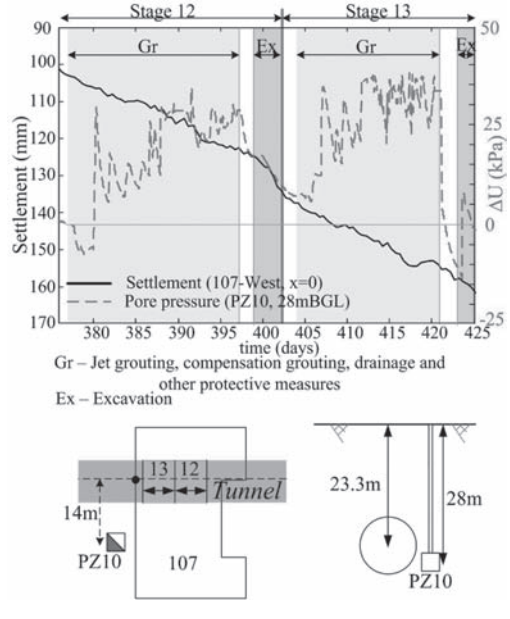

Figure 9. Variation in pore pressure and settlement during construction of stages 12 and 13.

Table 1. Reduction factors (α) for EI based on the percentage wall openings (from Melis and Ortiz, 2001).

Percentage openings	Reduction factor, α	
	$L < H$	$L > 2H$
0	1	1
0–15	0.7	0.9
15–25	0.4	0.6
25–40	0.1	0.15
>40	0	0

neutral axis of each component is taken about that of the individual member itself. The stiffness of all components are reduced to per metre length values in the plane of bending. E values for load bearing masonry and reinforced concrete are taken as 3×10^6 kN/m^2 and as 27×10^6 kN/m^2 respectively. Dimmock and Mair (2008) have demonstrated the importance of accounting for the effect of openings on the building stiffness. These effects are accounted for by applying the reduction factors in Table 1 (Melis and Ortiz, 2001) to the EI values for walls.

$$EI_{building} = \sum EI_{walls} + \sum EI_{slabs} + \sum EI_{footings} \qquad (4)$$

Using this approach, the bending stiffness for the western section of building 106 in the plane transverse to the tunnel heading was estimated as 4.9×10^6 kNm^2/m. EI for building 107 was estimated to be almost two orders of magnitude higher, at 2.3×10^8 kNm^2/m. For both buildings the internal and external walls were found to contribute to the majority of the bending stiffness. By summing the axial stiffness of each component in a similar manner to that outlined above, EA for buildings 106 and 107 has been estimated as 9.3×10^6 kN/m and 2.5×10^7 kN/m respectively.

The relative bending stiffness, ρ^*_{mod}, has been estimated (from Equation 1) for buildings 106 and 107 to be 6.7×10^{-2} and 3.5×10^0 respectively. Note that for each case, z_0 has been adjusted to account for the foundation depth and the soil stiffness (E_s) has been taken as 90 MPa. A value for L is not required as the building stiffness has been evaluated per metre length.

6 BUILDING RESPONSE

The following section outlines the response of buildings 106 and 107 to the tunnelling works. An assessment of current tools for quantifying the soil structure interaction, based on the observed settlement response, is also presented.

6.1 *Settlements*

Observed settlements of the western façade of building 106, the eastern and western façades of building 107 and of the greenfield section S-TE are illustrated in Figure 10. It is apparent that building 107 responded rigidly and simply tilted towards the tunnel centreline with no distinct hogging or sagging regions observable. This tilt response is observed to result in settlements at the northern edge (x = 10 m) that are significantly larger (265 mm) than the equivalent greenfield settlements (130 mm). Settlements of building 107 around the trough shoulders are also larger than the greenfield values indicating that the building embeds into the soil. This embedment is likely to have resulted from a redistribution of the building weight as the tunnel excavation progresses towards the building.

In contrast to building 107, the response of building 106 is seen to be relatively flexible with clear regions of hogging and sagging observable. Slight modification to the greenfield settlement profile can be seen, particularly towards the north of the building (x > 0 m) where, similar to building 107, settlements (200 mm) are larger than the equivalent greenfield values (130 mm). This embedment of the building is probably also due to the redistribution of the building weight as the excavation progresses beneath the building. However, as building 106 behaved relatively flexibly, this redistribution is not as significant as for building 107. The lower weight of building 106 relative to 107 may also explain why the embedment of building 106 is smaller.

6.2 *Quantifying soil structure interaction*

As discussed in Section 1, the deflection ratio is commonly used to quantify settlement distortions.

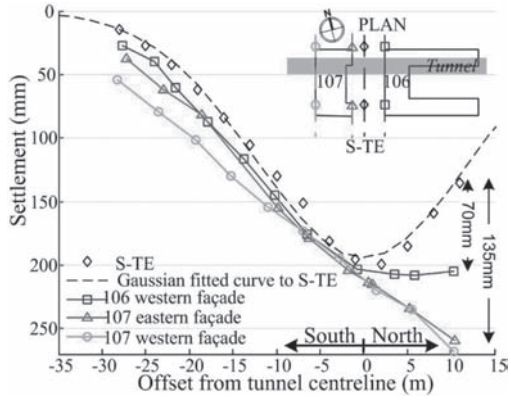

Figure 10. Building and greenfield settlement profiles.

This section investigates the modification to the settlement distortions that buildings 106 and 107 display in relation to their relative building stiffness. All deflection ratios have been estimated from the settlement profiles illustrated in Figure 10.

Values for DR^{GF} after construction are determined from cross section S-TE and have been calculated to be 0.13 and 0.27 in hogging and sagging respectively. Due to the rigid response of building 107, DR^{str} values and corresponding modification factors equal zero in both hogging and sagging. DR^{str} values for the western façade of buildings 106 are calculated as 0.06 and 0.19 in hogging and sagging respectively. Corresponding modification factors for building 106 are 0.46 and 0.7 respectively. Interestingly, these modification factors indicate that building 106 responded more flexibly in sagging than in hogging. This is contrary to evidence in the literature which suggests that buildings behave more flexibly in hogging due to the inability of masonry walls to sustain tensile strains near the roof and the reinforcement provided by the foundations in sagging (Burland & Wroth, 1974). For the case of building 106 however, the foundations are not reinforced which may explain this observation.

Upper bound design lines which relate M^{DR}, in both hogging and sagging, to the relative soil structure stiffness (ρ^*_{mod}) have been proposed by Franzius et al. (2006), as illustrated in Figures 11 and 12 respectively. Good agreement between the design lines, for e/B = 0.2, and the measured modification factors can be observed. The increased flexibility of building 106 in sagging is also predicted from the design lines, indicating that the building response to tunnelling is also a function of its location relative to the settlement trough.

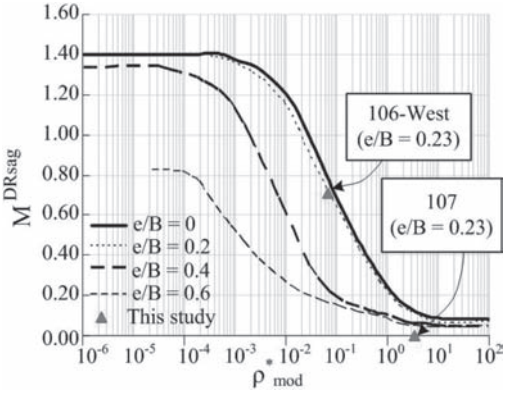

Figure 11. Modification factors versus relative building stiffness for buildings in sagging with design lines (from Franzius et al. 2006).

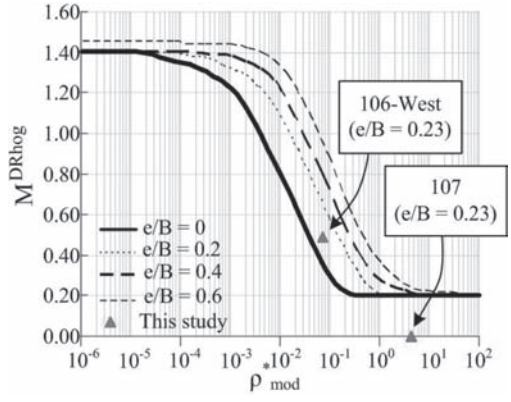

Figure 12. Modification factors versus relative building stiffness for buildings in hogging with design lines (from Franzius et al. 2006).

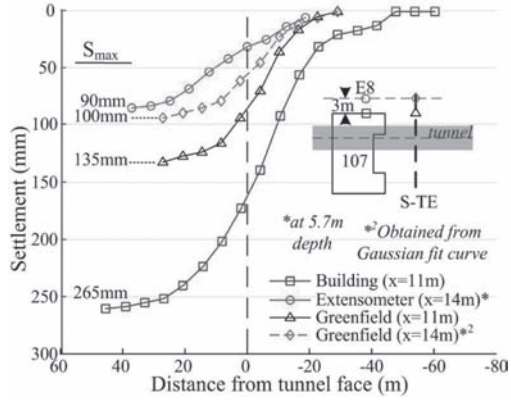

Figure 13. Comparison of settlement of building 107 with adjacent ground settlements.

7 SOIL RESPONSE

The redistribution of stress beneath rigidly responding buildings has been shown to cause buildings to embed into the soil, resulting in settlements that are significantly larger than greenfield settlements (see Figure 10). The response of the soil adjacent to the northern façade of building 107, measured at foundation level from an extensometer located 3 m away from the building facade, is illustrated in Figure 13. Building and greenfield settlements are also shown. Settlement measurement locations are indicated by the inset and on Figure 2.

Reasonable agreement between the maximum subsurface settlement at the extensometer and the maximum greenfield surface settlement at an offset from the tunnel centreline, x, of 14 m can be observed, indicating that the building did not

influence soil settlements at this location significantly. The maximum settlement of building 107 is, however, substantially larger (265 mm) than the greenfield settlement (130 mm), for reasons already outlined. It can therefore be deduced that close to greenfield settlements are restored within a relatively short distance from the building (less than 3 m).

This sharp settlement gradient between the building and the extensometer—roughly 175 mm over 3 m—could pose a significant risk to connecting services, particularly when the additional distortion arising from the building tilt is considered. Similar observations from centrifuge modelling have been made by Taylor and Grant (1998) and Farrell (2010). While finite element models have identified trends of building embedment into the soil, buildings have generally been modelled as weightless beams and so are perhaps missing an important aspect of the soil structure interaction.

8 BUILDING DAMAGE

Damage to building 106 was found to cause jamming of doors and windows and severe cracking. Re-pointing of brickwork was also required. Based on definitions of levels of damage proposed by Burland et al (1977), the level of damage to building 106 can be classified as category 3 or 'Moderate'.

Building 107, which responded rigidly and simply tilted, displayed only minor cracking of internal plastering resulting from shear strains. Cracking of the external façade was minimal and the maximum crack width was measured as 1.1 mm. No significant structural damage was observed. The level of damage can be classified as 'Very Slight to Slight'.

However, an assessment of the risk of damage to buildings 106 and 107 using simple beam theory, proposed by Burland & Wroth (1974), suggests that had the building been subjected to greenfield distortions, the damage in both cases would have been in the 'Severe to Very Severe' category. This is clearly a significant overestimation of the risk of damage to both buildings and highlights the importance of considering the soil-structure interaction when estimating potential tunnelling induced damage. It should be mentioned that the influence of horizontal distortions which contribute substantially to the estimated risk of damage, have not been addressed in this paper.

9 CONCLUSIONS

The settlement response of two buildings to the construction of a 12 m diameter SCL tunnel with face reinforcement, in Quaternary fluvial deposits has been presented. The following conclusions can be made:

1. Large volume losses, in the region of 5%, resulted in maximum greenfield settlements of 200 mm.
2. Assuming buildings to settle according to the greenfield settlement profile can provide highly conservative estimates of the risk of damage. The observed response of the two buildings analysed in this paper have demonstrated that these settlements can be modified to varying degrees, depending on the relative building stiffness. This agrees with observations from finite element analyses, centrifuge studies and previous case studies (Standing, 2001; Mair, 2001, Farrell, 2010).
3. The observed relationship between M^{DR} values and the relative building stiffness (ρ^*_{mod}) was found to agree well with relationships proposed by Franzius et al. (2006).
4. The redistribution of building weight due to tunnelling can significantly influence both the response of the building itself and of the subsoil. Rigid buildings tend to redistribute their weight and embed into the soil while flexible buildings simply deform according to the greenfield settlement profile.
5. Embedment of rigid buildings into the soil can result in settlements that are larger than the greenfield values. It has been shown however that the greenfield settlement profile is restored within a relatively short distance from the building. This response, coupled with the tilting response of the building, may have an adverse effect on connecting infrastructure such as services.

ACKNOWLEDGEMENTS

The authors would like to thank the EPSRC and the Cambridge European Trust for funding this research.

REFERENCES

Burland, J.B. & C.P. Wroth (1974). Settlement of buildings and associated damage. *Settlement of Structures*, Cambridge, pages 611–654. Pentech Press, London, Cambridge.

Burland, J.B., Broms, B.B. & De Mello, V.F.B. (1977). Behaviour of foundations and structures. *Proceedings of the 9th International Conference on Soil Mechanics and Foundations Engineering*, volume 2, pages 495–546. Tokyo.

Dimmock, P.S. & R.J. Mair (2008). Effect of building stiffness on tunnelling-induced ground movement. *Tunnelling and Underground Space Technology*, 23, no. 4, pages 438–450.

Duncan, M.J. & A.L. Buchignani (1976). *An engineering manual for settlement studies*. Berkley, University of California.

Farrell, R.P. (2010). Tunnelling in sands and the response of buildings. *PhD thesis*. University of Cambridge.

Franzius, J.N., Potts, D.M. & Burland, J.B. (2006). The response of surface structures to tunnel construction. *Proceedings of the Institution of Civil Engineering—Geotechnical Engineering*, 159, no. 1, pages 3–17.

Mair, R.J (2003). Research on tunnelling-induced ground movements and their effects on buildings—lessons from the Jubilee Line Extension. *Response of buildings to excavation induced ground movements. Proceedings of the international conference, Imperial College London, 17–18 July 2001*, pages 3–26, Jardine F.M. (eds), CIRIA SP199.

Mair, R.J., Taylor, R.N. & Burland, J.B. (1996). Prediction of ground movements and assessment of risk of building damage due to bored tunnelling. *Geotechnical Aspects of Underground Construction in soft ground*, pages 713–718. Balkema, London.

Mair, R.J. & Taylor, R.N. (1993). Prediction of clay behaviour around tunnels using plasticity solutions. In *Predictive Soil Mechanics—Proceedings of the Wroth Memorial Symposium*, pages 449–463. Thomas Telford, Oxford, UK.

Mair, R.J. & Taylor, R.N. (1997). Bored tunnelling in the urban environment. *Proc. 14th international conference on Soil Mechanics and Foundation engineering*, Vol. 4, pages 2353–2385. Hamburg: Balkema.

Mair, R.J. & Taylor, R.N. (2001). Settlement predictions for Neptune, Murdoch and Clegg Houses and adjacent masonry walls. *Building Response to tunnelling—Case studies from construction of the Jubilee Line Extension, London*. Vol. 1: Projects and Methods. In Burland J B, Standing J R, and Jardine F M, (eds) *CIRIA SP200*, pages 217–228.

Melis, M.J. & J.M. Rodriguez Otiz (2001). Consideration of the stiffness of buildings in the estimation of subsidence damage by EPB tunnelling in the Madrid subway. *International conference on the response of buildings to excavation induced ground movements*, pages 387–394. CIRIA SP 201.

O'Reilly, M.P. & New, B.M. (1982). Settlements above tunnels in the United Kingdom—their magnitude and prediction. In *Tunnelling '82*, pages 173–181. IMM, London.

Peck, R.B. 1969. Deep excavations and tunnelling in soft ground. *7th International Conference on Soil Mechanics and Foundation Engineering*, pages 225–290. Mexico City.

Potts. D.M. & Addenbrooke, T.I. (1997). A structures influence on tunnelling induced ground movements. *Proc. Inst. Civ. Engrs. Geotechnical Engineering*, Vol. 125, pages 109–125.

Standing, J.R. (2001). Paper on Elizabeth House. *Building response to tunnelling–case studies from the Jubilee Line extension. Vol. 2: Case studies, CIRIA SP2000,* pages 735–754. London: CIRIA and Thomas Telford.

Taylor, R.N & Grant R.J. (1998). Centrifuge modelling of the influence of surface structures on tunnelling induced ground movements. In Negro Jr & Ferreira (eds). *Tunnels and Metropolises,* pages 261–265. Rotterdam: Balkema.

This page intentionally left blank

Geotechnical Aspects of Underground Construction in Soft Ground – Viggiani (ed)
© 2012 Taylor & Francis Group, London, ISBN 978-0-415-68367-8

The response of piled buildings to deep excavations

M. Korff
Deltares, Delft, The Netherlands
Cambridge University, Cambridge, UK

R.J. Mair
Cambridge University, Cambridge, UK

A.F. van Tol
Deltares, Delft University of Technology, Delft, The Netherlands

F.J. Kaalberg
Witteveen + Bos, Amsterdam, The Netherlands

ABSTRACT: This paper explores the influence of the piled foundation on the building response to excavation-induced deformations. The influence of the type of foundation, the position of positive and negative skin friction zones, and the flexibility of the piles is evaluated with respect to both horizontal and vertical soil deformations. Case histories from the Netherlands are included from Amsterdam (North South Line) and Rotterdam (a building adjacent to the Willemspoortunnel). Most of the buildings are founded on timber piles ranging in length from 12–17 m. Conclusions are drawn about the interaction between the piled building and the soil deformation.

1 INTRODUCTION

The response of piled buildings near deep excavations is governed by the effect of the deep excavation on the soil, the interaction between the soil and the pile and the interaction between the pile and the building. In general, the unloading effect of the deep excavation will lead to deformations and changes in stresses behind the wall. Due to these excavation-induced changes, the nature of the interface between the pile and the soil changes.

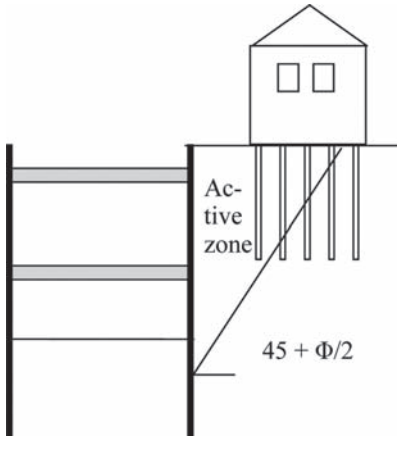

Figure 1. Active zone behind the wall.

This means that the soil around the piles is subject to vertical settlements and horizontal displacements, similar to the ground surface. In stress terms the vertical and horizontal stresses around the pile decrease. Outside the active zone (see Fig. 1 in the case of sandy soils) the stresses are assumed to remain approximately constant. For end bearing piles which settle less than the surrounding soil, negative skin friction may develop in the active zone.

Some general aspects of the behaviour of piled buildings due to horizontal and vertical ground deformations can be found in the literature, for example related to tunnelling-induced deformations.

2 PILE RESPONSE TO TUNNELLING

Jacobsz et al. (2005) describe the settlement predictions and measurements for the effects of tunnelling on piled structures for crossing of three bridges on the Channel Tunnel Rail Link project. Their cases indicate that a difference is found between end bearing and friction piles. End bearing piles were found to follow the green field settlement at the pile base for small volume losses. A reduction in the pile base capacity and subsequent load (due to stress relief

caused by tunnelling) will result in the mobilisation of additional positive shaft friction. The soil and pile will settle the same amount as the neutral level. Friction piles alter the green field subsurface displacements and can be assumed to follow more or less the surface settlements as a conservative approach.

Chen et al. (1999) present an analytical method to determine the influence of tunnelling on a single pile or a pile group, which led to the following conclusions related to pile response due to tunnelling:

- Lateral pile deflections are very similar to the soil deflections.
- The pile-head settlement is less than the maximum vertical soil movement.
- Tunnelling below the pile tip leads to smaller bending moments and deflection of the piles than for shallower tunnels. The behaviour of a pile is influenced significantly by whether the pile tip is above or below the tunnel axis.
- Disturbing effects on the piles should be added to the existing loading and stresses in the piles.

Kaalberg et al. (2005) describe the results of an extensive programme in the Netherlands to find the influence of tunnelling on piles, for which measurements and a field test were performed at the Second Heinenoordtunnel. They showed that deformation of piles due to shield tunnelling consists of settlement of the soil layer around the pile toe plus settlement caused by stress relief around the pile toe.

The following similarities and differences between the effects due to tunnelling and deep excavations have to be taking into account when assessing the response of piled buildings to deep excavations:

- The general movement of the pile towards the tunnel or excavation and downwards is similar.
- An approximately triangular zone of influence behind the wall or beside the tunnel is expected.
- Below the mid height of the tunnel, the ground settlements reverse to heave, which is probably not the case for deep excavations.
- The 3D effect for a passing TBM is not present at deep excavations, but other 3D effects such as those arising from corners of the excavation or the limited size of an adjacent building could still be significant.
- Installation effects of retaining walls present additional changes of stress in the case of deep excavations (unloading in case of excavation for diaphragm wall or bored piles, loading due to concrete pressures or densification due to vibrations).

3 PILE RESPONSE TO DEEP EXCAVATIONS

Very few papers describe the response of piled buildings due to excavations, with some exceptions shown here.

Davies & Henkel (1982) describe the construction of Chater Station in Hong Kong. It is made clear that piled foundations adjacent to deep excavations can experience serious settlements due to negative skin friction caused by the lowering of the water table. The settlement of the building behind the wall during excavation was about 1.5 times the maximum deflection of the wall.

Lee et al. (2007) describe the result of a building damage assessment for a multi-propped excavation in Singapore. At 6 m behind the diaphragm wall, a 12-storey building founded on 37 m long piles settled less than 10 mm (30% of the surface settlement) due to the presence of the pile foundation. Since the deep excavation was 15–17 m deep, this effect is probably caused by an increase in negative skin friction leading to some (minor) pile tip deformations.

Negative skin friction development is an important contributor to piled building response. The concept of pile response to negative skin friction is reported by Fellenius (2006) based on long term measurements of piles. He describes the concept of the pile moving with the neutral plane at the location of the force equilibrium between positive and negative skin friction.

Elshafie (2008) has studied the effect of deformations caused by deep excavations on buildings with experimental modelling. Elshafie concludes that buildings with individual spread footings experience large differential settlements, because footings outside the zone of influence do not follow the influenced part of the building. This results in significant distortions and tensile strains concentrating at the weak parts of the buildings.

Conclusions for piled buildings adjacent to deep excavations based on both tunnelling and deep excavation related papers are:

- Piled buildings tend to follow the soil deformations at the neutral plane, leading to a difference in response of end-bearing and friction piles; end bearing piles follow the soil deformations at pile tip level, friction piles as a conservative approach relate more to ground settlement at the surface.
- Piles might settle by an extra amount due to negative skin friction caused by soil settlement due to draw down of the ground water and/or diaphragm wall installation.
- Stress relief around the pile tip can lead to mobilisation of positive shaft friction.
- The presence of the piles influences the subsurface ground displacements.
- Piles are rather flexible in horizontal loading and tend to follow the soil deformations.
- Disturbing effects on the piles should be added to the existing loading and stresses in the piles.

Several questions remain specific for the response of piled buildings to deep excavations, such as the effect of installation of the retaining wall. It is also not clear to what extent the presence of the piles will strengthen and reinforce the soil. To address some of these questions three cases of piled buildings adjacent to deep excavations are presented in this paper.

4 CASE STUDY 'WITTE HUIS' ROTTERDAM

4.1 *Introduction and soil conditions*

In a case study by Brassinga & van Tol (1991) the response of a piled high rise building to a deep excavation in Rotterdam is presented. Additional information can be found Sarlemijn et al. (1993), who report on the construction of the Willemspoortunnel. The 'Witte Huis (white house)' 11-storey high rise building, dating from the end of the 19th century is located at 10 m distance from the 18 m deep excavation.

The soil conditions are rather typical for Rotterdam and the Western part of the Netherlands. The high phreatic level is found at 1–2 m below ground level (NAP +3.0 m). About 2–7 m of sand is found as the top layer, underlain by clay and peat layers to a depth of about 20 m (NAP –17 m). Below that the Pleistocene sand layer, commonly used as a foundation layer for piles, is found. Figure 2 shows a typical CPT.

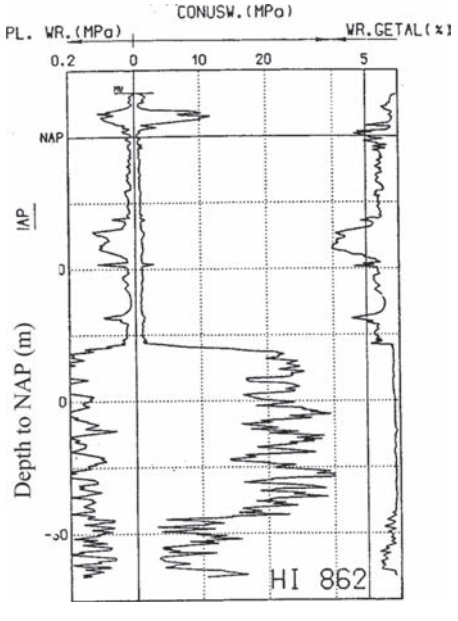

Figure 2. Typical CPT near Witte Huis.

4.2 *Details of the Witte Huis foundation*

The building is founded on wooden piles in the Pleistocene sand layer, with the diameter of the piles being about 250 mm. The design drawing shows in total about 750 piles for the foundation, placed in rows of 2–4 under the main walls, with a centre-to-centre spacing of 450–500 mm. Almost 9% of the total foundation area was filled with piles. During installation of the piles, a significant heave of the ground level of about 1.0 m was reported (Wikipedia).

Brassinga & van Tol (1991) report that the foundation had a low factor of safety before the deep excavation started. However, in the past no significant differential settlements of the Witte Huis had been noticed.

4.3 *Characteristics for tunnel construction*

Near the Witte Huis the cut-and-cover tunnel excavation crosses a canal from the harbour, leading to unequal loads on both sides of the excavation, see Figures 3 and 4.

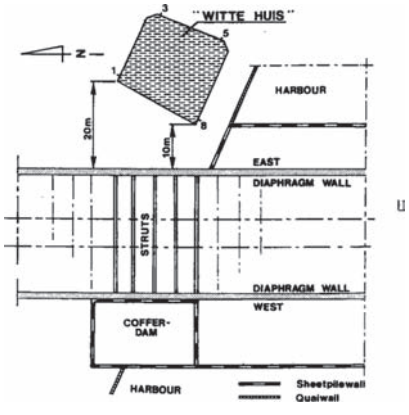

Figure 3. Plan view near the Witte Huis (Brassinga & van Tol, 1991).

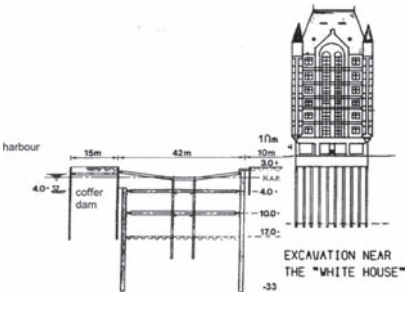

Figure 4. Excavation near the Witte Huis (Sarlemijn et al. 1993).

This caused horizontal displacements of the building. The excavation depth reached 20 m (NAP –17 m), just at the base of the pile foundation of the Witte Huis.

4.4 *Response of the 'Witte Huis'*

The building settled 6 mm during the D-wall construction, 12 mm in total including the first excavation phase (to NAP –4 m), and after extra prestressing of the struts an additional 5 mm (17 mm total) during the rest of the excavation. See Figure 5 for the development of the settlements of the four corners of the building with times.

Since no soil deformation was measured near the Witte Huis, it was calculated by FEM using the observed wall deflection as input. Vertical settlements of the building occur due to the combination of the ground deformation of the pile tip level and an increase in negative skin friction leading to increased pile tip load. Due to a low factor of safety of the original pile foundation, the neutral level is found clearly above the pile tip (where negative and positive skin friction meet). The measured deformation of the building is compared with the calculated green field settlement over the soil depth in Figure 6.

After the first excavation stage the settlement of the Witte Huis was 6 mm at measuring point 8 and 5 mm at point 1. Vertical soil displacements of this amount calculated using FEM were found at NAP –12 m at both distances from the wall for measuring points 8 and 5. This is assumed to be the level of the neutral point, which was used for prediction for the further excavation stages, see Figure 6.

It should be noted that the calculated ground settlement with depth in the soil turned out to be very sensitive to the assumed stiffness of the struts. This makes it difficult to define the neutral level accurately.

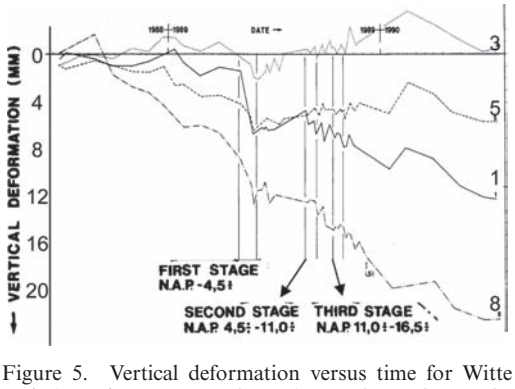

Figure 5. Vertical deformation versus time for Witte Huis (Brassinga & van Tol, 1991). Numbers relate to the settlement markers shown in Figure 3.

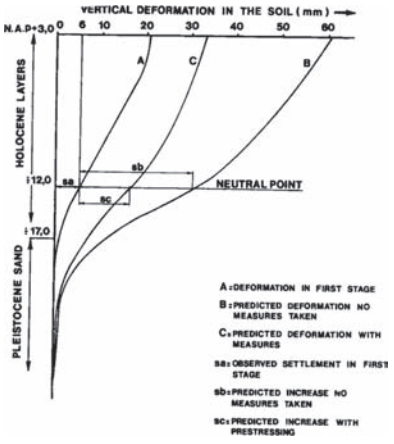

Figure 6. Calculated soil deformations with depth Witte Huis (Brassinga & van Tol, 1991).

Deformations after this stage (between August and November 1989) for the building were 10–12 mm. This value compares well with the calculated values based on the assessed neutral level, which was 11 mm.

4.5 *Analysis of the building response*

Figure 7 shows the settlement of the building at the points 1, 3, 5 and 8 at two stages: halfway down the full excavation depth and at full depth. Based on the regular distance between the lines of equal settlements, it is concluded that the building mostly tilted, without sagging or hogging deformation. The tilt is not exactly in the direction of the deep excavation due to the unequal loading on the harbour side, where the ground level is at NAP –4 m. Due to the extra struts in the second stage of the construction, the tilt at this stage is directed more towards the diaphragm wall.

The measured deflection is very small. No actual damage due to the deep excavation was observed in the building.

Horizontal deformation data are not available anymore, but deformations were larger than expected due to the soft response of the cofferdam on the opposite site of the excavation. No damage was observed as a consequence, so it is likely that the building moved rather uniformly. The maximum calculated horizontal deformation at point 8 was 20 mm after stage 1 and 25 mm at the end of construction. If the rear of the building did not move at all, the resulting horizontal strain would have been $7*10^{-4}$ and $1.2*10^{-3}$ respectively, based on the FEM results. The L/H ratio of the building is 20 m/43 m = 0.47. Combined with negligible deflection ratio this would have resulted in 'very

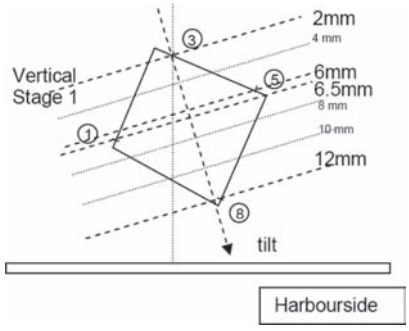

Figure 7a. Top view with vertical deformation of Witte Huis halfway excavation with direction of tilt indicated.

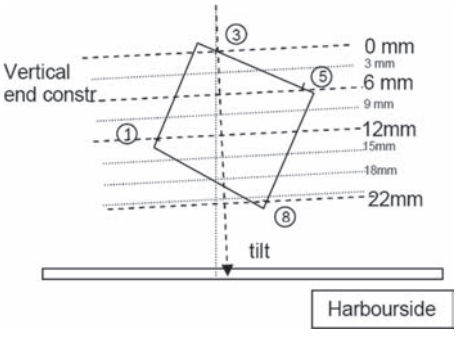

Figure 7b. Top view with vertical deformation of Witte Huis and at the end of construction (below) with direction of tilt indicated.

slight' or 'slight' damage respectively (Mair et al. (1996) and Cording et al. (2001)).

4.6 *Stiffness of the building*

The building shows no signs of bending in the structure at all. This means it is relatively stiff compared to the soil. The relative bending stiffness, defined as the stiffness of the building relative to the stiffness of the underlying ground, is compared using different methods. The concept of relative bending stiffness is described for tunnelling by Potts & Addenbrooke (1996) and Franzius et al. (2006). Since these require a depth of the tunnel, they can not easily be used for deep excavations. Recently, Goh (2010) and Goh & Mair (2011) adjusted the relative bending stiffness for deep excavations to:

$$\rho^*_{Goh} = EI/E_s L^3 \quad (1)$$

where EI is the building stiffness, E_s a representative soil stiffness and L the length in either hogging or sagging.

The bending stiffness of the building can be assessed by taking into account the base slab, the floors and/or the walls and the amount of interaction between them. In this case the masonry walls, with a width of over 1 m in the basement and about 0.4 m at the top of the building, provide most of the stiffness. Based on an average width of 0.6 m, a height to the roof of 30 m and 2 walls in the 20 m building, the EI of the building would be $810*10^6$ kN m^2/m. If a correction is made for the openings in the wall, based on Dimmock & Mair (2008), the actual stiffness would be about one order of a magnitude lower at about $80*10^6$ kN m^2/m. (If only the stiffness of the slab and the floors is considered, the EI would be about a thousand times smaller at $100*10^3$ kN m^2/m.)

The estimated relative bending stiffness values are calculated and presented in Table 1 and Figure 8.

Table 1. Calculated (relative) bending stiffness Witte Huis.

Description	Calculated value
Number of storey's	11 + basement, floor slabs 0.2 m
Width building	$20*\sqrt{2} = 28$ m
Length of building	$20*\sqrt{2} = 28$ m
Foundation	Slab cement/masonry 0.3 m + piles
E soil	$E_{0,01\%} = 3$ MPa soft clay
E slab and floors/wall	10 GPa/6 GPa
I building m^4/m:	
Slab + floors	$1\ m*0.3^3/12 + 11 \times 0.2^3/12 = 0.01$
2 walls 0.6 m	$2*b_{wall}/b_{building}*H_{wall}^3/12 = 2*0.6/20 *30^3/12 = 135$
$\rho^*_{Goh} = EI / E_s L^3$	
Slab + floors	$1.5*10^{-3}$
2 walls 0.6 m	1.2 (including reduction for openings)

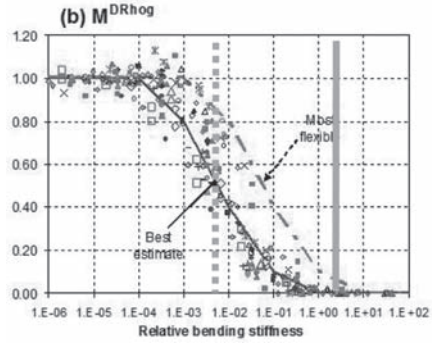

Figure 8. Design curves from Goh (2010), modified modification factor for hogging with results for Witte Huis in green lines (solid for walls, dashed for slab and floors).

In reality very little hogging deformation was observed, which is consistent with the estimated relative bending stiffness based on the walls (allowing for openings) leading to a modification factor of 0. The interaction based only on the individual slabs and floors underestimates the relative bending stiffness for this building. Methods for frame structures such as presented by Goh (2010) and Potts & Addenbrooke (1996) are not considered realistic for this type of masonry bearing structures.

4.7 *Conclusions*

The deep excavation mainly caused tilt in the Witte Huis. The amount of differential settlement (and associated deflection ratio) was negligible and so was the corresponding damage. The building shows no signs of bending in the structure at all. This means it is relatively very stiff compared to the soil, which is confirmed by Goh (2010) for the upper bound of EI values calculated for the building based on the stiffness of the walls (allowing for openings).

The effect of the pile foundation could only be evaluated using FEM results, because no deformations of the wall were measured locally. These calculations indicate that the piles follow the soil deformations at about NAP –12 m, while the bearing layer is situated at NAP –17 m. The neutral point is thus assumed at that level. The level of the neutral point did not change between stage 1 and the end of construction, based on the FEM analysis.

Horizontal deformations were larger than expected due to the translation of the whole excavation in the direction of the cofferdam.

5 CASE STUDY NORTH-SOUTH LINE

5.1 *Deep excavation and soil conditions*

The North-South Line in Amsterdam passes under the historical centre of the city in twin tunnels. Five underground stations are under construction. Ceintuurbaan Station is one of the deep stations in the historic city centre. The station is 220 m long, only 11 m wide and a maximum of 31 m deep. It is built by means of a top down construction, with 1.2 m thick diaphragm walls extending to a depth of NAP (Dutch reference level) –45 m. Details of the construction and soil profiles can be found in Kaalberg et al. (2005).

Fill and soft Holocene deposits are present to a level of about NAP –11.0 m (ground level around NAP +1.0 m). These are underlain by the 1st sand layer. The 2nd sand layer is found at about NAP –16 m, extending to NAP –25 m. Below the 2nd sand layer a stiff clay layer of around 15 m thickness (the Eem clay) is underlain by the 3rd sand layer.

A cross section of the excavation, soil profile and monitoring instruments is shown in Figure 9. The monitoring instruments include extensometers behind the wall, inclinometers in the soil and in the wall, manual levelling of the surface and the buildings and automatic monitoring of the buildings. Details about the construction and monitoring of Ceintuurbaan Station are given in De Nijs & Buykx (2010).

The buildings considered, see Figure 10, are built with masonry walls, wooden floors and timber pile foundations, reaching into the First Sand Layer at about 12 m below the surface level. Based on several pile load tests in the historic centre it is known that the wooden pile foundations have low factors of safety of around 1.0, if negative skin friction is assumed over all but the first sand layer.

Over a period of about 8 years, preparations for the construction and the subsequent excavation of the deep station to a depth of about 25 m took place, see Table 2.

The preliminary activities include raising the ground level (≈0.7 m), diaphragm wall construc-

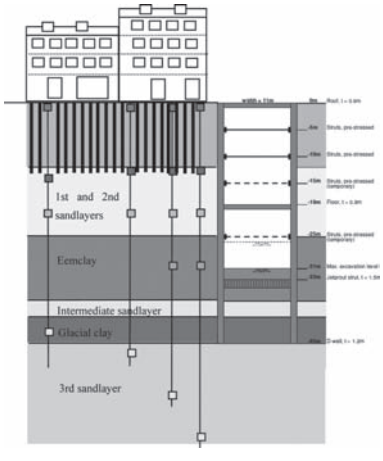

Figure 9. Cross section of Ceintuurbaan station with soil profile and extensometer locations.

Figure 10. Historic buildings at Ceintuurbaan station (dated 1880–1920).

Table 2. Construction activities and dates for Ceintuurbaan.

Construction activity	End date
Base monitoring start 2001	2003-11-01
Preliminary activities	2007-04-01
Excavation to NAP –6.2 m	2007-09-13
Excavation to NAP –15.3 m	2007-12-10
Excavation to NAP –19.4 m	2008-03-01
Excavation to NAP –24 m	2008-08-01
Excavation to NAP –25.6 m, floor construction, pumping test	2009-06-24

tion, jet grout strut installation, excavation to NAP –2 m, construction of the roof, refill on the roof and a pumping test for water tightness of the D-wall in the 1st and 2nd sand layers.

5.2 *Response during construction*

The building deformation and the soil deformations are compared in Figure 11 for the final date in Table 2.

Ground surface settlements measured by ground points (manual, 'GroundSurface') and extensometers (automatic, 'ExtensoSurface') are similar, but not exactly the same. This might be caused by the construction of the instruments itself, such as the size and weight of the base plates and some axial stiffness of the extensometer instruments in the borehole.

The settlement of the piled buildings (Leveling N and Leveling S) is larger than the ground settlement at pile tip level (ExtensoNAP –12 m), but smaller than the ground surface settlements. This indicates mobilization of positive shaft friction over parts of the 'soft layers'. The neutral level is found well above the foundation layer. For the buildings presented the neutral level is found at about NAP –4 m to NAP –9 m, assuming a linear variation of settlement between ground surface level and pile tip level.

Figure 12 shows the development of the building deformation during the construction stages presented in Table 2. The largest settlement of the buildings is due to the preliminary works and background settlement over 4 years between 2003 and 2007. During excavation of the station, the additional building deformations are less than 10 mm. Relative rotations are small (of the order of 10^{-4} or smaller).

Figure 13 shows the horizontal deformations of the building for both the North and South facades and for the MidHeight and Toplevel (respectively at heights of about 5–6 m and 12–13 m from street level). The amount of tilt can be derived from the difference between the prisms at these levels. This difference is 3–7 mm, leading to a tilt of 1: 1000 to 1:2000. Extrapolating this tilt results in a horizontal

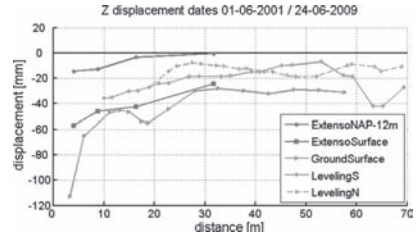

Figure 11. Building and soil deformations for North and South façade at Jan van der Heijdestraat East.

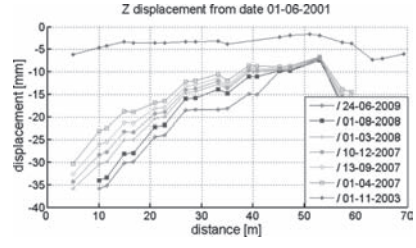

Figure 12. Building deformations for different construction stages for South façade with distance from the diaphragm wall perpendicular to the station.

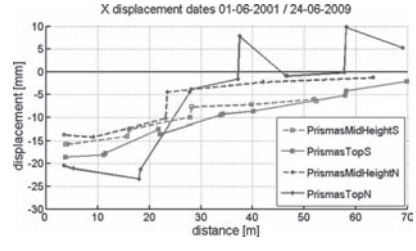

Figure 13. Horizontal building deformations (North and South facades) with distance from the diaphragm wall perpendicular to the station.

extension of 8–12 mm at street level. This is about 25–50% of the vertical settlement of the building at that point.

The horizontal extension diminishes to zero at a distance of about 28 m (north façade) and 52 m (south facades) respectively. The resulting average horizontal strain is of the order of 0.02–0.03%. Horizontal deformations of the soil have been measured automatically, but the results can not be presented here due to accuracy problems with the readings.

5.3 *Conclusions*

The settlement of the piled buildings is larger than the ground settlement at pile tip level, but smaller than the ground surface settlements. This indicates a neutral level above the pile tip level.

The largest settlement of the buildings is due to the preliminary works and background settlement over 4 years between 2003 and 2007. During excavation of the station, the additional building deformations are less than 10 mm. Horizontal building deformations at street level are about 25%–50% of the vertical building settlement.

6 CONCLUSIONS

Some of the conclusions for piled buildings adjacent to deep excavations set out at the start of this paper are confirmed by the case studies presented, as follows:

- Piled buildings tend to follow the soil deformations at the neutral level. Usually it is assumed that the building follows the ground deformation at the tip of the piles. The case studies presented in this paper confirm that it would be better to focus on the neutral level of the piles. For piles that are completely end-bearing in a competent stratum, this level would be the same as the tip level. For all other pile foundations the deformation should be calculated at a higher level, which depends on the equilibrium of the piles.
- Piles settle due to negative skin friction and soil settlement due to draw down of the ground water and/or diaphragm wall installation may cause a significant part (or even the main influence) of the overall construction effect.

Case studies with piled buildings adjacent to deep excavations are rare, especially information related to pile deformation and/or soil deformation at depth. The North-South Line project presents possibilities to investigate the vertical interaction, but unfortunately not the horizontal interaction, due to the limited availability of reliable inclinometer data.

ACKNOWLEDGEMENTS

This research is performed as part of a PhD study at Cambridge University, in cooperation with Deltares and the Dutch Centre for Underground Construction (COB). The authors would like to thank the Dienst NoordZuidlijn and the city of Amsterdam for the authorization to use and publish the monitoring data.

REFERENCES

Brassinga. H.E. & Tol. A.F. van. 1991. Deformation of a high-rise building adjacent to a strutted diaphragm wall. *11th European Conference of Soil Mechanics and Foundation Engineering* Hamburg. Balkema. pp. 787–790.

Cording, E.J., Long, J.H., Son, M., & Laefer, D. 2001. Modelling and analysis of excavation induced building distortion and damage using a strain-based damage criterion. *London Conference on Responses of Buildings to Excavation-Induced Ground Movements*, Imperial College, London.

Chen, L.T., Poulos, H.G., Loganathan, N. 1999. Pile responses caused by Tunneling. *Journal of Geotechnical en Geoenvironmental Engineering*; 207–215.

Davies, R.V. & Henkel, D. 1982. Geotechnical problems associated with the construction of Chater Station, Hong Kong. *The Arup Journal* 17(1): 4–10.

de Nijs. R.E.P. & Buykx. S.M. 2010. Instrumentation and Monitoring at Deep Excavation in Historic City of Amsterdam. Design and Performance Analysis of Monitoring System at Ceintuurbaan Station. *ITA 2010*. Vancouver.

Dimmock, P.S. & Mair, R.J. 2008. Effect of building stiffness on tunnelling-induced ground movement. *Tunnelling and Underground Space Technology* 23 (2008) 438–450.

Elshafie. M.Z.E.B. 2008. Effect of building stiffness on excavation induced displacements. *Geotechnical Department. Cambridge. University of Cambridge*. PhD.

Fellenius, B.H. 2006. Results from long-term measurement in piles of drag load and downdrag. *Canadian Geotechnical Journal*, Vol. 43, No. 4, pp. 409–430.

Franzius. J.N. & Potts. D.M. 2006. The response of surface structures to tunnel construction. Proc. Inst. Civ. Engrs Geotech. Eng. 1591: 3–17.

Goh. K.H. 2010. Response of ground and buildings to deep excavations and tunnelling. In preparation. Ph.D. thesis. University of Cambridge.

Goh. K.H. & Mair, R.J. 2011. Response of ground and buildings to deep excavations and tunnelling. *Geotechnical Aspects of Underground Construction in Soft Ground,* Roma.

Jacobsz, S.W.; Bowers, K.H.; Moss, N.A.; Zanardo, G. (2005). The effects of tunnelling on piled structures on the CTRL. *Geotechnical Aspects of Underground Construction in Soft Ground,* Amsterdam, Taylor&Francis Group, London.

Kaalberg, F.J., Teunissen, E.A.H., Van Tol, A.F., Bosch, J.W. 2005. Dutch research on the impact of shield tunnelling on pile foundations, *Proceedings of the XVI Intern. Conf. SMGE*, Osaka; 123–131.

Lee, S.J., Song, T.W., Lee, Y.S., Song Y.H. and Kim H.K. 2007. A case study of building damage risk assessment due to the multi-propped deep excavation in deep soft soil. *4th Int. Conf. Soft Soil Eng. Vancouver*, London, Taylor Francis.

Mair. R.J. & Taylor. R.N. 1996. Prediction of ground movements and assessment of risk of building damage due to bored tunnelling. *Int. Symp. Geotech. Aspects Underground Constr. Soft Ground.* London. April 1996. Rotterdam: Balkema.

Potts. D.M. & Addenbrooke T.I. 1996. The influence of an existing structure on the ground movements due to tunnelling. *Geotechnical Aspects of Underground Construction in Soft Ground.* London.

Sarlemijn, B.M.M., Bijkerk, J., Gerritsen, J., van Tol, A.F., Racke, H.K.; 1993; The Rotterdam Railway tunnel—desing, construction, organisation, *Options for Tunnelling 1993*, ed. H. Burger, p.p. 203–230.

Wikipedia. 2011. http://nl.wikipedia.org/wiki/Witte_Huis_(Rotterdam).

Geotechnical Aspects of Underground Construction in Soft Ground – Viggiani (ed)
© 2012 Taylor & Francis Group, London, ISBN 978-0-415-68367-8

The horizontal response of framed buildings on individual footings to excavation-induced movements

K.H. Goh
Land Transport Authority, Singapore (formerly from University of Cambridge)

R.J. Mair
University of Cambridge, UK

ABSTRACT: Deep excavations and tunnelling can cause ground movements that affect buildings within their influence zone. The current approach for building damage assessment is based on tensile strains estimated from the deflection ratio and the horizontal strains at the building foundation. This paper examines the significance of horizontal strains in buildings on individual footings. The first part of the paper presents a case study of a framed building in Singapore which was subjected to the effects of bored tunnelling, where significant horizontal strains were observed. The second part of the paper suggests a method to relate the horizontal strains induced in a building to the stiffness of the frame structure. Using a combination of simplified structural analysis and finite element models, design guidance is proposed to estimate excavation-induced horizontal strains in frame buildings on individual footings.

1 INTRODUCTION

Activities associated with deep excavations and tunnelling can cause ground movements that affect buildings within their zone of influence. The current approach for building damage assessment is based on the maximum tensile strains estimated from the deflection ratio and the horizontal strains at the foundation level (Mair et al, 1996). Recent studies have shown that the deflection ratio and the horizontal strains induced in the building can be reduced significantly if the building is on continuous footings (Mair, 2003). In contrast, the response of buildings on individual footings is not as well investigated.

Goh & Mair (2010) presented a case history on the settlement response of two reinforced concrete framed buildings above the bored tunnelling works for a section of the Singapore Circle Line, and showed that the inherent stiffness of framed buildings can influence their settlement response to tunnelling- and excavation-induced movements. To quantify this influence, a column stiffening factor was suggested to relate the bending stiffness of framed buildings to that of simple beams so that the deflection ratio of the building can be estimated from plots of building modification factors against relative bending stiffness (similar to the design curves proposed by Potts & Addenbrooke, 1997).

In terms of horizontal strains, Elshafie (2008) conducted centrifuge experiments of buildings behind a cantilever excavation in sand. He observed that a building modelled using a block sitting directly on the ground has horizontal strains which are low compared to the greenfield condition and depend on the stiffness of the building block. However, when the building is modelled using a block supported on two footings at each end, significant horizontal distortion to the building was observed especially at the block-footing interface.

In this paper, the behaviour of framed buildings on individual footings in terms of horizontal strains induced by tunnelling and deep excavations is examined. The first part of the paper presents a case study of two rows of shop houses that were subjected to the effects of bored tunnelling—this is the same site in Goh & Mair (2010) except that this paper focuses on the horizontal strain response in the framed buildings whilst the previous paper focused only on the settlement behaviour. For completeness, a summary of the settlement behaviour is also given in this paper.

In the second part of the paper, an attempt to quantify the influence of building stiffness is made for frame structures on individual footings. Using structural analysis, a method to estimate the horizontal stiffness of framed buildings is suggested. The finite element method was then used to study the response of frame structures adjacent to deep excavations, and to suggest design guidance for rigidly-connected frame buildings on individual footings.

2 CASE STUDY OF THE PASIR PANJANG SHOP HOUSES

2.1 *Site description*

A section of the tunnels in Contract 856 of the Singapore Circle Line was constructed using twin bored tunnelling drives, below two blocks of shop houses along the Pasir Panjang (PPJ) Road. These units were labelled as A29 and A32 during construction (Fig. 1). The bored tunnelling was done using earth-pressure balance shield machines, and was described by Venkta et al (2008). The first (inner) tunnel was constructed away from the shop houses, whilst the second (outer) tunnel was constructed directly below the shop houses. The depths to the tunnel axis ranged from 16 m to 19 m at this location.

Constructed together in the 1960s, the shop houses are two-storey, reinforced-concrete framed buildings. The columns are supported on shallow foundations of individual footings supported by timber bakau piles, whose lengths were estimated to be from 6 m to 9 m. At the ground floor, there are tie-beams connecting the main columns of the frame, but not all columns are connected in both directions. In particular, the columns along the five-foot-way—a common corridor which is about five foot wide—are unconnected at the ground floor level. The ground floor slab is of a non-suspended type. At the first floor, the beams connect all the columns together in a grid (including the columns above the five-foot-way) as they transfer the loads from the first floor slabs down to the foundation. The first floor slab is about 100 mm thick. As the roof is pitched and tiled, the roof beams are lightly loaded and mainly used for tying the main columns together. The building façade and internal walls are mostly formed using brick in-fills, whilst the walls at the rear of the shop houses are supported on strip footings and unconnected to the frame structure.

The geology at this location comprises the fluvial and marine deposits of the Kallang Formation over-lying the soils and rocks of the Jurong Formation whose members have varied sedimentary origins but commonly exhibiting evidence of metamorphism. Along this section of the bored tunnels, the ground typically consists of about 3 m of Fill underlain by a 9 m–14 m thick layer of Kallang Formation (of estua-rine, fluvial sand, fluvial clay and marine clay), and overlying the various weathering grades of Jurong Formation rocks. Locally, there is a thick layer of fluvial sand under shop house A32 and a substantial layer of compressible clays below the shop house A29. The bored tunnels were constructed in a mixed face condition of the Kallang Formation and the Ju-rong Formation, with a −2.5% gradient dip in the vertical alignment westwards along the tunnel drive. Figure 2 shows the cross sections of the shop houses and the soil profiles.

A detailed instrumentation programme was implemented during the bored tunnelling works. This included ground and building settlement markers, and tape extensometers measurements between columns. Whilst the settlement response

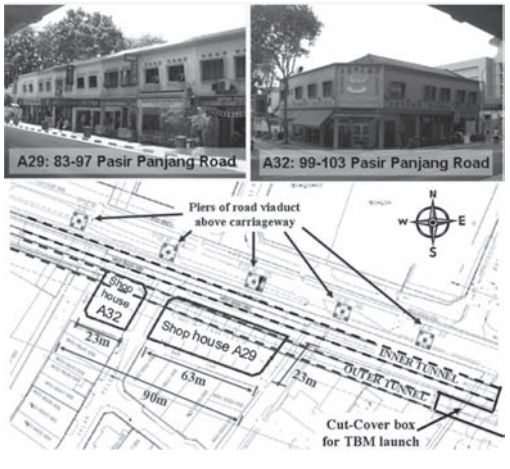

Figure 1. Location of the PPJ shop houses.

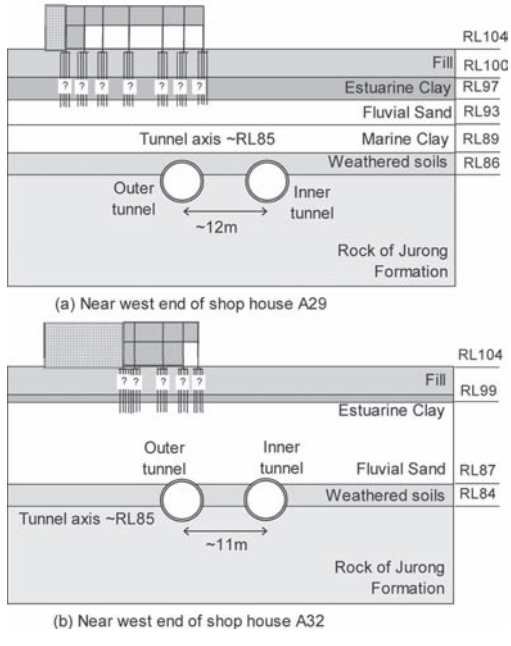

Figure 2. Cross-sections of the shop houses and soil profiles.

of the PPJ shop houses was described in Goh & Mair (2010), the monitoring results from the tapeextensometer are presented in this paper. Figure 3 shows the layout of the settlement monitoring and Figure 4 shows the tape extensometer measurements in the shop houses.

2.2 *Settlement behaviour*

As presented in Goh & Mair (2010), the settlement of the shop houses was monitored in four arrays. At the eastern-most section of shop house A29, there is a ground settlement array E14 (Fig. 3a) alongside to the building settlement array A29east (Fig. 3b). The ground and building settlement markers were observed to be settling several months after the passage of the first tunnel, and this makes it difficult to differentiate settlements due to the second tunnel drive alone. As such, the ground and building settlement troughs transverse to the direction of tunnel drive, were presented for the first tunnel drive and for both tunnels at the end of the second tunnel drive (see Fig. 5). At this location, the ground surface is settling in a hogging deformation for both tunnel drives. Furthermore, the hogging deformation of the building is very similar to the ground settlement—the building is deflecting very flexibly in this location.

That was the only location where ground settlement markers were monitored alongside building settlement markers. Elsewhere, a greenfield surface settlement trough can be assumed by using a theoretical Gaussian curve and considering the effects of the two tunnel drives separately. This is possible because the building settlement markers at these locations showed that the settlements due to the first tunnel drive had stabilised before the second tunnel drive started. The Gaussian settlement function is given by:

$$S_v = S_{max} e^{(-x^2/2i^2)} \quad (1)$$

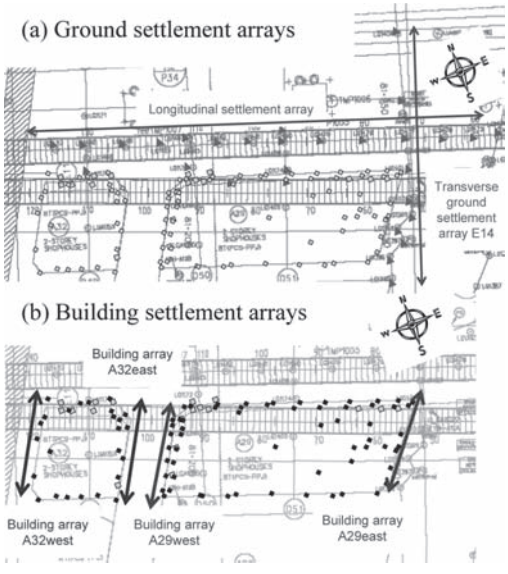

Figure 3. Layout of building and ground settlement markers.

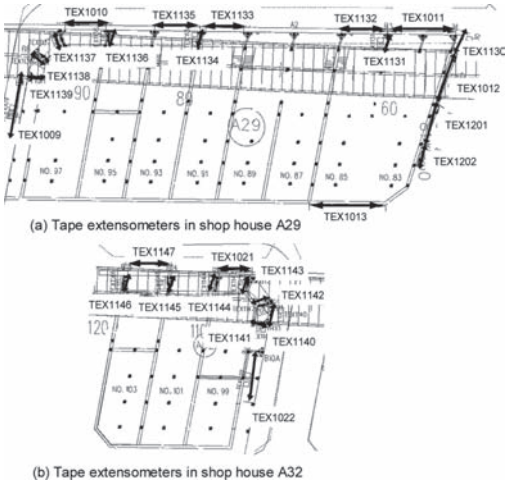

Figure 4. Layout of tape extensometer monitoring.

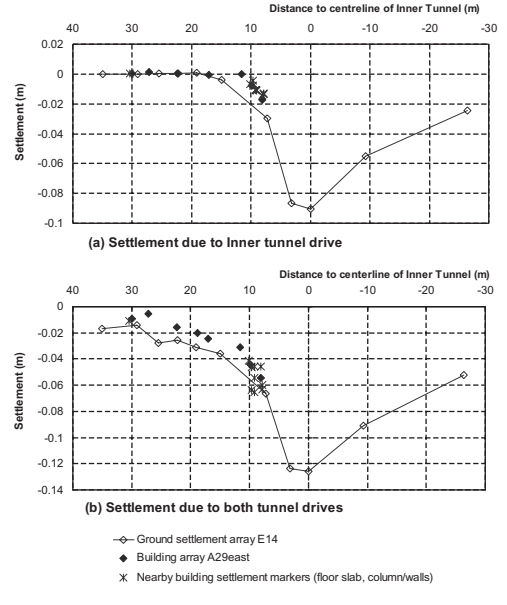

Figure 5. Ground and building settlement at east end of shop house A29.

where S_v is the ground surface settlement with a maximum value $S_{max} = V_L * \pi D^2/4/\sqrt{2\pi} * i$, V_L being the volume loss encountered during tunnelling, D is the tunnel diameter, and the width of the settlement trough, $i = K*z_0$ where K is a trough width parameter and z_0 is the depth to tunnel axis. The trough widths and volume losses can be varied to obtain various greenfield settlement curves.

Figure 6 shows the building settlement at the west end of shop house A29, and a particular greenfield settlement curve assumed using the Gaussian function in each tunnel drive. It was found that a narrow trough width for the Gaussian settlement curve provided a good match to the building settlement behaviour during the first (inner) tunnel drive. This could be due to the fluvial sand layer settling with a narrower trough, and also due to the effect of the bakau pile foundation causing the building to settle with the narrower subsurface settlement trough corresponding to a depth nearer to the pile toe level.

Nevertheless, using the same trough width parameter for the second tunnel drive, the building would be in the sagging deformation region directly above the tunnel and in the hogging deformation region further away from the tunnel. As seen in Figure 6(b), the settlement response of the building is semi-rigid during the second tunnel drive, compared to the greenfield settlement trough. This is in contrast to the flexible behaviour when the building is purely in the hogging deformation mode during the first tunnel drive.

Figure 7 shows the building settlement at both the east end and west end of shop house A32, and a specific greenfield settlement curve using the Gaussian function for each tunnel drive. The behaviour of shop house A32 is similar to that

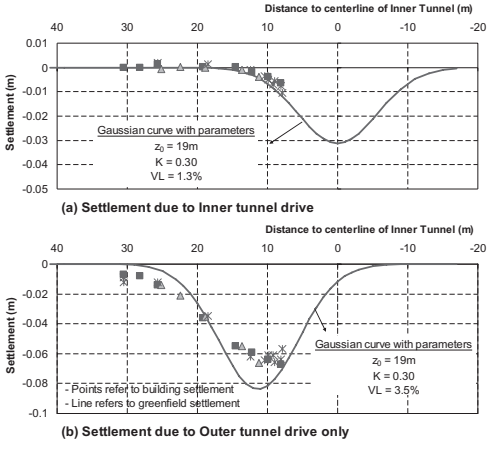

Figure 6. Greenfield and building settlement at west end of shop house A29.

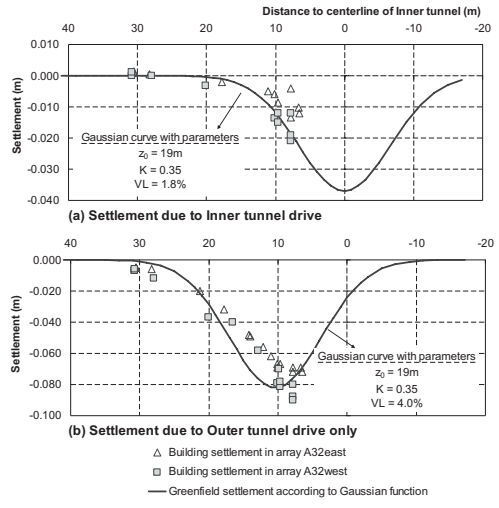

Figure 7. Greenfield and building settlement at both east end and west end of shop house A32.

of shop house A29. When the building is in a purely hogging deformation mode during the first (inner) tunnel drive, the building is very flexible and its settlement behaviour is similar to that of the greenfield. During the second (outer) tunnel drive, the building response is semi-rigid with a sagging deformation mode directly above the tunnel changing to a hogging deformation mode away from the tunnel. Venkta et al (2008) reported that the total building settlement of shop house A32 was up to 100 mm. Although cracks were found on the brick walls and column-brickwall interface, these were non-structural and did not affect the structural integrity of the building. Furthermore, Liew et al (2008) reported that the crack widths generally ranged from 0.3 mm to 1.5 mm, except for an isolated location registering 9.8 mm at an end wall. The crack widths are low as compared to the building settlements.

Using the PPJ shop houses, Goh & Mair (2010) illustrated that the inherent stiffness of framed buildings can influence their settlement response to tunnelling-induced movements. The horizontal response of the PPJ shop houses to tunnelling-induced movements will now be presented.

2.3 *Transverse horizontal strains*

Due to the orientation of the framed building with respect to the tunnelling drive, it is possible to categorise the tape extensometer measurements into those that are transverse to the tunnelling drive and those that are longitudinal. Moreover, the horizontal strains inferred from the tape extensometer measurements were low during the first tunnel

drive, and this is due to the inner tunnel being further away from the building. These became significant during the second tunnel drive when the outer tunnel is directly below the shop houses. As such, only the horizontal strains for the second tunnel drive will be presented.

Figure 8 plots the inferred horizontal strains that are transverse to the tunnelling drive in shop house A29, whilst Figure 9 plots the transverse horizontal strains in shop house A32. Some observations can be made by reviewing the character of the horizontal strains. Firstly, the horizontal strains are mostly compressive. This is due to the tape extensometer measurements made within the sagging trough of the settlement curve where the greenfield horizontal strains are compressive. The tape extensometer measurements showing tensile horizontal strains were further away from the tunnel centreline, and coinciding with the hogging zone of the surface settlement curve. Secondly, the highest horizontal strains occur between columns that are unconnected at the ground floor level and these are mostly along the five-foot-way area. The horizontal strains were as much as 0.24% in compression. This is in contrast to previous case histories of buildings on continuous footings where the horizontal strains in the building were low. Thirdly, for columns that are connected by ground beams, the horizontal strains are much lower (less than 0.04%).

Moreover, it was noted that some of the transverse horizontal strains were initially tensile in

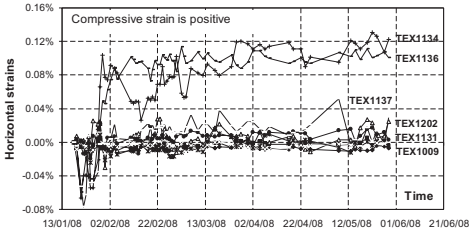

Figure 8. Development of transverse horizontal strains during second tunnel drive in shop house A29.

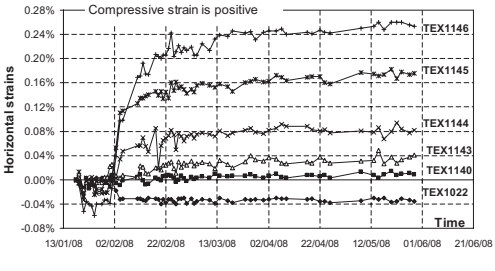

Figure 9. Development of transverse horizontal strains during second tunnel drive in shop house A32.

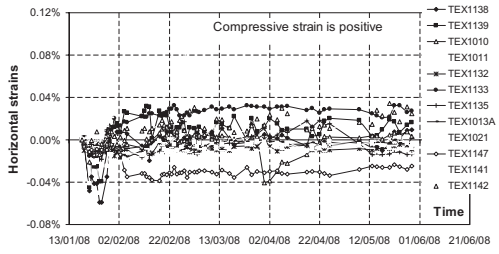

Figure 10. Development of longitudinal horizontal strains in shop house A29 and shop house A32.

nature (up to 0.08%) but changed to compressive at a later stage of the tunnelling. This is probably due to the effects of the advancing tunnelling trough in the longitudinal direction.

2.4 *Longitudinal horizontal strains*

Figure 10 plots the horizontal strains monitored from the tape extensometers that are parallel to the tunnelling direction. Longitudinal horizontal strains (of not more than 0.04%) are lower than the transverse strains, and the occurrence of the maximum strains coincided with the change in the maximum surface settlement monitored in the longitudinal direction. It may be inferred that when the volume loss remains reasonably constant for the tunnelling, the longitudinal horizontal strains would be low.

In general, horizontal strain was observed to be more critical in the transverse direction than the longitudinal direction. Moreover, there is some influence of ground beams on the horizontal strains induced in buildings on individual footings. This is investigated using the finite element method, as described in the following section.

3 NUMERICAL STUDY

3.1 *Finite element analysis*

To investigate the behaviour of framed buildings on individual footings, models of frame structures were simulated adjacent to a multi-propped excavation using the finite element method. Figure 11 shows the parameters of the frame and excavation model used in the study, where the frame columns are unconnected at the footing level. The excavation is 20 m deep and simulated in an undrained condition, whilst the frame is modelled as a weightless structure. The 20 m thick deposit of soft clay overlying a stiff clay stratum is modelled using the Modified Cam Clay, with soil parameters taken from recent soil investigation works in the Singapore Marine Clay.

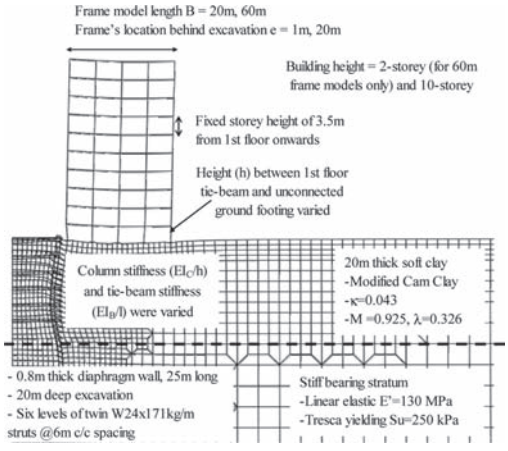

Figure 11. Excavation and soil parameters in model UD_A.

The weightless frame is modelled with various configurations of beam and column stiffness, and the height between the first floor beam and footing was varied. Table 1 shows the variation of frame models for the 20 m and 60 m long buildings, at 1 m and 20 m behind the excavation.

From the finite element models, it was observed that the horizontal displacement of the frame is different from that of the footings. From the first floor upwards, the frame appeared to be moving as a rigid body with very little horizontal strains—this is similar to structures on continuous footings. At the ground floor, there is relative horizontal displacement between the unconnected footings due to the induced movements. As the columns are restrained by the tie-beam at the first floor but much less constrained by the footings at the ground floor, the ground floor columns were showing various tilts in different bays of the frame structure. Due to the differential horizontal movements, substantial horizontal strains occurred between adjacent columns at the ground floor.

Potts & Addenbrooke (1997) proposed the modification factor approach to describe the building response to tunnelling in relation to the greenfield deformation. Specifically in this paper, to describe the average horizontal strains between the footings in terms of the corresponding horizontal strains in the greenfield, the modification factor $M^{\varepsilon h}$ is defined as

$$M^{\varepsilon h} = \frac{\varepsilon_{h,Bldg}}{\varepsilon_{h,GF}} \qquad (2)$$

where $\varepsilon_{h,Bldg}$ and $\varepsilon_{h,GF}$ refer to the maximum of the average horizontal strains between adjacent columns in the building and in the greenfield condition respectively.

Table 1. Configuration of frame structure models.

Beam type	1st floor tie-beam type	Column type
100 mm RC slab, with 5 m bay length	100 mm RC slab	150 × 150 mm RC column @5 m 150 mm RC wall
	300 × 300 mm RC beam@5 m	150 × 150 mm RC column @5 m 100 mm RC wall
	250 mm RC slab	150 × 150 mm RC column @5 m 150 mm RC wall
100 mm RC slab, with 10 m bay length	100 mm RC slab	150 × 150 mm RC column @5 m 150 mm RC wall
	250 mm RC slab	150 × 150 mm RC column @5 m
	300 × 300 mm RC beam@5 m	150 × 150 mm RC column @5 m

Furthermore, for buildings on continuous footings, Potts and Addenbrooke proposed a design chart to estimate the horizontal strain modification factor from the relative axial stiffness of the building. Following their definition, the relative axial stiffness (α^*) was calculated for each of the frame models in this study using Equation 3 below:

$$\alpha^* = \frac{EA}{E_S(B/2)} \qquad (3)$$

where the axial stiffness of the frame model (EA) is estimated by summing up the axial stiffness of all the individual beams, Es is a representative soil stiffness corresponding to mid-depth of the excavation, and B is the length of the building.

When the horizontal strain modification factors were plotted against the corresponding relative axial stiffness in each frame model, it was found that the modification factors varied from 0 to 1 irrespective of the relative axial stiffness (Fig. 12). Although the axial stiffness for a framed building may be sufficiently high that horizontal strains in the building are small, unconnected footings would still cause significant horizontal strains to the columns at ground floor level. Moreover, there is an important influence of the distance from the footings to the lowest tie beam, as shown in Figure 12. The relative axial stiffness alone does not describe the horizontal response of framed buildings on separate footings.

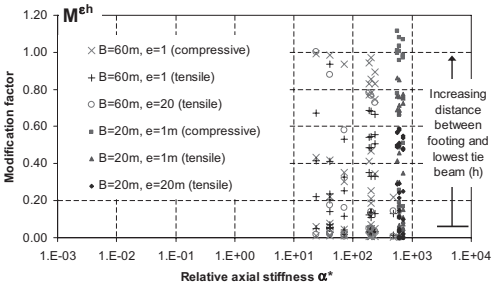

Figure 12. Horizontal strain modification factors for different relative axial stiffness values of frames on separate footings.

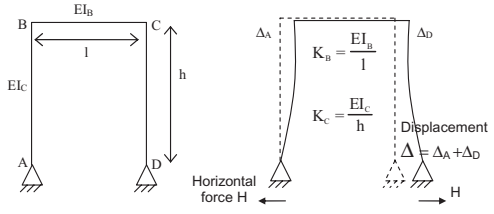

Figure 13. Schematic of simple portal frame.

3.2 *Frame stiffness factor*

A measure of horizontal stiffness for the frame action in the ground floor can be obtained, by determining the force needed to move the support of a structure frame horizontally by a unit displacement. As an approximation, a simple portal frame with a single bay was analysed. As the individual footing is deemed to be unable to offer much moment restraint to the column in the building frame, the simple portal frame was assumed to be pin-supported. A schematic of this portal frame is shown in Figure 13.

The derivation of the stiffness relationship was done by structural analysis using the slope deflection method (Goh, 2010). From the analysis, a frame stiffness factor (α_f) may be defined as

$$\alpha_f = \frac{H}{\Delta} = \frac{3K_B K_C}{h^2(2K_B + 3K_C)} \quad (4)$$

The frame stiffness factor has a dimension of kN/m per metre run, and is dependent on the column height at the ground floor (h), as well as the bending stiffness of the column ($K_C = EI_C/h$) and the first floor tie-beam ($K_B = EI_B/l$).

3.3 *Design guidance for the horizontal strain modification factor*

When the modification factors in Figure 12 are re-plotted against this frame stiffness factor, the results from the different frame-on-individual-footing models appear to fall within a reasonably close band as shown in Figure 14. It is possible to define an upper bound curve with all the modification factors obtained from the various finite element models of the frame structure. This upper bound may be used for design guidance to estimate the horizontal strains in buildings on individual footings or buildings on strip footings that are transverse to the deformation trough.

Using a simple portal frame to derive the frame stiffness factor is clearly a simplification of the actual problem. In reality, frame structures would have bays of different lengths as well as different numbers of upper storeys that would have an influence on the framing action at the ground floor. Furthermore, the portal frame in the structural analysis was pin-supported at its ends. In the actual building, the footing foundation would restrain the rotation of the ground floor columns, and the extent of this restraint—depending on the footing stiffness—would also have an influence on the frame stiffness.

To cope with the simplification, a reasonable upper bound can be derived from amongst all the frame models whose structural elements were varied. For example, additional finite element analyses were completed for frame models above various soil profiles of soft clay and firm soil (Goh, 2010). As shown in Figure 15, the modification factors when plotted against the frame stiffness factor fall within the upper bound curve suggested for design.

Design guidance defined using an upper bound curve will estimate a more flexible response of the horizontal strains for framed buildings on individual footings—this is conservative but acceptable. Nevertheless, it is noted that there is a considerable spread in the modification factors corresponding to each frame stiffness factor. This can be improved by using more rigorous structural frame analysis to define a more refined frame stiffness factor—but which may become complicated to compute.

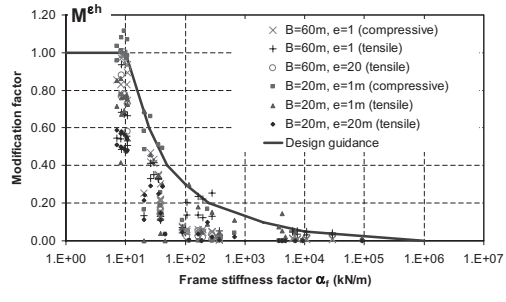

Figure 14. Horizontal strain modification factors for different frame stiffness factors.

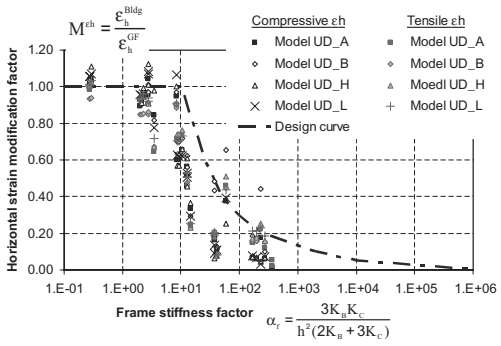

Figure 15. Modification factors for 60 m long, 2-storey frames at 1 m behind excavation in different soil profiles (refer to Goh, 2010 for details of models UD_A, UD_B, UD_H and UD_L).

4 CONCLUSIONS

The horizontal displacement behaviour of buildings on individual footings—including buildings on strip footings that are transverse to the induced ground displacement troughs—is investigated in this paper. While recent research has shown that the horizontal strains for most buildings on continuous footings is reduced significantly, the approach for buildings on individual footings has been to assume the horizontal strains in the greenfield condition.

The case study of the PPJ shop houses has shown the significance of horizontal strains in buildings on individual footings. More importantly, it has illustrated the difference in horizontal strains between columns that are connected by ground beams and columns that are unconnected at ground level but connected at first floor upwards. It was also observed that the transverse horizontal strains in the PPJ shop houses were more significant than the longitudinal horizontal strains.

To study the horizontal displacement behaviour of the rigidly-connected framed building on individual footings, models of frame structures with various configurations behind a multi-propped excavation were analysed using the finite element method. The greatest horizontal strains occur at the ground floor between the unconnected columns, and were observed to be related to the frame stiffness. Using structural analysis of a simple, pin-supported portal frame, a new frame stiffness factor has been defined to describe the horizontal stiffness of a frame structure. By plotting the horizontal strain modification factor against the frame stiffness factor, an upper bound curve has been developed to suggest guidance for estimating the maximum horizontal strains in rigidly-connected frame buildings on individual footings.

ACKNOWLEDGEMENTS

The authors would like to thank Mr. Rama Venkta for providing the information on the bored tunnelling works and the instrumentation monitoring at the PPJ shop houses. The first author would also like to thank the Land Transport Authority of Singapore for sponsoring his research study at the University of Cambridge.

REFERENCES

Elshafie, M.Z.E.B. 2008. *Effect of building stiffness on excavation induced displacements*. Ph.D. thesis, Cambridge University, UK.

Goh, K.H. 2010. Response of ground and buildings to deep excavations and tunnelling. Ph.D thesis, Cambridge University, UK.

Goh, K.H. & Mair, R.J. 2010. Settlement response of framed buildings to movements from tunnelling and deep excavations, *Proc. of World Urban Transit Conference, 20–22 Oct 2010, Singapore*.

Liew, Y.K., Veluvolu, H., Kho, C.M. & Sigl, O. 2008. Risk assessment for earth pressure balancing bored tunnelling under shophouses along Pasir Panjang Road, *Proc. of International Conference on Deep Excavations, 10–12 Nov 2008, Singapore*.

Mair, R.J. 2003. Keynote lecture: Research on tunnelling-induced ground movements and their effects on buildings—lessons from the Jubilee Line Extension. *In F.M. Jardine (ed.), Response of buildings to excavation induced ground movements, Proc. intern. conf., London, 17–18 July 2001*: 3–26. London: CIRIA.

Mair, R.J., Taylor, R.N. & Burland, J.B. 1996. Prediction of ground movements and assessment of risk of building damage due to bored tunnelling, In R.J. Mair and R.N. Taylor (eds.), *Proc. intern. symp. on Geotechnical Aspects of Underground Construction in Soft Ground, London, 15–17 April 1996*: 713–718. Rotterdam: Balkema.

Potts, D.M. & Addenbrooke, T.I. 1997. A structures influence on tunnelling-induced ground movements. *Proc. Institution of the Civil Engineers, Geotechnical Engineering* 125(2): 109–125.

Venkta, R., Hoblyn, S., Mahatma, S. & Lim, H.C. 2008. EPB tunnelling under 2-storey shophouses in mixed face conditions, *Proc. of International Conference on Deep Excavations, 10–12 Nov 2008, Singapore*.

Geotechnical Aspects of Underground Construction in Soft Ground – Viggiani (ed)
© 2012 Taylor & Francis Group, London, ISBN 978-0-415-68367-8

The response of buildings to movements induced by deep excavations

K.H. Goh
Land Transport Authority, Singapore (formerly from University of Cambridge)

R.J. Mair
University of Cambridge, UK

ABSTRACT: Deep excavations and tunnelling can cause ground movements that affect buildings within their influence zone. The current approach for building damage assessment is based on tensile strains estimated from the deflection ratio and the horizontal strains at the building foundation. For tunnelling-induced deformations, Potts & Addenbrooke (1997) suggested a method to estimate the building response from greenfield conditions using the relative building stiffness. However, there is not much guidance for building response to excavation-induced movements. This paper presents a numerical study on the response of buildings to movements caused by deep excavations in soft clays, and proposes design guidance to estimate the deflection ratio and the horizontal strains of the building from the building stiffness.

1 INTRODUCTION

Activities associated with deep excavations and tunnelling can cause ground movements that affect buildings within their zone of influence. The current approach for building damage assessment is based on the maximum tensile strains estimated from the deflection ratio and the horizontal strains at the foundation level (Mair et al, 1996). Potts & Addenbrooke (1997) proposed the modification factor and relative stiffness approach to incorporate the influence of building stiffness for predicting building response to tunnelling-induced movements. This has since been updated by Franzius et al (2006). However, there is not much guidance on how building stiffness can be included to estimate building response to movements induced by deep excavations.

A preliminary numerical study on the influence of building stiffness and the building's deformation response to excavation-induced movements was presented by Goh & Mair (2008). Using the Plaxis finite element software, a total stress analysis was carried out for a 20 m deep excavation in soft clay where the building was modelled as an elastic beam with axial and bending stiffness properties. In general, a building with low axial and bending stiffness is flexible and would follow the ground deformations in the greenfield condition, while a stiff building with high axial and bending stiffness would tend to rotate and move as a rigid body. Specifically, the preliminary study showed that the modification factor for horizontal strains induced in the building depends just on its axial stiffness, whilst the modification factor for deflection ratio depends on both the axial and bending stiffness. However, when the axial stiffness is high enough and in the range corresponding to actual buildings, the modification factor for deflection ratio depends mainly on the bending stiffness of the building.

A detailed numerical study was since completed to investigate the response of buildings to movements caused by deep excavations in soft clays, using the finite element software Abaqus. In this investigation, more parameters related to the building and excavation characteristics were varied, including the building length, building location, excavation depth, consolidation effects, etc. This paper presents the findings of the detailed study, and the development of design guidance to include building stiffness when estimating the building's deflection ratio and horizontal strains from the greenfield response.

2 INFLUENCE OF STRUCTURAL STIFFNESS AND GEOMETRY

2.1 *Finite element modelling*

To understand building behaviour under the influence of excavation-induced movements, a 2D finite element study was conducted using Abaqus. The building was modelled as a weightless, elastic beam with axial and bending stiffness properties—this is

similar to the elastic beam simplification used in Potts & Addenbrooke's study of buildings under the influence of tunnelling-induced deformations. The excavation is done in soft clay, undrained, and is supported using a multi-propped earth retaining wall with adequate toe embedment into stiff clay. A soil-structure interface was modelled between the soil and the building and between the soil and the wall, so that slipping will occur when the shear stress at the interface exceeds a maximum value of 20 kPa. Figure 1 shows the key elements and parameters in the base model of the analysis, where a 20 m deep excavation was simulated in a 20 m thick deposit of soft clay. The building's length and its location behind the excavation were varied—together with various combinations of axial and bending stiffness—to investigate the influence of structural stiffness and geometry on the building response to excavation-induced deformations.

Following the findings from the preliminary study (Goh & Mair, 2008), the stiffness values of the elastic beam were chosen to reflect realistic combinations in actual buildings so that the axial stiffness is not too low in comparison to the bending stiffness. Table 1 shows the combinations of bending and axial stiffness generally assumed in the study, although additional stiffness combinations were sometimes included to refine the results.

Furthermore, Potts & Addenbrooke's approach of using the building modification factors to describe the deformation behaviour in buildings is also used in this paper. Essentially, the modification factors of deflection ratio (M^{DRsag}; M^{DRhog}) and the modification factors of horizontal strains ($M^{\varepsilon hc}$; $M^{\varepsilon ht}$) are defined as follow:-

$$M^{DRsag} = \frac{(\Delta/L)_{sag,Bldg}}{(\Delta/L)_{sag,GF}} \quad (1)$$

$$M^{DRhog} = \frac{(\Delta/L)_{hog,Bldg}}{(\Delta/L)_{hog,GF}} \quad (2)$$

$$M^{\varepsilon hc} = \frac{\varepsilon_{hc,Bldg}}{\varepsilon_{hc,GF}} \quad (3)$$

$$M^{\varepsilon ht} = \frac{\varepsilon_{ht,Bldg}}{\varepsilon_{ht,GF}} \quad (4)$$

where $(\Delta/L)_{sag}$ and $(\Delta/L)_{hog}$ are the sagging and hogging deflection ratios, ε_{hc} and ε_{ht} are the maximum compressive and tensile horizontal strains, and the subscripts refer to the Building (Bldg) and the GreenField condition (GF).

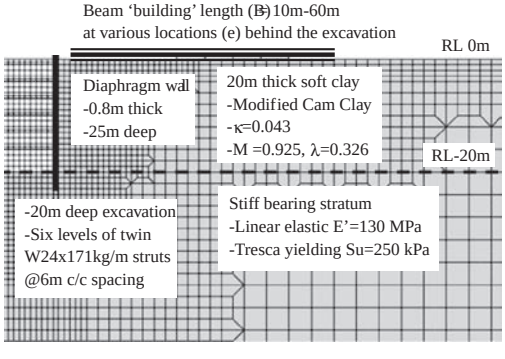

Figure 1. Key elements and parameters in excavation model.

Table 1. Bending stiffness and axial stiffness of building model.

EI (kNm²/m)	10^3	10^4	10^5	10^6	10^7	10^8	10^9
EA (kN/m)	10^3	10^4	10^5	10^6	10^7	10^8	10^9

2.2 *Effect of building length*

The length of a building is an important parameter affecting its stiffness. This is analogous to beam behaviour where a longer beam would deflect more than a shorter beam under the same loading and support conditions. To investigate this, the length of a building—the nearest edge of which is 1 m behind the excavation—was varied from 10 m to 60 m in the finite element analysis. In the base excavation model (model UD_A), the sagging trough is 20 m long—this was found by interrogating for the point of inflexion on the surface settlement curve. Thus, the 10 m and 20 m long buildings would be completely within the sagging zone of the greenfield settlement trough, whilst the 40 m and 60 m long buildings would show both sagging and hogging deformation.

Figure 2 plots the modification factors for deflection ratio and horizontal strain against the bending stiffness and axial stiffness, for various building lengths. In terms of deflection ratio, it is observed that a shorter building would have a lower modification factor compared to a longer building with the same bending stiffness. In terms of horizontal strains, a shorter building also appears to have a lower modification factor than a longer building, when the axial stiffness is low.

Moreover, it is noted that the horizontal strain modification factor is close to zero when the axial stiffness is sufficiently high, i.e. when axial stiffness is of the order 10^5 kN/m. This threshold is below the axial stiffness of actual buildings. For example, a 100 mm thick reinforced concrete slab will have an axial stiffness that is in the order of 10^6 kN/m.

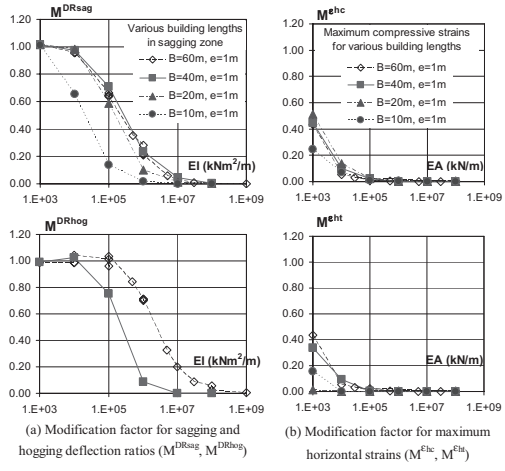

(a) Modification factor for sagging and hogging deflection ratios (M^{DRsag}, M^{DRhog})

(b) Modification factor for maximum horizontal strains ($M^{\varepsilon hc}$, $M^{\varepsilon ht}$)

Figure 2. Modification factors for various building lengths (nearest edge at 1 m behind excavation).

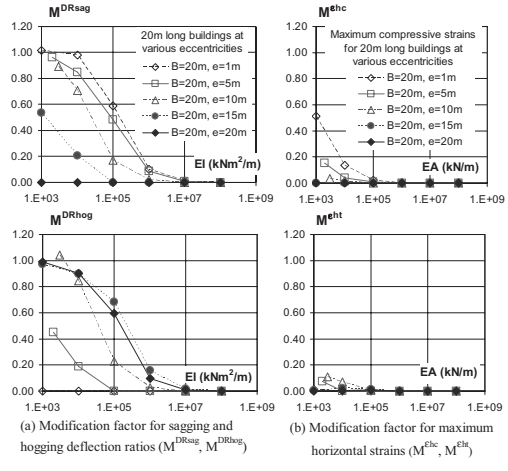

(a) Modification factor for sagging and hogging deflection ratios (M^{DRsag}, M^{DRhog})

(b) Modification factor for maximum horizontal strains ($M^{\varepsilon hc}$, $M^{\varepsilon ht}$)

Figure 3. Modification factors for 20 m long building at various distances (e) behind the excavation.

This implies that the horizontal strains in most buildings on continuous foundations would be negligible.

However when the axial stiffness is low, the horizontal strain modification factor is near to 0.5. This is due to the effect of a slipping interface modelled between the soil and the building. If an interface without slipping is modelled (i.e. where the soil nodes are rigidly connected to the building nodes), the horizontal strain modification factor would be near to unity when the axial stiffness is low.

2.3 *Effect of building location*

To investigate the influence of building location, the distance of the nearest edge of a 20 m long building to the excavation—defined as building eccentricity in this paper—is varied from 1 m to 20 m. The modification factors are shown in Figure 3. In the sagging zone, the deflection ratio modification factor for a building nearer to the excavation is higher than that of a building further away from the excavation. The converse is true in the hogging zone, as the deflection ratio modification factor of a building nearer to the excavation is lower than that of a building further away from the excavation. In terms of horizontal strains, there is a similar observation that the modification factors are near to zero when the axial stiffness is sufficiently high and of the order 10^5 kN/m.

2.4 *Relative bending stiffness of building*

Further finite element analyses were completed for buildings that are 40 m and 60 m long and at various eccentricities behind the same excavation (model UD_A). The deflection ratio modification factors for all the buildings are plotted against the bending stiffness in Figure 4. There is a wide spectrum in the modification factors between different buildings with the same bending stiffness. This implies that the deflection ratio in a building depends on factors other than simply its stiffness.

Since the modification factor is a measure of building response relative to the greenfield response, a parameter that gives the flexural stiffness of the building with respect to the soil can be similarly defined. Such a relative bending stiffness parameter should include the factors affecting the settlement behaviour of the building, such as its bending stiffness, its length, and its eccentricity, and possibly the excavation depth. Other than soil stiffness, a geometric parameter influenced by these factors is the sagging (and hogging) length of the building. Hence, it is proposed to define a new dimensionless relative bending stiffness factor (ρ_{sag} and ρ_{hog}) as

$$\rho_{sag} = \frac{EI}{E_S * L_{sag}^3} \tag{5}$$

$$\rho_{hog} = \frac{EI}{E_S * L_{hog}^3} \tag{6}$$

where EI (in kNm²/m run) is the bending stiffness of the building, E_s (in kN/m²) is a representative elastic stiffness of the soil defined as the weighted average of the soil stiffness above the excavation level, and L_{sag} and L_{hog} (in m) are the sagging and hogging lengths of the building in the greenfield condition.

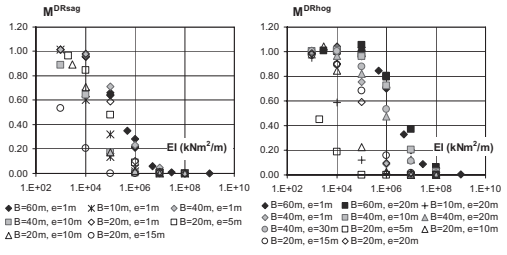

Figure 4. Deflection ratio modification factors for different building bending stiffness values.

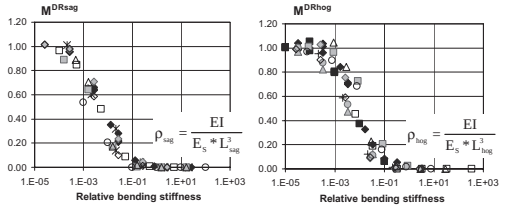

Figure 5. Deflection ratio modification factors for the new relative bending stiffness values.

When the deflection ratio modification factors are re-plotted against the new relative bending stiffness as shown in Figure 5, the data points converge into a narrow band. This suggests that the newly defined relative bending stiffness is a more useful parameter to describe the deflection behaviour of a building, compared to just using its bending stiffness.

3 INFLUENCE OF UNDRAINED EXCAVATION CHARACTERISTIC

3.1 *Depth of excavation*

To investigate the influence of excavation depth on building response, additional analyses were completed where the soil profiles were varied and final excavation depths changed. Table 2 summarises the excavation configurations varied in the study. For each excavation, the point of inflexion was found by interrogating for the point of maximum slope in the surface settlement curve. It is observed that the inflexion point which defines the length of the sagging trough may be different even though the excavation depth is the same. For example, the sagging trough in model UD_B is wider than in base model UD_A although the excavation depths are the same, and this is due to the thicker soft clay layer. This is because ground deformation in a multi-propped excavation is usually controlled by deep-rooted movements near the excavation level. The sagging length would give a better sense of the size and characteristics of induced ground deformations, as compared to the excavation depth. Although the elastic modulus of the soil—defined as the weighted average of the Young's modulus above the excavation level—does not describe the non-linear stiffness of soil exactly, it is noted that the different relative stiffnesses between buildings are in the orders of magnitude and such approximations on soil stiffness would be acceptable.

For a 60 m long building with the nearest edge at 1 m behind each of the different excavation depths, the modification factors for deflection ratio are plotted against the bending stiffness of the building in Figure 6a, and against the newly defined relative bending stiffness in Figure 6b. The spread in the modification factors is reduced when they are plotted against the relative bending stiffness. This shows that the sagging (and hogging) length for the greenfield condition is a suitable parameter to normalise the effects of excavation depth on building stiffness.

3.2 *Design guidance on modification factors for deflection ratio*

As with the base model, the buildings behind each of the excavation models were also varied in terms of the lengths (B = 10 m–60 m) and the locations (e = 1 m–30 m). The deflection ratio modification factors from all the models in Table 2 are plotted against the relative bending stiffness in Figure 7.

The modification factors for both sagging and hogging deflection fall into a narrow band. When the relative bending stiffness is less than 10^{-4}, the modification factor is close to unity and the flexible building would have a deflection ratio similar to that of the greenfield. When the relative bending stiffness is more than 10^{0}, the modification factor is close to zero and the stiff building would have zero deflection. Between the two values, the modification factor decreases rapidly from unity to zero, and this can be defined approximately using two curves—a mean curve for the best estimate response and an upper bound curve for the most flexible response. These two curves are the same for sagging deflection and hogging deflection modification factors. This can be used as a design guidance to estimate the modification factors and hence the deflection ratio in buildings adjacent to deep excavations in soft clay.

3.3 *Relative axial stiffness of building*

Earlier, it was pointed out that the horizontal strain modification factors depend mostly on the

Table 2. Excavation configurations varied in the study.

	Base UD_A	Model UD_B	Model UD_C	Model UD_D	Model UD_E	Model UD_F
Excavation depth	20 m	20 m	16 m	10 m	10 m	30 m
Soft clay thickness	20 m	30 m	16 m	12 m	12 m	32 m
Wall depth	25 m	35 m	20 m	15 m	15 m	40 m
Thickness of wall	0.8 m	1.0 m	0.6 m	0.6 m	0.6 m	1.0 m
No. of props	6 nos.	6 nos.	5 nos.	3 nos.	3 nos.	10nos.
1st activity	Excavate to RL-1.0 m				Prop at RL-0 m	
2nd activity	Excavate to RL-0.5 m				Prop at RL-3 m	
Location of inflexion pt.	21 m	29 m	17 m	11 m	11 m	30 m
Soil elastic modulus Es (kPa)	4709	4709	3767	2355	2355	7064

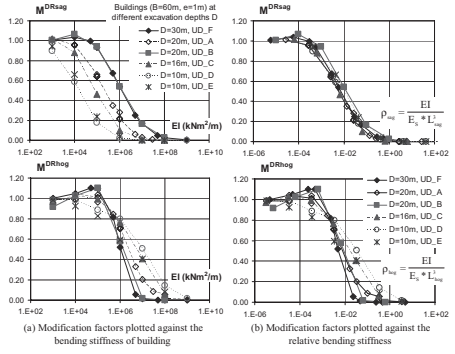

Figure 6. Effect of excavation depth on modification factors for deflection ratio.

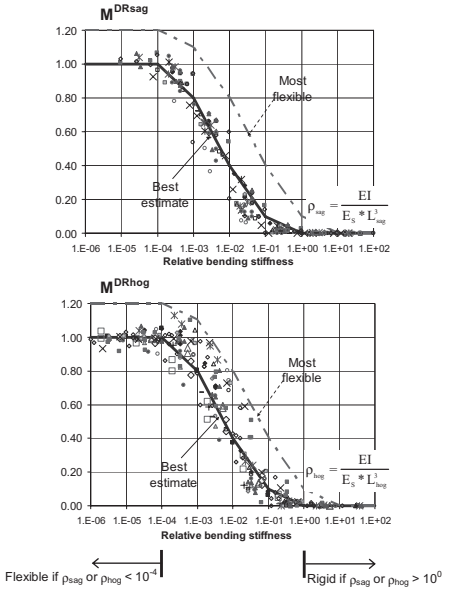

Figure 7. Deflection ratio modification factors for various buildings adjacent to different excavation depths.

axial stiffness of the building, but also depend (to a lesser extent) on the length of the building. In a similar way, a dimensionless relative axial stiffness (α) can be defined for buildings.

$$\alpha = \frac{EA}{E_S * B} \tag{7}$$

where EA (in kN/m run) is the axial stiffness of the building, Es (in kN/m^2) is the representative soil stiffness and B (in m) is the total length of the building.

Unlike deflection ratios where the modification factors between a building with slipping interface to the soil and a building without slipping interface were similar, the horizontal strains in the building can be influenced by the modelling of the soil-building interface. The maximum horizontal strains in the building were simulated using the most extreme situation where slippage is prevented at the soil-building interface. Figure 8 plots the horizontal strain modification factors against the relative axial stiffness using a non-slipping interface in the models under various excavation depths. An upper bound (shown on Fig. 8 as 'design estimate') can be used to estimate horizontal strain modification factors for buildings on continuous footings. Furthermore, for a 100 mm thick reinforced concrete slab that is 100 m long and continuous and for Es around 20 MPa, the relative axial stiffness is in the order of 10^0. This gives an indication on the range of the realistic axial stiffness of actual buildings, where the modification factor of horizontal strain would be near to zero as shown in the figure.

3.4 *Other parametric studies of the excavations in undrained conditions*

Other than excavation depths, parametric studies were also completed for other factors that would have an influence on the characteristics of the

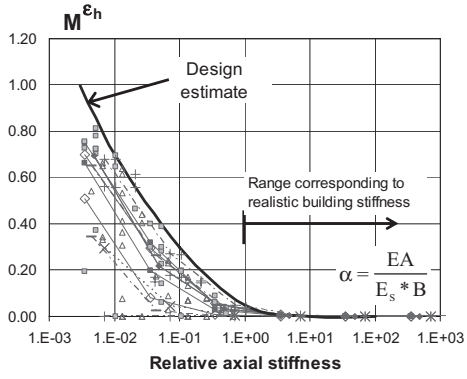

Figure 8. Horizontal strain modification factors for different relative axial stiffness values of buildings on continuous footings.

ground deformation caused by an adjacent deep excavation. These factors include:

- the stiffness of the excavation support system where the wall stiffness and prop spacing were varied in various excavation models,
- the effect of including building weight where a 40 kPa surcharge was placed on the 'beam' building with and without considering building stiffness,
- the effect of soil stiffness and constitutive modelling where the soft clay was modelled using a Strain Dependent Modified Cam-Clay model and then with a linear elastic, perfectly plastic Tresca model,
- the effect of composite soil profiles, where a thinner layer of firm soil was added into the otherwise homogeneous soft clay layer.

Full details of the procedures and results are given in Goh (2010). The soil stiffness and the composite soil profile studies showed that using the weighted average of soil stiffness above the final excavation level gives a reasonable estimate for the representative elastic stiffness of the soil. Furthermore, it was found that although ground and building deformation can be significantly influenced by the various factors in the parametric study, the building modification factors are much less affected when building behaviour is described using the proposed definition of relative stiffness. The design guidance shown in Figure 7 would still be applicable.

4 INFLUENCE OF CONSOLIDATION

4.1 *Effect on ground deformation*

Prior to this section, all the building responses were investigated during excavations in undrained condition. This is a reasonable approach only if the speed of excavation is quick relative to the time needed for pore water to flow in a low permeability soil so that consolidation is inhibited. However, there are many instances in published case histories where consolidation settlements are significant for excavations in soft clays (e.g. Nicholson, 1987, Wallace et al, 1993, Wen & Lin, 2002).

Using the same base model for the undrained analysis (i.e. model UD_A as shown in Figure 1), a coupled consolidation analysis was performed for the finite element models by allowing pore water flow according to the boundary conditions and then allowing the soil elements to deform to the pore pressure changes (i.e. model CON_A). This is done by setting the time step to coincide with a realistic time required for each construction sequence. Apart from the first 1 m excavation and the first prop installation (which are assumed to be quick and undrained as before), consolidation was allowed with every metre of excavation taking 10 days and every prop installation taking 30 days. The total excavation duration is about 12 months (see Fig. 9).

Figure 10 compares the wall deflection, the surface settlement and the horizontal displacement profile at the ground surface in the undrained

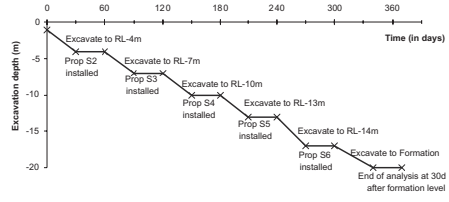

Figure 9. Excavation schedule for consolidation analysis.

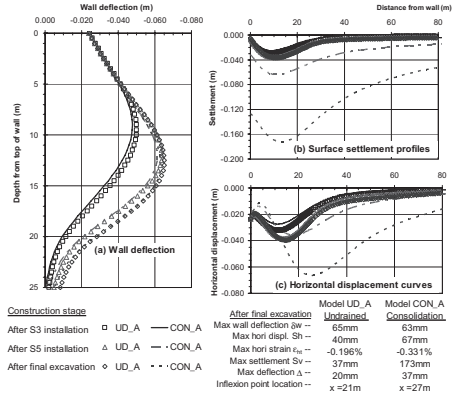

Figure 10. A comparison of wall and ground deformations between undrained (UD_A) and coupled consolidation (CON_A) analysis.

condition and with coupled consolidation. The wall deflection curves are similar between undrained and consolidation analysis at various stages of the excavation. However, the surface settlement and horizontal displacements increased substantially—and this can be up to four times the undrained deformations. The displacement troughs also became wider due to the effect of consolidation.

Figure 11 shows the change in groundwater pressure in the undrained excavation compared to the consolidation analysis, when the excavation has reached formation level. Arising from the significant reduction of vertical overburden within the excavation area, there is a reduction of water pressure across the bearing stratum below the compressible clay layer. This lowering of pore water pressure causes the soft clay layer to consolidate, and is similar to the field behaviour observed by Wen & Lin (2002) on the consolidation settlements being caused by under-drainage of the soft marine clay in Singapore. In comparison, the generation and dissipation of negative excess pore pressures directly behind the wall due to horizontal stress relief is much less dominant.

Additional analyses were also completed to investigate the factors that affect the extent of consolidation and ground deformation in the soil during excavation. These are detailed in Goh (2010), but can be summarised as follows:

– When the permeability of the wall was increased from being completely impermeable to 1×10^{-9} m/s, to simulate a leaking wall, there was an increased consolidation deformation which was more skewed towards the wall.

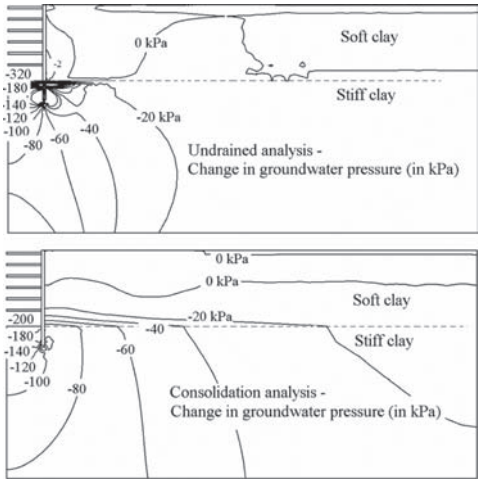

Figure 11. Change in groundwater pressure at final formation level for undrained analysis and consolidation analysis.

– When the total excavation period was shortened from 12 months to 6 months, the reduction in pore water pressure behind the wall and the resulting consolidation of the soft clay decreased.
– When the wall toe cut-off length was increased substantially from 5 m to 15 m in the stiff bearing stratum, there is some decrease in the consolidation movements.
– Reducing the permeability of the underlying bearing stratum from 1×10^{-7} m/s to 5×10^{-9} m/s significantly reduced the consolidation deformation so that the behaviour is near to the undrained deformation.
– Increasing the soft clay thickness from 20 m to 28 m resulted in a deeper excavation mechanism and increased the wall and ground movements, but also resulted in a longer drainage path that inhibited seepage in the bearing stratum and reduced consolidation in the overlying soft clay.

4.2 *Effect on building modification factors*

To investigate the influence of consolidation on the building modification factors, a few variations of the consolidation analysis were performed with a 60 m long building at 1 m behind the excavation. Table 3 shows the parameters that were varied in the consolidation analysis of the 20 m deep excavation.

The building stiffness values were varied in each of the consolidation models, and the modification factors of deflection ratio and horizontal strains are plotted against the relative building stiffness in Figure 12. Despite differences in the actual surface displacement profiles, the building modification factors from the consolidation analysis—plotted against the relative building stiffness—fall within the design guidance developed from the undrained analysis. Thus, the modification factor design curves can be used to estimate the response of a building from the deflection ratios and horizontal strains in the greenfield excavation, even when consolidation effects are significant.

Table 3. Variation of consolidation parameters.

	Permeability of wall	Excavation duration	Soft clay thickness
Model CON_A	Impermeable	12 months	20 m
Model CON_A1	10^{-9} m/s	12 months	20 m
Model CON_A2	Impermeable	6 months	20 m
Model CON_A3	Impermeable	12 months	28 m

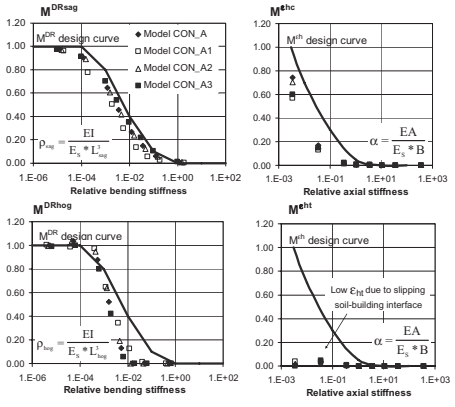

Figure 12. Building modification factors taking account of consolidation movements during excavation.

5 CONCLUSIONS

Using an elastic beam to model the building, it was observed that the deflection behaviour of the building depends mainly on its bending stiffness, while the horizontal displacement response depends on its axial stiffness. A building with higher bending and axial stiffness has a lower deflection ratio and horizontal strain. Therefore, by realistically including the influence of building stiffness to estimate deflection ratios and horizontal strains, the maximum tensile strains induced in the building can be reduced to result in a lower risk of building damage.

Other than bending stiffness, there are several factors related to the building and the excavation that would have an influence on the building deformation behaviour. For example, a shorter building will have a stiffer deflection response compared to a longer building with the same elastic stiffness in bending, and a building adjacent to a deeper excavation generally has a higher modification factor compared to another building with the same elastic and geometric properties adjacent to a shallower excavation.

Through a rigorous investigation of the parameters affecting ground deformations during a deep excavation, it has been found that there is a well-defined relationship between the building modification factors and the relative building stiffness. This makes it possible to use the modification factor and the relative stiffness approach to derive design guidance to estimate the influence of building stiffness on the actual deformation response of the building from the greenfield condition. As presented in this paper, a guidance to estimate the modification factors for buildings adjacent to deep excavations in soft clays has been proposed.

On a final note, it is likely that the proposed design guidance could be more dependent on the shape of the induced settlement trough, rather than on the construction process. In this study, the design curves were derived based on a concave settlement trough during a multi-propped excavation. For a convex settlement trough as observed during cantilever wall excavations, the different restraint conditions provided by the ground could well result in different design curves. On the other hand, a tunnelling-induced settlement curve that is similar to the concave settlement trough could have building modification design curves that are similar to the current study. These can be verified using findings from other research works.

ACKNOWLEDGEMENTS

The first author would like to thank the Land Transport Authority of Singapore for sponsoring his research study at the University of Cambridge.

REFERENCES

Franzius, J.N., Potts, D.M. & Burland, J.B. 2006. The response of surface structures to tunnel construction. *Proc. Institution of the Civil Engineers, Geotechnical Engineering* 159(1): 3–17.

Goh, K.H. 2010. Response of ground and buildings to deep excavations and tunnelling. Ph.D thesis, Cambridge University, UK.

Goh, K.H. & Mair, R.J. 2008. Response of a building under excavation-induced ground movements, *Proc. of International Conference on Deep Excavations, 10–12 Nov 2008, Singapore*.

Mair, R.J., Taylor, R.N. & Burland, J.B. 1996. Prediction of ground movements and assessment of risk of building damage due to bored tunnelling, In R.J. Mair and R.N. Taylor (eds.), *Proc. intern. symp. on Geotechnical Aspects of Underground Construction in Soft Ground, London, 15–17 April 1996*: 713–718. Rotterdam: Balkema.

Nicholson, D. 1987. The design and performance of the retaining walls at Newton Station. *Proc. conf. Singapore Mass Rapid Transit Conference, Singapore, 6–9 April 1987*: 147–154.

Potts, D.M. & Addenbrooke, T.I. 1997. A structures influence on tunnelling-induced ground movements. *Proc. Institution of the Civil Engineers, Geotechnical Engineering* 125(2): 109–125.

Wallace, J.C., Ho, C.E. & Long, M.M. 1993. Retaining wall behaviour for a deep basement in Singapore marine clay. *Proc. conf. on Retaining structures, July 1992, Cambridge*: 195–204.

Wen, D. & Lin, K.Q. 2002. The effect of deep excavation on pore water pressure changes in the Old Alluvium and under-drainage of marine clay in Singapore. In R. Kastner, F. Emeriault, D. Dias & A. Guilloux (eds), *Proc. 3rd intern. symp. on Geotechnical Aspects of Underground Construction in Soft Ground, Toulouse, 23–25 October 2002*: 447–452. Lyon: Spécifique.

Geotechnical Aspects of Underground Construction in Soft Ground – Viggiani (ed)

3D numerical modelling and settlement monitoring during excavation of the Metro-Torino South extension

G. Barla, M. Barla, & G. Leuzzi
Department of Structural and Geotechnical Engineering, Politecnico di Torino, Italy

ABSTRACT: The Metro-Torino South extension is under construction. The excavation of a 3.9 km long tunnel was recently completed by a 7.8 m diameter EPB Tunnel Boring Machine. A critical section of the line is represented by the underpass of Corso Spezia, in the Lingotto area, where the main difficulties are associated with the high water table and the poor ground conditions encountered. Concern was also raised due to the influence of the excavation on two adjacent masonry buildings of 1930. This required an intensive monitoring system to be designed and installed. Monitoring took place continuously during excavation and allowed one to infer a time dependent function which describes the settlement history satisfactorily. A 3D finite element model was also created to simulate the excavation process and its effects on the adjacent buildings. This model was validated through a back analysis procedure in order to assess the soil parameters and simulate the tunnel excavation in stages. This paper will describe the case study and the 3D numerical modelling work by comparing the results obtained with the monitoring data.

1 INTRODUCTION

Tunnelling in Torino took place extensively in the last decades involving a number of interferences with the built environment that needed high engineering expertise to be dealt with. This paper will focus on one of these interferences occurred during the construction of the South extension of the Metro Torino Line 1.

In the Corso Spezia area, the excavation of the tunnel is adjacent to two sensible buildings and below an underground car pass. The tunnel axis is located at about 15–20 m depth while the water table is 12 m below the surface. A poor quality soil layer characterises the stratigraphic sequence in this area and ground improvement techniques were used in the attempt to limit settlements.

With the great number of monitoring data recorded during and after excavation it was possible to describe successfully the time dependent displacements occurred at the site. Given the complexity of the case study, it is of interest to create a three dimensional model and back analyse the problem, although by using a simple constitutive law.

This paper will describe the results obtained. In situ monitoring data will be compared with the results of modelling.

2 METRO TORINO LINE 1

Construction of the completely automatic underground Metro Torino Line 1 represented a dramatic innovation of the city transportation system. The system started to play its role in the early 2006 just a week prior to the Winter Olympic Games that took place in the city.

The total length of the line in service is about 9.6 km and includes 15 stations connecting the city centre with the western suburbs. A new South extension of the line is now under construction between Porta Nuova and Lingotto (Figure 1). Construction works started in 2006 and are expected to be completed by 2011. Works include a 3.9 km long tunnel and 6 stations. An extension of the line (1.9 km and 2 stations) towards Piazza Bengasi is expected to be constructed starting with 2011.

The main tunnel was excavated at an average depth of 15–20 m using three EPB Tunnel Boring Machines, 7.8 m in diameter and 80 m in length. The tunnel lining is formed with precast concrete segments (7 sections a day were completed for an average progress rate of 10 m/d). Another EPB machine has just completed the excavation of the new extension between Porta Nuova and Lingotto.

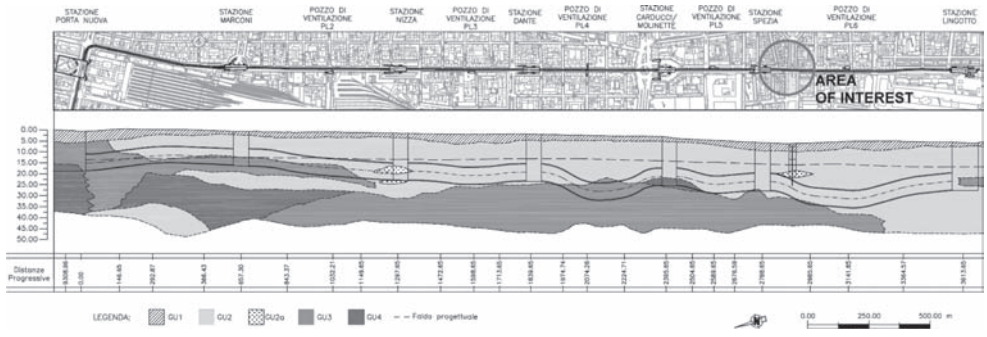

Figure 1. Plan view and geological longitudinal cross section of the Porta Nuova–Lingotto extension.

3 SUBSOIL CONDITIONS

Torino metropolitan area, located at the western edge of the Po valley, has an overall surface of about 130 km^2, 80% of which are a level area enclosed by the rivers Stura di Lanzo, Po and Sangone, while the remaining 20% are made up by a hilly area connected to the low reliefs of Monferrato. The city area is situated on the end section of the great alluvium fan of the Dora Riparia river and, from the morphological point of view, appears to be almost flat with a weak dip starting from West and going towards East, with elevation ranging from 260–270 m a.s.l. to about 220 m a.s.l. (Bottino and Civita, 1986).

The subsoil conditions in Torino are characterized by sand and gravel deposits, with different cementation degrees increasing with depth. Lenses of cemented soil or conglomerate are often present, down to a depth of 8–10 metres. The ground water level along the tunnel axis is well known based on piezometric measurements and predictions on long term conditions have also been carried out.

With the available data from geotechnical investigations and numerical analysis performed in the past, a geotechnical model for the subsoil conditions has been derived. For the depth relevant to tunnelling, four soil layers (Geothecnical Units, GU) were defined (Barla & Vai 1999, Barla & Barla 2005, Barla et al. 2010):

– GU1: superficial layer (filling and clayey sandy silt);
– GU2: sand and gravel from loose to slightly cemented;
– GU3: sand and gravel from slightly to medium cemented;
– GU4: sand and gravel from medium to heavily cemented.

The stratigraphic sequence is variable along the line. Figure 1 shows the longitudinal geological profile of the South extension, of interest in this paper.

4 CASE STUDY

Immediately out of the Spezia station, the tunnel passes close to two 1930 sensible 5-storey masonry buildings (named 973 and 974) and below an underpass (Figures 1 and 2). Ground improvement measures were therefore commissioned as defensive means for the buildings.

A comprehensive monitoring plan was set up in order to monitor the building response during the grouting process and tunnelling. Surface settlements were monitored using a number of inclinometers, extensometers, as well as traditional and state of the art monitoring techniques. Monitoring included a computerised total station with optical targets installed on the surrounding buildings in order to measure the induced settlements continuously.

Detailed site investigations including borehole drilling with core recovery (Figure 2a) and the retrieval of undisturbed samples of the cohesive layers allowed one to obtain a stratigraphic section as shown in Figure 2b. In addition to the usual stratigraphic sequence of the Torino subsoil, with the GU1, GU2, and GU3 units, the presence of a silt layer (GU2a) containing a lens of even weaker properties (GU2a mod) was found.

This unit (GU2a), based on the results of laboratory tests, exhibits a time dependent behaviour. An additional feature to be underlined in the section is the presence of an ancient river bed along the Corso Spezia underpass alignment, filled with poor quality landfill of anthropic origin. The ground water table is well known and located about 12 m below the ground surface.

During excavation, the EPB-machine suddenly lost face pressure and mud when driven through the underpass. Cracking and collapse of a number of waterproof panels in the underground pass did take place, in conjunction with floor heave just above the tunnel. As a consequence car traffic was stopped for some time to allow for repair work to take place.

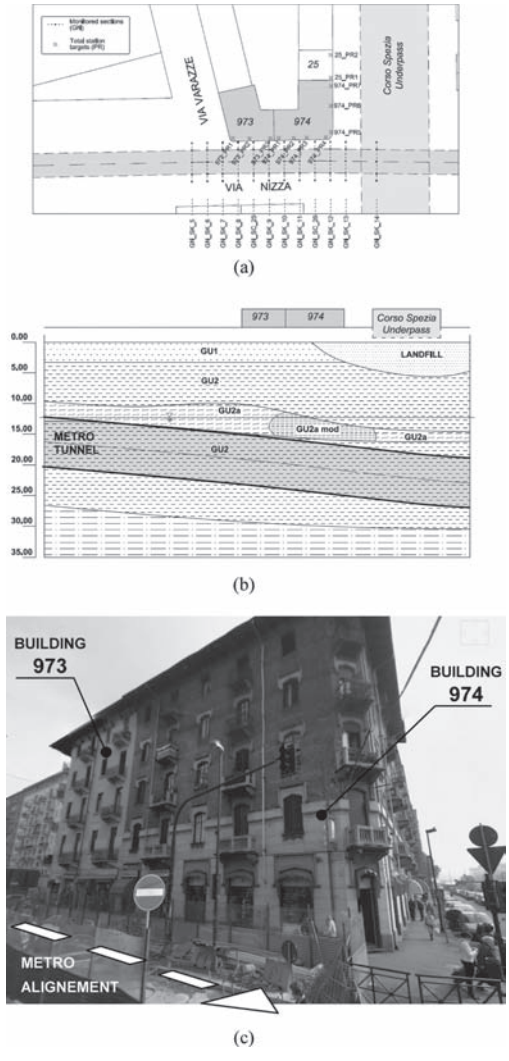

Figure 2. Plan view (a), geological profile (b) and photograph (c) of the area where the Metro Tunnel reaches the Spezia underpass.

5 ANALYSIS OF SETTLEMENT MONITORING

TBM monitoring took place systematically during excavation in order to measure the machine parameters such as mud pressure at the tunnel face, rotational speed, penetration, advancement rate, thrust, torque, etc.

Figure 3 shows a typical plot of the specific energy versus chainage during TBM advancement along the Spezia-Lingotto section. Specific energy is computed by the following equation:

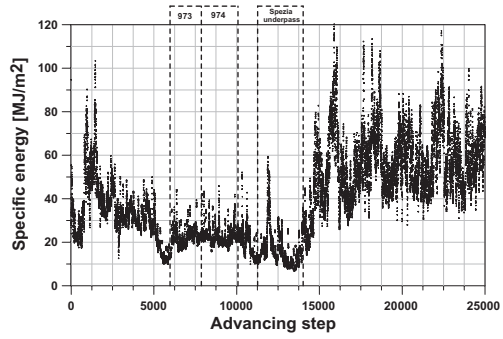

Figure 3. Specific energy versus chainage monitored by the TBM during face advancement along the Toino Metro Line 1 Extension from Porta Nuva Station to Lingotto.

$$E_s = \frac{F}{A} + 2 \times \pi \times \frac{N \times T}{u \times A} \quad (1)$$

where:

– F is the thrust force applied on the cutting wheel;
– N is the number of revolutions per second;
– T is the torque;
– A is the tunnel cross sectional area;
– u is the rate of penetration.

It is shown that starting with advancing step 1000 (i.e. at chainage 1400) the specific energy drops dramatically to reach an average value of 20 MJ/m^2 under the 973 and 974 buildings. As the underpass is being reached the specific energy drops again to its minimum of 10 MJ/m^2 under it. Therefore, as anticipated, the poor ground conditions below buildings 973 and 974 and the underpass itself is well underlined.

Based on conventional topographic surveys of target points on the ground surface (1 target point above the tunnel crown and 2 additional ones on each side of the tunnel axis, to reach a total of 5 monitoring points in every monitoring section) the settlement through above the tunnel could be obtained. The monitoring data were interpreted by using the well known settlement equation (Peck, 1969):

$$s_v = s_{v,\max} \exp(-y^2 / 2i^2) \quad (2)$$

where s_v = settlement, $s_{v,max}$ = maximum settlement on the tunnel centre-line, y = horizontal distance from the tunnel centre-line and the i horizontal distance from the tunnel centre-line to the point of inflexion of the settlement trough.

The surface settlements were found to be well related to TBM advance, i.e. to the distance of the monitored section from the TBM head, according

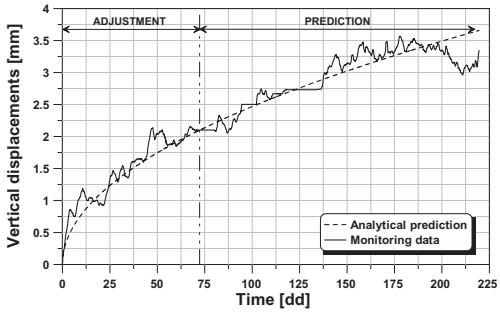

Figure 4. Vertical displacement versus time of target point GN SK 9 placed on the 974 building.

to the usual face influence functional relationship. However, it soon became apparent that settlements in the zone of interest (Figure 2), were heavily time dependent and likely related to the creep properties of the silt layer (GU2a).

With consideration given to this time dependent behaviour a thorough analysis of the available monitoring data was undertaken in order to find out a functional relationship describing settlement versus time, following the TBM passage in the cross section being monitored. Given that the total station targets were measured every half an hour and the traditional topographic surveys took place twice per day, most of the attention in the analysis was devoted to the former set of data.

At first, to minimize the temperature variation influencing data collection, all the monitoring data were averaged over a 24 hours duration. Also, fluctuations caused by extraordinary weather events were minimised accounting for the weather station charts recorded close to the area of interest. Based on the above, it was possible to define the following functional relationship by fitting the monitored settlements being measured at all the monitoring targets (Figure 4).

$$w(t) = A \times \left(\frac{t}{b}\right)^n \tag{3}$$

where:

$w(t)$ = time dependent displacement;
A = scale factor;
t = time;
b = shape factor;
n = exponent shape factor.

As shown typically in Figure 4, for a target point placed on building 974, fitting took place with equation (3) by considering the data obtained in the first 75 days of observation (adjustment period). Then this function could be used as a means of forward prediction of the expected settlement versus time. Figure 4 shows the comparison between monitored and computed data over a 6 months time span.

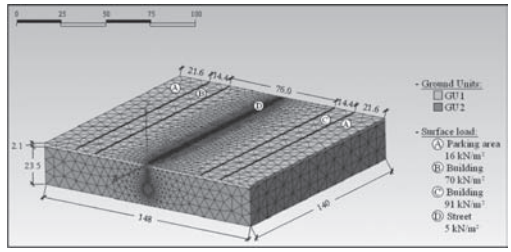

Figure 5. 3D validation model used for validation studies along the Nizza–Dante section.

6 3D NUMERICAL MODELLING

6.1 *Parametric analyses*

A 3D validation model based on the Finite Element Method and the MIDAS/GTS code (Midas 2005) was created first to simulate the monitored ground response when tunnelling along the Nizza–Dante section. Different overburden depths, model widths, distances of bottom depth boundary were considered with the Mohr-Coulomb elastic perfectly plastic model used for representing the soil behaviour.

As shown in Figure 5, the 3D validation model finally adopted considers a tunnel diameter of 7.80 m, at a depth of 15.70 m. The outer boundaries (left and right) have been modelled at a distance of about 10 diameters from the tunnel in both directions to minimize the boundary effects. The model extends about 20 tunnel diameters along the axis. The optimal distance between the bottom boundary and tunnel invert was set equal to 0.75 tunnel diameter, a distance which is recognised to minimize the uplift effects on the invert zone and has negligible influence on the computed surface settlements.

Efforts were placed on the appropriate method to simulate tunnel excavation when accounting for the interaction of the ground with the EPB shield. Most attention was posed in reproducing the influence of the gap existing between the excavation boundary and the shield as a number of alternatives exist to simulate this influence (Potts and Zdravkovic 2001). The method adopted consists in the simulation of excavation by a radial pressure reduction at the tunnel boundary, while activating step by step the plate elements representing the shield and the lining in order to reproduce face advancement.

The radial pressure distribution was assumed to vary from the TBM head (equal to the face pressure), to the shield tail, so as to simulate effectively the size of over excavation and the conical shape of the shield. Different distributions of radial pressure along the shield were tested and the optimal ground parameters were searched for capturing the observed settlement trough. The Mohr-Coulomb model was used for the GU units, while the structural elements were all considered elastic. A linear increase of the deformation modulus with depth was assumed for the GU2 unit, starting with a depth of 3.3 m below the ground surface.

6.2 *Analyses of the tunnel response and interaction with the neighboring buildings*

Based on the results of the parametric analyses above, the 3D FEM model shown in Figure 6 was set up to analyse the tunnel excavation and its interaction with the neighboring buildings 973 and 974 in detail. This model contains about 190.000 tetrahedral 4 noded solid elements. The shield and the lining are represented with about 40000 3 noded triangular plate elements, each 0.30 m thick.

The zone to be modelled is characterized by the presence of a series of buildings of a different year of construction, type (made of concrete or brick masonry materials), and height, on each side of the tunnel alignment as depicted in Figure 6. The foundations of the buildings were discretised into finite elements to a depth of 2 m below surface and modelled as elastic solid boxes with the unit weight equal to that of the soil and Young's modulus about 4 times that of the GU2 soil. A specific study was undertaken for the 974 building to account for its true geometrical and stiffness properties. As shown in Figure 6, loading of the buildings was applied to the soil surface below the foundation level as a uniform surcharge depending on the type of buildings. A constant pressure of 5 kPa was also applied to the free surface to simulate traffic loads.

The Spezia underpass, which is perpendicular to the tunnel axis as shown in Figure 6, was introduced in the model by accounting for its structural components which consist of 3 walls formed with contiguous concrete piles placed on the lateral and centre sides and a series of pre-cast concrete beams on the top. Both the lateral walls (0.6 m thick) and the central wall (0.9 m thick) reach a depth of 14 m below the street level. The tunnel is 1 m below the pile walls. Interface elements with poor shear and normal stiffness values were introduced in the model between the soil and the undersides of the lateral walls.

The TBM advance was simulated in stages with 1.4 m advance each stage (equal to the lining segment length) and with a shield length equal to 8.4 m. Based on the results of the 3D validation model, a pressure distribution on the shield during excavation in controlled conditions was assumed as shown in Figure 7, with a maximum value at the tunnel face and minimum on the shield tail. The maximum value applied at the face of 150 kPa is equal to the face pressure obtained from the available TBM monitoring data. With the intent to simulate the pressure drop which occurred as soon

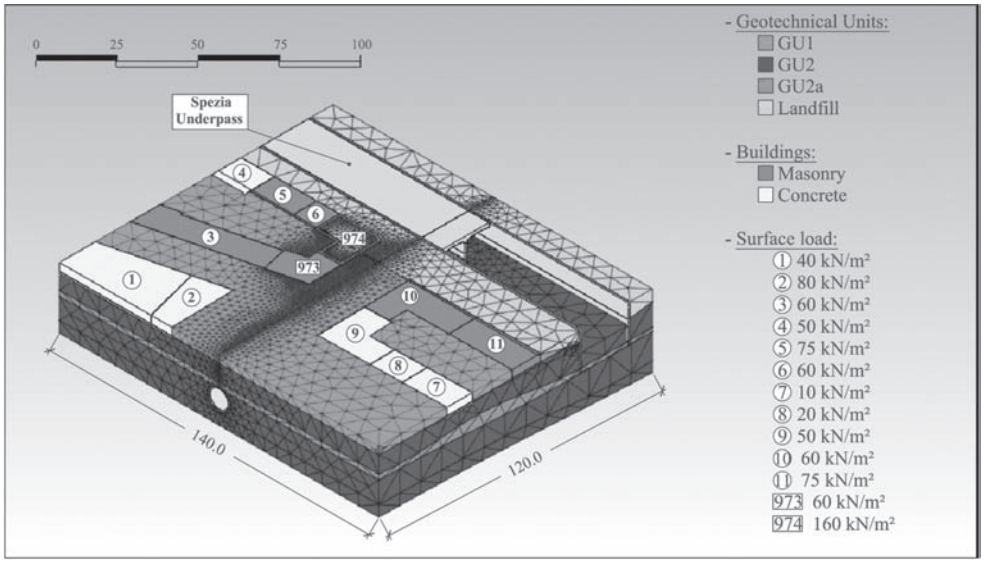

Figure 6. FEM model of Corso Spezia-underpass cross section.

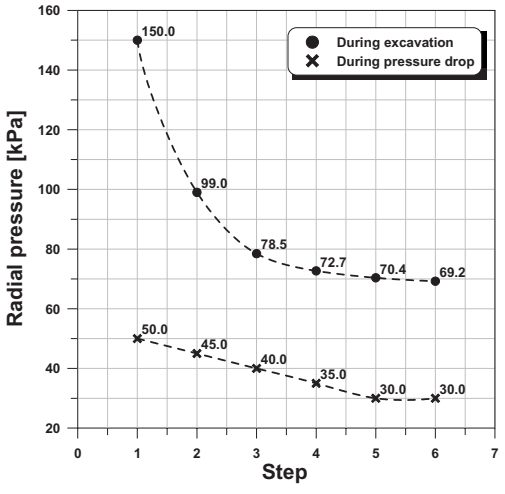

Figure 7. Radial pressure used to simulated the TBM both during excavation and during the pressure drop occurred below the underpass.

the TBM head reached the underpass section, the pressure distribution was changed as shown in the same Figure 7.

The initial stress conditions in the model were simulated by assuming gravity loading with a stress ratio equal to 0.5. Based on the experience gained with the 3D validation model, the outer boundaries (left and right) are introduced at a distance of approximately 10 diameters from the tunnel in both directions and the model extends about 20 tunnel diameters along the axis. The bottom boundary is placed at a distance of 0.75 tunnel diameters from the invert.

With the Mohr-Coulomb model used for the soil behaviour, two series of analyses were performed with the intent to match the surface settlements measured in the short term (i.e. during excavation, when the TBM head has reached a distance of a few diameters from the monitored section) and in the long term (i.e. with the tunnel excavation completed). The values of the soil parameters assumed for such conditions are given in Tables 1 and 2.

Figure 8 illustrates subsequent screenshots of the computed displacements occurring during face advance. Figure 9 compares the computed and monitored longitudinal displacements for short and long term conditions. The computed displacements show a good agreement with the monitoring data. It is noted that the adoption of interface elements between the soil and the undersides of the lateral walls was a key factor to allow to obtain a more realistic displacement pattern. Some differences between the computed and monitored values may however be underlined between 20 and 25 m probably due to some local disturbances (e.g. caused by grout injection operations).

Table 1. Geotechnical properties for short term behaviour used in the numerical analyses.

	Young's modulus	Poisson's ratio	Dry unit weight	Cohesion	Friction angle
	MPa	-	kN/m^3	kN/m^2	°
GU1	15	0.35	15.0	1	32.5
GU2	190 + 1.85 MPa/m	0.33	16.5	7	38.0
GU2a	60	0.33	16.5	10	29.0
GU2a mod	20	0.33	16.5	10	29.0
Landfill	12.5	0.33	18.0	1	34.0
Buildings	500	0.25	19.0	–	–
Underpass	40300	0.25	16.0	–	–
Lining	40300	0.24	25.0	–	–

Table 2. Geotechnical properties for long term behaviour used in the numerical analyses.

	Young's modulus	Poisson's ratio	Dry unit weight	Cohesion	Friction angle
	MPa	–	kN/m^3	kN/m^2	°
GU1	15	0.35	15.0	1	32.5
GU2	190 + 1.85 MPa/m	0.33	16.5	7	38.0
GU2a	30	0.33	16.5	10	29.0
GU2a mod	10	0.33	16.5	10	29.0
Landfill	1	0.33	18.0	1	34.0
Buildings	500	0.25	19.0	–	–
Underpass	40300	0.25	16.0	–	–
Lining	40300	0.24	25.0	–	–

Plots of the computed settlement troughs are shown in Figure 10 compared with the monitored data at the target points on the surface. It is possible to notice that the monitored values exhibit a non symmetric distribution. The presence of a pipe located at a distance of 5 m to the left of the tunnel axis may have reduced locally the monitored settlements.

The axial thrust and bending moment along the lining were also evaluated. Figure 11 shows the result for a cross section located at a distance of 42 m from the left boundary in the model, between the two buildings 973 and 974. Both short and long term computed values are shown. The maximum axial thrust is obtained on the left side of the tunnel, where the building foundations may very likely affect the stress distribution in the lining (maximum values being 346 kN for the short term and 352 kN for the long term conditions respectively).

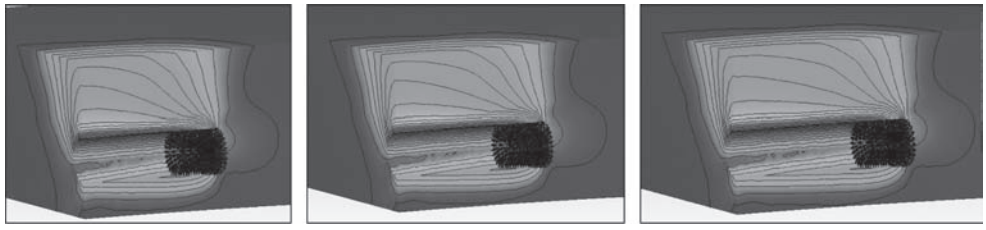

Figure 8. Subsequent screenshots of vertical displacement pattern around the tunnel during TBM advance.

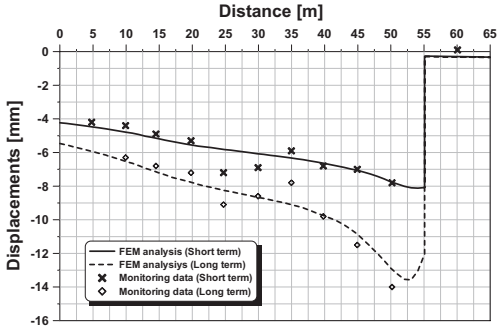

Figure 9. Comparison of the computed and monitored displacements along the tunnel axis.

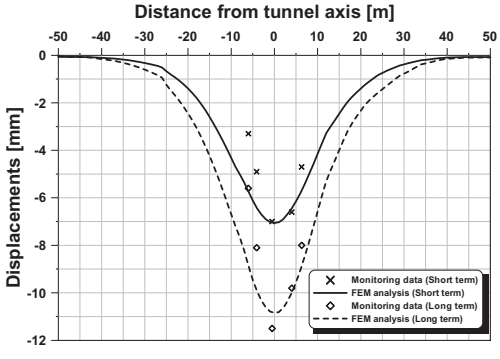

Figure 10. Comparison of computed settlement troughs with monitored values at target points above the tunnel for short term and long term conditions.

The variation of the bending moment at the crown shown in Figure 11 is due to the change in the soil geotechnical properties (GU2a soil is located in the upper part, while GU2 lies below). Maximum and minimum values of the bending moment are respectively 4.2 kNm at the crown and −3.5 kNm on the left sidewall for short term, and 4 kNm at the invert and −4 kNm on left sidewall for long term conditions. In terms of stresses, the lining is always under compression and the maximum tangential stress values are located on left sidewall: 1.35 MPa for short term and 1.41 MPa for long term conditions respectively.

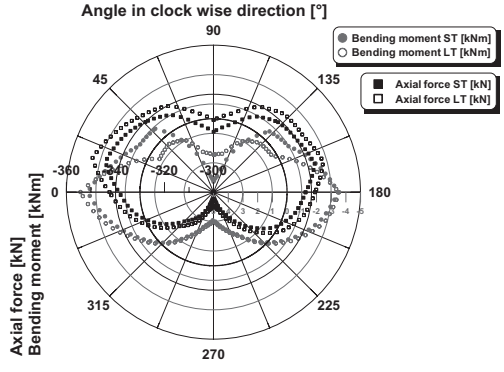

Figure 11. Computed axial thrust and bending moment in the segmental lining for short and long term conditions.

7 CONCLUDING REMARKS

This paper has described a case study of tunnel excavation and interaction of two sensible buildings preceding an underpass in the Corso Spezia area, along the South extension of the Metro Torino Line 1. The tunnel axis is located at a depth of about 15–20 m with the water table 12 m below the ground surface. The attention was posed on the observed time dependent vertical settlements above the tunnel and on the computed values in the short and long term conditions by using a 3D finite element model which takes into account the important features of the problem.

The authors are well aware of the limitations of the Mohr-Coulomb model used for representing the soil behavior. The short and long term response of the soil to tunnel excavation in terms of the induced settlement troughs at the ground surface, in both short term and long term conditions, could be well represented. However, in order to simulate the response time history as observed through settlement monitoring, advanced time dependent constitutive laws need be implemented in the model. This is being done at present and the results will be reported in the future.

ACKNOWLEDGEMENTS

The authors would like to thank GTT S.p.A. Divisione Metropolitana for providing the monitoring data and for direct access to the site. The work presented in this paper was performed during and following a consulting contract between GTT S.p.A. and Politecnico di Torino, Department of Structural and Geotechnical Engineering, under the coordination and responsibility of Professor Giovanni Barla.

REFERENCES

Barla G., Vai, L. 1999. Indagini geotecniche per la caratterizzazione del sottosuolo di Torino lungo il tracciato del passante ferroviario. *XX Convegno Nazionale di Geotecnica*, Parma.

Barla, M., Barla, G. 2005. Assessing design parameters for tunnelling in a cemented granular soil by continuum and discontinuum modelling. *Proc. 11th Iacmag Conference*, Torino, 19–24 June 2005, Vol. 4, pp. 475–484, Patron Editore.

Barla G., Barla M., Camusso M. 2010. Geotechnical characterization of the Torino subsoil by combining site investigations and numerical modeling. *ASCE J. of Geotechnical and Geoenvironmental Eng*. Under review.

Bottino, G., Civita, M. 1986. Engineering geological features and mapping of subsurface in the metropolitan area of Turin, North Italy. 5th International IAEG Congress, Buenos Aires, pp. 1741–1753.

Midas Information Technology Co. Ltd. 2005. MIDAS/GTS (Geotechnical and Tunnel analysis System). Ver 3.00.

Peck, R.B. 1969. Deep excavations and tunnelling in soft ground. *Proc. 7th International Conference on Soil Mechanics and Foundation Engineering*, Mexico City. State of the Art Volume, pp. 225–290.

Potts, D.M., Zdravkovic, L 2001. Finite element analysis in geotechnical engineering—theory. Thomas Telford.

Geotechnical Aspects of Underground Construction in Soft Ground – Viggiani (ed)
© 2012 Taylor & Francis Group, London, ISBN 978-0-415-68367-8

3D Numerical modelling of tunnelling intersecting piles

S.W. Lee, C.K.M. Choy & S.C. Tse
Geotechnical Consulting Group (Asia) Ltd, Hong Kong

F.R. van Gool, W.W.L. Cheang & R.B.J. Brinkgreve
Plaxis BV, Delft University of Technology, The Netherlands

ABSTRACT: Tunnelling beneath existing buildings supported by large numbers of piles is a three-dimensional (3D) soil-structure interaction problem. 3D finite element analyses (FEA) have been carried out to model construction of a 6 m diameter tunnel intersecting the lower portion of a building piled foundation system comprising 50 nos. of 0.6 m diameter, 21.5 m long friction piles. A total of 15 obstructing pile toes are cut off. A step-by-step pressure method is used to model the progressive advance of tunnelling. Two parametric study analyses are carried out to investigate the effects of the upper half of and a full 3 m thick grouted annulus around the tunnel. Results are presented for the responses of selected piles and building settlements. Both grouting schemes are found to be effective in reducing tunnelling-induced ground movements.

1 INTRODUCTION

Tunnelling in densely built-up urban areas often encounters obstructions such as buried utilities/services and existing pile foundations. In some cases the proposed tunnelling alignments were diverted to minimise any potential effect of tunnelling on existing structures. Due to reasons of construction costs, engineering challenges and land resumption, there were cases in which the diversion of tunnel alignments was not feasible, resulting in the tunnels intersecting the toes of existing piles (GCO 1985). In this scenario, the obstructing pile toes were cut off as the tunnel boring machine (TBM) passed through. Protective measures in the forms of superstructure strengthening and grouting beneath the building/around the tunnel were typically carried out prior to tunnelling. The process of pile-cutting was normally carried out manually with temporary stoppage of TBM operation (Pang 2006).

There are limited case histories reporting on the responses of cut piles due to tunnelling, mainly because of the difficulty associated with installing strain gauges in existing piles. This motivates the Authors to carry out 3D finite element analyses (FEA) to investigate the behaviour of piles in a large pile group and associated building in response to tunnelling involving pile-cutting. Parametric studies are carried out to investigate the effectiveness of grouting around the tunnel in mitigating pile/building movements.

2 BACKGROUND INFORMATION

Figure 1 shows the tunnelling problem investigated in this paper. A 6 m diameter bored tunnel will be constructed using a slurry shield Tunnel Boring Machine (TBM) passing through the lower portion of a 10×5 pile group supporting a 23-storey high-rise building. The tunnel axis level is –23 metres Principal Datum (mPD). The segmental tunnel linings are 0.25 m thick. The geometry of the reinforced concrete frame structure building is 17.8 m wide × 8.8 m long × 70 m high, orientated perpendicularly to the tunnel alignment. The pile cap geometry is 17.8 m × 8.8 m × 1.5 m thick. The piled foundation system comprises 50 nos. of 0.6 m diameter (d) Franki piles, spaced at 3d c/c. The Franki pile is a cast-in-situ concrete pile with an enlarged base and a cylindrical shaft. The pile head and toe levels are –1.5 and –23 mPD respectively. In plan view, 15 nos. of obstructing pile toes are cut off as they intersect the tunnel. The pile toes in Column 2 and Column 1/3 are cut to a level of –19.7 mPD and –20.3 respectively, i.e. 0.3 m above the tunnel extrados.

The ground conditions comprise a 1.5 m thick sandy Fill layer, a 38.5 m thick sandy Completely

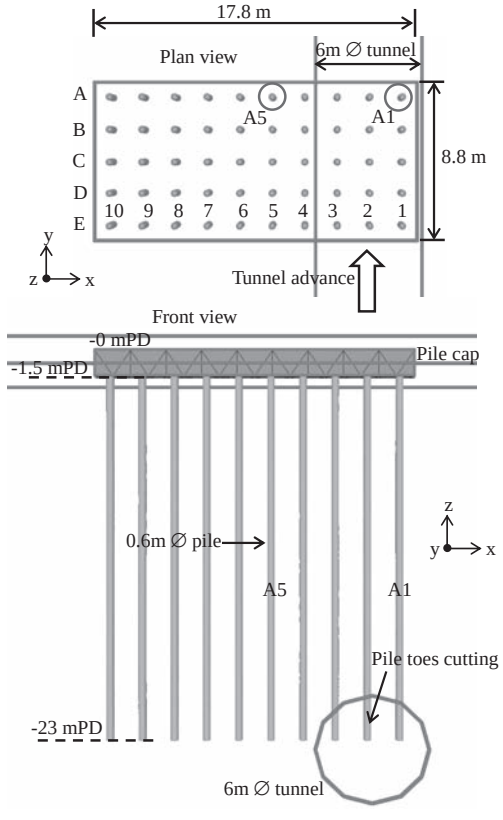

Figure 1. Investigated tunnelling problem.

Decomposed Granite (CDG) layer and bedrock. The ground surface and groundwater levels are 0 mPD and –1.5 mPD respectively.

3 DETAILS OF FEA

The tunnelling problem is analysed using a new commercial 3D FEA programme, Plaxis 3D 2010. Figure 2 shows the 3D model with the mesh refined around the tunnel and in the piled building area. The model geometry is 150 m wide × 120 m long × 40 m high, comprising 79,404 nos. of 10-noded tetrahedral elements. The top of the bedrock corresponds to the bottom boundary of the 3D model.

The non-linear stiffness of the CDG from very small strains ($\varepsilon = 1 \times 10^{-5}\%$) to engineering strain level ($\varepsilon = 1 \times 10^{-2}\%$ to 1%) is modelled using the Plaxis Hardening Soil-Small Strain Stiffness (HSsmall) constitutive model (Benz et al. 2009). The input parameters were calibrated by Lee et al. (2008) against Ng et al.'s (2000) triaxial results on CDG samples carried out at a mean effective stress

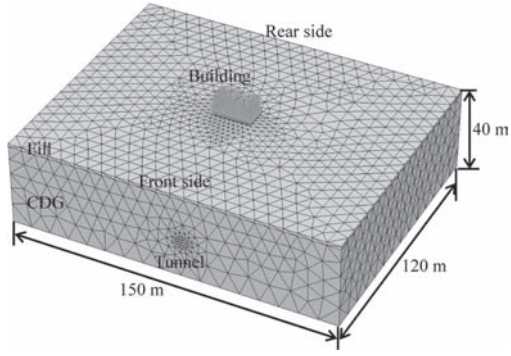

Figure 2. 3D FE model.

Table 1. Soil input parameters.

Parameters*	Fill	CDG
Soil model	HS	HSsmall
Material type	Drained	Drained
γ (kN/m^3)	19	20
E_{50}^{ref} & E_{oed}^{ref} (MPa)	20	39
E_{ur}^{ref} (MPa)	60	117
m [–]	0.5	0.5
c' (kPa)	0.1	5
ϕ' (Deg)	30	35
ν_{ur} [–]	0.2	0.2
p^{ref} (kPa)	100	200
K_0^{nc} [–]	0.5	0.43
G_0^{ref} (MPa)	-	200
$\gamma_{0.7}$ [–]	-	$5(10^{-5}$

* γ = unit weight, $E_{50}^{ref}/E_{oed}^{ref}/E_{ur}^{ref}$ = reference secant/tangent/unloading-reloading stiffness, m = power for stress-dependent stiffness, c' = effective cohesion, ϕ' = effective friction angle, ν_{ur} = Poisson's ratio for unloading-reloading, p^{ref} = reference stress for stiffness, K_0^{nc} = coefficient of earth pressure for normal consolidation, G_0^{ref} = reference shear modulus at very small strains, $\gamma_{0.7}$ = shear strain at $G = 0.722G_0$.

of 200 kPa. The Fill layer is modelled using the Plaxis Hardening Soil (HS) model, which considers the degradation of soil stiffness from a strain level of $1 \times 10^{-2}\%$. Table 1 presents the input parameters for the Fill and CDG.

The pile cap is modelled using linear elastic solid (or volume) elements with a Young's modulus (E) of 20 GPa and a Poisson's ratio (ν) of 0.15. A building loading of 350 kPa (or 47.6 MN) is applied on the top of the pile cap.

The piles are modelled using "Embedded Pile" structural elements. The embedded pile is a slender beam element connected to the surrounding soil by embedded skin (or shaft) and foot (or toe) interfaces (Engin et al. 2008). The pile diameter is input as 0.6 m with an E of 20 GPa, The pile heads are mod-

elled as pinned connections. The enlarged Franki pile base is not modelled. Break points are specified at the pile cutting levels of -19.7 and 20.3 mPD, and the process of pile toe-cutting is modelled by deactivating the pile sections below the two levels.

Potts & Addenbrooke (1997) proposed that the superstructure flexural rigidity (EI) could be estimated using either the Parallel Axis Theorem (i.e. bending about the building neutral axis) or the sum of EI for individual building storeys. The latter is adopted in the 3D analysis, where the superstructure rigidity is modelled using a "Plate" structural element located on the top of the pile cap with a conservative input EI of 3.1×10^8 kNm^2/m and an EA (axial rigidity) of 7.2×10^7 kN/m.

"Plate" structural elements are also used to model the tunnel linings with an input E of 30 GPa and a lining thickness of 0.25 m.

A step-by-step pressure method is used to model the progressive advance of tunnelling. For bored tunnelling in sandy soils, tunnelling contractors will usually apply a tunnel confinement (or face support) pressure defined as: confinement pressure = hydrostatic pore water pressure (pwp) + overpressure. Figure 3 shows the profiles of slurry pressure applied on the tunnel face and grout pressure applied along and around the TBM shield. For a hydrostatic pwp of 185 kPa at the tunnel crown, the modelled face pressures correspond to an overpressure of 20 kPa. The modelled linear varying pressure profile along the shield is to consider the conical shield where its diameter is slightly larger in the front than at the rear, over-cutting and relatively large volume loss into the tail void occurring at the rear of the shield. The pressure profiles could be varied to study the effect of varying the slurry/grouting pressure. It is noted that the shield itself is not modelled in the analysis.

For each advance of the tunnel face, the support pressures shown in Figure 3 are shifted forward by a lining ring width of 1.5 m and correspondingly, a new ring is erected behind the shield. This process is repeated as tunnelling progresses.

In total, three 3D analyses have been carried out as summarised in Table 2.

Analysis 1 is the baseline analysis with no grouting. Analysis 2 investigates the effect of the upper half of a 3 m thick grouted annulus around the tunnel over a horizontal distance of 12 m on reducing tunnelling-induced ground movements, see Figure 4a. The grout is modelled as a linear elastic, perfectly plastic Mohr Coulomb material with an E of 150 MPa, effective cohesion (c') of 100 kPa and effective friction angle (ϕ') of 35°. Analysis 3 models a full 3 m thick grouted annulus, see Figure 4b. Other modelling details for the three analyses remain the same.

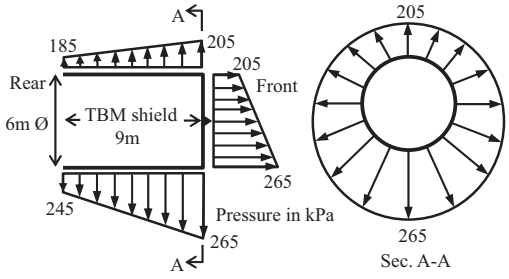

Figure 3. Modelled tunnel support pressures.

Table 2. Details of 3D analyses.

Analyses	Grout
1	No
2	Upper Half of 3 m thick annulus grout
3	Full 3 m thick annulus grout

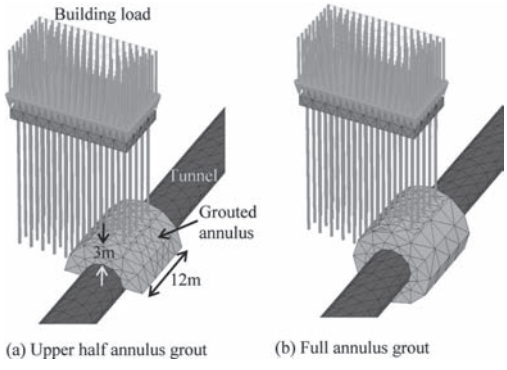

Figure 4. Parametric analyses on grouting effectiveness.

4 RESULTS OF 3D ANALYSES

Figure 5 shows the predicted deformations of the pile group when the tunnel face is well past the rear edge of the pile cap by 53 m for the baseline Analysis 1. The piles settle and displace horizontally towards the tunnel.

Due to space limitations, only results for the most critical pile A1 will be discussed in detail. In general, the A row of piles located in the rear edge of the pile cap show higher pile displacements/stresses. Figure 6 shows the tunnelling stages selected for presentation of results, which correspond to the tunnel face positions at 13 m, 7 m, 1 m before reaching the row A piles (denoted as –13 m, –7 m and –1 m respectively) and at 2 m, 53 m passing beyond the row A piles (denoted as +2 m and +53 m respectively).

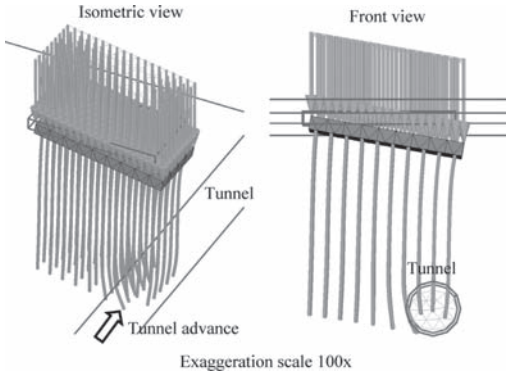

Figure 5. Predicted pile group deformations.

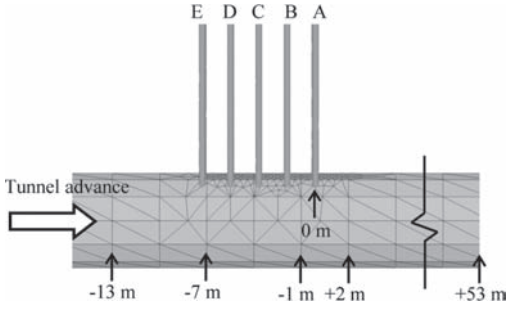

Figure 6. Selected tunnel face positions relative to row A piles.

Figure 7(a) shows the predicted settlements (u_z) of pile A1. At Stage –1 m prior to the pile cutting, the maximum pile u_z is 22 mm and the settlement at the pile head is larger than the pile toe. Immediately after the pile cutting (Stage +2 m), the maximum u_z increases to 29 mm and the settlement in the pile mid-section is smaller than the pile head and toe. At Stage +53 m, the final maximum u_z is 38 mm occurring at the pile toe.

Figure 7(b) shows the predicted axial forces (N) of pile A1. Up to Stage –1 m, the pile N increase due to negative skin friction induced by tunnelling. As the pile toe is cut at Stage +2 m, the pile N decrease due to undermining below the cut pile toe and correspondingly mobilisation of positive skin friction. At the final Stage +53 m, a portion of the cut pile toe experiences tensile forces with a maximum of –160 kN. Compared to the initial pile N profile before tunnelling (denoted as Initial), the final pile N has increased in the upper levels from –1.5 to –10 mPD and decreased in the lower levels from –10 to –20.3 mPD.

Figure 8(a) shows the predicted transverse horizontal displacements (u_x) of pile A1. The direction of u_x is perpendicular to the tunnel alignment.

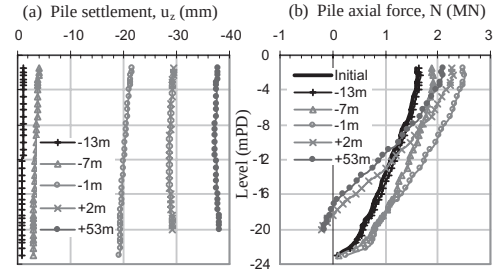

Figure 7. Predicted pile settlements and axial forces of A1.

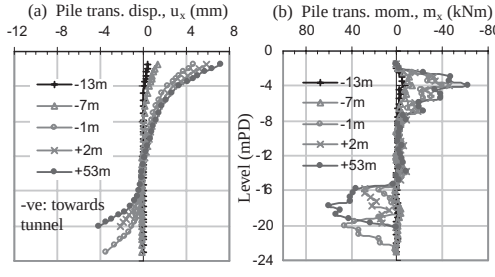

Figure 8. Predicted pile transverse u_x and m_x of A1.

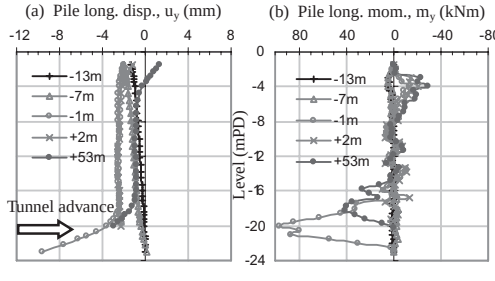

Figure 9. Predicted pile longitudinal u_y and m_y of A1.

The rate of pile u_x increases when the tunnel face approaches (Stage –1 m) and passes (Stage +2 m) pile A1. The final maximum pile u_x is 7 mm. The pile head u_x show positive values following the direction of pile cap/building horizontal displacements, whereas the pile toe u_x show negative values towards the tunnel centreline. Figure 8(b) shows the predicted transverse bending moments (m_x) of pile A1. A maximum pile m_x of 60 kNm is predicted at the –18 m PD level.

Figure 9(a) shows the predicted longitudinal horizontal displacements (u_y) of pile A1. The direction of u_y is parallel to the tunnel alignment. At Stage –1 m immediately prior to the pile-cutting, the pile toe shows a drastic increase in u_y to 10 mm towards the tunnel face, which is a transient value as the pile toe is cut off later. At Stage +53 m,

the final maximum u_y at the cut pile toe is 3 mm. Figure 9(b) shows the predicted longitudinal bending moment (m_y) of pile A1. A maximum m_y of 96 kNm is predicted at the –20 mPD level at Stage –1 m, which is a transient value. At Stage +53 m, the final m_y is 41 kNm occurring at the -18 mPD level. It is noted that the final pile horizontal displacement and bending moment are more critical in the transverse direction (final max. $u_x = +7$ mm, $m_x = 60$ kNm) than in the longitudinal direction (final max. $u_y = –3$ mm, $m_y = 41$ kNm).

Figure 10(a) shows the predicted settlements (u_z) of pile A5 located a horizontal distance of 2.4 m from the tunnel springline (see Figure 1). At Stage +53 m, the final maximum u_z is 25 mm. The pile head settlement is slightly larger than the pile toe settlement, indicating that negative skin friction is induced on the pile shaft due to tunnelling. Figure 10(b) shows the predicted axial forces (N) of pile A5. The pile N increase due to tunnelling, and the pile head N increases from an initial of 1003 kN to the final of 1191 kN at Stage +53 m.

Figure 11(a) shows the predicted transverse horizontal displacements (u_x) of pile A5. The whole pile has displaced horizontally towards the tunnel with a final maximum of 7 mm at the pile head. Figure 11(b) shows the predicted transverse bending moments (m_x) of pile A5. The final maximum m_x is 48 kNm occurring at the -18 mPD level.

Figure 12 shows the predicted building settlements (s_z) at the selected tunnelling stages for Analysis 1. The settlements are on the building rear edge. About 65% of the total building settlements occur up to Stage -1 m. The final maximum s_z is 40 mm, and the building settles and tilts as a rigid body.

Figure 13 compares the predicted greenfield ground surface settlement curve with the building settlement curve at Stage +53 m for the baseline Analysis 1. The greenfield curve represents a transverse section far away from the building, the location of which is not affected by the building/pile stiffness. The maximum building settlement of 40 mm is about 7 times larger than the maximum greenfield surface settlement of 6 mm, due to the pile-cutting and undermining below the cut pile toes. GCO (1985) observed the similar behaviour of building settlements being larger than greenfield surface settlements on a tunnelling project which involved cutting of pile toes located at the tunnel axis level. Lee et al. (2010) and Lee et al. (2011) also predicted the behaviour of building settlements being larger than greenfield surface settlements in 3D FEA analysing a building supported by a group of friction piles with the pile toe levels corresponding to the tunnel crown level.

Results for the parametric study Analyses 2 and 3 are compared to the baseline Analysis 1 in terms

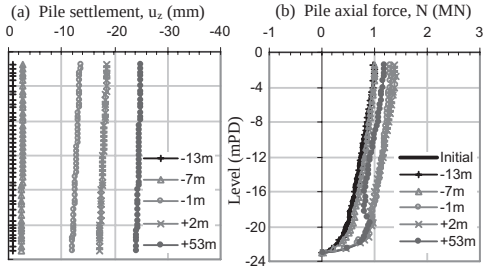

Figure 10. Predicted pile settlements and axial forces of A5.

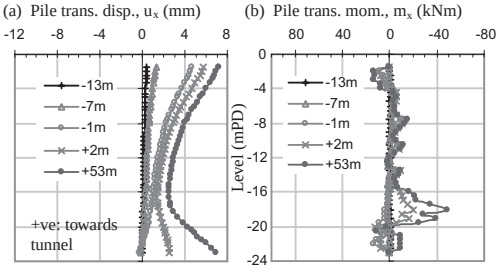

Figure 11. Predicted pile transverse u_x and m_x of A5.

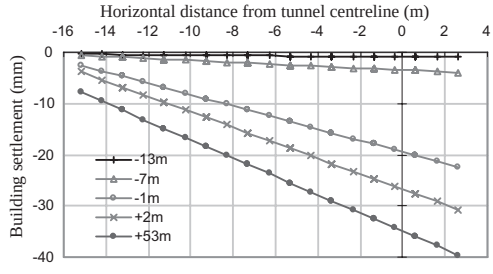

Figure 12. Predicted building settlements for Analysis 1.

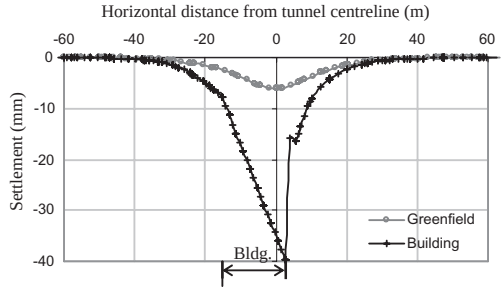

Figure 13. Greenfield & building settlements for Analysis 1.

of the predicted building settlements and selected responses of pile A1. Figure 14 compares the predicted final building settlements (s_z) at Stage +53 m between the three analyses. Analysis 2 modelling the upper half of a 3 m thick grouted annulus predicts 16 mm, whereas Analysis 3 modelling a full 3 m thick grouted annulus predicts the least maximum building settlement of 11 mm. This result suggests that if the grouting work is carried out close to the source of ground movements immediately around/in the tunnel area, the movement of the piles/building can be significantly reduced by 60% to 73%. To reduce further the building settlement, the thickness and length of the grouted annulus have to be increased.

Figure 15(a) compares the predicted settlements (u_z) of pile A1 at Stage +53 m between the three analyses. The half and full grouted annulus schemes reduce the maximum pile u_z from 38 mm (no grouting) to 15 mm and 11 mm respectively. Figure 15(b) compares the predicted axial forces (N) of pile A1 at Stage +53 m between the three analyses. Both grouting schemes predict compressive N throughout the pile length. This demonstrates the effectiveness of the grouted annulus schemes in reducing pile settlements and preventing the cut pile toe from experiencing tensile forces.

The predicted final pile N and m_x of pile A1 from the three parametric study analyses are checked against the pile axial force-moment (N-M) interaction chart of structural capacity, see Figure 16. Analyis 3 with a full 3 m thick grouted annulus has a higher margin of safety against exceeding the pile capacity envelope, followed by Analysis 2 with the upper half of a 3 m thick grouted annulus and Analysis 1 without grouting.

Figure 17 shows the predicted final building horizontal displacements and horizontal strains for Analysis 1. The maximum tensile horizontal strain (ε_h) is 1.7×10^{-4}%. The results from Analyses 2 and 3 are not presented because they are smaller than Analysis 1.

A check on the risk of building damage is carried out using Burland's (1995) assessment chart based on buildings deflection ratio (Δ/L) and ε_h. Please note that parameter Δ is relative deflection and L is length over the relative deflection range. For Analysis 1 the predicted maximum Δ/L is 7.1×10^{-4}% and maximum $_h$ is 1.7×10^{4}%. Figure 18 shows that the predicted category of risk of building damage is Category 0 (or Negligible) due to consideration of the building superstructure rigidity.

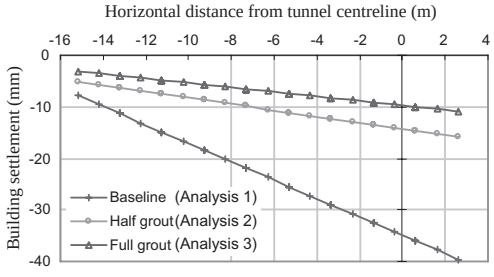

Figure 14. Building settlements for parametric analyses.

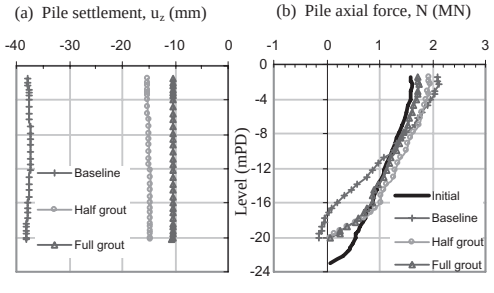

Figure 15. Results of parametric analyses for pile A1.

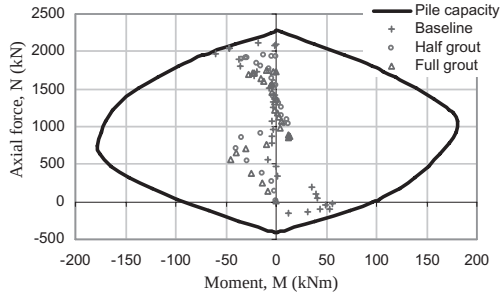

Figure 16. N-m_x of pile A1 vs. pile N-M interaction chart.

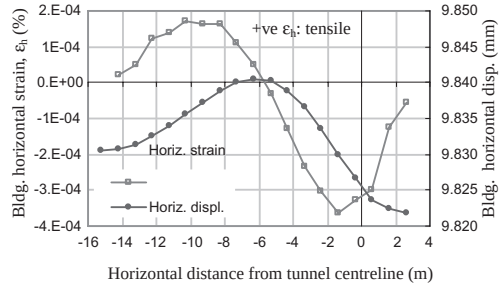

Figure 17. Building horizontal displacements and strains.

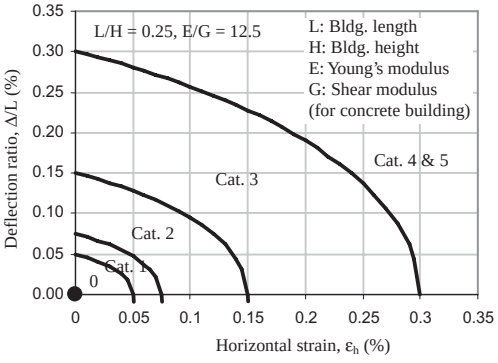

Figure 18. Burland's building assessment chart.

5 CONCLUSION

3D FEA have been carried out to model construction of a 6 m diameter bored tunnel intersecting the lower portion of a large pile group comprising 50 nos. of 0.6 m diameter friction piles supporting a high-rise building. The pile toe levels correspond to the tunnel axis level and 15 nos. of the obstructing pile toes are cut off as the tunnel passes through. A step-by-step pressure method is used to model the progressive advance of tunnelling with an overpressure of 20 kPa (i.e. the confinement pressure hydrostatic pore water pressure 20 kPa).

The most critical corner pile subjected to pile-cutting is predicted to settle by 38 mm. The pile axial force is reduced due to undermining below the cut pile toe, and a portion of the pile toe experiences tensile forces. The predicted final pile horizontal displacement (u) and bending moment (m) are more critical in the transverse direction (final max. u_x 7 mm, m_x 60 kNm) than in the longitudinal direction (final max. u_y -3 mm, m_y 41 kNm). An edge pile located at a horizontal distance of 2.4 m from the tunnel springline is predicted to settle by 25 mm and the pile axial force is increased due to the negative skin friction induced by tunnelling. The predicted maximum building settlement is larger than the maximum greenfield surface settlement by about 7 times without any protective measure.

Protective measures in the forms of the upper half of and a full 3 m thick grouted annulus around the tunnel are predicted to reduce the maximum building settlement from 40 mm (no grouting) to 16 mm and 11 mm respectively. Both grouting schemes can prevent the most critical cut pile from experiencing tensile forces near the toe. This result suggests that grouting work carried out close to the source of ground movements around/in the tunnel area is effective in mitigating tunnelling-induced ground movements.

The predicted pile axial forces (N) and bending moments (M) of the most critical pile are compared to the pile N-M interaction chart of structural capacity to check for potential over-stressing of the pile structurally. The predicted maximum building deflection ratio and horizontal tensile strain are plotted on Burland's assessment chart to determine the category of risk of building damage.

The numerical work presented in this paper has demonstrated the merits of using 3D FEA in analysing tunnel-soil-pile-building interaction problems in a rigorous manner. With advances in computing technologies, 3D FEA of practical geotechnical problems is now possible complementing conventional methods of analysis.

REFERENCES

Benz, T., Vermeer, P.A. & Schwab, R. 2009. A small-strain overlay model. *Int. J. Numer. Anal. Meth. Geomech*. 33: 25–44.

Burland, J.B. 1995. Assessment of risk of damage to buildings due to tunnelling and excavations. *Invited Lecture to IS-Tokyo'95, Int. Conf. on Earthquake Geotechnical Engineering*.

Engin, H.K., Septanika, E.G. & Brinkgreve, R.B.J. 2008. Estimation of pile group behaviour using embedded piles. *Proc. Int. Conf. 12th Int. Assoc. Comp. Methods Advances Geomech., Goa, India*: 3231–3238.

GCO 1985. MTR Island Line: Effects of construction on adjacent property. Geotechnical Control Office, Engineering Development Department, Hong Kong.

Lee, S.W., Choy, C.K.M., Cheang, W.W.L., Swolfs, W. & Brinkgreve, R. 2010. Modelling of tunnelling beneath a building supported by frictional bored piles. *Proc. of 17th Southeast Asian Geotechnical Conference, Taipei, May*: 215–218.

Lee, S.W., Choy, C.K.M., Tse, S.C., van Gool, F.R., Cheang, W.W.L. & Brinkgreve, R.B.J. 2011. Modelling of tunnelling near a building supported by large numbers of piles. *Proc. of 14th Asian Regional Conf. on Soil Mech. & Geot. Engrg., Hong Kong, May*: in press.

Lee, S.W., Pickles, A.R., Henderson, T.O., Li, E.S.F. & Cheang, W.W.L. 2008. 3D modelling of deep excavation in decomposed granite: influence of small strain stiffness and presence of individual piles. *Proc. of Applications on Innovative Technologies in Geotechnical Works, HKIE, Geot. Div. 28th Annual Seminar*: 171–180.

Ng, C.W.W., Pun, W.K. & Pang, R.P.L. 2000. Small strain stiffness of natural granitic saprolite in Hong Kong. *J. Geotech. & Geoenv. Engrg., ASCE* 126(9): 819–833.

Pang C.H. 2006. The effects of tunnel construction on nearby pile foundation. PhD thesis, National University of Singapore.

Plaxis 2010. Plaxis 3D Reference Manual, Version 2010, Release Candidate 1.

Potts, D.M. & Addenbrooke, T.I. 1997. A structure's influence on tunnelling-induced ground movements. *Geotechnical Engineering Proc. ICE* 125: 109–125.

This page intentionally left blank

Geotechnical Aspects of Underground Construction in Soft Ground – Viggiani (ed)
© 2012 Taylor & Francis Group, London, ISBN 978-0-415-68367-8

Geotechnical cut-off diaphragms for built-up area protection in urban underground development

N.S. Nikiforova & D.A. Vnukov
Gersevanov Research Institute of Foundations and Underground Structures, (NIIOSP), Moscow, Russia

ABSTRACT: Urban underground development necessitates protection of existing buildings, located within the zone of construction operations influence. Geotechnical cut-off diaphragm walls, erected between underground excavations (pits or tunnels) and existing buildings, are an effective protection tool. The paper describes cut-off diaphragm walls, made of steel pipes, cast-in-situ and deep-mix soil-cement piles and implemented on Moscow construction sites. Numerical and field data is presented, pertaining to geotechnical barriers erection between deep excavations or service tunnels and existing buildings. Recommendations are given for effective application of geotechnical cut-off diaphragm walls.

1 INTRODUCTION

Excavation of pits below 5.0 m depth and new service 2.5–4.0 m dia tunneling at 12.0 m depth in big cities for newly erected buildings with an underground basement requires protection of existing buildings within the influence zone of construction activities. Cut-off diaphragm walls between an underground excavation (a pit or a tunnel) and an existing building is an effective tool. Cut-off diaphragms can differ by their design (cast and intermittent walls, e.g. slurry walls, cast piles, steel piling walls) and by their erection technology (cast piles, secant cast piles, non-secant piles, cast screw piles and deep-mix piles) Geotechnical cut-off diaphragms are broadly applied in the city of Moscow for underground development. A cut-off diaphragm wall design depends on geotechnical and hydro-geological site conditions, on the distance of the existing building from subsurface excavation and on the respective "technological" settlement value i.e., the one, caused by a cut-off diaphragm wall erection. Comparison of settlement field data with PLAXIS 2D FEM simulation data enabled the authors to elaborate recommendations for effective application of cut-off diaphragms.

2 CUT-OFF DIAPHRAGM WALLS TO PROTECT DEEP EXCAVATIONS

Since 2008 a trade and business complex has been being erected in Moscow (1–24, 26/2/3 Arbat Str.). This is a framed multi-story building with two underground parking lots, having cast concrete bearing columns and floors. The building sits on a cast concrete slab. The excavation banks are retained by a cast slurry wall ~10.0 m deep.

The site is located within a densely built-up area. The subsoil is sand fill to 2.2–4.9 m depth with inclusions of construction debris, below till 15 m depth there occur interstratied sands of loose to medium density. Ground water occurs at 28 m depth.

The excavation pit influence zone reaches the E.Vakhtangov Theater (26, Arbat Str.), a historical brick three-story building, based on 0.48–5.73 m deep strip footings, erected in 1949 and now is at ~1,0 m off the excavated pit bank.

As per archive data the strip footing was partly strengthened by pressed-in 6 to 7 m long piles, not designed to bear extra loads from the new complex underground portion.

Maximum admissible extra deformations of the Theater building, as per Moscow Construction Code, are: settlement 10.0 mm, differential settlement 6×10^{-4}. Numerical analysis, made by Moscow State Building Construction University, forecast their value to be 12.0 mm. Therefore, prior to diaphragm slurry wall erection, a cut-off Ø250 mm piling diaphragm wall, reinforced with Ø219 × 8 mm steel tubes, was erected (Fig. 1).

The cut-off diaphragm wall was erected stepwise in the following sequence: at first a hole was augered under clay mud to the depth as per project design, then the hole was filled with cement-sand slurry through an injector-pipe, then welded steel pipe segments were sunk in (Fig. 2).

The geotechnical diaphragm wall erection was accompanied by considerable up to 20.0 mm extra settlements of the Theater office building (Fig.3). These settlements of the Theater footing sand bed

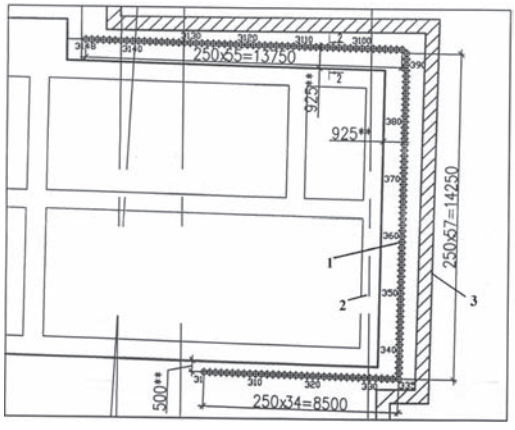

Figure 1. Geotechnical cut-off diaphragm layout.
1 – geotechnical cut-off diaphragm,
2 – Vakhtangov Theater building,
3 – slurry wall.

Figure 2. Geotechnical diaphragm wall for protecting the office building of the Vakhtangov Theater.

possibly resulted from soil loosening due to cut-off wall erection process.

The Theater building deformations, monitored during underground construction of the new complex, showed low effectiveness of the geotechnical cut-off diaphragm wall, as the maximum footing settlement was 40.0 mm i.e., more than threefold greater than the forecast value of 12 mm (Fig. 3).

Geotechnical cut-off diaphragm walls used at construction of tunnel-viaduct segment of the 3rd Transport Ring in Lefortovo district of Moscow in order to reduce deformations of nearby buildings (6, Tankovy Proezd and 8, Gospital'ny Pereulok).

Building 6, Tankovy Proezd, is a brick 4-story structure with longitudinal walls. The timber floors are supported by steel H-beams. The 2.1 to 2.4 m deep strip footings are made of crushed stone, fixed with lime mortar. Prior to tunnel construction the primary survey data showed unsatisfactory condition of the building. The bearing walls had cracks up to 3.0 mm wide.

Prior to the tunneling operations the building footings were strengthened by 160 mm dia 17 m long root piles. The maximum measured settlement during piling operations was 15 mm.

The admissible extra settlement of the building footings is 10.0 mm. The analytical extra settlement of the footings is 16 mm, and 7.0 mm if underpinned by piles, after cut-off wall erection the settlement is 8.0 mm.

During 4.5 m deep pilot pit excavation a 5.0 mm wide crack appeared in the building, extending from the 1st to the 4th story. The crack was caused by long-term soil saturation by a leak from a water line, coming from heating water line entry inside the building. After the leaks near the building were stopped a cut-off secant Ø650 mm 18 m long piling diaphragm wall was installed along the tunnel route and along two side façades of the building (Fig. 4). The piles were topped with 0.5 m thick cast concrete cap.

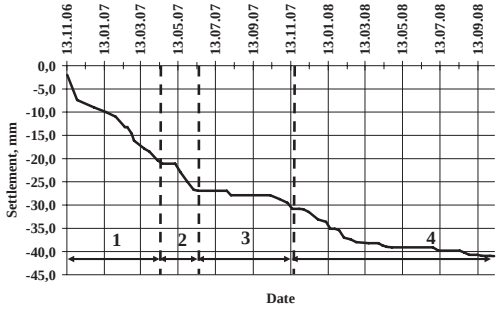

Figure 3. Vakhtangov Theater building maximum settlements.
1 – geotechnical cut-off diaphragm wall erection,
2 – slurry wall erection,
3 – excavation of pit,
4 – basement structures erection.

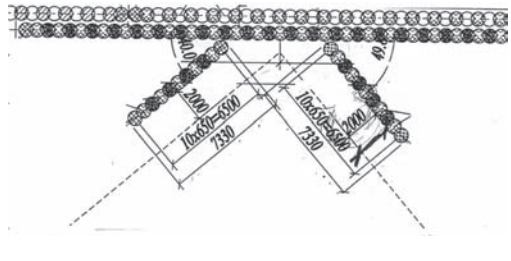

Figure 4. Overview plan of geotechnical cut-off diaphragm wall around a building (6, Tankovy Proezd).

Maximum registered settlement of the building footings, caused by protection measures influence, was, as follows: by root piling 15.0 mm, by cut-oft diaphragm wall 10.0 mm. Maximum registered settlement, caused by tunnelling, was 45 mm i.e., 5.5 times greater than the forecast 8.0 mm value. The forecast values did not take "technological settlement" into account.

3 APPLICATION OF CUT-OFF DIAPHRAGM WALLS TO PROTECT SEWAGE LINES

In the period from 2002 to 2003 service line tunnels for the Lefortovo tunnel were excavated, extending from substation 622 to Bakyninskaya Str. and along Lefortovo Embankment in parallel to N.E. Bauman Moscow State Technical University buildings.

The tunnel for underground cable service lines from substation 622 to Lefortovo tunnel was excavated with the help of 3.6 m dia shield.

The tunnel along building 61/67 on Bolshaya Poctovaya Str. was excavated in Jurassic stiff clays. The bottom of the tunnel was located at ~15.5 m depth from the surface. The distance from the tunnel axis to the building, along which the tunnel was excavated, was 8.0 to 9.0 m.

Geotechnical conditions along the tunnel route are, as follows: surface fill, underlain by water-saturated medium sands, underlain by clay loams on top of Jurassic clays, underlain by carbonaceous clays and fissured limestone.

The residential 5-story prefab panel house (61/67–5, Bolshaya Pochtovays) has 2.2 m deep basement. The building sits on 2.2 to 2.9 m deep strip prefab concrete footing.

The forecast deformations of 61/67, Bolshaya Pochtovaya Str. building were: maximum settlement 15.0 mm, differential settlements 0.0005.

Since Jurassic clay above the tunnel face is just from 1.0 to 2.0 m thick, the occurrence of unstable silt soft clay loams, and the fact that the forecast differential settlement reached the admissible limit of 0.0005 necessitated respective protection measures. NIIOSP recommended erection of a cut-off diaphragm wall between the footings of the building and the tunnel route.

The predicted deformations of the footings of building 61/67 on Bolshaya Pochtovaya, caused by the service tunnel with the protection cut-off diaphragm, were: maximum settlement 5.0 mm, differential settlement 0.0 i.e., less than the admissible extra values.

The geotechnical cut-off diaphragm wall was made of Ø159 × 10 mm 16.0 m long steel pipes, spaced 0.25 m in row, and topped by a cap made of B20 concrete. The cut-off diaphragm wall was continuous in order to exclude the barrage effect along the protected building. The diaphragm wall could be a dam for underground water (Fig. 5).

Measured mean building footing settlements on Fig. 6 caused by.

- Cut-off diaphragm wall erection: maximum settlement 6.0 mm, differential settlement 0.00046 i.e, less than admissible settlements;
- Cut-off diaphragm wall erection plus service line shield tunneling: maximum settlement 15.5 mm, differential settlement 0.00089.

The measured settlement was less than the admissible extra value of 20.0 mm, while differential settlement was times 1.8 less than admissible extra settlement value of 0.0005.

The authors analyzed the measure values of deformations and fixed the real quantity of volume loss 2.5%. After that the FEM analysis was made with volume loss 2.5%. Model Mohr-Coulomb was used. Grounds conditions were described at the beginning of this part of the paper. The tunnel was modeled by Plaxis 2D v. 8.

Figure 5. Erection of a cut-off diaphragm wall, made of bore steel pipes between the service tunnel and the existing building 61/67, Pochtovaya Str. in Moscow.

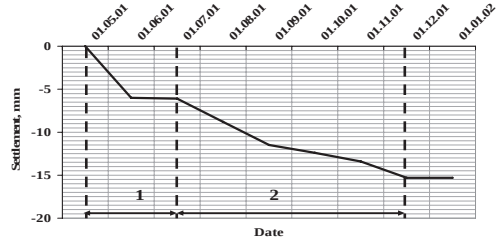

Figure 6. Mean footing settlements of building 61/67, Bolshaya Pochtovaya Str.
1 – cut-off diaphragm wall erection.
2 – service tunnel shield driving.

Also, for calculation scheme (Fig. 7) there has been identified for buildings of different structural design and condition, with due account of admissible extra deformations of the ground under footings and technological settlements, caused by screw bore pile cut-off diaphragm wall erection, a zone i.e., a distance from the building to the service tunnel axis, in which the cut-off diaphragm wall reduces the deformations of the ground to the admissible value (Table 1). If this distance is less than the one, given in Table 1, than the cut-off diaphragm wall application is ineffective. We established additional admissible values of deformations (settlements and relative difference of settlements) earlier and included it to Moscow normative document (Ilyichev V. A. et al., 2005).

Thus, footing "technological settlement" shall be taken into account for buildings at the project design stage, caused by geotechnical cut-off diaphragm wall erection. It is necessary to know the settlements of the ground surface, caused by shield tunneling, from the monitoring data of projects in similar geotechnical conditions in order to establish the actual value of soil excess excavation ratio.

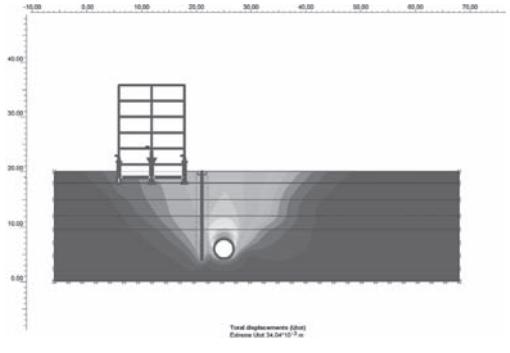

Figure 7. Geotechnical situation simulation.

The service tunnel dedicated to Lefortovo tunnel along Lefortovo Embankment was mined in parallel to the North and South Buildings of N.E. Bauman Moscow State Technical University with the help of 2.56 m dia shields at 6.0 to 8.0 m from the building at 3.5 m depth from the ground surface. The shield tunneling was conducted under 3.5 m fill layer in soft sand loams.

Building 5 on Lefortovskaya Embankment (Bauman Moscow State Technical University, North Building) is 6-story, built in early 1950s, has internal frame with concrete columns and steel girders, no basement, on 1.4 m deep concrete strip footing. A 7.0 m deep cut-off diaphragm wall, made of two rows of deep-mix 1200 mm dia piles is 1.4–2.8 m off the building. The piles in the row, nearest to the service tunnel route, were reinforced (Fig. 8).

Admissible extra settlement of the building is 10 mm. Numeric Plaxis geotechnical simulation was conducted as a part of the geotechnical monitoring package. The results showed that the value of extra footing settlement, caused by service tunnel driving, with no cut-off diaphragm wall, is 25 mm, while that with the cut-off diaphragm wall is just 7.0 mm. Mean measured settlement, caused by erection of the cut-off diaphragm wall was 8,0 mm and 4.0 mm from service tunnel construction 4.0 mm (Fig. 9).

Hence, deep-mix pile cut-off diaphragm wall along the North Building of the Bauman Moscow State Technical University enabled two-fold reduction of footing settlements, induced by service tunnel shield driving in soft clay soils.

The authors investigated behavior of cut-off deep-mix piling diaphragm walls in loose water-saturated sands, erected to protect the existing built-up area on Gruzinsky Val Str. for the project "Traffic Interchange, Multi-Level Underground Parking Lot and Trade Complex on Tverskaya Zastava Sqr." in Moscow. Notably, the service tunnel construction at 4 m depth below the ground

Table 1. The zone of effective application of cut-off diaphragm wall for service tunnel driving from substation 622 to Bakuninskaya Str. along the building 61/67 on Bakuninskaya Str.

Type of building	Admissible value (settlements/ relative difference of settlements)	Technical condition of the building	Distance from the building to the service tunnel axis, for which cut-off diaphragm wall application is feasible (m)
Multi-story no-frame buildings with large prefab panel bearing walls.	30 mm/0.0008	Satisfactory	9 to 11
	20 mm/0.0005	Unsatisfactory	Not feasible
Multi-story no-frame buildings with bearing walls, made of large-size blocks or non-reinforced brickwork	30 mm/0.0010	Satisfactory	6 to 9
	10 mm/0.0007	unsatisfactory	13
Multi-story buildings with bearing walls with reinforced concrete belts	20 mm/0.0010	unsatisfactory	6 to 9

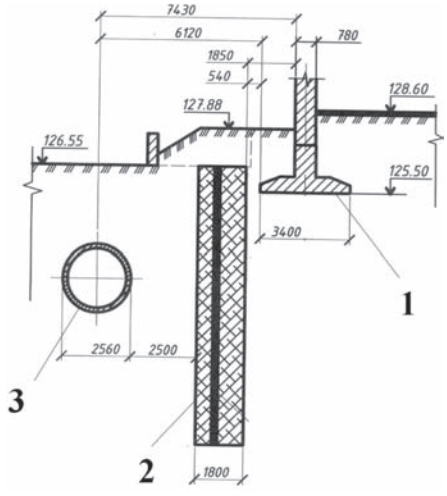

Figure 8. Geotechnical cut-off diaphragm wall near North Building of Bauman Moscow State Technical University.
1 – footing,
2 – geotechnical cut-off diaphragm wall,
3 – service tunnel.

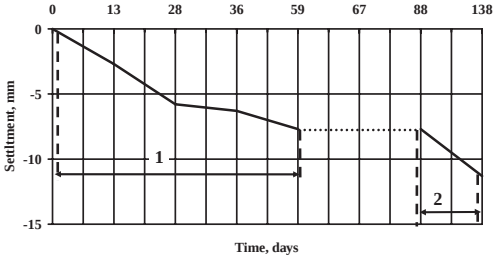

Figure 9. Footing settlements vs time. North Building of Bauman Moscow State Technical University.
1 – cut-off diaphragm wall erection,
2 – service tunnel shield driving.

surface in up to 5 m thick fill, with inclusions of construction waste, and in underlying loose water-saturated sands with the help of shield tunneler Lovat RME 163 SE was done for the first time in Moscow, and the tunnel route was viewed by NIIOSP as a test site. "Lovat" guaranteed the value of soil excess excavation ratio to be 1.78, however, NIIOSP performed the analysis for two values of excess excavation ration: 1.78 and 3.0. Cut-off diaphragm walls were recommended for two buildings, located on the service tunnel route 10.12 m deep, made of combination of concrete tubes and deep-mix piles. Geotechnical cut-off deep-mix piling diaphragm walls were applied as

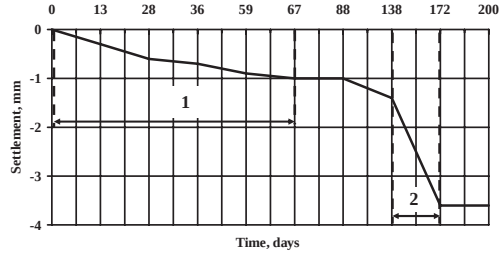

Figure 10. Footing settlement diagram of the building on 11–5, Gruzinskaya Str.
1 – geotechnical cut-off diaphragm wall erection,
2 – shield mining of service tunnel.

emergency to control water saturated sands breakthroughs into shield driving face space.

Cut-off diaphragm walls were erected, as follows: concrete tube piles were first installed through Ø180 mm pilot holes, spaced at 400 mm, in which Ø159 × 6 mm steel pipes were sunk, further filled with cement-sand grout, then deep-mix piles were cast in the space between the deep-mix piles. The Ø110 mm pilot holes were advance-drilled to the design depth, then back jet-grouted.

The building measured settlement, caused by cut-off diaphragm wall erection, was 1 to 3 mm, while the settlement, caused by service tunnel shield mining, was 2 to 5 mm, with admissible additional value for such buildings being 10.0 mm (Fig. 10). No new defects or existing defects evolution were observed.

The authors obtained empirical dependencies, based on of field data during service tunnels mining on Gruzinsky Val Str. and on Lefortovskaya Embankment for evaluation of technological settlements of building footings, starting from erection of the cut-off diaphragm deep-mix Ø700 mm piling wall in loose water-saturated sands and Ø1200 mm piling wall in soft clay soils (Nikiforova, N.S. & Vnukov D.A. 2010).

4 CONCLUSIONS

1. Numerical and field investigations showed that vertical cut-off diaphragm walls do not always reduce settlements of footings of buildings within the zone of deep excavations influence to admissible value. The measured final settlements of building footings are found to be 4.0–5.5 times greater than the forecast analytical values.
2. Diaphragm wall installation settlements were equal to 20 to 50% measured final settlements.
3. It is recommended to consider the option of tilted cut-off diaphragm walls for deep excavations.

4. Vertical continuous cut-off diaphragm walls option may be viewed as an emergency counter-measure to control water-saturated sands breakthrough into the face space in front of the shield or into the slurry wall trench.
5. Vertical cut-off diaphragm walls shall be used to reduce settlements of existing buildings and to evaluate the distance from the building to the service tunnel route. If this distance is less than a certain value then a cut-off diaphragm wall is ineffective.

REFERENCES

Ilyichev, V.A. et al., 2005. *Grounds, footings and underground structures. MGSN 2.07–01.* Government of Moscow, Russia.

Nikiforova, N.S. & Vnukov, D.A. 2010. Cut-off diaphragm walls to protect buildings during service tunnels excavation.

Geotechnical Aspects of Underground Construction in Soft Ground – Viggiani (ed)
© 2012 Taylor & Francis Group, London, ISBN 978-0-415-68367-8

Greater Metro Line 3, Cairo: Installation of underground construction pits using cut-off-wall and soft-gel-grouting

L. Liersch
Technical Services, BAUER Spezialtiefbau GmbH, Schrobenhausen, Germany

M. Baltruschat
Grouting Department, BAUER Spezialtiefbau GmbH, Schrobenhausen, Germany

ABSTRACT: The publication will give an overview on the preparation and execution of applied special foundation methods and a detailed description regarding installed soft-gel-plugs at the Greater Cairo Metro Line 3. Detailed description will explain general assumptions during tendering and design of grout-plugs, preparation of equipment, grouting procedure during execution and quality assurance activities (checking of drilling inclination, reporting of grouting) as well as reached final results.

1 GENERAL INTRODUCTION

Cairo, biggest city of the Islamic hemisphere, has approx. 25 Million inhabitants. Due to increase of local traffic, narrow streets, construction sites or broken cars, daily traffic jams (Fig.1) and chaos on streets can be seen as usual.

The first tramway opened in 1896 and tram is still an important part of public transportation. Additionally, there are approximately 2600 busses and countless mini busses, transporting approximately 1.3 Billion customers per year. Anyhow, they are also depending on free and accessible roads.

The most important public transport system therefore is the Metro (Fig. 2), existing since 1987. Two lines with a total length of 61.5 km are already in operation and transporting approximately 950 Million customers a year (2004). Metro Line 3, connecting the airport to the city of Cairo, is already under construction and planned in several parts. The "National Authorization for Tunneling"(NAT), a Department of Ministry of Transport is the client for all construction activities.

2 CONSTRUCTION ACTIVITIES

2.1 *Design and methods*

BAUER Egypt, contracted as a subcontractor of Metro Line 3 JV, executed the installation of open excavation pits for the start shaft of TBM and 4 stations with several ventilation shafts. Excavation and foundation levels for stations (Fig. 3) had been planned up to 26 m below ground water level and required cut-off-retaining-walls and soft-gel-grouting-plugs down to 60 m depth. Retaining walls, as well as separating trenches in the construction area had been installed as reinforced concrete cut-off-walls (cow) using several BAUER-cutters. Soil conditions at given sites had been investigated being cultural refill material (stones, concrete) and sand with silt or clay layers.

After enclosing of a complete box, grouting activities started by installation of multi-stage valves at the design depth of soft gel plug. Installation had been done by two phase method: drilling with 133 mm drilling rods and grouting with soft gel. Soft gel prepared as a mixture of sodium silicate and reactant had been prepared by a continuous mixer and grouted by using 13 pumps grouting container. Soft-gel-plugs had a thickness from 4.5 to 8.5 m.

Stations are located under existing roads. Depending on traffic, the roads had to be closed completely or half-side and traffic temporary diverted. Stations had been executed as water tight construction with cut-off-walls and grouting plug. Afterwards, the JV started excavation and construction of interior parts using top down method with temporary stiffening (Fig. 4).

The tunneling machine (TBM), installed as a slurry-shield machine by Herrenknecht, has a diameter of 9.8 m and is driving from one station to the next station and manual shifted within the stations (Fig. 5). Connections to the stations, as well as to maintenance and to air circulation shafts had been made with installing a sealing block by cut-off-wall, cut by the TBM.

Figure 1. Traffic jam in Cairo.

Figure 2. Roadmap of Metro Lines in Cairo.

2.2 *Staff and equipment*

All together 100,000 m² cut-off-wall in different thicknesses and approx. 18,000 m² soft-gel-plug, installed with 360,000 m drilling holes had to be executed. Main equipment had been chosen to BAUER-cutters BC20, BC30, BC40 and CBC 25 (at low head room) for cut-off-wall and two B28 with 42 m one-shot-drilling boom extension for soft-gel-plug. Grouting had been done using two fully automatic 13-pumps-grouting-container. BAUER Egypt executed the project under there own responsibility, supported by technical preparation, management engineering as well as

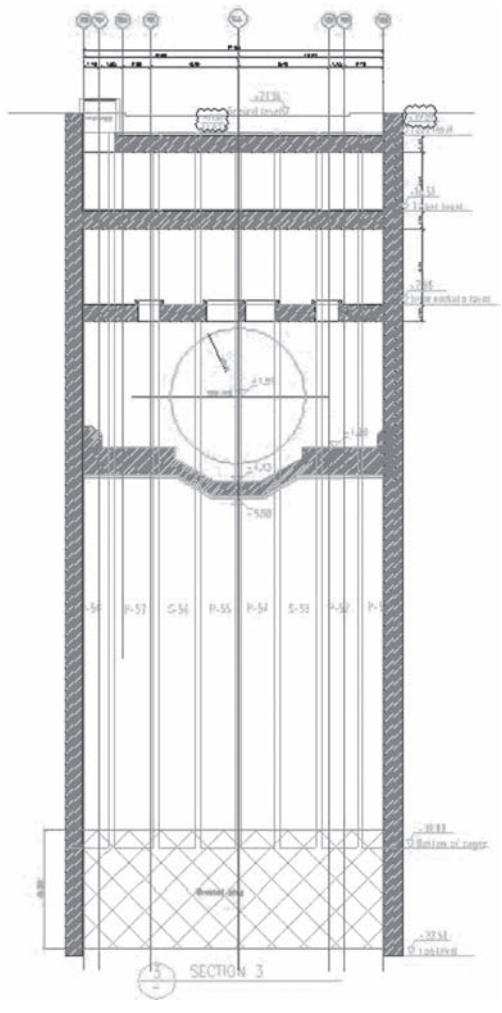

Figure 3. Cross section of a station.

Figure 4. Top down excavation with temporary stiffening.

Figure 5. Slurry-shield-TBM during shifting.

Figure 6. Site installation for cut-off-wall.

supervising staff at site. During the main activities approx. 400 people as local staff had been employed at site.

3 CONSTRUCTION OF CUT-OFF-WALL

3.1 *Design and method*

During the installation of cut-off-walls, the excavation of trenches down to the final depth usually will be done using cutters. Cutter wheels are cutting the soil and spoil will be removed mixed with bentonite slurry. Bentonite slurry is used as supporting as well as transportation fluid for spoil. De-sanding units, installed at site separate excavated spoil from the Bentonite slurry, see Figure 6.

At the Metro Cairo, perimeter cut-off-walls had been designed using steel reinforcement. Considering a cutting of cow along the axis by the TBM, these sections had been fitted by installing fibered glass reinforcement. Generally, cow dimensions had been chosen to a thickness of 1.2 to 1.5 m and a depth of 30 to 60 m following the primary–secondary sequence, primary panels had a length of 8 m and secondary of 2.8 m.

Following a usual method steps, the cow will be installed by cutting an open trench, stabilized with Bentonite slurry, followed by the de-sanding and cleaning of the trench. After the installation of the reinforcement cages, concrete has to be poured into the trench without any break using several tremie pipes.

3.2 *Production*

Considering the previously mentioned traffic problems, all site deliveries (steel, bentonite) and removal of spoil or wasted bentonite had been done during night shift. Especially during the pouring of concrete at the primary panels (requiring in part more than 500 m^3 of concrete), the main focus had been on a stable concrete supply. Therefore, the JV installed close to the sites two ready-mix-concrete-plants allowing a stable supply 24 hours a day.

Reinforcement cages had been prefabricated delivered to the site and ready assembled at a yard on site. After finishing a complete panel, cages had been lifted, using a table, and installed into the trench lengthwise by coupling of several cages.

Stations had been planned using the complete space under existing roads. So, space at site had been limited by the width of the road and the planned length of a station. Using the complete area for production, only at the front faces of each station site installation for offices, batching, storage and recycling of slurry was possible. Using the complete width of the already existing roads, at several stations no public traffic, except pedestrian traffic was possible along the site. Increasing the challenges, a road had been closed only half

Figure 7. BAUER-cutter in front of occupied houses.

side at Bab El Sharia (Fig. 8) leading to only half a space at site and finally double organization expense.

The complete utilization of the street width implied the installation of cow direct in front of partly more than 100 years old houses with unknown foundation design and in a state of disrepair.

Considering a lot of houses in state of disrepair, in preparation of the project all houses surrounding the stations had been investigated and documented according their conditions. Having doubts of sufficient stability, houses had been bought or evacuated before starting activities (Fig. 9).

Another challenge had been handled by execution of cow under several existing bridges with maximum limited working high of 5 m. In this area activities had been executed using a BAUER CBC 25 low head room (Fig. 10).

All together 10 construction sites, distributed over a wide area of Cairo, had completely different soil conditions, but had to be handled with the given equipments and methods. So, in some areas clay layers had to be penetrated with the cutter, leading to well known problems with sticky cutter wheels and thickening of bentonite slurry.

3.3 *QA/QC*

Walls had to be installed as permanent walls under very sensitive conditions (refilled substrata, houses in a state of disrepair). To ensure no collapse or insufficient durability, monitoring instrumentation had been installed for the installation of cow and the behaviour of the structure and the surrounding buildings.

The installation of cow had been done under very close monitoring and supervision. A fully automatic documentation for deviation and twist *etc*. installed into the cutter gave a complete picture for predicting overlapping of joints and location of

Figure 8. Production during half side diverted traffic.

Figure 9. Old houses had to evacuated before starting cutting activities.

Figure 10. Low head room CBC-cutter under a existing bridge.

wall for excavation phase. Additional monitoring for rheological properties of slurry (viscosity, yield point, sand content, filtrate loss and filter-cake) and workability as well as hardened properties of concrete had been done assuring integrity and durability of wall.

Considering adjoining buildings as well as different static retaining systems during excavation and strutting, a surveying system (fixed points, inclination, movements of walls) had been installed and operated during the complete construction.

All together, the monitoring showed a very safe installation of cow, without any collapses and no water and soil delivering gabs during excavation.

4 GROUTING PLUGS

4.1 *Design and tendering*

Considering the soft ground with high water levels, open construction pits have to be sealed by a grout plug in a depth, safe against uplift forces. The installation procedure for grout-plugs is shown in Figure 11. To have proper sealing against water access, the cow had to be installed up to the depth of plug and the plug grouted afterwards. Depending on water level, excavation depth and specific soil gravity, the cow had been designed at depth between 37 m (Abassia station) and 60 m (El Geish station).

Considering a required excavation level of 20 to 27 m and an existing water pressure of 14 to 25 m the thickness of plug can be calculated. For all plugs a gradient of i = 3 for the existing water pressure had been requested by the client. Grouting plugs had been chosen to a thickness of 4.5 m (Abassia station) to 8.5 m (Bab El Sharia station). All together, more than 120,000 m³ of soil had to be treated and sealed.

Considering a deviation of 1 to 2% for drilling, grid had been fixed, assuring both: no exceeded space between grouting points with insufficient treatment of soil and less overlapping of drilling points with the risk of damage grouting points. Finally, triangular grid usually had been considered with a space of 1.5 to 2.5 m.

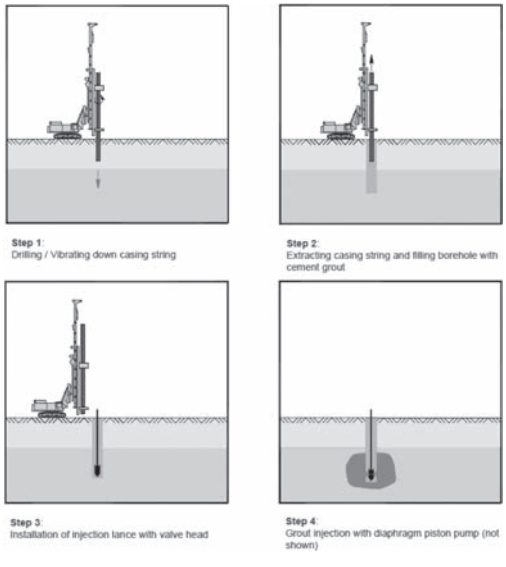

Figure 11. Installation procedure for grout-plugs.

4.2 *Adaption of the BAUER grouting system*

Following grouting activities at the Metro Line 1 and 2, the client requested Grouting by TaM-pipes and the application of cement-grout/chemical-grout with Sodium-bi-carbonate. During the tender stage and approval by the client, BAUER negotiated recommended grouting system and own experiences as following:

4.2.1 *TaM-pipes vs. multi-stage-valve-system*

Knowing advantages and disadvantages of the system like less vertical space between grouting stages or grouting, stage wise with intensive flushing of pipes, BAUER decided to install a multi-stage-valve-system (Fig. 12) as a bundle of several valves, fitted to a multiple-grouting-pipe. At every drilling point one bundle with valves distributed over the thickness of plug had been installed. This was the first time, the valve system had been applied at Metro Cairo, anyhow the system had been approved at many projects before.

4.2.2 *Grouting of cement/chemical grout with Sodium-bi-carbonate*

BAUER executed several grouting-plugs with cement-grout as well a chemical-grout using Sodium-bi-carbonate or Sodium-aluminate as reactant. Knowing risks of insufficient penetration and permeation of soil by cement grout, caused by soil fracturing, or insufficient stability of carbonated hardener, BAUER decided to use Chemical Grout with Sodium-aluminate hardener only.

Figure 12. Grouting valve for installation of grout-plug.

Figure 13. Chemical grouting body at a test field excavation.

4.2.3 *Grouting depth vs. uplift force*
Installation of up to 8.5 m thick grout plugs has to assure getting the lowest permeability at a depth, save against buoyancy. Especially at sites with irregular soil composition, minimum two grouting stages and main grouting quantities had been positioned two meters below depth of buoyancy.

4.2.4 *Design volume*
Considering the soil investigation reliable, the volume of grout had been calculated according grain size distribution and given void ratio of 30 to 40%. Anyhow, the volume had been overestimated by an additional grout volume considering a worst case event to compensate a given average drilling deviations in opposite directions as well as a partly escape of grout upwards. Final grout volumes for main points at plug had been fixed to partially more than 2400 l/point.

4.2.5 *Grouting procedure*
Depending on plug thickness and number of grouting stages, an individual grouting procedure had been fixed for every site. Usually, the procedure involves several phases of grouting vertical, to assure a covering from top and an increased treatment at bottom. Grouting in horizontal direction usually had been considered as fresh grouting in fresh grouting following the wave-theory.

4.2.6 *Grouting pressure*
Grouting pressure has not chosen to a fixed value, but tried to avoid pressures above 25 bar. During the grouting, the residual grouting pressure had been monitored and recorded automatically by measuring the total grouting pressure, reduced by the measured skin friction for every line.

4.2.7 *Estimation of flow rate*
Flow rate had been prefixed to a certain value, considering experienced monitoring at previous sites, theoretical assumptions based on soil permeability and finally reviewed regarding the pressure development and pressure drops monitored during the grouting.

4.3 *Production*

Following the tendered requirements, as well as explained and negotiated procedure, BAUER installed grouting valves, using two BG 28 with a 50 m boom extension, fitted to a one-stage-drilling-depth of 42 m (Fig. 14). Grouting holes had been refilled with Bentonite-Cement-Grout as a sleeve mix to seal installed valves. Grouting had been done using two 13 pumps grouting containers. Material had been delivered by trucks and stored in silos. Considering a scheduled time space between drilling and grouting, the grout–plug had been installed very fast and efficiently.

In order to reduce the risk of failure, as well as having an early handing over of already finished areas, station pits had been separated into several (max. 5) segments using concrete participants walls. Before handing over, every segment had been checked for water access by a pumping test.

4.4 *QA/QC and pumping tests*

In order to achieve a prediction for ground treatment, drilling and grouting had been monitored automatically as well as manually and fitted by additional features as visible below:

4.4.1 *Drilling*
Fully automatic documentation with records for every drilling point showing different graphs vs. depth for speed, thrust, torque, flow rate, flow pressure, used mixture, execution time. Multi-stage

Figure 14. Installation of 60 m deep grouting hole for soft-gel-plug using BG28.

grouting valves had been assembled at site and checked for length of tubes and positioning of valves. Confirming and reviewing the grout quantities, valve position had been checked at 20% of holes by inclinometer measurement.

4.4.2 *Grouting*

Grouting also had been documented using the full automatic documentation unit of the grouting container with following parameters: grouting time, Grout mixture, graphics for flow rate, quantity and pressure. Additional manual record sheets for the grouting procedure with executed numbers of grout valves, sequence and additional information for fresh grout gravity, shear strength of the sleeve mix, setting time of grout or unexpected occurrences, being prepared by the grouting operator.

4.4.3 *Pumping test*

Checking all documentation records, main point had been considered for perfect numbering and documentation of drilling points, as well as drilling deviation. For the grouting phase, main attention was laying on grouted points as well as pressure development. After reviewing all documents, site management decided executing of pumping tests. For every pit segment a pumping test had been done. After leveling down the water to the target level, remaining water access had been evaluated. Results showing values for dewatering of 0.03 to 0.85 l/sec*1000 m^2, which corresponds to a permeability of $7*10^{-7}$ to $2*10^{-8}$ m/sec

5 RESULT AND PERSPECTIVES

Reviewing on results of the project, BAUER had to handle a lot of technical challenges, all production deadlines had been followed, without any disturbance or collapses or increased water accesses. Using the well known cow method, BAUER also introduced a lot of changes for grouting with procedures, which are widely different from the previous applied grouting techniques at Metro Line 1 and Metro Line 2. The method itself had been applied at many projects with more than 300,000 m^2 plug installation, but anyhow hasn´t offered to the NAT before. After an initial review and skepticism regarding success and risk management by the JV and the client (NAT), the grouting method could be shown as an effective and safe method for soil treatment. A high leveled quality work handed over to the full convenience of the JV and the client. All unexpected problems had been solved in cooperation of the BAUER-Network in a current interest, leading to new contracts for BAUER at Phase 2 of Metro Line 3. Furthermore, BAUER executed the installation of a 97 m deep cut-off-wall-shaft and soil stabilisation with freezing method for rescuing of lost slurry-shield-machine.

This page intentionally left blank

Geotechnical Aspects of Underground Construction in Soft Ground – Viggiani (ed)
© 2012 Taylor & Francis Group, London, ISBN 978-0-415-68367-8

An interpretation of jet grouting effects on the retaining structures of a deep excavation and on adjacent buildings

E. Fontanella, L. Callisto & A. Desideri
University of Rome 'La Sapienza' Rome, Italy

A. Sciotti & C. Ottaviani
Roma Metropolitane Rome, Italy

ABSTRACT: This paper deals with the effect that an extensive jet grouting treatment produced on pre-existing structures. For the excavation of the new underground station of Conca d'Oro in Rome, adjacent jet grouted columns were created, that connected the two opposite diaphragm walls to provide horizontal contrast, and to reduce the hydraulic flow into the excavation. The jet grouting operations induced significant movements of the diaphragm walls and of the adjacent buildings, that were monitored carefully during the entire construction process. The monitored quantities allowed to establish relationship between the induced structure deformations and some jet grouting parameters, such as the daily production rate and the cumulative number of the jet grouted columns. On the basis of the monitoring results, it was also possible to devise an interpretation of the mechanisms that regulate the jet grouting-induced soil displacements.

1 INTRODUCTION

Displacements induced by deep excavations on the adjacent structures are becoming a basic concerns related to the construction of new underground infrastructures in urban areas.

Vertical displacements at surface points are a result of displacements induced at larger depths, that propagate upwards. Schematically, the main sources of vertical settlements at the ground surface can be thought to be (a) the horizontal displacements of the retaining structures; and (b) the stress-relief-induced heave of the soils located below the bottom of the excavation (Burland *et al*. 1979).

Horizontal wall displacements can only partially be limited by props or anchors, because these constrains can be installed only after the excavation has reached the corresponding elevation. Bottom heave is a direct consequence of the reduction in vertical stress associated with the excavation, and cannot be limited with ordinary support techniques. It is therefore tempting to improve the mechanical properties of deep soil layers within two facing retaining walls in a construction stage that antecedes the commencement of the excavation (pre-strutting), in order to restrict the horizontal wall movements from the earliest excavation stages, and to limit the bottom heave.

Soil improvement at large depths may be achieved with jet grouting, producing secant jet grout column to form a treated layer characterized by increased stiffness and strength. If the jet grouting-treated soil is coarse-grained, the treatment has also the beneficial effect of reducing the soil permeability and hence to minimize any water inflow related to the hydraulic head difference between the external soil and the excavation bottom. This technique was used in a number of projects (Gaba 1990, Sugawara et al. 1996), often involving jet grouting in fine-grained soils.

Jet grouting consists of an erosion of the soil through a very high fluid pressure, with a concurrent injection of grout. Because of the high pressures employed, the soil is not only cut, but also displaced laterally; this effect is more evident in fine-grained soil, and can lead to significant soil movements that can affect the retaining walls and may propagate up to the soil surface (Wong & Poh 2000). The following sections illustrate the ground and structure displacements produced by an extensive jet grouting treatment employed for the pre-strutting of a deep excavation. It is shown that it is possible to relate these detrimental effects to the main characteristics of the grouting and to the specific soil profile encountered.

2 PROJECT DESCRIPTION

The line B of the Rome underground is being extended northwards, (B1 extension) with the

addition of three new stations. Figure 1 shows a plan view of the deep excavation needed to accommodate the Conca d'Oro Station: it has an elongated shape, with a length of about 170 m and a width variable between 22 and 35 m. This plan view also shows the location of four boreholes and three CPT verticals, and the position of a portion of the monitoring instruments that is relevant to the data presented in this paper. This instrumentation consists of inclinometer tubes, inserted both into the diaphragm wall and in the soil external to the excavation; and a large number of topographical benchmarks for the precision levelling of six buildings adjacent to the excavation.

Figure 1 also shows a longitudinal and a transversal section through the new subway station. The soil profile consists of a top layer of made ground, with a thickness of 7 to 9 m, overlying a thick alluvial deposit of medium-soft silty clay. The clay fraction of this deposit increases below the depth of 17–18 m and the soil becomes less consistent, with an undrained shear strength of the order of 80-100 kPa, that becomes lower than 50 kPa in the central zone of the excavation. A sandy gravel layer is found below this soft fine-grained deposit, at depths generally larger than 40 m, with the exception of the North-East section of the excavation, where it emerges and is encountered at depths smaller than 30 m.

The excavation has a depth of 24.6 m and is retained by two facing reinforced concrete diaphragm with a thickness of 1.2 m, reaching a

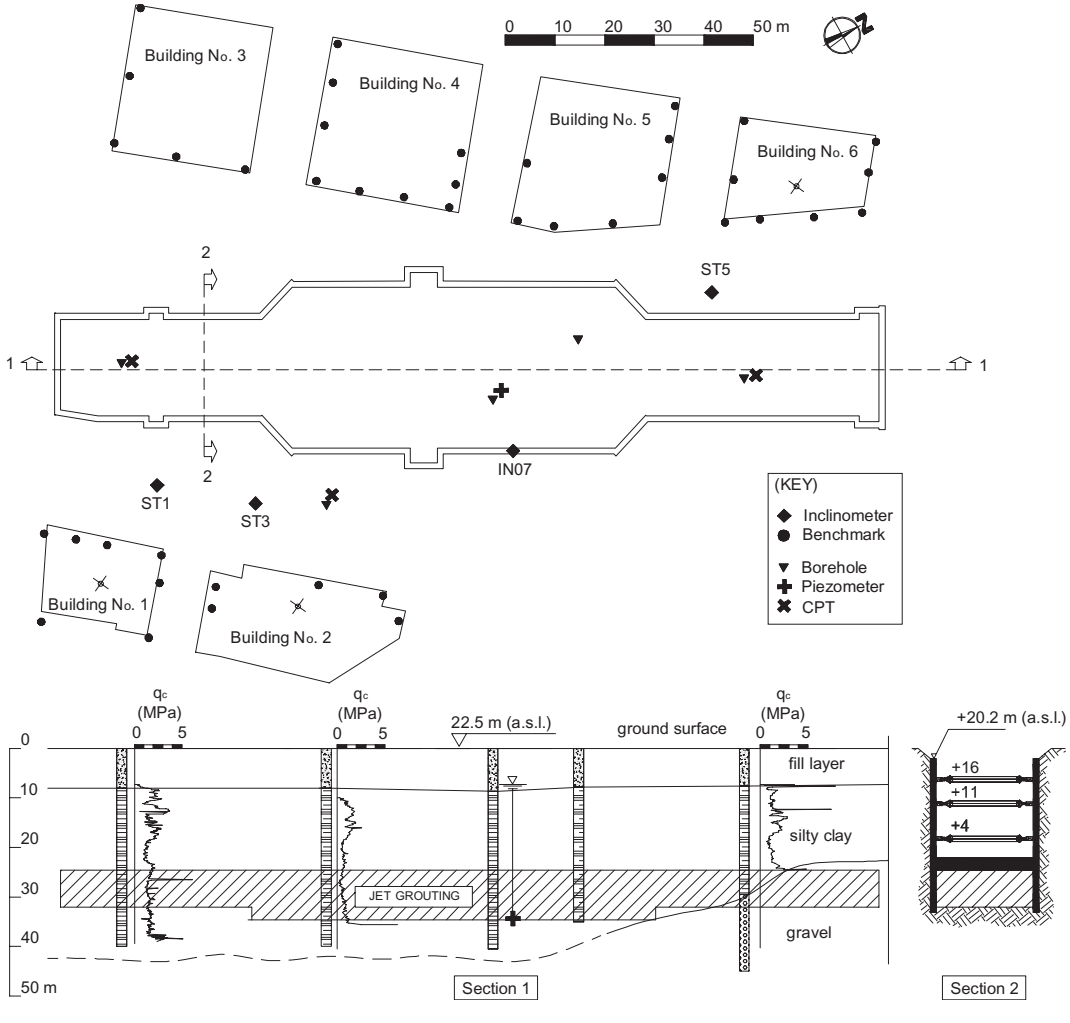

Figure 1. Conca d'Oro subway station in Rome: plan view with an indication of the monitoring instruments mentioned in this paper, and vertical sections with soil profile and jet-grouted levels.

depth of 33.1 m. The excavation was carried out with the bottom-up technique, installing progressively three levels of temporary tubular steel struts, casting a bottom concrete slab, and erecting the internal reinforced concrete structure that gradually replaced the temporary struts.

After a preliminary excavation down to the depth of 2.3 m, a pre-strutting soil treatment was carried out by jet grouting into the soil encountered at a depth interval of 25 to 32–35 m, as indicated in Figure 1. The soil treatment consisted of the formation of secant jet-grouted soil columns, with a diameter of 1.5 m, arranged in a triangular pattern with a spacing of 1.04 m, as shown in Figure 2. The nominal overlapping percentage associated with this pattern is equal to 73%. Figure 1 shows that the treated soil belong mostly to the fine-grained alluvial deposit, with the exception of the North-East section of the station, where the sandy gravels are encountered below the bottom of the excavation.

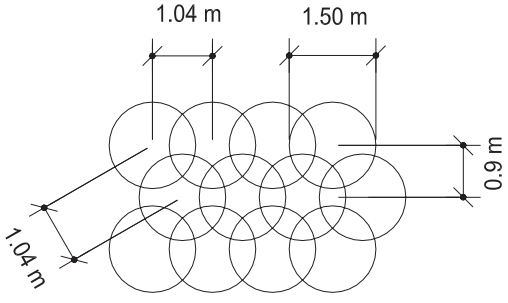

Figure 2. Planimetric arrangement of the jet-grouted columns.

The project area was sub-divided into three sectors: A, B, and C. Table 1 reports the main jet grouting parameters used in the different sectors. In Figure 3, for each sector a temporal bar chart shows the actual daily rate of treatment performed, and, on a separate scale, the cumulative number of columns produced. The grouting operations started in Sector A, with a gross average rate of about 7 columns per day, but with peaks of 22 col./day. The jet grouting was of the double-fluid type, involving a fast rod rotation (12 rpm) and a 45 MPa grout injection pressure.

The jet grouting in Sector C was carried out initially at an average rate of 8.5 col./day for the first 3.5 months, and then proceeded at a very slow

Table 1. Jet grouting parameters.

Operation parameter	Value
Sector A	
Specific energy	57.82 MJ/m
Grout injection pressure	45 MPa
Grout flow rate	0.275 m^3/min
Air pressure	1 to 1.2 MPa
Rod withdrawal rate	0.21 to 0.37 m/min
Rod rotation rate	12 rpm
Water cement ratio	1:1
Sectors B and C	
Specific energy	55.19 MJ/m
Grout injection pressure	41 MPa
Grout flow rate	0.340 m^3/min
Air pressure	1 MPa
Rod withdrawal rate	0.25 to 0.26 m/min
Rod rotation rate	5 rpm
Water cement ratio	1:1

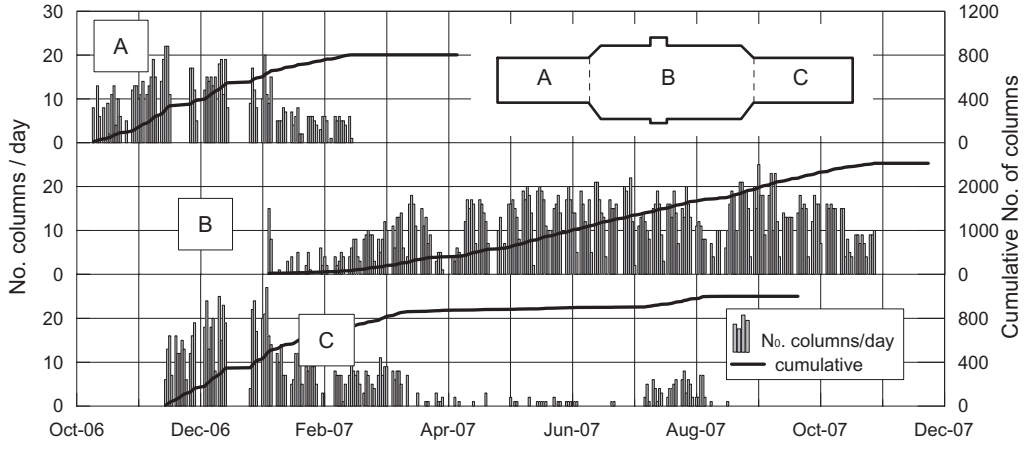

Figure 3. Daily and cumulative production rates of the jet grouted columns.

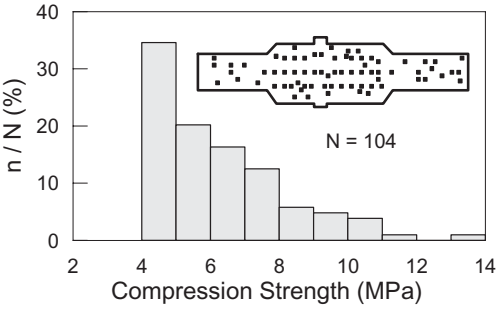

Figure 4. Distribution of the unconfined compression strength measured on core samples retrieved from the jet grouting columns.

rate. Peak rates over the first two months exceeded 25 col./day. In Sector B, after a low initial treatment rate, an average rate of about 11 col./day was maintained, with daily peaks of 20 columns. The jet grouting parameters in the B and C sectors were different, however, involving a much slower rod rotation and a somewhat larger grout flow rate (see Table 1).

A total of 104 core samples of jet-grouted soil were retrieved below the final excavation level, and were subjected to unconfined compression tests. The histogram of Figure 4 shows the distribution of the observed unconfined strength. All the tested samples showed a strength larger than the contractual requirement of 4 MPa. The effectiveness and spatial continuity of the treatment was also checked using a cross-hole seismic tomography. The measured shear wave velocities ranged between 900 and 1100 m/s.

3 INTEPRETATION OF THE MONITORING RESULTS

Figure 5 shows the horizontal displacements of the inclinometer tube IN07, measured during the jet grouting operation. This inclinometer was installed into a wall panel, and the horizontal displacement at the tube head was monitored with an independent topographic survey. Figure 5a shows the displacement time history of the inclinometer head, while Figure 5b shows the profiles of the measured horizontal displacements at selected time instants. In July and August 2007 the topographical measurements were temporary suspended: hence, the observations carried out after August 2007 were corrected on the basis of the previous displacement gradient, as shown in Fig. 5a.

The inclinometer IN07 is located in Sector B, and was very sensitive to the soil treatment carried out in this area: the jet grouting operations

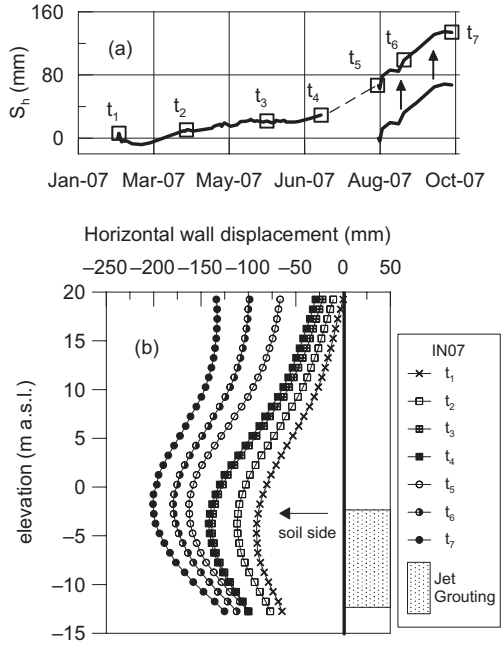

Figure 5. Horizontal displacements induced by the jet grouting, measured at inclinometer IN07, installed in the diaphragm wall.

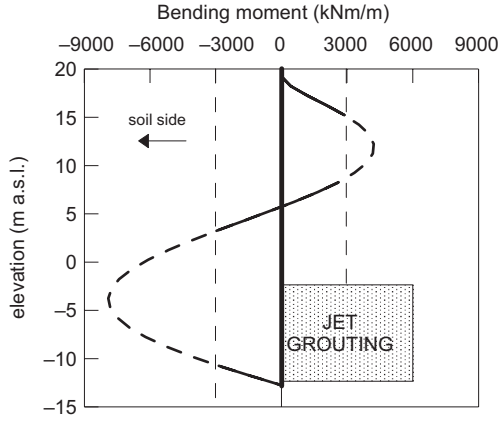

Figure 6. Bending moment profile in diaphragm wall, computed from the measurements shown in Figure 5.

displaced the wall panel away from the prospective excavation by an amount as large as 130 mm. The temporal increase of the horizontal displacements resembles closely that of the cumulative number of columns produced in sector B (see Fig. 3). An estimate of the bending moments in the panel associated with this displacement was obtained through a numerical differentiation of the displacements profile, assuming a nominal bending

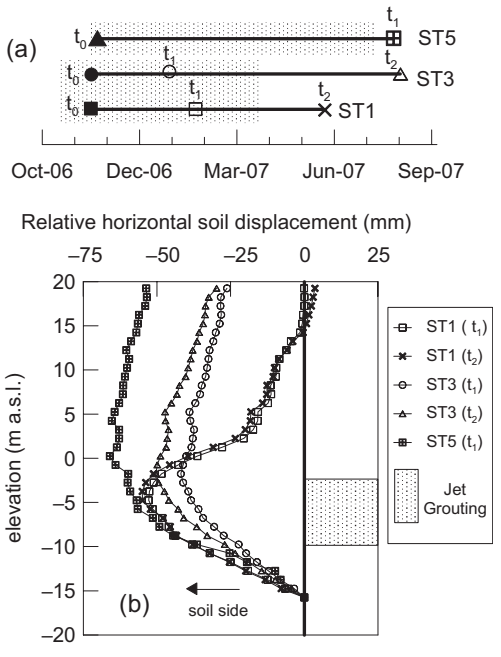

Figure 7. Horizontal displacements induced by the jet grouting at inclinometers ST1 and ST3, installed in the soil, external to the excavation.

stiffness $EI = 5.33$ GNm^2/m. The resulting bending moments are shown in the plot of Figure 6: as the wall bending capacity is close to 3000 kNm/m, it can be seen that the displacements induced by the jet grouting produced an extensive yielding of the diaphragm wall.

Figure 7 shows profiles of the horizontal displacements measured at inclinometer tubes ST1, ST3, and ST5, installed in the soil, midway between the excavation perimeter and Buildings No. 1, 2, and 6, respectively. As no independent measurement of the tube head displacement was carried out, the profiles in this figure represent merely the horizontal displacement relative to the tube toe. The maximum relative displacement induced by the jet grouting along these verticals is similar, reaching 50 to 65 mm, but the shape of the profiles is different: the displacements along the vertical ST1 show much larger gradients at an elevation corresponding roughly to that of the grouted layer, suggesting the occurrence of some grout leakage from the panel joints. The displacement profiles of inclinometers ST3 and ST5 have a gentler slope, that is probably a result of a more uniform displacement of the diaphragm wall away from the excavation.

The horizontal displacements induced by the jet grouting in the wall panels and in the surrounding soil resulted in appreciable movements of the six buildings adjacent to the excavation perimeter. The vertical movements of the topographic benchmarks of Figure 1 were precision-levelled continuously. This paper presents data relative to Buildings No. 1, 2, and 6, that are all founded on bored piles. For a single building, the vertical displacement at a given time instant were least-squares fitted with an interpolating plane. Figure 8 shows, for this three buildings, the vertical displacement w of the reference points shown in Figure 1, read on the interpolating plane, and the slope (α) of the plane in a direction orthogonal to the excavation. Positive values of w denote heave, while positive values of α signify a rotation of the building away from the excavation area (see Figure 8a).

The composite diagram of Figure 8b is relative to Building No. 1, and shows the time histories of w and α, together with that of the horizontal relative displacement of the inclinometer tube ST1 (located between the building and the excavation perimeter) at an elevation of –4 m a.s.l. These time histories are compared with the daily production rate and with the cumulative column production for Sector A. (Note that monitoring of the ST inclinometer tubes was commenced somewhat later than the initiation of the jet grouting.) As a consequence of the jet grouting, the building heaves, reaching a maximum vertical displacement of 7.5 mm, and rotates away from the excavation ($\alpha_{max} = 1.2 \times 10^{-2}$ deg).

A salient feature of Figure 8a is that the horizontal displacements have a temporal trend analogous to that of the cumulative jet grouting production, while the trend of the vertical displacements and rotations of the building is very similar to that of the daily production rate. Any pause in the jet grouting production rate resulted very clearly in a reduction of the building heave and rotation. After the completion of the treatment in Sector A, the horizontal soil displacements remained about constant, while a progressive reduction of the building displacements was observed, down to the somewhat constant residual values of $w = 2$ mm and $\alpha = 3 \times 10^{-3}$ deg.

A possible interpretation of the mechanism at stake for this building is schematically depicted in Figure 9. Because the soil encountered at the jet grouting elevation is fine-grained, it can be expected that the horizontal deformation induced by the formation of the jet-grouted column is, at least partially, undrained. In the short term, the volumetric strains in the soil can only be very small, and any horizontal displacement must be accompanied by a vertical heave, and by a corresponding increase in the pore water pressures (Figure 9a). The nature of the horizontal displacements is largely permanent because the hardened treated columns constitute a rigid inclusion in the soil. After any pause in

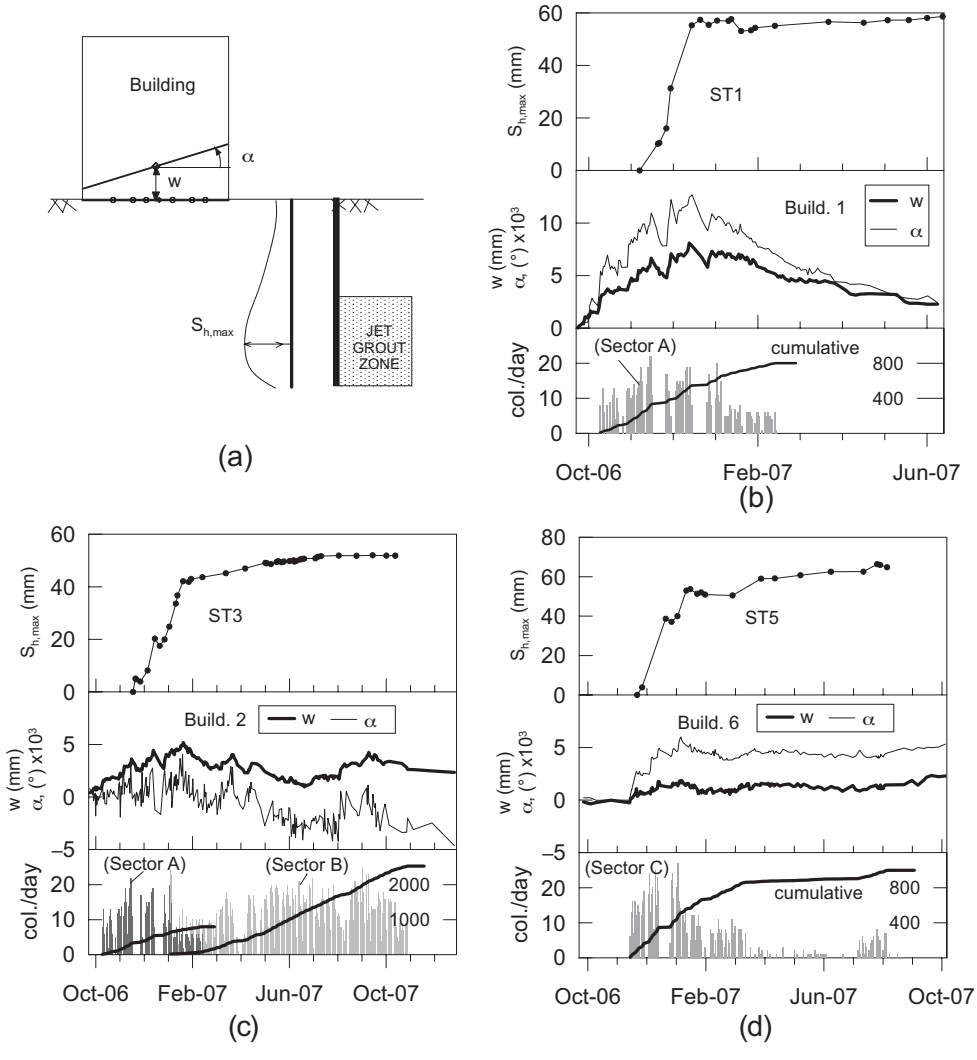

Figure 8. Time histories of horizontal displacements in the inclinometer tubes and vertical displacements of the corresponding buildings, compared to the jet grouting daily and cumulative production rates.

the treatment, and at the end of the jet grouting process, consolidation takes place, involving a reduction of the excess pore water pressures and a recovery of most of the vertical displacements (Figure 9b). Residual vertical displacements may be ascribed to the deviatoric components of the strains induced by the jet grouting, and to some leakage of the grout through the panel joints.

The displacement pattern for Building No. 2 is more complex (Figure 8b), because arguably this building was influenced by the jet grouting carried out in both Sector A and Sector B. However, the overall behaviour is quite similar to that outlined for Building No. 1: jet grouting caused an horizontal permanent displacement of the soil located between the building and the excavation area, as indicated by inclinometer ST3. The building heaved (w_{max} = 5 mm) and showed a very slight rotation, initially away from the excavation, and subsequently in the opposite direction. Once again, vertical displacements are very sensitive to the daily treatment rate, and are partially recovered as a consequence of any pause in the treatment. Between February and July 2007, jet grouting was carried out predominantly in the North-East portion of Sector B, and therefore interested only marginally the building, that recovered a significant portion of the previous heave. Subsequent jet

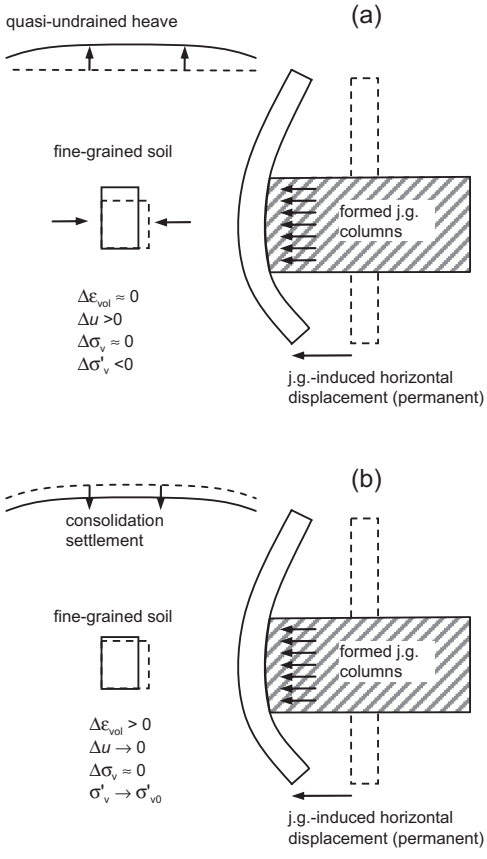

Figure 9. Interpretation of the observed horizontal and vertical displacements induced by the jet grouting.

grouting in the portions of Sector B closer to the building produced an additional heave, that was partially recovered after the completion of the jet grouting works.

Building No. 6 was affected by the jet grouting activities carried out in Sector C. Inspection of Figure 8d showed that for the present building a somewhat different behaviour was observed. The movements of the soil between the building and the excavation (inclinometer ST5) showed the usual trend: a permanent horizontal displacement comparable with that of other areas, with a temporal trend strongly related to the cumulative number of treated columns. Conversely, the building showed very small vertical displacements (w < 1 mm) and rotations, that were only marginally sensitive to the daily production rate, but rather increased progressively with the cumulative number of treated columns.

This atypical behaviour is to be related to the local soil profile: Figure 1 shows that Building No. 6 is situated in the North-East area, where a coarse grained gravel deposit is found at the jet grouting elevation. It can then be argued that the horizontal strains imposed by the jet grouting in this layer occurred in a drained manner, producing volumetric compression strains in the gravelly soil and little or no vertical displacements. The sensitivity to the treatment rate that is still perceptible in the plot of Figure 8d was probably due to the fine grained upper deposit, that were deformed in undrained conditions, but were only marginally interested by the displacements resulting from the jet grouting treatment.

4 CONCLUSIONS

The formation of a jet-grouted layer between facing diaphragm walls at the Conca d'Oro station produced large horizontal displacements in both the walls and the surrounding soil. The distortions in the reinforced concrete walls were significant, reaching in some cases the structure's bending capacity.

One of the reasons that prompted the use of a pre-strutting technique for this excavation was the need to minimize any effect of the excavation on the existing buildings located next to the excavation. However, the jet grouting itself produced, together with horizontal soil movements, vertical displacements and some distortion of these buildings.

A comparison between the temporal variations of several quantities, including the production details of the jet grouted columns and the displacements of the soil and the buildings, provided some insight into the mechanics of the jet grouting-induced displacements. Specifically, the vertical heave associated to jet grouting was seen to depend strongly on the local soil profile.

Jet grouting can be thought to create an inclusion between the two facing diaphragm walls that progressively expands, displacing the walls, but also hardens, making the horizontal displacements irreversible. If this expansion process were drained, it would cause only marginal vertical heaves, because the pore water pressures would remain stationary, and the total vertical stresses cannot vary for equilibrium. If the displaced soil is fine-grained, it is forced by its low permeability to deform at quasi-constant volume. Therefore, excess pore water pressures are generated, that cause a decrease in the effective vertical stresses and substantial vertical strains. This effect is mostly temporary, because the excess pore water pressures are dissipated during consolidation, and in the long term the vertical effective stresses recover their initial value.

It follows form this discussion that the vertical heave produced by jet grouting can be somewhat mitigated by performing the treatment with a low production rate, while the horizontal displacements of the walls cannot, being directly related to the geometry of the planned treatment, e.g. the amount of column overlapping and the planimetric extension of the treated area.

Admittedly, the present interpretation is partially speculative, since it is based on the measurement of integral quantities only, such as the horizontal and the vertical displacements at selected points. To be further substantiated, it would benefit of additional measurements of local quantities, and particularly of the observation of the variation of pore water pressures in fine-grained soils, with appropriate quick-responding piezometric cells.

REFERENCES

Burland J.B., Simpson B. & St John H.D. (1979). Movements around excavations in London Clay. In: *Design parameters in geotechnical engineering*. VIII ECSMFE Brighton Sept 79. BGS, London, Vol. 1, 13–29.

Gaba A.R. (1990). 'Jet grouting at Newton Station, Singapore. Proc. 10th Southeast Asian Geotech. Conf. Chinese Institute of Civil and Hydraulic Engineering, Taipei, Taiwan, 77–79.

Sugawara S., Shigenawa S. Gotoh H. & Hosoi T. (1996). Large-scale jet grouting for pre-strutting in soft clay. Proc., 2nd Int. Conf. on Ground Improvement Geosys.: Grouting and Deep Mixing, Balkema, Rotterdam, The Netherlands, 353–356.

Wong I.H. & Poh T.Y. (2000). Effects of jet grouting on adjacent ground and structures. *Journal of Geotechnical and Geoenvironmental Engineering*, Vol. 126, No. 3, 247–256

Geotechnical Aspects of Underground Construction in Soft Ground – Viggiani (ed)
© 2012 Taylor & Francis Group, London, ISBN 978-0-415-68367-8

Compensation grouting of piled foundations to mitigate tunneling settlements

F.J. Kaalberg
Adviesbureau Noord/zuidlijn/Witteveen + Bos, The Netherlands

R.D. Essler
Adviesbureau Noord/zuidlijn/RD Geotech Ltd, UK

Remco Kleinlugtenbelt
Dienst Noord/zuidlijn/Witteveen + Bos, The Netherlands

ABSTRACT: The Amsterdam North/South Metro line is a challenging project in an adverse urban environment of very soft soil and historical buildings founded on wooden piled foundations close to the tunnels. Following successful full scale trials, compensation grouting was selected as the most preferable method for mitigating movements. The final design was optimised by introducing an "interception design philosophy" with the TAMs installed midway between the tunnels and the pile toes, minimizing the risk of settlements during drilling. Being novel, an observational approach was applied, installing a single layer initially. Hydraulically jacked segmental shafts, new to the Netherlands, were able to meet the very strict settlement criteria and significantly reduce the hindrance to the urban environment. During the preconditioning phase, the buildings were heaved by approximately 4 mm. During tunnelling the single layer of TAM's provided good control and compensated the tunnelling induced settlements. In this paper the innovative design and observational construction approach will be explained and the results discussed.

1 INTRODUCTION

The Amsterdam North/south Metro scheme includes 3.8 km of twin tunnels of diameter 6.5 m. which pass through the centre of the city from Central station in the North to RAI in the south.

The tunnels are constructed using an Mixshield tunnel boring machine to reduce volume loss and disturbance to the environment. The previous section of the Amsterdam Metro was constructed in the 1970s through the city centre using cut and cover techniques and resulted in significant disruption and damage. The City Council was determined that the North-South section would be constructed with minimum environment disruption and so settlement mitigation was considered necessary for certain locations along the route.

Along the tunnel route more than 1000 historical buildings exist mainly all founded on wooden piles driven through the very soft clays to a sand layer. At locations where the tunnels are curving, volume loss would be expected to be higher and the design recognized that at these locations, mitigation of tunneling settlements would be needed (Kaalberg *et al*, 1999).

Design for the scheme commenced in 1995 and at an early stage (1999), compensation grouting was identified as a suitable solution to mitigate the settlements. As the use of compensation grouting in association with wooden piled foundations was not known, the project carried out a full scale trial (van der Stoel *et al*, 2002 and Hasnoot *et al*, 1999). Model foundations were constructed at a location along the line of the Sophia tunnel and compensation grouting during TBM passage was successfully carried out. This trial gave confidence to the use of this technique in Amsterdam and it then formed part of the contract requirements.

2 GROUND CONDITIONS

The ground conditions relating to the tunneling and compensation grouting comprised the following strata (and thicknesses):

1. Fill (1 m)
2. Very soft clays (12 m)
3. 1st Sand layer (2 m)
4. Allerod (2 m)
5. 2nd Sand layer (6 m)

The Allerod is a silty/clayey strata of variable composition. The general succession is illustrated on Figure 1 and 2.

Groundwater is very close to ground level.

3 CONTRACT DESIGN

The contractor initially had design responsibility for the compensation grouting and submitted an outline design for the required grouting and shafts specified within the documents.

3.1 *Compensation grouting design*

The contractor, as part of his bid submission, had produced an outline design which followed the geometry of the trial very closely with the injection pipes installed in a horizontal layer very close (1 m) to and below the pile toes, Figure 1. This had been necessary for the trial at Sophiatunnel as the TBM passed very close to the model pile foundations.

For the Amsterdam contract situation, the tunnels were significantly deeper and thus there was more leeway in positioning the pipes. As North/Southline in the end was carrying the associated risks for Compensation Grouting, the Adviesbureau North/Southline (ABNZL) changed the bid design so that the pipes were positioned further away from the piles, midway between the pile toes and tunnel crown, and installed at an angle to intercept the settlement contours. Figure 2 shows the redesign by ABNZL for the first location. Advantages of this design would be less potential settlement during installation of the pipes and the grout injection would be in a more uniform stress zone rather than very close to the end loaded driven piles. In addition it was felt that a single layer would provide sufficient control and thus would be trialed at the first location to be drilled and grouted.

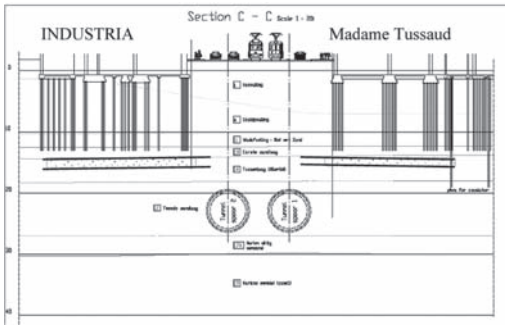

Figure 1. Original compensation grouting design section.

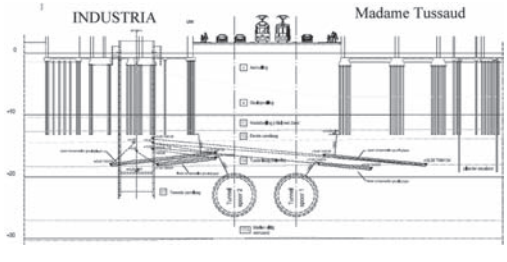

Figure 2. Revised compensation grouting design section.

3.2 *Grouting shaft design*

The Contractor had offered two types of shaft construction within his design:

Combi-shaft: Secant piled + freezing.
Caisson.

The Combi-shaft was designed on the basis of constructing the shaft using interlocking piles and then using ground freezing in the sandlayers to exclude the groundwater. The caisson type was designed using cast in situ concrete rings and then sinking the shaft by excavating the inside and then placing the base slab using underwater concrete.

The contractor advised that the caisson type was to be utilized where the shaft was relatively remote (10 m) from the nearest building as they predicted up to 50 mm of settlement and the Combi-shaft would be used close to the piled buildings as minimal settlements would arise.

The cost of the Combi-shaft was relatively high given the required use of ground freezing and therefore ABNZL suggested to the contractor that based on UK experience a jacked segmental shaft could be constructed without settlement close to a building.

This methodology differed from the conventional caisson in that the bottom edge of the shaft was jacked ahead of the excavation within the shaft which prevented loss of ground and hence settlement being generated. Special precast concrete segments were used which allowed Bentonite to be injected at the cutting edge through pipe channels that were aligned when the segments were bolted together. This provided a friction reduction and assisted the jacking process. In operation, the bottom edge would be jacked into the ground with the excavation being no closer than 0.5 m above the base. The segments were 1 m in depth, thus the jacking operation consisted of constructing a 5.2 m internal diameter ring of nine segments, jacking and excavating 1 m and repeating the process.

Therefore in addition to trialing the compensation grouting layout, the Industria location was chosen to trial this form of shaft construction.

3.3 *Monitoring*

The movements of the buildings during shaft sinking, drilling and grouting operations were extensively monitored. Monitoring was installed within the buildings, generally in the basement. The system chosen was a water level cell system where a reference cell is fixed remotely and provides a constant water level. Movement of the other cells connected to the reference cell then reflect a change in local head of water pressure at each location and thus the relative movement can be calculated. All cells were logged automatically and accessible through a web based system for all parties to follow.

In addition to the internal monitoring for the buildings a project wide system of remotely read total stations was installed along the line of the tunnels and could be also used to monitor external movements and would provide long term absolute level control.

The advantage of the water leveling cells was that they could be interrogated at very short intervals of time to allow control of the grouting and they had a high resolution of 0.1 mm to 0.2 mm.

3.4 *Performance requirements*

The contract specification set out the limits of movement for the buildings to be protected by compensation grouting and they were as follows:

Pretreatment Phase:.
- Maximum upward movement 2 mm.
- Maximum settlement 2 mm.
- Maximum angular rotation 1 in 2000.

Compensation Grouting Phase:
- Maximum upward movement 2 mm.
- Maximum settlement 3 mm.
- Maximum angular rotation 1 in 2000.

The movement limits for the compensation grouting phase were to be following pretreatment so that the maximum upward movement could technically be 4 mm and the maximum settlement could be 5 mm.

The contractor accepted the movement limits but it was agreed that the 1 in 2000 distortion limits would be a target with the contractor committed to pursuing these limits.

4 CONSTRUCTION

Construction on site commenced at the location of the Industria building.

4.1 *Shaft construction*

The works at the location of the Industria building commenced in March 2007 with removal of existing obstructions. It was decided that because there was the risk of historical masonry and wooden structures at the shaft location, predrilling using 1500 mm dia overlapping piles would be carried out to the first sand layer, a depth of around 12 m. The piles were backfilled with a special mix, DiWa Mix 230 produced by Heidelberg Cements which had a 28 day strength of less than 1 MPa. This was important to allow the follow on shaft jacking operation to be carried out without hindrance of any strong material being present.

Following the removal of obstructions the shaft was jacked in and the base slab cast during the period April to June 2007. Figure 4 shows the results of the monitoring of the prism attached to the building immediately opposite the shaft.

The results showed that the shaft had caused virtually no movement to the building and therefore this type of construction was then adopted for all the remaining shafts.

4.2 *Drilling and installing injection pipes*

Following completion of shaft sinking, a drill mounted on a rotating and jackable drill stand was installed within the shaft. The rotation allows the drill to be easily positioned for each drill hole and the jacking frame allows the drill to be simply

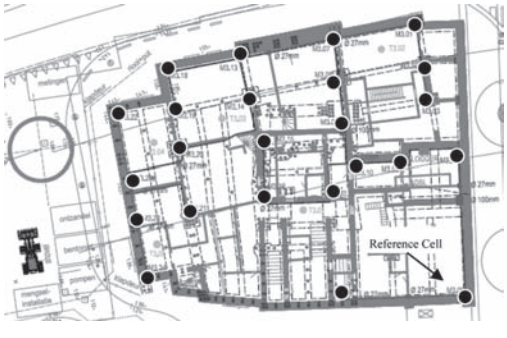

Figure 3. Monitoring layout within Industria.

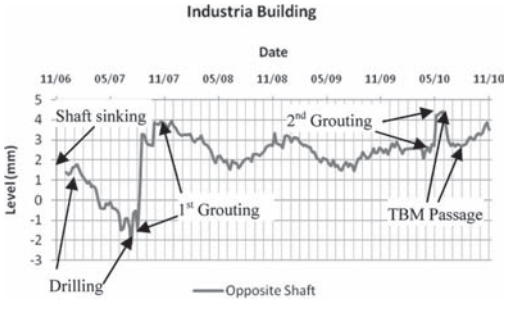

Figure 4. Monitoring of Industria building.

moved up and down. In order to accommodate the drill and frame around 3 m of space was required below the drilling level.

In order not to compromise the structural integrity of the shaft construction, special segments were installed during jacking at the levels of drilling. These segments allowed the drills to penetrate without cutting the reinforcement. In order to provide sufficient space between each drill hole, a number of entry levels had to be used. Figure 5 shows the entry hole layout for the Bijenkorf shaft.

At this time the design still incorporated the second lower layer of holes 201 to 212. The heavy dashed line shows the joints between rings of segments.

Drilling was carried out using special preventers to deal with the 1.5 Bar water pressure. Initially a number of systems were trialed by the contractor until the most suitable system was developed. Initially there was some settlement from the drilling as shown on Figure 4 however as the system was developed this did not continue.

In order to minimize the number of shafts, trial drilling with lengths of 60 m and 90 m were carried out to establish whether these design lengths could be utilized in the design. It was established that both 60 m and 90 m length holes were feasible in the first sand layer/Alleroid. Consequently the shaft opposite Madame Tussaud could be cancelled and all the work carried out from the Industria shaft.

On completion of drilling, the steel injection pipe was installed and with the help of a seal between the injection pipe and the drill casing, the casing was withdrawn while grouting the hole under pressure.

4.3 *Pregrouting*

It is always important to carry out a pregrouting exercise to ensure that there is a good contact

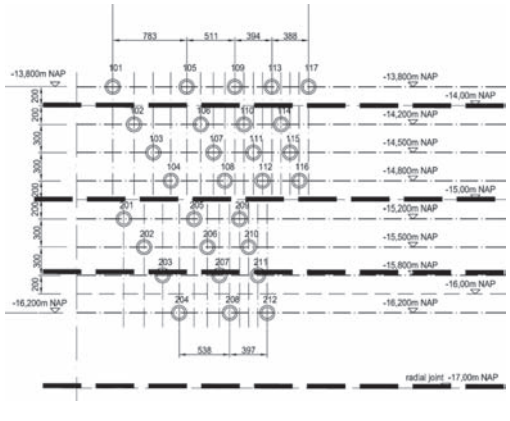

Figure 5. Layout of holes at entry level in shaft.

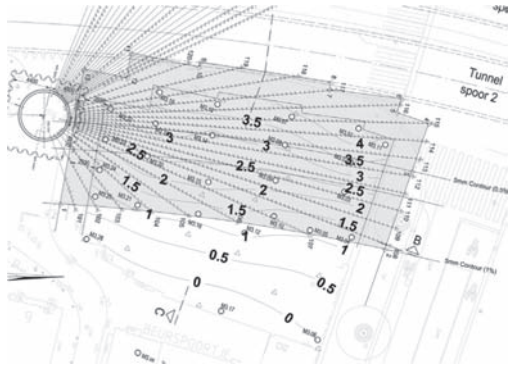

Figure 6. Pre-heave applied to Industria and Madam Tussaud-Building.

between the foundations and the grouting zone. Additionally the injection of the grout can stiffen the ground and reduce movements (Essler, 2000).

Pregrouting was carried out immediately after drilling. It was decided that it would be beneficial to incorporate a small tilt of the buildings away from the tunnel drive to compensate for the settlement during TBM passage. The control of the grouting was very precise and the tilt was applied to the building with 4 mm at the façade and 1 mm at the rear of the building.

The grout utilized was a preblended mix provided by Heidelberg known as Blitzdammer 750. The inital water solids ratio was set at 2.0 but it was decided that a better response was noted with a water cement ratio of 1.4 and this was then adopted for all future grouting. Grout volumes varied from 20 to 100 litres.

The single layer was grouted and found to be successful in lifting and maintaining the building and was adopted for all other locations.

The initial conditioning of the ground required around 250 litres of grout to be injected for each square meter of grouting area. This is relatively high when compared to some other projects (Chambosse, 2002) and is probably attributed to the potential flexibility of the wooden piling system and the reestablishment of the ground stresses which may have been reduced due to settlement caused by the drilling. Figure 7 shows the actual distribution of grouting intensity. Very high grout quantities were required in the south east part of Industria to correct for the initial settlement caused by the drilling development.

5 TBM PASSAGE

Due to programme difficulties, although the pregrouting at Industria was completed in late 2007, the TBM was only launched in the summer of

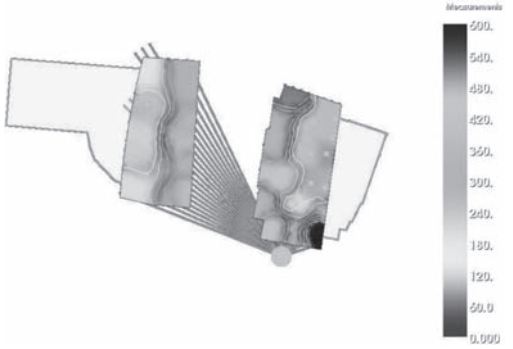

Figure 7. Variation in grouting intensity for Industria and Madam Tussaud.

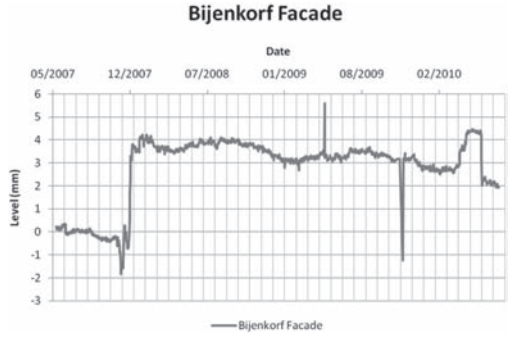

Figure 8. Change in level of Bijenkorf building.

2010 and thus Industria, Madam Tussaud and Bijenkorf buildings sustained the preheave for nearly three years. Figure 4 shows that in addition to seasonal variations there was a slight loss of level of around 1 mm.

Immediately prior to tunneling the contractor remobilised to the shaft which had been covered over and carried out some reinjections to regain the required tilt levels. It was noted that grouting efficiencies were higher than the initial grouting which is a further justification in carrying out pre-grouting to stiffen the ground. Around 27 litres m^2 were injected and an additional 2 mm heave was re-established on the façade.

The reaction of the other buildings were similar and Figure 8 shows the change in level for one of the settlement cells within the basement and adjacent to the Bijenkorf façade.

The TBM passed the grouting zone of the Bijenkorf building on 9th June 2010. Figure 8 shows that there was only around 2 mm of movement. Figure 9 shows the change in level of the Bijenkorf during TBM passage.

This shows that in general the settlement contours are parallel to the line of the tunnel drive and quite smooth indicating that the grouting zone not only stiffens the ground but can smooth out movements.

No grouting was carried out as the settlement was not excessive. It had been decided that the levels of the buildings following TBM passage should be maintained at 50% of the initial preheave limit, thus the façade would only require grouting if the levels dropped below 2 mm.

The east TBM reached the Industria building on the 16th June 2010. It was interesting that the building did not move initially until the face of the TBM was well past the northern corner. This is probably attributed to the 3D effect of the corner providing more support by arching. Figure 4 shows the change in level of the building during TBM

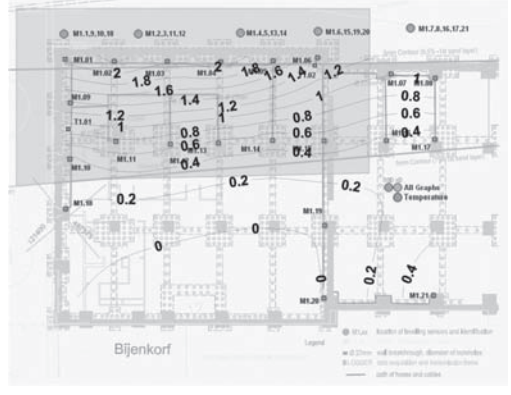

Figure 9. Change in level (mm) for Bijenkorf during TBM passage.

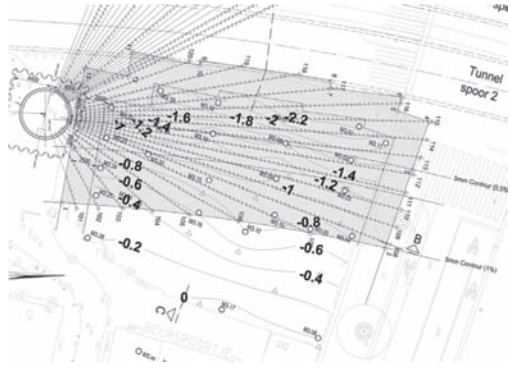

Figure 10. Change in level (mm) for Industria during TBM passage.

passage. The heave following TBM passage is most probably a seasonal effect as can be seen by the variation during 2008 and 2009.

Figure 10 shows the change in level of Industria as the TBM passed by.

Grouting was carried out on the 18th and 19th June 2010 to maintain the levels within specified limits. Approximately 4,500 litres of grout was injected, initially in volumes of 35 to 50 litres and then later with volumes of 150 litres.

For the Industria building the response was slightly more localized and this is probably due to the more complex shape of the building.

Based on the building settlements, the likely volume loss achieved was around 0.3% which indicated excellent TBM control and operation by the contractor Saturn (Zublin/Vermeer JV).

6 CONCLUSIONS

The redesign of the injection pipes was successful in that minimal effect was noticed on the building during drilling and the buildings could be compensated during TBM passage. The single layer approach was also successful in allowing good control of the building both during initial grouting and during TBM passage.

Increasing the drilled lengths to around 60 m allowed some shafts to be deleted with a significant cost saving.

The jacked segmental shaft construction was very successful in limiting settlements and providing an economical and efficient method of construction.

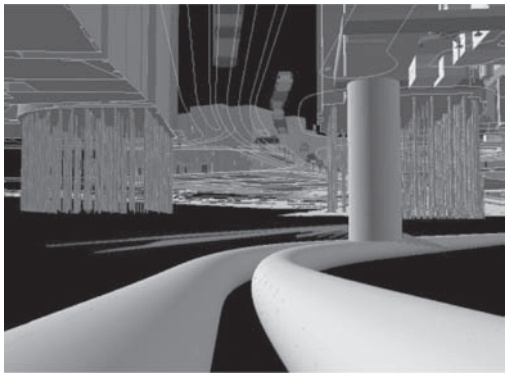

Figure 11. 3D of the single layered design based on the interception approach for Industria.

Figure 12. Working site at Industria from above.

ACKNOWLEDGEMENTS

The authors would like to thank the Dienst Noord/zuidlijn for the authorization to publish this paper.

REFERENCES

Chambosse G & Otterbein R, State of the Art of Compensation Grouting in Germany, *XVth International Conference on Soil Mechanics and Geotechnical Engineering,* Istanbul 2002.

Essler R.D, Droof E.R. & Falk E, Compensation grouting Concept, Theory and Practice*, Geotechnical Special Publication No.104*, Geo-Denver 2000.

Haasnoot J.K., A.E.C. van der Stoel, F.J. Kaalberg, 2002, *Fracture Grouting to mitigate settlements of wooden pile foundations*. Proc. Of AITES-ITA World Tunneling Down Under Conference, Sydney, Australia.

Kaalberg, F.J., Hentschel, V., 1999, *Tunneling in Soft Soil with a High Water Level and Pile Foundations, Towards the development of settlement-oriented and settlement-minimizing TBM operation*. Proceedings of ITA World Tunnel Congress, Oslo.

Van der Stoel A.E.C., Haasnoot J & Essler R.D.,1999, Feasibility of compensation grouting of timber pile foundations to mitigate TBM settlements—a full-scale trial for the North–South line, Amsterdam. *Response of buildings to excavation-induced ground movements, Proceedings of the international conference held at Imperial College, London, UK, on 17–18 July 2002.*

Geotechnical Aspects of Underground Construction in Soft Ground – Viggiani (ed)
© 2012 Taylor & Francis Group, London, ISBN 978-0-415-68367-8

Settlement behaviour after compensation and corrective grouting

A. Bezuijen,
Deltares/Delft University of Technology, The Netherlands

F.J. Kaalberg
Adviesbureau Noord/zuidlijn/Witteveen + Bos, The Netherlands

Remco Kleinlugtenbelt
Dienst Noord/zuidlijn/Witteveen + Bos, The Netherlands

R.D. Essler
Adviesbureau Noord/zuidlijn/RD Geotech, England

ABSTRACT: Settlement of buildings on piles after compensation grouting and corrective grouting is studied for 2 different locations in Amsterdam. The following situations have been studied: Long term settlement behaviour after pre-grouting, settlement behaviour after corrective grouting and short term settlement behaviour after TBM passage. Settlement was measured with liquid level systems as well as with prisms. Differences between these systems will be discussed. The settlement behaviour appears to be time dependent with periods of one day and a longer period of one year, but the permanent settlement is only very small (1 mm in 3 years). Long term settlement of adjacent buildings, is measured after corrective grouting that was performed to stabilize the foundations after an incident with a leaking D-wall joint. This is likely to be caused by the soil disturbance due to the incident and such settlements were not measured at locations without soil disturbance. The passage of a TBM close to one building leads to a settlement of 2 mm at maximum during passage. Further settlement could be adequately arrested by compensation grouting.

1 INTRODUCTION

The importance of the compensation grouting technique is that it is capable to create heave in the soil or heave of buildings. This makes it possible to compensate for settlement that had occurred or that is likely to occur without compensation grouting.

The success, or failure, of a compensation grouting project depends on the heave that can be created. During the metro building in Barcelona, it appeared that it was not possible to create heave with the compensation grouting system (but only more unwanted settlement) and therefore the project was abandoned, and the metro was finished without compensation grouting. This is quite an unusual result and will be discussed further in this paper.

The construction of the underground North/South line in Amsterdam offered the opportunity to measure the heave and settlements of buildings close to this metro line. This heave was measured in the relative short periods that compensation grouting was performed. At locations where compensation grouting was planned, an accurate liquid leveling system was applied. This provides the opportunity to investigate the long term settlement behaviour.

The paper deals with the short and long term heave and settlement. The settlement discussed is the settlement of the foundations of buildings. All buildings are supported on piled foundations. Measurements are presented and possible explanations are discussed. Settlement measurements from the locations dealt with have been published before Bezuijen et al. (2009) and Bezuijen (2010). In this paper the measurements stretch out over a longer period, showing also yearly fluctuations and for one location the TBM has passed the location and the influence of this passage regarding settlements will be shown.

2 LOCATIONS

This paper is focused on the measurements of two locations. One location is the building 'Industria' at the 'Rokin' close to the Dam square in Amsterdam.

Pre-grouting was performed as a start of compensation grouting because one TBM of the North/South line passes close to this historical building. The results of these measurements are representative for the results obtained at other locations along the North/South line.

The second location was at the Vijzelgracht station where a leakage had occurred in a diaphragm wall (Korff et al. 2009). This had led to settlements of up to 0.25 m for the historic houses close to the building pit. Corrective grouting was applied to re-strengthen the subsoil and arrest the settlements.

Monitoring was performed at both locations by means of a liquid leveling system. The reference position was remote from the tunnel so as not to be affected by the construction process.

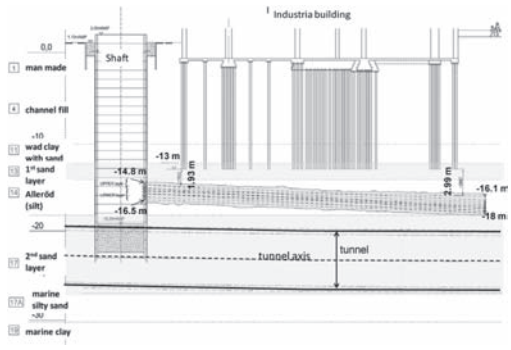

Figure 1. Cross-section installation shaft, pile foundation and TAM positions in the Amsterdam subsoil at the Rokin pre-grouting trial. Only the upper TAMs were used.

2.1 *Location Industria*

The pre-grouting at Rokin was performed in 2007. TAMs were installed from an installation shaft at 15–18 m depth, see Figure 1. The subsoil consists of a silt called the Alleröd and a sand layer.

After the installation of the TAM's (Tubes à Manchettes, the injection tubes), grout was injected to create a few millimetres of pre-heave in the part of the building that is closest to the TBM passage. The idea of this pre-grouting is that it allows for some settlement when the tunnel passes before more grout has to be injected and that importantly the soil is improved, which will also lead to a reduction of settlements at the moment the TBM passes. The TBM passed this location 2.5 years after the pre-grouting, in 2010. Shortly before the TBM passage about 16,000 l of grout was injected to compensate for settlements that had occurred after the pre-grouting. The grouting area underneath the Industria building is approximately 636 m^2. The average heave in this area is 1.3 mm and this means that the efficiency (defined as the average heave times the grouting area divided by the total volume of grout injected) of this second pre-grouting is 4.8%.

During TBM passage (from 18-06-2010, 9:00 until 19-06-2010, 3:40) 5,000 l of grout was injected.

Figure 2. Top view of corrective grouting location, Vijzelgracht (distances between TAM's in mm).

2.2 *Location Vijzelgracht*

The layout of the location Vijzelgracht is shown in Figure 2. The diaphragm wall is shown on the right side of the picture. The big grey area is the corrective grouting area, the lines are the TAMs and the thick, grey lines show the positions of the foundations of the settled buildings.

The foundations of these 17th century buildings consist of a row of 2 wooden piles under the brick walls to a depth of –13 m below surface into the 1st sand layer, see Figure 3. The positions of the liquid

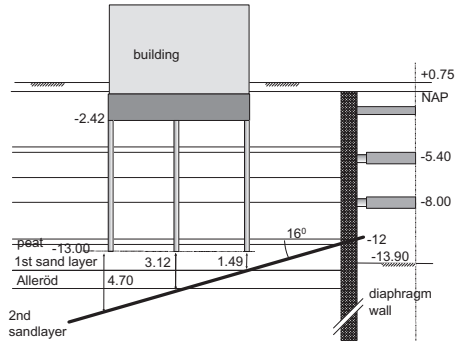

Figure 3. Sketch cross-section location. Dimensions in m.

leveling instruments (LL1 through LL14) attached to basement walls that were used for the displacement monitoring, are presented in Figure 2 as well

Table 1. Data on injection grout mixtures used, see also text.

Mixture	Binder/ water ratio	Density (kg/m^3)	No of injections	Total litres	Average date
M6	0.714	1360	1636	41735	24-09
M8	0.625	1323	1298	29315	09-09
MF	0.5	1269	601	12500	23-08
Total			3535	83550	

as the position in the diaphragm wall where the leakage occurred (between panels 89 and 90).

The TAM's were placed at an angle of 16 degrees (see also Figure 3). Horizontal TAM layout was not possible because after the incident it was not allowed to excavate the box further before stabilizing the buildings.

Grouting was performed using Biltzdämmer, a hydraulically-setting premixed dry mortar (Heidelberg, 2009). Three different mixtures were used, see Table 1. The different mixtures were used for all pumps, sleeves and in the beginning and end of the grouting operations. However, mixture MF was used more in the beginning, M8 in the middle and M6 was mostly used at the end. In this table the average date is the mean date of all injections with this mixture. Grout was injected using different TAMs at the same time in the injection periods.

3 RESULTS OF MEASUREMENTS

3.1 *Location Industria*

3.1.1 *Liquid level measurements*

The results of the first pre-heave show that a very controlled heave of the buildings was achieved, see Figure 4.

The grout was injected at 10 l/min. 50 to 200 litres were injected at one injection point during one injection. The upper bound of 200 litres is quite high compared to the volumes injected in other programs where normally up to 50 litres was injected during one injection at one opening.

Figure 5 shows the heave and settlement as a function of time for the various measurement points indicated in Figure 4, from the start of the measurements (28 March 2007) until the 2nd of August 2010. Just after installation of the measurement system, there is some settlement (up to 3 mm) for some of the instruments, caused by the installation of the TAM's. This is followed by the heave caused by the pre-grouting in September/ October 2007. After the pre-grouting there is some small settlement, as will be discussed later. There was some disturbance in the measurement system in the second half of 2009. In spring 2010, just

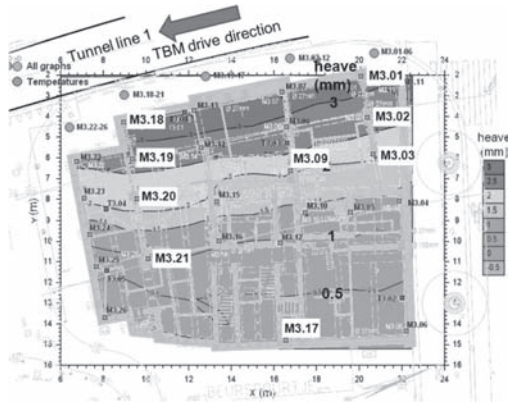

Figure 4. Result of pre-grouting: Measured heave after pre-grouting. Note that the lines of equal heave are parallel to the tunnel axis. The gray lines show the walls of the building that were heaved. The contours present the heave created in mm (21-10-2007).

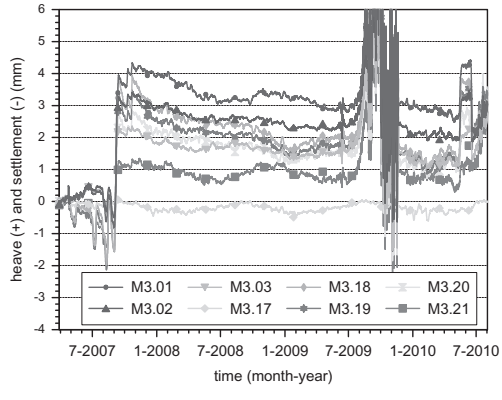

Figure 5. Measured heave and settlement from March 2007 up to 2 August 2010 on both sides of the building. Locations are indicated in Figure 4 (2 of these lines and M3.09 near the middle of the building are shown in Figure 10). Data taken every 2 hours with a moving average over 31 data points to reduce noise.

before the passing of the TBM, some extra pre-grouting was performed to reach the original level that was reached after the first pre-grouting. The passage of the TBM results in some settlement and after the passage of the TBM there is some heave which occurs relatively slowly and appeared to be caused by a measurement error as happened one year earlier, see Figure 5. Building prisms showed no such movement, see below.

3.1.2 *Prism measurements*

The liquid level system is an accurate measurement system that can deliver data with a relative high frequency as is necessary to follow the heave created

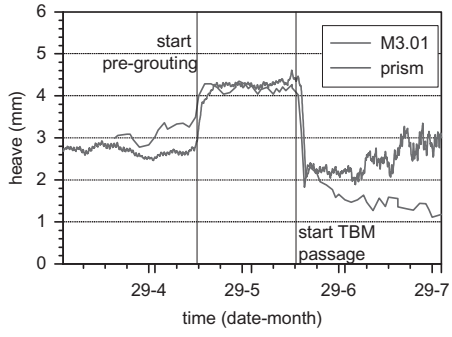

Figure 6. Industria,. Comparison of data liquid level system with prism, during second pre-grouting and TBM passage in 2010.

during compensation grouting. However, it is susceptible to disturbance or drift, as was the case in the second half of 2009. Therefore the results of this system have been compared with the results of the prism measurement system that operates with a lower frequency but are more reliable. The results for Industria are shown in Figure 6.

The results show that the liquid level system results in quite comparable results as the prism measurements during TBM passage, but the slow heave that is measured after TBM passage with the liquid level system is very likely a measurement error, since this is not found in the prism measurements.

3.2 *Location Vijzelgracht*

3.2.1 *Liquid level measurements*

Figure 7 shows an overview of the corrective grouting site near the Vijzelgracht station. The figure shows in plan view the position of the piled foundations (the black lines), the positions of the liquid leveling points (the black dots), the total amount of grout injected in litres during the project at that particular injection point (the grey circles, proportional with the amount of grout injected) and the heave created at the end of the corrective grouting project. The heave indicated is the heave of the basement walls and is interpolated from the results of the liquid leveling system. The heave is shown just after the corrective grouting campaign.

The corrective grouting campaign resulted locally in a significant increase in cone resistance (Bezuijen et al. 2009, Bezuijen 2010) as was the primary objective. Remarkable was that after the compensation grouting campaign there was ongoing settlement for quite some time. For this paper it was possible to extend the measurements over a longer period, see Figure 8.

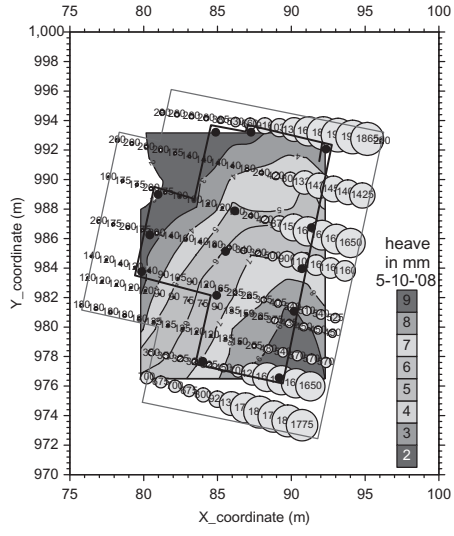

Figure 7. Corrective grouting Vijzelgracht. Volumes injected and heave created at 5–10–2008.

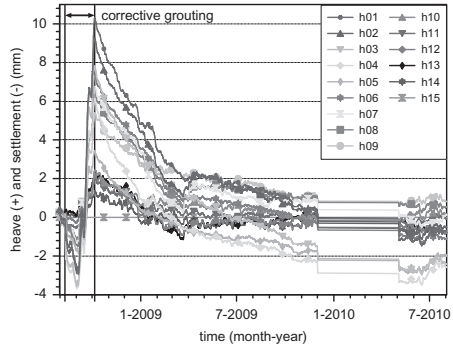

Figure 8. Heave and settlement measurements, Vijzelgracht location. Data taken every hour with a moving average over 31 data points to reduce noise.

The figure shows that although the grout injections start on 10th August 2008, at first the settlement rate increased, probably due to disturbance of the 1st sand layer by the TAM installation and the first injections. Most settlement was recorded at the instruments h03 and h04 at some distance from the leakage, see Figure 2. The injection of the first 21,000 litres of grout did not directly reduce the settlements but were needed to strengthen the soil and to reduce the progress of ongoing settlements. Grouting in September and the beginning of October of 2008, when another 62,000 litres were injected, led to heave of the buildings. Significant settlement occurred after the ending of the grout injection. This will be analysed further in the next sections.

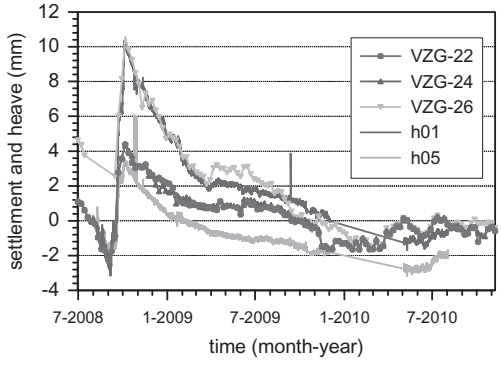

Figure 9. Vijzelgracht. Data liquid level system and prisms compared. (data every hour no averaging)

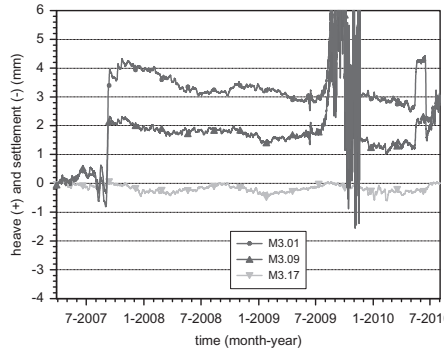

Figure 10. Three instruments selected for analysing the settlements (same averaging as Figure 5). Locations are indicated in Figure 4.

It was not possible to find a relation between the location of the heave, measured at the building and the location of the injection. This is caused by the stiffness of the building that was strengthened by wooden beams after the incident (Bezuijen, 2010).

Injection pressures vary significantly during the project. No clear correlations were found with the location, time and the number of injections (Bezuijen & Tol, 2011).

3.2.2 *Prism measurements*

Three prisms where attached to the houses that were subject to corrective grouting. One, VZG26, is above the LL1 instrument (see Figure 2), two other prisms VZG24 and VGZ22 are close to each other above LL5. Figure 9 compares the results of the instruments mentioned. The results show that there is good agreement between both measuring systems. Only the dip measured in h01 (data from LL1) was not found in VGZ26, because some data points fail in VGZ26 (around August 2008). Furthermore, the ongoing settlement measured with h05 (data from LL5) after November 2009 was not measured with VGZ22 and VGZ24. This may be caused by drift of LL5.

4 LONG TERM SETTLEMENTS

4.1 *Location Industria*

Three instruments were selected to investigate the long term settlement behaviour after compensation grouting. The one which showed the largest heave after the first pre-grouting M3.01, one which an average heave, M3.09 and one which hardly any heave (M3.17) after the first pre-grouting, see Figure 10.

The lines show that there is some seasonal variation of approximately 0.5 mm in the measurements. This may be temperature influences. It is not known whether this seasonal variation is instrument or structure driven or a combination. On top of that variation, there is a limited long term settlement for the locations where heave was created by compensation grouting. The settlement was measured just after the pre-grouting (from 24-10-2007 until 13-03-2008), called settlement short and over the whole period until the 2nd pre-grouting from 24-10-2007 until 01-04-2010, called settlement long. The results are presented in the table below.

The short term settlement rate is determined by linear regression. For the long term settlement rate this appeared to be complicated because this is disturbed by the long term fluctuations. Therefore the long term settlement rate was determined by the straight line that fits the data points from just after the first pre-grouting with the data points just before the second pre-grouting. Assuming that M3.17 presents the background situation, the results show that more than halve of the settlement measured on the short term is caused by the seasonal variations. The long term settlement rate after grouting is limited to 1 to 2 micron a day and is only slightly higher just after pre-grouting compared to the whole grouting period. From this it can be concluded that the settlements in the five months after pre-grouting are very limited.

Table 2. Settlement rate measured at Vijzelgracht.

Instr.	Settlement short (mm/day)	Settlement long (mm/day)
M3.01	$3.7*10^{-3}$	$1.5*10^{-3}$
M3.09	$3.2*10^{-3}$	$1.0*10^{-3}$
M3.17	$1.9*10^{-3}$	$1*10^{-4}$

4.2 *Vijzelgracht location*

A much larger settlement rate was found at the Vijzelgracht location compared to the Industria location. This was explained by the disturbance of the soil after the incident. Settlement rates up to 0.2 mm a day were reported (Bezuijen et al. 2009). The average settlement recorded by h01 between 5-10-2008 and March 2009 was 0.05 mm a day. Looking at Figure 8, this fast settlement seems to stop at the end of March 2009, there is even a temporary heave. However, after that the settlement goes on with a lower rate until approximately November 2009. The rates measured for the different instruments over this period vary between 0.51 until 8.6 micron a day, but only 5 instruments recorded a settlement of less than 2.5 micron a day (approximately 3 and 1 mm a year respectively). The prism measurements show that the measurements are stable after November 2009.

From these results it can be concluded that for more than a year the settlement rate is increased, compared to the Industria location. Note that there were no measurements recorded from approximately October 2009 until May 2010, (the straight lines in Figure 8).

5 SETTLEMENT AND HEAVE DURING TBM PASSAGE

On the 18th and 19th of June 2010 the TBM passed the Industria location. The amount of grout injected and the settlement variations found just before and during TBM passage, are shown in Figure 11 for the same 3 measurements points that were also shown in Figure 10. Figure 11 is a zoom of Figure 5 and shows the total injected volume and deformations at the Industria location just before and during TBM passage. From the results it appears that the grouting prior to the TBM passage directly led to heave. During the TBM passage there is a settlement of 2 to 2.5 mm close to the tunnel. This settlement stops after the TBM passage and the compensation grouting. During TBM passage approximately 5,000 litres are injected, this did not lead to any heave but it effectively stops the settlement, which was the primary objective.

Also for this location it was not possible to relate the injection at one location to heave or slowing down of the measured settlement rate. Figure 12 shows a further detail of the measured settlements, now for all measurements points, at the moment of TBM passage and showed measurement fluctuations that were measured with a daily period.

The daily variations were caused by temperature fluctuations and instrument problems. Figure 12 shows that measurement point M3.01starts

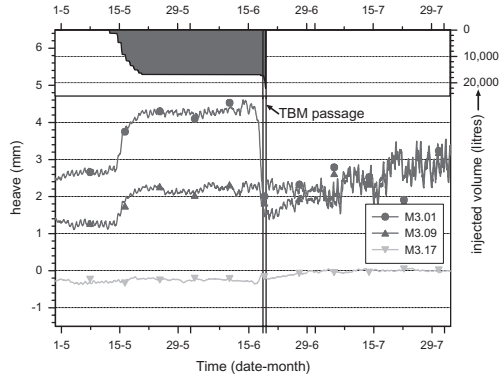

Figure 11. Injection and heave during TBM passage at the Industria location, (data every hour, moving average over 17 data points to reduce noise).

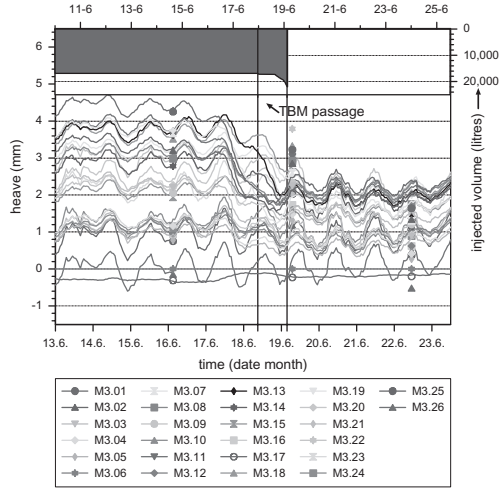

Figure 12. Detail injection and heave during TBM passage at the Industria location, (data every hour, moving average over 5 data points to reduce noise).

to settle when the TBM passes. This measurement point is at the upper right part of the Industria building (see Figure 4), where the TBM first passed close to the building. During TBM passage the other points close to the TBM start to settle later. The heave that should be the result of the grout injections is masked by the daily fluctuations and the ongoing settlement that is corrected.

6 DISCUSSION ON THE RESULTS

The results of the measurements at Industria show that it is possible to control settlement and heave of piled foundations by means of compensation grouting in saturated dense sand within millimeters.

In more disturbed soil, for example after an incident as occurred at Vijzelgracht Station, long term settlements after corrective grouting can be significant, although the CPT's show that there is a significant improvement of soil properties after the corrective grouting. This may be caused by movement of the piles with respect to the soil. Up to a bit more than one year after the grouting there was still a slightly increased settlement rate. The different results compared to the ones found at Industria, are most probably caused by the very different disturbed soil conditions. Compensation grouting works with millimeter accuracy is possible in undisturbed soil conditions. In disturbed soil conditions it is possible to create a significant soil improvement as appears from CPT tests, Bezuijen et al. 2009). However, in the Vijzelgracht case the layers above the layer where compensation grouting is applied most likely influenced the pile foundations leading to long term settlements.

The passage of the TBM at the Industria location led to only a few millimeters of settlement. This could be stopped effectively by compensation grouting. Since compensation grouting was carried out, it is not known what would be the result without the compensation grouting during TBM passage. However, based on the settlement and heave registrations the injections carried out were effective in maintaining the building within the required limits. The injection of 16,000 litres of grout just before the TBM passage led to a maximum heave of 2–3 mm, see Figure 11. From that it can be expected that the injection of 5,000 litres during TBM passage led to a comparable heave (or a reduction of settlement) of 2–3 mm or less, considering the much smaller area of building affected.

The Barcelona case, mentioned in the introduction has possibly to do with the unsaturated conditions that were present. In unsaturated conditions it is possible to over excavate for example during the installation of the TAM's without settlement of buildings on top as a direct result. During TBM-tunnelling in Toulouse, also under unsaturated conditions, settlements due to over excavation appeared at the surface months after the TBM had passed. In the saturated conditions present in Amsterdam there is an immediate response. This can be seen at the beginning of the measurements at the Industria location. The installation of the TAM's resulted directly to some millimeters of settlement. This is an advantage when compensation grouting is used in saturated conditions and makes 'surprises' as in Barcelona unlikely for the compensation grouting works in Amsterdam.

7 CONCLUSIONS

Although measurements are extended over a longer period now, the conclusions are not really different from the conclusions in earlier publications (Bezuijen et al. 2009, Bezuijen 2010): For the soil conditions present in Amsterdam, and only limited soil disturbance, compensation grouting is able to control the settlement and heave of buildings on piled foundations within millimeters. The settlement of the Industria building due to the passage of the TBM could be halted effectively.

For really disturbed soil conditions, long term settlements might be expected, that can be quite significantly (nearly 10 mm was measured at the Vijzelgracht location).

When analyzing the reaction of buildings due to compensation grouting, even in pre-grouting without soil settlement, it is difficult to find the influence of a single grout injection due to the stiffness of the building.

In the saturated soft soil conditions present in Amsterdam all soil disturbances immediately lead to soil movements and thus to movement of the foundations. For compensation grouting this is an advantage, because it is possible to compensate promptly. From this experience it seems that compensation grouting in sand is more suitable when saturated conditions are present, compared to unsaturated conditions.

A liquid level system is very useful to measure settlements during compensation grouting. When such a system is used for several years to determine long term settlements, there has to be a control system, as for example prism measurements, to detect possible instrument drift or disturbance of the system.

REFERENCES

Bezuijen A., Tol A.F. van, (2011). Compensation grouting, Mechanisms determining the shape of the grout body. *To be published proc. IS TC28 Roma.*

Bezuijen A., (2010). *Compensation and corrective grouting in sand, Experiments and modelling. Phd-Thesis.* Delft University of technology.

Bezuijen A., Kaalberg F.J., Kleinlugtenbelt R.E., Roggeveld, R.P., (2009) Corrective grouting in sand to restore pile foundations, Vijzelgracht, Amsterdam. *Int. Conference of Soil Mechanics and Geotechnical Engineering*, Alexandria, Egypt, pp. 2449–2452.

Heidelberg (2009), http://www.heidelbergcement.com/de/en/geotechnik /produkte /Blitzdaemmer.htm (March 2009).

Korff M., Mair R.J. and Tol A.F. van, (2009). Building damage examples due to leakage at deep excavations in Amsterdam. *Int. Conference of Soil Mechanics and Geotechnical Engineering*, Alexandria, Egypt, pp. 2060–2063.

This page intentionally left blank

Geotechnical Aspects of Underground Construction in Soft Ground – Viggiani (ed)
© 2012 Taylor & Francis Group, London, ISBN 978-0-415-68367-8

South Toulon tunnel: Analysis of an instrumented section

J.P. Janin, D. Dias & R. Kastner
Université de Lyon, INSA-Lyon, LGCIE, Villeurbanne, France

F. Emeriault
Grenoble INP, Laboratoire 3SR, CNRS UMR 5521, Grenoble, France

A. Guilloux & H. Lebissonnais
TERRASOL, Montreuil, France

ABSTRACT: Large tunnels in soft rock or hard soil are now often constructed using full face excavation associated with ground reinforcement. Such works induce complex interactions between the soil, the reinforcements and existing structures, which are difficult to model precisely. In order to improve the understanding of ground response to this tunnelling method, and to collect precise data for validating numerical models, two comprehensive monitoring sections have been installed during the construction of the south Toulon tunnel (France). The monitoring results of the "Alexander I" section are analyzed in this paper and a first example of 2D numerical back analysis is presented.

1 INTRODUCTION

The south Toulon tunnel will connect motorways A50 and A57 (direction Marseille-Nice). It is an urban shallow tunnel (12 m of diameter), excavated through very difficult heterogeneous soils. The construction method associates full face excavation and ground reinforcement ahead of the tunnel face by pipe umbrellas and face bolting. This construction technique induces complex interactions between the ground, the umbrella pipes, the face bolts and the surrounding existing structures. In an urban site such as the town of Toulon, it is essential to adapt the construction sequences and the amount of reinforcement in order to avoid a failure and to control the settlements. In the Toulon tunnel, the surface and building deformations are measured, with high frequency, by automatic theodolites (Cyclops). Every 9 m there is a measure profile. All measurements are immediately stored in a database with real time access for all the actors. This represents an efficient tool permitting to continuously adapt the tunnelling process as described by Janin *et al* (2011). But at the design phase, it remains difficult to assess the effect of the different construction and reinforcement elements on the control of the ground movements and settlements. Therefore, in addition to these regular measures, two particular sections were studied in further details, with additional instruments, to improve the understanding of ground response and to collect precise data for validating numerical models. The aim of this paper is to present the most important results obtained on one of the sections, followed by a first example of 2D numerical back analysis.

2 PRESENTATION OF THE ANALIZED SECTION

The section analysed in this paper is situated in garden "Alexandre I" in the west side of Toulon at chainage PM 882.

2.1 *Instrumentation*

The instruments set up from the surface in the section are (see Fig. 2.1):

- 2 inclinometers, 52 m deep, on both sides of the tunnel and 13 m from the axis;
- 1 vertical extensometer on the tunnel axis, 20 m long;
- 3 target prisms close to the previous instruments.

The instruments set up from the tunnel are:

- 4 radial extensometers, 13 m long;
- 6 vibrating strain gauges placed on the steel rib;
- 5 pressure cells;
- Convergence targets.

Table 2.1 shows the accuracy of each instrument and measures:

Table 2.1. Precision of instruments and measures:

Instrument/measures	Precision
Inclinometer	1 mm
Extensometer	0.5 mm
Theodolites—prism	0.5 mm
Radial extensometer	0.1 mm
Strain gauges	1 à 10 microstrains
Pressure cells	2 kPa
Tunnel convergence and settlements	2 mm

2.2 *Geology*

Based on the drilling information a geological profile has been proposed (see Fig. 2.1). It shows that the geological stratigraphy is generally horizontal and it highlights the high degree of alteration of the Basement. This alteration causes important variations of material characteristics.

The average ground properties of the different strata of the section, as retained for the detailed design, are presented in the table below:

Table 2.2. Hypothesis – geotechnical parameters Mohr-Coulomb.

Soils	γ (kN/m³)	E (MPa)	c (kPa)	φ (°)	ψ (°)	υ
Colluviums	20.8	40	10	30	0	0.3
Basement	24.2	120	30	25	0	0.3

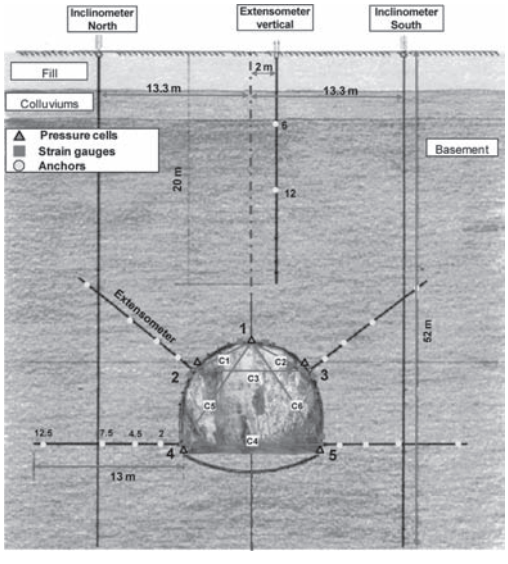

Figure 2.1. Geological section and instruments.

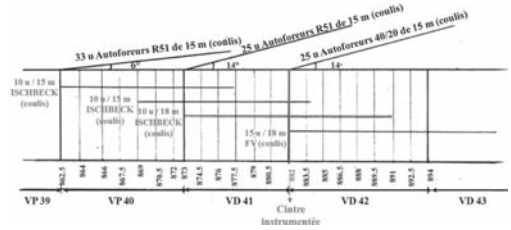

Figure 2.2. Prereinforcements applied at the studied section zone.

2.3 *Excavation method*

The south Toulon tunnel is excavated on the basis of the so-called "ADECO-RS" method developed by Lunardi (2008). This method is based on the principle that protecting and improving the strength and deformation characteristics of the ground ahead of the tunnel face permits to realize full face excavations of tunnels even under difficult ground conditions. Controlling the deformation response of the ground in the core ahead of the face tunnel is essential to increase tunnel stability and to reduce tunnel deformations and also surface settlements in case of shallow tunnels (Lunardi, 2008).

The reinforcements installed in the ground mass surrounding the monitoring section are (see Fig. 2.2):

- an umbrella composed by 25 autodrilling steel tubes, 14° of inclination, sealed by grout and renewed just after the analyzed section. The umbrella represents in Lunardi's theory a "protective conservation": it has to channel the stresses around the advance core in order to maintain the natural soil strength.
- 10 horizontal steel bolts (anchorage > 9 m), sealed by grout and renewed just after the section. They correspond to "reinforcement conservation": the bolts improve directly the natural strength and deformation characteristics of ground in the core ahead of the tunnel face.

The excavation progresses generally by 1.5 m steps and after each step one HEB 180 steel rib is installed. The tunnel invert, in this zone, was realized with a distance to tunnel face of about 40 m.

3 MEASUREMENT RESULTS

In the following paragraph, the major monitoring results on this section are presented and analysed.

3.1 *Inclinometers*

Figure 3.1 shows, in the transverse plane, the lateral displacements of the inclinometer tubes at the most significant moments. The measures were

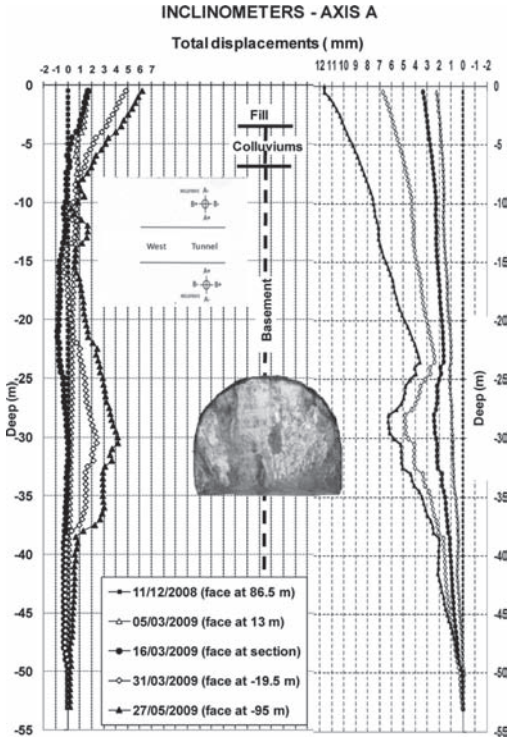

Figure 3.1. Inclinometers—Axis A.

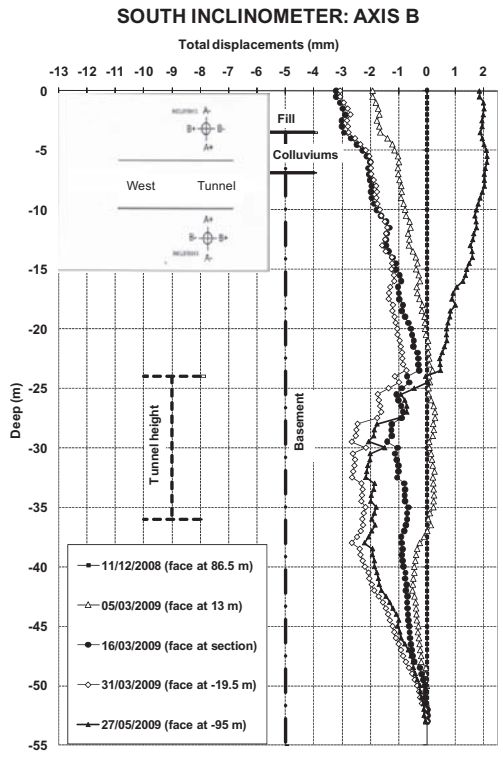

Figure 3.2. South Inclinometer—Axis B.

corrected taking into account the horizontal movements of the surface target prisms recorded by theodolites. One further correction was made after spiral inclinometer surveys.

The analysis of the curves shows two phenomena:

– the first few meters of inclinometers converge towards the tunnel;
– a local convergence ("belly") is also observed at the tunnel level.

Both phenomena increase until stabilization approximately 80 m after the tunnel face has crossed the section.

Some movements appear 1.5 times the tunnel diameter below the tunnel invert. This confirms the necessity to install the inclinometer base largely below the tunnel in order to ensure an anchored zone and be able to accurately analyse the monitoring data.

The measurements also show a dissymmetry of the ground structure caused by local effects due to soil heterogeneity.

The inclinometers movements parallel to the tunnel axis (Axis B) were analyzed as well. Figure 3.2 shows the South inclinometer movements.

The upper 25 m move towards the tunnel when it approaches. This movement is maximum when the tunnel face reaches the instrumented section. Then, the horizontal displacement decrease, go back to their initial values and in a last phase increase in the direction of the tunnel face progression.

At the same time, a local displacement at the tunnel level ("belly") appears and increases as the tunnel face approaches. This demonstrates that the extrusion movements concern not only the tunnel face but also an area of the ground which is at least 13 m far from the tunnel axis. Contrary to what happens in the first meters, this "belly trend" remains even after the tunnel face has passed the monitoring section. This local displacement is an indicator of the volume loss taking place ahead of the face and which will not be recovered.

The results obtained with the inclinometers are in agreement with those analysed by Serratrice (1999) in the north Toulon tunnel in the so-called "plot Chalucet" transverse section. They clearly show that the deformation field induced by the tunnel excavation process is three-dimensional. This does not result in a transverse 2D displacement field when the excavation is completed.

3.2 *Analysis of surface target prisms movements*

Automatic stations measured the X, Y, Z movements of the target prisms situated close to the two inclinometers and the extensometer heads. Unfortunately, the target prism next to the North inclinometer was damaged, therefore the measures can not be used.

The horizontal displacements in a direction parallel to the tunnel axis are shown in Figure 3.3, and confirm the inclinometer measurements. When the tunnel face is at approximately 35 m, the target prisms start to move towards the excavation.

As in the inclinometers results along axis B, the targets movements attain their maximum approximately at the tunnel face passage. Then, the target prisms start to move in the opposite direction, first coming back to their initial position and then reaching a final positive value. The stabilization is observed when the tunnel face is 80 m away from the section.

The vertical prisms movements were analyzed as well (Fig.3.4). They confirm the excavation starts to have an influence on settlements 35 m ahead of the tunnel face. When the excavation reaches the section the movements accelerate. Then, the settlements velocity decreases and a final stability appears over 90 m behind the tunnel face. The maximum observed settlement is about 20 mm.

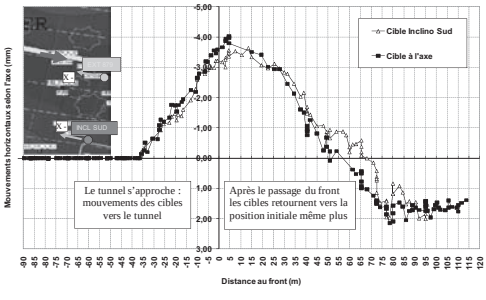

Figure 3.3. Prisms horizontal movements along tunnel axis.

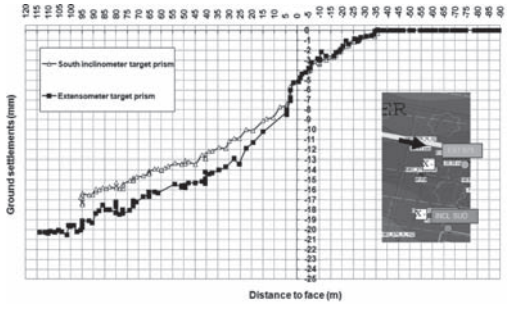

Figure 3.4. Prisms vertical movements.

Some of these results are in accordance with Rankin (1988) who founds that, at a distance to the face equivalent to twice the tunnel cover, the subsidence reaches a value equal to 84% of the expected subsidence. In the studied case, at 60 m far from the face (2 times the overburden), the measured settlement is about 16 mm, 80% of the final settlement (20 mm).

Thanks to the other surface measures close to the section a transverse settlement profile was studied.

With the advance of the tunnel excavation, a three-dimensional settlement trough is developed at the ground surface. On the basis of many field observations, Peck (1969) showed that this shape in a plane transverse to the axis of the tunnel can be represented by a Gaussian normal distribution curve, defined by 2 parameters: S_{max}, the settlement on the tunnel axis and i, the distance of the inflection point to the axis. This assumption was confirmed by the results of numerous in situ measurements conducted by Schmidt (1969), Attewell and Farmer (1974) and from small scale laboratory models carried out by Atkinson and Potts (1977).

A Peck optimization with the method of least squares was made on in situ measures (Fig. 3.5). In order to have more data, the settlement profiles of the sections close to the studied one were considered as well. The measures were normalized on the maximum settlement of each section. In comparison to the classical Gauss formulation, an x_0 parameter was added to represent an horizontal translation of the settlement trough. The formula becomes:

$$S(x) = S_{\max} \exp\left(\frac{-(x-x_0)^2}{2i^2}\right) \quad (1)$$

The optimization confirms a translation value of 2.1 m towards the South. This was also found by Serratrice (1999) for the analysis of the transversal settlement profiles of the North Toulon tunnel. It is caused by a dissymmetry of the soil structure.

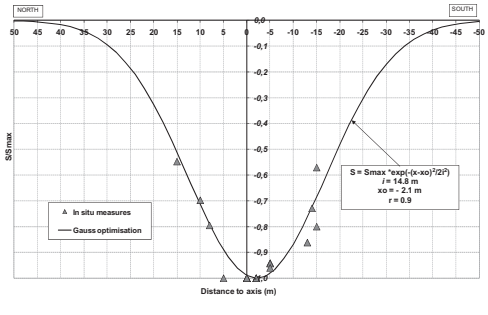

Figure 3.5. Gauss optimization of settlements profile.

The width of the settlement trough is taken equal to 14.8 m. O' Reilly and New (1982) made the hypothesis that this width can be estimated by an empirical parameter K, such as $i = K.Z_0$ (with Z_0 the depth of the tunnel axis) depending on the ground conditions. Values close to the lower limit (K = 0.2) are characteristic of loose grounds while values close to the higher limit (K = 0.7) can be associated to cohesive grounds (O'Really and New 1982, Yeates 1985).

Based on a large number of observations, Mair and Taylor (1997) concluded that K varies from 0.25 to 0.45 for sands and gravels and is close to 0.5 for short term settlement of clays, whether they are stiff or soft.

With the i value obtained from optimisation, K is, in the case of the monitored section, equal to 0.48.

Bilotta, Russo and Viggiani (2002) have collected approximately 90 cases of green field transverse settlement troughs of urban shallow tunnels. As in this study, they have interpolated with Gaussian curve the measures and, thanks to an optimization with the least squares method, they obtained the i parameters. Then they studied the K variation for all cases (see Fig. 3.6). The calculated arithmetic mean is 0.43 and the mean square deviation is equal to 0.20. Therefore the K obtained with our measures is within the average of their study.

It is possible also to calculate the ground settlement volume (Vs) using the following formula (for i = 14.8 m, S_{max} = 0.020 m):

$$V_S = i \cdot S_{MAX} \cdot \sqrt{(2 \cdot \pi)} = 0.74 m^3/m \qquad (2)$$

The volume loss in comparison to the theoretical excavated volume (120 m^3) is V' = 0.62%. This result agrees with the V' values calculated by Bilotta, Russo and Viggiani (2002) on in situ cases.

3.3 *Vertical extensometer*

The extensometer is composed by 5 anchors at 5 different deeps (6, 12, 16, 18 and 19 m from the surface). The displacements between each anchor and the instrument head were recorded with a micrometer. The settlements of the prism placed close to the extensometer head were added to obtain the total anchors movements. Due to problems with embedded instruments, only the measures of the two upper anchors are active.

Figure 3.7 shows the settlement of these 2 anchors plotted against the distance between the instrument and the tunnel face. The settlement trend of the two anchors is very similar and indicates that the upper twelve meters of soil above the tunnel crown behave as a rigid block.

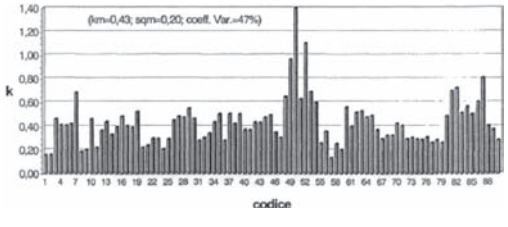

Figure 3.6. Barr chart of k values obtained from studied case - Bilotta, Russo and Viggiani (2002).

3.4 *Pressure cells*

The pressure cells were placed between the soil and the shotcrete when the tunnel face reached the analysed section. The installation was difficult due to the over-excavations beyond the rib that induces a bad contact between the soil and the instrument. The measures obtained are not very satisfactory due to the installation and to the high sensibility to temperature variation.

3.5 *Vibrating strain gauges*

Six couples of strain gauges (intrados and extrados) were welded on the rib directly above the analysed section. The strain gauges permit to calculate forces in the rib by measuring the steel deformation.

Just after the gauges installation, measures appear to be extremely sensitive to temperature variation. Then, a direct relation appears between each new step of excavation and stress increasing on the rib. There is a regular increase of the above mentioned stress till the tunnel face is 20 m away from the instrumented section. Afterwards, the measures show a small stress increase and a final stability appears after 100 m. The stabilised measures analysis indicates that the stress decreases from the crown to the tunnel invert.

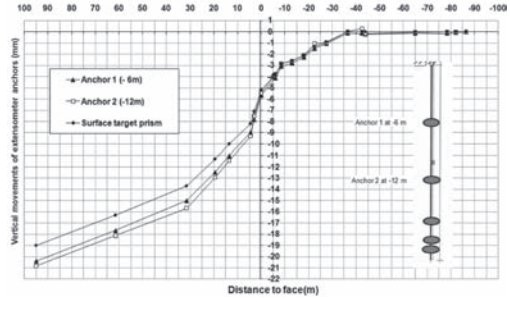

Figure 3.7. Total vertical movements of extensometer anchors.

The final values at the extrados (σ_e) and intrados (σ_i) measured by the gauges are used to calculate the axial force (N) and the bending moment (M) in 5 different positions along the rib (see Fig. 2.1). One of the gauges, placed at the tunnel crown, did not work.

Table 3.1 presents the forces calculated on the steel rib. The average axial force presents its maximum at the tunnel crown and decreases progressively towards side walls. The bending moment is positive and maximum at the tunnel crown. Then, at points 2 and 3 it becomes negative. Finally, the values show a dissymmetry in the steel rib lower parts.

3.6 *Convergence and tunnel settlements*

In the Toulon tunnel, the convergence in six directions and the settlement of five targets have been regularly measured by traditional topography.

The tunnel deformation was compared with the ground surface settlements in the analysed section. The results show that the underground deformations propagate towards the ground surface approximately with no delay and no damping.

Considering the stabilised final convergence, it is possible to draw the tunnel section deformation (see Fig. 3.8). This represents a qualitative interpretation based on the previous calculated bending moment and the following hypothesis:

– the horizontal movement of tunnel crown target is equal to zero;
– the convergences are symmetrical.

Table 3.1. Axial forces and bending moments on the rib.

	σ_e (MPa)	σ_i (MPa)	N (MN)	M (KN·m)
1	175.9	142.6	0.96	12.37
2	76.4	106	0.60	–6.32
3	95.1	107.4	0.66	–2.61
4	42.2	42.5	0.28	–0.07
5	60.5	36.1	0.32	5.18

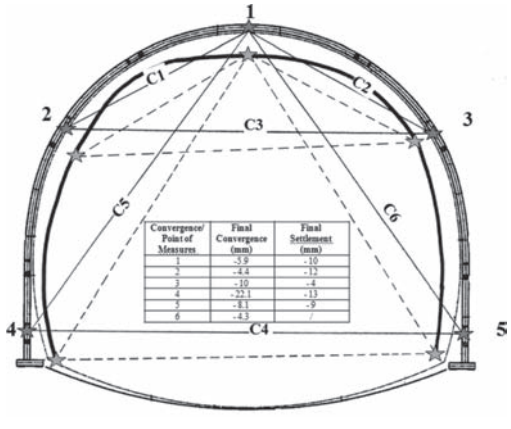

Figure 3.8. Rib deformation, qualitative interpretation.

3.7 *Radial extensometers*

Four radial extensometers were installed from the tunnel (see Fig. 2.1). Their installation was very difficult because after each drilling the hole was closing and it was not possible to easily set the instrument inside.

As an example, Figure 3.9 shows in the case of extensometer #4 the variations of the distance between the anchors and the extensometer heads (see Fig. 2.1) in relation with time and the underground activities. Negative distance corresponds to an extension between the anchor and the extensometer head. The anchors at 7.5 m and 4.5 m seem to belong to a homogeneous ground mass. On the contrary, the anchor at 2 m is in a more deformable part. It is evident that the excavation progress, i.e. VD 42, causes movement acceleration. This phenomenon ends once the tunnel face arrives 60 m away from the section and the radial displacements stabilises.

3.8 *Correlation between the different measures*

The data recorded by different instruments are compared (see Fig. 3.10).

The Northern and Southern vertical inclinometers both cross the radial extensometers n°4 and n°5 respectively in the vicinity of the anchor located 7.5 m from the tunnel. Thanks to this, the radial movements of the two tunnel side walls can be calculated.

In fact, the radial movement (Ur) is equal to the sum of the extension between the extensometer head and the anchor at 7.5 m and the horizontal

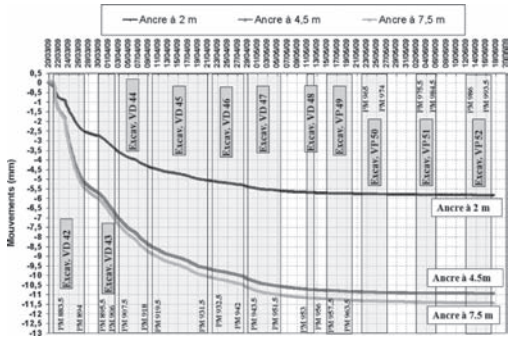

Figure 3.9. Anchors movements of extensometer # 4.

displacement of the same anchor which was measured by the inclinometer, since the tunnel face reaches the instrumented section.

The sum of the two abutment movements (23.1 mm) should then be equal to the convergence C4 measured by topography (22 mm). The comparison between the two above mentioned methods is very satisfactory and such results confirm the good accuracy of measurements.

4 2D NUMERICAL SIMULATION

All these measurements have permitted to create a significant database. The objective of the study is to carry out a back analysis on these data with numerical calculations. The main goal is to improve the settlements prediction, based on numerical approach, for the tunnels excavated with the prereinforcement techniques.

The first simulation was carried out with the finite element code PLAXIS 2D. The model represents the geometry of the section previously described. A linear elastic perfectly-plastic constitutive model with a Mohr-Coulomb failure criterion is considered for the soil layers. The steps of the calculation are the following:

1. Ground stress initialization (drained conditions).
2. Tunnel excavation with a stress release coefficient λ_1.
3. Application of reinforcement on side walls and key tunnel with a stress release coefficient λ_2.
4. Setting up of the tunnel invert and full stress release ($\lambda = 1$).

The comparison between the numerical outcomes and in situ measurements shows that it is not possible to represent the correct trend of inclinometer horizontal movements using a homogeneous Young's modulus (E) for the Basement layer. In order to solve this problem the Basement is divided in three layers with different moduli, that increase with depth (Fig 4.1).

This solution permitted to obtain numerical results that fit well the in situ measures. Figure 4.2 and Figure 4.3 show the settlement profile in the transverse section and the horizontal movements of the lateral inclinometer. These numerical results are obtained with stress release coefficients λ_1 and λ_2 respectively equal to 0.4 and 0.5.

This first simulation highlights that the used simple constitutive model is not able to represent the real soil behavior. It is necessary to adopt a more complex constitutive model that is able to take into account the non-linearity of soil behavior before

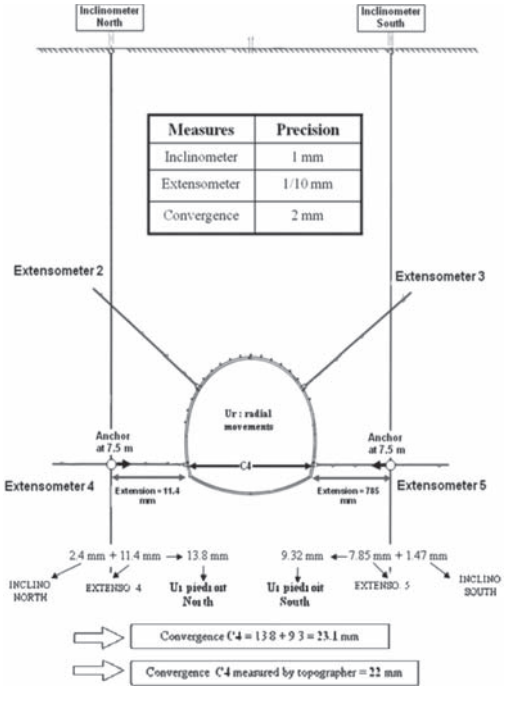

Figure 3.10. Correlation between the different measures method.

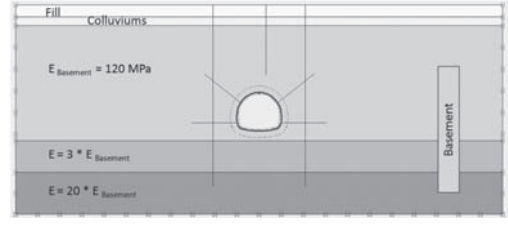

Figure 4.1. 2D numerical model (PLAXIS 2D).

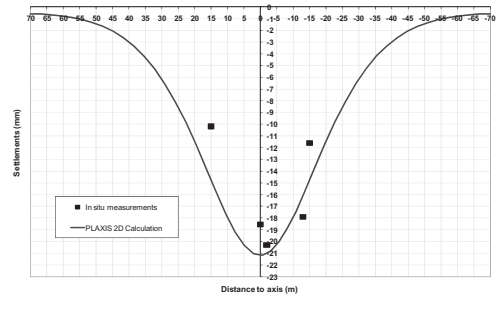

Figure 4.2. Settlement profile in the transverse section - comparison between 2D numerical simulation and in situ measures.

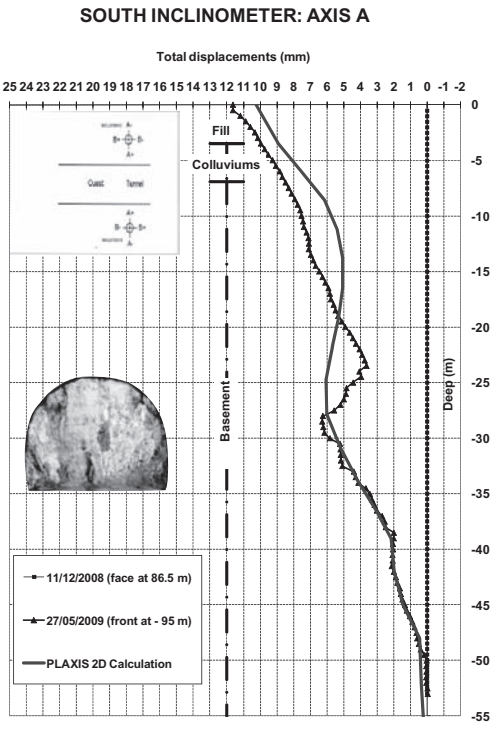

Figure 4.3. Inclinometer horizontal movements - comparison between 2D numerical simulation and in situ measures.

failure. This constitutive model must simulate unloading stress paths using a modulus that is different from the loading one.

5 CONCLUSION

The monitoring section, installed during the construction of the south Toulon tunnel, has permitted to analyse the evolution of soil deformation with the excavation progress. The comparison between the measures realized from the ground surface with those carried out from the tunnel proves the global coherence and accuracy of results.

The experimental data show that the excavation has an influence of 3 times the tunnel diameter ahead of the tunnel face. Then, a global stabilisation is reached about 90 m behind the tunnel face.

The analysis of inclinometers results highlights that the deformation field induced by the tunnel excavation process is fully three-dimensional.

The extensometer outcomes display that the upper twelve meters of soil above the tunnel crown behave as a rigid block.

The instruments placed close to the rib show a direct relation between the excavation progress and the increasing stress on the reinforcement.

Finally, this monitoring section has permitted to create a database of accurate measures that allow validating numerical simulations. Through 2D and 3D numerical approaches, based on the monitoring section, the effects of the prereinforcement techniques on the stress release will be studied.

REFERENCES

Atkinson, J.H. & Potts D.M. 1977. Subsidence above Shallow Tunnels. *Journal of Geotechnical Engineering,* ASCE, Vol. 103, No.4: 307–325.

Attewell, P.B & Farmer I.W. 1974. Ground deformation resulting from shield tunnelling in London clay. *Canadian Geotechnical Journal*, Vol. 11: 380–396.

Attewell, P.B., Yeats, J. & Selby, A.R. 1986. Soil movements induced by tunnelling and their effects on pipelines and structures. Glasgow: Blackie.

Bilotta, E., Russo, G, & Viggiani, C. 2002.Cedimenti indotti da gallerie superficiali in ambiente urbano. XXI Convegno Nazionale di Geotecnica: 487–494. L'Aquila.

Janin, J.P., Dias, D., Emeriault, F., Kastner, R., Lebissonnais, H. & Guilloux, A. 2011. Settlement monitoring and tunneling process adaptation—case of South Toulon Tunnel. *The seventh International Symposium on "Geotechnical Aspects of Underground Construction in Soft Ground", tc28 Rome*. Rome.

Mair, R.J., Taylor, R.N., 1997. Bored tunneling in the urban environment. *Proc. Conf. on Soil Mechanics. and Foundation Engineering*, Theme lecture. Hamburg.

Lunardi, P. 2008. Design and construction of tunnels—Analysis of controlled deformation in rocks and soils (ADECO-RS): 577. Springer—Verlag Berlin Heidelberg.

O'Reilly, M.E., New, B. 1991, Tunnelling induced ground movements predicting their magnitude and effects. *4th Internatinal Conference on Ground Movements and Structure.* Cardiff.

Peck, R.B. 1969. Deep excavation and tunnelling in soft ground 7th ICSMFE. *State of the art Volume*: 225–290. Mexico City.

Rankin, W.J. 1988. Ground movements resulting from urban tunnelling: prediction and effects. *Engineering Geology of Underground Movements:* 79–92. London: F.G. Bell et al.

Serratrice, J.F. 1999. Suivi du plot Chalucet, application à la prevision des tassements de surface pendant le creusement du tunnel de Toulon, Journée de Mècanique des Sols et des Roches d'Aix en Provence: 31.

Schmidt, B. 1969. Settlements and ground movements associated with tunneling in soil. *PhD thesis.* University of Illinois.

Geotechnical Aspects of Underground Construction in Soft Ground – Viggiani (ed)
© 2012 Taylor & Francis Group, London, ISBN 978-0-415-68367-8

Prediction of the effects induced by the Metro C construction on an old masonry building

F. Buselli, A. Logarzo & S. Miliziano
Dipartimento di Ingegneria Strutturale e Geotecnica "Sapienza" Università di Roma, Roma, Italia

F. Formato
DMS Geotechnical Engineering, Roma, Italia

G. Simonacci & A. Zechini
Roma Metropolitane, Roma, Italia

ABSTRACT: The paper reports the main results obtained through a numerical study aimed to predict the effects induced on an old masonry building by the tunnelling operations for the construction of Metro C line, in Rome. To achieve high quality of prediction, full 3D finite elements numerical analyses are carried out. The most important features simulated are: *i)* the advancement of tunnel front; *ii)* the pressure for front support; *iii)* the TBM geometry (weight and conicity of shield); *iv)* the tail void grouting; *v)* the building structure. A simple elastic perfectly plastic model with Mohr-Coulomb strength criterion and tension cut off is used for describing both soil and masonry behaviour. Preliminary analyses using different mesh density and tolerated error are carried out to optimize the complete analyses achieving an acceptable compromise between calculation time and accuracy of the results. In the usual range of pressure distributions for front support, the study underlines the light influence on stresses and strains distribution of the values adopted. The analysis of stress and strain distributions in the building structure before and after tunnel construction, numerically obtained, allows us to assess the category of damage in term of potential cracks induced and also in term of reduction of structural safety level.

1 INTRODUCTION

It is important to predict settlements due to excavation of tunnels in urban area to evaluate the effects induced on pre-existing structures. This prediction is very difficult because of the tridimensionality of the problem and due to the large number of factors that influence the interaction between soil-tunnel-surface structures. Many Authors are interested in three dimensional finite element analyses in which the tunnel, the soil and a building are all treated in a single analysis (Burd *et al*., 2000; Buselli *et al*., 2010). Using 3D numerical analysis it is possible to reproduce realistically the main features of the excavation process, without those assumptions that are necessary when the problem is approached by plain strain analysis. In detail, a 3D approach allows the easy simulation of the main excavation features via Tunnel Boring Machine (TBM): the front support, the conicity of the shield and the grouting in pressure of the tail void between the excavation profile and the lining. Moreover, in 3D numerical analysis it is possible to introduce 3D building structures into the model without conceptual difficulties.

Settlements profile and volume of subsidence basin obtained performing 3D simulations are analysis results which depend on geometry, soil characteristics and modality of excavation. Numerically obtained stress and strain distributions in the building structure can be analyzed to assess the level of damage induced both in term of cracks formations and reduction of structural safety level.

The case study presented in this paper is a real case: the interaction between Metro C line and an old masonry scholastic building, "Diaz-Carducci" located near S. Giovanni Station of Metro A, in Rome. The main south-east façade of the building is parallel to the axis of the tunnels.

Two circular cross-section tunnels will be driven by Earth Pressure Balanced Shield (EPB), to minimize the excavation-induced settlements as much as possible.

Full 3D numerical analyses are carried out modeling the most important aspects of the excavation process. To study the interaction between soil-tunnel-structure, both the stiffness and the weight of the building are taken into account. The whole

building is simulated adopting a simplified model for the geometry of structure framework and assumed to behave as elastic perfectly plastic.

Also soil behaviour is modeled as simply elastic perfectly plastic with Mohr-Coulomb strength criterion.Three types of finite element analyses are carried out using Plaxis 3D Tunnel code (Plaxis 3D Tunnel, 2007): *i) preliminary analyses,* to study the influence of mesh density and tolerated error on results accuracy and calculation time using a simplified model; the aim of those analyses is to achieve an acceptable compromise between accuracy and calculation time; *ii) greenfield analysis*, that involves only the construction of Tunnel B (the building is not simulated); *iii) interaction analysis,* to study the interaction between soil, tunnel and preexisting building.

In this paper, the geotechnical characterization of the site is reported after the descriptions of the building structure and the tunnels. Then, main features of the numerical models are described and the main numerical results are presented and discussed. Finally, the main conclusions of this research are summarized.

2 TUNNELS AND BUILDING

The Metro C project includes the construction of two single track tunnels: Tunnels A and B; the circular cross-section will be excavated with a Tunnel Boring Machine equipped with an Earth Pressure Balanced Shield technology (EPB). The shield diameter (D) is 6.7 m and the permanent lining outside diameter is 6.4 m, consisting of seven pre-cast reinforced concrete elements of 0.30 m thick. As a result the ring cluster between the lining and the excavation profile is 0.15 m thick.

The tunnels layout lies beneath the historic center of the city where a number of buildings of historical and social interest are located; among the most important structures, the "Diaz-Carducci School" is placed between 7.2 m and 9.3 m from Tunnel B axis; Tunnel A is 23 m far away.

The soil cover is about 22 m, near the building area, and the machine operates under the water table.

Fig. 1 reports a plan view of the building and the relative position of the tunnels.The building, located near the existing San Giovanni Station, is about 10 meters tall and its ground plan is almost rectangular (Fig. 2).

The structure is made up of two sections: the main original body, along Via La Spezia, was built around 1912; in the 1940s it was extended and, two extreme portions were added both on the left and on the right side.

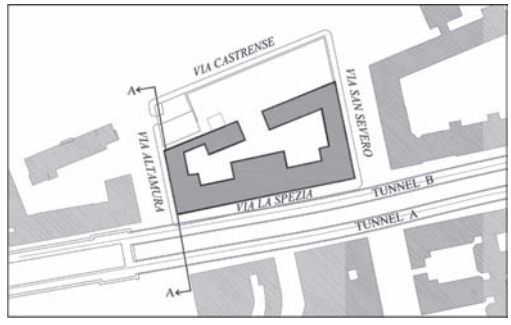

Figure 1. Plan view of building and tunnels.

Figure 2. Building involved in this study.

Fig. 3 illustrates the main façade by the side of Via La Spezia. Fig. 4 shows the building ground plan of the oldest part.

The building under investigation is a "Roman masonry" made up of bricks alternating at tuff bachelors in elevation.

Regarding the oldest body (constructed in 1912), the foundation is continuous on isolated masonry piers with the foundation level approximately 10 m below the ground surface; the foundation of the new portion of the building (constructed in 1934) is a shallow concrete slab placed 4.5 m below the ground surface.

The quality and the maintenance of the building are poor; the building suffers some damage and a large number of cracks were detected.

3 GEOTECHNICAL CHARACTERIZATION

Soil profile and hydraulic conditions have been determined on the basis of an extensive geotechnical investigation involving laboratory and *in-situ* tests. The main results of the geotechnical characterization are reported in Formato (2009). The building area is located close to the "Marana of Acqua Mariana", an ancient ditch which has completely eroded the volcanic sediments. As a result

Figure 3. The main façade of the building by the side of Via La Spezia.

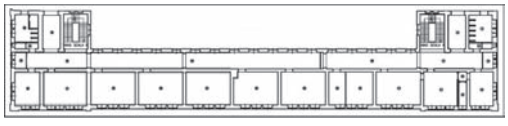

Figure 4. The building ground plan of the oldest body.

the hard rock layers of lithoid tuff are completely absent immediately beneath the building. The engraved area of the ditch was subsequently filled by fluvial-alluvial deposits. The underlying fluvial pre-volcanic deposit is made up of three main slightly over-consolidated levels.

From the ground surface (38 m amsl) the following layers are encountered:

- man made ground (**R**): medium to loose granular soil, including relicts of ancient structures; the thickness of this layer varies between 13 m to 17 m along the line and it is approximately 16 m at the building site;
- recent alluvial deposit (**LSO**): clayey silt and sandy silt, locally reaches a thickness of 18 m;
- a very dense silty sand and clayey silt **(St)**;
- a clayey silt and silty clay **(Ar)**;
- a sandy gravel cohesionless layer **(Sg)**.

The bedrock is at the bottom of a Pleistocenic fluvial deposit: it consists of a hundred of meters of stiff and over-consolidated Pliocenic clay, **Apl**. Geotechnical cross section is represented in Fig. 5. Based on piezometric measurements, pore pressure distribution in the man made ground and in the **Sg** granular layer is hydrostatic with piezometric surfaces at an elevation of 28 m amsl and 18 m amsl, respectively.

Pore pressure distribution in clayey strata (**LSO**, **St**, **Ar**) varies according to steady state flow downwards directed.

The tunnels will be excavated under the water level. The constitutive model adopted for soil

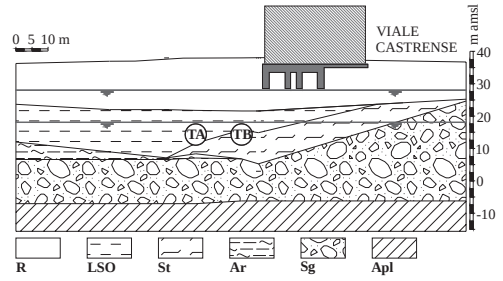

Figure 5. Geotechnical soil profile.

Table 1. Physical and mechanical parameters of soils.

Soils	γ (kN/m^3)	c' (kPa)	φ' (°)	E' (MPa)	K_0 –	ν' –
R	17.5	10	32	15	0.47	0.3
LSO	17.0	15	32	15	0.47	0.3
St/Ar	20.0	10	35	25	0.43	0.3
Sg	20.0	0	40	80	0.36	0.3

behaviour is elastic perfectly plastic with Mohr-Coulomb strength criterion. Young's moduli are assumed to increase with depth, according to the relationship proposed by Hardin (1978).

The horizontal effective stresses are calculated according to the classical equation $K_0 = 1 - \sin\varphi'$ and each layer is characterized by a Poisson's ratio, $\upsilon = 0.3$ assumed constant for all soils.

The physical-mechanical soil parameters adopted in the analyses are summarized in Tab. 1.

4 NUMERICAL MODELING

4.1 *Geometry*

Finite element mesh for soil is generated using "Plaxis 3D Tunnel v.2" commercial code. The model is 140 m wide, 45 m deep, and the total length in the z direction is 225 m (Fig. 6). In order to minimize the influence of mesh boundaries, according to Franzius & Potts (2005), the longitudinal distance

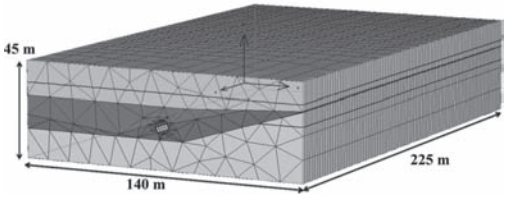

Figure 6. Adopted mesh.

between the tunnel face and the remote vertical boundary are fixed equal to 7×D and 13×D, ahead and behind the position of the studied structure building, respectively.

The mesh is divided, in tunneling direction, in slices of 2.5 m thick.

The deformation analyses do not extend into the deeper layer **Apl**.

Since the bottom boundary is assumed to represent such a stiff ground layer, both horizontal and vertical total fixities have been adopted as displacement restraints.

Roller supports are applied to all vertical sides. Due to non-symmetric geometry, it was necessary to mesh the complete problem; a coarse mesh is considered in the analyses, (Fig. 6), with a local refinement of the clusters around the tunnel.

The Tunnel Boring Machine has a 6.7 m diameter and the shield is 10 m long.

It is modeled as a four slices long ring of plate element; the weight of the plate is 56 kN/m^2, representing the full weight of the TBM including equipment for each meter.

4.2 *Tunnel construction*

The construction process is simulated discontinuously removing slices of elements inside the profile of excavation 2.5 m thick for each step, while at the same time the TBM shield advances, activating shell on front and deactivating shell on tail. The shield is slightly conical: the tail radius is 10 mm less than the frontal one. In order to simulate a reduction of the tunnel cross section area, the shield has a truncated cone shape. The continuous homogeneous final lining is switched on from behind the tail of the shield. Both TBM and tunnel lining are modeled as linear elastics, using shell elements with flexural stiffness, EI, and normal stiffness, EA, as reported in Tab. 2.

The distribution of pressure support at the front is assumed according to the adopted pressure distribution for front support (active total horizontal pressure); this pressure is about 150 kPa at the crown and increases linearly (8 kPa/m) moving to the invert.

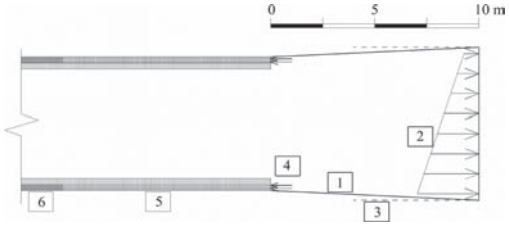

Figure 7. Scheme of excavation simulation: (1) TBM plate; (2) Front pressure; (3) Conicity of the shield; (4) Grout injection; (5) Fresh grout; (6) Hard grout.

Table 2. Plate characteristics.

Plate	E GPa	υ –	EA kN/m	EI kNm^2/m
TBM	210	0.3	$7.1 \cdot 10^7$	$6.8 \cdot 10^5$
Lining	38	0.2	$1.1 \cdot 10^7$	$8.6 \cdot 10^4$

The tail void injection is simulated using an axial pressure applied to the ring cluster between the lining and the excavation profile, opposite to the direction of tunnel advancement (Fig. 7), 50 kPa higher than the maximum value of the pressure at the front.

The stage construction process considers the ageing process of the grout: fresh grout is characterized by a low shear modulus and incompressibility (γ= 21 kN/m^3, E = 3 MPa, υ = 0.49), while hard grout is very stiff (γ= 21 kN/m^3, E = 14 GPa, υ = 0.15). Volume elements are activated to fill the tail void (15 cm) assuming linear elastic properties for them. The grout is assumed to be hardened after four slices.

Only excavation of the tunnel B is simulated; preliminary simplified analyses have showed that the settlements induced by Tunnel A are negligible.

4.3 *Building model*

Complete analysis study the influence of building presence; both the stiffness and the weight of the building are taken into account adopting a simplified model to simulate the structure framework.

The main part of the building structure is simulated modeling the load bearing and gable walls by means of elastic perfectly plastic continuum elements with Mohr-Coulomb strength envelope and a tension cut off (Fig. 8 and 10).

Average values of uniaxial compressive strength (σ_c = 120 kPa) and and Young's Modulus (E = 1.3 GPa) were obtained on uniaxial compression tests carried out on specimens retrivied from the

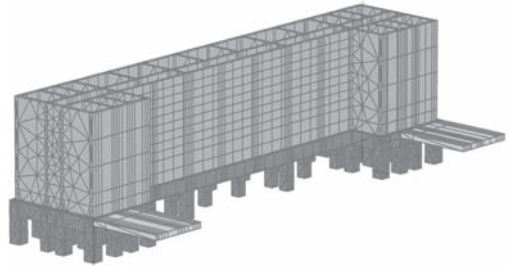

Figure 8. Building model.

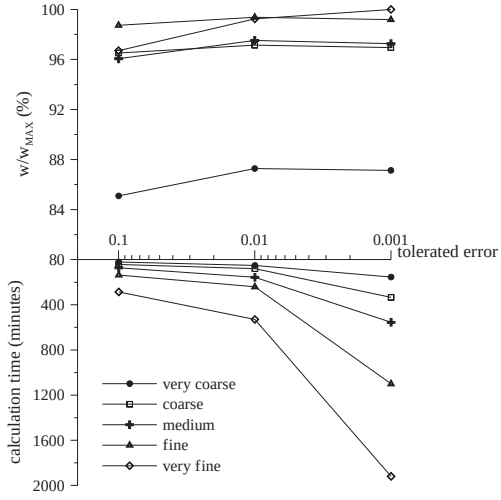

Figure 9. Results of preliminary analysis.

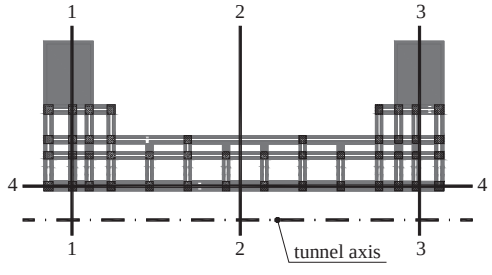

Figure 10. Plan view of the model with location of cross section for the representation of numerical results.

masonry of the building. Assuming a value of 40° for ϕ parameter, a value of 280 kPa results for cohesion, c. Tensile strength, σ_t, is assumed 1/20 σ_c.

The floor slabs are missing, but its weight and surcharges are taken into account applying an equivalent uniform load (15 kPa for each level) on bearing walls. Due to the large distance from Tunnel A, only the concrete slab foundation of the new portion of the building is modeled; to take into account its weight (a distributed load of about 10 kPa for each of the levels), distributed load is applied to the upper bound of the foundation. Foundation consists of elastic cluster of elements with a Young's Modulus E = 31 GPa and Poisson's ratio 0.15.

The interaction between soil and structure is done via an interface using a value of 0.5 for the strength reduction factor (the strength of the interface is half the strength of surrounding soil). In the first phase of full interaction analysis the building is "constructed" activating the solid elements and the distributed load representing the building.

5 NUMERICAL RESULTS AND DISCUSSION

5.1 *Preliminary analyses: influence of mesh density and error tolerance*

In order to achieve an acceptable compromise between accuracy of results and calculation time in the complete analyses (*greenfield* and interaction), the influence of mesh density and tolerated error is studied on a simplified model.

A small portion of the complete mesh has been adopted; the mesh is reduced in longitudinal direction only (60 m instead of 225 m).

Geotechnical profile and geometry are the same as in the complete analyses. Fig. 9 shows the maximum vertical displacement (at ground level above the tunnel crown) and the calculation time obtained varying the density of the mesh (very coarse, coarse, medium, fine, very fine) and the tolerated error (0.1, 0.01, 0.001).

The accuracy of the solution increases by increasing the density of the mesh and decreasing the tolerated error, but the calculation time increases quickly. An acceptable compromise between calculation time and accuracy of the results is obtained adopting a coarse mesh density (number of elements: 6800, average dimension of elements about 1 m) and a tolerated error equal to 0.01 (Fig. 9).

In fact, the difference between this solution and the most accurate solution obtained adopting a *very fine* mesh (number of elements: 37145, average elements size 0.40 m) and a value of 0.001 for tolerated error is less than 3%; moreover, the calculation time is 1/20 of the calculation time of the most accurate analysis carried out.

5.2 *Greenfield analyses*

Greenfield analysis involves only the construction of tunnel B (the building is not simulated). Fig. 11 shows the evolution of the *greenfield* settlements profile calculated along the vertical plain for cross section 4 (see Fig. 10), during the tunnel construction. The settlement profile reaches stationary trend very soon: the boundary condition effects are apparent for about 30 m (about 4.5D) from the boundary. The maximum value of the settlement is about 6 mm and, as expected (due to the small amount of plastic deformation developed), the settlement at the front is about 1/3 of the final total settlement. Fig. 12 reports the settlement profile along cross section 1 at the foundation level (10 m below the ground level) at the end of excavation process. The maximum settlement is about 8 mm; due to stratigraphic heterogeneity the settlement curve appears a bit nonsymmetrical.

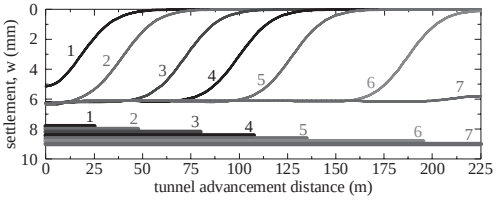

Figure 11. *Greenfield* settlement evolution during the advancement of Tunnel B construction simulation (vertical axial section).

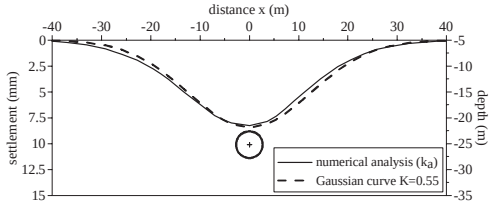

Figure 12. *Greenfield* settlement profile in cross section 1 obtained numerically and comparison with Gaussian curve.

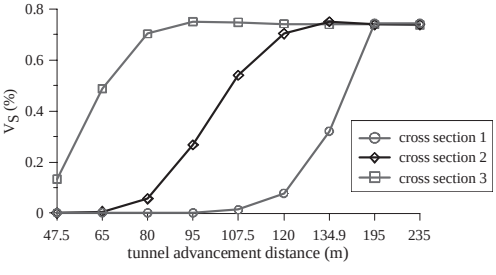

Figure 13. *Greenfield* analysis: Vs on tunnel advancement, cross section 1, 2, 3.

The numerical result matches quite well the Gaussian distribution originally proposed by Peck (1969) and successively adapted by Moh et al. (1996) for calculation of the settlement profile under ground level; calculated assuming the volume of subsidence curve numerically obtained and selecting a value of 0.55 for *K* parameter.

The volume of subsidence curve normalized to the nominal excavation volume, V_S, calculated from numerical results, regularly increases and reaches its maximum value of about 0.75% when the front is about 5D from the generic reference section.

Further tunnel advancements do not affect the value of V_S (Fig. 13).

5.3 *Interaction analyses*

Full interaction analyses are carried out to study the interaction between soil, tunnel and pre-existing

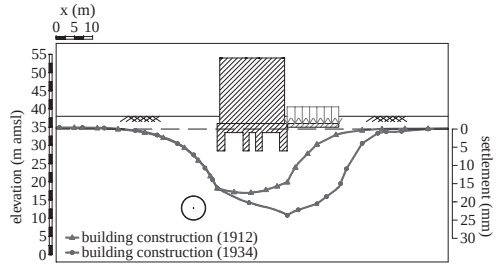

Figure 14. Settlement profile induced by building construction.

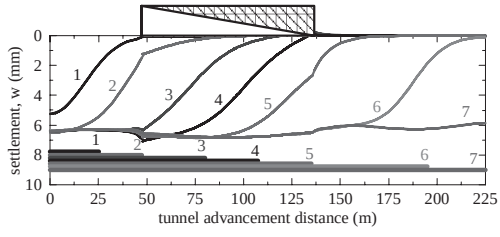

Figure 15. Interaction analysis: Settlement profile in longitudinal direction.

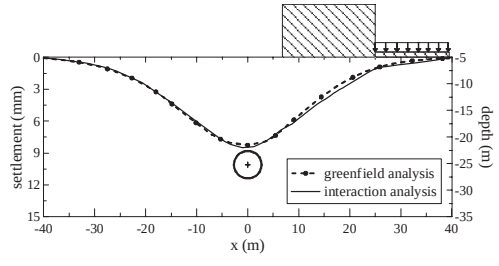

Figure 16. Interaction analyses: Settlement profile in cross section 1 and comparison with *greenfield* analysis.

building. Before the simulation of the Tunnel excavation the building is introduced into the model. Fig. 14 shows the vertical settlements induced by the building construction; the maximum calculated settlement is about 25 mm; the main structure (old portion, 1912) has just suffered a light distortion; after the more recent body construction (1934), the main structure experienced a small rotation (tilting), which is still visible. Displacements are set equal to zero before starting the construction of the Tunnel. The effects on profile settlement due to the presence of the building are clearly evident in Fig. 15 and Fig. 16. A small increment of settlements under the building foundation is noted. Due to the building stiffness, however, angular distortions are smaller compared to those calculated in *greenfield* condition (0.0016% and 0.0038% respectively) and are essentially inappreciable.

5.3.1 *Damage of the building*

Numerically obtained stress and strain distributions in the building structure can be analyzed to assess the level of damage induced both in terms of potential crack formations and reduction of structural safety levels. For this purpose the tensile stress and the shear strength mobilization levels are particularly relevant. As expected because of the small level of distortion experimented by the building structure, the severity of stress is practically unchanged due to tunnel construction. In Fig. 17, for example, the distributions of the shear strength mobilization ratio τ/τ_{max}, (τ is the current shear stress while τ_{max} is the maximum shear strength available) are shown before and after tunnel excavation, for cross section 1; τ/τ_{max} equal to 1 means that shear strength is completely mobilized. The effects induced by tunnel construction on the building are very small.

6 CONCLUSIONS

In order to simulate accurately the effects induced on surface structures by tunneling operations, full 3D finite elements numerical analyses shall be carried out. The simulation shall include the main aspects on which the amount and the distribution of the settlements depend: the support of the tunnel face, the conicity and weight of the shield as well as the grouting in pressure of the *annulus* between lining and excavation profile. Settlement profile and volume of subsidence basin obtained numerically are simple analysis results depending on geometry, soil characteristics and modality of excavation.

In 3D analysis, it is very important to carry out preliminary analyses on a small portion of the complete mesh, using different mesh density and tolerated error, to optimize the complete analyses achieving an acceptable compromise between calculation time and accuracy of the results.

The face pressure distribution considered in the model has been assumed within the design range. Under this assumption, the model gives a maximum settlement of about 8 mm, corresponding to a subsidence curve volume of 0.75%.

The study clearly underlines the necessity to incorporate the presence of the building into the model. For the case under investigation, the presence of the building induces a small increment of settlements. Due to structure stiffness, the building distortions are smaller than those calculated in *greenfield* condition (0.0016% and 0.0038% respectively). Consequently, the expected class of damage, according to Burland classification (Burland, 1995), is near to zero. As expected because of the small level of distortion experimented by the building structure, the severity of stress numerically obtained due to tunnel construction is practically unchanged.

Despite the very low class of damage expected, due to the very poor quality of the masonry, the building suffers some damage and a large number of cracks were detected, before the tunnel construction the structure of the building will be refurbished and the foundation system will be reinforced by micropiles.

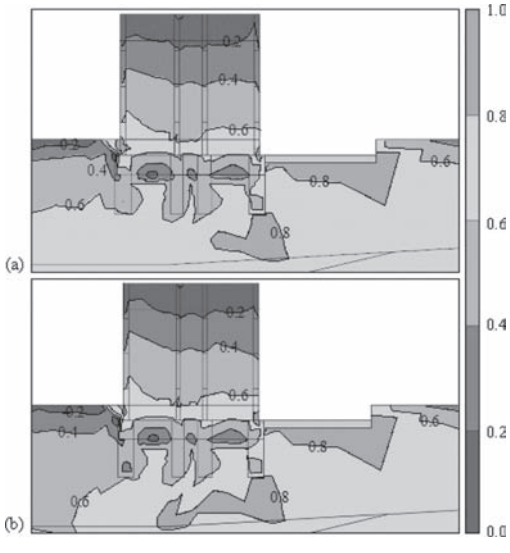

Figure 17. Mobilized shear strength, τ/τ_{max}, in cross section 1: a) after the building construction; b) after Tunnel B excavation.

REFERENCES

Burd H.J., Houlsby G.T., Augarde C.E. & Liu G. 2000. Modelling tunnelling-induced settlement of masonry building. Proc. ICE, Geotechnical Engineering, 143, 17–29 ISSN.

Burland, J.B. 1995. Assessment of risk of damage to building due to tunnelling and excavation. Invited special lecture to IS-Tokio: 1st Int. Conf. On Earthquake Geotechnical Engineering.

Buselli F., Logarzo A., Miliziano S. & Zechini A. 2010. Class A prediction of the effects induced by the Metro C construction on a preexisting building, in Rome. 7th European Conference on Numerical Methods in Geothecnical Engineering, NUMGE, Trondheim, Norway.

Formato, F. 2009. Analisi dell'interazione tra lo scavo delle gallerie della Linea C della metropolitana di Roma e l'edificio della scuola A. Diaz/G. Carducci

nel quartiere San Giovanni. Tesi di laurea. Sapienza, Università di Roma.
Franzius, J.N. & Potts, D.M. 2005. Influence of Mesh Geometry on Three-Dimensional Finite-Element Analysis of Tunnel Excavation. International journal of geomechanics, ASCE.
Hardin, B.O. 1978. The nature of stress-strain behaviour for soils. State of the Art. Proc. Geotechnical Eng. Division Specialty Conference on Earthquake Engineering and Soil Dynamics, ASCE, Pasadena, California.
Moh, Z.C. & Hwang, R.N. 1996. Ground movements around tunnels in soft ground. London, UK.
Peck, R.B. 1969. Deep excavations and tunnelling in soft ground. Proc., 7th Int. Conf. Soil Mech., Mexico City, State of the art 3. pp. 225–290.
PLAXIS, Plaxis 3D Tunnel Version 2.4, 2007. Finite Element Code for Soil and Rock Analyses.

Geotechnical Aspects of Underground Construction in Soft Ground – Viggiani (ed)
© 2012 Taylor & Francis Group, London, ISBN 978-0-415-68367-8

Ground movements induced by tunnel boring in Naples

E. Bilotta & G. Russo
University of Napoli Federico II, Naples, Italy

ABSTRACT: Major underground works have been carried out in the city of Naples (Italy) in the last two decades to enhance the public transport system and they are still in progress. Very densely urbanized areas of the city were interested, including historical and monumental buildings. Therefore, prediction and control of ground movements have been issues of great concern for designers and contractors. The paper refers about the ground movements measured during the excavation of tunnels of stretches belonging to Line 1 and Line 6 of the underground railway system. The collected data confirmed that the use of tunnel boring machines has nowadays largely reduced the level of ground loss during excavation and, consequently, the concern for possible interaction with the existing buildings.

1 INTRODUCTION

The ground movements induced by tunnel excavation are mainly generated by the larger volume of soil removed during operations compared to the volume occupied by the tunnel. This 'loss' of volume occurs at the front of the excavation ('face loss') and around the lining in radial direction ('radial loss'): both these components can be controlled during mechanised tunnelling. By using a Tunnel Boring Machine the face loss can be largely reduced by pressurising the front while the radial loss can be controlled by the volume and pressure of the backfilling grout. As a matter of fact, these parameters are also used as input value for advanced numerical predictions of TBM-induced ground movements (Koelewijn & Verruijt, 2001; Moller & Vermeer, 2008).

During the construction of new stretches of the underground in Naples, the ground movements were monitored for two main reasons: (i) controlling the construction processes and (ii) accumulating experimental data for the advancement of the knowledge on the topic. Some of the collected data are reported in this paper and discussed also in the light of the key parameters of the mechanised excavation (Bakker & Bezuijen, 2009), which were routinely controlled during the TBM driving procedures.

2 UNDERGROUND WORKS

2.1 *Line 1 extension*

The lower stretch of the Naples Metro Line 1 was constructed underground by boring two parallel tunnels at variable depth in various ground conditions (Fig. 1). From the intake located in a shaft at about 17 m below the ground level, the tunnels were bored in alluvial sands and silty sands, below the groundwater table (typically a few metres below the ground level). At 1 km far from the intake the two tunnels enter a soft rock formation (Yellow Tuff). The paper deals with the measurements carried out in the first part of the line where the two tunnels were excavated by two earth pressure balance shields (D = 6.74 m) through sandy soils and installing a precast r.c. segmental lining (5.85 m ID, 6.45 m OD).

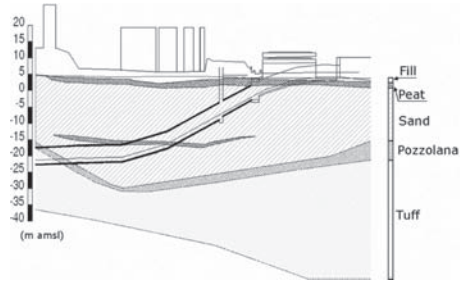

Figure 1. Ground conditions of Line 1 extension.

The average values of the properties of the sandy soil present in the first part of the line are summarized in Table 1.

2.2 *Line 6 extension*

The line 6 was partially constructed several years ago and a new long stretch is under construction. The terminal part of the existing line and the beginning of the new stretch are mainly excavated through sandy soils (Fig. 2).

The shallower layer is usually constituted by antropic fills, with thicknesses that reach up to

Table 1. Average values of geotechnical parameters.

	Sand
Dry unit weight, γ_d [kN/m^3]	15
Saturated unit weight, γ_{sat} [kN/m^3]	19
Permeability, k [m/s]	10^{-6}–10^{-7}
Cohesion, c' [kPa]	0
Friction angle, ϕ'	38°
Small strain shear modulus, G_o [MPa]	$10 + 5z$ (z = depth)
Earth pressure coefficient, K_o	0.4–0.5

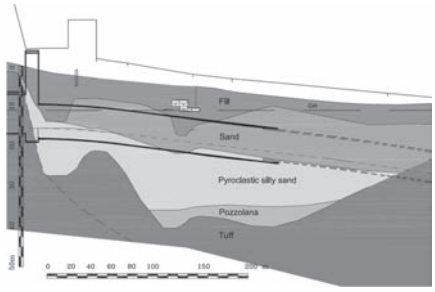

Figure 2. Ground conditions of Line 6.

Table 2. Average values of geotechnical parameters.

	Sand	Pyroclastic soils
Dry unit weight, γ_d [kN/m^3]	16	14
Saturated unit weight, γ_{sat} [kN/m^3]	18	16
Permeability, k [m/s]	10^{-6}–10^{-7}	
Cohesion, c' [kPa]	0	
Friction angle, ϕ'	37°	36°
Small strain shear modulus, G_o [MPa]	$10 + 5z$	(z = depth)
Earth pressure coefficient, K_o	0.4–0.5	

ten meters. The groundwater table is a few meters below surface. Both pyroclastic soils and landfills are characterized by medium-high density and high permeability. The sandy layers are limited at the bottom by the tuff formation. The average values of the main soil properties are shown in Table 2.

In the paper displacements obtained by two monitoring sections in the terminal part of the existing line will be presented and discussed. The stretch was bored by means of a hydroshield (D = 9.25 m) at a depth almost constant around 12 m bgl (axis depth, z_0), and lined by bolted rings of precast reinforced concrete segments. In the area the groundwater table is found around 7 meter deep, that is on average at the roof of the tunnel.

3 SOIL MONITORING DURING EXCAVATION

3.1 *Line 1 monitoring set-up*

The lower stretch of line 1 approaching the Garibaldi Station from the intake shaft located about 1 km away was partly (about 400 m) excavated in soft ground (sand) and partly excavated in the upper part of the underlying tuff formation, under a cover of overburden layers of sand (Fig. 1). Due to the presence in the area of several infrastructures, as the highway entrance and a regional railway embankment, and several buildings, among which the city main railway station, particular care was dedicated to control the ground movements induced by the excavation. Survey of ground surface was performed by levelling optical landmarks regularly deployed along the tunnel longitudinal axes. Moreover a number of tranverse sections were equipped for measuring the ground movements both at surface and in depth. A plan view of the line with the traces of the fifteen monitored sections is shown in Figure 3.

All the fifteen sections were provided with arrays of landmarks for measuring settlements at the ground level. In some of them also vertical tubes were installed with inclinometer casing and magnetic ring targets for measuring deep vertical and horizontal displacements by means of inclinometer and extensometer probes. A sketch of a typical monitoring section is shown in Figure 4: A, B, and C are the verticals along which both settlements and horizontal displacements were measured while S and N are centered on the tunnel vertical axes and for this reason only settlements were measured. In Table 3 the distance of the tubes A, B and C from the vertical axis of the tunnels are reported for each section.

3.2 *Line 6 monitoring set-up*

The extension of Line 6 under construction is being monitored similarly to Line 1 for both surface and deep ground movements. These data are still being collected and they will not be available for an overall interpretation before the works will be completed.

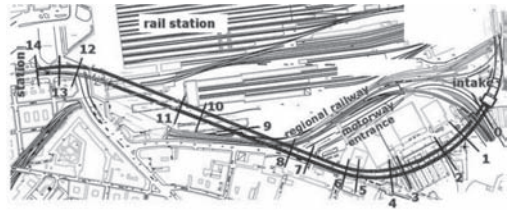

Figure 3. Plan view of the monitored stretch of Line 1.

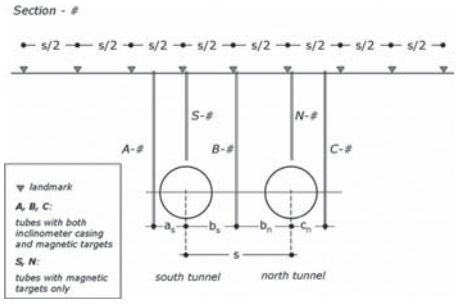

Figure 4. Sketch of a typical monitoring section.

Table 3. Distance of tubes from the tunnel axis.

Section	1		2		3		5		6	
a_s; b_s (m)	8.1	5.8	–	6.6	6.5	7.4	8.1	8.1	4.5	–
b_n; c_n (m)	8.0	8.5	8.4	–	8.0	6.0	5.5	–	–	–

Two monitoring sections belonging to the terminal part of the old existing stretch of the Line 6 are reported in Figure 5.

3.3 *Surface settlements*

Figure 6 shows the evolution of the maximum measured vertical displacement at four of the monitored sections of Line 1 during the construction of both south and north tunnels. The north tunnel was excavated after the south tunnel and for each section a new zero reading was taken before the contruction of the north tunnel started. Therefore the values of surface settlement shown for the north tunnel are to be considered as increments subsequent the completion of the south tunnel. As shown in the figure, settlement started before the arrival of the excavation front to the monitored section: around 50 m before for the north tunnel and a bit less for the south tunnel.

The settlements measured along the monitoring sections after plane strain condition were reached are shown in Figures 7 and 8. In the same figures the relevant Gaussian best fits are also shown. It is worthy reminding that the widely used Gaussian curve is represented by the following equation:

$$w = w_{\max} \cdot \exp\left(\frac{-x^2}{2i^2}\right) \tag{1}$$

With w_{max} equal to the maximum settlement above the tunnel axis, x equal to the horizontal distance from the tunnel axis, i equal to the distance of the inflexion point from the tunnel axis. The parameter i and the maximum settlement, w_{max}, are further

Figure 5. Plan view of the two monitoring sections along the tunnel of Line 6.

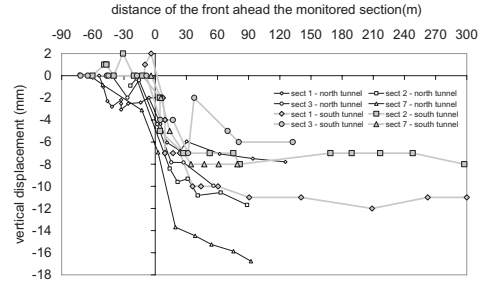

Figure 6. Evolution of vertical displacement as long as the front advances.

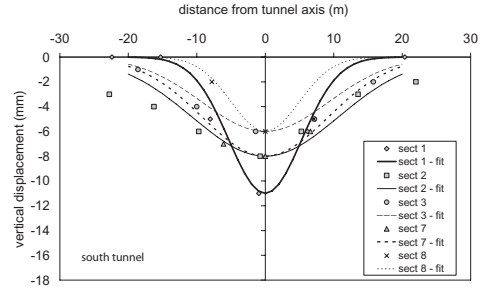

Figure 7. Measured settlements and Gaussian fit—Line 1 south tunnel.

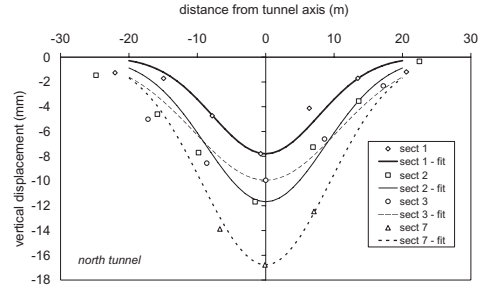

Figure 8. Measured settlements and Gaussian fit—Line 1 north tunnel.

linked by the following equation which introduces the volume loss, V':

$$V' = w_{max} \cdot 4\sqrt{\frac{2}{\pi}}\frac{i}{D^2} \quad (2)$$

The values of the parameter V' range between 0.3% and 0.5%, except for the section 7 of the north tunnel where $V' = 1\%$ was back-calculated. The values of the parameter K (= i/z_0) are in the range between 0.3 (section 1-south tunnel) and 0.65 (section 7-north tunnel) an average value being around 0.5. The upper bound of the range is consistent with the indication of Peck (1969) for tunnels in sand below the water table.

Figure 9 shows the longitudinal profiles of the maximum settlements, w_{max}, measured over a span of about 80 m when the south tunnel front was at five different locations between chainages 236 m and 378 m. In the figure are also shown the fitting curves based on the integration of the normal cumulative curve (Attewell & Woodman, 1982) and assuming: $w_{max}(-\infty) = 6$ mm according to measurements; the inflexion distance, i_{long}, equal to that of the Gaussian fit of the nearest monitored transverse section, i_{trasv}.

Although the plane strain maximum settlement, $w_{max}(-\infty)$, over the considered span is the same, the settlement at TBM face is different and ranges between 25% $w_{max}(-\infty)$ and 0. According to Craig (1975) this is to be expected for shielded tunnels in sand below the water table.

Similar plots are shown in Figure 10 referring to a larger span (from chainage 99 m to 513 m). The plane strain maximum settlement varies between 6 mm and 15 mm without correlation with the front settlement.

During the excavation of the stretch of Line 6 tranverse and longitudinal profiles of settlement were measured and results similar to those for Line 1 were obtained. In this case values of the parameter V' equal to 0.18% (section 1) and 0.33% (section 2)

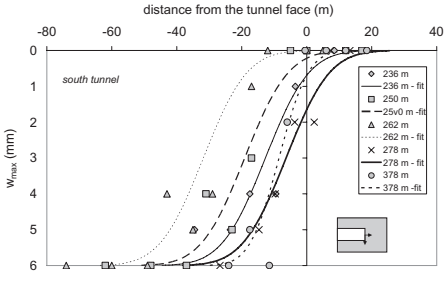

Figure 9. Longitudinal profiles of the maximum settlements, w_{max} between chainages 236 m and 378 m (Line 1 south tunnel).

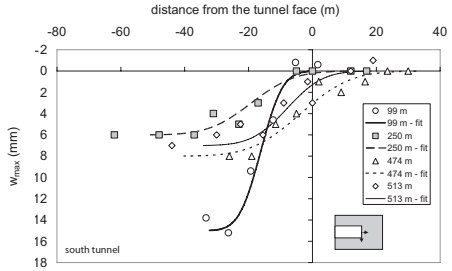

Figure 10. Longitudinal profiles of the maximum settlements, w_{max} between chainages 99 m and 513 m (Line 1 south tunnel).

and corresponding values of K equal to 0.43 and 0.27 were determined by Gaussian fit of the measured settlement in the tranverse section. The settlements measured in the longitudinal direction were best-fitted by assuming $i_{long} = 2 \cdot i_{trasv}$, the front settlement at section 2 being almost negligible.

3.4 *Deep displacements*

The deep settlements measured along the extensometer tubes (Fig. 4 and Table 3) are shown in the following Figures 11–13. The relative settlements measured between the magnetic targets in the tubes were referred to the top settlement of the extensometer tube, which was separately determined by optical levelling.

The vertical displacements (negative = downward) are plotted along the elevation from the tunnel axis.

It can be seen that the maximum settlement measured at the ground level generally increases with the tunnel depth. Furthermore this settlement tends to remain constant with the depth, at least until the tunnel section is approximately met. Suddenly the observed settlements decrease and below the tunnel axis they are very small: in some cases the displacements at that level are directed downward and in some others upward.

The vertical displacements measured in section 3 above the crown of both south and north tunnels (S-3 and N-3 in Figure 13) are substantially the same, indicating the same performance of the TBMs at that section. This is confirmed also by the corrisponding measurements at the lateral tubes (A-3 and B-3 in Fig. 11 and B-3 and C-3 in Fig. 12) and by the similar values of V' and K back-calculated for the two tunnels at that section.

On the other hand, the settlements measured in section 1 above the tunnel crown (S-1 and N-1 in Figure 13) are significantly different. In fact the settlement trough of the north tunnel was wider and lower settlements were measured at surface

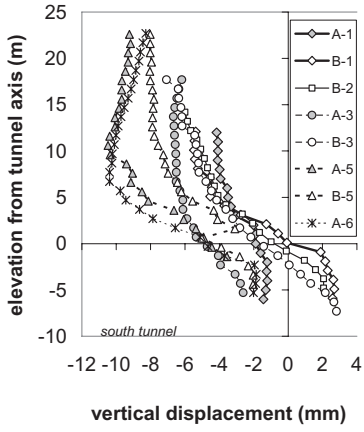

Figure 11. Vertical displacement with depth along the lateral extensometer tubes (Line 1 south tunnel).

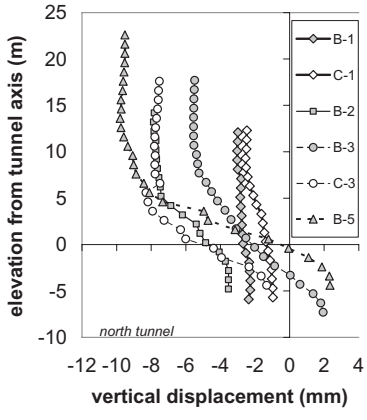

Figure 12. Vertical displacement with depth along the lateral extensometer tubes (Line 1 north tunnel).

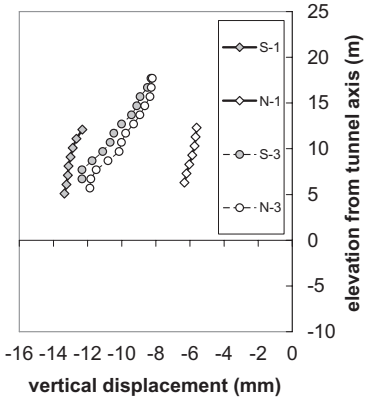

Figure 13. Vertical displacement with depth along the central extensometer tubes (Line 1 both tunnels).

(Figs. 7 and 8), although the same V' was back-calculated for the two tunnels at that section.

The deep settlements above the crown of both tunnels at sections 1 and 3 have been fitted by means of several Gaussian curves. It was found that the parameter V' generally increased with depth: a volume loss at the tunnel crown almost double than that back-calculated at surface was obtained for both sections. This measurements simply confirm that tunnel escavations in sandy soil is not an undrained process (as it is in clayey soil) which should imply costant volume loss from the tunnel upwards to the ground surface. Moreover, the distance from the axis of the tunnel to the inflexion point, i, decreased with depth, as shown in Figure 14.

Moh et al. (1996) proposed a formula to evaluate the trough width parameter, i, at a depth of z:

$$i(z) = bD\left(\frac{z_0 - z}{D}\right)^m \tag{3}$$

Where D is the tunnel diameter, $(z_0–z)$ the elevation from the tunnel axis depth, z_0, and b and m two parameters. Following Moh et al. (1996), the exponent m was determined from the settlement profiles above the tunnel centre shown in Figure 13 as the slope of the same profiles plotted in a bi-logarithmic plane. The coefficient b was obtained by fitting the settlement trough at surface. The results are shown in Table 4.

The corresponding profile i $(z–z_0)$ are shown in Figure 14 as fitting curves. A further profile is shown ($m = 0.8$, $b = 0.7$) as this fitted better the set of data corresponding to the south tunnel at section 3. However, in three over four cases the Eq (3),

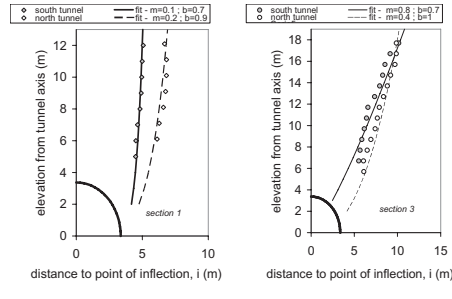

Figure 14. Profiles of i above the tunnel crown (Line 1 both tunnels).

Table 4. Back-calculated values of m and b.

	m (south)	b (south)	m (north)	b (north)
Section 1	0.1	0.7	0.2	0.9
Section 3	0.4	1	0.4	1

calibrated on the deep settlements above the tunnel centre and on the surface trough, enabled an accurate prediction of the profile of i (z) that was back-calculated by Gaussian fitting the deep settlements measured along different vertical lines.

The horizontal (in-plane) displacements measured in the transverse sections along the inclinometer tubes (Fig. 4 and Table 3) are shown in the following Figure 15 for the south tunnel. In most cases the horizontal components of ground movements at the tunnel sides were directed towards the tunnel (positive in the figures) and a significant decrease of their magnitude was observed with the depth. The horizontal displacements below the tunnel invert are generally very small.

The direction of the vectors of total displacement above the tunnel crown level are represented in Figure 16 as a ratio between the in-plane horizontal displacements, u_h, and the settlement, w. The ratio u_h/w is plotted against the ratio $x/|z_0 - z|$,

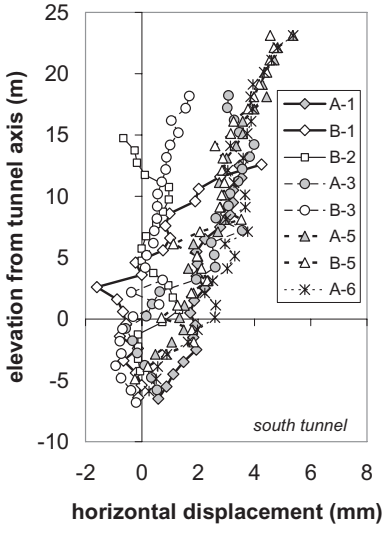

Figure 15. Horizontal displacements with depth along the inclinometer tubes (Line 1 south tunnel).

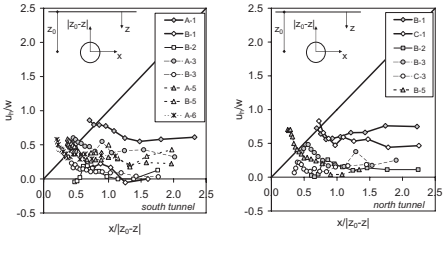

Figure 16. Direction of the vectors of displacement (Line 1).

indicating at each point in the ground the inclination of a vector pointing to the tunnel centre. It is worth noting that in most cases the vectors of displacement close to surface were directed toward the tunnel centre ($u_h/w = x/|z_0 - z|$). The plot shows also that the ratio u_h/w presents only minor changes with the depth indicating that the displacement vectors keep parallel with the depth pointing at different locations below the tunnel axis.

4 DISCUSSION

The results of monitoring presented in the previous section have been intrepreted in the light of the usual empirical criteria based on the Gaussian fit of surface and subsurface ground movements. The influence of the excavation technology was already evidenced by the low values of volume loss back-calculated from the experimental data, typical of a TBM excavation. For both case histories the value of V' derived by surface settlement troughs were rather small, ranging in the field 0.2%–0.5%. The values of the parameter K were on the average higher for Line 1 compared to Line 6. The difference is expected if the different groundwater table location is considered: for Line 1 the most of the covering sandy soil is under the groundwater table while for Line 6 the most of the covering sandy soil is above the groundwater table.

However the observed pattern of movements appeared in some cases locally conditioned by parameters related to the control of the tunnelling machine which are usually neglected in the design stage. Therefore, available parameters such as the applied face pressure, the volume and weight of the excavated soil, the volume and pressure of the injected grout at the shield tail, registered during the excavation, are analysed and discussed in the following.

A key parameter to control ground movements during the TBM excavation is the ratio between the volume of extracted soil and the theoretical volume of the excavation. The average value of such a ratio over the south tunnel of line 1 was roughly equal to 1 and over the north tunnel it was equal to 1.1. This would indicate an ideal performance of the TBM excavation, according to AFTES (2001), and would justify the low volume loss generally back-calculated. However, despite the low variability of such a ratio, along the tunnel a significant variability of the magnitude and of the shape of surface settlement through was observed. Such a variability cannot be explained by the typical suggestions of the so called Gaussian method which only asks for the definition of the type of subsoil and of the amount of volume loss V'.

Another parameter which could in principle be important to control settlement induced by excavation is the back-filling grout volume. In Figure 17, for instance, the maximum surface settlements measured along the south tunnel of Line 1 are plotted against the volume of the grout injected at the shield tail in the corresponding tunnel section. Although the large scattering of the experimental data, it clearly appears that the settlement decreases as far as the injected grout volume increases.

In Figure 18 the same data are plotted in another and more complex form to take into account all the main factors. The dimensionless ratio between the measured and the theoretical grout volume was computed as:

$$R_{inj} = \frac{4 \cdot V_{GROUT,meas}}{\pi\left(D_S^2 - D_L^2\right)} \tag{4}$$

Where $V_{GROUT,meas}$ is the measured injected grout volume per ring of lining, D_S is the diameter of the TBM shield and D_L the external diameter of the lining. Such a ratio was plotted on the left y-axis (grey line) along the corresponding chainages of the south tunnel (the fifteen monitored sections are also indicated on the chainage axis) together with the maximum settlement measured at surface

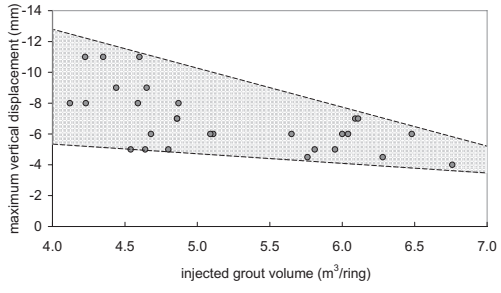

Figure 17. Influence of injected grout volume on settlement (Line 1—south tunnel).

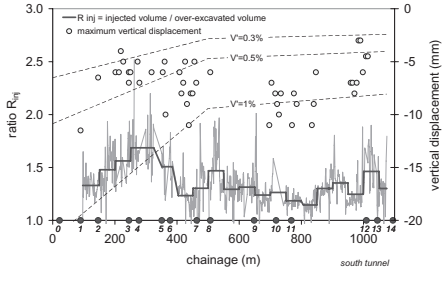

Figure 18. Relative injected grout volume and settlement along the south tunnel of Line 1.

(light grey dots, right y-axis). The stepwise black line is the average value of R_{inj} over 50 m.

The three dashed lines represent a simplified prediction of the maximum settlement by assuming a constant value of $K = 0.5$ (average value in the monitored section, see §3.3) and three different values of $V' = 0.3\%$, 0.5% and 1%. Such lines show clearly that in the first stretch of the Line 1, due to the shallower location of the tunnel axis, larger settlement at the surface should occur at the same fixed volume loss V'. As a matter of fact, even with some scattering, the recorded surface settlements along the whole stretch of the line fall always in the same range 3 mm–12 mm, independently from the depth of the tunnel axis. Such a finding may be explained by the higher values of the injected volume in the initial stretch of the line.

Further parameters which could help in explaining such a finding is the average earth pressure measured in the excavation chamber (at face) or at the shield tail. These values as recorded during the excavation process of the stretch are plotted in Figure 19. In the same chart two continuous lines labeled as the upper and lower allowable pressure at face are also plotted. The upper allowable pressure has been assumed as equal to the total vertical stress at the tunnel axis level, following a practical "rule of thumb" to avoid the risk of "blow out" of the ground. The lower allowable pressure has been calculated as the hydrostatic pressure at the tunnel axis incremented of the effective stress needed to balance the unstable wedge in front of the tunnel face, according to the Anagnostou and Kovàri (1996) method. While the pressure at the face is almost constantly close to the lower bound, the pressure at tail is closer to the upper allowable bound in the first part of the stretch, getting closer to the lower bound in the second part of the stretch.

Again, the use of relatively higher pressure at tail in the initial part of the stretch together with the use of larger volume of grout volume seem the main factors successfully adopted to prevent larger

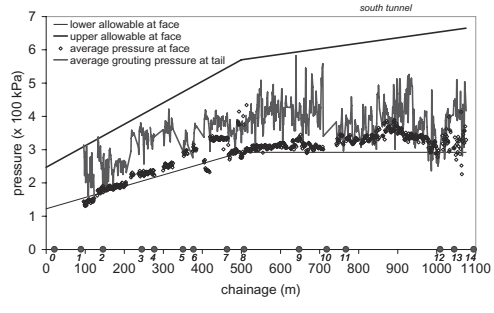

Figure 19. Face and grout pressures measured along the south tunnel of Line 1.

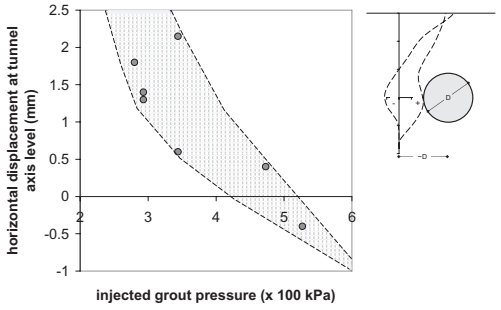

Figure 20. Horizontal displacement measured at the tunnel axis level versus the injected grout pressure.

settlement in the initial part of the stretch were the tunnel was located at shallower depth.

The patterns of the measured deep horizontal displacement (Fig. 15) are schematically summarised by the sketch in Figure 20. It has been observed in section 3.4 that the horizontal displacement around the tunnel axis level are directed sometimes toward the tunnel (positive) and sometimes outwards (negative). In Figure 20 the horizontal displacements measured about one tunnel diameter away at the tunnel axis level are plotted versus the injected grout pressure, showing a general trend of the ground movement to be directed outwards when the back-filling grout pressure increases.

5 CONCLUSIONS

The paper reports data obtained by the observations of both surface and deep movements recorded during the excavation of new tunnels with TBM in Naples (Italy). It is important to underline that very often tunnels excavated in urban areas interact also with buried structures: in such cases the empirical methods such as the Gaussian one should be adapted in the design stage to predict both surface and deep movements. To date the experimental evidence on deep movements around tunnels is rather scanty especially when compared to the data available on surface induced settlements.

The excavations in Naples were mainly carried out in sandy soil below the groundwater table. Surface settlements were measured using precision survey. Deep ground movements were measured using down hole extensometer and inclinometer probes.

Volumes of the surface trough as low as 0.3–0.5% of the tunnel volume were back-calculated; the volume of the trough deduced by deep movements data increased with depth up to values about twice the volume observed at the surface. The distance of the inflexion point from the tunnel axis, i, allowed the empirical parameter K of the Gaussian fit to be calculated: the values varied in the typical range proposed by literature suggestions, with an average value of 0.5. The distance to the inflexion point, i, decreased with depth slightly less than linearly, with power law with exponents between 0.7 and 1.

Interestingly, the vectors of displacements measured along vertical at the tunnel sides pointed towards different focuses located mainly below the tunnel axis.

The paper has shown also, at least on a qualitative basis, that the movements induced by TBM around the tunnel depend on technological and constructional procedures and details, usually non completely defined at the design stage. By a careful record of many operational parameters governed by the TBM drivers it has been possible to demonstrate that the volume of the injected grout at the tail and the pressure adopted for such injections are indeed factors controlling the induced surface and deep movements.

REFERENCES

AFTES 2001. Synthèse Eupalinos 2000. French National Project on Mechanized excavation in Heterogeneous Ground Earth Pressure Balance Shield.

Anagnostou, G. and Kovári, K. 1996. Face stability conditions with Earth-Pressure-Balanced Shields. *Tunnelling and Underground Space Technology*, Vol 11, No. 2, 165–173.

Attewell, P.B. and Woodman, J.P. 1982. Predicting the dynamics of ground settlement and its derivatives caused by tunnelling in soil. *Ground Engineering*, vol.15, no.7, 13–22.

Bakker, K.J. and Bezuijen, A. 2009. Ten years of bored tunnels in The Netherlands: Part I, geotechnical issues. *Geotechnical Aspects of Underground Construction in Soft Ground*–Ng, Huang & Liu (eds). Taylor & Francis Group, London. 243–248.

Koelewijn, A.R. and Verruijt, A. 2001. Simplified three-dimensional numerical modelling of shield tunnel advancement. *Proc. XV Int. Conf. Soil Mech. and Geotech. Engng. Istanbul 27–31 August 2001*. 1463–1466.

Mair, R.J. and Taylor, R.N. 1997. Bored tunnelling in the urban environment. State-of-the-art report and theme lecture, *Proceedings 14th International Conference Soil Mechanics and Foundation Engineering*, Hamburg vol. 4, Balkema, Rotterdam. 2353–2385.

Moeller, S.C. and Vermeer, P.A. 2008. On numerical simulation of tunnel installation. *Tunnelling and Underground Space Technology* 23. 461–475.

Moh, Z.C., Hwang, R.N. and Ju, D.H. 1996. Ground movements around tunnels in soft ground. *Geotechincal Aspects of Underground Construction in Soft Ground*—Mair & Taylor (eds), Balkema, Rotterdam. 725–730.

Peck, R.B. 1969. Deep excavations and tunnelling in soft ground, *Proc. 7th ICSMFE, Mexico City*, State of the Art Volume, 225–290.

Geotechnical Aspects of Underground Construction in Soft Ground – Viggiani (ed)
© 2012 Taylor & Francis Group, London, ISBN 978-0-415-68367-8

EPB tunnelling in deltaic deposits: Observations of ground movements

A. Gens, A. Di Mariano & M.T. Yubero
Department of Geotechnical Engineering and Geosciences, Technical University of Catalonia (UPC), Barcelona, Spain

ABSTRACT: The Line 9 of Barcelona Metro is currently under construction. The southern part of the line connects the city to the airport and is completely excavated in soft deltaic deposits of Holocene age. In this part, tunnelling is performed by two EPB machines of 9.4 m diameter. The paper first describes the specific geology of the area. Information derived from the excavation of this part of Line 9 is presented and reviewed. In particular, the following issues are addressed: history of volume loss distribution along the line, magnitude and shape of subsidence troughs, influence of pressures used during tunnelling on observed movements, and contributing causes to observed instances of larger ground movements. The paper may constitute a useful case record for other EPB tunnelling projects in soft soil.

1 INTRODUCTION

A new Metro line, named Line 9, is currently under construction in the Barcelona metropolitan area (Di Mariano et al., 2007; Gens et al., 2006). It has a total length of 47.8 km, out of which nearly 44 km correspond to tunnelling. The project includes the construction of 52 stations. For civil engineering planning purposes, the project was divided into 4 major parts (Fig. 1): Part 1, the southern part, connects Barcelona city to its airport; Part 2, the south-eastern part, links to the Logistic Activities Zone of the Port of Barcelona; Part 3, the central part, runs through the high part of the city and, finally, Part 4, the northern part, connects Barcelona to the densely populated cities of Badalona and Santa Coloma de Gramanet (Ormazabal et al., 2008). The southern part of the line, i.e. Part 1, is completely excavated in soft deltaic deposits of Holocene age, which constitute, at the larger scale, a rather homogeneous geological profile. In this area, tunnelling is performed by means of two 9.4 m diameter EPB machines excavating in opposite directions from Mas Blau Station (Fig. 1).

Figure 1. Plan view of the full route of the Line 9.

The present paper specifically refers to the excavation of the Line 9 between Mas Blau Station and Barcelona airport (Fig. 1). This 4.33 km-long section of the Line crosses an urban area close to some sensitive structures. Ground movements have therefore been a special concern during tunnel design and construction. An extensive instrumentation system has been deployed to control the magnitude and distribution of ground movements and also displacements of the structures during and after the excavation of the line. The article first summarily describes the special geology of the area and its implications for tunnelling. Afterwards, the information derived from this part of the excavation is presented and reviewed. In particular, the following issues are addressed: history of volume loss distribution along the line, magnitude and shape of subsidence troughs, and influence of pressures used during tunnelling on observed movements. Attention is also paid to contributing causes to observed instances of larger ground movements.

2 LOCATION AND GROUND CONDITIONS

The part of the Line 9 (L9) route described in this paper was constructed under L9 Contract T1D that starts at Mas Blau Station and ends at Terminal entre Pistes Station, inside Barcelona airport (Fig. 1). Tunnelling works started in April 2008 and lasted approximately one year. Figure 2 shows a plan view of this part of the line. It also indicates the location of the three instrumented reference sections present, the four stations of this route

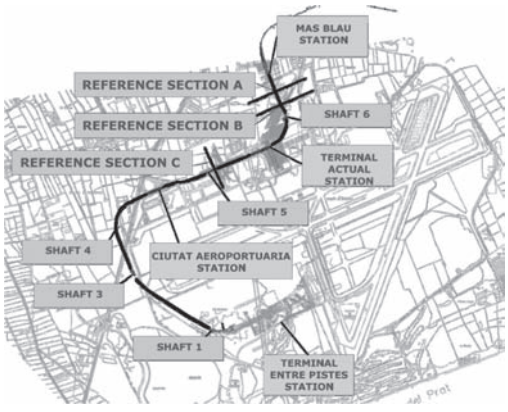

Figure 2. Plan view of the L9 contract T1D route.

and, finally, the five intermediate ventilation and emergency shafts. Of the four stations only one, the Terminal Actual Station, has been fully constructed underground and lacks a structure above ground. It will provide access to the old Barcelona Airport Terminal.

The longitudinal section shown in Figure 3 summarizes the geology along the tunnel route of Contract T1D. The top layer comprises made ground (R) of varying thickness overlying a thin stratum of brown fine silts (Ql1). Below it, gray fine sands, with some gravel inclusions (Ql2) are encountered which are in turn underlain by a gray layer (Ql3) of mixed composition: silty clays with some interlayered sands, sandy silts, clays and silts. The Ql3 layer is the main soft deposit and it reaches depths of approximately 50 m below ground level. It overlies the base gravels (QL4) where a confined aquifer is located. All of these materials are of Quaternary age and layers QL2 to QL4 belong to the deltaic deposits of the Llobregat River (Fig. 1). The water table is nearly horizontal and is located 0–1 m above sea level.

Except in the proximity of the Stations, the ground cover of the tunnel is about 16 m, with a cover/diameter (C/D) ratio of approximately 1.7. Around the Stations this ratio decreases reaching a minimum value of 1.0 in the area of Terminal Actual Station.

3 TUNNEL EXCAVATION

Tunnelling of Contract T1D was performed using a Herrenknecht Earth-Pressure-Balance (EPB) boring machine. The running tunnel was lined with 8.43 m Inner Diameter (ID) pre-cast segmental concrete rings, the segment length along the tunnel being 1.5 m. Six segments plus one key formed a full ring of 0.32 m thickness.

The advantage of EPB tunnelling is the possibility of providing substantial support to the excavated face at all times, thus allowing good ground movements control (Mair, 2008). During the excavation of the L9 Contract T1D, bentonite was systematically injected in the over-excavated annulus around the shield and the tail void was always grouted simultaneously to the EPB shield advance, in order to improve ground movement control (Wongsaroj et al., 2006).

Three different pressures were applied: the face pressure (Pf), a bentonite pressure (Pb) and the grouting pressure (Pg) (Di Mariano et al., 2009; Gens et al. 2009). Pf represents the support pressure to the excavation face provided partly by the thrust from the cutter head and partly by the chamber pressure (Mair, 2008); pressure Pb is the pressure of the bentonite injection around the shield, in the annular void between the shield and the ground due not only to the over-excavation of the cutter head but also to the conicity of the shield; pressure Pg corresponds to the pressure of the grouting injection that fills the gap between the extrados of the lining and the excavated ground (tail void). Typical face pressure values were in the range 2.0–3.0 bars, while shield pressures varied approximately from 1.3 to 2.0 bars and grouting pressures from 2.0 to 3.5 bars.

In order to achieve optimum performance with EPB machines, the excavated soil must form a suitable plastic mass of soft consistency and low friction that can readily be extruded from the head chamber through the screw conveyor (Peña Duarte, 2007). Natural ground does not usually have ideal properties when excavated, so modifications of its properties through soil conditioning may be necessary. The most common conditioners used in the tunnelling process are foams, polymers and clays (Peña Duarte, 2007). Foams were the only spoil conditioning agent used inside the chamber pressure in Contract T1D. Actually, when the excavated section was entirely in the Ql3 layer and its composition was mostly clayey, no spoil conditioning agent was needed.

After the first 250 m of the tunnel drive, access into the chamber pressure, by means of compressed air, was considered necessary to check the state of the cutting tools. No maintenance works were required. Afterwards, all the interventions at the cutter head were done at atmospheric pressure in the ventilation and emergency shafts and also in the Terminal Actual Station. In general, the wear and damage of the cutting tools was very limited in this section of the Line.

The advance of the EPB face with time is shown in Figure 4, together with the advancing tunnelling rates. The overall average advance rate, along the route of Contract T1D, was about 28.5 m/day,

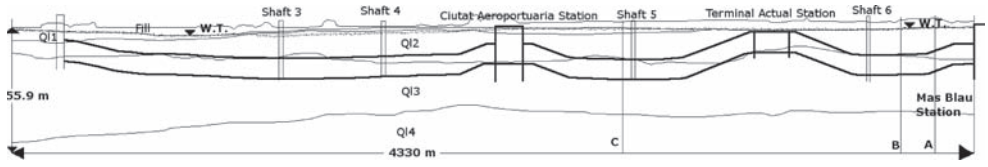

Figure 3. Sketch geological profile along the tunnel route of Contract T1D. Sections A, B and C are the instrumented reference sections at chainage 4150 m, 4000 m and 2750 m, respectively.

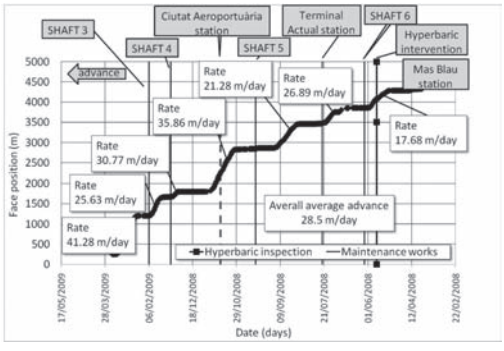

Figure 4. EPB face position vs. time. The Figure also indicates the advancing tunnelling rates.

i.e. 19 rings per day (stoppage periods are not included in these values) (Fig. 4). The maximum recorded daily advance was 90 m, or 60 rings. In Figure 4, the continuous vertical black lines indicate the positions of the shafts and the station where maintenance works were performed. The discontinuous line, which corresponds to Ciutat Aeroportuaria Station, indicates that the latter was constructed after the passage of the EPB machine and could not be used for maintenance. Finally, the vertical line, with solid black points, designates the location of the boring machine during the hyperbaric inspection.

4 GROUND MOVEMENT OBSERVATIONS

4.1 *Volume loss*

An extensive monitoring program was commissioned prior to the start of the excavation. Instrumentation was installed to measure not only the movements of nearby buildings, but also surface and subsurface movements as well as pore water pressures. Surface movements were monitored through levelling points and automatic sensors installed on the surface along longitudinal and transverse sections of the tunnel. Three instrumented reference sections were also installed to keep track of the deep ground movements at sections in greenfield situations with no buildings located nearby. Figure 5 shows, as an example, the instrumented section at chainage 4 + 000 m. The following instrumentation is deployed: seven levelling points along the transverse section of the tunnel, three extensometers (left, right and centre), two inclinometers (left and right), four open standpipe piezometers and three vibrating wire piezometers.

Two transverse settlement profiles, measured after the passage of the EPB beyond the zone of influence, are shown in Figure 6. Both of them refer to the instrumented section at chainage 4 + 000 m. The open points and the discontinuous line indicate the surface ground movement while the solid points and the continuous line represent the settlement trough at a depth of 9.5 m. Both profiles can be reasonably approximated in the form of a Gaussian distribution (Mair et al., 1993). In that case, the volume of the settlement trough per unit length, V_s is:

$$V_s = S_{\max} i \sqrt{2\pi} \tag{1}$$

where, S_{max} represents the ground vertical movement at the tunnel centre line and i the distance of the point of inflection of the curve from the tunnel centre line. The settlements caused by tunnelling are usually characterized by the volume or ground loss, V_l, which is the volume V_s expressed as a percentage of the notional excavated volume of the tunnel (Burland, 2001):

$$V_l = \frac{V_s}{\pi (D/2)^2} \tag{2}$$

Where D is the tunnel diameter. For practical purposes, the trough-width parameter at surface level (i) can be estimated with the following expression (O'Reilly & New, 1982):

$$i = K \cdot H_0 \tag{3}$$

where the parameter K depends on soil type and H_0 is the depth of the tunnel axis. For subsurface

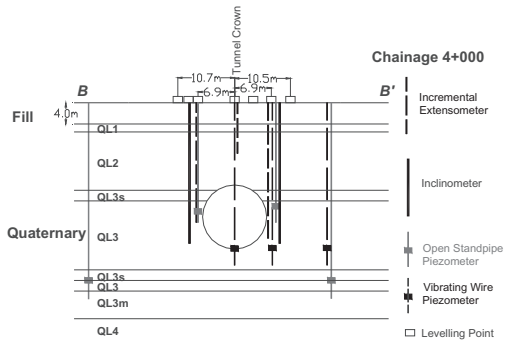

Figure 5. Instrumented reference section at chainage 4 + 000 m.

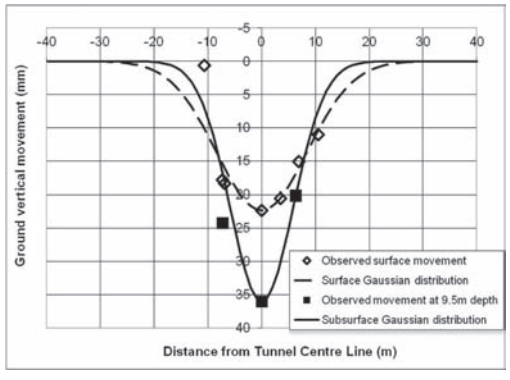

Figure 6. Surface and subsurface transverse settlement profiles in the instrumented reference section at chainage 4 + 000 m.

settlement profiles the trough-width parameter $i_{sub}(z)$ can be expressed as (Mair et al., 1993):

$$i_{sub}(z) = K_{sub}(z) \cdot (H_0 - z) \quad (4)$$

z being the depth at which the distribution of settlements is considered and $K_{sub}(z)$ the subsurface parameter K at a depth z.

For the surface settlement trough in Figure 6, equation (2) gives a volume loss of 0.68% and a trough-width parameter (i) of 8.5 m resulting in a K parameter equal to 0.42. At a depth of 9.5 m, the subsurface parameters i_{sub} and K_{sub} equal to 5.9 m and 0.55 respectively. Table 1 summarizes the values of K, and i, relative to both surface and subsurface Gaussian distribution curves at the three instrumented reference sections. The subsurface curves are always calculated at a depth of 9.5 m. In common with field measurements in other cases, the parameter K appears to increase with depth,

Table 1. K parameter and total volume loss at the three instrumented reference sections.

Reference section	Depth of tunnel axis	Volume loss	Surface settlement trough		Settlement trough at 9.5 m depth	
Chainage (m)	H_0 (m)	V_l (%)	K (–)	i (m)	K_{sub}* (–)	i_{sub}* (m)
4 + 150	18.7	0.22	0.51	9.5	0.59	5.4
4 + 000	20.2	0.68	0.42	8.5	0.55	5.9
2 + 750	21.4	0.50	0.52	11.1	0.70	8.3

*The subscript "sub" stands for subsurface.

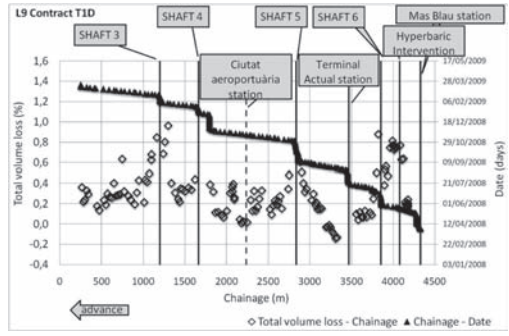

Figure 7. Total volume loss along the route of contract T1D.

giving proportionally wider settlement profiles closer to the tunnel (Mair et al., 1993).

In addition to the three instrumented reference sections, several additional transverse sections were installed on which surface settlements were measured (Nyren et al., 2001). Field observations indicated that the parameter K assumes an average value of approximately 0.50 at ground level, on nearly the entire route of Contract T1D. This value was hence used to evaluate volume losses along the excavation using only the settlement above the axis of the tunnel. Figure 7 shows the computed volume loss along the route, after the passage of the EPB beyond the zone of influence. The majority of values lie between 0.0 and 0.6 per cent, a rather low range of values given the soft nature of the excavated ground. Higher volume losses were observed in two areas: the first one close to chainage 3 + 851 m where shaft 6 is located and the second one in the area of chainage 1 + 201 m, corresponding to shaft 3. Usually, the shafts along the route were used to carry out scheduled maintenance works to the cutter head under atmospheric conditions. The process of the boring machine entering into a shaft or exiting from it caused sometimes difficulties for

maintaining the required face pressure. That is why volume losses in the proximity of the shafts were usually higher than in the rest of the L9 route. Moreover, whenever the EPB machine stopped, as in the case of the hyperbaric inspection, the restart of the excavation works generally represented a critical phase with higher ground losses.

Negative values of volume losses in Figure 7 refer to negative ground vertical movements, i.e. ground heave. Such negative values were registered in about 140 m of tunnelling in the gray fine sands of the Ql2 layer, just after the exit of Terminal Actual Station. Although the heave values are quite small, they probably indicate an excessively high face pressure.

4.2 *Components of ground movements associated with EPB tunnelling*

An example of the ground movements commonly associated with EPB tunnelling is shown in Figure 8 (Cording, 1991; Mair and Taylor, 1997; Dimmock, 2003 and Wongsaroj et al., 2006). Three components of settlements are indicated: the ground vertical movement measured when the face of the EPB machine is at the monitoring section (S_{Face}), the settlement due to the passage of the shield (S_{Shield}), and the settlement caused by both the closure of the tail void behind the shield and the deflection of the lining (S_{Tail}). Finally, the total settlement (S_{Total}) is defined as the sum of the three previous components. Delayed settlements caused by creep and/or consolidation are not explicitly considered in this paper. When measured, they were generally much smaller than the excavation-induced settlements.

As an example, Figure 9 shows the variation of the ground vertical movement with distance from the tunnel face, at a measuring point at chainage 2 + 900 m. The movement directly above the tunnel face, S_{Face}, is here less than 2 mm. In this

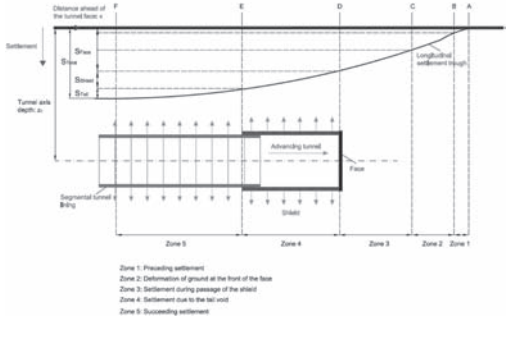

Figure 8. Components of ground settlements due to EPB tunnelling (Wongsaroj et al., 2006).

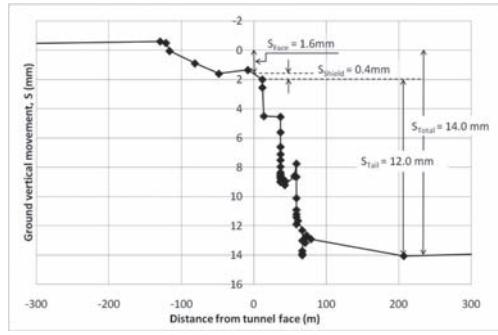

Figure 9. Ground vertical movement vs. distance from tunnel face at chainage 2+900 m.

case, S_{Face} represents approximately 10% of the total settlement. Generally, in the route of Contract T1D, the proportion of S_{Face} with respect to S_{Total} is quite low and often below 10%. Indeed, in some cases the arrival of the EPB face causes a small heave. At the same point (Fig. 9), the vertical movement due to the passage of the shield, S_{Shield}, is only 0.4 mm. The proportion of S_{Shield} with respect to S_{Total} varies greatly along the route, depending on several factors such as the excavated materials, the efficiency of the bentonite injection and the EPB rate of advance. In any case, the largest proportion of settlement by far corresponds to the closure of the tail void and the deflection of the lining (S_{Tail}). This applies to the entire route of Contact T1D and it is in fact very characteristic of EPB tunnelling.

5 INFLUENCE OF EPB OPERATING PRESSURES ON VOLUME LOSS

During the EPB advance in the Contract T1D route, face, shield and grouting pressures were measured at the injection points every ten seconds. A large amount of field data is therefore available to examine the potential influence of such pressures on volume loss. A drawback, however, lies in the fact that the range of variation of the pressures employed is limited, thus reducing the scope for examining the effect of large pressure variations. Three components of volume loss have been defined (Wongsaroj et al., 2006): the volume loss measured as the tunnel face reaches the monitoring section (V_{LF}), the volume loss measured when the end of the shield passes the monitoring section (approximately 10 m after the passage of the EPB face) (V_{LS}) and the tail volume loss when the EPB has advanced enough, beyond the monitoring section, and the surface settlement has stabilised (V_{LT}). All three components defined are incremental. Accordingly, three pressure

ratios have been introduced: the Face Pressure Ratio (FPR), the Bentonite Pressure Ratio (BPR) and the Grouting Pressure Ratio (GPR). The three ratios represent the face pressure, the bentonite pressure and the grouting pressure, respectively, normalised with respect to the overburden pressure at tunnel axis.

Figure 10 shows the relationship between the face volume loss, V_{LF}, and the face pressure ratio. It can be observed that the face volume loss is quite small in all cases and even negative at times. It can be concluded that, in this case, when face pressures are in the range 48–78% of the overburden pressure, the face volume loss is maintained well inside the ±0.2% range.

The volume loss V_{LS} measured when the end of the shield passes the monitoring section versus the bentonite pressure ratio is shown in Figure 11. Again, the volume loss is often very low and close to zero. The highest value of shield volume loss observed along the route of Contract T1D is only a little over 0.2%. Bentonite pressures in the range 33–74% of the overburden pressure are capable to keep the shield volume loss below 0.3% and generally much lower.

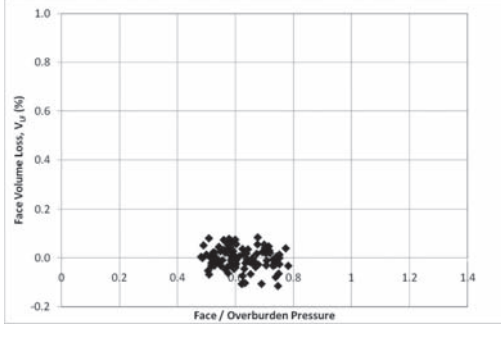

Figure 10. Face volume loss vs. face pressure ratio.

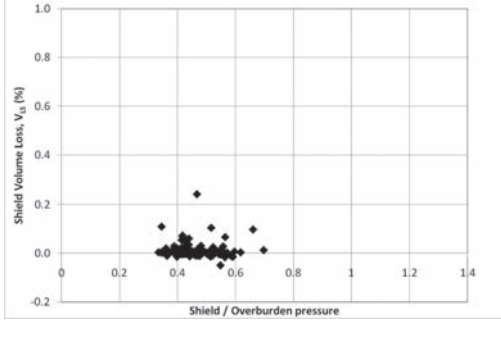

Figure 11. Shield volume loss vs. bentonite pressure ratio.

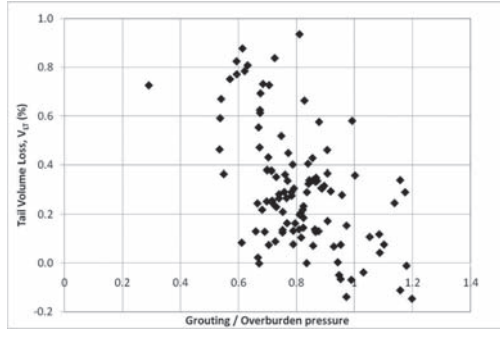

Figure 12. Tail volume loss vs. grouting pressure ratio.

The effect of the normalized grouting pressure on the tail volume loss is shown in Figure 12. Despite the large scatter in the data, there appears to be a rough tendency of the tail volume loss to decrease as the grouting pressure ratio increases. Identifying the causes of such scatter is not easy, as a number of additional factors (e.g. advanced rate, lining deflection, creep deformations) may contribute to it. As mentioned above, the volume loss due to the closure of the tail void represents the greatest percentage of the total volume loss, so the grouting injection has always been considered a very important operation. In the case described here, a full closure of the tail gap with no grouting applied would result in a volume loss of approximately 7%.

In any case, the good control of the three EPB operating pressures has resulted in quite low overall volume losses taking into consideration the soft characteristics of the ground.

6 SUMMARY AND CONCLUSIONS

The paper describes the excavation of a 4.33 km-long section of the Metro Line 9 between Mas Blau Station and Barcelona airport. The excavation has been performed in soft deltaic deposits with a number of sensitive structures close to the alignment.

The overall average advance rate of the EPB machine along the route was 28.5 m/day Volume losses lie generally in the range 0.0–0.6%, even though higher values have been observed at times. Most of the larger volume losses are associated with the entrance to or exit from shafts used for maintenance purposes. The parameter K that defines the width of the surface settlement trough has generally a value of about 0.5. Data from deep instrumentation confirms that K appears to increase with depth.

The face settlements and volume loss are always quite small and, sometimes, even negative indicating heave ahead of the EPB machine. The shield volume loss is more variable but also normally small. Most of the volume loss is associated with the closure of the gap after the passage of the shield. In spite of a large scatter of the data, there appears to be a correlation between the grouting pressures used and the tail volume loss.

In any case, the volume loss observed in the majority of cases is quite limited and the range of pressures adopted has been successful in reducing settlements to quite acceptable values in spite of the poor geotechnical characteristics of the excavated ground.

ACKNOWLEDGEMENTS

The authors thank GISA for the technical and financial support provided for the performance of the work reported in this paper. The contribution of the Ministry of Education and Science through research grant BIA2008-06537 is also gratefully acknowledged.

REFERENCES

Burland, J.B. (2001). Assessment methods used in design. In *Building response to tunnelling. Case studies from construction of the Jubilee Line extension (1)*: 23–43. London: J.B. Burland, J.R. Standing & F.M. Jardine (eds.)

Cording, E.J. (1991). Control of ground movements around tunnels in soils. General Report, *9th Pan-American Conference on Soil Mechanics and Foundation Engineering*, Chile.

Di Mariano A., Gesto J.M., Gens A. & H. Schwarz (2007). Ground deformation and mitigating measures associated with the excavation of a new Metro line. *Proceedings of the 14th European Conference on Soil Mechanics and Geotechnical Engineering*: 1901–1906. Madrid.

Di Mariano A., Persio R., Gens A., Castellanza R. & Arroyo M. (2009): Influence of some EPB operation parameters on ground movements. *2nd Int. Conf. On Computational Methods in Tunnelling*: 43–50. Bochum: Aedificatio Publishers.

Dimmock, P.S. (2003). Tunnelling induced ground and building movement on the Jubilee Line Extension. Ph.D. Thesis, University of Cambridge.

Gens A., Di Mariano A., Gesto J.M. & H. Schwarz (2006). Ground movement control in the construction of a new metro line in Barcelona. *Geotechnical Aspects of Underground Construction in Soft Ground*: 389–395. Taylor & Francis eds., Rotterdam: Balkema.

Gens A., Persio R., Di Mariano A., Castellanza R. & Arroyo M. (2009). Relación entre parámetros de una tuneladora EPB y los movimientos del terreno. *3as Jornadas Hispano-Portuguesas de Geotecnia*: 433–441. Madrid: Cedex.

Mair, R.J. Taylor, R.N. & Bracegirdle A. (1993). Subsurface settlement profiles above tunnels in clays. *Géotechnique* 43(2): 315–320.

Mair, R.J. & Taylor, R.N. (1997). Theme Lecture: Bored tunnelling in the urban environment. *Proc. 14th International Conference on Soil Mechanics and Foundation Engineering (4)*: 2353–2385. Hamburg: Balkema.

Mair, R.J. (2008). Tunnelling and geotechnics: new horizons, *Géotechnique* 58(9): 695–736.

Nyren, R.J., Standing J.R. & Burland J.B. (2001). Surface displacements at St. James's Park Greenfield reference site above twin tunnels through the London Clay. In *Building response to tunnelling. Case studies from construction of the Jubilee Line extension (2)*: 387–400. London: J.B. Burland, J.R. Standing & F.M. Jardine (eds.).

O'Reilly, M.P. & New, B.M. (1982). Settlements above tunnels in the United Kingdom—their magnitude and prediction. *Tunnelling '82*: 173–181. London: IMM.

Ormazabal G., Viñolas B. & Aguado A. (2008). Enhancing Value in Crucial Decisions: Line 9 of the Barcelona Subway. *Journal of Management In Engineering:* 265–272. ASCE.

Peña Duarte, M.A. (2007). Foam as a soil conditioner in tunnelling: physical and mechanical properties of conditioned sands. Ph.D. Thesis, University of Oxford.

Schwarz H., Boté R. & Gens A. (2006). Construction of a new Metro line in Barcelona: design criteria, excavation and monitoring. *Geotechnical Aspects of Underground Construction in Soft Ground*: 757–762. Taylor & Francis eds., Rotterdam: Balkema.

Wongsaroj J., Borghi F.X., Soga K., Mair R.J., Sugiyama T., Hagiwara T. & Bowers K.H. (2006). Effect of TBM driving parameters on ground surface movements: Channel Tunnel Rail Link Contract 220. *Geotechnical Aspects of Underground Construction in Soft Ground*: 335–341. Taylor & Francis eds., Rotterdam: Balkema.

This page intentionally left blank

Geotechnical Aspects of Underground Construction in Soft Ground – Viggiani (ed)
© 2012 Taylor & Francis Group, London, ISBN 978-0-415-68367-8

Mitigation of the effects induced by shallow tunneling in urban environment: The use of 'compensation grouting' in the underground Line B1 works in Rome

A. Sciotti
Roma Metropolitane S.r.l., Rome, Italy

A. Desideri
Università degli Studi 'La Sapienza', Rome, Italy

G. Saggio
Salini Costruttori S.p.a., Rome, Italy

C. Kummerer
Keller Fondazioni S.r.l., Verona, Italy

ABSTRACT: The new Underground Line B1 works in Rome involve the construction of three new stations and of about 7 km of single-track tunnels (i.d. 5.80 m) by means of two TBMs. The tunnels must be realized in heavily built-up areas, often with multi-storey buildings, both in masonry and in concrete. In the stretch near Bologna Station of the already operating Line B, the tunnels run at only few meters from building foundations. The settlements analyses carried-out in the design stage indicated the necessity of mitigation measures. Environmental constraints, building characteristics, geometric and geotechnical situations directed the choice towards the 'Compensation grouting' method as the best mitigation measure. Numerical analyses and one trial-field were used for exhaustive design definition. At the end of September 2010 the first tunnel under compensation grouting area was completed and the in situ monitoring data confirm the effectiveness of the chosen mitigation.

1 THE NEW METRO LINE B1 IN ROME

1.1 *General information*

Line B1 is a branch line of the existing "Line B" and extends for about 7.5 km, from Piazza Bologna to the Rome orbital motorway. Its catchment area is the northeast quadrant of Rome—in Municipal District II, III and IV—where more than half a million people live.

The section currently under construction starts from Bologna Station of the already operating Line B; it stretches entirely underground over a distance of about 4 km; it involves 3 new planned stations and about 7 km twin single-track tunnels. The Client is Roma Metropolitane, as an independent subdivision of the Municipality of Rome. The main contractor is Salini Costruttori Spa while the main designer is Tecnimont Spa (Rome, Italy). For the Compensation Grouting the sub-contractor is Keller Fondazioni Srl and the specialist designer is Stone Srl.

The construction works started in November 2005 and the planned schedule foresees the completion in October 2011. The tunnel excavation has just started at the end of 2008 and it takes place from the Conca d'Oro station towards the Bologna station, which is the connection to the existing line.

1.2 *Geological features*

On the whole Line B1, the typical excavated soils consist of fluvial-lacustrine recent sedimentary formations. The geological sequence comprises a base deposit of fluvio-palustrine gravel of Pleistocene age, overlain by a layer of clayey silts and sandy silts, both of Pleistocene age. Frequent and relatively deep ancient ditches filled by alluvial silty–clayey and sandy deposits cut into the Pleistocene deposits. A layer of made ground of varying thickness including relicts of ancient structures covers everywhere the natural soil profile. The piezometric level is few meters below ground level.

Several geotechnical site investigations have been performed during the designing phases. The main geotechnical parameters of soils to excavate are reported in Table 1.

Table 1. Geotechnical parameters.

Unit	c [kPa]	phi [°]	E [MPa]	cu [kPa]
Man made soils	0	30	20–70	
Pyroclastic soils	0–20	28–38	90–400	
Recent alluvial OC soils	15–45	19–27	60–160	60–160
Recent alluvial NC soils	0–5	28–30	60–160	30–110
Paleotevere—sand	0–30	26–37	80–200	60–260
Paleotevere—silt and clay	5–30	20–34	80–200	80–200
Paleotevere—gravel	0–10	32–41	100–300	

1.3 *Tunnel design*

The Line B1 projects involve tunneling and deep excavations in densely developed areas of Rome. As a consequence, the main issue of the B1 line design has been to minimize the impact on the urban environment. An impact of tunnelling is subsidence and its effects on structures and services. Thus, in the planning process it was decided to set the tunnels relatively deep (30–35 m below ground level) in order to mitigate interactions with pre-existing structures (building foundations, gas and water pipelines, etc.).

Tunnels are excavated through recent alluvial soils, characterized by poor geotechnical properties, below groundwater table (up to 25–30 m).

Due to complex geotechnical conditions and potential risks for buildings and services, tunnel excavation by closed-face shield machines, in which a pressure is applied to the tunnel face, has been considered the most reliable method to control surface displacements. Taking into account the variability of geotechnical conditions along the route, an Earth Pressure Balance Shield has been chosen.

The evaluation of face stability pressure was performed considering different conditions ("earth pressure at rest", "active earth pressure") by means of analytical analyses (characteristic line method, Anagnostou and Kovari (1996) equations, finite difference numerical analyses on cross and longitudinal sections). In this way the upper and lower limits for the face pressure were defined as well as possible in design phase.

The study of the tunnelling-induced settlements has been performed following different approaches, depending on the complexity and peculiar conditions along the route. In most cases the displacements fields induced by tunnel construction activities in greenfield conditions have been computed using well established empirical relationships based on the Gaussian settlement profiles (*e.g.* Peck 1969, Attewell & Farmer, 1974; Attewell, 1977; O'Really & New 1982; Shirlaw & Doran, 1988). Some specific cases, characterized by shallow cover or large predicted settlements, required a more detailed study, carried out by means of numerical analyses, which also allowed to evaluate the effectiveness of remedial measures.

The empirical predictions were performed considering the following input parameters range: a volume loss from 0.6% to 2%. The smaller values are the design values and the most likely considering the excavation techniques and the mechanical characteristics of the soil, the larger values was adopted as a worst scenario values.

The assessment of risk of damage to buildings due to tunneling has been developed according the Mair, Taylor & Burland approach (1996), which is based on the relationship between category of damage and limiting tensile strain. The acceptable damage categories have been considered from degree 0 to 2, when structural integrity is not at risk and damage can be repaired readily and economically. For degrees of damage higher than 3, protective measures have been planned.

2 MITIGATION MEASURES: COMPENSATION GROUTING APPLICATION

Generally the excavation by TBM must be considered as the first mitigation measure with regard to settlements. A correct approach and an effective management of TBM boring are essential and indispensable for a safety tunneling in an urban environment.

As mentioned above, when the design analysis (carried out on the basis of predictable TBM performance) pointed out situations in which the risks exceed the acceptable values, other protective measures were planned since the design stage.

Where the tunnels run to the side of buildings, the mitigation measures consist of jet grouting treatments to protect the foundations, bounding subsidence effects outside from the 'effective foundation volume'. The execution of vertical jet-grouting columns row from the ground level (just between the building and the tunnel), of a sufficient length to cover the whole subsidence curve induced by tunneling, is able to minimize foundation settlements.

In the last stretch towards the existing Bologna Station of the already operating Line B the tunnels have instead to run under existing buildings, at only few meters from their foundations.

Most of the buildings under-passed in the above identified stretch of Line B1 were built among

1930 and 1940: only two more recent buildings were built in 1954 and in 1960. Eleven buildings are made in masonry, and only three in reinforced concrete. The buildings have several main storeys—up to ten—with one basement under road level. Some of the buildings have direct (shallow) foundations, at about 3–5 m below ground level. The others have indirect (deep) foundations—as 'pozzi e barulle'—up to 12–15 m below ground level.

In this stretch the geological sequence is mainly characterized by volcanic deposits. The Pleistocene deposits (fluvio-palustrine gravel, clayey silts and sandy silts) are covered by pyroclastic soils, pozzolanic ash and not-well-cemented tuffs, with granular and/or cohesive behavior—both of Pleistocene age. A layer of made ground of varying thickness covers everywhere the volcanic deposits.

In this situation it was necessary to identify a different protective measure. Environmental constraints, building characteristics, geometric and geotechnical situations directed the choice toward the 'Compensation grouting' method. By means of empirical methods and numerical analysis, the study of the tunneling-induced settlements performed the effectiveness of 'compensation grouting' as remedial measure theoretically considered to be the most valid.

3 COMPENSATION GROUTING METHOD

Grouting as a measure for the settlement correction dates back in the 1930s where it was applied for the re-levelling of pavement slabs. From then, displacement grouting was frequently used to deal with settlement problems where active control of the deformation according to the observational methods was needed. Various grouting technologies such as compaction grouting or fracture grouting were developed for different soil conditions (Harris 2001). Recently compensation grouting was employed in infrastructure projects with challenging geotechnical conditions.

Compensation grouting is performed by introducing a grouting array between the structure and the source of the settlement, *i.e.* the tunnel excavation (see Fig. 1). The reduction of the settlements has to be established during the design process and is triggered by the allowable settlements of the structure.

In the majority of settlement compensation projects the fracture grouting technology is adopted. Soil fracturing means to fracture the ground in a controlled manner in order to create a skeleton of cement fractures (see Fig. 2). By repeating the process of fracturing several times, it is possible to obtain the designed settlement reduction along with an improvement of the mechanical properties of the soil.

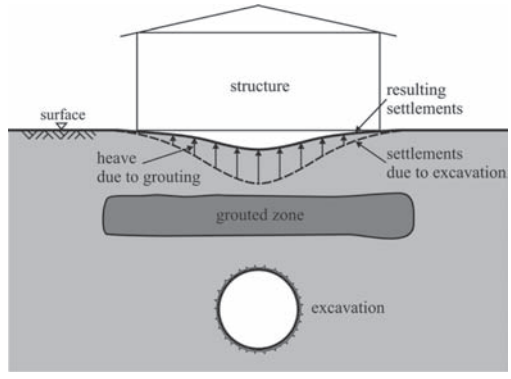

Figure 1. Principle of compensation grouting.

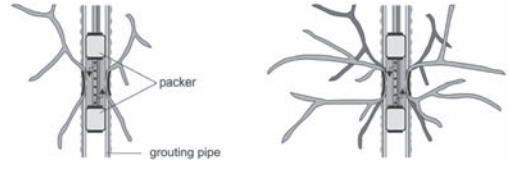

Figure 2. Phases of soil fracture grouting.

4 DESIGN OF THE COMPENSATION GROUTING APPLICATION

For the design of the project detailed analyses were carried out. The considerations included the settlement prediction with numerical and analytical methods as well as the structural analyses of the buildings potentially affected by the tunnels excavation.

In the first step of the design the expected deformation was calculated using the empirical Gauss method. With this method reliable settlement patterns were obtained for each building assuming a "design" volume loss of 0.6%.

These settlement troughs were used as the deformation load case for the structural analyses. In Figure 3 an example of the structural deformation is given.

By comparing the excavation induced stresses and the structural resistances the allowable absolute and differential settlement/rotation of the treated buildings was determined, considering two different building types (see Table 2). Building type 1 is the standard type with larger allowable settlements, whereas type 2 is more sensitive to settlements.

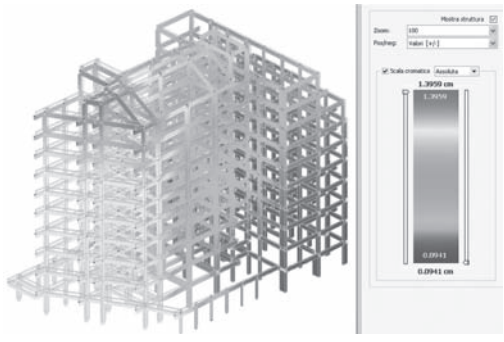

Figure 3. Imposed settlements as load case for the structural analyses.

Table 2. Allowable deformation in function of building type.

	Attention	Alert	Limit
Type 1			
Absolute settlement	–5 mm	–10 mm	–15 mm
Rotation	1/1000		1/500
Type 2			
Absolute settlement	0 mm	–5 mm	–10 mm
Rotation	1/1000		

All above mentioned values refer to the absolute zero-measurement (before any activity).

The allowable deformation was divided in three different intermediate levels. The aim of the compensation grouting activity was to maintain recorded settlement within the "alert level". To this scope specific procedures were established on the basis of monitoring data. Below the "attention-level", the equipment is kept ready for grouting, but grouting activity is generally not performed. Between the "attention-level" and the "alert-level" compensation grouting has to be performed in order to keep the deformation below the "limit-level". Moreover, a reduction of the TBM-speed was considered as additional measure. Beyond the "limit-level, the tunnel excavation would have been stopped and additional measures implemented.

5 FIELD TRIAL TESTS AND OPERATIVE CHOICES

A comprehensive field trial (Fig. 4) was performed prior to the compensation grouting job in order to verify the applicability of the proposed technology to the geotechnical and structural situation of Piazza Bologna and to establish the operative details and choices. The location of the field trial was chosen close to Piazza Bologna where very similar soil conditions were given. The aims of the field trial where:

- to identify a suitable drilling method from shafts;
- to verify that a controlled lift of the foundation element was achievable;
- to establish the grouting parameters in terms of grout mix, volumes pumping rates as well as grouting efficiency;
- to test the appropriate monitoring systems for real-time measurement.

The field trial was started in December 2008 with the construction of a footing consisting of 9 bored piles with 600 mm diameter and a length of 7.5 m. This foundation was chosen in order to simulate the special "shaft"-type foundation which is typical for this zone of Rome. The head of the piles were connected with a concrete block of dimensions of 2.2 × 2.2 m and 0.5 m thickness. Moreover a shaft was realized by means of 21 bored piles, 600 mm in diameter and ca. 12 m long. This circular shaft had an inner diameter of 3.6 m and ca. 10.6 m depth.

Thereafter a monitoring system was installed, integrated 13 liquid leveling points including the reference point, 38 precise leveling points and 3 inclinometers. The plan view of the field trial with the shaft, the theoretical position of the grouting pipes and the monitoring system is depicted in Figure 5. The field trial area was divided in two distinct zones—one with the "footing-zone", the other as "green field"-area. This choice was made to investigate to which extent the grouting would influence the adjacent area. For the installation of the grouting pipes (Tube a Manchettes) nine drillings were made, five drillings reaching the zone of the more distant footing zone and four additional for the green field area. The maximum drilling length was 28 m (see cross section in Fig. 5).

For the drilling a casing of 114 mm with controlled back-flush was utilized. After the completion of each drilling, the deviation was monitored with the Maxibor II equipment. A maximum horizontal deviation of 1.3% and vertical deviation of 0.9% was measured.

After these measurements the casing was withdrawn while filling the annular ring with appropriate sleeve grout. The settlement of the footing during the drilling phase was 1 mm.

At the beginning of the grouting works it was verified that all sleeves were groutable. Thereafter the heaving of the footing was commenced. The goal of the trial was to heave the footing up to 40 mm in various steps. This is the maximum

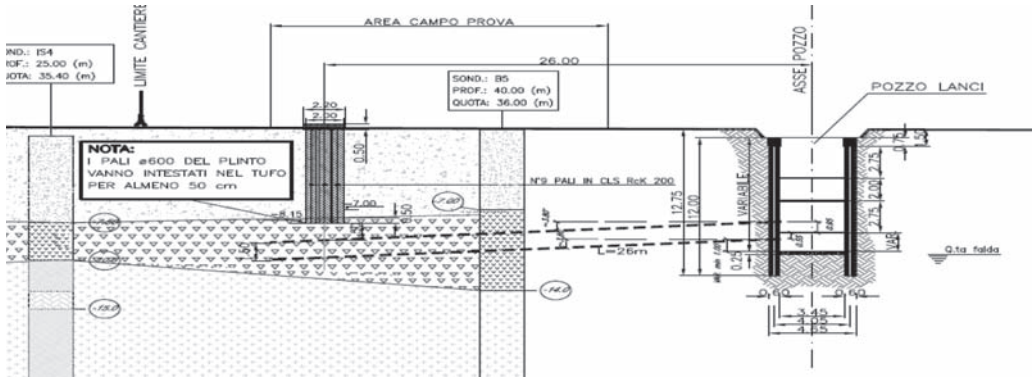

Figure 4. Compensation grouting field trial-cross section.

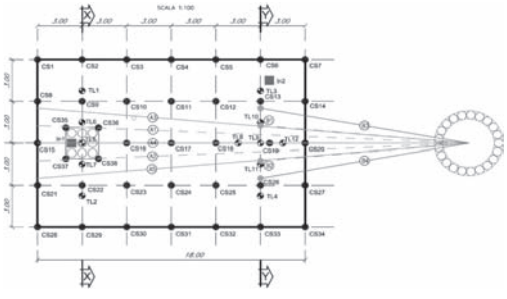

Figure 5. Compensation grouting field trial-plan view.

expected value for settlement in greenfield conditions in the area of compensation grouting application.

For the evaluation of the grouting process the specialist software GroutControl was applied. This software allows for the combined visualization of grouting and monitoring data.

The grouting phase was divided in the following steps:

- Pre-treatment grouting
- Conditioning grouting
- Compensation grouting

5.1 *Pre-treatment grouting phase*

The aim of this phase was to generate an initial heave of the footing by 1–2 mm in order to establish the appropriate grouting parameters for controlled heave. The uniform heave was obtained after up to 5 grouting steps per sleeve with volumes of 50–100 l/sleeve. The total volume grouted in this phase was 5.1% of the volume of grout treated underneath the footing.

5.2 *Conditioning grouting phase*

A uniform uplift of 5 mm had to be obtained in this phase. In a maximum number of 4 grout steps/sleeve this phase was completed. It was shown that no influence of the grouting underneath the footing was measured in the green field area.

5.3 *Compensation grouting phase*

In this phase an absolute heaving to 40 mm had to be achieved, corresponding to a tunnel induced volume loss of more than 1%. Figure 6 shows the vertical displacement of selected points in course of the field trial. A heave of 40 mm was measured on the footing (TL 5) and the adjacent water levels (e.g. TL 7). The final uplift of the distant water level TL 2 was only 6 mm. The Field trial finished in March 2009.

After the field trial an inspection of the grouted area was made. Therefore a borehole was drilled and disturbed soil samples were taken.

Figure 7 shows the result of one soil sample with the cement fractures (red color due to colored grout).

The grout take during the whole field trial was evaluated with GroutControl utilizing a 3 × 3 m grid showing the mean pressure and the volume grouted in the unit area (Fig. 8). Moreover the theoretical and real position of the grouting pipe with the sleeves is depicted.

The maximum grout take was 350 l/m² with the mean injection pressure ranging from 16.5 to 25 bar.

Based on the above mentioned grid the grout efficiency was determined. The grout efficiency is defined as ratio of "heave volume" and "grout volume" where the heave volume is the uplift measured by means of monitoring points. For the

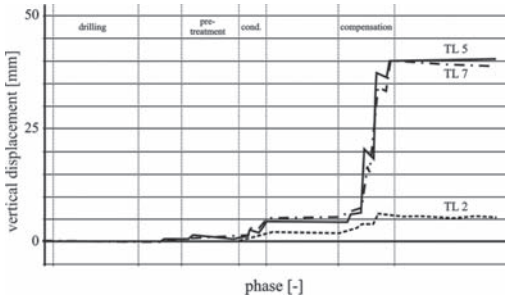

Figure 6. Vertical displacement of selected points.

Figure 7. Soil samples with coloured fracs.

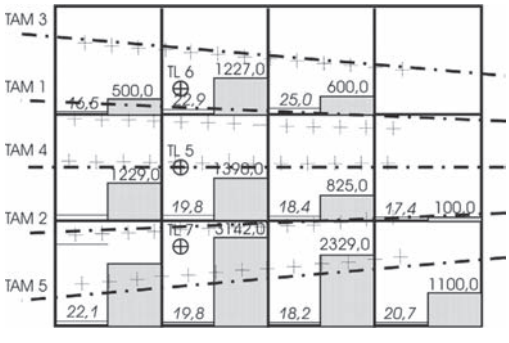

Figure 8. GroutControl plot of the area of the footing.

area of the footing with 16 m² of influence, the mean grout efficiency during the heaving phase was about 7%.

6 SITE PERFORMANCES

The compensation job had the aim to cover eight buildings where the design showed that high damage risk was likely without protective measures. Especially two buildings were particularly critical, namely Building No. 1 and 16.

Works were started in October 2009 with the installation monitoring system and the construction of the shafts.

Building No. 1 was constructed in 1935 and has a masonry structure with six floors. During the construction of the Metro B line this building experienced significant deformation, so the soil conditions can be considered to be disturbed (Fig. 9).

The Grouting pipes were installed from the exit shaft of the TBM, but due to geometrical circumstances straight drillings were not feasible. Therefore curved directional drillings from the first excavation level had to be made. The curvature of the drillings is about 120 m, the minimum distance to the foundation ca. 1 m.

A Paratrack probe was utilized for the directional drilling. The three-dimensional reference for the steering process was generated by means of an artificial magnetic field. After completing the pilot hole a casing was washed over the drilling rods in order to have defined conditions for the installation of the 2″ grouting pipes with a valve distance of 50 cm. In total 25 drilling were made for the protection of this building (see plan view in Fig. 10).

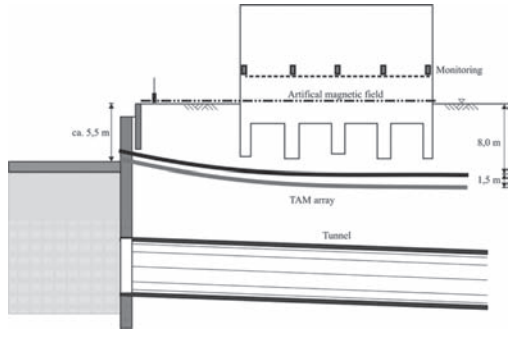

Figure 9. Schematic section of building 1.

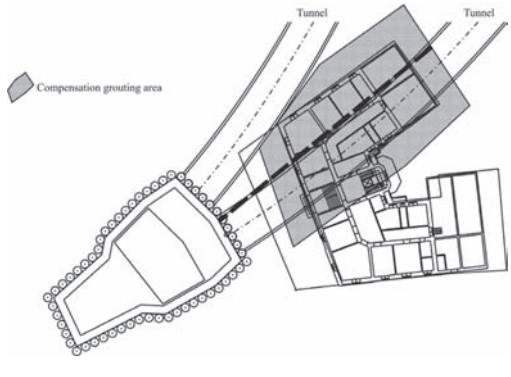

Figure 10. Plan view of building 1.

The concrete structure Building 16 was constructed in 1963 with 8 floors. Due the large basement floor, the cover between the foundation and the tunnel crown is only 2.8 m (Fig. 11). The TAM array with four layers was drilled from a shaft with elliptical shape of about 6.5 × 4.2 m. Two layers with 2″- steel pipes were used for compensation grouting purposes. Due to the very limited cover additional soil treatment was made with two layers of fiberglass-tubes in the crown of the tunnel section.

In the course of the projects, a total of 197 drillings were made with a length of ca. 6,700 m from 4 shafts. With the concept of two layers a better pre-treatment of the soil was achieved as well as more operational reliability. The maximum distance between the TAMs was ca. 3 m. The drilling deviation measured with the Paratrack probe and checked with the Maxibor system for 50% of the drillings turned out to be about 1%. Drilling induced settlements were 1–2 mm.

The mixing and grouting plant was selected according to the experiences made with the field trial. The main components are a Keller colloidal mixer, 12 pumps for a maximum pressure of 80–100 bar and 2 silos. With this plant various grout mixes based on water, cement and filler were mixed in place. From the central mixing plant the grout was pumped to the two grouting containers which distributed the suspension to the four shafts. The mixing/grouting capacity was estimated for an average TBM advance up to 20 m per day, considering a grout efficiency of about 7%. In spring 2010 grouting was started with the pre-treatment. Figure 12 shows the grouting process form the exit shaft close to Building 1.

In the site office located next to the plant all data from the project are collected and in progress analyzed: data from the real-time monitoring system, from the TBM excavation control system and from the grouting work012

According to the preliminary settlement analyses the designer decided to introduce a pre-heave

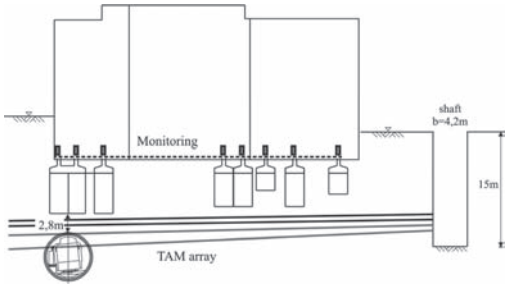

Figure 11. Schematic section of Building 16.

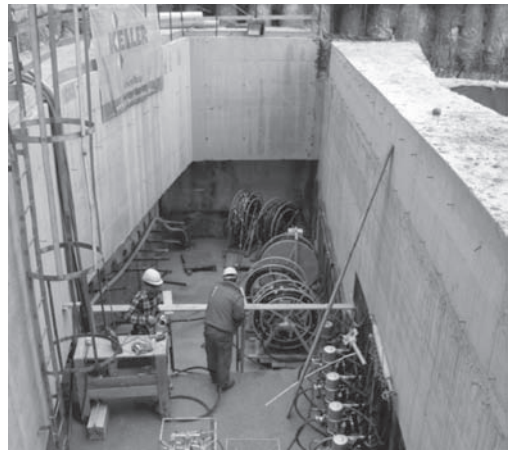

Figure 12. Grouting activity from the exit shaft.

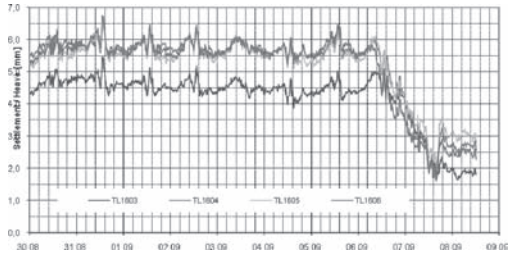

Figure 13. Settlement-time diagram for building 16.

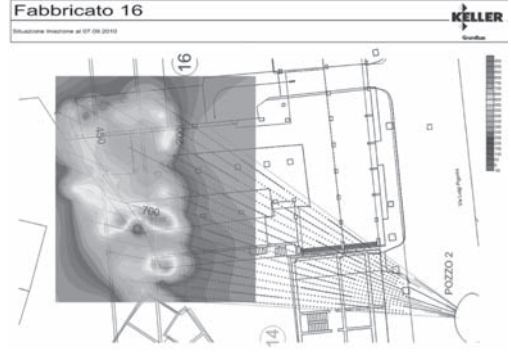

Figure 14. Contour plot of total grout take.

to all the buildings after the pre-treatment of the soil was finished. With the pre-heave more operational range was gained as it increases the allowable deformation range. The value of 5 mm was considered to be a reasonable value as it represents 30 to 50% of the expected settlement for a standard volume loss.

Figure 15. TBM breakthrough at the end of the tunnel, under building 1.

This phase was terminated in July 2010.

Compensation grouting was performed in September 2010 for the first tunnel (shallow tunnel) buildings under-passing. The duration of the compensation period was 16 days.

Due to correct design and adequate operative in progress management of compensation grouting activity, the recorded settlements were generally rather limited and always lower than alert-level values.

Particularly the vertical displacements of monitoring points of Building 16 during the tunnel excavations (referred to the absolute zero) are shown in Figure 13, with displacements of less than 5 mm.

The total injected volume is shown in Figure 14.

On the whole intervention area for the first tunnel, the total grout volume for the pre-treatment, pre-heaving and compensation was 515 m^3.

No interference with the tunnel operation due to grouting was observed.

7 CONCLUSIONS

On the new Line B1 works a correct design and operational approach have allowed to face—with excellent results—a situation particularly complex, by means of 'compensation grouting' method. The recorded site performances show an efficacious control of building settlements induced by mechanized excavation of the tunnel. The calibration of compensation grouting application by a field trial test has been a key to success (Fig. 15).

REFERENCES

Anagnostou, G. and Kovari, K. (1996). Face Stability Conditions with Earth-Pressure-Balanced Shields. Tunn. Undergr. Sp. Tech. 11(2), 1996, pp. 165–173.

Harris, D.I. (2001). Protective measures. In: Burland et al. (eds.), Building response to tunnelling. Case studies from construction of the Jubilee Line Extension, 2001, London. 135–176. Th. Telford, London.

Mair, R.J., Taylor, R.N. and Burland, J.B. (1996).

Prediction of Ground Movements and Assessment of Risk of Building Damage Due to Bored Tunnelling. In: R.J. Mair and R.N. Taylor (eds): Geotechnical Aspects of Underground Construction in Soft Ground, London, 1996. pp. 713–718. Balkema.

Geotechnical Aspects of Underground Construction in Soft Ground – Viggiani (ed)
© 2012 Taylor & Francis Group, London, ISBN 978-0-415-68367-8

Jacked piles as mitigation measure of surface settlements due to tunneling in clay

M. Marchi, G. Gottardi & G. Marchi
DICAM University of Bologna, Italy

P.M. Masoli
Società Italiana per Condotte d'Acqua S.p.A., Roma, Italy

L. Zambianchi & G. Zattoni
Soles S.p.A., Forlì, Italy

ABSTRACT: Tunnelling in highly urbanized areas very often leads to ground movements and subsequent potential risks of damage to adjacent structures and infrastructures. Intensive soil strengthening interventions ahead of and on the excavation face are usually carried out, but they are not always sufficient to keep soil movements within acceptable limits. The paper describes a well documented case-history of a shallow tunnel in clay in which, after the execution of a preliminary support by a pipe-roofing technique, jacked piles were eventually installed in order to stiffen the foundation soil under the base of the ribs and to further reduce tunnel-induced surface settlements. The reported case-history is a novel application of jacked piles as settlement reducers. The pile installation sequence during the tunnel excavation is described herein. A set of installed piles were provided with extensometers: records of monitoring data show the evolution of the load transfer mechanism from the tunnel structure to the piled foundation during excavation as function of the subsequent construction steps.

1 INTRODUCTION

Mitigation measures for the reduction of surface settlements due to shallow tunnel excavation is a recurrent challenge for geotechnical engineers, especially for shallow tunnels in soft soils and highly urbanized areas (Attewell *et al.,* 1986, Mair & Taylor, 1997). The final part of the access tunnel to the new underground high-speed railway station in Bologna (Italy), on the Milano-Napoli line has been excavated in such difficult conditions. Figure 1 shows the overall plan of the intervention area together with the indication of the tunnel excavation sectors (from 1 to 34) and the details of the location. A typical stratigraphic section of underground conditions along the tunnel axis is reported in Figure 2 (section A-A in Figure 1), which summarizes the results of extensive site investigations. In Figure 3 a more detailed view, transversal to the tunnel direction (section B-B in Figure 1), is also provided: the soil profile consists of four distinct units:

- Unit R: silty-sandy backfill with brick inclusions;
- Unit 1: clay, silty clay and clayey silt, with local sandy lenses, from brown to green-grey, deriving from alluvial fan and paleo-riverbed deposits. From soft to moderately compact (piezocone tip resistance q_t from 0.6 to 1.8 MPa). Local inclusions of Unit 2 can be found.
- Unit 2: silty sand, with gravel and cobble and local silty and clayey lenses, from alluvial fan and paleo-riverbed deposits. From moderately to very compact ($q_t > 10$ MPa).
- Unit 3 and 3a: clay, silty clay and clayey silt, with local rare slightly sandy lenses, from brown to green-grey. Unit 3 is moderately compact ($q_t = 1 \div 4$ MPa), Unit 3a is from compact to stiff ($q_t = 4 \div 7$ MPa).

Note that a few piezocone tests have been carried out from the tunnel bottom level, at a depth of about 22 m below the ground surface. The tunnel excavation, around 140 m^2 wide and 23 m deep (Fig. 3), has been carried out in such heterogeneous formations made up of alternating layers of coarse-grained and fine-grained soils, with different local water levels. Standard soil improvement techniques, such as jet grouting ahead the face and umbrella jet columns, adopted along most of the tunnel length, were replaced here by special mitigation measures due to the very limited thickness of the overlying soil and the densely populated intervention area, close to the Bologna central railway station.

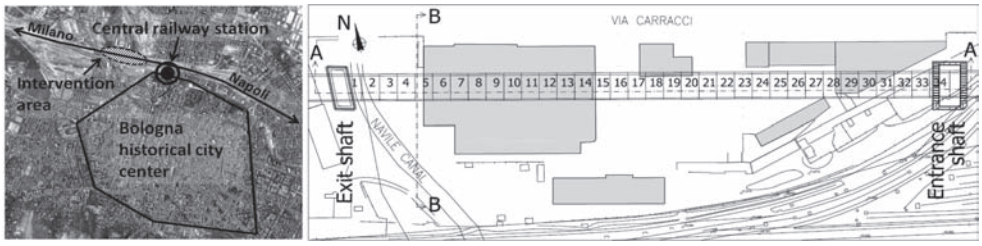

Figure 1. Plan view of the intervention area with location details and indication of excavation sectors.

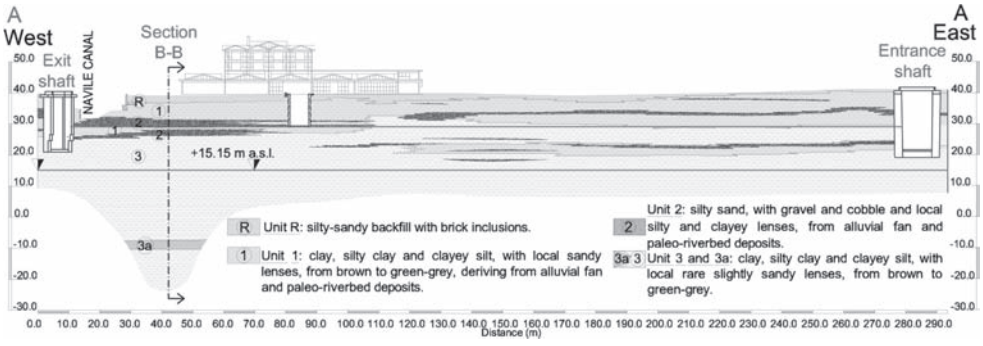

Figure 2. Schematic geological section along the tunnel axis (section A-A in Figure 1).

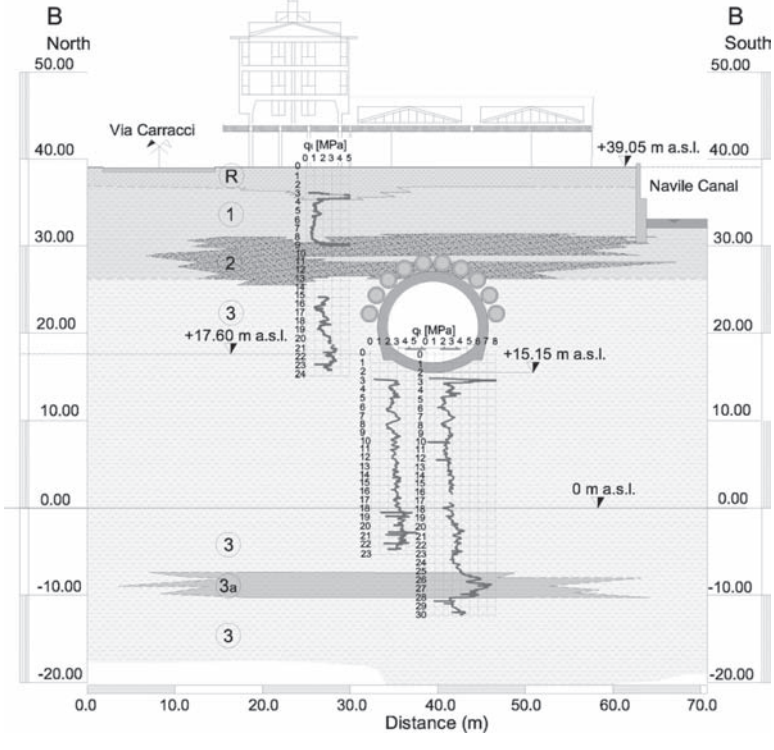

Figure 3. Schematic stratigraphic section of the subsoil and typical tunnel cross section (section B-B in Figure 1).

In order to further reduce surface settlements in this area, a rather elaborate preliminary structural support, has been carried out by microtunnelling, an assisted pipe-roofing technique. Nevertheless, settlement monitoring showed that during the excavation of the initial sectors (from number 1 to number 3 in Figure 1) and before the construction of the permanent liner, the structure of the tunnel itself could settle in the lower clayey layer due to the load transferred from the microtunnells to the steel ribs (Broere, 2000; Duan, 2001). In order to prevent tunnel structure subsidence, an array of jacked piles was eventually installed under the steel ribs. In the case-history described the innovative application of jacked piles as steel rib support, and hence as settlement reducers, is presented and relevant data recorded during the excavation and the subsequent construction steps is discussed.

2 THE REINFORCEMENT BY JACKED PILES AS SETTLEMENT REDUCERS

2.1 *The jacked piling technique*

The jacked piling technique, used in this application, is relatively new (Fig. 4): piles are installed by means of special hydraulic jacks (Fig. 5) and cast in-situ. The schematic section of Figure 4 shows the main pile components. The hollow tube steel pile (Fig. 4b) is driven into the ground via a quasi-static jacking force applied by hydraulic jacks (Fig. 5). The foundation raft serves as counterweight and creates a connection between piles and superstructure by means of the driving assembly, previously positioned inside the concrete foundation. In this specific case, a beam has been created at the base of the steel ribs in order to house the driving assembly. The pile base is closed by two flanges, a base flange and a widening flange. During installation, the flanges create an annular space between pile and soil which is filled with micro-concrete, maintained

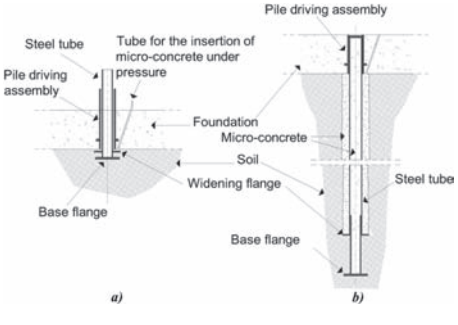

Figure 4. Pile sections: (a) detail of foundation with pile installation assemblies; (b) pile driving operations.

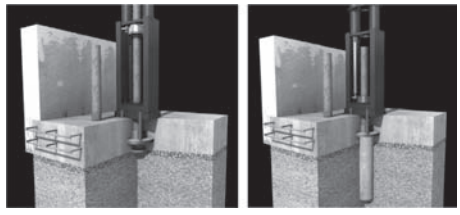

Figure 5. Schematic of the pile installation process.

under pressure during installation. Consequently, the pile-soil contact surface is quite rough and the shaft resistance improved. During the installation the jacking force can be recorded and provides a measure of the soil resistance very similar to the CPT tip resistance (Marchi *et al.* 2010). At the end of the installation process, the inner part of the pile is filled with concrete.

This technique, together with the typical benefits of displacement piles, has been chosen because of its potential advantages over traditional dynamic pile driving:

- no vibrations are produced, which is clearly a crucial aspect in urban areas;
- the small-size installation equipment can be easily handled in restricted spaces, hence, it is compatible with the narrow space in front of the excavation face of the tunnel;
- due to the characteristic slenderness of the pile (typically L/D > 20), the shaft resistance is the most important contribution to the pile overall bearing capacity. On the other hand, the jacking installation force is only due to the base resistance because of the lateral fluid micro-concrete maintained under pressure during installation.

2.2 *Tunnel excavation, pile installation sequence and monitoring*

The double-track tunnel construction was preceded by the execution of the pre-support along the intervention stretch (272 m long). This ground reinforcement consisted of 10 large diameter (1.6 m) concrete pipes installed longitudinally on top of the tunnel section and excavated through microtunnelling, a remotely controlled, guided pipe jacking process. All operations were carried out from two shafts, an entrance and an exit shaft showed in Figures 1 and 2. The pipes were installed one adjacent to the other, along an 'umbrella' shape but without any reciprocal interconnection, to form a pipe-roof above the tunnel excavation (Fig. 6) and then filled with reinforced concrete. As the excavation progresses, the pipe-roof provides continuous support for to the excavation face, carrying the over-burden load by the longitudinal beam action.

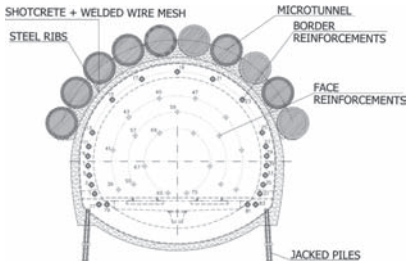

Figure 6. Typical tunnel cross section.

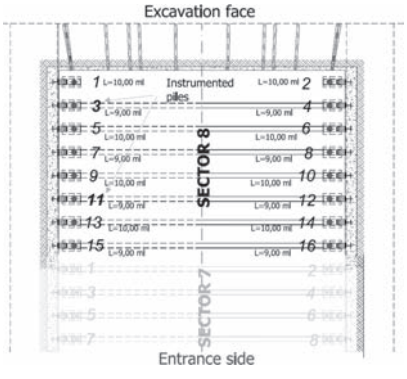

Figure 7. Plan of a typical sector (i.e. number 8 in Figure 1) with the installation lay-out of jacked piles (pile spacing 1 m).

Thus, this ground improvement technique helps to stabilise the face and reduces ground movements (Stein et al., 1989, Thompson, 1993). However, to this purpose in this case, as already mentioned a layout of jacked piles was also eventually installed. The subsequent tunnel construction (a typical cross section is shown in Figure 6) was executed by sequential excavation. For each excavation sector, 8 m long (Fig. 7), the sequence of operations was:

- execution of drainages and, at the same time, face and border reinforcement with fibreglass rods injected every meter;
- excavation and execution of the temporary liner using shotcrete and steel ribs;
- jacked piles installation (plan in Figure 7);
- proofing and casting of the invert;
- permanent liner installation.

Figure 7 shows the lay-out of piles installed in a typical sector, from number 4 to number 34 (Fig. 1). No piles were installed in sectors number 1 to number 3. Two rows of 8 piles, 9 m and 10 m long in turn, with a diameter of 320 mm and spaced at 1 m (about 3 diameters) were installed in each of the other sectors. In addition, two of them (pile number 3, close to the excavation face and pile number 11, in the middle of the sector, in Figure 7) were provided with two extensometers located at pile extremities. An additional pile was installed in sector 4 in order to perform a load test. Data from the load test, shown in the next section, has been used in the interpretation of instrumented piles monitoring data.

3 DATA ANALYSIS

3.1 *Load test*

A preliminary load test was carried out in order to investigate pile performance in relation to the existing soil conditions. For this purpose, a pile, 11 m long, was installed in the middle of sector 4 and instrumented with three extensometers (one in the middle and two at the ends). The test (Fig. 8) was performed according to maintained load test procedure i.e. by applying monotonic increasing constant load steps. The interpretation of measurements enabled the typical load vs head displacement curve and the load distribution along the shaft to be plotted, via the pile extrapolated elastic modulus (Figs. 9–11). Figure 9 shows the load vs displacement curves and provides the size of the pile ultimate load. Notice that the final load steps were not fully stabilized. In addition, Figure 10 shows the estimation of the composite pile elastic modulus obtained during the load test, as usual, from the comparison between the total applied load and the measurements of the extensometer located at the top of the pile.

Note that, according to the general rule, the elastic modulus tends to a constant value as deformations increase (i.e. with load increment): $E = 30.000$ MPa is therefore the reference value used in the monitoring data analysis. Figure 11, representing the

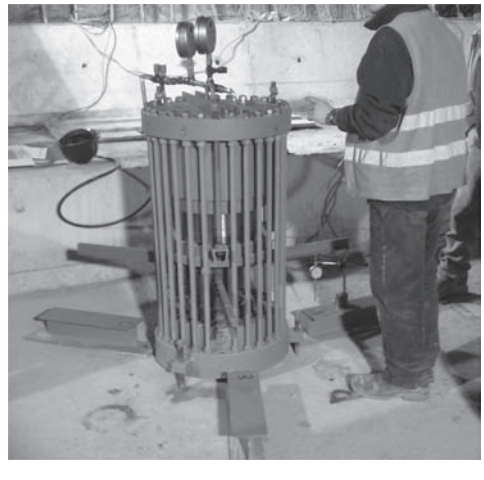

Figure 8. Pile load test set-up.

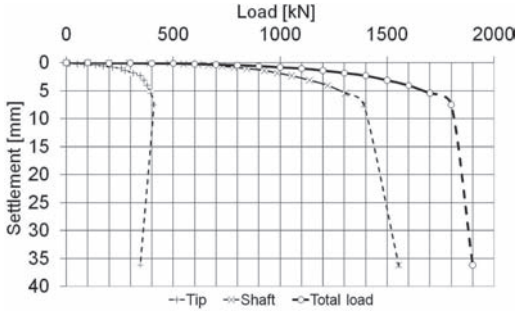

Figure 9. Load vs pile settlement.

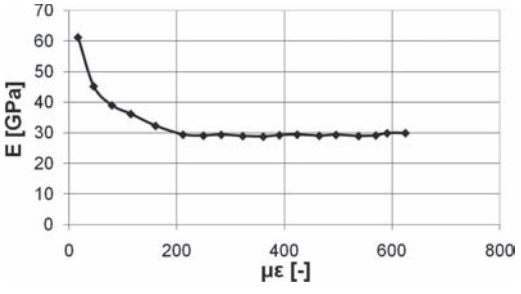

Figure 10. Pile elastic modulus derived from the load test.

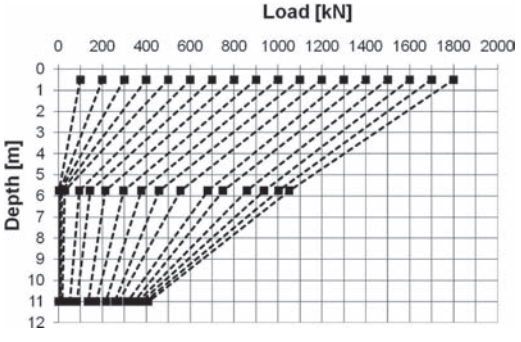

Figure 11. Load transfer curves.

load transfer curves along the pile shaft, shows that load at the pile toe starts to increase when the head load is already about 300 kN; lower loads are almost completely taken by the upper shaft. Data in Figures from 9 to 11 are a useful tool for the interpretation of monitoring data.

3.2 *Monitoring data analysis*

Figure 12 shows a significant example of the recorded monitoring data. Every extensometer provided three data logs and their average has been elaborated in order to obtain the size of the load resting on piles. The calculations of loads, starting from the $\mu\varepsilon$ records, have been carried out assuming E constant and equal to 30.000 MPa, as suggested by the load test (Fig. 11). Figures from 13 to 15 show the analysis results for the instrumented piles in sectors 5, 6 and 8. These sectors have been selected among the whole database because of their representativeness and their location below a very densely built area (see Fig. 1). The period covered by the records is very variable, from about 15 days (19 days in sector 8, shown in Figure 15) to about 2 months (60 days in sector 5, shown in Figure 13). As a consequence, the load evolution on every single pile is shown for a variable number of subsequent excavated sectors (5 in Figure 13, 4 in Figure 14 and 2 in Figure 15). The superimposition of the works timetable and data enables the in situ interaction mechanisms between piles and the tunnel structure in relation to the various excavation and construction phases to be identified. The pile load patterns in sector 5 (Fig. 13) shows that load taken by piles 3 and 11 increases during excavations of the subsequent sectors and execution of temporary liner. In particular, the load increase due to the excavation of the closest sector (sector 6) is higher than the increase due to the excavation of the subsequent sectors (7, 8, 9 and 10). During face reinforcement no clear trend can be identified, while the installation of piles clearly causes unloading, particularly on pile 3, close to the excavation face. Comparing pile 3 and 11 a final head load, common to both piles, of about 500–600 kN can be identified. This

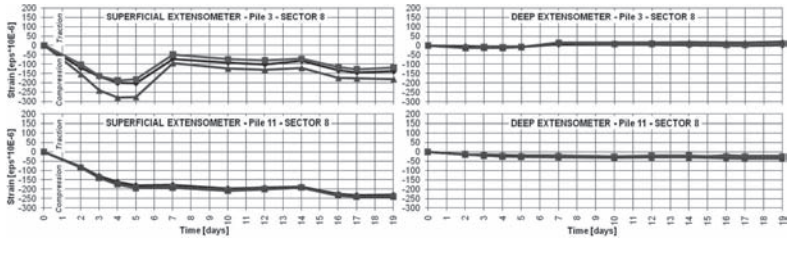

Figure 12. Monitoring data of sector number 8.

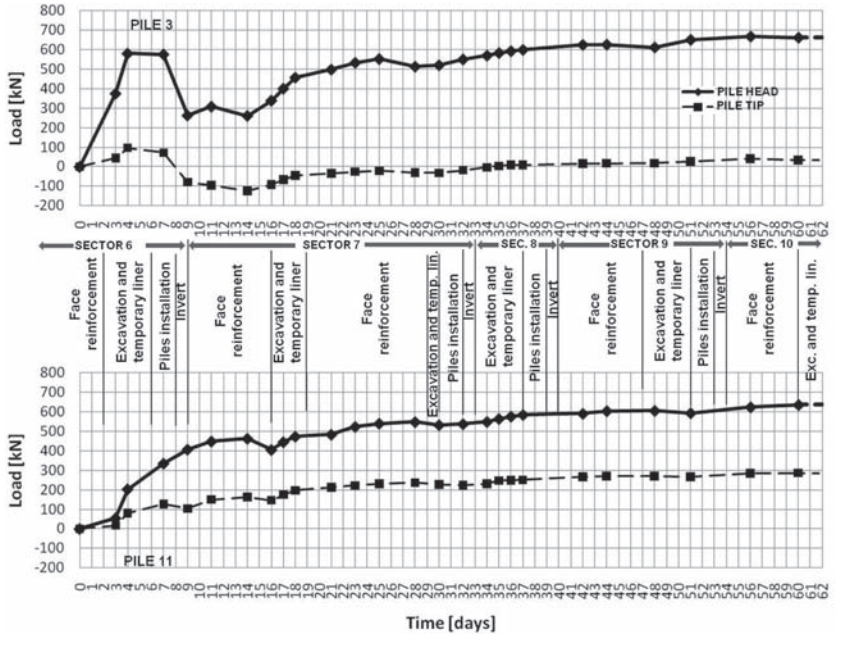

Figure 13. Evolution of the load applied to: (a) piles number 3 and (b) pile 11 in sector 5, during the tunnel construction.

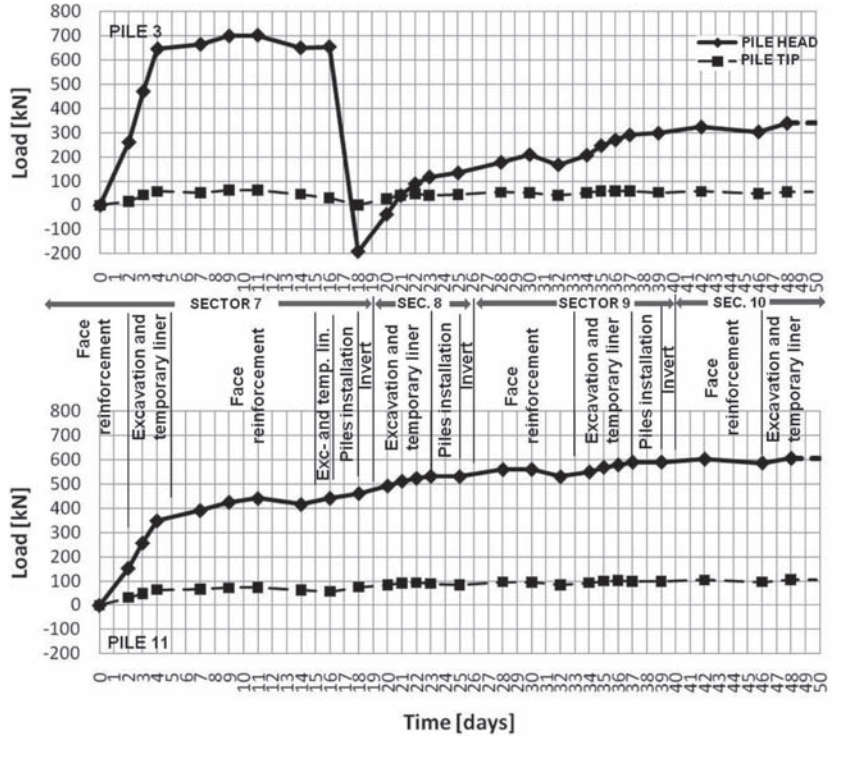

Figure 14. Evolution of the load applied to: (a) piles number 3 and (b) pile 11 in sector 6, during the tunnel construction.

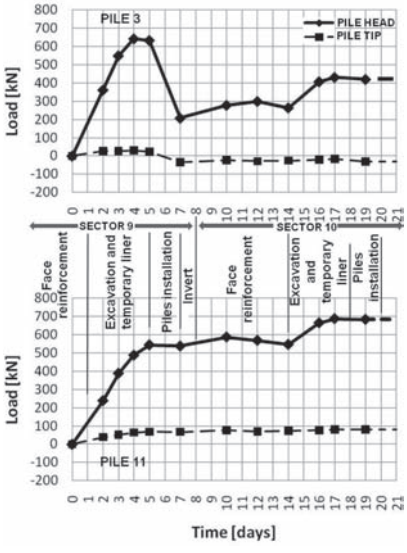

Figure 15. Evolution of the load applied to: (a) piles number 3 and (b) pile 11 in sector 8, during the tunnel construction.

load is almost constant after the excavation of sector 9, and is completely taken by the shaft in pile 3 and partly by the tip in pile 11. Similar results have been obtained for piles in the others sectors. Note that in sector 6 (Fig. 14), the unloading due to the piles installation in sector 7 generates a tensile load in pile 3. As a consequence the final head load in this pile is about 300 kN, half of the final load taken by most of them. Sector 8 in Figure 15 confirms the data trend shown in Figures 13 and 14. In particular, in pile 11 of sector 8 the final load is also higher than the other analysed cases, about 700 kN.

Note that, considering the whole database, the average maximum load taken by piles is about 600 kN, much less than the piles ultimate load shown in Figure 9. Assuming that the over-burden load due to the soil resting over the crown of the tunnel (about 100 m^3 per metre and a soil unit weight of about 20 kN/m^3) and neglecting the weight of the few light buildings, the maximum load taken by the piles (600 kN) corresponds to about half the estimated over-burden load resting on every single pile (about 1000 kN).

Finally, no actual data of pile head displacements are available, even if from Figure 9 it can be deduced they must have been extremely limited. Such mitigation measure was designed to stiffen the tunnel basement and therefore to reduce the effects of its settlement on the ground surface. The issue of other tunnel induced ground movements and records of surface displacements carried out in this site are beyond the scope of the paper.

4 CONCLUSIONS

This paper describes a well-documented case-history of jacked piles being used as provisional steel rib support during excavation of an urban tunnel in clay. A preliminary ground reinforcement intervention by a microtunnelling—an assisted piperoofing technique—was carried out before the tunnel excavation, but additional mitigation measures were needed in order to further reduce tunnel-induced ground settlements. Jacked piles were eventually installed under the steel ribs and several piles were instrumented in order to investigate the evolution of the load transfer mechanism from the tunnel structure to the pile foundation during excavation phases. Analysis of the data clearly shows the pile load pattern, characterized by loading during excavation phases and evident unloading during pile installation in subsequent excavation sectors. This novel application of jacked piles as settlement reducers has been therefore documented and the relevant monitoring data used to better understand their possible positive contribution to prevention of tunnel induced ground settlement.

ACKNOWLEDGEMENTS

The Authors are grateful to staff and engineers at the Bologna work site, in particular the Work Supervisorship (Direzione Lavori) and Italferr S.p.A, for enabling the monitoring of such an innovative tunneling intervention.

REFERENCES

Attewell, P.B., Yeates, J., & Selby, A.R. (1986). *Soil movements induced by Tunnelling. Chapman and Hall,* New York.

Broere, W. (2000). Settlements of Micro-Tunnels in relation to their use in Underground Logistic Systems. *Proceedings of the 2nd International Symposium of Underground Freight Transport by Capsule Pipelines and Other Tube/Tunnel Systems, Delft, 28–29 September.* Visser and van Binsbergen (eds.), 1–10.

Duan, Z. (2001). *Ground Movement Associated with Microtunnelling*. Ph.D. Dissertation, Louisiana Tech University.

Mair, R.J. & Taylor R.N. (1997). Bored tunnelling in the urban environment: State-of-the-art report and theme lecture. *Proc. 14th Int. Conf. Soil Mechanics and Foundation Engineering, Hamburg* 4, 2353–2385.

Marchi, M., Balbarini, L., Gottardi, G., Zambianchi, L. (2010). Comparing in-situ cone resistance and pile jacking force. *2nd International Symposium on Cone Penetration Testing. Huntington Beach, California, USA, May 9–11, 2010*.

Stein, D., Mollers, K., Bieleki, R. (1989). *Microtunnelling*. Ernst & Sohn, Berlin.

Thomson, J. (1993). *Pipejacking and Microtunnelling*. Blackie Academic and Professional, London.

This page intentionally left blank

Geotechnical Aspects of Underground Construction in Soft Ground – Viggiani (ed)
© 2012 Taylor & Francis Group, London, ISBN 978-0-415-68367-8

Observed and predicted settlements induced by the construction of hydraulic tunnels in Buenos Aires

A. Logarzo & S. Miliziano
Department of Structural and Geotechnical Engineering "Sapienza" University of Rome, Italy

V. Floria & M. Pescara
Geodata Engineering S.p.A. Turin, Italy

ABSTRACT: The paper deals with the main results of 3D numerical analyses carried out in order to simulate the tunnel construction for the real case of "*Túneles aliviadores del emisario principal del arroyo Maldonado*" in Buenos Aires. Full 3D numerical analyses are also developed to study the interaction between tunneling excavation and a tall concrete building. The numerical models take into account the main features of excavation process with Tunnel Boring Machine (presence of shield, face pressure, tail void grout injection); a realistic structural model of the building is also used. Due to the very small level of deformation expected, a simply elastic perfectly plastic with Mohr Coulomb strength criterion is adopted; values of stiffness parameters are selected at very small deformation level. Soil parameters were determined by means of in situ and in lab experimental test results. Comparison between the monitoring data and numerical results shows the good forecast capacity of the geotechnical model developed and encourages utilizing of 3D analysis as a valuable tool in tunnel design in urban areas.

1 INTRODUCTION

Urban areas pose challenging conditions for underground construction due to the presence of structures (both above and below the surface) and limitations on the ground improvement (narrow streets, buildings, unexpected materials intercepted during excavation). Difficulties increase in complex geological context with variable ground conditions.

In an urban context, an accurate prediction of ground movements, in addition to the stresses on the structures, is extremely important. Numerical modeling is a useful tool assisting the choice of the best design solution; in particular, a three dimensional numerical approach is very powerful in realistically simulating soil-structure interaction during tunnel construction also in the presence of existing structures. As an example, the case of the Maldonado head-race in Buenos Aires is analyzed.

The 3D numerical simulations presented here take into account the physics of the problem: face supporting, over cut of the machine, the injection of grout into the annular void and its hardening. Similar analyses were carried out by Melis et al. (2002) for the metro of Madrid, Kasper and Meschke (2007) and Buselli et al. (2010) for the metro C in Rome. In the analyses a realistic structural model of the building is also introduced.

After a description of the main features of the urban context and the project of "*Túneles aliviadores del emisario principal del arroyo Maldonado*", the geological and geotechnical aspects are illustrated. Successively, the numerical models developed and the techniques adopted to simulate the main factors of tunnel construction inducing settlements are then described. Finally, the results of numerical models are discussed and compared to the available monitoring data.

2 TUNNELS AND BUILDINGS

2.1 *The urban context*

Buenos Aires is one of the largest cities in the world with over eleven million inhabitants in both the city and its surroundings; the megalopolis is periodically affected by huge floods with enormous impact on the economy.

Hydraulic problems, due to the weak slope of the land, low altitude and low hydraulic conductivity of the soil are exacerbated by the recent increase in rainfall. As a result of climate change, the frequency of flood events has increased in the last 40 years.

In addition to the short and intense rainfall located in different parts of the city, it is worth considering the occasional elevations of the

"Rio de la Plata" level. One of the sectors most affected by these types of events corresponds to the bottom of the Maldonado river basin, which originates in the province of Buenos Aires and across the city towards west-northwest. In the late 1930s, the Maldonado River was piped along its entire length within the capital and reaches 21.3 km before emptying into the "Rio de la Plata" (7.2 km and 14.1 km in the province capital).

The total area is about 97 Km^2: 46 Km^2 located in the province and the remaining 51 Km^2 in the capital city; the latter representing 25% of Buenos Aires total area, hence the basin constitutes the largest area in the city. Topographic levels of travel range from heights of greater than 20 m in the upper basin to values of less than 5 m in its lower part.

The Maldonado rain collector divides the city of Buenos Aires in two macro-areas so that flood events affect movement of people and vehicles and interrupt the normal functioning of the city causing considerable social and economic costs.

2.2 *The project*

The proposed solution is considered the most important hydraulic structure (Fig. 1) for the urban area in the last century and it will definitely change the life of the biggest district of the city (Palermo).

The project conceived in the hydraulic system and flood control master plan by the Government of the City of Buenos Aires is seen as a definitive solution to alleviate the Maldonado collector through two hydraulic tunnels (T1, 4579 m long and T2, 9864 m long; the inner diameter is 6.90 m).

The works started in 2008 and after two years the tunnel T1 was completely excavated; it will be functional in May 2011. The second tunnel (T2) is under construction (pk 2300 m) and crosses the principal tall buildings of Palermo district.

The Punta Carrasco shaft (Fig. 2) represents the endpoint of collecting water drained through the two-tunnel reliever and is in turn shaped by a channel discharge that drains surplus rain flow to the Rio de la Plata. It was also the starting point of the project, where the two tunnel boring machines (TBM) started. Punta Carrasco is a huge shaft (40 m diameter, 55 m deep) and it was excavated without soil treatments, representing a massive application of hydromill trench cut technology.

The two tunnels run mainly under the main streets and interact with big infrastructural works such as two metro lines (B and D), an aqueduct, a railway line, a highway line and three viaducts.

In some stretches the tunnels underpass big towers (more than 25 floors high and 3 floors below surface level) with about 20 m of overburden (Fig. 3).

Taking into account the difficult aforementioned conditions and the presence of the groundwater table, tunnels are excavated by EPB (two Lovat EPB TBM) with control of the pressure at the face, based on the ground to be excavated.

The tunnel segmental lining consists of rings of 1.50 m each formed by 7 concrete reinforced steel elements 35 cm thick.

2.3 *Monitoring system*

In urban underground construction it is very important to measure the ground deformation around the excavation to validate the design previsions and to ensure integrity on preexisting structures.

In the Maldonado project the monitoring system includes several sections with: precise leveling and

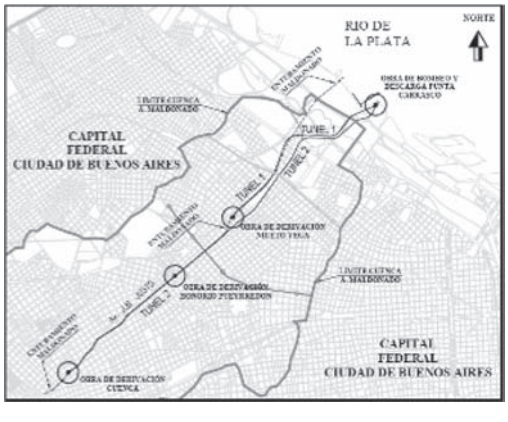

Figure 1. General layout of the project.

Figure 2. Punta Carrasco shaft: The starting point of the TBM.

Figure 3. The tunnels underpass big towers.

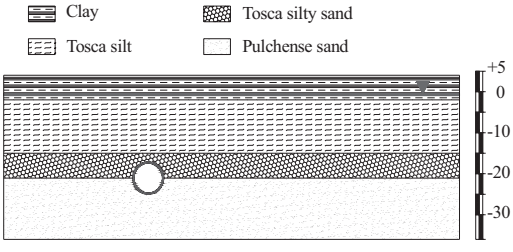

Figure 4. Geotechnical soil profile.

façade monitoring (accuracy is ±0.3 mm), extensometer in place installed from ground surface, inclinometer, Casagrande and standpipe piezometer.

3 GEOLOGICAL AND GEOTECHNICAL ASPECTS

The soil is mainly characterized by silty clay alternancy, arenaceous deposits and sands.

Regional-scale works are in a territory characterized by alluvial terrace formed deposits typical of a transitional continental environment (fluvial sandy loam, gravel). This layer is genetically related to the erosion and deposition of the River Plate. These continental deposits are interspersed with silt-clay lenses associated with deposition or sedimentation of marine environments (Sainato et al., 2000). Continental deposits form two terraced slope basins separated by 10–15 m of height: called "low terrace" closest to the area of the Rio de la Plata, and known as "terrace Pampa" or "high terrace", with altimetry position higher compared to the previous.

The soil profile and hydraulic conditions have been determined on the basis of the geotechnical investigation carried out in the design phase, involving laboratory and in-situ tests.

The soil (Fig. 4) consists of a top layer (6 m) of soft clay, overlaying an eolic soil deposit (Tosca), characterized by alternation of silt (10 m) and silty sand (5 m) and layers of monogranular sand (Puelchense).

Groundwater conditions are hydrostatic with the water table located 3.5 m below the ground level. Therefore, the tunnel will be excavated under the water level.

Further laboratory tests (Oedometric, Resonant Column, Triaxial and Shear test) have been carried out in the geotechnical laboratory of the Department of Structural and Geotechnical Engineering of *Sapienza*, University of Rome, on samples retrieved during the construction.

Due to the adopted excavation modality (TBM, EPB), small strain levels are expected in the soil around the tunnel. Small strain stiffness moduli determined by Resonant Column test (Fig. 5) were selected. Due to the geological history, the deposit is essentially normally consolidated then the horizontal effective stresses are calculated according to the classical equation $K_0 = 1 - \sin\varphi'$. A constant value of 0.3 for Poisson's ratio, ν', was assumed.

The constitutive model adopted for soil behaviour is elastic perfectly plastic with Mohr-Coulomb strength criterion. The physical-mechanical soil parameters adopted in the analyses are summarized in Tab. 1.

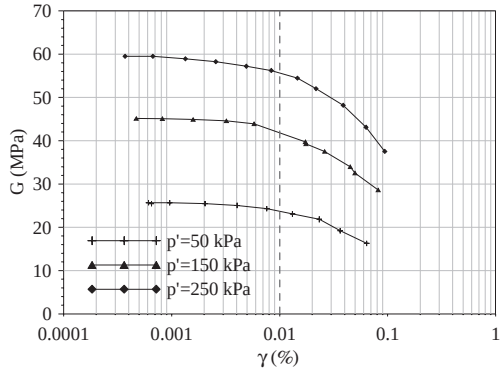

Figure 5. Results of Resonant Column tests.

Table 1. Physical and mechanical parameters of soils.

Soil	γ (kN/m^3)	c' (kPa)	φ' (°)	E' (MPa)
Clay	18.0	15	26	5
Tosca silt/silty sand	16.5	35	24	150
Pulchense sand	20.0	0	35	250

4 NUMERICAL MODEL OF TBM TUNNEL CONSTRUCTION

The main elements modeled are: the front pressure support; the TBM shield (geometry and weight); the grouting in pressure; the ageing process of grout; the lining rings.

The construction process is simulated discontinuously removing slices of elements inside the profile of excavation 2 m thick for each step, while at the same time the TBM shield advances, activating shell on front and deactivating shell on tail. In the model the real weight of the TBM (about 5000 kN) is simulated; to this aim, a fictitious unit weight of 450 kN/m^3 is attributed to the shell material.

A total pressure equal to the horizontal earth pressure at rest is applied to the front to support the soil during excavation. This pressure is about 260 kPa at the crown and increases linearly (13 kPa/m) moving to the invert (Fig. 6). The final lining is switched on from behind the tail of the shield. Both TBM and tunnel lining are modeled as linear elastics, using shell elements with the properties reported in Tab. 2.

The tail void injection is simulated using a pressure applied to the ring cluster between the lining and the excavation profile, opposite to the direction of tunnel advancement (Fig. 6), 20 kPa higher than the maximum value of the pressure at the front. The stage construction process considers the ageing of the grout: fresh grout is characterized by a low shear modulus and incompressibility (γ = 24 kN/m^3, E = 1 MPa, ν = 0.49), while hard grout is very stiff (γ= 24 kN/m^3, E = 8 GPa, ν = 0.15). Volume elements are activated to fill the tail void (15 cm) assuming linear elastic properties for them. The grout is assumed to be hardened after five slices (10 m).

Complete analysis studies the influence of a tall building (Fig. 7).

The building with reinforced concrete structure is composed of 29 storeys (100 m). The foundation, located 6.0 m under the ground level is a 1 m thick slab. The minimum distance between the building and the tunnel axis is 11.0 m, the overburden is 19.0 m. The foundation is connected to the soil by an interface, using a value of 0.5 for the strength reduction factor (the strength of the interface is half of the strength of surrounding soil). In the first phase of complete interaction analysis the building is activated; the resulting displacements are set equal to zero before starting the construction of the tunnel.

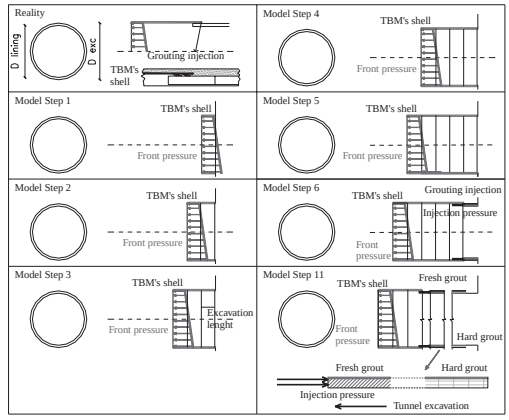

Figure 6. Excavation process model. numerical model of the building.

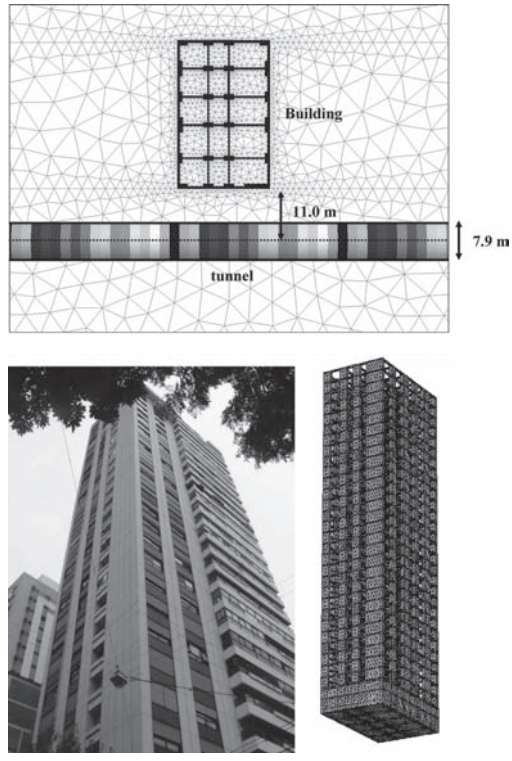

Figure 7. Building and numerical model.

Table 2. Shell properties.

Shell	s (m)	γ (kN/m^3)	E (GPa)	v (–)
TBM	0.04	450	210	0.15
Lining	0.35	25	31	0.15

5 NUMERICAL ANALYSIS

To minimize the boundary effects on settlements profile, the mesh dimensions both in the longitudinal and transversal direction are assumed according to the literature suggestions (Franzius and Potts 2005). Horizontal restraints are applied at the vertical boundary and total restraints are applied at the model base. The initial stress distribution is assigned according to the unit weight of the soils and the assumed coefficient of earth pressure at rest.

All the analyses are carried out in drained conditions; this choice is advisable for two reasons: *i)* the permeability of silt, silty sand Tosca (the deposits within which the tunnels are mostly bored through) is relatively high; *ii)* the monitoring field data doesn't show appreciable settlements due to consolidation phenomena.

5.1 *Preliminary analyses*

In preliminary analyses, a small portion of complete mesh (the mesh was reduced in longitudinal direction: only 50 m instead of 228 m) has been adopted (Fig. 8). Geotechnical profile and geometry are the same as in the complete analyses.

Fig. 9 shows the maximum vertical displacement at ground level, the vertical stress on tunnel crown and the calculation time obtained varying the density of the mesh (100000, 250000 and 500000 elements).

The accuracy of the solution increases by increasing the density of the mesh but the calculation time increases quickly. An acceptable compromise between calculation time and accuracy of the results is obtained adopting an average mesh density and an unbalanced force equal to 1 kN. In fact, the difference between this solution and the most accurate solution obtained adopting a very dense mesh is only about 5% (for displacement). However, the calculation time reduces drastically.

5.2 *Green field analysis*

The mesh used in *green field* analysis is depicted in Fig. 10. Fig. 11 shows the evolution of the *green field* settlements profile calculated along the tunnel axis during the construction of the tunnel for three points (ground surface, near tunnel crown and tunnel invert). The settlements begin to appear when the front of excavation is about 1.5 diameters behind the reference section (located in the middle of the mesh); only 25% of maximum settlement develops when the tunnel face is in the control section. Steady state conditions establish when the front of excavation is about 30 m faraway (4D).

Fig. 12 shows the surface settlements for different tunnel position (front in the reference section, tail shield in the reference section, front far from the reference section). The maximum value is 2.6 mm at the end of the tunnel excavation.

In Fig. 13 the tunnel axis ground surface settlements are depicted; it shows that the steady state settlement conditions were achieved at distance of

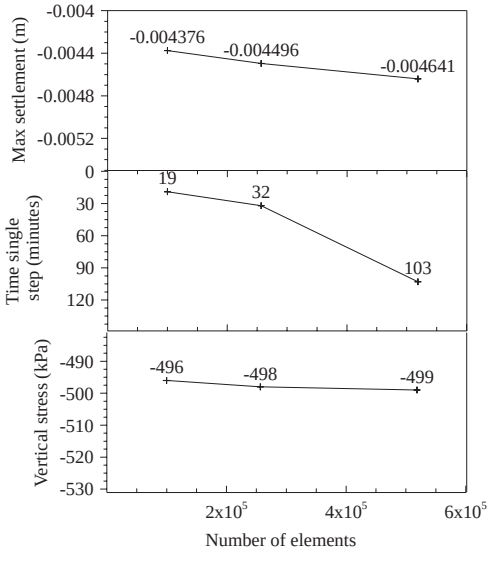

Figure 9. Results of preliminary study (Maximum surface settlement and vertical stress on tunnel crown).

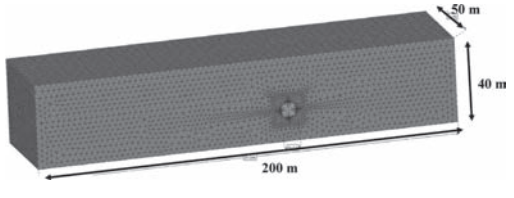

Figure 8. Mesh used in preliminary analyses.

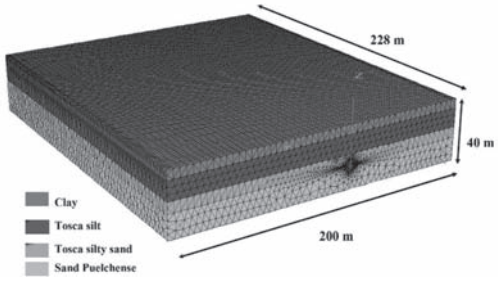

Figure 10. Mesh adopted in *green field* analyses.

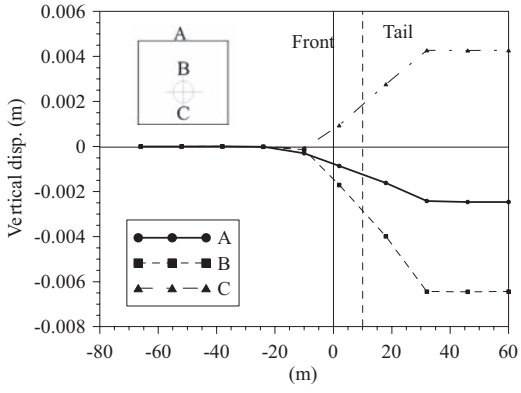

Figure 11. Computed settlement: A ground surface, B tunnel crown and C tunnel invert.

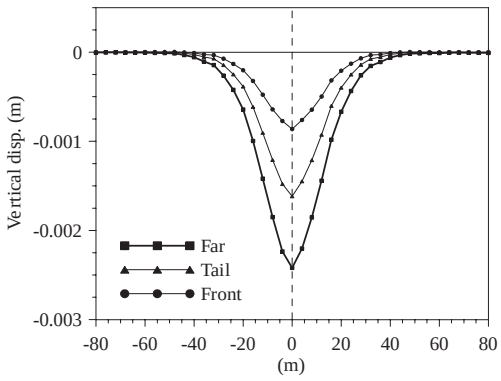

Figure 12. Computed settlement for different tunnel position.

5 diameter from the start boundary; the pre-settlement is 25% of maximum settlement.

The numerical result (Fig. 14) matches quite well the Gaussian distribution originally proposed by Peck (1969) and successively adapted by Moh et al. (1996) for calculation of the settlements profile under ground level, selecting for K a value of 0.45 and a value of 0.08% for the volume loss, V_L; it match quite well with the field data, also (section 5).

It is important to notice that V_L is a result of the analysis and not a design assumption; the volume loss calculated from numerical analysis is in good agreement with the field data, while the design value is bigger than them (Fig. 15). The value of V_L = is 0.5% in the design, 0.08% in this numerical analysis and it varies in the range 0.05–0.1% from field data.

As expected, in the analysis the ground around the tunnel remain in elastic condition and the strain levels are very small.

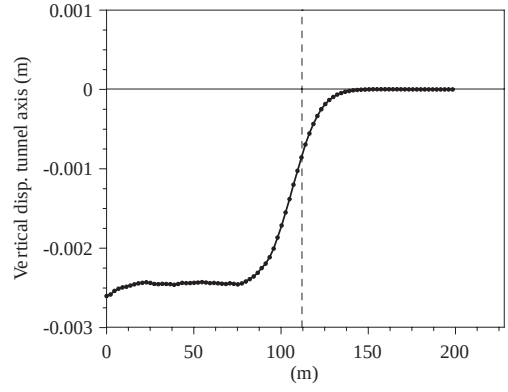

Figure 13. Longitudinal settlement profile.

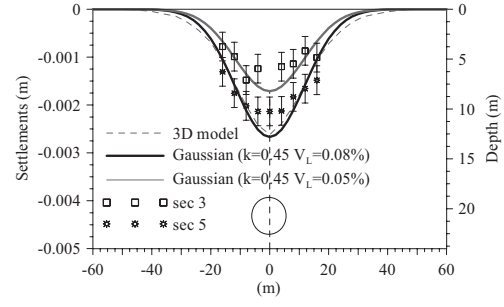

Figure 14. Computed, monitored and empirical settlement trough.

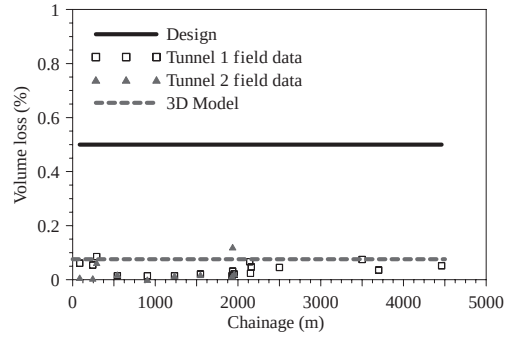

Figure 15. Design, computed and monitored volume loss.

5.3 *Interaction analysis*

In the interaction analysis the building was modeled with frame structure (Fig. 16).

The weight and the stiffness of the building modify the subsidence trough (Figs. 18, 19 and 20). The presence of the building slightly reduces the settlements and the curvature of settlement profile

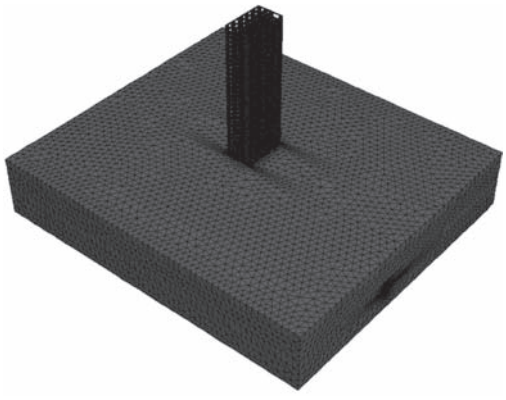

Figure 16. Mesh adopted in interaction analyses.

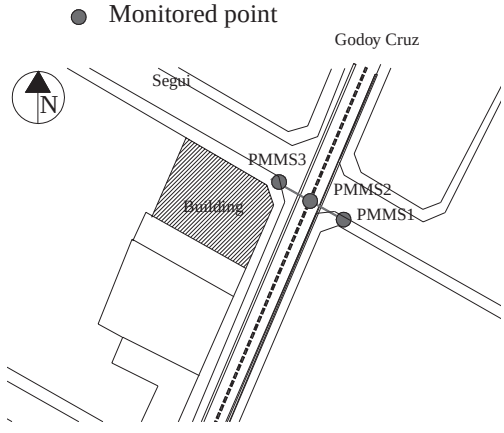

Figure 17. Monitoring instrumentation around the building.

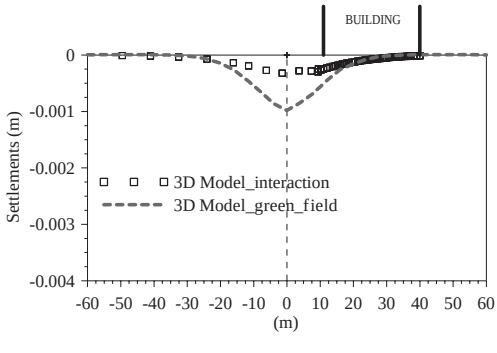

Figure 18. *Green field* and interaction settlements (tunnel face in the reference section).

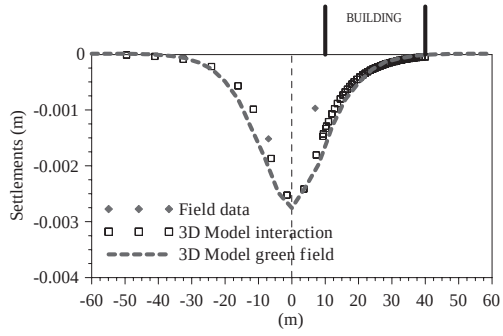

Figure 19. *Green field*, interaction and monitored settlement (tunnel totally excavated).

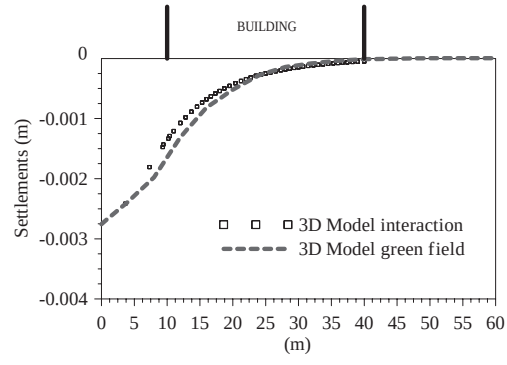

Figure 20. Settlement in foundation zone.

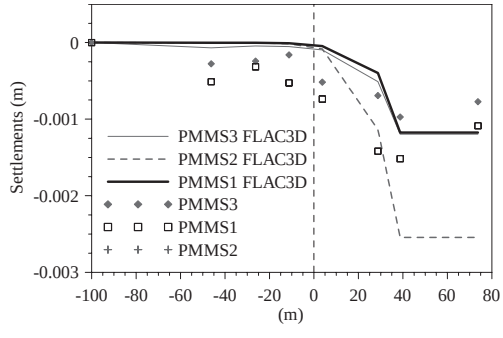

Figure 21. Computed and monitored settlement during tunnel construction (PMMS2 is out of service).

(Fig. 20). This result is attributed to: *i)* the relative position: the building is located at 11 m to the tunnel axis; *ii)* the building is set partially in the sagging area (where the settlements are reduced) and partially in the hogging area (where the settlements are increased) of the *green field* settlements profile.

Due to the stiffness of the building, however, the angular distortions, Δ/L, introduced by Burland and Whroth (1974), reduce about 30% ($1.02 \cdot 10^{-5}$ instead of $1.40 \cdot 10^{-5}$). According to classification proposed by Burland (1995), due to the very small distortion, the expected class of damage of the building is "0".

In Fig. 21 the comparison between the predicted longitudinal settlements and the field data (Fig. 17) at ground surface is reported. The results of the numerical model seem to provide a good match with the field data.

6 CONCLUSIONS

In this paper the main results of 3D numerical analyses carried out in order to simulate the tunnel construction process for the real case of "*Túneles aliviadores del emisario principal del arroyo Maldonado*" in Buenos Aires, are reported.

In order to obtain realistic results about the settlements induced on surface and on surface structures by tunneling operations, full 3D finite elements numerical analyses were performed. The analyses include the simulation of the main factors inducing settlements: the support of the tunnel face, the geometry and the weight of the shield, the grouting in pressure of the annulus between lining and excavation profile, the lining. In the interaction analysis also a realistic model of the building structure was also introduced.

The analysis of the numerical results and the comparison with field data obtained from monitoring systems allow us to draw the main conclusions reported in the following.

The settlements profile and volume loss obtained numerically are simply analysis results depending on geometry, soil characteristics and excavation process.

The field of settlements and, consequently, the volume loss estimated by numerical simulations are in good agreement with the field data.

Realistic values of volume loss can be obtained via 3D numerical analysis introducing the main factors by which the displacements field depends into the model.

For the case examined, the presence of the building does not modify the amount of settlements significantly; this phenomenon is essentially due to the relative position between the building and the tunnel. Due to the very small distortion, the expected class of building is "0".

Finally, the results obtained in this paper encourage the use of full 3D numerical analysis as a valuable tool in tunnel design in urban areas.

ACKNOWLEDGMENTS

The authors wish to thank Professor Luigi Callisto for his contribution in laboratory tests and Dr. Juan Silva Meche, Eng. Stefano Festa and Eng. Carlos Julian Civelli for their help in obtaining field data.

REFERENCES

Burland J.B. (1995)—*Assessment of risk of damage to building due to tunnelling and excavation*. Invited special lecture to IS-Tokio: 1st Int. Conf. On Earthquake Geotechnical Engineering.

Burland J.B. & Wroth C.P. (1974)—*Settlement of structures and associated damage*. State of the Art Review. Conf. On Settlement of Structure, Cambridge.

Buselli F., Logarzo A., Miliziano S. & Zechini A. (2010)—*Class A prediction of the effects induced by the Metro C construction on preexisting building, in Rome*. Numerical Method in Geotechnical Engineering (NUMGE, 2010), Trondheim 2010.

Franzius, J.N. & Potts, D.M. (2005)—*Influence of Mesh Geometry on Three-Dimensional Finite-Element Analysis of Tunnel Excavation.* International Journal of Geomechanics, ASCE.

Gunther M., Nagel1 F., Stascheit J. & Kasper T. (2007)—*Advanced numerical simulation of shield tunnelling And its role in the design process*. ECCOMAS Thematic Conference on Computational Methods in Tunnelling (EURO:TUN 2007).

Itasca Consulting Group 2006—FLAC3D *Fast Lagrangian analysis of continua in 3-D*. Version 3.1. Minneapolis, Minnesota.

Melis M., Medina L. & Rodríguez J. M. (2002)—*Prediction and analysis of subsidence induced by shield tunnelling in the Madrid Metro extension*. Canadian. Geotech. Journal. 39.

Moh Z.C., Daniel H. Ju & Hwang R. N. (1996)—*Ground movements around tunnels in soft ground*. Proceedings of Symposium on Geotechnical Aspects of Underground Construction in Soft Ground, London: 725–730.

Peck, R.B. (1969)—*Deep excavations and tunnelling in soft ground*. Proc. 7th Int. Conf. Soil Mech., Mexico City, State of the art 3.

Sainato R. (2000)—*Hydrogeological sections of the Pergamino basin (Buenos Aires province, Argentina), audio magnetotelluric and geochemical results.* Braz. J. o Geoph., Vol. 18, 2000.

Geotechnical Aspects of Underground Construction in Soft Ground – Viggiani (ed)
© 2012 Taylor & Francis Group, London, ISBN 978-0-415-68367-8

On the effects of Line 6 tunnel excavation in Naples

B. Bitetti & A. Mandolini
S.U.N.—Second University of Naples, Aversa, Italy

A. Frits Van Tol, W. Broere & R.B.J. Brinkgreve
Delft University of Technology, Delft, The Netherlands

ABSTRACT: The ever increasing demand for new transport routes led to the need of improving the current Naples underground system. It is actually composed by 7 lines connecting most of the suburban areas of the Neapolitan environment to the city center. Line 6 is one of the under construction lines of the system. Although the digging operations are still in progress, the line is already operating among Mostra and Mergellina Stations. Nowadays a 3 km tunnel, from Mergellina to Municipio Station is missing. This paper aims to discuss the tunnelling induced effects of the upcoming part of the line. A number of Finite Element Analysis has been performed with Plaxis 3D Tunnel, as to predict the tunnelling induced displacements field and the role played by both soil and machine parameters on it. The monitoring data will then be compared with the numerical analysis results in order to verify and validate them.

1 INTRODUCTION

The control of ground movements induced by tunnel excavation in urban areas is a key issue of concern for designers and many techniques are used in practice to minimize the effect of the excavation on existing buildings. This is particularly important when historical sites are affected by underground works and the limits on allowable movements are very onerous. Therefore the analysis of induced tunnelling displacements on ground surface and at depth is required.

Empirical methods have been developed on the basis of experimental data as to define the displacements field induced by tunnelling in greenfield hypothesis. However, numerical analyses can be used when more complex situations have to be analyzed.

Several Finite Element analyses have been performed, by Plaxis 3D Tunnel, in reference to the Line 6 tunnel in Naples in order to understand the soil behaviour and to back-analyze the observed induced displacements.

On the basis of collected monitoring data concerning the ground and the buildings displacements, as the machine applied pressures (front and grout pressure), the real tunnel excavation process has numerically been simulated by means of 13 construction stages. Moreover, parametric studies on soils parameters and machine pressures have been performed in order to observe their influence on induced displacements field, in terms of volume loss and maximum settlement at the ground surface.

1.1 *The Line 6*

Line 6 is a 6 km long line linking the Northern suburb of Fuorigrotta (Mostra Station) to the historic city center (Municpio Station), passing through one of the most urbanized areas of the city (Riviera di Chiaia). Nowadays the initial part of the line, between Mostra and Mergellina Stations, is already working, whereas 3 km of tunnel between Mergellina Station and Municipio Station have to be excavated as to finalize the line (Fig. 1).

The stratigraphic sequence featuring the area where the tunnel has to be excavated is made by an upper loose soils layer resting on a Yellow Neapolitan Tuff bedrock. The tunnel passes mainly through the loose soils layer, within 11 m up to 20 m depth and it is always located above the groundwater level (3 m a.m.s.l.).

An 8.15 m diameter Earth Pressure Balance (EPB) machine has been chosen to excavate the tunnel, while the final lining is made by ($1.50 \times 1.70 \times 0.30$) m segments made of RcK 45 MPa concrete.

Several investigation campaigns performed all over the years led to define the main geotechnical parameters for the soils affected by the tunnel excavation, as resumed in Table 1.

To supervise and control the tunnelling induced displacements, several monitoring instruments have been installed on the ground surface transversely to the tunnel track, and on preexisting buildings 'facades.

Figure 1. Line 6 plan.

Table 1. Geotechnical parameters.

	γ	c	φ	ψ	E
Soil layers	[kN/m³]	[kPa]	[°]	[°]	[MPa]
Loose soils	16	0	35	0	50
Tuff	14	500	27	0	1000

2 LINE 6: MONITORING DATA

2.1 *Tunnel excavation*

Up to August the 31st, 423 m of tunnel have been excavated and 250 lining segments have been installed within Mergellina Station and the under construction Arco Mirelli Station. Because of technological problems, the tunnel production has been interrupted for several days between May and June (Fig. 2). The best tunnel production has been reached in May, when almost 150 m of tunnel have been excavated and 75 lining segments have been installed.

Thanks to a number of sensors on the EPB machine, measurements of front pressure (FP), grouting pressure (GP) and torque moments (TM), applied for advancing with the tunnel excavation, have been collected. Figure 3 shows their trend versus the tunnel advance production. The front pressure is always linearly increasing with the tunnel advance, whereas both the grouting pressure and the torque moments have a non uniform trend. For the grouting pressure peak values have been recorded between June the 18th and July the 28th when electrical problems with the cutterhead and water inflow from the front have been encountered. In the same interval an instantaneous 50% reduction of the torque moments has been measured.

2.2 *Ground and buildings measured displacements*

Up to August the 31st, 45 ground landmarks sections have been installed along Via Piedigrotta, transversely to the tunnel track.

Looking at the maximum measured displacements, 3 zones can be identified: zone A (w_{max} = 14 mm), zone B (w_{max} = 8 mm) and zone C (w_{max} = 5 mm), as shown in Figure 4.

Zone A mainly includes landmarks sections measuring the largest displacements, zone B features the middle part of the monitored stretch and zone C shows the smaller measured displacements.

Measured displacements, versus front-section distance, have been plotted in Figure 5, whereas Figure 6 depicts such displacements at the tunnel front and at the passage of tail of shield. According to indications from Craig & Muir Wood (1978), for unsupported tunnel front in sandy soils, an average of 20% of the maximum displacements has been measured at the tunnel front and of 80% at passage of tail of shield.

Regarding the collected buildings monitoring data, up to August the 31st, 29 buildings have been monitored by means of several landmarks installed on their facades. The maximum measured settlement is 8 mm for building n°23 along Riviera di Chiaia (Fig. 7), while the average displacement is 5 mm.

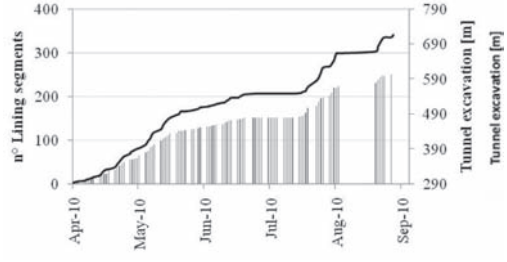

Figure 2. Tunnel advancing up to August the 31st.

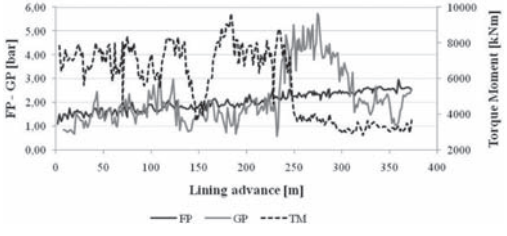

Figure 3. EPB measured pressures and torque moment.

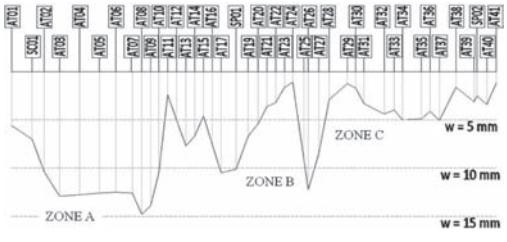

Figure 4. Landmarks on the ground surface: Maximum measured displacements in longitudinal profile.

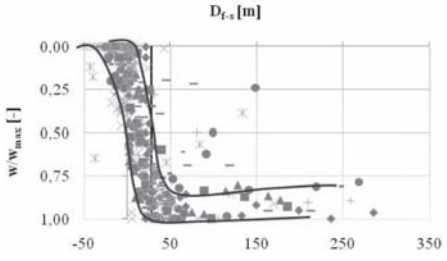

Figure 5. Maximum displacements in longitudinal direction.

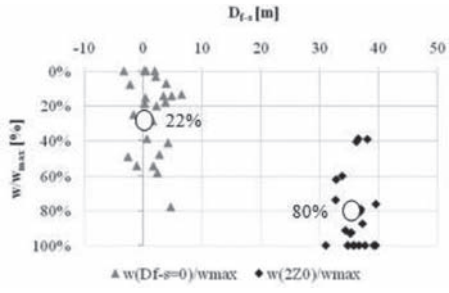

Figure 6. Maximum surface settlements at the tunnel front and at the passage of tail of shield.

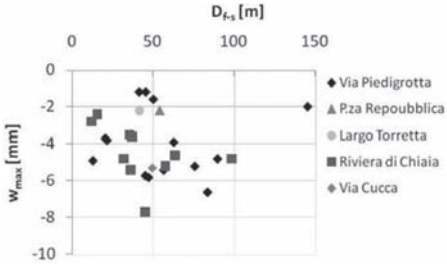

Figure 7. Maximum buildings settlements.

3 NUMERICAL ANALYSES

3.1 *The input model*

Several three-dimensional analyses have been performed by means of Plaxis 3D Tunnel, as to analyze the tunnelling induced soil behaviour.

Parametric studies have been carried on in order to observe the input soil parameters and machine pressures on the effects observed on the ground surface, hence to back-analyze the monitored effects induced by the Line 6 tunnel excavation. The monitoring data have been updated to August the 31st, and then the Mergellina-Arco Mirelli stretch has been back-analyzed.

The plane section shown in Figure 8, has been chosen along Via Piedigrotta as to perform the FE analyses. The tunnel mainly crosses the loose soil layer resting on the Tuff bedrock, 20 m deep, and is located 11 m below the groundwater table. The greenfield conditions have been considered for the analyses, then a symmetric section has been used, as to reduce the computation time.

To prevent the border effects influence on the excavation process, a (5D × 5D) size section has been defined. The number of planes in z-direction has been fixed as to reproduce at best the monitored excavation process day by day; in such a way a 125 m length model in z-direction has been constructed. The resulted 3D model is then featured by 44268 quadratic 15-node wedge elements and 122688 nodes.

Since the tunnel excavation affects at the most the upper layer made by sandy soils, "*drained*" analyses have been performed.

To describe soil and structures (EPB shield and concrete final lining) behavior, the Hardening Soil Model has been used for the former and the Linear Elastic Model for the latter; Table 2 resumes the used soils properties.

As the tunnel excavation implies recasting in soil properties, the model of soil-tunnel interaction has been required. Hence, soils materials with reduced strength parameters have been defined by means of the interface parameter R_{interf} set lower than 1.

3.2 *Parametric analyses on soil parameters*

In order to analyze the soils parameters influence on the surface effects induced by tunnelling, in terms

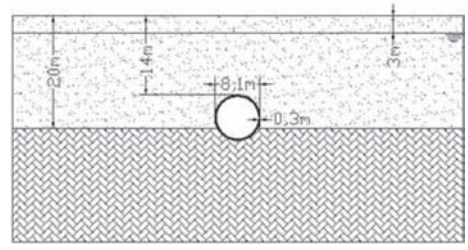

Figure 8. Plane section for 3D FE analyses.

Table 2. Geotechnical parameters of soils layers.

Soil layers		Loose soil	Tuff
γ_d	[kN/m^3]	13	14
γ_{sat}	[kN/m^3]	18	19
k	[m/sec]	1e^{-4}	1e^{-4}
ν	[–]	0.3	0.3
c	[kPa]	0	500
φ	[°]	35	27
ψ	[°]	0	0
E_{ed}	[kPa]	6.73e^4	1.35e^6
E_{ur}	[kPa]	2.02e^5	4.04e^6

of V_L and w_{max}, a number of FE analyses have been performed by varying soil strength and stiffness parameters within reliable ranges of values. As the deep Tuff layer did not reveal any influence on the surface displacements, a simplified homogeneous model, made only by loose soils, has been used. The soil parameters resumed in Table 2 have been used for the reference analysis, whereas Table 3 describes their ranges of variations. For all the above discussed analysis, the machine front and grout pressures have been kept constant (FP = 160 kPa, GP = 200 kPa).

Despite volume loss controlled analyses are possible with the used code, not any contraction has been imposed in this case, in order to observe the volume loss at the tunnel depth ($V_{L,d}$) changes, according to different soil parameters.

Results from the performed analyses showed a clear influence of the soil stiffness on $V_{L,d}$: the larger is the Young's modulus, the smaller is $V_{L,d}$, passing from 0.20% for $E = 1/3*E_{ref}$ to 0.02% for $E = 3*E_{ref}$. Regarding the surface effects in terms of volume loss (V_L), maximum settlement (w_{max}) and subsidence width (k), a great influence of the stiffness moduli on V_L and w_{max} (Figs. 9 and 10) has been noticed, whereas the stiffness moduli ratio $P = E_{ur}/E$ affects the subsidence width by leading to its extension up to 50% when it increases from 3 up to 12 (Fig. 11).

Clear relationships can be as well detected between γ and the effects on the ground surface. For three reference planes, at the tunnel front (Plane O), 2D (Plane U) and 3D (Plane AE) forward, an almost linear relation between γ, V_L and w_{max} has been detected (Figs. 12 and 13). Reductions, rather than increments, of γ up to 20%, leads to much more pronounced variations of k (–80%) (Fig. 13).

At the same time, not any particular relationship has been noticed between the friction angle (φ) and the dilatancy angle (ψ) with the volume loss and the maximum settlement on the ground surface. Nevertheless, a linear increase of the subsidence width up to 25% has been noticed for reduction of φ up to 40%. Conversely, not any effects on the

Table 3. Ranges of variations for soil parameters.

γ	φ	ψ	E	$P = E_{ur}/E$
(±20%)	(–40÷0)%	(0÷10)°	$(1/3÷3)E_{ref}$	(3÷12)

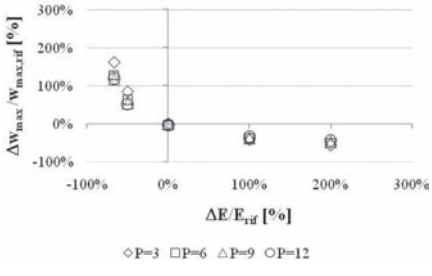

Figure 9. Effect of stiffness modulus variations on the maximum settlement on the ground surface.

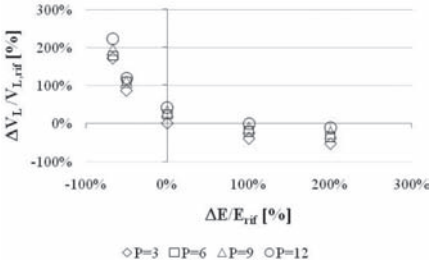

Figure 10. Effect of stiffness modulus variations on the volume loss on the ground surface.

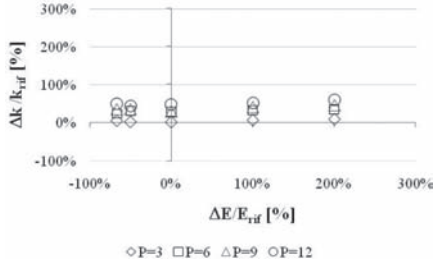

Figure 11. Effect of stiffness modulus variations on the subsidence width.

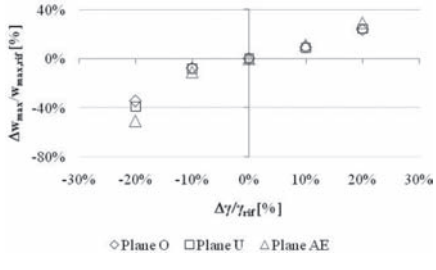

Figure 12. Effect of γ variations on the subsidence width. On the maximum settlement on the ground surface.

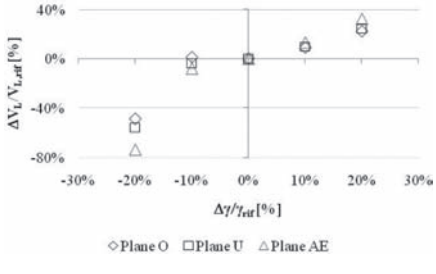

Figure 13. Effect of γ variations on the volume loss on the ground surface.

subsidence width has been detected for ψ increments less than 15%, from which an instantaneous enlargement of the surface subsidence basin, up to 20%, has been observed.

3.3 *Parametric analyses on EPB pressures*

When using and EPB machine in tunnelling, the effects on the ground surface are strictly dependant by the applied front and grout pressure.

Several FE analyses have been performed in order to identify any possible link between the applied pressures and the induced effects on the ground surface (V_L and w_{max}). Since such pressures concern also the Tuff layer, the two layered geometric shown in Figure 9 has been used.

The constitutive law describing the soil behaviour are the same as previously described, whereas volume loss controlled analyses have been performed, by imposing a 0.1% contraction at the tunnel depth.

Both front and grouting pressure have been varied within 100 kPa and 500 kPa, and 48 analyses have been carried on as to investigate their effects on the ground surface. Results have been plotted referring to a "reference" analysis where both front and grout pressures have been set equal to 100 kPa.

Looking at the front pressure (Figs. 16 and 17), beneficial effects in reducing the surface displacements (up to 30%) have been noticed, for pressures within a range of values preventing soil plastification. Indeed, results showed:

- face plastification, caused by large horizontal displacements toward the excavated tunnel, generate the lowest front pressure. This leads to the development of an active failure mechanism and of large surface settlements. Moreover, for front pressure within 100 kPa and 200 kPa, the larger is the applied pressure, the smaller are the V_L and w_{max}.
- soil plastification at the tunnel contour for front pressure exceeding 200 kPa. New increment in w_{max} and V_L developed together with horizontal displacements ahead the tunnel front, leading to a passive failure mechanism.

Concerning the grout pressure effects o the ground displacements, Figure 17 and Figure 18 show a linear reduction of both w_{max} and V_L for increasing grout pressure.

By comparing the front and the grout pressure influence, Figure 19 and Figure 20 show the

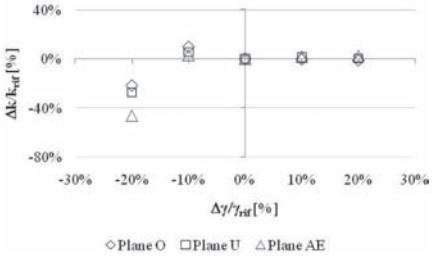

Figure 14. Effect of γ variations on the subsidence width.

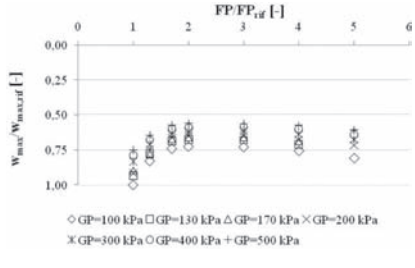

Figure 15. Front and grouting pressure effects on surface maximum settlements.

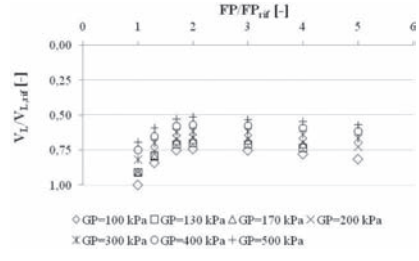

Figure 16. Front and grouting pressure effects on surface volume loss.

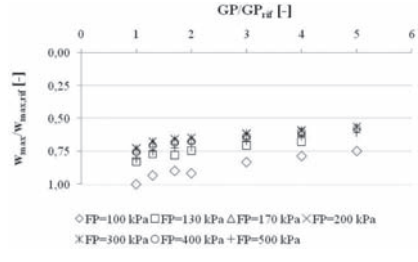

Figure 17. Front and grouting pressure effects on surface maximum settlements in dimensionless graph.

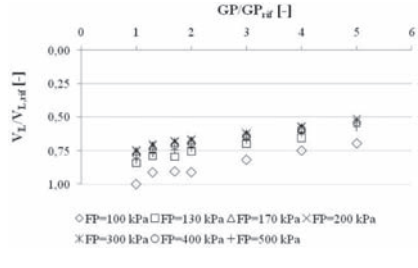

Figure 18. Front and grouting pressure effects on surface volume loss in dimensionless graph.

initial predominant effect of the front pressure up to 200 kPa (corresponding to 100% increment of the reference pressure).

Looking at the grout over the front pressure ratio effects on surface displacements, Figure 21 and Figure 22 show a sort of linear relationship in a range of values defined by the minimum and maximum front pressure values.

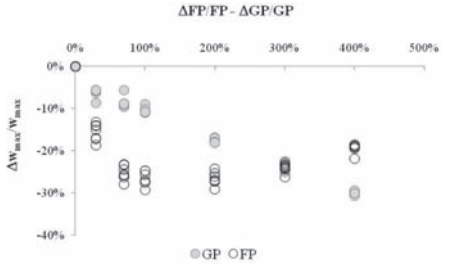

Figure 19. Comparison between the grout pressure (GP) and front pressure (FP) effects on maximum surface settlement.

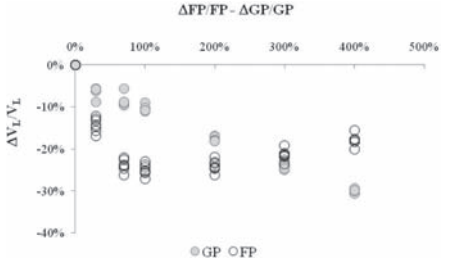

Figure 20. Comparison between the grout pressure (GP) and front pressure (FP) effects on surface volume loss.

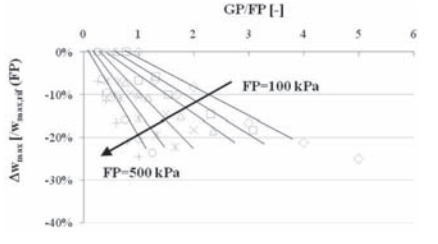

Figure 21. Influence of the grouting than the front pressure ratio on surface maximum settlement.

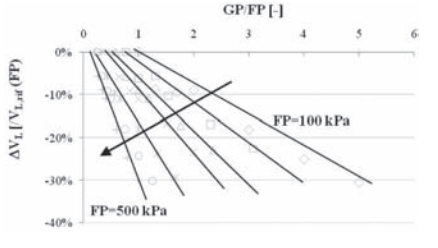

Figure 22. Influence of the grouting than the front pressure ratio on surface volume loss.

4 LINE 6: BACK-ANALYSIS OF MONITORED EFFECTS

In order to perform the Line 6 tunnelling back-analysis, the monitored construction process has been simulated and the volume loss or contraction method has been used. 13 calculation phases have been defined as to reproduce about 100 m of excavated tunnel. In each phase the same procedure to simulate the tunnel construction process has been repeated by:

- deactivating the soil clusters inside the tunnel lining.
- activating the shell elements representing the EPB shield behind the tunnel face and draining the water within it.
- applying the concrete properties to the clusters representing the installed final lining.
- applying the face and the grout pressure to prevent the tunnel collapse, and the forces the hydraulic jack driving the EPB machine, exert on the already installed lining.
- modelling the soil-tunnel interaction by assigning modified properties, with reduced strength parameters (by means of $R_{interf} < 1$), to the slices where between the tunnel front and the last lining segment.
- defining a tunnel contraction to simulate volume loss.

To reduce the influence of boundary conditions on the excavation process, 25 m of tunnel have been excavated at the start of the model and the induced tunnelling displacements have been set to zero. Both the front and grout pressure linearly increase with depth; 14 kPa and 20 kPa gradients (depending on the bentonite specific weight and on the mixture for the mortar injections) have then been used for the front and the grout pressure. On the contrary, as the hydraulic jacks' pressure on the final lining, related to the applied front pressure, is not depth dependent, a constant value has been defined.

In order to define the input values for the EPB pressures to apply in the analyses, on the basis of monitored EPB performances, the average value of measured front and grout pressures for each landmarks zone (A, B and C), has been estimated as resumed in Table 4.

On the contrary, no monitoring data about the volume loss, neither at the ground surface nor at the tunnel depth, is available. A 0.1% volume loss has then been considered as an initial reliable value

Table 4. Input EPB pressures in the FE analyses.

	Zone A	Zone B	Zone C
FE analyses	kPa	kPa	kPa
Front Pressure	160	190	240
Grout Pressure	150	150	370
Jacks Pressure	878	999	1202

Table 5. Input $V_{L,d}$ at the tunnel depth and resulting V_L at the ground surface.

FE analyses	Zone A	Zone B	Zone C
$V_{L,d}$ (Input)	0.25%	0.15%	0.10%
V_L (Output)	0.52%	0.34%	0.21%

to impose at the tunnel depth. Nevertheless, since the effects to be reproduced are significantly different from each other, on the basis of assumptions on soils behaviour and parameters, on geometric model and on applied pressures, different values for the volume loss at the tunnel depth have been needed. Table 5 resumes the required volume loss at the tunnel depth, and the consequent V_L at the ground surface, resulting always twice the imposed ones.

The analyses accuracy has been confirmed comparing the analyses results to the measured displacements both in transversal (Figs. 23, 24, 25) and longitudinal direction (Fig. 26).

5 CONCLUSION

Tunnelling in urban areas is of increasing importance over the past few decades. The prediction and the analyses of the induced effects, by means of analytical, numerical or experimental methods, play an even more important role, in order to prevent damage to the overlying buildings and services. Literature data reveal that the role of the excavation technique is far from negligible and a significant reduction in the induced effects due to the excavation techniques improvement over the years has been revealed.

Numerical analyses, by means of FE codes, represent a useful tool to account for the excavation method in the design process, since they enable the whole excavation process. In this context, the objective of this thesis has been to assess the influence of soil parameters and of technological factors on tunnelling induced displacements, thus several FE analyses, by means of Plaxis 3D Tunnel have been performed. Results have been used to back-analyze at the best the monitored surface effects induced by the Line 6 tunnel excavation.

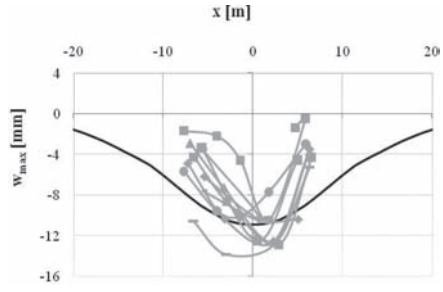

Figure 23. Transversal surface subsidence obtained by the back-analyses for Zone A.

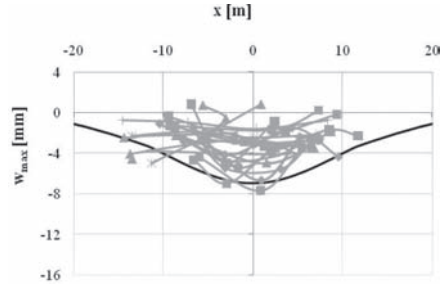

Figure 24. Transversal surface subsidence obtained by the back-analyses for Zone B.

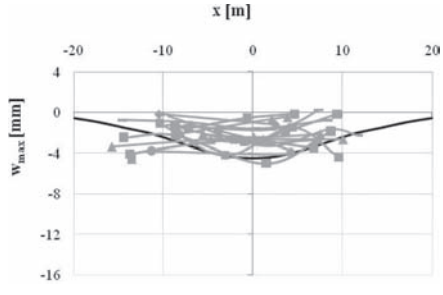

Figure 25. Transversal surface subsidence obtained by the back-analyses for Zone C.

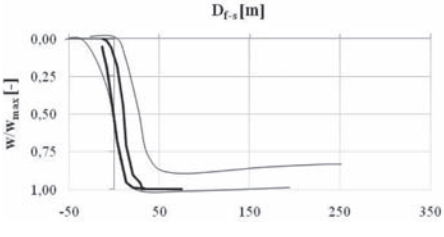

Figure 26. Longitudinal displacements obtained by the back-analyses compared to the range defined by collected monitoring data.

Looking at the soil parameters influence, main results of the parametric studies can be summarized in the following:

- the soil stiffness mainly affects V_L and w_{max} at the ground surface and influences the subsidence width (k) in a lesser degree: increasing the soil stiffness the subsidence becomes wider
- the soil stiffness moduli ratio does not significantly affects V_L and w_{max} but the subsidence width: the larger is such ratio, the larger is k
- linear relationship has been detected between γ, V_L and $w_{max;}$ however reduction of γ yields a shrinkage of the subsidence basin
- no clear relationships have been detected between φ and ψ with the surface displacements; conversely, reductions in φ lead to a sort of linear increase in k, whereas the dilatancy effect is evident only above a certain value when the subsidence width suddenly increases.

Regarding the EPB pressures effects, the main results can be resumed as follows:

- clear relationships between the applied pressures and the effects on the ground surface can be defined
- the positive effect of the front pressure on the induced displacements is evident up to a certain value, related to the front equilibrium, after which further increases leads to plasticization around the tunnel lining implying later growing in settlements and volume loss
- the face pressure governs the tunnel front behaviour leading to active or passive failure mechanism, thus strongly affecting the displacements at the ground surface
- the face pressure influence on both the volume loss and the maximum settlement at the ground surface, is much more pronounced than the grouting pressure, up to a certain value, when the observed behaviour changes and the grouting pressure becomes more influent in reducing the tunnelling induced effects
- looking at the pressures ratio, linear relationships with both the volume loss and settlement variations have been detected within a range defined by the minimum and maximum front pressure used.

As general conclusion, it seems reasonable to state that the design of tunnel cannot neglect (as usually done) technological factors, which have a strong influence on the tunnelling induced settlement.

In other words, good soil modelling coupled with advances numerical analyses, could give wrong results if technological aspects (grouting and front pressures) are not well considered at design stage and not well implemented at construction stage. A good design is based on a "right" balance of all above.

REFERENCES

Attewell, P.B. 1978. Ground movements caused by tunnelling in soil. *Large ground movements and structures*: 812–948. London: Pentech Press.

Attewell, P.B., Yeates, J. & Selby, A.R. 1986. Soil movements induced by tunnelling and their effects on pipelines and structures. Glasgow: Blackie.

Attewell, P.B. & Selby, A.R. 1989. Tunnelling in compressible soils: large ground movements and structural implications. *Tunnelling and Underground Space Technology* 4 (4)

Attewell, P.B. & Woodman, J.P. 1982. Predicting the dynamics of ground settlement and its derivatives caused by tunnelling in soil. *Ground Engineering* 15(8): 13–22.

Bloodworth A.G. 2002. Three-dimensional analysis of tunnelling effects on structures to develop design methods. Thesis (PhD). Oxford: University of Oxford.

Broms, B.B. & Bennermark, H. 1967. Stability of clay in vertical openings. *Journal of Soil Mechanics and Foundations,* ASCE, 193: 71–94.

Davis, E.H., Gunn, M.J., Mair, R.J. & Seneviratne, H.N. 1980. The stability of shallow tunnels and underground openings in cohesive material. *Géotechnique* 30(4): 397–416.

Franzius, J.N. (2003). *Behaviour of buildings due to tunnel induced subsidence.* Thesis (PhD). London: Imperial College, University of London.

Lake, L.M., Rankin, W.J. & Hawley, J. 1992. Prediction and effects of ground movements caused by tunnelling in soft ground beneath urban areas. CIRIA Funders Report/CP/5.

Macklin, S.R. & Field, G.R. 1999. The response of London clay to full-face TBM tunnelling at West Ham, London. In: *Proc. Int. Conf. On Urban Ground Engineering, Hong Kong, 11–12 November 1998*. London: Thomas Telford

Mair, R.J. 1979. Centrifugal modelling of tunnel construction in soft clay. Thesis (PhD). Cambridge: University of Cambridge.

Mair, R.J. & Taylor, R.N. 1993. Prediction of clay behaviour around tunnel using plasticity solutions. In: *Predictive Soil Mechanics: Proc. Wroth Memorial Symposium*, *Oxford, 27–29 July 1992*. London: Thomas Telford, 449–463.

Morton, K. & Au, E. 1975. Settlement observation on eight structures in London. In: *Proc. Conf. Settlement of Structures, Cambridge, April 1974*. London: Pentech Press, 183–203.

O'Reilly, M.P. & New, B. 1982. Settlements above tunnels in the United Kingdom—their magnitude and prediction. In. *Proc. Int. Symposium Tunnelling '82, London: 7–11 June.* London: Institution of Mining and Metallurgy, 173–181.

Nyren, R.J. 1998. Field measurements above twin tunnels in London clay. Thesis (PhD). London: Imperial College, University of London.

Peck, R.B. 1969. Deep excavation and tunnelling in soft ground. In: *Proc. 7th ICSMFE, State-of-the-art Volume, Mexico City*. Mexico: Sociedad Mexicana de Mecànica de Suelos, 225–290.

Simons, N.E. & Som, N.N. 1970. Settlements of structures on clay with particular emphasis on London clay. CIRIA Report 22.

Geotechnical Aspects of Underground Construction in Soft Ground – Viggiani (ed)
© 2012 Taylor & Francis Group, London, ISBN 978-0-415-68367-8

Long term environmental effect of tunnel construction in weak soils

M. Mets
Estonian University of Life Sciences, Tartu, Estonia

R. Raudsepp
Tallinn University of Technology, Department of Mining, Tallinn, Estonia

T. Ruben
Estonian University of Life Sciences, Tartu, Estonia

ABSTRACT: In the present paper the environmental effects of the construction of Tallinn's Merimetsa—Mehhaanika—Tihase sewage tunnel are analyzed, examining in closer detail the changes that occurred place during the construction works in 1987–1992, but also the later effects that only subsided during the last decade. Since three different technologies were used, acknowledging these effects might facilitate future endevours in similar circumstances.

1 INTRODUCTION

The tunnel is 2,2 meters in diameter is and it is supported with reinforced concrete elements; the length of the tunnel is 3 kilometres.

The geotechnical conditions on the line of the sewage tunnel are very complicated. It is situated in a buried primordial valley between Männiku and Pelguranna. According to data received from the Geological Survey of the Estonian SSR, the depth of the valley is about 100 meters. In the base of the valley, Lower Cambrian and Vendian sandstones are exposed. The valley is filled with fluvio-and limnoglacial deposits of different ice ages. The various glacial, fluvioglacial and layers are covered by Holocene deposits, which consist of marine sediments. A thin layer of fill and topsoil cover the marine sediments.

A typical geological section of the area is given in Figure 1.

2 GEOLOGICAL SECTION

2.1 *Soil layers*

Typical geological section of the area would be as follows (figure 1).

1. a thin layer of fill and topsoil (max 1,5 m); often the fill is missing;
2. a complex of marine sand that comprises mostly silty and fine sand interchanging with layers of medium and coarse sand;
3. a complex of weak clay layers; judging by the geotechnical properties, the most prevailing layer there should be limno-glacial deposits, which vary largely in their grading and thickness; the layer mostly consists of clay and silt; in general, clay content in clay complexes tends to diminish with depth and clay is usually located under marine sands; under the clay lies clayey silt;
4. fluvio-glacial sands with a variety of grading. In general, the grain size grows with depth: under the weak clayey silt lies silty- and fine sand, in deeper parts medium sand under which there can be found silty sand and clayey silt layers. Taking into account the grading curve and water content of latter, it can be asserted that the layer is mostly made up of redeposited till from the early formational stages of a glacial river;
5. Till—located 25 to 30 m from the ground level—is a dense, coarse grained sandy silt till; that lies in the depth 40 meters. The soil layers under the till were not geotechnically investigated.

2.2 *Ground water conditions*

On the investigated tunnel line there are two groundwater horizons above the till layer. The upper water horizon above the clay complex lies in marine sands and the fill deposit and gets its recharge from precipitation. The water table lies 0,3…1,0 meters beneath the ground level and the water there is fairly polluted, containing nitrates and phosphates. Under the clay complex there lies a layer of artesian groundwater that is connected with the upper unconfined groundwater horizon via the occasional "openings" in weak clay. From the onset of the excavation works, the pressure level

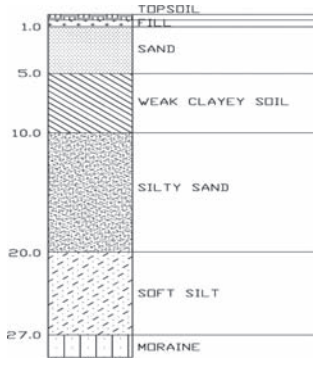

Figure 1. Geological section of the area.

of the artesian water horizon practically coincided with that of the upper groundwater horizon. The recharge area of the artesian groundwater layer extends relatively far—into the Männiku fluvioglacial delta—and has minimally polluted water.

3 GEOTECHNICAL PROPERTIES OF SOILS

The geotechnical properties of soils were examined with field and laboratory tests.

Meremeeste complex. The complex consists of silty-, fine- and medium sands. The upper part of the 0,5–1,2 m consists of silty sand (q_c = 1,2 MPa and $E_{0-0,8}$ = 4 MPa). Beneath the loose sand there lie dense sands with fine geotechnical properties – q_c = 4,0 to 15 MPa, E_{0-3} = 15 to 50 MPa, φ = 30 to 35° and **c** = 10–30 kPa.

Weak clay soils, silty clays and clayey silts and their geotechnical properties must be examined separately.

The natural water content of silty clay (with clay interlayers) is 45 to 60% (mean W_n = 57%). These soils are slightly overconsolidated, with the pressure (p_c) reaching up to 30 to 40 kPa. The yield limit during the plate load test was q_y = 70 kPa and the ultimate load q_t = 100 KPa. The modules of deformation reached 0,3 to 0,4 MPa. The shear strength parameters during the unconsolidated drained test were φ = 9 to 12° and c = 5 kPa. The undrained unconsolidated parameters based on field tests were the following: yield point C_{uy} = 14 kPa and maximum shear strength C_{uf} = 35 kPa.

The geotechnical properties of clayey silt improve with depth. In the upper layers, W_n = 27 to 28% and q_c = 2 to 5 MPa. Downwards, the water content becomes W_n = 22 to 25% and q_c = 12 to 18 MPa. In plate load tests, q_y = 120 kPa, q_f = 500 kPa and $E_{0-1,2}$ = 2,0 to 2,5 MPa. The unconsolidated drained shear test gave the following result φ = 30 and c = 0. The undrained shear strength parameters were C_{uy} = 20 kPa and C_{uf} = 50 kPa.

The soils that lie under the weak clayey layers were investigated only using cone penetration tests. Based on a field test, q_c = 9 to 23 MPa.

The coefficient of permeability in the upper ground water layer in silty sands was 3 m/d and 7 m/d in fine sand which corresponds with experiences from similar tunneling works. The water conductivity parameters in the artesian water layer depend on the grain-size distribution of the soil. The coefficient of permeability in silty sands was 2 to 3 m/d (lab tests and also field tests), in fine sands 5 to 10 m/d and in medium sands 10 to 30 m/d. The given data characterizes the industrial water lowering on the line of the sewage tunnel quite precisely.

4 GROUND WATER

During the first part of the excavation works the complex method of lowering the water table and caisson was used for penetrating the sewage tunnel. An extra pressure of 0,5 at was established in front of the tunnel and continuous water table lowering was implemented, lowering the pressure in such a way that the groundwater level was fixed to 1 to 2 m below the tunnel base. The complex method enabled the execution of normal and accident free excavation works and also the satisfactory advancement speed of 3,5 m/d. In the constructing conditions discussed above, this complex method can be considered the most optimal and best possible option.

The water table lowering along the sewage line was planned with 20 m deep boreholes (Ø = 500 mm) that did not penetrate the artesian water layer. The distance between the boreholes was 25 to 30 m. The boreholes in the artesian layer were equipped with ceramic filters, which worked quite well under the given geological conditions. The coefficient of permeability in medium sands was 20 to 30 m/d. Using this module in calculations coincided with the actual field works.

In September 1987 a groundwater monitoring grid was constructed in order to observe the settling of ground surface due to lowering groundwater levels, discussed further below. This borehole grid encompasses both upper and lower artesian water horizons. At the beginning, measurements were taken daily; later, the interval was 2 to 3 days. The grid was constructed in a beam-like pattern: two boreholes were situated perpendicularly across the construction line and one further downwards on the construction line. The length of the "beam" was 0,5 km and it gave good insight into the spreading of the drawdown and the change of pressure in the water horizons underneath the weak clay layers.

The boreholes describing the upper water horizon showed that the two water horizons were connected. The boreholes near the tunnel line reacted to

changes in the artesian water horizon with a delay of one day. A borehole which was located 60 m from the tunnel line reacted to the pressure drop of 1,5 m with a water level drop of 10 cm. No further reaction in the upper water horizon was detected. The reaction of the upper water horizon to precipitation was highly distinctive. A rainfall in September 1987 lifted the upper water table by 0,5 m in two days and this also resulted in an equivalent rise in the water table of the lower horizon (Figure 2). The drawdown of the upper horizon runs in an almost straight line. The pressure drop is 1 m per the 500 m long line, which results in a drawdown incline of 1:500.

The conditions were more complicated in the artesian horizon. Nearly all the boreholes on the "beam" reacted almost immediately to any changes in water pressure. In the reaction times between the boreholes nearest to the line and their neighboring boreholes, a few delays were registered. The formed depression curve can be tentatively divided into two. The first curve describes the distance of 0…130 m; at the minimal level the pressure drop was 2 m and 4 m during the maximum level. For the following 370 m, the corresponding figures were 0,8 and 2 m.

The extension of the depression curve indicates to the fact that the regular calculation schemes are not applicable in the cases of extensive and long-term lowering of water tables. The methods that give good results in calculating the criteria a single borehole tend to give a much lower figure than the actual result when used in cases of extensive water lowering works—hence the need for a separate hydrodynamic analyses of the obtained figures in order to be able to work out more realistic calculation schemes for the future.

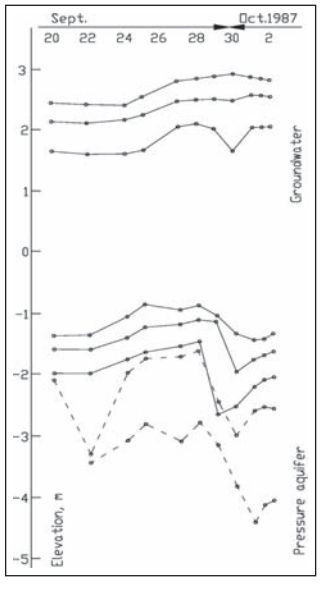

Figure 2. Changes in water table and pressure.

5 SETTLEMENTS

5.1 *Settlements caused by excavation*

Intensive water table lowering and excavation works resulted in settlements in the ground surface. These facts can be linked with two different processes. The first one of these is connected with the excavation works that caused the settlements directly above the tunnel line and the adjoining areas. The settlements were caused by an additional compaction of weak clay layers brought on by caisson and its pressure, the displacement of weak layers due to pressure and the soil outflow to the front of the tunnel. Settlements were smaller in sandy layers due to the greater excavation depth and the dilatation effect, but more significant in the clayey layer due to additional compaction and the soil outflow.

The deformations caused by excavation works were examined in 5 different profiles; the effect of excavations was also analyzed perpendicularly along the tunnel line. The selected profiles were situated in the area of the park, under the street and under the railroad.

The observations made along the line of the tunnel (Figure 3) revealed that the settling of the ground surface started to occur 15 to 20 m from the tunnel line. The main settlements occurred before the face (8 to 18 cm) and after and may continue for some years. The difference in benchmark behaviour cannot be explained with the geological situation, because geological conditions have not changed between the benchmarkers. Extensive ground settlements can be attributed to with the onset of excavation works.

Three of the four cross-sections behaved similarly (figure 3). The settlements on the axis of those three cross-sections were 8 to 14 cm and the extent of the settlement funnel was 7 m from the axis of the tunnel. The benchmarkers situated further on practically did not settle. The fourth cross-section that was located under the railroad settled up to 27 cm and the extension settlement funnel was 7,5 m. To minimize the effect of the tunnel works on the nearby building, a sheet-pile wall was constructed. Its effect was sufficient to prevent any further settlement on the building. An abandoned laboratory building got further settlements of 2 to 8 cm (less than on tunnel axis 12 cm) and developed cracks.

5.2 *Additional causes of settlements*

5.2.1 *Artesian water horizon*

Another cause for the settlements to take place was the pressure drop in the underlying artesian water horizon. It results in a rise of effective stress in weak

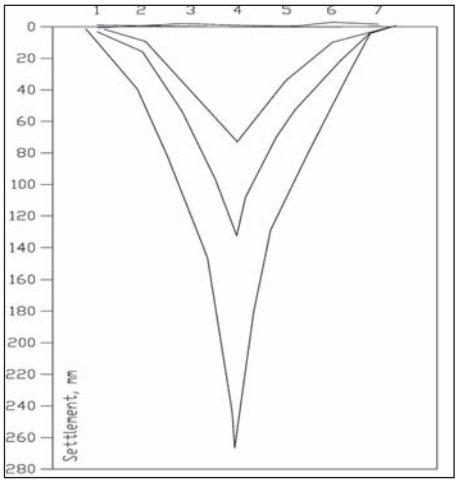

Figure 3. Settlements on cross-section a.

soils and in turn, consolidation takes place. In such cases, it is very important if the rise of effective stress exceeds p_c or not. Preliminary calculations estimated the settlement to be 4…10 cm and the lateral extension to be 0,5 to 1,0 km from the tunnels axis.

The development of actual settlements is a little different and smaller than in theoretical examples. Weak clay layers under pressure (less than p_c) are considerably less compressible than laboratory tests show (because of structural damage that gets done when obtaining probes and the preparation of probes in the laboratory). Analyzing settlements was difficult due to the fact that the geotechnical survey of the tunnel line started later than the actual excavation works, but was eventually somewhat facilitated by the relevant data that could be acquired from the one-time geodetical surveys that had been carried out there.

The settlements on the tunnel line lasted for 6 to 10 years. In area of the park, the settlements lasted for 3 years and in addition to the initial 18 cm settlements there were additional settlements of 5 cm during that time span. The street section with heavy traffic suffered an additional 10 cm settlements in the course of 10 years (initial 18 cm and additional 10 cm). The road surface needed additional maintenance every 3 to 4 years. Under the railroad, immediate settlements were 27 cm; during the next 8 years, the area settled another 6 cm.

5.2.2 *Construction and traffic*

Considering the common occurrence of weak clay layers and intensive construction activities and heavy traffic load, there has always been some settlement of buildings and ground surface. The intensity of the settlements has been quite big. For example bolts driven into asphalt constructed on fill settled for 3,5 years (1984 to 1987). These settlements of 20 to 90 mm depended on the geological section, the thickness of fill and the intensity of traffic: the settlements were 20 mm in places were the fill was absent, 60 mm in places where there was 1,5 m of fill with a low traffic load and 30 mm with the same fill thickness but a heavy traffic load.

Ground surface settlement took place before the lowering of water tables. In locations of thicker fill there may have been cases where the combination of hydrodynamic pressure drops and the loads inflicted by the fill caused the rise of effective stress that exceeded p_c values. However, considering the fact that weak soil layers have been compacted by the load of the fill material and its p_c has risen, it is unlikely that these spots could be very wide spread.

5.3 *Case examples of settlements*

The intensity of the settlement processes can be best described with the example of a school that was constructed on shallow foundations, which consist of differently loaded blocks. In the end of 1970s the maximum settlement for the school was 2,5 cm and minimal 1,5 cm, factoring in also the period during construction works and the time after completing the construction. Due to the uneven load scheme designed for the school, crack appeared in this particular building. The benchmark was levelled again in 1980 and 1986 and the settlement remained 4 mm. After the drop in groundwater levels, the settlements intensified and in the beginning of 1988 it had reached 39 mm. During the following three months, the settlement process slowed down.

The settlements in the Navy Hospital remained 7 mm during a 10 year period. During the first phase of water lowering works, the settlements were 25 mm; later, the settlements continued at the pace of 1 to 2 mm per month, until 1995.

An analysis of the two of afore-mentioned benchmarkers allows us to draw the conclusion that the settlement of 20 to 40 mm was caused by lowering the water table and the consolidation that had been induced by a pressure drop. Currently the consolidation caused by filtration has subsided and settlements occur due to creep (secondary consolidation). The settlements for the past half year were 3 to 15 mm (figure 8). Taking into account other similar surveys in the city district of Lilleküla, these settlements should subside in steady conditions in 2 to 3 years of time. Hence, the predicted settlements were 20 to 30% bigger than the maximum settlements in the area and 50 to 70% bigger than average settlements.

However, some of the benchmarkers behaved differently. These are the benchmarkers in the

catering block of the Navy Hospital and in the boiler-house of the Children's Hospital.

The floors in the catering block suffered the settlement of 11 mm, which can be explained by the fact that the backfill material under the floor had never been compacted evenly and thus it compacted unevenly after the completion of floors. The fill material also put a load on the weak clay layers, these compacted more and hence supplemented to the existing settlements. The maximum settlement under the floor happened in the middle zone of the floors, while the minimum settlement occurred near the grillage due to friction between the piles and the soil. During the lowering of the water table, the floors cracked off the grillage and there occurred additional settlements.

6 BUILDINGS ON PILE FOUNDATION

Two types of behaviour can be observed in buildings founded on pile foundations, depending on the soil layer the pile tips are inserted into. on to which. The first group consists of piles rammed into the fluvioglacial sands through weak clay. In accordance with the initial project, these piles were loaded with 30 to 40 tons (considerably less than prop limit). The buildings on these piles got settlements of 1 to 3 cm during the excavation works. The settlements faded in 1 to 2 years after the excavation works. The pressure drop in the artesian water horizon did not cause any additional settlements.

Different conditions appeared in Children's Hospital. The piles were driven into silty sand. The middle row of the piles was loaded over the yield limit. Due to this fact a large web of cracks developed in this building during its construction. After the completion of construction works these cracks were covered and forgotten. However, after the water table lowering these cracks reappeared and caused panic among the staff of the hospital, the children of the hospital were immediately evacuated. The immediately started geotechnical survey established that there were very little additional settlements (during the survey these never exceeded 2 to 6 mm).

The onset of cracks due to a drop in pressure has proved that those initial cracks must have been already there beforehand. At first, the cracks appear quite intensively, however, these are generally not dangerous and do not interfere with the normal exploitation of the building, except in the cases when the buildings have had dangerous cracks before the water lowering process. If this is the case, the building needs additional reinforcements, because the drop in pressure can cause the structure to collapse.

Additional cracks can also appear between two building blocks that are loaded differently, especially if the heavier blocks are loaded above the p_c level and the intensity of settlements rises abruptly. Fortunately these circumstances never appeared during this project. However, in the future these facts must be kept in mind.

Considering all the aspects discussed above, one can say that the technology chosen was the correct one. The problem with using this kind of technology is associated with the need for reinforcements in existing buildings and some renovation works; the expenses were small. The other option would have been to freeze the soil. It would have resulted in a somewhat lesser settlement caused by excavations and a reduction in the water pressure. These effects however would not be too significant.

7 BUILDINGS ON SHALLOW FOUNDATIONS

In the line of the excavations in question the buildings founded on shallow foundations received the settlement of 10 to 25 mm (depending on their weight). It is distinctive for this particular area that the settlements caused by consolidation cease within 2 to 3 years and the creep continues. Before the water lowering began, most of the older buildings had had settlements of 0,5 to 0,8 mm. Buildings on pile foundations had settlements of 2 to 4 cm (piles in sand layer) and 4 to 6 cm (piles in silty sand layer). The settlements had ceased before the water lowering process began.

The further behaviour of buildings was determined by their loading history.

A 3 to 5 storey building on shallow foundations had the additional settlements of 2 to 3 cm. The settlements in question were equable and no new cracks appeared, only some old ones reopened.

One-storey buildings developed further settlements of 3 to 4 cm, however no new cracks appeared either. The ground surface settlements were in the same magnitude. The sewage wells of the systems developed somewhat greater settlements of 4 to 6 cm.

The buildings that were founded on piles inserted into sand layers did not settle. However, the buildings with pile foundations which were inserted into silt settled 1 to 2 cm. The cellar floors behaved in a similar manner for both pile foundations, which received settlements of 4 to 6 cm. On the whole, the technology used induced settlements, but these were not dangerous and only reopened over existing cracks.

The geotechnical investigations conducted 25 years later revealed that the lowering of the water table had not permanently affected the properties of clay layers. However, a very substantial

effect was discovered in silty layers. The values of q_c had increased from 1 to 2 MPa up to 6 to 8 MPa. The water content had lowered by 3 to 6% and the bearing capacity of the pile tip had grown 3 times.

8 CONCLUSIONS ON DIFFERENT SEGMENTS OF THE TUNNEL LINE

8.1 *First segment*

The line segment ran along the streets where the private residences were dominant. The ditches to drain rain water had been dug to both sides of the street, between the streets and the residences. Since the thickness of the fluvioglacial sand layer was only 0,1 to 0,6 m, it was decided that no water lowering was to be used. Thus, the excavation works were carried out by using caisson technology. It proved to be successful, because no new cracks opened on private residences that were located in a 12 m radius from the tunnel axis. An exception was a terrace house situated 10 m from the tunnel axis that settled 3 to 10 cm and also developed some cracks. No other damage was registered on this line segment.

Considerably greater settlements occurred directly on the tunnel line. During the excavation works the area between the two drainage ditches settled 15 to 20 cm. After the completion of the excavation works, it settled another 10 cm in the course of 6 years.

On this segment a test polygon was established. Its aim was to register stresses accompanied with the excavation of the tunnel. The measuring station was situated 130 m from the tunnel front and ended at the excavation front. Pore water pressure and dead weight pressure were examined in the given depths. The pressure cells were installed into 4,3 m depth in the clay layer which lay above the tunnel ceiling. The next cell was installed in the depth of 6,0 m into silty layers that lay little above the tunnel base. The last cell was installed in the depth of 9,0 m, just under the base of the tunnel.

The pore pressure above the tunnel did not show any change during the excavation. In the depth of 6,0 m, a drop in pore pressure was registered. Probably the tunnel started to work as a drain. On the other hand, a slight rise in pore pressure was registered in a cell located 9,0 m deep.

8.2 *Second segment*

A situation concerning total stress is more complex. After the installation the cells showed that stabilisation had taken place. This was the case until the excavation works started. The beginning of excavation works is described in cells situated in the depth of 4,3 and 9,0 m with a sudden rise in pore pressure. The cell that was located 6.0 m deep did not react to the onset of the excavation works. This rise continued until the excavation shield was located 80 m from the cells. From this point forward, a slow decline in the total stress was registered. After the shield passed the monitoring station, a slow rise in total stress was observed and it probably continued until it reached the initial value.

The behaviour of the pore water pressure is understandable because all the changes appeared when the excavation shield passed the monitoring station. It is difficult to understand, however, why total stress grew in the course of the penetration of the excavation shield into the soil and then decrease until the shield reached the monitoring station. These measurements also do not explain the settlements under the streets.

8.3 *Third segment*

In the third section the thickness of fluvio-glacial sands and water pressure increased. Since the water conductivity of fluvio-glacial sand in this region is quite big, the cryogenic method was tested. Boreholes with the cap of 0,8 m were established and they reached 4 m into the fluvio-glacial sands. During the excavations, ground settlements were rare but after the melting, the ground settling continued and reached 35 cm in 12 years. The cryogenic method was also preferred because the constructed tunnel had to be connected with other collectors in the city.

One existing water pipe broke due to freezing and caused an outwash of soil and a settlement of 20 cm. Another problematic factor was the loss of strength in clay and silty sand layers after the melting. The decrease was 30 to 45%. To date, it is 85% from the initial strength. Due to loss in strength on one gathering shaft, a breakdown occurred during the construction works.

REFERENCES

Lill, H. 1988. Merimetsa tunnelkollektorist. *IX Eesti Geotehnika konverentsi teesid.* Tallinn, pp. 84–85 (in Estonian).

Mets, M., Saapar, L. 1988 Tunneli rajamisega kaasnevad geotehnilised nähtused. *IX Eesti Geotehnika konverentsi teesid.* Tallinn, pp. 86–87 (in Estonian).

Mets, M., Saapar, L. 1989. Tallinna Merimetsa tunnelkollektori geotehnikaprobleemid. *Ehitus ja Arhitektuur vol. 1*. Tallinn, pp. 56–61 (in Estonian).

Riet, K., Eller, E., Sedman, A., Podshibjakin, I. 1991. Tunnelkollektorite ehitusgeoloogiauuringute kogemusi. *Eesti geoloogiline ehitus ja maavarad: sümpoosiumi materjalid.* Tallinn, pp. 89–91 (in Estonian).

Geotechnical Aspects of Underground Construction in Soft Ground – Viggiani (ed)

Soft ground tunneling in urban areas—proximity effects

J.F. Chang, H.C. Chao & Z.C. Moh
MAA Group Consulting Engineers, Taipei, Taiwan

ABSTRACT: Transportation and lifelines play a crucial role in maintaining living functions of people in/around urban areas. Due to progressive development of major cities, bored tunneling has become one of the commonly adopted methods for constructing transportation and lifeline facilities. As ground deformation would inevitably be induced by tunneling, buildings or structures in the close proximity are subject to various levels of risk to damage. The soil/groundwater conditions as well as their interaction with tunnels and substructures have further made the situation of each case unique and full of challenges. This paper discusses 4 cases in the Taipei Rapid Transit System (TRTS) projects, where tunnels were bored in close proximity to or even in conflict with existing substructures and/or substructures to be constructed in the future. In addition to a review of possible consequence caused by the construction, numerical simulations are introduced to characterize important features and obtain insights of the problems. Engineering judgment and decision-making process to the ground deformation control and protection strategies are further presented for resolution of each case.

1 INTRODUCTION

With growing economical activities and transportation needs in the city, Taipei, the capital of Taiwan, has been developing its metro system for the past 25 years. As tabulated in Table 1, the Stage I Taipei Rapid Transit System (TRTS), with about 93-km routes and 82 stations, was completed and set out for revenue services in July 2009 (while the first line started the operation in March 1996). For the Stage II, which is currently under construction and is scheduled to be completed by 2018, additional 87-km routes and 76 stations would be added to the system. By the completion of the TRTS network in the Stage III, a total of 7 major lines with over 270-km routes and 250 stations will spread over the Taipei Metropolis (Fig. 1).

There are over 50% of total routes constructed by using the shield tunneling method. Due to limited spaces available in urban areas, tunnels are often bored in close proximity or even in conflict with existing substructures. Sometimes, there will be structures to be constructed in the proximity of tunnels in the future and provisions have to be made for protecting the tunnels. The so-called proximity effects have thus become a challenge to the TRTS projects. This paper discusses 4 cases in the Stage II construction of TRTS, including one with tunnels that are in close proximity to each other, one with tunnels in conflict with existing piled raft foundation, one with tunnels passing underneath existing tunnels, and one with tunnels affected by the constructions of adjacent pile foundations.

2 GEOLOGICAL CONDITIONS OF TAIPEI BASIN

The Taipei City is situated in a basin (the so-called Taipei Basin), which is surrounded by mountains, hills, and terraces (Fig. 2). Through a series of fluvial, lacustrine, estuarine, and brackish-water sedimentation process (*e.g.* Lin 1957), a sandy-clayey-interbedded stratum was formed at the surface. The interbedded Holocene deposit at surface is called the Sungshan Formation, and the underlain late Pleistocene gravel deposit is called the Chingmei Gravels.

Based on the data collected in decades, a geotechnical zoning map has been developed for Taipei City (MAA 1987) as shown in Figure 3. The zoning is mainly based on the distribution of sediments from the Hsintien, Tamshui, and Keelung Rivers. Figure 4 depicts typical soil profiles across the Taipei Basin. The ground surface is primarily within 10 m above the MSL (*i.e.* mean sea level). The Sungshan Formation consists of six sublayers (Hung 1966, Moh & Ou 1979) with total thicknesses varying from 40 m to 70 m, named sublayer I to IV from the bottom to the top. The underlying Chingmei Gravels is as thick as 140 m (Fu *et al.* 1990).

As can be noted from Figure 4, the six-sublayer sequence is evident in the central areas of the basin, where the Taipei Main Station of the TRTS is located. The silty clay sublayers (*i.e.* sublayer II, IV and VI) become dominant toward the north and the east of the basin. The interbedded sequence becomes complex toward the west of the

Table 1. Stations and routes planned in TRTS.

Stage	Station/Route length (km) Elevated	At grade	Under-ground	Total	Operation date
I	33/33.52	6/9.5	43/48.2	82/92.9	2009.07.
II	25/28.4	0/0	51/58.7	76/87.1	2018.12.
III	25/30.7	27/22.6	41/45.0	93/98.3	N.A.
Total	83/94.3	33/32.1	135/151.9	251/278.3	N.A.

Data obtained from TRTS (2010); N.A.: Not available.

Figure 1. Long-term route map for TRTS (after TRTS 2010).

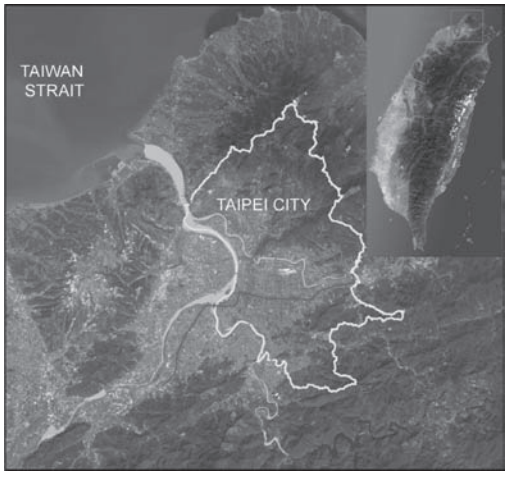

Figure 2. Satellite image of Taipei City (Copyright (c) CSRSR/CNES. 2004. Courtesy CSRSR, NCU).

Figure 3. Geotechnical zoning of Taipei Basin with first stage network of TRTS (after Chin *et al.* 2006).

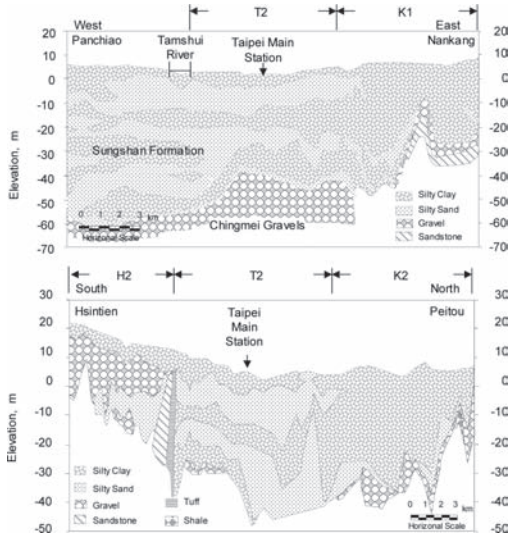

Figure 4. Typical stratification of Taipei Basin (after Chin *et al.* 1994).

basin. On the south side, gravels are even discovered in the sublayer V, where silty sand is present. Figures 5 and 6, respectively, illustrate typical CPT and soil strength profiles for the Sungshan Formation (Moh *et al.* 1999), and the engineering properties of the subsoils can be referred to Moh & Ou (1979).

With a maximum grain size of about 600 mm, the Chingmei Gravels is very permeable and rich in water-bearing. It used to be a primary source of

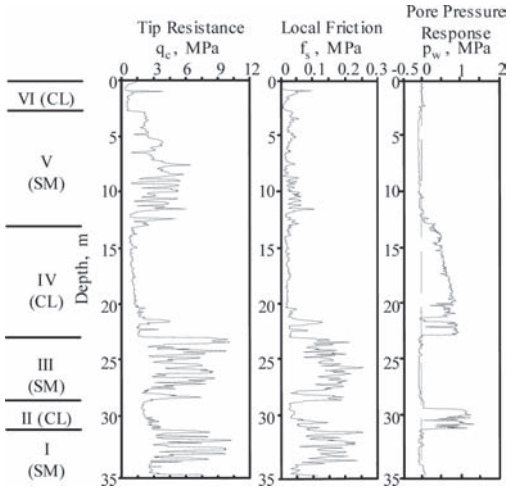

Figure 5. Typical CPT profile obtained in Taipei Basin (Moh *et al.* 1999).

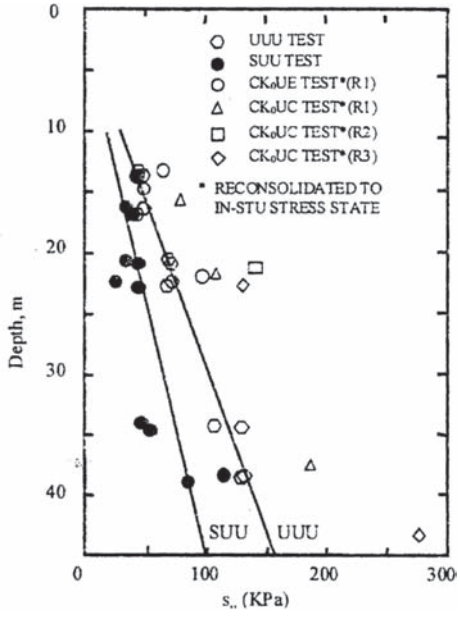

Figure 6. Distribution of undrained shear strength with depth in Taipei Basin (Moh *et al.* 1999).

water supply for people in the city. Figure 7 shows the variation of hydraulic pressure distribution with depth in the past 30 years. Excessive pumping from this gravel layer had led to significant drawdown of hydraulic pressures before 1970s. Pumping has been banned since 1968, and the water pressures in the Chingmei Gravels gradually recovered. According to the measurements taken in 2004,

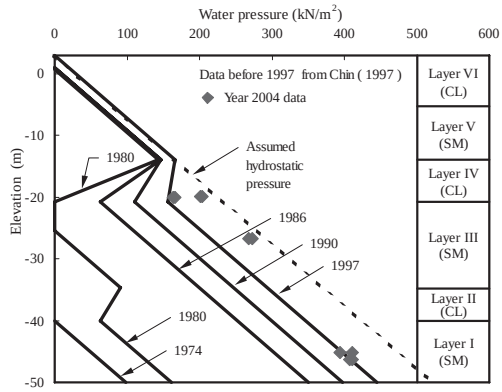

Figure 7. Distribution of hydraulic pressure with depth in Taipei Basin (after Chin *et al.* 2006).

the hydraulic drawdown was reduced to less than 100 kPa compared to the hydrostatic pressures. At present, about 10 kPa to 20 kPa of drawdown could be expected. The rising hydraulic pressure in the Chingmei Gravels has been reported as the main reason leading to critical tunnel failures in TRTS constructions (Ju *et al.* 1998, Hwang *et al.* 1998, Lin *et al.* 1997).

3 PROXIMITY EFFECTS OF TUNNELING

In general, the effects of driving a tunnel can be ignored if the clearance between the tunnel and the existing structures is larger than one diameter of the tunnel. However, with more and more routes constructed in the city, it becomes much more frequent to have situations where tunneling is to be carried out with smaller clearances. In some cases, tunnels to be constructed will encounter existing substructures and in some cases substructures are to be constructed in the proximity of existing tunnels. This section presents 4 such cases and explains how the problems were resolved.

3.1 *Case I—two tunnels in close proximity*

The Songshan Line is part of the Green Line in the Stage II construction of TRTS and is 8.5-km in length with 9 underground stations. Lot CG291 (Fig. 8) is one of the 3 construction lots in the Design Lot DG166 of the Songshan Line. The twin tunnels in this construction lot start from the north end of Beimen Station (G14) and end at Zhongshan Station (G16) with a total length of about 930 m.

An extensive study has been conducted to investigate the feasibility of constructing a station,

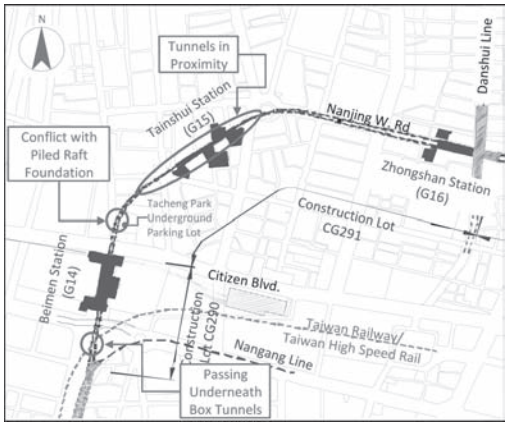

Figure 8. Scope of work for Lots CG290 and CG291.

Tienshui Station (G15), in the middle of the section. The station was finally cancelled because of the site constraints and the prohibitive cost of construction. The study is, however, of great interest because much has been learned on the interaction effects between the two tunnels.

3.1.1 *Lining design*

The limited space allowable at the mid-section of the route can only accommodate a narrow station with platforms at different levels. Therefore, the two tunnels have to switch from a parallel configuration at the G14 Station to a stacked position at the G15 and return to a parallel configuration at the G16. For a length of more than 350 m, the clearances between the two tunnels are smaller than 3 m with a minimum of 1.9 m (Fig. 9).

Figure 10 depicts the configuration of the precast reinforced concrete lining segments generally adopted for TRTS. The reinforced concrete rings are 6.1 m in outer diameter, 250 mm in thickness, and 1 m in length. Each ring consists of 6 segments. These segments are interlocked by curved galvanized bolts in the both radial and longitudinal directions. To prevent the presence of weakness along the connections of the rings and to increase the longitudinal rigidity of the tunnel lining, Type K segments are bolted with their adjacent counterparts by a certain degree of rotation (Fig. 10b).

The beam-spring model is most commonly adopted in the lining design as it can provide better simulations of joints that exhibit reduced bending rigidity on the circumference and longitudinal connections. Figure 11 shows the double-ring model where the segments are modeled as curved beam-frame elements. Figure 12 shows the loading combination adopted in the design.

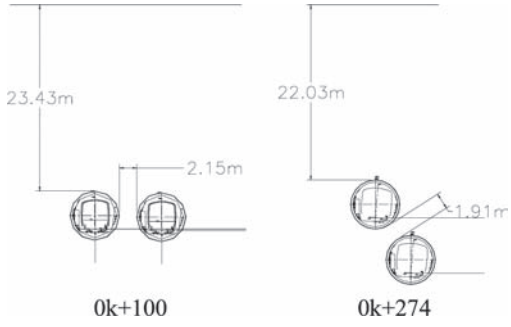

Figure 9. Twin tunnels in close proximity (after Kang *et al.* 2007).

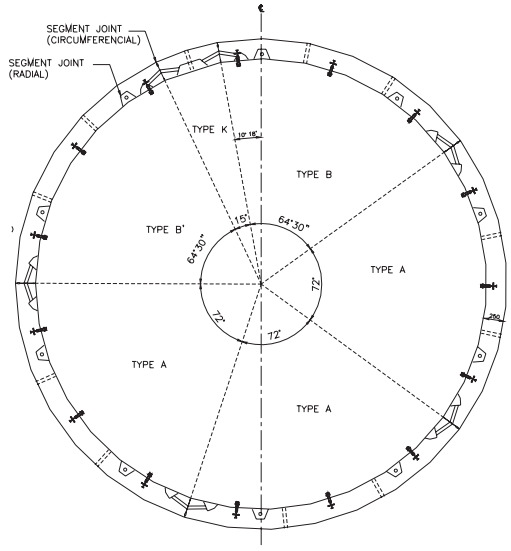

(a) Cross-section

(b) Segment arrangement

Figure 10. Typical layout of precast concrete lining segments for TRTS (after Kang *et al.* 2007).

3.1.2 *Analyses for proximity effects*

To investigate the effects of driving the second tunnel on the lining of the preceding tunnel, a series of 2-dimensional (2-D) numerical analyses were

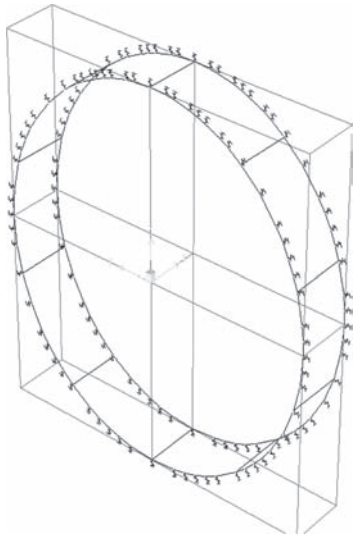

Figure 11. Double-ring model for lining design (Kang *et al.* 2007).

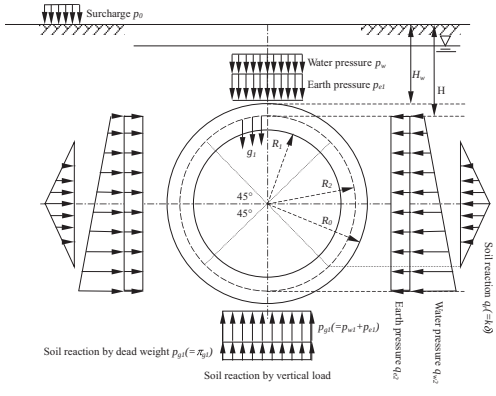

Figure 12. Design loads for lining design (Kang *et al.* 2007).

conducted using the computer program FLAC (ITASCA 2000) for various clearances between the two tunnels and various covers above these tunnels. Figure 13 shows the finite element mesh adopted for the purpose. The forces (in terms of stresses in elements) acting on top and on the both sides of the preceding tunnel induced by the driving of the second tunnel were computed. These forces would then be used to compute the stresses and the bending moments induced in the lining of the preceding tunnel.

A Mohr-Coulomb model with non-associated plastic flow rule was adopted to simulate soil behavior. The effects of construction and workmanship,

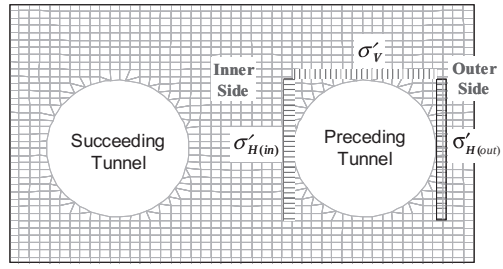

Figure 13. Numerical model for twin tunnel analysis (Kang *et al.* 2007).

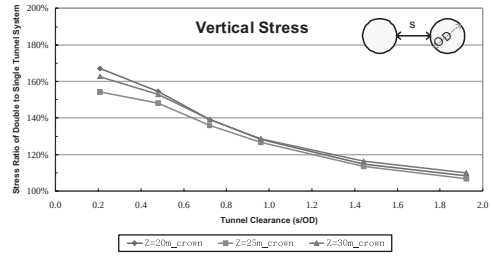

Figure 14. Variation of vertical stress along with tunnel clearance (after Kang *et al.* 2007).

such as delay of tail grouting (causing soil relaxation), excavation (inducing soil disturbance), and driving forces (increasing soil stress), are simulated by introducing the gap parameter suggested by Lee *et al.* (1992).

3.1.3 *Results of analyses*

As can be noted from Figure 14, the vertical stresses acting on top of the preceding tunnel increase as the clearance between the two tunnels decreases. This finding is in a reasonable agreement with the values suggested by JRCEA (1977), as tabulated in Table 2.

Figure 15 shows the corresponding lateral stresses on the two sides of the preceding tunnel. For the stresses on the outer side, a similar trend with those shown in Figure 14 is obtained. The values are however smaller. On the other hand, the induced stresses on the inner side are greater than the corresponding vertical stresses given in Figure 14 when the clearance between the two tunnels is larger than 0.8 times the tunnel diameter. A significant drop of stress is observed when the clearance is smaller than 0.8 times the diameter of the tunnel. Further, a significant difference (about 20%) of stress is observed between the two sides of the preceding tunnel when the clearance is about 0.2 times the tunnel diameter.

Table 2. Coefficient of additional vertical surcharge caused by proximity effects (after JRCEA 1977).

Clearance/Tunnel outer diameter (s/OD)	Additional surcharge/ Vertical earth stress
s/OD > 1.0	0
1.0 ≧ s/OD > 0.9	0.1
1.09 ≧ s/OD > 0.8	0.2
0.8 ≧ s/OD > 0.7	0.3
0.7 ≧ s/OD > 0.6	0.4
0.6 ≧ s/OD > 0.5	0.5

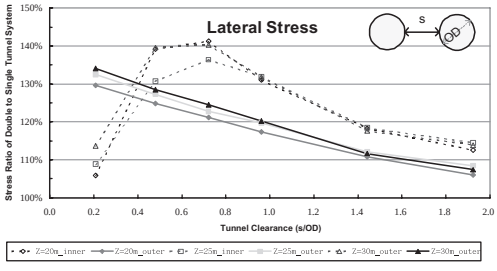

Figure 15. Variation of lateral stress along with tunnel clearance (after Kang *et al.* 2007).

Table 3. Comparison of response of lining with/without proximity effect (after Kang et al. 2007).

Design condition	Bending moment (kN-m)	Axial force (kN)
Single Tunnel	206	2,630
Twin Tunnels (s = 0.3OD)	352	3,335

With the stress distribution derived from the interaction analyses, the software SAP2000 (CSI 2008) is applied to obtain the resulting bending moments and stresses on the lining of the preceding tunnel. Table 3 shows the results obtained for a clearance of 1.9 m (about 0.3 times the tunnel diameter) between the two tunnels. The bending moment and axial force increase about 70% and 30%, respectively, as compared to those induced without the interaction effects.

The results of the analyses will suggest the following:

– Spherical graphite cast iron segments (*i.e.* ductile segments), rather than steel ones or precast concrete ones with increased thickness, are necessary for the preceding tunnel lining segments for the section of route with clearances less than 0.5 times diameter between the two tunnels. The ductile segments will be 250 mm thick and 1.25 m long. Each ring will consist of six segments with equal size, as shown in Figure 16.
– To reduce driving force effects on the preceding tunnel, it should be propped by steel frames for the section of the route with clearances less than one diameter between the two tunnels during the driving of the succeeding tunnel.
– To reduce disturbance to surrounding soils and stress relaxation induced by the driving of the succeeding tunnel, low-pressure grouting should be adopted to improve the soils around the two tunnels.

3.2 *Case II—tunnels in conflict with existing foundations*

In the same construction lot as in Case I, this case shows that the twin tunnels will pass underneath an underground parking lot at Tacheng Park (Fig. 8). As depicted in Figure 17, there are a total of 37 bored piles of 1.5 m in diameter and 42.3 m in length installed on the bottom of the raft foundation to increase its capacity against uplift forces. Six of them are in conflict with the up-track tunnel at depths of about 25 m to 27 m where sublayer III (a permeable, sandy silt to silty sand layer) of the Sungshan Formation is present, as shown in Figure 18.

Since the shield machine is incapable of cutting through reinforced concrete piles with such a large size, the piles in conflict have to be removed before tunneling. To maintain the safety of the

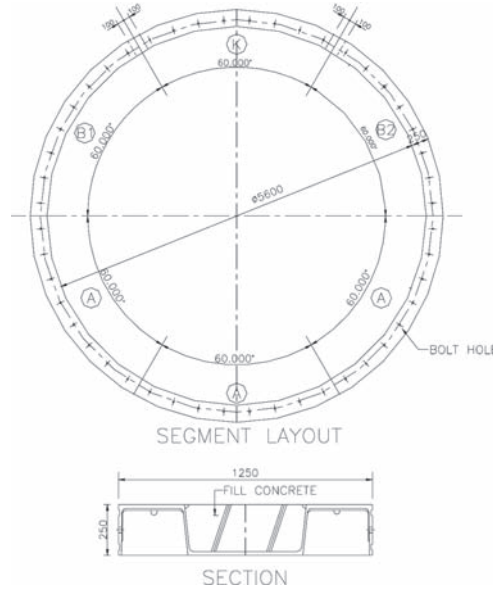

Figure 16. Typical layout of cast iron lining segments (after Kang *et al.* 2007).

Figure 17. Plan view of underground parking lot and conflicted tunnels.

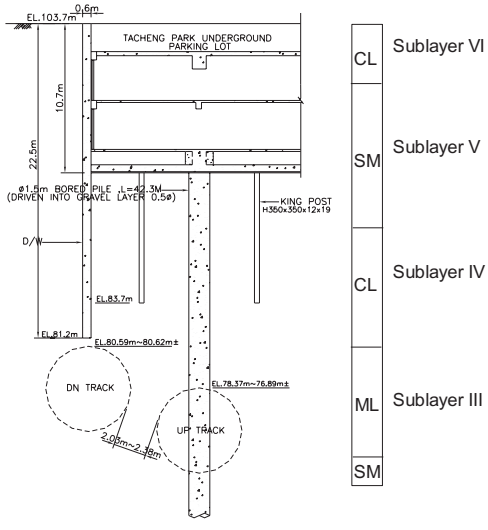

Figure 18. Schematic of bored piles in conflict with tunnels.

existing structure and to allow workers to walk out of the shield machine to remove the sections of piles in conflict with the tunnel, it is necessary to apply ground improvement around the piles with the use of compressed-air as a contingency measure. Figure 19 depicts pile sections to be removed and the range of ground improvement, and Figure 20 shows the procedures to be adopted.

3.2.1 *Analyses for proximity effects*

Analyses were carried out by using the software SAP2000 for computing the stress redistribution

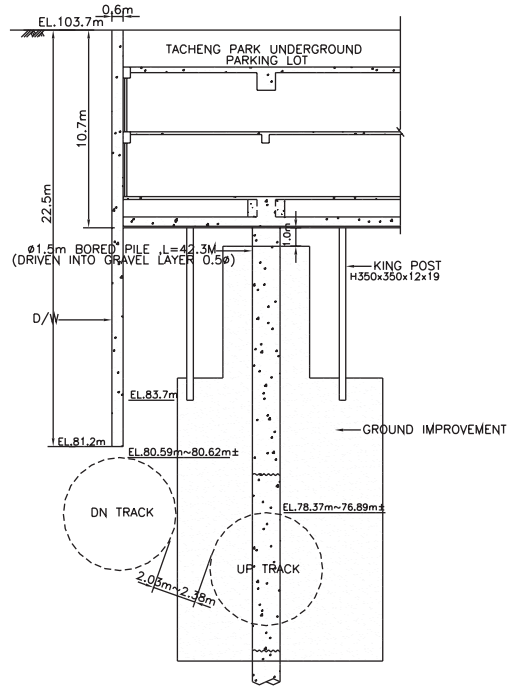

Figure 19. Schematic of ground improvement range for pile removal.

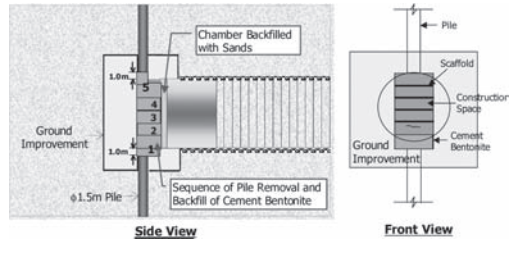

Figure 20. Procedures of pile removal ahead of shield machine.

and resulting settlements in the structure of the parking lot. Figure 21 shows the finite element models adopted for analyzing the interaction effects between the tunnel, piled raft foundation and the substructure of the parking lot. Soils were modeled as nonlinear springs whereas raft, grade beams, and piles were modeled as a series of plate or beam elements.

3.2.2 *Results of analyses*

The results indicate that the remaining piles could provide sufficient bearing capacity against the redistributed stress. The resulting differential settlement between nodes of the pile head and the

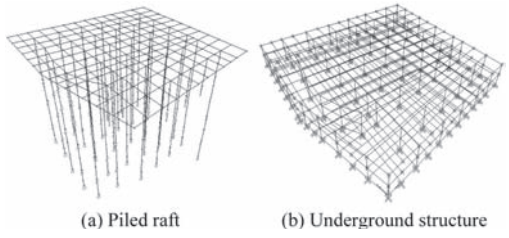

Figure 21. Numerical models for underground parking lot in conflict with tunnels (after Kao *et al.* 2007).

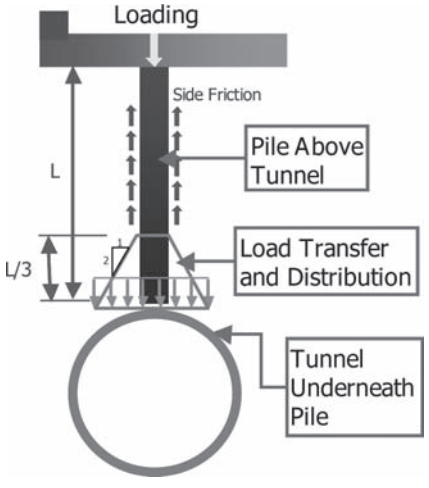

Figure 22. Sketch of load transfer of piles to tunnel passing underneath.

surrounding raft is in a range between 1.8 mm and 2.8 mm. As to the substructure of the parking lot, the additional stresses induced by pile removal are found to concentrate in the grade beams. The induced stresses in the rest of the structural components are negligible. Although additional bending moments are induced in the grade beams as a result of pile settlements, results show that they still meet design requirements.

The additional loading transferred from the piles that are to be removed is incorporated in the lining design. Figure 22 illustrates the load transfer of piles to the crown of the tunnel. The results of analysis show that the bending moment in the lining increases by about 60% (Kao *et al.* 2007) and, thus, the cast iron segments adopted in Case I are also suggested for the case.

3.3 *Case III—tunneling underneath existing box tunnels*

The case is in Construction Lot CG290, which includes the construction of the G14 Station and the twin tunnels to the south of the station (Fig. 8). Figure 23 depicts the 3-D presentation of the case, in which the two tunnels will pass the existing box tunnels for Taiwan Railway and Taiwan High Speed Rail. It is thus crucial to maintain the safety of the railway operation during tunneling.

3.3.1 *Analyses for proximity effects*

Preliminary 2D analyses were first carried out for the presumed most critical cross-section using PLAXIS (PLAXIS 2002), as shown in Figure 24a. Soils were modeled by Mohr-Coulomb criteria under a plane strain condition.

To further refine the analyses and verify the validity of the 2-D simplification, a series of 3-D numerical analyses were performed using ABAQUS (ABAQUS 2004). The 3-D structural mesh adopted is illustrated in Figure 25.

3.3.2 *Results of analyses*

From the 2-D analyses, Figure 24b presents the computed vertical displacement of the box tunnel slab on the basis of two ground loss ratios. The maximum deformation for the ground loss ratio of 2% (24.4 mm) is almost three times larger in magnitude than that for the ratio of 1% (8.4 mm). It implies the importance of tunneling control to prevent from excessive ground loss.

From the 3-D analyses, on the other hand, Figure 26 shows the vertical displacement of the twin-box tunnels induced by the driving of the metro tunnels. Unlike the results in the 2-D analyses, the variation of deformation along the longitudinal axis of the box tunnels can be numerically evaluated. The maximum deformation is on the order of 8 mm. A favorable agreement was obtained for the trend of the structure response between the

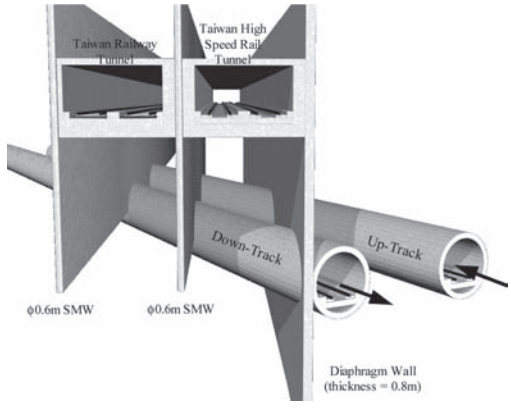

Figure 23. 3-D presentation of twin tunnels passing underneath existing box tunnels.

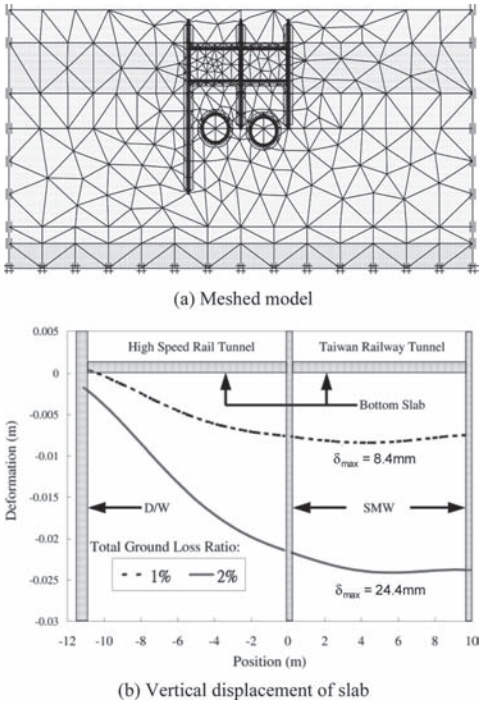

Figure 24. 2-D simulation on tunnel excavation (after Chao *et al.* 2005).

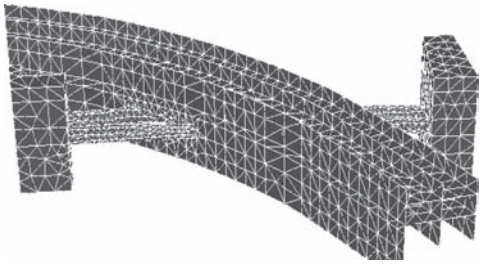

Figure 25. 3-D meshed model for case III (Chao *et al.* 2005).

2-D and 3-D analyses. Since the induced differential settlement in the slab is below the tolerance, it is then suggested a quality construction control and monitoring system for the safety of the railway operation.

3.4 *Case IV—pile effects on existing tunnels*

The case is in the Phase I construction of the Circular Line, which is an elevated line of approximately 15.4-km in length with 14 stations. In Design Lot DF113, the viaduct is to cross the existing underground Banqiao-Nangang Line of TRTS on Wenhua Road of Banqiao City. Figure 27 shows the alignment of the viaduct and a typical configuration of the tunnels and the piles supporting the piers of the viaduct.

There will be 21 piers (*i.e.* P15–8~P15–28) to be installed in the spaces between the up- and down-track tunnels of the Banqiao-Nangang Line that is currently in services. The covers above the tunnels vary from 11.0 m to 21.2 m, with an average of 16.0 m. The clearances between the two tunnels vary from 7.0 m to 9.3 m (about 1.1 to 1.5 times tunnel diameter). Piles of 1.2 m in diameter are to be installed to support these piers. Since the gaps between piles and tunnels are as small as 1.5 m or even less at places, piles are constructed using the casing method.

3.4.1 *Analyses for proximity effects*

A series of 3-D analyses were carried out by using Midas/GTS (Midas/GTS 2009). The finite element model covers a region of 120 m*120 m*70 m, as shown in Figure 28. Simulation was conducted for five major procedures, including initial stress state, tunnel construction, pile construction, cap construction, and loading of superstructure. The lining and casings were modeled by plate elements with elastic modes whereas the soil mass comprised of a series of 4-node-tetrahedron, solid elements with the Mohr-Coulomb soil model.

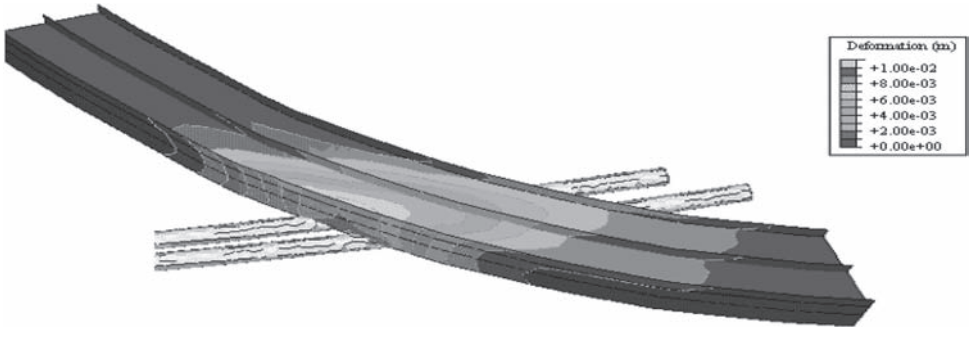

Figure 26. Vertical displacement of box tunnels induced by tunneling passing underneath (after Chao *et al.* 2005).

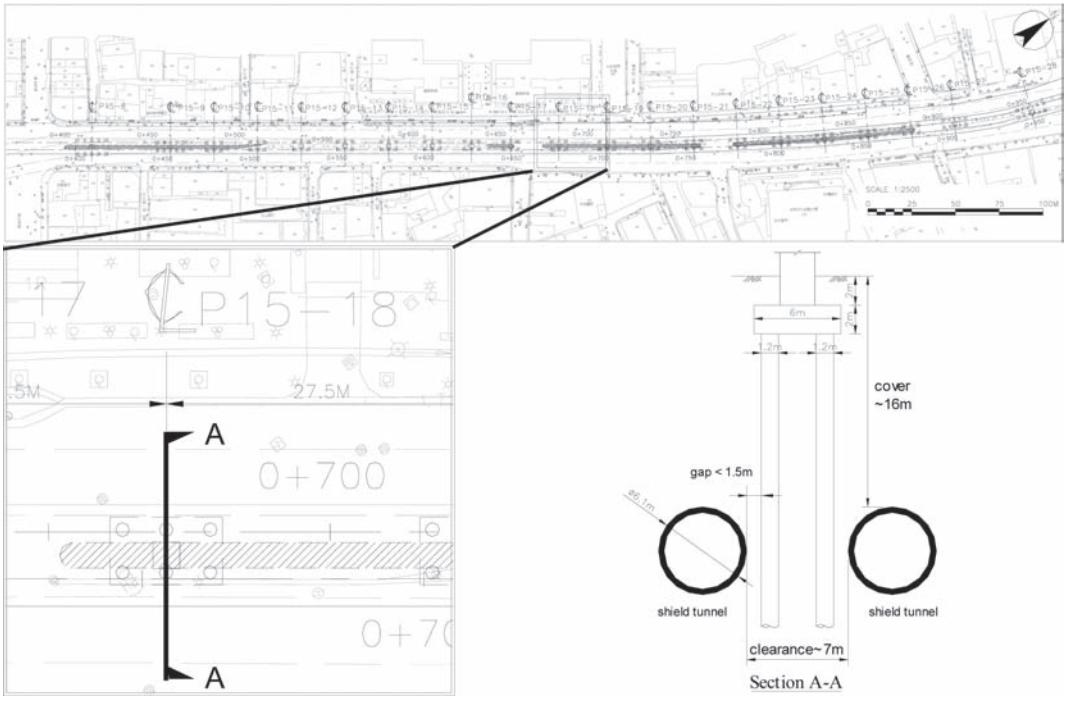

Figure 27. Schematic of plan view and typical cross-section of case study (Chang *et al.* 2010).

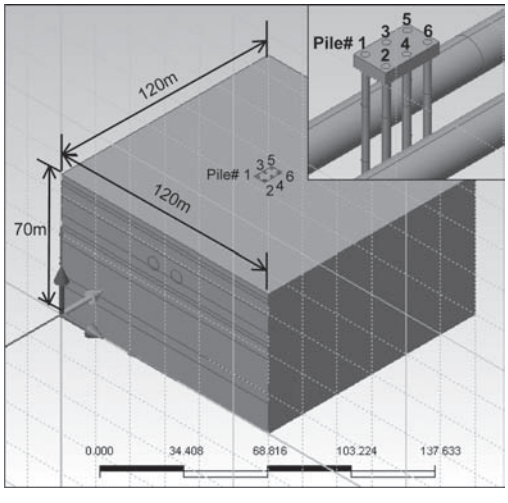

Figure 28. 3-D geometric model for case study (Chang *et al.* 2010).

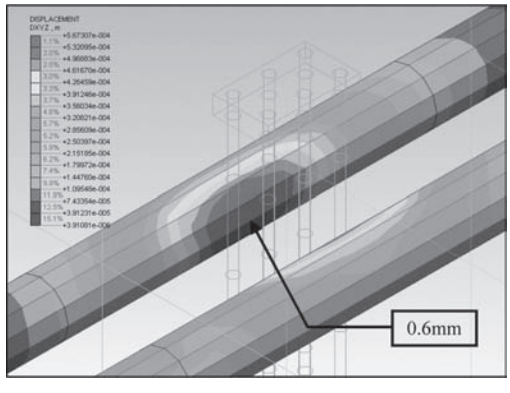

Figure 29. Computed tunnel deformation induced by pile construction (Chang *et al.* 2010).

3.4.2 *Results of analyses*

Figure 29 presents tunnel deformations induced by pile construction. The maximum deformation is about 0.6 mm after all the 6 piles are installed. Figure 30, on the other hand, shows the deformations of tunnels induced by loading on the viaducts. As can be noted, the maximum occurs in the upper quadrant of the tunnel near the piles. Compared to pile construction effects, tunnel deformation induced by pier loading is remarkably larger. The maximum deformation is as large as 2.4 mm. Figure 31 shows the distribution of maximum vertical displacement on the bottom of the tunnel along with the construction steps.

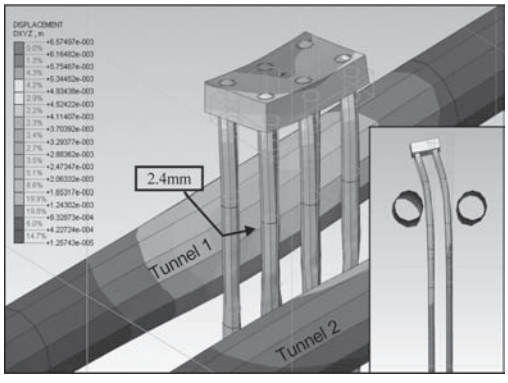

Figure 30. Computed tunnel deformation induced by pier loading (Chang *et al*. 2010).

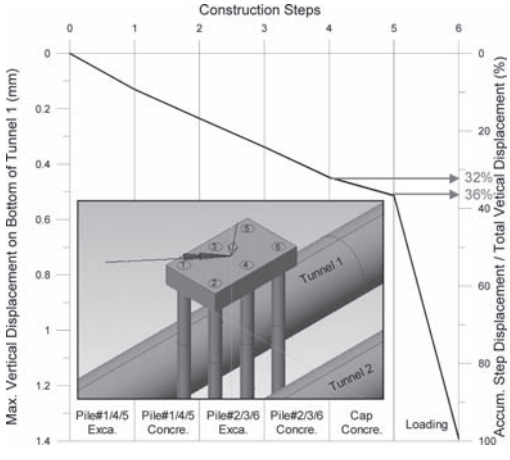

Figure 31. Variation of computed maximum vertical displacement on bottom of Tunnel 1 with construction steps (after Chang *et al.* 2010).

With covers above the tunnels varying from 11.0 m to 21.2 m (about 1.8 to 3.5 times tunnel diameter) and clearances between tunnels varying from 7.0 m to 9.3 m (about 1.1 to 1.5 times tunnel diameter), Figure 32 sketches the resulting distribution of maximum tunnel deformation. As can be noted, the deformations of the tunnels decrease about 40% as the covers above the tunnels increase from 1.8 to 3.5 times tunnel diameter. The deformations of the tunnels decrease about 8% as the clearances between the two tunnels increase from 1.1 to 1.5 tunnel diameter. From the results, the induced deformation remains on the safe side required by DORTS (2002). Therefore, cautious construction control and monitoring system is suggested to minimize the effects of piling and loading on the tunnels.

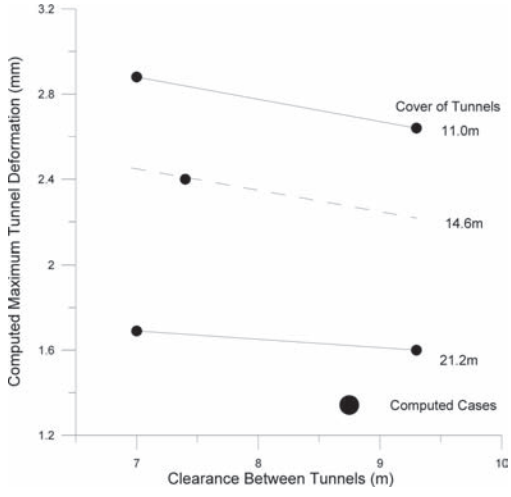

Figure 32. Schematic of maximum tunnel deformation distribution with various covers and clearances of tunnels (after Chang *et al.* 2010).

4 CONCLUSIONS

Proximity effects has become an important issue for soft ground tunneling in urban areas. It involves complex interaction between soil, tunnels, and substructures and, hence, application of more sophisticated geometric (3-D) and soil models (nonlinear or elasto-plastic models) would become popular in the practice. A proper numerical modeling requires in-depth understanding of soil mechanics, construction sequence, and theory underlying the algorithm. A well organized monitoring system that provides invaluable feedback data for the design and engineering judgment should always be emphasized.

ACKNOWLEDGEMENTS

Permission for publishing this paper from Moh and Associates, Inc. and Department of Taipei Rapid Transit System of Taipei City Government is gratefully appreciated. Special thanks to Dr. R.N. Hwang and Mr. T.C. Su who help prepare the manuscript.

REFERENCES

ABAQUS. 2004. *ABAQUS/CAE User's Manual*, Version 6.5, ABAQUS, Inc.

Chang, J.F., Hu, I.C., Su, T.C. & Chao, H.C. 2010. 3D modeling of pile construction and loading effects on adjacent shield tunnels - a case study. *Proc. of the*

17th Southeast Asian Geotechnical Conference, Taipei, Taiwan, 10–13 May, 483–486.

Chao, H.C., Hsieh, Y.M., Ju, D.H. & Chuang, C.H. 2005. 2-D and 3-D numerical analyses of tunneling. *Proc. of the 2nd World Forum of Chinese Scholars in Geotechnical Engineering, Nanjing, China*.

Chin, C.T. 1997. Groundwater control during the construction of Taipei MRT. *Proc. of the 14th Int'l. Conference on Soil Mechanics and Foundation Engineering. Hamburg, Germany, 6–12 September*, 2343–2346.

Chin, C.T., Crooks, A.J.H. & Moh, Z.C. 1994. Geotechnical properties of the cohesive Sungshan deposits, Taipei. *Geotechnical Engineering Journal*, 77–103.

Chin, C.T., Chen, J.R., Hu, I.C., Yao, D.T.C. & Chao, H.C. 2006. Engineering characteristics of Taipei Clay. *Proc. of the 2nd International Workshop on Characterisation and Engineering Properties of Natural Soils* 3: 1755–1803.

CSI. 2008. SAP 2000 *integrated software for structural analysis & design*, Version 12, Computer & Structures, Inc.

DORTS. 2002. *Taipei metropolitan rapid transit system – civil engineering design manual (CEDM),* Version 11, Department of Rapid Transit System, Taipei City Government. (in Chinese)

Fu, Y.J., Chin, C.T., Wang, Y.L. & Chen, M.S. 1990. The distribution of the gravel layer in the Taipei Basin. *Journal of the Civil and Hydraulic Engineering*, 16(4): 59–69. (in Chinese)

Hung, J.J. 1966. Physical properties of Quaternary sediments in Taipei Basin. *Bulletin of the College of Engineering*, National Taiwan University, 10: 1–24.

Hwang, R.N., Moh, Z.C., Yang, G.R., Fan, C.B., Chao, C.L. & Wong, R.K. 1998. Ground freezing for repairing a damaged tunnel. *Proc. of the 13th Southeast Asian Geotechnical Conference, Special Lecture, Taipei, Taiwan, 16–20 November*, 16–20.

ITASCA. 2000. *FLAC user's guide*, Ithasca Consulting Group, Inc.

JRCEA. 1977. *Guide of design and construction of shield tunnel,* Japanese Railway Civil Engineering Association. (in Japanese).

Ju, D.H., Duann, S.W. & Tsai, K.H.H. 1998. Ground freezing for restoration of damaged tunnel. *Proc. of the 13th Southeast Asian Geotechnical Conference, Taipei, Taiwan, 16–20 November*, 615–620.

Kang, S.M., Guo, J.H., Chua, H.Y., Whang, Y.H. & Kao, C.C. 2007. Design of the bored tunnel lining segments with close proximity effects for Songshan Line of Taipei MRT System. *Proc. of the 4th International Structural Engineering & Construction Conference (ISEC-4), Melbourne, Australia, 26–28 September*.

Kao, C.C., Kang, S.M., Lin, C.T., Su, T.C. & Whang, Y.H. 2007. Design consideration and evaluation of building protection on shield tunneling underneath piles of underground parking lot. *Proc. of the 4th Cross-Strait Conference on Structural and Geotechnical Engineering, Hangzhou, China, 24–26 April.* (in Chinese).

Lee, K.M., Rowe, R.K. & Lo, K.Y. 1992. Subsidence owing to tunneling I: estimation the gap parameter. *Canadian Geotechnical Journal* 29: 929–940.

Lin, C.C. 1957. The Taipei Basin. *Historical studies of Taiwan Province* 1: 303–314. (in Chinese).

Lin, L.S., Ju, D.H. & Hwang, R.H. 1997. A case study of piping failure associated with shield tunnelling, *Proc. of the 15th International No-Dig'97, Taipei, Taiwan, 26–28 November*, 6B-1-1~6B-1-13.

MAA. 1987. Engineering properties of the soil deposits in the Taipei Basin. *Report No. 85043*, Ret-Ser Engineering Agency and Taipei Public Works Department, Taipei. (in Chinese).

Midas/GTS. 2009. *Midas/GTS 03. Analysis*, MidasIT.

Moh, Z.C. & Ou, C.D. 1979. Engineering characteristics of Taipei silt. *Proc. of the 6th Asian Regional Conference on Soil Mechanics and Foundation Engineering, Singapore, July*, 1:155–158.

Moh, Z.C., Chang, J.L. & Hwang, R.N. 1999. Soft ground tunneling in Taipei—problems and solutions. *Proc. of Dr. Tan Swan Beng Memorial Sympos. Excellence in Infrastructure Engineering, Singapore, 18–19 March*, 87–97.

PLAXIS. 2002. *Plaxis 2D—version 8*, Plaxis b.v.

TRTS. 2010. *Department of Rapid Transit System Web Site*, http://www.dorts.gov.tw/.

Activities of TC204 working groups

This page intentionally left blank

Geotechnical Aspects of Underground Construction in Soft Ground – Viggiani (ed)
© 2012 Taylor & Francis Group, London, ISBN 978-0-415-68367-8

Urban tunnels in soft ground: Review of current design practice

Vinicius da Mota Wedekin
Bureau de Projetos e Consultoria Ltda, Sao Paulo, Brazil

Richard Kastner
Université de Lyon, INSA Lyon, LGCIE, France

Alain Guilloux
Terrasol, Paris, France

Adam Bezuijen
Delft Geotechnics, Delft, The Netherlands

Jamie Standing
Imperial College, London, UK

Arsenio Negro Jr.
Bureau de Projetos e Consultoria Ltda, Sao Paulo, Brazil

ABSTRACT: Current design practice for urban tunnel construction in soft ground as perceived worldwide is reviewed and discussed. The review is based on answers to a questionnaire prepared and sent out by a TC204 working group in 2010 to practitioners involved in the design or in the design supervision of tunnelling projects. The results of this investigation are carefully considered to identify trends and needs for development.

Keywords: urban tunnels, soils, design practice, survey.

1 INTRODUCTION

The first assessment of the design practice involving urban tunnels driven in soft ground (i.e. not rock) was carried out in 1993 through a survey performed in Brazil. The results from this were published in the 1st International Symposium on Underground Construction in Soft Ground in New Delhi by the former TC28 now TC204 (Negro and Leite, 1995).

In 2006 another Brazilian assessment was made, but this time cut-and-cover structures were not included and the review covered underground openings of any shape with more than 0.5 m diameter; directional drilling was not included. The survey was not limited to tunnels built in Brazil but covered any tunnel project conducted with criteria and procedures presently adopted in Brazil. Results from the second assessment were published in the TC28 Shanghai International Symposium (Negro, 2008). TC204 then created a working group to adapt this survey format to review the world design practice.

The present survey focuses on underground openings of any shape with more than 0.5 m diameter and covers tunnel projects conducted all around the world. In all cases tunnels were designed and built in areas with overlying surface buildings and subsurface utilities, both liable to damage induced by ground movements associated with tunnel excavation.

Multiple choice questions to which one or more answers could be selected were sent to professionals involved in the design or in the design supervision of tunnel projects over the past few years. Considering the multi-disciplinary nature of tunnel design, the questionnaire, with 46 questions, was sent to practitioners with a variety of expertise and included topics beyond a strict geotechnical context. Accordingly, questions were sent to geotechnical engineers, geologists, structural engineers and experts in numerical modelling.

These professionals could opt not to answer questions outside their fields of specialisation. In 51% of the cases the respondents were consultants working on tunnelling projects and 15% referred to

contractors (Figure 1). Note that TBM suppliers were not involved in this assessment.

Most questions asked for answers that would express the practitioners' current preference on each technical aspect of tunnel design, in such a way that they would reflect the respondents' routine design practice. The questionnaire was answered by 47 specialists in tunnel design from 15 different countries.

Figure 2 shows the distribution of respondents from around the world, revealing a significant concentration in Europe (41%) and an absence of the professionals from North America and Africa.

The results that follow are grouped according to related topics in a sequence that is not necessarily related to that of the questionnaire. One should note that respondents sometimes offered more than one answer to a question. Therefore, frequencies shown refer to the percentage of total answers offered or to the percentage of respondents as appropriate.

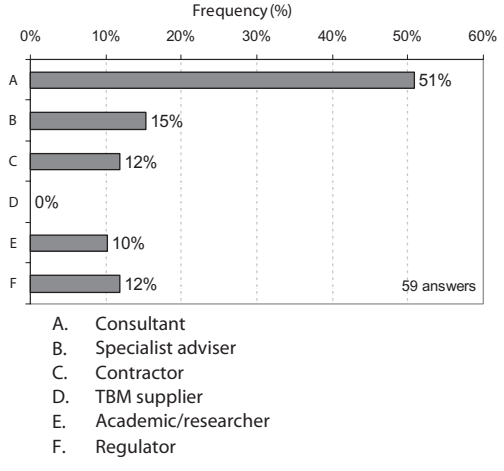

Figure 1. Types of companies/professionals involved.

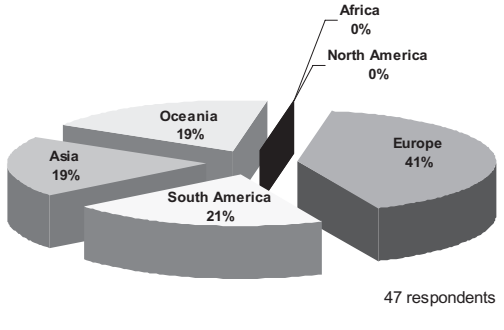

Figure 2. Frequency distribution of respondents from around the world.

2 TUNNEL TYPES AND SCENARIOS

To make the analysis of the answers simpler, a few questions were formulated to define the scenario of the design practice being referred to.

More than three quarters of the answers refer to tunnels built for trains, metro systems and vehicles in general (Figure 3).

Accordingly, more than four fifths of the answers (from 37 given) refer to tunnels of more than 6 to 10 m diameter (almost half with diameters in excess of 10 m—see Figure 4).

The ground conditions most frequently encountered were either mixed conditions at the face or hard soil/soft rock tunnelling (Figure 5). Tunnelling through granular (cohesionless) ground seems to be the least common. In most situations tunnelling takes place below the water table (Figure 6).

3 GEOTECHNICAL DESIGN AND CONSTRUCTION

3.1 *Tunnelling general*

Figure 7 indicates that conventional tunnelling with a sprayed concrete primary lining is the most frequently specified construction process. The responses are consistent with the large cross-section tunnels involved, since smaller tunnels are almost always built by mechanized shields.

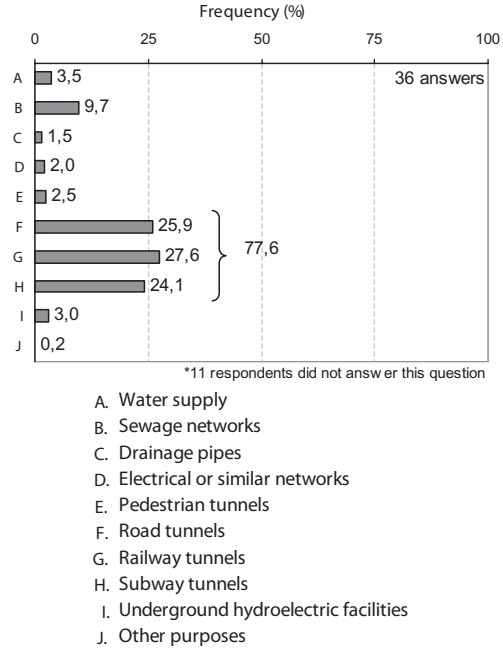

Figure 3. Purpose of tunnels designed.

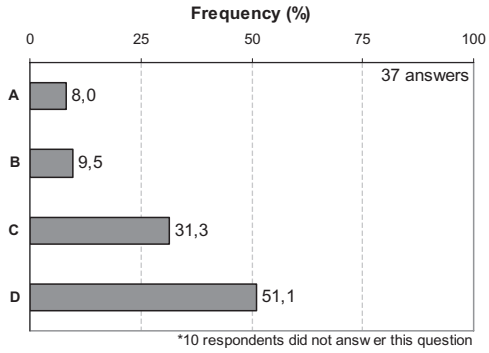

Figure 4. Equivalent diameters of tunnels designed.

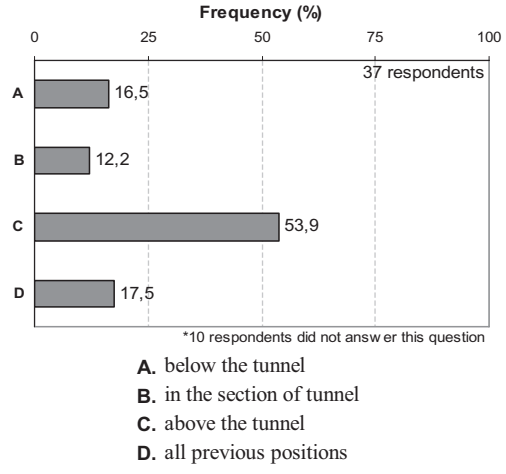

Figure 6. Water table position related to the tunnel.

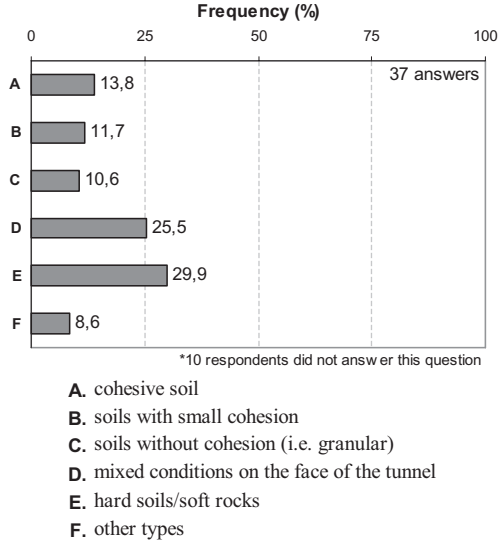

Figure 5. Excavated ground mass.

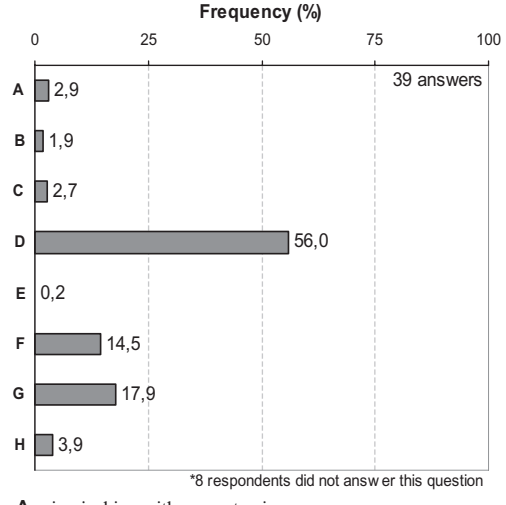

Figure 7. Construction processes used.

When asked whether they usually specify the construction sequence for conventional tunnelling with sprayed concrete, 28.9% of respondents replied that they do not design or do not specify such a type of tunnel construction procedure whereas the others respondents answered that they do. Those who answered affirmatively stated which construction procedures they specify out of the three listed: a) partial excavation of the tunnel heading face, b) ground conditioning of the tunnel face and c) maximum distance of the primary lining invert closure from the tunnel face. Figure 8 shows that the responses indicated no preference for any of the three procedures listed, which all received exactly the same number of indications.

Figure 9 shows that the majority of the respondents specify all procedures listed. It appears that

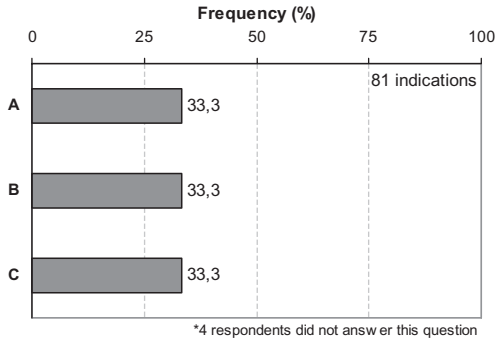

A. I specify the partial excavation of the tunnel heading face
B. I specify the ground conditioning of the tunnel face
C. I specify the maximum distance of the primary lining invert closure from tunnel face

Figure 8. Construction procedures specified for conventional tunnelling.

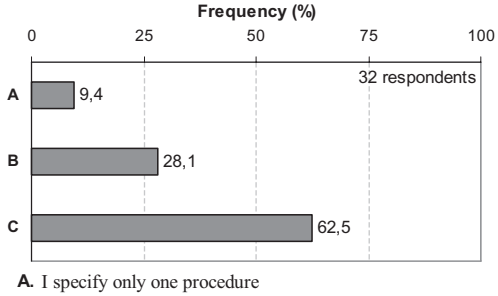

A. I specify only one procedure
B. I specify two procedures
C. I specify all three procedures

Figure 9. Number of construction procedures specified in conventional tunnelling.

there is a general concern to minimize instabilities during excavation as well as damage associated with tunnelling-induced settlements, by specifying stringent construction procedures.

3.2 *TBM Tunnelling*

When referring to mechanized driven tunnels with a shield, the most frequently used type of equipment is the earth pressure balance shield (46%°), while slurry shields are used in 33% of cases, and other types of tunnel boring machine (open face, compressed air or mixed TBMs) appear marginally, as indicated in Figure 10.

Likewise for the question on conventional tunnelling, for the TBM operations three construction procedures which have a strong influence on settlements were offered for selection by respondents: specifications for a) lining grout, b) tunnel face pressure and c) maximum overcutting at the cutting wheel. As indicated in Figure 11, face pressure control is the most frequent specification made.

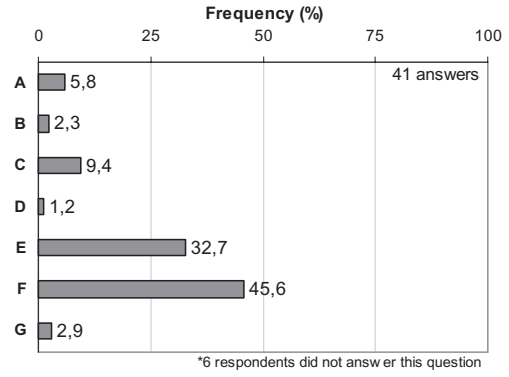

A. I do not design shield-driven tunnels
B. I do not specify shield-driven tunnels
C. open face shield
D. air pressure shield
E. slurry shield
F. earth pressure balanced shield
G. other types

Figure 10. Types of TBM chosen for shield driven tunnels.

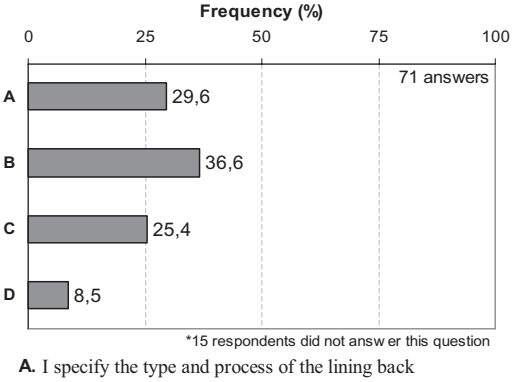

A. I specify the type and process of the lining back filling (tail skin grouting)
B. I specify the pressure on the face
C. I specify of the maximum ground over-cutting
D. others

Figure 11. Specifications for the operation of the machine for shield driven tunnels.

In urban areas, one of the main concerns is to avoid over-excavation and sinkholes.

For this problem (Figure 12), the TBM control parameter which is most often monitored is the face pressure (48% of the answers). Next comes

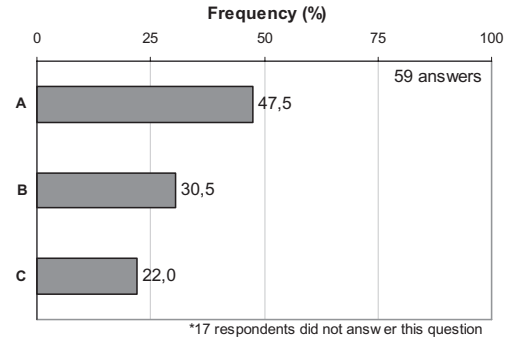

Figure 12. Shield driven tunnel parameters for TBM operation control.

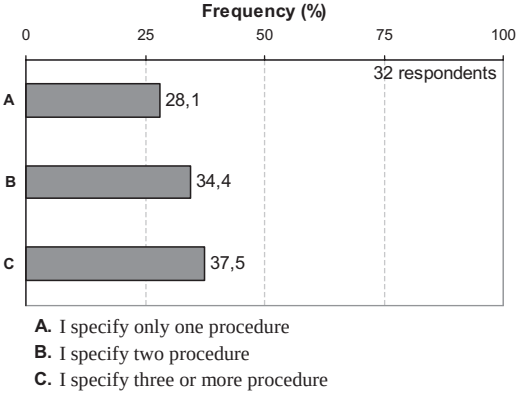

Figure 13. Number of construction procedures specified in TBM operation.

the weight of excavated ground which is monitored in 30% of cases. Additional observations are also often taken into account (22%). Among these additional observations are: the density of the mud, the volume of the excavated ground measured by combining weighing on the conveyor belt and a volume measurement by laser, the injection pressure of the annular void at the shield tail, and the volume of grout injected, followed by other machine parameters such as thrust combined with the torque on the cutting wheel and the use of various methods of field monitoring (e.g. extensometers, radial penetrometers installed in the machine).

Figure 13 shows that only slightly more than a third of the respondents specify three (or more) construction procedures, as opposed to almost two thirds, in conventional tunnelling. In the latter, only 9.4% of respondents specify just one procedure whereas in TBM construction 28.1% specify only one procedure. This may indicate that a more relaxed attitude prevails in the design of TBM driven tunnels compared with conventional tunnelling design.

3.3 *Conventional tunnelling*

Investigating further the importance of construction procedures to be specified in the design, Figure 14 shows the reasons for requiring the closure of the primary lining invert at a certain distance behind the face of conventional tunnels. The majority of the answers indicate stability issues as the main reason, especially in less competent ground, followed second by control of settlements.

When asked how the tunnel designer can act to control the face stability of a conventionally mined tunnel with sprayed concrete as primary lining, the experts (see Figure 15) revealed that their most preferred control measure is face nailing (73% of the cases). Other methods such as forepoling, partial excavation and reduced distance of closure of the invert are also commonly used. The least preferred measure is forepoling using steel piles driven into the ground; a technique popular in the 1970s.

3.4 *Groundwater control*

Figure 16 presents the preferences of distinct measures for groundwater control in conventional and TBM tunnelling. Clearly, with the former, preference is given to de-watering from inside the tunnel and with the latter the use of earth pressure balance systems.

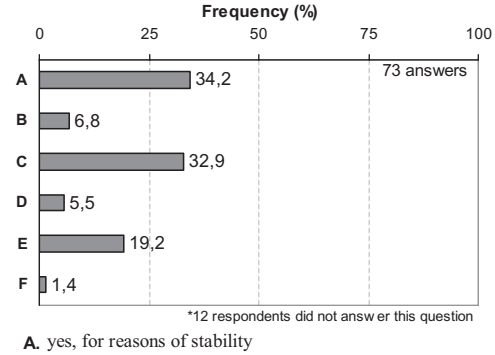

Figure 14. Reasons for closure of primary lining invert at a certain distance behind the face.

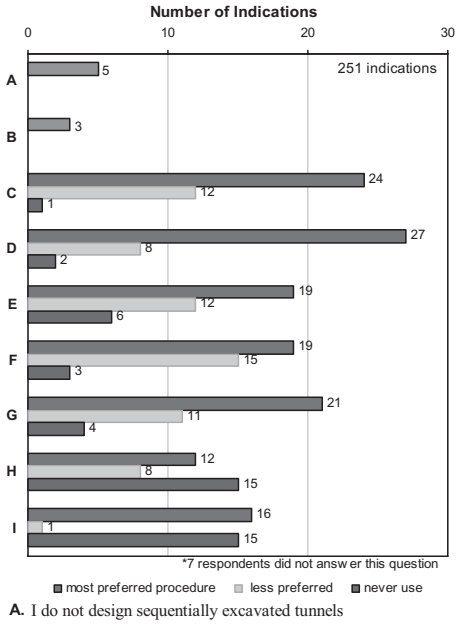

A. I do not design sequentially excavated tunnels
B. I do not design mined tunnels that require control of the stability of the face
C. cement injected tubular forepoling
D. face nailing
E. reduction of the distance of invert closure to the tunnel face
F. forepoling and / or face nailing with jet grouting
G. partial excavation of the face (use of side drifts, of temporary invert, etc)
H. steel piles driven (forepoling)
I. other methods

Figure 15. Preferences on measures for face stability control in conventional tunnelling with sprayed concrete primary lining.

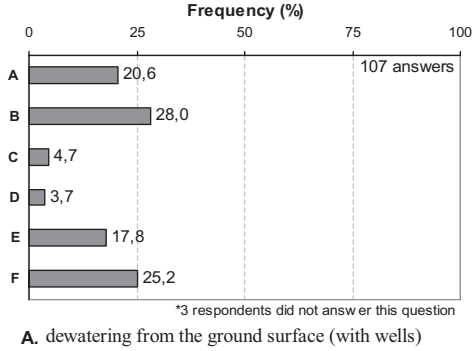

A. dewatering from the ground surface (with wells)
B. dewatering from in-side the tunnel
C. dewatering from drainage tunnel
D. closed face system: Compressed Air
E. closed face system: Slurry shield
F. closed face system: EPBS

Figure 16. Groundwater control measures.

4 LINING DESIGN AND WATER PROOFING

In TBM driven tunnels, the type of lining most frequently used is bolted concrete segments (74% of the answers), as shown in Figure 17. Other types are divided between non-bolted concrete segments (15%), ductile iron segments (7%) and 4% other types of linings, such as concrete pipes installed by jacking, or a concrete cast-in-place lining. From these answers, it is not possible to establish a correlation between the tunnel diameter and the lining type.

For primary linings in TBM construction or conventional tunnelling with sprayed concrete primary lining, wet-mix is most frequently used (83% of the respondents indicated it, see Figure 18) and the least used is the cast-in-place concrete (never used by almost 49% of the respondents, Figure 18).

On the other hand, the most commonly used secondary lining (see Figure 19) is cast in-place concrete, with 78% of the respondents opting for this. Moreover, 68% of the respondents indicated that dry-mix sprayed concrete and steel lining are never used. The responses are consistent with the large cross-section tunnels built in practice. Abandoning steel as a secondary lining material is likely to be connected to its susceptibility to chemical and electrical corrosion frequently present in urban environments. In some parts of the world it might also be because of cost.

Figure 20 shows that steel bars and welded steel meshes are the most common type of reinforcement used in concrete secondary linings. It is worth noting that synthetic fibres and steel sets are rarely used.

The majority of respondents (78%) require minimum reinforcement in the secondary lining.

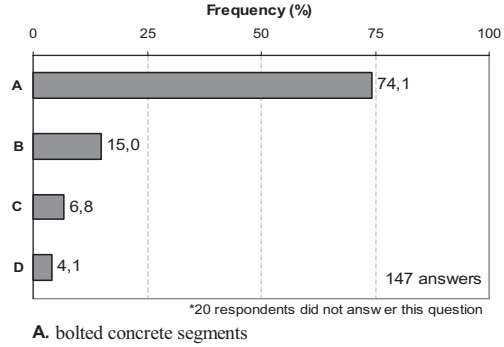

A. bolted concrete segments
B. wedge-block concrete segments
C. bolted SGI (spherical graphite iron) segments
D. other

Figure 17. Secondary lining types used for TBM driven tunnels.

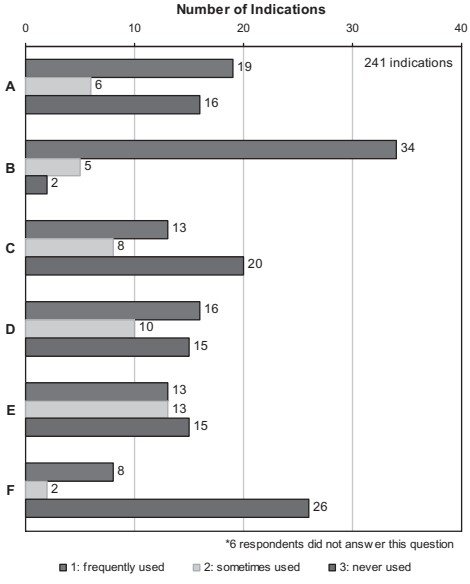

A. dry-mix sprayed concrete
B. wet-mix sprayed concrete
C. cast-in-place concrete
D. pre-cast concrete (segmental or not)
E. steel
F. others

Figure 18. Primary linings for tunnels.

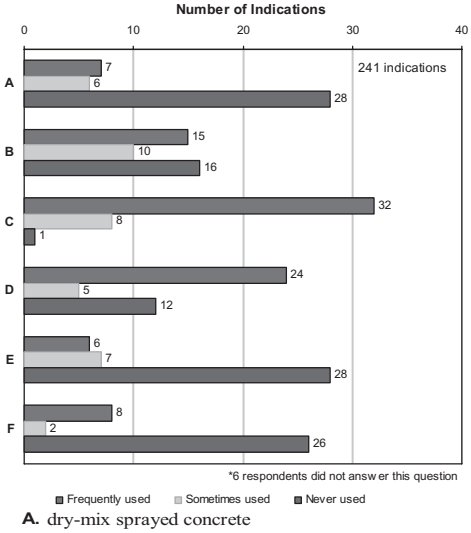

A. dry-mix sprayed concrete
B. wet-mix sprayed concrete
C. cast-in-place concrete
D. pre-cast concrete (segmental or not)
E. steel
F. others

Figure 19. Secondary lining for tunnels.

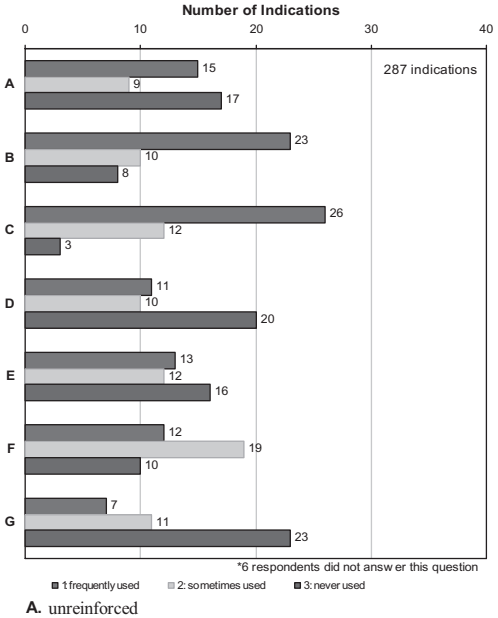

A. unreinforced
B. welded steel meshes
C. steel bars
D. steel sets
E. lattice girders
F. steel fibres
G. synthetic fibres

Figure 20. Concrete reinforcement types in secondary lining.

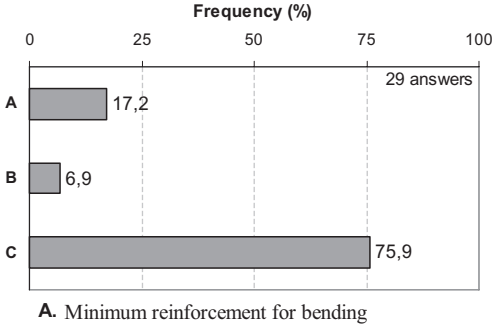

A. Minimum reinforcement for bending
B. Minimum reinforcement for shrinkage
C. both of them

Figure 21. Type of minimum reinforcement adopted.

Only a minority accept reinforcement less than the minimum. When asked what kind of minimum reinforcement is required (Figure 21), 17.2% of the respondents indicated that they adopt the minimum reinforcement for bending only and the majority (75.9%) consider the minimum reinforcement both for bending and shrinkage.

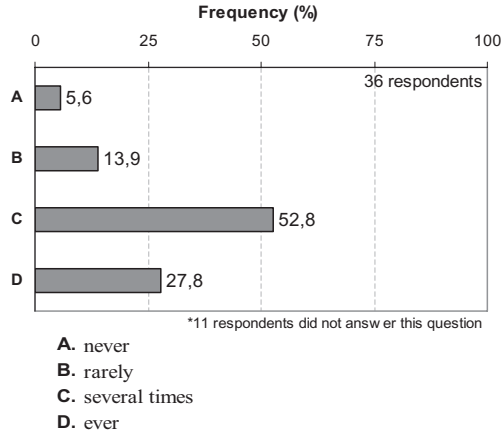

Figure 22. Lining designed to be waterproof or watertight.

When asked about the frequency of linings designed to be waterproof or watertight (Figure 22), 19.5% of the respondents declared that they either never or rarely design tunnels for those conditions. The majority of the respondents indicated that they have done it several times (52.8%) or always do it (27.8%).

The most frequent waterproofing measures for groundwater infiltration control (Figure 23) are the use of impervious membranes and of limiting the concrete cracking, with indications from 59% of respondents for each. It can be also seen that sprayed membranes are not used much for this purpose.

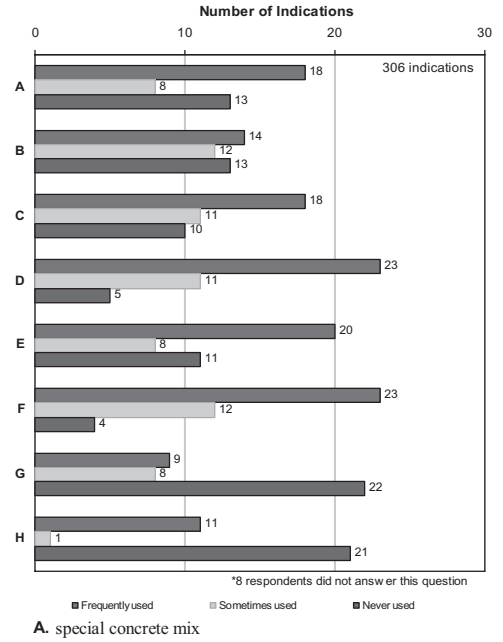

Figure 23. Groundwater infiltration measures adopted.

5 DESIGN PROCEDURES

5.1 *Stability analyses*

The great majority of respondents (97%) perform stability analyses of the tunnel heading excavation. As shown in Figure 24, limit equilibrium methods are used the most for tunnel excavation stability analyses (25.8%) despite being inaccurate. These are followed by stress-strain analyses and by empirical methods. More rigorous approach of limit analyses by the lower bound and upper bound theorems of plasticity are not used much.

A new class of solutions of tunnel stability analyses by numerical limit analyses (NLA) that combines finite element numerical methods with optimization procedures to find the maximum magnitude of a stress field to cause the collapse of the ground around the tunnel heading face without violating the failure criteria does not seem to be used much yet in practice.

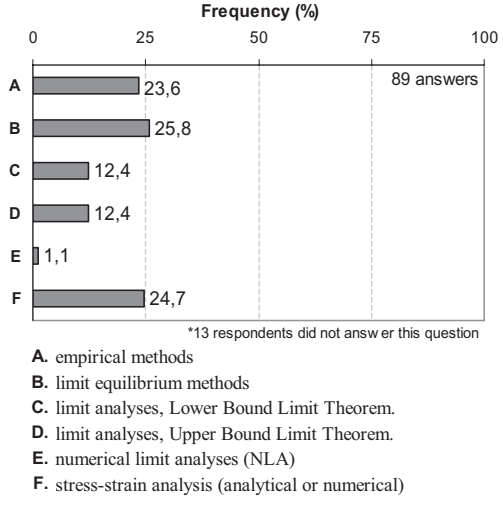

Figure 24. Methods for stability analyses of tunnel headings.

The final questions of the part related to TBMs concern the specification of the confining pressure at the face.

According to Figure 25, two thirds of respondents use distinct procedures for stability analyses of headings of conventional and of TBM driven tunnels.

Those that use different approaches were asked how the pressure to be applied at the tunnel face is to be defined. They showed a preference for limit equilibrium solutions (Figure 26), despite their theoretical limitations. It should be noted that, in most cases, several approaches are used. Thus, a detailed examination of responses shows that the empirical approach is never used alone. Similarly, with one exception, the numerical stress-strain analysis is always used in conjunction with other methods. Generally the simplified approaches might be considered as inadequate as they are not accurate for assessing the stability of the face and are used only as a first estimate. Usually they are supplemented at a later stage by more rigorous approaches.

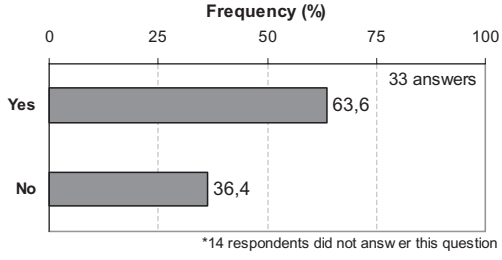

Figure 25. Use of distinct approaches for stability analyses of tunnel heading in conventional and TBM driven tunnels.

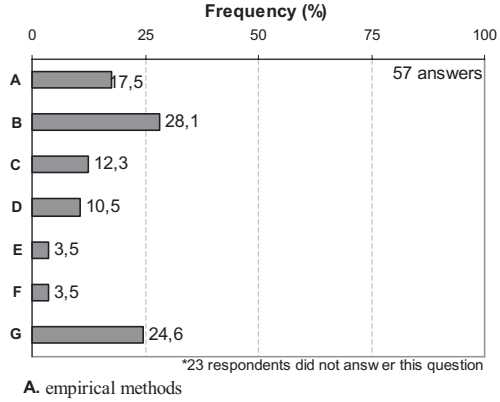

A. empirical methods
B. limit equilibrium methods
C. limit analyses, Lower Bound Limit Theorem.
D. limit analyses, Upper Bound Limit Theorem.
E. numerical limit analyses (NLA)
F. analytical stress-strain analysis
G. numerical stress-strain analysis (FEM, FDM, etc.)

Figure 26. Approaches used to define the pressure to be applied at the tunnel face.

5.2 *Settlements and their influence on surroundings*

Almost all respondents (97.8%) routinely perform predictions of settlement associated with tunnel excavation. More than 50% of the answers indicated numerical methods (finite element or finite difference) as the usual tools for such predictions (Figure 27). It should be noted that empirical and semi-empirical methods are also still in use for this purpose, summing 45% of the answers.

For the assessment of potential damage to surface structures by tunnelling-induced soil displacements, preference is given to the method by Mair, Taylor and Burland (1996) in 34.3% of the answers (Figure 28).

It was noted (Figure 29) that the majority of respondents (74%) always perform preliminary studies to evaluate the sensitivity of existing buildings and structures to tunnelling-induced damage.

When using finite element or finite difference approaches, a key aspect is the choice of the soil model: in the survey various types of model were considered and can be grouped into two main categories.

– Category A: includes two models that at very small strain ranges display linear responses; they are the linear elastic model and the elastic linear-plastic model associated with the Mohr-Coulomb failure criterion.
– Category B: includes models that at small strain ranges display non-linear responses; they are nonlinear models able to represent more accurately the actual behaviour of most soils.

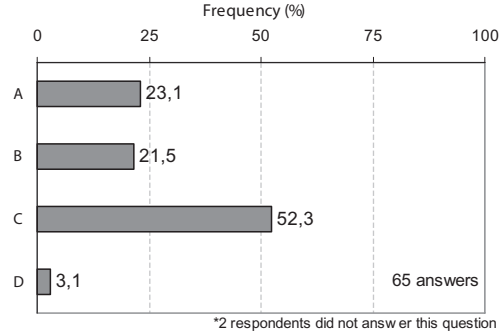

A. empirical methods
B. semi-empirical methods
C. numerical methods
D. numerically derived methods

Figure 27. Methods used for estimating settlements.

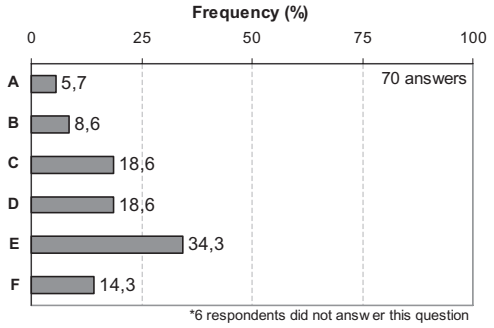

A. Skempton and MacDonald (1956) criterion
B. Bjerrum (1963) criterion
C. Burland and Wroth (1974) method
D. Boscardin and Cording (1989) method
E. Mair, Taylor and Burland (1996) approach
F. other method

Figure 28. Methods for assessment of potential damage induced in surface structures by tunnelling-induced soil displacements.

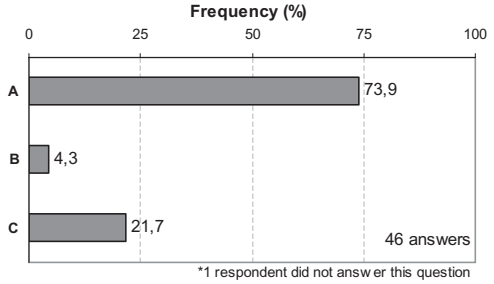

A. yes
B. no
C. in some cases

Figure 29. Preliminary assessment of the sensitivity of existing buildings to settlement damage induced by tunnelling in urban areas.

Figure 30 shows that two thirds of the answers refer to models of category A, which do not represent accurately the behaviour of actual soils. Only one third of the answers indicate that these respondents use non-linear models. This may reflect that practitioners are better acquainted with category A models, being part of a standard knowledge to many and, more importantly, available in most commercial computer codes, particularly because of its numerical simplicity and hence ease of use. Models within category B were developed later, are not always available in commercial codes and tend to be more cumbersome in handling both numerically and practically, although they portray better the real soil response.

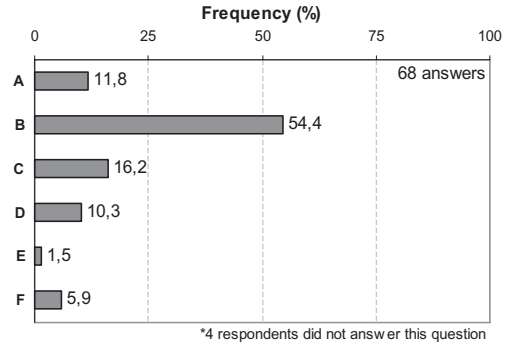

A. Linear elastic model
B. Linear elasto-plastic model associated to the Mohr-Coulomb failure criterion
C. Non-linear elastic model
D. Cam-clay model type
E. Lade model
F. Others

Figure 30. Constitutive model of soil behaviour adopted in numerical analysis for tunnelling projects.

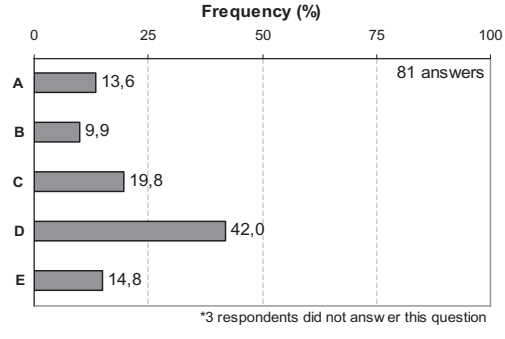

A. closed-form analytical solutions considering continuum mechanics theory
B. analytical solutions with springs
C. numerical solutions with discrete bar and spring representations
D. finite element numerical models
E. finite differences numerical models

Figure 31. Plane-strain solutions for the interaction between lining and soil.

5.3 *2-D Lining and soil interaction*

For the assessment of the interaction between lining and soil, in plane-strain conditions, a variety of solutions was offered to the practitioners as indicated in Figure 31.

By and large, numerical solutions by finite elements or differences are the most quoted solutions adopted in practice. However, the oldest simplified approaches largely coexist with the finite element

or finite difference method approaches. This coexistence is reflected by the fact that there are many multiple responses (50% of the respondents use two methods or more).

It has been noted that when calculating the primary lining using plane-strain solutions, two thirds of the practitioners assume a reduced overburden (see Figure 32). Methods most frequently used for estimating the reduction in the ground overburden are numerical or numerically derived (for instance, Negro and Eisenstein, 1997). These are followed in popularity by Terzaghi's arching theory (see Figure 33), despite the fact that this method implies a considerable ground stress reduction which is associated with large ground deformations and settlements, a situation to be avoided in an urban environment, besides being unsafe.

When analysing the secondary lining (see Figure 34) the reduced overburden assumption still prevails but less than noted for primary lining case and the full overburden assumption is increased in frequency. Perhaps this minor trend reflects attachments to the old hypothesis that long-term creep of any geological material eventually results in null shearing strength.

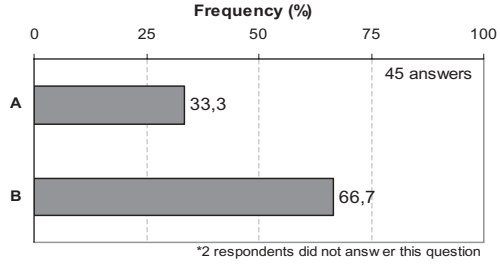

A. full overburden (without stress reduction)
B. reduced ground overburden

Figure 32. Overburden load assumptions on primary lining.

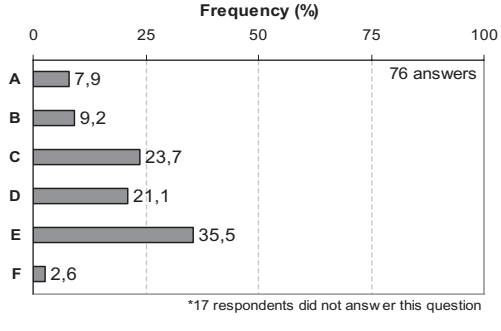

A. using empirical relations
B. using semi-empirical relations
C. using Terzaghi´s arching theory
D. using convergence/confinement type analysis
E. using numerical analysis
F. using other methods

Figure 33. Methods for estimating the ground overburden reduction.

5.4 *Pore water pressures*

With respect to the effect of pore water pressure on the behaviour of the soil (Figure 35), it is somewhat surprising to note that the water pressure on the lining is taken into account by only 41% of the answers.

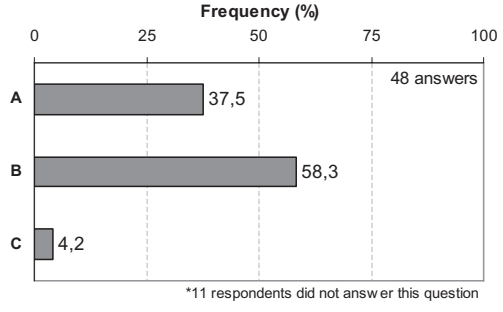

A. full overburden (no ground stress release)
B. reduced ground overburden
C. other assumptions

Figure 34. Overburden load assumptions on secondary lining.

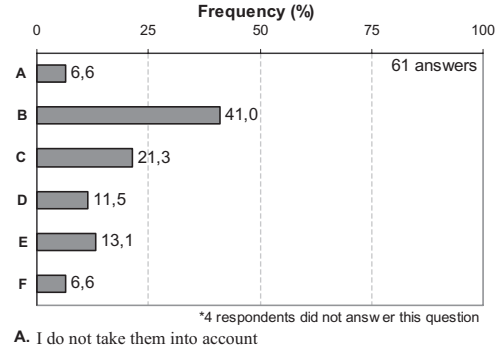

A. I do not take them into account
B. I consider only the water pressure on the lining
C. I perform coupled analysis of soil stresses and pore
D. I perform uncoupled analysis
E. I use flownets to evaluate the pore pressures associated with the induced drainage
F. I take into account the induced changes in pore water pressure furnished by analytical or numerically derived solutions.

Figure 35. The effect of pore water pressure on soil behaviour.

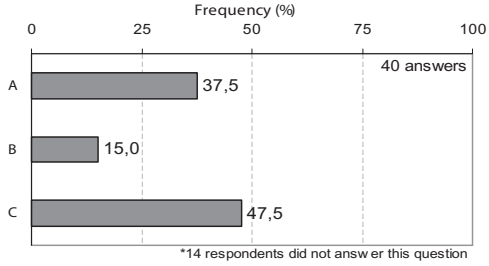

A. I do not take it into account: I assume the soil mass as fully drained
B. I assume the soil mass fully drained and consider the seepage forces
C. I take into account the pore pressures and effective stresses (reduced or not)

Figure 36. Account of groundwater loading on the primary lining in tunnels below water table.

Figure 36 presents how practitioners take into account the groundwater loading onto the sprayed concrete primary lining of conventional tunnels below the water table. It is interesting to note that more than a third of the answers indicate they assume the soil mass totally drained and neglect any water pressure acting on the lining.

5.5 *Numerical modelling*

Concerning stress-strain analyses, the questionnaire focuses on the type of finite element analysis (2D or 3D) and the soil models. The use of 2-D finite element or finite difference models is now widespread, and codes have pre-processors specifically designed for the simulation of tunnelling. More recently, 3-D models, adapted to geotechnical problems, have been developed and are commercially available.

Despite the fact that the ground stress redistribution around a tunnel heading is essentially three-dimensional, Figure 37 shows that 55% of respondents rarely or never perform 3-D analyses. This can be explained by the fact that 3-D analysis is still a very time-consuming engineering exercise. On the other hand, it is promising that the remaining 45% of the respondents perform 3-D analyses 'sometimes' to 'always', something that would not have been seen a decade or two ago. Also promising is the fact that those who always perform 3-D analysis are consultants, a sign that this tool is increasingly being used in practice. No correlation was found between use of 3-D models and tunnel diameter, and thus size of the project.

It should be interesting to review these figures in a few years time, as the development of effective pre—and post-processors in 3-D numerical codes may lead to a wider use of 3-D modelling.

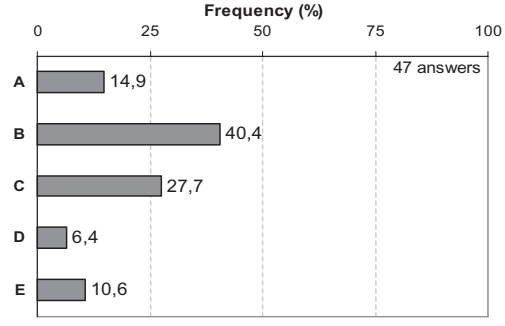

A. never
B. rarely
C. sometimes
D. often
E. always

Figure 37. Use of 3-D stress-strain analyses in tunnel projects.

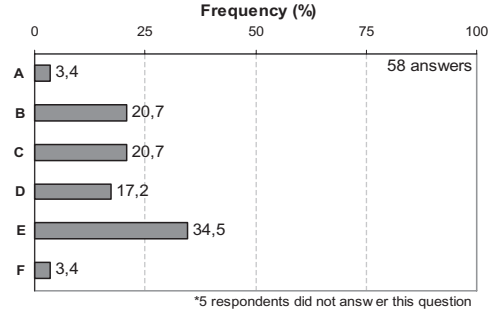

A. I do not use numerical methods for these purposes or I do not use 2D numerical analyses.
B. I consider a ground stiffness reduction.
C. I consider an imposed tunnel convergence (displacement boundary condition).
D. I consider a progressive tunnel core removal.
E. I consider a ground stress reduction in the tunnel perimeter.
F. none of above

Figure 38. Account of 3D effects in plane-strain analyses to estimate ground settlements and lining loads.

Bearing in mind that 2-D analyses are still used more than 3-D, the survey investigated how three-dimensional effects are accounted for in estimating lining loads and displacements, when using plane-strain analyses in practice. Figure 38 shows that the procedure most used, as indicated by more than a third of answers, involves a ground stress reduction around the tunnel perimeter. The next most popular approach is to use an imposed displacement boundary condition in which the transformation from the 3-D problem to the simplified 2-D section is achieved by progressively simulating

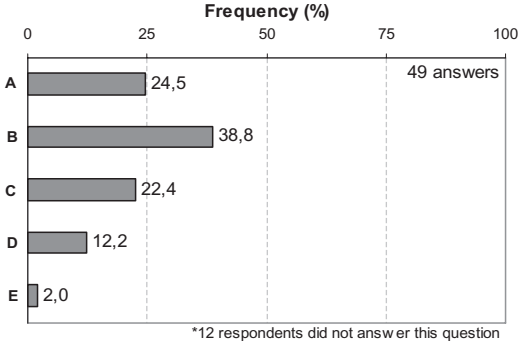

A. solid finite elements
B. solid finite elements and shells
C. shell elements plus bars or springs
D. finite differences
E. boundary elements

Figure 39. Three-dimensional numerical analyses used for tunnel design.

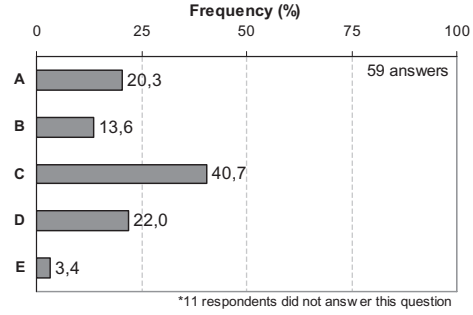

A. consider the two layers of concrete working together
B. consider the two layers of concrete working separately
C. consider only the second layer of concrete (the secondary lining) and neglect the primary layer
D. assume a partial decay of the primary lining
E. make other assumption.

Figure 40. Account of layered construction in the design of reinforced concrete lining.

a volume loss over the tunnel section, and finally installing the lining. Note that the other remaining methods have also a similar and significant use by 17 to 21% of respondents.

Whichever approach is chosen, the problem remaining is the assessment of the degree of reduction of either ground stiffness, ground stress or tunnel volume, which means that going from a 3-D analysis to 2-D is not a rigorous process. None of the methods in use can be regarded as superior, as they all depend on user experience. Because of the diversity of these 2-D approaches, it would be interesting in the future to investigate how the reduction factors are assessed in practice to simulate successive stages of excavation.

Whenever a 3-D analysis is used in practice (see Figure 39) preference is given to the use of solid finite elements to represent the ground and shells to represent the lining.

In conventional tunnelling the primary and secondary lining are installed separately in time and eventually with different specifications.

The survey questioned how practitioners account for this layered lining construction in the reinforced concrete lining design (Figure 40).

It was noted that in the majority of cases only the second layer of concrete is taken into consideration and the primary lining is fully neglected, a very conservative and frequent assumption. On the other hand more than 40% of the answers indicate that respondents consider the two layers of concrete working together, sometimes assuming a partial decay of the primary lining, perhaps a more realistic hypothesis.

6 GROUND INVESTIGATIONS AND MONITORING

Practitioners were also invited to share their preferences regarding field and laboratory geotechnical investigations in their routine practice. In a 0 (never use) to 3 (always use) scale they had to show their preference regarding each investigation type. The results obtained are depicted in Figure 41.

It can be noted that soil characterization tests in the laboratory are almost always performed as much as Standard Penetration Tests (SPT) are performed in the field. However, plate bearing tests, dilatometer and pressuremeter tests are not used much in routine practice.

With respect to field monitoring Figure 42 shows that more than 70% of respondents indicated that it is always used in routine projects, and less than 9% never or seldom use it. This seems to reveal that practitioners are usually concerned about the risks involved and any damage potentially caused by their works.

Another question posed to respondents was whether they have been involved in the analysis of the monitoring results. 89% of respondents answered yes to this question, showing that there is no longer a strong "dichotomy" between designers and site engineers.

Types of monitoring equipment preferred (Figure 43) are still very traditional: levelling of surface markers and settlements points on buildings; convergence measurements inside the tunnel and pore-water pressure indicators (e.g. piezometers) are the most frequently used techniques. On the other

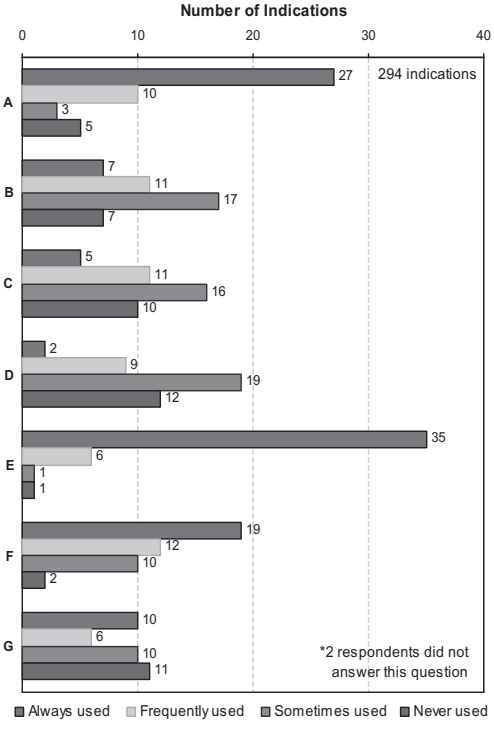

A. SPT or SPT-T (with torque measurement)
B. CPT, Deep sounding
C. Marchetti dilatometer (DMT) or pressuremeter tests
D. plate bearing test
E. soil characterization tests
F. special laboratory tests on intact samples
G. others

Figure 41. Preferences regarding geotechnical investigations.

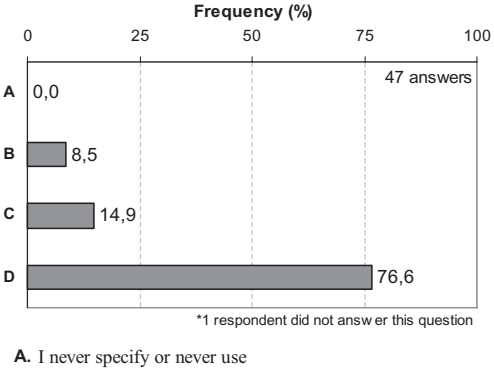

A. I never specify or never use
B. I seldom or rarely use
C. I frequently specify or use
D. I always specify or always use

Figure 42. The use of field instrumentation.

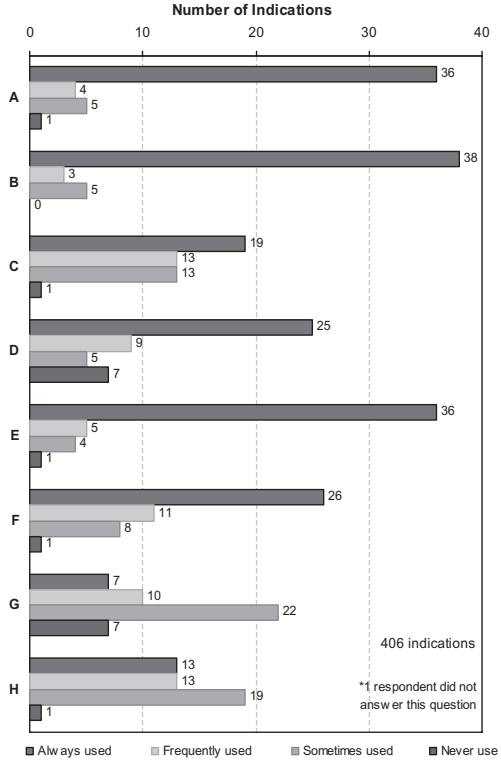

A. levelling of surface points (greenfield or near-greenfield)
B. levelling of settlements points in surface structures
C. levelling of deep settlement points
D. levelling of settlements points in the lining
E. convergence measurements
F. piezometers or water level indicators
G. load cells, stress or strain meters in the lining
H. inclinometers or slope indicators

Figure 43. Types of monitoring instruments.

hand, measurements of loads, stresses or strains in the tunnel linings are far less common.

Figure 44 shows that the most popular way of transmitting instrumentation results (almost 30% of the cases) is to send it by e-mail. Note that more than 40% of answers refer to more up-to-date forms of data publishing (E to I), including use of more elaborate databases that seems to be becoming more widespread.

Another point addressed in the survey was reflected by the question: if real-time monitoring was implemented, was the excavation process, the ground reinforcement, the tunnel lining or other processes continuously adapted to the monitoring results? As shown in Figure 45, 74% of respondents replied that monitoring in real time is widely used for continuous adaptation of works. This is an encouraging result, since monitoring is not only

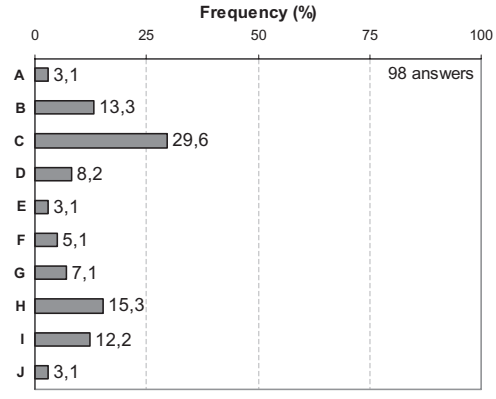

A. site only
B. paper reports faxed to other offices
C. emailed
D. shared on a VPN or FTP site
E. mounted statically on a website
F. mounted automatically on a web site
G. data sent to a web database server
H. data sent to a web database server with graph and reporting front end
I. data sent to a web database server with graph and reporting front end and GIS display
J. other

Figure 44. Forms of reporting field monitoring data.

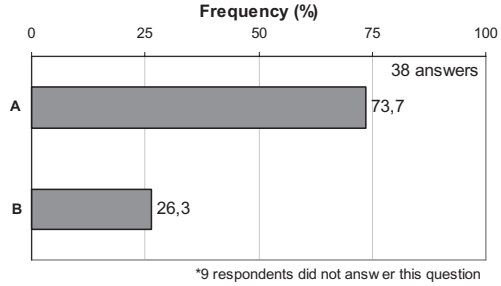

A. yes -
B. no -

Figure 45. Continuously adaptation of the excavation process, the ground reinforcement, the tunnel lining or other processes considering real time monitoring results.

being used to check the performance, but is also used to optimize tunnel construction (by either increasing or decreasing tunnel support).

Regarding the costs of the geotechnical investigations in relation to the total costs of the projects (see Figure 46), it was noted that in 50% of the cases it ranks between 1 to 2% and in 30% of the cases it is below 1%, fairly low ratios possibly explained by the magnitude of costs associated with the larger

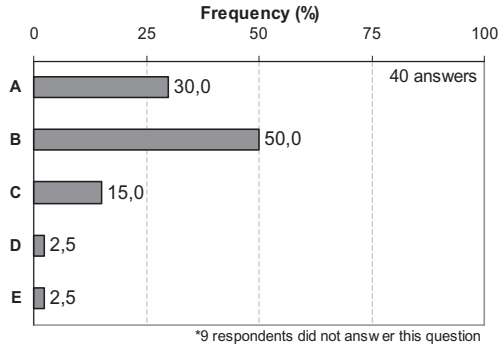

A. less than 1%
B. between 1% & 2%
C. between 2% & 4%
D. between 4% & 6%
E. between 6% & 8%

Figure 46. Costs of geotechnical site investigation in relation to the total cost of the project.

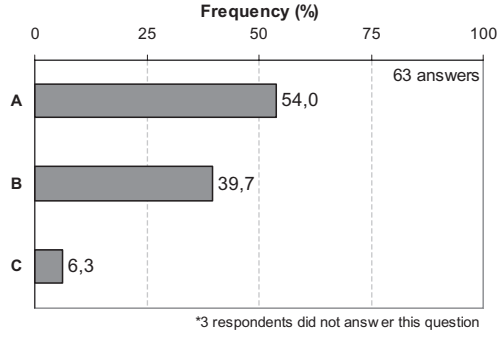

A. performing deterministic analysis with average ground properties and using adequate factors of safety.
B. performing deterministic analysis with "worst" case assumptions and using adequate factors of safety.
C. performing probabilistic analysis, assessing or not a probability of occurrence of an event.

Figure 47. How variability and uncertainty of geotechnical parameters are accounted for in the design.

tunnels and projects that are often represented in the survey.

7 RISK ASSESSMENT

It is interesting to note (see Figure 47) that probabilistic analyses are very infrequently performed, preference being given to more traditional deterministic approaches. This seems somewhat in

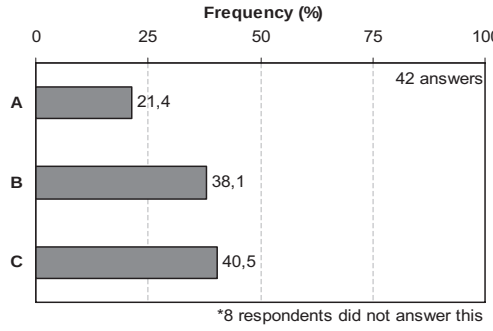

A. the owner employs a third specialised organisation to undertake the risk assessment

B. the risk factors are considered during the design stage, but no specific risk assessment is prepared

C. others

Figure 48. Approaches to risk assessment.

conflict with the perception discussed earlier that practitioners are usually concerned about the risks involved in urban tunnelling and about damage potentially caused by their works.

When asked about risk assessment as part of the design of the tunnel, 83% of the respondents confirmed that some element of risk assessment is always performed in their practice. On the other hand, for the implementation of these assessments in the tunnel design, frequently specific approaches are used, as indicated by Figure 48.

Combining the last two findings, one can speculate that practitioners do not perform probabilistic analyses in practice either because they are not familiar with the subject or because they do not have the resources to do so.

8 SATISFACTION WITH PRACTICE

Finally, the survey investigated the areas where practitioners are not satisfied with the current state-of-the-practice and understand that developments are required (see Figure 49).

The largest satisfaction levels were found with the current tunnel construction methods and with the lining types available. The least satisfaction levels were detected in the area of tunnel water-proofing which also showed one of the highest ratios of disapproval to approval levels with existing practice. In broad terms, respondents have shown to be moderately satisfied with all aspects investigated.

An evaluation of the practitioners' global satisfaction was calculated by the sum of all evaluated items shown in Figure 49, where the value zero was assigned for not satisfied answers, one for moderately satisfied and two for fully satisfied.

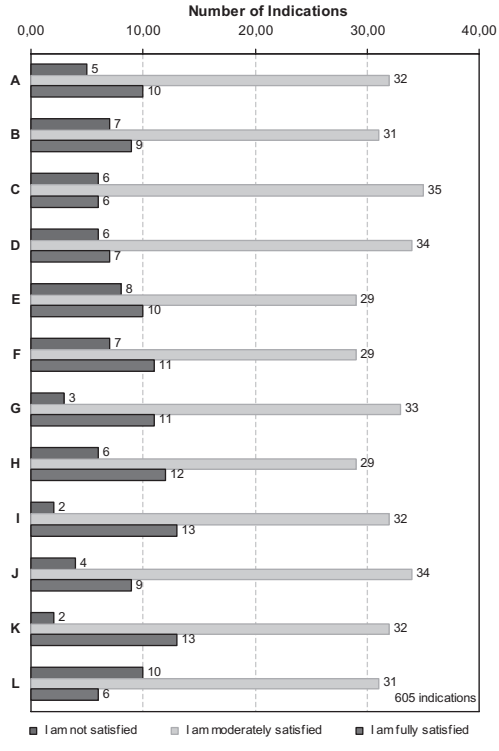

A. tunnels stability analysis

B. soil-structure interaction & deformation analysis

C. Face stability

D. settlements and induced damage estimates

E. estimates of lining loads and structural design of the lining

F. pore pressures and water flow estimates

G. field monitoring

H. field or laboratory investigations

I. available construction methods for tunnels

J. available methods for ground improvement

K. available types of lining

L. available types of water proofing

Figure 49. Satisfaction with the current practice.

Considering a total of 12 items, the maximum satisfaction with the current practice would ideally get a 24 mark and the minimum zero.

A correlation attempt was to relate the total satisfaction as defined above, with the recent experience of the respondents directly measured by the total number of tunnel designs each respondent conducted over the last five years. This correlation is presented in Figure 50. It appears that experienced tunnel designers are slightly less satisfied on average than designers with less experience.

However, it is worth noting that outlying points A and B are responsible for the negative linear correla-

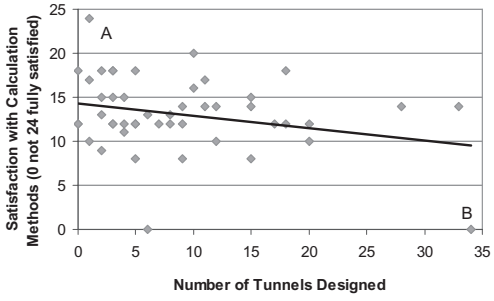

Figure 50. Comparison between total satisfaction degree and designer's experience.

tion shown. If these points were excluded it could be concluded that this correlation may not exist.

9 FINAL REMARKS

This survey focused on underground openings of any shape with more than 0.5 m diameter and covered many tunnel projects from around the world. The questionnaire was sent to geotechnical engineers, geologists, structural engineers and experts in numerical modelling, involved in the design or in the design supervision of tunnel projects over the past few years.

It is noteworthy that most of the professionals involved are related to tunnel consulting and construction and that the response was concentrated in Europe with no participation of professionals from Africa or North America.

The conclusions found refer to the most frequent practice scenarios representing the experience of the respondents. The scenarios are defined in broad terms by the respondents as covering: large size tunnels, with equivalent diameter larger than 6 m, designed for railways, metros, highways, driven under mixed face condition, in cohesive soils and soft rocks, below water table using sprayed concrete as lining (conventional tunnelling).

The assessment indicates that the design of conventional tunnels is conducted more rigorously than that for mechanized tunnelling, with the regard to the specification of construction procedures.

It was also noted that practitioners are concerned with the closure of the primary lining invert at a certain distance behind the face, for reasons of stability, quality of the lining and in order to control settlements. For face stability control, the preferred method is face nailing. The use of forepoling with driven steel piles is indicated to be the least preferred, despite being a popular technique in the 1970s.

The lining type most frequently used in mechanized excavations with a shield is bolted concrete segments. For conventional excavation, the most frequently used primary lining type is wet-mix sprayed concrete and for secondary lining, there is a preference for cast-in-place concrete.

There is a high frequency in the use of limit equilibrium methods and of empirical methods to assess the stability of the tunnel heading and face, although it is recognised that these approaches may not be accurate.

The use of numerical methods (FE or FD) is widespread in the local practice for estimating settlements or for tunnel lining design. Equally widespread is the assumption of reduced ground overburden in 2-D tunnel models. However, the persisting practice of using Terzaghi's arching theory to estimate the reduction of geostatic stresses is unjustified as it is potentially unsafe.

Due attention is being considered in practice to potential damage caused to surface structures, including preliminary assessments of sensitivity of these structures.

When designing primary and secondary lining the reduced overburden assumption is adopted by most, but the full overburden is also used by a significant number of the respondents, indicating possibly some prevalence of the questionable hypothesis of long-term creep of geological material eventually leading to zero shearing strength.

The majority of tunnel designers take into account pore water pressures, but this is often limited to accounting only for the effect of pore-water pressures on the lining. However, for primary lining, it is significant the amount of respondents who consider a fully drained situation.

A simplistic and incorrect hypothesis of ignoring the primary lining when the secondary lining is designed should be reconsidered. It should be possible to simulate and design linings taking into account both layers working separately.

The most used constitutive models in numerical analysis are those with elastic-plastic behaviour and a Mohr-Coulomb failure criterion. These models when applied to tunnels built with limited relaxation of ground stresses, resulting from restrictive construction methods, used to inhibit ground movements and associated damage in an urban scenario, result in linear elastic soil responses, with inhibited or limited plastic zones. This does not represent the now well-known non-linear behaviour of soils even at small strains: there is a clear need to use more appropriate and adequate soil models in local practice.

The use of three-dimensional modelling in practice is still limited, but it is believed that the increased use of this type of modelling, will be seen in practice soon.

A poor practice in geotechnical investigations for tunnel design was noted. It tends to be limited to soundings with SPT blow counts and simple laboratory testing on disturbed soil samples. This may be because of the emphasis on urban tunnels in environments which are, in general, well known both in geological and geotechnical terms, for which sizeable data banks are available. Perhaps a way to compensate such a deficiency is to stimulate the use of more sophisticated in-situ tests such as cone penetrometers, pressuremeters, dilatometers and others.

It is noteworthy that operating parameters are commonly monitored in shield tunnel projects, as they can be used as preventive measures to avoid excessive soil loss.

A favourable situation is seen in practice, in terms of field monitoring. Field instrumentation is always present. The noted deficiency is the lack of measurements of lining loads. There are a number of procedures to assess loads in concrete linings that could be used with variable degrees of success and cost but these are seldom used in practice.

Another important finding is that monitoring results are frequently used for the continuous adaptation of the excavation process, optimizing the tunnel lining and ground reinforcement.

Probabilistic analyses are still used very seldomly, preference being given to deterministic approaches, which is currently considered more traditional and conservative. On the other hand, risk assessments are often performed for tunnel projects.

Overall, respondents were found 'moderately satisfied' with current design and construction practice for tunnelling projects. However, the respondents believe that the area in need of further technical development is that of available techniques for water proofing tunnels. Nevertheless, they seem satisfied with the available construction methods and lining types. The survey indicates areas in current practice where academic institutions may contribute significantly to technology advancement.

ACKNOWLEDGEMENTS

This survey was only possible thanks to the kind attention of all those who replied the questionnaire. The authors acknowledge all of them and thank them for the time invested in the replies. They are: Pal Gyorgy, Alejo Oscar Sfriso, Roberto Terzariol, Mayer Zublin, Andrea Sciotti, Johannes Jäger, Enrico Maria Pizzarotti, Andreas Werth, Massimo Marchettini, Alessandra Sciotti and Andrea Pigorini, Yoshihiro Terashima and Hiroshi Dobashi, Takaaki Nishimura, Tomomi Iura, Thomas Böhme, Adri Vervuurt, R.W. den Hertog, Predrag Jovanovic, Stavroula Schina, Carlos Takashi Mitsuse, Sallo van der Woude, Erik Taffijn, IMM—Ingenieurbüro Maidl GmbH & Co. KG, Didier Subrin, Luis Eduardo Sozio, Daniel Scott, Alain Guilloux, Freyer Rudolf and Bayer Franz, Jacques Robert, Ana Cristina A. Hatori, Claudio Casarin, Fernando Stucchi, Marcelo Massaki Matsui, Werner Bilfinger, Arsenio Negro, Linn Nordstrom, Ernst-Rainer Tirpitz, Antonella Antonelli, Max Kitson, Thomas Lam, Johnny Cheuk, Dazhi Wen, Eric Chui Hon Man, Bai Yun, Gang Zheng, Saeid Khazaei and George Dounias.

REFERENCES

Bjerrum, L. (1963): Discussion to European Conf. On Soil Mech. Found. Eng. (Wiesbaden), Vol. II, p. 135.

Boscardin, M.D. & Cording, E.J. (1989). Building response to excavation induced settlement. *Journal of Geotechnical Engineering*, *ASCE*, 115, 1, pp. 1–21.

Burland, J.B. & Wroth, C.P. (1974). Settlement of buildings and associated damage. *Conf. on Settlement of Structures*, London, pp 611–654.

Mair, R.J., Taylor, R.N. & Burland, J.B. (1996): Prediction of Ground Movements and Assessment of Risk of Building Damage due to Bored Tunnelling. *Proceed. Intl. Symp. Geotechnical Aspects of Underground Construction in Soft Ground*, London, UK, pp. 713–718.

Negro A. (2008). Urban Tunnels in Soil: Review of Current Design Practice in Brazil. *The 6th International Symposium on Geotechnical Aspects of Underground Construction in Soft Ground*, Shanghai, China, pp. 640–645.

Negro, A. & Eisenstein, Z. (1997). Delayed Lining Activation and Ground Stress Relaxation in Shallow Tunnels. *Proc. of The 4th Intl. Conference on Soil Mechanics and Foundation Eng*, Hamburg, Germany, pp. 2391–2396.

Negro, A. & Leite. R.L.L. (1995). Design of Underground Structures in Brazil—National Report on Tunnelling and Braced Wall Excavation in Soft Ground. *Proc. Intl. Symposium on Underground Construction in Soft Ground*, New Delhi, India, pp. 49–56.

Skempton, A.W. & Macdonald, D.H. (1956). The allowable settlements of buildings. *Proc. Inst. Civ. Eng.* Part III 5, 727–768. Discussion closure: 783–784.

Geotechnical Aspects of Underground Construction in Soft Ground – Viggiani (ed)

Guidelines for comparing field or physical model observations with numerical simulations

G.M.B. Viggiani
Università di Roma Tor Vergata, Italy

ABSTRACT: This paper presents short report on the activities of TC204 Working Group on "Guidelines to compare field or physical model observations with numerical simulations". The main objective of the WG is that of proposing recommendations concerning the comparison between calculated and observed behaviour, specifically adapted for the type of works covered by TC204, *i.e.* tunnels and open excavations in soft ground.

1 INTRODUCTION

At the TC28 Meeting held in Madrid in 2007, the decision was made to set up a Working Group (WG) devoted to the compilation of guidelines to compare field or physical model observations with numerical simulations. The general objective of the WG was to propose recommendations concerning the comparison between calculated and observed behaviour, specifically adapted for the type of works covered by TC204, *i.e.* tunnels and open excavations in soft ground.

It is clear that the activities of the WG will have to deal with the two rather different aspects of numerical prediction and field or model observation, and the best way to present them together so that their value can be enhanced. On the one end, there is the observed behaviour of a prototype structure or a physical model, on the other there are numerical simulations, necessarily obtained with some theory.

The real world provides performance, by which we mean the measured response of the structure under working conditions and in some—hopefully less common—cases, at failure. Prediction is an estimate of the expected behaviour of the structure under the working loads and in the conditions that are likely to occur during its life. Prediction is different from design, which must consider also extreme and unlikely events, and would not necessarily relate to measurable performance parameters.

The object of engineering computations is the behaviour of engineering structures (or physical models of structures) such as tunnels and excavations; the goals of engineering are successful design, construction and maintenance. On the other hand, theories typically deal with abstract entities, such as isotropic elastic bodies, or point loads. Starting from a small number of axioms and principles, for instance conservation laws or thermodynamics, theorems are obtained by demonstration and calculus. The goal, always achievable in the realm of theory, is that of obtaining exact, repeatable results.

The process that translates the real world into the theory is the so-called process of *modelling*, involving simplifications and assumptions. In order to be treated by theory, real objects such as engineering structures must become abstract entities. On the other hand, *predictions* obtained through analysis (the deflection of an elastic beam representing a retaining wall, the pore pressures generated around an expanding cylindrical cavity representing a tunnel, *etc.*) translate the results of theory to the real world.

2 MOTIVATION

The creation of the WG was partly motivated by the ever-increasing rate of publication of papers reporting some comparison between computed predictions and observed performance.

For instance, Figure 1 reports the number of published papers containing a comparison between predicted and observed behaviour of bored tunnels as a function of time. The situation is not significantly different if one considers published papers open excavations.

In the present Symposium, every session, with the exception of the present one devoted to the activities of TC204, contained some papers comparing the results of numerical calculations with some observations, see Figure 2.

The percentage number of such papers is obviously maximum in Session 5, devoted to design methods and predictive tools, where more than

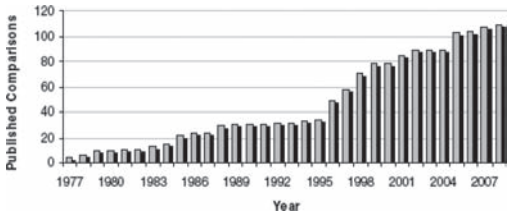

Figure 1. Number of published comparisons of predicted and observed behaviour for bored tunnels as a function of time (Negro *et al*, 2009).

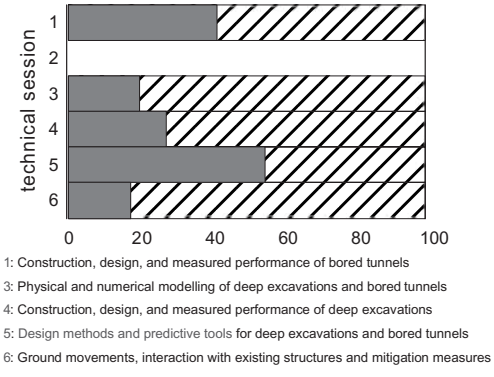

Figure 2. Percentage of papers containing comparison of predicted and measured behaviour of tunnels and open excavations in different sessions of TC28 IS-Roma 2011.

one half of the papers fall in the category, but it is interesting that even the mere illustration of a case history tends to be more and more often accompanied by some form of numerical calculation.

This is probably due to the rapid development of accessible numerical tools, such as Finite Element and Finite Difference codes, which makes it relatively easy to produce numerical computations, and yet, quite often, these comparisons are not very useful, or at least, not as useful as they could be, because they are not clearly or completely described.

Typical comments received by reviewers to papers submitted to this Symposium often included statements such as: "[…] more details are strongly needed about: drainage conditions, soil parameters, measured displacement, instruments and period of observation […]" or "[…] please provide information on the values of pore water pressure and, more generally, on the hydraulic conditions […]"; this is unfortunate as TC204 would like to set a virtuous example.

3 SCOPE

After the TC28 meetings of Shanghai (2008), Moscow (2010), and Alexandria (2010), the scope of the work of the WG, at least in a first stage, was narrowed down to deal primarily on reporting, rather than on providing recipes on how to design field instrumentation or carry out the predictions.

The guidelines will contain minimum requirements for meaningful reporting of comparisons of predicted and measured behaviour. Some of these are very general, such as a brief description of the general layout of the project and of the geological setting. These are typically included in most of the papers received to this conference, such as in the example given in Figure 3, extracted from Oteo *et al*. (2011), describing a new tunnel bored in alluvial soft soil under the Malaga Airport.

Information must also be contained on local soil conditions, including geometry of layers, groundwater conditions, and engineering properties of the ground, (unit weight, at rest horizontal stress, overconsolidation ratio, effective strength parameters, undrained shear strength, stiffness..). In other words some synthetic description of the geotechnical characterisation, leading to the definition of a geotechnical model of the site. It is obvious that not all the layers identified in the geological section need to be distinguished, as geotechnical layering may be simplified based on similar engineering properties.

Surprisingly, this was not often very well described in the papers to this Symposium, with comments received such as: "[…] add a figure with

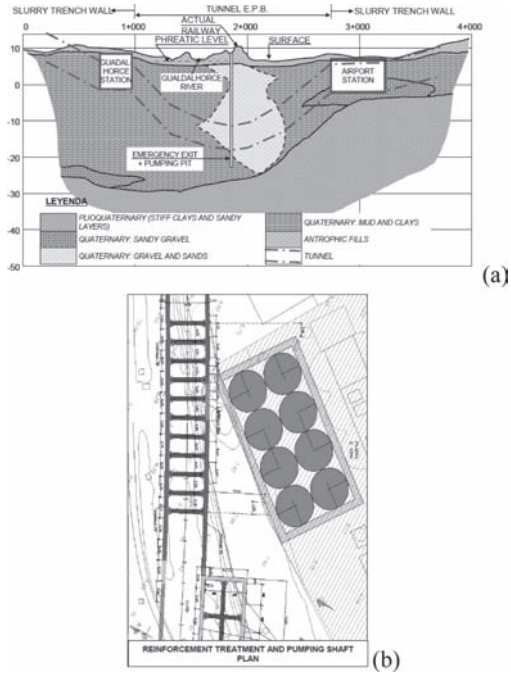

Figure 3. (a) Schematic geological profile of the area under examination, (b) detail of ground plan of the works.

the subsoil profile. The initial pore water pressure distribution has also to be defined […]" or "[…] please report in the paper the adopted mechanical parameters […]".

3.1 *Case history description*

Some details should be given on the case history at hand, such as construction and monitoring details. Of course this is going to be rather job specific and the guidelines by necessity will have to detail about different types of work, *e.g.* open excavation or tunnel. Despite the fact that no recipes are going to be provided in the guidelines, they may serve as a sort of checklist leading to better design of monitoring for more comprehensive comparisons of field and experimental data with the results of numerical modelling.

Some consideration will have to be given to the main factors affecting the behaviour of the structures. For instance, for open excavations, these will include the geometry of the excavation, not just its depth but also its plan area, as this may determine a particular behaviour, all other factors being the same. For instance, construction of a new conference centre required a very wide excavation (240 m × 35 m, for a total plan area of 32400 m^2) for a depth of about 15 m b.g.l., see Figure 4.

The purple area in the map corresponds to a tower founded on a piled raft, with 1 m diameter and 25 m long piles, the green area to the foundations of an auditorium resting on strip footings and localised pads, again with 1 m diameter and 30 m long piles. The rest of the foundation is a raft with a thickness of about 1 m. Because of the significant unloading of the underlying clay layers, if the joints between the raft and the piled foundations are sealed too early very large swelling pressures are expected. This is a case where an observational approach may be adopted in which the consolidation phenomena and the excess pore water pressures in the clay layer are monitored to optimise the construction process. For tunnels, geometrical details will include depth of the tunnel axis or cover and diameter of the tunnel.

Factors relating to construction will also have to be reported, for instance, again for open excavations, the procedures for the installation of the retaining structure, *e.g.*: slurry trenching and concreting of diaphragm walls, but also the maximum depth of excavation before any support is provided, the sequence of construction stages, details of the support structures such as struts, whalers, anchors, pre-stressing, etc., likely pore water pressure reductions due to water ingress in the excavation or dewatering, any ground treatment, etc.

If structures exist near the excavation there will be external loads to be detailed and the position of the structures relative to the excavation will have to be considered.

3.2 *Layout of instrumentation*

The guidelines will contain examples of typical layout of instrumentation for specific geotechnical purposes, similar to those reported in Figure 5 and Figure 6.

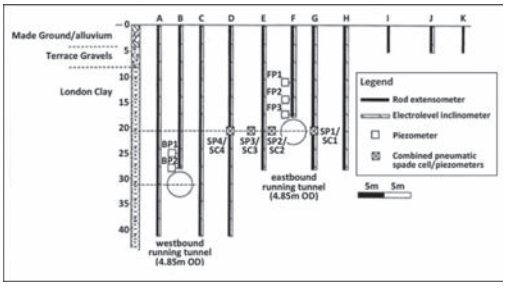

Figure 5. Layout of instrumentation at St. James's Park. (after Nyren, 1998).

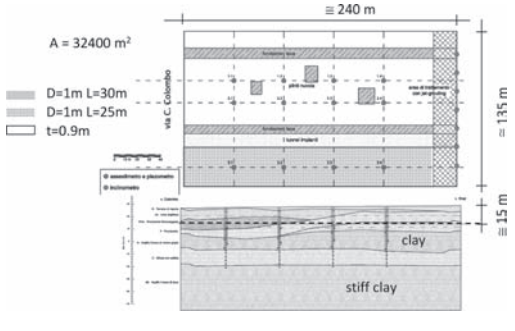

Figure 4. (top) Plan and (bottom) section of large excavation.

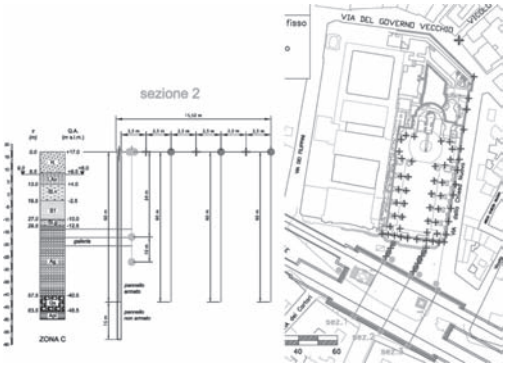

Figure 6. Proposed layout of instrumentation at Chiesa Nuova Station (courtesy of Metro C spa).

Figure 5 is the green field control section installed at St. James Park to monitor the effects of excavation of the of the running tunnels of the Jubilee Line Extension (Nyren, 1998), including surface levelling points, inclinometers, extensimeters and piezometers.

Figure 6 is the proposed layout of instrumentation around the deep open excavation for Chiesa Nuova Stations of contract T2 of Line C of Roma Underground, presently at the design stage.

In this case instrumentation includes reference points for precision levelling, both of the ground surface and of the nearby church, inclinometers and extensimeters for subsurface displacements, piezometers in the fine grained layers. In the same sections where bending moments are measured on the retaining structures by means of strain gauges, inclinometers are cast in the panels to measure horizontal deflections of the wall, to verify design assumptions and control construction.

Special monitoring schemes may be devised for particular purposes, such as, for instance, control sections to measure ground movements and stress redistribution due to slurry trenching and concreting.

4 CLASSIFICATION OF PREDICTION

A number of papers apply the term "prediction" when describing the results of numerical or analytical calculations, without clarification of when the prediction was carried out. Following a recommendation by Boone (2005), in the guidelines it will be strongly recommended that, if the term "prediction" is to be used in future publications, it must be explicitly described in terms of a "prediction class" as introduced by Lambe (1973) nearly 40 years ago, who classified the type of predictions according to whether they are made before (class A) during (class B) or after (class C) construction, and according to whether or not the results were known or not known to the authors of the prediction (see Table 1).

Most of so-called predictions are in fact class C1, so they should be better described as back analyses of the observed behaviour.

Another important classification which was introduced by Negro (1998) with specific reference to tunnel works regards the thoroughness of the prediction (see Table 2). Four categories of increasing thoroughness are defined depending on what was the object of the prediction. Ideally, a prediction should include comparisons of the complete ground displacement field and lining loads. In practice, the easiest predicted feature is a surface settlement trough, but very rarely is the field of subsurface or horizontal displacements predicted or compared with field observations.

Table 1. Classification of prediction (Lambe, 1973).

Class	Time of prediction	Results
A	before	–
B	during	not known
B1	during	known
C	after	not known
C1	after	known

Table 2. Thoroughness of tunnel predictions (Negro, 1998).

Category	Vertical displ.		Horizontal displ.		Lining loads
1	X	or	X	or	X
2	X	and	X	–	–
3	X	or	X	and	X
4	X	and	X	and	X

This can be easily adapted to the case of supported excavations, by looking not only to the horizontal deflections of the wall, which are generally easily matched by numerical calculations, but also to vertical displacements of the ground behind the retaining structure or subsurface vertical displacements, bending moments in the wall or strut forces and anchor loads.

5 NUMERICAL SIMULATION

The minimum requirements for reporting should also include details on the prediction, which will include a model of the problem, some constitutive assumptions for the soil and a procedure of analysis.

The geometry of the adopted mesh, the boundary and initial conditions and their changes due to excavation and loading should be specified.

Clear statements will also be needed on the adopted constitutive model for the soil, the parameters required by the model and if and how they are determined from the available data. In some cases, some if not all the parameters, might be obtained by back analyses of some of the available data and used to predict the rest of the data, using an inverse analysis procedure that uses construction monitoring data to update predictions of deformations for supported excavation systems (Finno & Calvello, 2005).

This all seems quite obvious and yet, in the comments of the reviewers we find requests such as: "[…] an example of mesh used (or its dimension) should be included […]", "[…] boundary conditions at wall position must be better specified […]", "[…] finite element analyses are mentioned in the paper, but no details of the analyses are provided: code? constitutive equation? […]",

"[…] the complete set of soil model parameters (unit weights, strength (cohesion, friction and dilation) should be presented […]".

Finally, the procedures of analysis have to be specified. Here we are not thinking of fine numerical issues such as integration schemes, but rather basic information on the ways the analyses were carried out: three- or two-dimensional (plane strain, axi-symmetric), by finite element or finite difference method, drained or undrained, coupled or uncoupled, with or without interfaces at soil structure contacts, etc.

Again from the comments of reviewers: "[…] a series of numerical analyses (perhaps 3D? it is unclear) […]", "[…] no information on whether these are effective stress or total stress […]", "[…] explain whether numerical analyses are carried out in terms of total or effective stress, and hydraulic boundary conditions for the saturated case […]".

6 PERSPECTIVE AND CONCLUSIONS

The activities that the working group has been busy with are a systematic review of case histories to identify areas of weakness in reporting. The questions we would like to answer to are: what is it that is missing in most cases? And how can this be improved? This will be mostly carried out with reference to case histories of deep open excavations, as there is already quite a lot of work that has been carried out on tunnel case histories.

An attempt to identify the scope of measurements (*i.e.*: verification of basis for design, document effects on surrounding structures, basic research, *etc.*) and relevance of particular instrumentation for scope is currently under way. Also an effort is being made to rationalise recommendations for standard ways to reduce and, represent data.

REFERENCES

Boone, S.J. (2005). General Report: Deep Excavations. 5th International Symposium on Geotechnical Aspects of Underground Construction in Soft Ground, Amsterdam, 81–92.

Finno, R.J. & Calvello M. (2005). Supported Excavations: Observational Method and Inverse Modeling. J. Geotech. Geoenviron. Eng. 131, 7, 826–837.

Lambe, W.T. 1973. Prediction in soil engineering. Géotechnique, 23(2), 149–202.

Negro, A. (1998). General report: Design criteria for tunnels in metropolises. Proc. World Tunnel Congress on Tunnels and Metropolises, Vol. 1, 201–214.

Nyren, R.J. (1998). Field measurements above twin tunnels in clay. Ph.D. thesis, Imperial College of Science, Technology & Medicine, London.

Oteo C.S., García Pérez J., Moreno H., de La Fuente P. & Oteo Escobar J. (2011). A new tunnel bored in alluvial soft soil under the Malaga Airport. *This Symposium*.

This page intentionally left blank

Geotechnical Aspects of Underground Construction in Soft Ground – Viggiani (ed)
© 2012 Taylor & Francis Group, London, ISBN 978-0-415-68367-8

A predictive exercise on the behaviour of tunnels under seismic actions

E. Bilotta & F. Silvestri
University of Napoli Federico II, Napoli, Italy

ABSTRACT: The calibration of numerical procedures for the prediction in design of the behaviour of tunnels under seismic conditions should be validated against experimental data. Centrifuge tests were carried out at the University of Cambridge (UK) on tunnel models in sand, for the assessment of different analytical methods developed in the framework of Italian ReLUIS-DPC Project. After the end of the research project, the experimental data have been made available online to the scientific community to be used for benchmarking simplified to complex dynamic numerical methods. This paper describes the organization of such a predictive exercise, promoted by TC204 together with TC104 and TC203 of ISSMGE.

1 INTRODUCTION

The behaviour of urban tunnels under seismic actions can be predicted by simplified (based on the pseudo-static approach) and dynamic methods, i.e. more complex procedures that take into account the dynamic nature of the seismic loads and the cyclic soil behaviour. These latter methods can either uncouple the analysis of free-field soil response from that of the tunnel ('*simplified dynamic analysis'*), or use complex numerical procedures (*full dynamic analysis*) accounting for soil-structure interaction, which is basically kinematic (*cfr.* Owen & Scholl, 1981; JSCE, 1992; AFPS/AFTES Guidelines, 2001; ISO TC 98, 2003; AGI, 2005). The calibration of all such methods should require validation against experimental data, which are seldom available at the prototype scale: centrifuge modelling is therefore an alternative powerful tool to produce 'artificial case histories' for calibration, back-analysis or benchmarking between different analytical approaches.

Centrifuge tests were carried out by researchers of the University of Napoli Federico II at the Schofield Centre of the University of Cambridge (UK) on tunnel models in sand (Lanzano, 2009), for the assessment of different analytical methods developed in the framework of ReLUIS Project 2005–2009 (Bilotta et al. 2007 and 2008). After the end of the research project, the experimental data can now be made available to the scientific community.

The experimental activity will be briefly described in this paper, further details can be found in referenced papers (Bilotta et al, 2009, Lanzano et al, 2009, Lanzano et al. 2010).

2 BACKGROUND

A systematic collection of data concerning damages to underground structures and tunnels after seimic events was carried out only after the San Fernando earthquake in 1971 ($M_w = 6.6$). In 1974 the American Society of Civil Engineers published some data about the damage to underground structures in the Los Angeles area following that event. Later the database of observed damages grew up in the years, mainly with data from cases occurred during earthquakes in the United States and in Japan (*cfr* Dowding & Rozen, 1978; Owen & Scholl, 1981; Sharma & Judd, 1991; Power et al., 1996; Lanzano et al., 2008).

A typical damage pattern due to the longitudinal and transversal components of ground motion is that of extension cracks along the tunnel lining. In the transverse section of a circular tunnel, for instance, the ground shaking induces ovalisation of the lining (Owen & Scholl, 1981). Hence, depending on the stress level of the lining under 'static' conditions, cracks may open where tensile stress increments arise during shaking (Fig.1).

Although it is quite difficult to measure such increments of internal forces during real earthquakes, centrifuge modelling allowed an experimental assessment of these quantities during 'artificial seismic events'; the results may be used for benchmarking simplified to complex prediction methods.

3 CENTRIFUGE TESTING PROGRAMME

Four centrifuge tests were carried out on tunnel models in dry sand at two different values of relative density, in a laminar box ($500 \times 250 \times 300$ mm^3).

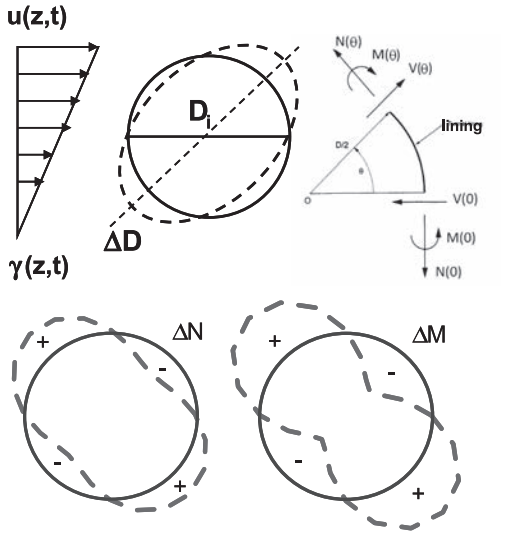

Figure 1. Typical increase of the lining internal forces due to ground shaking in the transverse section of a tunnel.

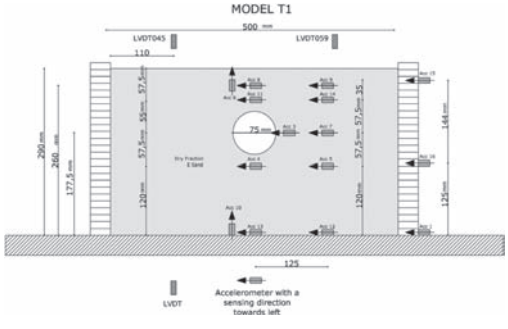

Figure 2. Schematic setup of model T1.

Table 1. Centrifuge tunnel tests.

Model	D (mm)	C (mm)	D_r	N
T1	75	75	~80%	80
T2	75	75	~40%	80
T3	75	150	~80%	80
T4	75	150	~40%	80

A schematic setup is shown in Fig. 2. The testing programme is summarized in Table 1 (model scale), where D is the diameter of the tunnel, C is the cover, D_r is the relative density of the sand and N is the g-level (Lanzano and Madabhushi, 2007a, b).

4 FACILITIES

4.1 *Philip Turner centrifuge*

The centrifuge tests at Schofield centre were carried out in a 10 m beam centrifuge, named from the engineer, P.W. Turner, who designed this facility in the early 1970's (Schofield, 1980).

The centrifuge consists essentially of a beam-like structure, which rotates about a central vertical axis. Dynamic tests can be carried out at centrifuge acceleration in the range of 40 to 100 g. In the performed tests, a swinging platform carrying the model and the dynamic SAM actuator was installed on one end of the beam and the required counterweight was placed on the other end.

4.2 *SAM actuator*

The Stored Angular Momentum (SAM) is an earthquake actuator developed at Cambridge University (Madabhushi et al.1998). The SAM actuator is a powerful tool and allows simulating strong earthquakes at high acceleration level; it can fire series of earthquakes at different frequencies, duration and g-level.

Very high levels of energy can be stored in a fly wheel spinning at high angular velocities. The energy stored in the fly wheel may be used to subject the centrifuge model to earthquakes. The angular velocity of the fly wheel determines the frequency of the earthquake. The duration of the earthquake is controlled by a fast acting clutch which starts and ends the earthquake. The strength of the earthquake can be controlled by altering the pivot point of the lever.

The soil model is shaken in the direction of centrifuge flight and the fly wheel rotates in the plane of rotation of the centrifuge arms. The variables that can be changed during the tests are:

- the level of inertial acceleration 'g';
- the frequency of the signal;
- the amplitude of the signal;
- the duration of the signal.

4.3 *Laminar Box (LB)*

The tests were performed using a Laminar Box (Fig. 3). This box is made by a series of stacked rectangular frames which can slip reciprocally through ball bearings. This solution is useful to minimize the friction between the laminae and to allow the horizontal movements of the whole box. The model container has inner sizes of $500 \times 250 \times 200$ mm^3 and a mass of 93.5 kg.

A plate is put at the base of the box to connect the container with the SAM actuator so to fire the earthquake on the model. The weight of the plate is 58 kg.

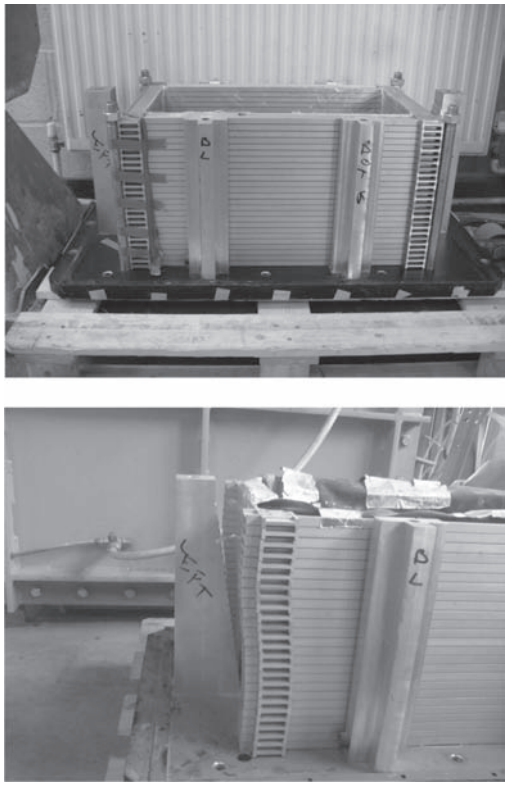

Figure 3. Undeformed (above) and deformed (below) Laminar Box.

5 MATERIALS

5.1 *Sand—Leighton Buzzard*

All the models were made using dry Leighton Buzzard sand (grade E) reconstituted at two different relative densities Dr (about 50% and 80%). The specific gravity of the sand is 2.65 and the maximum and minimum void ratios are 1.014 and 0.613 respectively (Jeytharan, 1991). A detailed characterization of the sand used in tests was performed in laboratory by means of triaxial and resonant column tests at the University of Napoli Federico II (Visone, 2009).

5.2 *Alloy (Dural)*

The tunnel lining was modelled using an aluminium tube having an external diameter D = 75 mm and a thickness t = 0.5 mm. The unit weight of aluminium is 2770 kg/m^3. At N = 80 g, the model would correspond to a 6 m diameter prototype tunnel with a shotcrete lining of about 6 cm.

6 INSTRUMENTATION

6.1 *Accelerometers*

Miniature piezoelectric accelerometers manufactured by D.J. Birchall Ltd™ were used to measure horizontal and vertical acceleration in the soil and on the model container during earthquakes (see Fig. 2). The device has a resonant frequency of about 50 kHz and maximum error of 5%; the transducer weight is about 5 grams.

6.2 *Strain gauges*

The tube has been instrumented in order to measure bending moments (BM) and hoop forces (HS) at 4 locations along 2 transverse sections (Figs. 4 & 5).

The main instrumented section was located at the mid-span of the tube and a second section 50 mm aside. This second section was needed for two reasons: checking the plane strain behaviour of the tunnel model (BM and HS at corresponding locations of

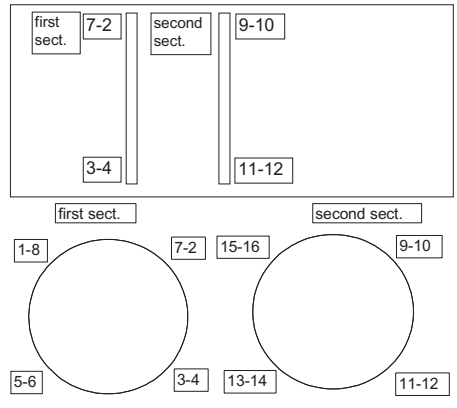

Figure 4. Strain gauges position.

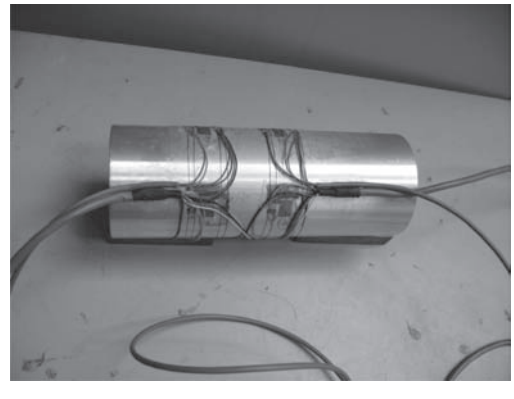

Figure 5. Instrumented tube.

different sections should be the same) and for redundancy of experimental data. In total 16 Wheatstone bridges (4 locations × 2 sections × 2 force measurements) were glued to the tube and wired.

6.3 *Displacement measuring device (LVDTs)*

The vertical displacement of the surface during centrifuge tests was measured by linear variable differential transformers (LVDTs) manufactured by Sangamo™. Each transducer weighs about 36 grams. LVDTs were placed in two gantries above the model.

7 INSTRUMENTATION

7.1 *Container preparation*

The Laminar Box was initially cleaned from the remains of previous test. At this stage the container was blocked with four columns at the corners of the box to prevent the movements during the model preparation, transportation and assembly. A grease layer was interposed between the box and an internal rubber lining. The internal rubber was stretched and was fixed at the box top by aluminium tape. The sockets for the external accelerometers were glued on the lateral surface of the box. A paper ruler was stuck on the internal wall to control the level of the sand during the pouring phase. Before pouring the sand, the external walls of the box were protected by black plastic liners that were removed at the end of the deposition: this was to avoid that sand grains could accidentally enter between the laminae.

7.2 *Sand pouring*

To make the "loose sand models", the sand was poured into the strongbox through a simple hopper system. The void ratio was therefore dependent on the height of the hopper and the opening of the slot at the bottom that controlled the rate of flow of the sand. A few trial tests were performed in advance to calibrate these values. After that the required height of the sand layer was achieved, the surface of the sand was levelled by a modified vacuum cleaner.

To make the "dense sand models", the sand was poured into the strongbox through an automatic hopper system which adopted a multiple sieving pluviation technique (Miura & Toki, 1982). The pouring of the sand was controlled by a computer. The parameters that played a crucial role in order to obtain the desired density were the height of fall and the nozzle diameter. During each pluviation step the sand was poured first longitudinally and then transversally with an offset of 15 mm. At the end of the step the hopper was lifted up by 10 mm (the height corresponding to the thickness of the layer poured in each step). During the sand deposition the instruments and the model tunnel were positioned in the model.

7.3 *Accelerometers positioning*

Before each test a layout drawing of the model was prepared, where the position and the sensing direction of every accelerometer was shown, such as in the example shown in Fig. 2. The accelerometers were placed in the model (Fig. 6) according to the indications of the layout. A vertical array of three accelerometers was deployed laterally to the laminar box, including one at the bottom identifying the 'bedrock reference motion'.

7.4 *Tunnel placement*

Once the level of the sand in the container reached the level of the tunnel invert, the instrumented tube was placed in the model (Fig. 7) according to the test layout (see Fig. 2). As the tunnel tube is shorter

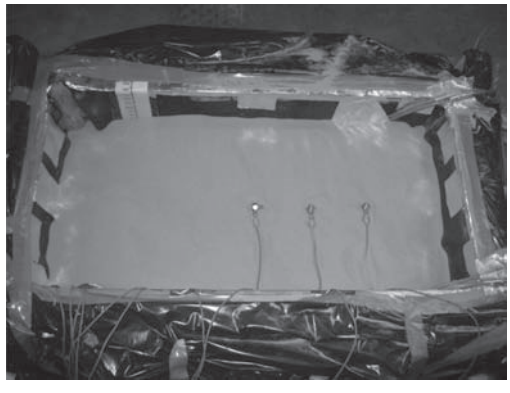

Figure 6. Accelerometers positioning.

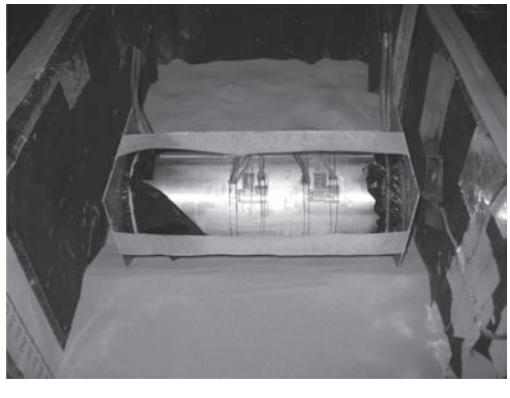

Figure 7. Tunnel placement.

than the box width by 50 mm (to avoid interaction with the container during shaking), two square plates were also placed at each end of the tunnel to avoid loss of sand inside the tube during the test. To reduce friction between the plates and the tube, the plates were lubricated and a black plastic liner patch was inserted in between.

8 TEST PROCEDURE

Before starting the centrifuge flight, the corner columns were removed. When the test started the centrifuge was swung up in steps of 10 g, from 10 g to 80 g. At each stage the readings of strain gauges transducers were recorded. Then the first earthquake was fired. After 4 earthquakes at 80 g, the centrifuge was slowed down at 40 g to fire another earthquake. Then the centrifuge was swung down. The model was permanently monitored through a camera installed on the beam.

9 TEST DATA

The channels for the measurements were 32 in all: 16 for the accelerometers and 16 for strain gauges or LVDTs. The data were plotted out channel by channel and recorded in a text file both for the swing up phase and every earthquake. All the data were acquired using the software CDAQS (Centrifuge Data AcQuisition System), a system that minimizes the noise derived by electrical interference of the SAM actuator. The earthquake data were sampled at a rate of 4 kHz. A typical set of records is shown in Fig. 8.

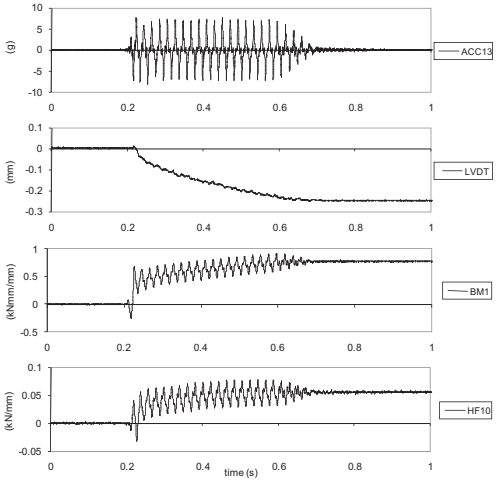

Figure 8. Typical outputs of an accelerometer, a LVDT, a BM and a HS strain gauges during T1 test (EQ3).

10 BENCHMARK TEST T3

The test initially selected for the benchmark, T3, is a model of dense sand and deep tunnel, the layout of which is drawn in Fig. 9. The internal available volume of the box (without the volume of the tunnel) is 3.32*107 mm^3 and the mass of the used sand is 51.5 kg. These values give a void ratio of 0.710 and a relative density of 75.9%. A total of 31 transducers were used in this test: 16 accelerometers, 13 strain gauges and 2 LVDTs. Four earthquakes were fired at 80 g and one at 40 g, with variable nominal peak acceleration amplitude and frequency. The main features of each earthquake are shown in Table 2, at the model and prototype (bracketed values) scales; their time histories, as recorded by the reference accelerometer Acc13, are resumed in Fig. 10.

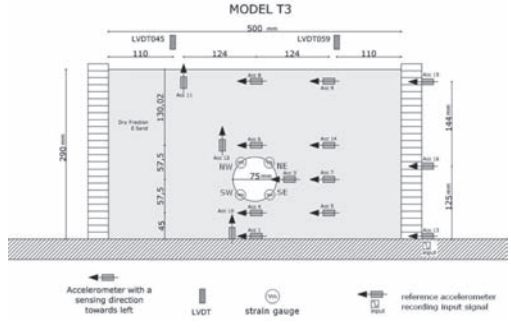

Figure 9. Layout of the model T3.

Table 2. Earthquakes fired in test T3.

Earthquake #	*N*	Frequency (Hz)	Duration (s)	Nominal *PGA* (g)
1	80	30 [0.375]	0.4 [32]	4 [0.05]
2	80	40 [0.5]	0.4 [32]	8 [0.10]
3	80	50 [0.625]	0.4 [32]	9.6 [0.12]
4	80	60 [0. 75]	0.4 [32]	12 [0.15]
5	40	50 [1.25]	0.4 [16]	12 [0.30]

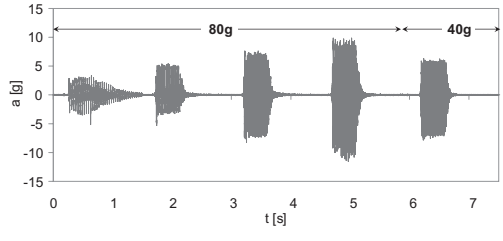

Figure 10. Time histories of input signals recorded by Acc13.

11 ROUND ROBIN TUNNEL TEST ORGANIZATION

The Round Robin Tunnel Test (RRTT) is jointly promoted by three ISSMGE Technical Committees, i.e. TC104 (*Physical modelling in Geotechnics*), TC203 (*Earthquake Geotechnical Engineering*) and TC204 (*Underground construction in soft ground*). Both researchers and practitioners are welcome to participate by writing to the Authors (emilio.bilotta@unina.it, francesco.silvestri@unina.it).

All participants will be enabled to use the selected test data, i.e. the reference accelerograms (Fig. 10) and the results of laboratory tests on LB sand, which are delivered through ftp with a restricted access. The analyses will be intended as 'blind' predictions.

Each participant will specify: (i) people involved and expected time of accomplishment (no. of months), (ii) the types of analyses which will be carried out (approach, numerical code, constitutive model, prototype or model scale), (iii) the output data to be benchmarked (e.g. acceleration amplitudes, soil strains, surface settlements, load increments in the lining), (iv) the will of participate to periodic meetings to be scheduled on purpose and/or during next international symposia related to tunnels and geotechnical earthquake engineering.

At his point they will receive a ftp address together with username and password to download the required input data and to upload the output data at the end of the analyses. Upon delivering the numerical output data, they will receive the corresponding experimental values to be taken as a reference for the benchmarking.

Finally, each attendant also will submit to the organizers a synthetic report with details on the numerical procedure and comparisons between numerical and experimental data. The reports may be collected in a short volume, jointly edited by TC203 and TC204. In the meantime, the participants will also be free to publish, either individually or through jointed co-operation with other groups subscribing the RRTT, any comparison between numerical and experimental data, provided the data source be properly quoted.

ACKNOWLEDGEMENTS

The organizers wish to acknowledge the promotion of the initiative by the Technical Committees TC104, TC203 and TC204 of the ISSMGE and the support of the Research Project DPC-RELUIS 2010–2013.

REFERENCES

AFPS/AFTES (2001). Guidelines on earthquake design and protection of underground structures.

AGI (2005). Aspetti geotecnici della progettazione in zona sismica—Linee Guida AGI, Associazione Geotecnica Italiana, Patron, Bologna (in Italian).

ASCE (1974). Earthquake damage evaluation and design considerations for underground structures, February, American Society of Civil Engineers, Los Angeles Section.

Bilotta E., Lanzano G., Russo G., Santucci de Magistris F., Aiello V., Conte E., Silvestri F. & Valentino M. (2007). Pseudostatic and dynamic analyses of tunnels in trasversal and longitudinal direction. Proc. 4th International Conference on Earthquake Geotechnical Engineering (Pitilakis ed.), Thessaloniki, Springer.

Bilotta E., Lanzano G., Russo G., Santucci de Magistris F. & Silvestri F. (2008). An early-stage design procedure for circular tunnel lining under seismic actions. Proc. 14th World Conference on Earthquake Engineering, Beijing, China.

Bilotta E., Lanzano G., Russo G., Silvestri F. & Madabhushi G. (2009). Seismic analyses of shallow tunnels by dynamic centrifuge tests and finite elements. Proc. 17th Int. Conf on Soil Mechanics and Geotechnical Engineering, Alexandrìa, Egypt.

Brennan A.J., Madabhushi S.P.G. & Houghton N.E. (2006). Comparing laminar and equivalent shear beam containers for dynamic centrifuge modelling, Proceedings of Physical Modelling in Geotechnics ICPMG '06.

Coelho P.A. (2007). In situ densification as a liquefaction resistance measure for bridge foundations, PhD Thesis, University of Cambridge.

Dowding C.H. & Rozen A. (1978). Damage to rock tunnels from earthquake shaking, ASCE, Journal of Geotechnical Engineering Division, Vol.104, p. 175–191.

ISO TC 98/SC 3 N229 (2003). Bases for design of structures—Seismic actions for designing geotechnical works.

Jeyatharan K. (1991). Partial liquefaction of sand fill in a mobile arctic caisson under ice loading, PhD Thesis, University of Cambridge.

JSCE (1992). Earthquake resistant design for civil engineering structures in Japan, The Japanese Society of Civil Engineers.

Lanzano G. (2009). Physical and analytical modelling of tunnels under dynamic loadings. Ph.D. Thesis, Università di Napoli Federico II.

Lanzano G., Bilotta E. & Russo G. (2008). Tunnels under seismic loading: a review of damage case histories and protection methods (Fabbrocino & Santucci de Magistris eds.) pp. 65–74.

Lanzano G., Bilotta E., Russo G., Silvestri F. & Madabhushi G. (2009). Experimental assessment of performance-based methods for the seismic design of circular tunnels, IS-Tokyo 2009.

Lanzano G., Bilotta E., Russo G., Silvestri F. & Madabhushi S.P.G. (2010). Dynamic centrifuge tests on shallow tunnel models in dry sand, VII International Conference on Physical Modelling in Geotechnics, Zurich.

Lanzano G. & Madabhushi G. (2007a). Dynamic centrifuge tests, ReLUIS Project – Tunnels, Internal Data Report, Tests T-2 & T-4, SC-CUTS-0706-R00.

Lanzano G. & Madabhushi G. (2007b). Dynamic centrifuge tests, ReLUIS Project – Tunnels, Internal Data Report, Tests T-1 & T-3, SC-CUTS-0707-R00.

Madabhushi S.P.G., Schofield A.N. & Lesley S. (1998). A new Stored Angular Momentum (SAM) based earthquake actuator, Centrifuge 98, Balkema, Rotterdam.

Miura S. & Toki S. (1982). A simple preparation method and its effect on static and cyclic deformation-strength properties of sand, Soils and Foundations, 22(1), 61–77.

Owen G.N. & Scholl R.E. (1981). Earthquake engineering of large underground structures, Report no. FHWA/RD-80/195. Federal Highway Administration and National Science Foundation.

Power M.S., Rosidi D. & Kaneshiro J.Y. (1998). Seismic vulnerability of tunnels and underground structures revisited, Proceedings of North American Tunneling '98, Newport Beach, CA, Balkema Rotterdam, p. 243–250.

Schofield A.N. (1980). Cambridge Geotechnical Centrifuge Operations, Geotechnique 30, No.3, 227–268.

Sharma S.W.R. & Judd (1991). Underground opening damage from earthquakes, Engineering Geology, vol.30, p. 263–276.

Taylor R.N. (1995). Geotechnical centrifuge technology, Blackie Academic & Professional.

Visone C. (2009). Performance based design of embedded retaining walls. Ph.D. Thesis, Università di Napoli Federico II.

Zeng X. (1992). Dynamic Centrifuge tests on Quay Wall Models, Internal Report, University of Cambridge.

This page intentionally left blank

This page intentionally left blank

Geotechnical Aspects of Underground Construction in Soft Ground comprises a collection of 118 papers, four reports on symposium themes, and four invited lectures presented at the seventh International Symposium on Geotechnical Aspects of Underground Construction in Soft Ground, held in Rome, Italy, 16-18 May 2011.

The symposium was organized by the Technical Committee TC28 "Underground Construction in Soft Ground" of the International Society for Soil Mechanics and Geotechnical Engineering (ISSMGE). This is the latest in a series which began in New Delhi in 1994, and was followed by symposia in London (1996), Tokyo (1999), Toulouse (2002), Amsterdam (2005), and Shanghai (2008). The Rome symposium was organised by the Italian Geotechnical Society (AGI), under the auspices of the International Society for Soil Mechanics and Geotechnical Engineering (ISSMGE) and the Italian Ministry for Public Works, and sponsored by various national and international companies.

Geotechnical Aspects of Underground Construction in Soft Ground includes contributions from 30 countries on research, design and construction of underground works in soft ground. The contributions cover:

- Construction, design, and measured performance of bored tunnels
- Physical and numerical modelling of deep excavations and bored tunnels
- Construction, design, and measured performance of deep excavations
- Design methods and predictive tools for deep excavations and bored tunnels
- Ground movements, interaction with existing structures and mitigation measures
- Activities of TC204 working groups

The general reports give an overview of the papers listed in the symposium's technical sessions. The proceedings include the written version of the four invited lectures covering topics ranging from the geotechnical aspects of construction of the new Mexico City deep sewerage system (as a special contribution of TC214 "Soft Soils"), to the long-term settlement mechanisms of tunnels in Shanghai, the lessons learned from the deep excavations for the North-South Line in Amsterdam, and the evaluation of the effects of tunnel excavation on historical buildings, drawing on experience gathered during construction of subway line C in Rome.

Similar to previous editions, Geotechnical Aspects of Underground Construction in Soft Ground represents a valuable source of reference on the current practice of analysis, design, and construction of tunnels and deep excavations in soft ground. The book is particular aimed at academics and professionals interested in geotechnical and underground engineering.

ISBN-13: 978-0-415-68367-8
9 780415 683678

CRC Press
Taylor & Francis Group
an informa business
www.crcpress.com

6000 Broken Sound Parkway, NW
Suite 300, Boca Raton, FL 33487
Schipholweg 107C
2316 XC Leiden, NL
2 Park Square, Milton Park
Abingdon, Oxon OX14 4RN, UK

an informa business